Special Issue No. 75 • Vol.2

Journal of Coastal Research

Proceedings of the 14th International Coastal Symposium
Sydney, 6-11 March 2016

Edited by:
Ana Vila-Concejo, Eleanor Bruce,
David M. Kennedy, and R. Jak McCarroll

THE UNIVERSITY OF SYDNEY

GEOCOASTAL RESEARCH GROUP

COASTAL EDUCATION & RESEARCH FOUNDATION, INC. CERF

JCR

JOURNAL OF COASTAL RESEARCH

An International Forum for the Littoral Sciences

CHEF-HERAUSGEBER

EDITOR-IN-CHIEF

Charles W. Finkl

RÉDACTEUR-EN-CHEF

Coastal Education and Research Foundation, Inc. *[CERF]*

Editorial Offices:

25 Jake Ridge Trail
Fletcher, NC
28732, U.S.A.

5130 NW 54th Street
Coconut Creek, FL
33073, U.S.A.

(Editorial Office, Coconut Creek)
CERF/JCR Website: http://www.CERF-JCR.org
e-mail: cfinkl@cerf-jcr.com

BOOK REVIEW EDITOR
J. Andrew G. Cooper
School of Environmental Sciences
University of Ulster
Coleraine, N. Ireland
jag.cooper@ulster.ac.uk

DEPUTY EDITOR-IN-CHIEF
Christopher Makowski
Coastal Education and Research
Foundation, Inc. *[CERF]*
5130 NW 54th Street
Coconut Creek, FL 33073, U.S.A.
cmakowski@cerf-jcr.com

EDITORIAL ASSISTANT
Barbara Russell
Coastal Education and Research
Foundation, Inc. *[CERF]*
5130 NW 54th Street
Coconut Creek, FL 33073, U.S.A.
barbara@cerf-jcr.com

WEB DESIGN & DEVELOPMENT
Jon Finkl
Media Mine
15014 Stonegreen Lane
Huntersville, NC 28078, U.S.A.
jon@mediamine.net

MITHERAUSGEBER

ASSOCIATE EDITORS

COMITÉ DE REDACTION

Edward J. Anthony
Coastal Geomorphology
Dunkerque, France

Kenneth Banks
Coral Reef Geomorphology
Plantation, Florida

Patrick Barnard
Coastal Geomorphology
Santa Cruz, California

Lindino Benedet
Oceanography, Modeling
Florianopolis, SC, Brazil

David M. Bush
Coastal Geology & Hazards
Carrollton, Georgia

Ilya V. Buynevich
Coastal Geology
Philadelphia, Pennsylvania

Javier A. Carrió
Sediment Processes
Valencia, Spain

Mark Crowell
Coastal Zone Management
McLean, Virginia

Omar Defeo
Sandy Beach Ecology
Montevideo, Uruguay

J. Javier Diez
Coastal Geomorphology
Madrid, Spain

Joseph F. Donoghue
Coastal Morphology & Hazards
Orlando, Florida

Jean Ellis
Aeolian Sediment Transport
Columbia, South Carolina

Luciana Esteves
Coastal Flooding & Erosion
Bournemouth, United Kingdom

Oscar Manuel Ferreira
Storm Impacts
Faro, Portugal

Duncan M. FitzGerald
Sediment Transport
Boston, Massachusetts

Chip Fletcher
Coastal Geology
Honolulu, Hawaii

Kazimierz K. Furmańczyk
Marine Cartography
Szczecin, Poland

Gary B. Griggs
Coastal Engineering & Hazards
Santa Cruz, California

Pramod Hanamgond
Coastal Geomorphology
Belgaum, India

Hans Hanson
Coastal Protection
Lund, Sweden

Simon Haslett
Paleoceanography
Wales, United Kingdom

David Hill
Nearshore Hydrodynamics
Corvallis, Oregon

Michael Hilton
Dune Geomorphology & Ecology
Dunedin, New Zealand

Carl H. Hobbs, III
Coastal Geology, Sand Mining
Gloucester Point, Virginia

James R. Houston
Sea-Level Change
Vicksburg, Mississippi

Wenrui Huang
Coastal Hydrodynamics
Tallahassee, Florida

Michael G. Hughes
Coastal Morphodynamics
Canberra, ACT, Australia

Federico I. Isla
Sea-Level Change
Mar Del Plata, Argentina

Nancy L. Jackson
Coastal Geomorphology
Newark, New Jersey

Markes E. Johnson
Paleoshores, Coastal Sand Dunes
Williamstown, Massachusetts

Timothy R. Keen
Waves & Circulation
Stennis Space Center, Mississippi

Dieter H. Kelletat
Coastal Geomorphology
Essen/Cologne, Germany

Joseph T. Kelley
Sea-Level Change
Orono, Maine

Vic Klemas
Remote Sensing
Newark, Delaware

Nobuhisa Kobayashi
Coastal Engineering
Newark, Delaware

Vladimir N. Kosmynin
Coral Reefs, Coastal Ecology
Tallahassee, Florida

Joseph L. Kowalski
Estuarine Plant Ecology
Edinburg, Texas

Michael J. Lace
Coastal Landforms & Processes
West Branch, Iowa

Stephen P. Leatherman
Barrier Islands, Beach Erosion
Miami, Florida

Charles Lemckert
Environmental Fluid Dynamics
Queensland, Australia

Ioannis Liritzis
Geophysical Proxy Data
Rhodes, Greece

Jeffrey H. List
Shoreline Change Processes
Woods Hole, Massachusetts

Michel M. de Mahiques
Sediment Processes
São Paulo, Brazil

Gonzalo C. Malvárez-Garcia
Beach Morphodynamics
Seville, Spain

Ashish J. Mehta
Coastal Engineering
Gainesville, Florida

Nobuo Mimura
Environmental Engineering
Ibaraki, Japan

Robert Nicholls
Global Climate Change
Southampton, United Kingdom

Karl F. Nordstrom
Coastal Geomorphology
New Brunswick, New Jersey

Julian Orford
Gravel Beaches, Storm Events
Belfast, Northern Ireland, UK

Phil D. Osborne
Sediment Dynamics
Shoreline, Washington

Hugh Parker
Airborne Lidar Bathymetry
Adelaide, SA, Australia

Charitha B. Pattiaratchi
Physical Oceanography
Crawley, WA, Australia

Carlos Pereira da Silva
Coastal Zone Management
Lisbon, Portugal

Michael Phillips
Coastal Geomorphology
Swansea, Wales, UK

Orrin H. Pilkey, Jr.
Coastal Geology
Durham, North Carolina

Paolo A. Pirazzoli
Sea-Level Changes
Paris, France

Nobert P. Psuty
Coastal Geomorphology
New Brunswick, New Jersey

Ulrich Radtke
Coastal Geomorphology
Duisburg-Essen, Germany

Elijah W. Ramsey, III
Coastal Image Processing
Lafayette, Louisiana

Kirt Rusenko
Sea Turtles, Dune Restoration
Boca Raton, Florida

Anja Scheffers
Coastal Evolution
Lismore, NSW, Australia

Vic Semeniuk
Coastal Sedimentation,
Mangroves
Perth, WA, Australia

Andrew D. Short
Coastal Geomorphology
Sydney, NSW, Australia

Pravi Shrestha
Coastal Engineering
Irvine, California

Alejandro J. Souza
Coastal & Sediment Processes
Liverpool, United Kingdom

Tom Spencer
Biogeomorphology
Cambridge, United Kingdom

Marcel Stive
Coastal Hydrodynamics
Delft, The Netherlands

Vallam Sundar
Coastal Engineering
Chennai, India

Adam D. Switzer
Coastal Hazards, Sea-Level Change
NTU, Singapore

E. Robert Thieler
Marine Geology
Woods Hole, Massachusetts

Arthur C. Trembanis
Coastal Morphodynamics
Newark, Delaware

Frank Van Der Meulen
Coastal Zone Management
Delft, The Netherlands

Ian J. Walker
Coastal Dunes & Sediments
Victoria, BC, Canada

Ping Wang
Beach Morphodynamics
Tampa, Florida

Allan Williams
Coastal Geology
Swansea, Wales, UK

Harry F. Williams
Paleotempestology
Denton, Texas

Colin D. Woodroffe
Coastal Geomorphology
Wollongong, Australia

Robert S. Young
Coastal Processes
Cullowhee, North Carolina

Guoliang Yu
Sediment Transport
Shangai, China

THE *JOURNAL OF COASTAL RESEARCH* (JCR) (ISSN 0749–0208) IS PUBLISHED BIMONTHLY FOR $115.00 FOR INDIVIDUAL US CERF MEMBERS, $125.00 FOR INDIVIDUAL INTERNATIONAL CERF MEMBERS, $519.00 FOR US INSTITUTIONS, AND $541.00 FOR INTERNATIONAL INSTITUTIONS BY THE COASTAL EDUCATION AND RESEARCH FOUNDATION, INC. (CERF), 5130 NW 54TH STREET, COCONUT CREEK, FL 33073–3713. PERIODICALS POSTAGE PAID AT FORT LAUDERDALE, FL AND ADDITIONAL MAILING OFFICES. **POSTMASTER:** SEND ADDRESS CHANGES TO *JOURNAL OF COASTAL RESEARCH*, ALLEN PRESS ASSOCIATION MANAGEMENT, P.O. BOX 1897, LAWRENCE, KS 66044–3018.

© 2016 Coastal Education and Research Foundation, Inc. *[CERF]*.

♾ This paper meets the requirements of ANSI/NISO Z39.48-1992 (Permanence of Paper).

JOURNAL OF COASTAL RESEARCH

An International Forum for the Littoral Sciences

Supporting Scientific Institutions

- Consorzio Nazionale Interuniversitario per le Scienze del Mare (Co.N.I.S.Ma.) [Rome, Italy; www.conisma.it/]
- Delft University of Technology [Department of Hydraulic Engineering, Delft, The Netherlands; http://www.citg.tudelft.nl/over-faculteit/afdelingen/hydraulic-engineering/]
- Duke University [Earth and Ocean Sciences Division, Durham, North Carolina, U.S.A.; https://nicholas.duke.edu/marinelab]
- Griffith University [Center for Infrastructure Engineering and Management, Southport, Queensland, Australia; https://www.griffith.edu.au/]
- Ibaraki University [Center for Water Environmental Studies, Mito, Japan; http://www.cwes.ibaraki.ac.jp/]
- International Geographical Union (IGU) [Commission on Coastal System (CCS); http://www.igu-ccs.org/]
- Royal Belgian Institute of Natural Sciences [Management Unit of the North Sea Mathematical Models (MUMM), Brussels, Belgium; http://www.mumm.ac.be/EN/index.php]
- Rutgers University [Institute of Marine and Coastal Sciences (IMCS), New Brunswick, New Jersey, U.S.A.; http://marine.rutgers.edu/main/]
- Universidad de la República [Marine Science Unit, Montevideo, Uruguay; http://www.imber.info/Science/National-Network/URUGUAY]
- Universidade Nova de Lisboa [e-Geo Center for Geographical and Regional Planning Studies, Lisbon, Portugal; http://e-geo.fcsh.unl.pt/]
- University of California, Santa Cruz [Institute of Marine Sciences, Santa Cruz, California, U.S.A.; http://ims.ucsc.edu/]
- University of Delaware [School of Marine Science and Policy, Newark, Delaware, U.S.A.; http://www.ocean.udel.edu]
- University of Maine [Climate Change Institute, Orono, Maine, U.S.A.; http://climatechange.umaine.edu/]
- University of Sydney [Coastal Studies Unit, Sydney, New South Wales, Australia; http://sydney.edu.au/]
- University of Szczecin [Institute of Marine and Coastal Science, Szczecin, Poland; http://www.wnoz.ztikm.szczecin.pl/en/1/inom/structure/]
- University of Ulster [Environmental Sciences Research Institute, Coleraine, Northern Ireland; http://www.ulster.ac.uk/es/research/]
- University of Wales, Trinity Saint David [Swansea Metropolitan University, Mount Pleasant, Swansea, South Wales, U.K.; http://www.uwtsd.ac.uk/]
- U.S. Army Corps of Engineers [Coastal and Hydraulics Laboratory (CHL), Vicksburg, Mississippi, U.S.A.; http://chl.erdc.usace.army.mil/]
- U.S. Geological Survey [National Wetlands Research Center, Lafayette, Louisiana, U.S.A.; http://www.nwrc.usgs.gov/]

Aims and Scope of the Journal

Journal of Coastal Research, an International Forum for the Littoral Sciences, is dedicated to all aspects of coastal research. These include geology, biology, geomorphology (physical geography), climate, littoral oceanography, hydrography, coastal hydraulics, environmental (resource) management, engineering, and remote sensing. Although each field functions effectivelywithin itsownpurview, the cross-disciplinarynature of coastal studies requires familiarity with other fields as well. Hence, the scope of topics is necessarily broad in order to address the complexity of coastal biophysical and socio-economic interactions. Because of the wide range of interrelated topics, the journal invites original contributions and manuscripts dealing with theory, methodology, techniques, and field or applied topic studies on interdisciplinary coastal issues.

The journal encourages the dissemination of knowledge and understanding of the coastal zone by promoting cooperation and communication between specialists in different disciplines. Natural scientists, for example, are encouraged to collaborate with professionals in other fields to prepare contributions relating to the coastal zone that foster increased appreciation of coastal environments and processes. By means of this journal, with its scholarly and professional papers, systematic review articles, book and symposia reviews, communications and news, and special topical issues, an international forum for the development of integrated coastal research is provided.

Advertising, Editorial, and Subscription Information

Advertising and Editorial Office: All advertising and editorial correspondence should be sent to Dr. Charles W. Finkl, Editor-in-Chief, Journal of Coastal Research, 5130 NW 54th Street, Coconut Creek, FL 33073, U.S.A. PHONE: 828-333-2300. E-MAIL: cfinkl@cerf-jcr.com

Subscription Information: The *Journal of Coastal Research* is a bimonthly publication. Calendar-year (2016) print and online subscription prices for the JCR are: $115.00 for US CERF members / $125.00 for International CERF members ($95.00 for online only), and $519.00 for US institutions / $541.00 for International institutions ($437.00 for online only). Additional surface charges may apply to subscribers located outside of the USA. For additional membership and subscription forms and information, please go to www.CERF-JCR.org. To obtain a membership or subscription form by mail, please send request to Journal of Coastal Research, P.O. Box 7065, Lawrence, KS 66044. Back Issues and Special Issues of the JCR, when available, can be directly purchased at www.CERF-JCR.org.

The *Journal of Coastal Research* is currently surveyed in *Applied Science & Technology Abstracts; Applied Science & Technology Index (H.W. Wilson); Aquatic Sciences & Fisheries Abstracts; BIOBASE; Biological Abstracts; BIOSIS Previews (Thomson); CAB International Abstracts (CABI); CSA Civil Engineering Abstracts (ProQuest); Current Awareness in Biological Sciences (Elsevier); Current Contents/Agriculture, Biology, & Environmental Sciences (Thomson); Ecology Abstracts (ProQuest); Environmental Sciences & Pollution Management; GeoAbstracts [Geographical Abstracts: Physical Geography; Ecological Abstracts; Geological Abstracts; GEOBASE] (Elsevier); GeoRef; Meteorological & Geoastrophysical Abstracts (ProQuest); Oceanic Abstracts (ProQuest); Oceanographic Literature Review (Elsevier); Physical Sciences Digest (CSA, Ebsco); Pollution Abstracts (ProQuest); Referativnyi Zhurnal; Science Citation Index; SciSearch (Thomson); SCOPUS; Water Resources Abstracts (Bethesda); Zoological Record (Thomson).*

JCR- SI75

Proceedings of the 14th International Coastal Symposium

ICS2016

Sydney, NSW, Australia

6th-11th March 2016

Volume 2

Edited by:

Ana Vila-Concejo[1], Eleanor Bruce[1], David M. Kennedy[2] and R. Jak McCarroll[1].

Coastal Education Research Foundation (CERF)

[1]Geocoastal Research Group, School of Geosciences, The University of Sydney.

[2] School of Geography, The University of Melbourne.

Acknowledgements

Putting these volumes together has required a lot of effort, dedication and enthusiasm. We would like to thank everyone involved in this process: Lee Devereux, Andrew Broderick, Tommy Fellowes, Jordan Gacutan, Madi Patterson, Steph Duce, Susan Warner. Mandi Thran not only helped with text formatting; she designed the artwork for the cover.

Journal of Coastal Research Special Issue No. 75

14th International Coastal Symposium ICS2016

Sydney, NSW, Australia

6th-11th March 2016

Local Organising Committee

Ana Vila-Concejo, Conference Chair, ARC Future Fellow, Associate Professor, School of Geosciences, The University of Sydney.

Elaine Baker, Professor, UNESCO Chair in Marine Science, School of Geosciences, The University of Sydney.

Eleanor Bruce, Senior Lecturer, School of Geosciences, The University of Sydney.

Ross Coleman, Associate Professor, School of Biological Sciences, The University of Sydney.

Peter Cowell, Associate Professor, School of Geosciences, The University of Sydney.

Filippo Dall'Osso, School of Geosciences, The University of Sydney.

William Figueira, Associate Professor, School of Biological Sciences, The University of Sydney.

Daniel Harris, School of Geosciences, The University of Sydney (Present address MARUM, University of Bremen).

Thomas Hubble, Associate Professor, Pro-Dean, Faculty of Science, School of Geosciences, The University of Sydney.

R Jak McCarroll, Associate Lecturer, School of Geosciences, The University of Sydney.

Phil McManus, Professor, Head of School of Geosciences, The University of Sydney.

Daniel Penny, Senior Lecturer, School of Geosciences, The University of Sydney.

Tristan Salles, Lecturer, School of Geosciences, The University of Sydney.

Andrew Short, Professor, School of Geosciences, The University of Sydney.

Jody M Webster, Associate Professor, School of Geosciences, The University of Sydney.

International Advisory Committee

Charles W Finkl, President, Executive Director, CERF.

Chris Makowski, Senior Vice President, Assistant Director, CERF.

International Scientific Board

Troels Aagard
Irene Alejo
Clara Armaroli
Elaine Baker
Javier Benavente
Rob Brander
Eleanor Bruce
Helene Burningham
Bruno Castelle
Insik Chun
Paolo Ciavola
Samantha Clarke
Ross Coleman
Peter Cowell
Filippo Dall'Osso
Robin Davidson-Arnott
Laura del Río
Irene Delgado
Paula Diz
Luciana Esteves
Samuel Etienne
Óscar Ferreira
William Figueira
Charles W. Finkl
Duncan FitzGerald
Conceição Freitas
William Glamore
Lluis Gómez-Pujol
Ian Goodwin
Sarah Hamylton
Mitchell Harley
Daniel Harris
Javier Hernández-Molina
Patrick Hesp
Thomas Hubble
Michael Hughes
Jennifer Irish
Nancy Jackson
José Jiménez
David M Kennedy
Chang S. Kim
Michael Kinsela
Antonio Klein
Hak Soo Lin
Chris Makowski
Gonzalo Malvárez
Gerd Masselink
Ana Matias
R Jak McCarroll
Tonatiuh Mendoza
Graziela Miot da Silva
André Pacheco
Kate Panayotou
Charitha Pattiaratchi
Daniel Penny
Marta Pérez-Arlucea
Hannah Power
Roshanka Ranasinghe
Amaia Ruíz de Alegría-Arzaburu
Tristan Salles
Marcello Sano
Nadia Sénéchal
Jae Seol Shim
Andrew Short
Wayne Stephenson
Bruce Thom
Ian Turner
Adriana Vergés
Ana Vila-Concejo
Jody Webster
Jon J Williams
Kathelijne Wijnberg

ISSN 0749-0208

Front cover photo: Ana Vila-Concejo
Back cover photos: Peter Frith (Top), Bottom (Geocoastal Research Group)

Published by
Geocoastal Research Group,
School of Geosciences F09, The University of Sydney,
http://www.grgusyd.org/
http://sydney.edu.au/science/geosciences/index.shtml

All the authors are responsible for the contents of their papers. The University of Sydney and CERF can not be held responsible for any opinions and statements made by them.

To view the links to papers of volume 1, please open the Volume 1 document

TABLE OF CONTENTS

COASTAL STUDIES UNIT

Surfzone-Beach-Dune interactions: Flow and Sediment Transport across the Intertidal Beach and Backshore
Patrick A. Hesp and Thomas A.G. Smyth 1

The Coastal Studies Unit and Development of the Australian Beach Models
Andrew D. Short 8

RIVERS

Using simplified bathymetry and SAR imagery in the validation of a hydraulic model for the Tagus River floodplain
Maria Amélia V.C. Araújo, Rita Pestana, Magda Matias, Dora Roque, António Trigo-Teixeira, and Sandra Heleno 13

Runoff and sediment Transport of Portel-Melgaço Water System in an Amazonian estuarine System
Mauricio S. Costa, Marcelo Rollnic, Yuri O. Prestes, Renan P. Rosário andThais A. C. Borba 18

Acoustic attenuation due to bi-modal size distributions of suspended sediment
Daniel M. Hanes 23

Simulation of Tsunami Runup in the Tone River Using Generalized Coordinate System and Influence of River Mouth Bar on Tsunami Water Level
Ryuji Nikaido, Shin-ichi Aoki, Hirotoshi Tamura, and Masanobu Jinbo 28

ESTUARIES

GIS-based modelling of vulnerability of coastal wetland ecosystems to environmental changes: Comerong Island, southeastern Australia
Ali K. M. Al-Nasrawi, Brian G. Jones, Sarah M. Hamylton 33

Modern sedimentary processes and seasonal variations of organic matter in an urban tropical estuary, Jaboatão River (PE), Brazil
Roberto L. Barcellos , Manuel J. Flores-Montes, Tatiana M. F. Alves, Plínio B. Camargo 38

Runoff quantification on Amazonian Estuary based on hydrodynamic model.
Thais A.C. Borba, and Marcelo Rollnic 43

Spatiotemporal variation in salinity during drought years in an Amazonian estuary (Taperaçu)
Ádila K. R. da Costa, Luci C. C. Pereira, Suzane F.S. Costa, Natália R. Leite, Manuel de J. Flores-Montes, and Rauquírio M. da Costa 48

Effective Roughness Height in High-Concentrated Flows
Jiayu Fang, Yongping Chen· Peng Yao, and Min Su 53

Mixing and Dispersal of Low Saline Waters in Estuarine Coastal Waters of the Yellow Sea
ChangShik Kim 58

Stratification of tidal influenced navigation channel
Nam-Hoon Kim· Jin Hwan Hwang and Hyeyun Ku 63

An Influence of Salinity on Resuspension of Cohesive Sediment
Kyunghoi Kim, Han-sam Yoon, In-Cheol Lee and Tadashi Hibino 68

Applicability of 3D Beach Evolution Model with Wave-current Interaction to River-mouth Bar Formation
Masamitsu Kuroiwa, Yoko Shibutani, Yoshiyuki Yasumoto , Hajime Mase, and Yuhei Matsubara 73

Biological response of a coastal plain estuary to torrential episodes: a modelling study
Longo, R.S., Picado, A., Vaz, N., Dias, J.M. 78

Depositional evolution in a estuarine lagoonal system under a port influence in Northeastern Brazil
Silvio E. M. Martins, Roberto L. Barcellos Manuel J. Flores-Montes and Elvis J. de França 83

Changes in the Frequency and Duration of Closures of the Opihi Hapua Following Construction of the Opuha Dam
Sarah L. McSweeney, Deirdre E. Hart, Derek J. Todd and David M. Kennedy 88

Salinity variation in the macrotidal mixing zone: the Paracauari River estuary, Marajó Island (Northern Brazil)
Sury M. Monteiro and Maâmar El-Robrini 93

The Trophic Status of an Amazonian Estuary Under Anthropogenic Pressure (Brazil)
Marcela C. Monteiro, Luci C. C. Pereira, and José A. Jiménez 98

Random Wave-Induced Onshore Scour Characteristics around Submerged Breakwaters on Mild Slopes
Dag Myrhaug and Muk Chen Ong 103

Downscaled Numerical Modelling to Study the Climate Change Effects on the Estuarine Stratification
Dongmin Jang, Hwan J. Hwang, and Thao T.H. Nguyen 108

Use of Groundwater-table To Establish a Buffer Zone In a Barrier Island, Nakdong River Estuary, South Korea
Junghyun Park, Chang-Ill Yoo and Han-sam Yoon 113

Deposition in Flowing Water of Fine Sediments under Different Salinity Conditions
Luís Ivens Portela, Ana Custódio, and António Trigo Teixeira 118

David and Goliath Revisited: Joint Modelling of the Tagus and Sado Estuaries
Américo S. Ribeiro, Magda C. Sousa, João D. Lencart e Silva and João M. Dias 123

Variability of Salinity in Pará River Estuary: 2D Analysis with Flexible Mesh Model
Renan P. Rosário, Thaís A.C. Borba, Arthur S. Santos, and Marcelo Rollnic 128

Intermittent Estuaries: Linking Hydro-geomorphic Context to Climate Change Resilience
Neil Saintilan, Kerrylee Rogers, Christina Toms, Eric D. Stein and David Jacobs 133

Sediment re-deposition in the mangrove environment of Can Gio, Saigon River estuary (Vietnam)
Klaus Schwarzer, Nguyen Cong Thanh, and Klaus Ricklefs 138

Environmental Dynamics of the Estuary of the Pacoti River in Ceará, Brazil: Proposals for Management and Environmental Planning
Edson V. Silva, Juliana F. Farias, Larissa N. Barbosa, Victor Gabriel F. Lima and Adryane Gorayeb 143

Effect of Particle Size on Calibration of Schmidt Number
Minwoo Son, Jisun Byun, Sang Ug Kim, and Eun-Sung Chung 148

Spatial and Temporal Variability of Residual Volume Transport according to Artificial Freshwater Discharge in Yeoungsan River Estuary, South Korea
Jin Il Song , Jong Wook Kim, Byung Il Yoon, and Seung-Buhm Woo 153

Effects of Sewage on Natural Environments of the Amazon Region (Pará-Brazil)
Natália S. S. Sousa, Marcela C. Monteiro, Adryane Gorayeb, Rauquírio M. Costa, Luci C. C. Pereira. 158

The Change of Tidal Characteristics under the Influence of Human Activities in the Yangtze River Estuary
Ya Tan, F. Yang, Danghan Xie 163

The Influence of Urban Effluents on the Elemental C/N Ratio in a Tropical Coastal Area of Northeastern Brazil
Rysoaurya K. Travassos, Manuel J. Flores Montes, Bruno V. Motta da Costa, and José Martins da Silva Júnior 168

Application of Terrestrial 3D Laser Scanning to Monitor Changes of Beach Landforms
Hyung-Seok Lee, In-Ho Kim, and Han-Gwun Kim 173

Primary production of the benthic microalgae in the bottom sediments of Ria de Aveiro lagoon
Leandro Vaz., Marcos Mateus., João Serôdio., João M. Dias, and Nuno Vaz 178

The Retention and Transport Patterns of Pollutants in the Radial Sand Ridges of the South Yellow Sea
Jie Yang and Jianfeng Tao 183

Wind-Induced Water Exchange between Stratified Basins
Jin-Hee Yuk, Shin-ichi Aoki, and Minsu Joh 188

Numerical Study on the Transport Timescale in a River-influenced Macro-tidal Estuary
Qin Zhang, Jian Feng Tao, and Jie Yang 193

Physical Study on Interactions between Waves and a Well-mixed Seabed
Jisheng Zhang, Ke Sun, Yanyan Zhai, Huashan Zhang, and Chi Zhang 198

Dynamic analysis of riverbed evolution: Chengtong Reach of Yangtze Estuary
Yongping Chen, Jiangxia Li, Zhigang Wu and Shunqi Pan 203

Integral Tide-Surge-Wave Model of the Yellow Sea for Understanding Local Sediment Transport
Byung Ho Choi, Jin-Hee Yuk, and Kyeong Ok Kim 208

Hydraulic and Environmental Stability Analysis in the Estuary of Gahwa River and Sacheon Bay by the Change of Discharge of Namgang Dam in South Korea
Tae Woo Kim, Woo Dong Lee, Dong Soo Hur, Jung Lyul Lee and Jong Sung Yoon 213

Short and Medium Term Variation in the Dynamics of the Mesozooplankton Community of an Amazonian Estuary
Natália R. Leite, André Magalhães, Leiliane M. Silva, Thamara P. Andrade, Jislene B. Matos, Ádila K. R. Costa,Luci C. C. Pereira, Manuel J. Flores-Montes, and Rauquírio M. Costa 218

TIDAL INLETS

An Analytic Approach to Model the Tidal Circulation in a Double-inlet Estuary
Moacyr Araujo, Carmen Medeiros and Jean-Philippe Endres 223

Records of Migration and Ebb-Delta Breaching at Historic and Ancient Tidal Inlets along a River-Fed Paraglacial Barrier Island
Christopher J. Hein, Gregory G. Fitzsimons, Duncan M. FitzGerald, and Andrew R. Fallon 228

Evolution of a relocated inlet migrating naturally along an open coast
Chiara Popesso, André Pacheco, Óscar Ferreira, and Giorgio Fontolan 233

Morphological evolution of the Nerang River Entrance ebb-tidal delta
Mahnaz Sedigh, Rodger Tomlinson, Nick Cartright and Amir Etemad-Shahidi 238

ESTURINE BEACHES

Validation of Empirical Wave Run-up Formulas to the Polish Baltic Sea Coast
Paulina Aniśkiewicz, Rafał Benedyczak, Kazimierz Furmańczyk, and Paweł Andrzejewski 243

Shoreline Change Rate of the Barrier Islands in Nakdong River Estuary over the Southern Part of Korea
Sang-Hun Jeong , Boo-Keun Khim, Yeong-Heon Jo, Beack-Oon Kim, Sang-Ryong Lee and Kwang-Soon Park 248

Stability of artificial beaches in Port Phillip Bay, Victoria, Australia
Meagan K. Lowe and David M. Kennedy 253

Morphodynamic of a sandy-muddy macrotidal estuarine beach under contrasted energy conditions (Vilaine estuary, France)
Morio O. , Sedrati M. , Goubert E. , Floc'h F. , Furgerot L. and Garlan T. 258

Typhoon Impact and Recovery from Continuous Video Monitoring: a Case Study from Nha Trang Beach, Vietnam
Duong H. Thuan, Le T. Binh, Nguyen T. Viet, Dong K. Hanh, Rafael Almar, and Patrick Marchesiello 263

DUNES

Downwind Sedimentation and Habitat Development Following Ammophila arenaria Removal and Dune Erosion, Mason Bay, New Zealand
Ella E.C.B. Buckley, Michael J. Hilton, Teresa M. Konlechner and Janice M. Lord 268

Wave Energy as a Control on Dune Development on two Regressive Barriers in Southern Brazil
Sergio Dillenburg, Patrick Hesp, Renato Cecilio, Graziela Miot da Silva 273

Foredune Morphological Changes by Offshore Winds Revealed By Ground-Penetrating Radar: Massambaba Beach – Rio de Janeiro, Brazil
Guilherme B. Fernandez, Mariana S. Figueiredo, Thais B. da Rocha, Victor B. Maluf, Caroline Martins and Martim A.B. Moulton 278

Downwind Sedimentation and Habitat Development Following Ammophila arenaria Removal and Dune Erosion, Mason Bay, New Zealand
Lynda M. Hanlon, Lynette K. Abbott, and David M. Kennedy 283

Flow within a Trough Blowout at Cape Cod
Patrick A. Hesp, Thomas A.G. Smyth, Ian J. Walker, Paul A. Gares, Thad Wasklewisz 288

Flow Deflection and Deceleration Across a Simple Foredune
Michael J. Hilton, Scott V. Hatcher, Sarah J. Wakes, and Teresa M. Konlechner 293

Downwind dune dynamics following Ammophila arenaria invasion
Teresa M. Konlechner, Ella E.C.B Buckley, Michael J. Hilton, and Sarah J. Wakes 298

Coastal Dunes and Plants: An Ecosystem-Based Alternative to Reduce Dune Face Erosion
M. Luisa Martinez, Rodolfo Silva, Edgar Mendoza, Itxaso Odériz, and Octavio Pérez-Maqueo 303

A Review of Coastal Dunefield Evolution in Southeastern Queensland
Graziela Miot da Silva and James Shulmeister 308

The Presence of Foredune Strip as Key Factor for the Integral Beach-dune System Conservation
Miquel Mir-Gual, Guillem X. Pons 313

Chronology, Morphology and GPR-imaged Internal Structure of the Callala Beach Prograded Barrier in Southeastern Australia
Thomas S. N. Oliver, and Colin D. Woodroffe 318

Ground Penetrating Radar applied to the Characterization of the Itapeva Dunefield, Torres, Brazil
Gabriela C. Rockett, Eduardo G. Barboza, Maria Luiza C.C. Rosa 323

Numerical Modelling of Turbulent Flow Structures in a Trough Blowout
Thomas A.G. Smyth and Patrick A. Hesp 328

Wind Turbulence Effects on Dune Sand Transport
Keiko Udo 333

Aeolian Sediment Flux Derived from a Natural Sand Trap
Alida J. van der Weerd, Kathelijne M. Wijnberg 338

Topographic Steering of Oblique Incident Winds Across a Foredune-Parabolic Topography, Mason Bay, Stewart Island, New Zealand
Sarah J. Wakes, Michael J. Hilton, and Teresa Konlechner 343

OCEAN BEACHES

Surf-Swash Interactions on a Low-Tide Terraced Beach
Rafael Almar, Pedro Almeida, Chris Blenkinsopp, Patricio Catalan 348

Seasonal Variations in Recovery Timescales of Shorelines on an Embayed Beach

Melanie Biausque , Nadia Senechal, Brice Blossier, and Karin R. Bryan 353

The Role of Beach and Wave Characteristics in Determining Suitable Habitat for Three Resident Shorebird Species in Tasmania
Anja Bock, Michael R. Phillips and Eric Woehler 358

Velocity of RFID Tagged Gravel in a Non-uniform Longshore Transport System
Tony Dolphin, Janette Lee, Roger Phillips, Colin J.L. Taylor and Keith R. Dyer 363

Prograded Barriers + GPR + OSL = Insight on Coastal Change over Intermediate Spatial and Temporal Scales
Amy J. Dougherty, Jeong-Heon Choi, and Anthony Dosseto 368

Morphological Response of a Macrotidal Embayed Beach, Porsmilin, France
France Floc'h, Nicolas Le Dantec, Clara Lemos, Romain Cancouët, Damien Sous, Lise Petitjean, Frédéric Bouchette , Fabrice Ardhuin, Serge Suanez and Christophe Delacourt 373

Pulsations in Surf Zone Currents on a High Energy Mesotidal Beach in New Zealand
Shari L. Gallop, Karin R. Bryan, Sebastian J. Pitman, Roshanka Ranasinghe, and Dean Sandwell 378

Wind-energy Development Causes Social Impacts in Coastal Ceará state, Brazil: The Case of the Xavier Community
Adryane Gorayeb, Jocicléa de Sousa Mendes, Antonio Jeovah de Andrade Meireles, Christian Brannstrom, Edson Vicente da Silva, Ana Larissa Ribeiro de Freitas 383

Beach response to Australian East Coast Lows: A comparison between the 2007 and 2015 events, Narrabeen-Collaroy Beach
Mitchell D. Harley, Ian L. Turner, Kristen D. Splinte, Matthew S. Phillips and Joshua A. Simmons 388

Shoreline-Sandbar Dynamics at a High-Energy Embayed and Structurally-Engineered Sandy Beach: Anglet, SW France
Jean-Remy Huguet, Bruno Castelle, Vincent Marieu, Denis Morichon, Inaki de Santiago 393

Wave attenuation and Coastal Protection by Shelly Ridges: Mont-Saint-Michel Bay, France
Matthieu Jeanson, Samuel Etienne, Antoine Collin 398

Morphological Change near Artificial Reefs as a Beach Erosion Countermeasure
Kyu-Han Kim, Kyu-Tae Shim, and Bumshick Shin 403

On Eddy-Mixed Longshore Currents: Video Observation and 3D Modeling off Grand Popo Beach, Benin
Patrick Marchesiello, Rafael Almar, Rachid Benshila, Stanislas Larnier, Bruno Castelle and James C. McWilliams 408

Phytoplankton Dynamics in Three Metropolitan Beaches of the Amazon Littoral (São Luís-Maranhão)
Jislene B. Matos, Antonio R.G. Oliveira, Wellington N. Trindade, Natália R. Leite, Maria L. Koening, Luci C.C. Pereira and Rauquírio M. da Costa 413

Bathymetric controls on very low frequency rip current motions
R. Jak McCarroll, Robert W. Brander, and Ian L. Turner 418

Small Scale Bedform Types off the South-Holland Coast
Saulo Meirelles, Martijn Henriquez, Alejandro J. Souza, Alexander R. Horner-Devine, Julie D. Pietrzak, Sabine Rijnsburg, Marcel J. F. Stive 423

Morphodynamic Processes on a Macrotidal Beach in the Eastern Amazon
Anderson T. do Nascimento and Luci C. C. Pereira 427

Estimation of Infragravity Waves inside Pohang New Port
Jung Eun Oh, Kyung-Duck Suh, Sang-Ho Oh, and Weon-Mu Jeong 432

Nearshore Dynamics and Holocene Evolution of the Coastal Barrier South of the Santa Marta Cape, Southern Brazil
Julio F. de Oliveira, Eduardo G. Barboza and Javier Benavente 437

Potential of Video Cameras in Assessing Event and Seasonal Coastline Behaviour: Grand Popo, Benin (Gulf of Guinea)
Abessolo Ondoa, G., Almar, R., Kestenare, E., Bahini, A., Houngue, G-H, Jouanno, J., Du Penhoat, Y., Castelle, B., Melet, A., Meyssignac, B., Anthony, E.J., Laibi, R., Alory, G., and Ranasinghe, R 442

Beach Morphological Predictions: The Impact of a Temporally Varying Sediment Fall Velocity
Sam Prodger, Paul Russell, Mark Davidson and Jon Miles 447

Equilibrium Beach Profile in the Presence of Beachrocks
Marcelo Rollnic and Carmen Medeiros 452

The Effects of Beach Morphology Variations on the Profile of Nearshore Currents on a Gently Sloping Mesotidal Beach
Amaia Ruiz de Alegria-Arzaburu, Mario Arturo Arreola-Cortez, Héctor García-Nava, Rafael Hernández-Walls and Adán Mejía-Trejo 457

Recovery Assessment of Two Nearby Sandy Beaches with Contrasting Anthropogenic and Sediment Supply Settings
Nadia Senechal, Jonathan Pavon, Remy Asselot, Mohammed Taaouati, Sophie Ferreira, and Stéphan Bujan 462

An artificial reef improves coastal protection and provides a base for coral recovery
Rodolfo Silva, Edgar Mendoza, Ismael Mariño-Tapia, María Luisa Martínez and Edgar Escalante 467

Subtidal and Intertidal Three-Dimensionality at a High Energy Macrotidal Beach
Christopher Stokes, Paul Russell, and Mark Davidson 472

Analysis of Coastal Erosion due to the 2011 Great East Japan Tsunami and its Recovery Using Ground Penetrating Radar Data
Maya Takamura, Keiko Udo, Motoyuki Sato, and Kazunori Takahashi 477

Subaerial Rotation on an Open Coast Beach: Pendine West Wales, UK

Tony Thomas, Nelson Rangel-Buitrago, Michael R. Phillips, Giorgio Anfuso, Allan T, Williams and Judith, A. Oakley 482
Tidal Modulation of Moderate Wave Energy on a Sandy Tidal Flat on the Macrotidal Amazon Littoral
Wellington Trindade, Luci C. C. Pereira, and Ana Vila-Concejo 487
Swash Motion Driven by the Bore and Prediction of Foreshore Profile Change
Jun Wang, Bingchen Liang, Huajun Li, Xinying Pan, Dongyoung Lee, Yu Xu 492
Laboratory Experiment on the Bed Load Sediment Transport over a Rippled Bed
Zhengtong Yang, Huajun Li, Bingchen Liang, Dongyoung Lee, Xinying Pan, Yu Xu 497
3D Morphodynamic Modeling of a Sand Recycling System
Yoshiyuki Yasumoto, Masamitsu Kuroiwa, Yoko Shibutani, Yuki Osakada, and Yuhei Matsubara 502
Hydraulic and Sediment Dynamics at times of Very Shallow Water on Intertidal Mudflats: The Contribution of Waves
Qian Zhang, Zheng Gong, Changkuan Zhang, Zeng Zhou, Ian Townend 507

CONTINENTAL SHELVES AND SLOPES

Spatial-Temporal Variability of the Thermohaline Properties in the Coastal Region of Fernando de Noronha Archipelago, Brazil
RamillaV. Assunção, Alex C. Silva, José Martins, and Manuel Flores Montes 512
Multi-Year Observation of Holloway Current along the Shelf Edge of North Western Australia
Mohammad Hadi Bahmanpour, Charitha Pattiaratchi, E.M.S Wijeratne, Craig Steinberg, and Nick D'Adamo 517
Modelling of Extreme Wave Climate in China Seas
Jiangxia Li, Yongping Chen and Shunqi Pan 522
Factors influencing the occurrence of Dense Shelf Water Cascades in Australia
Tanziha Mahjabin, Charitha Pattiaratchi, and Yasha Hetzel 527
Seasonal Variations of the Amazon River Plume with Focus on the Eastern Sector
Angela C.C. Mascarenhas , Gabriela S. Gomes, Antônia P.Y. Lima, Heriton K.N. da Silva, Leandro S. Santana, Renan P. Rosário, and Marcelo Rollnic 532
Sediment Dynamics from Coast to Slope – Southern Canadian Beaufort Sea
Philip D. Osborne, and Alexandre Forest 537
Internal Tide-Induced Enhancement of Cold Water Intrusion on the Continental Shelf of the Korea Strait
Jae-Hun Park, Ye Sol Kim, Ho Jin Lee, Hee-Yeol Lee, Ho Kyung Ha, Young-Gyu Park, Chanhyung Jeon, and Naoki Hirose 542
3-D Comprehensive Hydrodynamic Modelling in the Arabian Gulf
Zhong Peng and Jill Bradon 547
Coastal Fronts Utilized by Migrating Humpback Whales, Megaptera novaeangliae, on the Gold Coast, Australia
Joshua Reinke, Charles Lemckert, and Jan-Olaf Meynecke 552
Internal Tides in the Southwestern East/Japan Sea from Observation and Simulation
Seongbong Seo, Young-Gyu Park, Jae-Hun Park, Chanhyung Jeon , Chang Woong Shin and Hee-Dong Jeong 557
A Comparison of Geomorphic Settings, Sediment Facies and Benthic Habitats of Two Carbonate Systems of Western Mediterranean Sea and South Western Australia: Implications for Coastal Management
Sira Tecchiato, Carla Buosi, Angelo Ibba, David A. Ryan and Sandro De Muro 562
The Influence of the Subtropical High-Pressure Ridge on the Western Australian Wave Climate
Moritz Wandres, Charitha Pattiaratchi, E.M.S Wijeratne, Yasha Hetzel 567

CORAL REEFS

Three-dimensional structure of coral reef boulders transported by stormy waves using the very high resolution WorldView-2 satellite
Antoine Collin, Samuel Etienne, and Matthieu Jeanson 572
Atoll-scale comparisons of the sedimentary structure of coral reef rim islands, Huvadhu Atoll, Maldives
Holly K. East, Chris T. Perry, Paul S. Kench, and Yiqing Liang 577
Wave modifications across a coral reef: Cap Chevalier, Martinique Island.
Matthieu Jeanson, Franck Dolique, Mouncef Sedrati, Oliver Cohen, Jimmy Bertier, Alan Cavalin, Jessica Charpentier and Edward J. Anthony 582
Lagoonal reef sediment supply and island connectivity, Huvadhu Atoll, Maldives
Yiqing Liang, Paul S. Kench, Murray R. Ford, and Holly K. East 587

ROCKY COASTS

The Drowned Apostles: The Longevity of Sea Stacks over Eustatic Cycles
Rhiannon Bezore, David M. Kennedy, and Daniel Ierodiaconou 592
Modelling the Development of Varied Shore Profile Geometry on Rocky Coasts

Hironori Matsumoto, Mark E. Dickson, and Paul S. Kench 597
Observation of Wave Transformation on Macro-tidal Rocky Platforms
Timothy Poate, Gerd Masselink, Martin Austin, Mark Dickson, Paul Kench 602
Measuring Coastal Boulder Movement Under Waves Using Tri-Axial Accelerometers
Wayne J. Stephenson and Alenka Abazović 607
What controls the geometry of rocky coasts at the local scale?
Zuzanna M. Swirad, Nick J. Rosser, Matthew J. Brain, and Emma C. Vann Jones 612

MANAGING THE PRESENT

Video assessment of nearshore and beach evolution following the deployment of a submerged geotextile wave breaker
Yann Balouin, François Longueville, and Yohan Colombet 617
Stakeholder Perceptions of a Coastal Marine Protected Area
Beverley Clarke, Ruth Thurstan, and Katherine Yates 622
Which is the Best Predictor of Sea Temperature: Satellite, Model, or Data Logger Values? A Case Study from the Maltese Islands (Central Mediterranean)
Alan Deidun , Adam Gauci, Joel Azzopardi, Denis Cutajar, Hazel Farrugia and Aldo Drago 627
Defining the Trophic Status of Maltese (Central Mediterranean) Coastal Waters through the Computation of Water Quality Indices Based on Satellite Data
Hazel Farrugia , Alan Deidun, Adam Gauci, and Aldo Drago 632
Aquaculture Pond Precise Mapping in Perancak Estuary, Bali, Indonesia
Niken F. Gusmawati , Cheng Zhi, Benoît Soulard, Hugues Lemonnier and Nazha Selmaoui-Folcher 637
Managing Threats to the Marine Estate in New South Wales (Australia) to Maximise Community Wellbeing
Alan Jordan, Sarah Fairfull, Bob Creese 642
Data-driven Modeling of Coastal Water Quality using the Bayesian Method for Coastal Management
Jinah Kim and Jungwoon Choi 647
The Effects of Groundwater Pumping and Infiltration on Seawater Intrusion in Coastal Aquifer
Hojin Lee , Sungduk Kim, Kye-Won Jun, Hyung-Keun Park, and Jae-Sung Park 652
M2, overtides and compound tides generation in the Strait of Messina: the response of a non-hydrostatic, finite-element ocean model
Giovanni Quattrocchi, Gerard J. Gorman, Matthew D. Piggott and Andrea Cucco 657
New Coastal Regulation in Spain. A roadmap to a better approach to coastal environment
José Santos López-Gutiérrez, Vicente Negro, and M. Dolores Esteban 662
Review of coastal Land Reclamation situation in the World
Mario Martín-Antón , Vicente Negro, José María del Campo, José Santos López-Gutiérrez, and M. Dolores Esteban 667
Communicating beach management: educators; coastal engineers and local governments collaborating to create successful education programs.
Maggie Muurmans Peta Leahy Laura Richards 672
Evaluation of Life Cycle Cost for Wave-dissipating Works Considering Occurrence Probability of High Waves
Takao Ota, Hiroyuki Kawamura, Yoshiharu Matsumi and Takayuki Hirayama 675
Beach carrying capacity and protected areas: management issues in Arrábida Natural Park, Portugal
Carlos Pereira da Silva, Ricardo Nogueira Mendes, Gonçalo Moutinho, Vanessa Mota, Catarina Fonseca 680
Spatial Analysis of a Coastal Area for Conservation and Fishery of Mangrove Edible Crab (Ucides cordatus)
Luciana C. M. Santos, Mario M. Rollo Jr., Tânia M. Costa, Marcelo A. A. Pinheiro, Farid Dadouh-Guebas and Marisa D. Bitencourt 685
Ecosystem-Based Knowledge and Management as a tool for Integrated Coastal and Ocean Management: A Brazilian Initiative
Marinez E.G. Schererand Milton L. Asmus 690
Effect of the Coastal Protection using the Beach Nourishment at Tottori Sand Dune Coast, JAPAN
Yoko Shibutani , Masamitsu Kuroiwa, and Yuhei Matsubara 695
An Extreme Event as a Game Changer in Coastal Erosion Management
Carlo Sorensen, Nils K. Dronen, Per Knudsen, Jürgen Jensen, and Per Sorensen 700
Estuarine Beaches of the Amazon coast: Environmental and Recreational Characterization
Rosigleyse C. de Sousa, Luci C.C. Pereira, and José A. Jiménez 705
Development of Beach Health Index for the Gold Coast, Australia
Derek J. Todd and Kim Bowa 710
Gold Coast Seawall: Status Investigations and Design Review
Rodger B. Tomlinson, Angus (L.A.) Jackson, and Kim Bowra 715

Anchor Collision Analysis of Stone-filled Bags for Submarine Power Cable Protection using a Smoothed Particle Hydrodynamics Method
Jinho Woo, Dongha Kim, and Won-Bae Na 720
Connectivity between Sediment Storage in Dam Reservoir and Coastal Erosion: Implications Through Zonal Mappings of Monitoring Data
Yoshiyuki Yokoo and Keiko Udo 725

VOLUME 2

PAST CLIMATE AND SEA LEVEL CHANGE

Ground Penetrating Radar Observations of Present and Former Coastal Environments, Great Sandy National Park, Queensland, Australia – Focus on Moon Point, Fraser Island
Allen M. Gontz, Adrian B. McCallum, Patrick T. Moss, and James Shulmeister 730
Analysis of Wave Climate around Korea Based on Long-Term Hindcast and Coastal Observation Data
Weon-Mu Jeong, Sang-Ho Oh, and Ho Sik Eum 735
Testing versions of the Bruun rule for low energy macro-tidal tropical beaches against a theoretical late Holocene sea-level high-stand and beach ridge evidence of late Holocene beach faces
Andrew Kerans and Nick Cartwright 740
A Hierarchical Bayesian Model based Nonstationary Frequency Analysis of Extreme Sea Level under Climate Change along the Shorelines in South Korea
Yong-Tak Kim, Hye-Rin Cho, Sumiya Uranchimeg, Seung-Oh Lee, and Hyun-Han Kwon 745
Geological and Stratigraphic Characteristics of a Holocene Regressive Barrier in Southern Brazil: GIS and GPR Applied for Evolution Analysis
Renato A. Leal, Eduardo G. Barboza, Volney Jr. Bitencourt, Anderson Biancini da Silva and Rogério P. Manzolli 750
Effect of Large-Scale Atmospheric Circulation and Wind on Storm Surge Occurrence
Anne-Lise Montreuil, Jihane Elyahyioui, and Margaret Chen 755
Increasing the highest storm surge in Busan harbor
Sang Myeong Oh, Il-Ju Moon, and Suk Jae Kwon 760
Tidal Asymmetry and Energy Variation Due to Sea-Level Rise in a Macro Tidal Bay
Seung-Won Suh 765
Estimating the Accelerated Sea Level Rise along the Korean Peninsula Using Multiscale Analysis
Sumiya Uranchimeg, Hye-Rin Cho, Yong-Tak Kim, Kyu Nam Hwang, and Hyun-Han Kwon 770
Past extreme events recorded in the internal architecture of coastal formations in the Baltic Sea Region
Kadri Vilumaa, Hannes Tõnisson, Shinya Sugita, Ilya V. Buynevich, Are Kont, Merle Muru, Frank Preusser, Stefan Bjursäter, Tiit Vaasma, Egert Vandel, Anatoly Molodkov, and Johanna I. Järvelill 775
How to improve estimates of real-time acceleration in the mean sea level signal
Phil J. Watson 780
Tidal Evolution in the Yellow and East China Sea during Holocene
Chunyan Zhou, Jinhai Zheng, Ping Dong, Jisheng Zhang, Yuliang Zhu and Zhiheng Zhang 785

DECADAL COASTLINE AND ESTUARINE EVOLUTION

Sturgeon Bank, Fraser River Delta, BC, Canada: 150 Years of Human Influences on Salt Marsh Sedimentation
Rowland J. Atkins, Morgan Tidd, and Gord Ruffo....790 **Coastal Observation through Cosmo-SkyMed High-Resolution SAR Images**
Maria Francesca Bruno, Matteo Gianluca Molfetta, Michele Mossa, Raffaele Nutricat, Alberto Morea and Maria Teresa Chiaradia 795
Comparative spit dynamics. The case of deltaic river mouth spits
Zăinescu I. Florin, Vespremeanu-Stroe Alfred, Tătui Florin 800
Decadal Evolution of Mond River Delta, the Persian Gulf
S. Abbas Haghshenas, Azadeh Razavi Arab, Arash Bakhtiari, Morteza Jedari Attari, and Michael John Risk, ... 805
A Multiscale Simulation Approach for Linking Mangrove Dynamics to Coastal Processes using Remote Sensing Observations
Christophe Proisy, Pascal Degenne, Edward J. Anthony, Uta Berger, Elodie Blanchard, François Fromard, Antoine Gardel, Adewole Olagoke, Valdenira Santos, Romain Walcker, Danny Lo Seen 810
Ponta Negra Beach, Natal, Brazil: A Roll and Rock Story
Ada C. Scudelari, Claudio F. Neves, Venerando E. Amaro, and Olavo F. Santos 815

HYDRODYNAMICS (CONTEMPORARY PROCESSES)

3D numerical model of ecohydrodynamics for shallow waters
Roman Bezhenar , Kyung Tae Jung, Vladimir Maderich, and Kyeong Ok Kim 820
Field Observations, Video Monitoring and Numerical Modeling at Poetto Beach, Italy
Walter Brambilla, Arnold van Rooijen, Simone Simeone, Angelo Ibba, Sandro DeMuro 825
Numerical Modeling of Wave Transformation and Runup Reduction by Coastal Vegetation of the South China Sea
Haijin Cao, Weibing Feng, and Yujin Chen 830
Generation of Free Infragravity Waves by Time-Varying Breakpoint with Real Wave Conditions
Stephanie Contardo , Graham Symonds 836
Software for Predicting Hydrodynamic Pressures on Offshore Pile Foundations: The Next Step in Ocean Energy Development
Adrian Escobar, Vicente Negro, Jose Santos Lopez-Gutierrez , and M. Dolores Esteban 841
Experimental Study on Upstream-Advancing Waves Induced by Currents
Jun Fan, Jin-hai Zheng, Ai-feng Tao, Hao-feng Yu, Yi Wang 846
Effects of Ultra-Porous 3D Printed Reefs on Wave Kinematics
Lorenzo Frau, Andrea Marzeddu, Enrico Dini, Vicente Gracia, Xavier Gironella, Alessio Erioli, Alessandro Zomparelli, Agustín Sánchez-Arcilla 851
Effects of Gravity Waves on Turbulence and Processes That Contribute to Mixing at a Submarine Groundwater Discharge
Gabriel Gallegos D. B, Ismael Mariño-Tapia, and Arnoldo Valle Levinson 856
Theoretical and Observed Breaking Wave Height on a Barred Macrotidal Beach: Implications for Estimation of Breaker Index
Arnaud Héquette and Adrien Cartier 861
Variability of Benthic Communities in Relation to Hydrodynamic Conditions in the North-Eastern Baltic Sea
Kristjan Herkül , Kaire Torn, Ülo Suursaar, Victor Alari, and Anneliis Peterson 867
Prediction of the 2011 Tohoku Tsunami Scouring near Structures
Tatsuki Iida, Shuich Kure, Keiko Udo, Akira Mano, and Hitoshi Tanaka 872
Accurate Estimation of Wave Reflection on a High Energy, Dissipative Beach
Kris Inch, Mark Davidson, Gerd Masselink, and Paul Russell 877
Wave Set-up and Run-up Variability on a Complex Barred Beach During Highly Dissipative Storm Conditions
Alexandre Nicolae Lerma, Rodrigo Pedreros and Nadia Senechal 882
Morphological Response to the Installation of Detached Breakwaters along the Cigu Coast of Tainan, Taiwan
Tsung-Yi Lin 887
Hydrodynamic Regimes in Offshore Wind Farms
Clara Matutano, Vicente Negro, José-Santos López-Gutiérrez∞, M. Dolores Esteban, ... 892
Understanding Strandings: 25 years of Humpback Whale (Megaptera novaeangliae) Strandings in Queensland, Australia
Jan-Olaf Meynecke , Justin J. Meager 897
Three-Dimensional Numerical Simulation of Nonlinear Internal Waves in the St. Lawrence Estuary, Canada
Van Thinh Nguyen 902
Depression Waves Generated by Large Ships in the Venice Lagoon
Kevin E. Parnell , Luca Zaggia, Tarmo Soomere, Giuliano Lorenzetti, and Gian Marco Scarpa 907
Synthetic Imagery for the Automated Detection of Rip Currents
Sebastian Pitman, Shari L. Gallop, Ivan D. Haigh, Sasan Mahmoodi∞, Gerd Masselink and Roshanka Ranasinghe 912
Wave Height Distributions in the Surf Zone on Natural Beaches
Hannah E. Power, Peter Nielsen, Michael G. Hughes, Troels Aagaard and Tom E. Baldock 917
Physical and Numerical Modeling of Irregular Wave Transformation over a Fringing Reef
Sungwon Shin , Young-Taek Kim, and Jong-In Lee 922
Seasonal and Intraseasonal Variability of Wave Climate on the NE Brazilian Coast using a Nautical Radar System
Alex C. da Silva, Cristiane S. Bezerra, Roberto L. Barcellos, Moacyr Araújo, Nadège Bouchonneau, Valdir Manso 927
Empirical Parameterization of Wave Runup and Dune Erosion during Storm Conditions on a Natural Macrotidal Beach
Serge Suanez, Emmanuel Blaise, Romain Cancouët, and France Floc'h 932
Cusp Development on a Gravel Beach
Jinkang Wang and Douglas J. Sherman 937
Investigation of Wave Breaking Turbulence in Morphodynamic Modelling
Hyun-Doug Yoon, Minsang Cho, and Sang-Young Son 942

FUTURE FORECASTS

Sensitivity of shoreline-recession forecasts to sediment budget uncertainties
Salette A. de Figueiredo and Peter J. Cowell 947

A Flexible Approach to Forecasting Coastline Change on Wave-Dominated Beaches
Michael A. Kinsela, Bradley D. Morris, Marc J. A. Daley and David J. Hanslow 952

Interoperability as supporting tool for Future Forecasting on coastal and marine areas
Fatima Navas, Emilia Guisado-Pintado and Gonzalo Malvárez 957

On the Long-term Changes of Extreme Wave Heights at the German Baltic Sea Coast
Zhenshan Xu, Norman Dreier, Yongping Chen, Peter Fröhle and Dongmei Xie 962

MANAGING THE FUTURE

A Comparison of Shoreline Changes Estimated Using the Base of Beach and Edge of Vegetation Line at North Keeling Island.
Farrah A. F. Adnan, Sarah M. Hamylton , and Colin D. Woodroffe 967

Regional Environmental Sensitivity Index (RESI) Classification of Estonian Shoreline (Baltic Sea)
Robert Aps, Hannes Tõnisson, Ülo Suursaar, and Kaarel Orviku 972

Design Policy Options supported by Marine and Coastal Ecosystem Services Assessment and Valuation: a Case Study in Portugal
Maria da Luz Fernandes, Inês C. Antunes, Eduardo R. Oliveira, Fátima L. Alves 977

Measuring Success of Ocean Governance: a Set of Indicators from Portugal
Maria Adelaide Ferreira , David Johnson, and Carlos Pereira da Silva 982

Regional Scale Coastal Mapping to Underpin Strategic Land Use Planning in South East Australia.
David J. Hanslow, Jocelyn Dela-Cruz, Bradley D. Morris, Michael A. Kinsela, Edwina Foulsham, Michelle Linklater and Tim R. Pritchard 987

Coastal Impact of Onshore Wind Farms in Australia
Nick Harvey and Romana E.C. Dew 992

Outlining an approach to address Geospherical and Biospherical aspects of Coastal Squeeze in the Mediterranean
Annette Hildinger, Andreas Braun 997

The Management of Information to Identify the Submarine Cable Route: the Case Study of Campania islands
Ornella Nonnis, Chiara Maggi, Pasquale Lanera, Raffaele Proietti, Alessia Izzi, Pietro Antonelli, Massimo Gabellini 1002

Key Environmental Factors in the Management of Ciguatera
Leanne Sparrow and Kirsten Heimann 1007

Projected Changes in Wave Conditions in the Baltic Sea by the end of 21st Century and the Corresponding Shoreline Changes
Ülo Suursaar, Hannes Tõnisson, Victor Alari, Urmas Raudsepp, Henri Rästas, and Agnes Anderson 1012

COASTAL HAZARDS

Numerical Study on Tsunami Propagation into a River
Yasuhisa Aoyama, Mohammad Bagus Adityawan , Wahyu Widiyanto, Yuta Mitobe, Daisuke Komori, and Hitoshi Tanaka.. 1017

Video Observation of Waves and Shoreline Change on the Microtidal James Town Beach in Ghana
Donatus B. Angnuureng, Rafael Almar, Kwasi Appeaning Addo, Bruno Castelle, Nadia Senechal, Sowah W. Laryea, George Wiafe 1022

Alongshore variations in morphology and incident wave energy on a human-impacted coast: Agadir, Morocco
Ismail Aouiche, Lahcen Daoudi, Edward J. Anthony, Mouncef Sedrati, Abdelhadi El Mimouni, Philippe Dussouillez 1027

Open Sandy Beach Morphology and Morphodynamic as Response to Seasonal Monsoon in Kuala Terengganu, Malaysia
Effi Helmy Ariffin, Mouncef Sedrati, Mohd Fadzil Akhir, Rosnan Yaacob and Mohd Lokman Husain 1032

Fuzzy Control for Impact Mitigation of Coastal Infrastructure Equipped with Magnetorheological Dampers
Kemal S. Arsava, Yeesock Kim, and Kyu Han Kim 1037

Spatio-temporal Variability in the Tipping Points of a Coastal Defense
Jennifer M. Brown, Thomas Prime, Jack J.C. Phelps, Andrew Barkwith, Martin D. Hurst, Michael A. Ellis, Gerd Masselink, and Andrew J. Plater 1042

Coastal Impacts Induced by Storm Waves between Cape Frio and Cape Buzios, Rio de Janeiro, Brazil
Eduardo Bulhões, Guilherme B Fernandez, Silvio R Oliveira Filho, Thiago G Pereira 1047

Beach response to consecutive extreme storms using LiDAR along the SW coast of England
Olivier Burvingt, Gerd Masselink, Paul Russell and Tim Scott 1052

Development of Hazard Map with Probable Maximum Tsunamis
Yong-Sik Cho, Hyung-Sik Hwang, Jin-Young Kim, and Hyun-Han Kwon 1057

Migration of Coastal Erosional Hotspots due to Coastal Protection Structures
Kwang Hee Choi, Jang Soo Kim, Jong Chun Lee 1062

Using LiDAR Topographic Data for Identifying Coastal Areas of Northern France Vulnerable to Sea-Level Rise
Adrien Crapoulet, Arnaud Héquette, Franck Levoy and Patrice Bretel 1067

Multiple-Source Cliff Erosion in Southern Spain: Current Risk and Future Perspectives
Laura del Río, F. Javier Gracia, and Javier Benavente 1072

Fast Ensemble Forecast of Storm Surge along the Coast of China
Xuelin Ding, Yongping Chen, Yi Pan and Dominic Reeve 1077

Efficient Integration of a Storm Surge Model into a Multidisciplinary Agent Based Model Framework
Juan L. Garzon, Celso Ferreira, Robert A. Dalrymple, and Seth D. Guikema 1082

Hindcasting Tropical Storm Events in the Oman Sea
Sarmad Ghader, Daniel Yazgi, S. Abbas Haghshenas, Azadeh Razavi Arab, Morteza Jedari Attari, Arash Bakhtiari , and Hamid Zinsazboroujerdi 1087

Estimating Flooding Level Through the Brazilian Coast Using Reanalysis Data
Paula Gomes da Silva, Charline Dalinghaus, Mauricio González, Omar Gutiérrez, Antonio Espejo, Ana J. Abascal, and Antonio H. F. Klein 1092

Ecosystem Services and Their Benefits as Coastal Protection in Highly Urbanised Environments
Emilia Guisado-Pintado, Fatima Navas and Gonzalo Malvárez 1097

Synoptic Study on Forecasting Large Swell Waves along the Eastern Coast of Korea Using the Operational System
Taemin Ha, Cheolwoo Park, Jaeseon Yoon, and Ki-Young Heo 1102

Producing the Hindcast of Wind and Waves Using a High-Resolution Atmospheric Reanalysis around Korea
Ki-Young Heo and Taemin Ha 1107

Factors Controlling Coastal Erosion During Storm Events
Darius Jarmalavičius, Virmantas Šmatas, Gintautas Stankūnavičius, Donatas Pupienis, and Gintautas Žilinskas 1112

A Comprehensive Sensitivity Analysis of Tsunami Model System to the Parametric and Input Uncertainties
Tae-Hwa Jung, Sangyoung Son, Patrick J. Lynett 1117

Typhoon Morakot Induced Waves and Surges with an Integrally Coupled Tide-Surge-Wave Finite Element model
Kyeong Ok Kim, Jin-Hee Yuk, Han Soo Lee, and Byung Ho Choi 1122

Simulation Of Typhoon Bolaven Using Integrally Coupled Tide-Surge-Wave Models Based On Locally Enhanced Fine-Mesh Unstructured Grid System
Kyeong Ok Kim, Jin-Hee Yuk, and Byung Ho Choi 1127

Probabilistic Coastal Storm Surge Analyses using Synthesized Tracks Based on Historical Typhoon Parameters
Hyeon-Jeong Kim and Seung-Won Suh 1132

Resonance of 2011 East Japan Tsunami over Continental Shelf along Ibaraki Coast of Japan
Gun Hyeong Kim, Sobeom Jin, Seung Gyu Hyun , and Sung Bum Yoon 1137

Double Resonance Effect at Daeheuksando Port Caused by Air Pressure Disturbances in Yellow Sea on 31 March 2007
Myung-Seok Kim, Hyunsu Kim, Yoo-Keun Kim, Bon-Ho Gu, Ho-Jae Lee, and Seung-Buhm Woo 1142

Seasonal Characteristics and Mechanisms of Meteo-tsunamis on the West Coast of Korean Peninsula
Hyunsu Kim, Myung-Seok Kim, Ho-Jae Lee, Seung-Buhm Woo, and Yoo-Keun Kim 1147

Overview of Super Typhoon Haiyan and Characteristics of Human Damage due to its Storm Surge in the Coastal Region, Philippines
Shuichi Kure, Yasuhito Jibiki, Kanako Iuchi, and Keiko Udo 1152

A Hierarchical Bayesian Model-Based Uncertainty Analysis for Tsunami Heights along Shorelines in Korea
Hyun-Han Kwon, Jin-Young Kim, Byoung Han Choi, and Yong-Sik Cho 1157

Detecting errors in coastal databases using Bayesian Networks
Gonéri Le Cozannet, Thomas Bulteau, Manuel Garcin, Christophe Garnier, Heloise Müller, Anaïs Hoareau and Cyril Mallet 1162

The Application of a Rip Current Warning Decision-Process System, Haeundae Beach, South Korea
Jooyong Lee, Won Chul Cho, and Jung Lyul Lee 1167

Multi-Criteria Surge Vulnerability Assessment with Long-term Reanalysis
Gyumin Lee, Byoung-Il Min, and Kyung Soo Jun 1172

Lagrangian Observation of Rip Currents at Haeundae Beach Using an Optimal Buoy Type GPS Drifter
Jooyong Lee, Dong Hee Kim, Sahong Lee, and Jung Lyul Lee 1177

Synoptic Systems Generators of Extreme Wind in Southern Brazil: Atmospheric Conditions and Consequences in the Coastal Zone
Arthur A. Machado, and Lauro J. Calliari 1182

Evaluation of Runup Characteristics on the NSW Coast
Bradley D. Morris, Edwina Foulsham, Raymond Laine, Daniel Wiecek and David Hanslow 1187

Hurricane-induced shoreline change and post-storm recovery: northeastern Yucatan Peninsula, Mexico
Nicholas Mulcahy, David M. Kennedy, and Paul Blanchon 1192

A Framework for Modelling Shoreline Response to Clustered Storm Events: A Case Study from Southeast Australia
Scott L. Nichol, Andrew McPherson, Gareth Davies, Wenping Jiang, Floyd Howard, Uriah Gravois, David Callaghan and Tom Baldock 1197

Simulation of Inundation along the West Coast of Korea from the Meteo-Tsunami of 2007
Sae Chan Oh, Choong Hun Shin , and Sung Bum Yoon 1202

New Understanding on the Distribution of Individual Wave Overtopping Volumes over a Levee under Negative Freeboard
Yi Pan, Lin Li, Farshad Amini, Cuiping Kuang, and Yongping Chen..... 1207

Impacts of Submerged Breakwaters on Nearshore Sediment Transport
Shunqi Pan and George Fairbairn 1212

Beach Hazard and Risk Perception of Lifeguards Working in a Macrotidal Amazon Beach
Wilson C. Brito, Luci C.C. Pereira, Rosygleyse C. Sousa and Andrew D. Short 1217

Water Quality during the Recreational High Season for a Macrotidal Beach (Ajuruteua, Pará, Brazil)
Rubem M. C. Pessoa, Luci C.C. Pereira, Rosigleyse C. Sousa, and Rauquírio M. Costa..... 1222

Geological evolution and inundation hazard: an analysis through geotechnologies
Maria Luiza C.C. Rosa, Eduardo G. Barboza, Bruno S. Menegon, Priscila C. Frota, and Ricardo A.O. Anoni..... 1227

Natural and Anthropogenic Coastal System Comparison Using DSM from a Low Cost UAV Survey (Capão Novo, RS/Brazil)
Frederico M. Scarelli, Luigi Cantelli, Eduardo G. Barboza, Maria Luiza C.C. Rosa, and Giovani Gabbianelli..... 1232

Lagrangian Coherent Structures and the Dispersion of Green Algal Bloom in the Yellow and East China Sea
Young Baek Son, Yong Hoon Kim, Byoung-Ju Choi, and Young-Gyu Park..... 1237

Quantitative Behaviour Characteristics Analysis of GPS Buoy in Rip Current Generation
Dongseob Song, Giyoung Kim, and Junglyul Lee..... 1242

A New Computation Method of Bottom Shear Stress under Tsunami Waves
Hitoshi Tanaka, Mohammad B. Adityawan, Yuta Mitobe, and Wahyu Widiyanto..... 1247

Characteristics of Beach Erosion due to the 2011 Tohoku Earthquake and Tsunami and Its Recovery across the Entire Inundated Area
Kaoru Tojo and Keiko Udo 1252

Measurement and Model Simulations of Hydrodynamic Parameters, Observations of Coastal Changes and Experiments with Indicator Sediments to Analyse the Impact of Storm St. Jude in October, 2013
Hannes Tõnisson, Ülo Suursaar, Victor Alari, Merle Muru, Reimo Rivis, Are Kont, and Marili Viitak..... 1257

Tsunami Inundation Modelling in Estuaries: Sensitivity to Variation in Tide from an Emergency Management Perspective
Olivia A. Wilson, Hannah E. Power 1262

Probabilistic Tsunami Hazard Analysis － Application to Maanshan Nuclear Power Plant in Taiwan
En-Chi Wu, Wan-Hua Ma, Yen-Lung Chen, Han-Lun Wu, Kai-Cheng Hu, Shih-Chun Hsiao, and Yuan-Chieh Wu..... 1267

Erodibility assessment of Armour Blocks causing Damage to Breakwaters
Dong Hoon Yoo and Hak Soo Lim..... 1272

Minimisation of the Uncertainty in Estimation of Extreme Coastal Wave Heights
Zai-Jin You, Baoshu Yin, Zezhou Ji, and Cong Hu..... 1277

BLUE CARBON

Restoration of the Chandeleur Barrier Arc, Louisiana
Duncan M. FitzGerald, Ioannis Georgiou, and Mark Kulp..... 1282

Identification and Mapping of Marine Submerged Aquatic Vegetation in Shallow Coastal Waters with WorldView-2 Satellite Data
Tin Hoang, Rodrigo Garcia, Michael O'Leary, and Ravi Fotedar 1287

Integrating Seafloor Habitat Mapping and Fish Assemblage Patterns Improves Spatial Management Planning in a Marine Park
Hamish A. Malcolm, Alan Jordan, Arthur L. Schultz, Stephen D.A. Smith, Tim Ingleton, Edwina Foulsham, Michelle Linklater, Peter Davies, Renata Ferrari, Nicole Hill, Vanessa Lucieer 1292

Spatial Variation in Carbon Storage: A Case Study for Currambene Creek, NSW, Australia
Christopher J. Owers, Kerrylee Rogers, Debashish Mazumder, and Colin D. Woodroffe 1297

Beaches Morphological Variability Along a Complex Coastline (Sinis Peninsula, western Mediterranean Sea)
Simone Simeone, Giovanni De Falco, Giovanni Quattrocchi, Luca Palombo, Andrea Cucco 1302

SOUTH KOREA SESSION

Textural facies and distribution of surface sediments and morphology on Korean tidal flats
YoungSook Baek, SuHwan Lee, SangHoon Lee, Han-Joon Kim, Hyeong-Tae Jou, and SangOk Ryu 1307

Mud Deposition on a Macrotidal Beach: Dasari Coastal Dune, West Coast of Korea
Tae Soo Chang, Hun Jun Ha , and Seok Hwi Hong..... 1312

The Economic Benefit of Coastal Erosion Control in Korea
Jeong-In Chang Sungsoon Yoon 1317

Partitioning of Grain-size Component Populations in Bimodal Sediments
Tae-Jin Choi, Jun-Yong Park, and Jin-Yong Choi..... 1322

A Laboratory Experiment on beach profile evolution induced by two wave conditions dominated in the Haeundae Coast of Korea
Junwoo Choi, Min Roh, and Young Taek Kim..... 1327

A Boussinesq Modeling of a Rip Current at the Daechon beach in Korea
Junwoo Choi and Hyung Suk Kim 1332

Analysis of Positioning Accuracy Using Multi Differential GNSS in Coast and Port Area of South Korea
Wonseok Jang, Hansan Park , Kiyeol Seo, Youngki Kim 1337

Coastal Water Quality Modeling in Tidal Lake: Revisited with Groundwater Intrusion
Chang S. Kim, Jinah Kim, Haksoo Lim, Younghoon Jeong, and Kwang Soon Park 1342

The Impacts of Debris Torrents in Caribbean Coast of Honduras, Central America
Sungduk Kim, Hojin Lee, and Kye-Won Jun 1347

Study on Rip Current Generated by Submerged Breakwaters: Field Observation and Numerical Simulation
In Ho Kim , Woo Dong Lee, Sungwon Shin, Jin Hoon Kim, Dong Soo Hur, and Won Chul Cho 1352

Effects of Obliquely Incident Waves on Overtopping for Vertical Walls
Young-Taek Kim, Sungwon Shin, Jun-Woo Choi , and Jong-In Lee 1357

Morphodynamic behaviors of macrotidal ridge and runnel beaches during winter: The case of Baeksajang Beach, South Korea
Chan Woong Kim, Young Ho Shin, Keun Bae Yu, and Hosahng Rhew..... 1362

Numerical Simulations of Flow Patterns and Possible Implications for Deposition around Circular Patches of Vegetation
Hyung Suk Kim , Junwoo Choi, and Moonhyeong Park 1367

Analysis of Beach Deformation according to Nourishing Sand in Haeundae Beach, Korea
Woo Dong Lee, In Ho Kim, Jong Sung Yoon, Won Chul Cho and Dong Soo Hur..... 1372

Application of EurOtop to Improve Simulations of Coastal Inundations due to Wave Overtopping
Hwa-Young Lee, Seung-Won Suh 1377

The Scour Depth Prediction of the Submarine Pipeline Area on the Algorithm of the Radial Basis Function
Hojin Lee , Sungduk Kim, and Kye-Won Jun..... 1382

Second-mode semidiurnal internal tides on the continental slope of the southwestern East/Japan Sea
Hee-Yeol Lee, Jae-Hun Park, Chanhyung Jeon, Seongbong Seo, Dong Guk Kim, Young-Gyu Park, Hong Sik Min, and Sug-Dae Kim..... 1387

Wave-induced current simulated by wave–current coupled model in Haeundae
Hak Soo Lim, Insik Chun, Jae-Seol Shim, and Chang S. Kim 1392

Recent record-breaking high ocean waves induced by typhoons in the seas adjacent to Korea
Il-Ju Moon, Minyeong Kim∞, Minsu Joh, Jooneun Ahn, **Jae-Seol Shim,** and Jinyoung Jung 1397

Vertical Structure of Rip-currents in the Nearshore Circulation
Sangyoung Son , Tae-Hwa Jung, and Fengyan Shi 1402

Evaluating of Coastal Erosion Status from CEMP results in Eastern Coast, South Korea
Dongseob Song , Inho Kim, Jaeseok Choi, and Hyungseok Lee 1407

Seasonal Changes in Sediment Characteristics on the Tidal Flat in Geunso Bay, West Coast of Korea
Han Jun Woo, Jeongwon Kang, Jun-Ho Lee, and Seok Jang 1412

Rip Currents Generated by Distant Typhoons at Haeundae Beach of Korea: Forecast and Warning
Sung Bum Yoon, Ji Hoon Song, Min Roh, and Junwoo Choi 1417

Study of the Residual Flow and Salinity during the Spring and Neap Tides at the Seokmo Channel, South Korea
Byung Il Yoon, Nakyong Choi, Bon-Ho Gu, Jong Wook Kim, Jin Il Song, Chaewook Lim,
Myung-Seok Kim, and Seung-Buhm Woo 1422

Development of a near real-time forecasting system for storm surge and coastal inundation
Jong-Joo Yoon , Jae-Seol Shim 1427

Analysis of long-period sea-level variation around the Korean Peninsula
Jong-Ju Yoon..... 1432

Analyzing the relationship of meiobenthic community with geochemical factors in a coastal rocky shore of the East/Japan Sea, Korea
Ki Young Choi, Won Gi Min, Young Il Kim, and Hyun Soo Rho 1437

Influence of wave direction on uplift force of sloping high piled wharf
Chen Jia†, Yan Yixin†, Chen Guoping†, and Tan Huiming..... 1442

Land Subsidence Survey and Policy Development in Pantai Mutiara, Jakarta Bay, Indonesia
Hansan Park, Suk-jae Kwon, Safwan Hadi..... 1447

Journal of Coastal Research	SI	75	730-734	Coconut Creek, Florida	2016

Ground Penetrating Radar Observations of Present and Former Coastal Environments, Great Sandy National Park, Queensland, Australia – Focus on Moon Point, Fraser Island

Allen M. Gontz [†*], Adrian B. McCallum[‡], Patrick T. Moss[††], and James Shulmeister[††]

[†]School for the Environment
University of Massachusetts Boston
Boston, MA, USA

[‡]School of Engineering and Science
University of the Sunshine Coast
Sippy Downs, QLD, AU

[††]School of Geography, Planning and Environmental Management
University of Queensland
St. Lucia, QLD, AU

www.cerf-jcr.org

www.JCRonline.org

ABSTRACT

Gontz, A.M; McCallum, A.B., Moss, P.T., and Shulmeister, J., 2016. Ground penetrating radar observations of present and former coastal environments, Great Sandy National Park, Queensland, Australia. *In:* Vila-Concejo, A.; Bruce, E.; Kennedy, D.M., and McCarroll, R.J. (eds.), *Proceedings of the 14th International Coastal Symposium* (Sydney, Australia). *Journal of Coastal Research*, Special Issue, No. 75, pp. 730-734. Coconut Creek (Florida), ISSN 0749-0208.

The world's large sand islands and mainland sand masses dominate the coastal system of southeastern Queensland with dunes exceeding 240 m in height. Previous work using sediment cores and TL/OSL dating has estimated the age of the dunes at 730,000 years. This system, the world's largest downdrift sand system, has Fraser Island and the Coolala Sand Mass as the two northern-most members. Combined, these form the Fraser Island UNESCO World Heritage Site and the Great Sandy National Park. Between 2012 and 2015, a series of high-resolution, reconnaissance-level GPR lines were acquired on Fraser Island and on the northern end of the Coolala Sand Mass; totalling over 75 km. The lines provide insight into sea-level fluctuations that drive large-scale coastal evolution and reveal the presence of past shoreline complexes that are proposed to be associated with the mid Holocene highstand and the previous interglacial. The generalized sequence is interpreted as a variable thickness of aeolian sand over beach deposits with a transgressive unconformity at the base of the beach deposits, which is interpreted as the Mid Holocene-to-present system. The Mid Holocene system overlies an older system that has variable preservation and is composed of beach deposits with a transgressive unconformity at the base. In places, portions of the sequence are lightly consolidated with organic material, locally known as "coffee rock". The coastal sequences hold the potential to host an archive of storm, sea level and sediment supply records over at least two interglacial periods.

ADDITIONAL INDEX WORDS: *Fraser Island, Coastal Change, Sea Level Change, Palaeoenvironments*

INTRODUCTION

Coastal systems are some of the most dynamic environments on the planet. Changes in water level on time scales ranging from seconds to thousands of years are constantly reshaping the landscape. In low latitude sandy systems such alterations can be preserved within the sedimentary record of the coastal zone. Unraveling the history of change and linking changes to processes and climate variation is key in developing an understanding of how the environment will change in the future.

Great Sandy National Park is located in southeast Queensland, Australia (Figure 1). It is composed of two major section; Fraser Island (K'Gari) and the Cooloola Sand Mass (Johnson, 2009; Gontz *et al*., 2015). Fraser Island is the world's largest sand island and is the terminal island in the world's largest down drift sand system. Sand, eroded from sandstone deposits in eastern New South Wales is carried north by long shore transport to form numerous pocket and barrier systems south of the New South Wales-Queensland border (Harris *et al*., 1996). North of the border, the depositional style shifts and large sand islands and coastal sand masses dominate the coast (Harris *et al*., 1996; Johnson, 2009).

Research on the timing of emplacement of the sand islands of the Queensland coast has suggests the islands have grown during times of lower sea levels due to increased sediment availablility from the exposed continental shelf (Ward) or from highstand strandlines (Thompson, 1981). The sediment is mobilized by aeolian processes and dunes on the islands expand. Moreton Island, south of Fraser Island, shows a strong correlation of dune forms to changing aeolian regimes in recent years (Levin *et al*., 2014) while the core of the island contains dunes older than 400,000 years (Brooke *et al*., 2015).

Over the past ~130,000 years, global sea levels have fallen from slightly above present to -125 m below present and then

DOI: 10.2112/SI75-147.1 received 15 October 2015; accepted in revision 15 January 2016.
*Corresponding author: allen.gontz@umb.edu
©Coastal Education and Research Foundation, Inc. 2016

risen to modern levels (Bard *et al*., 1990). The record in Australia is different (Lewis *et al*., 2013). Sea levels were high (~+5 m) during MIS5 and dropped, following the global pattern to reach a lowstand (~-120 m) that coinicided with the Last Glacial Maximum (Lewis *et al*., 2013). During the post-glacial warming, sea levels rose and passed present levels approximately 8000 years ago and continued to about 1.5 to 2 m above present levels at about 7000 years ago. For the past 7000 years, sea levels in eastern Australia have been falling (Lewis, *et al*., 2013; Switzer *et al*., 2010). It is only in the past few decades that tide gages suggest an end to the falling levels and the beginnings of a rise (Gontz *et al*., 2015).

Ground penetrating radar (GPR) has proven to be a useful tool in assessing the stratigraphic architecture (Gontz, *et al*., 2014; Hein *et al*., 2012), reconstructing palaeoenvironments (Switzer *et al*., 2010) and interpreting processes (van Dam *et al*., 2003).

As a part of a larger effort to understand the Great Sandy system, we began a campaign to map areas of the region to develop a stratigraphic understanding. The knowledge gained from the GPR-based stratigraphy will be used to develop a targeted surface and subsurfce sampling regime. The samples will be used to extract subsamples for chronological control, analysis for climate and palaeoenvironmental proxies and ultimately create a robust palaeogeographic reconstruction.

METHODS

Over the course of several years (2012-2014) ground penetrating radar surveys have been conducted in Great Sandy National Park to relate Quaternary landscapes and evolutionary processes to climate variation. Nearly 75 km of radar profiles were acquired using MALA Geoscience GPR, ProEX amd GX systems with antenna frequencies ranging from 160 MHz to 500 MHz. All GPR data was acquired using time-firing (10Hz) and integrated DGPS for poitioning. GPR antennas were hand-towed in areas of rough terrain or narrow trails. Where possible, antennas were vehicle-towed. In both cases, survey speed was maintained at approximately 4 km/hr.

GPR data were post processed using GPR Slice v7. Radar lines were de-wow'ed, gained with a user-defined gain, bandpass filtered, depth-time corrected, topographically corrected, and spatially corrected. Radar data were exported as image files for qualitative and stratigraphic analysis as well as reflector mapped in GPR Slice and exported as ascii text files for spatial analysis in ArcGIS 10.

Due to dense vegetation and steep aeolian topography, initial GPR surveys were focused along existing unimproved roads and trails. A focus was placed on areas identified from aerial photographs that showed evidence of beach ridge topography and small topographic breaks below 10 m in elevation. This included the areas of Moon Point and Dilli Village on Fraser Island and Inskip Point, Rainbow Beach, Freshwater Beach and Teewah on the Cooloola Sand Mass. This manuscript will focuses on the information extracted from 10 GPR lines with a total line length of 4.6 km that were collected during July 2014 in the Moon Point area of Fraser Island. (Figure 1).

RESULTS

GPR data from Moon Point, Fraser Island were acquired perpendicular to the present-day coastal system along the Moon Point-Happy Valley Road. The survey began at the present-day beach and terminated at the intersection of the Moon Point-Happy Valley Raod and Bullock Road. A major break in slope occurs within 50 m of the road intersection (Figure 1).

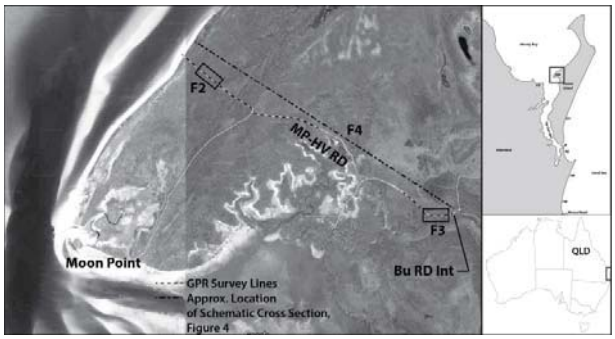

Figure 1. The Moon Point study area. (a) shows the generalized southeastern Queensland coastal system. (b) shows the location of Moon Point on Fraser Island. MP-HV RD is Moon Point to Happy Valley Road; Bu RD Int is Bullock Road Intersection. Boxes F2 and F3 indicate figures.

Analysis of GPR lines resulted in the identification of five (5) radar facies. Each of the facies is characterized by the geometric relationships of the internal reflections, relationships between internal reflections and facies bounding surfaces and the intensity of reflections (Figures 2 and 3).

FACIES1 – was observed on each of the 10 radar lines acquired along the Moon Point-Happy Valley Road. The upper bounding surface was coincident with the ground surface in all cases. The lower bounding surface was variable, but generally parallel to subparallel with respect to the ground surface. Internal reflections were parallel to subparallel with respect to the ground surface. Reflections exhibited extremely high intensity. Intensity of reflection was reduced from the upper bounding surface toward the lower bounding surface.

FACIES2 – was observed noncontinuously throughout the 4.6 km survey. When present, the upper bounding surface was coincident with the lower bounding surface of FACIES1. Internal reflection were generally wavy to subparallel with low intensity. Internal reflection were generally tangential to the lower bounding surface. Discontinuous areas of transparency to very low reflector intensity exist. The lower bounding surface was of medium intensity and exhibited an unconformable contact with the upper bounding surface of underlying facies.

FACIES3 – was observed in the northwestern poriton of the survey transect. When obserseved, it was continuous. The upper bounding surface truncates internal reflection and internal reflections of facies above are tangential to the upper bounding surface. Internal reflections are characterized by seaward (NW) dipping sigmoind clinoforms. The pattern of internal reflections is not consistent and exhibits numerous minor internal truncation surfaces. Internal reflections are generally tangential with the lower bounding surface. The lower bounding surface is continuous and exhibits a medium to high intensity. It truncates reflectors in the facies that underly FACIES3.

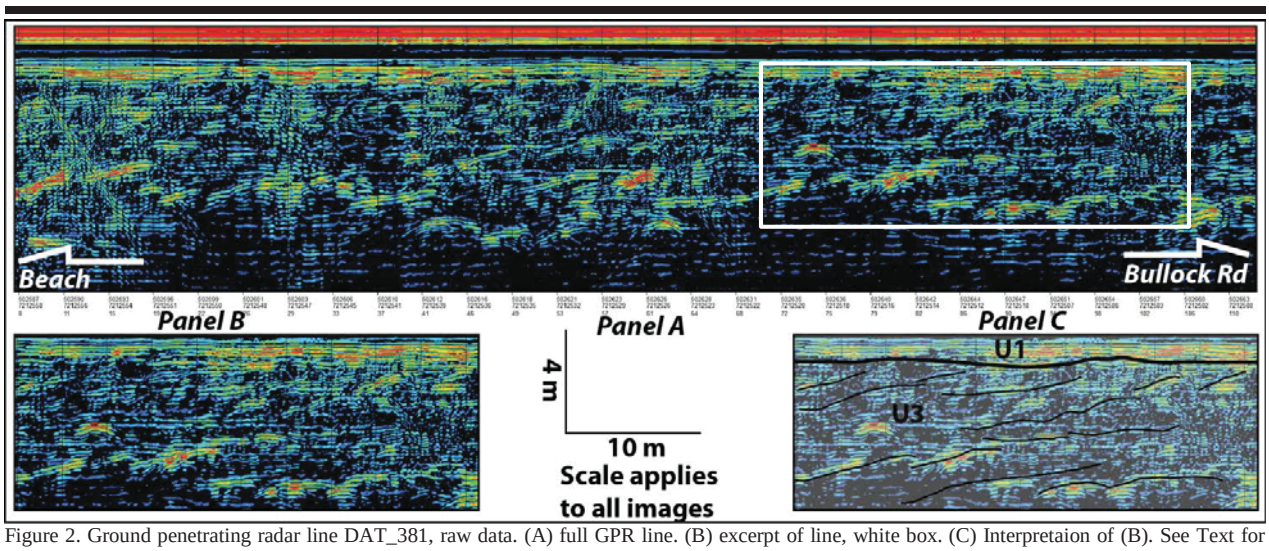

Figure 2. Ground penetrating radar line DAT_381, raw data. (A) full GPR line. (B) excerpt of line, white box. (C) Interpretaion of (B). See Text for description of units and Figure 1 for location of survey line. U1 is Unit 1; U3 is Unit 3.

FACIES4 – was observed in the southeastern portion of the survey transect. Where present, the unit was characterized by extremely high intesity reflections. The increase in intensity was not restricted to a specific package of reflections, rather as an overprint over existing GPR stratigraphic features. FACIES4 is a secondary feature and the GPR signature orignates from post-depositional alteration of the sediments.

FACIES5 – was observed on the southeastern section of the survey transect. The character of the upper bounding surface truncated reflections below. Internal reflections were characterized by parallel to subparallel, wavy and slightly sigmoid clinoforms. Minor internal truncation surfaces were regognized. FACIES5 was recognized at depth in the northwestern portions of the profile and shallower in areas where FACIES3 was absent.

Each of the facies were interpreted for depositional environment, processes and evidence for post depositional alteration (Figures 2 and 3).

UNIT1 – Anthropogenic Unit – FACIES1 exhibits the high-intensity reflectors at the surface and in the shallow sub surface. The facies was observed throughout the entire survey with a varied thickness. GPR lines were acquired on unimproved or slightly improved sand roads that experience various degrees of vehicle traffic. FACIES1 with its high intensity, surface parallel reflections is indicative of overcompaction. Based on the geospatial association with roads and the character of the facies, FACIES1 is interpreted as UNIT1 – Anthropogenic Unit, primarily roads.

UNIT2 – Dune Sediments – FACIES2 was observed in areas where the surface topography away from the road was hummocky to vegetated low ridges. The low ridges are not consistently orientated with the present beach positon. The wavy character coupled with the stratigraphic character are indicactive of low relief aeolian deposits (van Dam *et al*., 2003). UNIT2 contains a sub unit, UNIT2a that is interpreted as potential wetland deposits based on comparison of GPR signature to previous work in the area (Gontz *et al*., 2014; Gontz *et al*., 2015; van Dam, *et al*., 2003).

UNIT3 – Upper Beach System – FACIES3 was observed in the northwestern portion of the transect. The seaward-dipping sigmoid clinoforms coupled with minor internal truncation surfaces are indicative of beach ridge deposition (Switzer *et al*., 2010; Gontz *et al*., 2014). As the lower bounding surface of the facies is an unconformity related to transgression, it is proposed that the facies above relates to the regressive beach system formed during sea level fall from the mid-Holocene highstand as observed in other locations (Gontz *et al*., 2014; Switzer, *et al*., 2010; Barboza *et al*., 2009)

UNIT4 – Coffee Rock – FACIES4 was observed discountinuously throughout the Moon Point-Happy Valley Road transect. The facies was present in the southeastern portion of the profile and absent in the northwestern portion of the profile. The character of FACIES4 observed is similar in geophysical stratigraphy and environment of occurrence to units observed on GPR and ground truthed on the North Island of New Zealand (van Dam *et al*., 2003) and known occurrences in the area (Cox *et al*., 2000).

UNIT5 – Lower Beach System – FACIES5 was observed throughout nearly the entire transect. It was absent only in areas where saline ground water intrusion prevented penetration to depth. The internal character of the facies suggests that FACIES5 is a former beach system. The sigmoind clinoforms with minor truncation surfaces are similar to those found stratigraphically higher in FACIES3. A similar unit has been recognized at other locations in Australia (Gontz *et al*., 2014; Switzer *et al*., 2010; Barbosa *et al*., 2009). Based on the internal character, geographic position and stratigraphic location, FACIES5 is interpreted as UNIT5 – lower beach system.

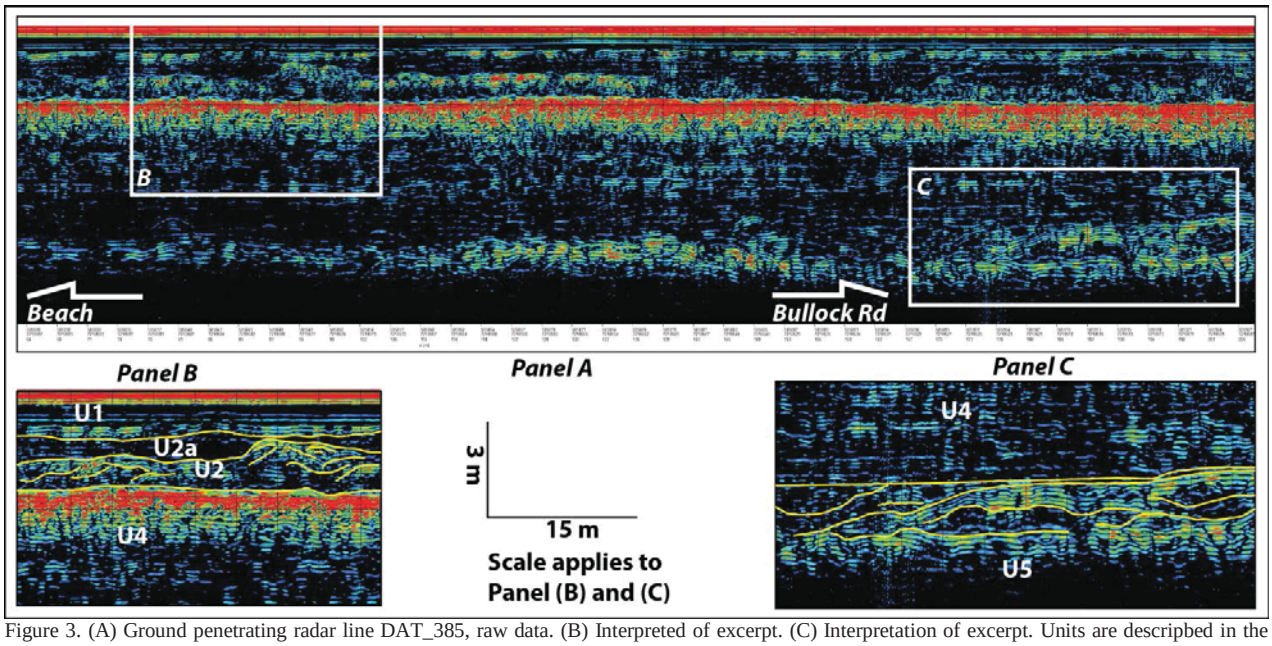

Figure 3. (A) Ground penetrating radar line DAT_385, raw data. (B) Interpreted of excerpt. (C) Interpretation of excerpt. Units are descripbed in the text. See Figure 1 for location of survey line. U1 is Unit1; U2 is Unit 2; U2a is Unit 2a; U3 is Unit 3; U4 is Unit 4; U5 is Unit 5.

DISCUSSION

The progression of units from the present coast towards the southeast exhibits a pattern that is indicative of a regressive coastal plain (Gontz *et al*., 2014). Moving further away from the coast to the southeast, the sequence transitions from one that is beach ridge deposition over a transgressive unconformity (Gontz *et al*., 2013) with a lower beach ridge system beneath the unconformity to a less-clear dune sequence over coffee rock with indications of a beach ridge system below the coffee rock (Figure 4).

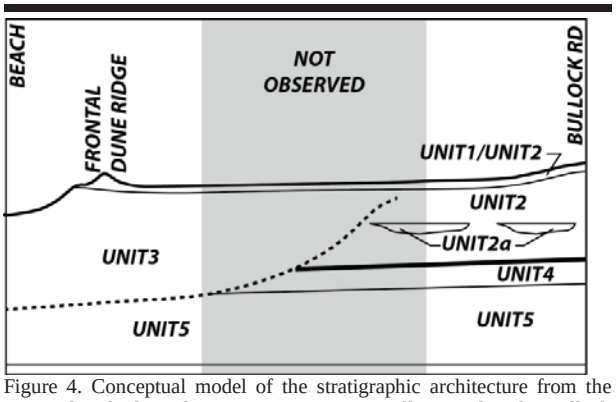

Figure 4. Conceptual model of the stratigraphic architecture from the present beach along the Moon Point Happy Valley Road to the Bullock Road intersection. See Figure 1 for location. Not to Scale

The patterns observed in UNIT3 and to some degree in UNIT5 exhibit similarities to other beach systems worldwide that have been correlated to periods of storm erosion and beach recovery (Dougherty, 2013). Previous work (van Heteren, et al., 1998) suggest that sea level elevations can be extracted from the changes in reflector morphology.

Similar work on North Stradbroke Island shows a similar pattern of low dunes capping a prograding beach ridge system over a transgressive unconformity with a lower beach ridge system underlying the sequence (Gontz *et al*., 2014). The Moon Point sequence contains a unit not observed in other locations that has been interpreted as “coffee rock”. Coffee rock is a dark brown to black lightly cemented sandstone. Cementation is through organic compunds (Van Dam *et al*., 2003). It is a barrier to shallow hand coring and has been encounted during coring in the pattern fens of Moon Point (Moss et al. in press). The GPR observations at Moon Point suggest the coffee rock layer ~ 1.5-2 m thick and cuts across the regional stratigraphic sequence. This supports previous research that suggests the deposition of corganic compound to cement the layer is a result of downward migration of pore fluids and leaching from layers above or through long-term groundwater flow (Cox *et al*., 2000). The GPR clearly shows reflectors crossing the boundaries of the high-intensity coffee rock (UNIT4; FACIES4). In Northern Queensland, deposits of coffee rock have been dated at 48,000 ybp based on roots contained within the deposit (Pye, 1982). The survey did not observe the northwestern edge of UNIT4 due to a large saline wetland complex. If the age of the Fraser Island coffee rock correlates with those in Northern Queensland, then the northwestern edge of the deposit may correlate with the location of the mid-Holocene highstand.

CONCLUSIONS

The GPR survey presented clearly shows several stratigraphic packages. These are interpreted as relating to present and former coastal systems. The stratigraphic relationships observed suggest that the following units exist:

1. An anthropogenically altered unit;
2. Present-day transgressive beach system;
3. Mid-to-Late Holocene regressive beach system;
4. Early-to-Mid Holocene transgressive beach system;
5. Buried wetlands;
6. Coffee rock; and
7. Late Pleistocene regressive beach system

Presently, dates are unavailable to correlate the stratigraphic packages and sequences across the Great Sandy region. However, this work presents the first step in understanding the dynamics of the system and how it has changed and evolved during the Late Quaternary. Work is ongoing to develop chronologies associated with the GPR stratigraphy, extract climate proxies from preserved coastal systems and reconstruct the palaeogeography.

ACKNOWLEDGMENTS

The research that supported this publication was funded by the Burrnettt Mary Regional Group (Moss), the Australian Research Council (Shulmeister), the University of Massachusetts Boston (Gontz) and the University of Queensland (Moss & Gontz). During field data collection, University of Queensland students provided assistance with field data acquisition. We would like to thank the Butchella People, the traditional owners of the Great Sandy region.

LITERATURE CITED

Barbosa, E.G., Dillenburg, S.R., Rosa, M.L.C.C., Tomazelli, L.J., and Hesp, P.A., 2009. Ground penetrating radara profiles of two Holocene regressive barriers in southern Brazil. *Journal of Coastal Research SI 56*, Proceeding of the 10th International Coastal Symposium, 579-583.

Bard, E., Hamelin, B., and Fairbanks, R.G., 1990. U-Th ages obtained by mass spectrometry in corals from Barbasos: sea level during the past 130,000 years. *Nature*, 346, 456-458.

Blackemore, A.G., Murray-Wallace, C.V., and Lachlan, T.J., 2014. First recorded evidence of subaqueosly-deposited late Pleistocence interstadial (MIS5c) coastal strata above present sea level in Australia. *Marine Geology* 355, 377-383.

Brooke, B.P., Pietsch, T.J., Olley, J.M., Sloss, C.R., and Cox, M.E., 2015. A preliminary OSL chronology for coastal dunes on Moreton Island, Queensland, Australia – marginal deposits of a large-scale Quaternary shelf sediment system. *Continental Shelf Research*, 105, 79-94.

Cox, M., Harbison, J., Ezzy, T., Preda, M., Brooke, B., Lee, R., Lester, J., and Oberhardt, M., 2000. "Coffee rock": an overview of its character and occurrence in the Pumistone region. *PASSCON 2000*, 23-25.

Dougherty, A.J., 2014. Extracting a record of Holocene strom erosion and depostion preserved in the morphostratigraphy of a prograded coastal barrier. *Continental Shelf Research*, 86, 116-131.

Gontz, A.M., Maio, C.V., and Rueda, L., 2013. The sunken forest of Duxbury, MA – constraints on sea level, coastal erosion and palaeoenvironments. *Journal of Coastal Research*, 29(6A), 168-176.

Gontz, A.M., Moss, P.T., and Wagenknecht, E.K., 2014. Stratigraphic architecture of a regressive coastal plain, Flinders Beach, North Stradbroke Island, Queensland, Australia. *Journal of Coastal Research*, 30(3), 575-585.

Gontz, A.M., Moss, P.T., Sloss, C.R., Petherick, L., McCallum, A.P., and Shapland, F., 2015. A review of the physcial environments of Fraser Island, Australia – toward understanding past climate variation and environmental change. *Australasian Journal of Environmental Management*, 22(2), 105-123.

Harris, P.T., Tsuji, Y., Marshall, J.F., Davies, P.J., Honda, N., and Matsuda, H., 1996. Sand and rhodolith-gravel entrainment on the mid- to outer-shelf under a western boundary current: Fraser Island continental shelf, eastern Australia. *Marine Geology* 129(3-4), 313-330.

Hein, C.J., FitzGerald, D.M., Carruthers, E.A., Stone, B.D., and Gontz, A.M., 2012. Refining the model of back barrier formation along a paraglacial coast in the Gulf of Maine. *Marine Geology*, 307, 40-57.

Hesp, P.A., 2006. Sand beach ridges: definitions and re-definition. *Journal of Coastal Research SI 39*, Proceedings of the 8th International Coastal Symposium, 72-75.

Johnson, D., 2009. *The Geology of Australia*. Cambridge: Cambridge University Press, 347p.

Levin, N., Neil, D., and Syktus, J., 2014. Spatial varibility of dune form on Moreton Island, Austrlaia and its correspondence with wind regime derived from observing stations and reanalysis. *Aeolian Resarch*, 15, 289-300.

Lewis, S.E., Sloss, C.R., Murray-Wallace, C.V., Woodroffe, C.D., and Smithers, S.G., 2013. Post-glacial sea-level changes around the Australian margin: a review. *Quaternary Science Reviews*, 74, 115-138.

Moss, P., Tibby, J. Shapland, F., Fairfax, R. Steward, P. Barr, C. Petherick, L., Gontz, A., and Sloss, C., 2015. Pattern fen formation and development from the Great Sandy Region, south east Queensland, Australia. *Marine and Freshwater Research*. (In press)

Pye, K., 1982. Sharacteristics and significance of some humate-cemeted sands (humicretes) at Cape Flattery, Queensland, Australia. *Geological Magazine*, 119(3), 229-242.

Switzer, A.D., Sloss, C.R., Jones, B.G., and Bristow, C.S., 2010. Geomorphic evidence for mid-late Holocene higher sea level from southeastern Australia. *Quaternary International*, 221(1-2), 13-22.

Thompson, C.H., 1981. Podzol chronosequences on coastal dunes of eastern Australia. *Nature*, 291, 59-61.

Van Dam, R.L, Nichol, S.L., Augustinus, P.C., Parnell, K.E., Hosking, P.L., and McLean, R.F., 2003. GPR stratigraphy of a large active dune on Parengarenga Sandspit, NZ. *The Leading Edge*, 22(9), 865-870.

Ward, W.T., 2006. Coastal dunes and stradndplains in southeast Queensland: sequencces and chronology. *Australian Journal of Earth Sciences*, 53(2), 363-373.

Journal of Coastal Research	SI	75	735-739	Coconut Creek, Florida	2016

Analysis of Wave Climate around Korea Based on Long-Term Hindcast and Coastal Observation Data

Weon-Mu Jeong[†], Sang-Ho Oh[†§*], and Ho Sik Eum[‡]

[†]Coastal Engineering Division
Korea Institute of Ocean Science and Technology
Ansan, Republic of Korea

[‡]Geosystem Research Co.
Gunpo, Republic of Koreaión, Chile

[§]Department of Convergence Study on the Ocean Science and Technology
Ocean Science and Technology School
Korea Maritime and Ocean University
Busan, Republic of Korea

www.cerf-jcr.org

www.JCRonline.org

ABSTRACT

Jeong, W.-M., Oh, S.-H., and Eum, H.S., 2016. Analysis of wave climate around Korea based on long-term hindcast and coastal observation data. *In:* Vila-Concejo, A.; Bruce, E.; Kennedy, D.M., and McCarroll, R.J. (eds.), *Proceedings of the 14th International Coastal Symposium* (Sydney, Australia). *Journal of Coastal Research*, Special Issue, No. 75, pp. 735-739. Coconut Creek (Florida), ISSN 0749-0208.

Understanding long-term trends of wave climate is important to establish proper mitigation and adaptation strategies for possible coastal erosion and loss of safety in maritime structure due to climate change. In this study, a 36-year (from 1979 to 2014) wave hindcasting was carried out and detailed analysis was made to recognize long-term changes in coastal wave climate of Korea. The reanalysis wind data provided by ECMWF are applied to the simulation of wave fields over sea waters around Korea. The SWAN model was used to obtain the wave fields from the longitude 120° to 150° East and from the latitude 22.4° to 47.6° North with a grid resolution of 1/12° by 1/12°. Comparison of the hindcasted waves with available wave observation data shows that the simulated wave field agrees fairly well with the observation although extreme values of the significant wave height are slightly underestimated. On average, the annual average and maximum values of the significant wave height showed increasing trend along the coasts of Korea.

ADDITIONAL INDEX WORDS: *Climate change, wave climate, long-term hindcast, wave observation, Korea.*

INTRODUCTION

Nearshore wave climate is fundamental information for understanding of various physical processes and management of human activities around coastal zones. In particular, its long-term variation over decades are main interest in context of future climate change on the global and regional scales. Proper estimation of long-term trend in parameters related to wave climate is the key factor for establishing future mitigation and adaptation strategies against wave-induced coastal disasters and change of coastal environment.

Up to now, a number of studies have been carried out to understand variability of global wave climate based on wave hindcasting (*e.g*. Sterl and Komen, 1998; Cox and Swail, 2001) or projection of future wave climate (*e.g*. Hemer *et al*. 2013a; b). Many more studies investigated regional change of wave climate over specific sea waters on the globe (*e.g*. Wang and Swail, 2002; Weisse and Günter, 2007; Grabemann and Weisse, 2008).

For the coastal waters around Korea, however, only a few studies have investigated long-term variation of the regional wave climate in the past or future. Yamaguchi and Hatada (2003) performed wave hindcasting on the coasts of Korea by using a shallow water wave model and found a slight decrease or no trend of wave climate between 1958 and 1998. Meanwhile, Lee and Jun (2006) evaluated design wave height based on a 25-year hindcasted wave data from 1979 simulated by HYPA (HYbrid PArametrical, Hasselmann *et al*., 1979) and WAM (WAMDI Group, 1988) wave models. Regarding the prediction of future wave climate, Lim *et al*. (2013) compared the wave climate of 1979-2003 and 2075-2099 by using the data sets of Mori *et al*. (2010). They reported increase of 50-year return period wave height in summer season while decrease of the quantity in winter season in general.

As there are very few literatures regarding wave hindcasting around Korea and no studies have been performed to simulate wave climate including the recent decade, a new wave modeling was carried out in the present study to provide assessment results of past wave climate from 1979 to 2014 around Korea. By using the SWAN (Simulating WAves Nearshore, Booij *et al*. 1999) wave model with ECMWF (European Centre for Medium-range Weather Forecast) reanalysis wind data, wave hindcasting was carried out over the 36 years. The modeled wave data were validated based on the field observation data obtained at various wave monitoring stations along the Korean coasts. Then, investigation was made to find long-term wave climate variability over the coastal waters of Korea.

DOI: 10.2112/SI75-148.1 received 15 October 2015; accepted in revision 15 January 2016.
*Corresponding author: coast.oh@gmail.com
©Coastal Education and Research Foundation, Inc. 2016

METHODS

Numerical simulation was made with SWAN (version 40.91) model with a Cartesian coordinate system. Computational domain covers a large-scale area of the longitude 120° to 150° East and the latitude 22.4° to 47.6° North with a grid resolution of 1/12° by 1/12°. Figure 1 shows the sea bottom bathymetry of the computational domain. The model was configured with 21 exponentially spaced frequencies ranging from 0.04 to 0.4 Hz, 36 evenly spaced directions, and a time step of 10 min. The default parameterisation was adopted for the source and sink terms of physical processes implemented in the model. More detailed description on the mathematical and numerical expressions of each forcing term is presented in SWAN technical documentation (SWAN team, 2013).

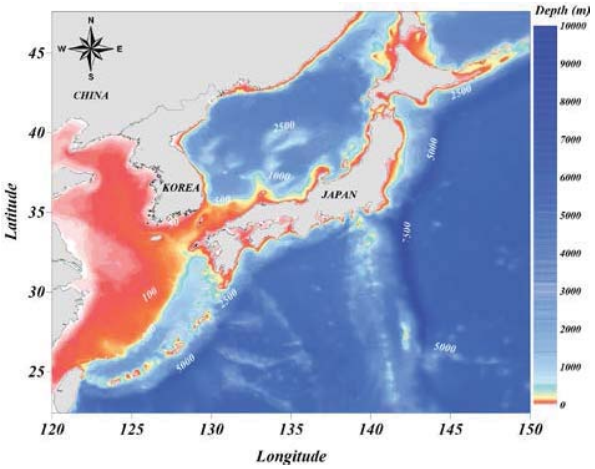

Figure 1. Sea bottom bathymetry of the geographical area simulated by the SWAN model.

Based on the reanalysis wind data provided by ECMWF, sea surface wind field at 10 m height from 1979 to 2014 at every 6 hours are prepared as input data for the SWAN model. The ECMWF wind data set available for the present wave modeling are composed of three different periods of different grid resolutions (1.125° for 1979-1993, 0.5° for 1994-2005, and 0.25° for 2006-2014). Hence, they were recompiled through a spatial interpolation onto the grid system of the model.

The simulated wave fields were validated with the field observation data acquired at various wave monitoring stations placed in the coastal zone of Korea. Figure 2 shows some of the available coastal stations where consecutive long-term wave monitoring has been performed by both Korea Institute of Ocean Science and Technology (KIOST) and Korea Meteorological Agency (KMA).

Figure 3 shows an exemplary comparison between the measured and computed significant wave height (H_s) at Namhangjin station located on the east coast of Korea, during the whole year 2014. Although the simulation shows reasonably good agreement with the measurement in terms of overall temporal variations of the wave height, the model tends to slightly underestimate peak values of relatively high wave events. This feature is also found in Figure 4, where the scatter diagram for the data shown in Figure 3 is presented. The difference between the measurement and computation becomes larger with increase of the wave height. There can be two reasons for the underestimation of the wave height. The ECMWF wind input is likely to be smaller than the real wind fields actually formed over the sea area around Korea. Another possibility is that the model might be unable to perfectly simulate the wave generation and propagation processes of relatively high wave events. More detailed investigation is required to lessen the gap between the measurement and simulation. In general, similar results as in Figures 3 and 4 were also obtained for the rest of the wave stations shown in Figure 2.

In order to more quantitatively assess the model performance by using reliable statistical parameters, two well-applied indices evaluating model accuracy were used in the present study: the index of agreement (d) suggested by Willmott (1981) and the Pearson's correlation coefficient (r), which are respectively calculated as follows.

$$d = 1 - \frac{\sum_{i=1}^{N}(x_i - y_i)^2}{\sum_{i=1}^{N}(|x_i - \bar{x}| + |y_i - \bar{x}|)^2} \quad (1)$$

$$r = \frac{\sum_{i=1}^{N}(x_i - \bar{x})(y_i - \bar{y})}{\left(\sum_{i=1}^{N}(x_i - \bar{x})^2 \sum_{i=1}^{N}(y_i - \bar{y})^2\right)^{1/2}} \quad (2)$$

where N is the number of data points of the time series that are considered, x_i and $\bar{x}$ denote the observed data and their mean value, and y_i and $\bar{y}$ are the modelled data and their mean value. For most of the measurement sites, good agreement is obtained for H_s with both indices of d and r over 0.9 on average.

Figure 2. Locations of the wave observation stations around Korea. AWAC (Acoustic WAve and Current profiler) and bottom-mounted pressure-type gauges operated by KIOST are shown in blue and red, respectively. Wave buoys managed by KMA are shown in white. Typical water depth at pressure-type gauges range from 15 to 20 m whereas AWAC and wave buoys are deployed at 30 to 40 m.

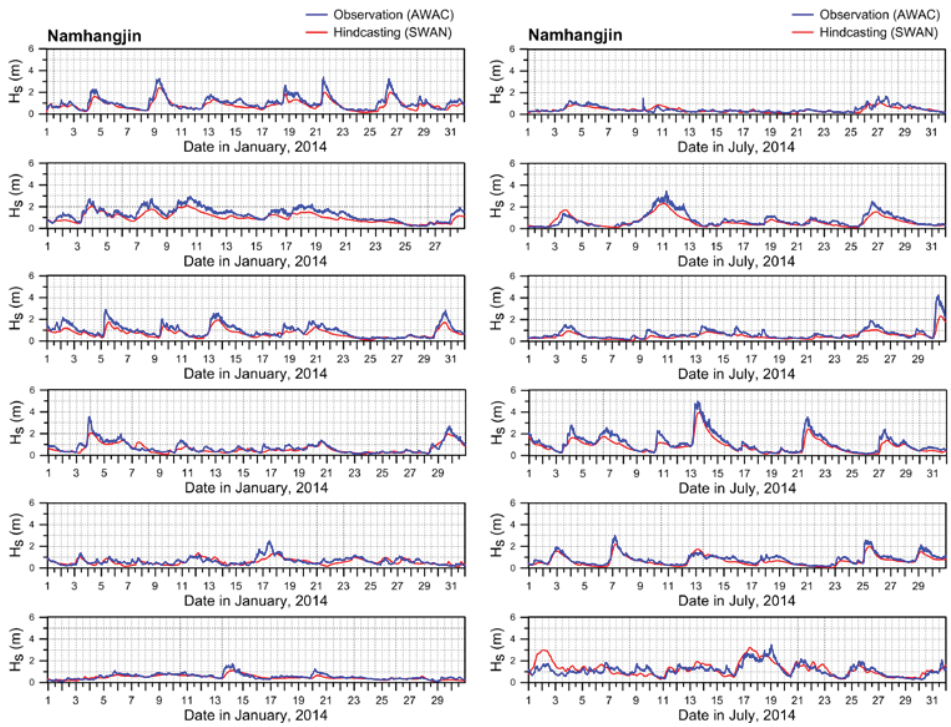

Figure 3. Measured and computed time series of the significant wave heights at Namhangjin station during the year 2014. The measured data obtained from AWAC are shown in blue line whereas the hindcasted by the SWAN model in red line.

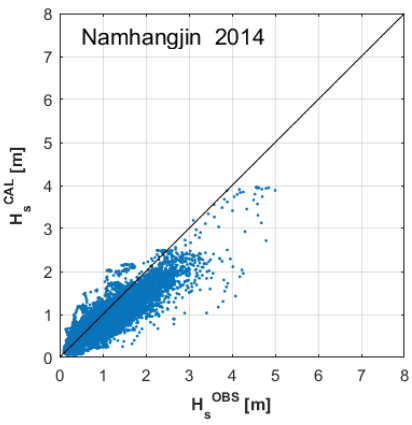

Figure 4. Scatter diagram between the measured and hindcasted significant wave height at Namhangjin station during 2014.

RESULTS

The 36-year wave hindcasting data allow investigation of the long-term change of wave climate on the coasts of Korea. Figure 5 shows yearly variation of the significant wave height in terms of its annual mean on the west, south, and east coast of Korea. In each of the three panels in Figure 5, time histories at three different sites are shown, which reveal very similar temporal variation one another. Meanwhile, among the three panels representing different sea area, slightly dissimilar overall trend is recognized.

For all the three panels shown in Figure 5, little significant trend was identified for the first 15 years (1979-1993), while apparently increasing trend appeared for the subsequent 21 years (1994-2014). Such a discrepancy in yearly variation of the mean wave height between the two time periods might be affected by the difference in the spatial resolution of the wind field used for the simulation. As mentioned above, the spatial resolution of the original ECMWF wind data for 1979-1993 is 1.125 degree, while more fine resolution of 0.5 or 0.25 degree for 1994-2014. Due to this discontinuity with respect to the spatial resolution of wind data, it is likely to obtain less reliable overall tendency of wave climate change over the whole simulation period. Nonetheless this limitation, it is still possible to recognize apparently increasing tendency of the annual average of H_s during the simulated time period.

Similar plots for the annual maximum of H_s is presented in Figure 6. Compared to the plots for the annual average of H_s, temporal variations in Figure 6 involve higher fluctuation of the parameter. Influenced by this feature, the variational tendency reveal more discrepancy among the three panels in the figure and among the three time series therein as well.

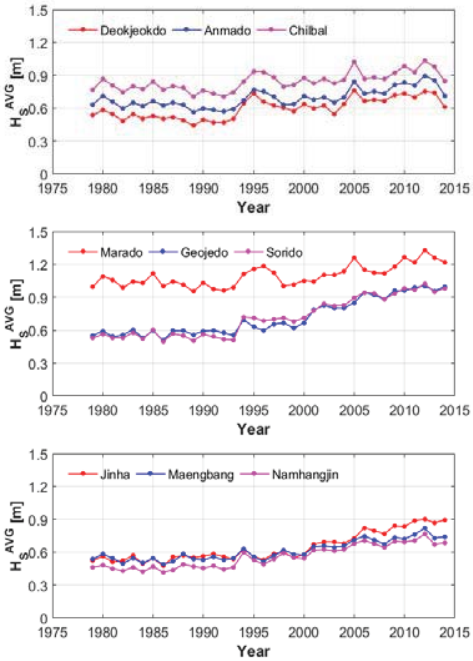

Figure 5. Yearly variation of the annual averages of the significant wave height at the locations on the west coast (top panel), south coast (middle panel), and east coast (bottom panel) of Korea.

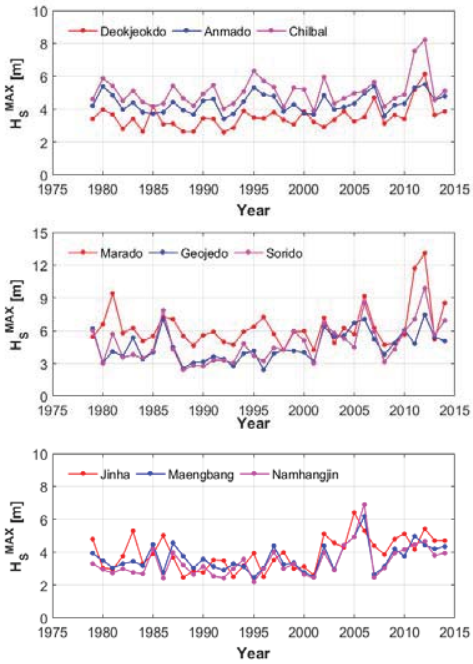

Figure 6. Yearly variation of the annual maxima of the significant wave height at the locations on the west coast (top panel), south coast (middle panel), and east coast (bottom panel) of Korea.

DISCUSSION

Based on the yearly variation of the annual averages and maxima of the significant wave height, it is able to estimate the mean changing rate over the hindcasted years. Considering possible influence of the discontinuity in the spatial resoultion in between 1993 and 1994, the analysis was conducted by using the simulated data over the total 36-year from 1979 and the recent 21-year period from 1994 separately. For the two different time spans, the mean changing rates of the annual averages and maxima were evaluated based on a simple linear regression analysis for the 20 locations shown in Figure 2.

Figure 7 shows the result obtained from such an analysis for the annual average of H_s. The label of the vertical axis, a_{Hs} denotes the fitted coefficient corresponding to the mean changing rate for the analyzed quantity. It is clearly seen that the annual average of H_s shows increasing trend all the locations along the Korean coasts. The increasing rate is within 1 cm per year on the west coast and northern part of the east coast, but greater than the value on the south coast and southern part of the east coast. In these regions, the influence of time period used for the trend analysis is significant, showing higher increasing rate for the 21-year period.

Similar figure for the annual maximum of H_s is presented in Figure 8. In this case also, positive values of the fitted coefficient are obtained over the all 20 locations examined. In contrast to the previous figure, the increasing rate becomes larger for most of the locations when the estimation was made by using the shorter period data of 1994-2014. The maximum value of the increasing rate, estimated based on the 21-year hindcasting data, is greater than 0.1 cm per year for the stations situated on the south coast.

CONCLUSIONS

This study presented the result of investigation on the long-term trends of nearshore wave climate of Korea based on 36-year hindcasted wave field over the sea waters around Korea. The wave hindcasting was conducted by using the SWAN wave model with ECMWF reanalysis wind data from 1979 to 2014 and validated with some available field observation data. Although the model slightly underestimated magnitudes of relatively large wave height, the hindcasted wave field showed fairly good agreement with the measured temporal variations of the wave height in general.

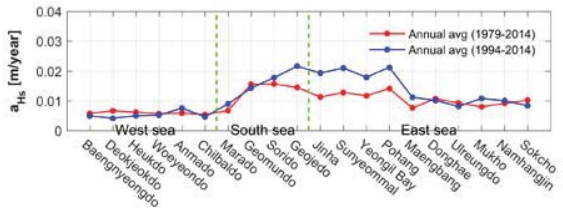

Figure 7. Spatial distribution of the mean increasing rate of the annual average of the significant wave height along the coasts of Korea, which is estimated by the regression analysis by using the total 36-year simulation data (red line) and the recent 21-year data (blue line).

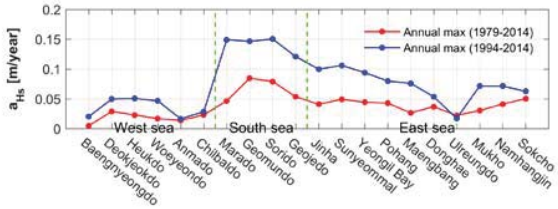

Figure 8. . Spatial distribution of the mean increasing rate of the annual maximum of the significant wave height along the coasts of Korea, which is estimated by the regression analysis by using the total 36-year simulation data (red line) and the recent 21-year data (blue line).

Then the long-term trend of the annual average and maximum of the significant wave height was analyzed based on linear regression analysis with the hindcasted wave data. In order to consider possible influence of different resolution of the original wind field on the yearly variation of the parameters, the analysis was carried out separately with two different time periods from 1979 to 2014 (the whole data) and from 1994 to 2014 (the recent 21-year data). Apparently increasing trend was identified both for the annual average and maximum of H_s for all the stations along the coasts of Korea, irrespective of the difference in the time span subjected to the analysis. Comparatively higher values of the yearly increasing rate of both quantities appeared at the sites located on the south coast and southern region of the east coast. Meanwhile, the influence of restricting the time period for the trend analysis to 21-years appeared as escalating magnitudes of the increasing rate.

It is noted that the results presented in the present work require further validation with more available field observation data to provide a better hindcasted wave data set showing enhanced agreement with the measured wave field. This may include more careful compilation of the wind data used for the model input and possible adjustment of some parameterization in the wave model. In addition, more investigation is needed in terms of the long-term variation of wave period and direction as well. In this context, care must be taken with regard to the understanding of yearly variation of the significant wave height shown in this study.

ACKNOWLEDGMENTS

This work has been supported by the research project (PE99326) of Korea Institute of Ocean Science and Technology.

LITERATURE CITED

Booij, N.; Ris, R., and Holthuijsen, L., 1999. A third-generation wave model for coastal regions: I-Model description and validation. *Journal of Geophysical Research* 104(C4), 7649-7666.

Cox, A.T. and Swail, V.R., 2001. A global wave hindcast over the period 1958-1997: validation and climate assessment. *Journal of Geophysical Research*, 106(C2), 2313-2329.

Grabemann, I. and Weisse, R., 2008. Climate change impact on extreme wave conditions in the North Sea: an ensemble study. *Ocean Dynamics*, 58, 199-212.

Hasselmann, K. and Ewing, J.A., 1979. A hybrid parametrical wave prediction model. *Journal of Geophysical Research*, 84, 5727-5738.

Hemer, M.A.; Katzfey, J., and Trenham, C. 2013a. Global dynamical projections of surface ocean wave climate for a future high greenhouse gas emission scenario. *Ocean Modelling*, 70, 221-245.

Hemer, M.A.; Fan, Y.; Mori, N.; Semedo, A., and Wang, X.L., 2013b. Projected changes in wave climate from a multi-model ensemble. *Nature Climate Change*, 6p, doi:10.1038/nclimate1791

Lee, D.Y. and Jun, K.C., 2006. Estimation of design wave height for the waters around the Korean Peninsula. *Ocean Science Journal*, 41, 245-254.

Lim, D.-U.; Suh, K.-D., and Mori, N., 2006. Regional projection of future extreme wave heights around Korean peninsula. *Ocean Science Journal*, 48, 439-453.

Mori, N.; Yasuda, T.; Mase, H.; Tom, T., and Oku, Y., 2010. Projection of extreme wave climate change under global warming. *Hydrological Research Letters*, 4, 15-19.

Sterl, L. and Komen, G.J., 1998. Fifteen years of global wave hindcasts using winds from the european centre for medium-range weather forecasts reanalysis: validating the reanalyzed winds and assessing the wave climate. *Journal of Geophysical Research*, 103(C2), 5477-5492.

SWAN team, 2013. *Scientific and technical documentation, Technical Report (version 40.91)*, Delft University of Technology.

WAMDI Group, 1988. The WAM model - a third generation ocean wave prediction model. *Journal of Physical Oceanography*, 18, 1775-1810.

Wang, X.L. and Swail, V.R., 2002. Trends of Atlantic wave extremes as simulated in a 40-yr wave hindcast using kinematically reanalyzed wind fields. *Journal of Climate*, 15, 1020-1035.

Weisse, R. and Günter, H., 2007. Wave climate and long-term changes for the Southern North Sea obtained from a high-resolution hindcast 1958-2002. *Ocean Dynamics*, 57, 161-172.

Willmott, C.J., 1981. On the validation of models, *Physical Geography*, 2(2), 184-194.

Yamaguchi, M. and Hatada, Y., 2003. Estimation of wave climate and its long-term variability around the coasts of Korea. *Proceedings of the 13th International Offshore and Polar Engineering Conference* (Honolulu, Hawaii), pp. 182-188.

Journal of Coastal Research	SI	75	740-744	Coconut Creek, Florida	2016

Testing versions of the Bruun rule for low energy macro-tidal tropical beaches against a theoretical late Holocene sea-level high-stand and beach ridge evidence of late Holocene beach faces

Andrew Kerans[†*] and Nick Cartwright[‡]

[†]Griffith Centre for Coastal Management (Gold Coast Campus) Griffith University, QLD, 4222 Australia

[‡]Griffith School of Engineering (Gold Coast Campus) Griffith University, QLD, 4222 Australia

www.cerf-jcr.org

www.JCRonline.org

ABSTRACT

Kerans, A.J., and Cartwright, N., 2016. Testing versions of the Bruun rule for low energy macro-tidal tropical beaches against a theoretical late Holocene sea-level high-stand and beach ridge evidence of late Holocene beach faces. *In:* Vila-Concejo, A.; Bruce, E.; Kennedy, D.M., and McCarroll, R.J. (eds.), *Proceedings of the 14th International Coastal Symposium* (Sydney, Australia). *Journal of Coastal Research*, Special Issue, No. 75, pp. 740-744. Coconut Creek (Florida), ISSN 0749-0208.

Significant evidence of late Holocene beach faces is presented in beach ridges along the North Queensland coast between Mackay and the Daintree region. The ages of these ridges has in some cases been dated giving confidence that the rearmost ridges are the result of a combination of cyclone activity and a late Holocene sea level high-stand. The height of this high-stand is the subject of debate, however the level may be confidently predicted through careful and extensive measurement of relict oyster beds in the region. Using pre-existing beach ridge research together with existing and new measurements of oyster beds on Magnetic Island, North Queensland a value for the late Holocene sea level high-stand is proposed which can be compared to the position of the coast on certain beaches during this period. These measurements are a good basis to test the applicability of the Bruun rules and some proposed modifications for the low energy beach systems of tropical North Queensland. This paper firstly examined the late Holocene sea level evidence stored in relict oyster beds and from that proposes a sea level to be used in the analysis. This sea level is then used to test the Bruun rule and variants and examine the differences between dated Holocene beach faces and the recession predicted by these models.

ADDITIONAL INDEX WORDS: *Magnetic Island; sea-level change; sea level high-stand, Saccostrea Cucullata; late Holocene; Bruun rule; coastal recession.*

INTRODUCTION

This work analyses the application of the Bruun Rule (a simple and a more comprehensive version) and modified Bruun Rule (Rosati *et al.*, 2013) for low energy macro-tidal coasts (LEMC) in North and Far North Queensland.

The first and best known model relating shoreline retreat to an increase in local sea level is that proposed by Per Bruun (1962). A simple application of the Bruun Rule finds that 1 cm rise in sea level erodes beaches about 1 m horizontally inland.

The Bruun rule states that as a result of a given sea level rise a typical concave-upward beach profile erodes sand from the beach face and deposits it offshore to maintain constant water depth out to a depth called 'the depth of closure' which is often taken to be ten metres.

The Bruun Rule estimates the response of the shoreline profile to sea-level rise. This simplified model states that the beach profile is a parabolic function whose parameters are entirely determined by the mean water level and the sand grain size. The analysis by Bruun assumes that with a rise in sea level, the equilibrium profile of the beach and shallow offshore moves upward and landward.

The Bruun Rule has been challenged in recent times (Cooper and Pilkey 2004) state "Several assumptions behind the Bruun Rule are known to be false and nowhere has the Bruun Rule been adequately proven; on the contrary several studies disprove it in the field. No universally applicable model of shoreline retreat under sea-level rise has yet been developed. Despite this, the Bruun Rule is in widespread contemporary use at a global scale both as a management tool and as a scientific concept".

Certainly on North Queensland beaches, where a late Holocene sea level high stand is estimated at 1.55 metres some coastal features, such as beach ridges formed by cyclones, are somewhat further inland than suggested by a simple interpretation of the Bruun Rule for this sea level.

This research investigates linkages between dated and undated beach ridges and the widely accepted late Holocene sea levels.

METHODS

Identifying Late Holocene Sea Levels: In order to determine recession due to sea level a Holocene sea level high-stand must be determined and this then compared to dated beach ridges in the area. The first part of this paper looks at published and new work on determining sea level, particularly using relict oyster beds in the otherwise stable area around Magnetic Island.

DOI: 10.2112/SI75-149.1 received 15 October 2015; accepted in revision 15 January 2016.
*Corresponding author: andrew.kerans@gmail.com
©Coastal Education and Research Foundation, Inc. 2016

Six areas of remnant oyster bed were identified over a 300 metre length of eastern Horseshoe Bay, the northern most bay on the island. For each remnant bed a nearby contemporary oyster line was also identified. For each of these locations the distance between the top of the remnant oyster line and the thickening element of the contemporary lines (about 10 cm below the vertical extent of oysters) was made using a spirit level.

Oyster bed measurements: Measurements were in a manner similar to that suggested by Lewis *et al.* (2013) and were made from the topmost visor of the remnant structure to ensure as far as possible that the measurement represented the highest point of the high-stand and to eliminate any pauses in either the rise or fall of the sea in the late Holocene period.

The authors note that Beaman *et al.* (1994) suggest the sea level retreated gradually and linearly post 4040 years BP because there was a tapering of the remnant oyster bed and no thickening suggesting any halt during the sea level fall.

The differences between the visor measurements give a good record of the difference in sea level between now and the time of the remnant beds but with the assumption that the wave climate in terms of direction and wave height are the same. However the contemporary beds are now on the beach at low tides they are exposed to breaking waves. The Bruun rule suggests the bed-form would have been filled as sea level rose and then presumably fallen to re-establish equilibrium as the sea level fell. Thus it is assumed that the seabed was relatively the same distance from both relict and contemporary oyster beds.

Finally the cave close to where Beaman *et al.* made the 1994 measurements on Balding Bay was revisited and a single measurement made. Using our method of measuring to the thickening of the contemporary oyster bed delivered an average difference of 1.50m

Using a method similar to that suggested by Lewis *et al.* (2013) the thickest uppermost point of each remnant oyster bed was identified and the difference in height between this and the visor a nearby similarly facing modern oyster bed was determined. Measurements were made using a measuring tape and a long water filled tube as there was often a considerable distance between the remnant fossil bed and the modern one.

Figure 1. Solitary Rock with Oyster Beds on Horseshoe Bay.

These differences were measured for six different relict oyster beds and are shown in Table 1. From the average these measurements a sea level highstand of 1.45 was determined.

No dating of the relict bed was undertaken, we assume the age of the upper beds (around 1.5m) are similar to those dated by Beaman.

Examination of Figures 1 and 2 show a similarity between the shapes of the modern and relict oyster beds. This similarity allows some confidence in the methods but is obviously subject to a potential error or around 20cm. The measurement technique is accurate and has a low error but the natural differences in modern oyster beds was measure also as plus or minus approximately 10cm in any one area between similar growths.

During the period where the highstand is believed to have been relatively stable, (7000 – 4000 ybp) a sea level of 1.45 metres above present appears to be a valid conclusion. This is the value we use to test the various versions of the Bruun Rule for this area.

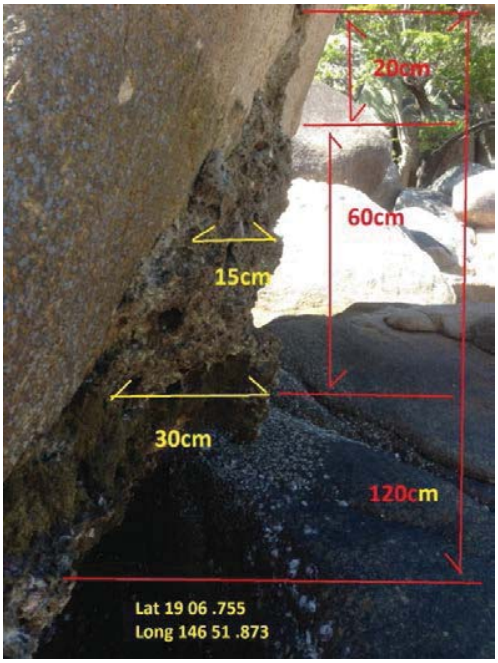

Figure 2. Relict Oyster Bed, Horseshoe Bay.

Table 1. *Height Differences of a Relict Oyster Bed on Horseshoe Bay.*

Site	Distance (R – C) m
1	1.57
2	1.55
3	1.33
4	1.28
5	1.28
6	1.70

While we have a degree of confidence in this value we note the sensitivity of the various versions of the Bruun rule naturally linear with about a 700:1 change for an active zone of 10,000m. There are many other relict oyster beds around Magnetic Island which will be measured in the future to add to the knowledge base.

This derived sea level rise (1.45m) will now be used to examine the accuracy of the original Bruun rule and two modified versions compared with dated and assumed relict coastlines between Cape Bowling Green and just north of Cairns, Queensland Australia. The 1.45m level is shown as a red line in Figure 3 which depicts various high-stand measurements.

Depth of Closure and Width of Active Zone: Some constants in the simple Bruun rule are often misused. These are depth of closure, beyond which wave action no longer shapes the sea bottom and the corresponding width of the active zone; that is the distance to the depth of closure. The depth of closure (h) is often taken to be ten metres (10m).

The fetch to most parts of the coast from Townsville to Cairns depends on the proximity of the Great Barrier Reef and in some cases continental islands such as Palm Island. This distance varies from about 80km to around 40 km further north.

Taking a category Three Cyclone blowing with wind speeds (at 10m) of 50m/s for 5 hours over a 75 km fetch theory suggests a significant wave height of 9.6 metres. This wave height is fetch limited.

Taking depth of closure to be given approximately by Equation 1 (Kamphuis, 2008).

$$d_c = 1.6\, H_s \qquad (1)$$

The depth of closure in cyclonic conditions is approximately 15 metres. The sensitivity of the complex Bruun equations is inverse logarithmic but tends to linear beyond 10 metres. A change of plus 1m introduces a change of about 5% in the estimated recession.

The width of the active zone, measured to a depth of 10m at low tide ranges around 10km in North Queensland. Complications arise due to continental islands where the free movement of sediment is blocked and currents appear to play a role. Measurements are based on Admiralty charts and are considered accurate to within +/- 50 metres as sands may shift over time and these widths may not be the same now as in the late Holocene.

Relict Cyclone Ridge Coastlines: The work of Tony Forsyth and his PhD Thesis on measuring and dating cyclone ridge relict coastlines in North Queensland has been vital to this work. Ridge systems dated by Forsyth, a system mapped and dated by Treziese (1994) at Pallarenda near Townsville and other systems identified from Google earth and examined and compared to the various Bruun Rules. Each ridge system is briefly discussed and conclusions presented regarding the accuracy of measurement.

Yabulu: Yabulu is a northern beaches district of Townsville and home to a nickel refinery. This ridge system is remarkably similar to dated systems to the north and so the assumption that they are the same age is valid. The structure is well defined on Google Earth and so the ridge measurement is considered to be accurate within +/- 10 metres.

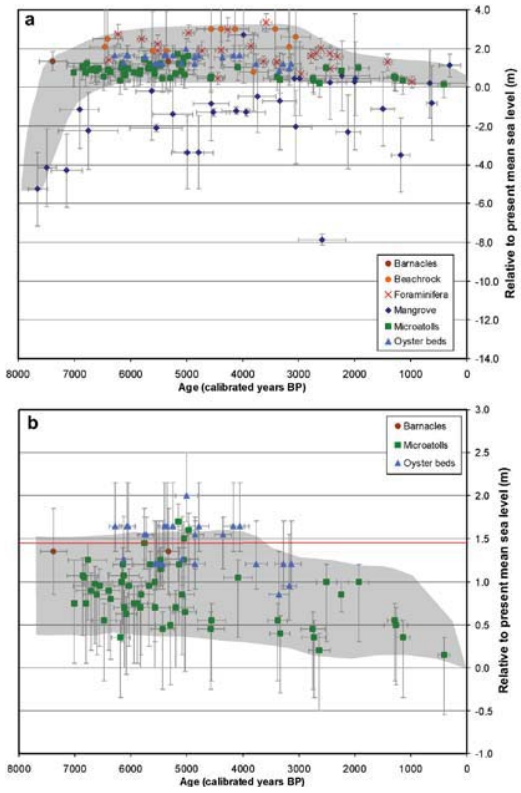

Figure 3. Sea level Highstand (Lewis 2013 with permission).

Pallarenda: The measurements for Pallarenda were undertaken by Trziese (1994) along with carbon dating of fossilised corals to give a date to the ridge system and the location is shown in Figure 4. These measurements are therefore considered to be accurate within +/- 5 metres.

Figure 4. Pallarenda ridges (Author from Treziese, 1994 and Google Earth)

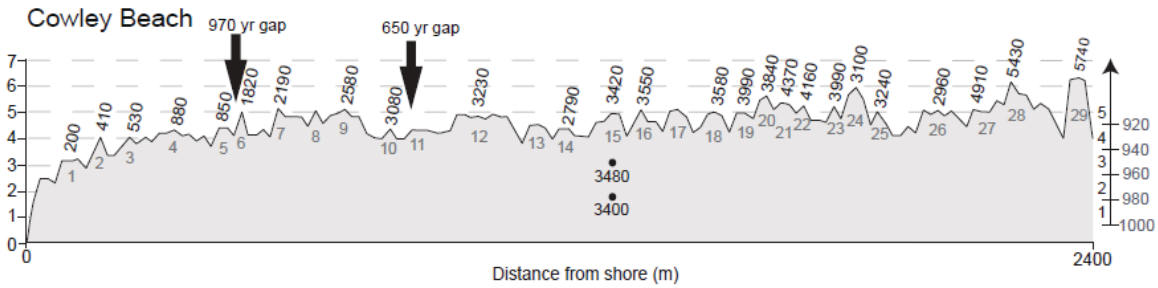

Figure 5. Cowley beach profile (Forsyth, 2015 with permission).

Halifax Bay: This is a complex system approximately 40 km to the north of Townsville. There is a structural similarity to measured systems and so the date of the oldest ridge is assumed to be late Holocene. However to the north the ridge system extends 550 metres inland while adjacent to the creek it extends 995 metres inland. As such this is not considered to be an accurate set of data and additional work will be required to properly measure and date this system.

Taylors Beach: Taylors Beach is east of Ingham and this system lies just to the south of that hamlet. The system is directly adjacent to agricultural land and in at least one area there may be regrowth over previously levelled land. The measurements from this system remain uncertain and will require further work to identify the ridge structures.

Kennedy (Rockingham Bay): This structure lies within the Kennedy national park north of Cardwell. The site was extensively surveyed by Forsyth and the ridges dated. This data is therefore considered to be accurate within +/- 5 metres.

Cowley Beach: Cowley beach lies 65 km to the north of Cardwell. This is a well-defined structure altered only by an airstrip. Again this is surveyed and dated data which is depicted in Figure 5. This data is considered accurate to +/- 5 metres.

South Townsville: This is a ridge and swale system to the south of Townsville. It is also the site of a refinery which has altered part of the system. The area, but not the actual ridges, was dated by Woodroffe (2009). This system is considered to be a reliable set of data but with and error in the range of +/- 100 metres because the action of the flooded swales (creating a spit) is unknown.

Cape Bowling Green: This system was identified by Forsyth who considered it to be a mix of cyclone beach ridges and Aeolian dunes. Because this system, when flooded, would be exposed to open sea from two directions this complexity makes the measurement unreliable.

Rowes Bay: This system was measured and dated by Mabin (2002) and is easily identified fr lnom Google earth despite being adjacent to Townsville Airport, a cemetery and has also been subject to various works. This data is considered accurate to +/- 10 metres.

Wonga Beach: Wonga beach is 68 km north of cairns on the Mossman to Daintree road. This system was measured and dated by Forsyth and as such is considered accurate with an error of +/- 5m.

The Bruun Rule and Variations: The Bruun Rule relates shoreline retreat, R, to sea level rise S (earlier derived to be 1.45m), by the ratio of horizontal and vertical profiles within the active zone by:

$$R = SW/(h + B) \qquad (2)$$

Where W is the width of the active zone or the distance out to the closure depth h.

Dean and Dalrymple (2002) suggested a modification to the Bruun Rule to take into account the diminishing height of the berm as sea level rises which was not considered by Bruun where:

$$R = W.\ln((h + Bo)/h + Bo - S) \qquad (3)$$

Which reduces to the simple Bruun rule for very small S. Finally, to account for landward transport, which for cyclone ridges is the sediment thrown up onto the landward side of the beach face Rosati, Dean and Walton (2013) proposed the following equation:

$$R = (W + VD/S)\ln((h + Bo)/(h + Bo - S)) \qquad (4)$$

Where V_D is the volume of sand per unit of beach length stored in the berm. In this case an average of 250 cu m per metre has been assumed. Each equation was tested against the physical beach data discussed above and a simulated active zone of 1000 metres. The results are presented in Table 2 for berm height B of 5m and closure depth h of 10m.

DISCUSSION

It is evident the improved equations reduce the error associated with the original Bruun Rule for the ridge systems analysed. If we consider the ridge systems that are both measured and dated that observation holds except for Rowes Bay where Bruun appears to be more accurate and the modifications over-estimate the recession. The reasons for this are unknown, however immediately seaward of Rowes Bay is Magnetic Island and at a tangent to the beach the depth never reaches the assumed closure depth of 10 metres. In addition Magnetic Island protects Rowes Bay from waves with a

Table 2. *Comparison of Bruun Rule versions and actual Holocene coasts*

	Ridge Location									
	Yabulu	Pallarenda	Halifax Bay	Taylors Beach	Kennedy	Cowley	Sth Tvl	Cp Bowl Green	Rowes Bay	Wonga
Distance to h (W)	9100	13000	9200	8300	13800	6700	17200	7300	17500	3950
Tidal Range	3.56	3.56	3.55	3.55	3.55	3.5	3.56	3.56	3.56	3.52
Recession (Bruun)	880	1257	889	802	1334	648	1663	706	1692	382
Recession (C-Bruun)	880	1257	889	802	1334	648	1663	706	1692	382
Recession (Dean)	925	1322	935	844	1403	681	1749	742	1779	402
Holocene Dune	943	1339	953	861	1420	699	1766	760	1797	419
Error Bruun	950	2120	995	730	1700	2400	1865	950	1700	1000
Error C Bruun	-7.4%	-40.7%	-10.6%	9.9%	-21.5%	-73.0%	-10.8%	-25.7%	-0.5%	-61.8%
Error Dean	-2.6%	-37.7%	-6.0%	15.6%	-17.5%	-71.6%	-6.2%	-21.9%	4.7%	-59.8%

northerly aspect although it remains exposed to the South East and North West.

For the other beaches all equations underestimate the recession from between 37 percent to 72 percent. This is a significant underestimation where data is needed for planning purposes on occupied beaches. A major assumption of this work, that the ridge systems of the late Holocene were deposited in a way that followed the physics of a more gradual contemporary sea level rise is also unproven.

CONCLUSIONS

It can be concluded that provided the same physics applied to the formation of the Holocene beach ridges examined that the three versions of the Bruun rule examined significantly underestimate coastal recession. No linkage to tidal range has been found as yet nor has an investigation of sediment size and its relationship to recession been undertaken.

More work is required in these areas and also on the processes of sediment transport during cyclonic conditions and the beach restoration processes under the low energy beach states that dominate between cyclones.

LITERATURE CITED

Beaman, Larcombe and Carter, 1994. New evidence for the Holocene sea level high from the inner shelf, central Great Barrier Reef, Australia. *Journal of Sedimentary Research*, 44(4), 881 – 885.

Bruun, 1962. Sea level rise as a cause of shore erosion. *Journal of Waterways and Harbour Divisions*, ASCE 88, 117 – 130.

Cooper, J.A.G. and Pilkey, O.H, 2004. Sea-level Rise and Shoreline Retreat: Time to Abandon the Bruun Rule. *Global and Planetary Change*, 43(3), 157-171.

Dean and Dalrymple, 2002. *Coastal Processes with Engineering Applications*, Cambridge University Press, Cambridge UK, 475.

Forsyth, A.J., 2015. *Beach Ridge Records of late-Holocene Tropical Cyclone Behaviour*. PhD Thesis, James Cook University School of Earth and Environmental Sciences.

Kamphuis, J.W., 2008. *Introduction to Coastal Engineering*, Worlds Scientific 2008.

Lewis, Wust, Webster, Collins, Wright and Jacobsen, 2013. *Rapid relative sea level fall along north-eastern Australia between 1200 and 800 cal. Years BP: An appraisal of the oyster evidence*, Unpublished, James Cook University School of Earth and Environmental Sciences.

Mabin, M.C.G, 2002, *Environmental History of Rowes Bay*, Tropical and Environmental Studies and geography, James Cook University, Townsville. (Prepared for Townsville City Council).

Rosati, 2013. The modified Bruun Rule extended for landward transport, *Journal of Marine Geology*, 340, 77 – 81.

Treziese, 1990, *Rocks and Landscapes of the Townsville District*, Queensland Department of Resource Industries (via Townsville library).

Journal of Coastal Research	SI	75	745-749	Coconut Creek, Florida	2016

A Hierarchical Bayesian Model based Nonstationary Frequency Analysis of Extreme Sea Level under Climate Change along the Shorelines in South Korea

Yong-Tak Kim[†], Hye-Rin Cho[‡], Sumiya Uranchimeg[†], Seung-Oh Lee[§], and Hyun-Han Kwon[†*]

[†]Department of Civil Engineering
Chonbuk National University, 567 Baekje-daero,
Deokjin-gu Jeonju-si, Jeollabuk-do 54896, Korea

[‡]Korea Institute of Civil Engineering and Building
Technology, 283 Goyangdae-ro, Ilsanseo-gu,
Gyeonggi-Do 10223, Korea

[§] Department of Civil Engineering
Hongik University, 72-1 Sangsoo-dong, Mapo-gu,
Seoul 04066, Korea

www.cerf-jcr.org

ABSTRACT

o, H.-R.; Uranchimeg, S.; Lee, S.O., and Kwon, H.-H., 2016. A hierarchical Bayesian model based nonstationary frequency treme sea level under climate change along the shorelines in South Korea. *Proceedings of the 14th International Coastal* ney, Australia). *Journal of Coastal Research*, Special Issue, No. 75, pp. 745-749. Coconut Creek (Florida), ISSN 0749-0208.

www.JCRonline.org

Urban development and population increases have continuously progressed in the coastal areas in Korea; thus, it is expected that vulnerability towards coastal disasters by sea level rise (SLR) would accelerate. This study investigated the trend of the sea level data using Mann-Kendall (MK) test, and the results showed that the increasing trends of annual average sea level at 17 locations were statistically significant. For annual maximum extremes, seven locations exhibited statistically significant trends. In this study, nonstationary frequency analysis for the annual extreme data, together with average sea level data as a covariate, was performed. Nonstationary frequency analysis results showed that sea level at the coastal areas of the Korean Peninsula would be increased from a minimum of 60.33mm to a maximum of 214.90mm. The future mean sea level rise (MSLR) increases in the year 2100 estimated in this study suggested that rises in the sea level at the sea near the Korean Peninsula would be rather less compared with global MSLR by RCP(AR5) scenarios. Nevertheless, the SLR is still very high and we need to evaluate the risk for the marine structures and coastal areas due to the acceleration of the sea level and to prepare adaptation strategies at the national level. Furthermore, it is necessary to carry out a nonstationary frequency analysis considering the representative concentration pathways (RCP) scenario and more reliable information for acceleration characteristics as a future study.

ADDITIONAL INDEX WORDS: *Bayesian, climate change, nonstationarity, risk, sea level rise*

INTRODUCTION

Climate change poses a fundamental threat to many things on which human life depends—safety, water resources, food, and agriculture. Sea level rise (SLR) due to climate change is one of the most serious threats worldwide, particularly since the low-lying coastal areas are vulnerable to sea level extremes (IPCC, 2001). In light of climate change, many studies for the estimation of the mean sea level rise (MSLR) have been conducted in recent decades. Changes in the sea level occurred in the context of different spatio-temporal scales along with various other factors attributed to climate changes (Milne *et al.*, 2009). Coastal areas in Korea surrounded by the ocean on three sides have various vulnerable factors such as urban development and population increases, thus if countermeasure for such factors are not considered in the end, serious damages could ensue.

Continuation of the rises of mean sea level (MSL) has been an evident even in the future as reported by the research results led by Intergovernmental Panel on Climate Change (IPCC).

IPCC published that sea level would rise around more than 100cm in the year 2100 if a representative concentration pathway (RCP) of carbon dioxide as published in the Climate Change 2014 Synthesis Report is considered. This result presents increases in the sea level at a large scale compared with the sea level rise of 59cm indicated in the IPCC 4th report.

Numerous studies have been conducted for the investigation of the SLR under climate change (Rahmstorf, 2007; USACE, 2011). Obeysekera and Park (2013) calculated future return periods of extreme sea levels from MSL acceleration scenarios and storm tide statistics. In Menendez and Woodworth (2010), the statistics of a global network of historical tide gauges, including statistics of the peak storms or maxima of the gauge time series (Kriebel *et al.*, 2015), have been calculated. However, uncertainty in the estimation of MSLR is an issue that has been discussed in the literatures. For instance, if the starting year is differently applied with the same data, the estimated MSLR would be different. There are some issues in terms of accounting for the interannual variation of sea level at a specific location and obtaining the reliable relationship between local MSL and a geodetic datum (Flick *et al.*, 2013).

The future extreme sea level scenario is essential to design and evaluate the project life cycle in managing, planning,

DOI: 10.2112/SI75-150.1 received 15 October 2015; accepted in revision 15 January 2016.
*Corresponding author: hkwon@jbnu.ac.kr
©Coastal Education and Research Foundation, Inc. 2016

engineering, constructing, operating, and maintaining completed and ongoing projects. In this regard, this study aims to investigate the risk informed by the MSLR. A probabilistic risk analysis has been used extensively for the estimation of extreme return levels. A main assumption in the probabilistic risk analysis is that the errors (*e.g.*, uncertainty) associated with parameter are assumed to be normally distributed. However, it has been largely acknowledged that the geophysical data including annual extremes of sea level data showed heavy tails (Kwon *et al*., 2008; Lee *et al*., 2010). In addition, the sampling errors in the frequency analysis model have been generally ignored in estimating the parameters (Kim *et al*., 2015). Recorded historical tide gauge data showed that extremes were generally modulated by the rise in MSL over time. In this study, we propose a Hierarchical Bayesian model (HBM) based nonstationary frequency analysis model to better estimate the extreme values along with the mean sea level as an exogenous variable that allows us to combine local and global sea level rise simultaneously within a linear or nonlinear regression framework. The HBM can adequately take into account for uncertainties.

The nonstationarity in the time series data can be evaluated by various statistical techniques (Kim, 2006). As trend analysis methods, numerous approaches (*e.g.*, Mann-Kendall [MK] test, Hotelling-Pabst test, Spearman's Rho test, linear regression test, CUSUM test, Cumulative Deviation test, Worsley likelihood test, Rank-Sum test, and Student's-t test) have been widely applied to the time series data (Oh *et al.*, 2005). Among these, MK test has been used as the most commonly adopted method. Kendall and Gibbons (1990) proposed a nonparametric MK test that was not affected by the characteristics of underlying distribution.

To begin with, the MK trend test was applied to evaluate the significance of the trend in sea level data. Second, the proposed Bayesian modeling frameworks were applied to tide gauge data at several locations in the Korean Peninsula for the estimation of the future changes in terms of the risk. In the next section, methods for the nonstationary frequency model based on HBM and the MK test were presented. The results and conclusions were then summarized in the final section.

METHODS

In this study, the Mann-Kendall (MK) test is used in place of a parametric linear regression model to analyze significant changes in sea level data. The purpose of the MK test (Mann, 1945; Kendall, 1975; Gilbert, 1987) is to statistically assess if there is a monotonic trend of the variable of interest over time. The monotonic trend indicates that the variable consistently increases (or decreases) over time, but the trend may be linear or nonlinear. The residuals from the linear regression model are assumed to be normally distributed while the assumption is not required by the MK test. In other words, the MK test is a non-parametric (distribution-free) test (Stalnacke *et al.*, 2014). In this study, the trend of the sea level was analyzed by using the MK test among the nonparametric methods. If the test statistics is significantly different from zero, the Null hypothesis (H_0) of no monotonic trend is rejected, and the alternative hypothesis (H_a) of monotonic trend is accepted and vice versa (Lee *et al.*, 2014).

A Hierarchical Bayesian-based nonstationary frequency analysis model is proposed to accommodate climate variability and nonstationarity using time-dependent climate predictors. An objective of Bayesian methods is to compute the posterior distribution of the desired variables; in this case, such are the parameters of the annual MSLR and the annual extremes distribution. The posterior distribution of the parameter vector, $\boldsymbol{\theta}$, is $p(\boldsymbol{\theta}|\mathbf{x})$, given by Bayes Theorem as follows:

$$p(\boldsymbol{\theta}|\mathbf{x}) = \frac{p(\boldsymbol{\theta}) \times p(\mathbf{x}|\boldsymbol{\theta})}{p(\mathbf{x})} = \frac{p(\boldsymbol{\theta}) \times p(\mathbf{x}|\boldsymbol{\theta})}{\int_{\Theta} p(\boldsymbol{\theta}) \times p(\mathbf{x}|\boldsymbol{\theta}) d\theta} \propto p(\boldsymbol{\theta}) \times p(\mathbf{x}|\boldsymbol{\theta}) \quad (1$$

In this equation, $\boldsymbol{\theta}$ is the vector of parameters of the distribution to be fitted, Θ is the space parameter, $p(\mathbf{x}|\boldsymbol{\theta})$ is the likelihood function, $\mathbf{x}$ is the vector of observation, and $p(\boldsymbol{\theta})$ is the prior distribution. Here, we present a method for incorporating the annual MSLR into updated estimates of the parameters for the extreme value distribution used to represent the annual extremes. The model is expressed in terms of both a location parameter $\boldsymbol{\mu}(\mathrm{t})$ and a scale parameter $\boldsymbol{\sigma}(\mathrm{t})$, which both change with time, *t*.

The parameters of extreme distribution associated with the annual extremes are hypothesized to be functions of the MSLR that are generally recognized as climate change features with expected local impacts.

Given a goodness-of-fit test (*e.g.*, Chi-square test and KS test), the annual MSLR $\mathbf{S_{mean}}(t)$ is assumed to be normally distributed and can be written as follows:

$$\mathbf{S_{mean}}(t) \sim Normal(\boldsymbol{\mu}_\mathbf{m}(t), \boldsymbol{\sigma}_\mathbf{m}(t)) \quad (2$$

Here, the symbol "~" denotes that the variable is assumed to be normally distributed with mean $\boldsymbol{\mu}_\mathbf{m}(t)$ and standard deviation $\boldsymbol{\sigma}_\mathbf{m}(t)$.

In the present application, $\boldsymbol{\sigma}_\mathbf{m}(t)$ is not found to vary significantly as a function of time. As a result, equation (2) is changed as follows:

$$\mathbf{S_{mean}}(t) \sim Normal(\boldsymbol{\mu}_\mathbf{m}(t), \sigma_m) \quad (3$$

$$\boldsymbol{\mu}_{\boldsymbol{m}}(\mathrm{x}) = \alpha_0 + \alpha_1 t + \alpha_2 t^2 \quad (4)$$

Here, α is a vector of regression parameters which are also normally distributed.

In this study, GEV distribution was selected to describe the annual extremes $\mathbf{S_{max}}(t)$ based on the goodness-of-fit test. Again, note that this study assumed that the annual extremes were hypothesized to be functions of the MSLR and can be written as follows:

$$\mathbf{S_{max}}(t) \sim Gev(\boldsymbol{\mu}_\mathbf{mx}(t), \sigma_{mx}, \xi_{mx}) \quad (5)$$

$$\boldsymbol{\mu}_\mathbf{mx}(\mathrm{x}) = \beta_0 + \beta_1 \mathbf{S_{mean}}(t) + e \quad (6)$$

This employs the Gibbs sampler, a Markov Chain Monte Carlo (MCMC) method for simulating the posterior probability distribution of the data field conditional on the current choice of parameters (Gelman, 2006). The Gibbs sampler explores the multivariate parameter space by fixing all but one of the parameters, sampling from the conditional distribution of the unfixed parameter and then repeating for the next parameter. The conditional distribution is conditioned on the fixed values of the other parameters. Most statistical applications of MCMC methods use the Gibbs sampler. For further reading on the use of MCMC methods for Bayesian inference, and specifically the Gibbs Sampler, see Gilks *et al.*, (1995) and Kwon *et al.* (2009).

RESULTS

In this study, time series data from 45 tide gauge stations operated by the Korea Hydrographic and Oceanographic Administration (KHOA, http://www.khoa.go.kr/) were used in order to construct MSLR and annual extremes of tide data. Twenty gauge stations where a data period of more than twenty years among forty-five tide gauge stations were selected and were further used for analysis.

Our present analysis confirms that there has indeed been an increase in extreme high water levels worldwide since 1970 (Menendez and Woodworth, 2010). In this paper, however, this data could not be confirmed for a shorter duration.

The MK statistics were estimated to identify long-term trends at each station. Temporal trends of the sea level time series were tested at the $\alpha = 0.05$ and $\alpha = 0.10$ significance level. The temporal trend in annual MSL and annual extremes were shown in Figure 2. Note that the upward trend of the sea level indicated that future risk would be rather severe while the downward trend was vice versa. The results showed that the upward trend in the annual MSLR for 17 locations were statistically significant except in Wido, Heuksando, and Anheung gauge stations, while annual extremes were statistically significant in the seven gauge stations including Mokpo, Jeju, and Busan. Jeju station, in particular, showed a high trend in both annual MSL and annual extremes with the lowest p-value.

If the correction is not conducted with respect to autocorrelation, the oscillations can conclude that it is not significant so easily (Foster and Brown, 2015). However, this paper is an analysis of the short period of data by units. Years were deemed insufficient errors that occurred without autocorrelation analysis.

Figure 1. Locations of tide gauge stations. (KHOA, http:// www. khoa.go.kr/)

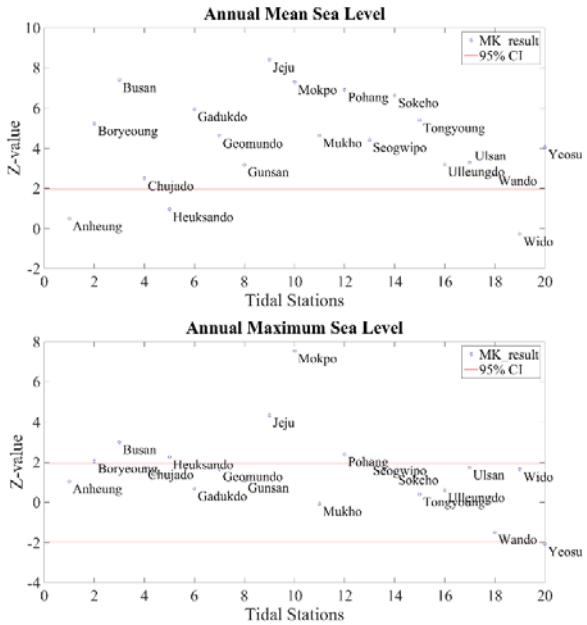

Figure 2. Results of significance test of trend of annual MSL and annual maximum extremes of sea level (X axis means station numbering in the study)

In order to combine nonstationary evolution of sea level extremes, potential acceleration was estimated by constructing quadratic regression proposed by the National Research Council (NRC) (1987) which was one of the equations to estimate sea water level increases. The acceleration used in this study for annual average tide data was at -0.0080 to $0.0081 mm/year^2$, while for annual maximum tide level -0.0316 to $0.0101 mm/year^2$.

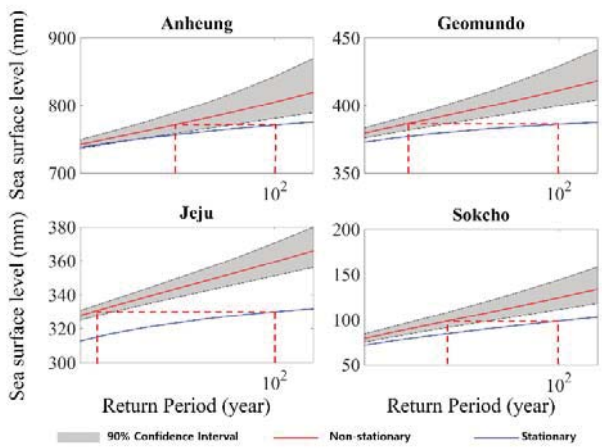

Figure 3. A comparison of frequency analysis for annual extremes between stationary and nonstationary items

To investigate nonstationarity in return periods, the nonstationarity frequency analysis was performed for the coastal areas in South Korea as illustrated in Figure 3 and Table 1. As the representative stations, four stations (Anheung, Geomundo, Jeju and Sokcho) were used to demonstrate the nonstationarity in annual extremes of sea level. Some interesting features of nonstationary behavior are a noticeable reduction in return period in a changing climate. For example, in case of Anheung gauge station, the corresponding sea level for a 100-year return period in stationary frequency analysis can be a 16-year return period under nonstationary condition. These results are similar to that reported by Obeysekera *et al.* (2013). For other stations, SLR appeared rather higher in the nonstationary frequency analysis compared to that in the stationary frequency analysis.

Table 1. *A comparison of design sea level according to return periods between stationary and nonstationarity frequency analysis*

Station Name		Return Period (year)			
		10	50	100	200
Anheung	Stationary	763.1	791.6	805.1	819.6
	5%	752.8	772.4	781.0	789.5
	Median	764.6	796.4	812.0	829.5
	95%	776.5	820.3	843.0	869.4
Geomundo	Stationary	390.3	404.7	411.3	418.2
	5%	384.7	395.3	399.8	404.3
	Median	390.9	406.9	414.5	422.9
	95%	397.1	418.6	429.1	441.5
Jeju	Stationary	339.0	353.3	359.6	366.0
	5%	334.7	346.3	351.3	356.3
	Median	339.3	354.2	361.1	368.2
	95%	343.8	362.0	370.8	380.0
Sokcho	Stationary	91.3	111.2	120.2	129.4
	5%	84.6	100.3	107.0	113.7
	Median	91.9	112.9	122.7	133.0
	95%	99.2	125.5	138.4	152.2

From posterior distributions of the parameters, one can estimate the Bayesian credible region, which is an interval that contains 95% of the probability. The estimated parameters is further used to investigate the temporal variation of future 100-year sea levels as computed using Equations 9-12, as shown in Figure 4. The results clearly show an increase tendency based on historic tide gauge data using the HBM.

DISCUSSION

This study confirmed that sea level trend around Korean Peninsula is significantly increasing. It suggests that existing frequency analysis techniques for estimating the return level of the sea level is not likely to be appropriate for the future plan-

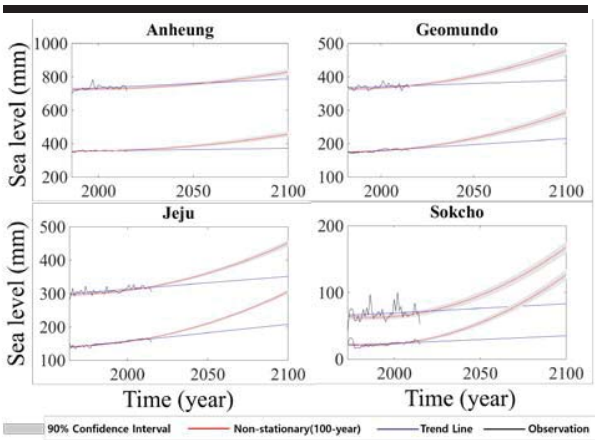

Figure 4. Temporal variation of future 100-year sea level changes under nonstationary condition

ning. Lee et al (2010) pointed out that there exists a difficulty in establishing a link between nonstationary trend and frequency analysis for extremes. In this study, we adopted a nonstationary model to incorporate the trend in sea level rise into frequency analysis. Particularly, there are statistically significant upward trend in the annual maximum SLR for 7 locations and annual mean SLR for 17 locations. The nonstationary frequency results showed that Anheung station is likely to increase 114mm. - Geomundo 111mm, Jeju 145mm, Sokcho 72mm given the future accelerations in the mean sea level. However, the increases in sea level are rather small compared to sea level rise presented in the IPCC. This is because the trend and acceleration were not consistent between nearly located tide gauge stations. This study concluded the main reason of such result may be the length of tide gauge records. The further development of this study could be related to Paleo data to better estimate reliable trend and acceleration in sea level.

CONCLUSION

Urban development and population increases continuously progress in the coastal areas in Korea, thus it is expected that vulnerability towards coastal disasters by SLR would accelerate. In this study, trend analysis and nonstationary frequency analysis using long-term historic tide gauge data in the coastal areas in Korean Peninsula were carried out. The presented nonstationary frequency analysis model is a flexible approach that allows one to accommodate time-varying effects in the frequency analysis, and better quantify uncertainties associated with model parameters. The research results from this study are summarized as follows:

First, the MK test results showed that the increasing trends of annual average sea level at 17 locations were statistically significant. In cases of annual maximum extremes, seven locations exhibited statistically significant trends.

Second, nonstationary frequency analysis results showed that sea level at the coastal areas of Korean Peninsula is likely to increase from a minimum of 60.33mm to a maximum of 214.90mm. These results are rather less compared to the mean seal level rise that considered RCP scenarios.

One of the interesting features is the temporal variation of future 100-year sea levels that shows a clear increase tendency and the noticeable reduction in the return period under nonstationary condition. The results presented here were based on historical data so that the uncertainties in the estimated future sea level rise would be high due to the short length of data. In this regard, future work will be focused on combining multiple climate change scenarios with the proposed HBM approach.

ACKNOWLEDGMENTS

This paper is a part of the results of a Research Project titled "Development of Coastal Erosion Control Technology" funded by the Ministry of Oceans and Fisheries, Korea, and this support was greatly appreciated.

LITERATURE CITED

Flick, R.E.; Knuuti, K., and Gill, S.K., 2013. Matching mean sea level rise projections to local elevation datums. *J. Waterway Port Coastal Ocean Eng*, 139(2), 142-146.

Folland, C.K.; Karl, T.R.; Christy, J.R.; Clarke, R.A.; Gruza, G.V.; Jouzel, J.; Mann, M.E.; Oerlemans, J.; Salinger, M.J., and Wang, S.W., 2001: Observed Climate Variability and Change. In: *Climate Change 2001: The Scientific Basis. Contribution of Working Group I to the Third Assessment Report of the Intergovernmental Panel on Climate Change* [Houghton, J.T.,Y. Ding, D.J. Griggs, M. Noguer, P.J. van der Linden, X. Dai, K. Maskell, and C.A. Johnson (eds.)]. Cambridge University Press, Cambridge, United Kingdom and New York, NY, USA, 881pp.

Foster, G. and Brown, P.T. 2015. Time andtide: analysis of sea level time series. *Climate Dynamics*, 45(1-2), 291-308.

Gelman, A., 2006. Prior distributions for variance parameters in hierarchical models. *Bayesian Analysis*, 1(3), 515–533.

Gilbert, R.O., 1987. *Statistical methods for environmental pollution monitoring*. John Wiley & Sons.

Gilks, W. R.; Best, N.G., and Tan, K.K.C., 1995. Adaptive rejection metropolis sampling within Gibbs sampling. *Journal of the Royal Statistical Society. Series C (Applied Statistics)*, 44(4), 455–472.

IPCC., 2014: *Climate Change 2014: Synthesis Report. Contribution of Working Groups I, II and III to the Fifth Assessment Report of the Intergovernmental Panel on Climate Change* [Core Writing Team, R.K. Pachauri and L.A. Meyer (eds.)]. *IPCC*, Geneva, Switzerland, 151 pp.

Kendall, M. and Gibbons, J.D., 1990. *Rank correlation methods.* E.Arnold, London, 260.

Kendall, M., 1975. *Multivariate analysis*. Charles Griffin, Londres, 0-85264-234-2

Kim, G.S., 2006. *Review of Statistical Methods for Hydrologic - Meteorological Data Analysis.* 2006 Subcommittee Research Task, *Report*, 373-398p.

Kim, K.B.; Kwon, H.H., and Han, D., 2015. Bias correction methods for regional climate model simulations considering the distributional parametric uncertainty underlying the observations. *Journal of Hydrology*, doi:10.1016/j.jhydrol. 2015.10.015

Kriebel, D.L.; Geiman, J.D., and Henderson, G.R., 2015. Future Flood Frequency under Sea-Level Rise Scenarios. *Journal of Coastal Research*, 31(5), 1078-1083.

Kwon, H.H.; Brown, C., and Lall, U., 2008. Climate informed flood frequency analysis and prediction in Montana using hierarchical Bayesian modeling. *Geophysical Research Letters*, 35, L05404, doi:10.1029/2007 GL032220.

Kwon, H.H.; Brown, C.; Xu, K., and Lall, U., 2009. Seasonal and annual maximum streamflow forecasting using climate information: application to the Three Gorges Dam in the Yangtze River basin, China. *Hydrological Sciences Journal des Sciences Hydrologiques*, 54(3), 582-595.

Lee, C.E.; Kim, S.U., and Lee, Y.S., 2014. Estimation of the regional future sea level rise using long-term tidal data in the Korean peninsula. *J. Korea water resources association*, 47(9) 753-766.

Lee, J.J.; Kwon, H.H., and Kim, T.W., 2010. Concept of trend analysis of hydrologic extreme variables and nonstationary frequency analysis. *Korean Society of civil engineers*, 30(4B), 389-397.

Mann, H.B., 1945. Nonparametric tests against trend. *Econometrica*, 13(3), 245-259.

Menéndez, M. and Woodworth, P.L., 2010. Changes in extreme high water levels based on a quasi-global tide-gauge data set. *Journal of Geophysical Research*, 115, C10011, doi:10.1029 /2009JC005997.

Milne, G.A.; Gehrels, W.R.; Hughes, C.W., and Tamisiea, M.E., 2009. Identifying the causes of sea-level change. *Nature Geoscience*, 2(7), 471-478.

Obeysekera, J., and Park, J., 2013. Scenario-Based Projection of Extreme Sea Levels. *Journal of Coastal Research*, 29(1), 1-7.

Obeysekera, J., and Salas, J.D., 2013. Quantifying the uncertainty of design floods under nonstationary conditions. *Journal of Hydrologic Engineering*, 19(7), 1438-1446.

Oh, J.S.; Jang, D.W.; Kim, H.S., and Seo, B.H., 2005. A study on trend analysis of time series data. *Korean Society of Civil Engineers*, 1408-1411.

Pollack, E.S. and Keimig, D.G., 1987. *Counting injuries and illnesses in the workplace: proposals for a better system*. National Academies, National Research Council (US), Panel on Occupational Safety, & Health Statistics.

Rahmstorf, S., 2007. A semi-empirical approach to projecting future sea-level rise. *Science*, 315(5810), 368-370.

Stålnacke, P.; Aakerøy, P.A.; Blicher-Mathiesen, G.; Iital, A.; Jansons, V.; Koskiaho, J.; Kyllmar, K.; Lagzdins, A.; Pengerud, A., and Povilaitis, A., 2014. Temporal trends in nitrogen concentrations and losses from agricultural catchments in the Nordic and Baltic countries. *Agriculture, Ecosystems and Environment*, 198, 94-10

U.S. Army Corps of Engineers (USACE)., 2011. *Sea-level change considerations for civil works programs.* Washington DC, Circular No.1165-2-212.

Journal of Coastal Research	SI	75	750-754	Coconut Creek, Florida	2016

Geological and Stratigraphic Characteristics of a Holocene Regressive Barrier in Southern Brazil: GIS and GPR Applied for Evolution Analysis

Renato A. Leal[†*], Eduardo G. Barboza[‡], Volney Jr. Bitencourt[†], Anderson Biancini da Silva[†] and Rogério P. Manzolli[†]

[†] Programa de Pós Graduação em Geociências, Universidade Federal do Rio Grande do Sul, Porto Alegre - RS -, Brasil

[‡]Centro de Estudos de Geologia Costeira e Oceânica, Instituto de Geociências, UFRGS, Porto Alegre 91509-900, Brasil

www.cerf-jcr.org

www.JCRonline.org

ABSTRACT

Leal, R.A.; Barboza, E.G., Bitencourt, V.Jr. Biancini da Silva, A. and Manzolli, R.P., 2016. Geological and Stratigraphic Characteristics of a Holocene Regressive Barrier in Southern Brazil: GIS and GPR Applied for Evolution Analysis. *In:* Vila-Concejo, A.; Bruce, E.; Kennedy, D.M., and McCarroll, R.J. (eds.), *Proceedings of the 14th International Coastal Symposium* (Sydney, Australia). *Journal of Coastal Research*, Special Issue, No. 75, pp. 750-754. Coconut Creek (Florida), ISSN 0749-0208.

The observation of geological and geomorphological factors in coastal barriers to allows interpret the processes involved and the temporal trends over time. During the Holocene, the Balneário Torneiro barrier, located in the southern coast of Santa Catarina, prograded approximately 1.3 km, preserving the records of Urussanga river's system dynamics in surface and subsurface paleochannels. The presence of such features close to the boundary with the Pleistocene deposits up to the present coastline indicates that the evolutionary behavior of the barrier is progradational. The identification of superficial morphological features interpreted on the barrier such as transgressive dune sheets and beach ridges corroborates this interpretation. In subsurface, three main radar facies (RF-1, RF-2, RF-3), a surface radar (erosive surface) and a subsurface feature (SF) were identified in the Ground Penetrating Radar (GPR) profiles. Continuous to discontinuous reflectors, sub parallel with high amplitude, were interpreted as corresponding to the beach/shallow marine environment (RF-1) formed by the barrier progradation. An erosive surface in concave form truncating these reflectors, with onlap and downlap reflectors in the concave face, and truncation in the convex base, was interpreted as the base of a paleochannel. The others radar facies (RF-2 and RF-3) are related to the filling of the channel. The integrated interpretation of GIS and GPR data have allowed to interpret evolutionary characteristics at different time scales of the studied barrier sector.

ADDITIONAL INDEX WORDS: *Paleochannels, Ground Penetration Radar (GPR), Deposicional architecture.*

INTRODUCTION

The Holocene coastal barriers started its development approximately 17.5 ky BP, after the end of the last glacial maximum, associated with the beginning of the Post-Glacial Marine Transgression – PMT (Field & Duane, 1974; Swift, 1976; Swift & Thorne, 1991; Roy *et al*., 1994; Cowell *et al*., 1999). This feature is the most important depositional element of low gradient, wave dominated coasts (Dillenburg & Hesp, 2009; Otvos, 2012). The observation of geological and geomorphological factors in this environment allows to interpret the processes involved and their temporal trends over time. During the late Holocene shoreline progradation on the coast of Balneário Torneiro barrier, located in the southern littoral of tSanta Catarina state (SC), the record of sediment dynamics of a river system (Urussanga river) was preserved in surface and subsurface paleochannels. Thus, for a detailed geomorphological and stratigraphic study, it is very important to combine geoprocessing techniques (GIS) with the geophysical method of Ground Penetration Radar (GPR).The use of GPR has allowed the stratigraphic interpretation of several coastal depositional systems (Bridge *et al*., 1995; Bristow and Jol, 2003; Bristow *et al*., 2007; FitzGerald *et al*., 2007; Barboza *et al*., 2011, 2013, 2014; Biancini da Silva *et al*., 2014; Buynevich *et al*., 2011; Dillenburg *et al*., 2014) and the time-series analysis with aerial photographs also provides important geological and geomorphological indicators. Therefore, this work focuses on the evolution of the Holocene coastal barrier based on the features interpreted in surface and subsurface through GIS techniques and geophysical surveys.

Regional Settings

The study area is located in the Pelotas Basin, a marginal sedimentary basin with approximately 40,000 km² emerged area (Dias, 1994), covering the southern portion of the continental margin of Brazil (Figure 1). The coastal plain of this basin was formed during the Quaternary by the juxtaposition of sedimentary deposits of four lagoon-barrier systems, designated I, II, III (Pleistocene) and IV (Holocene) (Villwock *et al*., 1986). The latest system began its formation about 7 ky BP in

DOI: 10.2112/SI75-151.1 received 15 October 2015; accepted in revision 15 January 2016.
*Corresponding author: relealsc@gmail.com
©Coastal Education and Research Foundation, Inc. 2016

consequence of the PMT. At that time, the sea level reached approximately 3 m above the present level (Angulo *et al*., 2006) and enabled the formation of a barrier that consists essentially of sand that has been transported by longshore drift (Dillenburg *et al*., 2000).The regressive barrier Balneário Torneiro is located at Jaguaruna city in the north end of the Pelotas Basin, in Tramandaí-Cape Santa Marta sector (Dillenburg & Barboza, 2014) segmented by Urussanga river's fluvial system (Figure 1). The climate is subtropical with average temperatures of 23ºC in summer and 14ºC in winter. The Anticyclone Tropical South of Atlantic predominates in spring and summer months, bringing easterly winds to northeast and autumn-winter the area is affected by Polar Mobile Anticyclone, with southerly winds southwest (Orselli, 1986). The waves reflect the characteristics of the winds, so during the spring and summer the predominant wave direction is east quadrant, and in the months of autumn and winter the passage of frontal systems produces winds and waves of southern quadrant. The significant wave height is 1.15 m (east) and 2 m (south) with periods in the range of 08 and 12 seconds, respectively (Araújo *et al*., 2003).

The tidal regime is characterized by semi-diurnal tides with microtidal range (average of 0.5 m tidal amplitude). Associated with the meteorological tides, the amplitude can reach more than 1 m (Giannini, 1993). Northeastward-orientated paleochannels along the coast of Santa Catarina suggest a drift to the same quadrant, as well as identified in the Rio Grande do Sul coast by Tomazelli & Villwock (1992) and Toldo Jr. *et al*., (2003). However, it is relevant to point out that Siegle & Asp (2007) concluded that the longshore drift close to the region, in an annual period, has a two-way character and shows a clear decrease in transport potential.

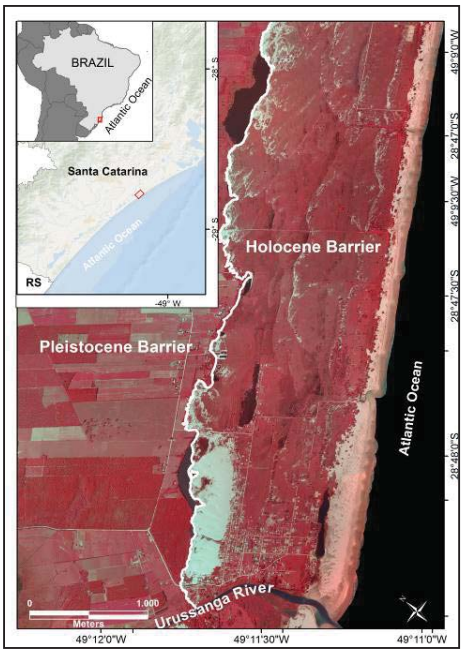

Figure 1. Study area location showing the boundary between Holocene and Pleistocene barrier.

METHODS

Geomorphological data were obtained through analysis of aerial photographs from 1938, 1957, 1978 and 2010 (scale 1: 25.000). Superficial morphological features were identified with the aid of GIS techniques in ArcGIS™ 10.2 software. Furthermore, GPR profiles were performed in order to show the stratigraphy of depositional systems. The equipment used for data acquisition was a SIR-3000 model from GSSI™ company (Geophysical Survey Systems, Inc.), with a contact antenna (200 MHz). The Common Off-set array was used. The constant dialetric of 10 was used to convert travel-time into depth, representing velocity 0.09 m/ns, usually related to sand deposits (Davis & Annan, 1989). The geophysical profiles were performed perpendicular (dip) and parallel (strike) to the coastline. The signal penetration varies between 7 and 12 m, in which different radar facies were identified. Topographic corrections were made by the coupling of the GPR system to the high precision differential positioning system (DGPS). The processing of the profiles was performed in two distinct softwares: Radan® e Prism®. The data interpretation followed the method of sismoestratigraphy (Payton, 1977) adapted to GPR by Neal (2004) which consisted in the interpretation of terminations (onlap, toplap, downlap and truncation), geometry and the pattern of reflectors (Mitchum Jr. *et al*., 1977).

RESULTS

The results are presented subdivided into subheadings according to the method applied. Environment surfaces are the result of GIS techniques and stratigraphic surfaces are the interpretations of geophysical data.

Environments of Surface

The barrier of Torneiro prograded about 1.3 km. Three depositional environments were recognized in the Holocene barrier: beach/shallow marine, alluvial and aeolian. From the geomorphological point of view, four main kinds of features were identified: transgressive dune sheets, beach ridges, precipitation ridges and paleochannels. Aerial photography analysis allowed to characterize the behavior of these environments and features over the past 72 years. The major change concerns the stabilization of the dunefield that covered the barrier which currently appears featured into four stages/periods of transgressive dune sheets demarcated by precipitation ridges. The presence of coastal lagoons and wetlands became evident with the stabilization of the dunefield. Due to the parallel orientation to the coast, with elongated forms and SW-NE direction, these water bodies were interpreted as paleochannels of Urussanga river. Associated to these paleochannels beach ridges are found which were probably built during the processes of abandonment and clogging of the channel.

Stratigraphic Surfaces – Characteristics and Intepretations of Radar Reflection

Eighteen GPR profiles were acquired measuring a total length of approximately 14 km. Two sections of these profiles were selected to illustrate the internal depositional architecture of the barrier (Figure 3). The location of the sections is shown in Figure 2D. Three main radar facies (RF-

1, RF-2, RF-3), a surface radar (erosive surface) and a subsurface feature (SF) were identified in the GPR dataset. RF-1 is located at a depth between 4.5 and 10 m. Reflectors are continuous to discontinuous, sub parallel with high amplitude, interpreted as corresponding to the beach/shallow marine environment (upper shoreface) formed by the barrier progradation. Similar deposits were observed in GPR profile for Dillenburg *et al*. (2011) and Barboza *et al*. (2009, 2010, 2011, 2013). An erosive surface in concave form truncates the reflectors of RF-1, with onlap and downlap reflectors in the concave face, and truncation in the convex base. This erosive surface was interpreted as the base of a paleochannel. In the second GPR profile, the surface is 2.5 m deep. Above the surface, low amplitude reflectors were interpreted as channel filling, subdivided into two radar facies, RF-2a and RF-2b, based on the pattern of the reflectors. The RF-2a corresponds to a sandy filling by Aeolian influence as a result of NE winds (cross-onshore), acting in the region. Reflectors are parallel and sub parallel, average inclination angle, alternating high and medium contrasts, and terminations downlap on the erosive surface towards the channel depocenter. The RF-2b reflectors are parallel, continuous and low contrast. This radar facies represent the channel filling by fine sediments related to low energy period which occurred after the channel migration. On top of the profiles, wavy reflectors, continuous, high contrast and low inclination angle in both directions represent the aeolian capping of the transgressive dune sheets (RF-3).

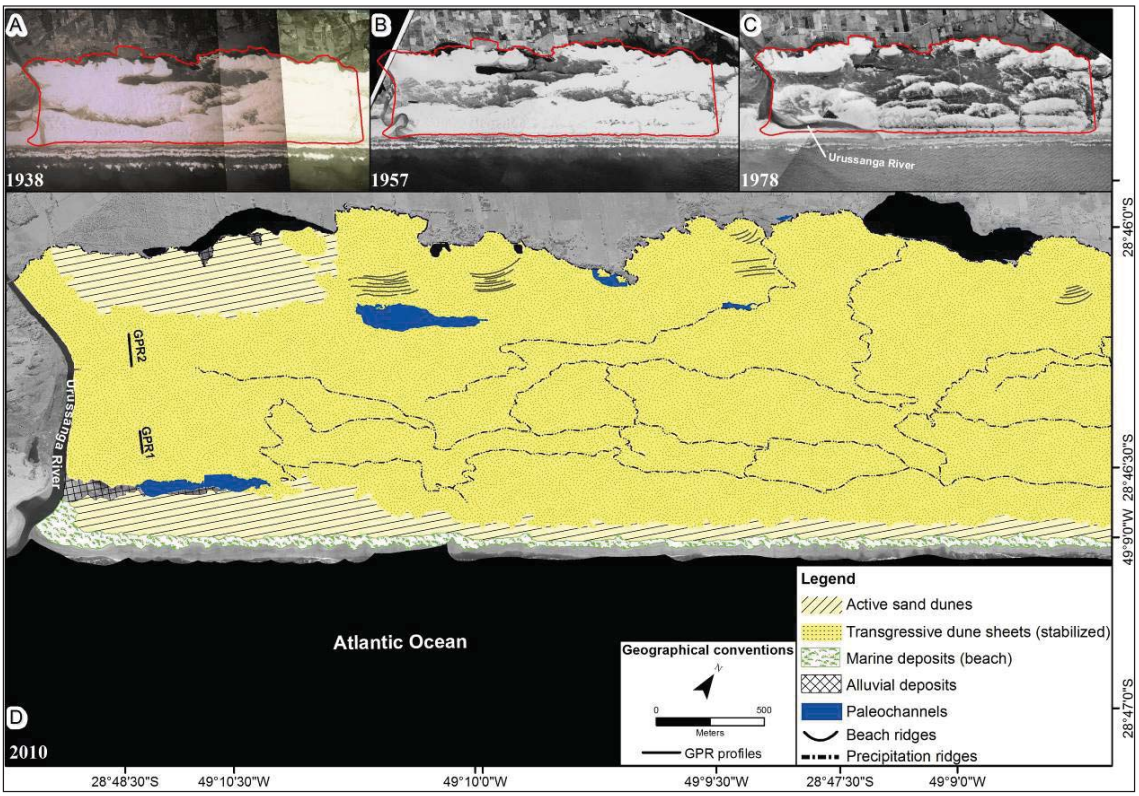

Figure 2. A,B,C) Analysis of historical aerial photographs showing stabilization of the dunefield. D) Geomorphological features identified in the barrier and GPR profiles location.

DISCUSSION

The presence of paleochannels close to the boundary with the Pleistocene deposits toward the present coastline indicates that the evolutionary behavior of the barrier is progradational (regressive coastline). The identification of stage/periods of transgressive dune sheets and beach ridges corroborates this interpretation as well as discribed by Barboza *et al.*, (2011), Hesp *et al*., (2005, 2007), Dillenburg *et al*., (2000) e Dillenburg & Barboza (2009) along the Rio Grande do Sul state (RS), around 60 km towards south.

The change in aeolian deposits decorating the barrier was already a target of several studies. Miot da Silva *et al*. (2013) discusses these geomorphological changes in the dunefields of southern Brazil, and attributes as the main factor the regional climate changes arising from the Pacific Decadal Oscillation and El Niño events. Another important feature is the water bodies and wetlands that truncate (erode) the dunefield and other features present in the barrier. They have elongated forms, with NE-SW orientation, parallel to the coastline, and were interpreted as paleochannels related to the dynamics of the Urussanga river. The NE-SW orientation is the result of the

predominant longshore drift which inflects the mouth of the rivers to northeast, as represented in Figure 2C. Nevertheless, at certain times the drift exhibits a marked decrease in transport potential, causing the mouth of the river to stay perpendicular to the coast, and even with a slight inflection to the south (Figure 2D).

About the subsurface data of Holocene coastal barriers, the analysis of the stratigraphic behavior has been carried out based on the patterns of the reflectors in two ways: landward dipping reflectors and seaward dipping reflectors, interpreted as retrogradational and progradational barriers, respectively (Barboza *et al*., 2011; Dillenburg & Barboza, 2014; Dillenburg *et al*., 2011; Fitzgerald *et al*., 2007). However, when barrier development is closely related to a river system, hardly these records are preserved in the subsurface, and other approaches must be conducted to characterize the system. The barrier of Torneiro has a dominant feature in the profiles which is the presence of erosional surfaces that represents the base of paleochannels. These channels are present in basically two different depths: 5 m and 2.5 m approximately. The deepest base indicates active channels for a longer time or moments of higher fluvial energy. The shallower channels were less worked with moments of lower energy fluvial. These channels reworked the beach/shallow marine environment during the progradation of the barrier and this process occurred throughout evolution, resulting in the interdigitation of shallow marine, alluvial and aeolian deposits. As viewed in the profiles, the paleochannels have two different fillings patterns: the RF-2a corresponds to a filling with aeolian influence as a result of NE winds (cross-onshore), acting in the region. This pattern suggests that the pattern of evolution of the barrier was analogous to Figure 2D, in which the channels were located parallel to the coastline and behind the backshore. Over time, with the barrier progradation, the river migrated concomitant with the barrier, leaving abandoned channels which later became coastal lagoons, a low energy environment that subsequently underwent colmatation by fine sediments represented by RF-2b. After this process, the transgressive dune sheets has shrouded most of the paleochannels, or, in some places, they became wetlands along the barrier.

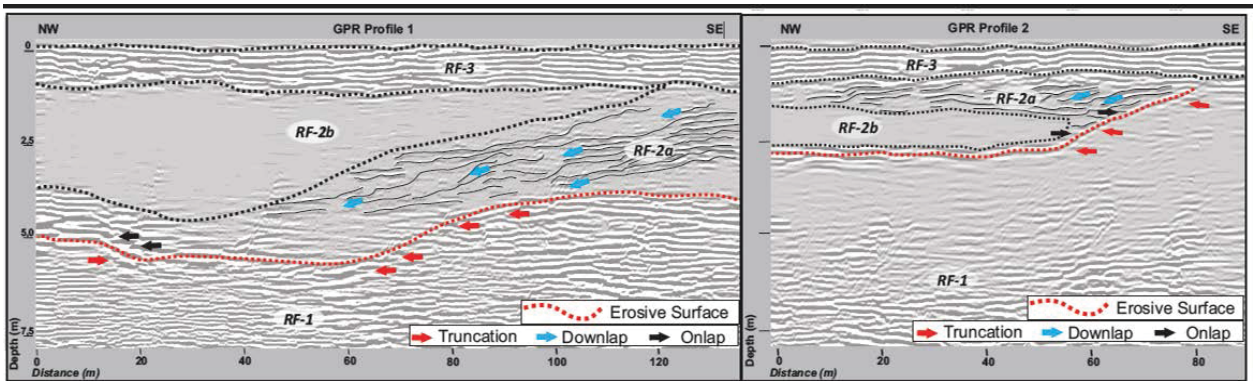

Figure 3.GPR profiles acquired with a frequency of 200 Mhz showing the paleochannels and its filling. RF-1 is characterized by deposits generated in shallow marine environment. This deposit is truncated by an erosive surface interpreted as the base of the paleochannel. The others radar facies (RF-2a, RF-2b, RF-3) represent the paleochannel fillings.

CONCLUSIONS

Both techniques used in conjunction allowed the interpretation of evolutionary characteristics at different time scales of the studied barrier sector. For the most recent scale, the use of GIS techniques permitted identifying important morphologies surface for evolutionary characterization of Holocene barrier, in addition to monitoring the behavior of these features in the last 72 years. The geophysical profiles allowed us to visualize the depositional architecture and stratigraphic deposits in the subsurface, showing the regressive behavior of this barrier sector. The GPR also revealed the interdigitation among the marine, alluvial and aeolian deposits in subsurface. This information has important implications for geotechnical studies related to planning and area management for urban development in this stretch of coastline. In subsurface these deposits have different mechanical resistance; at surface the paleochannels may represent humid environments and wetlands inappropriate for occupancy.

ACKNOWLEDGMENTS

The authors thank CAPES and CNPq for their research fellowships.

LITERATURE CITED

Angulo, R.J., Lessa, G.C. and Souza, M.C., 2006. A critical review of Mid - to Late-Holocene sea-level fluctuations on the eastern Brazilian coastline. *Quaternary Science Reviews*, 25, 486-506.

Barboza, E.G., Rosa, M.L.C.C., Hesp, P.A., Dillenburg, S.R., Tomazelli, L.J. and Ayup-Zouain, R.N., 2011.Evolution of the Holocene Coastal Barrier of Pelotas Basin (Southern Brazil) - a new approach with GPR data. Journal *of Coastal Research*, SI 64, 646-650.

Barboza, E.G., Rosa, M.L.C.C., Dillenburg, S.R. and Tomazelli, L.J., 2013. Preservation potential of foredunes in the stratigraphic record. *In*: Conley, D.C., Masselink, G., Russell, P.E. and O'Hare, T.J. (eds.), *Proceedings 12th*

International Coastal Symposium (Plymouth, England), *Journal of Coastal Research*, SI No. 65, pp. 1265-1270.

Barboza, E.G., Rosa, M.L.C.C., Dillenburg, S.R., Biancini da Silva, A. and Tomazelli, L.J., 2014. Stratigraphic analysis applied on the recognition of the interface between marine and fluvial depositional systems. *In*: Green, A.N and Cooper, J.A.G. (eds.), *Proceedings 13th International Coastal Symposium* (Durban, South Africa), *Journal of Coastal Research*, SI No. 70, pp. 687-692.

Biancini da Silva, A., Barboza, E.G., Rosa, M.L.C.C. and Dillenburg, S.R., 2014. Meandering Fluvial System Influencing the Evolution of a Holocene Regressive Barrier in Southern Brazil. *In*: Green, A.N. and Cooper, J.A.G. (eds.), *Proceedings 13th International Coastal Symposium* (Durban, South Africa), *Journal of Coastal Research*, SI No. 70, pp. 205-210.

Buynevich, I.V., Klein, A.H.F., FitzGerald, D.M., Cleary, W.J., Hein, C.J., Veiga, F., Angulo, R.J., Asp, N.E., and Petermann, R.M., 2011. Geological legacy of storm erosion along a high-energy indented coastline: northern Santa Catarina, Brazil. *Journal of Coastal Research*, SI 64, 1840-1844.

Cowell, P.J., Roy, P.S., Cleveringa, J. and DeBoer, P.L., 1999. Simulating coastal systems tracts using Shoreface-Translation Model. *International Association of Sedimentologists Special Publication*, Oxford, *Blackwell Scientific* Pub 62, 165-175

Davis, J.L. and Annan, A.P., 1989. Ground-penetrating radar for high-resolution mapping of soil and rock stratigraphy. Geophysical Prospecting, 37, 531-551.

Dias, J.L, Sad, A.R.E, Fontana, R.L. and Feijó, F.J., 1994. Bacia de Pelotas. *Boletim de Geociências da Petrobrás*, 8, 235-245.

Dillenburg, S.R. and Barboza, E.G., 2009. Long and short term progradation of a regressive barrier in southern Brazil. *Journal of Coastal Research*, SI, No 56. (*Proceedings of the 10th International Coastal Symposium*) 599-601. Lisbon, Portugal

Dillenburg, S.R. and Barboza, E.G., 2014. The Dip and Strike-Fed Sandy Coast of Southern Brazil. *In*: Martini, I.P. and Wanless H.R. (eds.). Sedimentary Coastal Zones from High to Low Latitudes: Similarities and Differences, *Geological Society*, London, Special Publications 388, 333-352.

Dillenburg, S. R., Roy, P. S., Cowell, P. J. & Tomazelli, L. J. 2000. Influence of antecedent topography on coastal evolution as tested by the shoreface translation-barrier model (STM). *Journal of Coastal Research*, 16, 71–81.

Dillenburg, S.R., Barboza, E.G., Tomazelli, L.J., Hesp, P.A., Clerot, L.C.P. and Ayup-Zouain, R.N.. 2009. The Holocene coastal barriers of Rio Grande do Sul. *In*: Dillenburg, S.R. & Hesp, P.A. (eds.) *Geology and Geomorphology of Holocene Coastal Barriers of Brazil*. Lecture Notes in Earth Sciences, Springer, Berlin, 107, 53-91.

Field, M.E., and Duane, D.B., 1974, Geomorphology and sediments of the inner Continental Shelf, Cape Canaveral, Florida: *U.S. Army, Corps of Engineers*, Coastal Engineering Research Center Technical Memorandum 42, 87 p.

Fitzgerald, D.M., Cleary, W.J., Buynevich, I.V., Hein, C.J., Klein, A.H.F., Asp, N.E. and Angulo, R.J., 2007. Strandplain Evolution along the Southern Coast of Santa Catarina, Brazil. *Journal of Coastal Research*, SI 50, 152-156.

Hesp, P.A., Dillenburg, S.R., Barboza, E.G., Clerot, L.C.P., Tomazelli, L.J. and Ayup-Zouain, R.N., 2007. Morphology of the Itapeva to Tramandaí transgressive dunefield barrier system and mid- to late Holocene sea level change. *Earth Surface Processes and Landforms*, 32, 407-414.

Hesp, P.A., Dillenburg, S.R., Barboza, E.G., Tomazelli, L.J., Ayup-Zouain, R.N., Esteves, L.S., Gruber, N.L.S., Toldo Jr., E.E., Tabajara, L.L.C.A. and Clerot, L.C.P., 2005. Beach Ridges, Foredunes or Transgressive Dunefields? Definitions and an Examination of the Torres to Tramandaí Barrier System, Southern Brazil. *Anais da Academia Brasileira de Ciências*, 77 (3), 493-508.

Miot Da Silva, G.; Martinho, C.T.; Hesp, P.A.; Keim, B.D., and Ferligoj, Y., 2013. Changes in dunefield geomorphology and vegetation cover as a response to local and regional climate variations. *In*: Conley, D.C., Masselink, G., Russell, P.E. and O'Hare, T.J. (eds.), *Proceedings 12th International Coastal Symposium* (Plymouth, England), *Journal of Coastal Research*, SI No. 65, pp. 1307 – 1312.

Mitchum Jr., R.M., Vail, P.R. and Sangree, J.B., 1977. Seismic Stratigraphy and Global Changes of Sea Level, Part 6: Stratigraphy interpretation of seismic reflection patterns in depositional sequences. *In*: Payton, C.E. (ed.), Seismic *Stratigraphy — Applications to Hydrocarbon Exploration*. Tulsa, AAPG, 26, 117-133.

Neal, A., 2004. Ground-penetrating radar and its use in sedimentology: principles, problems and progress. *Earth Science Reviews*, 66, 261-330.

Orselli J., 1986. Climatologia. In: GAPLAN – SC. Atlas de Santa Catarina. Rio de Janeiro, pp 38–39

Otvos, E.G., 2012.Coastal barriers – Nomenclature, processes, and classification issues. Geomorphology, 139 (140), 39-52.

Payton, C.E., 1977. Seismic Stratigraphy — Applications to Hydrocarbon Exploration.Tulsa, AAPG, (Memoir # 26), 516 p.

Roy, P.S.; Cowell, P.J.; Ferland, M.A., and Thom, B.G. 1994. Wave Dominated Coasts. *In*: Carter, R.W.G., Woodroffe, C.D. (eds.), *Coastal Evolution, Late Quaternary shoreline morphodynamics*. Cambridge. Cambridge University Press, pp. 121-186.

Siegle, E. and Asp, N.E. 2007. Wave refraction and longshore transport patterns along the Southern Santa Catarina coast. *Brazilian Journal of Oceanography*, v.55, n. 2, p. 109-120.

Swift, D.J.P, 1976. Continental shelf sedimentation. *In* D.J. Stanley, D.J.P, Swift (eds.), *Marine sediment transport and environmental management*, pp. 311-350. New York: Wiley.

Swift, D.J.P. and Thorne, J.A., 1991. Sedimentation on Continental Margins, I - A general model for shelf sedimentation. *Special Publication of the International Association of Sedimentologists*. vol. 14, pp. 3-31.

Villwock, J.A., Tomazelli, L.J., Loss, E.L., Dehnhardt, E.A., Horn Fº, N.O., Bachi, F.A. and Denhardt, B.A., 1986. Geology of the Rio Grande do Sul Coastal Province. *In*: Rabassa, J. (ed.), *Quaternary of South America and Antartic Peninsula*, 4, 79-97.

Journal of Coastal Research	SI	75	755-759	Coconut Creek, Florida	2016

Effect of Large-Scale Atmospheric Circulation and Wind on Storm Surge Occurrence

Anne-Lise Montreuil[†*], Jihane Elyahyioui[†], and Margaret Chen[†]

[†]Department of Hydrology and Hydraulic Engineering
Vrije Universiteit Brussel (VUB)
Brussels, Belgium

www.cerf-jcr.org

www.JCRonline.org

ABSTRACT

Montreuil, A-L.; Elyahyioui, J., and Chen, M., 2016. Impact of local wind and atmospheric circulation patterns on coastal morphological changes along the Belgian coast. *In:* Vila-Concejo, A.; Bruce, E.; Kennedy, D.M., and McCarroll, R.J. (eds.), *Proceedings of the 14th International Coastal Symposium* (Sydney, Australia). *Journal of Coastal Research*, Special Issue, No. 75, pp. 755-759. Coconut Creek (Florida), ISSN 0749-0208.

Large scale atmospheric circulation is an important component of wind forcing which in turn control strom surge generation. The study aim is to evaluate the impact of large-scale atmospheric flow and wind on the occurrence of storm surges causing significant morphological impacts along the Belgian coast. An objective classification scheme of the atmospheric circulation affecting the North Sea basin is used for almost 150-years (1871-2014). The observed storm surge events associated with erosion are examined with respect to the circulation weather types (CWTs) and the winter North Atlantic Oscillation (NAO) phases under which they occur. It is shown that although the Anticyclonic (A) type being the most frequent in winter (27%) and also over the entire year (28%) gives less than 1-10% of contribution to the occurrence of observed storm surges. However, the Cyclonic (C), Northerly (N), Northwesterly (NW), Westerly (W) and Southwesterly (SW) types happen less often, they account together for more than 82% of the observed storm surges. Also, the observed storm surges primarily occurred during a moderately positive winter NAO index while strong winter NAO index rarely accounted for the storm surge events. Results highlight the inter-connections between the occurrence of observed storm surges, interannual variability of CWTs and winter NAO index. These data are also investigated to examine their evolutionary trends in order to detect any ongoing trends of climate change. Identify any link and trend between storminess and atmospheric circulation pattern could help to better prepare coastal communities and coastal managers for future storm surges.

ADDITIONAL INDEX WORDS: *Forcing factors, storm surges, erosion, Belgian coast.*

INTRODUCTION

There is a large variety of natural processes acting on any coast in the world over wide ranges of spatial and temporal scales. Their consequences are multiple and some of them can be catastrophic, given the high degree of development of human activities along the coasts. Coastal erosion is an important consequence of these natural processes. It originates from interactions between external driving forces occurring at different spatio-temporal scales. Coastal erosion is thus dynamic and is expected to intensify due to sea-level rise and also human interferences (Leatherman *et al.*, 2000). Erosion results in coastline retreat and in loss of land, which become critical problems when the coastal zone is strongly developed and that there is no space to adapt to these changes.

The Belgian coast, facing the North Sea basin, is no exception of this phenomenon. About 50% of the coast suffers from erosion (Haerens *et al.*, 2012). Hard and soft engineering schemes are already being implemented such as groynes, breakwaters, seawalls, beach nourishments, *etc*.

It is important to identify the nature of the main processes dominating the sediment exchanges in order to take adequate actions and to implement the necessary structures.

Marine and atmospheric forcing factors bring energy in the coastal zone and take part to its shaping by transporting sediments and modifying coastal morphology. Marine factors include waves, tides, currents and sea level. Atmospheric factors concern climate weather and local wind. Several studies have investigated the action of forcing factors and their impacts on the coastal erosion along the Belgian coast (Haerens *et al.*, 2012; Ullmann and Monbaliu, 2010; Van den Eynde *et al.*, 2012). The conclusions are very case-specific and highlight the need for detailed studies at short (seasonal) and long-term (>5 years). Here, the potential impacts of the atmospheric circulation weather types (CWTs) and the winter North Atlantic Oscillation mode (NAO) are investigated on the local storminess. This study aims to achieve a better understanding of the relation between large scale atmospheric circulation, winds and the occurrence of storm surges along the Belgian coast.

Background

The study site is located along the Belgian coast which extends up to 67km. It forms more or less a straight line directed SW to NE from the French Opal coast to the nature reserve Zwin at the border with the Netherlands (Figure 1).

DOI: 10.2112/SI75-152.1 received 15 October 2015; accepted in revision 15 January 2016.

*Corresponding author: anne-lise.montreuil@vub.ac.be

©Coastal Education and Research Foundation, Inc. 2016

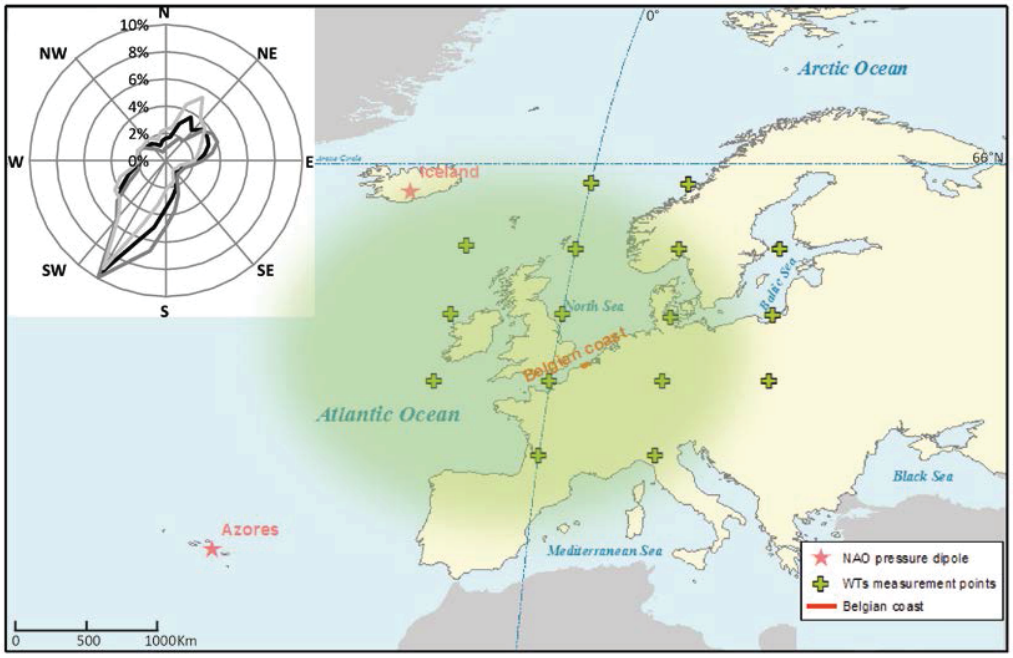

Figure 1. Location of the study site. The inset shows the wind rose. Black, dark grey and light grey lines correspond to annual, winter and summer winds respectively.

In general, the coast consists of a broad gentle sloping sandy beach backed by dykes, while in the shallow continental numerous sand banks occur, the Flemish Banks. The Belgian coast is mainly erosive (Haerens *et al.*, 2012). Hard and soft engineering schemes are already being implemented. From 50% to 60% of the coastline would be erosive if there were no human intervention to protect it and there would be a progressive landward retreat.

Along the coast, the tide is semi-diurnal. All beaches are in a macro-tidal regime and the tidal range is between 3.5m at neap tide and 5m at spring tide. The wind regime is characterized by typical wind speeds between 3 to 8m/s, coming from SW (Figure 1). There are no significant changes between summer and winter except for the intensity of winds. The strongest period is between November and February (Van den Eynde *et al.*, 2012). High wind speeds (>10m/s) are generally coming from WSW to NW, which are susceptible to have a devastating impact considering the coastline orientation since wind would produce piling up of water at the coast. Verwaest *et al.* (2008) have found that the wind direction is strongly correlated with the wave directions. Along the coast, the wave climate is typically characterized by wave height between 0.5 and 1m at the shore, and with wave period of 6s.

METHODS

In this study, the Lamb daily circulation weather type (CWT) and the winter North-Atlantic Oscillation (NAO) index were used to investigate the impact of the atmospheric circulation and wind forcing on the occurrence of storm surges. The advantages of using CWTs and NAO index are their large spatial coverage and also long-term records.

A method of classifying the CWT of the British Isles was described by Lamb (1972), in which the daily atmospheric pressure charts are used to examine the surface airflow pattern and steering of the circulation system. This was further developed by Jenkinson and Collison (1977) and Jones *et al.* (1993) who extended this classification based on mean sea level pressure measured at 16 fixed locations covering the British Isles and surrounding area (Figure 1). Eight main directional types in the classification are recognized as the directional types North (N), North-West (NW), West (W), South-West (SW), South (S), South-East (SE), East (E) and North-East (NE). In addition, there are 2 non-directional types: Anticyclonic (A), Cyclonic (C), and also an unclassified type which is not considered in this study. There is further an estbalished set of index associated with the directional (D) and total flow (F), and shear vorticity (Z) of the geostrophic wind. From this, a gale index $G = \sqrt{(F^2 + (0.5Z)^2)}$ was developed. For this study, the daily CWT data above the North Sea basin from 1871 to 2014, measured at synoptic hour 12, were collected from the Climate Research Unit of the University of East Anglia (UK). For the 10-types classification, each hybrid day was counted as half a day for one type and half a day for the other type (*e.g.* an 'Anticyclonic North-East type ANE' day counts for 0.5 day for type A and 0.5 day for type NE).

The NAO is a large-scale mode of atmospheric pressure variation that governs the climate variability in mid-latitudes of the North Atlantic ocean (Hurrell, 1995). It is defined as the fluctuation in sea level pressure difference between the Icelandic

Low and the Azores High (Figure 1). The NAO interacts on interannual-to-decadal time scales with other important phenomena dominant in the Northern Atlantic ocean. It is present the whole year, but its influence is particularly visible during winter season. The NAO index is computed from regional differences in normalized pressure anomalies and is used to quantify its state. Positive phases in the index often correspond to wet and stormy weather in Northwest Europe, dominated by strong mid-latitude westerlies, while negative phases are associated with dry, calm weather in Northwest Europe (Hurrell, 1995). Time serie of standardized monthly NAO index was provided from the National Oceanic and Atmospheric Administration. The winter NAO indices were here calculated for each winter corresponding to the period from October to March.

Haerens *et al.* (2012) analyzed topographic, bathymetric and hydrodynamic data to define a series of criteria to assess the happening of a storm surge of sufficient importance to cause significant morphological changes of Belgian sandy beaches. They identified 22 storm surges from 1993-2007 affecting the Belgian coast, and also concluded that a storm surge causing erosion must be characterized at least by marine conditions of a maximum significant offshore wave height higher than 4 m, maximum water level above 5 m TAW (*Tweede Algemene Waterpassing*, corresponding to the mean sea level at low tide in Ostend harbor), storm duration longer than 12 h. These criteria were used in this study to extract potential storm surges between 2008 and 2014 when 14 events were recorded.

RESULTS

The classification of the daily CWTs and the flow characteristics data is approximately centred in Belgium, but they also cover the entire North Sea basin and thus accounting for some spatial variability. The frequency of occurrence of each weather type for the whole year and for winter and summer seasons is shown in Figure 2 for a period covering 143-years (1871-2014). The A type is dominant over the North Sea in all seasons (27%) and also over the entire year (28%). Next to it, the C type occurs at 14% in winter, 16% in summer and over the year. The dominant directional types are SW and W in winter accounting together for 24.5%, but they are also very frequent in summer and over the whole year. One observes a shift in the direction towards more western conditions in summer compared to winter. The NW and S types are also common, each occurring for more than 8% at seasonal and annual scale. Thus, the sector SW-W-NW is dominant in all seasons, reflecting the influence of the westerlies, controlled by the mutual adjustment of the pressure gradient between the 30° and 60°N latitudes and the Coriolis force.

The mean gale index, computed from the daily total flow and the total shear vorticity over the North Sea, is shown per weather type in Figure 2. The SW-W-NW weather types are associated with high wind speed over the year. An average maximum gale index of 24.4m/s is measured for the W type, following by the type C which is 1.2 times higher than the type A. As expected, the gale index in winter is much higher than in summer for all the types, and in particular for the SW-W-NW and C types for which the difference exceded 6m/s.

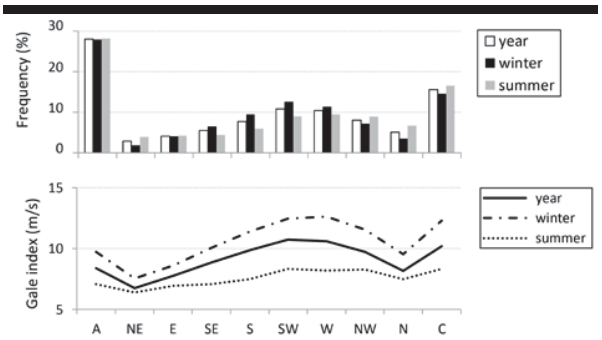

Figure 2. Annual and seasonal frequencies of occurrence (top panel), gale index of each CWT from 1871 to 2014 (lower panel).

Figure 3 presents the frequency of obseved storm surges, inducing erosion along the coast, which are associated with the weather types and the winter NAO index. Observed storm surges occur under C type for 40% time, following by N, NW, and W types (35.7% time). They are related to high gale index, except for NW type. Also, their maximum and average winter NAO is usually positive. It suggests that the most threatening types for the occurrence of surge are C, NW, N and W types. The frequency of storm surge events associated with SW type is only 6.3%. However, it is associated with relatively high wind speeds (maximum gale of 20.2m/s) and with positive trend of NAO index. Thus, SW type might be also a threatening type for the occurrence of storm surge. The A type gives less than 5% of contribution to the occurrence of storm surges, although it is the most frequent weather types as previously observed. Interestingly, the storm surge events happened during a moderately positive winter NAO index (<1.2), while stronger winter NAO index was not accounted for the storm surge events.

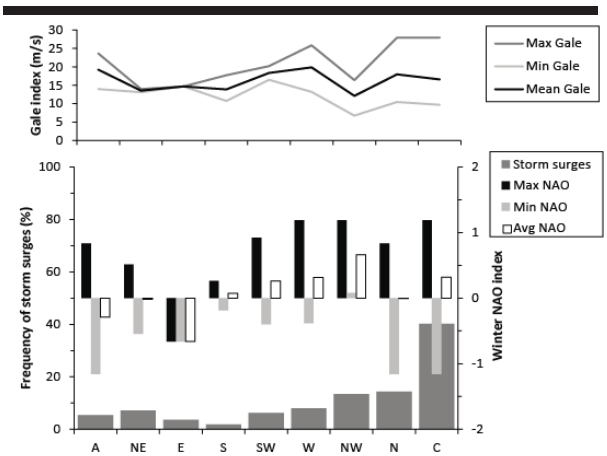

Figure 3. Observed storm surges associated with the CWTs, gale index and the winter NAO index from 1983 to 2014. Note: no storm occurred under type SE.

The results described above suggest a correspondence between the local storm surge events and the regional CWTs so that the long-term trends of these latter were examined at seasonal and annual scale. Table 1 presents the annual and seasonal linear trends for each weather type. The occurrences seem rather stable for most of weather types at seasonal and annual scales. However, some types still show a noticeable positive trend. Type W is getting more frequent with 11.4 days (0.08 days/year) and also A and NW types with 7.1 days from 1871 to 2014 (0.05 days/year). Although the trend is slightly lower, the N and SW types indicate an increase of days over time. In contrast, the E, SE and S types are getting less frequent. In general, the trends are slightly weaker in summer than in winter, indicating more stable regional weather conditions in summer than in winter.

Table 1. *Annual and seasonal trends of occurrences of each weather type. Positive trend is in italic (α 0.05).*

	Trend (days/year)		
Weather type	**Annual**	**Winter**	**Summer**
A	*0.05*	*0.04*	*0.01*
NE	-0.02	0.00	-0.01
E	-0.07	-0.03	-0.04
SE	-0.08	-0.04	-0.03
S	-0.04	-0.03	-0.01
SW	*0.03*	*0.02*	*0.01*
W	*0.08*	*0.05*	*0.03*
NW	*0.05*	*0.03*	*0.03*
N	*0.03*	*0.01*	*0.02*
C	-0.02	-0.03	*0.01*

The correlation between the temporal values of winter NAO index and of the seasonal and annual frequencies of each weather type is evaluated with the linear correlation coefficients, for the common period of data (*i.e.* 1951 to 2014) and shown in Figure 4. It seems that the winter NAO only impacts some of the directions. Positive correlation coefficients are noticeable for types SW, W and NW in winter and over the whole year. The frequencies of sectors NE, E and SE are also sensitive (negative correlation). Types A and C, which are particularly frequent over the North Sea, are not significantly correlated to the winter NAO index.

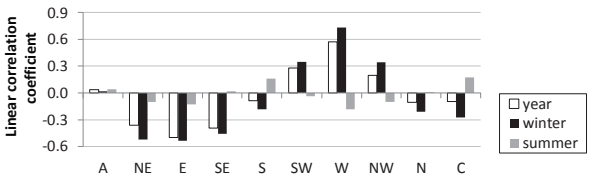

Figure 4. Linear correlation coefficients between the winter NAO index and the anual and seasonal occurrences of each weather type.

DISCUSSION

The Lamb CWT method is often applied to classify large-scale weather situations assimilated with local environmental variables. For example, it has been used to different European regions, in the context of investigating rainfall-relevant regimes and also the occurrence of severe storms (*e.g.* Fernandez-González *et al.*, 2012; Donat *et al*., 2010; Montreuil and Bullard, 2012). In this study, this CWT method was used, for the first time, to examine the contribution of each type to the observed storm surges impacting the Belgian coast.

The results suggest that C, N, NW, W and SW types are the most frequent (82%) for the occurrence of surge storm and wich are generally associated with high gale index. According to the coastline orientation, these CWTs could be the most threatening for causing coastal erosion. These observations at regional scale are in agreement with previous studies which found that the most devastating local winds and waves are known to come from the N-NW sector along the Belgian coast (Haerens *et al*., 2012; Verwaest *et al*., 2008).

The CWT method in conjunction with the winter NAO index presented in this study provides realistic and rational results for the investigation of storminess. The observations agree with findings from other studies on the significance of northerly, westerly and southerly flows for the occurrence of storms travelling from the North Atlantic to the British Isles, the North Sea and southern Scandinavia; and which also happen primarily during positive winter NAO index (*e.g.* Donat *et al*., 2010). Here, the storm surges coming from the N-NW-W sectors were for 51% associated with modest positive NAO index (<1.5), while no storm event happened with a strong NAO index (>1.5). In coastal studies, the winter NAO index is often used as a proxy for storminess (Pirazzoli *et al.*, 2004; Esteves *et al*., 2011; Thomas et al., 2011), but the link is not systematic. The NAO has not been not identified as the only responsible for the changes in storminess everywhere in Europe (Clarke and Rendell, 2009) since it could be supplanted by other modes in summer time (*e.g.* ENSO, AMO, summer NAO). In Belgium, Ullmann and Monbaliu (2010) have reported that the Atlantic Ridge weather pattern might play an important role in surge occurrence.

The results here suggest a slight increase of the frequency of the NW and W types especially in winter which are the most threatening for the occurrence of storm surges. Ullmann and Monbaliu (2010) have indeed shown that the number of extreme surges values has been increasing from 1925 to 2000 by +3mm/year. However, other studies do not conclude to a statistically increasing or decreasing storminess in Belgium (Bijl *et al.*, 1999; Van den Eynde *et al.*, 2012). The long-term sea level rise is estimated to +1.67mm/year from 1997 to 2007 (Van den Eynde *et al.*, 2012). MacDonald and O'Connor (1996) have shown by simulation that the sea level rise will impact the Belgian coast by decreasing the offshore sandbanks capacity to dissipate the wave energy and thus likely modifying the coastline.

The inter-connection between the positive winter NAO index and the CWTs to the occurrence of storm surges suggests an interesting way of forecasting the potential erosive events in the North Sea basin. Thus, if we were able to predict the value of the winter NAO index, for instance based on the sea surface temperature, and also the CWT in advance, then we would be able to know the risk of storm event occurrence and eventually degree of severity. Also, any possible changes or trend of storminess or having morphological impacts on the coast will be

relevant to better prepare coastal communities and coastal managers.

CONCLUSIONS

Large scale atmospheric circulation is an important component of wind which in turn control storm surge generation. The Lamb CWT method was used, for the first time, to examine the contribution of each type to the occurrence of observed storm surges impacting the Belgian coast. Seasonal and annual variations of the frequency of the CWTs were observed for which the A and C types clearly dominate over almost 150-years. The SW-W-NW weather types also are frequent and associated with high wind speed over the year. Also, the CWTs and the contemporaneous winter NAO index were considered for the observed storm surges impacting the Belgian coast from 1993 to 2014. This study has shown that the C, N, NW, W and SW types account for 82% of time for the occurrence of storm surges. Since these types are generally assimilated to high gale index and moderate positive winter NAO, they thus could be the most threatening types for the occurrence of a storm surge index. The results further suggest an increase of the frequence of the most threatening types up to 11.4 days from 1871-2014. Also, these types are generally correlated to positive winter NAO index. Therefore, some inter-connections exist between the CWT pattern, the winter NAO index and the occurrence of storm surge along the coast. Being able to forecast the CWT and the winter NAO index might be a way to predict the risk and severity of storm surge.

ACKNOWLEDGMENTS

The authors are grateful to the Climate Research Unit of the University of East Anglia, UK; and the National Oceanic and Atmospheric Administration for access to data.

LITERATURE CITED

Bijl, W.; Flather, R.; de Ronde, J.G., and Schmith, T., 1999. Changing storminess? An analysis of long-term sea level data sets. *Climate Research*, 11, 161-172.

Clarke, M.L. and Rendell, H.M., 2009. The impact of North Atlantic storminess on Western European coasts: a review, *Quaternary International*, 195(1-2), 34-41.

Donat, M.G.; Leckebusch, G.C.; Pinto, J.G., and Ulbrich, U., 2010. Examination of wind storms over Central Europe with respect to circulation weather types and NAO phases. *International Journal of Climatology*, 30, 1289-1300.

Esteves, L.S.; Williams, J.J., and Brown, J.M., 2011. Looking for evidence of climate change impacts in the eastern Irish Sea, *Natural Hazards and Earth System Sciences*, 11, 1641-1656.

Fernández-González, S.; del Río, S.; Castro, A.; Penas, A.; Fernández-Raga, M.; Calvo, A.I., and Fraile, R., 2012. Connection between NAO, weather types and precipitation in León, Spain (1948-2008), *International Journal of Climatology*, 32, 2181-2196.

Haerens, P.; Bolle, A.; Trouw, K., and Houthuys, R., 2012. Definition of storm thresholds for significant morphological change of the sandy beaches along the Belgian coastline. *Geomorphology*, 143, 104-117.

Hurrell, J.W., 1995. Decadal trends in the North Atlantic Oscillation: regional temperatures and precipitation. *Science*, 269, 676-679.

Jenkinson, A.F. and Collison, F.P., 1977. *An initial climatology of gales over the North Sea*. Synop. Climatology Branch Memorandum. 62, Meteorological Office, Bracknell, pp 7.3-7.5.

Jones, P.D.; Hulme, M., and Briffa, K.R., 1993. A comparison of Lamb circulation types with an objective classification scheme. *International Journal of Climatology*, 13, 655-663.

Lamb, H.H., 1972. *British Isles weather types and a register of the daily sequence of circulation patterns, 1861-1971*. Geophysical Memoirial: HM Stationery Office, 88p.

Leatherman, S.P.; Zhang, K., and Douglas, B.C., 2000. Sea level rise shown to drive coastal erosion. *Eos Transactions, American Geophysical Union*, 81, 55-57.

MacDonald, N.J. and O'Connor, B.A., 1996. Changes in wave impact on the Flemish coast due to increased mean sea level. *Journal of Marine Systems*, 7, 133-144.

Montreuil, A-L. and Bullard, J.E., 2012. A 150-year record of coastline dynamics within sediment cell: Eastern England. *Geomorphology*, 179, 168-185.

Pirazzoli, P.A.; Regnauld, H., and Lemasson, L., 2002. Changes in storminess and surges in western France during the last century. *Marine Geology*, 210, 307-323.

Thomas, T.; Phillips, M.R.; Williams, A.T., and Jenkins, R.E., 2011. Medium timescale beach rotation; gale climate and offshore island influences. *Geomorphology*, 135, 97-107.

Ullmann, A. and Monbaliu, J., 2010. Changes in atmospheric circulation over the North Atlantic and sea-surge variations along the Belgian coast during the twentieth century. *International Journal of Climatology*, 30, 558-568.

Van den Eynde, D.; De Sutter, R., and Haerens, P., 2012. Evolution of marine storminess in the Belgian part of the North Sea. *Natural Hazards Earth System Science*, 12, 305-312.

Verwaest, T.; Doorme, S.; Verelst, K., and Trouw, K., 2008. The wave climate in the Belgian coastal zone. *Proceedings 9th International Conference LITTORAL: A Changing Coast: Challenge for the Environmental Policies* (Venice, Italy), pp. 1-8.

Journal of Coastal Research	SI	75	760-764	Coconut Creek, Florida	2016

Increasing the highest storm surge in Busan harbor

Sang Myeong Oh †, Il-Ju Moon††∞, and Suk Jae Kwon§,

†Climate Research Department/APEC Climate Center, Busan, Republic of Korea

§Ocean Research Division, Korea Hydrographic and Oceanographic Administration, Busan, Republic of Korea

††Typhoon Research Center, Jeju National University, Jeju, Republic of Korea

www.cerf-jcr.org

www.JCRonline.org

ABSTRACT

Oh, S.M.; Moon, I.-J., and Kwon, S.J., 2016. Increasing the highest storm surge in Busan harbor, *In:* Vila-Concejo, A.; Bruce, E.; Kennedy, D.M., and McCarroll, R.J. (eds.), *Proceedings of the 14th International Coastal Symposium* (Sydney, Australia). *Journal of Coastal Research*, Special Issue, No. 75, pp. 760-764. Coconut Creek (Florida), ISSN 0749-0208.

One of the most pronounced effects of climate change in coastal regions is sea level rise and storm surges. Busan in particular, the fifth largest container handling port in the world, has suffered from serious storm surges and experienced a remarkable mean sea level (MSL) rise. This study investigates a long-term variation of annual maximum surge height (AMSH) using sea level data observed in Busan over 53 years (1962~2014). The decomposition of astronomical tides and surge components shows that the AMSH has increased 18 cm over 53 years (*i.e.*, 3.5 mm/year), which is much larger than the MSL trend (2.5 mm/year) in Busan. This significant increase in AMSH is mostly explained by the increased intensity of landfall typhoons over the Korean peninsula (KP), which is associated with the increase of sea surface temperature and the decrease of vertical wind shear at mid-latitudes of the western North Pacific. In a projected future warming environment, the combination of an increasing MSL and AMSH will accelerate the occurrence of record-breaking extreme sea levels, which will be a potential threat in Busan harbor.

ADDITIONAL INDEX WORDS: *Storm surge, sea level rise, Busan, typhoon, global warming*

INTRODUCTION

After the late 19th century, the rate of sea level rise associated with global warming has significantly increased. Research indicates that global sea level rose at a rate of 1.7 mm/yr. for the period between 1900–2009 based on tide gauge observations (Church and White, 2011). The Intergovernmental Panel on Climate Change's (IPCC) Fifth Assessment Report (AR5) also noticed that by the late 21st century, about 95% of the world's oceans will experience a sea level rise, with 70% of global coastlines affected. As three-quarters of all large cities are established on coastal regions and half of the world's population lives within 200 km of a coastline, future sea level rise is a potential threat for all people living in coastal regions. In particular, the coastal regions of the Korean peninsula (KP) have experienced the rapidest sea level rise, largely exceeding the global mean (Choi *et al.*, 2004; Ha *et al.*, 2006; Kang *et al.*, 1985; Kang *et al.*, 2005; Kang *et al.*, 2008). Future projections predict that the largest increase in sea level will take place over the western North Pacific, including the Kuroshio region and the KP (Choi *et al.*, 2002; Landerer *et al.*, 2007; Oh *et al.*, 2011).

Another future danger for coastal regions is the increase of storm surge height, which is mostly caused by tropical cyclones (TCs) and extratropical cyclones. Most projections based on climate modeling indicate that extreme surge events will globally increase under the warmer climate, although regional differences exist (Oh and Moon, 2013; Sterl *et al.*, 2009; Wang *et al.*, 2008; Woth *et al.*, 2006). The combined increase in storm surges and mean sea level (MSL) will aggravate coastal damages. Therefore, preparation for potential coastal hazards requires an investigation on the variability of not only MSL, but also storm surges.

Although a number of studies have attempted to examine variations in the regional MSL, long-term variations for storm surge, particularly in the KP coasts, have hardly been studied (Kwon *et al.*, 2008; Oh and Moon, 2013). This paper aims to examine long-term variability in the annual extreme storm surge heights in Busan, the largest harbor in Korea, with a special focus on investigating the cause of the variability and the importance of tidal phases in the occurrence of extreme sea levels. Finally, this study suggests the worst scenario with extreme sea levels in Busan harbor.

METHODS

To investigate a long-term trend of storm surge in Busan, we used sea level data measured in 1-hour intervals at Busan harbor from 1962 to 2014. Surge heights were calculated by subtracting the predicted tidal elevation from the observed sea level. The predicted tidal elevation was estimated using a harmonic analysis. For the analysis and verification of the estimated surge heights, we also used wind speed and sea level pressure data from the Korea Meteorological Administration (KMA). Figure 1 is an example that shows the time series of observed sea level,

DOI: 10.2112/SI75-153.1 received 15 October 2015; accepted in revision 15 January 2016.

∞Corresponding author: ijmoon@jejunu.ac.kr

©Coastal Education and Research Foundation, Inc. 2016

the predicted tide, the estimated surge height, and the observed wind speed/surface pressure in September 2003 when Typhoon Maemi occurred. From the monthly-based analysis over 53 years using this method, we calculated the annual maximum surge heights (AMSH).

Information on TCs was obtained from the Regional Specialized Meteorological Center (RSMC) in Tokyo. To investigate the environmental changes influencing TC activity in the western North Pacific, we used the atmospheric data from the National Center for Environmental Prediction-Department of Energy's (NCEP-DOE) reanalysis 2 (Kanamitsu *et al.*, 2002) and sea surface temperature (SST) from National Oceanic and Atmospheric Administration's (NOAA) Extended Reconstructed SST version 3 (ERSSTv3; Smith *et al.*, 2008) for the period of 1979–2014. Vertical wind shear (VWS) was calculated using the difference in wind vector between 200 and 850 hPa pressure levels. The linear regression analysis of SST and VWS were conducted using the averaged values over the TC peak season (June – October) using the NCEP-DOE reanalysis and ERSSTv3 data, respectively. Significance tests on linear trends were conducted using the Mann-Kendall trend test (Kendall, 1970; Mann, 1945).

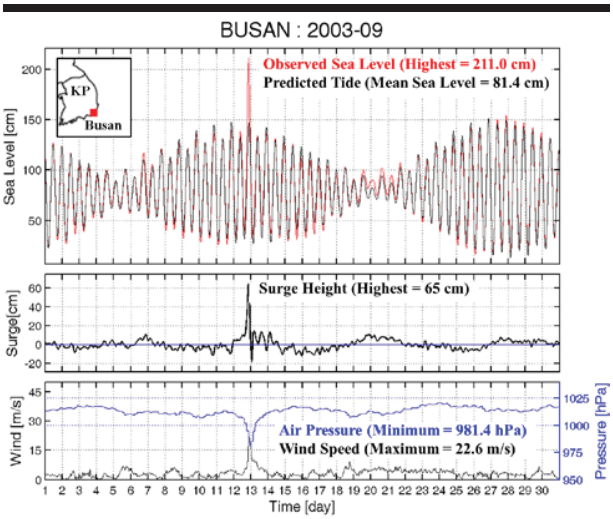

Figure 1. Time series of the observed sea level (red line in upper panel), the predicted tide (black line in upper panel), the estimated surge height (black line in middle panel), and the observed atmospheric pressure and wind speed (blue and black lines in lower panel, respectively) at the Busan tidal station in September 2013 when Typhoon Maemi occurred. The location of Busan tidal station is indicated in the upper left corner.

RESULTS

The long-term variation of AMSH in Busan over 53 years (1962-2014) exhibits a clear uptrend of 3.5 mm/year, which is statistically significant with 95% confidence (Figure 2A) and much higher than the rates previously reported at Sokcho (2.4 mm/year) and Mukho (2.6 mm/year) along the east coasts of the KP (Kwon *et al.*, 2008). The uptrend is associated with the fact that 80% of the top 20 peak surge events were recorded after 1990 (Table 1). It is also surprising that 14 among the top 20 (70%) occurred after 2000. A similar uptrend (2.5 mm/year) is found in the time series of the MSL, but the rate is smaller than that of AMSH (Figure 2B). The increase in MSL is believed to be connected with global warming and relevant local oceanic environmental changes (Kang *et al.*, 2008). Although both storm surges and MSL contribute to the occurrences of extreme sea levels, the significant uptrend in the AMSH has been mostly ignored in previous studies on coastal sea level changes. Our results indicate that the increase of the AMSH in Busan has also played a critical role in the recent increase in the occurrence of peak sea levels, in addition to MSL rise. This is well supported by Table 2 which shows that 75% and 60% of the top-twenty peak sea level events were recorded after 1990 and 2000, respectively, which is consistent with the tendency of the AMSH.

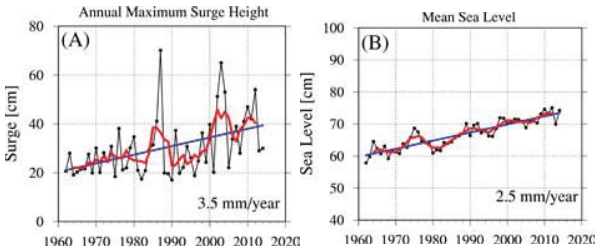

Figure 2. Variations of (A) annual maximum surge heights and (B) mean sea level in Busan during 1962-2014. The red and blue lines represent the 5-year running average and linear regression, respectively. The rates of the variation are denoted in the lower right corner.

70% of the top-twenty peak surge events were related to TC activities (see Table 1). This suggests that the rapid increase of surge heights in Busan is connected with the changes in TC activity in this region (Choi and Moon, 2008). To prove this assumption, we investigated variations in the annual records of minimum central pressure of TCs that made landfall over the KP during 1975-2012. Figure 3 reveals that the intensity of TCs increased with time, with a trend that is statistically significant with 95% confidence.

It is known that SST and vertical wind shear (VWS) are the most important environmental parameters related to the change in intensity of TCs (Wang and Wu, 2004). Warm SST and weak VWS provides a more favorable condition for the development and intensification of TCs. We analyzed the linear trend of SST and VWS over the western North Pacific from 1979 to 2014 (Figure 4). The uptrend of SST is the most dominant in the mid-latitudes (> 30ºN) including seas adjacent to the KP and Japan, as well as the eastern seas of Taiwan and the Philippines, in which the maximum trend is about 0.2 degC/decade. It is interesting that the high uptrend regions are consistent with the typical tracks of TCs heading for the KP. We also found that the VWS decreased with time in the middle latitude where TCs heading for the KP pass. These overall results suggest that atmospheric and oceanic conditions became favorable for TC development in the mid-latitudes of East Asia, contributing to the recent uptrend in the intensity of KP-landfall TCs.

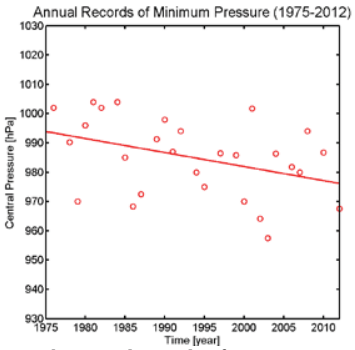

Figure 3. Variations in the annual records of minimum central pressure during typhoon events in the KP for the period 1975-2012. The red line represents the linear regression.

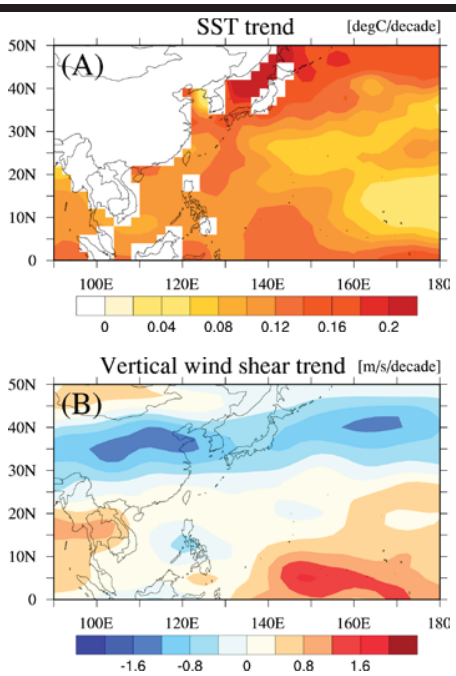

Figure 4. Linear trend of (A) sea surface temperature on 2°×2° grid and (B) vertical wind shear on 2.5°×2.5° grid during 1979-2014.

In this section, we examined the importance of tidal phases in the occurrence of extreme sea levels in Busan. For this, we compared two surge events for typhoon Dinah in 1987 and Typhoon Maemi in 2003. Typhoon Dinah recorded the highest peak surge height (70.1 cm) during 53 years in Busan. However, at the same time, the observed peak sea level (PSL) was only 128.7 cm, which is below normal (see Table 1). When the second highest surge peak (65 cm) was recorded by Typhoon Maemi in 2003, the observed PSL was 211 cm, which was the record-breaking highest value (Table 1). The large discrepancy in the observed PSLs between the two big surge events with similar heights is explained by the difference in tidal phases for the two events: ebb and near-low tide (B2) for Dinah; and spring and high tide (A1) for Maemi (see Figure 5 & Table 1). This implies that the occurrence of a record-breaking high sea level requires not only a high storm surge, but also high/spring tides. Actually, all of the top-twenty PSLs are recorded during high and spring tides (Table 2). The importance of tides in the extreme sea levels in Busan is also explained by the fact that the tidal range (~150 cm) in Busan is about twice the highest surge peak (70.1 cm).

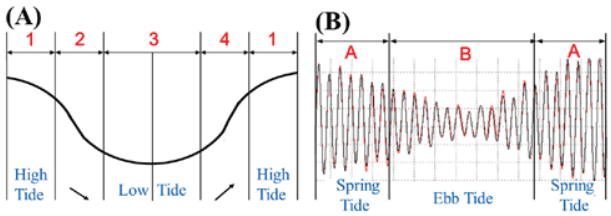

Figure 5. Definitions of four (1, 2, 3, 4) and two (A, B) phases divided for (A) high and low tides and (B) spring and ebb tides, respectively, which are used in Table 1 and 2.

If we simply assume that the peak surge events in Table 1 occurred during the nearest spring high tide (*i.e.*, A1 in Figure 5), the extreme (worst-case) PSL scenario in Busan can be estimated (see the 9th column (E) of Table 1). The results reveal that the extremes reach up to 200 cm for Typhoons Dinah, Sanba, Megi, and Rusa, which are comparable with typhoon Maemi in 2003. Proper preparedness with consideration of these worst-case scenarios as well as the increase of surge and MSL due to climate change will require Busan to reduce the potential for damages.

DISCUSSION

The characteristics of the landfall TCs over the KP may be influenced by periodic climate variability in the Pacific such as El Niño/Southern Oscillation (ENSO) and Pacific Decadal Oscillation (PDO). However, previous studies revealed that the variability of the intensity and frequency for the landfall TCs over the KP is little connected with the climate variability since the KP is located far from topical regions and the landfall TCs are mainly affected by regional steering flows and local oceanic and atmospheric conditions around the KP where TCs pass (Moon and Kwon, 2012; Oh and Moon, 2013; Choi and Moon, 2012). Therefore, this study focused on the changes in local environments related to TC development around the KP to explain the long-term variations of surge heights in Busan.

CONCLUSIONS

This paper examined the long-term variability in annual maximum surge heights (AMSH) and mean sea level (MSL) in Busan, the largest harbor in Korea, using 53-year sea level data measured from a tidal gauge. From the separate analysis of predicted tides and surge components, we found a significant long-term uptrend for the AMSH (3.5 mm/year), which is statistically significant with 95% confidence and also higher than the uptrend of the MSL (2.5 mm/year). The uptrend of the

surge heights is associated with a recent increase of extreme surge events (*i.e.*, 80% of the top-twenty peak surge events were recorded after 1990).

Since the occurrence of extreme sea levels in a specific region is caused by contributions of both storm surge and MSL, the significant uptrend in the AMSH, which has been mostly ignored in the studies on the coastal sea level rise, should be considered when calculating extreme values for the design of offshore and coastal structures.

We found that the rapid increase of the extreme surge heights in Busan is connected to the increasing intensity of TCs that made landfall over the KP. A trend analysis of sea surface temperature and vertical wind shear, the most important environmental parameters related to TC intensity change, reveals that atmospheric and oceanic conditions for TCs heading for the KP are changing to be favorable, which has led to the uptrend of TC intensity.

Finally, we emphasize the importance of tidal phases in the occurrence of the extreme sea levels at Busan from statistics on the top 20 extreme sea level events. The analysis reveals that it is impossible to break previous extreme sea level records without spring and high tides in Busan. Therefore, to prepare for potential threat of record-breaking sea level extremes in Busan, we require proper preparedness for the worst-case scenario, assuming the coincidental timing of historical big surge events and high/spring tides, as well as considering the increase of surge and MSL due to climate change.

ACKNOWLEDGMENTS

This work has been performed as a subproject of KISTI's project "*Building Response System for National-Wide Issues Based on High-performance Supercomputer*" as well as a part of the project titled "*Construction of Ocean Research Stations and their Application Studies*" funded by the Ministry of Oceans and Fisheries, Korea. Oh, S. M. would also like to acknowledge the support from the APEC Climate Center.

Table 1. *Top 20 of the peak surge heights (P) recorded at Busan during 1962–2014 and additional information on the observed sea level (O), the nearest spring high tide level (S), and the extreme sea level scenario (E, i.e., P+S), the name of influencing tropical cyclone, tidal phases, wind speed, and surface pressure at the time of the surge peak.*

Rank	Year	Month	Day	TC Name	Peak Surge Height (P), [cm]	Observed Sea Level (O), [cm]	Nearest Spring High Tide Level (S), [cm]	Extreme Sea Level Scenario (E), [cm]	Tidal Phase	Wind Speed [m/s])	Surface Pressure [hPa]
1	1987	8	31	DINAH	70.1	128.7	142.6	212.7	B2	15.7	971.0
2	2003	9	12	MAEMI	65.0	211.0	147.6	212.6	A1	22.6	981.4
3	2012	9	17	SANBA	54.0	168.0	153.0	207.0	A2	10.1	987.7
4	2004	8	19	MEGI	53.0	134.8	148.0	201	A4	8.8	981.5
5	2002	8	31	RUSA	51.2	152.7	158.1	209.3	B1	10.1	988.5
6	2010	3	1	-	47.0	113.0	127.0	174.0	A2	5.4	1010.3
7	2011	7	21	MA-ON	42.0	126.5	139.0	181.0	B1	1.9	1004.2
8	1986	8	28	VERA	41.1	147.6	144.8	185.9	B1	14.7	987.5
9	2009	2	14	-	41.0	129.0	129.0	170.0	A1	2.5	1010.0
10	2009	12	3	-	41.0	80.0	125.0	166.0	A3	2.0	1015.7
11	2000	9	16	SAOMAI	39.8	102.0	155.1	194.9	A3	18.6	979.5
12	2007	9	16	MARI	39.0	88.0	144.0	183.0	A3	6.0	1002.8
13	2009	11	15	-	39.0	82.0	125.0	164.0	A4	2.3	1025.8
14	1976	9	28	-	38.1	130.2	154.7	192.8	B4	2.3	1013.3
15	2011	9	19	TALAS	38.0	109.0	140.0	178.0	B1	5.2	1013.9
16	1991	7	29	CAITLIN	37.3	74.3	139.0	176.3	A3	15.7	979.3
17	1998	10	1	YANNI	36.3	106.4	147.8	184.1	B3	10.7	999.8
18	2010	9	8	MALOU	36.0	45.0	144.0	180.0	A3	3.4	1011.3
19	2010	1	4	-	35.0	132.7	128.0	163.0	A1	10.4	1005.1
20	1980	9	11	ORCHID	34.7	69.0	142.6	177.3	A3	6.0	987.7

LITERATURE CITED

Choi, B.H.; Kim, D.H., and Kim, J.W., 2002. Regional responses of climate in the northwestern Pacific Ocean to gradual global warming for CO2 quadrupling. *Journal of Meteorological Society*, 80, 1427–1442.

Choi, B.J.; Haidvogel, D.B., and Cho, Y.K., 2004. Nonseasonal sea level variation in the Japan/East Sea from satellite altimeter data. *Journal of Geophysical Research*, 109, C12028, doi: 10.1029/2004JC002387.

Choi, E.S. and Moon I.-J., 2008. The variation of extreme values in precipitation and wind speed during 56 years in Korea. *Korean Meteorological Society*, 18(4), 397–416.

Choi, K.S. and Moon, I.-J, 2012. Changes in tropical cyclone activity that has affected Korea since 1999, *Natural Hazards*, 62, 971–989.

Church, J.A. and White, N.J., 2011. Sea-level rise from the late 19th to the early 21st century. *Surveys in Geophysics*, 32(4-5), 585–602.

Ha, K.J.; Jeong, G.Y.; Jang, S.R., and Kim, K.Y., 2006. Variation of the Sea Surface Height around the Korean Peninsula with the Use of Multi-satellite Data (Topex/Poseidon, Jason-1, ERS, Envisat) and its Association with Sea Surface Temperature. *Korean Journal of Remote Sensing*, 22(6), 519–531.

Kang, Y.Q. and Lee, B.D., 1985. On the annual variation for mean sea level along the coast of Korea. *The Journal of the Oceanological Society of Korea*, 20, 22–30.

Kang, S.K.; Cherniawsky, J.Y.; Foreman, M.G.G.; Min, H.S.; Kim, C.H., and Kang, H.W., 2005. Patterns of recent sea level rise in the East/Japan Sea from satellite altimetry and in situ data. *Journal of Geophysical Research*, 110, doi: 10.1029/2004JC002565.

Kang, S. K.; Cherniawsky, J.Y.; Foreman, M.G.G.; So, J.K., and Lee, S.R., 2008. Spatial variability in annual sea level variations around the Korean peninsula. *Geophysical Research Letters*, 35, L03603, doi: 10.1029/2007GL032527.

Kanamitsu, M.; Ebisuzaki, W.; Woollen, J.; Yang, S.K.; Hnilo, J.J.; Fiorino, M., and Potter, G.L., 2002. NCEP-DOE AMIP-2 reanalysis(R-2). *Bulletin of the American Meteorological Society*, 83, 647–664.

Kendall, M.G., 1970. *Rank Correlation Methods*, 2nd Ed., New York: Hafner.

Kwon, S.J.; Moon, I.-J., and Lee, E.I., 2008. A Study on the Long-term Variations of Annual Maximum Surge Heights at Sokcho and Mukho Harbors. *Journal of Korean Society of Coastal and Ocean Engineers*, 20(6), 564–574.

Landerer, F. W.; Jungclaus, J.H., and Marotzke, J., 2007. Regional dynamic and steric sea level change in response to the IPCC-A1B scenario. *Journal of Physical Oceanography*, 37, 296–312.

Mann, H.B., 1945. Nonparametric tests against trend, *Econometrica*, 13, 245–259.

Moon, I.-J. and Kwon, S. J., 2012. Impact of upper-ocean thermal structure on the intensity of Korean peninsula landfall typhoons, *Progress in Oceanography*, 105, 61–66.

Oh, S.M.; Kwon, S.J.; Moon, I.-J., and Lee, E.I., 2011. Sea level rise due to global warming in the Northwestern Pacific and seas around the Korean peninsula. *Journal of Korean Society of Coastal and Ocean Engineers*, 23(3), 236–247.

Oh, S.M. and Moon, I.-J., 2013. Typhoon and storm surge intensity changes in a warming climate around the Korean Peninsula. *Natural Hazards*, 66, 1405–1429.

Smith, T.M.; Reynolds, R.W.; Peterson, T.C., and Lawrimore, J., 2008. Improvements to NOAA's historical merged land-ocean surface temperature analysis (1880-2006). *Journal of Climate*, 21, 2283–2296.

Sterl, A.; van den Brink, H.; Vries, de.; Haarsma, R., and van Meijgaard, E., 2009. An ensemble study of extreme North Sea storm surges in a changes climate. *Ocean Science*, 6, 1031–1059.

Wang, Y. and Wu, C.-C., 2004. Current understanding of tropical cyclone structure and intensity changes – a review. *Meteorology and Atmospheric Physics*, 87, 257–278.

Wang, S.; McGrath, R.; Hanafin, J.; Lynch, P.; Semmler, T., and Nolan, P., 2008. The impact of climate change on storm surge over Irish waters. *Ocean Modelling*, 25(1-2), 83–94.

Woth, K.; Weisse, R., and von Storch, H., 2006. Climate change and North Sea storm surge extremes: an ensemble study of storm surge extremes expected in a changed climate projected by four difference Regional Climate Models. *Ocean Dynamics*, 56, 3–15.

Table 2. *Top 20 of the peak sea levels recorded in Busan during 1962-2014 and additional information on the name of influencing tropical cyclone, surge height, wind speed, surface pressure, predicted tidal level, and tidal phases at the time of the sea level peak.*

Rank	Year	Month	Day	Hour	Peak Sea Level [cm]	TC Name	Surge Height [cm]	Wind Speed [m/s])	Surface Pressure [hPa]	Predicted Tidal Level [cm]	Tidal Phase
1	2003	9	12	21	211.0	MAEMI	64.7	22.6	981.4	146.3	A1
2	2012	9	17	10	184.0	SANBA	45.0	6.1	988.4	139.0	A1
3	1975	9	6	20	174.3	-	2.1	4.3	1010.4	172.2	A1
4	2010	9	7	20	171.0	MALOU	29.0	5.3	1008.5	142.0	A1
5	2014	8	11	21	170.0	HALONG	13.0	2.7	1002.9	157.0	A1
6	2001	8	21	22	169.2	PABUK	7.0	1.4	996.9	162.2	A1
7	2004	8	31	21	168.5	CHABA	9.9	2.1	1006.4	158.6	A1
8	1991	8	10	20	168.2	-	6.2	7	1003.4	162.0	A1
9	2005	8	21	22	168.1	-	12.5	3.2	1008.4	155.6	A1
10	2000	9	15	21	167.9	SAOMAI	14.2	5.2	996.8	153.7	A1
11	1964	8	23	21	167.0	KATHY	5.8	9.7	997.4	161.2	A1
12	1975	8	23	21	166.0	RITA	8.9	6.0	1011.0	157.1	A1
13	1999	9	24	7	165.1	BART	11.5	4.2	996.4	153.6	A1
14	2002	9	6	20	165.0	-	11.8	8.0	1012.3	153.2	A1
15	2010	8	11	22	164.0	DIANMU	19.0	4.9	1002.8	145.0	A1
16	1974	8	18	21	164.0	-	4.1	8.3	1007.5	159.9	A1
17	2000	7	31	20	163.1	BOLAVEN	15.0	3.8	994.4	148.1	A1
18	1974	7	6	21	163.0	GILDA	22.8	10.7	993.8	139.2	A1
19	2006	10	9	9	161.7	-	5.3	2.2	1018.0	156.4	A1
20	1999	8	12	21	161.2	-	4.2	4.2	1006.6	156.8	A1

Journal of Coastal Research	SI	75	765-769	Coconut Creek, Florida	2016

Tidal Asymmetry and Energy Variation Due to Sea-Level Rise in a Macro Tidal Bay

Seung-Won Suh[†*]

[†]Department of Ocean Science and Engineering
Kunsan National University
Kunsan, Republic of Korea

www.cerf-jcr.org

www.JCRonline.org

ABSTRACT

Suh, S.W., 2016. Tidal asymmetry and energy variations due to sea-level rise in a macro tidal bay. *In:* Vila-Concejo, A.; Bruce, E.; Kennedy, D.M., and McCarroll, R.J. (eds.), *Proceedings of the 14th International Coastal Symposium* (Sydney, Australia). *Journal of Coastal Research*, Special Issue, No. 75, pp. 765-769. Coconut Creek (Florida), ISSN 0749-0208.

Multiple coastal constructions at shallow depths in macro tidal environments, have resulted in remarkable coastal hydrodynamic alteration resulting in tidal asymmetry, energy flux, and dissipation. Consequently, the temporal aspect of sedimentation has changed abruptly and can eventually cause long-term variations. These anthropogenic alterations should be precisely investigated in relation to sea-level rise (SLR) in order to mitigate unexpected consequences. To understand alteration of tidal asymmetry due to SLR, gamma parameters that combine the traditional tidal amplitude ratio of M_4/M_2 and phase-lag difference were evaluated using the ADvanced CIRCulation (ADCIRC) model under finely resolved complex coastal geometry. Moreover, tidal energy flux and dissipation changes, in relation to tidal-flat area, were examined in Gyeonggi Bay, South Korea. As a result of SLR, spatial change in tidal asymmetry would occur; moreover, gamma parameter intensity, which shows flood dominance, would attenuate. M_2 and M_4 tidal energy flux would be lessened by SLR. For the energy dissipation, slight change appeared in M_2, while lessening tidal flat area directly affected reduction in M_4 based on SLR scenarios. Because a small change in tidal asymmetry could yield long-term morphological changes in the macro tidal environment, these alterations should be treated as important. A numerical restoration test removal of Siwha Dike, which behaved as a tipping point on tidal asymmetry, revealed that even a SLR scenario did not have significant effect if the natural shoreline persists. Thus, future studies should be focused on the importance of long-term impact on tidal alteration induced by coastal construction.

ADDITIONAL INDEX WORDS: *Tidal flat, ADCIRC, artificial coast, anthropogenic, flood dominance.*

INTRODUCTION

Multiple coastal constructions in the macro tidal environment in Gyeonggi Bay (GGB) [west coast of Korea (WCK), a part of the Yellow Sea (YS)], have resulted in remarkable coastal hydrodynamic alteration involving tidal asymmetry, energy flux, and dissipation. The mean spring tidal ranges along the WCK from the south-west of the Korea Peninsula to GGB vary from 3.8 to 8.0 m, and the GGB is well known as one of the most remarkable macro tidal basins in the world. The tidal form factor, $F = (K_1+O_1) / (M_2+S_2)$ is less than 0.20 thus, the WCK belongs to a semi-diurnal dominant region.

The GGB has been influenced by the coastal anthropogenic activities of Korean and China (Song *et al*. 2013; Suh *et al*. 2014) in terms of the near- and far-field effects during the last several decades. Suh *et al*. (2014) revealed that completion of the Siwha Dike, among a series of coastal developments, has behaved as a tipping point in tidal hydrodynamic changes from ebb to flood dominance. Pelling *et al*. (2013) showed that land-reclamation construction caused significant changes in tidal amplitude throughout the Bohai Sea because of extensive natural and anthropogenic activities. Moreover, this tidal basin will be influenced by global environmental changes and human interference within and adjacent to it (Wang *et al*., 2015). Thus, the necessity of understanding tidal hydrodynamics is greatly increasing, if we are to figure out how tidal hydrodynamic change will continue or be altered by sea-level rise (SLR). SLR would alter tidal dynamics, morphological change, and possibly the associated ecosystem of the tidal basin over the long-term.

Lopes and Dias (2014) attempted to quantify changes in tidal patterns for a coastal lagoon, in response to the local mean sea level rise. They found tidal alteration due to variation of depth toward shallowness in the lagoon under mean SLR conditions. SLR alters tidal asymmetry and hence affects coastal or estuarine morphological environments. Chernetscky *et al*. (2010) revealed how tidal asymmetry due to the intensifying nonlinear effect could alter sediment equilibrium dynamics. Van Maanen *et al*. (2013) simulated the morphological evolution of a tidal embayment to explore its response to rising sea level for semi-circular idealized basin with a barrier, and found SLR affected the exchange of sediment between the different morphological elements. Besides the impacts on sedimentation, the tidal energy variations associated with SLR were deeply investigated (Clara *et al*., 2015) in a series of scenarios that

DOI: 10.2112/SI75-154.1 received 15 October 2015; accepted in revision 15 January 2016.
*Corresponding author: suh@kunsan.ac.kr
©Coastal Education and Research Foundation, Inc. 2016

represented the present and future conditions due to SLR.

It is difficult to distinguish natural and artificial changes in tidal hydrodynamics of GGB because there is insufficient historical data recorded from 1959 to now (2015). Moreover, long-period tidal fluctuation, such as the nodal factor arising every 18.6 years, was not clearly discerned earlier. Thus, in analysis of future tidal alteration, by perhaps 2100, special causative factors should be included. This is because a modulation factor for M_2 of 3.7% for a corresponding amplitude of 3 m could be a variation of at least 11 cm of water surface elevation (WSE). Haigh *et al.* (2011) depicted variations in high tides that arise because of the 18.61-yr lunar nodal cycle and the 8.85-yr cycle of lunar perigee. Hence, not only for assessment of tidal asymmetry but also for the purpose of preventing coastal disaster, the long-term decadal modulation should be considered in tidal hydrodynamic analysis, especially in a macro tidal bay like GGB.

In this paper, the trend of tidal asymmetry, energy flux, and dissipation in the GGB will be touched upon, as well as how those would respond with respect to SLR. In the analysis, ADCIRC (Luettich *et al.*, 1992) was applied to provide several simulated scenarios corresponding to increments of SLR on finely resolved meshes considering inter-tidal flat variations and the impacts of artificial coastal structures that prevent overland flooding.

METHODS

According to the tidal asymmetry study along the WCK (Suh *et al.*, 2014), GGB in particular, showed abrupt change of tidal hydrodynamics from ebb to flood dominance. In this paper, the region of interest (ROI) is confined to the GGB to examine the tidal hydrodynamic alteration there. To analyze past changes in the tides, harmonic analysis and fast Fourier transformation have been applied to data from the recording period 1959–2015 at the Incheon tidal recording station shown in Figure 1.

SLR Scenarios and numerical parameters

For the future SLR, we followed IPCC RCP (IPCC, 2014) scenarios 4.5 and 8.5; thus, 0.64 and 0.82 m of mean SLR would be expected by 2100 in GGB (KMA, 2012). In addition, hypothetical SLR scenarios were incorporated to assess further possible rise, (*i.e.*, 1.0 and 2.0 m after Pelling *et al.* (2013), who added SLR of 1, 2, or 3 m in scenarios). Clara *et al.* (2015) considered even 10 m of SLR to get insight into potential future SLR. In addition, a nodal factor of 18.6 years was included in the analyses, and hypothetical cases involving removal of the Siwha Dike were tested to assess the potential for restoration, with or without consideration of potential SLR.

After setting up the grid, an unstructured circulation model, ADCIRC was applied with harmonic constants of eight major tidal constituents on open boundaries extracted from FES2004. The ADCIRC is a continuous-Galerkin finite element model that solves the generalized wave continuity equation, which is a modified form of the shallow water equations, and momentum equations on unstructured meshes in a Cartesian or spherical coordinate system. Solution in time can be performed using a semi-implicit or explicit time stepping algorithm. Subsequent improvements, details of code, manuals, and related utilites can be found at http://adcirc.org. Details of nodal intensity and other numerical parameters in modeling of ADCIRC can be found in a related article (Suh *et al.*, 2014).

Because tidal modeling in shallow regions with inter-tidal flats is greatly dependent on bottom friction, precise resolving of coastal lines and bathymetry is necessary. To meet this requirement, the study domain was discretized with great care on this point. For the bottom friction, a quadratic formula was adopted and spatially varying coefficients of 0.02 to 0.03 were assigned to account for the frictional losses in a shallow coastal region. Moreover, a coefficient higher than 0.2 was assigned to represent a land canopy for area flooding due to sea-level rise, because energy dissipation in this area is directly affected by surface roughness coefficients (Pelling and Green, 2013).

Tidal asymmetry and energy flux

Tidal distortion can be determined by the relationship with the major lunar semidiurnal constituent and its overtide (*i.e.*, the asymmetry intensity) by taking the amplitude ratio of M_4/M_2 and phase difference of $2\varphi M_2 - \varphi M_4$. In addition, the gamma parameter expressed in Equation (1) was applied for the purpose of simplification (Song *et al.*, 2013). In this paper, the strength of asymmetry was determined using the gamma parameter.

$$\gamma_{M_2/M_4} = \frac{\frac{3}{2}a_{M_2}^2 a_{M_4}\sin(2\varphi_{M_2}-\varphi_{M_4})}{\left[\frac{1}{2}\left(a_{M_2}^2+4a_{M_4}^2\right)\right]^{\frac{3}{2}}} \quad (1)$$

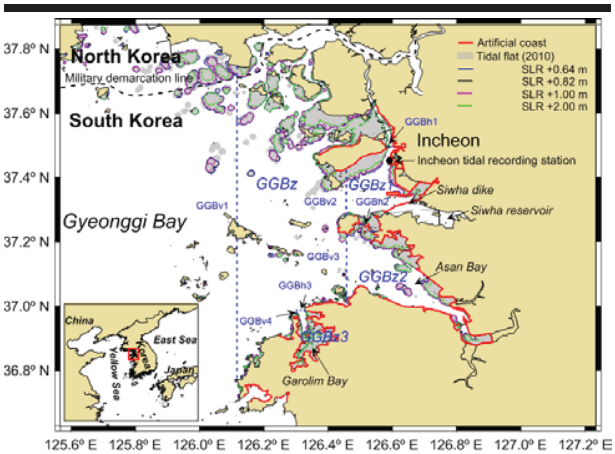

Figure 1. Map showing the study area, Gyeonggi Bay in Korea. Artificial coast (in red line) and tidal flat (in grey) retreats are depicted by color lines corresponding sea-level rise scenarios. Spatially divided zones with vertical and horizontal cross-sections are represented for the tidal energy flux comparison.

To understand precisely spatial tidal distortion, tidal energy flux, and dissipation, GGB was divided into sub zones as in Figure 1: main GGB zone, Incheon Harbor zone, Asan Bay zone, Garolim Bay zone. These were denoted GGBz, GGBz1, GGBz2, and GGBz3, respectively. The tidal-energy flux crossing sections for the sub zones were also shown as vertical and horizontal sections. Energy flux and dissipation averaged over a tidal cycle were computed using Equation (2) and Equation (3) (Pugh, 1987).

$$\text{Average energy flux} = \frac{1}{2}\rho g D H_0 U_0 \cos\left(g_{\zeta_0} + g_{U_0}\right) \quad (2)$$

$$\text{Average energy dissipation} = \frac{4}{3\pi} C_D \rho U_0^3 \text{ per unit area} \quad (3)$$

in which, ρ , g, and D are water density, gravitational acceleration, and water depth, respectively. H_0 and g_{ζ_0}(U_0 and g_{U_0}) represent the amplitude and phase of the surface elevation (current components), respectively. C_D is bottom friction.

Tidal asymmetry can be analyzed using tidal record data or by numerical modeling. The future SLR was predicted using the ADCIRC. Tidal amplitudes and phases of M_2 and its overtides M_4 and M_6, were extracted from simulated results for one year with SLR scenarios in year 2090 or 2100.

RESULTS

It would be meaningful to assess how alterations persist and how tidal asymmetry continues where anthropogenic impacts cause crossing of a tipping point. Among many construction projects over the last four decades in the GGB, clearly the most influential alteration would be the Siwha Dike and its tidal power plant. Among several future physical changes due to SLR, the foremost variation could be lessening of inter-tidal flat areas. Hence, we calculated the variations and found that sea level rise of 0.64, 0.82, 1.0, and 2.0 m would cause reductions of 19.2, 23.6, 28.0, and 47.1% of total inter-tidal area, respectively, in the GGB. This major reduction of shallow intertidal area (shown in Figure 1) acts as the primaryfactor slowing or intensifying of tidal distortion.

Simulation showed that the gamma parameters lessened gradually from 0.148 in 2010, to 0.122, 0.114, 0.108, and 0.084 for the corresponding SLR of 0.64, 0.82, 1.0, and 2.0 m, respectively, in 2100. Hence, the tidal asymmetry amplitude ratio M_4/M_2 would shrink from 0.045 to 0.038, 0.035, 0.033, and 0.021 (in the same order), though computed asymmetry showed somewhat higher value compared to the one observed in the present condition. However, phase differences $2\varphi M_2 - \varphi M_4$, show almost the same result, 129.0–130.2°, except for 112.7° for the 2.0 m SLR scenario.

To understand spatial tidal distortion distribution, gamma parameter tests were done and typically represented in the case of SLR +1.0 m (assigned as additional forthcoming anthropogenic rise effect based on SLR of 0.82 m in accordance with the IPCC RCP 8.5 scenario). Comparison of simulated results to present sea level condition is depicted in Figure 2. Most regions along coasts are flood dominant; however, the intensity gradually decreases with SLR. It is noted that sub-zone GGBz3 (Garolim Bay), will be slightly changed from flood to ebb dominance.

Tidal distortion might alter the tidal energy flux and/or dissipation variations. Under the present condition, strong flux of M_2 tidal energy occurs (on the order of 10^5–10^6 W/m) along channels surrounded by islands (Figure 3a). However, when sea level becomes 0.82 m higher, the tidal flux will be lessened by about 10^3–10^4 W/m in main channels, as seen in Figure 3b. The shrinking of tidal energy flux is due to de-amplification of M_2 caused by increasing mean depth, and to lessening of tidal flat area owing to SLR. On the other hand, M_2 energy did not dissipate regardless of changes in the area of tidal flats. Especially in GGBz3, tidal energy will be more dissipated than at present. This might be the result of ebb dominant change in the tidal characteristics. Besides tidal energy flux variations, SLR would cause reduction of the tidal power-generating capability at Siwha by 1.56, 1.92, 2.57, and 5.76%, corresponding with SLR of 0.64, 0.82, 1, and 2 m, respectively.

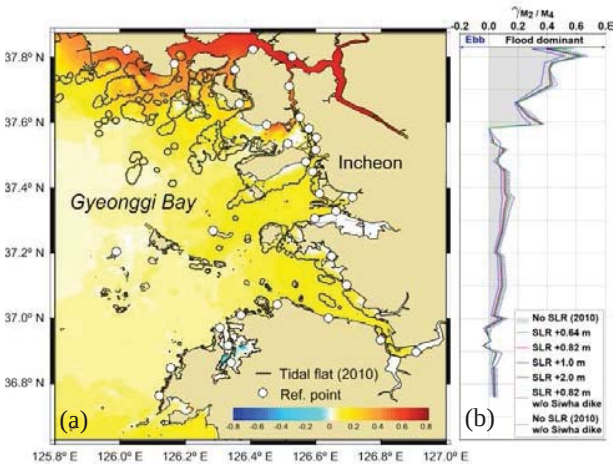

Figure 2. Tidal asymmetry: (a) Spatial distribution owing to a 1.0 m SLR scenario, (b) Temporal variations at coastal reference points for all scenarios in terms of γ_{M_2/M_4}.

However, results on shallow overtides showed lessening of M_4 energy influx through the main cross section of GGBv1. Even so, the magnitude of efflux dominant M_6 energy would be less due to SLR. M_4 energy would be dissipated mainly in GGBz and GGBz3 due to nonlinear energy dissipated by M_2 interaction and geometry. However, the M_6 component, which is more influenced by bottom friction, will lose energy only inGGBz. It is noted that there is strong correlation of M_4 energy flux and dissipation with tidal flat area variation as seen in Figure 4. This means that the non-linear shallow tidal energy and dissipation of M_4 in GGB, are directly affected by topology and hence would show a gradual decrease with SLR, owing to lessening of tidal flat area.

DISCUSSION

The morphological developments in estuaries and tidal basins are influenced by global environmental changes and human interference within and adjacent to them (Wang *et al.*, 2015). Owing to SLR, strengthening of tidal asymmetry might be attenuated in GGB, where critical change from ebb to flood dominance was recorded due to anthropogenic coastal construction (particularly the Siwha Dike, see Suh *et al.*, 2014). Van Maanen *et al*. (2013) have shown that tidal asymmetry related to morphological change during SLR cannot be neglected. This aspect, as found in this paper, is important because small changes in tidal asymmetry can yield long-term morphological changes in strong tidal currents in macro tidal environments such as GGB (Choi and Jo, 2015).

In this paper, the impacts of artificial coast on future tidal hydrodynamic changes were evaluated, because it is getting familiar as a hard-treating methods for coastal hazards protection. Pelling and Green (2013) pointed out that if permanent flooding of land were allowed, the response of the tides to SLR is dramatically different because permanent flooding of new land significantly alters the tidal response.

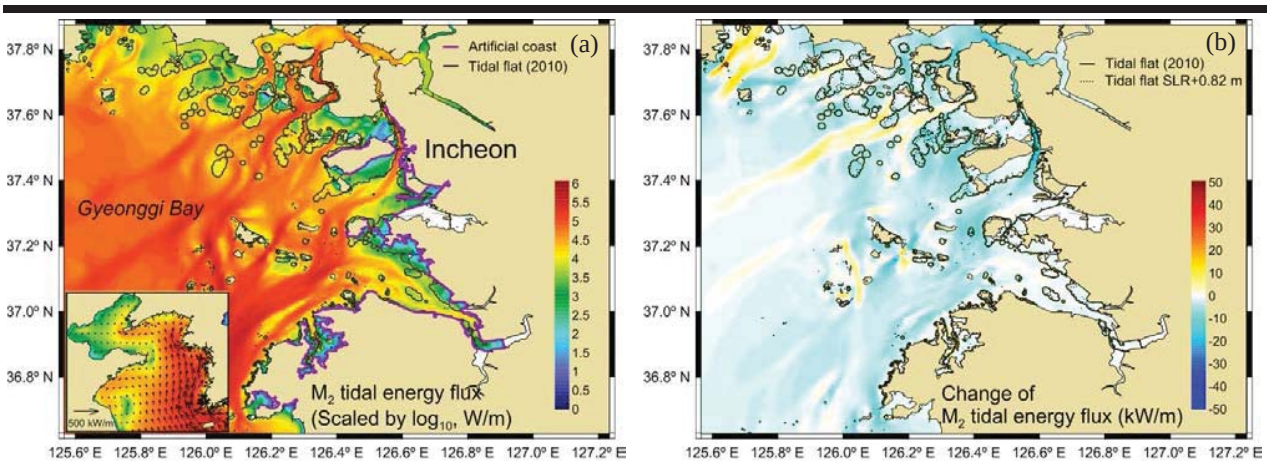

Figure 3. Tidal energy flux: (a) Distribution at present condition, (b) Differences due to SLR of 0.82 m by 2100.

However, 54% of the total coast in the GGB has already been made into artificial coast, so permanent flooding due to SLR is only valid for a restricted natural region. Thus, analysis should be done with intense care with much finer grid resolution and selection of proper roughness coefficients corresponding to surface canopy conditions.

Through recorded tidal data analyses, the 18.6-yr nodal factor variation was not clearly distinguishable because of the mixed effects of nearby large reclamation and dike construction. Although the length of the tidal record is about 65 yr long, inconsistency caused by re-installation or malfunctions reduced the record of reliable data by about 40 yr. Thus, careful attention is necessary in this analysis of tidal data as pointed by Houston and Dean (2011). It is manifest that the long-term period of constituents should be incorporated into the analysis of SLR (Haigh *et al.*, 2011; Pelling *et al.*, 2013). However, it is still not accounted properly in extrapolation due to limitations or lack of records from past years. Thus, further study is clearly required.

The study area is a very shallow, macro tidal environment thus, the intertidal flat area behaves as the main source of tidal distortion. Simulated results for SLR very clearly indicate decreasing M_4 tidal energy and dissipation, with lessening of tidal flat area. Because tidal distortion is mainly produced within a tidal basin by a combination of frictional effects and the interaction of the tide with the bathymetry, this can describe how the M_4 tidal energy has strong correlation with the decreasing tidal flat area due to SLR. Furthermore, tidal distortion with respect to SLR could alter not only the existing tidal power generating capability at the Siwha plant, but also a considerable amount at Asan and Garolim Bay (Figure 1: GGBz2 and GGBz3, respectively).

To investigate the impact of an anthropogenic tidal barrier, removing the Siwha Dike was tested and assessed by means of hypothetical simulations. The hypothetical modeling might give some insight into indiscriminate dike construction in other coastal bays. Through the recorded tidal data analysis, we now better understand how completion of the dike acted as a flood-dominating tipping point in the GGB. Through this hypothetical analysis, we found there might not be big impacts on coastal tidal hydrodynamics even with SLR of 0.82 m, if the natural condition (*i.e.*, without Siwha Dike), persists or is restored by 2100. Thus, any anthropogenic activity should be investigated profoundly, because unwanted impacts could arise in the near-field as short-term effects but also basin-wide over the long term. In addition, ongoing and future coastal projects in China and Korea could continuously distort the YS tidal hydrodynamics. Such artificial effects will complicate predictions related to natural sea-level change on both sides of the YS. It is essential to discern the anthropogenic impacts by precise analyses.

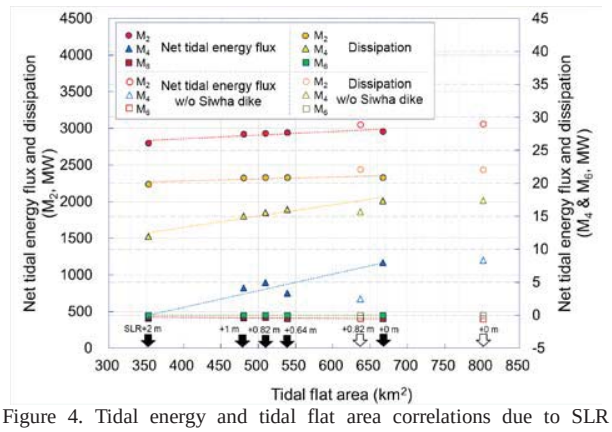

Figure 4. Tidal energy and tidal flat area correlations due to SLR scenarios for the GGB.

CONCLUSIONS

To understand the intensification of tidal asymmetry due to SLR, a gamma parameter that combines the traditional tidal amplitude ratio of M_2/M_4 and phase lag difference was evaluated using the ADCIRC model under finely resolved complex coastal geometry. Through this study, the author determined the trend in tidal asymmetry in the GGB, which has crossed a tipping point from ebb- to flood-dominance due to multiple coastal developments, which continue regardless of SLR and lessening of tidal flat area. Although the importance of the 18.6-yr periodic nodal factor under the condition of M_2 tidal amplitude of 3 m, could not be explicitly distinguished due to the mixture of anthropogenic coastal construction and relatively short period of observation (55 yr). Thus, inclusion of pure impact by the nodal factor should be accounted correctly in future research intended to account for sea-level variation. Model simulation results showed SLR, based on IPCC RCP scenarios with hypothetical cases, could lessen tidal asymmetry, and reduce tidal energy influx of M_4 by 50%, as a result of reduction of tidal flat area.

Through a numerical restoration test involving removal of the Siwha Dike, it is expected that even SLR of 0.82 m would not alter the tidal system of the bay greatly, if natural shoreline persists. Tidal hydrodynamic alterations could influence morphological change in estuaries and tidal basins as a result of global sea-level change and human interference. Thus, future studies should be focused on addressing the importance of any impact of tidal hydrodynamic alteration induced by coastal construction, using a well-designed numerical model. This is because anthropogenic land reclamation and/or tidal barriers have led to significant changes in semi-closed basins.

ACKNOWLEDGMENTS

This research is a part of the projects entitled “Countermeasure system against hazards of typhoons and tsunamis in harbor zones—Stage 2” and “Development of coastal erosion control technology” funded by the Ministry of Oceans and Fisheries, Korea.

LITERATURE CITED

Chernetscky, A.S.; Schuttelaars, H.M., and Talke, S.A., 2010. The effect of tidal asymmetry and temporal settling lag on sediment trapping in tidal estuaries. *Ocean Dynamics*, 60, 1219-1241.

Choi, K. and Jo, J., 2015. Morphodynamics and stratigraphic architecture of compound dunes on the open-coast macrotidal flat in the northern Gyeonggi Bay, west coast of Korea. *Marine Geology*, 366, 34-48.

Clara, L.M.; Simionato, C.G.; D’Onofrio, E., and Moreira, D., 2015. Future sea level rise and changes on tides in the Patagonian Continental Shelf. Florida Coconut Creek (U.S.A.). *Journal of Coastal Research*, 31(3), 519–535.

Haigh, I. D.; Eliot, M., and Pattiaratchi, C., 2011. Global influences of the 18.61 year nodal cycle and 8.85 year cycle of lunar perigee on high tidal levels. *Journal of Geophysical Research*, 116, C06025.

Houston, J.R. and Dean, R.G., 2011. Accounting for the nodal tide to improve estimates of sea level acceleration. *Journal of Coastal Research*, 27(5), 801-807.

IPCC, 2014. *Climate Change 2014: Synthesis Report. Contribution of Working Groups I, II and III to the Fifth Assessment Report of the Intergovernmental Panel on Climate Change.* IPCC, Geneva, Switzerland, 151p.

KMA, 2012. *Climate Change Forecast Report for Korean Peninsula*. Korea Meteorological Administration, 151p (in Korean).

Lopes, C.L. and Dias, J.M., 2014. Influence of mean sea level rise on tidal dynamics of the Ria de Aveiro lagoon, Portugal. *In:* Green, A.N. and Cooper, J.A.G. (eds.), *Proceedings 13th International Coastal Symposium (Durban, South Africa), Journal of Coastal Research*, SI 70, 574-579.

Luettich, R.A.; Westerink, J.J., and Scheffner, N.W., 1992. *ADCIRC: An Advanced Three-Dimensional Circulation Model for Shelves Coasts and Estuaries Report 1: Theory and Methodology of ADCIRC-2DDI and ADCIRC-3DL*. Vicksburg, MS: US Army Corps of Engineers Waterways Experiment Station, *Dredging Research Program Technical Report DRP-92-6*, 141p.

Pelling, H.E. and Green, J.A.M., 2013. Sea level rise and tidal power plants in the Gulf of Maine. *Journal of Geophysical Research: Oceans*, 118, 2863-2873.

Pelling, H.E.; Uehara, K., and Green, J.A.M., 2013. The impact of rapid coastline changes and sea level rise on the tides in the Bohai Sea, China. *Journal of Geophysical Research: Oceans*, 118, 3462-3472.

Pugh, D.T., 1987. *Tides, Surges and Mean Sea-Level*. New York: John Wiley & Sons, 472p.

Song, D.; Wang, X.H.; Zhu, X., and Bao, X., 2013. Modeling studies of the far-field effects of tidal flat reclamation on tidal dynamics in the East China Seas. *Estuarine, Coastal and Shelf Science*, 133, 147-160.

Suh, S.W.; Lee, H.Y., and Kim, H.J., 2014. Spatio-temporal variability of tidal asymmetry due to multiple coastal constructions along the west coast of Korea. *Estuarine, Coastal and Shelf Science*, 151, 336-346.

Van Maanen, B.; Coco, G.; Bryan, K.R., and Friedrichs, C.T., 2013. Modeling the morphodynamic response of tidal embayments to sea-level rise. *Ocean Dynamics*. 63(11), 1249-1262.

Wang, Z.B.; Van Maren, D.S.; Ding, P.X.; Yang, S.L.; Van Prooijen, B.C.; De Vet, P.L.M.; Winterwerp, J.C.; De Vriend, H.J.; Stive, M.J.F., and He, Q., 2015. Human impacts on morphodynamic thresholds in estuarine systems. *Continental Shelf Research*, CSR3681.

Journal of Coastal Research	SI	75	770-774	Coconut Creek, Florida	2016

Estimating the Accelerated Sea Level Rise along the Korean Peninsula Using Multiscale Analysis

Sumiya Uranchimeg[†], Hye-Rin Cho[‡], Yong-Tak Kim[†], Kyu Nam Hwang[†], and Hyun-Han Kwon[†*]

[†] Department of Civil Engineering, Chonbuk National University, 567 Baekje-daero, Deokjin-gu Jeonju-si, Jeollabuk-do 54896, Korea

[‡]Korea Institute of Civil Engineering and Building Technology, 283 Goyangdae-ro, Ilsanseo-gu, Gyeonggi-Do 10223, South Korea

www.cerf-jcr.org

www.JCRonline.org

ABSTRACT

Uranchimeg, S.; Cho, H.-R., Kim, Y.-T., Hwang, K.N., and Kwon, H.-H., 2016. Estimating the accelerated sea level rise along the Korean Peninsula using multiscale analysis. In: Vila-Concejo, A.; Bruce, E.; Kennedy, D.M., and McCarroll, R.J. (eds.), Proceedings of the 14th International Coastal Symposium (Sydney, Australia). Journal of Coastal Research, Special Issue, No. 75, pp. 770-774. Coconut Creek (Florida), ISSN 0749-0208.

An accelerated sea level rise has recently been detected in many parts of the world. It has been acknowledged that isolation of the acceleration in the long-term is difficult due to the fact that there is an embedded low frequency associated with the climate variability. In light of this, this paper aims to provide a new multiscale assessment tool for the estimation of sea-level acceleration for tide gauge data along the Korean peninsula. This study employed the wavelet transform (WT) and the Ensemble Empirical Mode Decomposition (EEMD) methods to better isolate time varying oscillation and estimate reliable sea-level acceleration of the trend. This paper first examined the WT and the EEMD methods to fully understand their capability using synthetic data, and then further investigated the acceleration rates of the historical tide gauge records. It was found that the EEMD showed more reliable estimates than the WT in terms of the trend error. The smooth increase in the trend at all stations, except Wido, and acceleration in southern coastlines of South Korea was identified through the EEMD. Future work must be focused on developing a Bayesian-based nonstationary frequency analysis model in which the estimated acceleration rates are used to evaluate the risk associated with sea-level rise.

ADDITIONAL INDEX WORDS: *Wavelet transform, ensemble empirical mode decomposition, sea level rise*

INTRODUCTION

The 3rd Assessment Report (AR3) of the Intergovernmental Panel on Climate Change (IPCC) found that global warming has accelerated during the 21st century due to human activities, thereby increasing steric sea-level rise and producing significantly adverse effects on the natural and human systems in coastal zones (IPCC, Climate Change, 2001). In the AR4 it was projected that global sea level would rise by up to -60 cm by 2100 in response to ocean warming and glaciers' melting (IPCC, Climate Change, 2007). Adding to this, recently the identified accelerated decline of polar ice sheet mass has raised the possibility of future sea level rise (SLR) of 1 m or more by 2100 (Lowe *et al*., 2009). A rise in sea level affects the inundation and displacement of lowlands and wetlands, intensifies coastal erosion and storm flooding, and increases the salinity of estuaries and salt water intrusion into freshwater aquifers (Nicholls *et al*., 1999), leading to a wide range of socioeconomic consequences, including crop production loss, decline in land value, changes in human health, deterioration of water and habitat quality, etc. According to McGranahan *et al*. (2007) 10% of the world's population lived in low elevation coastal zones, below 10 m elevation. Regional variations of sea level changes will be significant compared to the global mean value (Gregory et *al*., 2001). Therefore the assessment of regional long-term sea level changes in relation to global warming is important to understand the impact of sea level change in the future that is expected to accelerate in the 21st century.

The long-term sea level increase was investigated at all stations around the Korean Peninsula (Seo *et al*., 1999). A vertical land movement was not considered in earlier studies of sea level change. However, tide gauges were installed on the land and measured the relative seal level to land; thus, tide gauge data contained both oceanic and vertical land movements, which needed to be separated. According to this study, a vertical land movement component could be removed from tide gauge records by correcting tide gauge data with Glacial Isostatic Adjustment (GIA) model information, which is a solid Earth deformation associated with changes in ice mass distribution.

In recent decades, the trend in sea level data has been estimated using its oscillatory behavior, which extracts all periodic components from original data until there is no periodic component left, and then the trend is estimated from the residual. The Wavelet Transform (WT) is one of the multiscale analysis methods. The WT has been widely used for nonstationary processes such as hydro-meteorological time series (Pisoft *et al*., 2004). In meteorology and climatology particularly, such analysis seems to be advantageous and successfully applied to climate characteristics analysis (Smith *et al*., 1998), relationship between the North Atlantic oscillation and sea level changes (Yan *et al*., 2004), interannual temperature events, and shifts in the global temperature (Park and Mann, 2000). Recently, sea

DOI: 10.2112/SI75-155.1 received 15 October 2015; accepted in revision 15 January 2016.
*Corresponding author: hkwon@jbnu.ac.kr
©Coastal Education and Research Foundation, Inc. 2016

level change studies (Breaker and Ruzmaikin, 2011, 2013; Ezer, and Corlett, 2012) have adopted an approach of the Empirical Mode Decomposition (EMD) (Huang *et al*., 1998; Wu and Huang., 2009) which considers oscillatory contributions in a data-adaptive manner. Using EMD, Breaker and Ruzmaikin (2011) decomposed the sea level record from San Francisco (California, USA) to examine the temporal behavior of different modes, such as the interdecadal variability related to the Pacific Decadal Oscillation and Ezer, whereas Corlett (2012) found a statistically significant accelerating sea level trend in a sea level record from the Chesapeake Bay in Virginia, USA.

This paper aims to investigate sea level variations, both trend and acceleration, around the Korean Peninsula using tide gauge data. To improve understanding about estimated trend, we evaluated the performance of the WT and the EEMD on synthetic data and tide gauge records.

METHODS

The tide gauge records were obtained from the Korean Hydrographic and Oceanographic Administration (KHOA) (Figure 1). However, there were many studies suggesting a minimum record length in excess of 50-60 years (Douglas, 1992) to estimate sea level rise, while some other studies showed that trend could be found from relatively short length of record (Trupin and Wahr, 1990). In this paper, due to lack of long enough tide gauge records, 20 station data that had longer than 30 years record and less than 5% missing value were used for the analysis (Table 1).

Table 1. *The tide gauge records.*

Station		Data	
#	Name	Length (year)	Missing value (%)
1	Anheung	30	0.327
2	Boryeoung	31	2.479
3	Busan	60	1.391
4	Chujado	33	2.765
5	Daeheuksando	51	3.950
6	Gadukdo	39	1.430
7	Geomundo	34	0.016
8	Gunsan	36	0.942
9	Jeju	52	0
10	Mokpo	60	4.011
11	Mukho	51	1.942
12	Pohang	45	1.755
13	Seogwipo	31	0.009
14	Sokcho	43	2.173
15	Tongyoung	40	0.645
16	Ulleungdo	38	2.126
17	Ulsan	54	2.084
18	Wando	33	0.017
19	Wido	31	4.322
20	Yeosu	51	1.389

In this study, the continuous WT (CWT) method and the Ensemble Empirical Mode Decomposition (EEMD) method (Wu and Huang, 2005) were used to identify and estimate sea level trend and acceleration. The EMD method posed a major problem with mode mixing processes. In this regard, Wu and Huang introduced the EEMD method which used white noise to overcome this problem. Those approaches were widely used for decomposing nonstationary and oscillatory time series into periodic components and the residual. In this paper, we will investigate the residuals which are used to identify the trend of the time series being analyzed. Wu and Huang (2009) suggested adding noise with an amplitude that is approximately 0.2 times the standard deviation of the data, although the exact value of R_std is not a critical choice. They also noted that an ensemble number of a few hundred would lead to very good results and that the remaining noise would cause less than a fraction of 1% of error obtained using the reasonable amplitude of the added noise. In this study, added noise amplitude was R_std=0.2 and the estimated ensemble number was N_ens=300. For the CWT the Morlet mother wavelet transform was chosen with wave number ω_0=6 (Farge, 1992). We have monthly data, thus dt=1/12 years, and the smallest resolvable scale is s_0=2 dt. The largest scale chosen should be less than half of the length of the entire time series. The detailed descriptions of the WT and EEMD can be found in Daubachies (1990) and Wu *et al*. (2005). After decomposition, the most important task is to judge whether each of these periodic components (including trend) is useful information or just noise (Huang *et al*., 2003). Torrence and Compo (1998) developed a statistical significance test for WT spectrums, based on the Fourier power spectrum and global wavelet spectrum conducted with Monte-Carlo Simulation. Wu and Huang (2004) estimated the statistical significance test for EMD by conducting Monte-Carlo experiment on white noise.

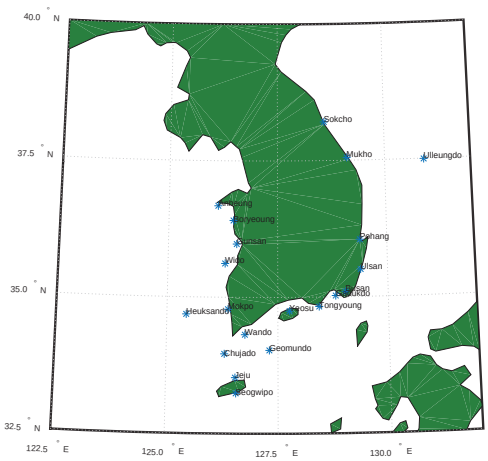

Figure 1. KHOA tide gauges along South Korea coastlines.

Based on the residual of the CWT and EEMD method, trend and acceleration were derived by fitting the second order equation. In general, the residuals of the methods are sigmoid-shaped. Visser *et al* (2015) mentioned that second-order polynomial fitting on sigmoid shaped curve would be outperformed by many other trend methods. The estimated trend was corrected with GIA model information (ICE-5G, VM2).

The performance of the two methods was evaluated using two types of synthetic data (Figure 2): Type-I synthetic data have the

same length and different magnitudes of trends, SD11 has no trend, SD12 has linear trend, and SD13 has accelerated trend; Type-II data have different lengths of data and different magnitudes of trends. SD21 has only a linear trend and its length is 100, SD22 has a linear trend and its length is 250, and SD23 has an accelerated trend and its length is 500. The trend and acceleration were added to the signals based on existing studies on sea level trend and acceleration around Korea (Kim and Cho, 2014). Since true trends in the synthetic data are clearly known, they can be compared with the identified trends for verification.

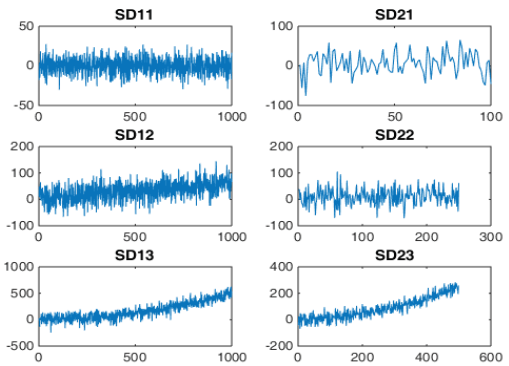

Figure 2. Two types of synthetic data used in this study, Type-I (left panels) and Type-II (right panels).

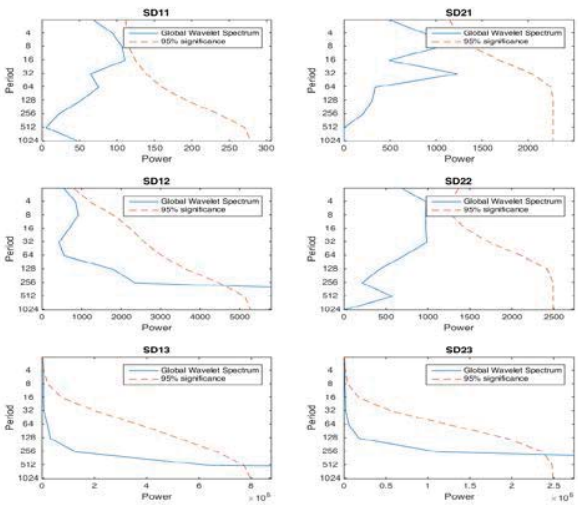

Figure 3. Significance test results of CWT spectrums by considering 95% confidence level, Type-I (left panels) and Type-II (right panels).

RESULTS

The performances of the two methods were evaluated using a significance test of the synthetic data. If any components had power above 95% confidence level, it was regarded as statistically significant in CWT method. The trends of the Type-I synthetic data were identified correctly by CWT method (Figure 3). However, trends of Type-II synthetic data were not correctly identified while the significant trend was found in only SD23. From the result of the CWT method, one can say that the CWT method's performance depended on the length of data. It meant that the CWT method could not correctly identify a trend of data for a short length of data. In the EEMD method, if any components had energy above 95% confidence level, it was regarded as statistically significant. The results of EEMD method (Figure 4) showed more reliable results than the CWT method. All the trends were identified correctly in the result of the EEMD method. Comparing the significance test results, the EEMD method performed better than the CWT for trend identification, and the EEMD was not affected by the length of the data.

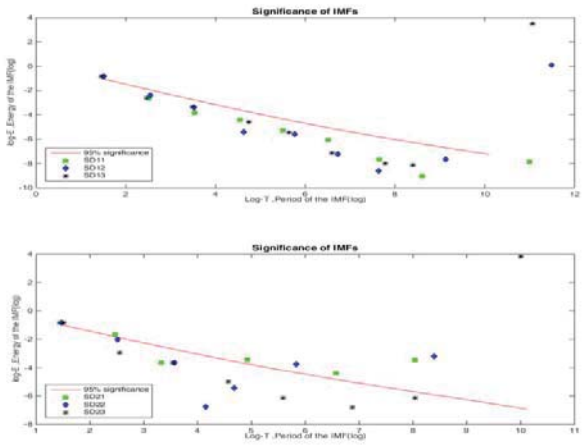

Figure 4. Significance test results of IMFs of EEMD by considering 95% confidence level, Type-I (top panels) and Type-II (bottom panels).

The proposed approaches were applied to the tide gauge records, and the significance test results of the CWT and the EEMD are presented in Table 2. The significance test of CWT method showed that trends in tide gauge records of Busan, Jeju, Pohang, and Sokcho were statistically significant at 95% confidence level, and there was no statistically significant trend in other tide gauge records. At the same time, the significance test of EEMD method showed that trends in tide records of Chulado, Gadukdo, Geomundo, Gunsan, Jeju, and Mokpo were statistically significant at 95% confidence level, and no statistically significant trend was presented in the other tide gauge records. The comparison of significance test results was presented in Table 2. Only two stations (i.e. Jeju and Mokpo) showed statistically significant trends in both methods. Kim and Cho (2014) also found that these tide gauges had a strong upward trend among the tide gauges around South Korea. And also Table 2 includes trends of the relative sea level were first estimated using the residuals of both methods, and then the trends were corrected with GIA model information. All the

trends had a strong upward trend regardless of the methods, except Wido station. The highest SLR was identified in Mokpo, followed by Jeju and the lowest (negative) SLR was identified in Wido and Mukho. The EEMD method showed almost a linear increase or decrease in sea level trend over the historical period, and also a much narrower confidence interval than the CWT method.

Table 2. *Comparison of estimated trends magnitude of tide gauge records using the CWT method and the EEMD method at 95% confidence interval.*

Station		Trend (mm/year)				
#	Name	CWT		EEMD		GIA
1	Anheung	1.558±1.653	N	1.225	N	-0.44
2	Boryeoung	1.999±0.364	N	4.547	N	-0.45
3	Busan	2.354±1.125	Y	2.107	N	-0.43
4	Chujado	0.405±0.183	N	0.721±0.005	Y	-0.33
5	Daeheuksando	0.240±0.339	N	0.305	N	-0.33
6	Gadukdo	1.384±0.472	N	3.034±0.014	Y	-0.44
7	Geomundo	1.688±0.370	N	3.364	Y	-0.37
8	Gunsan	0.763±0.222	N	3.899	Y	-0.44
9	**Jeju**	**6.151±2.431**	**Y**	**6.380**	**Y**	**-0.31**
10	**Mokpo**	**8.488±3.835**	**Y**	**6.461**	**Y**	**-0.39**
11	Mukho	1.141±0.940	Y	0.579	N	-0.30
12	**Pohang**	**3.625±1.058**	Y	**6.053±0.026**	N	**-0.38**
13	Seogwipo	1.250±0.349	N	3.588	N	-0.29
14	Sokcho	1.488±0.390	Y	2.920	N	-0.32
15	Tongyoung	0.927±0.327	N	1.770±0.168	N	-0.44
16	Ulleungdo	1.879±0.646	N	3.746	N	-0.13
17	Ulsan	0.513±0.435	N	1.563	N	-0.41
18	Wando	0.333±0.121	N	1.145	N	-0.37
19	**Wido**	**-0.552±-0.132**	N	**-1.163**	N	**-0.42**
20	Yeosu	1.218±0.533	N	1.062	N	-0.43

Accelerations of the trends were estimated using the residuals of both methods. Since our interest was in acceleration, lower accelerations (or decelerations) were not accounted (Table 3). The strong acceleration was found in Ulleungdo, following Pohang, Mopko, and Mukho tide gage stations based on the residual of the EEMD.

DISCUSSION

In terms of detecting trend and acceleration based on synthetic data, EEMD method showed better performance over CWT method regardless of data length and degree of the trend. We see that sea level trend around Korean Peninsula is significantly increasing except only Wido station. It suggests that ongoing climate change impact is likely to affect to some degree the sea level around the Korean Peninsula and a significant consideration in the increasing sea level is needed for coastal area protection. Particularly, sea level rise in tide gauge records from southern part was higher than the other tide gauge stations ranging from 6 mm/year to 8.5 mm/year. However, the estimated accelerations in sea level trend are rather ambiguous showing both acceleration and deceleration, and the accelerations in sea level rise were only found in the southern part. In our results, the trend and acceleration were not consistent between nearly located tide gauge stations. We concluded the main reason of such result may be the length of tide gauge records. The further development of this study could be related to Paleo data to better estimate reliable trend.

Table 3. *Comparison of estimated acceleration of tide gauge records using the CWT method and the EEMD method at 95% confidence interval.*

Station		Acceleration ($\mathrm{mm}/year^2$)	
#	Name	CWT	EEMD
1	Anheung	**-0.297±0.0294**	-0.380
2	Boryeoung	-0.010±0.005	-0.073
3	Busan	0.003±0.003	0.004
4	Chujado	0.013±0.007	**0.107**
5	Daeheuksando	-0.028±0.025	-0.151
6	Gadukdo	0.018±0.014	-0.047
7	Geomundo	-0.010±0.006	-0.106
8	Gunsan	0.001±0.001	-0.069
9	Jeju	-0.028±0.028	-0.098
10	Mokpo	0.016±0.016	**0.161**
11	Mukho	0.074±0.071	**0.161**
12	Pohang	0.042±0.032	**0.301**
13	Seogwipo	-0.026±0.013	-0.415
14	Sokcho	-0.004±0.003	-0.114
15	Tongyoung	-0.007±0.006	0.009
16	Ulleungdo	0.041±0.030	**0.470**
17	Ulsan	0.016±0.016	-0.022
18	Wando	-0.004±0.002	-0.030
19	Wido	-0.029±0.021	-0.382
20	Yeosu	-0.008±0.008	-0.043

CONCLUSION

An accelerated sea level rise has recently been detected in many parts of the world. Identifying the underlying trend of sea level plays an important role to better understand and manage the problems associated with climate change. However, it has been acknowledged that isolation of the acceleration in the long-term trend is still difficult due to the fact that there is an embedded low frequency associated with the climate variability. In light of this, this study aimed to provide a new multiscale assessment tool for the estimation of sea-level acceleration for tide gauge data along the Korean peninsula. This study employed the CWT and the EEMD methods to better isolate time varying oscillation and estimate a reliable sea-level acceleration of the trend.

This study first examined the CWT and the EEMD methods to fully understand their capability using synthetic data, and then further investigated the acceleration rates of the historical tide gauge records. For the synthetic data, the EEMD method showed better performance than the CWT method in terms of detecting the underlying trend, regardless of the data length and degree of the trend. The CWT method could not accurately identify the trend for a short length of data. However, the EEMD method showed a capability of identifying statistically significant seasonal to interannual trends.

The results confirmed that the EEMD showed more reliable estimates than the CWT in terms of detecting the underlying trend. The smooth increase in the trend at all stations, except Wido, and acceleration in southern coastlines of South Korea was identified through the EEMD. Future work would be focused on developing a Bayesian-based nonstationary frequency analysis model in which the estimated acceleration rates were used to evaluate the risk associated with sea-level rise.

ACKNOWLEDGMENTS

This research was supported by a grant (14AWMP-B082564-01) from Advanced Water Management Research Program funded by Ministry of Land, Infrastructure and Transport of Korean government.

LITERATURE CITED

Breaker, L. C. and Ruzmaikin, A., 2011. The 154-year record of sea level at San Francisco: extracting the long-term trend, recent changes, and other tidbits. *Climate dynamics*, 36(3-4), 545-559.

Breaker, L. C. and Ruzmaikin, A., 2012. Estimating rates of acceleration based on the 157-year record of sea level from San Francisco, California, USA. *Journal of Coastal Research*, *29*(1), 43-51.

Daubechies, I., 1990. The wavelet transform, time-frequency localization and signal analysis. *Information Theory*, IEEE Transactions on, 36(5), 961-1005.

Douglas, B. C., 1992. Global sea level acceleration. *Journal of Geophysical Research*: Oceans (1978–2012), 97(C8), 12699-12706.

Ezer, T., and Corlett, W. B., 2012. Is sea level rise accelerating in the Chesapeake Bay? A demonstration of a novel new approach for analyzing sea level data. *Geophysical Research Letters*, 39(19).

Farge, M., 1992. Wavelet transforms and their applications to turbulence. *Annual review of fluid mechanics*, 24(1), 395-458.

Haines, A., 2003. Climate Change 2001: The Scientific Basis. Contribution of Working Group 1 to the Third Assessment report of the Intergovernmental Panel on Climate Change. JT Houghton, Y Ding, DJ Griggs, M Noguer, PJ van der Winden, X Dai. Cambridge: Cambridge University Press, 2001, pp. 881,£ 34.95 (HB) ISBN: 0-21-01495-6;£ 90.00 (HB) ISBN: 0-521-80767-0. *International Journal of Epidemiology*, 32(2), 321-321.

Huang, N. E.; Shen, Z.; Long, S. R.; Wu, M. C.; Shih, H. H.; Zheng, Q., and Liu, H. H., 1998. The empirical mode decomposition and the Hilbert spectrum for nonlinear and non-stationary time series analysis. In *Proceedings of the Royal Society of London A: Mathematical, Physical and Engineering Sciences. The Royal Society*, 454(1971), 903-995.

Huang, N. E.; Wu, M. L. C.; Long, S. R.; Shen, S. S.; Qu, W.; Gloersen, P., and Fan, K. L., 2003. A confidence limit for the empirical mode decomposition and Hilbert spectral analysis. In *Proceedings of the Royal Society of London A: Mathematical, Physical and Engineering Sciences. The Royal Society*, 459(2037), 2317-2345.

Huang, N. E. and Shen, S. S., 2005. Hilbert-Huang transform and its applications (Vol. 5). *World Scientific*.

Kim, Y., and Cho, K., 2014. Sea level rise around Korea: Analysis of tide gauge station data with the ensemble empirical mode decomposition method. *Journal of Hydro-environment Research*. doi:10.1016/j.jher.2014.12.002

Koren, V. I.; Finnerty, B. D.; Schaake, J. C.; Smith, M. B.; Seo, D. J., and Duan, Q. Y., 1999. Scale dependencies of hydrologic models to spatial variability of precipitation. Journal of Hydrology, 217(3), 285-302.

Lowe, J.; Howard, T.; Pardaens, A.; Tinker, J.; Holt, J.; Wakelin, S., and Bradley, S., 2009. *UK Climate Projections science report: Marine and coastal projections*.

McGranahan, G.; Balk, D., and Anderson, B., 2007. The rising tide: assessing the risks of climate change and human settlements in low elevation coastal zones. *Environment and urbanization*, 19(1), 17-37.

Nicholls, R. J.; Hoozemans, F. M., and Marchand, M., 1999. Increasing flood risk and wetland losses due to global sea-level rise: regional and global analyses. *Global Environmental Change*, 9, S69-S87.

Park, J. and Mann, M. E., 2000. Interannual temperature events and shifts in global temperature: a "multiwavelet" correlation approach. *Earth Interactions*, 4(1), 1-36.

Partal, T. and Küçük, M., 2006. Long-term trend analysis using discrete wavelet components of annual precipitations measurements in Marmara region (Turkey). *Physics and Chemistry of the Earth, Parts A/B/C*, 31(18), 1189-1200.

Pišoft, P.; Kalvová, J., and Brázdil, R., 2004. Cycles and trends in the Czech temperature series using wavelet transforms. *International Journal of Climatology*, 24(13), 1661-1670.

Sang, Y. F., 2012. A practical guide to discrete wavelet decomposition of hydrologic time series. *Water resources management*, 26(11), 3345-3365.

Sang, Y. F.; Wang, Z., and Liu, C., 2014. Comparison of the MK test and EMD method for trend identification in hydrological time series. *Journal of Hydrology*, 510, 293-298.

Smith, L. C.; Turcotte, D. L., and Isacks, B. L., 1998. Stream flow characterization and feature detection using a discrete wavelet transform. *Hydrological processes*, 12(2), 233-249.

Torrence, C. and Compo, G. P. (1998). A practical guide to wavelet analysis. *Bulletin of the American Meteorological society*, 79(1), 61-78.

Trupin, A., and Wahr, J., 1990. Spectroscopic analysis of global tide gauge sea level data. *Geophysical Journal International*, 100(3), 441-453.

Visser, H.; Dangendorf, S., and Petersen, A. C., 2015. A review of trend models applied to sea level data with reference to the "acceleration-deceleration debate". *Journal of Geophysical Research*: Oceans.

Wu, Z. and Huang, N. E., 2004. A study of the characteristics of white noise using the empirical mode decomposition method. In *Proceedings of the Royal Society of London A*: Mathematical, Physical and Engineering Sciences. The Royal Society, 460(2046), 1597-1611.

Wu, Z., and Huang, N. E., 2009. Ensemble empirical mode decomposition: a noise-assisted data analysis method. *Advances in adaptive data analysis*,1(01), 1-41.

Journal of Coastal Research	SI	75	775-779	Coconut Creek, Florida	2016

Past extreme events recorded in the internal architecture of coastal formations in the Baltic Sea Region

Kadri Vilumaa[†*], Hannes Tõnisson[†], Shinya Sugita[†], Ilya V. Buynevich[††], Are Kont[†], Merle Muru[‡], Frank Preusser[§], Stefan Bjursäter[†§], Tiit Vaasma[†], Egert Vandel[†], Anatoly Molodkov[§§], and Johanna I. Järvelill[†]

[†]Institute of Ecology, Tallinn University, Tallinn, Estonia
[††]Department of Earth and Environmental Science, Temple University, Philadelphia, U.S.A.
[†§]Department of Natural Geography, Stockholm University, Stockholm, Sweden
[‡]Department of Geography, Institute of Ecology and Earth Sciences, Tartu University, Tartu, Estonia
[§]Institute of Earth and Environmental Sciences, Albert-Ludwigs-Universität Freiburg, Freiburg, Germany
[§§]Institute of Geology, Tallinn University of Technology, Tallinn, Estonia

www.cerf-jcr.org

www.JCRonline.org

ABSTRACT

Vilumaa, K.; Tõnisson, H.; Sugita, S.; Buynevich, I.V.; Kont, A.; Muru, M.; Preusser, F.; Bjursäter, S.; Vaasma, T.; Vandel, E.; Molodkov, A., and Järvelill, J.I., 2016. Past extreme events recorded in the internal architecture of coastal formations in the Baltic Sea region. *In:* Vila-Concejo, A.; Bruce, E.; Kennedy, D.M., and McCarroll, R.J. (eds.), *Proceedings of the 14th International Coastal Symposium* (Sydney, Australia). *Journal of Coastal Research*, Special Issue, No. 75, pp. 775-779. Coconut Creek (Florida), ISSN 0749-0208.

The postglacial uplift and transgressive-regressive phases of the Baltic Sea have affected the formation and displacement of sandy accumulation forms in the region. The dune-ridge complexes preserve a geological record of past sea-level fluctuations, coastal evolution, and extreme events, and offer insights into major driving mechanisms. This study aims to improve methodologies for identifying different storm signatures in coastal deposits using examples from Estonia and Latvia. The paleo-beach ridges are typically covered by aeolian sand, and the inter-ridge swales are mostly filled with organic sediments. Ground-penetrating radar surveys corroborate distinct textural patterns in sand layers underneath the ridges and swales. In the ridges, sharp seaward-dipping reflections represent storm scarps. The ridge sequences without dipping reflections suggest either aeolian origin or longshore transport; smaller sandy ridges, which are buried under peat layers, reflect prolonged, calmer phases. Compound dunes with ridges in their cores indicate major coastal events or shifts in atmospheric conditions that would have exposed wide sand areas to wind and facilitated dune development. This study demonstrates that the aeolian processes and changes in storminess have played an important role in the genesis of ridge-swale complexes in the Baltic Sea Region.

ADDITIONAL INDEX WORDS: *Beach ridges, dunes, heavy minerals, geophysical survey, luminescence.*

INTRODUCTION

Prograded coastal ridges and dunes are valuable archives of Holocene shorelines, past sea-level history, extreme events, paleo-storm morphostratigraphy, and medium-term variations in coastal processes (Björck and Clemmensen, 2004; Tamura, 2012; Bendixen *et al*., 2013; Hede *et al*., 2013; Dougherty, 2014; Nott *et al*., 2015). Beach ridge plains are found worldwide, where tropical cyclones or storm surges affect a spectrum of accumulation forms (Scheffers *et al*., 2012; Nott *et al*., 2015). These sandy shorelines are highly susceptible to erosion. Wave-eroded scarps in beach deposits are visible in subsurface ground-penetrating radar (GPR) records, indicating past high-energy events (Clemmensen and Nielsen, 2010; Nott *et al*., 2015). Heavy-minerals concentrations (HMCs) in dune scarps produce distinctive reflections in GPR images and are the evidence of erosional episodes in a long-term record of shoreline progradation (Buynevich *et al*., 2004; Dougherty, 2014).

Over the past 50 years, storminess has increased in northern Europe because of the changes in cyclonic activity. The number of cyclones moving over the area has increased in winter, shifting stormy season from autumn to winter (Suursaar *et al*., 2015). The Baltic Sea is essentially tideless, so that sea-level fluctuations are generally induced by wind direction and intense storms. Due to the isostatic uplift and sediment deficiency on the NE coast of the Baltic Sea, short-term relative sea-level changes (*e.g.* regressive and transgressive phases, extreme storms) are the main factor shaping regional coastal formations.

This study examines different storm signatures in beach deposits of Estonia and Latvia and discusses its relationships with the past changes in storminess. At an Estonian site, aeolian sand influx into peat sediments of a raised bog is used as a proxy for storminess.

METHODS

High-resolution topographic maps (LiDAR) were used for selecting the study areas and the locations of topographic transects. Field studies were conducted on two strandplains along the eastern Baltic Sea region (Figure 1). The Estonian study area is located at the northern end of Tahkuna Peninsula, Hiiumaa Island. The area is open to W and N winds. The shore-parallel ridges are fronted by a large dune belt containing relict blowouts and backed by lower foredunes. The aeolian processes have formed a large dune belt up to 17.5 m high. The GPR transect is >1 km long and traverses the ridges with altitudes of

DOI: 10.2112/SI75-156.1 received 15 October 2015; accepted in revision 15 January 2016.
*Corresponding author: Kadri.Vilumaa@tlu.ee
©Coastal Education and Research Foundation, Inc. 2016

5.5-7.5 m a.s.l. The ridge system shows evidences of removal of several ridges in the past. The surface deposits include reworked sand comprising the ridges that formed during sea-level fall, and peat accumulating in swales. The ridge-swale landscape is covered by a pine (*Pinus sylvestris*) forest.

The Latvian study area of Siltere is located over 20 km SW from Cape Kolka, ~2.5 km from the shoreline (Figure 1). The study was carried out across a single relic dune at ~20 m a.s.l., which is backed by a bog-covered terrace. The dune is mostly composed of fine sand, whereas the terrace consists of a 1.5-m-thick sand layer on top of stiff clay. The length of the topographic/geophysical transect is ~100 m. There are no coastal formations in a landward direction. Seaward, several higher dune-ridge systems and low ridge sets occasionally separated by lakes, are the most characteristic physiographic features.

Shore-normal subsurface surveys have been collected with a digital GSSI SIR-3000 georadar with a 270 MHz antenna, with a range of 250 ns and trace spacing of 0.05 m for each site. The GPR data post-processing and analyses were performed using *Road Doctor* and *Radan* 7 software. The selection of the 270 MHz antenna favored deeper signal penetration (>10 m), while still providing dm-scale vertical resolution. The electromagnetic wave velocities were estimated using a depth-to-target method. Interpretation of GPR facies was based on hand auger and window sampler coring, which provided accurate depths of key stratigraphic boundaries and bounding surfaces.

Samples for luminescence dating of the Estonian study site were collected from the base of a large dune belt (Hiiu-2; 5 m a.s.l.; sampling depth 1.1 m) and a relict foredune ridge 270 m landward from it (Hiiu-1; 7 m a.s.l.; 1.3 m) using opaque plastic tubes. The material was composed of mixed medium-to-coarse grained sand, with the 200-250 µm fraction extracted by wet sieving and treated with HCl, H_2O_2, and $Na_4P_2O_4$. Potassium feldspar and quartz grains were enriched through heavy-liquid separation and quartz grains etched using HF. The measurements were performed on a Freiberg Instruments Lexsyg Research instrument (Richter *et al*., 2013). As quartz did not emit any detectable luminescence emissions, the subsequent analyses focused on feldspar. A modified protocol (Murray and Wintle, 2003) was used with adopted stimulation temperatures from Reimann and Tsukamoto (2012), relying on infrared light stimulation at 50°C ($IRSL_{50}$) and at 150°C ($pIRIR_{150}$). The central age model (Galbraith *et al*., 1999) was used to obtain a weighted average dose equivalence (D_e) value for each sample. Age calculations were performed in *Adele Software* using an assumed internal K content of 12.5±0.5% and alpha efficiency of 0.07±0.02. High-resolution gamma spectroscopy was used for the determination of dose rate of the relevant elements. IRSL dates for the Latvia site were analyzed in the Research Laboratory for Quaternary Geochronolgy (RLQG), Institute of Geology, Tallinn University of Technology (see Molodkov and Bitinas, 2006 for detailed methodology).

Peat sediments were collected from a small bog at the Estonian study site using Russian peat sampler. The core was described, documented, and photographed in the field, and packed into bisected PVC tubes. In the laboratory the core was subsampled continuously at 1 cm intervals. The chronology of the core was based on ten AMS ^{14}C dates using terrestrial plant macro-remains. All dates were obtained at Poznan Radiocarbon Laboratory, Poland, and calibrated using the IntCal13 curve (Reimer *et al*., 2013) with Clam ver. 2.2 (Blaauw, 2010). The standard lithological content was assessed using the thermogravimetric analysis (Precisa prepASH 340 Series). The content of dry matter in the sediment was determined by heating the samples at 105 °C to the constant weight. Loss-on-ignition (LOI) at 550 ºC was used to establish the organic and mineral matter contents.

Boreholes were drilled and small pits were dug at the locations with strong subsurface reflections to calibrate GPR images and for textural analyses. Several HMC layers were analysed using immersion method with a polarized microscope.

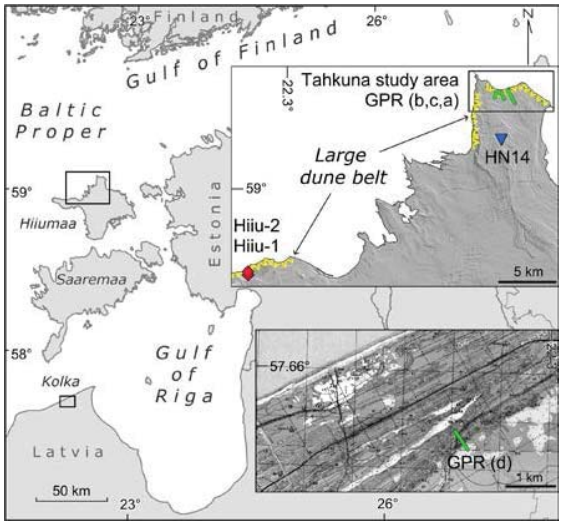

Figure 1. Location of study areas in the Baltic Sea region, LiDAR map (by Estonian Land Board) of Estonian study area with sampling sites of $IRSL_{50}$ (Hiiu-1, Hiiu-2) and peat core (HN14). And topographic map of the Latvian study area. a-d – locations of GPR profiles.

RESULTS

The results of geophysical and stratigraphic surveys, HMC analyses of sand and minerogenic fraction of peat, as well as ^{14}C and luminescence dates are summarized below.

Geophysical and sedimentological database

The morphology and internal patterns of the coastal formations were studied both in Estonia and Latvia. The Estonian profile was divided into three sections (Figure 2a-c) to ensure the quality of the data (parallel profiles in the locations where initial ridge-swale complexes were covered by dunes) and to avoid inaccessible sites (lakes, waterlogged bogs, streams).

The Estonian profile was divided into sections with different geomorphology and development history. The first section (Figure 2a1) includes the highest ridge in the profile. Similar ridges separated by former lagoons and filled with peat occurred landward of the profile. These ridges appear to be formed as spits as the result of longshore sediment transport (no seaward-dipping layers). This spit is followed by a 150-m-long section of large ridges (Figure 2a2). Extensive seaward-dipping reflections are clearly visible in GPR images. They are groundtruthed as

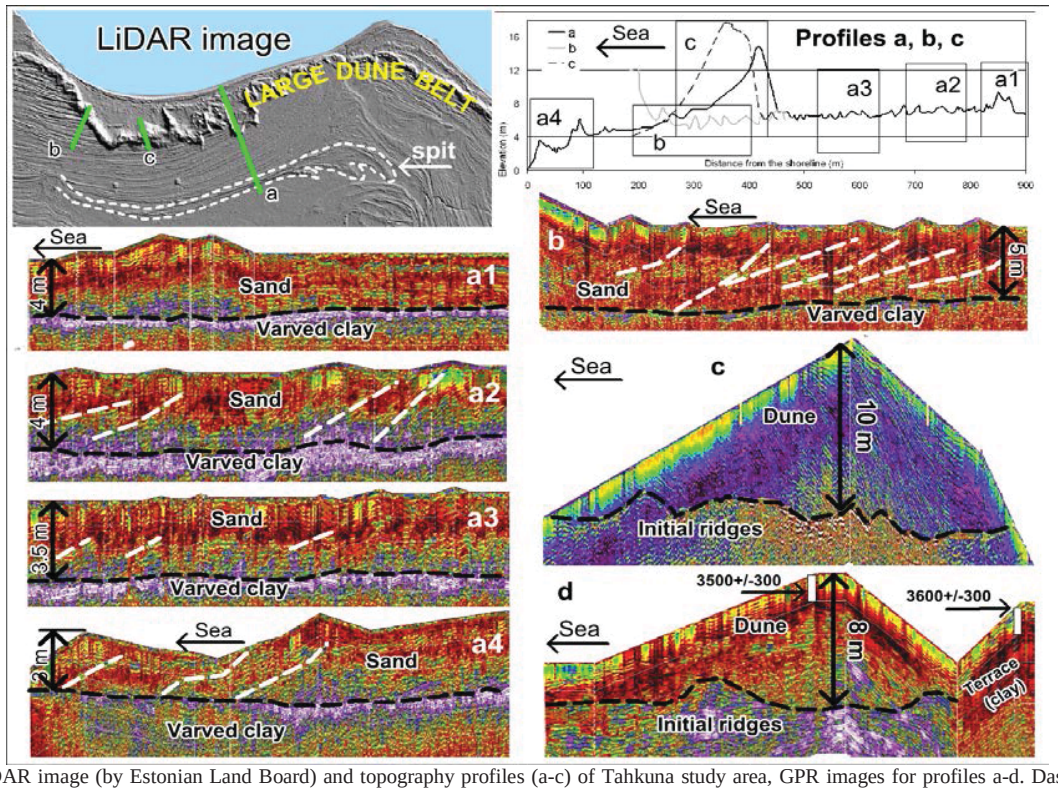

Figure 2. LiDAR image (by Estonian Land Board) and topography profiles (a-c) of Tahkuna study area, GPR images for profiles a-d. Dashed white lines – dipping layers with coarser sand or HMC. Two IRSL dates obtained in RLQG for the Latvian site shown in GPR image (d).

coarser-grained strata or those with higher HMC content. The next 250-m-long section (Figure 2a3) is characterized by low ridges with minor seaward-dipping layers. Most of the depressions between the ridges are filled by peat, resulting in almost flat topography. A parallel profile (Figure 2b) was used to establish a complete series of ridge-swale formation. The large ridges with long tilted layers have been formed in the result of cross-shore sediment accumulation. The final ridge in this section is covered by a large dune shown on another parallel profile (Figure 2c). The primary ridges are still visible under the 10-m-high dune. The landward tilted lamination on the leeward side of the dune is also clearly visible in the GPR image. As seen from the final section of the profile a (Figure 2a4), the seaward side of the large dune is flattened, probably due to dune migration and aeolian activity, until the last 100 m of the profile with two relatively large foredune ridges having seaward-dipping erosional surfaces.

At the Latvian study site typical, dune accretion mode is visible from the GPR reflection pattern (Figure 2d). According to the IRSL dating, this complex has been formed 3500 ± 300 years ago. The dates from the landward terrace and the seaward side of the dune fit the limits of calculated error indicating its rapid development.

IRSL$_{50}$ dates

The IRSL$_{50}$ ages are represented by lower and more clustered single aliquot D_e values compared to the pIRIR$_{150}$ ages, likely reflecting that the IRSL$_{50}$ signals were successfully bleached prior to deposition while the pIRIR$_{150}$ signals were only partially bleached. Preusser *et al*. (2014) have shown that samples for the region give IRSL$_{50}$ ages consistent with radiocarbon ages and hence the effect of anomalous fading on this signal is considered negligible. Furthermore, these provide a more plausible fit with the recent apparent land uplift rates in Estonia. Therefore, IRSL$_{50}$ ages are used to set the time of the formation of the ridge system in Tahkuna (Table 1) and the dune belt started to form 1210±80 years ago.

Peat core

The core in Tahkuna study area (coring site HN14) is 171-cm-long and records the entire thickness of the bog. The bog is located 3-4 km from the profiles and *ca* 2 km from the W-coast of Tahkuna Peninsula, 15 m a.s.l. The lowermost 6 cm is sand; the 165-68 cm section consists of highly decomposed peat with layers of wood (116-110; 97-94; 98-97; 89-88 cm) and some plant (mainly *Eriophorum vaginatum*) remains (110-100; 94-72 cm). The 72-68 cm section is reed peat, followed by 68 cm of well-preserved *Sphagnum* peat. The minerogenic matter content in the core is low in general with some exceptions (Figure 3). The highest concentration (54.9-99.4%) of mineral matter is at the bottom (171-165 cm - not shown on the Figure 3). The upper part of the core at 58 cm (*ca* 730 cal BP) and above contains 2.5-10.8% inorganic fraction. The mineral matter concentration before, during, and after the formation (2,200-1,100 cal BP;

107-73 cm) of the large dune belt is low (<2.4%) and monotonous.

HMC

HMC-rich layers coincide with prominent reflections GPR images as their electric susceptibility is much higher. Such layers suggest eroded slipfaces. We took several samples from the beach, dune and the ridges with similar properties along the Estonian coast. The fraction of heavy minerals on eroded beaches around Tahkuna Peninsula range between 13-18% (mostly ferromagnesian minerals and garnet), whereas the concentration on the top of the highest dune is only 1%. Several tests taken from similar ridges along the Estonian coast yield HMC content up to 4%. Therefore, we assume that the erosional slip-faces can be distinguished, because the HMC in these layers is many times higher than in aeolian deposits.

Table 1. *Feldspar measurement details: water content (WC), overdispersion value (OD), radionuclide concentration (Ra, Th, K), D_e, dose rate and inferred ages (before 2014). Number of accepted aliquots passing internal recycling ratio criteria (≤10%) was 12 in each case.*

Sample	Protocol	*WC* (%)	*OD* (%)	^{226}Ra (Bq kg^{-1})	^{232}Th (Bq kg^{-1})	^{40}K (Bq kg^{-1})	D_e (Gy)	Dose rate (Gy ka^{-1})	Age (ka)
Hiiu-01	$IRSL_{50}$	20±5	6.9	14.3±0.4	20.1±1.3	274.6±6.7	**2.20±0.14**	4.80±0.1	2.18±0.14
	$pIRIR_{150}$	13.4					**4.93±0.35**	10.74±0.43	2.18±0.15
Hiiu-02	$IRSL_{50}$	8±4	9.8	14.6±0.6	23.1±1.1	439.0±6.9	**1.21±0.08**	3.49±0.11	2.88±0.19
	$pIRIR_{150}$	14.2					**3.00±0.21**	8.64±0.26	2.88±0.20

DISCUSSION

The beginning of the Estonian section (Figure 2a1) was formed as a result of longshore sediment transport. Our previous studies have revealed that each increment of such drift-aligned recurved spits reflects changes in climatic and hydrodynamic conditions (Suursaar *et al*., 2015). Therefore, we hypothesize that each segment of the paleo-spit system reflects a climatic event in the past, possibly a major storm event or period.

Because the study region is experiencing sediment deficit, sea-level changes or extreme storms can create extensive ridges and dunes. A clear evidence of rapid formation of large dunes is the Latvian study area (Figure 2d). The first set of OSL dates indicates that the terrace behind the dune is almost of the same age, suggesting that the landform was created in a short time period or some re-deposition occurred during the Late Holocene The open sands are quickly covered by vegetation due to the influx of organic material from both seaward and landward sources (roots, seeds, *etc*.).

Stormy periods associated with high sea levels cause erosion of large volumes of coastal deposits from both erosional and accumulative sections. Our profiles were sited in the net accumulative sections of the shores where erosional bounding surfaces (truncations) archive the signatures of extreme events. These are often complemented with higher concentrations of heavy minerals (mineralogical lag; Smith and Jackson, 1990) and coarser fraction (textural lag). Most of the eroded material is accumulated either on shore or on the nearshore seabed. Therefore, the erosional layers are quickly buried by re-transported aeolian material from the exposed beach. These layers are clearly visible in the GPR images, with seaward-dipping layers in short succession indicating a longer stormy period. More extensive layers reflect stronger storm events with higher water levels. Large amounts of sand in nearshore zone contribute to the formation of larger ridges, their height being a function of aeolian aggradation, which seems to be characteristic for sections a2, b and a4 on the Estonian profile.

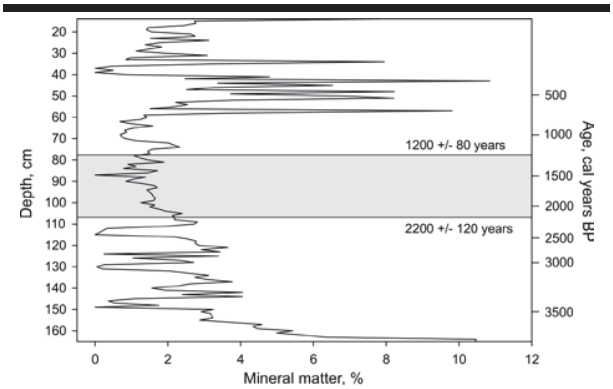

Figure 3. Concentration of mineral matter in the bog core from Tahkuna. The gray area represents the time period between two $IRSL_{50}$ samples.

The sections with small ridges with short tilted layers in deeper horizons are probably formed during relatively calm periods. Such short seaward tilted layers refer to low sea levels during their formation. Many ridges in this section are buried under peat layer today. Based on the GPR wave reflections, the section a3 was likely formed during a particularly calm period. Some slightly larger ridges in this section may have been formed as a result of a single stronger storm event.

The exceptionally high dune ridge, up to 17.5 m a.s.l., and extending across most of the northern coast of Hiiumaa Island, is an outstanding morphological feature in this region. Such high dunes are usually formed during periods of major sea-level fluctuations. However, the $IRSL_{50}$ dating confirmed, no sea-level fluctuations can be reported during the period of its formation. The formation of this dune cannot be connected with major storm events either, because this period is characterized by the lowest influx of mineral material into the bog a few km from the current shoreline (Figure 3). An alternative hypothesis is that this large dune was formed by an extreme event such as a tsunami about 1,200 years ago; however, historical documents or local folklores, referring to any such event, do not exist. On the contrary, the results of our current study suggest that this dune ridge was formed during a calm period with low cyclonic activity. Most of the Baltic Sea is covered by ice only in very cold and calm winters. If the sea ice cover breaks up during a NW storm, the sea ice may pile up on the shore. Sometimes such ice-ridges move hundreds of meters inland from the shoreline (Orviku *et al*., 2011), wiping out the vegetation and exposing wide areas of sand to wind activity. Thus, it is plausible to hypothesize that: (1) *ca* 1,200 years ago the winters were long and cold with less snow – a difficult condition for re-vegetating an open strandplain – and fewer major storms than usual, and (2)

because of those situations, a background aeolian activity alone helped form such a large dune belt. Low content of mineral material in peat is also supporting the idea of calm and cold winters at that time.

CONCLUSIONS

High-resolution georadar profiles, in combination with drilling data, detailed LiDAR maps, radiocarbon and luminescence dating, HMC analysis of sand, as well as assessment of minerogenic fraction in peat, allow for a detailed reconstruction of past climatic conditions along sections of Estonian and Latvian coasts. Changes in storminess, including the character of storm periods, are reflected in the internal patterns of ancient coastal formations. Based on changes in topography and internal architecture of beach/dune lithosomes, we propose at least three periods with high cyclonic activity and two relatively calm periods punctuated by few intense storms.

Future studies will focus enhancing the chronology of coastal events to clarify the periodicity of storminess over the past two millennia in this part of the Baltic Sea. In addition, a comparative study of the erosional paleo-surfaces and recent storm monitoring data is necessary for a better understanding, and thus a better reconstruction, of the past storm parameters. Our findings are part of a valuable contribution to the forecasting of future scenarios in regional storm risk assessment by providing a deep-time perspective.

ACKNOWLEDGMENTS

This work has been funded by the Estonian Ministry of Education and Research and by the Estonian Science Foundation grants No. 7564, 8549, 9191, 9011, IUT18-9, PUT456, the BONUS project BaltCoast and Doctoral School of Earth Sciences and Ecology (EU Structural Support), and Temple University Internationalization Program Award (IB).

LITERATURE CITED

Bendixen, M.; Clemmensen, L.B., and Kroon, A., 2013. Sandy berm and beach-ridge formation in relation to extreme sea-levels: A Danish example in a micro-tidal environment. *Marine Geology*, 344, 53-64.

Björck, S. and Clemmensen, L.B., 2004. Aeolian sediment in raised bog deposits, Halland, SW Sweden: a new proxy record of Holocene winter storminess variation in southern Scandinavia. *The Holocene*, 14, 677-688.

Blaauw, M., 2010. Methods and code for ‘classical’ age-modelling of radiocarbon sequences. *Quaternary Geochronology*, 5, 512-518.

Buynevich, I.V.; FitzGerald, D.M., and van Heteren, S., 2004. Sedimentary records of intense storms in Holocene barrier sequences, Maine, USA. *Marine Geology*, 210, 135-148.

Clemmensen, L.B. and Nielsen, L., 2010. Internal architecture of a raised beach ridge system (Anholt, Denmark) resolved by ground-penetrating radar investigations. *Sedimentary Geology*, 223, 281-290.

Dougherty, A.J., 2014. Extracting a record of Holocene storm erosion and deposition preserved in the morphostratigraphy of a prograded coastal barrier. *Continental Shelf Research*, 86, 116-131.

Galbraith, R.F.; Roberts, R.G.; Laslett, M.G.; Yoshida, H., and Olley, J.M., 1999. Optical dating of single and multiple grains of quartz from Jinmium Rock Shelter, Northern Australia: Part I, experimental design and statistical models. *Archaemetry*, 41(2), 339-364.

Hede, M.U.; Bendixen, M.; Clemmensen, L.B.; Kroon, A., and Nielsen, L., 2013. Joint interpretation of beach-ridge architecture and coastal topography show the validity of sea-level markers observed in ground-penetrating radar data. *Holocene*, 23(9), 1238-1246.

Molodkov, A. and Bitinas, A., 2006. Sedimentary record and luminescence chronology of the Lateglacial and Holocene aeolian sediments in Lithuania. *Boreas*, 35(2), 244-254.

Murray, A.S. and Wintle, A.G., 2003. The single aliquot regenerative dose protocol: potential for improvements in reliability. *Radiation Measurements*, 37(4-5), 377-381.

Nott, J.; Forsyth, A.; Rhodes, E., and O'Grady, D., 2015. The origin of centennial- to millennial-scale chronological gaps in storm emplaced beach ridge plains. *Marine Geology*, 367, 83-93.

Orviku, K.; Tõnisson, H., and Jaagus, J., 2011. Sea ice shaping the shores. *In*: Furmańczyk, K. (ed.), *Proceedings of the 11th International Coastal Symposium* (Szczecin, Poland). *Journal of Coastal Research*, Special Issue No. 64, pp. 681-685.

Preusser, F.; Muru, M., and Rosentau, A., 2014. Comparing different post-IR IRSL approaches for the dating of Holocene coastal foredunes from Ruhnu Island, Estonia. *Geochronometria*, 41(4), 342-351.

Reimann, T. and Tsukamoto, S., 2012. Dating the recent past (<500 years) by post-IR IRSL feldspar – Examples from the North Sea and Baltic Sea coast. *Quaternary Geochronology*, 10, 180-187.

Reimer, P.J.; Bard, E.; Bayliss, A.; Beck, J.W.; Blackwell, P.G.; Bronk Ramsey, C.; Buck, C.E.; Cheng, H.; Edwards, R.L.; Friedrich, M.; Grootes, P.M.; Guilderson, T.P.; Haflidason, H.; Hajdas, I.; Hatté, C.; Heaton, T.J.; Hoffmann, D.L.; Hogg, A.G.; Hughen, K.A.; Kaiser, K.F.; Kromer, B.; Manning, S.W.; Niu, M.; Reimer, R.W.; Richards, D.A.; Scott, E.M.; Southon, J.R.; Staff, R.A.; Turney, C.S.M., and van der Plicht, J., 2013. IntCal13 and Marine13 radiocarbon age calibration curves 0-50,000 years cal BP. *Radiocarbon*, 55(4), 1869-1887.

Richter, D.; Richter, A., and Dornich, K., 2013. Lexsyg – A new system for luminescence research. *Geochronometria*, 40(4), 220-228.

Scheffers, A.; Engel, M.; Scheffers, S.; Squire, P., and Kelletat, D., 2012. Beach ridge systems: archives for Holocene coastal events? *Physical Geography*, 36(1), 5-37.

Smith, A.W. and Jackson, L.A., 1990. Assessment of the past extent of cyclone beach erosion, *Journal of Coastal Research*, 6, 73-86.

Suursaar, Ü.; Jaagus, J., and Tõnisson, H., 2015. How to quantify long-term changes in coastal sea storminess? *Estuarine, Coastal and Shelf Science*, 156, 31-41.

Tamura, T., 2012. Beach ridges and prograded beach deposits as palaeoenvironment records. *Earth-Science Reviews*, 114, 279-297.

Journal of Coastal Research	SI	75	780-784	Coconut Creek, Florida	2016

How to improve estimates of real-time acceleration in the mean sea level signal

Phil J. Watson†

†School of Civil and Environmental Engineering,
University of New South Wales,
Kensington, NSW, Australia.

www.cerf-jcr.org

www.JCRonline.org

ABSTRACT

Watson, P.J., 2016. How to improve estimates of real-time acceleration in the mean sea level signal. *In:* Vila-Concejo, A.; Bruce, E.; Kennedy, D.M., and McCarroll, R.J. (eds.), *Proceedings of the 14th International Coastal Symposium* (Sydney, Australia). *Journal of Coastal Research*, Special Issue, No. 75, pp. 780-784. Coconut Creek (Florida), ISSN 0749-0208.

One of the most critical environmental issues confronting mankind into the foreseeable future remains the ominous spectre of climate change, in particular the pace at which impacts will occur and our capacity to adapt. Sea level rise is one of the key artefacts of climate change that will have profound impacts on global coastal populations. Although extensive research has been undertaken into this issue, there remains considerable conjecture and scientific debate about the temporal changes in mean sea level and the climatic and associated physical forcings responsible for them. Over recent years, significant debate has centered around the issue of a measurable acceleration in mean sea level, a feature central to projections based on the current knowledge of climate science. To reduce this uncertainty, it is necessary to determine the better performing analytical approaches for isolating the mean sea level signal from long, individual ocean water level time series with improved temporal resolution. This paper summarises the testing and development of an analytical tool designed specifically to enhance real-time estimates of velocity and acceleration in mean sea level derived from contemporary ocean water level data sets. The long ocean water level record at San Francisco, USA has been used to highlight the application and utility of the improved approach.

ADDITIONAL INDEX WORDS: *Mean sea level, acceleration, improved analytical tool.*

INTRODUCTION

One of the most critical environmental issues confronting mankind into the foreseeable future remains the ominous spectre of climate change, in particular the pace at which impacts will occur and our capacity to adapt. Sea level rise is one of the key artefacts of climate change that will have profound impacts on global coastal populations (Nicholls and Cazenave, 2010).

Although extensive research has been undertaken into sea level rise, there remains considerable conjecture and scientific debate about the temporal changes in mean sea level and the climatic and associated physical forcings responsible for them (Watson, 2015a). Of keen interest is whether there is a measurable acceleration in ocean water level records (*e.g.*, Baart, Van Koningsveld, and Stive, 2011; Donoghue and Parkinson, 2011; Houston and Dean, 2011a; Houston and Dean, 2011b; Rahmstorf and Vermeer, 2011; Visser, Dangendorf, and Petersen, 2015; Watson, 2011], a feature central to projections based on the current knowledge of climate science (Stocker *et al.*, 2013). In particular, the published works of Watson (2011) and Houston and Dean (2011a) generated extensive political, social and media debate around the issue.

Much of the professional debate concerns the manner in which acceleration is estimated. Almost exclusively, estimates of acceleration in global or basin scale mean sea level studies have been derived from the ubiquitous simplicity afforded by doubling the quadratic coefficient after fitting a second order polynomial function (*e.g.*, Church and White, 2006; 2011; Douglas, 1992; 1997; Hay *et al.*, 2015; Houston and Dean, 2011a; Jevrejeva *et al.*, 2006; 2008; 2014).

Other techniques applied infer acceleration as a change in the average velocity between differing time slices (*e.g.*, Bindoff *et al.*, 2007; Calafat and Chambers, 2013; Hansen, Aagaard, and Binderup, 2012; Kemp *et al.*, 2009; Merrifield, Merrifield, and Mitchum, 2009). Both techniques are comparatively limited, especially the fitting of a second order polynomial whose acceleration term assumes a constant rate of acceleration applies over the course of the record.

It's well understood that long records and global mean sea level reconstructions contain well recognized signatures of positive and negative "inflexions" (Woodworth *et al.*, 2009) as well as key influences driven ostensibly by climate modes (Cazenave *et al.*, 2012; Fasullo *et al.*, 2013; Hamlington *et al.*, 2013).

As a result, acceleration determined through simple quadratic fits are likely to be unduly influenced by the particular time slice chosen (Rahmstorf and Vermeer, 2011). These comparatively simple approaches work well at a coarse scale where real-time changes in these key characteristics are unimportant.

However, the importance of mean sea level acceleration and its intrinsic linkages to climate change science, demand more sophisticated measures and tools. Improving knowledge of acceleration in mean sea level lies principally with improving

DOI: 10.2112/SI75-157.1 received 15 October 2015; accepted in revision 15 January 2016.
*Corresponding author: philwatson.slr@gmail.com
©Coastal Education and Research Foundation, Inc. 2016

the temporal resolution of the trend signal. This is no trivial task given that ocean water level records are a complex composite of numerous dynamic influences of largely oceanographic, atmospheric or gravitational origins operating on differing temporal and spatial scales, superimposed on a comparatively low amplitude signal of sea level rise driven by climate change influences (Watson, 2015a).

The mean sea level (or trend) signal results directly from a change in volume of the ocean attributable principally to melting of snow and ice reserves bounded above sea level (directly adding water), and thermal expansion of the ocean water mass. This low amplitude, non-linear, non-stationary signal is quite distinct from all other known dynamic processes that influence the ocean water surface which, are considered to be stationary; that is, they cause the water surface to respond on differing scales and frequencies, but do not change the volume of the water mass.

Improved real-time knowledge of velocity and acceleration rests entirely with improving the temporal resolution of the mean sea level signal. Therefore it is essential to use enhanced time series analysis techniques to better isolate noise and remove the key contaminating signals that influence such records at inter-annual to decadal (and longer) timescales, revealing a more "refined" trend signal.

From this improved signal, the first and second differences provide real-time estimates of velocity and acceleration that are far more instructive in readily identifying key physical changes in mean sea level over time.

Background

Watson (2015b) provided the most extensive appraisal yet of time series analysis techniques for their utility to isolate the trend with improved temporal accuracy from conventional, long, individual ocean water level data sets. A broad range of analytical techniques were tested including linear and polynomial regression, LOESS smoothing, smoothing splines, moving averages, structural models, digital filters, singular spectrum analysis (SSA), empirical mode decomposition, wavelets and their respective derivatives. Sensitivity testing around key parametrization was undertaken to optimize performance of each of the analytics specifically for application with conventional ocean water level data.

In total some 1450 separate analyses were applied to a complex synthetic data set (Watson, 2015a), resulting in 21 million individual time series analyses. Key findings from this analysis were that enhanced accuracy in resolving the temporal resolution of the trend were achieved through the use of longer, annual average data, coupled with the use of so called "data adaptive" analytics, in particular, SSA and multi-resolution wavelet decomposition. SSA is more instructive and convenient for the process in hand given the techniques enhanced capability to seperate key harmonic components of the time series.

SSA is a powerful data adaptive technique capable of decomposing the observed time series into the sum of interpretable components with no a priori information about the time series structure (Alexandrov *et al.*, 2012; Golyandina and Zhigljavsky, 2013). Based upon detailed analysis of numerous long records in the Permanent Service for Mean Sea Level (PSMSL) data holdings (Holgate *et al.*, 2012), Watson has optimized the parameterization and performance of SSA to isolate the mean sea level (or trend) signal from long ocean water level data sets with improved accuracy.

The long annual average record at San Francisco, USA has been used to highlight the application and utility of the analytical approach within this paper.

METHODS

There are 4 key steps involved in isolating the trend signal from long individual ocean water level records with improved temporal resolution and improving estimates of the associated real-time (or instantaneous) velocity and acceleration.

Step 1: Gap Filling. In order to perform SSA, the time series data under consideration must be complete. Thus the initial step in the process involves filling any gaps in the annual average time series record under consideration. Although the San Francisco record used in this paper is one of the longer, more complete records available world-wide, there is a small gap in the time series for 2012. Numerous methods are available for gap filling time series data however, for ocean water level records it is recommended to fill the gaps using SSA and recurrent forecasts from complete parts of the record (Golyandina and Osipov, 2007). This process has been undertaken for the San Francisco record by reconstructing the gap from the combination of SSA components in which the peak spectral energy is ≤ 0.2 (alternatively, corresponding to peak periods ≥ 5 years). With this approach, the principal spectral structures evident in the complete parts of the record can be used to forecast with greater precision across the data gap.

Step 2: Isolating Trend Using SSA. Once gap filling has been completed, the time series is then decomposed using 1D-SSA via the "Rssa" Package in R (Golyandina *et al.*, 2015). The main step of the SSA method is the singular decomposition of the so-called series trajectory matrix. The time series is decomposed into a series of components of slowly varying trend, oscillatory components with variable amplitude and a structureless noise (Golyandina, Nekrutkin, and Zhigljavsky, 2001), with components ranked in order of their contribution to the original time series.

The trend can be isolated by reconstructing only the components that possess distinctly "trend-like" characteristics. Analysis of numerous long ocean records in the data holdings of the PSMSL demonstrate trend components are isolated effectively when a contribution threshold of $\geq 75\%$ is contained within a frequency bin of ≤ 0.01. The grouping of relevant components can be automatically detected (Alexandrov and Golyandina, 2005) and reconstructed via the Rssa Package. In the case of the gap-filled San Francisco time series, the first and second components of the SSA decomposition form the trend (or relative mean sea level) signal (Figure 1).

Step 3: Estimating Real-Time Velocity and Acceleration. A cubic smoothing spline is then fitted to the trend determined in Step 2 to estimate the real-time or instantaneous velocities and accelerations corresponding to each data point in the original time series. As the trend by definition is comparatively smooth, the fitted smoothing spline has been limited to 1 degree of freedom for every 8 data points. The coefficient of determination (R^2) between the SSA derived trend and the fitted cubic smoothing spline for the San Francisco record exceeds 0.9999, representing a near mathematically perfect model fit.

The instantaneous velocity and accelerations can be readily estimated from the first and second derivatives of the fitted smoothing spline, respectively. However, care is required in fitting smoothing splines and deriving second derivatives near the end of the time series. The reason for this is that the knots at the end of a fitted cubic smoothing spline are fixed in order to be differentiable, resulting in a second derivative at the ends which must converge to zero. For this reason, the first and last three derived acceleration points on the time series will likely have reduced accuracy and should not be included in the analysis.

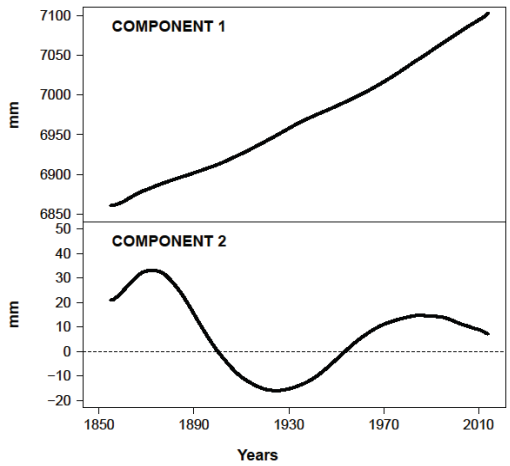

Figure 1. Components of the SSA decomposition of the San Francisco record which form the trend signal.

Step 4: Calculation of Errors. Errors in estimating the trend and associated instantaneous velocity and accelerations have been determined using block bootstrapping techniques with 10,000 iterations. This process initially involves fitting an autoregressive time series model to remove the serial correlation in the residuals between the SSA derived trend and the gap filled time series (Forster and Brown, 2015).

The uncorrelated residuals are then tested to identify change points in the statistical variance along the time series using the "Changepoint" Package in R (Killick and Eckley, 2014). A changepoint was not detected for the San Francisco record. However, in a time series where there is a changepoint detected in the variance, the recommended procedure involves block bootstrapping of residuals quarantined between identified variance change points and then adding the sections to the SSA derived trend prior to running steps 2 and 3 some 10,000 times. The standard deviations are then readily calculated for the trend and associated velocity and accelerations from which to directly derive confidence intervals (CI).

RESULTS

The application of the advised methodology to the long San Francisco tide gauge record is graphically depicted at Figure 2.

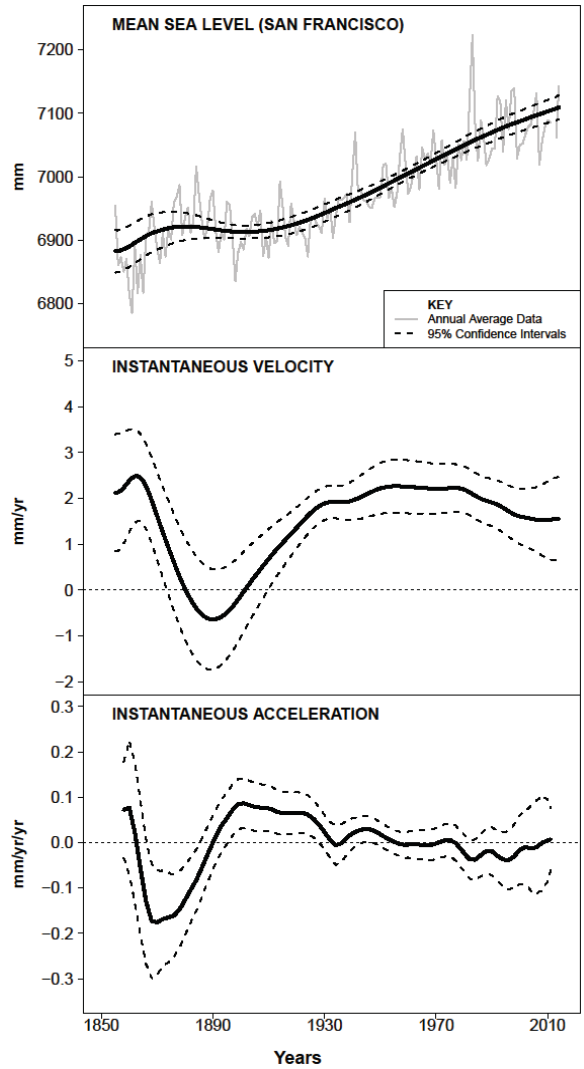

Figure 2. Refined trend and associated real-time velocity and acceleration for relative mean sea level at San Francisco, USA. Annual average data obtained from Permanent Service for Mean Sea Level (UK).

Whilst the record provides very clear evidence of significant relative sea level rise, of the order of 189 ± 52 mm (95% CI) over the course of the historical record, it is clear that the rate at which relative mean sea level has risen has fluctuated substantially over this period. Despite this rise, there is evidence of a fall in the mean signal of the order of around 9 mm between 1880 and 1901.

Interestingly the peak instantaneous velocity of 2.5 ± 1.0 mm/yr (95% CI) occurred early in the record (1863). The second highest velocity of 2.3 ± 0.6 mm/yr (95% CI) occurred in a block between 1950 and 1980, falling moderately to present day (2014) where the velocity is currently 1.6 ± 0.9 mm/yr (95%

CI). Another interesting artefact of the velocity time series is that the last time the mean velocity was as low as present was in 1922.

The peak instantaneous acceleration of 0.09 ± 0.03 mm/yr^2 (95% CI) occurred in 1901. However, over the period from 1928 to present, the instantaneous acceleration has not been statistically different to zero at the 95% confidence level.

DISCUSSION

The methodology advised in this paper and "road-tested" against the long San Francisco record, highlight the enhanced level of information which can be gleaned from the real-time (or instantaneous) velocity and acceleration derived from more accurate isolation of the relative mean sea level signal.

In reality the search for acceleration in any particular record need not be restricted to inspection of the instantaneous accelerations alone. Although this provides some instruction, an acceleration might also be inferred by considering whether or not peaks in the instantaneous velocity time series are increasing, becoming more sustained or abnormal over time in the context of the historical record. The decomposition of the San Francisco record highlights the virtue of considering acceleration from this new perspective, particularly when the mean sea level signal is dynamically changing over time.

Although this methodology provides enhanced levels of temporal understanding of the mean sea level trend signal, caution should be exercised in interpreting results as the quality of the data sets generally degrades (and in some cases substantially) back through time due to numerous factors that include technology and record keeping. Although the technique is based on relative mean sea level changes, the information gleaned could be further enhanced through consideration of land form movements (where relevant), particularly as the length of collocated continuous GPS measurements increases.

CONCLUSION

Based on extensive testing of time series analytics against the variety of complex signals and noise embedded within ocean water level data sets, SSA has proved an optimum choice for resolving the trend component with improved temporal precision for long, individual records (Watson, 2015a; 2015b).

These improved techniques are far more instructive than traditional methods used to date and provide a refreshing pathway forward to resolve some of the considerable ongoing professional debates over measures of acceleration in mean sea level records. This procedure is currently being developed into an analytical package for sea level researchers and is scheduled for release in 2016 as part of the R Project for Statistical Computing (R Development Core Team, 2015).

By enhancing the temporal resolution of the mean sea level signal, researchers can be more confident of identifying real changes to this signal at the earliest possible point in time which in turn might indicate the realisation of key climate change thresholds. These techniques will improve understanding of regional (and more localised) scales of sea level rise influence to better inform adaptation planning for this threat around the coastlines of the world.

ACKNOWLEDGMENTS

The genesis of this research initiative to improve measures of acceleration in mean sea level records has benefited significantly through encouragement from the late Professor Bob Dean (amonst others). The author also acknowledges the guidance and advice provided by Associate Professor Nina Golyandina (Department of Statistical Modelling, Saint Petersburg State University, Russia) in relation to the Rssa Package and SSA.

LITERATURE CITED

Alexandrov, T. and Golyandina, N., 2005: Automatic extraction and forecast of time series cyclic components within the framework of SSA. *Proceedings of the 5th St.Petersburg Workshop on Simulation* (St.Petersburg State University, St.Petersburg), pp. 45–50.

Alexandrov, T.; Bianconcini, S.; Dagum, E.B.; Maass, P. and McElroy, T.S., 2012. A review of some modern approaches to the problem of trend extraction. *Econometric Reviews*, 31(6), 593-624.

Baart, F.; Van Koningsveld, M. and Stive, M., 2011. Trends in sea-level trend analysis. *Journal of Coastal Research*, 28(2), 311-315.

Bindoff, N.; Willebrand, J.; Artale, V.; Cazenave, A.; Gregory, J.; Gulev, S.; Hanawa, K.; Le Quéré, C.; Levitus, S. and Nojiri, Y., 2007. *Observations: in Climate Change and Sea level, Climate Change 2007: The Physical Science Basis.* Contribution of Working Group 1 to the Fourth Assessment Report of the Intergovernmental Panel on Climate Change.

Calafat, F. and Chambers, D., 2013. Quantifying recent acceleration in sea level unrelated to internal climate variability. *Geophysical Research Letters*, 40(14), 3661-3666.

Cazenave, A.; Henry, O.; Munier, S.; Delcroix, T.; Gordon, A.; Meyssignac, B.; Llovel, W.; Palanisamy, H. and Becker, M., 2012. Estimating ENSO influence on the global mean sea level, 1993–2010. *Marine Geodesy*, 35(sup1), 82-97.

Church, J.A. and White, N.J., 2006. A 20th century acceleration in global sea-level rise. *Geophysical Research Letters*, 33(1).

Church, J.A. and White, N.J., 2011, Sea-level rise from the late 19th to the early 21st century. *Surveys in Geophysics*, 32(4-5), 585-602.

Donoghue, J.F. and Parkinson, R.W., 2011. Discussion of: Houston, J.R. and Dean, R.G., 2011. Sea-Level Acceleration Based on US Tide Gauges and Extensions of Previous Global-Gauge Analyses. *Journal of Coastal Research*, 27 (3), 409-417, *Journal of Coastal Research*, 27(5), 994-996.

Douglas, B.C., 1992. Global sea level acceleration. *Journal of Geophysical Research: Oceans* (1978–2012), 97(C8), 12699-12706.

Douglas, B.C., 1997. Global sea rise: a redetermination. *Surveys in Geophysics*, 18(2-3), 279-292.

Fasullo, J.T.; Boening, C.; Landerer, F.W. and Nerem, R.S., 2013. Australia's unique influence on global sea level in

2010–2011. *Geophysical Research Letters*, 40(16), 4368-4373.

Foster, G. and Brown, N., 2015. Time and tide: analysis of sea level time series. *Climate Dynamics*, 45, 291–308.

Golyandina, N.; Korobeynikov, A.; Shlemov, A. and Usevich, K., 2015. Multivariate and 2D Extensions of Singular Spectrum Analysis with the Rssa Package. *Journal Of Statistical Software*, 67(2), 1-78.

Golyandina, N.; Nekrutkin, V. and Zhigljavsky, A.A., 2001. *Analysis of time series structure: SSA and related techniques*. CRC press.

Golyandina, N. and Osipov, E., 2007. The "Caterpillar"-SSA method for analysis of time series with missing values. *Journal of Statistical Planning and Inference*, 137(8), 2642–2653.

Golyandina, N. and Zhigljavsky, A., 2013. *Singular Spectrum Analysis for time series*, Springer Science & Business Media.

Hamlington, B.; Leben, R.; Strassburg, M.; Nerem, R. and Kim, K.Y., 2013. Contribution of the Pacific Decadal Oscillation to global mean sea level trends. *Geophysical Research Letters*, 40(19), 5171-5175.

Hansen, J.M.; Aagaard, T. and Binderup, M., 2012. Absolute sea levels and isostatic changes of the eastern North Sea to central Baltic region during the last 900 years. *Boreas*, 41(2), 180-208.

Hay, C.C.; Morrow, E.; Kopp, R.E. and Mitrovica, J.X., 2015. Probabilistic reanalysis of twentieth-century sea-level rise. *Nature*, 517(7535), 481-484.

Holgate, S.J.; Matthews, A.; Woodworth, P.L.; Rickards, L.J.; Tamisiea, M.E.; Bradshaw, E.; Foden, P.R.; Gordon, K.M.; Jevrejeva, S. and Pugh, J., 2012. New data systems and products at the permanent service for mean sea level. *Journal of Coastal Research*, 29(3) 493-504.

Houston, J.R. and Dean, R.G., 2011a. Sea-level acceleration based on US tide gauges and extensions of previous global-gauge analyses. *Journal of Coastal Research*, 27(3), 409-417.

Houston, J.R. and Dean, R.G., 2011b. Reply to: Rahmstorf, S. and Vermeer, M., 2011. Discussion of: Houston, JR and Dean, RG, 2011. Sea-Level Acceleration Based on US Tide Gauges and Extensions of Previous Global-Gauge Analyses. *Journal of Coastal Research*, 27 (3), 409-417, Journal of Coastal Research, 27(4), 788-790.

Jevrejeva, S.; Grinsted, A.; Moore, J. and Holgate, S., 2006. Nonlinear trends and multiyear cycles in sea level records. *Journal of Geophysical Research: Oceans* (1978–2012), 111(C9).

Jevrejeva, S.; Moore, J.; Grinsted, A. and Woodworth, P., 2008. Recent global sea level acceleration started over 200 years ago? *Geophysical Research Letters*, 35(8).

Jevrejeva, S.; Moore, J.; Grinsted, A.; Matthews, A. and Spada, G., 2014. Trends and acceleration in global and regional sea levels since 1807. *Global and Planetary Change*, 113, 11-22.

Kemp, A.C.; Horton, B.P.; Culver, S.J.; Corbett, D.R.; van de Plassche, O.; Gehrels, W.R.; Douglas, B.C. and Parnell, A. C., 2009. Timing and magnitude of recent accelerated sea-level rise (North Carolina, United States). *Geology*, 37(11), 1035-1038.

Killick, R. and Eckley, I., 2014. Changepoint: An R package for changepoint analysis. *Journal of Statistical Software*, 58(3), 1-19.

Merrifield, M., S. Merrifield, and G. Mitchum (2009), An anomalous recent acceleration of global sea level rise. *Journal of Climate*, 22(21), 5772-5781.

Nicholls, R.J. and Cazenave, A., 2010. Sea-level rise and its impact on coastal zones. *Science*, 328(5985), 1517-1520.

R Development Core Team (2015). R: A language and environment for statistical computing. R Foundation for Statistical Computing, Vienna, Austria. ISBN 3-900051-07-0, URL http://www.R-project.org.

Rahmstorf, S. and Vermeer, M., 2011. Discussion of: Houston, J.R. and Dean, R.G., 2011. Sea-Level Acceleration Based on US Tide Gauges and Extensions of Previous Global-Gauge Analyses. *Journal of Coastal Research*, 27 (3), 409-417, *Journal of Coastal Research*, 27(4), 784-787.

Stocker, T.; Qin, D.; Plattner, G,; Tignor, M.; Allen, S. and Boschung, J., 2013. Summary for Policymakers in Climate Change 2013: The physical science basis, contribution of working group I to the fifth assessment report of the intergovernmental panel on climate change, edited, Cambridge University Press, Cambridge, New York, USA.

Visser, H.; Dangendorf, S.and Petersen, A.C., 2015. A review of trend models applied to sea level data with reference to the “acceleration-deceleration debate”. *Journal of Geophysical Research: Oceans*, 120(6), 3873-3895.

Watson, P.J., 2011. Is there evidence yet of acceleration in mean sea level rise around mainland Australia? *Journal of Coastal Research*, 27(2), 368-377.

Watson, P.J., 2015a. Development of a Unique Synthetic Data Set to Improve Sea-Level Research and Understanding. *Journal of Coastal Research*, 31(3), 758-770.

Watson, P.J., 2015b. Identifying the best performing time series analytics for sea-level research: in *Contributions to Statistics*, Springer Science & Business Media (in press).

Woodworth, P.; White, N.J.; Jevrejeva, S.; Holgate, S.; Church, J. and Gehrels, W., 2009. Evidence for the accelerations of sea level on multi-decade and century timescales. *International Journal of Climatology*, 29(6), 777-789.

Journal of Coastal Research	SI	75	785-789	Coconut Creek, Florida	2016

Tidal Evolution in the Yellow and East China Sea during Holocene

Chunyan Zhou[†‡], Jinhai Zheng[†*], Ping Dong[††], Jisheng Zhang[†], Yuliang Zhu[†] and Zhiheng Zhang[§]

[†]State Key Laboratory of Hydrology-Water Resources and Hydraulic Engineering
Hohai University
Nanjing, China

[‡]State Key Laboratory of Hydraulics and Mountain River Engineering
Sichuan University,
Chengdu, China

[††]School of Engineering, Physics and Mathematics
University of Dundee
Dundee, United Kingdom

[§]The First Institute of Oceanography
State Oceanic Administration
Qingdao,China

www.cerf-jcr.org

www.JCRonline.org

ABSTRACT

Zhou, C.Y.; Zheng, J.H.; Dong, P.; Zhang, J.S.; Zhu, Y.L., and Zhang, Z.H., 2016. Tidal evolution in the Yellow and East China Sea during Holocene. *In:* Vila-Concejo, A.; Bruce, E.; Kennedy, D.M., and McCarroll, R.J. (eds.), *Proceedings of the 14th International Coastal Symposium* (Sydney, Australia). *Journal of Coastal Research*, Special Issue, No. 75, pp. 785-789. Coconut Creek (Florida), ISSN 0749-0208.

The impact of the sea level (SL) change on the propagation of tides in the Bohai Sea, Yellow Sea and East China Sea (BYECS) during Holocene was investigated by a 3D numerical model with SL of -60, -30, -15, 0 and +2 m, respectively. Same amplitude and phase of tidal constituents M2, S2, K1 and O1 were applied along the open boundaries in all the cases. The results showed that the number of amphidromic points of M2 increased from 2 to 4 while that of K1 increased from 1 to 2 as the SL rising. Both M2 and K1 co-phase lines rotated anti-clockwise as sea-level rising. S2 shared similar evolution pattern with M2 while O1 evolved similarly with K1. The +2 m SL can have significant influence on the tide pattern. Mainly because the new basin area enlarged, especially the vast area around the Subei and Changjiang estuary, also very near the amphidromes in the south Yellow Sea, which dissipated large amount of tide energy. The new coastline and bathymetry changed the propagation pattern of M2, the tide energy decreased significantly at the north Yellow Sea and Bohai Sea while increased along the Yangtze estuary and Korea west coast. The strong tidal current area corresponded well with the sand ridges during Holocene while weaker tidal current area corresponded with finer muddy deposit, indicating tide force is the dominate factor controlling the bedform generation and sediment distribution in BYECS.

ADDITIONAL INDEX WORDS: *Tidal current, East China Sea, paleo-enviornment, Holocene.*

INTRODUCTION

Sea level (SL) change since the Last Glacial Maximum (LGM) has had a great impact on tides due to changes in ocean bathymetry (Green, 2010; Zhou *et al.*, 2013). Much numerical work has been done globally to investigate the evolution of tidal characteristics during the Holocene, such as European Shelf modeling (Uehara *et al.*, 2006) and sediment transport regimes in Fundy Bay (Greenberg *et al.*, 2012).

Geological records indicated that the geometry of the Bohai Sea, Yellow Sea and East China Sea (BYECS) has experienced significant changes due to SL rising by over 100 m since the last glacial maximum. Most of the BYECS region consists of a continental shelf shallower than 100 m. As basin geometries play an important role in tide propagation, tidal fields in this region must have been variable during the Holocene period. It is therefore necessary to evaluate the paleotidal properties when recovering the paleo shelf sea environments during the Holocene in the BYECS area.

DOI: 10.2112/SI75-158.1 received 15 October 2015; accepted in revision 15 January 2016.
*Corresponding author: jhzheng@hhu.edu.cn
©Coastal Education and Research Foundation, Inc. 2016

Although the paleo-tidal regime in regional area of BYECS due to sea lever rise has been studied by many researchers (Uehara *et al.*, 2002), corresponding dynamic sediment processes such as bedform generation (Zhang *et al.*, 2013), have barely been investigated systematically in the BYECS.

There are many sand ridges and muddy deposits in the BYECS (Figure 1), some of which are not located consistently with modern tidal current regime. For example, modern tidal-current conditions seem to be insufficient to form the sand ridges in the central East China Sea. Furthermore, radiocarbon dates from the sand-ridge region in the middle shelf, show mostly 7-11 ka B.P. and are thought to be deposited as deltaic sediments during the low stand of sea-level (Liu *et al.*, 2000). As tidal current is one of the most energetic hydrographic features in the modern BYECS, the information on the paleo-tidal regimes is essential for understanding the distribution of sand ridges and muddy deposits in the BYECS.

This study aims to reconstruct paleo-tidal fields and investigate their relationship with the distribution of sand ridges and muddy deposits in the BYECS during Holocene. Numerical scenarios were carried out to study the tidal regime and the corresponding dynamic sediment environment when sea-level was 60 m, 30 m, 15 m lower and 2 m higher than present SL.

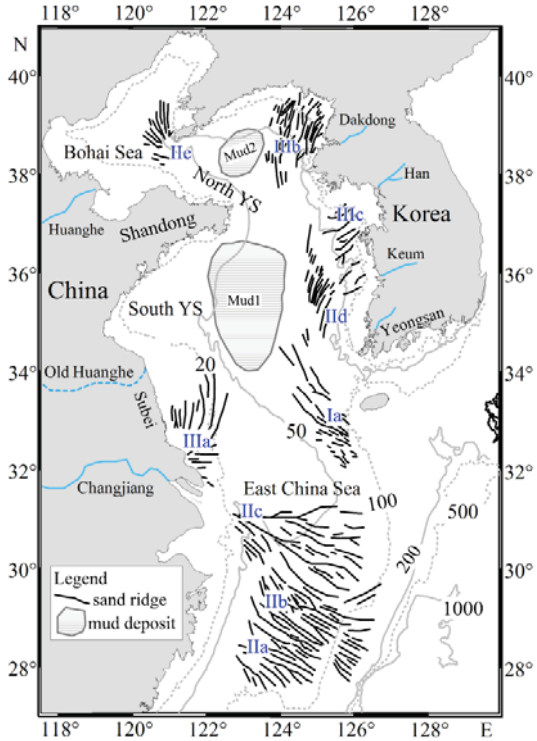

Figure 1. Regional map and depth contours of the BYECS. Contour unit is meter. The sand ridges are derived from Li *et al.* (2014), Ⅰ, Ⅱ and Ⅲ denote the first, second and third phase sand ridges, the following notes a-e of the same period denote the order of the spatio-temporal evolution of sand ridges.

METHODS

The paleo-tides during Holocene were simulated by an open source numerical model MITgcm (MIT General Circulation Model). The model is governed by the following equations:

$$\frac{1}{\rho}\frac{D\rho}{Dt}+\vec{\nabla}\cdot\vec{u}=0 \qquad (1)$$

$$\rho\frac{D\vec{u}}{Dt}+\rho 2\vec{\Omega}\times\vec{u}=-\nabla p+\rho\vec{g}+\mu\nabla^2\vec{u} \qquad (2)$$

where $\vec{u}$ is the three dimensional velocity vector, ρ is the density, $\vec{\Omega}=(0,\Omega\cos\varphi,\Omega\sin\varphi)$ is the forces due to earth rotation, where φ is latitude, p is the fluid pressure, $\vec{g}=(0,0,-g)$ is the gravitational acceleration constant; μ is the dynamic viscosity.

The model domain is 27.0625°N-41.125°N and 117.5°E-128.3125°E, with a horizontal resolution of 1/16 °× 1/16 °. There are 40 levels in the vertical with 20 levels of grid 5 m in the top 100 m, and then 10 levels of 25 m, 5 levels of 100 m and 5 levels of 180 m downwards. And piece-wise linear representation (shaved cells) is applied so that the minimum water depth can be 0.5 m.

The paleo-tides were driven by water levels along the open boundaries at the east and south. The tidal harmony constituents (M2, S2, K1 and O1) at the boundaries are interpolated from a Global Tide Model in the present SL with resolution of 0.125º × 0.125º, developed by DTU Space in collaboration with DHI (Cheng and Andersen, 2011).

The tidal forcing in the open boundaries of the domain is assumed not to change with the SL rising. Similar approach has been applied in many simulation studies on tide at different sea levels (Uehara *et al.*, 2002), because the relative change due to SLR along the open boundaries of our regional model (where depth is large) was small (less than 0.05 m) according to the global paleo-tidal model (resolution of 1º) since LGM carried out by Thomas and Sundermann (1999). Though this is not strictly true in the northern part of the east open boundary, it is assumed that the associated error is negligible, given that almost all tidal energy reaches the domain from the south (Uehara *et al.*, 2002).

The cases were carried out by lowering the SL from the present state to -60, -30, -15 m respectively, whereas the last one by increasing the SL by 2 m which corresponding to the highest SL around 7 ka B.P., using the present bathymetry. Water depths shallower than 0.5 m were set as 0.5 m to prevent numerical instabilities. The -60, -30, -15, 2 m represent the sea-level at 11600, 9400, 9000, and 7000 a B.P. according to the sea-level curve of Liu *et al.* (2004). All runs were initiated from rest and integrated for 2 months, and data of the last 30 days were used for tidal harmonic analyses by T_tide at each grid point. Additionally, modern tide regime, verified in the earlier study (Zhou *et al.*, 2015), was used for comparison with paleotidal regime.

RESULTS

When the SL was -60 m, there were only two degenerated amphidromes in the paleo-Yellow Sea (Figure 2a), and most of the co-phase lines aligned in direction normal to the axis of the bay. Large M2 tidal amplitude (>1.4 m) appeared along the southern coast of Korea, just outside the mouth of the paleo-Yellow Sea. M2 tide range was also large at around the paleo-Changjiang estuary (29°N, 124.5°E) with amplitude of 1.6 m. When SL was -30 m (Figure 2(e)), the shoreline moved towards to the strait of Bohai Sea (BS), the two amphidromes in the (YS) shifted to the west (Table 1). The M2 tidal amplitude decreased around the southern coast of Korea while increased significantly in the paleo-Changjiang estuary. When SL rose to -15 m (Figure 2 (i)), the other two amphidromes appeared in the BS. The amplitudes in the YS and BS enlarged, mostly because the basin geometry benefits the M2 propagation into the Yellow Sea and Bohai Sea. When the SL was 2 m higher than present, there are still four amphidromes in BS and YS (Figure 3(a)). The amplitude obviously decreased in the north YS and BS, which is shallow area with water depth mostly 20-50 m. The 2 meters increase in depth can have significant influence on the tide in the north YS and BS. Mainly because the new basin area enlarged in the +2 m case, especially the area around the Subei and Changjiang estuary, also very near the amphidromes in the south Yellow Sea, which dissipated large amount of tide energy, and the tide energy propagated to the north YS and BS decreased significantly. A radial current pattern appeared near the mouth of the paleo-Changjiang river since SL of -30 m (Figures 2(f), 2(j), 2(n) and 3(b)).

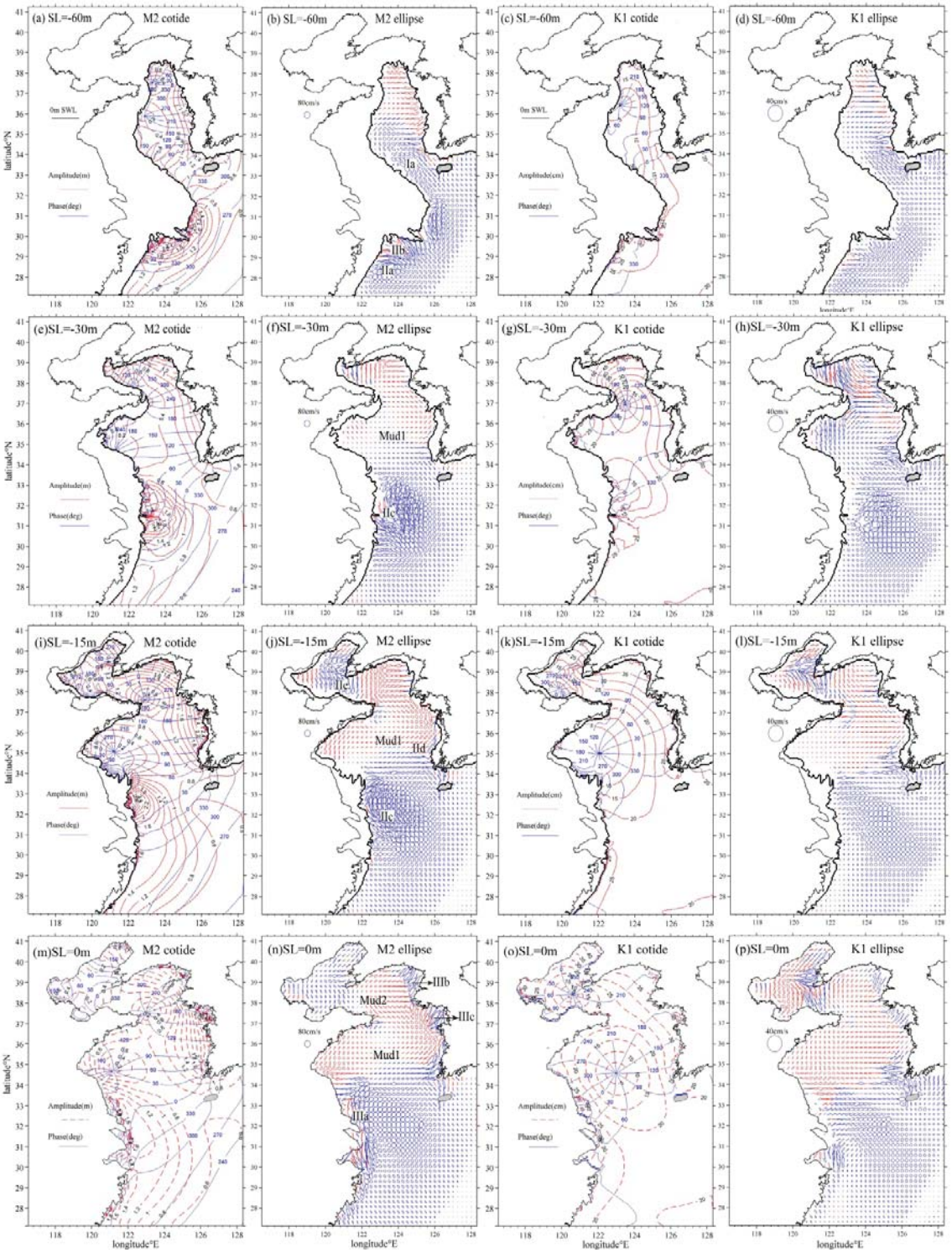

Figure 2. Co-tidal chart and current ellipse of M2 and K1 in BYECS under SL of -60, -30, -15 and 0m (ellipse: blue-clockwise; red-anticlockwise).

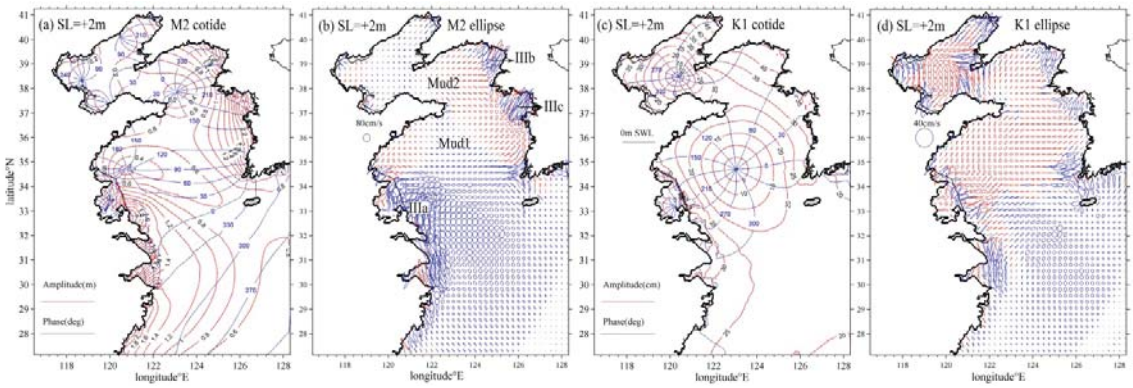

Figure 3. Co-tidal chart and current ellipse of M2 and K1 in BYECS under SL of +2m (blue ellipse- clockwise; red ellipse-anticlockwise).

For the K1 constituent, only one amphidrome exists off the southeast of Shandong peninsula in the Yellow Sea when SL was -60 m (Figure 2(c)), K1 amplitude maximum value is 0.15-0.2 m in the paleo-Yellow Sea, K1 tide retains its amplitude along the central axis of the paleo-Yellow Sea basin, as can be recognized from the 0.1 m contour, which is quite different with M2 tide amplitude decreasing rapidly as it enters the Yellow Sea (from about 1.2 m to less than 0.4 m). As the SL rose to -30 m (Figure 2(g)), the amphidromic point shifted northeastward in the Yellow Sea (Table 2). The large K1 amplitude value (0.5 m) appeared in the BS strait (122.5°E, 38.4°N), much larger than present value (0.2 m). With SL increasing to -15 m (Figure 2(k)), another amphidrome appeared in the BS, the amplitudes decreased in general compared with modern state. In the case of SL 2 m higher than present, there are still two K1 amphidromes totally in Bohai and Yellow Sea (Figure 3(c)). The K1 amplitude, however, increased in the north YS and BS while decreased slightly in the south YS, the change trend of which is contrary to that of M2 at +2 m SL. Thus, the K1 current even large enough to be comparable with M2 in the BS. Because the amphidromic point of K1 in the South Yellow Sea are relatively far away from the enlarged Subei and Changjiang estuary area, and the new coastline and bathymetry benefit the K1 propagating into the north YS and Bohai Sea.

Furthermore, both the M2 and K1 co-phase lines rotated anti-clockwise as the sea water level increased. S2 (not shown in this paper, referred to Zhou (2014)) shared the similar evolution pattern with M2 while O1(not shown in this paper, referred to Zhou (2014)) had the similar change pattern with K1 as SL rose from -60 m to 2 m. Overall speaking, the M2 and K1 changed unevenly with the SL rise. Sea level change affected the tidal regime mainly through changing geometries of the sea and thus tidal wavelength, because tidal wavelength is proportional to a square root of the water depth.

DISCUSSION

As mentioned earlier, there are many sand ridges and muddy deposits in the BYECS shelf, some of which were considered to form when the sea level was low based on geological analysis, such as sediment core dating, stratigraphy, sedimentary facies analysis, *etc*. However, the relationship of these sand ridges and muddy deposit with the tidal regime evolution is barely discussed before.

Table 1. *M2 amphidromic points position under different sea levels*

Sea area / SL(m)	BS North	BS South	North YS	South YS
-60	—	—	123.358°E	122.876°E
	—	—	37.523°N	35.908°N
-30	—	—	122.246°E	121.312°E
	—	—	37.903°N	34.768°N
-15	120.28°E	119.196°E	122.916°E	121.224°E
	39.924°N	38.115°N	37.587°N	35.055°N
0	120.126°E	118.911°E	123.095°E	121.239°E
	40.073°N	38.082°N	37.582°N	34.829°N
+2	120.480°E	118.725°E	123.074°E	120.764°E
	40.154°N	38.353°N	37.868°N	34.653°N

Table 2. *K1 amphidromic points position under different sea levels*

Sea area / SL(m)	Bohai Sea	Yellow Sea
-60	—	123.227°E
	—	36.423°N
-30		123.499°E
		36.893°N
-15	119.877°E	122.001°E
	38.125°N	35.008°N
0	120.526°E	123.113°E
	38.519°N	34.732°N
+2	120.345°E	123.055°E
	38.455°N	34.699°N

Sand ridges can form in the estuaries and nearshore areas with strong current of 0.5-1.0 m/s and the ellipticity of the M2 must be less than 0.4 (Liu *et al.*, 1998) and muddy deposit is formed in the area with very weak current field. According to the M2 tidal ellipse, the sand ridges and muddy deposits

formed in stages probably corresponding to paleo-tidal current as shown in Figures 2 and 3 and Table 3.

Ⅰa sand ridge formed in the Yellow Sea trough when the SL was -60m or below and Ⅱa and Ⅱb formed off the paleo-changjiang estuary at SL of -60m. As SL rose to -30m, radial current pattern off the paleo-changjiang mouth appeared and Ⅱc formed. When SL was -15m, Ⅱd and Ⅱe formed at the strong tidal current area along the Korea coast and Bohai Sea strait, respectively. For the SL of 0m and +2m, sand ridge Ⅲa corresponded to the radial current pattern and Ⅲb and Ⅲc formed along the Korea coast.

The formation of ridges is not only influenced by tidal currents but also by the sand sources. If there is not enough sand material, the sand ridge can not be formed even with favorable tidal conditions. Both the sand material carried out by rivers around the BYECS and the eroded relict sediment can affect the formation of sand ridges.

The tidal current of Mud1 area was very weak since SL of -30 m, providing an ideal environment for mud deposit there continuously. Mud2 formed later in the North YS under tidal regime similar with modern tidal current pattern.

Table 3. *Corresponding sediment formation along with the SL rise*

SL(m)	Figures	Sand ridges or muddy deposit
-60	Figure 2(b)	Ⅰa, Ⅱa, Ⅱb
-30	Figure 2(f)	Ⅱc, Mud1
-15	Figure 2(i)	Ⅱc, Ⅱd, Ⅱe, Mud1
0	Figure 2(n)	Ⅲa, Ⅲb, Ⅲc, Mud1,Mud2
+2	Figure 2(j)	Ⅲa, Ⅲb, Ⅲc, Mud1,Mud2

CONCLUSIONS

Numerical scenario were carried out in this research to study the tidal regime during the Holocene due to sea level change and then their relationships with distribution of sand ridges and muddy deposits were discussed.

Tidal regimes of both M2 and K1 varied significantly and changed unevenly along with sea level rise. S2 shared similar evolution pattern with M2 while O1 evolved similarly with K1. The +2 m SL can have significant influence on the tide pattern, and the change trends of M2 and K1 were contrary at +2 m SL case, and the K1 current in the BS and North YS became larger and even large enough to be comparable with M2, suggesting that the effects of diurnal constituents can not be neglected when investigating the tidal current at sea level higher than present.

The strong tidal current area corresponded well with the sand ridges during Holocene while weaker tidal current area corresponded with finer muddy deposit, indicating tide force is the dominate factor controlling the bedform generation and sediment distribution in BYECS.

ACKNOWLEDGMENTS

This work is funded by the National Science Fund for Distinguished Young Scholars (Grant No. 51425901), the Open Fund of State Key Laboratory of Hydraulics and Mountain River Engineering (Grant No. SKHL1428), Project Funded by China Postdoctoral Science Foundation (Grant No. 2015M581708), Jiangsu Planned Projects for Postdoctoral Research Funds (Grant No. 1501151B) and the Fundamental Research Funds in the Central University (Hohai University, Grant No.2014B04114).

LITERATURE CITED

Cheng, Y., and Andersen, O.B., 2011. Multimission empirical ocean tide modeling for shallow waters and polar seas. *Journal of Geophysical Research*, 116, C11001.

Green, J., 2010. Ocean tide sand resonance. *Ocean Dynamics*, 60, 1243-1253.

Greenberg, D.A.; Blanchard, W.; Smith, B., and Barrow, E., 2012. Climate Change, Mean Sea Level and High Tides in the Bay of Fundy. *Atmosphere-Ocean*, 20(3), 261-276.

Li, G.; Li, P.; Liu, Y.; Qiao, L.; Ma, Y.; Xu, J., and Yang, Z., 2014. Sedimentary system response to the global sea level change in the East China Seas since the last glacial maximum. *Earth-Science Reviews*, 139, 390-405.

Liu, J.P.; Milliman, J.D.; Gao, S., and Cheng, P., 2004. Holocene development of the Yellow River's subaqueous delta, North Yellow Sea. *Marine Geology*, 209(1-4), 45-67.

Liu, Z.; Berne, S.; Saito, Y.; Lericolais, G., and Marsset, T., 2000. Quaternary seismic stratigraphy and paleoenvironments on the continental shelf of the East China Sea. *Journal of Asian Earth Sciences*, 18(4), 441-452.

Liu, Z.; Xia, D.; Berne, S.; Wang, K.; Marsset, T.; Tang, Y., and Bourillet, J.F., 1998. Tidal deposition systems of China's continental shelf, with special reference to the eastern Bohai Sea. *Marine Geology*, 145(3-4), 225-253.

Thomas, M., and Sundermann, J., 1999. Tides and tidal torques of the world ocean since the last glacial maximum. *Journal of Geophysical Research*, 104(C2), 3159-3183.

Uehara, K.; Saito, Y., and Hori, K., 2002. Paleotidal regime in the Changjiang (Yangtze) Estuary, the East China Sea, and the Yellow Sea at 6 ka and 10 ka estimated from a numerical model. *Marine Geology*, 183(1-4), 179-192.

Uehara, K.; Scourse, J.D.; Horsburgh, K.J.; Lambeck, K., and Purcell, A.P., 2006. Tidal evolution of the northwest European shelfseas from the Last Glacial Maximum to the present. *Journal of Geophysical Research*, 111, C09025.

Zhang, C.; Zheng, J.; Dong, X.; Cao, K., and Zhang, J., 2013. Morphodynamic response of Xiaomiaohong tidal channel to a coastal reclamation project in Jiangsu Coast, China. *In*: Conley, D.C.; Masselink, G; Russell, P.E., and O' Hare, T.J. (eds.), *Journal of Coastal Research*, SI 65, pp. 630-635.

Zhou, C., 2014. Hydrodynamic Processes and Their Impacts on the Mud Deposit in the Southern Yellow Sea, China. Dundee, UK: University of Dundee, Ph.D dissertation, 161p.

Zhou, C.; Dong, P., and Li, G., 2015. Hydrodynamic processes and their impacts on the mud deposit in the Southern Yellow Sea. *Marine Geology*, 360, 1-16.

Zhou, X.; Zheng, J.; Doong, D.-J., and Demirbilek, Z., 2013. Sea level rise along the East Asia and Chinese coasts and its role on the morphodynamic response of the Yangtze River Estuary. *Ocean Engineering*, 71, 40-50.

Journal of Coastal Research	SI	75	790-794	Coconut Creek, Florida	2016

Sturgeon Bank, Fraser River Delta, BC, Canada: 150 Years of Human Influences on Salt Marsh Sedimentation

Rowland J. Atkins[†*], Morgan Tidd[†], and Gord Ruffo[‡]

[†]Golder Associates Ltd
2nd Floor, 3795 Carey Road
Victoria, BC V8Z 6T8, Canada

[‡]Port Metro Vancouver
100 The Pointe, 999 Canada Place
Vancouver, BC V6C 3T4, Canada

www.cerf-jcr.org

www.JCRonline.org

ABSTRACT

Atkins, R.J.; Tidd, M., and Ruffo, G., 2016. Sturgeon Bank, Fraser River Delta, BC, Canada: 150 Years of Human Influence on Salt Marsh Sedimentation. *In:* Vila-Concejo, A.; Bruce, E.; Kennedy, D.M., and McCarroll, R.J. (eds.), *Proceedings of the 14th International Coastal Symposium* (Sydney, Australia). *Journal of Coastal Research*, Special Issue, No. 75, pp. 790-794. Coconut Creek (Florida), ISSN 0749-0208.

The Fraser River Delta in south western British Columbia, Canada, is a relatively recent geologic feature being only approximately 10,000 years old. The delta environment, and the intertidal banks, are the cumulative effect of flood and sediment discharges over the post-glacial interval. The salt marsh of Sturgeon Bank, on the northwest side of the delta, has been identified as under threat from erosion. The occurrence, cause and extent of erosion have been a subject of speculation, investigation and conclusion for several decades; however, dissenting opinions on the persistence of erosion over the last fifty years are numerous. To explore potential causes of the erosion further, publically available historical datasets of natural phenomena were re-examined relative to records of human activities to enable development of a conceptual model. Historical datasets of natural phenomena included sedimentary geology, post-glacial history, bathymetry, flood discharge records, sediment discharge/basin sediment yield, sediment grain size data, wind-waves, and tides. Human activity, stretching back to the late 1800's, included navigation dredging, aggregate resource dredging, river training, river diversion, flood protection dyking, land-use changes, and ongoing habitat management activities. From this review, a conceptual model of physical constraints on deltaic environments was developed. The various phenomena are discussed, the integration of those phenomena as processes affecting deltaic habitat explored, and potential management strategies identified to address the sedimentary consequences of the last 150 years of human influence on the salt marshes of Sturgeon Bank.

ADDITIONAL INDEX WORDS: *Salt marshes, coastal development, coastal processes.*

INTRODUCTION

The Fraser River delta, in southwestern BC, Canada, is a relatively recent geologic feature (Clague *et al.*, 1983). The delta includes salt marshes that have been the subject of ongoing debate about whether they are eroding or accreting (Luternauer and Murray, 1973, Levings, 1980, Luternauer *et al.*, 1995, Clague *et al.*, 1998, Hales, 2000). A study was undertaken to review available data and assess the sedimentary regime of the marshes of Sturgeon Bank over the last 150 years to explore the likelihood that they are eroding. The work was undertaken in support of Port Metro Vancouver's Habitat Enhancement Program. The salt marshes of Sturgeon Bank were identified in the program as a potential area for management.

Background

The Fraser River delta is the largest river draining the west coast of Canada. It is approximately 1,400 km long and drains a basin over 234,000 km^2 in area (Clague *et al.*, 1983). Located south of Vancouver, BC, the delta is situated on the eastern shore of the Strait of Georgia, a semi-enclosed marine basin (Figure 1). The delta extends 15 km south and 23 km west from New Westminster (Clague *et al.*, 1983).

Lulu Island is situated at the mouth of the delta, immediately north of the main distributary channel (Main Arm). The island is bounded in the north by the North Arm distributary channel (North Arm) and a smaller secondary channel (Middle Arm). Middle Arm and Main Arm define the northern and southern limits of Sturgeon Bank whose tidal flats and upper inter-tidal and supra-tidal marshes mark the seaward edge of Lulu Island. The salt marshes are situated on shallowly-sloped (typically less than 0.5%) topset sediments (Luternaer *et al.* 1995). The tidal flats extend westwards into sub-tidal shallows to a water depth of approximately 13 m below mean sea level. Seaward of the sub-tidal shallows, the deltaic sediments form more steeply sloped foreset beds with slope gradients typically between 2% and 5%, which descend to between 150 m and 300 m below mean sea level (Clague *et al.* 1998).

METHODS

The assessment of human influences on the sedimentary environment of the upper inter-tidal and supra-tidal areas of Sturgeon Bank included a literature review and summary of current information and data available on the physical and human factors influencing Sturgeon Bank and the salt marsh. Conceptual models of pre-development and post-development geomorphological regimes were developed based on the data reviewed.

DOI: 10.2112/SI75-159.1 received 15 October 2015; accepted in revision 15 January 2016.
*Corresponding author: ratkins@golder.com
©Coastal Education and Research Foundation, Inc. 2016

Figure 1. Modern environment showing Sturgeon Bank situated on the western edge of Lulu Island and the present extent of dykes and jetties. Green polygon shows location of the salt marsh. Red arrows show sediment pathways, larger arrows imply more sediment. Base Image: Google Earth. Inset map of Fraser River watershed from FREMP, 2006.

REVIEW SUMMARY

The sedimentary environment of the Fraser River delta is summarized from the perspective of the deltaic regime, the geomorphological history, and the human influences.

Deltaic Regime

The Fraser River discharge regime is dominated by a late May-early June freshet. Flows range from 1,500 m^3/s up to a maximum of 17,000 m^3/s with a mean of 3,400 m^3/s (nhc, 2008, Clague *et al*., 1991). Maximum estimated discharges were 15,200 m^3/s for the 1948 flood and 12,900 m3/s for the 1972 flood (nhc, 2008). The average annual sediment load is 1.2×10^7 m^3/yr. (Thomson, 1981). Of the annual river discharge 65% is silt and clay and 35% sand (Milliman, 1980, NRC, 2007).

Tides for the Fraser River delta, as measured at Sand Heads (Station #7594, Fisheries and Oceans Canada, 2015), at the mouthof Main Arm, are predominantly mixed, semi-diurnal with a typical tidal range of 5.0 m and an extreme range of 5.9 m. Tidal currents on Sturgeon Bank typically flood to the northwest and ebb to the southeast. The northwest flood tide is the dominant tide therefore sediment transport from the Fraser is typically deflected to the northwest (Thompson, 1981, Fisheries and Oceans Canada, 2015).

Tidal influence within the river extends up Main Arm in the form of a salt wedge as far inland as New Westminster (Clague *et al*., 1983). The location of the salt wedge varies based on tidal height and river discharge but causes tidal effects on Fraser River ~80 km upstream during low flow conditions and ~100 km upstream during freshet conditions (Thomson, 1981, nhc 2008).

The tidal flats of Sturgeon Bank consist of sand flats, mud flats, eelgrass and intertidal marshes (Pharo and Brnes, 1976, Williams et al. 2009). The marshes of Sturgeon Bank include salt, brackish and freshwater marshes extending approximately 1 km offshore of the dykes. The salt marshes have historically experienced erosion and accretion (Hales, 2000).

Geomorphological History

The formation of the Fraser River delta initiated following deglaciation of the Fraser Lowland around 11,000 years before present (BP) (Clague *et al*., 1991). The delta initially formed as sediments deposited by Fraser River advanced down a partially submerged, glacially scoured trough (Clague *et al*., 1983). The delta reached New Westminster around 10,000 years BP then expanded south and west into the Strait of Georgia. Progradation of the delta continued westwards while sea level dropped relative to the land (Clague *et al*. 1983).

Post-glacial sea level stabilized around 8,000 years BP at 12 m below modern mean sea level and then began to rise relative to the land (Clague *et al*. 1983). Two general periods of marine transgression occurred around 7,000 and 5,000 years BP (Clague *et al*. 1983). The rising sea levels slowed sub-aerial delta development and growth to the west and south. The easternmost 10 km of the delta stabilized around 5,000 years BP allowing the accumulation of organic material in areas which are now the location of several large peat bogs (Clague *et al*., 1983).

From 5,000 years BP to present, the Fraser River discharged westwards into the Strait of Georgia (Clague *et al*., 1983). Tidal forcing tends to deflect Main Arm and its plume north as it advances westwards (Pharo and Barnes, 1976). In the 1700s, Main Arm of Fraser River was situated approximately 10 km southeast of its present location (Clague *et al*., 1983).

The current delta is approximately 975 km^2 in area (Milliman, 1980). A model of the sedimentary development of Fraser River delta over the last 10,000 years is presented in Figure 2.

Once deposited, the deltaic sediments tend to compact under gravity and the weight of overlying sediments (Mazzotti *et al*., 2009). The compaction leads to settlement of the ground surface or subsidence. The presence of anthropogenic structures can increase this settlement due to the weight of the structures. Mazzotti et al., (2009) have estimated settlement of 1 to 2 mm/yr for the native deltaic sediments and upwards of 3 to 8 mm/yr in association with large structures.

Human Influences

Natural development of the delta has been limited since the early 1800's due to human activity (Isfeld *et al*. 1996). This activity has included dredging for shipping and navigation, diversion of portions of the Fraser River watershed, land use changes within the watershed, channelization by river training for navigation, extraction of sediment for construction purposes (borrow dredging), narrowing of the floodplain by the construction of dykes for flood management, construction of jetties and ocean outfalls, filling in of distributary channels, and armouring of riverbanks. Table 1 summarizes major historical influences affecting the sedimentary regime of Sturgeon Bank.

Table 1. *Summary of Major Historical Influences on Sturgeon Bank*

Date	Event	Implications	Reference
1800s to present	Dredging commences	Sediment removal Channel deepened	Ferguson, 1991
1894	Largest documented flood (>1948)	Large sediment pulse	nhc, 2008
1906 to present	Dyke construction	Flood prevention Flood sediment distribution restricted	Richmond, 2000
1912	Steveston Jetty construction	Channel stabilized Marshes isolated from sediments	FREMP, 2006 Levings, 1980
1913	North Arm dredging	Sediment removal Channel deepened	FREMP, 2006
1917	North Arm Jetty construction	Channel stabilized Marshes isolated	Levings, 1980
1930s	South Jetty construction	Channel constricted Marshes isolated	Medley and Luternauer 1976
1935	Steveston Jetty extension	Channel stabilized further westwards	Levings, 1980
1948	Flood of record	Large sediment pulse	nhc, 2008
1951	North Arm Jetty extension	Channel stabilized further westwards	Levings, 1980
1954	Nechako diversion	Fraser River watershed area reduced	French and Chambers, 1997 Kellerhals *et al.*, 1979
1961	Iona causeway constructed	Natural sediment regime altered	Levings, 1980
1972	Large flood	Large sediment pulse	nhc, 2008
1973-75	Trifurcation works completed	Natural flow and sediment regime altered	Milliman, 1980
1978 to present	Steveston Jetty reconstruction	Water and fish (and sediment) released onto Sturgeon Bank	Levings, 1980
Late 1990s	Borrow dredging reduced	Sediment removals reduced	Bros, 2007
2007	Large flood event	Large sediment pulse	nhc, 2008

DISCUSSION

The review of available data, allows for an evaluation of the sedimentary regime of Sturgeon Bank over the historical period. Comparing Figures 1 and 2, the extent of dykes and river training jetties can be seen to isolate Sturgeon Bank (Figure 1) from the historical sediment pathways as discussed below.

The construction of flood protection dyking within the delta, especially around Lulu Island, has been ongoing since 1906 (Richmond, 2000). The construction of dykes has limited the dispersion of sediment-laden flood waters onto Sturgeon Bank. Floods in deltaic environments are a naturally occurring mechanism for sediment deposition which acts to counterbalance settlement and contribute to aggradation (Milliman, 1980, Clague *et al*. 1983, FREMP, 2006).

In addition to the constructed dykes, river training infrastructure and channelization devices have restricted the delivery of sediment to the delta (Isfeld *et al*. 1996). Steveston Jetty, constructed in 1912 (Richmond, 2000) along the north bank of Main Arm, has directed river water and sediment out to the seaward edge of the tidal flats and away from southern Sturgeon Bank (Levings, 1980). In 1978, alterations were made to the jetty by installing several gaps to allow both fish and water to transit the jetty and reach Sturgeon Bank (Williams and Hamilton, 1995). Fine sediments such as silt and clay pass through these openings onto Sturgeon Bank but limited sand is delivered this way (Luternauer *et al*., 1995, Hales, 2000). The stratigraphy of the bank sediments (Clague *et al*., 1983) indicate that historically, sand and fine sediment would have been delivered to the bank.

Figure 2. Model of post-glacial sedimentary regime of Fraser River, delta. Green polygon shows location of modern salt marsh. Orange dashed lines mark approximate delta front at 10,000 years BP and 5,000 yrs BP. Red arrows indicate sediment pathways, larger arrows imply more sediment. Base Image: Google Earth.

The construction of North Arm Jetty in 1917 has resulted in the deflection of flow and sediment away from the north end of Sturgeon Bank (Levings, 1980). The North Arm was also dredged for navigation, whereas Middle Arm was not, and thus sand-sized sediment is now transported within North Arm and deposited north of Sturgeon Bank (Isfeld *et al*., 1996). Furthermore, the north end of Sturgeon Bank was closed off in 1961 at McDonald Slough as part of a sewage treatment plant

project and this helped further isolate North Arm flows and sediment from Sturgeon Bank (Levings, 1980).

Channel training works on Main Arm, substantially completed by 1975 with the construction of the trifurcation project at New Westminster (Milliman, 1980), has resulted in 85% of Fraser River discharge and nearly 100% of the sedimentary load being transported through Main Arm (Isfeld *et al*. 1996). The remaining 15% of the Fraser River discharge is directed through North Arm (Milliman, 1980, Thomson, 1981) whereas historically 10% of the Fraser River discharge passed through this distributary channel carrying both water and sediment (Isfeld *et al*. 1996). The diversion of sediment has reduced sediment transport within North Arm (FREMP, 2006).

Navigation dredging has been occurring since the 1800s and represents a net loss of sediment to the delta (FREMP, 2006, Ferguson, 1991, Isfeld *et al*. 1996). Approximately 2.0×10^6 m^3 of sand is dredged each year from the various arms of Fraser River and deposited in the deeper waters of the Strait of Georgia. Annual dredging removes 2.5×10^5 m^3 of sediment from secondary channels (FREMP, 2006). As late as the 1990's, navigation dredging occured in North Arm on an as needed basis only (Isfeld *et al*. 1996).

Prior to 1998, non-navigational dredging (borrow dredging) was carried out to support the aggregate industry. This borrow dredging removed approximately 5×10^6 m^3 of sand from the river annually (Isfeld *et al*. 1996). Post-1998, borrow dredging volume decreased significantly (Bros, 2007). The effect of both types of dredging has resulted in increased channel deepening and a reduction of sediment delivery to the banks of the delta (Church, 2010). Table 2 summarizes the net effect of the human modifications to the delta.

Table 2. *Summary of Inferred Effect of Sedimentation*

Event/Modification	Inferred Implication to Marsh
Lower Sediment Discharge	Less sediment reaching marsh
River Training	Fewer sediment pathways to marsh
Flood Protection Dyking	Flood sediment diverted from marsh
Causeway/Jetty Construction	Isolated Sturgeon Bank from North and Main Arms, less sediment raching marsh. Wave protection from storms, less sediment transported onto the marsh
Borrow Dredging	Less sediment retained in channel
Navigation Dredging	Deeper channels capture sediment

Of the three distributary arms of Fraser River (Main, North and Middle in order of decreasing size), only Middle Arm is currently able to discharge to Sturgeon Bank without obstruction (McLaren and Ren, 1995). Middle Arm accounts for approximately 4% of total Fraser River discharge and little to no sediment delivery is occurring through this channel onto Sturgeon Bank (McLaren and Ren, 1995).

Coincident with these human alterations to water and sediment transport over and through the delta, the largest floods of record occurred in 1894 and 1948 (nhc, 2008). Thus natural variation in river discahrge over the historical period would suggest that sediment delivery has been lower in the latter half of the historical era (e.g. since 1950) than in the former half (e.g. before 1950). If there is less sediment being delivered to the delta now than 150 years ago, the sediment limiting effects of the flood protection dyking, channel training, and channel dredging would likely be amplified.

Management Concepts

Under present sedimentation conditions the marshes on Sturgeon Bank are likely erosional. Sediment delivery to Sturgeon Bank has been reduced over the last 150 years by human activity; therefore increased delivery is a potential design strategy to restore sedimentation. Based on the conceptual models (Figures 1 and 2), four concepts were prepared as potential strategies for restoring sediment delivery to Sturgeon Bank: (i) placement of sediment in the upper intertidal area, (ii) placement of sediment in the intertidal area, (iii) construction of armoured offshore wave breaks, and (iv) placement of sediment in offshore sources. Table 3 presents a preliminary evaluation of these options.

Table 3. *Preliminary Evaluation of Management Concepts*

Option	Pros	Cons
i) Upper Intertidal	Deliver from land Small footprint	Covers existing marsh May require rock
ii) Intertidal	Deliver from land Raises large area	Requires rock armour at toe Requires extensive grading
iii) Wave Breaks	Small footprint Standard design	Requires rock armour Limited marsh habitat value
iv) Offshore	Avoids marsh area Does not use rock	Wave redistribution needed Requires time to function

Of the four concepts, the offshore sediment source concept appears to be the best concept to restore sediment delivery. It neither impacts the existing marsh nor requires the use of rock armour in the intertidal area, but it requires wave redistribution of sediments so it will take time to realize a benefit.

An estimate of the necessary volume required as a source to replenish sediment delivery is approximately 525,000 m^3/yr (Luternauer and Murray, 1973), which is comparable to the natural accretion rate of 0.03 m/yr proposed by Hart *et al.* (1998). A volume of 5×10^5 m^3/yr represents approximately one-quarter of the sediment volume dredged annually from the river for navigational purposes (Isfeld *et al*., 1996).

CONCLUSIONS

Human activities undertaken on the Fraser River delta over the last 150 years have served to reduce the delivery of sediment to Sturgeon Bank. The reduction in sediment delivery to the marsh areas of the bank over the historical period has likely resulted in a modern erosional regime on what would naturally have been accreting salt marshes. A potential management strategy is to enhance delivery of sediment by discharge of dredged sediments from Main Arm to replenish the sediment delivery to the banks. Dredged sediment from channel maintenance activities could be used for this purpose.

ACKNOWLEDGMENTS

The authors would like to thank the habitat banking project team at Port Metro Vancouver's Habitat Enhancement Program for supporting this review. The authors would also like to thank the authors of the many papers that were reviewed to prepare this summary. Without their hard work and dedication this review would not have been possible.

LITERATURE CITED

Ausenco Sandwell, 2010. *Climate Change Adaptation Guidelines for Sea Dikes and Coastal Flood Hazard Land Use: Draft Policy Discussion paper*. Vancouver, BC: BC Ministry of Environment, 75 p.

Bros,W.J. 2007. Sustainable Dredging Program on the Lower Fraser River. Burnaby, BC: Simon Fraser University, Master's thesis, 125 p.

Clague, J.J, Luternauer, J.L., Pullen, S.E., and Hunter, J.A. 1991. Postglacial deltaic sediments, southern Fraser Delta, British Columbia. *Canadian Journal of Earth Sciences*, 28, 1386-1393.

Clague, J.J., Luternauer, J.L, Monahan, P.A., Edwardson, K.A., Dallimore, S.R., and Hunter, J.A. 1998. Quaternary stratigraphy and evolution of the Fraser delta. *In*: Clague, J.J., Luternauer, J.L., and Mosher, D.C. (eds.) *Geology and Natural Hazards of the Fraser River Delta, British Columbia, Bulletin 525*, Vancouver, Geological Survey of Canada, pp. 57-90.

Church, M. 2010. *Sustaining Fraser Estuary: Bases for a sediment management plan*. Vancouver, BC: FREMP, 39p.

Ferguson, Alan. 1991. *Navigation, dredging and environment in the Fraser River Estuary*. Vancouver, BC: FREMP, Navigation and Dredging Workgroup, 89 p.

Fisheries and Oceans Canada. 2015. *Canadian Tide and Current Tables, Volume 5, Juan de Fuca Strait and Strait of Georgia*. Ottawa, Ontario: Environment Canada, 120p.

Fraser Estuary Management Program, 2006. *Fraser River Estuary Management Plan*. Vancouver, BC: FREMP, 67 p.

French, T.D., and Chambers, P.A., 1997. Reducing flows in the Nechako River (British Columbia, Canada): potential response of the macrophyte community. *Canadian Journal of Fisheries and Aquatic Sciences*, 54, 2247-2254.

Hales, W.J., 2000. The Impact of Human Activity on Deltaic Sedimentation, Marshes of the Fraser River Delta, British Columbia. Canada: University of British Columbia, Ph.D. dissertation, 178p.

Hart R.S., Hamilton, T.S., and Barrie, J.V., 1998. Sedimentation on the Fraser Delta slope and prodelta, Canada, based on high resolution seismic stratigraphy, lithofacies and 137Cs fallout stratigraphy. *Journal of Sedimentary Research*, 68, 556-568.

Isfeld, E.O., Stepchuk, F, and Atkins, R.J. 1996. A Channel Maintenance Management Study: Lower Fraser Sandheads to Patullo Bridge including North and Middle Arms. *Proceedings Watercourses, Getting on Stream with Current Thinking* (Vancouver, BC, Canada, CWRA), pp. 191-196.

Kellerhals, R., Church, M., and Davies, L.B., 1979. Morphological effects of interbasin river diversions. *Canadian Journal of Civil Engineering*, 6, 18-31.

Levings, C.D., 1980. Consequences of Training Wall and Jetties for Aquatic Habitats at Two British Columbia Estuaries. *Coastal Engineering*, 4, 111-136.

Luternauer, J.L., and Murray, J.W., 1973. Sedimentation on the Western Delta-front of the Fraser River, British Columbia. *Canadian Journal of Earth Sciences*, 10, 1642-1663.

Luternauer, J.L. Atkins, R.J., Moody, A.I., Williams, H.E.I., and Gibson, J., 1995. Salt Marshes. *In:* Perillo, G.M.E. (ed.) *Geomorphology and Sedimentology of Estuaries*. Amsterdam: Elsevier, pp. 307-332.

Mazzotti, S., Lambert, A., Van der Kooji, M., and Mainville, A., 2009. Impact of anthropogenic subsidence on relative sea-level rise in the Fraser River delta. *Geology*, 37, 771-774.

McLaren, P. and Ren, P., 1995, *Sediment Transport and its Environmental Implications in the Lower Fraser River and Fraser Delta*. Vancouver, BC: Environment Canada, 113 p.

Medley, E., and Luternauer, J.L., 1976. Use of Aerial Photographs to map Sediment Distribution and to Identify Historical Changes on a Tidal Flat. *Paper 76-1C* (Vancouver, BC, GSC), pp. 293-304.

Milliman, J.D, 1980. Sediment in the Fraser River Delta and its Estuary. *Estuarine Coastal Marine Science*, 10, 609-633.

NRC. *Municipal Case Studies: Climate Change and the Planning Process: Delta, 2007*. http://www.cip-icu.ca/ CMS/Files/070504_delta.pdf.

nhc, 2008. *Comprehensive Review of Fraser River at Hope, Flood Hydrology and Flows – Scoping Study*. Vancouver, BC: BC Ministry of Environment, 63p.

Pharo, C.H. and Barnes, W.C., 1976. Distribution of surficial sediments of the central and southern Strait of Georgia, British Columbia. *Canadian Journal of Earth Sciences*, 13, 684-696.

Richmond. *City of Richmond Dyke System, 2000*. http://www.richmond.ca/asp2/HeritageInv/details.aspx?ID=161.

Thomson, R.E., 1981. *Oceanography of the British Columbia Coast*. Victoria, BC: Environment Canada, Department of Fisheries and Oceans, No. 56, 291p.

Williams, H.F.L. and Hamilton, T.S., 1994. Sedimentary dynamics of an eroding tidal marsh derived from stratigraphic records of 137Cs fallout, Fraser Delta, British Columbia, Canada. *Journal of Coastal Research*, 11, 1145-1156.

Williams, G., Zimmerman, A., Ray, D., and Menezes, C., 2009, *Roberts Bank and Sturgeon Bank Reach Overview: Backgrounder*. Vancouver, BC: FREMP, 90 p.

Journal of Coastal Research	SI	75	795-799	Coconut Creek, Florida	2016

Coastal Observation through Cosmo-SkyMed High-Resolution SAR Images

Maria Francesca Bruno†, Matteo Gianluca Molfetta†, Michele Mossa†, Raffaele Nutricato‡, Alberto Morea†† and Maria Teresa Chiaradia††

† DICATECh
Technical University of Bari
Bari, Italy

‡Geophysical Applications Processing (GAP) s.r.l.
Bari, Italy

††, Department of Physics "M. Merlin",
Technical University of Bari
Bari, Italy

www.cerf-jcr.org

www.JCRonline.org

ABSTRACT

Bruno, M.F.; Molfetta M.G.; Mossa, M., Nutricato, R., Morea, A., and Chiaradia, M.T., 2016. Coastal observation through Cosmo-SkyMed high-resolution SAR images. *In:* Vila-Concejo, A.; Bruce, E.; Kennedy, D.M., and McCarroll, R.J. (eds.), *Proceedings of the 14th International Coastal Symposium* (Sydney, Australia). *Journal of Coastal Research*, Special Issue, No. 75, pp. 795-799. Coconut Creek (Florida), ISSN 0749-0208.

The study deals with the application and further improvement of an advanced Earth Observation system, named COSMO-Beach, developed for semi-automatic shoreline extraction and coastal morphology identification. The system exploits SAR Single-Look-Complex data acquired by the COSMO-SkyMed constellation, which is able to provide X-band images with a short revisiting time. The implemented procedures have been tested over a very popular beach in Apulia Region (Italy), affected by erosion problems induced by human activities. The outcomes of the COSMO-Beach system are presented and discussed.

ADDITIONAL INDEX WORDS: *Earth Observation • Integrated Coastal Zone Management • COSMO-SkyMed.*

INTRODUCTION

The monitoring of the shoreline position and of the factors that, at different scales, affect the coastal dynamics is a relevant topic of the Integrated Coastal Zone Management (ICZM).

The correct setting of a continuous monitoring program involves the identification of survey methods and data analysis approaches capable to ensure: (i) reliability and accuracy of the measurements, (ii) acquisition and processing time efficiency, (iii) sustainable costs.

Given the length of the coast and the widespread erosion, traditional *in situ* investigations are not realistically and logistically conceivable for this purpose. On the contrary, remote sensing appears attractive and able to provide information on coastal evolution trend and to observe the impact of coastal protection structures, over a wide scale.

The present work is focused on the use of satellite Synthetic Aperture Radar (SAR) data and the application of robust imaging processing algorithms for monitoring both the coastal strip and the evolution of sandy coasts.

Semi-automatic techniques for shoreline extraction and coastal morphology identification have been developed aiming at fully exploiting the potentialities of the high-resolution SAR images acquired by the COSMO-SkyMed (CSK) constellation, and of the MapItaly acquisition plan, devised by the Italian Space Agency (ASI), able to provide X-band images covering the Italian territory with a 16 days revisiting time (ASI, 2007).

The developed system, called COSMO-Beach, is able to: (i) perform automatic selection of all archive radar data suited for precise shoreline identification (based on weather and sea conditions in the investigated area); (ii) extract the coastline; (iii) classify the shoreline according to the coastal morphology and (iv) correct the shoreline position in case of tidal fluctuations.

Figure 1. Geographic location of the test site along the Apulian Coast, Southern Italy, Ionian Sea. (Google Earth, 2015).

DOI: 10.2112/SI75-160.1 received 15 October 2015; accepted in revision 15 January 2016.
*Corresponding author: mariafrancesca.bruno@poliba.it
©Coastal Education and Research Foundation, Inc. 2016

One of the key elements of the COSMO-Beach system consists in its capability to integrate remotely sensed and *in-situ* data for an effective monitoring of the coastal strip and the evolution of sandy coasts. Meteo-marine measures are indeed extremely helpful for the proper selection of SAR images and their accurate processing, as discussed in the next sections.

Study Area and In-situ Data

The area of interest is *Bacino Grande* beach, a popular site located in the southern part of the Porto Cesareo municipality, Apulia Region, southeastern Italy (Figure 1). It is a 3000 m long sandy beach facing the Ionian Sea, and oriented W-E.

The sandy beach is backed by a sub-parallel coastline dune ridge. Coastal dunes in the area can reach 10 meters in height and are breached in several locations with clear signs of stress on vegetation, caused by the intense anthropic pressure along the coast. The inland area is characterized by the presence of wetlands and includes natural protected areas.

Since 2006, the area of interest has been constantly monitored by Apulia Region Meteomarine Network (Damiani *et al.*, 2007; Bruno, 2010), that includes: (i) an anemometric station, (ii) a tide gauge located a few hundred meters towards South, and (iii) a wave buoy moored installed off-shore Taranto city, about 60 km north of Porto Cesareo. The widespread availability of *in-situ* data over the years has allowed for a complete characterization of meteo-marine climate and erosion phenomena.

A shoreline evolution analysis has been carried out through long-shore transport mathematical models and by comparing the available cartography (DICATECh, 2014). Both the approaches highlight that there is not a prevailing direction of longitudinal sediment transport: beach morphodynamics is highly correlated to meteo-marine conditions, *i.e.* storms intensity and directionality. Shoreline changes have been detected by analyzing 1992 and 2011 aerial orthophotos. According to this analysis, the beach had retreated an average of about 6 m from 1992 to 2011, with the majority (82 percent) of transects indicating a trend of erosion.

MATERIALS AND METHODS

Shoreline position is constantly changing over time, mainly due to sea level oscillations. In order to define and quantify erosion phenomena, the coastline must be hence observed for a period sufficiently long to eliminate tidal influence, storm events and local sedimentary dynamics.

Background

SAR image segmentation aimed at shoreline extraction is generally performed using two different methods: radiometric approach, certainly the most used, and interferometric approach. The radiometric method attempts to identify edges in intensity images pixel values (Lee and Jurkevich, 1990; Niedermeier *et al.*, 2000, Liu and Jezek, 2004) while the interferometric approach exploits the loss of coherence usually observed in water-covered areas (Dellepiane *et al.*, 2004)

To overcome the issues related to speckle noise in SAR images, different approaches have been tested, ranging from classic edge detection methods, to those based on more complex mathematical models such as Active Contour Model (Mason and Davenport, 1996), Level Set Functions (Osher and Sethian, 1988; Shu *et al.*, 2010) and Snake models (Sheng *et al.*, 2012). In the last years, a considerable improvement in coastline mapping has been achieved using CSK data (Palazzo *et al.*, 2012; Braga *et al.*, 2013).

In the present research, the coastal evolution has been studied through SAR satellite imagery dataset taken from 2009 to 2015. SAR images have been processed using an advanced Earth Observation system, named "COSMO-Beach" (Bruno, 2014). The system takes advantage of the data pre-processing and interferometric processing libraries available in the software SPINUA (Bovenga *et al.*, 2005), whereas original tools have been implemented for image quality control, image segmentation and post-processing. The coastline extraction is based on a radiometric approach based on the use of SAR complex data, in terms of both amplitude and phase, since the phase information can be fruitfully used to extract information about shoreline morphology.

SAR Data Takes

As mentioned before, the availability of meteo-marine measures is extremely helpful for the accurate selection of SAR acquisitions available in the CSK archive, based on a preliminary check on the weather and sea conditions at the acquisition time. According to the outcomes of this preliminary analysis, the selected SAR images are part of two distinct CSK data takes, acquired in the framework of the MapItaly plan with an off-nadir angle of 24.13 deg and 24.67 deg (beams H4-01 and H4-02, respectively), along ascending orbits. The images are all HH polarized and captured by the SAR1 satellite of the CSK constellation in StripMap HIMAGE mode (spatial resolution: 3 m); their ground coverage is shown in Figure 2. Data take H4-01 consists of 6 images, acquired in the period 2009÷2011, while data take H4-02 is composed of 32 images acquired between 2010 and 2015.

Methodology

The data flow diagram of the COSMO-Beach system is sketched in Figure 3, where the processing steps carried out for the experimental analysis are highlighted.

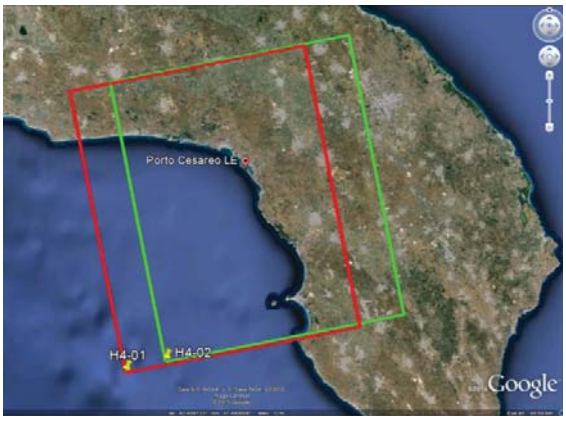

Figure 2. Ground coverage of the two CSK data takes over the study area: beam H4-01 (red frame) and H4-02 (green frame).

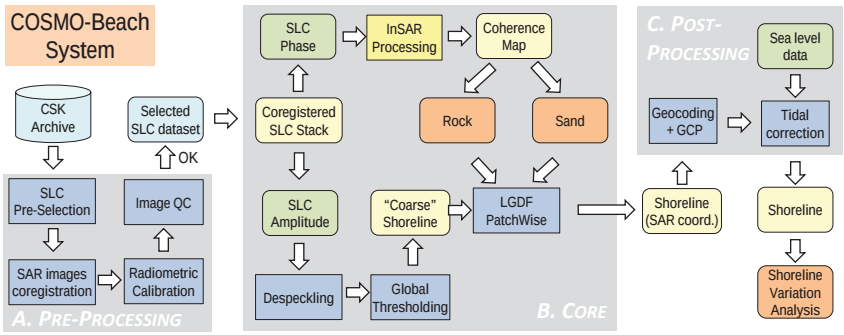

Figure 3. COSMO-Beach data flow diagram: (A) preprocessing steps; (B) algorithmic core; (C) post-processing steps.

The first step consists in the initial pre-selection of the SLC acquisitions best-suited for the coastline evolution analysis, based on (i) the availability of precise orbital records (necessary for accurate geocoding of the final extracted shoreline), and (ii) optimal weather conditions, as derived from meteo-marine measures. As general rule, it should be also verified that no significant meteorological event (like storms or very intense rainfalls) are recorded in the days preceding the SAR acquisition, in order to avoid any temporary phenomenon (like erosion profiles or flooded areas along the coastal zone) that could affect the final results derived by the processing chain, thus leading to wrong interpretations of the coastal dynamics.

According to Figure 3-A, further pre-processing steps are: fine coregistration (Nitti *et al.*, 2011), radiometric calibration and image Quality Check (QC). Image quality assessment is based on a number of tests, such as:

– Land/sea contrast: in general, this parameter is also significantly influenced by the look angle, and increases with it, as expected by the Rayleigh or the Frauenhofer criteria (Ulaby *et al.*, 1982).
– Sigma Naught (σ^0) evaluation over coastal sea: the check is passed if the backscattering coefficient is lower than a threshold (typically set to -19 dB).

Only the images that passed all QCs are provided in input to the COSMO-Beach Engine (Figure 3-B). The selected Single-Look-Complex (SLC) images are processed separately with radiometric and interferometric techniques, respectively: (i) amplitude images are despeckled (Lee, 1981) and segmented using a global thresholding algorithm (Otsu, 1975), in order to extract a "first-guess" shoreline; (ii) selected pairs of SAR images are processed interferometrically to generate coherence maps (Ferretti *et al.*, 2007). A segmentation algorithm is hence applied to both amplitude and coherence map. By properly setting threshold values for the coherence and for the signal amplitude, image pixels are classified as "rock" or "anthropogenic feature" if coherence and amplitude values are both over threshold; otherwise, they are classified as "sand".

The "coarse" land/sea interface and coastal morphology information are thoroughly exploited in the subsequent advanced segmentation stage, that includes the application of an active contour model, named Local Gaussian Distribution Fitting (LGDF) (Wang *et al.*, 2009), to identify coastline boundaries. The LGFD model, originally developed for applications in the bio-medical field, has proved to be effective and successful in shoreline detection providing errors lower than image resolution (Bruno, 2014). In fact, SAR amplitude images, being affected by speckle noise, have much in common with diagnostic images, which are hard to be segmented using classical edge detection techniques.

As proved by recent studies (Bruno, 2014), the LGDF approach showed higher performances with reference to other segmentation techniques (e.g., thresholding and region growing), in terms of position accuracy of the detected shorelines (for both sandy and rocky beaches) and robustness to SLC intensity artifacts.

At the end of the segmentation stage, in case of noticeable presence of speckle noise that still corrupts the expected results, images can be re-analyzed and the operator, during this "refinement" step, is allowed to change input parameters.

Once the shoreline has been accurately detected in SAR geometry, it must be geocoded in order to derive its position in geodetic coordinates (Post processing steps of Figure 3-C). In order to enhance the accuracy of the geocoding process, the following steps are performed: (i) the Atmospheric Path Delay on the radar signal propagation is estimated through NWP models, according to the procedure proposed in (Nitti *et al.*, 2015); (ii) Ground Control Points (GCP) are ingested by the geocoding tool chain, if available over the study area and recognizable on the SAR amplitudes (*i.e.*, artificial Corner Reflectors). Thanks to the availability of meteo-marine measures, the extracted sea/land interface is finally corrected to account for tidal influence and obtain shoreline position at 0.00m a.s.l.

RESULTS

As mentioned before, a data set of 38 archive CSK images – acquired between 2009 and 2015 – has been initially selected in the CSK catalogue, covering the study area, according to the indications provided by the meteo-marine measures. A large percentage (close to 90%) of them has passed all the QCs and shorelines have been detected for all of them through the COSMO-Beach system.

The comparison between 2009 and 2015 coastlines draws much attention to severe erosion phenomena in those years, with

peaks of retreatment of about 20 m in the southern area, as shown in Figure 4, where the shorelines extracted from only few CSK images are shown (just one shoreline per year), in order to aid the readability of the image.

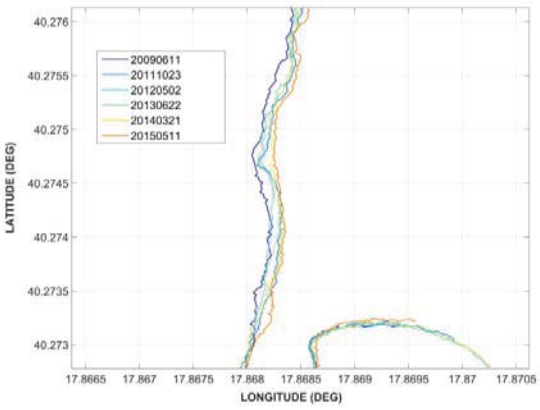

Figure 4. Shoreline evolution from 2009 to 2015 in the southern area.

DISCUSSION

The *in-situ* survey of the shoreline evolution (Figure 5) confirms a significant coastline retreatment: sandy beach sections are almost gone and dune ridges, already greatly degraded since long time, suffer a further dismantling by the storms that occurred in later years.

Figure 5. Erosion trend and damages caused by erosion at Porto Cesareo (A) shoreline during 2004 (from Google Earth), (B) shoreline during 2015 (from Google Earth), (C) and (D) sea water reaching the houses and destroying fences (2015).

Further analyzing shoreline evolution in Figure 4, a significant coastline retreatment is visible between 2009 and 2011, and since 2013, while a coastline progradation appears between 2011 and 2013. This can be explained by tracing the interventions occurred over the last years. Indeed, in February 2011, on an experimental basis, a protective breakwater was realized with 600 sand filled geotubes placed to a depth of 1 m and about 18 m from the shoreline. This barrier was much visible even from SAR images, as can be observed in Figure 6. In 2012, a large nourishment has been observed behind the breakwater, with a coastline progradation greater than 15 m. Following the dismantling of the barrier, which took place before the 2013 summer season, the nourishment disappeared and the erosion trend still persists, despite a number of localized interventions to protect constructions and beach clubs.

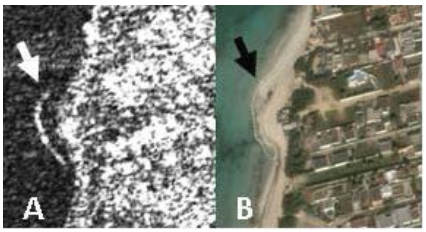

Figure 6. Sand bag barrier realized in February 2011: (A) SAR amplitude image (2012) and (B) aerial ortophoto (2012).

In order to perform a preliminary assessment of the accuracy achievable by the COSMO-Beach system, the shoreline detected by analyzing the CSK acquisition of May 11th, 2015, has been compared to ground truths collected through a GPS survey carried out in the same date. After tidal correction, the extracted coastline has been compared to the contour line at 0.00m a.s.l. obtained along 50 surveyed topographic transects (Figure 7). Results have shown an overall mapping accuracy of only 2 meters, *i.e.* lower than image pixel resolution, unless the high noise level of the SAR image acquired on May 11th, 2015, due also to the presence of Posidonia banks or small boats.

Figure 7. Shoreline accuracy assessment.

CONCLUSIONS

Thanks to the short revisiting time, CSK constellation opens new perspectives for coastal management through SAR satellite data. Furthermore, the MapItaly acquisition plan offers a wide archive of CSK data over the Italian territory. High resolution X-band SAR images, acquired in StripMap mode, have proved to be very effective in coastal zone monitoring, thus allowing the implementation of innovative reliable remote sensing services devoted to the study of beach morphodynamics and processes and to the analysis of shoreline variations over time.

In the near future, the continuity of service will be ensured by CSK Second Generation (CSG) mission, through which ASI intends to offer a system with enhanced performances with reference to current one, also in terms of image spatial resolution.

ACKNOWLEDGMENTS

This work is one of the results of the project "Towards COast to COast NETworks of marine protected areas (from the shore to the high and deep sea), coupled with sea-based wind energy potential (CoCoNET)". Project carried out using CSK® Products, © of the Italian Space Agency (ASI), delivered under a license to use by ASI. The authors are grateful to Prof. A.F. Petrillo and Prof. L. Guerriero for their suggestions and precious supervision and to dr. Davide Oscar Nitti for the fruitful collaboration.

LITERATURE CITED

ASI, 2007. *COSMO-SkyMed system description & userguide*. Rome, Italy: Agenzia Spaziale Italiana, 49p.

Bovenga, F.; Refice, A., Nutricato, R, Guerriero, L. and Chiaradia, M.T., 2005. SPINUA: a flexible processing chain for ERS/ENVISAT long term interferometry. *Proceedings of the 2004 Envisat & ERS Symposium* (Salzburg, Austria), pp 76.1-76.6.

Braga, F.; Tosi, L., Prati, C. and Alberotanza, L., 2013. Shoreline detection: capability of COSMO-SkyMed and high-resolution multispectral images. *European Journal of Remote Sensing*, 46, 837-853.

Bruno, M.F, 2010. La rete di monitoraggio meteomarina della Regione Puglia: elaborazione dei dati ondametrici. *Atti del XXXII Convegno Di Idraulica E Costruzioni Idrauliche* (Palermo, Italy).

Bruno, M.F., 2014. Valutazione delle potenzialità delle immagini SAR COSMO-SkyMed per il monitoraggio della fascia costiera. Politecnico di Bari, PhD dissertation, 154p.

Damiani, L.; Bruno, M.F., Molfetta, M.G. and Nobile, B., 2007. Coastal zone monitoring in Apulia region: first analysis on meteomarine climate. *CD ROM Proceedings of Vth International Symposium on Environmental Hydraulics (ISEH 2007)* (Tempe, Arizona (USA)).

Dellepiane, S.; De Laurentiis, R. and Giordano, F., 2004. Coastline extraction from SAR images and a method for the evaluation of the coastline precision. *Pattern Recognition Letters*, 25(13), 1461-1470.

DICATECh, 2014. *Supporto scientifico per la redazione del Piano Comunale delle Coste del Comune di Porto Cesareo (LE)*. Bari, Italy: Politecnico di Bari, 227p. Available at http://www.comune.portocesareo.le.it.

Dolan, R.; Hayden, B.P., May, P. and May, S., 1980. The reliability of shoreline change measurements from aerial photographs. *Shore and Beach*, 48(4), 22-29.

Ferretti, A,; Monti-Guarnieri, A., Prati, C., Rocca, F. and Massonet, D., 2007. *InSAR Principles-Guidelines for SAR Interferometry Processing and Interpretation.* Noordwijk, the Netherlands: ESA Publications.

Lee, J.S., 1981. Speckle analysis and smoothing of synthetic aperture radar images. *Computer graphics and image processing*, 17(1), 24-32.

Lee, J.S. and Jurkevich, I., 1990. Coastline detection and tracing in SAR images. *IEEE Transactions on Geoscience and Remote Sensing*, 28(4), 662-668.

Liu, H. and Jezek, K., 2004. A complete high-resolution coastline of Antarctica extracted from orthorectified Radarsat SAR imagery. *Photogrammetric engineering and remote sensing*, 70(5), 605-616.

Mason, D. and Davenport, I., 1996. Accurate and efficient determination of the shoreline in ERS-1 *IEEE Transactions on SAR images. Geoscience and Remote Sensing*, 34(5), 1243-1253.

Niedermeier, A.; Romaneessen, E. and Lehner, S., 2000. Detection of coastlines in SAR images using wavelet methods. *IEEE Transactions on Geoscience and Remote Sensing*, 38(5), 2270-2281.

Nitti, D.O.; Hanssen, R. F., Refice, A., Bovenga, F. and Nutricato, R., 2011. Impact of DEM-assisted coregistration on high-resolution SAR interferometry. *IEEE Transactions on Geoscience and Remote Sensing*, 49(3), 1127-1143.

Nitti, D.O.; Nutricato, R., Lorusso, R., Lombardi, N., Milillo, G., Bovenga, F., Bruno, M.F. and Chiaradia, M.T., 2015. On the geolocation accuracy of COSMO-SkyMed products. *Proceedings of SPIE Remote Sensing Europe 2015 SAR Image Analysis, Modeling, and Techniques XV, 96420D* (Toulouse, France).

Osher, S. and Sethian, J.A., 1988. Fronts propagating with curvature-dependent speed: algorithms based on Hamilton-Jacobi formulations. *Journal of Computational Physics*, 79(1), 12-49.

Otsu, N., 1975. A threshold selection method from gray-level histograms. *Automatica*, 11, 285-296.

Palazzo, F.; Latini, D., Baiocchi, V., Del Frate, F., Giannone, F., Dominici, D. and Remondiere, S., 2012. An application of COSMO-SkyMed to coastal erosion studies. *European Journal of Remote Sensing*, 45, 361-370.

Sheng, G.; Yang, W., Deng, X., He, C., Cao, Y., and Sun, H., 2012. Coastline detection in synthetic aperture radar (SAR) images by integrating watershed transformation and controllable gradient vector flow (GVF) snake model. *IEEE Journal of Oceanic Engineering*, 37(3), 375-383.

Shu, Y.; Li, J. and Gomes, G., 2010. Shoreline extraction from RADARSAT-2 intensity imagery using a narrow band level set segmentation approach. *Marine Geodesy*, 33(2-3), 187-203.

Tarquini, S.; Vinci, S., Favalli, M., Doumaz, F., Fornaciai, A. and Nannipieri, L., 2012. Release of a 10-m-resolution DEM for the Italian territory: Comparison with global-coverage DEMs and anaglyph-mode exploration via the web. *Computers & geosciences*, 38(1), 168-170.

Ulaby, F. T.; Moore, R. K. and Fung, A. K., 1982. Microwave Remote Sensing, Volumes 1, 2, and 3, Massachusetts: Addison-Wesley, 2162p.

Wang, L.; He, L., Mishra, A. and Li, C., 2009. Active contours driven by local Gaussian distribution fitting energy. *Signal Processing*, 89(12), 2435-2447.

Journal of Coastal Research	SI	75	800-804	Coconut Creek, Florida	2016

Comparative spit dynamics. The case of deltaic river mouth spits

Zăinescu I. Florin †, **Vespremeanu-Stroe Alfred**†, **Tătui Florin**†

† Faculty of Geography,
University of Bucharest, Romania

www.cerf-jcr.org

www.JCRonline.org

ABSTRACT

Zăinescu, I.F.; Vespremeanu-Stroe, A. and Tătui, F., 2016. Comparative spit dynamics. The case of deltaic river mouth spits. *In:* Vila-Concejo, A.; Bruce, E.; Kennedy, D.M., and McCarroll, R.J. (eds.), *Proceedings of the 14th International Coastal Symposium* (Sydney, Australia). *Journal of Coastal Research*, Special Issue, No. 75, pp. 800-804. Coconut Creek (Florida), ISSN 0749-0208.

This paper presents a comparison of evolution and dynamics of selected representative deltaic spits. Although recently receiving more attention, deltaic barrier spits still remain poorly understood in terms of long term evolution. Water, sediment and wave interactions at the river mouth are highly nonlinear such that hydrodynamic groin effects and sediment trapping mechanisms generate behaviours such as cyclic lobe progradation, as it is the case of some deltaic lobes, or conversely impose river mouth deflection when the wave influence becomes dominant. River mouth spits can be part of a prograding lobe (*e.g.* Sacalin and the paleo-spits of the Danube Delta lobes, Ba Lat spits) or can be a sign of lobe abandonment due to lobe switching, geoengineering or extreme reduction in sediment supply (*e.g.* La Banya, Ebro; Gracieuse, Rhone; Damietta, Nile). Human-induced reductions in river solid discharge have affected the majority of Mediterranean deltas and there is a wealth of other examples worldwide (*e.g.* Krishna & Godawari deltas). Dependent on the wave climate and especially the wave direction, cuspate features, migrating sand waves or flying spits form at the downdrift side of lobes. Comparison of dynamics shows that spits experience high temporal (inter-decadal), spatial (alongshore) and inter-landform variability. Dynamics is complex, often resulting from different interrelating effects which importance in control can change over time.

ADDITIONAL INDEX WORDS: *Spit dynamics, evolution, delta, river mouth, Landsat.*

INTRODUCTION

Deltaic spits are amongst the most dynamic features of the earth's surface often with rates of change that can reach hundreds of meters per year. They represent the time integral of the beach (Hesp and Short, 1999) and often comprise 3 distinct barrier sectors: an attached section, which usually fringes on the neighbouring deltaic deposits, a "free" barrier or neck, usually dominated by overwash and breach processes, backed by a lagoon, and a downdrift distal tip composed of multiple parallel or fan shaped beach ridges forming a small beach ridge plain. Spits are the morphologic expression of the littoral cell, reflecting the erosion-accumulation transition along the barrier.

Within deltas, spits form at the downdrift side, or less commonly flank the both sides of river mouths, and require very particular conditions which include low tides, a relatively high wave influence and oblique incidence and usually a shoreline protuberance or subaqueous bulge from which it can emerge and evolve. In contrast to the majority of barrier islands and spits, these landforms are highly sensitive and influenced by changes in the parameters of their updrift river mouths (Qs and Q). Delta mouths can be a fertile ground for the apparition of spits due to the protruding nature of the river mouths which deposit sediments and construct new land into the sea, causing the shorelines of lobes to become oriented acutely to wave angles when river strength is sufficient.

Spits on deltas may also arise as a consequence of deltaic lobe abandonment following drastic sediment reduction under highly oblique wave incidence (Nienhuis *et al.*, 2015) or may be part of the constructive process driving the formation of a delta lobe (Van Maren *et al.*, 2005; Preoteasa et *al.*, 2016) as is the case of the Sacalin (Danube) and Ba Lat (Red River) spits. In the latter case, barriers emerge from the edge of the river mouth platform which acts as a shoreline protuberance and present an initial elongated shape where cross-shore processes through onshore sediment transport are dominant. Van Maren (2005) tackled the question of emergence during either high energy storm or flood events or during fair-weather and found out that the Ba Lat spits emerge as a result of onshore sediment transport by waves between 1 and 3 meters due to the re-establishment of the equilibrium beach profile in response to an excess of sediment in the offshore profile. Emergence of an initial barrier island dominated by cross-shore processes blurs the definition limits between barrier islands and spits in the cases of Sacalin (Danube) and Ba Lat (Red River) that evolved into fully developed spits with a flying spit morphology in their later stages. In this paper we try to get insights into the development of spits from the comparison of largest examples.

METHODS

Shoreline positions were obtained from LANDSAT Multispectral Scanner (MSS), Thematic Mapper (TM) and Operational Land Imager (OLI) satellites at a decadal time

DOI: 10.2112/SI75-161.1 received 15 October 2015; accepted in revision 15 January 2016.
*Corresponding author: florinzainescu@yahoo.com
©Coastal Education and Research Foundation, Inc. 2016

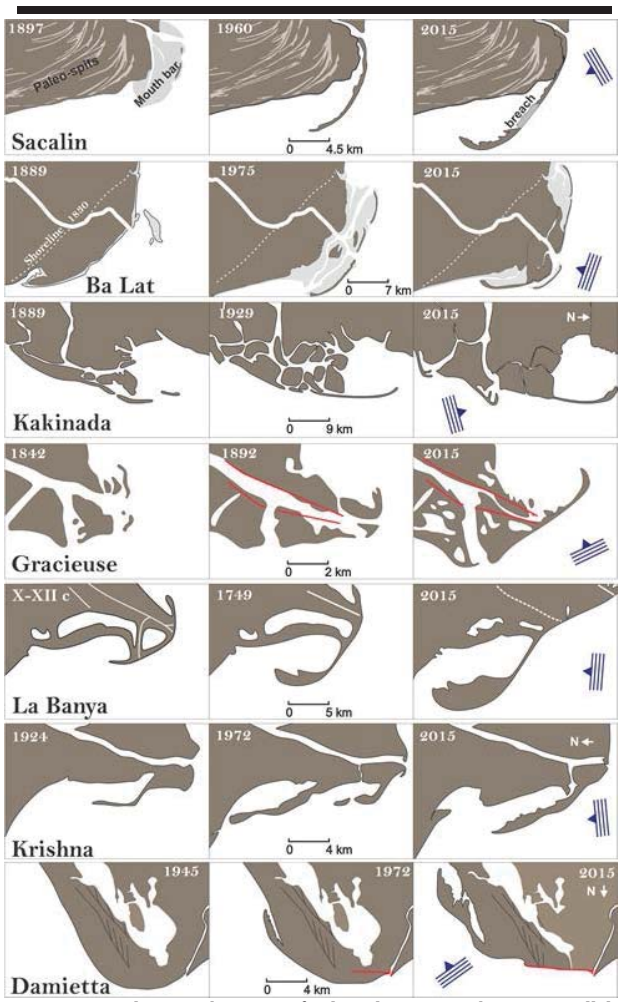

Figure 1. Development histories of selected river mouth spits. Parallel lines and arrow tip indicate wave incidence; red lines indicate engineering structures. Different scales are used for each spit. Sources of pre-1972 shoreline configuration (from top to bottom starting with second panel): Van Maren, 2005; Nageswara Rao, 2005; Sabatier and Suanez, 2003; Canicio and Ibanez, 1999; Nageswara Rao, 1985; Frihy and Lawrence, 2004.

interval between 1972 and 2015. The shoreline positions identified in Landsat images is not influenced by tidal fluctuations as the majority of study sites are microtidal. Only in the case of Red River delta spits, shorelines were obtained for the high tide level. Attention was given to the manual tracing of the shoreline and images were edge enhanced and resampled using cubic convolution to smooth the pixels in order to increase the accuracy of the digitization.

In order to quantify shoreline change, Digital Shoreline Analysis System 4.3 (DSAS) (Thieler *et al.*, 2009) was used in ArcGIS 10.1 to cast 100 m spaced apart transects for seven case study spits. The resulted rates were processed in Microsoft Excel to produce heatmaps for a graphically expressive visualization.

Data on long term shoreline configuration (before 1972) were compiled from available scientific publications and provide valuable qualitative information for assessment of long term spit dynamics.

RESULTS

The fast evolution of deltaic spits from initial embryo barriers to fully developed flying spits can take place in just a few decades. Considering that many of these landforms appeared and evolved in the last ~150 years, their evolution was documented by the first accurate and georeferenced historical and topographic maps of the XIX century and, starting with 1972, by the now freely available Landsat satellite imagery. This is an advantage compared to millennial scale spits for which historical maps and satellite imagery is available only in their last part of development.

Long term evolution

The Danube delta coast supports a wealth of barrier islands and spits, recently reviewed by Vespremeanu-Stroe and Preoteasa (2016). The Sacalin is the oldest and best developed of these presently evolving barriers and marks the 10th iteration in the cyclic evolutionary model of the Sf. Gheorghe lobe wich contains successive ridges (derived from former islands and spits) that are encased in the delta plain forming a barrier-marsh plain (Preoteasa *et al.*, 2016). It emerged initially in the 1890's as a barrier at the edge of the mouth bar platform and then it rapidly elongated and transgressed passing through successive stages from barrier island to attached spit with a distal beach ridge plain progressively increasing in morphological diversity

The Ba Lat distributary of the Red river forms two flanking spits in the north and south of the river mouth (Figure 1). These spits have appeared half a century ago and, similarly to the Sf. Gheorghe lobe, encased barriers are present on the delta plain that suggest a cyclic recurrence interval of ~100 years (Van Maren, 2005).

The late 1889 map shows a barrier and bars already formed in the northern side of Gautami mouth which later developed into the Kakinada spit (Nageswara Rao, 2005). The spit is morphologically similar with the Sacalin and Ba Lat which display an attached barrier, an elongated thin neck and a distal growing beach ridge plain. These first examples can be regarded as spits which initially formed under onshore sediment transport, where cross-shore processes are significant and cause the emergence of bars on the very low slope of mouth bar platforms (crest), which are the result of a positive sedimentary budget in the front of the river mouth. After some time (years), longshore currents strengthen and begin elongating the barrier which evolves into an arcuate bar with recurved tip morphology.

The Damietta (Nile), Krishna and Tinajones (Sinu) lobes in Egipt, India and Columbia appear very similar with highly protruding river mouths and multiple branches for the last two cases which suggests high river influence. These spits formed in very acute wave angles conditions and display fast elongation rates. Often, the distal beach ridges remained preserved along the whole length of the spit even though the spit retreats. Although previous spits have formed and remained encased or sometimes disintegrated on the downdrift side of the lobes, the present conditions of evolution for the Damietta and Krishna are of extreme sediment supply reduction as the solid inputs have

been completely halted from reaching the coast (Frihy and Lawrence, 2004; Venot *et al.*, 2008).

The La Banya spit (Ebro) has a rather long evolution, determined by the overgrowth of the southern Ebro delta until the 14th century (Somoza *et al.*, 1998), and the subsequent abandonment which resulted in the oldest and the largest deltaic spit in terms of distal beach ridge plain accumulation. The Ebro also presents a northern, smaller flanking spit (the El Fangar) which developed in a similar context of lobe abandonment.

On the Rhone delta coast, three spits can currently be observed: Gracieuse, Beauduc and Espiguette formed in 1892, 1711 and between the XVIII and XIX centuries respectively (Sabatier *et al.*, 2006). The spits from the Rhone delta are either fully attached, as the Beaduc and Espiguette, or have a flying spit shape sourced mainly by the erosion of adjacent lobes. The Gracieuse spit began forming under a dominant drift driven by waves from the SW after the Pegoulier outlet began experiencing significant erosion due to the opening of the Roustan outlet which resulted in the diversion of the liquid and solid discharge (Sabatier and Anthony, 2015). Erosion appears to have happened more rapidly on its first phase of development until the 1970's which later stabilized as the shoreline became more rectilinear. Although Gracieuse spit is more similar in morphology with the first spits analyzed in this study (Sacalin, Ba Lat, Kakinada), it develops in a less oblique wave climate and its shape may be due to its context of evolution.

A recent publication of Anthony (2015a) reviews two examples of deltaic spits, the Langue de Barbarie (Senegal) and Volta (Volta), in the context of strongly wave influenced river deltas and deflected river mouths. Growth of the Volta spit appears to have occurred relatively recently, in response to a westward shift in the river mouth and increased sequestering of sand by the Volta through enhanced wave refraction in the area downdrift of the spit tip (Anthony, 2015a). It formed downdrift of the mouth of the Volta river and displays an attached barrier morphology with an elongated accumulative end composed of juxtaposing sandy barriers. On the other hand, the Langue de Barbarie (Senegal) spit advances from the updrift side of the river mouth which suggests considerable sediment trapping. Sand bypassing occurs when the elongated spit breaches and the river outlet is relocated further updrift. These type of spits are quite common at river mouths (*e.g.* Chilia outlets in the Danube delta, updrift side of Grand Rhone mouth) and may cause the deflection of the river channel when the river flow is weak.

Similarities between the Ebro, Rhone and possibly Volta spits include lobe abandonment or updrift erosion under slightly oblique wave conditions which creates similar morphologies of attached/ detached spit in association with the downdrit orientation of the shoreline, which in the case of just slightly protruding lobes results in an attached spit morphology.

Recent dynamics

The variability of spits dynamics involves causal links between processes and resultant morphologic response.

A first analysis of the dynamics of the Sacalin spit (1898-present) finds that until the 1940's, very low retreat rates of ~5 m/yr. are related to the higher fluvial control exerted by the Sf. Gheorghe mouth (Zăinescu *et al.*, 2015). The narrow and low topography makes the spit highly affected by the wave climate and since the 1940's, variability in retreat rates correlate well with observed storminess change. Shoreline retreat rates on the Danube delta coast have also been found to be highly dependent on storm intensity and frequency (Vespremeanu-Stroe *et al.*, 2007), linked with the major modes of atmospheric teleconnections (*e.g.* NAO). The present analysis shows that for the last decade (2005-2015), the Sacalin experienced highest rates of shoreline retreat of ca. -50 m/yr. (Figure 2) in the context of an extraordinary large breaching (3.6 km) occurred in the 2012-2013 winter. However, the same period is characterized by the lowest storminess since 1949 (Zăinescu *et al.*, submitted). The extreme retreat rates have been promoted by a breach on the central sector of the barrier which occurred in the December 2012 in the absence of extreme or at least severe storms, which implies that the dynamics of the central sector of the Sacalin barrier is also modulated by breach dynamics in relation with the barrier width. The central barrier (neck) displays a periodic cyclic behavior oscillating in width from 400-600 m to 50-150 m just before breaching because washover penetration is inhibited by the reeds (*Phragmites australis*) which build a mud and root platform that dissipates wave energy. Consequently, because of the inhibiting effect of the reeds, significant barrier widening occurs only through breaching and produces a predictable 15 to 30 years recurrence period for breaches.

On the Trabucador bar of the La Banya spit (Rhone) breaches occured during extreme storms in Oct 1990, Nov 2001, Oct 2003 (Gracia *et al.*, 2013). These breaches are related to extreme storms and help explain the high retreat rates between 1992 and 2004 (8 m/yr.).

Breaches are also visible in 2005 on the neck sector of the Kakinada spit, corresponding to the 2004 tsunami which affected the Krishna and Godawari fringes by significant run-up levels and inundation distances (Nageswara Rao *et al.*, 2007). Moreover, the retreat patterns of Kakinada spit appear to be highly variable (on shorter spatial scales) at least on the attached sector, which indicates an effect of the vegetation and the small tidal channels in the back-barrier over which migration can occur very rapidly.

It is clear that drastic reduction in sediment supplied by river mouths triggers erosion downcoast (*e.g.* Nile, Krishna) but less certain is the effect of a 50% to 75% decrease may have on the decadal scale shoreline dynamics when storminess modulates the shoreline change rates. In addition, it is highly probable that the reduction in the Danube's sand supply especially after the 1950's contributed to the downdrift enlargement of the erosion sector of Sacalin compared to older spits which were cyclically encased within the Sf. Gheorghe lobe. The influence of sediment input to spit dynamics should be critical for its entire lifespan (decades, centuries), although floods and storms are expected to influence its dynamics on a yearly to decadal scale.

The Grand Rhone river mouth is still strong as indicated by the slight accumulative or stable shoreline downdrift of the river mouth on 2 km. The higher retreat/progradation rates near the river mouth are caused by a migrating shoreline bulge generated by the wave shadowing from the river mouth bar (Figure 2A).

The protruding river mouth under slight asymmetric wave climate creates a counter-drift as a result of gradients in wave dissipation between the mouth zone and the adjacent coast

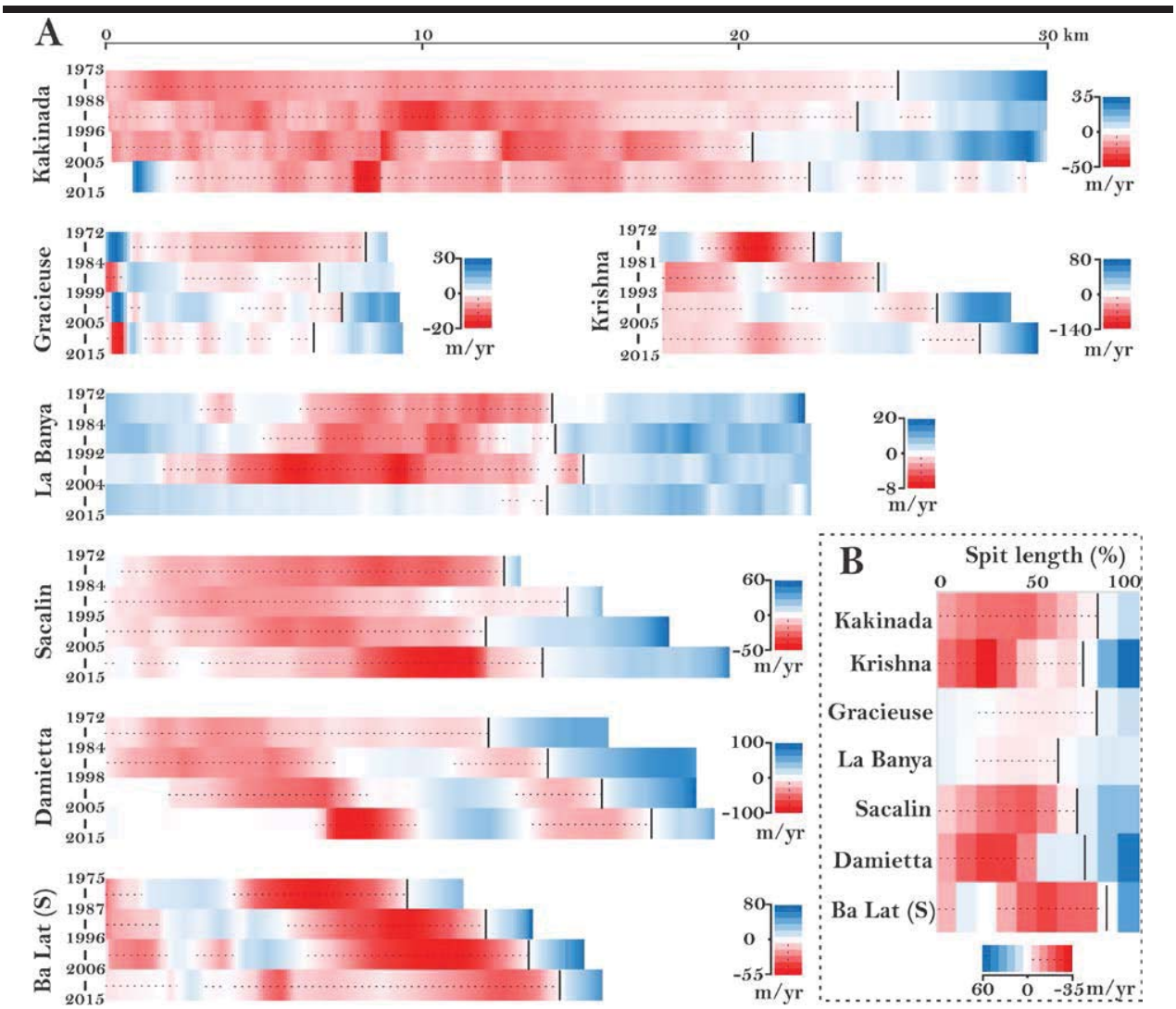

Figure 2. A: Decadal spit dynamics inferred from Landsat images; note the separate scales used for each spit; B: Comparative dynamics of spits (1972-2015). Spit lengths were standardized to 100%. Black vertical bars indicate fulcrum points. Dashed lines overlie negative values.

(Anthony, 2015b) which helps trapping the sediment. Strong mouth influence on the immediate downdrift sector is also encountered on the southern Ba Lat spit, which was sheltered by a newly emerging barrier from the mouth bar crest. The Ba Lat also experiences significant tide influence which causes the barriers to display the thinnest widths from all the studied spits.

On the Damietta distributary mouth jetties and 6 km long seawalls were erected at the river mouth to counteract erosion in the area, but aggravated erosion downdrift, which helped feed a migrating downdrift sandwave generating a pattern of alternating erosion-progradation sectors along the spit. The same pattern can be observed on the Krishna spit even though anthropic structures are absent, suggesting that this is common on spits with very acute wave angles of approach.

Shoreline dynamics varies significantly between spits (Figure 2B). A comparison between spit rates of change for the last 4 decades shows that the lowest rates occur on the Mediterranean spits of Gracieuse and La Banya with ca. -2 m/yr. for the spit neck and 8 m/yr. for the prograding distal spit which suggests lower values for both storm wave heights (wave run-up) and LST gradients. Other spits display a shoreline migration that reaches on average several tens of meters per year. The analysis of the dynamics of the fulcrum point, which marks the tipping from retreat to accumulation alongshore a spit, shows different behavior: downdrift migrating, stationary, or updrift migrating which can be related to changes in the geometry of the spit and wave refraction patterns and decadal variations in wave direction.

CONCLUSIONS

Comparative analysis of deltaic spits offers insight into the entire lifespan development and the morphodynamic behavior of these landforms.

Spits on deltas originated and evolved in diverse conditions: from the edge of the river mouth bar under onshore sediment transport or from alongshore wave transport under oblique wave conditions or in the context of abandoned deltaic lobes which either created attached spits or flying spits depending on the initial lobe protuberance or spits dominated by gradients in alongshore sediment transport. These situations represent a framework of interpreting the landform taking into account formation, evolution histories and resultant morphology.

Comparison of dynamics shows that spits experience high 3 dimensional variability: temporal (inter-decadal), spatial (alongshore) and inter-landform. Dynamics is complex, often resulting from different interrelating effects which importance in control can change over time. It is expected that due to their dynamic nature, sea level rise should have little influence on the last century evolution of the spits, and other forcings such as storminess (wave climate) and recent modification in sediment discharged by neighboring river mouths controlled their evolution. Although storms modulate the general geomorphic change, local, very diverse factors which are often predictable (*e.g.* the 15-30 year recurrence of breaches on the central Sector of the Sacalin spit), sometimes drives dramatic retreat rates in the following few years .

Every spit is in the end a truly unique landform, each with its own particular evolution history, shaped by numerous interchanging environmental conditions, and sometimes influenced by the effects of anthropogenic interventions, all of which gives rise to the wide range of forms, sizes and dynamics.

ACKNOWLEDGMENTS

This study was supported by the project “Climate changes influence on the erosion intensities along the critical sectors of the Danube and Rhone deltas coastlines” (PN-II-CT-RO-FR-2014-2-0062). FT was supported by the strategic grant POSDRU/159/1.5/S/133391.

LITERATURE CITED

Anthony, E. J., 2015a. Patterns of Sand Spit Development and Their Management Implications on Deltaic, Drift-Aligned Coasts: The Cases of the Senegal and Volta River Delta Spits, West Africa. In G. Randazzo, D. W. Jackson, J.A.G. Cooper (Eds.), *Sand and Gravel Spits*, pp. 21-36, Springer International Publishing.

Anthony, E. J., 2015b. Wave influence in the construction, shaping and destruction of river deltas: A review. *Marine Geology*, 361, 53-78.

Canicio, A. and Ibanez, C., 1999. The holocene evolution of the Ebre delta catalonia, Spain. Acta Geographica Sinica Vol. 54.

Frihy, O. and Lawrence, D., 2004. Evolution of the modern Nile delta promontories: development of accretional features during shoreline retreat. *Environmental Geology*, 46(6-7), 914-931.

Gracia, V., García, M., Grifoll, M., & Sánchez-Arcilla, A., 2013. Breaching of a barrier under extreme events. The role of morphodynamic simulations. *J. Coastal Res.*, 65, 951-956.

Hesp, P.A., Short A.D., 1999. Barrier morphodynamics. In: Short AD (ed), *Handbook of beach and shoreface morphodynamics*. John Wiley, pp 307-333.

Nageswara Rao, K., 1985. Evolution and dynamics of the Krishna delta, India. N*ational Geographical Journal of India*, 31(1), 1-9.

Nageswara Rao K, Sadakata N, Hema Malini B, Takayasu K., 2005. Sedimentation processes and asymmetric development of the Godavari deltas, India. In: *River Deltas-Concepts, Models and Examples*, Bhattacharya JP, Gioson L (eds). SEPM Special Publication 85; 435–451.

Nageswara Rao, K., Vardhan, D.A., Subraelu, P., 2007. Coastal topography and tsunami impact: GIS/GPS based mobile mapping of the coastal sectors affected by 2004-tsunami in Krishna-Godavari delta region. *Eastern Geographer*, 13, 67–74.

Nienhuis, J. H., Ashton, A. D., Roos, P. C., Hulscher, S. J., & Giosan, L., 2013. Wave reworking of abandoned deltas. *Geophysical research letters*, 40(22), 5899-5903.

Preoteasa, L., Vespremeanu-Stroe, A., Tătui, F., Zăinescu, F., Timar-Gabor, A., Cârdan, I., 2016. The evolution of an asymmetric deltaic lobe (Sf. Gheorghe, Danube) in association with cyclic development of the river mouth bar: long-term pattern and present adaptation to human induced sediment depletion, *Geomorphology*, 253, 59-73.

Sabatier F, Maillet G, Fleury J, Provansal M, Antonelli C, Suanez S, Vella C., 2006. Sediment budget of the Rhoˆne delta shoreface since the middle of the 19th century. *Marine Geology*, 234:143–157

Sabatier, F., & Anthony, E., 2015. The Sand Spits of the Rhône River Delta: Formation, Dynamics, Sediment Budgets and Management. I*n Sand and Gravel Spits*, pp. 259-274. Springer International Publishing.

Thieler, E.R., Himmelstoss, E.A., Zichichi, J.L., and Ergul, Ayhan, 2009, Digital Shoreline Analysis System (DSAS) version 4.0— An ArcGIS extension for calculating shoreline change: *U.S. Geological Survey Open-File Report 2008-1278.*

Van Maren, D. S., 2005. Barrier formation on an actively prograding delta system: The Red River Delta, Vietnam. Marine Geology, 224(1), 123-143.

Venot JP, Sharma BR, Rao KVGK., 2008. Krishna basin development: interventions to limit downstream environmental degradation. *Journal of Environment & Development*,17, 269–290.

Vespremeanu-Stroe, A., Constantinescu, S., Tatui, F., & Giosan, L., 2007. Multi-decadal evolution and North Atlantic Oscillation influences on the dynamics of the Danube Delta shoreline. *Journal of Coastal Research*, 50, 157-162.

Vespremeanu-Stroe, A., & Preoteasa, L., 2015. Morphology and the Cyclic Evolution of Danube Delta Spits. *In Sand and Gravel Spits*, pp. 327-339. Springer International Publishing.

Zăinescu, F., Vespremeanu-Stroe, A., Tătui, F., Constantinescu, Ş., 2015. Storm driven evolution and morphodynamic feedbacks. Sacalin spit, Danube delta. *European Geosciences Union General Assembly*, Viena, Austria.

Zăinescu F., Vespremeanu-Stroe A., Valchev N, Tătui F. 2015, Storm climate on the Danube delta coast. Evidence of recent storminess change and links with large scale teleconnection patterns (in Press).

Journal of Coastal Research	SI	75	805-809	Coconut Creek, Florida	2016

Decadal Evolution of Mond River Delta, the Persian Gulf

S. Abbas Haghshenas [†*], Azadeh Razavi Arab [†], Arash Bakhtiari[†], Morteza Jedari Attari[†], and Michael John Risk [††],

[†]Institute of Geophysics
University of Tehran
Tehran, Iran

[††]McMaster University
Ontario, Canada

www.cerf-jcr.org

www.JCRonline.org

ABSTRACT

Haghshenas, S.A.; Razavi A., A.; Bakhtiari, A., Jedari Attari, M., and Risk, M.J., 2016. Decadal Evolution of Mond River Delta, the Persian Gulf. *In:* Vila-Concejo, A.; Bruce, E.; Kennedy, D.M., and McCarroll, R.J. (eds.), *Proceedings of the 14th International Coastal Symposium* (Sydney, Australia). *Journal of Coastal Research*, Special Issue, No. 75, pp. 805-809. Coconut Creek (Florida), ISSN 0749-0208.

This paper studies the results of multi-disciplinary investigations on different features of evolution of the Mond River delta during the past five decades. Considering the high importance of Mond River and corresponding sediment discharge, physiography and watershed analysis of Mond River is investigated and sediment discharge from the river and its sand content are estimated in the first step. A numerical model has been utilized to investigate cases of flow and sediment transport behaviour in the coastal Mond area and annual rates of longshore sediment transport are estimated. The shoreline changes are investigated by analysing thirty four sets of aerial photos and satellite imagery taken between 1967 and 2014 to investigate decadal evolution of Mond River Delta during the past three decades. Eventually, numerical results are compared with field observations and comprehensive GIS based analysis of historic shoreline changes from aerial photos and satellite imagery.

ADDITIONAL INDEX WORDS: *Morphological change, Satellite imagery analysis, Mond River Delta.*

INTRODUCTION

The Mond River is the major Iranian seasonal river discharging in to the Persian Gulf, with a considerable amount of annual sediment load, which is supposed to be the most important cause for the formation of the river delta as well as down-stream sand spits in the area and makes this coastal area known as one the most dynamic environments in the Persian Gulf (Figure 1). The latest part of the river is completely meandered and the migration of the river mouth has been captured twice during the past 50 years based on available aerial photos and satellite imagery. Mond River flows through the valley between Darang and Mond anticlines and discharges considerable amount of sediment into the Persian Gulf. An analysis of Mond River watershed indicated that every year the river discharges more than one million cubic meter of sand which has created a large delta and has significantly affected the morphology of the area featuring extensive shallow water regions and intertidal zones. Ra's-e-Motaf Point is located in the eastern part of downstream sand spits. There is a large shallow region in the described area formed by the sediment discharge from Mond River and then transported to the site by longshore currents. Nearshore wave transformation over this shallow area may involve concentration of wave energy as a result of wave focusing which could be a hazard to the smaller fishery vessels. The morpho-dynamic of entire environment of the Mond River – Mond Delta highly affects marine environment in the surrounding area and is to be well studied.

The main objective of this study is to find out whether or not the area is in an equilibrium condition and to investigate how dynamic the area is from morpho-dynamic point of view.

REGIONAL SETTING

The geomorphology of the Ra's-e-Motaf-Mond area is governed by the sediment discharge of the Mond River. Hence a comprehensive study is completed based on a set of 37 year river hydrometric data from Qantareh Station, the nearest hydrometric station to the shoreline, between 1969 and 2005. The data are taken from Jamab (1999, 2005). This watershed physiographic study revealed that every year the river carries about 11.6×10^6 m^3/a sediment on average into the Persian Gulf. Of this volume, about 12% was estimated to be sand and 88% silt and clay. Therefore, it was estimated that on average approximately 1.39×10^6 m^3 of sand is delivered every year to the littoral system by Mond River. Most of this sand is subsequently carried towards the south by longshore currents and deposited around the sand spits and in Motaf Area.

The wave climate of the area is governed by frequent waves coming the north-west as well as less frequent waves coming from the south-east. Figure 2 shows the deep water wave rose in front of the river mouth for a 25-year hindcast data in the period of 1983 to 2008. The offshore waves are adopted from 25-years hindcast data of the Persian Gulf (Baird and Associates, 2010).

Tidal fluctuations of the water level is bounded to +/- 1 m with respect to the MSL in front of the river mouth. Figure 3 presents tidal level variations at the mentioned location (51.35 E, 27.76 N) from general tidal modeling of the Persian Gulf.

DOI: 10.2112/SI75-162.1 received 15 October 2015; accepted in revision 15 January 2016.
*Corresponding author: sahaghshenas@ut.ac.ir
©Coastal Education and Research Foundation, Inc. 2016

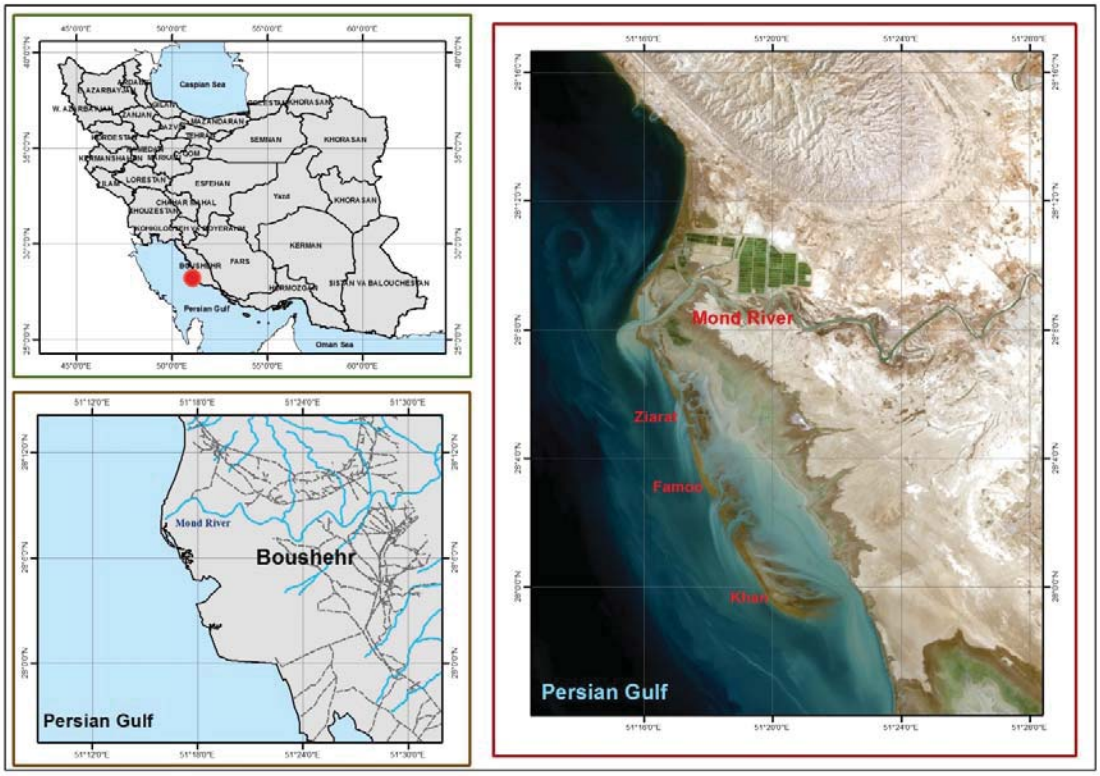

Figure 1. Study area and a satellite view of the Mond River Delta and downstream sand spits.

METHODS

The dynamics of Mond River Delta are investigated through shoreline change analysis and numerical modeling of sediment transport at the mentioned delta. Evolution of Mond River delta is studied by analyzing two sets of aerial photos taken in 1967 and 1993 and 32 series of satellite images from 1967 to 2014. In the first step, long-term shoreline changes are investigated generally by analyzing two sets of aerial photos taken in 1967 and 1993 and a series of satellite images from 2008. Analysis of historic shorelines in GIS indicated that the sand spits south of the Mond River mouth have experienced considerable accretion and erosion in both study periods. There are evidences in the area (such as finding several untouched parts of riser clams during a field investigation program) reveals frequent erosion and deposition over the sand spits. Moreover there is not reliable bathymetry data in near the spits location. Consequently, it is not possible to quantify the change in the volume of sand spits.

Calculation of potential longshore sand transport rate for the shoreline at the mouth of Mond River is performed by using Delft 3D Model. The bathymetry of the area in question is derived from extensive hydrographical campaign in the nearshore zone coupled with admiralty and Iranian National Cartographic Center bathymetric data in the deeper sections. Upon acquisition of the proper bathymetry of the region, a representative cross-shore profile was extracted at the river mouth extending to the depth contour of 20 m. Of particular attention is a notable mild slope between the depth of 0 and 1 m in form of a quasi-bar as a result of heavy Mond-driven contribution of riverine sediments.

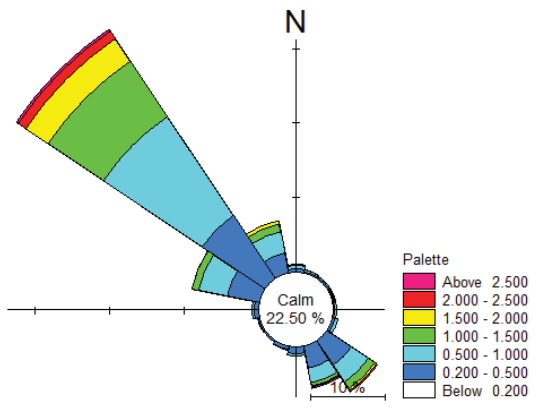

Figure 2. Deepwater wave rose in front of the river mouth – data adopted from 25-year wave hindcast data.

Delft 3D package, capable to simulate the transport processes of riverine deposits including sands and fine sediments, is employed here to model the sediment transport and morphodynamic changes at the site. The approach of Bailard (1981) implemented in Delft3D (Deltares, 2010) in the transport formulae of Bijker (1971) is adopted to simulate the sediment transport by combined effects of waves and currents in the study area.

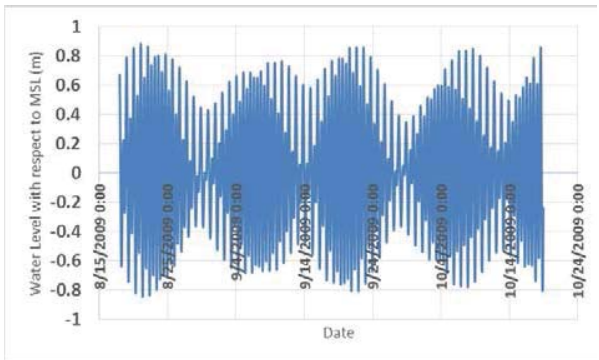

Figure 3. Sample data of tidal variations in front of Mond River Delta.

RESULTS

Investigation of the shorelines during 1967 to 1993and 1993 to 2008 periods reveals that there have been several progressions and recessions over the area. Studying the limits of the sand spits formed in the southern part of the Mond River mouth and comparison of shoreline position in 1967, 1993 and 2008 reveals that the morpho-dynamic conditions around the river mouth are very active and slight accretion on the southern part of the delta could be observed. The downstream sand spits consist of three separated parts, which are named Ziarat, Famoo and Khan, respectively from the north to the south. The estuary located at the conjunction location of Mond River and the Persian Gulf is called Ziarat Estuary. The location of Ziarat Estuary and the river mouth has changed between 1967and 1993 and the mouth direction has transmitted to the south. The southern part of the delta located in the downstream side of the river mouth in 1967 acted as a shelter in the northern part of the new mouth and simplified the development of new delta of the river in the northern part during the years after 2008. By the change in the river mouth position, the Ziarat Spit experienced extensive erosion between 1967 and 1993 and recovered during the second period, i.e. between 1993 and 2008. On the other hand, the Famoo Spit limits was extended, especially on the western (seaward) side. Associated with the changes in third spit limits, called Khan, it should be noted that it seems that the 1967 photo was taken during high tidal conditions, while the 1993 photos and 2008 image show lower sea level conditions. Considering this issue and the general patterns of the morpho-dynamic changes in the area and by looking at the submerged features, recognizable changes around the Khan Spit could be observed; although the changes are not so highlighted. The changes of the outer front of the spit may be attributed to the sand sediments coming from Mond River, while the changes of the inner side, more or less, can be attributed to the long-term deposition of the fine fracture of the Mond River sediments in the relatively calm sea conditions in the sheltered area. Local observations confirm the existence of fine deposits in the inner part of the spits. It should be noted that the surface of mentioned spits are subjected to frequent cycles of intensive erosion and deposition. During the field investigations occurred three days after a common storm (Baird and JWERC, 2010), several untouched parts of riser clams were found on the surface of Khan and Famoo Spits which imply a multi centimeters erosion in the area. Also other evidences of the ripple shaped features revealed erosion in some points and deposition some other ones of the spit. Moreover, by interview with local fishermen, it was specified that the spits get fully submerged once or twice a year during extreme storm events while occurred in high tide conditions. These evidences could be assumed as a proof for active morpho-dynamical conditions of the N-S section and confirms the discussion provided above based on the historical limits of the spits. Limits of the sand spits and relevant changes over the study periods, including Ziarat, Famoo and Khan Spits, as well as Nakhiloo Island in the south are presented in Figure 4.

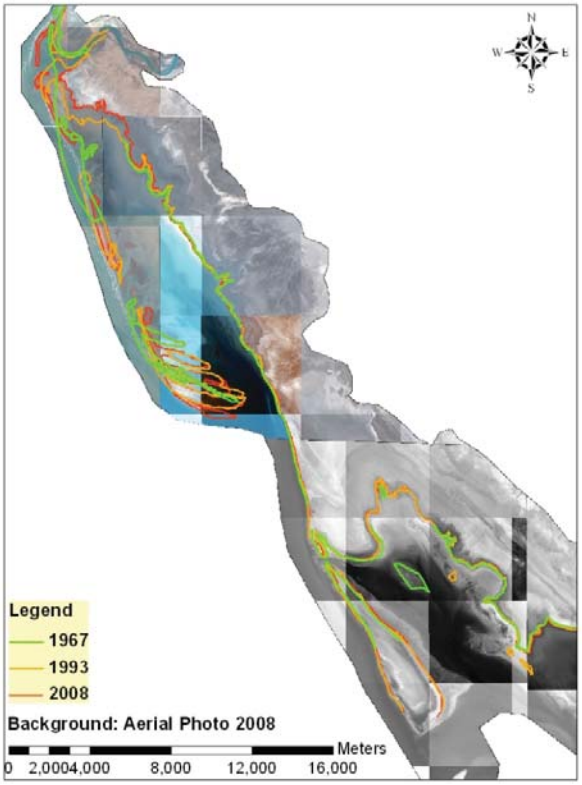

Figure 4. General pattern of shoreline changes in the study area in the periods of 1967 to 1993 and 1993 to 2008.

The moving river mouth in these three sets of historical data shows that this area might have experience several other

changes that has not captured in the primary study and raised the important question that how active is the main delta area is. To find an appropriate answer to this question the changes of shoreline in 34 sets of satellite data and aerial photos were analyzed in a 4 km buffer from the average center location of the river mouth. Figure 5 summarize the almost yearly shoreline position next to the Mond River mouth.

From this analysis it is obvious that although the average position of the river mouth is stable, the sand sits and shoreline is experiencing repetitive sequences of erosion and deposition.

Calculation of potential longshore sand transport rate for the shoreline at the mouth of Mond River is performed by using Delft 3D Model. Using the online hydrodynamic model of wave and currents of Delft 3D software, 2DH wave-induced currents and tidal currents are calculated and introduced to the sediment transport model. Figure 6 presents the employed grid for simulations. The cross section at the river mouth is defined perpendicular to land boundary to obtain the longshore sediment transport rate at the inlet.

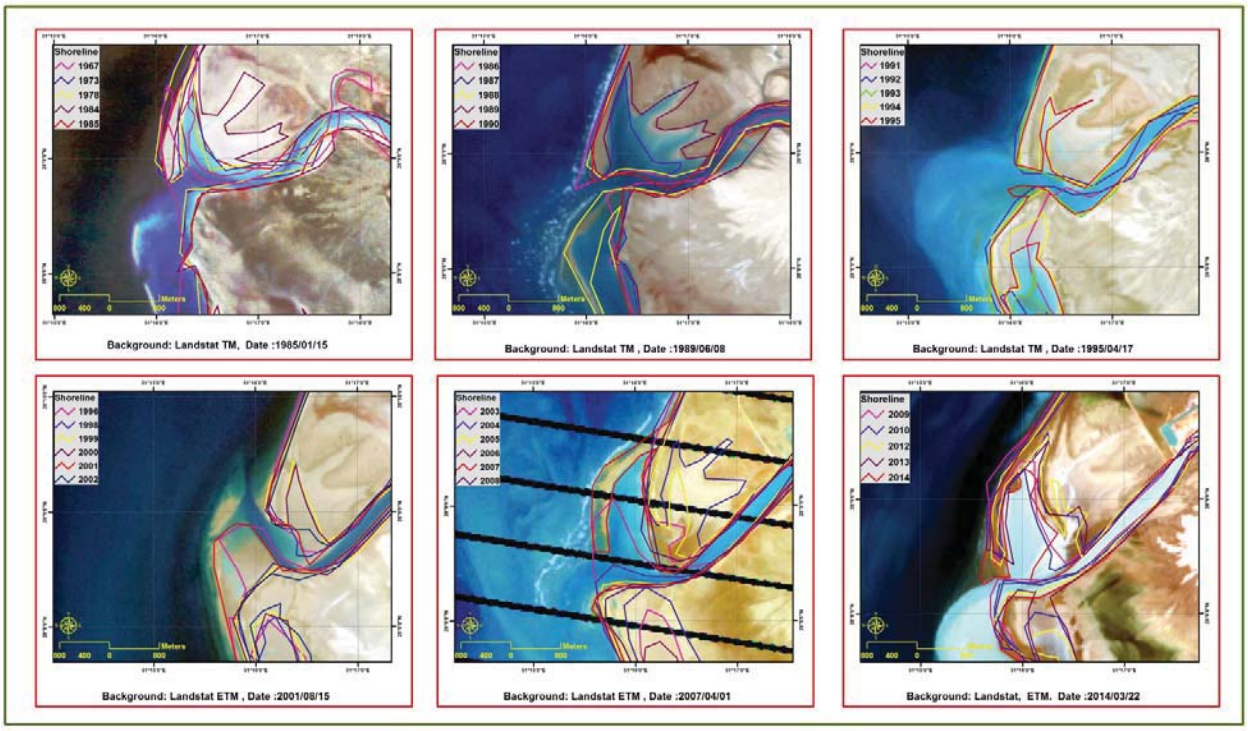

Figure 5. Decadal shoreline changes at the Mond River Mouth area extracted from GIS based shoreline change analysis of 32 sets of historical satellite data.

The hydrodynamic and wave input data at the offshore boundary of the model are tidal water level and wave characteristics (Figures 2 and 3). Figure 7 presents estimated annual potential longshore sand transport rates during the period of 1983 to 2008. Calculation of potential longshore sand transport rate for the shoreline at the mouth of Mond River indicated that the wave forcing in the region is capable of transporting approximately 1.3×10^6 m^3/a of sand on average with a net direction towards the southeast. Most of the sand discharged from the river mouth is therefore expected to be carried away from the river mouth towards the south contributing to further growth of the sand spits and deposition in Motaaf Area. The flow pattern around the down-stream sand spits of the Mond River is able to take the suspended load discharged (fine sediments) by the Mond River in to the sheltered area behind the sand spits; where the suspended sediments are supposed to be deposited.

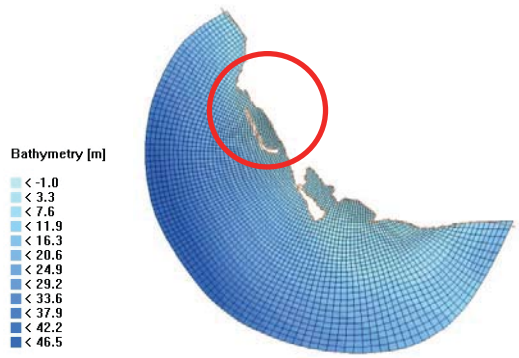

Figure 6. Delft 3D model domain for sand transport simulations.

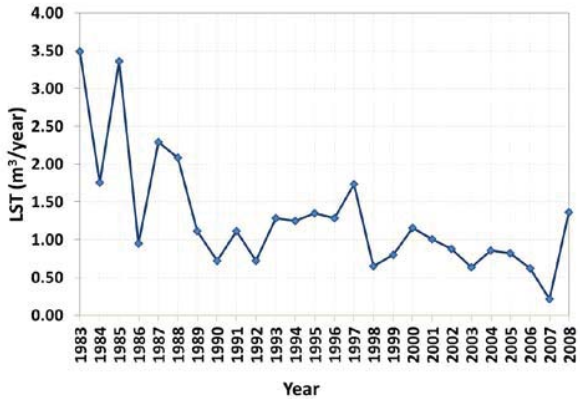

Figure 7. Variations of LST rate at the Mond River mouth during the period of 1983 to 2008.

Table 1. *Deepwater wave rose in front of the river mouth – data adopted from 25-year wave hindcast data*.

Year	River Sand discharge	LST	Period of Shoreline Analysis	Accretion/Erosion
1983	4.75E+05	3.49E+06		
1984	7.21E+05	1.76E+06	1978-1984	-168.69
1985	1.09E+06	3.36E+06	1984-1985	183.75
1986	1.55E+06	949705	1985-1986	201.36
1987	5.66E+05	2.29E+06	1986-1987	-103.50
1988	9.88E+05	2.08E+06	1987-1988	154.43
1989	9.29E+05	1.12E+06	1988-1989	-366.91
1990	1.87E+06	723894	1989-1990	-134.37
1991	3.92E+06	1.12E+06	1990-1991	-21.63
1992	5.74E+05	723894	1991-1992	158.37
1993	1.90E+06	1.28E+06	1992-1993	-25.50
1994	4.24E+06	1.25E+06	1993-1994	-159.94
1995	9.44E+05	1.35E+06	1994-1995	29.38
1996	2.29E+06	1.29E+06	1995-1996	79.11
1997	1.37E+06	1.74E+06	1996-1997	-15.91
1998	5.61E+05	646995	1997-1998	0.42
1999	3.42E+05	797647		
2000	1.20E+06	1.16E+06	1999-2000	-27.75
2001	5.76E+05	1.00E+06	2000-2001	305.34
2002	9.37E+05	876272	2001-2002	-320.54
2003	1.96E+06	633573	2002-2003	-2.97
2004	6.35E+05	854403	2003-2004	-297.09
2005	5.87E+05	821463	2004-2005	371.61
2006	5.87E+05	620953	2005-2006	-160.55
2007	1.50E+05	215400	2006-2007	182.97
2008	4.22E+05	1.37E+06	2007-2008	6.52

DISCUSSION

The present study offers the results of multi-disciplinary investigations of various features of river-delta-coastal environment interaction in Ziarat Estuary and the Mond Delta area. Considering the high importance of Mond River and corresponding sediment discharge, physiography and watershed analysis of Mond River is investigated and sediment discharge from the river and its sand content are estimated in the first step. Consequently, a numerical model has been utilized to investigate sediment transport rates in the coastal Mond area. The shoreline changes are investigated by analyzing thirty two sets of aerial photos and satellite images taken between 1967 and 2014 in a GIS framework. Table 1 encapsulates the summary of achieved annual data for river sediment discharge, longshore sediment transport rate and shoreline erosion accretion rates between 1983 and 2008. Figure 8 shows the comparison of the river sand discharge and potential LST rates against shoreline accretion/erosion.

As it is observed, the shoreline has experienced several cycles of erosion accretion during the past decades depending on the river sand discharge and wave climate which induced LST potential rate.

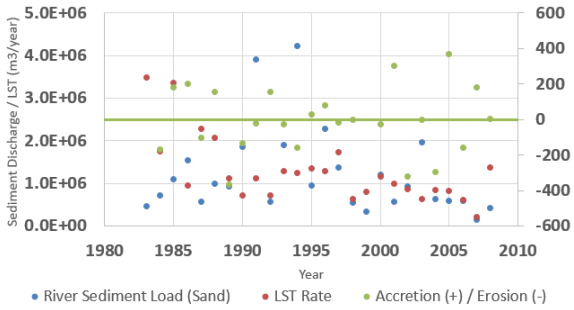

Figure 8. Summary of river sand discharge, potential LST rate and shoreline accretion/erosion in the period of 1983 to 2008.

ACKNOWLEDGMENTS

The Authors are grateful to Dr. Ali Naeimi for his valuable contribution to this study.

LITERATURE CITED

Baird and Associates, 2010. 25-Year Wave Climate Hindcast for the Persian Gulf, *Ports and Maritime Organization (PMO)*, 79p.

Baird and JWERC, 2010. Site Visit Report, Monitoring and Modeling Studies of Iranian Coastline-Phase III; *Report submitted to PMO*, 135p.

Deltares, 2010. Delft3D-FLOW. Simulation of multi-dimensional hydrodynamic flow and transport phenomena, including sediments – User Manual. Version 3.04, rev. 11114. *Deltares*, Delft, The Netherlands.

Jamab, 1999. Integrated water management plan of Iran – Mond River Watershed, *Jamab Consulting Engineers*, Tehran, Iran.

Jamab, 2006. Optimum monitoring system of Iran water resources – Mond River Watershed, *Jamab Consulting Engineers*, Tehran, Iran.

Journal of Coastal Research	SI	75	810-814	Coconut Creek, Florida	2016

A Multiscale Simulation Approach for Linking Mangrove Dynamics to Coastal Processes using Remote Sensing Observations

Christophe Proisy[†], Pascal Degenne[‡], Edward J. Anthony[††], Uta Berger[§], Elodie Blanchard[†], François Fromard[$], Antoine Gardel[Φ], Adewole Olagoke[§†], Valdenira Santos[#], Romain Walcker[!$], Danny Lo Seen[‡]

[†]UMR AMAP, Institut de Recherche pour le Développement, Montpellier, France
[‡] UMR TETIS, CIRAD, Montpellier, France
[††]Institut Universitaire de France, CEREGE, Aix-Marseille Université, Aix en Provence, France
[§]Institute of Forest Growth and Computer Science, Technische Universität, Dresden, Germany
[$]CNRS-UMR ECOLAB, Toulouse, France
[Φ]Université du Littorale Côte d'Opale-CNRS-Guyane, Cayenne, French Guiana
[#]Instituto de Pesquisas Científicas e Tecnológicas do Estado do Amapá (IEPA), Macapá, Amapá, Brazil
[!]Université Paul Sabatier, Toulouse, France

www.cerf-jcr.org

www.JCRonline.org

ABSTRACT

Proisy, C., Degenne, P., Anthony, E.J., Berger, U., Blanchard, E., Fromard, F., Gardel, A., Olagoke, A., Santos, V.F., Walcker, R., & Lo Seen, D. (2016). A multiscale simulation approach for linking mangrove dynamics to coastal processes using remote sensing observations. *In:* Vila-Concejo, A.; Bruce, E.; Kennedy, D.M., and McCarroll, R.J. (eds.), *Proceedings of the 14th International Coastal Symposium* (Sydney, Australia). *Journal of Coastal Research*, Special Issue, No. 75, pp. 810-814. Coconut Creek (Florida), ISSN 0749-0208.

We present a new landscape-modelling framework based on a domain-specific language called Ocelet that is used to question our understanding of how mangrove forests cope with fast-changing muddy seashores. For the demonstration, we selected the coast of French Guiana where mangrove physiognomy and extent continuously vary due to successive and recurrent erosion or accretion phases resulting from the alongshore migration of mud banks originating from the Amazon River. We modelled the French Guiana coastal system as a set of ecological and physical processes involving *entities* (*e.g.* ocean, mangrove shoreline, mud bank) that are in *relation* with each other. Interaction functions are written to specify how the entities change when they interact, according to the level of understanding and knowledge available. The *scenario* then describes what interaction functions are activated at each time step. We applied the approach to explain mangrove shoreline variations from 1986 to 2009 over 45 kilometres, and examined the contribution of alongshore and cross-shore wave energy and current velocities. The model was run with daily ERA-Interim/ECMWF waves and Mercator-Ocean currents as input data, whereas a time series of remote sensing images was used during the initialization and validation phases. We then discuss the flexibility of our approach to integrate existing models of mangrove forest dynamics.

ADDITIONAL INDEX WORDS: *mangrove coasts, coastal modeling, ERA-Interim, coastal currents.*

INTRODUCTION

The capability of mangroves to cope with coastal changes will remain a challenging question in the coming decades (*e.g.* Ellison, 2015). The future of mangroves is now doubly jeopardized by direct human pressures (Duke *et al.*, 2007) that compound effects of sea level rise and coastal erosion induced by changes in hydrodynamic and sedimentary processes or increasingly stronger storms. Among pending difficulties in forecasting changes in the extent and functioning of mangrove ecosystems is describing how multiple biotic and abiotic factors interplay at the local scale (*e.g.* Alongi, 2009) to regulate mangrove development, knowing that these factors are themselves constrained at larger scales by tides, winds, waves, nearshore currents or sediment transport (*e.g.* Anthony *et al.*, 2010).

Reciprocally, mangrove forests play an important role in the functioning of the coastal zone. Several models have been developed to address the dynamics of these forests (Berger *et al.*, 2007). They simulate growth of mangrove trees under different but stationary environmental conditions that are described in maps of abiotic factors obtained at forest stand or landscape scales. They are not designed to directly tackle the issue of real-world changing coasts. This may be one of the reasons why coastal zone management policies are still far from integrating all the knowledge acquired from scientific studies of mangrove ecology (Lewis, 2009). In our opinion, a considerable potential for groundbreaking research would consist in coupling actual forest dynamics models with hindcast, nowcast and forecast scenarios of coastal changes.

Remote sensing observations have proved useful in monitoring decadal-scale changes in mangrove shoreline and extent in many regions (*e.g.* Nascimento *et al.*, 2013). The knowledge thereby obtained on real case studies by observing decadal changes at a regional scale is not yet exploited sufficiently to forecast mangrove changes. Modeling of forest dynamics does not yet assimilate such pivotal information. Remote sensing data are also at the basis of global and regional climate simulations due to their multiple potential for monitoring oceans and atmosphere parameters. Hindcast data sources such as ERA-Interim wave or oceanic current signals provided by, respectively, the European Centre for Medium-

DOI: 10.2112/SI75-163.1 received 15 October 2015; accepted in revision 15 January 2016.
*Corresponding author: christophe.proisy@ird.fr
©Coastal Education and Research Foundation, Inc. 2016

Range Weather Forecasts (ECMWF) and Mercator Ocean provide crucial data to understand changes that have affected mangrove coasts over the last decades. However, to our knowledge, no mangrove studies have exploited this potential yet. One of the reasons that come to mind could be the need for a flexible modelling approach capable of handling the coupling of various types of data and factors at various time and spatial scales in order to go further in the understanding of what has been observed for decades in satellite images. We present a new landscape-modelling framework based on a domain-specific language called Ocelet that is used here to address the question of mangrove forest dynamics in the context of fast-changing muddy seashores.

METHODS

Recently, Walcker *et al.* (2015) found a significant relationship between multi-decadal fluctuation of mangrove shorelines and wave regimes in French Guiana. In this coastal region influenced by the massive fine-grained discharge from the Amazon River, hydrodynamics and sedimentary processes regulating the extent and physiognomy of mangroves are interwoven at many spatial and time scales (Figure 1). Hindcast, nowcast, and forecast coastal changes are particularly difficult to address.

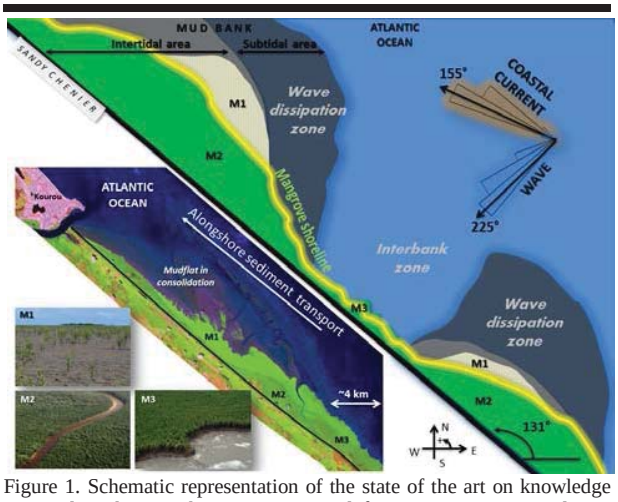

Figure 1. Schematic representation of the state of the art on knowledge acquired on the French Guiana. Bottom left pictures present a real case study near Kourou. *In situ* and aerial photographs are laid over a color composite extract of a SPOT-4 multispectral image acquired in 2005 to illustrate mangrove dynamics (M1-3). Top right diagram illustrates how ocean waves and coastal currents impact the mangrove shoreline as a function of the presence and size of two mud banks identified by their subtidal and intertidal parts. The orientation of the coast remains nearly at 131° counter clockwise from the east.

Study area and data used

For the demonstration, we focused our work on the coast of French Guiana where mangrove physiognomy and extent continuously vary due to successive and recurrent erosion or accretion phases originating from the alongshore transport of sediments (mud banks) from the mouth of the Amazon River towards the northwest.

Previous results suggest a complementary role of wind waves in the 'welding' of mobile mud banks to the shoreline (Gratiot *et al.*, 2007) while geostrophic currents parallel to the coast may control alongshore sediment transport (Bourret *et al.*, 2008). During the accretion phase, mudflats formed on the upper intertidal portions of mud banks undergo continuous consolidation (Gensac *et al.*, 2015) and, generally the latter process is followed by rapid and extensive mangrove colonization over hundreds of hectares (Proisy *et al.*, 2009). Shoreline retreat during erosion phase is mainly attributed to the impact of waves propagating across stretches of coast between banks, called inter-bank zones (Figure 1; Anthony *et al.*, 2010). Massive and rapid removal of mangroves can be observed over several square kilometres in a few years in inter-bank zones.

In this work, we used a subset of eleven SPOT-1/2/4/5 multispectral satellite images to obtain mangrove shoreline positions from a simple visual analysis as already done by Fromard *et al.* (2004) or Walcker *et al.* (2015). These data imaged the 45 km long coastline between Cayenne and Kourou from 1986 to 2009. Spatial resolutions ranged from 4 m to 20 m. Coastal orientation over the study area remains nearly constant and about 141° *w.r.t.* east. Additionally, we downloaded ERA-Interim reanalysis data from the European Centre for Medium-Range Weather Forecasts reanalysis products (ECMWF) website and focused on 1° daily ocean wave data available since 1986. We analyzed ocean wave data provided at the node 6°N, 53°W, which is located about 60 km north of Sinnamary. We considered this node the most suitable to study ocean waves that predominantly propagate southwestward (Figure 1). We combined wave height H and period T to produce the ratio H^3/T^2, a relevant parameter for describing wave forcing (Gratiot *et al.*, 2007). The average wave energy from 1986 to 2009 was about 0.066 ±0.04 $m^3.s^{-2}$ and maximum values regularly observed between January and March reach 0.15 $m^3.s^{-2}$. The high-energy season from October to May is characterized by wave incidence nearly orthogonal to the coastline. During the low-energy season from June to September, the incidence angle of ocean waves decreases to 70°. Data on coastal currents since 1986 were freely provided by Mercator-Ocean at 0.5° from the PSY2G2R1 analysis system. The node closest to the coast was at 6°N, 51.5°W and corresponded approximately to a distance of 140 km northeast of Cayenne. Coastal currents are continuously oriented alongshore with a direction remaining nearly constant around 115° *w.r.t.* east. Seasonal variations in coastal currents are observed with the highest velocities of 0.3 $m.s^{-1}$ occurring between February and June. The average velocity rate between 1986 and 2009 was 0.1 ± 0.07 $m.s^{-1}$. We centered and scaled the ocean wave and current signals in order to have them on an equal basis relative to their variation and, to enable evaluation of their respective contributions to changes in the mangrove shoreline.

Modelling with Ocelet

We used Ocelet (Degenne et al, 2009; 2010), which is a domain-specific language for modelling spatial dynamics within a model-building environment called the Ocelet Modelling Platform (OMP). Compared to other modelling approaches such as Systems Dynamics or Agent-Based systems, Ocelet proposes a more flexible way of handling space within processes, due to usage of *interaction graphs*. Ocelet introduced an extension to

the concept of *graph* (a set of *vertices* connected with *edges*) wherein appropriate semantics are attached to the vertices and edges so that they can be defined to represent a dynamic system in space and time. For example, a landscape can be represented by landscape elements (vertices) that are linked (through edges) to each other. During a simulation, *interaction functions* can be applied on the edges to change the state of the entities connected. Interaction graphs are thus dynamic (vertices changing state), with dynamic structure, as vertices and edges can be added or removed during a simulation. Among the properties included by the modeller to describe an entity, one is usually dedicated to its spatial representation, with points, lines, polygons and cells as possible data types. In certain models, it may be necessary to use vector and raster entities together, and interaction graphs in Ocelet appropriately embrace both types.

Once the main processes at work in the system studied are identified, they can be modeled with Ocelet one after the other, starting with the process expected to be the most relevant. Other processes can then be added in turn, and interactions between processes included whenever necessary. For a given process, the different types of entities involved are first identified and described. Then, relations are built by stating which entity interacts with which other entity (the graph structure), and describing each of the functions that can be applied when the entities interact (the interaction functions). These functions are used in the *scenario*, which comprises an initialization part, to define the initial state of the system, and the simulation part that describes, for each time step, which functions are executed, and in what sequence. Ocelet uses a different *datafacer* to interface with the different types of data sources possible (GIS database, text file, shapefile, kml file, raster image). No specific mechanism has yet been included to track the properties of the entities or other state variables. Therefore, the scenarios must also contain instructions to save the required variables into a file for display and analysis. The OMP environment groups within the same interface all the tasks required when building a model with Ocelet: model creation and maintenance, Ocelet code edition, compilation, simulation run, display and export of simulation results. Ocelet and the Ocelet Modelling Platform are released under the CECILL V2.1 license and can be downloaded from http://www.ocelet.org.The sources are for now available on demand. They are currently being properly formatted and will be openly available on GitHub soon.

Application to the French Guiana coast

We limited the spatial extent of the modelling study to the 45 km long coastal area between Cayenne and Kourou for which the maximum number of satellite images was available. With the benefit of hindsight of observations and analysis of changes that occurred over the last 60 years (Walcker *et al.*, 2015), we decided to start modelling using only three main interactions noted *f1-3* (Figure 2) and empirical equations given in table 1.

- *f1: Mud bank displacement along the coast.* The relation *f1* between *Ocean* and *Mud bank* entities describes how mud banks move under current and wave forcing. The displacement of the mud bank *Dm* is assumed to be linearly related to the alongshore components of ocean waves W_{al} and currents C_{al} by the coefficients k_{cc} and k_{cw}. From the observation of oceanic water areas displaying high turbidity in the 1986 satellite image, we roughly delineated the contour of two mud banks as semi-ellipses (Figure 2). The one near Kourou was larger than the second near Cayenne. We assumed that their size and direction of movement remained unchanged from 1986 to 2009.
- *f2: Mangrove shoreline exposure to wave-induced erosion depending on the degree of protection by a mud bank.* Mud banks are expected to offer some protection to mangroves by attenuating the erosive forces of waves. The exposure factor F_{exp} is computed as a function dependent on the distance r_{attn} a wave has to travel over a mud bank to reach a given point of the shoreline. This point is expected to be totally protected by the mud bank when r_{attn}>20 km. The exposure equation also includes a scale factor S_f and a shape parameter *n* of the attenuation function.
- *f3: Mud bank colonization by mangroves.* Mangrove seaward progression is due to complex colonization processes occurring at microtopography level (Proisy *et al.*, 2009) that could not be taken into account in the model at this time (Figure 1). Instead, we used a very simple constant rate of progression of the mangrove shoreline perpendicularly to the overall coastal orientation. This function is set proportional to ($S_f - F_{exp}$) and weighted by a scale factor β_{col}. When and where ($S_f - F_{exp}$) is greater zero, the mangrove shoreline is expected to shift seaward.
- *Initial state:* The simulation process starts from the 1986 observation. Two polylines were drawn: one for the chenier (the boundary inland that is considered stable) and the other for the mangrove shoreline that is subject to wave erosion.

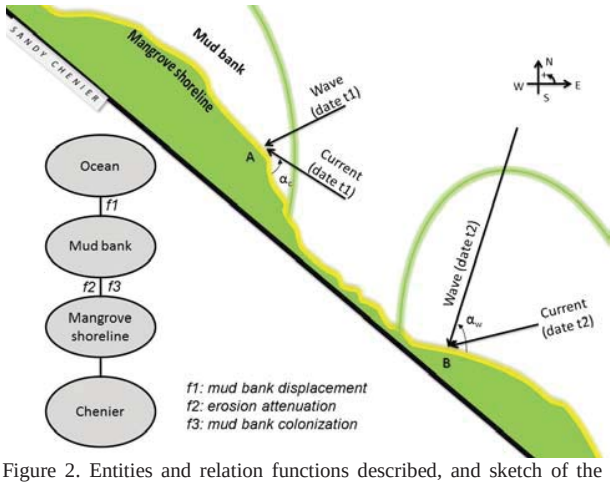

Figure 2. Entities and relation functions described, and sketch of the modeling approach in its present state. The mangrove shoreline is subjected to the energy of waves and coastal currents propagating along different directions. At a given time, the energy of waves that induce erosion is dampened by intertidal and subtidal areas that the forcing signal must go through following a given approach angle (α_w or α_c). Point A at t1 is less protected than point B at t2. For the moment, a mud bank is considered without influence on the neighboring mud bank to the northwest. The chenier (sand ridge) is considered as the landward limit of the mangrove area.

In the equations below, five parameters had to be estimated: the linear relation coefficients k_{cc}, k_{cw} and the shape and scale factors *n*, S_f and β_{col}. These were obtained by minimization of the differences between the simulated mangrove shoreline

between Cayenne and Kourou and the same shoreline observed in the satellite image acquired in 2001, this year lying close to the middle of the 1986-2010 period of study. Initial values for these five parameters (Table 1) were rounded estimates obtained using average values of observed shoreline displacements and ocean wave and current data (not shown for reasons of conciseness). The coast function used was defined as the root mean square error between simulated and observed shoreline positions along transect lines spaced 500 m and all directed perpendicular to the coast. The downhill simplex method (Nelder and Mead, 1965) was used to search for the optimal parameter values. Simulations were then carried out for the whole 45 km long studied coastal area between 1986 and 2009 with this parameter set.

Table 1. *Equations used in the main processes modelled.*

Process and function	Equations	Initial state	Final state
Mud bank displacement along coast (*f1*)	$\boldsymbol{D_m}$ (m.day^{-1}) = $\mathbf{k_{cc}}.\boldsymbol{C_{al}} + \mathbf{k_{cw}}.\boldsymbol{W_{al}}$	k_{cc}=30.0 k_{cw}=30.0	k_{cc}=21.7 k_{cw}=35.1
Mangrove shoreline exposure to erosion (*f2*)	$\overrightarrow{\boldsymbol{d_w}} = \boldsymbol{F_{exp}}.\overrightarrow{\boldsymbol{W}}$ with $\boldsymbol{F_{exp}} = \boldsymbol{S_f}.(\mathbf{1} - \frac{\boldsymbol{r_{attn}}}{\mathbf{20000}})^{\boldsymbol{n}}$	S_f = 6.0 n = 3	S_f = 2.5 n = 4.75
Mud bank colonization by mangroves (*f3*)	$\boldsymbol{d_{col}}$ (m.day^{-1}) = $(\boldsymbol{S_f} - \boldsymbol{F_{exp}}).\boldsymbol{\beta_{col}}$	β_{col} = 0.1	β_{col} = 0.13

RESULTS

The most salient result obtained from our modeling work concerns the confirmation that the iteration procedure converges, this meaning that our equations and thus the description of the underlying processes were suitable enough to explain some of the fluctuations in the mangrove shorelines. It is to be noted that the minimum was reached after 240 iterations of 2.8 min of computing time each (under Windows 7, 64 bits, 8 GB of RAM).

Resulting simulated mangrove shorelines for the ten images acquired after 1986 have been recorded in a kml format and displayed directly in Google Earth®. A relatively good visual agreement between satellite-observed and simulated fluctuations in mangrove shorelines was noted for each of the 14 years between 1987 and 2009, as shown in part in Figure 3 for only 1987, 1999 and 2009. Overall, our model makes the mangrove shoreline retreat in interbank zones during erosion phases and prograde when a mud bank protects a given area. The values obtained for the 5 parameters (table 1, right column) describe mangrove coast dynamics over 90 points of observation (every 500 m) with an averaged root mean square error increasing, except in 2001, and reaching a maximum of 360 m in 2006, 20 years after (Figure 3, bottom left).

DISCUSSION

The flexibility of the Ocelet language allowed us to intuitively establish a relationship between entities, such as the ocean, the mud banks and the mangrove areas. To our knowledge, these entities have remained unlinked in most of the studies dealing with mangrove changes. Our preliminary results suggest that the impact of waves on mangrove shorelines is almost two times more (k_{cw}=35.1; ~62% of the total contribution) than that of coastal currents do (k_{cc}=21.7; ~38%). These findings are in support of statistical evidence of a clear relationship between the extent of mangroves and large-scale, low-frequency changes in North Atlantic waves (Walcker *et al.*, 2015). We have therefore started developing a tool capable of steering and spatializing mangrove forest dynamics models from the simulated impacts of large-scale oceanic processes that should yield, for example, the timing and location of mangrove colonization and erosion processes. For these purposes, high spatial resolution images could be used to detect the initial time (Proisy *et al.*, 2009), the mangrove growth stage (Proisy *et al.*, 2007) and mangrove destruction.

The convergence of the modelling approach based on simple equations proves that ocean wave and coastal current signals 'force' the mangrove shoreline to adapt itself to different levels and types of processes, such as erosion associated with sediment remobilization by ocean waves (Gratiot *et al.*, 2007) or mud bank colonization by mangroves following substrate consolidation (Proisy *et al.*, 2009). A next step would be to integrate a forest dynamics model in the modelling approach, which can also be tested in other regions of the French Guiana coast, especially in the extreme western sector of the coast where shoreline orientation approaches 180° and mud banks become very elongated.

CONCLUSION

In this paper, we have presented preliminary milestones towards the simulation of the dynamics of mangrove coasts. The Ocelet modelling approach highlighted a good potential for addressing coastal processes involved in decadal changes in mangrove extent. We have succeeded, to a certain degree, in tracking and explaining mangrove shoreline variations using both widely available satellite and ocean data. Rapidly changing pristine mangrove coasts demonstrate fascinating capacities to cope with coastal changes. These capacities need to be properly addressed through interdisciplinary research in order to anticipate the highly variable future of coastal areas.

ACKNOWLEDGMENTS

This work was conducted in the framework of the 'STAMP', 'INFOLITTORAL-1' and 'MANGWATCH' projects funded, respectively, by the ANR Blanc, the French "Unique Inter-ministerial Fund", certified by the “Aerospace Valley competitiveness cluster" and CNRS 'Incubator for interdisciplinary research projects in French Guiana' research programmes. Mr. Olagoke acknowledges the "Erasmus Mundus" Forest for Nature programme (FONASO). We thank Mercator Ocean (http://www.mercator-ocean.fr/) for providing ocean current data. Mercator Ocean cannot be held responsible for the results nor for the use to which they are put.

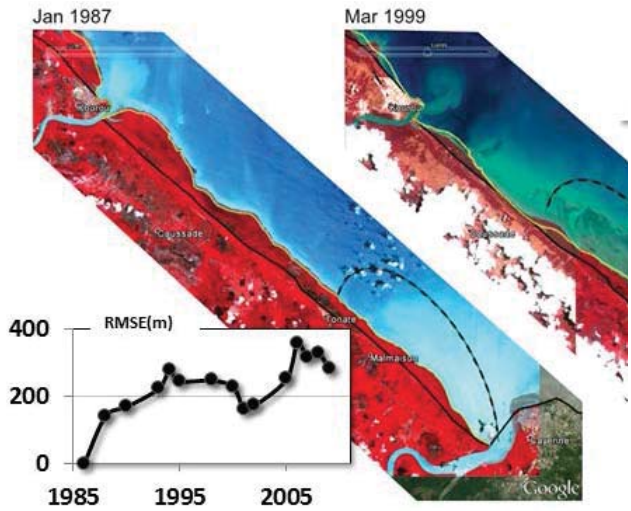

Figure 3. Simulated mangrove shorelines (yellow line) overlain on SPOT satellite images, Kourou-Cayenne region from 1987 to 2009.

LITERATURE CITED

Alongi, D.M., 2009. Paradigm shifts in mangrove biology. *In*: Perillo G.M.E.; Wolanski, E.; Cahoon, D.R., and Brinson, M. M. (eds), *Coastal wetlands: An integrated ecosystem approach*. Amsterdam: Elsevier, pp. 615-640.

Anthony, E.J.; Dolique, F.; Gardel, A.; Gratiot, N.; Proisy, C., and Polidori, L., 2008. Nearshore intertidal topography and topographic-forcing mechanisms of an amazon-derived mud bank in French Guiana. *Continental Shelf Research*, 28(6), 813-822.

Anthony, E.J.; Gardel, A.; Gratiot, N.; Proisy, C.; Allison, M.A.; Dolique, F., and Fromard, F., 2010. The Amazon-influenced muddy coast of South America: A review of mud-bank-shoreline interactions. *Earth-Science Reviews*, 103(3-4), 99-121.

Berger, U.; Rivera-Monroy, V.H.; Doyle, T.W.; Dahdouh-Guebas, F.; Duke, N.C.; Fontalvo-Herazo, M.L.; Hildenbrandt, H.; Koedam, N.; Mehlig, U.; Piou, C., and Twilley, R.R., 2008. Advances and limitations of individual-based models to analyze and predict dynamics of mangrove forests: A review. *Aquatic Botany*, 89(2), 260-274.

Bourret, A.; Devenon, J.L., and Chevalier, C., 2008. Tidal influence on the hydrodynamics of the French Guiana continental shelf. *Continental Shelf Research*, 28(7), 951-961.

Degenne, P.; Lo Seen, D.; Parigot, D.; Forax, R.; Tran, A.; Ait Lahcen, A.; Curé, O., and Jeansoulin, R., 2009. Design of a domain specific language for modelling processes in landscapes. *Ecological Modelling*, 220(24), 3527-3535.

Degenne P, Ait Lahcen A, Curé O, Forax R, Parigot D, Lo Seen D, 2010. Modelling with behavioural graphs. Do you speak Ocelet? Proc. of the International Congress on Environmental Modelling and Software, July 5-8, Ottawa, Ontario, Canada. http://www.iemss.org/iemss2010/proceedings.html

Duke, N.C.; Meynecke, J.O.; Dittmann, S.; Ellison, A.M.; Anger, K.; Berger, U.; Cannicci, S.; Diele, K.; Ewel, K.C.; Field, C.D.; Koedam, N.; Lee, S.Y.; Marchand, C.; Nordhaus, I., and Dahdouh-Guebas, F., 2007. A world without mangroves? *Science*, 317(5834), 41 - 42.

Ellison, J., 2015. Vulnerability assessment of mangroves to climate change and sea-level rise impacts. *Wetlands Ecology and Management*, 23(2), 115-137.

Gensac, E.; Gardel, A.; Lesourd, S., and Brutier, L., 2015. Morphodynamic evolution of an intertidal mudflat under the influence of amazon sediment supply – Kourou mud bank, French Guiana, South America. *Estuarine, Coastal and Shelf Science*, 158(5), 53-62.

Gratiot, N.; Gardel, A., and Anthony, E.J., 2007. Trade-wind waves and mud dynamics on the French Guiana coast, South America: Input from era-40 wave data and field investigations. *Marine Geology*, 236(1-2), 15-26.

Lewis III, R.R., 2009. Knowledge overload, wisdom underload. *Ecological Engineering*, 35(3), 341-342.

Nascimento Jr, W.R.; Souza-Filho, P.W.M.; Proisy, C.; Lucas, R.M., and Rosenqvist, A., 2013. Mapping changes in the largest continuous Amazonian mangrove belt using object-based classification of multisensor satellite imagery. *Estuarine, Coastal and Shelf Science*, 117, 83-93.

Nelder, J.A., and Mead, R., 1965. A simplex method for function minimization. *The Computer Journal*, 7(4): 308-313.

Proisy, C.; Couteron, P., and Fromard, F., 2007. Predicting and mapping mangrove biomass from canopy grain analysis using Fourier-based textural ordination of Ikonos images. *Remote Sensing of Environment*, 109(3), 379-392.

Proisy, C.; Gratiot, N.; Anthony, E.J.; Gardel, A.; Fromard, F., and Heuret, P., 2009. Mud bank colonization by opportunistic mangroves: A case study from French Guiana using LIDAR data. *Continental Shelf Research*, 29(3), 632-641.

Walcker, R.; Anthony, E.J.; Cassou, C.; Aller, R.C.; Gardel, A.; Proisy, C.; Martinez, J.-M., and Fromard, F., 2015. Fluctuations in the extent of mangroves driven by multi-decadal changes in north Atlantic waves. *Journal of Biogeography*, 42(11), 2209-2219.

Journal of Coastal Research	SI	75	815-819	Coconut Creek, Florida	2016

Sturgeon Bank, Fraser River Delta, BC, Canada: 150 Years of Human Influences on Salt Marsh Sedimentation

Ada C. Scudelari [†], Claudio F. Neves[‡*], Venerando E. Amaro[§], and Olavo F. Santos[††]

[†]PPgES, Civil Engineering Department
Federal University of Rio Grande do Norte
Natal, RN Brazil

[‡]Ocean Engineering Program - COPPE
Federal University of Rio de Janeiro
Rio de Janeiro, RJ Brazil

[††]PPgEC, Civil Engineering Departament
Federal University of Rio Grande do Norte
Natal, RN Brazil

[§]PPgGG, Department of Geology
Federal University of Rio Grande do Norte
Natal, RN Brazil

www.cerf-jcr.org

www.JCRonline.org

ABSTRACT

Scudelari, A.C.; Neves, C.F.; Amaro, V.E., and Santos, O.F., 2016. Ponta Negra Beach, Natal, RN, Brazil: A roll and rock story. *In:* Vila-Concejo, A.; Bruce, E.; Kennedy, D.M., and McCarroll, R.J. (eds.), *Proceedings of the 14th International Coastal Symposium* (Sydney, Australia). *Journal of Coastal Research*, Special Issue, No. 75, pp. 815-819. Coconut Creek (Florida), ISSN 0749-0208.

The paper presents a case study of the erosion process at Ponta Negra Beach, important touristic destination located 15 km south of the downtown area of the city of Natal, capital of the State of Rio Grande do Norte, Northeast Region of Brazil. Unplanned urbanization was followed by an attempt in late 1990's to improve the use of the beach front area. A 4 km long walkway was built along the beach on top of the foredunes, water supply and sewage pipes were buried into the landfill, and a seawall was built to contain the landfill. A slow unattended erosion process was initiated, until in 2012 the seawall and the walkway were severely damaged by waves. Possible causes are discussed and the adopted remedial solutions are presented. The paper should be viewed as a critical reflection on the role of coastal zone management in order to promote sustainable development, based on a tripod: continuous environment monitoring, engineering, and society engagement.

ADDITIONAL INDEX WORDS: *Beach erosion, coastal processes, coastal management.*

INTRODUCTION

The city of Natal (5°47'42" S , 35°12'34" W), State capital of Rio Grande do Norte, Brazil (Figure 1), was founded on Christmas Day of 1599, at the mouth of Potengi River, where a fortress had been built on top of the reefs (Figure 2). Population grew from 55,000 in 1940 to 870,000 in 2015. During the decades of 1980 and 1990, population of the city grew at a much faster pace than that of the State. As a result, urbanization expanded towards South, an area composed mostly of 30 m high, vegetated dunes (Figure 3a).

Ponta Negra Beach, 15 km south of the downtown area of Natal, a fishermen village since the beginning of XVIII century, became a touristic attraction in the 1940's. Since the 1980's the area has undergone heavy urbanization and the afflux of tourists has grown significantly although, more recently, it has declined, mainly after beach erosion and destruction of the walkway.

The beach extends for 4 km in the N-S direction from Morro do Careca, a 30m high dune on top of the promontory which gives its name to the beach (meaning Black Point). It has a typical spiral shape in planform, and is backed by a field of dunes, partly vegetated, partly urbanized (Figure 3a).

Rolling down the dune at Morro do Careca and diving into the sea (the location is shown as a white stripe on the background of Figure 3b) used to be a favorite amusement, until the State Environmental Agency blocked the access to the dune. Today, one can observe sand rolling downhill, mainly after raining, and, in low tide, water flows from the dune's water table towards the beach, carrying sand.

Analyzing aerial views of Morro do Careca, it is right to assume that the dune originally fed sediments to the beach, at an amount which has not yet been computed or estimated. Because

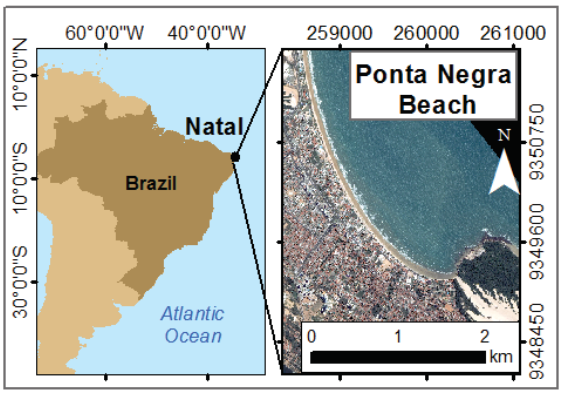

Figure 1. Location of the city of Natal and Ponta Negra Beach, Northeast Brazil.

DOI: 10.2112/SI75-164.1 received 15 October 2015; accepted in revision 15 January 2016.
*Corresponding author: neves@peno.coppe.ufrj.br
©Coastal Education and Research Foundation, Inc. 2016

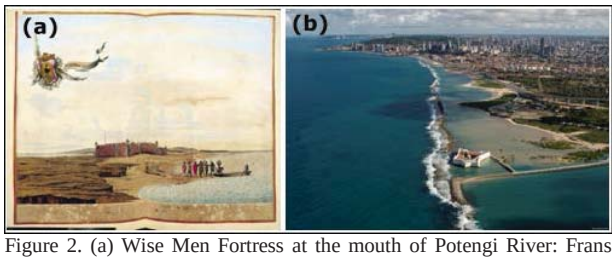

Figure 2. (a) Wise Men Fortress at the mouth of Potengi River: Frans Post illustration of Barlæus book (1647), and (b) contemporary aerial view of the fortress and the city on the background).

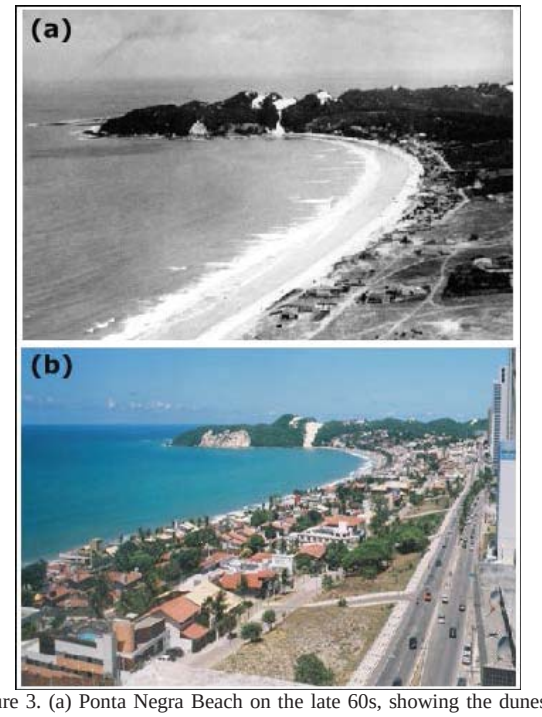

Figure 3. (a) Ponta Negra Beach on the late 60s, showing the dunes of Morro do Careca on the background and the unvegetated stripe where people used to roll down into the sea, compared to the present (b).

main littoral drift is oriented from South to North, the dunes of Ponta Negra should be the natural source of sand for the beaches to the North.

Urbanization started in 1980's at the southernmost portion of the beach. Along the beach, Erevan França Avenue was built, together with the first culverts, which discharged directly on the beach. Other water contributions were diverted into the drainage system though: illegal sewage connections, leaking pipes, watered lawns and drained swimming pools. All this excess water flowed towards the beach and, in low tide, it carried sand from the upper portions of the beach towards the swash zone.

The beach, which had always been considered as stable, has begun to show signs of erosion in 2010. Although this fact was initially disregarded, in 2012 the erosion process intensified. The lack of coastal monitoring left room for speculation on possible causes: natural oceanic agents (e.g. waves, sea level rise), urbanization related factors (e.g. loss of feeding sand, drainage), and other causes unusually associated to beach processes (e.g. tectonic displacement). It became as well an invitation for various creative "solutions", some of them not sound enough on an engineering or scientific basis.

City administration did not act to control the erosion until the sea front urbanization was seriously damaged. Low cost remedial works were ineffectively attempted. Legal action by the State of Rio Grande do Norte was finally taken against the City administration. Among several remedial options, artificial nourishment was recommended, but the City has chosen a hard solution, which not only did not stop the erosion process, but also caused the complete loss of the beach, as it will be shown later, besides other problems (difficulty of access, loss of area for fishermen boats, reduced consumption of food or beverage).

The paper describes the authors' quest to explain the causes for the erosion problem at Ponta Negra Beach.

METHODS

Information about the coastal environment is very scarce and thus quite unreliable (for instance, too many gaps in time series, visual observation of waves, and no record of sea level variation referred to a fixed datum).

Oceanographical data

Tidal records inside the Potengy River estuary have been obtained by the Hydrographic Service of the Brazilian Navy (DHN). Tide is semidiurnal and spring tidal range is about 2.5 m; there are two year-long records, one in 1959 and the other in 2004-2005, besides a few short term records. During 45 years, the morphology of the estuary has undergone major changes. Unfortunately, those tide records are not referred to the official Brazilian Vertical Datum (IBGE Imbituba datum), hence long term trends of sea level cannot be investigated.

Isolated measurements of currents near the promontory of Ponta Negra indicate values of the order of 10 to 50 cm/s, with strong shear between surface and bottom. At the mouth of Potengi River, tidal charts from the DHN indicate spring tide currents of the order of 1.7 m/s. However, due to persistent wind action, the combined effect of tidal currents and wind drift should be closely investigated, mainly in regard to their effect on wave propagation and local wave generation.

Wave data

The only measurement in Natal happened from April 1977 to April 1978 at a location 20 m deep; a bottom mounted pressure sensor was used, recording every six hours, and visual observations of direction were made twice a day. Average significant wave height was 120 cm, period 6.1 s and most frequent directions were E and ESE (Valentini 1981).

More recently, Global Wave Statistics has been used for designing the sewage outfall of Natal. The area covers the entire Northeast Region of Brazil and so it is not a good estimate for the local wave climate.

Wind data from reanalysis has also been used to generate wave climate at Ponta Negra Beach using WAVEWATCH III model, within the system SMC-Brasil (SMC, 2014). Joint distributions of Hs-Tp and Hs-Dir showed that most frequent waves had Hs between 1.3 and 1.7 m, and Tp around 8s, from E to SE direction. The portion of the beach closest to Morro do

Careca could be eventually exposed to waves 1.5 m high during storms (Almeida *et al.* 2015).

Precipitation

Rainy season runs from March to July with mean monthly precipitation between 200 and 270 mm; otherwise it is between 10 and 100 mm. Mean yearly accumulated precipitation is about 1,500 mm. Regional climate is much influenced by the latitudinal oscillations of the Intertropical Convergence Zone (ITCZ). Based on data from the National Meteorological Institute (INMET), the authors computed the running 7-day accumulated rainfall and counted the number of days in a year that this value has remained above a given threshold. Results are shown in Figure 4 for threshold values from 50 mm to 500 mm.

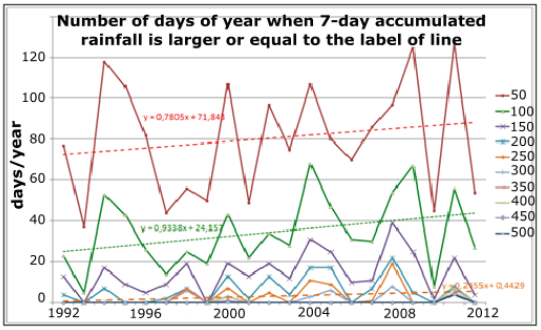

Figure 4. Pattern of annual precipitation in Natal. Each line represents the number of days of the year when the 7-day accumulated rainfall is larger or equal to the label of the respective line.

In this figure, for the value 100 mm (green curve), there are peaks in years 1994, 2000, 2004, 2009, and 2011. In those years, accumulated precipitation in 7 days was larger than or equal to 100 mm during 40 to 60 days a year (wet years), whereas in other years, the same value happened between 20 to 40 days.

Higher precipitation results in larger volumes of water drained directly towards the beach or infiltrating into the dunes' water table. After each event of more intense rainfall the beach face is excavated at the mouth the culverts (Figure 5), creating 50 cm deep and 3 m wide trenches. Because a culvert has been placed every 100 m, after many years there will be a net transport of beach sand to lower portions of the profile as a whole.

Figure 5. Loss of sediment due to pluvial drainage flow. (a) 23 January 2011 (Photo: Flavia Janiny); (b) 13 July 2012 (Photo: V. E. Amaro).

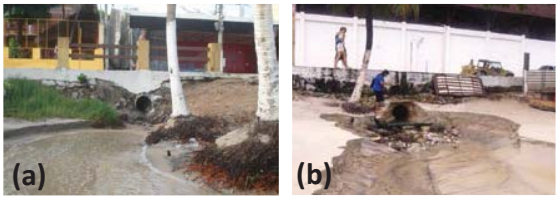

Water table dynamics

In falling tide, the beach face is always glassy or wet (Figure 6a), showing that significant seepage from the background dunes exists (Figure 6b). This flowing water carries sediments towards the sea and, if the water table rises (due to higher precipitation or increased infiltration from water supply pipes, septic tanks, sewage pipes, swimming pools), this excess water will emerge finally on the beach face. This is a very slow process which may contribute to a background erosion of the beach (Nielsen, 2012; Bird and Lewis, 2015).

Figure 6. (a) and (b) Seepage at beach face.

Wind data

The entire State of Rio Grande do Norte is under the influence of Southeastern trade winds and weather is influenced by the ITCZ. Local seas and aeolian sediment transport are two natural features observed at several coastal locations, including Natal, and easily identified in satellite images. As a matter of fact, several wind farms have been installed along the coast.

Prevailing winds in Natal come from SE direction (45%), with an average speed of 5.5 m/s; 90% of wind direction fall between ESE and S directions (Amaro *et al.* 2012).

Sediment processes

Sediment sizes vary along Ponta Negra beach. Samples were taken along three profiles, the first one near Morro do Careca, and the other two at 1km and 2km northward. Near Morro do Careca median diameter is 0.10 mm, increasing to 0.38 mm close to the seawall. Granulometric distribution in phi units shows clearly that two types of sediments are present. Moving northward away from Morro do Careca, sediment size increases to 0.24 and 0.33 mm in the swash zone (Amaro *et al.* 2012).

Valentini (1981) estimated 400,000 to 700,000 m^3/yr as the net longshore sediment transport due to waves at Areia Preta Beach, 10 km North of Ponta Negra Beach.

Aerial views and local inspection show that sand is drifted by wind from one side of Ponta Negra promontory, builds the dune (Figure 7b), and then slides downhill to the cove side (Figure 7a). As a matter of fact aeolian sediment transport is found along the entire coast of Rio Grande do Norte. The original beach (Figure 3a) must have been fed with sand from the dune, this process being interrupted after urbanization and construction of Avenue Erevan França and the walkway along the shore.

Morphological surveys

Amaro *et al.* (2014) described an application of remote sensing multitemporal analysis based on moderate and high-resolution images, a Post-Processing Kinematic (PPK) GPS survey for 3D modeling of the beach face, GIS spatial analysis, and field studies to get the time-series shoreline database for the long-term study (1973-1986 and 1986-2012) and the short-term study (from 2003 to 2011) of the erosion/accretion patterns on Ponta Negra Beach. This study was complemented by field surveys and local inspections.

The PPK GPS survey used a GPS antenna adapted on a quad-motorcycle as a rover receiver connected to a GPS antenna at the base station. The shoreline position and 3D morphological features were determined with high accuracy and precision using a GPS receiver Trimble Model R3 L1 Frequency whose nominal horizontal accuracy was 5 mm + 1 ppm and a vertical accuracy of 5 mm + 2 ppm. A total of 9 images from various satellites (QUICKBIRD, LANDSAT-1, LANDSAT-5, IRS-6, IKONOS-2, WORLDVIEW-2), with appropriate corrections for water and land differentiated reflectance, atmospheric interference and other effects. All this data was combined with *in situ* information and appropriately georeferenced.

RESULTS

For many years various research groups of the Federal University of Rio Grande do Norte (UFRN), mainly LABGEOFIS, LARHISA, GEOPRO, have carried on local inspections, photographic recording, expedite beach profiles, and analysis of remote sensing images about Ponta Negra Beach. This section describes some of these results, which support the evidence that background erosion had been under way for many years, mainly between 1973 and 2012.

Local inspections

Photographic records have been taken on a regular basis since 2009 (Janiny 2012; Amaro *et al.* 2012). Progressive failures of the seawall, loss of the landfill behind it and destruction of the walkway have been monitored. It was evident that an erosive process was under way, without any action to control it, nor any program for monitoring environmental conditions, such as wave climate or sea level.

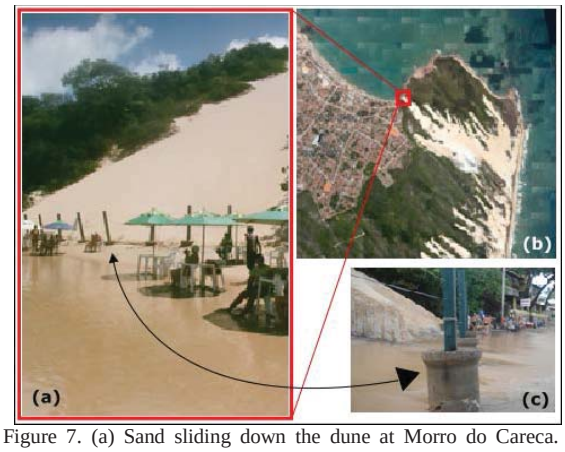

Figure 7. (a) Sand sliding down the dune at Morro do Careca. (b) Dune location, showing direction of sand drift by wind, from one side of the point to the cove. (c) Example of beach erosion response at the toe of Morro do Careca.

Remote sensing data

Results indicated shoreline recession rates of the order of 1.77 m/yr between 1973 and 1986 and 1.44 m/yr between 1986 and 2012, at the portion of the beach closest to Morro do Careca (Amaro *et al.* 2014). In the middle stretch of the beach, erosion rates for the same periods were 1.23 and 1.4 m/yr. At the North end of the beach, there was accretion at a rate of 4.23 m/yr in the period 1973-1986, followed by erosion at a rate of 1.65m/yr in the period 1986-2012. Total areas of erosion or accretion for different sectors of Ponta Negra Beach are shown on Table 1.

Table 1. *Summary of sedimentary balance (erosion/accretion) for each sector classified according to erosion damage to seaside structures*

Year		Sector			
		South end (m^2)	Very Strong (m^2)	Strong (m^2)	Moderate (m^2)
1973 to 1986	accretion	303	521	4,179	30,888
	erosion	24,661	15,859	1,765	0
1986 to 2012	accretion	1,005	371	0	0
	erosion	16,378	15,993	8,041	38,798

Remedial measures

The erosional process continued until the Public Prosecutor's Office took legal action against the City Administration. The first response was to put plastic bags filled with sand from the beach and then to drag sand from the beach face in low tide towards the upper portions of the beach, next to the debris of the destroyed seawall (Figure 8a). The erosional processes evidently increased, as higher waves reached the upper portions of the beach. Sand fill behind the seawall seeped through the crevices, as water from broken waves spilled over and infiltrated into the land fill. Water supply and sewage pipes were damaged, huge craters opened along the walkway (Figure 8b and c).

DISCUSSION

Analysis of satellite images shows signs of beach erosion occurring much earlier than the actual destruction along Erevan França Avenue and walkway. Yet coastline monitoring is not part of the actions of environmental agencies who deal with coastal zone management in Brazil.

Erosion on a sandy beach means essentially sand starvation. Two questions must be answered: (1) where does the sand come from? (2) where has the sand moved to? Neither of these questions has been addressed in the study for the recovery or protection of Ponta Negra Beach. Technical, social and economic justifications were not sufficient to face the really urgent problem of reinstalling the sewage and water supply lines. The shear view of destruction along the beach put enormous pressure on the City Administrators by public opinion and justice officials. Placing rocks or building seawalls may certainly protect shoreline assets but it will never attract sand back to the beach.

However other questions should be raised. Might the coast of the State of Rio Grande do Norte be undergoing a long term subsidence? According to the Brazilian Institute of Geography and Statistics (IBGE), the Natal GNSS Station displaces by 13 mm/yr towards N and 5.5 mm/yr towards W. Upward crustal movement is small, but the Recife GNSS station, 250 km South of Natal, shows a downward movement of 2mm/yr. Therefore, tectonic movements might be a possible cause for the erosion.

Figure 8. (a) Beach protection: first remedial measures, August 2012, (b) and (c) Failure of walkway, October 2012. (Photo: C. F. Neves).

Figure 9. Beach protection adopted solution: (a) low tide (b) high tide. (Photo: C. F. Neves, August 2012).

Rainfall water and eventually sewer, contaminated water, and oil from cars continue to be drained to the beach. During low tide, sand is slowly removed from the upper portions of the beach at the stormwater outlets and it is deposited at a lower location in the beach profile, where it is transported by waves at high tide towards North.

So, at a beach where people used to roll-down the dunes directly to the sea, where sand from the dunes used to roll-down, feed the beach, and be transported northward, nowadays there is a long stretch of rubble mound seawall, which demand beachgoers abilities of rock climbers.

City administrators guarantee that beach nourishment will be executed. However, poor economic conditions, lack of actual valuation of benefits and costs of beach recovering, lack of personnel with adequate technical education about coastal processes and/or coastal engineering in environmental agencies, and lack of public awareness about natural and man-made processes which have led to the erosion of Ponta Negra Beach, all these factors add together to this very sad roll-and-rock story.

CONCLUSIONS

The case study of severe coastal erosion in Ponta Negra beach, which has always been considered as stable, is presented. Possible causes are addressed: interruption of sediment supply from the dunes, sediment losses due to drainage outlets, interaction between water table dynamics and sediment at the beach face. Other plausible causes (sea level variations, changes in wave climate) cannot be verified due to lack of data. Analysis of remote sense images has shown that Ponta Negra beach has been undergoing a steady process of erosion since 1973, which accelerated after 1986. Crustal movements were also identified.

On the other hand, poor planning which resulted in building seawalls within the dynamic beach profile, disregard of natural processes of beach dynamics, lack of continuous morphological and environmental monitoring, and no planned response, all this contributed to the final critical situation in 2013.

An important lesson to be learned from this case can be translated into one concept: urgent need of coastal management based on monitoring, engineering and society participation.

ACKNOWLEDGMENTS

This publication results from the cooperation group "*Friends of Boussinesq Research Network*", sponsored by CAPES Foundation, Brazilian Ministry of Education, project PROCAD.

LITERATURE CITED

Almeida, L.R.; Amaro, V.E.; Marcelino, A. M.T.; Scudelari, A.C., 2015. Wave Climate Assessment on the Ponta Negra Beach (RN, Brazil) using SMC-Brasil and its contribution to coastal management. *Journal of Integrated Coastal Zone Management*. 15(2):135-151. DOI:10.5894/rgci532

Amaro, V.E.; Gomes, L.R.S.; Lima, F.G.F.; Scudelari, A.C.; Neves, C.F.; Busman, D.V.; and Santos, A.L.S. 2014. Multitemporal analysis of coastal erosion based on multisource satellite images, Ponta Negra Beach, Natal City, Northeastern Brazil. *Marine Geodesy*, 38(1):1-25.

Amaro, V. E.; Scudelari, A. C. ; Neves, C. F.; Tabosa, W. F. ; Lima, Z. M. ; Santos Jr, O. F. ; Ferreira, A. T. S.; Santos, A. L. S.; and Busman, D. V. 2012. *Indicação das obras emergenciais de contenção e reparação dos equipamentos públicos e de segurança dos frequentadores da Praia de Ponta Negra, Natal, RN*. Expert Report, Natal, 254p.

Bird, E. and Lewis, N. (2015). *Beach Renourishment*. Springer-Verlag: pp.7-28.

Janiny, F. 2012. *Vulnerability analysis of Natal,RN, to climate changes*. Master's Thesis. Sanitary Engineering Program, Federal University of Rio Grande do Norte. (*in Portuguese*).

Nielsen, P. (2012). *Coastal and Estuarine Processes*. World Scientific. Singapore: pp.301-316.

SMC-Brasil (2014) – *Documento temático de Ondas*. 155p. Instituto de Hidráulica Ambiental, Universidad de Cantabria, Santander, Spain. Available on-line at http://smcbrasil.ihcantabria.com/wpcontent/uploads/2013/06/Documento_Tematico_de_Ondas.pdf/ .

Valentini, E.M.S. (1981). *Methods for computing litoral drift and their application to Natal – RN*. MSc. Thesis, Ocean Engineering Program, COPPE/UFRJ. (in Portuguese)

Journal of Coastal Research	SI	75	820-824	Coconut Creek, Florida	2016

3D numerical model of ecohydrodynamics for shallow waters

Roman Bezhenar [§*], Kyung Tae Jung[‡], Vladimir Maderich[§], and Kyeong Ok Kim[‡]

[§] Institute of Mathematical Machine and System Problems
Kiev, Ukraine

[‡] Korea Institute of Ocean Science and Technology
Ansan, Republic of Korea

www.cerf-jcr.org

www.JCRonline.org

ABSTRACT

Bezhenar R.; Jung K.T.; Maderich V., and Kim K.O., 2016. 3D numerical model of ecohydrodynamics for shallow waters. *In:* Vila-Concejo, A.; Bruce, E.; Kennedy, D.M., and McCarroll, R.J. (eds.), *Proceedings of the 14th International Coastal Symposium* (Sydney, Australia). *Journal of Coastal Research*, Special Issue, No. 75, pp. 820-824. Coconut Creek (Florida), ISSN 0749-0208.

A new modeling system for the calculation of ecohydrodynamics in shallow water bodies is developed. It consists of three interacting components: hydrodynamics, sediment transport and ecodynamics. The system takes into account changes in the light absorption in the water due to presence of phytoplankton and suspended sediments as well as in the bottom friction due to presence of bottom vegetation. The bottom friction in turn affects the currents and turbulence that govern the transport and dispersion of nutrients which are necessary for the growth of phytoplankton and bottom vegetation. The turbulent mixing influences the resuspension of sediments that changes absorption of light in the water, affecting the bottom vegetation growth. The influence of model feedbacks on the biochemical characteristics of shallow Lake Markermeer (the Netherlands) was studied. Results of modeling show good quantitative agreement with measurements of temperature, nutrients, and dissolved oxygen. Good qualitative agreement of bottom concentration of periphyton with measured field of bottom plants was also obtained.

ADDITIONAL INDEX WORDS: *Shallow water, modeling system, ecodynamics.*

INTRODUCTION

The main indicator of ecological conditions in open water systems which include rivers, inland waters and coastal zone of seas is the concentration of human activity-originated organic and mineral pollutants contained in water. High concentration of related nutrients and the increase of water temperature in summer create a favorable condition for the intensive growth of microorganisms and plant populations, damaging the ecosystem of the water body and limiting the drinking and sanitary quality of water.

Ecohydrodynamic issues described in this study are concerned with the shallow water body (SWB) which could be characterized as the one in which: 1) wind currents and waves penetrate to the bottom, 2) suspended sediments are distributed throughout the whole water column and 3) bottom vegetation growth on the bottom is pronounced. Although there may be all kinds of bottom vegetation, we consider the growth and mortality processes of a gross form of bottom vegetation – periphyton. Well-known examples of such SWB are lakes Taihu (China), Okeechobee (USA), Balaton (Hungary) and Markermeer (the Netherlands). A good example is Lake Markermeer situated in the region with intensive agriculture. Besides it is a source of drinking water for Amsterdam, the capital of the Netherlands.

Main processes that take place in SWB are shown in Figure 1. Currents generated by wind induce turbulent mixing that leads to the erosion of bottom sediments. Currents also transport the nutrients which are necessary for the growth of phytoplankton and periphyton. On the other hand, periphyton plays a role of slowing down the flow velocity, leading to sedimentation of suspended sediments. The thermal state of SWB is determined by heat exchanges with the atmosphere including solar radiation, evaporation, and so on. In the daytime the light is absorbed by water and bottom whereas at night the inverse process takes place: water returns the heat to the atmosphere and the heat from bottom enter into the water column. It is important to note that for heat balance light absorption coefficient depends upon concentrations of phytoplankton and suspended sediments in the water.

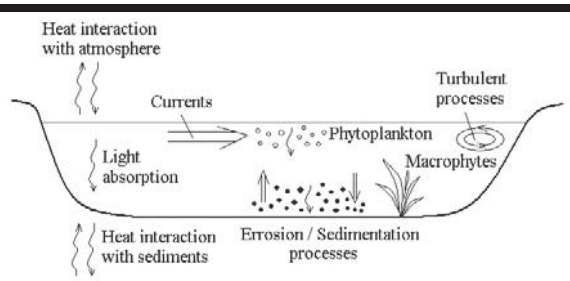

Figure 1. Thermohydrodynamical processes in shallow water body.

MODELING SYSTEM

A new 3D numerical modeling system is based on the model THREETOX (Maderich *at al.*, 2008) and includes three interactive models: circulation, sediment transport and

DOI: 10.2112/SI75-165.1 received 15 October 2015; accepted in revision 15 January 2016.
*Corresponding author: romanbezhenar@gmail.com
©Coastal Education and Research Foundation, Inc. 2016

ecodynamics with kinetics of the WASP model (Ambrose *et al.*, 2005). The main difference from the original model THREETOX is the introduction of new feedback processes between components of the modeling system.

Circulation Model

The circulation model describes the motion of an incompressible fluid by a system of Reynolds-averaged equations of continuity and horizontal momentum in Boussinesq and hydrostatic approximations. The system includes the heat transport equation and the equation of state describing the dependence of the density of water on its temperature and pressure. The coefficients of the vertical turbulent viscosity and diffusion are calculated using k-ε turbulence model, where k and ε are the kinetic turbulent energy and dissipation rate, respectively. The coefficients of the horizontal viscosity and diffusion are determined by the Smagorinsky formula. The detailed description of circulation part of THREETOX model with corresponding boundary conditions are given in Maderich *et al.* (2008).

Correct description of heat fluxes in the system of atmosphere – water – bottom sediments is very important for the simulation of the SWB thermal regime. In the model the total heat flux through the surface of the water includes the flux of solar radiation (Zillmann, 1972), the flux of longwave radiation (Zapadka *et al.*, 2001), as well as the turbulent heat flux and heat losses by evaporation (Blackadar, 1979). The model takes into account the absorption of light by water according to the Lambert-Beer Law: $I(z) = I_0 \exp(-K_d\, z)$, where I_0 is the part of the flux of solar radiation which has passed through the surface; K_d is a coefficient of vertical attenuation of light in the water; z is the vertical coordinate. The temperature of the bottom surface is obtained from the solution of the heat conduction equation in bottom sediments.

Sediment Transport Model

The transport of three fractions of sediments with different particle sizes (sand, silt and mud) can be considered in the modeling system. The advection-diffusion equation for the calculation of the concentration of each fraction of suspended sediments S_d in the water is given by

$$\frac{\partial S_d}{\partial t} + u\frac{\partial S_d}{\partial x} + v\frac{\partial S_d}{\partial y} + \left(w - w_g\right)\frac{\partial S_d}{\partial z} = \frac{\partial}{\partial z}\left(\nu_t'\frac{\partial S_d}{\partial z}\right) + \frac{\partial}{\partial x}\left(K_T\frac{\partial S_d}{\partial x}\right) + \frac{\partial}{\partial y}\left(K_T\frac{\partial S_d}{\partial y}\right), \quad (1)$$

where t is time, x, y are horizontal Cartesian coordinates, respectively, u, v denote the corresponding velocity components, w is the velocity component in vertical direction, w_g is the depositional velocity of solid particles in the water column, ν_t' and K_T are coefficients of vertical and horizontal diffusion, respectively.

For sand we used formula of van Rijn (1984) to calculate w_g, namely

$$w_g = \frac{10 g D_0^2}{\nu_w D_*^{3/2}}\left(\sqrt{1 + 0.01 D_*^3} - 1\right), \quad (2)$$

where D_0 is the average diameter of sand particles, g is the gravitational acceleration, ν_w is the kinematic viscosity of water, D_* is the dimensionless parameter of particles that depends on their density and diameter (van Rijn, 1984).

For silt we used the Stokes formula to determine w_g. For the cohesive sediments (mud) the extended Stokes formulae is employed that relates to increasing of particles size due to their flocculation (Winterwerp, 1999)

$$w_g = \frac{\left(\rho_s - \rho_0\right) g D_0^2}{18\rho_0 \nu_w} + \frac{k_A}{k_B} D_0 \frac{\rho_s - \rho_0}{18\nu_w}\frac{S_d}{L^{1/2}}, \quad (3)$$

where ρ_0 and ρ_s are densities of water and sediments, respectively, $L = \left(\varepsilon / \nu_w\right)^{1/2}$, k_A and k_B are empirical parameters defined in Winterwerp (1999).

At the free surface no vertical flux of the sediment is assumed. The net vertical flux of suspended sediments at the bottom is given by the difference in the resuspension and sedimentation rates.

Ecodynamics Model

The model describing the ecodynamics contains transport and biochemical transformation equations for 9 state variables, which could be combined into four inter-related processes: primary production growth, nitrogen cycle, phosphorous cycle and balance of dissolved oxygen (Figure 2). Circulation of substances in the water can be represented in the following way: phytoplankton and periphyton grow in a daytime using nutrients (inorganic nitrogen and phosphorus) and producing oxygen; their death result in excretion of organic nitrogen, phosphorus and carbon, which are mineralized and oxidized to inorganic matters.

In the water column the equations of mass balance for eight variables are considered

$$\frac{\partial C_i^w}{\partial t} + u\frac{\partial C_i^w}{\partial x} + v\frac{\partial C_i^w}{\partial y} + (w - f_{pi}^w w_{gi})\frac{\partial C_i^w}{\partial z} = \frac{\partial}{\partial z}\left(\nu_t'\frac{\partial C_i^w}{\partial z}\right) + \frac{\partial}{\partial x}\left(K_T\frac{\partial C_i^w}{\partial x}\right) + \frac{\partial}{\partial y}\left(K_T\frac{\partial C_i^w}{\partial y}\right) + S_i, \quad (4)$$

where C_i^w (i = 1, …, 8) is the concentration of ith substance in the water column (index 1 denotes ammonia nitrogen NH4, 2 – nitrates NO3, 3 – phosphates PO4, 4 – phytoplankton, 5 – carbonaceous biochemical oxygen demand CBOD, 6 – dissolved oxygen, 7 – organic nitrogen, 8 – organic phosphorus); the CBOD, organic nitrogen and organic phosphorus exist simultaneously in dissolved and particulated forms (parameter f_{pi}^w defines content of particulate fraction), phytoplankton is assumed to be fully particulate (that is, $f_{p4}^w = 1$), the rest of substances are fully dissolved (that is, $f_{pi}^w = 0$); w_{gi} is the settling velocity of ith particulate matter under a gravitation, which is defined using formula for cohesive sediments (3); the term S_i describes chemical transformation of variables and is defined in a way similar to well-known model WASP (Ambrose *et al.*, 2001).

Boundary conditions for these 8 variables at the surface and bottom take the flux form. At the surface the fluxes of all

variables, except oxygen, are set to zero. Exchange of oxygen with atmosphere is described by a coefficient depending on the average water velocity, depth, wind speed, and temperature (O'Konnor, 1983). Fluxes of the chemicals through the bottom boundary are described in the form which takes into account the diffusion of the dissolved fraction and the resuspension and settling-down of the solid fraction.

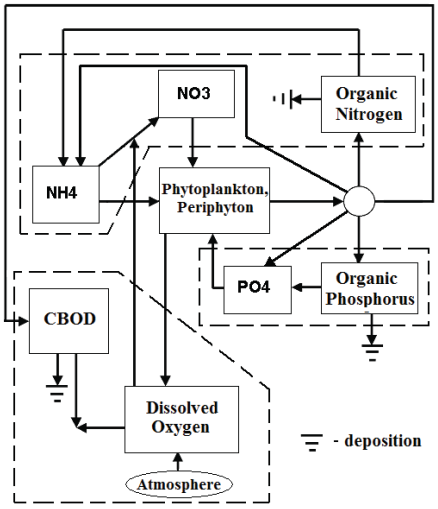

Figure 2. Variables of ecodynamics model and scheme of their transformations (three groups of substances mentioned above are encircled by dashed line, phytoplankton and periphyton makes fourth group – primary production).

The dynamics of the near-bottom region are characterizes by the presence of periphyton. For that, the 9th equation is introduced to the ecodynamics model which includes the term S_P describing the growth and death of periphyton. That is,

$$\frac{\partial C_P}{\partial t} = S_P \,. \tag{5}$$

According to Martin *et al.* (2006) S_P depends on water temperature, light and nutrient conditions, and available free space for further growth. It is noted that the equation does not describe advection and diffusion processes because periphyton is attached to the bottom.

Feedbacks in the Modeling System

A set of feedbacks coupling various system components introduced in this work are described. The influence of periphyton on the hydrodynamics of SWB is realized by changing the bottom friction coefficient. Total bottom friction coefficient describes friction of clear bottom and friction due to seagrass or periphyton. The friction of clear bottom is denoted by symbol C_{DZ}, whereas C_{DP} means friction component due to periphyton stems. We used the approach given by Nepf (1999) to express the total bottom friction coefficient C_D as

$$C_D = \left(1 - ad\right) C_{DZ} + \frac{1}{2} C_{DP}\, ad \frac{D}{pd} \,, \tag{6}$$

where ad is part of volume occupied by periphyton, pd is diameter of periphyton stems, D is the water depth. Dependence of C_{DP} on ad was approximated by Chen *at al.* (2007) as

$$C_{DP} = -0.255 \cdot \ln(ad) \,. \tag{7}$$

The presence of periphyton results in slowing down the near-bottom currents which are closely related to the sedimentation and resuspension of bottom sediments. We assumed that the near-bottom flow velocity decreases proportionally to height of periphyton stems and their concentration.

Described feedbacks change sediment dynamics that may strongly affect the concentration of suspended sediments in the water column. The presence of periphyton increases bottom friction which in turn results in the intensification of turbulence and the increase of resuspension of the bottom sediments. On the other hand, high concentration of periphyton reduces the near-bottom current and then increases sedimentation. Concentration of suspended sediments and phytoplankton determines the underwater light attenuation, proper description of which is important in modeling the temperature regime of SWB, heating of bottom sediment and the rate of the biochemical processes. For SWB we assume that short wave radiation is absorbed in the thin surface layer of water. Long wave component of sun radiation exponentially decreases with depth and could be approximated by Lambert-Beer's Law (see above), where K_d defines the vertical attenuation of light in the water. To determine K_d we used the simplified approach (van Duin *at al.*, 2001) given by

$$K_d = \frac{a_{dw} + a_{ds} + a_{dg}}{\cos\theta} \sqrt{0.81 + 0.425\cos\theta} \,, \tag{8}$$

where θ is the angle of incoming sun radiation, a_{dw}, a_{ds} and a_{dg} corresponds to absorption of sun radiation by pure water itself, suspended sediments, and phytoplankton, respectively. The dependence of absorption coefficients on concentration of suspended sediments and phytoplankton is described by empirical relations (Prieur and Sathyendranath, 1981) as

$$a_{ds} = c_s \cdot S_d \quad \text{and} \quad a_{dg} = c_g \cdot C_4^w \,, \tag{9}$$

where c_s varies in a range 0.4 – 1.5 $m^{-1}mg^{-1}l$ and depends on size of particles (Hekkink and Blom, 1984); c_g varies in a range 1.7 – 2.5 $m^{-1}mg^{-1}l$ (Prieur and Sathyendranath, 1981).

Numerical Setup

Model equations are solved semi-implicitly using the finite difference technique applied on a staggered Arakawa C grid. The numerical algorithm is implemented in the horizontal curvilinear-orthogonal coordinate system with σ-coordinate transformation. Splitting of the external and internal modes is using (Blumberg and Mellor, 1987). The advection terms in equations for transport of scalars are approximated by the high order TVD scheme (van Leer, 1979). The model code was parallelized using MPI. More details of solution technique are given by Maderich *et al.* (2008).

RESULTS

The developed modeling system was applied to the Lake Markermeer which is part of former Zuiderzee Bay. More than half of this lake has depth 4-6 m and there are wide shallow areas with depth 1-3 m (Figure 3). The calculations were carried out for the period from March to October 2004 with observed meteorological forcing. Curvilinear nonuniform grid with horizontal resolution in a range 100 – 1000 m and 12 σ-layers were used. Initially a uniform concentration of periphyton was set. For comparison purpose we used the measurements data set for water temperature, concentration of nutrients, and dissolved oxygen at the surface available from the Waterbase of Rijkswaterstaat (http://www.rijkswaterstaat.nl/water/scheepvaartberichtenwaterdata/historische_waterdata/waterbase/index.aspx). The set of data is available only for one point (Markermeer midden). Its location is shown in Figure 3 (point A).

Comparison of calculated and measured values in Figure 4 shows better agreement in the case with feedbacks between models. We obtained very good agreement for temperature (Figure 4a), confirming the proper description of the thermodynamic part of modeling system especially the heat fluxes in a system atmosphere – water – bottom and the description of light attenuation in the water column using its dependence on concentration of suspended sediments and phytoplankton. The model with feedbacks reproduced the time dependence of concentration of nutrients (Figure 4b) and dissolved oxygen (Figure 4c) with accuracy comparable with measurements.

The main effect of feedbacks between models on the concentration of organic and inorganic matters in the lake is dependence of the light attenuation coefficient on the concentration of suspended sediments and phytoplankton in water column. This coefficient determines the vertical distribution of light and temperature that are crucial for growth rates of phytoplankton and periphyton. The weak currents in the lake result in clear water with a small light attenuation coefficient causing intensive growth of periphyton. Accordingly high currents cause lower growth rate that leads to more rapid decrease of periphyton concentration. The other feedback has the influence of periphyton on resuspension rate of bottom sediments. Periphyton decreases the resuspension rate that leads to reduction of concentration of suspended sediments in the water column and clearer water.

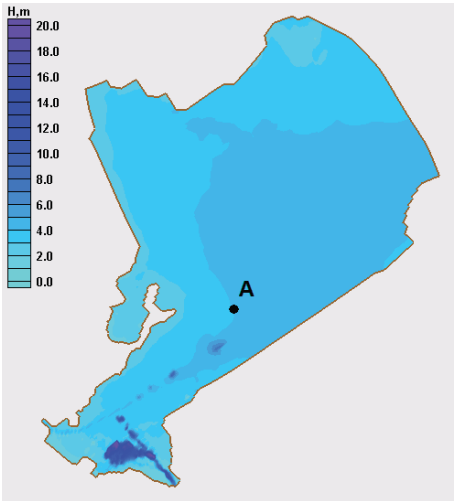

Figure 3. Bathymetry of lake Markermeer. Here point A denotes location of measurements.

The comparison between calculated concentration of periphyton and available observed distribution of bottom plants (Smits and Postema, 2005) are shown on the Figure 5. On the map the maximal level of bottom covering is named “class 7” and denoted by red color. We choose same colors for qualitative representation of the model results: red color denotes maximal concentration of periphyton and dark blue – minimal. Both maps demonstrate very similar patterns with maximal concentration of bottom plants in shallow areas of Markermeer.

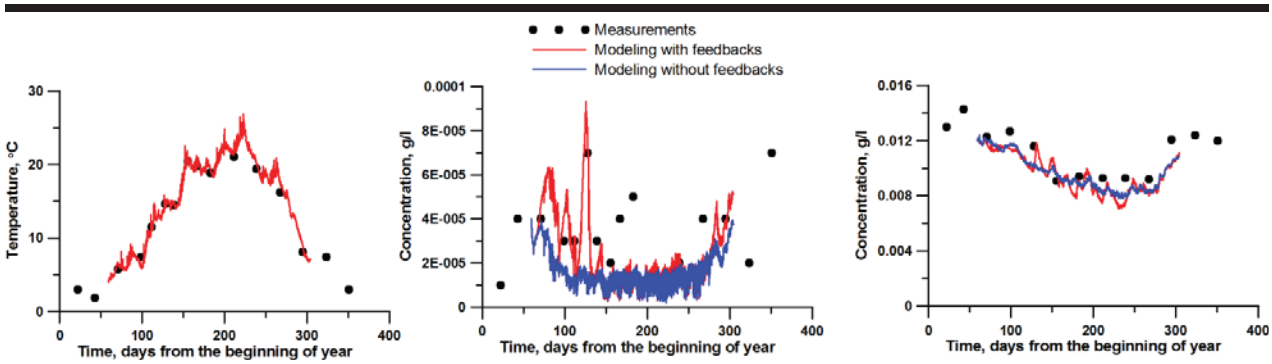

(a) (b) (c)

Figure 4. Surface temperature (a), concentration of ammonia nitrogen (b), and dissolved oxygen (c) in point A (see Figure 3).

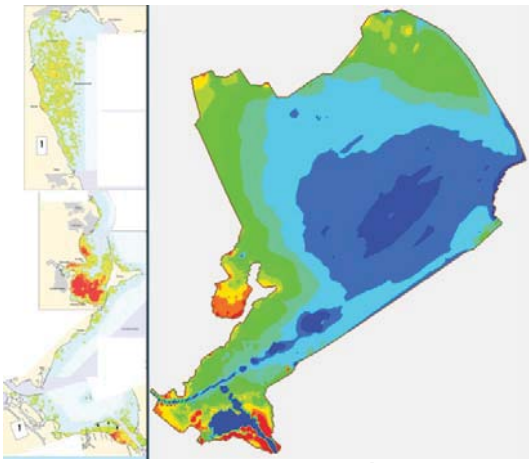

(a) (b)

Figure 5. Observed field of bottom plants in Markermeer (a) and modeled concentration of periphyton (b).

CONCLUSIONS

The main result of the present work is the development of a new modeling system for SWB which includes three interacting models: hydrothermodynamics, sediment transport, and ecodynamics. Set of feedbacks such as influence of periphyton concentration on both bottom friction coefficient and conditions of sedimentation and resuspension as well as influence of concentration of suspended sediments and phytoplankton in water column on light attenuation coefficient are included in the model. Application of the developed modeling system to Lake Markermeer shows a good quantitative agreement for temperature, nutrients, and dissolved oxygen at the measurement point and a good qualitative agreement of concentration of periphyton with measured field of bottom plants. It was shown that periphyton in SWB decreases the concentration of suspended sediments in the water that leads to better illumination of the near-bottom regions and subsequently provides a favorable environment for the growth of periphyton.

ACKNOWLEDGMENTS

This work has been supported by KIOST major project (PE99304).

LITERATURE CITED

Ambrose, R.B.; Wool, T.A., and Martin, J.L., 2001. *The Water Quality Analysis Simulation Program WASP6 (User Manual)*. Athens, Georgia: U.S. Environmental Protection Agency.

Blackadar, A., 1979. High resolution models of the planetary boundary layer. *In*: Pfafflin, J., and Ziegler, E. (eds.), *Advances in Environmental Science and Engineering*, 1, No 1. New York: Gordon and Briech, pp. 50-85.

Blumberg, A.F, and Mellor, G.L., 1987. A description of a three-dimensional coastal ocean circulation model. *In*: Heaps, N.S. (ed.), *Three-Dimensional Coastal Ocean Models*, *Coastal and Estuarine Science*, vol. 4 (American Geophysical Union), pp. 1-19.

Chen, S.N.; Sanford, L.P.; Koch, E.W.; Shi, F., and North, E.W., 2007. A nearshore model to investigate the effects of seagrass bed geometry on wave attenuation and suspended sediment transport. *Estuaries and Coasts*, 30, 296-310.

Hekkink, A., and Blom, G., 1984. *Lichtklimaat in Ondiepe Meren*. Wageningen, The Netherlands: Wageningen Agricultural University, 47p.

Maderich, V.; Heling, R.; Bezhenar, R.; Brovchenko, I.; Jenner, H.A.; Koshebutskyy, V., and Terletska, K., 2008. Development and application of 3D numerical model THREETOX to the prediction of cooling water transport and mixing in the inland and coastal waters. *Hydrological Processes*, 22, 1000-1013.

Martin J.L.; Ambrose R.B., and Wool T.A., 2006. *WASP7 Benthic Algae – Model Theory and User's Guide*. Athens, Georgia: U.S. Environmental Protection Agency, 26p.

Nepf, H.M., 1999. Drag, turbulence and diffusion in flow through emergent vegetation. *Water Resources Research*, 35, 479-489.

O'Konnor, D.J., 1983. Wind Effects on Gas-Liquid Transfer Coefficient. *Journal of Environmental Engineering*, 109, No 9, 731-752.

Prieur, L., and Sathyendranath, S., 1981. An optical classification of coastal and oceanic waters based on the specific absorption curves of phytoplankton pigments, dissolved organic matter and other particulate materials. *Limnology and Oceanography*, 26, 671-689.

Smits, J.B., and Postema, J., 2005. *Monitoring van Waterplanten en Perifyton in het IJsselmeergebied 2004 (Markermeer)*. Rijkswaterstaat, The Netherlands, *IJG-Rapport 2005-7, ISBN 903691338-1*, 86p.

Van Duin, E.H.S.; Blom, G.; Los, J.M.; Maffione, R.; Zimmerman, R.; Cerco, C.F.; Dortch, M.S., and Best, E.P.H., 2001. Modeling underwater light climate in relation to sedimentation, resuspension, water quality and autotrophic growth. *Hydrobiologia,*, 444, 25-42.

Van Leer, B., 1979. Toward the ultimate conservative difference scheme. V: A second order sequel to Godunov's method. *Journal of Computational Physics*, 32, 101-136.

Van Rijn, L.C., 1984. Sediment transport. Part I: Bed load transport. *Journal of Hydraulic Engineering*, 110, 1431-1456.

Winterwerp, J.C., 1999. On the Dynamic of High-Concentrated Mud Suspensions. Delft, The Netherlands: Delft University of Technology, Ph.D. dissertation, 204 p.

Zapadka, T.; Wozniak, S.B., and Wozniak, B., 2001. A simple formula for the net long-wave radiation flux in the southern Baltic Sea. *Oceanologia*, 43, 265-277.

Zillman, J.W., 1972. *A Study of Some Aspects of the Radiation and the Budgets of the Southern Hemisphere*

Journal of Coastal Research	SI	75	825-829	Coconut Creek, Florida	2016

Field Observations, Video Monitoring and Numerical Modeling at Poetto Beach, Italy

Walter Brambilla[†]*, Arnold van Rooijen[††], Simone Simeone[‡], Angelo Ibba[†], Sandro DeMuro[†]

[†] Chemical and Geological Sciences Department, Cagliari University, Cagliari, Italy

[††]Deltares, Dept. of Marine & Coastal Systems, Deltares, Delft, the Netherlands

[‡] Istituto per l'Ambiente Marino Costiero - C.N.R., Oristano, Italy

www.cerf-jcr.org

www.JCRonline.org

ABSTRACT

Brambilla, W.; van Rooijen, A.; Simeone, S.; Ibba, a.; DeMuro, S., 2016. Field observations, coastal video monitoring and numerical modeling of coastal processes at Poetto Beach, Italy. *In:* Vila-Concejo, A.; Bruce, E.; Kennedy, D.M., and McCarroll, R.J. (eds.), *Proceedings of the 14th International Coastal Symposium* (Sydney, Australia). *Journal of Coastal Research*, Special Issue, No. 75, pp. 825-829. Coconut Creek (Florida), ISSN 0749-0208.

This work presents an analysis of hydrodynamics and morphological evolution during one year at Poetto Beach (South Sardinia, Gulf of Cagliari - Italy). The results, in the form of a numerical model, Delft3D, were validated using data obtained from a very reproducible low-cost video monitoring system. Subsequently, the model was used to study local hydrodynamics (Delft3D) during wave events. Poetto Beach is a wave-dominated urban beach system characterized by an inner shelf with Posidonia oceanica meadows. Bathymetric and topographic surveys were carried out every three months in order to understand the beach morphology. Sediment grain samples were taken alongshore/cross-shore in correspondence with the main morphologies. The Delft3D model was used to simulate waves and hydrodynamics. The numerical simulation (Delft3D) showed good agreement with the field data and video image analyses for the distribution and direction of the rip and longshore currents. This approach, which can be easily replicated on other urban beaches, could provide beach managers with useful information on how to prevent and minimize the effects of storms and flooding.

ADDITIONAL INDEX WORDS: *Morphodynamics, numerical model, Delft3D, coastal videomonitoring.*

INTRODUCTION

In the Mediterranean Sea, the increased demand for infrastructure development and the use of a coastal area for recreational purposes has increased the threat of coastal erosion. Indeed, there is an acceleration of erosion and a reduction of natural habitats along several km of the Italian coast (DeMuro *et al.*, 2015). Furthermore, the impact of storms on a sandy coast can drastically modify the geomorphological aspect of beaches, including along the coastal zone where intense human activities on beaches can cause coastal damage, as well as civil protection issues.

This factor is particularly relevant along urban beaches, where managing coastal erosion and maintaining beaches are the most important forms of defence against flooding and storms. In Sardinia (western Mediterranean), the most important urban beach, Poetto, is a wide, semi-enclosed beach that is about 8 km in length (Figure 1) and fronts the city of Cagliari. Poetto Beach is a wave-dominated urbanized sandy beach that is characterized by an inner shelf with large seagrass (*Posidonia oceanica*) meadows that are mainly developed on the eastern side of the submerged beach. In 2002, on the western side, sand nourishment of about 350,000 m^3 was used to prevent flooding of the inland area and promote beach tourism.

DOI: 10.2112/SI75-166.1 received 15 October 2015; accepted in revision 15 January 2016.
*Corresponding author: walter.bra@hotmail.it
©Coastal Education and Research Foundation, Inc. 2016

The aim of this paper is to investigate the morphodynamic behaviour of a Mediterranean urban beach using a multidisciplinary approach that includes remote sensing, field surveys and numerical models. In particular, the use of video monitoring techniques and numerical modelling provides a low cost and very reproducible methodology for: evaluating urban beach processes, including the effects of storms and human stressors; and helping local managers to properly manage the beach space.

Wave data, beach profiling, sediment sampling and analyses, low-cost video monitoring techniques and numerical modelling were used to investigate the beach dynamics.

METHODS

A multidisciplinary methodology coupling wave data, sediment sampling and analyses, beach profiling, video monitoring techniques and numerical modelling was used to investigate the Poetto Beach dynamics.

Climate data

The wave data (Bencivenga *et al.*, 2012) were obtained from an offshore buoy located in the Gulf of Cagliari (Lat: 39 ° 6 '52 "- Long: 9 ° 24 '20 ") (ISPRA - R.O.N.), while the wind and tidal data were taken from a wind station in Cagliari Harbour (ISPRA, R.M.N.). The Gulf of Cagliari is characterized by low energy waves with a significant wave height (Hs) of at least 1 m

(80% of cases). Thirty/40 cm was the maximum tidal range recorded during the study.

The studied area is mainly exposed to wind and waves coming from the south. The prevailing direction of the waves is linked to the SW (225° direction) and SE winds (135° direction), with the latter generating the events prevalent for intensity and wave height (Figure 2).

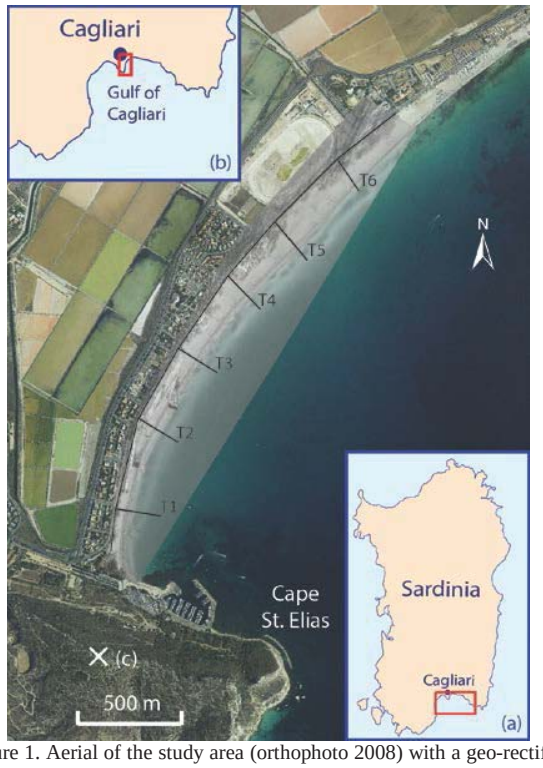

Figure 1. Aerial of the study area (orthophoto 2008) with a geo-rectified image Timex overlapped and measured beach profiles (shown in black). In The location of the video monitoring station (c) is indicated with the white cross. The measured beach profiles are shown in black.

Sediment

Sediment grain size and mineralogy were determined in order to define the beach type and to set up numerical morphodynamic models. Sediment samples were collected along the beach profiles, with the sub-aerial beach sediment sampled using hand corers, while the submerged beach sediment was sampled using a 5 L Van Veen grab. The samples were washed and dried in an oven for about 24 h at 80°C (De Muro *et al.*, 2013). The grain size distribution was determined following the ASTM international standard methodology, with sieves spaced on 1/4Ω between 2000 and 63 µm (Wentworth, 1922) (DeMuro *et al.*, 2015). The statistical parameters used (Folk and Ward, 1957) were obtained using the Gradistat software (Blott and Pye, 2001).

The density was determined for each sample using a pycnometer.

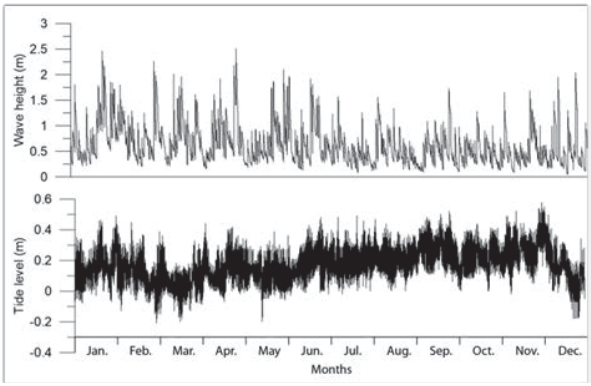

Figure 2. Hydrodynamics data: offshore significant wave height (Hs) and tide level acquired during 2014.

The sediment fall velocity was determined for each sample by considering the mean diameter (M_z) and density (ρ_s) using the Le Roux (1996) formula (Equation 1).

$$Ws=\frac{W_{ds}}{\sqrt[3]{\rho_f^2 / \mu g(\rho_s-\rho_f)}} \quad (1)$$

Beach profiles

Cross-shore beach profiles (spaced about 400 m apart) (Figure 1) were obtained using a differential global positioning system (DGPS) following the methods reported in Morton *et al.* (1993). Along the submerged beach, the profiles were obtained by coupling a single beam (Reson Navisound 215 echosounder) with a DGPS (Omnistar 8300HP DGPS). The beach profiles were obtained every three months for about 18 months, starting in October 2012. The surveys were conducted by referring to a geodetic net based on the IGM95 ETRF2000 n. 234802 point located in Cagliari Harbour.

On the basis of the data obtained from the investigations described above, it was possible to apply the morphodynamic classification method of Short (1999). The classification is based on the dimensionless fall velocity Ω (Dean, 1973) (Equation 2):

$$\Omega=\frac{H_b}{W_s T} \quad (2)$$

where (Hb) is the breaker wave height, (T) is the wave period and (Ws) is the fall velocity. The wave period (T) is the average value of the data recorded by a R.O.N. buoy.

The breaking wave height was calculated using the Kamphuis formula (Equation 3):

$$H_b=0.56 \exp(3.5m)\ h \quad (3)$$

where (m) is the average slope of the bottom, and (h) is the depth in the point where the waves break. 0.56 and 3.5 are constants. The Ω parameter (Dean, 1973) was calculated on six profiles acquired along the beach. The mean values of wave periods, breaker wave heights and sediment fall velocity were

calculated for each profile (Table 1). The dimensionless fall velocity allowed us to classify the beach morphodynamic state as reflective (Ω <1), intermediate (1 <Ω <6) and dissipative (Ω> 6). The intermediate state was subdivided into four more classes: Longshore Bar and Trough (LBT - $\Omega \sim 5$), Rhythmic Bar and Beach (RBB – $\Omega \sim 4$), Transverse Bar and Rip (TBR - $\Omega \sim 3$), and Low Tide Terrace (LTT - $\Omega \sim 2$) (Peron *et al.*, 2011).

Video monitoring

A low-cost coastal video monitoring station was installed on an edge of the promontory of Cape St. Elias at an altitude of 129 m (Lat: 39 ° 11'24 "Lon: 9 ° 09'29"). The images were acquired twice a day. In total, 180 snapshots were captured during each interval. The snapshot images were processed to obtain Timex images, which were georectified. The image processing was performed using developed algorithms on Matlab2013b. The georectification of the Timex images was achieved using the package "g_rect" for Matlab (Pawlowicz, 2003). The method considers the geometric characteristics of the field of view of the digital camera.

A total of 22 ground control points (GCP) were used that represent the latitude-longitude positions associated with the coordinates of the image pixels. Georectification was conducted based on a 2008 LIDAR survey with a 20x20 cm resolution. The relative horizontal error due to the geopositioning of the image is about 4 m. The Timex images present clear bands of high luminous intensity which correspond to zones where the waves break above the breaker bars and near the shore. The georectification of the Timex images allows for a planimetric view of the presence and evolution of breaker bars, especially during high-energy wave events. The images were used to visually classify the morphodynamic state of the beach according to the classification of Short (1999) (LBT; LTT; TBR; and RBB). The sandbars' shape (linear to crescentic), orientation (perpendicular to shore-parallel) and connection to the upper beach were also used to classify the morphodynamic state (Péron and Sénéchal, 2011) of Poetto Beach.

Numerical modelling

The climate data (wave and wind) and morphodynamic and sedimentological characteristics of the study area were utilized to set up the numerical model. Both the Delft3D-FLOW (Lesser *et al.*, 2004) and Delft3D-WAVE (which utilizes the SWAN model by Ris *et al.*, 1999, and Booij *et al.*, 1999) models were used to simulate the hydrodynamics and waves forcing on to Poetto Beach. The main hydrodynamic scenario identified in the area of Poetto Beach was simulated.

These typical wave events are induced by wind blowing from the SE. This characteristic scenario has a duration of 24 hours with 2 m wave heights, 7 seconds of wave periods and a 10 m/sec wind from the SE (135°). Three computational grids with increasing detail to simulate the wave approach to the coast were produced. The first grid (coarse) covers the Gulf of Cagliari up to a -125 m depth contour. The depth limits of the grid were chosen based on the wavelength maximums recorded in the Gulf. The intermediate grid (medium) was created in front of the study area. The detailed grid (order) was made on Poetto Beach. Medium and coarse grids were only used in the wave model. Meanwhile, a fine grid was used in both the wave and flow models that run in terms of online coupling. The simulated event was compared with the results obtained from the coastal video monitoring system to obtain visual feedback.

RESULTS

The results derived from the wave data and sediment and beach profile analyses were coupled with a video monitoring analysis to classify Poetto Beach's morphodynamic state.

Morphodynamic classification

The results of the morphodynamic classification of the beach profile (Short, 1999) are shown in Table 1.

Table 1 - *Summary of morphodynamic classification (Short, 1999). The table shows average of annual values for each beach profile (Figure 1). (ρ_s) is sediment density, (M_z) is the average diameter, (H_b) is the breaker wave height, (W_s) the sediment fall velocity, (Ω) the dimensionless fall velocity, (Type) are the morphotypes associated with Ω value.*

Profile	ρ_s (kg/m^2)	M_z (m)	H_b (m)	W_s	Ω	Type
T1	2665	0.000195	0.57	0.02	7.12	DB
T2	2664	0.000336	0.85	0.05	5.24	LBT
T3	2664	0.000326	0.6	0.04	3.83	TBR/ RBB
T4	2660	0.0003	0.45	0.06	4.23	RBB
T5	2657	0.000326	0.48	0.04	3.08	TBR
T6	2666	0.00032	0.63	0.04	4.11	RBB

From the images acquired with video monitoring, four homogeneous areas were recognized along the stretch of beach studied (Figure 3). The amplitude of this zone varies throughout the year. Furthermore, the morphological characteristics of the submerged bars (shape, orientation and access to the emerged beach) vary according to the characteristics of the recorded wave event. The first area extends from Cape Sant' Elia for about 300 m. This shows a linear shoreline without cusps in this zone, and the bars are devoid of rip channels. Therefore, it presents the typical morphology of a dissipative beach which is maintained throughout the year (Figure 3).

The second zone extends for 500 m and ends at a bathing establishment that breaks the continuity of the shoreline (Figure 3). The second area has morphologies classifiable as LBT. It also has a regular external bar separated by about 40 m from the inner bar, with a significant depression. The inner bar, which is very close to the foreshore, has weak rip channels that tend to accentuate during the spring/summer period, with small crescentic bar forms (25 m).

A third area extends for about 200 m (Figure 3). In spring/summer, crescentic bars are visible that change regularly during the winter in cross-bars with deep and marked rip channels. The beach in this area is classified as RBB and TBR morphotypes.

The fourth zone is characterized by strong spatial variability in its morphology during the year (Figure 3). Complex morphologies could be seen in March 2014, which were created by double bars. The external bar is connected to the inner bar with transverse bars. Well-developed rip channels that are oriented according to the direction of the waves can be seen. The

inner bar is connected to the shoreline and is characterized by cross-channel rips. In the fourth area, it is possible to observe an RBB morphology, with the inner bar welded to the linear shoreline, whereas the outdoor bar becomes almost the only bar with crescentic forms. In the images from December 2014, a TBR morphology can be seen that features cusps on the shoreline and cross-bars alternating with pronounced and profound rip channels.

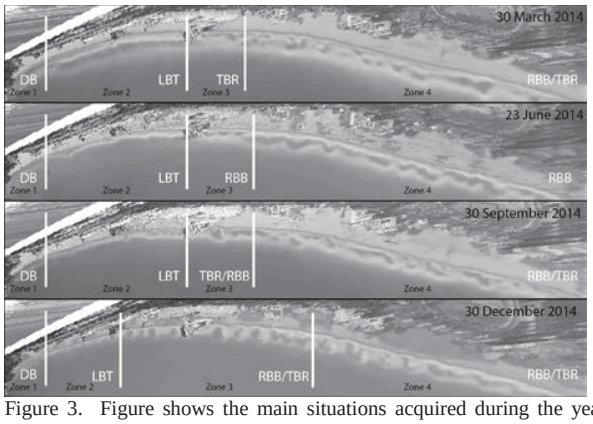

Figure 3. Figure shows the main situations acquired during the year. The images georectificated, were acquired in March (a), June (b), September (c) and December (d) 2014. Also shows 4 homogeneous areas recognized along the stretch of beach studied durante l'anno 2014.

The numerical model is set up to simulate a characteristic scenario generated by a SE event (Figure 4). The SE event generates a longshore current in the SW sector which flows towards the NE, generating longshore solid transport in the same direction. The longshore current is interrupted after about 800 m by rip currents perpendicular to the shoreline. A few hours after the event begins, another rip current is generated in the NE sector that is orientated SW. This current triggers several cell circulations that alternate clockwise and anti-clockwise. A longshore current directed towards the SW flows from the opposite direction. There are several flow rip currents perpendicular to the coastline along its flow. After a few hours from the start of the event, a big rip current length of about 800 m is created which extends outwards towards the SE.

DISCUSSION

The results of the morphodynamic classification (Short, 1999) applied to the Poetto Beach profiles show dimensionless fall velocity value (Ω) trends that decrease towards the central and NE sectors. This trend emphasizes that the beach is dissipative in areas near the promontory of Cape St. Elias in the SW. These areas have values of $5.24 < \Omega < 7.12$ (DB, LBT). In the central and NE areas, the values of $\Omega > 3.8$ Ω and <4.23 (TBR, RBB) suggest a beach with intermediate characteristics. The morphodynamic classification results (Short, 1999) are compatible with morphologies detected with a coastal video monitoring system. From the image processing acquired with the video monitoring, there are four homogeneous areas that vary in amplitude during the year. The profiles T1 and T2, which fall in the area of the SW beach, have values of Ω that are compatible with the morphotypes DB and LTB that were detected, respectively, in zones 1 and 2. The T3 and T4 profiles have values of Ω that are compatible with the morphotypes TBR and RBB detected in zone 3. Finally, profiles T5 and T6 in the NE sector have values of Ω that are compatible with the morphotypes RBB and TBR detected in area 4.

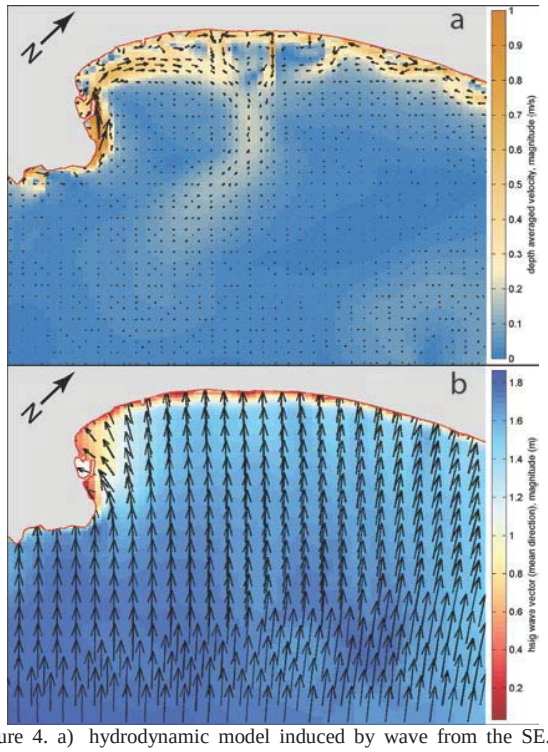

Figure 4. a) hydrodynamic model induced by wave from the SE. b) wave model induced by winds blowing from the SE.

The classification performed on the profiles (Table 1) is consistent with the morphotypes recognizable by the images (Figure 3). Moreover, submerged bars take on complex shapes during the autumn and winter (increased intensity and frequency of storm). In these seasons, the most important wave events originate from the SE. To obtain a knowledge hydrodynamics framework, we used the numerical model Delft3D. The event simulated generates a longshore current in the SW field of the area. This trend is confirmed by the LBT morphology detected in the same area by video monitoring.

The longshore current is interrupted by rip currents, which take different directions. From feedback with the georectified images, it can be seen that the LBT morphology is interrupted by RBB and TBR morphologies. Furthermore, knowledge of morphodynamic states could be useful for individuating an area of beach where flooding or erosion could occur (Benavente *et al.*, 2002). For an urban beach, this information could be very important, because the effect of storms can affect human activities. In this direction, our results highlighted, as for urban

beaches, the proposed methodology for investigating the beach dynamics, and can also provide information on the potential effect of storms. In fact, the areas more susceptible to flooding were zones 3 and 4 (REF), which both the video monitoring and field survey identified as intermediate with respect to zone 1, which was identified as dissipative. Finally, this study highlighted that the application of a low cost and easily reproducible methodology (video monitoring) can be very useful for investigating the dynamics of an urban beach, and can provide a helpful tool for beach managers to plan how to prevent and minimize the effects of storms and flooding.

CONCLUSIONS

This paper presents a study on coastal processes along a wave-dominated microtidal Mediterranean urbanized beach. In the study, several pieces of data were collected at Poetto Beach (Sardinia, Italy), including sediment data, bathymetry data, and hydrodynamic (waves, tide) and meteorological data (wind). The use of a low-cost video monitoring system is a good method for validating the morphodynamic beach classifications and providing useful information on the potential areas where flooding could affect the beach.

This approach, which can be easily replicated on other urban beaches, could provide beach managers with useful information on how to prevent and minimize the effects of storms and flooding.

ACKNOWLEDGMENTS

This work was funded by the Regione Autonoma della Sardegna – L.R. 7/2007 – project B.E.A.C.H.. The authors would like to thank ‘Marina Militare Italiana’.

LITERATURE CITED

Benavente, J.; Del Rio, L.; Anfuso, G.; Gracia, F.J., and Reyes, J.L., 2002. Utility of morphodynarnic characterization in the prediction of beach damage by storms. *Proceedings of the 7th International Coastal Symposium. Journal of Coastal Research*, Special Issue No.36, 56-64.

Bencivenga, M.; Nardone, G.; Ruggiero, F., and Calore, D., 2012. The Italian Data Buoy Network (RON). *Proceedings of the Advances in Fluid Mechanics IX. Edited by WIT, UK*, ISBN: 978-1-84564-600-4, 2012, 321-332.

Blott, S. J. and Pye, K., 2001. GRADISTAT: A grain size distribution and statistics package for the analysis of unconsolidated sediments. *Earth Surface Processes and Landforms*, 26(11), 1237–1248.

Booij, N.; Ris, R.C., and Holthuijsen, L.H., 1999. A third-generation wave model for coastal regions, Part I, Model description and validation. *Journal of Geophisical Research*, 104(C4), 7649–7666.

Dean, R.G., 1973. Heuristic models of sand transport in the surf zone. *Proceedings of the Conference on Engineering Dynamics of the Coastal Zone*, Sydney, N.S.W., Australia, pp. 208-214.

De Muro, S.; Brambilla, W.; Kalb, C., and Ibba, A., 2013. Medium and short-term evolution of a microtidal wave dominated Mediterranean beach seaward bordered by *Posidonia oceanica* meadow. The example of the Poetto beach (South Sardinia, Gulf of Cagliari-Italy). *Proceedings of 30th IAS Meeting of Sedimentology Manchester UK* (p. T3S1_P21). Manchester.DOI: 10.13140/RG.2.1.2676.6802.

De Muro, S. and De Falco, G., 2015. Handbook of best practices for the study, monitoring and management of Sardinian beaches. *University press - Scienze Costiere e Marine, CUEC Editrice*, pp.100. ISBN 978-88-8467-953-6.

De Muro, S.; Ibba, A., and Kalb, C., 2015. Morphosedimentology of a Mediterranean microtidal embayed wave dominated beach system and related inner shelf with Posidonia oceanica meadows: the SE Sardinian coast. *Journal of maps*, DOI:10.1080/17445647.2015.1051599.

Folk, R. L., and Ward, W., 1957. Brazos river bar: a study in the significance of grain size parameters. *Journal of Sedimentary Petrology*, 27(1), 3-26.

Le Roux, J.P., 1996. An EXCEL program for computing the dynamic properties of particles in Newtonian fluids. *Computer & Geosciences*, 23(6), 671-675.

Lesser, G.R.; Roelvink, J.A.; van Kester, T.M., and Stelling, G.S., 2004. Development and validation of a three-dimensional morphological model. *Coastal Engineering*, 51(8-9), 883-915.

Morton, R. A.; Leach, M. P.; Paine, J. G, and Cardoza, M. A., 1993. Monitoring Beach Changes Using GPS Surveying Techniques. *Journal of Coastal Research*, 9(3), 702-720.

Pawlowicz, R., 2003. Quantitative Visualization of Geophysical Flows Using Low-Cost Oblique Digital Time-Lapse Imaging. *Journal of Oceanic Engineering*, 28(4).

Péron, C. and Sénéchal, N., 2011. Dynamic of a meso to macro-tidal double barred beach: inner bar response. *Proceedings of the 11th International Coastal Symposium. Journal of Coastal Research*, Special Issue No. 64, pp. 120-124.

Ris, R.C.; Booij, N., and Holthuijsen, L.H., 1999. A third-generation wave model for coastal regions, Part II, Verification. *Journal of Geophisical Research*, 104(C4), 7667-7681.

Short, A.D., 1999. Handbook of Beach and Shoreface Morphodynamics. *Wiley, Chichester*, pp. 171-203, ISBN 0471965707.

Wentworth, C.K., 1922. A scale of grade and class terms for clastic sediments. *Journal of Geology*, 30(5), 377-392.

Journal of Coastal Research	SI	75	830-835	Coconut Creek, Florida	2016

Numerical Modeling of Wave Transformation and Runup Reduction by Coastal Vegetation of the South China Sea

Haijin Cao[†*], Weibing Feng[†], and Yujin Chen[‡]

[†]College of Harbor, Coastal and Offshore Engineering
Hohai University
Nanjing 210098, P. R. China

[‡]Research Institute of Tropical Forestry
Chinese Academy of Forestry
Guangzhou 510520, P. R. China

www.cerf-jcr.org

www.JCRonline.org

ABSTRACT

Cao, H.; Feng, W., and Chen, Y., 2016. Numerical modeling of wave transformation and runup reduction by the coastal vegetation of the South China Sea*:* Vila-Concejo, A.; Bruce, E.; Kennedy, D.M., and McCarroll, R.J. (eds.), *Proceedings of the 14th International Coastal Symposium* (Sydney, Australia). *Journal of Coastal Research*, Special Issue, No. 75, pp. 830-835. Coconut Creek (Florida), ISSN 0749-0208.

The aim of this study is to examine wave transformation and runup using a numerical model of coastal conditions including vegetation. Based on the previous field study, the drag coefficient was estimated using an analytical model. After that, numerical modeling of wave dissipation in SWASH (Simulating WAves until SHore) was conducted and validated with the observed data. Furthermore, calibrated SWASH was used to inspect the wave runup under vegetated and non-vegetated cases. For the flexibility of numerical modeling, We also used the numerical model to assess various vegetation parameters and beach slopes to inform the characteristics of wave runup reduction. The results of the model indicate that SWASH with proper parameters accurately simulated wave dissipation. Wave runup and setup were significantly reduced by the coastal vegetation. The numerical results suggest that vegetation parameters and beach slope are important factors when analyzing the wave runup reduction rate.

ADDITIONAL INDEX WORDS: *observed drag coefficient, wave dissipation by vegetation, wave runup reduction.*

INTRODUCTION

Recently, coastal vegetation has drawn substantial attention from natural scientists for its contribution to protecting coasts and infrastructures from storms, wind, and wave damage (Gedan *et al.*, 2011). This ecosystem serves as a transitional zone between water and land and conserves coastal habitats. Coastal vegetation provides a win-win solution for ecological balance conservation and development (Pinsky, *et al.*, 2013). However, due to global climate change, Phan *et al.* (2015) found that the mangroves have suffered severe degradation in recent years. It is imperative to explore how the underlying processes work in order to take measures to protect this ecosystem. Recently, the characteristics of wave attenuation were sufficiently presented by field investigations (Horstman *et al.*, 2014) and numerical methods (Cao *et al.*, 2015). Nevertheless, our understanding of wave runup reduction by vegetation remains limited due to the difficulty of monitoring wave runup on actual coasts. As far as coastal stabilization is concerned, wave runup is more significant and directly correlated to the protective effects.

Field studies of the mangrove forests along the South China Sea coast (Cao *et al.*, 2015) have been undertaken to inspect the mangrove traits and wave conditions to establish the exact wave dissipation rate by mangroves. While given the impracticality of conducting field work at every location under various hydrodynamic and vegetative conditions, numerical simulation calibrated with field data are a reasonable option to supplement the scarcity of field studies. Moreover, providing that the wave Characteristics are verified, the numerical model is capable of predicting the wave runup.

Based on previous data analysis in Cao *et al.* (2015), this study describes an analytical method to derive the bulk drag coefficient of vegetation. With all necessary parameters obtained, SWASH (Simulating WAves until SHore) model is employed to simulate wave attenuation over the vegetated coast. Afterwards, making use of SWASH's advantage in modeling moving shoreline, wave runup effects are numerically presented under both vegetated and non-vegetated conditions for comparison. The results indicate that wave runup is significantly reduced by vegetation fields. The suggested computational tests show that the wave runup reduction rate is closely related to vegetation parameters and beach slope. Numerical methods consider all underlying effects (wave shoaling, breaking, bottom friction, vegetation-induced dissipation and wave setup) and display wave transformation and runup along the sloping beach.

Background

As shown in Figure 1, field investigations were undertaken to reveal wave and vegetation characteristics at the coast of interest in Lei Zhou Bay (Cao *et al.*, 2015). Measurements were conducted in April of 2013 under a spring tide and windy weather. Wave gauges (from P1 to P5) were mounted every 25 m along a landward cross-shore transect in the mangrove forest to monitor the water surface elevation. For tidal variation, mangroves serve as the wet-dry interface. The largest significant wave height recorded was 23.5 cm at the outermost gauging position P1 with a water depth of 1.76 m. The traits of local flourishing mangroves, *Avicennia marina*, were also surveyed. In the sampling fields, the averaged vegetation density was 1.21-2.52 units/m^2, the plant trunk width at the breast was 7.8-10.2

DOI: 10.2112/SI75-167.1 received 15 October 2015; accepted in revision 15 January 2016.
*Corresponding author: hohaijin@gmail.com
©Coastal Education and Research Foundation, Inc. 2016

cm, the plant height was 0.93-1.92 m, the tree crown accounted for 40% of the height of a single tree with a branch width of 2.6-4.9 cm and a branch number of 4.05-8.57, and the pneumatophores (7.5-12 cm high and 1.3-2.2 cm wide) around the root had a density of 88-236 units/m^2. Further details regarding the measurement methods and data processing can be found in Cao *et al.* (2015).

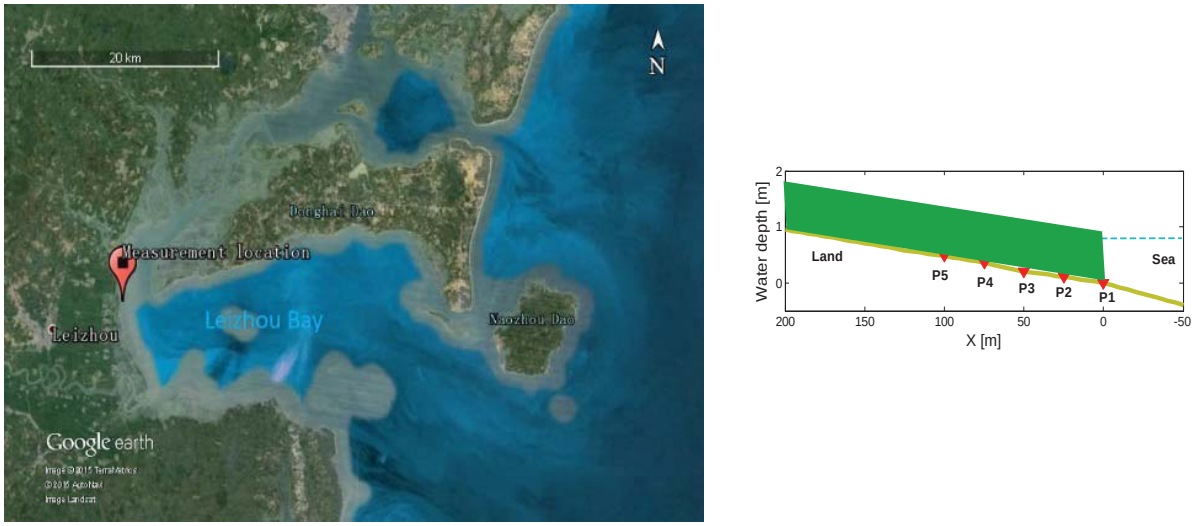

Figure 1. Landscape of Leizhou Bay and the beach profile of the field measurements.

METHODS

To achieve the objective of this study, relevant parameters, including vegetation and hydrodynamic parameters, are needed. Hydrodynamic parameters (wave and water depth) are not difficult to obtain from existing data. Vegetation traits, such as plant height, trunk width, branch number, root system, vegetation density, were also surveyed in the field work. Although the structure of a real mangrove is quite complex, the above-mentioned quantities can be represented by average sample values. The only exception is the drag coefficient which affects the vegetation-induced wave dissipation to a large extent. Hereafter, an analytical solution is used to solve for the drag coefficient.

Calculating the drag coefficient of vegetation

As discussed in a previous study (Mendez and Losada, 2004), drag coefficient is potentially related to both wave conditions and vegetation traits and plays a significant role in wave dissipation capabilities. Empirical models of solving the drag coefficient are distinctive for the diverse vegetation species (Pinsky *et al.*, 2013); therefore, these models cannot be generalized. Thus, for a specific case, the ideal method to determine the drag coefficient accurately is with the aid of measurement data. The derivation of the drag coefficient is based on the data analysis by Cao *et al.* (2015), in which wave attenuation is well presented and net dissipation by vegetation is isolated from the integrated wave effects (wave breaking, bottom friction, shoaling, etc.) by comparing the results of vegetated and bare coasts.

In consideration of practical cases (random waves and sloping beaches), a random wave model is employed using Rayleigh wave distribution, and an analytical solution for sloping beaches (Mendez and Losada, 2004) is used to solve the drag coefficient. The random wave dissipation model is presented as follows,

$$\frac{\partial E c_g}{\partial x} = -\varepsilon_v \quad (1)$$

$$\varepsilon_v = \frac{1}{2\sqrt{\pi}} \rho C_d b_v N_v \left(\frac{k_p g}{2\omega_p}\right)^3 \times \frac{\sinh^3 k_p \alpha h + 3\sinh k_p \alpha h}{3k_p \cosh^3 k_p h} H_{rms}^3 \quad (2)$$

where, E is the wave energy, c_g is the group velocity, ρ is the density of water, b_v is the plant width, N_v represents the vegetation density, k_p is the peak wave number, ω_p is the peak circle frequency, h is the water depth and h_v is submerged vegetation height. α denotes the relative vegetation height (h_v/h), and H_{rms} is the root-mean-squared wave height. For a sloping beach, the wave height is described as:

$$H = H_0 K_v K_s \quad (3)$$

$$K_v = \frac{1}{1 + \frac{2\beta H_{rms,0}}{m}(h_0^{1/4}/h^{1/4} - 1)} \quad (4)$$

$$K_s = h_0^{1/4}/h^{1/4} \quad (5)$$

$$\beta = \frac{C_d b_v N_v \alpha}{2\sqrt{\pi}} \quad (6)$$

in which, K_v denotes the dissipation coefficient by vegetation and K_s is the shoaling coefficient according to the Green Law. m is the beach slope.

A detailed deduction can be found in Mendez and Losada (2004). The drag coefficient can be obtained from Equation 4 and Equation 6 as

$$C_d = \frac{\sqrt{\pi} m}{b_v N_v \alpha H_{0,rms}(K_s - 1)}\left(\frac{1}{K_v} - 1\right) \quad (7)$$

With regard to the vegetation parameters, mean values are used. Since a mangrove plant has three layers (crow, stem and root), a characteristic value is defined for the plant width as:

$$\bar{b}_v = \mu_1 b_{v1} N_1 + \mu_2 b_{v2} N_2 + \mu_3 b_{v3} N_3 \quad (8)$$

in which, μ_1, μ_2 and μ_3 are the weight coefficients (the relative height of each layer) and N_1, N_2 and N_3 are the numbers of each part of a tree. With the available data, the observed drag coefficient can be determined.

Numerical methods

1-D SWASH (Simulating WAves until SHore) model was constructed to simulate wave transformation and runup in the coastal vegetated waters. SWASH is a non-hydrostatic wave-flow model applied to simulate wave transformation in the surf zone and swash zone. A slot technique is used in the model for moving shoreline (Zijlema *et al.*, 2011). On account of its computational stability and efficiency, this model is appropriate for actual scale modeling. With regard to the model setup, measured random wave conditions at P1 were used as incident wave conditions. Physics of bottom friction, wave breaking, and vegetation dissipation were activated to comply with a realistic coastal environment.

RESULTS

Drag coefficient

As analyzed by Mendez and Losada (2004), K_C (Keulegan-Carpenter number) is a better parameter to build the relationship with the drag coefficient, C_d. Thus, a K_C-related empirical model is introduced to establish the correlation between C_d and K_C. The fitting expression is written as:

$$C_d = \frac{2.95}{K_C^{0.522}} \quad 5.9 < K_C < 120.1 \quad (9)$$

$$K_C = \frac{u_{c,rms} T_p}{b_v} = \frac{\pi g k_p H_{rms,0}}{b_v \omega_p^2} \frac{\cosh(k_p \alpha h)}{\cosh(k_p h)} \quad (10)$$

where, $u_{c,rms}$ is the characteristic velocity at $h=h_0$, and k_p is the peak wave number. Based on above equations, we can correlate C_d with K_C as shown in Figure 2 (R^2 = 0.52). The results suggest that C_d tends to decline with increasing K_C.

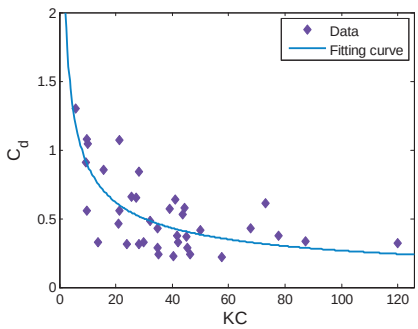

Figure 2. Correlation between C_d and K_c.

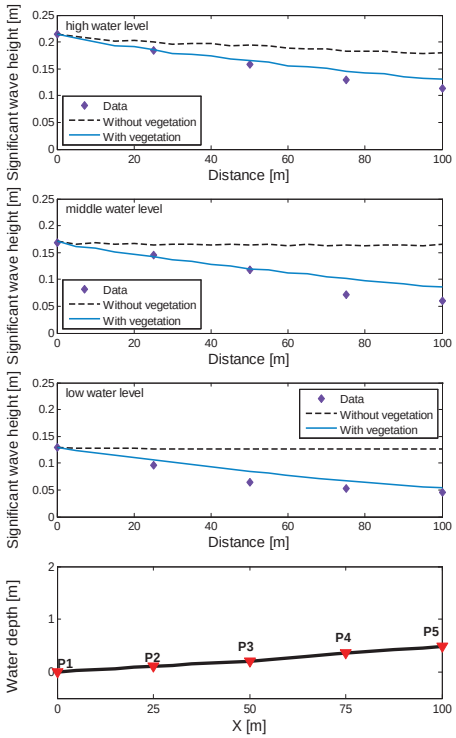

Figure 3. Comparison of wave propagation with and without vegetation; high water level: H_s = 21.39 cm, T_p = 3.02 s, C_d = 0.46, h_{p1} = 1.76 m; middle water level: H_s = 16.95cm, T_p = 3.68s, C_d = 0.68, h_{p1} = 1.43 m; and low water level: H_s = 12.96cm, T_p = 3.75s, C_d = 0.81, h_{p1} = 1.12 m. (The bottom of *P1* is defined as 0 m of water depth).

Numerical modeling

Numerical modeling of wave transformation and wave run up can be conducted based on the above parameterization. Numerical models were set up for three water level scenarios (high level, middle level and low level) according to observed hydrodynamic processes. In Figure 3, numerical results are compared to the measurement data. Overall, SWASH is able to predict wave dissipation accurately with appropriate parameters, despite existing slight underestimation of dissipation capabilities in presented cases. Compared to the non-vegetated cases, waves over the vegetated beach showed a remarkable dissipation by mangroves both in the numerical and observed results. By contrast, for the non-vegetated cases, waves presented minor dissipation only at the high water level.

Furthermore, the calculated and observed wave reduction rates (P5 relative to P1) are compared as a general validation in Figure 4. The comparison shows that the simulations of SWASH correlate well with the observed results (R^2 = 0.701). For varying hydrodynamic conditions (waves and water depth), the wave reduction rate varies from 0.4 to 0.8 in the 100-meter mangrove environment. Most cases present a reduction rate of more than 50%.

SWASH performs well when modeling wave runup effects (Zijlema *et al.*, 2011). Therefore, since wave attenuation was

validated with observed data, it is reasonable to predict wave runup at the land-sea interface (as marked in Figure 5b) using SWASH. In Figure 5 at the high water level, the wet-dry interface position of the still water level is at 358 m and Figure 5a shows the random wave runup under both vegetated and non-vegetated conditions. Due to wave setup and runup, the water surface elevation at this point was above 0 m. For the non-vegetated case, the water surface can reach a peak of around 4 cm over the still water level; while for the vegetated case, wave runup nearly vanished.

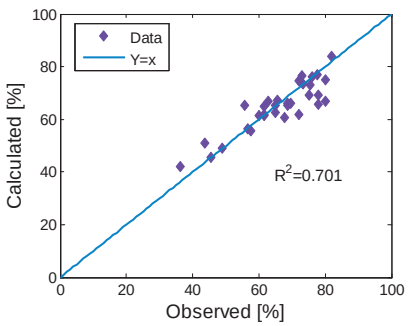

Figure 4. Comparison of observed and calculated wave reduction rates.

For random waves, it is difficult to define the wave runup reduction rate. Hence, $H_{2\%}$ is normally used to evaluate the wave runup reduction rate quantitatively (Bonakdar and Etemad-Shahidi, 2011). Figure 6 presents some simulations of wave runup under vegetated and non-vegetated conditions using $H_{2\%}$ corresponding to the waves in Figure 3. All cases show remarkable wave runup reduction by the vegetation. In contrast with the non-vegetated cases, wave runup at the high and middle water level are very similar, while the peak wave runup at the low water level was relatively small. For the vegetated cases, all results show that wave runup was significantly reduced at the mangrove coast.

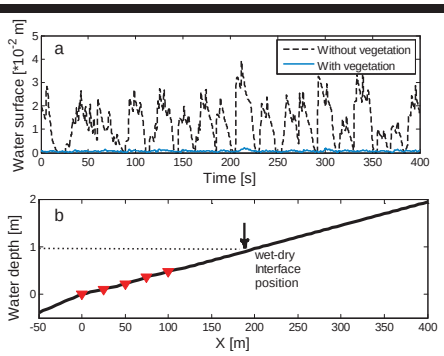

Figure 5. Wave runup at the wet-dry interface.

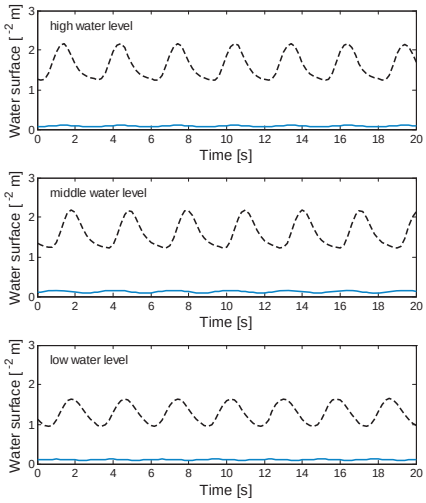

Figure 6. Wave reduction using $H_{2\%}$ corresponding to the waves in Figure 3 for the high level ($H_{2\%}$ = 0.298 m, T = 3.01s), middle level ($H_{2\%}$ = 0.235 m, T = 3.05s) and low level ($H_{2\%}$ = 0.181 m, T = 2.81s). The dashed lines represent the non-vegetated cases and the real lines represent the vegetated cases.

The remarkable reduction rates imply that the different hydrodynamics did not largely contribute to the wave runup reduction rate. To gain further insight into the nature and function of vegetation, different vegetation coefficients were assumed to examine the homologous wave runup reduction rates. Here, a comprehensive parameter V_f was defined as $C_d \times b_v \times N_v$ to simply the vegetation coefficients. Calculation checks were performed to verify the relationship between the wave runup reduction rate and V_f under the high water level and corresponding wave heights. Figure 7 shows that the wave runup reduction is poor for sparse vegetation, but increases sharply with the increase of V_f. For $V_f > 1$, the wave runup reduction rate was greater than 95% and presents a very slowly climbing trend.

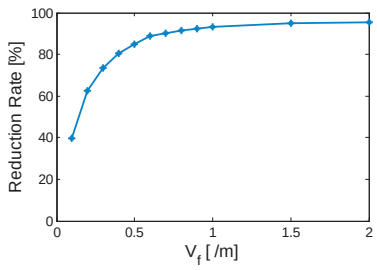

Figure 7. The relationship between the wave runup reduction rate and V_f.

The investigated beach had a mild slope of ~1:200, which could provide rationale for the small wave runup in non-vegetated cases. According to the field survey, the slope of local coasts ranges from 1:200 to 1:100. Calculation checks using $H_{2\%}$

at the high water level were conducted for different beach slopes to examine the variation in the reduction rate as the slopes change. Figure 8 presents a decreasing trend between the wave runup reduction rate and the slope. Even if the slope increases to 1:50, the wave runup reduction rate remains above 50%.

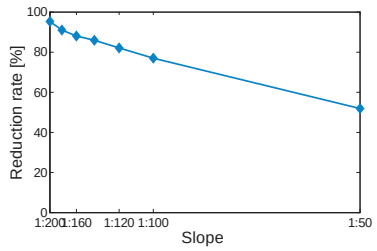

Figure 8. The relationship between the wave runup reduction rate and slopes.

DISCUSSION

The ability of solving the velocity in shallow water conditions is the major benefit of adopting SWASH. Thus, it can account for wave shoaling and transformation in shallow water conditions quite well. Additionally, the numerical study is able to integrate all the underlying functional effects of wave propagation at the nearshore zone of the coast. Compared to field studies, numerical studies provide the advantage of flexibility in that various conditions (hydrodynamic and vegetation conditions) can be simulated. We can use the numerical model to compare the vegetated and non-vegetated cases to evaluate the impact of vegetation in the numerical modeling. More detailed results can be obtained from numerical modeling in order to analyze unknown properties. For example, wave runup at the wet-dry interface is difficult to monitor or define in field studies, but can be modeled effectively with numerical modeling.

However, parameterization is critical to the accuracy of numerical simulations and can only be achieved through field studies. Consequently, field investigations are essential and preliminary work. Among the parameters, the drag coefficient is of great importance when assessing wave attenuation and shoreside wave runup, but it cannot be derived directly. Based on the fact that natural mangroves have several layers (crown, stem and root), it is challenging to define the drag coefficient for each layer. The drag coefficient was estimated as the bulk coefficient using average values of the entire vegetation canopy. Hence, the correlation in Figure 2 is not optimal. While in general, the proposed empirical model can basically reflect the drag resistance by the vegetation.

The numerical modeling results of wave attenuation indicate that with proper parameters SWASH is capable of simulating wave propagation into the mangrove environment. In Figure 3, although large waves occur at the high water level, the attenuation was greater due to the more submerged portion of the mangroves (normally, mangrove trees are tall enough to emerge from the water). After calibrating the wave dissipation in SWASH (Figure 4), wave runup was simulated. In Figure 5 and Figure 6, the comparison of vegetated and non-vegetated circumstances explicitly shows that vegetation did affect wave setup and runup. For large waves at the high water level, waves propagated over a longer flooded distance (longer vegetation scale) from the mangrove frontage to the land-sea interface. Combining bottom friction and possible wave breaking, the wave runup at the high water level was not prominently higher than that at the other two water levels. Figure 5 and Figure 6 indicate that, in the non-vegetated cases, wave setup raised the sea level at the beach. While in the vegetated cases, wave setup declined. Theoretically, the disappearance of wave setup signifies that waves does not break nearby. This means that the presence of vegetation fields inhibited the breaking of waves, which prevents the flushing flow of broken waves from stirring the coastal sands and contributes to coastal stabilization against the rising sea level.

The computational tests with additional vegetation parameters help explain the relationship between the wave runup reduction rate and vegetation traits. Although the tests are merely at the high water level, it can be inferred that the relationship will present a similar trend for other water levels. Figure 7 shows that the wave reduction rates are sensitive to vegetation parameters in a sparse vegetation environment. In Figure 8, with the increase of the beach slope, the flooded vegetation scale is decreased under the settled water level. This is the main cause of the decrease in the wave runup reduction rate. The wave setup also increased with the increase of the slope, indicating that wave breaking was activated for the increasing inclination of the beach profile.

CONCLUSIONS

When parameterizing the vegetation-induced dissipation, the drag coeffient is the most important parameter which normally can only be obtained from data analysis. SWASH is able to model wave transformation and runup at vegetated coasts with proper parameters. Compared to field studies, numerical studies provide a greater level of flexibility in investigating the nature of complex dynamic physical mechanisms. Wave setup and runup are of great significance to coastal stabilization, and vegetation parameters and the beach slope are crucial influencing factors to the wave runup reduction rate. In consideration of the peculiarity of every unique coast, a combination of observational and numerical studies is recommended.

ACKNOWLEDGMENTS

This publication is extends the field observation study supported by project grant No. CAFYBB2012018. We also thank the great efforts of Ye Tian for data collection in the intertidal flat. The authors also would like to acknowledge the support provided by the National Natural Science Foundation of China (grant No. 51279055).

LITERATURE CITED

Bonakdar, L. and Etemad-Shahidi, A., 2011. Predicting wave runup on rubble-mound structures using M5 model tree. *Ocean Engineering*, 38(1), 111-118.

Cao, H.; Feng, W.; Hu, Z.; Suzuki, T., and Stive, M.J.F., 2015. Numerical modeling of vegetation-induced dissipation using

an extended mild-slope equation. *Ocean Engineering*. 110, 258-269.

Cao, H.; Chen, Y.; Tian, Y., and Feng, W., 2015. Field investigation into wave attenuation in the mangrove environment of the South China Sea coast. *Journal of Coastal Research*. (In press)

Gedan, K.B.; Kirwan, M.L.; Wolanski, E.; Barbier, E.B., and Silliman, B.R., 2011. The present and future role of coastal wetland vegetation in protecting shorelines: answering recent challenges to the paradigm. *Climatic Change*, 106(1SI), 7-29.

Horstman, E.M.; Dohmen-Janssen, C.M.; Narra, P.M.F.; van den Berg, N.J.F.; Siemerink, M., and Hulscher, S.J.M.H., 2014. Wave attenuation in mangroves: A quantitative approach to field observations. *Coastal engineering*, 94, 47-62.

Phan, L.K.; de Vries, J.S.M.V., and Stive, M.J.F., 2015. Coastal mangrove squeeze in the Mekong Delta. *Journal of Coastal Research*, 31(2), 233-243.

Pinsky, M. L.; Guannel, G., and Arkema, K. K., 2013. Quantifying wave attenuation to inform coastal habitat conservation. *Ecosphere*, 4(8), UNSP95.

Mendez, F. J. and Losada, I. J., 2004. An empirical model to estimate the propagation of random breaking and nonbreaking waves over vegetation fields. *Coastal Engineering*, 51(2), 103-118.

SWASH model. http://swash.sourceforge.net/.

Zijlema, M.; Stelling, G., and Smit, P., 2011. SWASH: An operational public domain code for simulating wave fields and rapidly varied flows in coastal waters. *Coastal Engineering*, 58(10), 992-1012.

Journal of Coastal Research	SI	75	836-840	Coconut Creek, Florida	2016

Generation of Free Infragravity Waves by Time-Varying Breakpoint with Real Wave Conditions

Stephanie Contardo *, **Graham Symonds***

*CSIRO Oceans and Atmosphere, Floreat, Western Australia, Australia

www.cerf-jcr.org

www.JCRonline.org

ABSTRACT

Contardo, S. and Symonds, G., 2016. Generation of free infragravity waves by time-varying breakpoint with real wave conditions. *In:* Vila-Concejo, A.; Bruce, E.; Kennedy, D.M., and McCarroll, R.J. (eds.), *Proceedings of the 14th International Coastal Symposium* (Sydney, Australia). *Journal of Coastal Research*, Special Issue, No. 75, pp. 836-840. Coconut Creek (Florida), ISSN 0749-0208.

Breakpoint forcing is one of the major mechanisms for generation of free infragravity waves in the surf zone. Steep bed slopes, normalised to the incident sea-swell wavelength, are recognized to favor breakpoint forcing, but no study assesses the infragravity energy generated by breakpoint forcing in real conditions. We extend the breakpoint forcing model from bichromatic to spectral forcing and dimenzionalize the model output, and we estimate the sensitivity of the model to various spectral parameters on a plane beach. Steep beaches and short period waves (wind-sea) are favourable to breakpoint forcing, as expected. We also find that more energy is generated with real, multipeak, spectral forcing than with Jonswap spectra. The predicted infragravity response is consistent with observations on a barred beach suggesting breakpoint forcing is a major mechanism for the generation of free infragravity waves in the surf zone.

ADDITIONAL INDEX WORDS: *Nearshore processes, surf beat, breakpoint forcing, infragravity waves.*

INTRODUCTION

Long waves, also referred to as infragravity (IG) waves, are highly energetic in the surf zone, and their effect on the beach morphology has been widely reported in the literature since the 1970's. The interest in modelling free IG waves extends beyond the nearshore, for seismic measurements (Webb *et al.*, 1991) and for satellite altimetry data correction (Ardhuin *et al.*, 2014).

Munk (1949) and Tucker (1950) observed outgoing long waves in the nearshore region, correlated to incoming wave groups (Tucker, 1950). Longuet-Higgins and Stewart (1962, 1964) demonstrated the existence of bound long waves forced by the waves groups, and suggested these bound waves, reflected at the shoreline could explain the "surf beat" observed by Munk (1949) and Tucker (1950). Battjes (1988) suggested that the reflection of bound long waves was not sufficient to explain why the correlation between wave groups and outgoing waves would be stronger than the correlation between waves groups and incoming bound waves, as observed by Tucker (1950). In particular, important long wave dissipation in the surf zone (Henderson et al., 2002; de Bakker *et al.*, 2014) makes it unlikely that incoming long waves would remain energetic after propagating across the surf zone and reflecting at the shoreline.

Symonds *et al.* (1982) proposed a mechanism for the generation of free long waves based by the time-varying position of the breakpoint, due to the incoming group structure. The long waves propagate away from the breakpoint, both shoreward and seaward. The reflected incoming long waves add to the outgoing long waves, and are positively correlated with the incoming wave groups, with a time lag.

Several studies attempted to determine which, of the bound wave release and breakpoint forcing mechanisms, is dominant using numerical models, laboratory experiments or field observations. Schäffer (1990) and List (1992) estimated, based on modelling results and comparison with laboratory experiments, that breakpoint forcing was negligible in comparison to bound wave release. However, in a series of laboratory experiments, Baldock and his collaborators (Baldock *et al.*, 2000; Baldock and Huntley, 2002) concluded that breakpoint forcing is the dominant mechanism. Baldock (2012) introduced the surf beat similarity parameter based on the normalized beach slope for IG waves and the square root of the short wave (sea and swell) steepness. Using the surf beat similarity parameter, Baldock (2012) suggested that conditions such as a steep normalized bed slope and short wave steepness were favourable to breakpoint forcing, while bound wave release would be dominant otherwise. Contardo and Symonds (2013) reported observations of IG waves forced by wind-sea and swell, on a barred beach. Their results showed more IG energy in response to swell than wind-sea and they concluded that the bound wave release mechanism is present with swell forcing only, while breakpoint forcing is present with both wind-sea and swell forcing. Pomeroy *et al.* (2012) observed than on the steep fore-reef of a fringing reef, the generation of IG waves was dominated by breakpoint forcing.

Previous studies have demonstrated the presence of one or both mechanisms. Here we use the breakpoint forcing model to quantify the IG energy generated by breakpoint forcing, and we compare it with observations on a barred beach (Contardo and Symonds, 2013).

DOI: 10.2112/SI75-168.1 received 15 October 2015; accepted in revision 15 January 2016.
*Corresponding author: stephanie.contardo@csiro.au
©Coastal Education and Research Foundation, Inc. 2016

The method section describes how we extend the breakpoint forcing model from bichromatic to spectral forcing and dimensionalize the model output, and the results section presents a sensitivity study of the model to forcing wave parameters and beach slope, and a comparison between model results and the observations.

METHODS

The time-varying breakpoint model (Symonds *et al.*, 1982, hereafter: S82) parametrizes the radiation stress, in two dimensions, in a surf zone where the breakpoint position varies with time, due to normally incident wave groups. Standing wave solutions are found in the surf zone and, seaward of the breakpoint, the solutions are in the form of outgoing waves. Solutions are found at the group frequency and its higher harmonics. The results are presented as a function of the nondimensional parameter χ:

$$\chi = \frac{\sigma^2 X}{g \tan\beta} \tag{1}$$

with σ the group frequency, X the mean breakpoint position, β the beach slope and g the gravitational acceleration.

We coded the model with a time step of 2π / 64 s and a space step of 10^{-4} (nondimensional parameter). We studied the fundamental mode (group frequency) and neglected the harmonic solutions.

Figure 1 reproduces results reported in S82, namely elevation amplitude at the shoreline and the outer limit of the surf zone (see Figures 6 and 8 respectively in S82). Following S82 we limit the solutions to $\chi < \chi_{lim}$ with

$$\chi_{lim} = 0.1 \frac{\pi^2}{4\Delta a^2} \tag{2}$$

with Δa the difference of amplitude between the two waves in the group, as solutions are only valid for:

$$\chi \ll \frac{\pi^2}{4\Delta a^2} \tag{3}$$

Our results differ slightly from S82. While they found different values of elevation at the shoreline and the outer surf zone for different Δa, we find similar values. We tested the model with larger space steps and found that the elevation amplitude was underestimated. Hence, we assume the difference with S82 is due to the discretisation step chosen at the time. Although the value is not stated in their article, the step probably could not be small enough due to computing facilities available at the time.

From the figures, it appears that curves at different Δa, separate when $\chi > \chi_{lim}$ (dashed lines). We assume that the correct solutions should all follow the same curves, and we choose to make all the calculations with Δa = 0.1, so our solutions are not limited in χ.

We then calculate the elevation at different non-dimensional cross-shore locations (x), in the surf zone and offshore. Figure 2 shows the results with X = 1.

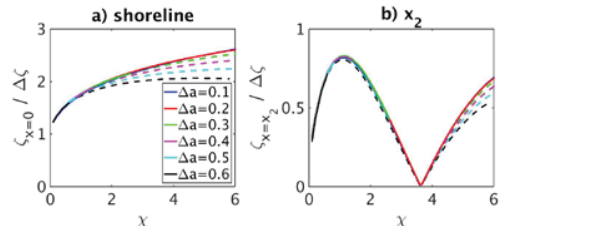

Figure 1. Elevation amplitude, ζ, normalised by $\Delta\zeta$ (half the nondimensional difference in setup), a) at the shoreline, b) at x_2 (offshore limit of breakpoint excursion), as a function of χ. Dashed lines are for $\chi > \chi_{lim}$.

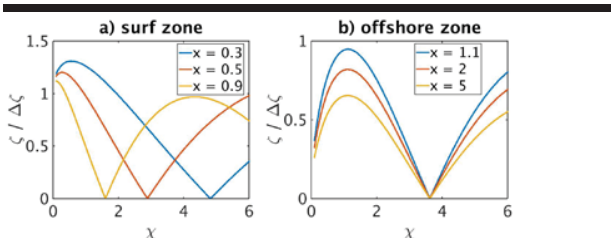

Figure 2. Elevation amplitude, ζ, normalised by $\Delta\zeta$, at different non-dimensional cross-shore locations, a) in the surf zone, b) in the offshore zone, as a function of χ.

The S82 model provides the elevation amplitude in the case of a forcing with bichromatic waves. We extend the model to spectral wave forcing. Using a prescribed spectrum, we run the model for all possible pairs of waves, with frequency differences between 0.01 Hz and 0.05 Hz. We then dimensionalize the output elevation amplitude and we calculate the total elevation amplitude, assuming, as the model is linear, that the total elevation amplitude is the summation of the elevation amplitude generated by each pair of waves in the group.

Jonswap spectra and real spectra are used to force the model. The real spectra were measured at Secret Harbour, a barred beach in the south west of Western Australia (Contardo and Symonds, 2013). When forcing with real spectra, we take shoaling into account, according to the linear wave theory.

RESULTS

We first assess the effect of a bathymetry parameter: beach slope, β, and different spectral wave parameters: sea-swell (short waves) significant wave height, $H_{m0,ss}$, peak period, T_p, spectral peakedness, γ, forcing the model with a Jonswap spectra. We then calculate the breakpoint forced IG wave generated using real wave spectra. Finally we compare the model results with observations.

Effect of beach slope

Plots of $H_{m0,IG}$ versus $H_{m0,ss}$, for different β and constant T_p and γ, using Jonswap spectra for forcing, are shown in Figure 3. The IG response increases with increasing beach slope, at the shoreline and away from the shoreline. The effect of beach slope is important: up to 10 cm between β = 0.02 and β = 0.04.

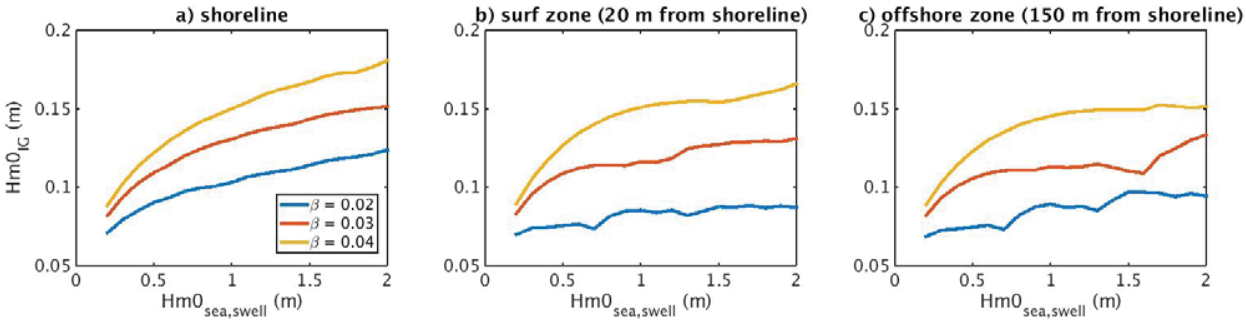

Figure 3. IG wave height versus short wave height, at three cross-shore locations, for three values of β (plane beach), T_p = 8s, γ = 3.3.

Peak period

For Jonswap spectra with the same peakedness, IG wave height increases with decreasing T_p (Figure 4). The effect is important with about 4 cm difference at the shoreline between T_p = 5 s and T_p = 12 s.

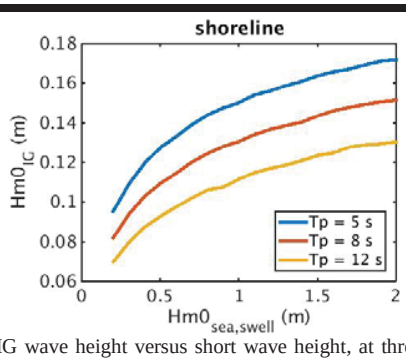

Figure 4 IG wave height versus short wave height, at three cross-shore locations, for three values of T_p, γ = 3.3, plane beach (β = 0.03).

Spectral peakedness

Figure 5 shows the IG wave height, $H_{m0,IG}$ at three cross-shore locations, and for different values of γ, as a function of $H_{m0,ss}$. At the shoreline the IG elevation amplitude decreases with increasing γ. It is also the case at other cross-shore locations, for small wave heights ($H_{m0,ss}$ < 1.2 m). The effect of γ is minor: 1 cm maximum between γ = 2 and γ = 6, at the shoreline.

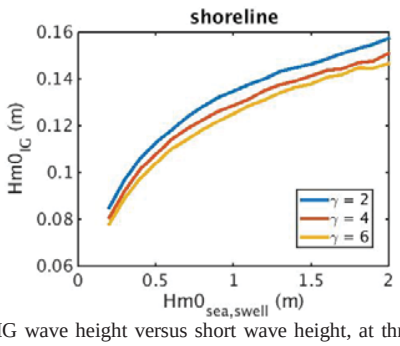

Figure 5 IG wave height versus short wave height, at three cross-shore locations, for three values of γ, T_p = 8s, plane beach (β = 0.03).

Wave height

At the shoreline, the IG wave height increases with increasing $H_{m0,ss}$ and from $H_{m0,ss}$ ~ 0.8 m the increase is almost linear with short wave height (*e.g.* Figure 3a). In the surf zone, it increases irregularly (Figure 3b), because of the presence of standing wave nodes. Offshore, it also generally increases (Figure 3c) although there are a few small decreases (*e.g.* at $H_{m0,ss} \approx 1.6$ m for β = 0.02 and at $H_{m0,ss} \approx 0.7$ m and $H_{m0,ss} \approx 1.3$ m for β = 0.03).

We can compare qualitatively the plots of $H_{m0,IG}$ versus $H_{m0,ss}$ for spectral forcing (Figure 3, Figure 4, Figure 5) to the plots of elevation amplitude versus χ for bichromatic forcing (Figure 1 and Figure 2), as χ is dependent on X (eq. 1), which increases with $H_{m0,ss}$.

In the case of bichromatic forcing, at the shoreline, the elevation amplitude increases with χ (Figure 1a). With spectral forcing (Figure 3a, Figure 4, and Figure 5), the increase of IG wave height is very similar to the bichromatic case (Figure 1a).

At locations in the surf zone, standing wave nodes cause null elevation amplitudes. The values of χ where the nodes occur, χ_{node}, depend on the cross-shore location, as shown in Figure 2a for three different locations. At all offshore locations (Figure *2* 2b), the elevation is null at χ = 3.665, corresponding to the case when no outgoing wave is generated (S82).

As we force the model with wave spectra and we plot the IG elevation amplitude versus $H_{m0,ss}$ (a dimensional parameter) instead of χ (a non-dimensional parameter), the zero values in amplitude are replaced with local minima or intermediate plateaux. There are local minima for example in Figure 4c, for $H_{m0,ss}$ = 0.7 or 1.3 m and β = 0.02 (blue line) and for $H_{m0,ss}$ = 1.7 m and β = 0.03 (red line), and a plateau in Figure 4b near $H_{m0,ss}$ = 1 m and β = 0.03 (red line).

Effect of spectral shape (real spectra)

To assess the effect of forcing with real spectra rather than Jonswap spectra, we force the model with wave spectra measured at Secret Harbour beach in summer (Contardo and Symonds, 2013). Figure 6 shows the modelled IG wave height versus the $H_{m0,ss}$, and T_p is indicated by the color scale. The values of IG wave amplitude are high, compared to the results with Jonswap spectra and β = 0.03 (red lines in Figure 3, and Figure 4 and Figure 5).

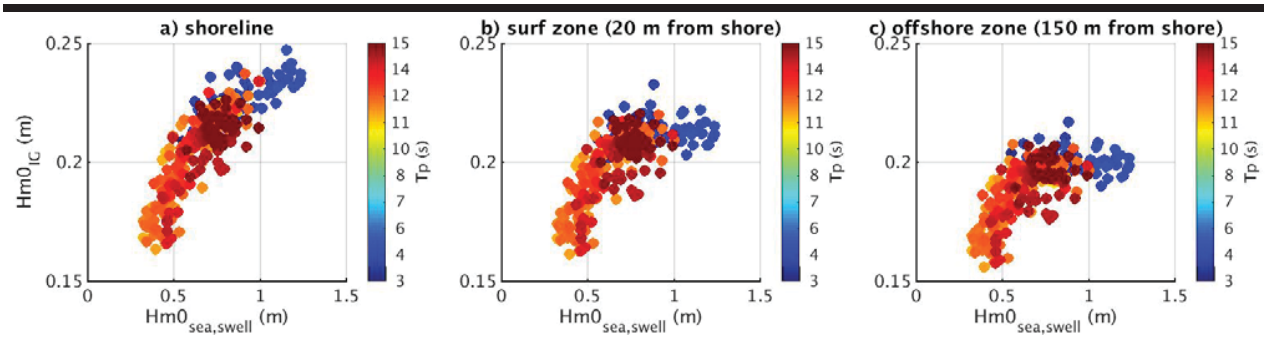

Figure 6. IG wave height versus short wave height, at three cross-shore locations, using real wave spectra, $\beta = 0.03$.

$H_{m0,IG}$ and $H_{m0,ss}$ are better correlated at the shoreline (Table 1), than away from the shoreline where the relationship is less linear. Although the peak periods vary from 3 to 15 s, it doesn't appear, with real spectra forcing, that shorter wave generated higher IG waves, as with Jonswap spectra forcing.

Table 1. *Correlation coefficients, r, between IG wave height and short wave height ($H_{m0,ss}$), at different distances from the shoreline, modelled with real spectra and measured at Secret Harbour (SH).*

		Shoreline	20 m	150 m
Model	Wind-sea	0.74	0.21	0.10
	Swell	0.84	0.75	0.70
SH	Wind-sea		0.87	0.86
	Swell		0.71	0.62

Comparison with observations

Figure 7 shows scatter plots between $H_{m0,IG}$ and $H_{m0,ss}$ as measured at Secret Harbour in the surf zone and offshore of the breakpoint (no measurements were made at the shoreline).

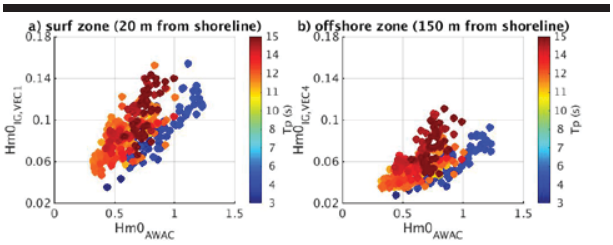

Figure 7. IG wave height versus short wave height, at two cross-shore locations, observed at Secret Harbour beach (Contardo and Symonds, 2013). Colour codes for T_p.

Overall the predicted values of $H_{m0,IG}$ are stronger than the observed values. This is expected as the model does not include dissipation. Observations show the response of IG waves to swell is stronger than the response to wind-sea. This does not appear in the model results in the plane beach case (Figure 6).

DISCUSSION

The extension of the breakpoint forcing model from bichromatic case to spectral forcing allows to compare model results with observations.

The beach slope and wave period are major parameters to predict IG energy generated by breakpoint forcing. Steeper beaches normalised to short wave wavelength are favourable to breakpoint forcing, as suggested by Baldock *et al.* (2000).

The shape of the wave spectra also has to be taken into account. The elevation amplitude decreases as the peakedness increases (Figure 5). When using real spectra for forcing, the energy in IG waves increases (Figure 6) compared to forcing with Jonswap spectra (Figure 3, Figure 4 and Figure 5). While the model forced with Jonswap spectra predicted higher IG waves generated with wind-sea than swell (Figure 4), the wave peak period doesn't affect the IG wave height prediction in the case of forcing with real spectra. Real spectra are more complex than Jonswap spectra. In particular, at Secret Harbour, swell and wind-sea co-exist, so some wave spectra have two peaks of energy, allowing for more forcing of IG waves.

The IG energy calculated for a plane beach using real wave spectra is lower than observed at Secret Harbour beach (Contardo and Symonds, 2013). Dissipation of IG waves (Henderson et al., 2002; de Bakker *et al.*, 2014), which is not included in the model could explain the difference.

Contardo and Symonds (2013) observed on a Western Australian barred beach, that swell conditions were forcing more IG waves than wind-sea forcing. Here we find that the peak period of the forcing wave does not affect the elevation amplitude of breakpoint forced IG waves. It agrees with their suggestion that an additional mechanism, bound wave release, was present during swell periods.

While IG wave height is usually calculated assuming a linear relationship with the incident short wave height (Ardhuin *et al.*, 2014; Webb *et al.*, 1991), our approach, although limited to breakpoint forcing mechanism, offers a finer approximation of IG energy.

We have limited the study to a plane beach case. This provides an order of magnitude of the elevation amplitude. However the morphology is an important factor in the generation of IG waves, and this model should be run for a barred beach case to add accuracy to the results. Using a barred beach profile, we could expect higher IG elevation amplitude

than for the plane beach case (Baldock and Huntley, 2000) and the appearance of quarter wave resonance.

CONCLUSIONS

The extension of the breakpoint forcing model, from bichromatic to spectral forcing, and the dimensionalization of the model output allow an estimation of the amplitude of breakpoint forced IG waves in the surf zone.

The IG energy generated by breakpoint forcing is of the same order of magnitude as the IG energy measured on a barred beach. The breakpoint forcing is sufficient to explain most the IG energy. However another mechanism, such as bound wave release, is necessary to explain why Contardo and Symonds (2013) observed a stronger IG response observed to swell than wind-sea.

For a more accurate study, the breakpoint forcing model should be run for a barred beach case, and dissipation of IG waves in the surf zone would need to be included.

ACKNOWLEDGMENTS

Financial support for this research is provided by CSIRO and the Royal Australian Navy.

LITERATURE CITED

Ardhuin, F.; Rawat, A., and Aucan, J., 2014. A numerical model for free infragravity waves: Definition and validation at regional and global scales. *Ocean Modelling*, 77, 20-32.

Baldock, T., 2012. Dissipation of incident forced long waves in the surf zone-implications for the concept of "Bound" Wave release at short wave breaking. *Coastal Engineering*, 60, 276-285.

Baldock, T. and Huntley, D., 2002. Long-wave forcing by the breaking of random gravity waves on a beach. *Proceedings of the Royal Society of London Series A-Mathematical Physical and Engineering Sciences*, 458(2025), 2177-2201.

Baldock, T.; Huntley, D.; Bird, P.; O'Hare, T., and Bullock, G., 2000. Breakpoint generated surf beat induced by bichromatic wave groups. *Coastal Engineering*, 39(2-4), 213-242.

Battjes, J.A., 1988. Surf-zone dynamics. *Annual Review of Fluid Mechanics*, 20, 257-293.

Contardo, S. and Symonds, G., 2013. Infragravity response to variable wave forcing in the nearshore. *Journal of Geophysical Research-Oceans*, 118(12), 7095-7106.

de Bakker, A.T.M.; Tissier, M.F.S., and Ruessink, B.G., 2014. Shoreline dissipation of infragravity waves. *Continental Shelf Research*, 72, 73-82.

Henderson, S.M. and Bowen, A.J., 2002. Observations of surf beat forcing and dissipation. *Journal of Geophysical Research-Oceans*, 107.

List, J., 1992. A model for the generation of 2-dimensional surf beat. *Journal of Geophysical Research-Oceans*, 97(C4), 5623-5635.

Longuet-Higgins, M. and Stewart, R., 1962. Radiation stress and mass transport in gravity waves, with application to surf beats. *Journal of Fluid Mechanics*, 13(4), 481-504.

Longuet-Higgins, M. and Stewart, R., 1964. Radiation stresses in water waves - a physical discussion, with applications. *Deep-Sea Research*, 11(4), 529-562.

Munk, W.H. 1949, Surf beats. *Trans. Am. Geophys. Union*, 30, 849-854.

Pomeroy, A.; Lowe, R.; Symonds, G.; Van Dongeren, A., and Moore, C., 2012. The dynamics of infragravity wave transformation over a fringing reef. *Journal of Geophysical Research-Oceans*, 117.

Ruessink, B., 1998. The temporal and spatial variability of infragravity energy in a barred nearshore zone. *Continental Shelf Research*, 18(6), 585-605.

Schäffer, H., and Jonsson, I., 2011. Theory versus experiments in two-dimensional surf beats. *Coastal Engineering Proceedings*, 1(22).

Symonds, G.; Huntley, D., and Bowen, A., 1982. Two-dimensional surf beat - long-wave generation by a time-varying breakpoint. *Journal of Geophysical Research-Oceans and Atmospheres*, 87(NC1), 492-498.

Tucker, M., 1950. Surf beats - sea waves of 1 to 5 min period. *Proceedings of the Royal Society of London Series a-Mathematical and Physical Sciences*, 202(1071), 565-573.

Webb, S. C.; X. Zhang, and W. Crawford, 1991. Infragravity waves in the deep ocean, *Journal of Geophysical Research-Oceans*, 96(C2), 2723-2736.

Journal of Coastal Research	SI	75	841-845	Coconut Creek, Florida	2016

Software for Predicting Hydrodynamic Pressures on Offshore Pile Foundations: The Next Step in Ocean Energy Development

Adrian Escobar †*, Vicente Negro†, Jose Santos Lopez-Gutierrez †, and M. Dolores Esteban†

†Research Group on Marine, Coastal and Port Environment and other Sensitive Areas
Technical University of Madrid
Madrid, Spain

www.cerf-jcr.org

www.JCRonline.org

ABSTRACT

Escobar, A.; Negro, V.; Lopez-Gutierrez, J.S., and Esteban, M.D., 2016. Software for predicting hydrodynamic pressures on offshore pile foundations. The next step in ocean energy development. *In:* Vila-Concejo, A.; Bruce, E.; Kennedy, D.M., and McCarroll, R.J. (eds.), *Proceedings of the 14th International Coastal Symposium* (Sydney, Australia). *Journal of Coastal Research*, Special Issue, No. 75, pp. 841-845. Coconut Creek (Florida), ISSN 0749-0208.

The purpose of this study is to carry out a thorough, critical analysis of the Morison equation as far as calculating wave action on large diameter piles like those used nowadays in offshore wind farms is concerned. The aim is to observe whether models currently used to estimate wave forces on piles are valid for large diameter piles apart from observing what the main forces in play in scouring are. This equation enables wave produced forces on a cylinder supported on the sea bed to be calculated. The study includes observations on the calculation model's sensitivity as to a variation in the cylinder's diameter, on the one hand and, on the other, as to temperature and salinity variation. With this in mind, specific software has been developed to simulate equations in fluid mechanics applied to solve the wave–structure interaction problem in the separation, inertial and diffraction range. This software will enable an iterative calculation to be made for finding out the shape of the pressure wave caused when a wave passes over and will show the results for different pile diameters and water temperature.

ADDITIONAL INDEX WORDS: *Morison equation, hydrodynamic wave actions, offshore foundations.*

INTRODUCTION

Nowadays, most standards applied in the world in the field of offshore wind farm design have the Morison formula as a main pylon of the calculation method for predicting hydrodynamic forces on a vertical circular cylinder. The following points will provide a brief description of the work performed by the main authors, who have developed the different theories solving the problem for all hydrodynamic ranges, and in addition, the main differences between the results obtained referring to those provided by the Morison equation will be shown. The whole analysis will focus on the estimation of stresses suffered by the pile foundation. Furthermore, as innovative approaches, two key points will be developed: temperature and salinity will be included as parameters of the calculation to observe their influence on the dynamic amplification factor and, an iterative method will be introduced for taking the interaction between structure and waves into account.

As the development of renewable energies increased, the main concern of researchers has been to find new sources for obtaining energy and new processes enabling cleaner, less expensive and, therefore, more efficient energy to be created. With this in mind, the use of offshore wind farms has been one of the major achievements of modern science for achieving this aim, as suggested by Esteban *et al*. (2011). The main difficulty these structures display from the construction standpoint lies in the correct estimation of hydrodynamic loads the structure will have to withstand. It could be said that calculating hydrodynamic forces in offshore structures is one of the major, key issues for design engineers participating in maritime engineering, as suggested by Negro *et al*. (2014). In addition, they will be very important for the study of the influence of each of the forces on possible scouring at the pile's base, as suggested by Matutano *et al*. (2013). Even though wave action is stochastic in nature, studying wave action as if it behaved in a regular fashion and estimating the hydrodynamic forces it will generate on the structure and its resulting movements are of the utmost interest to the engineer. This type of analysis is completely determinist and rests on two fundamental variables; the wave height and its period. On the other hand, there is another approach which, by using the probabilistic theory, works with the wave energy's spectra results.

Background

Morison *et al*. (1950) suggested that the two flow regimes generated by inertia forces and drag forces may be superimposed to obtain the total load varying in time per unit of length of an immobile cylinder in a plane flow field with an arbitrary free flow speed. The wave force on circular piles, within the diffraction range, was first calculated by MacCamy *et al*. (1954), who proposed that there was an exact mathematical solution presented by wave action according to the linear wave theory. Chakrabarti (1972) obtained the hydrodynamic forces

DOI: 10.2112/SI75-169.1 received 15 October 2015; accepted in revision 15 January 2016.
*Corresponding author: adrian.escobar.pastor@alumnos.upm.es
©Coastal Education and Research Foundation, Inc. 2016

caused by nonlinear waves on a vertical cylinder, including the use of the diffraction theory by means of a compact equation and then compared the equation proposed with experimental results. Lighthill (1979) made a methodological analysis describing the basic physical phenomena together with the applicable methods used for estimating hydrodynamic forces. His main contribution to the calculation of wave force by using the Morison equation lies in the proposal of a second order correction thereto. The 17th ITFC Ocean Engineering Committee undertook to compare the methods in order to calculate the movement of a semi-submergible body. They concluded with a summary of the final project results in which 34 computer programs from 28 different organizations were later described by Takagi *et al*. (1985).

Existing methods for finding hydrodynamic forces in offshore structures are mainly based on the following techniques: the use of the Morison equation or techniques using the potential of speeds for sources and sumps, in two-dimensional or three-dimensional flow. Faltinsen (1990) made a detailed analysis of wave induced linear movements and second order loads as well as nonlinear problems and viscous loads and concluded that the Morison equation and methods based on the theory of potential are favorably similar between them and with the field or laboratory made experimental measurements.

As computing power increased by means of the development of hardware and software engineering, new and more sophisticated methods have been introduced in recent years to calculate the wave–structure interaction problem. Koutandos (2009) presented a numerical study on wave interaction with rigid vertical barriers and computed the velocities and turbulence kinetic energy in the vicinity of the structure. Isaacson *et al.* (1998) and Zhu (2013) investigated wave interaction with a row of piles using the full wave theory. Zheng *et al.* (2015) presents an analytical model to predict the three-dimensional wave diffraction of a floating cylinder located in front of a vertical wall at a finite water depth. Feng *et al.* (2015), provide a solution for a two-dimensional non linear wave–structure interaction problem by a desingularized integral method in combination with a mixed Euler–Lagrange method. Dongfeng *et al.* (2015) develop a 1/10 scale model to study the influence of foundation degradation on the dynamic response of an offshore jacket platform, including the design of finite element models to analyze the dynamic behavior of the jacket platform.

METHODS

The methodology developed to suitably solve wave-structure interaction must be divided into three main sections or, in other words, into three separate problems. The first uses environmental conditions: wave period *(T)* and height *(H)* and sea depth *(d)* as first order variables which define the wave mechanics to develop in the calculation as a base for the whole assessment. Moreover, this section takes into account the influence of temperature *(Ta)* and salinity *(S)* over the water density *(ρ)* as a second order effect. In second place, section two is earmarked to assessing hydrodynamic loads on the basis of flow speeds *(v)* and accelerations *(a)* obtained in section one. This problem has the diameter of the pile *(D)* as a first order variable. Together with wave mechanics, the pile diameter defines the range (separate flow, inertial or diffraction) in which the problem must be solved. The sea temperature and salinity are included again because they play a key role in this part, due to their influence on water viscosity and, hence, on drag forces. Finally, the third section takes the sea wave loads *(F)* obtained from section two and assesses their effect on the foundation and on movements of the structure along the vertical axis. Finally, the structure movements and loads generated by them *(R)* feed the second section again and allow the calculation to be iteratively re-done until the final solution is achieved.

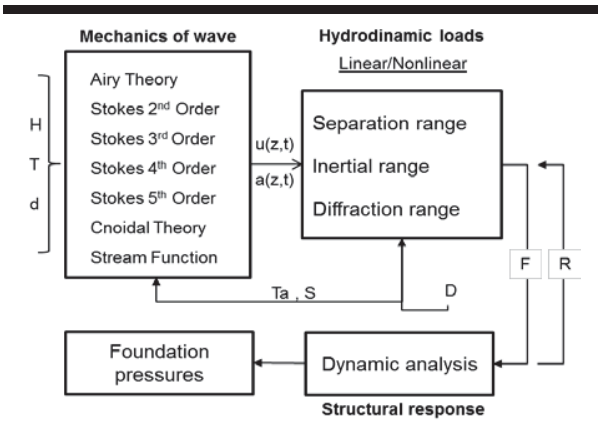

Figure 1. Calculation scheme as followed by the software

The wave mechanics model is designed to identify the range of the problem (deep water, intermediate depth and shallow water) and to solve the equations which define water wave motion (Euler equations of motion and continuity equation). To solve the system, the software will use the pertinent wave theory (such as Airy, Stokes, Cnoidal or Stream Function).

Hydrodynamic loads will be assessed by using six different calculation modules which provide the solution for one of the ranges: separate flow, inertial and diffraction; taking into account nonlinear effects when $H/L>0.5\cdot H/L_{max}$ (Table 1), where L is the wavelength.

Table 1. *Characterization of the hydrodynamic range performed by means of two parameters: Keulegan-Carpenter number (KC) and ratio D/L.*

Direction	KC < 4	KC > 4
D/L< 0.2	Inertial Range	Separate Flow Range
D/L> 0.2	Diffraction Range	-

The separate flow range is solved by means of the Morison equation. The Reynolds number, Re, is used to obtain the two parameters: coefficient of inertia due to the hydrodynamic mass C_M and drag coefficient C_D. Furthermore, nonlinear effects of wave motion will be introduced analytically for the cases in which the problem is located in the nonlinear separate flow range:

$$F(z,t) = F_1 + F_2 + F_3 + F_4 \quad (1)$$

$$F_1 = -\rho \int_{\partial\Omega} \left[\frac{\partial \varphi_1}{\partial t} n\right] ds \quad (2)$$

$$F_2 = \frac{1}{2} C_D \rho D \cdot u(z,t) \cdot |u(z,t)| \quad (3)$$

$$F_3 = \frac{1}{2} \rho \int_S (\nabla \varphi_1)^2 \cos\theta \, ds \quad (4)$$

$$F_4 = \frac{\rho}{2g} \oint_C \left(\frac{\partial \varphi_l}{\partial t}\right)^2 \cos\theta \, dl \quad (5)$$

The inertial range uses the same equation, shown above for the separate flow range, but removes the term F2 corresponding to the drag force. On the other hand, when the assumption that the kinematics of the undisturbed flow in the region near the structure does not change in the incident wave direction is not complied with, the diffraction theory has to be used. The theory provided by MacCamy *et al.* (1954) is used as a basis (F1) but adding additional terms to include the nonlinear effects in the calculation (F2).

$$F_1 = -D\rho \int_0^{2\pi} \left(\frac{\partial \varphi^{(1)}}{\partial t}\right)_{r=D} \cos(\pi - \theta) \, d\theta \quad (6)$$

$$F_2 = -D\rho \int_0^{2\pi} \left[\int_0^{\eta^{(1)}} \left(\frac{\partial \varphi^{(1)}}{\partial t} + gz\right) dz + \frac{\partial \varphi^{(2)}}{\partial t} + \frac{1}{2}\left(\frac{\partial \varphi^{(1)}}{\partial z}\right)^2 + \frac{1}{2D^2}\left(\frac{\partial \varphi^{(1)}}{\partial \theta}\right)^2\right]_{r=D} \cos(\pi - \theta) \, d\theta \quad (7)$$

The structural response is analyzed in the field of elastic deformation. The vertical circular cylinder is assumed to be a cantilever beam fixed in the sea bed. Calculations of structural movements and bending moments at a given time can be obtained by means of the superposition method as shown below:

$$x_{static}(z) = \int_{h=z}^{h=d} \left[\frac{z^2}{6EI}(3h - z)\right] dF - \frac{Fz^3}{3EI} + \int_{h=0}^{h=z} \left[\frac{h^2}{6EI}(3z - h)\right] dF \quad (8)$$

$$M_{static}(z) = \int_{h=z}^{h=d} (h - z) dF \quad (9)$$

The main problem shown in the above equation is that both expressions solve the static case without taking into account the inertial effects of the mass of the cylinder, so it is not suitable for applying in a dynamic analysis with dynamic loads. The calculation must apply a dynamic assessment in the frequency domain, which takes into account the inertial effects. The problem of that kind of analysis is the difficulty of finding a solution and has a substantial computing cost. However, this study has developed an efficient algorithm to solve these issues without increasing the calculation time or the computing cost. The differential equation which defines the behavior of the cantilever beam is:

$$EI \frac{\partial^4 x(z,t)}{\partial z^4} + m \frac{\partial^2 x(z,t)}{\partial t^2} = 0 \quad (10)$$

The above equation is best solved by separating variables. If it is assumed that the displacement can be separated into two parts, one depends on position and the other on time x(z,t) = Z·T, which are both independent of each other, so that the equation can now be written as two differential equations:

$$\frac{\partial^4 Z}{\partial z^4} - k_n^4 Z = 0 \quad (11)$$

$$\frac{\partial^2 T}{\partial t^2} + \omega_n^2 T = 0 \quad (12)$$

$$k_n^4 = \frac{w_n^2 m}{EI} \quad (13)$$

The solution to the system is given by:

$$x = \sum_{m=1}^{\infty} Z_n(z)[A_n \cos(\omega_n t) + B_n \sin(\omega_n t)] \quad (14)$$

A_n depends on the initial position at time t=0, B_n depends on the initial velocity, and both of them must be determined with the boundary conditions.

This kind of analysis leads to obtaining the speed and acceleration of each point of the structure as a response of hydrodynamic loads for a given time. These speeds and accelerations can be subtracted from the initial v(z,t) and a(z,t), and the process is repeated until its convergence for each fraction of time. The final result is a whole record of the movements of the structure along the whole length, as originated by sea waves. Finally, the bending moment on the foundation can easily be obtained from these structural movements.

RESULTS

The sensitivity of the model to temperature and salinity for the two extreme cases is shown below (Table 2). The percentage of error has been calculated as follows:

$$\%error = (M_2 - M_1)/M_1 \quad (15)$$

Table 2. *Differences in the model results with regard to the maximum bending moment on a pile foundation between using fresh water M_2 with low temperature S=0% and Ta=1ºC and saturated warm water water M_1 with S=3.5% and Ta=22ºC, for the case of H=7.0m, d=30.0m and values of T between 16 seconds and 6 seconds.*

Diameter	Max % error	Min % error
D=1m	1.77%	-0.07 %
D=2m	0.76%	-0.03 %
D=4m	0.45%	-0.01%
D=8m	2.02%	-0.04%
D=16m	10.73%	-0.07%
D=24m	10.52%	-0.07%

In addition, based on the above equation, results are shown (Figure 3) regarding the maximum bending moment on the pile foundation in terms of the ratio H/gT^2, and the flow of accelerations for the case of T=10s. Table 3 shows the error in using the simplified model (Airy & Morison) with regard to the results provided by the software which uses the correct formulation to match each calculation range.

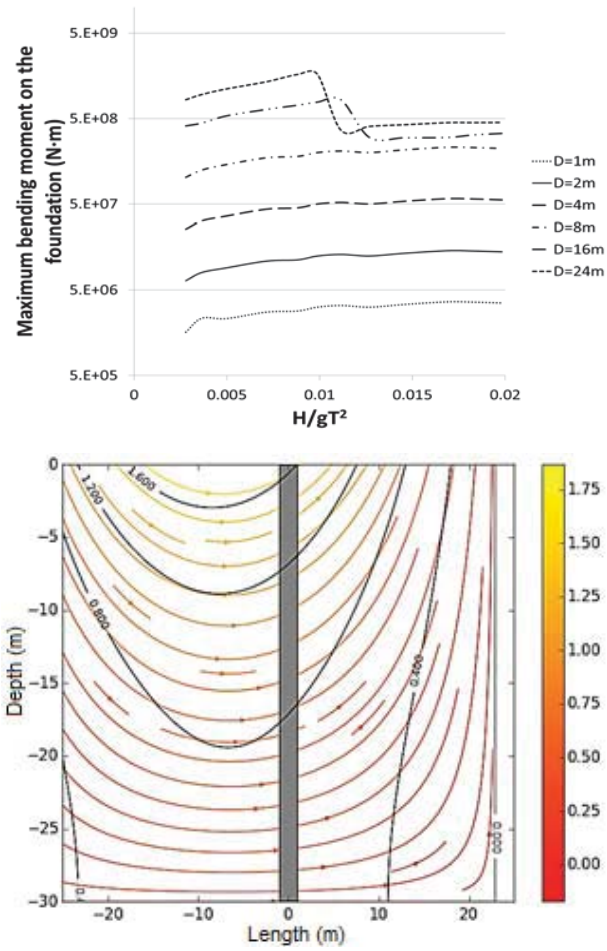

Figure 3. Maximum bending moment on the foundation for the case: H=7.0m, d=30.0m, S=3.5% and Ta=22.0 ºC (top figure); flow of accelerations (m/s^2) for the case of H=7.0m, d=30.0m, S=3.5%, Ta=22.0 ºC T=10s and D=2m, with depth as vertical axis (bottom figure).

Table 3. *Differences in the model results with regard to the maximum bending moment on a pile foundation between using Morison & Linear theory (M_2) or corresponding wave and hydrodynamic theory (M_1), for the case of S=3.5%, Ta=22ºC, H=7.0m, d=30.0m and values of T between 16 seconds and 6 seconds.*

Diameter	Max % error	Min % error
D=1m	122.05%	9.71%
D=2m	86.64%	8.74%
D=4m	68.76%	6.60%
D=8m	59.84%	5.54%
D=16m	232.33%	4.46%
D=24m	434.00%	9.07%

The loads over the cylinder are shown, for the case of T=10s, in Figure 4. The type of force acting on a foundation is then shown for several periods in Table 4.

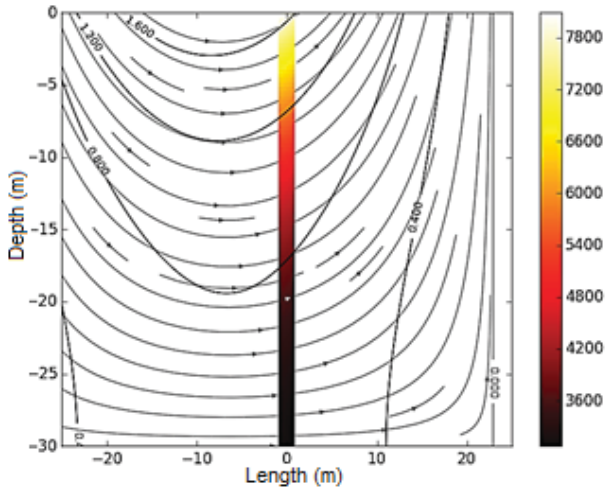

Figure 4. Wave generated loads (N) on the cylinder for the case of H=7.0m, d=30.0m, S=3.5% and Ta=22.0 ºC and D=2m.

Table 4. *Type of forces acting on the foundation for the case of H=7m, T=10s, d=30m,* S=3.5% and Ta=22ºC.

Diameter	Inertial F.	Drag F.
D=1m	205.42 N	0.031N
D=2m	273.90N	0.055N
D=4m	365.20N	0.098N
D=12m	469.55N	0.162N
D=16m	547.80N	0.220N

Finally, results from the Morison equation are compared against those provided by the diffraction theory for different diameters. It can be observed that for higher values of diameter, the effect of diffraction significantly increases the load dispersed.

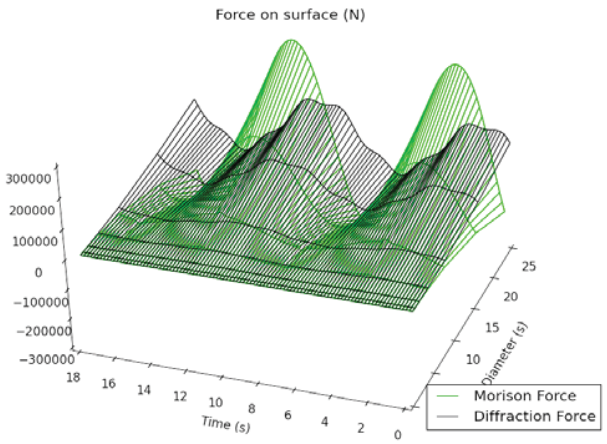

Figure 5. Comparison of Morison F. and Diffraction F. on surface for: H=7m, T=9s, d=30.0m, *S=3.5%, and Ta=22ºC* .

DISCUSSION

The large dispersion in the results which are shown in Table 3 has been a consequence of the choice of the range of pile diameters and the range of wave mechanic which is between 3rd Stokes and 5th Stokes ranges. The simulations which take into account large diameters have to be solved by means of diffraction models which consider the effects of the scatter flow in the calculation; this is the main cause that Morison formulation gives results four times higher, as shown Figure 5 for the biggest diameters. Furthermore, the nonlinear effects, which appear for some of the periods considered, have to be taken into account in the model in order to consider the real load profiles. This point is of key importance for assessing the foundation bending moment correctly, because nonlinear effects deform the distribution of loads along the whole pile, or in other words, they usually generate worse load cases than if only linear effects are considered. In addition, this dispersion is a consequence of vibration modes. For linear cases, vibration is harmonic and accumulates more energy in the pile. These three effects generate a difference in the results which shows that linear results can be four times higher than results taking all effects into account.

CONCLUSIONS

This study has shown the sensitivity of calculations with regard to the right choice of equations to characterize wave mechanics and hydrodynamic pressures. The results show a very important difference in the simplified model which is able to provide results up to five times higher than the results provided by using the suitable theory. In addition, the most important differences are caused in the diffraction range, where the simplified model considers that the scatter flow is negligible. In ranges with the smallest diameters, these differences are associated to the nonlinear effects, and mainly with drag forces, which are able to produce results up to two times higher. The smallest differences are produced for the cases of diameters of intermediate size because these calculations are mainly in the inertial range where diffraction effects and drag forces are neglected with regard to inertial forces. Hence, it has been demonstrated that the use of the Morison Equation and the Airy Theory is not valid to design large diameter offshore wind farms as used nowadays.

Furthermore, the effect of changing salinity and temperature has been presented and the conclusion drawn is that both of them have an insignificant effect in the total bending moment on the foundation. The maximum effect is found for the largest diameters and is 10.73%. This result is caused by the threshold between the diffraction theory and the inertial theory. Changes in salinity and temperature influence the wave length and this produces a light movement of the threshold to the left side generating a bigger difference. As a second conclusion, the differences in salinity and temperature cannot be neglected for the case of large diameter piles.

Finally, the predominance of inertial loads on foundation scouring is observed and this is due to of the high attenuation of drag forces with depth. Drag forces have attenuation with depth of a higher order than the attenuation of inertial forces. In the following years, more research and monitoring activities are needed in this regard.

LITERATURE CITED

Chakrabarti, S.K., 1972. Nonlinear wave forces on vertical Cylinder. *Journal Hydraulics Division*, ASCE, 98, No. HYll, 1895-1909.

Esteban, M.D.; Diez, J.J.; López-Gutiérrez, J.S., and Negro, V., 2011. Why Offshore Wind Energy?. *Renewable Energy Journal*, 36, 444-450.

Faltinsen, O.M., 1990. Wave loads on offshore structures. *Annual Review of Fluid Mechanics*, 22, 35-56.

Feng, A.; Chen, Z., and Price, W., 2015. A desingularized Rankine source method for nonlinear wave-body interaction problems, *Ocean Engineering*, 101, 131-141.

Isaacson, M.; Premasirl, S., and Yang, G., 1998. Wave interaction with vertical slotted barrier. *Journal of Waterway Port Coastal and Ocean Engineering*, 124 (3), 118–126.

Koutandos, E.V., 2009. Hydrodynamics of vertical semi-immersed slotted barrier. *WSEAS Transactions on Fluid Mechanics*, 4 (3), 85–96.

Lighthill, J., 1979. Waves and hydrodynamic loading. *Proceedings of the 2nd International Conference on the Behaviour of Offshore Structures*, (London, United Kingdom), pp. 1-40.

MacCamy, R.C. and Fuchs, R.A., 1954. *Wave forces on piles: a diffraction theory*. Washington: U.S. Corps of Engineers, Beach Erosion Board, Technical Memorandum No. 69.

Mao, D.; Zhong, C.; Zhang, L., and Chu, G., 2015. Dynamic response of offshore jacket platform including foundation degradation under cyclic loadings. *Ocean Engineering*, 100, 35-45.

Matutano, C.; Negro, V.; López-Gutiérrez, J.S., and Esteban, M.D., 2013. Scour Prediction and Scour Protection in Offshore Wind Farms. *Renewable Energy Journal*, 57, 358-365.

Morison, J.R.; Johnson, J.W., and Schaaf, S.A., 1950. The force exerted by surface waves on piles. *Journal of Petroleum Technology*, 2(5), 149-154.

Negro, V.; López-Gutiérrez, J.S.; Esteban, M.D., and Matutano, C., 2014, Uncertainties in the design of support structures and foundation for offshore wind turbines. *Renewable Energy Journal*, 63, 125-132.

Takagi, M.; Arai, S.I.; Takezawa, S.; Tanaka, K., and Takarada, N., 1985. A comparison of methods for calculating the motion of a semi-submersible. *Ocean Engineering*, 12, 45-97.

Zheng, S. and Zhang, Y., 2015. Wave diffraction from a truncated cylinder in front of a vertical wall. *Ocean Engineering*, 104, 329-343.

Zhu, D., 2013. Full wave solution for hydrodynamic behaviors of pile breakwater. *China Ocean Engineering*, 27(3), 323-334.

Journal of Coastal Research	SI	75	846-850	Coconut Creek, Florida	2016

Experimental Study on Upstream-Advancing Waves Induced by Currents

Jun Fan[†‡], Jin-hai Zheng[†‡*], Ai-feng Tao[†‡], Hao-feng Yu[‡], Yi Wang[‡]

[†]State Key Laboratory of Hydrology-Water Resources and Hydraulic Engineering
Hohai University
Nanjing, China

[‡]College of Harbour, Coastal and Offshore Engineering
Hohai University
Nanjing, China

www.cerf-jcr.org

www.JCRonline.org

ABSTRACT

Fan, J.; Zheng, J.; Tao, A.; Yu, H, and Wang, Y, 2016. Experimental study on upstream-advancing waves induced by currents. *In:* Vila-Concejo, A.; Bruce, E.; Kennedy, D.M., and McCarroll, R.J. (eds.), *Proceedings of the 14th International Coastal Symposium* (Sydney, Australia). *Journal of Coastal Research*, Special Issue, No. 75, pp. 846-850. Coconut Creek (Florida), ISSN 0749-0208.

Due to the widespread existence of large-scale continuous submarine sandbars the coasts and estuaries, the interaction between the ambient current and this kind of topography is important and complicated. It has been known that regular free surface waves can be generated and propagate in the upstream direction, when a steady current with specific depth and velocity flows past the fixed periodic wavy bottoms with large steepness. This particular free surface response, called the upstream-advancing wave, has drawn attention in the past few decades but still lacks detailed quantitative study identifying the critical conditions and the generation mechanism. A series of experiments in a large-sized flume were designed and performed to obtain the critical flow condition corresponding to the most intensive upstream-advancing waves. The wavy bottoms were formed by eight continuous fixed sinusoidal corrugated wood surfaces with wave steepness of 0.33. Wave height distributions were measured by adjusting the relative water depth (the ratio of the water depth to the bottom wavelength, 0.5-1.1, seven groups) and Froude number (0.15-0.35, 21 cases in each group). These distributions presented a unimodal pattern generally. It indicates that the critical relative water depth was 0.8 and the corresponding critical Froude number was 0.26. Once the waves were triggered, the wave periods concentrated on a small range between 1.2 s and 1.4 s. Wavelengths kept basically invariable along the propagating path.

ADDITIONAL INDEX WORDS: *Upstream-advancing waves, critical condition, periodic wavy bottoms.*

INTRODUCTION

Large-scale continuous submarine sandbars are mostly distributed in coastal regions, especially in estuary areas. These continuous sandbars present the periodic profiles with multiple undulations. Due to the existence of tidal and nearshore currents, when specific flow runs over the periodic profiles, these submarine wavy bottoms will evidently affect the ambient flow, particularly the free surface.

The initial research of this aspect dates back to the steady state of the free surface profile when steady currents flow over continuous sinusoidal wavy bottoms which are extended to both directions infinitely. These steady state of the free surface profile is called the stationary waves. Lamb (1932) summarized the linear solution of stationary waves and determined the critical flow velocity at which the amplitude of the free surface is unbound to infinity. This critical condition corresponds to the singularity of the linear solution with zero denominator.

Considering the limitation of the linear solution, the nonlinear analysis was given by Mei (1969). The results indicated that the amplitude of the stationary waves is finite in the vicinity of the critical flow velocity by removing the singularity. Then the instability features of the nonlinear steady solution of Mei (1969) were investigated to examine the possibility of chaos (Sammarco *et al*., 1994). Furthermore, the stationary wave profiles solved by perturbation method up to the second order were compared well with the experiments (Mizumura, 1995). It showed that the crest of the wave profile is flatter and longer than the trough in subcritical flow, and vice versa in supercritical flow. Besides, the free surface states were analyzed when the Froude number is close to unity (Binder *et al*., 2015).

Apart from the stationary waves for flow over wavy bed, the early experiment of steady flow over periodic wavy side walls indicated that strong instability occurs on the free surface in the form of self-stimulated unsteady waves on specific flow conditions (Binnie, 1960). The instability of the free surface waves is always one of the major topics in wave hydrodynamics (Tao *et al*., 2012; Zheng *et al*., 2014). The steady solution as well as the instability mechanisms involving the flow over wavy side walls have been investigated by various researchers (McHugh, 1988; Yih, 1982, 1983). Considering the presence of disturbances, the instability of the stationary waves for steady flow over periodic wavy bottoms was taken into consideration by linear instability analysis (Yih, 1976). The analysis showed that the stationary waves are unstable if the bottom wave number is larger than a critical value k_c and the Froude number is less than 1 (or for any bottom wave number if the Froude number is greater than 1).

The wave trains generated by steady flow over multiple sinusoidal wavy beds were investigated by a small-scale flume

DOI: 10.2112/SI75-170.1 received 15 October 2015; accepted in revision 15 January 2016.
*Corresponding author: jhzheng@hhu.edu.cn
©Coastal Education and Research Foundation, Inc. 2016

experiment with 8.0m total length (Kyotoh and Fukushima, 1997). In the experiment, the flow velocity and depth were adjusted by the discharge and flume's slope. The free surface waves were observed to propagate in the upstream direction so that they were called the upstream-advancing waves. These waves were found to be generated just with large wavy bottom steepness (0.31, the ratio of bottom wave height to wavelength). And the waves were stimulated by reducing the water depth (via decreasing the discharge) with fixed slope of the flume. All the flow velocity conditions corresponding to the wave occurrence were less than the critical value summarized by Lamb.

Although Kyotoh and Fukushima discovered the existence of upstream-advancing waves based on 19 cases with different discharge and slope values by experiment, the characteristics of the wave height, which represents the energy and intensity of the generated waves, were not given due to the experiment limits. So the critical flow condition corresponding to the strongest upstream-advancing waves cannot be determined because the excitation intensity of the waves has not been measured. Besides, in Kyotoh and Fukushima's experimental set-up, the base line of the sinusoidal bed's trough was in line of the flume's flat bottom so that the whole sinusoidal wavy topography was set above the flume's flat bottom. Because the average level of the sinusoidal bed is higher than the flume's flat bottom, this set-up of the topography was not consistent with the actual situation. It is also difficult to do further comparisons with the theoretical results.

In the present study, we performed a new experiment in a large-sized current flume in order to identify the wave height variation of the upstream-advancing waves by adjusting both the flow velocity and water depth. The wave height as well as the period and wavelength were analyzed to indicate the characteristics of generated waves. The particular critical condition which stimulates the strongest upstream-advancing waves was acquired. Besides, the average level of the sinusoidal wavy bottoms was set to be consistent with the level of the flume's flat bottom. It is more reasonable to be compared with further theoretical analysis for determining the generation mechanism of the upstream-advancing waves.

METHODS

The experiment was performed in a large scale wind-wave-current flume (Figure 1). In the longitudinal direction, the distance between the water outlet in the upstream side and inlet in the downstream side is 58.5m. The transverse width of the flume is 1.0m and the height is 1.5m. The flume is made of glass sidewalls and cement horizontal bottom. The steady flow is driven by bidirectional water bump beneath the flume and adjusted by electronic inverter which controls the rotation rate of the pump.

Continuous sinusoidal wooden bottoms were installed in the back side of the flume. The distance between the upstream flow outlet and the central part of the bottoms was 37.5m. These continuous wavy bottoms were sinusoidal profiles and consisted of eight crests and seven troughs. Their wavelength was 24cm and the wave height was 8cm. The steepness of the sinusoidal bottom was 0.33 which is large enough to induce the upstream-advancing waves in subcritical flow condition. The total length of the wavy topography was 1.80m and the transverse width was 1.0m, same as the flume. The average elevation of the sinusoidal wavy bottoms was set to accord with the level of the flume's flat bottom.

The free surface elevations were measured by 16 capacitive wave gauges along the longitudinal central axis of the flume. Three pairs were set on the upstream side. One single gauge was set on the downstream side. Nine wave gauges were equally spaced with 12cm interval above the upstream side of the wavy bottoms (Figure 1). The sampling interval was 0.006s. Before the experiment, all wave gauges were calibrated that the relative errors were less than 1.5%.

For flow velocity measurement, the Acoustic Doppler Velocimetry (Sontek 16MHz MicroADV: Up, Down and Side probes) was utilized. The sampling rate of ADV was 50Hz.

For stabilizing the flow, the cellular flow stabilizer made by circular plastic tubes (11mm diameter and 150mm length) was installed in the upstream cross-section (1.0m width and 0.6m height) near the flow outlet of the flume. And the vertical distributions of horizontal flow velocity over flat bottom were measured before installing the sinusoidal wavy bed. The velocity distribution at the target position (the location of wavy bottoms) was almost identical (average deviation 1.1%) to the upstream side positions (3.0m and 6.0m upstream from the target position). So the flow pattern in the region for installing the wavy bed was stable and fully developed. Meanwhile, this cellular facility can dissipate the free surface wave energy in order to reduce the reflection when upstream-advancing waves propagate through it.

The basic parameters of the steady flow are non-dimensionalized water depth and flow velocity. For nondimensionalization, the dimensionless water depth (relative water depth) is defined as $h'=h/L_b$, where h is the undisturbed water depth (water depth on horizontal bottom) and L_b is the wavelength of the wavy bottoms.

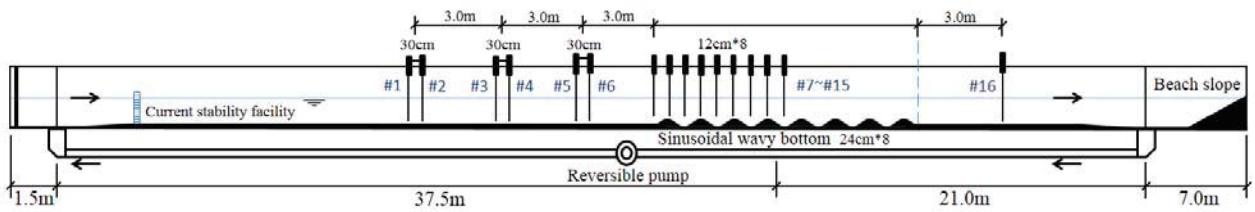

Figure 1. Experimental set-up of upstream-advancing waves.

And the Froude number $F=U/(gh)^{0.5}$ is utilized to represent the flow velocity, where g is the gravitational constant and U is the average flow velocity of the cross-section at the front edge on the upstream side of the wavy bottoms.

In this experiment, the relative water depth varies from 0.5 to 1.1 with the interval of 0.1 and the Froude number varies between 0.15 and 0.35 with the interval of 0.01 in different relative water depth groups. So there were seven groups for different water depth. And in each group, there were 21 cases with different Froude numbers.

In order to calibrate the flow in 147 cases with various combinations of water depths and flow velocities, for simplicity, the flow velocity was defined by average flow velocity of the full depth and calculated through the discharge divided by cross-sectional area.

Besides, due to the water surface slope in the flat bottom flume, the controlling position of water depth was on the flat bottom and located at the upstream side with 0.5m distance from the first crest of wavy bottoms. During the experiment, in each group, the water depth was kept constant and the flow velocity was adjusted gradually. For each case, five minutes was used to stabilize the flow. Then the measuring time in each case was 60s. The cases in the groups of relative water depth 0.6-1.0 were repeated three times, and the group of 0.5 were repeated twice.

RESULTS

Because the relative water depth and Froude number are important factors to indicate the critical condition and exact domain of existence. The generation processes of the upstream-advancing waves are addressed firstly. Then the detailed characteristics of the waves are stated.

Generation process of the upstream-advancing waves

The process of the free surface variation by increasing the Froude number from 0.15 to 0.35 with constant relative water depth (0.8) is illustrated as an example.

For the free surface response on the upstream side (from wave gauge No.1), when the Froude number was less than 0.22, there was no obvious fluctuation. Then the free surface began to fluctuate obviously when the Froude number increased to 0.24. Once the Froude number reached 0.26, the strongest upstream-advancing waves occurred with the average wave height up to 1.36cm. These intensive waves presented monochromatic (focused on a single frequency) and regular pattern (symmetrical profile).

However, when the flow velocity rose continuously, the wave height declined sharply. Once the Froude number raised to 0.30, the regular free surface fluctuation disappeared and only small random disturbances existed. So the upstream-advancing waves just appeared in a narrow range of the flow velocities. It can be shown clearly by the wave surface elevation time series as plotted in Figure 2 (Left).

At the same time, on the downstream side of the wavy bottoms, the free surface elevations (from wave gauge No.16) presented no regular wave profile in all the corresponding cases (Figure 2, Right). While the turbulence was strong when the Froude number was larger than 0.26.

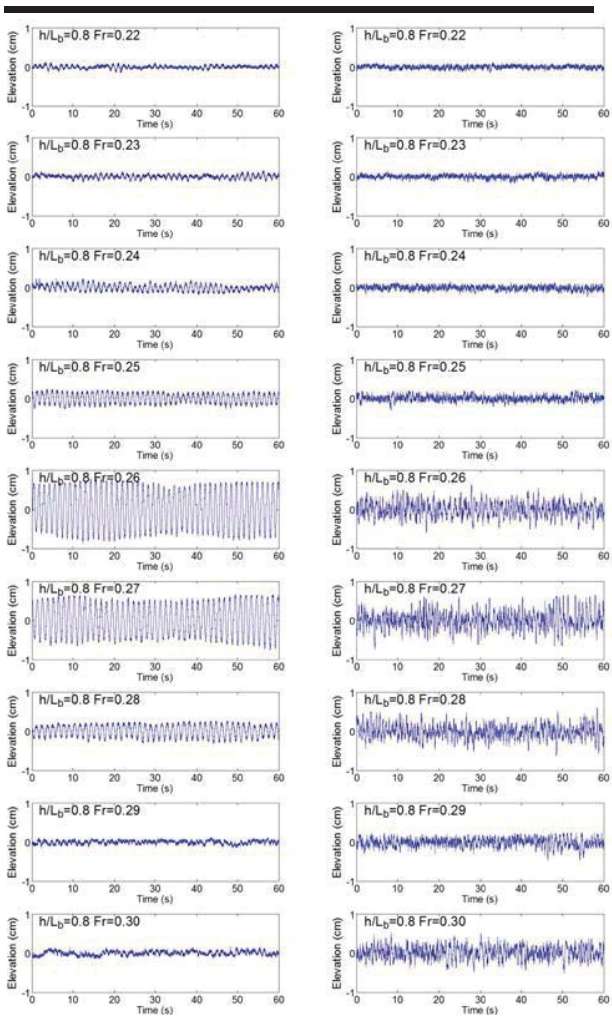

Figure 2. Free surface elevations from upstream side wave gauge No.1 (Left) and from downstream side wave gauge No.16 (Right) during the increasing process of the Froude number (0.22-0.30) with fixed relative water depth (0.8).

Wave heights and critical condition

Because the wave height reflects the intensity of the generated waves directly, the wave heights correspond to all Froude numbers in all seven groups with different water depths were measured. The average wave heights are performed (Figure 3). And the data are also from gauge No.1 as an example.

When the relative water depth is larger than 1.0, no upstream-advancing waves were generated in the flow velocity range. When the relative water depth ranged from 0.6 to 1.0, the wave height of the upstream-advancing waves influenced by flow velocity showed the unimodal pattern, similar to the generation process.

The flow velocity range, which corresponds to the existence of the upstream-advancing waves, declined with the increasing

relative water depth. The Froude number for the maximum wave height in each group decreased with the water depth growth. The maximum wave heights correspond to different water depths presented the unimodal pattern as the relative water depth covered from 0.6 to 1.0.

So the critical condition with the maximum wave height of the upstream-advancing waves was available. The critical relative water depth is 0.8 and the corresponding Froude number is 0.26.

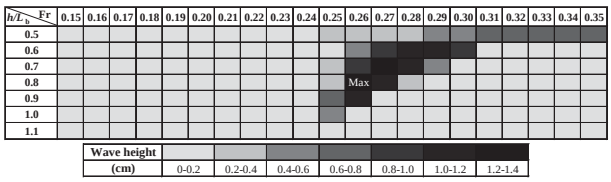

Figure 3. Average wave height distribution of the upstream-advancing waves (the 'Max' is at the critical condition corresponding to the maximum wave height).

Wave periods and wavelengths

The periods of the upstream-advancing waves are represented by the peak periods of the wave energy spectrum. The wave periods in the domain of existence concentrated on a narrow range between 1.2s and 1.4s (Figure 4). Because the variation range of the periods is so narrow that it can be regarded as irrelevant to the water depth and flow velocity.

The wavelengths of upstream-advancing waves were measured and calculated by three pairs of wave gauges on the longitudinal centerplate of the flume with 30cm interval for each pair. Three pairs' distances to the wavy bottoms were 3.0m, 6.0m and 9.0m respectively. The free surface elevations measured simultaneously by each pair of the wave gauges were calculated for the correlation coefficient. Then the time interval of upstream-advancing waves propagating through the neighboring wave gauges was obtained. The wave velocity was the distance of two neighboring wave gauges divided by the time interval. The wavelength was the product of the wave velocity and spectrum peak period.

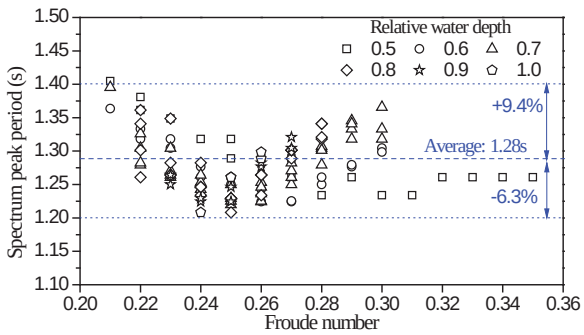

Figure 4. Peak periods with the variation of Froude number and relative water depth.

The wavelengths from the selected cases (with relatively intensive waves) concentrated on a small range between 0.95m and 1.15m. And there were no obvious differences of the wavelengths with different distances to the wavy bed. So the wavelength of the upstream-advancing waves can be regarded as unchanged when the waves propagated upstream (Figure 5).

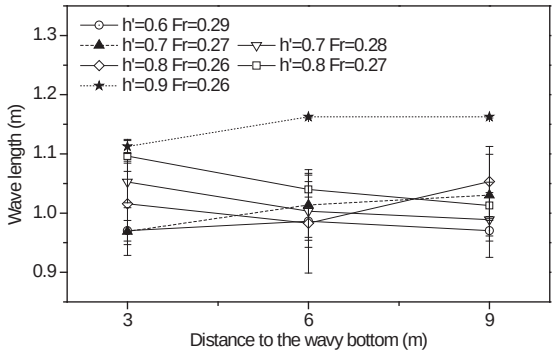

Figure 5. Wavelength distribution with the variation of flow factors and the distance to the wavy bottom (the error bar is the standard deviation).

DISCUSSION

Our findings identify the wave height variation of the upstream-advancing waves by adjusting the flow velocity with seven relative water depth values. For the relative water depths ranging from 0.6 to 1.0, the quantitative wave height variation illustrates that the wave generation is sensitive to the flow velocity with the unimodal pattern and the narrow range of existence. This experiment reflects the wave generation process from a new aspect through the flow velocity variation, because in Kyotoh and Fukushima's experiment, the waves were only stimulated by reducing the water depth.

Based on the measured wave height variation, a more specific domain of existence was acquired. The upper limit of relative water depth in the domain of existence is 1.1. When the water depth exceeds this limit, no regular waves occur. Also the exact boundary values of the Froude number in the domain of existence for various relative water depths were obtained.

More importantly, the particular critical condition which stimulates the strongest upstream-advancing waves was determined. When the relative water depth was 0.8 and the corresponding Froude number was 0.26, the wave height reached the maximum value. It is the crucial value to ascertain the most unstable condition of the wave generation.

Besides, when the waves were generated, the energy spectrum showed the obvious single peak at the corresponding period. And the wave period acquired by spectral peak in the domain of existence showed that it kept constant basically and is irrelevant with the flow conditions. So the wave component has the single and constant frequency once induced by the interaction among free surface, steady flow and periodic wavy bottoms. The wavelength was also irrelevant with the flow condition and kept constant specially. It showed that the wave

became stable and did not evolve in the propagating process which has the property of the free surface dispersive waves.

In general, the phenomenon observed by experiment indicates a special type of the instability. And this instability exists on the subcritical flow condition in which the flow velocity is less than the critical value from Lamb. To be more important, the upstream-advancing waves were just generated in a narrow specific range of current velocities and water depths. The unimodal patterns of the wave height distribution influenced by relative water depth as well as the flow velocity indicate the feature of resonance. The critical flow condition acquired by this experiment is the resonant condition. Because when the flow condition was away from this critical value, the wave height declined correspondingly and obviously. On the contrary, at the critical condition, the most intensive waves were triggered.

However, when the relative water depth was 0.5, the wave height grew monotonically with the Froude number from 0.22 to 0.35 which was different with the unimodal pattern. The reason could be that the flow velocity range is not wide enough to present the complete wave height variation for this water depth. Because the flow velocity range, which corresponds to the existence of the upstream-advancing waves, increased with the decreasing relative water depth. So a wider range of flow condition need to be investigated in the future work. Besides, the number and the steepness of the wavy bottoms need to be taken into further consideration.

Due to the energy is transferred from steady flow to the free surface wave component persistently and steadily when the upstream-advancing waves occur, this process could be an alternative to generate the wave energy by extracting it from the flow. And it may affect the wave field in the nearshore areas to a certain extent when continuous submarine sandbars exist and the corresponding flow conditions are satisfied.

CONCLUSIONS

The present experimental study identifies the wave height variation of the upstream-advancing waves by adjusting the flow velocity and water depth. A more definite domain of existence was acquired. It showed that the waves were only generated in a small specific range of current velocities and water depths along with the unimodal pattern of the wave height distribution. The particular critical condition which stimulates the strongest upstream-advancing waves was determined with the relative water depth of 0.8 and the Froude number of 0.26. Once generated, the wave periods kept constant and concentrated on a narrow range between 1.2s and 1.4s. And the wavelengths kept invariable basically along the propagating path.

ACKNOWLEDGMENTS

This research is funded by the National Natural Science Fund (51379071), the National Science Fund for Distinguished Young Scholars (51425901), the Fundamental Research Funds for the Central Universities of Hohai University (2014B04114, 2014B30614, KYLX_0483) and the Basic Research Fund From State Key Laboratory of Hydrology-Water Resources and Hydraulic Engineering, Hohai University (20145027512, 20145028412).

LITERATURE CITED

Binder, B.J.; Blyth, M.G., and Balasuriya, S., 2015. Steady free-surface flow over spatially periodic topography. *Journal of Fluid Mechanics*, 781, R3.

Binnie, A.M., 1960. Self-induced waves in a conduit with corrugated walls. I. Experiments with water in an open horizontal channel with vertically corrugated sides. *Proceedings of the Royal Society of London A: Mathematical, Physical and Engineering Sciences*, 259(1296), 18-27.

Kyotoh, H. and Fukushima, M., 1997. Upstream-advancing waves generated by a current over a sinusoidal bed. *Fluid Dynamics Research*, 21(1), 1-28.

Lamb, H., 1932. *Hydrodynamics*. Cambridge: Cambridge University Press, 409p.

McHUGH, J.P., 1988. The stability of stationary waves in a wavy-walled channel. *Journal of Fluid Mechanics*, 189, 491-508.

Mei, C.C., 1969. Steady free surface flow over wavy bed. *Journal of the Engineering Mechanics Division*, 95(6), 1393-1402.

Mizumura, K., 1995. Free-surface profile of open-channel flow with wavy boundary. *Journal of Hydraulic Engineering*, 121(7), 533-539.

Sammarco, P.; Mei, C.C., and Trulsen, K., 1994. Nonlinear resonance of free surface waves in a current over a sinusoidal bottom: a numerical study. *Journal of Fluid Mechanics*, 279, 377-405.

Tao, A.; Zheng, J.; Mee Mee, S., and Chen, B., 2012. The most unstable conditions of modulation instability. *Journal of Applied Mathematics*. doi:10.1155/2012/656873

Yih, C.S., 1976. Instability of surface and internal waves. *Advances in Applied Mechanics*, 16, 369-419.

Yih, C.S., 1982. Binnie waves. *Fourteenth Symposium on Naval Hydrodynamics* (Ann Arbor, Michigan), pp. 89-102.

Yih, C.S., 1983. Waves in meandering streams. *Journal of Fluid Mechanics*, 130, 109-121.

Zheng, J.; Wang, G.; Dong, G.; Ma, X., and Ma, Y., 2014. Numerical study on Fermi–Pasta–Ulam–Tsingou problem for 1D shallow-water waves. *Wave Motion*, 51(1), 157-167

Journal of Coastal Research	SI	75	851-855	Coconut Creek, Florida	2016

Effects of Ultra-Porous 3D Printed Reefs on Wave Kinematics

Lorenzo Frau[†], Andrea Marzeddu[†], Enrico Dini[†*], Vicente Gracia[†], Xavier Gironella[†], Alessio Erioli[§‡], Alessandro Zomparelli[‡], Agustín Sánchez-Arcilla[†]

[†] Laboratori d'Enginyeria Marítima, Universitat Politècnica de Catalunya (LIM/UPC), Barcelona 08034, Spain

[†*] Monolite UK Ltd, 101 Wardour Street, London W1F 0UN

[§]Universitá degli studi di Bologna, dipartimento di architettura (DA), viale Risorgimento 2, Bologna 40136, Italy

[‡] Co-de-iT

www.cerf-jcr.org

www.JCRonline.org

ABSTRACT

Frau, L.; Marzeddu, A.; Dini, E; Gracia, V.; Gironella, X.; Erioli A.; Zomparelli, A. and Sánchez-Arcilla, A., 2016. Effects of Ultra-Porous 3D Printed Reefs on Wave Kinematics. *In:* Vila-Concejo, A.; Bruce, E.; Kennedy, D.M., and McCarroll, R.J. (eds.), *Proceedings of the 14th International Coastal Symposium* (Sydney, Australia). *Journal of Coastal Research*, Special Issue, No. 75, pp. 851-855. Coconut Creek (Florida), ISSN 0749-0208.

Present 3D printing technology allows the efficient design and construction of structures with complex shapes and high porosity satisfying biological and coastal protection demands. In this case, an array of ultra-porous tetrahedron-shaped 3D printed artificial reef (UPTSAR) is proposed to be used as a submerged breakwater for both environmental enhancement and wave protection. The aim of this study is to analyse the wave-structure interaction effects and the resulting velocity and wave height fields. For this, two-dimensional small scale tests (1:15) using irregular waves were carried out in a wave flume facility at BarcelonaTech. The influence of wave steepness, relative freeboard, relative water depth and the porosity on wave Kinematics have been analysed. The paper will describe in detail the results obtained for the different tests. These results are used to evaluate the functionality of the UPTSAR as coastal protection structures.

ADDITIONAL INDEX WORDS: *submerged breakwater, reef, biotope, wave transmission, D-shape.*

INTRODUCTION

Submerged breakwaters are commonly considered as a "soft" solution for coastal protection or stabilization, as these structures do not present a visual impact from the land and do not change radically the behavior of the sea surface. Submerged breakwaters have been commonly constructed using rocks or concrete elements. These concrete blocks, specially designed and developed from an engineering point of view. Several studies on submerged breakwaters and their hydraulic performance have been widely conducted in the past (Hayakawa *et al*., 1998; Kawasaki and Iwata, 1998; Seabrook, 1997; Tsujimoto *et al*., 1999).

The performance of submerged breakwaters is mainly influenced by the local bathymetry, local wave characteristics, design and placement pattern of the breakwater units and the relative submergence (Herbich, 2000). In particular, submerged depth (h/d, where h is the water depth and d is the breakwater's height) and crest width (B) are supposed to be important factors influencing the transmission process (Dattatri *et al*., 1978; Dick and Brebner, 1968; Seabrook, 1999). Also the relative water depth (d/H_i, where H_i is the incident wave height) (Saito *et al*., 2002), wave steepness (H_s/L_{op}, where H_s is the significant wave height and L_{op} is the wave length in open water) (Van der Meer, 1988) and relative freeboard (R_c/H_s, where R_c is the freeboard of the structure) (Goda, 1974) contribute to wave transmission.

Submerged breakwaters are typically placed in the shallow water domain and because of this they are also frequently used as artificial reefs.

Artificial reefs have been traditionally used to create a sheltered area for fish and, thus, regenerate damaged ecosystems or create diving areas (Bohnsack *et al*., 1991; Ino, 1974). The first artificial reef was built in South Carolina in 1860s (Stone, 1985) using logs, while large scale ocean artificial reef constructions were made in 1935 using boat and other material in New Jersey (McGurrin and Reeff, 1986).

The use of such materials is no longer considered acceptable for a number of reasons including cost, pollution potential, biological effectiveness and long-term stability in the marine environment. This is why specific structures were designed for this purpose. The best known among all are the Reef Balls™, hemispherical concrete units mainly used to restore ailing coral reefs and to create new habitat for fish and other marine or freshwater species (Armono and Hall, 2003).

Most recently, Erioli and Zomparelli, (2012) developed an ultra-porous tetrahedron-shaped 3D printed artificial reefs as a benchmark test piece under the Emergent Reefs project. This project draws on the potential that emerges from a coherent utilization of the environment's inherent ecological structure using an approach based on digitally simulated ecosystems and sparked by the possibilities and potential of D-Shape large-scale 3D printing technology. The project's purpose is to establish, through strategies based on computational design tools and machine-based fabrication, seamless relations between three different aspects of the architectural process: generation, simulation, and construction (tailored to site-specific

DOI: 10.2112/SI75-171.1 received 15 October 2015; accepted in revision 15 January 2016.
*Corresponding author: lfraupons@gmail.com
©Coastal Education and Research Foundation, Inc. 2016

conditions), which can be specified as guided growth and articulates in the following design principles (Graziano and Erioli, 2013).

The aim of this paper is to investigate the hydrodynamic effects of such ultra-porous tetrahedron-shaped 3D printed artificial reefs, here referenced as UPTSAR. Since there are no previous studies on wave energy dissipation through UPTSAR breakwaters, two dimensional small scale tests using irregular waves were conducted in a small Wave Flume (CIEMito) at the Laboratori d'Enginyeria Marítima in the BarcelonaTech University (LIM/CIIRC-UPC).

METHODS

A set of small scale tests considering different water depth and sea conditions were developed for this study. Nevertheless, due to the lack of pieces, the tests were only carried out for a single row of three UPTSAR units, so the influence of the crest width on the wave energy dissipation could not be proved.

The aim of these tests was to provide efficient information about the UPTSAR hydraulic performance, in terms of wave transmission and kinematics and, thus, defining the right emplacement of the UPTSAR for their correct operation.

A model for wave transmission past a submerged breakwater made of multiple UPTSAR units has been developed in this study, besides determining the optimum configuration of the reef that will minimize the incident wave energy. The transmission coefficient, K_t, which is defined as the ratio between transmitted and incident wave (H_t/H_i), will be expressed taking into account the depth submergence, wave steepness, UPTSAR units' porosity and reef configuration to observe if any relationships or trends are present.

UPTSAR description

The pieces used for the tests are small scale models (1:15) from the original. The base is equilateral triangular, side 15.5 cm, and it is 6.5 cm high (Figure 1). Two types of units have been tested: porous and non-porous. Small scale porous models have an average weight of 344.2 g and an average volume of 197.4 cm^3, which corresponds to a density of 1.93 g/cm^3. The non-porous unit has a volume of 355.4 cm^3.

By comparing the volume from porous and non-porous units, it can be concluded that UPTSAR units have an average porosity of a 44.4%.

Experiment Set-up

Two-dimensional small scale tests were carried out in the CIEMito Wave Flume facilities at LIM/CIIRC-UPC, in Barcelona. The flume is 18 m long, 0.38 m wide and 0.56 m high and is equipped with a piston type wave maker driven by software developed at LIM/UPC, which allows generating regular and irregular waves up to 0.28 m wave heights and wave periods up to 2 seconds. A ramp with a slope of 1:13 is located at the end part of the flume, simulating a beach slope. At the ends of the flume, a passive wave absorber is located to minimize reflected wave energy. A total of nine different storm conditions with irregular waves have been defined by the JONSWAP spectrum, with prior determination of the significant wave height (H_s) and the peak period (T_p). These wave conditions have been used in all the tests for this study.

The selected wave configurations have been grouped using their wave steepness at the piston as H_s/L = 0.04; 0.05; 0.06. For each wave steepness, the configuration for three waves has been obtained by fixing three different significant wave heights (H_s = 0.04; 0.06; 0.08 m) where chosen. The nomenclature used for these nine different wave conditions are shown at Table 1.

Wave motions were measured by using four resistive wave gauges, with an accuracy of 0.1 mm. The probes were positioned at different points both seaward and landward of the breakwater, in order to measure the generated, transmitted and reflected waves, decomposing incident/reflected waves with the Mansard and Funke method (Mansard, 1980).

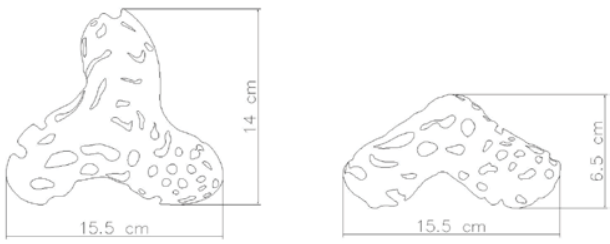

Figure 1. Small scale UPTSAR unit measurements. The left image corresponds to the plan view; the right image corresponds to a front view.

Considering the very low reflection it will be possible, with minimal errors, to measure and compare the wave height at the rear side of the structure, by assuming the incident wave height (H_i) as the wave height measured without the presence of the breakwater ($H_{without}$). Thus, in both free surface and wave currents tests, a comparison between the measurements obtained by carrying out the same test with and without the UPTSAR breakwater was developed.

Six different positions in the flume for the UPTSAR breakwater were considered for the tests, spread over the sloped section of the flume (Figure 2).

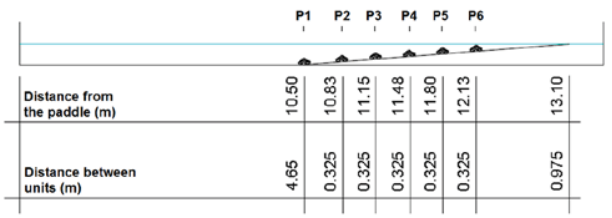

Figure 2. UPTSAR breakwaters positions. It represents the six different positions along the sloped plane (P1 up to P6).

A total of 212 tests were carried out in order to find out the transmission coefficient for the artificial reefs. Two situations were differentiated: tests developed on the horizontal bottom and tests carried out along the sloped plane. The same set of

tests were carried out with the flume empty (without breakwater and sloped beach), with porous units and non-porous ones.

Several tests were carried out with different water depths when the artificial reef was placed at the horizontal bottom. Nevertheless, a low depth makes the wave generation less controllable, producing several breaking waves before the structure and, thus, obtaining irrelevant results for this study. This is why no results for the horizontal bottom tests were used in this work to define the performance of the UPTSAR breakwater.

Table 1. *Wave reanalysis data provided by SMCBrazil software for Marinha Farinha beach (Oliveira et al., 2013)*

Test number	H_s (m)	Tp(s)	Nomenclature
1	0.04	0.67	T1
2	0.04	0.75	T2
3	0.04	0.87	T3
4	0.06	0.87	T4
5	0.06	0.99	T5
6	0.06	1.17	T6
7	0.08	1.07	T7
8	0.08	1.24	T8
9	0.08	1.50	T9

After a preliminary analysis of the results of the first set of tests, it was decided to move the UPTSAR breakwater at the end of the flume, on the sloped plane, and perform the same tests at the six different positions along the sloped plane, as described before (Figure 2). This configuration allows studying the performance of the breakwater with varying water depth (h).

Transmission coefficient

The transmission coefficient for both porous and non-porous structure was estimated by comparing the wave heights measured at the landward side of the breakwater with (H_{with}) and without ($H_{without}$) the presence of the UPTSAR breakwater.

$$K_t = \frac{H_{with}}{H_{without}}$$

Three sets of tests were developed in order to correctly define the transmission coefficient of the structure, differentiating tests with the empty flume (without any obstacle), with porous and non-porous units.

In order to find physical relations between the transmission coefficient and some dimensionless factors, different analyses have been performed: relative freeboard (R_c/H_s), relative depth (h/d) and wave steepness (H_s/L_{op}).

The relative depth is a dimensionless factor obtained as the ratio between the depth (h) and the breakwater's height (d). This will offer an idea about the position of the breakwater and allow studying its behaviour regardless of the scale of the tests.

RESULTS

Figure 3 shows the relationship found between K_t and R_c for porous and non-porous structure's tests. Despite the correlation coefficient (R^2) for the regression line is not so high, it is clearly appreciated a linear relation between the relative freeboard and the transmission coefficients. As seen in Figure 3, a linear relation between the relative freeboard (R_c/H_s) and K_t starts at a relative freeboard of about -1.7.

When the relative freeboard increases, the transmission coefficient gets lower and seems to do it linearly. For lower values of R_c/H_s, no effects on the free surface seem to be caused by the UPTSAR breakwater. It is appreciated a more dissipating behaviour of the non-porous structure in comparison with porous one, with a difference of about 8% of the transmission coefficient at the point with freeboard equal to zero.

It is also observed that results obtained for porous units have slightly more scatter versus the non-porous ones.

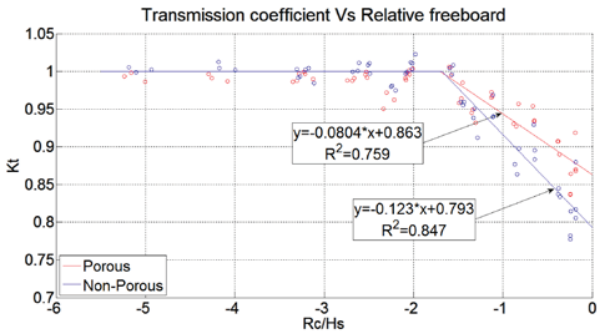

Figure 3. Transmission coefficient (K_t) *versus* relative freeboard (R_c/H_s) with both porous and non-porous units.

The comparison between Kt and the relative depth for porous and non-porous structures is shown in Figure 4. As can be seen, the tests with the high relative depth ratios had the larger K_t values. This behaviour is observed up to a value of 2.3 where no longer energy dissipation is observed.

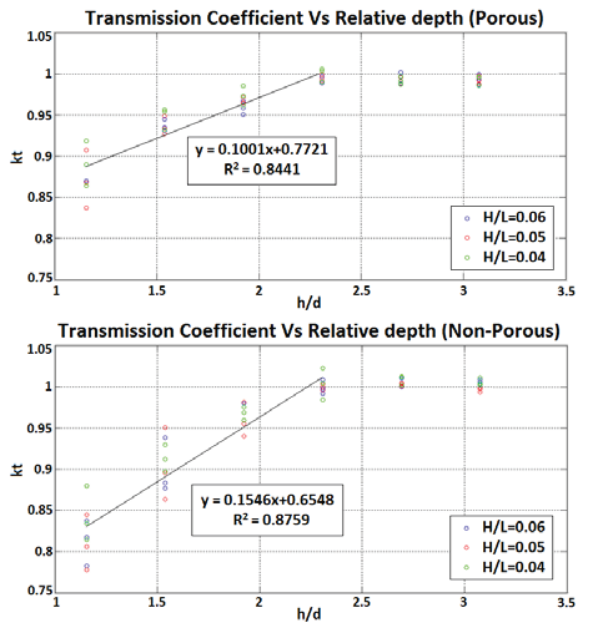

Figure 4. Comparing Transmission coefficient (K_t) Vs relative depth (h/d) with both porous and non-porous units.

Results obtained for the non-porous breakwater are about 8% lower than the obtained in tests for porous units. These results are more dispersed for the non-porous tests and get more spread as the relative depth decreases (higher dispersion at $h/d \approx 1$).

It is also observed, especially at the porous tests, a slight trend to increase the value of K_t as the wave steepness decreases. Nevertheless, it is not too significant to affirm this relation.

The wave steepness refers to the stability of the waves and is expressed as the ratio between the wave height and the wave length. In shallow water, wave height increases and wave length decreases, so the wave steepness clearly increases too.

An attempt to find a relation between the wave steepness and the transmission coefficient was carried out in this study. The results for porous and non-porous structures were plotted on two different graphs (Figure 5).

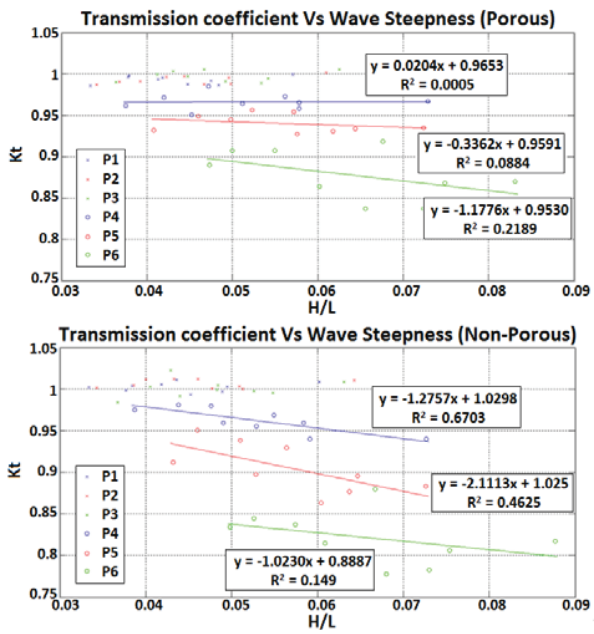

Figure 5. Comparing Transmission coefficient (K_t) and wave steepness (H_s/L) with both porous and non-porous units.

No conclusive relations between wave steepness (H_s/L) and transmission coefficient (K_t) can be extracted at first instance from these tests.

Nevertheless, it is appreciated a slight trend for the K_t to decrease when the wave steepness rises. These effects seem to be higher in tests with non-porous units, where lower values for K_t are obtained.

It is also seen that the effect of the UPTSAR breakwater on the transmission coefficient is irrelevant for deeper positions (P1, P2, P3) and the effects get higher as the depth decreases.

CONCLUSIONS

The 3D printing technology has allowed the construction of a 44.4% porosity element. An effect of the porosity on the wave transmission is appreciated. The results show that non-porous units offer higher performance than porous ones.

Wave height reduction was found to be influenced by the wave steepness, relative freeboard, relative depth and reef porosity, being the relative freeboard the most influencing factor. As Van der Meer (1990) defined, a linear equation depending on the relative freeboard is proposed to predict the transmission coefficient for the one-row UPTSAR breakwaters:

Porous
$$K_t = \begin{cases} 1 & \frac{R_c}{H_s} < 1.70 \\ -0.080 \cdot \frac{R_c}{H_s} + 0.863 & 1.70 < \frac{R_c}{H_s} < 0 \end{cases}$$

Non Porous
$$K_t = \begin{cases} 1 & \frac{R_c}{H_s} < 1.68 \\ -0.123 \cdot \frac{R_c}{H_s} + 0.793 & 1.68 < \frac{R_c}{H_s} < 0 \end{cases}$$

The obtained R2 for porous and non-porous structures is 0.759 and 0.847 respectively.

The minimum transmission coefficient (Kt), obtained at a freeboard close to zero, is 0.863 for the porous units and 0.793 for the non-porous ones.

Future works

The influences of wave steepness, relative freeboard, relative depth and reef porosity on wave energy transmission have been studied in this thesis. Nevertheless, an equation depending only on the relative freeboard has been proposed to predict the transmission coefficient. This is why large scale tests should be carried on in order to determinate the influence of these factors and be capable to propose a more robust relations.

On the other hand, the influence of the crest width (B) (equivalent to study the influence of the number of rows used for the UPTSAR breakwater), should be studied, as its effects on wave transmission are significant, according to previous studies by Armono (2003), Buccino and Calabressi (2013), Cappietti *et al* (2013), D'angremont *et al*. (1996) or Seabrook & Hall (1998). To bear out this, more UPTSAR units would be needed.

ACKNOWLEDGEMENTS

The first author acknowledges the Student Scholarship from the Civil Engineer School (ETSECCPB-UPC, 2014-2015) and has been partially supported by the iCOAST EU-project (contract agreement Nº ECHO/SUB/2013/661009) and the RISES-AM EU-project (FP7-ENV-693396).The Authors want to acknowledge NYXO ltd (formerly disguincio&co) for the collaboration.

Special thanks are due to the personal of the CIEMLAB at the LIM-UPC (Barcelona).

LITERATURE CITED

Armono, H.D. and Hall, K.R., 2003. Wave transmission on submerged breakwaters made of hollow hemispherical shape artificial reefs. *Proceedings of the 31st Annual Conference of the Canadian Society for Civil Engineering* (CSCE), pp. 1–13.

Bohnsack, J.A.; Johnson, DL., and Ambrose, RF., 1991. Ecology of Artificial Reef Habitats and Fishes. *In:* Seaman

Jr., W. and Sprague, L.M., (eds.), *Artificial Habitats for Marine and Freshwater Fisheries*, Academic Press, Inc., 285 p.

Buccino, M.; Vita, I. Del; Calabrese, M., and Civile, I., 2013. Predicting wave transmission past Reef Ball TM submerged breakwaters. *Journal of Coastal Research*, Special Issue No. 65, pp. 171-176.

Cappietti, L.; Gironella, X., and Marzeddu, A., 2011. Laboratory experiments on wave-induced fluxes over and through shore-defense detached permeable breakwaters. *Journal of Coastal Research*, Special Issue No. 64, pp. 484-487.

Dattatri, J.; Raman, H., and Shakar, N.J., 1979. Performance Characteristics of Submerged Breakwaters. *Proc. 16th International Conference on Coastal Engineering*, Hamburg, Germany, pp. 2152-2171

Dick, T.M. and Brebner, 1968. A Solid and Permeable Submerged Breakwaters. *Proceeding of 11th International Conference on Coastal Engineering.* London, UK, pp. 1141-1158.

Erioli, A. and Zomparelli, A., 2012. Emergent Reefs. *Proceedings of the 32nd Annual Conference of the Association for Computer Aided Design in Architecture.* pp. 139-148.

Goda, Y., 1969. *Re-analysis of Laboratory Data on Wave Transmission*. Report of the Port and Harbour Research Institute, 18(3).

Goda, Y., 1974. Estimation of wave Statistics from Spectra Information. *Proceedings of the International Symposium on Ocean Wave Measurement and Analysis* (ASCE), Vol. 1, pp 320-337.

Graziano, A. and Erioli, A., 2013. From shaping matter to informing matter. *In:* R. Armstrong, R. and Ferracina, S., (curators), *Unconventional Computing*.

Hall, K.R., 1999. Wave Transmission On Submerged Breakwaters Made. *Canadian Coastal Conference*, pp. 1-13.

Hayakawa, N.; Hosoyamada. T.; Yoshida, S., and Tsujimoto, G., 1998. Numerical Simulation of Wave Field around The Submerged Breakwater with SOLA-SURF Method. *Book of Abstracts of 26th International Conference of Coastal Engineering*, Copenhagen Denmark, Paper No. 78, pp. 156-157.

Herbich, J.B., 2000. *Handbook of Coastal Engineering*, McGraw-Hill, New York, USA.

Ino, K., 1974. Historical Review of Artificial Reef Activities in Japan. *Proceeding of an International Conference on Artificial Reefs*, pp. 1-23.

Kawasaki, K. and Iwata, K., 1998. Numerical Analysis of Wave Breaking Due to Submerged Breakwater in Three Dimensional Wave Field. *Book of Abstracts of the 26th International Conference of Coastal Engineering,* Copenhagen, Denmark, Paper No. 79, pp. 158- 159.

Mansard, E.P.D. and Funke, E. R., 1980. The measurement of Incident and Reflected Spectra Using a Least Squares Method.*Proceedingsof 17th International Conference on Coastal Engineering*, pp. 154-172.

McGurrin, J.M. and Reeff, M.J., 1986. Artificial Reef Development and Deployment. *Marine Technology Society Journal*, 20(3), 3-9.

Saito, M.; Watanuki, A.; Nishigori, W. and Hanzawa, M., 2002. Stability of New Type Submerged Breakwater and Its Effect on Ecosystem. *Proceedings of the 28th International Conference on Coastal Engineering*, Cardiff, Wales, UK, poster paper No 33.

Seabrook, S.R., 1997. *Investigation of the Performance of Submerged Breakwaters*. Master Thesis, Queens University, Kingston, Ontario, Canada.

Seabrook, S.R. and Hall, K.R., 1998. Wave transmission at submerged rubble mound breakwaters. *Proceedings 26th International Conference on Coastal Engineering*, ASCE, pp. 2000-2013.

Stone, R.B., 1985. History of Artificial Reef Use in the United States. *In:* D'itri, F.M., (ed), *Artificial Reefs: Marine and Freshwater Applications.* Lewis Publishers. Inc., 2nd ed., pp. 3-9.

Tsujimoto, G.; Kakuno, S.; Shigematsu, T.; Kurata, K., and Hosoyamada, T., 1999. Numerical Simulation of Turbulent Flows around a New Type of Reef Breakwater with Perforations by the k-ε Turbulence Model. *Coastal Structures '99* (Abstract), pp. 158-159.

Seabrook, S. and Hall, K., 1998. Wave Transmission at Submerged Rubblemound Breakwaters. *Coastal Engineering Proceedings*, pp. 2000-2013.

Van der Meer, 1990. *Rock slopes and gravel beaches under wave attack*. PhD Thesis Delft University of Technology, Delft Hydraulics publication No. 396.

Van der Meer, 1990. Stability of Low-Crested and Reef Breakwaters. *Proceedings of the 22th International Conference on Coastal Engineering* (ASCE), pp. 1375- 1388.

Journal of Coastal Research	SI	75	856-860	Coconut Creek, Florida	2016

Effects of Gravity Waves on Turbulence and Processes That Contribute to Mixing at a Submarine Groundwater Discharge

Gabriel Gallegos D. B. †*, Ismael Mariño-Tapia †, and Arnoldo Valle Levinson ††

†Laboratorio de Procesos Costeros y Oceanografía Física
Departamento de Recursos del Mar
Centro de Investigación y Estudios Avanzados del I.P.N.
Mérida, México

††Coastal and Civil Engineering
Department, University of Florida,
Gainesville, Florida, USA.

www.cerf-jcr.org

www.JCRonline.org

ABSTRACT

Gallegos, G.; Mariño-Tapia, I., and Valle-Levinson, A., 2016. Effects of gravity waves on turbulence and processes that contribute to mixing at a submarine groundwater discharge. *In:* Vila-Concejo, A.; Bruce, E.; Kennedy, D.M., and McCarroll, R.J. (eds.), *Proceedings of the 14th International Coastal Symposium* (Sydney, Australia). *Journal of Coastal Research*, Special Issue, No. 75, pp. 856-860. Coconut Creek (Florida), ISSN 0749-0208.

Submarine ground water discharges (SGD) around the coasts of the Yucatán Península are very common due to the karstic origin of the rocks, and the abundant rain. These discharges of brackish water into the coastal sea are strong enough to alter the thermohaline conditions, they can be preferential routes for salt intrusion, and also represent an important input of nutrients and pollutants. The mixing on these SGDs is a spontaneous and turbulent process, and its study is important for the understanding of dispersion of materials in regions influenced by these features. A set of measurements with two acoustic Doppler velocimeters (Nortek-Vector) were done in a very active SGD in the coast of Quintana Roo, Mexico. The first instrument was installed in the entrance of the cave and the other one ~2m above, both sampling at 64 Hz. Consistent with previous studies, results show that sea level variability (waves and tides) dominates the flow and the turbulence levels. When the spring is inactive wave frequencies (short 0.1 Hz, and 0.03 Hz long waves) have a clear peak in η and w, but when the spring is active, turbulence (Kolmogorov law) permeates to short wave frequencies, and IG frequencies diminish in η, but bulge in w at lower frequencies (0.01 Hz). Numerical modelling with Open Foam suggests that the shift in IG frequency could be driven by the spring geometry (depth and cave size) rather than forced by the incident waves.

ADDITIONAL INDEX WORDS: *Infragravity driven mixing, turbulent flow modeling, wave set up.*

INTRODUCTION

Wave propagation all over the ocean has been a widely studied topic in ocean science. In deep waters it is generally accepted that waves transfer energy and there is almost no mass transport. There are many assumptions in the way the wind generated waves are conceptualized, like the orbital motion of particles in a wave is irrotational,

$$\frac{\partial u}{\partial z} = \frac{\partial w}{\partial x}$$

Even though the principal theories consider the velocity field as irrotational, and therefore vorticity (and turbulence) would be suppressed, there are some authors that suggests there is a threshold of critical Reynolds number that enhances the change from laminar flux to a turbulent one, this value is around Re_{cr}=2000 (Babanin, 2006) . This turbulence is only due to non breaking surface waves.

Further experiments have been made to support the idea of turbulence generated by non breaking surface waves (Babanin, 2009). These experiments were done under controlled conditions in a wave tank, where the only forcing agent was mechanically generated waves. Results show that in fact there is turbulence production under non-breaking surface waves since there is a good correspondence in the velocity spectra and the Kolmogorov power law $k^{-5/3}$.

Other experiments show the contribution of non breaking waves to vertical mixing (Dai *et.al*, 2010). Again the only forcing agent is mechanically generated waves in a flume, but in this case they propagate in a thermally stratified media, The results show that when no waves are present, thermal destratification can take about 20 hours, and molecular diffusion is not enough to break entirely the stratified conditions, but under non-breaking waves, the stratified wave tank is mixed in the order of minutes. This study shows that the strength of mixing is an inverse function of the wave amplitude and wave length. These results imply that waves at infragravity frequencies would be the most important for the mixing processes in coastal zones.

The aim of this work is to distinguish the contribution of non-breaking waves at short and infragravity frequencies to the turbulent energy observed at the entrance of a submarine spring (SGD) with the use of *in situ* observations and numerical modeling. It is known that the SGD dynamics are dominated by the pressure gradient between the inland piezometric level and the sea surface elevation, so the input of water from land to sea will be modulated mainly by the tides (Valle-Levinson *et al*., 2011). TKE has also been observed to depend mainly on sea

DOI: 10.2112/SI75-172.1 received 15 October 2015; accepted in revision 15 January 2016.
*Corresponding author: malhaya@gmail.com
©Coastal Education and Research Foundation, Inc. 2016

level with a non-negligible contribution of wave set up in reef lagoons (Parra *et al*., 2014). Jet temperatures and salinities display semidiurnal oscillations with minimum salinity and temperature values during maximum discharge. Therefore, the outflow of less dense SGD water will have an important buoyant force that contributes to turbulence.

METHODS

The site of study, Puerto Morelos, is located in the northeast region of the Yucatan Peninsula, 30 km south of Cancun. It is part of the Mesoamerican Reef, the second largest reef coral barrier in the world.

This lagoon has ~4km longshore length and a varying width that goes from ~500m to ~1500m. The average depth inside the lagoon is ~ 5m. The circulation of the lagoon is dominated by wave induced flow (Coronado *et al*., 2007; Mariño-Tapia, *et al.*, 2010). Inside the lagoon there are several submarine groundwater discharges (Figure 1), but the SGD that is analyzed in this work is known as Pargos, situated at ~500 m from the shoreline (pointed with the black arrow). This spring is part of a complex cave system that runs under the seafloor and carries important amounts of recirculated water. The entrance of the cave is at 6m depth and the surrounding seabed is about ~4m depth. Figure 1 shows the bathymetry map and the location of several SGDs.

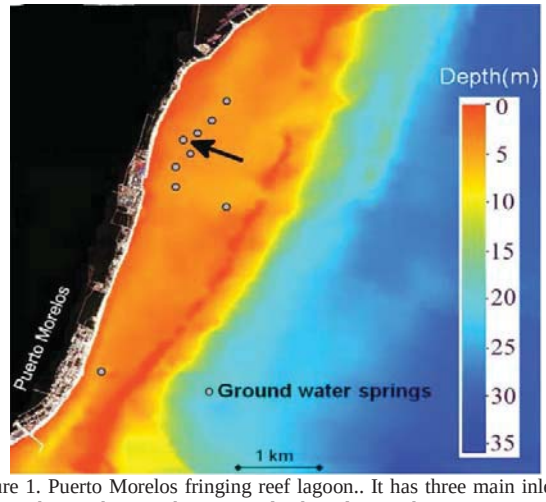

Figure 1. Puerto Morelos fringing reef lagoon.. It has three main inlets. One at the south it is about 10m depth and it works as a navigation channel. The other two inlets are gaps in the coral wall

Data Collection

Two acoustic Doppler velocimeters (ADV, Vector-Nortek) were moored at the spring (Figure 2). ADV1 was deployed at the very cave entrance, at the base of a small vertical drop in the bathymetry (~6m depth), and ADV2 was installed at the lagoon bed level (~4m depth). Both instruments were programmed to sample at 64Hz, in bursts of 10 minutes every 30 minutes. This deployment was designed to detect the vertical difference in the evolution of turbulence and the transference/dissipation of energy in the water column. The sampling period was from 21 March to 2 April 2014.

The detailed bathymetry on the vicinity of the spring was performed with an ADCP (Sontek-M5) with bottom tracking capability. The instrument was installed in a catamaran and synchronized with a Differential GPS (Leica-Geosystems), to have an accurate position (x,y,z) of the sea floor and the capability of filtering sea surface noise with an adequate post processing routine

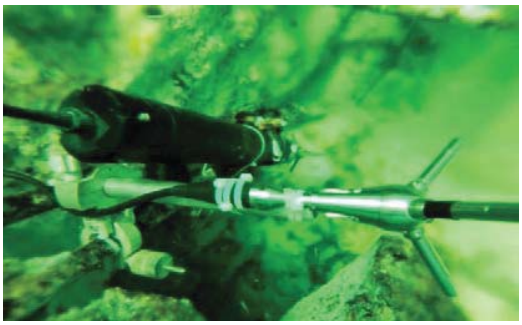

Figure 2. Photo of the moored ADVs. In the bottom is the ADV1 located at the mouth of the cave. Above is the ADV2 located at the surrounding lagoon bed level.

RESULTS

Spring dynamics are dominated by sea level variability, which include the astronomical tidal signal and the wave-driven set up. Even though Puerto Morelos is a place of micro tidal ranges, a variation of a few centimeters ~0.17m is enough to reverse the flow in the springs, this is indicated in a time series of ADV1 (Figure 3).

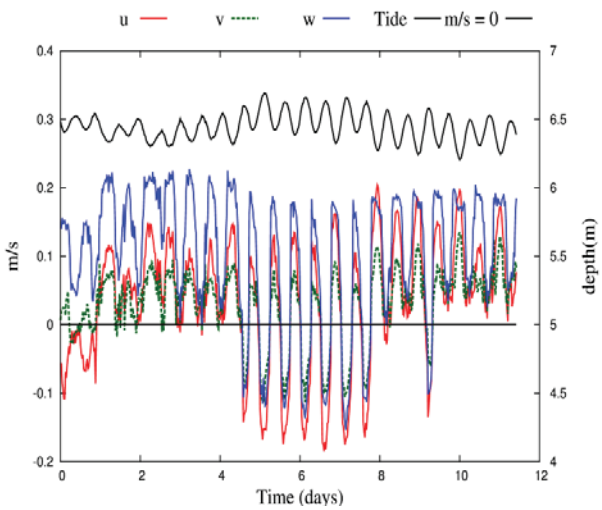

Figure 3. .Medium term (O[days]) behavior of the outflow and sea level measured at ADV1. This figure shows the three components of velocity u(cross-jet red), v(along-jet green), w(vertical blue), which are inversely proportional to the sea level (black).m).

Valle-Levinson *et al*. (2011) suggested that the dynamics of the water spring is dominated by the pressure gradient between the aquifer and the sea level, the later being the most dynamic part. The sea level inside the lagoon is mainly governed by tides, and wave set up has been detected to have also a significant contribution (Franklin *et al.*, 2013; Mariño *et al*., 2010; Parra *et al*., 2014). Figure 4 shows the contribution of waves to the sea level fluctuations, where wave set up (blue dotted line) can contribute significantly to the sea level fluctuation. On the other hand, the presence of infragravity energy (red line) is also notorious when wave climate is more energetic. This infragravity waves ought to be important in the mixing processes.

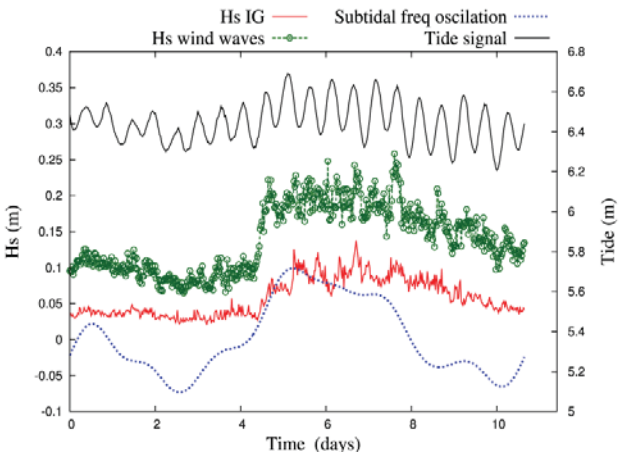

Figure 4. Measured sea level (black), Hs of incident waves (green) and IG waves (red). The low frequency sea level variation is shown in blue (sub tidal frequencies).

Waves contribution to turbulence.

It is known that turbulent energy dissipation would have to obey the $k^{-5/3}$ Kolmogorov law, therefore power spectral analysis for each ADV data set was performed to look for such behavior in the spectra of the vertical velocity (w) for each burst. The rate of energy transferred from great eddies to smaller ones in the inertial range of a turbulent process satisfies the Kolmogorov power law $k^{-5/3}$. In order to distinguish the energy content of different wave frequencies, power spectra was also performed of the surface elevation signal (η) for each 10 minute burst. A logarithm slope of -5/3 was done to the Fourier transform of w in two different moments, i) when the SGD was active and the outflow intense (w > 0) *i.e*. buoyant forces and wave effects would co-exist; and ii) when the SGD was inactive and the outflow ceases (w ~ 0) *i.e*. only waves are acting. This analysis is shown in Figure 5.

The surface elevation spectra (F[η]) when the jet is active is very similar to F[η] when inactive (lines with markers). Both have a very clear peak at 11 seconds (0.09 Hz) and a big drop in energy at 0.5 Hz. Frequencies above 0.5 Hz show sea surface variability that could fit the -5/3 slope criteria. The main difference between F[η] is at the infragravity (IG) frequencies. When the jet is active, IG has no clear peak, and a bulge at lower frequencies (0.01 Hz) occurs. On the other hand, the vertical velocity spectra F[w] when the jet is inactive (solid red line) shows a very strong resemblance to F[η], clear peaks at 0.03 and 0.09 Hz, turbulence dissipation occurs between frequencies of 0.6 and 2.5 Hz.

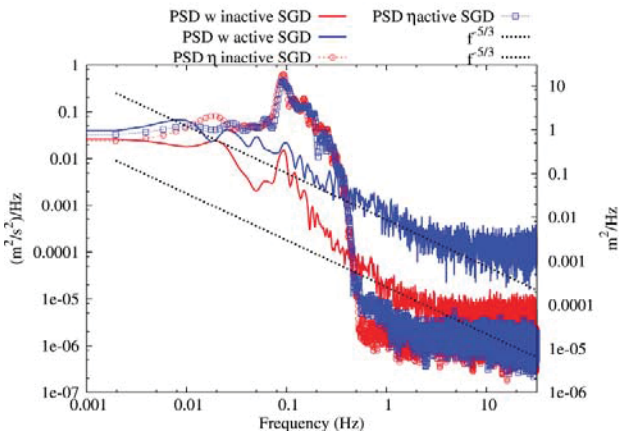

Figure 5. Power Spectral Density of surface elevations (F[η]) in dotted dash lines. Vertical velocity (F[w]) in solid lines. Two different moments are presented: active jet (blue) and inactive jet (red.) The black dashed line has a slope of -5/3 that shows the typical ratio of energy transfer of a turbulent flow according the Kolmogorov power law. The left axis shows the F[w] and the right axis the F[η].

When active, F[w] (green solid line) has a better fit to the Kolmogorov law in a larger range of frequencies, (0.1 to 2.5 Hz), including wave frequencies. This suggests that there is interaction between the outflow and the waves which behave like turbulence. Worth noting there is an increase in IG energy on F[w], which occurs at lower frequencies when the jet is inactive (0.01 Hz), and is also more notorious than the IG bulge in F[η]. The relevance of infragravity waves in mixing terms is that they should be capable of enhancing the vertical mixing even more than the short waves, since there is a inverse relation between the mixing and wave period (Dai *et al.*, 2010)

To show that this behavior is consistent in time, a cross spectra between η and w was done for all the sampling period. In Figure 6 the results are shown. Is very clear that there are high coherence values in the incident frequencies ~0.1Hz (green colors), but the for the IG frequencies the high values observed at low tides are not over the confidence limit. This happens for every single burst when the jet is active, so during those moments, the variation of w in the IG frequencies is not consistently related to surface elevation IG energy levels

Numerical Modelling with OpenFOAM

To find the origin of w oscillations in the IG band a numerical model was used. As a first approximation a bidimensional configuration was used to explore possible answers. The bathymetry measured with the M5-ADCP was used to generate the grid. Two numerical experiments are presented: a) Force the domain only with the SGD input without the density contrast. b) Add to the first case a monochromatic wave train with Hs=0.7m, T=7s, k=0.13761/m. The data acquisition was done through control points situated near the SGD with 100Hz sampling frequency for velocity and free surface. A mean velocity map of the control points is presented in Figure 7, which shows vortex structures like those found in the northern Yucatan coast with point source SGD (Valle-Levinson *et al*, 2011).

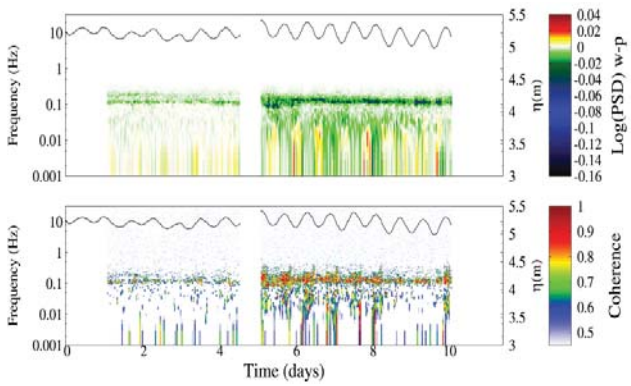

Figure 6. Cross spectra analysis F(w-η). On top is the cospectra and below is the coherence that is very poor for the IG frequencies

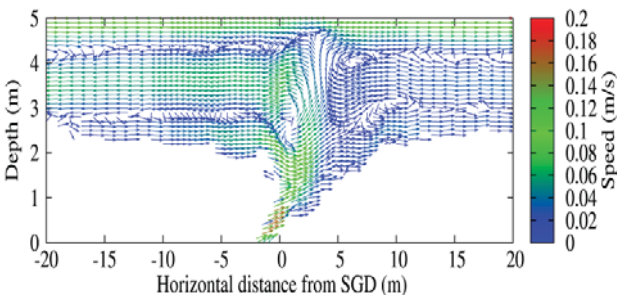

Figure 7. Mean velocity map result of a mean time of the velocity field over the control points.

Because of its nature, the turbulence is conceived as an unpredictable flow, hence comparison of modeled data could be performed in the frequency domain with Fourier transform (Figure 8). The model was run for the burst duration (10 minutes). To have certainty that the numerical model can solve turbulent flows the Kolmogorov test was made for the same position of the ADV1 deployment in the field.

As is expected F[w] is in good correspondence with the F[η]in frequency and magnitude. The Kolmogorov power law fits approximately the behavior between 0.1 and 2 Hz in similitude with the observations in the field. The occurrence of superharmonics is thought to be an artifice of feeding a monochromatic signal. Interesting to note is the existence of a bulge in IG energy of about 0.01 Hz and lower, similar to that observed in the field. It should be stressed that no IG energy forcing occurs in the model.

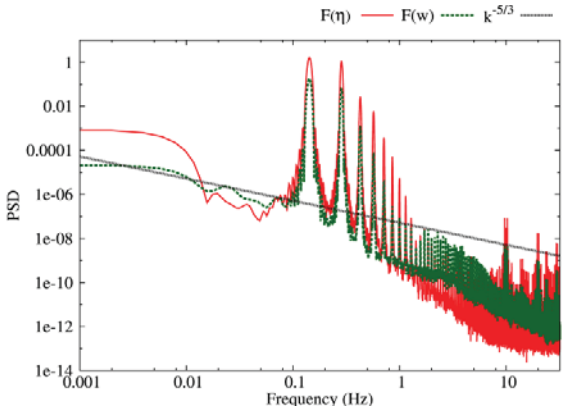

Figure 8. Fourier transform of η (red line), w' (green line) and the ratio of turbulent energy transference in black line.

DISCUSSION

The dynamics of the SGD is governed by the tide signal, but incident waves through wave set up also have a relevant influence. This is because the equilibrium between the piezometric level and the sea level is very delicate, so if the waves add an extra pressure over the SGD the outflow is stopped and flow reversal is likely. This is very clear in Figure 3 from days 4 to 8 when the mean w is negative and Hs increases.

The Kolmogorov power law establishes the transference rate of energy from great eddies to smaller ones in the inertial range. This rate is a temporal-scale transference of energy that has a -5/3 in a logarithm scale, so if F[w] fits well with this slope it is a clear proof that there are turbulent processes occurring. The SGD turbulence input can be easily differentiated from the non-breaking wave turbulence input. When the jet is active, turbulence has a much larger frequency range of inertial transfer , showing evidence of interaction with wave frequencies, and also much more energy levels than F[w] with an inactive jet, when the non-breaking waves dominate the dynamics.

When the jet is active, F[w] shows IG oscillations that do not have a correspondence in F[η] (no coherence in the cross-spectra). Since the numerical model replicates such frequency at the IG band without any direct forcing, it is hypothesized that the geometry of the jet (size of the hollow, speed of the flow and its depth) and the persistent eddy structure that is generated is responsible for such oscillation in the vertical velocity with frequencies of 0.01 Hz and below.

CONCLUSIONS

Incident wave conditions are fundamental to control the dynamics in the SGD, even to determine when a haline intrusion can happen in the aquifer system. The turbulent flow when the jet is active interacts with wave frequencies making a Kolmogorov law applicable for a larger range of frequencies. The geometry of the SGD can promote the local mixing in the water column due the recirculation cells that take place in the neighborhood of the discharge, being the likely origin of the increase in energy at infragravity frequencies, but unrelated to wave forcing, as suggested by a model forced without IG energy.

LITERATURE CITED

Babanin. A.V., 2006. On a Wave-induced turbulence and a wave-mixed upper ocean layer. G*eophysical Research Letters*, 33(20), L20605

Babanin, A.V. and Haus, B.K., 2009. On the Existence of water Turbulence Induced by Non-breaking Surface Waves. *Journal of Physical Oceanography*, 39(10), 2675-2679.

Coronado, C.; Candela, J., Iglesias-Prieto, R., Sheinbaum J., Lopez, M., and Ocampo-Torres, F.J., 2007. On the circulation in the Puerto Morelos fringing reef lagoon. *Coral Reefs*, 26(1), 149-163.

Dai, D., Qiao, F., Sulisz, W.; Han, L., and Babanin, A.V., 2010. An experiment on the Non Breaking Surface-Wave-Induced Vertical Mixing. *Journal of Physical Oceanography*, 40(9), 2180-2188.

Franklin, G.; Mariño-Tapia, I., and Torres-Freyermuth, A., 2013. Effects of reef roughness on wave setup and surf zone currents. *Journal of Coastal Research*, Special Issue No. 65, pp. 2005-2010.

Mariño Tapia, I.; Silva, R.; Enriquez, C.; Mendoza-Baldwin, E,; Escalante Mancera, E., and Ruiz Rentería, F., 2010. Wave Transformation and Wave-Driven Circulation on Natural Reefs Under Extreme Hurricane Conditions. *Proceedings of the ICCE Conference*, (Shangai, China). 1(32).

Parra, S. M.; Mariño-Tapia, I.; Enriquez, C., and Valle-Levinson, A., 2014. Variations in turbulent kinetic energy at a point source submarine groundwater discharge in a reef lagoon. *Ocean Dynamics*, 64(11), 1601-1614.

Valle-Levinson, A.; Mariño-Tapia, I.; Enriquez, C., and Waterhouse, A.F., 2011. Tidal variability of salinity and velocity fields related to intense point-source submarine groundwater discharges into the coastal ocean. *Limnology and Oceanography*, 56(4), 1213-1224.

Journal of Coastal Research	SI	75	861-866	Coconut Creek, Florida	2016

Theoretical and Observed Breaking Wave Height on a Barred Macrotidal Beach: Implications for Estimation of Breaker Index

Arnaud Héquette[†*] and Adrien Cartier[‡]

[†]Laboratoire d'Océanologie et de Géosciences, UMR CNRS 8187
Université du Littoral Côte d'Opale
Wimereux, France

[‡]GEODUNES
Dunkirk, France

www.cerf-jcr.org

www.JCRonline.org

ABSTRACT

Héquette, A. and Cartier, A., 2016. Theoretical and observed breaking wave height on a barred macrotidal beach: implications for the estimation of breaker index on beaches with large tidal range. *In:* Vila-Concejo, A.; Bruce, E.; Kennedy, D.M., and McCarroll, R.J. (eds.), *Proceedings of the 14th International Coastal Symposium* (Sydney, Australia). *Journal of Coastal Research*, Special Issue, No. 75, pp. 861-866. Coconut Creek (Florida), ISSN 0749-0208.

Although a large number of studies were dedicated to the observation and prediction of wave height at breaking, field investigations were essentially carried out in micro- to mesotidal environments. Here we report the results of a study conducted on a barred macrotidal beach of northern France during which video observations of wave breaking were carried out simultaneously with measurements of wave data using a series of hydrodynamic instruments deployed across the intertidal and the nearshore zones and an offshore wave buoy. Our results show that waves were breaking when the ratio of wave height to depth (H_b/h_b) was comprised between approximately 0.2 to 0.45, the lower value being slightly lower than what is commonly reported in the literature for macrotidal beaches. Comparison of measured and calculated wave height at breaking using a series of predictive equations revealed that the Rattanapitikon *et al.* (2003) formula gave the best results for our data set. Predicted breaker heights were nevertheless overestimated when using offshore wave measurements and better results were obtained with wave data recorded in 5 m water depth instead. This can be explained by the presence of offshore tidal sand banks that are responsible for significant wave refraction and wave energy dissipation. These results contribute to determine more precisely the range of appropriate breaker index values for barred macrotidal beaches and highlight that nearshore wave parameters should be used rather than offshore wave statistics for predicting breaking wave height and breaking depth where sand banks strongly alter wave characteristics.

ADDITIONAL INDEX WORDS: *Breaker height prediction, macrotidal beach, coastal hydrodynamics.*

INTRODUCTION

Wave metrics are essential parameters in a wide range of theoretical as well as applied studies dealing with the hydrodynamics and morphodynamics of the coastal zone. If deep-water wave statistics can commonly be obtained from offshore buoy measurements, wave characteristics in the nearshore zone are generally seldom available due to the paucity of *in situ* wave measurements in the shallow depths of the coastal zone. Nevertheless, breaking wave parameters such as significant breaker height (H_{sb}) or ratio of breaking wave height to breaker depth (H_b/h_b), also known as beaker index (γ_b), are required in most coastal sediment transport and morphodynamic models, but also for the design of coastal structures and other coastal engineering applications. This can explain why so much effort was dedicated for years for trying to predict breaking wave height and breaking depth. These investigations resulted in the development of a significant number of predictive equations based on laboratory experiments or on field measurements using deep-water and breaking wave observations (e.g., Le Mehaute and Koh, 1967; Kamphuis, 1991; Komar and Gaughan, 1972; Rattanapitikon and Shibayama, 2006).

The reliability of these empirical or semi-empirical equations for accurately predicting breaking wave parameters is extremely variable (Camenen and Larson, 2007; Robertson *et al*., 2013) and seems to depend on several site-specific characteristics (beach and/or surf zone slope, grain-size, bedforms,…) and wave characteristics (regular or irregular waves, initial deep-water wave steepness,..), as well as wind and tidal currents that may also interact with breaking wave processes.

Most of the studies aimed at predicting breaking wave height and breaking depth were conducted under microtidal or stable, laboratory-controlled, water level conditions. Although the prediction of breaking parameters is a complex task when mean water level changes are limited, it is even more complex in macrotidal environments where large vertical tidal fluctuations induce significant horizontal translations of the different hydrodynamic zones (shoaling, breaker and surf zones) across the bar-trough topography of the nearshore and intertidal zones (Levoy *et al*., 2001). In comparison with micro- to mesotidal coastal settings, investigations aiming at determining the height and depth at which waves break on macrotidal beaches are extremely limited. The objective of this paper is to present the results of a study conducted on the macrotidal coast of Northern France during which wave height and water depth at breaking were measured. *In situ* measured wave breaker heights were

DOI: 10.2112/SI75-173.1 received 15 October 2015; accepted in revision 15 January 2016.
*Corresponding author: arnaud.hequette@univ-littoral.fr
©Coastal Education and Research Foundation, Inc. 2016

compared with theoretical breaker heights calculated from several predictive equations using offshore and nearshore wave data.

The field measurements were carried out on a low-gradient (tanβ = 0.019) barred beach located at Zuydcoote near the Belgium border, facing the North Sea (Figure 1). The beach is composed of fine sand (mean grain-size: 0.2 mm) and comprises a series of 4 to 5 shore-parallel intertidal bars ranging from about 0.8 to 1.1 m high and 50 to 90 m wide (Figure 1B). Mean tide at Zuydcoote is approximately 4.5 m, but the tidal range exceeds 5.5 m during spring tides. This high tidal range is responsible for relatively strong tidal currents that flow parallel to the shoreline in the coastal zone, the ebb being directed westward and the flood eastward. Current measurements conducted in previous studies show that the speeds of flood currents exceed those of the ebb, resulting in a flood-dominated asymmetry responsible for a net regional sediment transport to the east-northeast (Héquette *et al*., 2008).

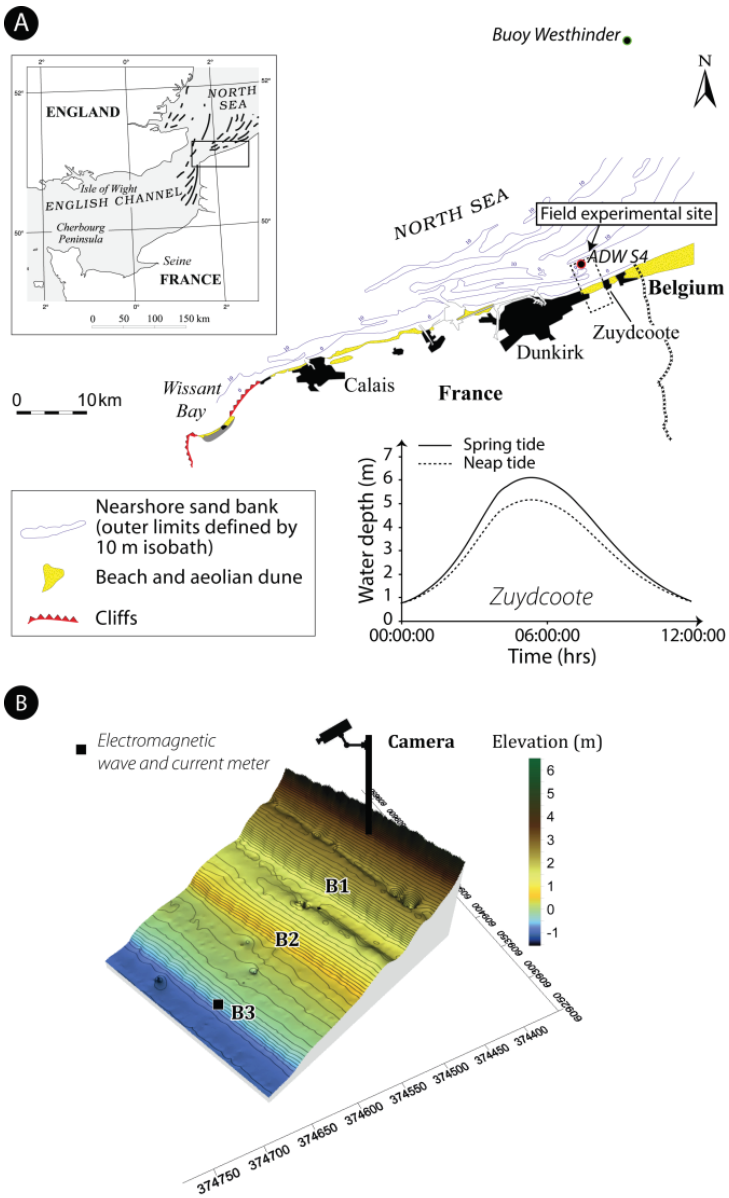

Figure 1. Location of (A) study area and (B) field experimental site.

The region is dominated by waves from southwest to west, originating from the English Channel, followed by waves from the northeast to north, generated in the North Sea. The presence of several sand banks on the shoreface and the inner shelf and the gentle beach slopes that characterize the coast of Northern France are responsible for strong wave energy dissipation, resulting in modal significant wave heights lower than 0.6 m in the intertidal zone (Héquette *et al*., 2009). Wave heights can nevertheless exceed 1.5 m on the foreshore during extreme events.

METHODS

Wave parameters were measured at different locations from the beach to the offshore zone from 2 to 9 June 2013. A Midas Valeport electromagnetic wave and current meter was deployed on the stoss side of an intertidal bar on the lower beach (bar B3, Figure 1B) in order to record breaking waves at mid-tide or higher. An InterOcean ADW S4 wave and current meter was moored in the subtidal zone (Figure 1A) in water depth of -5 m below Hydrographic Datum (*i.e*., approximately lowest astronomical tide level). Both instruments operated during 9 minutes intervals every 15 minutes at a frequency of 2 Hz. The duration of each burst of hydrodynamic measurements was chosen as a compromise between two opposite constraints. It had to be long enough to allow wave spectral analysis, but it also had to be short enough to respect stationary conditions as water depth is continuously changing over a tidal cycle on macrotidal beaches. Wave characteristics were obtained by spectral analysis, providing almost continuous records of significant wave height (Hs), wave period (T) and direction. Offshore wave data were also obtained from an offshore wave buoy (Westhinder) in 27 m water depth, approximately 36 km seaward of the Belgian coast (Figure 1A), providing significant wave height and wave period every 30 minutes.

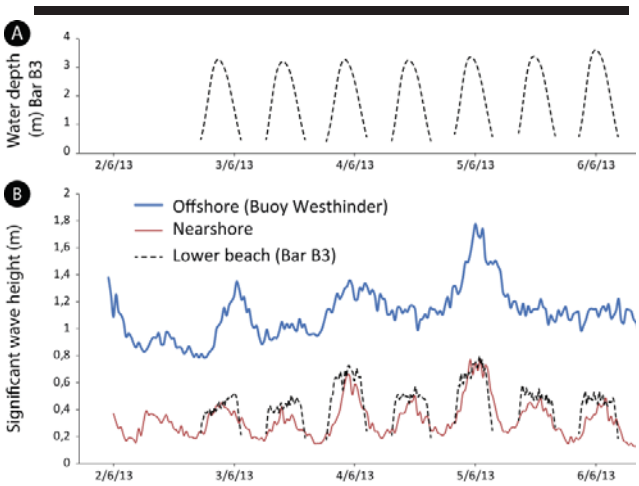

Figure 2. Time-series of (A) water depth on the lower beach and of (B) significant wave height recorded at different water depths from 2 to 9 June 2013 (see Figure 1 for location of the instruments)

resulted in a delay generally comprised between 1.0 to 1.5 hours between deep-water and nearshore/beach wave measurements.

During each day of the field experiment, beach morphology was surveyed at low tide using a very high resolution Differential Global Positioning System (Leica TPS Syst1200)

A video camera was installed in the backshore at an elevation of 10 m above the mean tide level and was programmed for recording a photograph of the beach and nearshore zone every 10 seconds. Series of 60 consecutive photographs were used for producing mean images of the coastal zone that were used for distinguishing the shoaling, breaking and surf zones during each burst of hydrodynamic measurements realized during day time (Figure 2). This enabled to determine what wave processes (shoaling, breaking or surf) were occurring near each hydrographic instrument during each measurement period. These observations allowed the calculation of a breaker index (H_b/h_b) when waves were observed to break over an instrument, using the breaking wave height (H_{bm}) and water depth (h_{bm}) measured by the instrument.

The *in situ* measured breaking wave heights (H_{bm}) were compared with calculated breaker heights (H_{bc}) according to different predictive equations developed from laboratory experiments and field data for regular and irregular waves (Goda, 2010; Kamphuis, 1991; Komar and Gaughan, 1972; Le Mehaute and Koh, 1967; Smith and Kraus, 1991; Rattanapitikon *et al*., 2003; Rattanapitikon and Shibayama, 2006; Van Dorn, 1978) applicable for the environmental conditions observed at the experimental site, notably beach slope and offshore wave steepness. Because the deep-water wave data were measured at a distance of about 36 km offshore, the wave travel time between the offshore wave buoy and the surveyed beach was estimated based on wave celerity incrementally computed for decreasing water depths according to linear wave theory. These calculations with vertical and horizontal accuracy of +/- 2.5 cm and +/- 1.5 cm respectively, allowing the determination of the beach slope seaward of the break point shortly before or after the breaking wave height measurements. The beach/nearshore slope was calculated for each wave breaking measurement down to the daily low-water line and was extended to a water depth of -5 m using available bathymetry data in order to consider a sufficiently long nearshore profile since it has been shown that the length of the effective seafloor slope over which waves undergo shoaling transformations and eventually breaking is of major importance for predicting breaking wave height (Robertson *et al*., 2015).

RESULTS

Deepwater significant wave height ranged from approximately 0.85 m to 2.0 m during the field experiment (Figure 2B). Wave heights were considerably lower in the intertidal and nearshore zones, however, due to significant refraction and energy dissipation of the incident waves originating from the NNE to NE that propagated over the offshore sand banks and gently sloping inner shelf of the southern North Sea. Our measurements also show that significant wave height is strongly modulated by water depth in the coastal zone, the higher wave heights being always recorded at high tide while much lower wave heights were observed during the rising or falling tide (Figure 2A & 2B), this dependence of wave height on water depth having been commonly observed in previous studies conducted on beach

hydrodynamics in the region (Anthony *et al*., 2004; Héquette *et al*., 2009).

Wave height/depth ratio measured on the lower beach (H_{lb}/h_{lb}) were compared with nearshore wave steepness (H_n/L_n) calculated from wave data, where H_n is the nearshore significant wave height recorded in 5 m water depth and L_n is the computed nearshore wave length at the same depth according to linear wave theory (Figure 3). Our results indicate that the highest H_{lb}/h_{lb} values, which correspond to breaking to surf zone conditions (as determined from video imagery), are associated with low H_n/L_n values, showing that low nearshore wave steepness allows waves to break in shallower water. In comparison, lower ratios of breaking wave height to water depth (H_{lb}/h_{lb}), corresponding to waves breaking in deeper water (for a given wave height), tend to be associated with higher wave steepness values although a relatively wide range of H_n/L_n values is observed, which can be explained by tidal water level hanges that partly control wave steepness in the nearshore zone.

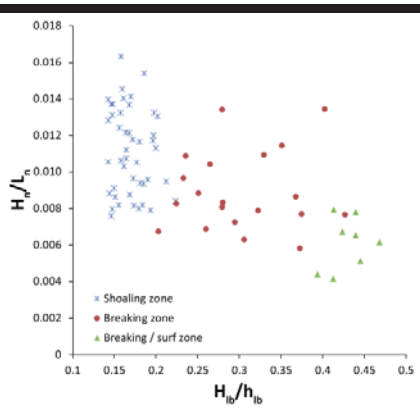

Figure 3. Relationship between nearshore wave steepness (H_n/L_n) measured in 5 m water depth and wave height to depth ratio (H_{lb}/h_{lb}) measured on bar B3 on the lower beach (see Figure 1 for location). The distinction between shoaling, breaking and surf zones is based on visual determination from video images.

A broad range of H_n/L_n values is also observed for shoaling conditions, but only with low H_{lb}/h_{lb} values (<0.22) as water depth is always large compared to wave height in the shoaling zone.

Measured breaking wave heights were compared with theoretical breaker heights calculated from several predictive equations using deep-water wave characteristics (Komar and Gaughan, 1972; Van Dorn, 1978), notably wave steepness, and beach/surf zone slope (Goda, 2010; Kamphuis, 1991; Le Mehaute and Koh, 1967; Rattanapitikon *et al*., 2003; Rattanapitikon and Shibayama, 2006; Smith and Kraus, 1991). All equations overestimate breaking wave height, but the results given by the equations of Kamphuis (1991), Smith and Kraus (1991), Rattanapitikon *et al.* (2003) and Goda (2010) show a better fit between calculated and measured values as shown by linear regression coefficients ($R^2 \geq 0.78$) (Figure 4).

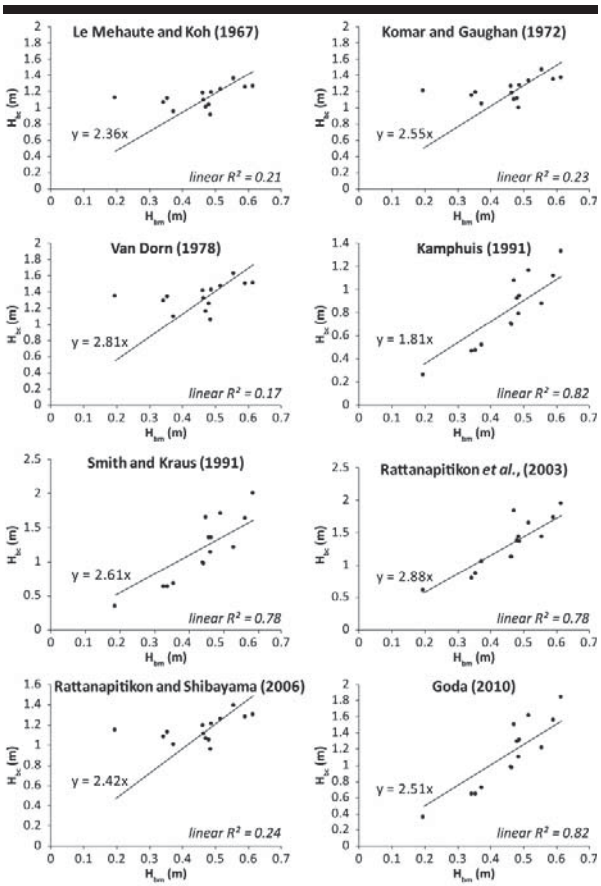

Figure 4. Comparison between measured (H_{bm}) and calculated breaking wave heights (H_{bc}) using various predictive equations.

It is noteworthy that these four equations, which gave more satisfactory results, are the only ones among the tested predictive formulas of breaker height that require some breaking parameter such as water depth at breaking or breaking wave length. These results suggest that predictive formulas of breaker heights using only offshore wave characteristics are not appropriate for estimating breaking wave height on the studied beach. In order to try to improve the results provided by these four equations, deep-water wave data were substituted by nearshore wave data measured in 5 m water depth. The use of nearshore wave data rather than offshore wave measurements lead to similar results with the Kamphuis (1991) and Goda (2010) equations (Table 1). In the case of the Smith and Kraus (1991) equation, a slightly better linear relationship between measured and predicted wave heights is obtained, but the overestimation of wave height is increased further. Results are significantly improved, however, when nearshore wave data are used with the Rattanapitikon *et al*. (2003) formula, the overestimation of breaking wave height decreasing from a factor of about 2.9 to approximately 1.7 with a best fit linear regression coefficient increasing from 0.78 to 0.86 (Figure 5).

Table 1. *Regression fit values for measured and calculated wave heights using different predictive equations.*

Equation	Offshore wave data		Nearshore wave data	
	$y=ax$	Linear R^2	$y=ax$	Linear R^2
Kamphuis (1991)	1.81	0.82	1.81	0.78
Smith and Kraus (1991)	2.61	0.78	2.93	0.75
Rattanapitikon *et al*. (2003)	2.88	0.78	1.72	0.86
Goda (2010)	2.51	0.82	2.62	0.78

The changes induced by the use of nearshore wave data in the equations of Kamphuis (1991), Smith and Kraus (1991) and Goda (2010) mainly result from the use of breaking wavelength instead of deep-water wavelength. Because only moderate variations were observed between deep-water and nearshore wavelengths (calculated from the wave periods measured in 5 m water depth), only minor differences were obtained between breaker height values computed with offshore or with nearshore wave data. In contrast, the Rattanapitikon *et al*. (2003) equation also includes a wavelength at breaking, which is always considerably shorter than the deep-water wavelength, which explains the significant decrease in calculated breaker heights.

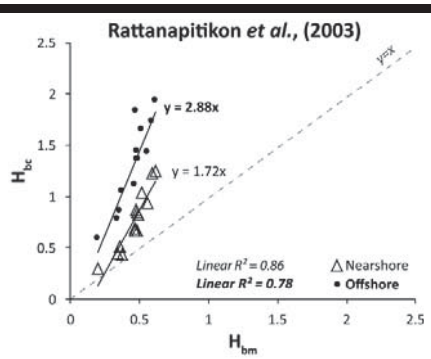

Figure 5. Comparison between measured (H_{bm}) and calculated breaking wave heights (H_{bc}) according to Rattanapitikon *et al*. (2003) predictive equation using offshore (27 m water depth) and nearshore (5 m water depth) wave data.

DISCUSSION

All the tested equations overestimate breaker heights. These differences between measured and predicted wave heights can probably be partly explained by strong wave energy dissipation during their propagation over the shallow sand banks on the gently sloping inner shelf and shoreface of the southern North Sea (Figure 1), resulting in a significant reduction in wave height at the coast (Figure 2). Nevertheless, better relationships between predicted and measured breaker heights were obtained with the equations of Kamphuis (1991), Smith and Kraus (1991), Rattanapitikon *et al*. (2003) and Goda (2010), which include some wave parameter at breaking. Our results also showed that the use of nearshore wave data instead of deep-water wave data can significantly improve breaker height prediction, notably when using the Rattanapitikon *et al*. (2003) equation in which a wavelength at breaking is considered, which can be explained by a change in wave period between the offshore and the nearshore zone. All these results suggest that breaker height can not be accurately estimated when using only deep-water wave data where waves propagate over a complex and dissipative shelf and coastal bathymetry responsible for a significant decrease in wave height.

The equations of Kamphuis (1991), Smith and Kraus (1991), Rattanapitikon *et al*. (2003) and Goda (2010), which gave better results than the other tested equations, all include the seafloor slope as an input parameter, suggesting that it represents an important factor for the prediction of breaking wave heights in the study area. These results are consistent with previous investigations that showed that the beach and nearshore slope represents an important parameter to consider for predicting breaking wave height (*e.g.*, Camenen and Larson, 2007; Robertson *et al*., 2015), which is presumably critical over highly dissipative, low-sloping, macrotidal beaches. Tidal currents may represent an additional factor influencing breaking wave processes in such environments.

Another factor that may explain some of the discrepancies between measured and predicted wave heights may also be due to the use of predictive equations that are based on regular wave tests which makes direct comparison difficult with irregular waves (Robertson *et al*., 2015). Some of the observed differences may also be related to the fact that calculated breaker heights correspond to a value at the breakpoint while our measurements of breaking wave height correspond to wave heights in the breaker zone, which can be slightly different.

CONCLUSIONS

Our results show that predictive equations based on deep-water wave characteristics overestimate breaking wave height on the studied beach. This can probably be explained by the presence of offshore sand banks and low-sloping inner shelf and shoreface that are responsible for significant wave refraction and wave energy dissipation. Our measurements also contribute to determine more precisely the range of appropriate breaker index values for barred macrotidal beaches and highlight that nearshore wave parameters should be used rather than offshore wave statistics for predicting breaking wave height and breaking depth where complex offshore and nearshore bathymetries strongly alter wave characteristics.

ACKNOWLEDGMENTS

This study was partly funded by the French *Centre National de la Recherche Scientifique* (CNRS) through operating funds to the *Laboratoire d'Océanologie et de Géosciences.* Offshore wave data recorded at the Westhinder buoy were kindly provided by the Flanders Marine Institute (VLIZ). The authors would like to thank all the personnel who participated in the field experiment for their help and technical assistance. Thanks are also due to D. Marin for drafting of the figures.

LITERATURE CITED

Anthony, E.J.; Levoy, F., and Montfort, O., 2004. Morphodynamics of intertidal bars on a megatidal beach,

Merlimont, Northern France. *Marine Geology*, 208(1), 73-100.

Camenen, B. and Larson, M., 2007. Predictive formulas for breaking depth index and breaker type. *Journal of Coastal Research*, 23(4), 1028-1041.

Goda, Y., 2010. Reanalysis of regular and random breaking wave statistics. *Coastal Engineering Journal*, 52(1), 71-106.

Héquette, A.; Hemdane, Y., and Anthony, E.J., 2008. Sediment transport under wave and current combined flows on a tide-dominated shoreface, northern coast of France. *Marine Geology*, 249(3-4), 226-242.

Héquette, A.; Ruz, M.H.; Maspataud, A., and Sipka, V., 2009. Effects of nearshore sand bank and associated channel on beach hydrodynamics : implications for beach and shoreline evolution. *Journal of Coastal Research*, SI 56, 59-63.

Kamphuis, J.W., 1991. Incipient wave breaking. *Coastal Engineering*, 15(3), 185-203.

Komar, P.D. and Gaughan, M.K., 1972. Airy wave theory and breaker height prediction. *Proc. 13th Conf. Coastal Engineering*, Vancouver, Canada, pp. 405-418.

Le Mehaute, B. and Koh, R.C., 1967. On the breaking of waves arriving at an angle to the shore. *Journal of Hydraulic Research*, 5(1), 67-88.

Levoy, F.; Monfort, O., and Larsonneur, C., 2001. Hydrodynamic variability on megatidal beaches, Normandy, France. *Continental Shelf Research*, 21(6-7), 563-586.

Rattanapitikon, W.; Vivattanasirak, T, and Shibayama, T., 2003. A proposal of new breaker height formula. *Coastal Engineering Journal*, 45(1), 29-48.

Rattanapitikon, W. and Shibayama, T., 2006. Breaking wave formulas for breaking depth and orbital to phase velocity ratio. *Coastal Engineering Journal*, 48(4), 395-416.

Robertson, B.; Hall, K.; Zytner, R., and Nistor, I., 2013. Breaking waves: Review of characteristic relationships. *Coastal Engineering Journal*, 55(1), 1-40.

Robertson, B.; Hall, K.; Nistor, K.; Zytner, R., and Storlazzi, C., 2015. Remote sensing of irregular breaking wave parameters in field conditions. *Journal of Coastal Research*, 31(2), 348-363.

Smith, E.R. and Kraus, N.C., 1991. Laboratory study of wave breaking over bars and artificial reefs. *Journal of Waterway, Port, Coastal, and Ocean Engineering*, 117(4), 307-325.

Van Dorn, W.G., 1978. Breaking invariants in shoaling waves. *Journal of Geophysical Research*, 83(C6), 2981-2988.

Journal of Coastal Research	SI	75	867-871	Coconut Creek, Florida	2016

Variability of Benthic Communities in Relation to Hydrodynamic Conditions in the North-Eastern Baltic Sea

Kristjan Herkül [†*], Kaire Torn[†], Ülo Suursaar[†], Victor Alari[‡], and Anneliis Peterson[†]

[†]Estonian Marine Institute,University of Tartu, Tallinn, Estonia

[‡] Helmholtz-Zentrum Geesthacht, Institute of Coastal Research, Geesthacht, Germany

www.cerf-jcr.org

www.JCRonline.org

ABSTRACT

Herkül, K.; Torn, K.; Suursaar, Ü.; Alari, V., and Peterson, A., 2016. Variability of benthic communities in relation to hydrodynamic conditions in the north-eastern Baltic Sea. *In:* Vila-Concejo, A.; Bruce, E.; Kennedy, D.M., and McCarroll, R.J. (eds.), *Proceedings of the 14th International Coastal Symposium* (Sydney, Australia). *Journal of Coastal Research*, Special Issue, No. 75, pp. 867-871. Coconut Creek (Florida), ISSN 0749-0208.

Wave forcing is an important hydrodynamic variable that influences spatial patterns and temporal dynamics of marine benthos. In this study, we used three principally different wave models – simplified wave model (SWM), spectral wave model SWAN (simulating waves nearshore), and locally calibrated point model (LCPM) – to assess the effects of wave forcing on the distribution and temporal dynamics of macrobenthos in the north-eastern Baltic Sea. Other important environmental variables like depth, salinity, turbidity etc., were also included into analyses of benthos distribution in order to quantify the relative importance of wave forcing. Following depth, SWM was the second most important environmental predictor of spatial distribution of benthos. The importance of SWAN was the lowest among environmental variables due to its low spatial resolution (1 nautical mile) compared to SWM (25 m). Considering the temporal dynamics of benthos, wave height significantly correlated with several benthic variables, but the direction and magnitude of effects were site-specific.

ADDITIONAL INDEX WORDS: *Wave hindcast, benthos, macrophytes, macroinvertebrates, SWAN.*

INTRODUCTION

Hydrodynamic energy is an important factor controlling the spatial distribution of benthic macrophytes and macroinvertebrates (Kautsky *et al*., 1999; Sousa, 1984). Hydrodynamics may act on biota in different ways. For example, wave action determines benthic habitat availability through direct physical disturbance, turbidity related light penetration, as well as reforming bottom substrates and nutrition conditions (Herkül *et al*., 2011; Sousa, 1984). Extreme waves during storms may rapidly reshape habitats on a local and sometimes even on a regional scale (*e.g.* Kim *et al*., 2015). In addition to temperature rise, the recent climate change also alters global wind conditions and storminess, which, in turn, affects the marine ecosystem through changes in hydrophysical conditions (Suursaar *et al*., 2015).

Spatial and temporal effects of hydrodynamics on subtidal benthic biota are still relatively poorly studied. The research obstacles may be related to mismatch of scales and disparate nature of hydrobiological and hydrophysical data, or collinearity of environmental predictors, i.e. many factors simultaneously affecting biota. Therefore, there is a lack of hydrobiological studies which use hydrodynamic models. Instead of sophisticated hydrodynamic models, simplified solutions are used. For instance, quite often, wave exposure is only indirectly and roughly considered through fetch and some geometric factor; instead of an appropriate temporal resolution, certain mean-states are assumed. Nevertheless, recent studies have shown that in addition to the commonly used biotic and abiotic drivers, hydrodynamic models may be helpful in accurately defining distributions of benthic communities and in explaining temporal variations in species distribution and abundance (Rattray *et al*., 2015). In this study we used both spatial and temporal hydrodynamic and hydrobiological data to clarify the role of hydrodynamic conditions in shaping the spatial and temporal patterns of marine macrobenthic communities.

METHODS

The study was conducted in Estonian waters, northern Baltic Sea (Figure 1). The study area is a nontidal brackish water (salinity < 8 PSU) marine area with depth mainly less than 50 m.

Benthos data

For studying the spatial patterns, coverage estimates of benthic macrophyte and macroinvertebrate species collected by SCUBA diving and underwater video from a total of 10112 sampling sites (Figure 1) in 2005–2015 were used. For each sampling site, percentage coverage of all visually distinguishable species and total coverage of macrophytes were estimated. The following benthos variables were used to study the spatial patterns: total coverage (percentage area of seabed covered) of macrophytes; species richness (total number of recorded macrophyte and invertebrates species in a site); coverage of charophytes (*Chara* spp, *Tolypella nidifica*); coverage of *Fucus* (*F. vesiculosus, F. radicans*); coverage of *Furcellaria lumbricalis*; coverage of *Zostera marina*; coverage of *Mytilus trossulus*. For temporal patterns, vegetation of the Pärnu, Eru and Kõiguste areas (Figure 1) was investigated in July or August 1996-2014. Along a transect line total coverage of phytobenthos community, coverage of individual species and

DOI: 10.2112/SI75-174.1 received 15 October 2015; accepted in revision 15 January 2016.
*Corresponding author: kristjan.herkul@ut.ee
©Coastal Education and Research Foundation, Inc. 2016

character of substrate was registered. Biomass samples were collected in three replicates from each community type along transects.

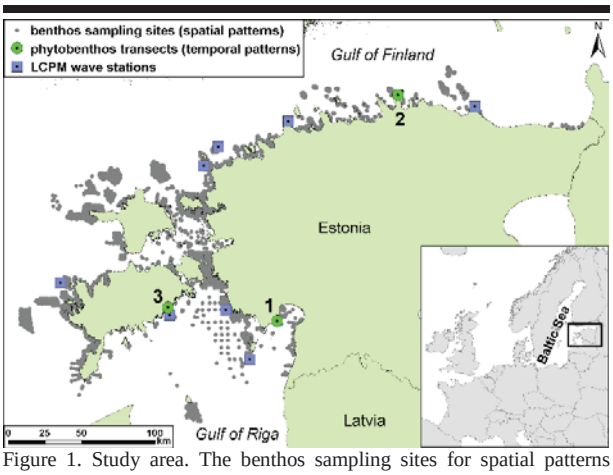

Figure 1. Study area. The benthos sampling sites for spatial patterns (n=10112) and transects for temporal variations (1 – Pärnu, 2 – Eru, 3 – Kõiguste) are shown.

The samples were stored in a deep freezer and later sorted and determined to species level in the laboratory. To study the effects of wave forcing on temporal variability of benthos, the following macrophyte variables were selected: depth distribution of macrovegetation and angiosperms, proportion of *Fucus vesiculosus* (based on coverage data), proportion of perennial species (listed in Torn and Martin, 2011, based on biomass data) and total number of macrophyte species in a transect.

Wave forcing and other abiotic data

Correlations between hydrodynamics and benthos variables were tested using three principally different wave models: simplified wave model (SWM), spectral wave model SWAN (Simulating Waves Nearshore), and locally calibrated point model (LCPM). The SWM is a wave exposure model that incorporates shoreline topography, fetch and wind data together with empirically derived algorithms to mimic diffraction (Isæus, 2004). The wave exposure estimates were computed in a geographic information system (GIS) with the software WaveImpact 1.0 (Isæus, 2004). Wind directions and speeds, obtained from the Estonian Environmental Agency (EEA) over a period of 1997–2006 were used for the model calculation. Nested grid sub-models together with highly detailed coastline layer resulted in final 25 m cell size (Figure 2).

The third generation spectral wave model SWAN (Booij *et al*., 1999) was applied to the Baltic Sea (629 meshes along longitudes and 734 along latitudes) with a grid of 1 nautical mile (1NM = 1852 m). It was forced by the winds from the Baltic Sea reanalysis database BaltAn65+ and wave hindcast for the period of 1965–2005 was obtained. For the Estonian coastal sea, a database of wave heights as well as near-bottom orbital velocities was created. To study the spatial relationships between wave forcing and benthic biota, georeferenced GIS-layer (average of a period 1989–2005) was produced.

Additionally to the wave data yielded by SWM and SWAN, five other environmental variables were used in the spatial pattern analyses of macrobenthos: depth, seabed slope, average ice thickness (based on meteorological radar data), water turbidity (based on satellite imagery), and salinity. All these datasets were available as raster layers in ArcGIS.

Mainly used in analysis of temporal variations, the LCPM provides hourly wave hindcasts at eight differently exposed Estonian coastal sea locations in 1966-2014. The hindcasts stem from extensive (1400 days-worth) measurements of currents and waves carried out in the Estonian coastal sea (2006-2014) using the bottom-mounted Recording Doppler Current Profiler RDCP-600. The measurements performed at the nearshore (10–15 m deep) study locations were used to calibrate a point model (Suursaar, 2013), which calculates the significant wave height (H_s) as a function of wind speed, fetch length and water depth. The model was forced by the wind data from the coastal meteorological stations (obtained from the EEA), where records were available since 1966. For comparing (cross-validating) the LCPM and SWAN results, a common period of the two independent wave hindcasts were used (Suursaar *et al*., 2014).

Statistical analyses

For analysis of spatial patterns, boosted regression trees (BRT) in the package “gbm” was used to quantify the magnitude of effects of wave forcing and other environmental factors on the benthic variables. BRT is an ensemble method that combines the strength of two algorithms: regression trees and boosting (Elith *et al*., 2008). Canonical correspondence analysis (CCA) in the package “vegan” was used to quantify and visually illustrate the strength and direction of effects of environmental variables on selected benthic species/groups (charophytes, *Fucus*, *Furcellaria*, *Zostera*, *Mytilus*). Both packages “gbm” and “vegan” were run in software R (R Core Team, 2014). BEST analysis using BIOENV method in software PRIMER 7 was run to study the relationship between the structure of benthos and environmental variables. Coverage data of all macrobenthic species (72 taxons, 10112 sites) was square root transformed before analysis to downweight the importance of species with very high coverage values (Anderson *et al*., 2008).

For temporal patterns, Spearman rank order correlation analysis was used to test relationships between wave heights (averages and 99th percentiles) and benthic variables. 99th percentile was used instead of maximum to avoid possible outliers. Average and 99th percentile of wave heights were calculated for the period of September to June preceding the yearly sampling of macrophytes. The analysis included paired up wave and biology data over the common period of 1995–2014 and three sites (Pärnu, Eru, Kõiguste; Figure 1).

RESULTS

Based on the BRT analysis, six out of seven models had depth as the most important environmental variable (Figure 3). The importance of depth was especially high in the models of total coverage and species richness. Depth was not the most important variable only in the model of *Mytilus* that had turbidity as the most influential environmental driver. Scoring the second most important variable, SWM was the most

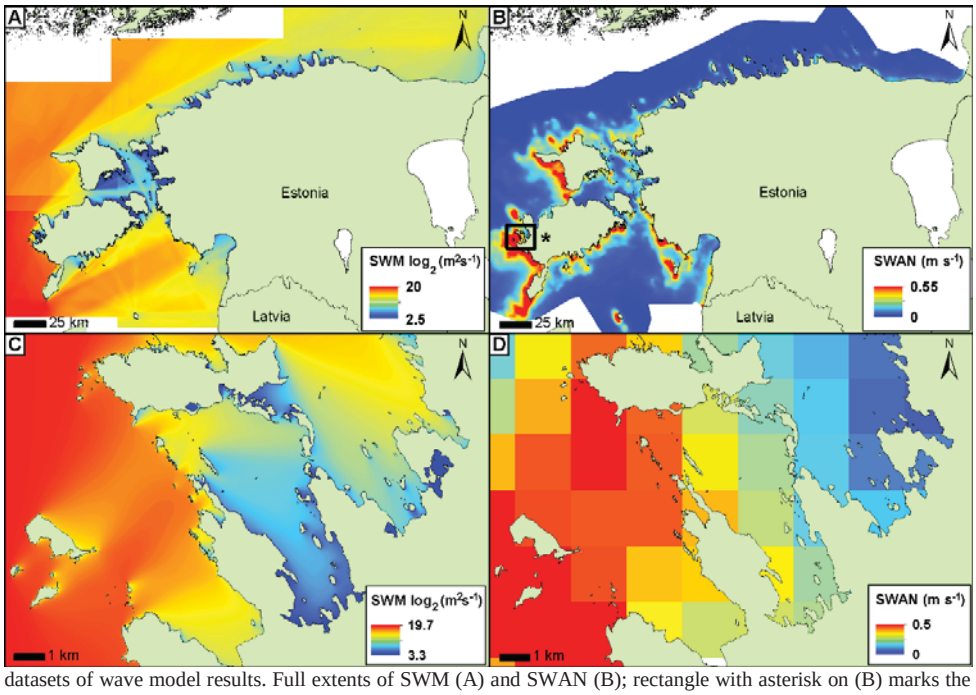

Figure 2. Spatial datasets of wave model results. Full extents of SWM (A) and SWAN (B); rectangle with asterisk on (B) marks the zoomed-in views of SWM (C) and SWAN (D) which illustrate their native spatial resolutions (25 m and 1 NM, respectively).

influential among hydrodynamic variables, while SWAN was the least important (Figure 3).

The CCA ordination clearly indicated a distinct layout of the selected benthic species/groups on environmental gradients and grouping of environmental variables with similar direction of change (Figure 4). Similarly to BRT, depth and SWM were the most influential variables and SWAN had the lowest contribution among environmental variables. Also the BEST analysis (Table 1) showed that the whole structure of benthos was most affected by depth and SWM. Remarkably, the model that included only depth appeared to be the second best result. Additionally, the influence of salinity was more pronounced on the whole structure of benthos compared to the effects on separate benthos variables (see the results on BRT and CCA).

In the temporal datasets, the relationships between wave height (H_s, H_{max}) and selected macrophyte variables differed in the case study areas (Table 2). Average wave height correlated negatively with all studied macrophyte variables in Pärnu. Controversial results were found between depth distribution of angiosperms, proportion of *Fucus* and wave height in Eru and Kõiguste.

DISCUSSION

Depth was by far the most influential environmental variable describing the spatial patterns of benthos (Figures 3 and 4; Table 2). This result is in good accordance with a multitude of previous studies (*e.g.* Wallin *et al.*, 2011) and is acknowledged as a general rule of spatial patterns of benthos. Depth was the most important environmental variable in all models of phytobenthic variables because the distribution of plants is strictly regulated by light availability (*e.g.* Kirk, 2011) that, in turn, is strongly correlated to depth. The importance of depth was most strongly expressed in the case of total coverage of phytobenthos where the contribution of other variables very low.

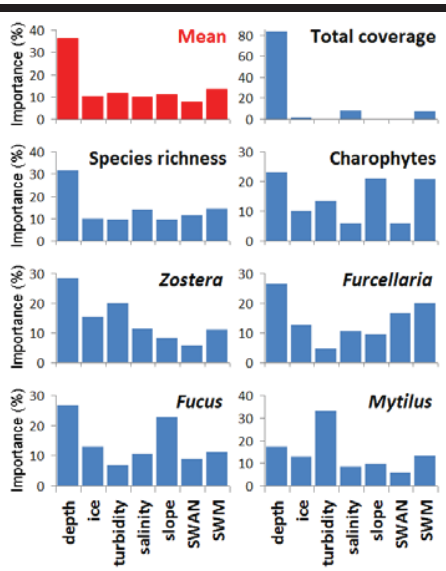

Figure 3. Relative importance of seven environmental variables (and their mean importance) predicting the spatial distribution of benthic variables based on BRT models.

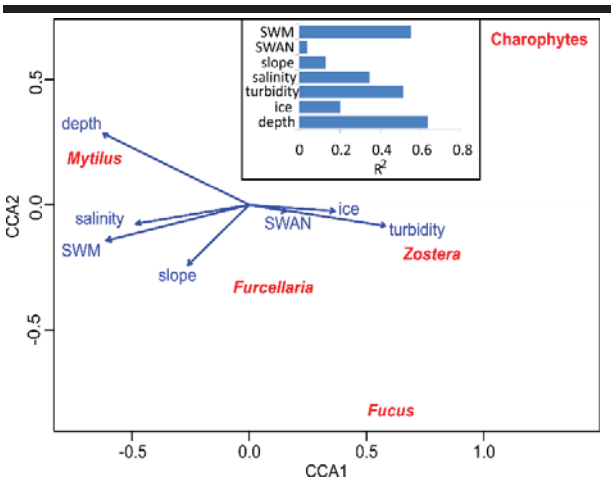

Figure 4. CCA ordination plot of selected benthic species and environmental variables. The determination coefficients (R^2) of the environmental variables are shown in the bar plot.

The importance of depth in describing general phytobenthos variables (like total coverage) was an expected result, although, the single predictor model that included only depth scoring the second best result in describing the total benthos structure, was a more notable result (Table 1). The inclusion of both depth and SWM into model scored the best overall result in BEST analysis. However, when adding further variables, the correlation started to decrease (Table 1). The overall pattern of the BEST analysis indicated that models with only few environmental variables with high predictive power (*i.e.* high data quality, ecological conformity, high spatial resolution) perform better than models with more environmental variables but with lower predictive power.

Depth was not the most influential environmental variable only in the case of the mussel *Mytilus.* Habitat preference of the invertebrate *Mytilus* is not directly driven by depth. Instead of depth, turbidity was found to be the most important driver of distribution of *Mytilus.* As a filter feeder, turbidity can be seen as a proxy for food to *Mytilus* – the phytoplankton (Lauringson *et al.*, 2009).

The influence of different wave models, including the relatively simplistic SWM and the rather advanced SWAN, was strongly contrasting. As shown by all analyses, SWM was the second important predictor after depth while SWAN placed as least important variable. The most likely reason for such a difference between SWM and SWAN lies in a fact that the spatial resolution of SWM was 25 m while that of SWAN was 1 NM. Most of the input benthos data originated from topographically complex coastal areas where 1 NM resolution is not enough to describe the actual variability (Figures 2C and 2D). However, refining the spatial resolution of the SWAN would obviously improve its applicability.

In the temporal dynamics dataset, the average wave height (based on LCPM) correlated well with the temporal trends of the depth distribution and composition of phytobenthic community in Eru and Pärnu.

Table 1. *Results of BEST analyses on the relationships between environmental variables and structure of macrobenthos. The five best combinations and single variable model correlations are shown.*

Number of variables	Correlation (ρ)	Selections of variables
Best overall results		
2	0.254	depth, SWM
1	0.248	depth
3	0.241	depth, SWM, salinity
4	0.223	depth, SWM, salinity, turbidity
2	0.218	depth, salinity
Single variable models		
1	0.248	depth
1	0.156	SWM
1	0.102	turbidity
1	0.088	salinity
1	0.020	ice
1	0.007	slope
1	-0.020	SWAN

Table 2. *Results of Spearman rank correlation analysis on the effect of wave height (LCPM) on the benthic variables. H_a–average wave height, H_m–99th percentile of maximum wave height. Statistically significant ($p<0.05$) correlations are marked in bold.*

Area	Benthic variables	H_a	H_m
Pärnu	Depth distribution of macrovegetation	**-0.54**	-0.08
	Depth distribution of angiosperms	**-0.56**	-0.20
	Proportion of *Fucus*	**-0.61**	**-0.65**
	Proportion of perennial species	**-0.64**	-0.51
	Species richness	-0.16	-0.11
Eru	Depth distribution of macrovegetation	**-0.53**	-0.03
	Depth distribution of angiosperms	-0.49	-0.74
	Proportion of *Fucus*	**0.64**	0.24
	Proportion of perennial species	0.25	0.30
	Species richness	-0.20	0.09
Kõiguste	Depth distribution of macrovegetation	0.24	0.02
	Depth distribution of angiosperms	0.28	**0.50**
	Proportion of *Fucus*	-0.22	-0.15
	Proportion of perennial species	-0.02	-0.07
	Species richness	-0.41	**-0.54**

The relationships were stronger with maximum wave height in Kõiguste area. The varying effects of wave height on submerged aquatic vegetation between areas can be explained by different substrate types. For example, fine sediments with some stony patches occurr at a depth of 1–3 m in Pärnu area. The majority of the stones in the area are small (<20 cm in diameter). This type of substrate is unstable and may be displaced under high wave events. Contrarily, large boulders prevail down to 6 m in Eru area. Under stable substrate conditions moderate wave exposure may have positive effect on *Fucus* recruitment due to the cleaning effect of hard substrate from soft sediments and epiphytic cover (Isæus, 2004).

Hydrodynamics and storms affect marine ecosystems via direct physical disturbance and decreased underwater light availability due to resuspension of soft bottom sediment. According to Blanchette (1997), extreme wave storms can erode the vegetation. Indeed, wave breaking during storms mainly occurs between 2–4 m depth in Estonian coastal sea (Suursaar *et al.*, 2014), which is usually a quite densely vegetated zone.

However, different species and organism groups are sensitive to wave impacts at a different degree. Disturbance caused by wave action reduced phytobenthos species richness in Kõiguste where species diversity was the highest among the studied areas.

Based on previous studies, species composition will recover during next vegetation season after small or medium scale physical disturbance (Herkül *et al*., 2011; Kim and De Wreede, 1996; Torn *et al*., 2010). However, after exceptionally violent storms, such as *e.g*. hurricane Katrina (Hill, 2012), the impacts may be long-lasting and profound.

CONCLUSIONS

The most important factor describing the coastal benthic communities was depth (which mainly applies through underwater light availability). Following the depth, wave forcing was the second most important predictor for spatial and temporal distribution of benthos. However, very high spatial resolution of hydrodynamic data is crucial for describing the spatial variability in (usually quite mosaic) nearshore benthos. It appeared that simple models with finer grid may yield better results than state-of-art models with coarser (~1 NM) grids. Still, wave activity is an essential driver in benthic habitats and it is a crucial component in refining the environment-biota relationships in the sea.

ACKNOWLEDGMENTS

The study was funded by the projects PUT595 and IUT02-20 and research grants 9439 and 8980 of the Estonian Research Council. The authors thank Holger Jänes for linguistically revising the manuscript.

LITERATURE CITED

Anderson, M.J.; Gorley, R.N., and Clarke, K.R., 2008. *PERMANOVA+ for PRIMER: Guide to Software and Statistical Methods*. Plymouth, UK: PRIMER-E.

Blanchette, C.A., 1997. Size and Survival of Intertidal Plants in Response to Wave Action: A Case Study with *Fucus gardneri*. *Ecology*, 78(5), 1563-1578.

Booij, N.; Ris, R.C., and Holthuijsen, L.H., 1999. A third-generation wave model for coastal regions: 1. Model description and validation. *Journal of Geophysical Research*, 104(C4), 7649-7666.

Elith, J.; Leathwick, J.R., and Hastie, T., 2008. A working guide to boosted regression trees. *Journal of Animal Ecology*, 77, 802-813.

Herkül, K.; Kotta, J., and Pärnoja, M., 2011. Effect of physical disturbance on the soft sediment benthic macrophyte and invertebrate community in the northern Baltic Sea. *Boreal Environment Research*, 16(A), 209-219.

Hill, D., 2012. The lessons of Katrina, learned and unlearned. *Journal of Coastal Research*, 29, 324-331.

Isæus, M., 2004. Factors structuring Fucus communities at open and complex coastlines in the Baltic Sea. Sweden, Stockholm: Stockholm University, PhD Thesis, 40p.

Kautsky, H.; Martin, G.; Makinen, A.; Borgiel, M.; Vahteri, P., and Rissanen, J., 1999. Structure of phytobenthic and associated animal communities in the Gulf of Riga. *Hydrobiologia*, 393, 191-200.

Kim, J.H. and De Wreede, R.E., 1996. Effect of size and season of disturbance on algal patch recovery in a rocky intertidal community. *Marine Ecology Progress Series*, 133, 217-228.

Kim, K.; Choi, J-K.; Ryu, J-H.; Jeong, H.J.; Lee, K.; Park, M.G., and Kim, K.Y., 2015. Observation of typhoon-induced seagrass die-off using remote sensing. *Estuarine, Coastal and Shelf Science*, 154, 111-121.

Kirk, J.T.O., 2011. *Light and Photosynthesis in Aquatic Ecosystems*. Cambridge: Cambridge University Press, 662p.

Lauringson, V.; Kotta, J.; Orav-Kotta, H.; Kotta, I.; Herkül, K., and Põllumäe, A., 2009. Comparison of benthic and pelagic suspension feeding in shallow water habitats of the northeastern Baltic Sea. *Marine Ecology*, 30, 43-55.

R Core Team, 2014. *R: A language and environment for statistical computing*. R Foundation for Statistical Computing. http://www.R-project.org/

Rattray, A.; Ierodiaconou, D., and Womersley, T., 2015. Wave exposure as a predictor of benthic habitat distribution on high energy temperate reefs. *Frontiers in Marine Science*, 2(8), 1-14.

Sousa, W.P., 1984. The role of disturbance in natural communities. *Annual Review of Ecology, Evolution, and Systematics*, 15, 353-391.

Suursaar, Ü., 2013. Locally calibrated wave hindcasts in the Estonian coastal sea in 1966–2011. *Estonian Journal of Earth Sciences*, 62, 42-56.

Suursaar, Ü.; Alari, V., and Tõnisson, H., 2014. Multi-scale analysis of wave conditions and coastal changes in the north-eastern Baltic Sea. *In*: Green, A.N. and Cooper, J.A.G. (eds.), Proceedings 13th International Coastal Symposium (Durban, South Africa). *Journal of Coastal Research*, Special Issue No. 70, pp. 223-228.

Suursaar, Ü.; Jaagus, J., and Tõnisson, H., 2015. How to quantify long-term changes in coastal sea storminess? *Estuarine Coastal and Shelf Science*, 156, 31-41.

Torn, K.; Martin, G.; Kotta, J., and Kupp, M., 2010. Effects of different types of mechanical disturbances on a charophyte dominated macrophyte community. *Estuarine Coastal and Shelf Science*, 87(1), 27-32.

Torn, K. and Martin, G., 2011. Assessment method for the ecological status of Estonian coastal waters based on submerged aquatic vegetation. *In*: Brebbia, C.A., and Beriatos, E. (eds.), *Sustainable Development and Planning V*. Southampton: WIT Press, pp. 443-452.

Wallin, A.; Qvarfordt, S.; Norling, P., and Kautsky, H., 2011. Benthic communities in relation to wave exposure and spatial positions on sublittoral boulders in the Baltic Sea. *Aquatic Biology*, 12(2), 119-128.

Journal of Coastal Research	SI	75	872-876	Coconut Creek, Florida	2016

Prediction of the 2011 Tohoku Tsunami Scouring near Structures

Tatsuki Iida[†], Shuich Kure[+*], Keiko Udo[+], Akira Mano[+], and Hitoshi Tanaka[++]

[†]Civil Engineering Div., Taisei Corporation
Shinjyuku Center Bldg., Nishi Shinjyuku 1-25-1,
Tokyo 1630606, Japan

[+]IRIDeS, Tohoku University
Sendai 9800845, Japan.
[++]School of Engineering, Tohoku
University, Sendai 9808579, Japan

www.cerf-jcr.org

www.JCRonline.org

ABSTRACT

Iida, T.; Kure, S.; Udo, K.; Mano, A., and Tanaka, H., 2016. Prediction of the 2011 Tohoku Tsunami scouring near structures. *In:* Vila-Concejo, A., Bruce, E., Kennedy, D.M., and McCarroll, R.J. (eds.), *Proceedings of the 14th International Coastal Symposium* (Sydney, Australia). *Journal of Coastal Research*, Special Issue, No. 75, pp. 872-876. Coconut Creek (Florida), ISSN 0749-0208.

The 2011 Tohoku Tsunami left innumerable sites with large scale scouring near failed coastal structures. This was a major cause of failure, and the reconstruction of these structures in a robust way requires determination of the mechanisms and prediction of the scouring. Two mechanisms are known for tsunami scouring: erosion by the bottom shear stress and liquefaction by the pore pressure, however, these mechanisms have not been compared yet in their effects. This study aims to quantify these mechanisms and predict the scouring by the 2011 Tohoku tsunami. For this approach, we developed a numerical model by the quasi-3D finite volume method by meshing horizontally in water and vertically in ground. After validating our model, we have applied it to the breach point of a coastal levee hit by the tsunami. We can conclude that erosion by the bottom shear stress has the major role, however, the fluidisation still has innegligible effect in 28% to the maximum erosion depth.

ADDITIONAL INDEX WORDS: *Liquefaction, pore pressure, quasi-3D finite volume method.*

INTRODUCTION

The 2011 Tohoku tsunami overtopped coastal levees in Miyagi and Iwate Prefectures, Japan, the most damaged prefectures, and delivered huge amounts of sea water on land. The water soon started to return to the sea. After the tsunami, there were innumerable sites with large scale scouring near the failed coastal structures.

Many “tsunami bays”, massive erosion behind the breach point of the coastal levee, and “tsunami channels”, long-extending erosion behind the alive levee, appeared along the Yamamoto Coast in the southern part of Miyagi Prefecture. Iida *et al*. (2014) analysed these phenomena and concluded that the return flow is the major reason of the erosion by using the materials of flow concentration at the breach points and turbid vortexes off the breach points clearly shown in the tsunami videos. Udo *et al*. (2012) examined morphological change on the coast and found significant deposition off the breach points. This also supports the above conclusion.

Before the tsunami, the two prefectures constructed gates at river mouths to prevent runup of tsunamis and storm surges into the rivers. For the most part, these gates were closed during the tsunami, effective to reduce the runup, and survived due to the strong structures of steel and concrete. However, the side of the gate was significantly eroded because the return flow, concentrated to the river, was prevented by the closed gate and bypassed at the side (Tanaka *et al*., 2012; TBJC, 2013).

Effective reconstruction of these structures robust for similar situations requires determination of the scouring mechanisms and prediction of the phenomenon.

Two mechanisms are known for the scouring: erosion by the high bed shear stress due to high velocity, and liquefaction by the excessive pore pressure in the ground. The former was taken into the simulation models: Takahashi *et al.* (2001), Gelfenhaum *et al*. (2007), and Ontowirjo and Mano (2013) for tsunamis, and Kobayashi and Lawrence (2004), and Pan *et al*. (2012) for solitary waves. Large tsunamis are generally characterized by high velocity on land and high shear velocity compared with the settling velocity of sediment. Sediment transport is fundamentally suspended load, and sediment concentration has vertical distribution. Therefore the sediment field is three dimensional.

The latter occurs when rapid decrease of water surface leaves high pore pressure force exceeding the soil weight above. Consequently, tsunami drawdown in the return flow tends to cause liquefaction. Tonkin *et al.* (2003) conducted a large scale experiment on the sand behavior around a cylinder under the act of a solitary wave. They measured pressure at several points in the sand layer and observed sand behavior by taking video. They found the most rapid scour at the end of drawdown and specified liquefaction by the pressure and video analysis.

The 2004 Indian Ocean tsunami also left numerous scouring sites around houses, railways, bridge peers, *etc.* EERI and FEMA published technical guidance on the tsunami (Francis and Yeh, 2006) and concluded high possiblity of liquefaction as the scouring mechanism by using generic parameters of tsunami period and height. However, it is not so sure because scouring by liquefaction is the localized phenomenon near structures.

Pan *et al*. (2012) conducted numerical simulation of the Tonkin *et al*.’s experiment by using shallow water equations and a sediment transport model considering erosion by the bottom

DOI: 10.2112/SI75-175.1 received 15 October 2015; accepted in revision 15 January 2016.
*Corresponding author: kure@irides.tohoku.ac.jp
©Coastal Education and Research Foundation, Inc. 2016

shear stress. They found that the simulation well reproduces the exprimental results except short-term bottom profile near the maximum erosion. This suggests that the scouring occurs by the mixed mechanisms of the erosion by bottom shear stress and the liquefaction by excessive pore pressure. These two mechanisms have not been compared yet in their effects. This study aims to quantify these mechanisms and predict the scouring by the 2011 Tohoku tsunami.

METHODS

This section shows theoretical solutions and their behaviors of porepressure for simplilfied conditions: one dimensional space, saturated soil by water, high soil compressibility than that of water, and a steady sinusoidal shallow wave on land with angular frequency ω. We define excessive porepressure p_e as the pressure deviation from the hydrostatic pressure, p_s, for the mean sea level, as seen in Figure 1,

$$p_e(z,t) = p(z,t) - p_s(z)\ . \tag{1}$$

This quantity is governed by the Terzaghi's consolidation equation (Terzaghi *et al*., 1996) ,

$$\frac{\partial p_e}{\partial t} = C_v \frac{\partial^2 p_e}{\partial z^2}\ , \tag{2}$$

$$C_v = \frac{k}{\rho g M_v}\ , \tag{3}$$

where k, ρ, g, and M_v are the permiability of the soil, the density of water, the gravity, and the compression of the soil, respectively.

The boundary conditions of the parabolic partial differential equation are,

$$p_e(o,t) = p_{e0}\cos(\omega t), \tag{4}$$

$$p_e(\infty,t) = 0, \tag{5}$$

$$p_{e0} = \rho g \eta_{\mathrm{amp}}, \tag{6}$$

where η_{amp} is the amplitude of the water surface change.

The specific solution for the boundary conditions is given by Hino (1974) and Francesco (2013) as

$$p_e(z,t) = p_{e0}\exp(-K_u z)\cos(\omega t - K_u z)\ , \tag{7}$$

where

$$K_u = \sqrt{\frac{\omega}{2C_v}}. \tag{8}$$

Hino introduced this functional form as the exact solution of the Navie Stokes equation for the fluid motion drived by a oscillating plate.

In the nondimensional form,

$$p_e^*(z^*,t^*) = \exp(-z^*)\cos(t^* - z^*), \tag{9}$$

where

$$p_e^* = \frac{p_e}{p_{e0}},\quad t^* = \omega t,\quad z^* = \frac{z}{z^+}\ ,\ z^+ = \sqrt{\frac{2C_v}{\omega}}. \tag{10}$$

Figure 2 plots Eq. (9) for each $t^*=n\pi/4$, n=0,1,2,.. The pressure is characterized by the phase lag and attenuation for larger z^*. The significant change is confined at $z < 3z^+$.

The characteristic depth, z^+, is plotted in Figure 3 for the typical wave period of wind waves to tsunamis, $T=2\pi/\omega$, and the consolidation coefficient in m^2/s unit. Here C_v <0.001, 0.01< C_v <0.1, and 1< C_v roughly corresponds to clay, sand, and pebble dominant soil, respectively. For the sand layer with lower C_v=0.01, the depth z^+ exceeds 1m for tsunamis with the period T > 300 s.

The liquefaction occurs for larger excessive pressure difference between the bottom surface and subsurface point. Figure 2 shows this occurs at the phase $t^*=\pi$ or the minimum water surface elevation. This accords with the observation by Tonkin *et al*. (2003) that the most rapid scour occurred at the end of drawdown.

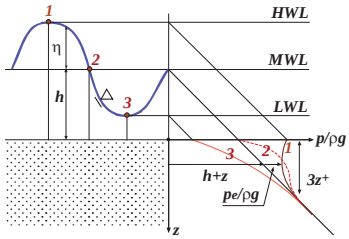

Figure 1. Porepressure change due to a shallow wave. Definitions of the cordinate z and the quantities.

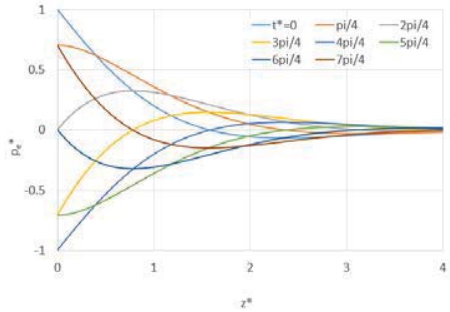

Figure 2. Excessive porepressure distribution, $p_e^*(z^*,t^*)$.

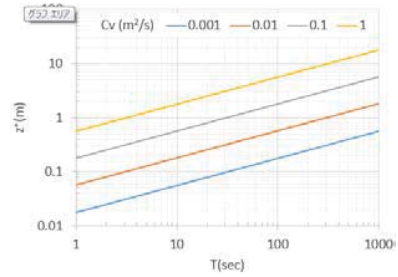

Figure 3. The characteristic depth z+ as a function of wave period and various values of consolidation coefficient.

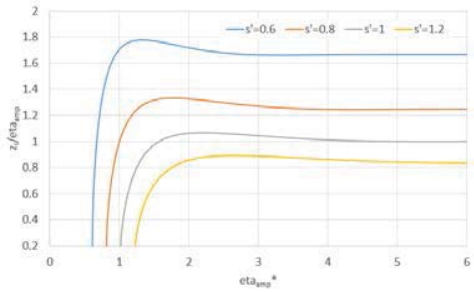

Figure 4. Nondimensional liquefaction depth, z_1/η_{amp}, as a function of η_{amp}^* with the various values of s'.

The mechanical equlibrium for the liquefaction initiation is given by,

$$\frac{p_e(z,t)-p_e(0,t)}{(\rho_s-\rho)gz(1-\lambda)} = \Lambda = 1, \quad (11)$$

where ρ_s is the density of the soil particle, λ the porosity of the soil layer. This condition is well established in geotechnology. Using (6), (9) and $t^*=\pi$, we have,

$$\eta^*_{amp}(1-\exp(-z^*)\cos(z^*)) = s'z^*, \quad (12)$$

where

$$s' = \frac{\rho_s-\rho}{\rho}(1-\lambda), \quad \eta^*_{amp} = \frac{\eta_{amp}}{z^+}. \quad (13)$$

We solved this equation by the Newton-Raphson method and plotted the solution, denoted as the liquefaction depth, $z_l=z$, in Figure 4. Here s'= 0.6 and 1.2 correspond to loose and dense soil layers, respectively.

z_l/η_{amp} tends toward $1/s'$ for large η_{amp}^* and has a peak near $\eta_{amp}^*=1$. The peak value is about 1.8 for the loose soil which corresponds to the condition that the liquefaction depth reaches 90% of the inundation depth. The peak value of about 0.9 for the dense soil corresponds to the condition that the liquefaction depth deminishes to 45% of the inundation depth because of the heavy soil weight. For the smaller value, $\eta_{amp}^*<1$, z_l/η_{amp} quickly drops to zero.

Quasi-3D Finite Volume Method

We developed a numerical model by a finite volume method to simulate tunami scouring on land. Suspended sediment is dominant in the sediment transport because of high bottom shear velocity compared to the settling velocity of soil particles. Vertical distribution of the sediment concentration is significant. Furthermore vertical distribution of the porepressure in the land is necessary to know the liquefaction initiation. We evolved a quasi-3D model to avoid the computational overload of full-3D models.

The shallow water equations with the Einstein summation convention are,

$$\frac{\partial q_j}{\partial x_j} = 0, \quad (14)$$

$$\frac{\partial q_i}{\partial t} + \frac{\partial}{\partial x_j}\frac{q_i q_j}{d} = -gd\frac{\partial \eta}{\partial x_i} + \nu_T\frac{\partial^2 q_i}{\partial x_j^2} - \frac{\rho n^2 g}{d^{7/3}} q q_i, \quad (15)$$

where q_j is the depth-integrated discharge per unit width in horizontal x_j direction (j=1,2), d is the depth from the bottom to the surface, ν_T is the depth-averaged eddy viscosity, n is the Manning's roughness coefficient, and q is the length of the vector (q_j). The eddy viscosity is formulated in an open channel flow as,

$$\nu_T = 0.11 d u_*, \quad (16)$$

where $u_*$is the bottom shear velocity and given as,

$$u_* = \sqrt{\frac{\tau_b}{\varrho}}, \quad \tau_b = \frac{\varrho n^2 g}{d^{7/6}} q^2. \quad (17)$$

The sediment transport equation averaged over the depth is,

$$\frac{\partial \bar{C}}{\partial t} + \frac{1}{d}\frac{\partial q_{sj}}{\partial x_j} = \frac{\bar{C}}{d}\frac{\partial q_{sj}}{\partial x_j} + \frac{\partial}{\partial x_j}\varepsilon_j\frac{q_{sj}}{\partial x_j} + \frac{w_0}{d}(C_a - C_b), \quad (18)$$

where $\bar{C}$ is the depth-averaged sediment concentration, q_{sj} is the depth-integrated sediment transport flux per unit width in x_j direction, ε_j is the depth-averaged diffusion coefficient in x_j direction, w_o is the settling velocity of the soil particles, and $w_0 C_a$ is the erosion flux from the bottom.

We assumed the diffusion coefficient same as the eddy viscosity in the value and used van Rijn' formula (van Rijn, 1993) for C_a ,

$$C_a = 0.015\frac{d_s}{a}D^{*^{-0.3}}\left(\frac{\theta-\theta_c}{\theta_c}\right)^{1.5}, \quad (19)$$

where d_s is the bottom particle diameter, a=50d_s, $D^*$is the nondimensional bottom particle diameter, θ is the Shields number, and θ_c is the critical value of θ. We also assumed equilibrium sediment concentration distribution by Rouse (1937) to know the bottom concentration, C_b from $\bar{C}$.

The morphological change by erosion and deposition is given by,

$$\frac{\partial Z_b}{\partial t} = \frac{1}{1-\lambda}(C_b - C_a)w_0, \quad (20)$$

where Z_b is the bottom elevation.

The generalized consolidation equation considering the compressibility of water and air in the soil layer is given by Nago (1982) and Nago and Maeno (1987),

$$f_d\frac{\partial p_e}{\partial t} + \rho g f_s\frac{\partial \eta}{\partial t} = \frac{k}{\rho g}\frac{\partial p_e}{\partial z^2}, \quad (21)$$

where

$$f_d = M_v + \beta\lambda_w + \frac{\lambda_a}{p_0+\rho g(\eta+h-z)}, \quad (22)$$

$$f_s = \beta\lambda_w + \frac{\lambda_a}{p_0+\rho g(\eta+h-z)}, \quad (23)$$

β is compression of water, λ_w and λ_a are the porosity for water and air, and p_0 is atmospheric pressure. Here the horizontal gradients of the pore pressure are negligible because the horizontal scale is much larger than the vertical scale. The modified consolidation coefficient is given by,

$$C'_v = \frac{k}{\rho g f_d}. \quad (24)$$

We can calculate the pore pressure up to the liquefaction initiation of the condition (11). Soil layer was assumed to remain in the same state after the liquefaction because softening and resettlement of the liquefied soil layer are unable to be treated by this model. The experiments by Tonkin *et al*. (2003) and the hindcasting by Pan *et al*. (2012) suggest that the liquefied soil is quickly resettled and the transport of the soil is small because the liquefaction occurs at the phase of the low flow and low shear stress.

These differential equations together with the boundary conditions of structure walls, wave input, wave front on a dry bed, *etc*. are discretized by the finite volume methods. Accurate discretization of the wall boundaries is necessary because flow concentration and rapid drawdown near the structures affect the scouring. We adopted the non-structure mesh by triangles which are flexible for finer meshing near the structures and used staggered scheme allocating η and p_e at the triangle's centroid and the discharge on the side because of the easiness of the boundary condition intake.

The dry bed meshes are judged by the depth less than the threshold depth, d_{min}. The discharge at the wave front boundary is calculated by using two ηs of the adjacent meshes: dry and non-dry bed meshes. To eliminate numerical oscillations induced by the wave front condition, we introduced the numerical viscosity term by Goto and Shuto (1980).

RESULTS

Model validation

Tonkin *et al*. (2003) conducted large scale experiments on the scouring by a cylinder of 0.5 m diameter at the shoreline on a uniform slope for a solitary wave incidence with various observations. They measured pore pressure at three different sand depths: 0.1 m, 0.2 m, and 0.3 m, of three different locations: front, side, and back points each 0.25 m apart from the cylinder surface.

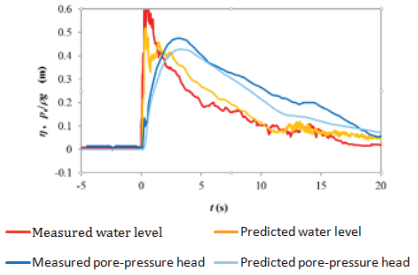

Figure 5. The water surface elevation and pore pressure head at the sand depth, 0.2 m in front of the cylinder. Comparison of the computed and measured values for Case *I*.

We conducted the simulation of the experiments by Tonkin *et al*. with the parameters: k=0.493x10^{-3}m/s, λ= 0.434 (Tonkin), M_v=1.0x10^{-9}Pa^{-1}, β=0.42x10^{-9}Pa^{-1}, λ_a=0.005, f_d=f_s=0.50x10^{-7}Pa^{-1}, (Nago). The air compression term is supremely dominant in f_d and f_s in spite of the tiny volume because of the high compressibility. Then, we get C_v'=0.98 m^2/s which is 12 times larger than that used in Tonkin *et al*. (2003). The value of 0.005 roughly corresponds to the residual air content in water saturated sand.

Figure 5 shows the time variation of the water surface elevation and pore pressure head at the sand depth, 0.2 m in front of the cylinder for their Case *I* with H_0=0.22 m. Our model well reproduces both the elevation and the pressure. It is concluded that the numerical model together with the condition (11) is able to predict the liquefaction initiation if we know the parameters.

Model Application

We applied this model for the scouring around a breached levee at Fujitsuka hit by the 2011 Tohoku tsunami (Iida *et al*., 2014) as shown in Figure 6(a). The boundary geometry was taken from the photo as Figure 6(b) with finer meshes near the breached openings of the size ranging 5.0 to 50.0 m. The levees were assumed to be high enough without overtopping. We set the following conditions: the ground slope S=1/500, the incident tsunami of a pseudo-solitary wave with the height 10 m, and period 50 min, the ground material with the sand diameter d_{50}=0.4 mm, k=1.7x10-5 m/s, λ=0.4, n=0.0035, and C_v'=3.4 m^2/s by assuming the same values for f_d and f_s as before. Computation time is 100 min.

Figure 7 shows the ground elevation change due to the bottom shear stress and sediment transport in which at t=55 min of the top plate, the area from the back of the right levee to the sea through the opening is eroded in the order of 3 to 6 m. The maximum erosion of about 13 m occurs near the tip of the right levee. However, at t=100 min in the bottom plate, this area is filled by the deposition. Thick deposition is found y > 1050 m. This final ground elevation change is similar to that found in the photo.

Figure 8 shows time variation of wave elevation, ground elevation change, and liquefaction depth at the center of the right opening. The rapid erosion occurs in the uprush phase reaching 15 m depth and soon filled by the deposition dominating the erosion in the stationary phase. Then withdrawal and liquefaction

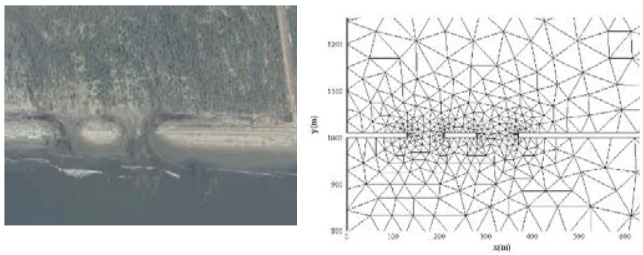

Figure 6. Breached levee and scouring at Fujitsuka. (a) Aerial photo taken by GSI, May 12, 2011 (left). (b) Wall boundaries and FVM meshing (right).

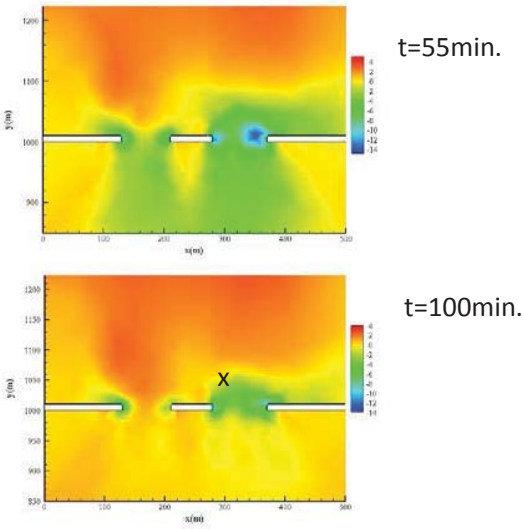

Figure 7. The gound elevation change in m.

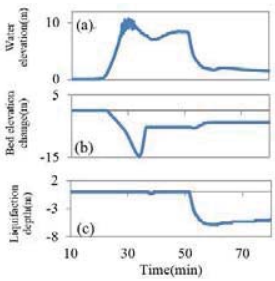

Figure 8. Time variation of wave elevation, ground elevation change, and liquefaction depth at the central point of the opening x.

starts at about t=50 min. The maximum liquefaction depth reaches 5.5 m. This is 28% of the maximum erosion depth due to shear stress.

Figure 9 shows the distribution of the maximum liquefaction depth. Deep liquefaction occurs at the two openings and the sea side of three tips of the coastal levees. These areas are characterized for the rapid withdrawal. Although the erosion by the bottom shear stress is dominant, the liquefaction is innegligible.

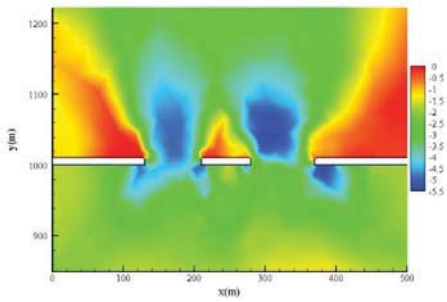

Figure 9. Distribution of the maximum liquefaction depth.

DISCUSSION

We used small values for the porosity of the air corresponding to saturated sand. However, the land inundated by tsunamis could have much larger air porosity which may change the liquefaction depth. We will examine the effects by using our analytical solutions. Equations (10), (21), and (24) give the relationship:

$$z^{+} \propto \lambda_a^{-\frac{1}{2}}. \qquad (25)$$

Then from Figure 4, η^*_{amp} becomes smaller for larger λ_a and

z_l/η_{amp} is stationary for η^*_{amp}>>1,

z_l/η_{amp} decreases for η^*_{amp}< 1,

z_l/η_{amp} slightly increases otherwise.

Therefore the liquefaction depth is mostly stationary or decreases with increase of the air in sand. Consequently, the bed shear stress is dominant in scouring and liquefaction is still innegligible depending on the place.

Tonkin *et al*.(2003) concluded Λ=1/2 by using approximate solution of (2), however, Λ=1 is established in geotechnology. Estimations of Λ and *Cv'* are sensitive to the air content.

CONCLUSIONS

Our conclusions are summarized as follows:

(1) We revealed synthetic characteristics on the liquefaction depth for wide range of wave heights, wave periods and bottom materials.

(2) We proposed a quasi-3D FVM model to predict scouring by the mechanisms of bottom shear stress and liquefaction which is validated with the experimental data.

(3) We applied this model to the scouring at Fujitsuka hit by the 2011 Tohoku tsunami and found the dominancy of the bed shear stress and innegligible effect of the liquefaction for the scouring depth.

ACKNOWLEDGMENTS

The authors would like to acknowledge the financial support of Grants-in-aid for Scientific Reasearch, (ID: 26289158), Japan Society for the Promotion of Science.

LITERATURE CITED

Francis., M.J. and Principal Adviser: Yeh, H., 2006. Tsunami Inundation Scour of Roadways, Bridges, and Foundations, Andaman Tsunami, EERI/FEMA NEHRP2006.

Francesco, R.D., 2013. Exact solution to Terzaghi's consolidation equation, *Applied Mathematics*, 4, 713-717.

Gelfenbaum, G.; Vatvani, D.; Jaffe, B., and Dekker, F. 2007. Tsunami inundation and sediment transport in vicinity of coastal mangrove forest, *Coastal Sediments* '07, 1117-1128.

Goto, T. and Shuto, N., 1980. Comparison between various tsunami runup computation methods and the wave front conditions, *Proc. Coastal Engineering*, 27, 80-84.

Hino, M., 1974. Fluid Mechanics, Tokyo: Asakura Books Co. Ltd., 275p.

Iida, T.; Mano, A.; Udo, K., and Tanaka, H., 2014. Destruction patterns and mechanisms of coastal levees on the Sendai Bay coast hit by the 2011 Tsunami, *Advances in Natural and Technological Hazards Research*, 35, 309-320.

Kobayashi, N. and Lawrence, A. R., 2004. Cross-shore sediment transport under breaking solitary waves, *JGR.*, 109(C3).

Nago, H., 1982. Pressure change and liquefaction in sand layers, *Water Engineering Series*, 82-A-9, JSCE Hyd. Committee.

Nago, H. and Maeno, S., 1987. Pore pressure and effective stress in a highly saturated sand bed under water pressure variation on its surface, *Natural Disaster Science*, 9(1), 23-35.

Ontowirjo, B.; Paris, R., and Mano, A., 2013. Modelling of coastal erosion and sediment deposition during the 2004 Indian Ocean tsunami in Lhok Nga, *Nat. Hazards*, 65, 1967-1979.

Pan, C. and W. Huang, W., 2012. Numerical modelling of tsunami wave run-up and effects on sediment scour around a cylindrical pier, *J. Engineering Mech.*, 138, 1224-1235.

Rouse, H., 1937. Modern coneptions of turbulence, *Trans. ASCE*, 102, 463-543.

Tanaka, H.; Tinh, N. X.; Umeda, M.; Hirao, R.; Pradjoko, E.; Mano, A., and Udo, K., 2012. Coastal and estuarine morphology changes induced by the 2011 Great East Japan Earthquake Tsunami, *Coastal Engineering J.*, 54(1), 1250010(25).

Takahashi, T.; Shuto, N.; Imamura, F., and Asai, D. 2001. Modelling sediment transport due to tsunamis with exchange rate between bed load layer and suspended load layer, *Coastal Engineering* 2000, 1508-1519.

Terzaghi, K.; Peck, R.B., and Mesri, G., 1996. Soil Mechanics in Engineering Practice, 3rd edit., New York: John Wiley and Sons, 592p.

The Tohoku Branch Joint Committee (TBJC), 2013. TBJC Scientific Research Report of the Great East Japan Earthquake and Tsunami Disaster, 1196p.

Tonkin, S.; Yeh, H.; Kato, F., and Sato, S., 2003. Tsunami scour around a cylinder, *J. Fluid Mech.*, 496, 165-192.

Udo, K.; Sugawara, K.; Tanaka, H.; Imai, K., and Mano, A., 2012. Impact of the 2011 Tohoku Earthquake and Tsunami on beach morphology along the northern Sendai Coast, *Coastal Engineering J.*, 54(1), 1250009(15).

Van Rijn, L.C., 1993. Principles of Sediment Transport in Rivers, Estuaries, and Coastal Seas, *Aqua Publications.*

Journal of Coastal Research	SI	75	877-881	Coconut Creek, Florida	2016

Accurate Estimation of Wave Reflection on a High Energy, Dissipative Beach

Kris Inch[†*], Mark Davidson[†], Gerd Masselink[†], and Paul Russell[†]

[†]School of Marine Science and Engineering
University of Plymouth
Plymouth, UK

www.cerf-jcr.org

www.JCRonline.org

ABSTRACT

Inch, K.; Davidson, M.; Masselink, G., and Russell, P., 2016. Accurate estimation of wave reflection on a high energy, dissipative beach. *In:* Vila-Concejo, A.; Bruce, E.; Kennedy, D.M., and McCarroll, R.J. (eds.), *Proceedings of the 14th International Coastal Symposium* (Sydney, Australia). *Journal of Coastal Research*, Special Issue, No. 75, pp. 877-881. Coconut Creek (Florida), ISSN 0749-0208.

Noise induced error in estimated wave reflection coefficients using an array method is investigated using simulated time series of water surface elevation with known reflection coefficients and added uncorrelated noise. Reflection coefficients are found to be increasingly overestimated with the addition of noise and this positive bias is more significant for lower levels of true reflection. Coherence between the water surface elevation time series changes systematically with the bias and, along with the estimated reflection coefficients, is used to create a "look-up table" which serves as a function to correct for the observed bias. Bias and corresponding coherence levels are found to be independent of frequency allowing the same correction function to be applied across all frequencies and for frequency-averaged (*e.g.*, across the infragravity band) reflection coefficients. Root-mean-square error associated with infragravity-averaged reflection coefficients, across all known reflection levels and noise-to-signal ratios up to 1, is reduced from 0.22 before the correction to 0.01 following the correction. Field data from a natural, dissipative beach is used to demonstrate the application of these results.

ADDITIONAL INDEX WORDS: *Incident and reflected waves, noise, frequency, linear wave theory.*

INTRODUCTION

As waves which are propagating towards a coastline reach shallow water they can dissipate, partially reflect, or fully reflect. The amount of energy that is reflected or dissipated is a function of the bed slope, wave height and wave period (Battjes, 1974). For example, on low gradient, dissipative beaches most waves dissipate their energy across wide surf zones and reflection is limited to low frequency (infragravity) waves. Conversely, on steep beaches or coasts backed by hard structures such as a sea wall, wave breaking is impeded allowing more reflection to occur and at higher frequencies. Wave reflection influences the hydrodynamics and sediment dynamics close to shore, and consequently the morphological response of the beach itself. Understanding and predicting the magnitude of wave reflection, particularly during energetic forcing conditions, is therefore important for estimating potential storm damage, modelling shoreline change, and the construction of marine structures.

Two general methods exist for measuring wave reflection; array methods and PUV methods. Array methods (*e.g.*, Battjes *et al.*, 2004; Gaillard *et al.*, 1980; Mansard and Funke, 1980) use a cross-shore array of spatially separated elevation or pressure sensors (ideally three or more) and the phase difference between each sensor pair in the array provides information on the shoreward and seaward propagating waves from which reflection coefficients (the ratio between seaward and shoreward propagating components) can be calculated. PUV methods (*e.g.*, Guza and Bowen, 1976; Sheremet *et al.*, 2002) use pressure and cross-shore current data from co-located sensors to estimate the shoreward and seaward propagating components using the slope of the sea surface. Whereas array methods provide a single estimate of wave reflection averaged over the entire spatial extent of the array, PUV methods have the advantage of estimating wave reflection at a single cross-shore location. However, pressure sensors are less intrusive to deploy in the field than current sensors and far more economical if reflection is required at several cross-shore locations; every additional pressure sensor deployed after the initial three allows for another sensor array from which wave reflection can be estimated.

Most array methods for calculating wave reflection are designed for waves propagating over a horizontal bed and do not account for sloping bathymetry such as that of a natural beach. However, Baldock and Simmonds (1999) used the method of Frigaard and Brorsen (1995) to demonstrate that relatively simple modifications are required for array methods to be adapted to account for shore-normal linear waves propagating over a sloping bottom. They also use numerically simulated data to show that neglecting the shoaling effects of waves on a sloping bed can lead to significant errors (up to 90%) in estimated reflection coefficients and amplitudes of the shoreward and seaward propagating waves, especially if the true reflection is low.

An additional source of error that may impact wave reflection estimates, particularly when using field data, is that of noise. Using simulated time series of elevation and current with known

DOI: 10.2112/SI75-176.1 received 15 October 2015; accepted in revision 15 January 2016.
*Corresponding author: kris.inch@plymouth.ac.uk
©Coastal Education and Research Foundation, Inc. 2016

true reflection coefficients and added uncorrelated noise, Huntley *et al.* (1999) show that the presence of noise in the data can introduce a significant positive bias to the estimated reflection coefficients from PUV methods. In an attempt to remove the bias found in some PUV methods, Tatavarti *et al.* (1988) used principal component analysis to separate the elevation and current time series into orthogonal eigenvector combinations, thus allowing the *correlated* parts of the two time series to be separated from unwanted noise. Applying this technique to field data did indeed provide lower reflection coefficient estimates than other PUV methods. Huntley *et al.* (1999) demonstrate that the bias in reflection coefficients from PUV methods can also be corrected for using the estimated reflection coefficient and coherence between the estimated shoreward and seaward propagating wave time series. A similar investigation of noise using array methods is currently lacking.

The aim of the present work is to use simulated time series of incident and reflected surface elevations to investigate noise induced error on reflection coefficients estimated using an array method. A technique is presented to correct for the observed error and this technique is applied to field data to demonstrate its value.

METHODS

The water surface elevation η at a single cross-shore location x is given by linear wave theory as

$$\eta(x,t) = a_i \cos(kx + \omega t + \phi_i) + a_r \cos(kx - \omega t + \phi_r) \qquad (1)$$

where t is time, a is wave amplitude, k is wavenumber ($2\pi/L$, where L is wavelength), ω is wave angular frequency ($2\pi f$, where f is frequency), ϕ is phase, and subscript i and r denote incident and reflected waves, respectively. The signs of the terms are for an offshore-directed x-axis. For multiple cross-shore locations separated by Δx, the incident and reflected waves are phase shifted by $-k\Delta x$ and $k\Delta x$, respectively.

Equation 1 is used to generate simultaneous time series of water surface elevation at three spatial locations. For the purpose of the simulations, a_i is set to 1 and $a_r$to a predetermined reflection coefficient at all frequencies. Furthermore, the time delay between spatial locations and between the incident and reflected waves, and the wave phase velocity are all independent of frequency. Uncorrelated, random noise is added to the time series at known noise-to-signal ratios and subsequent frequency dependant reflection coefficients are calculated as the ratio between the reflected and incident spectra using the array method of Gaillard *et al.* (1980) with modifications for wave shoaling and phase speed effects. To differentiate between known and estimated reflection coefficients they will be denoted by R and $\hat{R}$, respectively. The spectra used to calculate reflection coefficients were calculated from time series of 8192 points sampled at 4 Hz with 50% overlapping, hanning-tapered segments of 1024 points, giving a frequency resolution of 0.0039 Hz and 27 degrees of freedom (Nutall, 1971). Spectral coherence is calculated between each pairing of water surface elevation time series and subsequently averaged to obtain mean coherence over the array. The 95% confidence threshold on coherence is 0.19 (Shumway and Stoffer, 2000).

Simulations are run with known reflection coefficients between 0 and 1 at 0.05 increments and with noise-to-signal ratios between 0 and 2, also at 0.05 increments. The simulation for each reflection coefficient and noise-to-signal ratio combination is repeated 100 times to gain mean values of the error associated with each $\hat{R}$ estimate. While the use of constant wave amplitudes and reflection coefficients across all frequencies is not representative of real field data, it does allow the frequency dependence of noise induced error to be investigated as all $\hat{R}$ estimates represent independent realizations of the same conditions.

Whilst the results presented in the following section are applicable to all frequencies up to the Nyquist frequency of 2 Hz, the technique will later be applied to field data from the infragravity-dominated inner surf zone of a high energy, dissipative beach. Therefore, results from the numerical simulations will focus on infragravity reflection coefficients. For calculating frequency-averaged infragravity reflection coefficients $\hat{R}_{inf}$and corresponding coherence levels, the infragravity band is taken as 0.005-0.05 Hz.

RESULTS

Figure 1 shows the error associated with estimated infragravity-averaged reflection coefficients as a function of the true reflection coefficient and noise-to-signal ratio. It is clear that the addition of noise causes a positive bias in estimated reflection coefficients and that this bias is more significant when the true reflection coefficient is lower. For example, with a noise-to-signal ratio of 0.5, the positive bias is 0.25, 0.16 and 0.06 for true reflection coefficients of 0.2, 0.4 and 0.8, respectively. When the true reflection coefficient is 1, bias in the estimated reflection coefficient is negligible. The rate of increase in the bias with added noise is rapid up to a noise-to-signal ratio of around 1, above which it begins to slow.

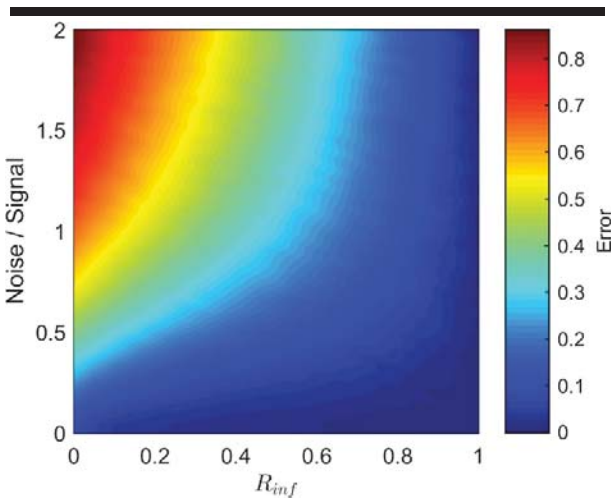

Figure 1. Error in estimated infragravity-averaged reflection coeffcients as a function of the known true reflection coefficient R and the noise-to-signal ratio.

Although the noise-to-signal ratio is unknown in real measurements, the spectral coherence between the water surface elevation time series can be considered an excellent proxy. Furthermore, the observed change in bias with coherence, as well as the modulation by R shown in Figure 1, is constant over all frequencies. This is demonstrated in the contour plot Figure 2 which shows the error associated with different levels of coherence over the infragravity frequency band with a true reflection coefficient of 0.2. The contour line corresponding to a positive bias of 0.5, for example, has a mean coherence of 0.27 across the infragravity frequency band and a maximum deviation away from the mean of 0.06. The consistency in bias across all frequencies, and thus range of wavelengths, implies that both array spacing and spectral smoothing will have little impact over the observed bias. Performing these simulations using a variety of different array set-ups and spectral analysis techniques (not shown) confirms this.

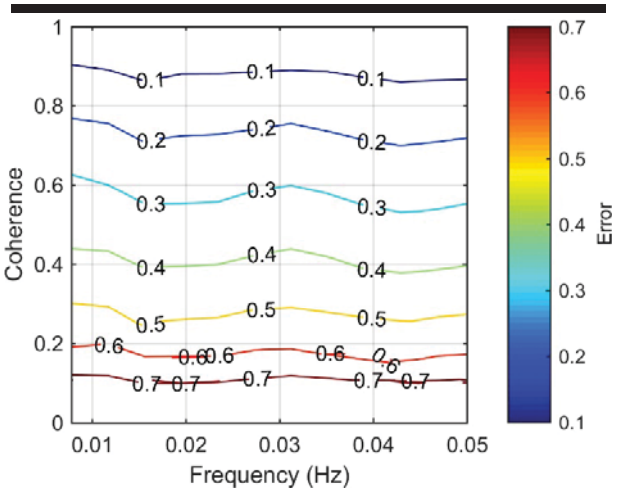

Figure 2. Contour plot showing the error in estimated reflection coefficients in the infragravity frequency band as a function of frequency and coherence. The true reflection coefficient is 0.2.

Whilst in real data the true reflection coefficient is unknown, the relationship between the bias and coherence, along with the knowledge that this relationship is independent of frequency, allows us to estimate and remove this bias. This is achieved by combining the estimated reflection coefficients, coherence levels, and associated bias from all simulations to create an algorithm based on a "look-up table" that can be applied across all frequencies, and indeed to frequency-averaged reflection coefficients. Figure 3 illustrates the data that are used to perform these corrections; where there is no data, a reliable estimate of the bias was unable to be made and the reflection coefficient must be assumed to be not significantly different from zero. Additionally, reflection coefficients must be assumed to be not significantly different from zero if the coherence is less than the 95% confidence threshold.

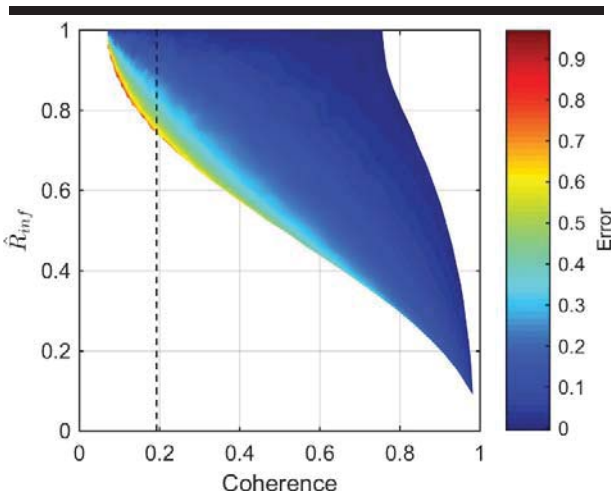

Figure 3. Error in estimated infragravity-averaged reflection coeffcients as a function of the estimated infragravity-averaged reflection coefficient $\hat{R}_{inf}$ and infragravity-averaged coherence between the water surface elevation time series. The black dashed line indicates the 95% confidence threshold for coherence.

To test the functionality of this correction technique, further simulations were run with the full range of known reflection coefficients and noise-to-signal ratios in order to obtain estimated reflection coefficients and associated coherence and error values that are not already contained in Figure 3. The outcome of applying the correction technique to this data is demonstrated in Figure 4A which shows the difference between the corrected estimate of the infragravity-averaged reflection coefficient $\hat{R}_{c,inf}$ and the known reflection coefficient as a function of the infragravity-averaged coherence. The correction technique is shown to be very effective with 94% of the corrected reflection coefficients having a residual error of < 0.02 and none with an error over 0.06. The correction performs slightly less well when coherence is low. For example, the mean residual error on reflection coefficients with corresponding coherence levels between 0.6 and 0.7 is 0.003, whereas this increases to 0.012 for coherence levels between 0.2 and 0.3. Corrections were not performed if the coherence was less than the 95% confidence threshold. This mainly occurs when the noise-to-signal ratio is above ~1.2. The results shown in Figure 4A are used to calculate 95% confidence limits on corrected reflection coefficients using the t-distribution. Confidence limits are calculated for separate coherence bands at increments of 0.1 and are shown in Figure 4B. The 95% confidence limits range from ± 0.003 for coherence levels between 0.9 and 1, to ± 0.035 for coherence levels between 0.2 and 0.3. The 95% confidence limits are well predicted using an exponential decay model with the equation $y = Ae^{bx}$ and coefficients A = 0.0824 and b = -3.6089. R^2 between the data and the exponential model is 0.9933.

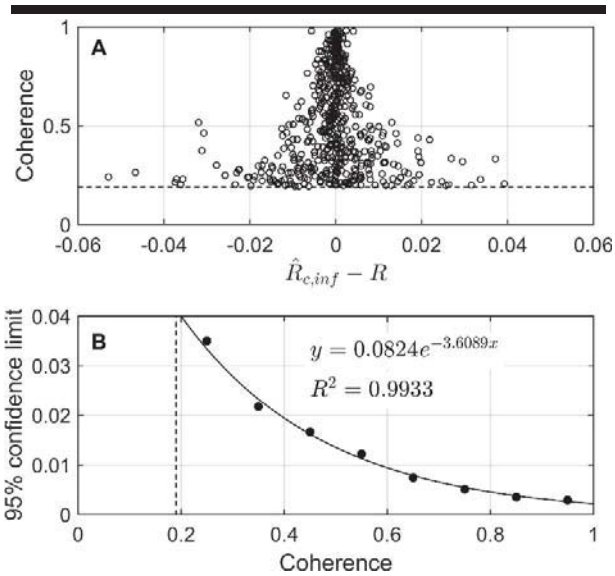

Figure 4. (A) Difference between corrected infragravity-averaged reflection coefficients $\hat{R}_{c,inf}$ and the known reflection coefficient R, versus infragravity-averaged coherence. (B) 95% confidence limits on $\hat{R}_{c,inf}$ for particular coherence bands at increments of 0.1, calculated using the t-distribution. Corrected reflection coefficients were not calculated if the coherence was below the 95% confidence threshold, identified by the black dashed line in (A) and (B). The solid black line in (B) is an exponential decay model with the equation $y = Ae^{bx}$ and coefficients A = 0.0824 and b = -3.6089. R^2 between the data and the exponential model is 0.9933.

DISCUSSION

To demonstrate the application of these results to field data, measurements are used from Perranporth Beach, Cornwall, UK. Perranporth is a macrotidal, dissipative beach exposed to both Atlantic swell and locally generated wind-sea. Water surface elevation data were collected during a field experiment in November 2014 by a cross-shore array of 15 buried pressure transducers logging at 4 Hz. Incident and reflected spectra and corresponding reflection coefficients are calculated as with the simulated data. The field data used here is from a single tide with an offshore significant wave height H_o of 2.06 m and a spectral peak period T_p of 14.3 s.

Measured and corrected frequency dependant reflection coefficients estimated from data collected in the inner surf zone at a mean depth of 1.5 m are shown in Figure 5B and corresponding coherence levels used in the correction are shown in Figure 5A. The measured reflection coefficients range from 0.38 to 0.85 and display the well documented pattern of low reflection at high infragravity frequencies (> 0.025 Hz) and higher reflection at low infragravity frequencies (< 0.025 Hz). Following the technique to correct for bias outlined in the previous section, the corrected reflection coefficients are lower than the measured values at all infragravity frequencies. The largest correction occurs at higher frequencies with a maximum bias of 0.39 at 0.0469 Hz. Lower infragravity frequencies have a smaller bias with a minimum of 0.005 at 0.0078 Hz. Levels of coherence are between 0.61 and 0.81 at all frequencies, corresponding to maximum and minimum 95% confidence limits of 0.007 and 0.004, respectively. The trend of increasing reflection coefficient with decreasing frequency is even more pronounced amongst the corrected reflection coefficients, with frequencies < 0.025 Hz having an average reflection coefficient of 0.53 and frequencies > 0.025 having an average of only 0.07.

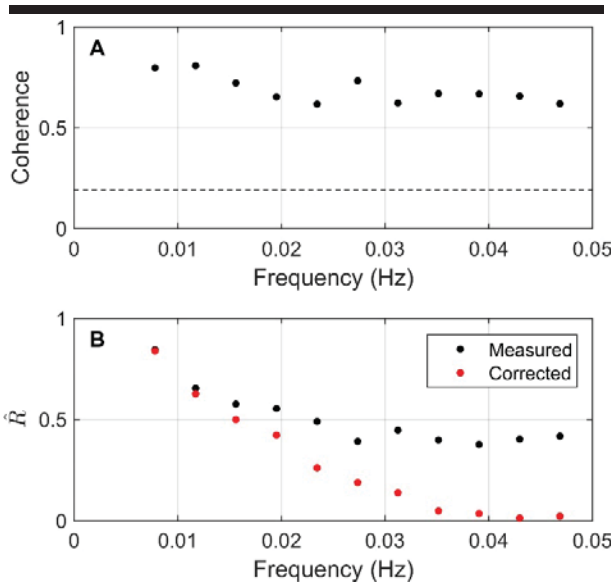

Figure 5. Data from the inner surf zone of Perranporth Beach, Cornwall, UK. (A) Infragravity coherence levels averaged over a cross-shore array of three pressure sensors. (B) Measured and corrected frequency dependant infragravity reflection coefficients $\hat{R}$. 95% confidence limits on the corrected reflection coefficients are negligible (max ± 0.007) and are thus not shown. The black dashed line in (A) indicates the 95% confidence threshold for coherence.

The data and techniques discussed in this paper are applicable to waves that approach the beach predominantly shore-normal. Whilst not presented herein, the results are found to be robust in terms of changing array size and spacing, spectral analysis technique, and the number of water surface elevation time series used in the decomposition method. However, the bias "look-up table" can not be applied confidently to reflection coefficients estimated using array methods other than that of Gaillard *et al*. (1980). Nevertheless, running the same simulations discussed in this paper with different array methods to calculate wave reflection coefficients would be relatively straight forward.

CONCLUSIONS

Synthetic time series of incident and reflected water surface elevation are used to investigate the impact of random noise on wave reflection coefficients estimated using an array method. Results show that noise introduces a positive bias into estimated reflection coefficients at all frequencies and that the bias is a function of the reflection coefficient itself and coherence

between the water surface elevation time series. Data from the numerical simulations is used to create a bias "look-up table" which is used to correct for bias in real reflection coefficient estimates from a high energy, dissipative beach. The results presented in this paper have important implications for studies of wave reflection using array methods and, while the correction technique is currently only applicable for the array method used herein, the process could be repeated using different array methods with relative ease.

ACKNOWLEDGMENTS

The authors would like to thank Sam Prodger, Kit Stokes, Tim Poate, Erwin Bergsma, Olivier Burvingt, and Peter Ganderton for their assistance during the Perranporth field experiment.

LITERATURE CITED

Baldock, T.E. and Simmonds, D.J., 1999. Separation of incident and reflected waves over sloping bathymetry. *Coastal Engineering*, 38(3), 167-176.

Battjes, J.A., 1974. Surf similarity. *Proceedings of the 14th Conference on Coastal Engineering* (Copenhagen, Denmark, ASCE), pp. 466-480.

Battjes, J.A.; Bakkenes, H.J.; Janssen, T.T., and van Dongeren, A.R., 2004. Shoaling of subharmonic gravity waves. *Journal of Geophysical Research*, 109, C02009.

Frigaard, P. and Brorsen, M., 1995. A time-domain method for separating incident and reflected irregular waves. *Coastal Engineering*, 24, 205-215.

Gaillard, P.; Gauthier, M., and Holly, F., 1980. Method of analysis of random wave experiments with reflecting coastal structures. *Proceedings of the 17th Conference on Coastal Engineering* (Sydney, Australia, ASCE), pp. 204-220.

Guza, R.T. and Bowen, A.J., 1976. Resonant interactions for waves breaking on a beach. *Proceedings of the 15th Conference on Coastal Engineering* (Honolulu, Hawaii, ASCE), pp. 560-579.

Huntley, D.A.; Simmonds, D., and Tatavarti, R., 1999. Use of collocated sensors to measure coastal wave reflection. *Journal of Waterway, Port, Coastal, and Ocean Engineering*, 125(1), 46-52.

Mansard, E.P.D. and Funke, E.R., 1980. The measurement of incident and reflected spectra using a least squares method. *Proceedings of the 17th Conference on Coastal Engineering* (Sydney, Australia, ASCE), pp. 154-172.

Nutall, A.H., 1971. *Spectral estimation by means of overlapped FFT processing of windowed data*. New London, Connecticut: Naval Underwater Systems Center (NUSC), *Report No. 4169*, 48p.

Sheremet, A.; Guza, R.T.; Elgar, S., and Herbers, T.H.C., 2002. Observations of nearshore infragravity waves: Seaward and shoreward propagating components. *Journal of Geophysical Research*, 107(C8), 3095.

Shumway, R.H. and Stoffer, D.S., 2000. *Time Series Analysis and Its Applications*. New York: Springer, 610p.

Tatavarti, R.V.S.N.; Huntley, D.A., and Bowen, A.J., 1988. Incoming and outgoing wave interactions on beaches. *Proceedings of the 21st Conference on Coastal Engineering* (Torremolinos, Spain, ASCE), pp. 136-150.

Journal of Coastal Research	SI	75	882-886	Coconut Creek, Florida	2016

Wave Set-up and Run-up Variability on a Complex Barred Beach During Highly Dissipative Storm Conditions

Alexandre Nicolae Lerma[†*], Rodrigo Pedreros[†] and Nadia Senechal[‡]

[†]BRGM (French Geological Survey), Risks and Prevention Division - Coastal Risks and Climate Change Unit, Orléans, France

[‡]CNRS, Université Bordeaux 1, UMR 5805-EPOC, Talence, France

www.cerf-jcr.org

www.JCRonline.org

ABSTRACT

Nicolae Lerma, A; Pedreros, R. and Senechal N. 2016. Wave set-up and run-up variability on a complex barred beach during highly dissipative storm conditions. *In:* Vila-Concejo, A.; Bruce, E.; Kennedy, D.M., and McCarroll, R.J. (eds.), *Proceedings of the 14th International Coastal Symposium* (Sydney, Australia). *Journal of Coastal Research*, Special Issue, No. 75, pp. 882-886. Coconut Creek (Florida), ISSN 0749-0208.

This study assessed the ability of the SWASH model to reproduce wave set-up and run-up on complex realistic 3D morphology during highly dissipative stormy conditions, based on the most energetic field data set reported in the bibliography (ECORS-Truc Vert'08 beach experiment). Several approaches (1D and 2D) and forcing methods (spectral and parametric) were applied. For the three days of high-energy conditions caused by the Johanna storm, wave set-up was accurately reproduced, with simulation performance in 1D and 2D at R^2 = 0.66, 0.81 respectively for all data considered; RMSE = 0.13 m, 0.08 m; bias = 0.06, -0.02. Run-up in the 1D configuration is significantly overestimated while in 2D, the reproduction of run-up using spectral forcing was very accurate with R^2 = 0.73; RMSE = 0.19; bias = 0.04, underlining the role of spectral frequency and directional spread to precisely reproduce the surf zone processes during a storm on a complex barred beach. The maximum estimated values for set-up, run-up and spatial variability of run-up are comparable with results from previous studies, even though significantly higher offshore wave conditions. These results support the hypothesis of a run-up saturation signature in dissipative contexts, mainly influenced by extreme offshore wave conditions.

ADDITIONAL INDEX WORDS: *Surf zone processes, 3D bathymetry, SWASH model, wave set-up, run-up*

INTRODUCTION

In coastal environments exposed to waves, processes caused by wave breaking play a critical role in foreshore changes, erosion and flood hazards. The main manifestation of surf zone processes on beaches is the time-varying vertical position of the water's edge, known as run-up. This is made up of a (quasi) steady component above the still water level (the wave set-up) and a fluctuating component that varies in time, the swash. Accurate estimations of wave set-up and run-up, particularly during storm conditions, are necessary to assess changes in beach face and dune front morphology or to quantify overtopping processes.

Predictions of wave run-up and its components have been the subject of numerous studies based, between many others, on laboratory or flume experiments (Mase 1989; Matias *et al.*, 2013), field observations (Holman and Sallenger 1985; Ruessink *et al.*, 1998; Ruggiero *et al.*, 2004) and numerical studies (Brinkkemper *et al.*, 2013; Guza and Feddersen 2012). However, given the complexity of deploying instruments and collecting field observations over time during high-energy events, most of these studies have focused on relatively moderate offshore wave conditions. Consequently, little is known on the performance of parametric or numerical models reproducing high-energy storm conditions.

Recent studies show that fundamental questions remain about interactions between waves and environmental parameters in highly dissipative conditions (Cox *et al.*, 2013; Guedes *et al.*, 2011; Senechal *et al.*, 2011a), and demonstrate the value of numerical modelling to estimate wave set-up and run-up (Brinkkemper *et al.*, 2013; Guza and Feddersen 2012) or to improve the performance of empirical models (Stockdon *et al.*, 2014) for extreme storm conditions. Recent developments in wave models and particularly non stationary models with a resolved phase, such as SWASH©, can theoretically reproduce surf zone processes such as wave-induced currents, set-up and run-up. However, most validation studies have been performed in flumes. Uses and validation of field data are highly experimental, and even more so for high-energy wave conditions and complex bathymetry.

The first objective of this study was to assess the ability of the SWASH model to reproduce wave set-up and run-up in highly dissipative stormy conditions, based on the most energetic field data set reported in the bibliography (Senechal *et al.*, 2011b; Pedreros *et al.*, in revision). The second aim was to assess the sensitivity of wave set-up and run-up to different model settings and data forcing. Finally, we evaluated the potential variability in time and alongshore of wave set-up and run-up during the studied period in the context of a complex 3D barred beach.

METHODS

For this study, we used data collected during the ECORS-Truc Vert'08 beach experiment (Aquitanian coast, France, Senechal *et al.*, 2011b). The field experiment lasted for 6 weeks, from 3 March to 13 April 2008. Truc Vert'08 was designed to

DOI: 10.2112/SI75-177.1 received 15 October 2015; accepted in revision 15 January 2016.
*Corresponding author: a.nicolaelerma@brgm.fr
©Coastal Education and Research Foundation, Inc. 2016

study beach dynamics during high-energy events, with a particular emphasis on large winter waves, three-dimensional morphology and macro-tidal conditions. All details about this experiment are described in Senechal *et al.* (2011b). The Truc Vert beach (Figure 1), located in SW France, is an open beach, where the wave climate is characterized by an annual mean significant wave height (Hs) of 1.4 m and an 8 s mean wave period (Butel *et al.*, 2002) but higher waves can reach Hs ≈ 10 m during severe offshore storms. The tide is semi-diurnal with an annual mean spring tide range of 3.7 m. Tidal currents are negligible, but wave-induced currents, such as rip currents, can reach 1m/s (Bruneau *et al*., 2011). The coast runs almost directly north to south and is characterized by a double-barred beach with the inner bar and outer bar generally exhibiting bar and rip morphology and crescentic patterns, respectively (Castelle *et al.*, 2007). During the experiment no beach cusps were observed and the upper beach face was relatively uniform in the alongshore direction.

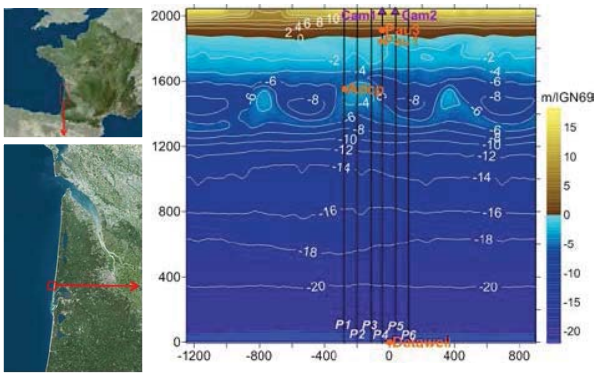

Figure1. Local bathymetric characteristics and sensor locations.

During the experiment period, a severe storm (Johanna) occurred, on 10 March 2008. This event was assessed as a 10-year return period storm and coincided with a large tidal amplitudes (more than 4 m, Figure 2). Sea state conditions were measured with a directional Mark III Datawell wave rider buoy anchored at a depth of 20 m offshore from the field area, about 1.5 km from the beach face (Figure 1). Wave conditions during the period studied (8 to 12 March 2008) reached Hs = 8.1 m and Tp = 17 s. Three sensors provided measurements of water level elevation: one ADCP current meter, located on the horn of the outer bar, and two pressure sensors (PAU1 and PAU3), located in the inner bar system (*cf.* Figure 1). The processing performed to estimate tide and storm surge contributions, and hence wave set-up, from the water level elevation are described in Pedreros *et al.*, (in revision). Because of their locations and the tidal variations, the ADCP sensor was alternatively located in the set-up and set-down areas and the two PAU sometimes emerged during low tide. It should be kept in mind that all the wave set-up values supplied at the ADCP, PAU1 and PAU3 locations are local values, and not the maximum value at the waterline.

Run-up on the beach was measured with two high-resolution digital cameras. Details on photogrammetric processing are given in Senechal *et al.* (2011a). Each observation was a 15-min time series measured along 2 individual cross-shore transects. Observations were concentrated around high tide to maximize stationarity of the wave-breaking location and area of the foreshore over which the run-up propagated. This also allowed measurements on steep beach slopes, since the high tide water level, and the swash region, reached as far as the upper beach face. Run-up elevation time series were acquired during rising conditions but, unfortunately, the storm tide reached its peak height during the night and because of the extreme climatic conditions (camera facing into wind and heavy rain), some data could not be used for analysis. The vertical resolution of the run-up elevation, depending both on lens properties and distance from the cameras, was estimated to be less than 0.10 m for all the data analysed.

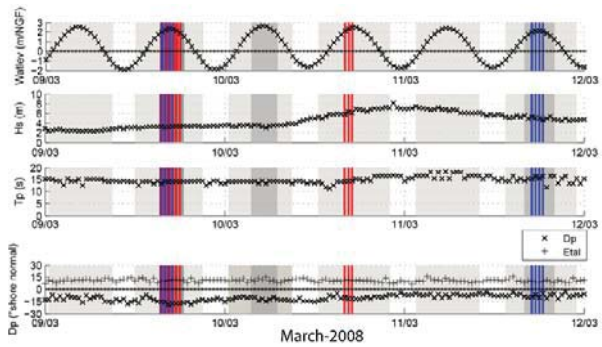

Figure 2. Observed wave conditions and reconstructed water level (tide and atmospheric surge) during the period studied from Pedreros et al., (in revision). The ADCP sensor functioned during the entire study period. Other acquisition periods are underlined as follows: light grey for PAU1, dark grey for PAU3, red for camera1 and blue for camera2.

The model used to simulate the free surface evolution in the surf zone was the SWASH 2.00A model (Zijlema *et al*., 2011). This model is based on nonlinear shallow water equations (NLSW) including non-hydrostatic pressure, and provides a general basis for describing complex changes in rapidly varying flows. It is considered as a valuable tool to reproduce wave propagation, wave breaking, energy dissipation and energy transfer from the incident frequency band to the infragravity band.

The model was run for the whole study period on a fixed topo-bathymetric model (2 m spatial resolution, Figure 2) constructed from a topo-bathymetric survey before the storm.

Because of the potential difficulty of securing full bathymetric survey data and observed wave data or to have available extended computing resources, the applicability of the SWASH model was assessed for several configurations. Two different simulation modes were used to reproduce wave set-up and run-up: in 1D mode with 6 cross-shore profiles to describe the bar and rip bathymetry at the centre of the domain and at the sensor location, and in 2D mode covering the entire domain. For each mode (1D and 2D) the model was forced with spectral and estimated parametric wave data from the offshore buoy (SHOM). The spectra (1D and 2D) comprise 32 frequencies from 0.7 to 0.04, and 24 directions for the 2D spectra.

Parametric and 1D spectral characteristics were computed every 30 minutes and 2D spectra only every 3 hours. In the present case, parametric forcing was integrated as a default TMA spectra computed by SWASH. Each simulation was computed from the initial stationary water level conditions. The simulation time was set at 20 min, with 5 min spin up and results output every 1s, equivalent to post-processing characteristics for wave set-up measurements and the acquisition time for video observations used to calculate run-up values. The simulation time step was set at 0.01 s, the minimum depth for computation at 0.01 m, bottom friction was integrated with a homogeneous Manning coefficient of 0.019 (default) and the CFL was around 0.4.

Wave set-up was calculated as the mean sea surface level during 15 min at the location of each sensor. Run-up height values were extracted every second, tracking the water line as the last wet cell where current values are null. To compare with previous observations (Senechal *et al.*, 2011a), the significant swash height (S) was calculated for cross-shore profiles computing energy spectra, PSD (*f*) from detrended, tapered run-up height time series as:

$$S = 4\sqrt{\sum PSD(f)df}$$

In the 1D configuration, simulated wave set-up for the ADCP location was calculated with profile P1. For the two PAU locations, it was calculated from simulations run in P4. In 2D, wave set-up was calculated for each location sensor. To compare observed and simulated run-up, results were computed along the cross-shore in front of the camera, i.e. for the P4 and P5 locations. Other analysis was performed based on the 2% maximum wave run-up, for comparison with other studies. $R_{2\%}$ was statistically obtained considering a normal distribution for all vertical run-up data series for each simulated case.

RESULTS

The simulated wave set-up was compared to sensor data post-processed as described in Pedreros *et al.* (in revision) (*cf.* Figure 3). The results presented here are from spectra forcing simulations. For the 1D configuration, comparisons were made every 30 min, while the 2D configuration was simulated only at 3h time step (corresponding to available 2D wave spectra). In 1D mode, the results concur with observations, showing high correlation and low RMSE, at R^2 =0.81, 0.82 and 0.77 and RMSE= 0.15 m, 0.09 m, 0.12 m for ADCP, PAU1 and PAU3 data respectively (*cf.* Figure 3). At the ADCP location, which is alternately in the set-up and set-down area due to tidal variations, the model does not reproduce well wave set-down. At this location, the simulations overestimate observations but with a reasonable bias (= 0.13m). For PAU1, wave set-up is reproduced even better, no bias (= -0.01m); the bias for PAU3 is slightly higher with a tendency towards underestimation (= -0.1m). In 2D mode, the results show a similar capacity for reproducing wave set-up accurately at each location. Given that comparisons are made with fewer data, the results show a similar or even better relationship, as for the ADCP location (R^2 = 0.85, RMSE = 0.07 m, Bias = 0.03 m).

When all available data are considered to evaluate the ability of the model to reproduce the spatial variability of wave set-up in the near shore area, the relationship between observations and simulations is better in 2D than in 1D. Results in 1D mode systematically display the highest RMSE and bias. Nevertheless, both configurations produce satisfactory results (*cf.* Table 1).

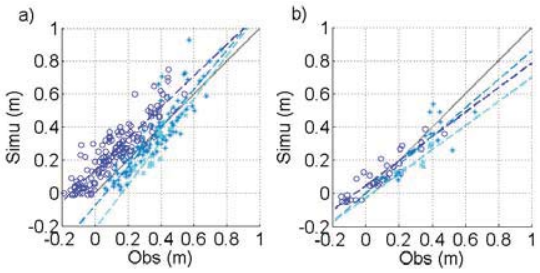

Figure 3. Observed versus simulated set-up: observed set-up (dark blue circles: ADCP; blue asterisks: PAU1; cyan crosses: PAU3) and linear regression versus simulations in 1D a), and 2D b), respectively.

Table 1. *Model performance in simulating wave set-up and run-up, spec = spectral forcing, para= parametric forcing*

Process	Sensor	Mode	R^2	RMSE(m)	Bias(m)
Setup	ADCP	1Dspec	0.81	0.15	0.13
		2Dspec	0.85	0.07	0.03
	PAU1	1Dspec	0.82	0.09	0.09
		2Dspec	0.76	-0.01	-0.04
	PAU3	1Dspec	0.77	0.12	-0.1
		2Dspec	0.76	0.09	-0.04
	All	1Dspec	0.66	0.13	0.06
		2Dspec	0.81	0.08	-0.02
Run-up	Camera	1Dspec	0.80	1.66	1.61
		1Dpara	0.67	2.36	2.32
		2Dspec	0.73	0.19	0.04
		2Dpara	0.71	0.43	0.27

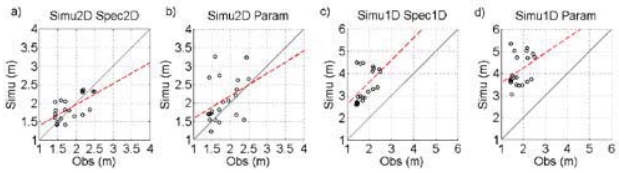

Figure 4. Observed versus simulated run-up.

For the run-up (Figure 4), comparisons between field results and simulations, the results show significant differences depending on the wave input characteristics and the model configuration (table 1, Figure 4). In the 1D configuration, the simulations show a strong correlation with observations for spectral forcing with R2 = 0.80 and 0.67 for parametric forcing, but a high overestimation of wave run-up values, with RMSE = 1.66 m and 2.36 respectively. This overestimation appears to be as a systematic bias (particularly for 1D spectral forcing).

The 2D configuration produces contrasting results. For 2D spectral forcing, results are good with R^2 = 0.73, RMSE=0.19

and a very weak positive bias = 0.04 m. In this configuration, the lowest run-up values are underestimated while the highest, corresponding to the peak of the storm, are more accurately reproduced. Model performance is poorest for 2D parametric forcing, with a comparable $R^2 = 0.71$ but a wider dispersion of results and a significantly higher RMSE = 0.43 m. However, the RMSE values are reasonable and bias is relatively low.

DISCUSSION

Given the natural instability of the run-up process, particularly during a storm, and the necessary approximation involved in assessing spectral energy density, simulations in 1D and 2D both produce acceptable results. In comparison with other recent studies, the ability of SWASH to reproduce wave set-up and run-up observed in the field is notably better than the performances presented by Stockdon *et al.* 2014 with the X-beach model. Inevitably, because of the non-integration of the alongshore wave-induced current and retro-actions, which are particularly intense in 3D morphologies, 1D simulation has a tendency to overestimate wave set-up and run-up values (Table 1). Results for the 2D mode are satisfactory but the use of spectral forcing clearly improves simulation performance. This is basically due to spectrum composition from parametric data, which cannot represent the complexity and nuances contained in the observed spectra. In this case, the 2D parametric reconstruction of the spectra was compared with the observed spectra at two moments, before and during the apex of the storm (*cf.* Figure 5). The figure clearly shows that the spread (more than 60°) and the second peak (particularly around 8s before the storm) of the observed spectrum cannot be reproduced by a TMA spectrum. This appears to be the main reason why simulations with parametric forcing produced the poorest results, and underlines the importance on complex barred beaches of taking into account the spectral spread to understand the wave-breaking process and the ensuing morphological changes.

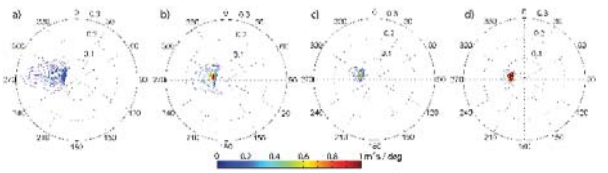

Figure 5. Observed and computed spectra used for 2D simulations, a), c) before the storm, b), d) during the peak respectively.

Taking into account the fact that the data observed over the entire period were simulated on a fixed bathymetry, the data presented in 2D mode show that potential morphological changes occurring during the storm have relatively little effect on set-up and run-up values. The morphological changes that occurred during the event in the foreshore area (straightening of the outer bar and its migration 100 m offshore after about one day (Almar *et al.*, 2010) were in fact expected to have little effect on run-up because of the distance between the position of the time-stacks and the closest onshore-protruding bar horn, which was observed as about 150 m alongshore and around 500 m in the cross-shore direction, at high tide (Senechal *et al.*, 2011a). Even though nearshore morphological characteristics and their potential evolution are expected to have relatively more influence during low or mid-tide, we decided to reconstruct the time-variable $R_{2\%}$ for the entire period studied (Figure 6). The results for the 1D and 2D configurations indicate comparable behaviour with (i) a higher $R_{2\%}$ value during the high tide period, (ii) $R_{2\%}$ variability of around 0.2 m at low tide and around 0.5 m at high tide. These results are comparable to observations of the Duck field experiments showed that the alongshore standard deviation of observed S showed differences of around 0.4 to 0.5 m (Stockdon *et al.*, 2006). During the storm peak, at high tide, spatial variability can be noticeably higher, up to 1.5 m in 2D and remaining at around 0.5 m during low tide.

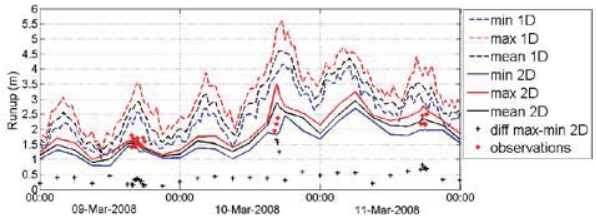

Figure 6. Alongshore variability of $R_{2\%}$ between 09-12 March 2008. Spatial variability is estimated based on 6 cross-shore profiles forced by 1D spectra every 30 min for the 1D mode and by 2D spectra every 3h for the 2D mode.

In previous study reporting higher values of set-up and run-up, Duck82 (Holman 1986), Duck94 (Holland and Holman, 1996) and Duck90 (Holland and Holman 1993), found set-up values at 1.5 m, 1.25 m, and around 1 m respectively. Observed run-up values were also higher, at more than 3 m, up to 2.7 m and between 2.5 and 2 m, respectively. Regarding the results obtained for 2D simulations with spectral forcing, the maximum set-up values during the peak of the storm, were around 1.5 m, which is comparable to the higher values observed in the Duck campaigns. Simulated run-up was around 3 m and up to 3.5 m, taking the spatial variability along the beach into account.

Surprisingly, although offshore wave conditions during the Truc Vert experiment (*cf.* Figure 2) were significantly higher than during the Duck 82 experiment (maxima Hs= 4.1 m and Tp=13.8), the set-up and run-up values observed, and simulated in this study, are quite similar. These observations need to be confirmed with other storm datasets, but they support the hypothesis of a saturation signature (Ruessink *et al.*, 1998; Senechal *et al.*, 2011a). In a dissipative context influenced mainly by extreme offshore wave conditions, saturation on the incident band extends to the infragravity band, which limits the $R_{2\%}$ values. This hypothesis was tested by Senechal *et al.* (2011a), who showed that when the entire Truc Vert campaign data set was taken into account, the best statistical predictor of run-up behaviour was hyperbolic tangent adjustment. This behaviour was also addressed by Brinkkemper *et al.* (2013) through numerical cyclonic wave modelling. This will be further investigated in forthcoming studies on wave-breaking parameterization to better reproduce wave set-down, and on the specific ability of the SWASH model to reproduce the behaviour

of the incident and infragravity bands in complex bathymetric conditions.

CONCLUSIONS

We explored the ability of the SWASH model to reproduce wave set-up and run-up in highly dissipative conditions. We found that the model performed well in reproducing the set-up process in the 1D and 2D modes, but produced more contrasting results when reproducing run-up. Predicting run-up accurately is clearly dependent on the integration of current water circulation (using the 2D mode), directional spreading and secondary spectral energy peaks. Nevertheless, have available observed spectral data is uncommon and so the use of parametric forcing in 2D produces reasonable results. However, further studies are needed to assess the specific ability of the SWASH model to reproduce the energy contained in the incident and infragravity bands and, in particular, to investigate reproduction of the saturation threshold and its consistency with studies performed in dissipative contexts that are mainly influenced by extreme offshore wave conditions.

ACKNOWLEDGMENTS

This work was financed by BRGM research founds. We thanks the all team of ECORS'08 project and especially EPOC and the SHOM (Fabrice Ardhuin). We are also grateful to Ifremer (Previmer), ANR (Vulsaco) and M. Yates for their work on the data used in the study.

LITERATURE CITED

Almar, R.; Castelle, B.; Ruessink, B.G.; Senechal, N.; Bonneton, P., and Marieu, V., 2010. Two- and three-dimensional double-sandbar system behaviour under intense wave forcing and a meso-macro tidal range.*Continental Shelf Research*, 30 (7), 781-792.

Brinkkemper J.A.; Torres-Freyermuth A.; Mendoza E.T., and B.G. Ruessink 2013. Parameterization of wave run-up on beaches in Yucatan, Mexico: a numerical study, *Coastal Dynamics 2013* No25, 225-234 p

Bruneau, N. ; Bonneton, P. ; Castelle, B., and Pedreros, R., 2011. Modeling rip current circulations and vorticity in a high-energy meso-environment, *Journal of Geophysical Research*, 116, C07026.

Butel, R. ; Dupuis H., and Bonneton P., 2002. Spatial variability of wave conditions on the French Aquitanian coast using in-situ data, Journal of Coastal *Research*., SI 36, 96-108.

Castelle, B.; Bonneton P.; Dupuis H., and Sénéchal N. 2007, double bar beach dynamics on the high-energy meso-macrotidal French Aquitanian coast, *Marine Geology*, 254, 216-223.

Cox, N.; Dunkin, L.M., and Irish, J.L., 2013.An empirical model for infragravity swash on barred beaches. *Coastal Engineering* 81, 44-50.

Guedes R.M.C.; Bryan K.R.; Coco G., and Holman R.A., 2011. The effects of tides on swash statistics on an intermediate beach. *J. Geophys. Res*. 116, C04008.

Guza, R. T. and F. Feddersen. 2012. Effect of wave frequency and directional spread on shoreline runup, *Geophys. Res. Lett*., 39, L11607.

Holland, K.T. and Holman, R.A., 1993. Statistical distribution of swash maxima on natural beaches. *Journal of Geophysical Research* 98 (C6), 10271–10278.

Holland, K.T. and Holman, R.A., 1996. Field observations of beach cusps and swash motions. *Marine Geology* 134, 77-93.

Holman, R.A. and Sallenger Jr., A.H., 1985. Setup and swash on a natural beach. *Journal of Geophysical Research* 90 (C1), 945–953.

Holman, R.A., 1986. Extreme value statistics for wave run-up on a natural beach. *Coastal Engineering* 9, 527–544.

Mase, H., 1989. Random wave runup height on gentle slope.*Journal of Waterway, Port, Coastal, and Ocean Engineering*, 115, 649-661.

Matias, A.; Masselink, G.; Kroon, A.; Blenkinsopp, C., and Turner, I.L., 2013. Overwash experiment on a sandy barrier *In:* Conley, D.C., Masselink, G., Russell, P.E. and O'Hare, T.J. (eds.), *Proceedings 12th International Coastal Symposium*, Journal of Coastal Research, Special Issue, No. 65, pp. 778-783 Plymouth, England, ISSN 0749-0208.

Pedreros, R.; Idier, D.; Muller, H.; Lecacheux, S.; Paris, F.; Yates-Michelin, M.; Dumas, F.; Pineau-Guillou, L.; Ardhuin, F., and Sénéchal N., 2015. Relative contribution of wave setup to the storm surge in complex and energetic environments: observation and modeling based analysis. *Coastal Engineering*. (in Press)

Ruessink, B.G.; Kleinhaus, M.G., and van den Beukel, P.G.L., 1998. Observations of swash under highly dissipative conditions. *Journal of Geophysical Research* 103(C2), 3111–3118.

Ruggiero, P.; Holman, R.A., and Beach, R.A., 2004. Wave run-up on a high-energy dissipative beach. *Journal of Geophysical Research* 109 (C6).

Senechal, N.; Coco, G.; Bryan, K.R., and Holman, R.A., 2011a. Wave runup during extreme storm conditions. *J. Geophys. Res. Oceans* 116 (C7), C07032.

Senechal, N.; Abadie, S.; Gallagher, E.; MacMahan, J.H.M.; Masselink, G.; Michallet, H.; Reniers, A.J.H.M.; Ruessink, B.G.; Russell, P.E.; Sous, D.; Turner, I.L.; Ardhuin, F.; Bonneton, P.; Bujan, S.; Capo, S.; Certain, R.; Pedreros, R., and Garlan, T., 2011b. The ECORS-Truc Vert'08 nearshore field experiment: presentation of a three-dimensional morphologic system in a macro-tidal environment during consecutive extreme storm conditions, *Ocean Dynamics*, 61

Stockdon, H.F.; Holman, R.A.; Howd, P.A., and Sallenger, A.H., 2006. Empirical parameterization of setup, swash, and runup. *Coastal Engineering* 53(7), 573–588.

Stockdon, H.F.; Thompson, D.M.; Plant, N.G., and Long, J.W., 2014. Evaluation of wave runup predictions from numerical and parametric models, *Coastal Engineering* 92, 1–11.

Zijlema, M.; Stelling, G.S., and Smit, P.B., 2011. SWASH: an operational public domain code for simulating wave fields and rapidly varied flows in coastal waters. *Coastal Engineering* 58, 992–1012.

Journal of Coastal Research	SI	75	887-891	Coconut Creek, Florida	2016

Morphological Response to the Installation of Detached Breakwaters along the Cigu Coast of Tainan, Taiwan

Tsung-Yi Lin

Department of Geography
National Taiwan Normal University
Taipei 10610, Taiwan

www.cerf-jcr.org

www.JCRonline.org

ABSTRACT

Lin, T.-Y., 2016. Morphological response to the installation of detached breakwaters along the Cigu coast of Tainan, Taiwan. *In:* Vila-Concejo, A.; Bruce, E.; Kennedy, D.M., and McCarroll, R.J. (eds.), *Proceedings of the 14th International Coastal Symposium* (Sydney, Australia). *Journal of Coastal Research*, Special Issue, No. 75, pp. 887-891. Coconut Creek (Florida), ISSN 0749-0208.

Coastal landforms represent a state of equilibrium between natural forces and geological resistance. Any hard structures constructed can interfere with the natural processes of the coastal system and initiate a series of reactions. This study investigates the morphologic changes after the installation of a group of eleven detached breakwaters at the Cigu coast of Tainan, Taiwan. Multi-temporal satellite images and aerial photographs, along with field data of beach profiles, are used to analyze the sequential landform changes before and after the construction of these engineering structures. During the late 1990s, the shoreline of the Ding-tou-er Barrier had retreated after a couple of typhoon events, and the coastal hazard prevention agency decided to install detached breakwaters to prevent further erosion. Due to the installation of detached breakwaters, the nearby shores, especially the down-drift side of the coast, experienced rapid erosion either during or after the construction. Only the four detached breakwaters at the most northern end had salients that formed on their back sides. The others yielded no sand accumulation at all. Moreover, the sand accumulates on the back side of the detached breakwaters at such a fast rate that vegetation cannot grow or expand. Thus, the bare surface sand became the source of wind-blown sand that moved over the dike during the winter season. These wind-blown sand first buried the road and large numbers of spare tetrapods, then encroached the nearby aqua-cultural ponds.

ADDITIONAL INDEX WORDS: *Engineering structures, detached breakwaters, morphological change, wind-blown sand, coastal management.*

INTRODUCTION

Coastal landforms represent a state of equilibrium between geological conditions and natural forces, such as waves, currents, tides, and wind. In a coastal system, constructions of engineering structures inevitably interfere with the natural state of equilibrium. Subsequently, coastal landorms will experience changes as a new state of equilibrium is established in response to such human intereference. Hsu *et al*. (2007) explored the effects of human activites on the problems of erosion along Taiwan's coastal lines. They found that around 80% of Taiwan's sandy coasts are currently experiencing erosion and that human activities are at the heart of why, after experiencing at least three hundred years of accumulation, these coasts are experiencing erosion. These human activities may include river regulation, construction of reservoir dams, the use of artificial structures on the coasts, and harbor construction.

In a comprehensive survey of the shoreline changes around Taiwan coast, Lin (2012) claimed that the installation of engineeringing structures is the main culprit responsible for most of the recent erosional hot spots. The current policies in Taiwan require that major construction projects, including the building of harbors and other coastal developments, be evaluated by their effects on the geomorphic environment.

Using various methods, such as physical modelling and numerical modelling of the hydraulics, evaluations and forecasts are made prior to construction. Yet, there lacks a requirement to track and verfiy the effects after construction begins. When it comes to coastal defence structures, such as the seawalls (dikes), groins, or detached breakwaters readily found in Taiwan, pre-construction evaluations, not to mention post-construction tracking or auditing, are frequently ignored under the pressures of emergency relief situations. Consequently, these engineering structures, which are built for coastal protection, often bring negative effects that are contrary to their purposes, as they cause other types of disasters and generate problems of erosion in nearby coasts.

This study investigates the series of landform changes in Cigu district in Tainan after the installation of a group of eleven detached breakwaters that between the years 1999 and 2001. These detached breakwaters are situated offshore of the Ding-tou-er Barrier. Using a varied collection of FORMOSAT-2 images, aerial photographs, as well as, the researcher's on-site photographs, along with field data of beach profiles, this study intends to reveal the geomorphological changes and processes that have occurred as a result of these detached breakwaters' installation. Further, this case study provides the government with empirical knowledge that may be referenced when coastal management is discussed. The study site has now been listed under the jurisdiction of the Taijiang National Park, thus making this research a valuable resource for Taijiang National Park to

DOI: 10.2112/SI75-178.1 received 15 October 2015; accepted in revision 15 January 2016.
**Corresponding author: aeolin@ntnu.edu.tw*
©Coastal Education and Research Foundation, Inc. 2016

develop practical strategies when managing the local environment. With Taiwan being an island country, such knowledge can prove useful to any future nationwide decisions related to coastal environments and their protection.

Background

The Ding-tou-er Barrier was originally part of a series of barrier islands located offshore of the Tainan coast (Figure 1). It is a long and narrow sand barrier, extending in the northeast-southwest directions, that was approximately parallel to and separated by lagoons from the shoreline of the main island of Taiwan. On its northern side, the barrier had been separated from Wan-tsu-liao, a barrier of the same orientation, by the southern inlet of the Cigu Lagoon. On its southern side, it had been one tidal inlet away from the Hsin-fu-lun Barrier, which is extending in the northwest-southeast directions. Evidently, the Ding-tou-er Barrier's location has a significant influence over the coastal environment of the southwestern coast of Taiwan.

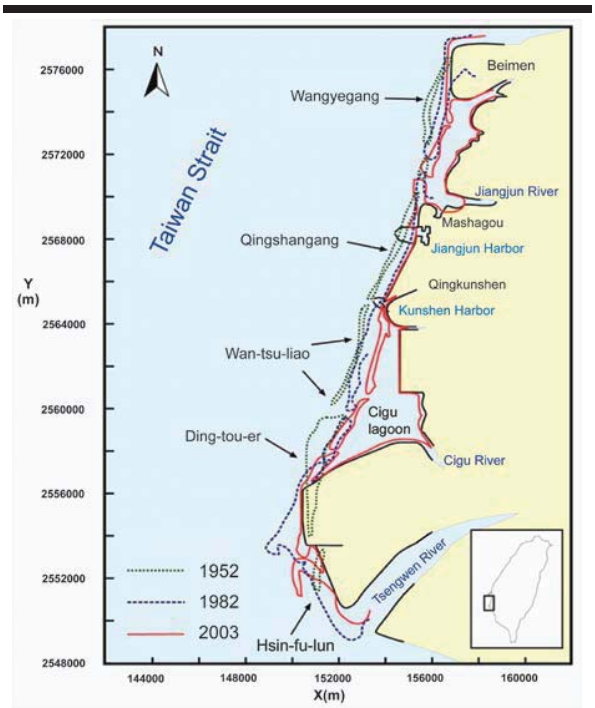

Figure 1. Location of the study area, Ding-tou-er Barrier of Cigu coast, Tainan, Taiwan. Shoreline change from 1952-1982-2003 is also shown.

As Lin (1997) noted, the Ding-tou-er barrier presents a significant turning point for the coastal processes of Taiwan's southwestern coast: not only do the shorelines on the northern and southern sides of the barrier move in different directions, such geomorphological differences also cause the sediment transport and other coastal processes to display contrasting features. On the coast of the northern side, the strong northeastern wind and the waves it induces control the littoral drifts in the winter, which prevail for the long-term. Both wind-driven currents and wave-induced longshore currents carry sediment from the North towards the South, which results in the deposition of sand on the protruding engineering structures' northern side, as well as, the erosion occuring on the southern side. In contrast, with these winter processes becoming less prominent at the relatively wind- and wave-sheltered southern side, the southeastern winds and waves in the summer turned into the main driving forces for the littoral drifts at the southern coast of the Ding-tou-er Barrier which carries sediment from the Southeast towards the Northwest. Later, with the development of fish ponds and the construction of roads, the use of land had stretched across the lagoons, which meant that the Ding-tou-er Barrier was no longer a separate sand barrier island, but a beach on the most outer edge of the main island's coast. In addition, a dike had been built to protect the fishing ponds, and the Cigu Lighthouse had been set up on a neighboring road for the fishing boats that pass by. During the late 1990s, the shoreline of the Ding-tou-er Barrier had been retreating after a couple of typhoon events when the coastal hazard prevention agency decided to install eleven detached breakwaters to prevent further erosion (Figure 2).

Figure 2. Eleven detached breakwaters off the Ding-tou-er Barrier of the Cigu coast, Tainan, Taiwan shown in this Google Earth image (Image source: GoogleEarth© 2007).

METHODS

To consider coastal changes, a researcher can make comparisons between photographs, maps, or satellite images that are taken or created at two different points in time at a specified area. Qualitatively, basic comparisons are made from identifiable landscape features photographed from certain angles and in certain directions. Quantitatively, on-site measurements made in selected locations, as well as, a wide variety of images, maps and geographical information systems, are used to detect and calculate changes. Thus, coastal changes may be monitored by appropriately utilizing the wide range of available images and information, which, as Pilkey *et al.* (1989) shows, can be accomplished by following these four steps: (1) selecting the materials, (2) capturing the shoreline, (3) measuring the before-

and-after differences found in the shoreline's locations, and (4) deducing the magnitude and rate of the changes. The notion that a shoreline is moving landwards, *i.e.* "retreating," can be interpreted as a sign of coastal erosion; conversely, the notion that a shoreline is moving oceanside, or "advancing," can be interpreted as a sign of coastal accumulation.

This study largely consists of gathering relevant aerial photographs and FORMOSAT-2 images of the Ding-tou-er Barrier in Tainan, Taiwan and its neighboring areas. Reference images from *before* the installation of the detached breakwaters, which are mostly aerial photographs taken prior to the year 1999, are used in comparison with photographs and the FORMOSAT-2 images taken between the years 2001 and 2012, *after* the installation. Some field data of beach profile measurements between July 2003- Feburary 2004 is also used for analysis. These reference images form the basis of analysis, as the changing locations of distinctive proxy-based shoreline indicators (Boak and Turner, 2005), such as the instantaneous water line, the dry/wet line, the first vegetation line, the inner beach edge line, the dune scarp line, *etc.*, are observed and considered (Lin, 2009). The distribution of various topographic features are used to interpret the changes brought to the Ding-tou-er Barrier. With long-term effects being observed, comparisons are also made specifically to distinguish the changes brought by seasonal influences before the installation of the detached breakwaters from those after. These analyses are further supplemented by on-site photographs taken by the researcher over many years, which provide an additional reference for confirming the accuracy of the analyses and for further investigating the causes of the observed landform changes.

RESULTS

In a series of aerial photographs, it can be observerved that, between the years 1996 and 1998, the sediment transport system along the northern side of the Ding-tou-er Barrier may have been affected by the construction of breakwaters at the Jiangjun Harbor (Figure 1). Due to an imablance within the sediment transport system, erosion began to occur in this area, prompting citizens to pressure the Sixth River Management Office to implement protective measures. Thus, the Sixth River Management Office planned the construction of detached breakwaters, hoping to preserve this section of the coast. The detached breakwaters were set up, one by one, in the direction of the drifting sand, north to south. With two to three breakwaters constructed per year, a total of eight were set up from 1999 to 2001. The total number would later be raised to 11, as breakwaters were set up along the southern side of the barrier. The height of the breakwaters had been three meters in the original design.

Three profile surveys were conducted between July 2003 and Feburary 2004 to study the seasonal morphologic changes of the barrier beaches. In a profile of the northern part of the Ding-tou-er Barrier (Cigu profile 2, near the site of 4th breakwater from the north), it is obvious that the beach had gradually grown taller and wider, especially with large amounts of sand having accumulated during the winter season. In contrast, a profile of the southern part of the barrier (Cigu profile 9, located about 800 meters south of the last breakwater) shows that the beach had narrowed in width from July to October, but remained about the same from October to the following February (Figure 3).

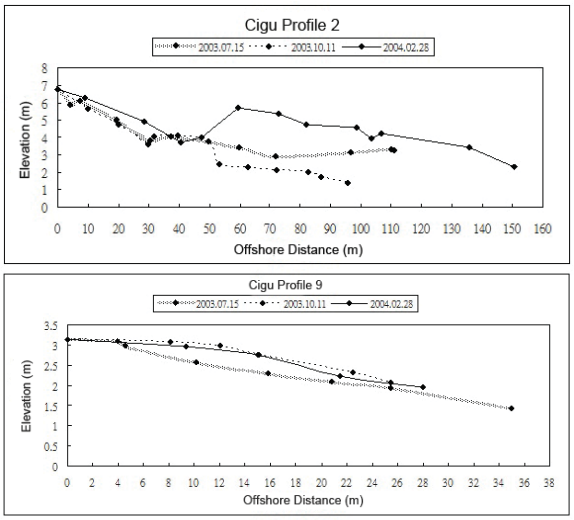

Figure 3. Beach profile surveys at the Ding-tou-er Barrier between July 2003-October 2003-Feburary 2004.

By comparing the aerial photographs of the northern reach of the Ding-tou-er Barrier from 1982 and from 2009 (Figure 4), it is clear that the shoreline is experiencing erosion due to the migration of the tidal inlet on the northern side. However, it is also evident that, behind the first four breakwaters (counting from north to south), sand accumulation had occurred and salient had formed. After this accumulation of sand had taken place on the northern side of a few detached breakwaters, it caused numerous problems at the downdrift side, including the obvious erosion of the beach, the retreat of the shoreline, the breach of the earth dike, and forest trees tumbling into waters. This rapid retreat of the coastal line, caused by the detached breakwaters, was named the "aka-groin effect" by Peng and Lin (2005), as it is just like the "groin effect," which usually shows erosion at the downdrift side of the groins.

Significant erosion had continued to occur at the southern reach of the barrier beach. The photograph image from 2009 shows that, due to a lack of sediment supply along the coast, the beach is mostly non-existent in the area in front of the four detached breakwaters located on the most southern side (Figure 4). This disappearance of the beach continued to take place even when the Sixth River Management Office tried to salvage the situation by adding a group of short groins, constructing a lengthened concrete seawall, and scattering tetrapods at the foot of the seawall (shown in photographs taken from 2005~2012, Figure 5). Moreover, large numbers of concrete tetrapods were stored in the space inside the seawall for emergency purposes during the typhoon season. The amount of sand being transported to the southern coast was, in fact, close to none, which meant that the windbreaking forest on the most southern edge of the coast retreated significantly as well.

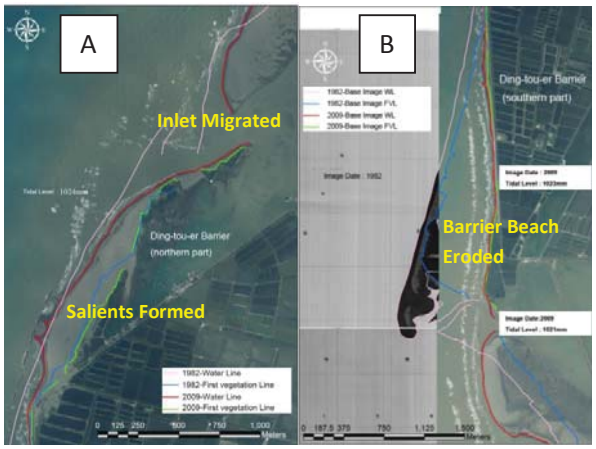

Figure 4. Comparison of the 1982 and 2009 shorelines of the Ding-tou-er Barrier, shown in aerial photos used to publish official maps. (A) is the northern part of the sand barrier, and (B) is the southern part.

Figure 5. (A) shows that, on the southern end of the group of detached breakwater, there had been a sandy beach 50m wide and a small dune in 2005 (2005/09/10). (B) is a photo taken at the southern side of the area shown in (A). During a 4-year period, the beach and the dune had eroded completely. The shoreline retreated at a very fast pace, and forest trees tumbled into the waters, leading the governmental agency to place stones and tetrapods as temporary protection (2009/08/27). (C) is taken at the same loaction as (B), which shows further beach erosion and more tumbling trees on the southern side. The earth dike was breached during a typhoon in the summer of 2012 (2012/07/23). The whiter part of the seawall shown in (D) is where the earth dike had been in 2012, which is also where the sandbags had been placed, as shown in (C) (2013/09/28). With the seawall being extended towards the South, the windbreaking forest is now completely outside the seawall and is expected to disappear completely. The beach in front of the seawall is predicted to be replaced by stones and tetrapods, (Photos: Tsung-Yi Lin).

When looking at images from 2009 to 2012 (Figure 6), it is evident that the coast continued to experience erosion, and only a small number of the windbreak forest tree remained. After an overtopping and dike-breaching event took place during the summer of 2012 at the earth dikes located behind this section of the windbreaking forest, sandbags were used as part of the emergency relief efforts, while new cement seawalls were built in 2013. Yet, the reality is that these detached breakwaters are only moving the problems of erosion to the downdrift side. Furthermore, the rapid speed of the sand accumulation occuring behind the detached breakwaters at the updrift side makes it difficult for vegetation to naturally spread across the beach. With the beach left bare, large amounts of sand are blown over the seawalls during the winter when the Northeast Monsoon prevails, thereby creating problems such as roads and tetrapods being buried and fishing ponds being invaded by sand (left lower corner in Figure 4(A) and Figure 7). Usually, the roads are cleaned each summer by moving the sand elsewhere. This meant that the sand is removed from the coastal system, thus forever diminishing the amount of sand supply within the system (Figure 7).

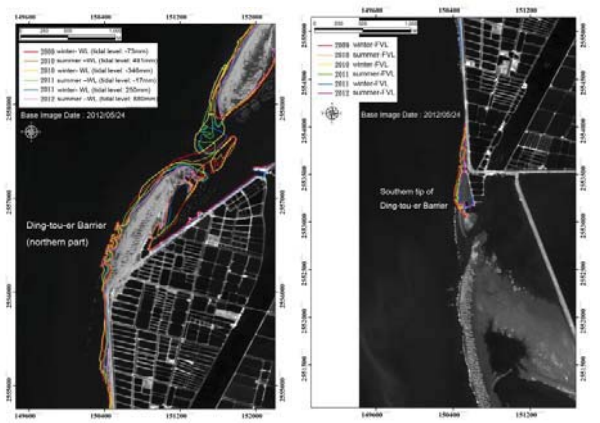

Figure 6. From 2009 to 2012, the northern tip of the the Ding-tou-er Barrier (with the tidal inlet migration) continued to be eroded and the area had shrunk. Only the parts behind the breakwaters kept their shapes. At the southern part of the barrier, the remains of the windbreaking forest continue to retreat and experience rapid erosion.

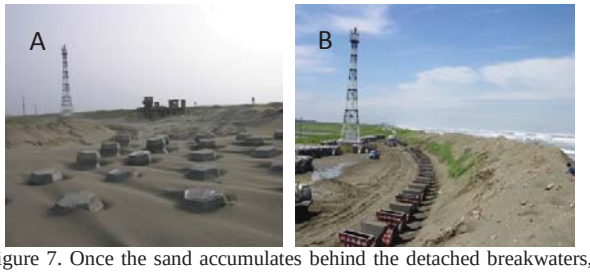

Figure 7. Once the sand accumulates behind the detached breakwaters, large amounts of sand are blown over the seawall during winter season, burying the roads and emergency tetrapod lot, as shown in (A). During the summer, sand is usually removed to clear the roads, but sometimes, the sand is used to make tetrapods on-site, as shown in (B).

DISCUSSION

As this study shows, the detached breakwaters did, in fact, fulfill the purpose for which it was designed and constructed: sand began to accumulate at the updrift side of the prevailing longshore currents, also known as the most northern side, forming salients on their backside. On the other hand, as the study indicates, the area of the windbreaking forests on the southern reach of the Ding-tou-er Barrier had decreased significantly, which leads to several occurances of waves crashing over the short earth dikes located behind the windbreaking forests. In order to combat the erosion issue, a group of short groins was installed on the southern side of the detached breakwaters. However, they clearly do not show much effect when it comes to trapping sand on the downdrift side. These detached breakwaters and groins lead to an insufficient amount of sediments on the southern side, as the sediments are trapped on the northern side instead. Meanwhile, an excess of sand accumulated at the most northern four detached breakwaters creates another problem: the bare sand surface becomes a source of wind-blown sand that invades the roads and fishing ponds.

The results of this study confirms a fundamental principle in geomorphology: an external impact on the environment is created whenever an engineering structure is constructed, which prompts the natural systems within the environment to direct themselves towards a new state of equilibrium. In a coastal system, various elements influence one another and are closely linked. This means that, when an engineering structure affects one of these elements and causes it to adapt, another element would also have to change in accordance, thus creating a chain effect. Although the sand did accumulate at the most northern four breakwaters during the period of observation, rapid and heightened erosion was also found at the southern side. Therefore, the traditional strategy of building rigid, engineering structures, such as sea walls, groins and detached breakwaters, in the face of coastal erosion problems is one that needs more consideration and discussion. Before any constructions are to occur on the coasts, complete evaluations of the long-term geomorphological impacts must be made in order to avoid the negative problems that are apparent in the case highlighted in this study. It is apparent from the geomorphologic processes observed that the beach and the windbreaking forest outside the seawall at the southern tip of the Ding-tou-er Barrier will be completely eroded away in the future.

CONCLUSIONS

This study's use of multiple sources of image data to illustrate the geomorphic impacts of external forces (*i.e.* the construction of detached breakwaters) on a coastal system represents the first in Taiwan to evaluate the problems with engineering structures through the lens of geomorphological principles. Such a study can provide an example that future research in the realm of engineering geomorphology can reference. The hope is that coastal management institutions within the nation will, when faced with problems of erosion and barrier island migration, be reminded of the need to develop well-thought-out strategies based on analyses of the laws of nature and to consider any establishment of engineering structures more thoroughly. When a governing institution considers how best to maintain important coastal landscapes and manage land development, it must include scientific research data as references for its decisions. Since the installation of detached breakwaters in 1999, their negative effects continue to be apparent today. Having examined the subsequent geomorphological changes closely, it can be concluded that the root of the problem lies within the imablance of the sediment transport system. Only after gaining a true sense of the effects of the geomorphological impacts of the detachted breakwater can Tailjiang National Park, the institution that now oversees the study area, develop informed management strategies and prevent the same mistakes in nearby beaches.

ACKNOWLEDGMENTS

This publication is financially supported by the former National Science Council (NSC), now the Ministry of Science and Technology (MOST) of Taiwan. The research project number: NSC 101-2119-M-003-004.

LITERATURE CITED

Boak, E.H. and Turner, I.L., 2005. Shoreline definition and detection: A review. *J. Coast. Res.*, 21(4), 688-703.

Hsu, T.-W.; Lin, T.-Y., and Tseng, I-F., 2007. Human impact on coastal erosion in Taiwan. *J. Coast. Res*, 23(4), 961-973.

Lin, T.-Y., 1997. Differences of sediments and coastal processes at north and south sides of Ding-Tou-Er Barrier. *Proceedings of the 19th Ocean Engineering Conference in Taiwan* (Taichung, Taiwan), pp. 547-552. (in Chinese with English abstract)

Lin, T.-Y., 2009. *Shoreline Change Mapping and Analysis Around the Taiwan Coast (1/4)*. Taipei, Taiwan: Central Geological Survey, Ministry of Economic Affairs, *Report 98-06*, 107p. (in Chinese with English abstract)

Lin, T.-Y., 2012. *Shoreline Change Mapping and Analysis Around the Taiwan Coast (2009-2012 Summary Report)*. Taipei, Taiwan: Central Geological Survey, Ministry of Economic Affairs, *Report 101-04*, 158p. (in Chinese with English abstract)

Peng, H.-H. and Lin, T.-Y., 2005. Impacts of Chiayi Hao-mei-liao's detached breakwater on coastal landforms. *Hwa Kang Geographical Journal*, 18, 2.1-2.13. (in Chinese with English abstract)

Pilkey, O.H.; Morton, R.A.; Kelley, J.T., and Penland, S., 1989. *Coastal Land Loss*. Washington, DC: American Geophysical Union, *Short Course in Geology*, 2, 73p.

Journal of Coastal Research	SI	75	892-896	Coconut Creek, Florida	2016

Hydrodynamic Regimes in Offshore Wind Farms

Clara Matutano†, Vicente Negro‡, José-Santos López-Gutiérrez∞, M. Dolores Esteban+,

† ‡ ∞ + Research Group on Marine, Coastal and Port
Environment and other Sensitive Areas
Universidad Politécnica de Madrid, E28040, Madrid

www.cerf-jcr.org

www.JCRonline.org

ABSTRACT

Matutano, C.; Negro, V.; López-Gutiérrez, J.S., and Esteban, M.D., 2016. Hydrodynamic regimes in offshore wind farms. *In:* Vila-Concejo, A.; Bruce, E.; Kennedy, D.M., and McCarroll, R.J. (eds.), *Proceedings of the 14th International Coastal Symposium* (Sydney, Australia). *Journal of Coastal Research*, Special Issue, No. 75, pp. 892-896. Coconut Creek (Florida), ISSN 0749-0208.

Offshore wind power has sharply increased its presence in the last few decades. This expansion has derived in much bigger structures to be placed on the seabed; however, no revision about hydrodynamic regimes that should be taken into account during the design of these facilities has been carried out. The equations developed by Morison *et al.* in 1950 to estimate the wave loads are commonly assumed as valid within professional and scientific activity, and no revision of their investigation has been carried out since then. The formulation developed 65 years ago may not be reliable enough to accurately predict the phenomena, since they were established for smaller bodies. This paper analyses the available data from several European offshore wind farms in order to determine their hydrodynamic domain and nature of forces that structures bear. The analysis has been performed with the aim of establishing the relationship between inertia and drag forces acting on piles under wave loading conditions. Different criteria from main standards within the sphere of maritime works have been followed for the analysis. Results clearly show how inertia dominates in most cases and, consequently, the acceleration of fluid particle motion is a critical variable for predicting coastal phenomena. In this sense, this research remarks the importance of that mathematical expressions incorporate this fact, both for structural calculation and coastal process prediction and they should be reviewed in future research studies.

ADDITIONAL INDEX WORDS: *Offshore wind farm, hydrodynamic regimes, Morison.*

INTRODUCTION

Offshore wind power is clearly increasing its presence within the renewable energy field. The number of facilities planned and constructed has increased sharply in the last few years (Esteban *et al.*, 2011). This development was first implemented in Europe, mainly the UK, but this type of energy source is spreading through other areas like Asia or the east coast of the USA (Esteban *et al.*, 2012).

This fact has promoted an increasing number of research studies in this field. Previous studies have developed the methodology for designing this kind of facility, with the aim of setting out the main steps of each phase (Esteban *et al.*, 2009; Esteban *et al.*, 2015). Additionally, further investigations have been addressed with respect to the scour phenomenon that jeopardizes the foundation elements of facilities and the whole structure's stability (Matutano *et al.*, 2013; Matutano *et al.*, 2015).

The majority of offshore wind farms installed are located in transitional waters, and their presence has a relevant influence on the coastal processes due to the associated changes in the hydrodynamic regime. In this sense, with the aim to better understand the effect of waves over offshore structures, classical theories for calculating these issues have been developed decades ago (Morison *et al.*, 1953). At that time, geometrical characteristics of bodies that took place within experimental analysis were considerably smaller, but the geometrical evolutions of offshore structures that have reached large dimensions have usually been linked to failures in the components and/or systems (Negro *et al.*, 2014). Hence it could be possible that relevant deviations at the time of making calculations were being disregarded, since forces could behave differently.

Nowadays, the nature of the wave forces that compromise the stability of offshore structures is a critical factor that determines the most suitable wave theory to be followed when calculating any parameter of the structure. The effect of waves that affects offshore structures is usually predicted according to a wave theory that is consequent with the force dominance at the location. Consequently, in the case of taking a non-reliable theory at any location, this may lead to errors in the following calculation and derive into inaccurate results.

In order to determine the location of offshore wind farms, as mentioned above, it is necessary to carry out an exhaustive study of the dominance of drag or inertia force with the objective of taking into account an adequate wave theory during de design phase. In this sense, knowing the main marine climate variables together with geometrical characteristics of offshore foundations in a two-way relationship, it is possible to determine the hydrodynamic domain and, therefore, the relation between

DOI: 10.2112/SI75-179.1 received 15 October 2015; accepted in revision 15 January 2016.
*Corresponding author: clara.mmolina@alumnos.upm.es
©Coastal Education and Research Foundation, Inc. 2016

inertia and drag forces and their dominance over offshore wind farms (Puertos del Estado, 2012).

With the aim to study the influence of the dominance of inertia or drag forces in the design of these facilities, an analysis of the wave forces applied on several offshore wind farms was carried out. The study developed according to the guidelines given by maritime works standards and previous studies, such as the Spanish ROM (Puertos del Estado, 2012), DNV-OS-J101 (Det Norske Veritas, 2011) and the Sarpkaya (2001), and Sarpkaya and Isaacson (1981) research and publications, took into account different offshore wind farms installed in the Irish Sea and the North Sea, all of them in transitional waters.

This analysis sets the foundations for revising the formulation that is currently used, analysing the accuracy of the expressions proposed and checking the calculations projected with the actual measured effects of the scouring phenomena.

The research analyses the nature of the force from the point of view of these structures having a small diameter if compared with the wavelength at the location, so the action of diffraction forces can be neglected. Hence, the traditional Morison theory has been followed for calculating the values of each force component, inertia and drag forces.

Background

The study began with the analysis of the validity of the theories according to Le Méhauté criteria (Mehaute, 1976). In 1976, Le Méhauté presented an important figure that showed the limits of validity of each wave theory. His criteria have also been adopted to validate different theories using standards within the maritime field, such as the ROM Standard (Puertos del Estado, 2012) or the Coastal Engineering Manual (US Army Corps Engineers, 2002). This figure was chosen as a reference for establishing the theory that should be taken in each wind farm.

In order to plot the offshore wind farms studied on Le Méhauté figure, the calculation of monomials (H/gT^2 and d/gT^2) was necessary. After calculations and plotting, as can be seen in the Figure 1, all offshore wind farms were located in an area of the figure where either Stokes theory (Stokes, 1851) or Cnoidal theory (Korteweg *et al.*, 1985) has to be followed.

It should be noted that selecting the theory that best fits each particular case is always a difficult issue. Different theories gave optimum results for different cases and there could be several possibilities. Due to the characteristics of this research that intends to establish a starting point for further investigations, calculations made for velocity and acceleration were based on the linear theory and assumed to be accurate enough.

Another calculations and assumptions about KC parameters and inertia and drag coefficients were established. The Keulegan and Carpenter number was one of the key ratios for establishing force dominance (Keulegan and Carpenter, 1958). The KC number is low for processes where the inertia force was the most important one. For higher values of the KC number, the drag force becomes more important and dominates the phenomena. The expression is as follows:

$$KC = \frac{u_{max} \cdot T}{D} \quad (1)$$

Where u_{max} (m/s) is the maximum flow velocity, T (s) is the wave period and D (m) is the diameter of the structure (the horizontal dimension normal to wave propagation).

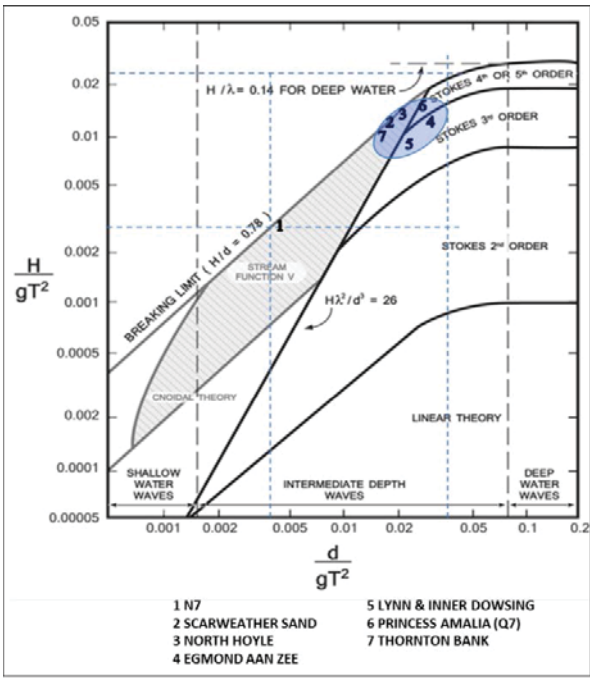

Figure 1. Validity domains of different wave theories of European offshore wind farms studied. Mehaute (1976).

The analysis of the wave force regimes was developed taking into account the Sarpkaya and Isaacson (1981) dissertations included in the book entitled Mechanics of wave forces on offshore structures as the basis for checking whether nonlinear effects have an important influence on each wind farm, and how significant they are.

Among a wide range of concepts analysed, the authors highlighted that the diameter- wavelength ratio (D/L) has to be low enough to use the Morison equation. Otherwise, if diffraction has a relevant effect on force calculations, it should be taken into account for calculating the loads by the diffraction theory, calculating the potential that solves the Laplace equation $\nabla^2 \emptyset = 0$

Calculation results under the Sarpkaya and Isaacson criteria showed that nonlinear effects were significant in most of the wind farms analysed. Only one, Egmond Aan Zee wind farm was outside the range where it was recommended to consider nonlinear effects.

Note that the wind farm N7 is out of the figure's domain, since its KC number is higher than 6 and, therefore, this calculation does not apply.

These results support the first calculation, and confirm that nonlinear effects would have to be considered and the higher order Stokes Theory should be addressed.

Finally, a discussion about the influence of flow velocity and acceleration in Morison equation was carried out, obtaining the inertia-drag force ratio.

From Airy wave theory (Airy, 1841), particle velocity (u (m/s)) and acceleration (a (m/s^2)) associated to the linear theory are given by the following expressions:

$$u = \frac{H}{2} \cdot \frac{gT}{L} \cdot \frac{\cosh\left(\frac{2\pi(z+d)}{L}\right)}{\cosh\left(\frac{2\pi d}{L}\right)} \cdot \cos\theta \tag{2}$$

$$a = \frac{H}{2} \cdot \frac{2\pi g}{L} \cdot \frac{\cosh\left(\frac{2\pi(z+d)}{L}\right)}{\cosh\left(\frac{2\pi d}{L}\right)} \cdot \sin\theta \tag{3}$$

Where,
d = water depth (m)
H = wave height (m)
T = wave period (s)
z = particle depth (m)
θ = wave phase (rad)
g = gravity acceleration (m/s^2)
$L = \frac{gT^2}{2\pi} \cdot \tanh(\frac{2\pi d}{L})$ = wave length (m)

Following the Morison Equation (Morison *et al.* 1953) the maximum value of inertia and drag forces, according to its theory, are the following:

$$|F_{imax}| = \frac{\pi D^2}{4} \cdot C_M \cdot \frac{2H\pi^2}{T^2} \cdot \frac{1}{\sinh\left(\frac{2\pi d}{L}\right)} \tag{4}$$

$$|F_{dmax}| = \rho \cdot \frac{D}{2} \cdot C_d \cdot \frac{H\pi}{T} \cdot \frac{1}{\sinh\left(\frac{2\pi d}{L}\right)} \cdot \frac{H\pi}{T} \cdot \frac{1}{\sinh\left(\frac{2\pi d}{L}\right)} \tag{5}$$

In order to find the force that dominates the wave forces, the ratio between the maximum inertia and drag forces is calculated as:

$$\frac{|F_{imax}|}{|F_{dmax}|} = \frac{C_M}{C_d} \cdot \frac{D\pi^2}{T} \cdot \frac{1}{u_{max}} = \frac{C_M}{C_d} \cdot \frac{\pi^2}{KC} \tag{6}$$

By introducing the most common values of inertia and drag coefficients, C_M = 2 and C_d = 1, the expression can be approximated to

$$\frac{|F_i|}{|F_d|} = \frac{20}{KC} \tag{7}$$

METHODS

Through the available data of European offshore wind market, seven wind farms were selected for the study, the majority of them located in the North Sea, but some installed in the Irish Sea and other points on the west coast of the United Kingdom. The location of each wind farm is shown in Figure 2. Different locations were taken with the aim of having a heterogeneous sample.

The main characteristics of facilities and wave climate variables about offshore wind farms used for the analysis were the foundation type, the monopile diameter, the water depth at location, and the significant wave height and the peak wave period.

Related to foundation types, most structures addressed in this research have a monopile foundation, although one of them belongs to the gravity based foundation group (Thornton Bank in Belgium). Diameters of foundations considered in the analysis range from a minimum 2.2 metres wide in Scarweather Sands (UK), to the GBS foundation of Belgium, where a foundation with 17 meters of diameter can be found.

All wind farms that form the database of the research are located in transitional waters; hence, the following expressions are fulfilled: 1/20 < h/L < 1/2 and π/10 < kh < π. Consequently, the formulation used in the following chapters is the most suitable for this water domain.

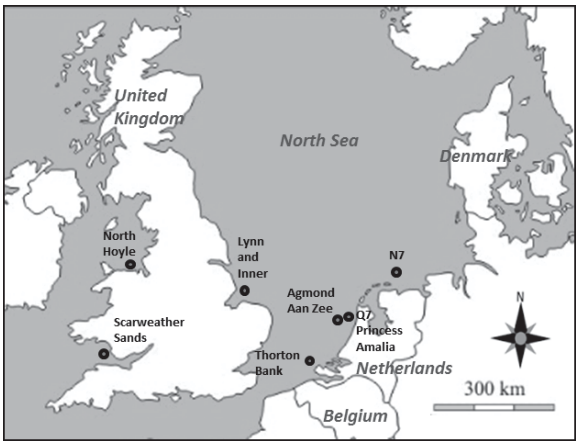

Figure 2. Location of European offshore wind farms studied.

Firstly, the validity of the theories for each location according to Le Méhauté criteria (Le Mehaute, 1976) was checked. After this pre calculation, and making assumptions that will be described later, the values required for the classification were calculated, at the bottom level, as is the aim of the paper. Secondly, monomials required for each standard were also calculated, plotted on the graphics and analysed for conclusions. And finally, an analysis of maximum velocity and acceleration of fluid particles was done, and their influence in the calculation of drag and inertia forces was proposed through the inertia-drag force ratio.

With the objective of checking how inertia and drag forces affect the wind farms analysed, Spanish ROM (Puertos del Estado, 2012), DNV-OS-J101 (Det Norske Veritas, 2011) and the Sarpkaya (2001), and Sarpkaya and Isaacson (1981) research and publications were taken as the chosen criteria to be followed in the study. These three standards present different methods for

establishing the inertia and drag dominance within structures located in marine environments.

In this sense, three analyses were performed following each standard, and their results were compared and discussed for obtaining conclusions based on different criteria.

The available data of offshore wind farms presented values as a range. This was an added difficulty since the precise data for each pile is unknown. Due to this lack of precision, results presented were calculated as the average of the combination of these ranges.

RESULTS

As mentioned above, ROM and DNV standards were followed in order to classify the drag-inertia force ratios. Furthermore, Sarpkaya and Isaacson (1981) gave some guidelines for knowing whether the diffraction and flow separation are important to the phenomenon.

The Spanish Recommendation for Maritime Constructions (Puertos del Estado, 2012) follows the criteria established by Chakrabarti (1987). The analysis made according to this technical Standard can provide further information about the characteristics of the phenomena since it shows six regions with different levels of force dominance.

Region III and low-side V of ROM figure (Puertos del Estado, 2012) were the zones where most of the wind farms are located, thus the inertia force is expected to dominate their hydrodynamic regimes. Only two wind farms (Scarweather Sands and Princess Amalia) are outside of Region III, but their positions are fairly close to the border, so drag force is likely to appear with a higher influence but still subordinated to inertia force effects.

Bodies located in Region III are stressed by forces where the dominating component is inertia and, hence, the acceleration of particles is critical at the time of calculating any other issues.

On the other side, the article 405 of the DNV standard (Det Norske Veritas, 2011) gives guidance for establishing the importance of drag, inertia and diffraction forces that stress the structure. It should be notice that no statistical description is recommended, so maximum wave height is assumed. No statistical information is given for the wave period either, so medium wave period was taken, as was done before.

Two parameters were required in the study of the influence of inertia and drag forces according to the DNV (2011) (Figure 3). The wave height-diameter ratio and the wave length-diameter ratio were needed.

The analysis carried out according to the DNV standard clearly showed that inertia forces totally dominate the nature of the hydrodynamic regimes. All wind farms are plotted in a zone where the inertia force is expected to be predominant. Moreover, the separation line between drag and inertia dominance seems to be far from the wind farms position in the figure.

As mentioned before, inertia and drag forces are going to reach very different values depending on the geometry and the maritime environment where the body is located. All structures referred in this research have a diameter (considered as the horizontal dimension normal to wave propagation) much smaller than the wavelength and then bodies act as if they were transparent to wave actions deriving from propagation phenomena. Hence, diffraction forces can be considered as insignificant and all calculations will be made under the Morison equation approximation. It is important to notice that maximum values for inertia and drag forces are 90 degrees out of phase.

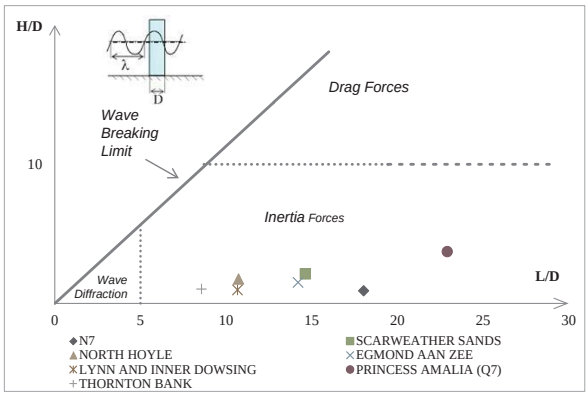

Figure 3. DNV classification of drag and inertia forces of European offshore wind farms analysed.

As mentioned before, in this section, the relation between force types is showed to analyse how much more significant inertial forces are compared with drag forces. Table 1 summarizes the results from calculations, taking into account the coefficients C_M and C_D described above and a seawater density of 1024 Kg/m^3.

Table 1. *Inertia-drag force ratio.*

Name	F_{dmax}	F_{imax}	$\frac{F_{i\,max}}{F_{d\,max}}$
N7	28.81	83.05	2.88
SCARWEATHER SANDS	4.58	19.73	4.31
NORTH HOYLE	10.42	64.37	6.18
EGMOND AAN ZEE	3.08	36.67	11.92
LYNN AND INNER DOWSING	7.01	65.88	9.4
PRINCESS AMALIA (Q7)	16.08	56.05	3.49
THORTON BANK	66.44	503.11	7.57

DISCUSSION

Throughout this research, different analyses were carried out in order to find out how forces disturb piles and how they are dealt with in different technical standards. All calculations made have yielded results in the same direction although they present some minor differences between them.

The first evidence was the absence of a consistent analysis for the validity of the Morison equation (Morison *et al.*, 1953) in all standards analysed, not only offshore wind industry standards, such as DNV (2011), Germanischer (2005) or International Electrotechnical Commission (2005, 2009), but also other standards like American Petroleum Institute (2000) within the Oil and Gas field, not include a validation theory check.

Secondly, the nature of wave forces was analysed, and the results clearly showed the dominance of inertia forces over drag forces for this kind of pile-shaped support structures. The dominance of inertia reached different values depending on the particular conditions of each facility, such as geometrical properties and wave climate variables. The inertia force calculated exceeded the drag force from 2.88 to 12 times.

CONCLUSIONS

With these results, the authors consider that it is important to be especially careful when it comes to predicting situations where inertia is the dominant force but is not properly included in the formulation taken for calculations. It should be noted that one of the most important variables that determines the inertia force is the fluid particle acceleration, so in one way or another, acceleration must be included in formulations related to the phenomena.

Hence, current formulations taken into account during the design phase of offshore wind farms need to be checked to predict the influence of inertia and drag component of wave force, and if not, it would be necessary to develop a new formulation for integrating the wave loading that affects offshore structures.

LITERATURE CITED

Airy, G.B., 1841. Tides and waves. *Encyclopaedia Metropolitana*, London, 241-396.

American Petroleum Institute, 2000. Recommended practice for planning, designing and constructing fixed offshore platforms–Working stress design.

Chakrabarti, S., 1987. Hydrodynamics of Offshore Structures. *Springer Verlag*.

Det Norske Veritas, 2011. DNV OS J101-Design of offshore wind turbine structures.

Esteban, M. D., Negro, V., and López-Gutiérrez, J.S., 2009. Integral Management Applied to Offshore Wind Farms. *Journal of Coastal Research*.

Esteban, M. D.; Negro, V., and López-Gutiérrez, J.S., 2011. Why offshore wind energy? *Renewable Energy*, vol. 36, 444–450.

Esteban, M. D.; López-Gutiérrez, J.S.; Negro, V.; Matutano, C.; Garcí-Flores, F.M., and Millán, M.A., 2015. Offshore Wind Foundation Design: Some Key Issues. *Journal of Energy Resources Technology*, vol. 137.

Esteban, M. and Leary, D., 2012. Current developments and future prospects of offshore wind and ocean energy, *Applied Energy*, no. 90, 128-136.

Germanischer Lloyd, 2005. Guideline for the Certification of Offshore Wind Turbines.

International Electrotechnical Commission, 2005. IEC 61400 - 1. Wind Turbines - Part 1: design requirements, Technical Standard.

International Electrotechnical Commission, 2009. IEC 61400 - 3. Wind turbines - part 3: Design requirements for offshore wind turbines, Technical Standard.

Keulegan, G.H. and Carpenter, L.H., 1958. Forces on Cylinders and Plates in a Oscillating Fluid. *Journal Research of the National Bureau of Standards*, 60(5), 423-440.

Korteweg, D.J. and De Vries, G., 1985. On the change of form of long waves advancing in a rectangular canal, and on a new type of long stationary waves. *The London, Edinburgh, and Dublin Philosophical Magazine and Journal of Science*, 39(240), 422-443.

Le Mehaute, B., 1976. An introduction to hydrodynamics and water waves. New York: Springer-Verlag .

Matutano, C.; Negro, V.; López-Gutiérrez, J.S., and Esteban, M.D., 2013. Scour prediction and scour protections in offshore wind farms. *Renewable Energy*, 57, 358-356.

Matutano, C.; Negro, V.; López-Gutiérrez, J.S., and Esteban, M.D., 2015. Design of Scour Protection Systems in Offshore Wind Farms. *Journal of Energy Resources Technology*, 137.

Morison, J.; Johnson, J.; O'Brien, M., and Schaff, S., 1953. Experimental Studies on Wave Forces on Piles. *Proc. 1st Conference Coastal Engineering*.

Negro, V.; López-Gutiérrez, J.S.; Esteban, M.D., and Matutano, C., 2014. Uncertainties in the design of support structures and foundations for offshore wind turbines. *Renewable Energy*, 63, 125-132.

Puertos del Estado, 2012. ROM 2.0-11 (Recomendaciones para el proyecto y ejecución en Obras de Atraque yAmarre).

Sarpkaya, T., 2001. On the force decompositions of Lighthill and Morison. *Journal of Fluids and Structures*. 227-233.

Sarpkaya, T. and Isaacson, M., 1981. Mechanics of Wave Forces on Offshore Structures.

Stokes, G.G., 1851. In On the effect of the internal friction of fluids on the motion of pendulums, vol. 9, Pitt Press, 1851, pp. 8-106.

US Army Corps Of Engineers, 2002. Coastal engineering manual.

Journal of Coastal Research	SI	75	897-901	Coconut Creek, Florida	2016

Understanding Strandings: 25 years of Humpback Whale (Megaptera novaeangliae) Strandings in Queensland, Australia

Jan-Olaf Meynecke [†‡], Justin J. Meager[§]

[†]Griffith Centre for Coastal Management, Griffith University, Gold Coast, Australia

[‡]Humpbacks & High-Rises Inc., Gold Coast, Australia

[§]Queensland Department of Environment and Heritage Protection, Australia

www.cerf-jcr.org

www.JCRonline.org

ABSTRACT

Meynecke, J-O. and Meager, J., 2016. Understanding strandings: 25 years of humpback whale strandings (*Megaptera novaeangliae*) in Queensland, Australia *In:* Vila-Concejo, A.; Bruce, E.; Kennedy, D.M., and McCarroll, R.J. (eds.), *Proceedings of the 14th International Coastal Symposium* (Sydney, Australia). *Journal of Coastal Research*, Special Issue, No. 75, pp. 897-901. Coconut Creek (Florida), ISSN 0749-0208.

Cetacean strandings are well-known phenomena in all parts of the world. In most cases the underlying reasons are unknown. Incidents have been associated with factors including changes in magnetic fields, diseases, unusual weather events, vessel strikes, pollution and fishing. Quantitative analyses over large spatial and time scales can provide insights into stranding hotspots, trends and relationships with physical drivers. Here we collated and combined available information on humpback whale (*Megaptera novaeangliae*) incidents that occurred in Queensland, on the east coast of Australia between 1989 and 2014. This study provides a first overview of incidents for humpback whales for the east coast of Australia over a 25 year period. Incidents included reports of carcasses, vessel strikes, injured animals found stranded, entrapped in shallow water, entangled or floating offshore. The location, timing, age class and types of over 200 incidents were analysed for trends and compared with oceanic and physical processes. The majority of incidents involving calves or juvenile humpback whales occurred during the austral winter (peak in August). The rate of strandings was associated with the position of the East Australian Current, and lagged Southern Oscillation Index (SOI). Our study demonstrates the importance of long-term strandings records to allow for the investigation of trends over spatial and temporal scales relevant to migratory species. A comprehensive strandings program is an important conservation and monitoring tool to better understand long-term trends and to quantify key threats to cetaceans.

ADDITIONAL INDEX WORDS: *Humpback whales, stranding, East Australian Current, SOI.*

INTRODUCTION

Strandings, entanglements and vessel strikes involving cetaceans often receive considerable public attention. The underlying patterns or causes of strandings are, however, not well known (Evans *et al*., 2005). Stranding records can provide valuable information for investigating trends on location, timing and type of incidents over long periods of time and large spatial scales (Evans *et al*., 2005; Meager and Limpus, 2014).

Humpback whales, *Megaptera novaeangliae*, are an iconic species of baleen whale that underpin a billion dollar commercial whale watching industry. Humpback whales in the southern hemisphere migrate annually between their summer feeding grounds in Antarctica and winter breeding grounds in the tropics (Dawbin, 1966). The movement along the migratory route is thought to be influenced by physical and biological factors resulting in the majority of the population passing within 10-30 km of the shore (Noad *et al.*, 2008). The Group V humpback whales travel along the east coast of Australia and are a distinct population. Recognised aggregation sites for resting or breeding of this population in Queensland, Australia, include the Gold Coast bay, Hervey Bay, Moreton Bay, the Swain Reefs, Whitsundays, southern Great Barrier Reef, Bell Cay and the Palm Island Group (DEWR, 2007; Meynecke *et al.*, 2013).

Strandings, mortalities and incidents involving humpback whales have been reported and investigated previously in other parts of the world. On the Pacific coast of Columbia most strandings (1986-2000) are calves and occur from August to October (Capella-Alzueta *et al.*, 2001). A similar trend was evident in Western Australia, where most humpback whale strandings occurred during the southern migration (August to October) and 44% of strandings were calves (Groom and Coughran, 2012). In New South Wales, Australia, the largest known cause of incidents was entanglement of cetaceans (134 individuals) with the majority being humpback whales caught in fishing gear (Lloyd and Ross, 2015). The reasons humpback whales strand are diverse, and can be influenced by behaviour and health of whales in addition to extrinsic factors such as the predation, geography of the coastline, proximity to shore, water temperature, wind and ocean currents (Geraci *et al.* 1993; Meager and Limpus, 2014).

DOI: 10.2112/SI75-180.1 received 15 October 2015; accepted in revision 15 January 2016.
*Corresponding author: j.meynecke@griffith.edu.au
©Coastal Education and Research Foundation, Inc. 2016

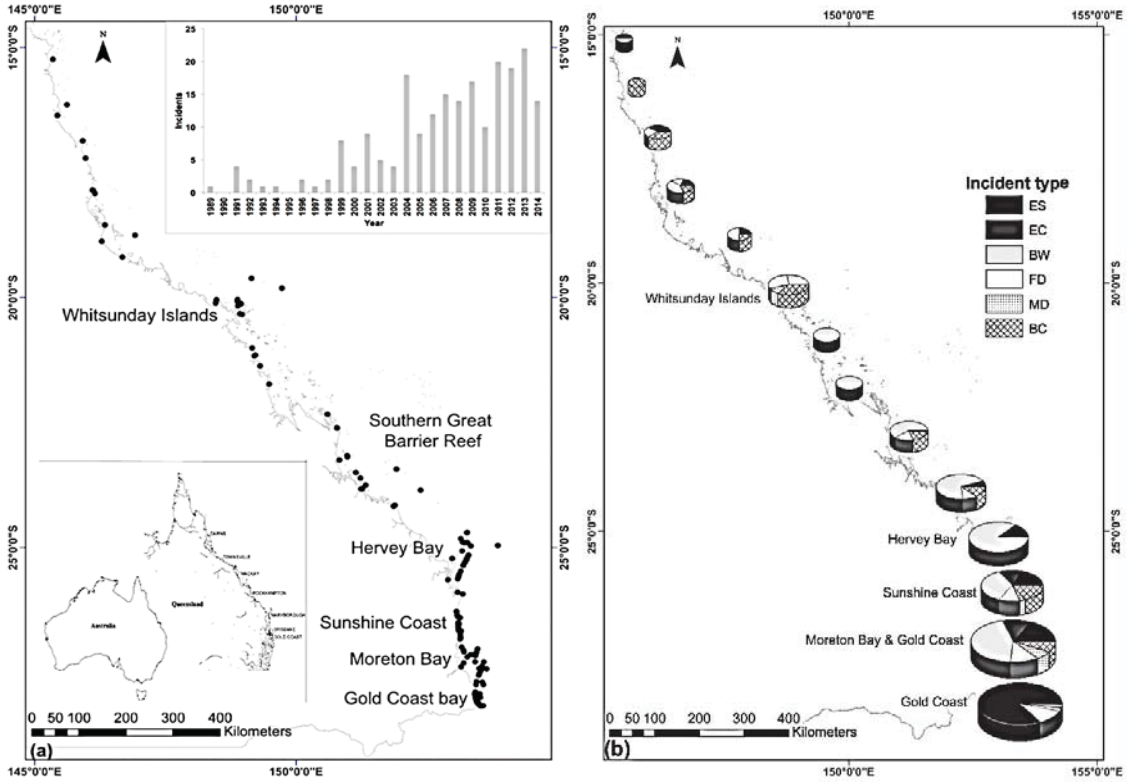

Figure 1. (a) Locations and number of strandings along the coast of Queensland, Australia (1989-2014); (b) incident types based on latitudes ranging from 28°S to 15° S with size of graphs proportional to the number of strandings. ES = entanglement in Queensland shark control program gear; EC = entanglement in commercial fishing gear; BW = washed ashore (dead or alive); FD = floating dead or alive; MD = entanglement in marine debris; BC =vessel interaction.

Humpback whale migration may be influenced by the environment (Ramp *et al.*, 2015), and large-scale oceanographic and climatic factors. Along the east coast of Australia the East Australian Current (EAC) flows in a southward direction as the western boundary current of the South Pacific sub-tropical gyre (Roughan and Middleton, 2002). The EAC strengthens during the austral summer and has weaker flows from May to July in the austral winter (Tranter *et al.*, 1986). Depending on the position of the EAC humpback whales may migrate closer or further to the shore utilising the current (Gaspar *et al.*, 2006). Another large scale climatic factor that may affect the whale population El Niño Southern Oscillation (ENSO) phenomenon, as measured by the Southern Oscillation Index (SOI). El Niño events generally bring warm and dry conditions with above average temperatures and below average rainfall to the Australian continent. It has been speculated that there is link between El Niño events and population dynamics of humpback whales, although the ecological link is unknown and may be a function of a complex relationship between climate and krill availability in the Antarctic foraging grounds (Chaloupka and Osmond, 1999; Murphy *et al.*, 2007).

This study aimed to investigate trends in reported humpback whale stranding incidents in nearshore waters of Queensland, Australia. We also aimed to explore the rates of humpback whale strandings in relation to major climatic (SOI) and the oceanic (EAC) factors.

METHODS

The Queensland east coast, ranging from Tweed Heads (28.1833°S, 153.5500°E) to the tip of Cape York (10.6833°S, 142.5333°E), was the focus of this study (Figure 1). The climate ranges from subtropical in the south-east to tropical in the north of Queensland.

Data were compiled from a number of sources, the Queensland Marine Wildlife Strandings and Mortality Program (StrandNet), the Sea World Rescue Foundation archive and newspaper articles for the time period 1989-2014. StrandNet records are based on information provided from government departments, community groups, businesses, environmental organisations, and the general public and were included from 1996-2014. Sea World Rescue Foundation has been involved in the rescue of marine wildlife for several decades and information from their archive was extracted. For the purpose of

this study strandings were defined as reports of carcasses, vessel strikes, injured animals found stranded, entrapped in shallow water, entangled or floating offshore. The final database included information on suspected and confirmed cases giving date, location, type, size, sex, fate, injuries, age and an

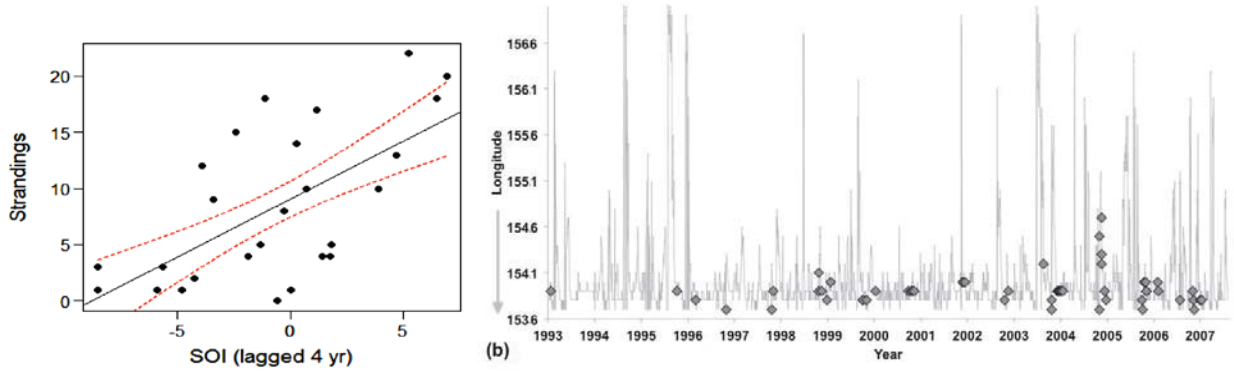

Figure 2. (a) Relationship between average SOI and the annual strandings rate from 1989 to 2014 (± 95% confidence intervals, β = 1.02, r^2 = 0.40, p = 0.02, robust regression), (b) position of the EAC (light grey line, arrow indicating direction to coast) over a 14 year period (1993-2007) with 58 stranding events (only beached or entanglement from Fraser Island to Tweed Heads, black diamonds).

incident description for 214 humpback whales ranging from 1989-2014.

The data was categorised into different incident types including beach washed, entanglement in gear from the QSCP gear, entanglement in commercial fishing gear, entanglement in marine debris, vessel collision and floating (dead or alive). The whales were classified in age groups of calves (<8 m in length), juveniles (<10 m in length), sub-adults (<12 m in length and adults (>12 m length) (Meynecke *et al.*, 2013). Data was mapped in ArcGIS (v. 10.1) to identify 'hot spots' of strandings and then summarised for each latitude. The annual summary of strandings was standardised by the estimated population (Franklin, 2014) to account for an 11% increase of population per year (Noad *et al.*, 2011).

Monthly SOI values (based on the difference in sea level pressures between Tahiti and Darwin, Australia) were obtained from the Australian Bureau of Meteorology. The location of the centre of the EAC was based on the CSIRO BLUElink Ocean Reanalysis model for 1992-2008. The longitude position of the EAC was measured daily from the centre of the main jet of the current with a relative high certainty south of Fraser Island (Oke *et al.*, 2008). Only stranding data south of Fraser Island (Hervey Bay) to Tweed Heads was compared with the position of the EAC. Incidents that were likely to have occurred offshore, such as vessel strikes and carcasses floating offshore were not included in this analysis. The relationship between SOI and strandings was examined using linear models. A range of SOI predictors were tested including SOI averaged over the year, SOI averaged over the migration season (May to October), lags of up to 4 years and moving averages of up to 4 years.

RESULTS

The highest number of reported incidents took place in south-east Queensland between 28 and 26°S with 124 incidents or 58% of all reported strandings during the observation period (Figure 1a). The southern Gold Coast bay had the most reported incidents for any of the regions with 73 records or 34%.

Of the 214 reported whales the age class of 54 was unknown or not reported. The majority were either calves or juveniles (55%) and only 34 involved adults (16%) (Table 1). The majority of strandings occurred during the austral winter (June to August, 58% of strandings) and spring (September to October, 40% of strandings). The annual summary of strandings indicated strong variability between years with higher strandings occurring approximately every 2-3 years (e.g. 2004-2007) In spite of this periodic variability, the number of strandings increased over the time period. A weak trend of increasing strandings remained when adjusted for the estimated annual population size. This was because of lower than expected strandings earlier in the study period, with the notable exception of 1991.

More than one third (37%) of the recorded incidents were a result of entanglements involving QSCP gear (27%), fishing gear (8%) or marine debris (2%). Another 87 whales (41%) washed up on beaches (dead or alive), while 23 (11%) whales were reported as floating dead or alive in the waters offshore. A total of 22 cases (10%) were attributed to interactions with vessels. The type of incident varied with location with entanglements being highest in south-east Queensland (Figure 1b).

Almost half of the stranded whales were reported as alive were either released alive, sighted alive but left in situ (91 whales or 43%), while another 89 whales (42%) were found dead, or died from their injuries sustained during the incident. (Table 1). In some cases a whale was euthanized and in other instances whales were able to release themselves.

A linear relationship was evident between the annual number of strandings and SOI, that was strongest for a 4 year moving average (r^2 = 0.40 p = 0.02, Figure 2a). The number of incidents was generally higher in strong La Niña events than in El Niño events (Figure 2a). Data were insufficient to analyse cause-specific trends.

The average position of the centre of the EAC during the observation period (1992-2008) was at longitude 154.03995°E.

In south-east Queensland, 89% of beach washed strandings and entanglement occurred when the centre of the EAC was closer to the coast than average (1993-2007). Most strandings took place when the centre of the EAC was between longitude 153.7° and 153.9°E (Figure 2b).

DISCUSSION

Our analysis of 25 years of humpback whale strandings records across the subtropical-tropical coastline of Queensland provided insights into spatial 'hotspots', temporal trends and variability associated with large-scale oceanic and climatic environmental factors. Strandings clustered in the regions recognised as resting, socialising or breeding grounds (DEWR, 2007). One key 'hotspot' for strandings was the Gold Coast, a region where the migratory corridor is close to the shore and where humpback whales are known to rest (Meynecke *et al*., 2013). It is also adjacent to a large metropolitan centre and therefore represents a site where anthropogenic interactions would be expected. Entanglements were the dominant known cause of strandings in the region and 75% of all reported entanglements occurred on the Gold Coast.

The increase of strandings is largely a reflection of the recovering humpback whale population (Noad *et al.*, 2011). However, the increasing trend of humpback whale strandings remains when adjusted for the estimated annual population for the time period 1989-2014, because few strandings occurred in the earlier years of the study period (<1996). Notwithstanding the possibility that the strandings reporting rate has changed over this period, this analysis suggests that other risk factors may have increased. Whether this is due to changes in anthropogenic sources such as vessel activity, fishing gear deployment, noise pollution, marine debris or water quality, or a natural driver is unknown.

Similar to findings elsewhere (Capella-Alzueta *et al.*, 2001; Holyoake *et al.*, 2012; Moura *et al.*, 2013), calves and juveniles dominated strandings with only 15-20% of the strandings involving adults, and the peak strandings rate occurred late in the austral winter (Meager and Sumpton, 2016). Mother and calf pairs are known to prefer to rest in shallow, sandy bays during the southern migration, which makes them more susceptible to anthropogenic impacts and strandings (Franklin *et al.*, 2011; Holyoake *et al.*, 2012; Meynecke *et al.*, 2013).

Individual animals attend the migratory flow at different times depending on sex, age and reproductive state (Dawbin, 1966) and calves traveling in August maybe in a state that makes them more vulnerable to strandings. The highest number of mother and calf pairs are seen travelling late in the southern migration (Paterson *et al.*, 1994). Females in advanced pregnancy are also the last to travel north, and some of the August strandings may be unsuccessful pregnancies. The proximate reasons for the peak of strandings of young humpbacks in August would be an important question for future research

The SOI represents large scale climate variability and showed a lagged, positive relationship with strandings Whether this was because of effects on the population size, the number of whales attending the migratory flow, health or another reason is unclear. Earlier research has noted the potential link between the number of humpback whales migrating along the Queensland coast and ENSO (Chaloupka and Osmond, 1999). Climate and oceanographic dynamics can influence the position and concentration of krill, which may have a direct effect on the timing of the northern migration of humpback whales (Paterson *et al.*, 1994), energy reserves or breeding success (see also Leaper *et al*., 2006).

Table 1. S*ummary of strandings per year (live or dead). M = male; F = female; UnS = unknown sex; ES = entanglement in QSCP; EC = entanglement in fishing gear; BW = washed ashore (dead or alive); FD = floating dead or alive; MD = entanglement in marine debris; BC = vessel interaction; UnA = unknown fate.*

Year	89	91	92	93	94	96	97	98	99	00	01	02	03	04	05	06	07	08	09	10	11	12	13	14
Total	1	4	2	1	1	2	1	2	8	4	9	5	4	18	9	12	15	14	17	10	20	18	22	13
M	-	-	-	-	-	-	-	1	1	1	1	1	2	3	1	1	-	1	2	2	2	5	2	1
F	-	-	-	-	1	-	-	-	5	1	2	-	-	1	1	-	3	1	1	1	2	2	3	1
UnS	1	4	2	1	-	2	1	1	2	2	6	4	2	14	7	11	12	12	14	7	16	11	17	11
ES	1	2	3	1	2	1	1	1	-	2	4	2	1	7	5	2	2	1	6	1	1	5	5	7
EC	-	1	-	-	-	-	-	-	-	-	-	-	-	3	-	4	5	-	-	-	-	1	3	-
BW	-	1	-	-	1	2	-	1	8	1	5	3	1	4	3	3	1	5	5	7	14	8	10	5
FD	-	-	-	-	-	-	-	-	-	-	1	-	1	-	1	2	4	2	5	1	2	3	2	-
MD	-	-	-	-	-	-	-	-	-	1	-	-	-	-	-	-	-	1	1	-	-	2	1	-
BC	-	-	-	-	-	-	-	-	-	-	-	-	1	4	-	1	3	5	-	1	3	1	2	1
Dead	-	-	-	-	-	-	-	-	6	1	7	3	2	4	2	4	5	5	11	6	13	10	7	3
Alive	1	4	2	1	1	1	1	2	2	2	2	1	2	9	7	5	7	4	6	3	5	7	7	9
UnA	-	-	-	-	-	1	-	-	-	1	-	1	-	4	-	3	3	5	-	1	2	1	8	2

The movement of the EAC core current to inshore waters can cause upwelling events and slope water intrusion bringing cooler waters to shore (Roughan and Middleton, 2002). Whales and other marine megafauna are known to use currents for navigation (Gaspar *et al.*, 2006) and prefer cooler temperatures (Dalla Rosa *et al.*, 2012). The encroachment of the EAC towards the coast may therefore result in a migratory corridor closer to the shore, and an increased likelihood of interacting with coastal human activities or stranding upon the shore. Other conditions such as wind and wave conditions, and sea surface temperature may also be useful for an improved prediction of humpback whale strandings, as would biological parameters such as calving rates and condition.

CONCLUSIONS

The increasing number of humpback whales and increasing number of users of the marine environment suggests that anthropogenic sources of strandings such as vessel interactions and entanglements will become more frequent into the future. Climatic and oceanic factors may act to mediate the number of these interactions, and therefore should be further understood. Such trends are best observed and monitored on a national or global scale, and by collaboration across jurisdictions.

Our descriptive approach detecting humpback whales stranding patterns and occurrence provides for the basis of a more in depth analysis to reveal underlying patterns, frequencies and dependencies on environmental factors. Understanding and predicting how the environment influences the vulnerability of humpback whales to natural and anthropogenic threats would support informed strandings management.

ACKNOWLEDGMENTS

The authors like to thank the Sea World Rescue Foundation, the Queensland Strandings and Mortality network and the Department of Fisheries and Agriculture for providing data; and T. Long, M. Horton and D. Kobashi for support. H. van de Sande, K. St Pierre, D. Teixeira, K. Gleeson, B. Lottes are thanked for assistance with data compilation of earlier versions of the database.

LITERATURE CITED

Capella-Alzueta, J.; Florez-Gonzalez, L., and Fernandez, F.P., 2001. Mortality and anthropogenic harassment of humpback whales along the Pacific coast of Colombia. *Memoirs of the Queensland Museum*, 47(2), 547-553.

Chaloupka, M. and Osmond, M., 1999. Spatial and seasonal distribution of humpback whales in the Great Barrier Reef Region. *American Fisheries Society Symposium*, 23, 89-106.

Dalla Rosa, L. and Ford, J.K., Trites, A.W., 2012. Distribution and relative abundance of humpback whales in relation to environmental variables in coastal British Columbia and adjacent waters. *Continental Shelf Research*, 36, 89-104.

Dawbin, W.H., 1966. *The seasonal migratory cycle of humpback whales.* In: Norris, K.S. (Ed.), *Whales, dolphins, and porpoises*. University of California Press, Berkley, CA, pp. 145-170.

DEWR, 2007. *The Humpback Whales of Eastern Australia*. Department of Environment and Water Resources, Canberra.

Evans, K.; Thresher, R.; Warneke, R.; Bradshaw, C.; Pook, M.; Thiele, D., and Hindell, M., 2005. Periodic variability in cetacean strandings: links to large-scale climate events. *Biology Letters*, 1(2), 147-150.

Franklin, W., 2014. Abundance, population dynamics, reproduction, rates of population increase and migration linkages of eastern Australian humpback whales *(Megaptera novaeangliae)* utilising Hervey Bay, Queensland. Lismore, NSW: Southern Cross University, PhD thesis, 364p.

Franklin, T.; Franklin, W.; Brooks, L.; Harrison, P.; Baverstock, P., and Clapham, P., 2011. Seasonal changes in pod characteristics of eastern Australian humpback whales (*Megaptera novaeangliae*), Hervey Bay 1992-2005. *Marine Mammal Science*, 27(3), E134-E152.

Geraci, J.R. and Loundsbury, V.J., 1993. Marine mammals ashore: A field guide for strandings. Texas A&M Sea Grant Publications, Galveston Texas.

Gaspar, P.; Georges, J.-Y; Fossette, S.; Lenoble, A.; Ferraroli, S., and Le Maho, Y., 2006. Marine animal behaviour: neglecting ocean currents can lead us up the wrong track. *Proceedings of the Royal Society of London B: Biological Sciences*, 273(1602), 2697-2702.

Groom, C. and Coughran, D., 2012. Entanglements of baleen whales off the coast of Western Australia between 1982 and 2010: patterns of occurrence, outcomes and management responses. *Pacific Conservation Biology* 18, 203.

Holyoake, C.; Stephens, N., and Coughran, D., 2012. *Collection of baseline data on humpback whale (Megaptera novaeangliae) health and causes of mortality for long-term monitoring in Western Australia.* Murdoch University, Perth.

Leaper, R.; Cooke, J.; Trathan, P.; Reid, K.; Rowntree, V., and Payne, R., 2006. Global climate drives southern right whale (*Eubalaena australis*) population dynamics. *Biology Letters*, 2(2), 289-292.

Lloyd, H.B. and Ross, G.A., 2015. Long-term trends in cetacean incidents in New South Wales, Australia. *Australian Zoologist*.

Meager, J.J. and Limpus, C., 2014. Mortality of Inshore Marine Mammals in Eastern Australia Is Predicted by Freshwater Discharge and Air Temperature. *PLoS ONE*, 9(4), e94849.

Meager, J.J. and Sumpton, W.D., 2016. Bycatch and strandings programs as ecological indicators for data-limited cetaceans. *Ecological Indicators* 60, 987-995.

Meynecke, J.-O.; Vindenes, S., and Teixeira, D., 2013. *Monitoring humpback whale (Megaptera novaeangliae) behaviour in a highly urbanised coastline: Gold Coast, Australia*, in: Moksness, E., Dahl, E., Støttrup, J. (Eds.), *Global Challenges in Integrated Coastal Zone Management - 2nd edition.* Wiley-Blackwell Ltd.

Moura, J.F.; Rodrigues, D.l.P.; Roges, E.M.; Souza, R.L.; Ott, P.H.; Tavares, M.; Lemos, L.S.; Tavares, D.C., and Siciliano, S., 2013. Humpback whales washed ashore in southeastern Brazil from 1981 to 2011: stranding patterns and microbial pathogens survey. *Biologia*, 68(5), 992-999.

Murphy, E.J.; Trathan, P.N.; Watkins, J.L.; Reid, K.; Meredith, M.P.; Forcada, J.; Thorpe, S.E.; Johnston, N.M., and Rothery, P., 2007. Climatically driven fluctuations in Southern Ocean ecosystems. *Proceedings of the Royal Society of London B: Biological Sciences*, 274(1629), 3057-3067.

Noad, M.J.; Dunlop, R.A.; Paton, D., and Cato, D.H., 2011. Absolute and relative abundance estimates of Australian east coast humpback whales (*Megaptera novaeangliae*). *Journal of Cetacean Research and Management* 3, 243-252.

Oke, P.R.; Brassington, G.B.; Griffin, D.A., and Schiller, A. 2008. The Bluelink Ocean Data Assimilation System (BODAS). *Ocean Modelling*, 20, 46-70.

Paterson, R.; Paterson, P., and Cato, D.H., 1994. The status of humpback whales *Megaptera novaeangliae* in east Australia thirty years after whaling. *Biological Conservation*, 70(2), 135-142.

Ramp, C.; Delarue, J.; Palsboell, P.J.; Sears, R., and Hammond, P.S., 2015. Adapting to a warmer ocean - Seasonal shift of baleen whale movements over three decades. *PLoS ONE*, 10(3), e0121374.

Roughan, M. and Middleton, J.H., 2002. A comparison of observed upwelling mechanisms off the east coast of Australia. *Continental Shelf Research*, 22, 2551-2572.

Tranter, D.J.; Carpenter, D.J., and Leech, G.S., 1986. The coastal enrichment effect of the East Australian Current eddy field. *Deep Sea Research* 33, 1705-1728.

Journal of Coastal Research	SI	75	902-906	Coconut Creek, Florida	2016

Three-Dimensional Numerical Simulation of Nonlinear Internal Waves in the St. Lawrence Estuary, Canada

Van Thinh Nguyen[†*]

[†]Department of Civil and Environmental Engineering, Seoul National University, South Korea

www.cerf-jcr.org

www.JCRonline.org

ABSTRACT

Nguyen, V. T., 2016. Three-Dimensional Numerical Simulation of Nonlinear Internal Waves in the St. Lawrence Estuary, Canada. *In:* Vila-Concejo, A.; Bruce, E.; Kennedy, D.M., and McCarroll, R.J. (eds.), *Proceedings of the 14th International Coastal Symposium* (Sydney, Australia). *Journal of Coastal Research*, Special Issue, No. 75, pp. 902-906. Coconut Creek (Florida), ISSN 0749-0208.

The existence of nonlinear internal waves (NIWs) running up a sloping boundary of the Ile-aux-Lievres Island in the St. Lawrence Estuary, Canada has been revealed by the researchers at Memorial and Dalhousie Universities of Canada. Unfortunately, there is no direct field observation of the generation of the NIWs in this region in order to determine where these waves be generated and emanated from. In this paper, a nonhydrostatic three-dimensional model, MITgcm model, is modified and applied to investigate the generation and propagation of NIWs by tidal forcing over an idealized depression simplified from the topography of the North Channel in the St. Lawrence Estuary. A comparison between the numerical results and the observations shows very good qualitative agreements. The results of the simulation is not only to explain above phenomenon, but also to show the mechanism of the NIWs in this region.

ADDITIONAL INDEX WORDS: *numerical simulation, nonlinear internal wave, non-hydrostatic, St. Lawrence Estuary*

INTRODUCTION

The breaking of nonlinear and nonhydrostatic internal gravity waves (NIWs) is an important source of turbulent mixing in ocean and coastal environments, such as redistribution of nutrients, pollutants and sediments in oceans, coastal and estuary regions. NIWs have length scales that are orders of magnitude smaller than the width or length of most coastal systems such as bays, estuaries and fjords. One particularly challenging aspect of turbulence caused by NIWs is that a wave can be generated at one spot but cause turbulence somewhere else, often tens or hundreds of kilometers from its generation site. One of such typical examples is the existence of NIWs running up a sloping boundary of the Ile-aux-Lievres Island in the St. Lawrence Estuary (SLE), which have been observed by Bourgault *et al.* (2003). Since there is no direct field observation of the generation of the NIWs in this region, they have hypothesized that a wavetrain emanated from somewhere near the 128 m deep trough off the Cap-de-la-Tete-au-Chien located in the North Channel of the SLE (Figure 1). Therefore, a comprehensive understanding of NIWs' generation, propagation and breaking in natural environments cannot be tackled from a local perspective because it depends on non-local properties. This poses difficulties not only to modelers but also to field experimentalists because it is difficult to obtain simultaneous direct observations of the full life cycle of a generating and propagating NIW. A combination of modeling efforts, field observations and laboratory experiments is required to tackle this problem. However, NIWs are neglected in most coastal ocean circulation models. The main reason for this lack comes from a limitation in available computational capability which restricts to achieve a real-time simulation for the realistic spatial and temporal scales.

The hydrostatic approximation breaks down for small-scale processes such as the steepening, formation and breaking of nonlinear internal and non-hydrostatic waves; therefore, a non-hydrostatic three-dimensional model is required to study such phenomena. Due to computational capability limitations, the problem of oceanic nonlinear internal wave's generation and propagation has been mostly addressed with two-dimensional non-hydrostatic numerical models, such as Bourgault *et al.* (2005), Lamb and Nguyen (2009), Warn-Varnas *et al.* (2010), *etc*., particularly Li *et al.* (2011) using 2D MITgcm to simulate internal solitary waves (ISWs) in the northern South China Sea. Recently, Guo *et al.* (2011) applied 3D MITgcm to study the ISWs for Luzon Strait, however their grid resolution is still very coarse (Δx=250m, Δy =1000m and Δz is from 10m to 150m). Hereby we used modern computational techniques to deal with higher resolutions to perform semi-realistic three-dimensional nonhydrostatic simulations of NIWs' generation and propagation over a three-dimensional topography in the North Channel of the SLE. The model geometry, background and forcing conditions are inspired from the conditions prevailing in the region of the SLE where the NIWs have been documented. Finally, in order to simulate the small-scale processes, a high spatial resolution is necessary; and consequently this requires the use of High Performance Computers (HPC).

DOI: 10.2112/SI75-181.1 received 15 October 2015; accepted in revision 15 January 2016.
*Corresponding author: vnguyen@snu.ac.kr
©Coastal Education and Research Foundation, Inc. 2016

METHODS

A summary of numerical model together with the study region and its boundary conditions are introduced in the following section.

Numerical Model

In this study, the simulations are based on the well-known open source MIT general circulation model (MITgcm) developed at MIT. The MITgcm model (http://mitgcm.org) is rooted in the incompressible Navier-Stokes equations under the Boussinesq assumption together with the continuity equation as shown in Marshall *et al*., (1997). The MITgcm solves the non-hydrostatic, nonlinear primitive equations using a finite volume formulation on an Arakawa C grid for the horizontal directions, and the cell center approach for the vertical direction. Topography is represented by lopped cells, whereby the intersecting boundary method (Adcroft *et al*., 1997) has been applied. This method allows the boundary of the topography to intersect with the regular grid cells, then the shape of the intersected cells has been modified in order to capture more precisely the bottom bathymetry. This feature can provide more accurate simulation of tide and topography interaction, and hence of the wave generation and propagation processes.

The initial background density based on the study of Bourgault *et al.* (2005), consists of a thin pycnocline separating a thin surface mixed layer from homogenous lower layer. It is given by

$$\rho_t(x,z)=\rho_c-\frac{\Delta\rho}{2}\left[1+\tanh\left(\frac{z-z_0}{\delta}\right)\right]$$

where

$$\rho_c=18.5\,kg/m^3;\ \Delta\rho=5.5\,kg/m^3;\ z_0=-10\,m;\delta=2\,m$$

To cope with this quasi-two layer stratification, the routine "find_rho.F" has been modified.

Study Region

As mentioned above, Bourgault *et al*. (2003) have revealed the existence of NIWs running up a sloping boundary of the Ile-aux-Lievres Island in the St. Lawrence Estuary, whereby the topography of the study region which is included in the North Channel in the SLE is shown in Figure 1 below. The channel has a width of about 15 km, the bottom of channel has a slope, which is shallow at the boundary of the Ile-aux-Lievres Island and gradually deeper to the North Shore.

The depression located next to the Cap-de-la-Tete-au-Chien has the depth of about 128 m. Figure 2 shows the topography of the numerical model which is an idealization from the topography of the North Channel. To minimize perturbations which may occur at the open boundaries and reflect into the study domain, the length of channel is extended towards two open boundaries and far away from the depression. The slope was modeled as close as possible to the bottom slope at the boundary of the Ile-aux-Lievres Island.

Boundary Conditions

In this simulation, no wind or thermal forcing at the free surface has been taken in account. At the bottom *z=H(x,y)*, no-slip condition is applied, *i.e*. all velocity components are set to zero on the bottom.

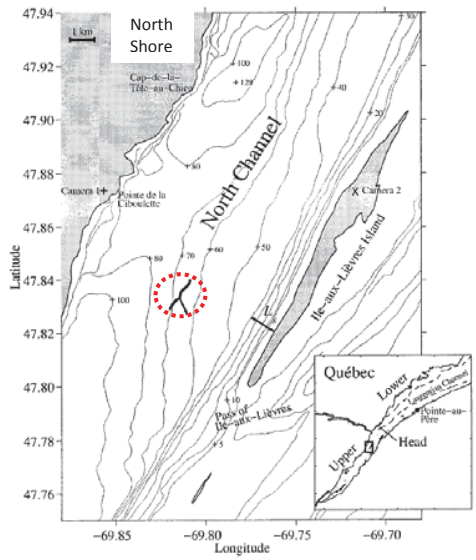

Figure 1. Map of the study region in the St. Lawrence Estuary, the red circle shows the observation site (Source: Bougault *et al.*, 2003).

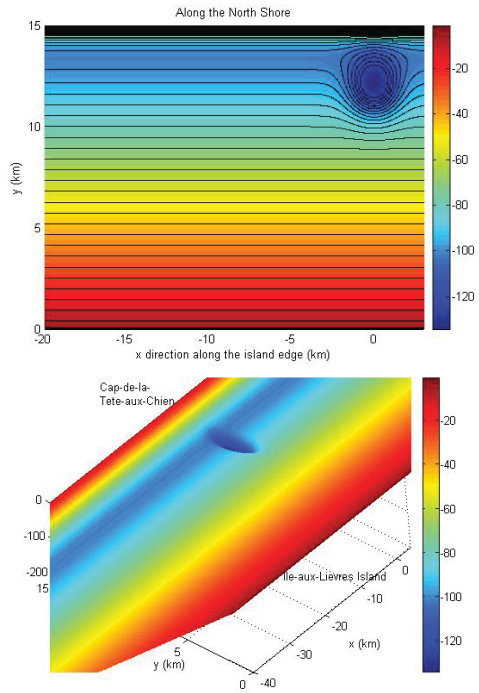

Figure 2. Top view of the idealized topography of the North Channel.

Bottom stresses were added as an additional source term in cells next to bottom boundaries. Bottom drag represents an additional friction, which is cast as a linear or quadratic function of the mean flow in the layer above the bottom, as follows:

$$\tau_{xz} = \left(\frac{2A_v}{\Delta r_c} + r_b + C_d \sqrt{2KE} \right) u$$

$$\tau_{yz} = \left(\frac{2A_v}{\Delta r_c} + r_b + C_d \sqrt{2KE} \right) v$$

where: $KE = \frac{1}{2}(u^2 + v^2)$ is the lateral kinetic energy, u and v are mean lateral velocity components in the layer above the bottom; $A_v = 10^{-3}$ (m^2/s) is vertical viscosity; Δr_c (m) is the distance from the center of adjacent cells to the bottom boundary; r_b (m/s) and C_d are bottom drag linear and quadratic coefficients, respectively. Using the same value as in the study of Bourgault and Kelly (2003), r_b and C_d were set to 0 and 0.003, respectively.

The domain was forced with a long plane wave of M_2 tidal frequency to study the interaction of the barotropic tide with the depression topography. This wave propagates forward and backward through the domain from SW to NE, and vice versa. At the open SW and NE boundaries, the boundary conditions were:

$$u = u(t) = u_0 \sin(\omega t), \qquad v = 0, \qquad and\ w = 0$$

where: u_0 = 1.5 m/s is the amplitude of the barotropic tide, and ω = 1.4075 x 10^{-4} s^{-1} (= M_2) is tidal frequency. To deal with reflecting waves from open boundaries, the routines "obcs_calc.F" and "obcs_sponge.F" have been modified.

A spatially uniform body force is added to the zonal momentum equation:

$$F_u = u_0 \cos(\omega t);\ and\ F_v = F_w = 0$$

where F_u, F_v and F_w are three components of the external force in the momentum equations. The calculation is initiated from state of rest, *i.e.* all velocity components in the simulation domain are initialized to zero.

RESULTS

The simulations using uniform and non-uniform grids with different resolutions have been implemented to test a sensitivity of the grid resolutions in x, y and z directions as follows:

1. A uniform grid with the resolution of 4000x100x60.
2. A non-uniform grid with the resolution of 4000x500x60, which has a non-uniform grid in the x direction with a coarser grid size (Δx=200m) at the open boundaries far away from the depression topography and gradually finer (Δx=25m) at the domain center where the depression located. The grid was uniform in the y and z directions with Δy = 30m and Δz = 2.15m, respectively.
3. A non-uniform grid with a resolution of 4000x750x72, where the grid in the x and z directions was non-uniform. The distribution of the grid size in the x direction was similar as in Case 2. In the y direction, the grid was uniform with Δy = 20m. In the z direction, there were 72 grid layers, which are distributed from finer at surface to coarse at bottom in such a way that 29 layers with Δz = 1m, 10 layers with Δz = 1.5m, 10 layers with Δz = 2.0m, 10 layers with Δz = 2.5m, and 13 layers with Δz = 3m.

The resolution in Case 1 was not fine enough to resolve the small scales of non-linear internal waves in y direction. However, the numerical results obtained from the grid resolutions of Cases 2 and 3 mentioned above were not significantly different, so the following results were taken from the resolution of 4000x500x60 with a time step Δt=1s.

Figure 3 shows the evolution of the temperature fields along the longitudinal section at y_0=12 km, which passes through the center of the depression. At the start of the simulation, with the initial condition that the flow over the depression is commenced from rest, the water initially in the depression is therefore heavier than at upper level, the flow is rapid supercritical on downslope at the right edge of the depression generating lee wave which moves to the right of the depression reaching its local maximum strength at t = 0.25 T (T =2π/ω = 44640s is the tidal period) as shown in Figure 3a. When the initial heavy water has swept out of the depression, the lee wave started to move to the left of the depression and reaching the second local maximum strength with an amplitude of about 17m at t=0.75 T as shown in Figure 3b; then the lee wave becomes steep and breaks, reaching again the local maximum amplitudes at t=1.25T and 1.75T, and so on. Eventually, in the zonal direction, the internal waves have moved forward (to the right of the depression) and backward (to the left of the depression) over the depression center (at x=0m), and the waves reached the local largest amplitudes at the deepest point of the depression, and had the period of 0.5 T; at t=0.25 T, 0.75 T, 1.25 T, 1.75 T, *etc.* as shown Figures 3a, 3b, 3c and 3d, respectively. Figure 4 shows the evolution of the temperature fields at the cross-section x=0m through the center of depression in the meridional and vertical directions. It shows that two internal solitary waves are generated at left and right edges of the depression. Subsequently, the wave on the left edge propagated towards the Island; another wave on the right edge propagated towards the North Shore, then collided with the boundary and formed a reflected wave propagated to the island. Consequently, two ISWs have been formed, propagated towards the Island and running on the slope of the Ile-aux-Lievres Island. This process has been repeated in each half tidal period T, at t=0.25, 0.75 T, 1.25 T, 1.75 T, so on. The results of NIWs running up on the slope of the Ile-aux-Lievres Island shown in Figures 4b and 4c are qualitatively similar to the observations of Bourgault *et al.* (2007).

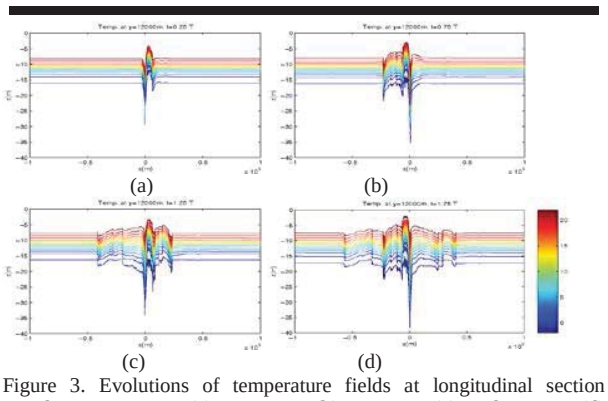

Figure 3. Evolutions of temperature fields at longitudinal section y=12km, at t=0.25 T (a); t=0.75 T (b), t=1.25 T (c), and t=1.75T (d) (location x=0 is center of the depression).

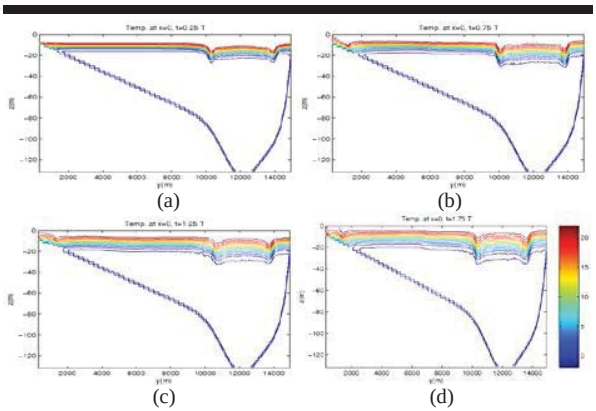

Figure 4. The evolution of the temperature fields at the cross-section x=0m through the center of depression at t=0.25 T (a); t=0.75 T (b), t=1.25 T (c), and t=1.75T (d).

DISCUSSION

An idealized bathymetry simplified from the North Channel in the SLE has been used to study the full life cycle of NIWs, which have been generated from the interaction of the barotropic tide with the depression topography in the North Channel, then they propagated over a distance of about 11km from the center of the depression to the slope of the Ile-aux-Lievres Island. A comparison between the numerical results and the observation of Bourgault *et al.* (2001, 2003) shows very good qualitative agreements as shown in the following discussions.

Figure 5 shows the wavetrain obtained from the numerical simulation at the free surface. Figure 6 shows the surface signature of the internal waves from the observation of Bourgault and Kelly. Due to the interaction of the barotropic tide with the depression, two wavetrains, named A and B as shown in Figures 5 and 6, have been generated at the depression region. The wavetrain B propagated towards and collided the Island with an angle of approximately 45°. The wavetrain B spreads out as wide as the North Channel width (15 km), and the distance between wave front positions is quite constant. Figure 5 (simulation) and Figure 6 (observation) show a very similar configuration between the simulation and observation. The wavetrain B collided with the Island, as well as with the waves reflected from the slope shown by a "turbulent" mixing region along the slope of the Island (Figure 5), where the velocity field of one advected each of the others. These interactions are complex, because they combine of nonlinearity internal waves, shoaling and turbulence mixing processes on the slope. Due to the resolution of the computational grid is coarse (Δy=30m and Δz=2.2m), these processes on the slope cannot be captured from this simulation. Regarding the propagation of the wavetrain A towards the North Shore, it shows a qualitative similarity between the simulation and the observation. However it should be stated that while it shows very good agreement between the simulation and observation of the wavetrain B's propagation, there still exists some differences between the simulation and observation of the wavetrain A's propagation. These differences may come from the implementation of the idealized bathymetry of the North Channel, where the bathymetry at the mild slope of the Ile-aux-Lievres Island are well approximated, while the bathymetry along the North Shore are not well represented in the numerical model due the irregular coastline and the abrupt slope near the Cap-de-la-Tete-au-Chien as shown in Figures 1 and 2.

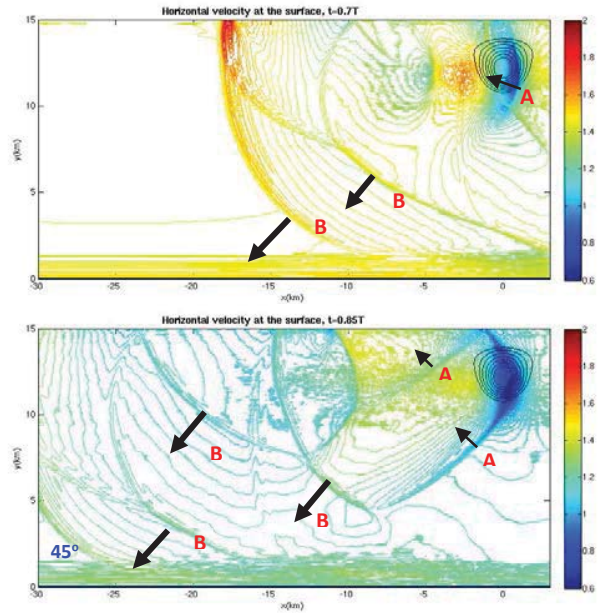

Figure 5. The arrows indicate the propagated directions of wavetrains from the depression region; wavetrain B propagated to the Ile-aux-Lievres Island; wavetrain A propagated to North Shore (Simulation).

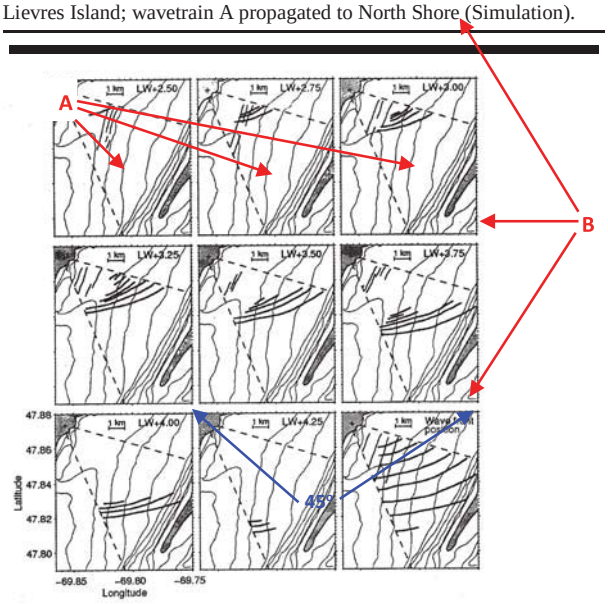

Figure 6. (a) Position of wavetrains obtained from observation; wavetrains A and B are depicted by thin and thick curves, respectively. (Source: Bougault and Kelly, 2003, page 561).

The maximum amplitude of the internal waves obtained from the simulation (about 17m) at the center of the depression (as shown in Figure 3d) is closed to the observation (15m) of Bourgault and Kelley. This difference may come from the implementation of the idealized bathymetry, and particularly the location where this maximum value was observed. As shown in Figure 1, the observed location (red circle) is located in the distance of about 10km away from the center of the depression, so the difference of 2 m can be occurred due to the wave damping from traveling over this distance.

As mentioned above, the numerical simulation has been carried out for a simplified bathymetry, however the number of grid cells are already up to $120x10^6$ (4000x500x60), which strongly requires a powerful computer facility. A real time simulation for each tidal period (T=44640s), using 80 CPUs (1CPU=2x2.6GHz) on a HPC distributed memory machine of the Shared Hierarchical Academic Research Computing Network (SHARCNET), Canada (https://www.sharcnet.ca), needed about 168 hours for the calculation and used 80 GB RAM. The number of CPUs used for this simulation has been optimized and scaled on this platform.

CONCLUSIONS

The objective of this paper is to study the full life cycle of generation and propagation of the NIWs in the North Channel of St. Lawrence Estuary using a fully 3D nonhydrostatic numerical model. The result of the simulation has not only verified the Bourgault and Kelly's hypothesis, but also shown the mechanism of the NIWs in this region. It has shown that due to the tidal forcing over the deep trough off the Cap-de-la-Tete-au-Chien, the internal waves were generated, then propagated over the distance of about 11km towards and collided the sloping boundary at the Ile-aux-Lievres Island with the angle of approximately 45° as shown in the observations of Bourgault and Kelley. In the zonal direction, the internal waves have been generated at the center of the depression, propagated forward and backward over the depression and reached local largest amplitudes at the center of depression in each half tidal period (=0.5T). The same as in the zonal direction, in each half tidal period two internal solitary waves were generated at the center of the depression, propagated and ran up on the slope of the Island.

As it is well-known that a simulation using a real SLE topography, including the wind forcing and river runoff from the Saint Lawrence River can provide a better information about the processes of NIWs propagation, steepening and interaction with boundaries at the slope of the Ile-aux-Lievres Island. However, a simulation with such completed inputs and using higher grid resolution to simulate small scale processes of non-linear internal waves will strongly require high performance computers facility (a large number of CPUs and memory), and the calculation definitely will consume a significant time and data storage space. This task is currently over the facility of our HPC.

ACKNOWLEDGMENTS

This work was supported by the Seoul National University Research Grant. The author also would like to thank Dr. Kevin G. Lamb for his supports to this research topic during the author's staying at the Department of Applied Mathematics, University of Waterloo, Canada.

LITERATURE CITED

Adcroft, A.; Hill, C., and Marshall, J., 1997. Representation of topography by shaved cells in a height coordinate ocean model, *Monthly Weather Review*, Vol. 125 (9), 2293-2315.

Bourgault, D.; F.J. Saucier, and C.A. Lin, 2001. Shear instability in the St. Lawrence Estuary: A comparison of fine-scale observations and estuaries circulation model results, *Journal of Geophysical Research*, 106, 9393-9409.

Bourgault, D. and D. E. Kelley, 2003. Wave-induced boundary mixing in a partially mixed estuary, Journal of Marine Research, 61 (5), 553-576.

Bourgault, D.; D.E. Kelley, and Galbraith, P.S., 2005. Interfacial solitary wave run-up in the St. Lawrence Estuary, *Journal of Marine Research*, 63, 1001-1015.

Bourgault, D.; Blokhina, M.D.; Mirshak R., and Kelley D.E., 2007. Evolution of a shoaling internal solitary wavetrain, *Geophysical Research Letters*, Vol. 34, L03601.

Guo, C.; Chen, X.; Vlasenko, V., and Stashchuk, N., 2011. Numerical investigation of internal solitary waves from the Luzon Strait: generation process, mechanism and three-dimensional effects, *Ocean Modelling*, Vol. 38, 203-216.

Lamb, K. and Nguyen, V. T., 2009. On Calculating Energy Flux in Internal Solitary Waves with an Application to Reflectance, *Journal of Physical Oceanography*, Vol. 39(3), pp. 559-580.

Li, D.; Chen, X. and Liu, A., 2011. On the generation and evolution of internal solitary waves in the northwestern South China Sea, *Ocean Modelling*, Vol. 40, 105-119.

Marshall, J.; Hill, C.; Perelman, L., and Adcroft, A., 1997. Hydrostatic, quasi-hydrostatic and nonhydrostatic ocean modeling, *Journal of Geophysical Research*, 102(C3), 5733-5752.

Warn-Varnas, A.; Hawkins, J.; Lamb, K.; Piacsek, S.; Chin-Bing, S.; King, D., and Burgo, G., 2010. Solitary wave generation dynamics at Luzon Strait. *Ocean Modelling*, 31(1-2), 9-27.

Journal of Coastal Research	SI	75	907-911	Coconut Creek, Florida	2016

Depression Waves Generated by Large Ships in the Venice Lagoon

Kevin E. Parnell [†*], Luca Zaggia[‡], Tarmo Soomere[§], Giuliano Lorenzetti[‡], and Gian Marco Scarpa[††]

[†]College of Marine and Environmental Sciences
James Cook University
Townsville, Australia

[‡]Institute of Marine Sciences
National Research Council
Venice, Italy

[§]Institute of Cybernetics
Tallinn University of Technology
Tallinn, Estonia

[††]Environmental Sciences, Informatics and Statistics
Università Ca' Foscari
Venice, Italy

www.cerf-jcr.org

www.JCRonline.org

ABSTRACT

Parnell, K.E.; Zaggia, L.; Soomere, T.; Lorenzetti, G., and Scarpa, G-M. 2016. Depression waves generated by large ships in the Venice Lagoon. *In:* Vila-Concejo, A.; Bruce, E.; Kennedy, D.M., and McCarroll, R.J. (eds.), *Proceedings of the 14th International Coastal Symposium* (Sydney, Australia). *Journal of Coastal Research*, Special Issue, No. 75, pp. 907-911. Coconut Creek (Florida), ISSN 0749-0208.

At present cruise ships use the Lido and Giudecca channels to berth at the Port of Venice, and cargo vessels use the Malamocco–Marghera channel to berth at the Marghera industrial area. Following a government decree to restrict large ship access to the Port of Venice through the Lido and Giudecca channels, the Port authority has been investigating the construction of a new channel between Marghera and the cruise terminal, to re-route all large vessels through the Malamocco lagoon entrance. Ships in the Venice Lagoon travel at low speeds with associated low depth-based Froude numbers (<0.5), and classical Kelvin wave effects are minimal. However, under certain channel geometries, depression waves (also known as Bernoulli wake) can be substantial with significant far-field effects. In the Malamocco–Marghera Channel, depression waves up to 2.5 m, with high (~1.5 m/s) near bed water speeds, transform into asymmetric Riemann waves, able to propagate large distances from the navigation channel into the shallow lagoon. By contrast, depression waves associated with large ships in the Lido and Giudecca channels are much smaller (~0.3–0.4 m). Rerouting large cruise ships entering the Port of Venice through the Malamocco–Marghera channel and a newly constructed channel will have adverse effects on the Venice lagoon with increased water velocities and sediment resuspension associated with the nonlinear Riemann waves. It is therefore essential that the potential effects be thoroughly evaluated using an appropriate methodology before the development of a new lagoon channel.

ADDITIONAL INDEX WORDS: *Bernoulli wake, vessel wakes, Riemann waves, nonlinear waves.*

INTRODUCTION

The classic theory of ship-generated wakes focuses on the properties of surface undulations created by moving vessels (Newman, 1977). In the open deep ocean the influence of wake waves on water mass dynamics is negligible. Wake waves and their specific nonlinear components (such as precursor solitons), particularly for vessels travelling at high speed, play a much larger role in shallower areas (Didenkulova *et al*., 2009; Erm and Soomere, 2006; Parnell and Kofoed-Hansen, 2001; Parnell *et al*., 2007; Soomere *et al*., 2011).

The governing parameter for wave generation is the depth-based Froude number F_d , the ratio of the vessel speed V and the maximum wave celerity for the depth d. If this parameter is below 0.6–0.7, the wave system resembles the Kelvin wake, while at values F_d in the high-speed subcritical range 0.7–1, various nonlinear phenomena become evident (Soomere, 2007). The structure of wave wake at supercritical speeds (F_d >1) is fundamentally different and resembles a Mach-type system (Pethiyagoda *et al*., 2014; Rabaud and Moisy, 2013).

While most components of wake waves are either almost linear or can be described by weakly nonlinear models, recent research has highlighted the effects of a depression wave, a strongly nonlinear ship-generated disturbance. Often called a Bernoulli wake, it is an intrinsic part of moving in shallow or narrow waterways. It becomes evident as 'squat' (Naghdi and Rubin, 1984) where lower pressure around the ship causes it to be closer to the seabed than in deep water. It is commonly thought that the resulting depression is located only in the immediate vicinity of the ship.

In certain geometries of the fairway, waves of elevation are almost negligible and almost all energy is concentrated in the depression wave. Such a situation occurs in the narrow and shallow navigation channels in the Venice Lagoon (Figure 1). Even though all large ships in the Venice Lagoon travel at low speeds with associated low depth-based Froude numbers (<0.5) and classical Kelvin wave effects are minimal, vessel-generated single depressions in an ~12 m deep waterway can be as much as 2.5 m (Parnell *et al*., 2015). These entities are highly nonlinear and they propagate over the shallow-water areas as long-living solitary depression waves at least ~1 km into the lagoon (Rodin *et al*., 2015). In the shallow and muddy

DOI: 10.2112/SI75-182.1 received 15 October 2015; accepted in revision 15 January 2016.
*Corresponding author: kevin.parnell@jcu.edu.au
©Coastal Education and Research Foundation, Inc. 2016

lagoon they create high water velocities and intense resuspension (Rapaglia *et al*., 2011), possibly leading to serious environmental consequences for large parts of the Venice Lagoon (Gelinas *et al*., 2013; Rapaglia *et al*., 2015).

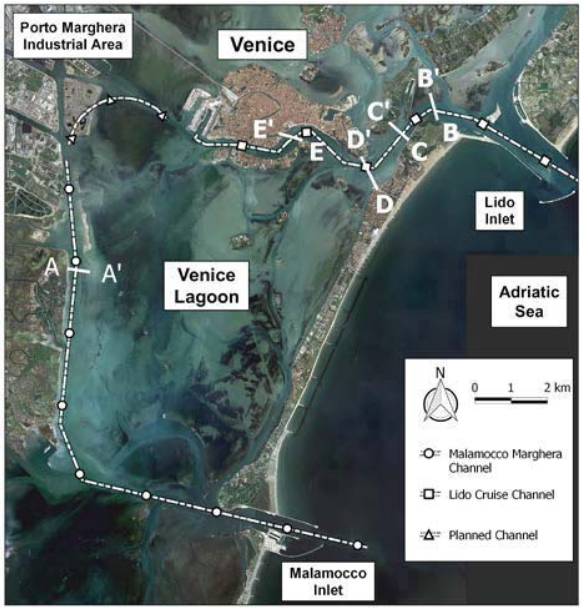

Figure 1. The Venice lagoon, showing the Malamocco–Marghera channel, used by cargo ships, the Lido channel used by cruise ships and the most recently suggested location of a channel that may be constructed so that cruise ships can reach the passenger terminal through the Malamocco entrance. The location of cross sections on which data were collected are also indicated. The cross section areas (at local datum level where MSL = –0.26 m) are: A 1910 m^2; B 5053 m^2; C 4301 m^2; D 3546 m^2; E 4080 m^2.

The largest depressions rapidly lose a large part of their height when travelling over the first 100–200 m in the lagoon and the amplitude of the depression wave in the shallow lagoon only weakly depends on the initial amplitude of the wave (Rodin *et al*., 2015). Therefore, even relatively modest depression waves, generated in narrow channels constructed in a shallow lagoon may penetrate to substantial distances into the lagoon provided their amplitude is large enough to ensure a strongly nonlinear regime of propagation.

At present, cruise ships use the Lido entrance to the Venice Lagoon and the Lido and Giudecca channels to berth at the Venice cruise ship terminal, and cargo vessels use the Malamocco entrance and the Malamocco–Marghera channel to berth at the Marghera industrial area (Figure 1). Pressure to restrict large ship access to the Port of Venice through the Lido and Giudecca channels increased after the 'Costa Concordia' disaster in the Tuscan archipelago, and the level of protest increased. Stated reasons to exclude large ships from the Lido and Giudecca channels include aesthetics, the risk of accidents, safety, and wake-wave effects, particularly on structures. The national government notified a future ban (by decree) that forced the Port of Venice to investigate the construction of a new channel between the Malamocco–Marghera channel and the cruise ship terminal, to enable the re-routing of all vessels through the Malamocco entrance.

In this paper we discuss the properties and propagation of ship-induced depression waves generated by ships in a section of the Malamocco–Marghera industrial channel. We compare these depression waves with those generated by cruise ships in the Lido and Giudecca channels, and consider the implications of re-routing cruise ships to the Malamocco-Marghera channel and a potential newly constructed channel providing access to the Venice cruise terminal.

METHODS

The Venice Lagoon has a surface area of 550 km^2 and average depth of 0.8 m (Brambati *et al*., 2003). Water circulation is mainly controlled by tides with tidal range between 0.3 and 1.1 m. The lagoon has three inlets with depths from about 10 m to > 17 m (the Malamocco inlet).

Ship wake measurements were performed in the Malamocco–Marghera navigation channel, south of the industrial area of Marghera (Figure 2). Self-recording pressure sensors housed in different instruments were deployed in 8 positions across a section (Parnell *et al*., 2015), from the channel margins, extending to the shoreline on the Eastern side ('B' locations in Figure 2) and to a breakwater protection on the Western side ('W' locations in Figure 2). At some locations InterOcean S4 current meters were deployed with directional currents being recorded. We underestimated the water speeds that the current meters would experience, and the current meters overturned due to insufficient anchor weight and drag on surface buoys. Consequently, on a number of occasions during early deployments, current data were lost. Therefore, where noted, the reported speeds are the highest recorded before the current meter tilted and are therefore likely to be less than the true maximums. Data were recorded at either 2 or 5 Hz acquisition frequency over four sampling periods of between 2 to 6 days in March and April 2014. Approximately 90 cargo vessel passages were recorded. Ships travelled at speeds of between 6 and 11.5 knots, with blocking ratios C^* (width W x draught D of the vessel / cross-sectional area of the channel), between 0.02 and 0.14, and with depth Froude numbers (F_d) between 0.3 and 0.55 (clearly in the sub-critical range). Two examples are shown (Table 1; Figure 3).

Table 1. *Vessel details for the Abu Dhabi Star and Domenico Ievoli (Malamocco–Marghera channel) and MSC Preziosa and Costa Fascinosa (Lido and Giudecca channels)*

Ship	*Length (m)*	*W (m)*	*D (m)*	*V (kn)*	C^*	F_d
Abu Dhabi Star	183	32	7.8	7.7	0.14	0.37
Domenico Ievoli	146	20	6.6	10.4	0.07	0.50
MSC Preziosa	333	38	8.6	5.2 to 7.5	0.06 to 0.09	0.23 to 0.35
Costa	289	36	8.3	5.7	0.05	0.23

Fascinosa	to 8.1	to 0.08	to 0.31

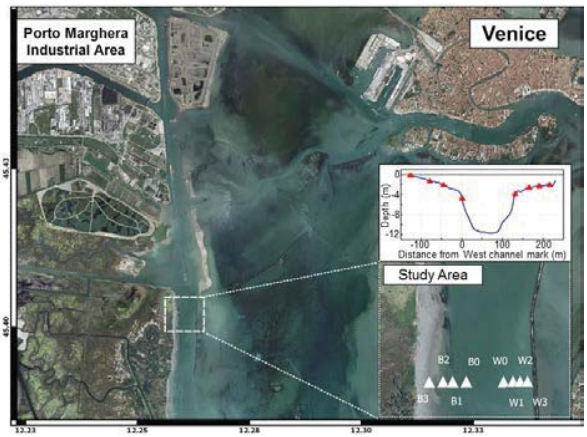

Figure 2. Study site in the Marghera–Malamocco channel.

Wake measurements of cruise ships MSC Preziosa on 5 April 2014 and Costa Fascinosa on 7 April 2014, passing through the Lido and Giudecca channels were obtained during a sampling period from 4 to 8 April 2014 (Table 1). Measurements were taken near the channel edge. Eight instruments were deployed, all measuring pressure with four InterOcean S4 current meters also measuring directional currents. Typically, cruise ships enter Venice in the early morning and depart in the late afternoon or early evening.

RESULTS

Two examples of depression waves from cargo vessels on a cross section in the Marghera–Malamocco channel are shown in Figure 3, and are presented as actual water depths at the time of the ships passage. Because of the low speed (7.7 and 10.4 knots, with corresponding F_d of 0.37 and 0.50) sign-variable wave groups or solitary waves of elevation were not evident. The most noticeable feature was a deep depression typically lasting ~80 s. Of the ~90 records, Abu Dhabi Star, an unremarkable ship in terms of its size and speed, produced the largest depression wave of 2.5 m from still water level. A common feature of the depressions was the difference in size at the opposite sides of the channel. On the lagoon side the depression wave generated by the Abu Dhabi Star was only 1.6 m. The depression wave of the Domenico Ievoli, travelling in the opposite direction, was larger on the lagoon side. The depressions were almost perfectly symmetric at the channel margins, but became asymmetric with the front slope becoming less steep and the rear slope becoming steeper, as the waves crossed the adjacent shoals. Virtually all records showed the development of a step on the rear slope of the depression wave. Parnell *et al.* (2015) show that these waves are described reasonably well as long-living strongly nonlinear solitary Riemann depression waves. At those sites where water speeds were also recorded (B1, B2, W1 and W2), even small depression waves generated high near bed speeds (greater than 0.65 m/s in the examples shown). In the case of Abu Dhabi Star, near bed speeds of at least 1.89 m/s were recorded before the current meter was overturned.

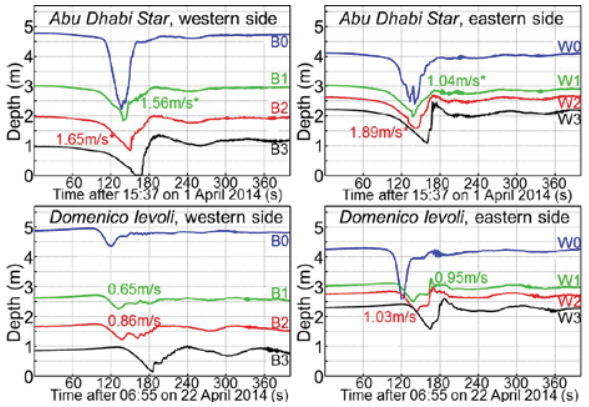

Figure 3. Depression waves in the Marghera–Malamocco channel. Water speeds are the maximum recorded ~20 cm above the seabed. Speeds labelled * are the maximum recorded before the instrument was overturned. Actual maximum speeds are likely to be higher.

Waves generated by MSC Preziosa in the Lido and Giudecca channels are presented in Figure 4. Depression waves generated by Costa Fascinosa, measured on a different day, were almost identical in shape but smaller in magnitude than those for MSC Preziosa. Data are not presented from sites B, C', D' and a site 250 m west of B', but they typically showed waves that were smaller than or similar to those illustrated. At site D', no depression waves were recorded.

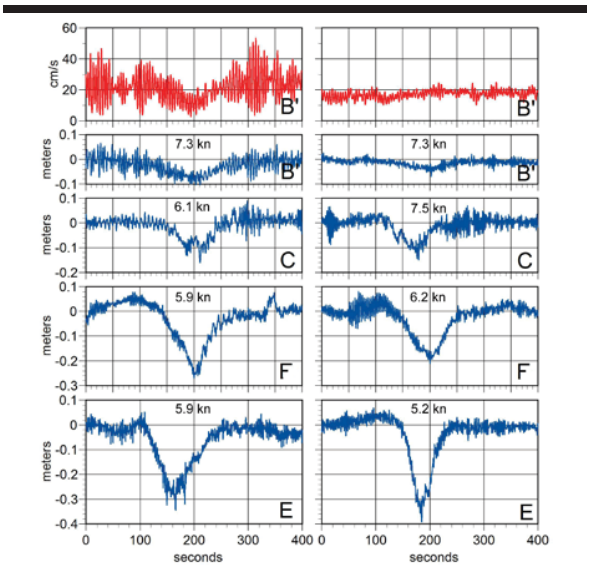

Figure 4. Depression waves generated by MSC Preziosa at sites in the Giudecca and Lido channels (see Figure 1), incoming to Venice on the left and outgoing on the right. Zero is the average water surface in the first 30 seconds of the record. The top graphs (red) show water velocities approximately 1 m from the bed at site B'. The speed of the

ship passing the site is shown in knots.

In the Lido and Giudecca channels, the largest measured depression wave was 0.4 m from still water level at site E., with the next largest wave (0.26 m, although preceded by a 0.04 m increase in water level) at site F. Smaller depression waves were observed at other measurement sites further east. This is surprising as the ships were at their slowest speeds at sites E and F, and the cross section area of the channel (and therefore the blocking ratios) were not significantly different to cross sections C and D, however, the ship tracks took them quite close to these two gauge sites. The depression waves (measured close to the channel edge) are all nearly symmetric.

The water level variations caused by the combined effects of wind generated waves and the multitude of smaller vessels are also clearly seen as background noise on the main trend. No sign-variable waves caused by the cruise ships are apparent in the record, although as evidenced by the water level rise in a few records, precursor solitons may occur, the magnitude of which is only in the order of a few centimeters.

The graphs in red in Figure 4 show the near bed water speeds associated with the passage of MSC Preziosa. Tidal currents at this site averaged 23 cm/s during the incoming passage. As MSC Preziosa had been announced to be the largest vessel ever to enter Venice through the Lido entrance, it was accompanied by a number of small spectator boats. The small boat wakes (and possibly some wind driven waves) can be seen. The effect of the depression wake on water speeds was to reduce the average (tidal) current and change the water movement direction. This was typical of all records for which we had water velocity data.

DISCUSSION

The depression waves generated by large cruise ships in the Lido and Giudecca channels are significantly smaller than those generated by cargo vessels in the Marghera–Malamocco channel. The precise combination of factors to explain this are not fully understood. Blocking ratios for cruise ships in the Lido and Giudecca channels were approximately the same as for the smaller cargo vessels in the Marghera–Malamocco channel (*e.g.* Domenico Ioveli), but significantly less than the larger cargo vessels (*e.g.* Abu Dhabi Star). The impact of channel geometry on the depression wave size has not been established. The cruise ships were travelling slightly slower than was typical for the cargo ships (with correspondingly smaller F_d), which may have been influential. The proximity of the ship to the measurement site is probably an important factor, to the extent that significantly different amplitudes of the depression are observed on different sides of the channel, although this is not tested in this study.

The potential impact of depression waves propagating as strongly nonlinear Riemann waves across wide and shallow shoals has been demonstrated by Parnell *et al.* (2015) and Rodin *et al.* (2015). Provided that their amplitude is large enough to ensure a strongly nonlinear regime of propagation, waves generated in a narrow channel constructed in a shallow lagoon may penetrate to substantial distances. Numerical simulations have shown that once established, the initial size of the depression wave is not significant, as the height of the wave reduces to a common level after some propagation time, meaning that depression waves of even a modest size may produce the theoretically maximum amplitude in the lagoon, potentially >0.3 m (Rodin *et al.*, 2015). The propagating wave becomes highly asymmetric, with a gently sloping front and a very steep rear, even at a distance >1 km from the navigation channel. Rapaglia *et al*. (2015) demonstrate the significant effect of such waves on water speeds and sediment resuspension and transport in the lagoon, including the resuspension of contaminated sediments, and safety issues, particularly associated with the steep rear slope of the propagating wave (Rodin *et al*., 2015).

The conditions described above, a channel with extensive adjacent shallow shoals, occurs over the entire length of the Marghera–Malamocco channel and in the eastern parts of the Lido channel. Whereas depression waves of sufficient amplitude to form nonlinear Riemann waves in the shallows always or almost always occur in the Marghera–Malamocco channel, our data suggests that waves of sufficient size are not generated by the cruise ships in the Lido channel. Once in the Giudecca channel, where larger depression waves apparently form, the morphological conditions for the development of nonlinear Riemann waves do not exist. The direct wake effects of cruise ships in the Lido and Giudecca channels therefore appear to be small, although increased velocities in adjacent channels may still result (Costa and Zuliani, 2004).

There is currently a directive to reroute cruise ships entering the cruise ship terminal in Venice through the Marghera–Malamocco channel and a new channel to be constructed. While there may be many reasons why such a move is the right thing to do (aesthetics, risks of spills or accidents, safety, conflict with other users), most wake related issues are almost certainly much less significant. However, an increase in the number of large ships with blocking ratios larger than those of cargo ships (calculated at cross section A of 0.18 for MSC Preziosa and 0.17 for Costa Fascinosa, compared to 0.14 for Abu Dhabi Star) in the Marghera-Malamocco channel and in a newly constructed channel could cause a significantly increased impact on the lagoon ecosystems in an area which has been already heavily impacted (Sarretta *et al*., 2010) and on the safety and convenience of other users of the lagoon.

Shipping channels with extensive adjacent shallow water areas are common on the approaches to ports. The far-field impact of depression waves generated in such channels has been demonstrated (Rapaglia *et al*., 2011, 2014; Parnell *et al*., 2015; Rodin *et al.*, 2015) and their further propagation has been acceptably replicated in the strongly nonlinear framework of Riemann waves (Parnell *et al.*, 2015; Rodin *et al.*, 2015). However, the physics of their generation is yet to be clarified. While the wakes generated by ships is now generally well understood and several features of the wake signature for particular ships are remarkably stable (Torsvik *et al*., 2015), it may be necessary to test ships sailing in navigation channels surrounded by wide and shallow banks with respect to their ability to excite potentially dangerous depression waves.

CONCLUSIONS

Although depression waves (otherwise called Bernoulli wakes), have been well known for some time, their structure and impacts after propagation over wide and shallow banks has only recently been described in the context of nonlinear Riemann wave theory, using the case of the Marghera–Malamocco channel in the Venice lagoon. We demonstrate that these wakes, generated by cargo vessels, can have significant amplitude. Even larger cruise ships transiting the Lido and Giudecca channels generate much smaller depression waves in the outer parts of the route, potentially too small to establish nonlinear effects, and on the inner section of the route, where waves of up to 0.4m were recorded, the lack of adjacent shallow areas means that the effects are likely to be minimal.

The proposal to reroute ships from the Lido and Giudecca channels through the Marghera-Malamocco channel and a newly constructed channel will lead to larger and more ships transiting this route, and may have significant further impact on lagoon morphodynamics with substantial effects on ecosystem services, and on the safety and convenience of other lagoon users. It is therefore essential that the effects of this change be investigated using an appropriate methodology before such a project is implemented.

ACKNOWLEDGMENTS

This work was supported by the institutional financing by the Estonian Ministry of Education and Research (grant IUT33-3), and the Estonian Science Foundation (from 2011 Estonian Research Council) grant 9125. The field studies were undertaken during Parnell's visit to CNR-ISMAR, Venice, Italy, and were funded by the project Ritmare (SP3-WP3-A1).

LITERATURE CITED

Brambati, A.; Carbognin, L.; Quaia, T.; Teatini, P., and Tosi, L., 2003. The Lagoon of Venice: geological setting, evolution and land subsidence. *Episodes*, 26(3), 264-265.

Costa, F. and Zuliani, A., 2004. *Analisi degli effetti idrodinamici indotti nei rii in corrispondenza del passaggio delle grandi navi da crociera: Relazione di sintesi*, CNR-ISMAR, Venezia, 17p. (in Italian)

Didenkulova, I.; Parnell, K.E.; Soomere, T.; Pelinovsky, E., and Kurennoy, D., 2009. Shoaling and runup of long waves induced by high-speed ferries in Tallinn Bay. *Journal of Coastal Research*, Special Issue No. 56, pp. 491-495.

Erm, A. and Soomere, T., 2006. The impact of fast ferry traffic on underwater optics and sediment resuspension. *Oceanologia*, 48(S), pp. 283-301.

Gelinas, M.; Bokuniewicz, H.; Rapaglia, J., and Lwiza, K.M.M., 2013. Sediment resuspension by ship wakes in the Venice Lagoon. *Journal of Coastal Research*, 29, 8-17.

Kelpšaite, L.; Parnell, K.E., and Soomere, T., 2009. Energy pollution: the relative influence of wind-wave and vessel-wake energy in Tallinn Bay, the Baltic Sea. *Journal of Coastal Research*, SI 56, 812-816.

Naghdi, P. and Rubin, M., 1984. On the squat of a ship. *Journal of. Ship Research*. 28, 107-117.

Newman, J.N., 1977. *Marine hydrodynamics*. Cambridge, Massachusetts: MIT Press, 402p.

Parnell, K.E. and Kofoed-Hansen, H., 2001. Wakes from large high-speed ferries in confined coastal waters: Management approaches with examples from New Zealand and Denmark. *Coastal Management*, 29 (3), 217-237.

Parnell, K.E.; McDonald, S.C., and Burke, A.E., 2007. Shoreline effects of vessel wakes, Marlborough Sounds, New Zealand. *Journal of Coastal Research*, SI 50, 502-506.

Parnell, K.E.; Soomere, T.; Zaggia, L.; Rodin, A.; Lorenzetti, G.; Rapaglia, J., and Scarpa, G-M., 2015. Ship-induced solitary Riemann waves of depression in Venice Lagoon. *Physics Letters A*, 379(6), 555-559.

Pethiyagoda, R.; McCue, S.W., and Moroney, T.J., 2014. What is the angle of a nonlinear Kelvin ship wave pattern? *Journal of. Fluid Mechanics*. 758, 468-485.

Rabaud, M. and Moisy, F., 2013. Ship wakes: Kelvin or Mach angle? *Physical. Review. Letters*. 110 (21), No. 214503.

Rapaglia, J.; Zaggia, L.; Ricklefs, K.; Gelinas, M., and Bokuniewicz, H., 2011. Characteristics of ships' depression waves and associated sediment resuspension in Venice Lagoon, Italy. *Journal of Marine Systems*, 85(1-2), 45-56.

Rapaglia, J.; Zaggia, L.; Parnell, K.E.; Lorenzetti, G., and Vafeidis, A.T., 2015. Ship-wake induced sediment remobilization: Effects and proposed management strategies for the Venice Lagoon. *Ocean & Coastal Management* 110, 1-11.

Rodin, A.; Soomere, T.; Parnell, K.E., and Zaggia, L., 2015. Numerical simulation of the propagation of ship-induced Riemann waves of depression into Venice Lagoon. *Proceedings of the Estonian Academy of Sciences*, 64 (1), 22-35.

Saretta, A.; Pillon, S.; Molinaroli, E.; Guerzoni, S., and Fontolan, G., 2010. Sediment budget in the Lagoon of Venice, Italy. *Continental Shelf Research*,. 30, 934-949.

Soomere, T., 2007. Nonlinear components of ship wake waves, *Applied Mechanics Reviews*, 60 (3), 120-138.

Soomere, T.; Parnell, K.E., and Didenkulova, I., 2011. Water transport in wake waves from high-speed vessels, *Journal of Marine Systems*, 88 (1), 74-81.

Torsvik, T.; Soomere, T.; Didenkulova, I., and Sheremet, A. 2015. Identification of ship wake structures by a time-frequency method. *Journal of Fluid Mechanics*, 765, 229-251.

Journal of Coastal Research	SI	75	912-916	Coconut Creek, Florida	2016

Synthetic Imagery for the Automated Detection of Rip Currents

Sebastian Pitman[†*], Shari L. Gallop[‡], Ivan D. Haigh[†], Sasan Mahmoodi[∞], Gerd Masselink[§] and Roshanka Ranasinghe[††]

[†]Ocean and Earth Science, National Oceanography Centre, University of Southampton, UK.

[‡]Department of Environmental Sciences, Macquarie University, Sydney, NSW, Australia.

[∞]School of Electronics and Computer Science, University of Southampton, UK.

[§]School of Marine Science and Engineering, Plymouth University, UK.

[††]UNESCO-IHE and Deltares, Delft, The Netherlands; and Australian National University, Canberra, Australia.

www.cerf-jcr.org

www.JCRonline.org

ABSTRACT

Pitman, S.J.; Gallop, S.L.; Haigh, I.D.; Mahmoodi, S.; Masselink, G., and Ranasinghe, R., 2016. Synthetic imagery for the automated detection of rip currents. *In:* Vila-Concejo, A.; Bruce, E.; Kennedy, D.M., and McCarroll, R.J. (eds.), *Proceedings of the 14th International Coastal Symposium* (Sydney, Australia). *Journal of Coastal Research*, Special Issue, No. 75, pp. 912-916. Coconut Creek (Florida), ISSN 0749-0208.

Rip currents are a major hazard on beaches worldwide. Although *in-situ* measurements of rips can be made in the field, it is generally safer and more cost effective to employ remote sensing methods, such as coastal video imaging systems. However, there is no universal, fully-automated method capable of detecting rips in imagery. In this paper we discuss the benefits of image manipulation, such as filtering, prior to rip detection attempts. Furthermore, we present a new approach to detect rip channels that utilizes synthetic imagery. The creation of a synthetic image involves the partitioning of the 'parent' image into key areas, such as sand bars, channels, shoreline and offshore. Then, pixels in each partition are replaced with the respective dominant color trends observed in the parent image. Using synthetic imagery increased the accuracy of rip detection from 81% to 92%. Synthetics reduce 'noise' inherent in surfzone imagery and is another step towards an automated approach for rip current detection.

ADDITIONAL INDEX WORDS: *rip channel, image filtering, remote sensing, coastal imaging, synthetic imagery.*

INTRODUCTION

Rip currents (rips) are seaward-orientated, jet-like flows originating in the surfzone (Short, 1985). They generally occur in channels incised into sand bars (Shepard *et al*., 1941; Bowen, 1969). Despite numerous field campaigns, studies have been unable to relate rip behaviour solely to the incident wave field, due to factors such as nonlinearity, time-lags, and the largely unknown effects of antecedent bathymetry (*e.g.*, Holman *et al*., 2006; Huntley and Short, 1992; Short, 1985). The inability to linearly link forcing and response of rip channels has resulted in a somewhat site-specific understanding on the key controls on rips. The main cause for this knowledge gap is the lack of adequate, long-term field data at multiple sites with different forcing. Field experimentation in the surfzone is difficult, expensive, and often dangerous. Therefore, remote sensing provides an attractive alternative.

Video imaging has been used to remotely sense the nearshore for about 25 years. Lippmann and Holman (1989) first realised the utility of time-lapse imagery in identifying the position of offshore sand bars, using areas of high light intensity generated by waves breaking over the bar. The development of bespoke coastal imaging methods such as Argus (Holman and Stanley, 2007), allows extraction of quantitative data from images. Such information includes bar position (Lippmann and Holman, 1989), wave period and nearshore bathymetry (Ranasinghe *et al.*, 2004; Stockdon and Holman, 2000), wave incidence angle (Lippmann and Holman, 1991), and alongshore rip channel locations (Ranasinghe *et al*., 1999).

Video imaging has been used to detect and measure rip channel parameters, such as quantity and alongshore location (*e.g.*, Ranasinghe *et al*., 1999). These techniques were used to extract datasets of up to 4 years (*e.g.*, Holman *et al*., 2006); timescales that would be unfeasible to measure *in-situ*. A major limiting factor on the length of rip datasets that can be generated is that all attempts thus far required various degrees of manual input (Bogle *et al.*, 2000; Gallop *et al.*, 2009; Holman *et al*., 2006; Quartel, 2009; Ranasinghe *et al*., 1999; Turner *et al*., 2007; Whyte *et al*., 2005). The majority of research using video images uses the raw image products (snapshot, timex, daytime, etc.) output from the cameras, which can often be inherently 'noisy', hindering robust rip channel detections.

Therefore, this research aims to investigate the merits of image manipulation, prior to the extraction of data from imagery. In particular, we consider the benefits of spatial filtering, and the use of synthetic images as it may provide an intermediate step overcoming previous problems with automated rip detection.

Image-Based Rip Detection

The favoured approach to date for automatic rip detection has been to use pixel intensity minima as indicative of rip channel location, because deeper channels appear as darker areas between the higher intensity wave breaking zones over shoals. It is also common to average the intensity values in the cross-shore

DOI: 10.2112/SI75-183.1 received 15 October 2015; accepted in revision 15 January 2016.
*Corresponding author: sjp1e13@soton.ac.uk
©Coastal Education and Research Foundation, Inc. 2016

direction. All values between the shoreline and the edge of the breaking region are averaged at each alongshore position, to compute one alongshore intensity profile (Ranasinghe *et al*., 1999). This method is appropriate for simple scenarios, where rip channels are orientated in shore-normal directions. It is inappropriate for complex bathymetries (Holman *et al*., 2006) such as the common cases where rip channels cut across the surfzone diagonally to form acute angles with the shoreline.

The intensity profiles generated have typically been subject to visual classification in order to ascertain rip locations (*e.g.*, Bogle *et al*., 2000). This is due to the resultant image intensity profiles containing a degree of 'noise' or 'fouling' that can act to obscure the main features. In this context, noise refers to artefacts introduced to the image during processing. Fouling refers to anything undesirably captured by the camera, such as rain drops and fog. Noise can be present in the image for a variety of reasons, such as environmental factors (i.e. sensor temperature) during image acquisition (Russ, 2007).

Analogue signals of the natural world are continuos (Bovik, 2005) and therefore need to be quantized to produce digital images before computer processing. In the literature pertaining to image-based rip detection and surfzone studies, pixel values know as intensities are usually quantized into 256 discrete levels [0-255]. This quantization process introduces a uniform noise to the digital image (Gonzalez and Woods, 2008). A common approach to reduce such noise in the field of image processing is to filter the image, yet this is rarely discussed in literature pertaining to image-based rip detection, or surfzone studies.

Image Filtering & Manipulation

To our knowledge, simple single-image filtering of nearshore images has not been widely used before, because the prevalent image type used for analysis is the so called timex image, which represents the time-mean of intensity in all frames collected at 2 Hz over a 10-minute period (Holman and Stanley, 2007). This constitutes a form of average filtering during the image acquisition stage; however, the resultant image may still include background noise or erroneous data. One such example is raindrops on the lens covering, which would appear in the rectified image, giving a false intensity signature for the pixel(s) concerned. Studies using video images tend to reject imagery where raindrops are visible on the lense for this reason. Holman *et al.* (2013) described how consecutive images in a time series can be used to create a running-average estimate (cBathy). cBathy uses wave celerity to estimate bathymetry, and the use of this running-average filter has been successful in removing fouling from subsequent images, such as rain drops or sun glare. Despite the assumption that a timex image is already prefiltered, it still contains noisy signals, representative of a very dynamic surfzone. Furthermore, inclement weather still appears as fouling in the imagery. Therefore, there is a need to pre-filter the image before processing, rather than relying on filtering the signal that is extracted as a result of processing.

METHODS

In this study we use images from Tairua beach in New Zealand, to investigate the benefit of simple spatial filtering, as well as the use of synthetic images for rip channel detection.

Field Site

Tairua beach, is located on the Coromandel Peninsula of New Zealand's North Island. This site was chosen because it exhibits a range of surfzone morphologies. Tairua is a 1,200 m-long embayment confined by a rocky promontory in the north, and an extinct volcano in the south (Figure 1). The beach faces east and receives medium energy (H_s = 1.5 m; T_m = 10 s) waves from the South Pacific (Almar *et al*., 2008). The beach generally exhibits an intermediate state (Masselink and Short, 1993), and is comprised of medium-coarse ($D_{50} \approx$ 0.6 mm) sands (van de Lageweg *et al*., 2013). The tidal regime is predominantly microtidal, with a range varying between 1.2 m (neap) and 2.0 m (spring) (van de Lageweg *et al*., 2013). The beach is monitored under the New Zealand National Institute of Water and Atmospheric Research (NIWA) Cam-Era scheme, which has collected images here since 1999. The camera is mounted at the southern end of the beach, at a height of 68 m above mean sea level (van de Lageweg *et al*., 2013).

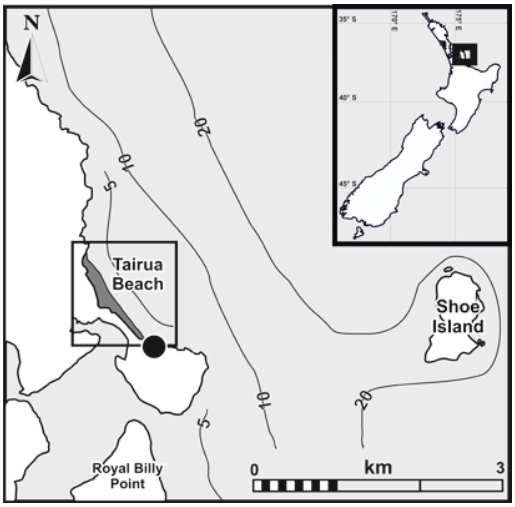

Figure 1. Map of Tairua study site (black box), including the location of the Cam-Era monitoring station (black circle).

Image Filtering

The first stage to create a synthetic image is filtering the parent image. A common approach to filtering is the use of high- and low-pass filters. These operate in the frequency domain of the image, akin to Fourier transforms. High frequency noise is introduced to imagery by sharp intensity transitions, such as edges observed at the shoreline. These high frequency signals can be smoothed using a lowpass filter, attenuating the high frequency components and therefore blurring the image (Gonzalez and Woods, 2008).

In simple cases, where only a few raindrops have fouled the image, spatial filtering can remove the effect of this noise. When the fouled image is rectified, the previously small element of noise (the rain drop), is projected across a wide area (*e.g.*, Figure 2a), as a result of the transformation between image co-ordinates [u, v] and real-world co-ordinates [x, y, z]. A Gaussian lowpass

filter (mask = 15 x 15, σ = 10) is applied to the rectified image (Figure 2b). Subsequently, pixel intensities from the same transect of pixels in each image are extracted (Figure 2c). The maximum gradient in intensity profile is used as an estimation of the onset of wave breaking. In the unfiltered image, large errors are evident in the detected location of wave breaking (Figure 2d) wherever rain fouls the lens. In contrast, the errors do not exist in the profile extracted from filtered imagery.

This example highlights the benefits to be gained from image manipulation prior to processing, such as the removal of small patches of lens fouling. As these sharp intensity transitions are often expected to represent the very feature we wish to investigate, such as the edge of a rip channel, filtering can smooth these features yielding more accurate results.

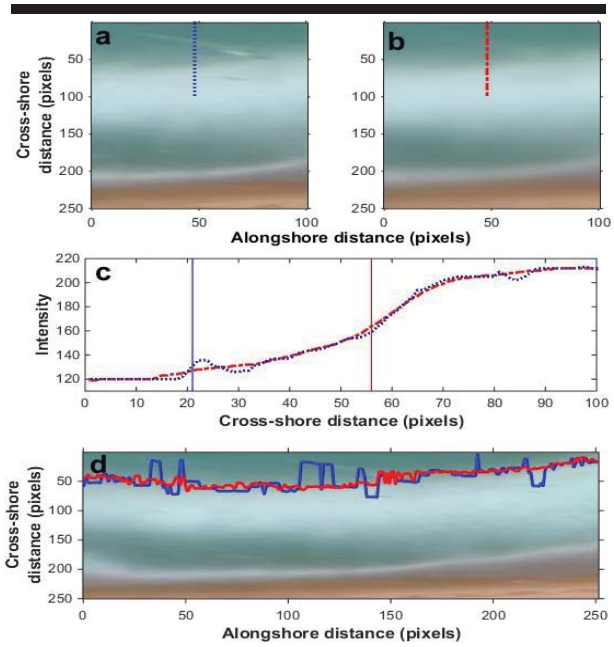

Figure 2. (a) Rectified timex image of Tairua beach, New Zealand. Rain drop fouling is evident in the region of the blue transect line. (b) Filtered version of (a) with red transect line. (c) Intensity profiles for both transect lines, with the maxima marked by horizontal lines. (d) Onset of wave breaking detected alongshore using intensity maxima transects, as per (c).

Synthetic Image Creation

Having filtered the parent image, the next stage is to segment it into distinct zones: beach, rip channels, breaking waves, and offshore. Rip channels and breaking waves form the surfzone. The offshore boundary of the surfzone is the limit of wave breaking which is defined by the first significant increase in the pixel intensity gradient (Bogle *et al*., 2000). The landward boundary of the surfzone is determine by the shoreline. This is detected using segmentation based on 3-banded *k-means* clustering (Wang and Adelson, 1994). This method identifies the beach by the dominance of the red pigmentation in the RGB signature. The surfzone must then be separated into rip channels and wave breaking regions. This is done by thresholding the extreme intensity values, and using the mid-point as a cut-off.

The image is now composed of 4 distinct zones (Figure 3b). All pixel values for each individual zone are collated, and used to create zone-specific histograms of red, green and blue pigments (Figure 3c-f). For each zone, the pixels are replaced with synthetic pixels. These synthetic pixels are generated from the normal distribution created in the previous stage. The pixel value is random, but weighted towards the higher probability occurrences from the distribution curve.

In order to estimate the utility of synthetic imagery for improved methods of automated rip detection, this study applies the rip detection method proposed by Ranasinghe *et al.* (1999) to both the original rectified imagery, and the corresponding synthetic image. The original image is manually digitized in a similar method to that described by Whyte *et al.* (2005) as a benchmark to assess the accuracy of the rip detection algorithm. The errors of such digitisation are documented in Holman *et al.* (2006), who report that two users digitising rips on average recorded the same number of rips in the imagery per day, but the recorded location of rips was more variable between digitizers. For the purposes of this study, the more consistent rip number parameter is used. The images selected are a random selection of 80 images from the archive.

RESULTS

Both image types produce a statistically significant (at 95%) correlation in the quantity of rips. Correlation in the original imagery (R = 0.28, P = 0.013) is poorer than that in the synthetic detections (R = 0.47, P = 1.2×10^{-5}). The correlation in synthetic imagery was statistically significant at 99%. Correlation alone is not a good measure of agreement; therefore, the error in each method has been presented here.

The user-digitized number of rips in each image varies between 1 and 4 (Figure 4). A nominal 'acceptable error' threshold of ±1 detected rip is plotted onto Figure 4. In total, the original imagery produces correct detections 34% of the time, compared to 41% in the synthetic imagery. The detections lay inside of the ±1 error threshold 81% of the time in the original imagery, compared to 92% of the time in the synthetic imagery, resulting in total error (> ± 1) in 19% of the original image detections, and 8% of the synthetic detections.

Of the detections that were incorrect in the original imagery (66%), 38% were under-predictions, compared to 62% over-predictions. The opposite is true of the synthetic imagery (59% incorrect), whereby 64% of erroneous detections were under-predictions and 36% were over-predictions.

In the original imagery, in all 4 scenarios (1 - 4 digitized rips), the standard deviations in the detection lie outside of the ±1 error threshold (Figure 4a), whereas only one scenario (4 rips) contains standard deviations outside this threshold in the synthetic imagery. Interestingly, both methods produce an under-estimation of comparable magnitude in the 4 rip scenario.

DISCUSSION

In this paper we have shown that simple image filtering can reduce small-scale fouling and noise in imagery. Previously, the signal extracted from the raw image would generally be filtered,

as opposed to filtering the image first. This is important as the extracted signal through a set of pixels is generally 1-directional and does not take account of neighbouring pixels and trends. The filtering of an image, rather than extracted signal, uses 2-dimensional filters and local pixel statistics to remove noise (Lee, 1980). This filtered image is then ready for quantitative analysis, or here, the creation of a synthetic image. We have also shown that the use of synthetic imagery as opposed to original images improves rip detection using the method outlined by Ranasinghe *et al.* (1999). The total error in detections with synthetics is halved when compared to original imagery.

The reported limitations of the Ranasinghe *et al.* (1999) method (Holman *et al*., 2006; Turner *et al*., 2007) were clear in the results, as detections on both the original and synthetic images produced considerable scatter. This is likely the result of the complex rip channel morphologies at Tairua, where rips orientated shore-normally are a minority occurrence. That said, there are significantly fewer rips detected in the synthetic imagery (n = 203), compared to the original imagery (n = 242), which infers that the synthetic images provide a dataset with much less unrelated extraneous noise.

The method used for rip detection oversimplifies the morphology qualitatively observed in the imagery, and therefore, it is expected that any results obtained via this method would under predict the occurrence of rip channels. Despite the oversimplification inherent in the method, detections based on the original imagery still produces over-estimation of rip number 41% of the time, which is perhaps indicative of the amount of noise the original image contains. In comparison, the synthetic imagery produces under-estimation (as would be expected using this method) on 38% of detections.

The work of Bogle (2000) used the same approach as Ranasinghe *et al.* (1999) on Tairua, but ultimately resorted to visual selection of intensity minima. This is presumably because the complex patterns observed in imagery made automation via the use of thresholds (such as in our approach using original imagery) unviable. The use of a simplified synthetic-type image may aid steps towards an automated approach to rip detection. We have shown here, for the same study site that the simplification of the imagery via the creation of a synthetic image, increases the number of correct detections, and also the number of predictions correct to within ± 1 rip. This new intermediate step may help overcome the documented limitations of current attempts to automatically detect rip channels in imagery.

CONCLUSIONS

This research investigated the effect of image manipulation, in the form of image filtering and synthetic image creation, on automated rip channel detection in surfzone imagery. Simple filtering methods were able to reduce the effects of small scale fouling and noise on image intensity signals. The use of synthetic imagery increased rip detections within the acceptable error threshold from 81% correct to 92%. Rip channel detection using synthetic imagery reduced the total number of detections by 16%, showing a reduction of extraneous noise inherent with the original image. A systematic underprediction was observed in the detection of rips using synthetic imagery, which is consistent with the detection method selected. This paper provides proof of concept for image manipulation prior to

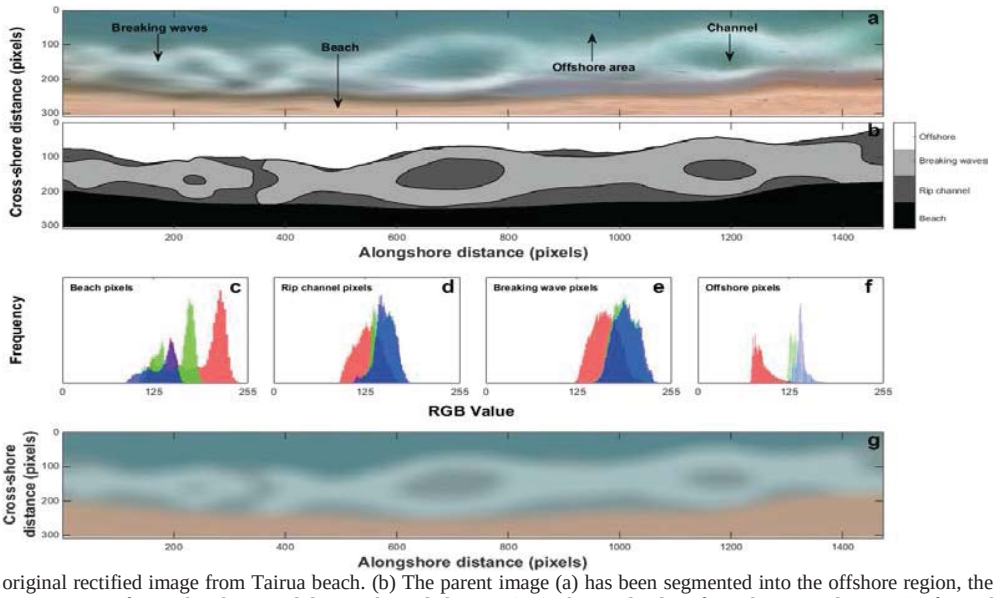

Figure 3. (a) An original rectified image from Tairua beach. (b) The parent image (a) has been segmented into the offshore region, the beach, and then within the surfzone into areas of wave breaking, and deeper channeled areas. (c-e) The pixel values from the original image (a) for each zone identified in (b) have been extracted, and presented in terms of their red, green, and blue pixel values. The zones in (b) are then filled with pixels randomly selected from the corresponding pixel value distribution curve in (c-f). The resulting image is the synthetic image, with each zone now exhibiting the dominant colour trend observed in the parent image.

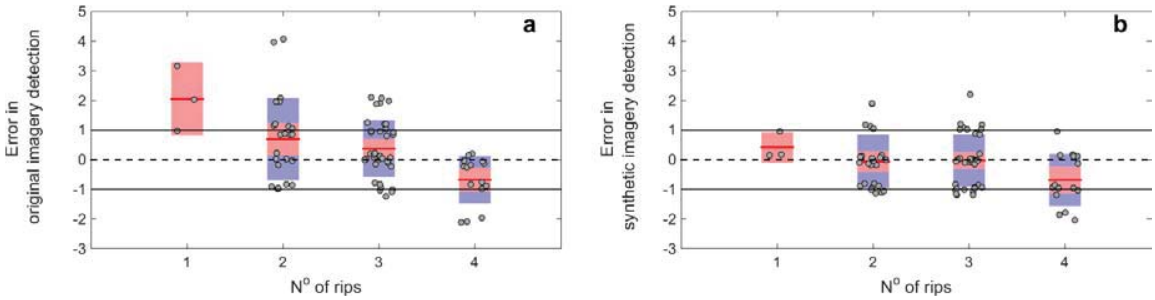

Figure 4. The user-digitized number of rips in each image obtained by digitization compared to the error in the number of rips detected in the corresponding original image (a) and synthetic image (b). Positive and negative numbers represent over- and under-predictions, respectively. Each prediction is represented as a scatter point. The data is binned by the user-digitized number of rips, with the mean (red line), the 1.96 standard error of the mean for each class (red bar), and the standard deviation (blue bar).

processing, in order to aid automated surfzone feature detection.

ACKNOWLEDGEMENTS

The authors acknowledge Waikato Regional Council and NIWA for the provision of Cam-Era images presented in this study. Thanks to Karin Bryan (University of Waikato) for help with image rectification. RR is supported by the AXA Research fund and the Deltares Deltares Harbour, Coastal and Offshore engineering Research Programme *'Bouwen aan de Kust'*.

LITERATURE CITED

Almar, R.; Coco, G.; Bryan, K.; Huntley, D.; Short, A., and Senechal, N., 2008. Video observations of beach cusp morphodynamics. *Marine Geology.* 254, 216-223.

Bogle, J.; Bryan, K.; Black, K.; Hume, T. and Healy, T., 2000. Video Observations of Rip Formation and Evolution, *in:* Healy, (ed) *Proceedings, International Coastal Symposium 2000. Journal of Coastal Research*, SI 34, 117–127.

Bovik, A.C., 2005. Introduction to digital image and video processing, *in:* Bovik, A. (Ed.), *Handbook of Image and Video Processing*., USA: Elsevier, pp. 3–20.

Bowen, A.J. 1969. Rip currents 1: Theoretical observations. *Journal of Geophysical Research*, 74, 5467-5478.

Gallop, S.L.; Bryan, K.R., Coco, G., 2009. Video observations of rip currents on an embayed beach, *in:* Da Silva (ed) *Proceedings, International Coastal Symposium 2009. Journal of Coastal Research*, Special Issue No. 56, pp. 49–53.

Gonzalez, R.C. and Woods, R.E., 2008. *Digital Image Processing*, 3rd ed. USA: Pearson.

Holman, R.A.; Plant, N.G. and Holland, K.T., 2013. cBathy: A robust algorithm for estimating nearshore bathymetry. *Journal of Geohpysical Research*, 118(5), 2595-2609.

Holman, R.A. and Stanley, L., 2007. The history and technical capabilities of Argus. *Coastal Engineering*, 54, 477–491.

Holman, R.A.; Symonds, G.; Thornton, E.B. and Ranasinghe, R., 2006. Rip spacing and persistence on an embayed beach. *Journal of Geohpysical Research* 111, C01006.

Huntley, D.A., and Short, A.D., 1992. On the spacing between observed rip currents, *Coastal Engineering.* 17, 211 – 225.

Lee, J-S., 1980. Digital image enhancement and noise filtering by use of local statistics. *IEEE Transactions on pattern analysis and machine intelligence*, PAMI-2 (2), 165-168.

Lippmann, T.C. and Holman, R.A., 1991. Phase Speed and Angle of Breaking Waves Measured with Video Techniques, in: *Coastal Sediments* (1991). ASCE, pp. 542–556.

Lippmann, T.C. and Holman, R.A., 1989. Quantification of Sand Bar Morphology : A Video Technique Based on Wave Dissipation. *Journal of Geohpysical Research*, 94, 995–1011.

Masselink, G. and Short, A.D., 1993. The effect of tide range on beach morphodynamics and morphology: A conceptual beach model. *Journal of Coastal Research*, 9, 785–800.

Quartel, S., 2009. Temporal and spatial behaviour of rip channels in a multiple-barred coastal system. *Earth Surface Proceeses and Landforms*, 34, 163–176.

Ranasinghe, R.; Symonds, G. and Holman, R.A., 1999. Quantitative characterisation of rip currents via video imaging, *in:* Kraus, N.C., McDougal, W.G. (eds.), *Coastal Sediments '99*. American Society of Civil Engineers, Reston, USA, pp. 987–1002.

Ranasinghe, R.; Symonds, G.; Black, K. and Holman, R.A., 2004. Morphodynamics of intermediate beaches: a video imaging and numerical modelling study. *Coastal Engineering.* 51, 629-655.

Russ, J., 2007. *Image processing handbook*, USA: CRC Press.

Shepard, F.; Emery, K. and LaFond, E., 1941. Rip currents: a process of geological importance. *J. of Geology*, 49, 337-369.

Short, A.D., 1985. Rip current type, spacing and persistence, Narrabeen Beach, Australia. *Marine Geology.* 65, 47-71.

Stockdon, H.F. and Holman, R.A., 2000. Estimation of wave phase speed and nearshore bathymetry from video imagery. *Journal of Geohpysical Research* 105, 22015-22033.

Turner, I.L.; Whyte, D.; Ruessink, B.G. and Ranasinghe, R., 2007. Observations of rip spacing, persistence and mobility at a long, straight coastline. *Marine Geology.* 236, 209–221.

Van de Lageweg, W.I.; Bryan, K.R.; Coco, G. and Ruessink, B.G., 2013. Observations of shoreline-sandbar coupling on an embayed beach. *Marine Geology*. 344, 101–114.

Wang, J. and Adelson, E., 1994. Represent moving images with layers. *IEEE Transactions on Image Processing*. 3, 625-638.

Whyte, D.; Turner, I.L. and Ranasinghe, R., 2005. Rip Characterisation on the Gold Coast, Australia: An Analysis using Coastal Imaging Techniques, in: *Coasts and Ports 2005: Coastal Living - Living Coast*. Adelaide, Australia.

Journal of Coastal Research	SI	75	917-921	Coconut Creek, Florida	2016

Wave Height Distributions in the Surf Zone on Natural Beaches

Hannah E. Power[†*], Peter Nielsen[‡], Michael G. Hughes[††], Troels Aagaard[§] and Tom E. Baldock[‡]

[†] School of Environmental and Life Sciences
University of Newcastle
Callaghan, NSW, Australia

[‡] School of Civil Engineering
University of Queensland
St Lucia, Qld, Australia

[††] School of Geosciences
University of Sydney
Sydney, NSW, Australia

[§] Institute of Geography and Geology
University of Copenhagen
Copenhagen K, Denmark

www.cerf-jcr.org

www.JCRonline.org

ABSTRACT

Power, H.E.; Nielsen, P.; Hughes, M.G.; Aagaard, T., and Baldock, T.E., 2016. Wave height distributions in the surf zone on natural beaches. *In:* Vila-Concejo, A.; Bruce, E.; Kennedy, D.M., and McCarroll, R.J. (eds.), *Proceedings of the 14th International Coastal Symposium* (Sydney, Australia). *Journal of Coastal Research*, Special Issue, No. 75, pp. 917-921. Coconut Creek (Florida), ISSN 0749-0208.

Wave height distributions in the surf zone are examined using a large existing field dataset. Observed distributions are compared to the Rayleigh distribution, the Weibull distribution, and the normal distribution. In more than half the 15-minute data runs (57%), wave height distributions were statistically significantly different to a Rayleigh distribution, of which the majority were more narrowly distributed, with fewer extrema. In contrast, only 6% of distributions were statistically significantly different to a normal distribution. The distributions were observed to become narrower with decreasing depth. Data were subsequently fitted to a Weibull distribution with a varying exponent to allow for a change in the shape of the distribution with changing depth. The data show distributions with a wide range of exponents, but a mean of 2.4 indicating that, on average, data are more narrowly distributed than a Rayleigh distribution (exponent of 2). The value of the exponent was observed to increase in shallower water, with a strong inverse correlation between depth and the exponent.

ADDITIONAL INDEX WORDS: *surf zone, wave breaking, wave height distribution, field data, Rayleigh distribution, Weibull distribution.*

INTRODUCTION

Effective coastal management requires accurate modelling of the processes that occur in the surf zone so as to predict changing coastal conditions due to changing offshore conditions. Wave height transformation models can be used to drive sediment transport models as well as to predict wave setup and runup and therefore assess coastal management options. Parametric wave transformation models are computationally efficient and are therefore the most widely used in cross-shore morphological models (Baldock *et al.*, 1998); however, in order to use parametric models to predict random wave behaviour, assumptions must be made about the wave height distribution function and the fraction of broken waves (Baldock *et al.*, 1998; Battjes and Janssen, 1978; Ruessink *et al.*, 2003; Thornton and Guza, 1983). This paper addresses the first part of this issue by investigating the wave height distribution in the surf zone on natural beaches.

For waves in deep water, Longuet-Higgins (1952) showed that for a linear model of waves with a narrow energy spectrum the heights of the waves fit a Rayleigh distribution well. The Rayleigh probability density function is given by:

$$f(x) = 2\frac{H}{H_{rms}} exp\left[-\left(\frac{H}{H_{rms}}\right)^2\right] \quad (1)$$

and the cumulative distribution function is given by:

$$F(X) = P(x < X) = 1 - exp\left[-\left(\frac{x}{H_{rms}}\right)^2\right] \quad (2)$$

where H_{rms} is the root mean square wave height (see Nielsen, 2009, for further details, pp. 56-61; thick solid line in Figure 1). Since the observations of Longuet-Higgins, numerous field observations have also shown that zero-crossing wave heights are approximately Rayleigh distributed in the surf zone (*e.g.*, Massel, 1996; Thornton and Guza, 1983). If waves are Rayleigh distributed, all the characteristic wave heights (H_{rms}, H_{sig}, $H_{1/10}$, etc.) can be calculated from the standard deviation of the water surface elevation using known constants.

After waves enter the surf zone, the natural variation of incident wave heights means that the cross-shore location of breaking is not a constant for every wave, with the largest waves breaking furthest offshore, and the smallest waves breaking well within the limits of the surf zone (Komar, 1998). In the deeper water depths of the surf zone, both broken and unbroken waves exist simultaneously. This breaking process strongly modifies the wave height distribution and may result in a distribution that is significantly different to the Rayleigh distribution. Relatively, few studies have examined the wave height distribution in the surf zone in detail and, of those that have, most studies have

DOI: 10.2112/SI75-184.1 received 15 October 2015; accepted in revision 15 January 2016.
*Corresponding author: hannah.power@newcastle.edu.au
©Coastal Education and Research Foundation, Inc. 2016

used data obtained from laboratory experiments (*e.g.*, Baldock *et al.*, 1998; Battjes and Groenendijk, 2000; Hamm and Peronnard, 1997; Mase and Iwagaki, 1982; Ting, 2001; van Vledder *et al.*, 2013).

The Rayleigh distribution is widely used as a parametric descriptor of ocean waves, including waves within the surf zone. As a result, it is used in numerous random wave transformation models, and therefore needs to be a correct descriptor of the actual wave height distribution if wave transformation models are to provide accurate results. As noted in several papers, significant differences exist between random wave model predictions and field data (see Apotsos *et al.*, 2008, for a review). A proportion of this error may be due to the assumption in some random wave models that the probability distribution of wave heights in the surf zone conforms to a Rayleigh distribution. It is this assumption, that wave heights in the surf zone of natural beaches conform to a Rayleigh distribution, which is assessed in this paper. Of the previous work discussed above, there has only been limited testing of the applicability of the Rayleigh distribution within the surf zone. There is also a limited range of field data analysed in the studies described above (Goda, 2010; Thornton and Guza, 1983). Consequently, the range of surf conditions included in such assessment is very narrow. This paper presents an analysis of an extensive set of field data from ten different beaches and broad range of wave conditions to address this issue.

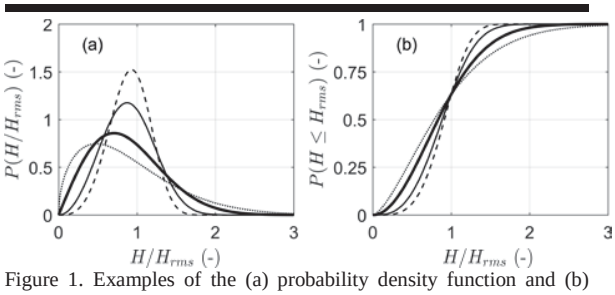

Figure 1. Examples of the (a) probability density function and (b) cumulative distribution function for the Rayleigh distribution (thick solid line), and Weibull distribution with p=1.5 (dotted line), p=3 (thin solid line), and p=4 (dashed line). The Rayleigh distribution is equivalent to a Weibull distribution with p=2.

METHODS

To investigate the assumption that wave heights in the surf zone are Rayleigh distributed, wave height distributions were calculated for a large existing dataset of experimental data. This dataset was collected in the surf zone of 10 different sandy beaches during 27 different instrument deployment periods over individual tidal cycles (*e.g.*, 12 h or less; Table 1). The instrument deployments include data from a large range of beach types (from reflective to dissipative; Wright and Short, 1984) and from both sea and swell conditions. For further details on the data collection, experimental setup, and data pre-processing, see Power *et al.* (2010).

All wave data were analysed in 15-minute time series to ensure stationarity with respect to the changing tidal water level (Hughes and Moseley, 2007; Power *et al.*, 2010). For each 15-minute time series, the heights of the individual waves were obtained using both a local minima analysis (Power *et al.*, 2010) and a zero down-crossing analysis. The distribution of individual wave heights calculated for each time series was then compared to a theoretical Rayleigh distribution. The cumulative probability distribution of wave heights was calculated for each time series and then normalised by H_{rms} to allow the record to be compared to a Rayleigh cumulative distribution function, Eq. (2).

Table 1. *Percentage of data records from each deployment with wave height probability distributions that were statistically significantly different to a Rayleigh distribution (Rayleigh) and a Weibull distribution (Weibull). Results are from a Kolmogorov-Smirnov test with confidence level α = 0.05. The offshore Iribarren number (ξ_o) is also shown for each deployment. Beaches are in New South Wales, Australia, unless specified. For further details on each deployment see Power et al. (2010).*

Location	Date	ξ_o	Rayleigh	Weibull
Seven Mile Beach (S.C.)	13/11/02	0.24	80.00	50.00
Seven Mile Beach (S.C.)	14/11/02	0.27	77.27	59.09
Seven Mile Beach (S.C.)	17/11/02	0.52	80.00	33.33
Seven Mile Beach (S.C.)	18/11/02	0.25	68.00	60.00
Seven Mile Beach (S.C.)	19/11/02	0.32	92.86	75.00
Seven Mile Beach (S.C.)	21/11/02	0.22	95.83	66.67
One Mile Beach, N.S.W.	6/05/04	0.22	14.29	0.00
Bluey's Beach	7/05/04	0.11	42.86	14.29
Elizabeth Beach	11/05/04	0.19	58.97	41.03
Avoca Beach	16/11/04	0.43	50.00	22.73
Avoca Beach	17/11/04	0.61	37.93	19.54
Vejers Beach, Denmark	4/10/06	0.08	17.65	21.57
Vejers Beach, Denmark	5/10/06	0.09	16.22	18.92
Vejers Beach, Denmark	7/10/06	0.08	24.69	9.88
Boomerang Beach	24/04/07	0.09	12.50	12.50
Seven Mile Beach (C.C.)	26/04/07	0.17	78.38	64.86
Bluey's Beach	27/04/07	0.19	71.43	71.43
Moreton Is., Qld.	10/12/07	0.23	34.09	30.40
Moreton Is., Qld.	11/12/07	0.22	26.74	31.94
The Spit, Qld.	1/10/08	0.20	30.16	34.92
The Spit, Qld.	18/11/08	0.38	12.50	12.50
Moreton Is., Qld.	7/12/08	0.15	50.44	14.16
Moreton Is., Qld.	8/12/08	0.19	89.80	32.65
Moreton Is., Qld.	9/12/08	0.21	89.10	26.92
The Spit, Qld.	10/03/09	0.12	55.56	7.41
The Spit, Qld.	11/03/09	0.21	24.44	6.67
The Spit, Qld.	12/03/09	0.22	42.55	12.77
Total	-	-	56.67	27.73

RESULTS

Here, observed wave data are compared against the Rayleigh and Weibull distributions.

Comparison with Rayleigh distribution

In the majority of deployments, the measured distribution of wave heights was qualitatively observed to be narrower than the Rayleigh distribution, with fewer than expected extreme values. Examples of comparisons between the Rayleigh distribution and measured wave height distributions for wave heights calculated using a local minima analysis are shown in Figure 2.

A goodness-of-fit, non-parametric, Kolmogorov-Smirnov hypothesis test was used to assess whether the observed differences between the measured wave height and Rayleigh distributions were significant. For each data record, the observed normalised cumulative wave height distribution was compared with a cumulative Rayleigh distribution. By way of summary, Table 1 shows the percentage of data records from each deployment that had a wave height probability distribution that was significantly different to a Rayleigh distribution at the confidence level α=0.05. Of the 27 deployments, there were six where 80% or more of the data records had a wave height distribution that was significantly different to a Rayleigh distribution and 14 where over 50% of data records had a wave height distribution significantly different to Rayleigh distribution (Table 1). Across the entire data set, >50% of data records were significantly different to a Rayleigh distribution (Table 1). This suggests that a different probability distribution, that more accurately represents the true wave height distribution, may improve predictions by parametric wave transformation models.

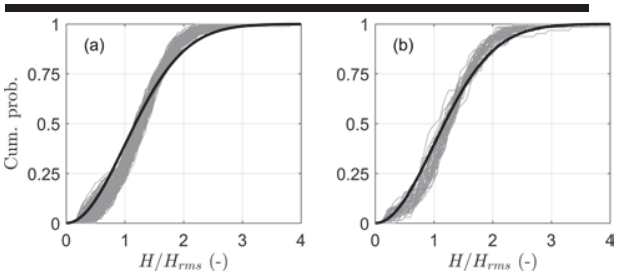

Figure 2. Cumulative probability distribution of normalised wave height, H/H_{rms}, for each run (grey lines) compared to the cumulative Rayleigh distribution function (black line) for two example deployments: (a) Moreton Island 8 December 2008, and (b) The Spit, Gold Coast, 12 March 2009.

Comparison with Weibull distribution

To obtain an improved wave height distribution function, a Weibull distribution was used, where the probability density function is given by:

$$f(x) = p\left(\frac{H}{H_{rms}}\right)^{p-1} exp\left[-\left(\frac{H}{H_{rms}}\right)^{p}\right] \quad (3)$$

and the cumulative distribution function is given by:

$$F(X) = P(x < X) = 1 - exp\left[-\left(\frac{x}{H_{rms}}\right)^{p}\right] \quad (4)$$

For a Rayleigh distribution, the exponent p=2 (see Figure 1). Observed wave height distributions for each 15-minute data record were fitted to the Weibull distribution by optimising the value of p. This was done by comparing the normalised descending ranked wave height, H_n/H_{rms}, with the probability of each wave height occurring, n/N, where n is the descending wave height rank, and N is the total number of waves in the data record. These data (H_n/H_{rms} and $-\ln(n/N)$) were then plotted in a log-log plot and a line of best fit was calculated to determine the optimal power p for the distribution in Eq. (3). If the data are Rayleigh distributed they will lie on a line with a slope, $1/p$, of 0.5. This procedure was repeated for each data record from the field data set.

Histograms of the optimal value of p for each data record are shown in Figure 3 for wave heights calculated using both a local minima analysis and a zero down-crossing analysis. For the majority of data records p>2.0 indicating that waves are more narrowly distributed than predicted by the Rayleigh distribution. For both of the wave-by-wave analysis methods, mean values of p were greater than 2.0. Some data records had p<2.0 indicating a wider distribution than a Rayleigh distribution.

While values of p are similar for wave heights obtained from the two different wave-by-wave analysis methods, there are some clear differences. Values for p obtained from data analysed using a zero-down-crossing method are more narrowly distributed than those obtained from a local minima analysis. Differences between results are likely to be due to the differences in the results of wave heights obtained using the two methods which is discussed in Power *et al.* (2010). While the zero-crossing method is more widely used, the local minima analysis is included here as it has been shown to be more appropriate for obtaining individual waves heights in the inner surf zone (Power *et al.*, 2010).

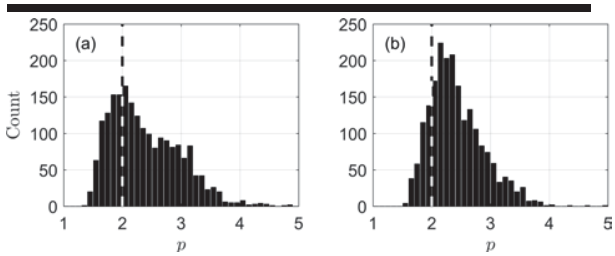

Figure 3. Histograms of the value of p calculated for each data record in the field data set (Table 1) calculated using wave heights obtained from (a) a local minima analysis, $\bar{p}$ =2.39, and (b) a zero down-crossing analysis, $\bar{p}$ =2.42. The value of p=2.0, which corresponds to a Rayleigh distribution, is shown in both panels (dashed line).

Values of p for each data record were compared to the mean water depth (h) and the normalised mean water depth (h/H_o) for p values from both a local minima analysis and a zero down-crossing analysis (Figure 4). Strong trends were observed in three of the four cases, with the value of p increasing with decreasing h and decreasing h/H_o. Least squares linear regression analysis was performed on binned data and high R^2 values were obtained for comparisons between p and h (p= −0.67(±0.15)h+3.03(±0.11), R^2=0.89) and p and h/H_o (p=−0.45(±0.08)h/H_o+2.81(±0.05), R^2=0.94)

for p values for wave heights obtained from a local minima analysis. A strong correlation was also observed between p and h/H_o for p values for wave heights obtained from a zero down-crossing analysis (p=−0.24(±0.07)h/H_o+2.62(±0.05), R^2=0.84), however, the correlation between p and h was poor (p=−0.2(±0.16)h+ 2.52(±0.12), R^2=0.37). Values of p were also compared to the local wave height to water depth ratio (γ) and the normalised local wave height (H_{rms}/H_o), however, no correlations were observed (not shown).

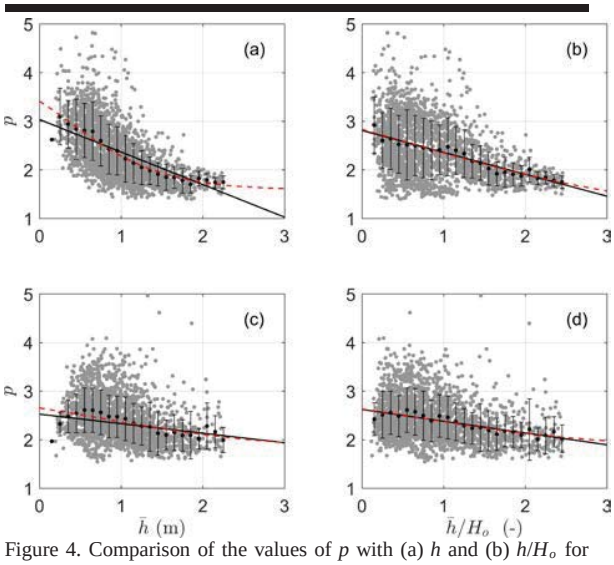

Figure 4. Comparison of the values of p with (a) h and (b) h/H_o for individual data records with wave heights obtained using a local minima analysis (grey circles), and a comparison of the values of p with (c) h and (d) h/H_o for individual data records with wave heights obtained using a zero-down crossing analysis (grey circles). Data are binned corresponding to h ± 0.05 and h/H_o ± 0.05. The means and standard deviation of the binned data are shown (black circles). Linear regression equations for binned data are shown (black solid lines). Non-linear regression equations that fulfil the criteria as $h\rightarrow\infty$, $p\rightarrow 2$ are also shown (dashed red lines). See text for full regression equations and R^2 values.

It should be noted that the linear regression equations derived here (Figure 4) should only be applied for values of h < 2.32 m and h/H_o < 2.46 m as this is the upper limit of the data. If these equations are applied more widely, *i.e.*, in deeper water depths or for smaller values of H_o, they lead to unrealistically small p which results in very broad wave height distributions. As such, additional regression equations are derived that have $p\rightarrow 2$ for $h\rightarrow\infty$ or $h/H_o\rightarrow\infty$ (Figure 4, dashed red lines), which is consistent with previous work that suggests offshore wave heights are Rayleigh distributed, *i.e.*, p=2. High R^2 values were obtained for comparisons between p and h (p=(3.83(±1.46)-2.78(±1.00)h)/(h^2+2.72(±1.19))+2, R^2=0.98) and p and h/H_o (p=(22.64(±62.91) - 12.8(±35.12)h/H_o)/((h/H_o)^2 + 27.22(±77.49)) +2, R^2=0.94) for p values for wave heights obtained from a local minima analysis. A strong correlation was also observed between p and h/H_o for p values for wave heights obtained from a zero down-crossing analysis (p=(7.47(±31.95)-2.66(±12.50)h/H_o) / ((h/H_o)^2 + 11.89(±51.20)) + 2, R^2=0.84), however, the correlation between p and h was not as robust (p=(7.34(±50.95) - 2.85(±21.53)h)/(h^2 + 11.24(±78.81)) + 2, R^2=0.71).

As with the comparison between the observed wave height distributions and the Rayleigh distribution a Kolmogorov-Smirnov test was also applied to assess the differences between the Weibull distribution with optimised p and observed wave height distributions. None of the 27 deployments had more than 80% of data records with a wave height distribution that was significantly different to the Weibull distribution and only 6 had more than 50% of data records with a wave height distribution significantly different to the Weibull distribution (Table 1). Across the entire data set, <30% of data records were significantly different to a Weibull distribution (Table 1). This distribution is therefore a statistically better descriptor of wave heights in the surf zone than the Rayleigh distribution.

DISCUSSION

The results presented in this paper clearly show that the majority of wave height distributions in the surf zones on these natural beaches differ from a Rayleigh distribution. Observed distributions are mostly narrower, with fewer extreme values than the Rayleigh distribution, as expected with depth controlled wave breaking. However, it should be noted that despite the distributions being narrower, no sharp cutoffs were observed at either end of the distributions such as those suggested by Kuo and Kuo (1975). While these differences have been observed before in several studies (*e.g.*, Battjes and Groenendijk, 2000; Hamm and Peronnard, 1997; Mase and Iwagaki, 1982; Ting, 2001; van Vledder *et al.*, 2013), this is a far more comprehensive field dataset that incorporates a range of wave and beach conditions. Importantly, the observations also show that there is a statistical difference between the majority of observed surf zone wave height distributions and the Rayleigh distribution (Table 1), which questions the use of that distribution as standard in parametric models. However, this observation is in contrast with the observations of Thornton and Guza (1983) who found that a Rayleigh distribution was qualitatively acceptable for surf zone wave heights.

Observed wave height distributions were broader than a Rayleigh distribution in the outer region of the surf zone and then became narrow as water depths decreased (Figure 4). This is consistent with suggestions by Goda (2010), whereby individual wave heights are enhanced by the shoaling process, thus making the wave height distribution broader than the Rayleigh distribution at the outer edge of the surf zone. However, in contrast to the observations of Goda (2010), the wave height distributions presented here were not observed to return to a Rayleigh distribution near the shoreline but continued to narrow beyond a Rayleigh distribution.

A Weibull distribution is shown to be a better representation of wave height distributions in the surf zone with no significant differences between the Weibull

distribution and observed wave heights for the majority of data runs (>72%). This is a similar approach to that taken by Battjes and Groenendijk (2000), however, the distribution utilised in this study is significantly simpler than that developed by Battjes and Groenendijk. The distribution used here also has the advantage of having a continuous probability density function, unlike that of Battjes and Groenendijk. Despite this, the observed mean and range of exponent values for the Weibull distribution used in this study ($\bar{p} \approx 2.4$, $1.40<p<5.86$) are comparable to those used by Battjes and Groenendijk ($\bar{p} = 2.0$ and $\bar{p} = 3.6$). It should be noted that high values of p could be considered equivalent to conditions on mildly sloping beaches where surf is more likely to be saturated and wave height distributions narrow, while low values of p are equivalent to steeply sloping beaches with unsaturated surf (Power *et al.*, 2010, 2013).

CONCLUSIONS

An analysis of wave height distributions within the surf zone has been presented from 10 sandy beaches and 27 different field deployments. The data show that observed wave height distributions on natural beaches are significantly different to a Rayleigh distribution in ≈57% of cases, with the majority of wave heights being more narrowly distributed than a Rayleigh distribution with fewer large or small extreme values. The data show that the distributions of wave heights become narrower as depth decreases, although a large amount of variation still remains unexplained.

Data are fitted to a Weibull distribution with a varying exponent of the exponential term. Fitting these empirical distributions to the data show distributions with a wide range of exponents, but a mean of 2.4, rather than 2 (*i.e.*, a Rayleigh distribution) with the exponent increasing in shallower water. The observed wave height distributions were statistically compared to the Weibull distribution and only ≈28% of data records were found to be significantly different from a Weibull distribution, *i.e.*, most data records are better approximated by a Weibull distribution than a Rayleigh distribution.

ACKNOWLEDGMENTS

The assistance of Dave Mitchell, Felicia Weir, Andrew Aouad, Aart Kroon, Nick Cartwight, Dave Callaghan, and Ph.D. students at UQ on field trips is much appreciated. The authors are grateful to the Queensland Government, Manly Hydraulics Laboratory, and Danish Coastal Authority for supplying offshore wave data.

LITERATURE CITED

Apotsos, A.; Raubenheimer, B.; Elgar, S., and Guza, R. T., 2008. Testing and calibrating parametric wave transformation models on natural beaches. *Coastal Engineering*, 55(3), 224-235.

Baldock, T. E.; Holmes, P.; Bunker, S., and van Weert, P., 1998. Cross-shore hydrodynamics within an unsaturated surf zone. *Coastal Engineering*, 34, 173-196.

Battjes, J. A. and Janssen, J. P., 1978. Energy loss and setup due to breaking of random waves. *Proceedings of the 16th International Conference on Coastal Engineering*, ASCE, pp. 569-588.

Battjes, J. A., and Groenendijk, H. W., 2000. Wave height distributions on shallow foreshores. *Coastal Engineering*, 40(3), 161-182.

Goda, Y., 2010. Reanalysis of regular and random breaking waves statistics. *Coastal Engineering Journal*, 52(1), 71-106.

Hamm, L. and Peronnard C., 1997. Wave parameters in the nearshore, A clarification. *Coastal Engineering*, 32(2–3), 119-135.

Hughes, M. G. and Moseley, A. S., 2007. Hydrokinematic regions within the swash zone. *Continental Shelf Research*, 27(15), 2000-2013.

Klopman, G., 1996. *Extreme wave heights in shallow water. Report H2486*, WL|Delft Hydraulics.

Komar, P.D., 1998. *Beach Processes and Sedimentation*. Prentice Hall, New Jersey, 544 pp.

Kuo, C. T. and Kuo, S. J., 1975. Effect of wave breaking on statistical distribution of wave heights. *Proceedings of Civil Engineering in the Oceans Conference*, ASCE, pp. 1211-1231.

Longuet-Higgins, M.S., 1952. On the statistical distribution of the heights of sea waves. *Journal of Marine Research*, 11(3), 245-266.

Mase, H. and Iwagaki, Y., 1982. Wave height distributions and wave grouping in the surf zone. *Proceedings of the 18th International Conference on Coastal Engineering*, New York, ASCE, pp. 58-76.

Massel, S. R., 1996. *Ocean surface waves, Their physics and prediction*. Singapore, World Scientific, 491 pp.

Nielsen, P., 2009. *Coastal and estuarine processes*. World Scientific, Singapore, 343 pp.

Power, H. E.; Hughes, M. G.; Aagaard, T., and Baldock, T. E., 2010. Nearshore wave height variation in unsaturated surf. *Journal of Geophysical Research*, 115(C8), C08030.

Power, H. E.; Baldock, T. E.; Callaghan, D. P., and Nielsen, P., 2013. Surf zone states and energy dissipation regimes - a similarity model. *Coastal Engineering Journal*, 55(1), 1350003.

Ruessink, B. G.; Walstra, D. J. R., and Southgate, H. N., 2003. Calibration and verification of a parametric wave model on barred beaches. *Coastal Engineering*, 48(3), 139-149.

Thornton, E.B. and Guza, R.T., 1983. Transformation of Wave Height Distribution. *Journal of Geophysical Research*, 88(C10), 5925-5938.

Ting, F. C. K., 2001. Laboratory study of wave and turbulence velocities in a broad-banded irregular wave surf zone. *Coastal Engineering*, 43(3–4), 183-208.

van Vledder, G. Ph.; Ruessink, G., and Rijnsdorp, D. P., 2013. Individual wave height distributions in the coastal zone, measurements and simulations and the effect of directional spreading. *Proceedings of Coastal Dynamics 2013*, pp. 1799-1810.

Wright, L. D. and Short, A. D., 1984. Morphodynamic variability of surf zones and beaches, a synthesis. *Marine Geology*, 56, 93-118.

Journal of Coastal Research	SI	75	922-926	Coconut Creek, Florida	2016

Physical and Numerical Modeling of Irregular Wave Transformation over a Fringing Reef

Sungwon Shin [†], Young-Taek Kim[‡], and Jong-In Lee[††*]

[†] Kangwon National University,
Environmental Technology Research Institute
Samcheok, Rep. of Korea

[‡] Korea Institute of Civil Engineering and Building Technology,
Hydro-Science and Engineering Research Institute
Goyang, Gyeonggi, Rep. of Korea

[††] Chonnam National University,
Department of Marine and Civil Engineering
Yeosu, Jeonnam, Rep. of Korea

www.cerf-jcr.org

www.JCRonline.org

ABSTRACT

Shin, S.; Kim, Y.T., and Lee, J.I., 2016. Physical and Numerical Modeling of Irregular Wave Transformation over a Fringing Reef. *In:* Vila-Concejo, A.; Bruce, E.; Kennedy, D.M., and McCarroll, R.J. (eds.), *Proceedings of the 14th International Coastal Symposium* (Sydney, Australia). *Journal of Coastal Research*, Special Issue, No. 75, pp. 922-926. Coconut Creek (Florida), ISSN 0749-0208.

Two-dimensional laboratory experiments were conducted to investigate cross-shore variations of wave transformation, setup, and breaking phenomena over a fringing reef. Various conditions of irregular waves were generated by changing a water depth, a wave period, and a wave height. A multi-layer Boussinesq model was used to predict the wave transformation and the results were compared to the experimental results. One-layer and two-layer model configurations were selected to figure out and compare the model capability. In the model and data comparisons, both models well predicted the wave transformation characteristics and setups when the nonlinearity was small. However, as the wave nonlinearity increased, two-layer model results were more stable in the wave breaking region than one-layer model results. The results also showed that the broken wave heights finally reached stable conditions on the reef flat section in all cases and the relative stable wave heights (the ratio of the stable wave height to the water depth) were found as approximately 0.56. This data set can be used to benchmark studies for numerical model developers.

ADDITIONAL INDEX WORDS: *Wave breaking, reef, experiment, Boussinesq modeling.*

INTRODUCTION

Wave transformation including wave breaking has been an important issue in terms of the beach morphological change, sediment transport as well as an impact on the coastal structures. As the waves approach the beach slope, they are transforming more steeply and start breaking in a certain ratio of a wave height to a water depth (Iverson, 1952). It is known that the wave breaking affects the wave energy dissipation, longshore currents, wave setup, turbulence, and sea bottom instability.

A fringing reef is a kind of coral reef, which is formed with mild or flat slope from the reef toe to the coast followed by the reef face slope. Fringing reefs are important in the context of protecting the coastal area by inducing wave breaking and energy dissipation. However, the modeling of wave transformation and energy dissipation on this kind of topography is still a challenging issue.

Smith (1993) reviewed the research work on the wave breaking and decay in the surf zone including reefs. Ting and Kirby (1994) investigated the wave transformation on a constant beach slope to estimate the wave breaking induced turbulence in the surf zone through the laboratory experiment and found that the turbulence transport is possibly correlated to the sediment transport. Other researchers (Svendsen, 1987; Nadaoka *et al*., 1989; Cox and Kobayashi, 2000; Shin, 2005; Shin and Cox, 2006) conducted both laboratory experiments and numerical modeling of the wave breaking mechanism on the constant sloped beach. Various numerical schemes have been developed and tested on the different beach slopes (Raubenheimer, 2002; Kirby *et al*., 1998; Lin and Liu, 1998; Christensen and Diegaard, 2001; etc). Lynette and Liu (2004) developed the multi-layer Boussinesq model to overcome the limitation of the conventional Boussinesq model that gives errors to solve the hydrodynamic problem with the higher nonlinearity.

While many researchers have studied the wave transformation and breaking on the constant sloped beach, few researchers have investigated those topics on the reef shaped beaches. Gourlay (1994) conducted laboratory experiments to understand the wave transformation characteristics over a fringing reef with a steeper slope. Goertz et al. (2012) used probabilistic bulk dissipation models to predict the wave energy dissipation on a reef structure and compared the results with the laboratory experimental data, but none of them successfully predicted the wave energy dissipation over the reef structure. Lee *et al*. (2014) conducted the laboratory experiments to investigate the wave transformation characteristics over a fringing reef in the

DOI: 10.2112/SI75-185.1 received 15 October 2015; accepted in revision 15 January 2016.
*Corresponding author: jilee@chonnam.ac.kr
©Coastal Education and Research Foundation, Inc. 2016

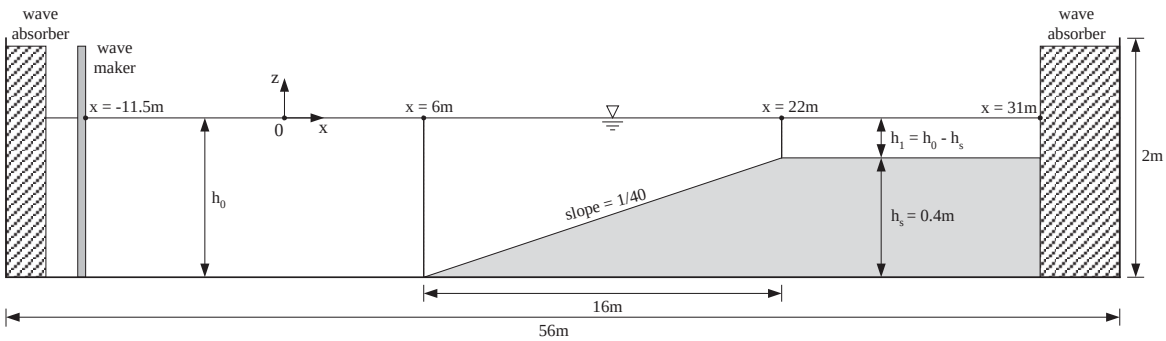

Figure 1. A cross-sectional view of experimental and numerical model setups (Lee *et al*., 2014).

monochromatic wave conditions and used multi-layer Boussinesq model (COULWAVE, Lynett and Liu, 2004) to test its capability of simulating the wave transformation, setup, and nonlinearity.

In this study, we extended the studies by Lee *et al.* (2014) to the irregular wave conditions not only for the model verification but for investigating the wave transformation and the formation of the stable wave on the reef flat section.

METHODS

Lynett and Liu (2004) showed that two-layer Boussinesq model accurately predicted the wave transformation and hydrodynamics in both linear and nonlinear wave conditions when *kh* is smaller than 8 and 6 respectively. Therefore, one-layer and two-layer models were used in this study to check the model capabilities on this reef topography. The two-layer model divides the water column into two vertical layers and integrates the fluid velocities and pressure on the boundary. This model employed the energy dissipation by wave breaking that was proposed by Kennedy *et al.* (2000). For a detailed description of the multi-layer and two-layer models used in this study see Lynett and Liu (2004) and Lee *et al.* (2014) respectively.

Two-dimensional laboratory experiments were conducted in a glass-walled wave flume in Korea Institute of Civil Engineering and Building Technology (KICT) as shown in Figure 1. The flume dimension is 56.0 m long, 1.0 m wide and 2.0 m deep. A 1/40 beach slope was installed in the and a flat section followed on from the top of the slope to reproduce the idealized fringing reef.

In the numerical model domain as shown Figure1, the wavemaker in the flume was located at x = -11.5 m. The beach slope started at x = 6 m and the flat section started at x = 22 m followed by the reef front. The reef flat elevation (h_s) was fixed to 0.4 m. Water surface elevations were measured using capacitance type wave gauges which were deployed every 0.5 m from the toe of the slope to the wave breaking region and every 0.25 m near the wave breaking region.

Total 18 different experimental scenarios were involved in this study by wave conditions and water depths. Table 1 shows the wave conditions and offshore side water depth. H_s, T_s, and h_0 represent a target significant wave height, a target significant wave period, and an offshore side water depth respectively. Irregular waves in each case were generated for 300 seconds by using a Bretschneider-Mitsuyasu spectrum. In the computational domain of the numerical model, the horizontal grid size (Δx) was set to 0.02 of the wavelength.

Table 1. *Wave condition and water depths for the experiments and the numerical simulations*

H_s (cm)	T_s (s)	h_0 (cm)
4.0	1.3, 1.6, 1.9, 2.2	45, 50
8.0	1.6, 1.9, 2.2	45, 50
12.0	1.6, 1.9	45, 50

RESULTS

In this study, the experimental and numerical simulation results in terms of the cross-shore variations of the wave heights, wave crest, and trough levels, and mean water level (setup) were compared each other under the same condition. Both one- and two-layer models were involved in predicting those quantities to check the capability of the two-layer model on the fringing reef bathymetry.

$(kH_{1/3})_0$ and k_0h_0 in this study ranged from 0.061 to 0.279 and from 0.653 to 1.360 respectively and no wave was broken at x = 0m. The significant crest and trough levels, as well as the significant wave heights, were examined in order to investigate if the numerical model successfully predicted the wave nonlinearity. Figure 2, 3, and 4 show the cross-shore variations of the wave heights, crest levels, trough levels, and setups when the offshore water depth was 45cm. In Figure 2 (a) through (d), the wave steepnesses ($(kH_{1/3})_0$) were 0.114, 0.087, 0.071, and 0.061 respectively. All four cases in Figure 2, one-layer model over-predicted the crest levels and wave heights near the wave breaking zone while the two-layer model precisely predicted those quantities.

In all three figures (Figure 2, 3, and 4), the results show that the shoaling effect appears earlier and the waves also break earlier as the significant wave period increase under the same wave height condition. On the reef flat section, wave heights decrease and reached equilibrium state after the waves break on the slope. Also, the difference between the crest level and the trough level increases on the reef flat section as the wave height

increases (see Figure 2, 3, and 4). In Figure 4, the maximum mean water level was 6% of the significant wave height when the offshore water depth was 45cm.

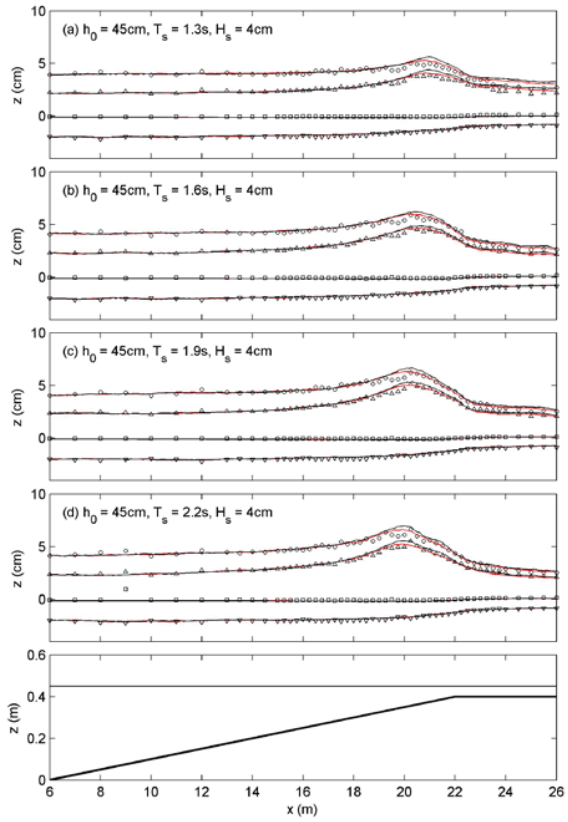

Figure 2. Numerical model and experimental results under the different wave conditions when H_s = 4cm and h_0 = 45cm. Solid lines are the numerical model results (black lines: one-layer model; red lines: two-layer model). Symbols are the experimental results (open circles: wave heights; triangles: wave crest levels; reverse triangles: wave trough levels; squares: mean water level or setup).

Figure 5, 6, and 7 show the experimental and numerical model results when the offshore water depth is 50cm and the water depth on the reef flat section is 10cm. Compared to the case of 45cm water depth, the wave heights decayed slowly after the wave was broken. In Figure 7, the maximum mean water level was 4~5% of the significant wave height when the offshore water depth was 45cm.

Under both water depth conditions, both one- and two-layer models successfully predicted the experimental results in all six figures, but one-layer model slightly over-predicted those quantities compared to the results of the two-layer model. Therefore, the energy dissipation scheme suggested by Kennedy *et al.* (2000) which was used in the Boussinesq model of this study can be applicable to this kind of experimental condition.

DISCUSSION

Stable wave heights after the wave breaking in terms of the water depth on the reef flat section (h_1) and the water depth on the reef flat section (h_1) were compared to the previous studies. Horikawa and Kuo (1966) conducted laboratory experiments under the reef-type bathymetry by using regular waves until x_1/h_1 = 20. Using the experimental results, they suggested the stable wave height after the wave breaking as H/h_1 = 0.35.

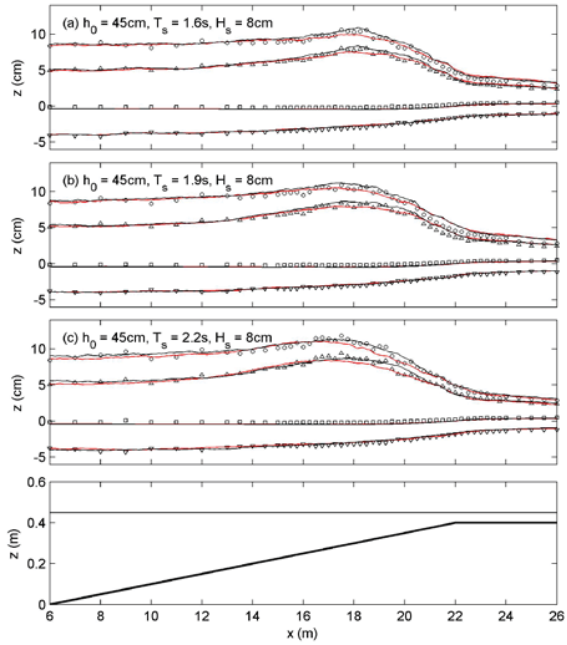

Figure 3. Numerical model and experimental results under the different wave conditions when H_s = 8cm and h_0 = 45cm. Figure configuration is same as Figure 2.

Lee et al. (2006) also conducted laboratory experiments over a fringing reef with the same slope as this study under the regular wave conditions. The stable wave height in their study was also approximately 0.35 near the x_1/h_1 = 20. Therefore, these results seem to be similar to those by Horikawa and Kuo (1966). However, the stable wave height converged 0.3 when x_1/h_1 = 40.

Figure 8 shows the experimental results of the stable wave heights on the reef flat section. As mentioned from the study of Horikawa and Kuo (1966), the stable wave height is defined as the ratio of the significant wave height at each horizontal location ($H_{1/3}$) to the water depth on the reef flat section (h_1) and was plotted as a function of the ratio of x_1 to h_1. Figure 8(a) shows the stable wave height including the wave setup and Figure 8(b) represents the stable wave height after eliminating the wave setup. Regardless considering the wave setup, the relative horizontal location (x_1/h_1) to reach the stable wave height was shown as approximately 30, which is the same location as regular wave cases by Lee *et al.* (2006).

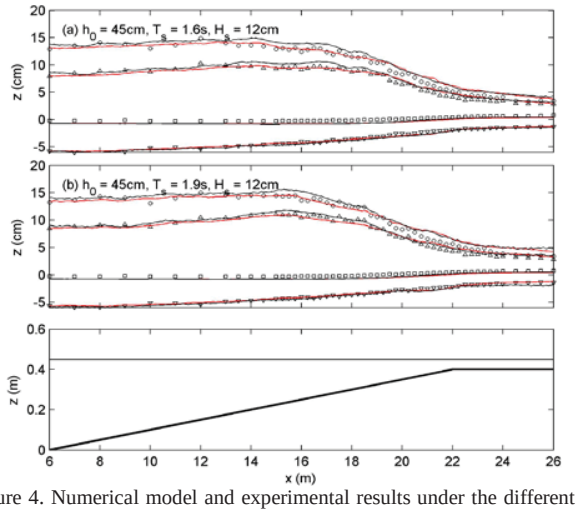

Figure 4. Numerical model and experimental results under the different wave conditions when H_s = 12cm and h_0 = 45cm. Figure configuration is same as Figure 2.

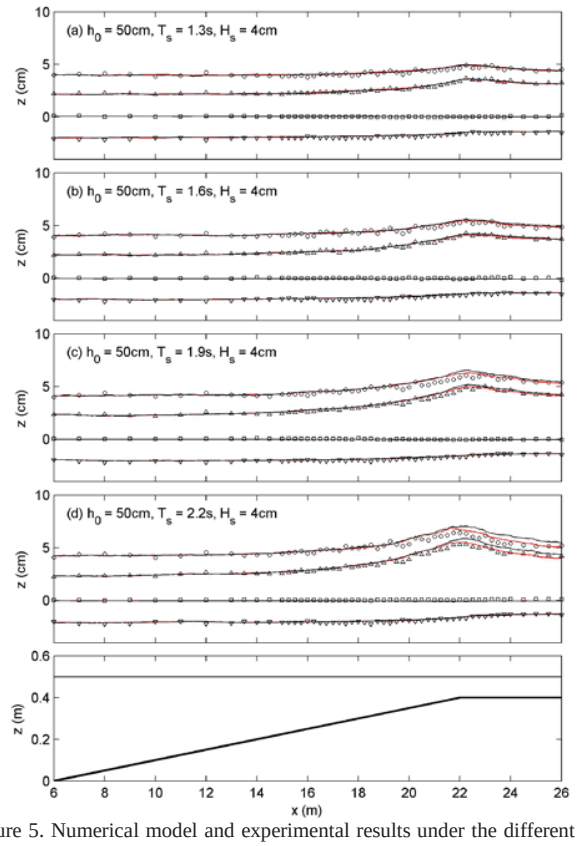

Figure 5. Numerical model and experimental results under the different wave conditions when H_s = 4cm and h_0 = 50cm. Figure configuration is same as Figure 2.

The stable wave height after the wave breaking on the reef flat section converged approximately 0.61 when the wave setup was included. The experimental results also showed that the stable wave height without the wave setup converged around 0.45. Therefore, the effect of the wave setup on the stable wave height was around 5%. The results also showed that the stable wave height under the irregular wave condition was twice larger than that under the regular wave condition.

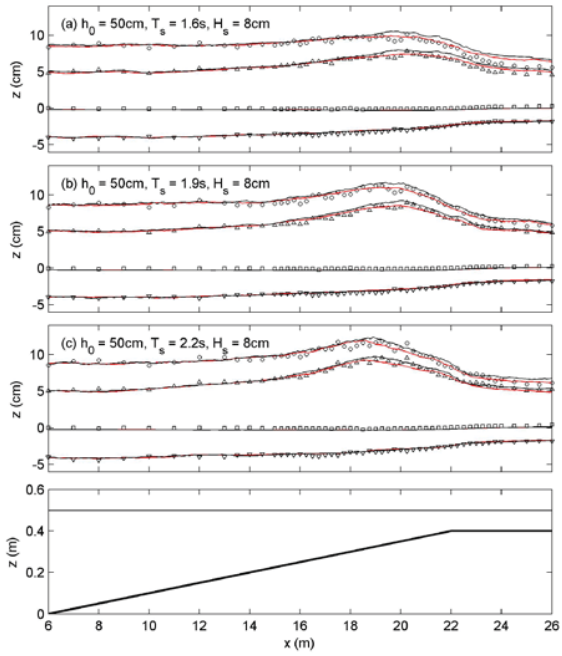

Figure 6. Numerical model and experimental results under the different wave conditions when H_s = 8cm and h_0 = 50cm. Figure configuration is same as Figure 2.

CONCLUSIONS

Two-dimensional laboratory experiments were conducted to investigate cross-shore variations of wave transformation, setup, and breaking phenomena over a fringing reef. Various conditions of irregular waves were generated by changing a water depth, a wave period, and a wave height. A multi-layer Boussinesq model was used to predict the wave transformation and the results were compared to the experimental results. In this study, conventional Boussinesq model (one-layer model) and two-layer model were tested their modeling capability over a reef-type bathymetry. Overall, both models successfully predicted the wave transformation but one-layer model a little over-predicted the wave heights and the crest levels near the surf zone. The results showed that two-layer model was more stable in all cases regardless of the wave nonlinearity.

The experimental results showed that the stable wave heights under the regular and irregular wave condition converged 0.3 and 0.56 respectively. The results from this study can be used to verify the modeling capability in the context of the wave transformation.

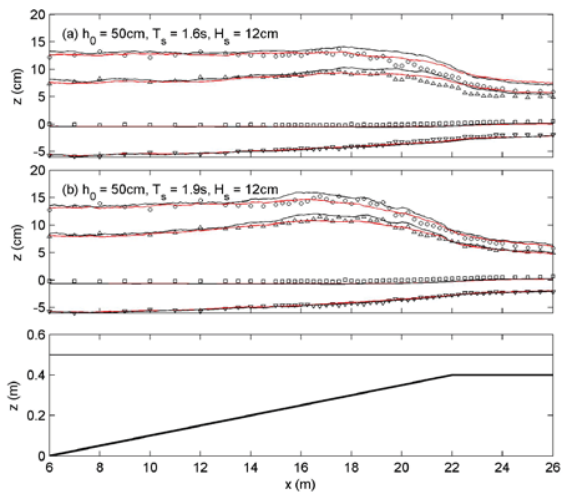

Figure 7. Numerical model and experimental results under the different wave conditions when H_s = 12cm and h_0 = 50cm. Figure configuration is same as Figure 2.

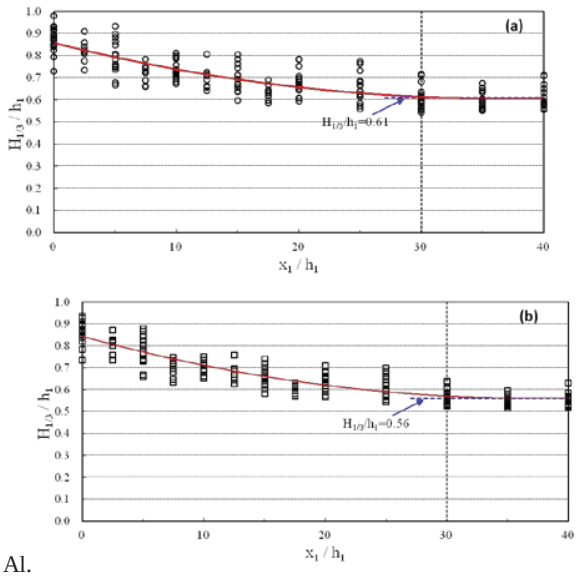

Al.

Figure 8. Stable wave height after wave breaking on the reef flat with wave setup (a) and without wave setup (b).

ACKNOWLEDGMENTS

This work was partially supported by the National Research Foundation of Korea (NRF) grant funded by the Korea government (MSIP) (No. 2011-0030040) and the Korea Institute of Marine Science & Technology Promotion funded by Ministry of Oceans and Fisheries (No. 20110131).

LITERATURE CITED

Christensen, E.D. and Deigaard, R. 2001. Large eddy simulation of breaking waves. *Coastal Engineering*, 42, 53 – 60.

Cox, D.T. and Kobayashi, N. 2000. Identification of Intense, Intermittent Coherent Motions under Shoaling and Breaking Waves," *Journal of Geophysical Research*, 105(C6), 14223 – 14236.

Goertz, J.T.; Kaihatu, J.M.; Sheremet, A.; Smith, E.R., and Smith, J.M. 2012. Long wave effects on breaking waves over fringing reefs. *Proceeding of 33th International Conference on Coastal Engineering (Santander, Spain)*, 1-8.

Gourlay, M.R. 1994. Wave transformation on a coral reef. *Coastal Engineering*, 23, 17-42.

Horikawa, K. and Kuo, C.T. 1966. A study of wave transformation inside the surf zone. *Proceedings of 10th International Conference on Coastal Engineering*, 217 – 233.

Iverson, H.W., 1952. Waves and breakers in shoaling water. *Proceedings of the 3rd International Conference on Coastal Engineering (Cambridge, USA)*, 51-58.

Kennedy, A.B.; Chen, Q.; Kirby, J.T., and Darlymple, R.A. 2000. Boussinesq modeling of wave transformation, breaking and runup I: 1D. *Journal of Waterway, Port, Coastal and Ocean Engineering*, 126(1), 39 – 47.

Kirby, J.T.; Wei, G.; Chen, W.; Kennedy, A.B., and Dalrymple, R.A. 1998. *FUNWAVE 1.0 Fully nonlinear Boussinesq wave model*. Documentation and user's manual, Tech. Rep. CACR-98-06, Center for Applied Coastal Research, Ocean Engineering Laboratory, Univ. Delaware.

Lee, J.I.; Shin, S., and Kim, Y.T. 2014. Experimental and Numerical Studies on Wave Breaking Characteristics over a Fringing Reef under Monochromatic Wave Conditions. *The Scientific World Journal*, Article ID 573025, 1-11.

Lin, P. and Liu, P.L.F. 1998. A numerical study of breaking waves in the surf zone. *Journal of Fluid Mechanics*, 359, 239 – 264.

Lynett, P. and Liu, P.L.F. 2004. A two-layer approach to water wave modeling. *Proceeding of Royal Society of London*, 460, 2637-2669.

Nadaoka, K.; Hino, M., and Koyano, Y., 1989. Structure of the turbulent flow field under breaking waves in the surf zone. *Journal of Fluid Mechanics*, 204, 359-387.

Shin, S. 2005. *Laboratory Observations and Numerical Modeling of Inner Surf and Swash Zone Hydrodynamics on a Steep Slope*. Oregon State University.

Shin, S. and Cox, D.T. 2006. Laboratory observations of inner surf and swash zone hydrodynamics on a steep beach. *Continental Shelf Research*, 26, 561-573.

Smith, J.M., 1993. *Nearshore Wave Breaking and Decay*. Technical report CERC-93-11, Vicksburg, Mississippi: U.S. Army Corps of Engineers.

Svendsen, I.A., 1987. Analysis of surf zone turbulence. *Journal of Geophysical Research*, 92(C5), 5115-5124.

Ting, F.C.K. and Kirby, J.T., 1994. Observation of undertow and turbulence in a laboratory surf zone. *Coastal Engineering*, 24, 51-80.

Raubenheimer, B. 2002. Observations and predictions of fluid velocities in the surf and swash zones. *Journal Geophysical Research*, 107(C11), 3190 – 3196.

Journal of Coastal Research	SI	75	927-931	Coconut Creek, Florida	2016

Seasonal and Intraseasonal Variability of Wave Climate on the NE Brazilian Coast using a Nautical Radar System

Alex C. da Silva[†*], Cristiane S. Bezerra[†], Roberto L. Barcellos[††], Moacyr Araújo[†], Nadège Bouchonneau[‡], Valdir Manso[§]

[†]Laboratório de Oceanografia Física Estuarina e Costeira - Departamento de Oceanografia
Universidade Federal de Pernambuco
Recife, Brazil

[‡]Departamento de Engenharia Mecânica
Universidade Federal de Pernambuco
Recife, Brazil

[††]Laboratório de Oceanografia Geológica
Departamento de Oceanografia
Universidade Federal de Pernambuco
Recife, Brazil

[§]Laboratório de Geologia e Geofísica Marinha
Departamento de Geologia
Universidade Federal de Pernambuco
Recife, Brazil

www.cerf-jcr.org

www.JCRonline.org

ABSTRACT

Silva, A.C.; Bezerra, C.S.; Barcellos, R.L.; Araújo, M.; Bouchonneau, N. and Manso, V., 2016. Seasonal and intraseasonal variability of wave climate in the NE Brazilian coast by using Nautical Radar System. *In:* Vila-Concejo, A.; Bruce, E.; Kennedy, D.M., and McCarroll, R.J. (eds.), *Proceedings of the 14th International Coastal Symposium* (Sydney, Australia). *Journal of Coastal Research*, Special Issue, No. 75, pp. 927-931. Coconut Creek (Florida), ISSN 0749-0208.

This paper presents a study about wave climate acting on the Northeast coast of Brazil (Recife, Pernambuco) from the use of X-band nautical radar, which runs through the emission of electromagnetic waves and receives the signal by backscattering the sea surface. The main objective of this work is to obtain information about the wave acting on this coast, by analyzing significant height, period and direction of the incident waves, which will be helpful to generate a solid database for future coastal measures, engineering works of contention for coastal and marine protection. Data were obtained from polar images of X-band nautical radar, from April 2010 to April 2011. By analysing the results, it was possible to observe the joint occurrence of waves wind sea and swell in the region of study. Wind sea waves occur predominantly at 90º - 135º, with higher values at the end of September (3.9 m). Swell waves were more frequent during June, October and December 2010, and February and March 2011. Moreover, we observed a change in direction of the waves and decrease in wave heights along the inner shelf of the coast, caused by variation in bathymetry and the presence of sandstone reefs. The results of this study demonstrated great efficiency in acquiring the physical parameters of waves through the X-band nautical radar system, proving to be an efficient tool for measuring physical parameters of waves in coastal regions.

ADDITIONAL INDEX WORDS: *NE Brazilian coast, swell, wind sea waves, X-band nautical radar.*

INTRODUCTION

Coastal erosion process due to wave action, occurring mainly during events of severe storms, is one major concern in various regions of the world. The necessity to better understand the dynamics of coastal areas has motivated wave climate monitoring and the development of models for waves prediction.

Near the equatorial belt of the Atlantic Ocean is formed a huge lane, where trade winds produce sea shakes characterized by local waves, which propagate from east to west, reaching the northeast Brazilian coast. The fluctuation of these trade winds on the north/northeast coast (N/NE) of Brazil suffers a seasonal latitudinal displacement depending on the position of the Intertropical Convergence Zone (ITCZ) (Hastenrath, 1985). From September to November the ITCZ is in its northernmost position, prevailing trade winds from SE, while from December to March the ITCZ is displaced southward, reaching the N-NE coastal area of Brazil, when northeast trade winds prevail (Silva *et al.*, 2011).

The waves generated and supported by the trade winds stress are called wind sea waves. Other weather events may also produce waves, Swell, on the coast of NE Brazil, as in the case of tropical cyclones, formed in the North or South Atlantic, and easterly African atmospheric disturbances that propagate westward across the Atlantic (Innocentini *et al.*, 2005, Melo *et al.*, 1995). Due to its geographical location, the coastal region of NE Brazil, highly urbanized, receives the swell-type waves. These large swells usually produce strong impacts on the natural dynamics of erosion, as well as overtopping and inundation.

The study area is located in Recife-PE near a coastal region presenting high population density and high level of tourism frequentation, and has in recent years suffered from coastal erosion actions. The understanding of coastal dynamics in the region is difficult to achieve due to the morphology

DOI: 10.2112/SI75-186.1 received 15 October 2015; accepted in revision 15 January 2016.
*Corresponding author: alex.csilva@ufpe.br
©Coastal Education and Research Foundation, Inc. 2016

characteristic of its background, illustrated in Figure 1(c), consisting in reef lines and flow channel.

Along the Brazilian coast still few studies are derived from *in-situ* waves measurements, and most of them were based on short-term observations (Melo *et al.*, 1995; Silva *et al.*, 2011). Numerical modeling studies of wave dynamics along Brazilian coastline are more numerous (Gomes and Silva, 2014; Oliveira, 2002; Parise, 2010; Pianca *et al.*, 2010), although the lack of sea data represents always a handicap for evaluating models validity and performance.

In the present work, we analyze the wave climate variability on the coast of NE Brazil by using polar images obtained through X-band nautical radar. The images are converted into wave parameters through a set of numerical routines known as Wave and Surface Current Monitoring System - WaMoS II. This system has been primarily used in the northwest Atlantic Northwest and northeast Pacific Northeast (Hessner *et al.*, 2006; Hessner and Hanson, 2010; Reichert and Lund, 2007). In this paper we present the first application of this technique in a coastal region of NE Brazil.

The study aims to determine and characterize the temporal variability of the types of waves (sea and swell) that affect the internal shelf of Boa Viagem (Recife-PE), which is an area less influenced by the sandstone reefs present along the intern continental shelf. The correct determination of the wave parameters in the region is fundamental to plan coastal erosion process, the prevention of risk factors to ships, offshore structures, coastal infrastructure and coastal ecosystems.

METHODS

Waves parameters (significant wave height - *Hs*, Peak Period - *Tp*, and direction – θ, maximum height – *Hmax*, mean period – *Tm*, wavelength - λ) were obtained from polar images of X-band nautical radar generated from the Wave and Surface Current Monitoring System - WaMoS II, developed by OceanWaves GmbH (Germany). This equipment was installed at Lat. 08°08.098 S and Long. 034°54.085 W (Figure 1(a)), in a fixed platform on the roof of a building 56 m above mean sea level (Figure 1(b)), on the coast of NE Brazil (Recife-PE). Data were collected between April 2010 and April 2011.

The system operates through the emission of electromagnetic waves pulses and later reception of the backscattered signal generated from the dispersion of electromagnetic waves in shallow ocean waves. The scope of the radar corresponds to an area that begins at a distance of 180 m from the antenna to 2080 m toward offshore.

The records of each data file obtained by X-band nautical radar were performed every 2 minutes. A data file consisted of the acquisition of 32 polar images, each one being generated after a full rotation cycle of the radar antenna (2.34 s). More information about the method by which the signal processing occurs until obtaining the wave parameters are described in the WaMoS II's operation manual (Wave Monitoring System, 2007) and Hessner (2007).

In order to better understand the wave climate in the region, a specific subregion of the entire region covered by the radar was selected to avoid changes in the physical parameters of the waves. This subregion covers 128x128 pixels, with approximately 1 km², lying at 1080 m offshore direction of the radar antenna. In this study, we use the data obtained farther from the coast, in an area located at about 1080 m distance from the radar antenna as shown in Figure 1(a), to better understand the physical parameters and the special variability of waves in the region.

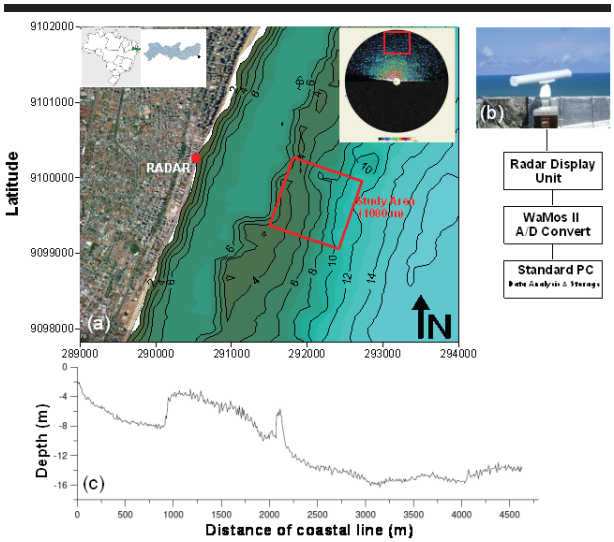

Figure 1. (a) Location of the X-band nautical radar system and representation of the study area, indicating the respective distance to the radar antenna and the bathymetry of the region - Source of bathymetry data: FINEP/UFPE, 2009. On the right corner is represented a polar image related to the coverage area of the radar; (b) Radar system antenna; (c) Topobathymetry profile next to Boa Viagem beach (Pernambuco, Brazil) - Source: FINEP/UFPE (2009).

The wind data used in this article were collected by the Bank of Climatological Data (BDC) of Brazil, assigned by the Subdivision of Climatology and Meteorological Archive (PBCA) and Research Sub-Directorate (SDP) of the Institute for Airspace Control (ICEA). In this study we used observational meteorological data of wind speed (daily means and maximums) and daily mean direction from a weather station located at 08 ° 07'S and 034 ° 55 'W coordinates. For September 2010, we used data of intensity and wind direction from the database of the National System of Environmental Data (SINDA) located in Recife-PE (Latitude: 8.06 ° S and Longitude: 34.92 ° W).

To realize the statistical analysis we applied the Mann-Whitney test in order to compare two independents and random samples. More details about this technique are described by Siegel and Castellan (2006).

RESULTS

During the study period, the wind sea waves showed predominantly direction between 90 ° and 135 ° (Figure 2(a)), with a percentage of 94.86% occurrence. For *Tp*, throughout the year, no defined predominance was observed, and waves with maximum and minimum values were present in the same month (Figure 2(a)). What differs this waveform from the others is the mean value obtained during each month. Thus, predominance of waves with average values of *Tp* between 6.6 s to 6.9 s were

registered between November 2010 and February 2011, and mean *Tp* values above 7 s were observed in the other months (April 2010 - October 2010 and March 2011 and April 2011, with a maximum value of 7.9 s obtained in September).

Significant waves height study showed higher occurrence of waves with *Hs* between 1.1 to 1.5 m between April 2010 and October 2010, and higher occurrence of waves with *Hs* between 0.5 - 1 m between November 2010 and April 2011 (Figure 2(b)).

In can be highlighted that during September 2010, the highest incidence of waves with high *Hs* values was registered and the highest wave height occurred at the end of this month (3.9 m), matching the period of greatest intensity of trade winds. During the period July 2010 - October 2010, highest daily means values of wind speed were registered (Figure 2(b) and (c)). The lowest *Hs* value recorded (0.4 m) was observed from December 2010 to April 2011, and may be associated to lower intensity of trade winds, which occurred between January 2011 and April 2011 (Figure 2(b) and (c)).

The swell-type waves were observed during the entire study period in the region, but with different amounts of records. The months with the highest occurrence of swell were June, October and December 2010 (with 287, 246 and 230 records, respectively) and February and March 2011 (with 320 and 404 records, respectively) (Table 1).

The highest *Hs* swell was 4.1 m observed in April 2011, and the lowest *Hs* swell was 0.2 m occurring in most months studied (Figure 2(d)). Greater occurrence of *Hs* swells values recorded was 0.5 m. During June 2010, January, February and March 2011, *Tp* values greater than 17 s were recorded, but periods between 10 and 15 s prevailed with most frequent wave period registered of 12.2 s. These swell waves showed direction mostly from the east (Figure 2(d)).

The swell waves directions were divided by sectors, namely: north (0°Az - 22°Az and 337°Az - 360°Az), northeast (23°Az - 67°Az), east (68°Az - 112°Az) and southeast (113°Az - 157°Az) (Table 1). The greater occurrence of waves came from the east, representing 45.72% of the occurrences throughout the study period. June and October 2010 and March 2011 had the highest occurrence of easterly swell with 198, 143 and 165 records of occurrence, respectively. The occurrence of north swell was quite low (6.97%), except during the months of June 2010 and March 2011, which presented 25 and 43 records of highest swell incidence from the north, respectively (Table 1).

The lower swell incidence throughout the study was from northeast (4.38%). In most months, swell incidence did not reach 10 wave records, except during January, February and March 2011, which presented higher amounts of records (17, 15 and 22 events, respectively).

The swell waves from the east and southeast were the ones that had higher observations, predominantly in June 2010 (222 records), October 2010 (178 records), but also significant in February 2011 (183 records) and March 2011 (209 records) (Figure 3 and Table 1).

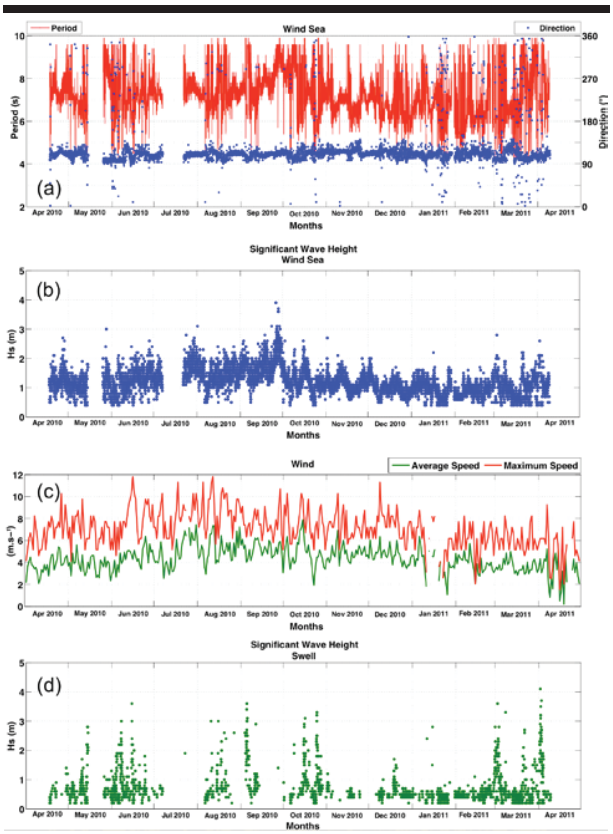

Figure 2. Physical wave parameters registered during the period: April 2010-April 2011: (a) Period and direction of wind sea waves; (b) Significant height (*Hs*) of sea wave; (c) Maximum and daily averaged wind speed; (d) Significant height (*Hs*) of swell wave.

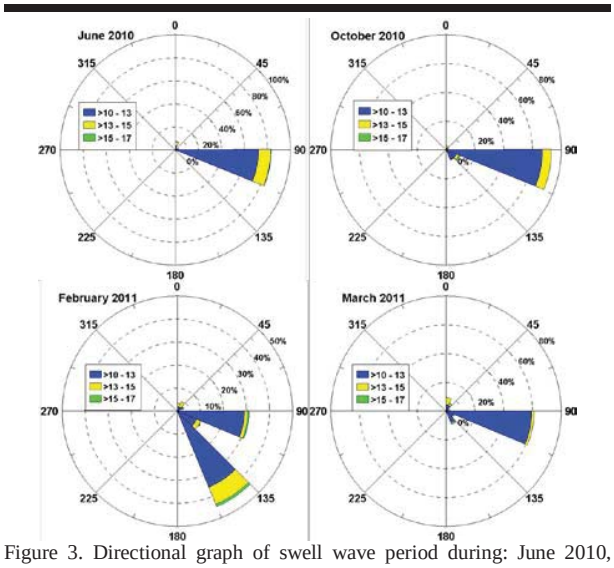

Figure 3. Directional graph of swell wave period during: June 2010, October 2010, February 2011 and March 2011.

Table 1. *Total swell records and classification regarding the wave origin, with their respective quantities of occurrence in each month studied. Swell from North (0°Az - 22°Az and 337°Az - 360°Az); Swell from Northeast (23°Az - 67°Az), Swell from East (68°Az - 112°Az) and Swell from Southeast (113°Az - 157°Az).*

	Apr 2010	May 2010	Jun 2010	Jul 2010	Aug 2010	Sep 2010	Oct 2010	Nov 2010	Dec 2010	Jan 2011	Feb 2011	Mar 2011	Apr 2011
Total Records	38	196	287	17	97	94	246	67	230	194	320	404	89
Swell from North	2	15	25	14	5	1	13	1	12	18	14	43	6
Swell from Northeast	3	10	9	0	1	1	8	2	8	17	15	22	4
Swell from East	17	99	198	0	75	90	143	36	76	23	66	165	54
Swell from Southeast	2	12	24	0	1	2	35	7	35	43	117	44	12

DISCUSSION

The sea wind waves that focus on the NE coast of Brazil (Recife-PE) are mostly from East-Southeast (ESE) in all months studied. These waves are directly related to the trade winds from the southeast.

The results of the physical parameters of wind sea waves (*Tp* and *Hs*) confirm that they are related to the local wind action. In the first Semester of the year there is the influence of NE trade winds in Tropical Atlantic region (in this case, wind with less intensity). Wind observational data collected in the second half of July until the early October show increased wind speed under the influence of the SE trade winds associated with the ITCZ migration to most northern position (Hastenrath, 1985; Silva *et al.*, 2011).

By comparing the results obtained through the X-band nautical radar system to historical data conducted in the same study area, we can conclude that these results are consistent with Rollnic (2008), who studied the NE coast of Brazil (Recife-PE) from observational data, and demonstrated higher wave heights in August and September. These results are also in accordance with Cunha (2004) and Silva *et al.* (2011), who also studied the waves in the NE region of Brazil (Natal-RN and Fortaleza-CE), and showed shortest wave heights at the beginning of the year and largest wave heights from June to September.

The occurrence of swell may be associated with tropical storms. The waves generated by such systems can propagate for thousands of kilometers in the deep ocean with little loss of energy, potentially affecting a larger number of more distant shorelines. Recent empirical studies have demonstrated that tropical storm and hurricane activity in the Atlantic Ocean vary on decadal and multi-decadal time-scales and that this variability is correlated with sea-surface temperature anomalies in the Main Development Region (Shapiro and Goldenberg, 1998).

Such storms occur mainly between June and August, when the ITCZ is displaced further north of its mean position and with waters in the east coast of the Northeast above 28 °C. Although records are realized during short-term period, tropical storms seem to be more common in La-Niña years (Molion and Bernardo, 2002). Its genesis is associated with the penetration of frontal systems or its remains, which can reach equatorial latitudes at this time of year. In addition, it is noteworthy that the study period (2010) was under the influence of a strong La Niña event. The highly active 2010 Atlantic hurricane season was associated with the onset of a La Niña event, which was well predicted several months in advance (Davey *et al.*, 2011).

The swells from the east and southeast in May and June may be related to the raid at least four frontal systems that penetrated the equatorial region from May 2010, which was responsible for the total rainfall in June 2010.

The occurrence of swell from the north and northeast showed a very low frequency. However it should be noted that the waves, until reaching the area, have undergone the refraction process due to bathymetry of the continental shelf of Pernambuco, justifying this low occurrence. This occurrence may be associated with events developed in the Northern Hemisphere. Innocentini *et al.* (2005) described that the extratropical cyclone developed in the North Atlantic and easterly wave disturbances are responsible for generating waves on the NE coast of Brazil.

According to the National Center of Hurricanes (NHC), the period of occurrence of hurricanes in the North Atlantic runs from June to November. However, it was between August and October that there was a higher development of hurricanes in the most central area of North Atlantic that may possibly have influenced the waves acting on the NE coast of Brazil, which may explain the high occurrence of swell in October 2010.

Melo *et al.* (1995) observed greater incidence of swell from December to March in the NE coast of Brazil (Ceará), as observed most recently in 1997, 2000 and 2001 by Silva *et al.* (2011). These waves, according to these authors, were associated with extratropical events in the North Atlantic Ocean. These studies corroborate the results obtained in this paper, regarding to the large amount of swell observed between December 2010 and March 2011.

CONCLUSIONS

By analyzing the wave climate for the study area during 13 months, combined occurrence of wind sea and swell waves has been highlighted. Wind sea waves showed preferential direction from ESE, with *Tp* between 7 and 8 s, and *Hs* of 1 to 1.5 m. Greater *Hs* values, as well as *Hmax* for wind sea, were obtained during periods presenting higher wind velocity (July-October 2010), whereas lower *Hs* values were registered during low wind velocity periods (December 2010-March 2011). Thus, the

analysis of these waves indicates great relationship with the local wind (trade wind system), which changed according to the variations occurring in atmospheric systems operating in the Atlantic Ocean.

Regarding to the swell waves, they showed very significant occurrence during the months of May, June, October and December 2010 and January, February and March 2011. These waves showed predominant period between 10 and 13 s with observations of maximum *Hs* swell between 1.2 to 4.1 m.

The greater occurrence of waves came from the east, representing 45.72% of the occurrences throughout the study period related to most energetic events occurring in the South Atlantic Ocean. Furthermore, waves coming from the North Atlantic Ocean (6.97% Swell from North and 4.38% Swell from NE) were also recorded.

The data were obtained from April 2010 to April 2011 (13 months), which is short term in dealing with wave climate, which should have a longer cycle (e.g. ENSO cycles). However, even though the data have been collected in a relatively short period, they can play an important role in determining other local climatic factors, as well as assuring the quality of wave forecast models.

ACKNOWLEDGMENTS

This work was supported by the National Council for Scientific and Technological Development (CNPq) and the Foundation of Support to Science and Technology of the State of Pernambuco (FACEPE) by the financing of PGEST and MC-MAR/NE Projects, allowing the deployment of the radar equipment along the coast of Pernambuco to monitor the wave climate; and Katrin Hessner for her help regarding to the radar system.

LITERATURE CITED

Cunha, E.M.S., 2004. Evolução atual do litoral de Natal-RN (Brazil) e suas aplicações a gestão integrada. Barcelona, Spain: Universidat de Barcelona, Ph.D. dissertation, 393 p.

Davey, M.; Huddeleston, M., and Brookshaw, A., 2011. Global impact of El Niño and La Niña: implications for financial markets. Advisor Report for the Lighthill Risk Network. UK: Met Office. SR3 19 Available from: https://ktn.innovateuk.org/web/financialservicesktn/articles/-/blogs/globalimpact-of-el-nino-and-la-nina-on-financial-markets.

FINEP/UFPE, 2009. Monitoramento ambiental integrado (MAI-PE), Relatórios 1, 2, 3, Financiadora de Estudos e Projetos – FINEP, Recife-PE, Brasil, 485 p.

Gomes, G., and Silva, A.C., 2014. Coastal Erosion Case at Candeias Beach (NE-Brazil). *J. Coastal Res*., 71, 30-40.

Hastenrath, S., 1985. *Climate and circulation of the tropics*. D. Reidel Publishing Company, Holland, 445 p.

Hessner, K., 2007. Wamos II wave analysis method, limitations and definitions, *Ocean Waves GmbH*, Lüneburg.

Hessner, K. and Hanson, J.L., 2010. Extraction of coastal wavefield properties from X-band radar. *Proceedings of the Geoscience and Remote Sensing Symposium (IGARSS)*, 2010 IEEE International (Honolulu, USA), pp. 4326-4329.

Hessner, K.; Reichert, K., and Dannenberg, J., 2006. 2D surface elevation measurements by means of X-band radar. *Proceedings of the 9th International Workshop on Wave Hindcasting and Forecasting* (Victoria, Canada), pp. 1-13.

Innocentini, V.; Arantes, F.O.; Ferreira, R.J., and Micheleto, R.G., 2005. A agitação marítima no litoral nordeste do brasil associada aos distúrbios africanos de leste. *Revista Brasileira de Meteorologia*, 20(3), 367-374.

Melo, E.; Alves, J.H.G.M.; Jorden, V., and Zago, F., 1995. Instrumental confirmation of the arrival of North Atlantic swell to the Ceará coast. *Proceedings of the 4th International Conference on Coastal an Port Engineering in Developing Countries (COPEDEC)*, Rio de Janeiro, Brazil, pp.1984-1996.

Molion, L.C.B. and Bernardo, S.D.O., 2002. Uma revisão da dinâmica das chuvas no nordeste brasileiro. *Revista Brasileira de Meteorologia*, 17(1), 1-10.

Oliveira, F.S.B.F., 2002. Wave climate modelling south of Rio de Janeiro in Brazil. *Cont. Shelf Res*., 22(14), 2021-2034.

Parise, C.K., 2010. Estudo da variabilidade de ondas no oceano atlântico sul e a contribuição energética de um ciclone extratropical intenso nos espectros das ondas ao largo do rio grande do sul. Porto Alegre, Brazil: Universidade Federal do Rio Grande do Sul, Master's thesis, 65 p.

Pianca, C.; Mazzini, P.L.F., and Siegle, E., 2010. Brazilian offshore wave climate based on nww3 reanalysis. *Braz. J. Oceanogr*., 58(1), 53-70.

Reichert, K., and Lund, B., 2007. Ground based remote sensing as a tool to measure spatial wave field variations in coastal approaches. *Proceedings of the 9th International Coastal Symposium* (Gold Coast, Australia), pp.1-5.

Rollnic, M., 2008. Dinâmica das ondas e circulação no litoral da região metropolitana do recife - implicações para o transporte de sedimentos e estabilidade da costa. Recife, Brazil: Universidade Federal de Pernambuco, PhD dissertation, 124 p.

Shapiro, L.J. and Goldenberg, S.B., 1998. Atlantic Sea Surface Temperatures and Tropical Cyclone Formation. *J. Climate*, 11(4), 578–590.

Siegel, S. and Castellan, Jr. N.J., 2006. Estatística não-paramétrica para ciências do comportamento, Porto Alegre, Artmed, 448 p.

Silva, A.C.; Façanha, P.; Bezerra, C.S.; Araújo, A., and Pitombeira, E., 2011. Características das ondas sea e swell observadas no litoral do Ceará-Brasil: Variabilidade anula e inter-anual. *Tropical Oceanography*, 39(2), 17-26.

Wave Monitoring System, 2007. *Operating manual version 3.03*, installation guide, Ocean Waves Gmbh, Lüneburg.

Journal of Coastal Research	SI	75	932-936	Coconut Creek, Florida	2016

Empirical Parameterization of Wave Runup and Dune Erosion during Storm Conditions on a Natural Macrotidal Beach

Serge Suanez[†*], Emmanuel Blaise[†], Romain Cancouët[†], and France Floc'h[‡]

[†]LETG-Brest-Géomer UMR 6554 CNRS, Institut Universitaire Européen de Mer, Technopole Brest-Iroise, Rue Dumont d'Urville, 29280 Plouzané, France

[‡] LDO UMR 6538 CNRS, Institut Universitaire Européen de Mer, Technopole Brest-Iroise, Rue Dumont d'Urville, 29280 Plouzané, France

www.cerf-jcr.org

www.JCRonline.org

ABSTRACT

Suanez, S.; Blaise E.; Cancouët R., and Floc'h F., 2016. Empirical Parameterization of Wave Runup and Dune Erosion during Storm Conditions on a Natural Macrotidal Beach. *In:* Vila-Concejo, A.; Bruce, E.; Kennedy, D.M., and McCarroll, R.J. (eds.), *Proceedings of the 14th International Coastal Symposium* (Sydney, Australia). *Journal of Coastal Research*, Special Issue, No. 75, pp. 932-936. Coconut Creek (Florida), ISSN 0749-0208.

An experimental study based on field measurements for runup parameterization was conducted on a high energy macrotidal beach located on North Brittany (Vougot Beach). The approach was based on morphological and hydrodynamic high frequency monitoring collected between 2008 and 2013. The aim was to quantify in-situ environmental conditions and dimensional swash parameters for the best calibration of Battjes (1971) runup formula. In addition, an empirical equation based on observed tidal water level and offshore wave height was produced to estimate extreme water levels defined as the sum of (*i*) astronomic tide, (*ii*) storm surge, and (*iii*) vertical wave runup. A good correlation between this empirical equation ($1.01H_{mo}\xi_o$) and field runup measurements (R_{max}) was obtained (R^2 85%). The goodness of fit given by the RMSE was about 0.29 m. Extreme water levels were then used to explain dune erosion processes that occured during the winter storms 2013-2014. A good relationship was noted between dune erosion and high water levels when they exceed the dune foot elevation.

ADDITIONAL INDEX WORDS: *Macrotidal beach, runup, storm, dune, erosion, extreme water level.*

INTRODUCTION

Runup corresponds to the time fluctuating vertical position of the wash limit on the upper part of the beach. It is defined as the difference between discrete water elevation maxima and still water level corresponding generally to observed tide level (Holman, 1986; Hunt, 1959; Stockdon *et al.*, 2006). Runup is one of the most important components that can generate extreme water levels, especially during storm condition. Therefore, it is a key factor during coastal erosion processes, when extreme water levels reach the toe of the dune (Hesp, 2002; Kriebel, 1986; Pye and Neal, 1994; Ruggiero *et al.*, 2001; Sallenger, 2000; Vellinga, 1982). Estimation of wave runup is a complicated issue because of the complex processes driving the swash zone related to incident band wave energy transferred to both higher and lower frequencies through the surf zone (Longuet-Higgins and Stewart, 1962; Stockdon *et al.*, 2006). Therefore, wave runup is largely dependent on environmental conditions such as the local beach slope (synthesized through dissipative to reflective context generally given by Iribarren number, see Battjes, 1974) and the infragravity-to-incident offshore wave energy which dominates the inner-surf zone (Guza and Thornton, 1982; Holman and Sallenger, 1985; Ruessink *et al.*, 1998; Ruggiero and Holman, 2004). A simple formula was first proposed by Hunt (1959) showing that runup (R) was proportional to significant wave height (H_s) and slope (S).

DOI: 10.2112/SI75-187.1 received 15 October 2015; accepted in revision 15 January 2016.
*Corresponding author: serge.suanez@univ-brest.fr
©Coastal Education and Research Foundation, Inc. 2016

Battjes (1971) has shown that runup was better related to a morphodynamic component defined by a dimensionless surf similarity parameter called the Iribarren number, expressed by the following equation:

$$\frac{R}{H_s} = C\xi_o \qquad (1)$$

where C is a constant, and ξ_o is the Iribarren number given by Battjes (1974):

$$\xi_o = \frac{\tan\beta}{(H_o/L_o)^{1/2}} \qquad (2)$$

where $\tan\beta$ is the beach slope, H_o corresponds to significant offshore wave (equivalent to H_s in deep water), and L_o is deep water wavelength.

Following this approach, Holman (1986) found a clear relationship between the 2% exceedence value of runup normalized by H_s and ξ_o, and fit this equation on a natural intermediate-to-reflective beach ($0.07 < \tan\beta < 0.2$). Based on the laboratory tests, Mase (1989) developed a predictive on uniform impermeable slopes ($0.03 < \tan\beta < 0.2$). He found that the runup was approximately twice as large as values measured in the field by Holman (1986), and explained this discrepancy by the effect of beach profile geometry. Nielsen and Hanslow (1991) indicated proportionality between the best-fit of runup elevation distribution and the beach slope for a steeper beach ($\tan\beta \geq 0.10$). For the flatter beaches ($\tan\beta \leq 0.10$), the slope became largely unimportant and the vertical scale of the runup

distribution was scaled directly with $(H_oL_o)^{0.5}$. Ruessink *et al.* (1998) came to the same conclusion under highly dissipative conditions ($0.01 < \tan\beta < 0.03$) and found that the significant infragravity swash height (R_{ig}) was about 30% of the offshore wave height H_0, and that the slope in the linear H_0 dependance of R_{ig} amounted to only 0.18. More recently, Stockdon *et al.* (2006) indicated that in an infragravity-dominated dissipative context, the magnitude of swash elevation $R_{2\%}$ was dependent only on offshore wave height and wavelength while in intermediate and reflective context with complex foreshore morphology, beach slope was on the contrary much more important. Therefore, the authors have elaborated different runup equations according to the beach morphodynamic context from a dissipated state ($\xi_o < 0.3$), to an intermediate state ($0.3 < \xi_o < 1.25$), to a reflective state ($\xi_o > 1.25$).

In a previous study already on the Vougot beach, a first methodological approach for calibrating runup equation suggested that on the macrotidal beach, the slope of the active section of the upper beach should be used to obtain the most relevant estimation of observed runup elevations (Cariolet and Suanez, 2013). The aim this study was to improve this simple parameterization approach for calculation of maximum runup elevation in order to estimate extreme water levels. Based on the Sallenger (2000) and/or Ruggiero *et al.* (2001) models, the aim was then to understand processes of the erosion of the dune of Vougot beach that occurred during the stormy winter 2013-2014.

STUDY SITE

The Vougot beach is located on the North coast of Finistère in Brittany (France) (Figure 1). It is formed by a massive foredune, anchored on the Zorn abandoned cliff, that stretches over about 2 km in a southwest to northeast direction. It culminates at an altitude of 13 m above sea level – asl.

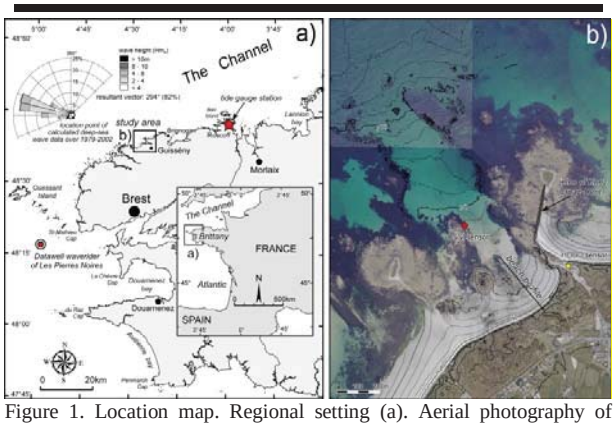

Figure 1. Location map. Regional setting (a). Aerial photography of Vougot beach showing the beach/dune profile location and both wave/water level and atmospheric pressure sensors (b).

Over the last decades, the eastern part of the dune has experienced erosion reaching about -0.6 m/yr between 1952 to 2014. This rate has increased to -1.5 m/yr over the last decade (from 2000 to 2009) due to the impact of a major storm on 10th March 2008 (Suanez *et al.*, 2010). Erosion was caused by the construction of the Enez Croas Hent jetty in 1974 (Figure 1b), which completely modified the hydrodynamics and interrupted the westward sand drift. However, from spring 2008 to summer 2013, almost 5 years of dune recovery occured inducing a maximum progradation of dune front reaching +12 m (Suanez *et al.*, 2012).

Incident waves come mostly from the west-north-west direction (242°) (Figure 1a). The most frequent wave height (H_{m0}) is between 1.5 and 3 m (average of 2.2 m), and the most frequent period (T_{pic}) is between 9 and 11 s (average of 10.6 s). The maximum wave height and period related to storm events reached respectively 14 m and 20 s. Macrotidal range is reaching about 7 m between MHWS and MLWS. The beach profile is characterized by different morphodynamic environments according to the composite slope and concave beach (Figure 2). The lower part of the tidal beach, between MHWN and MLWN, is characterized by dissipative context with a very gentle slope ($\xi_0 \leq 0.3$ and $0.034 < \tan\beta < 0.014$). In contrast, the upper beach up to MHWN, is characterized by intermediate to moderately reflective conditions ($0.72 < \xi_0 < 1.6$ and $0.081 < \tan\beta < 0.18$). Therefore, depending on the tide's water level, waves break on different morphodynamic environments. This is important because runup process differs between dissipative to reflective conditions (Senechal *et al.*, 2011; Stockdon *et al.*, 2006).

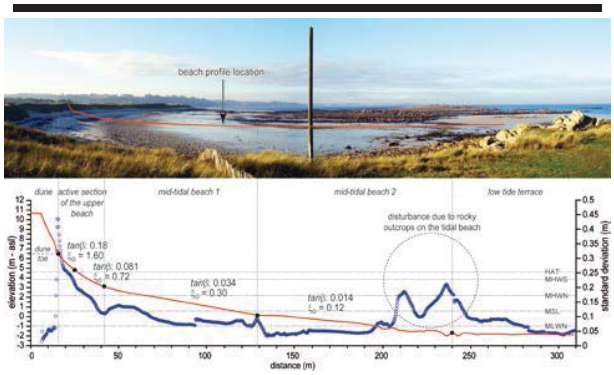

Figure 2. Mean cross-shore profile of the surveyed Vougot beach section (red line). Morphodynamic conditions (dissipative to reflective conditions) have been analyzed along the concave beach profile using Iribarren value.

METHODS

Two set of data collected along a transect situated on the eastern part of the beach (see Figure 1b) were used concerning the survey of beach profile and maximum swash elevation (runup) R_{max}. The first one concerns the data acquired between between 2008 and 2010 and already published in a previous study (see Cariolet and Suanez, 2013). The second one corresponding to the current data was collected between June 2012 and 2013 following the same approach as Cariolet and Suanez (2013). In total, a set of 90 morphological and runup measurements was used in this study. The maximum swash elevation was determined by the wrack deposit and/or the limit

of the water mark (Figure 3). We assume that this limit corresponded to the highest level reached by the runup during the previous high tide. Therefore, it corresponds to R_{max} (maximum runup) instead of the generally used random variable $R_{2\%}$ that corresponds to vertical runup distance exceeded by 2 percent of wave runups. Measurements were carried out using a Differential GPS in RTK mode. Measurements were calibrated using the geodesic marker from the French datum.

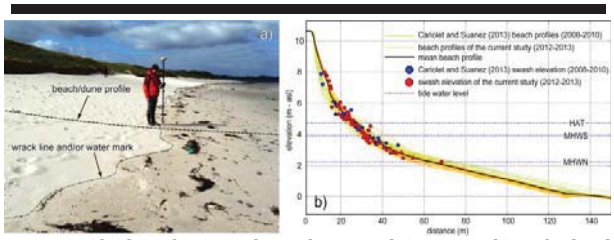

Figure 3. The limit between dry and wet sand (water mark) at the level of high tide deposit (wrack line) shows the level reached by the swash processes (a). Beach/dune profile measurements and the runup elevation R_{max} reached during the previous high tide (b).

Offshore wave analysis was based on data acquired from the WAVEWATCH III model (WW3) which reproduced the offshore wave conditions at the calculation point 4°29'24"W, 48°40'12"N at a water depth of 18.3 m. Wave parameters such as wave height (H_{m0}) and period ($T_{m0,-1}$) were extracted for the time periods corresponding to the high tide level.

Analysis of water levels was based on records achieved between June 2012 and 2013 on the intertidal zone using a pressure sensor deployed along the beach transect mentioned above (see Figure 1b). It was computed taking into account atmospheric pressure measured on the site. The data was smoothed to a moving average of 10 min to filter out wave deformations of the water surface, and water levels corresponding to both daily high tides were extracted (Figure 4a).

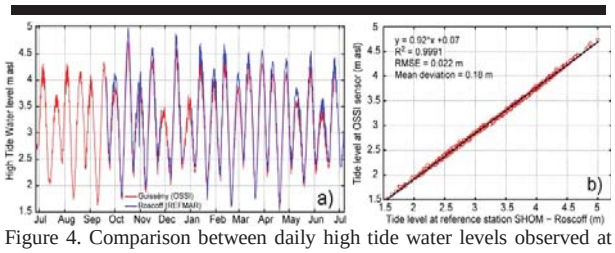

Figure 4. Comparison between daily high tide water levels observed at Vougot beach, using the OSSI-010-003C sensor, and at the permanent Roscoff tidal gauge station.

A similar calculation was done using data recorded at a permanent tide gauge station of Roscoff located at about 30 km east of the study site (Figure 1). Both the time series were used to estimate the differences in high tide water level between the two sites reaching 18 cm mean deviation (Figure 4b).

RESULTS

The results show the parameterization of a runup equation, and the use of this calibrated equation to analyze the dune erosion processes during the winter 2013-2014.

Runup parameterization

First, calibration of Battjes (1971) runup formula was achieved following the same methodological approach as the one used by Cariolet and Suanez (2013). Morphodynamic parameters such as $H_{m0}\xi_o$ and slope of the beach active section were used to estimate maximum runup elevation R_{max} (Figure 5). The correlation between observed runup and $H_{m0}\xi_o$ can be expressed as:

$$R_{max} = 0.68 H_{m0}\xi_o \quad (3)$$

It gives the same result as the previous Cariolet and Suanez (2013) study with a constant equal to 0.68 (95% confidence intervals [0.65; 0.71]).

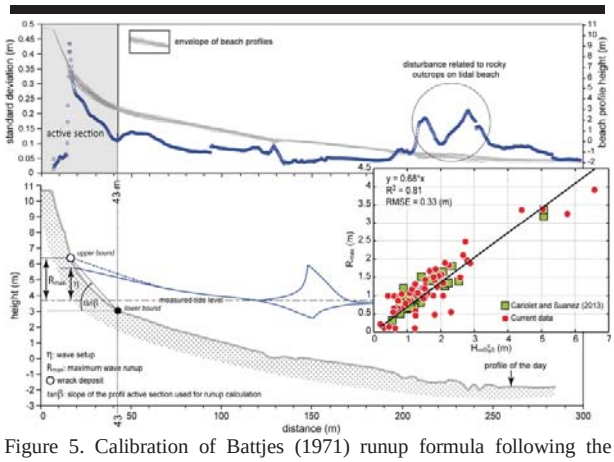

Figure 5. Calibration of Battjes (1971) runup formula following the method used by Cariolet and Suanez (2013) to calculate beach slope for the runup calculation. The lower bound corresponds to the limit of the profile section (called "active section") where changes of elevation are the most significant. This limit of 43 m has been defined by calculating the standard deviation of height changes of the beach profiles (gray lines). The upper bound corresponds to field measurements of the swash height given by the water mark limit or wrack line deposit.

Secondly, the parameterization of a general empirical equation of the runup was achieved using offshore wave and water level data. The slope was calculated using the observed high tide water level (*HTWL*) and a fraction of the offshore wave height (H_{m0}) from which the horizontal beach slope section (*HBSS*) was defined (Figure 6). Different correlation tests have shown that $1/4H_{m0}$ gives the best result in this case. Therefore, the upper and lower bounds of the beach slope profile width is calculated as follows:

$$Bound_{\text{up and low}} = HTWL \pm 1/4H_{m0} \quad (4)$$

Swash runup is in this case best parameterized with a best-fit R^2: 0.85 and Root Mean Squared Error (RMSE): 0.29 m. The coefficient of the regression line is 1.01 with 95% confidence

intervals [0.97; 1.05]. In this case, the relationship can be expressed as (Figure 6).

$$R_{max} = 1.01\ H_{m0}\xi_0 \qquad (6)$$

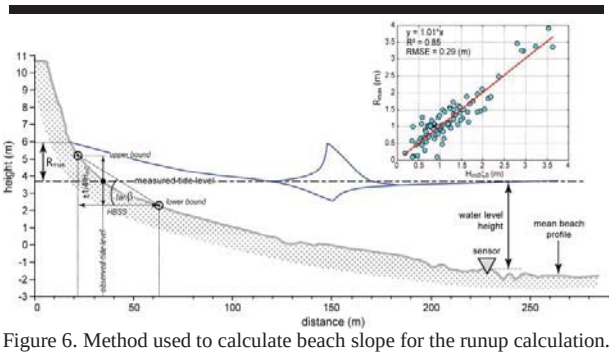

Figure 6. Method used to calculate beach slope for the runup calculation. It is based on measured tide level from which the beach section is defined. In contrast to the Cariolet and Suanez (2013) previous method, note that this approach is using the mean beach profile instead of daily beach profile.

Winter Storm 2013-2014 test case

Winter 2013-2014 (December 2013 to March 2014) was characterized by a series of about 12 storms that hit the Brittany coast (Blaise *et al.*, in press). It was in February that these storms were the most frequent and particularly virulent. The maximum wave heights measured off Finistère reached 23.5m during Petra storm of February 4-5 (Figure 7b). However, analysis of hydrodynamic conditions shows that only three episodes promoted extreme morphogenetic conditions because they were combined with high spring tide. The first one occurred on January 3-4, it was followed by events from February 1st to 3, and March 2-3 (Figure 7a).

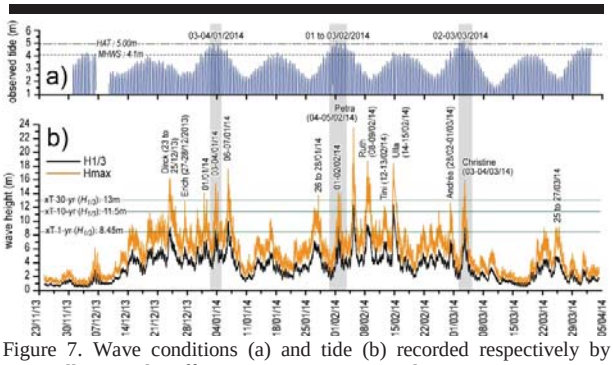

Figure 7. Wave conditions (a) and tide (b) recorded respectively by Datawell waverider off western Brittany peninsula at Les Pierres Noires and tide gauge at permanent Roscoff station (see Figure 1), during the winter 2013-2014. Grey lines show the three major storm events.

During these three extreme events the observed tide levels were above highest astronomical tide level (HAT) with maximum surge level up to 1m during Ulla storm of February 14-15.

Dune survey achieved during this winter period showed a retreat reaching about -7 m (Figure 8a). This erosion induced a net loss of sediment of about -20 m^3/l.m that occurred into three stages (Figure 8b). The first one is related to the January 3-4 storm event that generated extreme water levels reaching more than 9 m asl (Figure 8c). Nevertheless the erosion has not been not so important because the altitude of the dune foot was high at that period (about 8.25 m asl). The second storm event of the beginning of February generated a very significant dune érosion. It was associated to high extreme water levels reaching 9 m asl whereas the altitude of dune foot was considerably reduced due to the impact of the previous storm (6.7 m asl). The last storm event of March 2-3 has produced very few impact on dune erosion because a short phase of dune recovery occurred just after the 1-2 February storm event (see beach measurement of 16/02/2014 in Figure 8). Therefore, the altitude of the foot of the dune was higher due to accretion whereas the extreme water levels were lower (about 8.3 m asl).

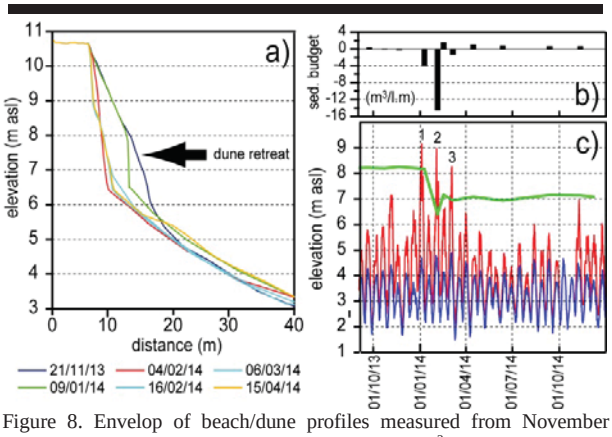

Figure 8. Envelop of beach/dune profiles measured from November 2013 to April 2014 (a). Dune sediment budget in m^3/l.m (b). Altitude of the dune foot (green line) related to observed tide level (bleu line) and extreme water level (observed tide level + runup elevation; red line) (c). 1, 2, and 3 indicate the three major storm events of the beginning of January, February, and March.

DISCUSSION AND CONCLUSIONS

Following the previous study of Cariolet and Suanez (2013) this experiment has more deeply examined new parameterization of the runup formula for predicting total swash elevation in the extreme water level calculation. The new set of data used in this study has confirmed the complexity of defining the best slope when the beach exhibits composite-slope and/or a concave profile in macrotidal environment. A best-fit was obtained when beach slope was calculated using observed water level (R^2: 85%; RMSE of 29 cm). This approach, based on sea level changes due to tides and/or storm surges, allows for better consideration of beach slope variations in the context of a concave beach profile. As already indicated by Mayer and Kriebel (1994) the use of fixed bounds (upper or lower bounds) or an averaged planar slope for the calculation of beach steepness is therefore inappropriate when beaches exhibit complex morphology with a composite-slope, especially in a

macrotidal environmental context. If we take into consideration the steep slope face of the upper concave beach ($0.08 > \tan\beta > 1.8$), this experiment also confirms the findings of Nielsen and Hanslow (1991), attesting that the best-fit distribution is proportional to the surf similarity parameter (ξ_o) on intermediate to reflective beaches in agreement with Hunt's formula for runup of regular waves on steep slopes.

Validation of this equation to calculate the runup during the stormy winter 2013-2014 shows very good applicability of this approach. The three significant morphogenetic events of the beginning of January, February and March are very well identified from the extreme water levels and explain very relevant way retreating of the dune. Refering to the Sallenger's model (2000), the type process controling the dune erosion corresponds to the collision regime. In this context, as R_{high} increases, runup collides with the base of the dune inducing erosion. The eroded sand is generally transported out of the system (offshore or longshore transfer) and does not return to recover the dune. In addition to the net erosion of the dune, the upper part of the tidal beach also experiences erosion. Nevertheless, depending on the post-storm weather conditions, eroded sand may be returned to the beach as a post-storm-recovery processes.

ACKNOWLEDGMENTS

This work was supported by the French government through the LabexMER ANR-10-LABX-19-01, and ANR COCORISCO ANR-10-CEPL-0001 research programs. It was also supported by the French Institut (INSU) under-program, SNO-DYNALIT. Tide data came from the REFMAR database (refmar.shom.fr).

LITERATURE CITED

Battjes, J.A., 1974. Surf similarity. *Proceedings of the 14th Conference on Coastal Engineering* (Copenhagen, Denmark), pp. 466–479.

Battjes, J.A., 1971. Run-up distributions of waves breaking on slopes. *Journal of Waterways, Harbors and Coastal Engineering Division*, 97, 91–114.

Blaise, E. ; Suanez, S. ; Stéphan, P. ; Fichaut, B. ; David, L.; Cuq, V. ; Autret, R. ; Houron, J. ; Rouan, M.; Floc'h, F. ; Ardhuin, F. ; Cancouët, R. ; Davidson, R. ; Costa, S., and Delacourt, C., 2015. Bilan des tempêtes de l'hiver 2013-2014 sur la dynamique de recul du trait de côte en Bretagne. *Géomorphologie*, 21(3), 267-292.

Cariolet, J.-M. and Suanez, S., 2013. Runup estimations on a macrotidal sandy beach. *Coastal Engineering*, 74, 11–18.

Guza, R.T. and Thornton, E.B., 1982. Swash oscillations on a natural beach. *Journal of Geophysical Research: Oceans*, 87(C1), 483–491.

Hesp, PA., 2002. Foredunes and blowouts: initiation, geomorphology, and dynamics. *Geomorphology*, 48(1-3), 245–268.

Holman, R.A., 1986. Extreme value statistics for wave run-up on a natural beach. *Coastal Engineering*, 9(6), 527–544.

Holman, R.A. and Sallenger, A.H., 1985. Setup and swash on a natural beach. *Journal of Geophysical Research: Oceans* 90(C1), 945–953.

Hunt, I.A., 1959. Design of seawalls and breakwaters. *Journal of the Waterways and Harbors Division*, 85(3), 123–152.

Kriebel, D.L., 1986. Verification study of a dune erosion model. *Shore & Beach*, 54(3), 13–21.

Longuet-Higgins, M.S. and Stewart, R.W., 1962. Radiation stress and mass transport in gravity waves, with application to 'surf beats'. *Journal of Fluid Mechechanics*, 13(4), 481–504.

Mase, H., 1989. Random Wave Runup Height on Gentle Slope. *Journal of Waterway, Port, Coastal, and Ocean Engineering*, 115(5), 649–661.

Mayer, R.H. and Kriebel, D.L., 1994. Wave runup on composite-slope and concave beaches. *Proceedings of the 24th Coastal Engineering Conference* (Kobe, Japan), pp. 2325–2339.

Nielsen, P. and Hanslow, D.J., 1991. Wave Runup Distributions on Natural Beaches. *Journal of Coastal Research*, 7(4), 1139–1152.

Pye, K. and Neal, A., 1994. Coastal dune erosion at Formby Point, north Merseyside, England: Causes and Mechanisms. *Marine Geology*, 119(1-2), 39–56.

Ruessink, B.G.; Kleinhans, M.G., and van den Beukel, P.G.L., 1998. Observations of swash under highly dissipative conditions. *Journal of Geophysical Research: Oceans*, 103(C2), 3111-3118.

Ruggiero, P.[Holman, R.A.; and Beach, R.A., 2004. Wave run-up on a high-energy dissipative beach. *Journal of Geophysical Research: Oceans*, 109(C06025), 1–12.

Ruggiero, P.; Komar, P.D.; McDougal, W.G.; Marra, J.J., and Beach, R.A., 2001. Wave runup, extreme water levels and erosion of properties backing beaches. *Journal of Coastal Research*, 17(2), 407–419.

Sallenger, A.H., 2000. Storm impact scale for barrier islands. *Journal of Coastal Research*, 16(3), 890–895.

Senechal, N.; Coco, G.; Bryan, K.R., and Holman, R.A., 2011. Wave runup during extreme storm conditions. *Journal of Geophysical Research: Oceans*, 116(C07032), 1–13.

Stockdon, H.F.; Holman, R.A.; Howd, P.A., and Sallenger, A.H., 2006. Empirical parameterization of setup, swash, and runup. *Coastal Engineering*, 53(7), 573–588.

Suanez, S. ; Cariolet, J.-M. ; Cancouët, R. ; Ardhuin, F., and Delacourt, C., 2012. Dune recovery after storm erosion on a high-energy beach : Vougot Beach, Brittany (France). *Geomorphology*, 139–140, 16–33.

Suanez, S. ; Cariolet, J.-M., and Fichaut, B., 2010. Monitoring of recent morphological changes of the dune of Vougot beach (Brittany, France) using differential GPS. *Shore & Beach*, 78(1), 37–47.

Vellinga, P., 1982. Beach and dune erosion during storm surges. *Coastal Engineering*, 6(4), 361–387.

Journal of Coastal Research	SI	75	937-941	Coconut Creek, Florida	2016

Cusp Development on a Gravel Beach

Jinkang Wang† and Douglas J. Sherman‡

†Legal Aid Foundation of Los Angeles
Los Angeles, CA 90019, U.S.A.

‡Department of Geography
Univesity of Alabama
Tuscaloosa, AL 35487, U.S.A.

www.cerf-jcr.org

www.JCRonline.org

ABSTRACT

Wang, J., and Sherman, D.J., 2016. Cusp development on a gravel beach. *In:* Vila-Concejo, A.; Bruce, E.; Kennedy, D.M., and McCarroll, R.J. (eds.), *Proceedings of the 14th International Coastal Symposium* (Sydney, Australia). *Journal of Coastal Research*, Special Issue, No. 75, pp. 937-941. Coconut Creek (Florida), ISSN 0749-0208.

Field experiments were conducted on a gravel foreshore at Portmore Beach, Ireland, to test edge wave, self-organization, and process-based hypotheses. The study site is on a 350 m long, meso-tidal beach, open to waves from the northeast. The gravel foreshore comprises 20-250 mm particles, and cusps are ubiquitous thereon. The foreshore is fronted by a sandy nearshore. Water levels, waves, and currents were measured with an instrument array that comprised seven Marsh-McBirney model 511, bi-directional current meters, and eleven KPSI pressure transducers. Prior to the experiment the study area was graded to remove existing cusps and a video camera installed to monitor morphological change. Beach cusps formed on the morphodynamically reflective foreshore within a few hours of inundation by the rising tide, with H_s = 0.66m, T= 12.2s: breaker heights exceeded 1.1 m and the surf similarity parameter was 0.83 for the foreshore. Mean cusp spacing and width were 7.6 m and 3.6 m. Analysis of phase relationships between waves and currents and the cross-shore structure of spectra indicated the presence of a mode 1, synchronous standing edge-wave that should have generated cusp spacing of 130 m. Analysis of video data indicated a mean swash excursion length of 4.66 m that should have generated cusp spacing of 7.9 m. The results support the self-organization hypothesis and suggest that although edge waves were present, they did not form the beach cusps.

ADDITIONAL INDEX WORDS: *Reflective beach, edge waves, self-organization.*

INTRODUCTION

There is a rich literature, spanning almost two centuries, concerned with the morphology of beach cusps (Palmer, 1834) and the processes associated with their formation. For much of the last three decades it has been mainly argued that cusps are formed on morphodynamically reflective beaches by edge waves (Guza and Inman, 1975; Huntley and Bowen, 1978) or by system self-organization (Almar *et al*., 2008; Coco *et al*., 2003; Werner and Fink, 1993). Field evidence has supported either or both concepts, but has not unambiguously ruled out one or the other (*e.g.*, Ciriano *et al*., 2005).

In this paper we present the results of a field experiment designed originally to test the edge wave vs. system self-organization hypotheses. A morphodynamically reflective gravel beach was instrumented with an array of pressure transducers and current meters to measure relevant hydrodynamics, pre-treated to remove existing cusps, and video-monitored to record subsequent cusp formation. The data are also used to test the empirically-derived Sunamura (2004) model for cusp spacing.

Background

Edge waves may form when beaches are morphodynamically reflective, often characterized using some version of a surf-scaling parameter, ε, such as that suggested by Guza and Inman (1975):

$$\varepsilon = a_b\sigma^2/g\tan^2\beta \qquad (1)$$

where a_b is the wave amplitude at breaking, σ is radian frequency ($2\pi/T$ where T is the incident wave period), g is the gravity constant and β is the beach slope. Guza and Inman (1975) found that reflection capable of generating edge waves occurred if $\varepsilon \leq 2.5$. The alongshore wave length, L_e of a standing edge wave is a function of T and β:

$$L_e = \left(\frac{g}{2\pi}\right) T_e^2 (1+2n)\tan\beta \qquad (2)$$

where T_e is edge wave period and n is the modal number of the edge wave, describing the across-shore structure of the edge wave in terms of the number zero-crossings of the mean water level. The oscillatory drift velocities associated with edge wave motion force divergent sediment transport patterns that generate rhythmic cusp morphology. For a synchronous edge wave, the cusp spacing $L_c = L_e$. For a subharmonic edge wave, $L_c = L_e/2$ (Guza and Inman, 1975). The presence and nature of a standing edge wave can be recognized by the across-shore structure of water surface elevations and by the at-a-point phase relationships between horizontal velocity components and water surface elevations. A standing edge wave has across-shore, u, and alongshore, v, wave-induced velocities that are in phase, and quadrature between η, the water surface elevation, and u and v (*e.g.*, Holman and Bowen, 1979).

The system self-organization model suggests that beach cusps form through initially positive feedback between swash flow, foreshore morphology, and sediment transport that enhances initial topographical irregularities (Coco *et al*., 2003). This forms rhythmic topography that scales with the swash excursion length, L_s, so that $L_c = fL_s$. According to Werner and Fink

DOI: 10.2112/SI75-188.1 received 15 October 2015; accepted in revision 15 January 2016.
*Corresponding author: sherman@ua.edu
©Coastal Education and Research Foundation, Inc. 2016

(1993) the value of the constant of proportionality, f, is between 1 and 3. Takeda *et al*. (1986), from their laboratory experiments, found a best-fit value of f = 1.2, for example, and Coco *et al*. (1999) found a best-fit value of 1.63.

Under typical surfzone and foreshore conditions, edge wave and self-organization models predict similar morphologies, making it difficult to discern the actual formative process from cusp spacing alone (Allen *et al*., 1996: Coco *et al*., 1999; Werner and Fink, 1993). There is some evidence from field experiments that cusps have been initiated without some forms of edge wave motion being detected (*e.g*., Almar *et al*., 2008; Ciriano *et al*., 2005; Masselink *et al*., 2004). The findings of field studies, however, remain somewhat ambiguous with regard to cusp formation processes because of potential template influences of pre-existing cusp patterns that interact with swash, for example, or because of incomplete hydrodynamic information.

A third cusp spacing model was developed by Sunamura (2004), based on the kinematics of swash and particle-size, D, dependent energy dissipation:

$$L_c = A\varnothing T(gH)^{0.5} \qquad (3)$$

where A is an empirical constant that averages 1.35, $\varnothing$ is the grain-size effect ($\varnothing = exp(-0.23D^{0.55})$), and H is the nearshore wave height. The model was successfully tested against Masselink's (1999) field results, and was found by Vousdoukas (2012) to provide better cusp spacing predictions than either edge wave or self-organization models.

In order to test the alternative models of cusp formation and their ability to explain cusp spacing in natural environments, measurements must be obtained to detect and characterize edge waves, and to represent foreshore morphology and sediment characteristics. We designed and implemented such an experiment at Portmore Beach, Malin Head, Donegal, Ireland in June, 1997 (Figure 1).

Portmore Beach is approximately 350 m long, with a gravel foreshore (D = 20 – 250 mm) approximately 30 m wide and 5 m high, perched on a sand apron (D = 0.15 – 0.25 mm). Maximum gravel slopes are about 13°, but are more commonly 5-7 ° on the ..lower foreshore. The nearshore sands slope at 1-2° (Sherman *et al*., 1993). The beach is open to Atlantic swell from the northeast, with typical breaker heights of 1 m and periods of 10 s. Tides are semi-diurnal with spring and neap ranges of 3.2 m and 1.2 m. Typical foreshore morphology comprises several tiers of cusps with spacing ranging from about 5 m to 50 m, with the largest cusps highest on the profile, where they are reworked only by extreme storms. The lower cusps are reworked during average wave conditions during high spring tides. Additional details for the site are presented in Wang (2003) and Sherman (1991).

METHODS

We deployed in an array designed to capture the alongshore and across shore structure of standing edge wave motion (Figure 2) comprising seven Marsh-McBirney bidirectional current meters (labelled 1 through 7 in Figure 2) and eleven KPSI pressure transducers (labelled 20 through 30). Each current meter was collocated with pressure transducer. All instruments were hard-wired to a data acquisition system and sampled at 2 Hz. A set of range poles was installed along the gravel profile to allow scaling of video of swash runup and beach response.

On June 18, the lower foreshore was graded to remove the cusp morphology (similar to the "Dozer Duck" experiments (Coco *et al*., 2003) and the gravels reworked with shovels to approximate a planar surface (Figure 3 A&B). Special attention was given to produce a straight gravel-sand boundary. After cusps formed during the morning high tide of June 19, the beach was surveyed, sediment samples obtained from the cusps and sand apron, and the beach re-graded. After the next high tide, the process was repeated.

Wave and current data were used to obtain spectral and co-spectral information to estimate wave heights and periods and phase relationships between waves and currents. Sediment samples were measured for size and shape analysis.

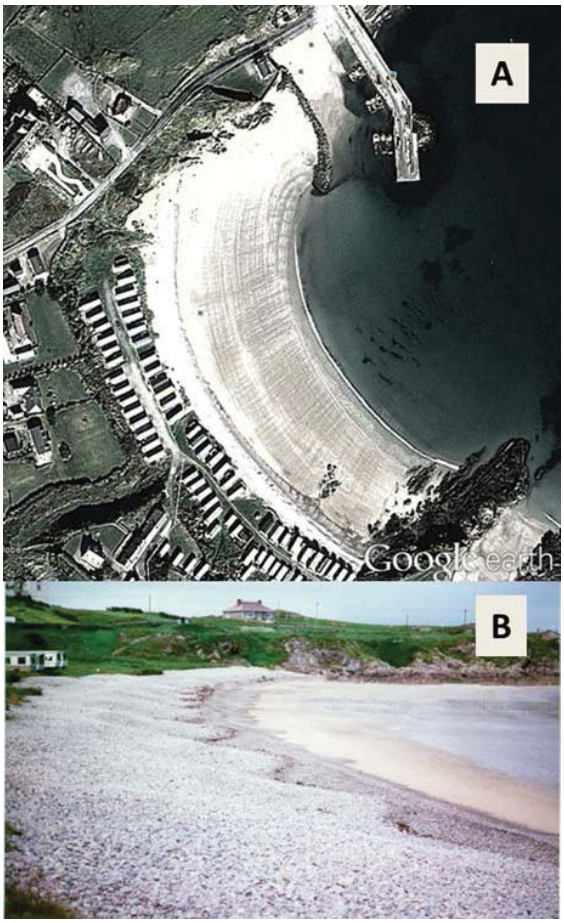

Figure 1. The study site at Portmore Beach. (A) Google™earth image of beach at low tide with ~ 75 m wide sand apron seaward of (bright) gravel foreshore. (B) Typical gravel cusp configurations near the center of the beach.

RESULTS

A moderate storm occurred during late June 18 and early June 19. On the 19th we began recording data at 04:42, with measured breaker heights up to 1.2 m with periods of 12.2 s. At high tide, waves were collapsing/plunging 3 – 4 m offshore of the toe of the gravel and the lower foreshore was inundated. At 05:00 there was no visual indication of cusp formation or of alongshore periodicity of run up (Figure 3C). By 06:00 there was obvious, but topographically subtle, cusp development and analogously variable swash motion. The cusp relief increased until about 08:00 (Figure 3D) when the morphology stabilized. Pressure Transducer 28 failed during the storm. Key information for the detection of edge waves include: for T = 12.2 s, wave data indicated a spectral trough at x = 6 m (x is distance offshore from base of gravel foreshore), while the current data showed a spectral peak in v. There was a 161^0 phase difference between wave motion recorded at PT24 and PT 30. Phase and coherence data for the remaining six instrument pairs (Table 1) are suggestive of the presence of a standing, mode 1, synchronous edge-wave between 05:00 and 05:59, the time of cusp initiation. Edge wave length was estimated with slope values from the sand apron and the foreshore. This produced L_e values of 38.4 and 129.2 m. Using the CERC (1984) formula, the estimated edge wave amplitude was 0.09 m.

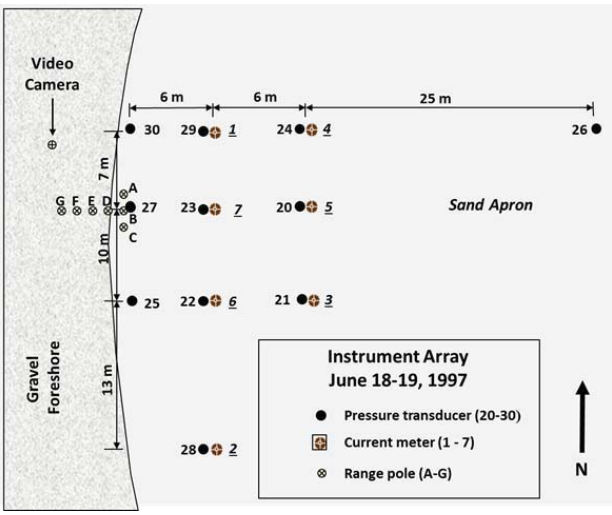

Figure 2. Schematic of experimental design used after foreshore grading. Arhythmic alongshore spacings were used to maximize detection potential for standing edge waves.

Analysis of swash video indicated a mean period of 11.9 with a spectral peak at 12.8 s, both values broadly consistent with the 12.2 s wave period. Mean uprush and backwash velocities were 1.08 ms^{-1} and 0.61 ms^{-1}, and mean and significant swash lengths were 4.66 m and 5.91 m. Swash pattern was horn-divergent and uprush at horns and bays was in phase.

Post-storm surveys made at low tide indicated that cusps on the lower foreshore had mean spacing (L_c) = 7.6 m and width = 3.6 m. Maximum alongshore relief (horn to trough) was about 0.3 m. Mean grain size of sediment from the sand apron was about 0.17 mm. Average lengths of a, b, and c axes of gravel sampled from the cusps were 42, 32, and 18 mm, respectively. Note that additional supporting hydrodynamical, morphological, and sedimentological data and interpretation are detailed in Wang (2003).

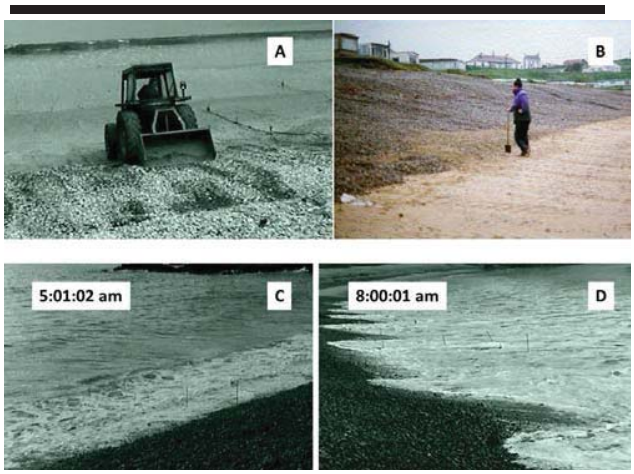

Figure 3. (A) Machine grading of cusps. (B) Hand leveling of surface and reworking the gravel-sand boundary. (C) June 19 Video image of foreshore and uprush before cusp initiation. (D) June 19 cusp morphology after three hours of gravel movement.

Similar results were obtained during the following high tide when cusps were formed on the regraded gravel beach. We began recording data when the rising tide reached the base of the gravel, at about 16:00. Breaking was collapsing/plunging about 3 – 4 m from the gravel, with breaker height about 1.1 m at periods of 10.7 s. Once again cusp formation was rapid, with distinctive morphology evident within about 120 minutes of reworking by swash. The new cusps on the lower foreshore had mean spacing (L_c) = 6.8 m and width = 3.2 m. Maximum alongshore relief (horn to trough) was about 0.4 m. There was

Table 1. *Phase (degrees) and coherence squared (coh.^{2})data, September 19, 1997. Coh.^{2}>0.25 is significant at 0.99. CM = current meter and PT = pressure transducer.*

Location	u-v phase (coh.^{2})	u-η phase (coh.^{2})	v-η phase (coh^2)
X = 6 m			
05:59			
CM1-PT29	178 (0.87)	-139 (0.40)	-43 (0.28)
CM6-PT22	115 (0.18)	8 (0.20)	-103 (0.13)
CM7-PT23	178 (0.91)	-156 (0.32)	-21 (0.26)
18:26			
CM1-PT29	174 (0.95)	112 (0.87)	62 (0.86)
CM6-PT22	-25 (0.61)	88 (0.91)	-109 (0.65)
CM7-PT23	180 (0.41)	108 (0.87)	76 (0.36
X= 12 m			
05:59			
CM3-PT21	177 (0.89)	98 (0.91)	78 (0.86)
CM4-PT24	180 (0.87)	106 (0.93)	74 (0.77)
CM5-PT20	175 (0.78)	106 (0.89)	68 (0.70)

evidence of synchronous, mode 1 standing edge-wave motion in the current meter and pressure transducer pairs located 6 m seaward of the foreshore (Table 1), with L_e = 29.0 or 99.4 m and an amplitude of 0.09 m. Swash video was not obtained for this period because of a logging error.

DISCUSSION

The data recorded during the high tides on June 19 allow us to compare and assess the predictions made by the edge wave, self-organization, and Sunamura models for beach cusp formation (Table 2). The cusp spacing associated with a synchronous edge wave is the same as the edge wave length. For the morning and evening high tides there are two potential edge wave lengths that depend on whether the slope of the sand apron or the gravel foreshore is used in equation 2. Similarly, for the Sunamura (2004) model, there are two possible cusp spacings, depending on whether sand size or gravel size (b axis) is used in equation 3. In table 2, the resulting predictions are labeled L_c (gravel) and L_c (sand) to distinguish the data used to estimate L_c.

Table 2. *Predicted and observed beach cusp spacing, June 19. The designations of gravel and sand refer to the environment represented by the data used in the models. Swash refers to predictions based on swash length (mean and significant excursions) .*

Model	Lc (gravel)	Lc (sand)	Lc (swash)	Lc
Edge Wave				
AM	129.2 m	38.4 m		
PM	99.4 m	29.0 m		
Sunamura				
AM	11.9 m	52.0 m		
PM	10.0 m	43.6		
Self-Organization				
mean			7.6 m	
significant			9.6 m	
Observed				
AM				7.6 m
PM				6.8 m

The data suggest that the system self-organization model, using mean swash length, produces results that are most consistent with the observed cusp spacing, although the Sunamura predictions based on the gravel particle b-axis length closely approximate the observations. It is unfortunate that the lack of video data for the afternoon of June 19 precluded measurement of swash. However, given that the sediment sizes and slopes remained essentially constant and breaker height was minimally different, only the decrease in peak period would have contributed substantially to a change in runup. The runup model of Lorang (2002) for gravel beaches and that of Stockdon *et al*. (2006) for sandy beaches each suggest that there would be a decrease in runup from the morning to the afternoon of about 10%, based on the decreased wave height and period. This should be reflected in a similar decrease in cusp spacing according to the self-organization model, very close to what was observed.

There is some ambiguity in the length scales associated with the edge waves. During the afternoon high tide on June 18, the pressure transducer measurements indicated the presence of a mode 1, subharmonic edge wave. The phase relationships correspond with those associated with edge wave motion, the period, 14.6 s, was twice that of the incident waves, and the across shore structure of the amplitude matches the mode 1 configuration with an antinode at x = 17.9 m (Figure 4). A similar modal structure could not be reproduced for synchronous edge waves on June 19, although the spectra and cospectra are suggestive of mode 1 motion. It is possible, therefore, that a mode 0 edge wave was present. In that case, the respective edge wave lengths would have been one third of those reported in Tables 1 and 2, and this would have produced cusps with spacing as short as 12.8 m in the morning and 9.7 m in the afternoon.

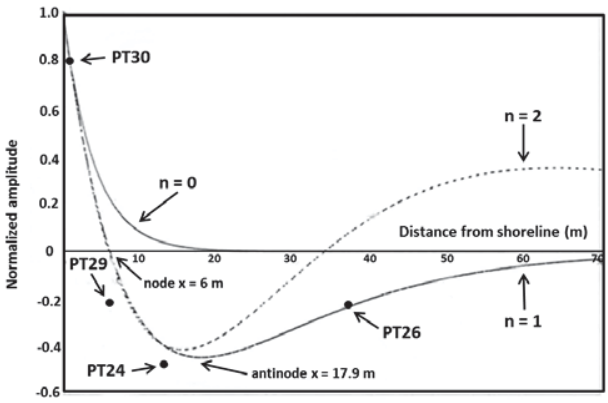

Figure 4. The across shore structure of edge wave amplitude as measured at PT30, PT29, PT24, and PT26 on June 18. Curves depict structure associated with the three lowest modes (n) of edge waves.

There is a theoretical argument that could support the occasional production of even smaller cusps by synchronous, standing edge waves. During storm conditions, if the edge wave amplitude is large relative to that of incident waves, cusps with lengths one half of the edge wave length could be formed (Bowen, 1972; Holland and Holman, 1996). This suggests that cusps with L_c = 6.4 and 4.9 m could have been formed during this storm. The edge wave amplitudes on June 19 at Portmore Beach, however, were only about 20% of the incident wave amplitude, thus negating this argument.

Time and resources did not allow additional grading and further sampling, so that our tests were admittedly limited. Nevertheless, our results suggest that the edge wave model is not viable for the cusp formation documented here and the system self-organization model is. The Sunamura model produces results that are quite similar to our observations and the self-organization model. We note that the process elements in the former are essentially those that control runup, so that the similarity is not coincidental.

In our tests of the self-organization concept we were unable to reproduce the time-scale of cusp formation as observed. We developed a simulation model similar to that of Coco *et al.* (2003) and Werner and Fink (1993) based on the conditions at Portmore Beach. For the swash velocities observed, the simulation indicated that the time required to reproduce the observed morphology was of the magnitude of 10^2 hours, as

opposed to the few hours needed in the field. Alternatively, we could drive cusp formation in a few hours if we increased swash velocities to the order of 10 ms^{-1}, about ten times that measured. We do not know how to reconcile these results with our observations. Because we graded only the surface gravels to remove cusps, it is possible that there remained buried templates within the beach, and the correspondence with contemporary processes was solely coincidental.

CONCLUSIONS

The formation of cusps on the gravel foreshore at Portmore Beach does not appear to have been driven by edge waves, even though our data indicate that mode 1, synchronous edge waves were present. We conclude, therefore, that cusp formation is driven by swash processes similar to those represented explicitly in the system self-organization models that link cusp spacing to the length of swash excursion, and implicitly in the runup-based model of Sunamura (2004). Both of the latter produce results that are in reasonable agreement with our observations. Our small sample size makes it difficult to argue more strongly for one approach over the other.

ACKNOWLEDGMENTS

This project was support by the Office of Naval Research (Award No. N000149710810) and a Doctoral Dissertation Improvement Grant from the National Science Foundation (Award No, 9628727). We gratefully acknowledge the tremendous field support provided by Eugene Farrell, James McDermott, and Alon Yaari. Special thanks to Derek Jackson and his team from the University of Ulster for support with the topographic surveys of the cusps. Professor Bernard Bauer made valuable comments on the dissertation upon which this paper is based. Errors or omission are our responsibility.

LITERATURE CITED

Allen, J. R.; Psuty, N. R.; Bauer, B. O., and Carter, R. W. G., 1996. A field data assessment of contemporary models of beach cusp formation. *Journal of Coastal Research*, 12(3), 622-629.

Almar, R.; Coco, G.; Bryan, K. R.; Huntley, D. A.; Short, A. D., and Senechal, N., 2008. Video observations of beach cusp morphodynamics. *Marine Geology*, 254(3), 216-223.

Bowen, A.J., 1972. Edge waves and the littoral environment. *Proceedings, 13th International Conference on Coastal Engineering, ASCE*, 1313-1320.

CERC, 1984. *Shore Protection Manual*. Coastal Engineering Research Center, *U.S. Army Corps of Engineers*, Vicksburg, VA.

Ciriano, Y.; Coco, G.; Bryan, K. R., and Elgar, S., 2005. Field observations of swash zone infragravity motions and beach cusp evolution. *Journal of Geophysical Research: Oceans*, 110, C02018, doi:10.1029/2004JC002485.

Coco, G.; O'Hare, T. J., and Huntley, D. A., 1999. Beach cusps: a comparison of data and theories for their formation. *Journal of Coastal Research*, 15(3), 741-749.

Coco, G.; Burnet, T. K.; Werner, B. T., and Elgar, S., 2003. Test of self-organization in beach cusp formation. *Journal of Geophysical Research: Oceans*, 108(C3), 3101, doi:10.1029/2002JC001496.

Guza, R. T. and Inman, D. L., 1975. Edge waves and beach cusps. *Journal of Geophysical Research*, 80(21), 2997-3012.

Holland, K. T. and Holman, R. A., 1996. Field observations of beach cusps and swash motions. *Marine Geology*, 134(1), 77-93.

Holman, R. A and Bowen, A. J., 1979. Edge waves on complex beach profiles. *Journal of Geophysical Research: Oceans*, 84(C10),6339-6346.

Huntley, D. A. and Bowen, A. J, 1978. Beach cusps and edge waves. *Proceedings, 16th International Conference on Coastal Engineering*, ASCE, pp. 1378-1393.

Lorang, M. S., 2002. Predicting the crest height of a gravel beach. *Geomorphology*, 48(1), 87-101.

Masselink, G., 1999. Alongshore variation in beach cusp morphology in a coastal embayment. *Earth Surface Processes and Landforms*, 24(4), 335-347.

Masselink, G.; Russell, P.; Coco, G., and Huntley, D., 2004. Test of edge wave forcing during formation of rhythmic beach morphology. *Journal of Geophysical Research: Oceans*, 109(C6). C06003, doi:10.1029/2004JC002339.

Palmer, H. R., 1834. Observations on the motions of shingle beaches. *Philosophical Transactions of the Royal Society of London*, 124, 567-576.

Sherman, D. J., 1991. Gravel beaches. *Research & Exploration*, 7(4), 442-452.

Sherman, D. J.; Orford, J. D. and Carter, R. W. G., 1993. Development of cusp-related, gravel size and shape facies at Malin Head, Ireland. *Sedimentology*, 40(6), 1139-1152.

Stockdon, H. F.; Holman, R. A.; Howd, P. A., and Sallenger, A. H., 2006. Empirical parameterization of setup, swash, and runup. *Coastal Engineering*, 53(7), 573-588.

Sunamura, T., 2004. A predictive relationship for the spacing of beach cusps in nature. *Coastal Engineering* 51(8): 697-711.

Takeda, I.; Terasaki, T. and Sunamura, T., 1986. Formation and spacing of beach cusps on a laboratory beach. *Annual Report of the Institute of Geosciences*, University of Tsukuba, 12, 55-58.

Vousdoukas, M. I., 2012. Erosion/accretion patterns and multiple beach cusp systems on a meso-tidal, steeply-sloping beach. *Geomorphology*, 141, 34-46.

Wang, J., 2003. *The Generation of Cusps on Gravel Beaches: An Evaluation of Edge Wave and Self-organization Hypotheses*. (Doctoral dissertation, University of Southern California), 161 pp.

Werner, B. T.; and Fink, T. M., 1993. Beach cusps as self-organized patterns. *Science*, 260(5110), 968-971.

Journal of Coastal Research	SI	75	942-946	Coconut Creek, Florida	2016

Investigation of Wave Breaking Turbulence in Morphodynamic Modelling

Hyun-Doug Yoon†, Minsang Cho†, and Sang-Young Son‡*

†Dept. Of Civil and Environmental Eng.
Myongji University
Yongin, Korea

‡School of Civil, Environmental and Architectural Eng., Korea University, Seoul, Korea.

www.cerf-jcr.org

www.JCRonline.org

ABSTRACT

Yoon, H.-D.; Cho, M., and Son, S.-Y., 2016. Investigation of wave breaking turbulence in morphodynamics modelling. *In:* Vila-Concejo, A.; Bruce, E.; Kennedy, D.M., and McCarroll, R.J. (eds.), *Proceedings of the 14th International Coastal Symposium* (Sydney, Australia). *Journal of Coastal Research*, Special Issue, No. 75, pp. 942-946. Coconut Creek (Florida), ISSN 0749-0208.

The effect of wave breaking turbulence on morphodynamics was investigated using Xbeach. To achieve this goal, the results from Xbeach simulation were compared with a large-scale laboratory experiment (CROSSTEX) and a numerical model (COBRAS) which is based on Reynolds-Averaged Navier-Stokes (RANS) equation. To incorporate the impact of wave breaking turbulence, a new near-bed turbulence estimation was suggested in addition to the existing turbulence options in Xbeach. Hydrodynamics results from Xbeach were generally in a good agreement with CROSSTEX and COBRAS. However, morphodynamics from Xbeach did not match well with CROSSTEX nor COBRAS, especially in the vicinity of a longshore bar. Most bathymetric changes occurred in the inner surf zone or swash zone, showing dune erosion. The possible causes of disagreement can be related to the limitation of the depth-averaged advection-convection equation used for sediment transport in Xbeach. Also, long wave motions dominates morphologic changes near the dune area. It is concluded that more investigation is still required to better simulate morphodynamics.

ADDITIONAL INDEX WORDS: *Xbeach, bathymetric change, longshore bar, coastal processes.*

INTRODUCTION

Wave breaking turbulence and sediment transport are important processes for understanding hydrodynamics and morphodynamics in the surf zone. Wave breaking turbulence enhances sediment suspension and vertical mixing, and thus affects beach profile change. However, interaction between hydrodynamics and morphodynamics is still unclear due to its complexity.

A number of researchers have tried to elucidate the effect of wave breaking turbulence on sediment suspension. Nadaoka *et al*. (1989) observed that "obliquely descending eddies" generated by wave breaking reached the bottom and caused sediment suspension in a laboratory experiment. Voulgaris and Collins (2000) argued that sediment suspension is highly dependent on wave breaking rather than bottom boundary layer turbulence. Aagaard and Hughes (2010) observed that coherent vortices generated by wave breaking significantly affect sediment suspension from field measurements. Findings of the impact of wave breaking turbulence on sediment suspension were considered in the cross-shore sediment transport modelling. For example, Roelvink and Stive (1989) examined the stirring effect due to breaking-induced turbulent flow on the energetic-based bar-generating model and achieved an improved beach profile prediction. Kobayashi *et al*., (2005) also added a wave energy dissipation term in the sediment transport model and obtained improved results.

The open source model, Xbeach, is widely used for the beach modelling. This model consists of formulations for short wave envelope propagation, nonstationary shallow water equations, sediment transport and bed updates. In this model, the depth-averaged advection diffusion equation was adopted for sediment transport model. Then, the gradient of suspended sediment concentration from the sediment transport equation was used for the calculation of morphological updates. For the calculation of equilibrium sediment concentration, the averaged velocity and wave induced oscillating velocity were combined to obtain the interaction between hydrodynamics and morphodynamics (van Thiel de Vries, 2009).

Recently, wave breaking turbulence was considered in the model which may be significant in modelling surf zone processes (Xbeach manual, 2015). However, it is still required more thorough study of the effect of wave breaking turbulence on morphodynamics.

In this context, the present study investigates the effects of wave breaking turbulence on sediment transport and morphologic changes using Xbeach. Numerical simulation results from Xbeach will be compared with large-scale laboratory experiment data, CROSSTEX (CROss-Shore Sediment Transport EXperiment) (Yoon and Cox, 2010). Also, Hydrodynamics from Xbeach is also compared with COBRAS (Cornell BReaking waves And Structures) model which is based on RANS (Reynolds-Averaged Navier-Stokes) equation. Yoon *et al*., (2015) investigated nearshore hydrodynamics over the

DOI: 10.2112/SI75-189.1 received 15 October 2015; accepted in revision 15 January 2016.
*Corresponding author: sson@korea.ac.kr
©Coastal Education and Research Foundation, Inc. 2016

evolving bathymetry during CROSSTEX, with numerical simulation using COBRAS.

METHODS

The simulation results of Xbeach were compared with a large-scale laboratory experiment (CROSSTEX) and a numerical model based on RANS equations (COBRAS) for validation. In this section, brief descriptions of Xbeach, CROSSTEX, and COBRAS are provided.

Xbeach

Xbeach consists of formulations for short wave envelope propagation, nonstationary shallow water equations, sediment transport and bed updates. The depth-averaged advection diffusion equation was adopted for sediment transport model. Then, the gradient of suspended sediment concentration from the sediment transport equation was used for the calculation of morphological updates. The entrainment or deposition of sediment is determined by the mismatch between the actual sediment concentration C and the equilibrium concentration C_{eq} thus representing the source term in the sediment transport equation. In Xbeach, to account for wave breaking turbulence, the orbital velocity is adjusted as follows (van Thiel de Vries, 2009) .

$$u_{rms,2}^2 = u_{rms}^2 + 1.45k_b \tag{1}$$

where $u_{rms,2}$ is the adjusted orbital velocity, u_{rms} is the root-mean-square of cross-shore velocity, k_b is turbulent kinetic energy (TKE) due to breaking of short waves. Three options were available for estimating k_b wave averaged near-bed turbulence energy, bore-averaged near-bed turbulence energy, and not taking into account the turbulence variance at the bed (Xbeach Manual, 2015).

In addition to these options, we applied a depth-averaged TKE based on the observation from CROSSTEX. Yoon and Cox (2010) found that the depth-averaged TKE is in proportional to wave energy dissipation by bores (Thornton and Guza, 1983). The wave energy dissipation by bores is given as:

$$\langle \varepsilon_b \rangle = \frac{3\sqrt{\pi}}{16}\rho g B^3 \bar{f} \frac{H_{rms}^{\ 5}}{\gamma^2 h^3}\left[1 - \frac{1}{\left(1+\left(H_{rms}/\gamma h\right)^2\right)^{5/2}}\right] \tag{2}$$

where, is the water density, g is the gravity acceleration, B is the breaker coefficient, $\bar{f}$ is the average frequency of waves, H_{rms} is the root-mean-square wave height, γ is the depth-limited breaking coefficient, h is the water depth. We used f_p =0.25 Hz for $\bar{f}$. From the linear relationship between the depth-averaged $\bar{k}$ and $(\langle \varepsilon_b \rangle / \rho)^{2/3}$ observed in Yoon and Cox (2010), $(\langle \varepsilon_b \rangle / \rho)^{2/3}$ was used for near-bed turbulence option in addition to the existing near-bed turbulence option in Xbeach. The total near-bed turbulence options in the present study are tabulated in Table 1. In Table 1, $\bar{k}_s$ is time-averaged TKE near water surface, L_{mix} is the mixing length, T_{rep} is the representative wave period, T_{bore} is the period of bores.

Table 1. *Near-bed turbulence option*

Option	Equation
Bore-averaged	$k_b = \dfrac{\bar{k}_s}{\exp(h/L_{mix})-1}$
Wave-averaged	$k_b = \dfrac{\bar{k}_s \cdot T_{rep}/T_{bore}}{\exp(h/L_{mix})-1}$
None (No near-bed turbulence)	-
Present study	$(\langle \varepsilon_b \rangle / \rho)^{2/3}$

Then, $u_{rms,2}$ is used for the equilibrium sediment concentration suggested by Soulsby- Van Rijn (1997) and van Rijn (1984)

$$C_{eq,b} = \frac{A_{sb}}{h}\left(\sqrt{v_{mg}^{\ 2} + 0.018\frac{u_{rms,2}}{C_d}} - U_{cr}\right)^{2.4} \tag{3}$$

$$C_{eq,s} = \frac{A_{ss}}{h}\left(\sqrt{v_{mg}^{\ 2} + 0.018\frac{u_{rms,2}}{C_d}} - U_{cr}\right)^{2.4} \tag{4}$$

where, A_{sb} and A_{ss} are the bed load and suspended load coefficients, v_{mg} is the velocity magnitude, C_d is the drag coefficient, and U_{cr} is the critical velocity.

For the simulations, some important input parameters were tabulated in Table 2. For other parameter, default values were used. The grid size was 1 cm both in *x, z* direction.

Table 2. *Input parameters for simuation of Xbeach*

Input parameter	Value
Morphological acceleration factor (morfac)	6
Wave boundary	jons
Significant wave height (m)	0.6
Peak frequency (Hz)	0.25
Boundary conditions	- Absorbing-generating (seaward, landward) - Wall (left and right)

CROSSTEX

CROSSTEX is the large-scale laboratory experiment conducted in the large wave flume at HWRL (104 m long, 3.7 m wide, and 4.6 m deep) at Oregon State University. A natural beach was installed using approximately 800 m^3 of Oregon beach sand with a median grain diameter (d_{50}) of 0.22 mm. Two types of irregular waves were generated to simulate the different types of morphological cases: the formation of a sand bar (erosive case) and restoration of a planar beach (accretive case). For the erosive conditions (significant wave height: 0.6 m, peak wave period: 4.0 s, peak enhancement: 3.3), the vertical instrument array was held fixed, while the bathymetry transformed from essentially a planar beach to a barred beach.

For each run, the same irregular waves were generated by the wavemaker for 15 min. In the present study, these six erosive runs (total elapsed time = 90 min) were adopted. More details about the experiment are referred to Yoon and Cox(2010).

COBRAS

The COBRAS model is a depth- and phase-resolving wave propagation model based on the RANS equation, where the instantaneous velocity and pressure fields are decomposed into mean and turbulence components:

$$\frac{\partial \langle u_i \rangle}{\partial x_i} = 0 \tag{5}$$

$$\frac{\partial \langle u_i \rangle}{\partial t} + \langle u_j \rangle \frac{\partial \langle u_i \rangle}{\partial x_j} = -\frac{1}{\rho}\frac{\partial \langle p \rangle}{\partial x_i} + g_i + \frac{1}{\rho}\frac{\partial \langle \tau_{ij} \rangle}{\partial x_j} - \frac{\partial \langle u_i' u_j' \rangle}{\partial x_j} \tag{6}$$

where u is the instantaneous velocity, p is the pressure, and the angle brackets(< >) is the mean component, and the prime is the turbulent component. The k–ε equations for turbulent kinetic energy (TKE) per unit mass, k, and the turbulent dissipation rate, ε, are given as follows:

$$\frac{\partial k}{\partial t} + \langle u_j \rangle \frac{\partial k}{\partial x_j} = \frac{\partial}{\partial x_j}\left[\left(\frac{\nu_t}{\sigma_k} + \nu\right)\frac{\partial k}{\partial x_j}\right] - \langle u_i' u_j' \rangle \frac{\partial \langle u_i \rangle}{\partial x_j} - \varepsilon \tag{7}$$

$$\begin{aligned}\frac{\partial \varepsilon}{\partial t} + \langle u_j \rangle \frac{\partial \varepsilon}{\partial x_j} &= \frac{\partial}{\partial x_j}\left[\left(\frac{\nu_t}{\sigma_\varepsilon} + \nu\right)\frac{\partial \varepsilon}{\partial x_j}\right] \\ &- C_{1\varepsilon}\frac{\varepsilon}{k}\nu_t\left(\frac{\partial \langle u_i \rangle}{\partial x_j} + \frac{\partial \langle u_j \rangle}{\partial x_i}\right)\frac{\partial \langle u_i \rangle}{\partial x_j} \\ &- C_{2\varepsilon}\frac{\varepsilon^2}{k}\end{aligned} \tag{8}$$

where i, j = 1,2 for a 2-D flow field, ρ is the fluid density, g_i is the i-th component of the gravitational acceleration, $<\tau_{ij}>$ is the viscous stress tensor of the mean flow, and ν_t is the eddy viscosity. Yoon *et al.*, (2015) applied COBRAS to CROSSTEX data and compared hydrodynamic parameters between them.

RESULTS

Figure 1 shows cross-shore distribution of hydrodynamic results of Xbeach(with near-bed turbulence options), COBRAS(RANS Equation) and CROSSTEX (large-scale laboratory experiment). Results from COBRAS and CROSSTEX were depth-averaged to compare with Xbeach results. Note that the coordinate system is x positive onshore and z positive up, with x=0 m at the wave maker and z=0 m at the still water level. In Figure 1(a), the depth-averaged cross-shore mean velocities (U_{mean}) of all near-bed turbulence options and COBRAS show similar values. Exceptionally, CROSSTEX data shows much larger mean cross-shore velocity in the offshore direction because the velocity was measured in the lower region of water column (within 50 cm from the bed). In Figure 1(b), the root-mean-square cross-shore velocity (U_{rms}) shows a good agreement between Xbeach, COBRAS, and CROSSTEX. It was found that COBRAS and CROSSTEX slightly overestimated U_{rms} at x~60 m. In Figure 1(c), near-bed turbulence (k_b) for bore-averaged option shows much larger values compared to others. In Figure 1(d), the bathymetric changes are shown. However, Xbeach model with all options does not simulate the bathymetric changes of the longshore bar.

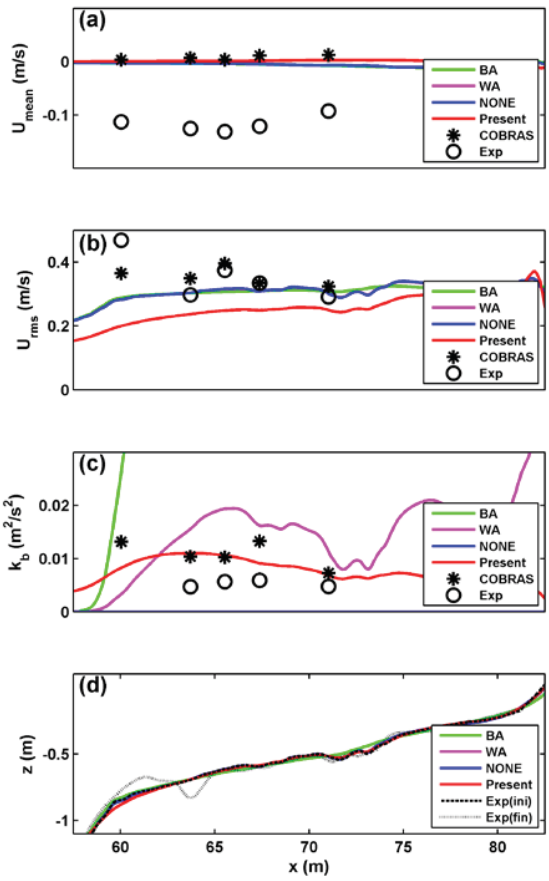

Figure 1. Cross-shore distributions of (a) depth-averaged mean cross-shore velocity, (b) depth-averaged root-mean-squared and (c) near-bed turbulence intensity and (d) bathymetry. BA represents Bore-Averaged. WA represents Wave-Averaged.

Figure 2 shows cross-shore distribution of sediment transport results, such as depth-averaged sediment concentration (C), depth-averaged equilibrium sediment concentration (C_{eq}), and depth-averaged cross-shore sediment flux(q_x). In Figure 2a and 2b, The maximum values of depth-averaged sediment concentration (C) and depth-averaged equilibrium sediment concentration (C_{eq}) were located far inner surf zone near dune, implying that most bathymetric changes occurred in this region as a form of dune erosion. Comparing the cases with near-bed turbulence options, the results from bore-averaged option is larger than other cases by a factor of 2. As expected, results with no turbulence option shows the smallest C and C_{eq} because

there is little stirring effect of wave breaking turbulence. In Figure 2c, strong offshore sediment flux (negative q_x) was found near the bar crest and inner surf zone.

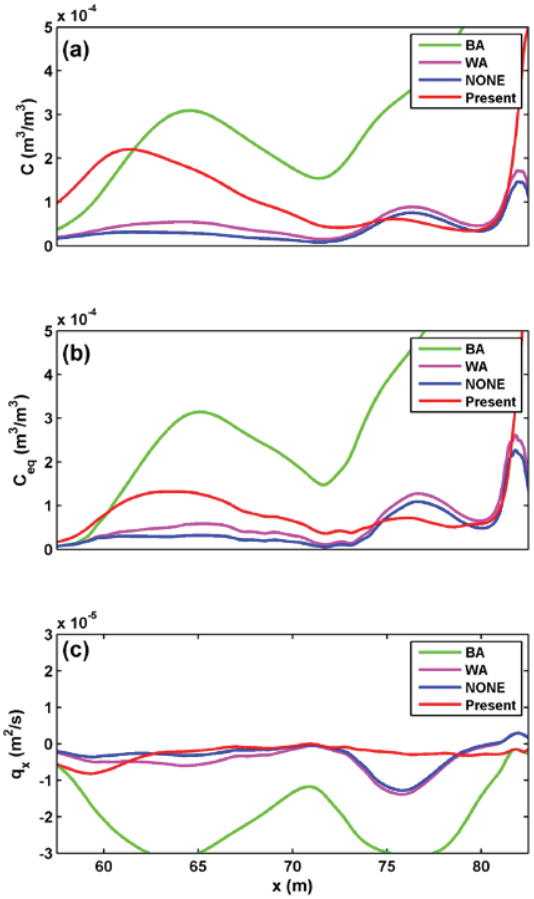

Figure 2. Cross-shore distributions of (a) depth-averaged sediment concentration, (b) depth-averaged equilibrium sediment concentration and (c) depth-averaged sediment flux in cross-shore direction. BA represents Bore-Averaged. WA represents Wave-Averaged.

Figure 3 shows the bathymetric changes with options used in this study. Xbeach results are compared with CROSSTEX data after 2700 s and 5400 s. Note that still water level (SWL) is located at z=0. The bathymetric changes mostly occurs inner surf zone in the case of bore-averaged option (Figure 3a). For wave-averaged and no turbulence options, there is little profile changes (Figure 3b and 3c). With modified near-bed turbulence option suggested in the present study, bathymetric changes are shown in the bar crest region (Figure 3d). However, the longshore bar feature was not successfully simulated for all near-bed options.

Comparing hydrodynamics, sediment transport, and bed updates resulted from Xbeach with CROSSTEX and COBRAS, it is found that hydrodynamics were generally in a good agreement. However, Xbeach could not successfully simulate the bed updates despite its near-bed turbulence consideration. Especially, longshore bar, which plays a significant role in nearshore processes in which strong wave breaking occurs, was not successfully generated with Xbeach. This is contrast to the results of Roelvink *et al.*, (2009) in which a longshore bar was successfully simulated.

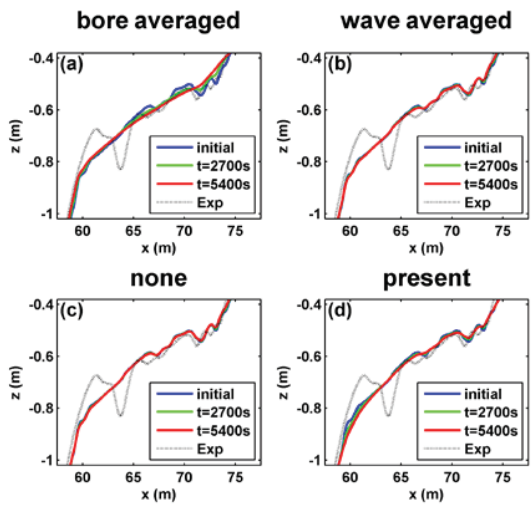

Figure 3. Bathymetric change with near-bed turbulence options: (a) bore-averaged, (b) wave-averaged, (c) no near-bed turbulence and (d) options given in present study

DISCUSSION

Since Xbeach was focused on the simulation of the bathymetry changes near dune, the longshore bar generation was not successfully simulated despite incorporating the effect of wave breaking turbulence. Most of bathymetric changes occur near far inner surf zone as a form of dune erosion as shown in Figure 4. This is due to long wave motions which are dominant inner surf zone.

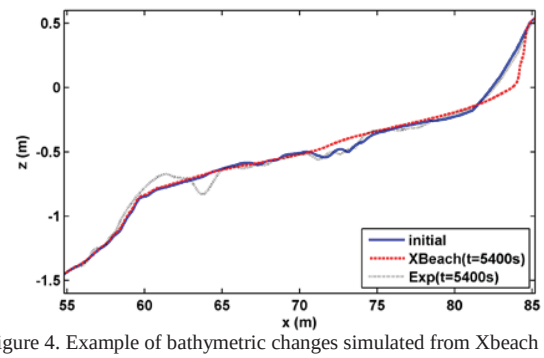

Figure 4. Example of bathymetric changes simulated from Xbeach

Sediment transport in Xbeach is modeled with a depth-averaged advection-diffusion equation with a source-sink term. This source-sink term are based on the difference of sediment concentration (C) from equilibrium sediment concentration (C_{eq}). However, because of the original limitation of the depth-averaged equation, the vertical distribution of sediment concentration and velocity cannot be carefully considered in the model. Especially, at the bar crest and trough where the vertical variation of sediment concentration is very strong (*e.g.*, Yoon and Cox, 2012), the vertical gradient of source-sink term and cross-shore sediment flux should be considered. At the bar crest and trough, sediments are transported predominantly near the bed, which cannot be exactly simulated with the depth-averaged advection-diffusion equation. This probably causes large error in simulating a longshore bar in Xbeach.

CONCLUSIONS

The effect of wave breaking turbulence was investigated with large-scale laboratory experiment data (CROSSTEX) and RANS numerical model (COBRAS). Hydrodynamics results from Xbeach were in a good agreement with CROSSTEX and COBRAS. However, bathymetric changes were not successfully simulated with Xbeach. Most of bathymetric changes occurred near dune. The nearshore (longshore) bar was not simulated satisfactorily. When we applied the average rate of energy dissipation by bores for estimating wave breaking turbulence in addition to the existing near-bed turbulence options in Xbeach, slight change of bed profile was found at the bar crest. However, more investigation is still required to simulate the feature of longshore bar successfully. Especially, the vertical gradient of sediment concentration should be incorporated in the model, because of the strong vertical variance of sediment concentration in the surf zone.

ACKNOWLEDGMENTS

This work was supported by Basic Science Research Program through the National Research Foundation of Korea (NRF) funded by the Ministry of Science, ICT & Future Planning (2014R1A1A1008095).

LITERATURE CITED

Aagaard, T. and Hughes, M.G. 2010. Breaker turbulence and sediment suspension in the surf zone, *Mar. Geol.*, *271*, 250-259.

Kobayashi, N.; Zhao, H., and Tega, Y., 2005. Suspended sand transport in surf zones, *Journal of Geophysical Research, 110 (C12)*, doi: 10.1029/2004jc002853.

Nadaoka, K.; Hino, M., and Koyano, Y., 1989. Structure of the turbulent flow field under breaking waves in the surf zone, *J. Fluid Mechanics*, *204*, 359-387.

Roelvink, D. and Stive, M.J.F., 1989. Bar-Generating Cross-Shore Flow Mechanisms on a Beach, *Journal of Geophysical Research*, *94 (C4)*, 4785-4800.

Roelvink, D.; Reniers, A.; van Dongerern, A., and van Thiel de Vries, J., 2009. Modelling storm impacts on beaches, dunes and barrier islands, *Coastal Engineering*, *56*, 1133-1152.

Soulsby, R. L. 1997. Dynamics of Marine Sands. London, *Thomas Telford Publications*

Thornton, E. B. and Guza, R. T. 1983. Transformation of wave height distribution, *Journal of Geophysical Research*, *88*, 5925-5938

Van Rijn, 1984. Sediment pickup functions, *Journal of Hydraulic Engineering*, *110*, 1494-1502.

Van Thiel de Vries, J. S. M., 2009. *Dune erosion during storm surges*, PhD thesis, Delft University of Technology, Delft.

Voulgaris, G. and Collins, M.B. 2000. Sediment resuspension on beaches: response to breaking waves, *Marine Geology*, *167(1)*, 167-187.

Xbeach Manual, 2015. *Deltares*, 135p.

Yoon, H.-D.; and Cox, D. T., 2010. Large-scale laboratory observations of wave breaking turbulence over an evolving beach. *Journal of Geophysical Research*, 115, doi:10.1029/2009jc005748.

Yoon, H.-D. and Cox, D. T., 2012. Cross-shore variation of intermittent sediment suspension and turbulence induced by depth-limited wave breaking. *Continental Shelf Research*, 47, 93-106.

Yoon, H.-D.; Cho, M.-S.; Shin, S.; Cho, K., and Cox, D. T., 2015. Numerical Modeling on the Hydrodynamics of Surf Zone over Movable Beach Profiles. *Proc. Of the 25th International Ocean and Polar Engineering Conference*, 1291-1296.

Journal of Coastal Research	SI	75	947-951	Coconut Creek, Florida	2016

Sensitivity of shoreline-recession forecasts to sediment budget uncertainties

Salette A. de Figueiredo † **and Peter J. Cowell**‡

† Instituto de Oceanografia
Universidade Federal do Rio Grande
Rio Grande, Brasil

‡Coastal Studies Unit
The University of Sydney
Sydney, Australia

www.cerf-jcr.org

www.JCRonline.org

ABSTRACT

Figueiredo, S.A.; Cowell, P.J., 2016. Sensitivity of shoreline-recession forecasts to sediment-budget uncertainties. *In:* Vila-Concejo, A.; Bruce, E.; Kennedy, D.M., and McCarroll, R.J. (eds.), *Proceedings of the 14th International Coastal Symposium* (Sydney, Australia). *Journal of Coastal Research*, Special Issue, No. 75, pp. 947-951. Coconut Creek (Florida), ISSN 0749-0208.

Intrinsic uncertainty associated with the stochastic nature of coastal processes and how they affect sediment budget estimates under present conditions already make predicting coastal change difficult. The possibility that under climate change conditions alteration of wave climate will have direct implications for alongshore transport in future, may complicate even more future forecasts of coastal change in response to sea-level rise. This study exploits the variability in sediment budgets along the Rio Grande do Sul coastal plain, in southern Brazil, to provide an experimental framework to evaluate the significance of such uncertainties in coastal response under the rising sea levels rates predicted for the next century. The analysis involved quantifying the variation in coastal recession sensitivity between different sectors along the coast (coastal cells), through the application of RanSTM (Random Shoreface Translation Model) using two different scenarios for the sediment-budget parameter. Sediment budget parameter was estimated based on historical shoreline changes and Holocene barrier stratigraphic data. The results show that forecasts for lower-magnitude coastal recession associated with more likely impacts (*e.g.* 90% risk) are more susceptible to uncertainties in littoral sediment budgets than high-magnitude less likely impacts (*e.g.* 10% risk). This is especially the case for coastal cells with low dune dimensions because in general such dunes have less capacity to buffer coastal-erosion effects. The reduced effect on high-end forecasts with respect to sediment budget uncertainties therefore favors better confidence in the forecasts.

ADDITIONAL INDEX WORDS: *Sea level rise, large scale processes, coastal response.*

INTRODUCTION

The combination of the geo-dynamical setting, substantial accommodation space and abundant shelf sand supply supported the development of a long and wide sand barrier, along Rio Grande do Sul (RS) state coastline in southern Brazil, with a general configuration that comprises a gentle undulating coast with embayed and protruding sectors (Dillenburg *et al.*, 2000). The evolution of the Holocene barrier along RS coast was primarily controlled by alongshore gradients on the littoral sediment budgets, a consequence of the changes in shoreline orientation and offshore gradients, under stable/slowly rising sea levels rates, which resulted in a diverse coastline configuration where progradational, retrogradational and aggradational barriers coexist (Dillenburg *et al.*, 2000; Dillenburg *et al*., 2009; Martinho *et al*., 2009).

Following the analysis of relevant inherited geological factors and external forcing that exert major control over long term coastal change, through application of coastal-tract concepts (Cowell *et al*., 2003), the Rio Grande do Sul state coastal region was subdivided into nine coastal cells (C1 to C9) that form the fundamental sediment budget control volumes. The basis for coastal cell delineation involves main changes in shoreline orientation, shoreface morphology, offshore gradients and accomodation space, which directly influence littoral transport patterns, sediment budgets and changes shoreline in position (Lélis and Calliari, 2006; Lima *et al*., 2001) as well as, in the longer term, barrier evolutionary types described in previous studies for the Rio Grande do Sul coast region (Dillenburg *et al.*, 2000; Martinho *et al.*, 2008; Dillenburg *et al*., 2009). Cell boundaries location are indicated in Figure 1.

Based on the assumption that protruding sectors are likely to undergo higher rates of erosion whereas coastal embayments undergo deposition (May and Tanner, 1973), it can be expected that the Rio Grande do Sul coastline will develop a tendency for becoming straighter into the future. As a consequence smaller gradients of littoral transport along the coast may be expected. Dillenburg *et al.* (2000) demonstrated that coastal change of this type has been underway throughout the late Holocene, under slow rates of sea level change. Under the current slowly rising rates of sea level change, White *et al.* (2005) show that the effects of positive sediment budgets can override shoreface sand-sink effects and the coast can continue to accrete, whereas a negative budget can produce erosion rates that exceed those expected due to sea-level rise alone. Nonetheless, Roy *et al.* (1994) points out that sediment budget effects on forecasts of

DOI: 10.2112/SI75-190.1 received 15 October 2015; accepted in revision 15 January 2016.
*Corresponding author: saletteoc@gmail.com
©Coastal Education and Research Foundation, Inc. 2016

coastal response are likely to be overridden under accelerated rates of sea level rise and mainly controlled by substrate morphology.

According to Rosati (2005) producing estimates of sediment budgets with confidence is still very challenging, and the calculation of sediment budgets not only includes determining the appropriate boundaries for the budget and interior cells estimates, defining possible range pathways and relative magnitudes of each, but also consist of properly representing the budgets by incorporating the uncertainty associated with values. Such uncertainties may be amplified along an oceanic open coast under climate-change conditions with alteration of wave climate further complicating the definition of precise values in future. This study will focus on evaluating the sensitivity of coastal response at each cell substrate to changes in sediment budget, by exploring the relative contribution of sediment imbalances to coastal response relative to effects of other controls of regional topography (*e.g.* shoreface slope; dune topography) under accelerated sea level rise conditions.

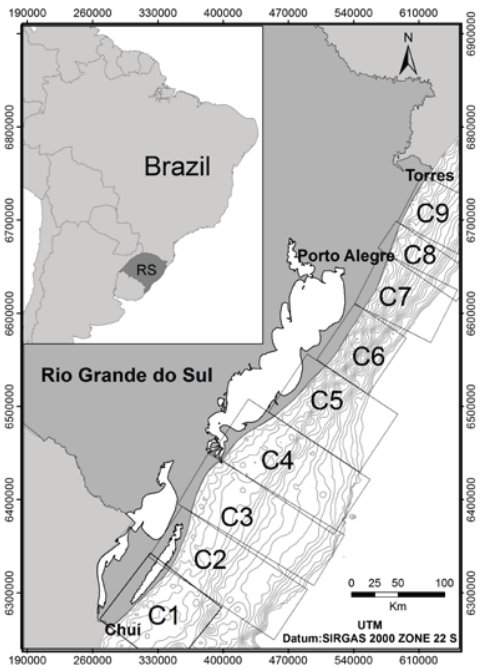

Figure 1. Coastal cells sub-divisions for model application along the study area.

METHODS

The effects that uncertainties in sediment budget estimates have on forecasts of coastal response in each coastal cell under rising sea levels rates (0.18 m; 0.89 m; 1.1 m) by the year 2100, on the Rio Grande do Sul coast were evaluated based on simulation experiments involving manipulation of the sediment budget parameter. Simulation of coastal response to sea level rise were performed for each coastal cell through the application of RanSTM (Random Shoreface Translation Model). It is a coastal geomorphic model which uses principles of sediment-mass balance to calculate shoreline migration and surface evolution in response to environmental influences such as sea level change and altered sedimentation regimes (Kinsela and Cowell, 2011). Two scenarios for the sediment-budget parameter were designed: one involving in littoral sediment budgets inferred from previous studies geo-historical (stratigraphy and historical) behavior on medium to long-term (Lima *et al.*, 2001; Lélis and Calliari, 2006; Dillenburg *et al.*, 2009), and another with moderated budgets.

The simulation design accounted for this possibility in the RanSTM by the adjustment of the sediment budget parameter, gains or losses due to alongshore sediment transport and transgressive dune migration (Table 1). The adjustment involved a 50 % moderation in the volumes calibrated based on historical and stratigraphic evidence. Consequently, the embayed coastal cells that initially were assigned strongly positive sediment-budgets were recalibrated to weaker positive-budget scenarios. Conversely, the sediment volume parameter in simulations of protruding sectors of the coast was adjusted to a 50% reduction of their negative sand-budgets. Recession distances obtained from model simulations with the alongshore-sediment budgets parameter calibrated based on geo-historical data were compared with those obtained from simulations with moderated sediments budgets accounting for the shoreline-equilibration tendency.

Table 1. *Sediment-budget volumes used in model simulation.*

Cell Location	Geo-historical (m^3.m)	Equilibrated (m^3.m)
C1	-594	-297
C2	-474	-237
C3	1496	738
C4	1457	728
C5	-460	-230
C6	-760	-380
C7	-600	-300
C8	-507	-253
C9	1492	746

Further analysis of these results was undertaken to examine the relative changes in coastal recession forecasts as a result of moderation in sediment budgets expected if the shoreline geometry adjusts toward equilibrium. Absolute differences were examined because it is the sensitivity to effects of the sediment budget that is of interest. This analysis was applied to remove effects of scale by expressing differences in recession distances between the two sediment budget treatments. Comparison of results between the two simulations addresses not just the difference between representative values (*e.g.* means), it also incorporates more extreme results (tails of the distributions), which are likely to be of greater relevance in risk assessment. Kolmogorov-Smirnov test was favored over the *t*-test because this type of test enables the comparison of the entire distribution of recession distances.

RESULTS

The results of simulation with the two sediment budget scenarios indicate that mean coastal response between sediment

budgets experiments is statistically different (Figure 2). Cells that initially had a positive budget had an increase in mean recession, and those that initially displayed a negative budget had a decrease in mean recession, with equilibration tendency budgets relative to the geo-historical calibration results. However, the regional alongshore vulnerability level initially observed with the geo-historical standard calibration was generally maintained at most cells. The only exceptions involved C4 and C1, where the former was originally less vulnerable than the latter due to more benign sediment budget estimates.

The 95% confidence intervals between simulations only overlap for C1 and C2, indicating that in this case sediment budget effects cannot be resolved from the effects of other factors. Results for the other cells show larger differences in mean recession distances between the two simulation designs. Regardless of the alteration in sediment budgets, the gentler shoreface slope southern four cells (C1 to C4) continue to display larger recession distances relative to the steeper northern cells (C5 to C9) (Figure 2). To determine if coastal response is significantly affected by changes in alongshore sediment budgets within each cell relative to all other effects, two sets of complete recession-distance distributions, and not just mean coastal recession, for each cell were compared.

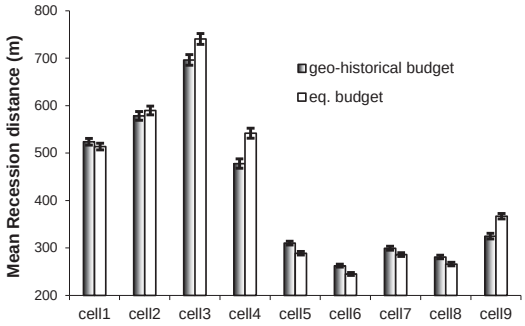

Figure 2. Comparison between mean recession distance (95% confidence interval) at each cell, calibrated for geo-historical sediment budget and equilibration tendency, under the projected range in sea level rise to 2100.

Results of the K-S test (Table 2) demonstrate that changes in alongshore sediment budgets produce a significantly different coastal response in all cells, except C2, where there is no significant difference in the results between the two experiments (P>0.349), corroborating with the results from the analyses of the means and 95% CI (Figure 2). However, C1, which showed no significant difference between means for the two experiments (Figure 2), was significantly affected by the changes in sediment budgets in terms of the overall recession-distance distributions. The most extreme differences, according to the K-S test occurred for C3, C4, C5, C6 and C9 (Table 2). These results are also consistent with the results obtained by comparison of mean recession distances (Figure 2).

Additional examination of the results of the K-S test reveals that C3, which displayed the second largest differences in mean recession between the two experiments, has its overall differences diminished when the entire distribution of recession distances is examined. The most extreme differences between the two treatments for C3 (0.083) are smaller than the other four aforementioned cells (Table 2).

Table 2 shows the results which indicate that, even when removing the scale effect of the absolute sediment-budget volumes, comparative differences between cells remains much the same. The simulated changes in sediment budgets did not alter the general geographic differences in vulnerability. C4 and C9, both located at prograted coastal sectors, remain the most affected by moderation in the sediment budget, followed by C6, C5, C3 and C8, which had intermediate proportional differences. Conversely, C1, C2 and C7 experience the smallest differences in recession distances between the two sediment budget scenarios.

Table 2. *Results of Kolmogorov-Smirnov (K-S) analyses testing for difference between output recession probability density functions (PDFs) from simulations with the sediment budget based on geo-historical data versus those calibrated for shoreline equilibration.*

Cell Location	Most extreme dif.	Z statistic	P
C1	0.062	1.961	< 0.001*
C2	0.030	0.933	> 0.394*
C3	0.083	2.609	< 0.000*
C4	0.115	3.637	< 0.000*
C5	0.112	3.542	< 0.000*
C6	0.101	3.178	< 0.000*
C7	0.074	2.324	< 0.000*
C8	0.076	2.403	< 0.000*
C9	0.130	4.111	< 0.000*

* Significant at 0.05

In addition, a detailed examination of the data reveals that those differences for the two treatments vary at different levels of risk amongst cells. The greatest differences in recession distances between the two experiments are associated with those at higher exceedance levels (90% risk) in most cells, and are generally followed by progressively smaller relative changes at successively lower probability-of-exceedance levels (Figure 3). That is, forecasts for lower-magnitude and more likely impacts are more susceptible to uncertainties or variations in littoral sediment budgets. Even though less likely, the high-magnitude impacts are probably of greater concern in contingency planning for coastal management.

An exception occurs in C4, for which changes in the sediment budget have greatest effect in both tails of the distribution (90% and 1%). Another minor departure from the general pattern described in the preceding paragraph occurs in C2 and C7. For these cells, moderation in sediment budgets has a slightly larger effect in the middle of the distribution (at the level of 50% risk), the mean recession. Apart from these anomalies, the results indicate that moderation in sediment budget imbalances is more likely to affect the lower half of the probability distribution for recession distances (smaller distances of shoreline recession), representing impacts with a higher likelihood of occurrence (90% risk). Risk of more extreme values of recession (10% risk) is less affected by uncertainty in sediment budgets. Still further exploration of the results was essential in order to investigate

why C4 is more susceptible to the sediment-budget uncertainties then C3.

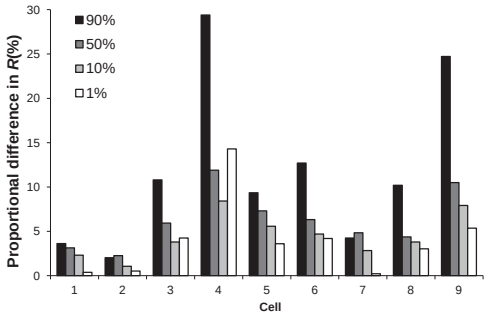

Figure 3. Sensitivity of coastal-recession forecasts to equilibrated sediment budgets, shown as proportional differences in recession distance(*R*) between the two sets of simulations for four levels of risk.

More specifically, when considering that C3 and C4 were calibrated for a similar sediment budget (Table 1) and do not display significant differences in offshore substrate morphology, both with gentler slopes (0.02° to 0.08°) (Dillenburg *et al*., 2000), compared to the adjacent cells (Table 1), it is likely that another factor may also be exerting control over regional variability in coastal response under conditions of sediment budgets alteration. To confirm that proposition, further investigation of onshore dune and offshore topography (upper and lower shoreface) dimensions was performed. Upper and lower shoreface offshore limits were also tested but neither showed a clear correlation to the proportional differences at 90% risk level in *R* and therefore do not seem to have any influence in such response. Dune volumes demonstrated a clear inverse correlation at the 90% risk level (Figure 4) to the proportional changes in recession distances. Cells with the smallest dune volumes, Cells 4 and 9, proved to be the most affected by equilibration tendencies, where a 50% change in sediment budget volume resulted in 12% and 11% difference in mean recession, respectively.

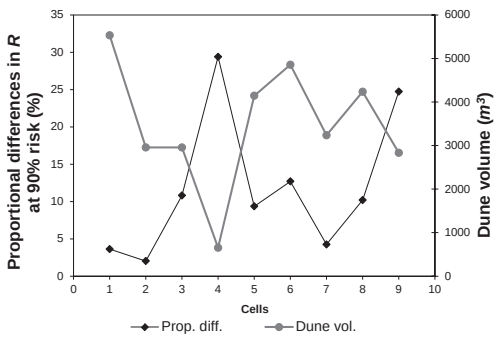

Figure 4. Proportional differences in recession distance (90% risk), between the two simulations design for sediment budget relative to dune volume.

DISCUSSION

The results presented here comparing coastal recession distances between sediment budget treatments, either from K-S test or for most of the 95% confidence intervals for means comparison, show that changes in sediment budget significantly affect coastal recession rates. These results are consistent with the principles discussed in Dillenburg *et al.* (2000), Stive (2004) and Stive *et al.* (2009), who demonstrated that net natural shoreline changes are influenced by sediment budgets, which can sometimes exceed shoreline rates of change due to a rise in sea level. In this study, through the comparison of recession distances from the two experimental sediment budget treatments demonstrate that the cells with the greatest sediment budget imbalance, generally those at coastal embayments and gentle slopes (C3, C4 and C9), also displayed the greatest differences in mean recession distances between the two experiments.

These results indicate a greater susceptibility to effects of shoreline equilibration in the lower gradient cells as the littoral supply weakens. A plausible explanation for the disparity may relate to the onshore sediment volumes, since cells with lesser dune volume are less capable of compensating a sediment deficit. As expected from first principles, when dune volume decreases coastal response presents a higher sensitivity to sediment budget alteration.

These results are also in line with analyses undertaken by List *et al.* (1997) along the low lying barrier islands of Louisiana coast which indicated that even under sea level rise, the effects of alongshore sediment budgets may play a major role in influencing shoreline behavior. Under the present slow rates of sea level rise (~2mm/yr) the alongshore transport uncertainties override the effects of rising sea levels, thus limiting the application of the *Bruun rule* (Bruun, 1962) principles when hindcasting shoreline position (Stive *et al*., 2009). Dillenburg *et al.* (2000) could only properly reconstruct steps in barrier formation and shoreline position for the Rio Grande do Sul coast since the last Post-glacial Marine Transgression, when taking into account the contribution from the alongshore sediment transport and onshore sediment supply from the shoreface, highlighting the relevance of sediment budgets for large scale coastal behavior and evolution under slowly changing sea levels.

In the present study, when evaluating the large scale geographic differences in vulnerability between cells associated with projected shoreline retreat, these are mostly preserved regardless of possible future changes in sediment budgets. That is, despite of the alteration in sediment budgets, the southern four cells, with gentler shoreface slope, continued to display larger recession distances relative to the steeper cells. On the 100 year time scale (*i.e.*, in forecasts to 2100) for which the experiments were conducted, the 50 percent moderation in sediment budgets applied in the documented experiments did not affect the alongshore ranking of cells with respect to vulnerability. These findings suggest that, given the simulated rates of sea level rise relative to the scale of sediment-budget alteration, substrate morphology also exerts some control over coastal response, as described by Roy *et al.* (1994). The only exceptions were C1 and C4 mainly because of its higher dunes (the former became less vulnerable than the latter), in which differences in dune heights became more important once the imbalance in littoral sediment budgets became more subdued,

highlighting the importance of such features in coastal protection in the future.

CONCLUSIONS

Subject to some anomalies, it can be inferred from the general results that shoreline-recession forescasts are sensitive to sediment budget alteration under rising sea levels. Nevertheless, site specific morphological controls also play a part in influencing coastal recession forecasts under the projected accelerated sea level rise rates.

Since initial conditions can be far more readily quantified with confidence for morphology than for sediment budgets, this inference also confers greater confidence on forecasts for coasts like that of Rio Grande do Sul and to coasts with significant variation in morphology and sediment budgets, but with little effect from tidal inlets as potential sinks for beach and dune sand.

ACKNOWLEDGMENTS

The authors thank CAPES (Centro de Aperfeiçoamento de Pessoal de Nível Superior) for providing a PhD scholarship at the University of Sydney for the first author during the development of this research.

LITERATURE CITED

Bruun, P., 1962. Sea-level rise as a cause of shore erosion. *Journal of Waterways Harbors Division, American Society of Civil Engineers*, 88(1), 117–130.

Cowell, P.J., Stive, M.J.. F., Niedoroda, A.W., De Vriend, H.J., Swift, D.J.P., Kaminsky, G.M., and Capobianco, M., 2003. The Coastal-Tract (Part 1): A Conceptual Approach to Aggregated Modeling of Low-Order Coastal Change. *Journal of Coastal Research*, 19(4), 812–827.

Dillenburg, S.R., Barbosa, E.G., Tomazelli, L.J., Hesp, P.A., Clerot, L.C.P., Ayup-Zouain, R.N., 2009. The Holocene Coastal barriers of Rio Grande do Sul. *In: Geology and geomorphology of Holocene Coastal Barriers of Brazil*. pp. 53–91.

Dillenburg, S.R., Roy, P.S., Cowell, P.J., and Tomazelli, L.J., 2000. Influence of Antecedent Topography on Coastal Evolution as tested by the Shoreface Translation-Barrier model (STM). *Journal of Coastal Research*, 16(1), 71–81.

Kinsela, M.A., and Cowell, P.J., 2011. Site geomorphology or inner shelf adjustments controls coastline response to climate change? *Proceedings 20th New South Wales Coastal Conference*, pp. 58–68.

Lélis, R.J.F., and Calliari, L.J., 2006. Historical Shoreline Changes Near Lagoonal and River Stabilized Inlets in Rio Grande do Sul State, Southern Brazil . *Journal of Coastal Research*, SI 39, 301–305.

Lima, S.F., Almeida, L.E.S.B., and Toldo Jr., E.E., 2001. Estimated of alongshore sediment transport from wave data at Rio Grande do Sul coast. *Pesquisas*, 28(1), 99–107.

List, J.H., Sallenger, J.A.H., Hansen, M.E., and Bruce, J.E., 1997. Accelerated relative sea-level rise and rapid coastal erosion: testing a casual relationship for the Lousiana barrier islands. *Marine Geology*, 140(3-4), 347–365.

Martinho, C.T., Dillenburg, S.R., and Hesp, P.A., 2009. Wave Energy and Longshore Sediment Transport Gradients Controlling Barrier Evolution in Rio Grande do Sul, Brazil. *Journal of Coastal Research*, 25(2), 285–293.

Martinho, C.T., Dillenburg, S.R., and Hesp, P.A., 2008. Mid to late Holocene evolution of transgressive dune fields from Rio Grande of Sul coast, southern Brazil. *Marine Geology*, 256, 49–64.

May, J.P., Tanner, W.F., 1973. The littoral power gradient and shoreline changes. *In:* Coates, D.R. (ed.), *Publications in Geomorphology*. Binghamton: State University of New York, pp. 43–60.

Rosati, J.D., 2005. Concepts in Sediment Budgets. *Journal of Coastal Research*, 21(2), 307–322.

Roy, P.S., Cowell, P.J., Ferland, M.A., and Thom, B.G., 1994. Wave-dominated coasts. *In*: Carter, R.W.C. and Woodrofe, C.D. (eds.), *Coastal evolution – late quaternary morphodynamics.* Cambridge University Press, pp.121–186.

Stive, M.J.. F., 2004. How important is global warming for coastal erosion? An Editorial Comment. *Climatic Change*, 64(1), 27–39.

Stive, M.J.F., Ranasinghe, R., Cowell, P.J., 2009. Sea Level Rise and Coastal Erosion. *In:* KIM, Y.C. (ed.) *Handbook of Ocean and Coastal Engineering.* Singapore: World Scientific Publishing,(Ch. 37), 1023-37.

White, N.J., Church, J.A., and Gregory, J.M., 2005. Coastal and global averaged sea level rise for 1950 to 2000. *Geophysical Research Letters*, 32(1), 2–5.

Journal of Coastal Research	SI	75	952-956	Coconut Creek, Florida	2016

A Flexible Approach to Forecasting Coastline Change on Wave-Dominated Beaches

Michael A. Kinsela[†*], Bradley D. Morris[†], Marc J. A. Daley[‡] and David J. Hanslow[†]

[†]Coastal and Marine Unit, Science Division
NSW Office of Environment and Heritage
Newcastle, NSW, Australia

[‡] Coast Estuary and Floodplains, Regional Operations
NSW Office of Environment and Heritage
Newcastle, NSW, Australia

www.cerf-jcr.org

www.JCRonline.org

ABSTRACT

Kinsela, M.A., Morris, B.D., Daley, M.J.A. and Hanslow, D.J., 2016. A Flexible Approach to Forecasting Coastline Change on Wave-Dominated Beaches. *In:* Vila-Concejo, A.; Bruce, E.; Kennedy, D.M., and McCarroll, R.J. (eds.), *Proceedings of the 14th International Coastal Symposium* (Sydney, Australia). *Journal of Coastal Research*, Special Issue, No. 75, pp. 952-956. Coconut Creek (Florida), ISSN 0749-0208.

Standard methods of predicting coastline change typically rely on the analysis and extrapolation of historical trends, or simple geometric rules that consider the response of idealised coastal morphology to environmental change – *e.g.* the Bruun rule of coastline retreat due to sea level rise. In practice, predictions based on such methods are often challenged, due to the limited capacity to characterise natural geomorphic complexity, and consequently, the inability to satisfy restrictive assumptions. While statistical simulation methods offer a means to manage uncertainty in environmental forcing, datasets, and predictive models, the continued reliance on simple geometric rules introduces unnecessary error into forecasts. The increasing coverage and detail of geomorphic datasets, provided by modern remote sensing techniques (*e.g.* LiDAR, GPR), means that more rigorous approaches are now achievable in many settings. This paper presents a simple yet flexible approach to forecasting coastline change on wave-dominated beaches. The method combines a Monte Carlo simulation approach with a volumetric coastline response model that features a parameterised sediment budget. Model complexity reflects the levels of topographic and geomorphic data typically available for beaches in southeastern Australia, allowing for the sediment budget parameterisation to be broad or refined. A volumetric implementation of all components of coastline variability and change ensures that forecasts are sensitive to the complex coastal geomorphology of individual beaches. Application of the method demonstrates the sensitivity of forecast coastline change to three-dimensional beach and dune morphology, irregular substrates comprising mixed hard and soft materials, and complex shoreface surfaces featuring submerged reef structures.

ADDITIONAL INDEX WORDS: *Coastal hazards, Probabilistic modelling, Sediment budget, Southeast Australia.*

INTRODUCTION

The average position of the shoreline on wave-dominated beaches is a product of sea level (affected by waves, tides, storm surge and climate variability), and the distribution of sand within the sub-aerial and sub-aqueous beach system. The latter varies in response to fluctuations in energy conditions (*e.g.* waves and currents), sediment supply, and sea level, which collectively control the distribution of sediments within the geomorphic framework (Cowell *et al.*, 2003). Redistribution of sediments in response to permanent change in one or more controls may modify shoreline migration relative to a simple passive response (*i.e.* passive retreat due to inundation by sea level rise only).

While the historical impacts of coastal erosion have been documented at many SE Australian beaches, predicting the potential reach of coastline variability at present, and coastline change into the future, are problems characterised by substantial uncertainty. Uncertainty is unavoidable due to an imperfect understanding of coastal sediment transport processes and future environmental conditions, and limited records of beach volume and shoreline change. Despite having some of the best long-term beach measurement records by global standards (Thom and Hall, 1991; Short *et al.*, 2014; Harley *et al.*, 2015), the diverse coastal geomorphology and beach types of the SE Australian coastline (Short, 2006) present challenges to generalising data and models, and thus assessing coastal hazards (Kinsela and Hanslow, 2013).

However, uncertainty is inherent to risk management and in no way precludes robust forecasts of coastline change. For example, the recent adoption of statistical modelling frameworks within coastal geosciences provides for more rigorous and transparent approaches to identify, manage and communicate uncertainty in predicted coastline response to storms and environmental change (Cowell *et al.*, 2006; Anderson *et al.*, 2015; Simmons *et al.*, 2015). Recognition of the importance of quantifying uncertainty and model error in order to support transparent evidence-based decision making has encouraged the application of probabilistic methods to coastal management and planning in practice (Woodroffe *et al.* 2012, Mariani *et al.*, 2013).

DOI: 10.2112/SI75-191.1 received 15 October 2015; accepted in revision 15 January 2016.
*Corresponding author: Michael.Kinsela@environment.nsw.gov.au
©Coastal Education and Research Foundation, Inc. 2016

Here we present a flexible approach to forecasting coastline change on wave-dominated beaches and consider the influence of geomorphic complexity on SE Australian beaches on uncertainty in coastline change predictions.

Regional Setting

The New South Wales (NSW) coastline forms the majority of the mircrotidal wave-dominated SE Australia coastal setting, spanning some 1,500 km at a NE-SW orientation. The coast features over 1,000 km of sandy beaches with reflective to rhythmic bar and beach modes, and longshore bar and trough and dissipative states periodically adopted at the more exposed beaches (Short, 2006). The coast experiences a moderate-high energy SE swell and storm wave climate (Shand *et al.*, 2011).

The geological framework of the coastline varies from north to south: the northern region features broad embayments, low relief and a shallow shelf; the southern region features deeper pocket embayments, rugged relief and a steeply sloping shelf (Roy and Thom, 1981). As such, compartmentalisation is more developed within the central to southern regions. Further to defining sediment accommodation, the framework has shaped beach types by modifying local energy regimes, resulting in considerable regional- and local-scale variability (Short, 2010). Additional geomorphic complexity is introduced by nearshore reefs and consolidated or cemented beach-dune substrates.

Sediment connectivity via littoral and shoreface sand transport means that many NSW beaches cannot be considered isolated features that vary independently from surrounding beaches (Goodwin *et al.*, 2013). Rather, most beaches are elements of larger *sediment-sharing systems*, and respond to the redistribution of sand within the system due to evolving forcing conditions, such as the energy climate or sea level (Cowell *et al.*, 2003). The magnitude and timescales of beach change reflect not only variability in forcing conditions, but also the spatial scales and connectivity (by sediment transport) of adjacent beaches within each sediment-sharing system.

METHODS

Informed decision-making in the face of uncertainty, necessitates a risk management approach to assess the costs and benefits of management options and planning strategies, in the context of the likelihood and consequences of impacts.

Here we use a statistical simulation method to characterise uncertainty in model inputs, and describe the likelihood of hazard scenarios within the feasible uncertainty space. Nested within the simulation framework is a volumetric coastline response model that uses detailed terrain data and a parametrised sediment budget (consistent with available data) to predict the potential range of present and future coastal erosion hazards.

Statistical simulation approach

The Monte Carlo method is a standard modelling approach that is typically used to explore the potential range of solutions where the precise values of model inputs is poorly defined. The method has been previously applied to manage uncertainty in forecasting coastline change, with uncertainty in model predictions typically described in terms of the probability of exceeding potential coastline positions, or as confidence intervals (Cowell *et al.*, 2006; Mariani *et al.*, 2013; Anderson *et al.*, 2015).

Key to the process is appropriately capturing the uncertainty space (*i.e.* feasible range of values) of model parameters and variables that are randomly sampled for each model iteration. Here we express the uncertainty space for most inputs as a triangular probability density function (pdf), which is suitable where the bounds of the uncertainty space can be estimated but little data exists to define the precise shape of the distribution. Triangular pdfs are defined by fixed lower and upper bounds, and a modal value that controls probability density (Figure 1).

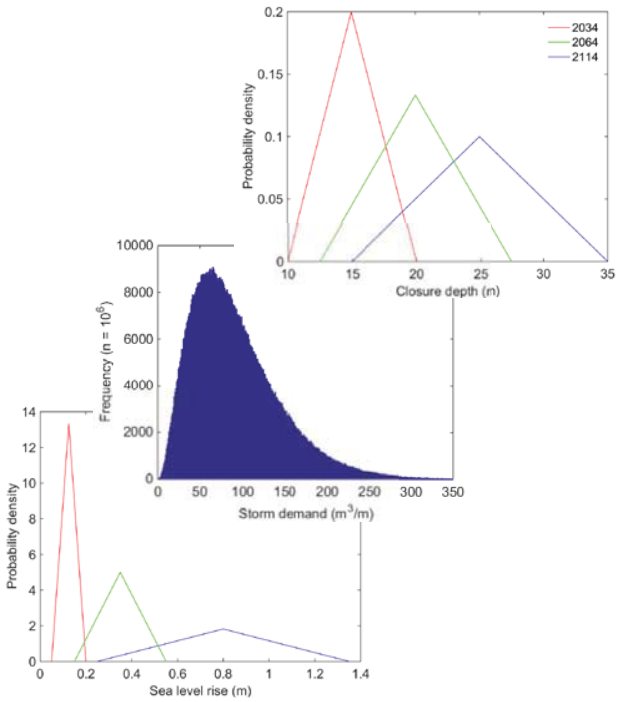

Figure 1. Triangular pdfs for sea level rise and closure depth for three forecast periods, and 10^6 samples from the storm demand gamma pdf.

The simulation method is carried out as follows (for further detail refer to Cowell *et al.*, 2006):

1. Input pdfs are defined using available data and expert reasoning to reflect the nature of the uncertainty space
2. The coastline response model is run many times (*e.g.* 10^6) with inputs sampled at random, unless correlation between particular inputs suggests proportionate sampling
3. A frequency histogram of model predictions is constructed
4. A continuous probability distribution (such as Generalised Extreme Value or Gaussian) is then fitted to the predictions
5. The cumulative probability function of the fitted distribution is derived to determine exceedance probabilities
6. Model predictions corresponding to relevant exceedance probabilities are derived from the fitted cumulative function
7. The zone of forecast coastline change is mapped for selected exceedance probabilities or confidence intervals

Volumetric coastline response model

The coastline response model treats each component of coastline variability and change as a sediment volume. For the chosen forecast period (t years), coastline change is solved as the sum of sediment volume flux per metre of beach (V_T):

$$V_T = C_F(V_F) + C_R\left[(q_x + q_y)t + C_S(V_S) + \left(\frac{A_D \cdot S}{L}\right) + \left(\frac{V_O + V_A + V_M + V_C}{L}\right)t\right]$$

q_x = historical shore-normal sediment flux rate [m^3/m/yr]
q_y = historical alongshore sediment flux rate [m^3/m/yr]
V_F = fluctuating erosion from storms and variability [m^3/m]
V_S = theoretical shoreface accommodation volume [m^3/m]
V_O = sediment loss via barrier overwash [m^3/yr]
V_A = sediment loss via aeolian transport to dunes [m^3/yr]
V_M = sediment loss via mega-rips during storms [m^3/yr]
V_C = carbonate sediment dissolution or production [m^3/yr]
A_D = surface area of marine (flood-tide) delta [m^2]
S = sea level change over forecast period [m]
L = alongshore length of sediment cell [m]

The parameterisation of all potential contributors to coastal erosion as volumetric sediment budget components allows for the distinctive morphology of each beach to be accounted for in coastline change predictions. The coastline change distance (R_T) is calculated by applying V_T to a beach profile derived from LiDAR topography (Figure 2), and includes an allowance for dune slumping (Nielsen *et al.*, 1992). Ideally, an alongshore-averaged beach profile is used where homogeneity of processes and morphology is satisfied, to account for the redistribution of sediments within the beach system (Cowell *et al.*, 2003).

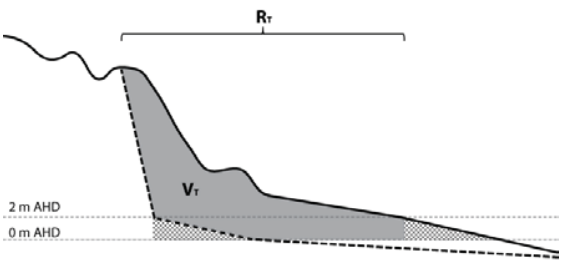

Figure 2. The forecast coastline change distance (R_T) is calculated by applying V_T above mean sea level and landward of 2 m elevation.

The solution features three scaling coefficients: *fluctuating* erosion (C_F) and coastline *recession* (C_R) account for reduced exposure to wave energy, or substrate resistance, for fluctuating and recession components; and, *shoreface* response (C_S) accounts for shoreface reefs that occupy space in the water column and reduce the theoretical sediment accommodation volume.

Fluctuating beach erosion due to storms (V_F) is handled using a gamma pdf (Figure 1), which better captures the frequency of occurrence of severe erosion events as estimated from historical records (Gordon, 1987). Where sufficient data (historical or geological) exists, shoreface-beach (q_x) and alongshore sediment exchange trends (q_x) can be included.

Coastline response to sea level rise is also considered as a volumetric component. First, an idealised shoreface profile of the form $h = Ax^m$ is fitted to available hydrographic data (Figure 3). For each model run, the profile is raised by the sea level rise sampled from the input pdf, and the area between the initial and raised profiles is calculated, although only to the limit of the sampled closure depth (Figure 1). The calculated area is then halved to derive V_S, in accordance with basic principles of sediment conservation (Bruun, 1962). Figure 1 shows that the profile closure depth increases with the forecast period, which is consistent with depth-increasing shoreface response timescales (Stive and de Vriend, 1995; Kinsela and Cowell, 2015). Flood-tide delta aggradation due to sea level rise (Eysink, 1990) is also considered using the active delta area (A_D) and sea level rise (S) values sampled in each model run from the respective pdfs.

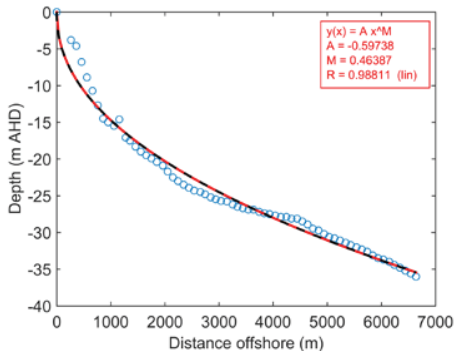

Figure 3. Shoreface profile fitted to hydrographic data (o) from Lake Cathie Beach to calculate the theoretical shoreface accommodation.

Other sediment budget components may be measured or estimated as gross fluxes within the sediment cell. The examples included here (V_O, V_A, V_M, V_C) are not exhaustive but are intended to capture processes relevant to the SE Australian coastal setting.

Application to Lake Cathie Beach

The volumetric coastline response model was applied to Lake Cathie Beach on the mid-north coast of NSW. Historical records from this beach suggest a trend of coastline recession, and properties and infrastructure have been identified as at risk from coastal erosion (SMEC, 2010; Cardno, 2014).

Lake Cathie Beach features geomorphic complexity in the form of indurated sand (coffee rock) within the beach and dune sands, and shoreface reef structures (Figure 4). A recent geotechnical study found coffee rock intermittently throughout the beach and dunes between 0-4 m elevation, with strength ratings ranging from extremely low to moderate (Cardno, 2014). The beach is also situated within a drift-aligned alongshore transport setting, and together these complexities invalidate traditional approaches to predicting coastline change such as the standard Bruun rule of coastline retreat due to sea level rise (Bruun, 1962).

Geomorphic complexity was accounted for by adjusting the response scaling coefficients to reflect the available data (Table 1). Analysis of historical erosion during severe storms (Cardno, 2014) indicates that the storm demand volume at Lake Cathie

Beach is about 70% (135 m^3) of the typical value for exposed NSW beaches (200 m^3), so C_F was set accordingly. However, geotechnical testing suggests that the coffee rock may not withstand prolonged erosion as would be anticipated during coastline recession (Cardno, 2014), and thus C_R allowed for a potential full response to sediment budget redistribution (*i.e.* C_R = 1). Detailed mapping of shoreface reefs by marine LiDAR indicated approximately 30% coverage (Figure 4), and so C_S was set accordingly, within a 20% uncertainty space.

Figure 4. LiDAR data showing shoreface reef off Lake Cathie Beach.

Table 1. T*riangular pdf values for coastal response scaling coefficients.*

Scaling coefficient	Lower	Mode	Upper
C_F	0.6	0.7	0.8
C_R	0.6	0.8	1.0
C_S	0.6	0.7	0.8

RESULTS

Applying the volumetric coastline response model using the statistical simulation method generates a frequency histogram of coastline change predictions for each forecast period that reflects the convolution of the various input pdfs. Figure 5 shows the results of a 50-year forecast for Lake Cathie Beach, with 50, 90, 99 and 99.9 percentiles marked in grey. Fitting a continuous probability distribution to the frequency histogram allows for the predictions to be interpreted in terms of exceedance probabilities. The cumulative function of the best-fit distribution - in this case Generalised Extreme Value (GEV) is plotted to show exceedance probabilities for the full range of predictions (Figure 5).

DISCUSSION

Comparison of the 50-year forecast results shown in Figure 5, with a previous 'best estimate' prediction for 2050 using standard approaches, provides an opportunity to demonstrate the utility of the probabilistic approach in communicating uncertainty in predictions, and to consider the influence of geomorphic complexity at Lake Cathie Beach on forecast coastline change.

Figure 6 compares the 50-year probabilistic forecast (2064) with the 'best estimate' hazard line for 2050, which was derived using extrapolation of historical trends and the standard Bruun rule (SMEC, 2010). It is seen that the 50% exceedance forecast for 2064 (red line) is consistent with the best estimate prediction for 2050. In this case, the geomorphic complexity of Lake Cathie Beach (irregular dune topography, coffee rock, shoreface reefs) accounted for by the volumetric coastline response model moderates forecast coastline change relative to the best estimate, suggesting a potential delay in the magnitude of coastline change experienced of 15-20 years relative to the standard approach.

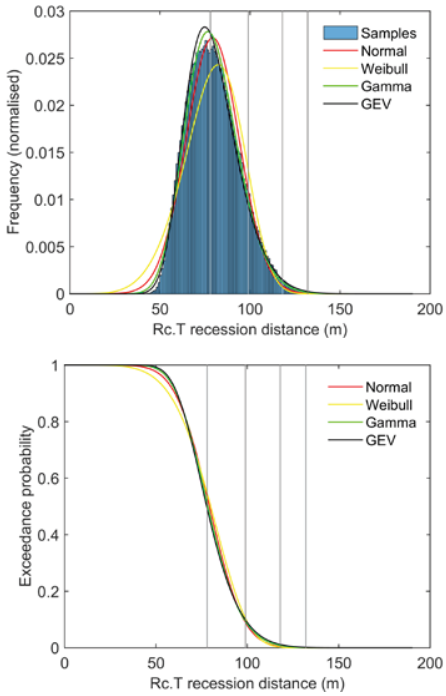

Figure 5. Frequency histogram (upper) and cumulative probability (lower) for a 50-year coastline change forecast at Lake Cathie Beach.

However, the 1% exceedance position marked by the green line indicates that 1% of feasible predictions exceeded that line, and thus some erosion risk exists beyond the 2050 best estimate line, which may need to be considered in future (Figure 6).

The flexibility of the volumetric coastline response model allows for the level of complexity to be adapted to suit the resolution and accuracy of data available to guide the sediment budget parameterisation, or the necessary resolution of forecasts. For example, a sediment cells framework characterising regional variability in coastal geomorphology and sediment transport has been developed for NSW to support regional-scale modelling to inform strategic planning (Hanslow *et al.*, 2016).

CONCLUSIONS

Uncertainty is characteristic of risk management and can be handled in predictions of coastline change through the use of statistical sampling techniques and flexible predictive models that account for the natural complexity of sediment-sharing systems. The method described here provides a pragmatic means to consider complexity due to three-dimensional morphology,

multiple sources and sinks, partially resistive substrates, and timescale-dependent shoreface response to sea level change, in a manner consistent with available data and current knowledge.

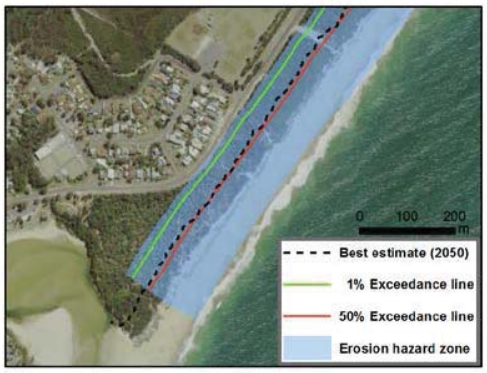

Figure 6. 50-year forecast for Lake Cathie Beach showing potential range of coastline change with 50% and 1% exceedance level lines.

ACKNOWLEDGMENTS

This study was partly funded by the NSW Government Natural Disasters Resilience Program. The authors are grateful for insightful comments and suggestions from Prof. Andrew Short, Angus Gordon and Prof. Bruce Thom.

LITERATURE CITED

Anderson, T.R.; Fletcher, C.H.; Barbee, M.M.; Frazer, N.L and Romine, B.M, 2015. Doubling of coastal erosion under rising sea level by mid-century in Hawaii. *Nat. Hazards*, 78, 75-103.

Bruun, P., 1962. Sea level rise as a cause of shore erosion. *Journal of Waterways and Harbors Division*, 88, 117-130.

Cardno, 2014, *Lake Cathie Hazard Study Review*. Cardno Pty. Ltd., 37 pp.

Cowell, P.J.; Stive, M.J.F.; Niedoroda, A.W.; de Vriend, H.J.; Swift, D.J.P.; Kaminsky, G.M. and Capobianco, M., 2003. The coastal-tract (part 1): A conceptual approach to aggregated modeling of low-order coastal change. *Journal of Coastal Research*, 19, 812-827.

Cowell, P.J.; Thom, B.G.; Jones, R.A.; Everts, C.H. and Simanovic, D., 2006. Management of uncertainty in predicting climate-change impacts on beaches. *Journal of Coastal Research*, 22, 232-245.

Eysink, W.D., 1990. Morphologic response of tidal basins to changes. *Proceedings of 22nd International Conference on Coastal Engineering* (Delft, The Netherlands).

Goodwin, I.D.; Freeman, R. and Blackmore, K., 2013. An insight into headland sand bypassing and wave climate variability from shoreface bathymetric change at Byron Bay, New South Wales, Australia. *Marine Geology*, 341, 29-45.

Gordon, A.D., 1987. Beach fluctuations and shoreline change – NSW. *Proceedings of 8th Australasian Conference on Coastal and Ocean Engineering* (Launceston, Australia).

Hanslow D.J.; Dela-Cruz J.; Morris B.D.; Kinsela M.A.; Foulsham E.; Linklater M. and Pritchard T.R., 2016. Regional Scale Coastal Mapping to Underpin Strategic Land Use Planning in South East Australia. *Proceedings of 14th International Coastal Symposium* (Sydney, Australia). *Journal of Coastal Research*, Special Issue 75 (this volume).

Harley, M.D.; Turner, I.L; Short, A.D.; Bracs, M.A.; Phillips, M.S.; Simmons, J.A. and Splinter, K.D., 2015. Four decades of coastal monitoring at Narrabeen-Collaroy Beach: the past, present and future of this unique dataset. *Proceedings of 22nd Australasian Coasts and Ports Conference* (Auckland, NZ).

Kinsela, M.A. and Cowell, P.J., 2015. Controls on shoreface response to sea level change. *Proceedings of Coastal Sediments '15* (San Diego, USA).

Kinsela, M.A. and Hanslow, D.J., 2013. Coast erosion risk assessment in New South Wales: limitations and potential future directions. *Proceedings of 22nd NSW Coastal Conference* (Port Macquarie, Australia).

Mariani, A.; Flocard, F.; Carley, J.T.; Drummond, C.D.; Guerry, N.; Gordon, A.D.; Cox, R.J. and Turner, I.L., 2013. *East Coast Study Project – National Geomorphic Framework for the Management and Prediction of Coastal Erosion*. Water Research Laboratory (WRL) Research Report 253, 41 pp.

Nielsen, A.F.; Lord, D.B.; Poulos, H.G. 1992, Dune stability considerations for building foundations, *Civil Engineering Transaction of the Institute of Engineers Australia, CE* 34.

Roy, P.S. and Thom, B.G., 1981. Late Quaternary marine deposition in New South Wales and southern Queensland - An evolutionary model. *Journal of the Geological Society of Australia*, 28, 471-489.

Shand, T.D.; Goodwin, I.D.; Mole, M.A.; Carley, J.T.; Browning, S.; Coghlan, I.R.; Harley, M.D.; and Peirson, W.L., 2011. *NSW Coastal Inundation Hazard Studies: Coastal Storms and Extreme Waves*. Water Research Laboratory (WRL), 45 pp.

Simmons, J.A.; Marshall, L.A.; Turner, I.L.; Splinter, K.D.; Cox, R.J.; Harley, M.D.; Hanslow, D.J. and Kinsela, M.A, 2015. A more rigorous approach to calibrating and assessing the uncertainty of coastal numerical models. *Proceedings of 22 Australasian Coasts and Ports Conference* (Auckland).

Short, A.D., 2006. Australian beach systems – nature and distribution. *Journal of Coastal Research*, 22, 11-17.

Short, A.D., 2010. Role of geological inheritance in Australian beach morphodynamics. *Coastal Engineering*, 57, 92-97.

Short, A.D.; Bracs, M.A. and Turner, I.L, 2014. Beach oscillation and rotation: local and regional response at three beaches in southeast Australia. *Proceedings of 13th International Coastal Symposium* (Durban, South Africa). *Journal of Coastal Research*, Special Issue 66, 712-717.

SMEC, 2010. *Lake Cathie Coastal Hazard Study – Revised*. SMEC Australia, November 2010, 23 pp.

Stive, M.J.F. and de Vriend, H.J., 1995. Modeling Shoreface Profile Evolution. *Marine Geology*, 126, 235–248.

Thom, B.G. and Hall, W., 1991. Behavior of beach profiles during accretion and erosion dominated periods. *Earth Surface Processes and Landforms*, 16, 113-127.

Woodroffe, C.D.; Cowell, P.J.; Callaghan, D.P.; Ranasinghe, R.; Jongejan R.; Wainwright, D.J.; Barry, S.J.; Rogers, K. and Dougherty, A.J., 2012. *Approaches to risk assessment on Australian coasts: A model framework for assessing risk and adaptation to climate change on Australian coasts*. NCCAR.

Journal of Coastal Research	SI	75	957-961	Coconut Creek, Florida	2016

Interoperability as supporting tool for Future Forecasting on coastal and marine areas

Fatima Navas[†], Emilia Guisado-Pintado[‡] and Gonzalo Malvárez[†]

[†]Physical Geography Area. Universidad Pablo de Olavide, Sevilla. CP 41013 (Spain)
fnavas@upo.es

[‡]Coastal Environments Research Group, Universidad Pablo de Olavide, Sevilla. CP 41013 (Spain)

www.cerf-jcr.org

www.JCRonline.org

ABSTRACT

Navas, F., Guisado-Pintado, E., and Malvárez, G., 2016. Interoperability as supporting tool for Future Forecasting on coastal and marine areas. *In:* Vila-Concejo, A.; Bruce, E.; Kennedy, D.M., and McCarroll, R.J. (eds.), *Proceedings of the 14th International Coastal Symposium* (Sydney, Australia). *Journal of Coastal Research*, Special Issue, No. 75, pp. 957-961. Coconut Creek (Florida), ISSN 0749-0208.

The powerful development of technology has allowed coastal sciences to advance significantly towards developing forecasting tools coupling empirical measurements with computer modelling, which proves to be of paramount importance for most decision making processes. However, coastal models and forecasting tools are data hungry and, whilst data and information availability for regional scales is more abundant than ever, the need for harmonised and compatible data-formats to integrate spatialised data continues to be an issue to feed these models. On the data and information side of development, interoperable systems appear to be somewhat limited to mapping agencies and computer scientists who focus on issues that are, to some extent, of limited relevance to coastal and marine scientists. In recent years however, this gap is being bridged by Spatial Data Infrastructures (SDI) in the framework of the INSPIRE Directive, which are showing to provide, via its integration with worldwide initiatives such as GEOSS and others, a source of great advances. In this paper we present two SDI designed, developed and implemented to be applied in coastal and marine management. Both platforms have taken a focused approach at spatial data manipulation favouring the use of specific viewers with circumscribed tools for making onscreen analyses and interpretations and capable of generating atlas-like products in real time dedicated to specific policies of relevance to the coastal and marine institutional framework.

ADDITIONAL INDEX WORDS: *Spatial Data Infrastructures, GEOSS, Geographic Information Sciences, Coastal and Marine Management.*

INTRODUCTION

In recent years coastal scientists and users at large have seen increasing access to an enormous and continuous flow of spatial information and much of this information is georeferenced. In the last 30 years, the amount of georeferenced data available has grown exponentially in line with the swift improvement of new communication channels and technologies such as the rapid development of spatial data capture technologies i.e. Global Positioning Systems (GPS), remote sensing images, sensors, etc. However, finding and accessing certain environmental and socioeconomic information is neither always straightforward nor adequate for further utilization of the data contained in the information (Albert and Dobbs, 2012). It appears that with the wealth of available spatialised information, a wider audience within the scientific and other user communities is demanding access to spatial information and, critically, to the data associated with maps and remote sensing products showing via internet resources such as map viewers (Cinnirella *et al*., 2012). Once a generalized use of geographic information technologies has demonstrated the widespread applicability, the first development of transforming maps into interoperability products affected cartographic outputs. These were maps visible via internet browsers without the need of extensive and expensive data transfer for processing on desktop applications.

Advanced mapping, achievable using web based technologies, allows the downloading of relevant data for more detailed local analysis by simple Geographic Information System (GIS) manipulation. However, beyond desktop solutions, online geospatial tools can assist in identifying ideal or potential locations for new projects in coastal areas. Other uses include discovery of new maps, visualization, and provide in some cases access to the raw data. This can be the case of dedicated Spatial Data Infrastructures (SDI) with an architecture developed through web-based geonodes (i.e. from data providers) that can integrate, through standardised services, significantly enlarged access to available geographical information. This implies using interoperable spatial information that allows coordination across organizations, joining together land and sea management bodies and reducing the costs of delivery. Likewise, managers and decision makers can create and evaluate different policy scenarios for coastal and marine management by examining the effects of different coastal activities in relation to policy targets. In certain circumstances, it can help visualize the consequences of different management approaches on coastal processes such as erosion, floods or other associated risks. Maps may be generated in support of disaster prevention efforts and response to emergencies.

DOI: 10.2112/SI75-192.1 received 15 October 2015; accepted in revision 15 January 2016.
*Corresponding author: fnavas@upo.es
©Coastal Education and Research Foundation, Inc. 2016

Interoperability requires the compliance with standards, normally driven by OGC (Open Geospatial Consortium), such as the Web Map Services (WMS) created to show, remotely, maps on the web in the form of services (Plesea, 2008). Like any other maps colours represented the different variables. Along with the mapped information (coloured) spatial information in the context of interoperability must also contain metadata, which consist of data about the spatial data. This accompanying database includes a variety of relevant information regarding geometric and cartographic details related to the map. This has been where the impact of the EU promoted INSPIRE Directive (European Union, 2007) has been greatest for all governmental agencies developing cartographic products, since the obligation to metadata maps has proved a colossal task. The positive effect is that nowadays, still within the scope of INSPIRE implementation at regional and national levels in Europe, most mapping agencies are complying with the requirements. However, this vision is not applicable to a significant amount of information being generated by scientists and other stakeholders who are not involved in the many requisites implicit in complying with the development of interoperable spatial information. Cartographic agencies are today the main agents and drivers of mapping services and tools.

Other types of web based services potentially of great usability by scientific users include Web Coverage Service (WCS) which offers multi-dimensional coverage data for access over the Internet or Web Feature Services (WFS), which are more adequate for data manipulation and further application. WCS and WFS are more complex and thus are infrequent as an output of scientific research results (other than geospatial research).

Commonly, national spatial data infrastructures have been directed toward terrestrial information, leaving marine data largely underdeveloped. Thematic SDIs can cover coastal and marine infrastructures, land uses changes as well as marine habitats and biodiversity (Fowler *et al.*, 2010), but, most importantly, they reinforce the need for a cohesive and decisive management and administration strategy for coastal zones (Binns 2004; Strain *et al*., 2006).

Finally, a future area for development of interoperable data systems is environmental process modelling. Many are the examples demonstrating the need for data accessibility for application in modelling of coastal and marine environments. The issues affecting the slow development of interoperable settings for modelling and forecasting are also related to the land-sea divide (a spatial problem in geodatabases) that prevents marine based models to integrate easily land data. Also, in purely marine datasets the inherent level of complexity requires addressing data processes at the individual data type level (Ojeda *et al.*, 2006). Issues like standardization, authoritative sources, and user needs are still being resolved for the more complex data in these contexts.

In terms of data input and output for modelling applications, SDI are currently finding quite challenging the transferability of results as well as general approaches to data use. For instance, in the development of marine ecosystem indicators the use of spatial data to feed computer based models (e.g. food chain models) could require time series at various depths as input. In the case of sea surface temperature models derived from satellite observation, the limitations are commonly related to harvesting of data sets shown just as “colour maps” where data is reduced in WMS to the colour pallet use to draw the map instead of the actual value represented. Another significant drawback is the need, in marine ecosystem modelling too, to use three-dimensional datasets (e.g. NetCDF files), which are frequently out of the scope of interoperable maps produced by mapping agencies. Three-dimensional variables (such as concentrations in the water column) can be incorporated as interoperable packages by using layered depth-variable maps. However, these and many examples continue to be specific developments and are not found in most SDI accessible on the web from mapping authorities.

Coastal and Marine scientists find frequently that the usual issues negatively affecting their research is still a limiting factor in data availability and quality despite the great wealth of data generated. In this paper, two dedicated SDI designed, developed and implemented for coastal and marine management are used as case study to provide the basis for discussion on the role of spatial data interoperability as supporting tool for future forecasting on coastal and marine areas. The PEGASO SDI (P-SDI) and the MEDINA e-Infrastructure (MeI) are two mapping platforms that have taken a focused approach at spatial data manipulation favouring the use of specific viewers to include tools for making onscreen analyses and interpretations capable of generating atlas-like products in real time dedicated to specific policies of relevance to the coastal and marine institutional framework.

Forecasting can be achieved in two ways in these mapping platforms: (i) producing new maps in an online Atlas based on trends, such as Interoperable versions of Cumulative Environmental Impact maps; and (ii) by creating interoperable maps based on modelling providing access to complex and comprehensive information for further forecasting tools (e.g. location of aquaculture industry, Posidonia oceanica occurrence).

CASE STUDY

The PEGASO SDI (P-SDI) and the MEDINA e-Infrastructure (MeI) are described in detail to illustrate their technical structure and their potential for addressing the challenges that stakeholders and scientific users could face.

The development of P-SDI responds to the need to establish a solid and interoperable distributed platform to support the implementation of the Integrated Coastal Zone Management Protocol for the Mediterranean (UNEP-MAP, 2008). Conceptually the P-SDI is built via a number of geonodes, which are centrally managed, but all serving their cartographic products to support the development of environmental indicators and other mapping tools, including land-sea interactions.

The MeI is a cyber infrastructure developed and registered in the GEOSS (Global Earth Observation System of Systems) which is fully devoted to showing and manipulating earth observation and modelling products in the context of marine ecosystem monitoring in North African Mediterranean countries.

Structure and components of the P-SDI.

The P-SDI is a distributed shared infrastructure made up of geonodes and with three main components: a map viewer, map services and a spatial catalogue. Thanks to this spatial data infrastructure, services and datasets related to the project PEGASO (www.pegasoproject.eu) can be used and shared by end users (stakeholders, researchers, communities, etc.) from a great variety of sources in a standardized, harmonized and interoperable way.

The P-SDI has been designed to support the PEGASO Shared Governance Platform for the delivery of Integrated Coastal Zone Management (ICZM), and the integrated assessments of coastal zones and marine areas in the Mediterranean and the Black Sea. All technologies employed in the development and implementation of P-SDI are open source with the structure of a composed stack of technologies both in the server and client side. On the server side, there is an implementation of an OGC (Open Geospatial Consortium) compliant server that delivers maps (WMS), geometric features (WFS) and coverages (WCS) on demand. MapServer was chosen as the leading server for online map delivery because of its speed and reliability.

A GeoNetwork catalogue server that implements OGC CSW protocol and ISO 19139 standards is used. The Java-based software has turned out to be a powerful tool with a graphic interface to manage metadata associated to the spatial datasets to create different user profiles and to visualize map images for published metadata. Moreover, it implements a powerful distributed search and harvesting engine across different catalogues implementing other protocols (OAI-MPH, etc). The GeoNetwork server is running on a server container called Apache Tomcat. This Java application server is connected to the most popular open source web server. All metadata managed by GeoNetwork are stored in a spatial-enabled database. Our election was PostgreSQL with its spatial extension PostGIS.

On the client-side a user interface is developed that renders map images and geometric features in any modern Internet browser. All libraries support cross-browser requirements and are written in Javascript implementing AJAX technology, releasing server load: OpenLayers, ExtJS and GeoExt. OpenLayers has been the most common open-source framework to display maps from different WMS servers to create authentic mash-ups. It contains a group of map controls to create interactive maps, enhancing the user experience supporting a great variety of OGC and Web 2.0 standards such as SVG, XML, GML, GeoJSON, GeoRSS and OGC Filter, for instance. ExtJS is a Javascript framework that allows users to create desktop-like web applications with interesting and interactive widgets.

The distinctive element developed for the P-SDI focused on providing interoperable products and forecasting tools to coastal and marine scientists is the P-SDI web-based Atlas. It is an online tool that is fully integrated in the P-SDI geoportal and combines interactive maps with text and images, organized in different sections or topics. The Atlas is one of the three components of the P-SDI (Map Viewer, Data catalogue and Atlas) developed to support coastal management in the framework of ICZM. The main focus for the development of the Atlas was to engage stakeholders and scientists in coastal management. The P-SDI Atlas consolidates essential data onto a state of the art mapping and visualization platform that allows end users to visualize, query, map, and analyse coastal data and various purpose built products (Indicators factsheets, Integrated Regional Assessments, Cumulative Impact Mapping and other relevant interoperable products).

Structure and components of the MeI.

The MeI is more than a geoviewer (www.medinageoportal.eu). It is an infrastructure that integrates all the results developed by the partners of the MEDINA Consortium. A geoviewer is at the front face and the public gateway to the information of the SDI. The MeI is a compound of services produced from Earth Observation, modelling and other analysis and transformed into interoperable services following OGC standards. The variety of thematic services and the capabilities of the viewer make the MeI a reference for scientist interested in topics related with monitoring marine ecosystems in North Africa. The MeI focuses in acting as a repository of spatial data for research centres and also as a tool for dissemination as well as a window to a very valuable set of data for the general public.

The Medina e-infrastructure is supported by an architecture based on an Open Source geomatic stack, being its basic components in the server side. There are a few components (hardware and software) that are completely necessary for the correct working of the Medina SDI, some belong to the server side and others to the client side.

On the server side an operating system Ubuntu 14.04.1 LTS from the OVH nodes network is used. The WMS server is an Open Source platform for publishing spatial data and interactive mapping applications to the web. Originally developed in 1997 as part of the ForNet project by the University of Minnesota in cooperation with NASA and the Minnesota Department of Natural Resources, MapServer is released under an MIT-style license. MapServer is an Open Source geographic data rendering engine written in the C language. Beyond browsing GIS data, MapServer creates “geographic image maps”, that is, maps that can direct users to content. Currently, MapServer is a project of OSGeo, and is maintained by a growing number of developers (nearing 20) from around the world. It is supported by a diverse group of organizations that fund enhancements and maintenance, and administered within OSGeo by the MapServer Project Steering Committee made up of developers and other contributors.

The CSW server, or GeoNetwork, has been developed to connect spatial information communities and their data using a modern architecture, which is at the same time powerful and low cost, based on the principles of Free and Open Source Software (FOSS) and International and Open Standards for services and protocols (a.o. from ISO/TC211 and OGC). The software provides an easy to use web interface to search geospatial data across multiple catalogues, combine distributed map services in the embedded map viewer, publish geospatial data using the online metadata editing tools and optionally the embedded GeoServer map server. Administrators have the option to manage user and group accounts, configure the server through web based and desktop utilities and schedule metadata harvesting from other catalogues.

An OpenDAP server from the Open Source OpenDAP NPO is combined with a Geographic database PostGIS which is a

spatial database extender for PostgreSQL object relational database. It adds support for geographic objects allowing location queries to be run in SQL. In MeI, a PostGIS database to store vector data which is located within the server. A supporting server-side programming for the browser front-end: several PHP programs (with CodeIgniter framework) is using PHP with a CodeIgniter framework.

On the client side (user interface) a custom Viewer developed with JavaScript (with jQuery) based on Leaflet integrates a dual panel, synchronized view, and an integrated catalog. In the client side, the technologies implemented are HTML5, CSS3 and JavaScript with a few libraries like JQuery 1.9.0, jQuery-ui 1.10.3, Leaflet and KineticJS 4.7.4. All the technology is accessible via the www.medinageoportal.eu with a custom application developed to access all spatial information (indicators and variables) as well as the relevant GEOSS catalogues.

For the interaction with desktop GIS the MeI has been adapted to the OGC standard, which means that can be accessed from any GIS application like QGIS, GvSIG, etc. Within the MeI, the server architecture is based on Linux, and the whole IT infrastructure is located in a server system.

DISCUSSION

By placing the Atlas directly in the hands of regional coastal and marine stakeholders via a powerful and simple to use interoperable mapping tool, the P-SDI Atlas supports collaborative decision making and robust regional and local coastal management and planning (Malvárez *et al.*, 2015). It acts as a repository of relevant documents, in different formats, accessible through the P-SDI. It improves the comprehension of tools and spatial information loaded on the viewer, it will support decision making process and contains predefined maps of main findings for both basins, with the interpretation of the results among other reports and suit of indicators.

Among other applications the P-SDI Atlas offers support to a multi-scale coastal risk index for the Mediterranean, an economic and social analysis of the uses of the coastal and marine waters, an integrated regional assessment in support of ICZM in the Mediterranean and Black Sea Basins (Santoro *et al.*, 2014). In relation to forecasting utilities all mapping products related to environmental and socio-economic indicators generated by the PEGASO project can be available to scientists and other stakeholders via the P-SDI Atlas including the Mediterranean scenario experiences developed within the ICZM platform where a cross-cutting approach between regional foresight analysis and participatory prospective can be integrated. Another significant development for further exploitation is the cumulative impact maps, currently shown as WMS, the first interoperable Land Use and Ecosystem Accounting maps for the entire Mediterranean basin comparing CORINE land cover land uses of 2000 and 2010 and mapped indicators of the State of the Mediterranean marine and coastal environment.

A key issue for the aperture of new communities to spatial data (such as scientists not necessarily involved in mapping science) is the efforts made in platforms such as MeI for the integration of indicators and model results. A key process that can be transferred to other initiatives is that model output are transformed into interoperable services following OGC standards as well as the INSPIRE EU Directive and the GEO System of Systems principles. In the MeI fully interoperability with the Global Common Infrastructure (GCI) and other systems is assured. Users are able to access key data sources and models, as well as to their associated metadata information. Metadata formats have been developed conforming to EN ISO 19115 and EN ISO 19119 for the Commission Regulation (EC) No 1205/2008 of 3 December 2008 implementing the INSPIRE Directive (European Union, 2007). Moreover, to guarantee applicability, close coordination with the GEOSS Architecture Data Committee (GEOSS ADC) and Science & Technology Committee (STC) ensures the common rules for the development and registration of the MeI and its services into the GCI. These are fully compatible with the GEOSS Infrastructure.

Purpose built forecasting environments based on web applications are enabling users to develop new spatial information by using, directly on the dedicated web services, existing interoperable data (Van Bemmelen and Craglia, 2013). These intelligent environments that link the appropriate information to promote new intended output and mapping products are technically achievable but far from standardize practice in most research projects dealing with coastal and marine science. As a tool for forecasting the immediate future challenge for SDI is the adaptation as architectures for web and cloud based services, including multidimensional interactive visualisation, collaborative user-driven environments and context-aware mapping environments.

CONCLUSIONS

A new paradigm has seen spatial data and information providers adapt to the interoperable ways for future forecasting based on web services. However, more demanding applications are arising due to the new possibilities offered by interoperability compliant data in coastal and marine modelling. Significant efforts are being made to reach the new demands of the scientific communities by offering specialized environments for mapping (such as purpose built Atlases) and modelling using interoperable input and output protocols. The two case studies presented in this paper, the P-SDI and the MeI contribute in providing prototype style mapping and viewing capacities but further development and awareness is needed to reach a wider scientific community. Online cloud-based modelling is increasingly the research area focusing on facilitating the bridge between data manipulation and powerful future forecasting online tools.

ACKNOWLEDGMENTS

The authors thank the PEGASO (supported by the European Union within FP7- ENV.2009.2.2.1.4 Integrated Coastal Zone Management. Contract n. 244170) and MEDINA (supported by the European Union Seventh Framework Programme FP7/2007-2013 under Grant Agreement n. 282977) consortia for the spatial information shared.

LITERATURE CITED

Albert, D. P. and Dobbs, R., 2012. Emerging Methods and Multidisciplinary Applications in Geospatial Research. IGI Global, Pennsylvania, USA, 386 p.

Binns, A., 2004. Defining a Marine Cadastre: Legal and Institutional Aspects. Melbourne, Australia: The University of Melbourne, M.Sc Thesis, 100 p.

Cinnirella, S., March, D., O'Higgins, T., Murciano, C., Sardà, R., Albaigés, J., and Pirrone, N., 2012. A multidisciplinary Spatial Data Infrastructure for the Mediterranean to support implementation of the Marine Strategy Framework Directive. *International Journal of Spatial Data Infrastructures Research*, 7, 323-351.

European Union, 2007. Directive 2007/2/EC of the European Parliament and of the Council of 14 March 2007 establishing an Infrastructure for Spatial Information in the European Community (INSPIRE). *Official Journal of the European Union.*

Fowler, C., Smith, B., and Stein, D., 2010. Building a Marine Spatial Data Infrastructure to support Marine Spatial Planning in U.S. waters. In: Calado H. and Gil A., (Eds.), *Geographic Technologies Applied to Marine Spatial Planning and Integrated Coastal Zone Management*. Ponta Delgada, Centro de informacao geografica e planeamento territorial, Unversidade dos Acores, 120-128.

Malvárez, G., Guisado-Pintado, E., Navas, F., and Giordano, A., 2015. Spatial data and its importance for the implementation of UNEP MAP ICZM Protocol for the Mediterranean. *Journal of Coastal Conservation*, 19 (5), 633-641. DOI: 10.1007/s11852-015-0372-1

Ojeda Zujar, J., Perez, J., and Gomez, A., 2006. Restitución Analítica, Estereocorrelación y Lídar para la Generación de Modelos Digitales de Terreno en Marismas Mareales. In Camacho, M.T, Cañete, J.A, and Lara, J.J. (Eds.), *El Acceso a la Información Espacial y Nuevas Tecnologías Geográficas*. Granada, Editorial de la Universidad de Granada, 1121-1134.

Plesea, L., 2008. The Design, Implementation and operation of the JPL OnEarth WMS Server. In Sample, T., Shaw, K., Tu, S., and Abdelguerfi, M., (Eds.), *Geospatial Services and Applications for the Internet*. US, Springer, 93-109.

Santoro, F., Lescrauwaet, A. K., Taylor, J., and Breton, F., 2014. *Integrated Regional Assessments In Support of ICZM In The Mediterranean And Black Sea Basins*. Intergovernmental Oceanographic Commission of UNESCO, IOC Technical Series, 111; IOC/2014/Ts/111, Paris, 84p.

Strain, L., Rajabifard, A., and Williamson, I., 2006. Marine administration and spatial data infrastructure. *Journal of Marine Policy*, 30 (4): 431-441.

UNEP-MAP (United Nations Environment Programme-Mediterranean Action Plan), 2008. Integrated Coastal Zone Management Protocol in the Mediterranean. Published by PAP/RAC. 89p.

Van Bemmelen, J., and Craglia, M., 2013. *GEOWOW: GEOSS Interoperability for Weather, Ocean and Water. IEEE.* Earthzine. http://earthzine.org

Journal of Coastal Research	SI	75	962-966	Coconut Creek, Florida	2016

On the Long-term Changes of Extreme Wave Heights at the German Baltic Sea Coast

Zhenshan Xu[†], Norman Dreier[‡], Yongping Chen[†*], Peter Fröhle[‡] and Dongmei Xie[††]

[†]College of Harbor, Coastal and Offshore Engineering
Hohai University
Nanjing, China

[‡]Institute of River and Coastal Engineering
Hamburg University of Technology
Hamburg, Germany

[††]Department of Civil and Environmental Engineering
University of Maine
Maine, U.S.A.

www.cerf-jcr.org

www.JCRonline.org

ABSTRACT

Xu, Z.S.; Dreier, N.; Chen, Y.P., Fröhle, P. and Xie, D.M., 2016. On the long-term changes of extreme wave heights at the German Baltic Sea Coast. *In:* Vila-Concejo, A.; Bruce, E.; Kennedy, D.M., and McCarroll, R.J. (eds.), *Proceedings of the 14th International Coastal Symposium* (Sydney, Australia). *Journal of Coastal Research*, Special Issue, No. 75, pp. 962-966. Coconut Creek (Florida), ISSN 0749-0208.

The assessment of extreme wave heights is of great importance for the design of coastal protection strucutres. This paper aims to present long-term changes of extreme wave heights at several selected locations at the German Baltic Sea Coast. Annual maximum significant wave heights were selected from the hourly wave data obtained from a hybrid approach (wind-wave-correlations combined with numerical simulations on the basis of the SWAN model) for a total period of 140 years, spanning from 1961 to 2100. The future projections of wind data were dreived from the regional COSMO-Climate Local Model for two emission scenarios A1B and B1. The extreme wave heights at each location were estimated from the respective best-fitting distribution, log-normal or Weibull distribution. The results indicate that, the long-term changes of extreme wave heights are related to the emission scenarios used in the regional climate model, the distribution chosen for the estimating (up to +9.6%) and also the sample size for the extreme value analysis (up to +8.7%). These factors should be carefully considered in the future coastal structure design.

ADDITIONAL INDEX WORDS: *Baltic Sea, extreme wave heights, extreme value distribution, Cosmo-CLM, SWAN*

INTRODUCTION

Coastal areas are the densely populated and highly industrialised parts of the world. The human activities there suffer from the coastal disasters caused by the local storms or wind waves. The coastal protection structures, such as groins, beach nourishments, breakwaters, are extensively used in these areas to eliminate those adverse effects. The design of these structures is dependent on the local wave conditions, especially the extreme wave conditions, which could be estimated by using the concept of return periods. Most of the existing coastal protection structures were designed based on the dataset of wave conditions in the past. Observed by IPCC (2007), climate change leads to significant changes of sea levels and wind events. These changes should be considered when determining the extreme wave conditions in the future design of coastal protection structures.

Recently, the future projection of the regional wave climate has become an interesting topic. It could be realised by applying spectral wave models, such as SWAN (Booij *et al.*, 1999) and WAM (The Wamdi Group, 1988). These models were driven by wind data obtained from regional climate models (RCMs). The boundary conditions of the RCMs were derived from the general circulation models (GCMs). Examples are given in the works of Grabemann and Weisse (2008), Casas-Prat and Sierra (2013), Groll *et al.* (2013). Examples of frequently used RCMs are the models Cosmo-CLM, HIRHAM5, RACMO2, and RCA3. The projection uncertainties are caused on the one hand side by different models and different scenarios of future climate change, which should be taken into account in the climate impact research (*e.g.*, Wang and Swail, 2006). On the other hand, the determination of extreme wave heights also relies on the distribution used and the time period for the selection of the samples.

This paper aims to present the long-term changes of extreme wave heights at selected locations along the German Baltic Sea Coast. Studies on the projections of the wave climate in the Baltic Sea have been conducted by different researchers, see BACC Author Team (2008, 2015). While most of the studies were focusing on the general changes in the region of Baltic Sea, we are focusing on several selected locations along the German Baltic Sea Coast in this study. Hourly wave data were obtained using the hybrid approach (wind-wave-correlations combined with the SWAN model simulations). The future projections of wind data were derived from the regional COSMO-Climate Local Model for two emission scenarios A1B and B1 from the IPCC Special Report. The extreme wave

DOI: 10.2112/SI75-193.1 received 15 October 2015; accepted in revision 15 January 2016.
*Corresponding author: ypchen@hhu.edu.cn
©Coastal Education and Research Foundation, Inc. 2016

heights were estimated by fitting annual maxima values of significant wave heights of 30 and 40 years to the Gumbel, Weibull and log-normal distribution. The confidence intervals were estimated by the Monte Carlo method. The results could be used to provide guidance in future coastal structure design.

METHODS

A hybrid approach was developed to calculate the wave data with the help of wind-wave-correlations and SWAN model simulations (Dreier *et al.*, 2013). On the basis of available synchronized local field data for wind and waves, the wind-wave-correlations have been derived for different locations at the German Baltic Sea Coast. The study area and the selected locations are shown in Figure 1. If the wind data used for the calculation of the past and future wave conditions exceeded the maximum wind velocities used for the derivation of the wind-wave-correlations, the wave heights were calculated with the help of stationary numerical simulations using SWAN. The numerical simulations were performed at a mean sea level and the resolution of ΔU_{10}=1m/s for the wind velocities and $\Delta\Theta_w$=10° for the wind directions as boundary conditions.

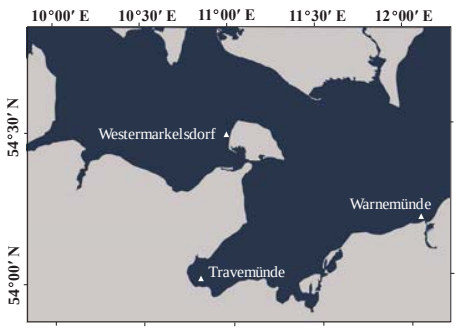

Figure 1. Study area and selected locations.

Table 1. *Cosmo-CLM runs. (Dreier et al., 2013)*

20th century (1961-2000) observed anthropogenic forcing	21st century (2001-2100) forced by emission scenario A1B	21st century (2001-2100) forced by emission scenario B1	transient time (1961-2100) series of wind parameter
C20_1	A1B	/	C20_1-A1B
C20_1	/	B1	C20_1-B1
C20_2	A1B	/	C20_2-A1B
C20_2	/	B1	C20_2-B1

The hourly wind data used in the hybrid approach were derived from the regional climate model Cosmo-CLM (Rockel *et al.*, 2008). The model Cosmo-CLM was forced by the global atmosphere-/ocean-ice-model ECHAM5/ MPI-OM. As shown in Table 1, two independent runs were available for the climate of 20th century (C20_1 and C20_2). For the future climate modelling both the two climate model runs for the 20th century were continued and forced by the SRES scenarios A1B (global economic) and B1 (global environmental), resulting in 4 independent runs, covering a period from 1961 to 2100. Figure 2 shows the comparisons of calculated and observed wave heights near Warnemünde. The calculated wave heights agree well with the observed data. More details of the model description and validation were given by Dreier *et al.* (2013).

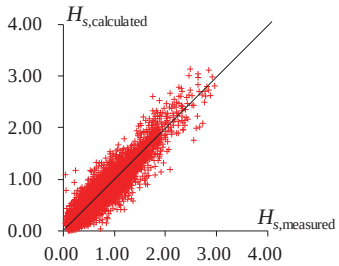

Figure 2. Comparisons of calculated and observed wave heights near Warnemünde.

From the time series of significant wave heights for each simulation run, the maximum wave height for each year was taken at the three locations shown in Figure 1. The annual maxima at each location in every 30/40-consecutive-year were fitted to three selected distributions, namely the Gumbel, Weibull and log-normal distribution. The cumulative distribution function (CDF) of Gumbel distribution is as follows,

$$F(x) = P(x < X) = \exp\{\exp[-(x-\alpha)/\beta]\} \quad (1)$$

where X is the random variable of the annual maxima, x is a possible value of X, α and β are location and scale parameters, respectively. The CDF of Weibull distribution is described as,

$$F(x) = P(x < X) = 1 - \exp\left[-(x/\beta)^{\alpha}\right] \quad (2)$$

where α and β are called the shape and scale parameters, respectively. The CDF of normal distribution is obtained by numerical integration of the probability density function (PDF). The PDF of normal distribution is described as,

$$f(y) = \frac{1}{\sigma(2\pi)^{0.5}} \exp\left[-(y-\mu)^2/(2\sigma^2)\right] \quad (3)$$

where μ and σ are the mean and standard deviation, respectively. If Y follows the normal distribution, and Y=ln(X) (X>0), X will follow the log-normal distribution. Then the PDF of the log-normal distribution can be derived. The parameters in the above theoretical CDFs or PDFs can be estimated using the maximum likelihood method. The empirical CDF was estimated as,

$$F_n(x_i) = \frac{i}{n+1} \quad (4)$$

where i= 1, 2, . . . , n denotes the rank of the annual maxima $x(i)$ in ascending order and n=30 or 40 in this study. The difference between the theoretical and empirical CDFs was represented by the absolute value of the average difference (D),

$$D = \frac{1}{n}\sum_{i=1}^{n}\left|F_n(x_i) - F(x_i)\right| \quad (5)$$

By comparing the D values regarding to different types of CDFs, the best-fitting CDF was determined. With the help of these theoretical CDFs, the return periods of extreme wave heights can be calculated. The relative changes of the extreme wave heights at the year m, which are calculated by using the data of the former 40 consecutive years, are defined as,

$$\Delta H_{s,m} = \frac{H_{s,l\sim m} - H_{s,1961\sim 2000}}{H_{s,1961\sim 2000}} \times 100\% \quad (6)$$

where m=2001,2002,…,2100 and l=1962, 1963,…,2061.

The confidence intervals of return periods were estimated by the Monte Carlo method, instead of the bootstrap resampling method. The Monte Carlo method is used to simulate the random process by a computer random number generator (see Chu, 1995). Based on the known theoretical CDF, 1000 batches of the simulated significant wave heights were generated by this method. Each batch contains 1000 significant wave heights, which means 1000 return periods calculated by the empirical CDF. There are 1000 significant wave heights with the same return periods for the 1000 batches. The confidence intervals can be estimated by sorting the above 1000 significant wave heights.

RESULTS

The performance of each theoretical CDF is examined by comparing with the corresponding empirical CDF, which is obtained by using the annual maxima data in every 40 consecutive years. The D values of each simulation run at three locations are shown in Figure 3 for the location Westermarkelsdorf and Figure 4 for the location Travemünde. Near the location of Westermarkelsdorf, the log-normal distribution is the best for the overall goodness of fit because the discrepancy is smallest, the same for the location Warnemünde. Near the location of Travemünde, the D values of log-normal and Weibull distributions are in the same level for the simulation runs C20_1-A1B and C20_1-B1, while the Weibull distribution fits better with the empirical CDF for the simulation runs C20_2-A1B and C20_2-B1. The Weibull distribution is chosen for the analysis of extreme wave heights near Travemünde.

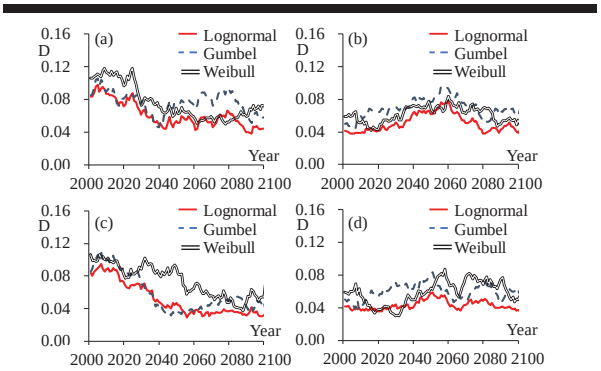

Figure 3. D values between theoretical and empirical CDFs of each simulation run near Westermarkelsdorf, (a) C20_1-A1B, (b) C20_1-B1, (c) C20_2-A1B, (d) C20_2-B1.

Figure 5 shows the relative changes of the extreme wave heights near Westermarkelsdorf, which are represented by the significant wave heights with a return period of 200 years obtained from the log-normal distribution. An increasing trend of relative changes is found for the simulation runs C20_2-A1B and C20_2-B1, while a decreasing trend is found for the other two runs. It should be also noted that, the magnitudes of the changes derived from log-normal distribution are depending on the sample size. Based on the analysis of the data in 30 consecutive years, the amplitude of changes for the simulation run C20_2-B1 is +19%, which is about twice of that obtained from the analysis of the data in 40 consecutive years. Similar results is found for the simulation run C20_2-A1B, while the differences between the results are slightly small for the simulation runs C20_1-A1B and C20_1-B1, around -8% and -16% respectively.

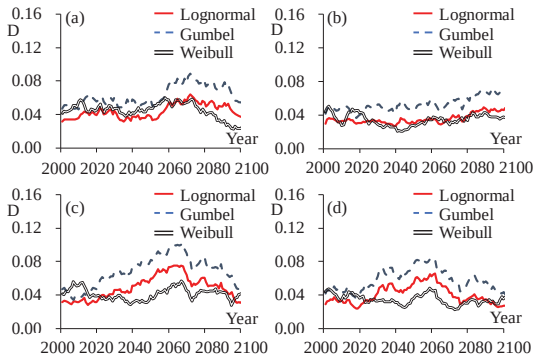

Figure 4. D values between theoretical and empirical CDFs of each simulation run near Travemünde, (a) C20_1-A1B, (b) C20_1-B1, (c) C20_2-A1B, (d) C20_2-B1.

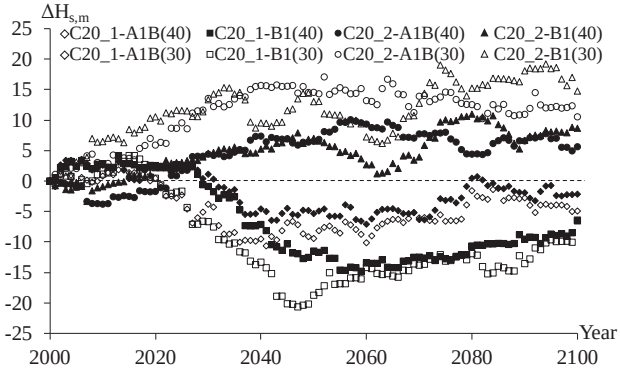

Figure 5. Changes of extreme wave heights near Westermarkelsdorf.

The relative changes of the extreme wave heights near Travemünde are shown in Figure 6. The results derived from the Weibull distribution for the sample size of 30 *resp.* 40 consequtive years are close to each other. The maximum difference is below ±3%. The changes of the extreme wave heights are around ±2.5% before the year 2030. After that, the changes could reach up to +10% or -6.5%, depending on different simulation runs. Figure 7 shows the relative changes of the extreme wave heights near Warnemünde. The results of log-normal distribution based on the analysis of the data in 40 consecutive years are not drawn here for the readability. From the beginning of the year 2040, the change of the extreme wave heights near Warnemünde shows in general a slight increasing trend with a maximum increase of up to +8%, except for the run C20_2-A1B which shows a maximum decrease of down to -7%.

Finally, the 95% confidence intervals of the 200 year return period for the extreme wave heights in all simulation runs at

three locations are illustrated in Figure 8. The absolute changes of the extreme wave heights for each simulation run and each location can be clearly seen in Figure 8. For example, the maximum extreme significant wave heights among the four simulation runs near the location of Warnemünde are 5.17m, 5.2m, 5.34m for the scenarios of 2000, 2050 and 2100, respectively. The extreme wave heights will not exceed 3m for all the scenarios of 2000, 2050 and 2100 near Travemünde. It is also found that the confidence intervals are quite broad, roughly 20% of the corresponding extreme wave heights.

DISCUSSION

As shown in Figure 5~7, the changes of the extreme wave heights at each location vary with different simulation runs. These differences may be attributed to the uncertainties in future social and economic development, which are represented by the different emission scenarios in this study. We are not able to state which scenario is more realistic in the near future. Each scenario should be considered equally in the analysis. Thus, the idea of ensemble projection could be applied in the estimation of the changes of the extreme wave heights along the German Baltic Sea Coast. Many studies (Donat *et al.*, 2010) suggest that an ensemble mean is better than a single model. For example, Grabemann and Weisse (2008) have conducted an ensemble study on the extreme wave conditions in the North Sea influenced by climate change. In our study, only two emission scenarios of one RCM were used for the simulation of the future wind conditions. In the next step, more samples of scenarios and models would be considered for deriving a robust conclusion.

Apart from the above uncertainties, some other aspects should also be considered with caution in the analysis of the future extreme wave heights. One is that the selection of the extreme value distribution, which might be a problem at certain locations. For example, the log-normal and Weibull distributions perform quite close with each other in the simulation runs C20_1-A1B and C20_1-B1 near the location of Travemünde. But, the extreme wave heights obtained from the log-normal distribution are 2.72m, 2.85m, 2.91m and from the Weibull distribution of 40 years 2.56m, 2.60m, 2.74m for the scenarios of 2000, 2050, 2100 respectively, for the simulation run C20_1-B1. The differences are ranging between +6.2% and +9.6%, which are quite large and will have a significant effect in the design of the coastal protection structures. The performances of different distributions are recommended to be compared comprehensively by use of more judging indexes.

The results of the extreme wave heights, which were obtained from the analysis of two sample sizes (30 and 40 years), are presented in this study. The difference between

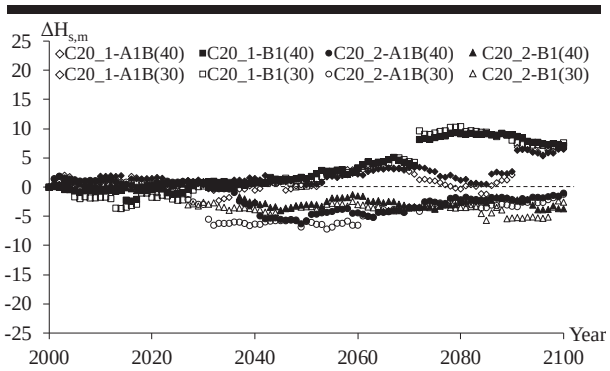

Figure 6. Changes of extreme wave heights near Travemünde.

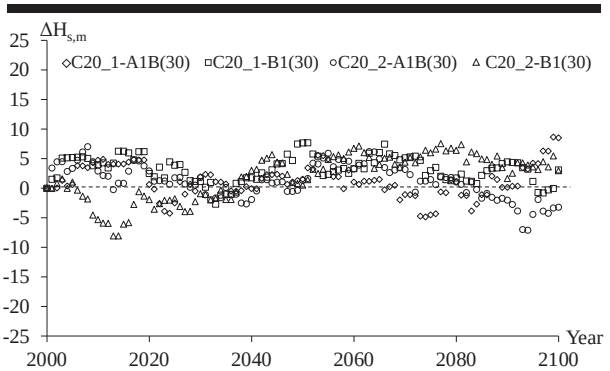

Figure 7. Changes of extreme wave heights near Warnemünde.

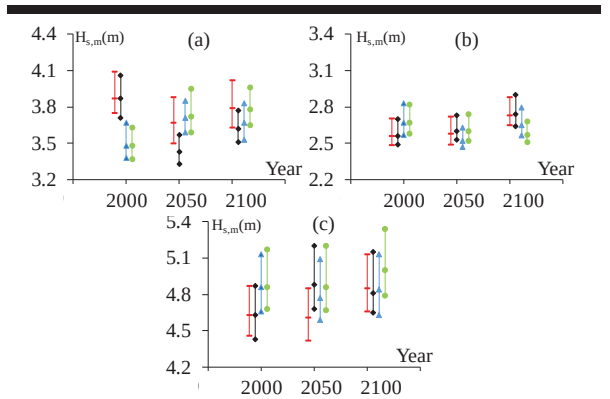

Figure 8. 95% confidence intervals of the 200 year return period for the extreme wave heights in all simulation runs (C20_1-A1B, Red‐ C20_1-B1, Black⋄ C20_2-A1B, Blue▵ C20_2-B1, Green&dot) near the locations (a) Westermarkelsdorf, (b) Travemünde, (c) Warnemünde.

them are quite obvious for some locations. As an example, the relative differences of extreme wave heights for the simulation run C20_1-B1 near the location of Westermarkelsdorf are shown in Figure 9. The maximum difference is +8.7%. The World Meteorological Organization (WMO) recommends in general a time period of 30 years for the assessment of climate

change and climate change inducted processes. In this study the sample size for the extreme value analysis was extended up to 40 years to get a larger sample size which gives better estimations of extreme wave heights due to the fitting of the extrem value function to the samples. In contrast a lower sample size (30 years) will lead to a higher uncertainty in the estimation of extreme wave heights, which is also reflected in larger confidence intervals for the 30 years sample size.

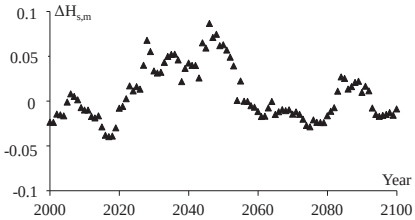

Figure 9. Relative differences of the extreme wave heights calculated for two sample sizes (30 and 40years) for the simulation run C20_1-B1 near the location of Westermarkelsdorf.

CONCLUSIONS

In this study the long-term changes of extreme wave heights were analysed at several selected locations of the German Baltic Sea Coast. Hourly wave data spanning from 1961 to 2100, were obtained using a hybrid approach. The future projections of wind data were derived from the regional COSMO-Climate Local Model for two emission scenarios A1B and B1. The log-normal distribution was assessed to be best fitted to the samples near the locations of Westermarkelsdorf and Warnemünde. In contrast near the location of Travemünde the Weibull distribution leads to the least differences in the goodness-of-fit test. Based on the analysis of the data in 30 consecutive years, an increasing up to 19% and a decreasing down to -20% were examined near the location of Westermarkelsdorf. The relative changes could reach up to 10% for increasing or -6.5% for decreasing, depending on different simulation runs for the location Travemünde. From the beginning of the year 2040, the change of the extreme wave heights near Warnemünde shows in general a slight increasing trend with a maximum increase of up to +8%, except for the simulation run C20_2-A1B which shows a maximum decrease of down to -7%. The relative differences of extreme significant wave heights obtained from the analysis of two series of data with different length (30 and 40 years) can reach up to 8.7% for the location Westermarkelsdorf.

ACKNOWLEDGMENTS

This publication was supported by the National Natural Science Foundation of China (Grant No. 51379072), the 111 Project of the Ministry of Education and the State Administration of Foreign Experts Affairs, China (Grant No. B12032), the research project RADOST (Regional Adaptation Strategies for the German Baltic Sea Coast, Grant No. 01LR0807F) as part of the research priority KLIMZUG (Managing Climate Change in Regions for the Future) funded by the German Ministry of Education and Research (BMBF) and the European Union Seventh Framework Programme (FP7/2007-2013) for the research project PEARL (Preparing for Extreme And Rare events in coastaL regions, Grant No. 603663). The paper reflects only the authors' views and the European Union is not liable for any use that may be made of the information contained herein.

LITERATURE CITED

BACC Author Team. 2008. *Assessment of climate change for the Baltic Sea basin.* Regional Climate Studies. Berlin: Springer.

BACC Author Team. 2015. *Second Assessment of climate change for the Baltic Sea basin.* Regional Climate Studies. Berlin: Springer.

Booij, N., Ris R.C., and Holthuijsen L.H., 1999. A third-generation wave model for coastal regions, Part I - Model description and validation. *Journal of Geophysical Research*, 104(C4), 7649-7666.

Casas-Prat, M., and Sierra, J.P., 2013. Projected future wave climate in the NW Mediterranean Sea. *Journal of Geophysical Research: Oceans*, 118, 3548-3568.

Chu, P.S., 1995. Hawaii rainfall anomalies and El Niño. *Journal of Climate*, 8, 1697-1703.

Donat, M.G., Leckebusch, G., Wild, S., and Ulbrich, U., 2010. Benefits and limitations of regional multi-model ensembles for storm loss estimations. *Climate Research*, 44(2-3), 211-225.

Dreier, N., Schlamkow, C., Fröhle, P., and Salecker, D., 2013. Changes of 21st Century's average and extreme wave conditions at the German Baltic Sea Coast due to global climate change. *Journal of Coastal Research*, Special Issue No. 65, pp.1921-1926.

Grabemann, I., and Weisse, R., 2008. Climate change impact on extreme wave conditions in the North Sea: an ensemble study. *Ocean Dynamics*, 58, 199-212.

Groll, N., Hünicke, B., and Weisse, R., 2013. Baltic Sea wave conditions under climate change scenarios. *Proceedings of the 7th Study Conference on BALTEX* (Borgholm, Sweden), pp.62.

IPCC AR4, 2007. *Climate change 2007. Fourth assessment report of the intergovernmental panel on climate change.* Cambridge University Press, Cambridge.

Rockel, B., Will, A., and Hense, A., 2008. The regional climate model COSMO-CLM (CCLM). *Meteorologische Zeitschrift*, 17(4), 347-348.

The Wamdi Group, 1988. The WAM model - a third generation ocean wave prediction model. *Journal of Physical Oceanography*, 18, 1775-1810.

Wang, X, and Swail, V., 2006. Climate change signal and uncertainty in projections of ocean wave heights. *Climate Dynamics*, 26, 109-126.

Journal of Coastal Research	SI	75	967 - 971	Coconut Creek, Florida	2016

A Comparison of Shoreline Changes Estimated Using the Base of Beach and Edge of Vegetation Line at North Keeling Island.

Farrah A. F. Adnan[†‡*], Sarah M. Hamylton [†], and Colin D. Woodroffe[†]

[†] School of Earth and Environmental Sciences,
University of Wollongong,
2522 New South Wales, Australia

[‡] Faculty of Science and Natural Resources,
Universiti Malaysia Sabah, Jalan UMS,
88400 Kota Kinabalu, Sabah, Malaysia

www.cerf-jcr.org

www.JCRonline.org

ABSTRACT

Adnan, F.A.F.; Hamylton, S.M., and Woodroffe, C.D., 2016. A Comparison of Shoreline Changes Estimated Using the Base of Beach and Edge of Vegetation Line at North Keeling Island. *In:* Vila-Concejo, A.; Bruce, E.; Kennedy, D.M., and McCarroll, R.J. (eds.), *Proceedings of the 14th International Coastal Symposium* (Sydney, Australia). *Journal of Coastal Research*, Special Issue, No. 75, pp. 967 - 971. Coconut Creek (Florida), ISSN 0749-0208.

The vulnerability of reef islands is often assessed by measuring changes in shoreline positions over time. Historical aerial photographs provide valuable information of past shoreline dynamics and are commonly incorporated in shoreline change assessment. Edge of vegetation line is the most common shoreline proxy adopted for assessments of reef island change because it is a visually distinguishable feature in aerial photographs, when compared to other coastal features such as high water line and base of beach. This study assesses shoreline changes of North Keeling Island from aerial photographs taken in 1987 and 2011 to evaluate the implications of adopting edge of vegetation line (EVL) and base of beach (BB) as shoreline proxies. The Digital Shoreline Analysis System (DSAS) (ArcGIS 10.2) method was applied to calculate shoreline changes using both proxies. Results indicate that EVL and BB generated different rates of change and variations of shoreline behaviour were observed at different locations around the island. The EVL indicated that the surface area of the island reduced in size over the 24 years, while in contrast, BB indicated that the island had accreted. Findings of this study imply that reef island shorelines are dynamic features which vary spatially and an improved understanding of the processes that underlie shoreline behaviour requires a geographical spread of sites for shoreline proxies when assessing shoreline change.

ADDITIONAL INDEX WORDS: *Reef island, DSAS, aerial photograph.*

INTRODUCTION

Reef islands are composed of largely unconsolidated sediments of calcareous sands and gravels that accumulate on the rim of atolls and other reef platforms (Kench *et al.*, 2005; Dawson and Smithers, 2014). Reef islands can be classified into sand cays and shingle cays (motu), depending on their morphology, sediment characteristics and vegetation (Stoddart and Steers, 1977). Many reef islands play important socioeconomic and ecological roles, such as providing areas for human settlements as in the Pacific and Indian Oceans (Woodroffe, 2008; Webb and Kench, 2010), and underpinning tourism revenue generated from activities such as fishing and resorts for many small island nations (Nunn *et al.*, 2015). Reef islands are perceived to be vulnerable to changing environmental conditions, particularly climate change and its associated impacts, such as the increased frequency and intensity of storms and sea-level rise (Church *et al.*, 2006; Biribo and Woodroffe, 2013). This vulnerability arises because they are low-lying, small in size and have sediments that are easily mobilised and reworked by waves and currents.

One of the great concerns of climate change is the loss of land area on reef islands due to erosion and inundation as a result of sea-level rise (SLR), especially in highly populated areas (Woodroffe, 2008). Assessments of reef island vulnerability often incorporate measurements of shoreline change over time. Despite limitations such as image quality and accuracies associated with older data, many studies acknowledge that historical data such as aerial photographs, topographical surveys and maps are valuable information for reef island studies. This is because they provide baseline information on past shoreline configurations against which changes can be monitored to provide insight on past reef island dynamics (Ford, 2013; Hamylton and Puotinen, 2015). Historical aerial photographs allow monitoring of shoreline changes for a longer period compared to more recent remote sensing satellite data; providing information that is not captured by modern technology.

Digital Shoreline Analysis System (DSAS) is a tool commonly used to determine the distance of digitised shoreline proxies along transects cast perpendicular to a baseline to compute shoreline change (Thieler *et al.*, 2009). Boak and Turner (2005) review examples of shoreline proxies from numerous studies, which suggest that edge of vegetation line, base of beach and the high water line are discernible features that can be detected in aerial photographs. Most studies of reef island change that incorporate aerial photographs usually adopt edge of vegetation line as shoreline proxy because it is easier to identify compared to other geomorphological features (Ford, 2013; Kench *et al.*, 2015). Biribo and Woodroffe (2013) in their study on reef islands of Tarawa Atoll, Kiribati suggested that base of the beach is also a good shoreline proxy as it is a prominent line that can easily be detected along the oceanward shore in aerial photographs.

DOI: 10.2112/SI75-194.1 received 15 October 2015; accepted in revision 15 January 2016.
*Corresponding author: fafa639@uowmail.edu.au
©Coastal Education and Research Foundation, Inc. 2016

A key issue for the selection of shoreline proxies in change analysis is the question of whether or not the proxies selected represent the actual shoreline position. Do movements in vegetation lines actually correspond well with movements of the adjacent beach areas over time? Ford (2012) noted that changes in beach area may not necessarily influence vegetation position. This calls into question the whole basis for using aerial photographs and remote sensing information for monitoring reef island changes. Here, we evaluate the implications of applying different definitions of the shoreline when using historical aerial photographs to assess island shoreline change over time. We compare estimates of shoreline change using the edge of vegetation line and base of beach as shoreline proxies of North Keeling Island for 1987 and 2011 (24 years).

Background

North Keeling Island (a.k.a. Pulu Keeling) is part of the Cocos (Keeling) Islands group that are located in the East Indian Ocean. North Keeling Island is an uninhabited island of about 2.1 km long and 1.3 km wide that is located 26 km north of the main Cocos Atoll (South Keeling Islands) (Woodroffe and Berry, 1994). It is a semi-crescentic, densely vegetated reef island resembling a small atoll with swampy lagoon (Woodroffe and McLean, 1994). The dominant vegetation types on this island are *Pisonia grandis* and *Cocos nucifera* forest, *Heliotropium foertherianum* shrublands, *Pemphis acidula* thickets and open grassy areas (Director of National Parks, 2015). Sediment varies from sand in the north to coarser coral rubble to the south and radiocarbon dates on corals suggest that the island developed more than 3000 years B.P. (Woodroffe and McLean, 1994). Outcrops of coral conglomerate and rubble ridges are common features found especially at the southern and eastern shores. Reef crest is present round the island except at the northwestern corner. A channel provides an entrance to the lagoon on the eastern, windward side of the island, which has undergone significant sedimentation in the past two decades. North Keeling was declared a National Park in 1995 due to the unique and pristine state of its flora and fauna and is administered by Parks Australia (Director of National Parks, 2015).

METHODS

Coloured vertical aerial photographs of North Keeling Island from 1987 and 2011 provided by Geoscience Australia were used in shoreline change assessment for this study as outlined in Figure 1. Both aerial photographs were independently georeferenced in ArcMap (ArcGIS 10.2) to the WGS 1984 UTM Zone 47S projected coordinate system using thirteen ground control points for permanent features such as beachrock, conglomerate platforms and reef patches that were extracted from Google Earth (version 2013). Images were transformed using the second order polynomial transformation in ArcMap, with both images having an associated RMSE <1 m.

The edge of vegetation line (EVL) and base of beach (BB) were selected as shoreline proxies in this study as both are visibly distinctive shoreline features in the datasets. EVL is indicated by the seaward edge of vegetation which is generally distinct due to the colour contrast between vegetation and beach sediment, particularly where dense vegetation is present. This study adopts the BB shoreline as suggested by Biribo and Woodroffe (2013), which is where the edge of beach sand meets the solid reef flat and can be indicated by the sudden change in substrate and beach slope. Shorelines were visually interpreted and manually digitised by a single operator at a fixed scale (1:1000) within ArcMap. Digitised shorelines were used to analyse changes in shoreline positions.

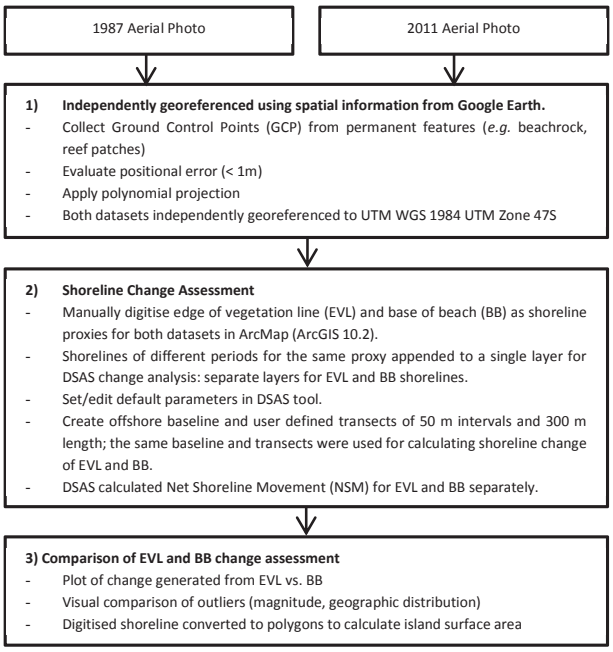

Figure 1. Methods used in assessing shoreline change using EVL and BB as shoreline proxies.

Shoreline proxies for the two periods were incorporated into DSAS for shoreline change analysis based on the methods by Thieler *et al.* (2009). DSAS offers various statistical measurements of shoreline change but only Net Shoreline Movement (NSM) was used for this study. NSM calculates the distance between oldest and youngest shoreline. To compare the shoreline change rate between EVL and BB, an offshore baseline was created and transects were cast at intervals of 50 m around the island using the DSAS tool. Transects length was set to 300 m to allow intersections with all shorelines for shoreline change calculation. NSM was calculated separately for each shoreline proxy, by using the same user-defined baseline and transects to allow for comparison between shoreline changes measured using EVL and BB for each transect. 139 transects were cast around North Keeling Island and shoreline change rates for each transects were calculated using DSAS, as outlined in Figure 1.

RESULTS

Analysis of reef island shoreline changes during the period 1987-2011 for North Keeling Island reveals that overall there is a weak correlation between rate of shoreline change indicated by

edge of vegetation line (EVL) and base of beach (BB) (Figure 2). Results show that there is correlation when there is accumulation and vegetation line is slowly advancing as the BB accretes with a succession of littoral plants. Conversely, it is apparent that there is no correlation between BB and EVL when erosion occurs.

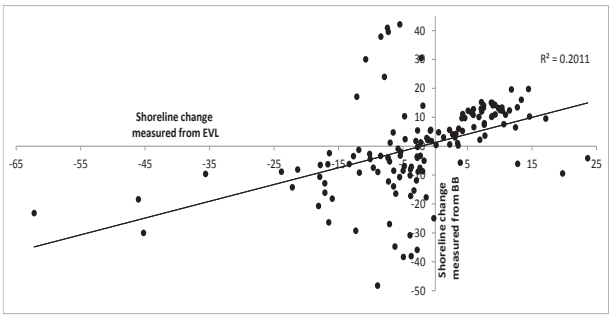

Figure 2. Shoreline change rates for each transect compared between EVL and BB based on NSM rates.

NSM values calculated for each transects around North Keeling Island ranged between -62.2 – 23.64 m and -48.24 – 42.13 m for EVL and BB respectively (Figure 3). When using EVL as shoreline proxy, 60 % of the transects indicated areas of erosion compared to the BB, where only 47 % of the transects had negative values of NSM. This implies that between 1987 to 2011, the vegetation line underwent more erosion than accretion. The total planform island area measured using EVL in 1987 was 2.066 km^2 and decreased to 2.059 km^2 in 2011. On the other hand, shoreline change analysis using the BB in this study showed that 53 % of the transects had positive NSM values indicating that the number of locations accreting was slightly higher compared to eroding areas. Island area measured using the BB increased from 2.194 km^2 in 1987 to 2.197 km^2 in 2011.

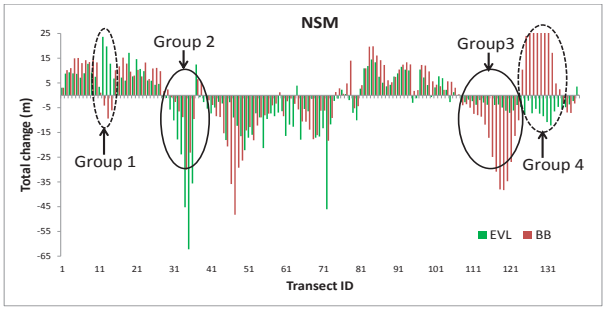

Figure 3. Shoreline changes around North Keeling Island (1987 to 2011) measured from both the EVL and BB shoreline, showing rates of change based on NSM. The circles mark some areas of substantial differences in shoreline changes measured between EVL and BB (Dashed line circles: examples of inverse relationship of accretion/erosion measured from the different shoreline proxies; Solid line circles: examples of direct relationship of accretion/erosion but with substantial difference in rate of change measured from the different shoreline proxies).

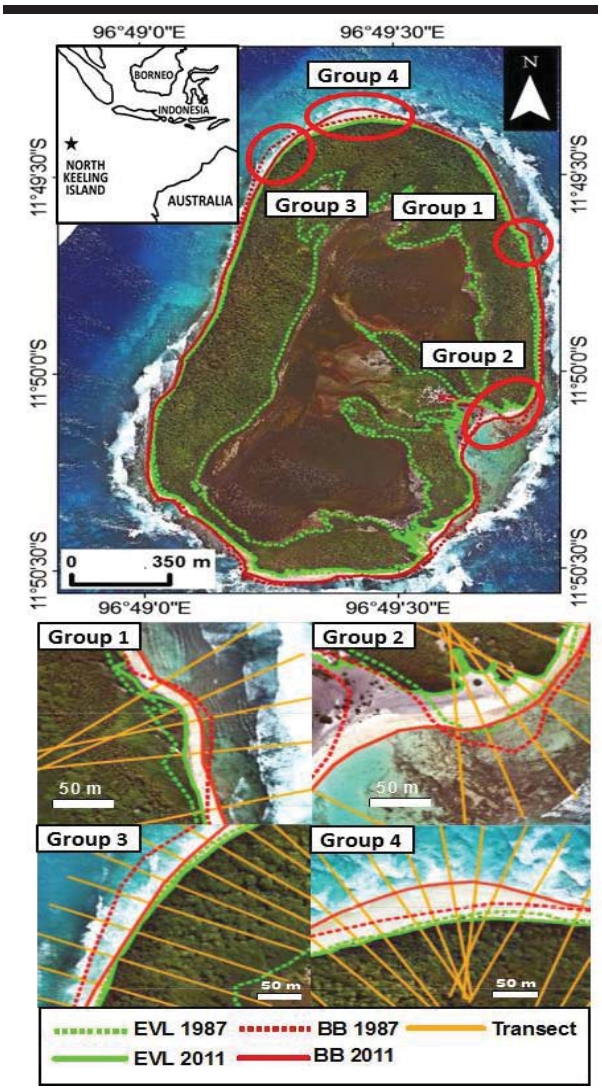

Figure 4. Aerial photo of North Keeling 2011 with digitised shorelines of EVL and BB for 1987 and 2011. Insets show Group 1 to 4; the areas where substantial shoreline differences between EVL and BB occurred (as depicted in Figure 3).

This study identifies four main types of deviation of shoreline change around North Keeling Island based on comparison between NSM measurements calculated using EVL and BB shoreline proxies (Figures 3 and 4). These four types represent inverse and direct relationships of shoreline behaviours between the EVL and BB and are described as follows:

Group 1: Inverse relationship; where EVL showed accretion while the BB indicated erosion as observed at northeast part of the island.

Group 2: Direct relationship; where both EVL and BB eroded but erosion of EVL is substantially greater than that of BB as observed near the lagoonal entrance, southeast of the island.

Group 3: Direct relationship; where both EVL and BB eroded but erosion of BB is substantially greater than that of EVL as observed at the northwest of the island.

Group 4: Inverse relationship; where BB showed accretion while EVL indicated erosion as observed at the northern part of the island.

Although areas of Group 3 and 4 are situated next to each other at the northern part of the island (Figure 4), the behaviour of their BB shorelines was totally opposite. BB shorelines of Group 3 indicate erosion and conversely in Group 4, the BB indicated shoreline accretion. Areas where sediments are coarser and cemented features are present, such as beachrock and outcrops of conglomerate platforms as described by Woodroffe and McLean (1994) especially at the southern part of the island, showed smaller range of deviation between the shoreline proxies.

DISCUSSION

This study presents the findings of two assessments of reef island change that adopt different shoreline proxies derived from aerial photographs. There appears to be little correspondence in movements of EVL and BB shorelines, suggesting that the processes that influence EVL differ from those that influence BB. Some possible explanations for the difference in shoreline behaviour could be attributed to the presence of different vegetation and geomorphic features, giving rise to different geomorphological processes around the island.

The variation of EVL behaviour around North Keeling Island could be influenced by the difference in vegetation type at a particular location and also by the absence/presence of shore protectors such as outcrops of beachrock and rubble ridges. Vegetation can provide stability compared to the beach area consisting of unconsolidated sand, especially where no cemented features are present (Dawson and Smithers, 2010). The stabilising effect of vegetation through binding of loose sediments and entrapment of sediments carried by wind, tide or overtopping waves may differ according to size, type and denseness of the vegetation (Stoddart and Steers, 1977). Therefore, vegetation that is more erosion-resistant might avoid erosion which is possibly the reason that the EVL shoreline did not exhibit recession when BB indicated erosion at the northeastern area of the island. On the other hand, ecological communities that comprise less erosion-resistant vegetation might slowly recede as the beach area erodes which can be observed at the southeastern area.

There is evidence that the geomorphic variations around reef islands can also result in different morphological responses around reef islands (Aston, 1995) which can be influenced by various processes such as wind and wave action. We suggest that substantial BB shoreline change observed at the northern shores of North Keeling could be attributed to the much finer grain size that is easier to be mobilised by waves and currents compared to the coarser sediment accumulated at the southern area. The waves generated from the windward, south direction, could potentially refract around the island and deposit the finer sands on the leeward (northern) facing shorelines, consequently producing a larger beach area as observed for the Group 4 shoreline change. Substantial BB shoreline recession at the northwestern area (Group 3) also suggests that this is an erosion area, which could potentially act as a sediment source to the neighbouring Group 4 beach. Continuous supply of sediment to the northern part of the island will favour beach accretion, although EVL undergoes erosion. Therefore, we are not able to find correlation between BB recession and EVL recession. Moreover, the elevation of the beach might decrease as a result of erosion but the BB shoreline might move towards the sea as a result of sediment addition from the eroded upper beach. However, current study is not able to estimate changes in elevation.

Over time, accumulation of sediment to the nearshore areas could favour seaward EVL accretion as it provides area for natural plant-cover succession to take place. Areas that have coarser sediment particles or have cemented structures such as rubble ridges and beachrock at the south and eastern shores denote similar trend of shoreline change between EVL and BB. Shoreline changes at these areas are more representative of a long term transition towards erosion and accretion states, instead of temporary or cyclic localised fluctuations that differ at other parts of the island. Temporary shoreline changes could be determined by more comprehensive study incorporating analysis of more shoreline records over time as suggested by Ford (2013).

Our results reveal that changes in shoreline of a vegetated reef island using EVL and BB as shoreline proxies generated differing results. This is consistent with findings of Biribo and Woodroffe (2013), where more transects cast using EVL at the lagoon shore indicated accretion compared to the transects using BB. They further suggested that BB would be a better indicator of shoreline as it captures the footprint of the island compared to the EVL but the difficulties in distinguishing the BB for certain locations may influence the accuracy of the results. Kench *et al.* (2015) adopted the EVL as the shoreline proxy to assess the reef islands of Funafuti Atoll in which 15 out of 29 islands indicate island area accretion over a period of more than 100 years. If BB were chosen as a shoreline proxy instead, the results would most likely be different because the studied reef islands varied in size and sediment composition. Differing behaviours of shoreline proxies were also observed by Hanslow (2007) for McMasters Beach, New South Wales where EVL and high water mark showed different changes.

Understanding the different processes that influence different types of shoreline is important for the selection of suitable shoreline proxies for assessing reef island change to yield results that represent actual shoreline movements. Considerable care is needed when choosing shoreline proxies as changes could be attributed to natural oscillation of the beach or episodic events that could mask actual island accretion or erosion. A more comprehensive study incorporating field data such as elevation to quantify island volume can further verify whether the change in planform area is caused by additional input of sediments from the surrounding reef or is merely a characteristic of island dynamism undergoing natural cyclic processes.

CONCLUSIONS

The following conclusions can be drawn from the present study: i) shoreline change assessment for North Keeling island adopting edge of vegetation line as shoreline proxy indicated erosion of island planform area and, conversely, the assessment

that adopted base of beach as a proxy indicated accretion, ii) shorelines exhibit various responses to coastal processes based on their geomorphological characteristics.

Results of assessments of shoreline change for a reef island are dependent on what shoreline indicator is selected. Deviation of shoreline changes likely occurred because the coastal processes influencing BB are different to the processes influencing EVL. BB shoreline represents a reef island in terms of sediment source and supply whilst EVL reflects the natural plant-cover succession. Careful interpretation of reef island change using BB shoreline is pivotal in order to distinguish temporary from long term changes. Our results also challenge the idea that reef island change is represented by changes in EVL as adopted in many studies. There is little evidence to support the idea that changes in natural plant-cover succession reflect actual island change. It is also important to note the uncertainties that arise when using shoreline proxies extracted from aerial photographs which is generally visually bias and could be reduced by conducting field groundtruthing. This study suggests that a more holistic measure of shoreline change might account for the numerous processes that underpin shoreline movements including the geographic variation that these might exhibit with local environmental features around an island periphery.

ACKNOWLEDGMENTS

The authors would like to acknowledge the University of Wollongong, Australia for providing technical support and facilities for spatial analysis work conducted for this study. We thank Parks Australia, particularly Ismail MacRae and Trish Flores in the Pulu Keeling National Parks Office and Geoscience Australia for providing various datasets of North Keeling Island for this study. This study is a part of an education scholarship aid by the Ministry of Higher Education Malaysia and Universiti Malaysia Sabah.

LITERATURE CITED

Aston, J. P., 1995. The relative mobilities of coral cays on the Great Barrier Reef can be modeled. Townsville, Queensland: James Cook University, Master's thesis, 267p.

Biribo, N. and Woodroffe, C.D., 2013. Historical area and shoreline change of reef islands around Tarawa Atoll, Kiribati. *Sustainability Science,* 8(3), 345-362.

Boak, E.H. and Turner, I.L., 2005. Shoreline Definition and Detection: A Review. *Journal of Coastal Research,* 214, 688-703.

Church, J.A.; White, N.J., and Hunter, J.R., 2006. Sea-level rise at tropical Pacific and Indian Ocean islands. *Global and Planetary Change,* 53(3), 155-168.

Dawson, J.L., and Smithers, S.G., 2010. Shoreline and beach volume change between 1967 and 2007 at Raine Island, Great Barrier Reef, Australia. *Global and Planetary Change,* 72(3), 141-154.

Dawson, J.L., and Smithers, S.G., 2014. Carbonate Sediment Production, Transport, and Supply To A Coral Cay At Raine Reef, Northern Great Barrier Reef, Australia: A Facies Approach. *Journal of Sedimentary Research,* 84(11), 1120-1138.

Director of National Parks, 2015. *Pulu Keeling National Park Management Plan 2015-2025.* Canberra: Australia.

Ford, M., 2012. Shoreline Changes on an Urban Atoll in the Central Pacific Ocean: Majuro Atoll, Marshall Islands. *Journal of Coastal Research,* 279, 11-22.

Ford, M., 2013. Shoreline changes interpreted from multi-temporal aerial photographs and high resolution satellite images: Wotje Atoll, Marshall Islands. *Remote Sensing of Environment,* 135, 130-140.

Hamylton, S.M., and Puotinen, M., 2015. A meta-analysis of reef island response to environmental change on the Great Barrier Reef. *Earth Surface Processes and Landforms.* doi: 10.1002/esp.3694

Hanslow, D.J., 2007. Beach Erosion Trend Measurement: A Comparison of Trend Indicators. *Proceedings of the 9th International Coastal Symposium (ICS2007). Journal of Coastal Research,* Special Issue No. 65, pp.588-593.

Kench, P.S.; McLean, R.F., and Nichol, S.L., 2005. New model of reef-island evolution: Maldives, Indian Ocean. *Geology,* 33(2), 145.

Kench, P.S.; Thompson, D.; Ford, M.R.; Ogawa, H., and McLean, R.F., 2015. Coral islands defy sea-level rise over the past century: Records from a central Pacific atoll. *Geology.* doi: 10.1130/g36555.1

Nunn, P.D.; Kumar, L.; Elliot, I., and McLean, R.F., 2015. *Regional coastal susceptibility assessment for the Pacific Islands: Technical Report.* Commonwealth of Australia, 2015, 122p.

Stoddart, D.R., and Steers, J.A., 1977. The Nature and Origin of Coral Reef Islands. *In:* Jones, O.A. and Endean, R. (eds.), *Biology and Geology of Coral Reefs (Vol. IV: Geology 2)*. New York: Academic Press, Inc.

Thieler, E.R.; Himmelstoss, E.A.; Zichichi, J.L., and Ergul, A., 2009. *Digital Shoreline Analysis System (DSAS) version 4.0 — An ArcGIS extension for calculating shoreline change.* U.S. Geological Survey Open-File Report 2008-1278.

Webb, A.P., and Kench, P.S., 2010. The dynamic response of reef islands to sea-level rise: Evidence from multi-decadal analysis of island change in the Central Pacific. *Global and Planetary Change,* 72(3), 234-246.

Woodroffe, C.D., 2008. Reef-island topography and the vulnerability of atolls to sea-level rise. *Global and Planetary Change,* 62(1-2), 77-96.

Woodroffe, C.D., and Berry, P.F., 1994. Scientific studies in the Cocos (Keeling) Islands: an Introduction. *In:* Woodroffe C.D. (ed.), *Ecology and Geomorphology of the Cocos (Keeling) Islands. Atoll Research Bulletin,* No. 399, 1-16.

Woodroffe, C.D., and McLean, R.F., 1994. Reef islands of the Cocos (Keeling) islands. *In:* Woodroffe C.D. (ed.), *Ecology and Geomorphology of the Cocos (Keeling) Islands. Atoll Research Bulletin,* No. 403, 1-36.

Journal of Coastal Research	SI	75	972 - 976	Coconut Creek, Florida	2016

Regional Environmental Sensitivity Index (RESI) Classification of Estonian Shoreline (Baltic Sea)

Robert Aps[†], Hannes Tõnisson[‡]*, Ülo Suursaar[†], and Kaarel Orviku[‡]

[†]Estonian Marine Institute, University of Tartu
Tallinn, Estonia

[‡]Institute of Ecology, Tallinn University
Tallinn, Estonia

www.cerf-jcr.org

www.JCRonline.org

ABSTRACT

Aps, R.; Tõnisson, H.; Suursaar, Ü., and Orviku, K, 2016. Regional Environmental Sensitivity Index (RESI) Classification of Estonian Shoreline (Baltic Sea). *In:* Vila-Concejo, A.; Bruce, E.; Kennedy, D.M., and McCarroll, R.J. (eds.), *Proceedings of the 14th International Coastal Symposium* (Sydney, Australia). *Journal of Coastal Research*, Special Issue, No. 75, pp. 972 - 976. Coconut Creek (Florida), ISSN 0749-0208.

Despite improving navigation safety measures, there is a growing risk of accidental oil spills and associated oil pollution on the Baltic Sea, an area which has been designated as a Particularly Sensitive Sea Area by the International Maritime Organization. Environmental Sensitivity Index (ESI) maps have been an integral component of oil-spill contingency planning and response in the United States since 1979, serving as a quick reference for oil spill responders. The ESI ranks shoreline into 10 classes in relation to sensitivity, natural persistence of oil, and ease of clean-up. Some countries outside the US have adopted the ESI approach to classify their own shorelines for similar oil spill contingency planning, the resulting maps being referred to as Regional Environmental Sensitivity Index (RESI) maps. However, problems arise when applying the classification system. This article highlights the difficulties of applying the standard ESI classification to the Estonian shoreline and suggests a potential RESI classification scheme for Estonia that would divide cliff shores among sensitivity classes 1 and 5, with most of them into class 5, the designation for those that are the most difficult to clean up (mixed sediments on the beach and no access from the land). An Estonian RESI map layers are integrated into the SmartResponse Web - an analytical tool for emergency response and recovery that is used to combine the information related to the accident, development of an oil spill and information on environmental sensitivity of the Baltic Sea shoreline. The SmartResponse Web enables the identification and dynamic assessment of environmental risks as a continuous process for purposes of determining best practices for reducing or even eliminating the risks, and it is used by the Estonian oil spill response authorities for contingency planning, training and in emergency situation.

ADDITIONAL INDEX WORDS: *ESI, RESI, STAMP, oil spill response, shoreline geology, shore types.*

INTRODUCTION

The Baltic Sea was designated as a Particularly Sensitive Sea Area (PSSA) at the International Maritime Organization's (IMO) Marine Environment Protection Committee's 53rd session in July 2005. The coastal waters of the Gulf of Finland constitute an environmentally rich ecosystem with unique natural beauty. Since the marine ecosystem in the Baltic Sea is fragile and highly sensitive to marine pollution (*e.g*. Sonninen *et al.*, 2006), the risk posed by heavy vessel traffic is especially acute. However, oil transportation in the Baltic Sea is growing significantly with the shipping routes through the Gulf of Finland being some of the busiest in the world. According to Brunila and Storgård (2012), every day more than 2000 ships sail in the Baltic Sea (almost 15% of the world's maritime transportation). Approximately 25% of them are oil tankers.

Developed by the NOAA (National Oceanic and Atmospheric Administration; 2002) for the US, Environmental Sensitivity Index (ESI) maps have been an integral component of oil-spill contingency planning and responsethere since 1979. Serving as a quick reference for oil spill responders, it addresses three categories: (1) shoreline. For purposes of this article, we focus only on shoreline classification. The NOAA scheme assesses shoreline based on its physical and biological characteristics in order to classify it on a 10-point environmental sensitivity scale, with class 1 being the least sensitive and class 10 being the most sensitive. Along this scale, there may be several sub-types (A, B, *etc*.) according to more site-specific environmental conditions. In the event of an oil spill, the Smart Response Web tool is used to support the decision-making by national response authorities. This tool is based on the Systems Theoretic Accident Modelling and Processes (STAMP) concept (Leveson, 2011). Thus, the main aim of this paper is to present the results of transformation standard ESI classification into the Regional Environmental Sensitivity Index (RESI) classification for Estonia, the Baltic Sea.

METHODS

This section introduces the methods for converting geology-based shore types used in ESI shoreline classification to the Estonian shoreline and the possibilities to use it in a rapid response to an oil spill. The suggested shoreline classification scheme for Estonia is based mostly on the substrate type and grain size. However, these two components often determine the physical and biological character of the shore environment as

DOI: 10.2112/SI75-195.1 received received 15 October 2015
accepted in revision 15 January 2016
*Corresponding author: Hannes.Tonisson@tlu.ee
©Coastal Education and Research Foundation, Inc. 2016

well as some habitats and ecosystems characteristic to specific geological shore types only.

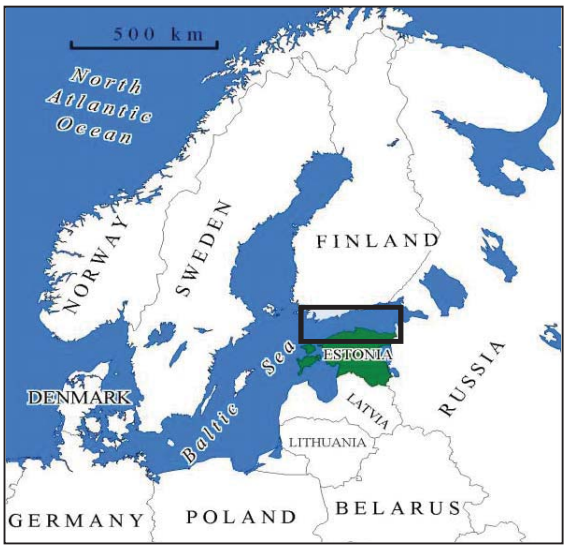

Figure 1. Study area. A detailed map is shown on Figure 3.

Study Area

The Gulf of Finland is a non-tidal bay (tidal range is less than 5 cm) exposed to the winds and waves (depending on the specific location) from the west, south-west or north (Figure 1). Despite virtually non-existent tides, the Gulf of Finland frequently experiences rapid meteorologically forced sea-level fluctuations, including up to 4.2 m high storm surges in the area of St. Petersburg and up to 2-3 m high surges along the North Estonian coast (Suursaar, 2010). Based on long-term studies of coastal geology, the Estonian shoreline of the Gulf of Finland may have one of the most detailed geological classifications of all the shore types found in Europe (Orviku *et al.*, 2010).

The length of the Gulf of Finland shoreline in Estonia is approximately 750 km. The most common shore types there are till shores (40%) and sandy shores (25%). (All percentages are approximate and real values may vary.) Long stretches of cliff shores (10%) and their accompanying gravel-pebble shores (15%) nearby are the most characteristic features of the Estonian coast of the Gulf of Finland. Silty shores and artificial shores make up the remaining 10% of the shoreline length. Over 2/3 of these shore types are with very high ESI values.

Shoreline Classification

There are no geological maps that apply the ESI standard classification to the Estonian shoreline. Mapping 4,000 km of shoreline and classifying it according to the NOAA's ESI scheme would be time-consuming and expensive. Therefore, this paper describes how the ESI maps could be adapted to Estonia's existing shoreline geological classification (Orviku *et al.*, 2010). Using such characteristics as the tilt of the primary relief, the geological character of initial rocks and the prevailing shore processes, Dr. K. Orviku has classified Estonia's Gulf of Finland coast into the following categories:

Cliff shore – Shoreline characterized by an abrasion escarpment in resistant Paleozoic rocks, with a wide talus base (mostly 10-100 meters wide). A sandy or mixed gravel beach a few meters wide is often between the talus and the shoreline. Cliffs without talus are rare. *Scarp shore* – Shoreline characterized by an abrasion bluff in brittle loose Quaternary deposits. *Rocky shore* – Shoreline characterized by an abrasion sloping shore in resistant Paleozoic rocks. This type of shoreline can be mostly found on the western coast of the West Estonian islands. *Till shore* – Shoreline characterized by an abrasion sloping shore with a protective cover of boulders. Finer grained material is often washed away on the tips of the peninsulas caused by high wave activity and steep coastal slope. Sheltered shores can be characterized by various sediment size and numerous boulders in the coastal sea. *Gravel-pebble shore* – Shoreline characterized by an accumulation shore with beach ridges of longshore and onshore drift or derived from the local bedrock. Usually located in zones of high wave activity. The mixing rate of the sediments can be high - formations up to 4 m high can form during one strong storm event (Tõnisson *et al.*, 2013). *Sandy shore* – Shoreline characterized by an accumulation sandy beach with ridges of foredunes or dunes. The width of the beach may vary from a few meters to few hundred meters. The sandy beaches of north Estonia are located mostly near the outlets of ancient valleys filled with loose Quaternary sediments. Some sandy beaches have a very thin sand layer (20-50 cm) and they may turn from sandy beaches to mixed beaches or even gravel and till beaches after major storm events. *Silty shore* - Shoreline characterized by an accumulation shore with an insignificant accumulation of silty-pelitic sediments. These shores are often located at river mouths and are characterized by large areas of reed-beds and shallow water. *Artificial shore* - Shoreline characterized by a shore with man-made coastal protective constructions including two main types: concrete walls and so-called "rip-rap." Both types are equally represented along the Gulf of Finland shores in Estonia.

The shore types are adapted and modified according to the environmental conditions of the Estonian coast of the Gulf of Finland and ranked according to substrate type and grain size in relation to the natural persistence of oil and ease of clean-up. The relative exposure to waves (hydrodynamic energy level; *e.g.* Suursaar, 2010) and the shoreline slope are characterized and taken into account. In the first stage, we took the shoreline geology layer (in scale 1:25,000) and refined it based on the shoreline visible on the latest orthophotos. In the second stage, we used the latest orthophotos, the Estonian soil, geology, landcover and the Estonian Base maps to refine the borders of different shore types. Fieldwork data from various projects and the results of the National Coastal Monitoring programme were also used as an additional data source. Finally, several existing shore types were divided between the ESI classes based on previously mentioned GIS data.

Smart Response Web application

The STAMP standard control loop (Leveson, 2011) based SmartResponse Web application is used to integrate on-line information from 1) collision/grounding model simulation (simulated depth, amount and duration of oil spill), 2) Seatrack

Web spilled oil trajectory simulations, and 3) environmental risk assessment based on sensitivity map layers imported as a Web Map Services into the system.

Performance of the SmartResponse Web is largely based on the distributed databases and the imported Web Map Services and, therefore, this application is of universal use in respect of the geographical area concerned. The SmartResponse Web application is expanded into an online, dynamic Common Operational Picture and Situation Awareness framework for oil spill accident emergency management. The user-centered design approach is implemented to ensure that the decision support tool is taking the needs, desires, and challenges of its users into account (Figure 2). As a result, the flexible Common Operational Picture enables the response authorities to fit it to their particular Situation Awareness needs, while still maintaining access to the overall picture.

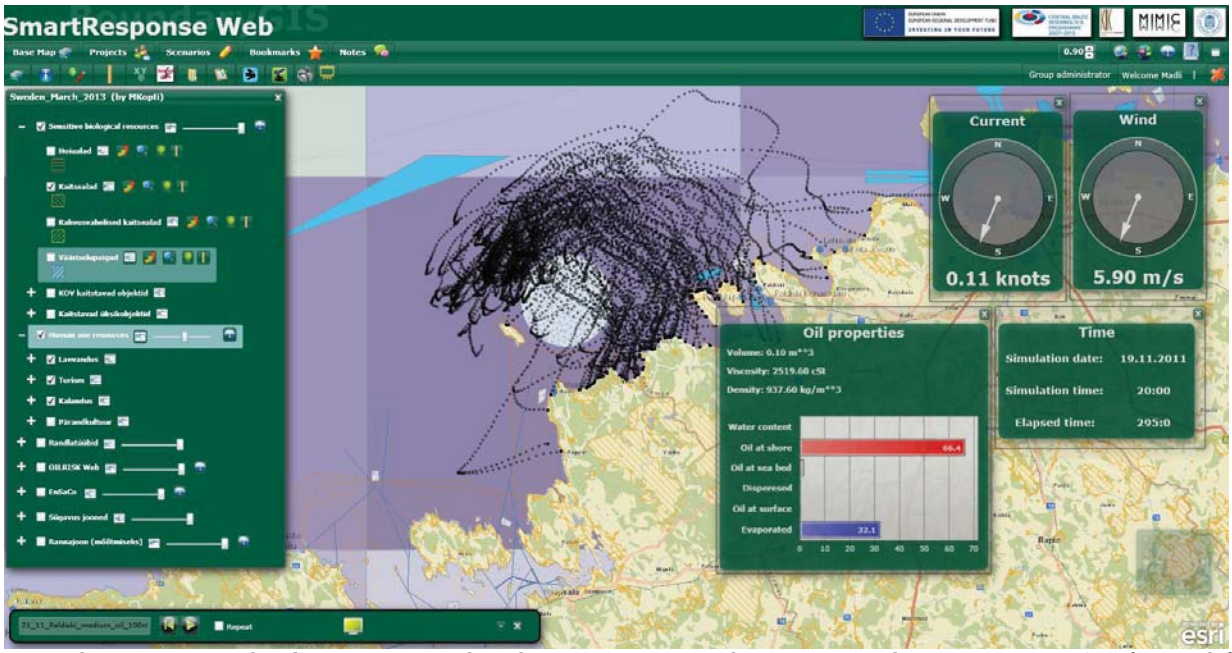

Figure 2. The STAMP concept based SmartResponse Web - online Common Operational Picture (COP) and Situation Awareness (SA) framework for accidental oil spill adaptive response management.

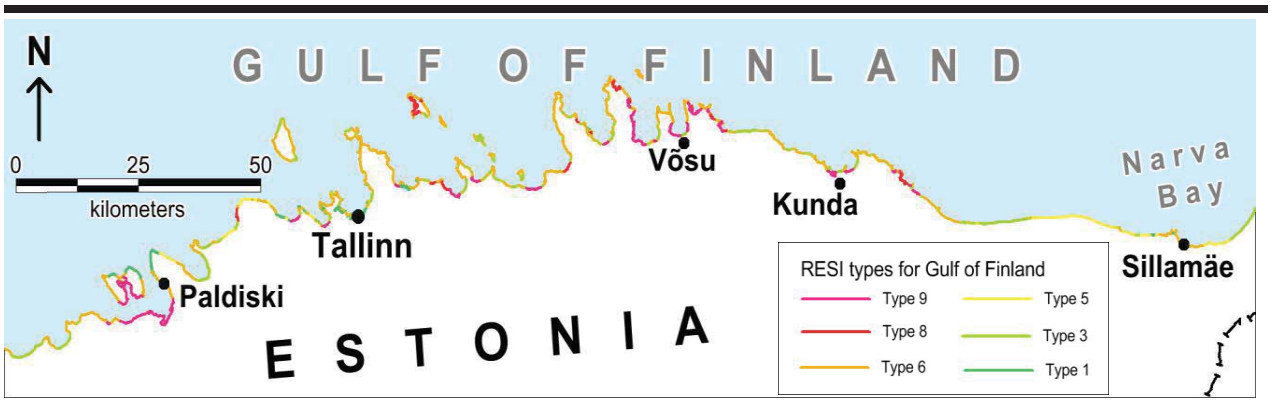

Figure 3. Regional Environmental Sensitivity maps for Gulf of Finland, Estonian coast. Type 1 is the least sensitive, type 9 is the most sensitive to oil pollution.

RESULTS

We have compared the NOAA's ESI classification and our local geological shore types' classification to create Regional Environmental Sensitivity Index (RESI) maps (Figure 3) for Estonia. As the Baltic Sea is a non-tidal sea we were not able to find all the ESI types here. However, several Estonian geology-based shore types can be fitted under some of the ESI tidal processes related types. Frequent strong storms (Orviku *et al.*, 2009), and associated storm surges create conditions similar to the conditions found in some tide-related ESI types (Table 1). Thus, only 11 out of 27 ESI types were found on the Estonian coast of the Gulf of Finland. Some geological shore types coincide directly with the ESI types (e.g., gravel-pebble shore and sandy shore), and some types can be divided between the types with very similar sensitivity class (e.g., scarp shore, silty shore and till shore). But some geological types may have very different sensitivity (e.g. artificial shore, cliff shore). Fortunately, both types can be easily divided into corresponding RESI classes using the available GIS data. Cliff shores should be divided into classes 1C and 5. Most of the Estonian cliff shores belong to class 5, and they are very difficult to clean up (mixed sediments on the beach and virtually no access from the land). Very few cliffs belong to class 1C, which are easily recognizable from the orthophotograph. Such tasks can be even carried out during the accident response period to avoid surprises caused by the shore dynamics (major collapses of the cliff, etc.). Similar solution can be found with the artificial shores. This type must be divided between the classes 1B and 5B. Dividing process can be done again by using orthophotos – it is relatively easy to separate concrete walls from rip-rap protection measures.

The SmartResponse Web enhances the potential for dynamic Situation Awareness by adding a dimension related to the properties and characteristics of the sea environment. Its performance is based on Web Map Services with GIS map layers. The Web Map Services are grouped according to the Environmental Sensitivity Index (ESI) framework, and they include the following map layers:

1. Shoreline classification, ranked according to a scale in relation to sensitivity, natural persistence of oil, and ease of clean-up.
2. Biological resources sensitive to oil spills include oil-sensitive plants, animals or habitats, or are used by oil-sensitive species.
3. Human-use resources, *i.e.* areas with increased sensitivity and values because of their use (*e.g.* beaches, parks, marine protected areas of different level, historic/cultural sites).

The GIS map layers of Regional Environmental Sensitivity Index (RESI) Classification of the Estonian shoreline are integrated into the SmartResponse Web operational framework and are used by the national oil spill response authorities for contingency planning, training and in emergency situations.

DISCUSSION

It is possible to successfully use the existing geological shore types to divide our shores into the ESI classes in order to create the RESI.

Table 1. *NOAA classification (ESI), NOAA types that can be found on the coast of Gulf of Finland (RESI) and corresponding Estonian shore types (RESI).*

Nr	ESI	RESI	Shore types
1a	Exposed rocky shores	X	X
1b	Exposed, solid man-made structures	Exposed, solid man-made structures	Artificial shore
1c	Exposed rocky cliffs with boulder talus base	Exposed rocky cliffs with boulder talus base	Cliff shore
2a	Exposed wave-cut platforms in bedrock, mud, or clay	X	X
2b	Exposed scarps and steep slopes in clay	Exposed scarps and steep slopes in clay	Scarp shore
3a	Fine- to medium-grained sand beaches	Fine- to medium-grained sand beaches	Sandy shore
3b	Scarps and steep slopes in sand	Scarps and steep slopes in sand	Scarp shore
3c	Tundra cliffs	X	X
4	Coarser-grained sand beaches	X	X
5a	Mixed sand and gravel beaches	Mixed sand and gravel beaches	Cliff shore
5b	Riprap gravel beaches (cobbles and boulders)	Riprap gravel beaches (cobbles and boulders)	Till shore/ Artificial shore
5c	Riprap	X	X
6a	Gravel beaches (granules and pebbles)	Gravel beaches (granules and pebbles)	Gravel-pebble shore
7	Exposed tidal flats	X	X
8a	Sheltered scarps in bedrock, mud or clay. Sheltered rocky shores (impermeable)	X	X
8b	Sheltered, solid man-made structures Sheltered rocky shores (permeable)	X	X
8c	Sheltered riprap	X	X
8d	Sheltered rocky rubble shores	Sheltered rocky rubble shores	Till shore
8e	Peat shorelines	X	X
9a	Sheltered tidal flats	Sheltered tidal flats	Silty shore
9b	Vegetated low banks	X	X
9c	Hypersaline tidal flats	X	X
10a	Salt- and brackish-water marshes	Salt- and brackish-water marshes	Silty shore
10b	Freshwater marshes	X	X
10c	Swamps	X	X
10d	Scrub-shrub wetlands, Mangroves	X	X
10e	Inundated low-lying tundra	X	X

However, several shore types are divided between two different ESI classes with notably different sensitivity values (Table 1). For instance, cliff shores (Figure 4) and artificial shores are both divided between class 1 and 5. These two types cover nearly 22% of the Gulf of Finland shore types, which demonstrates very clearly the need of the RESI to adequately estimate the sensitivity to possible oil spill. Till, silty and scarp shores were also divided between two different ESI classes, but their sensitivity to possible oil spill was not so significant ranging between 1 to 3 class differences. Moreover, we must keep in mind that the shore sediments are very diverse in Estonia.

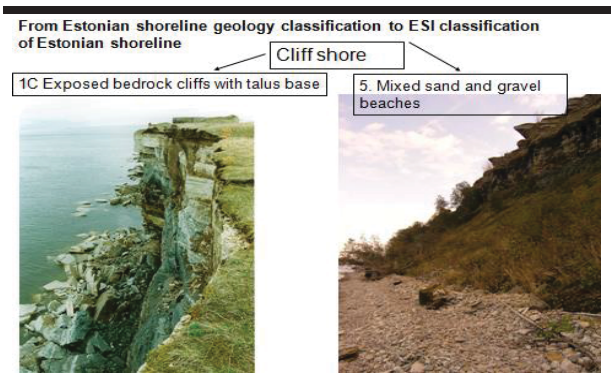

Figure 4. Cliff shore has been divided between two classes with very different ESI classes.

The layers of various shore sediments can be relatively thin and the shores might switch from one ESI class to another during major storm events (Aps *et al.*, 2014). So, there is a need to re-evaluate these classes in certain locations after extreme storms. In order to improve further the classification scheme, we should also strive to move from the standard ESI-related and locally-adapted static shoreline classification (RESI) towards a more dynamic shoreline monitoring-based characterization. This, in turn, is another challenging task that must be considered in the future. However, in such cases, we may be able to reduce the risk of inaccurate classification by using a methodology produced by Aps *et al.* (2014) designed to help us locate dynamic shore types and draw their borders.

The effectiveness of STAMP standard control loop based adaptive oil spill response management is largely dependent on the quality of available RESI classification accompanied by map layers more precisely ranked to a scale in relation to sensitivity, natural persistence of oil, and ease of clean-up map layers. Operational use of the SmartResponse Web application enables the oil spill response authorities to integrate the spill monitoring and evaluation functions directly into the actual oil spill response management processes. Based on operational analysis of the feedback information stream, the changes in oil spill response actions accompanied with reallocation of resources to response actions are decided and the adaptive response process continues.

CONCLUSIONS

Coastal geological classification together with various GIS data sources have been valuable inputs to produce RESI maps for the Estonian shoreline of the Gulf of Finland. In addition to finding similar ESI types compared to our geology-based shore types, we were able to divide several shore types into different ESI classes with very different sensitivity. Combining the static RESI types with the results of the studies related to dynamic shore types and incorporating it into the Smart response Web allows responders to take the most efficacious response to a possible oil spill, while minimizing the impact on nature and keeping clean-up costs to a minimum. Increasing amount of GIS data and the availability of ortophotographs allow us to cover the whole Estonian shoreline with RESI maps. Such methodology can be used in other countries bordering the Baltic Sea or other non-tidal coasts as well.

ACKNOWLEDGMENTS

This work was supported by ESF grant No. 9191, institutional research funding IUT18-9 of the Estonian Ministry of Education and Research, by the Estonian Research Council grant PUT595, and by the EstKliima project of the European Regional Fund program No. 3.2.0802.11-0043. The study was also supported by the Estonian Environmental Investment Centre and by the project "Strategic and Operational Risk Management for Wintertime Maritime Transportation System-STORMWINDS". The project was also supported by the BONUS, the joint Baltic Sea research and development program (Art 185), funded jointly from the Estonian Research Council and the Academy of Finland under the European Union's 7th Programme for research, technological development and demonstration. Special thanks to Dr A. Kont and D.A. Willis for their assistance in providing English language editorial comments and suggestions.

LITERATURE CITED

Aps, R.; Tõnisson, H.; Anfuso, G.; Perales, J.A.; Orviku, K., and Suursaar, Ü., 2014. Incorporating dynamics factor to the Environmental Sensitivity Index (ESI) shoreline classification – Estonian and Spanish example. *Journal of Coastal Research*, Special Issue No. 70, pp. 235-240.

Brunila, O.P. and Storgård, J., 2012. Oil transportation in the Gulf of Finland in 2020 and 2030. *Publications from the Centre for Maritime Studies.* Turku: University of Turku, A61, 72 p.

NOAA, 2002. *Environmental Sensitivity Index Guidelines, Version 3.* NOAA Technical Memorandum Nos OR and R11. Hazardous Materials Response Division, National Ocean Service. Seattle, WA: 192 p.

Leveson, N., 2011. *Engineering a Safer World: Applying Systems Thinking to Safety*. MIT Press.

Orviku, K.; Kont, A., and Tõnisson, H., 2010. Estonia. *In*: Bird, E. (Eds.), *Encyclopedia of the World's Coastal Landforms*. Dordrecht, Heidelberg, London, New York: Springer, pp. 605-611.

Orviku, K.; Suursaar, Ü.; Tõnisson, H.; Kullas, T.; Rivis, R., and Kont, A., 2009. Coastal changes in Saaremaa Island, Estonia, caused by winter storms in 1999, 2001, 2005 and 2007. *Journal of Coastal Research*, Special Issue No. 56, pp. 1651-1655.

Sonninen, S.; Nuutinen, M., and Rosqvist, T., 2006. Development process of the Gulf of Finland mandatory ship reporting system. Reflections on the methods. Espoo: *VTT Publications*, 614, 120 p.

Suursaar, Ü., 2010. Waves, currents and sea level variations along the Letipea – Sillamäe coastal section of the southern Gulf of Finland. *Oceanologia*, 52, 391-416.

Tõnisson, H.; Suursaar, Ü.; Rivis, R.; Kont, A., and Orviku, K., 2013. Observation and analysis of coastal changes in the West Estonian Archipelago caused by storm Ulli (Emil) in January 2012. *Journal of Coastal Research*, SI 65, pp. 832-837.

Journal of Coastal Research	SI	75	977 - 981	Coconut Creek, Florida	2016

Design Policy Options supported by Marine and Coastal Ecosystem Services Assessment and Valuation: a Case Study in Portugal

Maria da Luz Fernandes†, Inês C. Antunes†, Eduardo R. Oliveira†, Fátima L. Alves†

†CESAM, Environment and Planning Department
University of Aveiro
Aveiro, Portugal

www.cerf-jcr.org

www.JCRonline.org

ABSTRACT

Fernandes, M.L.,Antunes, I.C.; Oliveira, E.R., and Alves F.L., 2016. Design policy options supported by marine and coastal Ecosystem Services assessment and valuation: a case study in Portugal. *In:* Vila-Concejo, A.; Bruce, E.; Kennedy, D.M., and McCarroll, R.J. (eds.), *Proceedings of the 14th International Coastal Symposium* (Sydney, Australia). *Journal of Coastal Research*, Special Issue, No. 75, pp. 977 - 981. Coconut Creek (Florida), ISSN 0749-0208.

Marine and Coastal Ecosystems provide services and benefits to human well-being whose value is inadequately incorporated into decision-making. Studies are being developed on Ecosystem Services but the challenge remains on how can Ecosystem Services better inform policy options. This paper presents the governance framework analysis and assessment in the study area of Peniche-Nazaré, in Portugal. This research is part of the project on Economic Valuation and Governance of Marine and Coastal Ecosystem Services funded by Gulbenkian Oceans Initiative. This project aims to assess the economic value of Ecosystem Services provided by the region of Peniche-Nazaré (coastal and marine zones). The research started with the analysis of the governance framework (policies, strategies, plans, programmes and institutions). In the study area, this framework supported the characterization of activities and processes, providing inputs on key Ecosystem Services, environmental drivers of change and threats. This analysis demonstrated that the last decade has seen an intensification of strategic documentation and regional funding programmes, due to the European funding context. The assessment highlights the priority axes of investment which are Tourism, Nature Conservation, Fisheries and Energy. This investigation will clarify the key Ecosystem Services that are relevant to specific policies, strategies and programmes, in the region. The final results of this project will inform policy makers, NGOs and businesses in improving planning and regulatory decisions at different policy levels.

ADDITIONAL INDEX WORDS: *Governance, Planning Process, Decision-making; Nazaré-Peniche*

INTRODUCTION

The relation between Ecosystems Services (ES) and the human well-being is becoming more evident to policy makers. Several policies are assimilating the ES approach into planning process, making the concepts operational and linked to decision-making process (Dunbar *et al.*, 2013; Maes *et al.*, 2012; Ruckelshaus *et al.*, 2013). However, research points that integration of ES into day-to-day policy-making is far from being achieved. The 'integration of ES' into policies as defined in Helming *et al.* (2013) means the "*consideration of ES at all stages and for all sectors of policy making.* As stated in Kumar *et al.* (2013) at the beginning of the policy cycle is essential to clarify the key ES that are relevant to specific policies and framed as part of the problem concerned. In this process the threats to biodiversity caused by human-induced changes should be identified. Likewise trends and conditions of ES, their relationship with human-well-being and development goals needs to be assessed (Kumar *et al.*, 2013). In this context, the Convention on Biological Diversity (CBD) played a key role in bringing ES into policy agenda.

In 2010 the CBD adopted a strategic plan for biodiversity for the period 2011-2020 including 20 targets, known as the Aichi Targets (UNEP, 2010). These targets complement the previous conservation-based biodiversity targets and add the ES (Target 11). Following this tendency, in 2011, European Union (EU) also published a set of 6 targets for 2020 (EU Biodiversity Strategy 2020) to "*halt the loss of biodiversity and the degradation of ES and restoring them in so far as feasible while stepping up the EU contribution to averting global biodiversity loss*" (European Commission, 2011). This strategy is in line with other cross-cutting EU policies in the marine field as the Water Framework Directive (Directive 2000/60/EC) and, more recently, the Marine Strategy Framework Directive (Directive 2008/56/EC) that aims to improve the ecological and environmental status of European member-states waters. Portugal, as part of European Union is adopting and implementing new environmental targets and changing its marine policy landscape, in line with Europe 2020 Strategy (COM(2010) 2020 final), the Integrated Maritime Policy (IMP) (COM(2007) 575 final) or the Fisheries Policies (Regulation n.º 1380/2013). There is also a new marine and maritime policy agenda that is now being the focus of attention driven by the new legal framework for Portuguese maritime spatial planning (Law n.º 17/2014, April 10) developed in the last three years and supported by the new Ocean Strategy (RCM n.º 12/2004, February 12).

DOI: 10.2112/SI75-196.1 received received 15 October 2015 accepted in revision 15 January 2016
*Corresponding author: maria.luz@ua.pt
©Coastal Education and Research Foundation, Inc. 2016

With a vision of protection, conservation and management of oceans and marine ecosystems, in 2013, Calouste Gulbenkian Foundation (FCG) created the Gulbenkian Ocean Initiative (GOI). This initiative aimed to increase public and political understanding of the role of oceans in human well-being commissioning the research project "The Economic Valuation and Governance of Marine and Coastal Ecosystem Services" (MCES Project) focused on the region of Peniche and Nazaré districts (coastal and marine zone). The main goal of this project is to assess the economic value of coastal and marine ES, and how these contribute to improve decision-making processes and raise marine environmental awareness. This paper shows the relevance of the governance framework analysis and assessment within this context; how this can be a valuable method for identifying the key ES relevant to specific policies and how these policies can be designed in order to better integrate the ES status and conditions, targets and threats.

Study site

The study site is located in the west region of mainland Portugal, the study area is part of Oeste region (NUT III). (Figure 1).The characterization phase of MCES Project was focused on the bio-physical features, socio-economic dynamics and governance framework.

Around 360000 inhabitants live in this territorial area, circa of 2500 km^2 (FCG, 2015). In this study were considered five municipalities Alcobaça, Nazaré, Caldas da Rainha, Óbidos and Peniche. From the ecological point of view there is a wide representation of marine and coastal habitats: Berlengas archipelago, Óbidos coastal lagoon, São Martinho do Porto bay, supratidal and intertidal zones of sandy and rocky shores, dune fields, pelagic and benthic habitats from the coast line to the deep sea and the Nazaré canyon extending from near-shore to abyssal depths.

The importance of Berlengas as insular ecosystem, the biological value of the surrounding marine area, high botanical interest and the island's role in terms of marine birds were responsible factors for classifying the islands as a Natural Reserve (Decree-law n.º 264/81, September 3).

The variety of ES support several existing and potential activities and uses in the area such as fisheries, aquaculture and related transformation activities; shellfish collection, algae, sand and gravel extraction; shipbuilding industry, leisure and tourism activities, wave energy conversion, marine resources extraction, educational and research activities (FCG, 2015).

METHODS

The methodological approach to the analysis and assessment of the governance framework was a four step process consisting of: collection; analysis, assessment and stakeholders meetings. First, was done a collection of information from policy and strategic documents and from administrative structures of territorial scope in the area from 2000 onwards (*i.e.* legislative and strategic planning documents, projects, R&D projects, public or private initiatives). Second, the analysis of the information was supported by a literature review of policies, strategies, planning tools and projects. The level of the analysis was extended from local, regional, national and international level. The information was analyzed considering the relevance to MCES Project namely the hierarchy, degree of influence, sector of activity; associated institutions, competences and time frame. Third, information was assessed and combined in order to identify the main policy targets, key strategic activities and drivers of change and threats. Finally, two meetings with local stakeholders were held in Peniche in autumn 2014 to gather their perceptions on the information and to identify other documents of relevance.

RESULTS

Table 1 presents the condensed analysis and assessment of the policies, strategies, planning tools and projects and their relevance to MCES Project. The priority axes of development and the key activities and processes were extracted from the strategic policy documents and projects (Figure 2). The most relevant targets at the study area are connected with Europe 2020 (employment, climate change, R&D, education and poverty); IMP; Renewable Energy, and Nature Conservation Targets.

Drivers are here defined as anthropogenic activities that may generate environmental effects. Main environmental drivers of change and threats, identified from the analysis of the governance framework are: industrial and urban pressure and its related impacts on water quality; touristic pressure, land use changes in the coast, coastal erosion, fisheries and shipping (Figure 3). Their spatial distribution is focused in the urban area around Peniche, Nazaré, southern beaches of Peniche and, during the summer, in the Berlengas archipelago.

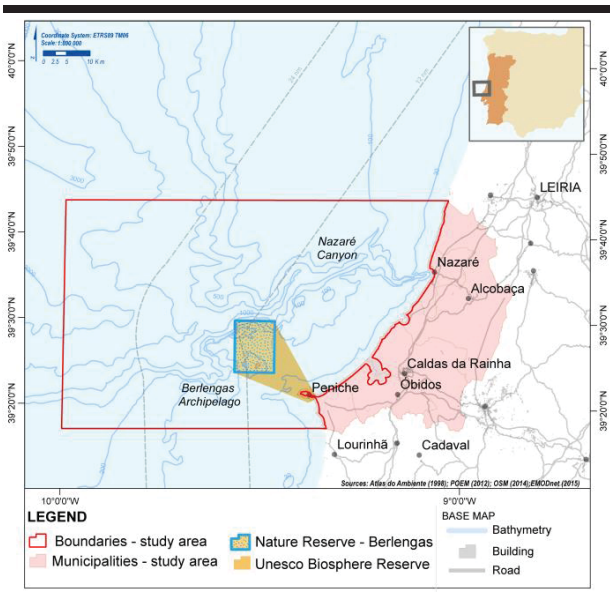

Figure 1. Location of study site area (adapted from FCG, 2015).

Table 1. *Main policies, strategies, planning tools and projects and its relevance for MCES Project at national and regional level*

Date	Legislation	Relevance to MCES Project
		NATIONAL
2007	Spatial Plan for the Nature Reserve of Berlengas (POAP) 2007-2013. (Decree-law nº 264/81, September 3)	Implementation programme to safeguard flora and fauna, to manage marine resources and also to contribute to the spatial management of touristic activities in the island.
2007	Strategic Plan for Fisheries (PEN Pescas) 2007-2013 (RCM nº 79/2008, May 16)	Promoted competitiveness of fisheries sector in adequacy to available and exploitable resources, to ensure the sustainable development of coastal areas dependent on fisheries.
2008	Portuguese Maritime Spatial Planning (POEM) (approved by Ruling No. 32277/2008)	Provides a survey of activities and uses (existing and potential) in the Portuguese maritime continental space.
2009	Strategy for Integrated Coastal Zone Management (ENGIZC) (RCM n.º 82/2009, September 8)	Establishes a long–term vision of 20 years incorporating a sustainable, well managed, competitive and safe coastal zone; reaffirms a new coastal zone paradigm.
2010	Strategy for Adaptation to Climate Change (ENAAC) (RCM n.º 24/2010, April 1)	Selects sectorial working groups for development of adaptation measures on territory and urban development; several measures are connected with preservation and protection and improving knowledge on marine and coastal ES
2012	Marine Strategy for the subdivision of the Continent (DQEM) (Decree-law nº 136/2013, October 7)	Establishes a framework to achieve or maintain the good environmental status in the marine environment by 2020. Next steps are the creation and implementation of regulatory measures.
20102013	Energy Strategy (ENE 2020) Action Plan for Renewable Energies 2020 (RCM n.º 29/2010, April and RCM n.º 20/2013, April 10)	Aims at ensuring 60% of produced electricity and 31% of energy consumption originate from renewable energy sources. Pilot area for waves and offshore wind energy production (off the coast of São Pedro de Moel). Estimated contribution of 6 MW for wave energy and for offshore wind energy of 27 MW installed capacity.
2013	National Ocean Strategy (ENM) 2013-2020 (RCM n.º 12/2014, February 12)	Strategy and action plan; selects several activities of interest present in the study area and provides visions, objectives and guiding principles for future development.
2013	Strategic Plan for Tourism (PENT) 2013-2015 (RCM nº 24/2013, April 16).	Highlights urban and environmental sustainability, service quality and Portugal Brand. Identifies different type of products in Centre Region: nature, sun and sand, gastronomic/wine tourism and health and nautical tourism as emerging trends.
2014	Strategic Plan for Aquaculture 2014-2020	Aims to promote aquaculture as a balance and alignment factor of production with the consumption needs.
2014	Basis of the Policy for Marine Spatial Planning and Management (LBOGEM) of the National Maritime Space (Law 17/20014, April 10)	Legal framework for spatial planning and management of national maritime space.
		REGIONAL
2002	Coastal Zone Management Plan (POOC), stretch Alcobaça – Mafra (RCM n.º 11/2002, January 17) Action Plan for Protection and Valuation of Littoral (PAPVL) 2012	POOC is a binding plan constraints coastal use for safeguard of ecosystems. Identified risk and assigns coastal protection works to locations in danger, such as reinforcement of dunes, coastal protection, stabilization of cliffs or protection of scarps. The most pressing measures still not implemented were recently updated to PAPVL
2005	Óbidos Lagoon Candidacy to Regional Protected Landscape	Joint proposal candidacy to Protected Landscape of Óbidos Lagoon at regional scale developed by ICNF (governmental body), municipalities and ONGs in the region.
20062009	Peniche Municipal Strategy for the Sea 2006-2010 Magna Carta Peniche 2025	Peniche, a touristic city focusing on tourism and surf center developed a strategy focusing mainly on sea economy, renewable energies, tourism and urban planning.
2007	ECOS Project and Berlengas Laboratório de Sustentabilidade	Two regional projects both started in 2007 and already finished. Developed by public entities focusing on tourism, sustainable development and renewable energies.
2007	Grupos Acção Costeira Oeste	Programme supporting the development of fisherman communities.
2009	SURGE Project	Private consortium installed a grid-connected wave energy converter (Waveroller) in Peniche and now developing a wave farm of several units.
2009	Regional Spatial and Management Plan for West and Tagus River Region (PROT-LVT) (RCM n.º 64-A/2009, August 26)	Identifies main trends for the region: territory strong development of the touristic sector; reinforcement of the local administrative and associative powers; strong pressures on land use.
2009	Rip Curl Pro Peniche	Touristic and sports events related with surf practice, one held in Peniche and other in Nazaré.
2010	North Canyon Project	
2011	Berlengas Biosphere Reserve Man and Biosphere Programme (Berlengas MAB UNESCO)	Plan of Action of the Biosphere Reserve.
2013	River Basin Management Plan (RBMP) of Ribeiras do Oeste and Vouga, Lis and Mondego (RCM n.º 16-B/2013. D.R. n.º 58)	Following the Water Framework Directive, includes ecological status as measure of quality of water bodies and establishes several measures for attaining this status, monitoring programmes.
2013	West Regional Strategy (OESTE 2020) Portugal	Regional strategy focus in tourism, fish and seafood industry, surf, shipbuilding and education.
2014	Operational programme and Strategy for the Centre Region 2014-2020 (CRER 2020). Research and Innovation Statregy (RI3 Centro)	Address the problems and challenges the region faces towards Europe 2020 Strategic goals. Main target areas are related with natural endogenous resources, aquaculture, fish, canned fish, salt, surf economy, renewable energy and tourism.

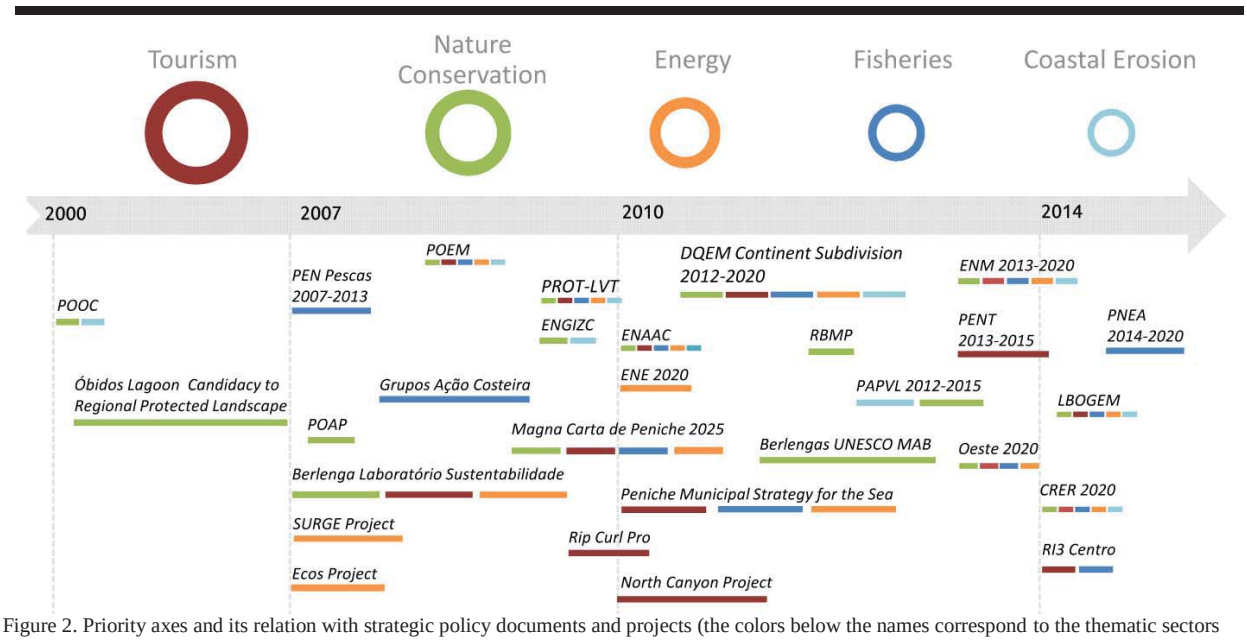

Figure 2. Priority axes and its relation with strategic policy documents and projects (the colors below the names correspond to the thematic sectors included and the size of the circles corresponds to the relevance of the themes).

DISCUSSION

From the analysis of Figure 2 we note that most of the documents presented were produced in the last 7 years (between 2007 and 2014), indicating that a strong revision effort of strategies and policy orientations was carried out in that period.

Nature conservation appears more often in the older documents, before 2010, mostly associated with protection of landscapes and biodiversity values that were being threatened, as the Spatial Plan for Berlengas. Also in the Óbidos Lagoon, for example, a candidacy supported by the municipality was developed in a time of high urban development in the region, likewise to what occurred in the rest of the country.

The region has two important fishing ports and fisherman community, in Nazaré and Peniche. Fishing has an historical importance and its continually referenced in the governance framework. In the last years the European legislation favored the diversification of fisherman communities promoting the Fisheries Task Groups (Grupos de Ação Costeira) aiming to provide fishing communities with tools for generating capacities and create value at all stages of the supply chain.

Between 2007 and 2010 energy related legislation has been increasing. The transposition of the Energy Directive (2001/77/CE) was first published in 2003 and at the time the high targets for renewable energies in Portugal induced the creation of wave energy projects. Surge Project appeared in this context along with other initiatives in Portugal. As of 2010 the renewable energy targets and tariffs were reviewed and the impetus for creation of a wave energy cluster decreased. Nevertheless, Surge Project is active and received EU funding in 2014 for improving the technology and growing up in scale.

The coastal erosion appearance is more evident after the publication of the National Strategy for Coastal Zone, in 2009 and also motivated by strong storms episodes that have gathered momentum, as the significant loss of territory. At the same time, tourism gathers more relevance at regional level showing up as main driver of change since projects as North Canyon in Nazaré and Rip Curl world tour in Peniche are occurring. Coastal erosion and tourism, both as threats and drivers of change are gaining relevance and prominence in the regional strategies and the interest demonstrated by touristic projects is arising.

In the last 10 years, the production of legislative acts in the coastal and maritime area has been intense. The creation of a legal framework for maritime spatial planning and management was driven by the increasing interest in the exploration of marine resources (within and beyond the continental shelf) and by the publication of the Integrated Maritime Policy and Blue Growth Agenda. This agenda aims to improve maritime sectors, as “an initiative to harness the untapped potential of Europe’s oceans, seas and coasts for jobs and growth” (European Commission, 2012). This perspective was also embedded in the National Ocean Strategy and reflected in the new legal framework for maritime spatial planning and management. These laws tend to relate more closely to maritime sectors of development, looking for a sustainable use of resources, and considering nature conservation as another sector to have into account.

Legislative documentation has been showing a multi-sectorial character, favoring the development of different activities strongly motivated by tourism. The European framework and funding schemes have widely contributed to this fact. The regional strategies favor the demand of the European funds in their texts and show an impressive fast embedment of the European 2020 targets and agenda.

The strategic policy documents and projects with relevance in the study area show that the main axes of development in the region are concerned with Tourism, Nature Conservation, Energy, Fisheries and Coastal Erosion. This is closely in line with the outputs extracted from MCES Project – Study site characterization that supported for further economic valuation the following activities and processes: fisheries, tourism, scientific and educational services.

Main drivers and threats presented in Figure 3 are more prominent in Peniche, as this is the major human settlement in the coastal area, a widely renowned spot for surfing practice and a departing point for Berlengas archipelago. Environmental threats are mostly related with water quality status and coastal erosion as spotted by the Berlengas Nature Reserve Plan and the Coastal Zone Management Plan.

The analysis of the main drivers of change and threats extracted from the policy analysis provides relevant information on the most pressing issues that the region is facing. This information allows the identification of the most vulnerable ecosystem and the ES which are more prone to be impacted by anthropogenic activities.

CONCLUSIONS

The study of the governance framework analysis is a valuable method for informing and improving the design of policies supporting ES. From the analysis of the policy documents were extracted the key activities and processes in the study area, which are nature conservation tourism, fisheries, energy and coastal erosion. The mapping of the threats and drivers contributes to the assessment of the most vulnerable ecosystems and ES in the study area. EU targets and funding are relevant drivers for the creation of new policies. This study shows that to have an effective ES integration into policies it is necessary to translate and combine the environmental concerns with the relevant axes of development and the main drivers of change into planning policies, at the different scales of action and since the beginning.

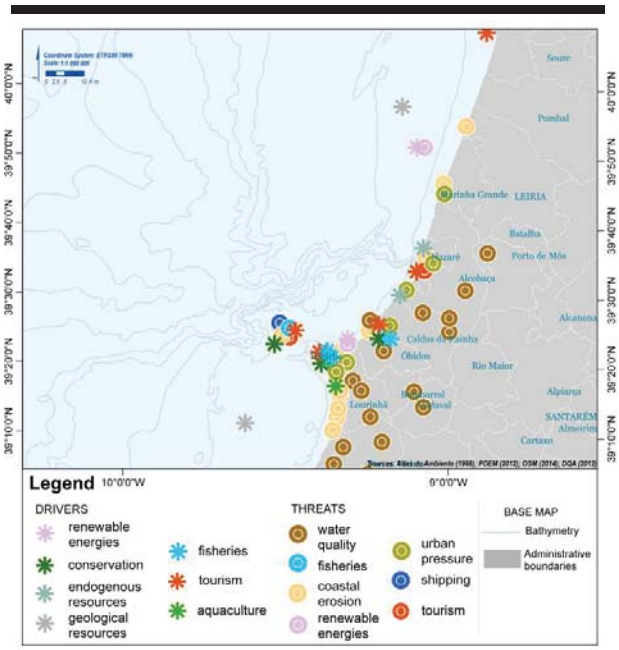

Figure 3. Main drivers of change and threats recognized in the study area and its surroundings.

ACKNOWLEDGMENTS

This work has been financed by the FCG "Gulbenkian Oceans Initiative", developed under the consortium between Nova School of Business and Economics and University of Aveiro. The first author is financed by GOI from MCES Programme (BCGT/GOI_DAO2014) and from a Do*Mar PhD grant from FCT. The second and third author were financed by MFEEE/EEA-Grants through Project ClimAdaPT.Local (BCGT /UA/ClimAdaPT.LOCAL/2014 and BI/UA/ClimAdaPT .LOCAL/2014).

LITERATURE CITED

Dunbar, M.B.; Panagos, P.; Montanarella, L., 2013. European perspective of ecosystem services and related policies. *Integrated Environmental Assessment and Management* 9, 231–236.

European Commission, 2011. Our life insurance, our natural capital: an EU biodiversity strategy to 2020 COM(2011)244 final 2020, 17p.

European Commission, 2012. Blue growth: opportunities for marine and maritime sustainable growth. COM(2012) 494 final. European Commission.COM(2012)494final,12p

FCG, 2015. *The Economic Valuation and Governance of Marine and Coastal Ecosystem Services.* Progress Report Task A4. Study Site Characterization - Assessment of the status and trends of marine and coastal Ecosystem Services. Fundação Calouste Gulbenkian, 157p.

Kumar, P.; Esen, S.E.; Yashiro, M., 2013. Linking ecosystem services to strategic environmental assessment in development policies. *Environmental Impact Assessment Review* 40, 75–81.

Maes, J.; Egoh, B.; Willemen, L.; Liquete, C.; Vihervaara, P.; Schägner, J.P.; Grizzetti, B.; Drakou, E.G.; Notte, A. La; Zulian, G.; Bouraoui, F.; Luisa Paracchini, M.; Braat, L.; Bidoglio, G., 2012. Mapping ecosystem services for policy support and decision making in the European Union. *Ecosystem Services* 1, 31–39.

Ruckelshaus, M.; McKenzie, E.; Tallis, H.; Guerry, A.; Daily, G.; Kareiva, P.; Polasky, S.; Ricketts, T.; Bhagabati, N.; Wood, S.; Bernhardt, J., 2013. Notes from the field: Lessons learned from using ecosystem service approaches to inform real-world decisions. *Ecological Economics* 115, 11–21.

UNEP, 2010. Conference of the Parties to the Convention on Biological Diversity UNEP/CBD/COP/DEC/X/2. Strategic Plan for Biodiversity 2011-2020, 13p.

Journal of Coastal Research	SI	75	982 - 986	Coconut Creek, Florida	2016

Measuring Success of Ocean Governance: a Set of Indicators from Portugal

Maria Adelaide Ferreira [†*], **David Johnson**[‡††], **and Carlos Pereira da Silva**[†]

[†]CICS.NOVA,
Interdisciplinary Center of Social Sciences,
FCSH/UNL, Lisboa, Portugal

[‡]Seascape Consultants Ltd.
Belbins, Romsey, UK;
[††]Advisory Committee on Protection of the Sea (ACOPS)
Trinity College, Cambridge, UK

www.cerf-jcr.org

www.JCRonline.org

ABSTRACT

Ferreira, M.A.; Johnson, D.; and Pereira da Silva, C., 2016. Measuring success of Ocean governance: a set of indicators from Portugal. *In:* Vila-Concejo, A.; Bruce, E.; Kennedy, D.M., and McCarroll, R.J. (eds.), *Proceedings of the 14th International Coastal Symposium* (Sydney, Australia). *Journal of Coastal Research*, Special Issue, No. 75, pp. 982 - 986. Coconut Creek (Florida), ISSN 0749-0208.

Evaluating the success of marine spatial planning (MSP) remains a challenging task. Portugal, one of the world's largest maritime nations, with its recent ocean governance framework, is an ideal case study for the development of an evaluation mechanism for MSP. This paper presents a brief characterization of Portugal's maritime area and of its legal regime, and a methodology for defining and selecting a set of indicators to evaluate MSP once it has been operational for a number of years. The resulting set of indicators is discussed, as are prospects for their development and generalization.

ADDITIONAL INDEX WORDS: *Maritime spatial planning, Portugal, indicators.*

INTRODUCTION

Ocean governance frameworks, including marine spatial planning (MSP), are increasingly being developed and implemented wordwide (Cicin-Sain *et al.*, 2015; Ehler, 2014). They are prompted by a growing competition for space and resources in this "last frontier" environment – the ocean, seen as a promising new source of opportunities, "an inexhaustible cornucopia" (Norse, 2005, p.423). However, they are also coupled with the recognition that the intensification of maritime activities has the potential to increase conflicting situations, and degrade the marine environment, upon which all of us depend (IOC, 2006). As such, evaluating the success of integrated ocean management initiatives, generally aimed at achieving sustainable use of the marine environment and its resources, is of the utmost importance (Ehler, 2014; IOC, 2006).

Evaluation is often achieved based on sets of indicators, understood as "quantitative/qualitative statements or measured/observed parameters that can be used to describe existing situations and measure changes or trends over time" (IOC, 2006, p. 11). In a management context, indicators should be directly linked to intended objectives (Day, 2008; Douvere and Ehler, 2011). They should also be measurable, interpretable and understandable, sensitive to changes in relevant aspects and responsive to management actions, be based on established scientific theory, and be cost-effective; to be manageable and effective, an ideal set should comprise as few indicators as possible (Douvere and Ehler, 2011; IOC, 2006).

In the context of the evaluation of ocean governance frameworks, and MSP initiatives in particular, indicators should highlight the effects of maritime activities (the focus of MSP), ideally establishing a clear link between a given activity and its impacts (positive and/or negative). Notwithstanding a growing literature on the subject of evaluation of MSP (*e.g.* Carneiro, 2013; Ehler, 2014), it remains a difficult issue to tackle in practice, as the Belgian MSP example, advocating the importance of indicators but proposing none, clearly demonstrates (Royaume de Belgique, 2014).

As one of the world's largest maritime nations, and with its ocean governance framework just finalized, Portugal emerges as an ideal case study for the development of an evaluation mechanism for its marine spatial planning and management (MSPM) system. At the current stage of the ocean governance cycle in Portugal, before any Marine Spatial Plans are in place, what indicators are most suited to evaluate progress towards sustainable ocean governance and can they be beneficially used in other contexts?

This paper presents a brief characterization of Portugal's national maritime space (NMS) and of the corresponding legal regime. It then presents a methodology for defining and selecting a set of indicators to evaluate the implementation of its MSPM system. The set of indicators obtained is briefly presented and discussed, as are prospects for their development and possible application to other contexts.

The Portuguese case

Portugal's maritime area (0-200 nautical miles, nm), including the Exclusive Economic Zones (EEZs) of the mainland and of the archipelagos of Madeira and the Azores totals c. 1 700 000 km^2. Portugal also has sovereign rights over the natural resources of the seabed and subsoil beyond 200 nm (a map of Portugal's maritime area can be found at http://www.emepc.pt/images/pdf/MapaPortugaleMar.pdf). This extended continental shelf adds another 2 100 000 km^2 of ocean seafloor to Portugal's NMS, which totals *c.* 3 800 000 km^2 (*c.* 4% of the Atlantic Ocean and 1% of the global Ocean) (Bessa

DOI: 10.2112/SI75-197.1 received received 15 October 2015 accepted in revision 15 January 2016
*Corresponding author: adelaide.ferreira@fcsh.unl.pt
©Coastal Education and Research Foundation, Inc. 2016

Pacheco, 2013). Portugal's NMS is potentially rich in living and non-living resources (Resolution 12, 2014). In recent years, several private sectors have shown a growing interest, *i.a.*, in the exploration and exploitation of renewable energies (including wave and wind), oil and natural gas extraction, massive sulphides on the sea bottom and offshore aquaculture (Ferreira *et al.*, 2015). Non-consumptive uses such as leisure and coastal and nautical tourism, of which surfing is one notable example, are growing activities and key drivers of the Portuguese economy (*ibid*.).

Since 2014, Portugal has been developing the political and legal framework for its NMS, very much aligned with the European Union's (EU) maritime policies:

- February 2014: National Ocean Strategy 2013-2020 (NOS 2013-2020). It adopted "Blue Growth" (COM(2012) 494 final) as its development model, and stated Portugal's strategic objectives for its NMS (Resolution 12, 2014);
- April 2014: Law establishing the Basis of the Policy for Marine Spatial Planning and Management of the NMS (MSPM Law). It stated the objectives of marine spatial planning and management (MSPM) of the NMS, and created two types of marine spatial plans (MSPlans): the Situation Plan for the entire NMS and smaller scale Allocation Plans (Law 17, 2014);
- March 2015: Decree-Law 38/2015 detailing aspects of the implementation of the MSPM Law and transposing the EU's MSP Directive (2014/89/EU of 23 July). It stated the objectives of future Portuguese MSPlans, and defined that until the adoption of the Situation Plan, the POEM (an MSPlan developed in 2008-2010 for the EEZ of mainland Portugal and published as a study in 2012) is to be considered as the reference situation for MSP of the entire NMS and for the allocation of new private use titles (Decree-Law 38, 2015; Ferreira *et al.*, 2015a).

As a contracting party to several international conventions and as a EU member state, Portugal fulfills a number of obligations concerning ocean issues, including the implementation of the monitoring programme for the EU's Marine Strategy Framework Directive (MSFD), which aims to achieve or maintain Good Environmental Status (GES) of the marine environment by 2020 (OJEU, 2008).

METHODS

The Portuguese legal framework for MSPM was analyzed to identify stated objectives of (future) MSPlans, through which the Portuguese MSPM system will be implemented.

A literature review of scientific and technical references on evaluation mechanisms and established indicators of Ocean governance with emphasis on MSP was carried out. It included a search for indicators of sustainable development, evaluation of MSP and MSPlans, and implementation of international conventions and commitments, and European Directives pertinent to maritime issues. Selected indicators were tentatively matched with stated objectives.

A review of ocean monitoring commitments assumed by Portugal was also carried out to identify and take advantage of potential areas of overlap, avoiding duplication of efforts, and minimizing implementation costs.

RESULTS

Decree-Law 38/2015 states the following objectives of future Portuguese MSP instruments (Decree-Law 38, 2015, p. 1526):

a) To implement the objectives of strategic development established in the strategic instruments of the spatial planning and management of the national maritime space, namely in the National Ocean Strategy;

b) To promote the sustainable economic, rational and efficient exploitation of marine resources and ecosystem services, ensuring the preservation, protection and recovery of natural values and coastal and marine ecosystems and the good environmental status of the marine environment, as well as of coastal and transition waters, preventing the risks of human action and minimizing the effects of natural catastrophes and climate change;

c) To align (order) the uses and activities to be developed in the national maritime space taking into account the marine ecosystems and the safeguard of underwater cultural heritage, aiming to ensure the sustainable use of resources and fostering creation of employment;

d) To prevent or minimize eventual conflicts among uses and activities developed in the national maritime space;

e) To ensure legal certainty and transparency of the procedures entrusting the rights of private use in the national maritime space;

f) To ensure the use of available information on the national maritime space.

Strategic development objectives stated in the NOS 2013-2020, the object of objective a), are presented in Table 1. The indicators for objective b) are presented in Table 2, and the indicators for objectives c) to f) are presented in Table 3.

International and/or European targets for selected indicators are indicated when available, as are existing monitoring programmes already being conducted by Portugal.

Table 1. *Strategic objectives of the Portuguese NOS2013-2020 and related indicators.*

Objective	Indicator
To reaffirm the national maritime identity in a modern proactive and entrepreneurial framework;	-
To bring to realization the economic, geostrategic and geopolitical potential of the national maritime territory, turning the Mar-Portugal into an asset with permanent economic, social and environmental benefits;	-
To create conditions for attracting investment, both national and international, in all sea economy sectors, promoting growth, employment, social cohesion and territorial integrity, and, until 2020, promoting an increase of the sea economy contribution to the GDP of about 50%.	contribution of the sea economy to the GDP (%)
To strengthen national scientific and technological capacity, stimulating development of new areas of action that promote the knowledge of the Ocean and effectively and sustainably enhance its resources, uses and activities as well as the ecosystem's services.	-
To make Portugal, on a worldwide level, a leading maritime nation and an undisputed partner of the IMP and of the EU maritime strategy in particular for the Atlantic area.	-

Table 2. *Proposed indicators for objective b). References: [1]MAOT, 2010; [2]GRA, 2011; [3]GGKP, 2013; [4]UNGA, 2015; [5]GFCM, 2013; [6]UNEP, 2010; [7]OJEU, 2013; [8]SIC, 2013; [9]SCBD, 2011; [10]Governo de Portugal, 2014; [11]IOC-UNESCO, 2011; [12]UNEP, 2014; [13]IEEP, 2003; [14]EC, 2010; [15]EC, 2011; [16]UNEP, 2006. *Monitoring planned or underway*.

Indicator	Unit
Requests to use the national maritime space[1]	No.
Changes in the use of maritime space[1]	%
Private investment in the national maritime space[1]	€
Public and private investment in RDT by sector of maritime activity[1]	€
Contribution of maritime economic activities in the trade balance[1]	€
GAV by sector of maritime economic activity[1]	€
GDP/*capita* of coastal residents[2*]	€/inh.
Electricity generated from marine renewables[1*]	%, GWh
New market niches explored and product diversification[1]	No./%
Trends in benefits that humans derive from ecosystem services: GAV in the Environmental Goods and services sector[3]	% GDP
Trends in benefits that humans derive from ecosystem services: employment in the Environmental Goods and services sector[3]	% total employment
Sustainability/quality certification schemes (fisheries, aquaculture)[4,5]	%
Green award certification (shipping)	No., %
Stocks at MSY (*Maximum Sustainable Yield*)[6*]	%
Stocks overfished[4]*	%
Unwanted catches& discards /catches landed[7]	%
Tourism figures for wildlife visitor attractions[8*]	No.
Benefit sharing with coastal communities[9]	
Shipping density[10*]	-
Coastal & marine area protected[1*]	%
Degraded ecosystems restored[1]	%
Developments permitted impacting designated sites/species[8]	No.
Condition of Marine Protected Areas[8*]	-
Conservation status of marine mammals[8*]	-
Conservation status of marine birds[8*]	-
Environmental Status of the marine environment[1*]	MSFD
State of coastal and transition waters[1*]	WFD
Trends of invasive alien species[1*]	No.
Escapement of cultured species	No.
Marine trophic index[11]	-
Red List Index[12]	-
Status of target species[13]	-
Food chain impacts[13]	-
Greenhouse Gas emissions from maritime transport[14, 15*]	g/tonkm
Energy efficiency[16*]	-
Specific CO_2 emissions[14*]	g/tonkm
Plastic materials entering ocean[4*]	ton/y
Pollution incidents reported[8]	No.
Incidents of dumping at sea[8]	No.
Applications with waste/litter management plan/measures[8]	No.
Operational pollution from ships[16]	No.
Port waste reception facilities available[12]	%
Noise[10*]	-
People & goods affected by storms	%, No.
Losses from climate related events[11]	€

Table 3. *Proposed indicators for objectives c), d), e), and f). [1]SDSN, 2015; [2]Ehler 2014; [3]SIC, 2013; [4]EC, 2010; [5]MAOT, 2010; [6]Ardron et al., 2014; [7]UNEP, 2014.*

Indicator	Unit
Objective c)	
Marine areas and coastline with formulated &adopted ICM/MSP plans[1]	%
Zoning plans and regulations completed, approved & implemented[2]	%
Applications where there are potential impacts on a site designated for historical environment[3]	No.
Condition of sites designated for historical environment[3]	-
Monitoring & mapping of new historical environment sites discovered as part of a development[3]	%
Employment rate of population aged 20-64[4]	%
Employment rate in maritime sectors[5]	%
Objective d)	
Conflicts in the use of maritime space by type and frequency	No.
Reported navigational accidents as a result of a marine development (construction or operation)[3]	No.
Applications refused due to incompatibility with other marine uses[3]	No.
Applications where there are potential impacts on the marine environment as a result of infrastructure development[3]	No.
Objective e)	
Licenses refused	No.
Conflicting processes at one-stop-shop	No.
Access to data (allowing for peer-reviewing of scientific advice)[6]	% requests
Access to meeting documents[6]	% requests
Rules concerning the participation of civil society observers[6]	-
Access to compliance and performance measures[6]	-
Objective f)	
Existence of a system of annual update	-
Incorporation of knowledge into management plans	-

DISCUSSION

To find indicators for the stated objectives of future Portuguese MSPlans, and to effectively articulate with the implementation of international commitments, such as the United Nation's Sustainable Development Goals (SDGs), particularly Goal 14 related to the conservation and sustainable use of "the oceans, seas, and marine resources" (UNGA, 2015), the present exercise drew information from a diversity of references related to ocean governance, including MSP, and specific maritime sectors.

The identification of potentially useful indicators for the evaluation of future Portuguese MSPM instruments was a challenging task for two main reasons: the general nature of the objectives, and the scarcity of currently available bibliography that comprehensively and effectively tackles the evaluation of MSP and related activities (especially considering the diversity of activities projected to take place in the Portuguese NMS).

Most of the stated objectives, particularly those of the NOS 2013-2020, can be equated to what Douvere and Ehler (2011) designated as "goals", *i.e.*, "statements of intent or general direction" as opposed to "objectives" defined as "statements of

measurable outcome" (*ibid.*, p.309). This vagueness promotes subjectivity in the indicator selection process. To assist in the identification of adequate indicators, objectives should be SMART: Specific, Measurable, Achievable, Relevant, and Time-bound (*e.g.*, Ehler, 2014). However, only one of the stated objectives meets these requirements ("*increase contribution of the sea economy to the GDP of about 50% by 2020*") allowing for a direct derivation of the corresponding indicator (cf. Table 1). The remaining strategic objectives of the NOS were found to be too broad or unclear to derive indicators, an unsurprising consequence of their strategic nature. The same difficulty was also felt with the objectives for MSP instruments, stated in Decree-Law 38/2015, due to their dubious/vague phrasing (Ferreira *et al.*, 2015b).

Related to this aspect is the differential complexity of the various objectives. While some are single and straightforward (*e.g.*, "prevent or minimize conflicts" or "ensure the use of available information"), others (*e.g.*, objectives b) and c)), are extremely complex, and multi-tiered. They are composed of a primary objective (respectively, exploitation of marine resources and ecosystem services, and organization of uses and activities), which is related to the achievement of underlying objectives (including preservation of the marine environment, while maintaining Good Environmental Status, in the first case, and respecting the marine ecosystem and underwater cultural heritage, and job creation, in the latter). This different complexity is inescapably reflected in the number of indicators proposed for each objective and, consequently, on the relative weight of each objective in the resulting indicator set.

The literature review carried out suggests that despite the existence of a great number of indicators to assess the state of the marine environment, very few references focus on their relationship with maritime activities and with the specificities of MSP. When they do (*e.g.*, Plan Bothnia), they only offer general pointers for measuring the effects of selected activities. It could be argued that the impacts of any given activity (environmental, social and economic), namely given their inherent specificities, are best evaluated at the project monitoring level ensuing from the corresponding Environmental Impact Assessment process. However, unless the effects of maritime activities integrate the higher ranking, global MSP evaluation framework, there will be a diminished possibility to act on existing stressors and to effectively adapt management actions to counter them.

For the reasons presented above, we believe that this set of indicators from Portugal, particularly considering the range of activities it encompasses, when fully developed and stabilized, can set the stage for improved evaluation frameworks in other MSP efforts worldwide. Next steps include: i) the verification and refinement of this indicator set by a panel of Portuguese and international experts on evaluation and MSP, and, building on it, ii) the development of a comprehensive framework for the evaluation of MSP initiatives. Such a framework should allow for the organization of these discrete indicators into a coherent whole, providing a measure of the distance from achieving sustainability objectives, the ultimate goal of MSP. It should also contribute to highlight gaps, not only in terms of needed information, but also in terms of important concerns for MSP that current frameworks may not address, such as impacts of MSP on human health or seascapes.

CONCLUSIONS

The set of indicators presented in this paper is a starting point for the development of a comprehensive evaluation framework of the MSPM of the Portuguese NMS. Given the size and geostrategic position of Portugal's maritime area, and the wide range of maritime activities it encompasses, despite the necessary adjustments related to the unique contexts of each individual case, it may constitute a useful tool in the emerging field of MSP evaluation worldwide, in articulation with the UN's Sustainable Development Goals (particularly Goal 14).

ACKNOWLEDGMENTS

This work was partly funded by Portuguese national funds through FCT/MEC in the framework of project UID/SOC/04647/2013. The first author is supported by a Ph.D. grant from the Portuguese Foundation for Science and Technology – FCT (ref. SFRH/BD/88549/2012). All translations from the Portuguese are by the first author. Thanks to Helena Calado for valuable suggestions on indicators, and to Francisco Andrade for insightful discussions and comments on an earlier version of this paper. We are also grateful to the reviewers, whose comments helped to improve the quality of the paper.

LITERATURE CITED

APA (Agência Portuguesa do Ambiente), 2010. *Sistema de Indicadores de Desenvolvimento Sustentável SIDS Portugal: Indicadores-chave 2010*. Lisboa: Agência Portuguesa do Ambiente, 69p. (in Portuguese)

Ardron, J.; Clark, N.; Seto, K.; Brooks, C.; Currie, D., and Gilman, E., 2014. Tracking twenty-four years of discussion about transparency in international marine governance: where do we stand? *Stanford Environmental Law Journal*, 33, 167-190.

Bessa Pacheco, M., 2013. *Medidas da Terra e do Mar*. Lisboa: Instituto Hidrográfico, 38p. (in Portuguese)

Carneiro, G., 2013. Evaluation of marine spatial planning. *Marine Policy*, 37, 214-229.

Cicin-Sain, B.; VanderZwaag, D.L., and Balgos, M.C., 2015. *Routledge Handbook of National and Regional Ocean Policies*. New York, NY: Routledge, 640p.

Day, J., 2008. The need and practice of monitoring, evaluating and adapting marine planning and management – lessons from the Great Barrier Reef. *Marine Policy*, 32, 823-831.

Decree-Law 38, 2015. *Decreto-Lei 38/2015 de 12 de Março*. Diário da República, I série, no. 50, p.1523–1549. (in Portuguese)

Douvere, F. and Ehler, C.N., 2011. The importance of monitoring and evaluation in adaptive maritime spatial planning. *Journal of Coastal Conservation*, 15, 305-311.

EC (European Commission), 2010. *EUROPE 2020: a strategy for smart, sustainable and inclusive growth*. COM(2010) 2020 final. Brussels: European Commission, 34p.

EC (European Commission), 2011. *EU biodiversity strategy to 2020*. COM(2011) 244 final. Brussels: European Commission, 16p.

EC (European Commission), 2011. *White paper: Roadmap to a Single European Transport Area*. COM(2011) 144 final. Brussels: European Commission, 30p.

Ehler, C., 2014. *A Guide to Evaluating Marine Spatial Plans*, Paris: UNESCO, IOC Manuals and Guides, 70, 84p.

Ferreira, M.A.; Calado, H.; Pereira da Silva, C.; Abreu, A.D.; Andrade, F.; Fonseca, C.; Gonçalves, E.J.; Guerreiro, J.; Noronha, F.; Pereira, M.; Pinto Lopes, C.; Ribeiro, M.C.; Stratoudakis, Y., and Vasconcelos, L., 2015. Contributions towards maritime spatial planning (MSP) in Portugal – Conference report. *Marine Policy*, 59, 61-63.

Ferreira, M.A.; Pereira da Silva, C.; Campbell, H.V.; Conway, F.; Andrade, F. and Johnson, D., 2015. Gold Rush or Pandora's Box? Toward a transparent and measured approach to MSP in Portugal. *The International Journal of Marine and Coastal Law*, 30(3), 418-444.

GFCM (General Fisheries Commission for the Mediterranean), 2013. *Indicators for sustainable aquaculture in Mediterranean and Black Sea countries*: *Guide for the use of indicators to monitor sustainable development of aquaculture*. Rome: FAO, GFCM Studies and Reviews, no. 93, 60p.

GGKP (Green Growth Knowledge Platform), 2013. *Moving towards a Common Approach on Green Growth Indicators*. Swiss Confederation: Green Growth Knowledge Platform, 44p.

Governo de Portugal, 2014. *Programa de monitorização e programa de medidas da Directiva-Quadro Estratégia Marinha: Subdivisões Continente, Açores, Madeira e Plataforma Continental Estendida*. Lisboa: Governo de Portugal, 228p. (in Portuguese)

GRA (Governo Regional dos Açores), 2011. *Manual de indicadores para a monitorização do ordenamento do território da Região Autónoma dos Açores*. Vol. 1: Modelo e Metodologia de Monitorização. Relatório Final – Fase 5. Fundação Gaspar Frutuoso/CEDRU, 64p. (in Portuguese)

HELCOM (Helsinki Commission), 2013. *HELCOM core indicators: Final report of the HELCOM CORESET project*. Baltic Sea Environment Proceedings No. 136. Vantaa: Helsinki Commission, 71p.

IEEP (Institute for European Environmental Policy), 2003. *Review and Gap analysis of environmental indicators for fisheries and aquaculture*. London, UK, 61p.

IOC (Intergovernmental Oceanographic Commission), 2006. *A Handbook for Measuring the Progress and Outcomes of Integrated Coastal and Ocean Management*. IOC Manuals and Guides, 46; ICAM Dossier 2. Paris: UNESCO, 217p.

IOC-UNESCO, 2011. *Methodology for the GEF Transboundary Waters Assessment Programme. Volume 6. Methodology for the Assessment of the Open Ocean*. UNEP, vi + 71p.

Johnson, D. and Ferreira, M.A., 2015. ISA Areas of Particular Environmental Interest in the Clarion-Clipperton Fracture Zone: Offsetting to fund scientific research. *The International Journal of Marine and Coastal Law*, 30(3), 559-574.

Law 17, 2014. *Lei no. 17/2014 de 10 de Abril*. Diário da República, I série, no. 71, 2358–2362. (in Portuguese)

MAOT (Ministério do Ambiente e Ordenamento do Território), 2010. *Vol. 2: Proposta de POEM. Tomo 4: Proposta de programa de monitorização*. Lisboa: MAOT, 16p. (in Portuguese)

Norse, E.A., 2005. Ending the Range Wars on the Last Frontier: Zoning the Sea, *In*: Norse E.A. and Crowder L.B. (eds.), *Marine Conservation Biology: The Science of Maintaining the Sea's Biodiversity*. Washington, D.C.: Island Press, pp. 422-443.

OJEU (Official Journal of the European Union), 2000. *Directive 2000/60/EC of 23 October 2000 (Water Framework Directive)*. L 327/1-72.

OJEU (Official Journal of the European Union), 2008. *Directive 2008/56/EC of 17 June 2008 (Marine Strategy Framework Directive)*. L164/19-40.

OJEU (Official Journal of the European Union), 2013. *REGULATION (EU) 1380/2013 of 11 December 2013 on the Common Fisheries Policy*. L354/22-61.

Plan Bothnia, 2013. *Planning the Bothnian Sea. Outcome of Plan Bothnia - a transboundary Maritime Spatial Planning pilot in the Bothnian Sea (Digital edition 2013)*. Backer, H., and Frias, M. (eds.). Helsinki: Helsinki Commission, 153p.

Resolution 12, 2014. *Resolução do Conselho de Ministros no. 12/2014 de 12 de Fevereiro.* Diário da República, I série, no. 30, 1310-1336. (in Portuguese)

Royaume de Belgique, 2014. *Arrêté royal relatif à l'établissement du plan d'aménagement des espaces marins. Annexe 2: Vision à long terme, objectifs, indicateurs et choix stratégiques*. 55p.

SCBD (Secretariat of the Convention on Biological Diversity), 2011. Nagoya Protocol on Access to Genetic Resources and the Fair and Equitable Sharing of benefits arising from their utilization to the Convention on Biological Diversity. Montreal: Canada, 25p.

SDSN (Sustainable Development Solutions Network), 2015. Indicators and a Monitoring Framework for the Sustainable Development Goals. Sustainable Development Solutions Network. 225p.

SIC (Shetland Islands' Council), 2013. *Shetland Islands' Marine Spatial Plan 4th edition: Strategic Environmental Assessment – Environmental Report*. Shetland Islands Council, 179p.

UNEP (United Nations Environment Programme), 2006. *Plan Bleu: Methodological sheets of the 34 priority indicators for the "Mediterranean Strategy for Sustainable Development" follow-up*. 80 p.

UNEP (United Nations Environment Programme), 2010. Strategic Plan for Biodiversity 2011-2020 and the Aichi Targets. https://www.cbd.int/doc/strategic-plan/2011-2020/Aichi-Targets-EN.pdf.

UNEP (United Nations Environment Programme), 2011. *Methodology for the GEF Transboundary Waters Assessment Programme. Volume 1*. UNEP, 60 pp.

UNEP (United Nations Environment Programme), 2014. *Measuring Success: Indicators for the Regional Seas Conventions and Action Plans.* UNEP Regional Seas Report and Studies No. 194. 214p.

UNGA (United Nations General Assembly), 2015. 2030 Agenda for Sustainable Development. http://www.un.org/sustainabledevelopment/

Journal of Coastal Research	SI	75	987 - 991	Coconut Creek, Florida	2016

Regional Scale Coastal Mapping to Underpin Strategic Land Use Planning in South East Australia.

David J. Hanslow†, Jocelyn Dela-Cruz†, Bradley D. Morris†, Michael A. Kinsela†, Edwina Foulsham†, Michelle Linklater† and Tim R. Pritchard†

†NSW Office of Environment and Heritage,
Newcastle, NSW 2300, Australia

www.cerf-jcr.org

www.JCRonline.org

ABSTRACT

Hanslow D.J., Dela-Cruz J., Morris B.D., Kinsela M.A., Foulsham E., Linklater M., and Pritchard T.R., 2016. Regional Scale Coastal Mapping to Underpin Strategic Land Use Planning in South East Australia. *In:* Vila-Concejo, A.; Bruce, E.; Kennedy, D.M., and McCarroll, R.J. (eds.), *Proceedings of the 14th International Coastal Symposium* (Sydney, Australia). *Journal of Coastal Research*, Special Issue, No. 75, pp. XX-XX. Coconut Creek (Florida), ISSN 0749-0208.

In the current study we develop spatial data to inform strategic land use and coastal planning which considers coastal hazards and the protection, maintenance and in some cases, restoration of our waterways. The benefits of sustainable coastal development underpinned by a well-established understanding of coastal processes and our ability to avoid negative impacts from inappropriate placement of development are well understood. With climate change and increasing use of coastal systems there is increasing need to identify and manage both current and possible future risk exposure. Mapping is undertaken to allow upfront identification of risks and benefits associated with potential future land use as well fundamental data to help inform coastal assessments. This will help ensure impacts on the coastal environment are minimised and impacts on proposed development from coastal hazards are avoided. The study has several parallel components addressing estuarine water quality and ecosystem health, sea level rise inundation, coastal erosion and sediment/geomorphic setting. Additional benefits of the project include risk based assessment to enable prioritisation of effort to address existing development which is either exposed to coastal hazards or having an impact on coastal waterways.

ADDITIONAL INDEX WORDS: *Coastal management, ecologically sustainable development, coastal hazards, coastal risk.*

INTRODUCTION

The benefits of sustainable development of the coast based on a sound understanding of coastal processes and avoidance of negative impacts from inappropriate placement of development are well understood. These benefits are likely to grow significantly over time with climate change and increasing use of coastal systems. Presently, considerable development in South East Australia is exposed to coastal hazards, while impacts from previous poorly considered development have included habitat degradation, declining water quality, resource depletion, and loss of coastal amenity.

Coastal development in New South Wales is subject to various controls through both coastal and estuarine planning and local and regional land use planning. The planning framework operates at different spatial scales and has been in place for some time through both coastal management legislative provisions (Coastal Protection Act, 1979) and environmental legislation (Environment Environmental Planning and Assessment Act, 1979). Under its coastal zone management program, the Office of Environment and Heritage (OEH) aims to reduce the impact of coastal hazards and maintain the ecological health of estuaries. The program has a long history of state and local government working collaboratively on coastal zone management. Much of this work is incorporated into coastal zone management plans (CZMPs), which are a requirement of the Coastal Protection Act 1979.

CZMPs can address risks from coastal hazards, threats to estuary health, and projected impacts of climate change such as sea level rise and risks of coastal erosion. The CZMPs are developed for local scale application, typically individual estuaries or beaches. They have been instrumental in providing detailed assessments of coastal and estuarine processes. However, not all estuaries and beaches have a CZMP to date, and there is limited ability to upscale existing assessments for use in strategic state-wide or regional planning and decision making due to inconsistencies in approach. There is a current pressing need for state-wide or regional assessments to help manage the regional growth that will occur over the next 20 years. Most of this growth is projected for the Greater Metropolitan Region, with continued demand for development along the coast placing increasing pressure on estuaries and coastal catchments.

The need for mapping at different spatial scales to inform national, regional and local risk assessment and management has been recognised previously both in the US and Australia (Titus and Richmond, 2001; Sharples *et al.*, 2008).

DOI: 10.2112/SI75-198.1 received received 15 October 2015 accepted in revision 15 January 2016
*Corresponding author: David.hanslow@environment.nsw.gov.au
©Coastal Education and Research Foundation, Inc. 2016

In this study, we fill the information gap by undertaking regional mapping of coastal erosion and inundation hazard and threats to estuary health. Results are presented for a case study location at Lake Illawarra on the south coast of NSW. For coastal erosion we developed a probabilistic approach that considers both short and long term sediment transport processes including storms, sediment supply and loss and response to sea level rise. For inundation we addressed differences in tidal processes between individual estuarine systems as well as along coast variability in tides and the longer term implications of sea level rise. For estuarine health we developed an effects based assessment, consisting of a coupled series of catchment, hydrodynamic and ecological response models, to predict the likely impact of coastal developments on the ecological condition of estuaries. Our overall objective was to provide maps that allow upfront identification of risks and benefits associated with planned future coastal development.

Regional Setting

The New South Wales (NSW) coastline stretches for over 1590 km (Figure 1) and has more than 750 sandy beaches (Short, 2007) and more than 184 significant estuaries (Roper *et al.*, 2011). Over 85% of the population live within 50 kilometres of the coast (ABS, 2004) which is known to be highly vulnerable to both erosion and inundation (DCC, 2009; Cechet *et al.*, 2012) and subject to various land use pressures which impact ecological health.

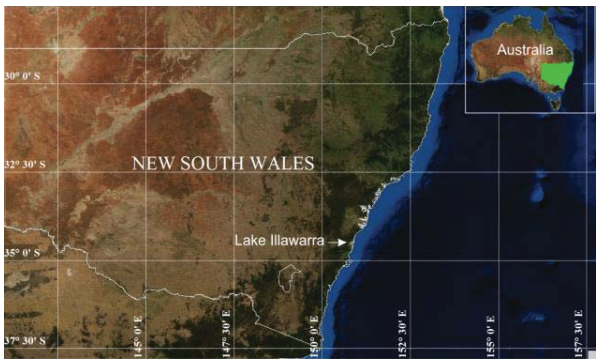

Figure 1. The NSW coast and case study location at Lake Illawarra.

The coast is aligned to the predominant south east swell and experiences a moderate to high energy wave regime (Shand *et al.*, 2011). Tides are microtidal and semi-diurnal with a pronounced diurnal inequality. The mean spring range is 1.2 m while the mean neap range is 0.8 m (AHS, 2011; MHL, 2012). Tidal range varies slightly along the coast with an increase of around 0.2 m from south to north (MHL, 2011).

The shoreline is comprised of areas of rocky cliffs and headlands joined by sandy beaches. On the south coast, the beaches are predominantly pocket beaches isolated by rocky headlands with little alongshore sand exchange from compartment to compartment. In the north of the state, these beaches tend to be longer and alongshore rates of sand movement are higher with sand moving from compartment of compartment, predominantly from south to north. Beaches are typically backed by high dunes which provide some protection against storm surge and wave runup.

Estuaries vary in shape and function along the NSW coast (Roper *et al.*, 2011) and have been classified by several authors using a variety of approaches (*e.g.* Roy, 1984; Roy *et al.*, 2001 and NSW Gov., 1992). These include drowned river valleys, tidal rivers, tidal lakes, intermittently open and closed lakes (ICOLLs) and lagoons and ocean embayments.

METHODS

Three types of maps were produced for all significant estuaries and beaches in NSW using the methods described below: i) maps showing the risk of coastal development on the ecological condition of estuaries under current and future regional growth scenarios, ii) maps showing the extent of inundation for 3 sea level rise scenarios of 0.5, 1 and 1.5 m, and iii) maps showing the potential extent of coastline change in the immediate and potential future coastal erosion and recession scenarios.

Estuary health (ecological condition)

Effects based assessment (EBA) focusses on the effect of management, that is, what we are trying to achieve (Scanes *et al.*, 2014). EBA is usually applied at the local scale but for this study, we adapted the assessment to produce maps at the subcatchment scale. The maps identify subcatchments upland of the estuary, where development controls would have the most benefit for protecting ecological condition. Typically, these are equivalent to areas that pose the highest risk of impact on ecological condition. The maps integrate the outcomes of sub-catchment scale surface runoff models that predict the quality and volume of runoff from land use (including new developments), and the outcomes of hydrodynamic and empirical ecological response models that predict the transport, retention and impact of the runoff within the major tributaries, reaches and basins of estuaries. Our EBA approach differs from current practice, which focusses solely on source control irrespective of the sensitivity of the receiving environment and/or the impacts on ecological condition.

The model outcomes were integrated using the ISO 31000 risk analysis approach, and included additional information on environmental assets that may be affected by the development and/or other processes not captured in the models. These included, for instance, the presence of ecologically endangered communities, acid sulfate soils, and proximity of the development to the estuary. We constrained the risk analysis to three risk levels corresponding to greater potential for impact on ecological condition. The risk levels can be matched with different types and levels of development and/or in intensity of water sensitive urban design to alleviate impact from both current and potential future development.

Inundation

To incorporate tidal and ocean inundation, we mapped estuarine inundation at the High High Water Solstice Springs (HHWSS) level. We used a mid-level approach to the modelling and mapping of water levels as outlined in Foulsham *et al.*, (2012) and Morris *et al.*, (2013). The approach is based on measured tidal plane data or berm heights for intermittently closed and open lakes and lagoons (ICOLL's). The method allows for variation in tidal levels both between and along estuaries and thus improves on simple bathtub type approaches

used in previous assessments (e.g. DCC, 2009; Cechet *et al.*, 2012).

For gauged estuaries we used tide gauge data from MHL (2012) to create interpolated tidal planes. These data are also used to categorise NSW estuary planes and identify characteristic tidal plane types for application to non-gauged estuaries. Within ICOLL's we adopt berm height to approximate inundation extent. The berm height was based on measured data or a formulation ($BH = 3.92*D_{50} + 1.12$) derived from Hanslow *et al.*, (2000) where no data were available.

Tidal planes were overlain on 1m resolution digital elevation models derived from high resolution LiDAR data. The liDAR data have a vertical accuracy of 0.3 m (95% CI). The resulting spatial model of inundation, greatly improves the representation of current inundation hazard areas and allows for improved assessment of the inundation hazard associated with potential sea level rise.

The impacts associated with sea level rise scenarios of 0.5 m, 1.0 m and 1.5 m were mapped and inundation extents were used to quantify risk, based on data from the geo-coded urban and rural addressing system database. The 0.5 m water level offset also allowed a first order estimation of effects of storm surge and other non-tidal processes (excluding wave setup and runup effects).

Erosion

We developed a volumetric coastal response model applied within a Monte Carlo statistical approach to map forecasts of immediate and potential future coastal erosion and recession (Kinsela *et al.*, 2016). The modelling builds on the approaches of Cowell *et al.*, (2006); Woodroffe *et al.*, (2012); and Mariani *et al.*, (2013). A probabilistic approach was adopted to help overcome uncertainty in historical measurements, understanding of coastal processes, potential future changes to environmental forcing, and our capacity to predict coastal responses. The method uses repeated random sampling of inputs to generate a probability distribution of model predictions based on the combined uncertainty spaces of the model inputs. In this application, the coastal response model is run repeatedly for each scenario, with model inputs chosen at random from their respective probability density functions (pdfs). Model inputs include variables such as sea level rise, and parameters of the coastal response model that is used to predict the potential extent of coastal erosion.

Model inputs include pdfs for short term storm response, sediment budget considerations including longshore transport, and predicted coastal response to sea level rise calculated from the sampled values of: sea level rise, shoreface closure depth and the surface area of connected and estuarine flood-tide deltas. The sea level rise and profile closure depth determine the theoretical shoreface sediment-accommodation volume generated by sea level rise. The shoreface accommodation volume can be scaled to account for the extent of shoreface reefs or other hard substrate, where present, which occupy volume in the water column above the shoreface and thereby reduce the theoretical accommodation volume. The scaled shoreface accommodation volume is then applied to the LiDAR beach-dune profiles to determine the coastline recession in response to sea level rise.

To parameterise the geomorphology and sediment budget of each sediment-sharing system along the NSW coast, a hierarchy of sediment cells were identified and mapped. These sediment cells reside within the secondary sediment compartments mapped by Geosciences Australia (McPherson *et al.*, 2015). They include primary, secondary and tertiary cells which define the boundaries of sediment-sharing systems at short to intermediate timescales.

The three levels of sediment cells allow for different sediment budget components to be defined along the coastline at spatial and temporal scales that are consistent with the scale of variation in the sediment transport processes that drive exchanges between sources and sinks. For example, sediment budget components that vary over short space and time scales (*e.g.* storm-induced beach erosion) can be defined at the tertiary cell resolution, whereas components that vary over longer timescales might be defined at the secondary or primary cell resolutions. The sediment cells framework supports further development of the coastal erosion hazard mapping approach described here, which may extend to higher resolution modelling and mapping based on a more refined parameterisation of coastal sediment budgets, and the inclusion of additional sediment budget components.

The sediment cells also provide a means to derive a regional shoreface bathymetry profile for each beach. Specifically, the average distance from sandy shorelines to the offshore depth limit of each primary (40 m), secondary (20 m) and tertiary (10m) cell was calculated, along with the average distance to the 30 m depth contour. An idealised shoreface bathymetry profile was then generated for each beach using the average distances to the 10, 20, 30 and 40 m depth contours, and the profiles were then used to calculate the theoretical shoreface sediment-accommodation volume generated by sea level rise. The resolution of the idealised shoreface profiles derived using that procedure is consistent with the regional-scale mapping approach.

RESULTS

The results described here are for Lake Illawarra, located ~100 km south of the Sydney Metropolitan Area (Figure1). We chose Lake Illawarra as a case study because of the large area of urban development in the west of the catchment (Figure 2), which will take place in the next 20 years to accommodate regional growth (Department of Planning and Environment, 2015).

Estuary health

Figure 2 shows the outcomes of the EBA under the future regional growth scenarios. The three colours on the map correspond to the three risk levels in the risk analysis. Developments in subcatchments that have been coloured red pose the greatest risk of impact on the ecological condition of the lake. These subcatchments are where management, such as water sensitive urban design or integrated water cycle management, will be of most benefit for protecting the ecological condition of the lake. Management in subcatchments coloured in yellow will have the next best benefit, and management in subcatchments in blue the least benefit because they pose the lowest risk of impact on ecological condition.

Inundation

Figure 3 shows the inundation map for Lake Illawarra. The varying shades of blue denote varying inundation levels corresponding to the existing surface area of the estuary (lightest blue) and the three sea level rise scenarios 0.5, 1.0 and 1.5 m (darkest blue). The map shows low lying areas such as the lake foreshores and major tributary inflows are the most vulnerable to future inundation.

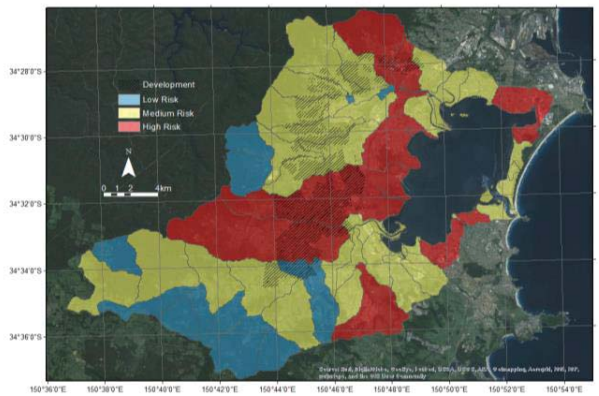

Figure 2. Estuary risk map for Illawarra showing low (blue), medium (yellow) and high (red) risk of impact of developments on estuary health.

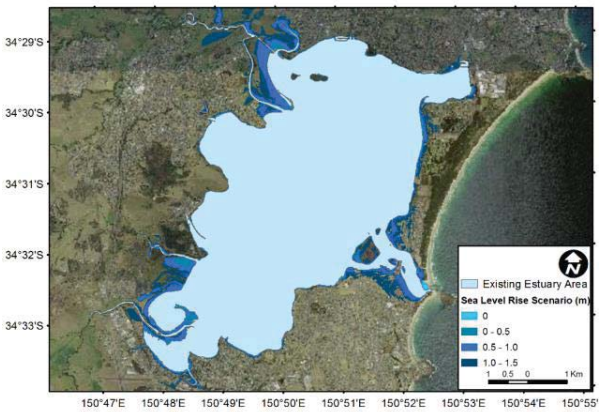

Figure 3. Inundation for different sea level rise scenarios around Lake Illawarra.

Erosion

For erosion the probabilistic modelling provides for the mapping of predicted coastal erosion and recession hazards at chosen confidence levels for each forecast period.

Figure 4 shows map output for a 50 year forecast of coastal change at Windang Beach, north of the entrance to Lake Illawarra. The blue hazard zone blue zone includes the erosion hazard zone mapped up to the 0.1% exceedance level. The red and green lines have a 50% and 1% chance of exceedance respectively, thus capturing the likely maximum reach of coastal erosion and recession over the next 50 years. The green line indicates a position consistent with 99% confidence that the coastline will not reach landward beyond that point.

DISCUSSION

In this study we developed maps showing the risks from subcatchment inflows, inundation and coastal erosion, which will allow upfront consideration in regional planning to enable impacts on the coastal environment to be minimised and potential

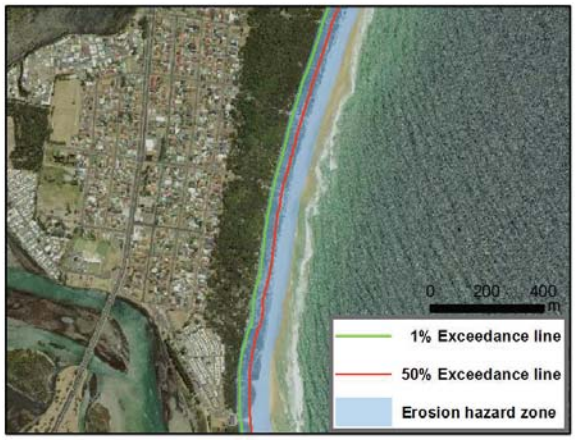

Figure 4. 50-year forecast of coastline change at Windang Beach. The blue zone includes the erosion hazard zone mapped up to the 0.1% exceedance level. The red and green lines have a 50% and 1% chance of exceedance respectively.

future impacts on new development from coastal hazards to be avoided. Some potential uses of the mapping for management of ecological health include the provision of spatial information to inform:

- strategic planning including information to help inform where developments are better placed. For example, blue and/or yellow subcatchments could be favoured over red subcatchments to reduce the potential impacts on estuary health.
- guidance in strategic impact assessments as part of preparations for Neighbourhood Plans. For example, knowledge of the required level of stormwater controls for a subcatchment can assist discussions between developers on optimal locations for the controls, and potentially reduce the number of future assets that Council will need to maintain.
- investigation of offset options in situations where management targets cannot be met at the site of development. The yellow areas within the same tributary as the site of development are potential offset sites. These are especially useful in situations where runoff from upstream land use activities impact on the effectiveness of stormwater controls at the development site.
- directions for setting management targets and options. For example, developments in red areas could be used to help improve the condition of the estuary through stringent

controls, whereas developments in yellow or blue areas could simply apply minimum controls such as used currently.

For inundation and erosion the mapping provides information to help decide where developments are better placed so as to avoid future impacts from coastal hazards. The mapping also provides information to inform risk scoping to identify the need for detailed risk assessment and need for detailed adaptation planning.

CONCLUSIONS

The maps are intended to guide strategic decision making at the regional level and to provide risk information to enable prioritisation of more detailed risk assessment. The mapping may form a default planning layer where risk is low or be refined though more detailed local process modelling and investigation.

ACKNOWLEDGMENTS

Part funding for the inundation mapping undertaken for this study was provided by the NSW Government Natural Disasters Resilience Program. Part funding for the erosion model development was provided through the NSW Environment Trust. Water level data was kindly provided by Manly Hydraulics Laboratory. Terrain data was provided by NSW Land and Property Information.

LITERATURE CITED

ABS, 2004. *Year Book Australia, 2004*. Australian Bureau of Statistics, 2004 1301.0., 872p.

AHS, 2011. *Australian Nation Tide Tables 2012*. Australian Government Department of Defence, Australian Hydrographic Service, Australian Hydrographic Publication 11.

Cechet, R.; Hazelwood, M.; Skene, D.; Griffin, C.; Dunford, M.; Power, L.; Canterford, S.; Nadimpalli, K.; Taylor, P.; Woolf, M. and Anderson, H., 2012. Impacts of climate change on human settlements and other nationally significant infrastructure in the coastal zone. *Record 2012/65*. Geoscience Australia: Canberra, 46p.

DCC, 2009. *Climate Change Risks to Australia's Coast: A first pass national assessment*. Australian Government Department of Climate Change, 168p.

Dela-Cruz, J., 2009. Threat of eutrophication. *Wetlands Australia*, 17:28.

Department of Planning and Environment, 2016, accessed 16 October 2015, <http://www.planning.nsw.gov.au/>.

Cowell, P. J., Thom, B. G., Jones, R. A., Everts, C. H., and Simanovic, D., 2006, Management of uncertainty in predicting climate-change impacts on beaches, *Journal of Coastal Research*, 22, 232-245.

Foulsham, E.; Morris, B. and Hanslow, D., 2012. Considering tidal modification when mapping inundation hazard in NSW estuaries. *Proceedings of 21st NSW Coastal Conference*, Kiama, Australia.

Hanslow, D.J., Davis, G.A., You, B.Z., Zastawny, J., 2000. Berm height at lagoon entrances in NSW. *Proceedings of 10th NSW Coastal Conference*, Yamba, Australia.

Kinsela, M.A.; Morris, B.D.; Daley, M.J.A. and Hanslow, D.J., 2016. A Flexible Approach to Forecasting Coastline Change on Wave-Dominated Beaches. *In:* Vila-Concejo, A.; Bruce, E.; Kennedy, D.M., and McCarroll, R.J. (eds.), *Proceedings of the 14th International Coastal Symposium* (Sydney, Australia). *Journal of Coastal Research*, SI, No. 75 (this volume), Coconut Creek (Florida).

Mariani, A.; Flocard, F.; Carley, J.T.; Drummond, C.D.; Guerry, N.; Gordon, A.D.; Cox, R.J. and Turner, I L., 2013. *East Coast Study Project – National Geomorphic Framework for the Management and Prediction of Coastal Erosion*, Water Research Laboratory, WRL Research Report 253, 41 pp.

McPherson, A.; Hazelwood, M.; Moore, D.; Owen, K.; Nichol, S. and Howard, F., 2015. *The Australian Coastal Sediment Compartments Project: methodology and product development*. Geoscience Australia, Canberra, 2015/25.

MHL, 2011. *New South Wales Ocean Water Levels*. Manly Hydraulics Laboratory, Report MHL1881, 29p.

MHL, 2012. *OEH NSW Tidal Planes Analysis: 1990-2010 Harmonic Analysis*. Manly Hydraulics Laboratory, Report MHL2053, 18p.

Morris, B.D., Foulsham, E., Hanslow, D., 2013. An improved methodology for regional assessment of tidal inundation hazards in NSW estuaries. *Proceedings of the 23rd Australasian Coastal Engineering Conference*, Sydney.

NSW Gov., 1992. *Estuary Management Manual*. NSW Government Printer.

Office of Environment and Heritage, 2011, Coastal Eutrophication Risk Assessment Tool, accessed 16 October 2015, <http://www.ozcoasts.gov.au/nrm_rpt/cerat/index.jsp>

Roper, T., Creese, B., Scanes, P., Stephens, K., Williams, R., Dela-Cruz, J., Coade, G., Coates B. and Fraser, M., 2011. *Assessing the condition of estuaries and coastal lake ecosystems in NSW, Monitoring, evaluation and reporting program*, Technical report series, Office of Environment and Heritage, Sydney.

Roy, P.S., 1984. New South Wales estuaries - their origin and evolution. In *Developments in Coastal Geomorphology in Australia* (Thom, B.G., ed.), Academic Press, New York, pp. 99 - 121.

Roy, P.S., Williams, R.J., Jones, A.R., Yassini, I., Gibbs, P.J., Coates, B., West, R.J., Scanes, P.R., Hudson, J.P. and Nichol, S., 2001. Structure and Function of South-east Australian Estuaries. *Estuarine, Coastal and Shelf Science*, 53, 351-384.

Scanes, P.; Dela-Cruz, J. and Ferguson A., 2014. Determining ecologically based targets for stormwater quality. *Stormwater Australia* Bulletin, 204, 2-5.

Sharples, C.; Attwater, C. and Carley, J.T., 2008. Three pass approach to coastal risk assessment *Proc. IPWEA National Conference Climate Change Response*, (Coffs Harbour, Australia).

Short A.D., 2007. *Beaches of the New South Wales Coast* (2nd ed), Sydney University Press, 398p.

Titus, J.G. and Richmond C., 2001 Maps of lands vulnerable to sea level rise: Modelled elevations along the US Atlantic and Gulf coasts. *Climate Research* 18 205-218.

Woodroffe, C. D., Cowell, P. J., Callaghan, D. P., Ranasinghe, R., Jongejan R., Wainwright, D. J., Barry, S. J., Rogers, K. and Dougherty, A. J., 2012, *Approaches to risk assessment on Australian coasts: A model framework for assessing risk and adaptation to climate change on Australian coasts*, National Climate Change Adaption Research Facility, 203 pp.

Journal of Coastal Research	SI	75	992 - 996	Coconut Creek, Florida	2016

Coastal Impact of Onshore Wind Farms in Australia

Nick Harvey [†§*] **and Romana E.C. Dew**[†]

[†]Centre for Coastal Research
The University of Adelaide
South Australia, 5005

[§]College of Marine and Environmental Sciences
James Cook University
Townsville, North Queensland, Australia 4811

www.cerf-jcr.org

www.JCRonline.org

ABSTRACT

Harvey N. and Dew, R.E.C. 2016. Coastal Impacts of Onshore Wind Farms in Australia *In:* Vila-Concejo, A.; Bruce, E.; Kennedy, D.M., and McCarroll, R.J. (eds.), *Proceedings of the 14th International Coastal Symposium* (Sydney, Australia). *Journal of Coastal Research*, Special Issue, No. 75, pp. 992 - 996. Coconut Creek (Florida), ISSN 0749-0208.

The global expansion of wind-generated power has resulted in a rapid proliferation of both onshore and offshore wind farms, particularly in Europe. Australia like the rest of the world has experienced a rapid increase in wind power over the last decade but unlike Europe, its coastal wind farms are all located onshore mostly in the southern part of the country where wind energy resources are high. Around half of the wind farms are located in rural coastal locations. This paper discusses the various environmental, social and political issues associated with coastal wind farm development in Australia by assessing the coastal impact of wind farms and the adequacy of coastal management strategies for dealing with such impacts. The paper concludes that the technological pace of coastal wind farm development has outstripped the development control process, which has resulted in a largely unforeseen cumulative impact on the Australian coast.

ADDITIONAL INDEX WORDS: *Coastal Management, wind farms, aesthetics, coastal landscapes*

INTRODUCTION

There has been a rapid global expansion of wind-generated power, which has risen from a global cumulative installed capacity of 6,100 MW in 1996 to 369,553 MW at the end of 2014 (GWEC, 2015). This demand has been met by the installation of wind turbine arrays referred to as wind farms around the globe. The growth in the wind energy industry worldwide has seen a simultaneous increase in the number of coastal wind farm developments. This increased capacity for electricity generation is due to the higher wind speeds associated with coastal areas and the potential for wind farms to be in close proximity to human settlements. Consequently, there has been a rapid expansion of both onshore and offshore wind farm developments. In Europe, due to the inherent difficulties in finding suitable onshore open spaces in coastal areas, offshore wind energy is becoming a much more viable option (Diesendorf, 2011). This phenomenon in Europe has also resulted in reduced siting and environmental issues typically associated with the objections to onshore wind farm developments (Diesendorf, 2011).

In Australia, recent wind farm development has mirrored the global experience with a rapid increase in output capacity, particularly over the last decade (Figure 1). As of August 2015, there were 73 wind farms operating in Australia incorporating a total of 2,022 turbines with a capacity to produce an output of approximately 4,135 MW of electricity. This rapid development of Australian wind farms includes a

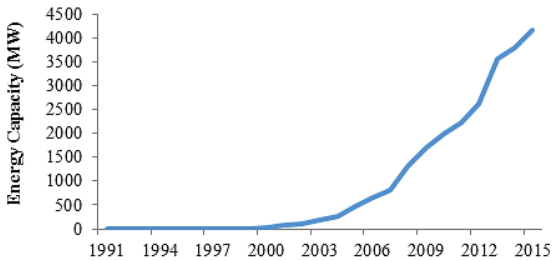

Figure 1. Graph illustrating the total Australian installed capacity of wind energy since 1991. Source: GWEC (2015).

significant proportion located around the coast due to a reliable wind environment. This has resulted in wind farm sites in close proximity to population centers and electricity grids, mostly on the southeast coast.

Unlike Europe, due to Australia's abundance of open spaces and most of its coastal waters being too deep for offshore wind farm technology, all current wind farm developments are land-based (Diesendorf, 2011). Over a decade ago, Mercer (2003) noted the start of this rapid development and potential impact on the Australian coast. Since then there have been a number of site-specific coastal wind farm studies and papers on planning approvals and legal issues but there is a gap in the literature relating to the national impact of this form of coastal development or its broader implications for coastal management.

Concerns about impacts of windfarms are often focused on their visual and aesthetic qualities, land-use impacts, community

DOI: 10.2112/SI75-199.1 received received 15 October 2015 accepted in revision 15 January 2016
*Corresponding author: nick.harvey@adelaide.edu.au
©Coastal Education and Research Foundation, Inc. 2016

health and wildlife especially bird mortalities. In addition, offshore wind farms produce a set of specific marine impacts including marine ecosystem disturbance and navigational safety (REN 21, 2014). Given a lack of such offshore developments in Australia this paper focuses on issues associated with the siting of onshore wind farms such as socio-cultural and environmental impacts and technological factors.

Visual impacts are among the most commonly expressed concerns about wind energy development projects in the United States and Europe, in both onshore and offshore settings (Diesendorf, 2011; Firestone *et al.* 2015; Pasqualetti, 2012). Pasqualetti (2012) addressed the criticisms and future potential for wind power within the context of the UK, USA and Mexico. This study concluded that objections to wind farms can be largely reduced to their effects on the community's quality of life and it is not simply the landscape, but rather the cultural connection that individuals have with it (Pasqualetti 2012). Erickson *et al.* (2005) estimate in an American study that, wind turbines, comprise only 0.003 percent of bird fatalities. Nevertheless, there is no doubt that in some locations, such as Altamont Pass in California, the incidence of wind-related bird fatalities is unacceptably high, especially of 'charismatic birds', such as falcons and eagles (Pasqualetti, 2012). From a technological perspective, wind turbines emit a mechanical sound from their gearbox and an aerodynamic noise from the rotation of the blades (Firestone *et al.* 2015). Turbines have been under past scrutiny due to purported problems including a variety of alleged interference (noise, electromagnetic, electrical, radar and navigation), the blade glint and flicker, stray voltage, oil leaks, fires, ice toss and collapse (Pasqualetti, 2012). There has also been a recent increase in the attribution of symptoms and diseases to wind turbine exposure and sub-audible sound for humans and animals, coined the 'wind turbine syndrome' (Crichton *et al.*, 2014).

This paper focuses on coastal impacts from onshore wind farms, which are of relevance in Australia. The paper analyses the nature, growth and distribution of the Australian wind farm industry illustrating the extent, timing and impact of wind farm development on the coast. In particular, this paper examines the various issues associated with coastal wind farm development and the extent to which these have been addressed in coastal management and planning legislation and policies. This is linked in general to the uptake of science into environmental policy. The paper concludes that the rapidity of this form of development has largely moved ahead of specific policies and development controls regulating the industry and this has created a significant impact around the southern half of the Australian coast.

METHODS

Wind farm geo-referenced location data were obtained predominantly from the Wind Energy Market Intelligence for all Australian wind farms installed as of mid-2015 and compiled and digitized into an ArcGIS shapefile in order to examine the geographic distribution of all Australian wind farms. From this information, a Euclidean distance between each wind farm and its nearest coastline was calculated and grouped into farms less than 5 km, 10 km, 25 km and 50 km or greater from the coast.

These data were then used to determine the relative concentration of wind farms near the Australian coast. Data on the number of wind turbines and their installed wind generating capacity was also recorded for each wind farm. This was important as an individual wind farm may have a larger number of wind turbines or a greater total generating capacity than the cumulative output of a number of smaller wind farms.

In addition, government reports such as planning documents, conditions of approval and any environmental impact assessment (EIA) documents were examined to identify potential impacts and proposed mitigation measures for all coastal wind farms. These impacts were categorized and comparisons made with examples from the international wind farm literature. Site visits were also conducted to selected coastal wind farms.

Following the assessment of coastal wind farm impacts, a brief review was undertaken of government policies and legislation, which relate to the facilitation or control of coastal wind farm development and mitigation of any impacts. It is likely that variable state coastal management and planning policies will influence the siting of wind farms and in a more general sense variable state and federal renewable energy policies will influence the extent of wind farm development.

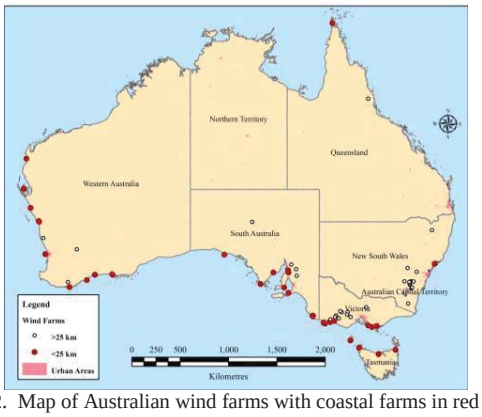

Figure 2. Map of Australian wind farms with coastal farms in red

RESULTS

In this study, coastal wind farms have been defined as being within 25 km of the coast. A map constructed from the wind farm locational GIS data-base (Figure 2) illustrates the distribution of all constructed wind farms in Australia revealing that nearly two thirds (64%) of these are located near the coast. Each wind farm contains a different number of wind turbines. There is also a variation in the energy output of the turbines depending on the type and make of the turbine. In general, there has been an increase in the size and efficiency of turbines over time.

Wind energy represents the fastest growing source of renewable energy in Australia with an overall 47% compound annual growth rate from 1991 to 2015. Analysis of the Australian wind farm data shows that the coastal zone not only contains the majority of wind farms but also half (50%) of the total number of the country's installed wind turbines. Similarly,

coastal regions also contain about half (51%) of the total national installed capacity of 4,135 MW since the MW output capacity is more closely aligned with the number of turbines, rather than the number of wind farms. The extent of Australia's coastal wind farm developments also varies considerably on a state-by-state basis.

An analysis of government reports, EIA statements and planning approvals indicates a number of impacts associated with coastal wind farms although many non-coastal wind farms have similar impacts. These coastal impacts have been categorized in Table 1 according to; a) socio-cultural impacts, in particular aesthetic impacts on landscapes, visual and amenity impacts; b) biophysical impacts such as construction impacts, ecological impacts and bird and bat strikes, and; c) economic and technological impacts.

Table 1. *Coastal impacts of wind farms tabulated from literature*

Wind Farm Impacts	References
a) Aesthetics and visual amenity; cultural heritages and norms; wind turbine syndrome	Lothian 2008; Chapman 2015; Crichton *et al.* 2014
b) Landscape scarring & erosion; biota danger especially bird and bat; water contamination; habitat loss; life-cycle global warming emissions	Mercer 2003; Lothian 2008; Pasqualetti, 2012; Arnett *et al.* 2010
c) Property loss; navigational safety; noise	Pasqualetti, 2012

An Australian study (Lothian 2008) provides empirical evidence to demonstrate the aesthetic impacts of wind farms on the landscape and specifically coastal landscapes of high scenic value. He concluded that wind farms had a greater negative impact on coastal landscapes of high scenic quality compared to lower rated coasts. The aesthetic impact on coastal landscapes is identified as a major impact, particularly given the predominantly unspoiled rural coastal locations of many wind farms sites.

Examples of aesthetic impacts on rural coastal landscapes can be seen in South Australia, which has the highest proportion of the country's wind farms.

Figure 3. Starfish Hill windfarm, Fleurieu Peninsula, South Australia (illustrating visual impact on rural cliffed-coastal landscape)

The Starfish Hill wind farm (Figure 3) near Cape Jervis south of Adelaide comprises 23 wind turbines built on Starfish and Salt Creek Hills where folded meta-sedimentary rocks of the Adelaide Geosyncline are exposed in the coastal cliffs at the southern end of the Fleurieu Peninsula. Environmental impacts, including visual impacts were assessed prior to approval as a Crown Development in 2002.

A second example comes from the Wattle Point wind farm on Yorke Peninsula comprising 55 turbines located across an area of 17.5 km^2. Apart from the illustrated visual impacts on the low-lying sandy coast, there were also impacts on indigenous heritage issues, which required the re-positioning of a number of the turbine locations.

Figure 4. Wattle Point wind farm, Yorke Peninsula, South Australia (illustrating visual impact from nearby beaches)

A third example (Figure 5) comes from the southeast coast of South Australia where there are 23 wind turbines in the Canunda wind farm plus 112 wind turbines in the adjacent Lake Bonney wind farm complex stretching across 24 km^2 of the Woakwine Range formed from older Pleistocene coastal dunes. The total of 135 turbines create a significant visual impact on the rolling dune landscape as shown in Figure 5 where the turbines stand out against the backdrop of the adjacent Lake Bonney and the coastal Canunda National Park.

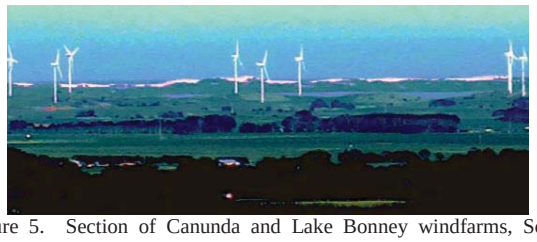

Figure 5. Section of Canunda and Lake Bonney windfarms, South Australia (illustrating visual impact on the coastal dune landscape)

A fourth example (Figure 6) comes from the southwest coast of South Australia where the Cathedral Rocks wind farm contains 33 wind turbines stretching over an area of 29 km^2 above the scenic Pleistocene aeolianite coastal cliffs of the Coffin Bay Peninsula. This aerial view demonstrates the aesthetic impact on a relatively pristine section of coast, which has restricted access for the general public because the wind farm has been built on private farming land.

These four examples of wind farm development, including one of Australia's largest wind farm developments at Canunda/Lake Bonney, illustrate significant visual changes to rural coastal landscapes. In Lothian's empirical study he demonstrated a negative impact of wind farms on perception of

South Australian coastal landscape quality, although it is noted that there are also anecdotal reports in the international literature of positive visual impacts (Firestone *et al.* 2015).

Figure 6. Aerial view of Cathedral Rocks wind farm, Eyre Peninsula, South Australia (illustrating visual impact on a relatively pristine coastal landscape: Photo Coast Protection Board of South Australia)

A perhaps unforeseen impact is the potential for turbine failure to initiate bushfires in the summer months. So far there have been turbine fires in South Australia at the Lake Bonney complex in January 2006; in the Wattle Point wind farm in February 2009; and then a major fire and destruction of one of the Starfish Hill turbines in October 2010. In the latter instance fire crews had major difficulties in getting close to the fire.

Another potential impact is for bird strikes on coastal species of raptors or migratory birds. The Bald Hills wind farm development in Victoria had potential impact on a rare and endangered species of coastal migratory bird, the orange-bellied parrot. This triggered the national environmental legislation (the Environmental Protection and Biodiversity Act, EPBC) causing the federal Environment Minister to stop the project in 2006, although his decision was subsequently overturned.

There have also been reports of the wind turbine syndrome, although this is not specifically a coastal issue. Reviews of the medical literature by Chapman *et al.* (2013) found the evidence for attribution was very poor and conclude that sub-audible, low-frequency sound and infrasound does not pose a direct risk to human health. Chapman, who has been critical of Australian claims of ill-effects from wind turbine syndrome has himself been criticized by the Senate Committee on Wind Turbines (2015; p18-22) which questioned a number of Chapman's assertions. The committee called for further high-quality research on this issue to determine cause and effect.

Development and management of the Australian coast lacks a consistent national policy approach, a victim of the federated system of government (Wescott, 2012). Coastal policy remains the jurisdiction of state governments, despite four separate national inquiries since the 1980s recommending a national coastal policy. Hence, coastal wind farms are assessed on a state-by-state basis according to relevant state planning and development processes, legislation and controls rather than as a coastal management issue.

The influence of wind energy policy is an important factor in the extent of wind farm development, particularly at the state level. South Australia (SA) has ambitious targets and supporting policies, which have resulted in the highest number of wind farms in Australia and 40 percent of the nation's wind capacity (Climate Council, 2014).

In contrast, Victoria which previously had strong support for renewable energy and wind farms with development of its WindAtlas in 2001, changed its policy and planning regulations to restrict wind farm development (Climate Council, 2014). Victorian guidelines now focus on coastal siting issues related to minimizing the impacts on primarily 'visually significant' landscapes. This includes a turbine setback distance of 2 km from dwellings. Victoria's largest wind farms located within 5 km of the coast are positioned linearly behind vegetated dunes on existing cleared pastoral land in order to complement the landscape. These planning changes protect the state's key tourist and coastal regions such as the Great Ocean Road and Mornington Peninsula.

New South Wales planning guidelines for wind farms do not specifically mention coastal issues whereas Queensland does not have specific policies for wind farms. Similarly Tasmania has no wind farm policies, although it is of note that all of Tasmania's wind farms have coastal locations.

Western Australia planning guidelines focus on minimizing coastal visual impacts and coastal vegetation removal. The guidelines include a 1 km setback distance from 'noise-sensitive buildings', based on SA noise guidelines for wind farms. Wind turbines within 5 km of the coastline have typically been placed linearly along coastal ridgelines to reflect and complement landscape and topographical features. The more sizeable coastal wind farms in Western Australia are located on existing cleared pastoral and grazing land less than 25 km from the coast.

The relatively low level of environmental impact of wind energy developments together with favorable planning and policy frameworks has been a major factor in their rapid introduction in rural coastal areas. Notwithstanding this, they have attracted criticism particularly related to aesthetics and siting issues, noise pollution and well as the impacts on local bird and bat populations.

DISCUSSION

The advent and rapid growth of onshore wind farm development in Australia, represents a significant impact on the Australian coast. Coastal wind farms have generally not been classified as coastal development limiting the extent to which coastal management issues have been considered in the planning process.

The major impact of wind farms appears to be the aesthetic impact on the visual quality of coastal landscapes as demonstrated by Lothian (2008). It is interesting to note that Victoria has introduced planning restrictions to protect highly valued coastal landscapes such as the Great Ocean Road, whereas the Cathedral Rocks coastal landscape in SA (Figure 6) for example has comparable landscape qualities but was subject to a routine local government approval process as it was on private land and not visible to the general public. There is clearly a need to incorporate aesthetic impact guidelines into coastal policies to allow for the assessment of different levels of visibility based on location and population.

Unlike the aesthetic issues, mitigation is possible for the many of the environmental issues (Mercer 2003; Lothian 2008; Pasqualetti, 2012) include scarring and erosion, biota danger (especially birds), water contamination and habitat loss. Negative impacts on flora and fauna, namely through land clearance, as well as bird and bat strikes have been a common factor in arguments against wind farm developments (Arnett *et al.*, 2010). These are usually assessed through a formal state-based EIA process unless any species of flora and fauna constitutes a matter of 'national significance', which could trigger the federal EPBC legislation.

One impact identified in the current paper, but not apparent in the general wind farm literature, is the risk of coastal wind turbine failure and its potential to trigger summer bushfires.

CONCLUSIONS

The rapid growth rate in the Australian wind farm industry over the last 25 years has led to half of the wind farms being located around southern coasts where wind energy resources are high. These developments have been assessed on a case-by-case basis under separate state planning legislation. There does not appear to be any national strategic approach to the siting of wind farms and nor has it been treated as a coastal management issue. The result has been a largely unforeseen and unplanned cumulative impact on the visual quality of many Australian rural coastal landscapes.

ACKNOWLEDGMENTS

The authors acknowledge research funding of the CSIRO Flagship Collaboration Fund (coastalcluster.org.au). Photographs were taken by the authors unless otherwise stated.

LITERATURE CITED

Arnett, E.B.; Huso, M.M.P.; Hayes, J.P., and Schirmacher, M., 2010. *Effectiveness of changing wind turbine cut-in speed to reduce bat fatalities at wind facilities.* A final report submitted to the Bats and Wind Energy Cooperative. Austin, Texas: Bat Conservation International.

Chapman, S.; St. George, A.; Waller, K., and Cakic, V., 2013. The Pattern of Complaints about Australian Wind Farms Does Not Match the Establishment and Distribution of Turbines: Support for the Psychogenic, 'Communicated Disease' Hypothesis. *PLoS ONE* 8(10), 1-11.

Crichton, F.; Dodd, G.; Schmid, G.; Gamble, G.; Petrie, K.J., 2014. Can expectations produce symptoms from infrasound associated with wind turbines? *Health Psychology*, 33(4), 360-364.

Climate Council, 2014. *The Australian Renewable Energy Race: Which States Are Winning or Losing?* Climate Council of Australia Limited, 47p.

Diesendorf, M., 2011. *Europe has offshore wind farms … why can't Australia?* https://theconversation.com/europe-has-offshore-wind-farms-why-cant-australia-3574

Erickson, W.P; Johnson, G. D., and Young, D. P., 2005. *A summary and comparison of bird mortality form anthropogenic causes with an emphasis on collisions.* Albany, California: U.S. Department of Agriculture Forest Service, *General Technical Report PSW-GTR-191*, pp. 1029-1042.

Firestone J.; Bates, A., and Knapp, L.A., 2015. See me, Feel me, Touch me, Heal me: Wind turbines, culture, landscapes, and sound impressions. *Land Use Policy*, 46, 241-249.

Global Wind Energy Council (GWEC) Staff, 2015. *Global Wind Statistics 2014*. Brussels, Belgium: Global Wind Energy Council, 4p.

Hindmarsh, R., 2010. Wind farms and community engagement in Australia: a critical analysis for policy learning. *East Asian Science, Technology and Society: An International Journal*, 4, 541–563.

Hindmarsh, R. and Matthews, C., 2008. Deliberate Speak at the Turbine face: Community Engagement, Wind Farms, and Renewable Energy Transitions, in Australia. *Journal of Environmental Policy & Planning*, 10(3), 217–232.

Lothian, A., 2008. Scenic Perceptions of the Visual Effects of Wind Farms on South Australian Landscapes. *Geographical Research*, 46(2), 196-207.

Mercer, D., 2003. The great Australian wind rush and the devaluation of landscape amenity. *Australian Geographer*, 34, 91–121.

Pasqualetti, M.J., 2012. The Misdirected Opposition to Wind Power. *In*: Szarka, J.; Cowell, R.; Ellis, G.; Strachan, P.A., and Warren, C. (eds.), *Learning from Wind Power*. Hampshire, England: Palgrave Macmillan, pp.133-152.

Senate Select Committee on Wind Turbines, 2015 *Final Report of Senate Select Committee on Wind Turbines*, August 2015, Australian Government, 350p.

Wescott, G., 2012. Disintegration or disinterest? Coastal and marine policy in Australia. *In:* Crowley, K., and Walker, K. (eds.), *Environmental Policy Failure: the Australian story*. Victoria, Australia: Tilde University Press, pp. 88-101.

Journal of Coastal Research	SI	75	997 - 1001	Coconut Creek, Florida	2016

Outlining an approach to address Geospherical and Biospherical aspects of Coastal Squeeze in the Mediterranean

Annette Hildinger[†*], **Andreas Braun**[†]

[†]Institute of Regional Science
Karlsruhe Institute of Technology
Karlsruhe, Germany

www.cerf-jcr.org

www.JCRonline.org

ABSTRACT

Hildinger, A.; Braun, A. 2016. Outlining an approach to address geospherical and biospherical aspects of Coastal Squeeze in the Mediterranean. *In:* Vila-Concejo, A.; Bruce, E.; Kennedy, D.M., and McCarroll, R.J. (eds.), *Proceedings of the 14th International Coastal Symposium* (Sydney, Australia). *Journal of Coastal Research*, Special Issue, No. 75, pp. 997 - 1001. Coconut Creek (Florida), ISSN 0749-0208.

Sea level changes and growing anthropogenic pressures on coasts worldwide represent a pressing matter that urges investigations across disciplines. The Coastal Squeeze concept is appropriate for this purpose. It addresses coastal dynamics regarding geomorphological and anthropogenic impacts like landward constructions *i.e.* barrages, with a focus on coastal management. Regarding the role of coastal ecosystems in mitigation to climate change and sea level rise the ecological impacts caused by coastal squeeze can no longer be neglected. The paper develops a research concept to link geospherical and biospherical aspects of Coastal Squeeze within a Mediterranean study site. In order to understand coastal squeeze dynamics along a coastline complex, an integrating approach should address the whole coastline working from a regional to a local scale. The regional scale encompasses coastal types, changes in sea level, sediment supply, flooding, inundation, salt water intrusion and landward barriers (geosphere). On the local scale an integrated approach should take into account significant environmental parameters as they will determine the localization of future coastal ecosystems (biosphere).For the study area a coast of the Mediterranean Sea that is made up of different coastal types, high anthropogenic impacts and micro-tidal dynamics was chosen. Due to also being a biodiversity hotspot this region represents a suitable study site for ecosystem related coastal squeeze research. This work in progress will be presented and discussed at the International Coastal Symposium 2016.

ADDITIONAL INDEX WORDS: *Coastal processes, Coastal Squeeze, Mediterranean Sea*

INTRODUCTION

Coastal Squeeze has gained an amount of significance in science in recent years. This might be probably due to the growing awareness of the increasing pressures on coasts worldwide due to sea level changes and anthropogenic influence (Martínez *et al.* 2007).

In its origin the Coastal Squeeze concept addresses coastal dynamics regarding geomorphological and anthropogenic impacts form the coastal manager's point of view (Pontee 2013). Recognized under the label "Coastal Squeeze" in the frame of coastal management in Great Britain in the 1980s the concept has been introduced to the scientific community by (Doody 2004). Since then it has been worked on under various aspects in different regions of the world. As examples might serve: Jolicoeur and O'Carroll (2007), Martínez *et al.* (2014), Phan *et al.* (2015), Schleupner (2008), Torio and Chmura (2013).

Jolicoeur and O'Carroll (2007) examine changes to highly dynamic coastal habitats induced by a coastal-near highway located on sandy barriers at Gulf of St. Lawrence (Québec, Canada) under a historical perspective. Coastal protection structures have been built to prevent the highway from erosion. The study is based on an analysis of historical developments by aerial photograph series. The findings on two study sites show that these measures led to a coastal squeeze since the 1940 between protecting structures and retreating shoreline.

Schleupner (2008) focuses on coastal development in the context of tourism infrastructure in Martinique choosing a future perspective. Analysis is done via a digital terrain model (DTM) in which sea level and erosion scenarios are implemented. The applied coastal squeeze index takes into account migration opportunities related to coastal elevation and infrastructure, sea level rise based on sea level rise scenarios and including erosion and accumulation as well as the coastal wetland type (beach, mangrove). Results suggest that almost half of Martinique's coasts is very sensitive to Coastal Squeeze assuming a sea level rise of 25 cm.

Torio and Chmura (2013) develop a "Coastal Squeeze Index" in order "to identify locations where coastal squeeze is likely to occur" (p. 1049) in a first step and rank the threats faced by wetlands along a particular coast. Such information is needed for a coastal management that tents to prevent migrating wetlands from disappearance or degradation through Coastal Squeeze. Their approach focuses on marsh ecosystems which they examine at a complex of marshes in the Gulf of Main (USA) and the Gulf of Saint Lawrence (Canada). They suggest to derive topography of the study area from LIDAR and ASTER data sets to establish a digital elevation model (DEM). Aerial photographs serve to approach particular study sites. Elevation limit and tidal datum information are taken into account. Based on the DEM and a sea level rise scenario of 2,5m they determine

DOI: 10.2112/SI75-200.1 received received 15 October 2015 accepted in revision 15 January 2016
*Corresponding author: annette.hildinger@kit.edu
©Coastal Education and Research Foundation, Inc. 2016

the flooded upland. The index *i.e.* the coastal squeeze potential is then derived by classifications of slope and imperviousness of the future flooded upland, proceeded by an uncertainties analysis. Both attributes determine the migrating potential of marshes and are thus indispensable to be taken into account when studying marsh ecosystems.

This exemplary choice of studies – which, due to space limits, does not claim to be exhaustive – shows some methodological preferences in coastal squeeze research: many studies work spatially explicitly on particular study sites and take into account local terrain and environmental properties like at least elevation (*i.e.* DEM), sea level (*e.g.* tidal information), erosion and land use (*e.g.* protecting structures, roads etc). Additionally, certain ecosystem types are taken into account (*e.g.* beaches, marshes, mangroves). Departing from the geographical base coastal squeeze is studied (mostly in a GIS) either via a historical perspective (using *e.g.* aerial imagery or remote sensig) that determines changes of the coastal setting over a certain period between the past and the present. Or the study is done with a perspective to possible future conditions using spatially explicit modeling approaches by implementing *i.e.* SLR scenarios and/or projected trends from historical coastal squeeze analysis. The historical perspective has a more explanatory dimension. It helps to find out about areas where Coastal Squeeze already has taken place in order to e.g. to develop a coastal zone management that minimizes the consequences. The forward-looking perspective tents to predict the location of future Coastal Squeeze areas in order to develop a management that will limit these impacts to a minimum.

It should be mentioned that some authors choose a very specific focus within their coastal squeeze studies even if they use similar methodological approaches like the studies mentioned above. (Mazaris *et al.* 2009) *e.g.* examine the impacts of coastal squeeze on sea turtle nesting (scenarios of habitat loss due to sea level rise linked to hatchling production; study area: western Greece, forward looking perspective). Other authors focus on mangrove squeeze due to anthropogenic impact like *e.g.* Phan *et al.* (2015) examine mangrove degradation and depletion due to the construction of sea dikes (study site: Mekong Delta).

The differences in focus, research subject and methods suggest that Coastal Squeeze represents a matter that urges a definition beforehand. According to Pontee (2013) the meaning of changes of the coast's geospherical environmental conditions to the extent of ecosystems related to the coast (coastal habitats) should not be neglected. Furthermore, he suggests to use the term Coastal Squeeze only when taking about coastal habitat changes resulting from a combination of sea level rise and anthropogenic structures that hinder landward migration of the coastal habitat. In contrast a coastal habitat decline due to naturally induced decreases in coastal zone width should be referred to as "coastal narrowing" (Pontee 2013). Our approach will be based on this interpretation of Coastal Squeeze.

In our study we intend to pick out explicitly the link between geosphere and biosphere in the context of Coastal Squeeze by an integrated approach on two aspects: (1) link the abiotic environmental conditions and the environmental parameters relevant to particular ecosystems of the studied coastal area to the occurrence behavior of the ecosystem, not to forget about the anthropogenic influence, and (2) take into account the terrestrial as well as the marine part of the coast. An approach very similar to ours concerning the first aspect is described by Martínez *et al.* (2014).

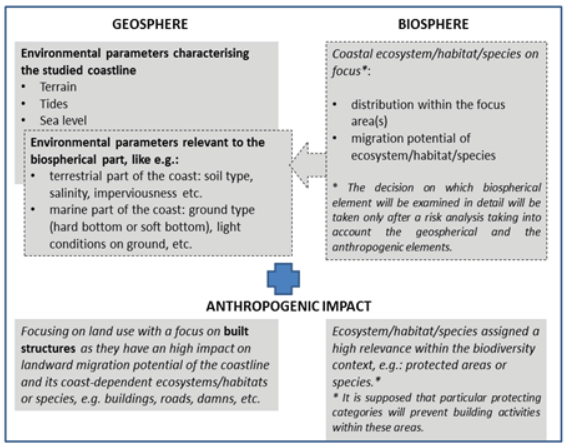

Figure 1. Elements of an approach to coastal squeeze that integrates geospherical, biospherical and anthropogenic elements

In our opinion Coastal Squeeze should be addressed in a way that scenarios of future developments of a specific coast could be combined with changes in coastal ecosystems evoked by those potential developments. This would help to build up an anticipatory coastal management. Thus we choose a forward-looking perspective.

As study area we chose the Mediterranean coast of France, which is a micro-tidal coast of high biodiversity relevance and important ecosystem services that suffered and still does high anthropogenic impact in form of near-coast built structures in last decades, especially due to rising tourism since the 1970s (Cori 1999). (Brunel and Sabatier 2009) *e.g.* find a relative sea level rise over the 20th century of 1,1-2,2mm/y along the coasts of the region "Provence". This accounts for a high vulnerability of the French Mediterranean Coast facing a potential sea level rise.

METHODS

Coasts are highly dynamic places on an ecological point of view. Thus coastal ecosystems must adapt to terrestrial and marine environmental parameters and permanently changing conditions. They face frequent changes in geomorphological, hydrographical, sedimentological conditions. Related to a sea level rise coasts would change for example by permanent flooding of terrestrial coastal zones, increase in damage due to more frequent inundation events, rising erosion rates or, on the marine side of the coast, by changing light conditions. This means a serious change of the abiotic conditions at coasts threatened by sea level rise. As these abiotic conditions build the framework for the occurrence of specific coastal ecosystems on a certain coast, they had to be considered when approaching possible future coastal squeeze dynamics from an integrating point of view.

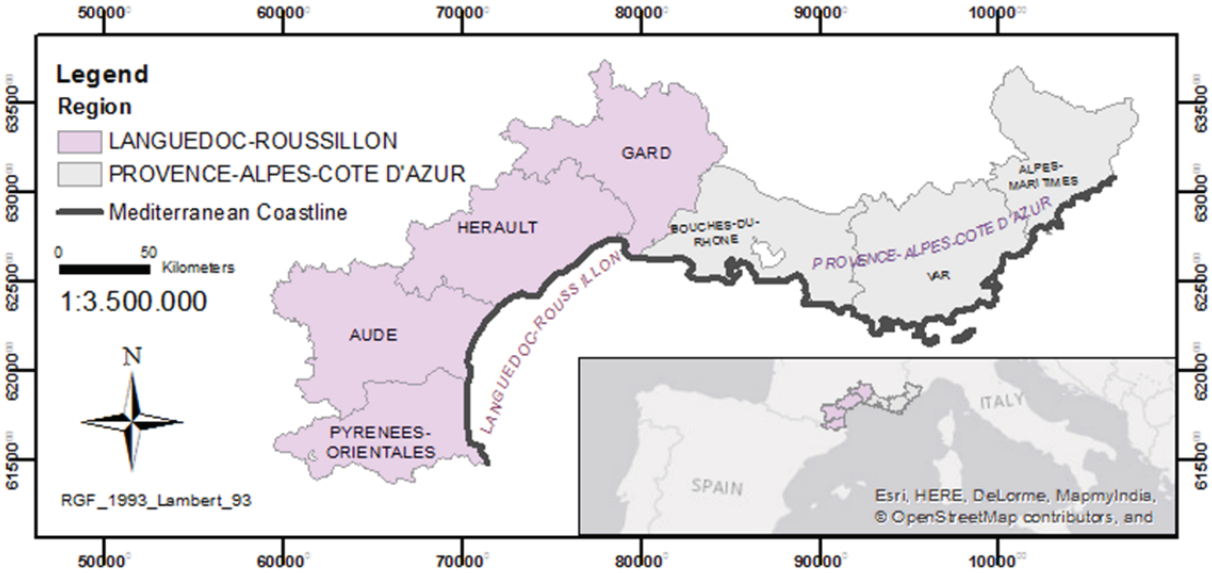

Figure 2. Location of study area. The inset shows the administrative regions of the Mediterranean coast of France.

Additionally, it is supposed that coastal squeeze is induced by anthropogenic structures built up near shore (Doody 2004), which hinder (terrestrial) coastal ecosystems to move unhindered landward in case of a landward movement of the coastline.

The methodological approach should therefore take into account three main aspects that determine coastal squeeze dynamics (Figure 1): (1) geosphere: referring to the environmental conditions resulting from the geospherical situation at the studied coast, and parameters relevant to the biospherical part. (2) biosphere: focusing on an ecosystem, habitat or species with particular relevance at the studies coast. In our study the decision on what biospherical element the focus will be, will be taken only after a risk analysis based on geopherical and anthropogenic key elements whilst having in mind the meaning of this element to biodiversity context in the study area. Categories for the risk analysis need to be defined in a further step. Depending on what element the study will focus on additional geospherical parameters can become relevant and thus should be taken into account. (3) anthropogenic impact, referring to land use categories and ecosystem "value", assigned by protection status.

Altogether the approach consists of two main parts:

1) Large-scale analysis of coastal situation. It will serve to identify areas at risk where a small-scale analysis would be reasonable to be executed (focus areas):
   a) Probable risk due to already existing conflicts in land use between built structures and protected nature. It is supposed that built structures lying close or within protected natural areas result in hindered migration of the biospherical element due to these built structures.
   b) Future risks referring to sea level rise scenarios and erosional trends.
2) Small-scale analysis in the focus areas. It will serve to link the environmental changes of the coastline to the biosphere.
   a) First we identify focus biospherical elements within the focus areas relying on an already existing protection status, the geospherical factors relevant for this element, actual distribution of the element.
   b) Potential future distribution of the focus biospherical element taking into account the risks defined in 1b and possible land use changes.

Steps 1a and 2a refer to the present situation while 1b and 2b refer to a possible future situation. 1b will be based on a scenario for sea level rise that will be developed from literature (*e.g.* IPCC 2013) taking into account also erosion trends (*e.g.* Sabatier *et al.* 2011). From this a future coastal setting will modelled. 2b will be based on the results of 1b. Environmental parameters that limit the distribution of the examined habitat or species will be implemented in a species (or habitat) distribution model (SDM). A land use scenario that still needs to be developed will help to limit the distribution of the environmental parameters. It could be based *e.g.* on regional land development plans and indicate future built areas. This planning aspect will limit the time frame of our projection to a maximum of 30 years as this represents a usual administrative planning horizon.

Data and models to be used

In Europe the CORINE Land Cover data (raster resolution 100x100 m, (European Environment Agency, EEA 2013) and Natura 2000 (resolution 1:100000, EEA 2011) data could be used before referring to more detailed national and local data. We used this data for the first part of the large-scale analysis taking land use information out of the CORINE data set and areas protected areas out of the Natura 2000 dataset. Preliminary results are presented in the Results section.

Beyond this digital terrain data is indispensable to include sea

level changes in the study. For the large-scale analysis we want therefore use ASTER Global Digital Elevation Model (GDEM) Version 2 (resolution 30x30m, Toutin 2008).

To address 1b the open source software Delft3D-Flow (www.deltares.nl) will be used. This is a 3D/2D modelling suite developed for the simulation of multi-dimensional hydrodynamic and morphodynamic flows, especially on coasts (Deltares). Sea level rise will be implemented by a vertical offset within this model.

Potential focus areas will be identified out of part 1. For this categorical risk classes will be determined. They are not defined yet but will take into account the key elements of coastal squeeze (sea level, erosion, anthropogenic impact). We suppose that there will be a need to further limit the number of areas to one or two where we will exceed an exemplary study. This will be based on the meaning of the biospherical element within the biodiversity context. Selection criterial still need to be defined.

For the small-scale analysis (part 2) Litto3D® (Institut National de l'Information Geographique et Forestière, IGN 2015), a DEM of the French coastline, will be used. On the terrestrial part it includes altitude up to +10m at a minimum of 2km inland (resolution 5x5m, 0,2m in altitude) and on the marine part of the coast it includes bathymetric information up to 10m depth and 6km of the coast (resolution 5x5m, 0,4m in depth). We intend to work on a 10x10m resolution in the focus areas as this seems suitable to study the biospherical elements as well as the land use change.

The potential future distribution (2b) will be modelled via an SDM that is designed to include geospherical and anthropogenic impact information and thus indicates the potential future distribution out of the environmental space binding the bio-spherical element to geospherical elements. It should be one designed to predict the possible future distribution, based on *e.g.* a machine learning model using maximum entropy or genetic algorithms) (Elith and Leathwick 2009). Which model this could be, will be defined in a future step.

Large-scale analysis of potential conflicting areas between built structures and protected nature

This first step of our approach helps to identify future coastal squeeze areas which could be of a high relevance to the biosphere. The analysis was based on large-scale data sets (CORINE -> artificial areas, Natura 2000 -> protected areas) that were treated in a GIS. As the anthropogenic impact represents a key factor the analysis is limited to the terrestrial part of the coast, which therefor was limited to a coastal strip of 500m inland and 500m to the sea. The coastal strip then served as mask to extract the near coast information out of the abovementioned datasets into new layers. The layers where intersected to find out about the location of areas where artificial areas touch or even lay in areas that are protected under Natura 2000. We presume to find conflicting use in these areas with a negative impact on the migration potential of the protected natural element. The situation might be aggravated in case of additional coastal squeeze dynamics.

RESULTS

This part presents preliminary results of the first part of the large-scale coastal analysis. The coastline length of the Mediterranean coastline of France adds up to around 770 km, of which around 0,5 km belong to two near-coast islands (Iles d'Hyères, Ile du Levant) (Figure 3). On the coastal strip areas of 304 km² are identified as artificial area by the CORINE Land Cover analysis. Other area belongs to the categories "wetlands", "agricultural areas", "forests" and "seminatural areas".

Areas with relevance to biodiversity and reported under Natura 2000 (European Commission DG Environment 2013) cover about 460 km² within the coastal strip. They belong to coastal and halophytic habitats like estuaries, sandbanks, coastal inlets with mixing of freshwater and sea water typical for estuaries, mudflats, coastal lagoons, reefs, Posidonia beds (*Posidonia oceanica*), sea cliffs and shingle or stony beaches sometimes vegetated with en-demic *Limonium spp*., areas

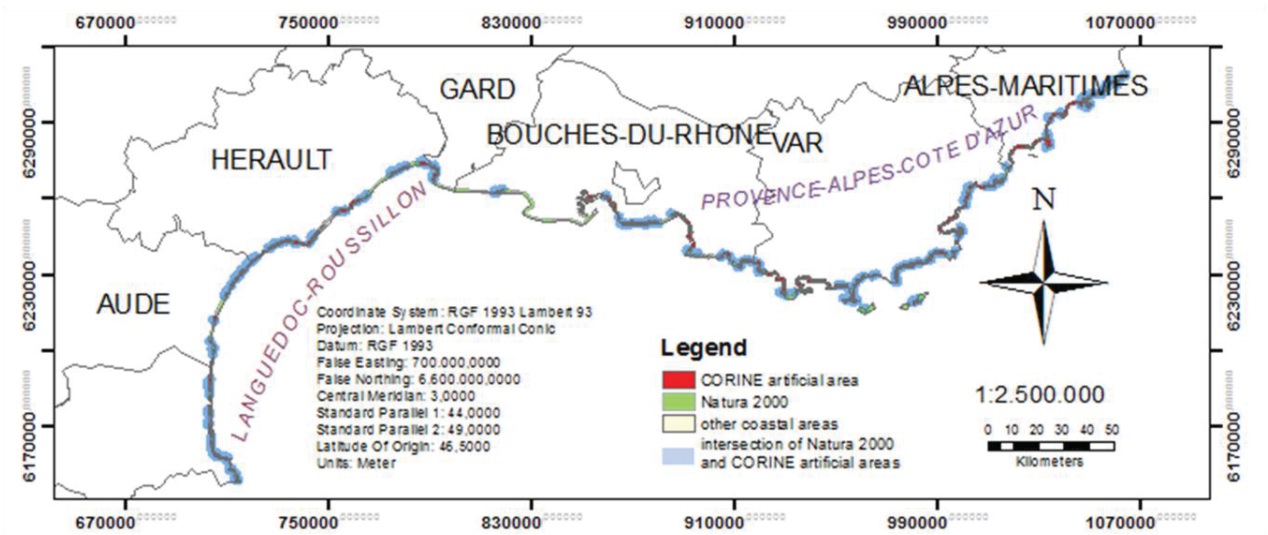

Figure 3. Potentially conflicting areas along the analyzed coastal strip. CORINE artificial area (red), Natura 2000 area (green) and intersection of both (blue) is shown. The intersections show areas of probable actual coastal squeeze.

composed of *Salicornia* and similar annuals, mediterranean salt meadows (*Juncetalia maritimi*), halophilous scrubs (*Sarcocornetea fruticosi*) and halo-nitrophilous (*Pegano-Salsoletea*), mediterranean salt steppes (*Limonietalia*). These are found mainly along the sandy shores of departements Aude, Hérault, Gard and Bouches-du-Rhone. There are also coastal sand dunes like embryonic shifting dunes and dunes with *Ammophila arenaria*, humid dune slacks and sea dunes typical for the Mediterranean coast (with *e.g. Crucianellion maritimae, Euphorbia terranica*). sometimes wooded with *Pinus.* At the rocky shores of the departments Pyrenees-Orientales, Var and Alpes-Maritimes submerged or partially submerged sea caves could be found.

By the first step of the holistic approach to this coast, areas where artificial areas and areas of high relevance for biodiversity protection could be identified. There are more than 200 points where artificial areas touch or intersect Natura 2000 areas covering about 25km² (Figure 3).

CONCLUSIONS

The GIS analysis based on the CORINE and the Natura 2000 data has been indeed executed on a rather large area. Anyway it helps to give a first hint on areas where coastal squeeze dynamics could be expected due to spatial conflicts between anthropogenic artificial and natural area. It gets evident that the French Mediterranean coast undergoes a high anthropogenic influence but at the same time is of relevance to biodiversity.

The presented results are a first and preliminary result to establish the approach presented herein, which will be discussed at the conference and – after taking into account suggested changes – be realized in future work.

LITERATURE CITED

Brunel, C. and Sabatier, F., 2009. Potential influence of sea-level rise in controlling shoreline position on the French Mediterranean Coast. *Geomorphology* 107(1-2): 47–57.

Cori, B., 1999. Spatial dynamics of Mediterranean coastal regions. *Journal of Coastal Conservation* 5(2): 105–112.

Deltares. *Delft3D-FLOW User Manual*. https://www.deltares.nl.

Doody, J.P., 2004. 'Coastal squeeze' – an historical perspective. *Journal of Coastal Conservation* 10(1), 129–138.

Elith, J. and Leathwick, J.R., 2009. Species Distribution Models: Ecological Explanation and Prediction Across Space and Time. *Annual Review of Ecology, Evolution, and Systematics* 40(1), 677–697.

European Commission DG Environment, 2013. *Interpretation Manual of European Union Habitats*.

EEA, 2011. Natura 2000 data - the European network of protected sites. http://www.eea.europa.eu/data-and-maps/data /ds_resolveuid /6330966da3fa1aff9eb900a5540eacb5

EEA, 2013. Corine Land Cover 2006. Raster data on land cover for the CLC2006 inventory. http://www.eea.europa.eu/data-and-maps/data/ds_resolveuid/ a47ee0d3248146908f72a8fde9939d9d.

Institut National de l'Information Geographique et Forestière (IGN), 2015. Litto3D Version 1.0. http://www.ign.fr

IPCC, 2013. *Climate Change 2013: The Physical Science Basis. Contribution of Working Group I to the Fifth Assessment Report of the Intergovernmental Panel on Climate Change.* Cambridge University Press, Cambridge, United Kingdom and New York, NY, USA.

Jolicoeur, S. and O'Carroll, S. 2007. Sandy barriers, climate change and long-term planning of strategic coastal infrastructures, Îles-de-la-Madeleine, Gulf of St. Lawrence (Québec, Canada). *Landscape and Urban Planning,* 81(4), 287–298.

Martínez, L.; Mendoza-González, G.; Silva-Casarín, R. and Mendoza-Baldwin, E., 2014. Land use changes and sea level rise may induce a "coastal squeeze" on the coasts of Veracruz, Mexico. *Global Environmental Change*, 29, 180–188.

Martínez, M.L.; Intralawan, A.; Vázquez, G.; Pérez-Maqueo, O., Sutton, P. and Landgrave, R., 2007. The coasts of our world: Ecological, economic and social importance. *Ecological Economics*, 63(2-3), 254–272.

Mazaris, A.D.; Matsinos, G. and Pantis, J.D. 2009. Evaluating the impacts of coastal squeeze on sea turtle nesting. *Ocean & Coastal Management* 52(2), 139–145.

Phan, L.K.; van Thiel de Vries, Jaap S.M., and Stive, M.J., 2015. Coastal Mangrove Squeeze in the Mekong Delta. *Journal of Coastal Research* 300, 233–243.

Pontee, N., 2013. Defining coastal squeeze: A discussion. *Ocean & Coastal Management*, 84, 204–207.

Sabatier, F.; Anthony, E.J.; Héquette, A.; Suanez, S.; Musereau, J.; Ruz, M.-H. and Regnauld, H., 2011. Morphodynamics of beach/dune systems: examples from the coast of France. *Géomorphologie: relief, processus, environnement*,1, 3–22.

Schleupner, C., 2008. Evaluation of coastal squeeze and its consequences for the Caribbean island Martinique. *Ocean & Coastal Management*, 51(5), 383–390.

Torio, D.D. and Chmura, G.L., 2013. Assessing Coastal Squeeze of Tidal Wetlands. *Journal of Coastal Research*, 290, 1049–1061.

Toutin, T., 2008. ASTER DEMs for geomatic and geoscientific applications: a review. *International Journal of Remote Sensing*, 29(7), 1855–1875.

Journal of Coastal Research	SI	75	1002 - 1006	Coconut Creek, Florida	2016

The Management of Information to Identify the Submarine Cable Route: the Case Study of Campania islands

Ornella Nonnis[†*], Chiara Maggi[†], Pasquale Lanera[†], Raffaele Proietti[†], Alessia Izzi[†], Pietro Antonelli[‡], Massimo Gabellini[†]

[†] ISPRA, via Vitaliano Brancati 60, 00144 Rome, Italy

[‡]Terna S.p.A. - Rete Elettrica Nazionale
Roma - Viale Egidio Galbani, 70 - 00156

www.cerf-jcr.org

www.JCRonline.org

ABSTRACT

Nonnis, O.; Maggi, C., Lanera, P.; Proietti, R.; Izzi, A.; Antonelli, P. and Gabellini, M., 2016. The management of information to identify the submarine cable route: the case study of Campania island. *In:* Vila-Concejo, A.; Bruce, E.; Kennedy, D.M., and McCarroll, R.J. (eds.), *Proceedings of the 14th International Coastal Symposium* (Sydney, Australia). *Journal of Coastal Research*, Special Issue, No. 75, pp. 1002 - 1006. Coconut Creek (Florida), ISSN 0749-0208.

Offshore pipelines and cables are infrastructures frequently located in the midst of delicate marine ecosystems. The route definition is one of the more complex and strategic aspect for the operation of laying a submarine cable or pipeline. In the designing phase different cable's routes are selected analyzing in detail the natural and/or anthropogenic constraints of the areas to be crossed, to identify the optimal alternative with less environmental impact. A multidisciplinary approach is needed to group all the area's and infrastructure's information, like bathymetry, regional geology, environmentally sensitive areas, shipwrecks, existing infrastructures, potential geohazards, geomorphology, meteocean observations and boundary information. Through an instrument named Desk Top Study (DTS), the information are analyzed and overlapped for the evaluation of the different route hypothesis and the design of appropriate survey programs. In this context TERNA S.p.A. (concessionaire company in Italy for the transmission and dispatching of electricity) charged ISPRA to perform the Desk Top Study for the connection between the coast of Campania peninsula and the islands of Capri and Ischia. Data relating to the areas affected by the electrical connections, collected through the DTS, were managed by a geographic information system (GIS), capable to organize different types of information, thus providing substantial support for the definition of the preliminary route. This work presents the methodology and the main results of the Desk Top Study, carried out for the electric cables laying between the coast of Campania peninsula and the islands of Capri and Ischia.

ADDITIONAL INDEX WORDS: *Marine cable, Desk Top Study, Campania islands, Tyrrhenian Sea.*

INTRODUCTION

The global growing demand for energy and the need to connect mainland with offshore environments are forcing energy companies to enhance their underwater cables and pipelines networks in order to allow an effective, continuous and reliable transport of energy resources (Bacci *et al.*, 2013).

A linear engineering project covers a long distance and, therefore, usually cuts through a series of ecosystems of varying importance from the point of view of conservation, functionality and socioeconomic value. Therefore the realization of a linear engineering project, such as a cable or a pipeline, may cause important environmental repercussions that can be mitigated by awareness, understanding and appropriate environmental management strategies (Rescia *et al.*, 2006).

Characterization of the positioning area, to identify route and landing points, plays a central role also for the laying of submarine cables and pipelines, due to possible risks linked to the installation of these infrastructures. The definition of best positioning scenarios requires a multidisciplinary approach. In fact, besides the evaluation of cable or pipeline technical features (e.g. minimum bending radius) and of seabed nature (geomorphological structure of substrate, marine biodiversity and ecosystems protection), the various uses of the sea near the coast must also be taken into account (tourism, fishing and aquaculture, urban settlements, maritime traffic). Therefore the cable route shall as far as possible avoid hazardous points or areas (*i.e.* navigation routes, anchorage areas, port entries, intensively-trawled areas, seabed with rock outcrops, submarine canyons or steep slopes, areas with presence of shipwrecks or unexploded devices or any other obstacles and areas subject to strong bottom currents) and points or areas subject to constraints (Marine Protected Areas, SCI, SPA, sensitive ecosystems, archaeological areas). With regards to the environmental aspects, the choice of route and landing points must take into account the possible environmental disturbing actions, such as the excavation activities for cables burial (Bacci *et al.*, 2013; Nonnis *et al.*, 2010). The main impacts associated with submarine cables and pipelines installation are: the removal or temporary modification of biocoenosis in the area of interest, the increased turbidity and the possible remobilization of hazardous substances and, in general, all disturbances on marine organisms (Boudouresque *et al.*, 2008).

DOI: 10.2112/SI75-201.1 received received 15 October 2015 accepted in revision 15 January 2016
*Corresponding author: ornella.nonnis@isprambiente.it
©Coastal Education and Research Foundation, Inc. 2016

The TERNA project for the connection of the Campania region islands (Italy) with the mainland, is part of this context. TERNA S.p.A is the concessionaire company in Italy for the transmission and dispatching of electricity on the high and very high voltage; the project in question consists of an "electricity ring" connecting the Campania region islands (central-southern Tyrrhenian Sea). The submarine electricity ring will connect the islands of Capri and Ischia with the mainland (Figure 1). This development measure is necessary mainly due to the unreliability of the electricity production systems currently in use (generally supplied with fuel oil) and to the lack of a direct connection with the mainland grid. Both these factors increase the risk of blackouts particularly during the summer months, thus reducing the electricity service's quality (Terna, 2015).

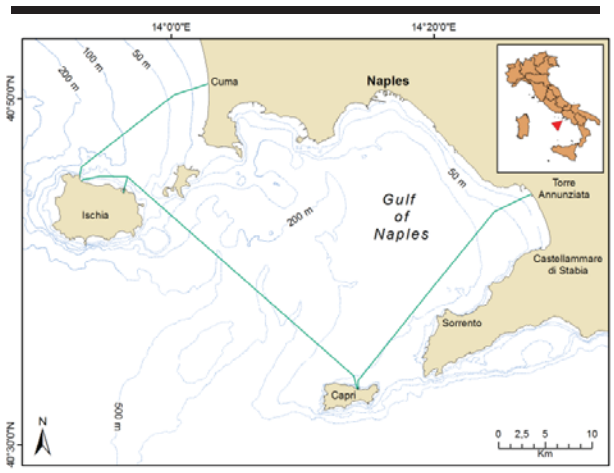

Figure 1. Connection among the coast of Campania peninsula and the islands of Capri and Ischia (Italy).

As part of the project for the electricity interconnection of the Campania region islands, ISPRA was tasked to perform a Desk Top Study (DTS) that consists of the collation, evaluation and integration of project relevant information already available for preliminary assessment of site conditions and conceptual design.

In the case of the Campania islands, the preliminary routes identified through the DTS performed in 2009, were later subject to a marine survey and to a detailed geophysical survey in order to define the best suited route for cable-laying.

In this paper we present the methodology and the main results of the Desk Top Study, conducted for the electricity interconnection project between the mainland and the archipelago of Campania (Capri and Ischia islands) in order to identify the preliminary route and the potential risks.

Study area

The study areas are situated in the Gulf of Naples, a wide bay located on the continental shelf south east of the Tyrrhenian Sea, off the Campania region coast (Italy). With an area of about 870 km^2 and an average depth of about 170 m, the Gulf is delimited to the North by Ischia and Procida islands, and to the south by Capri Island and the Sorrento Peninsula. The Gulf continental slope is marked by the presence of the Magnaghi and Dohrn submarine canyons, with depths of 600 and 800 m. The Gulf presents a very strong population density and consequent human pressure, especially in its central part (mainly from the metropolitan area of Naples), up to Castellammare di Stabia. This pressure inevitably produces environmental degradation events. In addition, the Sarno river mouth represents a major source of pollution in the Gulf. This river is in fact considered the most polluted river in Europe (Cicchella *et al.*, 2014).

METHODS

The fundamental objective of the DTS is to identify the landing points and preliminary marine path taking into account the feasibility study, any existing constraints and technological and environmental aspects. Relevant information contained in a desktop study can include bathymetry, regional geology, environmentally sensitive areas, shipwrecks, existing infrastructure, potential geohazards, geomorphology, metocean observations and boundary information. The more detailed and comprehensive the DTS is, the easier will be for technicians to evaluate the various route proposals, and the more focused will be the following pre-installation survey.

In general, a very wide corridor is firstly identified, where to carry out data acquisition. On the basis of information obtained, the survey area is then restricted and the search is refined until the identification of landings and optimal route, also highlighting any issues that may require specific study.

In the DTS for the Campania islands project, a corridor of 2,5Km was firstly identified, followed by a systematic gathering of topic-based information, for example collecting science research papers and nautical thematic maps, contacting research institutions, protected areas management authorities, local authorities (region, province, municipalities), maritime authorities, owners of submarine transport services and on websites (Table 1).

The set of acquired data allowed the creation of a dedicated geodatabase, which enabled the management of spatial data as well as the processing of cartography needed to support the design choices adopted to overcome existing constraints along routes or at landings. Essential to the collation and review of various spatial datasets is the development of a geographical information system (GIS) framework for geodata management. GIS is a powerful mapping and analysis technology that allows large quantities of information to be viewed and analyzed within a geographical context. A GIS provides a platform from which to efficiently display multiple datasets as layers, to query and interrogate those data, and to facilitate interpretation in an effective visual manner (Denis and Nash, 2012).

RESULTS AND DISCUSSION

From the information acquired, as shown in Table 1, it results that the Gulf of Naples can be divided into two sectors: the South-east sector, which is partly carbonatic (Sorrento peninsula and Capri island) and partly alluvial (Sarno river mudflat), and the North-west sector (Campi Flegrei area, Ischia and Procida islands), volcanic and characterized by shallows and submerged banks, as well as by the presence of submarine canyons (Aiello *et al.*, 1999; Menna, 2007).

Moreover, it results that it is relevant for both natural and environmental aspects, so that 3 Marine Protected Areas and 15 Natura 2000 Sites of Community Importance were established in the area. Also present are several biological protection areas and shallows of great biological interest.

Table 1. *Data acquired during the DTS for Campania region islands project.*

Topic	Information	Data source
Landing sites	Description and photographic documentation of the area (presence of activities that may interfere with the facility installation, existing constraints, interference with other services).	Surveys/Inspections.
Maritime traffic	Maritime connections. Public transport service. Cruisers, recreational, commercial and other maritime trades traffic.	Sea transport companies web sites.
Bathymetry and morphology	Bathymetry and morphology of marine areas.	Scientific articles, nautical maps.
Legitimate uses and services installed on the seabed	Submarine transport system, and identified services. Obstacles occurring on seabed and restrictions to navigation. Regulated areas (military use, reserved for anchoring, anchoring and/or fishing ban, reserved for dredging, landfill and mining). Limit of territorial waters and exclusive economic zones.	Official cartography of the Italian Navy Hydrographic Institute, reports of Port Captaincies.
Fishing and aquaculture	Size of the fishing fleet. Bottom trawling. Fishing gears used (hydraulic dredge, rake, and other fishing systems). Fishing activities within Marine Protected areas. Impact assessment of trawling, hydraulic dredge and rake and risks of mechanical aggression of cable in all routes. Aquaculture facilities.	Italian Ministry for Agriculture, Food and Forestry, and scientific articles.
Areas subject to constraints	Marine Protected Areas (Area of Punta Campanella, istituenda of Isle of Capri, Neptune's Kingdom). Natura 2000 sites. I.B.A. Zones. Sites of National Interest (SNI). Areas of biological protection and shallows. Archaeological constraints.	Studies on marine protected areas, Natura 2000 sites, biological protection areas and shallows, archaeological constraints.
Geology and sedimentology	Geology of the Tyrrhenian- Campania margin; geology and geomorphology of marine areas; morphostructural elements; sedimentological characteristics of seismic facies stratigraphy; instability phenomena along underwater embankments of the continental shelf.	Scientific papers, feasibility studies.
Physical oceanography	Hydrological structure, current metric measures and dynamics of water masses.	Current and CTD measurements in the Gulf of Naples, scientific articles
Report on meteorology	Characteristics of the Mediterranean climate and of Italy. Meteorology and climate of the Gulf of Naples. Winds analysis, winds interannual analysis and seasonal variability; marine weather characterization; considerations on the interference with installation activities.	Dataset of Hydrographic and Tidal National Service (SIMN), Air Force Weather Service and National waves measure Network, scientific articles.
Flora and fauna	Characteristics and distribution of seagrasses; characteristics and distribution of benthic biocoenoses; Cetaceans (Guidelines for mitigating impacts; species occurring among stranded cetaceans; studies in nature, potential impact of cable-laying on cetaceans).	Scientific articles.
Laying methods and protection of cables in the sea	Pre-installation survey and seabed cleaning. Cable laying. Cable protection. Areas colonized by Posidonia oceanica. Rocky bottom. Uneven bottom. Areas of loose or low-cohesion sediments and of cemented sediments.	Past ISPRA experiences, scientific literature, gray literature, technical reports.
Methods for ecosystem protection in submarine cables laying and operation stages	Environmental aspects linked to materials used for cable construction; methods for ecosystem protection after the laying and protection of submarine cables; alteration of sediment dynamics, seagrasses, morphological structures and hydrodynamics; generation of noise; methods for ecosystem safeguard following the operation of submarine cables.	Scientific articles, technical reports, manuals.
Analysis of project connections	Listings of the track major points. Summary of existing and planned services within the area affected by the project connections and interference with foreseen connections.	

In seabed in front of Ischia and Capri islands, there are wide meadows of *Posidonia Oceanica*, forming an almost continuous belt around each island. In addition, the presence of cliffs in large stretches of coast allows the presence and wide distribution of Coralligenous biocenosis and pre-coralligenous (Relini and Blasi, 2002). As for cetaceans, the area immediately north has frequent sightings, since the Cuma submarine canyon is a feeding and breeding site for different types of cetaceans (Miragliuolo *et al.*, 2005). Despite its significant environmental value, in the Gulf of Naples there are however several Sites of National Importance (SNIs) which represent very large contaminated areas in need of remediation, to avoid health and environmental damages.

With regards to legitimate uses and services installed on the seabed, the information was obtained from various competent authorities and administrations (municipalities, offices of the maritime state property, Port Authorities). In the study area, all cable and pipeline services, in use and out of operation, under construction and in planning, were surveyed. Sunken wrecks and unexploded remnants of war were also surveyed, and information were collected on areas intended for military exercises (a more extensive one north of Ischia and a smaller

one West of Ischia). In the stretch of coast off the port of Torre Annunziata and Castellammare di Stabia there are two anchorage areas intended for merchant ships of large tonnage, while a buoy area for pleasure craft is located NNW of Ischia. In addition, areas where anchoring and fishing are prohibited are present in the islands of Procida, Ischia and Capri and between Torre Annunziata and Castellammare di Stabia.

Among the legitimate uses of the sea, due consideration must be given to fishing, which may be relevant during the cable laying and later may pose a risk to the safety of powerlines (Sala *et al.*; 2009). Therefore information were extrapolated on ships carrying out their fishing activities in the Gulf of Naples, analysing all those using bottom trawls, hydraulic and shellfish dredges, all these being fishing gears acting on the seabed that may therefore impact on submerged structures (AAVV, 2004).

Considering the maritime orientation of the Gulf of Naples, extensive investigations were conducted on maritime traffic, which included means for public transport service (for connection to and from the islands), means for traffic cruiser, pleasure craft and freight transport ships (Gentile, 2008).

Besides small ports, the Gulf of Naples it is characterized by the presence of the homonymous Port of Naples, considered one of the most important ports in Europe (Aramu, 2009). The Gulf of Naples as a whole, has thus many peculiarities, including the relevant special features of its environment, a substantial human pressure and the diversified uses of sea and coastal environment.

The definition of the routing hypotheses, one of the most complex and strategic part of cable-laying, led to a careful assessment of all scenario aspects in order to minimize impacts on the environment and reduce the overall cost of the work. Therefore, upon acquisition of available data and information, specific Reports were prepared for each route, containing all relevant information for the definition of the route in question (ISPRA, 2010). Each report is structured around the themes presented in Table 1.

These reports aim to provide a complete analysis of the area where cable-laying is foreseen and they also include the inspections at the hypothetical landing points. About 70 thematic maps were produced, in which the achieved results are represented and summarized, geo-referenced and reported with appropriate graphics and symbols. As baseline data, each map shows all coastlines with major names, as well as geographical and UTM grids and available bathymetry.

The thematic maps are divided in 4 types with different scale, on which the information is differently represented, based on the area and on the purpose of the map itself (Table 2).

Table 2. *Type thematic maps at different scales.*

Landing point (scale 1:2.500)	Landing area (scale 1:25.000)	Route (scale 1:25.000-40.000)	Synthesis map (scale 1:50.000)
Map of Landing (bathymetric map).	Bathymetric map; Map of legitimate uses and of services installed on the seabed; Map of environmental constraints; Sediments and morphological map; Map of seagrasses.	Route profile and plans, with legitimate uses and services installed on the seabed, environmental constraints, sediments and morphological elements, seagrass distribution.	Bathymetric map; Map of legitimate uses and of services installed on the seabed; Map of environmental constraints; Sediments and morphological map and seagrass distribution; Fishing and aquaculture.

Therefore, in the landing points and landing areas a scale was used, allowing adequately detailed information for bathymetric trend, legitimate uses of sea and presence of services on the seabed, environmental and archaeological constraints, morphological and sediment characteristics, and presence of seagrasses.

For the entire cable route, the bathymetric profile was drawn associated with geomorphological features and fishing activities existing in the area. Track plans were also drawn up with all the information acquired (bathymetry, legitimate uses, services installed on the seabed, environmental constraints, geomorphological elements, sedimentology, seagrass distribution, shipping routes, etc.) in order to have an overview of the context in which the work is placed.

Finally some synthesis maps were produced with the same themes used for the other maps, including areas subject to trawling, to make an overall assessment of the project routes with respect to the peculiarities of the Gulf of Naples.

The identified routes (Figure 2), besides being graphically represented, were processed in a table format so that each row contains a point locating specific positions (T/M coupling, point of intersection with coastline, point of intersection of cables or other existing services, point of intersection with significant bathymetries, coordinates, depth, progressive kilometrics, *etc.*).

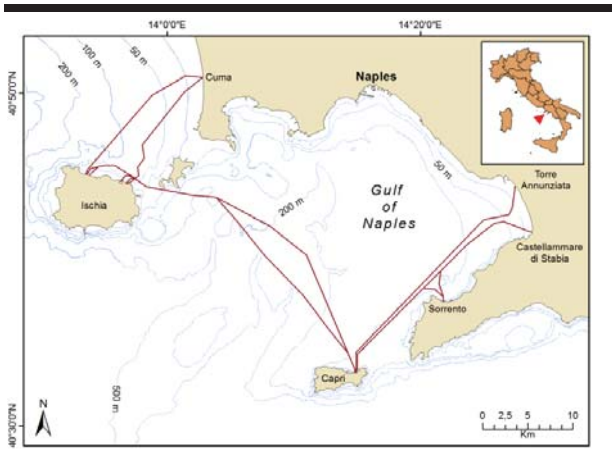

Figure 2. Preliminary route of cable following the DTS.

The drafting of the DTS was a re-iterative work. So, the cable route was gradually updated on the base of acquired information and of technical requirements linked to cables features and to installation technologies.

CONCLUSIONS

Desktop studies are high value, relatively low cost products, which can identify potential geo‑constraints to support pipeline routing activities in the early stage of the project. Performing a DTS at an early stage in cable routing assessment can ease planning and decision making processes by firstly identifying a suitable corridor(s), secondly guiding the remainder of the data acquisition programmes, enabling the selection of the most appropriate survey technologies and analysis techniques and, thirdly, highlighting any issues that may exist along the route that may require specific study (Denis and Nash, 2012). DTS also offers the possibility to optimize fit for purpose site investigation programmes that would otherwise be reduced to a costly random search of data. Desktop studies improve project efficiency and reduce costs, by providing a clearer understanding of future challenges by identifying potential problem areas that may have otherwise been overlooked.

In the Campania islands interconnection project, the set of acquired data enabled the creation of a dedicated geodatabase. This geodatabase allowed to manage spatial data and to produce the maps required for documenting design choices progressively adopted to overcome the existing constraints along routes or at landings. As a result of this search, it was possible to define the preliminary routes and landings for each segment. The DTS enabled the scheduling of subsequent field surveys to obtain detailed characteristics and possible route refinement, for a careful planning of cable installation.

ACKNOWLEDGMENTS

The authors thank the many co-authors and colleagues for their valuable contributions to the preparation of DTS for the electricity interconnection of the Campania region islands, and to the translation of this paper.

LITERATURE CITED

Aramu, L., 2009. *La Camera sul porto (il porto di Napoli dall'unità d'Italia al fascismo)*. Colla Passaggi Editore, 2009. Codice ISBN 9788887501827 (in italian).

AAVV. 2000. *La gestione della pesca in Campania sviluppo di sistemi innovativi e analisi della sostenibilità economica ed ecologica della pesca a strascico*. Progetto P.O.R. Campania, misura 4.23 “Interventi di contesto ed a sostegno dell’adeguamento infrastrutturale del settore della pesca” - sottomisura 6 – Reg. (CEE) 2792 (in Italian).

Aiello, G.; Budillon, F.; Cristofalo, G.; D'Argenio, B.; De Alteriis, G.; De Lauro, M.; Ferraro, L.; Marsella, E.; Pelosi, N.; Sacchi, M., and Tonielli, R., 1999. Marine geology and morphobathymetry in the Bay of Naples. A multidisciplinary approach to the recent evolution of the sea floor. In: F.M. Faranda, L. Guglielmo, G. Spezie (eds.) *Mediterranean Ecosystems: structures and processes*. Springer Verlag, 1-8.

Bacci T., Rende F.S., Nonnis O., Maggi C., Izzi A., Gabellini M., Massara F., Di Tullio L., 2013. Effects of laying power cables on a *Posidonia oceanica* (L.) Delile prairie: the study case of Fiume Santo (NW Sardinia, Italy). *Journal of Coastal Research*, Special Issue, No. 65, 868-873

Boudouresque, C.F.; Bernard, G., Bonhomme, P., Charbonnel, E., Diviacco, G., Meinesz, A., Pergent, G., Pergent-Martini, C., Ruitton, S., and Tunesi, L., 2008. *Tutela e conservazione delle praterie a Posidonia oceanica*. RAMOGE pub. 1-202 (in Italian).

Cicchella, D.; Giaccio, L.; Lima, A.; Albanese, S.; Cosenza, A.; Civitillo, D.; De Vivo, B., 2014. Assessment of the topsoil heavy metals pollution in the Sarno River basin, south Italy. *Environmental Earth Sciences*, 71(12), 5129-5143.

Denis, R. and Nash, I., 2012. Desktop study: the un-exploited resource. *World Pipelines magazine*. February 2012.

Gentile, D., 2008. I collegamenti marittimi nel Golfo di Napoli. C*onvegno di Federmobilità “Trasporto sostenibile: i servizi marittimi”* (in Italian).

ISPRA, 2010. *Desk Top Study relativo all’interconnessione delle isole minori della Regione Campania al Sistema Elettrico Nazionale*. Rome, Italy (in Italian).

Menna, M., 2007. Misure di correnti superficiali nel Golfo di Napoli eseguite con radar costiero. Tesi di Dottorato. *Dottorato in Scienze ed Ingegneria del Mare XX ciclo. Università degli Studi di Napoli “FEDERICO II”* (in Italian).

Miragliuolo, A.; Mussi, B. and Bearzi, G., 2005. Observations of driftnetting off the island of Ischia, Italy, with indirect evidence of dolphin bycatch. *European Research on Cetaceans*, 16.

Nonnis, O.; Maggi, C.; Bacci, T.; Izzi A.; Massara, F.; Rende, F.S.; Trabucco, B.; Gabellini, M., 2014. An Environmental Monitoring Plan Related to the Laying of Marine Power Cables: The Case Study of SAPEI Project. *Proceedings of the 2014 International Conference on Environmental Science and Geoscience (ESG 14)*, 24-29.

Relini, G. and Blasi, C., 2002. *Distribuzione delle specie protette nei mari italiani. Modulo e: Descrizione di Base delle Biocenosi Marine Costiere.* Ministero dell’Ambiente e della Tutela del Territorio. SIBM – DIP.TE.RIS (in Italian).

Rescia, A.J.; Astrada, E.N.; Bono, J.; Blasco, C.A.; Meli, P.; Adamoli, J.M., 2006. Environmental analysis in the selection of alternative corridors in a long-distance linear project: A methodological proposal. *Journal of Environmental Management*, 80, 266–278.

Sala, A.; Lucchetti, A.; Ferretti, M., Mariani, A. and Serra, S., 2009. *Indagine preliminare dell’impatto sul fondale marino esercitato dalla pesca con reti a strascico gemelle e prime valutazioni dell’efficienza di pesca*. Rapporto finale. (in Italian).

Terna S.p.A.http://www.terna.it/

Journal of Coastal Research	SI	75	1007 - 1011	Coconut Creek, Florida	2016

Key Environmental Factors in the Management of Ciguatera

Leanne Sparrow †* **and Kirsten Heimann**†

†Centre Sustainable Tropical Fisheries & Aquaculture
James Cook University
Townsville, Australia

www.cerf-jcr.org

www.JCRonline.org

ABSTRACT

Sparrow, L. and Heimann, K., 2016. Key parameters in the management of ciguatera. *In:* Vila-Concejo, A.; Bruce, E.; Kennedy, D.M., and McCarroll, R.J. (eds.), *Proceedings of the 14th International Coastal Symposium* (Sydney, Australia). *Journal of Coastal Research*, Special Issue, No. 75, pp. 1007 - 1011. Coconut Creek (Florida), ISSN 0749-0208.

Ciguatera is a tropical illness that has expanded its geographic range through international travel, frozen tropical fish exports and the expansion of ciguatera-causing dinoflagellates into temperate coastal marine habitats. The drivers in the distribution of *Gambierdiscus* spp. and other ciguatera-causing dinoflagellates on their macroalgal substrates were investigated in this study. Palatability and macroalgal growth morphology were identified as important drivers in the heterogenetic distribution of *Gambierdiscus* populations. Higher *Gambierdiscus* densities were not always associated with fish-palatable macroalgal substrates. At mid-reef sites, *Gambierdiscus* populations were only found on flattened macroalgal substrates that were palatable to gastropods. Although there was no trend in substrate preference, there were site-specific preferences. This needs further investigation to identify environmental factors that influence the composition and distribution of macroalgae and thereby the potential expansion of ciguatera-causing dinoflagellates into new coastal marine habitats. This research is essential in developing ciguatera monitoring tools as marine fisheries are an integral part of the economy, diet and lifestyle of coastal populations throughout the world.

ADDITIONAL INDEX WORDS: *Gambierdiscus, macroalgae substrates, disturbance events, grazers.*

INTRODUCTION

Ciguatera is a tropical illness induced when people consume contaminated reef fish. Fish species in tropical regions bioconvert and trophically accumulate ciguatoxins derived from the dinoflagellate, *Gambierdiscus* spp. Ciguatera is endemic to tropical regions and affects 50,000 to 500,000 people annually worldwide (Arena *et al.*, 2004; Chinain *et al.*, 2010). Ciguatera incidence rates for tropical island nations have been based on reported ciguatera cases and/or questionnaires (Azziz-Baumgartner *et al.*, 2012; Chateau-Degat *et al.*, 2007; Lawerence *et al.*, 1980; Skinner *et al.*, 2011). Estimated rates ≥ 1000 cases / 100,000 population are referred to as ciguatera hotspots, and while many vary between years or decades, French Polynesia Islands have consistently recorded high estimated rates (Chinain *et al.*, 2010; Skinner *et al.*, 2011).

The variability in estimated incidence rates is due to a complexity of factors that can influence the probability of consuming contaminated fish (Sparrow *et al.*, *unpub. data*). Artificial increases in incidence rates can be triggered by factors, such as seasonal migrations of predatory fish *e.g.* mackerel and barracuda. However other factors such as government bans and restrictions are likely to artificially decrease incidence and the interaction of such factors can result in relatively stable rates (Figure 1). Affordable tourism-associated travel and increased demands for tropical fish exports are factors that affect incidence rates but also contribute to geographic expansion of ciguatera (Heimann and Sparrow, 2015). Disturbance events, both natural and anthropogenic are influential factors (Figure 1) that can trigger temporary and permanent expansions of ciguatera-causing dinoflagellates, including *Gambierdiscus* spp.

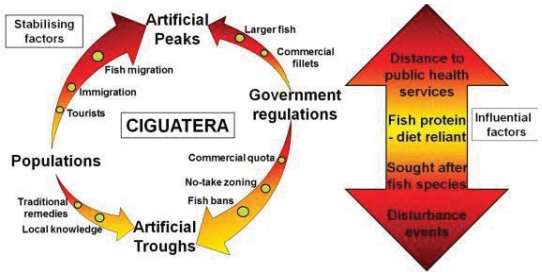

Figure 1. Schematic diagram of factors which play a role in estimated ciguatera incidence rates and the minor fluctuating but stable rate of ciguatera incidence due to the interaction of these factors. Larger fluctuations in incidence rates are a response to influential factors that impact on the stable state.

In tropical regions, the causative benthic toxic dinoflagellate, *Gambierdiscus* spp. is found on coral reefs. It is frequently associated with macroalgae as a substrate along with other benthic toxic dinoflagellates (BtD), including *Prorocentrum* spp., *Ostreopsis* spp., and *Coolia* spp. Coral reefs are a dynamic ecosystem where large-scale disturbance events such as cyclones, crown-of-thorns (COTs) outbreaks and coral bleaching can lead to temporary or permanent phase shift from coral- to macroalgal-dominated reefs (Heimann *et al.*, 2011), which is thought to be followed by the range expansion of BtD.

DOI: 10.2112/SI75-202.1 received received 15 October 2015 accepted in revision 15 January 2016
*Corresponding author: leanne.sparrow@my.jcu.edu.au
©Coastal Education and Research Foundation, Inc. 2016

On the Great Barrier Reef (GBR), cyclones can result in extensive flood plumes with nutrient-rich waters triggering trophic blooms. Coral bleaching events are triggered by warmer sea surface temperatures that can also trigger population growth of *Gambierdiscus* spp. and other BtD (Heimann *et al.*, 2011). Positive correlations have been shown between warmer sea surface temperatures and the increase in ciguatera incidence (Hales *et al.*, 1999; Llewellyn, 2010; Tester *et al.*, 2010). The frequency and intensity of large-scale disturbance events have also shown strong correlations with increases in ciguatera incidence (Rongo and van Woesik, 2011).

Climate change affects weather patterns, extending warmer sea surface temperatures and strengthening ocean currents into temperate waters, which promote temporary and permanent range expansion of ciguatera-causing dinoflagellates into new coastal habitats (Heimann *et al.*, 2011). However, the drivers in the patchy distribution of *Gambierdiscus* spp. and other BtD on macroalgal substrates are still poorly understood.

This study hypothesised that the patchy distribution is likely driven by predation as well as morphology of macroalgal substrates. The aims of this study were to investigate potential preference in the distribution of BtD on macroalgal substrates.

METHODS

Two separate surveys were conducted in the central GBR during 2008 – 2009. One survey was conducted in Nelly Bay, Magnetic Island (Figure 2), with samples collected monthly as weather conditions permitted. Nelly Bay is on the south-eastern side of Magnetic Island and has a sub-tidal fringing reef.

The other survey was based at Orpheus Island Research Station and was conducted on three separate 10-day periods in November 2008, March and August 2009, to represent seasonal differences between the Austral wet and dry seasons (Heimann *et al.*, 2010).

Data from four of the sites collected in August 2009, as part of the Austral dry season, are reported here: two mid-shelf reefs: Lodestone and Keeper Reefs; and two inshore-reefs: Pioneer Bay on Orpheus Island and Pelorus Island (Figure 2). The fringing reef at Pioneer Bay had an extensive inter-tidal reef flat, while the fringing reef at Pelorus Island was sub-tidal, remaining submerged at low-tide. Benthic toxic dinoflagellates were collected from their macroalgal substrates, which were sampled and processed as described by Heimann *et al.* (2010).

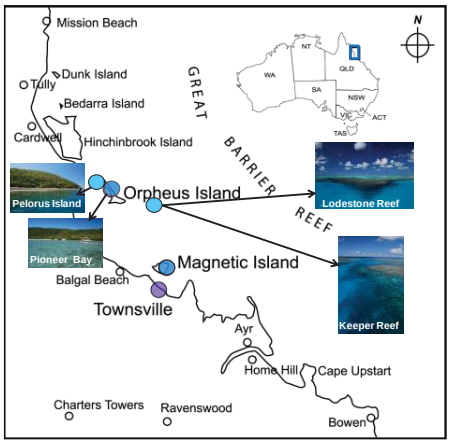

Figure 2. The location of survey sites on fringing reef at Nelly Bay, Magnetic Island and on Orpheus and Pelorus Islands as well as two mid-reef sites, in the central Great Barrier Reef, Australia.

All benthic toxic dinoflagellate (BtD) cell counts were standardised as mean abundance per wet weight (g) of macroalgal substrate sampled and to number of macroalgal samples collected.

To determine if BtD had a preference between macroalgal substrates, macroalgae were firstly investigated by growth morphology, with three categories: flattened; leathery; or terete. Secondly, by palatability of macroalgae between grazers: fish; urchins; crustaceans; gastropods; mesograzers; and sea turtles (Cruz-Rivera and Villareal, 2006).

RESULTS

Total abundance of BtD at Nelly Bay, Magnetic Island was variable over the months surveyed with the highest abundance in May 2008 (1914 cells/g. ww/substrate) followed by a decrease in June at 96 cells/g. ww/substrate (Figure 3A). Higher BtD abundance at 1406 cells/g. ww/substrate also occurred in October 2009 (Figure 3A).

Composition of the BtD community was comparable within all months sampled at Nelly Bay and was dominated by the dinoflagellate, *Ostreopsis* spp. (Figure 3A). Although *Gambierdiscus* spp. was a minor component of the BtD community, an increase in abundance was observed in August 2008.

The total abundance of BtD at Pioneer Bay for August 2009 (Orpheus Island Research Station (OIRS) based survey) was comparable to the total abundance for Nelly Bay in August 2008 (Figure 3A and D). Total BtD abundances were significantly different between the mid-reefs, Lodestone and Keeper Reefs ($T\text{-test}_{df28}$; $p<0.05$); as well as between inshore-reefs ($T\text{-test}_{df28}$; $p<0.05$) at Pioneer Bay and Pelorus Island (Figure 3D). Similar to Nelly Bay, *Gambierdiscus* spp. was a minor component of the BtD community; however in contrast *Prorocentrum* spp. dominated (Figure 3A and D).

There was no clear seasonal trend in BtD substrate preference when based on macroalgae growth morphology for Nelly Bay (Figure 3B). Flattened macroalgal substrates were more frequently associated with higher BtD abundances at Lodestone Reef and Pioneer Bay for August 2009 (Figure 3E). BtD abundances were higher on terete macroalgal substrates at Keeper Reef and Pelorus Island, which was similar to BtD preference observed at Nelly Bay in August 2008 (Figure 3B and E).

BtD abundances were often associated with macroalgae known to be palatable to crustaceans, urchins and sea turtles as well as fish in all months surveyed at Nelly Bay (Figure 3C). In comparison, macroalgal substrates palatable to fish and urchins had the least BtD abundances associated at both Lodestone and Keeper Reefs (Figure 3F). Higher BtD abundances were associated with macroalgal substrates known to be palatable to gastropods at Lodestone and Keeper Reefs as well as Pelorus Island. Macroalgal substrates known to be palatable to mesograzers recorded highest BtD abundances at Lodestone Reef but were low or absent at other reefs (Figure 3F). At Pioneer Bay, higher BtD abundances occurred on macroalgal

substrates known to be grazed by urchins as well as fish and crustaceans (Figure 3F).

Gambierdiscus cells were absent in June 2008 at Nelly Bay (Table 1) and the lowest abundance were recorded in May 2008, however showing the highest BtD abundance (Figure 3B and Table 1). In May 2008, *Gambierdiscus* cells were only

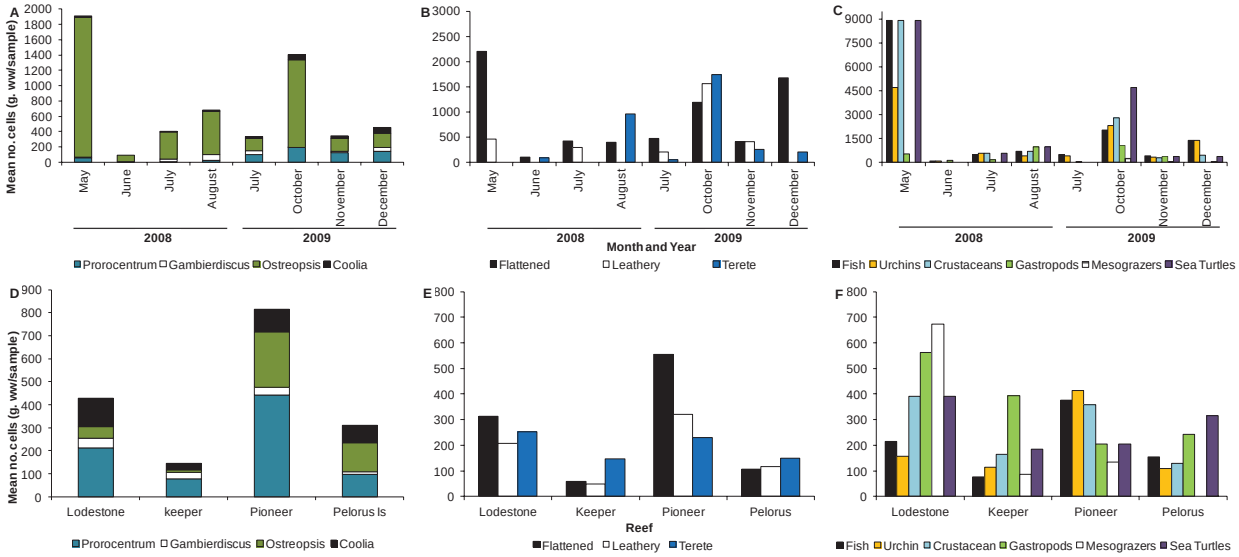

Figure 3. Mean abundances of benthic toxic dinoflagellates observed in two surveys: monthly seasonal survey at Nelly Bay, Magnetic Island (A-C); and within the Orpheus Island Research Station based survey (D-F). For both surveys, mean benthic toxic dinoflagellate abundances were shown: for community composition (A and D); in preference to macroalgae growth morphologies (B and E); and in preference to known palatability of grazers on surveyed macroalgal substrates (C and F). Mean abundances were standardised to macroalgal substrates by wet weight (g. ww) and number of samples.

Table 1. *Mean abundance of Gambierdiscus cells (# cells.g^{-1} ww of sample) relative to macroalgal growth morphologies and known grazer palatability at Nelly Bay, Magnetic Island between 2008 and 2009.*

Macroalgal morphology and grazer palatability	2008			2009			
	May	Jul	Aug	Jul	Oct	Nov	Dec
FISH							
Flattened		17.67	23.96	118.49	4.44	6.88	197.60
Leathery		11.72				6.50	
Terete			135.14			26.09	37.35
URCHINS							
Flattened		17.67	23.96	118.49	5.92	6.88	197.60
Leathery	2.88						
Terete						4.22	37.35
CRUSTACEAN							
Flattened		17.67	23.96		4.44	2.30	42.74
Leathery							
Terete			135.14			26.09	37.35
GASTROPODS							
Flattened		68.34			1.72		
Leathery							
Terete			135.14			27.75	
MESOGRAZER							
Flattened							
Leathery							
Terete					1.81	6.61	3.41
SEA TURTLES							
Flattened		17.67					
Leathery							
Terete			135.14			26.09	37.35

recorded on leathery macroalgal substrates that were palatable to urchins (Table 1). In contrast, BtD cells were more frequently associated with flattened macroalgal substrates known to be palatable to fish, crustaceans and sea turtles (Figure 3B and C).

Higher abundances of *Gambierdiscus* cells were associated with flattened macroalgal substrates known to be grazed by gastropods in July 2008 and by fish and urchins in July and December 2009 (Table 1). In August 2008 and November 2009, higher abundance of *Gambierdiscus* cells were associated with terete macroalgal substrates known to be grazed by fish, crustaceans, gastropods and sea turtles. This was similar to frequent high BtD abundances with terete substrates in August 2008, but contrasted with November 2009 when terete was least preferred by BtD (Figure 3B and Table 1).

Highest abundance of *Gambierdiscus* cells within the OIRS-based survey was recorded at Lodestone Reef and was associated with terete macroalgal substrates known to be palatable to crustaceans and sea turtles (Table 2). Higher *Gambierdiscus* spp. abundances were associated with terete macroalgal substrates compared with highest BtD abundances associated with flattened macroalgal substrates at Lodestone Reef and Pioneer Bay (Figure 3E and Table 2). Macroalgal substrates known to be palatable to urchins was least preferred by *Gambierdiscus* cells at Lodestone and Keeper Reefs but were preferred in association with terete and leathery macroalgal substrates at Pioneer Bay (Table 2). High BtD and *Gambierdiscus* abundances were recorded for macroalgal substrates known to be palatable to gastropods at both mid-reefs.

However, *Gambierdiscus* cells were recorded on flattened macroalgal substrates only known to be gastropod palatable (Table 2).

Table 2. *Mean abundance of Gambierdiscus cells (# cells.g^{-1} ww of sample) relative to macroalgal growth morphologies and known grazer palatability at mid- and inshore-reefs within OIRS survey.*

Macroalgal morphology and grazer palatability	MID-REEFS		INSHORE-REEFS	
	Lodestone Reef	Keeper Reef	Pioneer Bay	Pelorus Island
FISH				
Flattened			3.12	11.16
Leathery	8.93	1.59	10.13	
Terete	35.04	26.33	16.72	1.38
URCHINS				
Flattened			3.12	9.33
Leathery	8.93	1.59	18.69	
Terete	4.01	13.87	20.29	2.31
CRUSTACEANS				
Flattened				5.39
Leathery				
Terete	50.56	46.49	6.04	
GASTROPODS				
Flattened	29.38	23.38		
Leathery				
Terete	20.22	34.93	6.04	
MESOGRAZERS				
Flattened				
Leathery	8.93	1.59		
Terete	26.52			
SEA TURTLES				
Flattened				8.09
Leathery				
Terete	50.56	63.84	6.04	

DISCUSSION

It is hypothesised that herbivorous fish grazing on macroalgae inadvertently transfer *Gambierdiscus* spp. and other BtD into marine fish food chains, with their toxins then bioconverted into ciguatoxins and bioaccumulated into larger predatory fish (Heimann *et al.*, 2011). However, links in the transfer of ciguatoxins from *Gambierdiscus* populations into marine fish food chains in the GBR remain unclear. This study identified potential key parameters in the distribution of *Gambierdiscus* populations in the central GBR.

The hypothesis that fish grazing on macroalgae transfer ciguatoxins into fish food chains, suggests that *Gambierdiscus* populations are uniformly distributed on macroalgal substrates. In this study BtD populations, in particularly *Gambierdiscus* spp. had a heterogenic distribution on macroalgal substrates. Previous field surveys have shown similar heterogeneity in *Gambierdiscus* spp. distribution on macroalgal substrates (Ballantine *et al.*, 1985; Gillespie *et al.*, 1985). This suggests that palatability of macroalgal substrates has an influence on the distribution of BtD, including *Gambierdiscus* spp.

Predation by grazers other than herbivorous fish is thought to contribute in the transfer of ciguatoxins into fish food chains (Heimann *et al.*, 2011) leading to the patchy distribution of BtD on macroalgal substrates. The higher abundances of *Gambierdiscus* populations found on flattened macroalgal substrates at Lodestone and Keeper Reefs in this study were only palatable to gastropods. In Nelly Bay, higher *Gambierdiscus* densities were found on macroalgal substrates palatable to crustaceans, urchins and gastropods, as well as fish and varied between months. It is thought that population estimates from field samples have been based on remnant macroalgae after grazing pressures and therefore do not reflect accurate distribution and preference trends for *Gambierdiscus* populations. Herbivory exclusion experiments showed macroalgal composition changed in response to grazing pressures (Diaz-Pulido and McCook, 2002; McClanahan *et al.*, 2002). Further field and laboratory experiments are needed to investigate accurate distribution of *Gambierdiscus* and other BtD populations. This is essential in identifying key vectors in the transfer of ciguatoxins into fish food chains.

Gambierdiscus population densities were also found to vary between macroalgal growth morphologies, which differed between sites. Higher densities of BtD were associated with flattened substrates at inshore-reefs, terete substrates at mid-reefs and varied between months in Nelly Bay, Magnetic Island. This study is the first to investigate substrate preference through macroalgal growth morphology influenced by environmental factors which has flow-on effects on macroalgal composition in addition to herbivory pressures. Large-scale disturbance events have been shown to positively correlate with increases in ciguatera incidence (Llewellyn, 2010; Rongo and van Woesik, 2011). The impact of small-scale disturbances on the distribution and abundances of BtD, in particularly *Gambierdiscus* spp., such as fishing, wave action from boat traffic and competition for space on reefs are poorly understood. Competition for space between corals and macroalgae is well known (McCook, 2001), however, competition between macroalgal growth morphologies have not been explored, such as growth rates, overshadowing and abrasive action. The influence of these factors on macroalgal composition is likely to have a flow-on effect to the distribution of BtD.

Gambierdiscus spp. co-occur on macroalgal substrates with other BtD (Heimann *et al.*, 2011), however, interactions between BtD is poorly understood. This study showed that higher *Gambierdiscus* populations were not always associated with the same macroalgal growth morphology in contrast to higher BtD populations. In Pioneer Bay, higher *Gambierdiscus* abundances were on terete macroalgal substrates, which were least preferred by BtD populations. Highest BtD abundance was on flattened macroalgal substrates in May 2008 at Nelly Bay, however, *Gambierdiscus* cells were only recorded on leathery macroalgal substrates. Allelopathic interactions have been shown to influence composition of temperate bloom-forming toxic dinoflagellates (Hakanen *et al.*, 2014). The dominance of *Ostreopsis* spp. in Nelly Bay and *Prorocentrum* spp. at mid- and inshore-reefs suggest potential allelopathic interaction could play a role in population growth of *Gambierdiscus* spp.

CONCLUSIONS

Range expansions of *Gambierdiscus* populations in tropical regions following large-scale disturbance events have been correlated with increases in ciguatera incidence. The growth morphology and palatability of macroalgal substrates have an important role in the distribution and abundance of *Gambierdiscus* populations. To understand the significant role these factors play in ciguatoxin transfers to marine food chains,

it is essential to explore the role of herbivory pressures, grazer abundances, competition and allelopathic interactions on macroalgal composition and abundance.

Changed weather patterns under current climate warming conditions have promoted the expansion of *Gambierdiscus* populations into temperate coastal habitats. There is concern that colonisation by *Gambierdiscus* spp. into new coastal habitats will be followed by ciguatoxins accumulating in local fish populations and fisheries. It is essential for more research to continue investigating key factors that influence distribution of *Gambierdiscus* populations and key vectors in the transfer of ciguatoxins into fish food chains. Without this, monitoring reported ciguatera cases and implementing fisheries management strategies, such as bans and restrictions, will not pay tribute to the continued geographic expansions by *Gambierdiscus* spp.

ACKNOWLEDGMENTS

The author gratefully acknowledges funding for field work to David Blair and Kirsten Heimann through the Marine and Tropical Sciences Research Facility (MTSRF); use of equipment at the North Queensland Algal Identification and culturing Facility (NQAIF), James Cook University, Townsville, Australia; volunteers that assisted with field work; the Orpheus Island Research Station managers, Rob and Kylie.

LITERATURE CITED

Arena, P.; Levin, B.; Fleming, L.E.; Friedman, M.A., and Blythe, D. 2004. A pilot study of the cognitive and psychological correlates of chronic ciguatera poisoning. *Harmful Algae*. 3:51-60.

Azziz-Baumgartner, E.; Luber, G.; Conklin, L.; Tosteson, T.R.; Granade, H.R.; Dickey, R.W., and Backer, L.C. 2012. Assessing the incidence of ciguatera fish poisoning with two surveys conducted in Culebra, Puerto Rico, during 2005 and 2006. *Environmental Health Perspectives*. 120:526-529.

Ballantine, D.L.; Bardales, A.T., and Tosteson, T.R. 1985. Seasonal abundance of Gambierdiscus toxicus and Ostreopsis sp. in coastal waters of southwest Puerto Rico. *Proceedings of the Fifth International Coral reef Congress*, Tahiti.4,417-422.

Chateau-Degat, M.L.; Dewailly, E.; Cerf, N.; Nguyen, N.L.; Huin-Blondey, M.O.; Hubert, B.; Laudon, F., and Chansin, R. 2007. Temporal trends and epidemiological aspects of ciguatera in French Polynesia: a 10-year analysis. *Tropical Medicine and International Health*. 12, 485-492.

Chinain, M.; Darius, H.T.; Ung, A.; Fouc, M.T.; Revel, T.; Cruchet, P.; Pauillac, S., and Laurent, D. 2010. Ciguatera risk management in French Polynesia: The case study of Raivavae Island (Australes Archipelago). *Toxicon*. 56, 674-690.

Cruz-Rivera, E., and Villareal, T.A. 2006. Macroalgal palatability and the flux of ciguatera toxins through marine food webs. *Harmful Algae*. 5, 497-525.

Diaz-Pulido, G., and McCook, L. 2002. The fate of bleached corals: patterns and dynamics of algal recruitment. *Marine Ecology Progress Series*,. 232, 115-128.

Gillespie, N.C.; Holmes, M.J.; Burke, J.B., and Doley, J. 1985. Distribution and periodicity of Gambierdiscus toxicus in Queensland, Australia. In: Anderson, D.M.; White, A.W., and Baden, D.G. (eds.), *Toxic Dinoflagellates*. Elsevier, New York. 183-188.

Hakanen, P.; Suikkanen, S., and Kremp, A. 2014. Allelopathic activity of the toxic dinoflagellate Alexandrium ostenfeldii: Intra-population variability and response of co-occurring dinoflagellates. *Harmful Algae*. 39:287-294.

Hales, S.; Weinstein, P., and Woodward, A. 1999. Ciguatera (fish poisoning), El Nino, and Pacific sea surface temperatures. *Ecosystem Health*. 5:20-25.

Heimann, K.; Capper, A., and Sparrow, L. 2011. Ocean surface warming: Impact on toxic benthic dinoflagellates causing ciguatera. In *The Encyclopaedia of Life Sciences* A23373. Wiley Publishing.

Heimann, K., and Sparrow, L. 2015. Ciguatera: Tropical reef fish poisoning. In: Se-Kwon, K. (ed.), Handbook of marine microalgae: biotechnology advances. *Academic Press*, USA. 547-558.

Heimann, K.; Sparrow, L.; Capper, A., and Blair, D. 2010. Final report on seasonal sampling of toxic microalgae from the central GBR. June Final Report to the Marine and Tropical Sciences Research Facility, *Reef and Rainforest Research Centre Limited*, Cairns. 19.

Lawerence, D.N.; Enriquez, M.B.; Lumish, R.M., and Maceo, A. 1980. Ciguatera fish poisoning in Miami. *Journal of the American Medical Association*. 244:254-258.

Llewellyn, L.E. 2010. Revisiting the association between sea surface temperature and the epidemiology of fish poisoning in the South Pacific: Reassessing the link between ciguatera and climate change. *Toxicon*. 56:691-697.

McClanahan, T.R.; Cokos, B.A., and Sala, E. 2002. Algal growth and species composition under experimental control of herbivory, phosphorus and coral abundance in Glovers Reef, Belize. *Marine Pollution Bulletin*. 44:441-451.

McCook, L.J. 2001. Competition between corals and algal turfs along a gradient of terrestrial influence in the nearshore central Great Barrier Reef. *Coral Reefs*. 19:419-425.

Rongo, T.,van Woesik, R., 2011. Ciguatera poisoning in Rarotonga, southern Cook Islands. *Harmful Algae*. 10, 345-355.

Skinner, M.P.; Brewer, T.D.; Johnstone, R.; Fleming, L.E., and Lewis, R.J. 2011. Ciguatera Fish Poisoning in the Pacific Islands (1998 to 2008). *Plos Neglected Tropical Diseases*. 5.

Sparrow, L.; Heimann, K.; Capper, A., and Blair, D. unpub. data. Managing ciguatera - implications of recorded incident (2001-2012), distribution, seasonality and trophic interactions.

Tester, P.A.; Feldman, R.L.; Nau, A.W.; Kibler, S.R., and Litaker, R.W. 2010. Ciguatera fish poisoning and sea surface temperatures in the Caribbean Sea and the West Indies. *Toxicon*. 56:698-710.

Journal of Coastal Research	SI	75	1012 - 1016	Coconut Creek, Florida	2016

Projected Changes in Wave Conditions in the Baltic Sea by the end of 21st Century and the Corresponding Shoreline Changes

Ülo Suursaar[†*], Hannes Tõnisson[‡], Victor Alari[&], Urmas Raudsepp[§], Henri Rästas[#], and Agnes Anderson[‡]

[†] University of Tartu, Estonian Marine Institute, Tallinn, Estonia

[&] Institute of Coastal Research, Helmholtz-Zentrum Geesthacht, Germany

[#] University of Tartu, Institute of Physics, Tartu, Estonia

[‡] Tallinn University, Institute of Ecology, Tallinn, Estonia

[§] Marine Systems Institute at Tallinn University of Technology, Tallinn, Estonia

www.cerf-jcr.org

www.JCRonline.org

ABSTRACT

Suursaar, Ü.; Tõnisson, H; Alari, V.; Raudsepp, U.; Rästas, H., and Anderson, A., 2016. Projected changes in wave conditions in the Baltic Sea by the end of 21st century and the corresponding shoreline changes. *In:* Vila-Concejo, A.; Bruce, E.; Kennedy, D.M., and McCarroll, R.J. (eds.), *Proceedings of the 14th International Coastal Symposium* (Sydney, Australia). *Journal of Coastal Research*, Special Issue, No. 75, pp. 1012 - 1016. Coconut Creek (Florida), ISSN 0749-0208.

The aim of the study is to analyse possible future changes in the Baltic Sea wave conditions and to project coastal changes in six differently exposed Estonian coastal sections resulting from changing wind climates. In the open parts of the Baltic Sea, the SWAN model with 3 NM spatial resolution was used for simulation of wave fields in 1966–2100. Regional climate projection EUR-11 assuming the RCP4.5 greenhouse gas scenario was used as wind forcing. In addition, using a site-dependently calibrated fetch-based wave model, a set of semi-realistic scenario calculations was obtained by modifying the baseline wind input data in order to investigate the reaction of wave climates and coastal developments. For coastal change, past developments in the shoreline and accumulation-erosion areas were tracked using repeated GPS measurements and GIS-overlaid cartographic and photographic material. The projections showed spatially and temporally varying wave fields and a slight overall increase, which corresponds to increased south-westerly winds. Depending on exposition, the wave climates would change differently even within a single semi-enclosed sea. Using the previously established empirical relationships between wave parameters and shoreline changes, we predict that erosion will probably increase in transitional zones while accumulation increases within bays. Sea-level rise and shortening of the sea-ice duration will probably have a remarkable contribution.

ADDITIONAL INDEX WORDS: *Wave hindacst, SWAN, coastal change, future projections, climate change.*

INTRODUCTION

In coastal zone management and for design of coastal defence structures, the influences of climate change on wave conditions, as well as on coastal geomorphic processes, have to be analysed. At the international level, a large number of global climate change scenarios have been produced over the recent decades, often in connection with work on the latest Intergovernmental Panel on Climate Change (IPCC) assessment reports in 2001, 2007 and 2014. At European level, some of the scenario calculations have been dynamically or statistically downscaled for detailed analysis of climate change and its impacts on a regional scale (Kjellström *et al.*, 2011; Jakob *et al.*, 2012). In atmosphere, temperature and precipitation projections have gained most of the attention, while changes in the wind climate are considered as the most uncertain (Christensen *et al.*, 2015). This has probably also hindered the development of wave projections. Although some studies applying advanced wave models for the Baltic Sea have been recently published (Weisse and Günther, 2007; Dreier *et al.*, 2013), there is still a lack of such nowledge, including on the impacts of wave climate changes on sea-coasts in the future.

Our aim is to present a study on wave conditions based on the SWAN (Simulating Waves Nearshore) model calculations for the Baltic Sea for the period of 1966–2100. Wind forcing for the SWAN was downscaled from the coupled Max Planck Institute Earth System Model at base resolution (MPI-ESM-LR) by the Regional climate Model (REMO) EUR-11 under the EURO-CORDEX project (Jacob *et al.*, 2012). A discussion on reliability of such wave projections is also presented. For illustrating dependencies between (possible) future wind and wave climates, as well as their impacts on seacoasts (Tõnisson *et al.*, 2008), a study of semi-realistic scenario calculations is presented for six differently exposed Estonian coastal sections (Figure 1). Based on hindcast wave conditions, we tried to find simple relationships between forcing conditions and the shoreline change rates and to discuss possible future developments in coastal change.

METHODS

Two different approaches were used for projecting future wave conditions. First is the full calculation of Baltic Sea wave fields using the downscaled REMO EUR-11 daily wind with a spatial resolution of 0.11 degrees (~12 km) as input. The third generation phase averaged spectral wave model SWAN (Booij *et al.*, 1999) cycle III, version 40.91, with a 3 nautical mile spatial resolution, was run in a non-stationary mode with a 30 minute integration time step. Twice-daily significant wave

DOI: 10.2112/SI75-203.1 received received 15 October 2015 accepted in revision 15 January 2016
*Corresponding author: ulo.suursaar@ut.ee
©Coastal Education and Research Foundation, Inc. 2016

height (H_s) output was saved for the Baltic Sea within the period 1966–2100. The hindcast results (1966–2006) were previously validated. For changes in wave climate in response to the RCP 4.5 greenhouse gas emission scenario, the control (baseline) period was 1990–1999 and the scenario period was 2090–2099. For this study, differences both in wind and wave conditions between the two time spans were considered. Usually, wave models are capable of describing offshore wave conditions, as the closest reasonable marine grid-cell may lay 1 to 3 km off the coastline. Although one can assume that wave energy does not transform significantly until reaching the coast, it would be advisable to spatially refine the wave energy calculations. Thus, wave energy flux and absorption of energy by the shoreline were estimated. Using SWAN output, the calculations (Rästas, 2015) took into account the shoreline orientation relative to wave direction. The distances between the neighboring coastal points were about 1 km and varied depending on the geometry of the (refined) coastline between 0.2 and 17 km.

The second, simplified approach tries to find out what happens to wave conditions (and coastal processes) if the wind conditions change in certain prescribed ways. The study stems from long-term wave hindcasts using a semi-empirical model, which was calibrated against the wave measurements made in six coastal sections with different expositions using ADCPs in 2006–2014 (Suursaar, 2013). A locally calibrated point model (LCPM, a type of the significant wave method), was used to calculate variations in H_s as a function of wind speed, effective fetch length and depth. For each of the locations, the data from the closest meteorological station were used to supply the wave model with wind speed and direction. For the comparison with the SWAN, see Suursaar *et al.* (2014). As the full calculation period (1966–2013) might suffer from inhomogeneity of wind input data, a homogeneous time cut (2004–2013 with hourly resolution) was chosen as a baseline (control) period. For projecting the future changes, an ensemble of nine semi-realistic scenario calculations were obtained by modifying the original wind input data in line with greenhouse gas scenarios (RCP2.6, RCP4.5) and the corresponding narratives for future wind ("increase in geostrophic wind by 5% above the Northern Atlantic; increase in westerly wind in winter", *etc.*). They included: increase in all wind speed modula by 1 m/s (scenario No.1), adding 1 m/s (No.2) or 2 m/s (No.3) to the *u*-component (which leads to an increase in westerly and a decrease in easterly winds), adding 1 m/s to both *u* and *v* (No.4), increase *u* by a factor of 1.1 (No.5); No's. 6–9 included the same manipulations as in 2–5, but only from October to March.

Among the chosen six Estonian coastal study sites, the Cape Kelba at Harilaid (code HAR; see Figure 1) is the most thoroughly studied, where both annual and long-term coastal data are available (Tõnisson *et al.*, 2008). From 2000 until 2010, shoreline positions were measured using handheld GPS instruments (accurate to within 3 m). After 2010, a RTK-GPS (accurate to within 1–2 cm) was used. The shoreline contours obtained from the GPS surveys, as well as from the digitized maps (from the years 1900, 1946, 1988) and aerial photographs (1951, 1981, 1995, 1998, 2005, 2008, 2011, 2012) were overlaid and analysed using the MapInfo software. The rate of coastal change was calculated as a ratio of volume change to the duration of the period (and per shoreline meter).

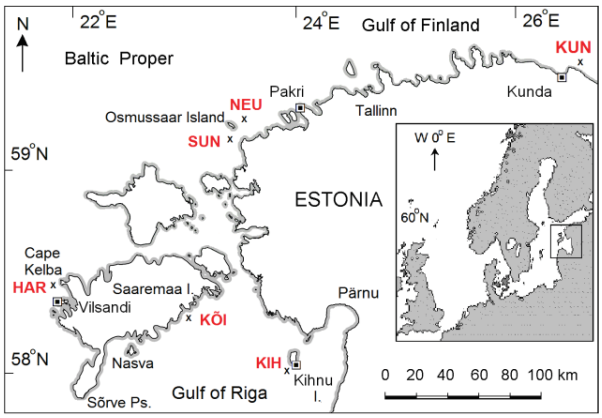

Figure 1. The study area. The codes for LCPM wave hindcast: HAR – Harilaid (Cape Kelba), KÕI – Kõiguste, KIH – Kihnu, SUN – Sundgrund, NEU – Neugrund, KUN – Kunda.

Areal changes over the sub-periods (mainly determined by the availability of map and photographic sources) were calculated. At Harilaid (exposed to SW), those sub-periods were 1955–1980–1997–2013; at Kunda–Sillamäe (N) 1968–1979–1995–2013; at Kõiguste–Nasva (SE) 1959–1987–1998–2013; at Kihnu–Pärnu (S) 1964–1988–2001–2013; and at two sides of the Osmussaar Island (exposed to W, N; Figure 1), 1962–1981–1998–2013. Based on recorded and hindcasted changes in wind-driven wave conditions, a set of relationships between forcing conditions and the rates at which shorelines are changing (both for displacement and area change) have been studied.

RESULTS

According to the REMO EUR-11 projections in response to the RCP 4.5 scenario, using the (past) control period and the scenario period 2090–2099, a slight overall wind speed increase is anticipated over the Baltic Sea. The increase would be stronger in the south-eastern Baltic Sea and in the eastern Gulf of Finland. When we considered winter months (December to February), the increase in wind speed was higher and spatially more uniform over the north-eastern Baltic Sea. Close to the West Estonian Archipelago, winds from the south would increase by about 0.7 m/s while winds from the north will decrease by 0.4 m/s. Zonal winds continue to increase because the winds from the east would decrease slightly and westerly winds would remain nearly unchanged. Westerly winds already prevail in the region and their share has increased over the last half century (Weisse and Günther, 2007; Suursaar, 2013).

Calculated using the SWAN, the wave energy flux close to West Estonia would follow the wind climate changes. Although spatially, the energy fluxes seem quite similar for the both time periods (Figure 2a,b), the differences between the hindcast and the scenario would still have distinct change patterns. There would be an increase over the sea along western and south-western coasts (Figure 2c). The opposite tendency can be seen at the northern coast. Nominally, the increase in energy flux will be

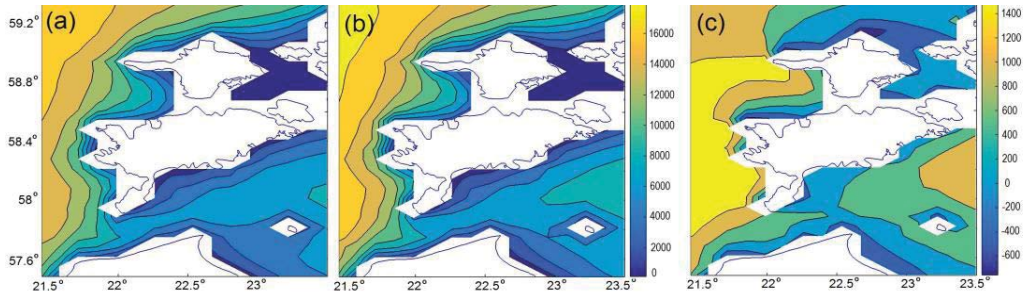

Figure 2. Mean wave energy fluxes (W/m) calculated with SWAN over the period 1990–1999 (a), over the period 2090–2099 (b), and the differences between the periods of 2090–2099 and 1990–1999 (c).

higher (up to 1400 W/m) offshore, but considering the high base levels, the relative increase is about 10%.

In areas closer to the S-SW coast of the Saaremaa Island, the relative increase would be up to 15–20%, and the decrease in some northerly and easterly exposed coastal sections about 5–10%. The results were generally the same when coastal exposition was taken into account in greater detail (Figure 3). Wave action increases over western and southern coasts, which already suffer the most from wave action, and the mean wave pressure reduces on the northern coasts. The long-term scenario calculations showed some temporal variations in different scales. Still, the future projections results did not change significantly when we extended the 10-year analysis periods into 30-years (1970–1999 and 2070–2099, respectively).

Wave conditions in the medium-size and semi-enclosed Baltic Sea basically follow those of so-called wind-seas which means that the impact of wind climate changes on wave conditions should be relatively straightforward. Thus, an additional set of wave projections was made in order to illustrate such cause-consequence type relationships using the LCPM (Figure 4a). According to the envelope (Figure 4) of chosen scenarios (which all could be considered quite realistic based on current knowledge), the largest increase (by up to 13–22%) is expected at the westerly exposed locations with long fetches (NEU, HAR, SUN; Table 1). The relative increase in the 99th percentile wave heights seemed smaller (increase by 7–15%), but assuming higher values, the absolute increase was still higher. The scenarios worked differently on southerly exposed Kihnu and northerly exposed Kunda. Moreover, at Kõiguste, which mainly catches waves over relatively short fetch from SE and E, had decreases in wave heights by 5–9%.

Coastal Changes

Regression analysis was used to investigate the possible developments at selected coastal sections if wave and wind conditions would change in some prescribed ways. Coastal changes over the selected sub-periods were calculated using ArcGIS and these changes were matched with the statistics of past and future wave conditions in those areas. Several types of relationships were tested, *e.g*. wave heights on one side, and quantifications of accumulation, accumulation plus erosion (intensity), or accumulation minus erosion (saldo), on other side. The most meaningful results seemed to be with the saldo as a function of average H_s (Figure 5). Placing the projections for "future" waves into the relationship, indications for future coastal changes could be found. Although the relationships seem rather confident, they are in fact quite uncertain and only some rough inferences could be drawn here. We have found that the current rates of coastal changes in the West Estonian study sites are already 2–3 times higher than in the 1950s (Suursaar *et al.*, 2015) and rapid coastal change will continue in the future. We predict that erosion will probably increase in transitional zones (annual shoreline recession may reach to 2 m) while accumulation increases within bays. Siltation will affect ports and navigational channels; flattening of the coastal zone may increase the risk of inundation during storms. Still, notable changes will take place on geomorphically active coasts, leaving roughly half of the Estonian coastline practically unchanged (at least until the sea level rise rate will not exceed 2–3 mm/yr). The rate of coastal changes would not change much on the northern coasts unless an unexpectedly strong northern storm causes rapid event-driven coastal destruction.

We have also studied annual increments of the Cape Kelba (Figure 6). Accumulations of new beach ridges gradually elongate the spit while historical changes in shoreline position reflect past changes in wind and wave climate. The elongation (by about 30 m a year) occurs mainly during winter storms.

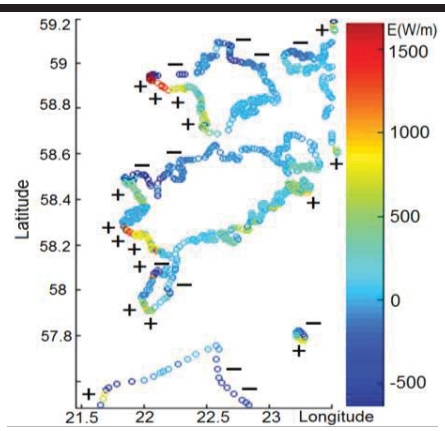

Figure 3. Absorption of wave energy (W/m) at the coast, the difference between 2090–2099 and 1990–1999. In addition to the colour code,

increase (+) and decrease (-) zones are marked on the Figure.

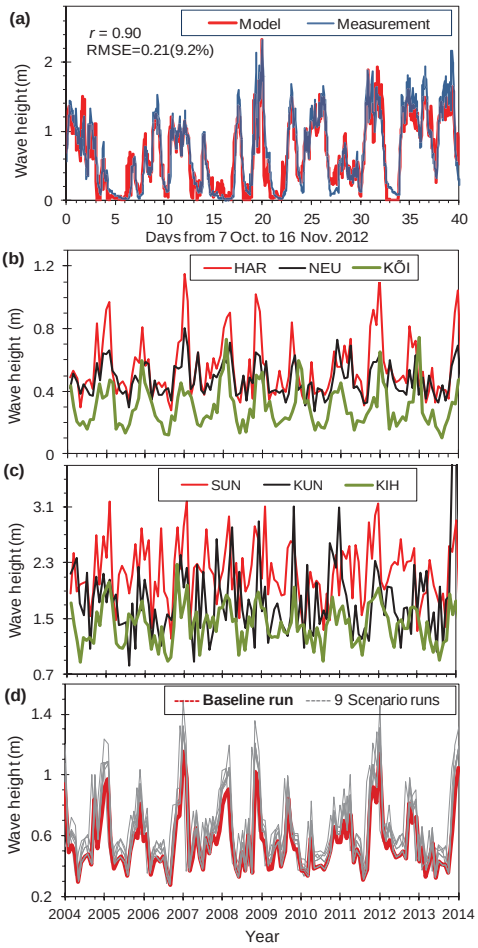

Figure 4. An example of LCPM calibration at KIH (a); variations in average H_s wave heights (b) and 99th percentiles (c) computed on monthly basis; exemplified for HAR, the realistic hindcast (baseline run) and an envelope of manipulated scenario runs (d).

Table 1. *Compared to baseline run, change (%) in average and 99% wave heights in the locations (with given exposure) according to a set of wind change scenarios (see Figure 4d).*

Location	Exposure	1	2	3	4	5	6	7	8	9	**Av.**
		Scenarios 1–9; average wave heights									
HAR	SW	20	14	33	16	12	7	15	8	12	**15**
KIH	S	23	2	14	3	13	-2	3	-1	5	**7**
KÕI	SE	25	-17	-20	-10	13	-12	-15	-8	-3	**-5**
SUN	W	29	20	43	30	11	10	21	16	21	**22**
NEU	NW	26	4	17	21	11	2	8	11	17	**13**
KUN	NE	33	13	38	11	12	7	18	6	12	**17**
		99th percentiles									
HAR	SW	10	12	23	12	11	6	12	6	11	**11**
KIH	S	10	4	12	5	11	1	5	1	6	**6**
KÕI	SE	14	-21	-24	-15	12	-14	-16	-11	-6	**-9**
SUN	W	12	11	18	12	9	6	10	6	10	**10**
NEU	NW	12	2	9	10	11	1	4	4	9	**7**
KUN	NE	14	-4	4	-8	12	-1	2	-4	1	**2**

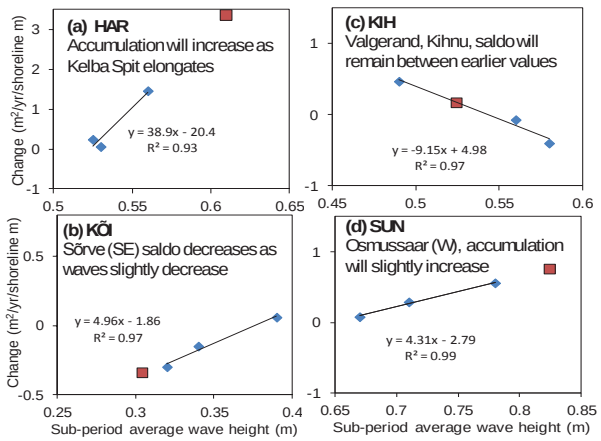

Figure 5. Selected relationships between average H_s (LCPM) and coastal change rates in the studied sub-periods. The future coastal change rates (relative to wave projections) are given by large markers.

In certain prominent storms (such as Gudrun on January 9, 2005), the increment could reach 80 m in length (Figure 6).

DISCUSSION

Putting our findings on the Baltic Sea wave conditions into a wider perspective, we must admit that our calculation is just one out of many possible scenario calculations. Obviously, the crucial role in wave modelling lies on correct and representative calculations of future winds. However, a large number of wind climate projections exist with remarkable scatter, which may depend on many factors, such as models used, greenhouse gas scenarios, assimilated data properties, meshes, scaling procedures etc. The results diverge and it is not possible to estimate whether there will be a general increase or decrease in wind speed in the future. For the Baltic Sea, a projected wind speed change scatter could be from -2% to +14% (Kjellström *et al.*, 2011). Christensen *et al.* (2015) claimed that future changes in wind speed above the Baltic Sea are highly dependent on changes in the large-scale atmospheric circulation simulated by global models. Hence, uncertainties in global scale are translated into uncertainties in regional reanalyses and subsequently into wave model outputs. Wave projections cannot be more reliable than the respective wind projections.

The results obtained using the two different approaches were quite similar. Of course, the scenarios mainly favoured increases in W or SW winds and also assumed a slight increase in overall wind speeds. If we had favoured *e.g.* easterly winds, the results would have been correspondingly different. Still, our simulations indicated, that (1) depending on exposition, the wave climates would change differently within a water body. Although wave heights may even slightly decrease at some locations under specific scenarios, the ensemble means predicted increases in wave heights by about 5–20% in most parts of the Estonian coastal sea. Also Dreier *et al.* (2013) found spatial patterns for changes in wave conditions in the Baltic Sea,

which included increases of H_s at westerly exposed locations up to 7% and small decreases at easterly wind exposed locations.

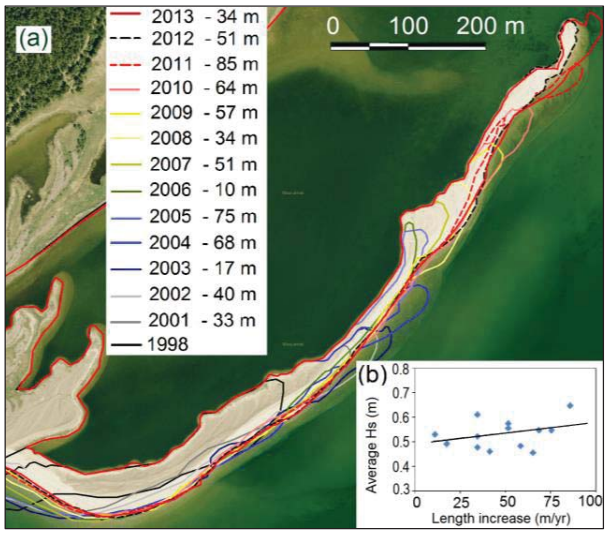

Figure 6. Annual increments of Cape Kelba; the length increase is given in the legend (a) and the relationship with average wave heights in (b).

Secondly, no matter what the (realistic or semi-realistic) wind change details are, the wave conditions do not alter too drastically. Wave conditions have changed cyclically within a range of ±30% around long-term mean over the past 50 years (Suursaar *et al.*, 2015), and the future changes will not fall much outside these limits as well. However, wave action is just one factor for coastal changes in the future. Not considered in this study, both gradual shortening of the winter sea-ice duration and the impact of the global sea level rise will have a remarkable contribution. As opposed to future changes in wind climates in mid-latitudes, these projections have much smaller scatter for the 21st century. Whether there is a reduction in sea-ice cover depends mainly on the projected change in air temperature over the Baltic Sea in winter, and most likely the temperature will rise (*e.g.* Christensen *et al.*, 2015) and ice cover continues to shrink. Sea level rise will probably exceed the local land uplift effect, and that will lead to intensified coastal erosion.

CONCLUSIONS

Wave climates could change differently even within a single semi-enclosed sea. Although wave heights may slightly decrease at northerly or easterly exposed sites under specific scenarios, the ensemble means predicted increases in wave heights by about 5–20% in most parts of the Estonian coastal sea. Still, compared to the past long-term variations, the wave conditions will not alter too drastically. According to the wind-wave-coastal change relationships, coastal erosion will continue to increase in the westerly exposed coasts and in transitional zones while accumulation increases within bays. While changes in wind conditions can directly be linked to changes of wave conditions, the fate of the coasts additionally depends on winter ice conditions and the sea level rise, which should be also taken into account in more detailed future studies.

ACKNOWLEDGMENTS

The study was financially supported by the projects IUT18-9 and IUT19-6 of the Estonian Ministry of Education and Research and by the Estonian Research Council grant PUT595.

LITERATURE CITED

Booij, N.; Ris, R.C., and Holthuijsen, L.H., 1999. A third-generation wave model for coastal regions; 1. Model description and validation. *Journal of Geophysical Research C: Oceans*, 104 (C4), 7649–7666.

Christensen, O.B.; Kjellström, E., and Zorita, E., 2015. Projected change – atmosphere. *In*: The BACC II Author Team. *Second Assessment of Climate Change for the Baltic Sea Basin*. Cham: Springer, pp. 217–233.

Dreier, N.; Schlamkow, C.; Fröhle, P., and Salecker, D., 2013. Changes of 21st Century's average and extreme wave conditions at the German Baltic Sea Coast due to global climate change. *In*: Conley, D.C., Masselink, G., Russell, P.E. and O'Hare, T.J. (eds.), *Proceedings 12th International Coastal Symposium* (Plymouth, England). *Journal of Coastal Research*, Special Issue No. 65, pp. 1921–1926.

Jacob, D.; Elizalde, A.; Haensler, A.; Hagemann, S.; Kumar, P.; Podzun, R.; Rechid, D.; Remedio, A.R.; Saeed, F.; Sieck, K.; Teichmann, C., and Wilhelm, C., 2012. Assessing the transferability of the regional climate model REMO to different coordinated regional climate downscaling experiment (CORDEX) regions. *Atmosphere*, 3, 181–199.

Kjellström, E.; Nikulin, G.; Hansson U.; Strandberg, G., and Ullerstig, A., 2011. 21st century changes in the European climate: uncertainties derived from an ensemble of regional climate model simulations. *Tellus A*, 63, 24–40.

Rästas, H., 2015. Spatial distribution of absorption of wave enery along the shoreline of the Baltic Sea. Tartu: University of Tartu, BSc Thesis, 31 p.

Suursaar, Ü.; Alari, V., and Tõnisson, H., 2014. Multi-scale analysis of wave conditions and coastal changes in the north-eastern Baltic Sea. *In*: Green, A.N. and Cooper, J.A.G. (eds.), *Proceedings 13th International Coastal Symposium* (Durban, South Africa). *Journal of Coastal Research*, Special Issue No. 70, pp. 223–228.

Suursaar, Ü.; Jaagus, J., and Tõnisson, H., 2015. How to quantify long-term changes in coastal sea storminess? *Estuarine Coastal and Shelf Science*, 156, 31–41.

Suursaar, Ü., 2013. Locally calibrated wave hindcasts in the Estonian coastal sea in 1966–2011. *Estonian Journal of Earth Sciences*, 62(1), 42–56.

Tõnisson, H.; Orviku, K.; Jaagus, J.; Suursaar, Ü.; Kont, A., and Rivis, R., 2008. Coastal damages on Saaremaa Island, Estonia, caused by the extreme storm and flooding on January 9, 2005. *Journal of Coastal Research*, 24(3), 602–614.

Weisse, R. and Günther, H., 2007. Wave climate and long-term changes for the southern North Sea obtained from a high-resolution hindcast 1958–2002. *Ocean Dynamics*, 57(3), 161–172.

Journal of Coastal Research	SI	75	1017 - 1021	Coconut Creek, Florida	2016

Numerical Study on Tsunami Propagation into a River

Yasuhisa Aoyama [†*], Mohammad Bagus Adityawan [‡], Wahyu Widiyanto[††], Yuta Mitobe[††], Daisuke Komori[†], and Hitoshi Tanaka[††]

[†]Hydro-environmental System Laboratory, Graduate School of Environment Studies, Tohoku University, Sendai, Japan

[‡] Water Resources Engineering Research Group, Faculty of Civil and Environmental Engineering, Institut Teknologi Bandung, Bandung, Indonesia

[††] Department of Civil Engineering, Tohoku University, Sendai, Japan

www.cerf-jcr.org

www.JCRonline.org

ABSTRACT

Aoyama, Y.; Adityawan, M.B., Widiyanto, W., Mitobe, Y., Komori, D., and Tanaka, H., 2016. Numerical Study on Tsunami Propagation into a River. *In:* Vila-Concejo, A.; Bruce, E.; Kennedy, D.M., and McCarroll, R.J. (eds.), *Proceedings of the 14th International Coastal Symposium* (Sydney, Australia). *Journal of Coastal Research*, Special Issue, No. 75, pp. 1017 - 1021. Coconut Creek (Florida), ISSN 0749-0208.

The Tohoku Earthquake and Tsunami in 2011 caused serious damage not only to coastal structures, but also to riverine infrastructure due to long distance of wave propagation into rivers located on the coast facing the Pacific Ocean. Although there have been numerous investigations on tsunami, limited number of studies have been made for tsunami propagation into a river channel. This study investigates tsunami propagation into a river numerically by comparing with laboratory experiment data. The present numerical simulation is based on shallow water equations, which are solved with the MacCormack scheme. Difference between calculated and experimental results are evaluated in terms of root mean square error. It is concluded that the present numerical simulation yields good agreement with experimental data in a wave flume. In addition it is observed that geographical characteristics in the river channel, such as sandbars and estuarine sand spits, highly affect tsunami propagation process in a river, causing lowering water level along with late arrival of tsunami peak.

ADDITIONAL INDEX WORDS: *Numerical simulation, tsunami propagation into a river, shallow water equation, the 2011 Tohoku Earthquake Tsunami.*

INTRODUCTION

The Tohoku Earthquake, which had Mw.9.0 seismic intensity, occurred off the coast of the Pacific Ocean on March 11, 2011. The tsunami induced by this earthquake overtopped existing coastal embankments in Japanese, and inundated the coastal area facing the Pacific Ocean. The maximum tsunami run-up height attained was around 40m. Because of such extreme energy, the tsunami propagated far upstream of rivers as well. The maximum tsunami run-up distance in a river was observed along the Kitakami River located in Miyagi Prefecture, resulting in serious damage to riverine structures (Tanaka and Tinh, 2012). In addition to the tsunami propagation into the river, the subsequent return flow caused considerable change to fluvial river topography such as erosion of sand bars and sand spits at the river entrance.

There have been several studies dealing with tsunami behavior within a river channel, e.g., Goto and Shuto (1981), Murashima *et al*. (2010), Adityawan *et al*. (2012), Tanaka *et al*. (2012), Fukushima *et al*. (2013), and Fukazawa *et al*. (2014). According to Adityawan *et al*. (2012), tsunami wave propagating into a river has higher celerity as compared with that over land area. However, field data available for numerical model verification is highly limited.

Fukushima *et al*. (2013) used measured tsunami height data along the Kitakami River in their study to verify numerical modelling, and found that the conventional shallow water equation model gives underestimation for water level in the river by 2m. Other numerical studies for the Kitakami River have been carried out by Imai *et al*. (2015) and Matsui *et al*. (2015). However it is quite difficult to thoroughly verify models due to limitations in available field data.

In the present study, instead of utilizing field data, detailed experimental results from physical model for the Kiatakami River mouth are used for comparison with numerical simulation. The laboratory experiment has been carried out using a fixed bed model by National Institute for Land and Infrastructure Management (NILIM), Japan.

STUDY AREA

The Kitakami River is a large river in Japan flowing through the southern part of Iwate Prefecture and the northern part of Miyagi Prefecture (Figure 1). The downstream river branches into two channels: the Old-Kitakami River and the Kitakami River. The Old-Kitakami River flows on a fertile plain which has been highly developed for agriculture and industry, while the Kitakami River flows through a narrow valley into a small bay facing the Pacific Ocean. The Kitakami River has a sharp bend about 10km upstream from the river mouth as seen in Figure 1. In this study, the numerical simulation domain is set up in the downstream of the bend.

It is noted that there is a sandbar and an elongated river mouth spit in the Kitakami River as seen in Figure 2, which might affect tsunami ascending in the river. Thus laboratory experiment has been carried out for both with and without sandbar and sand spit as explained later.

DOI: 10.2112/SI75-204.1 received 15 October 2015; accepted in revision 15 January 2016.
*Corresponding author: yasuhisa.aoyama.q6@dc.tohoku.ac.jp
©Coastal Education and Research Foundation, Inc. 2016

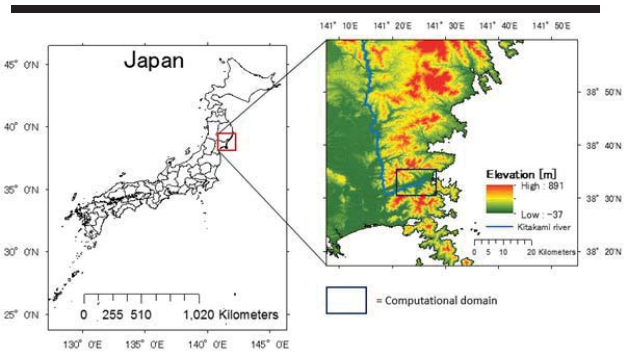

Figure 1. Location of study area. The black square in the figure corresponds to the computational domain.

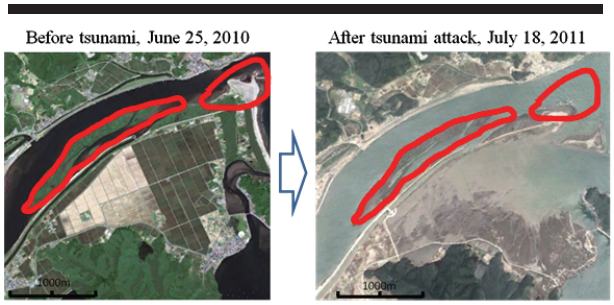

Figure 2. Geographical feature change of river mouth. The red lines indicate eroded sandbar and sand spit. The huge tsunami occured on March 11, 2011 (Image source: GoogleEarth©).

METHOD OF NUMERICAL SIMULATION

In this study, a shallow water equation model with fixed bed in a two-dimensional plane coordinate system is used. Here, the following basic equations are solved numerically using a finite difference method applying the MacCormack scheme (e.g., Kusuma *et al*., 2008).

$$\frac{\partial h}{\partial t}+\frac{\partial(uh)}{\partial x}+\frac{\partial(vh)}{\partial y}=0 \tag{1}$$

$$\frac{\partial u}{\partial t}+u\frac{\partial u}{\partial x}+v\frac{\partial u}{\partial y}+gh\frac{\partial(h+z)}{\partial x}=-ghS_{fx} \tag{2}$$

$$\frac{\partial v}{\partial t}+u\frac{\partial v}{\partial x}+v\frac{\partial v}{\partial y}+gh\frac{\partial(h+z)}{\partial y}=-ghS_{fy} \tag{3}$$

$$S_{fx}=n^2u(u^2+v^2)^{\frac{1}{2}}/h^{\frac{4}{3}} \tag{4}$$

$$S_{fy}=n^2v(u^2+v^2)^{\frac{1}{2}}/h^{\frac{4}{3}} \tag{5}$$

where (x, y): the plane coordinates as defined in Figure 3, h: the depth of water, u: the velocity in an x-direction, v: the velocity in y-direction; t: the time, g: the gravitational acceleration, S_{fx}: the friction slope in x-direction, S_{fy}: the friction slope in y-direction, and n: Manning's roughness coefficient.

The range of a computational domain is 10km x 8km as seen in Figure 3, in which squared mesh of 10m length and n=0.03 are used in the numerical simulation.

LABORATORY DATA

Using a 1/330 scale model of the Kitakami River mouth, comprehensive laboratory experiments have been carried out in a wave flume of NILIM (Fukushima *et al*., 2013). A pneumatic wave generator, consists of air chamber of 30 m wide and 3 m heigh, was used to generate a tsunami-like wave. Detail of the wave generator can be found in Noguchi *et al*. (1995).

Two input waves generated by this system are shown in proto-type scale in Figure 4. The water level is measured at the bay entrance located at the right hand end of the flume in Figure 3. The first input wave corresponds to the 2011Tsunami wave which will be referred to as "Level 2 (L2) Tsunami", while the second input wave is the maximum tsunami height that can be generated by the present generation system, named as "Class-25m Tsunami" hereafter.

Temporal variation of water level has been measured using water level gauges deployed at 22 places along the model river as illustrated in Figure 5.

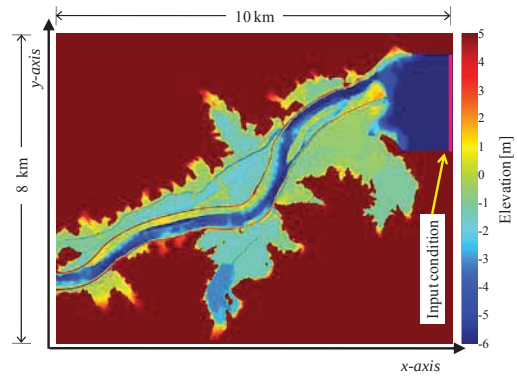

Figure 3. Computational domain in proto-type scale.

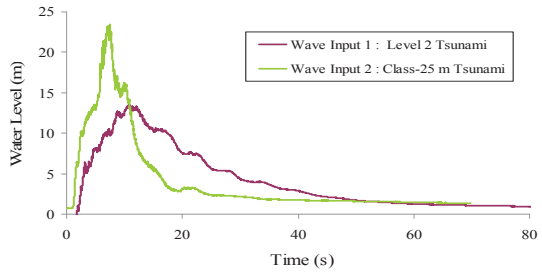

Figure 4. Input wave for numerical simulation consists of "Level 2 Tsunami" and "Class-25m Tsunami" shown in prototype scale.

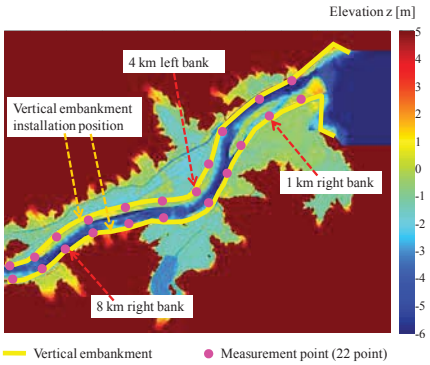

Figure 5. Water level measuring points in the NILIM laboratory flume.

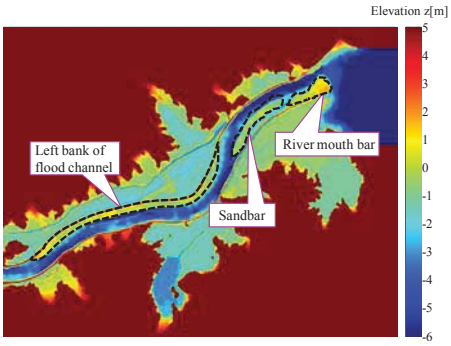

Figure 6. Geographical features of river channel at the Kitakami River mouth.

Two geographical features were used in order to investigate the influence of topography on tsunami propagation into a river. The first is based on the actual geographic features precisely reproduced in the laboratory flume (Figure 6), while in the latter case, sand spit at the entrance and sandbar are removed to investigate the influence of these sediment deposit. Figures 7 and 8 indicate examples of the cross section in these two cases at 0km and 1km points, respectively.

In order to implement the experiment under simplified flow condition, river embankment indicated by yellow lines in Figure 5 was installed high enough to avoid overflowing water over the river embankment.

Investigation cases in the present study are summarized in Table 1, categorized with respect to terrain and input wave in the experimental flume.

Table 1. *Investigation case.*

	Case	Terrain	Input wave
1	Normal terrain	Normal	L2, Class-25m
2	Without sandbar	Without sandbar	L2, Class-25m

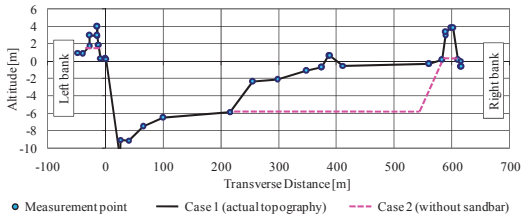

Figure 7. Cross section of 0 km of river mouth point. Pink dotted lines indicate the removed part for Case 2 simulation.

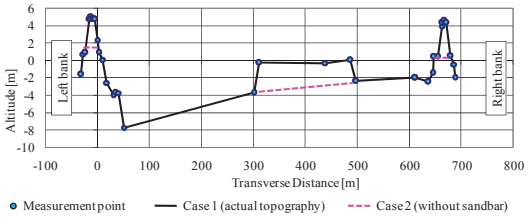

Figure 8. Cross section of 1 km of river mouth point. Sandbar in the middle of river is erased in the simulation of Case 2.

RESULTS AND DISCUSSIONS

It is noted that all variables shown hereafter are expressed in terms of prototype scale by converting from the model test scale, 1/330. In addition water level is defined as $\eta=h+z$.

In order to evaluate reproducibility of water level from the numerical model, the following root mean square error (*RMSE*) will be used to make quantitative comparison.

$$RMSE=\sqrt{\frac{1}{N}\sum_{i}^{N}(\eta_{cal,i}-\eta_{\exp,i})^2} \qquad (6)$$

where *RMSE*: the root mean square error, *N*: the total number of computational time steps, η_{cal}: the calculated water level, and η_{exp}: the experimental water level. Although detailed water level measurement has been carried out at 22 points as shown in Figure 5, detailed graphical comparison will be made for the measurements at 1km, 4km and 8km from the river mouth.

Case 1 (with actual geographical features)

Temporal variation of the water level at three points are shown in Figure 9. Good agreement between the experimental results and the numerical calculation can be seen, although the numerical model gives slight overestimation after the passage of the peak.

In addition *RMSE* value obtained from whole of the 22 measuring points are summarized in Table 2. For L2 Tsunami Level, most of the value of *RMSE* is less than 1m, and the averaged value is *RMSE*=0.74m as seen in Table 2.

As for 25m Tsunami, the value of *RMSE* at any point in the range of 1 m with an average of *RMSE*=1.18m. There is only one point with an error more than 2m, located at the mouth of the river. In general, the amount of error is almost constant.

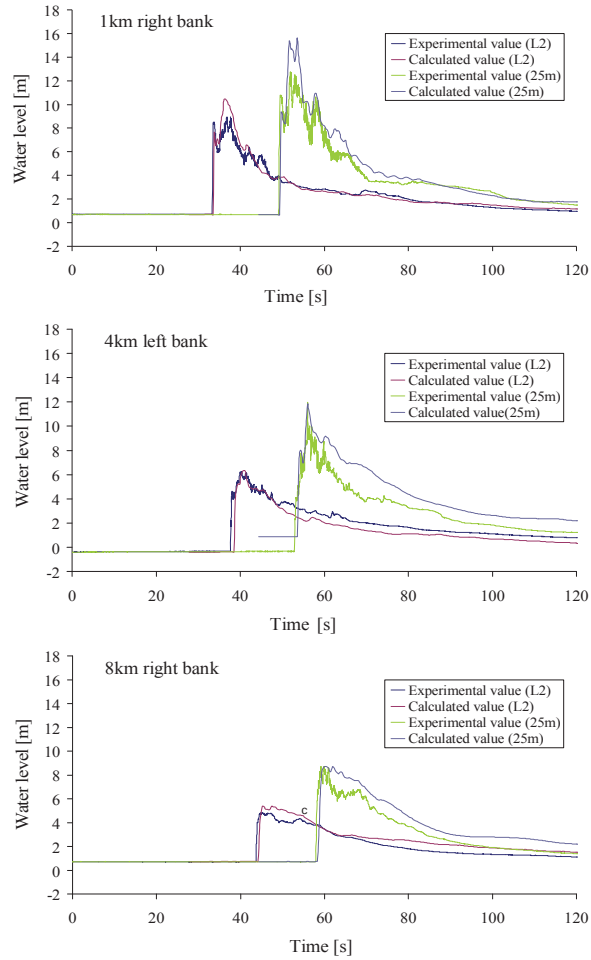

Figure 9. Comparison of water level between numerical and experimental results for Case 1.

Case 2 (without sand spit and sandbar)

Figure 10 shows the temporal variation of water-level for Case 2 with a modified river bed topography. Similar to Case 1, the numerical simulation overestimates results as a whole. The biggest difference occurs at about 2m at the river entrance. It should be noted that the removal of sand spit and sand bar causes water level rise as compared with Case 1 both in laboratory experiment and numerical analysis.

For L2 tsunami, most of the value of *RMSE* is less than 1m, with the average of *RMSE*=0.74m as shown in Table 1. As for the 25m Tsunami, the *RMSE* values are approximately 1 m, with an average *RMSE*=0.99m. The error around the river mouth is relatively large. At the maximum water level, the error is 10% or less, so that the results of numerical computation shows good agreement.

Table 2. *RMSE values (m) for Case 1 and Case 2.*

Meas. Point (L:left,R:right)	Case 1		Case 2	
	L2 Tsunami	25m Tsunami	L2 Tsunami	25m Tsunami
0km/L	0.57	1.30	0.52	1.20
1km/L	0.53	1.20	0.42	0.96
2km/L	0.66	1.16	0.58	1.03
3km/L	0.56	0.92	0.44	0.76
4km/L	0.65	1.41	0.60	0.75
5km/L	0.58	0.94	0.59	0.81
6km/L	1.00	0.93	0.63	0.90
7km/L	0.85	0.97	0.56	0.95
8km/L	0.80	1.84	0.62	0.82
9km/L	1.16	0.62	0.77	1.01
10km/L	0.63	1.12	0.94	1.24
0km/R	1.50	2.08	1.63	1.78
1km/R	0.57	1.19	0.59	1.14
2km/R	0.75	1.51	1.27	1.23
3km/R	0.57	1.31	0.71	1.01
4km/R	0.56	1.20	0.69	1.00
5km/R	0.50	0.96	0.69	0.76
6km/R	0.61	1.09	0.46	0.55
7km/R	0.62	1.02	0.68	1.04
8km/R	0.56	1.05	0.74	0.98
9km/R	0.48	1.05	0.81	1.13
10km/R	1.47	1.09	1.49	1.32
Averaged	0.74	1.18	0.74	0.99

It is noted that results from both experiment and numerical simulation show that arrival time of tsunami peak is earlier in Case 2. This indicates that sediment deposit in the river channel could hamper tsunami energy intrusion into a river. The presence of sandbar and sand spit causes roughness to increase, resulting in retardation of tsunami arrival. The effect of energy dissipation by sandbar and sand spit also induces a lowering of tsunami height in a river. For example, at 4km/L for L2 Tsunami, the highest water level is 6 m in Case 1 as shown in Figure 9, whereas it attains 8m in Case 2 in Figure 10.

The calculated value is slightly larger than the experimental value after the peak at 4km and 8km in Case 1. In Case 2, however, good agreement can be seen. This result indicates that the accuracy of 2-D flow in the river is influenced by river bed topography. Hence greater attention should be paid to input river bed elevation in order to obtain more precise results.

Accuracy of the simulation can be improved by applying a dynamic grid. For example, by making the size of the grid finer in the river channel. Adaptive mesh refinement method could be an option for this purpose.

CONCLUSIONS

In this study numerical simulation has been carried out for tsunami propagation into a river, and computation results are compared with 1/330 scale experiments in a laboratory. *RMSE* value for both cases with and without geographical modification is about 0.75m for L2 Tsunami, while the *RMSE* value for 25m Tsunami is about 1.0m. In general the numerical simulation results based on shallow water equations are highly satisfactory. Geographical characteristics of river affect the propagation of tsunami in a river, causing lowering of water level and delay of tsunami peak arival. This behavior can be successfully reproduced by the present numerical model, although the numerical simulation shows slight underestimation by 1 to 2m as compared with experiments in several simulation. Nevertheless, it is still around 10-20% of the maximum water level.

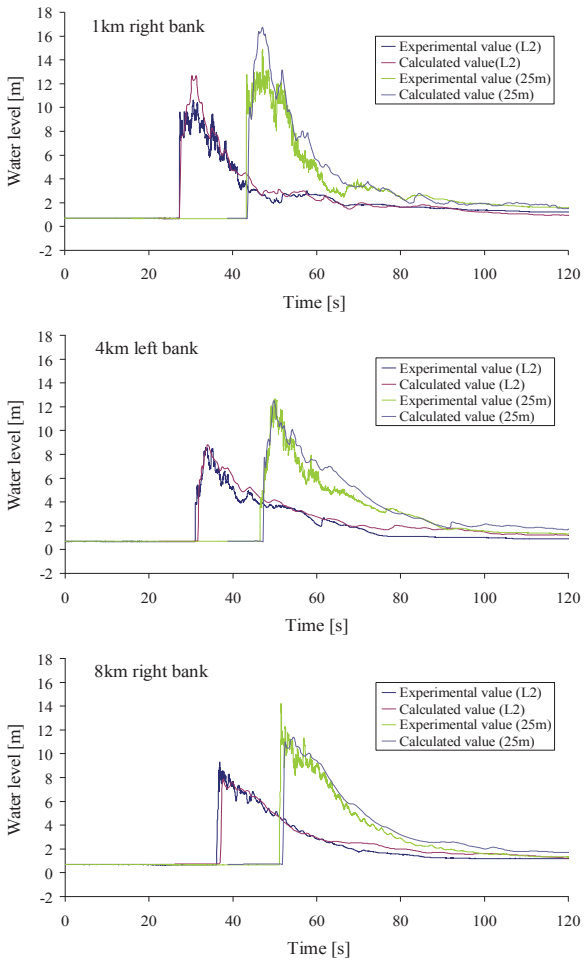

Figure 10. Comparison of water level between numerical and experimental results for Case 2.

ACKNOWLEDGMENTS

The hydraulic model test data used in this study were obtained and provided by the National Institute for Land and Infrastructure Management, Japan. Authors wish to express deep gratitude.

LITERATURE CITED

Adityawan, M.B., Roh, M., Tanaka, H., Mano, A. and Udo, K., 2012. Investigation of tsunami propagation characteristics in rivers and on land induced by the Great East Japan Earthquake 2011. *Journal of Earthquake and Tsunami,* 6(3).

Fukazawa, S., Sanuki, H. and Tajima, Y., 2014. Characteristics of tsunami run-up around the Kido River mouth based on video-image analysis and numerical experiments. *Journal of JSCE B-2 (Coast. Eng.)*, 70(2), 146-150. (in Japanese)

Fukushima, M., Matsuura, T., and Hattori, A., 2013. Experimental study on the characteristics of river tsunami. *Journal of JSCE B-2 (Coast. Eng.)*, 69(2), 261-265. (in Japanese)

Goto, T. and Shuto, N., 1981. Run-up calculation of river tsunami. *Journal of Coastal Engineering JSCE*, 64-68. (in Japanese)

Imai, K., Sugawara, D., Takahashi, T., Iwama, S., and Tanaka, H., 2015. Numerical study for sediment transport due to tsunami around the Kitakami River mouth. *Journal of JSCE B-2 (Coast. Eng.)*, 71(2), 247-252. (in Japanese)

Kusuma, M.S.B., Adityawan, M.B. and Farid, M., 2008. Modeling two dimension inundation flow generated by tsunami propagation in Banda Aceh City. *Proceedings of International Conference on Earthquake Engineering and Disaster Mitigation*, 407-414.

Matsui, T., Uchida, T., Nakamura, Y., and Hattori, A., 2015. Analysis of tsunami run-up into the Kitakami river using a quasi-3D numerical model. *Journal of JSCE B-2 (Coast. Eng.)*, 71(2), 181-186. (in Japanese)

Murashima, Y., Koshimura, T., Oka, H., Murata, Y. and Imamura, F., 2010. Development of the practical river run-up model of tsunami based on non-linear dispersive wave theory. *Journal of JSCE B-2 (Coast. Eng.)*, 66(1), 201-205. (in Japanese)

Noguchi, K., Sato, S. and Tanaka, S., 1995. Propagation of Hokkaido Nansei-Oki earthquake tsunami around Cape Aonae. *Coastal Engineering in Japan*, 38(2), 133-142.

Tanaka, H. and Tinh, N.X., 2012. The 2010 Chilean and the 2011 Tohoku Tsunami waves impact to rivers in the Tohoku Region, Japan. *Proceedings of 33rd International Conference on Coastal Engineering*, 2012.

Journal of Coastal Research	SI	75	1022 - 1026	Coconut Creek, Florida	2016

Video Oberservation of Waves and Shoreline Change on the Microtidal James Town Beach in Ghana

Donatus B. Angnuureng[‡†*], Rafael Almar[‡], Kwasi Appeaning Addo[§], Bruno Castelle[†], Nadia Senechal[†], Sowah W. Laryea[§], George Wiafe[§]

[†]UMR EPOC, University of Bordeaux / CNRS, Bordeaux, France. [‡]IRD/UMR, LEGOS, Toulouse, France.

[§]MAFS/Remote Sensing Lab., University of Ghana, Accra, Ghana.

www.cerf-jcr.org

www.JCRonline.org

ABSTRACT

Angnuureng, D. B., Almar, R., Appeaning Addo, K., Senechal, N., Castelle, B., Laryea, S. W., Wiafe, G., 2016. Video observation of waves and shoreline change on the microtidal James town Beach in Ghana.. *In:* Vila-Concejo, A.; Bruce, E.; Kennedy, D.M., and McCarroll, R.J. (eds.), *Proceedings of the 14th International Coastal Symposium* (Sydney, Australia). *Journal of Coastal Research,* Special Issue, No. 75, pp. 1022 – 1026, Coconut Creek (Florida), ISSN 0749-0208.

The morphology of sandy beaches is highly dynamic. They are influenced by the geology of the coastal area and external hydrodynamic forcing. On long timescales (years to decades), it is more efficient and convenient to monitor beach evolution through remote sensing technics rather than through direct field measurements. Erosion is a major problem along the coastline of Ghana with over 25 erosion hotspots, including James town. Here, tides, ECMWF EraInterim re-analysis wave data and images covering the beach area have been obtained for the 2013-2014 period. This paper presents preliminary results of the first efforts in processing video-derived observations of waves and shoreline change in Ghana. The pilot application shows a strong potential of the video system in providing fair quality wave data for beach management purposes where video wave characteristics are in good agreement with EraInterim global reanalysis (daily RMSE = 0.8 m and 0.7 m for H_b and T_p, respectively). Shorelines extracted from video suggest large monthly variability driven by wave seasonality while shoreline change shows a subsequent erosion/accretion cycle.

ADDITIONAL INDEX WORDS: *Shoreline location, wave modeling, beach profile changes.*

INTRODUCTION

Understanding coastal processes in the nearshore at different time scales is crucial, especially in the present context of vulnerability to sea level rise (Sagoe-Addy and Appeaning, 2013;Stive *et al.,* 2002). Vulnerability of beaches to natural forcing and anthropogenic factors has been addressed through both hard (*e.g.* revetments, jetties or breakwaters, and groins (Angnuureng *et al.,* 2013)) and soft (*e.g.* revegetation and beach nourishment) approaches in attempts to control the changes (*e.g.* French, 2001;Turner and Leatherman, 1997) yet both methods are debatable. Traditionally, studies in the nearshore have been realised via topographic surveys and in-situ measurements (Stockdon and Holman, 2002). However these measurements are intermittent both in space and time and the distance covered is often limited. The nearshore is a very variable system constantly changing at various timescales (Puleo *et al.,* 2003) and require a high frequency of sampling for adequate characterization. Remote video imagery has been used to measure nearshore processes (*e.g.* Aarninkhof *et al.,* 2003; Armaroli and Ciavola, 2011; Holman and Stanley, 2007; Plant and Holman, 1997) over the past two decades. According to Holman and Stanley (2007), the video system gives good resolutions (cm to m), and is safe and cheap.

From video images, wave height, celerity and period (*e.g.* Almar *et al.,* 2008; Holman and Stanley, 2007); break point and intertidal sandbar locations (Holman and Stanley, 2007; Ruessink *et al.,* 2007), beach profiles, and shoreline position (Almar *et al.,* 2012a; Smith and Bryan, 2007; Plant and Holman, 1997) can be remotely estimated.

Along the Ghanaian coast, erosion has been observed to be increasing over the last decades (Appeaning Addo *et al.,* 2008; Boateng *et al.,* 2009) with over 25 erosion hotspots identified. On the eastern part, this is due to the method of management (*e.g.* groynes and revertment) which affects the sediment budget (Jayson *et al.,* 2013; Ly, 1980). Angnuureng *et al.* (2013) observed that erosion has increased from about 3 to about 17 m/yr. from 2001 to 2011, which has been probably enhanced by sand mining along the coast.

Monitoring of the Ghanaian coastline is mainly done using satellite images albeit rough resolution, aerial photographs and field observation using DGPS on an irregular basis. Though portions of the unmonitored coast remains, a well planned and reliable monitoring scheme with such methods does not guarantee the capture of the short term temporal shoreline evolution. It is then essential for the data gathering strategy to include events in all times and space, that such video system provides.

In the methods section, the James town study area is described and daily nearshore measurements from video imagery presented. The goal is to analyse the shoreline

DOI: 10.2112/SI75-205.1 received 15 October 2015; accepted in revision 15 January 2016.
*Corresponding author: angnuureng@yahoo.com
©Coastal Education and Research Foundation, Inc. 2016

evolution and the potential of the video system in providing fair quality wave data for beach management purposes.

METHODS

Shoreline and beach profiles were automatically extracted from the timex (or averaged) images and shoreline positions resampled into daily and 15-day values. The shoreline location can be obtained using various definitions (Boak and Turner, 2005) but here the procedure followed minimum shoreline variability (MSV) video technique (Aarninkhof *et al.,* 2003; Almar *et al.,* 2012a). Wave properties (e.g. breaker wave height H_b and peak wave period T_p) at breaking are extracted from video images to compare with hindcast wave data (WAM model, The Wamdi Group, 1988).

Study area

James town is a major fishing community in Ghana (Gulf of Guinea, West Africa) on the eastern part (Figure 1) of the Korle lagoon, which is a major ecological site in Accra under the Ghana wetlands management project. The shoreline erosion in Ghana has risen from 1.13 m/yr. (Appeaning Addo *et al.,* 2008) to a rate of about 2 m/yr. (Wiafe *et al.,* 2013). The increasing coastal erosion threatens the community, the lighthouse and the old Accra harbor presently being used as a fishing harbor.

The nearshore bathymetric profile is relatively gentle (Sagoe-Addy and Appeaning Addo, 2013) and the area experiences periodic high-wave conditions (*e.g.* Sagoe-Addy and Appeaning Addo, 2013). The mean wave incidence is SSW, mean peak period T_p and the mean significant wave height are 10.9 s and 1.4 m (Angnuureng *et al.*, 2013; Appeaning Addo *et al.,* 2008), , respectively, but these could periodically rise to 20 s and 3 m. Tide range is micro-tidal with mean value of 1 m. Oblique waves drive alongshore drift of about $2*10^5$ m^3/yr. (Wellens-Mensah *et al.,* 2002) on this gentle beach (slope <0.03).

The 40-m high lighthouse was built in the for navigation (insert, Figure 1). A video camera was mounted on the lighthouse on 14/09/2013, inclined to the beach at an angle of 20° covering about 1.3 km across shore and 2 km along shore and recording from 6 - 18 hours GMT at 2 Hz. Three kinds of images are collected every 15 min: snapshot (Figure 2a); time exposure (timex) (Figure 2b) and time stacks (Figure 2c). Timex images are 15 min averaged of snapshot images into a single image (Almar *et al.,* 2012b; Holland *et al.,* 1997) while timestacks are obtained by stack of single cross shore section. The origin of the coordinate system (cross-shore X=720, longshore Y=0) is the lighthouse.

Geo-rectification of oblique images to plan view

Seven ground control points on site (Figure 2b, red circles) were taken with GPS and converted to Universal Transverse Mercator, UTM (Easting and Northing) coordinates. Including camera location (5.5265, 0.2121) at 30 N UTM zone, images were geo-rectified from oblique to plan view images by applying the method of direct linear transformation (*e.g.* Argus, Holland *et al.,* 1997). To get the rectified data, two approaches were applied. First, a zone of interest covering the beach and water (Figure 2a, white patch) was selected on the image and rectified at a 1-m resolution before desired information was extracted. We used for the rectification, the focal length (4m) based on a least square error minimization method. For shorter processing time purpose, the shorelines were detected (*see next section*) on the oblique images before the rectification.

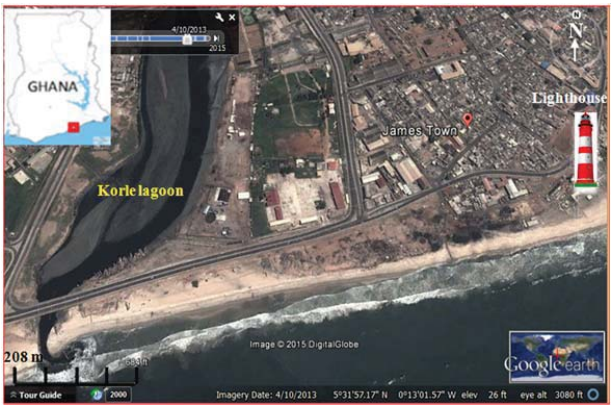

Figure 1. James Town Beach. Camera is mounted on lighthouse.

Because of the oblique camera view angle, the pixel resolution at the shoreline for the image lateral edges can be about 0.5 m, whereas it is about 0.1 m at the lower beach in front of the video system (Almar *et al.,* 2012a), increasing to 1 and 2 m at the lateral edges.

Automated shoreline delineation

Following Almar *et al.* (2012a), a region of interest (ROI) is demarcated on the oblique images to cover both wet (sea) and dry (land) pixels. Beach pixels display high red-channel values and low green values giving high *R:G* ratio, whereas water pixels exhibit strong green-channel values and low red values (*i.e.* low *R:G*). Within the ROI (*see* Figure 2a), the *R:G* ratios are computed for all pixels. These low and high values of *R:G* mark water and beach respectively based on some bimodal distribution (Almar *et al.,* 2012a). The local minimum stands for the transition between water and beach, that is, the shoreline. In other words the shoreline is represented by the time averaged waterline. Figure 2b shows the location of the shoreline X delineated automatically. This was repeated for all images, and converted to metric values. To reduce uncertainties, a 1-hr moving average (4 points) was done. The overall error (0.5m) rises from water level uncertainties due to wave breaking or atmospheric pressure variations or wrong shoreline detection. 2D shoreline migration was estimated via the alongshore averaged cross-shore 2D location $<X>$ (Figure 2c). 3D shoreline behaviour (non-uniformities development) was estimated through the standard deviation of cross-shore location along Y.

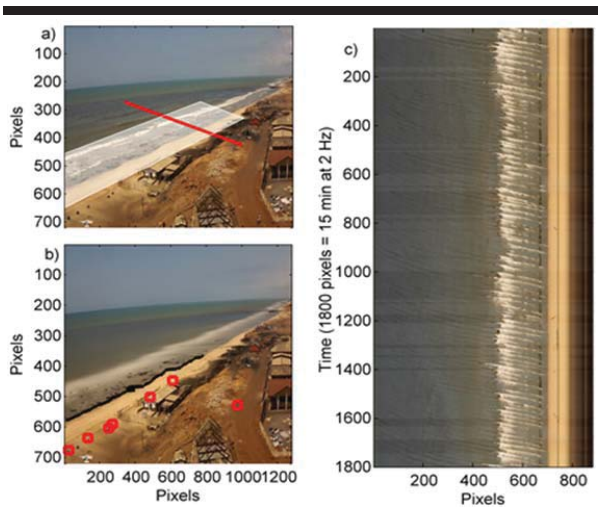

Figure 2. Video image types: a)snapshot; selected zone is shaded white while timestack profile is red line b) timex: shoreline is shown black line and GPS points in red circles c) timestack (vertical is time (1800 pixels =15 min at 2 Hz).

Wave and tide data from models

To validate video estimates of wave properties, hindcast data of significant wave height H_s, direction and peak period T_p have been obtained from EraInterim global reanalysis (WAM model, The Wamdi Group, 1988) at 0.5° and 6 hr spatial and temporal resolution, respectively (Sterl and Caires, 2005) at the grid point 30°N, 30°W. The wave data spans from Sep. 2013 to Oct. 2014. Tide was extracted from WXtide model. Because there is no tide gauge at the study site, the tidal subordinate at Accra (0°12' W, 5°32' N), from the nearest tide gauge station, Takoradi (~200 km) was used as the reference point. H_s and T_p were transformed into breaker conditions $H_{b(lm)}$ and $T_{p(lm)}$, respectively, following Larson *et al.* (2010). Beach states were computed using the formulation of Dean parameter (*see* Wright and Short, 1984), $\Omega = H_{b(lm)}/T_{p(lm)}w_s$, where w_s is sediment fall velocity, using the reanalysed wave data. A w_s of 0.05 m/s was used in consistence with similar sandy beaches (*e.g.* Masselink *et al.*, 2009).

Wave characteristics from video images

Wave breaker height H_b and T_p were obtained from time stack images and compared to the model data. T_p was computed from the offshore pixel intensity timeseries using mean zero-crossing method (Almar *et al.*, 2008). Following the wave signature induced by breaking, sudden variation in intensity values were identified on the image. For each breaker, standard deviation δ of the pixel intensity time series is estimated on a time window about the break point time. Almar *et al.* (2012b) showed that the width of the peak of δ marks the horizontal projection of wave face covered by the roller (L) which is subsequently projected into vertical H_b, $H_b = L\tan\beta$, where β is the camera view angle. H_b is obtained as the wave height of the average of all passing breakers over the timestack duration (1800s or stacking).

H_b and T_p were respectively regressed with $H_{b(lm)}$ and $T_{p(lm)}$, propagated from deep water to the breakpoint and a relationship established. Breaker parameters H_b and T_p from video followed this relationship.

Beach types were assessed from timex images. To estimate the beach profile evolution, 3D data (x, y, z) is needed. The shoreline location constitute 2D (x and y) which means a third axis (z-elevation) is needed. Subsequently profiles (not shown) were inferred from interpolated tide values at the different shoreline times where the profile of the beach at each time follow the tide values. The monthly average profiles were then estimated.

RESULTS

Preliminary findings of this West Africa pilot video system are given in the following subsections. They include the validation of video-derived wave parameters (RMSE, correlation with hindcast) and a brief description of the temporal evolution, extraction of shoreline and slope linked to wave and then tide forcing.

Validation of vide-derived wave characteristics

Figure 3 represents H_b and T_p obtained from regressed video-derived values as a function of hindcasted ones $H_{b(lm)}$ (and modelled $T_{p(lm)}$ from transformation of H_s, *see method section*) following Larson *et al.* (2010). Figure 3a shows that corrected video-derived T_p correlates strongly with hindcast (r = 0.9, daily RMSE = 0.7). Result error is due to variation in image quality. In Figure 3b it is showed that corrected video-derived H_b is in agreement with $H_{b(lm)}$ (r=0.9, daily RMSE=0.8). Overall, these results show the reasonable skills of the video in estimating wave conditions from daily to monthly scale for this beach.

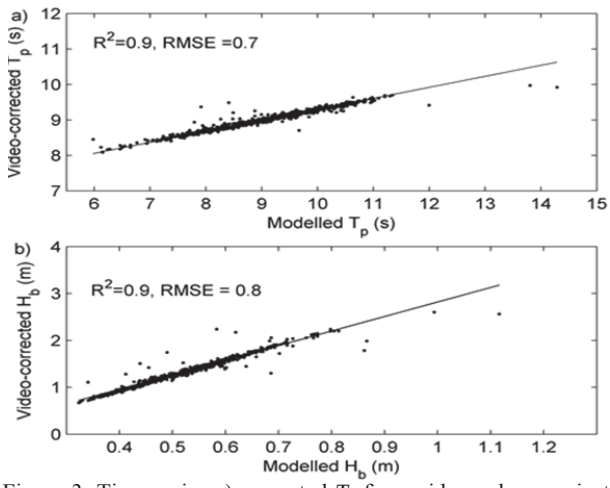

Figure 3. Time series a) corrected T_p from video values against model T_p b) corrected H_b from video values against model H_b. Model values are Larson's model H_b and T_p. Sloping solid lines are the best linear fits.

Shoreline and morphological evolution: event and overall evolution

During the observation period, from Sep. 2013 to Jul. 2014, alongshore averaged shoreline positions <*X*> ranged from 127 to 211 m with an average at 151 m. Figure 4c gives the daily <*X*> relative to the initial position <X_i>. It shows that shorelines retreat beyond the <X_i> more than they advance. Shoreline alongshore non-uniformity *Δ(X)*, *i.e,* standard deviation of shoreline *X*, is 8 m on average due to the presence of cuspate pattern but can fall to 3 m during energetic conditions. H_b ranges from 0.3 to 2.5 m while literature reported between 0 and 2.8 (Angnuureng *et al.,* 2013). T_p ranges from 7 to 14 s at the zero mean crossing shown on the images. Figure 4d shows that H_b decreases from September, 2013 to January, 2014 concomitant to beach advance while after January, 2014, H_b increases progressively corresponding to shoreline recession till June, 2014. In Figure 4c, 15-day averaged shoreline positions are shown; September to early November period recorded beach advance gradually till it peaks in January. Shoreline retreats from January onward (Austral winter) when waves averagely become larger (Figure 4d).

Daily waves (H_b and T_p) did not correlate with shoreline positions as beach morphologies do not respond instantaneously to the changing wave field. Interestingly, similar results were found at a nearby beach (Grand Popo, Bénin) where the short term evolution of the shoreline seems to be more affected by tidal cycles from neap to spring (Bahini, 2015). This is due to the large Relative Tide Index (Masselink and Short, 1993) value which is around 1, even though the environment is microtidal. On the other hand, at the event scale, waves have more influence on *Δ(X)* development. *Δ(X)* is observed to correlate significantly at 95% (p = 0.03) with H_b though with low value (r ~0.16).

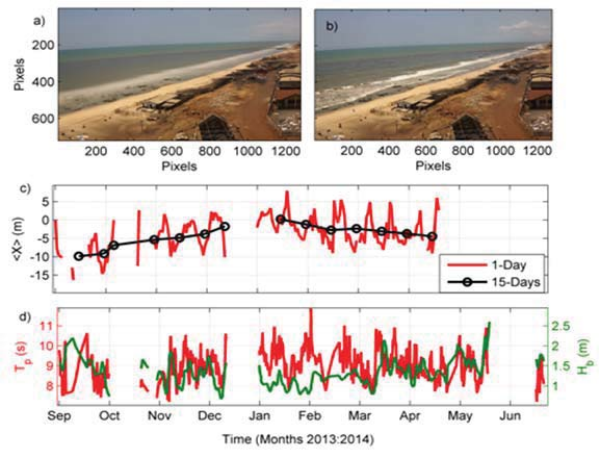

Figure 4. a) Timex b) Snapshot c) Daily (4 point moving average) and 15-Day shoreline locations <*X*> relative to the initial position <X_i> d) estimated H_b and T_p from video.

At the monthly scale, waves showed large correlation (r = 0.87) with <*X*> and *Δ(X)* than tides, *TR* (r = -0.57). This suggests waves have a strong influence on the shoreline location at seasonal scale. <*X*> correlates with alongshore non-uniformity (r= 0.3, significant at 95%) which means errors in <*X*> decrease with decrease in its values. Though it is too early to conclude, a preliminary recessive change of the beach is envisaged. This is in line with previous studies (Appeaning Addo *et al.,* 2008) who observed an erosion of 1.13 m/yr. along the Accra Coast. Mean beach slope of 0.03 from tides against the horizontal shoreline positions indicates dissipative characteristics based on Wright and Short (1984) classification.

Noteworthy, video-derived beach slopes showed seasonal changes that can be attributed to an adaptation to wave energy modulation: with Ω ranging from 2 (intermediate beach state) in summer to 5 (dissipative) in winter, with steeper and gentle slopes in summer and winter periods

Beach profiles are estimated over a distance of 500 m from camera location and seaward. However, the estimation of topography from video at James town should be further validated using field measurements in order to get more confidence and robust conclusions on beach state evolution and variability.

DISCUSSION AND CONCLUSIONS

On a Ghana coastline of over 550 km presenting a large diversity (embayed and open beaches, sandbarriers, rivermouths) with recurrent shoreline problems, this is the first video system that has been used to continuously collect information on nearshore waves and beach changes.

The predictions of the H_b and T_p from video images and hindcast data are in good agreement, with RMSE of 0.7 and 0.8, respectively. This highlights the accuracy of the video in estimating waves parameters. Shoreline changes at James town show a seasonal response to waves with accretion during the austral summer months (Nov-Jan) and retreat during the winter months. The link between short-term shoreline evolution and waves conditions is less clear, as found at Grand Popo beach, Benin (Bahini, 2015) where short term evolution is attributed to tidal modulation. Overall, beach profile is in more dissipative state than predicted by Wright and Short (1984) classification with the absence of intertidal sandbars as one might expect. Although small, the variability of the beach profile is detectable. The results of the beach profiles show minor features probably due to the presence of small rocks observed around the study area. These rocks are well exposed on the images during low tides.

Beach and shoreline change analysed using video data covering 11 months suggest that breaking wave conditions and intertidal beach morphology can be continuously monitored. The results are consistent with previous findings though we suggest that large number of images be taken to give large seasonal shoreline data and minimise errors. Video deriving wave characteristics and shoreline change from a long-term monitoring perspective proved to be doable along this Ghanaian beach.

ACKNOWLEDGMENTS

The authors give appreciation to the French institute of research for development (IRD), the Office of Naval Research (US-ONR) prioject and Ghana ports and Harbour Authority for their support and also grateful to Benjamin Okyere, Alexander Boateng, Agbemebiase Nunana and Wilson Ako for their

assistance. This research has received support from French grants through French INSU/CNRS EC2CO-LEFE/IRD and ANR (COASTVAR: ANR-14-ASTR-0019).

LITERATURE CITED

Aarninkhof, S.G.J., Turner, I. L., Dronkers, T. D.T. , Caljouw, M., and Nipius, L., 2003. A video-based technique for mapping intertidal beach bathymetry. *Coastal Engineering*, 49, 275–289.

Almar, R, Ranasinghe, R., Catalan, P. A., Senechal, N., Bonneton, P., Roelvink, D., Bryan, K. R., Marieu, V., and Parisot J. P., 2012a. Video-based detection of shorelines at complex meso-macro tidal beaches. *Journal of Coastal Research*, 28(5), 1040-1048.

Almar R, Cienfuegos R, Catalan PA, Michallet H, Castelle B, Bonneton P., and Marieu V., 2012b. A new breaking wave height direct estimation from video. *Coastal Engineering*, 61, 42-48.

Almar, R., Senechal, N., Bonneton, P., 2008. Wave celerity from video imaging: validation with in-situ Pre-ECORS data. *Proc. I. C. C. E.* 1 (5), 661–673.

Angnuureng, D.B., Almar, R., Senechal, N., Castelle, B., Appeaning Addo, K., Marieu, V., and Ranasinghe, R., 2015. Shoreline evolution under sequences of storms from video observation at a meso-macrotidal beach*. Geomorphology with major revision.*

Angnuureng, B. D., Appeaning Addo, K., and Wiafe G., 2013. Impact of sea defense structures on downdrift coasts: The case of Keta in Ghana. *Academia Journal of Environmental Sciences* 1(6), 104-121.

Appeaning Addo, K., Walkden, M., and Mills, J. P., 2008. Detection, Measurement and Prediction of Shoreline Recession in Accra, Ghana*. ISPRS Journal of Photogrammetry and Remote Sensing*, 63(5), 543-558.

Armaroli, C., and Ciavola, P, 2011. Dynamics of a nearshore bar system in the northern Adriatic: A video-based morphological classification. *Geomorphology*, *126*(1), 201-216.

Bahini, A., 2015. Etude par imagerie video de la reponse du Littoral de grand popo benin de 2013 a 2015. Implications pour la stabilite de la plage. CIPMA-Chaire UNESCO, Université d'Abomey-Calavi, M.Sc. Thesis, 21p.

Banno, M., and Kuriyama, Y., 2012. Multiple regression analysis of effects of bar and tide on shoreline change. *The Port and Airport Research Institute,* Kanagawa, 3-1-1, 239-0836.

Boak, E.H., and Turner, I.L., 2005. Shoreline Definition and Detection: A Review. *Journal of Coastal Research,* 21(4), 688–703.

Boateng, I., 2009. Development of Integrated Shoreline Management Planning: A Case Study of Keta, Ghana. *Paper presented at the FIG Working Week 2009.*

French, W. P., 2001. Coastal Defences: Processes, Problems and Solutions. *Psychology Press*, pp 5.

Holman, R.A., and Stanley, J., 2007. The history and technical capabilities of Argus. *Coastal Engineering,* 54, 477 – 491.

Jayson-Quashigah, P. N., Appeaning Addo, K., and Kufogbe, S.K., 2013. Shoreline monitoring using medium resolution satellite imagery, a case study of the eastern coast of Ghana. *Journal of Coastal Research*, 65, 511-516.

Ly, C. K., 1980. The role of the Akosombo Dam on the Volta river in causing coastal erosion in central and eastern Ghana (West Africa). *Marine Geology, 37*(4), 323-332.

Masselink, G., Russell, P., Turner, I., and Blenkinsopp C., 2009. Net sediment transport and morphological change in the swash zone of a high-energy sandy beach from swash event to tidal cycle time scales. *Marine Geology,* 267, 18–35.

Masselink, G., and Short, A., 1993. The Effect of Tide Range on Beach Morphodynamics and Morphology: A Conceptual Beach Model. *Journal of Coastal Research,* 9(3), 785-800.

Plant, N. G., and Holman, R. A., 1997. Intertidal beach profile estimation using video images, *Marine Geology*, 140, 1-24.

Puleo, J.A., Farquharson, G., Fraiser, S.J., and Holland, K.T., 2003. Comparison of optical and radar measurements of surf and swash zone velocity fields. *Journal of Geophysical Research*, *108*(3), 3100-3112.

Ruessink, B. G., Kuriyama, Y., Reniers, A. J. H. M., Roelvink,J. A., and Walstra, D. J. R., 2007. Modeling cross-shore sandbar behavior on the timescale of weeks. *Journalof Geophysical Research,* 112.

Sagoe-Addy, K., and Appeaning Addo, K., 2013. Effect of predicted sea level rise on tourism facilities along Ghana's Accra coast. *Journal of Coastal Conservation and Management*. 17(1), 155-166.

Smith, R. K., and Bryan, K. R., 2007. Monitoring beach face volume with a combination of intermittent profiling and video imagery. *Journal of Coastal Research*, 892-898.

Sterl, A., and Caires, S., 2005. Climatology, variability and extrema of ocean waves- the web-based KNMI/ERA-40 Wave Atlas. *International Journal of Climatology,* 25, 963–977.

Stive, M. J.F.,Aarninkhof, S. G.J., Luc Hamm., Hanson, H., Larson, M., Wijnberg, K. M., Nicholls, R. J., and Capobianco, M., 2002. Variability of shore and shoreline evolution. *Coastal Engineering.* 47, 211–235.

Stockdon, H.F., Sallenger, A.H., List, J.H. and Holman, R.A., 2002. Estimation of shoreline position and change using airborne topographic lidar data. *Journal of Coastal Research,*18(3), 502–513.

Stokes, C, Davidson, M., and Russell P., 2015. Observation and prediction of three-dimensional morphology at a high-energy macrotidal beach. *Geomorphology*, 243,1–13.

The Wamdi Group, 1988. The WAM Model-A Third generation ocean wave prediction model*. Journal of Physical Oceanography,* 18, 1775–1810.

Turner, I.L., and Leatherman,S.P., 1997, Beach Dewatering as a 'Soft' Engineering Solution to Coastal Erosion – History and Critical Review. *Journal of Coastal Research*, 13(4), 1050-1063.

Wiafe G., Boateng I., Addo, A. K., Quashigah, P.N., Ababio S.D. and Laryea S. W., 2013. Handbook of Coastal Processes and Management in Ghana. *The Choir Press*, pp., 274.

Wright, L.D., and Short, A.D., 1984. Morphodynamic variability of surf zones and beaches: A synthesis. *Marine Geology*, 56, 93-118.

Journal of Coastal Research	SI	75	1027 - 1031	Coconut Creek, Florida	2016

Alongshore variations in morphology and incident wave energy on a human-impacted coast: Agadir, Morocco.

Ismail Aouiche[‡*], Lahcen Daoudi[‡], Edward J. Anthony[†], Mouncef Sedrati[††], Abdelhadi El Mimouni[‡], Philippe Dussouillez[†]

[‡] Laboratoire de Géosciences et Environnement, Faculté des Sciences et Technique, Université Cadi Ayyad - Marrakech, B.P.549, Marrakech, Morocco.

[††]Equipe Géosciences Marines et Géomorphologie du littoral Domaine océanique UMR6538 GMGL Université de Bretagne sud, Vanne, France.

[†] Aix Marseille Univ, Institut Universitaire de France, CEREGE, UM 34, Europôle Méditerranéen de l'Arbois, B.P. 80, 13545 Aix en Provence, France.

www.cerf-jcr.org

www.JCRonline.org

ABSTRACT

Aouiche, I.; Daoudi, L.,Anthony, J.A.,Sedrati, M., and Dussouillez, P., 2016. Alongshore variations in morphology and incident wave energy on a human-impacted beach: Bay of Agadir, Morocco. *In:* Vila-Concejo, A.; Bruce, E.; Kennedy, D.M., and McCarroll, R.J. (eds.), *Proceedings of the 14th International Coastal Symposium* (Sydney, Australia). *Journal of Coastal Research*, Special Issue, No.75, pp. 1027 - 1031.Coconut Creek (Florida), ISSN 0749-0208.

Beaches in developing countries are increasingly affected by human impacts, notably the construction of harbors and tourist infrastructure. In Morocco, the city of Agadir is a fine example of this situation. Agadir was destroyed by an earthquake in 1960 (5.7 on the My scale and 60,000 dead). The Agadir city front corresponds to a semi-sheltered bay that has been strongly impacted by economic development and rapid (> 10% a year) demographic growth in the course of its recovery following this earthquake. The northern sector of the bay is sheltered by a commercial harbor constructed in 1988. In order to understand how this harbor has affected sediment circulation, the morphology and hydrodynamics of the beach have been monitored since 2012. This study discusses beach morphological variations between the harbor-sheltered northern sector and the exposed southern sector. The offshore and nearshore wave regime, analysed using the MIKE 21 coupled model Fm, is largely dominated by waves approaching from the north. The modeling results show that wave energy attenuation between the inner shelf and the shore in the northern sector ranges from 30% to 80% as a result of diffraction caused by the harbor breakwater, whereas the southern sector is exposed to much higher waves. Two digital elevation models obtained in March 2012 and April 2015, confirm these expected results from the alongshore wave-energy gradient, and show that the northern sector of the beach is largely dominated by accretion, whereas the southern sector is undergoing erosion.

ADDITIONAL INDEX WORDS: *Intertidal beach evolution, Wave-current modelling, Sediment transport capacity.*

INTRODUCTION

Coastal systems where sediment transport is perturbed by engineering structures on the shoreline and shoreface provide examples that throw light on sediment exchange links between coastal units. The impacts of engineering structures on embayed beaches can, for instance, lead to various types of departures from the 'static bay beach' plan shape (Hsu *et al.*, 2010), depending on the dimensions of these structures, and bay beach planform aspects such as wave incidence angle (Hsu *et al.*, 1989) and degree of bay beach indentation (Spagnolo *et al.*, 2008; Uda *et al.*, 2010; Schiaffino *et al.*, 2011; Sedrati and Anthony, 2007). Achieving the objective of highlighting these links on coasts requires methods that jointly address coastal morphological change and hydrodynamic forcing.

The Agadir coast of Morocco shows a typical dilemma facing many developing countries, where economic activities are exerting an increasingly stronger stranglehold on coastal resources, making the coast susceptible to erosion and sediment loss. Agadir Bay is one of the most clearly anthropogenic sectors of Morocco's coasts, and one of the country's major urban poles. The coastal region and the city of Agadir (city population in 2012: 600,000) were struck in 1960 by an earthquake (5.7 on the MyScale) that virtually completely destroyed the city. The rapid reconstruction and strive to achieve economic development in the region in the wake of this earthquake have had, unfortunately, a heavy toll on shoreline stability. Agadir Bay epitomizes the effects of dwindling sediment supplies caused by coastal constructions and aeolian dune destruction, but has also hosted a rapidly growing city (annual population growth > 10%) whose twin economic drivers are the commercial harbor and tourism.

In the past three decades, various significant structures have been built along Agadir Bay. In addition to the commercial harbor, a fishing harbor and marina, and a beach defense system,

DOI: 10.2112/SI75-206.1 received received 15 October 2015; accepted in revision 15 January 2016.
*Corresponding author: aouiche31@gmail.com
©Coastal Education and Research Foundation, Inc. 2016

and in the near future many more developments are planned. Optimal planning and management of a coast depends on its stability, which, in the case of coasts bound by sandy beaches, is directly linked to the surf zone dynamics. Sea surface waves (short- to long-period waves) dissipate their energy at the coast, deforming the coastline. The installation of coastal structures, especially in bays, influences the characteristics of waves, mainly by diffracting them (*e.g*, Sedrati and Anthony, 2007).

Using a combined methodological approach based on wave-current modeling and beach topographic surveying, the present study highlights the close links between variations in the bed of the intertidal beach and the cross-shore and longshore sand transport pathways prevailing in the surf zone. In this paper, we also explore the wave-generated longshore current patterns and associated littoral processes predicted using the Mike-21 suite of numerical models (developed by the Danish Hydraulic Institute).

STUDY AREA

Located on the Atlantic coast of Morocco (Figure 1), the Agadir coast is the central part of a 35 km-long sandy shoreline bound in the north by Cape Ghir and in the southwest by Cape Aglou. Agadir Bay and the adjacent smaller Anza beach north of the commercial harbor belong to the Souss Massa plain which covers an area of about 23,950 km2. The climate of the Souss Massa plain is arid to semi-arid. The proximity of the ocean and the influence of the cold Canary Current mitigate the arid climate (Aouiche *et al.*, 2013).

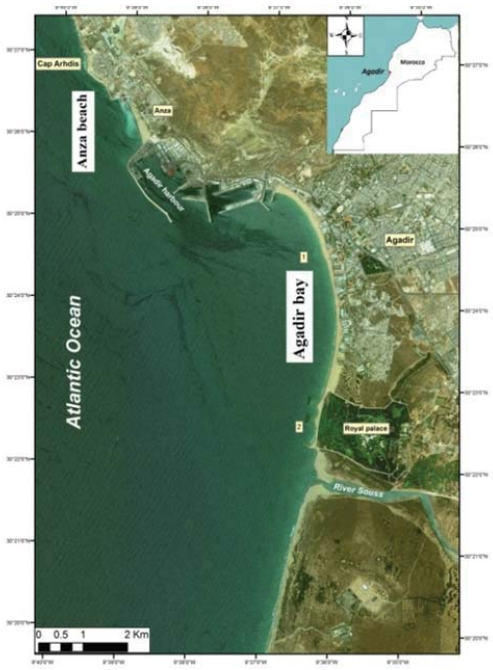

Figure 1. Agadir Bay and the adjacent Anza pocket beach on the Atlantic coast of Morocco (Google Earth, 2013). Numbers 1 and 2 show breakwater constructed in 1968 and beach defence system composed of two breakwaters and a groyne constructed in 1994 (Image source: GoogleEarth©).

The evolution of the coastline of Agadir is related to a complex combination of natural and anthropogenic factors. Harbour development, tourism, and urban growth have seriously disrupted the natural sediment balance of the coast. Since the 1990s, foredunes have been largely destroyed by overbuilding and linear shoreline urbanization driven by tourism. In places, the foredunes have been completely flattened and the sand used to build infrastructure and hotels along the beach (Aouiche *et al.*, 2015). The pocket beach of Anza is a product of these developments, having formed against part of the main harbor breakwater

Agadir Bay is exposed to relatively energetic waves from the North Atlantic. Daily forecasts from the wave monitoring station SIMAR 44 (with coordinates 35.5 N and 10 E and run by the Ports Authority of Spain (http://www.puertos.es) offshore of Agadir, show that waves from NW largely dominate in both winter and summer. More than 70% of waves in winter have significant heights ranging from 1.5 to 3.5 m, and typical peak periods of 11 to 15 s. In summer, the directional range is also dominantly from the north, and more than 90% of incoming waves during this season have significant heights ranging from 1 to 2 m and typical peak periods of 8 to 10 s. Tides in Agadir Bay are semi-diurnal and mesotidal with a mean spring range of 2.9 m and a mean neap range of 1.3 m. Tidal currents are very weak, of the order of 0.1 m/s, with a circular pattern within the bay (Aouiche *et al.*, 2015). The bay is composed of sandy facies. The coarse fraction (> 80 µm accounts for 78.7% to 99%, the rest composed of finer sand fine) (Aouiche *et al.*, 2015).

METHODS

In order to characterise morphological changes and sand transport in Agadir Bay and Anza beach, and derive a sediment budget, two methodological approaches have been adopted in this study. The first relates to topographic surveying of the bay beach and the second the application of the hydrodynamic model MIKE 21 in order to understand the hydrodynamic functioning of the bay.

Offshore wave parameters (mean significant wave height Hs, peak wave period Tp, and direction θ) over the survey time-span (see below) were obtained from daily forecasts generated by the Spanish network of wave measurements mentioned above).

Sediment budget determinations were obtained from two digital elevation models, the first in March 2012 and the second in April 2015, from the harbor entrance to the limits of the royal palace. The surveys were carried out using a Leica Total Station, with an accuracy of 5 cm, and covered the beach down to a depth of approximately 1.3 m below the local mean spring low tide level. We condensed the data to extract digital elevation models, based on kriging, which has been demonstrated by several authors (Robinson, 1994; Bourgault and Marcotte, 1997; Guillaume, 1977) as being the most appropriate method for digital elevation model construction. 53 sediment samples were collected in the intertidal zone, and mean size determined by wet laser scattering

The mapping of hydrodynamic forcing conditions is a preliminary phase in producing model simulations. For each combination of wave parameters, the frequency of occurrence (p) is calculated. Eight scenarios having a significant contribution and being representative of swell waves offshore of

Table 1. *Wave reanalysis data provided by Puertos del estados (based on 58-year wave dataset).*

Wave conditions	Hs (m)	Tp (s)	Direction (N°)	Probability of Occurrence
1	1.5	11	337.5	34
2	2.5	12	337.5	16
3	3.5	14	337.5	4
4	1.5	11	315	12
5	2.5	13	315	7
6	3.5	14	315	3
7	1.5	11	292.5	3
8	2.5	13	292.5	3
			Total	82

the limits of the model were selected. Their characteristics are summarized in Table 1.

Model bathymetries were created on the basis of the survey realized by the Moroccan Ports Authority in 2012 and data points prepared using triangulation. The alongshore transport was estimated using the empirical formula of Soulsby (1997). Though many formulas exist for the computation of longshore drift, the best known and the simplest is the CERC formula (Coastal Engineering Research Center, 2001). A variety of versions have been used in modelling, differing chiefly in their treatment of the wave group velocity Cg and wave-breaking criterion. The CERC formula can be converted (Fredsoe and Deigaard, 1992) to a dimensionally consistent form (Soulsby, 1997). It uses the longshore flow pattern generated from wave heights and hydrodynamic modeling (HD model) obtained from the spectral wave model (SW) as input. The annual sediment transport at 20 points was estimated by computing the longshore drift for each combination of wave height, period and direction, and assigning the associated probability for the particular combination.

RESULTS

The DEM differentials for the intertidal beach between 2012 and 2015 are shown in Figure 2. Areas of erosion and accretion were identified by overlay of the two DEM maps. We note that the northern half of Agadir beach is largely dominated by accretion, whereas the southern half clearly evinces erosion, evidenced by significant bed lowering. The sediment budget calculated from the DEM differentials shows a net subaerial beach loss of about 219,000m^3, which corresponds to an annual loss of 73,000 m^3/year.

Wave simulations show that the breakwater and dike of the commercial harbour implanted in 1989 lead to a significant decrease in wave energy, as expected, as a result of wave diffraction (Figure 3). This decrease in energy is very notable in the northern part of the bay. The south of the bay is exposed to much higher levels of incident energy (Figure 3). The modeling results show that offshore swells reach the southern sector of the bay from N290°, resulting in an incidence angle of 6° to 14° relative to the shoreline. Artificial structures such as the breakwaters and groynes on the coast, especially those in the south in front of the royal palace, modify the direction of nearshore wave propagation.

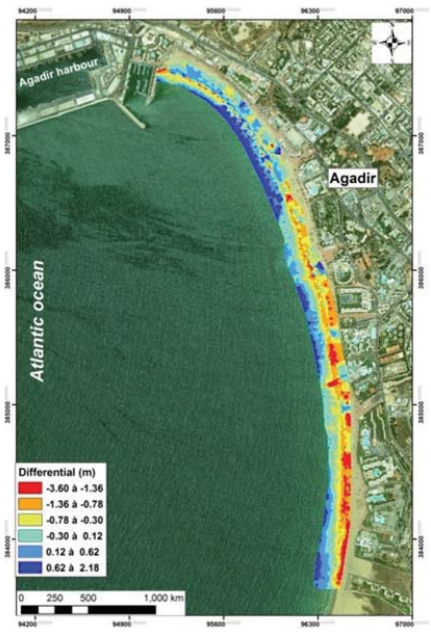

Figure 2: Differential between digital elevation models (March 2012-April 2015) of the intertidal beach in Agadir Bay (Image source: GoogleEarth©).

The nature of the generated currents is primarily influenced by the angle of incidence of the waves during breaking near the shore. The focus here is on the currents for the two areas: at Anza beach, situated between Cape Arhdis and the commercial harbour (Figure 1), and Agadir Bay (Figure 1). At Anza beach, the longshore flow pattern is towards the south whatever the angle of incidence of the swell. The speeds are high throughout the study area (greater than 0.5m/s). For most of the swells, flows diverge at the breakwater of the commercial harbour, with oriented offshore at the foot of the breakwater (Figure 4). In Agadir Bay, the computed current vectors, for the majority of conditions tested, show two major trends with two potential drift directions: one oriented to the north and the second to the south, creating a divergence in the centre of the bay (Figure 5). For all conditions, a recirculation of the current is observed in the shadow area of the harbour, in the north of Agadir Bay, generating currents towards the north (Figure5). In the southern sector, we note that the current speed increases gradually as one moves from north to south (Figure5). Artificial structures in the southernmost sector in front of the royal palace generate spreading of the wave rays and a decrease in wave energy and wave height. We note also the formation of rip currents in this southernmost sector, just updrift of the beach breakwaters (Figure 5). The average annual sediment transport volumes are extracted from the model for each wave height, period and direction combinations and the associated probability is assigned. The net annual volumes for 20 points are presented in Figure6. The results show large quantities of sand moving

alongshore due to the action of waves. The highest transport rate, of the order of 440,000 m³/year is observed at Anza beach (Point 1). As sand approaches the foot of the harbor breakwater, it is diverted seaward, to the tune of 76,600 m³/year. Within Agadir Bay, the sediment volume drifting along shore becomes gradually more significant from north to south, increasing from 20,000 to 200,000 m³/year.

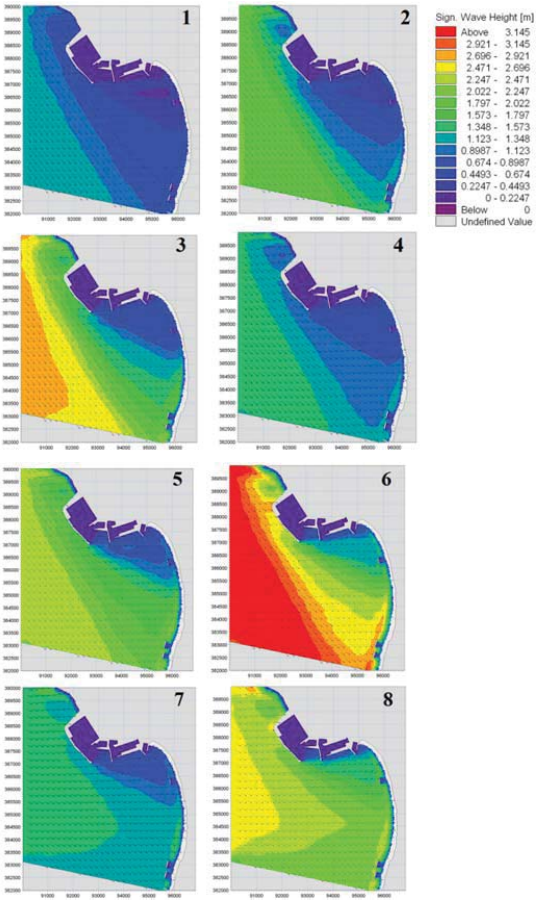

Figure 3. Wave height contours for different conditions (1 to 8, See Table 1).

In the north of Agadir Bay, the sediment transport capacity varies from 20,000 to 40,000 m³/year. A drift divergence zone is present in the centre with a convergence area behind the breakwater built in 1968. In the southern sector of Agadir Bay, the sediment transport capacity varies from 30,000 to 200,000 m³/year. In the southern sector of the bay, there are two convergence zones behind the breakwaters constructed in 1994 in front of the royal palace. About 4000 m³/year are transported offshore at the updrift part of this defense system.

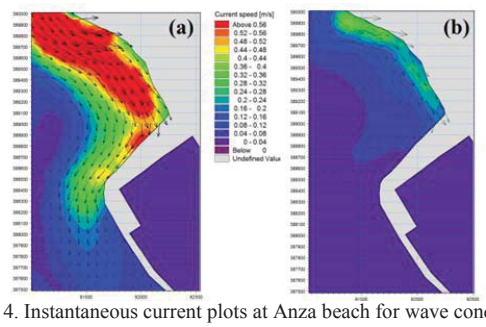

Figure 4. Instantaneous current plots at Anza beach for wave conditions 1 and 7. (a) Condition 3; (b) Condition 7.

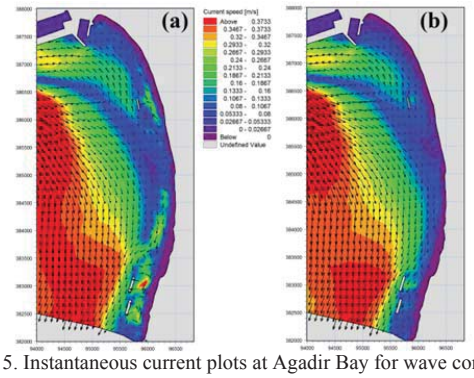

Figure 5. Instantaneous current plots at Agadir Bay for wave conditions 1 and 7. (a) Condition 3; (b) Condition 7.

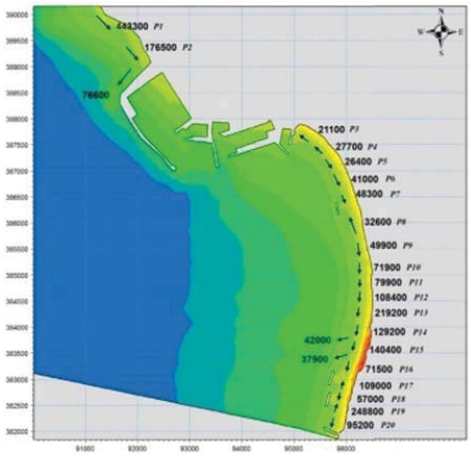

Figure 6. Net longshore transport volumes at selected sections of the Agadir coast.

If we calculate the total annual loss of sand from point P3 to point P13, which corresponds to the area of the DEMs, we obtain a value of around 60,000 m³/year which is largely in agreement with the value of 73,000 m³/year obtained from the two DEMs of March 2012 and April 2015.

DISCUSSION

In this study, intertidal beach change over 2 years has been monitored in order to obtain a partial regional sediment budget of Agadir and Anza beaches. Wave-current modelling was used to characterize the hydrodynamics, and more specifically the impact of coastal engineering structures in sand transport pathways involved in these changes. These approaches yield concordant results that clearly demonstrate the linkages between the intertidal beach sediment balance, and coastal sand transport pathways at a medium-term scale. The results from wave propagation simulation and wave incidence at the coast and the resultant current vectors agree well with intertidal beach changes in terms of accretion and recession.

The study of intertidal beach evolution highlights two contrasting sectors between 2012 and 2015; accretion tends to increase as we move north. In contrast, the southern part of Agadir Bay shows overall erosion. At Anza beach, parallel to the commercial harbor jetty, as sand drifting alongshore is trapped against the northern harbor breakwater flank there will be progressive subaqueous accretion and storage over an increasingly deeper shoreface.

The important role of Agadir harbor, both in its smaller ancestral form as a fishing harbour built in 1918, and since 1988 in the form of the present large commercial harbor, in promoting these changes is manifest. Shoreline orientation and the commercial harbour are responsible for a complex hydrodynamic pattern. The northern sector is protected from wave action as the harbour breakwaters have reduced the incident wave energy, leading to deposition. In contrast, the southern sector is exposed to direct wave action and characterized by severe erosion. The situation is critical in this dominantly eroding southern sector, where seaside tourist facilities and the seafront promenade are now increasingly exposed to waves as the beach has narrowed. Artificial structures such as the breakwaters and groynes, especially those in front of the royal palace, disrupt the wave energy, resulting in both erosion and accretion. The downdrift erosion is a classic illustration of what Hsu *et al.* (2010) have referred to as 'bay beach reshaping' resulting from harbour effects on longshore sediment transport.

CONLUSION

The results shown in this work provide a key element in understanding the evolution of a beach strongly impacted by coastal engineering and development infrastructure. The erosion problem in the southern sector of Agadir Bay is delicate, and has several causes, among which dune destruction and the effects of Agadir harbour on alongshore sand transport.

The two complementary approaches, very-high resolution beach topographic surveys and hydrodynamic modeling, yielded concordant results that clearly demonstrate the linkages between sand transport pathways and intertidal beach sediment storage or loss. Successful management of the coastal zone in Agadir Bay, as elsewhere, requires a good grasp of these linkages and the way they are perturbed by developments on the seafront.

ACKNOWLEDGEMENTS

Financial support for this study was provided by the Projet d'Action Intégrée Hubert Curien "Volubilis" N° MA/13/290.Mr AOUICHE receives a scholarship from the National Center for Scientific and Technical Research (CNRST, Morocco) that we like to thank. LPEE-Casablanca and DPDPM-Rabat are thanked for the various supporting documents provided.

LITERATURE CITED

Aouiche, I. ; Daoudi, L., Anthony, E.J., Sedrati, M., Ziane, E., Harti, A. and Dussouillez, P., 2015. Anthropogenic effects on shoreface and shoreline changes: Input from a multi-method analysis, Agadir Bay, Morocco. *Geomoropholgy* 254, 16-3 doi:10.1016/j.geomorph.2015.11.013.

Aouiche, I.; Daoudi, L., Harti, A., Ziane, E., and Ouahmane, B., 2013. Etude multidisciplinaire de l'impact des aménagements côtiers sur l'évolution du littoral de la baie d'Agadir (Maroc atlantique). *Actes du Colloque Quaternaire du Nord-Ouest de l'Afrique*, 21-22.

Bourgault, G. and Marcotte, D. 1997. Multivariable variogram and its application to the linear model of co-regionalization. *Mathematical Geology*, 23, 899-928.

Coastal Engineering Research Center, 2001.*CoastalEngineering Manual, fifthed. U.S. Army Corp. Eng., Washington, D.C.*

Fredsoe, J. and Deigaard, R., 1992. Mechanics of coastal sediment transport. In: Advanced Series on Ocean Engineering, vol. 3.*World Scientific Publishing*.

Guillaume, A. 1977. Analyse des variables régionalisées. *Editions Doin, Paris*, 180 p.

Hsu, J.R.C.; Silvester, R., and Xia, Y.M., 1989. Generalities on static equilibrium bays. *Coastal Engineering,* 12, 353–369.

Hsu, J.C.R.; Yu, M.J., and Yu, Lee, F.C., 2010. Static bay beach concept for scientists and engineers: A review. *Coastal Engineering,* 57, 76-91.

Robinson, G.J., 1994. The accuracy of digital elevation models derived from digitized contour data. *Photogrammetric Record,* 14, 805-814.

Schiaffino, C.F.; Brignone, M., and Ferrari, M., 2011. Application of the parabolic bay shape equation to sand and gravel beaches onMediterranean coasts. *Coastal Engineering,* 59, 57-63.

Soulsby, R.; 1997.Dynamics of Marine Sand andannual forPractical Application.Thomas Telford Publications.

Spagnolo, M.; Llopis, I.A., Pappalardo, M., and Federici, P.R., 2008. A new approach for the study of the coast indentation index. *Journal of Coastal Research,* 24, 1459-1468.

Uda, T.; Serizawa, M., Kumada, T., and Sakai, T., 2010. A new model for predicting three-dimensional beach changes by expanding Hsu andEvans' equation. *Coastal Engineering* 57, 194-202.

Sedrati, M. and Anthony, E.J., 2007. A brief overview of plan-shape disequilibrium in embayed beaches: Tangier Bay, Morocco, revisited*. Méditerranée*, 108, 125-130.

Journal of Coastal Research	SI	75	1032 - 1036	Coconut Creek, Florida	2016

Open Sandy Beach Morphology and Morphodynamic as Response to Seasonal Monsoon in Kuala Terengganu, Malaysia

Effi Helmy Ariffin[1, 2], Mouncef Sedrati[1], Mohd Fadzil Akhir[3], Rosnan Yaacob[2] and Mohd Lokman Husain[2,3]

[1]Equipe Géosciences Marines et Géomorphologie du Littoral, Domaines Océaniques UMR6538-GMGL, Université de Bretagne-Sud, Vannes, France

[2]School of Marine Science and Environment, Universiti Malaysia Terengganu, Kuala Terengganu, Malaysia

[3]Institute of Oceanography and Environment, Universiti Malaysia Terengganu, Kuala Terengganu, Malaysia

www.cerf-jcr.org

www.JCRonline.org

ABSTRACT

Ariffin, E.H.; Sedrati, M., Akhir, M.F., Yaacob, R., and Husain, M.L,. 2016. Open Sandy Beach Morphology and Morphodynamic as Response to Seasonal Monsoon in Kuala Terengganu, Malaysia. *In:* Vila-Concejo, A.; Bruce, E.; Kennedy, D.M., and McCarroll, R.J. (eds.), *Proceedings of the 14th International Coastal Symposium* (Sydney, Australia). *Journal of Coastal Research*, Special Issue, No. 75, pp. 1032 – 1036, Coconut Creek (Florida), ISSN 0749-0208.

Understanding beach morphology and morphodynamic changes is important in regions where there is a large amount of recreation and development. Kuala Terengganu beaches has many anthropogenic infastructure such as an extension to an airport runway similar in design to a groin which affect morphology and morphodynamics in response to seasonal monsoon storms. Seasonal monsoon storms are one of the most important controls on the cycle of erosion and accretion on beaches. Beach profile data and wave modelling were used to determine the response of five beaches on the north of Kuala Terengganu to Northeast and Southwest seasonal monsoons. The beaches along the Kuala Terengganu state coast before the construction of the airport extension exhibited a classical morphodynamic response. This includes erosion during Northeast monsoon and accretion/recover during Southwest monsoon. The airport construction disturbed and changed normal coastal evolution. Two distinct sediment cells were generated, each having developed a proper morphodynamic response within the Northeast and Southwest monsoon wave regimes.

ADDITIONAL INDEX WORDS: *Beach Morphology and Morphodynamic; Northeast Monsoon Storm.*

INTRODUCTION

The open sandy beach is a natural sediment buffer for coastal systems. Erosion and accretion this buffer are correlated with high and low energy wave conditions. High energy waves erodes sand from the beach, while low energy waves supplies causes it to accrete. Stive *et al.* (2002) created a storm model which predicts rapid sediment erosion during storms and subsequent slower accretion in the post-storm period. This model may be applied to natural areas expressing a seasonal variable wave energy regime. However, anthropogenic impacts on coastal areas (eg Harbor jetties, groins and breakwaters) may affect sediment supply and transport. The coastal areas under both natural and anthropogenic impacts can suffer from severe erosion as the case of Taiwan and Sulawesi (Indonesia) coasts (Hsu *et al*., 2007) and Umar *et al*., 2015).

The coast of Peninsular Malaysia can be divided into two parts, West and East. The West Coast express a low wave energy regime because of the protection of Sumatera, whereas the East Coast faces the South China Sea is experiences high wave energy (Ghazali, 2006). Kuala Terengganu in the East Coast of Peninsular Malaysia territory is governed by two monsoonal wind and waves regimes.

The Northeast Monsoon lasts from the end of October to middle of March and produces strong waves along the eastern coast of Peninsular Malaysia. However, during the Southwest Monsoon, which lasts from the middle of May till September, moderate waves are generated along the east coast of Peninsular Malaysia. The significant wave height during Northeast and Southwest Monsoon conditions on the east coast of Peninsular Malaysia varies from 2 m and 0.5 to 1 m respectively. The Sulawesi coast (Indonesia) is affected by the same two monsoonal regimes has a maximum significant wave height up to 3 meters and is affected by a severe erosion (Umar *et al*., 2015). Furthermore, the strong waves can affect and modify erosion in coastal zone areas during a monsoon storm (Chempalayil *et al*., 2014).

Considering the seasonal changes in wind-wave monsoon regimes and the net longshore drift from the southeast to northwest, two morphological annual stages which evolve erosional and depositional phases were defined in this coast (Rosnan *et al.,* 2003). Recently, the construction of Kuala Terengganu airport extension (similar to a groin) and several coastal protection structures along this coast perturbed the natural sediment balance equilibrium and the longshore

DOI: 10.2112/SI75-207.1 received 15 October 2015; accepted in revision 15 January 2016.
*Corresponding author: effihelmy@umt.edu.my
©Coastal Education and Research Foundation, Inc. 2016

sediment drift circulation under the variable monsoonal waves regimes.

Using a beach profile survey and wave modelling parameters, this paper investigates seasonal patterns of beach erosion and accretion along the Kuala Terengganu coast. Furthermore, we focused on the interpretation of longshore processes prevailing on this coast in term of natural versus human-induced perturbation of a natural/anthropogenic beach system.

Study Area

The study area comprises almost 15 km of the Kuala Terengganu coastline areas, extending from Kampung Batu Rakit to Kampung Seberang Takir (Figure 1). This coast is backed by a Quaternary coastal plain for most of its length. A 1km airport tarmac extension was constructed in 2010 (Figure 1). This construction interrupted the longshore drift circulation and resulted in marked variations in shoreline width. A number of rivers, the largest of which is Terengganu River occur on this coast (Figure 1).

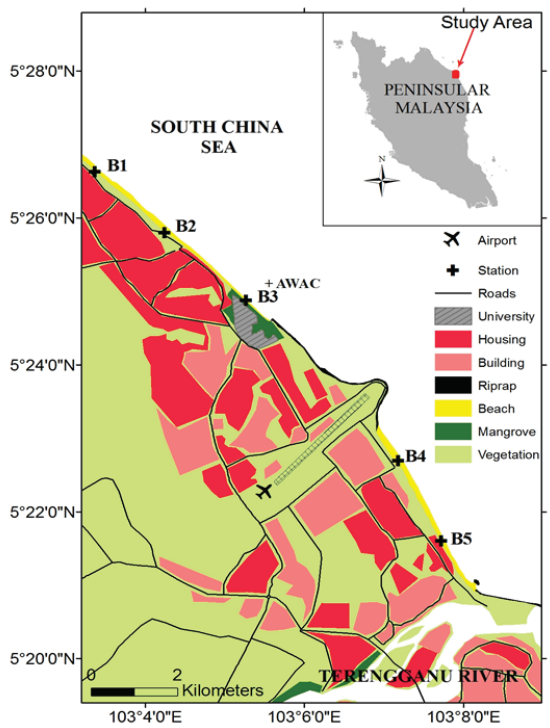

Figure 1. Study area with the location of the five surveyed beaches and the extended airport tarmac (form of a groin) constructed in 2010.

The coastal current at the Kuala Terengganu coastline flows more or less parallel to the coastline. Akhir and Chuen (2011) noted that during the Northeast Monsoon season, the surface current runs southward along the east coast of Peninsular Malaysia. However, during the Southwest Monsoon, the current moves to the north and the currents change with similar strength running to the south. Strong waves are prevalent during the Northeast Monsoon when the winds are onshore; during the southwest monsoon the winds are offshore and low energy (Rosnan *et al.*, 2003).

Tides are semi-diurnal and micro to meso-tidal. The Terengganu coast has a wet equatorial climate, which is which experiences high temperatures all year round and sporadic heavy rainfall, specifically during the Northeast Monsoon (Figure 2) when the average annual rainfall is 2987.9 mm/ year. The major weather systems, determining the wind speed in Sultan Mahmud Airport, Kuala Terengganu, during Northeast and Southwest Monsoon, are approximately 3.0 m/s and 1.7 m/s respectively.

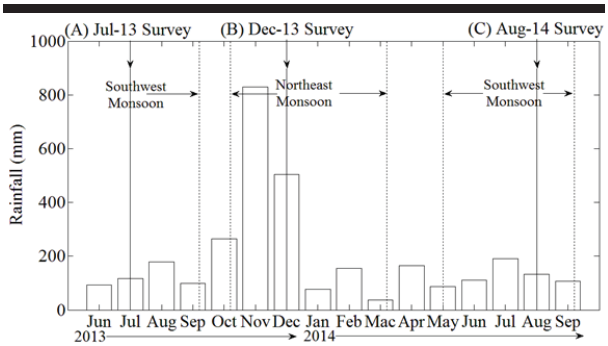

Figure 2. Monthly-average rainfall measured at the Sultan Mahmud Airport, Kuala Terengganu from June 2013 to September 2014 (refer to Figure 1 for location). Arrow line represents a profile survey: (A) July 2013; (B) December 2013; and (C) August 2014.

METHODS

Beach profile surveys were performed fourteen times (monthly) from July 2013 to August 2014 on the five studied beaches (B1 to B5, Figure 1). Beach profile surveys conducted at low tide using a theodolite, levels, and a Total Station (Topcon GPT-3100N). The profile started in the dunes (start vegetation) at a benchmark and ended in about 0.5 m water depth with the average of beaches width between 40-80 m. The benchmark elevations for each of the beaches were adjusted to the DTGSM datum.

The seasonal volume change of beach sand was initiated during the Southwest Monsoon in July 2013 (base profile), followed by profiling in Northeast Monsoon on December 2013. However, to quantify the cycle of seasonal change, profiling on August 2014 (Southwest Monsoon) was also undertaken. For each season, profiling was compared to the base profile of July 2013.

Wave measurements (*in-situ* data) were recorded with a current profiler and a wave directional system (AWAC) deployed in bottom-mounted frame at sub- tidal zone areas (10 m depth) from 28 November 2013 to 28 February 2014 in front of B3-UMT beach (Figure 1). Wind and wave modelling was generated by Mike-21 to estimate wave pattern during the survey period (June 2013 to September 2014).

The Spectral Wave Flexible Mesh (SW) was calibrated by testing the influence of bottom friction and its influence on wave breaking at the AWAC measurement location. It was shown that the combination of adjustable parameters leading to the best

agreement between the measured and calculated data sets could adjusted by using a wave growth formula. Bottom dissipation gives no significant effect on the wave height and wave period since the AWAC measurement point is located in deep water. The significant wave height comparison shows close correlation between measured and modelled results; with the root mean squared value calculated is larger for significant wave height (RMSE=0.29).

RESULTS

The beach volume changes of the five surveyed beaches between July 2013 and August 2014 is summarised in Table 1 and the morphological changes of these beaches are shown in Figure 3. This study showed B1, B2 and B3 in the north (Zone A) part of the airport; while, B4 and B5 in the south (Zone B) part (Figure 4).

Batu Rakit (B1)

Batu Rakit is located on the north of Kuala Terengganu coastline (Figure 1). Figure 3 shows sediment deposition on backshore and foreshore with an increase of 10% in beach volume during Northeast Monsoon. During Southwest Monsoon deposition on the backshore and foreshore are shown; whereby this season still shows deposition with a decrease on percentage of beach volume (7.39 %).

Pengakalan Maras (B2)

Pengkalan Maras located on the north of Kuala Terengganu coastline and the extended Sultan Mahmud Airport (Figure 1). Backshore and foreshore on B2 show erosion during both Northeast Monsoon (-5.08 %) and Southwest Monsoon (-11.35 %) respectively (Figure 3).

UMT (B3)

B3 is Universiti Malaysia Terengganu beach located 3 km near the northern part Sultan Mahmud airport. Universiti Malaysia Terengganu (UMT) beach was resurfaced (on 20-30 m distance) on November 2013 after been victim of a major erosion from September to October 2013. However, we measured significant backshore accretion (6.33 %) during the Northeast Monsoon. In April 2014, the entire UMT beach was collapsed (Figure 3); while the beach eroded during the Southwest Monsoon by 2.65 % of the entire sand volume.

Teluk Ketapang (B4)

Teluk Ketapang is located south of the Kuala Terengganu coastline and the Sultan Mahmud Airport (Figure 1). Figure 3 shows the deposition and erosion on backshore and foreshore respectively, with a percentage of sand volume loss of 3.27 % during Northeast Monsoon. However, during the Southwest Monsoon deposition the accretion on backshore and foreshore reached 2.07% of the initial profile sand volume.

Seberang Takir (B5)

Seberang Takir is located along the south of Kuala Terengganu coastline and the extended Sultan Mahmud Airport (Figure 1). During the Northeast Monsoon, the profile loss of sediment reached up -10.69 % while during the Southwest Monsoon, 19.27 % of sediment gain was measured on backshore and foreshore areas of this profile.

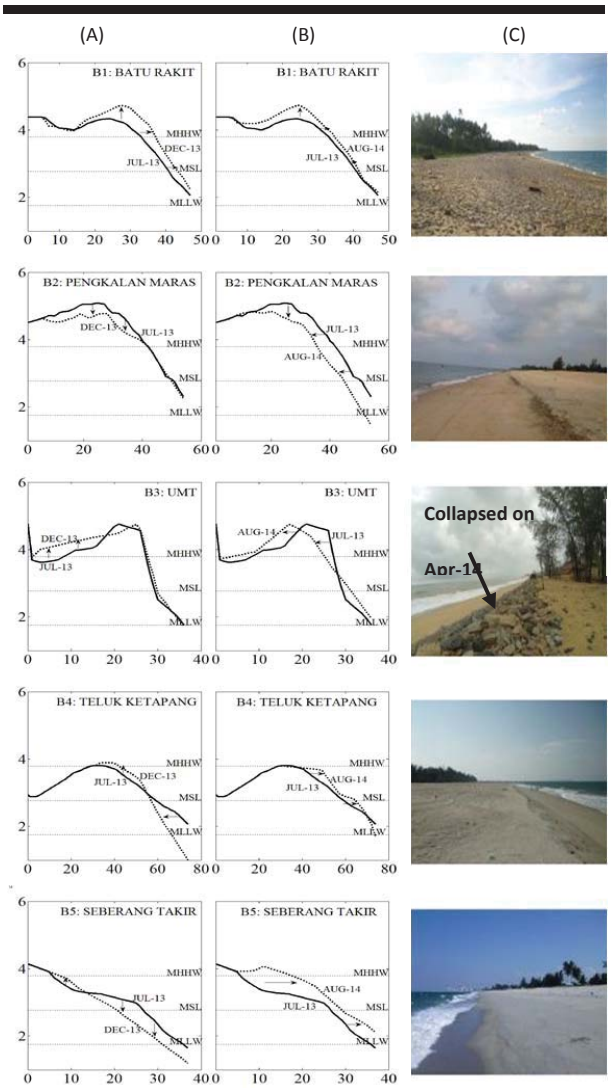

Figure 3. Beach profile sequences for the five surveyed beaches along Kuala Terengganu coast (elevation are relative to DTGSM datum) and July 2013 referred as base profile: (A) Northeast Monsoon-December 2013; (B) Southwest Monsoon-August 2014; and C) field observation on August 2013. The solid line represents the beach profile during July 2013 and the dashed line represents December 2013 and August 2014 profiles.

The volume sediment variation *i.e.* erosion and deposition, was referenced to July 2013 profile considered as a base profile; volume changes during seasons are compared and presented in

Table 1 and Figure 4. The north (Zone A) of the study area shows B1 and B3 accretion during Northeast Monsoon and decrease in volume during Southwest Monsoon. However, B2 is moderately and highly erosional during the Northeast and Southwest Monsoon respectively. Lastly, B4 and B5 located in the south (Zone B) of the study area show erosion and deposition during Northeast and Southwest Monsoon respectively.

Table 1. *Beach volume sequence for five beaches along Kuala Terengganu coast with comparison profile of seasons. The minus '-' value indicates the volume of sand eroded; plus '+' value indicates the volume of sand deposited (refer to Figure 3 for the 2-D graph).*

Profile Name	Jul-13	Dec-13	Aug-14	A	B
	Volume in cubic meters				
B1	109.72	120.69	117.83	10.00	7.39
B2	179.95	170.81	159.53	-5.08	-11.35
B3	90.90	96.66	93.31	6.33	2.65
B4	236.10	228.39	240.98	-3.27	2.07
B5	76.31	68.15	91.02	-10.69	19.27

**A: Northeast Monsoon (from July 2013 to December 2013); B: Southwest Monsoon (from July 2013 to August 2014).*

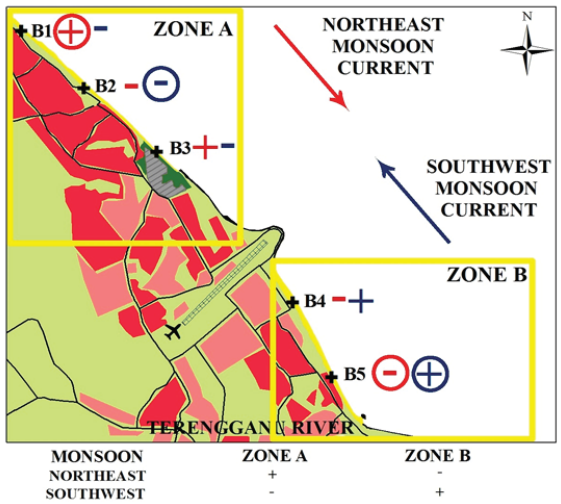

Figure 4. Volume changes during Northeast (Red) and Southwest (Blue) Monsoon. The minus '- and +' value indicates the volume of sand eroded and deposited respectively; and circle indicates heavy erosion or deposition.

Inshore Wind and Wave Conditions

Figure 5 represents the responses observed by the modelled wind and waves in this study. The wind speed shows an increase during the Northeast Monsoon (November 2013) and at the end of the post-Northeast Monsoon (March 2014). The storms started from November 2013 to March 2014 and three major storms took place during this season. The first and second storms were in December 2013 and the third occurred in January 2014. The highest Northeast Monsoon storm of January 2014 produced the largest significant wave height of 1.48 m, while another two storms during Northeast Monsoon reached 1.45 m wave height. Southwest Monsoon did not include any storms and the average of significant wave height was < 0.66 m

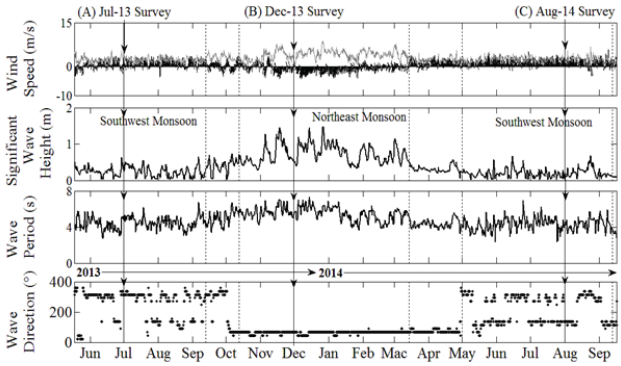

Figure 5. Wind and wave modelled from July 2013 to September 2014: (A) wind speed and direction; (B) significant wave height; (C) wave period; and (D) wave direction. Arrow line represents a profile survey: (A) July 2013; (B) December 2013; and (C) August 2014.

DISCUSSION

This study demonstrates that morphological changes (Northeast Monsoon effect) on the majority of the beaches along the Kuala Terengganu coasts are triggered by variations in wave energy and relate seasonal changes in the littoral drift direction; (Masselink and Pattiaratchi, 2001; Mishra *et al.,* 2011; Rosnan and Mohd Lokman, 2005; and Wong, 1981). Normally, during the Northeast Monsoon storms, the beaches on the north subsequently shows deposition when the long-shore sediment transport operates toward the south. Furthermore, the beaches located on south become narrower during the Northeast Monsoon and wider during the Southwest Monsoon. B1 and B3 beaches.

To the north of the study area (Zone A with B1 to B3 beaches), the Northeast monsoon is responsible for significant accretion along the zone (except B2) when the Southwest monsoon generates erosion of this area. The B2 beach remains the exception by having intensive erosion during this period. To the south of the study area (Zone B with B4 and B5 beaches), the Northeast monsoon storms cause erosion while the Southwest monsoon conditions lead to significant accretion. This zone highlights a contrasted morphological model compared to the northern zone which presents normal hydrodynamic and sedimentological processes under the Northeast and Southwest Monsoons impacts.

However, it is challenging to generalize a simple morphodynamic model for this coast (seasonal accretion/ erosion cycle) with a reversal in littoral drift under Northeast and Southwest monsoon's wave regime. Longshore wave energy gradients and littoral drift may undergo medium-term (order of several years) modifications in one of at least three ways, rarely in combination: (1) commonly cyclic changes in deep-wave approach directions due to climatic oscillations; (2) cyclic changes in nearshore bathymetry due to large-scale intrusion of longshore migrating sediment bodies into the wave field

affecting bays; and (3) perturbation of the wave field by human constructions, notably port breakwater structures (Sedrati and Anthony, 2007). Type 3 modifications are perfectly exemplified by Terengganu Coast evolution (the extension of Terengganu airport tarmac in 2010).

Rosnan and Mohd Lokman (2005) states that there are two net directions of sediment transport by littoral drift along the Terengganu state coast; a north-westward transport and southward transport, to the north-west, and south of Kuala Terengganu respectively. Terengganu state coast exhibited a relatively consistent beach width before the extension of the Terengganu Airport tarmac. This construction acted like a groin and was responsible of the generation of two separately and distinguishes sediment cells. These multiple cells are suggested to explain longshore changes in beach morphology, and the marked spatio-temporal variability in morphology. Over shorter time scales, Mohd Radzi *et al.* (2014) revealed that on the beaches located between groins, variations in beach volume may arise as a result of a short-term reversal of longshore transport.

Normally, during Northeast Monsoon the beaches are eroded and recover on Southwest Monsoon (classic monsoonal morphodynamic model) however, this study represents developed beaches that did not recover. Hill *et al.,* (2004); and Quartel *et al.,* (2008) also demonstrated that the developed beaches did not recover from their post-storm conditions as quickly as the developed beaches. The developed beaches are unlikely to naturally regain an equilibrium state that the undeveloped beaches do, and are hence, more directly impacted by strong meteorological circumstances.

CONCLUSIONS

The main dynamic model of the evolution of Terengganu state coast was completely disturbed by human constructions. Since 2010s, several strategies to prevent further erosion or to rebuild and protect the eroded beaches of Terengganu coast and to restore acceptable beach widths have been realised by Terengganu authorities. These projects that consist in the construction of a series of groins or breakwaters have been implemented. Few years later, the installed structures turned out to be ineffective in reducing erosion. It's however clear there is a need of management strategy involving a good understanding and an integrated view of beaches and coastal dynamics, as well as defence strategies covering not only the beaches but also the dunes and the nearshore zone.

ACKNOWLEDGMENTS

This research was funded by Institute of Oceanography and Environment, Universiti Malaysia Terengganu, Malaysia. We would like to thank the Laboratory of Physical Oceanography and Geology, for making the physical data available.

LITERATURE CITED

Akhir, M.F.M., and Chuen, Y.J., 2011. Seasonnal Variation of Water Characteristics during Inter-Monsoon along the East Coast of Johor. *Journal of Sustainability Science and Managment*, 6(2), 206–214.

Chempalayil, S.P.; Kumar, V.S.; Dora, G.U. and Johnson, G., 2014. Near shore waves, long-shore currents and sediment transport along micro-tidal beaches, central west coast of India. *International Journal of Sediment Research*, 29(3), 402–413.

Ghazali, N.H.M., 2006. Coastal erosion and reclamation in Malaysia. *Aquatic Ecosystem Health & Management*, 9(2), 237–247.

Hill, H.W.; Kelley, J.T.; Belknap, D.F., and Dickson, S.M., 2004. The effects of storms and storm-generated currents on sand beaches in Southern Maine, USA. *Marine Geology*, 210(1-4), 149–168.

Hsu, T.W; Lin, T.Y, and Tseng, I.F., 2007. Human impact on coastal erosion in Taiwan. *Journal of Coastal Research*, *23*(4), 961–973.

Masselink, G., and Pattiaratchi, C.B., 2001. Seasonal changes in beach morphology along the sheltered coastline of Perth, Western Australia. *Marine Geology*, 172, 243–263.

Mishra, P.; Patra, S.K.; Ramana, M.V.; Mohanty, P.K., and Panda, U.S., 2011. Interaction of monsoonal wave, current and tide near Gopalpur, east coast of India, and their impact on beach profile: a case study. *Natural Hazards*, 59(2), 1145–1159.

Mohd Radzi, A.H.; Nor Aslinda, A., and Kartigeyan, V., 2014. Physical modelling on coastal erosion due to runway extension at Terengganu Airport. *Journal of Malaysia Water Research*, *5*(1), 1–11.

Quartel, S.; Kroon, A., and Ruessink, B.G., 2008. Seasonal accretion and erosion patterns of a microtidal sandy beach. *Marine Geology*, 250(1-2), 19–33.

Rosnan, Y., and Mohd Lokman, H., 2005. The realtionship of Sediment Texture with Coastal Environments along the Kuala Terengganu Coast, Malaysia. *Environmental Geology*, 48, 639–643.

Rosnan, Y.; Raj, J.K.; Tajuddin, I., and Mohd Lokman, H., 2003. Coastal Processes Study along the East Coast of Malaysia. *In Investing in Innovation*, pp. 19–24.

Sedrati, M., and Anthony, E.J., 2007. A brief overview of plan-shape disequilibrium in embayed beaches: Tangier bay (Morocco). *Méditerranée*, 108, 125–130.

Stive, M.J.F.; Aarninkhof, S.G.J.; Hamm, L.; Hanson, H.; Larson, M; Wijnberg, K.M.; Nicholls R.J., and Capobianco, M., 2002. Variability of shore and shoreline evolution. *Coastal Engineering*, 47(2), 211–235.

Umar, H.; Rahman, S.; Baeda, A.Y., and Klara, S., 2015. Identification of Coastal Problem and Prediction of Coastal Erosion Sedimentation in South Sulawesi. *Procedia Engineering*, 116(Apac), 125–133.

Wong, P.P., 1981. Beach changes on a monsoon coast, Peninsular Malaysia. *Bulletin of the Geological Society of Malaysia*, 14, 59–74.

Journal of Coastal Research	SI	75	1037 - 1041	Coconut Creek, Florida	2016

Fuzzy Control for Impact Mitigation of Coastal Infrastructure Equipped with Magnetorheological Dampers

Kemal S. Arsava[†], Yeesock Kim[†*], and Kyu Han Kim[‡*]

[†]Civil and Environmental Engineering Department
Worcester Polytechnic Institute, Worcester 01609, U.S.A

[‡]Civil Engineering Department, Catholic Kwandong University, 24, Beomil 579, Gangneung, Gangwon 25601, South Korea

www.cerf-jcr.org

www.JCRonline.org

ABSTRACT

Arsava, K.S., Kim, Y., and Kim, K.H., 2016. Automatic control for hazard mitigation of coastal infrastructures. *In:* Vila-Concejo, A.; Bruce, E.; Kennedy, D.M., and McCarroll, R.J. (eds.), *Proceedings of the 14th International Coastal Symposium* (Sydney, Australia). *Journal of Coastal Research*, Special Issue, No. 75, pp. 1037 - 1041. Coconut Creek (Florida), ISSN 0749-0208.

This paper proposes to develop an acceleration feedback-based smart fuzzy controller for coastal bridge piers employing magnetorheological (MR) dampers. The proposed system reduces nonlinear structural responses to collision forces so that the risk of collapse is minimized. Based on the American Association of State Highway and Transportation Officials (AASHTO, 2012) specifications, a scaled coastal bridge pier was manufactured to mimic a full scale coastal bridge pier that has three columns and a pier cap. The scaled coastal bridge pier is equipped with an MR damper, accelerometers, an LVDT, strain gages, load cells, data acquisition systems, and a voltage-current converter. A variety of experimental studies were conducted on the smart coastal bridge pier under a variety of impact loads and control signals to generate sets of input data to train the proposed smart fuzzy controller. Passive and the proportional integral derivative controller (PID) were used as baselines. The performances of controllers were compared with those of the uncontrolled system in order to determine which system effectively reduces the collision responses of the coastal bridge pier. Comparisons of the smart fuzzy controller with the benchmark controllers demonstrated that the smart fuzzy controller is the most effective way to mitigate the structural collision response of integrated coastal bridge pier-MR damper systems subjected to various impact loadings.

ADDITIONAL INDEX WORDS: *fuzzy logic controller, coastal bridge pier; high impact load, magnetorheological (MR) damper, collision, and smart control technology.*

INTRODUCTION

Coastal bridge piers are very susceptible to collision loads. The collision-induced excessive forces can affect the structural integrity of the coastal bridge by causing fracture or excessive deformations. Although a great deal of interest has been paid to structural control systems subjected to earthquakes (Mitchell *et al.*, 2013, 2015), very little has been done regarding the application of smart control technology to collision-induced impact response mitigation of large-scale coastal bridge piers (Arsava *et al.*, 2013; Arsava and Kim, 2015; Arsava *et al.*, 2015; Das and Dey, 1992; Hughes *et al.*, 2015; Patten *et al.*, 1996; Wilde and Fujino, 1993).

In recent years, magnetorheological (MR) dampers, which uses a magnetic fluid that can change its rheological properties with the application of a magnetic field, has attracted a great deal of attention in the area of vibration control (Carlson, 2005; Hu *et al.*, 2012; Yang *et al.*, 2002; Mitchell *et al.*, 2012; Mohammadzadeh *et al.*, 2015; Kim *et al.*, 2014; Kim *et al.*, 2015). The MR damper can be operated either as a passive or as an active control device. In active cases, the MR fluids change into a semi-solid state in a few milliseconds with the application of a magnetic field. This unique aspect allows the MR damper to remain operable as a passive damper even when the control feedback components are not functioning properly.

Other distinguishing properties of the MR damper are its mechanical simplicity, fast response, high dynamic range, low manufacturing cost, large force capacity and robustness (Dyke *et al.*, 2001; Kim *et al.*, 2009; Yi *et al.*, 1999). However, the development of an effective control algorithm for time-varying smart coastal bridge pier-MR damping systems is challenging due to the nonlinear impact behavior (Arsava *et al.*, 2013).

In this study, a fuzzy controller is proposed to optimize the magnetic field on MR fluids for mitigation of structural impact responses (Kim and Clark, 1999; Zhou and Chang, 2000). Many investigators have demonstrated that the fuzzy controller-based MR damping system shows great deal of promise for civil engineering applications (Jansen and Dyke, 2000; Kim and Clark, 1999; Liu *et al.*, 2001; Zhou and Chang, 2000; Kim *et al.*, 2009; Kim *et al.*, 2010a-c; Sharifi *et al.*, 2010). Liu *et al.* (2001) proposed a closed-loop control system based on fuzzy logic to suppress the bridge deck motion under random excitations. It was demonstrated that the fuzzy control system significantly reduced the deck displacement, while the absolute deck acceleration remained unchanged. Wilson and Abdullah (2005) developed a fuzzy controller to regulate the damping properties of structure-MR damper systems under four different earthquake loads. They demonstrated that both displacement and acceleration responses were successfully reduced. However, most of the studies on fuzzy controller-based MR damping technology has focused on seismic or wind load dissipation while relatively little research has been carried out on high impact collision forces (Hu *et al.*, 2012; Liu and Chen, 2011). Liu and Chen (2011) proposed a hybrid fuzzy-PID controller to

DOI: 10.2112/SI75-208.1 received 15 October 2015; accepted in revision 15 January 2016.
*Corresponding authors: yeesock@wpi.edu and khkim@cku.ac.kr
©Coastal Education and Research Foundation, Inc. 2016

optimize the damping force of MR dampers under high impact loads. Displacement, the impact force and the damper chamber pressure were used as inputs to obtain the optimum current signal. Experimental studies were performed using a single bar long-stroke MR damper. It was demonstrated that the performance of the fuzzy-PID control algorithm is better than the maximum current control for the dynamic system stabilization. Hu *et al*. (2012) designed an MR shock absorber to control the recoil dynamics of a gun. To control the applied current of the piston coil in an MR damper, three control algorithms, an on–off control, a PID control, and a fuzzy control algorithm, were used. The results showed that the fuzzy control significantly reduced the stroke and pressure peak of the MR shock absorber. Arsava *et al.* (2015) numerically demonstrated the effectiveness of fuzzy controllers in reducing structural impact responses using a simply supported concrete beam.

The focus of this paper is to experimentally demonstrate the capacity of the MR damping system employing the fuzzy controller to mitigate collision-induced impact responses of coastal bridge piers over a wide range of collision loading conditions. The performance of the proposed fuzzy controller is compared to that of a passive control, a PID controller, and an uncontrolled bridge pier.

METHODS

This research experimentally evaluates the impact response mitigation of the smart fuzzy control system while passive and PID controls are used as baselines. In this context, a scaled coastal bridge pier is selected to obtain input-output data to train the proposed fuzzy controller. Based on the AASHTO specifications (AASHTO, 2012), it is designed to have the same stiffness with the full scale pier. This single structure is then scaled down to fit in the drop tower test facility. The 1/150 scale is used for the dimensions of the coastal bridge pier.

A scaled down bridge pier with a size of 15×25×100 cm is constructed. One end of the member is clamped in order to act as a fixed end while the other end is left free just like a real bridge pier. The modulus of elasticitiy and the compressive strength of the concrete was estimated as 15 GPa and 26 MPa, respectively.

An MR damper is placed under mid-span of the coastal bridge pier in order to investigate the performance of smart control system (Fig. 1). The coastal bridge pier is tested under various collision loads and voltage signals for the MR damper.

The collision test facility in Structural Impact Mitigation and Mechanics Laboratory in the Civil and Environmental Engineering Department at WPI is used to apply collision loads to the coastal bridge pier. A total of 210 impact tests are performed to investigate the structure with and without an MR damper. Five different impact force levels (free fall from 30, 60, 80, 110 and 130 mm) are evaluated under different control signals generated by uncontrolled, passive, PID and fuzzy controls. For each drop release height and current on the MR damper, the collision test is performed three times to validate the proposed control strategy.

Passive Control

Passive control can be simply described as an energy dissipation mechanism, which is designed to modify the stiffness of structures without requiring an external power supply. Passive control adjusts the structural damping through coupling with passive devices: i.e., it generates counter acting forces without the use of a real-time structural response feedback. This non-optimal behavior of passive systems has an uncertainty about the responses to unexpected large events such as collisions. In this study, the passive control is simulated by applying a constant voltage (0-5V) to the MR damper.

Control algorithms are developed in dSPACE to collect structural responses and send control signals to the MR damper simultaneously. For the passive control, the algorithm sends the previously defined current signals to the MR damper, and measures the structural responses. Then the collected data set is processed and evaluated by using MATLAB software.

Figure 1. Scaled down coastal bridge pier employing an MR-damper.

PID Control

In this study, a proportional integral derivative (PID) controller is used first as a benchmark because the PID controller is one of the most commonly used algorithms in the field. The description of a PID controller is as follows (Kim *et al*., 2010b).

$$Cu(t) = K_p Out(t) + K_I \int_0^t Out(t)dt + K_D \frac{dOut(t)}{d(t)}, \quad (1)$$

where $Cu(t)$ is the current value of the MR damper at time t, and K_P, K_I and K_D are the weight factors of the PID controller, which are determined via many trial and errors. The structure-MR damping system employing the PID controller is implemented using dSPACE.

Experimental study showed that the PID controller is effective in mitigating the nonlinear dynamic response of the coastal bridge pier employing an MR damper under collision loads. For example, for the 30 mm drop release height, the maximum acceleration response of the smart bridge pier using the PID controller is 12.5 g, which is about 20% less than the uncontrolled system. Although the PID controller has a great performance on the impact response mitigation of the bridge pier, the PID weight factors would not be optimal for all the impact load scenario because each weighting factor is a optimum value for a single impact load. In this context, a fuzzy logic control algorithm is proposed to improve the reliability and robustness of the smart bridge pier system.

Fuzzy Logic Control

Fuzzy control is one of the most effective smart control strategies to improve the dynamic performances of structures

(Casciati *et al*., 1994; Choi *et al*., 2004; Dounis *et al*., 2007; Gu and Oyadiji, 2008; Nomura *et al*., 2007; Pourzeynali *et al*., 2007; Kim *et al*., 2011).

Based on an identifed model (Kim *et al*., 2013b; Kim *et al*., 2014a; Kim *et al*., 2014c), an effective control algorithm can be developed to optimize the current values of the MR dampers. The acceleration feedback is used to calculate the optimum current signals. The conceptual configuration of the proposed fuzzy control is shown in Fig. 2. The fuzzy control model is as follows.

$$\begin{aligned} &Rule\ c: If\ A_c^{t-d}\ is\ X_c, \ldots, and\ V_c^{t-d}\ is\ Y_c, \\ &\qquad Then\ V_c^t = p_c A_c^{t-d} + q_c V_c^{t-d} + r_c \end{aligned} \tag{2}$$

where A^{t-d} and V^{t-d} are inputs at time *t-d* while V^t is the otuput at time *t* of the fuzzy system. $c = 1,2,\ldots,h$; h is the number of rules. The delay term is represented by *d*. In the model consequent parameters are represented as p_c, q_c and r_c. The functions of Layer 1 is presented as

$$O_c^1 = \mu \begin{bmatrix} X_C\left(A_c^{t-d}\right) \\ Y_C\left(V_c^{t-d}\right) \end{bmatrix} \tag{3}$$

where μ is the appropriate parameterized membership function (MF), and O_c^1 (c = 1,2,3) is the output that specifies the degree to which the given input A^{t-d} satisfies the quantifier. In Layer 1 MFs are applied to each input and send to the second layer, which combines all the inputs. The product of Layer 2 is the combination of all incoming outputs that is called 'firing strength' of a fuzzy control rule

$$w_C^t = \mu X_C(A_C^{t-d}) \times \mu Y_C(V_C^{t-d}) \tag{4}$$

In Layer 3 the output of Layer 2 is normalized by taking the ratio of the firing strength

$$\overline{w}_C^t = \frac{w_C^t}{\sum w_C^t} \tag{5}$$

As a next step, node functions $V_c^t = p_c A_c^{t-d} + q_c V_c^{t-d} + r_c$ are applied to output of Layer 3

$$O_C^4 = \overline{w}_C^t \times V_C^t = \overline{w}_C \times \left(p_C A_C^{t-d} + q_C V_C^{t-d} + r_C\right) \tag{6}$$

In the last step, Layer 5 summates the layer inputs

$$O_C^5 = overall\ \ output + \sum_c \overline{w}_C^t \times V_C^t = \frac{\sum_C w_C^t \times V_C^t}{\sum_C w_C^t} \tag{7}$$

It is observed that the fuzzy controller significantly improves the dynamic behavior of the smart coastal bridge pier under impact loads. For the 130 mm collision test, the maximum acceleration response of the fuzzy control system is about 18*g*, which is 76%, 49% and 56% less than the uncontrolled, PID and passive (with optimum current) controllers, respectively. The fuzzy controller decreased the maximum deflection by 58%, which is 44% and 47% better than the PID and passive controllers. The quantitative evaluation of the proposed fuzzy control system is presented in detail in the following section.

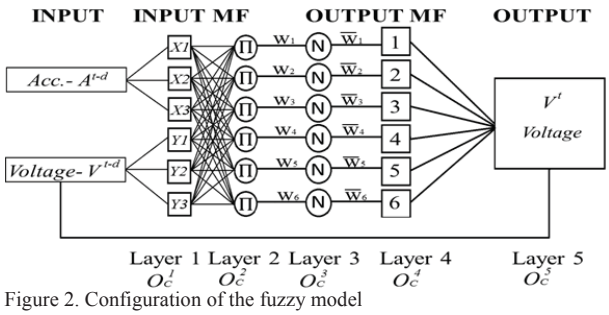

Figure 2. Configuration of the fuzzy model

Table 1. *Evaluation of control models*

		Drop Release Height				
		30 mm	60 mm	80 mm	110 mm	130 mm
J_1	F	**8.5450**	**11.4811**	**12.5462**	**15.6323**	**18.3340**
	PID	12.5830	12.9873	15.0557	18.3337	36.3676
	PA	12.8674	20.5250	24.1537	26.2165	41.7610
	Unc	15.7589	24.7759	32.8513	33.9016	76.8240
J_2	F	**0.1576**	**0.1951**	**0.1829**	**0.2253**	**0.3425**
	PID	0.1930	0.1964	0.2068	0.2611	0.5044
	PA	0.2207	0.3519	0.4381	0.4859	0.5768
	Unc	0.3698	0.3955	0.5673	0.6093	0.6839
J_3	F	**25.8503**	**34.1772**	**33.6442**	**40.1765**	**63.9279**
	PID	34.2712	36.3477	40.0007	48.4878	84.7655
	PA	40.4374	57.8880	68.7813	85.0856	96.2351
	Unc	47.8073	65.5764	86.2201	102.0797	155.6425
J_4	F	**0.0254**	**0.0315**	**0.0304**	**0.0339**	**0.0344**
	PID	0.0336	0.0347	0.0373	0.0433	0.0618
	PA	0.0268	0.0372	0.0461	0.0558	0.0660
	Unc	0.0376	0.0539	0.0646	0.0729	0.0824
J_5	F	0.0054	0.0069	**0.0066**	**0.0075**	**0.0065**
	PID	0.0067	0.0069	0.0069	0.0083	0.0145
	PA	**0.0040**	**0.0066**	0.0078	0.0077	0.0108
	Unc	0.0082	0.0075	0.0097	0.0113	0.0109
J_6	F	0.4976	0.6359	**0.6092**	**0.6866**	**0.6249**
	PID	0.6397	0.6466	0.6590	0.7960	1.3272
	PA	**0.3832**	**0.6090**	0.7420	0.7885	1.0672
	Unc	0.6958	0.7687	1.0349	1.1003	1.1715

RESULTS

To evaluate the performance of the proposed fuzzy control approach, several evaluation indices are used. J_1, J_2 and J_3 are the max, mean and norm values of the acceleration response in units of *g*, respectively. J_4, J_5 and J_6 are the max, mean and norm values of the deflection response in units of mm.

Table 1 shows a detailed comparison of the studied controllers. The optimum voltage signals are used in the evaluation of the passive control. Fig. 3 and Fig. 4 depict the detailed comparison of the studied controllers for different drop release heights. The low value in J_1 represents the good acceleration response reduction. In the 110 mm drop release height, the J_1 value of fuzzy controller is about 15g, which is about 53%, 40% and 14% less than the uncontrolled, passive and PID controlled cases, respectively. The J_4 value of the fuzzy controller is about 39% and 21% less than the passive and PID controllers.

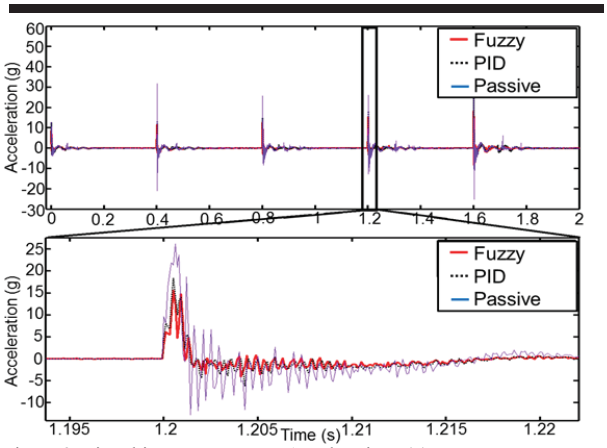

Figure 3. Time history responses: Accelerations (g).

For the 130 mm drop release height, the J_2 value of the fuzzy controller is 50%, 59% and 67% of the uncontrolled, passive and PID control systems, respectively. The J_5 value of the fuzzy control system is about 1.67, 1.66 and 2.23 times smaller than the uncontrolled, passive and PID controlled systems. For the 80 mm drop release height, the J_3 value of the fuzzy control system is about 1.18, 2.04 and 2.56 times smaller than the uncontrolled, passive and PID control systems. The PID and passive controllers produced the J_5 values of about 0.65 mm and 0.74 mm, which are 7% and 22% higher than the fuzzy contoller. It is observed that the smart fuzzy controller produced the lowest values for almost all the indices, which means that the fuzzy model is very effective in mitigating the collision responses of the smart coastal bridge pier under a variety of impact loadings. The repair/replacement of damaged coastal bridges is very costly. In addition to the direct cost, there is a more significant indirect cost due to loss of use of the coastal bridge, user delay cost, and loss due to related economic activity prevented by the coastal bridge closure or construction delays. This of course does not take into consideration any potential for loss of life or injury to the coastal bridge users.

CONCLUSIONS

This paper represents a smart fuzzy controller for coastal bridge piers employing MR dampers to mitigate collision-induced impact responses. To demonstrate the effectiveness of the proposed fuzzy controller, a scaled coastal bridge pier was manufactured that has the same stiffness with a full scale coastal bridge pier. Then the smart coastal bridge pier was tested under a variety of impact loads. To train the fuzzy controller, acceleration responses were used as input while the optimum voltage of the MR damper is output. As baseline models, a passive and a PID controller were used. The performances of the controllers are compared with those of the uncontrolled system. It is demonstrated that the proposed fuzzy controller is very effective in mitigating complex dynamic responses of smart coastal bridge piers under various impact loads. By employing the proposed system, it is expected that the cost and time to repair or replace coastal bridge systems after collisions will be significantly reduced.

AKNOWLEDGEMENTS

This research was partially supported by Regional Technolgy Innovation Program funded by Ministry of Land, Infrastructure and Transport of Korean Government (12-RTIPB01)

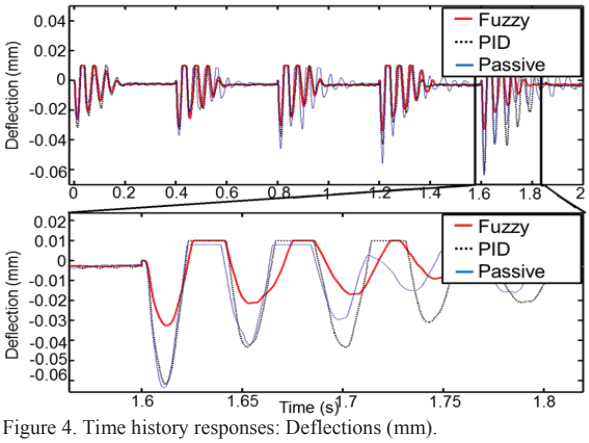

Figure 4. Time history responses: Deflections (mm).

LITERATURE CITED

American Association of State Highway and Transportation Officials, 2012. *AASHTO LRFD Bridge Design Specifications: Customary U.S. Units 2012.* Washington D.C.

Arsava, K.S.; Kim, Y.; El-Korchi, T., and Park, H.S., 2013. Nonlinear system identification of smart structures under high impact loads. *Journal of Smart Materials and Structures*, 22(5), 1-30.

Arsava, S.K. and Kim, Y., 2015. Modeling of magnetorheological dampers under various impact forces, *Shock and Vibration*, Article ID 905186, In Press.

Arsava, S.K.; Nam, Y. and Kim, Y., 2015. Nonlinear system identification of smart reinforced concrete structures under high impact loads, *Journal of Vibration and Control*, In Press.

Arsava, S.K.; Kim, Y.; Kim, K.H., and Shin, B.S., 2015. Smart fuzzy control of reinforced concrete structures excited by collision-type forces, Expert Systems with Applications, 42, 7929-7941.

Carlson, J.D., 2005. MR fluids and devices in the real world. *International Journal of Modern Physic*19(07n09),1463-1470.

Casciati, F.; Faravelli, L., and Yao, T., 1994. Application of fuzzy logic to achieve structural control. *Proceedings of the Second European Conference on Smart Strucutres and Materials* (Glasgow, Scotland), 206-209.

Choi, K.M.; Cho, S.W.; Jung, H.J., and Lee, I.W., 2004. Semi-active fuzzy control for seismic response reduction using magneto-rheological dampers, *Earthquake Engineering & Structural Dynamics*, 33(6), 723-736.

Das, A.K. and Dey, S.S., 1992. Effects of tuned mass dampers on random response of bridges. *Computers and Structures*, 43(4), 745-750.

Dounis, A.I.; Tiropanis, P.; Syrcos, G.P., and Tseles, D., 2007. Evolutionary fuzzy logic control of base-isolated structures in response to earthquake activity. *Structural Control and Health* Monitoring, 14(1), 62–82.

Dyke, S.J.; Yi, F.; Caicedo, J.M., and Carlson, J.D., 2001. Experimental verification of multinput seismic control strategies for smart dampers. *ASCE Journal of Engineering Mechanics*, 127(11), 1152-1164.

Gu, Z.Q. and Oyadiji, O., 2008. Application of MR damper in structural control using Anfis method. *Computers and Structures*, 86(3-5):427–436.

Hu, H.; Jiang, X.; Wang J., and Li, Y., 2012. Design, modeling, and controlling of a large-scale magnetorheological shock absorber under high impact load, *Journal of Intelligent Material Systems and Structures*, 23(6), 635-645.

Hughes, J.E.; Kim, Y., and El-Korchi, T., 2015. Radar-based impact load prediction for damage mitigation of infrastructure, *Journal of Vibration and Control*, DOI: 10.1177/1077546315603856, In Press.

Jansen, L.M. and Dyke, S.J., 2000. Semiactive control strategies for MR dampers: comparative study. *Journal of Engineering Mechanics*, 126(8), 795-803.

Kim, S. and Clark, W.W., 1999. Fuzzy logic semi-active vibration control. *Adaptive Structures and Material Systems*, 59(87), 367-372.

Kim, Y.; Langari, R., and Hurlebaus, S., 2009. Semiactive nonlinear control of a building structure equipped with a magnetorheological damper system, *Mechanical Systems and Signal Processing*, 23, 300-315, 2009.

Kim, Y.; Langari, R., and Hurlebaus, S., 2010a. Control of seismically exited benchmark building using linear matrix inequality-based semiactive nonlinear fuzzy control. *ASCE Journal of Structural Engineering*, 136(8), 1023-1026.

Kim, Y.; Langari, R., and Hurlebaus, S., 2010b. Model-based multi-input, multi-output supervisory semiactive nonlinear fuzzy controller, *Computer-Aided Civil and Infrastructure Engineering*, 25, 387-393.

Kim, Y.; Kim, C., and Langari, R., 2010c. Novel bio-inspired smart control for hazard mitigation of civil structures, *Journal of Smart Materials and Structures*, 19, 115009, 2010.

Kim, Y.; Hurlebaus, S., and Langari, R., 2010d. Control of a seismically excited benchmark building using linear matrix inequality-based semiactive nonlinear fuzzy control, ASCE *Journal of Structural Engineering,* 136(8), 1023-1026.

Kim, Y.; Langari, R., and Hurlebaus, S., 2011. MIMO fuzzy identification of building-mr damper system. *International Journal of Intelligent and Fuzzy Systems*, 22(4), 185-205.

Kim, Y.; Mallick, R.; Bhowmick, S., and Chen, B., 2013. Nonlinear system identification of large-scale smart pavement systems, *Expert Systems with Applications*, 40, 3551-3560.

Kim, Y.; Shin, S.S., and Plummer, J.D., 2014. A wavelet-based autoregressive fuzzy model for forecasting algal blooms, *Environmental Modeling & Software*, 62: 1-10.

Kim, Y.; Bai, J.W., and Albano, L.D., 2014. Fragility estimates of smart structures with sensor faults, *Journal of Smart Materials and Structures*, 22 125012.

Kim, Y.; Kim, K.H., and Shin, B.S., 2014. Fuzzy model forecasting of offshore bar-shape profiles under high waves, *Expert Systems with Applications*, 41, 5771-5779.

Kim, Y.; Kim, Y.H., and Lee, S., 2015. Multivariable nonlinear identification of smart buildings, *Mechanical Systems and Signal Processing*, 62-63, 254-271.

Liu, B. and Chen, J., 2011. Control system design of magneto-rheoloical damper under high-impact load. *Modern Applied Science*, 5(5), 253-258.

Liu, Y.; Gordaninejad, F.; Evrensel, C.A., and Hitchcock, G., 2001. An experimental study on fuzzy logic vibration control of a bridge using fail-safe magneto-rheological fluid dampers. *Smart Structures and Materials*, 4330, 281-288.

Mitchell, R.; Kim, Y., and El-Korchi, T., 2012. System identification of smart structures using a wavelet neuro-fuzzy model, *Journal of Smart Materials and Structures*, 21, DOI:10.1088/0964-1726/21/11/115009.

Mitchell, R.; Kim, Y.; El-Korchi, T., and Cha, Y.J., 2013. Wavelet-neuro-fuzzy control of hybrid building-active tuned mass damper system under seismic excitations, *Journal of Vibration and Control*, 19(12), 1881-1894.

Mitchell, R.; Cha, Y.J.; Kim, Y., and Mahajan, A., 2015. Active control of highway bridges subject to a variety of earthquake loads, *Earthquake Engineering and Engineering Vibration*, 14(2), DOI:10.1007/s11803-015-0021-6.

Mohammadzadeh, S.; Kim, Y., and Ahn, J., 2015. PCA-based neuro-fuzzy model for system identification of smart structures, *Journal of Smart Structures and Systems*, 15(5).

Nomura, Y.; Furuta, H., and Hirokane, M., 2007. An integrated fuzzy control system for structural vibration. *Computer-Aided Civil and Infrastructure Engineering*, 22(4), 306–316.

Patten, W.N.; Sack, R.L., and He, Q., 1996. Controlled semiactive hydraulic vibration absorber for bridge. *Journal of Structural Engineering*, 122(2), 187-192.

Pourzeynali, S.; Lavasani, H.H., and Modarayi, A.H., 2007. Active control of high rise building structures using fuzzy logic and genetic algorithms. *Engineering Structures*, 29(3), 346–357.

Sharifi, R.; Kim, Y., and Langari, R., 2010. Sensor fault isolation and detection of smart structures, *Journal of Smart Materials and Structures*, 19, 105001.

Wilde, K. and Fujino, Y., 1993. Aerodynamic control of bridge deck flutter by active surfaces. *Journal of Engineering Mechanics*, 124(7), 718-727.

Wilson, C.M.D. and Abdullah, M.M., 2005. Structural vibration reduction using fuzzy control of magnetorheological dampers. *ASCE Structures Congress*, (New York, New York), 1-12.

Yang, G.; Spencer, B.F.; Carlson, J.D., and Sain, M.K., 2002. Large-scale MR fluids dampers: modeling and dynamic performance consideration. *Engineering Structures*, 24(3), 309-323.

Yi, F.; Dyke, S.J.; Caicedo, J.M., and Carlson, J.D., 1999. Seismic response control using smart dampers. *Proceedings of the 1999 American Control Conference*, 1022-1026.

Zhou, L. and Chang, C.C., 2000. Adaptive fuzzy control for a structure-MR damper system. *Proceedings of SPIE 3988,Smart Structures and Materials: Smart Systems for Bridges, Structures, and Highways*, 105-115.

Journal of Coastal Research	SI	75	1042 - 1046	Coconut Creek, Florida	2016

Spatio-temporal Variability in the Tipping Points of a Coastal Defense

Jennifer M. Brown[†*], Thomas Prime[†§], Jack J.C. Phelps[†§], Andrew Barkwith[‡], Martin D. Hurst[‡], Michael A. Ellis[‡], Gerd Masselink[††], and Andrew J. Plater[§]

[†]Marine Physics and Ocean Climate
National Oceanography Centre
Liverpool, UK

[‡]Environmental Modelling directorate
British Geological Survey
Nottingham, UK

[††]School of Marine Science and Engineering
Plymouth University
Plymouth, UK

[§]Department of Geography and Planning
University of Liverpool
Liverpool, UK

www.cerf-jcr.org

www.JCRonline.org

ABSTRACT

Brown, J.M.; Prime, T.; Phelps, J.J.C.; Barkwith, A.; Hurst, M.D.; Ellis, M.A.; Masselink, G., and Plater, A.J., 2016. Spatio-temporal Variability in the Tipping Points of Coastal Defense. *In:* Vila-Concejo, A.; Bruce, E.; Kennedy, D.M., and McCarroll, R.J. (eds.), *Proceedings of the 14th International Coastal Symposium* (Sydney, Australia). *Journal of Coastal Research*, Special Issue, No. 75, pp. 1042 - 1046. Coconut Creek (Florida), ISSN 0749-0208.

To enable effective adaptive management, early warning of when a 'tipping point' within a system's defense may occur is vital. A tipping point is a critical threshold at which the state of a system is altered, perhaps irreversibly. After the extremity of the UK's 2013/2014 winter, many coastal systems have undergone a change in state. For example, the conversion of a sandy beach into a rocky platform or an increase/decrease in flood hazard due to a defense breach or new intervention. Coastal monitoring networks around the UK have enabled data collection of these extreme events to drive model applications to assess plausible changes in coastal conditions that trigger a sudden change in a system's state and conditions that enable recovery. Using available UK monitoring networks and a numerical approach, we focus on Dungeness and Rye Bay, a region of high value in terms of habitat and energy, to assess (i) how the natural variability within the profile of the gravel barrier modifies the overwash rates that can occur and (ii) how ambitious human intervention that re-scape the geomorphic character of the shoreline could impact the critical point at which overwash occurs.

ADDITIONAL INDEX WORDS: *Morphological tipping point, flood risk, erosion risk, sandscaping.*

INTRODUCTION

After the extremity of the UK's 2013/2014 winter many coastal systems have undergone a change in state (Masselink *et al*., 2015). This has highlighted the need to identify triggers that change the resilience of a system to inform shoreline managers of future conditions (beach and sea levels) that could require a change in management strategy (*e.g.*, Figure 1, that shows a beach stripped of sediment). In the last decade a wave monitoring network, WaveNet supported by the Centre for Environment, Fisheries and Aquaculture Science (Cefas), has complimented the long-term tide gauge network, which is part of the National Tidal & Sea Level Facility (NTSLF). Together these networks record conditions to improve our understanding of the joint probability of combined wave and water level events, which is important for coastal managers to assess the defense level provided by naturally evolving systems, such as gravel barriers and dunes, and ageing engineered structures (Wadey *et al*., 2015).

At many locations the level of defense offered by a natural barrier varies in both time and space as the geomorphic system evolves in response to the prevailing coastal conditions, which in turn are changing as a consequence to climate change and sea-level rise. This is also true for engineered structures, which sit within a naturally evolving system. For example, seasonally changing beach levels modify the wave impact at the toe of a structure as offshore conditions are transformed as they propagate across the coastal zone. To enable effective adaptive management, spatial vulnerability assessments are required alongside progress assessments in relation to changing climate conditions (Sano *et al*., 2015). More recently, 'softer' interventions for flood and erosion risk management are being considered to support habitats at risk from coastal squeeze. Some examples are the consideration of intertidal wetlands to attenuate storm tide elevations (Smolders *et al*., 2015) and ambitious geomorphic interventions that nourish vulnerable coastline beyond decadal timescales (Stive *et al*., 2013).

After the Dutch initiative of 'The Sand Engine' (http://www.dezandmotor.nl/), the consideration of 'Sand and Gravel Engines' is becoming a consideration for 'important' sites within the UK. In support of this management approach, this research starts to identify the uncertainty in the flood hazard due to non-uniform changes in geomorphic systems over time and space, and also, the possibility of using 'advance the line' management options to support existing natural and engineered structures through increased beach width in the UK. This

DOI: 10.2112/SI75-209.1 received 15 October 2015; accepted in revision 15 January 2016.
*Corresponding author: jebro@noc.ac.uk
©Coastal Education and Research Foundation, Inc. 2016

modelling study is the first in the UK to identify numerical methods as briefly described in Section 2 for such a feasibility study. The results presented in Section 3 are the initial results that will form the basis to start the development of a decision support tool for adaptive coastal management (extending the approach of Knight *et al*., 2015). The findings are discussed in relation to the formation of new habitat and coastal resilience in Section 4, before the conclusions are drawn in Section 5.

Figure 1. Storm impact (a) before and (b) after the winter 2013/2014 for Whipsiderry beach, north of Newquay, north Cornwall, England.

METHODS

We focus on Dungeness Foreland and Romney Marsh, a site where alternative solutions for coastal protection are being considered (Figure 2). Dungeness is a gravel foreland with extant and reclaimed wetlands (Plater *et al*., 2009). It is largely designated as a Site of Scientific Special Interest (SSSI) for international geological and ecological interests, but also supports valuable infrastructure and assets: a nuclear power station, electricity sub-station and Military of Defence (MoD) ranges. The area experiences a bi-modal wave climate (Mason *et al*., 2008) with waves from northeast and southwest and skew surge elevations of the order of tens of centimeters (Idier *et al*., 2012). The flood defense is variable in width and height (Figure 3), comprising a gravel barrier (Figure 2) that is reinforced by hard defense at either end.

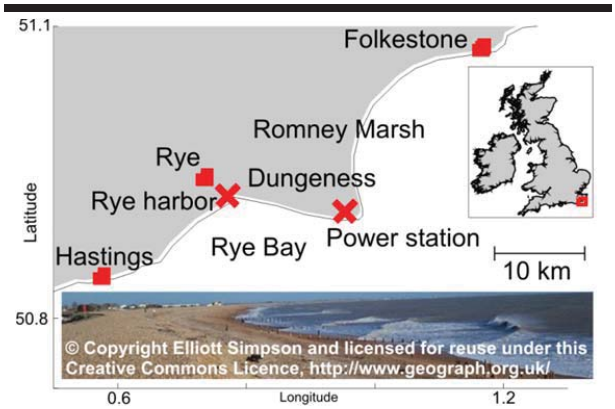

Figure 2. Dungeness Foreland and located within the UK.

To assess the flood and erosion hazard under present day sea levels a modelling approach is adopted. XBeach-G, a model that simulates gravel barrier evolution and overwash during storm events (McCall *et al*., 2014; 2015), is first applied to beach profiles obtained from the UK Environment Agency (Figure. 3). Variable overwashing discharges and event-driven morphological evolution are simulated along the barrier's length for the same joint 1 in 200 year wave and water level event (H_s = 4.67 m; T_p = 9.1 s; η = 4.32 m ODN, where ODN represents c. 0.2 m below mean sea level in England), defined by analysis of nearby and available long-term monitoring. This defense level is chosen for the study because it represents the typical defense design standard applied in new schemes across the UK (McMillan *et al*., 2011). Following initial simulations for the observed beach profiles, the beach is widened to identify the point at which a management option of 'advance the line' could noticeably reduce the flood hazard. Here, the beach width is defined as the distance between the barrier toe and the point at which the gradient of the lower profile flattens, below 0 m ODN.

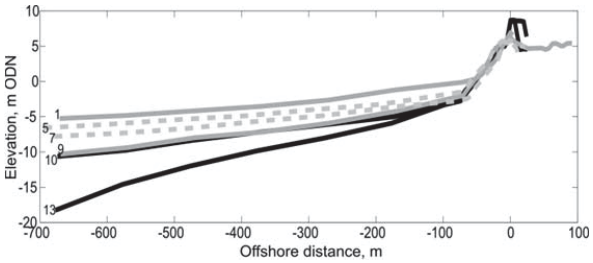

Figure 3. The alongshore variability in the natural (lines 1 – 9) and hard-engineered (lines 10 – 13) beach profiles between Rye harbor and the power station (Figure 2). The dashed profiles (5 and 7) depict the lowest barrier heights.

To represent the impact of a 'gravel engine' on the overwashing hazard, the beach is extended by a continuous elevation equal to the level of the barrier toe across 50%, 100%, 150%, 200%, 250% 300% and 400% of the beach width in profile 5. We chose this profile because it represents the lowest barrier crest level, but is also associated with a naturally wide beach-barrier system compared with the other profiles, so already has some resilience to overwashing. It is also fairly central along the natural frontage, with no support from hard-engineering. It does not have the deepest or shallowest subtidal profile, so does not represent the extremes in the subtidal profile. In addition, to assess the potential evolution of an ambitious advance the line option such as a gravel engine, a coastal evolution model (CEM, Barkwith *et al*., 2014) is applied at a 100-m resolution. By calibrating the setup for gravel transport (USACE, 1984), using historic rates of shoreline recession (1 m/yr, from Google Earth images) confirmed by the local authorities, a baseline shoreline erosion rate with 'no intervention' is first created. The impact of different spit features on the shoreline erosion is then simulated. The interventions are scenarios introduced to explore the potential support to existing defense and areas at risk of erosion through beach nourishment using natural processes, over a management epoch (100 years), to redistribute the initial large scale nourishment.

RESULTS

For the chosen 1 in 200 year event, the natural barrier profiles are overwashed, with larger rates occurring between profiles 2 – 9 (Figure 4a), while the hard-engineered profiles remain resistant. Along the naturally defended section of coast, the rate of overwash does not decrease with increasing barrier height (Figure 4b). There seems to be no clear correlation with beach width either (Figure 4c), while there seems (Figure 4d) to be a weak relation with the beach height when the 4 hard-engineered profiles are neglected (Figure 3). The lack of correlation between overwashing and the initial beach profile is likely to be due to the event-driven profile evolution. In general, the alongshore barrier beach response to the event is to form a more uniform slope between the barrier and beach, with erosion at the upper elevations and deposition at the lower elevations. The only noticeable change in crest elevation is for profile 5 and 7 (the two low profiles, Figure 3), which build in elevation. In the case of profile 7 the crest retreats. The only profile not to conform to this pattern is profile 1, which already has a fairly uniform frontage slope; in this case, the lower beach erodes, thereby increasing the shoreline depth.

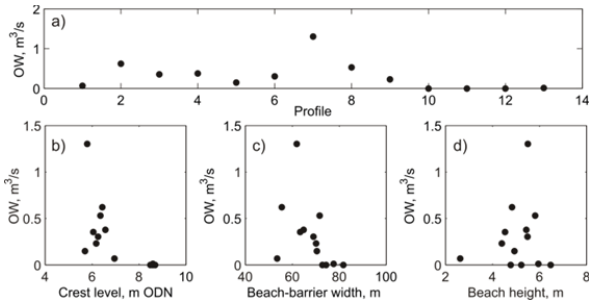

Figure 4. The 95th percentile overwash rate (OW) for (a) each profile, versus the initial (b) defense crest level, (c) barrier-beach width and (d) beach height from the subtidal to the barrier toe.

Initial analysis of the spatial pattern in overwash seems to relate to:

$$(\widehat{C-T})(\hat{C}-C)/D^2 \quad (1)$$

where C = the initial crest level, T = the initial toe level of the beach frontage, D = the initial width of the defense barrier positioned on the upper undisturbed beach and ^ = the maximum value along the (13 profile) frontage. This suggests the spatial resilience is correlated to the variability in crest level relative to the highest point in the system, the maximum change in elevation from the beach level to the barrier crest, and the local barrier-beach width (Figure 5).

We use profile 5, with the lowest crest level, to show how incrementally increasing the beach width (Figure 6a) reduces the flood hazard of the 1 in 200 year event considered (Figure 6b). For this profile an increase in beach width of 200 - 250%, at an elevation equal to the barrier toe, creates a change in the rate of reduction in total overwash volume, after which continued increase in beach width has limited impact. This is due to a secondary bar building towards the seaward limit of the widened beach platform during the event. This morphological response occurs only when the artificial beach is imposed to be ≥250% wider than the observed beach width.

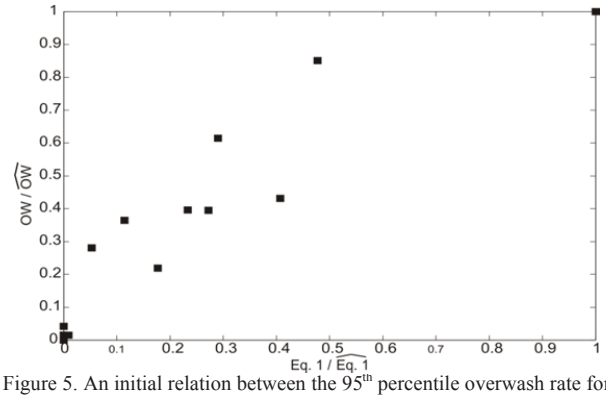

Figure 5. An initial relation between the 95th percentile overwash rate for each profile normalized by the maximum rate along the frontage and Eq. 1 normalized by the maximum value along the frontage.

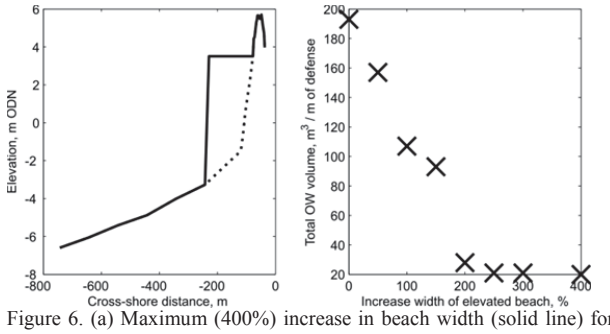

Figure 6. (a) Maximum (400%) increase in beach width (solid line) for profile 5 (dashed line) and (b) the total overwash volume during the event for each increased beach width considered.

For this case study, the consideration of 'sand scaping' to reshape the shoreline by 'advancing the line', with a gravel engine, has varied alongshore impact on the recession rates relative to a baseline 'do nothing' scenario. We show three scenario interventions, of interest to managers, that are representative of different nourishment schemes to explore location, size, number and shape of the intervention(s) on the long-term coastal response (Figure 7). It is clear that the impact is variable along the frontage and can act to either increase or decrease the local erosion over a 100-year period (Figure 8). The increased erosion in I3, Figure 8b, is likely to be a consequence of this intervention restricting the natural long-shore sediment drift to this shoreline, which may also be helping to sustain this intervention over the 100 year period. Multiple small interventions (Figure 7a) or a single large intervention positioned to the western end of the natural barrier (Figure 7b) have a wide spread reduction in erosion.

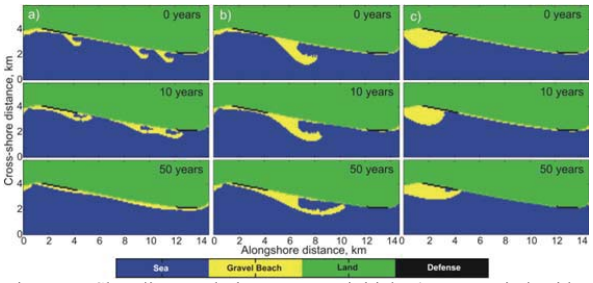

Figure 7. Shoreline evolution over an initial 50-year period with the consideration of 3 scenario interventions. (a) Intervention 1 (I1) considers multiple small recurved spits, (b) intervention 2 (I2) considers a single large recurved spit and (c) intervention 3 (I3) considers a large peninsula.

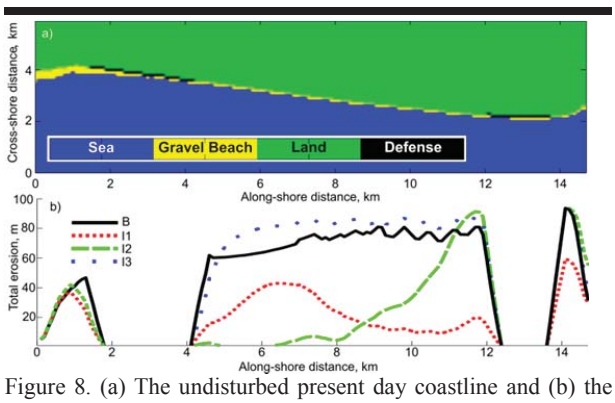

Figure 8. (a) The undisturbed present day coastline and (b) the shoreline recession after 100 years for the baseline simulation (B) without intervention and for each scenario intervention simulated (I1, I2 and I3, Figure 7).

DISCUSSION

This research, has worked with energy stakeholders (EDF, Magnox, National Grid), land owners/managers (MoD, Royal Society for the protection of Birds), and environmental regulators (Environment Agency (EA), Natural England) to examine the potential of an 'advance the line' option for future defense of the southern Dungeness shoreline. This is a critical area at the down-drift limits of the EA's responsibilities for coastal resource management. Current EA proposals explore 'do nothing' and 'retreat the line' options. The future decision on this specific coastal juncture clearly impacts on essential infrastructure and assets, not just in terms of the power station, but also in relation to the MoD ranges.

The 95th percentile value in overwash is initially used to incorporate the influence of event-scale evolution of the natural defense system on the time-varying flood hazard. By assessing the wave overwash hazard for 13 different profiles we capture the long-term variability in resilience due to the natural evolution of the defense system; the present-day frontage representing different alongshore barrier-beach profiles in response to the prevailing coastal conditions.

Although the offshore beach profiles deepen from west to east there is no clear trend in increasing overwash with increased water depth fronting the beach-barrier system. The overwashing is minimal for the shallowest beach profile in the west (profile 1 most likely due to wave dissipation) and limited by the presence of the high engineered structure (profiles 10-13) in the east. The proposed equation is an initial attempt at representing the spatial variability in the overwash hazard for a barrier-beach system. However, to improve the correlation the grain size and representation of the event-driven system evolution needs consideration.

Repeat simulations of identical wave and water levels for a range of beach profiles enables us to focus on the morphological impacts on tipping points in flood hazard from wave overwash. The overwashing is repeatedly simulated for a range of widened beach morphologies, chosen to explore the tipping point in wave overwash events for 'advance the line' management options. This will inform managers of the additional beach width required along the frontage to prevent, or noticeably limit, overwash fans occurring along the frontage. Initial simulations were performed for profile 5, which naturally has a low overwash hazard relative to the other profiles due to its relatively wide barrier-beach. This profile is therefore likely to require less intervention than other locations to reduce the flood hazard. The elevation of the barrier toe in profile 5 is just below the extreme water level considered. Although the widened beach is acting to absorb the wave energy it is not preventing the water elevation reaching the barrier. Further simulation will continue to explore the variability in required beach width along this frontage to limit overwashing for a 1 in 200 year event considering the natural variability in the barrier-beach profile. By simulating both the width required for reducing the flood hazard and the coastal evolution to project changes in beach width in response to 'advance the line' schemes, a time period over which a proposed intervention will be effective at increasing coastal resilience can be determined.

Here, the coastal evolution indicates how the different nourishment schemes might impact coastal recession. However, a higher resolution model is required to assess the changing beach width to accurately assess a change in overwash hazard. The 'advance the line' scenarios considered show the possibility of the recurved spit forming a natural lagoon as the recurve reattaches to the coast. This intervention could therefore also provide increased habitat in a region where the marsh is becoming squeezed. The use of multiple smaller scale interventions enables more targeted reductions in erosion, in this case across the full barrier frontage between the engineered structures. Multiple small lagoons are formed and the most eastward intervention is sustained by the adjacent one to the west. However, the smaller interventions more rapidly loose there shape and form a wide beach after 50 years. The peninsula shaped intervention does evolve to create a small lagoon, but the influence alongshore is limited within the 100 year period considered. This is due to its position in the sheltered corner of this coastline. However, it does maintain the beach width beyond 100 years providing support to the existing engineered structure, possibly extending its design life.

CONCLUSIONS

Using XBeach-G and CEM we have explored the overwashing hazard in response to 'advance the line' management options and the long-term (100 yr.) evolution of plausible options and surrounding coastline. For the southern shore of Dungeness overwashing is found to be more sensitive to the dissipative nature of the beach slope, than the barrier height. This is important as this site could be a possible location for a future gravel engine, creating greater beach volume increasing the system's resilience. However, the size of the engine is critical for sustained impact. Small interventions are found to collapse within 50 years, while larger schemes can last a century, forming recurved spits suitable for developing long-term sites for nature conservation. This is of interest as the current site forms a globally important wildlife reserve that is at risk of erosion.

By carrying out sensitivity analysis we find that increasing the beach width by ~250% noticeably reduces the overwashing volume for the beach profile with lowest crest elevation under a 1 in 200 year storm event. The overwashing is not prevented due to the extreme water level exceeding the elevation of the widened beach. To dissipate enough of the wave energy to prevent overwashing would require a much larger beach width as the change in total overwash volume is minimal with continued increase in beach volume. Further work will extend this analysis to the full range of barrier heights across this domain. By combining knowledge of the required beach width to prevent overwashing with long-term projections of shoreline evolution under managed scenarios will allow more informed decisions to be made to improve adaptive coastal planning at this site.

Continued research will aim to develop the CEM to include a more sophisticated representation of a gravel barrier and increase the model resolution to enable a high resolution numerical assessment of alongshore vulnerability to determine the spatial variability in the overwash hazard as an intervention evolves.

ACKNOWLEDGMENTS

This research was funded through the ERIIP "Sandscaping for Mitigating Coastal Flood and Erosion Risk to Energy Infrastructure on Gravel Shorelines: a case study approach" project (NERC NE/M008061/1) and the ARCC "Adaptation and Resilience of Coastal Energy Supply" (ARCoES) project (EPSRC EP/I035390/1). The Crown Estate and Tom Dauben at the EA are thanked for contributing to this research. The Channel Coastal Observatory, the EA, CEFAS and, NTSLF, BODC are thanked for the provision of beach survey, Lidar, WaveNet wave rider and UK tide gauge data at the study site.

LITERATURE CITED

Barkwith, A.; Hurst, M.D.; Thomas, C.W.; Ellis, M.A.; Limber, P.L., and Murray, A.B., 2014. Coastal vulnerability of a pinned, soft-cliff coastline, II: assessing the influence of sea walls on future morphology. *Earth Surface Dynamics*, 2, 233-242.

Idier, D.; Dumas, F., and Muller, H., 2012. Tide-surge interaction in the English Channel. *Natural Hazards Earth System Science*, 12, 3709-3718.

Knight, P.J.; Prime, T.; Brown, J.M.; Morrissey, K., and Plater, A.J., 2015. Application of flood risk modelling in a web-based geospatial decision support tool for coastal adaptation to climate change. *Natural Hazards Earth System Science*, 15, 1457-1471.

Masselink, G.; Scott, T.; Poate, T.; Russel, P.; Davidson, M., and Conley, D., 2015. The extreme 2013/14 winter storms: Hydrodynamic forcing and coastal response along the southwest coast of England. *Earth Surface Processes and Landforms*, in press, DOI: 10.1002/esp.3836

Mason, T.; Bradbury, A.; Poate, T., and Newman, R., 2009. Nearshore wave climate of the English Channel - evidence for bi-modal seas. *Proceedings of the 31st International Conference on Coastal Engineering* (New York, USA, ASCE), pp. 605-616.

McCall, R.T.; Masselink, G.; Poate, T.G.; Roelvink, J.A.; Almeida, L.P.; Davidson, M., and Russell, P.E., 2014. Modelling storm hydrodynamics on gravel beaches with XBeach-G. *Coastal Engineering*, 91, 231-250.

McCall, R.T.; Masselink, G.; Poate, T.G.; Roelvink, J.A., and Almeida, L.P., 2015. Modelling the morphodynamics of gravel beaches during storms with XBeach-G. *Coastal Engineering*, 103, 52-66.

McMillan, A.; Batstone, C.; Worth, D.; Tawn, J., and Horsburgh, K., 2011. *Coastal flood boundary conditions for UK mainland and islands. Project: SC060064/TR2: Design sea levels*. Bristol, Environment Agency, 142p.

Plater, A.J.; Stupples, P., and Roberts, H.M., 2009. Evidence of episodic coastal change during the Late Holocene: The Dungeness barrier complex, SE England. *Geomorphology*, 104(1–2), 47-58.

Sano, M.; Gainza, J.; Baum, S.; Low Choy, D.; Neumann, S., and Tomlinson, R., 2015. Coastal vulnerability and progress in climate change adaptation: An Australian case study. *Regional Studies in Marine Science*, 2,113-123.

Smolders, S.; Plancke, Y.; Ides, S., Meire, P., and Temmerman, S., 2015. Role of intertidal wetlands for tidal and storm tide attenuation along a confined estuary: a model study. *Natural Hazards Earth System Science*, 15, 1659-1675.

Stive, M.J.F.; de Schipper, M.A.; Luijendijk, A.P.; Aarninkhof, S.G.J.; van Gelder-Maas, C.; van Thiel de Vries, J.S.M.; de Vries, S.; Henriquez, M.; Marx, S., and Ranasinghe, R., 2013. A new alternative to saving our beaches from sea-level rise: The Sand Engine. *Journal of Coastal Research*, 29(5), 1001-1008.

USACE, 1984. Shore protection manual. Vicksburg, Mississippi: *U.S. Army Corps of Engineers*, Coastal Engineering Research Center, 656p.

Wadey, M.P.; Brown, J.M.; Haigh, I.D.; Dolphin, T., and Wisse, P., 2015 Assessment and comparison of extreme sea levels and waves during the 2013/2014 storm season in two UK coastal regions. *Natural Hazards Earth System Science*, 15, 2209-2225.

Journal of Coastal Research	SI	75	1047 - 1051	Coconut Creek, Florida	2016

Coastal Impacts Induced by Storm Waves between Cape Frio and Cape Buzios, Rio de Janeiro, Brazil.

Eduardo Bulhões [†§*], Guilherme B Fernandez[‡§], Silvio R Oliveira Filho[§], Thiago G Pereira[††§]

[†] Laboratório de Geografia Física
Departamento de Geografia.
Universidade Federal Fluminense
Campos dos Goytacazes, Brazil

[‡]Departamento de Geografia
Universidade Federal Fluminense
Niterói, Brazil

[††] Instituto de Geografia
Universidade do Estado do Rio de Janeiro
Rio de Janeiro, Brazil

[§] Laboratório de Geografia Física
Universidade Federal Fluminense
Niterói, Brazil

www.cerf-jcr.org

www.JCRonline.org

ABSTRACT

Bulhoes, E.; Fernandez, G.; Oliveira Filho, S.R., Pereira, T.G., 2016. Coastal Impacts Induced by Storm Waves between Cape Frio and Cape Buzios, Rio de Janeiro, Brazil. *In:* Vila-Concejo, A.; Bruce, E.; Kennedy, D.M., and McCarroll, R.J. (eds.), *Proceedings of the 14th International Coastal Symposium* (Sydney, Australia). *Journal of Coastal Research*, Special Issue, No. 75, pp. 1047 – 1051, Coconut Creek (Florida), ISSN 0749-0208.

The wave field in deep waters is notable for its variability and dictates the energy that will be directed towards the coast. Morphological impacts on coastal environments depend on the magnitude of the meteorological and oceanographic forcings and the beach capabilities of absorbing this energy. In the analysis between Cabo Frio and Cape Buzios, we considered the textural characteristics of the inner continental shelf from the analysis of 394 sediment samples, the volumetric variability of 438 surveys along 17 beach profiles and characteristics of 75 storms between 2003 and 2014. Results showed that sedimentation in the nearshore, through the mean grain size parameter, reflects the areas with higher or lower wave energy. The results also indicated the occurrence of a "storm waves season" between April and September, and this is the main element associated with erosion and volume variation of subaerial sand stock on beaches. A period with no occurrence of these storm waves (extended summer season) lead to the recovery of this subaereal sandy stock. The different segments of beaches show the greater or lesser magnitude of these effects, depending primarily on the orientation and exposure of each beach segment and also beach morphodynamics. Isolated storms with greater magnitude tend to promote severe erosion, especially if they occur at the beginning of this "season of storm waves".

ADDITIONAL INDEX WORDS: *Morphological change, beach profiles, season of storm waves.*

INTRODUCTION

The main impacts on coastal environments depend on the magnitude of atmospheric and oceanographic forces and on the capacity of beaches in absorbing it. The coastal segment between Cape Frio and Cape Buzios (Figure 1) is marked by the presence of rocky headlands which divides the coast in several cove beaches with different directions, exposition and morphological patterns that leads to the occurrence of the whole set of morphodynamic stages. In this sense, different are also the impacts and morphological changes produced in those beaches, regarding the alternating incoming storm and fair weather waves. This is the central theme on this paper.

Embayed or cove beaches are sandy deposits bordered by rocky or artificial headlands that influence the availability of sediment and the pattern of hydrodynamic circulation induced by waves. Jackson *et al.* (2005) redeems the idea that all beaches are supported on an antecedent geological structure and it is this structure that determines the limits for a beach to spatialize. Hydrodynamic processes that influence the dynamics of beach environments can be highly controlled by the provision of this geological structure, such as the presence of rocky shores, islands, submerged slabs etc. Short (1999) adds that, despite the rock structure be totally independent of the formation of beaches, plays a fundamental role in plan shape, sediment transport and their morphodynamics aspects.

In Brazil, Mahiques *et al.* (1998) argued that (i) the interaction between the mean wave direction, with (ii) the extent and orientation of the openings of coves, and also (iii) the presence of islands or rocky slabs on the inner continental shelf, lead the variations in the nearshore dynamics. The differences in energy levels between the beaches are associated to the direction of wave incidence and with the orientation of these beach openings. Also according to the authors, the bottom sediments distribution data shows the possibility of establishing an energy gradient of hydrodynamic agents acting on the surface of certain embayed beaches. Similarly, Loureiro *et al.* (2009) and Bulhoes *et al.* (2013) suggest that main differences in morphological impacts during storm events are associated with the relative position of beaches to the inputs of the wavefronts.

Storm events and Morphological Change of the Coastline

DOI: 10.2112/SI75-210.1 received 15 October 2015; accepted in revision 15 January 2016.
*Corresponding author: eduardobulhoes@id.uff.br
©Coastal Education and Research Foundation, Inc. 2016

According to Innocentini *et al.* (2003) most intense waves that occurs in South Atlantic ocean is caused by migratory cyclones, whose displacement, according to Satyamurty and Mattos (1989), follows the direction SW - NE. Parise *et al.* (2009) describe three patterns of storm tracks over the Southwestern Atlantic based on the minimum relative vorticity in the center of cyclones: a) cyclogenesis south of Argentina shift eastward and trajectory between 47.5ºS and 57.5ºS; b) cyclogenesis south of Uruguay with displacement east and trajectory between 35ºS and 42.5ºS; c) cyclogenesis south of Uruguay with displacement to the southeast and trajectory between 35ºS and 57.5ºS. Additionally, Reboita *et al.* (2005) and Parise *et al.* (2009) identify cyclonic activity on the south and southeast coast of Brazil (between 20ºS and 35ºS), the latter being closer to the Rio de Janeiro coast.

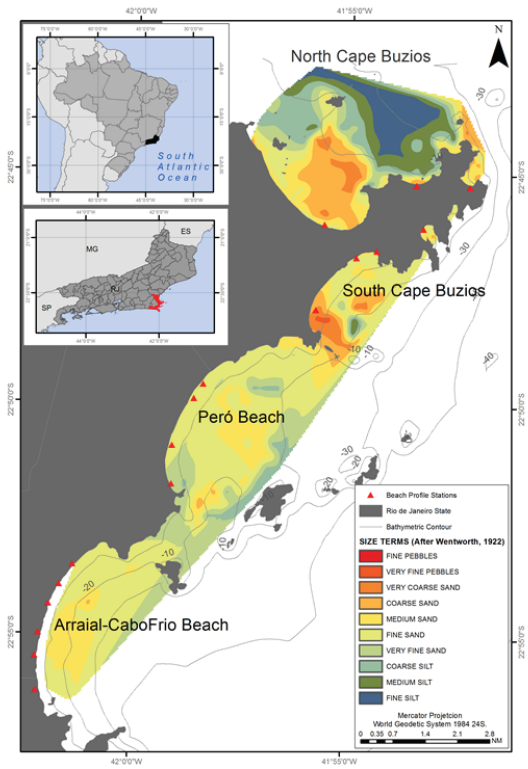

Figure 1. Study area, beach profile stations and surface sediment size distribution.

In coastal areas, storm events have been characterized from the moment that the significant wave height (Hs) exceeds the threshold of 3 meters (You and Lord, 2008; Loureiro *et al.* 2009; Jacob *et al.* 2009) for more than 12 hours (Rangel-Buitrago and Anfuso, 2011; Santiago *et al.* 2013). In this sense, output data from NOAA Wave Watch III model, compiled between 2003 and 2014 to a position nearby the study site, show the total number of events and some of their main characteristics, summarized in Table 1.

The central aim of this paper is to diagnose the morphological behavior of beach profiles selected in the coves between Cabo Frio and Cabo Búzios (RJ), and test the hypothesis that exposure or relative protection of each segment of the coast ahead of the storm waves input is the main element in driving these changes.

Table 1. *Basic characteristics of storm events between 2003 and 2014 period for the offshore section of the study site. Source: NOAA Wave Watch III model.*

Years	No. of Storm Events	Mean Duration (h)	Mean Sign. Wave Height (m)	Mean Wave Direction (°N)	Max. Wave Height (m)
2003	6	30	3.07	180'00	3.60
2004	11	34	3.07	180'00	3.40
2005	3	54	3.17	180'00	3.40
2006	10	43	3.31	178'82	4.10
2007	9	39	3.36	180'00	4.50
2008	9	32	3.1	172'29	3.90
2009	9	32	3.17	180'00	3.70
2010	3	48	3.51	167'14	4.70
2011	5	37	3.32	176'25	4.00
2012	-	-	-	-	-
2013	4	32	3.33	189'64	4.30
2014	6	27	3.09	184'50	3.70
2003 - 2014	75	38	3.09	178'41	3.94
Month	**No. of Storm Events**	**Month**	**No. of Storm Events**	**Month**	**No. of Storm Events**
Jan.	1	May.	13	Sep.	10
Feb.	1	Jun.	10	Oct.	3
Mar.	1	Jul.	7	Nov.	7
Apr.	8	Aug.	12	Dec.	2

METHODS

Beach profile monitoring at 17 positions along the study site resulted in a total of 438 profiles used for calculations of volume changes over the subaerial portion of beaches. Volumetric variation over time aims to highlight the fluctuation of the seasonal sand stock. In addition, bottom information was compiled from surface sediment samples in the inner continental shelf. In total 394 samples were collected and analysed between 2008 and 2011. All sediment analysis followed dry sieving method, except for 38 silt samples analysed by laser diffractometry. Results were interpolated to assess whether areas of greatest wave energy corroborate the distribution of particle size in the coves. Finally, simulations of wave energy distribution were performed in shallow waters to the main inputs of storm waves. 75 storms were identified between April 2003 and December 2014 (Table 1) to position (24º0'S, 41º40'W) that met the standardization of bigger waves than 3 meters occurring for at least 12 hours. From these storms we used the maximum significant wave height values plus the standard deviation and also maximum peak period. These conditions were simulated for three different directions: mean wave direction, mean wave direction minus the standard deviation and the mean wave direction plus the standard deviation. The wind data used were the average conditions.

RESULTS

Sediment Distribution

The results of the distribution (Figure 1) and average diameter of the particles indicate that the occurrence of fine sediment prevails (63%). On south, they occur in the classes of fine (43%) and very fine (5%) sands, while to the north prevails the classes of coarse silt (6%), medium silt (4%) and fine silt (5 %). In the central portion of the coves and nearby rocky headlands, there are spots with coarser sediments, such as medium sands (22%) both in Arraial-Cabo Frio and Pero beach arches and coarse (10%) and very coarse (6%) sand deposits occurring to the north and south of Cape Búzios.

Shallow Water Wave Distribution

Table 2 presents the basic statistics of the 75 storm events identified in the 2003-2014 period.

Three hypothetical simulations of incident wave were prepared with the following basic characteristics input:

- Simulation 01 – Hs: 5,1m; T: 16s; Mean Wave Direction: 179 (South); Wind Speed: 11 kn; Mean Wind Direction: 145 (South Southeast)
- Simulation 02 – Hs: 5,1m; T: 16s; Mean Wave Direction: 154,7º (South-Southeast); Wind Speed: 11 kn; Mean Wind Direction: 145 (South Southeast)
- Simulation 03 – Hs: 5,1m; T: 16s; Mean Wave Direction: 203,3º (South-Southwest); Wind Speed: 11 kn; Mean Wind Direction: 145 (South-Southeast).

Table 2. *Storm events basic statistics for the offshore portion of study site. Source: NOAA Wave Watch III model.*

Storm Event Stats	Sign. Wave Height (m)	Mean Wave Direction (°N)	Period (s)	Wind Velocity (knots)	Mean Wind Direction (m)	Storm Duration (h)
Max.	4.7	247'5	16.0	27.0	337'5	105'0
Mean	3.2	179'0	11.6	11.20	145'1	36'2
Min.	2.2	112'5	6.0	1.0	0	18'0
St. Dev.	0.4	24'3	1.7	4.4	72'8	16'9

Results presented in Figure 2 were extracted from these simulations from the exactly submerged portion adjacent to each monitoring stations of beach profiles.

The maximum wave height occurred in the P3 position of Arraial - Cabo Frio beach arch which is exposed to storm waves from South and Southeast. In Pero beach, the profile position that received most energy was North Center Pero, for all simulations. In South Buzios, positions South Geribá and South Tucuns received larger waves also from any of the simulated directions. North Buzios is full protected against storm waves. For storm waves from South-Southwest, the beach arch Arraial-Cabo Frio is also protected.

Volumetric variability of subaerial profiles.

In Arraial-Cabo Frio beach arch (Figure 3) the central profile (P3) is the most stable and P5 profile the most unstable, presenting his lower volumes in autumn and winter months (i.e. April 2005, August 2010 and July 2012). The peaks of sand accumulation occurred in March 2006 for P6 profile (200m³/m); October 2007 for P5 profile (192.5m³/m);

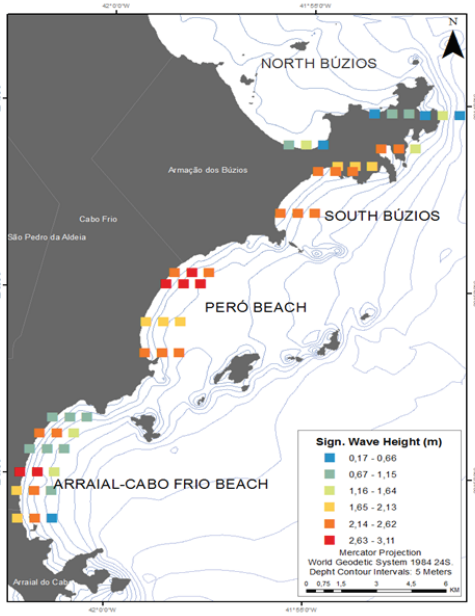

Figure 2. Result of simulations of storm waves. The colored squares represent from left to right, the maximum heights Resulting from simulations 01, 02 and 03 and their location represent each of the 17 stations of monitoring beach profiles.

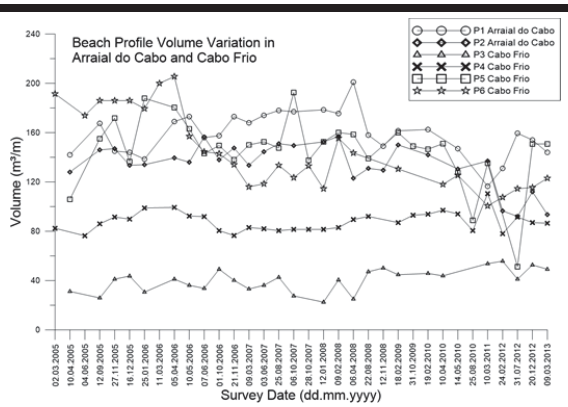

Figure 3. Beach profile volume variability for Arraial-Cabo Frio beach arch.

March 2011 for P4 profile (110.5m³/m); February 2012 for P3 profile (55.7m³/m); June 2006 for P2 profile (156.5m³/m); and April 2008 for P1 profile (201m³/m). The biggest losses in subaerial stock occurred in P6 profile, located further north of the beach arch, between April 2006 (205m³/m) and March 2007 (116m³/m) which represents a loss of 43% of the previous volume. In these 11 months, 11 storms were identified according to Table 1, and it is suggested that, by cumulative effect, the subaerial profile has not recovered.Figure 4 shows the volumetric variation of seven beach profiles in the coves of Cape Buzios. The South Tucuns profile has the highest

volumetric variability, accumulating a significant loss (38m³/m) between January and November 2008, during which 10 storms were recorded. Between February and May 2010, there were only two storms, these being the largest magnitude since 2003 to date. Such a storm, whose morphological impacts on beaches were recorded by Fernandez *et al.* (2011), promoted losses in all sections of the southern area of Cape Buzios, with 39m³/m in North Geriba profile; 7.4m³/m in South Geriba profile; 19m³/m in South Tucuns profile; 5.5 m³/m in Ferradura profile; and 1.5 m³/m in Center Canto profile. When these changes are compared with the preceding volume for subaerial profiles, it equates to a loss of, respectively, 73%, 72%, 22%, 11% and 33%.

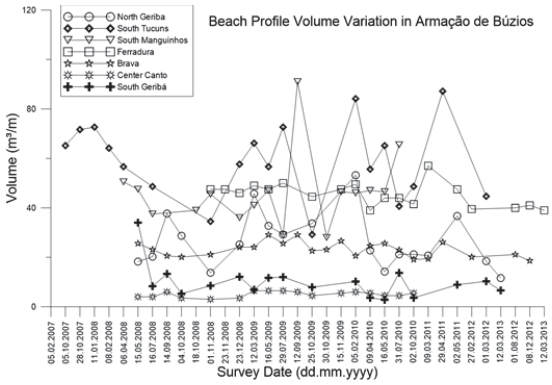

Figure 4. Beach profile volume variability for Cape Buzios.

Figure 5 shows the volumetric variation of beach profiles established along Pero beach arch. The largest accumulation occurred between August 2008 and May 2009 to North Center Pero profile. Among May 2010 and March 2011 there were gains for all profiles. In this period only two storms were identified, which may explain the cumulative pattern. Biggest losses occurred for North Center Pero profile during the period from May 2009 (165m³/m) to May 2010 (91.9m³/m) when 10 storm events were identified. In the same period, continual losses occurred in all profiles: North Pero (-30.5m³/m); South Pero (-21.4m³/m); South Center Pero (-19m³/m). Note that these losses corroborate the pattern of greater or lesser exposure to storm waves shown in Figure 2.

DISCUSSION

Grain size distribution results represent two distinct sources of sedimentation to the study area, as already suggested by Saavedra (1994). To the south of Cape Buzios the relict fine sands of inner continental shelf supplies the beaches and dune fields along these arcs. North of Cape Buzios, the silts represent a neoteric (modern) fluvial sedimentation that overlies the palimpsest sedimentation (Bulhoes and Fernandez, 2011). The coarse sands indicate, north of Cape Buzios, greater agitation by waves, making it impossible to fine sediment (neoteric) to deposit, according to results of Tavares *et al.* (2010). South of Cape Buzios, coarse sediments indicate gravelly areas mostly composed by biogenic fragments, especially in the vicinity of rocky headlands and submerged rocky slabs.

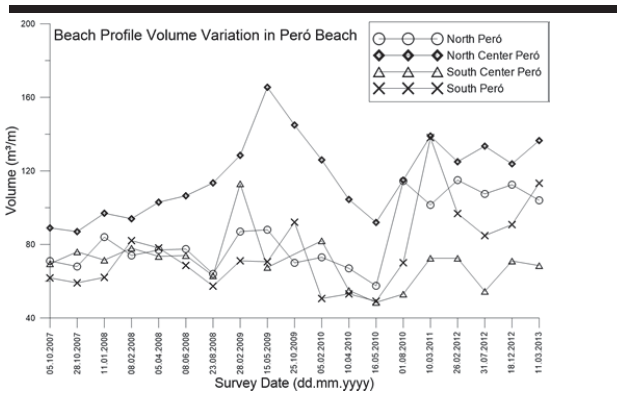

Figure 5. Beach profile volume variability for Peró beach arch.

In Pero beach arch, Guerra *et al.* (2005), Muehe *et al.* (2010) and Oliveira Filho (2011) found similar results such as: medium sands in the central portion of the beach and fine sands towards the beach ends, pattern that repeats for inner continental shelf. The interpretations were different: while the first author attributed the standard particle size distribution to the convergence of longshore drift, leading to the accumulation of sediments, the second author considers that the central portion of the beach arch is a scattering area of fine sands; and third author considers the effect of wave diffraction due to the islands positioning. Despite these interpretations and agreeing that the main depositional agent is the movement promoted by waves, it is important to consider that the average sediment diameter describes the average kinetic energy of the depositional agent (Sahu, 1964) and therefore is a good indicator of the action waves on the shallower areas of the continental shelf.

For profile results, in the south portion of the study site (P1 and P2) and in protected coves in North Cape Buzios there is an increase in sand stock of beach profiles during the storm waves season, as these areas are highly protected from direct incidence of storm waves. In profiles of the central and northern segment of Arraial-Cabo Frio beach arch (P3 to P6), the sediment accumulation is greatest during the fair weather season. In Pero beach it was observed in six years that only South Center Pero position has downward trend in the volume of sediments of subaerial portion of the profile, and all others showing an increase in the stock of sediment over the period, with seasonal fluctuations, which by that time is not a global trend of erosion or accumulation but the morphodynamic variability of the intermediate type beaches, agreeing with what Muehe *et al.* (2010) also pointed to this area.

CONCLUSIONS

Three topics can be presented as conclusive in this work:

• Size distribution of medium and coarse sands in the shoreface and inner continental shelf indicates that greatest wave energy occurs in the central position of the coves. While this is a good result, the interpretation of the distribution of fine and very fine sand and preferred erosion areas, transport and deposition of sediments needs analysis, among others, using some dispersion parameters such as standard deviation, skewness and kurtosis, which was not proposed in this work.

• The distribution of storm waves over time showed that they occur mostly between April and September (80%) and this is the "storm waves season". In this period larger waves can reach up to 5 meters in deep water, incoming between the South-Southeast and South-Southwest directions, with most energy towards the central and northern portions beach arches between Cape Frio and Cape Buzios. Thus positions to the south of these arches remain protected as does the coves in the northern portion of the Cape Buzios.

• Volume variations of beach profiles, over time, shows oscillations of templating agents, as are the waves. During the "storm waves season" there is a general trend of loss in the stock of sediments of subaerial portion of monitoring profiles (a 73% rate of loss was measured for South Geriba). The volume of loss accompanying the relative position of the profiles, which are greater in those more exposed and lower among those most protected from storm waves. Analysis of the morphological effects of storm waves can be subdivided into two: the first analysis should consider the "cumulative effect" which is caused by a period of successive storms (e.g. 11 storms at 11 months), while the second can be called of "personal effect" and is the most common type of analysis, such as the case cited the April event in 2010. As the number of morphological surveys on the beaches becomes greater, we can try to understand this first type of effect and then being appointed morphological trends in the role of beaches in protecting mainland.

ACKNOLEDGEMENTS

The authors thank FAPERJ and CNPq for granting daily for field surveys and CAPES for granting scholarships for postgraduate studies. The authors also thank the many students who collaborated with field surveys and analyzes in the laboratory.

LITERATURE CITED

Bulhões, E. and Fernandez, G.B., 2011. Analysis of shallow water wave propagation and coastal response in embayed beaches. Case study in Cape Buzios, Rio de Janeiro, Brazil. *J. Coastal Res.*, SI 64: 2022-2026.

Bulhões, E.; Fernandez, G.B., and Rocha, T.B., 2013. Morphodynamics of embayed beaches. Case study in Cape Buzios, Rio de Janeiro, Brazil. J. Coastal Res., SI 65, 1739-1744.

Fernandez, G.B.; Bulhões, E.; and Rocha, T.B., 2011. Impacts of severe storm occurred in April 2010 along Rio de Janeiro coast, Brazil. *J. Coastal Res.*, SI 64, 1850-1854.

Guerra, J.V.; Schmitt, R.S.; Souza, J.H.M.; Skrepnek, C.C.; and Bentes, A.M.L., 2005. Sedimentologia das praias arenosas da região costeira situada entre o Cabo Frio e o Cabo Búzios. X *Congresso da Associação Brasileira dos Estudos do Quaternário*. (Guarapari, ES).

Innocentini, V.; Arantes, F.O.; and Prado, S.C.C., 2003. Modelo de Ondas Aplicado ao Caso 5-8 de Maio de 2001. *Revista Brasileira de Meteorologia*, 18 (01): 97-104.

Jackson, D.W.T.; Cooper, J.A.G.; and Del Rio, L., 2005. Geological control of beach morphodynamic state. *Marine Geology*, 216, 297-314.

Jacob, J.; Gama, C.; Salgado, R.; Liu, J.T.; and Silva, A., 2009. Shadowing effects on beach morphodynamics during storm events on Tróia-Sines embayed coast, southwest Portugal. *J. Coastal Res.*, SI 56, 73-77.

Johnson, D.W. 1919. Shore Processes and Shoreline Development. John Wiley & Sons, Inc. London, 584 p.

Loureiro, C.; Ferreira, Ó.; and Cooper, J.A.G., 2009. Contrasting morphologic behavior at embayed beaches in Southern Portugal. *J. Coastal Res.*, 56, 83-87.

Mahiques, M.M.; Tessler, M.G.; and Furtado, V.V., 1998. Characterization of energy gradient in enclosed bays of Ubatuba region, South-Eastern Brazil. *Estuar. Coast. Shelf Sci.*, 47:431-446.

Muehe, D.; Belligotti, F.M.; Lins-de-Barros, F.M.; Oliveira, J.F.; Maia, L.F.P.G., 2010. Potential vulnerability to climate change of the beach-dune system of the Peró coastal plain – Cabo Frio, Rio de Janeiro state, Brazil. *Panam J Aquat Sci.* 5(2):267-276.

Oliveira Filho, S.R. 2011. Morfodinâmica Associada entre Duna, Praia e Zona Submarina como Subsídio a Adequada Ocupação do Espaço Costeiro na Praia do Peró – RJ. Dissertação de Mestrado. Centro de Ciências e Tecnologia. Universidade Estadual do Ceará. 96p.

Parise, C.K.; Calliari, L.J.; Krusche, N., 2009. Extreme storm surges in the South of Brazil: Atmospheric conditions and shore erosion. *Brazilian Journal of Oceanography,* 57(3):175-188.

Rangel-Buitrago, N., Anfuso, G. 2011. An application of Dolan and Davis (1992) classification to coastal storms in SW Spanish littoral. *J. Coastal Res*., SI 64:1891-1895.

Saavedra, L., 1994. Dinâmica sedimentar na plataforma continental interna entre a Ilha do Cabo Frio e Cabo Búzios. Dissertação de Mestrado. Programa de Pós-Graduação em Geografia. Universidade Federal do Rio de Janeiro. 125p.

Sahu, B.K. 1964. Depositional mechanisms from the size analysis of clastic sediments. *Journal of Sedimentary Petrology*, 34(1), 73-83.

Santiago, I.; Morichon, D.; Abadie, S.; Liria, P.; and Epelde, I.; 2013. Effect of winter storms on a partly engineered embayed beach: The case of Zarautz beach (North of Spain). *Coastal Dynamics*, 2013, 487-498.

Satyamurty, P.; and Mattos, L.F., 1989. Climatological lower tropospheric frontogenesis in the midlatitudes due to horizontal deformation and divergence. *Monthly Weather Review*, 117, 1355-1364.

Short, A.D. 1999. Handbook of Beach and Shoreface *Morphodynamics*. John Wiley & Sons Ltd. New York. 379p.

Tavares, A. C. A.; Bulhões, E.; and Estrada, A. F. D., 2010. Distribuição de fácies sedimentares e tendências de transporte de sedimentos na enseada de Manguinhos, Armação dos Búzios, *Revista de Geografia,* 27(2), 81-97

You, Z.J.; and Lord, D. 2008. Influence of the El-Niño-Southern Oscillation on NSW coastal storm severity. *J. Coastal Res.*, 24(2A), 203-207.

Journal of Coastal Research	SI	75	1052 - 1056	Coconut Creek, Florida	2016

Beach response to consecutive extreme storms using LiDAR along the SW coast of England

Olivier Burvingt[†*], Gerd Masselink[†], Paul Russell[†] and Tim Scott[†]

[†]School of Marine Science and Engeenering Plymouth University, UK

www.cerf-jcr.org

www.JCRonline.org

ABSTRACT

Burvingt, O.J.P.; Masselink, G., Russell, P.,and Scott,T. 2016. Beach response to consecutive extreme storms using LiDAR along the SW coast of England. *In:* Vila-Concejo, A.; Bruce, E.; Kennedy, D.M., and McCarroll, R.J. (eds.), *Proceedings of the 14th International Coastal Symposium* (Sydney, Australia). *Journal of Coastal Research*, Special Issue, No. 75, pp. 1052 - 1056. Coconut Creek (Florida), ISSN 0749-0208.

On the south west coast of England, the 2013/14 winter has been the most energetic period over the past 60 years, counting over 22 storms with recorded wave heights exceeding 10 meters. Pre- and post-storm aerial LiDAR surveys have been carried out by the Environmental Agency along the entire SW coastline. A total of 157 beaches have been selected from this dataset and morphological changes over the stormy period have been calculated and studied by processing the LiDAR data. This analysis shows the varying response of the beaches to the extreme storms and highlights two mechanisms involved in sediment transport. The results show that North coast beaches exposed to the main storm waves eroded, losing sediment offshore by cross-shore transport processes. Conversely, on the South coast beaches, where wave approach was more oblique, sediment was mainly transported along-shore resulting in beach rotation.

ADDITIONAL INDEX WORDS: *Storm, extreme events, coastal prossesses, morphological changes, LiDAR.*

INTRODUCTION

The vulnerability of coastal areas is becoming an increasingly important social, economic and environmental issue. Sea level rise, leading to higher risk of flooding events along coastal areas (Milly *et al*., 2002), has already been observed in many areas of the world and quantified (Rhein *et al*., 2013). In addition, climate change also disrupts atmosphere physical properties and is likely to be responsible for more variable and extreme weather conditions. At the same time, coastal population growth is expected to continue in the future (Neumann *et al*., 2015). Thus, the question of how coastal areas and populations will cope with increasing water levels combined with extreme storms is a big challenge in coastal sciences.

Western European countries along the North Atlantic Ocean such as the UK, France and Portugal were impacted by extreme storm events during the 2013/2014 winter. A sequence of 22 storms hit the south west coast of England between October 2013 and April 2014. Waves higher than 10 meters with exceptionally long periods, often over 20 seconds, were recorded 30 kilometres off the tip of SW England. These waves, when associated with spring high tide levels, caused damage and flooding in a large number of coastal locations round SW England (Devon County Council, 2014) (Fig. 1). In addition to infrastructural and environmental damage, beach erosion in SW England was wide-spread and this had significant economic consequences. A large number of beaches in the area offer recreational activities and stimulate tourism, representing one of the major sources of economy in the region. The extreme events that occurred during the 2013/14 winter provided a unique opportunity to better understand the impact of storms on coastal areas.

DOI: 10.2112/SI75-211.1 received 15 October 2015; accepted in revision 15 January 2016.

*Corresponding author: olivier.burvingt@plymouth.ac.uk

©Coastal Education and Research Foundation, Inc. 2016

If the conditions during the 2013/14 winter are likely to occur more often during the next decades, an improved understanding of storm-induced morphological changes along this coastline is a priority for the future. This better understanding comes through more field or lab data collection, which is essential to improve the models used to describe and forecast coastal hydrodynamics and sediment transport.

Thanks to recent advances in technology, different techniques for recording beach morphological change are available, including ground-based GPS beach surveys (*e.g.* Stephan *et al*., 2012), airborne LiDAR (*e.g*. Houser *et al*., 2013) and satellite imagery (*e.g*. Castelle *et al*., 2015). Aerial LiDAR surveys offer large spatial data with a relatively good resolution and form the basis for this regional spatial study of morphological changes caused by extreme storms covering over 150 diverse beaches (Fig.3).

The aim of this article is to give an overview of the coastal impact of the unprecedented extreme winter storms of 2013/2014 in SW England and to use aerial LiDAR datasets to examine the resulting coastal morphological changes.

Background

Winter 2013/2014 was characterised by an exceptional sequence of storms. Most of the European western coast was affected over that period, from Ireland to Portugal and some detailed studies about those events have already been presented (Masselink *et al*., in press; Castelle *et al*., 2015). Focusing on SW England, records from the Sevenstones Lightship buoy located 30 km offshore of the coast of Cornwall and at 70 metres depth (Fig.3) have been studied. While definition of storm events are site-specific (Almeida *et al*., 2012), Masselink *et al*.,(in press) -

defined a storm as a wave event during which the maximum Hs exceeds the 1% exceedance wave height (5.9 m for this winter period), where the start and end of the storm is defined when *Hs* exceeds or falls below 4.5 m (Fig. 2, horizontal lines) corresponding to the 5% exceedance height.

The upper panel of Figure 2 shows the 22 storms that were recorded between October 2013 and April 2014. During this 6-month period, average peak and mean significant wave height *Hs* were respectively 8.1 m and 6.1 m, with an average storm duration of 29 hours. These wave conditions were exceptional, while the westerly wave direction was typical of Atlantic storms. Furthermore, to highlight the exceptional nature of this winter period, Masselink *et al*., (in press) –analysed the 8-week moving average of modelled (1953-2011; WWIII data from Dodet *et al*., 2010) and measured (2008-2014, http://www.previmer.org/) significant wave height at Sevenstones Lightship buoy (Fig. 2; lower panel). These records show that this winter represents at least a 1:60 year event for the SW coast of England; such wave conditions have not been recorded since at least 1953.

Figure 1. Pictures of wave conditions during extreme storms in 2013/2014 at different locations along the SW coast of UK. Clockwise from top left: Porthcothan, North Cornwall; Sennen Cove, West Cornwall; Dawlish, South Devon and Porthleven, West Cornwall.
Source: Telegraph, Western Morning News

In addition to the unique conditions of the winter 2013/2014, the south west peninsula represents a ideal study area because of its diversity. Indeed, from Weston-Super-Mare (Somerset) in the north of the SW peninsula to Seaton (Devon) on the south coast, over 150 beaches are present that are spread along the 1000 km of coastline. Among these beaches, there is a high diversity in terms of dynamic (waves, tides) and static (shoreline orientation, geology, sediment size and abundance) boundary conditions, giving this part of England a special character which attracts a large number of tourists every summer and represents 25% of all employment in the region (Research–Visit Cornwall, 2011). A study about morphodynamic characteristics from 92 beaches within this area resulted in the identification of 9 distinct beach types (Scott *et al*., 2011). Although tidal range is highly variable throughout the region, all beaches are macro-tidal, with mean spring tide range varying from 11.4 m (Weston-Super-Mare, the most northern site on the North coast) to 3.6 m (West Bay, the easternmost site on the South coast).

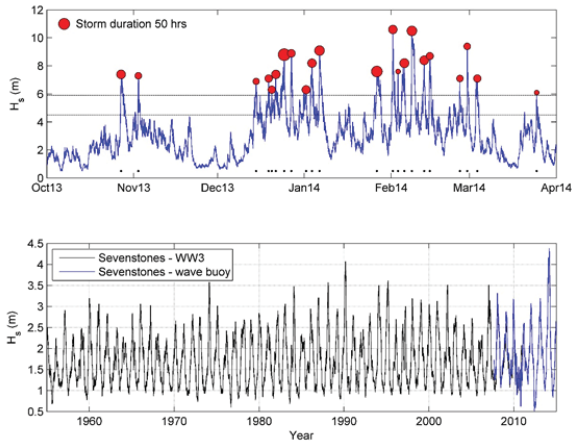

Figure 2. Upper panel shows time series of significant wave height *Hs* measured at Sevenstones Lightship (location in Figure 3). The horizontal lines represent the threshold *Hs* level used for delineating the strom events. Lower panel shows time series of 8-week moving average of WWW III modelled (1953-2011; Dodet *et al*., 2010) and measured (2008-2014) significant wave height at Sevenstones Lightship.
Source: Masselink *et al*., in press.

Figure 3. Location of the study area (left panel). SW peninsula of England with study beaches locations in blue and Sevenstones Lightship buoy location in yellow (right panel).

METHODS

Aerial LIDAR uses a laser to measure the distance between the survey aircraft and the ground surface, and then collects millions of XYZ georeferenced points. The use of LiDAR data to assess geomorphological changes in coastal science is relatively new.

Given the amount of data collected, it represents a good compromise in terms of time, effort and cost, in comparison with other survey techniques, such as RTK-GPS surveys. The vertical accuracy of LiDAR is estimated in the range of 0.05 m to 0.15 m, which is appropriate for studying beach morphological changes observed during such extreme events. Furthermore, the spatial resolution in the order of 1 m, is comparable to other survey techniques commonly used. However, aerial LiDAR does have some limitations in terms of surface coverage as the laser cannot survey through water so beach coverage is rarely 100% and data are missing where the beach surface is covered with water (*e.g.* in intertidal channels). Airborne LiDAR surveys for coastal areas are usually carried out during spring tides, offering the largest surface of the exposed beach at spring low tides. Every beach for which LiDAR coverage was estimated to be less than 70% of the whole surface area has been removed from our list of study sites. Commissioned by the Environment Agency (EA), the coastline of SW England is surveyed every few years by airborne LiDAR. Different sections of the coast are surveyed in different years, but the whole coast has been surveyed in spring 2014 following the extreme events of the winter 2013/2014. The timing of the *pre*-storm datasets was, however, an issue since LiDAR campaigns do not run every year for every site. The most recent *pre*-storm surveys dated from April 2012 while the oldest *pre*-storm surveys dated from October 2010. Our study focuses on the changes that occurred during the winter of 2013/14; therefore, several of our *pre*- and *post*-storm datasets actually represent a 2-4 year period, making the comparison between *pre* and *post* storm morphology potentially problematic. However, the study of another dataset provides confidence in the methodology used here. The Coastal Processes Research Group (CPRG; Plymouth University) has been surveying Perranporth beach monthly since 2006 (Fig. 4). Perranporth is a macro-tidal beach located on the north coast of Cornwall in SW England and is 4 km long. This beach faces the Atlantic Ocean and is fully exposed to the prevailing swell and wind-waves. Figure 4 shows the evolution of volumetric sediment change at Perranporth beach from 2006 to 2014.

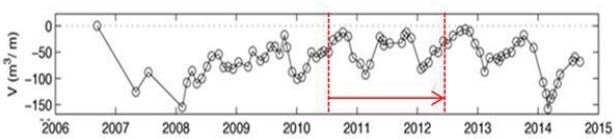

Figure 4. Volumetric net change of sediment per meter witdh ($m^3.m^{-1}$) at Perranporth beach between 2006 and 2014. The red window indicates the *pre* storm LiDAR survey period.
Source: Modified from Scott *et al*.,(2015).

Seasonal changes in beach volume due to the difference of wave climate between winter and summer can be observed, with erosion from October to April and accretion from May to September. There is a severe loss of sediment during the winter 2013/14 and the volume changes that occurred from winter 2010/11 to summer 2013 are considerably less than that occurred during the 2013/14 winter. The beach volume time series from Perranporth shows that the time delay between the *pre*-storm LiDAR surveys and the onset of the 2013/14 winter is only expected to have limited impact on our analysis.

All data from the different aerial LiDAR surveys have been compiled by the Plymouth Coastal Observatory. Every beach from our study area where the LiDAR coverage was satisfactory was selected resulting in 157 study sites spread all over the SW peninsula with 56 beaches located on the north coast and 101 on the south coast (Fig. 3).The first step was to extract the data corresponding to the sediment areas for all these beaches. LiDAR surveys generally extend from Spring Low Water Level to several 100's m landward (Fig. 5a) and, the beach area cannot be directly identified. Therefore, every single beach area was digitized by drawing polygonal shapefiles on ArcMap 10.2.2 software (Fig. 5c). The 157 shapefiles were drawn using high resolution aerial pictures (Fig. 5b) and, beach areas were digitized with high precision and leaving out obstacles (cliff, infrastructure on the beach). Then, using the same coordinate system (British National Grid Projected Coordinates System), both shapefiles and LiDAR rasters were overlapped (Fig. 5d) and the overlapped data were extracted. Figure 5 shows the process described above for two different beaches located on the north coast of Cornwall (Crantock and Fistral). The extraction is done twice (*pre*- and *post*-storm rasters) for each of the 157 beaches leading to new rasters. These rasters are then converted into ASCII files, to be next processed with Matlab R2013®.

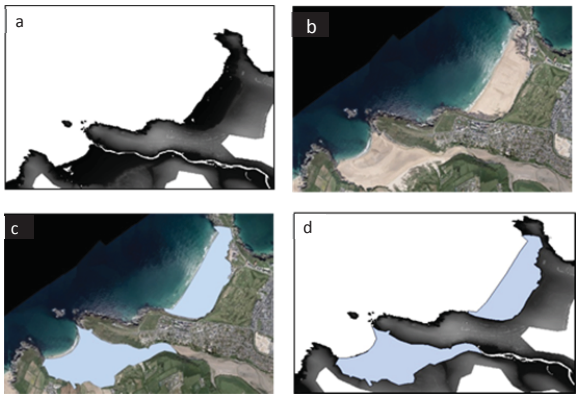

Figure 5. Illustration of the process of extracting useful data from the LiDAR tiles: (a) raw LiDAR data; (b) aerial picture of the same area; (c) digitized shapefiles drawn around the two beaches (Crantock and Fistral); and (d) digitized shapefiles overlapped with LiDAR data. Once the process is complete, relevant LiDAR data can be extracted.

The 157 pairs of XYZ georeferenced points with a horizontal resolution of 1 m corresponding to both *pre*- and *post*- storm surveys can therefore be compared and analysed in order to estimate the morphological changes caused by the extreme wave conditions during the winter 2013/2014.

RESULTS

The LiDAR datasets provide the unique opportunity to quantify the sediment change that has occurred over a 1:60 year event for 157 beaches in the SW of England. The total volumetric change dQ_{tot} corresponds to the sum of every topographic change between *pre* and *post* storm datasets and is expressed in m^3 (Equation 1).

$$dQ_{tot} = \sum_1^N dQ_i \quad (m^3) \qquad (1)$$

Results show that104 (66%) of the beaches lost sediments while the other 53 (34%) beaches gained sediment during the 2013/14 winter. Figure 6 shows the geographical distribution of the eroding (red symbols) and accreting beaches (blue symbols). Volumes of sediment that were lost are in line with the exceptional nature of that winter period. Perranporth and Bude beaches, which are wide open beaches located on the North coast that receive the full brunt of the swell and storm waves, lost up to 700 000 m^3 of sediment.

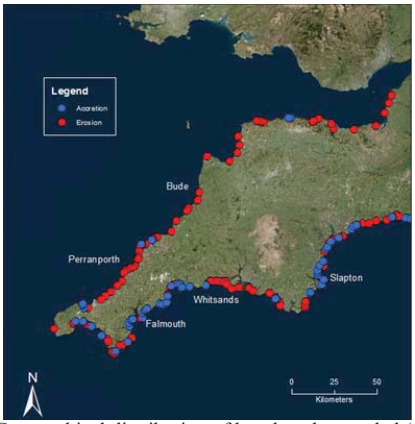

Figure 6. Geographical distribution of beaches that eroded (red symbols) and accreted (blue symbols) during the 2013/2014 winter.

The total volumetric change for each beach dQ_{tot} was converted to a volumetric change per unit m beach width dQ by dividing dQ_{tot} by the length of the beach. Figure 7 plots dQ for all 157 beaches, geographically ordered from north (left) to south (right). On the north coast, almost all beaches lost sediments (88%). During those extreme events, the main offshore wave direction was from the west; therefore, the west- and north-west-facing beaches were fully exposed to the storm waves. Widespread and extensive erosion of the north coast beaches is thus not very surprising. However, the observed beach response on the south coast is more complex. Erosion and accretion are balanced with 46 (45%) beaches gaining sediment while sediment losses are observed for the other 55 (55%) beaches. This non-uniform beach response among south coast beaches can be partly explained by their variable shoreline orientation relative to the storm wave direction; the storm waves usually approached obliquely from the west and the south-west causing beach to rotate.

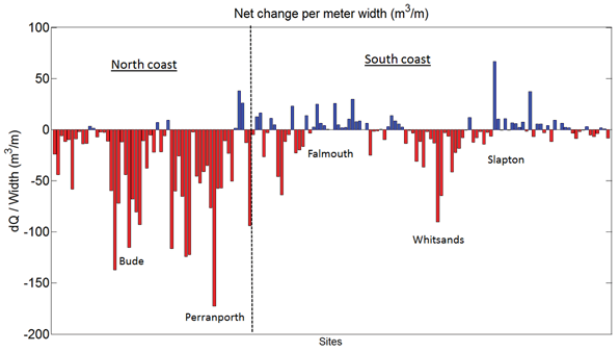

Figure 7. Volumetric net change per meter width (m^3/m) between *pre* and *post* storm periods for all 157 beaches. Bars are geographicaly ordered from North to South, red color corresponds to erosion and blue color to accretion.

DISCUSSION

Large volumes of sediment, of up to 100-200 m^3/m, were lost by several beaches on the SW coast during the 2013/14 winter and illustrate the significant coastal impacts of such a sequence of extreme storms. Unsurprisingly, the fully exposed beaches located on the north coast lost larger quantities of sediment than most of the beaches located on the south coast. However, inspection of the LiDAR data (Fig. 8 and 9), reveals varying patterns of response along north and on the south coast beaches (see also Masselink *et al*., in press). Most of the beaches located on the North coast are dominated by cross-shore sediment transport (Fig.8). On the other hand, many sites located on the south coast show a clear eastward long-shore sediment transport leading to a rotation of the beach (Fig.9). The different wave approach between both coasts is certainly something to consider about the difference in sediment transport. A method that could allow quantifying the cross-shore and long-shore character of the beach response will be examined in future work.

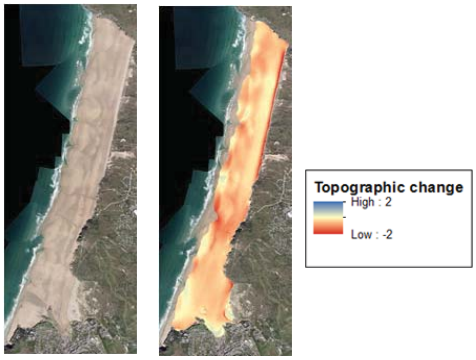

Figure 8: Aerial picture (left panel) overlapped by topographic change LiDAR data in m (right panel) of Perranporth beach on the north coast.

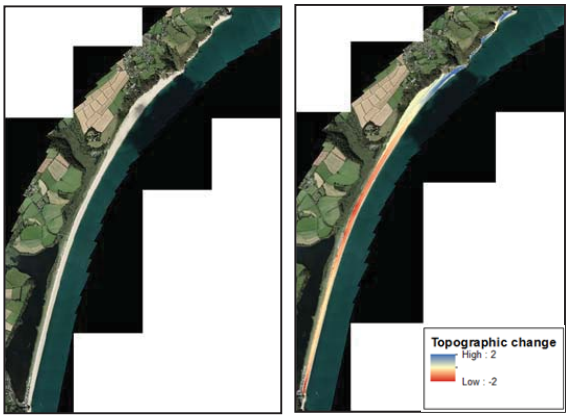

Figure 9: Aerial picture (left panel) overlapped by topographic change LiDAR data in m (right panel) of Slapton beach on the south coast.

CONCLUSIONS

The 2013/14 winter was characterised by a rare and intense sequence of storms hitting the Atlantic coast of Europe. The analysis based on modelled and observed offshore wave conditions described this period as a 1:60 year event. The impact of the waves caused by the storms on coastal housing and infrastructure has been widely reported in the local and national news. Scientific interest has focused on the impact of these storms on the coastline. A campaign of airborne LiDAR surveys has been carried out a few weeks after the end of the winter period all along the SW coast of England. The large spatial coverage of these surveys allows the investigation of the storm response of practically all beaches along the SW peninsula. A methodology concerning the LiDAR data process has been presented. Preliminary results from this analysis have quantified the volume of sediment that has been lost or gained by 157 beaches during the 2013/14 winter. North coast beaches were exposed to the large storm waves and most were characterised by a shore-normal storm wave approach, leading to a dominance of cross-shore transport. The beach response to these waves was erosion, with very high volumes of sediment up to 200 m^3/m eroded from the large exposed north coast beaches. South coast beaches are more sheltered from the storm waves and at most locations the storm waves approach obliquely from the west and south-west leading to dominant eastwards longshore transport and beach rotation. Overall some south coast beaches eroded and some accreted and there was less erosion/accretion than on the more exposed north coast beaches. This dataset has a wider potential and future work will focus on investigating in more detail the relationship between the type and quantity of the coastal response, and the, static (shoreline orientation, geology, sediment size and abundance) and dynamic (waves, tide) boundary conditions.

ACKNOWLEDGMENTS

This study has been possible thanks to the Environmental Agency which lead the airbone LiDAR surveys via the South West Regional Coastal Monitoring Programme. The authors would like to acknowledge the help of the Plymouth Coastal Observatory directed by Emerald Siggery.

LITERATURE CITED

Almeida, L.P., Vousdoukas, M.V., Ferreira, O., Rodrigues,B.A, Matias, A., 2012. Thresholds for storm impacts on an exposed sandy coastal area in southern Portugal. *Geomorphology*, 143-144, 3-12.

Castelle, B., Marieu, V., Bujan, S., Splinter, K.D., Robinet, A., Sénéchal, N. and Ferreira, S., 2015. Impact of the winter 2013-2014 series of severe Western Europe storms on a double-barred sandy coast: beach and dune erosion and megacusp embayments. *Geomorphology*, 238, 135-148.

Devon County Council, 2014. *Reviewing the impacts, responses and resilience of people and places in Devon to the winter storms of 2013/2014*.http://www.devonmaritimeforum.org.uk.

Dodet, G., Bertin, X. and Taborda, R., 2010. Wave climate variability in the North-East Atlantic Ocean over the last six decades. *Ocean Modelling*, 31, 120-131.

Houser, C., 2013. Alongshore variation in the morphology of coastal dunes: implications for storm response. *Geomorphology*, 199, 48-61.

Masselink G., Scott T., Davidson M., Russell P., and Conley D., in press. The extreme 2013/2014 winter storms: hydrodynamic forcing and coastal response along the southwest coast of England. *Earth Surface Processes and Landforms*.

Milly, P. C. D., Wetherald R. T., Dunne K. A. and Delworth,T. L., 2002. Increasing risk of great floods in a changing climate. *Nature* ,415, 514-517.

Neumann, B., Vafeidis, A.T., Zimmermann, J., and Nicholls R.J., 2015. Future coastal population growth and exposure to sea- level rise and coastal flooding, a global assessment. *PLoS One* 10 (3).

Previmer, Observations et previsions cotieres. http://www.previmer.org.

Research–Visit Cornwall. https://www.visitcornwall.com/sites/default/files/generic_files/Value%20of%20tourism-2011.pdf

Rhein, M., Rintoul S.R., Aoki S., Campos E., Chambers D., Feely R.A., Gulev S., Johnson G.C., Josey S.A., Kostianoy A., Mauritzen C., Roemmich D., Talley L.D. and Wang F., 2013. *Climate Change 2013: The Physical Science Basis*. Contribution of Working Group I to the 5th Assessment Report of the IPCC. Cambridge: Cambridge University Press.

Scott, T., Masselink, G. and Russell, P., 2011. Morphodynamic characteristics and classification of beaches in England and Wales. *Marine Geology*, 286, 1-20.

Stephan, P., Suanez, S. and Fichaut, B., 2012. Long-term morphodynamic evolution of the Sillon de Talbert gravel barrier (Brittany, France). *Shore & Beach*, 80, 19-36.

Journal of Coastal Research	SI	75	1057 - 1061	Coconut Creek, Florida	2016

Development of Hazard Map with Probable Maximum Tsunamis

Yong-Sik Cho[†], Hyung-Sik Hwang[†], Jin-Young Kim[§], and Hyun-Han Kwon[§*]

[†]Dept. of Civil and Environmental Engineering
Hanyang University, 222 Wangsimni-ro,
Seongdong-gu, Seoul 04763, Korea

[§]Dept. of Civil Engineering
Chonbuk National University, 567 Baekje-daero
Deokjin-gu Jeonju-si, Jeollabuk-do 54896, Kore

www.cerf-jcr.org

www.JCRonline.org

ABSTRACT

Cho, Y.-S.; Hwang, H.-S.; Kim, J.-Y., and Kwon, H.-H., 2016. Development of Hazard Map with Probable Maximum Tsunamis. *In:* Vila-Concejo, A.; Bruce, E.; Kennedy, D.M., and McCarroll, R.J. (eds.), *Proceedings of the 14th International Coastal Symposium* (Sydney, Australia). *Journal of Coastal Research*, Special Issue, No. 75, pp. 1057 – 1061, Coconut Creek (Florida), ISSN 0749-0208.

The disaster prevention against unexpected tsunami events has attracted much attention due to huge casualties resulting from the Sumatra Tsunami on December 26, 2004 in Indonesia and the East Japan Tsunami on March 11, 2011 in Japan. Research on how to mitigate the damage by unexpected tsunami events should be completed, because of the significant number of human deaths and property damage from these events. An effective and economic way for the tsunami hazard mitigation planning is to develop a hazard map along those coastlines vulnerable to tsunami events. In order to create a hazard map for unexpected tsunami events, numerical modelling for several tsunami events should be carried out. The Eastern Coast of the Korean Peninsula is vulnerable to tsunami events generated the Western Coast of Japan. In 1983, the Central East Sea Tsunami caused 3 fatalities and property damage. Furthermore, several nuclear power plants are now under operation and several more are scheduled to be constructed. Thus, a tsunami hazard map should be made based on the probable maximum tsunami events. The developed hazard map could be used by the civil defence organizations to make evacuation plans in the real tsunami event.

ADDITIONAL INDEX WORDS: *Tsunami, Hazard map, Probable maximum tsunami, Numerical model, Inundation*

INTRODUCTION

Recently, devastating tsunamis triggered by undersea earthquakes in subduction zones around the Pacific Ocean have frequently caused the loss of a large number of human lives as well as property damage. The Sumatra Tsunami event that occurred on December 26, 2004, caused approximately 220,000 human deaths and 10 billion US dollars in property damage (http://www.ngdc.noaa.gov/hazard/26dec2004.html). The East Japan Tsunami event occurred on March 11, 2011, caused approximately 20,000 casualties (including missing people) and approximately 300 billion US dollars in property damage (http://www.ngdc.noaa.gov/hazard/11mar2011.html). This loss of human lives and extensive property damage led to considerable attention from the public and research community focused on tsunami disaster prevention. Traditionally, most of available studies on tsunamis have focused on the predicted tsunami flooding areas and the run-up heights based on numerical simulations.

It is difficult to reproduce tsunami inundation by hydraulic modeling, because the observation data of tsunami flooding heights are very limited. The employment of numerical models of behaviors and the associated run-up process of tsunamis is plausible and frequently used to investigate the behaviors of tsunamis. Therefore, many researchers have focused on numerical modeling to understand inundation. In most of the numerical models, the model consists of propagation and the associated run-up process.

In this study, eleven virtual and three historical and tsunami events are employed to predict the maximum flooding area at specific locations at eastern coast of the Korean Peninsula (Lee *et al.*, 2012). The eleven cases of virtual tsunamis suggested by the Korea Peninsula Energy Development Organization (KEDO, 1999) are selected to generate the initial conditions of free surface displacement. Furthermore, three historical tsunamis recorded during last few decades in East Sea which caused damage to Korea are also selected in this study. These historical tsunamis are Niigata Tsunami in 1964, Central East Sea Tsunami in 1983 and Hokkaido Tsunami in 1993. Thus, the probable maximum tsunamis consist of eleven virtual and three historical tsunamis in this study. Figure 1 shows areas of the initial free surface displacement and earthquake sources of the eleven virtual and three historical tsunamis.

A combined numerical model of propagation and run-up process is used to simulate the projected tsunami events. The sum of maximum inundated areas based on 14 tsunamis is then estimated and used to make a hazard map at certain location. The generated hazard map could be used by the each civil defense organizations to make evacuation plans in the event of a real tsunami event.

DOI: 10.2112/SI75-212.1 received 15 October 2015; accepted in revision 15 January 2016.
*Corresponding author: hkwon@jbnu.ac.kr
©Coastal Education and Research Foundation, Inc. 2016

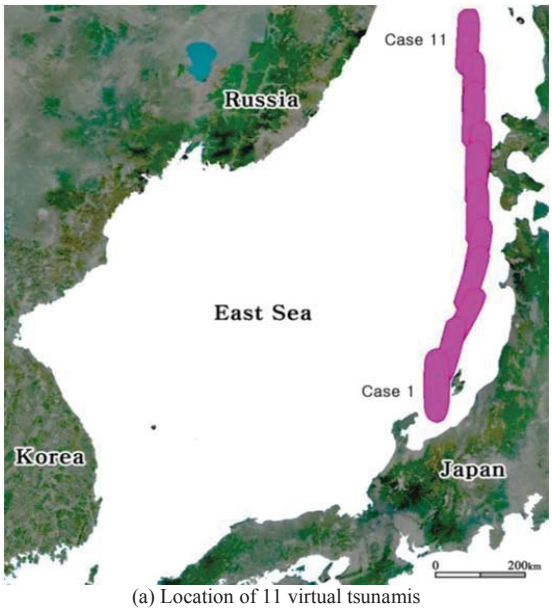

(a) Location of 11 virtual tsunamis

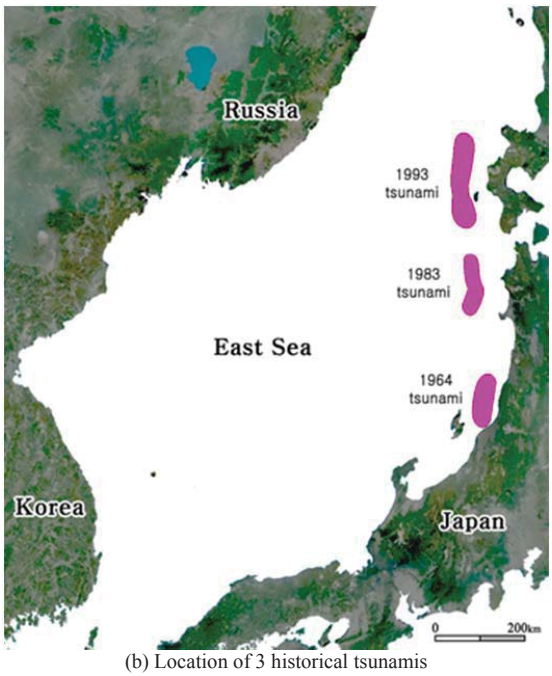

(b) Location of 3 historical tsunamis

Figure 1. Location of 11 virtual and 3 historical tsunamis.

PROPAGATION AND RUN-UP OF TSUNAMIS

The nonlinear convective terms of the momentum equations can be ignored in the numerical simulation for tsunami propagation, because the free surface displacement for tsunamis is relatively less than the water depth. On the other hand, the frequency dispersion effects play important roles in distant propagation and should be taken into consideration in its governing equations, because the wave length of tsunamis compared to the tide is relatively short and the tsunamis are propagated over a long distance. Therefore, the governing equations that address the dispersion effect, namely the linear Boussinesq equations, should be used in the numerical simulation of tsunami propagation (Cho, 1995).

To address the numerical difficulty of the linear Boussinesq equations, a set of lower-order partial differential equations (the linear shallow-water equations) were solved using the leap-frog scheme, and the frequency dispersion terms were replaced by manipulating the numerical dispersion results from the leap-frog scheme. Recently, a new modified scheme is proposed for the linear shallow-water equations as follows (Ha and Cho, 2015):

$$\frac{\zeta_{i,j}^{n+1/2}-\zeta_{i,j}^{n-1/2}}{\Delta t}+\frac{P_{i+1/2,j}^{n}-P_{i-1/2,j}^{n}}{\Delta x}+\frac{Q_{i,j+1/2}^{n}-Q_{i,j-1/2}^{n}}{\Delta y}=0 \tag{1}$$

$$\begin{aligned}&\frac{P_{i+1/2,j}^{n+1}-P_{i+1/2,j}^{n}}{\Delta t}+gh_{i+1/2,j}\frac{\zeta_{i+1,j}^{n+1/2}-\zeta_{i,j}^{n+1/2}}{\Delta x}\\&+\frac{\alpha}{12\Delta x}gh_{i+1/2,j}\left[\zeta_{i+2,j}^{n+1/2}-3\zeta_{i+1,j}^{n+1/2}+3\zeta_{i,j}^{n+1/2}-\zeta_{i-1,j}^{n+1/2}\right]\\&+\frac{\gamma}{12\Delta x}gh_{i+1/2,j}\left[\left(\zeta_{i+1,j+1}^{n+1/2}-2\zeta_{i+1,j}^{n+1/2}+\zeta_{i+1,j-1}^{n+1/2}\right)-\left(\zeta_{i,j+1}^{n+1/2}-2\zeta_{i,j}^{n+1/2}+\zeta_{i,j-1}^{n+1/2}\right)\right]\\&-\frac{\beta}{12}gb\left(\zeta_{i,j+1}^{n+1/2}-2\zeta_{i,j}^{n+1/2}+\zeta_{i,j-1}^{n+1/2}\right)-\frac{\delta}{12}gb\left(\zeta_{i+1,j}^{n+1/2}-2\zeta_{i,j}^{n+1/2}+\zeta_{i-1,j}^{n+1/2}\right)=0\end{aligned} \tag{2}$$

$$\begin{aligned}&\frac{Q_{i,j+1/2}^{n+1}-Q_{i,j+1/2}^{n}}{\Delta t}+gh_{i,j+1/2}\frac{\zeta_{i,j+1}^{n+1/2}-\zeta_{i,j}^{n+1/2}}{\Delta y}\\&+\frac{\alpha}{12\Delta y}gh_{i,j+1/2}\left[\zeta_{i,j+2}^{n+1/2}-3\zeta_{i,j+1}^{n+1/2}+3\zeta_{i,j}^{n+1/2}-\zeta_{i,j-1}^{n+1/2}\right]\\&+\frac{\gamma}{12\Delta y}gh_{i,j+1/2}\left[\left(\zeta_{i+1,j+1}^{n+1/2}-2\zeta_{i,j+1}^{n+1/2}+\zeta_{i-1,j+1}^{n+1/2}\right)-\left(\zeta_{i+1,j}^{n+1/2}-2\zeta_{i,j}^{n+1/2}+\zeta_{i-1,j}^{n+1/2}\right)\right]\\&-\frac{\beta}{12}ga\left(\zeta_{i+1,j}^{n+1/2}-2\zeta_{i,j}^{n+1/2}+\zeta_{i-1,j}^{n+1/2}\right)-\frac{\delta}{12}ga\left(\zeta_{i,j+1}^{n+1/2}-2\zeta_{i,j}^{n+1/2}+\zeta_{i,j-1}^{n+1/2}\right)=0\end{aligned} \tag{3}$$

where ζ is the free surface displacement, h is the still water depth, P and Q are the depth-averaged volume fluxes in the $x-$ and $y-$ axis directions, respectively, and g is the gravity acceleration. In Eqs. (1)-(3), a staggered grid system is used both in space and time (Cho and Yoon, 1998).

The numerical dispersions generated by Eqs. (1)-(3) are matched with the physical dispersion effects of the linear Boussinesq equations by assuming the water depth as a linear plane surface. That is, the modified equation of the new scheme is identified with the governing equation up to the third order accuracy by using the new dispersion correction factors β and δ:

$$\beta=\frac{-20h^2+gh\Delta t^2+\Delta x^2}{\Delta x^2},\ \delta=\frac{\Delta x^2-24h^2}{\Delta x^2} \tag{4}$$

Since a local approximation is employed the coefficients a and b are obtained at each grid as:

$$h=ax+by+c\ ,\ \frac{\partial h}{\partial x}=a\ ,\ \frac{\partial h}{\partial y}=b \tag{5}$$

The linear Boussinesq equations are no longer valid as the governing equations in the nearshore region, because the wave length of tsunamis becomes shorter and the amplitude becomes larger as the tsunami propagates in the coastal region. In addition, the bottom friction effects become more important in the coastal region. Therefore, the nonlinear convective inertia force and the bottom friction terms become increasingly important, while the frequency dispersion terms become less relevant. As a result, the nonlinear shallow-water equations that include the bottom friction term should be used as the governing equations to simulate run-up process of tsunamis. The nonlinear shallow-water equations are represented as followings:

$$\frac{\partial \zeta}{\partial t}+\frac{\partial P}{\partial x}+\frac{\partial Q}{\partial y}=0 \tag{6}$$

$$\frac{\partial P}{\partial t}+\frac{\partial}{\partial x}\left(\frac{P^2}{H}\right)+\frac{\partial}{\partial y}\left(\frac{PQ}{H}\right)+gH\frac{\partial \zeta}{\partial x}+\tau_x H=0 \tag{7}$$

$$\frac{\partial Q}{\partial t}+\frac{\partial}{\partial x}\left(\frac{PQ}{H}\right)+\frac{\partial}{\partial y}\left(\frac{Q^2}{H}\right)+gH\frac{\partial \zeta}{\partial y}+\tau_y H=0 \tag{8}$$

where H is the total water depth, and τ_x and τ_y are the bottom friction terms represented by the Manning formula. The Manning formulas can be written in the following form, where n is the Manning coefficient:

$$\tau_x=\frac{gn^2}{H^{10/3}}P\left(P^2+Q^2\right)^{1/2},\quad \tau_y=\frac{gn^2}{H^{10/3}}Q\left(P^2+Q^2\right)^{1/2} \tag{9}$$

A detailed description of the finite difference approximations for Eqs. (6)-(8) including Eq. (9) can be found in the literature and not repeated here (Cho, 1995; Cho *et al.*, 2007; and Sohn *et al.*, 2009).

GENERATION OF HAZARD MAP

In this study, Donghae Port located on eastern coast of Korea is selected as a target port, because the port is one of the important ports as the nationally managed trade ports designated by the Korean Government (Figure 2). The maximum inundation map is needed to evacuate the people from tsunami flooding. The inundation area comes from the numerical simulation results of 14 selected tsunami cases. The maximum inundation area is obtained by summing up of 14 inundation areas.

Figure 3 shows the arrival time of the leading parts of the Niigata Tsunami which occurred in 1964. The arrival time is estimated by a numerical model based on Eqs. (1)-(3). As shown in the figure, the leading parts reach the eastern coast of Korea after about 140 minutes. Thus, the authority may have 140 minutes to prepare for the disaster. In Korea, the Korea Meteorological Agency (KMA) is in charge of the first warning of a tsunami. The Ministry of Public Safety and Security is in charge of emergency preparedness and civil defense. In general, 30 minutes is defined to prepare against any tsunami strike triggered by undersea earthquakes off the western coast of Japan.

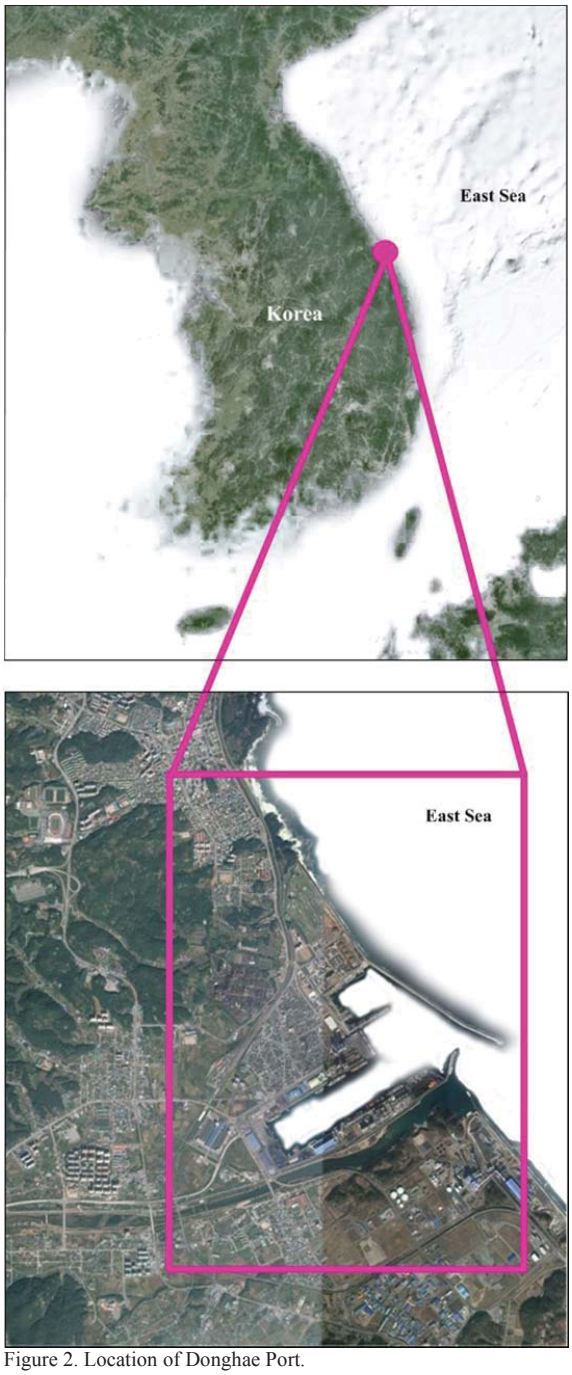

Figure 2. Location of Donghae Port.

The object of tsunami hazard map is to evacuate quickly and safely from tsunami hazard. Thus, the evacuation routes and shelters have to be added to the tsunami hazard map.

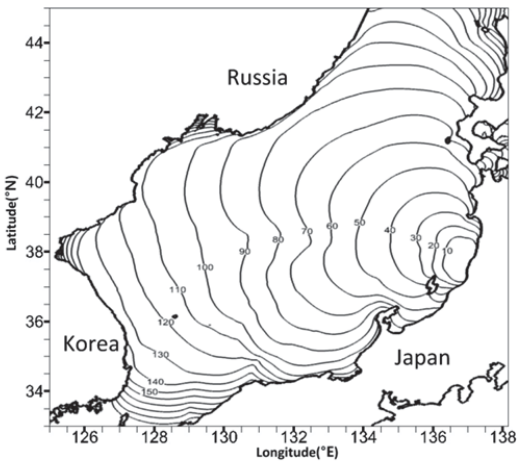

Figure 3. Predicted arrival time of leading tsunamis for 1964 tsunami event (unit: min).

To collect data such as efficient evacuation routes, location of shelters and topography information, a field survey should be carried out. Figure 4 displays a tsunami hazard map at Donghae Port. In the figure, the shelters are selected to evacuate promptly, and the other shelters are chosen where people who lost their living space can reside temporarily for flood refuge. These shelters have to be safe from tsunami hazard. In the inundation danger area, the shelters should be built by reinforced concrete and have three floors and account for the numbers of people who would require shelter during an event.

The disaster due to tsunamis should not be overlooked in Korea because it can cause a lot of damage even in a single occurrence. Thus, recently, the Korean Government is pursuing more proactive disaster prevention measures against unexpected tsunami events. Among these measures, the hazard map is more efficient and economic measure than others. The hazard map can be utilized in situation of real tsunami events at any target location. It is also used to educate local residents and officials about tsunamis. Although the hazard map of the study covers topographical map of target location, shelter information, emergency contacts list, tsunami characteristics, legend and symbols, any other local information can be included if necessary.

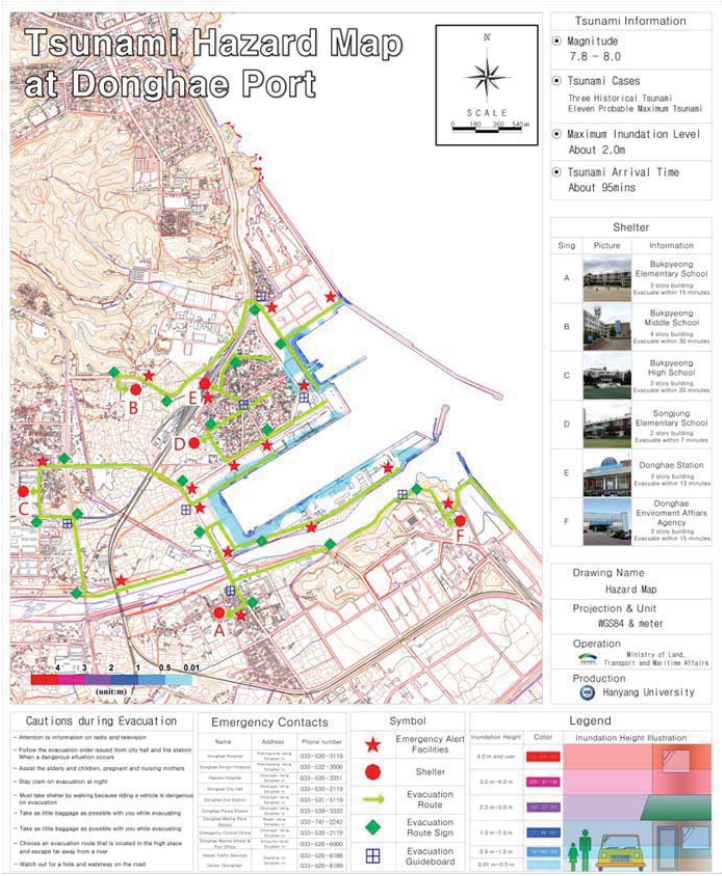

Figure 4. Tsunami hazard map at Donghae Port.

CONCLUSION

An effective and economic way for tsunami hazard mitigation planning is to develop hazard maps at those coastal communities vulnerable to tsunami. If a hazard map is provided, local residents near a vulnerable area can evacuate safely based on their own knowledge. The hazard map should contain emergency contacts and information on shelters. In addition, because transit times between the shore and shelter are contained, people can see how far the nearest shelters are from their location. The ground levels of each shelter are added to allow people to be aware of the safe height from inundation.

This study will enable disaster managers and policy makers to decide the safe location of critical infrastructure. Although the hazard map developed in this study covers a large amount of information, the map should be updated and revised at regular intervals.

ACKNOWLEDGMENTS

This work was supported by the National Research Foundation of Korea(NRF) grant funded by the Korea government(MSIP) (No. 2015R1A2A1A15054097).

LITERATURE CITED

Cho, Y.-S., 1995. Numerical simulations of tsunami propagation and run-up. Ithaca, New York, USA: Cornell University, Ph.D. thesis, 264p.

Cho, Y.-S.; Sohn, D.-H., and Lee, S.-O., 2007. Practical modified scheme of linear shallow-water equations for distant propagation of tsunamis. *Ocean Engineering*, 34(11), 1769-1777.

Cho, Y.-S. and Yoon, S.B., 1998. A modified leap-frog scheme for linear shallow-water equations. *Coastal Engineering Journal*, 40(02), 191-205.

Ha, T. and Cho, Y.-S., 2015. Tsunami propagation over varying water depths, *Ocean Engineering*, 101, 67-77.

Imamura, F. and Goto, C, 1988. Truncation error in numerical tsunami simulation by finite difference method, C*oastal Engineering in Japan*, 31(2), 245-263.

Korean Peninsula Energy Development Organization (KEDO), 1999. Estimation of Tsunami Height for KEDO LWR Project. Yongin-Si, Korea: *Korea Power Engineering Company*, Inc.

Lee, H.W.; Shin, J.W.; Kim K.Y., and Cho Y.-S., 2012. Database for tsunami hazard at harbor zones, Journal of *Korean Society of Hazard Mitigation*, 12(6), 305-314, (in Korean).

Sohn, D.-H.; Ha, T., and Cho, Y.-S., 2009. Distant tsunami simulation with corrected dispersion effects. *Coastal Engineering Journal*, 51(02), 123-141.

Yoon, S.B., 2002. Propagation of tsunamis over slowly varying topography. *Journal of Geophysical Research*, 107(C10), 1-11.

Journal of Coastal Research	SI	75	1062 - 1066	Coconut Creek, Florida	2016

Migration of Coastal Erosional Hotspots due to Coastal Protection Structures

Kwang Hee Choi †*, Jang Soo Kim ‡, Jong Chun Lee†

†Environmental Resources Research Department, National Institute of Environmental Research, Incheon, South Korea

‡ Chungnam Institute, Chungnam-do, South Korea

www.cerf-jcr.org

www.JCRonline.org

ABSTRACT

Choi, K. H. and Kim, J. S. and Lee, J.C., 2016. Migration of coastal erosional hotspots due to coastal protection structures. *In:* Vila-Concejo, A.; Bruce, E.; Kennedy, D.M., and McCarroll, R.J. (eds.), *Proceedings of the 14th International Coastal Symposium* (Sydney, Australia). *Journal of Coastal Research*, Special Issue, No. 75, pp. 1062 - 1066 . Coconut Creek (Florida), ISSN 0749-0208.

Measures to protect coasts with artificial structures have recently become popular for beach management, notably in the east coast of South Korea. In many cases, however, some structures induced unwanted effects on adjacent beaches. Yet local governments continue to build these kinds of structures to solve erosion problems. In this study, coastline changes due to such construction were investigated by comparing historical aerial photographs, taking two beaches (Gusan-Wolsong coast and Osan-Yeongsin coast) as examples. In these two beaches, submerged artificial breakwaters and groins were constructed to reduce erosion which had been accelerated since the extension of the existing harbors in the north. These defence measures seemed to work successfully initially, but they soon caused new erosional problems on the neighboring beaches. Historical changes of the two shorelines for the last 30-40 years showed that the standard deviations of beach widths estimated from the sections comprising the entire coastline have been continuously increased since the construction of the artificial structures, with minimal changes of mean beach width or total areas. The beach width of protected areas was largely increased but that of neighboring coast was severely affected. These findings indicate that the artificial structures in the east coast of the peninsula may cause erosion on the adjacent beaches, simply moving the erosional hotspot to the south.

ADDITIONAL INDEX WORDS: *Beach erosion, shoreline change, breakwaters, coastal disaster*

INTRODUCTION

Sandy coastal areas are very sensitive to changes in climate and sea level, and can be largely affected by the coastal disasters including climatic events. However, the magnitude and frequency of these disasters are reported to be increasing because of the recent sea level rise associated with global warming (Goldenberg *et al.*, 2001; Holland and Webster, 2007; Grinsted *et al.*, 2013). The long-term variations of annual maximum surge heights along the east coast of South Korea are also reported to have a clear increasing tendency for the last 34 years (Kwon *et al.*, 2008).

Such sandy coastal systems are also vulnerable to anthropogenic interference (Choi *et al.*, 2007). Over the past few decades, many coasts have been developed for huge fishery ports, recreational areas, and power plant construction. As a result, the sandy beaches are continuously eroded and the safety of the coastal residents is threatened by increasing typhoon disasters (Uda *et al.*, 2007; Cooper and Lemckert, 2012). Beach erosion along the east coast is getting worse and is emerging as a social issue as the existing fishery ports are expanded (Kim *et al.*, 2014). Therefore, many local governments try to develop effective policies to reduce erosion and prepare for disasters. Artificial protection structures including groins, submerged breakwaters, and artificial headlands are some of the defence measures popular for beach management. However, these hard defences may have undesirable effects on adjacent beaches (Uda *et al.*, 2007). In addition, they may deteriorate the quality of coastal landscape and adversely affect coastal ecosystems. Therefore, these measures should be evaluated in the light of overall contribution of beach protection with sustainability. In this study, the coastline changes were investigated to review the effectiveness of the artificial defences on the two beaches in South Korea.

STUDY AREA

The two study areas (Osan-Yeongsin and Gusan-Wolsong) are located on the eastern shoreline of Uljin County in Gyeongbuk Province, South Korea (Figure 1). Both coasts are wave-dominated, with tidal ranges between 0.2 and 0.3 m during spring tides. The dominant waves are from east and northeast in winter, while southerly or southeasterly waves are common in summer (Kim *et al.*, 2014; Ryu and Hong, 2012). Wave roses for Pohang Buoy indicates that northerly and southerly waves were dominant during the last 5 years (Figure 2). Typhoons pass through the study area once every 2–3 years on average, resulting in significant erosion. Each study area has large fishing port. These ports are open to the south, avoiding the strong northeasterly winds.

Doeksin Beach, c. 1.5 km in length, is located in Wonnam-myeon, facing the Osan Harbor in the north and Yeongsin Beach in the south. Osan Harbor was originally constructed before 1945 and had been used as a fishing port since 1946 (MMAF, 2003). The harbor was designated as 'national fishing port' in 1991. The 85 m long breakwater was constructed to extend the north breakwater between 1991 and 1993 (MLTMA, 2011).

DOI: 10.2112/SI75-213.1 received 15 October 2015; accepted in revision 15 January 2016.
*Corresponding author: geoist@korea.kr
©Coastal Education and Research Foundation, Inc. 2016

Subsequently, 670 m north breakwater, 485 m south breakwater, and three offshore sand groins (300 m in total) were constructed before 2002. Between 2005 and 2010, three submerged breakwaters were built to these groins, to prevent erosion in Doeksin Beach. Eventually, the beach was surrounded by the artificial structures in 2010.

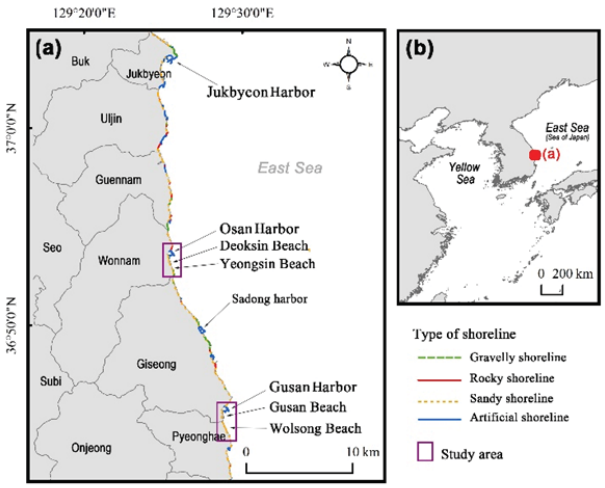

Figure 1. Study area (a) located along the east coast of South Korea (b).

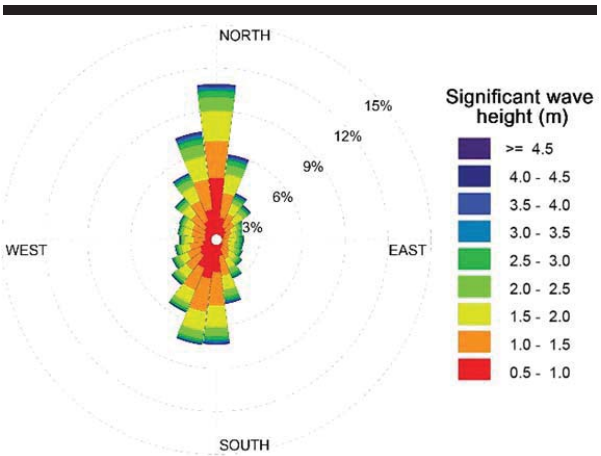

Figure 2. Wave rose for Pohang Buoy wave data for last 5 years (Jan. 2010 – Dec. 2014). The station is located 50 km south of the study area.

Gusan-Wolsong coast is located about 15 km south of Osan area, and stretches along two administrative districts, Giseong-myeon and Pyeonghae-eup. The coast extends from Gusan Harbor in the north to the mouth of Namdae River to the south and its total length is c. 3.0 km including the inner harbor shoreline. Several beach-foredune ridges or coastal dunes are well developed behind the beach, which must have prograded since the Mid-Holocene (Choi *et al.*, 2014). After the designation of Gusan Harbor as fishing port in 1991, 650 m long north breakwater and 560 m long south breakwater were constructed between 2002 and 2005. In addition, submerged breakwaters and artificial reefs amounting to 500 meters in total length were put in place from the south breakwater in order to prevent beach erosion in Giseong-myeon. This construction was completed in the early 2009.

METHODS

The aerial photographs taken between 1971 and 2013 were used to estimate and analyze the past position of shoreline and coastline of the two study areas (Table 1). The photographs from 1970s were available for Gusan area (1970, 1980, 1991, 1995, 2005, 2009, 2010, 2011, and 2013) but those of Osan area were obtainable only after 1980s (1980, 1988, 1991, 1995, 2005, 2009, 2010, 2011, and 2013). The images taken before 2010 were orthographically corrected using the ERDAS Imagine 9.1 software except some ortho-rectified ones which were provided as preprocessed formats by NGII (National Geographic Information Institute). After completion of all the preprocessing procedures such as ortho-rectification, geometric correction and georeferencing, every past shoreline and coastline was extracted from the corrected images by the unsupervised classification method (wet and dry) using the same software.

Table 1. *Series of aerial photographs used in this paper.*

Location	Type[1]	Year	Month	Day	No. GCP	RMSE
Gusan	AP	1971	Aug.	-	7	1.579
	AP	1980	Dec.	-	7	1.732
	AP	1991	Jun.	5	8	1.737
	AP	1995	Dec.	-	7	2.107
	AP	2005	May.	29	8	1.522
	AP	2009	Mar.	12	7	1.614
	OP	2010	Dec.	15	-	-
	OP	2011	Dec.	2	-	-
	OP	2013	Dec.	28	-	-
Osan	AP	1980	Dec.	28	10	1.718
	AP	1988	Sep.	-	7	2.500
	AP	1991	May.	5	5	1.923
	AP	1995	Nov.	5	9	1.635
	AP	2005	May.	27	10	1.401
	AP	2009	Mar.	1	10	0.948
	OP	2010	Dec.	15	-	-
	OP	2011	Dec.	4	-	-
	OP	2013	Dec.	24	-	-

[1]AP: Aerial photograph, OP: Ortho-rectified photograph

When detecting the shoreline and coastline, the concept of coastal profile suggested by Davidson-Arnott (2010) was applied. According to the concept, the shoreline is defined as the intercept of the mean water level along the beach, and the coastline is the boundary between back shore and dunes or sea walls. Because the location of the shoreline depends on tides at the time of imaging, the shoreline position should be adjusted to specific tidal data. However, in this study, the tidal level was not considered because there was lack of continuous tidal data in the past and the tidal range is negligible (<0.3 m) in this area. Considering the spring tidal ranges and the steep inter-tidal beach slope (7~10˚) in the study areas, the estimated shorelines may have comparatively small (~2 m) errors in beach width estimation. For quantitative comparison of the spatial changes

with time, the extracted shorelines and coastlines were segmented at 50 m intervals, dividing the beach into many cells (Figure 3). The total numbers of segments in Gusan area and Osan area were 60 and 48, respectively.

RESULTS

The multi-temporal aerial photographs showed that anthropogenic shoreline changes following the construction of artificial structures created new erosional hotspots south of the construction. In the case of Osan coast, the segments between 3 and 15 were severely eroded between 1991 and 1995 at the time of harbor expansion (Figure 5-(a)). The estimated total beach area of 13.50 ha in 1980 had decreased to 9.57 ha in 1995 after the harbor expansion (Figure 4-(a)). However, due to the countermeasures against erosion such as construction of sand groins and offshore breakwaters, the area of Deoksin Beach continuously increased after 2005, but at the same time sacrificing Yeongsin Beach next to the Deoksin Beach. Therefore, due to the countermeasures, the total beach area in 2013 (9.90 ha) remained almost the same as that in 1995.

The shoreline changes in Gusan-Wolsong coast during the last 20 years were similar to that of Osan coast (Figure 4-(b)). The harbor expansion and countermeasures against coastal erosion resulted in the loss of sand beaches. Before the expansion of Gusan harbor, the total beach area was estimated to 15.61 ha in 1971 and 18.48 ha in 1995 (Figure 5-(b)). Then, the beach surface was decreased to 15.35 ha in 2013. Although the construction against the beach erosion in front of Gusan Beach helped to increase the sandy area in Giseong-myeon, it also induced the severe sand loss in Wolsong Beach instead. Therefore, the beach area of 9.36 ha that belongs to Wolsong Beach in 1995 decreased to 4.73 ha in 2013, while the Gusan Beach increased from 9.11 ha in 1995 to 10.61 ha in 2013. It is clear that the construction of artificial structures on one beach caused erosion on the neighboring beaches.

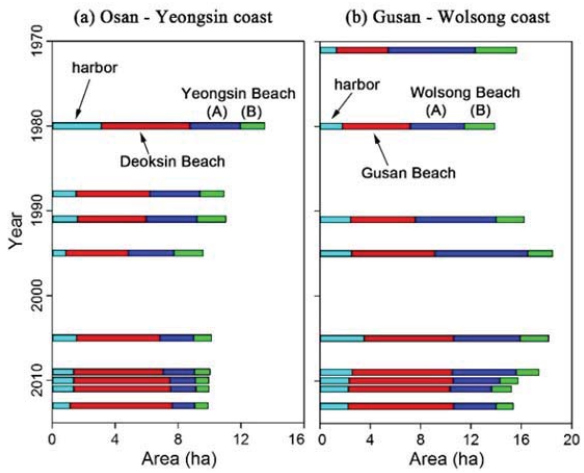

Figure 4. Areal changes of sand beach in the two study areas.

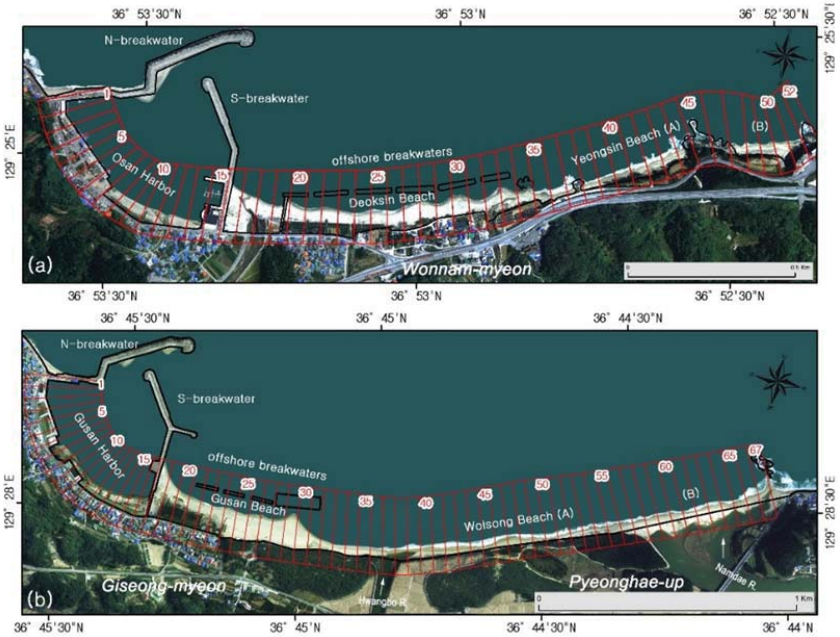

Figure 3. Both coastlines were divided by a 50-m interval to analyze the beach area with time. (a) Osan-Yeongsin coast, (b) Gusan-Wolsong coast.

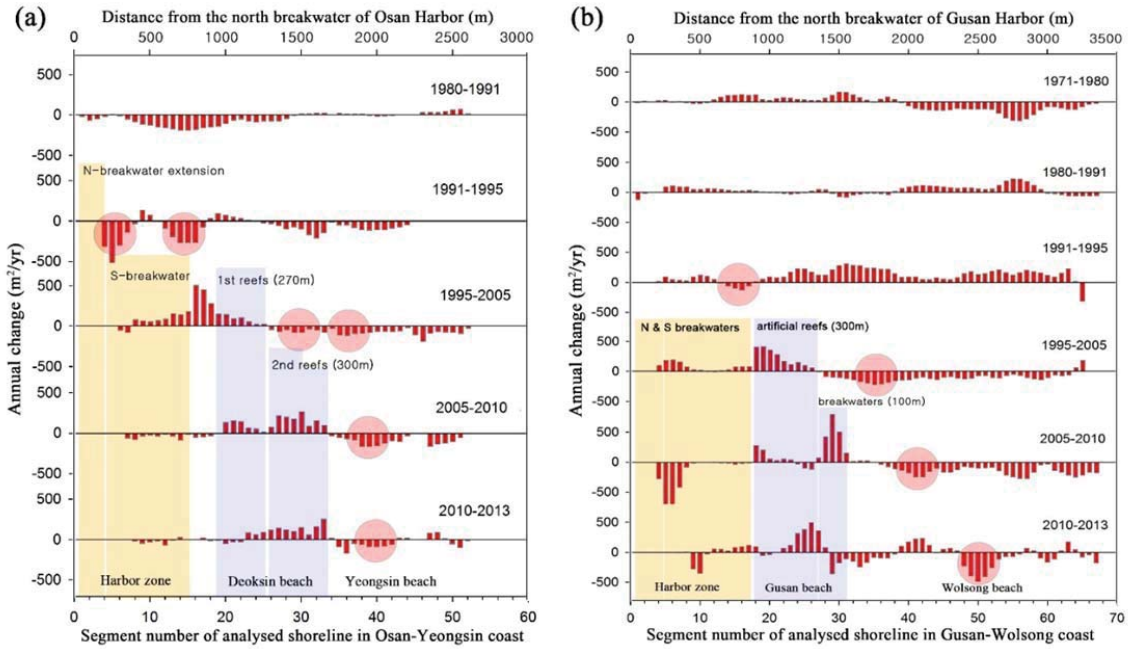

Figure 5. Annual changes of beach area in the two study areas showing the erosional hotspots (red circles) moving southward with time. Both coasts started to be eroded after expansion of the existing harbors and their neighboring beaches are now suffering from beach erosion.

Annual analyses of beach width of each cell in the two study areas (Table 2 and 3) showed that the total deviation at the mean in each area have a tendency to increase since the harbor expansion around 1995, which implies the disruption of natural coastline. On the other hand, the mean beach width of entire coast (N=52, N=62, respectively with each area) were not largely affected during the same period. Widening of the two protected beaches (Deoksin and Gusan) could be confirmed by the increase in the mean beach widths, but severe decrease in their neighboring beaches (Yeongsin and Wolsong) after 1995 was observed. In 1980, the mean beach width in Osan-Yeongsin coast varied between 38.4 and 63.3 m (Table 2). However, in 2013, the mean width of protected Deoksin Beach (67.3 m) was three times wider than that of Yeongsin B (20.8 m). The situation of Gusan-Wolsong coast is comparable, as the protected beach, Gusan Beach, boasts its mean width three times wider than that of its neighboring beaches (Table 3). This indicates the construction of artificial defences against beach erosion in the two study areas led to regional disparity of beach width as well as areal imbalance.

DISCUSSION

Along the eastern shoreline of South Korea, northerly and northeasterly winter waves are generally strong. In addition, the wind waves are intensified by the occasional typhoons passing through the Korean Peninsula from spring to autumn. Therefore, the main forcing of beach erosion or landform development could be related to wind waves but not tides. Erosion and recovery in sandy beaches are natural in this regard. However, due to construction or expansion of fishing ports along the eastern coastline of South Korea, many beaches have suffered from severe erosion. Furthermore, the risk of natural disasters such as typhoons, storm surges and tsunamis are increasing because of the recent sea level rise related with the global warming (Goldenberg *et al.*, 2001; Holland and Webster, 2007; Kwon *et al.*, 2008; Grinsted *et al.*, 2013). Thus, the government constructed various artificial defences such as sand groins, offshore breakwaters, and artificial headlands. These countermeasures have been considered to be effective to solve erosional problems in the target areas. However, these countermeasures might not be a sustainable solution as expected because of the complicated coastal hydraulic phenomena (Kim *et al.*, 2014). In addition, they may cause new erosional problems in adjacent regions. However, this is often neglected because the causal relationship of this problem is not clear.

The multi-temporal analyses of coastline changes in this study area during the last decades showed that the construction of artificial defences on one beach caused erosion on the neighboring beaches, merely moving the erosional hotspot to another area. Beach erosion in Deoksin and Osan beaches seemed to be restrained due to these measures and the beach area and width were recovered. Therefore, the countermeasures following the harbor expansion seemed to be successful. On the other hand, however, their neighboring districts of Yeongsin and Wolsong face new problems in their beach management, because of the rapid beach erosion. They now also have to devise plans for their own sake to prevent from the erosion. Probably their solution may also be the similar artificial defences to protect their own coastline, passing on the erosional hotspots to other districts. This could create a chain reaction of

moving the erosion hotspots southward along the coastline, deteriorating the quality of entire coastal landscape and the coastal ecosystem. In other words, the artificial breakwaters may result in significant shoreline recession (Uda *et al.*, 2007). Therefore, in order to break the vicious cycle of the anthropogenic beach erosion, it is recommended to avoid constructing such artificial structures and use natural defences such as coastal dunes, wetlands, and forests as alternatives.

Table 2. *Changes of mean beach width taken at each cell in Osan – Yeongsin coast.*

Year	Osan Harbor (N=15)	Deoksin Beach (N=19)	Yeongsin Beach (A) (N=10)	Yeongsin Beach (B) (N=8)	Total (N=52)
1980	41.0±19.7	58.5± 9.3	63.3±13.3	38.4±18.6	51.3±17.9
1988	19.8± 8.4	48.5±11.6	63.3±13.3	38.4±18.6	41.5±19.9
1991	21.1± 2.6	45.1±12.2	63.8±12.5	46.1±22.7	41.9±20.5
1995	11.2±13.0	41.2±12.5	57.4±11.5	46.1±22.7	36.4±22.2
2005	20.2±19.2	54.9±25.1	42.4±9.9	28.1±23.8	38.4±25.3
2009	17.7±17.8	59.0±24.8	39.5±9.5	24.6±21.0	38.0±26.4
2010	17.7±17.8	63.5±20.3	32.3±8.8	20.7±18.9	37.7±26.7
2011	17.7±17.8	63.8±20.1	32.3±8.8	20.7±18.9	37.8±26.7
2013	14.8±16.9	67.3±17.9	28.5±8.5	20.8±18.2	37.5±28.2

Note: N indicates the number of analyzed cells.

Table 3. *Changes of mean beach width taken at each section in Gusan – Wolsong coast.*

Year	Gusan Harbor (N=17)	Gusan Beach (N=20)	Wolsong Beach (A) (N=20)	Wolsong Beach (B) N=10)	Total (N=67)
1971	15.0±8.0	41.6±14.5	68.9±2.0	65.7±4.8	46.6±23.5
1980	20.9±12.9	53.9±13.0	43.2±14.9	47.7±10.0	41.4±18.2
1991	28.6±16.9	51.4±11.2	64.5±7.2	44.0±10.5	48.4±17.9
1995	29.6±16.1	65.9±14.9	74.1±6.7	49.1±18.6	56.9±22.7
2005	41.5±24.5	71.0±29.9	53.1±5.7	44.7±9.7	54.2±23.8
2009	30.0±24.5	79.6±32.2	50.9±7.0	35.9±9.9	51.9±29.4
2010	27.0±21.7	82.8±36.1	37.1±6.8	29.0±10.6	47.0±33.0
2011	26.6±21.3	80.8±34.6	33.0±9.8	31.7±11.3	45.5±32.3
2013	26.2±23.2	83.8±39.1	34.0±9.5	26.6±6.8	45.8±35.2

Note: N indicates the number of analyzed cells.

CONCLUSION

To investigate the effect of the protection structures to coastal areas, this study examined the shoreline changes along Osan – Yeongsin coast and Gusan – Wolsong coast during the last few decades using aerial photographs. Even though such structures contributed to increase the beach area in the target coast, but at the same time, they caused unexpected erosional problems on their neighboring beaches. The southward shifting of the erosional hotspots left minimal changes in total beach areas, but making regional disparity of beach width as well as interfering the natural coastal system. Therefore, such artificial structures should be used in discretion for coastal area protection in landscape planning process.

ACKNOWLEDGMENTS

This publication was performed as a part of the project "Reduction of natural disaster risk due to climate change of coastal area (NIER-RP-2014-286)". The authors thank Dr. Ngoc for her thorough review, and Dr. P.M. Jung (NIE), Ms. Y. Kim and Ms. J.Y. Kim for their helps in collecting data.

LITERATURE CITED

Choi, K.H., Yoon, K.S., Choi, J.-H., Shin, Y.K., Lee, J.C., Suh, M.H., Munyikwa, K., and Oh, K.H., 2007. Anthropogenic geomorphological changes during the last century in the Kangneung area along the east coast of Korea. *Journal of Coastal Research,* SI50, 1015-1022.

Choi, K.H., Choi, J.-H., Kim, J.W., 2014. Reconstruction of Holocene coastal progradation on the east coast of Korea based on OSL dating and GPR surveys of beach-foredune ridges. *The Holocene*, 24, 24-34.

Cooper, J. and Lemckert, C., 2012. Extreme sea-level rise and adaptation options for coastal resort cities: A qualitative assessment from the Gold Coast. *Australia. Ocean & Coastal Management,* 64, pp.1-14.

Davidson-Arnott, R.G.D., 2010. *Introduction to Coastal Processes and Geomorphology*, Cambridge, Cambridge University Press.

Goldenberg, S.B., Landsea, C.W., Mestas-Nunez, A.M., and Gray, W.M., 2001, The recent increase in Atlantic hurricane activity: causes and implications. *Science*, 293, 474-479.

Grinsted, A., Moore, J.C. and Jevrejeva, S., 2013, Projected Atlantic hurricane surge threat from rising temperatures. *Proceedings of the National Academy of Sciences of the United States of America*, 110, 5369-5373.

Holland, G. and Webster, P., 2007, Heightened tropical cyclone activity in the North Atlantic: natural variability or climate trend? *Philosophical Transactions of the Royal Society A*, 365, 2695-2716.

Kim, I.H., Lee, H.S., Kim, J.H., Yoon, J.S., Hur, D.S., 2014. Shoreline Change due to Construction of the Artificial Headland with Submerged Breakwaters. *Journal of Coastal Research,* SI 72, 145-150.

Kwon, S.J., Moon, I., and Lee, E., 2008. A study on the long-term variations of annual maximum surge heights at Sokcho and Mukho Harbors. *Journal of Korean Society of Coastal and Ocean Engineers*, 20, 564-574.

MLTMA, 2010. *A guidebook to management of erosion in coastal improvement projects*, 207p.

MMAF, 2003. *Fishing ports of Korea*. 112p.

Ryu, H-J., and Hong, S.Y., 2012. Study on Freak wave characteristics and approximation of wave spectrum in Uljin Sea area. *Journal of Ocean Engineering and Technology*, 26, 8-13.

Uda, T., Hoshigami, Y., Seino, S., and Ozawa, H., 2007. Increase in disaster potential caused by excess use of land in coastal zone. *Journal of Coastal Research,* SI50, 140-146.

Journal of Coastal Research	SI	75	1067 - 1071	Coconut Creek, Florida	2016

Using LiDAR Topographic Data for Identifying Coastal Areas of Northern France Vulnerable to Sea-Level Rise

Adrien Crapoulet[†], Arnaud Héquette[†*], Franck Levoy[‡] and Patrice Bretel[‡]

[†]Laboratoire d'Océanologie et de Géosciences, UMR CNRS 8187
Université du Littoral Côte d'Opale
Wimereux, France

[‡] Laboratoire M2C, UMR CNRS 6143
Université de Caen Basse Normandie
Caen, France

www.cerf-jcr.org

www.JCRonline.org

ABSTRACT

Crapoulet, A., Héquette, A., Levoy, F. and Bretel, P., 2016. Using LiDAR topographic data for identifying coastal areas of northern France vulnerable to sea-level rise. *In:* Vila-Concejo, A.; Bruce, E.; Kennedy, D.M., and McCarroll, R.J. (eds.), *Proceedings of the 14th International Coastal Symposium* (Sydney, Australia). *Journal of Coastal Research*, Special Issue, No. 75, pp. 1067 - 1071. Coconut Creek (Florida), ISSN 0749-0208.

A major portion of the coast of northern France consists of wide macrotidal beaches and coastal dunes protecting low-lying backshore areas (mostly reclaimed lands) from marine flooding. Although the shoreline was stable or even prograded seaward in places during the last decades, several coastal areas underwent severe erosion during the same period, while flooding sporadically occurred locally during major storms. A study of the potential impacts of sea-level rise on the coast of northern France was conducted based on airborne LiDAR topographic data collected from 2008 to 2014. Mapping of areas at risk of erosion and flooding during storm-induced events associated with high water level with a 100-year return period by 2050 was carried out using high water level statistics derived from tide gauge measurements, offshore wave climate statistics, and a sea-level rise projection based on RCP6.0 scenario (IPCC, 2013). Wave run-up was computed based on the Cariolet and Suanez (2013) equation developed for macrotidal beaches and using beach topographic profiles extracted from the LiDAR data. Results show that marine flooding would still be limited in 2050 even with a higher sea-level, but reveal that coastal dune erosion will most likely be widespread (Fig. 1). However, our study also shows that if coastal retreat proceeds during the next decades at the same or higher rates as today, several coastal dune systems will be entirely eroded in the near future, which would result in extensive storm-induced marine flooding in several coastal areas.

ADDITIONAL INDEX WORDS: *Coastal hazards, marine flooding, climate change.*

INTRODUCTION

Although demographic projections for the 21st century only show a slight increase of population living along European coasts, about 50 million people in Europe are living in low lying coastal areas exposed to coastal hazards (Neumann *et al*., 2015). This is particularly the case in the densely populated coastal areas bordering the North Sea, such as in Belgium, the Netherlands, and Denmark, where reclaimed lands below mean sea level are subject to marine flooding. The northern coast of France is part of this extensive set of low-elevated shorelines exposed to coastal risks that are likely to worsen in the next decades with predicted sea level rise associated with climate change (IPCC, 2013).

It is well established that global sea-level has been rising since the late 19th century and that the rate of sea-level rise increased during the last decades (Church and White, 2011). However, tide-gauge data as well as satellite altimetry clearly show that the rate of rise displays strong regional variations due to climate-related processes, such as steric effects and water mass redistribution, and/or to vertical land movement caused by natural or anthropogenic geological processes (Nichols and Cazenave, 2010). Recent observations of mean sea-level records from tide gauge sites along the North Sea and English Channel coastlines revealed that the rate of (local) sea-level rise was particularly high in the North Sea, exceeding 4.0 mm yr^{-1} between 1993 and 2009 (Wahl *et al*., 2013) which is significantly higher than mean rate of global sea-level rise of 3.2 mm yr^{-1} measured by altimeter satellites during the same period (Church and White, 2011).

In this paper, we present the results of a study carried out along the coast of northern France, using a series of LiDAR topographic data collected between 2008 and 2014 which were used for analyzing shoreline change and for mapping areas at risk of erosion and flooding. The possible impacts of future sea-level rise by 2050 are also assessed based on a moderate scenario of greenhouse gas emissions from the IPCC (2013) Fifth Assessment Report.

STUDY AREA

The coast of northern France is located in the eastern English Channel and southern North Sea (Figure 1). A major portion of this coast consists of wide dissipative barred beaches (300-600 m) and coastal dunes protecting low-lying backshore areas (mostly reclaimed lands) from marine flooding, despite a considerable expansion of urban and port areas during the 20th century (Figure 1). Although the shoreline was stable or even prograded seaward in places during the last decades, several coastal areas underwent severe erosion during the same period (Chaverot *et al*., 2008), while flooding sporadically occurred locally during major storms (Maspataud *et al*., 2012).

DOI: 10.2112/SI75-214.1 received 15 October 2015; accepted in revision 15 January 2016.
*Corresponding author: arnaud.hequette@univ-littoral.fr
©Coastal Education and Research Foundation, Inc. 2016

The tidal regime in the region is semidiurnal and macrotidal, the tidal range increasing from the North Sea to the English Channel, with a mean spring tidal range of more than 5.4 m at Dunkirk to approximately 8.5 m at Berck-sur-Mer (Figure 1). Due to the large tidal amplitude, tidal currents are strong along the northern coast of France with a flood-dominated asymmetry responsible for a net regional sediment transport to the north in the coastal zone of the English Channel and to the east-northeast along the North Sea coast (Héquette *et al*., 2008).

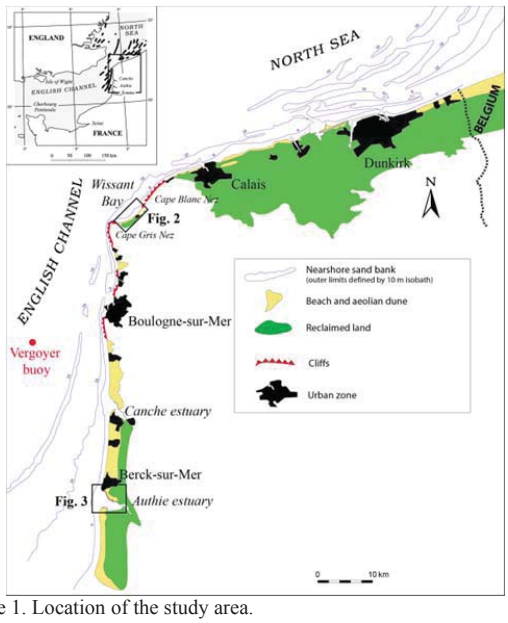

Figure 1. Location of the study area.

The dominant winds in the eastern English Channel and southern North Sea are from west-southwest and from north to northeast. In response to these winds, the offshore wave regime is characterized by short-fetch waves from southwest to west, originating from the English Channel, followed by waves from the northeast to north, generated in the North Sea. Most waves have periods and significant heights of less than 5 s and 1.5 m, respectively, but may episodically exceed heights of 4 m during major storms (Ruz *et al*., 2009). Wave heights are much lower at the coast, however, due to significant wave refraction and shoaling over the tidal sand banks of the eastern Channel and southern North Sea (Héquette *et al*., 2009).

METHODS

The potential impacts of sea-level rise on the coast of northern France were assessed based on high-resolution topographic data of the intertidal zones and coastal dunes, which were obtained from airborne LiDAR surveys carried out between 2008 and 2014. A complete topographic coverage of the coast of northern France from the Authie estuary to the Belgium border (Figure 1) was obtained in May 2008, March 2011 and December 2013/January 2014. Partial LiDAR surveys were also conducted in November 2012 in specific areas.

The 2008 survey was carried out with an Optech ALTM 1020 LiDAR having a planimetric position accuracy of ± 0.25 m and a vertical accuracy of ± 0.1 m over bare surface areas. The other surveys were conducted using a Leica ALS60 LiDAR system that acquired topographic data with a planimetric accuracy ranging from ± 0.1 to 0.17 m with a vertical accuracy < ± 0.10 m as verified by several ground control points using a very high resolution differential GPS (Leica TPS Syst1200). The vertical error range can easily increases to ± 0.25 m or more in areas covered by dense vegetation (Saye *et al*., 2005).

A density of data points of 1.2 to 1.4 points/m^2 was obtained during the different LiDAR survey. LiDAR topographic data were filtered to remove vegetation, buildings and other objects. Filtered data were then used to create contour Digital Terrain Models (DTM) using Golden Software Surfer™. The DTMs were obtained by linear interpolation using a Delaunay triangulation resulting in a grid with a 1 m resolution, a grid cell resolution of 1 m^2 appearing to provide reliable representation of topography and accurate volumetric measurements in coastal dunes using LiDAR data (Woolard and Colby, 2002).

Shoreline evolution between 2008 and 2014 was calculated based on different sets of LiDAR topographic data mentioned above. Shoreline position was determined from each DTM as the upper beach/coastal dune limit based on a change in slope gradient on the upper beach calculated as:

$$\|\vec{g}\| = \sqrt{\left(\frac{\partial z}{\partial x}\right)^2 + \left(\frac{\partial z}{\partial y}\right)^2} \qquad (1)$$

Where $\vec{g}$ is the slope gradient, z the elevation, x and y the coordinates of each point of the calculation of the grid. The value of the gradient is 0 for a horizontal surface and tends to infinity for a slope approaching the vertical. The transition between the upper beach and the coastal dunes corresponds to a sharp increase in the value of the slope gradient that is then selected for mapping shoreline position. To validate this semi-automatic shoreline extraction method, shoreline position detected from LiDAR data was compared at several sites with the position of the dune toe simultaneously determined in the field using a high-resolution differential GPS. The comparison of these two shoreline indicators usually showed small position differences, especially along erosive shoreline stretches, with a standard deviation of approximately 1.5 m. The margin of error associated with the delimitation of the shoreline was thus estimated at ± 1.5 m based on this comparison. Shoreline change measurements were carried out on cross-shore transects spaced every 50 m along the shore for each period between the different LiDAR surveys. When comparing shoreline position between two dates, the error margin can be considered to be ± 3 m.

To assess the risk of coastal erosion and marine flooding, critical high water levels were determined based on storm surge observations from Boulogne-sur-Mer, Calais and Dunkirk tide gauge stations (Figure 1) and tidal predictions computed by the French Hydrographic Service (SHOM). A joint probability method was used for determining the 100-year return period high water level for each tide gauge station based on the probability distributions of extreme water levels (observed positive surges and predicted high tide levels) (SHOM, 2012).

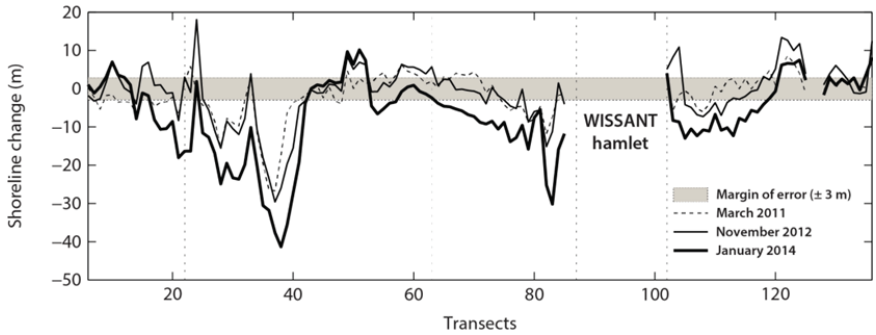

Figure 2. Shoreline changes along the coast of Wissant Bay between May 2008 and January 2014. The shoreline positions are extracted from LiDAR Digital Terrain Models (see text for explanation) and are relative to the May 2008 shoreline.

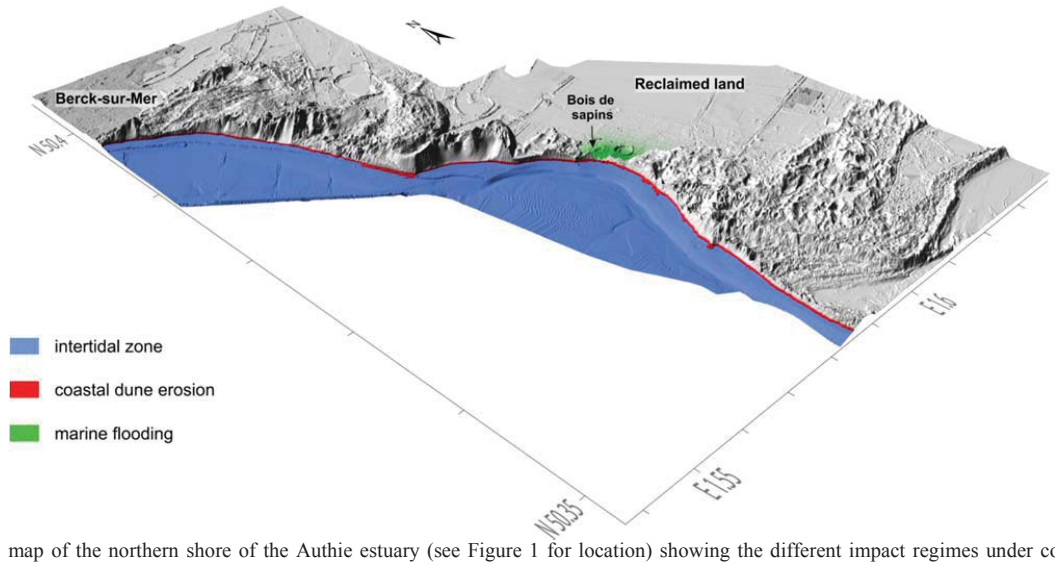

Figure 3. 3D map of the northern shore of the Authie estuary (see Figure 1 for location) showing the different impact regimes under conditions of extreme storm waves (H_o = 6 m, T = 10 s) associated with a 100-year return period water level that would result in a maximum wave run-up elevation of 6.95 m above French vertical datum (IGN69).

In order to evaluate the maximum elevation reached by waves during extreme high water events, wave run-up was estimated according to Cariolet and Suanez (2013) equation based on run-up measurements on a macrotidal beach:

$$R_{max} = 0.67\, \xi_o\, H_o \qquad (2)$$

Where R_{max} is the maximum wave run-up elevation, H_o is the significant offshore wave height and ξ_o is the Iribarren parameter $(tan\beta/(H_o/L_o)^{1/2})$, L_o is the deep water wavelength and $tan\beta$ is the beach slope. The beach slope was measured between the dune toe and the mean high water level, which closely corresponds to the active section of the beach defined by Cariolet and Suanez (2013) to be used in Equation (2). Run-up was computed for two storm wave conditions based on wave statistics from the Vergoyer wave buoy off Boulogne-sur-Mer (Figure 1), using H_o = 3.5 m and T = 9 s for moderate storm conditions and H_o = 6 m and T = 10 for extreme storm conditions.

Sea level rise by 2050 was estimated based on the RCP6.0 scenario from the last IPCC report (IPCC, 2013). Under this scenario, the increase will be 7.3 mm yr^{-1} by 2050, or about + 29 cm (relative to 2010). This value was added to the high water levels and run-up elevations previously calculated as explained above for estimating water levels in 2050.

Coastal hazard mapping was conducted using the latest LiDAR topography data set (December 2013 and January 2014), based on the method of Sallenger (2000) which allows to distinguish coastal dune erosion (*collision regime*) when the maximum run-up elevation reaches an altitude between the dune toe and the dune crest and marine flooding (*overwash* and *inundation regimes*) when run-up reaches or exceeds the elevation of the dune crest. Overwash and inundation were not

discriminated from one another because both processes can be responsible for marine flooding since overwash may lead to dune breaching and eventually to flooding. Foreshore erosion (i.e., Sallenger's *swash regime*) was not considered in the present study, because the beaches of the region do not necessarily undergo erosion during storms as intertidal bars prove to be remarkably stable even during high wave-energy events (Anthony *et al*., 2004).

RESULTS

Mapping of high water levels over the LiDAR-generated DTMs showed that most of the region's coastline is subject to erosion under present sea level conditions, even during moderate storm events. Coastal erosion is already significant at several sites along the coast of northern France such as in Wissant Bay where the shoreline locally retreated by more than 250 m during the second half of the 20th century (Chaverot *et al*., 2008). Our LiDAR surveys revealed that the coast of Wissant Bay continued to erode during recent years, the shoreline having retreated landward by more than 20 m in several places between May 2008 and January 2014, with a maximum retreat of about 40 m in the western part of the bay (Figure 2), corresponding to annual retreat rates on the order of 3.5 to 7.0 m yr^{-1}. The shoreline was stable or slightly prograded seaward in some areas however, notably east of the village of Wissant, which is likely due to the redistribution of eroded material along the coast.

Most of the coastline retreat took place between November 2012 and January 2014 with shoreline retreat in excess of 7 m along extensive stretches of the coast and up to nearly 20 m at several locations (Figure 2). These high values of coastal retreat can be explained by the occurrence of extreme water levels (return period > 100 years) associated with a series of severe storms during the fall and early winter of 2013 (Daubord, 2014). These storms were responsible for significant coastal erosion at several other sites along the coast of northern France like along the northern shore of the Authie estuary where shoreline retreat ranged from approximately 15 to 30 m between March 2011 and December 2013, reaching about 70 m along a low-elevated stretch of coastal dunes named "Bois de sapins" (Figure 3).

The determination of coastal areas subject to marine flooding based on LiDAR-generated DTMs and storm-induced high water levels (including maximum run-up elevation) showed that only localized and spatially restricted, low-elevated, coastal areas would be at risk of inundation along the coast of northern France during a 100-year return period event. One of these areas is the "Bois de sapins" mentioned above, on the northern shore of the Authie estuary, where a breach has formed through the dune crest that hardly exceeds 7 m above French vertical datum (IGN69) (Figure 4). Even under present sea level, our data show that marine flooding could occur in this area under high-energy storm wave conditions associated with a 100-year return period water level, which would result in partial inundation of the low-lying reclaimed land located behind the coastal dunes (Figure 3).

With a 29 cm higher sea level in 2050, as projected with the RCP6.0 scenario (IPCC, 2013), this area would obviously be more easily and more completely flooded as an inundation regime would last a longer period of time at or near high tide (Figure 4A) and would affect a longer stretch of coast. Similar storm impact regimes would prevail in the western part of Wissant Bay where overwash and limited inundation could occur locally under present sea level conditions during an extreme storm event associated with a 100-year return period, while more extensive inundation would take place in 2050 with a higher sea level (Figure 4B). However, our results suggest that although a higher proportion of coastal dunes would undergo erosion with a higher sea level in 2050, marine flooding would still be essentially restricted to the shores of the Authie estuary and Wissant Bay.

DISCUSSION AND CONCLUSION

This study shows that the dune coast of northern France is subject to widespread shoreline erosion during high-energy wave events associated with a 100-year return period water level, even under present sea level. Severe coastal dune erosion is already taking place at a number of sites along the northern coast of France, notably in Wissant Bay and the Authie estuary where the shoreline retreated by tens of meters in places in response to the storms that hit western Europe during the fall and winter of 2013-2014 (Castelle *et al*., 2015). With a higher sea level in 2050, coastal dune erosion would not only be more widespread, but also more severe since the dune front should generally experience a collision regime up to a greater height.

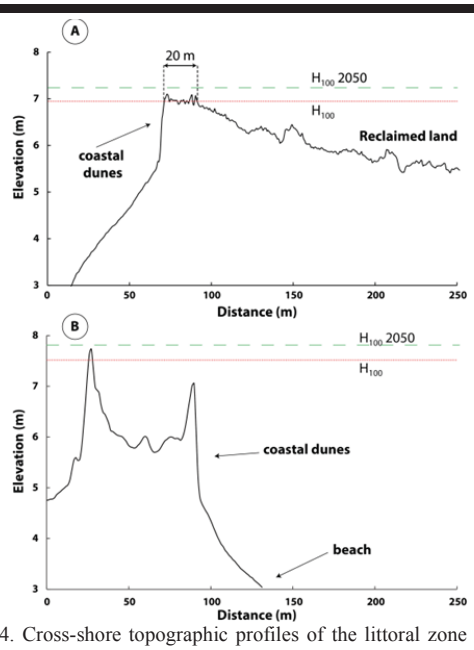

Figure 4. Cross-shore topographic profiles of the littoral zone showing maximum run-up elevation during extreme storm wave conditions (H_o = 6 m, T = 10 s) associated with a 100-year return period water level with present sea level (H_{100}) and with predicted sea level rise in 2050 (H_{100}2050); (A) "Bois de sapin" on the northern shore of the Authie estuary, (B) western shore of Wisant Bay.

Moreover, a rising sea-level will also result in a higher frequency of extreme water levels (Haigh *et al.*, 2011), which will also result in intensified coastal erosion.

Our results show that the risk of marine flooding is currently limited to a few sites. This work also suggests that although an

increase of 29 cm in mean sea level by 2050 would induce more extensive flooding at sites already vulnerable to this hazard, flooding would still be essentially limited to the same sites. Such interpretation only based on the mapping of storm-generated high water levels over LiDAR-generated DTMs could be misleading, however, because coastal dunes are already eroding at high rates in places and coastal erosion will likely increase during the next decades with rising sea level (Nicholls and Cazenave, 2010). On the northern shore of the Authie estuary, for example, the low-elevated polders are only protected from marine flooding by a narrow (20 m) dune barrier that is affected by considerable erosion. If coastal erosion continues to proceed at the same or higher rates, coastal flooding will certainly take place well before 2050 at this location. The same situation occurs at a number of sites along the northern coast of France where coastal flooding is not an immediate threat, but where coastal dunes protecting low-elevated coastal lowlands are presently undergoing erosion, which could lead to flooding hazards in the near future.

ACKNOWLEDGMENTS

Financial support for this work was provided by the *Fondation de France* through a Ph.D. scholarship to A. Crapoulet. LiDAR data were obtained through the CLAREC project funded by Regional Councils of France and by the French *Centre National de la Recherche Scientifique*. Additional funding was provided by DREAL of *Nord-Pas de Calais*.

LITERATURE CITED

Anthony, E.J., Levoy, F. and Montfort, O., 2004. Morphodynamics of intertidal bars on a megatidal beach, Merlimont, Northern France. *Marine Geology*, 208(1), 73-100.

Cariolet, J.-M. and Suanez, S., 2013. Runup estimations on a macrotidal sandy beach. *Coastal Engineering*, 74, 11-18.

Castelle, B., Marieu, V., Bujan, S., Splinter, K. D., Robinet, A., Sénéchal, N. and Ferreira, S., 2015. Impact of the winter 2013–2014 series of severe Western Europe storms on a double-barred sandy coast: Beach and dune erosion and megacusp embayments. *Geomorphology*, 238, 135‑148.

Chaverot, S., Héquette, A. and Cohen, O., 2008. Changes in storminess and shoreline evolution along the northern coast of France during the second half of the 20th century. *Zeitschrift für Geomorphologie*, Suppl.-Bd., 52(3), 1‑20.

Church, J.A. and White, N.J., 2011. Sea-level rise from the late 19th to the early 21st century. *Surveys in Geophysics*, 32(4), 585-602.

Daubord, C., 2014. *Caractérisation de 7 évènements de tempête de l'automne-hiver 2013-2014 à partir des données disponibles au SHOM*. Technical report from the French Service Hydrographique et Océanographique de la Marine n° 001/2014, Brest, 31 pp.

Haigh, I., Nicholls, R. and Wells, N., 2011. Rising sea levels in the English Channel 1900 to 2100. *Proceedings of ICE-Maritime Engineering*, 164(2), 81-92.

Héquette, A., Hemdane, Y. and Anthony, E. J., 2008. Sediment transport under wave and current combined flows on a tide-dominated shoreface, northern coast of France. *Marine Geology*, 249(3–4), 226‑242.

Héquette, A., Ruz, M.-H., Maspataud, A. and Sipka, V., 2009. Effects of nearshore sand bank and associated channel on beach hydrodynamics: implications for beach and shoreline evolution. *Journal of Coastal Research*, SI 56, 59–63.

IPCC, 2013. *Climate change 2013: The Physical Science Basis*. Contribution of Working Group I to the Fifth Assessment Report of the Intergovernmental Panel on Climate Change , T.F. Stocker et al. (eds.), Cambridge University Press, Cambridge, 1535 pp.

Maspataud, A., Ruz, M.-H. and Vanhée, S., 2012. Potential impacts of extreme storm surges on a low-lying densely populated coastline: the case of Dunkirk area, Northern France. *Natural Hazards*, 66(3), 1327‑1343.

Neumann, B., Vafeidis, A. T., Zimmermann, J. and Nicholls, R. J., 2015. Future coastal population growth and exposure to sea-level rise and coastal flooding - A global assessment. *PLOS ONE*, 10(3), e0118571.

Nicholls, R.J. and Cazenave, A., 2010. Sea-level rise and its impact on coastal zones. *Science*, 328, 1517-1520.

Ruz, M.-H., Héquette, A. and Maspataud, A., 2009. Identifying forcing conditions responsible for foredune erosion on the northern coast of France. *J. Coast. Res.*, SI 56, 356‑360.

Sallenger, A.H. Jr., 2000. Storm impact scale for barrier islands. *Journal of Coastal Research*, 16(3), 890-895.

Saye, S. E., van der Wal, D., Pye, K. and Blott, S. J., 2005. Beach–dune morphological relationships and erosion/accretion: An investigation at five sites in England and Wales using LIDAR data. *Geomorphology*, 72(1–4), 128‑155.

SHOM, 2012. *Statistiques des niveaux marins extrêmes des côtes de France (Manche et Atlantique)*. Service Hydrographique et Océanographique de la Marine, Brest, 160 pp.

Wahl, T., Haigh, I. D., Woodworth, P. L., Albrecht, F., Dillingh, D., Jensen, J., Nicholls, R.J., Weisse, R. and Wöppelmann, G., 2013. Observed mean sea level changes around the North Sea coastline from 1800 to present. *Earth-Science Reviews*, 124, 51‑67.

Woolard, J. W. and Colby, J. D., 2002. Spatial characterization, resolution, and volumetric change of coastal dunes using airborne LIDAR: Cape Hatteras, North Carolina. *Geomorphology*, 48(1-3), 269‑287.

Journal of Coastal Research	SI	75	1072 - 1076	Coconut Creek, Florida	2016

Multiple-Source Cliff Erosion in Southern Spain: Current Risk and Future Perspectives

Laura del Río[†*], F. Javier Gracia[†], and Javier Benavente[†]

[†]Earth Sciences Department, CASEM
University of Cadiz
Puerto Real, Cadiz, Spain

www.cerf-jcr.org

www.JCRonline.org

ABSTRACT

Del Río, L.; Gracia, F.J., and Benavente, J., 2016. Multiple-source cliff erosion in Southern Spain: current risk and future perspectives. *In:* Vila-Concejo, A.; Bruce, E.; Kennedy, D.M., and McCarroll, R.J. (eds.), *Proceedings of the 14th International Coastal Symposium* (Sydney, Australia). *Journal of Coastal Research*, Special Issue, No. 75, pp. 1072 - 1076. Coconut Creek (Florida), ISSN 0749-0208.

This work analyses coastal erosion causes, impacts and management strategies in two sandstone cliffs in SW Spain: El Almirante (EA) and Fuente del Gallo (FG). Five sets of aerial photographs spanning the last 50 years were used, combined with detailed field inspection. Retreat rate of the cliff top in EA is 0.8-1.6 m/yr, increasing over the last decade to 4 m/yr at some points. This poses a serious risk for infrastructure located on the cliff top, and cliff recession leaves an outstanding palaeontological site exposed to wave attack. Erosion rates in FG are lower, but there is a significant risk to beach visitors due to mass movements involved in cliff retreat. Interventions to mitigate erosion impacts in EA have consisted in tetrapod deployment and concrete fencing, while in FG stabilization measures include removal of unstable blocks, soil nailing, draining tubes, seeding, a riprap and beach nourishments. However, these measures have only had a limited success, as the main causes for cliff erosion are related to marine and subaerial processes enhanced by rainfall and cliff fractures. Undermining of the cliff base by waves in FG and in eastern EA triggers rock falls, which are easily dismantled by waves, resulting in a rapidly retreating cliff face. In central EA rotational slides are responsible for cliff top recession, favoured by a plastic substratum of marls. Future projections of shoreline position indicate a likely increase in potential damage generated by erosion in both sites, leading to the need for adopting alternative mitigation measures.

ADDITIONAL INDEX WORDS: *Cliff retreat, coastal erosion, risk, mass movements, erosion management.*

INTRODUCTION

Coastal erosion is a problem of increasing magnitude in many areas around the world. Over the last decades, conflicts between natural dynamics of coastal environments and accelerating occupation of coastal zones by population have notably increased worldwide. Erosion processes occur in every type of shoreline, but most studies on these aspects have traditionally been focused on beaches and sandy coasts (Trenhaile, 1987; Naylor *et al.*, 2010). One of the main reasons lies in the difficulties of studying sea cliff dynamics and cliff erosion hazard, especially regarding the performance of field measurements and the prediction of the future behaviour of cliffs. This is mostly due to the complexity of the quantification of retreat rates on rocky coasts (Hapke, 2004). Sea cliff erosion is an episodic, site-specific phenomenon: cliffed areas usually recede at very slow rates until a low-frequency, high-energy event causes sudden erosion episodes of much higher magnitude than average retreat (Lee *et al.*, 2001; Moore and Griggs, 2002), generally in the form of different types of slope mass movement. These episodes are sporadic and unpredictable, thus rendering their observation and measurement difficult.

Furthermore, cliff recession causes are often complex to identify, due to the interactions between diverse types of marine and subaerial processes involved in cliff retreat. Overall, cliff evolution is controlled by a number of factors such as lithology, geological structure/tectonics, wave energy and sea level trend (Trenhaile, 1987). Lithology is probably one of the most important characteristics determining both the rate of cliff recession and the main types of erosion processes acting on the escarpments. When the cliff is formed by homogeneous rocks, cliff profile evolution depends on the relative influence of subaerial and marine processes, as defined by Emery and Kuhn (1982). However, the evolution of complex cliffs composed by different units and lithologies is more difficult to predict, as vertical and lateral facies changes introduce variations in the resistance and susceptibility of rocks to weathering and erosion (Montoya *et al.*, 2012).

This work is aimed at analysing coastal erosion causes, impacts and management strategies in two sandstone cliffs in SW Spain. In both cases, human infrastructure and activities are seriously threatened by cliff recession due to a combination of factors, which has led to a number of interventions in order to mitigate this risk.

STUDY AREA

The study area is located in the Gulf of Cadiz (SW Spain) facing the Atlantic Ocean (Figure 1). Climate is of Mediterranean type, with warm dry summers and mild humid

DOI: 10.2112/SI75-215.1 received 15 October, 2015; accepted in revision 15 January, 2015.
*Corresponding author: laura.delrio@uca.es
©Coastal Education and Research Foundation, Inc. 2016

winters. Mean annual precipitation in the area is around 600 mm and clearly seasonal, with autumn and spring being the main rainy seasons (López Geta, 2005). Prevailing winds blow from the WNW and ESE, giving rise to waves approaching from W and E. However, due to coastal orientation wave climate is dominated by the W and SW directions, and prevailing longshore drift flows to the SE. Winter storms come from the Atlantic Ocean, with mean significant wave heights of around 4 m, while fair-weather waves show an average height of 0.6 m, which classifies the area as a low-energy coast; tidal regime is mesotidal with a mean spring tidal range (MSTR) around 3 m (Benavente *et al.*, 2006).

The analysis is focused in two cliff sites: El Almirante (Rota) and Fuente del Gallo (Conil). El Almirante embayment (EA) extends along 1600 m in a WNW-ESE direction (Figure 1), limited by the headlands of La Puntilla to the West and Punta Huete to the East; the former is surrounded by a wide intertidal rocky shore platform. The cliff is composed of soft Pliocene sandstones and Miocene marls, with a height between 20-25 m (Del Río and Gracia, 2009). Cliff slope increases from West to East, showing a vertical profile at the eastern end of the embayment. A very narrow sandy beach extends at the cliff toe, being slightly wider at the western end; the beach is totally submerged during high tide. The area is located within the U.S. Naval Station at Rota, built in the mid-1950s, which includes a wide harbor with two jetties located immediately updrift EA embayment (Figure 1).

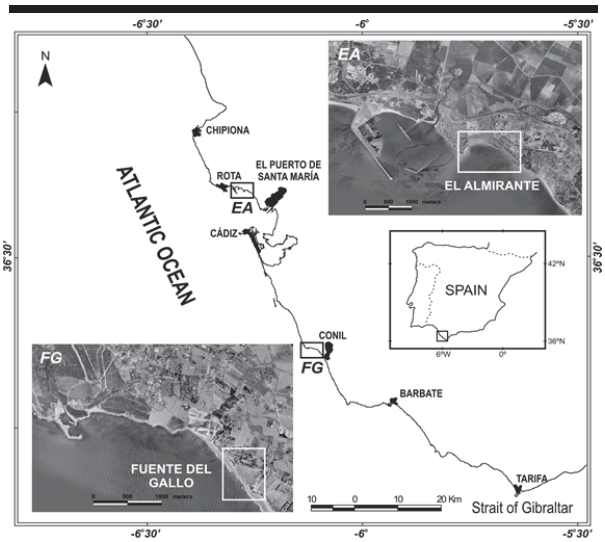

Figure 1. Location map of the study area.

About 40 km South of EA, Fuente del Gallo cliff (FG) extends along 900 m in a NW-SE direction (Figure 1). It is mainly composed of Late Miocene materials, namely calcareous sandstones on top of sandy marls, with a height about 15-20 m and a nearly vertical profile (Anfuso *et al.*, 2013). Also here a narrow sandy beach appears at the cliff toe, generally submerged during spring high tides and during storms. The cliff is located on a very touristic coastal area, and the beach is frequently used by visitors and locals. Due to ongoing erosion processes, FG has been classified as a high-risk cliff in previous works (Del Río and Gracia, 2009; Del Río *et al.*, 2009; Anfuso *et al.*, 2013).

METHODS

Detailed field inspections and digital photogrammetric techniques were combined in order to evaluate cliff erosion processes in the study sites. Field inspection included the identification of geological characteristics like lithologies, facies, joints and faults. Geomorphological indicators of activity or instability, as well as other micro and mesoforms related to erosional processes were also noted.

Recession rates were calculated based on 8 sets of vertical aerial photographs and orthophotographs dating between 1956 and 2013, at scales between 1:18,000 and 1:30,000. Photo censoring by military authorities reduced the availability of usable aerial photographs in EA site, so here only 5 sets of images could be analysed. On the other hand, the reduced dimensions of the cliff in FG site hampered the use of small scale imagery, so at this site only orthophotographs between 1977 and 2013 were used, with spatial resolutions between 0.5 and 0.7 m.

The contact prints were scanned and geometrically corrected by means of GIS tools in order to minimize photograph distortions. Then the top of the cliff was digitized on the georectified images and orthophotographs (Moore and Griggs, 2002). The resulting shorelines were compared in a GIS environment and cliff recession rates were calculated by using the DSAS 3.2 extension for ArcGIS ® (Thieler *et al.*, 2005). For this purpose, shore-normal transepts were drawn 10 m apart on the digitized shorelines; this distance was determined based on alongshore variation of cliff characteristics. Rates of cliff change were then computed on each transept by linear regression technique, as it is considered the most statistically robust quantitative method when a limited number of shorelines are available (Crowell *et al.*, 1997). The uncertainty of resulting rates was estimated by taking into account image pixel size and RMS error of the georeferencing process, as well as several parameters involved in photo distortions as a consequence of relief displacement, such as cliff height or image scale (Del Río and Gracia, 2013). The average errors in calculated recession rates were around ±0.10 m/yr.

Finally, in those cliffed sections where rates of shoreline change showed a clear trend, the future position of cliff top was roughly estimated by projecting calculated rates of change; for this purpose, the yearly rate was multiplied by a number of years into the future (Leatherman et al., 1997).

RESULTS AND DISCUSSION

Shoreline changes at EA show a very clear pattern (Figure 2) in which the Western area of the embayment has remained relatively stable during the study period, while the central and Eastern sectors have experienced remarkable erosion. Average retreat rates of the cliff top in this area between 1956 and 2010 range between 0.8-1.6 m/yr, notably increasing over the last decade at some points. In fact, cliff erosion rates in the central sector of EA have increased from 0.5 m/yr during the period 1956-1994, to 3.4 m/yr during 1994-2002 and up to 4.5 m/yr during 2002-2010. In absolute terms, at certain points the cliff

top has receded more than 60 m over the last decades. The high rates East of Punta Huete are related to the occurrence of a significant landslide at some moment between 1956 and 1994, affecting 120 m of coastline alongshore and with a total landslide area of around 7250 m^2. More recently this area has remained relatively stable, although field inspection reveals a slow movement of the landslide. Similar trends appear when analysing cliff toe evolution.

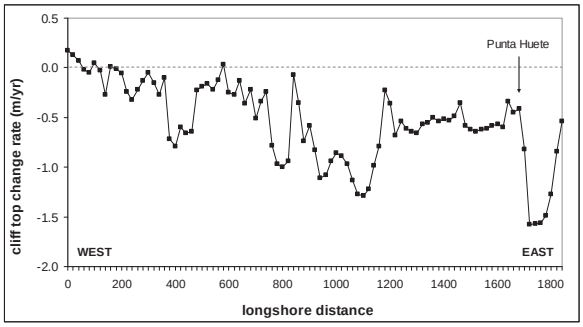

Figure 2. Rates of cliff top change in El Almirante between 1956-2010.

The differential behaviour of the Western and Eastern sectors of EA can be attributed to the contrasting degree of wave exposure, together with anthropogenic influence. The Western sector is protected from wave attack by La Puntilla headland and the rocky shore platform around it, so the beach at the cliff toe is wider and the cliff is more stable. Wave influence in the central sector of the embayment is more significant, so here cliff toe recedes due to the lack of a wide protective beach. At the same time, cliff top recession occurs by rotational slides favoured by the plasticity of marls. The result is a gently sloping cliff, with vegetation on the cliff face and semicircular scars at the edge (Figure 3A). It is likely that watering of the large garden areas located on top of the cliff contributes to mass movements, as the continuous supply of water helps in destabilizing sandy marls (Del Río *et al.*, 2009). Wave exposure is maximum at the Eastern sector of EA, triggering undermining of the cliff base and subsequent rock falls. These blocks are easily dismantled by waves, resulting in a rapidly retreating cliff toe and cliff top and hence a vertical profile without vegetation, as this is the most active sector of the embayment (Fig. 3B). In any case, the whole study area and nearby zones experience sediment starving due to the blocking of longshore drift by the wide harbour of the U.S. Naval Station (Figure 1) (Cooper *et al.*, 2009).

Different types of protection structures have been built to mitigate cliff erosion, namely concrete fences and tetrapods that were deployed at the base of the cliff in the 1980s. However, these structures have not been successful in preventing erosion of the central and Eastern sectors of EA, and in these areas cliff recession poses a serious risk for several houses and other infrastructure located on the cliff top. Moreover, cliff retreat leaves an outstanding palaeontological site located in the Eastern sector of the embayment exposed to wave attack. The fossils are embedded into the sandstone, ending up on the beach due to rock falls and dismantling of fallen blocks.

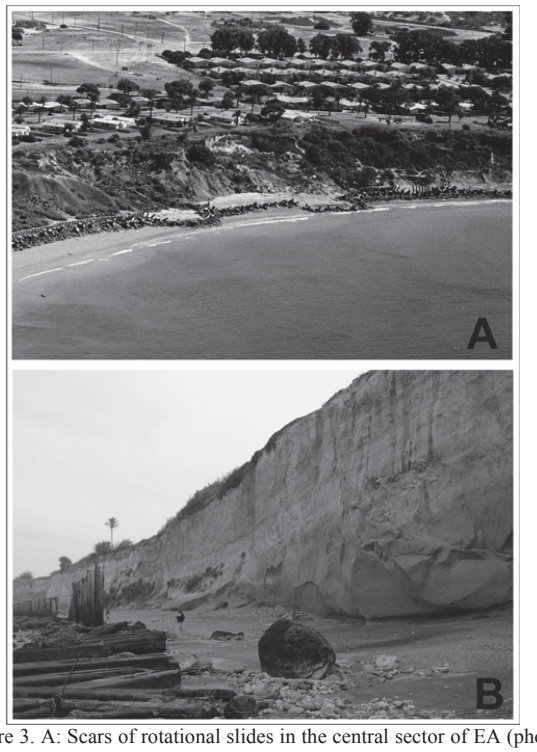

Figure 3. A: Scars of rotational slides in the central sector of EA (photo: Spanish Ministry of Environment). Note tetrapods at the cliff toe. B: Vertical cliff profile and fallen defenses in the Eastern sector of EA.

Figure 4 shows the 2035 set-back line for the cliff top, obtained by projecting past rates of change 25 years into the future. Even with the limitations of this method (Leatherman *et al.*, 1997), it can be observed that if past trends continue, several houses could be further affected by cliff retreat, as well as a road and a leisure area. In fact, the two houses that were located closest to the cliff edge were abandoned and dismantled between 2005 and 2007 due to the growing risk. Moreover, considering the recent increase in the penetration of rotational slides in the central sector of EA (see above rates), cliff top recession higher than predicted in Figure 4 could occur in the near future.

Shoreline erosion rates in Fuente del Gallo (FG) are lower than in EA and show a significant spatial variability. Cliff top recedes at an average rate of 0.3 m/yr in the Northern end and in the central sector, while other areas of the cliff have remained relatively stable over the last decades (Figure 5). Unlike continuous retreat being experienced in certain sectors of EA, cliff recession in FG is markedly episodic, with long periods of relative stability followed by sudden mass movements that generate fast retreat, usually during heavy rainfall events. For this reason, a set-back line showing future cliff top position could not be projected in this area.

FG is a clear example of interactions between marine and subaerial cliff erosion agents. Wave attack at the cliff base combines with water erosion and weathering in the upper layers,

resulting in a variety of mass movements favoured by rock discontinuities and contrasts in lithology (Del Río *et al.*, 2009; Anfuso *et al.*, 2013). This way, wave impact during high tide produces undermining of the cliff base and removal of fallen blocks and debris, due to the low resistance of sandstone blocks. The presence of cracks and joints increases the effect of wave impact, due to the sudden air compression within the cracks (Trenhaile, 1987). This in turns contributes to rock falls, due to the gravitational instability of upper cliff layers. In the central sector of FG, where the cliff is higher and shows a vertical profile, sandstone layers are notably fractured; cracks are vertical and parallel to the cliff face, thus favouring the occurrence of rock falls and topples (Dikau *et al.*, 1996).

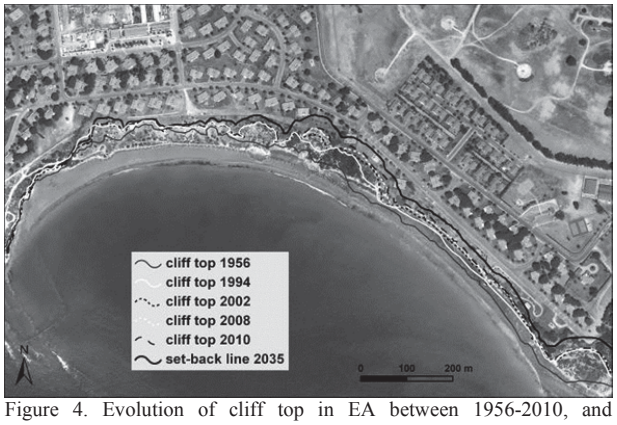

Figure 4. Evolution of cliff top in EA between 1956-2010, and projection of cliff top position in 2035.

Regarding water erosion, field inspection reveals numerous signs of piping processes affecting the soil on top of the upper sandstone layers, thus unstabilizing cliff edge and triggering debris falls.

Apart from falls and topples, rotational slides are the most widespread type of mass movement in FG, triggered by lithological contrasts within the cliff. Upper sandstones and lower marls have different permeability and mechanical behaviour, so rainfall water infiltrates through the sandstones and accumulates in the lower part of this layer due to the impervious character of the marls. The increase of hydraulic load contributes to the unstabilization of the cliff, by fluidizing the upper part of the marl layer, on which the over-saturated sandstones slide. This effect is especially important in the Southern sector of FG, due to the watering of gardens located on top of the cliff. Anthropogenic influence on cliff evolution is also clearly reflected in the reduction of sediment supply to the narrow beach fronting the cliff, since the building of Conil harbour in 1984, located updrift West of FG (Figure 1).

Despite the relatively low rates of shoreline change, the frequent occurrence of mass movements involved in cliff retreat pose a significant risk to beach visitors in this highly touristic area. For this reason, numerous and varied interventions have been carried out in FG since 2006 in order to mitigate erosion impacts. These include removal of unstable blocks, reduction of slope in the cliff edge, soil nailing, draining tubes, seeding, building of a riprap at the cliff base, and execution of repeated beach nourishments. However, this remarkable variety of stabilization measures has not been successful, as the lack of maintenance together with particularly heavy rainfall during 2010 winter led to the loss of most part of the structures (Figure 6) and increased cliff recession.

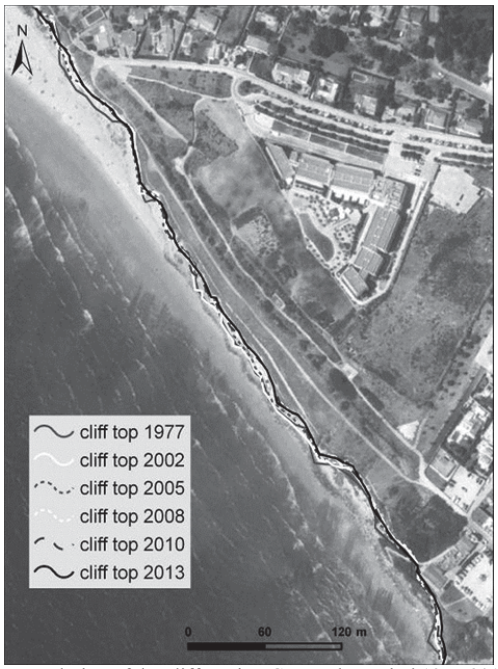

Figure 5. Evolution of the cliff top in FG over the period 1977-2013.

Figure 6. Massive rock falls in the central area of FG after heavy rainfall in winter 2010. Note the destruction of the wire mesh and soil nailing structures, and the presence of a fence hanging on the cliff edge.

Nowadays risk reduction in FG can only be achieved by reducing exposure (i.e. by limitation of visitor access to the cliff

base and top), as hazard and vulnerability have demonstrated to be extremely difficult to reduce, due to the intrinsically unstable nature of the cliff.

CONCLUSIONS

The analysis of recent evolution of two sandstone cliffs in SW Spain reveals clear erosional trends over the last decades, which in certain points create a considerable risk for human activities and infrastructure. Current interventions to mitigate the risk have proven unsuccessful in both sites, despite the variety of techniques employed. This is a concerning issue, especially considering the future context of climate change. As stated by Naylor *et al.* (2010), cliffs are erosional features and thus any climate change that increases the efficiency of processes acting on them will lead to increased rates of erosion. In EA and FG this involves a possible increase in the frequency and/or intensity of storm events in the area. Given the characteristics of both cliffs, this would probably intensify wave impact on the cliff base and thus cliff undermining and related rock falls; furthermore, it would increase surface runoff and thus water erosion and related mass movements, such as rotational slides. These perspectives imply an urgent need for adopting alternative mitigation measures, more focused on the reduction of the exposure (with strategies such as managed realignment) than on the current hold-the-line approach.

ACKNOWLEDGMENTS

This work is a contribution to the research group RNM-328 of the Andalusian Research Plan (PAI), the project RNM-6547 funded by the Regional Government of Andalusia, and the project ADACOSTA (CGL2014-53153-R) funded by the Spanish Ministry of Economy and Competitiveness.

LITERATURE CITED

Anfuso, G.; Gracia, F.J., and Battocletti, G., 2013. Determination of cliffed coastline sensitivity and associated risk for human structures: a methodological approach. *Journal of Coastal Research*, 29(6), 1292-1296.

Benavente, J.; Del Río, L.; Gracia, F.J., and Martínez, J.A., 2006. Coastal flooding hazard related to storms and coastal evolution in Valdelagrana spit (Cádiz Bay Natural Park, SW Spain). *Continental Shelf Research*, 26, 1061-1076.

Cooper, J.A.G.; Anfuso, G., and Del Río, L., 2009. Bad beach management: European perspectives. *Geological Society of America Series*, 460, 167-179.

Crowell, M.; Douglas, B.C., and Leatherman, S., 1997. On forecasting future US shoreline positions: a test of algorithms. *Journal of Coastal Research*, 13(4), 1245-1255.

Del Río, L., and Gracia, F.J., 2009. Erosion risk assessment of active coastal cliffs in temperate environments. *Geomorphology*, 112, 82-95.

Del Río, L.; Gracia, F.J., and Benavente, J., 2009. Mass movements and cliff retreat along the SW Spanish coast. *Journal of Coastal Research*, SI 56, 717-721.

Del Río, L., and Gracia, F.J., 2013. Error determination in the photogrammetric assessment of shoreline changes. *Natural Hazards*, 65, 2385-2397.

Dikau, R., Brunsden, D., Schrott, L., and Ibsen, M.L. (eds.), 1996. *Landslide Recognition*. Chichester, John Wiley and Sons, 251p.

Emery, K.O., and Kuhn, G.G., 1982. Sea cliffs, their processes, profiles and classification. *Geological Society of America Bulletin*, 93, 644-654.

Hapke, C.J., 2004. The measurement and interpretation of coastal cliff and bluff retreat. In: *Formation, evolution and stability of coastal cliffs*, USGS Professional Paper 1693, USGS, pp. 39-50.

Leatherman, S.; Douglas, B.C., and Crowell, M., 1997. Editorial: Beach erosion trends and shoreline forecasting. *Journal of Coastal Research* 13 (4), 3-4.

Lee, E.M.; Hall, J.W., and Meadowcroft, I.C., 2001. Coastal cliff recession: the use of probabilistic prediction methods. *Geomorphology*, 40, 253-269.

López Geta, J.A. (coord.), 2005. *Atlas hidrogeológico de la provincial de Cádiz. Instituto Geológico y Minero de España*, Excma. Diputación de Cádiz, Cádiz.

Montoya, I; Rodríguez-Santalla, I; Sánchez, M.J.; Alcántara-Carrió, J.; Martín, S. and Gómez Ortiz, D., 2012. Mapping of landslide susceptibility of coastal cliffs: the Mont-Roig del Camp case study. *Geologica Acta,* 10 (4), 439-455.

Moore, L.J., and Griggs, G.B., 2002. Long-term cliff retreat and erosion hotspots along the central shores of the Monterey Bay National Marine Sanctuary. *Marine Geology*, 181, 265-283.

Naylor, L.A.; Stephenson, W.J., and Trenhaile, A.S., 2010. Rock coast geomorphology: Recent advances and future research directions. *Geomorphology*, 114, 3-11.

Thieler, E.R.; Himmelstoss, E.A.; Zichichi, J.L., and Miller, T.L., 2005. Digital Shoreline Analysis System (DSAS) version 3.0: An ArcGIS extension for calculating shoreline change. *USGS Open-File Report* 2005-1304

Trenhaile, A.S., 1987. *The Geomorphology of Rock Coasts*. Clarendon Press, Oxford, 384p.

Journal of Coastal Research	SI	75	1077-1081	Coconut Creek, Florida	2016

Fast Ensemble Forecast of Storm Surge along the Coast of China

Xuelin Ding[†‡], Yongping Chen[†‡*], Yi Pan[‡] and Dominic Reeve[††]

[†]State Key Laboratory of Hydrology-Water Resources and Hydraulic Engineering, Hohai University, Nanjing, China

[‡]College of Harbor, Coastal and Offshore Engineering, Hohai University, Nanjing, China

[††]College of Engineering, Swansea University, Swansea, The United Kingdom

www.cerf-jcr.org

www.JCRonline.org

ABSTRACT

Ding, X. L.; Chen, Y. P.; Pan, Y., and Reeve, D., 2016. Fast Ensemble Forecast of Storm Surge along the Coast of China. *In:* Vila-Concejo, A.; Bruce, E.; Kennedy, D.M., and McCarroll, R.J. (eds.), *Proceedings of the 14th International Coastal Symposium* (Sydney, Australia). *Journal of Coastal Research*, Special Issue, No. 75, pp. 1077-1081. Coconut Creek (Florida), ISSN 0749-0208.

The uncertainties in typhoon wind field forecasts may introduce significant errors in storm surge forecasts. The common method to tackle this problem is based on ensemble forecasting of a typhoon wind field by using different initial and/or boundary conditions in the adopted weather forecast model. However, this method demands very high computational costs and therefore may not always be acceptable for operational use. In order to improve time efficiency, this paper introduces a new method which mainly relies on the forecast results from different weather forecast centres. With the bias modification, the control typhoon forecast is first generated by the weighted averaging of forecast results from individual forecast centres. The weighted factor for each centre is calculated under a dynamic training scheme. The ensemble typhoon forecasts are then generated by combination of five different typhoon tracks and three different wind speeds around the control forecast. The ensemble storm surge forecasts are conducted by running a well-validated storm surge model driven by the wind fields obtained from the above ensemble typhoon forecasts. Since each storm surge forecast can be calculated independently, the ensemble storm surge forecast can be fast conducted without significant increase in computational time. The above method is applied to the forecasting of storm surge in 2013 along the coast of China. By comparison with the traditional forecast, the control forecast exhibits a higher accuracy, and the ensemble forecasts provide more types of forecast results, such as the occurrence probability of storm surge over a certain surge level, which are useful for the probabilistic decision of protection measures against storm surge.

ADDITIONAL INDEX WORDS: *Multi-model super-ensemble, probability circle, storm surge, probabilistic forecast.*

INTRODUCTION

Typhoon-induced storm surge can cause severe damage to coastal areas. An accurate storm surge forecast needs to be provided in a fast way for early decision-making. However, the accuracy of storm surge forecast is likely to be affected by the uncertainties arising from the typhoon forecast. These uncertainties can stem from the settings of initial and boundary conditions in the weather forecast models adopted, and the errors of those models in the description of typhoon physical processes such as typhoon generation, development and dissipation. To reduce the effect of these uncertainties, the ensemble method was developed where small perturbances on initial conditions could be accounted for and the forecasting errors could be successfully reduced (Epstein, 1969). Subsequently the ensemble method, through perturbing initial conditions (e.g., Hoffman *et al*., 1983) and/or physical parameters (e.g., Buizza *et al*., 2000), were widely applied to solve the uncertainty problems.

Although the ensemble methods mentioned above were able to improve the accuracy of typhoon forecasts, two problems remained unsolved: (1) the uncertainty arising from the model selection was not considered; (2) the number of ensemble members should be large enough to obtain an acceptable forecast result, thus the computational costs were too expensive for operational use. To solve these problems, a multi-model super-ensemble method was proposed by Krishnamurti *et al.* (1999), which is based on the weighted averaging of the bias-removed forecast results from several selected weather forecast centres. The weighted factors for each forecast centre could be uniform or non-uniform. Previous studies show that this method performed well in the forecast of typhoon wind fields (e.g., Kumar *et al*., 2003).

Chen *et al.* (2014) used a similar method to forecast the ensemble typhoon wind fields, in which a fixed training scheme was proposed to calculate the weighted factors for each weather forecast centre. According to their results, the ensemble forecast method can effectively increase the reliability and accuracy of the storm surge forecast. This study aims to further improve this method by introducing a new training scheme, which dynamically determines the weighted factors for each forecast centre. The ensemble forecast wind fields will be used to drive a

DOI: 10.2112/SI75-216.1 received15 October, 2015; accepted in revision 15 January, 2015.
*Corresponding author: ypchen@hhu.edu.cn
©Coastal Education and Research Foundation, Inc. 2016

storm surge to conduct the ensemble storm surge forecast. Several types of new probabilistic forecast products obtained from the ensemble storm surge forecast will be introduced in this study.

Meteorological Data

The meteorological data used in this study was obtained from Fujian Province Water Conservancy Information Network (http://www.fjwater.gov.cn). The data includes the 24h, 48h and 72h forecast results of typhoon tracks and intensities (maximum wind speed) over the Western Pacific (0°N~50°N, 90°E~160°E) from four operational weather forecast centres: the China Meteorological Administration (CMA), Japan Meteorological Agency (JMA), Joint Typhoon Warning Centre (JTWC) of USA and Taiwan Meteorological Centre (TMC). The forecasts of typhoons were conducted four times a day at 02:00, 08:00, 14:00 and 20:00 (Beijing time ~ GMT+08).

METHODS

The fast ensemble forecast of storm surge consists of three steps: (1) using a modified multi-model super-ensemble method to generate a control typhoon forecast; (2) making perturbances on the control typhoon forecast to generate an ensemble of several typhoon forecasts, including one control forecast and fourteen perturbed forecasts; (3) using each typhoon forecast to drive the storm surge model and obtaining fifteen ensemble storm surge forecasts.

Control Typhoon Forecast

The control typhoon forecast is generated by using a modified multi-model super-ensemble approach. In this approach, the forecast procedure is divided into two periods, *i.e.*, training period and forecasting period. The weighted factors for each centre are determined by its perfomance of typhoon forecast in the training period, *i.e.*, a higher weighted factor will be assigned to the centre that performed more accurately in the training period. It can be numerically described as,

$$\alpha_i = E_i / \sum_{i=1}^{N} E_i \tag{1}$$

in which α_i is the weighted factor for the i-th forecast centre; E_i is the multiplicative inverse of the mean forecast errors of i-th forecast centre in the training period.

Once the weighted factor is determined, the control forecast can be calculated by using the bias-removed ensemble mean (WEM) method, which is described as:

$$F_{WEM} = \sum_{i=1}^{N} \alpha_i (F_i - \bar{e}_i) \tag{2}$$

in which F_{WEM} is the control forecast value; F_i is the forecast value of the i-th forecast centre; N is the number of the forecast centres, with N=4 in this study; $\bar{e}_i$ is the mean forecast bias of the i-th centre in the training period.

From the above equations, we can see that the forecast value is affected by the mean bias $\bar{e}_i$ and the weighted factor α_i of each centre, while the bias and the factor are both determined by the forecasting errors of each centre during the training period. Therefore, how to determine the training period becomes very important. The traditional way to determine the training period is based on the fixed training method, in which all the forecasting typhoons have the same training period (Figure 1). However, as the accuracy of forecast value relies on the consistency of forecasts between the training period and the forecasting period for each centre, the fixed training method may perform worse for the forecast typhoons which occurs far from the training period. To overcome this problem, this study proposes a new training method to dynamically determine the weighted factor for each centre. In this method, each forecasting typhoon has its own training period. The training period moves with the new occurence of tyhpoon, but the number of typhoons in the training period is fixed. The weighted factors are calculated based on this 'moving' training scheme (Figure 2). In this way, the forecast performance of each centre can be updated on a regular basis.

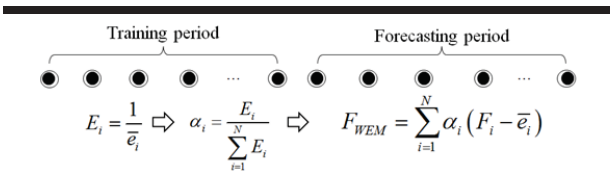

Figure 1. Illustration of a typical fixed training method.

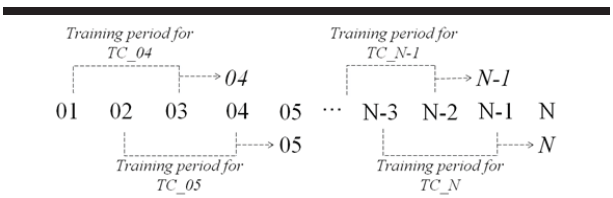

Figure 2. Illustration of a moving training method.

Perturbed Typhoon Forecasts

As the typhoon track and intensity (maximum wind speed) are two of the main factors used in the parametric typhoon wind model, the uncertainties during the forecast of these two parameters may introduce significant errors in the typhoon forecasts and subsequently in the storm surge forecasts. In order to generate the ensemble forecast, small perturbances are made on these two parameters, which values have been determined in the control typhoon forecast.

As for the perturbance on the typhoon tracks, the concept of "probability circle" (Wang *et al.*, 2010) is introduced. With these circles, four perturbed typhoon tracks are built according to the control typhoon track and the mean error of the corresponding centre in the training period. These four tracks are the left track, right track, quick track and slow track (Figure 3). As for the perturbance on the maximum wind speed, the mean absolute error of the maximum wind speed of all centres in the training period is used as a perturbed value. By adding and subtracting the error to and from the value of the control track, two perturbed maximum wind speeds can be generated.

By combining the five typhoon tracks (1 control track plus 4 perturbed tracks) with the three maximum wind speeds (1 control speed plus 2 perturbed speeds), an ensemble of fifteen groups of typhoon parameters can be obtained. Subsequently,

fifteen ensemble typhoon wind fields can be generated by substituting these parameters in the modified Jelesnianski parameteric typhoon model (Jelesnianski, 1965).

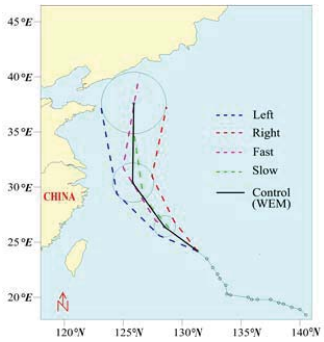

Figure 3. Ensemble typhoon tracks based on the concept of "probability circle".

Ensemble Storm Surge Forecast

The ensemble storm surge forecast is obtained by driving a well-validated storm surge model (Tan *et al.*, 2009) with the above ensemble typhoon wind fields. This surge model is robust with a high-precision, and has been used for the real-time forecasts along China coasts since 2007. Since each typhoon ensemble member is independent, the ensemble storm surge forecasts can be processed in parallel. If fifteen computers/CPUs were used for computation at the same time, the computational time for a 15-member ensemble of storm surge forecasts would remain almost the same as that for only one forecast. In this study, the computed period of a storm surge event includes a 2-day warm-up and 3-day forecast for 24h, 48h and 72h forecasts. It takes less than 10min for a 5-day ensemble storm surge forecast using this storm surge model on a 64-bit system, including the time of pre-processing, 15-member ensemble forecasting and post-processing.

RESULTS

Control Storm Surge Forecast Results

As the perturbed forecasts are built on the control forecast, the accuracy of the control one needs to be examined first. Due to the page limit, this paper only presents the results for the control storm surge forecast, which is obtained by adopting the control typhoon wind field forecast to drive the storm surge model. To show the relative accuracy of the control storm surge forecast (*i.e.*, WEM forecast), it is compared with the traditional storm surge forecast driven by the typhoon forecasting data from the CMA forecast centre.

The average improvement of storm surge forecast errors $\Delta\bar{E}_{MA}$ in 2013 along China coasts is shown in Table 1. The improvement is calculated as,

$$\Delta\bar{E}_{MA} = -(\bar{E}_{MA_EM} - \bar{E}_{MA_CMA}) \quad (3)$$

in which $\bar{E}_{MA_EM}$ is the average forecast error of control storm surge forecast; $\bar{E}_{MA_CMA}$ is the average forecast error of traditional storm surge forecast, which is based on the typhoon forecast from the China Meteorological Administration (CMA).

It can be seen that the control forecast is generally better than the traditional forecast, with the improvement of forecast errors in the range of 1~9 cm in the timely water level forecast and 1~14 cm in the maximum water level forecast at most of the tidal observation stations.

Table 1. *Average improvement of storm surge forecast errors of typhoons along China coasts in 2013 (unit: m)*

	$\Delta\bar{E}_{MA}$ (Timely water level)		$\Delta\bar{E}_{MA}$ (Maximum water level)	
Station	24h	48h	24h	48h
Luchaogang	0.02	0.03	0.03	0.02
Zhapu	0.03	0.08	0.09	0.03
Zhenhai	0.02	0.05	0.00	-0.01
Dinghai	0.01	0.00	0.03	0.01
Jiantiao	0.05	0.02	0.07	0.04
Haimen	0.02	0.09	0.14	0.08
Wenzhou	0.05	0.01	0.05	-0.06
Ruian	0.03	0.00	0.01	0.04
Chongwu	0.01	0.02	0.01	0.02

Ensemble Storm Surge Forecast Results

As the ensemble storm surge forecast can provide 15 different forecast results at the same time, several types of probabilistic products for the storm surge forecast can be obtained. As an example, Figure 4 shows the time series of ensemble forecast results of water level at Denglongshan Station. By taking the extreme values (maximum/minimum) and the average values of the 15 forecast results at each forecast time, the time series of the maximum envelope, minimum envelope and ensemble average forecast can be obtained. They can present the possible extreme large/small values and average value of storm surge forecast, respectively.

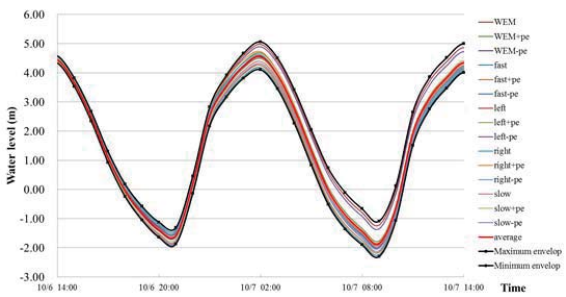

Figure 4. Time series of ensemble forecast of water level for Typhoon Fitow in 2013 at Denglongshan Station, with maximum and minumum envelopes shown in dotted black lines, and the ensemble average value shown in red line.

Apart from the product serving for a single station (Figure 4), other products serving for a specific region can also be developed. As shown in Figure 5, two filled contour maps showing the distribution of storm surge forecasting values in the

whole East China Sea are presented. They are plotted according to the results of ensemble average (on the left) and the ensemble values with 50% guarantee rate (on the right) in that region. It can be seen that there has a slight difference between these two coutour maps, particularly in the south part of East China Sea.

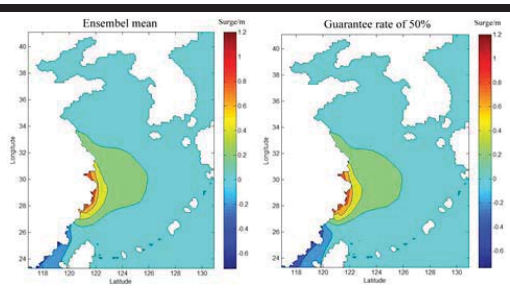

Figure 5. Filled contour maps of ensemble average (left) and ensemble value with guarantee rate of 50% (right) of storm surge forecast for Typhoon Fitow in 2013.

As the maps shown in Figure 5 can only present average status of the ensemble forecast results, some important details may be missing, particularly for some extreme cases. To avoid this problem, similar to those presented in the study of Flowerdew *et al.* (2009), the stamp maps are proposed to present all members' forecasts at the same time in Figure 6. The maps can present the results under different perturbances in a more straight way. As shown in Figure 6, the storm surge forecasts in a line have larger difference than those in a row, which indicates a bigger effect from perturbances on the typhoon track than on the maximum wind speed.

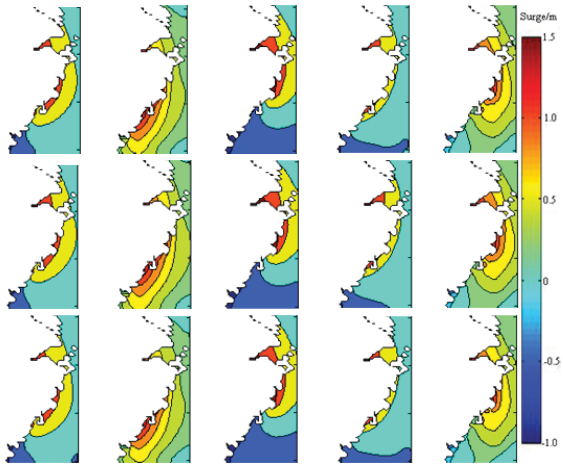

Figure 6. Stamp maps of ensemble storm surge members for Typhoon Fitow in 2013, with perturbances made on typhoon track between the members in a line and perturbances made on typhoon maximum wind speed between members in a row.

In addition, the occurrence possibility map (Figure 7) can be used to show the distribution of occurrence possibility of storm surge over a certain surge level at the interested sites. The occurrence possiblity is calculated by the equation below:

$$P(L > L_0) = n(f > L_0)/N \tag{4}$$

in which $P(L>L_0)$ is the possibility of forecast values exceeding a given value, L_0; $n(f>L_0)$ is the number of ensemble members that have forecasts exceeding the value of L_0; and N is the total number of ensemble members, with N=15 in this study.

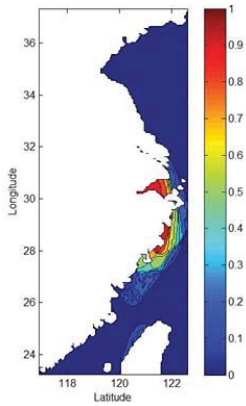

Figure 7. Occurrence possibility map of storm surge exceeding 0.6m for Typhoon Fitow in 2013.

DISCUSSION

The multi-model super-ensemble approach is one of the effective ways to reduce the effect of uncertainties in typhoon forecast (e.g., Chen *et al.*, 2014), and therefore the ensemble stom surge forecast shows improvement over the traditional storm surge forecast. As the maximum water level forecast is more sensitive to the uncertainties in typhoon forecast, it is understood that the multi-model super-ensemble approach contributes a more significant improvement in the maximum water level forecast than that in the timely water level forecast, as shown in Table 1. This improvement can help to make a better prevention decision against the storm surge, because the maximum water level is more concerned for the coastal disaster protection. Although this study has shown a promising result, more studies on the ensemble storm surge forecasts in other regions and time periods are necessary in the future to make a more general conclusion on the performance of ensemble storm surge forecasts.

As the ensemble storm surge forecasts can provide 15 forecast results at the same time, various types of probabilistic products can be generated. Those products can provide much more information than that from the traditional forecast. For example, the time series of ensemble forecasts, as shown in Figure 4, can show how the uncertainty varies by time at a specific site; the ensemble average and ensemble value with guarantee rate of 50%, as shown in Figure 5, can show the forecast uncertainty lying in selection of different statistical values of ensemble forecasts; and the stamp maps, as show in Figure 6, can clearly show the influence of perturbances on each parameter. In fact, some of these probabilistic products have already been proposed

in previous studies, such as in the storm surge prediction for Atlantic Canada (e.g., Bernier *et al.*, 2015) and the North Atlantic and European domain (e.g., Flowerdew *et al.*, 2009). This implies that those products can be generally used in the storm surge forecast in different regions.

The high time-efficiency of ensemble storm surge forecasts in this study is mainly due to three reasons: (1) the utilizing of the WEM method has small time requirement on the pre-processing; (2) the perturbances on forecast of typhoon parameters are based on the statistical forecast errors in the past, and thus no extra time is needed to generate the ensemble wind fields. (3) The computation of 15 ensemble storm surge members can be conducted in parallel. In fact, the overall time cost of a 5-day ensemble storm surge forecast takes less than 10 min on a single PC computer in this study. It is relatively small compared to many other ensemble storm surge forecast models, such as the model in the study of Suh *et al.* (2015), with the average time of 69 min for the storm surge forecast.

For future works, more case studies on multi-model super-ensemble forecast in different regions and periods will be conducted to show more general results; perturbances on more parameters other than the typhoon track and the maximum wind speed will also be considered. More types of probabilistic products will be proposed with the accumulative feedbacks from various operational users.

CONCLUSIONS

Based on the forecasts of typhoon tracks and intensities (maximum wind speed) from China Meteorological Administration, Japan Meteorological Agency, Joint Typhoon Warning Centre of USA and Taiwan Meteorological Centre, the control typhoon forecast is fast generated by using the weighted average of bias-removed forecasts from the four forecast centres. Based on the concept of "probability circle" and the parametric typhoon wind model, a 15-member ensemble of typhoon wind fields are then generated. The ensemble storm surge forecasts are conducted by running a storm surge model driven by the ensemble wind field forecasts. Since each ensemble member is independent and can be calculated in parallel, the ensemble forecast of storm surge can also be fast conducted.

The accuracy of the control storm surge forecast along China coasts in 2013 has been examined. The results show that the control forecast has a slightly better performance than the traditional forecast. Apart from the control forecast, several types of probabilistic storm surge forecasting products are generated based on the 15 ensemble forecast results. Those results are useful for the probabilistic decision of protection measures against the storm surge.

ACKNOWLEDGMENTS

The work in this paper was undertaken as part of the Ensemble Estimation of Flood Risk in a Changing Climate (EEFRaCC) project funded by The British Council under its Global Innovation Initiative. The authors also acknowledge the support of the National Natural Science Foundation of China (General Program, 51379072), the Key Research Project of Jiangsu Water Resources Department (2015006) and the 111 Project of the Ministry of Education and the State Administration of Foreign Experts Affairs, China (Grant No. B12032).

LITERATURE CITED

Buizza, R., Barkmeijer, J., Palmer, T.N., and Richardson, D.S., 2000. Current status and future developments of the ECMWF Ensemble Prediction System. *Meteorological Applications*, 7(2), 163-175.

Bernier, N.B., and Thompson, K.R., 2015. Deterministic and ensemble storm surge prediction for Atlantic Canada with lead times of hours to ten days. *Ocean Modelling*, 86, 114-127.

Chen, Y., Gu, X., and Ding, X., 2014. Fast Generation of Ensemble Typhoon Wind Field and Its Application. *Proceedings of the 24th International Ocean and Polar EngineeringConference*, Busan, Korea, v3, 438-442.

Epstein, E.S., 1969. Stochastic dynamic prediction. *Tellus*, 21(6), 739-759.

Flowerdew, J., Horsburgh, K., and Mylne, K., 2009. Ensemble Forecasting of Storm Surges. *Marine Geodesy*, 32(2), 91-99.

Hoffman, R.N. and Kalnay, E., 1983. Lagged average forecasting, an alternative to Monte Carlo forecasting. *Tellus A*, 35(2), 100-118.

Jelesnianski, C.P., 1965. A numerical computation of storm tides induced by a tropical storm impinging on a continental shelf. *Monthly Weather Review*, 93(16), 343-358.

Krishnamurti, T.N., Kishtawal, C.M., Larow, T.E., Bachiochi, D.R., Zhang, Z., Williford, C.E., Gadgil, S., and Surendran, S., 1999. Improved weather and seasonal climate forecasts from multimodel superensemble. *Science*, 285, 1548-1550.

Kumar, T.S.V.V., Krishnamurti, T.N., Fiorino, M., and Nagata, M., 2003. Multimodel superensemble forecasting of tropical cyclones in the Pacific. *Monthly Weather Review*, 131(3), 574-583.

Suh, S.W., Lee, H.Y., Kim, H.J., and Fleming, J.G., 2015. An efficient early warning system for typhoon storm surge based on time-varying advisories by coupled ADCIRC and SWAN. *Ocean Dynamics,* 65(5), 617-646.

Tan, Y., Zhang, J.L., and Zhang, D.S., 2009. The characteristic analysis of the storm surge in Fujian coastal area and its forecast. *The Proceedings of the 19th International Offshore and Polar Engineering Conference*, Osaka, Japan, 1259-1263.

Wang, P., Yu, F., Liu, Q., and Dong, J., 2010. Research and application of the ensemble refined numerical forecast of typhoon storm surge alone the coast of Fujian Province. *Marine Forecasts*, 27(5), 7-15. (in Chinese)

Journal of Coastal Research	SI	75	1082 - 1086	Coconut Creek, Florida	2016

Efficient Integration of a Storm Surge Model into a Multidisciplinary Agent Based Model Framework

Juan L. Garzon[†*], Celso Ferreira[†], Robert A. Dalrymple[‡], and Seth D. Guikema [††‡]

[†]Department of Civil, Infrastructure and Environmental Engineering
George Mason University
Fairfax, U.S.A

[‡]Department of Civil Engineering
Johns Hopkins University
Baltimore, U.S.A

[††]Deparment of Industrial and Operations Engineering
University of Michigan
Ann Arbor, U.S.A.

www.cerf-jcr.org

www.JCRonline.org

ABSTRACT

Garzon, J.L.; Ferreira, C.; Dalrymple, R. A., and Guikema, S.D., 2016. Efficient integration of a storm surge model into a multidisciplinary agent based model framework. *In:* Vila-Concejo, A.; Bruce, E.; Kennedy, D.M., and McCarroll, R.J. (eds.), *Proceedings of the 14th International Coastal Symposium* (Sydney, Australia). *Journal of Coastal Research*, Special Issue, No. 75, pp. 1082 - 1086. Coconut Creek (Florida), ISSN 0749-0208.

Multiple hurricanes have impacted coastal areas of the USA and they represent one of the most costly natural hazards in the country. In an effort to comprehend the regional vulnerability and resilience to these hazards, a multi-disciplinary team is developing an novel framework, the *Integrated Hazard, Impact, and Resilience Model (IHIRM)*. Storm surge modelling is a key role of this framework and inundation from multiple scenarios will be estimated by using a hydrodynamic model (ADCIRC) and a wave model (SWAN). Simulating a large number of storm surge scenarios requires a considerable computational effort and therefore the trade-offs between cost and accuracy must be investigated. Initially, model response sensitivity to numerical mesh resolution was performed for Hurricanes Irene (2011) and Sandy (2012). Results from the moderate and high resolution meshes provided similar values, while the increase of computational time was substantial. Secondly, we explored the difference between the maximum water levels simulated with ADCIRC and with the coupled version ADCIRC+SWAN (*i.e.*, contribution of wave setup during the peak of the storm). The contribution of wave setup to the overall water levels was less than 0.1 m inside the Chesapeake Bay and 0.5 m outside the Bay. Additionally, the computational time significantly increased for the coupled version simulation. Hence, neglecting the contribution of wave setup in areas like the upper Chesapeake Bay would not have a significant impact on the surge estimates and a considerable amount of resources would be saved. Conversely, wave setup must be considered at open coast areas.

ADDITIONAL INDEX WORDS: *Storm surge modeling, ADCIRC, Chesapeake Bay*

INTRODUCTION

The United States (US) North Atlantic Basin is prone to tropical storms and hurricanes events. The newest report conducted by the North Atlantic Coast Comprehensive Study, (NACCS) identified 153 severe land-falling storms and 37 bypassing storms for the US East Coast between 1851 and 2012. Some examples of these storms are Floyd (1998), Isabel (2003), Irene (2011) and Sandy (2012), and they represent some of the costliest natural disasters in the history of the US. Therefore, coastal areas of the US East Coast are highly vulnerable to coastal flooding driven by hurricane storm surge events. Additionally, repeated exposure to flood hazards might induce alterations in the evolution of regional vulnerability and resilience through changes in both individual and collective responses.

In an effort to comprehend regional vulnerability and resilience to these hazards, a multi-disciplinary team is developing a novel framework, the Integrated Hazard, Impact, and Resilience Model (IHIRM).This integrated approach will provide a basis for evaluating multiple influences and feedbacks that characterize hazard mitigation plans and measures, avoiding the limitations of single-discipline approaches. The IHIRM is based on an Agent Based Model (ABM) framework and will allow a rapid evaluation of the influences and feedbacks between the multiple agents of the project.

In this framework, the storm surge model component should be seamlessly integrated to the ABM, both accounting for the decisions and projections from the interdisciplinary framework and providing subsequent inundation results. These decisions and projections will be divided up into five blocks: modeling domain, mitigation scenarios, meteorological conditions, sea level rise and land use change, (Figure 1). The ABM will explore three spatial scales by modeling the response and behavior of its units for a local area (Anne Arundel County in Maryland), a regional domain (Baltimore-Washington DC region), and a continental scale (mid-Atlantic region). The mitigation scenarios consist of defining alternatives that help to prevent or reduce coastal flooding. Storm surge will be simulated for historical storms in order to calibrate and validate

DOI: 10.2112/SI75-217.1 received 15 October, 2015; accepted in revision 15 January, 2015.
*Corresponding author: patricio.catalan@usm.cl
©Coastal Education and Research Foundation, Inc. 2016

the ABM and the hydrodynamic model and for a large number of synthetic storms based on climate predictions. The sea level rise scenarios will be incorporated as an initial condition by the storm surge model. Finally, changes in land use or land cover will be integrated in the storm surge simulations. Therefore, generating a large number of scenarios and consequently a large number of different simulations will be performed.

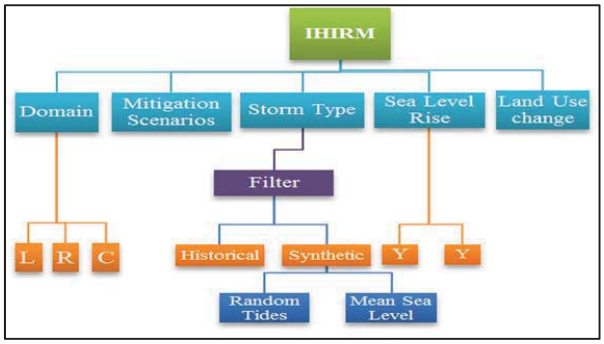

Figure 1. Information from IHIRM that will be integrated into the storm surge model

The numerical modeling of storm surge has improved significantly during the last decades and a wide number of storms have been validated successfully against observed data (*e.g.*, Dietrich *et al.* 2011b for ADCIRC). However, accurate solutions depend on the truthful representation of the storm surge physical processes and a high resolution numerical grid that represents complex domains and detailed topographies or bathymetries. As a consequence, simulations with highly complex numerical schemes on high resolution grids require significant computational time. Multiple studies are found in the literature discussing the relation between mesh resolution and the goodness of the results simulating water levels. Kerr *et al.* 2013 carried out a statistical analysis of maximum water elevations and showed that the higher resolution SL18TX mesh, the most recent mesh designed for the Gulf of Mexico, provided more accurate results than the moderate resolution ULLR mesh, developed for the U.S. IOOS study. On the other hand, the change in momentum flux of breaking waves contributes another forcing element of water levels. This extra elevation of the mean sea level is the wave setup, (Higgins and Stewart, 1963, 1964). Resio and Westerink 2008 stated that the relative wave contribution depends on the slope of the sea bed, and this contribution to the overall water levels could be significant.

In order to create an efficient integration of a storm surge model into the IHIRM, the purpose of this work is to assess the impact of mesh resolution and wave radiation stress gradients on the accuracy of the simulated results. In conclusion, we will discuss the cost-benefits analysis in terms of computational resources and accuracy of results. These findings will be used as recommendations or insights to configure the storm surge model integration to the IHIRM.

METHODS

Study Site

Two domains from the IHIRM, local, and regional, lie on potential flood areas inside the Chesapeake Bay, and the continental domain also includes the entire bay. Chesapeake Bay is the largest estuary of the US, lying between the North American mainland to the west and Delmarva Peninsula to the east. The bay is approximately 300 km long and less than 30 km in width. The main axis runs in north-south direction and the mean water depth is 6.5 m. Additionally, a large amount of available data to validate the storm surge model is found in this area. For example, National Oceanographic Atmospheric Administration, (NOAA) runs multiple tidal gage stations distributed throughout the whole bay. Besides NOAA, the US Geological Survey, (USGS), deployed sensors for monitoring storm surge during Hurricanes Irene or Sandy. For these reasons, Chesapeake Bay was selected as a study area for this work.

Numerical Methods

The coupled version of ADCIRC+SWAN represents a good trade-off between the computational cost and the representation of the physical processes. More computationally efficient models, such as SLOSH (Jelesnianski *et al.* 1992), have limited capacity to represent flow over different land covers. While higher fidelity three-dimensional models such as applied by Sheng *et al.* 2012 in a study of the reduction of storm surge by vegetation canopies in an idealized domain, are still computationally prohibitive in a real-world regional scale.

Two computational models were used in this study: ADCIRC, (Westerik *et al.* 2008) and the coupled version SWAN+ ADCIRC (Dietrich *et al.*, 2011b). ADCIRC is a continuous-Galerkin finite element model. It simulates water level by solving the generalized wave continuity equation (GWCE) and currents by using the vertically integrated shallow water momentum equations. In the coupled version ADCIRC passes water levels, currents and wind speeds to SWAN. SWAN is a third generation, phase integrated wave model (Zijlema, 2010). These inputs are used by SWAN to calculate wave parameters and wave radiation stress gradients. Finally, these gradients are sent back to ADCIRC to compute water levels.

Two numerical grids with different resolutions will be used to perform the model response sensitivity to the resolution. The first mesh used in this study is the Federal Emergency Management Agency, FEMA, region III. It has 1.875 million nodes. This mesh covers the western Atlantic Basin, the Gulf of Mexico, and the Caribbean Sea, and the finest resolution is observed at Chesapeake Bay and Delaware Bay. The minimum resolution found is 14 m. The open ocean tidally forced boundary lies on the 60ºW meridian. The second mesh is a modification of the FEMA region III mesh with the highest resolution around 130 m. We will refer this mesh as the moderate resolution mesh. The numerical grid has 0.381 million nodes. This coarser mesh was built based upon the same domain than the FEMA mesh. Figure 2 shows a comparison between the grid resolution of FEMA and moderate resolution mesh. The grid resolution is computed as the average distance between a node and its neighbors.

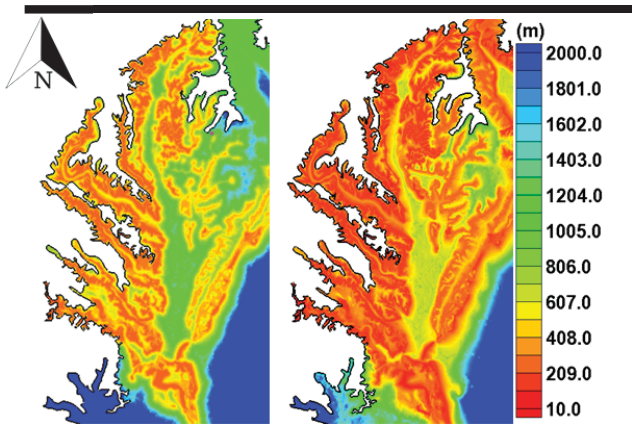

Figure 2. Grid resolution in meter within the Chesapeake Bay. Modified FEMA at the left side and original FEMA at the right side.

Water levels and waves were simulated using tides and meteorological data as forcing elements. Regarding meteorological forcing, we hindcasted Hurricanes Irene (2011) and Sandy (2012). Wind and pressure fields were generated by using a dynamic asymmetric Holland model (Holland, 1980). The primary parameters of those were extracted from the National Hurricane Center (NHC) Best Track database.

RESULTS

Impacts of mesh resolution

Hindcasts of Irene and Sandy storms were simulated on the FEMA region III mesh, and the moderate resolution mesh using ADCIRC model. Figure 3 shows maximum water levels observed against maximum modeled water levels at NOAA gage stations and temporary sensors deployed by USGS. Figure 3 (A) is the validation for Irene storm. The maximum peaks of this storm event were found in the lower Bay and at the Delmarva Peninsula, and the maximum elevations were lower in the middle and the upper Bay. Figure 3 (B) shows the scatter plot for Hurricane Sandy. It is important to highlight that the USGS sensors recorded water levels each 30 or 60 seconds. It reduced the quality of the measurements in terms of accuracy because other phenomena such as waves or currents are included in the measurements as well. Additionally, those sensors were deployed at inland zones with complicated morphological features such as channels, lagoons, marshes or protected areas. In contrast, NOAA tidal stations are situated at open sea areas, where the model theoretically provided more accurate results. Therefore, the agreement for NOAA data is noticeably better than for USGS data. Table 1 summarizes the statistical comparison of both storms and resolution levels. The statistical skill metrics used are: coefficient of determination, the slope of the fit line, standard deviation and mean normalized error. These skill metrics show a slightly better performance for the FEMA mesh Irene simulation than the moderate resolution mesh Irene simulation. For Sandy simulation, high resolution provided a higher coefficient of determination, but moderate resolution showed a lower error in the other metrics, (m, σ, E_{NORM}). Finally, we want to emphasize that the clock wall time of the simulation increased at the same proportion to the number of elements, *i.e.*, the computational time of the FEMA mesh simulations was 4.9 times higher than of the moderate resolution mesh simulations.

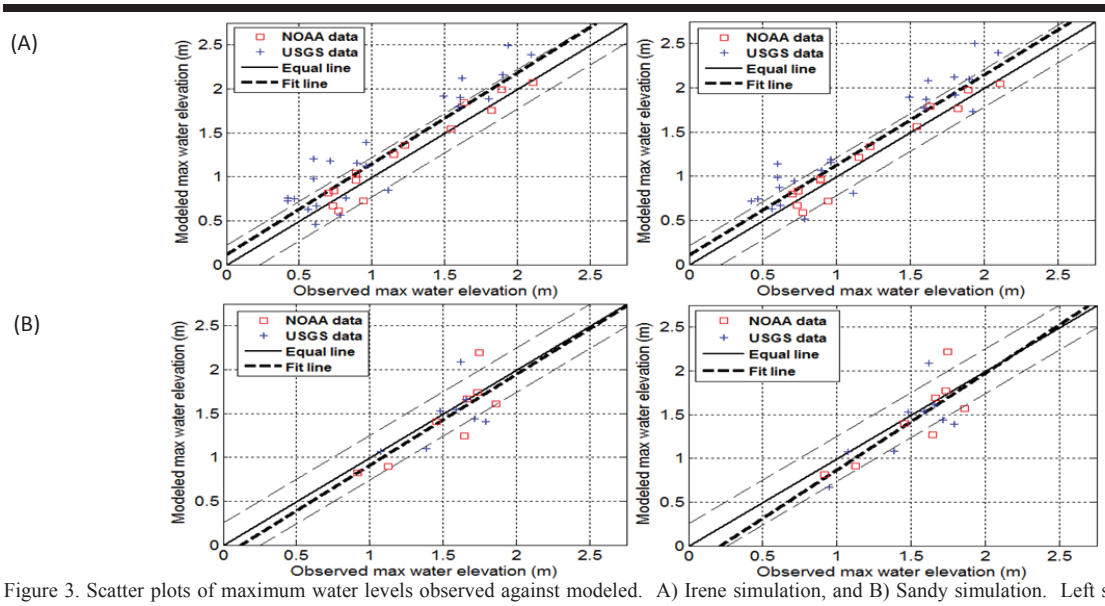

Figure 3. Scatter plots of maximum water levels observed against modeled. A) Irene simulation, and B) Sandy simulation. Left side plots represent the hindcast performed on the moderate resolution mesh and right side plots correspond to original FEMA mesh simulation.

Table 1. *Metric skills using in the statistical analysis.*

Storm	Resolution	R^2	m	σ	E_{NORM}
Irene	High	0.866	1.021	0.212	0.190
Irene	Moderate	0.856	1.035	0.224	0.217
Sandy	High	0.634	1.1066	0.256	0.170
Sandy	Moderate	0.564	1.0392	0.252	0.162

Wave radiation stress

Simulations of Irene and Sandy were performed on the moderate resolution mesh by using ADCIRC and ADCIRC+ SWAN. Then, maximum water levels simulated without waves were compared with maximum water levels obtained with the coupled version. It allows us to study the impact of the wave radiation stress on storm surge. The contribution of waves to water levels, wave setup, is driven by the wave radiation stress gradients. These gradients are formulated as:

$$\tau_{sx,waves} = -\frac{\partial S_{xx}}{\partial x} - \frac{\partial S_{xy}}{\partial y}, \text{ and } \tau_{sy,waves} = -\frac{\partial S_{xy}}{\partial x} - \frac{\partial S_{yy}}{\partial y}.$$

S_{xx}, S_{xy} and S_{yy} are the wave radiation stresses proposed by Longuet-Higgins and Stewart, 1964. Figure 4 (A) shows the difference between the maximum water levels simulated for Irene hindcast considering wind waves and without wind waves, *i.e.* the wave setup during the peak of the surge. The highest contributions of waves to maximum water levels were found at the open coast, where the applied wave radiation stress gradients were more significant, Figure 4 (B). The most energetic waves reaching the shoreline induced significant gradients, and wave setup drove increments in water levels ranging from 0.2 m to 0.5 m, especially behind the barrier islands. These increments led to a significant relative contribution of the wave setup to the total storm tide at the Delmarva Peninsula. Relative contributions of 20% in water levels were found in some USGS record stations. Even an unusual value of 84% was observed at one USGS sensor. However, as long as the waves propagated throughout the bay, their energy was reduced due to the shallow depth and limited fetch. As the energy reduced, the wave setup phenomenon was lower in this area. Maximum values of wave setup of 0.15 m were observed in the middle of the bay, and it represented a relative contribution of 15% or 17% at stations located at this region.

Only areas at the mouth and the open coast were analyzed for Hurricane Sandy. Sandy transitioned from tropical storm to extratropical storm, and therefore we considered the asymmetric parametric wind model did not represent correctly the wind field in the upper Chesapeake Bay. Consequently, we cannot extract conclusions from these simulations affecting to local and regional domain. However, this information results very important to understand the model response in inland and open seas areas for the continental domain. As we expected, wave setup during Sandy followed a similar pattern as Irene, Figure 5 (A). Wave setup values of as much as 0.5 m during the peak of the storm surge at the Delmarva Peninsula were observed. This increment represented a relative contribution of 15% at the USGS stations deployed the Delmarva Peninsula. Additionally, the contribution of waves to water levels in the lower Bay was

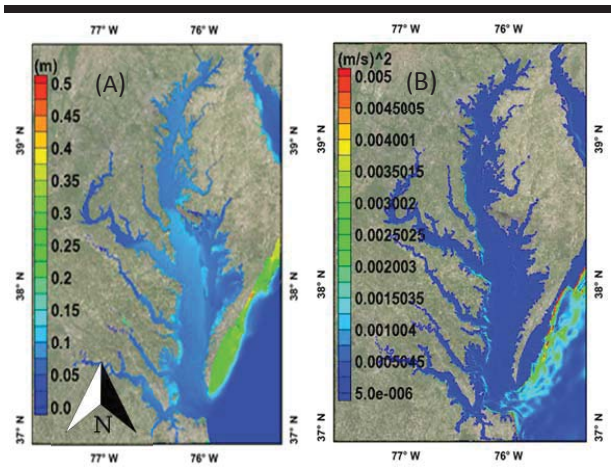

Figure 4. Contour plots of (A) Wave setup during the peak of the storm surge for hurricane Irene, and (B) Applied wave radiation stress gradients at the same moment. It was obtained by dividing the stress in units of force/area by the reference density of water.

significant. It varied between 0.20 and 0.25 m., (contrasting with 0.1 or 0.15 m observed for the simulation of Irene). The relative contribution of wave setup represented a 15-20% for several NOAA gage stations located at the mouth of the bay. The highest values were observed at the open coast, and they reduced inside the bay. Those values are directly related to the applied wave radiation stress shown in the Figure 5 (B). As a final point, the calculation of the evolution in geographical space and time of the wave radiation stress contribution increased the computational time 315 % for the Irene hindcast and 333% for Sandy.

DISCUSSION

From the metric skills and Figure 3, we concluded that the simulation of Hurricane Irene performed similarly on the high resolution and moderate resolution mesh. The level of resolution at inland and coastal locations of the moderate mesh was able to capture the same processes as the FEMA mesh. NOAA gage stations are mainly situated at locations with clear and well connections to open water. Therefore, ADCIRC performed well at these locations. However, most of the modeled USGS stations over-predicted the storm surge. This could be associated with a lower resolution at inland locations as Blain *et al* 1998 demonstrated for a hindcast of Hurricane Camille. Additionally, Keer *et al.* 2013 demonstrated that a coarser resolution at inland locations poorly represented the evolution and attenuation of the storm surge. Therefore, even the higher resolution of the FEMA mesh might not be appropriate to model inland surge dynamics. Likewise, Sandy hindcast showed a similar level of performance for both levels of resolution. The smaller number of stations studied for Sandy was not adequate for proper statistical analysis, and therefore, deeper studies were not carried out.

The wave setup is highly location dependent but the maximum values of wave setup simulated in this study at the Delmarva Peninsula for Hurricane Irene and Hurricane Sandy were similar to the study done by Kerr *et al. 2013* for the simu-

(A)

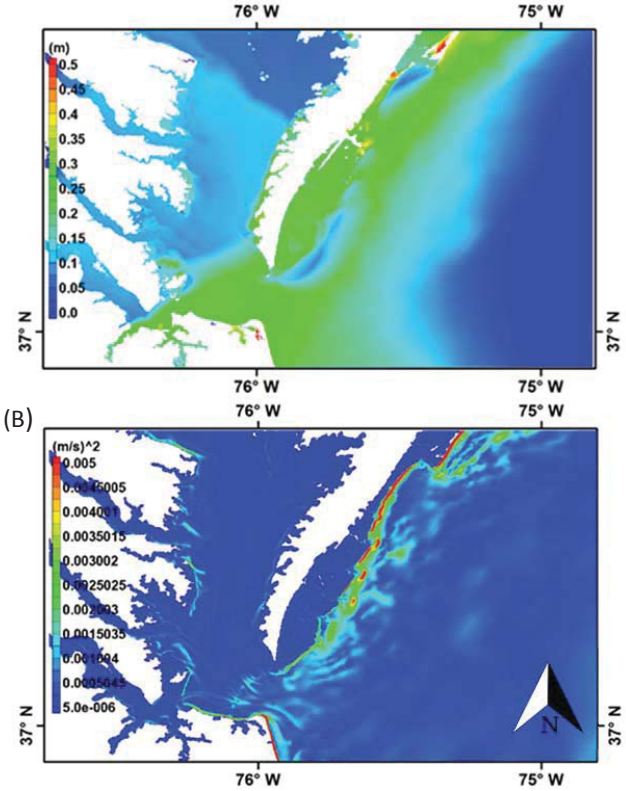

Figure 5. Contour plots of (A) Wave setup during the peak of the storm surge for hurricane Sandy, and (B) Applied wave radiation stress gradients at the same moment.

lation of Hurricane Ike. The relative contribution of waves to the total water level observed in this paper at the shore of the peninsula was, in general, slightly lower than the simulation of Katrina (2005) studied by Dietrich *et al*., 2010. However, an increment of 84% is very unusual, and a deeper analysis must be applied to this area.

CONCLUSIONS

This paper endeavors to assess a cost-benefit analysis between computational resources and the degree of accuracy of the storm surge simulation results. The incorporation of wave setup to the storm surge simulation and the level of numerical mesh resolution have a significant impact on the required computational resources.

The degree of accuracy of the results provided by the moderate and high resolution meshes was almost similar. The model represented well the peak of the storm surge at open areas, but it over-predicted the results at inland locations. It could be related to a lack of resolution, although deeper studies should be conducted in order to figure out what caused those errors. The local and regional domain covers areas at the upper Bay, and the wave setup observed at this region is less than 0.10 m. The uncertainties associated to other factors such as wind model, land cover or topography are more significant than 0.10 m, and therefore, we consider that contribution of wave setup to the overall water levels could be neglected at these two domains. Whereas the wave setup is essential to properly simulate water levels at the continental shoreline.

LITERATURE CITED

Blain, C.; J.; Westerink, J.J., and Luettich, Jr., 1998. Grid convergence studies for the prediction of hurricane storm surge. *International Journal of Numerical Methods in Fluid,* 26(4), 369-401.

Dietrich, J.C.; Bunya, S.; Westerink, J.J.; Ebersole, B.A.; Smith, J.M.; Atkinson, J.H.; Jensen, R.; Resio, D.,T.; Luettich, R. A.; Dawson, C.; Cardone, V.J.; Cox, A., T.; Powell, M. D.; Westerik, H. J., and Roberts H.J., 2010. A high resolution coupled riverine flow, tide, wind, wind wave and storm surge model for southern Louisiana and Mississippi: Part II — synoptic description and analyses of Hurricanes Katrina and Rita. *Monthly Weather Review,* 138, 378–404.

Dietrich, J., M. Zijlema, J. Westerink, L. Holthuijsen, C. Dawson, R. Luettich Jr., R. Jensen, J. Smith, G. Stelling, and G. Stone, 2011, Modeling hurricane waves and storm surge using integrally-coupled, scalable computations. *Coastal Engineering*, 58(1), 45–65.

Holland, G.J., 1980. An analytic model of the wind and pressure profiles in hurricanes. *Monthly Weather Review,* 108, 1212–1218.

Jelesnianski, C. P., Chen J., and Shaffer, W. A., 1992. SLOSH: Sea, Lake, and Overland Surges from Hurricanes. NOAA *Technical Report NWS 48. National Oceanic and Atmospheric Administration, U.S. Department of Commerce.*

Kerr, P.C.; Martyr, R. C.; Donahue, A.S.; Hope, M.E.; Westerink, J. J.; Luettich Jr., R. A.; Kennedy, A. B.; Dietrich, J. C.; Dawson, C., and Westerink, H. J., 2013. U.S. IOOS coastal and ocean modeling testbed: Evaluation of tide, wave, and hurricane surge response sensitivities to mesh resolution and friction in the Gulf of Mexico. *Journal of Geophysical Research: Oceans*, 118, 4633–4661.

Longuet-Higgins, M. S. and Stewart R. W., 1963. A note on wave set-up. *Journal Marine Reseach*, 21.4-10.

Longuet-Higgins, M.S., Stewart, R.W., 1964. Radiation stresses in water waves; physical discussions, with applications. *Deep-Sea Research,* 11, 529–562.

Resio, D.T. and Westerink, J.J., 2008. Modeling the physics of storm surges. *Physics Today,* 61 (9), 33–38.

Westerink, J.J.; Luettich, R.A.; Feyen, J.C.; Atkinson, J.H.; Dawson, C.; Roberts, H.J.; Powell, M.D.; Dunion, J.P.; Kubatko, E.J., and Pourtaheri, H., 2008. A basin- to channel-scale unstructured grid hurricane storm surge model applied to southern Louisiana. *Monthly Weather Review,* 136, 833–864.

Sheng, Y. P., Lapetina A., and Ma, G. 2012. The reduction of storm surge by vegetation canopies: Three-dimensional simulations. *Geophysical Research Letter*, 39.

Zijlema, M., 2010. Computation of wind–wave spectra in coastal waters with SWAN on unstructured grids. *Coastal Engineering*, 57, 267–277.

Journal of Coastal Research	SI	75	1087 - 1091	Coconut Creek, Florida	2016

Hindcasting Tropical Storm Events in the Oman Sea

Sarmad Ghader[†], Daniel Yazgi[†], S. Abbas Haghshenas[†*], Azadeh Razavi Arab [†], Morteza Jedari Attari [†], Arash Bakhtiari [†], and Hamid Zinsazboroujerdi[‡]

[†]Department of Space Physics
Institute of Geophysics
University of Tehran
Tehran, Iran

[‡]URS Corporation
Tallahassee, FL 32317, U.S.A.

www.cerf-jcr.org

www.JCRonline.org

ABSTRACT

Ghader, S.; Yazgi, D.; Haghshenas , S.A.; Razavi Arab, A., Jedari Attari, M., Bakhtiari, A., Zinsazboroujerdi, H., 2016. Hindcasting Tropical Storm Events in the Oman Sea. *In:* Vila-Concejo, A.; Bruce, E.; Kennedy, D.M., and McCarroll, R.J. (eds.), *Proceedings of the 14th International Coastal Symposium* (Sydney, Australia). *Journal of Coastal Research*, Special Issue, No. 75, pp. 1087 - 1091 Coconut Creek (Florida), ISSN 0749-0208.

Reliable coastal structure design, sediment transport predictions and future planning all depend on the use of accurate long-term wave data. The present study aims to reproduce measured data from the most important tropical storms in the Oman Sea whose observational data are available. This is assumed as a part of a new wave/wind hindcast for a period of about 30 years over Iranian waters of the Oman Sea. In order to provide a reliable assessment of the wave conditions for this area, three tropical cyclone events are selected for the hindcast model, including Gonu (2007), Phet (2010) and Nilofar (2014). The wind field is reproduced using a meso-scale numerical weather prediction model, namely, Weather Research and Forecast (WRF) model. The reproduced wind field is introduced to the 3rd generation wave model SWAN to hindcast wave characteristics for the most sever event of the mentioned three storms, i.e. Gonu event.

ADDITIONAL INDEX WORDS: *Hurricane, wave hindcasting, wind hindcasting, WRF, SWAN*

INTRODUCTION

The Oman Sea waters and coastline is subjected to tropical cyclone influence on an infrequent basis; however, these cyclones can generate relatively large sea states. At many locations along this coastline, particularly in the southern and northern central and eastern portions of the coast, tropical cyclone waves are the dominant coastal design wave condition as the wave heights can exceed those generated from other meteorological phenomena, such as the monsoon and the northerly Shamals. In early June 2007, Cyclone Gonu entered the Oman Sea and large waves were experienced even along the Iranian coastline; somewhere that has experienced rare tropical events. This cyclone had an unusual path, traveling much further west and north than the typical cyclone. Significant wave heights in excess of 4 meters were measured at Chabahar Bay during this event. Tropical cyclones generally travel from east to west with a velocity of 5 to 15 knots, although considerable variability may occur during the life of a storm. The paths of the cyclones tend to curve towards the north in the northern Indian Ocean and Arabian Sea. The rotating wind field and the forward motion of the cyclone combine to create a somewhat asymmetrical wind field, with the strongest winds found on the right side of the cyclone (in the northern hemisphere), in relation to the path of travel. Winds are relatively light at the center of the storm, while at a distance of 10 to 30 nautical miles from the center, the winds are most intense (radius of maximum winds, R_{max}). The wind strength generally decreases with distance (in an exponential manner) from the R_{max}, although the rate of decrease varies by storm. In addition, meso-scale wind systems, which are embedded in a synoptic scale tropical cyclone system, can also make the wind field somewhat asymmetrical. The meso-scale systems are usually located between the R_{max} and the outer periphery of the cyclone.

Numerical weather prediction models can be used as a tool to estimate marine surface winds and for providing input parameters to the sea surface wave and ocean circulation numerical models (Chen *et al*., 2005; Schulz, *et al*., 2007, Sousa, *et al*., 2013; Liu, *et al*., 2011). In addition, these models can be used for simulation of tropical storms and cyclones (Mukhopadhyay, *et al*., 2011, Nguyen and Chen, 2011). In this work, the weather research and forecasting (WRF) model (Skamarock, *et al*., 2008; Wang, *et al*., 2010) is exploited to hindcast of surface winds for three tropical cyclone events including Gonu (2007), Phet (2010) and Nilofar (2014) over the Oman sea (See Figure 1 for the tracks). This data is used to provide input parameters to the sea surface wave model.

The wind field in a tropical cyclone generates waves that radiate outward from the center of the storm in all directions. However, waves are typically most severe in the quadrant of the storm where the winds blow in the direction of cyclone travel. In addition, waves traveling in the same direction as the storm have an effectively longer fetch, allowing increased time for wave generation. Waves generated by a tropical cyclone reduce in intensity with distance from the center of the storm due to spatial dispersion. In this study the 3rd generation wave model SWAN is employed to simulate wave characteristics during Gonu Cyclone over Iranian coastline of the Oman Sea at Chabahar Bay. Model results are compared with field observations of Dibajnia *et al.* (2010) and

DOI: 10.2112/SI75-218.1 received 15 October, 2015; accepted in revision 15 January, 2015.
*Corresponding author: sahaghshenas@ut.ac.ir
©Coastal Education and Research Foundation, Inc. 2016

Soltanpour (2007). Dube *et al.* (2009) and Fritz *et al.* (2010) simulated wave parameters and storm surge values for Cyclone Gonu over Omani Coastline.

METHODS

In the present work, all wind simulation are carried out with the Advanced Research WRF (ARW) model developed at National Center for Atmospheric Research (NCAR). The WRF is a fully compressible, Euler non-hydrostatic mesoscale numerical weather prediction model (Skamarock *et al.*, 2008; Wang *et al.*, 2010).

In this study, the ARW dynamical core of the WRF model version 3.4.1 is used. The WRF model is configured with two nests with 0.3 degree and 0.1 degree horizontal grid resolutions in a Lat-Lon (latitude-longitude) projection, respectively. Figure. 1 shows that the finer (inner, d02) domain covers the Oman Sea and the Persian Gulf. Outer and inner domains have 103×76 and 256×194 grid points, respectively. For all domains 39 terrain following vertical levels are used.

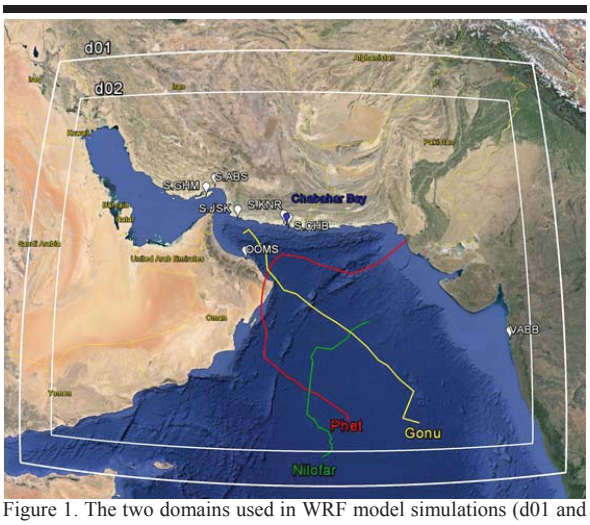

Figure 1. The two domains used in WRF model simulations (d01 and d02). The locations of observational stations, the location of Chabahar Bay and the tropical cyclone tracks (source: http://weather.unisys.com) are also depicted (background taken from Google Earth).

The parameterization schemes used in this study for physical processes in WRF model are as follows. The Lin, WRFSM3, WRFSM6, Thompson, Goddard and Ferrier methods for the microphysics, the rapid radiative transfer model (RRTM) scheme for the longwave radiation, Dudhia and Goddard methods for the shortwave radiation, the YSU, ACM2, MRF, MYJ, MYNN2.5 and QNSE schemes for the planetary boundary layer (PBL), Kain Fritsch, Grell, Grell Devenyi and BMJ for the cumulus parametrization, the MM5, revised MM5, Pleim Xiu, Eta, MYNN and QNSE methods for the surface layer, the Noah, Pleim Xiu, and 5-layer thermal diffusion methods for the land surface, are used. More details are given by Skamarock *et al.* (2008) and Wang *et al.* (2010).

These choices are used to create 13 WRF model configurations (see Table 1). To find the suitable WRF model configuration, the model is run with these 13 different physics configurations. Then, one of these configurations is selected to be suitable for wind simulation over water based on statistical analysis. To this end, all simulations differ only in the physical parameterization schemes listed in Table 1. These different configurations are given different names as in the second column in Table 1.

In this study, the reanalysis ERA-Interim data (Dee *et al.*, 2011) produced at the European Centre for Medium-Range Weather Forecasts (ECMWF) are used to provide the initial and boundary data for WRF model simulations. ECMWF ERA-Interim data set is selected after testing the National Centers for Environmental Prediction Final Operational Global Analysis (NCEP FNL; Kalnay *et al.* 1996) and the NCEP Climate Forecast System Reanalysis (CFSR; Saha *et al.*, 2010) data. Wind simulations of Gonu tropical cyclone showed using the three dataset with the same model set up (here we emphasize on the time step) shows that the most of the simulations with FNL and CFSR data sets caused the model to crash where ECMWF ERA-Interim data set did not. For this reason the assessment of the different model configurations are achieved using ECMWF ERA-Interim data to simulate the most intense tropical cyclone Gonu.

The selection of the suitable model configuration to regenerate the wind field was achieved by the evaluation of WRF model simulation from 1 to 6 June 2007 of the tropical cyclone Gonu. Hindcast verification was achieved using the Model Evaluation Tools (MET; Fowler *et al.* 2010) of the developmental testbed center (DTC) at NCAR.

To perform a hindcast for a specific period of time (namely, 7 days) first it is divided to daily periods. Then the WRF model is run for every 1.25 day with 6 hours of spin-up time. Finally, when all simulations are carried out, the first 6 hours of individual simulations (spin-up time) is discarded and daily simulations are concatenated to form a pseudo-continuous dataset (e.g., Lo, *et al.* 2008; Mentaschi *et al.* 2015).

At each observational station and along 24 hours of the day that have valid observation, the corresponding simulated wind speed and zonal and meridional components of the wind field are interpolated from WRF forecasts. Then, using MET, the root mean squared error (RMSE) and correlation coefficient (Wilks 2011) between observations and simulations are calculated. RMSE and correlation are the main statistical quantities used to select the proper model configuration.

A sample correlation coefficient (CC) and RMSE of the evaluation process of the tropical cyclone Gonu for the 10 m surface wind vector and its components are presented in Table 2 for different stations and different dates. The model setup is represented by numbers of Table 1. Observational stations that their measured data are used in this work are presented in Table 3 (locations are shown in Figure 1). Summary of statistical analysis for all observational stations and all dates lead to the suitable configuration of WRF model. Table 4 presents the final setup and configuration of WRF model.

The third-generation spectral wave model SWAN was employed in the present study to simulate wave generation and propagation over the physical model domain. Model runs were carried out for a one month period including the

observational studies during Gonu storm event. The results of the SWAN computations are presented and compared with the observed wave parameters recorded at the study site.

Table 1. *The different WRF model configurations. Long wave radiation scheme for all configurations is RRTM.*

No.	Configuration name	Microphysics	PBL	Cumulus	Short wave	Surface Layer	land surface
1	Phys01	WRFSM3	YSU	Kain Fritsch	Dudhia	MM5	Noah
2	Phys02	Lin	ACM2	Kain Fritsch	Goddard	Pleim Xiu	Pleim Xiu
3	Phys03	Lin	MRF	Kain Fritsch	Goddard	Revised MM5	Noah
4	Phys04	Lin	MYJ	Kain Fritsch	Goddard	Eta	Noah
5	Phys05	Lin	MYNN 2.5	Kain Fritsch	Goddard	MYNN	Noah
6	Phys06	Lin	YSU	Kain Fritsch	Goddard	revised MM5	Noah
7	Phys07	WRFSM6	MYJ	Kain Fritsch	Dudhia	Eta	Noah
8	Phys08	WRFSM3	MRF	Kain Fritsch	Dudhia	MM5	5-layer thermal diffusion
9	Phys09	WRFSM6	YSU	Kain Fritsch	Dudhia	MM5	5-layer thermal diffusion
10	Phys10	Lin	QNSE	Kain Fritsch	Goddard	QNSE	Noah
11	Phys11	Thompson	YSU	Grell	Goddard	MM5	5-layer thermal diffusion
12	Phys12	Goddard	MYJ	Grell Devenyi	Dudhia	Eta	Noah
13	Phys13	Ferrier	YSU	BMJ	Dudhia	MM5	Noah

Table 2. *A sample CC and RMSE of 10 m wind speed (SPD) vector and its components.*

Station	Model Setup	Date	SPD CC	SPD RMSE	U CC	V CC
OOMS	Phys02	6/6/2007	0.87	1.74	0.88	0.87
S.ABS	Phys04	6/3/2007	0.81	1.34	0.49	0.84
S.CHB	Phys08	6/3/2007	0.75	1.51	0.41	0.87
S.GHM	Phys11	6/3/2007	0.90	0.99	0.59	0.81
S.JSK	Phys04	6/4/2007	0.81	1.87	0.75	0.76
S.KNR	Phys11	6/3/2007	0.96	2.38	0.80	0.69
VABB	Phys05	6/3/2007	0.49	2.43	0.66	0.47

Table 3. *Observational stations.*

No.	Station Name	Country	Abbriv.	Latitude	Longitude
1	Bandar Abbas	Iran	S.ABS	27.2147	56.3728
2	Bombay Santa Cr	India	VABB	19.1200	72.8400
3	Chabahar	Iran	S.CHB	25.2811	60.6511
4	Gheshm	Iran	S.GHM	26.7519	55.8906
5	Jask	Iran	S.JSK	25.6378	57.7697
6	Kenarak	Iran	S.KNR	25.4333	60.3667
7	Seeb Int. Airport	Oman	OOMS	23.5800	58.2800

RESULTS

Figure 2 presents the distribution of 10 m wind vector and contours of the mean sea level pressure fields simulated by the WRF model over the Oman sea for three dates (one date for each tropical cyclone studied here). For comparison, the plots of ERA-Interim data are also shown.

Figures 3 to 5 presents the simulated wave parameters at Chabahr Bay in comparison with observational data, just for Gonu Storm, as reliable data were available to the authors just for this case. As it is observed acceptable accuracy has obtained with an RMSE value of 0.48.

Table 4. *Final WRF model configuration used to regenerate the wind field.*

Dynamics	ARW
Map projection	Lat-Lon
Domains count	2 nested domains
Resolution (horizontal)	Mother domain (d01) 0.3° Nested domain (d02) 0.1°
No. of vertical levels	39
Initial and boundary condition data	ECMWF ERA-Interim
Physical Parameterization configuration	Phys04 of Table 1.

DISCUSSION

Results of WRF model simulations presented in Figure 2, for instance, at 00 UTC 04 June 2007 (Gonu tropical cyclone period) shows that the minimum pressure of the Gonu cyclone center simulated by model is about 994 hPa; while for the ERA-Interim data it is 999 hPa. In addition, the observed value is 988 hPa (Pattanayakand and Mohanty, 2008). The strong wind simulations of the center of cyclones using the WRF model is also noticeable.

The wave height simulations for Cyclone Gonu shows an acceptable agreement with the observational data. It is while the model has partially failed to catch the high frequency periods in the very beginning; something that can be attributed to the limited domain of the model and applying no wave condition on the southern boundary. This deficiency may be solved by extending the model domain towards Antarctica. Model performance for the wave direction is acceptable as well.

The whole hindcasting system seems to be reliable for tropical cyclone wind and wave simulations over the Oman Sea and the Arabian Sea. Modifications are needed to improve wave period estimations.

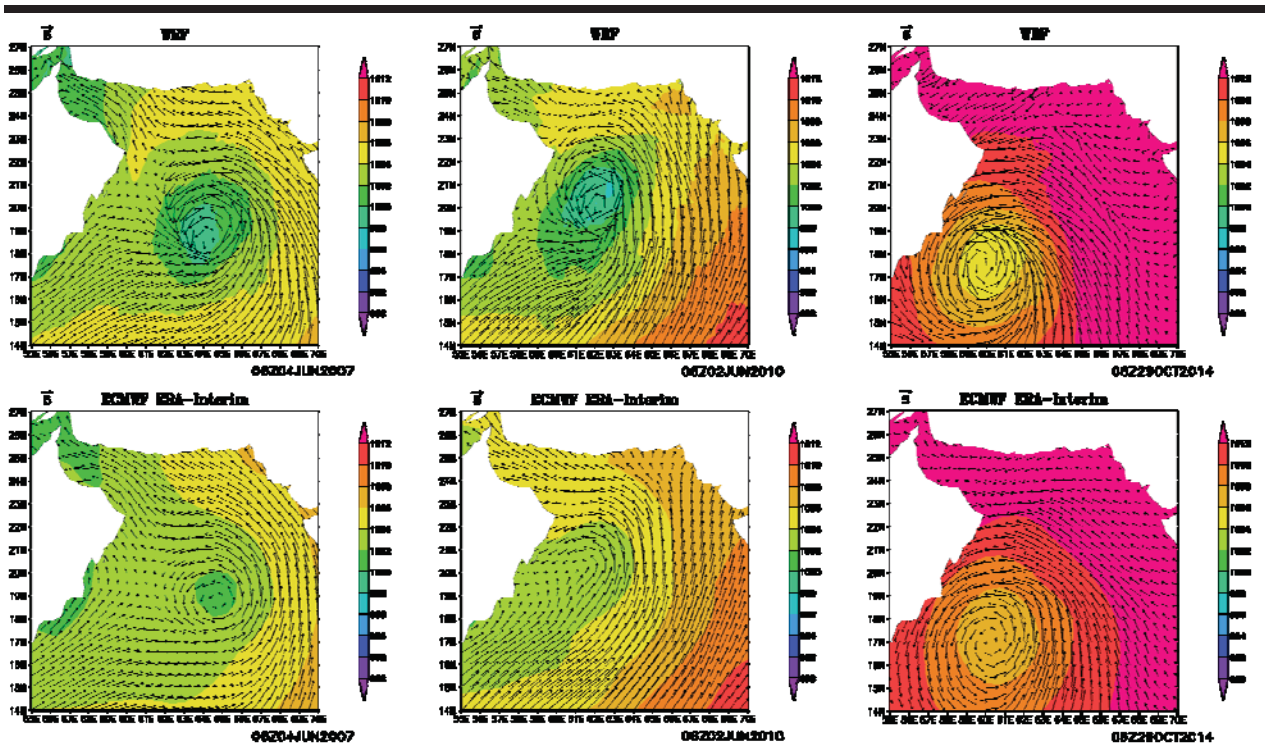

Figure 2. Horizontal 10 m wind vector (ms-1) and contours of the mean sea level pressure for WRF model simulations (top) and the ERA-Interim data (bottom). Date and times are 06 UTC 04 June 2007 (Gonu), 06 UTC 02 June 2010 (Phet) and 06 UTC 29 October 2014 (Nilofar), respectively.

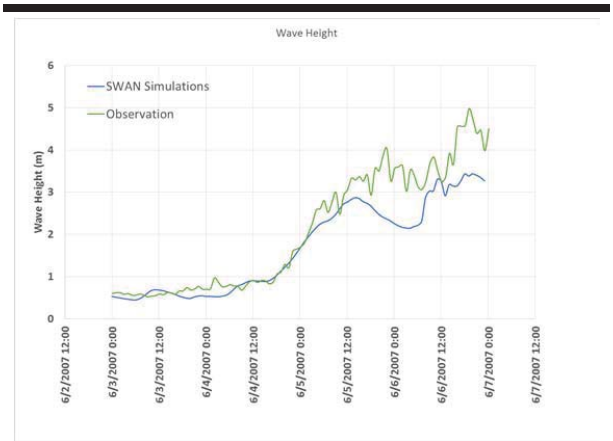

Figure 3. Simulated wave height for Gonu observations at Chabahar Bay.

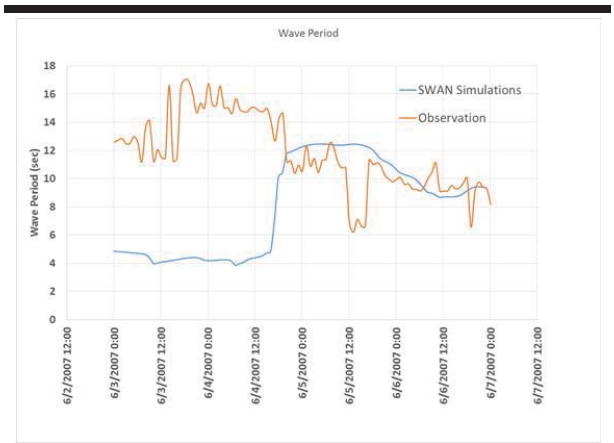

Figure 4. Simulated wave period for Gonu observations at Chabahar Bay.

Figure 5. Simulated wave direction for Gonu observations at Chabahar Bay.

CONCLUSIONS

A combination of WRF and SWAN modeling activities are adopted to simulate and regenerate Gonu storm wind and waves in the Oman Sea. Model setup for WRF model is selected by using three major tropical storms happened in the Oman Sea and the Indian Ocean since 2007. Regenerated wind field for Gonu Storm (2007) was introduced to SWAN wave model and wave parameters were hindcasted at Chabahar Buoy over Iranian Coastline of the Oman Sea. Regenerated waves are in reasonable agreement with observations in height and direction, but more attention should be paid for improving the accuracy of simulated periods.

LITERATURE CITED

Chen, C., Beardsley, R. C., Hu, S., Xu, Q., Lin, H., 2005. Using MM5 to hindcast the ccean surface forcing fields over the gulf of Maine and Georges bank region, *Journal of Atmospheric and Oceanic Technology*, 22, 131-145.

Dee, D. P.; Uppala, S. M.; Simmons, A. J.; Berrisford, P.; Poli, P.; Kobayashi, S.; Andrae, U.; Balmaseda, M. A.; Balsamo, G.; Bauer, P.; Bechtold, P.; Beljaars, A. C. M.; van de Berg, L.; Bidlot, J.; Bormann, N.; Delsol, C.; Dragani, R.; Fuentes, M.; Geer, A. J.; Haimberger, L.; Healy, S. B.; Hersbach, H.; Hólm, E. V.; Isaksen, L.; Kållberg, P.; Köhler, M.; Matricardi, M.; McNally, A. P.; Monge-Sanz, B. M.; Morcrette, J.-J.; Park, B.-K.; Peubey, C.; de Rosnay, P.; Tavolato, C.; Thépaut, J.-N.; Vitart, F., 2011. The ERA-Interim reanalysis: configuration and performance of the data assimilation system. *Quarterly J. of the Royal Meteorological Society*,137(656), 553-597.

Dibajnia, M., Soltanpour, M., Nairn, R., Allahyar, M. R., 2010. Cyclone Gonu, the most intense tropical cyclone on record in the Arabian Sea, *Indian Ocean Tropical Cyclones and Climate Change*, Springer, pp. 149-157 (ISBN 978-90-481-3109-9)

Dube, S., Jain, I.,Rao, AD.andMurty, TS., 2009. Storm surge modeling for the bay of Bengal and Arabian sea, *Nat Hazards*, 5, 3-27.

Fowler, T. L., T. Jensen, E. I. Tollerud, J. Halley Gotway, P. Oldenburg, and R. Bullock, 2010. New Model Evaluation Tools (MET) software capabilities for QPF verification. Preprints, Third Int. Conf. on QPE, QPF and Hydrology, Nanjing, China, *WMO/World Weather Research Programme*. [Code and documentation available online at http://www.dtcenter.org/met/users/metoverview/index.php]

Fritz, H.M, Blount, C.D, Albusaidi, F.B, AlHarthy, A.H.M, 2010. Cyclone Gonu storm surge in Oman, *Estuarine, Coastal and Shelf Science*, Vol. 86, P. 102-106.

Liu, B., Liu, H., Xie, L., Guan, C., Zhao, D., 2011. A coupled atmosphere–wave–ocean modeling system: Simulation of the intensity of an idealized tropical cyclone, *Mon. Wea. Rev.*, 139, 132-152.

Lo, J. C. F., Yang, Z. L., Pielke Sr. R. A., 2008. Assessment of three dynamical climate downscaling methods using the Weather Research and Forecasting (WRF) model. *J. Geophys. Res.*, 113, D09112.

Mentaschi, L., Besio, G., Cassola, F., Mazzino, A., 2015. Performance evaluation of Wavewatch III in the Mediterranean Sea, *Ocean Modelling*, 90, 82-94.

Mukhopadhyay, P., S. Taraphdar, and B. N. Goswami 2011, Influence of moist processes on track and intensity forecast of cyclones over the north Indian Ocean, *J. Geophys. Res.*, 116, D05116, doi:10.1029/2010JD014700.

Nguyen, H. V., Chen, Y. L., 2011. High-resolution initialization and simulations of typhoon Morakot (2009), *Mon. Wea. Rev.*, 139, 1463-1491.

Pattanayakand , S., U. C. Mohanty, 2008. A comparative study on performance of MM5 and WRF models in simulation of tropical cyclones over Indian seas. *Current Science*,95(7), 923-936.

Saha, S., and Coauthors, 2010: The NCEP climate forecast system reanalysis. *Bull. Amer. Meteor. Soc.*,91, 1015-1057.

Schulz, Eric W., Jeffrey D. Kepert, Diana J. M. Greenslade, 2007., An assessment of marine surface winds from the Australian bureau of meteorology numerical weather prediction systems, *Weather and Forecasting*, 22,613-636.

Skamarock, W. C., Klemp, J. B., Dudhia, J., Gill, D. O., Barker, D. M., Wang, W., Powers, J. G., 2008. A description of the advanced research WRF version 3. NCAR Tech. NCAR/TN–475+STR.

Soltanpour M., 2007. Cyclone Gonu, the most intense tropical cyclone in the Arabian Sea, *Proc. of Tsunami, Storm Surge and other Coastal Disasters ~Experiences of Indian Ocean Tsunami and Hurricane Katrina~*, Dar es Salaam, Tanzania, pp. 57-58

Sousa, M. C., I. Alvarez, N. Vaz, M. Gomez-Gesteira, J. M. Dias, 2013. Assessment of wind pattern accuracy from the Quikscat satellite and the WRF model along the Galician coast (northwest Iberian Peninsula), *Monthly Weather Review*, 141, 742-753.

Wang, W., Bruyère C., Duda M., Dudhia J., Gill D., Lin H., Michalakes J., Rizvi S. Zhang X., Beezley J. D., Coen J. L., and Mandel J., 2010. User's guide for the advanced research WRF (ARW), Version 3.5, NCAR.

Wilks, D. S., 2011. *Statistical methods in the atmospheric sciences*. 2nd ed. Elsevier, 704

Journal of Coastal Research	SI	75	1092 - 1096	Coconut Creek, Florida	2016

Estimating Flooding Level Through the Brazilian Coast Using Reanalysis Data

Paula Gomes da Silva[†*], Charline Dalinghaus[††], Mauricio González[†], Omar Gutiérrez[†], Antonio Espejo[†], Ana J. Abascal[†], and Antonio H. F. Klein[††]

[†] Environmental Hydraulics Institute "IH Cantabria"
Universidad de Cantabria
Santander, España

[††] Laboratório de Oceanografia Costeira,
Departamento de Geociências
Universidade Federal de Santa Catarina
Florianópolis, Brasil

www.cerf-jcr.org

www.JCRonline.org

ABSTRACT

Gomes da Silva, P.; Dalinghaus, C.; González, M., Gutiérrez, O., Espejo, A., Abascal, A.J., and Klein, A.H.F., 2016. Estimating flooding level through the Brazilian coast using reanalysis data. *In:* Vila-Concejo, A.; Bruce, E.; Kennedy, D.M., and McCarroll, R.J. (eds.), *Proceedings of the 14th International Coastal Symposium* (Sydney, Australia). *Journal of Coastal Research*, Special Issue, No. 75, pp. 1092 - 1096. Coconut Creek (Florida), ISSN 0749-0208.

This paper presents an estimative of coastal flooding level values distribution along the Brazilian coast by using reanalysis data and by simulating wave propagation with Snell approximation. The coast was divided into 24 zones and flooding levels series were calculated for each one. Mean and extreme distribution show higher flooding levels occurring in northern coast (3 m higher than beaches in central coast) followed by the southern coast (1 m higher than central coast). High values obtained on north region were associated with greater tidal elevations (maximum values > 3 m) while higher values in south were related to greater wave heights and higher storm surge elevations (~2 m and >7 m respectively). A comparison between beach types were also conducted and demonstrate higher values of flooding levels during reflective conditions (0.3 m higher for a specific beach condition), as a result of the runup model applied. Although simplifications were used to calculate this large scale variation of the flooding level along the coast, the results partially presented here can be of large usefulness in pre-design phases of coastal projects and in preliminary risk analysis.

ADDITIONAL INDEX WORDS: *Coastal flooding, Brazilian coast, reanalysis data.*

INTRODUCTION

Understanding sea surface variation is critical to determine safety guidelines for coastal engineering and navigation. Wave and level data are indispensable in establishing coastal engineering projects, vulnerability and risk analysis.

A coastal flood event consists initially in the mean sea level in a given stretch of the coast. Above this, the astronomical tide and storm surge induce the elevation of the sea surface, followed by waves that reach the beach at a certain height (runup). The sum of all these components is called flooding level (*FL*) (Medina and Mendez, 2006).

Problems related to coastal flooding levels have been observed throughout the world, especially in areas where the occupation of costal zones is more intense, as it is observed in several beaches all over Brazil. (Muehe, 2006). The lack of measured time series makes difficult the verification of flooding levels in most part of the Brazilian coast. Decisions are then taken based on few records which lead to higher uncertainties on both risk analysis and pre-design levels calculation. In these cases, reanalysis data can be especially important, since it can provide large temporal series with high homogeneous spatial and temporal resolutions.

Based on the facts presented above, the aim of this work is to present an estimate of coastal flooding distributions along the Brazilian coast, based on sixty years reanalysis data (wave, astronomical tide and storm surge series) and simulating wave propagation by Snell approximation.

Dynamics of the Brazilian coast

The Brazilian coast extends for near 9000 km, with 17 States bordering the Atlantic Ocean. Such extension gives the coast a variety of conditions, which results in very different environments. The predominant wave climate in the south part of Brazil (RS to RJ –Figure 1) comes from the south, southeast and northeast, with 6 to 15 s period and 1-3 m height, reaching more than 7 m during fall season (Pianca *et al*., 2010). From Rio de Janeiro (RJ) to Rio Grande do Norte (RN) the waves are predominantly from the east and southeast, with an average period ranging from 8 to 10 s and wave height between 1-2 m (Pianca *et al*., 2010). Eventually, during austral winter, waves generated by frontal systems coming from the south reach the state of Pernambuco (PE). These waves are typically from the south and southeast, with periods of 7 to 12 s and 1-2 m wave height (Tessler and Goya, 2005). Finally, waves in the coastline between RN and Amapá (AP) present directions from east and northeast, with shorter periods (6-8 s) (Pianca *et al*., 2010). Other ocean waves that affect this segment come from storms formed in the northern hemisphere. These swells, with longer

DOI: 10.2112/SI75-219.1 received 15 October, 2015; accepted in revision 15 January, 2015.
*Corresponding author: silvapgomes@gmail.com
©Coastal Education and Research Foundation, Inc. 2016

periods, may occur especially during boreal winter (Melo Filho *et al*., 1995).

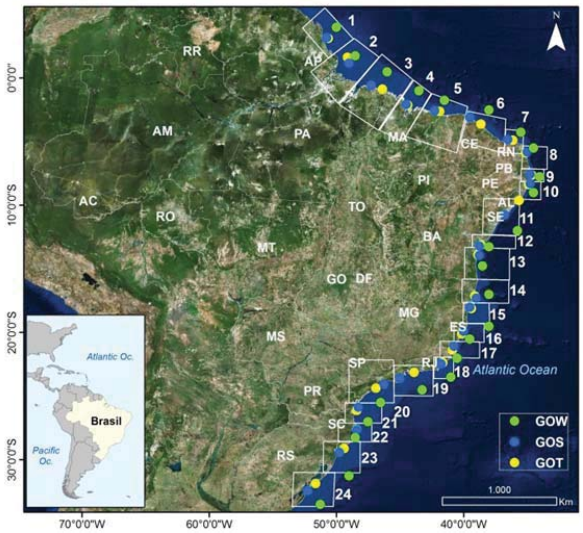

Figure 1. Map of Brazil with the GOW, GOT and GOS databases and the 24 divided zones.

The tidal regime is also variable along the coast, with tidal range values increasing from south to north. A large part of the coast (from Rio Grande do Sul – RS - to Alagoas - AL) presents tidal regimes with less than 2 m amplitude (microtidal regime). Some punctual elevations bigger than 2 m may occur in areas where geomorphology provides an increase in tidal current speed. Amplitudes greater than 4 m (macrotidal regime) are present only in the state of Maranhão (MA), in part of Pará (PA) and in southern Amapá (AP). Other shorelines and some places in Bahia (BA) and Sergipe (SE) present mesotidal regime with amplitudes between 2 and 4 m (Tessler and Goya, 2005).

METHODS

In order to calculate the coastal flooding level distributions across the Brazilian coast, four basic steps were taken (accordingly Medina and Mendez, 2006): i) the Brazilian coast was divided in 24 zones according to wave, tide, surge and coastal orientation; ii) waves were propagated from deep to coastal waters in each zone; iii) wave runup series were empirically calculated based on wave parameters and beach morphology and iv) coastal flooding levels were then calculated based on wave runup, tide and storm surge time series and values representative of extreme and mean distributions could be verified.

Data

Wave and sea level reanalysis used in this study were generated by the Environmental Hydraulics Institute "IH Cantabria": Global Ocean Waves (GOW), Global Ocean Tide (GOT) and Global Ocean Surge (GOS). These databases are composed of a set of 60 year (1948-2008) hourly time series of wave, tide and storm surge over the whole globe, including some points near the Brazilian coast (Figure 1).

GOW database was generated by simulation using the Wave Watch III model. Tidal database "GOT' was created based on the harmonic constants of TPXO Global Tidal Solution (Egbert and Erofeeva, 2002). Finally, the high-resolution hindcast of the meteorological sea level component "GOS" has been developed using the Regional Ocean Model System (ROMS). Detailed information about the generation of this series and respective validation can be found in Reguero *et al*. (2012) and Losada *et al*. (2013).

Coastal segmentation and beach orientation

The coast was divided into zones with similar physical characteristics namely: wave height, tidal range, storm surge values and coastal orientation. The zones were defined so that the wave model can better represent wave transformation along the coast (Figure 1).

For each zone, the orientation of the beaches with respect to the north was verified and classified in ranges of 22.5º (*i.e.* 348.75º to 11.25 º corresponds to N; 11.26 º to 33.75 º corresponds to NNE, *etc.*). This data was used as the final orientation of the bathymetry by the propagation model.

Wave propagation

Deep-water wave parameters were propagated from GOW points (Figure 1) to shallow water by Snell approximation. Wave rays were propagated considering three main bathymetric orientations. The last one represents the coastline orientation.

Snell approximation takes into account wave refraction and shoaling without considering the diffraction process. Wave propagation stops when the wave breaking occurs (*i.e.* H/h = 0.8m). Such propagation method was chosen as it is a simple model which requires low computational cost (this is very important when working with such a large study area and long time series) and simple input data (*i.e.* beaches information was obtained simply by verifying bathymetry and coastline orientation in Google Earth).

Wind data are not taken into account on wave propagation. Since the aim of this work is to obtain a primary analysis and a general view of the dynamics along the entire Brazilian coast, it was considered that local wind could be neglected when calculating wave transformation (still storm surge is considered on final flooding level).

Wave runup

Based on the wave values in shallow waters, runup series ($R_{2\%}$ - runup reached by 2% of the waves) were calculated using the empirical model proposed by Nielsen and Hanslow (1991) that differentiates beaches with gentle and steeper foreshore slope (eq. 1, 2 and 3):

$$Ru_{2\%} = 1.98L \quad (1)$$

$$L \sim 0.6(H_{orms}L_o)^{0,5} tan\alpha_F \text{ for } tan\alpha_F > 0.1 \quad (2)$$

$$L \sim 0.05\,(H_{orms}L_o)^{0,5} \text{ for } tan\alpha_F < 0.1 \quad (3)$$

where H_{orms} is the quadratic root mean square height, L_o is the wavelength and $tan\alpha_F$ is the foreshore slope.

The resultant runup series presented same length and temporal resolution as wave reanalysis series.

Coastal flooding levels

Coastal flooding level series for each beach orientation in each zone was calculated by summing mean sea level (MSL), wave runup ($Ru_{2\%}$), astronomical tide (AT) and storm surge (SS) level series (eq. 4):

$$FL = MSL + AT + SS + Ru_{2\%} \quad (4)$$

FLseries were then adjusted to mean and extremal distributions. The mean distribution, was expressed in terms of number of hours that some level is reached in a year, which is possible due to the hourly temporal resolution of the time series. The extreme values distribution were expressed in terms of return period of Gumbel (maximum) distribution based on annual maximum values.

The results are then assessed following three steps relative to the beach characteristics: a) zone in which the beach is located, b) orientation of the beach and c) foreshore slope.

RESULTS

The values of Hs, tide and storm surge from GOW, GOT and GOS series for each one of the 24 zones of Brazilian coast are presented in Figure 2. As can be seen, Hs presents higher values near the south, with a maximum of almost 8 m in comparison with 4 m values in northern coast. The same behavior is observed for the storm surge levels (elevations due to storm surge can present 1.5 m higher values than the northern coast), while astronomical tidal range present the opposite behavior with elevations in the northern coast having 2.5 m higher values than the southern coast.

With these reanalysis series, FL were calculated for each beach orientation and morphodynamic state (dissipative and reflective) in all 24 zones. As an example of the values obtained, the results of three beaches are shown in here: i) Futuro Beach (CE - Zone 6), ii) Atafona Beach (RJ - Zone 17) and iii) Morro dos Conventos Beach (SC - Zone 23). Studies carried out in these three beaches show foreshore slope values lower than 0.1 ($tan\alpha_F < 0.1$) (Albuquerque *et al*., 2009; Bastos and Silva, 2000; Machado, 2005), so the results presented here are representative of intermediate to dissipative beaches. Figure 3 shows the results of mean and extremal distribution of FL series. In Futuro Beach, flooding reaches levels 1 m higher than Morro dos Conventos and 2 m higher than Atafona levels during the same period in a year. Also, it shows higher FL values than the other two beaches for the same return period, as a result of tidal amplitude observed in this zone (4 m in zone 6). On the other hand, Morro dos Conventos beach presents higher flooding levels when compared to Atafona Beach, which is expected since wave heights and storm surges are significantly greater (until 1 m and 3 m higher, respectively) in this beach. This can suggest a general pattern of higher flooding levels in the north and south of the Brazilian coast, and lower values in the central part of the coast.

DISCUSSION

Based on the results presented above, two main topics deserve special attention: the distribution of FLalong the Brazilian coast and the influence of the beach type.

Dynamics and flooding level distribution along the Brazilian coast

The values presented by reanalysis series in each zone (Figure 2) agree with those presented in previous works which characterized the dynamics in the Brazilian coast.

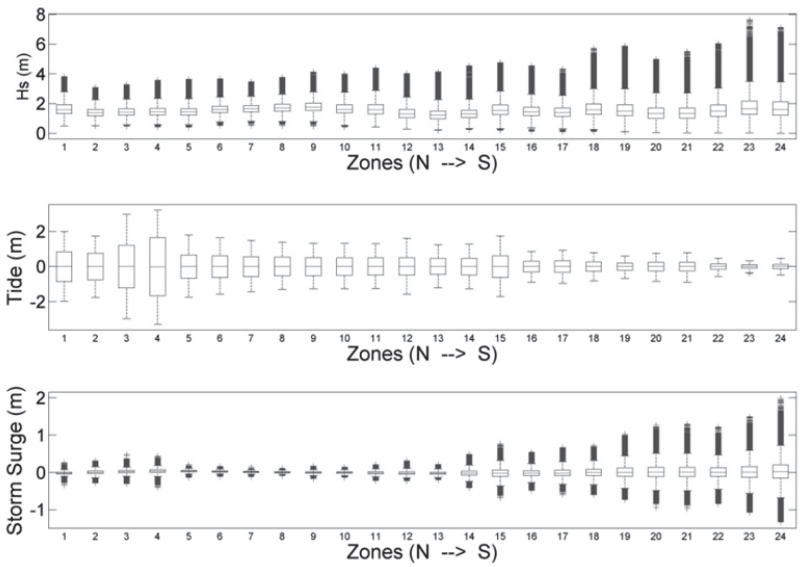

Figure 2. Wave height, tide and surge levels reanalysis series along the 24 zones (obtained in the points presented in Figure 1). Boxes represent values between quantiles Q25 and Q75, whiskers represent Q5 and Q95 and the central line represents the mean value of the series.

Hs values, for example, presented a similar pattern when studied by Pianca *et al.* (2010), who found that wave power presents a decrease in energy levels from the south to northern Brazil. The most energetic waves come from south and are

associated with the passage of cold fronts, which mainly affect the southern coast. In the north (zone 1 to 4) waves are usually lower than 1.5 m (Innocentini *et al*., 2000), although during summer, because of a change in the wind systems, waves of 3 m have been verified (Cachione *et al*. 1995). On the other hand, measured data in southern regions demonstrates that extreme Hs of 6 m (maximum individual height of 13.8 m) can occur (Melo *et al*., 2006).

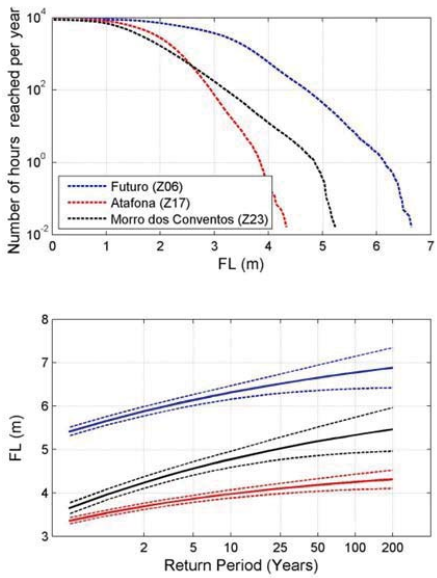

Figure 3. Mean (a) and extremal (b) distributions of the three beaches analyzed.

Tidal ranges reaching up to 5.5 m was also verified by Torres and El-Robrini (2006) in the northern part of Brazil. Ranges between 2 and 4 m and lower than 2 m in the central and south coast are described in FEMAR (2000). GOS reanalysis series in each zone also seems to be consistent with values presented in previous studies. Campos *et al*. (2010) showed that storm surge variation can reach 0.8 m in Espírito Santo (ES) coast (zone 18), which matches with the values presented by GOS series in the same zone. At the same time, Parise *et al.* (2009) verified that storm surge can generate 1.9 m surface elevation on the south coast (zone 24), which highlights the major influence of this parameter on coastal flooding levels in southern regions, different from the north where low values of storm surge must not present greatly influence this zone's dynamics.

Considering that Futuro, Atafona, and Morro dos Conventos represent north, central and south zones of the Brazilian coast, some relation between FL distribution and coastal dynamics parameters can be made. Higher values of FL in the north can be attributed to higher tidal elevations observed in these zones. The dynamics in this part of the Brazilian coast are dominated by tidal oscillations, with ranges of 4 m in Zone 6 where Futuro Beach is located. In contrast, high FL values occurring in south are related to wave heights and storm surges significantly greater and more frequent than in the central and northern part of the Brazilian coast (Parise *et al*, 2009). Still, even with tidal values dominating flooding levels in the north part of the Brazilian coast, waves can be very important on flooding process in all regions and so must be taken into account.

Influence of the beach type

Coastal flooding values can vary significantly from reflective to dissipative beaches. Since reflective beaches present steeper slopes, wave breaking usually occurs very close to the shoreline. This leads to less energy dissipation in the surf zone resulting in higher values of wave runup and consequently higher flooding levels (Nielsen and Hanslow, 1991).

Given the simplifications undertaken, the differences on wave propagation and breaking on distinct morphodynamic states are not taken into account. However, the runup model applied differentiates dissipative beaches ($tan\alpha_F < 0.1$) from reflective ones ($tan\alpha_F > 0.1$). Extreme flooding levels in reflective and dissipative conditions in beaches SE orientated in zone 23 are shown in Figure 4 as an example of such difference. For this specific situation, a difference of until 0.3 m can be verified between them.

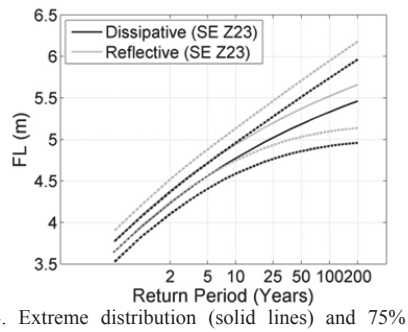

Figure 4. Extreme distribution (solid lines) and 75% confidence interval (dotted lines) of flooding level series in dissipative and reflective conditions in beaches SE orientated in zone 23.

Gomes da Silva (2014) showed a comparison between extreme coastal flooding levels generated with the method applied here and the values generated by propagating GOW series with a more complex model (SMC). The author found that such simplified methodology can cause some overestimation of FL in embayed beaches and beaches sheltered by islands where diffraction can be an important factor in wave energy dissipation. Furthermore, empirical runup formulas used here were generated with exposed oceanic beaches data. This may lead to additional overestimation of the results when the model is applied to beach zones protected by headlands. Previous studies carried out with the same runup model in embayed beaches showed good agreement between runup measurements and runup values calculated by applying Nielsen and Hanslow's formulation on the most exposed part of the beach (Vieira da Silva, 2012).This confirms that the results are reliable in areas where diffraction it is not an important dissipation factor.

CONCLUSIONS

This paper presented the calculation of flooding level distributions along the Brazilian coast based on wave, tide and storm surge reanalysis data. A methodology based on the use of simplified models to calculate wave propagation and runup values was applied.

A general pattern of *FL* values was observed along the Brazilian coast, where higher *FL* are observed in the northern coast (mainly a result of greater tidal elevation), followed by high *FL* in the south (mostly due to stronger wave energy and higher magnitudes of storm surge). It must be pointed out that tidal levels are very predictable and have a shorter return period when compared to high storm surge and wave events. The frequency of occurrence of each variable wasn't considered separately in this work when calculating *FL*, but it must be taken into account when comparing flooding risks in different parts of the Brazilian coast, since higher flooding levels in the northern coast will not always indicate higher risk. This is a topic for future works.

Although simplifications can lead to some overestimation of flooding levels, it was verified that the methodology is applicable to a great part of the Brazilian coast. Considering the need of available data and low computational cost methodologies during pre-design phases of coastal projects and preliminary risk analysis, the results partially presented here are important for areas of the Brazilian coast where diffraction it is not an important dissipation factor.

ACKNOWLEDGMENTS

The authors are thankful to the Brazilian government through the Ministério do Meio Ambiente (MMA), the Agência Brasileira de Cooperação (ABC) and the Agencia Española de Cooperación Internacional para el Desarrollo (AECID) for the financial support of this research.

LITERATURE CITED

Albuquerque, M. G., Calliari, L. J., Corrêa, I.C.S. and Pinheiro, L. S., 2009. Morphodynamic of Futuro Beach, Fortaleza-CE: a synthesis of two years of study. *Quaternary and Enviromental Geosciences*, 1(2), 49-57.

Bastos, A.C. and Silva, C.G., 2000. Coastal morphodynamics of the northern Rio de Janeiro State, Brazil. *Revista Brasileira de Oceanografia*, 48(1), 41-60.

Campos, R.M., Camargo, R. and Harari, J., 2010. Caracterização de eventos extremos do nível do mar em Santos e sua correspondência com as reanálises do modelo do NCEP no sudoeste do Atlântico Sul. *Revista Brasileira de Meteorologia,* 25(2), 175-184.

Cachione, D.A., Drake, D.E., Kayen, R.W., Sternberg, R.W., Kineke, G.C. and Tayle, G.B., 1995. Measurements in the Bottom boundary layer on the Amazon subaqueous delta. *Marine Geology*, 125, 235-239.

Egbert, G.D. and Erofeeva, S.Y., 2002. Efficient inverse modeling of barotropic ocean tides. *Journal of Atmospheric and Oceanic Technology,* 19, 183–204.

FEMAR, 2000. Catálogo das Estações Maregráficas do Brasil.

Gomes da Silva, P. 2014 Exposição à inundação costeira nas praias dos Ingleses, Moçambique e Barra da Lagoa. Florianópolis, Santa Catarina: Federal University of Santa Catarina, Master Thesis, 237p.

Innocentini, V., Prado, S.C.S.C., Pereira, C.S., Arantes, F.O. and Brandão, I.N., 2000. Marulhos no litoral norte do Brasil gerados por furacões: Caso 24 de outubro de 1999. *Proceedings of XI Congresso Brasileiro de Meteorologia* (Rio de Janeiro, Brazil)

Losada, I.J., Reguero, B.G., Méndez, F.J., Castanedo, S., Abascal, A.J. and Mínguez, R., 2013. Long-term changes in sea-level components in Latin America and the Caribbean. *Global and Planetary Change*, 104, 24-50.

Machado, C., 2005. Morfodinâmica do trecho praial entre Morro dos Conventos – Balneário Gaivota, SC. Florianópolis, SC: Federal University of Santa Catarina, Master Thesis, 117p.

Medina, R. and Méndez, F.J., 2006. Inundación costera originada por la dinámica marina. *Ingeniería y Territorio*. 74, 68-75.

Melo Filho, E., Alves, J.H.G.M., Jorden, V. and Zago, F., 1995. Instrumental confirmation of the arrival of north atlantic swell to the Ceara coast. *Proceedings of the IV COPEDEC* (Rio de Janeiro, Brazil), pp.1984-1996.

Melo, E., Hammes, G.R. and Franco, D., 2006. Estudo de caso: A ressaca de 2005 em Santa Catarina. *Proceedings of the II Seminário e Workshop em Engenharia Oceânica*, (Rio Grande, Brazil), pp. 1-16.

Muehe, D., 2006. *Erosão e progradação do litoral brasileiro*. Brasília: Ministério do Meio Ambiente, 476p.

Nielsen, P., Hanslow, D.J., 1991, Wav runup distributions on natural beaches. *Journal of Coastal Research*, 7(4), 1139-1152.

Parise, C.K., Calliari, L.J. and Krusche, N., 2009. Extreme storm surges in the South of Brazil: atmospheric conditions and shore erosion. *Brazilian Journal of Oceanography*, 57(3), 175-188.

Pianca, C., Mazzini, P.L. and Siegle, E., 2010. Brazilian offshore wave climate base don NWW3 reanalysis. *Brazilian Journal of Oceanography,* 58(1), 53-70.

Reguero, B.G., Menéndez, M., Méndez, F.J., Mínguez, R. and Losada, I.J., 2012. A global Ocean Wave (GOW) calibrated reanalysis from 1948 onwards. *Coastal Engineering,* 65, 38–55.

Tessler, M.G. and Goya, S.C., 2005. Processos costeiros condicionantes do litoral brasileiro. *Revista do Departamento de Geografia*, São Paulo, 17, 11-13.

Torres, A.M. and El-Robrini, 2006. Amapá. In: Muehe, D (Ed). *Erosão e progradação do litoral brasileiro*. Brasília, Ministério do Meio Ambiente.

Vieira da Silva, G.,2012. Cota de inundação e recorrência para a enseada do Itapocorói e praia de Morro dos Conventos, Santa Catarina. Porto Alegre, Rio Grande do Sul: Federal Universityof Rio Grande do Sul, Master Thesis, 98p.

Journal of Coastal Research	SI	75	1097 - 1101	Coconut Creek, Florida	2016

Ecosystem Services and Their Benefits as Coastal Protection in Highly Urbanised Environments

Emilia Guisado-Pintado[†*], Fatima Navas[‡] and Gonzalo Malvárez[‡]

[†]Coastal Environments Research Group, Universidad Pablo de Olavide of Sevilla. CP 41013, Spain
esguipin@upo.es

[‡]Physical Geography Area. Universidad Pablo de Olavide of Sevilla. CP 41013, Spain

www.cerf-jcr.org

www.JCRonline.org

ABSTRACT

Guisado-Pintado, E.; Navas, F., and Malvárez, G., 2016. Ecosystem Services and Their Benefits as Coastal Protection in Highly Urbanised Environments. *In:* Vila-Concejo, A.; Bruce, E.; Kennedy, D.M., and McCarroll, R.J. (eds.), *Proceedings of the 14th International Coastal Symposium* (Sydney, Australia). *Journal of Coastal Research*, Special Issue, No. 75, pp. 1097 - 1101. Coconut Creek (Florida), ISSN 0749-0208.

Coastal hazards from hydro-meteorological events such as flooding, shoreline erosion, storm surges and sea level rise, have been widely studied not least because they can have significant impacts on human activities and assets, adversely affecting the economy, well-being and safety of coastal communities. Coastal hazards are a major concern for local populations and authorities and recently European Union Directives and Horizon 2020 strategies have focussed on building a common framework to manage those events, to take adequate and coordinated measures to reduce it. As a result, the quantification and evaluation of ecosystem services provided by coastal systems for human populations have begun to be incorporated into policy and decision-making processes in order to preserve both ecosystems and the benefits these offer. Notwithstanding the considerable progress that has been made in recent years, successful delivery of indicators to evaluate and map the Coastal Protection ecosystem service at adequate spatial scale is still uncommon. In this paper existing indicators at a European scale for Coastal Protection service (capacity, flow and benefit) are adapted and applied to a coastal area in southern Spain where urban and tourism activities are the main drivers whilst coastal exposure to hazards is increasing. Results highlight the importance of scale and resolution when approaching coastal systems and the importance of using accurate and local-regional sets of data. Further, the need to understand the spatial and temporal variability of the Coastal Protection service and the non-linearity response is shown to be essential when developing coastal and marine management strategies.

ADDITIONAL INDEX WORDS: *Coastal hazards, habitats, vulnerability, Cascade model.*

INTRODUCTION

Natural hazards have become important forcing variables in their interaction with human activity (coastal vulnerability) and particularly in their negative impacts on the economy and the safety of coastal communities (McLaughlin and Cooper, 2010). The increasing impact of flood events, rising sea-levels and storm erosion effects is currently a major concern for coastal populations and authorities.

Growing demands placed on coastal and marine resources from various economic sectors have also led to habitat loss, pollution, over-exploitation and a general degradation of ecosystems (EEA, 2010). Recent policies and regulations (EU Biodiversity Strategy, Flood Directive) have clearly stated the need for inclusion of Ecosystem Services (ES) assessments in socio-economic analysis such as Cost-Benefits appraisals and risk reduction programmes. Ecosystem Services are usually viewed as providing benefits from natural systems to human well-being or as the actual benefits derived from nature to people (MEA, 2005). Coastal and marine ecosystems are particularly linked to the Coastal Protection (CP) service, namely the natural defence of the coastal zone against inundation, erosion from waves, storms and sea level rise, which contribute up to 77% of the global ecosystem service value (Martinez *et al*., 2007). Hence, CP can be interpreted as the ecosystem's capacity to supply natural hazard and erosion regulation (MEA, 2005), as well as the actual benefits derived from moderation of extreme events, regulation of water flows and erosion prevention (TEEB, 2010). Therefore, CP is a combination of the above services that act over a narrow coastal strip where both the drivers (waves, storms, sea-level rise) and the protection elements (geomorphology, emerged and submerged habitats) are interconnected.

Despite the considerable progress made in recent years, with wide-ranging assessments being conducted of the CP benefits from specific coastal ecosystems such as mangroves and estuaries (Barbier *et al*., 2011), wetlands (Costanza *et al.,* 2008) and protection against tsunamis (Danielsen *et al*., 2005), data and methods are still somewhat limited (Barbier, 2012). Compared to terrestrial ecosystem assessments, there is a low resolution and/or paucity of spatially explicit information on complex coastal and marine environments. This therefore presents a challenging problem when quantifying functions and benefits (Maes *et al*., 2012). Apart from a recent proposal of CP indicators at a continental European scale (Liquete *et al*., 2013) and the INVEST model, a decision support tool for local ecosystem mapping (Guerry *et al*., 2012), little progress has been made in providing a

DOI: 10.2112/SI75-220.1 received 15 October, 2015; accepted in revision 15 January, 2015.
*Corresponding author: esguipin@upo.es
©Coastal Education and Research Foundation, Inc. 2016

holistic approach to ES benefits in which all components of the continuum coastal-marine ecosystems are considered and further mapped. While different approaches can be considered in the assessment of ES, the *Cascade model* (CM) is the one adopted here, as it links both the biodiversity to human well-being through the flow of ES (Haines-Young and Potschin, 2010) and it supports the representation of ES at various scales (e.g. Maes *et al*., 2012; Liquete *et al*., 2013). The CM approach considers the *Capacity* of an ecosystem to deliver a service based on its internal structure (e.g. presence of sand dunes or cliffs), the exposure to processes (e.g. waves, tides, currents) and its ecological functions (e.g. wave attenuation, sediment redistribution). Those functions eventually can provide a *Flow* of ecosystem services (e.g. erosion protection) which might contribute to human well-being and thus could be rendered into specific *Benefits* (e.g. contribution to safety, reduction of risk). Additionally, benefits can be translated into monetary values, for example, the estimated damage from a storm event.

In this paper, the ecosystem service CP- Coastal Protection is assessed through the calculation of quantitative indicators and their metrics for a touristic area on the southern coast of Spain. The indicators (initially proposed at European scale by Liquete *et al*., 2013) have been significantly adapted to a local scale in order to consider key physical and socio-economic specificities of the study area.

STUDY AREA

The Costa del Sol, located along the Andalusia Mediterranean coast of Southern Spain, is a renowned global tourist destination, being one of the most visited places in Spain. The peak of tourist infrastructure development took place in the 1960's, resulting in a significant population growth and a corresponding transformation of the coastal landscape. This has resulted in irreversible environmental impacts from the aggressive urbanisation undertaken (Guisado *et al*., 2013). However, despite the fact that in 2012, the population of the littoral area was around 520,000 inhabitants, with an annual average increment of >20,000 inhabitants/year (IECA, 2013), well-preserved natural spots and low-urbanised areas still remain. The study area comprises eight coastal municipalities (Figure 1) that encompasses a coastal stretch of some 107 km long with a WSW-ENE orientation. The proximity of the Sierras to the Mediterranean coastline and the presence of a narrow continental platform with a predominance of soft coastal cliffs results in coastal plains associated with river mouths and narrow beaches where coastal dunes are rarely found. Nevertheless, at some spots medium to wide beaches are backed by small aeolian planes and other minor sedimentary formations. The dune field at Cabopino is probably the best representative of this type of environment. Seabed habitats are mainly composed of medium to fine sands, where seagrass meadows and other hard substrata are more scattered, only relevant to the west of Marbella. With a microtidal range, the wave action is the main hydrodynamic agent. Beach profiles are quite steep and the resulting surf zone is generally steep and narrow, which marks a concentration of wave action within a narrow fringe (Malvárez, 2012). These physical attributes along with a dense urban and touristic coastal area makes the Costa del Sol a highly vulnerable area, where flooding events are enhanced by the presence of narrow and steep rivers, and erosion effects by storms are of major concern to local and regional authorities, and population in general.

METHODS

For the purpose of this research, the coastal zone is defined as the area potentially affected by extreme hydrodynamic conditions and includes all coastal and marine systems (excluding habitats far inland). The coastal area is then delimited by the 100 m depth isobath (with a maximum extent of 1 nautical mile offshore from the territorial waters baseline following the Water Framework Directive) and 100 m height topographic contour given the existence of steep slopes (continental platform and coastal cliffs). From these limits, 76 calculation units (CU) of 1 km length perpendicular to the coast were delineated for geoprocessing and indicator calculation.

Following the CM approach and guided by previous studies (Liquete *et al*., 2013, CMA, 2011), the following indicators are proposed to assess CP along the Costa del Sol. The Inherent Capacity (CPcap) as the natural ability of coastal and marine ecosystems to protect against natural hazards (flood, erosion) based on their ecological and geological characteristics. The Natural exposure (CPexp) defined as the predicted need of protection based on oceanographic and climatic conditions (waves, tides, etc.). Then finally, Human demand (CPdem), as the calculated need of coastal populations for protection based on the presence of residents, tourists and assets. The CP service flow (combination of CPcap and CPexp) is understood as the potential of an ecosystem to deliver a service (capacity) and the need of doing it (exposure). On the other hand, the combination of the Cpflow and the specific demand (CPdem) of a given coastal area provides an indication of the benefit (CPben) for society.

Variables used and Indicators calculation

The spatial scale (here mainly local and municipal) determines the resolution and complexity that should be considered and so variables were fully adapted using locally updated data and based on specificities of the Costa del Sol. For *CPcap*, habitats and natural structures (Table 1) were selected following expert-based ranking (in agreement with previous studies from Pendleton *et al*., 2010; Liquete *et al*., 2013), and further ordered into a meaningfully sequence based on their influence and role in coastal protection. Additionally, for these qualitative variables (geomorphology, seabed and emerged habitats) weighting values were applied in order to assess their protection capacity in the study area. The resulting indicator is defined as $CPcap = 0.33geo + 0.25\ slope + 0.21\ seahab + 0.21\ emerhab$.

Regarding the *CPexp*, given that tide is insignificant in the Mediterranean (average of 0.8m), the influence of waves (especially high energy events), rising sea level and erosion impacts are very important. The exposure indicator is defined as $CPexp = 0.29\ wav + 0.29\ ero + 0.23\ slr - 0.19\ tide$.

Furthermore, a variable to account for tourism demand (hotel beds/coastal length) was also considered, resulting in *CPdem= 0.35 pop+0.25 inf +0.15 art + 0.10 her+ 0.25 tour*.

Table 1. *List of variables, data sources and geo-processes considered in the calculation of Coastal Protection indicators of CPcap, CPexp and CPdem.*

Variable	Database	Reference	Scale	Geoprocess
Bathymetry Topography	Topo-bathymetry integrated model from land-sea.	CMA-REDIAM, 2010	20x20 m	Delimitation of study site and mean slope (slope) *CPcap*
Geomorphology Seabed habitats	Coastal shoreline geomorphology and defence works. Seabed morphology: ecocartography from Málaga.	CMA-REDIAM, 2000 MMA, 2005	1:5000 1:5000	Weighted average based on coastal protection (geo, seahab, emerhab) *CPcap*
Emerged Habitats	EU Corine Land Cover (CLC) dataset from 2006.	EEA, 2012	100 m	
Waves	Modelled data (SWAN) from buoy records (WANA 2011011) of maximum wave height for the decade 2000-2010.	SWAN (Booij, 1999); Puertos del Estado, 2010.	20 m	Mean significant wave height (wav) *CPexp*
Erosion rates	Coastal Vulnerability Index. Indicator of Erosion trend measured from 1956-2005 (m/yr).	CMA, 2011	1:100.000	Mean Erosion rate (ero) *CPexp*
Sea level trend	Global grid of mean sea level trends (satellite altimetry 1992-2010).	Ssalto/Duacs /AVISO; CNES, 2010	1/3 deg.	Mean sea level trend (slr) *CPexp*
Tidal range	Tidal amplitude from M2 calculated for 1993- 2014 for Málaga.	Puertos del Estado, 2015		Mean tidal range (tide) *CPexp*
Population density	Spatial distribution of Andalusian population in 2013.	IECA/REDIAM, 2013.	250 m	Population density (pop) *CPdem*
Infrastructures	Infrastructures in the coastal zone represented by the regional roads network.	IECA, 2011	1:100.000	Infrastructures density (inf) *CPdem*
Artificial surface	EU Corine Land Cover (CLC) dataset from 2006.	EEA, 2012	100 m	% artificial surface (art) *CPdem*
Natural Heritage	Natural protected areas, Red Natura 2000 and Biosphere Reserves.	IECA/REDIAM, 2015.	1:10.000	% nat heritage (her) *CPdem*
Tourism demand	Socio-economic Coastal Vulnerability Index. Indicator for touristic accommodation by coastal length (hotel, beds).	CMA, 2011	1:100.000	Mean Touristic density (tour) *CPdem*

Note: Further information on variables used and full references can be found in this link (http://dx.doi.org/10.13140/RG.2.1.2389.1284).

A total amount of 13 biophysical variables (Table 1) were normalised and weighted, based on minima and maxima after aggregation within each CU. Resulting values are dimensionless and thus have no meaning in absolute terms but are designed for comparative analysis. For all indicators positive linear relationships between variables were assumed based on weights, except for the tide as it's considered to be defensive since it builds a protective buffer zone (lower values of CPexp). In addition, human structures (e.g. ports) are not taken into consideration in the assessment of ecosystem services as they cannot be considered natural systems.

RESULTS

Three qualitative indicators (CPcap, CPexp and Cpdem) ranked as low, medium and high based on 33rd and 66th percentile, were calculated and mapped along the 107 km of Costa del Sol. Lower values of CPcap, less capacity of adaptation to potential changes, are found around urban beaches of the municipalities of Estepona, Marbella and Mijas and are driven mainly by low values of *geo* (artificial beaches) and *emerhab* (open spaces with no vegetation). Conversely, high values are due to the combination of *geo* (well-developed beaches with dune systems or cliffs), the presence of seabed habitats with capacity to disrupt water movement (seagrass meadows, rock substrata), and are found around Cabopino and western of Punta de la Doncella, where valuable coastal ecosystems still persist (Figure 1a).

Across the study area, CPexp is mainly determined by waves and erosion rates (greater around ports and urban beaches) and to a lesser extent by mean sea level trends which increase towards the E. Therefore, lower values are found to the E of Marbella (around Cabopino) which is both sheltered from eastern storms (less exposed) and represents a dissipative environment, whereas the eastern and more exposed coastal strip from Mijas to Torremolinos shows higher CPexp values. Population density (that peaks in Mijas) and the presence of artificial surfaces (*art*) are the main drivers for higher values of CPdem encountered in Puerto Banús and the city of Marbella. Along the East part, where 49% of the coast has been deeply transformed, the tourism demand variable reaches the greatest values (around 60,000 touristic beds in 2014) and thus determines Cpdem values. Low values are scattered along the Ensenada de Marbella-Cabopino and from Estepona to Manilva. The joint effect of the capacity, exposure and demand affect ecosystem dynamics and functions, and thus the services (flow and benefit) that they can provide. The CPflow is found to be 'satisfactory' in 36% of the coast (CPcap=CPexp) and 'abundant' (CPcap>CPexp) across 30% of the study area (mainly around Cabopino and W of Estepona). However, around 33% of the Costa del Sol (mainly eastern municipalities) falls into the 'Deficient' category (CPcap<CPexp) and thus are less stable in terms of resilience as they lack sufficient protection capability under changing scenarios of coastal hazards.

Finally, the Coastal Protection benefit for society is determined as 'satisfactory' or 'abundant' along 60% of the area, while 39% is categorised as 'Deficient' (Figure 1b) due to the fact that the demand is greater than the capacity of the ecosystem to provide the services (Puerto Banús surroundings and scattered sites alongside the eastern municipalities).

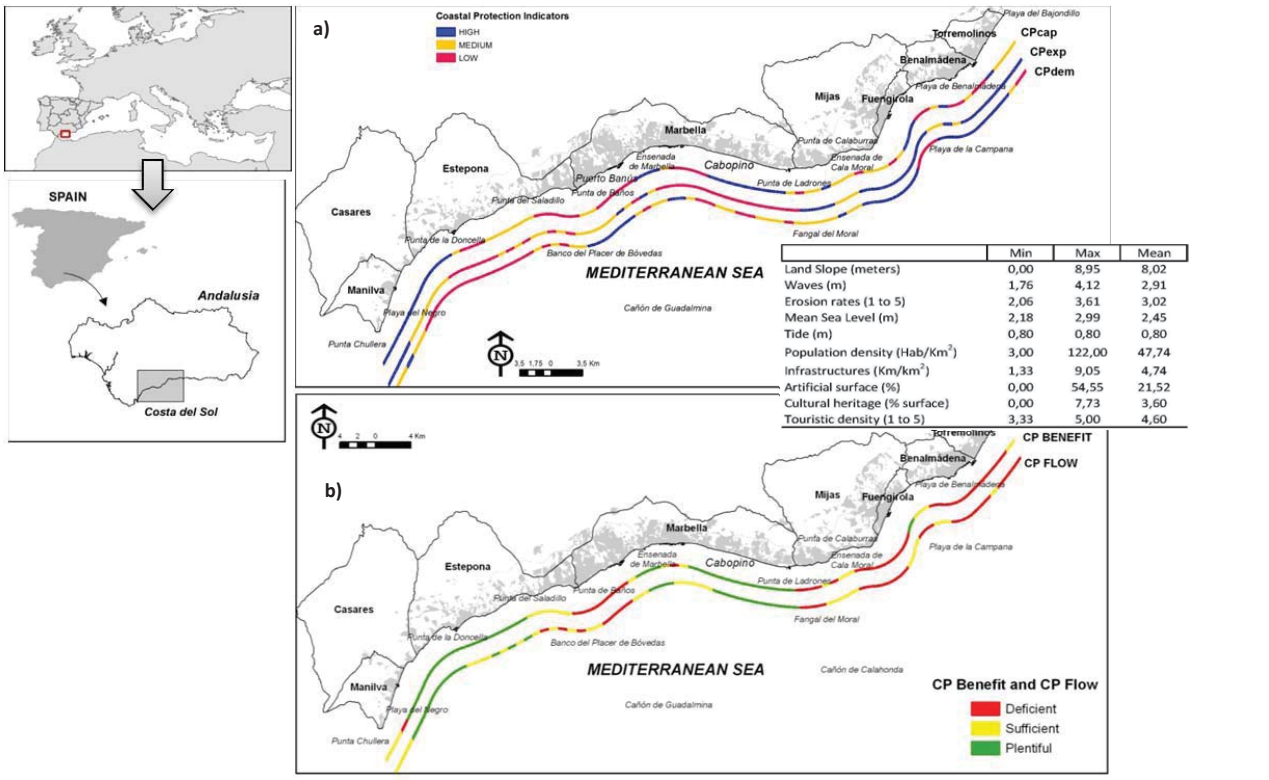

	Min	Max	Mean
Land Slope (meters)	0,00	8,95	8,02
Waves (m)	1,76	4,12	2,91
Erosion rates (1 to 5)	2,06	3,61	3,02
Mean Sea Level (m)	2,18	2,99	2,45
Tide (m)	0,80	0,80	0,80
Population density (Hab/Km^2)	3,00	122,00	47,74
Infrastructures (Km/km^2)	1,33	9,05	4,74
Artificial surface (%)	0,00	54,55	21,52
Cultural heritage (% surface)	0,00	7,73	3,60
Touristic density (1 to 5)	3,33	5,00	4,60

Figure 1. a) CP indicators of Capacity, Exposure and Demand and main statistics of variables. b) CP indicators of Flow and Benefit.

DISCUSSION

Natural ecosystems play an important role in hazards regulation and risk protection, which impacts have been increasing as population density and coastal and marine demands increase. However, the capacity of the ecosystems to provide services and their role of protection under extreme events is still poorly understood and thus benefits are undervalued or not considered in decision-making processes. Coastal management and prevention programmes, however, can no doubt be improved if the protective role of natural ecosystems and their relationship with Human, Social and Built capitals are considered (Pérez Maqueo *et al*., 2007).

In this approximation, the ES assessment evidences the deficient coastal zones in terms of coastal protection services. Thus, results can drive actions oriented to increasing resilience along low capacity areas with poor *flow* where significant erosion and flood problems occur (33% of the coast). Better management of low CPbenefit areas (39%) would also result where demand should be controlled in order to enhance ecosystem function for coastal hazards response.

Different areas along the Costa del Sol, with similar patterns and exposure to natural coastal hazards, have varying levels of capacity, depending on past socio-economic and urban development decisions, and on the status of their natural capital (ecosystem and habitats). Moreover, as CP varies in time (storms frequency, vegetation status) and space (heterogeneity across geomorphology and seabed and emerged habitats) non-lineal protection services against natural hazards should be considered when designing management plans and conservation strategies. Further, synergetic processes and complex relationships between coastal and marine variables will require cognisance of the entire land-sea continuum to guarantee the maintenance of functions and services. Here the *Capacity* and *Flow* indicators represent the current natural provision of coastal protection in the area, based on their geophysical attributes. However, given the accelerated degradation of ecosystems and facing the future consequences of climate change and growing coastal population, those areas with "covered" CPflow should also need to be included in adaptive strategies. Certainly, through this approach (CM) the capacity, exposure and demand of ecosystems, as well as their flow and benefit, could easily be translated into information that can ultimately

drive institutional and social responses (Daily *et al*., 2009).

Whilst maps of CP benefits show where future research and actions should be focused in protection of important areas, CPcap and CPdem provide an insight into vulnerable zones for potential intervention action (Cabopino dune system among others). Although some attempts have been made to integrate the economic valuation of the ecosystem, this still remains controversial and complex as it requires many assumptions to me made (e.g. ES provide many benefits yet most of them have no market value) and thus the translation of ecosystem values and their benefits into monetary terms, remains a huge challenge. Although in our approach the indicator of benefit could be used as a proxy for this (Liquete *et al*., 2013), in agreement with Heal (2000) we believe that the key issue is not to value ecosystem services in economic terms but to demonstrate the incentives and benefits for their protection.

CONCLUSIONS

In the present work, an approximation of coastal ecosystem services, including the provision of meaningful cartography of CP at adequate spatial scale, and the protective role from natural hazards is presented. Results enhance the inclusion of Ecosystem services' assessments in coastal management plans (ICZM strategies) as well as helping support current and future Directives implementation (e.g. Floods). The characterisation of CP indicators could help to drive strategies and actions as they are indicative of needed protection and vulnerable areas for intervention. However, further research should consider future scenarios of climate change, population and economic trends and their influence in the provision of the Coastal Protection service.

ACKNOWLEDGMENTS

Thank goes to C. Liquete and D.J. for their advices and to the Regional Government of Andalusia (CMA, IECA & REDIAM) for data provision.

LITERATURE CITED

Barbier. E., Hacker, S., Kennedy, C., Koch, E., Stier, A. and Silliman, B., 2011. The value of estuarine and coastal ecosystem services. *Ecological Monographs*, 81(2), 169-193.

Barbier, E., 2012. Progress and Challenges in Valuing Coastal and Marine Ecosystem Services. *Review on Environmental Economics and Policy* 6 (1), 1-19.

CMA, 2011. *Análisis preliminar de la vulnerabilidad de la costa de Andalucía a la potencial subida del nivel del mar asociado al cambio climático*. Edited by Regional Government of Andalusia (Spain), 154p.

Costanza, R., Pérez-Maqueo, O., Martinez, M.L., Sutton, P., Anderson, S.J. and Mulder, K., 2008. The value of coastal wetlands for hurricane protection. *Ambio* 37 (4), 241–248.

Daily, G., Polasky, D., Golfstein J., Kareiva P. et al., 2009. Ecosystem services in decision making: time to deliver. *Frontiers in Ecology and Environment,* 7, 21-28.

Danielsen, F., Sorensen, M.K., Olwig, M.F., Selvam, V., Parish, F. et al., 2005. The Asian Tsunami: a protective role for coastal vegetation. *Science*, 310, 643.

EEA (European Environment Agency), 2010. 10 Messages for Coastal Ecosystems. *Office for Official Publications of the European Union*, Luxembourg, 17 pp.

Guerry, A.D., Ruckelshaus, M.H., Arkema, K.K., Bernhardt, J.R., Guannel, G., Kim, C. *et al.*, 2012. Modeling benefits from nature: using ecosystem services to inform coastal and marine spatial planning. *Intern. J. of Biodiversity Science and Ecosystem Services Management*, 8 (1-2), 1–15.

Guisado, E., Malvárez, G. and Navas, F., 2013. Morphodynamic environments of the Costa del Sol, Spain. *Journal of Coastal Research*, SI 65, 500-505.

Haines-Young, R.H., and Potschin, M.P. 2010. The links between biodiversity, ecosystem services and human well-being. In: D. Raffaelli, C. Frid (Eds.), *Ecosystem Ecology: A New Synthesis*. Ecological Reviews Series, CUP, Cambridge, pp. 110–139.

Heal, G. 2000. Valuing ecosystems services. *Ecosystems* (3), 24-30.

IECA, 2013. Annual population density for Andalucia. Cartography and Statistics Institute of the Regional Government of Andalusia. Spain. Public dataset.

Liquete, C., Zuliana, G., Delgado, I., Stips, A and Maes, J. 2013a. Assessment of coastal protection as an ecosystem service in Europe. *Ecological Indicators*, 30.205–217.

Maes, J., Egoha, B., Willemena, L., Liquete, C. and Vihervaarab, P., 2012. Mapping ecosystem services for policy support and decision making in the European Union. *Ecosystem Services*, (1), Issue 1, 31–39

Malvárez, G.C., 2012. The history of Shoreline Stabilisation on the Spanish Costa del Sol. In: Cooper A. and Pilkey J. (ed.). *Pitfalls of Shoreline Stabilization: Selected Case Studies.* Springer, Netherlands, pp 235.

Martínez, M.L., Intralawan, A., Vázquez, G., Pérez-Maqueo, O., Sutton, P. and Landgrave, R., 2007. The coasts of our world: ecological, economic and social importance. *Ecological Economics*, 63 (2-3), 254–272.

McLaughlin, S. and Cooper, J.A.G., 2010. A multi-scale coastal vulnerability index: a tool for coastal managers. *Environmental Hazards,* 9(3), 233–248.

MEA (Millennium Ecosystem Assessment), 2005. Our human planet: summary for decision makers. In: *Millennium Ecosystem Assessment*. Island Press, 109 pp.

Pendleton, E.A., Thieler, E.R. and Williams, S.J., 2010. Importance of coastal change variables in determining vulnerability to sea- and lake-level change. *Journal of Coastal Research*, 26, (1), 176–183.

Pérez-Maqueo, O., Intralawan, A. and Martínez, M.L., 2007. Coastal disasters from the perspective of ecological economics. *Ecological Economics*, 63, (2-3), 273–284.

TEEB., 2010. *The Economics of Ecosystems and Biodiversity: ecological and economic foundation*. Kumar P, ed. London and Washington: Earthscan.

Journal of Coastal Research	SI	75	1102 - 1106	Coconut Creek, Florida	2016

Synoptic Study on Forecasting Large Swell Waves along the Eastern Coast of Korea Using the Operational System

Taemin Ha[†], Cheolwoo Park[†], Jaeseon Yoon[‡], and Ki-Young Heo[§*]

[†]Department of Civil Engineering
Kangwon National University
Samcheok, Korea

[‡]Hydraulic Research Division
Rural Research Institute
Ansan, Korea

[§]Operational Oceanography Research Center
Korea Institute of Ocean Science and Technology
Ansan, Korea

www.cerf-jcr.org

www.JCRonline.org

ABSTRACT

Ha, T.; Park, C.; Yoon, J., and Heo, K.-Y., 2016. Synoptic study on forecasting large swell waves along the eastern coast of Korea using the operational system. *In:* Vila-Concejo, A.; Bruce, E.; Kennedy, D.M., and McCarroll, R.J. (eds.), *Proceedings of the 14th International Coastal Symposium* (Sydney, Australia). *Journal of Coastal Research*, Special Issue, No. 75, pp. 1102 - 1106. Coconut Creek (Florida), ISSN 0749-0208.

In recent years, the eastern coast of Korea has been experiencing frequent large swell waves during winter. These waves, occasionally higher than 3 m, rarely occurred until recently and now cause severe casualties, damage to coastal structures, and extensive beach erosion along the eastern coast of the country. Therefore, the urgency for appropriately predicting large swell waves affecting these areas has increased. A convenient forecasting source is a numerical wave prediction system running in an operational mode. Since 2009, Korea Institute of Ocean Science and Technology (KIOST) has been developing and improving Korea Operational Oceanographic System (KOOS), funded by the Ministry of Oceans and Fisheries (MOF). The project aims at developing an integrated operational oceanographic system providing nowcasts and forecasts of ocean information around the Korean Peninsula. This study introduces an operational wave forecasting system using high-resolution multigrids, developed for its implementation in KOOS. A series of numerical experiments were conducted on previous cases of large swell waves along the eastern coast of Korea, using weather hindcasting products of KOOS. The new system was evaluated by comparing the obtained numerical results with data from the previous wave forecasting system and available observations. The wave forecasting system proposed yielded good qualitative and quantitative predictions for large swell waves in different locations. Furthermore, the obtained numerical results highly agree with available observational data.

ADDITIONAL INDEX WORDS: *wave model, atmospheric model, hindcast.*

INTRODUCTION

The eastern coast of Korea has experienced frequent large swell waves during winter in the past decade, resulting in repeated human casualties, due to their sudden occurrence near beaches, coastal structures, and navigating ships (Table 1). Additionally, winter storm waves higher than 3 m have often been recorded in recent years. Such events were responsible for severe casualties, damages to coastal structures, and extensive beach erosion along the eastern coast of Korea, seldom seen before the 21st century. Most of the victims were affected under mild rather than wild weather conditions when risk wariness was low (Oh and Jeong, 2013). However, since studies of these large swell waves are rare in the literature, researching their characteristics, leading up to accurate prediction models has become a crucial technical concern. A convenient source for forecasting large swell waves is the numerical wave prediction system, running in an operational mode.

Table 1. *Notable accidents of large swell waves along the eastern coast of Korea*

Date	Location	Victims	Human losses
Oct 2005	Sokcho, Gangneung, Donghae, Pohang, Ulsan	21	6
Oct 2006	Sokcho, Goseong, Ulleung	12	9
Oct 2007	Sokcho	1	1
Feb 2008	Gangneung	18	2
Jan 2009	Gangneung, Ulsan, Geoje	16	4
Sep 2011	Sokcho, Donghae, Samcheok	5	3
Jan 2012	Samcheok, Pohang	4	1
Dec 2012	Ulsan	15	4

Since 2009, Korea Institute of Ocean Science and Technology (KIOST) has been developing and improving Korea Operational Oceanographic System (KOOS), funded by the Ministry of Oceans and Fisheries (MOF). The goal of this project is to develop an integrated operational

DOI: 10.2112/SI75-221.1 received 15 October, 2015; accepted in revision 15 January, 2015.
*Corresponding author: kyheo21@kiost.ac.kr
©Coastal Education and Research Foundation, Inc. 2016

oceanographic system providing both nowcasts and forecasts of ocean information around the Korean Peninsula.

In this study, a set of hindcasts was conducted by applying the previous and present systems to past events of large swell waves occurring along the eastern coast of Korea. The results rendered by the new approach were then evaluated against those produced by the previous system and available observation data. The high-resolution multi-grid system qualitatively predicted the development of large swell waves in different locations, while returning numerical results highly agreeing with available observational data.

METHODS

A new operational wave forecasting system using high-resolution multi-grids has been developed to be implemented in KOOS. The key difference between the previous and present approaches lies in the facultative use of atmospheric data assimilation.

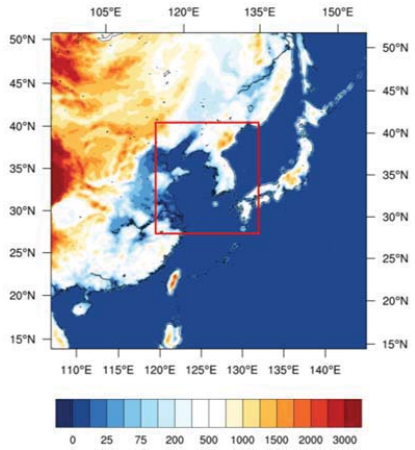

Figure 1. WRF domains and model topography with 20 km of horizontal resolution, used for model integration. Domain 2 is limited by the red frame and terrain height (shaded) is shown in meter.

The regional atmospheric run

In the present wave forecasting system, both Weather Research and Forecasting Model (WRF) version 3.7 and its variational data assimilation system (WRFDA) were employed to perform high-resolution regional atmospheric reanalysis, including 10-m wind fields necessary to force the wave hindcasts. Observational data were assimilated every 6-hour, using the three-dimensional variational data assimilation system (3DVAR) for initial conditions improvement. WRF version 3.5 was employed without WRFDA, representing the previous system approach. The modeling domain was configured to encompass the East Asian region and vicinities of the Korean Peninsula (Figure 1). We focused on a configuration with two nested domains of 20 km, and 4 km grid spacing. The model used 31 vertical levels, with the top located at 50 hPa.

Atmospheric modeling was initialized with the global final analysis (FNL) run by the National Centers for Environmental Prediction (NCEP) of 1° resolution, and the NCEP's daily global SST analysis. In the present system, in-situ measured data included surface observations from 236 widespread stations, alongside measurements from 78 radiosonde sites. In-situ surface data contained hourly temperature, humidity, wind, and pressure. Radiosonde profiles included 12-hourly temperature, humidity, and wind at vertical levels extending from the surface up to ~10 hPa.

The model was reinitialized every day, and run for 30 hours to generate the aimed hindcast products. In spite of frequent data assimilation usage, forecast errors increased dramatically after 1 day, hence the chosen 24 h re-initialization period. The results from the first 6 h of each run were used as model spin-up and disregarded afterwards, with the remaining 1-day periods pieced together, forming a continuous time series.

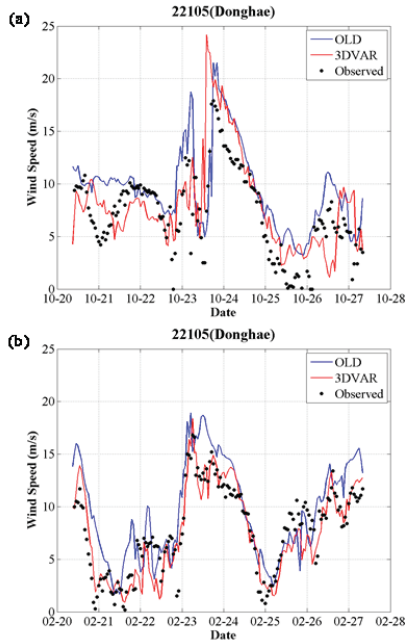

Figure 2. Comparison between wind speeds measured at an available buoy site and simulated products of previous (OLD) and present (3DVAR) wave forecasting system, during (a) October 2006 and (b) February 2008.

The regional wave run

The wave model WAVEWATCHIII (WW3) version 3.14, developed at the Marine Modeling and Analysis Branch (MMAB) of the Environmental Modeling Center (EMC) of NCEP (Tolman, 2009), was used to perform the hindcast of large swell waves along the eastern coast of Korea. WW3 was based on WAVEWATCHI and WAVEWATCHII, developed at Delft University of Technology, and NASA Goddard Space Flight Center, respectively (Tolman, 2009). For further details of the model, readers are referred to the works of Tolman (2002, 2009).

The computational grids were constructed by utilizing 30 arc-second KorBathy30s bathymetry data (Seo, 2008), 1 arc-minute global relief model ETOPO1 bathymetry data, and the electronic navigational charts produced by the Korea Hydrographic and Oceanographic Administration (KHOA). The present hindcast was performed using two grid resolutions: a coarse grid with 1/12° resolution and a finer with 1/60°, for both latitude and longitude. These two domains interacted through the two-way nesting method (Tolman, 2008; 2009).

RESULTS AND DISCUSSION

Figure 2 displays a comparison between simulated wind speed products obtained from the previous (blue line) and present (red line) wave forecasting systems, and real measurements gathered at an available buoy site.

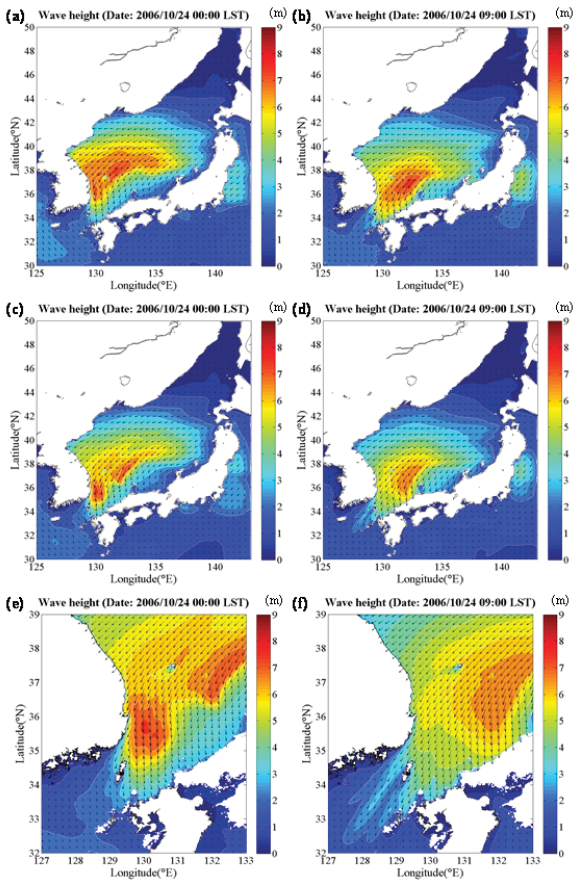

Figure 3. Comparison of significant wave heights distribution using different wave forecasting systems (October 2006). (a)-(b) the previous system. (c)-(d) the present system on a coarse grid. (e)-(f) the present system on a fine grid.

Large swell waves on 23 October 2006

On 23 October 2006, abnormally large swell waves hit the eastern coast of Korea, leading to a loss of human lives (Table 1). The observed significant wave height was 9.69 m, the highest recorded on the eastern coast of Korea. The wave forecasting system was employed to perform a hindcast of this event, using the products provided by KOOS. The present system reasonably reproduced the wind speeds measured at the buoy site, in spite of slightly overestimating peak values in October 2006 (Figure 2a).

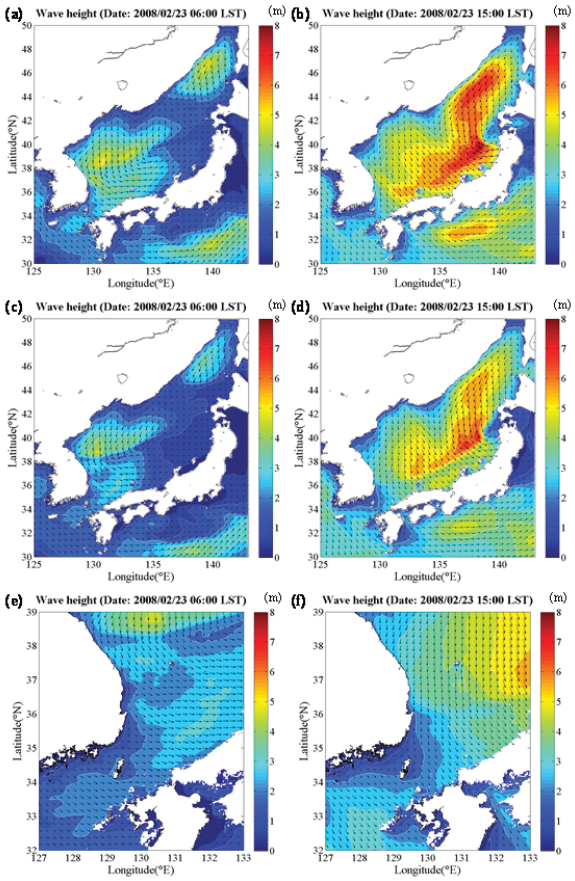

Figure 4. Comparison of significant wave heights distribution using different wave forecasting systems (February 2008). (a)-(f) are same as in Figure 3.

Figure 3 shows a comparison between previous and present wave forecasting systems, concerning simulated distribution of significant wave heights in the vicinities of the Korean Peninsula. The present system estimated slightly smaller wave heights and an earlier arrival of large waves to the eastern coast of Korea. The horizontal distribution of significant wave heights was similar in early stages for both models; however, large wave heights developed southwestwards in the previous system, while the present system indicated a southward propagation as time passed. As the first large wave

components decayed towards Japan, the remaining components exited through the Korea Straits (Figures 3e and f), followed by a double-peaked pattern of wave heights developed on the southeastern coast (Jinha) of Korea (Figure 5). Measured and simulated significant wave heights (H_s) and peak wave periods (T_p) are compared in Figure 5. Both forecasting systems adjusted well to measured data concerning these parameters, however, the present model enabled a more realistic simulation of development pattern and wave phase.

Large swell waves on 24 Feb 2008

The most recent remarkable winter event in the East Sea occurred on 24 February 2008, highlighted by a peak in significant wave height of 9.92 m at Toyama Bay, and consequent severe damaging of coastal facilities (Mase *et al.*, 2009; Oh and Jeong, 2013). The large swell waves also hit the eastern coast of Korea, causing the loss of human lives (Table 1). Oh and Jeong (2013) stressed the difference between the events of February 2008 and October 2006. Namely, significant wave heights rapidly increased, followed by a monotonous drop for more than two days in October 2006, while wave heights kept increasing on 24 February 2008, after the first height jump on the previous day. Thus, the development pattern of wave heights showed a double-peaked profile for the February 2008 event (Figure 6). The present system computed wind speeds at the buoy site more accurately, in terms of both development pattern and peak value (Figure 2b).

Table 2. *Statistical parameter for significant wave heights (Root Mean Square Error-RMSE).*

Location	Oct 2006		Feb 2008	
	Present	Previous	Present	Previous
Sokcho	0.818	0.861	0.288	0.527
Kangmun	0.571	0.596	0.297	0.459
Mukho	0.611	0.655	0.510	0.581
22105(Donghae)	1.217	1.439	0.624	1.111
Wangdolcho	0.814	0.655	0.528	0.468
Hupo	0.530	0.580	0.370	0.531
Jinha	0.596	0.698	0.699	0.754

As for October 2006 event, the present system estimated slightly smaller wave heights and a later arrival of large waves to the eastern coast of Korea. The horizontal distribution of significant wave heights depicted in Figure 4 reveals important differences between the two systems. In an early stage, the height distribution computed by the present system was divided into two parts along the eastern, while the previous system produced a single pattern. Thus, the present system performed better, as reflected by Figure 6. After the early developing stage, large swell waves were weakened near the western coast of Japan and later re-strengthened. This led to the development of double-peaked profiles in measured wave data. The simulated results thoroughly reproduced this double-peaked pattern in both models, but calculated Root Mean Square Errors (RMSE) values were much smaller for the present system (Table 2). Thus, the present model provided better results, both quantitatively and qualitatively.

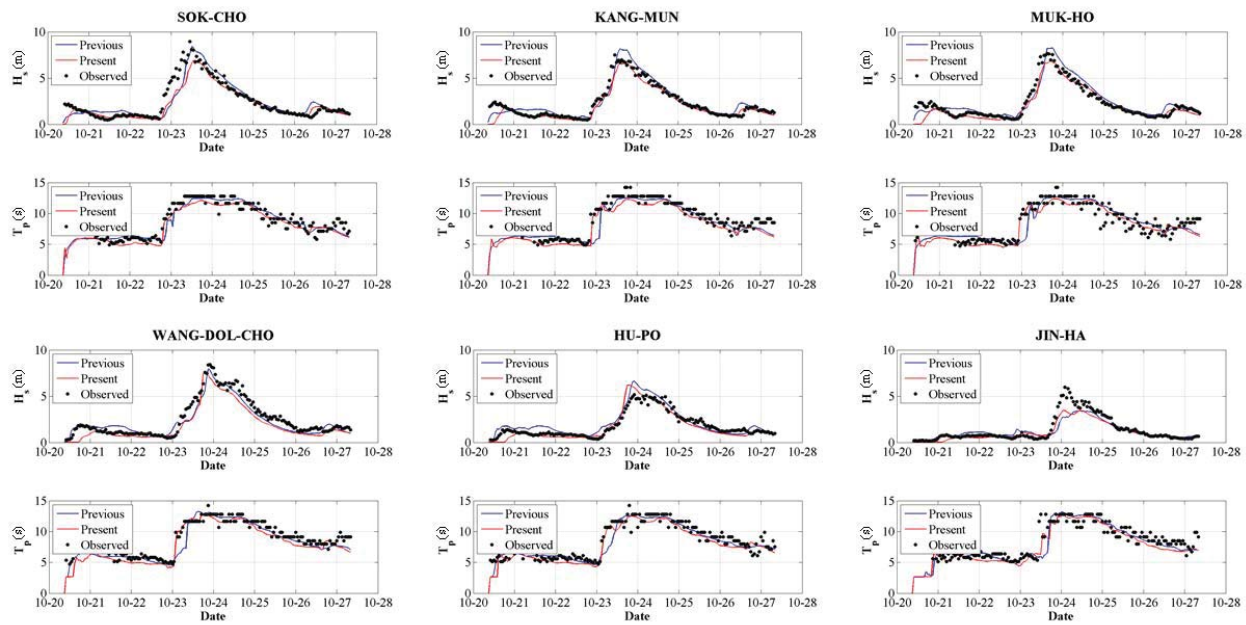

Figure 5. Comparison between significant wave heights (H_s) and peak wave period (T_p), measured at different wave stations sites, and simulated products of previous and present wave forecasting systems (October 2006).

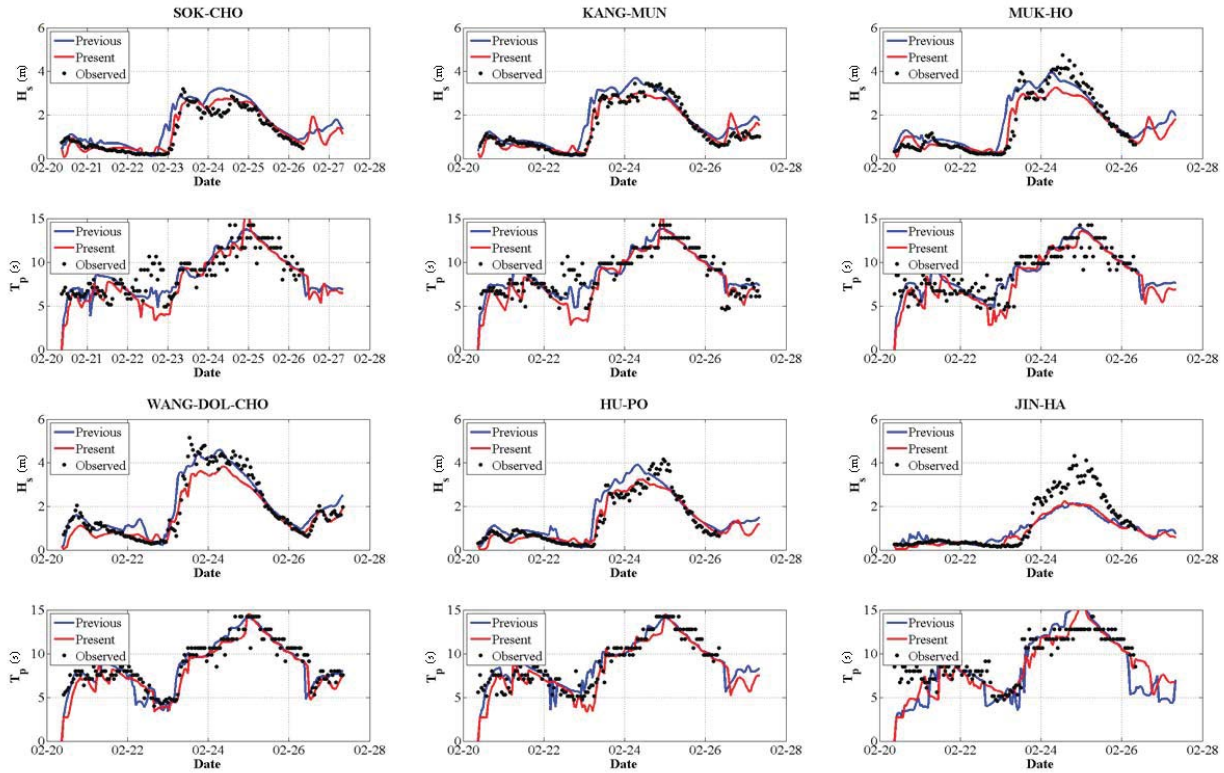

Figure 6. Comparison between significant wave heights (H_s) and peak wave period (T_p), measured at different wave station sites and simulated products of previous and present wave forecasting system (February 2008).

CONCLUSIONS

In this study, the previous and present operational wave forecasting systems in KOOS were evaluated using reference data concerning past events of large swell waves occurring along the eastern coast of Korea. The main difference between these systems regards the facultative usage of atmospheric data assimilation. In spite of small levels of discrepancy, the present forecasting system predicted reasonably well the observational wave data, from both qualitative and quantitative points of view. Therefore, the present system can be used to predict large swell waves affecting the eastern coast of Korea, being also suitable for operational wave forecasting in KOOS.

ACKNOWLEDGMENTS

This research was a part of the project titled "Development of Korea Operational Oceanographic System (KOOS), Phase 2" and "Investigation of Large Swell Waves and Rip Currents and Development of the Disaster Response System (no. 20140057)" funded by the Ministry of Oceans and Fisheries, Korea.

LITERATURE CITED

Mase, H., Yasuda, T., Tom, T. H., Tsujio, D. and Mori, N., 2009. Forecast and hindcast of waves which caused coastal disasters along Toyama Coasts on February 2009, *Proceedings of the 33rd IAHR Congress (Vancouver, USA)*, pp. 2854-2861.

Oh, S.-H. And Jeong, W.-M., 2013. Characteristics of high waves observed at multiple stations along the east coast of Korea. *National Hazards and Earth System Sciences*, 13, 3503-3514.

Tolman, H. L., 2002. *User manual and system documentation of WAVEWATCHIII version 2.22*. Technical Note 222. NOAA/NWS/NCEP/MMAB, 133p.

Tolman, H. L., 2008. A mosaic approach to wind wave modeling. *Ocean Modeling*, 25, 35-47.

Tolman, H. L., 2009. *User manual and system documentation of WAVEWATCH III^{TM} version 3.14*. Technical Note 276. NOAA/NWS/NCEP/MMAB, 194p.

Journal of Coastal Research	SI	75	1107 - 1111	Coconut Creek, Florida	2016

Producing the Hindcast of Wind and Waves Using a High-Resolution Atmospheric Reanalysis around Korea

Ki-Young Heo [†] **and Taemin Ha** [‡*]

[†]Operational Oceanography Research Center
Korea Institute of Ocean Science and Technology
Ansan, Korea

[‡] Departament of Civil Engineering
Kangwon National University
Samcheok, Korea

www.cerf-jcr.org

www.JCRonline.org

ABSTRACT

Heo, K.-Y., and Ha, T., 2016. Producing the Hindcast of Wind and Waves Using a High-Resolution Atmospheric Reanalysis around Korea. *In:* Vila-Concejo, A.; Bruce, E.; Kennedy, D.M., and McCarroll, R.J. (eds.), *Proceedings of the 14th International Coastal Symposium* (Sydney, Australia). *Journal of Coastal Research*, Special Issue, No. 75, pp. 1107 - 1111. Coconut Creek (Florida), ISSN 0749-0208.

The Weather Research and Forecasting Model (WRF) and its variational data assimilation system (WRFDA) are applied to all of the surrounding seas of the Korean Peninsula for a high-resolution regional atmospheric reanalysis study. Observational data are assimilated every 6 h, and the results are verified against unassimilated observations. In this study, three-dimensional variational data assimilation (3DVAR) has been adopted to improve the model's initial conditions and to generate the final high-resolution analysis. For the hindcast of the meteorological data, the real-time analysis field obtained from the global final analysis (FNL) operated by the National Centers for Environmental Prediction (NCEP) is taken as the initial and 6 h forecast files and as initial and lateral boundary conditions. For the wave hindcast, we used the third-generation spectral wave model, WAVEWATCH III (WW3). Both nested wave models consist of a coarse 9 km model covering the East Asian marginal seas and a nested 2 km resolution model covering all of the surrounding seas of Korean Peninsula forced with 20 km and 4 km resolution hindcasts of winds, respectively. A comparison against in-situ observations of wind and sea states reveals significant improvement in the mean values and upper percentiles of wind vectors and significant wave height. Improvement is also found in the mean wave period. The reanalysis data of wind with the data assimilation technique and waves in this study is also useful for computing the design wave.

ADDITIONAL INDEX WORDS: *Hindcast, wind, wave, reanalysis, design wave.*

INTRODUCTION

Sea surface wind plays a dominant role in oceanic phenomena such as oceanic seas, swells, and currents, which have an important effect on the climate. However, the lack of reliable historical weather observations and limited data make it difficult to effectively analyze climate variability and change over oceans. In contrast, numerical simulation data is used to analyze the spatiotemporal variation of sea surface wind. However, this method is fundamentally limited in the exact reproduction of atmospheric phenomena owing to initial uncertainty in the model initialization and the chaotic behavior of the nonlinear system governing the atmosphere (National Research Council, 1998).

To overcome this limitation, data assimilation techniques have been adopted to improve the model's initial conditions and to generate the final high-resolution analysis. Reanalysis includes a combination of state-of-the-art models and data assimilation methods with high-quality controlled surface-, upper-level sounding-, and satellite-based observations. Since the release of the original National Centers for Environmental Prediction/National Center for Atmospheric Research (NCEP/NCAR) Reanalysis Project (NCEP-1), the NCEP/NCAR, European Centre for Medium-Range Weather Forecasts (ECMWF), Japan Meteorological Agency (JMA), and the Central Research Institute of Electric Power Industry (CRIEPI) have produced reanalysis products covering 1979 to the present (Murakami, 2014). However, a limitation is present in detailed analyses of the impacts of climate characteristics in the Korean Peninsula when using these reanalysis products because they are designed and executed as global products with low resolution. To overcome this limitation, it is necessary to produce high-resolution regional reanalysis products that consider the various characteristics of climate in the East Asian region, particularly near the Korean Peninsula.

To improve the performance in modeling the regional atmosphere, significant efforts have been made using the state-of-the-art regional Weather Research and Forecasting Model (WRF). With the development of various remote sensing observations and improvements of in situ observation networks, the application of data assimilation techniques can truly improve the accuracy of the model's initial conditions and performance. The high-resolution atmospheric reanalysis around the Korean Peninsula will provide a unique opportunity to better understand the interaction of the changing climate with local fine-scale processes and their impact on the mesoscale meteorology of the surface wind field throughout the region. In this study, atmospheric reanalysis products are used to develop a long-term hindcast wave database by using the WAVEWATCH III (WW3) third-generation spectral wave model (Tolman, 2009).

DOI: 10.2112/SI75-222.1 received 15 October, 2015; accepted in revision 15 January, 2015.
*Corresponding author: tmha@kangwon.ac.kr
©Coastal Education and Research Foundation, Inc. 2016

MODEL AND DATA FOR REANALYSIS

To obtain the high-resolution reanalysis data, the Advanced Research core of WRF was used (ARW; Skamarock *et al.*, 2008). ARW is a mesoscale model developed through a community collaboration effort and managed by NCAR. The WRF is a limited-area, fully compressible, nonhydrostatic numerical model formulated in Arakawa C-grid staggering horizontal grid and a terrain-following hydrostatic pressure vertical coordinate. ARW has various dynamical and physical options and includes its own data assimilation system known as WRFDA (Barker *et al.*, 2012). In this study, the three-dimensional variational data assimilation (3DVAR) technique was adopted to improve the model's initial conditions and to generate the final high-resolution analysis. In WRFDA, the analysis field is generated by merging observations and background forecasts through iterative minimization of the cost function (Barker *et al.*, 2012). The background forecasts in this study are generated by WRF simulations, and the observations are quality controlled before being assimilated by WRFDA. The modeling domain for this study (Figure 1) was configured to encompass the East Asian region including Korean Peninsula area. The domains have a grid spacing of 20 km and 4 km with 31 vertical levels and a model top of 50 hPa. A summary of the model configuration parameters and physical schemes used is given in Table 1.

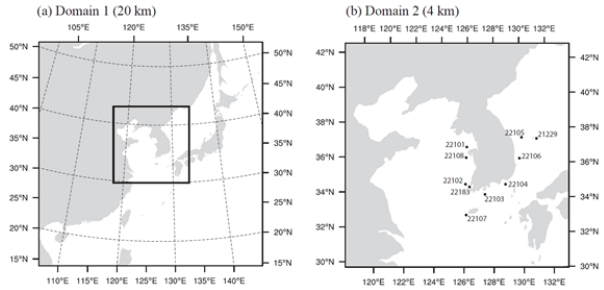

Figure 1. Weather Research and Forecasting Model (WRF) domains and model topography used for model integration. (a) Domain 1 with 20 km horizontal resolution; (b) Domain 2 with 4 km horizontal resolution. Domain 2 is indicated by the frame in (a). The locations of buoys are shown in (b).

The real-time analysis field obtained from the global final analysis (FNL) run by the NCEP with 1° resolution was used to provide atmospheric forcing (initial and lateral boundary conditions) and initial conditions for soil moisture and temperature. The FNL analyses were obtained from NCEP's Global Data Assimilation System (GDAS; Kanamitsu 1989). Because it was the final run, the analyses include all of the late-arriving conventional and satellite data. The NCEP's daily global SST analysis (RTG_SST_HR) was used in the meteorological model. We used 6 h sea surface temperature (SST) data interpolated from the RTG_SST_HR. In situ observational data used for assimilation and model verification in this study include surface observations from 236 stations distributed throughout the model domain, along with 78 radiosonde stations. The in situ surface observations contain hourly 2 m temperature and humidity, 10 m wind, and pressure data. The radiosonde profiles include 12 h temperature, humidity, and wind at vertical levels extending from the surface up to about 10 hPa.

For generating the reanalysis products, the model was reinitialized daily with NCEP FNL providing initial and lateral boundary conditions and was run for 30 h. Because forecast errors increase with time dramatically after one day even with frequent data assimilation, a one-day re-initialization was chosen, and available observational data were assimilated every 6 h including the initial hour. The results from the first 6 h of each run were used as model spinup and were removed from consideration; the remaining one-day periods were pieced together to form a continuous time series.

The computational grids of WW3 were constructed by utilizing 30 arc-second KorBathy 30s bathymetry data, the bathymetry data of the Earth Topography 1 arc-minute global relief model (ETOPO1), and the electronic navigational charts produced by the Korea Hydrographic and Oceanographic Administration (KHOA). The present hindcast was performed using two grid resolutions, a coarse grid with 1/12° resolution and a finer with 1/60°, for both latitude and longitude.

Table 1. *Weather Research and Forecasting Model (WRF) configuration.*

	Option	Configuration
Physics	Microphysics	WSM5 (Lim and Hong, 2005)
	Longwave radiation	RRTMG (Iacono *et al.*, 2008)
	Shortwave radiation	RRTMG (Iacono *et al.*, 2008)
	Planetary boundary layer	YSU PBL (Hong *et al.*, 2006)
	Surface layer	Monin–Obukhov (Janjic, 2002)
	Land surface model	Noah LSM (Mitchell, 2005)
	Cumulus	Kain–Fritsch (Kain, 2004)
Grid	Horizontal grid spacing	20 km, 4 km
	Vertical levels	31 levels with top at 50 hPa
WRFDA	Surface assimilation option	2

IN-SITU COMPARISON OF SEA SURFACE WIND

In this section, we compare wind speeds and wind directions measured at the buoy sites against the corresponding gridded hindcast data. A statistical comparison was performed using scatter diagrams, histograms, and standard parameters including mean bias error (MBE), root–mean–square error (RMSE), correlation coefficient (R), and slope and intercept of the regressed line. The comparisons and scatter plots of the wind speed between the hindcast and observation are shown in Figure 3. Buoys along the Korean coast shown in Figure 1 were included in the scatter plots. The observed and simulated values are displayed along the x-axis and y-axis, respectively. The total number of comparisons for each simulation time was 8760. The hindcast showed noticeable scatter but was in good agreement with observations. However, the model tended to underestimate high wind magnitudes and underestimate wind speeds greater than 15 m s^{-1}. The best performance was confirmed by the correlation coefficient value of 0.86 and the RMSE of 1.83 m s^{-1} at the 22108 buoy (Figure 2i; Table 2). The scatter of the 22107 buoy (Figure 2h) showed a behavior quite similar to that shown for the 22108 buoy, as confirmed by the statistical parameters (Table 2). In fact, the correlation coefficient was 0.86, and the RMSE was 1.98 m s^{-1}.

Over the Yellow Sea, the wind speed correlations were 0.81–0.86 except for the 22183 buoy, whereas the MBEs and RMSEs were 0.59–1.12 m s^{-1} and 1.83–2.24 m s^{-1}, respectively. These values of the buoys and hindcast correlated closely, as expressed by slopes of 0.75–0.81 and intercepts close to 0–0.5 m s^{-1}. The hindcast for the 22183 buoy (Figure 2j) showed a strong overestimation for winds. Although the spread of the data points near the regression line was similar to that observed at the other buoys over the Yellow Sea, the RMSE was higher, at 2.84 m s^{-1}, and the correlation coefficient was lower, at 0.77. Over the South Sea, the hindcast data was relatively low, with correlation coefficients of 0.78–0.86). The MBEs and RMSEs were −0.22–0.43 m s^{-1} and 1.98–2.25 m s^{-1}, respectively. The data of these buoys correlate reasonably with that of the hindcast, as expressed by slopes of 0.73–0.84 and intercepts close to 0.9–1.42 m s^{-1}. Over the East Sea, the correlation coefficients of 0.79–0.80, MBEs of 0.22–0.65, and RMSEs of 2.30–2.34 also showed good performance but with a sensible increase in the slopes and intercepts.

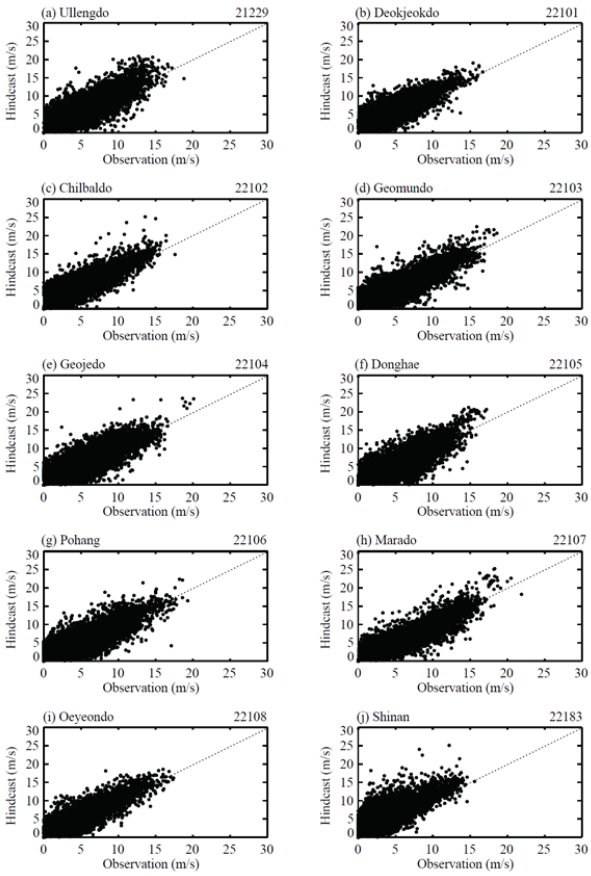

Figure 2. Scatter diagram of the wind speed observed from buoys versus hindcast using hourly data in 2014; the total number of data was 8760 for each buoy. The station locations are marked with dots in Figure 1. The dashed line denotes the perfect fit to hindcast and observed values.

Table 2. Statistical parameters for the wind speed including mean bias error (MBE), root–mean–square error (RMSE), correlation coefficient (R), and slope and intercept of the regressed line.

Location	Buoy	Intercept (m s^{-1})	Slope	R	MBE (m s^{-1})	RMSE (m s^{-1})	No. of pairs
ES	21229	1.21	0.71	0.80	0.65	2.31	8680
YS	22101	0.24	0.75	0.81	1.07	2.24	8639
YS	22102	0.00	0.81	0.85	1.12	2.21	8571
SS	22103	0.90	0.80	0.84	0.43	2.10	8475
SS	22104	1.42	0.73	0.78	0.32	2.25	8491
ES	22105	1.40	0.70	0.79	0.40	2.34	8019
ES	22106	1.34	0.76	0.80	0.22	2.30	8498
ES	22107	1.29	0.84	0.86	−0.22	1.98	7782
YS	22108	0.58	0.78	0.86	0.59	1.83	8426
YS	22183	0.08	0.65	0.77	1.85	2.84	8354

Note: YS: Yellow Sea; SS: South Sea; ES: East Sea

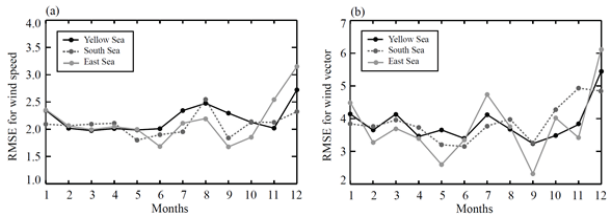

Figure 3. Seasonal variations in root–mean–square error (RMSE) for (a) wind speed and (b) wind vector averaged over the Yellow Sea (black solid lines), South Sea (gray dashed line), and East Sea (gray solid line) in 2014.

The results were again analyzed using the RMSE of the hindcast as calculated against the observations with the wind speed and vector. Figure 3 shows the seasonal variations of RMSEs for wind speed and vector averaged over the Yellow, South, and East seas throughout the year. The RMSEs of wind speed and vector were separately averaged over the three seas. The results demonstrate that errors are generally lower in the warmer months, when variability in atmospheric conditions is minimal, and increase significantly in winter. During February−September, the RMSE of wind vector is distinguished from that in the cold season. The effects of higher atmospheric variability can be attributed to the model's relatively poor performance with larger errors produced in winter.

The wind rose plots shown in Figure 4 include the observed and hindcast data over the Yellow, South, and East seas in 2014. Overall, the one-year hindcast tended to have good agreement with observations, producing an accurate distribution of wind direction. However, all of the simulations generated wind that was significantly more northwesterly than that in the observations. Over the Yellow Sea, the high frequency of northerly winds was captured effectively, although the hindcast generated wind that was significantly more north–northwesterly (Figures 4a and 4d). For the wind speed, the model reproduced the strong northerly components of wind. A comparison with the observations in Figure 5e revealed that the wind roses of the hindcast and the South Sea observation are very close (Figures 4b and 4e). The annual average wind speeds for the observed and hindcast were about 6.17 m/s and 6.48 m/s, respectively.

The dominant wind from the hindcast was northerly between northwesterly and northeasterly winds, at an annual average of 46.4%, which differed slightly from the observed value of 40.5%. Over the East Sea, the wind speed and direction from the hindcast were close to those of the observed, although the west–northwesterly (southwesterly) wind was overestimated (underestimated; Figures 4c and 4f). However, the results of the wind rose plots show satisfactory agreement between the measurements and hindcast for the buoys near the Korean coast.

IN-SITU COMPARISON OF WAVES

In this section, we compare the significant wave heights and peak wave periods measured at the buoy sites against the corresponding gridded hindcast data. A statistical comparison was performed using scatter diagrams and standard parameters. The comparisons and scatter plots of significant wave heights and peak wave periods between hindcast and observation are shown in Figure 5. The observed (simulated) values are displayed along the x-axis (y-axis) . The total number of comparisons for each simulation time was 8760. The hindcast of wave heights showed noticeable scatter but was in good agreement with observations. However, the distribution pattern of simulated values differed among the localities. Specifically, the model tended to overestimate wave heights at the 22103 and 22107 buoys, which are located in the southern sea of Korea, and slightly underestimate those at the other buoys. The best performance was confirmed by the R values of 0.95, 0.93, and 0.91 and the RMSE values of 0.343 m, 0.404 m, and 0.277 m at the 21229, 22107, and 22108 buoys, respectively (Figures 5a, 5h, and 5i; Table 3).

It should be noted that the hindcast of the wave periods suggests the inclusion of considerable numerical or measuring errors. The measured wave periods are clearly arranged at particular intervals, whereas the simulated wave periods varied by default. Furthermore, the model tended to overestimate the wave periods at small magnitudes; the estimation was more unpredictable as the magnitude increased. Both the measured and simulated data had only one peak wave period. Therefore,

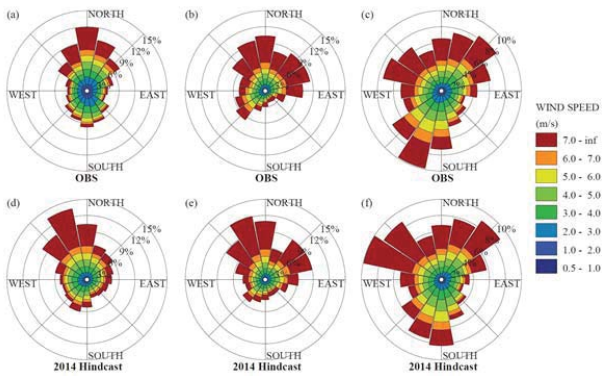

Figure 4. Comparison of 10 m wind roses between observations (OBS) (top) and the one-year hindcast in 2014 (bottom) over the Yellow Sea (left panel), South Sea (middle panel), and East Sea (right panel). The station locations are marked by dots in Figure 1.

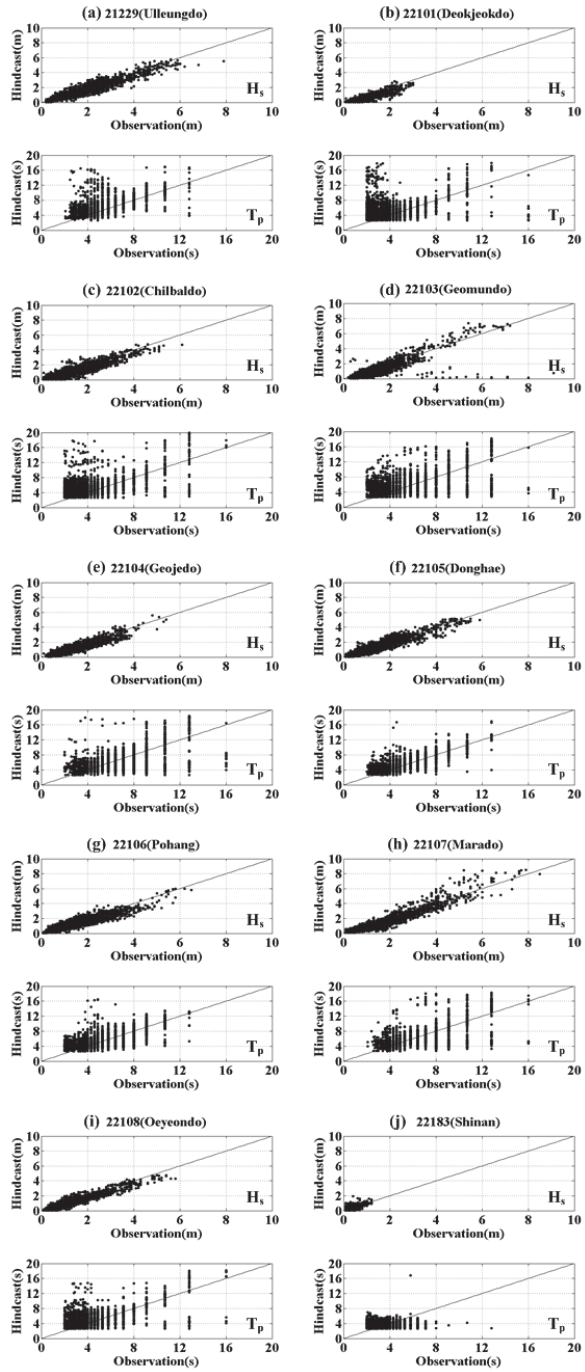

Figure 5. Scatter diagram of significant wave heights and peak wave periods observed from buoys versus Hindcast using hourly data in 2014. The solid line denotes the perfect fit to hindcast and observed values.

swell components were hidden in the data and induced inconsistency between the two datasets. Figure 6 shows additional numerical errors because the phase difference is treated as a numerical error.

Table 3. Statistical parameters for significant wave heights and peak wave periods based on the correlation coefficient (R), mean error (ME), and root–mean–square error RMSE.

Location	Buoy	Significant wave heights			Peak wave periods		
		R	ME (m)	RMSE (m)	R	ME (m)	RMSE (m)
ES	21229	0.95	0.255	0.343	0.64	1.048	1.718
YS	22101	0.64	0.286	0.340	0.47	1.504	2.582
YS	22102	0.75	0.295	0.383	0.52	1.345	2.247
SS	22103	0.78	0.423	0.865	0.57	1.619	2.447
SS	22104	0.76	0.285	0.390	0.57	1.526	2.340
ES	22105	0.81	0.236	0.316	0.57	0.852	1.208
ES	22106	0.83	0.252	0.339	0.58	0.967	1.420
ES	22107	0.93	0.301	0.404	0.60	1.371	2.246
YS	22108	0.91	0.217	0.277	0.58	1.114	1.799
YS	22183	0.84	0.137	0.168	0.52	0.960	1.327

Note: YS: Yellow Sea; SS: South Sea; ES: East Sea

SUMMARY AND DISCUSSION

In this study, wind and wave data were reanalyzed with the data assimilation technique by using numerical models including WRF as an atmospheric model and WW3 as a wave model. A comparison against in-situ observations was conducted near the Korean Peninsula. A comparison against in-situ observations of wind and sea states revealed significant improvement in mean values and in the upper percentiles of wind vectors and significant wave height. Improvement was also found in the mean wave period. The results of this study are also useful for design wave computation. Over the Yellow Sea, the difference in dominant wind between the hindcast and observation occurs mainly in spring, particularly during April–May, with rapidly changing pressure patterns owing to a migratory anticyclone. Over the East Sea, the difference occurs mainly in winter, particularly in December–January, with strong wind conditions owing to extension of the Siberian High. The WRF model has a limitation in simulating the expansion/contraction of the Siberian High despite the inclusion of data assimilation.

Although slight discrepancy was noted, overall agreement with observations was acquired. However, the analysis of peak wave periods revealed that considerable work remains for identifying certain discrepancies between measured and simulated data. This hindcast study is useful for offshore and coastal researchers in the development of reliable estimates of extreme wind, wave, surge, and current for the design of specific offshore and coastal structures.

ACKNOWLEGEMENT

This research is part of the project titled “Development of Korea Operational Oceanographic System (KOOS), Phase 2” and “Investigation of Large Swell Waves and Rip Currents and Development of the Disaster Response System (No. 20140057),” funded by the Ministry of Oceans and Fisheries, Korea. This work was also supported by the KIOST (Grant PE99325).

LITERATURE CITED

Barker, D.; Huang, X.; Liu, Z.; Auligné, T.; Zhang, X.; Rugg, S.; Ajjaji, R.; Bourgeois, A.; Bray, J.; Chen, Y.; Demirtas, M.; Guo, Y.; Henderson, T.; Huang, W.; Lin, H.; Michalakes, J.; Rizvi, S., and Zhang, X., 2012. The Weather Research and Forecasting Model’s Community Variational/Ensemble Data Assimilation System:WRFDA. *Bulletin of the American Meteorological Society*, 93, 831–843.

Hong, S.-Y.; Noh, Y., and Dudhia J., 2006. A new vertical diffusion package with an explicit treatment of entrainment processes. *Monthly Weather Review*, 134, 2318–2341.

Iacono, M.; Delamere J.; Mlawer, E.; Shephard, M.; Clough, S., and Collins, W., 2008. Radiative forcing by long-lived greenhouse gases: Calculations with the AER radiative transfer models. *Journal of Geophysical Research*, 113, D13103, doi:10.1029/2008JD009944.

Janjic, Z.I., 2002. *Nonsingular implementation of the Mellor–Yamada level 2.5 scheme in the NCEP Meso Model*. NCEP Office Note 437, National Centers for Environmental Prediction, 61 pp.

Kain, J.S., 2004. The Kain–Fritsch convective parameter-ization: An update. *Journal of Applied Meteorology*, 43, 170–181.

Lim, H. and Hong, S.-Y., 2005. Effects of bulk ice microphysics on the simulated monsoonal precipitation over east Asia. *Journal of Geophysical Research*, 110(D24), 06 166-06 181.

Mitchell, K., 2005. *THE COMMUNITY Noah LAND-SURFACE MODEL (LSM)*. (available from http://www.emc.ncep.noaa.gov/mmb/gcp/ noahlsm/).

Murakami, H., 2014. Tropical cyclones in reanalysis data sets, Geophysical Research Letters, 41, 2133–2141, doi:10.1002/2014GL059519.

National Research Council, 1998. *The Atmospheric Sciences Entering the Twenty - First Century*. Washington, USA: National Academy Press, 384p.

Skamarock, W.C., Klemp, J.B., Dudhia, J., Gill, D., Barker, D., Wang, W., Powers, J.G., 2008. *A description of the advanced research WRF version 3*. NCAR Tech. Note TN-475+STR, p. 113.

Tolman, H.L., 2009. *User manual and system documentation of WAVEWATCH III version 3.14*. Tech. Note 276, NOAA/NWS/NCEP/MMAB, 220 pp.

Journal of Coastal Research	SI	75	1112 - 1116	Coconut Creek, Florida	2016

Factors Controlling Coastal Erosion During Storm Events

Darius Jarmalavičius[†*], Virmantas Šmatas[‡], Gintautas Stankūnavičius[‡], Donatas Pupienis[†], and Gintautas Žilinskas[†]

[†]Nature Research Centre
Vilnius, Lithuania

[‡]Faculty of Natural Science, Vilnius University
Vilnius, Lithuania

www.cerf-jcr.org

www.JCRonline.org

ABSTRACT

Jarmalavičius, D.; Šmatas, V.; Stankūnavičius, G.; Pupienis, D., and Žilinskas, G., 2016. Factors controlling coastal erosion during storm events. *In:* Vila-Concejo, A.; Bruce, E.; Kennedy, D.M., and McCarroll, R.J. (eds.), *Proceedings of the 14th International Coastal Symposium* (Sydney, Australia). *Journal of Coastal Research*, Special Issue, No. 75, pp. 1112 - 1116. Coconut Creek (Florida), ISSN 0749-0208.

Extreme storms may induce major changes in coastal morphology which are usually short-term in nature. The storm-related effects are controlled by different factors such as storm intensity, sand composition and coastal morphology. The main task of this study is to identify the main factors controlling erosion processes in particular coastal sectors during an extreme event. We analysed three major storms that took place over the last 15 years on the Lithuanian Baltic Sea coast: 4th December, 1999, 9th January, 2005 and 11th January, 2015. The scale of storm impact has been assessed through annual and post-storm shore profile measurements (70 profiles). We estimated changes in beach volume (m^3/m) during each storm, post-storm recovery and for the whole 1995-2015 period, as well as analyzed sand composition and morphological parameters. Storm parameters, such as wind direction and speed were analyzed using Advanced Research, Weather Research and Forecasting Model (WRF-ARW). Our results demonstrate that despite wind field differences in particular coastal sectors during storms, scale of erosion mainly depends on coastal morphology and sand composition.

ADDITIONAL INDEX WORDS: *WRF-ARW model, coastal processes, Baltic Sea coast, Lithuania.*

INTRODUCTION

One of the main factors controlling coastal erosion are extreme storms which wash out large amounts of sand within short time periods. The scale of storm-induced erosion depends on wave height (Gervais *et al*., 2002; Regnauld *et al*., 2004), sea level (Suanez *et al*., 2012), duration and frequency of event (Ferreira, 2005; Karunaratha *et al*., 2014), and lithological composition and geomorphology of the coast (Keijsers *et al*., 2015; Loureiro *et al*., 2009).

The main element controlling sea level and wave regime in the Lithuanian part of the Baltic Sea coast is wind field. Thus, extent of erosion may be estimated using simulated near surface wind parameters and applying a numerical weather prediction model (NWP). Consequently, hydrometeorological conditions during extrem events are also possible to assess.

The main aim of this study is to assess a contribution of different factors to storm-induced erosion like the wind field, coastal geomorphology and lithology in various coastal sections, using Advanced Research, Weather Research and Forecasting Model (WRF), and direct measurements.

Background

The Lithuanian coast is usually divided into two segments of a different genesis: the Curonian Spit (51.0 km) and the mainland coast (38.5 km) (Fig. 1). On the Curonian Spit 30–80 m wide beaches are composed of fine and medium sand. The altitude of the foredune reaches up to 16 meters (Jarmalavičius and Žilinskas, 2006; Pupienis *et al*., 2013), and the volume of beach sediment ranges between 42 and 124 m^3/m. Beach sediment volume on mainland coast is 16–160 m^3/m. Also, the 20–85 meters wide beaches are mostly composed of fine and medium sand. The highest dune ridge at Šventoji reaches 14 meters while in Būtingė and Melnragė it is only 4 meters high (Jarmalavičius *et al.*, 2015). In addition, moraine cliffs dominate in coastal stretch extending between Šaipiai and Karklė.

The study has analysed three of the most destructive storms observed in the last 20 years on the Lithuanian sea coast. The maximal surface wind speed, during all three storms, exceeded hurricane force threshold (≥32.6 m/s) according to Beaufort wind scale. Stormy weather lasted minimum half a day; also, the sea level rose more than 130 cm.

In the morning of December 4th, 1999 a deep extratropical cyclone system struck Lithuanian coast. The cyclone has been named ”Anatol” in line with German Weather Service nomenclature. The mean maximal wind speed during the storm was 25.0 m/s, and prevailing wind direction – from SW to WSW. Moreover, the maximal gust wind speed reached 40.5 m/s. Klaipėda port gauge station recorded the maximum rise in sea level of 1.65 m. The stormy weather continued for approximately 20 hours. Lastly, coastal sediment losses related to wash out process were estimated on roughly 45.0 m^3/m of sand volume.

Another storm, named “Ervin“, touched the Lithuanian coast on January 8-9, 2005. Palanga meteorological station recorded gale of the mean maximal wind speed exceeding 25.0 m/s; moreover, gust wind speed reached 33.0 m/s. The strongest wind blew from W and WSW, and stormy weather continued for nearly 25 hours. The water level rose to 154 cm in Klaipeda port. Consequently, the coast beaches lost on average 3.1 m^3 /m of sand.

DOI: 10.2112/SI75-223.1 received 15 October, 2015; accepted in revision 15 January, 2015.
*Corresponding author: jarmalavicius@geo.lt
©Coastal Education and Research Foundation, Inc. 2016

The last analyzed storm came together with extratropical cyclone "Felix". The mean maximal wind speed of 25.0 m/s was observed in Klaipėda port; wind gusts reached 32.6 m/s. The prevailing winds blew from WSW. The storm remained for approximately 25 hours. Also, sea surge forced water level to rise up to 1.37 m. The sediment loss was estimated on 8.7 m^3 /m.

Since tides and river discharge are minor elements influencing sediment transport in the studied area, the main factor controlling coastal erosion during storm events is wind-induced waves.

METHODS

The scale of changes in coastal deposits volume are documented through cross-shore profile leveling. These measurements are performed every autumn in particular coastal sectors. Additional post-storm shore profile measurements were carried out immediately after the storm wind and waves ceased. Due to the unpredictable nature of a storms the scale of the identified erosion / accumulation usually reflects not only the aftermaths of the storm but also effects of conditions prevailing prior the storm, so covering wider period of time. The observations show that relatively calm conditions preceded the extreme storms. Thus, the measurements carried out even earlier than a month prior the particular storm allow to assess its impact on the coast. Furthermore, the estimated changes capture the effect of the extreme storms.

To assess the lithological sediment composition we analized sand texture of 1993, 2011 and 2014 samplings collected along the Lithuanian coast. A detailed description of the analysis and sampling methodology are provided in the recent Jarmalavičius *et al*. (2015) study.

Wave monitoring is performed visually on the Lithuanian coast, i.e. twice a day in the spring-summer season and once a day in the autumn-winter season (when the highest waves are observed). Thus, wave height data is insufficiently representative (Soomere and Zaitseva, 2007). Therefore, in this analysis we used wind data to determine storminess instead of wave height due to a significant correlation between these two indicators (Kriaučiūnienė *et al*., 2006; Kelpšaitė and Dailidienė, 2011). Westerly wind of 20 m/s speed generated the wave of 4.2 m height, whereas wind of 25 m/s speed generated 5.6 m height wave (Kriaučiūnienė *et al*., 2006). However, the storms reached its peak in the night when visual observations and assessment of wave height were impossible to carry out. For this reason wind data was used as a substitute of wave height.

Storm parameters such as wind direction and wind speed were analyzed using Weather Research and Forecasting, Environment Modeling System (WRF EMS) with Advanced Research WRF (ARW) core. The simulations helped to assess the spatial and temporal hurricane strength wind field within deep extratropical cyclones. The time span of the whole simulation was 48 hours and started approximately 24 hours prior the individual storm peak. Output data was recorded with 3 hours interval, likewise conventional meteorological observations. The vertical resolution of the model was increased up to 50 vertical levels. The Kain-Fritsch Cumulus scheme was selected for the convective parameterization, the Lin scheme - for microphysics, and the Mellor-Yamada-Janjic scheme - for Planetary Boundary layer. Input data with 0.5° lat/lon resolution from CFSR (Climate Forecast System Reanalysis) was used for "Anatol" and "Ervin" events. GFS (Global Forecast System) input data with 0.5° lat/lon resolution was used for "Felix" storm. CFSR and GFS reanalysis data is available for every 6 hours (00Z, 06Z, 12Z and 18Z). Model spatial resolution was reduced to 5 x 5 km. The simulated wind direction of the most extreme winds was the same as observed (SW-WSW); thus, we used only wind speed data for future analysis.

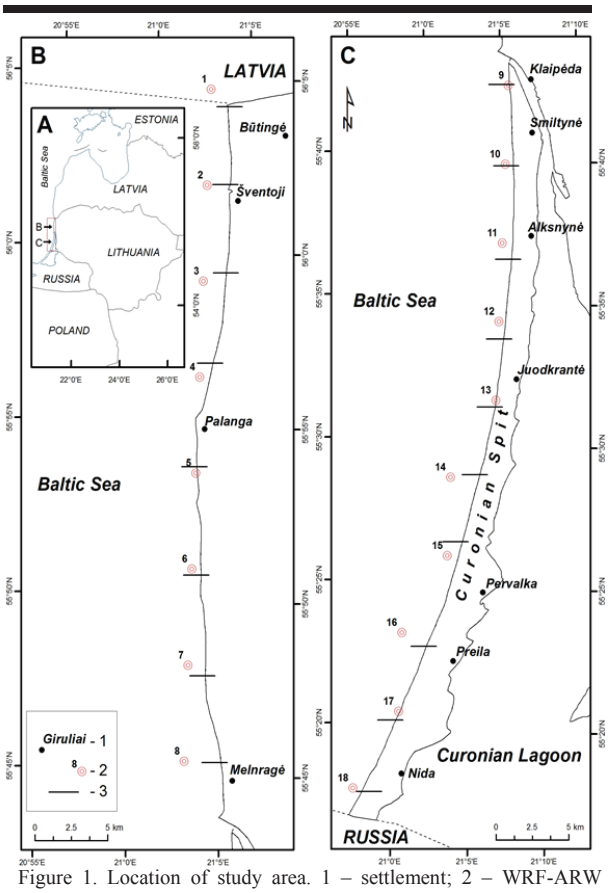

Figure 1. Location of study area. 1 – settlement; 2 – WRF-ARW model grid; cross-shore leveling site.

Figure 1 shows position of grid points for the wind speed data and shore profile leveling on the Lithuanian coast.

RESULTS

The analysis of the mean surface wind field during the "Anatol" storm revealed the stepwise increase in wind speed from north to south, i.e. from almost 21 m/s near Būtingė to 29 m/s near Nida (Fig. 2). We observed a similar tendency in the maximal wind gusts, i.e. from 31 m/s near Būtingė up to 37 m/s near Nida. The extent of coastal erosion during the storm shows almost the opposite tendency. Fig. 2 shows a decreasing volume washed out sand from the south to the north. The largest erosion was estimated near Lithuanian – Latvian border, i.e. near Palanga (20 km from Latvian border) and near Smiltynė (40 km

from Latvian border). The least erosion was observed near Juodkrantė (60 km from Latvian border) and near Lithuanian – Russian border (Fig. 2).

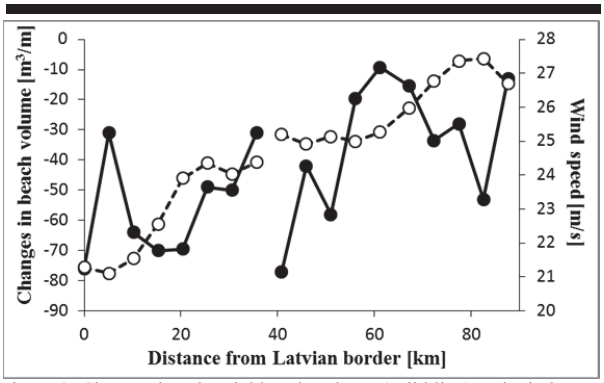

Figure 2. Changes in subaerial beach volume (solid line) and wind speed (dashed line) during storm on December 4th, 1999.

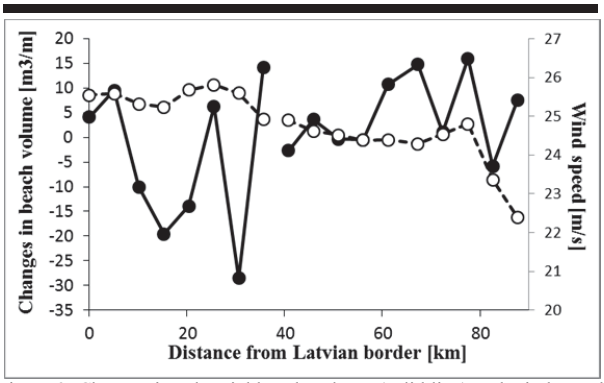

Figure 3. Changes in subaerial beach volume (solid line) and wind speed (dashed line) during storm on January 9th, 2005.

An almost uniform mean wind speed field was detected along Lithuanian coast during the "Felix" storm in 2015. The amplitude of the mean wind speed was only 2 m/s (from 22 to 24 m/s). Maximal wind speed in gusts shows similar distribution: from 32 to 33 m/s. Erosion was characterised by a very uneven distribution during this storm. We observed the most substantial erosion near Palanga (20 km from Latvian border), near Alksnynė (50 km from Latvian border), and along coastal section between Pervalka and Preila (75-85 km from Latvian border). Coastal section near Juodkrantė (60 km from Latvian border) suffered no damage related to erosion likewise during other analyzed storms (Fig. 4).

The mean wind speed during "Ervin" storm in January 2005 decreased from north to the south (Fig. 3). Maximal values of the mean wind speed (26 m/s) were detected near Būtingė while in the southernmost coastal section the maximal wind speed reached only 22 m/s. In addition, the maximal wind speed in gusts ranged from 35 m/s near Būtingė to 32 m/s near Nida. Despite clear tendency in wind speed along the coast, it was detected no substantial change in the storm induced erosion. It was determined that the largest volume of sand was washed out from the beach section between Šventoji and Palanga (10-20 km from Latvian border). On the contrary, the beaches in Melnragė (35 km from Latvian border) and e tsection between Juodkrantė and Preila (60-80 km from Latvian border) experienced only minor erosion (Fig. 3).

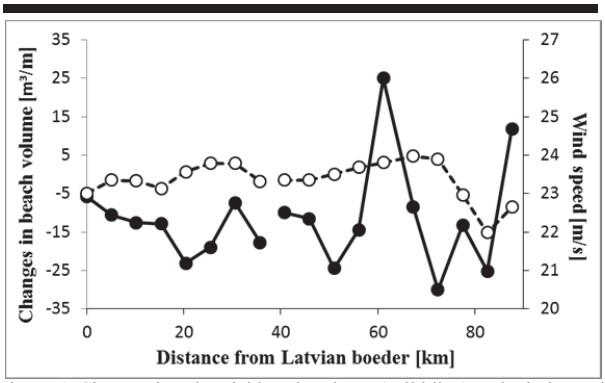

Figure 4. Changes in subaerial beach volume (solid line) and wind speed (dashed line) during storm on January 11th, 2015.

DISCUSSION

The analysis, refering to the surface wind field contribution to erosion extet along the coast, indicate rather weak correlation between the mean wind speed and changes in beach sand volume during high wind episodes. The investigation shows even contradictory results: during the storms in 4th December, 1999 and 9th January, 2005 the erosion was almost uniformly disributed along the coast while the maximal wind speed had an oposite gradient (Figs. 2-4).

Due to a lack of direct measurements of longshore transport and the fact that simulation model is based on visual wave observations, we can not evaluate the influence of storm-generated longshore current on erosion extent in particular beach sections. Besides, in our model sand particle size was assumed as contant, i.e. the model overlooked variation in grain size along the coast. Moreover, the posible influence of Klaipėda and Šventoji jetties in our analysis is also omitted (Viška and Soomere, 2013). Therefore, an effect of shore currents during storm is imposible to evaluate reliably.

The results reveal that losses in beach volume during extreme storms mainly depended on coastal lithology and geomorphology. The sand grain size analysis shows 0.2 – 0.3 mm sand dominating along the coast (Fig. 5); however, coarse sands prevail in coastal section near Melnragė (35 km from Latvian border) and in Juodkrantė (60 km from Latvian border) (Jarmalavičius *et al*., 2015).

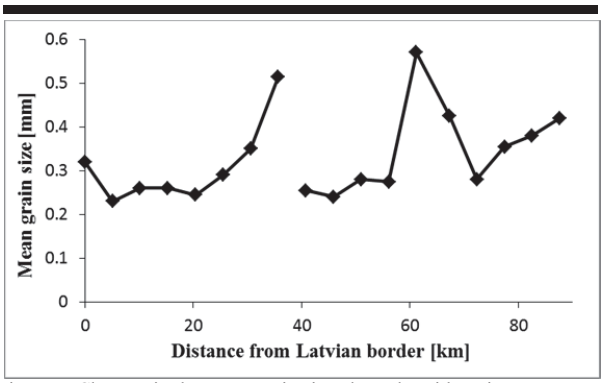

Figure 5. Changes in the mean grain size along the Lithuanian coast.

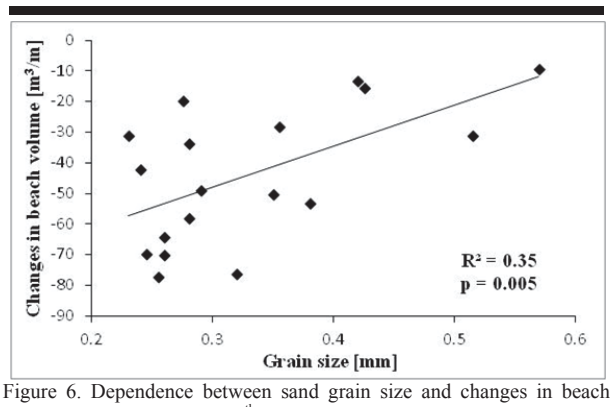

Figure 6. Dependence between sand grain size and changes in beach volume during the storm of 4th December, 1999.

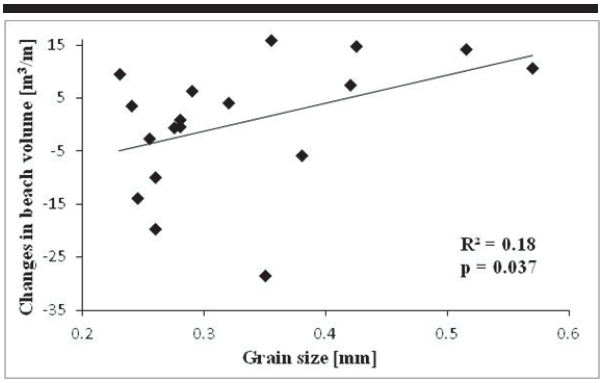

Figure 7. Dependence between sand grain size and changes in beach volume during the storm of January 9th, 2005.

We found clear correlation between the extent of coastal erosion and the variation in grain size along the coast (Figs. 6-8). In addition, the sand grain size composition determines also other coastal geomorphologic parameters. The Lithuanian coast beaches composed of fine sand are usually wide (up to 60-80 m), low sloped (Θ = 0.06-0.07), and bordered by the reclined high dune ridges (h = 9-12 m). Conversely, the beaches composed of the coarse sand are rather narrow (up to 20-40 m), high sloped (Θ = 0.13-0.14), and bordered by the low dune ridges (h = 3-5 m). Such differences in coastal geomorphology contributed to high variation in the coastal erosion during storms along the coast.

Figures 2-4, illustrating changes in beach volume along coast, indicate that erosion is negligible in the Juodkrantė coastal section where coarse sand dominates. Minor changes were also estimated in the section near Melnragė except the last storm in January 2015. However, such impact is predetermined by reconstruction of Klaipėda port jetties in 2002 when the jetties were far extended and the entrance channel deepened. Consequently, the reconstruction led to the erosion in the coast section near Melnragė (Jarmalavičius *et al*., 2012; Pupienis *et al*., 2013), and the effect of storm of January 2015 in this section was larger than expected.

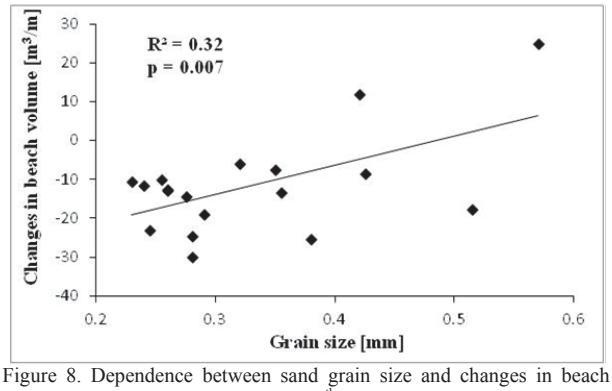

Figure 8. Dependence between sand grain size and changes in beach volume during the storm of January 11th, 2015.

CONCLUSIONS

The analysis of the effect of individual storms on the coast reveal that the scale of erosion in particular coastal sections can not be reliable determine if it is grounded just on visual wave observations and no direct measurements of shore currents are included.. This happens due to several uncertainities like network with rarely distributed points, visual observaitions, omitted variation in sand grain size along the coast, and the impact of hydraulic structures excluded from the analysis. Consequently, the storm model was base on wind speed and direction insted of wave height. The changes in wind speed along the coast during storm (together with water level and wave height) have no evident effect on coastal erosion. The variations in wind mean speed up to 6 m/s along the coast does not correlate with sediment volume losses. In such cases the coastal lithology and geomorphology played more decisive role.

The most extensive coastal erosion during storms took place in coastal sections with wild and low-sloped beaches where fine-grained sand dominates; the narrower beaches consisting of

coarse-grained sand and with larger slopes experience no substantial coastal erosion.

Hydrological and meteorological data (wind speed and direction, wave height or sea level) from Klaipėda hydrometeorological station could be sufficient for the assessment of the effects of the individual storms along the coast. The station location almost in the middle of the Lithuanian coastline and the variation of hydrometeorological parameters along the relatively short coastline (about 90 km) do not significantly affect coastal processes.

The Weather Research and Forecasting model reliably reproduces the wind field structure within extreme storm system. However, it can not properly assess the meso-scale extreme wind patterns since there are influenced by diverse coastal morphology, airflow convergence structure and the local convective clouds.

ACKNOWLEDGMENTS

This study was partly supported by Lithuanian Science Council Grant No. MIP-039/2014.

LITERATURE CITED

Ferreira, O., 2005. Storm groups versus extreme single storms: predicted erosion and management consequences. *In:* Finkl, C.W. (ed.), *The Sun, Earth, and Moon, Journal of coastal research*, Special Issue No. 42, pp. 221-227.

Gervais, M., Balouin, Y., and Belon, R., 2012. Morphological response and coastal dynamics associated with major storm events along the Gulf of Lions Coastline, France. *Geomorphology*, 143-144, 69-80.

Jarmalavičius, D. and Žilinskas, G., 2006. Peculiarities of sand sorting on the Lithuanian coast of the Baltic Sea. *Geologija*, 56, 36-42.

Jarmalavičius, D., Žilinskas, G., and Pupienis, D., 2012. Impact of Klaipėda port jetties reconstruction on adjacent sea coast dynamics. *Journal of Environmental Engineering and Landscape Management*, 20(3), 240-247.

Jarmalavičius, D., Pupienis, D., Buynevich, I.V., Žilinskas, G., and Fedorovič, J., 2015. Aeolian sand differentiation along the Curonian Spit Coast, Baltic Sea, Lithuania. Coastal Sediments 2015. *Proceedings of the Coastal Sediments 2015* (San Diego, USA), pp. 1-10.

Karunarathna, H., Pender, D., Ranasinghe, R., Short, A.D., and Reeve, D.E., 2014. The effect of storm clustering on beach profile variability. *Marine geology*, 348, 103-112.

Keijsers, J.G.S., Poortinga, A., Riksen, M.J.P.M., and Maroulis, J., 2014. Spatio-temporal variability in accretion and erosion of coastal foredunes in the Netherlands: Regional climate and local topography. *Plos One*, 9(3), e91115.

Kelpšaitė, L., and Dailidienė, I., 2011. Influence of wind wave climate change on coastal processes in the eastern Baltic Sea. *In*: Ahrens, L.H., Press, F., Rankama, K., and Runcorn, S.K. (eds.), *Proceedings of the 11th International Coastal Symposium* (Szczecin, Poland). Journal of Coastal Research, Special Issue No. 64, pp. 220-224.

Kriaučiūnienė, J., Gailiušis, B., and Kovalenkovienė, M., 2006. Peculiarities of sea wave propagation in the Klaipėda Strait, Lithuanica. *Baltica*, 19(1), 20-29.

Loureiro, C., Ferreira, O., and Cooper, J.A.G., 2009. Contrasting morphologic behavior at embayed beaches in Southern Portugal. *In:* Brock, J.C. and Purkis, S.J. (eds.), *Proceedings of the 10th International Coastal Symposium* (Lisbon, Portugal), *Journal of Coastal Research*, Special Issue No. 56, 83-87.

Pupienis, D., Jonuškaitė, S., Jarmalavičius, D., and Žilinskas, G., 2013. Klaipėda port jetties impact on the Baltic Sea shoreline dynamics, Lithuania. *In:* Conley, D.C., Masselink, G., Russell, P.E. and O'Hare, T.J. (eds.), *Proceedings 12th International Coastal Symposium* (Plymouth, England), *Journal of Coastal Research*, Special Issue No. 65, pp. 2167-2172.

Pupienis, D., Buynevich, I. V., Jarmalavičius, D., Žilinskas, G., and Fedorovič, J., 2013. Regional distribution of Heavy-mineral concentrations along the Curonian Spit coast of Lithuania. *In:* Conley, D.C., Masselink, G., Russell, P.E. and O'Hare, T.J. (eds.), *Proceedings 12th International Coastal Symposium* (Plymouth, England), *Journal of Coastal Research*, Special Issue No. 65, pp. 1844-1849.

Regnauld, H., Pirazzoli, P.A., Morvan, G., and Ruz, M., 2004. Impact of storms and evolution of coastline in western France. *Marine Geology*, 210 (1-4), 325-337.

Soomere, T., and Zaitseva, I., 2007. Estimates of wave climate in the northern Baltic Proper derived from visual wave observations at Vilsandi. *Proceeding of the Estonian Academy of Sciences Engineering*, 13, 48-64.

Suanez, S., Cariolet, J., Cancouët, R., and Ardhuin, F., 2012. Dune recovery after storm erosion on a high-energy beach: Vougot beach, Brittany (France). *Geomorphology*, 139-140, 16-33.

Viška, M., and Soomere, T., 2013. Simulated and observed reversals of wave-driven alongshore sediment transport at the eastern Baltic Sea coast. *Baltica*, 26(2), 145-156.

Journal of Coastal Research	SI	75	1117 - 1121	Coconut Creek, Florida	2016

A Comprehensive Sensitivity Analysis of Tsunami Model System to the Parametric and Input Uncertainties

Tae-Hwa Jung [†], Sangyoung Son [‡*], Patrick J. Lynett [§]

[†]Department of Civil and Environmental Engineering,
Hanbat National University,
Daejeon, South Korea

[‡‡]School of Civil, Environmental and Architectural Engineering,
Korea University,
Seoul, South Korea

[§]Department of Civil and Environmental Engineering,
University of Southern California,
Los Angeles, CA, USA

www.cerf-jcr.org

www.JCRonline.org

ABSTRACT

Jung, T.-H.; Son, S. and Lynett, P., 2016. A Comprehensive Sensitivity Analysis of Tsunami Model System to the Parametric and Input Uncertainties. *In:* Vila-Concejo, A.; Bruce, E.; Kennedy, D.M., and McCarroll, R.J. (eds.), *Proceedings of the 14th International Coastal Symposium* (Sydney, Australia). *Journal of Coastal Research*, Special Issue, No. 75, pp. 1117 - 1121. Coconut Creek (Florida), ISSN 0749-0208.

In the present study, it is examined the tsunami modelling sensitivity to the various input factors based on the simulation results of 2004 Indian Ocean Tsunami. The numerical tests were implemented using coupled shallow water equation model, COMCOT(Liu *et al.,* 1998) and Boussinesq model(Son *et al.,* 2011) on the multi-grid system. Four different configurations(CASE 1 through 4) where three factors were controlled independently had been set up and simulated. From the numerical results, it was examined that some of defined factors may have control over the level of prediction accuracy in tsunami impacts on the nearshore area. It was shown that hydrodynamic performances calculated by Boussinesq model(Son *et al.,* 2011) were very distinct from those by COMCOT-only. Most importantly, this study also suggests that more thorough and dedicated investigations on the diffusive errors embedded inherently in numerical models are required for the future study.

ADDITIONAL INDEX WORDS: *Tsunami modelling, sensitivity, run-up, inundations, numerical simulations, Boussinesq model.*

INTRODUCTION

Among other natural disasters, tsunami waves are undergoing increased due to their frequent occurrence in recent years as well as their related devastating natural impacts. Tsunamis are dangerous not only due to the overflow effects on the land, but also due to the strong currents induced in the nearshore (Lynett *et al.,* 2012, 2014).

Recently, various types of modelling have been developed for predictioning tsunami evolution. In most of the modelling efforts, however, many of optional parameters such as bottom friction coefficients and sub-closure model properties require greater accuracy. This highlights the importance of the right use of basic parameters when implementing tsunami models. For example, a range of friction factors or grids sizes can be adopted for the tsunami simulation, but this may potentially provide different prediction level on tsunami evolutions.

Tsunami waves are typically known to be solitary-wave-like belong to a long wave regime and this assumption brings about the use of long wave models as typical modeling approaches. Thus, either shallow water equation model or Boussinesq model are mostly preferred in simulations. Therefore, the choice of governing system in the modeling efforts may be another factor to be considered.

DOI: 10.2112/SI75-224.1 received 15 October, 2015; accepted in revision 15 January, 2015.
*Corresponding author: sson@korea.ac.kr
©Coastal Education and Research Foundation, Inc. 2016

The aim of this paper is to examine tsunami modelling sensitivity to the various factors used in numerical models. This paper is organized as follows. In the next section, different types of tsunami models and their governing physics are introduced ahead of their application to tsunami events. Then four different settings for test cases will be defined through combinations of three input factors. The following section will make use of tsunami models to simulate 2004 Indian Ocean Tsunami based on four different configurations. To examine the factor that may affect the level of predictions in tsunami impact on the coastal area, simulated results will be compared with observed data and analyzed.

NUMERICAL MODELS

Three types of tsunami models have been involved in the study for the tsunami simulations; conventional shallow water equation model (COMCOT), Boussinesq model and coupled model of both.

Shallow Water Equation Model (COMCOT)

Typically, numerical approaches to tsunami prediction are conducted through a shallow water equation model. Based on the long wave theory, frequency dispersion can be ignored and thus hydrostatic pressure field and depth-constant horizontal velocity can be feasibly derived. This has provided the great advantage to the numerical approach, but has also produced some potential errors especially relating to tsunami-

induced dispersive waves in the nearshore (Son *et al.*, 2011). However, tsunami models based on a shallow water equation is still being considered as typical by tsunami modelers.

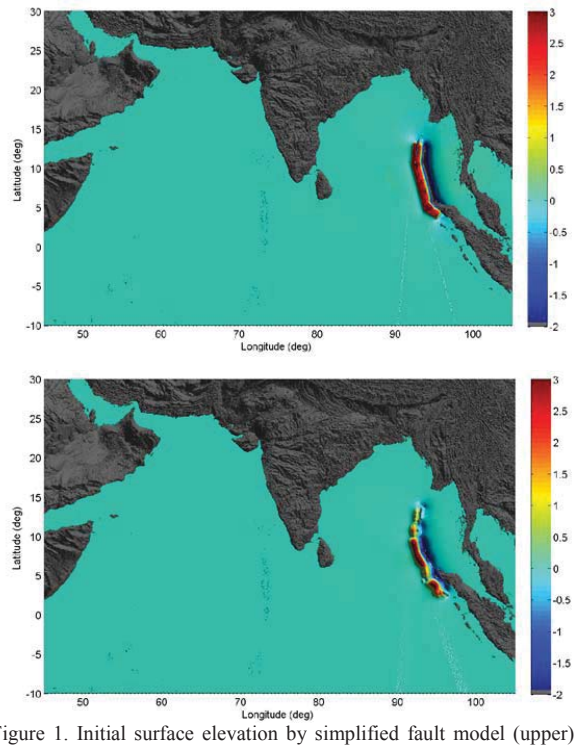

Figure 1. Initial surface elevation by simplified fault model (upper) and by finite fault model(lower)

In this study, Cornell multi-grid coupled tsunami model (COMCOT) model presented by Liu *et al.* (1998) was employed. This model adopts the staggered leap-frog integration with an upwind scheme for the nonlinear convective terms and can also include some nearshore physics such as inundations. Governing equation of COMCOT, i.e., nonlinear shallow water equations considering bottom shear stress can read as,

$$\frac{\partial \zeta}{\partial t} + \frac{\partial P_i}{\partial x_i} = 0 \tag{1}$$

$$\frac{\partial P_i}{\partial t} + \frac{\partial}{\partial x_j}\left(\frac{P_i P_j}{H}\right) + gH\frac{\partial \zeta}{\partial x_i} + R_i = 0 \tag{2}$$

where i, j = (1, 2), $H=\zeta+h$ is total water depth, ζ is surface elevation, h is water depth, and P_i is volume flux. R_i denote bottom friction term related to Manning's formulation.

Boussinesq Model for Rotational Flows

Boussinesq-type models, which include dispersive effects and/or rotational property of flows in the nearshore area, can be used to obtain more realistic wave predictions. Boussinesq equations add additional accuracy to the shallow water equation. However, Boussinesq model is still far from being in common use because of its computational complexity. To overcome this drawback, a coupled modelling technique between the shallow water equation model and Boussinesq model has been proposed and will be introduced in the following subsection.

The governing equations in the Boussinesq model are depth-integrated mass and momentum equations, which are given as,

$$\frac{\partial H}{\partial t} + \frac{\partial H\hat{u}_i}{\partial x_i} + \left(M + M^v\right) = 0 \tag{3}$$

$$\begin{aligned}\frac{\partial H\hat{u}_i}{\partial t} + \frac{\partial H\hat{u}_i\hat{u}_j}{\partial x_j} + gH\frac{\partial \zeta}{\partial x_i} + H\left(D_i + \xi_i + D_i^v + \xi_i^v\right) \\ + \hat{u}_i\left(M + M^v\right) - H\frac{\partial}{\partial x_j}\left(\nu_t^h\frac{\partial \hat{u}_i}{\partial x_j}\right) \\ + H\frac{\partial}{\partial x_i}\left(\nu_t^v\frac{\partial \hat{u}_j}{\partial x_j}\right) + \frac{\tau_i^b}{\rho} = 0\end{aligned} \tag{4}$$

where $\hat{u}_i$ is velocity at the depth, z(=-0.531h), and M and M^v represent second-order correction terms by frequency dispersion and bottom-induced turbulence effects respectively in the continuity equation. Similarly, D_i and D_i^v denote frequency dispersion and bottom-induced turbulence terms, respectively in the momentum equation. Turbulent eddy viscosity is also included as ν_t^h and ν_t^v, which denote decomposed horizontal and vertical components, respectively and τ_i^b is the shear stress on bed. Discretized forms of above set of equations for numerical implementation and the entire details about each terms included can be found in Son *et al.* (2011).

Coupled COMCOT-Boussinesq Model

The conventional approach in tsunami modelling has been advanced through the coupling between shallow water equation model and Boussinesq-type model which includes rotational property of flows in the nearshore area (Son *et al.*, 2011). The coupled modelling approach allows optimized tsunami modelling platform through the application of Boussinesq model. This spot-focused application of Boussinesq model within the shallow water equation model has proven to reduce computational costs and to increase simulation accuracy in calculating nearshore physical properties. Entire details about the coupling efforts between the shallow water equation model and Boussinesq model and about the validation of coupled model can be found in Son *et al.* (2011). Consequently, in the present study this advanced simulation technique was adopted to obtain more accurate and efficient modelling results.

TEST CASES

To examine factors that can contribute to the tsunami impact on the nearshore area, four different configurations (CASE 1 through 4) had been proposed and set up. In each case, three factors were independently considered and controlled. The first factor to be controlled was the fault model. Two types of models could be chosen; simplified fault model and finite fault model. Simplified fault model suggests the tsunami source can be approximated by three subfaults, while finite fault model tries to directly describe the slip distribution on the sea-floor in more detail. Thus it can be said that important information on the tsunami source can be included more accurately by finite fault model. Second factor for sensitivity tests was an addition of refined grid for the Maldives region. This site-dependent option was chosen for 2004 Indian Ocean tsunami because wave propagation was supposed to be affected significantly by the Maldives' geology. The third factor was bottom friction and the inclusion of this might be able to result in different nearshore- or overflow-dynamics of tsunami waves.

Table 1. *Simulation Cases.*

No.	Fault Model	Refined Layer for Maldives	Bottom Friction
CASE 1	Simple Fault	×	×
CASE 2	Finite Fault	×	×
CASE 3	Simple Fault	o	×
CASE 4	Simple Fault	×	o

By the free combination of these all factors, four cases were set. CASE 1 used simplified three subfaults for the generation of initial ocean surface elevation without the application of friction effects to the bottom and the refined Maldives layer. Parameters for simplified subfaults used here can be found in Wang and Liu (2006). CASE 2 is same as CASE 1 but employs the most recent version of finite fault solution by Chlieh *et al.* (2007), instead of simplified fault conditions. Initial ocean surfaces generated by either simplified fault or finite fault model are shown in Figure 1. Similarly, CASE 3 includes an additional refined layer for Maldives with keeping CASE 1 configuration unchanged. The refined layer around the Maldives, with a reduction factor of 4, is to better capture the evolution of the wave through this region. The bathymetry for Maldives had been obtained from SRTM30 PLUS (Becker *et al.*, 2009). Finally, for investigating the bottom friction effects on the results, bottom friction factor is added in CASE 4. COMCOT can consider it in terms of Manning's roughness coefficient whereas Boussinesq model does it by the equivalent sand roughness. COMCOT and Boussinesq model used 0.013 and 0.8mm for the bottom friction, relatively. Table 2 illustrates these combinations of parameters in four cases.

Table 2. *Grid setups for 2004 Indian ocean tsunami simulation.*

Layer No.	*x* range (lon., ° E)	*y* range (lat., ° N)	n*x*×n*y*	*dx*	*dt* (s)	Model
Layer 1	45°00′00″ ~ 45°17′12″	45°00′00″ ~ 45°17′12″	1801 ×1210	2′	1	LSW(S)[a]
Layer 2	45°00′00″ ~ 45°17′12″	45°00′00″ ~ 45°17′12″	2455 ×2405	24″	0.5	LSW(S)
Layer 2-1[b]	45°00′00″ ~ 45°17′12″	45°00′00″ ~ 45°17′12″	840 ×1560	30″	0.5	LSW(S)
Layer 3	45°00′00″ ~ 45°17′12″	45°00′00″ ~ 45°17′12″	2655 ×1455	4.8″	0.25	LSW(S)
Layer 4	45°00′00″ ~ 45°17′12″	45°00′00″ ~ 45°17′12″	600 ×600	18.5m	0.125	NLSW[c]
Layer 5	45°00′00″ ~ 45°17′12″	45°00′00″ ~ 45°17′12″	309 ×309	9.3m	0.125	BOUSS[d]

[a] Linear Shallow Water Model in Spherical Coordinates
[b] Optional layer for Maldives bathymetry to be employed in CASE 3
[c] Non-Linear Shallow Water Model in Cartesian Coordinates
[d] Boussinesq Model in Cartesian Coordinates

In addition to above cases, for the comparison of the performance of coupled model against the COMCOT-only, COMCOT-only had been run using the same condition as CASE 1. This meant to compare shallow water equation result with Boussinesq model result, explicitly. Due to the limited number of subgrid level (4th in COMCOT Ver. 1.6), however, different grid size in Layer 4 has been used to get the same resolution for port Salalah as in the coupled model simulation. Total run time for all cases is 16 hours after the first wave arrives at Port Salalah, Oman, to match up with the tidal station data. Grids system for the simulation has been organized using multi-grid system in COMCOT (Liu *et al.,* 1998); see Table 2 for details about grid set-up. Totally, 5 layers of grids with different domain sizes and resolutions were determined in the simulation while the final finest grid focused on the port Salalah in Oman.

RESULTS

Different numerical results resulted from four different configurations were compared either to other numerical results or to observed data. The runup heights along the southeast coast of Oman were recorded up to 3.3m and the inundation were as much as 447m from the shoreline under a runup height of 2.3m. A trend of larger runups mainly occurred in southernmost coast area of Oman was also established. Detailed features of surveyed data are summarized in Okal *et al.* (2006). Figure 2 shows numerical runup heights compared with observed records. Different runup heights were calculated from case to case, even though each case produced similar values in limited ranges. Fair agreements were found between observed and numerical data, but runups higher than 2.5m were not predicted well. Among

4 cases, CASE 2 was most distinguishable from others, which demonstrated that the application of different type of fault model (i.e., simplified fault model and finite fault model in this study) will cause significant variations in runup predictions. This will also be confirmed through the comparisons of other properties such as instant water level (Figure 4) and current speed (Figure 5).

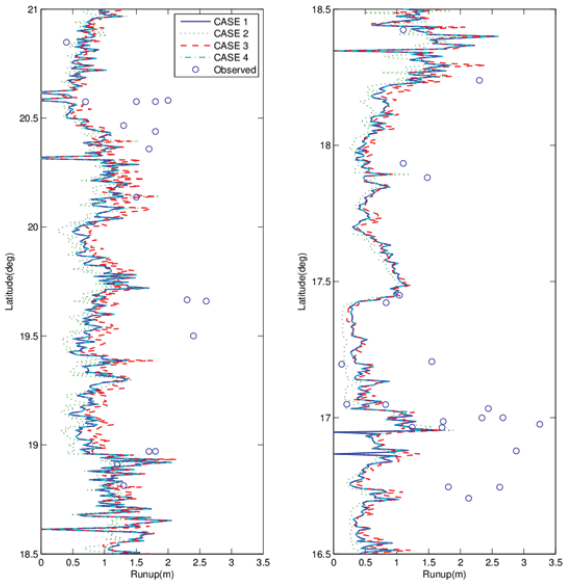

Figure 2. Comparison of numerical runup with observed record by Okal *et al.* (2006)

Calculated maximum free surface elevation was also examined by comparing CASE 1 with COMCOT-only case. This comparison is intended to identify the effects of dispersive and bottom-induced turbulence terms in Boussinesq model on the calculation accuracy of surface elevations. Figure 3 is showing maximum free surface elevation of both the Boussinesq and COMCOT-only results, and there exists no distinct difference between them.

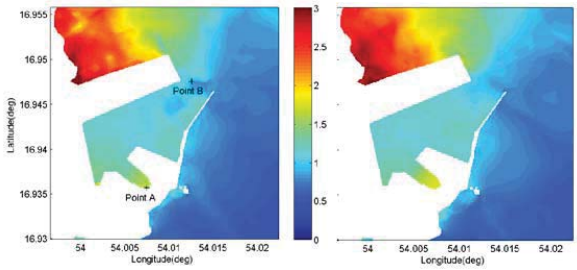

Figure 3. Maximum free surface elevation in port Salalah, Oman: COMCOT-only (left), CASE 1(right)

Figure 4 depicts time series of calculated surface elevation recorded at the tidal station ("Point A" in Figure 3). Instant surface elevation of each case has the similarity in that the arrival of initial tsunami wave at the recording location are almost identical except CASE 2 (finite fault model) and exhibits different pattern after 11.5 hrs. All the cases agree well with measured profile both in wave height and phase until about 11.5 hrs. In particular, CASE 1 and 4 produced almost identical results, indicating that bottom friction effects did not play a significant part in calculations of tsunami wave heights.

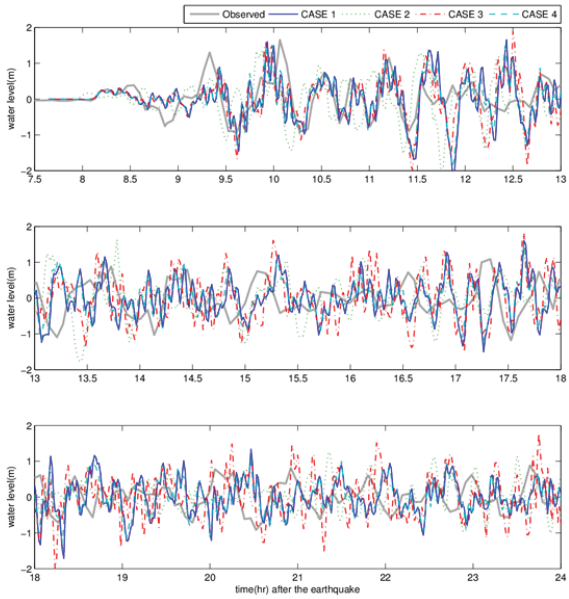

Figure 4. Comparison of calculated tsunami height at "Point A" with tidal station record

Now, our interest turns to the investigation on hydrodynamic properties of tsunami waves, i.e., current speeds. Tsunami-induced currents encompass various kinds of complex physics and thus more comprehensive approach is needed for understanding, especially in the nearshore area (Lynett *et al.*, 2014). For the present study, current speed at the entrance of the port ("Point B" in Figure 3) had been recorded and compared each other as shown in Figure 5. Overall current speed results have wide deviations each other and this is in contrast to the surface elevation results. For instance, current speeds in CASE 2 and 3 show quite different behaviors from others at the beginning of the record, while CASE 1 and 4 still show somewhat similar pattern with some discrepancies. It can be inferred from these results that the friction factor tends to give less impact on the hydrodynamic results than other factors. Nevertheless, maximum currents predicted at "Point B" range within limited values(3.5m/s ~ 4.0m/s) and almost coincide in the magnitude and timing of the first speeds peak.

Consequently, predicted hydrodynamic properties of tsunami waves are more sensitive to the three parametric and input factors defined in this study than other properties such as runup and surface elevation. This fact can be seen more

clearly from Figure 6, where the maximum current speed of CASE 1 and COMCOT-only were compared. Thus it can be said that strong sensitivity of tsunami models to the parametric and input factors will be closely related to the potential errors in the prediction of tsunami-induced current speed and coherent structures (Lynett *et al.*, 2012).

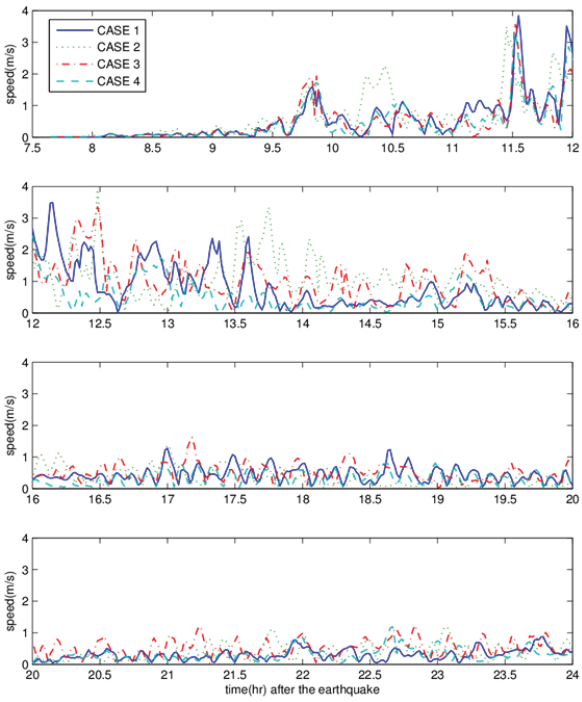

Figure 5. Numerical speed record at harbor entrance "Point B"

CONCLUSIONS

This study focuses on tsunami modelling sensitivity to the various input factors based on the simulation results of 2004 Indian Ocean Tsunami. Ahead of the application of tsunami model, three different factors including friction coefficients and the choice of fault models were considered, to produce four different configurations. Numerical tests were performed using coupled COMCOT and Boussinesq model on the multi-grid system. The simulation revealed that the choice of fault model and inclusion of refined grids could significantly control the estimation level of tsunami impacts on the harbor area. It was also shown that hydrodynamic performances calculated by Boussinesq model are very distinct from those by COMCOT-only, which had been previously described by Lynett *et al.* (2012).

Therefore, it should be noted that care must be taken when these factors are considered and tuned in numerical simulations for tsunami inundations. In other words, the parametric/input factors in the numerical model should be clearly defined before their use and be carefully set for the simulation, since different setting will produce equally inaccuracy. Most importantly, this study also suggests that wave-induced coherent structures which is strongly related to the hydrodynamic behavior of tsunami waves needs to be thoroughly examined and benchmarked on the dataset of simulations results based on the belief that they are more or less sensitive to the diffusive errors and friction factors.

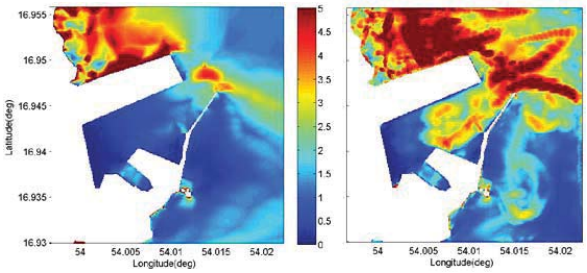

Figure 6. Maximum velocity in port Salalah, Oman: COMCOT-only (left), CASE 1(right)

ACKNOWLEDGMENTS

This research was supported by a grant 'Development of the Evaluation Technology for Complex Causes of Inundation Vulnerability and the Response Plans in Coastal Urban Areas for Adaptation to Climate Change' [MPSS-NH-2015-77] from the Natural Hazard Mitigation Research Group, Ministry of Public Safety and Security of Korea.

LITERATURE CITED

Becker, J.; D. Sandwell; W. Smith; J. Braud; B. Binder; J. Depner and D. Fabre *et al.*, 2009. Global bathymetry and elevation data at 30 arc seconds resolution: SRTM30_PLUS. *Marine Geodesy*, 32(4), 355-371.

Chlieh, M.; J.-P. Avouac; V. Hjorleifsdottir; T.-R. Alex Song; C. Ji; K. Sieh and A. Sladen et al., 2007. Coseismic slip and afterslip of the great Mw 9.15 Sumatra-Andaman earthquake of 2004. *Bulletin of the Seismological Society of America.* 97, S152–S173.

Liu, P.; Woo, S.-B., and Cho, Y.-S., 1998. Computer programs for tsunami propagation and inundation, *Technical report*, Cornell University.

Lynett, P.; Borrero, J.; Weiss, R.; Son, S.; Greer, D. and Renteria, W., 2012, Observations and modeling of tsunami-induced currents in ports and harbors, *Earth and Planetary Science Letters*, 327–328, 68–74.

Lynett, P.; Borrero, J.; Son, S.; Wilson, R. and Miller, K., 2014. Assessment of the tsunami-induced current hazard, *Geophysical Research Letters*, 41, 2048–2055.

Okal, E.; Fritz, H.; Raad, P.; Synolakis, C.; Al-Shijbi, Y. and Al-Saifi, M., 2006. Oman Field Survey after the December 2004 Indian Ocean Tsunami, *Earthquake Spectra*, 22, S203-S218

Son, S.; Lynett, P.; Kim, D.-H., 2011. Nested and Multi-physics Modeling of Tsunami Evolution from Generation to Inundation, *Ocean Modelling*, 38(1-2), 96-113

Wang, X. and Liu, P., 2006. An analysis of 2004 Sumatra earthquake fault plane mechanisms and Indian Ocean tsunami, *Journal of Hydraulic Research*, 44(2),147-154.

Journal of Coastal Research	SI	75	1122 - 1126	Coconut Creek, Florida	2016

Typhoon Morakot Induced Waves and Surges with an Integrally Coupled Tide-Surge-Wave Finite Element Model

Kyeong Ok Kim[†], Jin-Hee Yuk[‡], Han Soo Lee[††], and Byung Ho Choi[§*]

[†]Marine Radionuclide Research Center
Korea Institute of Ocean Science & Technology
Ansan, Korea

[‡]Disaster Management HPC Technology Research Center, Korea Institute of Science and Technology Information
Daejeon, Korea

[††]Graduate School of Science and Engineering
Saitama University
Saitama, Japan

[§]Department of Civil and Environment Engineering
Sungkyunkwan University
Suwon, Korea

www.cerf-jcr.org

www.JCRonline.org

ABSTRACT

Kim, K.O.; Yuk, J.-H.; Lee, H.S., and Choi, B.H., 2016. Typhoon Morakot induced wave and surges with an integrally coupled tide-surge-wave finite element model. *In:* Vila-Concejo, A.; Bruce, E.; Kennedy, D.M., and McCarroll, R.J. (eds.), *Proceedings of the 14th International Coastal Symposium* (Sydney, Australia). *Journal of Coastal Research*, Special Issue, No. 75, pp. 1122 - 1226. Coconut Creek (Florida), ISSN 0749-0208.

A coupled system of unstructured-mesh SWAN and ADCIRC, running on the same unstructured mesh, has been applied to simulate storm surges and waves during typhoon Morakot in August 2009. Emphasis is placed on the effect of wave-tidal current interaction on storm surges and wind waves. Two advantages of this system are that the physics of wave-circulation interactions can be satisfactorily resolved, and a large domain covering a deep ocean and shallow shelf can be dealt with seamlessly, requiring no mesh nesting. Wave refraction and directional spreading induced a wave-current effect, which was confirmed by the cross correlation between the observed significant wave periods and the wave-current angle. The results from the application of the system show that waves resulting from a typhoon can be reasonably simulated in a coastal area. The effect of coupling wave heights and wave periods is found to be approximately 5% and 10%, respectively. Spectral characteristics such as directional spreading and refraction support the influence of tidal current effects on wind waves. This coupled system is a good starting point for operational wave-tide-surge forecasting and can be easily extended to regional sites of interest without a significant increase in the computational burden. The system currently uses a set of depth-integrated equations that simplifies the vertical structure of the current, radiation stress, surface stress and bottom boundary layer.

ADDITIONAL INDEX WORDS: *Typhoon Morakot, tide-surge-wave interaction, finite element numerical model.*

INTRODUCTION

Typhoon Morakot was the most devastating storm of the 2009 Pacific typhoon season, and it was also the deadliest typhoon in the recorded history of Taiwan. A total of 461 people were killed in the typhoon and another 192 were missing. The entire village of Xiaolin was buried in the southern county of Kaohsiung, killing 439 people with many roads left damaged and the landscape changed. The damages totaled roughly $3.3 billion (USD). Morakot brought huge amounts of rainfall, peaking at 2,777 mm. The slow moving storm also caused widespread damage in China, leaving eight people dead and causing $1.4 billion (USD) in damages. This study attempts to simulate wind waves and storm surges near Taiwan during typhoon Morakot in August 2009 using a coupled system of unstructured-mesh SWAN and ADCIRC. Two advantages of this system are that the physics of wave-circulation interactions can be satisfactorily resolved and a large domain covering a deep ocean and shallow shelf can be dealt with seamlessly, requiring no mesh nesting. Focus is placed on the identification of the effect of wave-tidal current interaction on storm surges and wind waves. In this study, all numerical results have been calculated using both the fully coupled and uncoupled systems. Additionally, current-induced refraction and directional wave energy spreading induced by tidal currents are described through spectral analysis.

METHODS

The modeling system used in this study is composed of two sub-models, a wind wave model and a tide-surge model. The essential features of each sub-model are briefly described below.

Wind wave and tide-surge models

A sophisticated model known as SWAN, developed by Booij *et al.* (1999), incorporates depth-induced wave breaking and triad wave-wave interaction. This model predicts the evolution in geographic space and time of the wave action density spectrum with the relative frequency and the wave direction, as governed by the action balance equation (Booij *et al.*, 1999). The details of the equation have been described

DOI: 10.2112/SI75-225.1 received 15 October, 2015; accepted in revision 15 January, 2015.
*Corresponding author: bhchoi.skku @gmail.com
©Coastal Education and Research Foundation, Inc. 2016

in earlier studies (Booij *et al.,* 1999). ADCIRC (the ADvanced CIRCulation model) is a continuous-Galerkin, finite-element, shallow-water model that solves for water levels and currents at a range of scales (Luettich and Westerink, 2004). The details of this solution have been widely published (refer to http://www3.nd.edu/~adcirc/manual.htm for the User's Manual and Theory Report) and will not be stated here.

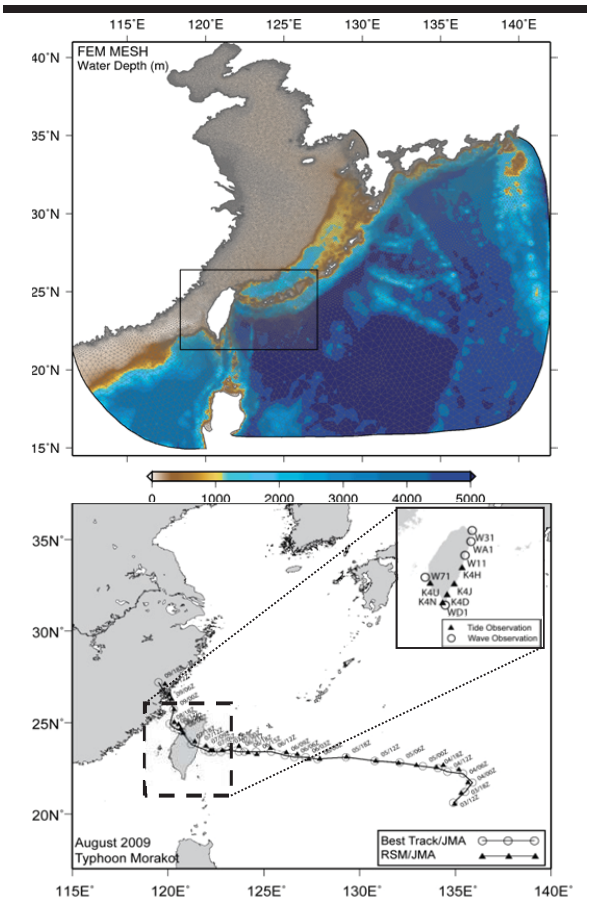

Figure 1. Model domain and water depth with FEM mesh composed of variable sizes (upper). Typhoon Morakot (2009) track of the RSMC/JMA best track and the RSM/JMA numerical model and locations of the 5 tidal stations used for tide-surge validation and 5 wave stations used for wave validation (lower).

Coupling of ADCIRC and SWAN

SWAN is driven by wind speeds, water levels and currents computed at the vertices by ADCIRC. Marine winds can be input to ADCIRC, and these winds are adjusted directionally to account for surface roughness. ADCIRC interpolates spatially and temporally to project these winds to the computational vertices, and then it passes them to SWAN. The water levels and ambient currents are computed in ADCIRC before being passed to SWAN, where they are used to re-compute the water depth and all related wave processes (wave propagation, depth-induced breaking, *etc.*). The ADCIRC model is driven partly by radiation stress gradients that are calculated with information from SWAN. ADCIRC and SWAN run in series on the same local mesh and core. The two models leap frog through time, each being forced with information from the other model. The coupling interval is set to be the same as SWAN's time step. The basic structure of this coupling system (ADCIRC-SWAN) was developed by Dietrich *et al.* (2010).

Mesh generation

To obtain stable and accurate solutions on the unstructured grids of the tide-surge model and spectral wind wave model, the mesh must be carefully generated to satisfy the requirements of both models. The ADCIRC model needs to satisfy the CFL condition for long wave propagation (or shallow water depth in the area). For the spectral wave model SWAN, steep topography can cause numerical instability, creating spurious wave refraction over an element. Preliminary calculations have also revealed that with the fully coupled wind wave, storm surge and tide model, computed radiation stress is very sensitive to grid size. For this study, we adopted BatTri to create a mesh that is a graphical Matlab interface to the C language two-dimensional quality grid generator (Bilgill *et al.*, 2006). Iterative calculations indicate that this generation method is very efficient and produces reasonable results. Figure 1 shows the mesh system ultimately used in this study, which is comprised of mesh sizes of 1 km on the continental shelf, less than 100 m in the wave breaking zones and inland, and as little as 20-30 m in coastal areas.

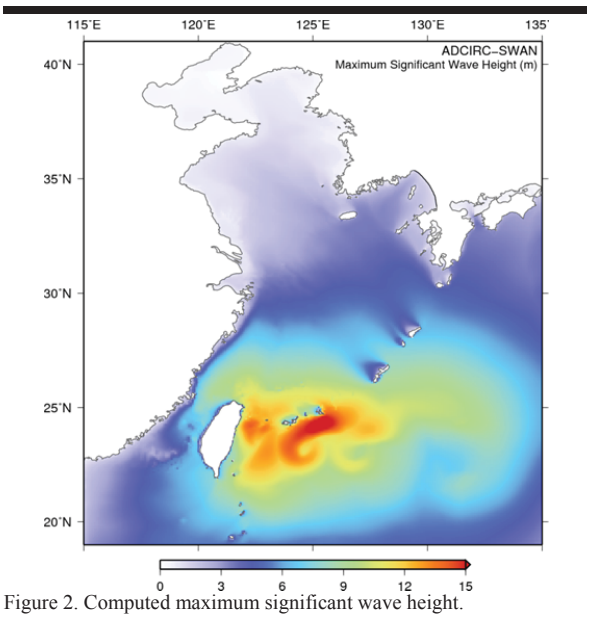

Figure 2. Computed maximum significant wave height.

Model setups for typhoon Morakot

Figure 1 shows the best track data from the Regional Specialized Meteorological Center (RSMC) from Japan Meteorological Agency (JMA) for comparison, including the

location of the pressure center in the Regional Spectral Model (RSM) of JMA data. Despite the low resolution (horizontally, 20 km) of the RSM data, it can be seen that the two datasets are in agreement. In particular, we can see that the time and location of landfall, which have important effects on our results, are in very good agreement. Sea level pressures and wind field data for storm surge and storm wave modeling were obtained from the RSM data, which generates predictions at three-hour intervals. Time steps for the ADCIRC and SWAN calculations are 3 and 300 seconds, respectively. The NAO's tidal predictions (Matsumoto *et al.*, 2000) are the source of real-time tidal elevation for the simulation.

RESULTS

Figure 2 shows the distribution of the maximum significant wave height. A maximum significant wave height over 15 meters is computed south of the Ryukyu Islands. Waves propagating to the East China Sea with long periods decay as they enter the Yellow Sea. Figure 3 compares computed sea levels from the uncoupled system (dashed line) and coupled system (triangle symbol) with measured sea levels (circle symbol) from the Central Weather Bureau in Taiwan at five stations (shown in Figure 1). The water elevation is relative to the Taiwan Vertical Datum (TWVD2001). Additionally, the peak sea level anomaly is shown in Taiwan during the summer season by the Kuroshio transport current (Gilson and Roemmich, 2002). Detailed information of the observation stations are also described in Lee *et al*. (2013). At Yongan (K4U), on the west side of Taiwan, water level predictions were reasonably accurate, within 0.16 cm of the measured peak surge values. However, at Shihit (K4H), on the east side of Taiwan, the model under-predicted the peak surge by approximately 0.5 m. Shihit was located at the center of Morakot's path from UTC August 6-8, 2009, but the model results hardly show the effect of the storm. Although it is difficult to isolate the cause, errors in meteorological forcing, which can be pronounced during the passage of a typhoon, are one possible explanation for the under-prediction. Systematic problems with the measurement instruments are another possible explanation, but no information is available to confirm or exclude this possibility.

Figure 4 shows changes in significant wave heights, wave period and mean wave direction with current direction over time during the passage of typhoon Morakot as measured at wave gauges in Taiwan. Early on August 7, the storm attained its peak intensity, with winds of 140 km/h (85 mph 10-minute sustained), according to the JMA. The JTWC reported the storm to be slightly stronger, with winds peaking at 150 km/h. Generally, all wave gauges show an increase in both significant wave heights and the wave period at this time. Typhoon Morakot weakened slightly before making landfall in central Taiwan later that day. Approximately 24 hours later, the wave height and period gradually decreased as the storm moved into the Taiwan Strait, weakening to a severe tropical storm before making landfall in mainland China on August 9. At Kenting (WD1), located left of Morakot's path, the model under-predicted the peak wave height by approximately 5 m. In contrast, the model largely agreed with observational data at Suao and Longdong, to the right of the typhoon's path, with a maximum difference of approximately 2.2 m between the model and observed peaks. Because typhoon winds blow counterclockwise, it is possible that the wind is strongly affected by Taiwan's topography on the left side of the typhoon. The grid resolution of the meteorological data (RSM/JMA) is approximately 20 km, and with this coarse resolution, the effect of the terrain may not be fully reflected. The right side of the typhoon may be relatively less affected by topography.

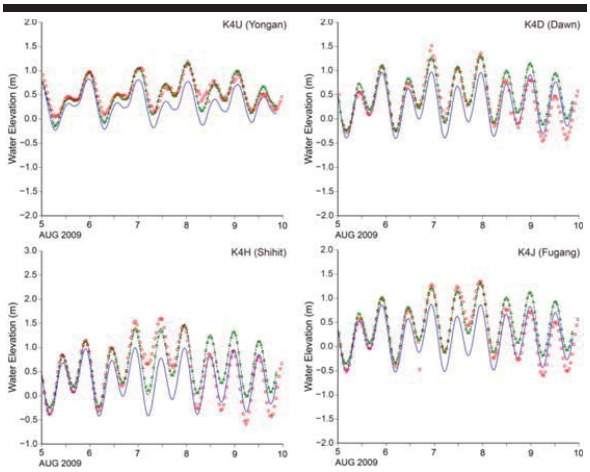

Figure 3. Hydrographs of modeled (dashed line and triangle) and recorded (circle). Water surface elevation relative to the tide level (TWVD2001).

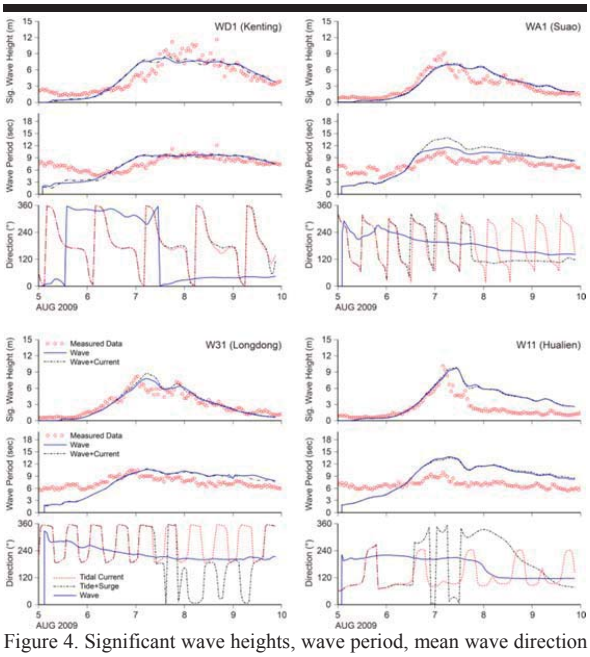

Figure 4. Significant wave heights, wave period, mean wave direction and current direction during typhoon Morakot.

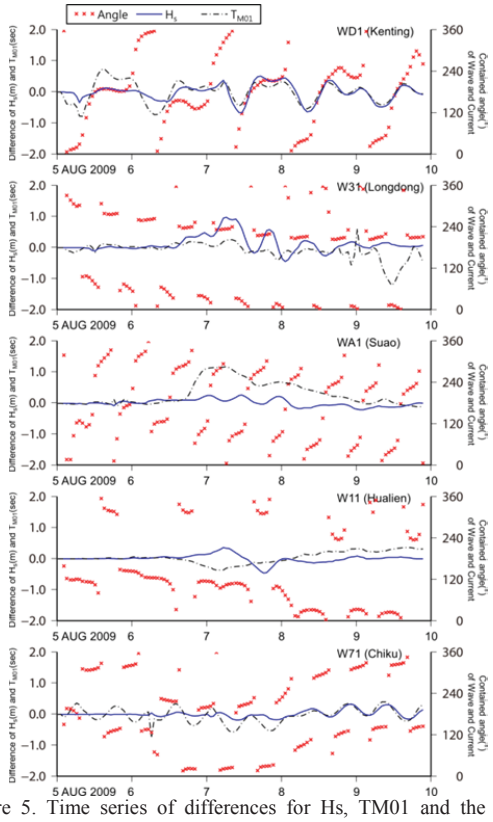

Figure 5. Time series of differences for Hs, TM01 and the angle between mean wave direction and current at each station.

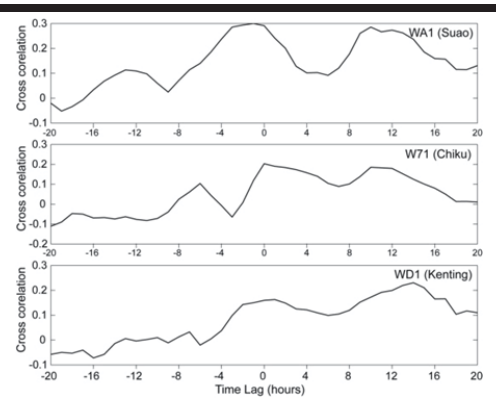

Figure 6. Cross correlation of observed significant wave period and wave-current angle.

DISCUSSION

Ou *et al.* (2002) observed an effect of semi-diurnal tides on waves, known as current-induced refraction. To quantify the impact of the coupling processes on waves, this study uses a series of statistical parameters to compute significant wave heights (H_s) and the mean period (T_{M01}) at each station during the passage of Morakot.

Figure 5 shows the time series of the differences in H_s and T_{M01} between the fully coupled and uncoupled systems. The influence of semi-diurnal tides on waves was clearly observed in the time series of both parameters, but the statistical parameters computed for the mean wave period, T_{M01}, were more sensitive to the tide/surge interaction than those for H_s. The difference in H_s between the fully coupled and uncoupled systems was approximately 2 cm, approximately 5% of the local values. These oscillations occur during strong wind conditions and are in phase with the depth variation of the water column. Positive differences (*i.e.*, higher values computed by the coupled system) in phase with the tidal signals are the main cause of the observed oscillations in the H_s time series. Oscillations induced by the tide/surge effect on T_{M01} were approximately 1.0 s, representing up to 10% of the local values. Stronger modulations were observed during typhoon Morakot, especially before and after the typhoon made landfall, when the current induced wave refraction and directional spreading were more visible. To aid identification of the current induced refraction and directional spreading effects, a cross correlation between the observed significant wave periods and the angle between the mean wave and current directions might be useful.

Figure 6 shows the cross correlation between the observed significant wave periods and the wave-current angle. The analysis period covered two days beginning August 7, when the wave modulation was pronounced. The semi-diurnal tidal effect was clearly observed during the time lags at 0 and 12 hours at Suao and Chiku. Figure 7 depicts the computed energy density spectra at Kenting (south of Taiwan) and Suao (east of Taiwan) every 6 hours. At Kenting station, the frequency dropped to a lower band than that of the uncoupled results at 21:00 UTC on August 7, 2009, when wind wave and current directions were nearly opposite (see Figure 5). After 12 hours, the wind wave and current directions were nearly the same, such that the spectral energies tended to spread out on the high frequency band. At Suao station, the wind wave and current directions were nearly orthogonal, and thus, the frequency moved counterclockwise compared with the uncoupled results at 15:00 UTC on August 8, 2009. The propagation of a wave across a current can be calculated as the sum of the propagation of the wave in the absence of the current and the bodily transport of the wave by the current (Holthuijsen, 2007). If the current is not uniform, the bodily transport of the wave will induce a change in the refraction of the wave.

CONCLUSIONS

The ADCIRC-SWAN coupled system, which uses a single unstructured-mesh, was employed to study the effect of currents on wave-current interaction during the passage of typhoon Morakot. Validation has shown that the model results, including sea levels and wind waves, are in reasonable agreement with observed values at several stations in Taiwan.

Examining differences in the wave height and wave period parameters between the coupled and uncoupled systems, the coupled system reproduces the wave period, T_{M01}, more accurately. The coupling effect on H_s is found to be marginal compared with T_{M01}.

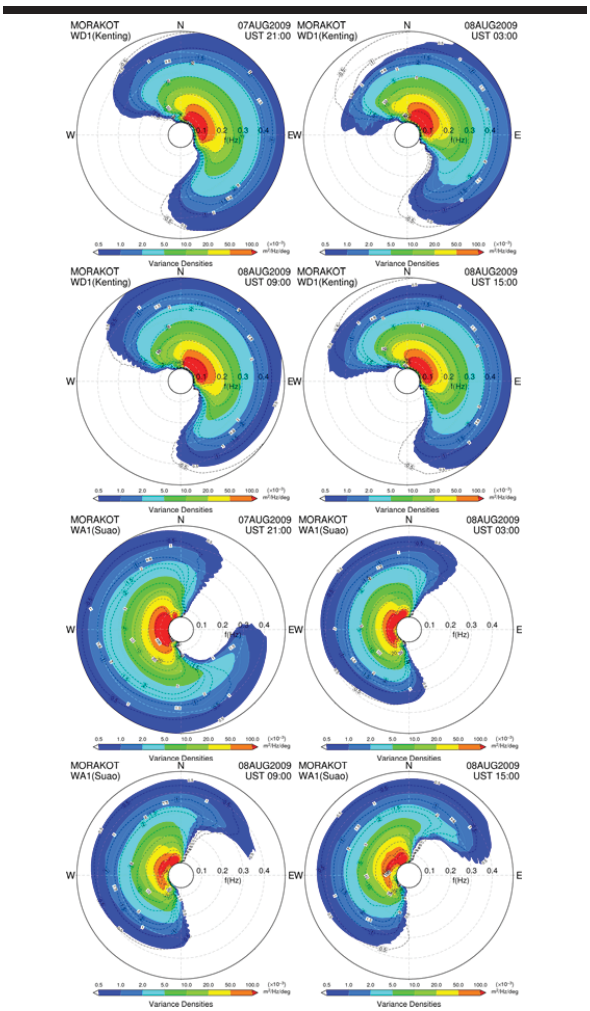

Figure 7. Computed energy density spectrum at Kenting (WD1) and Suao (WA1). Shaded colors represent the energy density considering coupled processes and the wave-only simulation results are shown in contours of dashed lines.

Wave refraction and directional spreading induced a wave-current effect, which was confirmed by the cross correlation between the observed significant wave periods and the wave-current angle. The current-induced refraction was also illustrated in the spectra of the computed energy densities.

In this study, ocean currents, including the north-flowing Kuroshio currents off the eastern coast of Taiwan, are not considered in the ambient currents. The Kuroshio currents in the open sea are considerably stronger than the tidal currents in the shallow water. Therefore, we have to take into account the effects of ocean currents, particularly Kuroshio currents, when interpreting the results of this study.

The ADCIRC-SWAN system was found to be sufficiently appropriate for the hindcast simulation of coupled processes of wave-tide-surges in both the deep open and shelf sea regions. This coupled system is a good starting point for operational wave-tide-surge forecasting and can be easily extended to regional sites of interest without a significant increase in the computational burden. There is, however, an obvious need further refinement and extension of the system. One immediate need is to introduce a diffraction term and higher-order propagation scheme into the spectral wind wave model, especially for application to engineering problems. The system currently uses a set of depth-integrated equations that simplifies the vertical structure of the current, the radiation stress, the surface stress and the bottom boundary layer. A future extension of the system with three dimensions will be needed.

ACKNOWLEDGMENTS

This study was supported by the China-Korea Cooperative Research Project funded by CKJORC, a major project titled “the development of the marine environmental impact prediction system” funded by KIOST and the project of KISTI for the development of a HPC-based management system against national-scale disaster.

LITERATURE CITED

Bilgill, A.; Smith, K.W., and Lynch, D.R., 2006. BatTri: A two-dimensional bathymetry-based unstructured triangular grid generator for finite element circulation modeling. *Computers & Geosciences*, 32(5), 632-642.

Booij, N.; Ris, R.C., and Holthuijsen, L.H., 1999. A third-generation wave model for coastal regions, Part I, Model description and validation. *J. Geoph. Res.*, 104, 7649-7666.

Dietrich, J.C.; Bunya, S.; Westerink, J.J.; Ebersole, B.A.; Smith, J.M.; Atkinson, J.H.; Jensen, R.; Resio, D.T.; Luettich, R.A.; Dawson, C.; Cardone, V.J.; Cox, A.T.; Powell, M.D.; Westerink, H.J., and Roberts, H.J., 2010. A high resolution coupled riverine flow, tide, wind, wind wave and storm surge model for southern Louisiana and Mississippi: Part II − Synoptic description and analyses of Hurricanes Katrina and Rita. *Mon. Weather Rev.*, 138(2), 378−404.

Gilson, J. and Roemmich, D., 2002. Mean and temporal variability of Kuroshio geostrophic transport south of Taiwan (1993–2001). *J. Oceanogr.*, 58, 183–195.

Holthuijsen, L.H., 2007. *Waves in Oceanic and Coastal Waters*. Cambridge University Press.

Lee, H.S.; Yamashita, T.; Hsu, J., and Ding, F., 2013. Integrated modeling of the dynamic meteorological and seasurface conditions during the passage of Typhoon Morakot. *Dynamics of Atmospheres and Oceans*, 59, 1-23.

Luettich, R.A. and Westerink, J.J., 2004. *Formulation and Numerical Implementation of the 2D/3D ADCIRC Finite Element Model, version 44.XX*, http://adcirc.org/adcirc_theory_ 2004_12_08.pdf.

Matsumoto, K.; Takanezawa, T., and Ooe, M., 2000. Ocean tide models developed by assimilating TOPEX/POSEIDON altimeter data into hydrodynamical model: A global model and a regional model around Japan. *Journal of Oceanography*, 56, 567-581.

Ou, S.-H.; Liau, J.-M.; Hsu, T.-W., and Tzang, S.-Y., 2002. Simulating typhoon waves by SWAN wave model in coastal waters of Taiwan. *Ocean Eng.*, 29(8), 947-971.

Journal of Coastal Research	SI	75	1127 - 1131	Coconut Creek, Florida	2016

Simulation of Typhoon Bolaven using Integrally Coupled Tide-Surge-Wave Models based on locally Enhanced Fine-Mesh Unstructured Grid System

Kyeong Ok Kim[†], Jin-Hee Yuk[‡], and Byung Ho Choi[††*]

[†]Marine Radionuclide Research Center
Korea Institute of Ocean Science & Technology
Ansan, Korea

[‡]Disaster Management HPC Technology Research Center,
Korea Institute of Science and Technology
Information, Daejeon, Korea

[††]Department of Civil and Environment Engineering
Sungkyunkwan University
Suwon, Korea

www.cerf-jcr.org

www.JCRonline.org

ABSTRACT

Kim, K.O.; Yuk, J.-H., and Choi, B.H., 2016. Simulation of Typhoon Bolaven using integrally coupled tide-surge-wave models based on locally enhanced fine-mesh unstructured grid system. *In:* Vila-Concejo, A.; Bruce, E.; Kennedy, D.M., and McCarroll, R.J. (eds.), *Proceedings of the 14th International Coastal Symposium* (Sydney, Australia). *Journal of Coastal Research*, Special Issue, No. 75, pp. 1127 - 1131. Coconut Creek (Florida), ISSN 0749-0208.

The integrally coupled wave-tide-surge models based on hydrodynamic and spectral wave models with an unstructured mesh system were tested in the typhoon Bolaven, which hit the Korean Peninsula in 2012 and caused the deaths of 19 victims. The identical and homogeneous mesh allows the physics of wave-circulation interactions to be correctly resolved in both models. The unstructured mesh can be applied to a large domain allowing all energy from deep to shallow waters to be seamlessly followed. The model results were compared with the observations, and the model performance was evaluated. The results show that it is important to incorporate the wave-current interaction effect into coastal areas in the wave-tide-surge coupled model. The model should consider effects of depth-induced wave breaking, wind field, currents and sea surface elevation in the prediction of waves. The resulting modeling system can be used for hindcasting (prediction) and forecasting the wave-tide-surge coupled environments at complex coastlines, shallow water and fine sediment areas, such as around the Korean Peninsula.

ADDITIONAL INDEX WORDS: *Typhoon Bolaven, tide-surge-wave interaction, finite element numerical model.*

INTRODUCTION

The recent introduction of unstructured wave models has made nesting unnecessary, and the coupled system can run on the same unstructured mesh. This identical and homogeneous mesh allows the physics of wave-circulation interactions to be correctly resolved in both models. The unstructured mesh can be applied to a large domain, allowing all energy from deep to shallow waters to be seamlessly followed. There is no nesting or overlapping of structured wave meshes, and no interpolation is required. The waves and storm surge were allowed to develop on the continental shelf and interact with the complex nearshore environment. The integrally coupled wave-tide-surge models were developed based on the hydrodynamic and spectral wave models, ADCIRC-SWAN and SELFE-WWMII. The two model systems use an unstructured mesh grid, but different numerical schemes and wave modules are used. The major difference of the hydrodynamic parts are that ADCIRC solves the 2-dimensional finite element equation designed in the focused coastal water dynamics in an explicit scheme, and SELFE solves the 3-dimensional equation, which can be used in 2-dimensions using one vertical layer in an implicit scheme. In this study, the tide, surge and wave were simulated to evaluate the model performances considering the tide-surge-wave interaction and coexistence with the local fine-mesh using two modeling systems during the typhoon Bolaven, which hit the Korean Peninsula in 2012 and caused the deaths of 19 victims.

METHODS

The ADvanced CIRCulation (ADCIRC) model is a finite-element hydrodynamic model based on the generalized wave continuity equation (GWCE) to render a smooth, noise-free, dampened solution. ADCIRC was developed to properly resolve the complex coastline and bathymetry of shallow water that results from artificial structures. ADCIRC was able to attain some success on large-scale tide, storm surge, and inundation simulations (Westerink *et al.*, 1994).

SWAN (Simulating WAves Nearshore) predicts the evolution in geographical space and time of the wave action density spectrum as governed by the action balance equation (Booij *et al.*, 1999). The associated SWAN parameterizations are provided by Booij *et al.* (1999), with all subsequent modifications as present in version 40.72, including the phase-

DOI: 10.2112/SI75-226.1 received 15 October, 2015; accepted in revision 15 January, 2015.
*Corresponding author: bhchoi.skku@gmail.com
©Coastal Education and Research Foundation, Inc. 2016

decoupled refraction-diffraction. The unstructured-mesh version of SWAN implements an analog to the four-direction Gauss-Seidel iteration technique employed in the structured version, and it maintains SWAN's unconditional stability (Zijlema 2010). SWAN computes the wave action density spectrum at the vertices of an unstructured triangular mesh and orders the mesh vertices to sweep through them and update the action density using information from neighboring vertices.

The coupled ADCIRC-SWAN model is highly scalable and seamlessly integrates the physics and numerics from deep ocean to shelf to floodplain. Waves, water levels and currents are allowed to interact in complex problems and in a way that is accurate and efficient to thousands of computational cores. ADCIRC-SWAN is well suited for the simulation of hurricane waves and surges (Dietrich, 2010).

SELFE (A Semi-implicit Eulerian-Lagrangian Finite-Element; Zhang and Baptista, 2008) is an open-source community-supported modeling system, based on unstructured grids and designed for the effective simulation of 3D baroclinic circulation. SELFE uses a semi-implicit finite-element Eulerian-Lagrangian algorithm to solve the Navier-Stokes equations (in either hydrostatic or non-hydrostatic form), written to realistically address a wide range of physical processes and of atmospheric, ocean and river forcings. The numerical algorithm is high-order, stable and computationally efficient.

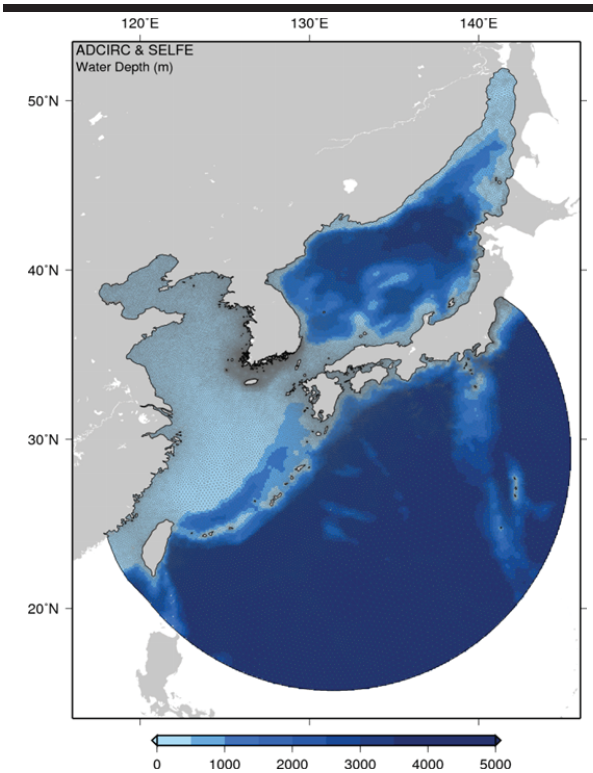

Figure 1. Mesh system for FEM numerical models

A new generation of the wind wave model (WWM) solves the Wave Action Equation on spatially unstructured grids (Roland *et al.*, 2012). This unstructured wind-wave model allows direct coupling with the circulation model. Initially, the finite element method (FEM) was implemented into the first version of WWM. However, this scheme is non-monotone and results in oscillations when strong gradients in the solution are present. To remedy this behavior, alternative numerical schemes have been implemented into the WWMII. Because the WWMII employs a Residual Distribution method for the discretization of the model area (unstructured mesh), the resolution can be enhanced near-shore and relaxed in deep water, allowing the model to simulate the wave evolution efficiently. Teng (2012) introduced a new community-driven, parallel, and innovative numerical framework that can be utilized to study the wave-current interaction processes based on unstructured meshes in geographical space. The wind wave model WWMII was coupled with the ocean circulation model SELFE, accounting for the wave-induced momentum flux from waves to currents, based on the radiation stress formulations, the wave boundary layer, surface mixing and the current-induced Doppler shift for waves.

Figure 1 depicts the whole mesh system in this study for FEM numerical models with approximately 100,000 nodes and 200,000 elements.

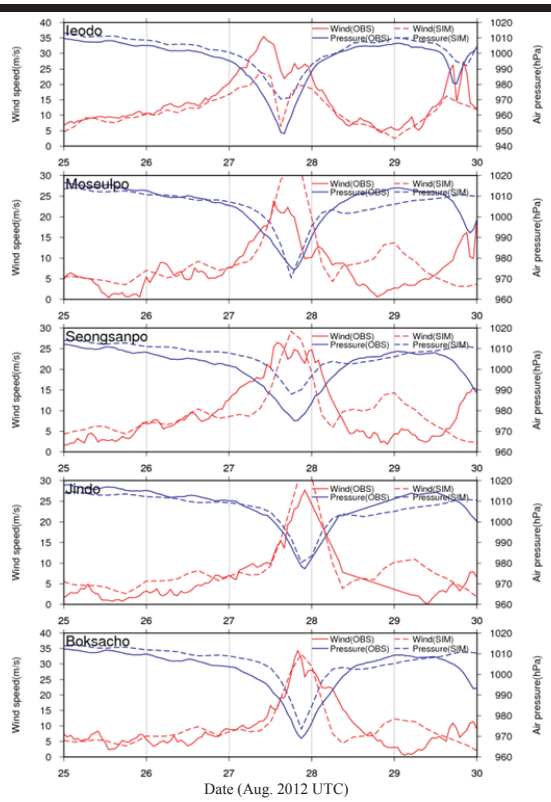

Figure 2. Comparison of the 10 meter wind speed and sea level pressure measured by the KMA observation system and simulated by the Holland model and NCEP dataset using the blending scheme.

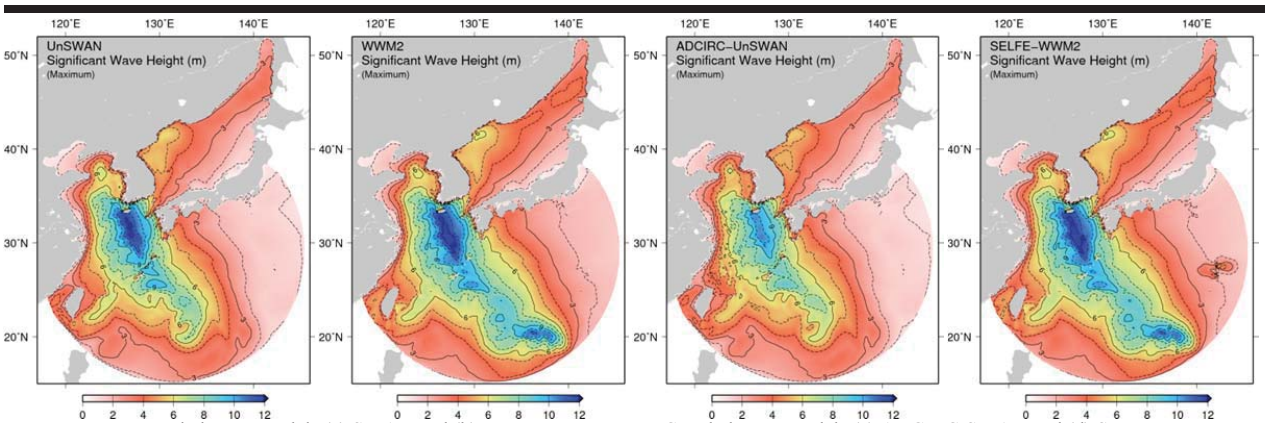

Uncoupled wave models (a) SWAN and (b) WWMII Coupled wave models (c) ADCIRC-SWAN and (d) SELFE-WWMII

Figure 3. The maximum significant wave height computed by uncoupled and coupled wave models during the typhoon event.

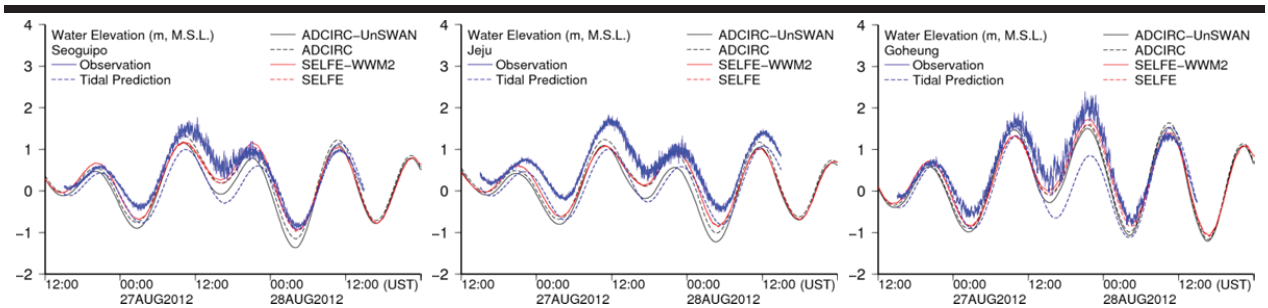

Figure 4. Observed and computed water elevations in Seoguipo, Jeju and Goheung.

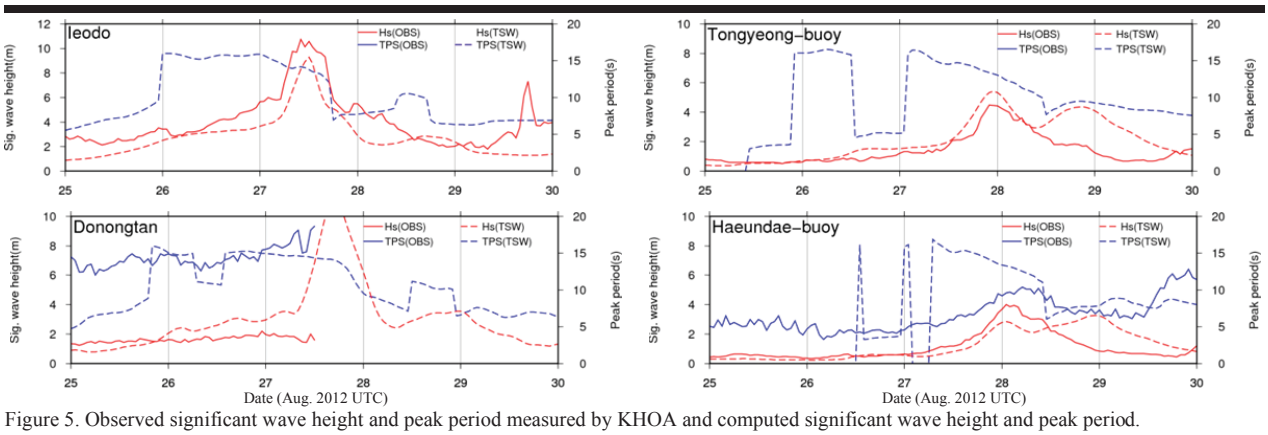

Figure 5. Observed significant wave height and peak period measured by KHOA and computed significant wave height and peak period.

RESULTS

Typhoon Bolaven was regarded as the most powerful storm to strike the Korean Peninsula in nearly a decade with wind gusts measured up to 50 m/s. Although Bolaven struck the Ryukyu Islands as a powerful typhoon, damage was less than expected in Japan. In South Korea, 19 people were killed by the storm. Many buildings were damaged and approximately 1.9 million homes were left without power. Losses in the country reached 420 billion won, the majority of which was due to destroyed apple orchards. Significant damage also occurred in North Korea where at least 59 people were killed and 50 others were reported missing. Additionally, 6,700 homes were destroyed. The wind and pressure field during Typhoon Bolaven was generated by the blending method (Kim, 2015). Figure 2 shows the comparison of the 10 meter wind speed and sea level pressure measured by the KMA observation system and simulated by the Holland model and the NCEP dataset using the blending scheme.

Figure 3 shows the maximum distributions of the significant wave heights computed by uncoupled (SWAN and WWMII) and coupled (ADCIRC-SWAN and SELFE-WWMII) wave models during the typhoon event. The significant wave height of SWAN was reduced after coupling with the hydrodynamic model, ADCIRC. However, the coupling results of SELFE-WWMII show similar results with the WWMII case. The negative coupling effect to wave height were observed in the SWAN models, but the effective differences were not observed in WWMII models.

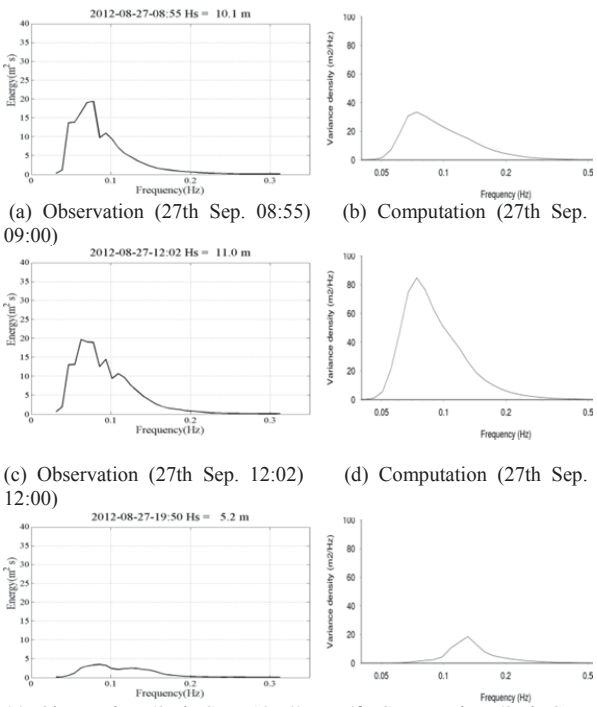

(a) Observation (27th Sep. 08:55) (b) Computation (27th Sep. 09:00)

(c) Observation (27th Sep. 12:02) (d) Computation (27th Sep. 12:00)

(e) Observation (27th Sep. 19:50) (f) Computation (27th Sep. 20:00)

Figure 6. Observed 1-dimensional wave energy spectrum in Ieodo and simulated wave energy using the ADCIRC-SWAN.

Figure 4 shows the computed results of water elevation using the coupling and single hydrodynamic models in Seoguipo, Jeju and Goheung. Models show similar results for water elevations to the positive effects in coupled models. Figure 5 shows the observed significant wave height and peak period in the Ieodo station, Tongyeong buoy, Donaongtan and Haeundae buoy and was computed using ADCIRC-SWAN coupled model. The wave heights and periods were well-simulated in the open ocean observatory. Figs. 6 and 7 are the observed 1 and 2 dimensional wave spectrums (27th September 08:55, 12:02 and 19:50) in the Ieodo observation station (Chae *et al.*, 2013) and the simulated wave spectrum (27th September 09:00, 12:00 and 20:00) using ADCIRC-SWAN coupled model.

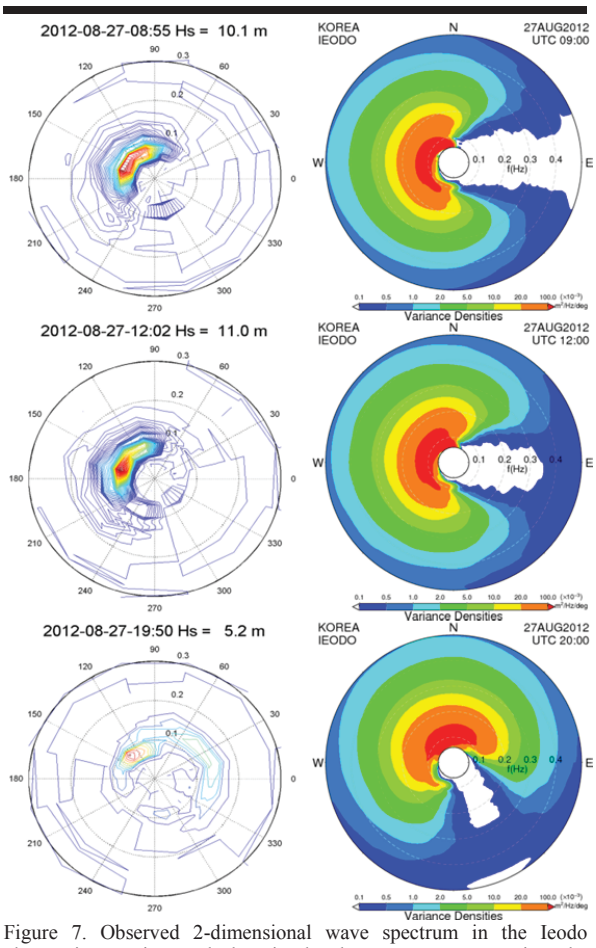

Figure 7. Observed 2-dimensional wave spectrum in the Ieodo observation station and the simulated wave spectrum using the ADCIRC-SWAN.

DISCUSSION

For the locally enhanced mesh system, the regions of Gageo Island (offshore southwestern corner of the Korean Peninsula) and south of Jeju Island (Gangjeong port and Seogwipo port) were refined in the whole YS-ECS mesh system (Figure 2).

The explicit and implicit numerical methods were selected to address the problem. The implicit methods use less computational resources with a comparably large time step and provided stable computation results. However, unexpected abnormal values resulted when an inappropriate time step was used. The time step is strongly dependent on the cell size and the water depth of the model domain.

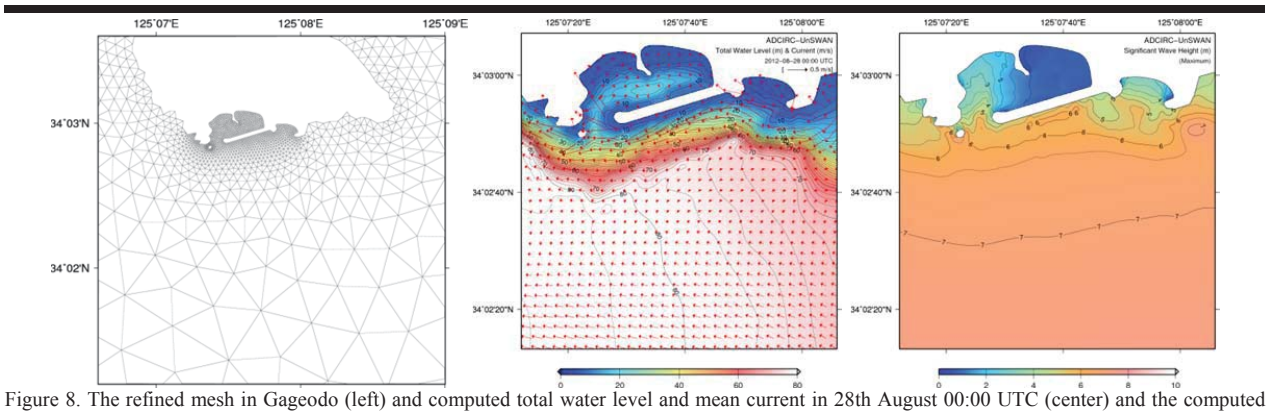

Figure 8. The refined mesh in Gageodo (left) and computed total water level and mean current in 28th August 00:00 UTC (center) and the computed maximum significant wave height (right) during the Typhoon Bolaven event using ADCIRC-SWAN coupled model near Gageodo. The refined mesh is overlaid.

When the numerical integration truncation error is ignored, the explicit method can use the smallest time step that satisfies the CFL condition, but contradiction exists in the implicit method to set the time step. A small time step is necessary to resolve the local fine mesh area, but this small time step creates unexpected results in the outer large mesh area. We could not determine the valid time step resolving fine and coarse meshes at the same time in the SELFE-WWM model.

Figure 8 shows the computed total water level and mean current on 28th August 00:00 UTC (up) and the computed maximum significant wave height (down) during the Typhoon Bolaven event using the ADCIRC-SWAN coupled Model near Gageodo.

CONCLUSIONS

The model results were compared with the observations, and the model performance was evaluated. The resulting modeling system can be used extensively for the prediction of the typhoon surge and usual barotropic forecast. The results show that incorporating the wave-current interaction effect into coastal areas is important in the wave-tide-surge coupled model. Additionally, the model should consider the effects of depth-induced wave breaking, wind field, currents and sea surface elevation in wave predictions. In particular, we found that the wind wave significantly enhances the current and surge elevation.

The local fine mesh system was tested using the ADCIR-SWAN coupled model near Gageodo. The resulting modeling system can be used for hindcasting (prediction) and forecasting the wave-tide-surge coupled environments at complex coastlines, shallow water and fine sediment areas, such as around Korean Peninsula.

ACKNOWLEDGMENTS

This study was supported by the China-Korea Cooperative Research Project funded by CKJORC, as well as a major project titled the development of the marine environmental impact prediction system funded by KIOST, the development of the safe voyage planning system for vessels operating by KIMST, and the project of KISTI for the development of HPC-based management system against national-scale disasters.

LITERATURE CITED

Booij, N.; Ris, R.C., and Holthuijsen, L.H., 1999. A third-generation wave model for coastal regions 1. Model description and validation. *J. Geophys. Res.*, 104(C4), 7649-7666.

Chae, J.W.; Jeong W.M.; Jun, K.C.; Choi, J.Y.; Park, W.S., and Park, W.K., 2013. Extreme waves generated by typhoon Bolaven (201215) in southern Korean waters. *Proceedings of the 7th International Conference on Asian and Pacific Coasts* (Bali, Indonesia), pp. 996-1001.

Dietrich, J.C., 2010. Development and Application of Coupled Hurricane Wave and Surge Models for Southern Louisiana, University of Notre Dame, Ph.D. dissertation, 310p.

Kim, K.O., 2015. Typhoon Storm Surge Simulation for Typhoon Haiyan. *J. Int. Dev. Coop.*, 21, 17-25.

Roland, A.; Zhang, Y.J.; Wang, H.V.; Meng, Y.; Teng, Y.-C.; Maderich, V.; Brovchenkod, I; Dutour-Sikiric, M., and Zanke, U., 2012. A fully coupled 3D wave-current interaction model on unstructured grids, *J. Geophys. Res.*, 117, C00J33, doi:10.1029/2012JC007952.

Teng, Y., 2012. Developing an Unstructured Grid, Coupled Storm Surge, Wind Wave and Inundation Model for Super-regional Applications. The College of William and Mary in Virginia, Ph.D. dissertation, 300p.

Westerink, J.J.; Luettich, R.A., and Muccino, J., 1994. Modeling tides in the western North Atlantic using unstructured graded grids. *Tellus*, 46A, 178-199.

Zhang, Y.-L. and Baptista, A.M., 2008. SELFE: A semi-implicit Eulerian-Lagrangian finite-element model for cross-scale ocean circulation. *Ocean Modelling*, 21(3-4), 71-96.

Zijlema, M., 2010. Computation of wind-wave spectra in coastal waters with SWAN on unstructured grids. *Coastal Engineering*, 57(3), 267-277.

Journal of Coastal Research	SI	75	1132 - 1136	Coconut Creek, Florida	2016

Probabilistic Coastal Storm Surge Analyses using Synthesized Tracks Based on Historical Typhoon Parameters

Hyeon-Jeong Kim[†] and Seung-Won Suh[†*]

[†]Department of Ocean Science and Engineering
Kunsan National University
Kunsan, Republic of Korea

www.cerf-jcr.org

www.JCRonline.org

ABSTRACT

Kim, H.J. and Suh, S.W., 2016. Probabilistic coastal storm surge analyses using synthesized tracks based on historical typhoon parameters. *In:* Vila-Concejo, A.; Bruce, E.; Kennedy, D.M., and McCarroll, R.J. (eds.), *Proceedings of the 14th International Coastal Symposium* (Sydney, Australia). *Journal of Coastal Research*, Special Issue, No. 75, pp. 1132 - 1136. Coconut Creek (Florida), ISSN 0749-0208.

Natural hazards driven by storm surge increasingly threaten low-lying coastal areas and infrastructures. Although several attempts have been made to minimize coastal hazards by incorporating probabilistic, deterministic, and hybrid analyses, the nonlinear interactions between the tide and surge makes difficulties in storm surge analyses. In this study, an efficient approach to assess the vulnerability to storms surges is developed by applying a random generation scheme called the Topical Cyclone Risk Model (TCRM). The maximum radii and wind speed of synthetic storms were adjusted with central pressure based on historical track data to represent the most appropriate probability. A total of 177,244 storms were synthesized by a fully automated procedure using a Perl script; these acted as forcing in ADvanced CIRCulation (ADCIRC) model incorporating random tidal motion. By comparing the results of the hypothetical typhoon surges with observed data showed that the suggested synthetic storms based on historical tracks satisfactorily reproduce probabilistic surge elevations and show almost similar characteristics in real situation. Moreover, the simulation results showed typhoons heading to the west coast could cause higher surge heights than those landing on the south coast because of superposition of high tidal fluctuations in a macro-tidal environment. Thus, this method can be applied to coastal hazards mitigation measures against return periods and future climate change. However, parameters such as moving speed and shape of the typhoon vortex would be important in surge simulations; hence, more appropriate treatment of these characteristics should be studied in future research.

ADDITIONAL INDEX WORDS: *TCRM, ADCIRC, probabilistic storm generation, typhoon characteristics.*

INTRODUCTION

Super storms such as Hurricane Katrina in 2005, Sandy in 2012, and Typhoon Haiyan in 2013 repeatedly remind us of the importance of preparedness against storm surges. Moreover, global warming causes not only a rise in the sea level but may also intensify storm strength. Typhoon Haiyan developed in the North Western Pacific Sea and landed at the province of eastern Samar, Philippine; it was the strongest typhoon ever recorded in terms of one-minute sustained wind speed of 315 km/h. According to the study by Kossin *et al*. (2014), the strongest genesis location of tropical cyclones, including typhoons and hurricanes, has been moving to higher latitudes from near the equatorial area. This kind of unexperienced environmental change could lead to greater coastal disasters on the mid-latitude area due to strengthening of storms in the future.

To minimize uncertainty, several studies providing a probabilistic understanding in storm surge prediction were conducted. Needham *et al*. (2012) analyzed frequency of surge height on the Gulf coast based on recorded surge data by using Pareto, Gumbel, beta-P distributions, and different regression methods. They showed that the surge height of frequency could be altered when using different methods. Suzuki *et al*. (2014) studied variability of central pressure depression (P_c), due to global warming. Atkinson *et al*. (2013) simulated storms with similar meteorological characteristics to examine the coastal features influenced by storm surges responding to increased sea levels. Moreover, they also noted that because of the complexities of storm-surge dependency on storm strength, track, and local topography, there is no one-size-fits-all response to sea-level rise descriptive for all locations. Lin *et al*. (2010) studied flood risk assessment on New York City for the return periods of 100 and 500 years based on 7,555 synthesized storms. They applied the Markov chain method (Emanuel *et al*., 2006) to allow for the future conditional probability to be dependent on the present condition and to be independent of the past environment. Hall and Jewson (2007) proposed a scheme for generating statistically synthesized storms by incorporating a normal distribution treatment for best track.

In this study, to analyze coastal hazards induced by storm surges, a series of synthetic storms were generated by incorporating a probabilistic method to overcome the limited historical data. Because randomly generated storms could show some deviation with historical track characteristics; thus, moderately modified values were assigned through correlation analyses in terms of probability distribution function based on historical storms. In multiple simulations, an automated Perl

DOI: 10.2112/SI75-227.1 received 15 October, 2015; accepted in revision 15 January, 2015.
*Corresponding author: suh@kunsan.ac.kr
©Coastal Education and Research Foundation, Inc. 2016

script command was applied to generate numerous tracks and analyze results.

METHODS

The characteristics of a synthesized storm mainly depend on the type of corresponding probability distribution function (PDF). In this study, to minimize uncertainty in purely statistically generating storm, we proposed a semi-empirical method in generating synthetic storms through statistical analyses of historical typhoon data to find a moderate PDF.

Although, the track generation scheme of TCRM (Summons and Arthur, 2011) follows the statistical Monte Carlo method, it would not reasonably consider regional or historical variations of storm characteristics at an optimum level. However, according to Vickery *et al*. (2000) and Willoughby *et al*. (2006), the radius at which the maximum wind occurred (R_{max}) has some relation with maximum wind speed (V_{max}) and, the latitude of the cyclone's track (φ). Thus, these relations should be incorporated after analyzing storm characteristics. Most typhoons affecting the Korean coast originated in the North Western Pacific (NWP) region and had an inflection point between latitudes 20°N–30°N. Thus, to find the most appropriate PDF, we analyzed every 1° for that region.

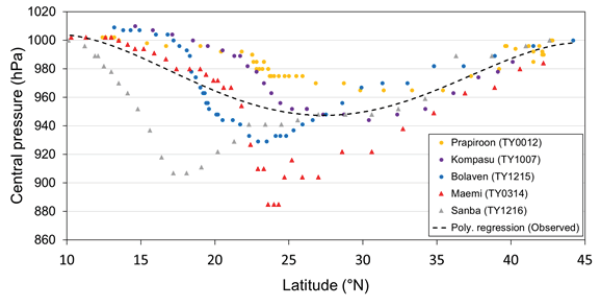

Figure 1. Variation in central pressure depressions with respect to latitude for the most significant typhoons that hit Korea.

As shown in Figure 1, most of the influential typhoons had a strong central pressure depression between the intervals of 20°N–30°N. For example, typhoon Maemi (TY0314) which is the strongest typhoon recorded in the history in Korea, marked P_c of 885 hPa at 24°N and attacked the south coast causing severe damages. Hence, defining moderate probabilistic distribution of P_c on those latitudes should be carefully analyzed, since it is directly correlated to V_{max} and R_{max} as suggested by Vickery *et al*. (2000) and Willoughby *et al*. (2006).

In probabilistic analyses using generated storm surges, it is recommended that multiple synthetic storms are provided to diminish uncertainties in a small group of generation. Lin *et al*. (2010) generated 7,555 storms. After the initial assessment via a relatively light model that had low accuracy, they applied a more complex and accurate surge model, ADCIRC (Luettich *et al*., 1992), to the selected storm tracks to find the vulnerability of low-lying coastal area in the future climate change case. The total number of storms varies according to research purposes; however, in the study by Berg (2013) they noted that 1 million of generation is recommended. Thus, at least several thousands of synthetic storms are required in the analyses of a probabilistic storm.

After several trials to provide statistically sufficient synthetic storm surges, 177,244 storms were generated to assign P_c, V_{max}, and R_{max}. In our simulation, ADCIRC was considered as the basic surge modeling under an unstructured grid named NWP-G57k, which has 56,617 vertices covering the NWP and can efficiently simulate tide and surge (Suh *et al*., 2015). Owing to the strong tidal current importance on surges in a macro-tidal environment, every synthetic storm track should be run by considering arbitrary tidal fluctuation, by which a combination of tidal coupling can be incorporated in probabilistic analyses. To run multiple series of storm surges, an automation scheme that includes not only the whole procedure of the typhoon track but also an analysis of the simulated results, should be considered to minimize the computational burden and maximize accuracy. To maintain computation efficiency, we used a Perl script file to run a series of storm surge computations on a parallel processor. At first, the tide is randomly simulated for 61 days from cold start. Then, the results for the last 30 days were archived for use in hot start condition in forthcoming storm surge simulation. After completion of a series of storm surge simulations, pure surge heights were extracted by eliminating the synthesized tide during that period.

RESULTS

The surge appearance on the west and south coast of Korea is somewhat different because of geophysical characteristics such as shallow depth, macro-tidal environment, and Kelvin effect along the west coast of South Korea (WCK). We categorized historical typhoons attacking as passing the influencing zones in East China Sea and Yellow Sea entrances as shown in Figure 2. As seen in the figure, 83.3% of the total typhoons passed southern boundaries, S1 and S2. In addition, 20.6% and 26.3% of the total typhoons affect the west and south coast, respectively. Among the historical typhoons, Bolaven (TY1215), Kompasu (TY1007), and Prapiroon (TY0012) affected typically the WCK passing the boundaries E2 and N1. Especially 1.52 m of surge height at the Incheon tidal station, as shown in Figure 2 occurred due to typhoon Bolaven passing. However, generated synthetic storms are mostly passing the S1 and S2 boundary; furthermore, no tracks were found through W1 and W2. However, focusing only on WCK, a comparison of track appearances for synthetic and best tracks crossing the E2 and N1 boundaries showed 11.4%, 15.8%, and 6.7%, 4.8%, respectively. Thus, it can be concluded that the generated tracks are acceptable, as they statistically hit the historical tracks.

To apply synthetic typhoons by TCRM with high reliability, the historical cyclone characteristics need to be captured. Because it was designed following statistical methods, it may have limitations in representing a real situation. Thus, we analyzed best track data to represent typical characteristics; V_{max}, R_{max}, and the shape parameter especially in the zones from 20°N to 30°N of latitude where the typhoon track has an inflection point turning to north-east, and finally hitting Korea. Moreover, parameter comparisons were conducted with empirical formulas suggested by Willoughby and Rahn (2004), Willoughby *et al*. (2006), and Vickery and Wadhera (2009).

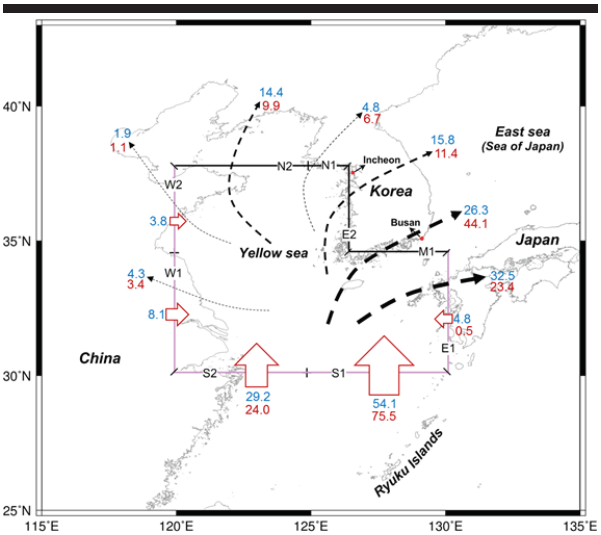

Figure 2. Frequency of typhoon passing tracks. Blue and red colors indicate historical and synthetic tracks, respectively.

Plotted results on the relation between R_{max} and P_c and V_{max} and P_c for historical data are shown in Figure 3a and 3b. Results showed that V_{max} decreased with a high value of P_c. Furthermore, the results showed a second-order polynomial regression following Vickery and Wadhera (2009) with correlation coefficients of 0.99, as shown in Figure 3a. However, as seen in Figure 3b, R_{max} did not show a distinct relationship with P_c. A weaker storm normally has large R_{max}, but the small size of the storm would not coincide with lower central pressure. On the other hand, V_{max} vs P_c is a highly inverse correlation, *i.e.*, low central pressure of storm yields high wind speed.

Additionally, the relationship of R_{max} with P_c showed an exponential variation and low correlation at $R^2 = 0.38$, as shown in Figure 3b. This poor correlation might have been because of less historical data available in the range of P_c 920 to 980 hPa corresponding with R_{max}. Central pressures of storms in that range assume importance in analyzing storm surge hazards in Korea. Moreover, it is noted that R_{max} values following Willoughby *et al*. (2006), as expressed in Equation (1), are normally underestimated, whereas R_m □ values as in Equation (2) by Vickery and Wadhera (2009) are overestimated when P_c is greater than 980 hPa. Comparison results of R_{max} for the historical typhoons, Maemi (TY0314), Kompasu (TY1007), Bolaven (TY1215), and Sanba (TY1216), showed almost coinciding patterns with fitted values within 5 km of discrepancies, especially for the range of 940 to 980 hPa of P_c.

$$R_{max} = 46.4exp(-0.0155V_{max} + 0.0169\varphi) \quad (1)$$

$$R_{max} = exp(3.015 - 6.291 \times 10^{-5}\Delta p^2 + 0.0337\varphi) \quad (2)$$

where, φ means latitude of typhoon location and Δp represents central pressure deficit.

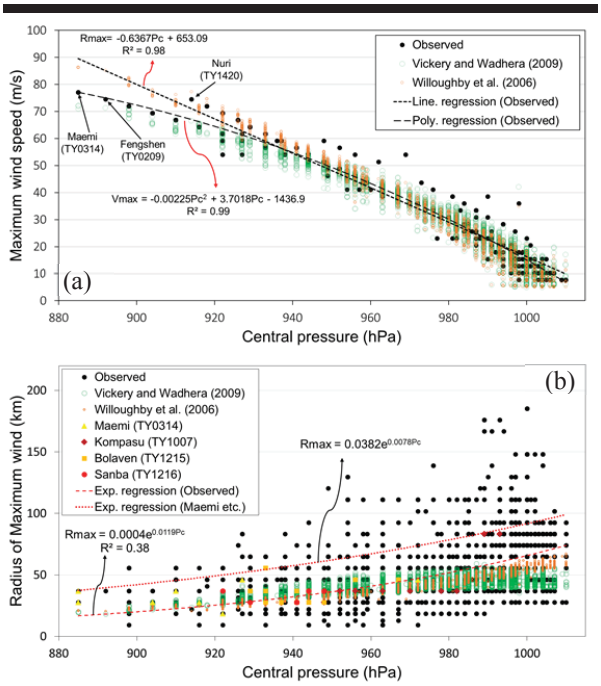

Figure 3. Comparison of historical typhoon characteristics with corresponding values suggested by relevant studies for (a) V_{max} vs P_c, and (b) R_{max} vs P_c.

To quantitatively compare the generated surges with historical recorded surge heights, the Incheon and Busan stations were selected as the representative locations for the two typical storms; the typhoons Bolaven in 2012 and Maemi in 2003 have influenced on the west and south coasts, respectively. Among the 177,244 cases of generated storm surges, we selected the five most similar storm surges for the corresponding typhoons. The recorded maximum surge height at the Incheon station was 1.52 m induced by typhoon Bolaven, whereas the generated surges were in the range of 1.1 to 1.57 m. Typhoon characteristics based on the best track were 960 hPa, 39 km, and 45 $m \cdot s^{-1}$ at landfall time, whereas the generated characteristics were in the range of 952–975 hPa, 36–48 km, and 34–48 $m \cdot s^{-1}$ for P_c, R_{max}, and V_{max}, respectively. At the Busan station, the surge elevation was 0.99 m because of the passing of typhoon Maemi, whereas the generated surge heights for five synthetic storms were in the range of 0.61 to 0.97 m. The characteristics of storms according to the best track were 950 hPa, 19 km, and 50 $m \cdot s^{-1}$ at landfall time; on the other hand, the generated values were 929–967 hPa, 27–42 km, and 40–60 $m \cdot s^{-1}$ for P_c, R_{max}, and V_{max}, respectively. Storm tracks, characteristics according to storm locations, and comparisons of surge elevation are shown in Figure 4. Not only the reproduced storm characteristics but also the simulated surge heights are in good agreement with the historical typhoon records. Thus the suggested synthesized storm surge generation scheme could be applied in coastal hazard preparedness with satisfactory results.

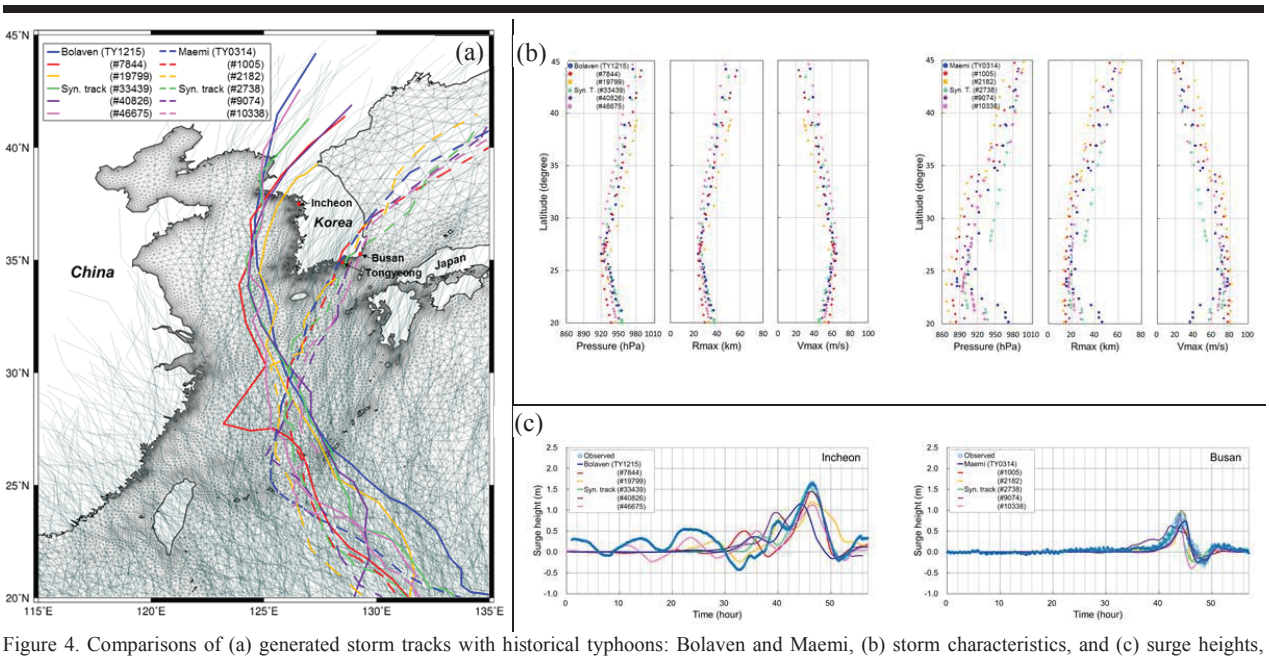

Figure 4. Comparisons of (a) generated storm tracks with historical typhoons: Bolaven and Maemi, (b) storm characteristics, and (c) surge heights, where synthesized storm numbers with corresponding values are represented by different colors.

DISCUSSION

There are several probabilistic methods for storm generation that account for different PDFs such as log or Weibull distributions for the maximum wind speed in the study area (Emanuel *et al*., 2006). However, such approaches have some limitation arising from the shape of tail because of assumed PDF. Moreover, generating synthesized storms based on insufficient historical data could yield some mismatch due to insufficient available wind or related data. To improve the reliability of generated synthetic storms, we compared typhoon parameters of the best tracks in terms of relations of R_{max} and V_{max} with P_c suggested by Willoughby *et al*. (2006) and Vickery and Wadhera (2009). In addition, in their expressions, another important parameter B, which represents typhoon vortex shapes, was expressed as R_{max} or V_{max} with corresponding latitudes of typhoon centers. However, if such deterministic shape parameter relationship is adopted in surge simulation regardless of high uncertainty, it may not reproduce appropriate V_{max} or R_{max} and may cause unwanted results. Thus, a modification is necessary by representing the time-varying shape parameters.

We evaluated storm surge height variations by assigning generated R_{max} in accordance with typhoon Sanba. The generated surge heights at the Tongyeong tidal station as in Figure 4 were 0.84 m with an R_{max} of 39 km. These can be compared with the recorded surge height of 0.85 m and the corresponding R_{max} of 37 km at landfall. However, application of an even larger R_{max} of 68 km (larger by 84%) showed only an 11.8% reduction in surge heights (0.75 m). Thus, it can be considered that surge heights are not sensitive to R_{max}. Even though several sensitivity tests were conducted by changing the parameter in synthetic storm analyses, it should be intensively studied further because surge heights are affected by several uncertain ambient environments.

In the statistical generation of storms using TCRM, P_c followed kernel density estimation based on assigned historical characteristics. Sufficient historical data for P_c with R_{max} could give high reliability; otherwise less data might yield more uncertainties. To overcome such limitation, we modified the probability of P_c corresponding latitudes of typhoon in accordance with the analyzed results of P_c of best track data, which is more close to generalized extreme value distribution. Thus, it is necessary to define a moderate probability density function in order to effectively analyze surge elevation by synthetic tracks.

In this study, V_{max} and R_{max} with P_c from the best fitted relation according to Weibull-type PDF were applied in generating 177,244 storms. The analysis results showed that the probabilistic generation method could reproduce almost similar storms to historical typhoons; hence, those were applied in the west and south coasts to assess hypothetical storm surges. Among the generated synthetic storms, the #7844 hypothetical typhoon yielded a surge height of 1.43 m at Incheon station with a central pressure of 966 hPa; in addition, the #2738 typhoon with a P_c of 967 hPa could raise the water surface by 0.61 m at Busan station. By comparison, in general, typhoons heading to the west coast could cause higher surge heights than those landing on the south coast. Thus, in a given condition of typhoons, a hazardous coastal situation may be severe when tracks enter the Yellow Sea and finally affect the west coast. Such a situation may originate from the macro-tidal environment in the shallow depth, which could yield a superposition of water level coinciding with the flood tide. More detailed study will be required to clarify the origins.

CONCLUSIONS

To analyze coastal storm surges in terms of statistical return periods, reliable synthetic storm generation is required. In this study, we adopted TCRM, a tool for cyclone generation based on kernel density estimation. However, randomly generated storms showed slightly deviated characteristic compared with historical tracks. Thus, it is needed to assign modified values representing typical probability distribution function through correlation analyses of P_c regarding past track data, and furthermore by referring to the empirical prediction equations of previous studies. Based on the analysis results, the central pressure related to the location of typhoon's latitude is an important factor in not only historical tracks but also generated storms. Thus, the typhoon locations between the middle of 20°N to 30°N, where most inflection points of typhoon tracks developed and where finally storm surge elevations in Korea have dominated, should be treated intensively because latitude of typhoon could be one of the most significant characteristics affecting P_c and V_{max}. However, a limited number of historical typhoons were referred in this study; thus, further study should be conducted to validate the approach taken. Moreover, the moving speed and shape parameter of typhoon vortices would be important factors; thus more profound approaches to evaluating these characteristics should be studied in further research. Comparison of results of storm surge elevation by probabilistically synthesized typhoons with observed surge elevation showed that the probabilistic storms accounting for historical characteristics satisfactorily reproduce realistic surge elevations. Thus, the study results can be applied in coastal hazard mitigation. Moreover, owing to the whole automatic procedure using a script, from storm generation to surge analyses, the computation can be easily conducted on an efficiently designed unstructured grid by using the ADCIRC model; thus this proposed approach can be applied in the analyses of vulnerability assessment in low-lying coastal areas, especially considering sea-level rise.

ACKNOWLEDGMENTS

This research is a part of the projects entitled "Development of coastal erosion control technology" and "Countermeasure system against hazards of typhoons and tsunamis in harbor zones—Stage 2" funded by the Ministry of Oceans and Fisheries, Korea.

LITERATURE CITED

Atkinson, J.; McKee Smith, J., and Bender, C., 2013. Sea-level rise effects on storm surge and nearshore waves on the Texas coast: Influence of landscape and storm characteristics. *Journal of Waterway, Port, Coastal, and Ocean Engineering*, 139(2), 98-117.

Berg, N.J., 2013. On the influence of storm parameters on extreme surge events at the Dutch coast. Enschede, The Netherlands: University of Twente, Master's thesis, 128p.

Emanuel, K.A.; Ravela, S.; Vivant, E., and Risi, C., 2006. A statistical deterministic approach to hurricane risk assessment. *Bulletin of the American Meteorological Society*, 87(3), 299-314.

Hall, T.M. and Jewson, S., 2007. Statistical modelling of North Atlantic tropical cyclone tracks. *Tellus A*, 59(4), 486-498.

Kossin, J.P.; Emanuel, K.A., and Vecchi, G.A., 2014. The poleward migration of the location of tropical cyclone maximum intensity. *Nature*, 509, 349-352.

Lin, N.; Emanuel, K.A.; Smith, J.A., and Vanmarcke, E., 2010. Risk assessment of hurricane storm surge for New York City. *Journal of Geophysical Research*, 115, D18121.

Luettich, R.A.; Westerink, J.J., and Scheffner, N.W., 1992. *ADCIRC : An Advanced Three-Dimensional Circulation Model for Shelves Coasts and Estuaries Report 1: Theory and Methodology of ADCIRC-2DDI and ADCIRC-3DL*. Vicksburg, MS: US Army Corps of Engineers Waterways Experiment Station, *Dredging Research Program Technical Report DRP-92-6*, 141p.

Needham, H.F.; Keim, B.D.; Sathiaraj, D., and Shafer, M., 2012. Storm surge return periods for the United States Gulf Coast. *Advances in Hurricane Engineering*, 715-740.

Suh, S.W.; Lee, H.Y.; Kim, H.J., and Fleming, J.G., 2015. An efficient early warning system for typhoon storm surge based on time-varying advisories by coupled ADCIRC and SWAN. *Ocean Dynamics*, 65(5), 617-646.

Summons, N., and Arthur, C., 2011. *Tropical Cyclone Risk Model. User guide*, *Geoscience Australia*. Commonwealth of Australia (Australian Government), 22p.

Suzuki, T.; Shibaki, H., and Suzuyama, K., 2014. Prediction of inundation disaster due to storm surge under global warming. *In*: Lynett, P.J. (eds.), *Proceedings of 34th Conference on Coastal Engineering* (Seoul, Korea), pp. 1-9.

Vickery, P.J.; Skerlj, P.F., and Twisdale, L.A., 2000. Simulation of hurricane risk in the U.S. using empirical track model. *Journal of Structural Engineering*, 126(10), 1222-1237.

Vickery, P.J. and Wadhera, D., 2009. Statistical models of Holland pressure profile parameter and radius to maximum winds of hurricanes from flight-level pressure and H*Wind data. *Journal of Applied Meteorology and Climatology*, 47(10), 2497-2517.

Willoughby, H.E. and Rahn, M.E., 2004. Parametric representation of primary hurricane vortex. Part I: Observations and evaluation of the Holland (1980) model. *Monthly Weather Review*, 132(12), 3033-3048.

Willoughby, H.E.; Darling, R.W.R., and Rahn, M.E., 2006. Parametric representation of the primary hurricane vortex. Part II: A new family of sectionally continuous profiles. *Monthly Weather Review*, 134(4), 1102-1120.

Journal of Coastal Research	SI	75	1137 - 1141	Coconut Creek, Florida	2016

Resonance of 2011 East Japan Tsunami over Continental Shelf along Ibaraki Coast of Japan

Gun Hyeong Kim†, Sobeom Jin‡, Seung Gyu Hyun††, and Sung Bum Yoon§ *

† Dept. of Civil and Environmental Engineering
Hanyang University
Seoul, Korea
kimgun@hanyang.ac.kr

‡ Dept. of Nuclear Emergency Preparedness
Korea Institute of Nuclear Safety
Daejeon, Korea
Jinsb@kins.re.kr

†† Dept. of Structural Systems and Site Safety
Evaluation Korea Institute of Nuclear Safety
Daejeon, Korea
mgodo@kins.re.kr

§ Dept. of Civil, Environmental and Plant Engineering
Hanyang University- ERICA Campus
Ansan, Korea
sbyoon@hanyang.ac.kr

www.cerf-jcr.org

www.JCRonline.org

ABSTRACT

Kim, G.H.; Jin, S.B.; Hyun S.G., and Yoon, S.B., 2016. Resonance of 2011 East Japan Tsunami over Continental Shelf along Ibaraki Coast of Japan. *In:* Vila-Concejo, A.; Bruce, E.; Kennedy, D.M., and McCarroll, R.J. (eds.), *Proceedings of the 14th International Coastal Symposium* (Sydney, Australia). *Journal of Coastal Research*, Special Issue, No. 75, pp. 1137 - 1141. Coconut Creek (Florida), ISSN 0749-0208.

From the wavelet analyses of the tsunami waveforms of the 2011 East Japan Tsunami measured at several stations it is found that the tsunami waves are resonated at the coast of Tokai-Daini nuclear power plant in Ibaraki bay of Japan. For the investigation of this phenomenon numerical simulations are conducted. From the numerical simulations it is understood that the trapping of incidence tsunamis due to the concave shape of the bay and the continental shelf near the entrance of the bay are responsible for the resonance of tsunami waves. The reflections of tsunami waves from land boundaries outside the Ibaraki bay contribute also to the long-lasting tsunami behavior in this bay.

ADDITIONAL INDEX WORDS: *Tusnami, Resonance, Spectral analysis, Wavelet, 2011 East Japan Tsunami.*

INTRODUCTION

A mega-thrust undersea earthquake of M_w 9.0 occurred off the east coast of Japan on 11 March 2011. This 2011 East Japan Earthquake is recorded as the fourth largest earthquake in the world since modern instrumental measurements began in 1900. The tsunami generated by the 2011 East Japan Earthquake caused 15,891 deaths, 2,584 missing persons, and 6,152 injured in Japan. This tsunami also caused nuclear accidents including meltdowns of reactors in the Fukushima Daiichi Nuclear Power Plant site. This 2011 tsunami was measured at plenty of wave gauges and buoys deployed along the Japanese coastline and the Pacific Rim. Moreover, accurate seismic data were also accumulated at many stations around Japan. The abundance of measured data can help understand in detail the generation, propagation, run-up and inundation processes of the tsunami.

In the early stage just after the tsunami event the research was mainly concentrated in identifying the initial shape of tsunami source using the inversion method based on the waveforms measured at various locations including the DART buoys along the Pacific Rim, the GPS buoys, the tide gauges and the wave gauges along the Japanese coast (Maeda *et al.*, 2011; Fujii *et al.*, 2011; Saito *et al.*, 2011). Those tsunami source models were verified by comparing the observed and numerically simulated time histories of water levels at various locations. Even though the shapes of initial tsunami source were different between the source models, all the models gave good agreements with the observed data. This controversy suggests that the inversion methods do not give a unique solution, but the solution of the inversion methods depends on the selection of locations of input data and the performance of the numerical models employed to calculate the Green function for an individual source. Another important point the early researches missed is the temporal behavior of the fault. Since the early researches assumed that the fault motion occurs instantly, it is not clear whether the waveforms at a specific locations are attributed to the initial shape of the tsunami source or the performance of the numerical model. Saito *et al.* (2011) has successfully reproduced the waveforms at the DART 21418 station with their source model using a linearized Boussinesq numerical model. Saito *et al.* (2011) stated that the second crest of the tsunami waves at the DART 21418 station was possible because the numerical model can handle the dispersion of waves. The mechanism of the second crest for the tsunami waves was attributed to the dispersive nature of the tsunami waves in a deep ocean.

Later on, some researchers were interested on the effect of time-dependent fault behavior on the shape of tsunami source. Sugino *et al.* (2012) and Satake *et al.* (2013) proposed time-dependent tsunami source models using the shallow water equations. Even though the numerical model cannot deal with the dispersion effects of waves, Satake *et al.* (2013)

DOI: 10.2112/SI75-228.1 received 15 October, 2015; accepted in revision 15 January, 2015.
*Corresponding author: sbyoon@hanyang.ac.kr
©Coastal Education and Research Foundation, Inc. 2016

demonstrated that the second crest of the tsunami waves at the DART 21418 station can be observed. For a clear understanding of the source mechanism of the 2011 East Japan Tsunami further research is necessary. Putting aside the validity of the various source models the behavior of the tsunami waves in a shallow water region along the coast line should be understood to investigate the resonance problem in a particular location.

In this study the tsunami waveforms measured at several stations along the East coast of Japan are compared. In general, the tsunami waves decrease with increasing time. However, the waveforms measured at Tokai-Daini NPP of Ibaraki area is significantly different from those of other stations. The waves persist in their large wave heights for five hours as shown in Figure 1. For the investigation of this interesting phenomenon numerical simulations are conducted for the 2011 East Japan Tsunami. The dispersion-correction finite difference numerical model based on the shallow water equations is employed with the time-dependent initial ground motion proposed by Sugino *et al.* (2012). The numerical model is verified by comparing the calculated free surface time histories with those measured at several wave stations. Additional numerical simulations are performed with all land boundaries except for the Ibaraki coast removed artificially to reduce the reflection of waves. The mechanism of wave trapping is then analyzed by comparing two time histories of waveforms.

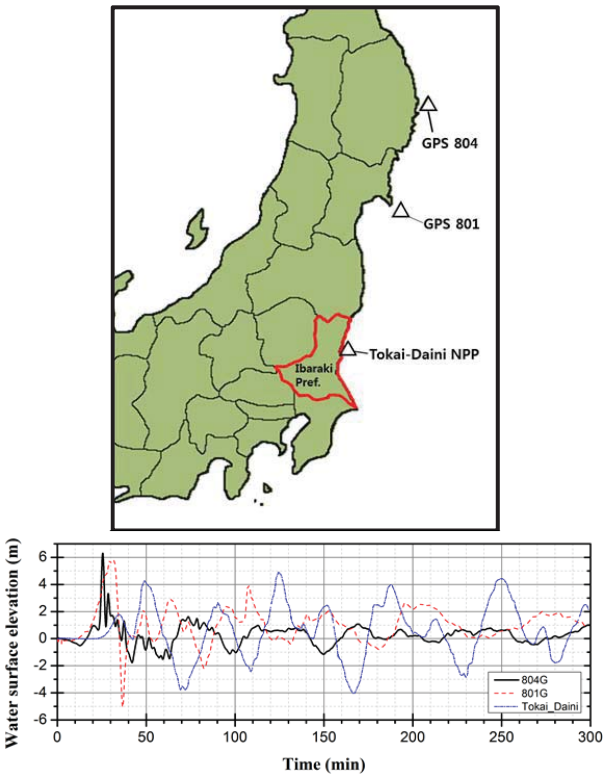

Figure 1. Locations of GPS 804 and GPS 801 offshore buoys and Tokai-Daini wave station (upper panel), and comparison of time histories of tsunami waves measured for 2011 East Japan Tsunami (lower panel).

METHODS

The 2011 East Japan Tsunami was measured at plenty of wave gauges and buoys deployed along the Japanese coastline and the Pacific Rim. The waveforms of the tsunami were analyzed by many researchers using spectral analysis and wavelet analyses (*e.g.*, Heidarzadeh and Satake, 2013). The power peaks of conventional wavelet (*e.g.*, Torrence and Compo, 1998) are slightly distorted such that the spectral powers with longer periods are exaggerated. Liu *et al.* (2007) proposed a technique to rectify the spectral powers by normalizing the results calculated using the conventional wavelet. The technique proposed by Liu *et al.* (2007), however, gives different levels of spectral power depending on sampling rates. Thus, in this study, a new technique is developed to give the same spectral power for the wave components of an equal wave height. The new technique is free of the wave period and the sampling rate of the data.

For the investigation of tsunami behavior in the coastal area numerical simulations are conducted for the 2011 East Japan Tsunami. The dispersion-correction finite difference numerical model based on shallow water equations is employed. The numerical model was originally developed by Cho *et al*. (2007), and further improved by Yoon *et al*. (2014) to include the Coriolis effect and the spherical effect of the computational domain. An efficient dynamic nesting scheme is also implemented in the numerical model of Yoon *et al*. (2014). Figure 2 shows the computational domains with different grid sizes. Table 1 presents the computational information for each subdomain. The time-dependent initial ground motion proposed by Sugino *et al.* (2012) is employed.

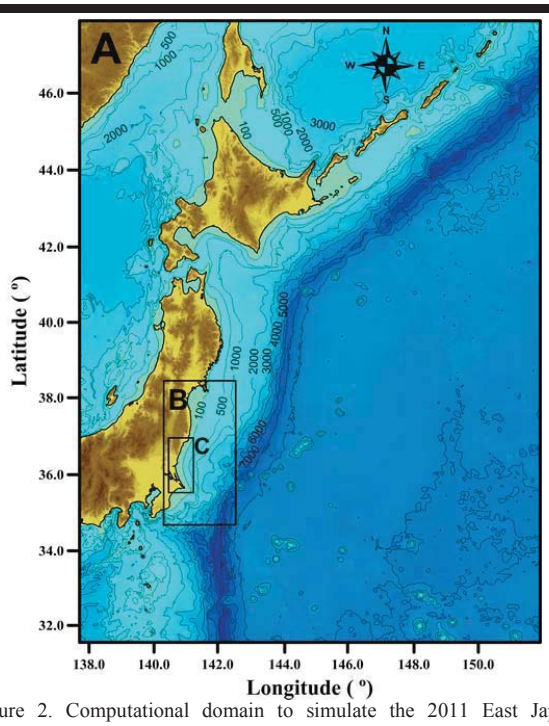

Figure 2. Computational domain to simulate the 2011 East Japan Tsunami.

Table 1. *Computational information for each subdomain.*

Region	Grid	$\Delta x\ (m)$	$\Delta t\ (sec)$	Remark
A	1000 × 1350	1350	3	LSWE
B	478 × 1051	450	1	NSWE
C	478 × 1108	150	0.333	NSWE
D	719 × 1349	50	0.111	NSWE
E	697 × 1225	16.667	0.037	NSWE
F	1610 × 1424	5.556	0.037	NSWE+MB

RESULTS

Wavelet spectral analyses are performed for the tsunami waveforms measured at four stations, *i.e.*, DART 21418 buoy, GPS 804 and GPS 801 buoys, and Tokai-Daini wave station presented in Figure 3.

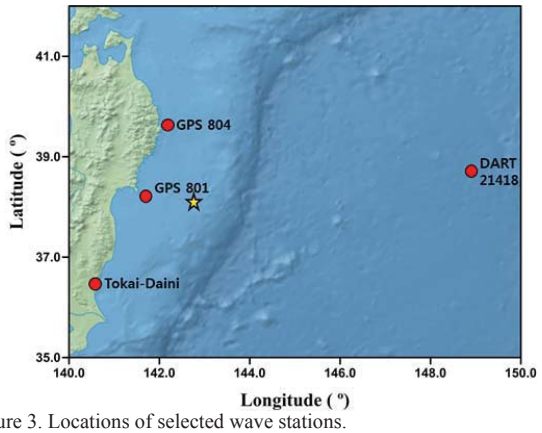

Figure 3. Locations of selected wave stations.

Figure 4 shows the wavelet analysis results for the tsunami waveforms measured at four stations. For the DART and GPS buoys located to the north of the epicenter the power levels in the shorter period range are significant, while the short period component is weak for the Tokai-Daini station located in the south of the epicenter. This shows that the short wave components were generated in the northern part of the epicenter near the trench. Another interesting point is that the spectral powers in the coastal area persist in their strength for a long time, while that of DART buoy decays in a relatively short time. This means that the tsunami waves propagated landward are trapped on the continental shelf. Among three coastal locations the Tokai-Daini station shows the longest duration of high spectral power level.

Figure 5 presents the wavelet spectral power averaged over 30-min. time spans denoted by three white dashed boxes in Figure 4. The first 30-min. time interval is set to cover the tsunami wave group arrived first at the given station. For two wave stations, GPS 801 and Tokai-Daini, located in the southern part of the east coast of Japan the power levels are higher, and the wave periods are longer, than those of the northern part. In particular the wave power or energy measured at the Tokai-Daini station remains strong, or becomes even stronger, while the wave power levels of other stations decay with time. This fact suggests that the tsunami waves are trapped in the coastal region near the Tokai-Daini NPP site.

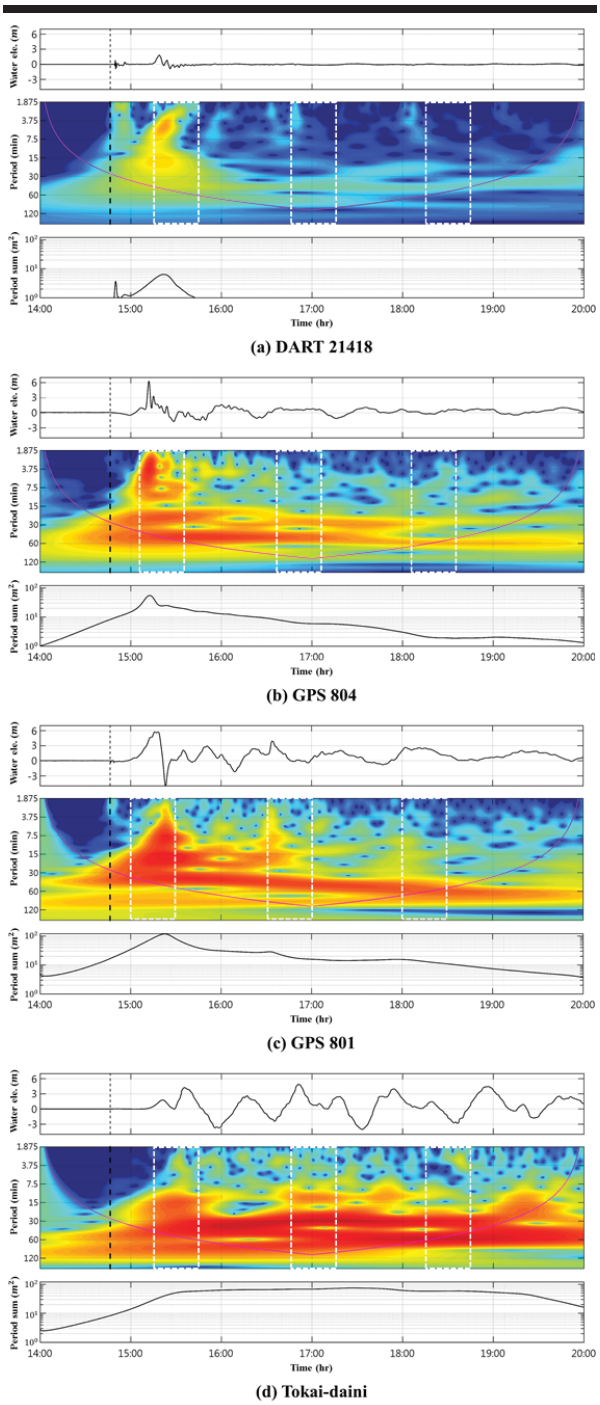

Figure 4. Wavelet specral power distribution for 11 March 2011 at selected wave gauge stations, (a) DART 21418 buoy, (b) GPS 804 buoy, (c) GPS 801 buoy, and (d) Tokai-Daini station, presenting the observed water elevation (upper panel), wavelet spectral power (middle panel), and sum of spectral power at a given time (lower panel).

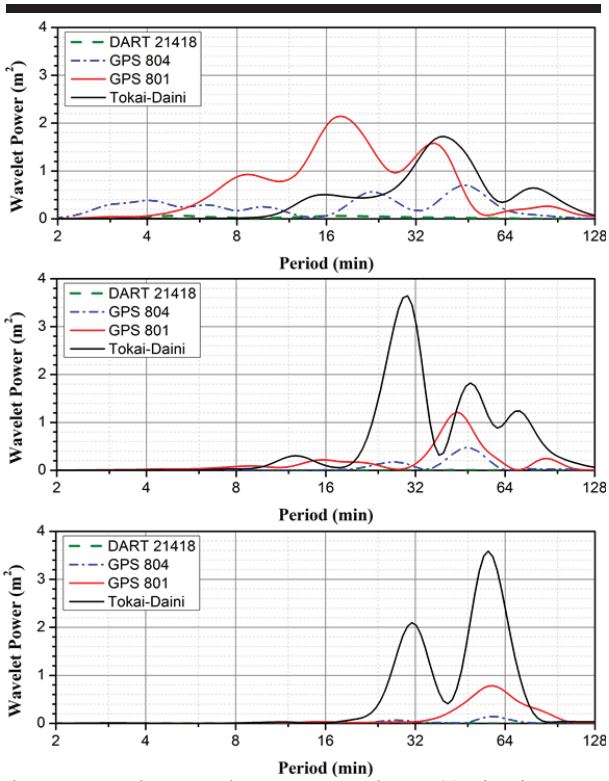

Figure 5. Wavelet spectral power averaged over 30-min. time spans denoted by three white dashed boxes in Figure 4.

Figure 6 shows the bathymetry in the neighborhood of Ibaraki bay area. The shape of the coastline of the bay resembles a concave mirror with a focus. Moreover, the water depths of the bay change suddenly to form a continental shelf, while those of other coastal area vary slowly as shown in the same figure. Due to this topography the tsunami waves reflected from the coastline can be concentrated at a topographical focus, and, in turn, can be re-reflected towards the coast. Thus, the tsunami waves can be possibly trapped in this bay. This wave trapping is called resonance.

Figure 7 shows the comparison of the observed and calculated free surface elevations at the Tokai-Daini wave station for the 2011 East Japan Tsunami. The calculated result agrees reasonably well with the measured one. The numerical model and the initial ground motion used in this study are verified to study the resonance mechanism of the 2011 East Japan Tsunami in Ibaraki bay.

To investigate the resonance problem further in detail, additional simulations are performed with suppressing the reflection of tsunami waves from the land boundaries other than Ibaraki bay. Figure 8 shows the comparison of the free surface elevations calculated with and without the reflection from the land outside the Ibaraki bay. When the reflection from the land outside the bay is suppressed, the tsunami waves maintain their strength for the first three wave periods, and then decrease with time.

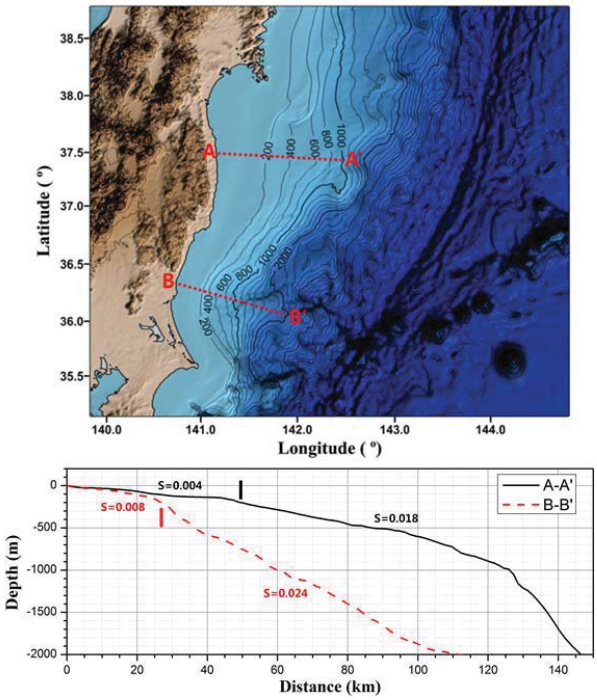

Figure 6. Bathymetry in the neighborhood of Ibaraki bay area, and the water depth distribution along two selected sections.

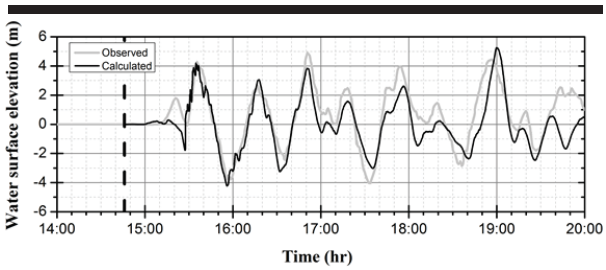

Figure 7. Comparison of observed and calculated free surface elevations at Tokai-Daini wave station for 11 March 2011.

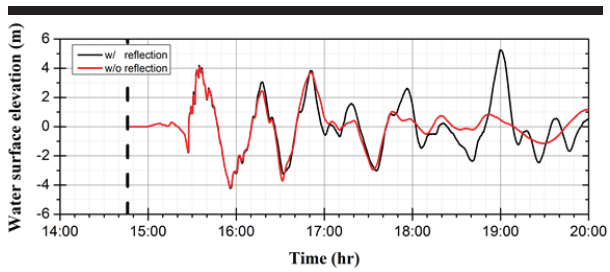

Figure 8. Comparison of free surface elevations calculated with and without reflection from land outside Ibaraki bay.

From this comparison it is understood that the first three waves are resulted from trapping or resonance of incident waves inside the bay system, and the waves arriving after the third one are due to the reflected waves from the land boundaries other than the Ibaraki bay. In particular, the video based on the calculated results with reflective boundaries shows that the waves at 17:00 h and 19:00 h are reflected from the Sendai bay located in the north of Ibaraki bay. From the simulation results it is found that the resonance of the tsunamis due to the continental shelf and the concave coastline of the Ibaraki bay are responsible for this interesting phenomenon. On top of this, the reflections of tsunami waves from land boundaries outside the Ibaraki bay contribute also to the long-lasting tsunami behavior. Thus, the appropriate estimation of the reflection of waves from the land boundary is one of the essential parts for the accurate simulation of tsunamis.

CONCLUSIONS

In this study the tsunami waveforms of the 2011 East Japan Tsunami measured at several stations along the East coast of Japan are compared. The wave forms at Tokai-Daini NPP coast of Ibaraki area shows resonance on a continental shelf. For the investigation of this phenomenon numerical simulations are conducted. The numerical model is verified by comparing the calculated free surface time histories with those measured at several wave stations. Additional numerical simulations are performed with all land boundaries except for the Ibaraki coast removed artificially to reduce the reflection of waves. The mechanism of wave trapping in the Ibaraki bay system is then analyzed by comparing two time histories of wave forms. The trapping of incidence tsunamis due to the concave shape of the bay and the continental shelf near the bay are responsible for the resonance of tsunami waves. On top of this, the reflections of tsunami waves from land boundaries outside the Ibaraki bay contribute also to the long-lasting tsunami behavior. Thus, the appropriate estimation of the reflection of waves from the land boundary is one of the essential parts for the accurate simulation of tsunamis.

ACKNOWLEDGMENTS

This research was a part of the project titled ‘Countermeasure System against Hazards of Typhoons and Tsunamis in Harbor Zones (South Coast) – Stage 2’, funded by the Ministry of Oceans and Fisheries, Korea. GHK and SBY thank Professor K. Satake of the University of Tokyo, Japan for providing the extensive observation data of the 2011 East Japan Tsunami.

LITERATURE CITED

Cho, Y.S.; Shon, D.H., and Lee, S.O., 2007. Practical modified scheme of linear shallow-water equations for distant propagation of tsunamis. *Ocean Engineering*, 34, 1769-1777.

Fujii, Y.; Satake, K.; Sakai, S.; Shinohara, M., and Kanazawa, T., 2011. Tsunami source of the 2011 off the Pacific coast of Tohoku Earthquake. *Earth Planets Space*, 63(7), 815-820.

Heidarzadeh, M. and Satake, K., 2013. Waveform and spectral analyses of the 2011 Japan Tsunami records on tide gauge and DART stations across the Pacific Ocean. *Pure and Applied Geophysics*, 170, 1275-1293.

Liu, Y.; Liang, X.S., and Weisberg, R.H., 2007. Rectification of the bias in the wavelet power spectrum. *Journal of Atmospheric and Oceanic Technology*, 24(12), 2093-2102.

Maeda, T.; Furumura, T.; Sakai, S., and Shinohara, M., 2011. Significant tsunami observed at ocean-bottom pressure gauges during the 2011 off the Pacific coast of Tohoku Earthquake. *Earth Planets Space*, 63(7), 803-808.

Saito, T.; Ito, Y.; Inazu, D., and Hino, R., 2011. Tsunami source of the 2011 Tohoku-Oki earthquake, Japan: Inversion analysis based on dispersive tsunami simulations. *Geophysical Research Letters*, 38, L00G19, doi:10.1029/2011GL049089.

Satake, K.; Fujii, Y.; Harada, T., and Namegaya, Y., 2013. Time and space distribution of coseismic slip of the 2011 Tohoku Earthquake as inferred from tsunami waveform data. *Bulletin of the Society of America*, 103, No. 2B, 1473-1492.

Sugino, H.; Iwabuchi, Y.; Ebisawa, K.; Nemoto, M., and Korenaga, M., 2012. Investigation of mechanisms causing ground motion and tsunami due to the 2011 Tohoku Earthquake at Nuclear Power Plant sites. *Proceedings of the 15th World Conf. on Earthq. Eng.* (Lisbon, Portugal), Paper 2671.

Torrence, C. and Compo, G.P., 1998. A practical guide to wavelet analysis. *Bulletin of the American Meteorological Society*, 79(1), 61-78.

Yoon, S.B.; Kim, S.C.; Baek, U., and Bae, J.S., 2014. Effect of bathymetry on the propagation of tsunamis towards the east coast of Korea. *In:* Green, A.N. and Cooper, J.A.G. (eds.), *Proceedings 13th International Coastal Symposium* (Durban, South Africa), *Journal of Coastal Research*, Special Issue No. 70, pp. 332-337.

Journal of Coastal Research	SI	75	1142 - 1146	Coconut Creek, Florida	2016

Double Resonance Effect at Daeheuksando Port Caused by Air Pressure Disturbances in Yellow Sea on 31 March 2007

Myung-Seok Kim[†], Hyunsu Kim[‡], Yoo-Keun Kim[‡], Bon-Ho Gu[†], Ho-Jae Lee[‡], and Seung-Buhm Woo[†*]

[†]Department of Ocean Science,
College of Natural Sciences, Inha University,
Incheon, South Korea

[‡]Department of Atmospheric Science,
Pusan National University,
Busan, South Korea

www.cerf-jcr.org

www.JCRonline.org

ABSTRACT

Kim, M.S.; Kim, H.S.; Kim, Y.K.; Gu, B.H.; Lee, H.J., and Woo, S.B., 2016. Double resonance effect at Daeheuksando Port caused by air pressure disturbances in Yellow Sea on 31 March 2007. *In:* Vila-Concejo, A.; Bruce, E.; Kennedy, D.M., and McCarroll, R.J. (eds.), *Proceedings of the 14th International Coastal Symposium* (Sydney, Australia). *Journal of Coastal Research*, Special Issue, No. 75, pp. 1142 - 1146. Coconut Creek (Florida), ISSN 0749-0208.

We found that an internal resonance, combined with other topographic effects, following an external resonance could significantly amplify insignificant sea-level oscillations in the open sea to wave heights of several meters in a coastal area. Sudden sea-level oscillations characterized by high frequencies (0.0042-0.5 min^{-1}) and a maximum wave height of about 1 m were observed at Daeheaksando Port (DP) on 31 March 2007. These sea-level oscillations, which caused heavy casualties and large economic loss, were also detected along the west coast of South Korea. Particularly, at DP, there were sea-level oscillations that had significant power spectrum in a specific period band. When the maximum power spectrum of the sea-level oscillations increased rapidly, the period of the maximum power spectrum converged toward the fundamental period of the port. However magnitude of the air pressure disturbance at DP could not make such sea-level oscillations. The resulting sea-level oscillations were likely amplified by the free waves generated by air pressure disturbances at KyukRyulbeedo (KR) and propagated to DP. The initial magnitude of the disturbances propagated from Shandong was approximately 2.5 hPa/10-min, based on results of the atmospheric model. Theoretically, a 2.5 hPa air pressure change can make sea-level oscillations of about 2.5 cm, but it made meteotsunamis in the port because of the double resonance effect on 31 March 2007.

ADDITIONAL INDEX WORDS: *Air pressure disturbances, meteotsunamis, double resonance effect.*

INTRODUCTION

Severe damage was caused at around 0000 KST on 31 March 2007 by an abnormal wave that occurred in Yellow Sea. “Abnormal wave” is a term that has been used in South Korea to describe the characteristics of a meteotsunami, which can generate sudden and very large waves near the coast like a tsunami. According to reports from the Korea Meteorological Administration (KMA), the meteotsunamis that occurred on 31 March 2007 caused a total of six human casualties (four dead and two injured) and property damage estimated at up to two million dollars, including flooded homes, capsized fishing boats, and losses of fish farm (Yoon and Eom, 2013).

Meteotsunamis associated with atmospheric instability were known in some countries as “abiki” in Japan, “rissagga” in Spain, “šćiga” in Croatia, “marrubbio” in Sicily, “milghuba” in Malta, “seebär” in Baltic coutries, “death waves” in Western Ireland and “inchas” in the Azores and Madeira islands (Vilibić *et al.*, 2014). The general mechanism of a catastrophic meteotsunami, according to the diagram suggested by Monserrat *et al.* (2006), is as follows.

(1) A small air pressure disturbance (3 hPa) over a short time interval that initially propagates from the open sea causes sea-level oscillations of approximately 3 cm due to the inverted barometer effect. (2) Then, as the phase speed of the propagating sea-level oscillations and the speed of air pressure disturbance become similar, Proudman resonance, which is an external resonance, occurs at the air-sea interface. The resonance amplifies the amplitude and lengthens the wavelength of the sea-level oscillations. (3) The amplitude of the propagating sea-level oscillations can increase again at the shelf region due to topographic properties. (4) Wave deformations near an inlet or artificial structure can also cause significant sea-level oscillations. When the period of the sea-level oscillations entering the harbor corresponds with the fundamental period of the harbor, harbor resonance, which is an internal resonance, occurs (1-5 m). The risk of the destructive meteotsunami is closely related to the shelf topography and coastline geography, which create a “double resonance effect” (Rabinovich, 1993) that is a combination of the resonances.

The generation of air pressure disturbances that resulted from atmospheric gravity waves that repeatedly propagated toward the west coast of South Korea produced meteotsunamis on 31 March 2007 (Choi *et al.*, 2008). During the meteotsunamis, both the air pressure disturbances and high frequency sea-level oscillations propagated in a south-easterly direction (Eom *et al.*, 2012). By applying crests of the air pressure disturbances derived from 3 hourly weather charts to a 2-dimensional shallow water wave model, they simulated sea-level oscillations amplified by the Proudman resonance effect. Kim *et al.* (2014)

DOI: 10.2112/SI75-229.1 received 15 October, 2015; accepted in revision 15 January, 2015.
*Corresponding author: sbwoo@inha.ac.kr
©Coastal Education and Research Foundation, Inc. 2016

showed that atmospheric instability, generated by the passing of a low pressure system accompanying a cold front, propagated across the Yellow Sea from Shandong (Figure 1) from the results of a synoptic analysis and the Weather Research and Forecast model (WRF).

In this study, we investigated the presence of harbor resonance after Proudman resonance and the degree of amplification due to each resonance at DP on 31 March 2007.

METHODS

Mean sea-level pressure at KR and DP at an interval of a 1-min was used for the analysis of the meteotsunamis that occurred at DP on 31 March 2007. Radar images that could show the evolution of atmospheric instability over the Yellow Sea at an interval of a 10-min were also used. These atmospheric data were provided by KMA. The tide level at DP at an interval of a 1-min was provided by the Korea Hydrographic and Oceanographic Administration (KHOA).

In general, signals in the time domain due to meteotsunamis are characterized by localized peaks at the specific time and are attenuated non-periodically. In order to analyze such non-stationary signals, the wavelet transform, which uses an isolated wave as a basis function, was used. Because time series can be converted into time–frequency domain through the wavelet transform, it is possible to analyze how the variability of interest changes with time and frequency. The Morlet wavelet was used as the wavelet basis function because the wavelet scale is almost equal to the Fourier period. To estimate power spectrum of tide level in the high frequency band during meteotsunamis, wavelet reconstruction and Scale Averaged Wavelet Power (SAWP) were used (Torrence *et al.*, 1997).

The Advanced Research WRF version 3.6.1 was used to simulate the atmospheric instability. To simulate fine air pressure at the lowest level in WRF, dense sigma levels and two nested domains were used. The grid information of each domain and the physical options of the model integration are shown in the Table 1. FNL (Final) Operational Global Analysis data, which are reanalysis data from the Global Forecast System (GFS), National Centers for Environmental Prediction (NCEP), and Real Time Global SST were used as initial boundary conditions. A total of 6 days, from 0900 KST on 27 March 2007 to 0900 KST on 02 April 2007, was simulated. Considering the spin-up time of 1 day, only the results for last 5 days were used.

Table 1. *Details of the grids and the physics options used in the WRF model (Kim et al., 2014)*

Scheme	Domain 1	Domain 2	Domain 3
Horizontal grid	165×150	271×226	289×307
Resolution	30 km	10 km	3.3 km
Vertical grid	48 layers (sigma coordinate)		
Microphysics	WSM3	Milbrandt-Yau 2-Moment	
Surface layer	Revised MM5		
Land Surface	Noah-LSM		
Boundary layer	YSU		
Cumulus	Kain-Fritsch		
Longwave radiation	RRTMG		
Shortwave radiation	RRTMG		

RESULTS

The results section is organized into three subsections. To explain the double resonance effect at DP, the organization is sea-level oscillations at the port, source of meteotsunamis, and evidence of harbor resonance in sequence.

Characteristics of sea-level oscillations at DP

There was mainly a dominant power spectrum at the diurnal and the semi-diurnal tidal cycle in the tide level of DP during 31 March 2007 and 01 April 2007 (Figure 2a and 2b). Additionally, in a short period of less than 4-h, sea-level oscillations similar to tsunami oscillations existed due to the meteotsunamis. As shown in the wavelet scalogram, the power spectrum of the tides distributed above 10^5 cm^2min and the power spectrum of the meteotsunamis distributed within 10^2 cm^2min and 10^5 cm^2min. In addition, sea-level oscillations with amplitude less than 30 cm also occurred before and after 31 March, the day on which human casualties and property damage were reported. As shown in Figure 2c, the maximum SAWP of the residual tide level (less than 4-h) occurred at 0056 KST on 31 March 2007 during high tide, indicating that the arrival time of the meteotsunamis. Subsequent disturbances occurred repeatedly after this time, and sea-level oscillation lasted approximately 18-h (Figure 2, gray dashed line). It is well known that meteotsunamis on 31 March first occurred at the tidal station near KR before reaching DP on 31 March (Eom *et al.*, 2012).

Air pressure disturbances propagated from Shandong

To understand the rapid evolution of air pressure disturbances in space and time, atmospheric pressure at an interval of a 1-min from the model results was analyzed.

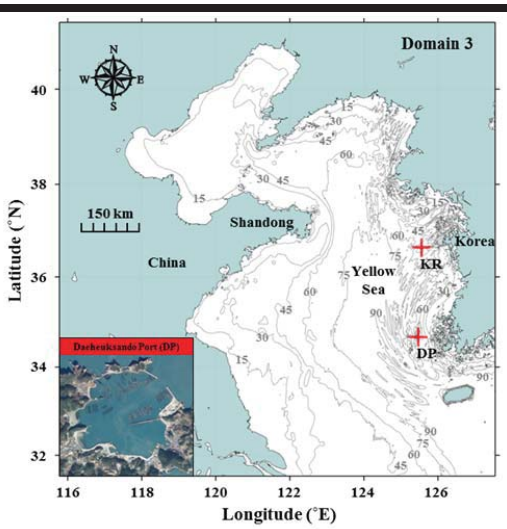

Figure 1. Study area (Domain 3) and satellite image of DP captured from Google Earth. Red cross markers indicate locations of KR and DP. Gray dashed lines are bathymetric contours.

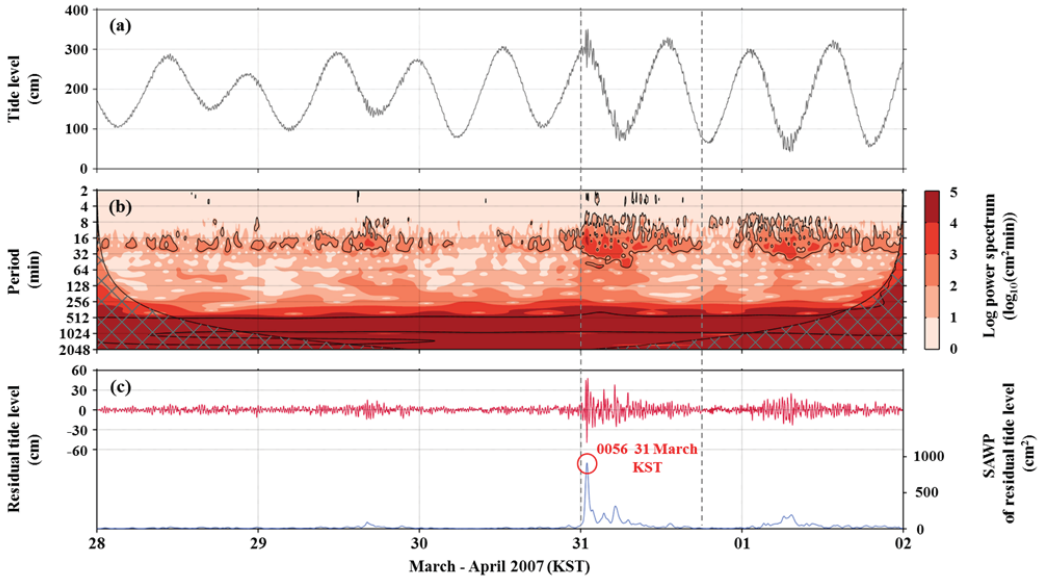

Figure 2. Tide level, wavelet scalogram of the tide level, and residual tide level (high pass filtered, 4-h) and Scale Averaged Wavelet Power (SAWP) of the residual tide level at DP. (a) Gray dashed lines indicate the time interval of occurrence of successive accidents. (b) The left axis is Fourier period (min). The thick contour encloses regions of greater than 95% confidence level for the power spectrum of tide level during the five days. Cross-hatched regions indicate the cone of influence, where edge effects become important. (c) Red circle indicates arrival time of meteotsunami.

The first air pressure disturbance at Shandong (Figure 3a, P0), which had a significant diameter of approximately 400 km at 2100 KST on 30 March, gradually developed into a wave crest line as it propagated (Figure 3b, P0). Then, at 0000 KST on 31 March, two wave crest lines divided from the initial P0, and P1 and P2 moved successively in an eastern direction toward the west coast of South Korea (Figure 3c, P1 and P2). At this time, the radar images indicated a high rain rate which is a sign of the atmospheric instability also propagated while showing a spatio-temporal distribution that was similar to the simulated air pressure disturbances (Figure 3e-3g). However, it was impossible to identify the location of P0 that appeared on the model with the radar images because of the limited coverage of the radar. Additionally, the air pressure disturbances derived from the model results tend to dissipate quickly at the west coast (Figure 3d and 3h).

The amplitude of the air pressure disturbance near Shandong was approximately 2.5 hPa/10-min at the maximum amplitude (Figure 3a, P0). The slopes of the wave crest lines (Figure 3c, P1 and P2) were 62˚ and 77˚ (clockwise from the northward direction), respectively, and the two wave crest lines propagated together in an eastward direction from 2230 KST on 30 March to 0330 KST on 31 March at an average speed of 28 m/s. Especially, they propagated by passing through the regions between KR and DP (Figure 3c and 3d). Considering the spatial scale of the wave crest lines, it can be assumed that the sea-level oscillations lasted for a long time because of the influence of P2 rather than P1 (Figure 3c). However, the critical meteotsunami was reported during propagation of P1, and the sea-level oscillations resulting from P1 had much more SAWP than those from P2 (Figure 2c, blue line).

Harbor resonance at DP

Air pressure disturbance was derived from the sea-level pressure at KR and DP to analyze the cause of the sea-level oscillations detected at DP. As a result, only insignificant air pressure disturbance (Figure 4a, bottom gray line) was examined at DP where meteotsunamis occurred. However, air pressure disturbance at KR (Figure 4a, bottom red line) was more significant (-4.1-3.0 hPa/10-min) during P1. Thus, it could be concluded that maximum power spectrum (10^3-10^4 cm^{2}min) at DP during P1 (Figure 4b), black line) resulted from the free waves propagated from KR because the magnitude of the air pressure disturbance that occurred at DP could not generate such sea-level oscillations. Similarly, the maximum power spectrum during P2 was also increased rapidly by the propagated sea-level oscillations originated from KR. After P1 and P2, the air pressure disturbance that occurred at DP increased up to 1.7 hPa/10-min at 0720 KST on 31 March, but power spectrum of the sea-level oscillations did not increase as sharply as before. It seemed that such air pressure disturbance at DP occurred because of the influence of the P2 wave crest line, which was elongated as shown in Figure 4d.

Before meteotsunamis arrived at DP almost until 0000 KST on 31 March, the period of the maximum power spectrum occurred near the cut-off frequency (Figure 4b, blue line). However, the period converged into a specific period band

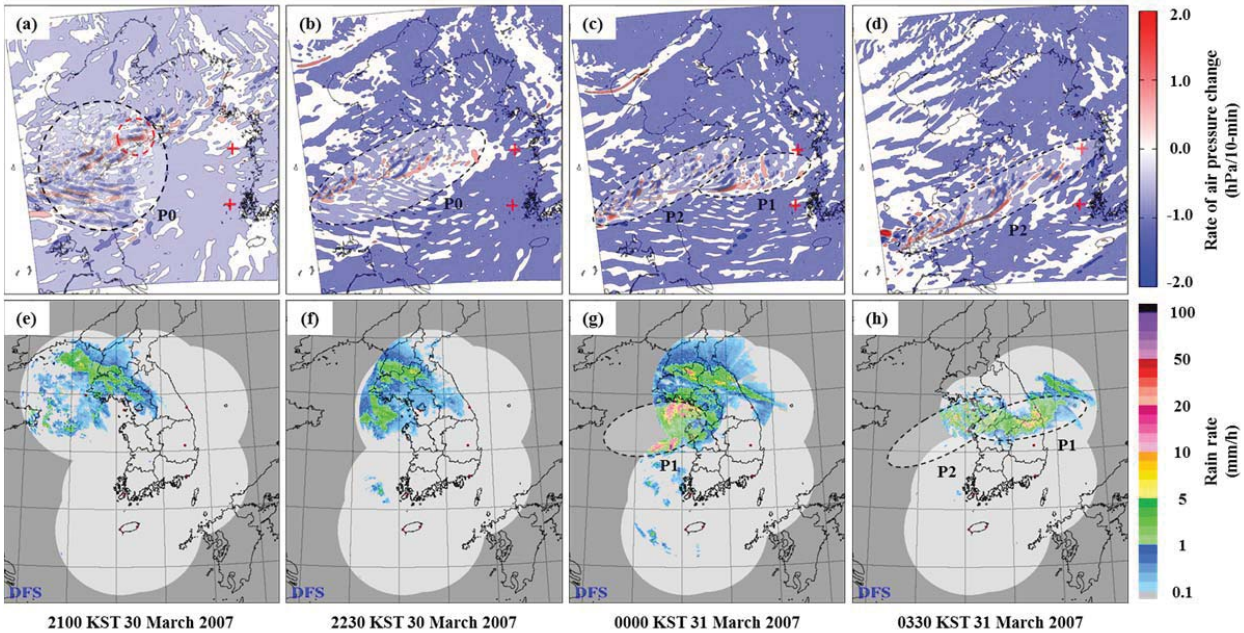

Figure 3. Horizontal distribution of the air pressure disturbances at the bottom layer derived from WRF 1-min interval results by using rate of air pressure change (Šepić and Vilibić, 2011) and radar images. P0, P1, and P2 indicate evolution of the atmospheric instability associated with pressure disturbances. Red cross markers indicate location of KR and DP (a-d).

when the maximum power spectrum increased (Figure 4b, red dashed line). Even after P1 and P2 passed, sea-level oscillations that exceeded the maximum power spectrum ranging from 10^2 cm^2min to 10^3 cm^2min in the same period band lasted until 1800 KST on 31 March. It was considered as continuing harbor resonance during and after meteotsunamis.

DISCUSSION

The rate of air pressure change derived from the air pressure in the model results was utilized to estimate the amplitude of sea-level oscillations that were amplified by the external resonance from Shandong. According to Proudman (1929), the resonance shown by the following formula occurs if the speed of air pressure disturbances propagated from open sea equals the longwave phase speed of ocean waves.

$$\Delta\eta = \Delta\eta^{*}/\left(1 - F_r^{\,2}\right) , \qquad (1)$$

where $\Delta\eta$ is the amplified amplitude in open ocean, $\Delta\eta$ = -$\Delta P_a/\rho g$, where ΔP_a is the air pressure disturbance and ρ is the water density, and F_r is the Froude number. Considering the average velocity of P1 (28 m/s) and the depth range of the Yellow Sea (60-90 m) from Shandong to DP, the range of the Froude number was calculated to be between 0.9 and 1.2, which is a favorable condition for meteotsunami. When the amplified amplitude by Proudman resonance is calculated by using (1), the $\Delta\eta$ caused by the resonance approaches infinity if F_r = 1. Thus, the amplified amplitude was calculated by using (2), which was suggested by Hibiya and Kajiura (1982).

$$\Delta\eta = -\Delta\eta^{*} x_f / 2L_1 , \qquad (2)$$

where L_1 is the width of an air pressure disturbance in its direction of propagation and x_f is the distance from the source area. The red dashed circle in Figure 3a represents the maximum magnitude of the air pressure disturbance (2.5 hPa/ 10-min) located at Shandong. The model results ($\Delta\eta^{*}$ = 2.5 cm, L_1 = 33 km, x_f = 320 km) were utilized with an assumption that the amplitude of the sea-level oscillation due to the air pressure disturbance would be approximately 2.5 cm based on the inverted barometer effect. Therefore, $|\Delta\eta|$ was 12.2 cm, which is 4.9 times the amplitude of $|\Delta\eta^{*}|$.

The fundamental period of DP was estimated from the spatial information in order to analyze the cause of the significant power spectrum at DP, which was frequently amplified in a specific frequency band after Proudman resonance. Basin's empirical formula of the fundamental period for a semi-elliptic geometry (Wilson, 1972), which is most similar to the geometric type of DP is given by

$$T_0 = 2.220[2L/(gh_1)^{1/2}] , \qquad (3)$$

where L is the length of the port, h_1 is the depth at the open mouth of the port, and g is gravitational acceleration. When the spatial information of DP was applied to (3), T_0 was calculated to be in the range between 14.3-min and 18.9-min (L = 1600 m, h_1 = 4-7 m). This implies that there was harbor resonance at DP because the range of the calculated T_0 approximated to the period band between 16-min and 32-min

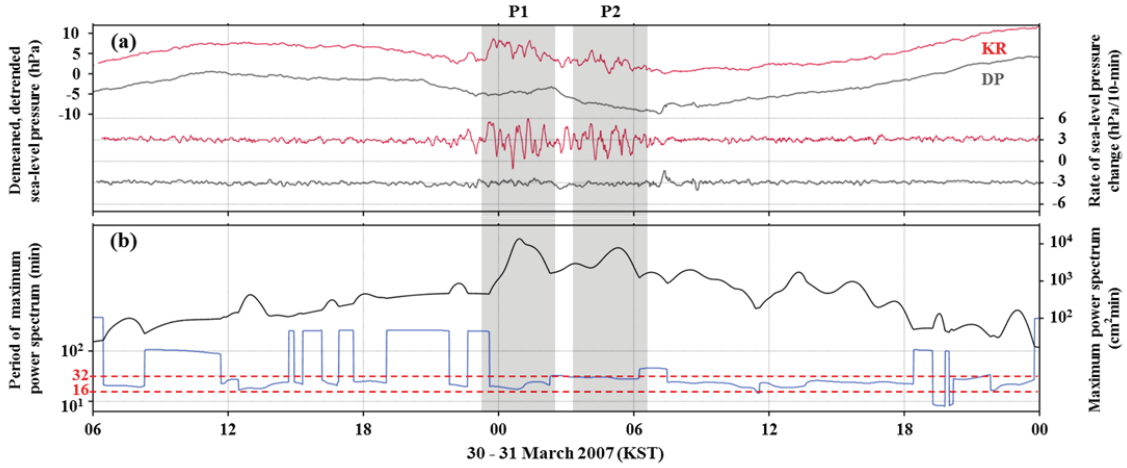

Figure 4. The evidence of harbor resonance at DP. (a) Demeaned, linearly detrended sea-level pressure (top) and rate of sea-level pressure (bottom) at KR (red line) and DP (gray line). Gray boxes indicate duration of the atmospheric instabilities (P1, P2). (b) Maximum power spectrum of the residual tide level (black line) and period of the maximum power spectrum (blue line). Red dashed lines indicate convergence to the specific period band when the maximum power spectrum increases.

whenever the maximum power spectrum increased suddenly (Figure 4b). Excluding the amplified amplitude caused by the external resonance from the initial amplitude (49.7 cm) when the meteotsunami first arrived at DP, approximately 75.5% (37.5 cm) of the amplitude was amplified by the internal resonance combined with other topographic effects.

CONCLUSIONS

In this work, we found that sea-level oscillations with amplitude of 2.5 cm that occurred in the open sea were amplified 20 times at DP by the harbor resonance succeeding Proudman resonance, when including the topographic effect. Therefore, the meteotsunamis at DP that occurred on 31 March 2007 were a phenomenon caused by the double resonance effect, which is the combination of an external resonance and an internal resonance. Further quantitative research using an atmosphere-ocean coupled model should be conducted to better understand how the sea-level oscillations that propagate with the air pressure disturbances evolve with time and how much they can be amplified by the resonances.

ACKNOWLEDGMENTS

This work was funded by the Korea Meteorological Administration Research and Development Program under Grant KMIPA 2015-1071.

LITERATURE CITED

Choi, B.J.; Park, Y.W., and Kwon, K.M., 2008. Generation and growth of long ocean waves along the west coast of Korea in March 2007. *Ocean and Polar Research*, 30(4), 453-466.

Eom, H.M.; Seung, Y.H.; Woo, S.B., and You, S.H., 2012. Analysis of abnormal wave at the west coast on 31 March 2007. *Journal of Korean Society of Coastal Ocean Engineers*, 24(3), 217-227.

Hibiya, T. and Kajiura, K., 1982. Origin of Abiki phenomenon (a kind of seiches) in Nagasaki Bay. *Journal of the Oceanographical Society of Japan*, 38, 172-182.

Kim, H.S.; Kim, Y.K.; Woo S.B., and Kim, M.S., 2014. Atmospheric analysis on the meteotsunami case occurred on 31 March 2007 at the Yellow Sea of South Korea. *Journal of Environmental Science International*, 23(12), 1999-2014.

Monserrat, S.; Vilibić, I., and Rabinovich, A.B., 2006. Meteotsunamis: atmospherically induced destructive ocean waves in the tsunami frequency band. *Natural Hazards Earth System Sciences*, 6, 1035-1051.

Proudman, J., 1929. The effects on the sea of changes in atmospheric pressure, *Geophysical Journal International*, 2(4), 197-209.

Rabinovich, A.B., 1993. Long Ocean Gravity Waves: Trapping, Resonance, and Leaking (in Russian). *St. Petersburg: Gidrometeoizdat*, 325p.

Šepić, J. and Vilibić, I., 2011. The development and implementation of a real-time meteotsunami warning network for the Adriatic Sea. *Natural Hazards and Earth System Sciences*, 11, 83-91.

Torrence, C. and Compo, G.P., 1998. A practical guide to wavelet analysis. *Bulletin of the American Meteorological Society*, 79, 61-78.

Vilibić, I.; Monserrat, S., and Rabinovich, A.B., 2014. Meteorological tsunamis on the US East Coast and in other regions of the World Ocean. *Natural Hazards*, 74, 1-9.

Wilson, B., 1972. Seiches. *Advances in Hydroscience*, 8, pp. 1-94.

Yoon, J.H. and Eom, H.M., 2013. Challenge to no casualty of the abnormal waves at the west coast of South Korea. *Seoul, South Korea: Observation Infrastructure Bureau of Korea Meteorological Administration*, 3p.

Journal of Coastal Research	SI	75	1147 - 1151	Coconut Creek, Florida	2016

Seasonal Characteristics and Mechanisms of Meteo-tsunamis on the West Coast of Korean Peninsula

Hyunsu Kim†, Myung-Seok Kim‡, Ho-Jae Lee†, Seung-Buhm Woo‡, and Yoo-Keun Kim†*

†Department of Atmospheric Sciences,
Pusan National University,
Busan, South Korea

‡Department of Ocean Sciences,
College of Natural Sciences

www.cerf-jcr.org

www.JCRonline.org

ABSTRACT

Kim, H.; Kim, M.-S.; Lee, H.-J.; Woo, S.-B., and Kim, Y.-K. 2016. Seasonal Characteristics and Mechanisms of Meteo-tsunamis on the West Coast of Korean Peninsula. *In:* Vila-Concejo, A.; Bruce, E.; Kennedy, D.M., and McCarroll, R.J. (eds.), *Proceedings of the 14th International Coastal Symposium* (Sydney, Australia). *Journal of Coastal Research*, Special Issue, No. 75, pp. 1147 - 1151. Coconut Creek (Florida), ISSN 0749-0208.

A meteo-tsunami is produced by atmospheric disturbances, such as pressure jumps, and the seasonal frequency changes of meteo-tsunamis might be dependent on the seasonal synoptic weather features. Therefore, an analysis of the synoptic atmospheric mechanism for the cause of meteo-tsunamis is important for predicting the meteo-tsunamis precisely and reducing the sudden damage. As the west coast of the Korean peninsula is a region with frequent meteo-tsunamis, the outcome of an analysis of the tidal level observation data at 1-min intervals shows that meteo-tsunami have occurred 92 times (3-SD(exceeding the 3 times of standard deviation): 28 times, 2-SD: 64 times) over the last 12 years (2002-2013). Meteo-tsunamis occur every season but have the greatest frequency in the spring (MAM; 53.3%) and winter (DJF; 26.1%). In particular, strong meteo-tsunamis in excess of 3-SD have occurred in spring (53.6%) and winter (28.6%). Climatologically, low pressure systems often passes through the Korean peninsula located in the mid-latitudes during spring. In this season, the potential instability of the atmosphere is increased on the Yellow sea. On contrast, the Siberian high pressure system periodically extends to the Korean peninsula during winter. This can cause atmospheric dynamic instability from the boundary between the land and sea.

ADDITIONAL INDEX WORDS: *meteo-tsunami, atmospheric disturbance, synoptic atmospheric mechanism.*

INTRODUCTION

Meteo-tsunamis in the Korean peninsula became more widely known because of the coastal disaster (*e.g.* meteo-tsunami) that occurred in the Yellow sea in March 2007 and May 2008. After that, several studies have been conducted (Choi *et al*., 2008; Eom *et al.*, 2012; Kim, 2014) (Figure 1). According to the existing accident and previous studies, meteo-tsunamis in the Korean peninsula occur mainly in the spring, and attempts have been made to analyze the causes primarily in oceanographic aspects. Previous studies have been conducted to estimate the speed and propagation of meteo-tsunamis using methods, such as propagating the virtual pressure jump in the different types to generate an external force to the numerical ocean model. However, as it can be seen in the name of "meteo-tsunami", a meteo-tsunami has a meteorological cause (*e.g.* fluctuations of air pressure). Therefore, a meteorological understanding is essential in meteo-tsunami research because the meteorology is a significantly contributiong factor to the propagating process in a meteo-tsunami. In this study, the meteo-tsunami events that occurred in the west coast of the Korean peninsula in the past were selected and the synoptic weather analysis on the meteo-tsunami events was carried out. Also, the seasonal characteristics and mechanisms of meteo-tsunamis occurring in the Korean peninsula were reinterpreted by analyzing the meteorological causes of the meteo-tsunamis and categorizing the events with similar synoptic patterns.

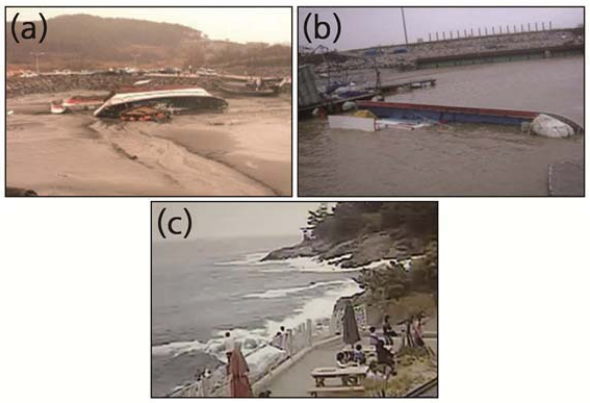

Figure 1. Damage images caused by meteo-tsumamis at the west coast of Korean peninsula: (a), (b) property damage caused by the meteo-tsunami in Younggwang on 31 March 2007 (Kim, 2014), (c) CCTV image of the meteo-tsunami in Boryeong on 4 May 2008 (Yoo, 2010).

DOI: 10.2112/SI75-230.1 received 15 October, 2015; accepted in revision 15 January, 2015.
*Corresponding author: kimyk@pusan.ac.kr
©Coastal Education and Research Foundation, Inc. 2016

METHODS

In this study, some research methods were set up to understand the seasonality and generation mechanism of the meteo-tsunami, as shown below.

Study area and observation sites

Various coastal disasters occur in the Korean peninsula, which is surrounded by the sea on three sides, but the west coast of Korean peninsula in the Yellow sea was set up as the local study area (LSA) because it is an area where meteo-tsunamis often occur. This study examined the generation mechanisms of meteo-tsunamis through synoptic weather analysis. The study area was divided into a synoptic study area (SSA) for the synoptic analysis and LSA for the tidal data analysis, as shown in Figure 2. Different types of weather and marine observation sites can be found over the coastal area in the LSA. As China and North Korea have not provided information on the weather and marine observations easily, the only values used in this study were the data of automatic weather systems (AWS) in the Korea Meteorological Administration (KMA) and tidal stations in the Korea Hydrographic and Oceanographic Administration (KHOA) in South Korea.

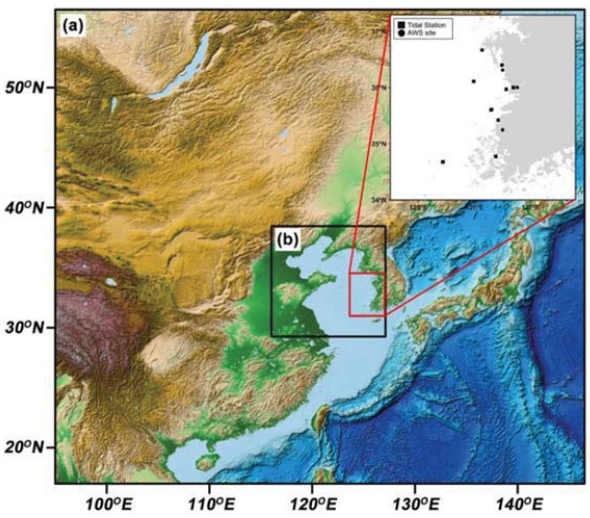

Figure 2. Map showing (a) a Synoptic study area (SSA) and (b) a Local study area (LSA) with tidal stations on the west coast of Korean peninsula (the minimap in the upper right corner).

Wavelet analysis

Monserrat *et al.* (2006) reported that the ocean oscillations by a meteo-tsunami almost always occurred in the periodic ranges between 1 minute and 2 hours. Eom *et al.* (2012) stated that most meteo-tsunamis in the Yellow sea occurred in the periodic ranges within 1 hour. As the Yellow sea is affected seriously by great tidal fluctuations compared to other seas around the Korean peninsula, an elimination of the tidal component is necessary to distinguish accurately the meteo-tsunamis from marine observations. The research methods of Kim *et al.* (2013) with a Butterworth low pass filter (Butterworth, 1930) were used to eliminate the tidal component in the marine observations and the period component between 2 and 60 minutes was extracted for the tide level data over last 12 years (2002-2013). Among the decomposed time series, those values with the maximum amplitude become the daily representative values. Daily representative values in excess of the 95% confidence interval at each tidal station will be classified as the occurrence of abnormal waves in terms of the power spectrum. A meteo-tsunami was concluded to have occurred along the west coast of the Korean peninsula if abnormal waves occur at more than three of the tidal stations at the same time (Kim *et al.*, 2013).

Synoptic weather analysis

After selecting the meteo-tsunami event days, synoptic weather analysis was carried out to analyze the synoptic causes of the meteo-tsunami using the standard weather charts (*e.g.* surface weather charts in 3 hour intervals and upper layers weather charts in 12 hour intervals) and auxiliary weather charts (*e.g.* local weather chart, radar images, lightening images, satellite images, and skew T- log P diagram) from every events. To understand the causes of the atmospheric disturbances related to the occurrence of meteo-tsunamis, every event was analyzed by synoptic weather analysis and was classified according to some synoptic types. In addition, an attempt was made to understand the seasonal characteristics and the generation mechanism of meteo-tsunamis according to each synoptic type.

RESULTS

Meteo-tsunamis selected by a wavelet analysis occurred a total of 92 times over the last 12 years. Spatial-temporal characteristics of meteo-tsunamis on the west coast of Korean peninsula were analyzed. Four types of meteorological causes were also categorized by synoptic weather analysis.

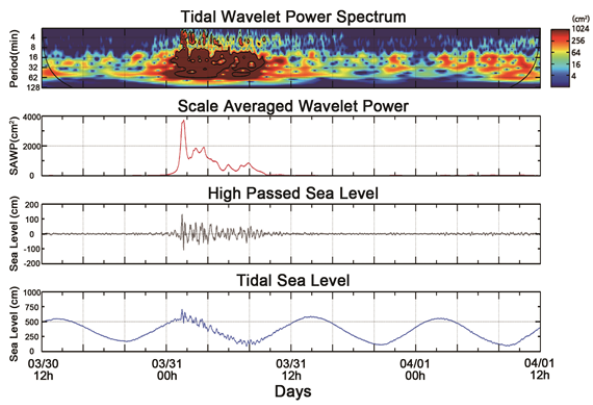

Figure 3. Examples of the wavelet and time series analysis on 31 March, 2007 in the Younggwang tidal station.

Table 1. *Dates of the meteo-tsunamis in excess of 3-SD and the maximum amplitudes of the ocean wave at each tidal stations (AH: Anheung, BR:Boryeong, CJ:Chujado, DH: Daeheuksando, EC: Eocheong, GS: Gunsan, JH: Janghang, WD: Wido, YG: Younggwang) during the last 12 years (2002-2013)*

(units: cm)

Event Day	YG	GS	CJ	JH	BR	WD	AH	DH	EC
2002. 04. 16	-27.3	25.7			-8.3	18.1	-22.6	-13.7	
2002. 10. 15	29.5	29.8			-8		32.8	14	
2002. 12. 05	-21	19.2						-17.3	
2003. 04. 25	-29.6	25.6					34.4		
2004. 09. 20	24.6	22.6			9.8				
2005. 02. 01	-25.1			106.7	-10.9				
2005. 04. 20		39.8		29.9	-19		36.3	27.3	
2005. 06. 02	23.2	-14.7		72.5			24.5		
2005. 12. 04	-24.6	-25.5			8.6				
2005. 12. 21	-26.1	14.1	-23.7		21.6				
2006. 04. 19		-31.7			-18.9	33.4	24.3		
2007. 03. 29	39.3	23.6				42.1		16.9	
2007. 03. 31	131.7	59.5	13.3	40.5	14.9	131.3	-70.2	-53.9	
2007. 05. 09	-23.5	-14	-20.8			21.5	-24.6	-19.8	
2008. 04. 25	-31.2		19	-21.6	6.7	-13.2	21.6	-23	10.4
2009. 04. 15	-38.1	15.3					42.1	30.9	-27.5
2009. 10. 17		-16.9			-18.1	-25.1			8.1
2010. 02. 10		-23.7	19.7		7.9	-21.7	19.1	-23.4	14.6
2010. 02. 11			18.2		0	-16.6		21.7	-14.5
2010. 03. 05			17.9					-19.5	8.5
2010. 05. 24			-15.1			18		-39.3	-11.2
2011. 04. 26			-24.3			23.2		-76.5	-24.2
2011. 04. 30			-11.5		-9.1	25.8	21.6	-23.2	23.7
2011. 05. 21		-15.2			-10.4	-18.5	19.8	13.4	-25.4
2011. 06. 08		-15.9			-7.6	-21.9	-185	-20.5	-25.6
2013. 02. 03			17.7			-15.4		19.4	-12.2
2013. 02. 04			-11.6			17.8		20.2	-17.1
2013. 03. 13			15			17.3		21.4	-12.5

Selection of the meteotsunami event

Table 1 lists the dates of meteo-tsunamis in excess of 3-SD and the maximum amplitudes of the ocean wave at each tidal station based on the selection established in this study. Twenty eight meteo-tsunamis in excess of 3-SD were found to have occurred over the last 12 years. In particular, an event of the maximum amplitude occurred in Younggwang on 31 March, 2007. Figure 3 shows the examples of the wavelet and time series analysis of ocean wave in the YG to determine an intensity and outbreak point in time of the meteo-tsunami.

Temporal characteristics of the meteo-tsunami

Ninety two meteo-tsunamis (3-SD: 28 times, 2-SD: 64 times) have taken place over the last 12 years (2002-2013) in the west coast of Korean peninsula (Figure 4). They occurred every season but the greaest frequency of occurrence was the spring (MAM; 53.3%) and winter (DJF; 26.1%) by 2-SD. In particular, strong meteo-tsunamis in excess of 3-SD have occurred in spring (53.6%) and winter (28.6%). Although there are differences according to the maximum amplitude criteria, they were concentrated in the spring and winter due to the continual passage of the low pressure system with a cold front and the expansion of the Siberian high pressure system, respectively. In addition, the frequency of the meteo-tsunamis is lower in the summer and autumn between June and November. The atmospheric instability caused by typhoons and localized torrential downpours often occurs in the summer season, but there are many cases that do not meet the criteria for the selection of a meteo-tsunami. On the other hand, the meteo-tsunami of the autumn has a stable atmospheric structure comparable to other seasons because of a migratory anticyclone. Therefore, the synoptic meteorological characteristics of the spring and winter season in the Korean peninsula are likely to affect the occurrence of meteo-tsunamis in the Yellow sea.

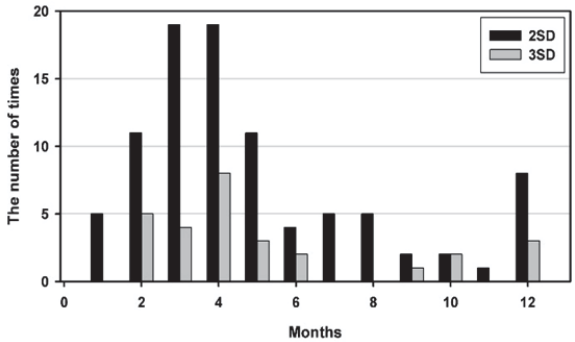

Figure 4. Monthly variations of the meteo-tsunami according to the the intensity over the last 12 years.

Spatial characteristics of the meteo-tsunami

Figure 5 shows the spatial distribution of the occurrence frequency of meteo-tsunamis at the tidal stations located in the west coast of the Korean peninsula. Meteo-tsunamis exceeding

2-SD tend to occur in the offshore areas (*e.g.* Daeheuksan and Eocheong) more than the inland area. In addition, meteo-tsunamis in excess of 3-SD often occur in Gunsan and Janghang without the distinction between the offshore and inland.

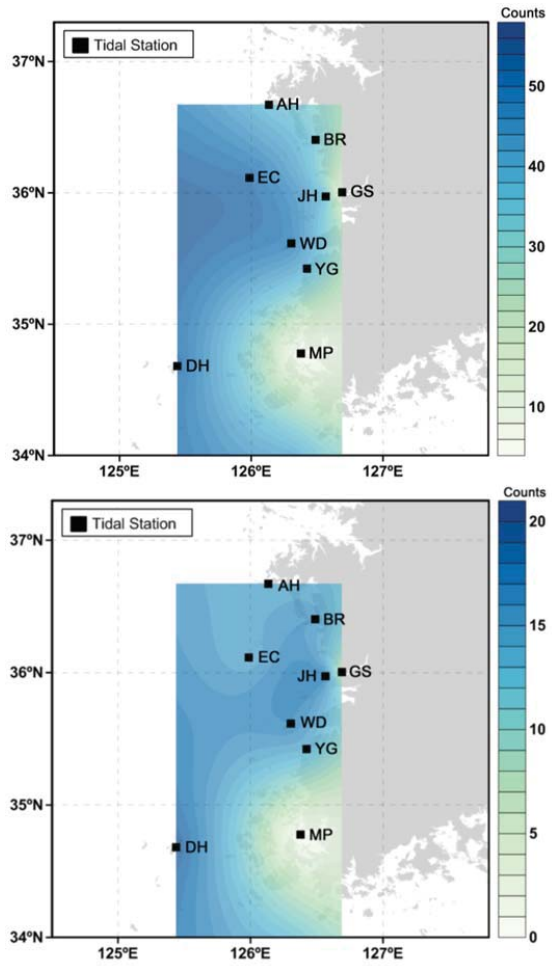

Figure 5. Spatial distributions of the meteo-tsunami by the intensity (2-SD (upper panel); 3-SD(bottom panel)) in the Yellow sea over the last 12 years.

Seasonal synoptic weather characteristics in Korean peninsula

According to previous results, the meteo-tsunamis in the west coast of the Korean peninsula occurred mainly in the spring and winter over the last 12 years. The Far East Asia region, including the Korean peninsula, is an area with four distinct seasons, and each season has representative characteristics climatologically. The spring in the Korean peninsula has the seasonal characteristics of a migratory anticyclone and an extratropical depression generated in Tibet and the Mongolian plateau passing through the Yellow sea every three or four days. The spatial distribution of this atmospheric pressure system generally increases the potential atmospheric instability in the Yellow sea. Atmospheric instability (*e.g.* pressure jump, low-level jet), which can lead to fluctuations of the sea level, often increase when a cold front in an extratropical depression passes through the Yellow sea (Figure 6(a)-(c)).

The Korean peninsula is generally dominated by the influence of the Siberian high pressure in winter, unlike spring. The Siberian high is characterized by having very cold and dry air, and causes a strong northwesterly wind expanding into the Korean peninsula. As the Siberian high is colder and drier, the temperature difference between the atmosphere and sea level over the Yellow sea increases with a change in wind speed. Changes in these meteorological factors can increase the instability of the sea level (Figure 6(d)).

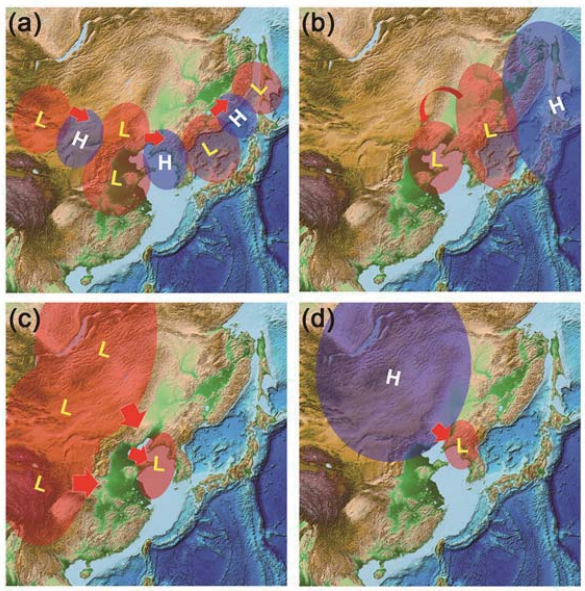

Figure 6. Examples of the typical distribution of atmospheric pressure system in the Korean peninsula ((a) type1, (b) type2, (c) type3, and (d) type4).

Synoptic weather mechanisms of meteo-tsunamis in Korean peninsula

According to the synoptic weather analysis performed in this study, meteo-tsunamis occurring in the Korean peninsula are largely caused by the four synoptic weather types. The three types of meteo-tsunamis that occur in the spring are caused mainly by a low pressure system. The first type (type 1) is caused by accumulation of the potential atmospheric instability in the low pressure system passing through the Yellow sea frequently (4-5 times over 5 days on average). The second type (type 2) is caused by the strong atmospheric instability of the secondary low pressure system generated by a blocking high

pressure system in the East sea or the Japanese islands. The last type (type 3) is caused by a strong travelling depression developed by the topographical difference passing through the west coast of the Korean peninsula. All three types of meteo-tsunamis have something in common in that they are accompanied by a strong cold front passing through the Yellow sea, but the meteorological reasons for the strong cold front are different.

A meteo-tsunami in winter is caused mainly by the Siberian high pressure expanded to the Yellow sea (type 4). Before the expansion of the Siberian high pressure to the Korean peninsula in winter, the weak low pressure system passing through the Shantung peninsula and Yellow sea causes a warm and humid atmosphere in the boundary layer and increases the potential instability of the boundary layer over the Yellow sea. After that, the dry and cold high pressure system passing over the warm sea surface increases the dynamical atmospheric instability in the Yellow sea.

CONCLUSIONS

Previous studies of meteo-tsunamis all over the world have shown that it is important to deal with both oceanographic and meteorological factors. The meteo-tsunami research in the west coast of the Korean peninsula for an analysis of meteorological causes has been somewhat inadequate. This study found that meteo-tsunamis in the west coast of the Korean peninsula often occurred in the spring and winter. In addition, a total of 92 meteo-tsunamis during last 12 years by 2SD criteria have occurred in the spring (53.3%) and winter (26.2%) (spring: 53.6%, winter 28.6% according to the 3SD criteria). The seasonal characteristics of meteo-tsunamis are believed to be related to the distinct four seasons in Korea. Moreover, it is closely related to the synoptic atmospheric structure or patterns caused by the atmospheric disturbances in the ocean boundary layer or on the sea level depending on each season. For further study, based on the results of synoptic weather analysis, additional efforts will be needed to reproduce the atmospheric instability in the ocean boundary layer or on the sea level by high resolution numerical modeling.

ACKNOWLEDGEMENT

This work was funded by the Korea Meteorological Administration Research and Development Program under Grant KMIPA2015-1073.

LITERATURE CITED

Butterworth, S., 1930. On the theory of filter amplifiers. *Experimental Wireless and the Wireless Engineer*, 7, 536-541.

Choi, B.-J.; Park, Y., and Kwon, K., 2008. Generation and growth of long ocean waves along the west coast of Korea in March 2007. *Ocean Polar Res.*, 30(4), 453-466.

Eom, H.-M.; Seung, Y.-H.; Woo, S.-B., and You, S.-H., 2012. Analysis of abnormal wave at the west coast on 31 March 2007. *Journal of Korean Society of Coastal Ocean Engineers*, 24, 217-227.

Kim, H.; Kim, Y.-K.; Woo, S.-B., and Kim, M.-S., 2014. Atmospheric analysis on the meteo-tsunami case occurred on 31 March 2007 at the Yellow sea of South Korea. *Journal of Environmental Science International*, 23(12), 1999-2014.

Kim, M.-S., 2014. Comparative analysis of propagation direction of abnormal waves in the Yellow Sea on 31 March 2007 and on 25 April 2008 by analysis methodology for abnormal waves. Incheon: Inha University, Master's thesis.

Kim, M.-S.; Woo, S.-B., and Eom, H.-M, 2013. Propagation of abnormal waves on 25 April 2008 at the west coast of South Korea. *Journal of Coastal Research*, SI 65, 731-735.

Monserrat, S.; Vilibić, I., and Rabinovich, A.B., 2006. Meteotsunamis: atmospherically induced destructive ocean waves in the tsunami frequency band. *Natural Hazards and Earth System Sciences*, 6, 1035-1051.

Yoo, J.; Lee, D.-Y.; Ha, T.-M.; Cho, Y.-S., and Woo, S.-B., 2010. Characteristics of abnormal large waves measured from coastal videos. *Natural Hazards and Earth System Sciences*, 10, 947-956.

Journal of Coastal Research	SI	75	1152 - 1156	Coconut Creek, Florida	2016

Overview of Super Typhoon Haiyan and Characteristics of Human Damage due to its Storm Surge in the Coastal Region, Philippines

Shuichi Kure[†*], Yasuhito Jibiki[†], Kanako Iuchi[†], and Keiko Udo[†]

[†+]International Research Institute of Disaster Science, Tohoku University
Sendai 9800845, Japan.

www.cerf-jcr.org

www.JCRonline.org

ABSTRACT

Kure, S.; Jibiki, Y., Iuchi K., and Udo, K., 2016. Overview of Super Typhoon Haiyan and characteristics of human damage due to its storm surge in the coastal region, Philippines. *In:* Vila-Concejo, A.; Bruce, E.; Kennedy, D.M., and McCarroll, R.J. (eds.), *Proceedings of the 14th International Coastal Symposium* (Sydney, Australia). *Journal of Coastal Research*, Special Issue, No. 75, pp. 1152 - 1156. Coconut Creek (Florida), ISSN 0749-0208.

Approximately 2 years have passed since the catastrophic damage caused by Super Typhoon Haiyan, which struck the Philippines on November 8, 2013. The purpose of this paper is to illustrate what actually happened during the Haiyan event, by examining observations and literature reviews. Our questionnaire survey results were analyzed to understand availabilities of opportunities to participate in disaster-related education programs and drill to local residents both before and after Haiyan. Following our analysis, we conclude that there were few opportunities for local residents to take part in disaster-related activities in the highly damaged areas in Leyte before Haiyan. After Haiyan, many opportunities for training were provided by non-governmental organizations (NGOs) and city and barangay officials. Residents leant about possible typhoon impacts during Typhoon Haiyan, and the educational activities that took place afterwards, facilitated successful evacuation during Typhoon Ruby. Based on our overview of Typhoon Haiyan and characterization of the human damage incurred by the storm surge in the target area, we recommend some future steps that contribute to reduce the risks posed by natural disasters in the Philippines.

ADDITIONAL INDEX WORDS: *Typhoon Haiyan, Storm Surge, Philippines, Disaster Education.*

INTRODUCTION

Approximately two years have passed since the catastrophic damage caused by Super Typhoon Haiyan, which struck the Philippines on November 8, 2013. Haiyan generated remarkably high wind speeds, storm surges and waves – of unprecedented magnitude – resulting in over 7,000 casualties.

Many surveys and analyses regarding the damage caused by Haiyan have been conducted. Tajima *et al.* (2014) conducted a detailed on-site survey regarding the damage caused by the wind and storm surge, and used the results to map the storm surge inundation areas in Leyte. Mas *et al.* (2015) identified severely damaged houses in Leyte by inspecting satellite images and confirmed the damage with on-site surveys.

In terms of the behavior of the storm surge in the Leyte Gulf, the local amplification of the water surface elevation due to seiche was significant (Mori *et al.,* 2014). This conclusion was based on an analysis of the best available hindcast results. Concerning the high waves observed in Samar, Roeber and Bricker (2015) found that the tsunami-like wave that struck Hernani was the result of the abrupt breaking of waves over the steep reef face, which generated an energetic surf beat.

Jibiki *et al.* (2016) found that more than 80% of local residents did not know the meaning of the term "storm surge" and Esteban *et al.* (2015) pointed out that local people underestimated the impact of Haiyan before its landfall. This kind of underestimation and lack of knowledge prevented local people from evacuating even though they received the storm surge warning almost 1 day before Haiyan's landfall. On the other hand, as Kure *et al.* (2016) reported, the performance and knowledge of barangay (the barangay is the smallest administrative division in the Philippines) captains contributed to a reduction in the number of human casualties during the storm. The number of casualties sustained during this event resulted from a combination of the massive force of Super Typhoon Haiyan and social factors, such as the low level of disaster education and awareness.

In this paper, an overview of the Haiyan event is presented, based on observation data. Using literature reviews, we characterize the human casualties caused by the storm surges in Tacloban, Palo and Tanauan, Leyte. Furthermore, the opportunities available for participating in disaster education and prevention activities, both before and after Haiyan, were evaluated. We based our evaluation on a questionnaire and interviews with local people and barangay captains. This helped us to understand the impact of the educational opportunities provided after Haiyan. One year after the Haiyan event, another powerful tropical cyclone, Typhoon Ruby, struck Visayas leaving 18 casualties. The evacuation situation, including how the training provided after Haiyan affected the behavior of local people during the Ruby event, are also discussed in this paper.

METHODS

In this section, we describe the characteristics of Haiyan, based on observational data, literature reviews and a questionnaire that enabled us to evaluate the opportunities for disaster education before and after the event.

DOI: 10.2112/SI75-231.1 received 15 October, 2015; accepted in revision 15 January, 2015.
*Corresponding author: kure@irides.tohoku.ac.jp
©Coastal Education and Research Foundation, Inc. 2016

Overview of typhoon Haiyan

On November 8, 2013, 4:40 A.M. Philippine time, Haiyan made its first landfall over Guiuan, Eastern Samar, with maximum wind speeds of 125 kt and a central pressure of 895 hPa (Category 5 on the Saffir-Simpson Hurricane Scale). Figure 1 shows the path of Haiyan. Tacloban, Palo and Tanauan were the hardest hit, as shown in Figure 2.

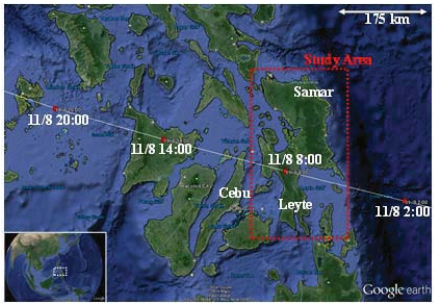

Figure 1. Path of Haiyan shown by white line (Google Earth).

Figure 2. Location of Tacloban, Palo and Tanauan.

Observations

Figure 3 shows the time series of the observed wind speed, mean sea level pressure and rainfall at the weather station in Tacloban. The data were provided by the Philippine Atmospheric Geophysical and Astronomical Services Administration (PAGASA). Haiyan made landfall in Tacloban at around 8:00 A.M (November 8). A rapid increase in wind speed and rainfall, and a decrease in the mean sea level pressure around the peak landfall time, can be seen clearly in Figure 3. The observation equipment was completely destroyed by the high winds and the inundation caused by the storm surge, so data recordings stopped around the peak time. This means the peak wind speed and pressure values may not have been recorded. This incident proves that the ground wind speed and storm surge associated with Haiyan were enormously strong. Figure 4 shows the time series of the predicted astronomical tide at Guiuan, from data provided by PAGASA. The tide levels are based on the average mean sea level. It can be seen from the figure that the tide level was not particularly high when Haiyan made landfall. If the landfall had occurred during high tide, the damage caused by storm surges and high waves would have been more serious.

Figure 5 shows the flood runoff response in the Lingayon River, flowing into San Pedro Bay through Palo, due to the heavy rainfall during Haiyan. In Figure 5 we see that the water depth increased due to the rainfall induced by Haiyan. The water depth data were measured visually at river gauge stations by members of the Department of Public Works and Highway (DPWH). It should be emphasized that there is a time difference between the rainfall-induced flood peak and the storm surge peak. Numerical simulations and local interviews confirmed that the storm surge occurred in San Pedro Bay at around 6:30–8:00 A.M. on November 8, 2013, but the rainfall-induced flooding in the rivers shows that the peak flood time was in the afternoon. If the peak flooding in the rivers had occurred during the storm surge peak, the damage caused by storm surges and river flooding would have been more serious. This is because the combination of the storm surge and flood would have significantly increased the water levels downstream of rivers.

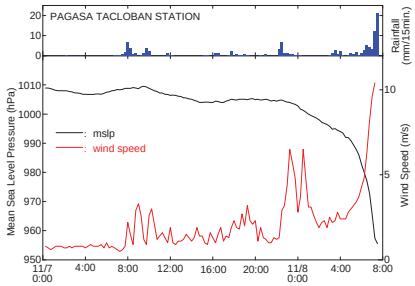

Figure 3. Time series of the wind speed and mean sea level pressure at Tacloban station, Leyte.

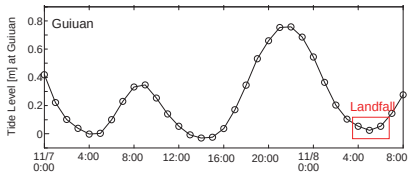

Figure 4. Time series of the predicted astronomical tide level.

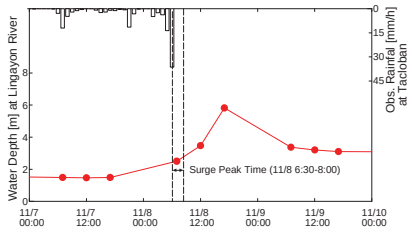

Figure 5. Observed water depth data at Lingayon River, Palo.

Damages

Haiyan caused massive damage to the Philippines. As of 6:00 A.M. on March 14, 2014, 6,268 individuals were reported dead, 28,689 were injured and 1,061 were missing. A total of 3,424,593 Filipino families were affected. The number of damaged houses was 1,140,332 (550,928 totally destroyed and 589,404 partially destroyed). The total direct cost of the damage

was estimated at PHP 39,821,497,852.17, with damage to infrastructure costing PHP 19,559,379,136.11 and damage to agriculture costing PHP 20,262,118,716.06 (NDRRMC, 2014). The number of human casualties in Tacloban, Palo and Tanauan in Leyte was very large due to the storm surge in San Pedro Bay. According to the information provided by each city, as of February 25, 2014, the number of people who died or missing from Tacloban, Palo and Tanauan counted 2,603, 1,101 and 859, respectively. This means that more than 60% of the casualties due by Haiyan were concentrated in these three cities in Leyte.

Warning

At 11:00 A.M., PAGASA announced Severe Weather Bulletin #3, a warning that the storm surge wave may reach a height up to 7 m in the coastal areas of Eastern Samar, Samar, Leyte and Visayas, Southern Leyte. It should be emphasized that PAGASA estimated and warned the 7 m wave height in coastal areas about 18 hours before the first landfall in Guinuan. This estimation was based on numerical simulations and historical records of waves. Several surveys confirmed after Haiyan that the estimations of wave height provided by PAGASA were accurate. In reality, Tacloban experienced a storm surge of 7 m.

Evacuation

Main problems hindering evacuation efforts prior to Haiyan were lack of disaster education, poverty and inappropriate evacuation facilities. As Jibiki *et al.* (2016) pointed out, many people did not know what a storm surge could do to them. They also explained that, if the warning included a word "tsunami," they would have evacuated. This incident clearly explains the importance of disaster education and the use of appropriate methods for transferring disaster-related information to local people. Poverty was another indirect cause to people not evacuating; strong young men stayed in their houses during Haiyan from the fear of their property being burgled while away. Evacuation facilities, which included schools and churches, were not structurally appropriate for Haiyan-like events with storm surge and enormously strong winds.

Evaluation of human loss and disaster education

In this paper, opportunities for disaster training and drills before and after the Haiyan were evaluated, based on a questionnaire survey targeting local residents and barangay captains. We conducted the survey in Tacloban, Palo, and Tanauan from March 14 to March 22, 2014 to assess local people's evacuation behavior at the time of Haiyan, as well as the availability of education before the event. Survey data was collected with the paper-based interviews, and 642 results were obtained from 12 barangays. Additional interviews were conducted in November 2014 and February 2015 targeting 33 barangay captains, to identify how they were engaged in disaster-related training after Haiyan. The target barangays were selected based on the number of deaths and missing persons due to Haiyan and the proportion of fatalities in each barangay.

RESULTS

In this section, we discuss human loss caused by Super Typhoon Haiyan. We also assess how the experience gained during Haiyan contributed to disaster education activities – and affected evacuation behaviors – during the Typhoon Ruby.

Characteristics of human loss

Kure *et al.* (2016) summarizes the factors that magnified the damage caused by Haiyan as: i) a massive external force; ii) concentrated population in coastal areas; iii) vulnerability of buildings and evacuation facilities; and iv) lack of awareness and preparation. Figure 6 shows a spatial distribution of the number of deaths and missing persons, and the fatality ratio, in each barangay in Tacloban, Palo and Tanauan. It can be clearly seen from Figure 6 that high numbers of deaths and missing persons were concentrated in the coastal areas. This is due to storm surge that occurred in San Pedro Bay.

Figure 7 shows the relationship between average inundation depth and proportion of fatalities in Tacloban, Palo, and Tanauan during the Haiyan event (Kure *et al.*, 2016). The fatality ratios increased as the average inundation depth increased. However, two trends can be seen in Tacloban and Tanauan. In all three cities, human losses increased rapidly when the surge depth was greater than 3 m. Some barangays in Tacloban and Tanauan, in the dotted circle found in Figure 7, show gradual increases in human losses. Kure *et al.* (2016) pointed out that the barangay captains' capabilities and performance affected these trends, and emphasized that the barangay captains may have played an important role in saving lives during the Haiyan event and could do so again during future typhoon events.

From the overview of the Haiyan event explained, we can conclude that disaster-related education and activities are extremely important for saving lives and reducing risk of human loss in a wake of future super typhoons.

Opportunity for disaster education

As we discussed in the previous section, underestimation of the wind speed of Haiyan prior to landfall, and the use of the terminology 'storm surge' in warning resulted people to stay on their land rather than evacuating. However, many barangay captains who encouraged local residents to evacuate saved many lives. As such, it is clear that disaster education and preparation is indispensable for reducing the future disaster risks.

Our survey results showed that many people did not have the opportunity to participate in disaster training courses or drills prior to Haiyan, as shown in Figure 8. Numerous respondents answered "Very low" to the question "Did you have any opportunities to learn about natural disasters before Typhoon Haiyan?" Many respondents indicated that they did not have the opportunity to attend evacuation training before Haiyan. As such, it is clear that local residents did not have the opportunity to learn about storm surge risks in their area. This could be because the typhoon risk in Leyte was estimated to be much smaller than that in the Samar and Luzon regions of the Philippines.

After Haiyan, apparent changes on local people's attitudes towards disaster prevention activities were identified in our survey results; 87.1% of barangay captains answered "Very high" on the question regarding the extent to which barangay residents changed their thinking concerning disaster prevention and preparation, and 100% of the barangay captains indicated that they want to attend future training pertaining to evacuation

during typhoons, storm surges, earthquakes and tsunamis. Furthermore, 74.2% of barangay captains indicated that they participated in activities relating to disaster prevention and preparation after Haiyan, including disaster-related seminars, training sessions, lifesaving drills, and evacuation drills, mainly provided by non-governmental organizations (NGOs) and city and barangay officials.

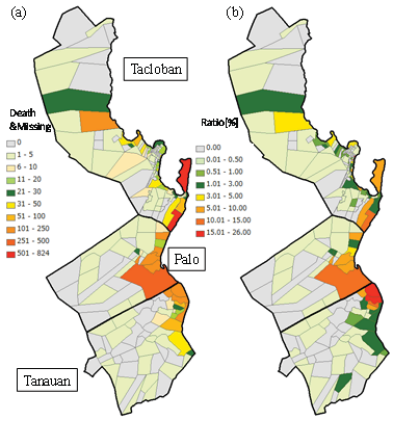

Figure 6. The number of deaths and missing persons (a) due to Super Typhoon Haiyan, and the proportion of fatalities [%] (b) (Kure *et al.*, 2016).

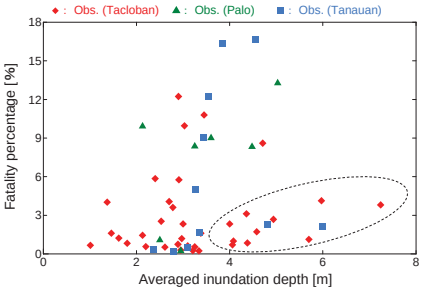

Figure 7. Relationship between average inundation depth and the proportion of fatalities (Kure *et al.*, 2016).

We found that these activities helped people evacuate during Typhoon Ruby: 88% of barangay captains indicated that the extent to which those activities helped was "Very high" during the Ruby event and 93.5% answered that the extent to which the experience of the Haiyan event helped during the Ruby event was "Very high."

From our survey results, we conclude that there were few opportunities to participate in disaster training activities in the highly damaged area of Leyte but, after Haiyan, many activities were available for local residents, provided by NGOs and city and barangay officials. The experience of Haiyan and subsequent training exercises helped ensure the success of the evacuation efforts undertaken prior to Typhoon Ruby. It should be emphasized that the Ruby event proves that much lessons on impact of typhoon disaster was learned from the Haiyan event. People properly prepared and evacuated well, and saved many lives during Ruby, and built foundation to practice well during the future super typhoons. However, it should be noted that comparing damage and loss results between Haiyan and Ruby directly could be misleading without approproiate interpretations, because external forces between the two were different, as in the stormsurge occurence observed in Haiyan. Also, relationship between opportunities of the disaster-related activity, the evacuation situation and damage in each barangay should be evaluated more quantitavely in the future study.

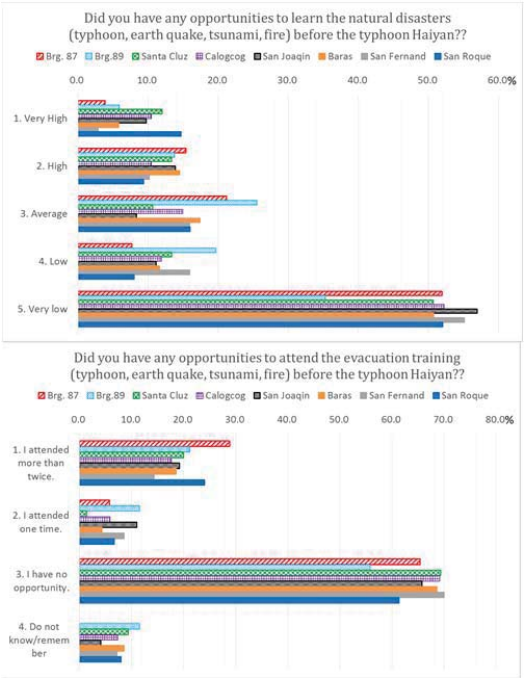

Figure 8. Opportunities for education and training.

DISCUSSION

Based on the observational data and literature review, we concluded that the external forces of Haiyan were enormously strong but the damage caused by storm surges would have been further devastating depending on the tidal conditions at the time of landfall. Another point to underscore is that the storm surge of a similar scale could happen again in this region because of the seiche in San Pedro Bay (Mori *et al.*, 2014). From the social aspects, we identified that the exerbated human losses by the typhoon Haiyan was due to lack of knowledge on 'storm surge' prior to the event in general (Jibiki *et al.*, 2016), yet the effort to lead evacuation by the barangay captains contributed to reduce additional loss of lives (Kure *et al.*, 2016). In the event of Typhoon Ruby that occurred about a year later, people successufuly evacuated because they were aware of appropriate procedures from the Haiyan experience and were involved in educational activities that took place afterwards. We underscore that sharing knowledge on disaster events and participating in evacuation training and disaster drills, to prepara for future typhoon events are extremely important.

We now address future challenges to reduce risks associated

with disasters in the Philippines. Two years have passed since the Typhoon Haiyan catastrophe. Now, robust efforts are being made to rebuild severely affected areas such as Tacloban. The DPWH began to construct a seawall along the coast of Tacloban, Palo, and Tanauan. The wall is planned to be built 4 m higher than the mean sea level. Although the relocation of houses in the newly designated no building zone along the coast to the northern area of Tacloban have started, not all of the residents near the ocean will be relocated to higher lands. Additionally, the construction of the seawall needs a significant amount of time. It means that residents in some areas along the coast continue to be exposed to disaster risks. Therefore, evacuation during typhoon continues to be the priority to save lives of population exposed to risks.

In order to do so, first, hazard maps should be carefully checked by city and barangay officials. For instance, the Japan International Cooperation Agency developed a detailed storm surge hazard map based on numerical simulations, and conducted a location and capacity assessment of evacuation centers using the map created. To help local people to understand the hazard risks and locate appropriate evacuation facilities, introducing people to, and explaining these hazard maps are strongly encouraged. Furthermore, the Department of Science and Technology developed multiple hazard maps illustrating the risks of storm surges and landslides. In addition to understanding hazards through such newly created maps, it is also vital for local people to understand what such hazards could result as potential damage. Jibiki *et al.* (2016) suggested that underestimation of damages was made by those who answered to be understanding technical terms, such as "wind speed," "maximum instantaneous wind speed," and "atmospheric pressure." This implies that there is a gap between understanding hazard risks and estimating damages, and thus filling such gap is critical as the future efforts.

Second, the warning transfer system at the local barangay level requires improvement. As we discussed, the capabilities and performance of barangay captains played important roles in ensuring appropriate evacuation of the barangay residents. The warning transfer system should be designed so that the warnings can be delivered directly to local residents by the barangay captains or officials. Many people claimed that if they had received the evacuation order directly from the barangay captain, they would have evacuated. Third, disaster-related education and training should be implemented at the barangay level. Based on the disaster-related education, evacuation drills, etc., a Community Based Disaster Risk Reduction (CBDRR) strategy should be developed at the city and barangay levels. The CBDRR strategy may be suitable to mitigate future disasters in the Philippines, because a system involving both barangay communities and captains enables action to be taken at a local level. Finally, we must never forget Super Typhoon Haiyan. As Jibiki *et al.* (2016) pointed out, there were similar storm surge disasters in Tacloban in 1897 and 1912, but only few local residents remember those disasters. To keep reminding people of the Haiyan event, continuous evacuation drills are strongly encouraged. Also, Haiyan-related ceremonies and activities, including the construction of monuments or statues, will help people to remember the disaster.

CONCLUSIONS

In this paper, we first reviewed Super Typhoon Haiyan based on the ground observations and literature reviews to understand what actually happened during the storm. Our investigation confirmed that, in addition to the large external force of Haiyan, insufficient preparation and lack of education contributed to the human cost incurred by Haiyan.

We analyzed our survey results, which helped us understand the opportunities available for local residents to participate disaster-related training courses in Tacloban, Palo and Tanauan before and after Haiyan. Based on our analysis, we conclude that the residents of highly damaged areas in Leyte had few opportunities to prepare for disasters. After Haiyan, many such opportunities were provided to local residents by NGOs and city and barangay officials, and these activities facilitated evacuation during the Ruby event. To reduce the risks of future disasters related to typhoons, the development of a CBDRR strategy is highly recommended. This should occur at both the city and barangay levels and comprise both education and evacuation drills. Remembering Haiyan will be critically important for ensuring the success of future disaster reduction exercises.

LITERATURE CITED

Jibiki, Y.; Kure, S.; Kuri, M., and Ono, Y., 2016. Analysis of early warning systems: the case of super-typhoon Haiyan. *Int. J. Dis. Risk Red.* In Print.

Kure, S.; Jibiki, Y.; Quimpo, M.; Manalo, U.; Ono, Y., and Mano, A., 2016. Evaluation of the characteristics of human loss and building damage and reasons for the magnification of damage due to Typhoon Haiyan. *Coastal Eng. J.* In Print.

Mas E.; Bricker, J.D.; Kure, S.; Adriano, B.; Yi, C.J.; Suppasri, A., and Koshimura, S., 2015. Field survey report and satellite image interpretation of the 2013 Super Typhoon Haiyan in the Philippines. *Nat. Hazards Earth Syst. Sci.* 15, 805-816.

Esteban, M.; Valenzuela, P.; Yun, N.Y.; Mikami, T.; Shibayama, T.; Matsumaru, R.; Takagi, H.; DahnThao, N.; Leon, M.D.; Oyama, T., and Makamura, R., 2015. Typhoon Haiyan 2013 Evacuation Preparations and Awareness. *J-SustaiN*, 3(1).

Mori, N.; Kato, M.; Kim, S.; Mase, H.; Shibutani, Y.; Takemi, T.; Tsuboki, K., and Yasuda, T., 2014. Local amplification of storm surge by Super Typhoon Haiyan in Leyte Gulf. *Geophysical Research Letters*, 41(14), 5106-5113.

NDRRMC, 2014. SitRep No.107, Available at: http://reliefweb.int/sites/reliefweb.int/files/resources/Update%20Yolanda%20Sitrep%20107.pdf

Roeber, V. and Bricker, J.D., 2015. Destructive tsunami-like wave generated by surf beat over a coral reef during Typhoon Haiyan. *Nat. Commun.*, 6:7854.

Tajima, Y.; Yasuda, T.; Pacheco, B.M.; Cruz, E.C.; Kawasaki, K.; Nobuoka, H.; Miyamoto, M.; Asano, Y.; Arikawa, T.; Ortigas, N.M.; Aquino, R.; Mata, W.; Valdez, J., and Briones, F., 2014. Initial report of JSCE-PICE joint survey on the storm surge disaster caused by Typhoon Haiyan. *Coastal Eng. J.* 56(1), 1450006-1-12.

Journal of Coastal Research	SI	75	1157 - 1161	Coconut Creek, Florida	2016

A Hierarchical Bayesian Model-Based Uncertainty Analysis for Tsunami Heights along Shorelines in Korea

Hyun-Han Kwon[†], Jin-Young Kim[†], Byoung Han Choi[††], and Yong-Sik Cho[§*]

[†]Department of Civil Engineering
Chonbuk National University, 567 Baekje-daero
Deokjin-gu Jeonju-si, Jeollabuk-do 54896, Korea

[§]Department of Civil and Environmental Engineering
Hanyang University, 222 Wangsimni-ro,
Seongdong-gu, Seoul 04763, Korea

[††]Rural Research Institute Korea Rural Community
Coporation, 870 Haean-ro Sangnok-gu Ansan-si,
Gyeonggi-do, 15634, Korea

www.cerf-jcr.org

www.JCRonline.org

ABSTRACT

Kwon, H.-H.; Kim, J.-Y.; Choi, B.H., and Cho, Y.-S., 2016. A hierarchical Bayesian model based uncertainty analysis for tsunami heights along shorelines in South Korea. *Proceedings of the 14th International Coastal Symposium* (Sydney, Australia). *Journal of Coastal Research*, Special Issue, No. 75, pp. 1157 - 1161. Coconut Creek (Florida), ISSN 0749-0208.

Uncertainties in estimation of tsunami inundation risk are mainly caused by limited information of tsunami characteristics associated with locations and propagation paths. It is common to use probability distributions in risk assessment so that a selection of the probability distributions and good estimates of the parameters are especially important to reduce the uncertainties in the assessment. The uncertainty in existing studies, however, has not been properly addressed. In this study, a new probabilistic tsunami-inundation risk assessment approach is proposed to characterize the uncertainties. A main objective of this study is to combine different sources of the uncertainties related to the attributes of earthquake (i.e., location and magnitude) and the estimation of the parameters of the distribution (i.e., Gamma distribution) in a Hierarchical Bayesian Model (HBM) framework. This study estimated the tsunami inundation risk with a Bayesian credible interval by combining the data of three historical tsunamis and 11 virtual tsunamis. The results indicate that the HBM well represented the underlying distribution and the associated uncertainties. In addition, the results confirmed that the proposed model was more relevant in quantitatively combining and estimating the uncertainties. The inundation risk information incorporating uncertainty could be used to better understand and manage tsunami-related hazards.

ADDITIONAL INDEX WORDS: *Hierarchical Bayesian model, Tsunami, Inundation risk, Uncertainty analysis*

INTRODUCTION

During the last few decades, many countries have suffered extensive property damage due to devastating tsunamis. Among these tsunamis, the most severe was the Sumatra Tsunami occurring in Indonesia in December 2004. The tsunami was triggered by an earthquake off Sumatra Island. About 230,000 people were killed, and massive property damage was reported. Also, during a tsunami in the South China Sea in 1782, around 40,000 casualties were recorded. In addition to these, tsunamis frequently occur in many places around the world. In Korea, the potential damage to coastal areas from unexpected tsunamis is relatively high. In particular, the East Sea has deep water and is surrounded by Korea, Japan, and Russia. Several devastating tsunamis have occurred off the western coast of Japan.

Human deaths and property damage occurred in the eastern coastal areas due to tsunamis in the East Sea in 1983 and 1993. Until now, though there have not been considerable casualties or property damage in Korea as in Indonesia and Japan, Korea is at potential risk of tsunami because eastern coastal areas are close to Japan. Thus, tsunami-induced inundation risk needs to be assessed in order to mitigate casualties and property damage. In this regard, a hierarchical Bayesian model was introduced to better identify the underlying distribution and to understand different sources of the uncertainties related to the attributes of earthquakes (i.e., location and magnitude) and the estimation of the parameters of the distribution (i.e., Gamma distribution) in a Hierarchical Bayesian framework.

Numerous studies have focused on the determination of optimal probability distribution and its parameters. Many studies were carried out to better identify probability distribution type and to better estimate the parameters of probability distribution through various methods (*e.g.,* L-moment and maximum likelihood method) (Hosking *et al.*, 1985; Hosking, 1990; Lee and Kwon, 2011; Heo *et al.*, 2007). However, the conventional approaches have focused less attention on the uncertainties associated with the parameters (Kwon *et al.*, 2013; Kim *et al.*, 2014).

Probabilistic risk analysis has been used for estimation of extreme return levels. A main assumption in probabilistic risk analysis is that the errors (*e.g.*, uncertainty) associated with parameters are normally distributed. However, it has been largely acknowledged that geophysical data including tsunami height and rainfall showed heavy tails (Kwon *et al.*, 2008). In addition, the sampling errors in the frequency analysis model have been generally ignored when estimating the parameters (Kim *et al.*, 2015). This study aims to develop a Hierarchical Bayesian Model (HBM) for the estimation of extreme return levels of tsunami height so that the uncertainty can be

DOI: 10.2112/SI75-232.1 received 15 October, 2015; accepted in revision 15 January, 2015.
*Corresponding author: ysc59@hanyang.ac.kr
©Coastal Education and Research Foundation, Inc. 2016

adequately considered. First, the tsunami heights corresponding to the eleven probable undersea earthquakes were obtained along the coastline using numerical simulation. The HBM was then applied to estimate the parameters of the probability density function of tsunami height.

The background and purpose of this paper are described in the Introduction. Then, the proposed approach for tsunami risk analysis in South Korea is briefly introduced, and the results are summarized.

METHODS

In this study, eleven virtual and three historical tsunami events are considered to investigate the maximum flooding depth at specific locations on the eastern coast of the Korean Peninsula (Lee *et al.*, 2012). The eleven virtual tsunamis suggested by the Korea Peninsula Energy Development Organization (KEDO, 1999) were selected to generate the initial conditions of free surface displacement. In addition, three historical tsunamis that occurred in the East Sea during the last several decades were also included in this study. These historical tsunamis are the Niigata Tsunami that occurred in 1964, Central East Sea Tsunami in 1983, and Hokkaido Tsunami in 1993. Thus, the probable maximum tsunamis consist of eleven virtual and three historical tsunamis in this study. Figure 1 shows the areas of initial free surface displacement and the earthquake sources of the eleven virtual and three historical tsunamis. Table 1 shows the genesis of earthquakes and fault parameters for tsunamis used in this study.

Table 1. *The genesis of earthquakes and the fault parameters for three historical and eleven virtual tsunamis*

Case	Location		θ	H	δ	λ	L	W	D	M
	Longitude	Latitude	(°)	(km)	(°)	(°)	(km)	(km)	(m)	
1964	139.4	38.7	189	1.0	56	90	80	30	3.3	7.5
1983	138.8	40.2	355	3.0	40	90	40	30	3.0	7.8
1993	139.3	42.3	175	5.0	60	105	30	25	2.5	7.8
Case 1	137.5	37.5	0	0.0						
Case 2	137.7	38.3	145	145						
Case 3	138.0	39.0	275	275						
Case 4	138.4	39.7	170	170						
Case 5	138.7	40.2	100	100						
Case 6	138.9	40.9	1.0	1.0	40	90	125	62	631	8.0
Case 7	139.0	41.7	1.0	1.0						
Case 8	139.1	42.1	4.0	4.0						
Case 9	139.1	42.9	2.0	2.0						
Case 10	139.2	43.5	2.0	2.0						
Case 11	139.2	44.4	3.0	3.0						

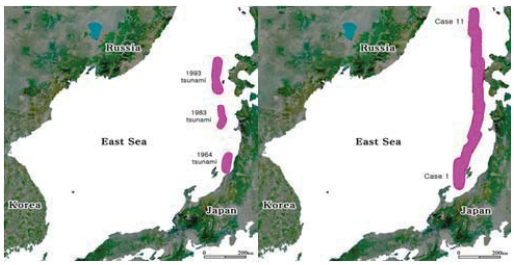

Figure 1. Location of historical and virtual tsunami events.

In Table 1, H is the depth of the fault plane, θ is the strike angle, δ is the dip angle of the fault, λ is the slip angle on which fault slips, L is the length of the fault, W is the width of the fault, D is the displacement of the fault, and W is the scale of the earthquake.

Different nesting of the tsunami propagation model combining small grid meshes and a moving boundary condition were employed to better simulate the run-up process in the coastal area A total of six computational domains were used in the numerical analysis as A~F and are shown in Figure 2. Region A used the free transmission condition, and the other regions used the dynamic linking method as a boundary condition for the open sea. From regions A to D, a fully reflected condition was used and regions E and F used a moving boundary condition for land (Kim *et al.*, 2012).

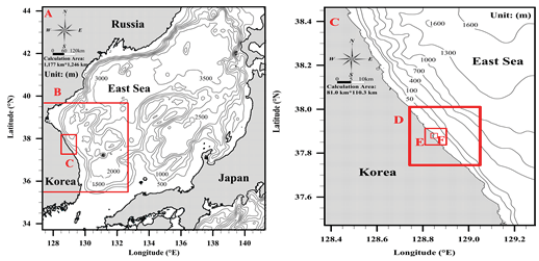

Figure 2. Computational domains and bathymetry of the East Sea.

This study first considered the Log-normal, Gamma, and Weibull distributions as candidate distributions for tsunami height. The three respective probability density functions can be written as follows:

$$f(X|\mu,\sigma) = \frac{1}{X\sigma\sqrt{2\pi}} exp\{\frac{-(lnX-\mu)^2}{2\sigma^2}\} \quad (1)$$

$$f(X|k,\theta) = \frac{1}{\theta^k \gamma(k)} x^{k-1} exp^{-\frac{X}{\theta}} \quad (2)$$

$$f(X|\lambda,k) = \frac{k}{\lambda}(\frac{X}{\lambda})^{k-1} exp^{-(\frac{X}{\lambda})^k} \quad (3)$$

This study investigated underlying distributions using the DIC (deviance information criterion). The DIC is similar to AIC (Akaike information criterion) and BIC (Bayesian information criterion), which have been used as compatibility methods in the conventional models. The DIC is particularly useful in Bayesian model selection problems where the posterior distributions of the models have been obtained by Markov chain Monte Carlo (MCMC) simulation. The DIC can be written as described in Spiegelhalter *et al.* (2002).

$$DIC = \overline{D} + P_D \quad (4)$$

$$\overline{D} = E_{\theta|y}[-2lnf(y|\theta)] \quad (5)$$

where $\overline{D}$ is a measure of fit between the model and the data; the larger is this value, the worse is the fit. In Equation (5), $f(y|\theta)$ represents a likelihood function, while P_D is the index expressing the complexity of the model representing the number of effective parameters. This study utilized DIC in order to

select the optimum probability distribution among the three chosen probability distributions, and the results are presented in Table 2.

Table 2. *Comparison of deviance information criterion for three distributions for three historical and eleven virtual tsunamis*

Case	Log-normal			Gamma			Weibull		
	$\bar{D}$	P_D	DIC	$\bar{D}$	P_D	DIC	$\bar{D}$	P_D	DIC
1964	20035	2.0	20037	21332	2.0	21334	23261	2.0	23263
1983	47375	2.0	47377	47010	2.0	47012	47423	2.0	47425
1993	49210	2.0	49212	48654	2.0	48656	49046	2.0	49048
Case1	51925	2.0	51927	51100	2.0	51102	51222	2.0	51224
Case2	50350	2.0	50352	49569	2.0	49571	49672	2.0	49674
Case3	46286	2.0	46288	45117	2.0	45119	45030	2.0	45032
Case4	46121	2.0	46123	45299	2.0	45301	45388	2.0	45390
Case5	39390	2.0	39392	39041	2.0	39043	39295	2.0	39297
Case6	29027	2.0	29029	28800	2.0	28802	29261	2.0	29263
Case7	20394	2.0	20396	20023	2.0	20025	20408	2.0	20410
Case8	1779	2.0	1781	2134	2.0	2136	2819	2.0	2821
Case9	24090	2.0	24092	22521	2.0	22523	22184	2.0	22186
Case 10	40204	2.0	40206	39436	2.0	39438	39505	2.0	39507
Case 11	36368	2.0	36370	35517	2.0	35519	35659	2.0	35661

As shown in Table 2, the Gamma distribution is most suited to the frequency analysis given the DIC. Therefore, the Gamma distribution was chosen as the underlying distribution for tsunami height in this study.

The HBM is a multi-level statistical model that estimates the posterior distribution of the parameters. The HBM is useful when information is available on several different levels of observation. The HBM helps in the understanding of multi-parameter problems and plays an important role in development of computational strategies (Gelman, 2004). The Bayesian approach allows us to carry the uncertainty associated with each parameter to the final estimated value (in this case, tsunami height). In order to do so, each parameter must have a distribution that reflects the prior belief regarding that parameter value (Kwon *et al.*, 2008). The parameters are then fit through sampling from these distributions to maximize the likelihood under the model; in this case, the Gamma distribution. We first assume that the tsunami height $(Y_{s,t})$ follows a Gamma distribution given the location s and time t. Here, we assign a Gamma distribution for $k_s$and $\theta_s$that are sampled from a common distribution defined by hyper-parameters. The parameters of the hyper-parameters, k_k, θ_k, k_θ, and $\theta_\theta$are also assigned distributions that reflect our prior beliefs regarding their values. We assign Gamma distributions for the hyper-parameters to constrain them to positive values (Gelman, 2004).

$$Y_{s,t} \sim Gamma(k_s, \theta_s), s = 1, \dots, n, t = 1, \dots, n \quad (6)$$

$$k_s \sim Gamma(k_k, \theta_k) \quad (7)$$

$$\theta_s \sim Gamma(k_\theta, \theta_\theta) \quad (8)$$

A concept of the proposed HBM for tsunami height is illustrated in Figure 3.

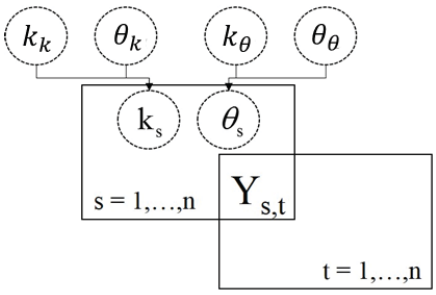

Figure 3. Directed a cyclic graph for hierarchical Bayesian model.

RESULTS

We generated three chains (MCMC) of length 100,000 and discarded the first 8,000 as burn-in. The estimated posterior density of the parameters based on 2,000 MCMC samples from a three-chain MCMC-based estimate is displayed in Figure 3. From this density, one can estimate the Bayesian credible region, which is an interval that contains 95% of the probability. The mean, standard deviation, and 95% credible interval are based on a Hierarchical Bayesian specification. The parameters were found to be statistically significant given their uncertainties.

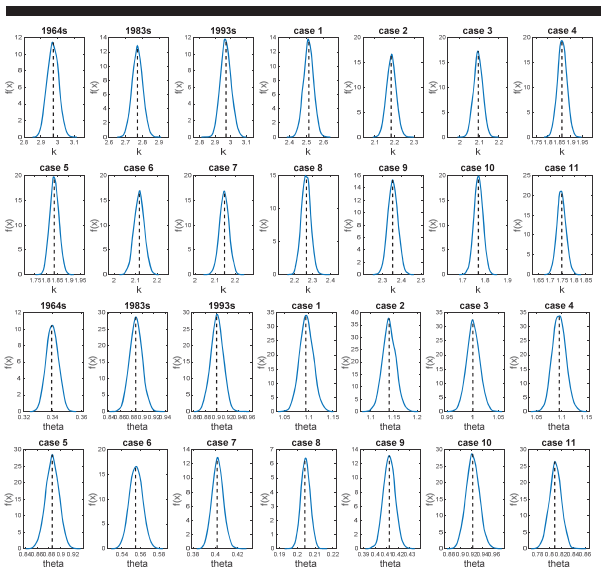

Figure 4. Bayesian posterior density of the parameters (k_s and θ_s) for 3 historical and 11 virtual tsunamis. The vertical black line shows the value obtained from maximum likelihood method.

In Figure 4, blue lines represent Bayesian credible intervals of the parameters, while black lines represent parameters estimated by the maximum likelihood method. All the parameters estimated by the maximum likelihood method are close to the median value of the posterior distribution. As shown in Figure 3,

the credible intervals did not intersect zero, indicating that all the estimated parameters are statistically significant.

Figure 5 shows posterior distributions of the parameters across locations s and the common parameter. The circles shown on the x −axis are the model parameters estimated by the maximum likelihood method, while the solid blue lines represent the posterior distribution of each case estimated through the HBM. All of the parameters had a decreasing tendency toward the common distribution.

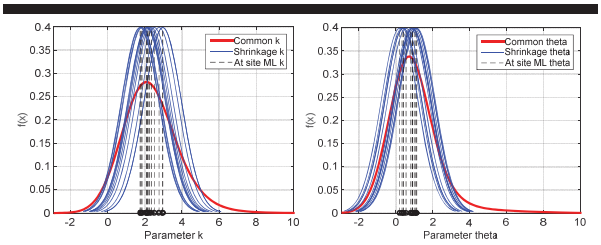

Figure 5. Marginal posterior distributions of Gamma parameters. The thick red line indicates regional parameters and the solid blue line represents individual parameters.

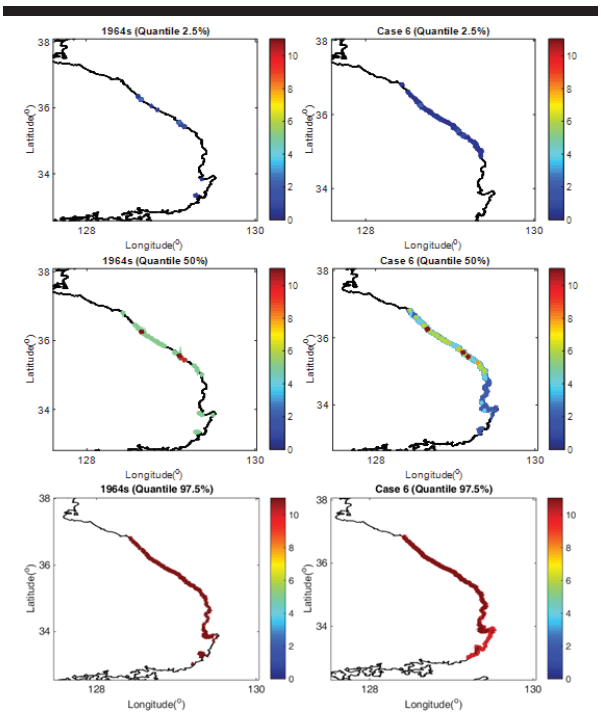

Figure 6. Spatial distribution of inundation levels and their uncertainties for the case year-1964 and Case 6.

Finally, a tsunami-induced inundation risk map and uncertainty are provided for the case year-1964 and case 6. The quantiles and uncertainties associated with parameters via Hierarchical Bayesian inference for the tsunami are presented in Figure 6. The quantiles (flooding depth) were calculated using the cumulative distribution functions corresponding to the determined probability (i.e., 2.5%, 50%, and 97.5%). The northern part of the eastern coast region showed relatively higher inundation stress compared to the southern area. This indicates that tsunami height is highly sensitive to the bathymetric impact and to the characteristics of the causative undersea earthquakes (Kim *et al.*, 2012). The results show that uncertainties in the inundation risk estimation can be effectively quantified in the proposed Bayesian framework, and this information could be used for protection and counteraction. The estimated tsunami height and Bayesian credible interval according to grid index number are also displayed. The index number of the grid starts from the southern end of the Korean Peninsula, as shown in Figure 7, and the uncertainties associated with the probabilistic model are noticeably high. The range of uncertainty is spatially quite similar along the grid, possibly due to the geographic environment tending to directly and indirectly influence tsunami height.

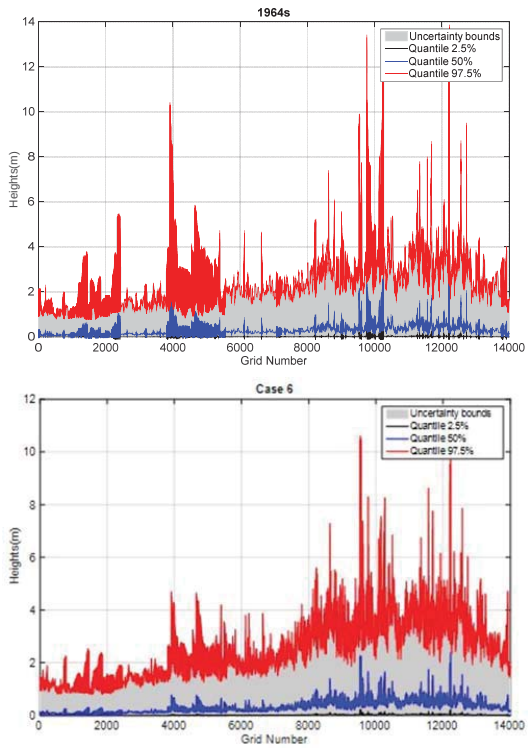

Figure 7. The estimated tsunami heights together with uncertainty bound according to grid number.

CONCLUSIONS

Tsunamis have complex characteristics, and it is difficult to forecast their patterns. Uncertainties in estimation of tsunami inundation risk are generally caused by limited information for accurately modeling all of the characteristics associated with tsunami location and propagation path. However, the uncertainty

in the existing studies has not been properly addressed. Hence, this study proposed a new probabilistic tsunami-inundation risk assessment approach to better characterize the uncertainties.

A main objective of this study was to combine different sources of the uncertainties related to the attributes of an earthquake (i.e., location and magnitude) and the estimation of the parameters of the distribution (i.e., Gamma distribution) in an HBM framework. The results indicate that the HBM well represented the underlying distribution and the associated uncertainties of tsunami height. In addition, the results confirm that the proposed model was more relevant in quantitatively combining and estimating the uncertainties of tsunami-inundation risk. The inundation risk information incorporating uncertainty can be used to better understand and manage tsunami-related hazards.

ACKNOWLEDGMENTS

This research was supported by a grant (MPSS-NH-2015-78) through the Natural Hazard Mitigation Research Group funded by Ministry of Public Safety and Security of Korean government.

LITERATURE CITED

Gelman, A.; Carlin, J.B.; Stern, H.S. and Rubin, D.B., 2004. Bayesian Data Analysis. SHAPMAN&HALL/CRC.

Heo, J.-H.; Lee, Y. S.; Shin, H. J., and Kim, K.-D., 2007. Application of Regional Rainfall Frequency Analysis in South Korea (I): Rainfall Quantile Estimation. *Journal of Korean Society of Civil Engineer, KSCE*, 27(2B), 101-111.

Hosking, J.R.M., 1990. L-moments: Analysis and estimation of distributions using linear combinations of order statistics. *Journal of the Royal Statistical Society, Series B*, 52(1), 105-124.

Hosking, J.R.M.; Wallis, J.R., and Wood, E.F., 1985. An appraisal of the regional flood frequency procedure in the UK Flood Studier Report. *Hydrological Sciences Journal*, 30(1), 85-109.

Kim, J.-Y.; Kwon, H.-H., and Lim, J.-Y., 2014. Development of Hierarchical Bayesian Spatial Regional Frequency Analysis Model Considering Geographical Characteristics. *Journal of Korea Water Resources Association, KWRA*, 47(5), 469-482.

Kim, K.B.; Kwon, H.-H., and Dawei, H., 2015. Bias Correction Methods for Regional Climate Model Simulations Considering the Distributional Parametric Uncertainty Underlying the Observations. *Journal of Hydrology*, doi: 10.1016/j.hydrol.2015.10.015.

Korean Peninsula Energy Development Organization (KEDO), 1999. *Estimation of Tsunami Heights for KEDO LWR Project*. Korea Power Engineering Company, Inc., Korea.

Kim, Y.C.; Choi, M.; Cho, Y.-S.; Tsunami Hazard Area Predicted by Probability Distribution Tendency, *Journal of Coastal Research*, 28(5), 1020–1031

Kwon, H.-H.; Kim, J.-Y.; Kim, O.-K., and Lee, J.-J., 2013. A Development of Regional Frequency Model Based on Hierarchical Bayesian Model. *Journal of Korea Water Resources Association, KWRA*, 34(2), 119-130.

Kwon, H.-H.; Brown, C., and Lall, U., 2008. Climate informed flood frequency analysis and prediction in Montana using hierarchical Bayesian modelling. *Geophysical Research Letters*, 35, L05404, doi:10.1029/2007GL 032220.

Lee, H.W.; Shin, J.W.; Kim K.Y., and Cho Y.-S., 2012. Database for tsunami hazard at harbor zones. *Journal of Korean Society of Hazard Mitigation*, 12(6), 305-314, (in Korean).

Lee, J.-J. and Kwon, H.-H., 2011. Analysis on Spatio-Temporal Pattern and Regionalization of Extreme Rainfall Data. *Journal of Korean Society of Civil Engineer, KSCE*, 31(2B), 129-146.

Spiegelhalter, D.J.; Best, N.G.; Carlin, B.P., and van der Linde, A., 2002. Bayesian Measures of Model Complexity and Fit (with discussion). *Journal of the Royal Statistical Society, Ser*, B (64), 583-639.

Journal of Coastal Research	SI	75	1162 - 1166	Coconut Creek, Florida	2016

Detecting errors in coastal databases using Bayesian Networks

Gonéri Le Cozannet[†*], Thomas Bulteau[‡], Manuel Garcin[‡], Christophe Garnier[‡], Heloise Müller[†], Anaïs Hoareau[‡] and Cyril Mallet[‡]

[†]BRGM, French Geological Survey
3 avenue Claude Guillemin
45000 Orléans, France

[‡] BRGM-Aquitaine
24 avenue Léonard de Vinci
33600 Pessac, France

www.cerf-jcr.org

www.JCRonline.org

ABSTRACT

Le Cozannet, G.; Bulteau, T., Garcin, M., Garnier, C., Müller, H., Hoareau, A. and Mallet, C., 2016. Detecting errors in coastal databases using Bayesian Networks. *In:* Vila-Concejo, A.; Bruce, E.; Kennedy, D.M., and McCarroll, R.J. (eds.), *Proceedings of the 14th International Coastal Symposium* (Sydney, Australia). *Journal of Coastal Research*, Special Issue, No. 75, pp. 1162 - 1166. Coconut Creek (Florida), ISSN 0749-0208.

With growing concerns regarding coastal planning, management and adaptation, coastal observatories are collecting an increasing amount of geographical datasets such as historical shorelines, descriptions of hydrodynamic processes, coastal geomorphology or hydrogeology. Evaluating the integrity of such databases is difficult in practice due to the volume and heterogeneity of data, as well as the number of persons involved in data collection and management. Here, we adress the question of error detection in coastal databases. We test the utility of Bayesian Networks to guide users toward subsets of the database, where errors are more likely. The approach is applied to two coastal databases: (1) the French Basque Coast geographical database, managed by the Aquitaine Coastal Observatory; (2) the Eurosion database, describing European coasts and resulting from the synthesis and aggregation of multiple datasets. We show that the approach is more useful in the second case, but that the method can also help to derive a probabilistic information from a regional deterministic database. Finally, we highlight the utility of improving current coastal data models, especially for improving the description of coastal cliffs evolutions in large aggregated databases.

ADDITIONAL INDEX WORDS: *Coastal databases, coastal observatory, bayesian networks, geoinformatics.*

INTRODUCTION

To inform coastal communities and practitioners concerned with coastal risks, a number of coastal observatories have been set up over the last decades (e.g. Aubié *et al.*, 2004; Howarth and Palmer, 2011; Jeanson *et al.*, 2014). These regional coastal observatories are collecting an increasing amount of data, which is revealed difficult to manage due to their fragmented nature, but also because of the number of different persons involved in in-situ data collection, data rescue and the management of geographical information systems where data are stored and analysed. As these databases are growing, the question of ensuring their integrity is coming into increased scrutiny.

In addition to data delivered by such regional coastal observatories, the need to provide statistics and information on coastal evolutions at national to global scales has stimulated the emergence of synthetic aggregated coastal databases (Quelennec *et al.*, 1998; Thieler and Hammar-Klose, 1999; Eurosion, 2004; Vafeidis *et al.*, 2008). Such datasets provide a consistent (but simplified) description of coastal settings and processes (e.g., coastal geomorphology, geology, wave and storm climates). They are largely based on a reinterpretation of existing regional coastal databases, complemented with additional data (Figure 1). Hence, new difficulties arise due to the heterogeneity of geographical scales, semantics and data models of existing local to regional coastal datasets (Vafeidis *et al.*, 2008). These difficulties introduce new potential source of errors that may affect the integrity of synthetic aggregated coastal databases.

DOI: 10.2112/SI75-233.1 received 15 October, 2015; accepted in revision 15 January, 2015.
*Corresponding author: g.lecozannet@brgm.fr
©Coastal Education and Research Foundation, Inc. 2016

This paper focuses on the issue of error detections in such coastal databases. As the amount of data is growing, detection of errors becomes extremely difficult to undertake without any supporting tool. Here, we test the utility of a Bayesian network approach to reveal inconsistencies in coastal databases. Bayesian networks provide a quantified statement of the probabilistic links between variables, and we use Bayesian networks to detect unlikely combinations of coastal settings (see part 2). We apply the approach to the regional coastal database of the Aquitaine Basque Coast (Data: Aquitaine Coast Observatory) and to the European aggregated coastal database Eurosion (Eurosion, 2004).

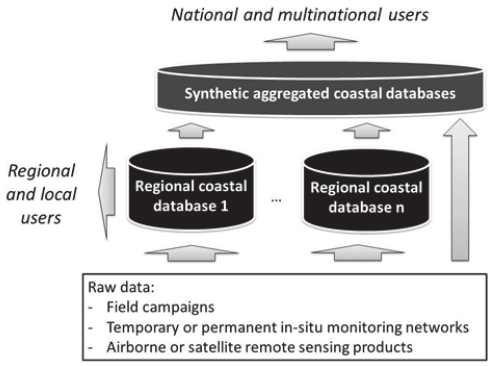

Figure 1. Data and information flows accross existing coastal databases.

METHODS

Use of Bayesian Networks for error detection

Coastal databases contain items that display conditional dependencies. For example, coastal geology and the slopes of cliffs are expected to be linked, as landslides and rock fall will be more likely if some layers are made of unconsolidated materials. Using Bayesian Networks, we identify unlikely combinations in coastal geographical databases.

Bayesian Networks are probabilistic models allowing to quantify dependancies between different state variables. In recent coastal research, Bayesian networks have been either used to test their predictive capabilities, or to identify statistical relationships between variables, that can potentially reflect a physical link, and, particularly, a role of sea-level rise in recent shoreline evolution (e.g., Hapke and Plant, 2010; Gutierrez *et al.*, 2011; Le Cozannet *et al.*, 2014; Bulteau *et al.*, 2015).

To build a Bayesian Network adapted to coastal databases, we follow the approach of Hapke and Plant (2010) and Gutierrez, *et al.* (2011). First, we elaborate a general scheme describing the statistical relationships between variables in the database (e.g., Figure 2). A learning phase follows, in which we use the information from the coastal database (e.g., Table 1) to compute a maximum likelihood estimation of the Bayesian Network parameters. This step provides a probabilistic estimation of the conditional distribution of each variable given its parents. Then, in the inference phase, we can compute the probability distribution of any variable given any combination of the others. In particular, we define a predictive model for a variable of interest V – for example coastal evolution, by assigning, for each combination of states of the other variables in the Bayesian Network, the state of V that has the maximum conditional probability.

Then we use the Bayesian Network predictions and skills to guide users toward potential errors in the database. We consider variables, whose prediction values diverge from their expected values (e.g. from the expertise of a coastal geologist). We also identify sites where the predictions of the Bayesian Networks do not correspond to observations, whereas the confidence in the prediction is high. The confidence of a prediction is given by the actual value of the probability of the predictive state. By doing this, we limit the investigations to a limited subset of the original database. While the approach does not guarantee to detect all errors, it is expected that when the content of the database is too large to be memorized by a single expert, it will make the detection of errors not only more efficient, but also manageable by a human.

Application: case studies in Europe and Aquitaine

We use the BNT Matlab toolbox (Murphy, 2011) to carry out all Bayesian Networks computations, and ArcGIS to manipulate and display the coastal database. We test the method in two cases: (1) the european coastal database Eurosion (Eurosion, 2004), where we use the Bayesian Netword previously established by Yates and Le Cozannet (2012); (2) the coastal database of the Basque coast, managed by the Aquitaine Coastal Observatory. We describe below the application in the second case.

The French Basque coast is constituted by heteregenous rocky cliffs alternated with pocket sandy beaches. Due to both marine and continental factors, mean cliff erosion rates are around 15 to 30cm/year (Garnier *et al.*, 2014). Since 1995, the Aquitaine Coastal Observatory aims to survey and analyse coastal erosion and marine submersion in order to carry out a coastal database and to deliver scientific expertise in support to Integrated Coastal Zone Management. The present status of the coastal database of the Basque coast is characterized by a very large amount of heterogeneous data, collected during several field surveys (e.g., Nedellec *et al.*, 2005; Peter-Borie, 2008; Aubié *et al.*, 2011).

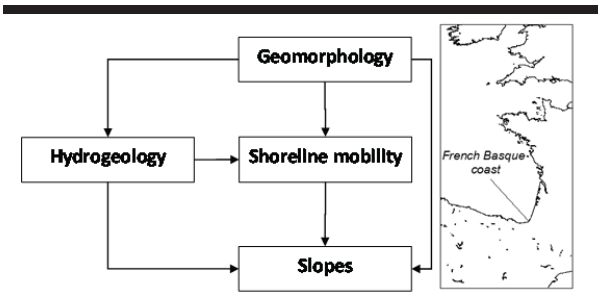

Figure 2. Left: Bayesian Network used for detecting errors in the regional coastal database of the Basque Coast (South Aquitaine). The parents of each variable are the ones from which arrows are pointing to the variable of interest. For example, the parents of the variable "shoreline mobility" are "hydrogeology" and "geomorphology". Right: location of the regional study site.

Establishing a Bayesian Network in this context is complex since each local coastal segment appears almost unique in the database. This case is characteristic of living coastal databases, so that it must be considered as representative of the difficulties encountered in applying our approach to this type of objects. To overcome this difficulty, we selected an homogeneous subset of the database corresponding to its initial status in 2005 (Nedellec *et al.*, 2005; Genna *et al.*, 2005), completed with a more recent analysis of shoreline retreat rates (Aubié *et al.*, 2011). This results in about 30 variables for 103 sites along a coast of about 40km. We tested several Bayesian Network structures to explore this database, and finally used the graph presented in Figure 2, where the four most important variables for explaining observed coastal recession rates remain (Table 1).

Table 1. *Description of the regional coastal data from the Basque coast incorporated in the Bayesian Network depicted in Figure 1.*

Variable	States
Geomorphology	6 cliffs settings (Genna *et al.*, 2005): (1) nearly horizontally stratified rocks with recent sediment and a thin alterite cover; (2) unconsolidated sediments covered by recent sediments and alterite; (3) folds in hard-rock covered by recent sediments and alterite; (4) folds in hard rocks covered by alterites only; (5) undeformed tilted hard rocks; (6) low-relief of alterite
Hydrogeology	2 states: absence or presence of spring water
Cliff Slopes	4 states: very high (90°-80°), high (80-55°), moderate (55-30°), gentle (30°, 0°)
Shoreline mobility	4 states (Aubié *et al.*, 2011): none, low (0-0.1m/yr), moderate (0.1-0.2m/yr), high (0.3-0.5m/yr)

RESULTS

Regional coastal database of the French Basque Coast

Table 2 shows the sum of log-likelihood ratios obtained for 2-variables Bayesian Networks. It indicates the order of importance of the explanatory variables in predicting the actual outcomes of shoreline mobility according to the coastal database of the French Basque coast (Gutierrez *et al.*, 2011). Therefore, Table 2 shows that as expected, geomorphology plays a key role as an explanatory variable of coastal erosion rates. This is consistent with previous observations that highlighted the key role of a regional layer of alterites (weathered rocks) to explain the regional variability of cliff retreat processes (Genna *et al.*, 2005). The surprising result in Table 2 is the minor role of hydrogeological factors in explaining the spatial variability of cliff retreats. This counterintuitive outcome may reflect a less important role of hydrogeological processes than expected. More probably, it could be due to missing observations in the database.

To investigate this hypothesis, we examine the 37 coastal sites where groundwater should be present according to the Bayesian Network in spite of the lack of observational evidences in the field work report of Nedellec *et al.* (2005). In 28 of these coastal sites where the Bayesian Network suggests the presence of water, Peter-Borie (2008) indeed observed some evidences of springwater (e.g., site 61 in Figure 3). 9 sites remain, where neither Nedellec *et al.* (2005) nor Peter-Borie (2008) observed spring waters, although the Bayesian network expects hydrogeological processes to take place. We examine these 9 sites in details: for 8 of these sites, no direct observation of spring water were observed during the additional field missions conducted by coastal geologists in charge of maintaining the regional database. However, the presense of hydrogeological processes was suspected for 7 of these 9 sites by indirect indices such as the presence of alteritic layers, of draining walls or landslides (indirect evidences). The 8th coastal site (site 601 in Figure 3) is highly urbanized, and the construction of water drainage infrastructures probably prevents from observing any source. Finally, the last coastal site appears as a false unappropriate prediction of the Bayesian Network, as the geomorphological context is not prone to the presence of groundwater at all.

In this regional coastal database, the Bayesian Network performs well in detecting errors: it allows to identify 35 coastal sites with missing information regarding the presence of spring water. Obviously, a minimum level quality is required for the initial database to ensure that the Bayesian Network learns parameters that make sense physically.

During the investigations, we saw that coastal geologists in charge of maintaining the database currently have a clear view of both the content and gaps of their database, thus limiting somehow the utility of the approach for error detection in this example. However, it was recognized useful for another application: indeed, part of the difficulties in gathering a complete inventory of spring water is due to the fact that many can not be observed all the time (role of rainfall variability, changing hydrogeological processes, rockfalls and landslides). Here, the Bayesian Network is useful to bring probabilistic information to field investigations necessarily sparsely distributed in time, and to highlight places where some variability can be expected over time.

Table 2. *Sum of the Log-Likelihood ratios computed for 2-variables subgraphs of Figure 2 (shoreline mobility and each variable indicated in the 1st column).*

Variable	Sum of Log-Likelihood ratios
Geomorphology	12.3
Cliff Slopes	5.5
Hydrogeology	0.7

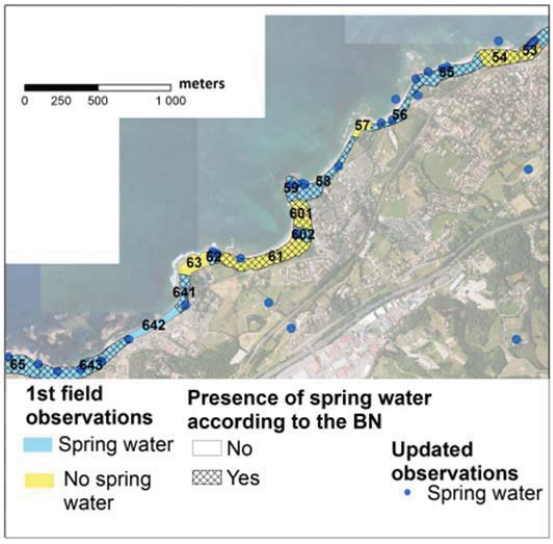

Figure 3. A section of the Basque coast showing prior and updated spring water observations together with the Bayesian Network (BN) predictions.

European database

We apply the same type of approach to detect potential errors in the european coastal database (Eurosion, 2004), using the Bayesian Network of Yates and Le Cozannet (2012). For each subset of data with the same forcing factors values (waves heigths, sea-level rise, etc.), this Bayesian network assigns the maximum probability of shoreline changes (accretion, erosion or stability). We immediately identify that the Bayesian Network expects the French Basque coast to be stable.

The French Basque coast is generally eroding according to the Eurosion database. This is in agreement with observations. Therefore, the errors (if any) should affect locations used in the same data sample as French Basque cliffs during the learning phase of our approach. These locations are displayed in Figure 4. They correspond to soft cliffs exposed to energetic waves conditions, high tidal range and sea-level rise comprised between 1 and 1.6mm/yr. All coastal sites meeting these criteria are located along the atlantic French and Spanish coast.

Figure 4 shows that a large part of these cliffs are stable according to Eurosion (2004). Therefore, the maximum probability event is stability, so that the Bayesian Network

predicts stability for all these coastal sites. However, other

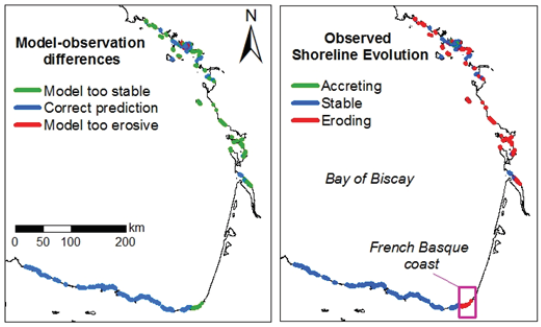

Figure 4. Observations and model predictions for coastal systems that fell in the same data sample than the French Basque coast during the learning phase of the Bayesian Network model of Yates and Le Cozannet (2012). The Figure is centered on the Bay of Biscay.

observations suggest that these cliffs in Spain are retreating slowly (Borja and Collins, 2004). The incorrect predictions are due to this subset of data being used for the learning phase. In this case, we used incorrect predictions of the Bayesian Network in a sector known to the authors to find a probable error affecting another location, where the authors have not made any investigations.

This error was not necessarily introduced when coastal data were collected. On the contrary, it is possible that different coastal geologists interpreted the meaning of the world "erosion" differently, so that coasts in moderate erosion (in the order of a few tens of centimeter per year) may have been considered as "stable" or "in erosion" depending on the organization in charge of providing national data to the European body aggregating all datasets. In this case, this would raise the issue of referring to shared semantics and ontologies when elaborating coastal databases (Wariyapol *et al.*, 1999; Stock *et al.*, 2012). This question is examined in the discussion.

Using the same approach, we found other inconsistencies between the Eurosion database and the existing literature, in particular for a few beaches of the Netherlands and France. For example, there are differences in beach erosion status description in southern Brittany (Pian and Meunier, 2011). However, more investigations are necessary to understand if these inconsistencies should be corrected, or if they just reflect different evolutions of the same beaches depending on the period of time of survey (e.g., role of storms, anthropogenic actions such as sand nourishment, etc.).

DISCUSSION

Utility and applicability of the method

The two examples above show that the Bayesian Network can be useful for error detections, especially for large coastal databases. For regional evolving coastal databases coastal geologists in charge of maintaining the database usually have a clear view of both the content and gaps of their database, and finally know much more from their field work experience than what the coastal database contains.

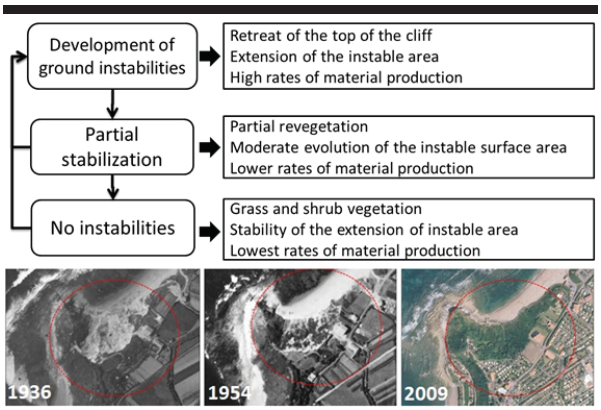

Figure 5. above: observed cliff states and transients between them in the case of the French Basque coast; below: an example of stabilization.

While this limits the interest of the approach in the regional case, we argue that the Bayesian Network can be useful to elaborate a probabilistic product from the existing deterministic coastal database, e.g. to show where temporary spring water could be observed along the French Basque coast.

The Bayesian Networks used here are simple, and are not conceived to integrate all available data. While more complex schemes can be elaborated, it must be kept in mind that they must remain a compromise between: (1) the complexity of processes in the real world, and (2) the necessity to keep a sufficient number of observations for each combination of states of variables for the learning phase of the Bayesian network. Hence, in applying the error detection approach, it is more efficient to test several simple Bayesian Networks rather than a single complex one, which drastically reduces the number of samples available during the learning phase of the approach (see e.g. Bulteau *et al.*, 2015).

Perspectives in geoinformatics applied to coastal systems

This study highligths some issues regarding the description of metadata and their quality. It is important to note that the processes to build the Eurosion database followed a strict quality control (Eurosion, 2004), and that the dataset is accurate in most cases. However, for specific questions, it remains uneasy for the user to understand the history of the data. In addition, we identified one case where different interpretation of the reference data model may have led to inconsistencies in the database. This raises the issue of working on an adapted ontology applied to coastal systems in order to avoid discrepancies when aggregating coastal data at larger scales (e.g. from regional or national levels to European, see Figure 1). A second reason for addressing this research topic is to better describe states of coastal evolution in coastal databases.

Indeed, a simple description such as the rate of erosion and/or fluctuations around a stable position appears too limited for systems such as the French coast cliffs. We undertook a further analysis of historical aerial images ranging acquired in 1938, 1954, 1968, 1977, 1996 and 2009 in Aquitaine, and delineated areas prones to slope instabilities (landslides, rockfall). This

analysis shows that the planimetric area of bare soils, taken as indicator of unstable areas on coastal cliffs, has drastically decreased from 1938 to 1977, and then remained almost stable. Errors due to georeferencing, interpretation and the quality of photographs can not explain this trend. While this information could be important for hazard assessment, the shift toward less erosion and rockfall events is missing in the present description of data at European scale. We identified different states and transients between them (Figure 5), which could be extended to develop an alternative model for describing shoreline evolution states in the case of erodible cliffs, using, for example, the formalism developed by Pchenichny and Kanzheleva (2011) to describe coastal geomorphic evolutions. The resulting large-scale coastal databases could benefit from such research and finally provide more applied information in support to coastal management and adaptation.

CONCLUSIONS

In this paper, we used Bayesian Networks to detect errors in two coastal databases. The method performs well in both cases, and appears useful for larger coastal databases, which contain so many coastal sites that a single coastal geologist could not manage to visit all of them. This study highlighted the need for new research in the field of geoinformatics and knowledge representation applied to coastal environments. We argue that such research will have tangible benefits for future versions of, for example, European coastal databases.

ACKNOWLEDGMENTS

This Project has been funded by BRGM through the PREVAQUI and CCRA projects (regional and European scale study respectively). We thank Bruce Ayache and Agnès Tellez Arenaz for their useful comments.

LITERATURE CITED

Aubié, S., Dumeix, C., Mallet, C., and Baudry, D., 2004. Mise en place du SIG de l'Observatoire de la côte Aquitaine. BRGM/RP-53362-FR.

Aubié, S.; Mallet, C. and Favennec, J., 2011. Caractérisation de l'aléa erosion (2020-2040) de la côte Aquitaine dans le cadre de l'étude stratégique de gestion du trait de côte. Rapport BRGM/RP-59095-FR.

Borja, A., and Collins, M.. 2004. Oceanography and marine environment in the Basque Country, vol. 70, Elsevier.

Bulteau, T.; Baills, A.; Petitjean, L.; Garcin, M.; Palanisamy, H., and Le Cozannet, G., 2015. Gaining insight into regional coastal changes on La Réunion island through a Bayesian data mining approach. *Geomorphology*, 228, 134-146.

Eurosion, 2004. www.eurosion.org

Gutierrez, B.T.; Plant, N.G., and Thieler, E.R., 2011. A Bayesian network to predict coastal vulnerability to sea level rise. *J. Geophys. Res. Earth Surf.,* 116, 15.

Garnier, C. and Millecamps, B., 2014. Agglomération Sud-Pays Basque: Evaluation de l'aléa erosion côtière en 2023 et 2043 dans le cadre de la stratégie locale de gestion de la bande côtière. Rapport BRGM/RP-63588-FR.

Genna, A.; Capdeville, J. P.; Dubreuilh, J., and Mallet, C., 2005. Recent and present evolution of the French Basque Coast (analysis and prediction). *Comptes rendus Géosciences*, *337*(16), 1474-1483.

Hapke, C., and Plant, N., 2010. Predicting coastal cliff erosion using a Bayesian probabilistic model. *Marine geology*, 278(1), 140-149.

Howarth, J., and Palmer, M., 2011. The Liverpool Bay Coastal Observatory.*Ocean Dynamics*, 61(11), 1917-1926.

Jeanson, M. ; Dolique, F., and Anthony, E. J., 2014. A GIS-based coastal monitoring and surveillance observatory on tropical islands exposed to climate change and extreme events: the example of Mayotte Island, Indian Ocean. *Journal of Coastal Conservation*, 18(5), 567-580.

Le Cozannet, G.; Garcin, M.; Yates, M.; Idier, D., and Meyssignac, B., 2014. Approaches to evaluate the recent impacts of sea-level rise on shoreline changes. *Earth-Science Reviews*, *138*, 47-60.

Murphy, K.P., 2001. The Bayes net toolbox for Matlab. *Comput. Sci. Stat.*, 33 (2), 1024–1034.

Nedellec, J.-L.; Zornette, N. and Mathon, C., 2005. Evaluation et cartographie de l'aléa movement de terrain sur la côte Basque. Rapport BRGM/RP-52783-FR.

Peter-Borie, M., 2008. Les massifs rocheux du Crétacé supérieur du labourd occidental: processus d'altération et instabilités littorales. PhD thesis, 370pp. (In French).

Pian, S., and Menier, D., 2011. The use of a geodatabase to carry out a multivariate analysis of coastline variations at various time and space scales. *Journal of coastal research*, *64*, 1722-1723.

Pshenichny, C. A., and Kanzheleva, O. M., 2011. Theoretical foundations of the event bush method. *Geological Society of America Special Papers*, 482, 139-164.

Quelennec, R.-E.; Oliveros, C.; Uhel, R., and Devos, W., 1998. Corine: érosion côtière. *Environmental and Quality of Life Series* Office for Official Publications of the European Communities, Luxembourg, pp.170. (In French)

Stock, K.; Stojanovic, T.; Reitsma, F.; Ou, Y.; Bishr, M.; Ortmann, J.; and Robertson, A., 2012. To ontologise or not to ontologise: an information model for a geospatial knowledge infrastructure. *Computers & Geosciences*, *45*, 98-108.

Thieler, E.R., Hammar-Klose, E.S., 1999. National assessment of coastal vulnerability to future sea-level rise: preliminary results for U.S. Atlantic Coast. *U.S. Geol. Surv. Open File Report*, Woods Hole, Massachusetts, pp. 99–593.

Vafeidis, A. T.; Nicholls, R. J.; McFadden, L.; Tol, R. S.; Hinkel, J.; Spencer, T.; Grashoff, P. S.; Boot, G., and Klein, R. J., 2008. A new global coastal database for impact and vulnerability analysis to sea-level rise. *Journal of Coastal Research*, 24(4), 917-924.

Wariyapol, P.; Abrams, S. L.; Robinson, A. R.; Streitlien, K.; Patrikalakis, N. M.; Elisseeff, P., and Schmidt, H., 1999. Ontology and metadata creation for the Poseidon distributed coastal zone management system. In *Research and Technology Advances in Digital Libraries, 1999. IEEE Proceedings,* 180-189.

Yates, M. L., and Le Cozannet, G., 2012. Brief communication" Evaluating European Coastal Evolution using Bayesian Networks". *Natural Hazards and Earth System Science*, 12(4), 1173-1177.

Journal of Coastal Research	SI	75	1167 - 1171	Coconut Creek, Florida	2016

The Application of a Rip Current Warning Decision-Process System, Haeundae Beach, South Korea

Jooyong Lee†, Won Chul Cho‡, and Jung Lyul Lee†*

† Construction and Environmental Research Center
Sungkyunkwan University
Suwon, Republic of Korea

‡Department of Civil and Environmental Engineering
Chung-Ang University
Seoul, Republic of Korea

www.cerf-jcr.org

www.JCRonline.org

ABSTRACT

Lee, J.; Cho, W.C., and Lee, J.L., 2016. The Application of a Rip Current Warning Decision-Process System, Haeundae Beach, South Korea. *In:* Vila-Concejo, A.; Bruce, E.; Kennedy, D.M., and McCarroll, R.J. (eds.), *Proceedings of the 14th International Coastal Symposium* (Sydney, Australia). *Journal of Coastal Research*, Special Issue, No. 75, pp. 1167 - 1171. Coconut Creek (Florida), ISSN 0749-0208.

Rip currents have the potential to pull swimmers into deep water, beyond offshore sand bars, posing a significant danger to beach goers worldwide. At Haeundae Beach in Busan, a south eastern region of South Korea, many rip current events have recently occurred, resulting in a number of people requiring rescue from these fast moving, seaward currents in 2014. The main objective of this study was to provide a warning decision-process for the occurrence of rip currents, to aid in the protection of human life in the areas where these rip currents occur. The rip current warning decision-process system developed in this work consists of both the NERiPS-H (Nearshore Rip current Prediction System for Haeundae Beach) and HAECUM (HAEundae Current Model) systems. By combining the predictive index model (NERiPS-H) and the numerical model for rip current forecasting (HAECUM), rip currents were forecasted using wave and wind data, along with forecasting information. Using this system, it possible to provide a 72-hour rip current forecast, which was made available on the KMA website. Four warning levels were chosen for forecasting of rip current occurrences by the KMA.

ADDITIONAL INDEX WORDS: *rip current, HAECUM, NERiPS-H, warning decision-process system*

INTRODUCTION

Recently, coastal disasters, such as rip currents, swells, and freak waves, have frequently occurred, resulting in not only the destruction of property, but the loss of human life. Many researchers have attempted to determine the mechanism behind the formation of rip currents and setup numerical models. The interaction of waves with currents is achieved by repetitively recalculating the wave field over the evolving flow field (Haas *et al*., 2003; Yu & Slinn, 2003). Although these models usually do not account for wave group related motions, they can be modified to include infragravity waves and wave-group induced vortical motions that constitute a significant part of thetemporal variability of the rip current flows (Long & O˙zkan-Haller, 2009; Roelvink *et al*., 2009). Another wave model for use as a wave driver, based on the time dependent Boussinesq equations for variable depth (Peregrine 1967), describes waves in shallow water and includes both frequency and amplitude dispersion. These time domain equations have been extended for greater applicability by Nwogu (1993), who introduced a modified depth, which gives better frequency dispersion than the usual formulations that use the bottom or the still-water elevation; by Madsen *et al*. (1991), who introduced new terms to allow the model to be used in deeper water; and by Wei *et al*. (1995), who added additional abilities to model more nonlinear waves.

In spite of numerical research, there is currently a lack of forecasting techniques for phenomena such as dangerous rip currents, and further, a distinct lack of effective systems that can send out severe warnings within Korea. An accurate and fast prediction of dangerous rip currents is essential to many coastal engineering projects, specifically for coastal disaster planning. The main objective of this study is to develop a practical rip current prediction system that can be conveniently used for the operational forecasting of wave-induced currents off the coast of Haeundae, Korea.

Rip currents became well-known in Korea during the summer of 2015. Haeundae Beach attracts approximately one million visitors every year, and more than fifty people have had to be rescued from rip currents each summer (Figure 1). The Korean Meteorological Administration (KMA) plans to set up automatic monitoring systems in order to forecast the occurrence of rip currents, to improve public safety at Haeundae Beach. In addition to the development of a model, there is a need to provide clear warning decisions so as to allow non-specialists to understand the resulting implications of the model.

This study focussed on developing an efficient rip current warning decision-process system that combines rip current predictive index model and rip current simulation model. Unfortunately, current understanding of the spatial and temporal behaviour of rip currents is limited. A lack of suitable field data has impeded the application of morphodynamic approaches to modelling natural rip current systems. Rip currents frequently occur at Haeundae Beach, and many people have been swept away by these fast-moving, seaward currents. In this study, intensive field monitoring experiments were carried out in order to subsequently issue rip current warnings for Haeundae Beach. These field experiments involved a comparison of the real, observed rip currents with the results of the model-generated rip

DOI: 10.2112/SI75-234.1 received 15 October, 2015; accepted in revision 15 January, 2015.
*Corresponding author: jooyong@gmail.com
©Coastal Education and Research Foundation, Inc. 2016

currents. These in-situ measurement data were then used to validate the modelling approach. This paper introduces, and describes, a rip current warning decision-process system. The current method for modelling rip currents used at Haeundae (HAECUM) is combined with a near-shore rip current predictive index model (NERiPS-H) with the aim of providing a warning decision for the likelihood of rip current occurrence.

Figure 1. Rip current occurrence at Haeundae Beach (August 04, 2012).

Site Description

Haeundae Beach, at a latitude 35.16° N and longitude of 129.17° E, is located in the south eastern corner of the Korean Peninsula, opening approximately southward, as shown in Figure 2. Because of a large population of Busan city, the beach receives a high number of visitors throughout the year. In particular, during the summer vacation period, over one million people visit the beach on a peak day. However, the beach is extremely small, with a length of only 2 km and average width of approximately 50 m. The mean tidal range is approximately 1 m, and the waves predominantly approach from the south during the summer swimming season. Thus, the approaching waves are approximately normal to the shoreline, which leads to the generation of rip currents.

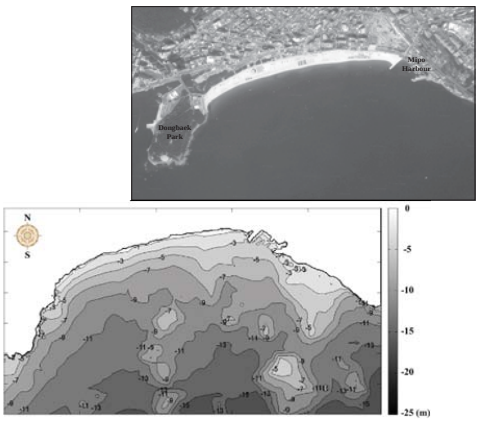

Figure 2. Location of Haeundae Beach. Isobaths are marked every 2 m, and the shoreline in bold.

A directional wave buoy is located 1 km offshore, and is used to gather data on incident waves. Moreover, the presence of several oversized sunken rocks, located a short distance offshore, results in a very uneven morphology. The highly uneven water depth acts to distribute the locations of the breaking waves. This is because the wave current is dependent on the hydraulic gradient of the mean water level. The presence of a large number of reefs on the beachfront results in changes to water levels due to their effect on wave height, and, additionally, creates partial cut-offs in sand bars (Figure 3). Rip channels were observed in the surf zone bathymetry. Haeundae Beach has an average seafloor inclination of 1:15 to 1:30, and a wave-dominated with a softer inclination along the eastern side. According to the tidal characteristics observed by the Busan harbour tidal observation station, Haeundae Beach has a mean sea level of 64.9 cm. In addition, the representative wave directions are southeast (SE), south (S), and southwest (SW), and the mean wave height reaches a significant 0.68–1.0 m, with a wave period of 5.7–6.0 s. The main wave direction in the summer of 2012 was approximately 210° (Kim *et al.*, 2014).

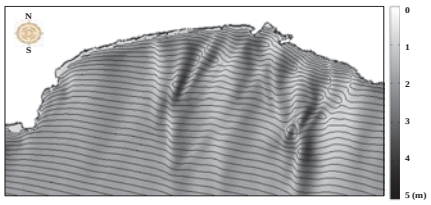

Figure 3. Wave crest distribution, Haeundae Beach.

METHODS

Through a research and development program, a rip current forecasting system was developed that considers both bathymetric and meteorological effects. The system is based on high-resolution topography measurements, and uses the direction, height, and period of incident waves, along with the tidal elevation and wind conditions. Following the occurrence of a number of rip current incidents at Haeundae Beach, the KMA began researching into establishing a forecasting system. The HAECUM system, which has been in use since 2012, involves observational monitoring and the use of a quantitative model.

Figure 4 shows the rip current warning decision-process in the form of a flowchart. This rip current warning decision-process system consists of the NERiPS-H model, HAECUM, and an information presentation system. In order to evaluate the performance of the system, the initial warning level uses the NERiPS-H method to calculate a rip current predictive index using wave height, wave period, and wave direction (provided by the regional Wave Watch 3 system). If the result of the NERiPS-H model shows that there is no risk of rip current occurrence, the decision-process system does not advance to the next level. However, if the result of the NERiPS-H modelling shows a strong possibility of rip currents, the warning decision-process system moves on to level two. The second level uses a rip current prediction model, HAECUM, which is a two-layer current model that forecasts rip current safety using depth, wave, wind, and tidal data. The HAECUM system plays an effective role in the forecasting of rip currents by significantly reducing the forecasting time required, particularly in the case where the result of the rip current occurrence probability, from the NERiPS-H model, is at danger level.

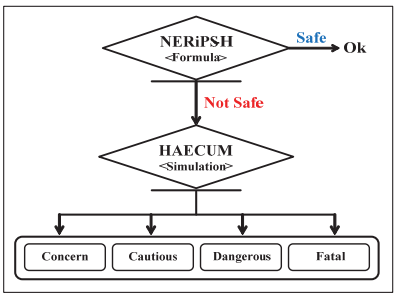

Figure 4. Flowchart for the rip current warning decision process system.

First Level: NERiPS-H

An extensive literature review of the current advanced research into the predictive index for rip currents was conducted. The National Weather Service (NWS), in the USA, has developed rip current forecasting techniques for the east coast of Florida. Lushine (1991) developed the Lushine Rip Current Scale (LURCS), an empirical forecasting technique that utilises wind direction and velocity, swell height, and the time of low tide, in order to forecast the danger of rip currents in South Florida. The LURCS forecasting technique was adapted for use in East Central Florida (ECFL LURCS) by Lascody (1998). The swell period was included as an additional factor, and the tidal factor was changed. Lascody noted that the ratio of true to false alarms raised by the ECFL LURCS scale indicated that there was a need for improvement. Engle *et al.* (2002), developed two predictive factors aimed at improving the ECFL LURCS scale: an improved tidal factor; and, a wave direction factor. The inclusion of these factors, in addition to the elimination of two wind scales, was found to improve the accuracy of the ECFL LURCS scale in Volusia County. However, the modified ECFL LURCS does not account for the correlation between the occurrence of rip currents and the Haeundae wave data.

According to the criteria on which the above studies are based, a modified predictive rip current index is applied, as shown in equations (1) and (2). H denotes the wave height, T denotes the wave period, θp denotes the incident angle of the wave with respect to north, and θ denotes the angle of the wave with respect to the normal to the shoreline. Wave forecasting information, which is one of the input parameters, was obtained from a wave prediction system currently operated in the field by the KMA. The KMA's Wave Watch III (WW3) is used twice a day to produce three-day forecasts. This formula is suitable for Haeundae Beach. Compared with the results obtained by applying the modified ECFL LURCS to data taken from Haeundae, the results of the NERIPS-H model were judged to be reasonable, and the model appropriate for use in predictive guidance (Lee *et al.*, 2013).

$$R = R_H R_T R_\theta = H^{\alpha} H^{\beta} H^{\gamma} \quad (1)$$

$$R = H^{1.0}[0.75 + 0.25\tanh(\frac{T-8}{2})] \times \{0.25 + 0.75[1 - \tanh^5(\frac{|\theta_p - \theta|}{5})]\} \quad (2)$$

Equations (1) and (2) are the basic expressions used in the calculation of rip current predictive indices. The determination of a predictive rip current index is vitally important to the protection of human life. Such an index allows government agencies to issue rip current warnings directly to the public, and allows preventative measures to be established based upon the magnitude of the rip current threat. Figure 5 shows a case study of the results of a rip current prediction system, applied in July and August of 2012, provided by the KMA. Rip currents occurred on the 15th and 19th of July, and 2nd and 4th of August. The red vertical lines indicate the instances where beachgoers were rescued, and the blue vertical lines show days when no swimming was permitted owing to the presence of rip currents. The probability of rip current occurrence is presented as a value ranging from 0.1 to 2.0. A value of 1.0 represents a definitive prediction (Fatal Level), a value greater than 0.4 represents a high probability of occurrence (Dangerous Level), and a value greater than 0.1 is a cautions level.

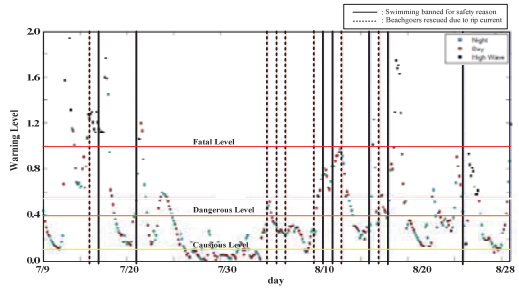

Figure 5. Results of the application of the NERiPS-H method to Haeundae Beach (July and August, 2012).

Second Level: HAECUM

The forecasting system outlined in this study uses HAECUM, a previously existing two-layer model to act as a user-friendly simulation tool for end users. The resolution of HAECUM is 1 km, and the calculation area includes the maritime territories of the regional administration (Eom *et al.*, 2014). This model automatically combines the effects of tides and currents, reflects the effects of wind, and separates the mass flux and undertow, to provide a more precise simulation of the flow of surface water in rip currents (Lee and Lee, 2011). Moreover, this model can primarily be used to provide rapid forecasting under spectral wave conditions over a broad band that does not show superior reflected waves, and is designed to easily combine nonlinear, three-dimensional, and vorticity models. HAECUM automatically uses wave and wind data to forecast rip currents. Lee's approach estimates the near-shore surface currents that result from breaking waves (Lee *et al.*, 2013). This study compared the data measured in the summer of 2012 with the results from the model, calculated using the recorded incident wave conditions. The rip current forecasting model used for Haeundae Beach was verified in order to assess weather conditions, and to issue rip current warnings for Busan's beaches in 2010 (Lee *et al.*, 2013). The user can view, explore, and print data from the results of the numerical prediction system. Finally, the near-shore current numerical prediction system simulation allows the user to monitor the results of the simulated current. The simulation results are saved in the data file, as shown in Figure 6.

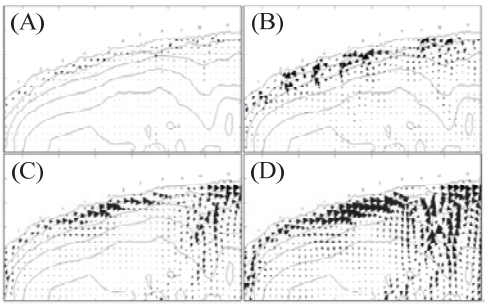

Figure 6. Four levels of HAECUM results, for the forecasting of rip currents (A) Level 1: Concern, (B) Level 2: Cautious, (C) Level 3: Dangerous, (D) Level 4: Fatal.

RESULTS

The rip current warning decision-process system, developed and detailed in this study, combines the NERiPS-H method and HAECUM system, as shown in Figure 4. The result of the NERiPS-H model was greater than 0.4, the probability of dangerous rip current occurrence was deemed to be high. In addition to this, based on field observations, it was verified that a rip current was not usually generated when the guidance result of the model was at 'Level 1: Concern'. The results of the HAECUM system, which quantitatively simulates rip currents, are presented on a more localised basis. As a result, lifeguards can take appropriate action in advance. The output from the HAECUM simulation is viewed as a safety factor, and it provides combined current vectors in order to make it easier for the emergency management officials to make decisions. This forecasting model can then be used to establish a control over safety at Haeundae Beach. These safety levels are usually displayed as numbers ranging from 0.1 to 2 (Concern = under 0.1, Cautious = 0.1~0.4, Dangerous = 0.4~1.0, and Fatal = over 1.0). By combining the predictive index model (NERiPS-H) and the rip current numerical forecasting model (HAECUM), rip current forecasts were made using wave and wind data, along with forecasting information, which made it possible to provide a 72-hour rip current forecast. This forecast was then displayed on the KMA website. In this study, the positions of swimmers were measured using closed-circuit television (CCTV). As shown in the middle of the left section of the CCTV image displayed in Figure 1, the spatial distribution of swimmers swept away by rip currents could be well represented by using a CCTV image. A rip current warning decision-process system was created using wave data, and provided the KMA with forecasting information four times a day (09:00, 12:00, 15:00, and 18:00). Figure 7 shows an example of a selection of forecasting results from the 19th to the 21st of August, 2014. The 2014 rip current forecasting results for the warning decision-process system are sent to the KMA and a notice is provided on their website (Lee *et al.,* 2014). The rip current warning decision-process system operated for: 51 days in 2012 (a total of 204 uses), from the 9th of July to the 28th of August; 34 days in 2013 (a total of 136 uses), from the 12th of July to the 14th of August; and, 94 days in 2014 (a total of 376 uses), from the 9th of June to the 10th of September. Figure 8 shows the total forecasting results of the rip current warning decision-process system in 2014. CCTV cameras were installed on tall buildings that were situated nearby, in order to investigate the occurrence of rip currents. By comparing the modelled results with the real, observed rip current occurrences, the results of the rip current warning decision-process system showed a prediction accuracy of approximately 72%, 75%, and 76% for 2012, 2013, and 2014, respectively (Lee *et al.*, 2014). These results show that, over the course of the entire period, there were more rip current occurrences than were predicted, and that the prediction accuracy increased over time.

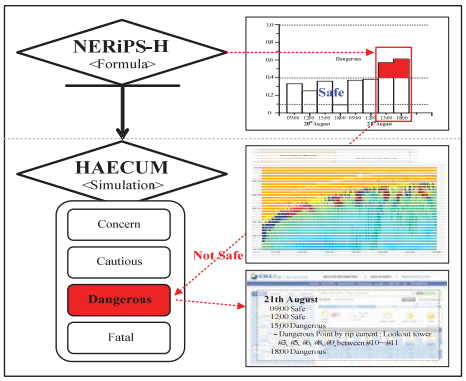

Figure 7. Rip current forecasting results (19st~21st August, 2014).

DISCUSSION

In this study, we focussed on developing an efficient rip current warning decision-process system in Korea. The results of the system showed a prediction accuracy of approximately 72%, 75%, and 76% for 2012, 2013, and 2014, respectively (Lee *et al.*, 2014). According to these results, this system could play an effective role in the forecasting of rip currents. To provide a user-friendly simulation for rip currents, a forecasting system had been built in the form of a software package. To predict wave-induced currents for the sake of public safety, coastal flows and waves were produced at each time step and grid point by means. To verify the accuracy of the HAECUM model, we compared rip current occurrence data with the results of the HAECUM simulation with incident wave conditions supplied by the KMA. In 2014, the reliability of the HAECUM system was lower than at other times. This is due to the fact that the topography of Haeundae Beach was altered by the construction of an offshore, submerged breakwater, in addition to the effects brought on by the beach nourishment conducted in 2014. The rip current warning decision-process system was updated in 2015 in order to account for the new Haeundae Beach topography. Rip current warning decision-process systems are in use at other locations across Korea where rip current-related accidents have also occurred. These locations include Jungmun beach in Jeju, and Naksan beach in Yangyang. The results of this study can be used to improve marine disaster-prevention techniques.

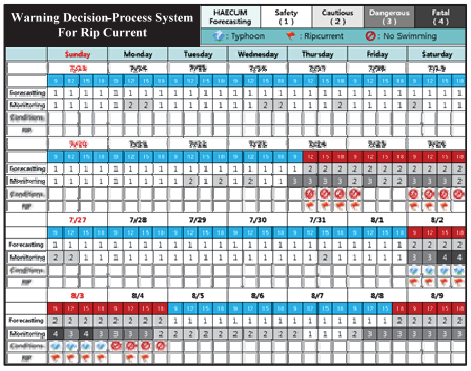

Figure 8. Comparison between the warning decision-process system results and the CCTV monitoring system, 2014 (Haeundae Beach).

CONCLUSIONS

Rip currents are not inherently dangerous, but a lack of education and awareness allows these important surf-zone circulations to become deadly. In order to provide reliable rip current forecasting results, a rip current warning decision-process system was developed in this study, using a combination of the NERiPS-H method and HAECUM system. By combining the predictive index model and the numerical rip current forecasting model, rip currents were forecasted using wave and wind data, along with forecasting information, which made it possible to provide a 72-hour rip current forecast. This forecast was then displayed on the KMA website. In the first stage of the rip current warning decision-process system, the NERiPS-H model is used to predict the occurrence of dangerous rip currents in advance during the swimming seasons. At Haeundae Beach, an observation system for investigating rip currents could provide basic rip current occurrence data in terms of oceanophysical phenomena, which, in turn, could be used to improve the economic value of coastal monitoring and warning systems. In the second stage, the HAECUM system automatically used wave and wind data in a simulation. In order to predict the expected wave-induced currents, simulated coastal flows and waves were produced at each time step and grid point, with the aim of improving public safety. The accuracy of the HAECUM system was verified by comparing the real, observed rip current occurrence data with the results of the HAECUM simulation, using the incident wave conditions supplied by the KMA as the inputs for the model. A rip current warning decision-process system could play an effective role in the forecasting of rip currents by significantly reducing the forecasting time required.

ACKNOWLEDGMENTS

This research was supported by Basic Science Research Program through the National Research Foundation of Korea (NRF) funded by the Ministry of Education (NRF-2013R1A1A2058707). This work was funded by the Korea Meteorological Administration Research and Development Program under Grant KMIPA 2015-1072.

LITERATURE CITED

Eom, H.; Yun, J.H.; Jeong, C.K.; Seo, J.W., and You, S.H., 2014. Introduction to KMA Operational Forecasting System for Rip Current, *J. Coast. Res.*, SI 72, 63-68.

Engle, J.; MacMahan, J.; Thieke, R.J.; Hanes, D. M. and Dean, R.G., 2002. Formulation of a Rip Current Predictive Index Using Rescue Data, *Proceedings National Conference on Beach Preservation Technology*, FSBPA, MS.

Haas, K.; Svendsen, I.; Haller, M., and Zhao, Q., 2003. Quasi-three dimensional modeling of rip current systems, *Journal of Geophysical Research: Oceans,* 108(C7), 3217.

Kim, I.; Lee, J.L.; Hwang, J.S.; Lee, S., and Lee, J., 2014. Vertical Structure of Rip Current Observed at Haeundae Beach, *Proceedings of 3rd International Rip Current Symposium* (Busan, Republic of Korea), *Journal of Coastal Research,* Special Issue No. 72, pp. 1–5.

Lee, J.; Yoo, C., and Lee, J.L., 2014. Introduction to Automated System in HAECUM (HAEundae Current Model), *Proceedings 3rd International Rip Current Symposium* (Busan, Republic of Korea), *Journal of Coastal Research*, Special Issue NO. 72, pp. 81-84.

Lee, J.Y.; Jun, K. C.; Lee, S. C., and Lee, J.L., 2013. A study on a Predictive Index for Dangerous Rip Current Generation at Haeundae Beach, *Proceedings 12th International Coastal Symposium* (Plymouth, England), *Journal of Coastal Research*, Special Issue NO. 65, pp. 754-759.

Lee, J.Y. and Lee, J.L., 2011. Verification of Rip Current Simulation Using HAECUM Compared with Field Observational Data, *Proceedings of the 6th International Conference on Asian and Pacific Coasts* (Hong Kong, China), pp. 877-884.

Lascody, R.L. 1998. East Central Florida rip current program. *National Weather Digest*, 22(2), pp. 25-30.

Long, J. W. and Ozkan-Haller, H. T., 2009. Low frequency characteristics of wave group-forced vortices. *Journal of Geophysical Research.* 114, C08004.

Lushine, J. B., 1991. A study of rip current drownings and related weather factors, *National Weather Service Forecast Office*, National Weather Digest, pp. 13-19.

Madsen, P. A.; Murray, R., and Sorensen, O., 1991. A new form of Boussinesq equations with improved linear dispersion characteristics, *Coastal Engineering,* 15, pp. 371–88.

Nwogu, O., 1993. Alternative form of the Boussinesq equations for nearshore wave propagation, *Journal of Waterway, Port, Coastal, and Ocean Engineering,* 119, pp. 618–38.

Peregrine, D. H., 1967. Long waves on a beach, *Journal of Fluid Mechanics,* 27, pp. 815–27.

Roelvink, J. A.; Reniers. A. J. H. M.; van Dongeren, A. R.; van Thiel de Vries, J. S. M.; McCall, R. T., and Lescinski, J., 2009. Modeling storm impacts on beaches, dunes and barrier islands, *Coastal Engineering,* 56, pp. 1133–1152.

Wei, G.; Kirby, J. T.; Grilli, S., and Subramanya, R., 1995. A fully nonlinear Boussinesq model for surface waves I. Highly nonlinear, unsteady waves, *Journal of Fluid Mechanics,* 294, pp. 71–92.

Yu, J., and Slinn, D., 2003. Effects of wave-current interaction on rip currents, *Journal of Geophysical Research,* 108, 3088.

Journal of Coastal Research	SI	75	1172 - 1176	Coconut Creek, Florida	2016

Multi-Criteria Surge Vulnerability Assessment with Long-term Reanalysis

Gyumin Lee[†], Byoung-Il Min[††], and Kyung Soo Jun[‡*]

[†]Construction and Environmental Research Center
Sunkyunkwan University
Suwon, Korea

[‡]Graduate School of Water Resources
Sungkyunkwan University
Suwon, Korea

[††]Nuclear Environment Safety Research Division
Korea Atomic Energy Research Institute
Daejeon, Korea

www.cerf-jcr.org

www.JCRonline.org

ABSTRACT

Lee, G.; Min, B., and Jun, K.S., 2016. Multi-Criteria Surge Vulnerability Assessment with Long-term Reanalysis. *In:* Vila-Concejo, A.; Bruce, E.; Kennedy, D.M., and McCarroll, R.J. (eds.), *Proceedings of the 14th International Coastal Symposium* (Sydney, Australia). *Journal of Coastal Research*, Special Issue, No. 75, pp. 1172 - 1176. Coconut Creek (Florida), ISSN 0749-0208.

Storm surges are one of the biggest natural disasters. In Korea, which has many of its important cities on its coast and since three sides of the country are bordered by the ocean, surges have the potential to generate great economic and social damage. The main factors causing surges are typhoons and tropical atmospheric pressure. Korea is affected by an average of 3.1 typhoons annually. In this study, we aim to evaluate the vulnerability of the Korean peninsula to typhoons. The best information on the tracks of past typhoons was collected and the hazard calculated by interpreting the typhoons' degree of influence and magnitude. Vulnerability was also estimated by considering the effects on society and the economy. At this point in time, the evaluation was based on the Driving force-Pressure-State-Impact-Response (DPSIR) framework. This framework is a set of sustainable development indicators that reflects the social structure and capability, including national efforts to respond to direct or indirect damage and disasters. As a result of calculating the vulnerability to surge, the cities of Busan, Ulsan, and Tongyeong, which are all located on the southern coast of Korea, were estimated to be the places of primary vulnerability.

ADDITIONAL INDEX WORDS: *Coastal hazard management, Costal hazard vulnerability, MDCM.*

INTRODUCTION

Storm surge is one type of natural disasters that cause great economic and social damage in Korea, which is surrounded by water on three sides. Surges may be caused by events such as typhoons and tropical anticyclones, and Korea experiences an average of three typhoons annually. The most damaging typhoon was Rusa, which occurred in 2002, which resulted in 246 casualties and property damage worth 5,147,900,000,000 won. In 2012, Typhoon Bolaven and Typhoon Tembin caused property damage worth 63,650,000,000 won (National Typhoon Center, 2010). The main reasons for such a large amount of damage are that most economic activity involves transport through seaports, and excellent dockyards were built in Korea with the development of ship building businesses. Another important reason is the fact that large cities are also located in coastal areas.

Accordingly, the vulnerability needs to be evaluated in order to take systematic counteractive measures against surges. In this study, vulnerability refers to the extent to which changes could harm a system, or to which a community could be affected by the impact of a hazard. Therefore, we aimed to use readily available data in this parametric approach to build a picture of the vulnerability of an area (Balica *et al.*, 2013).

In this study, we introduced the Driving force-Pressure-State-Impact-Response (DPSIR) framework, which is a European Environment Agency (1995) model for sustainability assessment that has recently been used in many fields in order to designate vulnerability parameters. The DPSIR framework provides a structure to the description of environmental problems by formalizing the relationships between various sectors of human activity and the environment as causal chains of links (Chung and Lee, 2009a). Under the DPSIR framework, the environmental management process may be described as a feedback loop that controls a five-stage cycle (Economic and Social Commission for Asia and the Pacific, 2004). We used this framework to include the social and economic influences and responses related to disasters. Storm surge hazard scenarios were established based on the long-term reanalysis of typhoons and the surge height was estimated from these data. The technique for order performance by similarity to ideal solution (TOPSIS), which is widely used at present, was employed as a vulnerability assessment technique.

DOI: 10.2112/SI75-235.1 received 15 October, 2015; accepted in revision 15 January, 2015.
*Corresponding author: ksjun@skku.edu
©Coastal Education and Research Foundation, Inc. 2016

Background

Most of the highly populated areas in Korea are located in lowland and coastal areas. Therefore, these areas are very vulnerable to fluvial or coastal flooding. In particular, coastal areas are directly exposed to natural disasters resulting from typhoons. Accordingly, it is very important to prepare effective measures to prevent coastal disasters. Typhoons are the primary cause of repeated natural disasters occurring in these coastal areas. Table 1 presents a summary of data for 10 typhoons that caused the greatest economic damage in the Korean peninsula from 1904 to 2014. The typhoon that caused the most damage in Korea's coastal areas was Typhoon Maemi, which occurred in 2003. According to the weather forecast provided in Korea, the pressure recorded at the center of Maemi was 950 hPa, which is the lowest pressure recorded, and this was accompanied by strong winds, surges, and waves. Maemi arrived in Korea simultaneously with a high tide, causing enormous amounts of damage to property and human lives. To make things worse, some areas that were damaged by Typhoon Maemi had not yet fully recovered from the damage caused by Typhoon Rusa in the previous year.

Table 1. *Rank of typhoon damage (National Typhoon Center, 2014; Statistics Korea; 2015).*

Typhoon	Date	Damage (10 billion won)
RUSA	2002.08.30~09.01	51,479 (0.530% of GDP)
MAEMI	2003.09.12~09.13	42,225 (0.424% of GDP)
OLGA	1999.07.23~08.04	10,490 (0.129% of GDP)
BOLAVEN & TEMBIN	2012.08.25~08.30	6,365 (0.048% of GDP)
JANIS	1995.08.19~08.30	4,563 (0.063% of GDP)
THELMA	1987.07.15~07.16	3,913 (0.108% of GDP)
SANBA	2012.09.15~09.17	3,657 (0.028% of GDP)
YANNI	1998.09.29~10.01	2,749 (0.037% of GDP)
PRAPIROON	2000.08.23~09.01	2,520 (0.029% of GDP)
MEGI	2004.08.17~08.19	2,508 (0.024% of GDP)

According to the Hyundai Research Institute (HRI) (2012), the total cost of restoration of an area is over 1.6 times that of the damage caused. This is due to the fact that when a damaged area is restored, there are intangible costs, such as running costs, and restoration entails improvement to ensure durability. The HRI estimated that these hazards could negatively affect the national economy due to consumer price distress and production decline.

Therefore, to decrease the damage, strategies were established with assessed vulnerable areas and criteria before hazards occurred.

METHODS

This study was carried out in four steps. Step 1 involved determining probable maximum surge heights using long-term wave data. In this study, we calculated the maximum probable storm surge height for every coastal locality using long-term reanalysis data. Step 2 involved the determination of the criteria to construct a data matrix. The surge vulnerability based on the DPSIR framework was estimated in this step. Step 3 involved the selection of all feasible proxy variables or indicators to quantify, measure, and communicate the relevant information and to collect all of the data. The data that was presented was grid-based. Step 4 involved estimation of the assessment results. The surge vulnerabilities were quantified and ranked using the TOPSIS method.

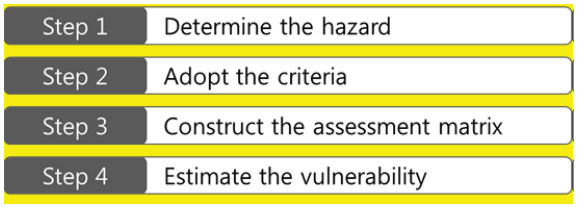

Figure 1. Study procedure.

In this study, the southern coast areas with a relatively high frequency of storm occurrence were selected as the target areas and the vulnerability assessment for each local government was performed as shown in Figure 2.

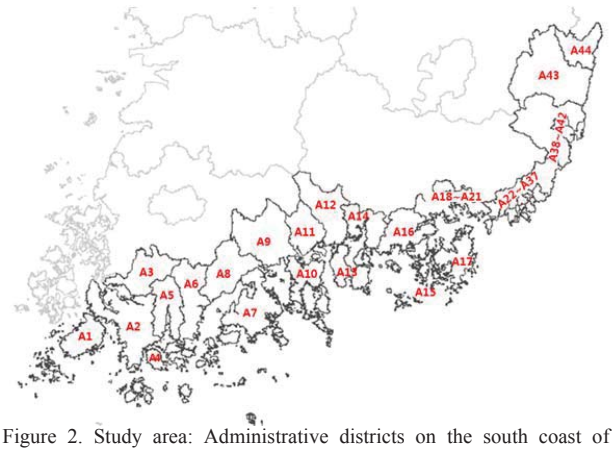

Figure 2. Study area: Administrative districts on the south coast of Korea.

Estimated surge risk with long-term reanalysis

The hazard risk of surges was estimated using long-term reanalysis data, which was provided by the Korea Institute of Ocean Science and Technology (KIOST). It was calculated on the grid cells with 18 km based on the long-term surge output of the numerical simulation using observation data for 25 years and the estimated storm surge data for primary storms for 53 years. The hazard risks of each of the cells were determined with the calculated probable maximum surge. Figure 4 shows the surge hazard level using an index that estimated the probable maximum surge heights from the 100-year return period.

Establishing vulnerability criteria

The DPSIR framework was adopted by the European Environment Agency (1995) to report the results of environmental monitoring from different environmental assessment tools, such as environmental impact assessments. The Water Strategy Man (WSM) (2004) developed strategies for integrated water resource management in water-deficient regions using the DPSIR framework. Lee *et al.* (2013) developed the integrated multi-criteria flood vulnerability assessment approach based on the DPSIR framework. This framework makes it possible to formalize all policy-making and management processes by identifying cause and effects links among complex elements of the chain of human-environment interaction.

Surge vulnerability is inherent in various circumstances including the possibility of disaster, the influence of the disaster on society, and society's ability to respond to the disaster. Therefore, we considered various aspects of the region such as: (1) damage, (2) exposure, and (3) response criteria, in this study in order to assess surge vulnerability. These sub-criteria were composed of combinations of the DPSIR framework (Table 2). All of the data for the sub-regions were collected from administrative sources, such as governmental agencies, the national statistical office, and the national emergency management agency.

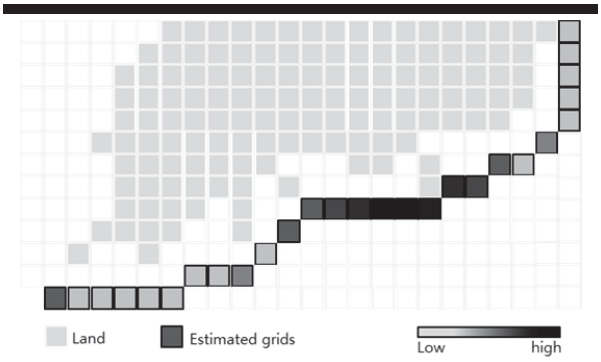

Figure 3. Estimated surge hazard.

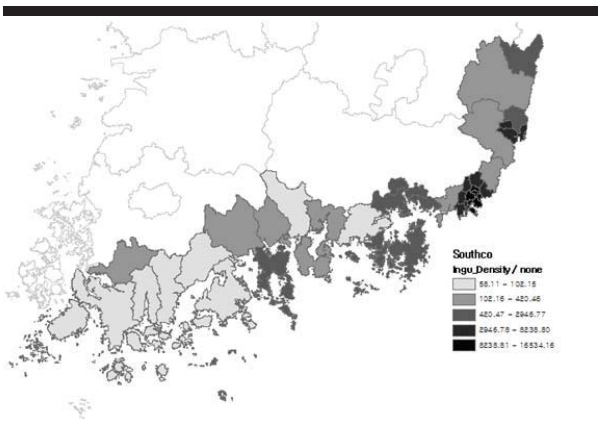

Figure 4. Collected assessment spatial criteria (ex. population density).

TOPSIS

TOPSIS, known as one of the most classical MCDM (Multi-Criteria Decision-Making) methods, is based on the idea that the chosen alternative should be closest to the positive ideal solution and furthest from the negative ideal solution (Hwang and Yoon, 1981; Lai *et al.*, 1994). This technique is based on the concept that the ideal alternative has the best level for all of the attributes, whereas the negative ideal is the alternative with all of the worst attribute values. A TOPSIS solution is defined as the alternative that is simultaneously farthest from the negative ideal and closest to the ideal alternative (Chu, 2002). According to Kim *et al.* (1997) and Shih *et al.* (2007), there are four advantages of using TOPSIS: (1) a sound logic that represents the rationale of human choice; (2) a scalar value that accounts for both the best and worst alternatives simultaneously; (3) a simple computation process that can be easily programmed; and (4) for any two dimensions, the performance measures for all of the alternatives can be visualized on a polyhedron.

The TOPSIS procedure can be expressed in a series of steps as follows:

- Calculate the normalized decision matrix as follows:
  $C_{ij} = x_{ij} / \sqrt{\sum x_{ij}^2}$, $i = 1, \cdots, m,\ j = 1, \cdots, n$
  (1);
- Calculate the weighted normalized decision matrix as follows:
  $r_{ij} = w_j C_{ij}$, $i = 1, \cdots, m,\ j = 1, \cdots, n$
  (2),
  where w_j is the weight of the ith attribute or criterion, and $\sum_{j=1}^{n} w_j = 1$;
- Determine the positive ideal solution (PIS) and negative ideal solution (NIS) as follows:
  $A^+ = \{r_1^+, \cdots, r_n^+\} = \{(\max_j r_{ij} \,|i \in I), (\min_j r_{ij} \,|i \in J)\}$ (3)
  and
  $A^+ = \{r_1^-, \cdots, r_n^-\} = \{(\min_j r_{ij} \,|i \in I), (\max_j r_{ij} \,|i \in J)\}$
  (4),
  where I is associated with the benefit criteria and J is associated with the cost criteria;
- Calculate the separation measures using the n-dimensional Euclidean distance. The separation of each alternative from the ideal solution is given as follows:
  $d_j^+ = \left\{\sum_{j=1}^{n} (r_{ij} - r_j^+)^2\right\}^{1/2},\ i = 1, \cdots, m$
  (5) and
  $d_j^- = \left\{\sum_{j=1}^{n} (r_{ij} - r_j^-)^2\right\}^{1/2},\ i = 1, \cdots, m$,
  (6);
- Calculate the relative closeness to the ideal solution. The relative closeness of the alternative A^- with respect to A^+ is defined as follows:
  $R_i = d_i^- / (d_i^+ + d_i^-),\ i = 1, \cdots, m$
  (7); and
- Rank the preference order. Using this index, the alternatives can be ranked in decreasing order.

The basic principle of the TOPSIS method is that the chosen alternative should have the "shortest distance" from the positive ideal solution and the "farthest distance" from the negative ideal

solution. The TOPSIS method introduces two "reference" points, but it does not consider the relative importance of the distances from these points.

Table 2. *Vulnerability criteria for assessment.*

DPSIR framework	Damage	Exposure	Response
Driving force		GRDP	Safety consciousness
Pressure		Population growth Rate of urbanization	Regional development plan
State	Damaged area	Population, land value Commercial zone Manufacturing area	Hazard response strategy Recovery plan
Impact	Value of damage, casualties	Distribution of the weak and the vulnerable Primary protection area	Disaster response officials Emergency rescue service Capability of emergency recovery
Response		The present condition of safety education Evacuation route maps and disaster shelters	Disaster mitigation activity program

RESULTS

In this study, we tried to identify surge vulnerable areas using long-term data reanalysis with the MCDM method. The weights set for the MCDM approach were the same value, 1.0. Figure 5 shows the results of the vulnerability assessment. The big city of Busan was the most vulnerable area. The primary cause of the results was that the levels of exposure criteria were high. Therefore, Ulsan, and Tongyoung were vulnerable areas in addition to Busan.

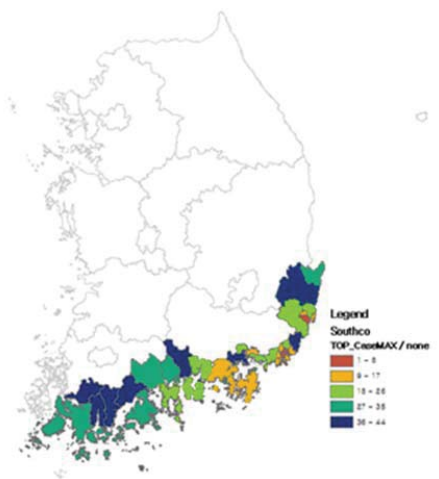

Figure 5. Results of the vulnerability assessment.

It seems to be the result of the commercial criteria and primary protection area criteria, such as power plants. The vulnerability of Tongyoung saw an increase in comparison to that in the study by Lee *et al.* (2015) who conducted a tsunami vulnerability assessment of the south coast of Korea. That study did not apply the same criteria , but the values of the dominant factors, such as the population density, primary protection area, and land value, were the same. The estimated results of the surge and tsunami hazard risks on the south coast of Korea were compared and are shown in Figure 6. Therefore, various hazards had to be taken into consideration in order to establish a strategy for natural hazards on the coast. The presented vulnerability assessment approach that could include the relationship between the human society and natural hazards could be widely used.

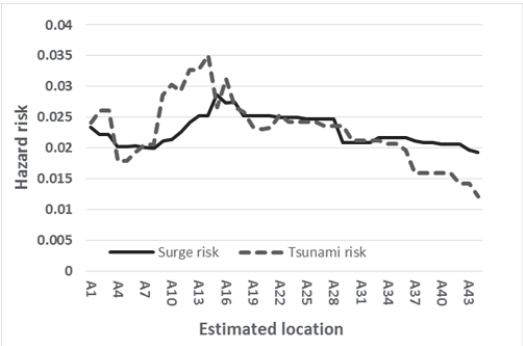

Figure 6. Comparison with the estimated hazard risk.

DISCUSSION

In the assessment conducted in this study, the hazard of surges was not entirely clear. The surge height in each area was analyzed according to the established scenarios and then the probability of the storm surge height was calculated to apply as a hazard risk in the assessment. However, this work was not completed in this study and further work will need to be done to continuously improve the research. At present, the damage caused by a storm surge is not considered separately in Korea when determining the damage caused by a typhoon. Therefore, it was difficult to obtain data for the damaged property to be considered in the vulnerability criteria. Thus, all of the damage caused by a typhoon was summed. Therefore, basic data have to be collected in advance for the places vulnerable to storm surges for assessment of the damage caused by a storm surge.

CONCLUSIONS

In this study, we established a storm surge vulnerability assessment technique. In this approach, we used both the vulnerability criteria based on the DPSIR framework and the maximum storm-surge height extracted from the scenario established by the long-term reanalysis as the hazard criteria. Thus, an assessment matrix was built and the vulnerability areas were determined by assessment with the MCDM technique. When this assessment technique was applied to the southern coastal areas of Korea, the regions of Busan, Ulsan, and Tongyoung appeared to have the highest vulnerability. However, in this assessment, the damage caused by the storm surge could not be extracted separately from the overall damage, which accounted for a big portion of the cause of vulnerability, thereby influencing the assessment results.

The assessment technique established in this study should be improved by supplementing the data and revising the assessment items. Thereafter, the technique can be applied to determine the areas vulnerable to storm surges on the Korean peninsula. In addition, it can contribute to the establishment of policies for taking counteractive measures against storm surges.

ACKNOWLEDGMENTS

This study was financially supported by the Basic Science Research Program of the National Research Foundation of Korea (NRF), which is funded by the Ministry of Education (NRF-2013R1A1A2060942).

LITERATURE CITED

Lee, G.; Jun, K.-S., and Chung, E.-S., 2013. Integrated multi-criteria flood vulnerability approach using fuzzy TOPSIS and Delphi technique. *Natural Hazards and Earth System Sciences*, 13, 1293-1312.

Hwang, C. L. and Yoon, K., 1981. *Multiple attributes decision-making methods and applications*. Springer, Heidelberg.

Chu, T. C., 2002. Selecting plant location via a fuzzy TOPSIS approach. *International. Journal of Advanced Manufacturing Technology*, 20, 859-864.

Kim, G.; Park, C. S., and Yoon, K. P., 1997. Identifying investment opportunities for advanced manufacturing systems with comparative integrated performance measurement. *International Journal of Production Economics,* 50, 23-33.

Shih, H. S.; Shyur, H. J., and Lee, E. S., 2007. An extension of TOPSIS for group decision making. *Mathematical and Computer Modelling.* 45, 801-813.

National Typhoon Center, 2014. Overview, http://typ.kma.go.kr/TYPHOON/index_eng.jsp (accessed October 10, 2015).

WSM, 2004. *A Comprehensive Decision Support System for the Development of Sustainable Water Management Strategies*, EU DG Research, Contract No: EVK1-CT-2001-00098.

Lee, G.; Min, B.I.; Suh, K.S., and Jun, K.-S., 2015. A study on tsunami vulnerability assessment in South Korea. *ISOPE* (Hawaii), 806p.

Yoon, J.J. and Shin, J.S., 2013. Estimation of storm surge inundation and hazard mapping for the southern coast of Korea. *Journal of Coastal Research*, Special Issue No. 65, pp. 856-861.

European Environment Agency, 1995. *Europe's Environment: The Dobris Assessment*. Copenhagen, Denmark.

Balica, S.F.; Popescu, I.; Beevers, L., and Wright, N.G., 2013.Parametric and physically based modelling techniques for flood risk and vulnerability assessment: A comparison. *Environmental Modelling and Software,* 41, 84-92.

Chung, E. S. and Lee, K. S., 2009. Prioritization of water management for sustainability using hydrologic simulation model and multicriteria decision making techniques. *Journal of Environmental Management*, 90, 1502–1511.

Economic and Social Commission for Asia and the Pacific, 2004. *Guidelines on Strategic Planning and Management of Water Resources*. New York, United Nations.

Hyundai Research Institute, 2012. *Rain and Economics, Issue and Assignment*. Seoul, Korea.

Journal of Coastal Research	SI	75	1177 - 1181	Coconut Creek, Florida	2016

Lagrangian Observation of Rip Currents at Haeundae Beach Using an Optimal Buoy Type GPS Drifter

Jooyong Lee†, Dong Hee Kim‡, Sahong Lee‡, and Jung Lyul Lee ‡*

† Construction and Environmental Research Center
Sungkyunkwan University
Suwon, Republic of Korea

‡ Interdisciplinary Program in Crisis, Disaster and Risk Management
Sungkyunkwan University
Suwon, Republic of Korea

www.cerf-jcr.org

www.JCRonline.org

ABSTRACT

Lee, J.; Kim, D.H.; Lee, S., and Lee, J.L., 2016. Lagrangian Observation of Rip Currents at Haeundae Beach Using an Optimal Buoy Type GPS Drifter. *In:* Vila-Concejo, A.; Bruce, E.; Kennedy, D.M., and McCarroll, R.J. (eds.), *Proceedings of the 14th International Coastal Symposium* (Sydney, Australia). *Journal of Coastal Research*, Special Issue, No. 75, pp. 1177 - 1181. Coconut Creek (Florida), ISSN 0749-0208.

In this study, we designed a new buoy type GPS drifter that is capable of measuring the rip current pattern in the surface layer particularly at Haeundae Beach, Korea. Our field test performance in August 2012 was successful using this new GPS drifter. Our GPS-tracked surf zone drifter can not only be easily affected by physical forces below the surface on the equipment's movement, but also unaffected by breaking waters. In this study, the design for a small, low-cost buoy type GPS drifter for collecting accurate Lagrangian data in the coastal zone is described.

ADDITIONAL INDEX WORDS: *rip current, buoy, GPS drifter, Lagrangian observation.*

INTRODUCTION

'Rip current' has recently become a well-known technical term in Korea. At Haeundae Beach, located on the southeastern corner of the Korean Peninsula, hundreds of people were swept away by a fast-moving seaward current and were rescued, as shown in Figure 1. In response, the Korean Meteorological Administration plans to set up monitoring systems to establish the mechanisms of the rip current generation at Haeundae Beach. A rip current can essentially be thought of as a localized river in the ocean, carrying water from the shoreline out to sea. Differences in bathymetry lead to variations in the breaking of waves along the shore, which cause a higher mean water level over shoals than over rip channels. Surf zone circulation, which is driven primarily by breaking waves, transports sediments, pollutants, and swimmers (Longuet-Higgins, 1970). Changes in the breaking of waves, owing to variations in wave height and direction along curving coastlines, irregular bathymetry, and man-made structures, are believed to cause complex surf zone circulation, including rip currents and mean longshore currents that can change direction across both the surf zone and along depth contours (Shepard *et al*., 1950). The resulting circulation pattern shown in Figure 2 (illustrated using the COMET Program) is offshore-directed flow in the rip channel and onshore flow over the shoals to either side. The rip head is the seaward tip of the rip, where rip currents diffuse and lower velocities are present.The flow in the rip head is less constrained by the bathymetry of the rip channel and spreads laterally. The returning onshore flow is funneled into the rip through longshore-directed feeder currents, which occur near the shoreline.

DOI: 10.2112/SI75-236.1 received 15 October, 2015; accepted in revision 15 January, 2015.
*Corresponding author: jooyong@gmail.com
©Coastal Education and Research Foundation, Inc. 2016

Hydrodynamic studies of open beach circulation have received significant attention in recent years, including Eulerian observations, Lagrangian observations, video observations, radar observations, physical models, and numerical modeling. Studies have also been conducted on embayed beaches under normal circulation. Many coastal scientists have been surveying rip currents by several methods, using various field measurement devices. A representative device is the Lagrangian drifter, which includes a Global Positioning System (GPS) module. Surf zone drifters have been used in oceanographic research for decades, as well as for experiments in physics (Shepard *et al*., 1941; Shepard and Inman, 1950). Advances in technology permitting the installation of small GPS receivers on drifters have improved measurement accuracy (Johnson *et al*., 2003; Schmidt *et al*., 2003; Schmidt *et al*., 2005).

Figure 1. Rip current occurrence at Haeundae Beach (August 04, 2012).

A GPS system provides simultaneous information on location and time during almost all weather conditions. Using these data, we can understand flow pattern, current speed, and flow direction. More recently, GPS-tracked drifters have further

improved our understanding of the surf zone (Schmidt *et al*., 2005) and have shown that the rip current intensifies as tide level decreases. Unfortunately, field observations of rip current flows in coastal zones are scarce in Korea but important for understanding the spatial variability of rip currents.

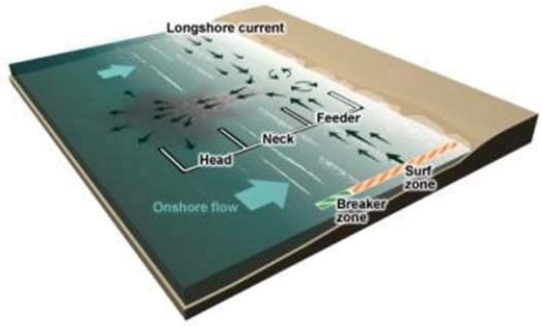

Figure 2. Conceptual representation of a rip current circulation system.

As part of this research, we specifically designed a new buoy type GPS drifter to measure the rip current pattern in the surface layer at Haeundae Beach, Korea. Our field test performance using this new GPS drifter in August 2012 was successful. Our GPS-tracked surf zone drifter can not only be easily affected by physical forces below the surface on the buoy's movement, but is also unaffected by breaking waters. Unlike other beaches worldwide, Haeundae Beach has a swimming restraint line for safety reasons, which is 50-100 m away from the shore. Since lifeguards keep the public within the swimming restraint line, we found it difficult to deploy general GPS drifters at Haeundae Beach. In this study, we describe field tests of a surf zone drifter and results from a deployment near a rip current. To our knowledge, this is the first study to comprehensively measure a nearshore rip current in a surf zone in Korea.

Site Description

Haeundae Beach, at a latitude 35.16° N and longitude of 129.17° E, is located on the southeastern corner of the Korean Peninsula and opens southward, as shown in Figure 3. Due to the large population of Busan City, the beach has many visitors throughout the year. During the summer vacation season in particular, over one million people may visit the beach on a peak day. However, the beach is extremely small, with a length of only 2 km. The average width of the beach is less than about 50 m. The mean tidal range is approximately 1 m, and waves mostly come from the south during the summer swimming season, and thus are nearly perpendicular to the shore, which generates rip currents. A directional wave buoy is located 1 km offshore to measure incident waves. Owing to the nearly perpendicular incident wave conditions, the rip channels seem to be stable over a measurement period. Mainly at night, the buildings hinder winds from the seaward direction, and this can decrease the incident wave height. This is because the beach has been exposed to higher wave height and beach erosion. Moreover, the presence of several oversized sunken rocks located a short distance from the beach results in a very uneven morphology. The very uneven water depth facilitates variation in the breaking of waves. This is because the wave current is the result of the hydraulic gradient of the mean water level. Change would be directed seaward by the almost identical current nearby. Rip channels were observed in the surf zone bathymetry. Haeundae Beach has an average seafloor inclination of 1/15 to 1/30 and a wave-dominated pocket shape with a softer inclination along the eastern side. According to the tidal characteristics observed by the Busan harbor tidal observation station, Haeundae Beach has a mean sea level of 64.9 cm. In addition, the representative wave directions (θ) are southeast (45°SE), south (S), and southwest (19°SW), with the waves reaching a significant wave height (H1/3) of 0.15-2.39 m (mean value is 0.61 m) and a wave period (T1/3) of 2.66-16.40 s (mean value is 5.42 s).

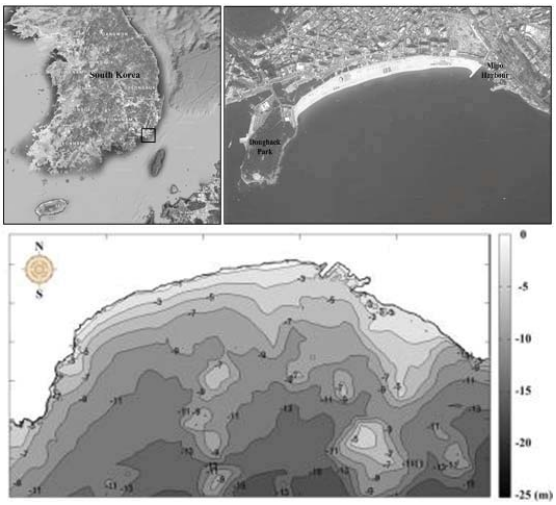

Figure 3. Haeundae Beach location and 2 m isobaths. The shoreline is in bold.

METHODS

Design of the GPS Drifter

The high cost of drifters commercially available drifters has made it difficult to obtain more than 10 drifters for any experiment and has resulted in limited detail (Schmidt *et al*., 2005). Less expensive drifters ($500) have been built, at the expense of either reduced accuracy or a time-consuming process to match the accuracy of those available commercially (Johnson *et al*., 2003). The focus of this research effort was to design an inexpensive drifter that uses handheld, off-the-shelf Differential GPS (DGPS) technology.

MacMahan and Brown (2007) modified a commercially available DGPS logger ($150) to obtain system accuracy in position (0.4 m) and velocity (0.01 m/s) after post-processing. The low cost (less than $250 each, without labor) of the drifters built with this technology allowed the construction of a fleet of 30 for about the same cost as a single commercially available drifter. In order to detect the velocities and directions of the long-shore current and rip current, we designed a GPS buoy system with a Satellite Based Argumentation System (SBAS). A

DGPS data logger is currently used with a floating platform. The small spatial (5 m) and short temporal (1 min) scales of interest in surf zone circulation are resolved with GPS techniques used in coastal and near ship drifters (*e.g.*, real-time DGPS, 3–5 m accuracy (George and Largier, 1996)). However, in the surf zone, submergence by breaking and broken waves prevents the reception of GPS signals, and upon surfacing and reacquiring signal, there is a delay in the estimation of GPS parameters. A small GPS drifter for current measurements in the coastal zone has been recently developed by Sabet *et al*. (2011). As part of this research, we designed a new buoy type GPS drifter to measure the rip current pattern in the surface layer at Haeundae Beach, Korea.

The new buoy type GPS drifter, shown in Figure 4, includes five primary components. These are a spherical shaped instrument casing, a handy GPS receiver, a weight to provide submergence equilibrium, and a casing cap for retrieval of the drifter. A damper is connected to the bottom of the casing with glue. The main casing is an approximately spherical compartment with an outer diameter of 30 cm and an overall height of 37 cm. The buoy type GPS drifter is made of yellow PVC, and a space for a GPS receiver is attached to the top of the body to house the DGPS logger. A transparent cap on the buoy can be easily closed and rapidly opened with a screw-type lock. When the cap of the casing is closed, the compartment is waterproof. A patch is attached to the bottom of the assemblage to improve the drifter's movement. The GPS receiver is a GPS742 high-sensitivity integrated receiver. The default receiver setting is data (position, time, and date). All initialization and satellite acquisition is carried out automatically by the receiver. The memory of the device can store 12,500 points, which is equivalent to approximately 25 h of continuous operation. The drifters store their latitude and longitude internally. Each drifter records GPS latitude and longitude and transmits this information to shore at 1-s intervals for real-time differential GPS (DGPS) tracking and partial data backup. The GPS unit can connect to a computer using a computer connector cable, Bluetooth communication, or USB communication and transfer the data stored in the memory of the device to a computer.

GPS drifters are deployed and recovered by hand and can easily be used for repeated runs over a short period of time. Their ease of deployment makes them effective for measuring rapidly developing transient features. To minimize wind resistance and inertial effects, the drifter units are nearly neutrally buoyant so that only the upper surface covering the internal GPS receiver is above water. The total weight of this GPS drifter is approximately 15 kg, and the drifter is much cheaper than the GPS drifters that have been made up until now. The advantages of the new buoy type GPS drifter include simplicity, compact size, reusability, and great maneuverability upon deployment. In the following section, an application of this small GPS drifter will be presented.

Field Test

The drifters permit data collection with greater spatial and temporal resolution than previously achieved. Figure 5 is a photo of a drifter. GPS buoys have been used to measure seas, rivers, and lakes for navigation purposes (Chen *et al*., 2004).

In this study, the design of a small, low-cost buoy type GPS drifter for collecting accurate Lagrangian data in the coastal zone is described. This new buoy type drifter that incorporates non-differential GPS technology has been constructed and is suitable for coastal investigations over short timescales (a few minutes to several hours) and distances and, in particular, for field surveying of the rip current at Haeundae Beach. A field experiment for measuring the rip currents at Haeundae Beach. The buoy type GPS drifters are intended for use in nearshore environments over timescales of a few minutes to several hours and are a low-cost alternative for applications that do not require buoys with sea-going capability (Song *et al*., 2011). The low cost makes it feasible to conduct experiments with buoy type GPS drifters in order to collect all data about circulation and dispersion in a system. To collect Lagrangian data, drifters were deployed on August 02, 2012. Deployment periods lasted for approximately 4 h on that day. On the day of deployment, four people initially started loggers for two drifters. The following day, August 03, 2012, a field rip current experiment was also conducted to examine rip current circulation patterns in greater detail.

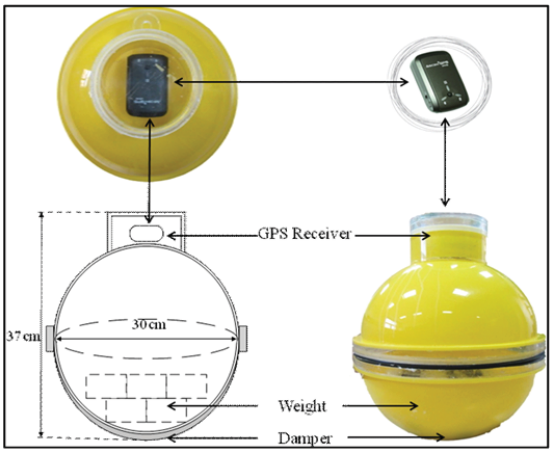

Figure 4. Design of a new buoy type GPS drifter.

Rip channels in bars and the associated seaward-directed rip currents have been a well-known phenomenon (Shepard *et al*., 1941; McKenzie, 1958; Sonu, 1972). Although the emergence of the rip channel morphology itself is still relatively poorly understood, the fundamental driving mechanism for the flow over a previously formed rip channel morphology is relatively well understood. Rip channels can be identified in the surf zone bathymetry. Bathymetric surveys were obtained during low tide using a NRTK-GPS surveying system on a personal watercraft. These surveys were performed 10 times in the summer season.

A rip channel can be found by surveying the surf zone depth using NRTK-GPS devices, which are accurate to within 2 cm (z values). The rip current morphology has a channel width of about 100 m, based on the bathymetry illustration in Figure 6. The rip channels are most noticeable in front of the number 8 lookout tower. Based on CCTV data, a rip current occurred near the number 8 lookout tower on August 10, 2012. Once the lights

of the loggers were flashing to indicate they were collecting data, the drifters were taken to the water and deployed so that their bodies did not interfere with each other. The drifters were removed from the water when they started to drag along shoals or when they left the swimming restraint line. Drifter trajectories at Haeundae Beach are displayed using Google Earth (Figure 7).

Figure 5. Close-up of the buoy type GPS drifter.

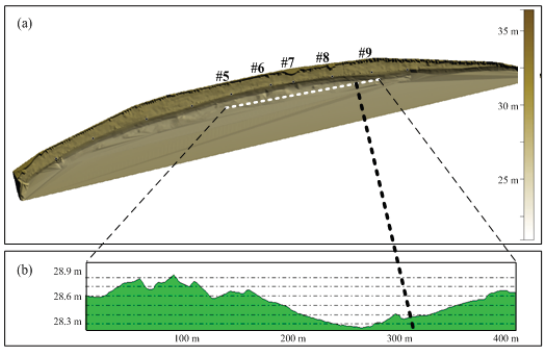

Figure 6. (a) Bathymetry plots using Global Mapper (August 13, 2012); (b) Longshore cross-section at dashed line.

Sources of Error

There were several sources of error introduced to the data during collection. Generally, the easiest source of error to identify was human influence on the drifters. Since the logging devices were turned on before the drifters were taken to the water, there were a few minutes of positional data at the beginning of each set that was unrelated to the flow field. The same is true whenever drifters were removed from the water. Additionally, when drifters would occasionally approach the shoreline close to a rip current, they were given a push to set them back in the current. While the drifters are designed to prevent excessive vertical oscillations due to waves, breaking waves affected the drifters by occasionally submerging their antennas. Drifters were designed to pass under oncoming waves (to prevent surfing), and their signal was periodically interrupted or degraded when this occurred.

RESULTS

Many coastal scientists have been surveying rip currents using several methods. However, due to the beach environment of Haeundae Beach, scientists could not use a typical drift buoy, which is why we designed the new buoy type GPS drifters for Haeundae Beach, as shown in Figure 4. Tracks for buoy type GPS drifters are shown in Figure 8. and the new buoy type GPS drifters performed well. To evaluate the incurrent measuring performance of the designed buoy type GPS drifters, we conducted experiments at Haeundae Beach, Korea. Observations were acquired out of the surf zone where the water depth was approximately 1.5-2 m.

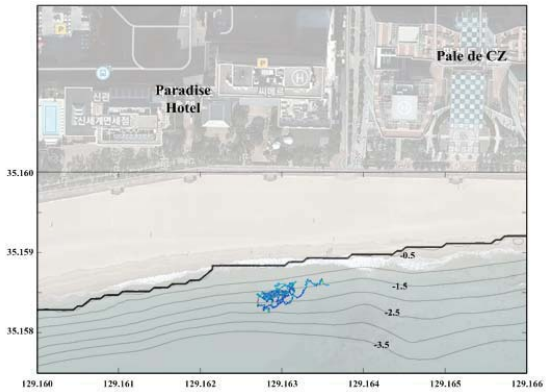

Figure 7. Data logging display using Google Earth.

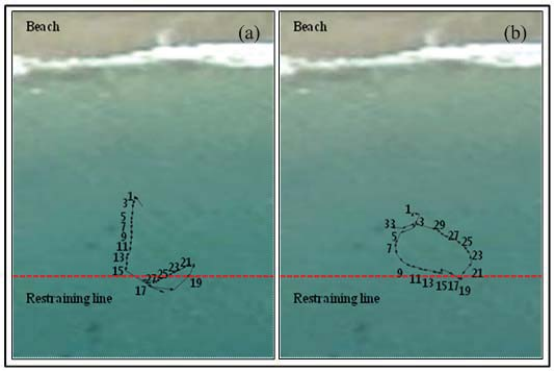

Figure 8. (a) Drifter flow patterns with rip current occurrence; (b) Drifter flow patterns with no rip current occurrence.

Drifters were deployed by swimmers inside the surf zone in a rip current throat. The release point location was determined by a bathymetric map, together with visual observations of circulation. Drifters were manually carried to the release point and released. Drifter motions were monitored visually from the beach. Figure 8 shows the routes tracked by a GPS drifter on August 02, 2012. The trajectories show a rip current flow which appears to spread and dissipate in the surf zone at 1.5 m water depth (relative to local MSL). Figure 8(a) shows the movement of the buoy type GPS drifter illustrated step-by-step in 1 min intervals due to the flow pattern of the buoy type GPS drifter

within the rip channel. After the buoy type GPS drifter was off the restraint line, the drifters were taken inside the restraint line. When rip currents did not occur, the movement of the buoy type GPS drifter showed circulation patterns, as shown in Figure 8(b). Tracks for a drifter deployment are shown in Figure 9 with the line color indicating instantaneous velocity. The average velocity of the buoy type GPS drifter going out into the open sea is 0.78 m/s, and the maximum velocity going out into the open sea is 3.34 m/s at that time. Comparing this velocity to the maximum velocity of the Beijing Olympic gold medal winning swimmer Park Tae-hwan, 2.3 m/s, the speed of this rip current is a danger to public safety.

CONCLUSIONS

This study has demonstrated a newly designed optimal buoy type GPS drifter and field application experiments at Haeundae Beach, Korea. We carried out a surf zone drifter deployment and test near a rip channel and described the design, construction, and application of a new buoy type GPS drifter. Despite the apparent difficulties of using GPS drifters in the coastal zone, deployment and retrieval were successful. We assume that the newly designed small size buoy type GPS drifter will be valuable equipment in the study of circulation and dispersion in coastal environments, such as rip currents and longshore currents, in which Lagrangian measurements are scarce. Our drifters make experiments more effective close to the shoreline. In addition, the buoy type GPS drifter is suitable for coastal investigations over short timescales and distances and for field surveying of rip currents at Haeundae Beach. Wave data will be improved in additional intensive field surveys investigating rip currents and measuring rip current patterns in the surface layer at Haeundae Beach.

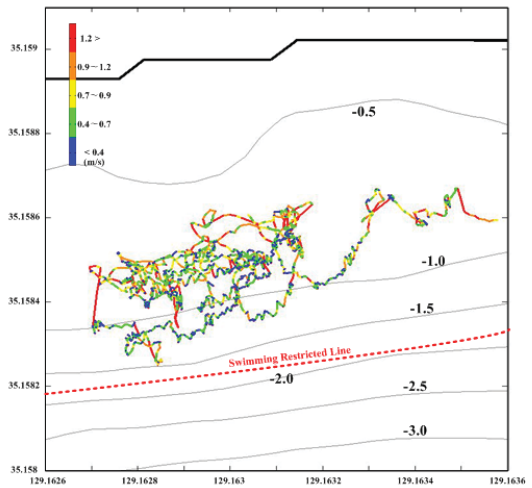

Figure 9. Lagrangian observations. Drifter tracks are colored by the magnitude of velocity with 0.5 m isobaths. The shoreline is in bold.

ACKNOWLEDGMENTS

This research was supported by Basic Science Research Program through the National Research Foundation of Korea (NRF) funded by the Ministry of Education (NRF-2013R1A1A2058707).

This work was funded by the Korea Meteorological Administration Research and Development Program under Grant KMIPA 2015-1072.

LITERATURE CITED

Brander, R. W. and Short, A. D., 2000. Morphodynamics of a large-scale rip current system at Muriwai Beach, New Zealand, *Marine Geology*, Vol 165, pp 27-39.

Chen, W.; Hu, C.; Li, Z.; Chen, Y.; Ding, X.; Gao, S., and Ji, S., 2004. Kinematic GPS Precise Point Positioning for Sea Level Monitoring with GPS Buoy, *Journal of Global Positioning Systems*, Vol 3, pp 302-307.

George, R. and Largier, J. L., 1996. Description and performance offinescale drifters for coastal and estuarine studies, *Journal of Atmospheric and Oceanic Technology*, Vol 13, pp 1322-1326.

Johnson, D.; Stocker, R.; Head, R.; Imberger, J., and Pattiaratchi, C., 2003. A Compact, Low-Cost GPS Drifter for Use in the Oceanic Nearshore Zone, Lakes, and Estuaries, *Journal of Atmospheric and Oceanic Technology*, Vol 20, Issue 12, pp 1880-1884.

Lee, J. Y. and Lee, J. L., 2007. Verification of the Rip Currents predictive model using the tube image detecting techniques, *Proceeding of 11th International Coastal Symposium* (Szczecin, Poland), Special Issue No.64, pp 917–921.

Longuet-Higgins, M. S., 1970. Longshore currents generated by obliquely incident seawaves, *Jornal of Geophysical Research*, Vol 75, pp 6790-6801.

MacMahan, J. H. and Brown, J., 2007. An inexpensive hand-held global positioning system for oceanographic drifters, *Journal of Atmospheric and Oceanic Technology*, Vol 165, pp 27-39.

Sabet, B. S. and Barani, G. A., 2011. Design of small GPS drifters for current measurements in the coastal zone, *Ocean & Coastal management*, Vol 54, Isuue 2, pp 158-163.

Schmidt, W. E.; Woodward, B. T.; Millikan, K. S.; Guza, R. T.; Raubenheimer, B., and Elgar Steve., 2003. A GPS-Tracked Surf Zone Drifter, *Journal of Atmospheric and Oceanic Technology*, Vol 20, Issue 7, pp 1069-1075.

Schmidt, W. E.; Guza, R. T., and Slinn, D. N., 2005. Surf zone currents over irregular bathymetry: Drifter observations and numerical simulations, *J. Geophys. Res.*, 110(C12).

Shepard, F. P.; Emery, K.O., and La Fond, E.,C., 1941. Rip currents: A process of geological importance, *Journal of Geology*, Vol 49, Issue 4, pp 337-369.

Shepard, F. P. and Inman, D. I., 1950. Nearshore water circulation related to bottom topography and wave refraction, *EOS, Trans. Am. Geophys. Union*, 49, 196-212.

Shepard, F. P., 1936. Undertow, rip tide or rip current, *Science* (New York), Vol 34, pp 181-182.

Sonu, C. J., 1972. Field observations of nearshore circulation and meandering currents, *J. Geophys. Res.*, 77(18), 3232-3247.

Song, D. S. and Bae, H. K., 2011. Observation and Forecasting of Rip Current Generation in Haeundae Beach, Korea Plan and Experiment, *Proceeding of 11th International Coastal Symposium* (Szczecin, Poland), pp 946-950.

Journal of Coastal Research	SI	75	1182 - 1186	Coconut Creek, Florida	2016

Synoptic Systems Generators of Extreme Wind in Southern Brazil: Atmospheric Conditions and Consequences in the Coastal Zone

Arthur A. Machado[†*], and Lauro J. Calliari[†]

[†]Geological Oceanography Laboratory, Institute of Oceanography
Federal Universityof Rio Grande - FURG
Rio Grande, Brazil

www.cerf-jcr.org

www.JCRonline.org

ABSTRACT

Machado, A.A. and Calliari, L.J., 2016. Synoptic systems generators of extreme wind in southern Brazil: atmospheric conditions and consequences in the coastal zone. *In:* Vila-Concejo, A.; Bruce, E.; Kennedy, D.M., and McCarroll, R.J. (eds.), *Proceedings of the 14th International Coastal Symposium* (Sydney, Australia). *Journal of Coastal Research*, Special Issue, No. 75, pp. 1182 - 1186.Coconut Creek (Florida), ISSN 0749-0208.

The coast of Rio Grande do Sul (RS), southern Brazil, suffers a seasonal variation due to the dynamics associated with the frequency and intensity of storms. These storms are mostly associated with high intensity extratropical cyclones that generate wind waves which can change a beach profile from its maximum accretion state to complete erosion during a period that can vary from few hours to a few days. Using the Generalized Pareto Distribution, we observe that the 0.01 probability density value of all the wind speed values studied was 17 ms^{-1}. Analyzing the storms that generate extreme winds (ie ≥ 17 m s^{-1}), an increase in the number of extreme events to the coast of RS was observed over the past 66 years (1948-2013). The increase in the frequency of extreme events of wind, will modify and increase flooding, storm surge, and erosion along the coast. It was observed that the main weather systems generating strong winds to the shore of the RS are extratropical cyclones, which are mainly formed between parallels 30°S to 40°S, with two preferred trajectories, east and southeast, generating both erosion and storm surges. The majority of extratropical cyclones presentend propagation velocities between 20-40 km h^{-1} (61.97%). The months with the highest number of extreme events were June (22), followed by October (16). The consequences of storms in RS coast were: erosion of 45 m^3m^{-1}, storm surge of 1.88 m, wind speed of 26.21 m s^{-1} and significant wave height of 8.79 m.

ADDITIONAL INDEX WORDS:*Extratropical cyclones, extreme events, storm surge.*

INTRODUCTION

Atmospheric fronts and frontal systems are central components of weather (and hence, climate) over much of the world. These frequent phenomena (every few days over many extratropical regions) are associated with precipitation, dramatic changes in temperature and changes in wind (direction and speed), among other factors (Simmonds *et al.,* 2012).

Extratropical synoptic systems compose the daily weather patterns in the mid and high latitudes (Lim and Simmonds 2007). The extratropical cyclones can cause severe coastal damage, such as beach erosion and storm surge (Machado *et al.*, 2010). Furthermore, intense cyclones and associated episodes of strong winds, high waves, and heavy precipitation are important in transmitting the effects of low-frequency climate variability to the environment and society (Graham and Diaz 2001).

In Rio Grande do Sul (RS), southern Brazil, storms are frequently associated with high intensity extratropical cyclones, which generate wind waves that can alter a beach profile from its maximum accretion state to a completely eroded state over a few hours to a few days (Calliari *et al.*, 1998, Machado *et al.*, 2010). Machado *et al.* (2010) studied extreme wave events at RS shore and showed that both extratropical cyclones and anticyclones generate extreme waves in the South Atlantic.

The southeast coast of South America is affected by atmospheric systems at synoptic and sub-synoptic scales, which are influenced by factors associated with circulations at large or local scales. Among the phenomena at the synoptic scale are frontal systems (Saraiva *et al.*, 2003).

Gan and Rao (1991) studied the surface cyclogenesis frequency over South America during a 10 year period and observed a larger number of extratropical cyclones in the winter (30.5 per year), followed by autumn (30.2 per year), spring (26.8 per year) and summer (20.7 per year). In addition to seasonal variations, Gan and Rao (1991) observed an interannual variation in the frequency of cyclogenesis over South America, with the incidence of higher cyclogenesis during El Niño years.

Therefore, the present work aims to describe the distribution of wind speeds over 66 years (1948-2013) and the probability of occurrence of extreme wind speeds along the RS coast (southern Brazil). Furthermore, the synoptic propagating systems that generate these strong winds and their consequences in the coastal zone are explored.

Background

The Holocene barrier system of RS occupies the entire 620 km length of coast. Discontinuities in the barrier occur only at two sites: in the south, at Cassino (Figure 1), where the inlet of the Patos Lagoon is located, and in the north, at the inlet of Tramandaí Lagoon. Both inlets are permanently open because of a continuous and large discharge of fresh water through their entrances. The entire RS coastline is gently undulating and

DOI: 10.2112/SI75-237.1 received15 October, 2015; accepted in revision 15 January, 2015.
*Corresponding author: oceaam@gmail.com
©Coastal Education and Research Foundation, Inc. 2016

consists of two large subdued seaward projections and two landward embayments. This is the longest barrier system of South America and certainly one of the longest in the world. The barrier display a NE-SW trend and is subject to dominant swell waves generated in southern latitudes and wind generated waves produced by strong spring-summer sea breezes from the northeast. The coast is microtidal with semidiurnal tides that have a mean range of only 0.5 m. Consequently, sediment transport and deposition along the open coast is primarily dominated by wave action (Dillenburg and Hesp, 2009).

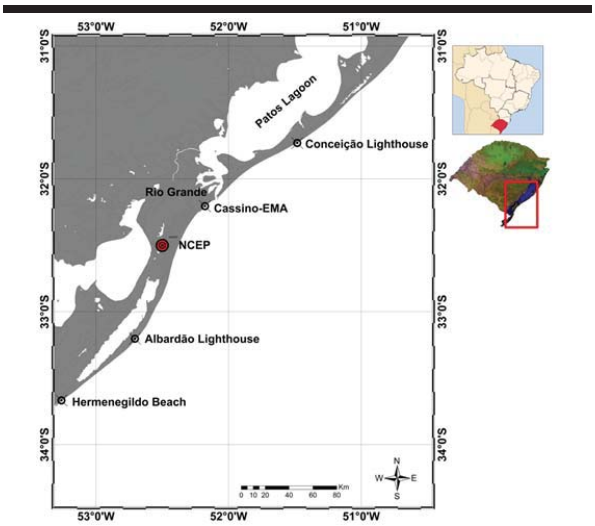

Figure 1. The study area, the grid point position of the NCEP/NCAR reanalysis data used in this work (red marker).

Observations of synoptic weather conditions and sea level elevation done by Parise *et al*. (2009) showed that the highest sea level elevation events resulted from the action of SW winds which blow parallel to the main NE-SW coastline orientation in the region, a result that can be explained by the pilling up of water at the coast due to the Coriolis effect (i.e. Ekman transport).

METHODS

The quality of hindcasts depends on the accuracy of the atmospheric wind and pressure fields as provided by operational analyses or (regionalized) ‘‘reanalysis’’ of atmospheric conditions. Prime examples of reanalysis datasets are those of the National Center for Atmospheric Research and National Centers for Environmental Prediction (NCAR/NCEP) (http://www.esrl.noaa.gov/psd/data/gridded/data.ncep.reanalysis.html) and ERA-40 (http://www.ecmwf.int/research/era) (Storch and Woth, 2008).

The reanalysis dataset used in the present work was created by the cooperative efforts of the NCEP and NCAR (Kalnay *et al.*, 1996) to produce relatively high-resolution global analyses of atmospheric fields over a long time period. Several studies have been conducted using NCEP/NCAR data (Simmonds and Keay, 200; Lim and Simmonds, 2007; Parise *et al*., 2009; Machado *et al.*, 2010).

The reanalysis dataset (R-1 of NCEP/NCAR) was used for characterizing the atmospheric conditions and for selecting extreme wind speed events. Meridional and zonal components of the wind and atmospheric pressure at the 995 mbar level were used. A spatial resolution of 2.5° x 2.5° and a temporal resolution of 6 hours (0000, 0600, 1200, 1800 UTC) for data restricted between 60°S - 15°S and 90°W - 20°W were adopted. To better characterize the path of the systems that generated extreme events, a threshold vorticity less than or equal to (ζ10) - 5 x 10^{-5} s^{-1} was adopted (Machado *et al*., 2010).

To select the extremes of wind speed, the database of the R-1 Project Reanalysis NCEP/NCAR cited above was used. We also used the zonal and meridional components of the wind at 32°50'S, 52°50'W, which is the grid point of the reanalysis data closest to Rio Grande (Figure 1). To increase confidence of the reanalysis data, we performed correlations with wind data from the Pilot Station (year 2009) located near the Pato Lagoon mouth (32°8'S, 52°6'W). Wind intensity and direction data were collected at a meteorological station by an automatic weather station installed at the top of the tower. The data are collected hourly and are based on sample averages of 5-minute data acquisitions per hour. However, the data have many gaps that preclude the generation of a continuous series.

Analyses of time series have been widely used for determining standards in environmental variables, investigating periodic phenomena and studying global-scale events (Sprott, 2003). To analyze the speed threshold of extreme wind was used the Generalized Pareto Distribution (GPD) (Brabson and Palutikof, 2000). The equation used for calculating the (GPD) was:

$$F(X) = \frac{1}{\sigma}\left(1 + K\frac{X}{\sigma}\right)^{-1-\frac{1}{K}}$$

where K = shape parameter, σ = scale parameter (Sigma) and X is the data of the wind speed.

To analyze the wind intensity during the 66 years of study, analysis of variance (ANOVA) was used. ANOVA was used for verifying the differences between numbers of events at 3-year intervals during the study period (1948-2013). Data normality was tested by the Kolmogorov-Smirnov test, and the homogeneity was determined by the Levene test. Because extreme wind speed data are not normal, we used the Kruskal-Wallis ANOVA, which is the analysis of variance method for nonparametric data.

To determine extratropical cyclone propagation velocities, the distances traveled in each time interval (6h) divided by the time were calculated. To calculate the propagation direction, the azimuth between the starting and ending point of each extratropical cyclone studied was computed. For correlations between the cyclone velocity propagations (first 24 hours and total) and the correlations between the propagation directions (first 24 hours and total), the averages were calculated.

RESULTS

Data from the NCEP/NCAR showed a moderate correlation (r = 0.65) with the data from the meteorological station of the Barra do Rio Grande Pilot Station. Note that the meteorological station of the Barra do Rio Grande Pilot Station is at a height of

25 m, and the results of the reanalysis represent an altitude of 10 m, i.e., the winds are stronger at greater heights. Thus, the measured winds were more intense than the reanalysis winds.

Regarding the distribution of wind speeds over 66 years (from 1948 to 2013), the speeds from 5 to 10 m s^{-1} represent approximately 53.89% of the data. The average wind speed was 6.29 m s^{-1}; the minimum was 0 m s^{-1}, the maximum was 26.21 m s^{-1}, and the standard deviation was 2.92 m s^{-1}. The percentage frequency distribution of the wind direction for all wind intensities (1948-2013) reveals that the main directions were east (20.09%) and northeast (19%).

When the probability density function is calculated using a normal distribution, the curve is centered on the average of 6.29 m s^{-1}. Using the Generalized Pareto Distribution, 0.01 (1%) probability density value of all the wind speed values studied was 17 m s^{-1} (Figure 2). For locations with frequent hurricanes, the starting point is 18.9 m s^{-1}, which is T0 on the T-Scale and B8 on the Beaufort Scale (Meaden *et al.*, 2007). The Brazilian coast has only one recorded hurricane, Hurricane Catarina in 2004, and the choice of threshold must be appropriate for the climatology of the site; thus, for this study, the threshold used for selecting the extremes of wind speed was 17 m s^{-1} (approximately 61 Km h^{-1}), which is equivalent to 7.4 on the Beaufort Scale according to George Simpson's table.

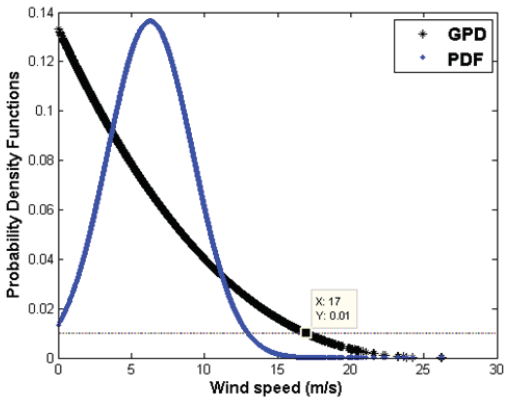

Figure 2. Graph of two probability density functions value of the wind speed, blue for PDF (normal distribution) and black for GPD (Generalized Pareto Distribution).

Analyzing only wind data with intensities greater than 17 m s^{-1}, main wind directions were west (53.89%) and southwest (17.53%).

Between 1948 and 2013, 93 events presented wind speeds above 17 m s^{-1}, considering 32°50'S, 52°50'W as the reference position. The mean number of events per year was 1.41 with a minimum of 0 events and a maximum of 4 events per year. The standard deviation was 1.25 per year. In 1998, 1999, 2000, 2008, 2010 and 2011, 4 extreme wind speed events occurred.

Because the data of wind speed extremes are not normal (Kolmogorov-Smirnov d = 0.21, p < 0.2), Kruskal-Wallis ANOVA test, which is the analysis of variance method for nonparametric data, was used. The Kruskal-Wallis ANOVA result of 22 groups in 3-year intervals showed significant differences in the number of extreme wind speed events during the 66-year period (H (21, N = 66) = 44.83 p = 0.0018, confidence interval 95%) (Figure 3). The correlation of the numbers of events and the 66-year period showed a positive correlation (r = 0.84). In the past 66 years, as shown in Figure 3, an increase in the number of extreme wind speed events occurred at the Rio Grande do Sul coast.

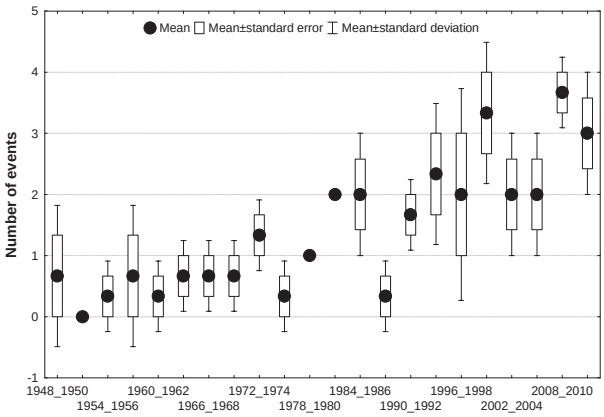

Figure 3. Average number of extreme wind speed events for the 22 groups. The vertical bars denote the standard deviations.

The monthly distribution exhibited a bimodal distribution, with peaks in June (22 events) and October (16 events). May had 12 events, January and March did not reportedly experience any extreme wind events over the 66 years. For the 93 events studied, 81 were generated by extratropical cyclones and 12 were generated by anticyclones.

Of the 81 events generated by extratropical cyclones, 71 (87.65%) were associated with cyclones that originated between 30°S and 40°S. There was no variation in the distribution of cyclogenesis locations over the 66-year period (r = 0.145). Within these latitudes, extratropical cyclones were displaced in four directions (east, southeast, south and southwest). The two preferred directions of displacement of extratropical cyclones were southeast (Figure 4) and east (Figure 5), accounting for 43 and 24 cyclones, respectively. Only four extratropical cyclones traveled in the other directions of south (3) and southwest (1).

The propagation velocities of extratropical cyclones that experienced cyclogenesis between 30°S and 40°S were mostly between 20 and 40 km h^{-1} (39); 24 cyclones were between 40 and 60 km h^{-1}, 5 were between 60 and 80 km h^{-1} and only 3 were below 20 km h^{-1}.

A good correlation (r = 0.76) was observed for the average propagation velocities of extratropical cyclones during their entire trajectories and during the first 24 hours of their lifecycles. These results showed that the extratropical cyclones that generate extreme wind events tend to maintain their initial propagation velocity. The average direction of extratropical cyclone propagation in the first 24 hours showed a moderate to strong correlation (r = 0.69) with the average total propagation direction of extratropical cyclones, i.e., a cyclone tends to maintain the same propagation direction that was reported in the first 24 hours.

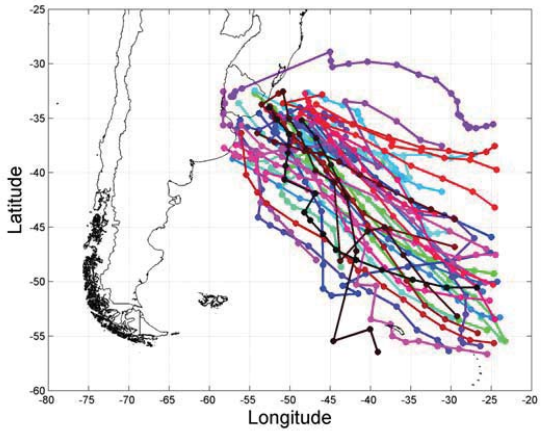

Figure 4. Trajectories of extratropical cyclones that experienced cyclogenesis within 30°S-40°S and propagated southeast.

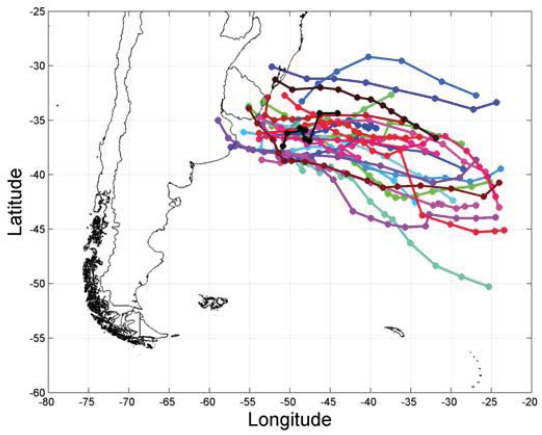

Figure 5. Trajectories of extratropical cyclones that experienced cyclogenesis within 30°S-40°S and propagated east.

Of the 93 extreme events studied, 12 were generated by anticyclones. Similarly to extratropical cyclones, strong winds are formed by a large pressure gradient; thus, the high pressure centers (anticyclones) are usually accompanied by low pressure centers (cyclones). It is interesting to note that from 1948 to 1977, no extreme wind events were generated by anticyclones, but between 1978 and 2013, 12 extreme wind events were generated by the passage of anticyclones.

DISCUSSION

The NCEP/NCAR reanalysis dataset proved being particularly useful in large scale analysis. Although the spatial resolution of the data was 2.5° x 2.5° (~277 x 277 km), the cyclones and anticyclones studied have diameters of 1.000 km or more. They are generated by baroclinic waves at the midlatitudes with a spatial scale of 3.000 km in regions of westerly winds. Thus the spatial scsale of the NCEP/NCAR reanalysis dataset proves reasonable for a synoptic evaluation of the extreme events studied.

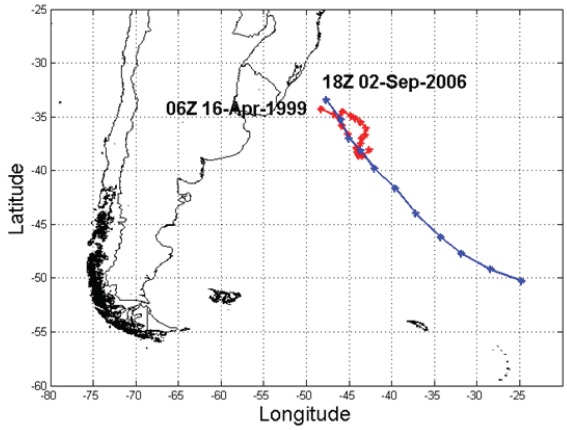

Figure 6. Trajectory of the extratropical cyclone on April 16, 1999 (Red), Trajectory of the extratropical cyclone on September 2, 2006 (Blue).

In the past 66 years, as shown in Figure 3, an increase in the number of extreme wind speed events occurred at the Rio Grande do Sul coast. Recent studies suggest that cyclone activity in both hemispheres changed over the second half of the 20th century. General features include a poleward shift in storm track locations, an increase in storm intensities, and a decrease in total storm numbers (Simmonds and Keay, 2000). According to (IPCC, 2007), midlatitude westerly winds have generally increased in both hemispheres. Significant increases in the strength of intense extratropical cyclone systems have been documented in several studies and are associated with changes in the preferred storm tracks (Kalnay *et al.*, 1996). Intense extratropical cyclones are often associated with extreme weather, particularly with severe windstorms.

The meteorological setup of April 17th, 1999 extreme event was unusual because the path of the cyclone that developed off the RS coast nearly formed a loop without much forward motion (Figure 6). The average propagation velocity of this cyclone was 12.66 km h^{-1} toward 131.21°.The wind speed was 18.46 m s^{-1} (226.97°). This extratropical cyclone presented the lowest propagation velocity of all cyclones studied. Machado *et al.* (2010) studied this event and observed significant wave heights (6.08 m) with periods of 12.95 s. This storm caused severe erosion at Hermenegildo Beach (45 m^3 m^{-1}).

The storm of September 2, 2006 had 17.26 m s^{-1} of wind speed and 255.23° of direction. This cyclone had a propagation velocity of 44.41 km h^{-1} and moved toward the southeast (Figure 6).This event coincided with one of the extratropical cyclones studied by Parise *et al.* (2009) and Machado *et al.* (2010). This particular cyclones caused a storm surge of 1.83 m and a significant wave height of 7.13 m (Tp=13.91 s). The effects of the passage this extratropical cyclone were not restricted just south of Brazil. Were recorded impacts on the coast of the city of Rio de Janeiro, as erosion and storm surge. Other storms

studied by Machado *et al.* (2010) showed Hs 8.79 m and storm surge of 1.88 m.

Based on the graphs in Figure 3, the distribution pattern of extreme wind speed events in the 1970s changed; this pattern coincides with the 1976-1977 climate shift (Miller *et al.*, 1994; Giese *et al.*, 2002). Observations from the Tropical Pacific Ocean show an abrupt change in the climate in the year 1976 in which the ocean surface temperature increased from colder than normal to warmer than normal over a period of one year (Giese *et al.*, 2002). This observed shift in the Pacific added more heat to the global atmosphere, i.e., more energy to the system. This phenomenon may cause an increase in the number of high energy storm events. An investigation by Graham and Diaz (2001) in the North Pacific indicates that there has been an increase in the intensity of storms since 1948, i.e., over at least half a century. They suggested that the progressive increase of the intensity of waves generated by the storms and winds may be the result of warmer water temperatures in the tropical western Pacific, providing a possible link to global warming.

CONCLUSIONS

During the 66 years studied, only 0.159% of the wind speed data were equal to or greater than 17 m s^{-1}. There was an increase in the number of extreme wind speed events along the coast of Rio Grande do Sul over the study period (1948-2013). The increase in the frequency of extreme events of wind, will modify and increase the coastal hazards like wind waves, storm surge, and erosion in southern Brazil.

The main weather systems that generate strong winds on the shore of Rio Grande do Sul are extratropical cyclones (87.1%) followed by anticyclones (12.9%). Extratropical cyclones have two preferred trajectories: southeast and east, both generate large waves, erosion and storm surges. The propagation velocity of extratropical cyclones is predominantly between 20 and 40 km h^{-1} (61.97%), followed by velocities between 40 and 60 km h^{-1} (38.03%).

The average propagation velocity and average propagation direction of extratropical cyclones are similar to the propagation velocity and propagation direction that occur during the first 24 hours of a cyclone's lifecycle. This can be useful for predicting the trajectories of extratropical cyclones.

The most severe effects of extreme events recorded at the Rio Grande do Sul coast were erosion up to 45 m^3 m^{-1}, a storm surge of 1.88 m, and a wind speed of 26.21 m s^{-1} (94.36 km h^{-1}).

ACKNOWLEDGMENTS

This article is a contribution of the Brazilian National Institute of Science and Technology (INCT) for Climate Change funded by CNPq Grant Number 573797/2008-0. This research is supported by Capes-EditalCiências do Mar 09/2009.

LITERATURE CITED

Brabson, B.B., and Palutikof, J.P.,2000; Tests of the Generalized Pareto Distribution for Predicting Extreme Wind Speeds. *Journal of Applied Meteorology*, 39, 1627–1640.

Calliari, L.J., Tozzi, H.A., and Klein, A.H.F., 1998. Beach morphology and Coastline Erosion Associated with Storm Surge in Southern Brazil- Rio Grande to Chuí, RS. *Anais da Academia Brasileira de Ciências*, 70, 231–247.

Gan, M.A., and Rao, V.B., 1991. Surface Cyclogenesis over South America. *Monthly Weather Review*,119,1293–1302.

Giese, B.S., Urizar, S.C., and Fuckar, N.S. 2002. Southern Hemisphere Origins of the 1976 Climate Shift. *Geophysical Research Letters*,29(2), 1-4.

Graham, N.E., and Diaz, H.F., 2001. Evidence for Intensification of North Pacific Winter Cyclones since 1948. *Bulletin of the American Meteorological Society*, 82, 1869–1893.

IPCC (2007), IPCC Fourth Assessment Report: Climate Change 2007: The Physical Science Basis: Contribution of Working Group I to the Fourth Assessment Report of the Intergovernmental Panel on Climate Change, edited by S. Solomon, D. Qin, M. Manning, Z. Chen, M. Marquis, K. B. Averyt, M. Tignor, and H. L. Miller, Cambridge University Press, Cambridge.

Kalnay, E., Kanamitsu, M., Kistler, R., Collins, W., Deaven, D., Gandin, L., Iredell, M., Saha, S., White, G., Woollen, J., Zhu, Y., Leetmaa, A., Reynolds, R., Chelliah, M., Ebisuzaki, W., Higgins, W., Janowiak, J., Mo, K.C., Ropelewski, C., Wang, J., Jenne, R., and Joseph, D., 1996. The NCEP/NCAR 40-year reanalysis project. *Bulletin of the American Meteorological Society*, 77, 437–471.

Lim, E-P., and Simmonds, I., 2007. Southern Hemisphere Winter Extratropical Cyclone Characteristics and Vertical Organization Observed with the ERA-40 Data in 1979–2001. *Journal of Climate*,20, 2675–2690.

Machado AA, Calliari LJ, Melo E, Klein AH da F (2010) Historical assessment of extreme coastal sea state conditions in southern Brazil and their relation to erosion episodes. *Pan-American Journal of Aquatic Sciences*,5, 277–286.

Meaden, G.T., Kochev, S., Kolendowicz, L., Kosa-Kiss,A., Marcinoniene, I., Sioutas, M., Tooming, H., and Tyrrell, J., 2007. Comparing the theoretical versions of the Beaufort scale, the T-Scale and the Fujita scale. *Atmospheric Research*,83, 446–449.

Miller, A.J., Cayan, D.R., and Barnett, T.P., 1994. The 1976-77 Climate Shift of the Pacific Ocean. *Oceanography*, 7, 21–26.

Parise, C.K., Calliari, L.J., and Krusche, N., 2009. Extreme storm surges in the south of Brazil: atmospheric conditions and shore erosion. *Brazilian Journal of Oceanography*, 57, 175–188.

Saraiva, J.M.B., Bedran, C., and Carneiro, C., 2003. Monitoring of Storm Surges on Cassino Beach, RS, Brazil. *Journal Of Coastal Research*, 35, 323–331.

Simmonds, I., and Keay, K., 2000. Mean Southern Hemisphere Extratropical Cyclone Behavior in the 40-Year NCEP–NCAR Reanalysis. *Journal of Climate*, 13, 873–885.

Simmonds, I., Keay, K., and Tristram Bye, J.A. 2012. Identification and Climatology of Southern Hemisphere Mobile Fronts in a Modern Reanalysis. *Journal of Climate*,25, 1945–1962.

Sprott, J.C., 2003. Chaos and Time-Series Analysis. *Oxford University Press*, 507p.

Storch, H., and Woth, K., 2008. Storm surges: perspectives and options. *Sustainability Science*, 3, 33–43.

Journal of Coastal Research	SI	75	1187 - 1191	Coconut Creek, Florida	2016

Evaluation of Runup Characteristics on the NSW Coast

Bradley D. Morris[†*], Edwina Foulsham[†], Raymond Laine[‡], Daniel Wiecek[‡] and David Hanslow[†]

[†]Coastal and Marine Unit
NSW Office of Environment and Heritage
Newcastle, NSW, Australia

[‡]Water, Floodplains and Coast
NSW Office of Environment and Heritage
Wollongong, NSW, Australia

www.cerf-jcr.org

www.JCRonline.org

ABSTRACT

Morris, B.D., Foulsham, E., Laine, R., Wiecek, D. and Hanslow, D., 2016. Evaluation of run-up characteristics on the NSW coast. *In:* Vila-Concejo, A.; Bruce, E.; Kennedy, D.M., and McCarroll, R.J. (eds.), *Proceedings of the 14th International Coastal Symposium* (Sydney, Australia). *Journal of Coastal Research*, Special Issue, No. 75, pp. 1187 - 1191. Coconut Creek (Florida), ISSN 0749-0208.

Communities and infrastructure along the coast of New South Wales, Australia, are vulnerable to coastal inundation from the combined impacts of ocean tides, storm surge, wave setup, wave run-up and wave overtopping. The focus of the current work is to examine the potential for coastal inundation on beaches and dunes on the open coast of NSW through the evaluation of wave run-up. To achieve this we combine information on tides, surge and wave run-up to examine dune overtopping potential. The study utilises data from the NSW wave and ocean tide gauge network and an extensive set of beach profile and grainsize data covering over 200 beaches as well as available photogrammetry and LiDAR data. Ocean still water level and design nearshore wave conditions are used together with beach slope data to calculate wave run-up height. Choice of appropriate wave run-up formulation is evaluated through the use of available long term datasets from Narrabeen and Moruya. Geographical variability in relevant beach/dune characteristics including beach slope and dune height are examined using survey (RTK-GPS), photogrammetry and LiDAR data. Overtopping potential for various design events (e.g. 5y, 20y, 100y storms) is examined through the overlay of predicted run-up heights on high resolution digital elevation models at each pilot study site.

ADDITIONAL INDEX WORDS: *.Inundation, Exposure, Coastal hazards, Coastal risk.*

INTRODUCTION

The New South Wales (NSW) coastline stretches for over 1590 km and has over 750 sandy beaches (Short, 2007). Over 85% of the population live within 50 kilometres of the coast (ABS, 2004) which is known to be highly vulnerable to both erosion and inundation (DCC, 2009; Cechet *et al.*, 2012).

Recent investigations into the extent of the risk posed by coastal hazards along the NSW coast has shown that on the open coast around 2100 properties are exposed to coastal erosion at present. With sea level rise, coastal recession is projected to increase the exposure of coastal properties to erosion. By 2050 total properties at risk is projected to increase to around 1900 primary and an additional 1900 secondary addresses and by 2100 to around 3200 primary and an additional 3700 secondary addresses (OEH, 2015).

On the open coast in NSW, waves are the dominant contributor to inundation. Wave runup is known to reach levels many meters above ocean tide still water level (NSW Government, 1990). The broad scale risk assessments undertaken to date (DCC, 2009; Cechet *et al.*, 2012) have not taken this into consideration, thus the extent of the problem here is largely unknown.

DOI: 10.2112/SI75-238.1 received 15 October, 2015; accepted in revision 15 January, 2016.
*Corresponding author: bradley.morris@environment.nsw.gov.au
©Coastal Education and Research Foundation, Inc. 2016

Wave runup in this study is defined as the landward extent of wave uprush measured vertically from the still water level. The runup includes the combined effects of wave setup (super-elevation of the mean water surface) and individual wave uprush. The still water level is the average water surface elevation at any instant including the effects of tides, storm surges and other contributors to regional ocean levels but excluding effects from waves.

In the current study we examine contributors to both still water levels and wave runup along the NSW coast and develop a pilot method for a first pass assessment of open coast inundation hazard.

Regional Setting

The NSW coast is aligned to the predominant south east swell and experiences a moderate to high energy wave regime. The shoreline is comprised of areas of rocky cliffs and headlands joined by sandy beaches. On the coast south of Sydney, the beaches are predominantly pocket beaches isolated by rocky headlands, whilst in the north of the state the beaches tend to be longer and alongshore rates of sand movement are higher, predominantly from south to north. NSW beaches also vary in type according to exposure to the modal SE-S wave direction and sediment grain size. Along shore variation in wave exposure also results in variation in characteristics within beaches with southern ends tending to be more sheltered than the exposed northern ends. Beaches in NSW are typically backed by high dunes which provide some natural defence against storm surge

and wave inundation. Dune height characteristically varies along shore with higher dunes to the northern ends associated with increased exposure to wave and wind.

Coastal water levels are influenced by a variety of astronomical, meteorological and oceanographic factors. These include both tidal and non-tidal contributors to regional still water levels as well as the effects of waves including wave setup and wave runup. Tides along the NSW coastline are semi-diurnal in nature and have a pronounced diurnal inequality. The mean spring range is 1.2 m while the mean neap range is 0.8 m (MHL, 2012). Tidal range varies slightly along the coast with an increase of around 0.2 m from south to north (MHL, 2011).

Variations in water level due to non-astronomic factors are common along the NSW coast and MHL (1992) shows that anomalies of 0.3 m occur at return intervals of months, and thus become a significant addition to tidal predictions. Drivers of tidal anomalies include variations in air pressure and wind stress which during storms is known as 'storm surge'; coastal trapped waves; ocean currents; steric effects; seiches; tsunamis; Rossby waves etc. These processes operate over a wide range of time frames.

The NSW coast is subject to a moderate to high energy wave climate predominantly from the south to south-east (Harley *et al.*, 2010). The average offshore significant wave height is ~1.5 m and average peak period is ~9.5 s (Lord and Kulmar, 2000). The wave climate is periodically affected by large wave events originating from coastal storm systems which vary both spatially and temporally in their genesis, intensity and track. Very large storm events also occasionally impact the coastline (Shand *et al.*, 2011).

At a regional scale the occurrence of and exposure to different storm types varies with latitude along the NSW coast (Shand *et al.*, 2011). The relatively steep and narrow nature of the continental shelf ensures that loss of wave power to bed friction is minimal across the shelf (Wright, 1976) although the presence of headlands and offshore reefs does lead to significant alongshore variation in wave climate.

METHODS

Available runup formulations are reviewed and evaluated against field runup observation data collected from a variety of sites along the NSW coast. To enable broader state-wide application a new relationship between beach slope and grainsize is developed. Nearshore wave transform relationships are used to address along shore variation in exposure to extreme storm waves and to predict runup height for a range of storm wave conditions.

Predicted runup is compared to dune crest elevation for pilot sites to provide a first pass indication of dune overtopping potential and open coast inundation hazard. The pilot sites are chosen to be representative of a diverse range of beach types, Figure 1. These include Kingscliff, Mooball/New Brighton, Brunswick Heads, Belongil, Main Beach/Clarks, Terrigal/Wamberal, Avoca, Narrabeen/Collaroy, Moruya Beach, and Pedro Beach.

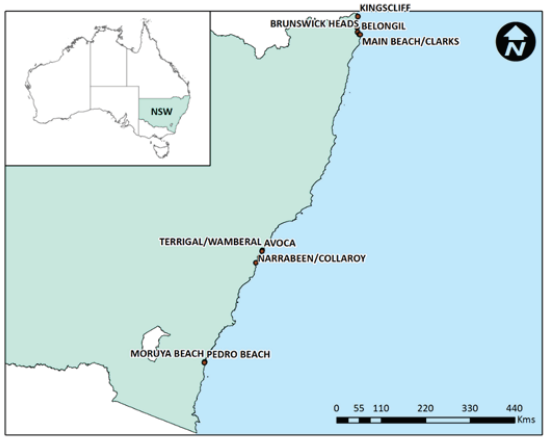

Figure 1. Map of New South Wales, Australia, showing location of pilot study sites.

The beach slope in the swash zone can be expressed as a function of the grain size, thus as part of the current project an extensive beach survey data set was collected from some 200 beaches along the NSW coast in 2013. These survey data include beach profiles using RTK-DGPS and sediment sampling. This data set (OEH) allowed the determination of the beach slope and grain size in the swash zone. A second, more comprehensive, set of grain size data (Short, 2007) which encompasses almost all of the 720 beaches in NSW was also obtained from Prof. Andrew Short (USyd).

These two data sets were collated taking into consideration the method of grain size analysis. It is well documented that the laser diffraction method generally measures larger particle sizes than when compared to results from sieve analyses (Baldock and Felder, 2013). The Short (2007) dataset, which was analysed using the sieving method, was converted to reflect a laser diffraction analysis following Rodríguez and Uriarte, (2009).

Using the measured swash slope and corresponding swash sediment grain size from the OEH survey data a linear fit was performed and was used to calculate swash beach slope for sites where only information on grain size was available. Settling velocity was also calculated using the grain size data following the methods of Hallermeier (1981).

In order to evaluate runup both offshore and nearshore wave parameters are required. In this study offshore wave height (H_0) and period (T_{p0}) for a set of three Annual Return Intervals (ARI), 5y, 20y and 100y, are used (Shand *et al.*, 2010). These offshore ARI wave data are directionally partitioned into north-east (0 - 90), east (90 – 135) and south-east (135 – 180). This allows for consideration of directionality in storm wave climate and in particular the lower probability of storm waves from the north.

To obtain a scaled nearshore wave height (H_S) the NSW Nearshore Wave Transfer Tool (Baird and MHL, 2015) was used. This tool transforms wave parameters from deep water (*i.e.* nearest wave buoy location) to the 10m depth contour. Transforms are performed on each of the three directionally

partitioned offshore wave heights to obtain directionally partitioned scaled nearshore wave heights which are then combined using directional likelihood tables to obtain a single H_S value.

Each of the pilot study sites were partitioned into three spatially equal sectors, nominally North, Central and South in order to reflect the potential differences in wave exposure within a beach embayment. A distinct H_S estimate was obtained for each of these sectors using the above technique.

Runup formulae have been recently reviewed for the NSW coast by Shand *et al.* 2011 and Power *et al.* 2013. In the current study the following formulae are used initially; Hunt (1959), Mase (1989), Nielsen and Hanslow (1991), Holman (1986), Hanslow and Nielsen (1995) and Stockdon *et al*. (2006). A seventh formula, Hunt (1959) scaled, was also included where H_0 was replaced with H_S in the original formula.

In order to determine the most appropriate formula, or set of formulae, to use in estimating maximum runup (Rmax) along the NSW coast a comparison was made between formula results and field data. Long term topographic survey data were obtained from Prof. Andrew Short for three beaches; Narrabeen/Collaroy, Moruya Beach and Pedro Beach (Figure 1). These survey data consist of nominally monthly surveys of several fixed profiles per beach. More details of these survey data are outlined in Short *et al.* (2014).

In addition to topographic beach profile data, these data sets also contain an estimate of maximum runup elevation at each profile location. These elevations were compared to runup values determined using the seven runup formulae. To obtain estimates of runup values for each of the three sites the grain size from the Short (2007) data set was used to calculate the swash beach slope. Offshore wave data for the day preceding each survey was filtered to obtain the maximum wave and water level conditions and these wave parameters were transformed to obtain the nearshore wave heights at each profile location. Using these data and the runup formulae a set of maximum runup estimates was obtained at each profile for each survey at the three sites.

The maximum of these runup estimates over the whole survey period at each of the three sites were then compared to the corresponding maximum measured runup values. The accuracy of the calculated maximum runup estimates as compared to measured values were then used to rank the seven formulae. The results from all three sites ranked the methods of Hunt (1959) scaled, Hanslow and Nielsen (1995) and Holman (1986) as the three 'best' methods and thus they were selected for use in the risk assessment.

In order to compare the calculated maximum runup elevation with the morphology of each study site, the location of the dune crest was manually digitised using hill-shaded topography DEM (created from best available LiDAR data) in association with the best available ADS40 aerial imagery. Elevations, relative to AHD, were extracted at each vertex in the dune crest linear feature, as well as at 10 m intervals along the feature.

The Still Water Level (SWL) was added to the calculated maximum runup (Rmax) values in order to compare with these dune crest elevations. For each study site the HHWSS values (MHL, 2012) from the nearest ocean tide gauging station were used as a basis for SWL. To account for non-astronomical water level variations the extreme water level values for each ARI scenario were added to the appropriate HHWSS water level to obtain the SWL. The values used in this study are 0.43, 0.47 and 0.51 m for the 5y, 20y and 100y ARI respectively (SMEC and UQ, 2013).

The elevation of the dune crest (E_D) for each study site was then compared with the elevation of the maximum runup (E_R = Rmax + SWL) to evaluate the inundation potential. The Rmax used in this comparison is the mean of the results for the top three ranked formulae along with the corresponding standard deviation (σR). Runup inundation potential is defined as High, Medium or Low as shown in Table 1. Since each of the pilot study sites were partitioned into North, Central and South sectors to reflect the potential differences in wave exposure a distinct Rmax value, and thus E_R, was calculated for each sector.

Table 1. *Definition of conditions used for assessment of runup inundation potential.*

Runup inundation potential	Condition
High	$E_D < E_R - \sigma R/2$
Medium	$E_R - \sigma R/2 < E_D < E_R + \sigma R/2$
Low	$E_D > E_R + \sigma R/2$

RESULTS

An example of the evaluation of runup inundation potential is shown in Figure 2 using 5y ARI runup values for the Avoca site.

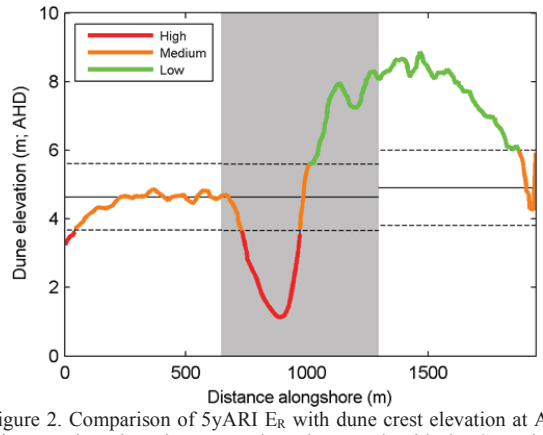

Figure 2. Comparison of 5yARI E_R with dune crest elevation at Avoca. Distance alongshore is measured south to north with the Central sector shaded. Estimated runup elevations and standard deviations are shown for each sector as solid and dashed lines respectively. Coloured lines indicate runup inundation potential.

In this figure the runup inundation potential is colour coded such that red, orange and green indicate high, medium and low respectively. The shading in the figure is to distinguish the three sectors, *i.e.* the Central sector is shaded, and the estimated runup elevations and standard deviations are shown as solid and dashed black lines respectively. The runup inundation potential can also be expressed quantitatively as a percentage of length of the beach or shown graphically as in Figure 3.

Figure 3. Map showing Avoca site with level of runup inundation potential shown for the 5y ARI case.

Examining the case of the Avoca site and using the 5y ARI values it can be seen (Figure 2) that the South sector dune field is between 3-5 m elevation and E_R is ~4.6 m resulting in the sector generally being classified as having Medium runup inundation potential. The exception in this sector is the far southern corner of the beach where runup inundation potential is high. Here a carpark has replaced the dune field. The Central sector includes the entrance to Avoca Lake with very low elevation and thus classified as High potential, however the remainder of the sector consists of a high (E_D > 6 m) dune field classified as Low potential since E_R in this sector is ~ 4.6 m. Likewise in the North sector the high dune field (E_D > 6 m) results in a Low potential classification generally despite E_R being larger (~4.9 m) in this sector, with the exception of a Medium potential area (E_D < 5 m) in the far north.

The evaluation of runup inundation potential was undertaken for all ten pilot study sites for the three ARI cases and a summary of the results, as a percentage of length of the beach, are shown in Table 2. The Medium and High potentials have been combined to obtain a conservative estimate of the inundation potential.

Table 2. *Runup inundation potential as percentage of length of beach for three ARI cases.*

Study Site	5y	20y	100y
Kingscliff	6	8	9
Mooball/New Brighton	8	10	13
Brunswick Heads	0	0	0
Belongil	7	7	7
Main Beach/Clarks	0	0	0
Terrigal/Wamberal	59	73	76
Avoca	56	63	69
Narrabeen/Collaroy	48	57	85
Moruya Beach	19	22	26
Pedro Beach	13	14	15

DISCUSSION

The findings from the evaluation of runup inundation potential at the ten pilot sites show similar trends despite the variations of conditions at each site, *i.e.* wave exposure, grain size, swash slope etc. Generally, there is less runup inundation potential at southern ends due to reduced exposure to predominant SE wave climate. This is highlighted in the extreme case of the Main Beach/Clarks site where there is almost no exposure to SE waves and hence no inundation potential even in the largest (100y) wave case (Table 2). At the central to northern end of the beach embayments the inundation potential is also decreased, in this case by the presence of higher elevation dune fields, even though the runup maximum values are greater due to greater wave exposure. In some cases (*i.e.* Avoca) the dune elevation is twice that of the runup elevations.

Runup formulations are generally sensitive to variations in both swash slope and wave height in particular since these are the primary drivers. Limitations of the method presented here thus include uncertainties in the swash slope which is highly spatially and temporally variable. Grain size is used in this study to calculate swash slope which decreases the variability and also allows assessment at sites where no survey data are available. Uncertainties in the wave heights are also a limitation of the method, however these have been mitigated by use of a nearshore wave transfer tool to obtain H_S. This is particularly important when considering that the three best ranked formulae used for the assessment are dependent on H_S.

CONCLUSIONS

The assessment of pilot sites using the method presented here shows sheltering from predominant SE wave climate decreases runup inundation potential at southern ends of beach embayments whilst higher elevation of dune fields at northern ends generally also decreases inundation potential despite higher wave and runup exposure.

The methodology used in this pilot study will be applied to beaches state wide in NSW to obtain a first pass assessment of runup inundation potential. Future work will also include the examination of storm runup and also an assessment of runup inundation under sea level rise which would affect the coastal water levels.

ACKNOWLEDGMENTS

Funding for this study was provided by the NSW Government Natural Disasters Resilience Program. Water level data was

kindly provided by Manly Hydraulics Laboratory. Terrain data was provided by NSW Land and Property Information. Grain size, beach profile and swash observations were provided by Prof Andrew Short (University of Sydney).

LITERATURE CITED

ABS, 2004. *Year Book Australia, 2004*. Australian Bureau of Statistics, 2004 1301.0., 872p.

Baird and MHL, 2015. *NSW Coastal Wave Model: State wide Inshore Wave Transformation Tool*. Report for NSW Office of Environment and Heritage, Baird Australia Pty Ltd & Manly Hydraulics Laboratory, 47p.

Baldock, T. and Felder, S., 2013. *Sediment Sizing of NSW Beach Sand Particle size distribution analysis of dune, berm and swash sand samples from NSW beaches*. School of Civil Engineering, University of Queensland, p8.

Cechet, R.; Hazelwood, M.; Skene, D.; Griffin, C.; Dunford, M.; Power, L.; Canterford, S.; Nadimpalli, K.; Taylor, P.; Woolf, M. and Anderson, H., 2012. *Impacts of climate change on human settlements and other nationally significant infrastructure in the coastal zone*. Record 2012/65. Geoscience Australia: Canberra, 46p.

DCC, 2009. *Climate Change Risks to Australia's Coast: A first pass national assessment*. Australian Government Department of Climate Change, 168p.

Hallermeier, R.J., 1981. Terminal settling velocity of commonly occurring sand grains. *Sedimentology*, 28, 859-865.

Hanslow, D.J. and Nielsen, P., 1995. Field Measurements of Runup on Natural Beaches. *Proceedings of the 12th Australasian Coastal & Ocean Engineering Conference*, (Melbourne, Australia), pp. 184-188

Harley, M. D.; Turner, I. L.; Short, A. D., and Ranasinghe, R., 2010. Interannual variability and controls of the Sydney wave climate. *International Journal of Climatology*, 30, 1322–1335.

Holman, R.A., 1986. Extreme Value Statistics for Wave Run-up on a Natural Beach. *Coastal Engineering*, 9(6), 527-544.

Hunt, I.A., 1959. Design of seawalls and breakwaters. *Journal of Waterways and Harbours Division*, ASCE 85 (WW3), 123-152.

Lord D.B. and Kulmar, M.A., 2000. The 1974 Storms Revisited: 25 years Experience in Ocean Wave Measurement Along the South-East Australian Coast. *Proceedings of the 27th International Conference of Coastal Engineering* (Sydney, Australia, ASCE), pp. 559-572.

Mase, H., 1989. Random Wave Run-up Height on Gentle Slopes. *Journal of the Waterway, Port, Coastal and Ocean Engineering Division*, American Society of Civil Engineers, 593-609.

MHL, 1992. *Mid New South Wales Coastal Region Tide-Storm Surge Analysis*. Manly Hydraulics Laboratory, Report MHL621, 39p.

MHL, 2011. *New South Wales Ocean Water Levels*. Manly Hydraulics Laboratory, Report MHL1881, 29p.

MHL, 2012. *OEH NSW Tidal Planes Analysis: 1990-2010 Harmonic Analysis*. Manly Hydraulics Laboratory, Report MHL2053, 18p.

Nielsen, P. and Hanslow, D.J., 1991. Wave Run-up Distributions on Natural Beaches. *Journal of Coastal Research*, 7(4), 1139-1152.

NSW Government, 1990. *NSW Coastline Management Manual*. NSW Public Works Department, 114p.

OEH, 2015. *Coastal Erosion Risk Assessment in NSW: Assessment of Exposure to Coastal Erosion Hazards*. NSW Office of Environment and Heritage, Draft Report 2015.

Power, H.E.; Atkinson, A.L.; Hammond, T. and Baldock, T.E., 2013. Accuracy of Wave Runup Formula on Contrasting Southeast Australian Beaches. *Proceedings of the 21st Australasian Coastal & Ocean Engineering Conference*, (Sydney, Australia), pp. 618-623.

Rodríguez, J.G. and Uriarte, A., 2009. Laser Diffraction and Dry-Sieving Grain Size Analyses Undertaken on Fine- and Medium-Grained Sandy Marine Sediments: A Note. *Journal of Coastal Research*, 25(1), 257-264.

Shand, T.D.; Goodwin, I.D.; Mole, M.A.; Carley, J.T.; Browning, S.; Coghlan, I.G.; Harley, M.D. and Peirson, W.L., 2010. *NSW Coastal Inundation Hazard Study: Coastal Storms and Extreme Waves*. Water Research Laboratory, Technical Report 2010/16, 41p.

Shand, R.D.; Shand, T.D.; McComb, P.J. and Johnson, D.L., 2011. Evaluation of empirical predictors of extreme run-up using field data. *Proceedings of the 20th Australasian Coastal & Ocean Engineering Conference*, (Perth, Australia), pp. 669-675.

Short A.D., 2007. *Beaches of the New South Wales Coast (2nd ed)*, Sydney University Press, 398p.

Short, A.D.; Bracs, M.A. and Turner, I.L., 2014. Beach oscillation and rotation: local and regional response on three beaches in southeast Australia. *In:* Green, A.N. and Cooper, J.A.G. (eds.), *Proceedings 13th International Coastal Symposium* (Durban, South Africa), *Journal of Coastal Research*, Special Issue 70, pp. 712-717.

SMEC and UQ, 2013. *Flooding Tailwater Levels for NSW Coastal Entrances*. Report for NSW Office of Environment and Heritage, SMEC Australia and University of Queensland, 97p.

Stockdon, H.F.; Holman, R.A.; Howd, P.A. and Sallenger, Jr., A.H., 2006. Empirical parameterization of setup, swash, and run-up. *Coastal Engineering*, 53(7), 573-588.

Wright, L.D., 1976. Nearshore wave-power dissipation and the coastal energy regime of the Sydney-Jervis Bay region, New South Wales: a comparison. *Australian Journal of Marine and Freshwater Research*, 27, 633-640.

Journal of Coastal Research	SI	75	1192 - 1196	Coconut Creek, Florida	2016

Hurricane-induced shoreline change and post-storm recovery: northeastern Yucatan Peninsula, Mexico

Nicholas Mulcahy [†‡*], David M. Kennedy[††], and Paul Blanchon[§]

[†]Coastal Research Ltd
Wellington, New Zealand

[‡]School of Geography, Environment, and Earth Sciences
Victoria University of Wellington
Wellington, New Zealand

[††]School of Geography
The University of Melbourne
Melbourne, Australia

[§]Reef Systems Unit, Institute of Marine Sciences and Limnology (ICML)
National Autonomous University of Mexico (UNAM)
Cancun, Mexico

www.cerf-jcr.org

www.JCRonline.org

ABSTRACT

Mulcahy, N.; Kennedy, D.M., and Blanchon, P., 2016. Hurricane-induced shoreline change and post-storm recovery: northeastern Yucatan Peninsula, Mexico. *In:* Vila-Concejo, A.; Bruce, E.; Kennedy, D.M., and McCarroll, R.J. (eds.), *Proceedings of the 14th International Coastal Symposium* (Sydney, Australia). *Journal of Coastal Research*, Special Issue, No. 75, pp. 1192 - 1196. Coconut Creek (Florida), ISSN 0749-0208.

Storms are major drivers of shoreline change on barrier beach systems. In tropical environments many such systems are fronted by coral reefs; however, little is known about how these reefal structures influence beach response during hurricanes. This study provides a detailed assessment of the impacts of Hurricane Wilma on the coral-fringed barrier beaches of the northeastern Yucatan Peninsula, Mexico. Hurricane Wilma made landfall in late October 2005 as a Category 4 storm, bringing sustained wind speeds of 67 ms^{-1}, and storm waves with significant wave heights (H_s) ≈ 13 m. To determine the impact of Hurricane Wilma, satellite imagery was used in conjunction with beach profile data to quantify immediate storm impacts and subsequent shoreline recovery. The beaches responded to storm waves in two broadly different ways. Reef-protected beaches accreted by between 2.1 and 24.6 m, while unprotected beaches underwent erosion of over 10 m. In the years following Hurricane Wilma, reef-protected beaches transgressed landwards as they readjusted to their pre-storm equilibrium shoreline position. Exposed beaches responded much more rapidly, with the majority of shoreline adjustment occurring within eight months of the storm; however, the responses were found to be highly variable alongshore. The results indicate that, under contemporary climatic conditions, hurricanes are key drivers of barrier beach evolution over the short to medium terms, but are not so influential over longer time scales.

ADDITIONAL INDEX WORDS: *Shoreline change, barrier beaches, hurricanes.*

INTRODUCTION

Barrier beaches are dynamic landforms, sensitive to changes in sediment supply, wind and wave conditions, sea level, and tectonics (Hesp and Short, 1999). Storms have historically been seen as important drivers of barrier beach evolution; however, the response of barrier beaches to storms can be highly variable, with geomorphic changes influenced by site-specific factors (Sallenger, 2000; Morton, 2002; Wang *et al*., 2006). Research to date has largely focused on the immediate impacts of storms, often neglecting short and medium-term post-storm responses. Additionally, research into the response of barrier beaches on coral-fringed coastlines is scarce, with most studies focused on the quartz-dominated barrier islands of the Gulf and East Coasts of the United States (Morton, 2002; Morton and Sallenger, 2003).

The northeastern Yucatan Peninsula, Mexico, provides an ideal location to study the significance of hurricanes to barrier beach evolution on coral-fringed coastlines. With the passage of Hurricane Wilma, 15-25 October 2005, the immediate geomorphic response of barrier beaches to a major hurricane could be assessed. The lack of geomorphically significant tropical storms or hurricanes since Hurricane Wilma also enabled the post-storm response to be evaluated.

This study aims to quantify the significance of tropical storms and hurricanes on the short to medium-term shoreline evolution of shore-attached barrier beaches on coral-fringed coastlines.

Background

The northeastern Yucatan Peninsula is characterised by shore-attached calcium carbonate barrier beaches, which are separated from a late Pleistocene dune-ridge system (Marine Isotope Stage (MIS) 5e) by mangrove wetlands; together they form a coastal plain of Holocene age (Szabo *et al*., 1978). The barrier beach is fronted by the Mesoamerican Reef Tract, which runs from the Yucatan Channel in the north to Honduras in the south (Coronado *et al*., 2007). The section of reef relevant to this study is characterised by discontinuous fringing reefs and shallow backreef lagoons; as such, both reef-protected and unprotected barrier beaches are present along this coastline (Ward, 1985; Coronado *et al*., 2007).

DOI: 10.2112/SI75-239.1 received 15 October, 2015; accepted in revision 15 January, 2016.
*Corresponding author: nick.mulcahy@coastalresearch.org.nz
©Coastal Education and Research Foundation, Inc. 2016

The northeastern Yucatan Peninsula is periodically exposed to tropical storms and hurricanes (Landsea, 1993). In the five years prior to Hurricane Wilma, six storm events, ranging from tropical depressions to category 4 hurricanes, tracked within 130 km of the study site.

Hurricane Wilma made landfall in late October 2005 as a Category 4 hurricane, bringing sustained wind speeds of 67 ms^{-1}, and storm waves with significant wave heights (H_s) ≈ 13 m; this is the most intense storm recorded to date in the Atlantic Basin (Pasch, 2006). The storm persisted for over 20 hours, while storm waves inundated the low lying barrier beaches and rainfall flooded inland wetlands and lagoons.

This study examines the immediate and post-storm shoreline response of shore-attached barrier beaches on predominately natural sections of the northeastern Yucatan Peninsula to Hurricane Wilma. The beaches studied are situated between Punta Nizuc in the north and Playa del Secreto in the south, an expanse of approximately 35 km (Figure 1). The study area has been broken into six zones based on the exposure to waves, barrier beach morphology (barrier beach width and foredune height), and the extent of coastal infrastructure development.

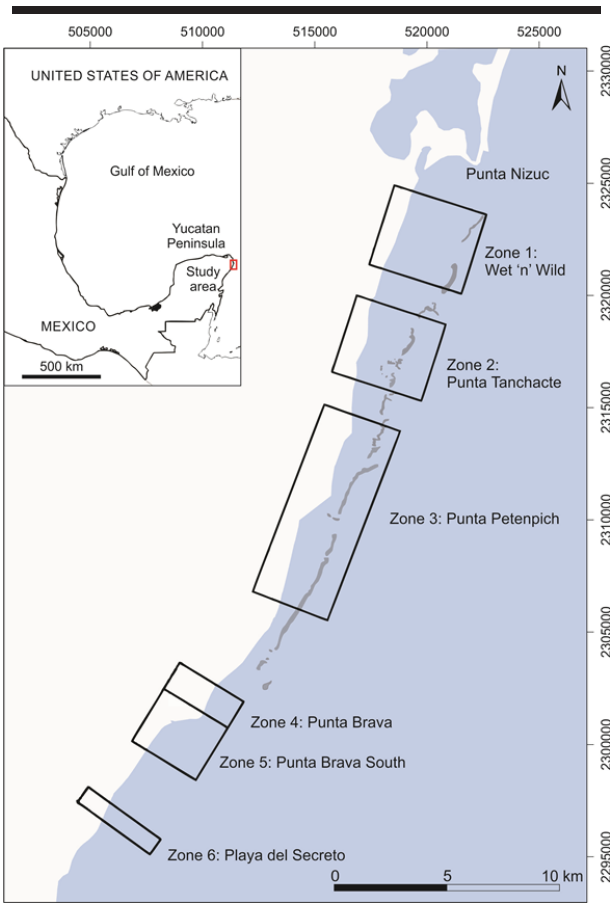

Figure 1. Location of the study area on the northeastern Yucatan Peninsula, Mexico. The six zones investigated in this study are outlined.

METHODS

Imagery from Digital Globe's Quickbird Two Satellite was used to map shoreline change resulting from Hurricane Wilma. The imagery was also used in conjunction with beach profile data to measure post-storm readjustment. The images analysed were taken prior to Hurricane Wilma, immediately following the passage of the storm, and a number of times following the event (2006 and 2010). The images were georeferenced and georectified, and ground truthed during on-site assessment in April 2010.

Dune crest data, captured using a GPS during ground truthing, was used as the baseline position from which all satellite imagery measurements of beach width were taken. The measurements were taken across-shore to mean high water (MHW), marked by the line of seagrass debris during calm periods and the wetted line following Hurricane Wilma. MHW is often used as a shoreline indicator when measuring shoreline change, and provides an accurate point of comparison under normal conditions (Moore, 2000; Boak and Turner, 2005). However, under storm conditions there is greater error (Boak and Turner, 2005).

RESULTS

Hurricane Wilma had a dramatic impact on the low-lying barrier beaches of northeastern Yucatan Peninsula. Results from two contrasting sites, Punta Tanchacte, a reef-protected barrier beach, and Punta Brava, an exposed section of coastline, are presented here in detail.

Punta Tanchacte is situated behind a fringing reef which encloses a lagoon 1.35 - 1.80 km wide and 3 - 4 m deep (Figure 2). It is characterised by the highest foredunes in the study area, which range from 3.0 - 6.5 m above MHW.

Figure 2. Punta Tanchacte, showing the location of the transects measured in this study.

Storm waves from Hurricane Wilma reworked the beach and part of the foredune at Punta Tanchacte. Lower sections of foredune were overtopped, and the beach widened to 78.2 ± 8.6 m. This represented an average increase of 16.3 ± 3.9 m, but varied from 24.6 m at the southern end to 7.7 m in the north.

By June 2006, eight months after Hurricane Wilma, the beach had narrowed to 74.7 ± 8.3 m. However, this was highly variable, with the greatest erosion experienced at the southern end (9.7 m), no change in the centre of the zone, and shoreline accretion further north (2.7 m). By April 2010, a further 48 months later, the beach had undergone continued erosion at all sites, with an average reduction of 11.8 ± 5.7 m since June 2006, amounting to 15.5 ± 4.9 m since Hurricane Wilma (Figure 3).

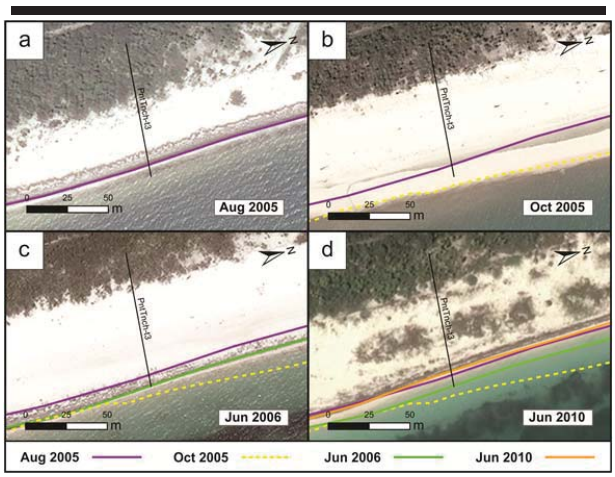

Figure 3. Shoreline change at Punta Tanchacte showing (a) pre-storm, (b) immediately post-storm, (c) and (d) following Hurricane Wilma.

In contrast, Punta Brava, situated in the south of the study area, is directly exposed to waves from the Caribbean Sea due to its location within a gap in the Mesoamerican Reef Tract (Figure 4). The site has a relatively steep shoreface, and the dunes reach up to 3.0 m above MHW.

Storm waves inundated the site during Hurricane Wilma, reworking and overwashing the beach and foredune. Considerable volumes of sediment, including large coral boulders, were transferred into the backdune and mangrove wetlands. As a result, the barrier beach eroded by an average of 5.3 ± 4.8 m, with the greatest erosion at the southernmost site.

By June 2006, the barrier beach had undergone some shoreline recovery. The response was, however, highly variable, with on average 6.3 ± 6.7 m of accretion. The barrier beach was therefore 1.1 ± 2.0 m wider than the pre-storm beach width, indicating the shoreline had largely recovered. By June 2010, the shoreline had shifted once again, with shoreline transgression of up to 4.4 m at the northern and southern ends of the site, contrasting beach accretion of 2.8 m in the centre (Figure 5). This indicates that the prevailing energy regime, and other site-specific factors, contribute to regular shoreline movement at Punta Brava.

Figure 4. Punta Brava (top box), showing the location of the transects measured in this study.

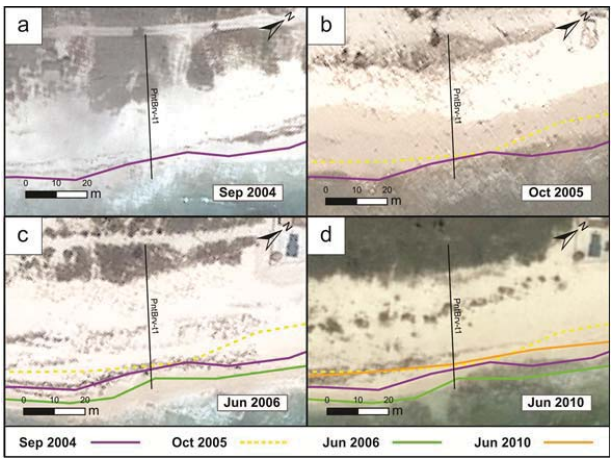

Figure 5. Shoreline change at Punta Brava showing (a) pre-storm, (b) immediately post-storm, (c) and (d) following Hurricane Wilma.

Shoreline response to Hurricane Wilma and post-storm recovery varied considerably across the other areas investigated (Table 1). Similar to Punta Tanchacte, Wet 'n' Wild and Punta Petenpich experienced storm-driven shoreline accretion, followed by post-storm shoreline erosion. However, shoreline response was highly variable, and was also influenced by coastal development at Punta Petenpich. Similar to Punta Brava, Punta Brava South and Playa del Secreto experienced storm-driven erosion, followed by regular post-storm shoreline fluctuations.

Table 1. *Variation in beach width (m) across the study area from 2004/05 to June 2010.*

Site	Pre-storm 2004/05	Immediate post-storm Oct 2005	Post-storm Jun 2006	Post-storm Jun 2010	Δ 2004/05 - Jun 2010
Wet 'n' Wild	34.5 ± 5.1	49.5 ± 5.2	45.3 ± 4.9	35.9 ± 5.7	+ 1.4
Punta Tanchacte	61.9 ± 9.0	78.2 ± 8.6	74.6 ± 8.3	62.9 ± 9.0	+ 1.0
Punta Petenpich	-	-	45.0 ± 16.4	37.5 ± 17.3	-
Punta Brava	29.3 ± 1.4	24.0 ± 5.2	30.3 ± 2.7	29.2 ± 1.6	- 0.1
Punta Brava South	26.1 ± 3.6	21.6 ± 1.4	22.8 ± 8.8	17.1 ± 6.9	- 9.0
Playa del Secreto	36.1	27.6	35.2	29.0	- 7.1

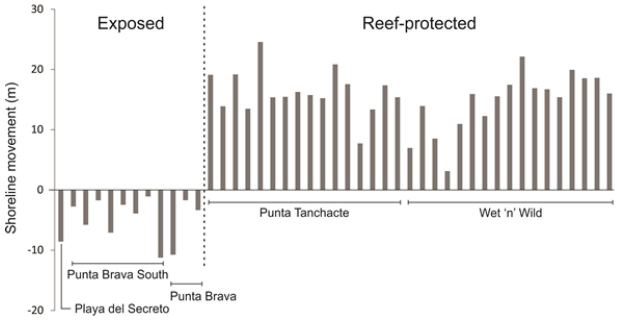

Figure 6. Immediate shoreline response driven by Hurricane Wilma.

DISCUSSION

Tropical storms can drive considerable geomorphic changes on barrier beaches in a short period of time. Storm surge, combined with large storm-generated waves, can remove large quantities of sediment from the beach and dune system and transport it offshore, alongshore, or, if the inundation is great enough, wash sediment inland (Morton and Sallenger, 2003).

Local environmental factors and conditions influence the distribution of wave energy at the shoreline, and therefore determine the way sediment is redistributed across the system. The presence of dissipative structures (such as coral reefs), pre-storm beach morphology, and storm duration and intensity can all influence storm-driven shoreline response (Sallenger, 2000; Morton, 2002).

Wave heights recorded during Hurricane Wilma showed that there was a significant difference between waves in the backreef lagoon and in areas exposed to the Caribbean Sea. Coral reefs were found to dissipate wave energy by over 80%; as such, reef-protected beaches were inundated by storm waves of up to only $H_s \approx 2.4$ m, while exposed sections of coastline were subject to waves of up to $H_s \approx 13$ m (Blanchon *et al*., 2010).

Based on the considerable difference in wave energy reaching reef-protected and unprotected beaches, it would be expected that different patterns of storm-driven sediment redistribution would result from Hurricane Wilma. As outlined earlier, a clear distinction was observed between the storm-driven response of reef-protected and unprotected barrier beaches in this study; the former accreted by up to 24.6 m, while the latter eroded by up to 11.3 m. While the magnitude of erosion and accretion varied alongshore, all sites followed this distinct pattern (Figure 6). The presence or absence of coral reefs evidently is the primary determining factor driving immediate shoreline response on these barrier beach systems.

In the months and years following tropical storms and hurricanes, barrier beaches tend to recover towards their pre-storm conditions (Morton *et al*., 1994). Following Hurricane Wilma, the wave energy regime of northeastern Yucatan Peninsula was characterised by relatively low energy conditions. Reef-protected and exposed barrier beaches again showed different responses.

Despite the low-energy conditions following Hurricane Wilma, approximately a quarter (24%) of the accreted shoreline on reef-protected barrier beaches eroded within eight months. This is likely due to the most easily reworked beach features, such as the beachface and sand bars, being realigned with wave swash under the prevailing conditions. This trend continued over the following years, with many of the beaches returning to their pre-storm shoreline position within 54 months. This likely represents the equilibrium shoreline position of these barrier beaches under current climatic conditions. However, the post-storm recovery was found to be more variable than the initial storm-driven response.

Exposed barrier beaches, in contrast, tended to return to their pre-storm shoreline position relatively quickly (within eight months of the storm), then fluctuated about this position. This indicates that the impact of tropical storms and hurricanes on exposed barrier beaches is only clearly evident in the short term, after which the prevailing conditions are the major control on shoreline position.

On the northeastern Yucatan Peninsula, the return period of storms similar to Hurricane Wilma where $H_s > 12$ m has been calculated by Silva-Casarín *et al*. (2009) to be 100 years; storms producing waves of $H_s \approx 8$-10 m have a calculated return period of 5-10 years. These lengthy return periods indicate that the barrier beaches of northeastern Yucatan Peninsula likely have sufficient time to readjust post-storm to their equilibrium shoreline position, prior to the landfall of another storm on a similar scale. Therefore, under current climatic conditions, tropical storms and hurricanes strongly influence barrier beach evolution over the short (0-8 months) to medium terms (8-54 months) on the northeastern Yucatan Peninsula; however, they may be less influential over the longer term. The varying responses of reef-protected and exposed barrier beaches to tropical storms and hurricanes, as they relate to storm intensity and return period, are conceptualised in Figure 7.

However, future climatic change is predicted to result in increased intensity of major tropical storms and hurricanes, and subsequently an increase in the scale of their geomorphic impacts. As a result, the barrier beaches of northeastern Yucatan Peninsula may be more frequently inundated by waves greater than 8 m or even 12 m, with the return period of the most intense storms likely to reduce. If this occurs, the difference

between the beach recovery time and the storm recurrence interval would become shorter. Over time, these high energy events may start to have greater influence on the longer-term evolution of barrier beaches, with successive catastrophic storms potentially making landfall prior to full beach recovery. This could result in a landward shift of the long-term equilibrium shoreline position.

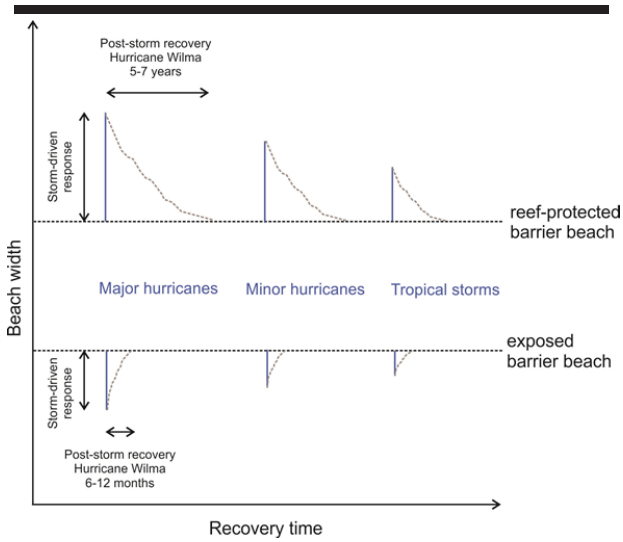

Figure 7. Conceptual model of barrier beach width change and post-storm recovery time, with respect to storm intensity.

CONCLUSIONS

This study found that the barrier beaches of the northeastern Yucatan Peninsula responded to Hurricane Wilma in two broadly different ways. Reef-protected beaches underwent rapid accretion during the passage of the storm, followed by gradual erosion over subsequent years. In contrast, exposed barrier beaches were eroded during the storm and then rapidly accreted back to their pre-storm shoreline position.

Under contemporary climatic conditions, tropical storms and hurricanes were found to be key drivers of barrier beach evolution over the short to medium terms. These events are considered less influential over longer time scales due to current storm recurrence intervals generally exceeding barrier beach recovery times. An expected increase in the intensity of major storms in the future may increase the significance of hurricanes to longer-term barrier evolution; storm impacts are likely to be greater and storm recurrence intervals may be shorter than the time required for recovery.

However, of potentially greater immediate impact to the study area, development on the Yucatan Peninsula is progressively extending along this coastline. The construction of seawalls and other structures will restrict shoreline movement and across-shore sediment exchange, inhibiting the natural dynamics of barrier beaches, and reducing their resilience to future storm events.

LITERATURE CITED

Blanchon, P.; Iglesias-Prieto, R.; Jordán Dahlgren, E., and Richards, S., 2010. Arrecifes de coral y cambio climático: vulnerabilidad de la zona costera del estado de Quintana Roo. *In*: A.V. Botello, S. Villanueva-Fragoso, J. Gutiérrez, J.L. Rojas Galaviz (eds.), *Vulnerabilidad de las zonas costeras mexicanas ante el cambio climático*. Semarnat-INE, UNAM-ICMyL, Universidad Autónoma de Campeche, 229-248.

Boak, E.H. and Turner, I.L., 2005. Shoreline Definition and Detection: A Review. *Journal of Coastal Research*, 21(4), 688-703.

Coronado, C.; Candela, J.; Iglesias-Prieto, R.; Sheinbaum, J.; López, M., and Ocampo-Torres, F., 2007. On the circulation in the Puerto Morelos fringing reef lagoon. *Coral Reefs*, 26(1), 149-163.

Hesp, P.A. and Short, A.D., 1999. Barrier morphodynamics. *In*: A.D. Short (ed.), *Handbook of Beach and Shoreface Morphodynamics*. Chichester: John Wiley & Sons, 307-333.

Landsea, C.W., 1993. A climatology of intense (or major) Atlantic hurricanes. *Monthly Weather Review*, 121(6), 1703-1713.

Moore, L.J., 2000. Shoreline Mapping Techniques. *Journal of Coastal Research*, 16(1), 111-124.

Morton, R.A.; Paine, J.G., and Gibeaut, J.C., 1994. Stages and Durations of Post-Storm Beach Recovery, Southeastern Texas Coast, USA. *Journal of Coastal Research*, 10(4), 884-908.

Morton, R.A., 2002. Factors Controlling Storm Impacts on Coastal Barriers and Beaches - A Preliminary Basis for Near-Time Forecasting. *Journal of Coastal Research*, 18(3), 486-501.

Morton, R.A. and Sallenger, A.H., 2003. Morphological impacts of extreme storms on sandy beaches and barriers. *Journal of Coastal Research*, 19(3), 560-573.

Pasch, R.J.; Blake, E.S.; Cobb III, H.D., and Roberts, D.P., 2006. *Tropical Cyclone Report, Hurricane Wilma 15-25 October 2005*. Miami, Florida: National Oceanic and Atmospheric Administration, 27p.

Sallenger, A.H., 2000. Storm Impact Scale for Barrier Islands. *Journal of Coastal Research*, 16(3), 890-895.

Silva-Casarín, R.; Mendoza-Baldwin, E.; Escalante-Mancera, E.; Mariño-Tapia, I., and Ruiz-Rentería, F., 2009. Wind waves induced by Hurricane Wilma in Puerto Morelos, Quintana Roo, Mexico. *Ingenieria Hidraulica en Mexico*, 24(2), 93-109.

Szabo, B.J.; Ward, W.C.; Weidie, A.E., and Brady, M.J., 1978. Age and magnitude of the late Pleistocene sea-level rise on the eastern Yucatan Peninsula. *Geology*, 6(12), 713-715.

Wang, P.; Kirby, J.H.; Haber, J.D.; Horwitz, M.H.; Knorr, P.O., and Krock, J.R., 2006. Morphological and sedimentological impacts of hurricane Ivan and immediate poststorm beach recovery along the northwestern Florida barrier-island coasts. *Journal of Coastal Research*, 22(6), 1382-1402.

Ward, W.C., 1985. Quaternary geology of northeastern Yucatan Peninsula. *In*: W.C. Ward, W.C.; Weidie, A.E., and Back, W. (eds.), *Geology and hydrogeology of the Yucatan and quaternary geology of northeastern Yucatan Peninsula*. New Orleans Geological Society, New Orleans, LA, pp. 23-95.

Journal of Coastal Research	SI	75	1197 - 1201	Coconut Creek, Florida	2016

A Framework for Modelling Shoreline Response to Clustered Storm Events: A Case Study from Southeast Australia

Scott L. Nichol[†*], Andrew McPherson[†], Gareth Davies[†], Wenping Jiang[†], Floyd Howard[†], Uriah Gravois[‡], David Callaghan[‡] and Tom Baldock[‡]

[†]Geoscience Australia
Canberra, ACT 2601, Australia

[‡]School of Civil Engineering
University of Queensland
Brisbane, QLD 4072, Australia

www.cerf-jcr.org

www.JCRonline.org

ABSTRACT

Nichol, S.L.; McPherson, A., Davies, G., Jiang, W., Howard, F., Baldock, T., Callaghan, D., and Gravois, U., 2016. A framework for modelling shoreline response to clustered storm events: A case study from southeast Australia. *In:* Vila-Concejo, A.; Bruce, E.; Kennedy, D.M., and McCarroll, R.J. (eds.), *Proceedings of the 14th International Coastal Symposium* (Sydney, Australia). *Journal of Coastal Research*, Special Issue, No. 75, pp. 1197 - 1201. Coconut Creek (Florida), ISSN 0749-0208.

An overview of a framework for modelling shoreline response to clustered storm events is presented for a case study area on the high energy coast of southeast Australia. We adopt the coastal sediment compartment as the functional management and modelling unit and use sub-surface information (ground-penetrating radar) to assess sediment thickness in the upper beach and foredune. Results for an actively eroding beach face at Old Bar Beach (New South Wales) indicate that sand cover is highly variable at the critical beach-dune interface, ranging from less than 1 m where bedrock occurs in shallow sub-crop to greater than 4 m across a former tidal inlet. The temporal distribution of storm events is examined through statistical modelling. For the duration of the data, modeled wave parameters are in good agreement with wave buoy observations. Event clustering does not appear to be stronger than is expected from events that occur randomly in time. Together, these data provide site-specific information necessary to inform shoreline response modeling to storms by establishing the requisite conditions describing the geomorphic setting and nearshore process regime.

ADDITIONAL INDEX WORDS: *Beach erosion, sediment compartment, time series, coastal management* .

INTRODUCTION

Coastal communities in Australia are particularly exposed to coincident natural hazards, whereby tropical cyclones and extra-tropical storms cause damage to infrastructure and shorelines from severe wind, flood and storm surge. Because the climatic drivers of severe storms are stronger under certain conditions (e.g. during La Niña periods for tropical cyclones), these events can repeatedly impact the coast over periods of weeks to months. Historically, major episodes of beach erosion in southeast Australia have occurred during every decade over the last century, with the most severe in 1974 resulting from two extra-tropical storms within two months (McLean *et al*., 2010).

While the process of beach erosion is well understood in general terms, the response of a specific sector of coast to clustered storms may not be. For effective coastal management, this site-specific knowledge becomes essential. Here we use a case study on the southeast coast of Australia to introduce a framework for integrating coastal geomorphology and storm event modelling to guide predictions of shoreline response to clustered storms at a spatial scale that can directly inform management agencies. We consider clustering of storms in the context of beach recovery time between successive events.

Study Site

Old Bar Beach is located on the mid-north coast of New South Wales (NSW), southeastern Australia (Figure 1). The beach-dune system is representative of an open-coast swash aligned sand-dominated shoreline, with the beach-type classified as intermediate with a transverse inner bar and rip system (Short, 2007). The modal beach state is characterised by a double bar system, with the inner bar intersected by a series of rips that locally erode sand from the beach face. Modal wave height is ~1.6 m with storm waves in the range of 5 to 8 m, as measured by a deepwater waverider buoy offshore Crowdy Head (Kinsela *et al*., 2014). Wave direction on the NSW coast prevails from the southeast, but larger wave events arrive from the south-south-east in Winter. Tidal range is microtidal.

Beach sediments are mixed sand and gravel, with the latter forming a discontinuous surface lag on the mid to upper beach face (Figure 2). Gravel beach cusps form periodically along the central section of the beach, usually during storms. Sediment cover in the nearshore is discontinuous with rocky reefs located at the southern end and central sector of the embayment where they extend from the intertidal zone to ~20 m water depth (Breen *et al*., 2004; NSW Office of Environment and Heritage, 2012). Wave modelling shows that these reefs influence wave refraction and nearshore circulation during storms, to the extent that a large rip cell forms between the reefs when significant wave height exceeds 5 m from the east-southeast (Worley Parsons, 2010). Under these conditions, the same modelling predicts depth-averaged current velocities of 0.5 m/s.

Dunes are continuous along the Old Bar shoreline, forming a stationary-type barrier up to 100 m wide and 10 m elevation and

DOI: 10.2112/SI75-240.1 received 15 October, 2015; accepted in revision 15 January, 2016.
*Corresponding author: nick.mulcahy@coastalresearch.org.nz
©Coastal Education and Research Foundation, Inc. 2016

mostly stabilised under vegetation cover. Erosion of the dune face is concentrated along the central section of the embayment where storm surge undercutting has destabilised the dune (Figure 2). This condition has prevailed as a recognised problem since the early 1970's, resulting in property loss and damage to access paths and other infrastructure (Department of Public Works, 1981; Kinsela and Hanslow, 2013). Continuing efforts to stabilise the dune have included placement of geotextile across the dune face along with planting of vegetation (grasses and sedges).

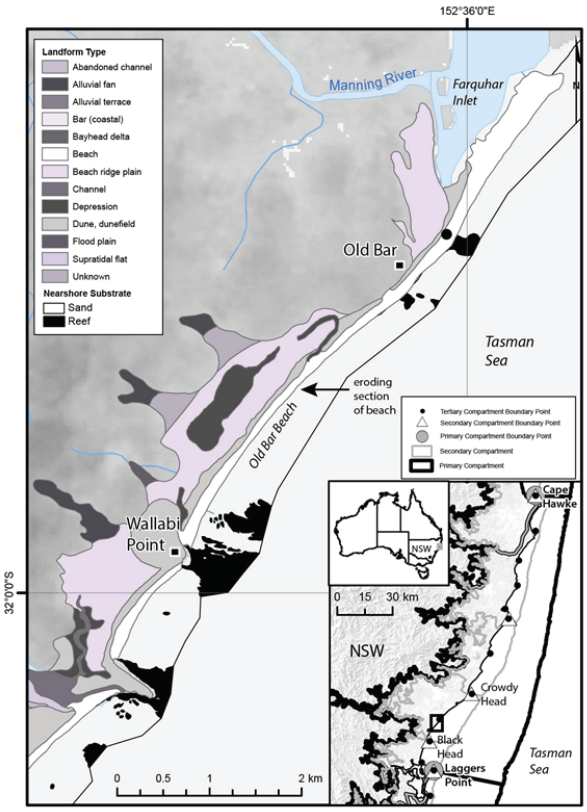

Figure 1. Location of study area, with inset showing Primary, Secondary and Tertiary coastal compartment boundaries for the NSW mid-north coast. For reference, Cape Hawke defines the southern Primary boundary and Laggers Point the northern boundary. Quaternary geology boundaries (Hashimoto & Troedson, 2007) have been re-mapped to landform types using the National Coastal Geomorphology Classification (Hazelwood *et al*., 2013)

METHODS

This study integrates information from desktop and field based analysis to define the physical characteristics and extent of the modelling domain, as follows:

Coastal Compartments

The coastal sediment compartments framework (Eliot *et al*., 2011a, b) uses a prioritised set of environmental attributes to sub-divide the Australian coastline into spatial units reflecting variation in the geological and geomorphic characteristics of the coast (Table 1; McPherson *et al*., 2015). Termed Primary and Secondary compartments, these spatial units were generated at 1:250,000 and <1:250,000 respectively; the boundary between each compartment was defined using one or more of the attributes shown in Table 1. At the local scale (<1:100,000), a higher spatial resolution (Tertiary) compartment data set has also been proposed, following the approach of Eliot *et al*. (2011a, b) and Stul *et al*. (2012) for mapping compartments in Western Australia. Mapping at this scale is based on landform information defined at the Landform Type and Subtype levels (e.g. beach, dune, beach ridge plain - Hazelwood *et al*., 2013). A preliminary point data set delineating Tertiary compartment boundaries around the Australian coast has been generated by Geoscience Australia (unpublished data) and was used in this study to define the alongshore extent and geomorphic units within the Old Bar sediment compartment to guide field work and shoreline response modelling.

Figure 2. Dune erosion at Old Bar beach. Note geotextile on dune face and gravel berm on the upper beach (photo taken 4 March 2015) .

Table 1. *Prioritised attributes used to determine the boundary points for Primary and Secondary coastal sediment compartments (modified after Eliot et al., 2011a, b).*

Priority	Physical Attribute	Example
1	Gross geological change	Volcanic outcrop
2	Geomorphic feature	Peninsula, headland, cliff
3	Dominant landform type	Pocket beach, tombolo
4	Change in shoreline aspect	--

Sub-surface Mapping

Ground-penetrating radar (GPR) data was acquired at Old Bar using a MALÅ ProEx system fitted with a sled-mounted 250 MHz shielded antenna. Data was collected between Wallabi Point and Farquhar Inlet (Figure 1) along shore-normal profiles (dune crest to beach face) at 21 locations and along a shore-parallel profile (toe of dune) as a series of lines that extend the ~5 km length of the study area. Additional profiles were

collected at sites where bedrock was exposed on the upper beach face, for the purpose of establishing the radar signature of the buried sand-rock contact.

Data processing was undertaken using RadExplorer™ software (Geomatrix Earth Science Ltd). Processing involved elevation correction to account for surface topographic variation (*e.g.* dunes), signal filtering (background removal, bandpass filtering) to reduce noise, and gain correction to compensate for reduced signal strength at depth. Limited migration was undertaken, although all profiles were time-depth converted to transform two-way time to depth. Radargrams were generated for profiles with acceptable penetration depth and data resolution, and reliable topographic correction.

Synthetic Storm Event Modelling

Extreme storm events at a given site can be described using multivariate summary statistics, including the maximum significant wave height (H_{sig}), median wave period, median wave direction, duration, peak storm surge, and time of occurrence. Here we define a storm event using a peaks-over-threshold approach, with a threshold equal to the 95% exceedance quantile of significant wave height. For the study site, we use waverider buoy data for Crowdy Head, located 25 km northeast of Old Bar in ~70 m water depth (Figure 1 inset). Data gaps were filled using the neighbouring Coffs Harbour and Sydney buoys. Spanning 30 years of observations, these data record a 95% threshold value for H_{sig} of 2.9 m. Consecutive events exceeding this threshold were manually checked against sea-level pressure data to determine if they were generated by the same meteorological system, and if so the events were combined. This then established a final storm event set that comprised meteorologically independent storm events.

A variety of statistical techniques were applied to model the magnitude and frequency of the extracted storm events. The event timings were modelled as a non-homogenous Poisson process, with finite storm durations during which no other storm can occur (Callaghan *et al.*, 2008). The model accounts for the sub-annual variations in the rate of storms (e.g. at Old Bar, storms are more frequent in the winter months than the summer months). It also accounts for temporal dependency between successive events, which is partly caused by the finite duration of events, and may potentially be affected by any over/under dispersion in the meteorological forcing. The multivariate distribution of event summary statistics was simulated by first fitting a particular marginal distribution to each variable, and then modelling their dependencies with a copula (Li *et al.*, 2013). A Generalised Pareto distribution was fitted to H_{sig} and a Pearson type 3 distribution to duration and tidal residual. Empirical marginal distributions were employed for wave period and direction. The dependencies among these marginals were modelled using Copulas. Two methods were tested: a Gaussian-copula, and a combination of a Gumbel Copula for H_{sig} and duration, and a Gaussian copula for H_{sig} and all other variables. Goodness-of-fit tests such as Kolmogorov-Smirnov (K-S) tests, Chi-square tests and AIC and BIC were used to quantitatively evaluate the fitting qualities and to assess model parsimony, along with graphical visualisations.

A long-term synthetic time-series of storm events (10^6 years) was generated using the event magnitude and timing simulated with the fitted models. These long-term synthetic events can be used to derive exceedance probabilities and to construct designed storm events to be applied to beach erosion modelling.

RESULTS

The eroding section of Old Bar Beach is located within a Tertiary sediment compartment defined by a bedrock headland at Black Head in the south and the transition from continuous beach-dune to inlet-beach at the southern end of Farquhar Inlet in the north (Figure 1). This transition also marks a subtle change in aspect, with the Old Bar compartment facing south-east into the prevailing deepwater swell direction, whereas the inlet-beach section faces east-south-east (*i.e.* more drift aligned). At the Primary and Secondary compartment scales, Old Bar Beach is located toward the southern end of a Primary compartment that extends ~170 km from Forster (Cape Hawke promontory) to South West Rocks (Laggers Point headland) that in turn comprises four Secondary compartments (Figure 1 inset). Of these, Old Bar sits within the second smallest Secondary compartment. Old Bar Beach is therefore at the southern end of a segmented northward littoral drift system with negligible sediment exchange at the Tertiary compartment scale.

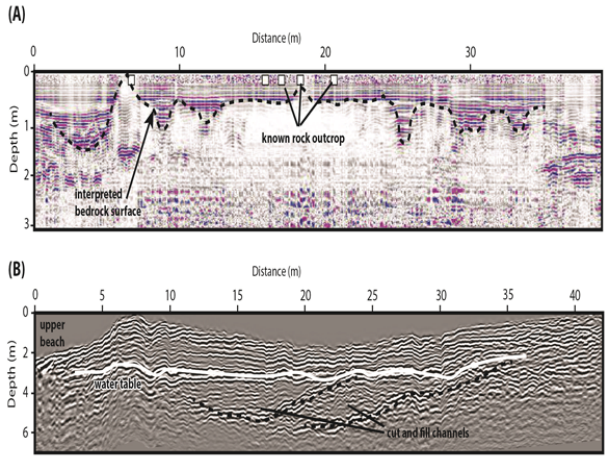

Figure 3. Representative GPR profiles (250 MHz antenna) for Old Bar Beach, showing: (A) Shore parallel section of horizontally-bedded sand less than 1 m thick over buried rock at the beach-dune interface. White squares show position of known rock outcrop located within 1-2 m of the profile; (B) Cross-shore section of cross-bedded dune sand and channel fill to ~6 m depth adjacent to Farquhar tidal inlet (now closed) at the northern end of Old Bar Beach.

Results from the GPR survey show sediment thickness in the upper beach ranges from zero to several metres, with a general trend of increasing thickess (and width) toward the north (Figure 3). In particular, at sites where bedrock outcrops on the upper beach (*i.e.* the eroding section) the GPR data reveals this bedrock continues in the shallow sub-surface, limiting the sand thickness to less than 1 m. Notably, this rock outcrop/subcrop surface is strongly dissected, resulting in variations in sand thickness of 1-2 m over distances of 5-10 m (Figure 3a). A

similarly irregular bedrock surface was observed on shore platforms and where exposed in the surf zone at low tide. In contast, toward the northern end of Old Bar beach (where bedrock outcrop or sub-crop is not evident), beach sediment thicknesses are shown to be a minimum of 4 m below ground surface, with some sites suggesting thicknesses of 6 m or more (Figure 3b).

The best-fitting statistical model of storm events with H_{sig} > 2.9 m replicates key properties of the observed record for Crowdy Head (Figures 4 and 5; see Figure 1 inset for location). Thus, H_{sig} for the largest storms ranged from the threshold of 2.9 m to sub-annual events of ~6 m and decadal events exceeding 7 m. Our model well matches the seasonal variation in the storm rate, and accounts for the finite duration of storm events. Of note, while sequences of closely spaced storm events occur in the model and data with similar frequency (~15 events per year over threshold H_{sig}), we do not find any evidence that the storms are clustered more than would be expected if their timings were random. The replication of observed storm events in the synthetic event series is also represented across wave period, storm duration, wave direction and time of year (season) (Figure 5).

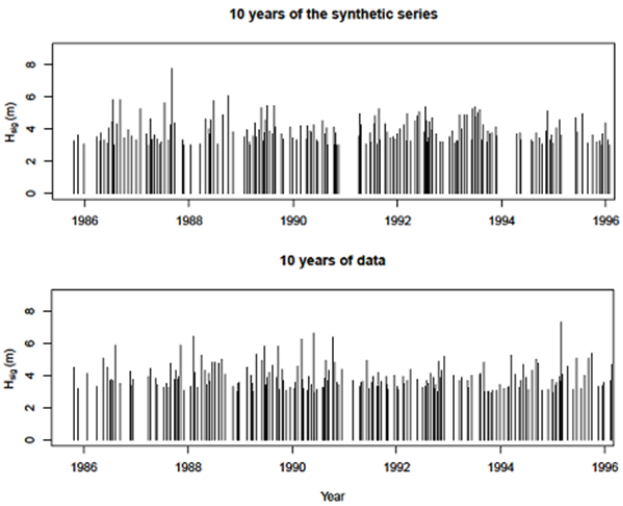

Figure 4. Example of a 10-year synthetic storm wave record time-series compared to observed data for Crowdy Head wave buoy, NSW.

DISCUSSION

The concept of the coastal sediment compartment is not new (Davies, 1974). However, defining compartments coastwise using a standarised method at multiple spatial scales is rarely applied yet provides the fundamental context for approaching issues of coastal management, particularly shoreline erosion. In the Old Bar case, it is clear that erosion (while localised) is in part a function of its location within a regionally small Secondary compartment at the up-drift end of a segmented Primary compartment. Sediment supply from external sources is therefore limited. This is further evident from mapping at the Tertiary scale which shows that erosion is ocurring immediately up-drift of the Tertiary compartment boundary, defined by an extensive offshore reef. Previous modelling studies have demonstrated the influence of this reef on nearshore circulation, with the development of a large rip cell during storms (Worley Parsons, 2010). The evidence presented here extends this understanding by showing that the onshore continuation of shallow bedrock locally controls sediment thickness on the beach, including at the critical beach-dune interface. This effectively limits the local sediment source for maintaining a stable beach-dune system. Furthermore, it sets the context for describing potential antecedent beach states prior to storm events.

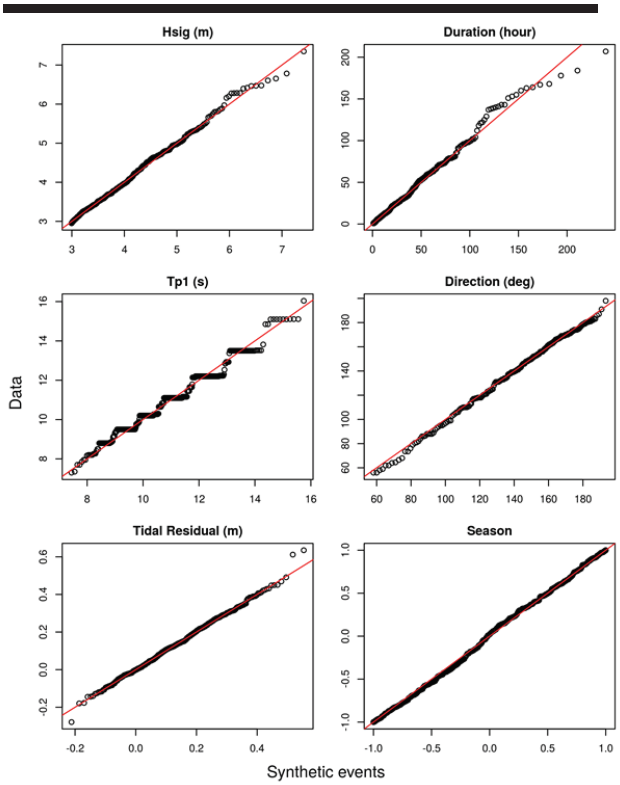

Figure 5. Observed versus modelled parameters for storm waves at Crowdy Head (central NSW coast), showing good model performance up to significant wave heights of 7 m.

The statistical analysis of the modelled wave record for Old Bar indicates that while closely spaced events occur in the observed data and the model, these do not appear to occur more frequently than expected for a model where the events occur randomly in time (subject to seasonal variations in the event rate and a finite event duration). Thus, event clustering does not appear to be strong. Regardless, the result does provide the necessary input for modelling shoreline response to successive events by defining the time available for beach recovery for a given antecedent beach state. Ongoing work is considering incorporating wave direction and climate cycles (*e.g.* ENSO) into this analysis.

CONCLUSIONS

The value of site specific information to inform shoreline response modelling is enhanced with the application of a standardised approach to defining sediment compartments at multiple spatial scales. Central to the value of the approach is an understanding of local scale variability in sediment distributions that might otherwise have been assumed uniform, particularly when supported by field measurements. Further, it supports the definition of potential antecedent conditions for a given beach type as a key input to response modelling. Finally, the temporal aspect of shoreline modelling can be considered through statistical hindcasting to develop a robust time series of storm events.

ACKNOWLEDGMENTS

This paper is a contribution to the Bushfire and Natural Hazard Cooperative Research Centre project "Storm surge: Resilience to clustered disaster events on the coast." We thank Brendan Brooke, Craig Arthur of Geoscience Australia, and an anonymous reviewer for their constructive reviews. Published with permission of the Chief Executive Officer, Geoscience Australia.

LITERATURE CITED

Breen, D.A., Avery, R.P., and Otway, N.M., 2004. *Broad-scale biodiversity assessment of the Manning Shelf marine bioregion*. NSW Marine Parks Authority. http://www.mpa.nsw.gov.au/psglmp-Manning-assessment.html

Callaghan, D., Nielsen, P., Short, A., and Ranasinghe, R., 2008. Statistical simulation of wave climate and extreme beach erosion. *Coastal Engineering* 55, 375-390.

Davies, J.L., 1974. The coastal sediment compartment. *Australian Geographical Studies* 12, 139-151.

Department of Public Works, 1981. *Old Bar Coastal Erosion Study*. Unpublished consulting report Sinclair Knight and Partners, 186p.

Eliot, I., Gozzard, R., and Nutt, C. 2011a., Geologic Frameworks for Coastal Planning and Management. *Proceedings of the 20th Australasian Coastal and Ocean Engineering Conference and the 13th Australasian Port and Harbour Conference*.

Eliot, I., Nutt, C., Gozzard, R., Higgins, M., Buckley, E., and Bowyer, J., 2011b. *Coastal Compartments of Western Australia: A Physical Framework for Marine and Coastal Planning*. Report 80-02. Damara WA Pty Ltd. Report to the Departments of Environment and Conservation, Planning and Transport and the Environmental Protection Authority.

Hashimoto, T.R. and Troedson, A.L., 2007. Taree Area 1:100 000 and 1:25 000 Coastal Quaternary Geology Map. *Coastal Quaternary Geology 1:100 000 and 1:25 000 Map Series*. Geological Survey of New South Wales, Maitand. http://www.resourcesandenergy.nsw.gov.au/miners-and-explorers/geoscience-information/products-and-data/maps/coastal-quaternary-maps/CQGT.

Hazelwood, M., Nicholas, W.A., and Woolf, M., 2013. *National Coastal Geomorphology Information Framework Implementation: Discovery and Distribution*. Geoscience Australia Record 2013/35, Geoscience Australia, Canberra, 33p.http://www.ga.gov.au/corporate_data/74294/Rec2013_035.pdf.

Kinsela, M.A. and Hanslow, D.J., 2013. Coastal erosion risk assessment in New South Wales: limitations and potential future directions. *Proceedings of the 22nd NSW Coastal Conference 2013*, Port Macquarie, 12-15 November 2013, www.coastalconference.com/papers.php

Kinsela, M., Taylor, D., Treloar, D., Dent, J., Garber, S., Mortlock, T., and Goodwin, I., 2014. NSW coastal ocean wave model: Investigating spatial and temporal variability in coastal wave climates. *Proceedings of the 23rd NSW Coastal Conference 2014*, Ulladulla, 11-14 November 2014, www.coastalconference.com/papers.php

Li, F., van Gelder, P., Ranasinghe, R., Callaghan, D., and Jongejan, R. (2014) Probabilistic modelling of extreme storms along the Dutch coast. *Coastal Engineering* 86, 1-13.

McLean, R., Shen, J., Thom, B., 2010. Beach change at Bengello Beach, Eurobodalla Shire, New South Wales: 1972-2010. *Proceedings 19th NSW Coastal Conference*, Batemans Bay, 10-12 November 2010. www.coastalconference.com/papers.php

McPherson, A., Hazelwood, M., Moore, D., Owen, K., Nichol, S. and Howard, F., 2015. *The Australian Coastal Sediment Compartments Project: methodology and product development*. Geoscience Australia Record 2015/25. Geoscience Australia, Canberra, 24p. http://dx.doi.org/10.11636/Record.2015.025.

NSW Office of Environment and Heritage, 2012. *Nearshore subtidal marine reef systems and soft sediment mapping, New South Wales*. [digital dataset]. NSW Office of Environment & Heritage, Sydney, http://mapdata.environment.nsw.gov.au/geonetwork/srv/en/main.home

Short, A.D., 2007. *Beaches of the New South Wales coast: a guide to their nature, characteristics, surf and safety*. 2nd edition. Sydney University Press, Sydney. 398 pp.

Stul, T., Gozzard, J.R., Eliot, I.G., and Eliot, M.J., 2012. *Coastal Sediment Cells between Cape Naturaliste and the Moore River, Western Australia*. 44 pp. Report prepared by Damara WA Pty Ltd and Geological Survey of Western Australia for the Western Australian Department of Transport, Fremantle.

Worley Parsons, 2010. *Black Head to Crowdy Head Coastline Hazard Definition Study*. Unpublished consulting report to Greater Taree City Council, 156p. http://www.gtcc.nsw.gov.au/assets/Main-Site/Files/FP-Strategic-Environment/

Journal of Coastal Research	SI	75	1202 - 1206	Coconut Creek, Florida	2016

Simulation of Inundation along the West Coast of Korea from the Meteo-Tsunami of 2007

Sae Chan Oh[†], Choong Hun Shin[§], and Sung Bum Yoon[§*]

[†]Department of Civil and Environmental Engineering
Hanyang University
Seoul, Korea

[§]Department of Civil, Environmental and Plant Engineering
Hanyang University- ERICA Campus
Ansan, Korea

www.cerf-jcr.org

www.JCRonline.org

ABSTRACT

Oh, S.C.; Shin, C.H., and Yoon, S.B., 2016. Simulation of Inundation along the West Coast of Korea from the Meteo-Tsunami of 2007. *In:* Vila-Concejo, A.; Bruce, E.; Kennedy, D.M., and McCarroll, R.J. (eds.), *Proceedings of the 14th International Coastal Symposium* (Sydney, Australia). *Journal of Coastal Research*, Special Issue, No. 75, pp. 1202 - 1206. Coconut Creek (Florida), ISSN 0749-0208.

On March 31, 2007 a destructive long wave occurred along the west coast of Korea. Due to this long wave, four human lives were lost and many of ships and houses were damaged. Because no earthquake or no strong wind was reported around the Yellow Sea by that time, this long wave is suspected to be a meteo-tsunami. This study focuses on the understanding of the generation mechanism of atmospheric pressure jump and its resultant meteo-tsunami. In this study, a new type of atmospheric pressure jump which generated the meteo-tsunami along the west coast of Korea on the 31st of March, 2007 is suggested. To confirm the relation between the atmospheric pressure jump and the meteo-tsunami, a numerical simulation using two dimensional nonlinear shallow water equations was conducted. The results agree well with the observed free surface data at the Younggwang tidal station and the measured inundation heights at the Beopsungpo area of Korea.

ADDITIONAL INDEX WORDS: *Meteo-tsunami, atmospheric pressure jump, inundation, numerical simulation.*

INTRODUCTION

A destructive long wave occurred along the west coast of Korea on March 31, 2007. This long wave superimposed on the high water of spring tide in the Yellow Sea. The surge heights observed at the tidal stations along the west coast of Korea range from 1 m to 1.7 m, and the long waves inundated some low lands where a nuclear power plant site is located nearby. The maximum surge height measured at the intake channel of the nuclear power plant site was 3.5 m above high tide level. Due to this long wave four lives were lost, 55 ships destroyed, and 120 houses inundated.

At this time no earthquake or no strong wind was reported in the Yellow Sea. However, rapid changes in the atmospheric pressure between 3 to 8 hPa in 15 minutes were observed at the several areas along the west coast of Korea. Thus, the long waves occurred in the Yellow Sea in 2007 were suspected as a meteo-tsunami. According to Monserrat *et al*. (2006) rapid changes in the atmospheric pressure will generate a localized rise or fall of sea level. When the translational speed of pressure jump equals the phase speed of wave, the Proudman resonance occurs and the wave height increases gradually with increasing propagation distance. The amplification of waves can be further intensified due to the shoaling and the harbor resonance. Flooding and damage caused by meteo-tsunamis have been reported over the world (Monserrat *et al.,* 2006). These destructive meteo-tsunamis have
specific local names: Rissaga in the Balearic Islands, Marubbio in Sicily, Milghuba in Malta, Abiki in Nagasaki Bay, Japan, and Seebar in the Baltic Sea. In China the meteo-tsunami has been also reported at the Longkou harbor located on the north-western coast of Shandong Peninsula.

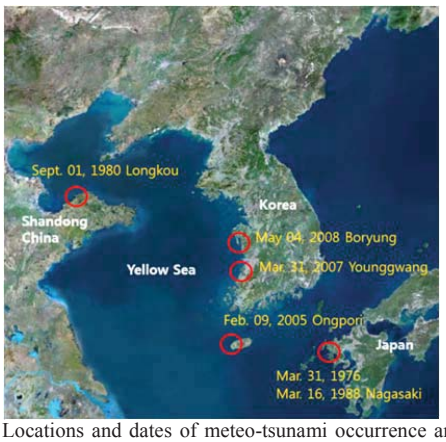

Figure 1. Locations and dates of meteo-tsunami occurrence around the Yellow Sea.

In Korea, as shown in Figure 1, the first meteo-tsunami was reported on Feb. 9, 2005 at Ongpori located on the west coast of Jeju Island. The meteo-tsunami of 2005 was so weak that it inundated the small fishing port with no noticeable damage. Thus, it did not draw much attention. The second meteo-tsunami of March 31, 2007, however, was destructive with four victims. The third meteo-tsunami occurred on May 4, 2008 at Juk Island of Boryung also located along the west coast of Korea. The

DOI: 10.2112/SI75-241.1 received 15 October, 2015; accepted in revision 15 January, 2016.
*Corresponding author: sbyoon@hanyang.ac.kr
©Coastal Education and Research Foundation, Inc. 2016

surge height of this meteo-tsunami was not so large. However, the surge occurred suddenly and nine people died. After these three events the meteo-tsunami become a growing concern of the scientists and engineers in Korea.

All of the meteo-tsunamis occurred in Korea, Japan and, China surrounding the Yellow Sea along their west coasts. This suggests that the meteo-tsunamis were generated in the western part of the Yellow Sea, and propagated easterly. Another common factor is that the meteo-tsunamis occurred mostly in the Spring season (except Longkou harbor case) when the sea water temperature is low. In the Spring the thermal inversion layer in the atmosphere develops easily in the Yellow Sea. Thus, any meteorological disturbance can easily induce the pressure jump and the pressure jump can propagate in the form of a bore within the inversion layer.

METHODS

In this study the generation mechanism of the atmospheric pressure jump and its resultant meteo-tsunami were investigated by various data analyses and numerical simulation. The weather charts, the observed atmospheric pressure data and the tidal records were used in the analyses. In order to verify the relation between the atmospheric pressure jump and the meteo-tsunami, a numerical simulation was performed. In this study, the two-dimensional nonlinear shallow water equations, (1) ~ (3), are employed. Additionally, the moving boundary technique developed by Yoon and Cho (2001) is applied.

$$\frac{\partial \zeta}{\partial t}+\frac{\partial P}{\partial x}+\frac{\partial Q}{\partial y}=0 \tag{1}$$

$$\frac{\partial P}{\partial t}+\frac{\partial (P^2/D)}{\partial x}+\frac{\partial (PQ/D)}{\partial y}+\mathrm{g}D\frac{\partial \zeta}{\partial x}+\frac{gn^2}{D^{7/3}}P\sqrt{P^2+Q^2}+\frac{D}{\rho}\frac{\partial P_a}{\partial x}=0 \tag{2}$$

$$\frac{\partial Q}{\partial t}+\frac{\partial (PQ/D)}{\partial x}+\frac{\partial (Q^2/D)}{\partial y}+\mathrm{g}D\frac{\partial \zeta}{\partial y}+\frac{gn^2}{D^{7/3}}Q\sqrt{P^2+Q^2}+\frac{D}{\rho}\frac{\partial P_a}{\partial y}=0 \tag{3}$$

where, ζ is water surface elevation from the still water level (m), P and Q are depth-averaged volume fluxes (m^2/s), g is gravity acceleration (m/s^2), D is total water depth (m), ρ is density of water (kg/m^3), n is Manning's coefficient (s/$m^{1/3}$), and P_a is air pressure (hPa). The nonlinear shallow water equations are solved using the conventional staggered leap-frog finite difference scheme.

The computational domain is divided into finite difference meshes with locally-square girds. A nested grid system is employed to resolve the complicated coastal structures near the coastline. Figure 2(A) shows the computational domains from region A to region E1 and E2. Figures 2(B) and 2(C) show the computational domains and the bathymetry of the detailed region E1 for Younggwang area and the detailed region E2 for Beopsungpo area, respectively. The grid size of the region A is 20 s. in longitudinal direction. Thus, the actual grid size of the region A varies from 465 m to 520 m according to the latitude of the local square grid. Each grid size of sub-regions is subsequently reduced by 1/3 as shown in Table 1. The grid size of detailed regions is 6.2 m to resolve the buildings and roads.

Table 1. *Computational information for Younggwang and Beopsungpo area.*

Region	No. of Grids	Δx (m)	Δt (sec)
A	1842×1918	465~520	
B	607×826	167.4	
C	790×799	55.8	0.3
D	1306×1048	18.6	
E1 (*Younggwang*)	964×1033	6.2	
E2 (*Beopsungpo*)	871×840	6.2	0.1

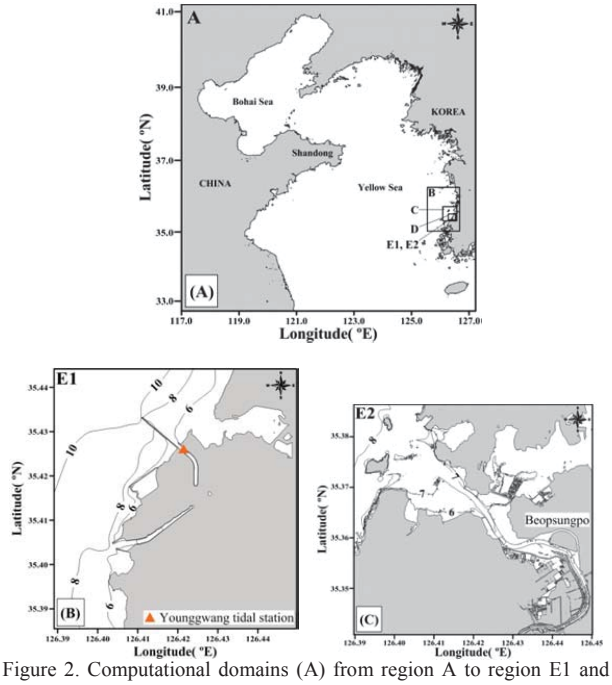

Figure 2. Computational domains (A) from region A to region E1 and E2, (B) region E1 for Younggwang area, and (C) region E2 for Beopsungpo area.

The results were compared with the observed data obtained from the tidal record at the Younggwang tidal station. Finally, the inundation of the meteo-tsunami was simulated for the Beopsungpo of Younggwang area, and the simulated inundation heights were compared with the measured data.

RESULTS

Figure 3 presents the weather charts of KMA (Korea Meteorological Administration) that show the distribution of atmospheric pressure when a meteo-tsunami occurred in 2007. At 21:00 KST (Korean Standard Time) on March 30 a high-pressure is located in the East Sea of Korean Peninsular and a low-pressure is located in the Yellow Sea. They moved eastward due to the westerly winds. This weather chart does not give too

much information whether the atmospheric pressure jump develops or not in this region, because the weather chart shows only the slowly varying changes in the atmosphere. To check the occurrence of pressure jump Eom *et al.* (2012) analyzed the 1-minute meteorological data measured at the AWS (Automatic Weather Station) of KMA as shown in Figure 4. The AWS data shows clearly the pressure jump (marked by two red lines) propagating south-easterly over the Korean Peninsula. The speed of pressure jump was about 25 m/s. Choi *et al.* (2008) was the first to investigate the meteo-tsunami of 2007 by analyzing the meteorological data measured at AWS by KMA.

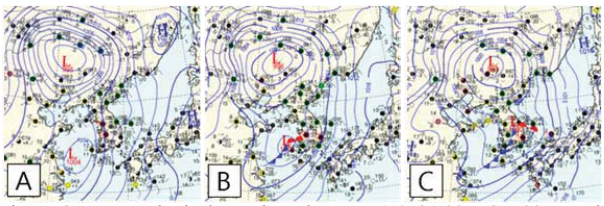

Figure 3. Meteorological weather charts at (A) 21:00 KST 30 March 2007, (B) 00:00 KST 31 March, (C) 03:00 KST 31 March.

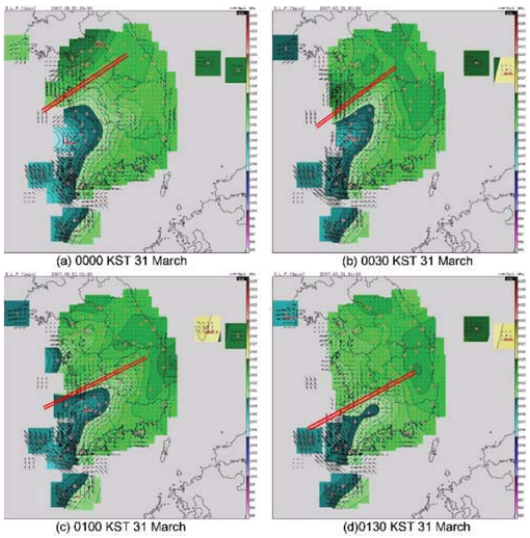

Figure 4. Mean sea level air pressure measured at AWS at (A) 00:00 KST 31 March 2007, (B) 00:30 KST, (C) 01:00 KST, (D) 01:30 KST (Eom *et al.*, 2012).

Figure 5 shows the locations of AWS of KMA along the west coast of Korea and the tidal stations of KHOA (Korea Hydrographic and Oceanographic Administration). Figure 6 shows the 1-minute pressure data observed at AWS at Baekryeong Island (BRI), Kyeokryeolbiyeol Island (KRI), Incheon (IC), Seosan (SS), Kunsan (KS) and Younggwang (YG) . The pressure jump passed over the BRI at 22:41 KST on March 30, 2007, the KRI at 23:46, the IC at 00:01 on March 31, the SS at 00:29, the KS at 01:05, and the YG at 01:29. These arrival times showed that the pressure jump moved south-eastward along the west coast of Korea.

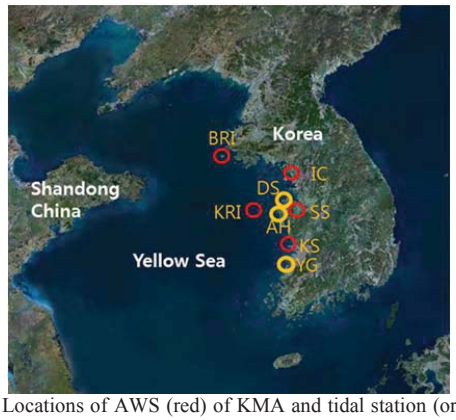

Figure 5. Locations of AWS (red) of KMA and tidal station (orange) of KHOA.

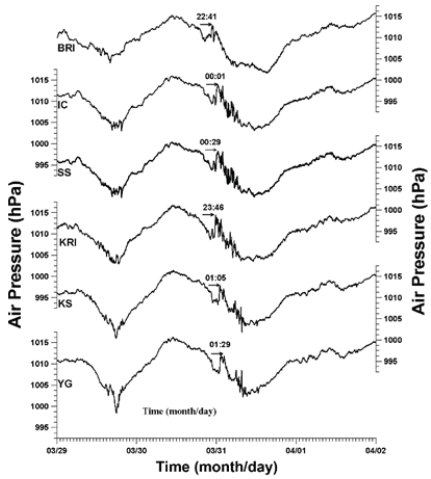

Figure 6. Time histories of atmospheric pressure recorded at various coastal locations for the meteo-tsunami in 2007 (Choi *et al.*, 2008).

Figure 7 shows the water surface displacement due to only the meteo-tsunami by removing the ambient tidal level, and shows also the arrival time of the meteo-tsunami with the surge period of meteo-tsunami. The meteo-tsunami of 2007 has 15-19 minutes of surge period, and it belongs to the intermediate level of long wave. Four surges arrived at most of the tidal stations, and the wave height of first surge was the largest and the second and third surges became weaker and the last surge increased again. At Younggwang tidal station, the third surge was not observed. Choi *et al.* (2008) conducted a numerical simulation of the meteo-tsunami of 2007 using one-dimensional shallow water equations with a simplified step-like atmospheric pressure jump. In the numerical simulation the pressure jump was over-simplified and two-dimensional amplification mechanisms of meteo-tsunami including the refraction and harbor resonance

were neglected. Thus, Choi *et al.* (2008) failed to reproduce well the meteo-tsunami measured at the tidal stations. However, the contribution of the pioneering work of Choi *et al.* (2008) cannot be underestimated in the study of meteo-tsunami occurred in 2007 along the west coast of Korea.

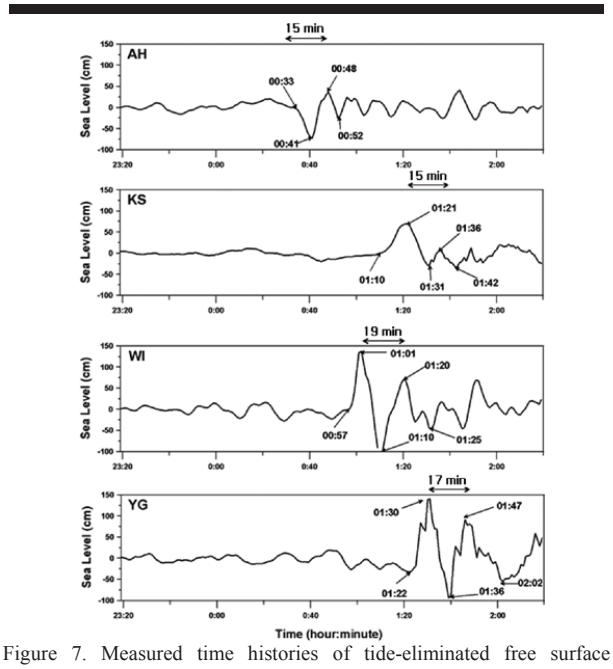

Figure 7. Measured time histories of tide-eliminated free surface displacement due to the 2007 meteo-tsunami at Anheung, Kunsan, Wi Island and Younggwang tidal stations (Choi *et al.*, 2008).

On the other hand, Bae (2012) analyzed the weather charts of KMA and the satellite cloud images on March 30 to 31, 2007 and suggested that the atmospheric pressure jump inducing the meteo-tsunami of 2007 was generated by the interaction of the warm updraft developed in the northern area of Shandong Peninsula and the cold front driven by the large-scale low-pressure located in the Liaoning of China as shown in Figure 8. Once the pressure jump developed, it can propagate in a form of a bore through the strong inversion layer over the Yellow Sea.

Figure 9 shows the shape of pressure jump obtained by removing the ambient pressure from the atmospheric pressure data recorded at Younggwang tidal station. The negative jump, *i.e.,* depression of pressure, occurred first, and then, the positive jump arrived next. The maximum pressure increase due to jump is approximately 9 hPa. The magnitude of pressure jump captured at other AWS locations along the west coast of Korea is smaller than that measured at Younggwang station. The actual shape of the pressure jump during the propagation cannot be obtained, because no meteorological station is deployed over the Yellow Sea. Thus, it is achieved by the so-called inversion problem. Figure 10 shows the free surface displacements corresponding to the elapsed time of the pressure jump propagation.

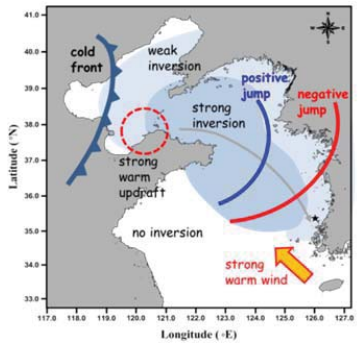

Figure 8. Schematic diagram to descibe the generation mechanism for atmospheric pressure jump occurred in the Yellow Sea in 2007.

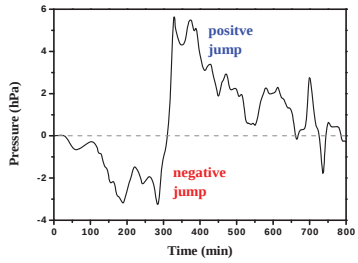

Figure 9. Atmospheric pressure jump obtained by removing the ambient pressure from the measured data at Younggwang tidal station.

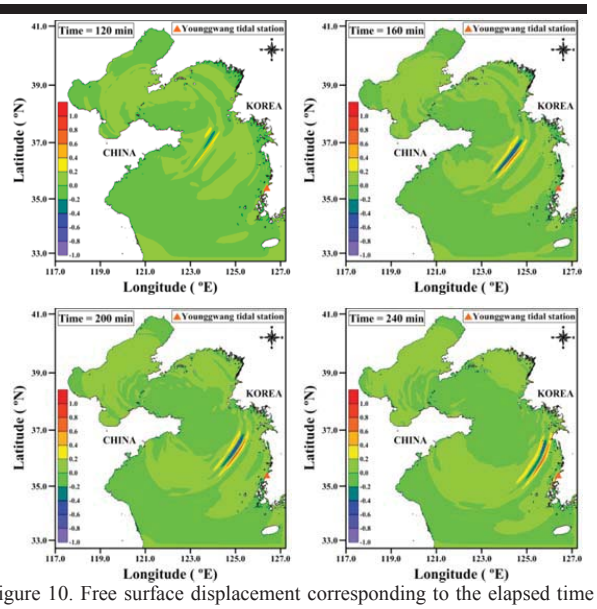

Figure 10. Free surface displacement corresponding to the elapsed time of the pressure jump propagation (Unit: m).

Figure 11 shows the comparison of the calculated and measured water elevations at the Younggwang tidal station. The comparison shows that the calculated wave period and

maximum water elevation of the meteo-tsunami agree well with those of the observations.

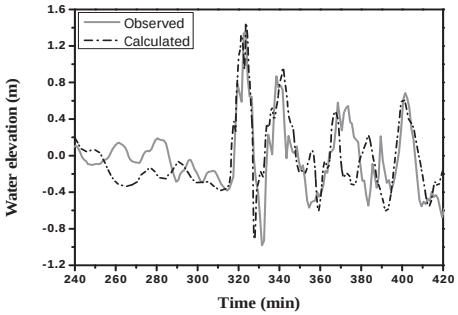

Figure 11. Comparison of observed and calculated time series at Younggwang tidal station.

Figure 12 shows the numerical simulation of the inundation of the buildings at Beopsungpo area. Good agreements are achieved between the simulated and measured maximum inundation heights of 5.61 m above mean sea level.

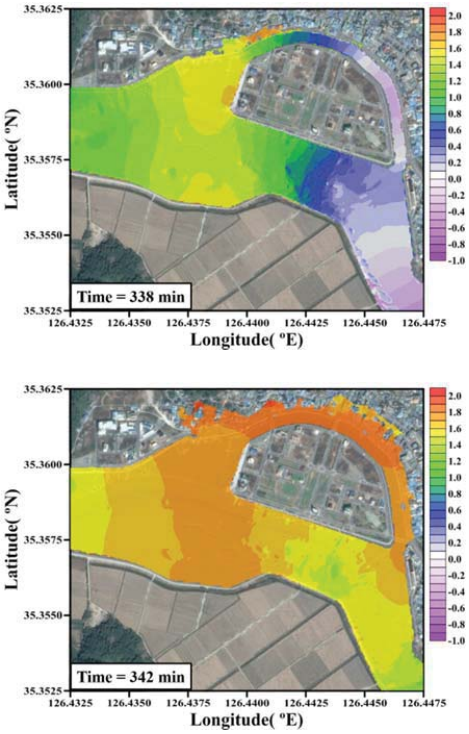

Figure 12. Inundation height at Beopsungpo due to the meteo-tsunami occurred in 2007 (Unit: m).

CONCLUSIONS

In this study the generation mechanism of the atmospheric pressure jump and its resultant meteo-tsunami were investigated by analyzing the weather charts, the observed atmospheric pressure data and the tidal records. In order to verify the relation between the atmospheric pressure jump and the meteo-tsunami, numerical simulations were performed. The calculated results were compared with the observed data obtained from the tidal record at the Younggwang tidal station. The inundation of the meteo-tsunami was also simulated for the Beopsungpo of Younggwang area, and the simulated inundation heights were compared with the measured data. Even though the comparisons showed good agreements, the information on the atmospheric pressure jump from the source region to the west coast of Korea was not verified due to the lack of detailed observed data. Thus, further efforts to secure the meteorological data from China is required.

ACKNOWLEDGMENTS

This study was performed by a project of “Investigation of large swell waves and rip currents and development of the disaster response system (No. 20140057)” sponsored by the Ministry of Oceans and Fisheries of Korea.

LITERATURE CITED

Bae, J.S., 2012. Study of Meteorological Tsunamis Generated in the Yellow Sea. Seoul, Korea: Hanyang University, Ph.D. dissertation.

Choi, B.J.; Park, Y., and Kwon, K., 2008. Generation and Growth of Long Ocean Waves along the West Coast of Korea in March 2007. *Ocean and Polar Research*, 30(4), 453-466.

Eom, H.M.; Seung, Y.H.; Woo, S.B., and You, S.H., 2012. Analysis of Abnormal Wave at the West Coast on 31 March 2007. *Journal of Korean Society of Coastal and Ocean Engineers*, 24(3), 217-227.

Monserrat, S.; Vilibic, I., and Rabinovich, A.B., 2006. Meteotsunamis: atmospherically induced destructive ocean waves in the tsunami frequency band. *Natural Hazards and Earth System Sciences*, 6, 1035-1051.

Yoon, S.B. and Cho, J.H., 2001. Numerical simulation of coastal inundation over discontinuous topography. *Water Engineering Research*, Korea Water Resources Association, 2(2), 75-87.

Yoon, S.B.; Shin, C.H., and Bae, J.S., 2014. Analysis of generation and amplification mechanism of abnormal waves occurred along the west coast of Korea. *Journal of Korean Society of Coastal and Ocean Engineers*, 26(5), 314-326.

Journal of Coastal Research	SI	75	1207 - 1211	Coconut Creek, Florida	2016

New Understanding on the Distribution of Individual Wave Overtopping Volumes over a Levee under Negative Freeboard

Yi Pan[†*], Lin Li[‡], Farshad Amini[‡], Cuiping Kuang[††], and Yongping Chen[†]

[†]College of Harbor, Coastal and Offshore Engineering
Hohai University
Nanjing, Jiangsu 210098, China

[‡]Department of Civil and Environmental Engineering
Jackson State University
Jackson, MS 39217, USA

[††]Department of Hydraulic Engineering
Tongji University
Shanghai 200092, China

www.cerf-jcr.org

www.JCRonline.org

ABSTRACT

Pan, Y.; Li, L.; Amini, F.; Kuang, C.P., and Chen, Y.P., 2016. New understandings on the distribution of individual wave overtopping volumes over a levee under negative freeboard. *In:* Vila-Concejo, A.; Bruce, E.; Kennedy, D.M., and McCarroll, R.J. (eds.), *Proceedings of the 14th International Coastal Symposium* (Sydney, Australia). *Journal of Coastal Research*, Special Issue, No. 75, pp. 1207 - 1211. Coconut Creek (Florida), ISSN 0749-0208.

This paper presents some new understanding on the distribution of individual wave overtopping volumes under combined wave and surge overtopping conditions. Two-parameter Weibull distribution was utilized to present the distribution of the individual wave overtopping volumes. In different studies, the best-fit values of Weibull factors were fitted with different proportions of the sample values, *e.g.*, all values, upper 50 % and upper 10 % of the values. In this paper, the performances of the Weibull factors fitted with different proportions of the data were assessed based on an analysis of the data of full-scale flume tests. Comparisons and discussions were made among the best fits with different proportions of the sample values. Mean and maximum values of the individual wave overtopping volumes calculated from the Weibull factors were compared to the measured ones. The results show that the maximum values are underestimated by the Weibull factors fitted with the upper parts of the data. It is suggested to use all proportion in Weibull curve fitting of individual wave overtopping volumes.

ADDITIONAL INDEX WORDS: *Weibull distribution, combined wave and surge overtopping, full-scale tests.*

INTRODUCTION

Combined wave and surge overtopping is the wave overtopping under negative freeboard (Figure 1). It means that the wave overtopping occurs at the same time as storm surge overflow and may cause more severe damage than wave-only overtopping and surge-only overflow (Hughes and Nadal, 2009). Combined wave and surge overtopping has become an issue of concern in coastal engineering since hurricane Katrina, where studies show that it may be responsible for a large part of the levee failures (ASCE Hurricane Katrina External Review Panel, 2007). Studies have been conducted on the overtopping discharge, flow structure, and levee erosion processes of combined wave and surge overtopping (*e.g.*, Hughes and Nadal, 2009; Reeve *et al.*, 2008; Li *et al*., 2012; Pan *et al.*, 2013; Pan *et al.*, 2015; Pullen *et al*., 2007; Schüttrumpf *et al*., 2001).

This paper presents some new discussion on the distribution of individual overtopping volume of combined wave and surge overtopping. The individual wave overtopping volume is one of the most concerned parameters of combined wave and surge overtopping as it is an important factor in design criteria of the sea defense structures, as suggested by Franco *at al*. (1994).

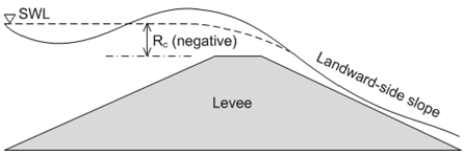

Figure 1. Combined wave and surge overtopping.

Franco *et al.* (1994) and van der Meer and Janssen (1994) used the Weibull distribution to represent the distribution of individual overtopping volumes under wave-only overtopping conditions. The research of Hughes *et al.* (2012), Nørgaard *et al*. (2014), Pullen *et al*. (2007), Victor *et al*. (2012) extend the understanding on the distribution of individual overtopping volume of wave-only overtopping under different water depth and levee slopes.

The Weibull distribution was also used to represent the distribution of individual overtopping volume of combined wave and surge overtopping (*e.g.*, Hughes and Nadal, 2009; Pan *et al.*, 2015). Flume experiments were conducted and equations were provided to estimate the shape factor and scale factor of Weibull distribution presenting the individual overtopping volumes.

DOI: 10.2112/SI75-242.1 received 15 October, 2015; accepted in revision 15 January, 2016.
*Corresponding author: panyi21hhu@gmail.com
©Coastal Education and Research Foundation, Inc. 2016

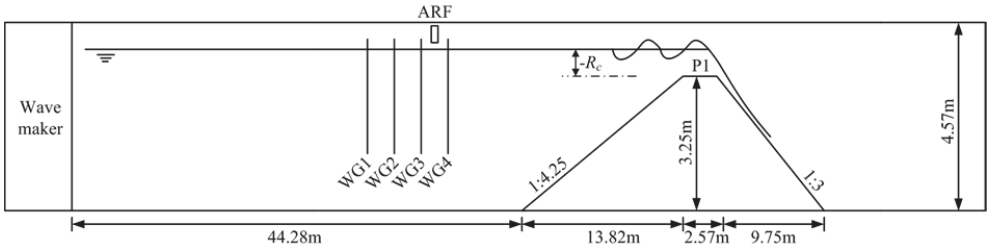

Figure 2. Illustration of the LWF and the full-scale test set-up.

However, in some cases the Weibull distribution could not fit all of the individual overtopping volumes well, and therefore in some studies only large individual wave volumes were used to achieve a best fit, *e.g.*, in Victor *et al*. (2012) only the individual volumes that larger than the average wave volume V_{mean} were used, and in Hughes *et al*. (2012) only the upper 10 % of the wave volumes were used. In this paper, different proportions of the individual wave overtopping volumes, *i.e.*, all values, upper 50 % and upper 10 % of the values, were used to get the best-fit Weibull factors, and new empirical relationships for the Weibull factors were proposed. The performances of different sets of Weibull factors were assessed by comparisons between the measured mean and maximum individual overtopping volumes and the estimated ones with different Weibull factors. The results suggest that the Weibull factors fitted with all values performs better in estimation of the characteristic individual overtopping volumes.

METHODS

The two-parameter Weibull distribution was used to present the individual wave overtopping volume of combined wave and surge overtopping. The measurements of full-scale flume tests of Li *et al*. (2012) and Pan *et al*. (2013) were used for analysis.

Laboratory experiments

The laboratory tests were conducted in the Large Wave Flume (LWF) of the O.H. Hinsdale Wave Research Laboratory (HWRL) at Oregon State University. A definition sketch of the test set-up is shown in Figure 2. The LWF is a 104 m × 3.66 m × 4.57 m (length × width × height) flume equipped with a unidirectional piston wave maker. The levee model was built with a sand core and a concrete cap. A test section was reserved in the landward-side slope to test the anti-erosion performances of different levee strengthening system; however, in this paper the erosion aspect is not discussed.

Irregular wave time series realization was generated conforming to the idealized TMA (Texel-Marsen-Arsloe) wave spectrum, which is a modified JONSWAP spectrum for better performance in shallow water. A total of 24 different conditions were designed with different upstream heads and incident wave conditions. Four surface-piercing wave gauges were placed near the seaward-side toe of the levee to record the time series of water level and separate the incident and reflected waves. The Acoustic Range Finder, ARF, placed between WG 3 and WG 4 was used to calibrate the wave gauges. The flow depths and flow velocities at P1 were recorded by ARF sensor and Acoustic Doppler Velocimetry (ADV) sensors, respectively. One ARF sensor and two ADV sensors at different elevations are installed. A pump system was used to provide return flow to counterbalance the overtopping discharge.

Weibull distribution

Weibull distribution is widely used to present the distribution of individual overtopping volumes under wave-only overtopping and combined wave and surge overtopping condition. The probability distribution function is given by

$$P_V = P(V_i \le V) = 1 - \exp[-(\frac{V}{a})^b] \tag{1}$$

where P_V is the probability of the overtopping volume per wave V_i being less than or equal to V, a is the scale factor and b is the shape factor.

The scale factor a and the shape factor b are the two factors that control the shape of the Weibull distribution. Based on the 25-to-1 laboratory tests, Hughes and Nadal (2009) gives equations to estimate the factors as

$$a = 0.79 q_{ws} T_p \tag{2}$$

$$b = 15.7\left(\frac{q_s}{gT_p H_{m0}}\right)^{0.35} - 2.3\left(\frac{q_s}{\sqrt{gH_{m0}^3}}\right)^{0.79} \tag{3}$$

where q_{ws} is the average discharge of combined wave and surge overtopping, T_p is the peak wave period, q_s is the surge-only overflow discharge under the same freeboard, H_{m0} is the energy-based significant wave height, g is the gravity.

It should be noted that the hydraulic parameters (*e.g.*, the average overtopping discharge q_{ws}) of the combined wave and surge overtopping show different behaviors in different ranges of the relative freeboard R_c/H_{m0} (*i.e.*, $R_c/H_{m0} < -0.3$ and $-0.3 \le R_c/H_{m0} < 0$), Pan *et al*. (2015) classified the cases with $R_c/H_{m0} < -0.3$ as surge dominated cases (SD hereafter) and the cases with $-0.3 \le R_c/H_{m0} < 0$ as wave dominated cases (WD hereinafter). For SD cases and WD cases, modified equations were proposed separately to provide better estimations of the shape parameter b. The equations are given as

$$b = 73.55\left(\frac{q_{ws}}{gH_{m0}T_p}\right)^{0.76} \quad \text{for} \quad R_c / H_{m0} \le -0.3 \tag{3}$$

$$b = 54.58\left(\frac{q_{ws}}{gH_{m0}T_p}\right)^{0.63} \quad \text{for} \quad -0.3 < R_c / H_{m0} < 0 \tag{4}$$

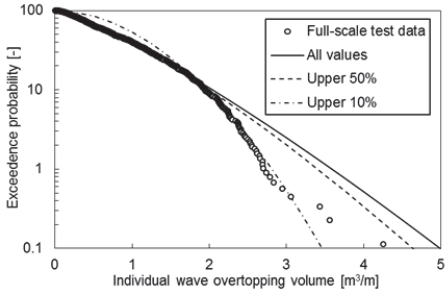

Figure 3. Example of the best fits of Weibull distribution to individual wave overtopping volume to different part of the data.

Pan *et al.* (2015) also proposed an equation for the scale parameter a based on the full-scale test data as

$$a = 1.017 q_{ws} T_{m-1,0} \tag{5}$$

where $T_{m-1,0}$ is the mean (energy) wave period.

Using both wave-only overtopping data and combined wave and surge overtopping data of van der Meer and Janssen (1994), Hughes and Nadal (2009) and Victor *et al.* (2012), Hughes and Nadal gives a general equation for both cases by

$$b = \left(\exp\left(-0.6 \frac{R_c}{H_{m0}} \right) \right)^{1.8} + 0.64 \tag{6}$$

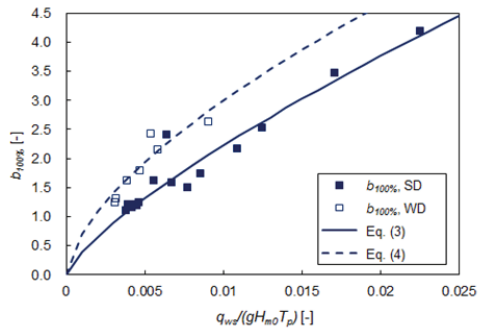

(a) $b_{100\%}$, Eqs. (3) and (4)

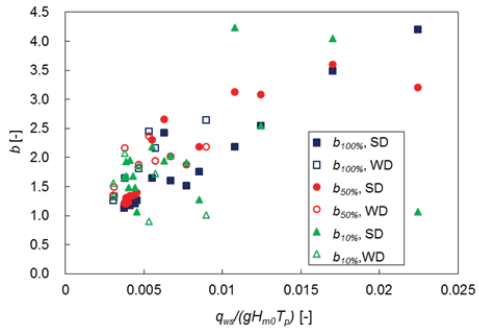

(b) $b_{100\%}$, $b_{50\%}$ and $b_{10\%}$

Figure 4. The Weibull shape parameters $b_{100\%}$, $b_{50\%}$ and $b_{10\%}$ versus dimensionless overtopping discharge.

RESULTS

All values, upper 50 % and upper 10 % of the values, were used separately to get the best fits of the individual overtopping volumes measured in the full-scale test data. Figure 3 shows an example of best-fits of Weibull distribution to different parts of the data. Different scale factors and shape factors were obtained with different parts of the data. For convenience, we used a subscript to denote the part of data used in the fitting, *e.g.*, $b_{50\%}$ denotes the shape factor *b* obtained with upper 50 % of the data.

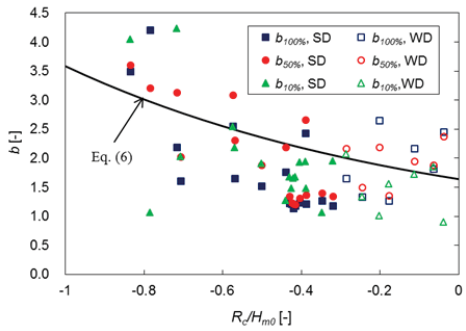

Figure 5. The Weibull shape parameters $b_{100\%}$, $b_{50\%}$ and $b_{10\%}$ versus relative freeboard.

The Weibull shape parameter *b*

The $b_{100\%}$ for SW cases and WD cases were plotted versus dimensionless overtopping discharge $q_{ws}/(gH_{m0}T_p)$ together with Eqs. (3) and (4) in Figure 4(a). The $b_{100\%}$, $b_{50\%}$ and $b_{10\%}$ for all the full-scale tests were plotted versus dimensionless overtopping discharge $q_{ws}/(gH_{m0}T_p)$ in Figure 4(b). As seen, the data spots of $b_{100\%}$ for SW and WD cases have good trends with the increase of the dimensionless parameter $q_{ws}/(gH_{m0}T_p)$, while the $b_{50\%}$ and $b_{10\%}$ show more scattered distributions. The general trends of the three sets of shape parameter *b* are similar, but the exclusive using of the upper parts of the data yields more scattered data. However, it should be mentioned that the scattered data might be induced by the limited numbers of samples after the removal of the small values.

It could also be noticed that in $b_{50\%}$ and $b_{10\%}$ cases (especially for $b_{10\%}$), the deviations between the distributions of surge dominated cases and wave dominated cases are not as significant as that of $b_{100\%}$. One possible explanation is that the upper parts of the data, *i.e.*, the individual overtopping volumes of the large waves, are more controlled by the wave breaking rather than the relative proportion of wave and surge.

Since the distributions of the $b_{50\%}$ and $b_{10\%}$ along the dimensionless overtopping discharge are relatively scattered, we also plot the $b_{100\%}$, $b_{50\%}$ and $b_{10\%}$ versus relative freeboard together with Eq. (6) in Figure 5. As it can be seen, the data spots of $b_{100\%}$, $b_{50\%}$ and $b_{10\%}$ distribute around Eq. (6), but the data spots are also scattered and no significant deviation are found among the general trends of the distributions of $b_{100\%}$, $b_{50\%}$ and $b_{10\%}$. After several attempts based on Figure 4(b) and Figure 5, we tentatively used different dimensionless parameters to

estimate the $b_{50\%}$ and $b_{10\%}$, as plotted in Figure 6. The best-fit curves in Figure 6 are given as

$$b_{50\%} = 25.05\left(\frac{q_{ws}}{gH_{m0}T_p}\right)^{0.5} \tag{7}$$

$$b_{10\%} = 5.004\left(\frac{R_c}{H_{m0}}\right)^{3.261} + 1.418 \tag{8}$$

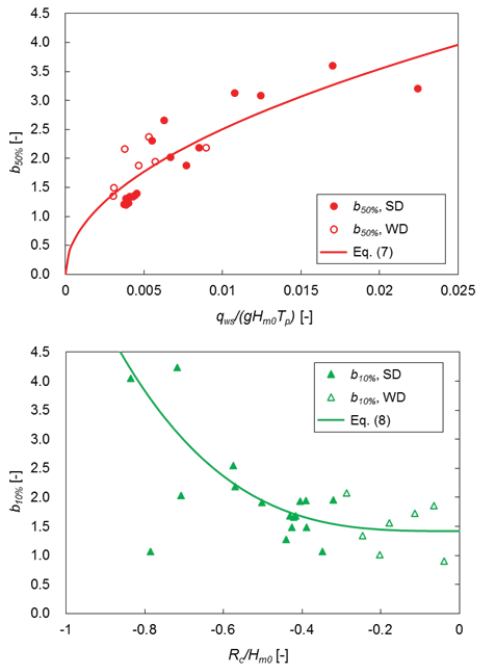

Figure 6. Estimations of the Weibull shape parameters $b_{50\%}$ and $b_{10\%}$ with dimensionless parameters.

The Weibull scale parameter *a*

The Weibull scale parameters $a_{100\%}$, $a_{50\%}$ and $a_{10\%}$ are plotted versus overtopping parameter $q_{ws}T_{m-1,0}$ in Figure 7. According to previous studies, the Weibull scale factor a has a linear relationship with the product of the overtopping discharge and the characteristic wave period of the incident wave, which confirms Figure 7. It can be seen that the distributions of $a_{100\%}$, $a_{50\%}$ and $a_{10\%}$ are close to each other, so we use a general form of equation to estimate Weibull scale factor a by

$$a = k_a q_{ws} T_{m-1,0} \tag{9}$$

where k_a is an empirical parameter, which could be taken as 1.017 for $a_{100\%}$, 1.041 for $a_{50\%}$ and 1.037 for $a_{10\%}$.

DISCUSSION

Now we have the $b_{100\%}$, $b_{50\%}$, $b_{10\%}$, $a_{100\%}$, $a_{50\%}$ and $a_{10\%}$, both best-fit values from the time series of overtopping discharge and estimations based on the overtopping parameters. However, the question is which ones are better, or which parts of the data should be used in the Weibull curve fitting?

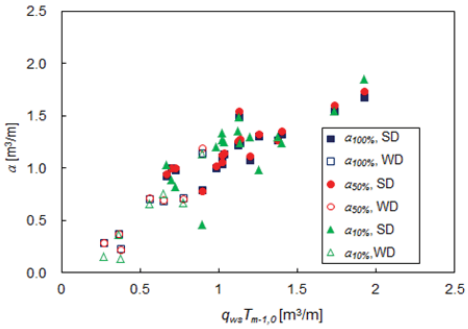

Figure 7. The Weibull scale parameter a versus overtopping parameter $q_{ws}T_{m-1,0}$.

One of the usages of the Weibull factors is the calculation of the mean and maximum values. In this paper comparisons between the measured mean/maximum individual overtopping volumes and the estimated ones with Weibull factors were conducted to study the performances of different sets of Weibull factors. The mean and maximum value of the Weibull distribution can be calculated in terms of the scale factor a and shape factor b as (*e.g.*, Victor *et al.*, 2012)

$$V_{mean} = a \cdot \Gamma\left(1 + \frac{1}{b}\right) \tag{10}$$

$$V_{\max} = a \cdot \left(\ln\left(N+1\right)\right)^{1/b} \tag{11}$$

where Γ is the gamma function and N is the overtopping wave number.

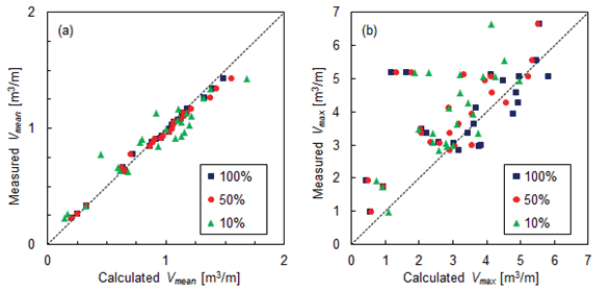

Figure 8. Comparison of measured characteristic overtopping volumes and calculated characteristic overtopping volumes with fitted a and b: (a) V_{mean}, (b) V_{max}.

Firstly the V_{mean} and V_{max} were calculated with the best-fit Weibull factors from the time series of overtopping discharge. The measured values versus calculated values were plotted in Figure 8. The estimation of the V_{mean} was good and the estimation of V_{max} was mediocre but reasonable. The root-mean-square errors (RMSE) of the calculations of V_{mean} with $a_{100\%}$ and $b_{100\%}$, $a_{50\%}$ and $b_{50\%}$, and $a_{10\%}$ and $b_{10\%}$ are 0.035, 0.053, and 0.133 respectively. The root-mean-square errors (RMSE) of the calculations of V_{max} with $a_{100\%}$ and $b_{100\%}$, $a_{50\%}$ and $b_{50\%}$, and $a_{10\%}$ and $b_{10\%}$ are 1.303, 1.330, and 1.332 respectively. It can be seen

that for the calculation of both V_{mean} and V_{max}, the fitted $a_{100\%}$ and $b_{100\%}$ perform better.

Then the V_{mean} and V_{max} were calculated with the estimations of Weibull factors based on the overtopping parameters. The measured value versus calculated value was plotted in Figure 9. The estimation of the V_{mean} was good and the estimation of V_{max} was mediocre but reasonable. The root-mean-square errors (RMSE) of the calculations of V_{mean} with $a_{100\%}$ and $b_{100\%}$, $a_{50\%}$ and $b_{50\%}$, and $a_{10\%}$ and $b_{10\%}$ are 0.142, 0.149, and 0.151 respectively. The root-mean-square errors (RMSE) of the calculations of V_{max} with $a_{100\%}$ and $b_{100\%}$, $a_{50\%}$ and $b_{50\%}$, and $a_{10\%}$ and $b_{10\%}$ are 1.389, 1.625, and 1.638 respectively. It can be seen that for the calculation of both V_{mean} and V_{max}, the estimated $a_{100\%}$ and $b_{100\%}$ perform better. Another noticeable thing is that the calculated $a_{50\%}$ and $b_{50\%}$ and $a_{10\%}$ and $b_{10\%}$ tend to underestimate the large waves.

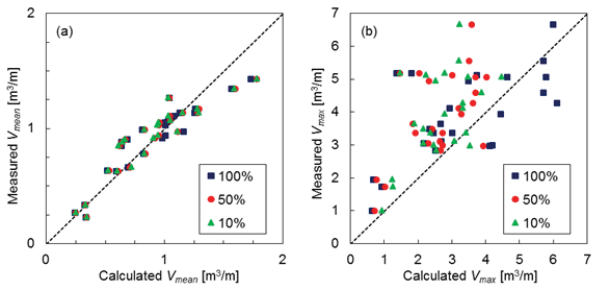

Figure 9. Comparison of measured characteristic overtopping volumes and calculated characteristic overtopping volumes with estimated *a* and *b*: (a) V_{mean}, (b) V_{max}.

CONCLUSIONS

In this work we present new understanding on distribution of individual wave overtopping volumes under combined wave and surge overtopping condition. The analysis was based on full-scale flume tests. Two-parameter Weibull distribution was used to present the distribution of the individual wave overtopping volumes. Different proportions of the sample values, *e.g.*, all values, upper 50 % and upper 10 % of the values, were used to get the best fit and calculate the corresponding Weibull factors. New empirical relationships for the Weibull factors $b_{50\%}$, $b_{10\%}$, $a_{50\%}$ and $a_{10\%}$ were proposed.

Mean and maximum values of the individual overtopping volume were calculated with both the fitted and estimated values of Weibull factors $b_{100\%}$, $b_{50\%}$, $b_{10\%}$, $a_{100\%}$, $a_{50\%}$ and $a_{10\%}$. Calculated values were compared to the measured ones. The comparisons show that for the calculation of the mean and maximum individual overtopping volume, the Weibull factors $a_{100\%}$ and $b_{100\%}$ perform better than then Weibull factors obtained from the upper parts of the data. Hence, it is suggested to use all proportion in Weibull curve fitting of individual wave overtopping volumes to have better performance in estimation of characteristic individual overtopping volumes.

However, it is noticeable that the poor performances of the Weibull factors fitted from the upper parts of the data may result from the limited numbers of samples after the removal of the small values. Future research is needed on this regard.

ACKNOWLEDGMENTS

We sincerely thank the supports from the National Natural Science Foundation of China (51309092, 51379072), the Natural Science Fund for Colleges and Universities in Jiangsu Province (BK20130833), the Fundamental Research Funds for the Central Universities (2015B16014).

LITERATURE CITED

ASCE Hurricane Katrina External Review Panel, 2007. *The New Orleans Hurricane Protection System: What Went Wrong and Why?* Reston, Virginia: American Society of Civil Engineers, 92p.

Franco, L.; de Gerloni, M., and van der Meer, J.W., 1994. Wave overtopping on vertical and composite breakwaters. *Coastal Engineering Proceedings*, 24, 1030-1044.

Hughes, S.A. and Nadal, N.C., 2009. Laboratory study of combined wave overtopping and storm surge overflow of a levee. *Coastal Engineering*, 56(3), 244-259.

Hughes, S.A.; Thornton, C.I.; van der Meer, J.W., and Scholl, B.N., 2012. Improvements in describing wave overtopping processes. *Coastal Engineering Proceedings*, 33, waves-35.

Li, L.; Pan, Y.; Amini, F., and Kuang, C.P., 2012. Full Scale Laboratory Study of Combined Wave and Surge Overtopping of a Levee with RCC Strengthening System. *Ocean Engineering*, 54(1), 70 – 86.

Reeve, D.E.; Soliman, A., and Lin, P.Z., 2008. Numerical study of combined overflow and wave overtopping over a smooth impermeable seawall. *Coastal Engineering*, 55, 155-166.

Pan, Y.; Kuang, C.P.; Li, L., and Amini, F., 2015. Full-scale laboratory study on distribution of individual wave overtopping volumes over a levee under negative freeboard. *Coastal Engineering*, 97, 11–20.

Pan, Y.; Li, L.; Amini, F., and Kuang, C. P., 2013. Full Scale HPTRM Strengthened Levee Testing under Combined Wave and Surge Overtopping Conditions: Overtopping Hydraulics, Shear Stress and Erosion Analysis. *Journal of Coastal Research*, 29(1), 182-200.

Pullen, T.; Allsop, N.W.H.; Bruce, T.; Kortenhaus, A.; Schüttrumpf, H., and van der Meer, J.W., 2007. *EurOtop: Wave Overtopping of Sea Defences and Related Structures: Assessment Manual*. http:// www.overtopping-manual.com

Schüttrumpf, H.; Möller, J.; Oumeraci, H.; Grüne, J., and Weissmann, R., 2001. Effects of natural sea states on wave overtopping of seadikes. *Proceedings of the 4th International Symposium Waves 2001, Ocean Wave Measurement and Analysis* (San Francisco, California, ASCE), pp. 1565-1574.

van der Meer, J.W. and Janssen, J.P.F.M., 1994. *Wave run-up and wave overtopping at dikes and revetments*. Delft, Netherlands: Delft Hydraulics, 22p.

Victor, L.; van der Meer, J.W., and Troch, P., 2012. Probability distribution of individual wave overtopping volumes for smooth impermeable steep slopes with low crest freeboards. *Coastal Engineering*, 64, 87–101.

Journal of Coastal Research	SI	75	1212 - 1216	Coconut Creek, Florida	2016

Impacts of Submerged Breakwaters on Nearshore Sediment Transport

Shunqi Pan[†*] and George Fairbairn[‡]

† Hydro-environmental Research Centre, School of Engineering, Cardiff University, Cardiff, UK

[‡]School of Engineering, Cardiff University, Cardiff, UK

www.cerf-jcr.org

www.JCRonline.org

ABSTRACT

Pan, S. and Fairbairn, G., 2016. Impacts of Submerged Breakwaters on Nearshore Sediment Transport. *In:* Vila-Concejo, A.; Bruce, E.; Kennedy, D.M., and McCarroll, R.J. (eds.), *Proceedings of the 14th International Coastal Symposium* (Sydney, Australia). *Journal of Coastal Research*, Special Issue, No. 75, pp. 1212 - 1216. Coconut Creek (Florida), ISSN 0749-0208.

Submerged breakwaters have been increasingly popular as the coastal defence structures due to the advantages of the low construction costs and less visual intrusion. However, the impacts of the structures on nearshore sediment transport and beach morphology remain unclear. This paper presents the results of beach morphological changes affected by different submergence of a group of shore-parallel breakwaters under the combined wave and tide conditions from a depth-average process-based coastal morphological model - COAST2D. In this study, different breakwater crest levels are used in the model under both storm waves and tides based on the field measurements at the Elmer breakwater scheme site to investigate the impacts of the breakwater submergence on nearshore hydrodynamics and morphological changes. The results show that the fully submerged breakwaters produce more stable and balanced sediment loss/gain in the protected area, and yield more desirable formation of salients behind the breakwaters. The results also reveal the complex nearshore processes and morphological changes under the extreme waves for further study.

ADDITIONAL INDEX WORDS: *Submerged breakwaters, morphological change, sediment transport.*

INTRODUCTION

Submerged breakwaters have been increasingly popular as the coastal defence structures due to the advantages of low construction costs and less visual intrusion. However, the impacts of the submergence of the structures on nearshore hydrodynamics, sediment transport and the resulting beach morphological changes remain unclear and hence further investigations are required to achieve a better understanding. This is particularly important for the UK coasts as the majority of the UK coasts experience meso- to macro-tide conditions (Chasten *et al.*, 1993). Traditionally, due to the large tidal ranges, it has been suggested that breakwaters are necessarily to be built as surface-piercing structures at a location closer to the shoreline to prevent waves from overtopping the structures (Dally and Pope, 1986). This will inevitably incur a high cost in construction and maintenance in severe wave conditions (Pilarczyk and Zeidler, 1996). In this study, a two-dimensional depth-average coastal morphological model is used to investigate in detail the impacts of submergence of a group of breakwaters on the nearshore hydrodynamics and morphological changes under the combined wave and tide conditions. The breakwaters used in this study are similar to those at Elmer, located in Bognor Regis on the southern coast of England, as shown in Figure 1. This breakwater scheme consists of 8 surface-piercing, shore-parallel breakwaters, which was built in response to serious storm flooding of the residential hinterland (Cooper *et al.*, 1996).

Figure 1. The Elmer breakwater scheme at high water level (top) and low water level (bottom) (Google Earth, 2015)

The scheme, completed in 1993, is currently managed by the local authority and the UK Environment Agency. Since the completion, the breakwater scheme has performed well in

DOI: 10.2112/SI75-243.1 received 15 October, 2015; accepted in revision 15 January, 2016.
*Corresponding author: PanS2@cardiff.ac.uk
©Coastal Education and Research Foundation, Inc. 2016

stabilising the beach. On the 28-29 October 1996, a severe storm occurred along the south coast of England, which was coincided with large spring tides and strong winds of 90 mph. Waves up to 3.6 m high were recorded. Despite these extreme conditions, no coastal flooding occurred and the breakwaters were considered to have fulfilled their design criteria. The coastal defence scheme was inspected by the Environment Agency in 2014 after the severe flooding experienced in the winter of 2013/14, and it was concluded that overall the defence scheme has been considered a success in protecting the neighbouring residential area.

Elmer Sands exhibits macro-tide conditions, with a mean tidal range of 5.3 m and net sediment drift from west to east (King *et al.*, 2000). The breakwaters at Elmer Sands were constructed to reduce nearshore wave energy and retain the sediment material as a principal form of protection against storm flooding (Holland and Coughlan, 1994). The length of breakwaters ranges from 80 to 140 m, and the gap between the breakwaters ranges from 75 to 130 m. The breakwaters are located approximately 130 m from the shoreline in general. Expect for the breakwater at the far east of the scheme where tombolo is formed, salients are formed behind all other breakwaters, as shown in Figure 1.

METHODS

The model used in this study is a process-based coastal morphological model – COAST2D, which has been developed and refined through a number of research projects. The model consists of fully coupled modules to simulate nearshore hydrodynamics and morphodynamics. The wave module computes wave-period averaged wave energy (wave height) and wave direction by taking account of wave refraction/diffraction, wave breaking and full wave-current interaction for wave transformation from offshore to nearshore. The flow module computes the depth-integrated current velocity and water surface elevation under both tide and wave actions. Morphological changes are determined by computing the sediment transport rates using equilibrium formulae (Soulsby, 1997) in the sediment transport module. The model uses explicit finite difference methods to solve the governing equations. Further details of the model can be found in Pan *et al.* (2009) and Du *et al.* (2010).

In this study, COAST2D is set to an idealised breakwater scheme similar to that at Elmer, and the main focus is to investigate the impacts of breakwater submergence on the nearshore hydrodynamics, sediment transport and the resulting beach morphological changes under different wave and macro-tide conditions. Figure 2 shows the computational domain used, in which 5 representative breakwaters are installed at approximately 250 m from the shoreline, where the mean water depth is approximately 12.5 m. The length of the breakwaters and the gap between breakwaters are both set to 250 m. The initial beach slope is 1:20 in the nearshore area and the beach is set to be flat from 20 m water depth seawards. Uniform sediment with the medium grain size (D_{50}) of 250 μm is used over the entire computational domain. To consider the breakwater submergence, 3 different crest levels (Zc) of the breakwaters are set. They are: 3.0 m above the mean sea level to represent the surface piecing breakwaters; 2 m below the mean sea level to represent the partly submerged breakwaters; and 4.5 m below the mean sea level to represent the fully submerged breakwaters, respectively. The breakwaters are treated as non-erodible in the morphological computations. M2 tides with a range of 5.5 m are assumed to represent the macro-tide condition at the site.

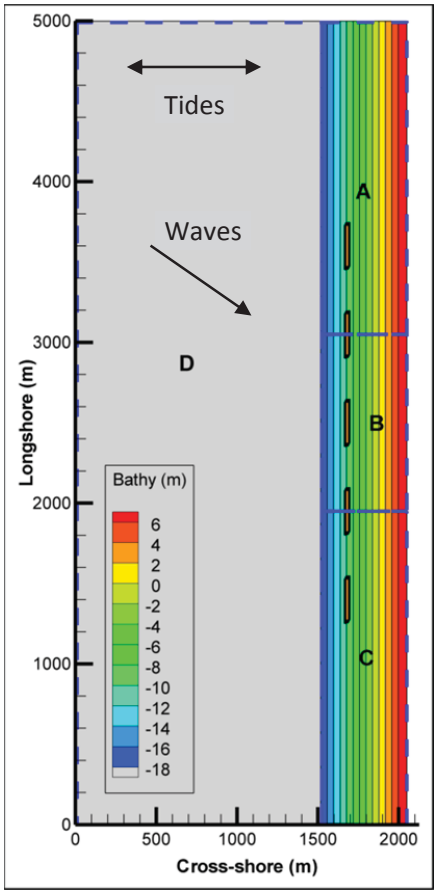

Figure 2. Computational domain and initial bathymetry

Wave data obtained from Channel Coastal Observatory (CCO – http://www.channelcoast.org/), a national network of the regional coastal monitoring programmes for England is used in this study. The wave data was measured at Rustington, some 10 km east of the site, at 30 mins intervals over a period of five years from 2008 to 2012. The data is fully re-analysed, and the results indicate that the majority of waves during this period are south-westerly (within the sector between 210° and 240° from North). Four wave heights, namely 1.5 m, 2.0 m, 2.5 m and 4.0 m, are found to represent approximately top 26% of all waves at the site. Therefore, it is decided that four wave heights described above are used as the incident wave conditions along the offshore boundary of the computational domain. All waves at the offshore boundary are assumed to be predominately south-westerly, *i.e.* at 225° from North. In total 12 cases, as summarised in Table 1, are considered in this study. The wave period is determined from the correlation of the measured wave heights and wave periods (not shown here).

Table 1. *Test Condition.*

Case	*Zc (m)*	H_s (m)	T_p (m)
1	3.0	1.5	7.0
2	3.0	2.0	7.5
3	3.0	2.5	8.0
4	3.0	4.0	8.5
5	-2.0	1.5	7.0
6	-2.0	2.0	7.5
7	-2.0	2.5	8.0
8	-2.0	4.0	8.5
9	-4.5	1.5	7.0
10	-4.5	2.0	7.5
11	-4.5	2.5	8.0
12	-4.5	4.0	8.5

RESULTS AND DISCUSSION

The COAST2D model is run for each case listed in Table 1 over a period of 126 hours in total, of which the morphological changes are computed for 120 hours, as the first 6 hours are used as the lead-in time to ensure the stability of the simulations. Figure 3 shows the computed wave heights (contours) and flow velocities (vectors) in the central area of the breakwater scheme with three different breakwater crest levels at the high water level. The incident wave height is 2.0 m and the wave period is 7.5 s for these cases.

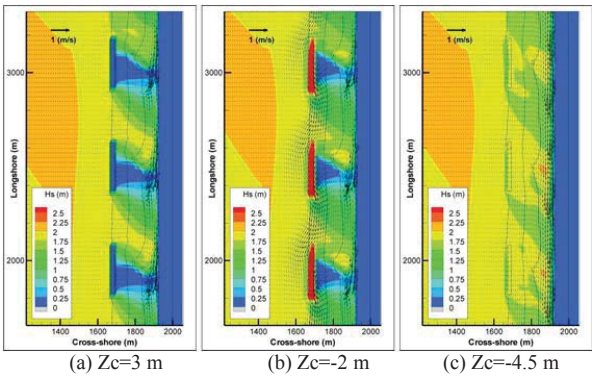

(a) Zc=3 m (b) Zc=-2 m (c) Zc=-4.5 m

Figure 3 Computed wave height (contours) and flow velocity (vectors) with different crest levels of breakwaters for Cases 2, 6 and 10 (Hs=2.0 m, Tp=7.5 s) at high water level

Figure 3(a) is for the case with the highest breakwater crest level (Zc=3 m). It can be found that waves are completely blocked by the breakwaters, resulted in a clear wave diffraction zone in the lee side of the breakwaters. The diffracted waves induce strong longshore currents along the shoreline. In Figure 3(b), the crest level of the breakwaters is 2 m below the mean sea level (Zc=-2 m) and the breakwaters are submerged at this tidal stage. It can be seen that the wave energy accumulates in the front of breakwaters, and the wave refraction from the breakwaters generates strong flow jets in the area adjacent to the breakwaters from top of the breakwaters to the gaps of embayment. The wave diffraction also induces strong circulations in the lee side of the breakwaters. For the fully submerged breakwaters (Zc=-4.5 m) as shown in Figure 3(c), the alongshore flow is slightly refracted by the breakwaters and the strong longshore currents are found to be close to shoreline. Changes in wave height are small in the nearshore area behind the breakwaters.

Figure 4 shows the computed wave heights and current velocities at the low water level in a similar way as those shown in Figure 3. At the low water level, both Figure 4(a) and Figure 4(b) show a similar flow pattern, indicating that waves are seen largely blocked by the breakwaters, where the strong alongshore currents are found parallel to the shoreline within the embayment. However, in Figure 4(c), the breakwaters are submerged, and the wave refraction over the breakwaters creates strong flow circulations in the updrift of the breakwaters and strong flow streams towards and over the embayment.

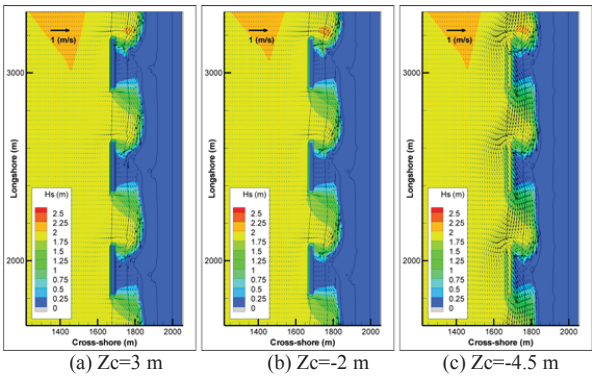

(a) Zc=3 m (b) Zc=-2 m (c) Zc=-4.5 m

Figure 4 Computed wave height (contours) and flow velocity (vectors) with different crest levels of breakwaters for Cases 2, 6 and 10 (Hs=2.0 m, Tp=7.5 s) at low water level

Figure 5 shows the final bathymetries for Cases 3, 7 and 11, where Hs=2.5 m and Tp=8.0 s, representing a moderate storm event. From Figure 5, it can be seen that the crest level of the breakwaters has a profound impact on the beach morphology. In Figure 5(a), tombolos are formed behind the surface piercing breakwaters over the duration of 120 hours. In Figure 5(b) with the partly submerged breakwaters, the formation of tombolos is also found. However, with fully submerged breakwaters, as shown in Figure 5(c), only salients are formed. The results show that for the storm conditions such as those used in this study, the fully submerged breakwaters can produce more desirable results for the coastal protection with the formation of salients. For the other cases where the wave heights are 1.5 m, 2 m and 4 m, the results (not shown here) also indicate the similar patterns. This clearly demonstrates that the fully submerged breakwaters can not only reduce the construction costs, but also yield more desirable outcome as the coastal defence structures.

Figure 6 shows the total bed level changes (BLC) in the central area of the computational domain for the cases shown in Figure 5 (*i.e.* Cases 3, 7 and 11, with Hs=2.5 m and Tp=8.0 s). In Figure 6(a), the sediment accretion occurs mainly in the lee side of the breakwaters and erosion occurs in the embayment. The maximum accretion is up to 5 m in the locations immediately behind the breakwaters, forming part of the tombolos. Erosion is found in the embayment up to -3 m. With the decrease of the breakwater crest level, the position of the sediment deposition tends to move seawards.

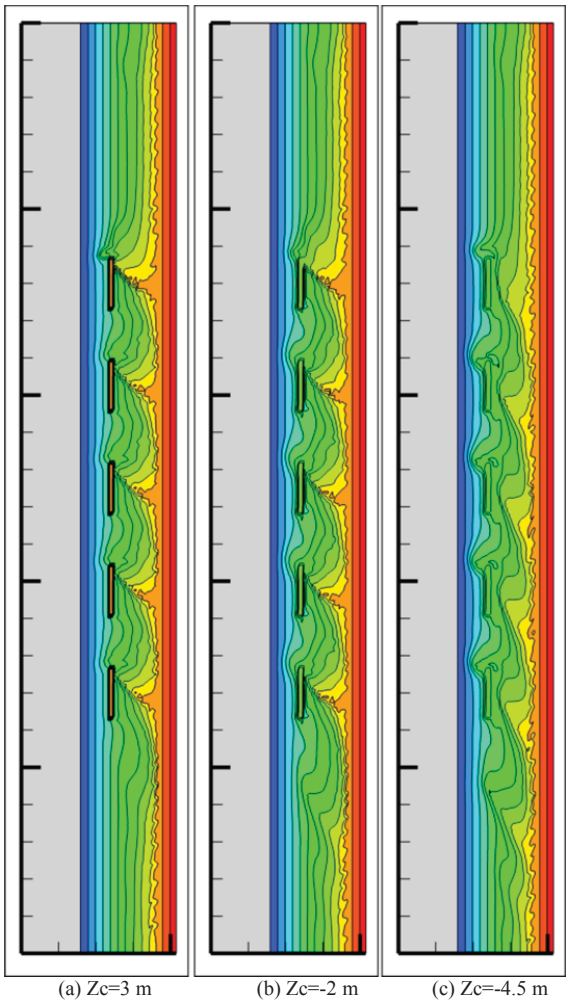

(a) Zc=3 m (b) Zc=-2 m (c) Zc=-4.5 m

Figure 5. Computed final bathymetries over 120 hours for Cases 3, 7 and 11 (Hs=2.5 m, Tp=8 s)

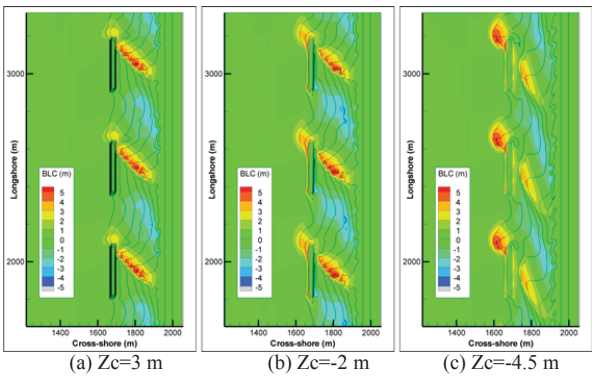

(a) Zc=3 m (b) Zc=-2 m (c) Zc=-4.5 m

Figure 6. Computed bed level changes (BLC) for Cases 3, 7 and 11 (Hs=2.5 m, Tp=8 s) (Isolines indicate the corresponding bathymetry)

Figure 7 shows the total bed level changes (BLC) for Cases 4, 8 and 12 with Hs=4 m and Tp=8.5 s, the highest waves amongst all test cases. For the surface piercing breakwaters, as shown in Figure 7(a), the sediment deposition in the area behind the breakwaters increases significantly, compared with that shown in Figure 6(a). The erosion in the embayment also increases. In Figure 7(b), although more sediment deposition is found in the front of breakwaters, the erosion in the embayment has further increased (deeper than 5 m). For the fully submerged breakwaters as shown in Figure 7(c), however, the deposition and erosion are more evenly distributed as those shown in Figure 6(c), which can be regarded as the more favourable outcome of the design of the breakwaters.

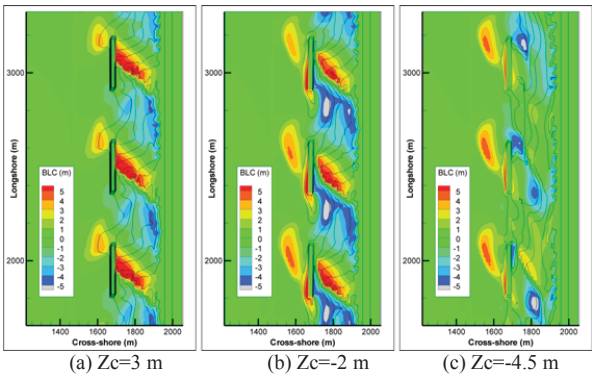

(a) Zc=3 m (b) Zc=-2 m (c) Zc=-4.5 m

Figure 7. Computed bed level changes (BLC) for Cases 4, 8 and 12 (Hs=4.0 m, Tp=8.5 s) (Isolines indicate the corresponding bathymetry)

The sediment volumetric changes over 4 areas in the computational domain, as indicated as A, B, C, and D in Figure 2, are calculated and analysed. Areas A, B and C are defined to examine the sediment volumetric changes in the nearshore zones strong affected by the breakwaters, and Area D is defined to examine effect of breakwaters on cross-shore sediment movement between offshore and nearshore areas. However, in this paper, only the sediment volumetric changes over the entire computational domain (A+B+C+D) are presented. Figure 8 shows the total sediment volumetric changes for all cases in 3 groups (Cases 1-4, 5-8 and 9-12) according to the breakwater crest level. It should be noted that since the sediment volumetric changes for cases with Hs=4 m and Tp=8.5 s are much larger than those for other cases, for the sake of clarity, the sediment volumetric changes for these 3 cases have been downscaled by a factor of 4 (as indicated as "/4") in Figure 8. For the surface piecing breakwaters, the net loss of the sediment volume is found for three different wave conditions to be in the range of: ~25,000 m^3 with Hs=1.5 m; ~250,000 m^3 with Hs=2.5 m; and ~1,200,000 m^3 for Hs=4 m over the computational duration (120 hours) due to the morphological changes. For the partly submerged breakwaters, the loss of sediment generally decreases when Hs<4 m. For case with Hs=4 m, the loss of sediment volume increases instead. However, the sediment volume changes for the fully submerged breakwaters appear to be more stable for all wave conditions, particularly when Hs<4 m. For Hs=4 m, the loss of the sediment volume is significantly reduced in comparison with other cases. The results clearly indicate the

complex processes and interaction between the hydrodynamics, morphodynamics and the nearshore structures. The reasons for having different patterns of sediment volumetric changes are unclear and further investigation is therefore required.

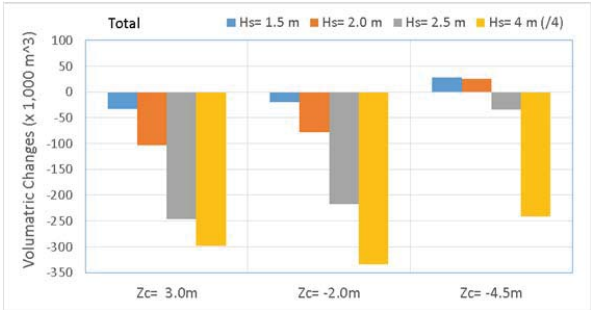

Figure 8. Total sediment volumetric changes for all 12 cases

CONCLUSIONS

In this study, a depth-average coastal morphological model - COAST2D is set up for an idealised breakwater scheme similar to that at Elmer in southern England. The model has been applied to the test site with 3 different crest levels of breakwaters ranging from surface piercing, partly submerged to fully submerged, combined with 4 different wave conditions under a constant macro-tide condition over a period of 120 hours. The impacts of the breakwater submergence on the beach morphological changes are investigated. The results show that the breakwater submergence can significantly change the hydrodynamics in the nearshore area and result in considerable changes of beach morphology under storm conditions. The fully submerged breakwaters produce more stable and balanced sediment loss/gain in the protected area, and yield more desirable formation of salients behind the breakwaters. Further to the previous studies on the submerged and/or low-crested breakwaters in Europe and worldwide (Kramer *et al.*, 2005; Lamberti *et al.*, 2006; Zanuttigh and Martinelli, 2008; Marcinkowski and Szmytkiewicz, 2013), the results presented in this paper reveal the complex nearshore processes and morphological changes under the extreme waves, particularly when Hs>4 m in this study, which require further investigations.

LITERATURE CITED

Chasten, A., Rosati, J., and McCormick, J., 1993. Engineering Design Guidance for Detached Breakwaters as Shoreline Stabilization Structures, *Coastal Engineering Research Center*, *U.S. Army Corps of Engineers, Waterways Experiment Station*, CERC-93-19.

Cooper, N.J., King, D.M., and Hooke, J.M., 1996. Collaborative Research Study at Elmer Beach, West Sussex, UK. In: Taussik, J., Mitchell, R. (Eds.), *Partnership in Coastal Engineering*. Samara Press, Cardigan, 369 – 376.

Dally, W.R. and Pope, J., 1986. Detached breakwaters for shore protection. *Coastal Engineering Research Center*, USACE

Du, Y., Pan, S. and Chen, Y., 2010. Modelling the effect of wave overtopping on nearshore hydrodynamics and morphodynamics around shore-parallel breakwaters, *Coastal Engineering*, 57(9), 812-826

Holland B. and Coughlan P., 1994. The Elmer Coastal Defence Scheme, *Proceedings of MAFF Conference of River and Coastal Engineers*, Paper 7.1

King, D.M., Cooper, N.J., Morfett, J.C., and Pope, D.J., 2000. Application of offshore breakwaters to the UK: a case study at Elmer beach. *Journal of Coastal Research,* 16 (1), 172 – 187

Kramer, M., Zanuttigh, B., Van Der Meer, J.W., Vidal, C. and Gironella, F.X., 2005. Laboratory experiments on lowcrested breakwaters. *Coastal Engineering,* 52(DELOS Special Issue), 867-885.

Lamberti, A., Zanuttigh, B. and Martinelli, L., 2006. Wave overtopping and transmission: an interpretation of spectral change at low crested rubble-mound structures. *Coastal Engineering 2006*, Vol. 5, 4628-4640.

Marcinkowski, T. and Szmytkiewicz, M., 2013. Performance of submerged breakwaters as improvement of beach fill effectiveness in Gdynia, Poland. *Journal of Coastal Research*, SI(65), 326-331

Pan, S., 2009. Beach nourishment modelling: impact of coastal structures, *Coasts, Marine Structures and Breakwaters 2009: Adapting to Change*, (ed.) N.W.H. Allsop, Thomas Telford Ltd, London, Vol 2, 25-35

Pilarczyk, K. and Zeidler, R., 1996. *Offshore breakwaters and shore evolution control*, A. A. Balkema Publishers

Soulsby, R. (1997), *Dynamics of marine sands*, Thomas Telford Ltd

Zanuttigh, B. and Martinelli, L., 2008. Transmission of wave energy at permeable low crested structures. *Coastal Engineering*, 55(12), 1135-1147.

Journal of Coastal Research	SI	75	1222 - 1226	Coconut Creek, Florida	2016

Beach Hazard and Risk Perception of Lifeguards Working in a Macrotidal Amazon Beach

Wilson C. Brito[†], Luci C.C. Pereira[†*], Rosygleyse C. Sousa and Andrew D. Short[‡]

[†]Coastal and Estuarine Laboratory,
Coastal Studies Institute
Federal University of Pará
Bragança, Brazil

[‡]School of Geosciences, University of
Sydney, Sydney, NSW 2006, Australia.

www.cerf-jcr.org

www.JCRonline.org

ABSTRACT

Brito, W.C..; Pereira, L.C.C.; Sousa, R.C., and Short, A.D., 2016. Beach hazard and risk perception of lifeguards working in a macrotidal Amazon beach. *In:* Vila-Concejo, A.; Bruce, E.; Kennedy, D.M., and McCarroll, R.J. (eds.), *Proceedings of the 14th International Coastal Symposium* (Sydney, Australia). *Journal of Coastal Research*, Special Issue, No. 75, pp. 1222 - 1226. Coconut Creek (Florida), ISSN 0749-0208.

Amazon sandy beaches attract a large number of beachgoers, mainly during July the school vacation period and beginning of the dry season. Local hydrodynamic processes are related to the presence of moderate wave energy (H_s up to 1.7 m and H_{max} up to 2.0 m), macrotides (around 5.0 m during spring tides), and strong currents (up to 1.5 m/s in the surf zone and more than 2.0 m/s in the tidal channels). These conditions represent hazards to beachgoers, and result in drowning and other injuries. Lifeguard services began in Ajuruteua (Pará) in 2008, however at present, the lifeguards have little knowledge about physical beach hazards and are provided with limited safety equipment and training. Thus, the lifeguards are not well equiped to protect and educate the beach users. Overall, the risks to the beachgoers result from a combination of factors including as the hazardous hydrodynamic conditions combined to the high number of beachgoers (around 15,000 beachgoers during summer vacation period) and their lack of knowledge of physical beach hazards. There is a clear need for the implementation of management initiatives in order to reduce the local risks, and consequently to guarantee the safety and the quality of the recreational experience of the beachgoers in this Amazon sector. This study investigated the perception of the lifeguards about the beach hazard and risks at Ajuruteua beach (Pará).

ADDITIONAL INDEX WORDS: *Lifeguard service quality, perception, Amazon beach.*

INTRODUCTION

Sandy beaches are destination of leisure and recreation that contain potential hazards for bathers, swimmers, surfers, amongst others (Heggie, 2013; Short and Hogan, 1994). Beach safety resources in the form of professional or volunteers lifeguards and a well-established system with flags and messages are an effective method for mitigate the potential hazards (Phillips and House, 2009; WHO, 2003). These methods are used in many countries such as New Zeland, Australia, EUA, UK, South Africa (McKay *et al.*, 2014). Professional lifeguards are well trained in water rescue and first aid, and also are excellent swimmers (Harada *et al*., 2011). Thus, lifeguards are able to reduce accidents, through education and information about water safety, provision of warnings, denial of access and supervision training in survival skills (Avramidis, 2009; Griffiths *et al*., 2002; Slovic *et al*., 1985).

Amazon beaches are exposed to maco to mega-tides (4-11m), moderate waves (H_s up to 2 m) and tidal currents with more than 1.5 m s^{-1} (Pereira *et al.*, 2012, 2013), which result in serious hazards to beachgoers, causing drownings and other injuries (Pereira *et al.*, 2014). At these beaches, firefighters work as lifeguards and the beaches are normally patrolled during the school vacation period (July) and other holiday periods in the second semester (Oliveira *et al.*, 2011; Pinto *et al.*, 2011; Silva *et al.*, 2011). However, these beaches are long (exceding normally 2 km) and the patrol covers only a narrow area. In addition, the majority of the lifeguards have no knowledge or special skills to recognize and avoid dangerous situations, to save lifes, to recognize hazardous conditions (Pereira *et al.*, 2014).

Lifeguard services began in Ajuruteua in 2008. In order to assess the perception of these lifeguards with respect to self knowledge or skills required to reduce drownings and water-related injuries, a study was made at one of the most visited beaches of northern of Pará State, Ajuruteua beach. The results could be used by the authorities to improve lifeguard training and equipment and implement beach safety programs to prevent drownings and injuries.

STUDY AREA

This study focuses on a macrotidal sandy beach located on the Amazon coast, in the northeastern corner of the Brazilian state of Pará (Figure 1). The beach is about 2.5 km-long faces the Atlantic Ocean and is bordered by two tidal channels "Chavascal" and "Barca". Local inhabitants survive through subsistence fishing and tourism (Oliveira *et al*., 2011). The Ajuruteua waterfront is occupied by a variety of wooden structures and has approximately 300 permanent inhabitants. The beach is one of the most popular

DOI: 10.2112/SI75-244.1 received 15 October, 2015; accepted in revision 15 January, 2016.
*Corresponding author: cajueiro@ufpa.br
©Coastal Education and Research Foundation, Inc. 2016

in the state of Pará, and typically receives in excess of 90,000 visitors during the vacation month of July (Pereira *et al*., 2007).

This beach is 300-400 m wide during low spring tides (Oliveira *et al*., 2014). Local tides are semidiurnal and asymmetric, and spring tide heights range are between 5.0 and 6.0 m (Pereira *et al*., 2014). Circulation patterns in the area are dominated by tidal currents which flow to the northwest during the ebb and to the southeast during the flood (Monteiro *et al*., 2009). Ebb tides are longer (6.5-7.5 h) than flood tides, resulting in strong flood-tide currents (above 1.0 m/s). Nearshore significant wave height (H_s) can exceed 1.5 m (Pereira *et al*., 2013) and, in general, spilling waves break on two or more sandbars.

The climate is humid equatorial with a period of relatively high rainfall (rainy season), typically between January and June, when total rainfall often exceeds 2000 mm and mean temperatures are around 26-27°C. During the second half of the year (dry season), monthly mean rainfall is normally about 200 mm and mean temperatures are around 28-29°C (INMET, 2014).

Beach hazards include the presence of tidal channels and moderate to high energy surf zone. The presence of beachfront structures adds another element of risk. Risk increases during the busy vacation periods with local lifeguards recording an increased number of drownings and other injuries. The large number of beachgoers raises the risks in July (scholar vacation) when the hydrodynamic energy is lower, as well as during equinoctial tides that occur around March-April (Easter) and September (Brazilian Independence Day) when the hydrodynamic energy is higher (Pereira *et al*., 2014; Sousa *et al*., 2011).

METHODS

In this study, 40 lifeguards, employees of the "12º Subgrupamento de Bombeiro militar (12º SGBM)" eho work in Ajuruteua beach during vacation periods were ask to complete a questionnaire designed to address seven main aspects: (i) the profile (age and education level) of the lifeguards; (ii) the lifeguard perception on local beach hazards and risks per lifeguards` age classes; (iii) the lifeguard perception on local beach hazards and risks per time working in this service (according to Short and Hogan, 1994, Short, 2006 and Szpilman, 2005 for beach hazard criteria); (iv) the lifeguard perception with respect to the different types of physical hazards; (v) the lifeguard ability to make safe choices, to prevent injuries, and to act in emergency and rescue situations; (vi) lifeguard opinion of the quality of the lifesaving service; and (vii) lifeguard perception about what is required to improve the lifesaving service and to guarantee the beach safety.

RESULTS

The lifeguards interviewed were all males. Table 1 shows their average age is 37 years, and 40% of them are between 34 and 39 years. The highest education levels (Graduate and Postgraduate) were recorded among lifeguards with 24-39 years old. The lifeguards between 34 and 39 had a higher perception on local beach hazards and risks, followed by those from 44 to 49 years old (Table 2).

The majority have worked as lifeguards between 2 and 10 years, and many of them consider that local hazards and risks are low or believe that those are non-existent (Table 3). About 40% of the lifeguards consider the intertidal tidal channels as the principal physical hazard and the presence of tidal channel

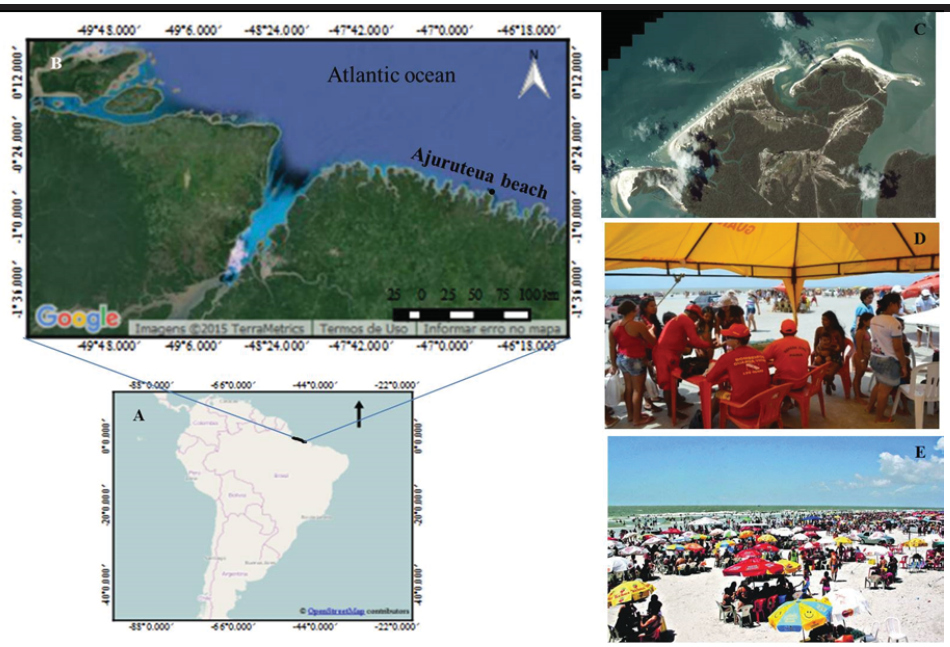

Figure 1. Study Area. (A) South America including Brazil; (B) Coastal zone of the Pará State; (C) Ajuruteua beach; (D) Lifeguards; and (E) Beachgoers on the beach.

(Chavascal and Barca) was almost neglected (Table 4). Unfortunately, many of them feel unable to take preventative actions, to prevent injuries, and only respond in emergency and rescue situations (Table 5). Only 57.5% believed they were well trained. With respect to lifesaving service quality, only 27.5% believe that the service is excellent (Table 6). As a consequence, the majority of them comment that improved lifeguard training is the best beach safety measure, followed by an increase in the number of lifeguards (Table 7).

Table 1. *Age and scholar degree of lifeguards represented in absolute (A) and relative numbers (R).*

Age (years)	HSG	UG	PG	A	R
24 - 29	0	4	3	7	17.5%
29 - 34	1	1	0	2	5.0%
34 - 39	1	15	0	16	40.0%
39 - 44	3	2	0	5	12.5%
44 - 49	7	2	1	10	25.0%
∑	12	24	4	40	100%

Table 2. *Lifeguards perception on local beach hazards and risks per age, represented in absolute (A) and relative numbers (R), according to Short and Hogan (1994), Short (2006) and Szpilman (2005).*

Age (years)	Hazard and risk perception					
	1	2	3	4	A	R
24 - 29	01	02	02	02	07	12.5%
29 - 34	01	00	01	00	02	5.0%
34 - 39	00	05	06	05	16	40.0%
39 - 44	00	01	02	02	05	12.5%
44 - 49	00	05	03	02	10	25.0%
∑	02	13	14	11	40	100%

1. None, 2. Few, 3. High, 4. High for kids.

HSG: High School Graduate; UG: University Graduate; PG: Posgraduate.

DISCUSSION

Beach safety depends on the implementation of prevention strategies required by a specific beach. At Ajuruteua, wind-waves can attain moderate energy during high tide period (H_s up to 1.7 m), the macrotides can reach up to 6.0 m and strong flood tide currents flowing in deep channels can be around 1.5 m s^{-1}. (Pereira *et al*., 2013). The level of beachgoers risk is a function of these physical hazards and the number of beachgoers (around 15,000 beachgoers during summer vacation period), their swimming ability, knowledge of local physical hazards, and level of safety equipment and lifeguards training (Pereira *et al.*, 2014). Also while public rescue equipment (life buoys, lifejackets and life rafts) is available on the beach, first aid equipment is usually not and hospitals are located dozens of kilometers from Ajuruteua.

Table 3. *Lifeguards perception on local beach hazards and risks per service time, represented in absolute (A) and relative numbers (R), according to Short and Hogan (1994), Short (2006) and Szpilman (2005).*

Time working in this service (years)	Hazard and risk perception					
	1	2	3	4	A	R
02-06	01	04	05	03	13	32.5%
06-10	01	03	02	04	10	25.0%
10-14	00	02	02	01	05	12.5%
14-18	00	01	00	00	01	2.5%
18-22	00	01	03	01	05	12.5%
22-26	00	02	02	02	06	15.0%
∑	02	13	14	11	40	100%

1. None, 2. Few, 3. High; 4. High for kids.

Table 4. *Lifeguards perception with respect to the diferent types of physical hazard, according to Short and Hogan (1994) and Short (2006), represented in absolute (A) and relative numbers (R).*

Physical hazard	A	R
Intertidal tide channels	16	40.0%
Macrotides	11	27.5%
Tidal currents	06	15.0%
Wind waves	03	7.5%
Depth	03	7.5%
Tidal channels	01	2.5%
∑	40	100%

Table 5. *Lifeguards perception to make safe choices, to prevent injuries, and to act in emergency and rescue situation, represented in absolute (A) and relative numbers (R).*

Personal Technical Condition	A	R
Highly prepared	23	57.5%
Moderately prepared	6	15.0%
No prepared	7	17.5%
Can not evaluate	4	10.0%
∑	40	100%

Table 6. *Lifeguard perception about the quality of the lifesaving service, represented in absolute (A) and relative numbers (R).*

Lifeguard Service Quality	A	R
Excelent	11	27.5%
Good	17	42.5%
Moderate	9	22.5%
Bad	2	5.0%
Can not evaluate	1	2.5%
∑	40	100%

Table 7. *Lifeguard perception about what is required to improve the lifesaving service and to maintain the beach safety, represented in absolute (A) and relative numbers (R).*

Beach safety Meassure	A	R
Training	13	32.5%
To increase the lifeguard numbers	10	25.0%
Education of beachgoers	8	20.0%
Availability of first-aid equipment	6	15.0%
Information with flags, board and maps	3	7.5%
∑	40	100%

DISCUSSION

Beach safety depend on the implementation of prevention strategies required by a specific beach. At Ajuruteua, wind-waves can attain moderate energy during high tide period (H_s up to 1.7 m), the macrotides can reach up to 6.0 m and strong flood tide currents flowing in deep channels can be around 1.5 m s^{-1}. (Pereira *et al*., 2013). The level of beachgoers risk is a function of these physical hazards and the number of beachgoers (around 15,000 beachgoers during summer vacation period), their swimming ability, knowledge of local physical hazards, and level of safety equipment and lifeguards training (Pereira *et al.*, 2014). Also while public rescue equipment (life buoys, lifejackets and life rafts) is available on the beach, first aid equipment is usually not and hospitals are located dozens of kilometers from Ajuruteua.

Other issues that need to be addressed are the lack of a zonation for different users (swimmer, surfers, kites, jetskis, etc.) to prevent conflict and injury, as well as the lack of information indicating the beach hazards (waves, currents, channel, etc.) and beach usage. The probability of the risks also increases during the popular vacation periods, when the highest number of drowning and other injuries are recorded by the lifeguards.

Beach patrol surveilance (lifeguards and flags) is an effective method for reducing the incidences of drownings in some parts of the world. In fact, almost all drownings in Australia and USA, for example, occur either on unpatrolled beaches, outside the flags, or after patrol hours (Mckay *et al.*, 2014; Wilks *et al.*, 2007). On Ajuruteua beach however drowning and incidents occur in both patrolled and unpatrolled areas.

The primary duty of lifeguards is to mitigate risk on beaches though preventative actions, rescues and use of safety equipment including first aid. But, if a lifeguard is not well-trained, the area will not be well-patrolled and incidents will be more frequent. The questionnaire results show that many of the lifeguards are unable or unwilling to take preventative action and only respond in emergency and rescue situations (also observed by Griffiths *et al*., 2002) It is also clear that local lifeguards have limited knowledge of local physical beach hazards. For example, one of the most dangerous areas along Ajuruteua beach are the Chavascal and Barca channels, which are usually neglected by lifeguards (Pereira *et al*., 2014).

The following actions are required to reduce public risk on beaches like Ajuruteua. Based on the lifeguard survey there is a need to improved lifeguard training particularly their perception of beach hazards and the need to take preventative actions. This should be coupled with an increase in the number of lifeguards, particularly during the vacation period, and an improvement in beach safety resources including safety equipment, flags, signage, vehicles and first aid. In addition there is an urgent need for beach safety campaigns including maps and buoys to indicate areas for different activities, signage to warn the beach goers about beach hazards, information about the role of lifeguards and where and how to bath safely, something similar to the beach safety program implemented in Santa Catarina state (Klein, *et al*., 2005). This should all be done in consultation with Sociedade Brasileira de Salvamento Aquatico (Brazilian Society for Aquatic Rescue) SOBRASA (http://www.sobrasa.org), the lead organization in Brazilian beach safety management.

CONCLUSIONS

Ajuruteua beach, like many Brazilian beaches, has a high level of public risk owing to a combination of hazardous beach conditions and a poor perception of these hazards by the beachgoers. This is compounded by an inadequate lifeguard service, that as identified by this study, is poorly trained and equipped, and has a poor understanding of the local beach hazards. A range of measures are required to both improve lifeguard effectiveness and inform and manage the beachgoers so as to mitigate the presently unacceptably high level of beach risk.

ACKNOWLEDGMENTS

The author Brito would like to thank the lifeguards of “12º Subgrupamento de Bombeiro militar (12º SGBM)” for participating in the interviews. The authors Sousa (141551/2012-7) and Pereira L.C.C. (310909/2014-7 and 200629/2014–0) would also like to thank CNPq for research grants. This research was supported by the CNPq (Universal project - 483913/2012-0) and CAPES (Ciências do Mar II, Edital 43/2013).

LITERATURE CITED

Avramidis, S., 2009. Lifeguard leadership: A review. *International Journal of Aquatic Research and Education*, 3(1), 89-100.

Griffiths, T., 2002. The vigilant lifeguard. *Aquatics International*, 14(4), 18-21.

Harada, S.Y.; Goto, R.S., and Nathanson, A.T., 2011. Analysis of lifeguard-record data at Hanauma Bay, Hawaii. *Wilderness & Environmental Medicine*, 22, 72-76.

Heggie, T.W., 2013. Sand hazards on tourist beaches. *Travel Medicine and Infectious Disease*, 11, 123-125.

Instituto Nacional de Meteorologia (INMET), 2014. Estação Automática de Bragança. Available at < http:// www. inmet.gov.br/sonabra> Access: nov.08th, 2014.

Klein, A.H.F.; Mocellim, O.; Menezes, J.T.; Berribilli, M.; Vintém, G.; Dafferner, G.; Diehl, F.L.; Sperb, R.M., and Santana, G.G., 2005, Beach safety management on the coast of Santa Catarina, Brazil. *Z. Geomorph* 141: 47-58.

McKay, C.; Brander, R.W., and Goff, J., 2014. Putting tourists in harms way.- coastal tourist parks and hazardous unpatrolled surf beaches in New South Wales, Australia. *Tourism Management,* 45, 71-84.

Monteiro, M.C.; Pereira, L.C.C., and Oliveira, S.M.O., 2009. Morphodynamic changes of a macrotidal sand beach in the Brazilian Amazon Coast (Ajuruteua-Pará). *Journal of Coastal Research*, SI56, 109-107.

Oliveira, S.M.O.; Pereira, L.C.C.; Vila-Concejo, A.; Gorayeb, A.; Sousa, R.C., and Costa, R.M., 2011. Natural and anthropogenic impacts on a macrotidal sandy beach of the Brazilian Amazon (Ajuruteua): guidelines for coastal management. *Journal of Coastal Research*, SI64, 1385-1389.

Oliveira, S.M.O.; Pereira, L.C.C., and Vila-Concejo, A., 2014. Morphodynamic processes in a macrotidal beach in the Amazon littoral. *Quaternary and Environmental Geosciences*, 5, 125-136.

Pereira, L.C.C.; Oliveira, S.M.O.; Costa, R.M.; Costa, K.G., and Vila-Concejo, A., 2013. What happens on an equatorial beach on the Amazon coastal when La Niña occurs during the rainy season? *Estuarine, Coastal and Shelf Science*, 135, 116-127.

Pereira, L.C.C.; Guimarães, D.O.; Costa, R.M., and Souza-Filho, P.W.M., 2007. Use and occupation in Bragança littoral, Brazilian Amazon. *Journal of Coastal Research*, SI50, 1116-1120.

Pereira, L.C.C.; Vila-Concejo, A.; Costa, R.M., and Short, A.D., 2014. Managing physical and anthropogenic hazards on macrotidal Amazon beaches. *Ocean & Coastal Management*, 96, 149-162.

Pereira, L.C.C.; Silva, N.I.S.; Costa, R.M.; Asp, N.E.; Costa, K.G. da, and Vila-Concejo, A., 2012. Seasonal changes in oceanographic processes at an equatorial macrotidal beach in northern Brazil. *Continental Shelf Research*, 43, 95-106.

Pinto, K.S.T.; Pereira, L.C.C.; Vila-Concejo, A.; Gorayeb, A.; Sousa, R.C., and Costa, R.M., 2011. Effects of the lack of coastal planning on water quality and land use on a macrotidal beach (Atalaia, Pará) in the Amazon region. *Journal of Coastal Research*, SI 64, 1401-1405.

Phillips M.R. and House, C., 2009. An evaluation of priorities for beach tourism: Case studies from South Wales, UK. *Tourism Management*, 30, 176–183.

Short, A.D. and Hogan, C.L., 1994. Rip currents and beach hazards: their impact on public safety and implications for coastal management. *Journal of Coastal Research*, SI12, 197-209.

Short, A. D. (2006). Beaches of the Northern Australian Coast The Kimberley, Northern Territory and Cape York - A guide to their nature, characteristics, surf and safety. Sydney University Press, Sydney 463 pp, 1-920898-16-6.

Silva, I.R. da; Pereira, L.C.C.; Sousa, R.C.; Oliveira, S.M.O de; Guimarães, D.O., and Costa, R.M., 2011. Amazon Beaches (São Luís, Brazil): Recreational use, environmental indicators, and perception of beachgoers. *Journal of Coastal Research*, SI 64, 1287-1291

Slovic, P.; Fischhoff, B., and Lichtenstein, S., 1985. Characterizing perceived risk. *In:* Kates, R. W.; Hohenemser, C., and Kasperson, J. X. (eds.). *Perilous progress: Managing the Hazards of Technology*, pp. 91-125.

Sousa, R.C.; Pereira, L.C.C.; Silva, N.I.S.; Oliveira, S.M.O. de; Pinto, K.S.T,. and Costa, R.M., 2011. Recreational carrying capacity of three Amazon macrotidal beaches during the peak vacation season. *Journal of Coastal Research*, SI 64, 1292-1296.

Szpilman, D., 2005. Afogamento na infância: epidemiologia, tratamento e prevenção (Drowning in childhood: epidemiology, treatment and prevention). *Rev. Paul Pediatria*, 23(3), 142-53.

Wilks, J.; De Nardi, M., and Wodarski, R., 2007. Close is not close enough: drowning and rescues outside flagged beach patrol areas in Australia. *Tourism in Marine Environments*, 4, 57-62.

World Health Organization (WTO), 2003. *Guidelines for safe recreational water environments*. Coastal and fresh waters. Geneva, Switzerland, 1, 20–35.

Journal of Coastal Research	SI	75	1222 - 1226	Coconut Creek, Florida	2016

Water Quality during the Recreational High Season for a Macrotidal Beach (Ajuruteua, Pará, Brazil)

Rubem M. C. Pessoa[†*], Luci C.C. Pereira[†], Rosigleyse C. Sousa[†], and Rauquírio M. Costa[†]

[†]Instituto de Estudos Costeiros,
Universidade Federal do Pará,
Bragança, 68600-000, Brazil

www.cerf-jcr.org

www.JCRonline.org

ABSTRACT

Pessoa, R.M.C.; Pereira, L.C.C.; Sousa, R.C., and Costa, R.M., 2016. Recreational Quality on a Macrotidal Beach (Ajuruteua, Pará, Brazil). *Proceedings of the 14th International Coastal Symposium* (Sydney, Australia). *Journal of Coastal Research*, Special Issue, No. 75, pp. 1221 - 1226. Coconut Creek (Florida), ISSN 0749-0208.

Coastal tourism in the Brazilian Amazon region is limited by logistic problems and climatic conditions, with recreation being concentrated in the school vacation period and bank holiday weekends. The present study evaluated the temporal variation in recreational, climatological, hydrodynamic, and microbiological processes among two bank holiday weekends and one weekend during the summer school vacation in July. One weekend was the Easter bank holiday in the rainy season in April, and the second was Brazilian Independence day, in the dry season in September. Data on hydrodynamics (tides and waves), climate (rainfall), and microbiological parameters (thermotolerant coliform levels) were collected, and the number of visitors was recorded every 3 hours between 07:00 h and 19:00 h (Friday through Monday), during each study period. The largest numbers of bathers were recorded during the dry season (July followed by September). The high precipitation levels recorded during the rainy season resulted in a reduced number of visitors and consequently low concentrations of thermotolerant coliforms. High rainfall rates are typical of Amazonian beaches and affect recreational activities. While there is no basic sanitation in the study area, the low concentrations of thermotolerant coliforms indicate that the water was safe for bathers In April and September. During the July vacation, however, high concentrations of beachgoers resulted in the contamination of the water, which was unsafe for bathing. Given this situation, management measures are urgently needed to increase the recreational quality of the beach and improve the water quality during the school vacation period.

ADDITIONAL INDEX WORDS: *Vacation period, water quality, Amazon beach.*

INTRODUCTION

The quality of the water in beach environments used for recreational activities that involve direct contact (swimming, bathing, diving, *etc*.) may be affected by a number of different factors, including the discharge of raw sewage into the environment (Fleisher *et al*., 2010). The presence of micro-organisms, such as bacteria, viruses, and protozoa, may affect the health of beachgoers, causing disorders such as gastroenteritis, primarily in children, the elderly, and individuals with low natural resistance (Soller *et al*., 2014).

One basic criterion for the evaluation of the suitability of a body of water for bathing is the concentration of thermotolerant coliforms (TC) found in the water (Fleisher *et al*., 2010; WHO, 2003). The contamination of water sources by TC is a major problem in many parts of the world (Abdallah *et al*., 2005; Fiorentino *et al*., 2014). In Brazil, the National Environment Council (CONAMA, 2005) determines the standards of water quality required for the recreational use of beaches, determining the criteria that have been adopted by the Blue Flag Program (IAR, 2015), which certifies the environmental quality of Brazilian beaches.

In the Amazon region, recreational beaches may be located on rivers, estuaries or coastlines, and may be associated with urban centers, semi-urbanized or rural environments, and suffer a range of different types of pressures and uses (Silva *et al.,* 2013; Sousa *et al*., 2011). Local coastal tourism and beachgoing is basically restricted to local residents and visitors from other urban centers within the region (Sansolo, 2003).

In the Brazilian state of Pará, the peak visitation periods coincide with the principal school vacation (July) and long bank holidays (Pessoa *et al*., 2013; Sousa *et al*., 2014). The intense rains during the first half of the year, together with the long distances between the Atlantic coast (in the case of oceanic beaches) and the state capital and other urban centers, are two of the principal factors that limit the numbers of beachgoers during other times of the year (Pinto *et al*., 2011).

While the local coastal tourism industry is poorly developed, very large numbers of beachgoers may visit the beaches of Pará during peak periods. Even so, the lack of public sanitation means that, during these peak periods, the increased influx of beachgoers results not only in an increase in the discharge of sewage, but also a peak in the thermotolerant coliform concentrations (Silva *et al*., 2013). In this context, the present study evaluated the temporal variation in recreational, climatological, hydrodynamic and microbiological variables on Ajuruteua beach in Pará, Brazil. The results of this study will provide an important database for the development of

DOI: 10.2112/SI75-245.1 received 15 October, 2015; accepted in revision 15 January, 2016.
*Corresponding author: rubempessoa@yahoo.com.br
©Coastal Education and Research Foundation, Inc. 2016

management plans for this beach, and for other similar beaches in the Amazon region.

STUDY AREA

Ajuruteua beach (Figure 1) is 36 km from the town of Bragança, on the Atlantic coast of the Brazilian state of Pará. The beach is 2.5 km long, and 200–400 m wide at low spring tide. The local climate is humid equatorial, with well-defined rainy and dry seasons, mean annual precipitation of more than 2000 mm, and mean annual temperature of 26°C (Martorano *et al*., 1993). Northeastern trade winds predominate in the study area, together with a semidiurnal macrotidal regime, tidal currents with mean velocities of over 0.5 m/s, and wave heights (H_s) up to 1.6 m (Pereira *et al*., 2014).

Ajuruteua has approximately 300 permanent residents, in addition to holiday home owners, although more than 90,000 visitors may pass through this beach in July (Pereira *et al*., 2007). This major peak in the concentration of visitors, together with the unregulated occupation of the study area, the lack of adequate services and infrastructure, in particular a public sanitation system, threaten the potential of this beach for recreational bathing and, ultimately, local tourism as a whole (Sousa *et al*., 2011).

METHODS

To understand the potential of Ajututeua beach for recreational bathing during different times of the year, this study focused on three distinct four-day periods (Friday-Monday): the Easter bank holiday (April 5-9, 2012) in the rainy season, the penultimate weekend of the summer school vacation (July, 20-23, 2012), and Brazilian Independence day weekend (September 7-10, 2012), in the dry season.

During this survey, the number of people present was counted every hour between 08:00 h and 18:00 h along a transect located in the central portion of the beach, which was divided into three zones: (i) zone 1 (100 x 20 m); (ii) zone 2 (40 m x the widest point between neap and spring tide levels); (iii) zone 3 (10 x 40 m).

The precipitation data were obtained from the National Meteorological Institute's (INMET) Tracuateua station (station 82145). The hydrodynamic data (waves and tides) were collected on site using tide and wave sensors (TWR-2050). The equipment was bottom-mounted at a depth of 1.7 m in the surf zone at low tide. The waves were measured at a rate of 4 *Hz* (512 samples every 10 minutes), and the tide data were collected every 2 seconds, with mean values being obtained every 10 minutes.

Water samples were collected daily every 3 hours between 07:00 h and 19:00 h in the surf zone, using a Niskin oceanographic bottle, and stored in sterilized containers. The thermotolerant coliform (TC) concentrations were determined by the multiple tubes method, as described by the American Public Health Association (2004).

Two statistical analyses were used, Lilliefors (Conover, 1971) and Cochran (Underwood, 1997) tests to verify the normality and homogeneity of variance (thermotolerant coliform numbers). When not normal, data were log-transformed (x+1) to achieve normality (Underwood, 1997; Zar, 1999) and tested by one-way ANOVA. Tukey`s (Tukey Honest significant difference - HSD test) post-hoc test was them employed to compare the averages when significant differences were found. The analyses were run in Statistica 6.0, considering a significance level of 5%.

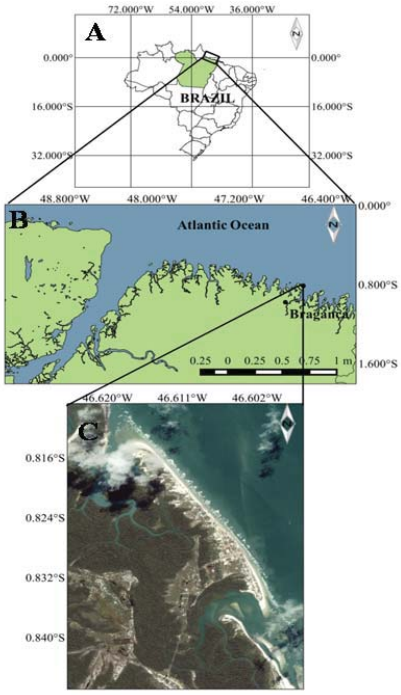

Figure 1. Study area. (A) Brazil, (B) Pará coast, (C) Ajuruteua beach.

RESULTS

In general, seasonal variation in the climate and the distance between Ajuruteua and the state's principal urban centers are the principal factors limiting the visitation of the study beach. On a local scale, tidal dynamics have a direct influence on the distribution of visitors along the profile of the beach. The influence of seasonal variables, the number of beachgoers, and the relationship between levels of bacteriological contamination and tidal dynamics during the three study periods are described below.

In April 2012, total precipitation was 341 mm. The Easter holiday coincided with the rainiest three months of the year, resulting in a considerable reduction in the number of beachgoers during this period, with only 314 visitors on the study area being recorded during the peak hour, that is, 12:00–13:00 h. The highest numbers of visitors were observed on Friday and Saturday (Figure 2).

The Easter holiday coincided with the equinox, and the tidal range exceeded 6.0 m, with significant wave height (H_s) of 1.8 m during high tide (Figure 3A). During this phase of the tide, there is no available area of intertidal zone or backshore, and bathing is relatively dangerous because of the high wave energy. The combination of these factors leads beachgoers to return to their homes, remain in the beachside bars or visit the only local

piazza until the intertidal zone once again has space available for recreational activities. During the high tide, the water reaches the cesspits located in the intertidal zone or among the frontal dunes (Figure 4A), while the reduced number of beachgoers (Figure 4B) and the high hydrodynamic energy during this month favored the dilution of the coliforms in the water (< 3 MPN/100 ml).

During the July vacation month, total precipitation was 198 mm, although virtually no rainfall was recorded during the study weekend. A much larger number of visitors was recorded in comparison with the Independence Day holiday. Saturday and Sunday were the most popular days, with the number of beachgoers peaking between 13:00 h and 15:00 h (1625 visitors) (Figure 2). The tidal range was 4.4 m, and wave heights (H_s) did not exceed 1.07 m (Figure 3B). During this period, the large numbers of bathers (Figure 4C) and the high tide levels, which reached the cesspits on the beach, contributed to the high thermotolerant coliform concentrations recorded (>1100 MPN/100 ml).

Total precipitation during September 2012 was only 2 mm, which contributed to a much larger number of visitors during the Independence Day weekend in comparison with the Easter holiday (Figure 2). During this period, the tidal range was only 3.0 m, and wave height (H_s), 1.21 m (Figure 3C). These conditions favored the presence of visitors on the beach (Figure 4D), even during the high tide. The most popular days were Saturday and Sunday, with a peak of visitation being reached between 11:00 h and 12:00 h (419 visitors). During this period, the high tide did not reach the cesspits, and the larger number of beachgoers on sunday resulted in higher coliform concentrations (11–460 MPN/100 ml), although the water was still considered adequate for bathing, according to CONAMA standards.

Significant differences in thermotolerant coliforms were found between the Easter bank and Brazilian Independence day holidays (p = 0.0001), school vacation and Easter bank periods (p = 0.00012) and school vacation and Brazilian Independence day (p = 0.0002). High TC during school vacation contrasted those obtained in the Easter bank and Brazilian Independence day periods, while the lowest concentrations recorded during Easter bank period were different from those found in the Brazilian Independence day holiday (Figure 5A-C). However, considering only the school vacation (June), thermotolerant coliform concentrations were above the limits permitted by CONAMA (2005).

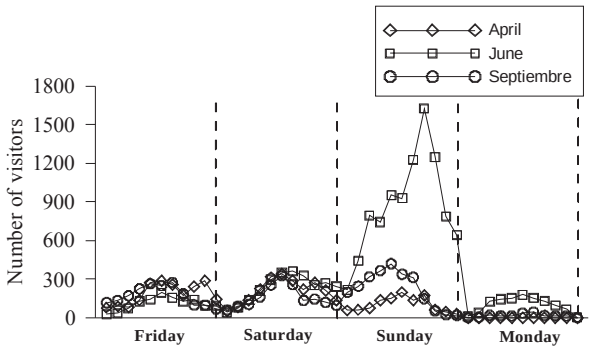

Figure 2. Data on the distribution of beachgoers.

DISCUSSION

The practice of recreational activities on beaches during holiday periods is a worldwide phenomenon influenced by a variety of anthropic and natural factors (Zacarias *et al*., 2011). On the Amazon coast, the region's distinctive rainy/dry climatic seasons is a natural feature that limits the potential for beachgoing and recreational activities in the beach environment. In contrast with other areas of the Brazilian coast, the principal school vacation period occurs in July, when the region's coastal and estuarine beaches become overcrowded (Pessoa *et al*., 2013; Sousa *et al*., 2014). Friday, is normally marked for the beginning of the recreational period, attracting a reduced number of visitors compared to the Saturday and Sunday.

In the Brazilian state of Pará, in addition to climatic factors, the large distances (typically 200–250 km) that separate the beaches of the Atlantic coast from major urban centers, such as the state capital, Belém, also limit visitation during shorter holiday periods (other than July), even during the second half of the year (Pessoa *et al*., 2013). The shorter distances between these urban centers and many local fluvial and estuarine beaches contributes to the popularity of these sites as an alternative recreational option for many beachgoers (Sousa *et al*., 2014). These considerations account for the much lower numbers of beachgoers observed in April and September, despite the popularity of Ajuruteua beach during the summer vacation period.

The lack of infrastructure and services, and the paucity of incentives from local administrators for the development of the

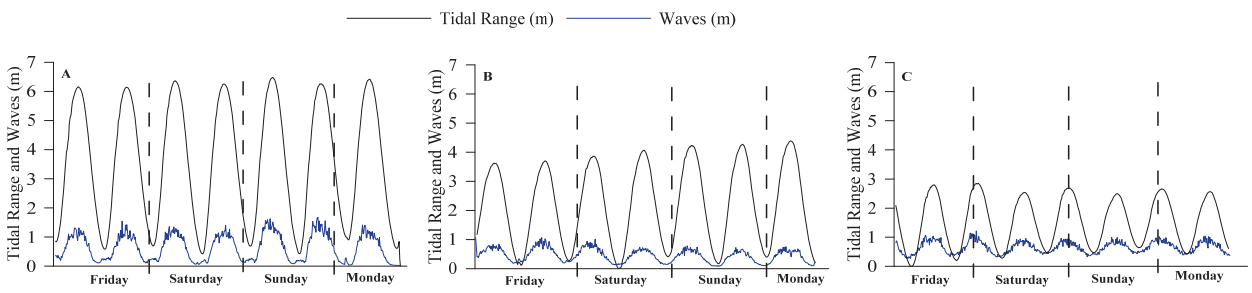

Figure 3. Data of hydrodynamic variables in (A) April, (B), July and (C) September 2012.

Figure 4. A) Cesspit in the intertidal zone being washed out during the high tide; B) Visitors in the beach during the Easter bank holiday (13:00 h); C) Visitors during the summer vacation (15:00 h); D) Visitors during the Brazilian Independence Day holiday (12:00 h);

local coastal tourism industry also limit the potential of Ajuruteua and other local beaches during other times of the year. Even so, the ongoing occupation of coastal areas and growing pressures on natural resources have been causing a variety of socio-environmental problems, including questions related to water quality.

The lack of basic public sanitation is one of the main issues affecting the quality of bathing water in many countries around the world (Saltaren *et al*., 2008; Soller *et al*., 2014), but the problems are most accentuated in the regions that lack effective regulatory policies, monitoring, and the enforcement of environmental legislation, such as in the Amazon region. In fact, the lack of a public sanitation system has resulted in the contamination of the Amazon region's waters by thermotolerant coliforms primarily during the vacation period on urban (Silva *et al*., 2013), semi-urban (Pinto *et al*., 2011) and rural beaches (Silva *et al*., 2011). This contamination is related directly to the large numbers of beachgoers, the lack of an adequate system for the collection and treatment of sewage, and the installation of cesspits in dunes and the intertidal zone, where they can be reached by the water of the highest tides. These cesspits are fragile structures not designed to prevent contamination during high tide (Pinto *et al*., 2011; Sousa *et al*., 2011). On Ajuruteua beach, in addition to these cesspits, domestic effluents are discharged directly into the intertidal zone from bars, guesthouses, and local homes. As a consequence, the highest TC numbers coincided with a higher number of beachgoers, as those recorded in July month.

CONCLUSIONS

In this study, the interaction among microbiological, climatological and hydrodynamic factors was analyzed in the context of distinct recreational periods (long bank holidays in the dry and rainy seasons, and the school vacation period). The quality of local bathing water was found to be adequate in all periods except the July vacation, when high concentrations of visitors on the beaches and in local guesthouses contributed directly to the contamination of the water with thermotolerant coliforms.

Effective incentives for local tourism, not only during periods of peak demand, such as the school vacation, but also other holiday periods, will depend on (i) the improvement of the quality of local infrastructure and services, (ii) the removal of cesspits from the beach environment, (iii) the installation of a public sewage treatment system, (iv) the interaction between public authorities and private interests for the creation of effective tools for the development of local tourism, and (v) the creation of a coastal management plan with the objective of developing a sustainable local tourism industry.

ACKNOWLEDGMENTS

This research was supported by CNPq (Universal project - 483913/2012-0) and FAPESPA (008/2013). The authors Pereira LCC (310909/2014-7 and 200629/2014–0) and Costa RM (306061/2011–2 and 200622/2014–5) would also like to thank CNPq for research grants. We also thank Dr. Stephen Ferrari for his careful revision of the English.

LITERATURE CITED

Abdallah, S.A.; Elmanama, A.A.; Fahd, M.I., and Afifi, S.,

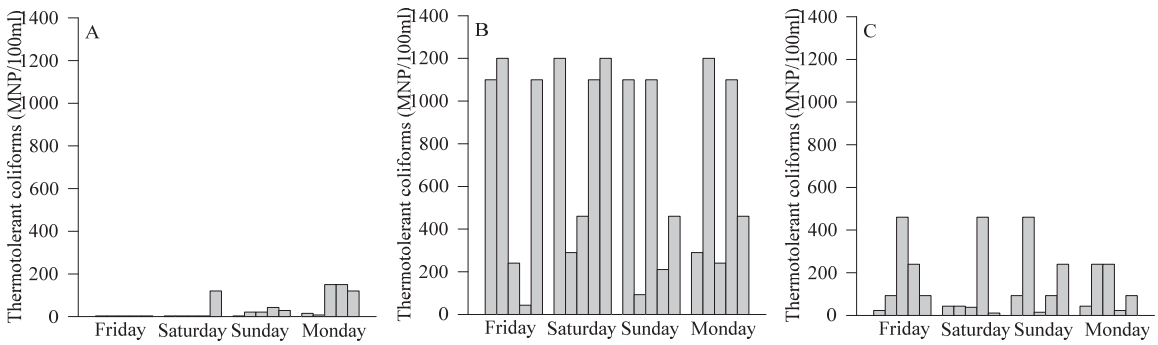

Figure 5. Data on coliform concentrations in (A) April, (B), July and (C) September 2012.

2005. Microbiological Beach Sand Quality in the Gaza Strip in Comparison to Seawater. *Polish Journal of Environmental Studies*, 14(6), 841–850.

American Public Health Association, 2004. *Standard Methods for Examination of Water and Wastewater*. Washington, D.C. http://www.standard.methods.org/Articles.cfm

Conover, W.O.J., 1971. *Practical nonparametric statistics. John* Wiley, New York.

Conselho Nacional de Meio Ambiente – CONAMA, 2005. Resolução nº 357, de 17 de março de 2005. Brasil: CONAMA.

Fiorentino, L.A.; Olascoaga, M.J., and Reniers, A., 2014. Analysis of water quality and circulation of four recreational Miami beaches through the use of Lagrangian Coherent Structures. *Marine Pollution Bulletin*, 83(1), 181–189.

Fleisher, J.M.; Fleming, L.E.; Solo-Gabriele, H.M., and Kish, J.K., 2010. The beaches study : health effects and exposures from non-point source microbial contaminants in subtropical recreational marine waters. *International Journal of Epidemiology*, 3, 1–8.

Instituto Ambiental Ratones – IAR, 2015. *Programa Bandeira Azul Praias – Brasil*: *Critérios e notas explicativas*. FEE, Brasil.

Martorano, L.G.; Pereira, L.C.; Cézar, E.G.M., and Pereira, I.C.B., 1993. Estudos Climáticos do Estado do Pará, Classificação Climática (KÓPPEN) e Deficiência Hídrica (Thornthwhite, Mather). Belém, SUDAM/EMBRAPA, SNLCS. 53p.

Pereira, L.C.C.; Guimarães, D.O.; Ribeiro, M.J.S., Costa, R.M., and Souza Filho, P.W.M., 2007. Use and Occupation in Bragança Littoral, Brazilian Amazon. *J. Coast. Res.*, SI 50, 1116-1120.

Pereira, L.C.C.; Pinto, K.S.T., and Vila-Concejo, A., 2014. Morphodynamic variations of a macrotidal beach (Atalaia) on the Brazilian Amazon Coast. *In:* Green, A.N., and Cooper, J.A.G. (eds.), *Proceedings 13th International Coastal Symposium* (Durban, South Africa). *J. Coast. Res.*, SI 66, 681-686.

Pessoa, R.M.C.; Pereira, L.C.C.; Sousa, R.C., and Costa, R.M., 2013. Recreational Carrying Capacity of an Amazon Macrotidal Beach During Vacation Periods. *In:* Conley, D.C.; Masselink, G.; Russell, P.E., and O'Hare, T.J. (eds.), *Proceedings 12th International Coastal Symposium* (Plymouth, England). *J. Coast. Res.*, SI 66, 1027-1032.

Pinto, K.S.T.; Pereira, L.C.C.; Vila-Concejo, A.; Gorayeb, A.; Sousa, R.C., and Costa, R.M., 2011. Effects of the lack of coastal planning on water quality and land use on a macrotidal beach (Atalaia, Pará) in the Amazon Region. *In:* Furmanczyk, K.; Giza, A., and Terefenko, P. (eds.), *Proceedings 11th International Coastal Symposium* (Szczecin, Poland). *Journal of Coastal Research*, Special Issue No 64, pp. 1401-1405.

Saltarén, C.M.; García, Y.H.; Porto, J.G.; Manjarrés, M.O., and Rocca, L.H.D., 2008. Metodología de cálculo de la capacidad de carga turística como herramienta para la gestión ambiental y su aplicación en cinco playas del caribe norte Colombiano. *Gestión y Ambiente*, 11(3), 109-122.

Sansolo, D.G., 2003. Turismo e sustentabilidade na Amazônia: um novo conteúdo territorial e a experiência do Município de Silves, Amazonas. *Pasos: Revista de Turismo y Patrimonio Cultural*, 1, 39-50.

Silva, I.R.; Pereira, L.C.C.; Trindade, W.N.; Magalhães, A., and Costa, R.M., 2013. Natural and anthropogenic processes on the recreational activities in urban Amazon beaches. *Ocean & Coastal Management*, 76, 75-84.

Silva, N.I.S.; Pereira, L.C.C.; Gorayeb, A.; Vila-Concejo, A.; Sousa, R.C.; Asp, N.E., and Costa, R.M., 2011a. Natural and social conditions of Princesa, a macrotidal sandy beach on the Amazon Coast of Brazil. *In:* Furmanczyk, K.; Giza, A., and Terefenko, P. (eds.), *Proceedings 11th International Coastal Symposium* (Szczecin, Poland). *Journal of Coastal Research*, Special Issue No 64, 1979-1983.

Soller, J.A.; Schoen, M.E.; Varghese, A.; Ichida, A.M.; Boehm, A.B.; Eftim, S.; Ashbolt, N.J., and Ravenscroft, J.E., 2014. Human health risk implications of multiple sources of faecal indicator bacteria in a recreational waterbody. *Water Research*, 66, 254–264.

Sousa, R.C.; Pereira, L.C.C.; Costa, R.M., and Jiménez, J.A., 2014. Tourism carrying capacity on estuarine beaches in the Brazilian Amazon region. *In:* Green, A.N., and Cooper, J.A.G. (eds.), *Proceedings 13th International Coastal Symposium* (Durban, South Africa). *Journal of Coastal Research*, Special Issue No. 66, pp. 545-550.

Sousa, R.C.; Pereira, L.C.C.; Silva, N.I.S.; Oliveira, S.M.O.; Pinto, K.S.T., and Costa, R.M., 2011. Recreational carrying capacity of three Amazon macrotidal beaches during the peak vacation season. *In:* Furmanczyk, K.; Giza, A., and Terefenko, P. (eds.), *Proceedings 11th International Coastal Symposium* (Szczecin, Poland). *Journal of Coastal Research*, Special Issue No. 64, pp. 1292-1296.

Statistica 6.0. Statsoft. http://www.statsoft.com

Underwood, A.J., 1997. *Experiments in ecology: their logical design and interpretation using analysis of variance*:. Cambridge University Press, Cambridge, 504p.

World Health Organization – WHO, 2003. Guidelines for safe recreational water environments.

Zacarias, D.A.; Williams, A.T., and Newton, A., 2011. Recreation carrying capacity estimations to support beach management at Praia de Faro, Portugal. *Applied Geography*, 31, 1075-1081.

Zar, J.H., 1999. *Bioestatistical analysis*: Prentice Hall, New Jersey, 909p.

Journal of Coastal Research	SI	75	1227 - 1231	Coconut Creek, Florida	2016

Geological evolution and inundation hazard: an analysis through geotechnologies

Maria Luiza C.C. Rosa[†§*], Eduardo G. Barboza[†‡], Bruno S. Menegon[††], Priscila C. Frota[††], and Ricardo A.O. Anoni[††]

[†]Centro de Estudos de Geologia Costeira e Oceânica, CECO
Federal University of Rio Grande do Sul
Porto Alegre, Brazil

[‡]Departamento de Paleontologia e Estratigrafia
Federal University of Rio Grande do Sul
Porto Alegre, Brazil

[§]Departamento de Geodésia
Federal University of Rio Grande do Sul
Porto Alegre, Brazil

[††]Instituto de Geociências, Curso de Geologia
Federal University of Rio Grande do Sul
Porto Alegre, Brazil

www.cerf-jcr.org

www.JCRonline.org

ABSTRACT

Rosa, M.L.C.C; Barboza, E.G.; Menegon, B.S.; Frota, P.C.; and Anoni, R.A.O., 2016. Geological evolution and inundation hazard: an analysis through geotechnologies. *In:* Vila-Concejo, A.; Bruce, E.; Kennedy, D.M., and McCarroll, R.J. (eds.), *Proceedings of the 14th International Coastal Symposium* (Sydney, Australia). *Journal of Coastal Research*, Special Issue, No. 75, pp. 1227 - 1231. Coconut Creek (Florida), ISSN 0749-0208.

In the southern coastal plain of Rio Grande do Sul, southern Brazil, part of the city of Santa Vitória do Palmar was studied to analyze inundation hazard and its relation to geological evolution. Remote sensing, GNSS, total station surveys, laser scanning and photogrammetric reconstructions with a low cost UAV were combined and compared aiming at defining four main units with different levels of inundation susceptibility, which correspond to geological units of different ages. The allogenic factor related to the development of these units is sea level, which controls lagoon level, and determines that younger areas have higher inundation susceptibility. An autogenic control was also verified and is related to the dynamics of the lagoon system, where spits are higher and have a lower susceptibility when compared to the plains of the same age.

ADDITIONAL INDEX WORDS: *Risk areas, digital surface models, topographic surveys.*

INTRODUCTION

The rapid development of urban areas in response to economic investments brings many challenges. Urban growth without planning may result in occupation of unsuitable areas. On coastal plains a clear risk is often related to inundation. The definition of risk areas is very helpful to coastal management and planning, but to set out land limits is not a simple task, as many considerations must be done.

The sedimentary record of the coastal plain of Rio Grande do Sul, southern Brazil, is mainly composed of four barrier-lagoon systems, which evolved during different glacioeustatic cycles (Villwock, 1984). The ages of these systems were first suggested by Villwock and Tomazelli (1995), based on correlation with marine oxygen isotope stages. The oldest system was named as System I, and the youngest as System IV. Then, absolute dating methods (^{14}C, thermoluminescence, electron spin resonance and OSL) were applied defining the ages of the systems as 325, 200, 125 and 7 ka to the present, respectively.

In terms of elevation, the oldest system is in a higher position, and the youngest in the lowest one (Villwock and Tomazelli, 1995). Studies along the coastal plain defined that sea level reached 9±1 m during isotope stage 7, related to System II; 7±1 m during isotope stage 5, related to system III; and 3±1m during isotope stage 1, related to System IV (Angulo and Lessa, 1997; Lopes *et al.*, 2014; Rosa, 2012; Tomazelli and Dillenburg, 2007).

In the southern portion of the coastal plain is the city of Santa Vitória do Palmar (Figure 1). This city has a high growth potential, as many investments have been carried out in this region during the past years. One possible area for expansion is in the direction of Mirim lagoon, where a road reaches a harbor and some houses are already located. An analysis of a digital elevation model shows how greatly the elevation varies from the urban area to the lagoon (Figure 1). This change in elevation is related to the geological evolution; the main urban area is positioned on top of Barrier II, and on the way to the harbor there are lagoonal deposits related to the evolution of Systems III and IV. As sea level controlled the lagoon levels during their evolution, it was hypothesized that risk areas are related to the age of lagoonal deposits.

Therefore, the aim of this study is to define the relationship between risk of inundation with geological evolution in the region between the urban area of Santa Vitória do Palmar and Mirim lagoon, which has a potential for city expansion. To test this hypothesis, different methods were applied, including the integrated application of geotechnologies with traditional methods. These technologies were tested to evaluate their results and efficiency to the proposed application.

DOI: 10.2112/SI75-246.1 received 15 October, 2015; accepted in revision 15 January, 2016.
*Corresponding author: luiza.camara@ufrgs.br
©Coastal Education and Research Foundation, Inc. 2016

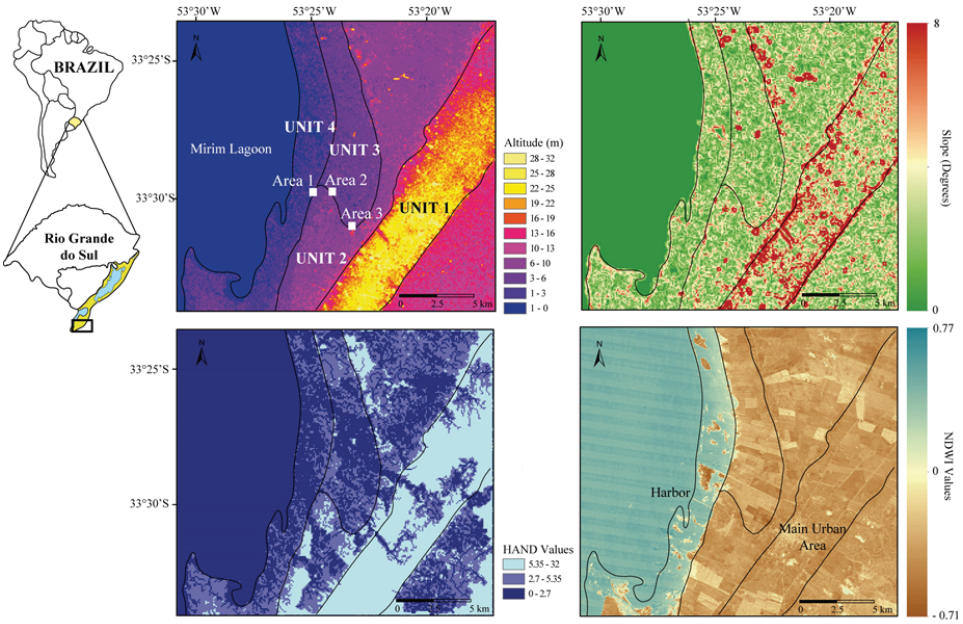

Figure 1. Remote sensing analysis of the study area, located in the southern portion of the coastal plain of Rio Grande do Sul. The left top image is the SRTM digital elevation model, from which was derived the slope (right top image) and the HAND model (left bottom image). In the bottom right image, NDWI values in blue represent flooded areas in September, 1998.

METHODS

To define the relation between risk areas with geological evolution, remote sensing was conducted to define the main geological boundaries and their susceptibility to inundation. The digital elevation model (DEM) of Shuttle Radar Topography Mission (SRTM), refined in the TOPODATA Project to achieve a resolution of 1" (about 30 m) was processed into a Geographic Information System (GIS), created with version 10.3 of ArcGIS®. As products, elevation and slope maps, and a HAND (Height Above the Nearest Drainage) model were created (Figure 1). The HAND model normalizes the topography in respect to the drainage network through the definition of level differences of the DEM in relation to the flow path of the closest drainage (Pires and Borma, 2013), which indicates inundation susceptibility. To build this model the plugin *Terrahidro* of the software Terraview 4.2.2 was applied. Classes are high, medium and low susceptibility, defined in relation to normal, low and high terraces levels, respectively, which are observed in the profiles. In the study area, the normal level of drainage ranges from 0 to 2.7 m HAND, the low terrace has 2.7 to 5.35 m HAND, and the high terrace has 5.35 to 32 m HAND.

With the same purpose, optical images of the satellite Landsat 7 were processed to create a NDWI (Normalized Difference Water Index) image (Figure 1). The NDWI is created with green and infrared bands (2 and 4 of ETM+ sensor), which are subtracted and divided by their sum. As water has a contrasting spectral behavior in these bands, this procedure amplifies the contrast and helps in identifying dry and wet areas, as well as water bodies (McFeeters, 1996). According to this author, an NDWI≥0 indicates the presence of water, while NDWI≤ 0 indicates dry areas. As the purpose of this study is to analyze inundation hazard, images of September 13th, 1998, were chosen because that was a period of high precipitation. The cumulative rainfall of July, August and September reached 260 mm. At Santa Vitória do Palmar the water level of Mirim lagoon reached 3.96 m in that date, well above the average of 1.60 m.

The regional analysis allowed the recognition of features related to the evolution of the lagoon system. The highest area, where most of the city is located, is related to Barrier II. In the region between Barrier II and Mirim lagoon at least three levels can be identified. The highest feature has a spit shape oriented to the north. Its boundaries are Barrier II to SE, an intermediate level to the NE, and the lowest level to the E. To define level differences, establish altitudes, and correlate these units with geological evolution, a fieldwork survey was designed to acquire detailed topographic data. Three target areas were selected to measure the boundary of the spit and lower regions (Figure 1). Measurements were performed in four ways: with a global navigation satellite system (GNSS), by a traditional trigonometric leveling with a total station, through a photogrammetric survey with a low cost unmanned aerial vehicle (UAV), and with laser scanning.

In each area 24 targets spaced 20 m apart were distributed and georeferenced with GNSS through the differential method (DGPS) using a Trimble® PRO-XRT equipment. The targets were measured during 60 sec., with exception of one main reference, measured during 1 hour. The data were processed using a public base station located about 200 km from the study area. The targets were measured also with a total station Ruide RTS-860R, positioned on the reference target to define its

elevation based on GNSS altitude. Then, the altitudes and level differences of the different methods were compared.

To obtain the DEM model and orthophoto through a photogrammetric reconstruction (Mancini *et al.*, 2013), a survey with a low cost UAV was held in each area. The flights were done with a DJI Phantom 2 vision+ quadcopter, with a 3-axis system for camera stabilization linked to a 14 Megapixel HD camera, which has a FOV (field of view) of 140° and f/2.8 focus. A GNSS eTrex®30-Garmin with barometric altimeter was coupled with the UAV in order to determine the position of each picture during acquisition. The flight was performed at two heights (25 and 50 m), with a speed of 3 m/s to guarantee an overlap of about 80% between the vertical aerial photos. The DEM was built using a Structure from Motion (SfM) approach by Agisoft Photoscan© workflow (Agisoft, 2013). Each target had the coordinates determined by GNSS (planimetric) and total station (altimetric) surveys. After the target recognition and the alignment of the photos, a point cloud was generated, the dense cloud, the mesh, and the texture. After this workflow, a DEM and an orthophoto were created.

Another technology applied to determine level differences was terrestrial laser scanning (FARO FOCUS 3D X330), which provides detailed and accurate plani-altimetric data. Based on the emission, reflection and detection of laser beams, a 3D point cloud is created for each station. To test its application, three scanning placed at a distance of about 50 m apart were acquired in each area, with 360º and 300º of horizontal and vertical coverage, respectively. The resolution was ¼ (about 6 mm for a distance of 10 m) and 4x quality, taking about 11 min to acquire each scene. After scanning the point cloud, photos were taken by the 70 Megapixel camera of the scanner, obtaining color in the scenes. An internal GNSS acquired the station coordinates, aiding positioning. As specific targets for the laser scan were not placed in the terrain, the scenes were positioned and aligned based on its overlap through cloud-by-cloud method, which was performed using the software Scene. After point cloud alignment, the dense cloud is built and color is applied. Measurements can be performed using targets created at the scenes or directly in the point cloud, which can be used to build a mesh and a DEM.

The products for each area are: coordinates of the targets with GNSS and Total Station; DEM and orthophoto from photogrammetric reconstruction; and 3D point cloud from laser scanning. All results were uploaded into the GIS project, where they were compared and interpreted.

RESULTS

The DEM of SRTM was classified with 11 colors ranging from 0 to 32 m, allowing four main elevation units to be distinguished (Figure 1). The higher unit ranges from 10 to 32 m, has an elongate shape with a SW-NE orientation, and an undulating morphology. Its border is evidenced in the slope image, achieving a maximum of 8º (Figure 1). This unit is defined as Barrier II (CPRM, 2008), which has its genesis related to a sea level elevation occurring at about 200 ka, and is where the main urban area of Santa Vitoria do Palmar is located. Except for areas of drainage, in the HAND model most of this unit is classified as low susceptibility, with 5.35 to 32 m. As well, NDWI values are all ≤ 0, indicating dry areas.

The second unit is at most 7.5 m high, with elevation ranging from 10 to 3 m. It has a curved form with the presence of a S-N spit shape. The terrain is plain to gently undulating and its borders are in contact with lower units which have slopes of about 1º. This unit is defined as lagoonal deposits, probably related to the evolution of System III, which has its genesis associated with a sea level maximum at about 120 ka. As sea level achieved a maximum of +3 m on the Rio Grande do Sul coast during the Holocene, the elevation of this unit allows an interpretation that it must have been formed during a higher sea level event, compatible with the one associated with System III (Tomazelli and Dillenburg, 2007). In the HAND model this unit contains all classes, where most of the low susceptibility areas are in the spit area. In the NDWI image the values are all ≤ 0, indicating dry areas.

Unit III is lower than 5 m and extends as an elongated area, with a gentle curved border limited to the east with Unit II, and to the west with Unit IV. It has a plain morphology and its border is in contact with Unit IV and has slopes less than 0.5º. In the HAND model this unit has medium and high inundation susceptibilities, and in the NDWI image the area was dry. This unit is mapped as part of System III (CPRM, 2008), but as it has altitudes close to the maximum of sea level during the Holocene, and as no absolute dating has been done, this definition is not precise.

Unit IV is in the margin of Mirim lagoon, it is plain, with an elevation lower than 3 m. In HAND model this unit has medium and high inundation susceptibilities, and NDWI indicates that most of the area was flooded. Dryer and medium susceptibility areas of Unit IV are related to spits developed on the lagoon margin. Unit IV is comprised of lagoonal deposits, related to the evolution of System IV, developed during the Holocene (CPRM, 2008).

For each of the three target areas the detailed surveys resulted in a series of data that were analyzed and compared. Area 1 is in the border of units II and IV. Elevation ranges from 7 to 1 m, defined with the DEM produced by photogrammetric reconstruction. The DEM has a resolution of 0.03 m and photos alignment achieved a precision of 0.26 m in relation to target positioning. Four profiles were conducted along the same place with the different methods (Figure 2). With the exception of the GNSS profile, all are similar, with lower values to the west (Unit IV) and higher to the east (Unit II), achieving a maximum difference of 2.2 m between SRTM and GNSS profiles. In the GNSS profile an elevation of about 1 m in its west portion is represented. Although it is overstated, it does exist and is represented in the photogrammetric model, with about 0.4 m. As well, laser scanner measurements allowed identification of the same feature, with a compatible level difference, which are not represented in total station and SRTM profiles because of their resolution – measurements only of targets with the total station, and a pixel size of 30 m for SRTM. Slopes defined with SRTM (1.05º), photogrammetric data (0.95º), and total station (0.85º) varies less than 0.2º.

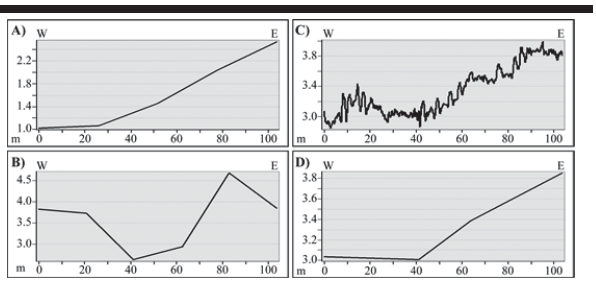

Figure 2. Profiles of Area 01, built with four methods: A) SRTM DEM; B) GNSS; C) Photogrammetric DEM; and D) Total Station. Higher areas are Unit II (E), and lower are Unit IV (W).

Area 2 is in the border of units II and III, with elevation ranging from 7 to 1 m in the photogrammetric DEM (Figure 3), which has a resolution of 0.03 m, and a precision in photo alignment of 0.78 m. With the exception of SRTM, the profiles have a similar trend, where higher values are to the west (Unit II) and lower to the east (Unit III). The maximum difference is of 2.6 m between SRTM and the other profiles. The slope defined with SRTM (1.2º) is twice that defined in the photogrammetric data (0.7º), total station (0.6º), and GNSS (0.6º).

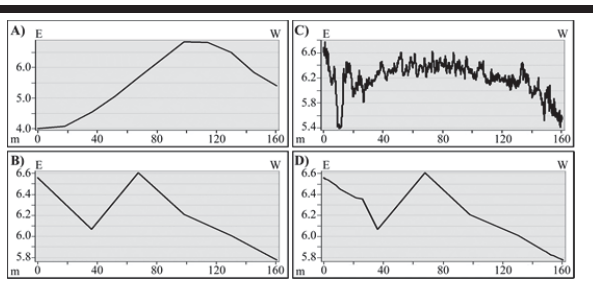

Figure 3. Profiles of Area 02, built with four methods: A) SRTM DEM; B) GNSS; C) Photogrammetric DEM; and D) Total Station. Higher areas are Unit II (W), and lower are Unit III (E).

Finally, Area 3 is in the internal region of the spit, in the border of units II and IV. The elevation of this area ranges from 8 to 2.5 m in the photogrammetric DEM, which has a resolution of 0.03 m, and a precision of 0.51 m (Figure 4). The profiles have similar trend, with the lowest values to the north (Unit III), the highest in the middle, and lower to the south (Unit II). While total station and GNSS profiles have almost identical altitudes, with low levels close to the SRTM, photogrammetric profile has high values close to the ones of SRTM. Slopes are higher in SRTM (1.9º), medium in total station and GNSS profiles (1.3º), and lower in photogrammetric model (0.7º).

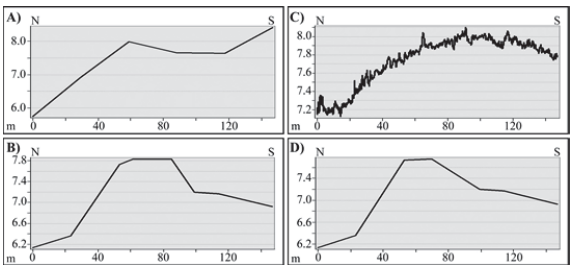

Figure 4. Profiles of Area 03, built with four methods: A) SRTM DEM; B) GNSS; C) Photogrammetric DEM; and D) Total Station. Higher areas are Unit II (S), and lower are Unit III (N).

Laser scanning provided dense point clouds for each area; however, as only three scans were acquired, many gaps are present in the scenes, especially because of shadow zones caused by vegetation. Thus, laser scanning data were applied only to compare dimensions and solve doubts of specific features observed through other methods.

DISCUSSION

The analysis performed at a regional scale through geoprocessing of remote sensing data, allowed the characterization of four morphological units, which are directly related to geological evolution and inundation hazard. Sea level fluctuations influenced lagoon and palaeo-lagoon level, controlling the development of sedimentary systems in specific positions. Related to the evolution of System III, at about 120 ka, Unit II has been deposited at higher levels than those achieved during the Holocene, determining low inundation susceptibility for this (Figure 1). Besides base level, susceptibility is also influenced by lagoon dynamics, as spit features have low susceptibilities than other areas in the same unit. It is verified in units II and IV (Figure 1), indicating that the inundation hazard is influenced by allogenic and autogenic factors.

Even though the age of Unit III is not well defined, as its altitudes are close to the maximum Holocene sea level and there is no absolute dating, it is possible to hypothesize three situations. The first one is to associate this unit to the evolution of System III, formed after and in a lower level than Unit II. Another possibility is to associate this unit with the Holocene maximum sea level, achieved at about 6 ka (Angulo and Lessa, 1997). A third possibility is that its development could be associated to a lagoon level oscillation of higher frequency, which may be related to the dynamics of the lagoonal system, more precisely to the moment when the inlet connecting Mirim lagoon with the Atlantic ocean, in the region of Taim Swamp, was closed. At any rate, from Unit I to IV the ages are progressively younger, and inundation susceptibility is progressively higher.

Comparing the four units it is clear that Unit IV has a higher inundation susceptibility. However it does not mean that it is the most dangerous area, as people are used to seeing those terrains flooded with frequency. Thus, although Unit III has a lower susceptibility, it is possible to see that it could be more

dangerous, as a lower frequency and greater magnitude event could flood that area. This in the year of 1941, when 431.6 mm fell in 21 days, between April 10th and May 14th. According to the dwellers, "the lagoon entered through behind", which is actually related to the fact that the flood skirted the spit of Unit II, reaching its inner edge.

In relation to detailed areas, altitudes and slopes were established, and the results of different methods were compared. As many works that aim at defining risk areas employ regional DEM as the one SRTM, it is fundamental to analyze its validation for this purpose. Despite that the SRTM DEM has a limited resolution, and some features are not represented, in a general way it has a correspondence to the topographic data acquired in the field. Morphological trends are recorded, but absolute elevations and slopes differ from those defined through the surveys. This may influence the details of forecast models relating precipitation, water level changes and risk areas, but for a regional analysis it can be satisfactorily applied.

Photogrammetric reconstruction proved to be an efficient way to acquire continuous and good quality topographic data with very low cost. The combination of a high resolution DEM with orthophotos provides detailed information that can be applied to improve models. Although the quality of the results have been varied among the areas, as the survey covered extensions larger than target allocation, it could be improved with a better target distribution. Professional UAV, specifically designed for mapping purposes, would enhance the results as well. Laser scanning is another good way to acquire detail topographic data, however many scans are necessary to a complete and continuous surface representation, implying significant field time and high performance computers for data processing. An alternative to have a better continuity in the mapped surface is to couple a laser scanning system with a UAV, for aerial acquisition.

CONCLUSIONS

In this work the application of different methods with an aim to analyze inundation risk and its relation with geological evolution is presented. It was possible to define four main units with different levels of susceptibility, which correspond to geological units with different ages. The allogenic control related to the development of these units is sea level, which controls lagoon level. An autogenic control was also noticed and is related to the dynamics of the lagoon system, where spits are higher and have a lower susceptibility when compared to the plains of the same age.

A qualitative assessment of three target-areas was developed defining the topography with GNSS, total station, laser scanning and through a photogrammetric reconstruction. The advantages and disadvantages of each method and its relation to the MDE of SRTM were analyzed. Although differences have been identified, for regional definitions, the SRTM data can be applied satisfactorily, as its relation to terrain morphology was checked. For detailed analyses the most effective method was the photogrammetric reconstruction. In this purpose, the combination with GNSS is fundamental for positioning. A closer base station could improve GNSS precision, excluding the need for a total station to define target position, especially elevations.

Finally, inundation susceptibility does not always reflect how dangerous an area can be, as more susceptible areas which flood frequently are less occupied by urban settlement than areas without such an obvious risk.

ACKNOWLEDGMENTS

The authors would like to acknowledge the Geosciences Institute of the Federal University of Rio Grande do Sul (UFRGS) for funding, and P. Hesp for his editorial assistance.

LITERATURE CITED

Agisoft PhotoScan, 2013. *User Manual: Professional Edition.* Version 0.9.1; AgiSoft LLC: Petersburg, Russia.

Angulo, R.J. and Lessa, G.C. 1997. The Brazilian sea-level curves: a critical review with emphasis on the curves from Paranaguá and Cananéia regions. *Marine Geology*, 140,141-166.

CPRM, 2008. *Geologia e recursos minerais do Estado do Rio Grande do Sul.* Programa de Geologia do Brasil. Integração, Atualização e Difusão de Dados de Geologia do Brasil. Mapas Geológicos Estaduais em Sistema de Informações Geográficas – SIG. 1:750.000. DVD Rom.

Lopes, R.P.; Kinoshita, A.; Baffa, O.; Figueiredo, A.M.G.; Dillenburg, S.R.; Schultz, C.L., and Pereira, J.C., 2014. ESR dating of Pleistocene mammals and marine shells from the coastal plain of Rio Grande do Sul state, southern Brazil. *Quaternary International*, 352, 124-134

Rosa, M.L.C.C., 2012. *Geomorfologia, estratigrafia de sequências e potencial de preservação dos sistemas laguna-barreira do quaternário costeiro do Rio Grande do Sul.* Porto Alegre, 251p. PhD Thesis, Instituto de Geociências, Universidade Federal do Rio Grande do Sul.

Mancini, F.; Dubbini, M.; Gattelli, M.; Stecchi, F.; Fabbri, S.; and Gabbianelli, G., 2013. Using Unmanned Aerial Vehicles (UAV) for High-Resolution Reconstruction of Topography: The Structure from Motion Approach on Coastal Environments. *Remote Sens.* 5, 6880-6898.

McFeeters, S.K., 1996. The use of the Normalized Difference Water Index (NDWI) in the delineation of open water features. *International Journal of Remote Sensing*, 17(7), 1425-1432.

Pires, E.G. and Borma, L.S. 2013. Utilização do modelo HAND para o mapeamento de bacias hidrográficas em ambiente de Cerrado. In: *Anais of 16th Simpósio Brasileiro de Sensoriamento Remoto.* Foz do Iguaçu, PR. Foz do Iguaçu: INPE, 5568-5575.

Tomazelli, L.J. and Dillenburg, S.R. 2007. Sedimentary facies and stratigraphy of a last interglacial coastal barrier in south Brazil. *Marine Geology*, 244, 33-45.

Villwock, J.A. and Tomazelli, L.J., 1995. Geologia Costeira do Rio Grande do Sul. *Notas Técnicas* 8, 1-45.

Villwock, J.A., 1984. Geology of the Coastal Province of Rio Grande do Sul, Southern Brazil. A synthesis. *Pesquisas*, 16, 5-49.

Journal of Coastal Research	SI	75	1232 - 1236	Coconut Creek, Florida	2016

Natural and Anthropogenic Coastal System Comparison Using DSM from a Low Cost UAV Survey (Capão Novo, RS/Brazil)

Frederico M. Scarelli[‡†*], Luigi Cantelli[†], Eduardo G. Barboza[††], Maria Luiza C.C. Rosa[††], and Giovani Gabbianelli[†]

[‡] Programa de Pós Graduação em Geociências, Universidade Federal do Rio Grande do Sul Porto Alegre, RS, Brasil.

[†] BiGeA, Università di Bologna, Ravenna, Italy.

[††] CECO, Instituto de Geociências, Universidade Federal do Rio Grande do Sul, Porto Alegre, RS, Brasil.

www.cerf-jcr.org

www.JCRonline.org

ABSTRACT

Scarelli, F.M.; Cantelli, L.; Barboza, E.G.; Rosa, M.L.C.C.; and Gabbianelli, G., 2016. Natural and Anthropogenic coastal system comparison using DSM from a low cost UAV survey (Capão Novo, RS/Brazil). *In:* Vila-Concejo, A.; Bruce, E.; Kennedy, D.M., and McCarroll, R.J. (eds.), *Proceedings of the 14th International Coastal Symposium* (Sydney, Australia). *Journal of Coastal Research*, Special Issue, No. 75, pp. 1232 - 1236, ISSN 0749-0208.

In many cases, unplanned urbanization is the main factor that causes a decrease in coastal resilience. This paper compares the differences between the anthropogenic and natural coastal zone, based on the morphological dune reconstruction, using a low cost UAV (unmanned aerial vehicle) survey and the photogrammetric reconstruction method. The study area is in the Northern Littoral of Rio Grande do Sul State, where the dunes have few man-changes and are adjacent to an anthropogenic zone with a highly modified beach/dune system. By photogrammetric reconstruction it was possible to obtain a high-resolution DSM (Digital Surface Model) and a high-resolution othophoto to analyse differences in morphology. Data acquired by UAV's are important to coastal managers and decision makers as they can collect high-resolution data and be used for Integrated Coastal Zone Management. Moreover this work propose a low cost method for obtaining a high-resolution data for researchers and local authorities.

ADDITIONAL INDEX WORDS: *ICZM; coastal morphology; coastal zone; photogrammetry.*

INTRODUCTION

To increase knowledge about coastal environmental behavior and to apply integrated coastal zone management (ICZM), it is essential to know about the pressures on the system and the interaction between the anthropogenic and natural factors (Psuty, 1988; Sherman and Bouer, 1993; Hesp, 2002; Carrasco *et al.*, 2012). This knowledge aids coastal managers in improving their choices for coastal resource management, decreasing vulnerability and hazard as well as attending to stakeholders interests (Kindermann, and Gormally, 2013). To acquire more information and to monitor the coastal environment, local authorities need a better cost-benefit tool to obtain data on natural factors such as the impact of the storm-surges on the coast, and anthropogenic pressure factors as the urban zone expands (Andrews *et al.*, 2002; Lambert and Zanuttigh, 2005; Davidson *et al.*, 2006; Tătui *et al.*, 2013).

This work proposes a methodology to acquire high-resolution Digital Surface Models (DSM) and ortho-rectified images (orthophotos) in the coastal environment (Mancini *et al.*, 2013) using a low cost and easy to operate unmanned aerial vehicle (UAV). Moreover, the data may be used in several disciplines, including engineering, urban planning, biological, geological and environmental sciences, archaeology and others (Gares *et al.*, 2006).

The study aims to investigate the morphology and the interaction between natural and anthropogenic features of a dune/beach system on a Brazilian coastal region, using aerial photos obtained from a UAV survey (Casella *et al.*, 2014; Gonçalvez and Henriques, 2015).

In this work we have done a qualitative analysis since the main aim is to propose the methodology to acquire environmental data at a low cost. In the region where this study was conducted, many features are present that may increase the vulnerability and the risks in the coastal zone such as small creeks, which are washouts through the foredunes and beach named "sangradouros", according to Figueiredo and Calliari, (2005). These are mainly pluvial water drainage channels that are about 0.8 m deep. These features may be observed along the entire Rio Grande do Sul (RS) coast and are mainly present in the urbanized stretches. These washouts represent a high coastal hazard, because in many cases the beaches are trafficked by cars and the washouts are hidden, causing severe accidents. In addition, due to the foredune fragmentation the sediment transport from dune and beach to the surf zone, mainly during storms, may create a sediment deficit, increasing coastal erosion. Finally, this work offers a good coast-benefit tool for local authorities to increase the investments in the local ICZM and in

DOI: 10.2112/SI75-247.1 received 15 October, 2015; accepted in revision 15 January, 2016.
*Corresponding author: frederico.scarelli@ufrgs.br
©Coastal Education and Research Foundation, Inc. 2016

the coastal urbanization planning, since many of the coastal settlements grow without an urban plan (Esteves *et al.*, 2003).

Background

The study area is in Capão Novo, a beach settlement in the Northern littoral stretch of Rio Grande Do Sul (RS), the southernmost state of Brazil (Figure 1). The RS coast is approximately 620 km length, has a gentle undulating barrier coast with a NE-SW orientation, and is characterized by a barrier-lagoon depositional system formed by sea level changes during the Quaternary (Villwock *et al.*, 1986; Dillenburg *et al.*, 2009). The coast is classified as dissipative and intermediate beaches; the beaches area about 60 m in width (Gruber *et al.*, 2006), and have a microtidal regime with a semidiurnal tide with a mean range of 0.5 m. It is a wave-dominated coast and the sediment supply is by littoral drift that is northward. The barrier deposits are dominated by very fine to medium grained quartz sand; the dominant winds are from NE during spring and summer, and from SW during autumn and winter (from April to July). The latter are responsible for the stronger storm surges (Dillenburg and Barboza, 2014). The average significant wave height is 1.5 m, and during storms the sea level may surge up to 1.3 m at the coast (Barletta and Calliari, 2001; Calliari *et al.*, 1998).

Figure 1. Study area in North Littoral of RS. The red polygon is the UAV survey area.

The study area is located in a mildly concave part of the coast in a regressive stretch of the barrier that was covered by transgressive dunefields during the barrier progradation (Dillenburg *et al.*, 2009; Barboza *et al.*, 2011 and 2013). In this stretch, the reduction and dispersion of wave energy resulted in a positive balance for the sediment budget, however, the anthropogenic activities and an unplanned development (Esteves *et al.*, 2003) increased the vulnerability along the coast. The foredunes have been subject to urbanization with sidewalks built directly above the dunes, beachfront properties and sand mining,

that affected the local sand balance (Dillenburg *et al.*, 2004). Capão Novo and near settlements represent the most developed and urbanized beaches in this stretch, principally by holiday houses that are engaged during the summer season. The beaches were classified as developed and mainly eroding beaches by Estves *et al.*, (2003). This study focuses on a 600 m stretch which includesa part of a dune in an urbanized zone and a part of dune in an adjacent non urbanized zone, with a washout in between.

METHODS

To do an high-accuracy analysis of the stretch under study a low coast UAV was used to obtain a high-resolution DSM and orthophoto from a photogrammetric reconstruction method (Mancini *et al.*, 2013). The flight was done in the final part of the summer season (mid-march) when the beach presented a summer profile. To collect the aerial photographs a DJI Phantom quadcopter was utilised, a smaller commercial UAV costing about USD$1,000. The advantages of this UAV are that it has an easy flight system platform allowing a safe control and operability and costs much more less than a professional UAV. The DJI Phantom UAV has an integrated GPS Positioning Module as ±0.8m vertical and ±2.5m horizontal accuracy, a Controlled Automatic Return to Home; an Intelligent Flight Battery; a 3-Axis Camera Stabilization; a 14 Megapixel HD camera, which has a FOV (field of view) 140° f/2.8 focus at ∞, with real-time Camera Preview on IOS and Android Device Application. A smartphone integrated with the the UAV Remote Controller is required to control the camera. The survey took about one hour, and was done in three flights in the entire stretch, flying at three different heights, ~16, ~30, and ~5 m above the washout to increase data resolution. The flight speed was ~1.5 m/s; and 689 photos were acquired, shot perpendicular to the ground, with about 80% overlap between the aerial photos to allow the creation of the DSM in Agisoft Photoscan software. The UAV flight was coupled with a Global Navigation Satellite System (GNSS) eTrex®30-Garmin with barometric altimeter and with the local topographic chart. The flight track acquired was used to insert a geotag in all the photos using BaseCampTM. For high-accuracy that allows one to use the model for a quantitative and future comparative analyses 36 Ground Control Points (GCPs) were used and georeferenced by Differential Global Navegation Satellite System (DGNSS) using a Trimble® ProXRT GNSS in UTM-WGS84-22S. These used in Agisoft as monument points in coded targets. Due to the FOV wide-angle camera on the UAV, a customized calibration profile to recover planarity in the potos was used, and this calibration allow us to obtain a higher accuracy orthophoto.. Using a Structure from Motion (SfM) approach (Snavely *et al.*, 2007) by Agisoft Photoscan Professional Edition algorithms workflow (Agisoft, 2013), after photo alignment and GCPs the following was accomplished: i) point cloud; ii) the dense cloud, where the model was cleaned, deleting the outlyer points and persons or other objects;iii) a mesh was built; and iv) the texture. After this workflow the model has been exported into a DSM in ascii format and an orthophoto in tiff extension, allowingthe data to be imported into a Geographic Information System (GIS) software.

RESULTS AND DISCUSSION

This survey allow us to obtain a DSM with a 0.3 m cell resolution and an othophoto with a pixel size of 0.05 m. The orthophoto was draped on the DSM to improve this analysis, allowing us to identify the features in the area, such as the vegetation density. In this model the features without interest were not eliminated such as the people, cars or trees, because these elements may indicate the survey quality. Based on the model results (Figure 2) it is possible to recognize clear differences between the natural and urbanized areas:

In the urbanized area (Figure 2E and 2F): the dune is very fragmented, the blowouts are visible, the anthropogenic pressure is very high with a walkway above the dune, and behind the dune facilities. In addition, a -controlled washout is present, which removes sediments from the foreshore/backshore and carries them to the surf zone, decreasing the dune resilience. Since according to Tomazelli *et al.* (2008) most of the sediment to the natural system nourishment of the dune system in the Northern Littoral of RS comes from the backshore/foreshore, that are transported by the NE wind.In the natural area (Figure 2C and 2D), an active dune field is present, with vegetation that increases in density inland. The sediment availability for the system equilibrium due to the seasonal beach profile changes is clearly higher and the washout is bigger than in the urbanized area and without human driven changes. Actually this area presents the same morphological characteristics of the zone in 1948 where it is possible to identify the dune fields with a NE orientation but without anthropomorphic pressures.

This survey has disadvantages and advantages, which are necessary to discuss to increase the potential of the method in future work. The disadvantages are the time to realize the workflow on Agisoft, mainly to obtain high-resolution data; a powerful computer is necessary; the cost of the GNSS equipment to do the GCPs survey with high accuracy; in the surveys where water and features in movement are present, there may be some gaps because, the vegetation is moved by wind, and the software is unable to point match between the potos. For a quantitative analysis of the volumumetric changes with high accuracy, the vegetation cover may be a problem because it interfers with accurate results. In addition, weather is another limiting factor because the Dji Phanton cannot fly in wind speeds above ~18 km/h winds. The advantages are the price to acquire high-resolution data if compared to the other UAV's or LiDAR surveys that may be able to provide the same data accuracy; the facility to operate the UAV with high security; the logistics are simpler allowing a quick organization for the surveys after an interesting event such as a storm appears; easily repeatability of the data to increase the database and to aid coastal monitoring; the data may be used in different disciplines for scientific work as well for management work.

CONCLUSIONS

Using a low coast UAV, it has been possible conduct a first high-accuracy DSM to study the coastal environment in the coast of RS. This has allowed us to investigate the factors that act in this zone and to understand in a detailed scale the environmental response to the urbanized areas. The results obtained from the aerial photographic survey are of great quality, which is ± 0.13 m accuracy, and in accordance with

other work (Mancini *et al.*, 2013; Casella *et al.*, 2014; Gonçalves and Henriques, 2015) where the same survey methodology was used using a SfM approach with a professional camera. This work provides a low cost methodology to aid the local authorities acquire high-resolution data in their area of interest and to improve the management and knowledge about the environment responses to natural and human pressures. In many cases, mainly in developing countries such as Brazil, the local authorities do not have funds to create a simple database to aid decision-makers in their actions, and this work and UAV provides a low cost alternative to support both scientific research or local authorities.

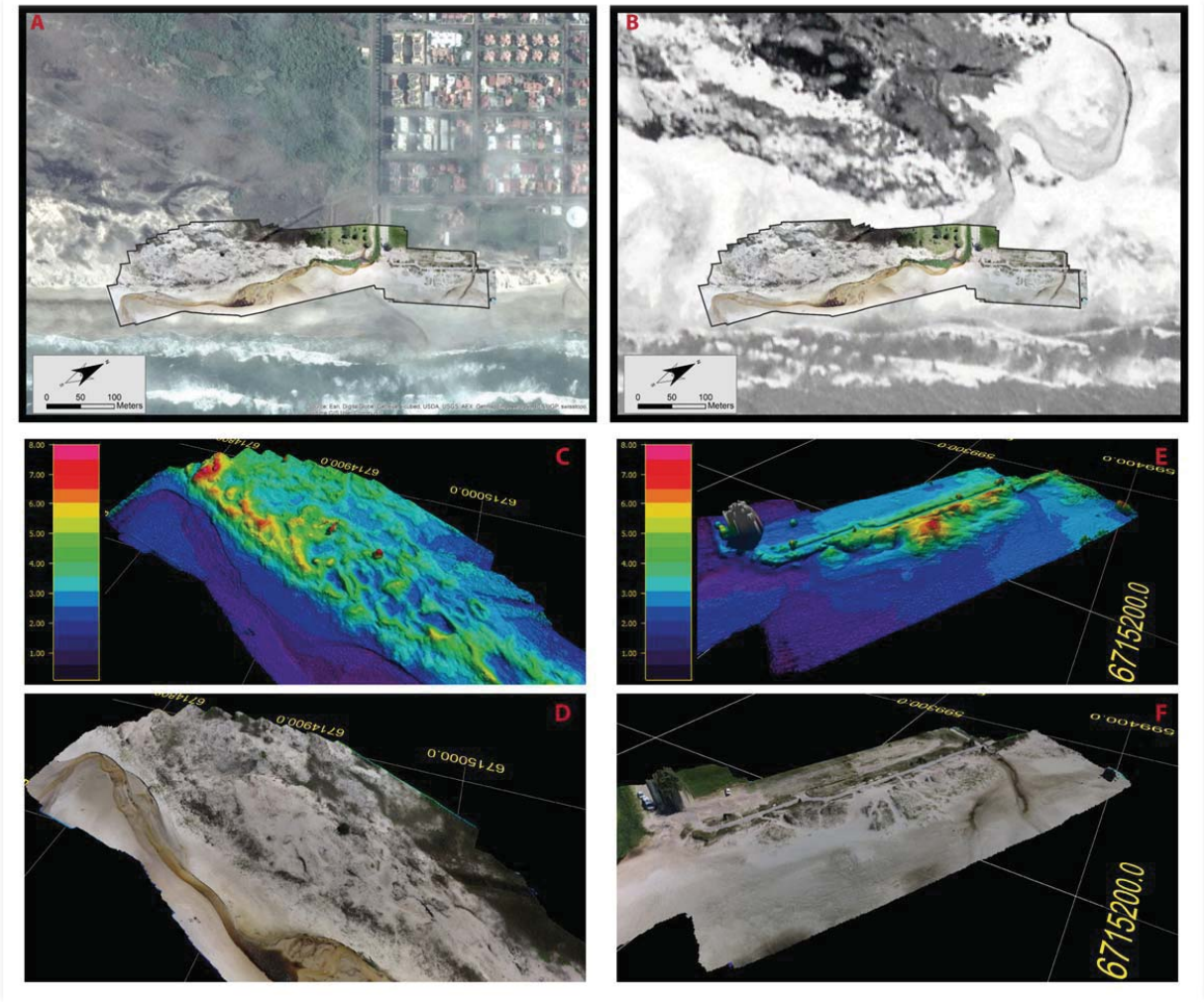

Figure 2. Results from the UAV survey: A) the orthophoto overlapping the World Imagery from ArcGIS Online data; B) the orthophoto overlapping the aerial photo from 1948; C) DSM in the natural area; D) orthophoto draped on the DSM in the natural area; E) DSM in the anthropogenic area; F) orthophoto draped on the DSM in the anthropogenic area

ACKNOWLEDGMENTS

This study has been done through the Joint Laboratory on Coastal Evolution between UFRGS and UNIBO; funded by Fondazione Flaminia (Italy) via project RIGED-RA; and Conselho Nacional de Desenvolvimento Científico e Tecnológico (CNPq – Brazil) via project n° 307856/2013-5. We are grateful for PPGGEO/IGEO/UFRGS and for all students who participated in the survey.

LITERATURE CITED

Agisoft PhotoScan, 2013. *User Manual: Professional Edition*; Version 0.9.1; AgiSoft LLC: Petersburg, Russia

Andrews B.; Gares P., and Colby J., 2002. Techniques for GIS modeling of coastal dunes. *Geomorphology,* 48, 289-308.

Barboza, E.G.; Rosa, M.L.C.C.; Hesp, P.A.; Dillenburg, S.R.; Tomazelli, L.J., and Ayup-Zouain, R.N., 2011. Evolution of the Holocene Coastal Barrier of Pelotas Basin (Southern Brazil) - a new approach with GPR data. *Journal of Coastal Research*, SI 64, 646-650.

Barboza, E.G.; Rosa, M.L.C.C.; Dillenburg, S.R., and Tomazelli, L.J., 2013. Preservation potential of foredunes in the stratigraphic record. *Journal of Coastal Research*, SI 65, 1265-1270.

Barletta, R.C. and Calliari, L.J., 2001. Determinação da intensidade das tempestades que atuam no litoral do Rio Grande do Sul, Brasil. *Pesquisas em Geociências*, 28(2), 117-124.

Calliari, L.J.; Tozzi, H.A.M., and Klein A.H. F., 1998. Beach Morphology and Coastline Erosion Associated with Storm Surges in Southern Brazil- Rio Grande to Chuí, RS. *Anais Academia Brasileira de Ciências,* 70, 231-247.

Casella, E.; Rovere, A.; Pedroncini, A.; Mucerino, L.; Casella, M.; Cusati, L.A.; Vacchi, M.; Ferrari, M., and Firpo, M., 2014. Study of wave runup using numerical models and low-altitude aerial photogrammetry: A tool for coastal management. *Estuarine, Coastal and Shelf Science*, 149, 160-167.

Carrasco, A.R.; Ferreira, O.; Matias, A., and Freire, P., 2012. Natural and human-induced coastal dynamics at back-back barrier beach. *Geomorphology*, 159 -160, 30-36.

Davidson, M.A.; Aarninkhof, S.G.J.; Van Koningsveld, M., and Holman, R.A., 2006. Developing coastal video monitoring systems in support of coastal zone management. *Journal of Coastal Research*, SI 39, 49-56.

Dillenburg, S.R. and Barboza, E.G., 2014. The Dip and Strike-Fed Sandy Coast of Southern Brazil. In: Martini, I.P. and Wanless H.R. (eds.). Sedimentary Coastal Zones from High to Low Latitudes: Similarities and Differences, *Geological Society, London*, Special Publications 388, 333-352.

Dillenburg, S.R.; Esteves, L.S., and Tomazelli, L.J., 2004. A critical evaluation of coastal erosion in Rio Grande do Sul, Southern Brazil. *Anais da Academia Brasileira de Ciências*, 76(3), 611-623.

Dillenburg, S.R.; Barboza, E.G.; Tomazelli, L.J.; Hesp, P.A.; Clerot, L.C.P., and Ayup-Zouain, R.N., 2009. The Holocene Coastal Barriers of Rio Grande do Sul. In: Dillenburg, S.R. and Hesp, P.A. (eds.), Geology and Geomorphology of Holocene Coastal Barriers of Brazil. *Lecture Notes in Earth Sciences*, 107, 53-91.

Esteves, L.S.; Silva, A.R.P.; Arejano, T.B.; Pivel, M.A.G., and Vranjac, M.P., 2003. Coastal development and human impacts along the Rio Grande do Sul beaches, Brazil. *Journal of Coastal Research*, SI 35, 548-556.

Figueiredo, S.A. and Calliari, L.J., 2005. Sangradouros: Distribuição Espacial, Variação Sazonal, Padrões Morfológicos e Implicação no Gerenciamento Costeiro. *Gravel*, 3, 47-57.

Gares, P.A.; Wang, Y., and White, S.A., 2006. Using LIDAR to monitor a beach nourishment project at Wrightsville Beach, North Carolina, USA. *Journal of Coastal Research*, 22(5), 1206-1219.

Gonçalvez, J.A. and Henriques, R., 2015. UAV photogrammetric for topographic monitoring of coastal areas. ISPRS *Journal of Photogrammetric and Remote Sensing*, 104, 101-111.

Gruber, N.L.S.; Toldo, E.E.; Barboza, E.G.; Nicolodi, J.L., and Ayup-Zouain, R.N., 2006. A shoreface morphodynamic zonation and the equilibrium profile variability on the northern coastline of Rio Grande do Sul, Brazil. *Journal of Coastal Research*, SI 39, 504-508.

Hesp P.A., 2002. Foredune and blowouts: initiation, geomorphology and dynamics. Geomorphology, 48, 245-248.

Kindermann, G. and Gormally, M.J., 2013. Stakeholder perceptions of recreational and management impacts on protected coastal dune systems: A comparison of three European countries. *Land Use Policy*, 31, 472-485.

Mancini, F.; Dubbini, M.; Gattelli, M.; Stecchi, F.; Fabbri, S., and Gabbianelli, G., 2013. Using Unmanned Aerial Vehicles (UAV) for High-Resolution Reconstruction of Topography: The Structure from Motion Approach on Coastal Environments. *Remote Sensing*, 5, 6880-6898.

Psuty, N.P., 1988. Sediment budget and beach/dune interaction, in: N.P. Psuty (Ed), Dune/Beach Interaction. *Journal of Coastal Research*, SI 3, 1-4.

Sherman, D.J. and Bauer, B.O., 1993. Dynamics of beach-dune interaction. *Progress in Physical Geography*, 17, 413-447.

Snavely, N.; Seitz, S., and Szeliski, R., 2007. Modeling the world from the internet photo collections. *International Journal of Computer Vision*, 80(2), 189-210.

Tătui, F.; Vespremeanu-Stroe, A., and Preoteasa, L., 2013. The correlated behavior of sandbars and foredunes on a nontidal coast (Danube Delta, Romania). *Journal of Coastal Research*, SI 65, 1874-1879.

Tomazelli, L.J.; Dillenburg, S.R.; Barboza, E.G., and Rosa, M.L.C.C., 2008. Geomorfologia e Potencial de Preservação dos Campos de Dunas Transgressivos de Cidreira e Itapeva, Litoral Norte do Rio Grande do Sul, Brasil. *Revista Pesquisas em Geociências*, 35(2), 47-55.

Villwock, J.A.; Tomazelli, L.J.; Loss, E.L.; Dehnhardt, E.A.; Horn, N.O.; Bachi, F.A., and Dehnhardt, B.A., 1986. Geology of the Rio Grande do Sul Coastal Province. In: Rabassa, J. (Ed.), *Quaternary of the South America and Antarctic Peninsula*, 4, 79-97.

Journal of Coastal Research	SI	75	1237 - 1241	Coconut Creek, Florida	2016

Lagrangian Coherent Structures and the Dispersion of Green Algal Bloom in the Yellow and East China Sea

Young Baek Son [†], Yong Hoon Kim[‡], Byoung-Ju Choi[††], and Young-Gyu Park[§*]

[†]Jeju International Marine Science Center for Research & Education
Korea Institute of Ocean Science and Technology (KIOST), Korea

[‡] RPS ASA (Applied Science Associate Inc.)
South Kingstown, RI, USA

[††] College of Ocean Science and Technology
Kunsan National University, Korea

[§]Ocean Circulation and Climate Research Center
Korea Institute of Ocean Science and Technology (KIOST), Korea

www.cerf-jcr.org

www.JCRonline.org

ABSTRACT

Son, Y.B.; Kim, Y.H.; Choi, B.-J., and Park, Y.-G., 2016. Lagrangian Coherence Structures and the dispersion of green algal bloom in the Yellow and East China Sea. *In:* Vila-Concejo, A.; Bruce, E.; Kennedy, D.M., and McCarroll, R.J. (eds.), *Proceedings of the 14th International Coastal Symposium* (Sydney, Australia). *Journal of Coastal Research*, Special Issue, No. 75, pp. 1237 - `1241. Coconut Creek (Florida), ISSN 0749-0208.

During the summer 2011, the Geostationary Ocean Colour Imager (GOCI) detected patches of the recurrent massive floating green algae in the central part of the Yellow Sea (YS) and East China Sea (ECS). This study utilizes the Lagrangian Coherent Structures (LCSs) analysis to demonstrate the horizontal dispersion pattern of algal bloom patches. This approach is based on the assumption that unstable manifolds such as ridges in the finite-time Lyapunov exponent (FTLE) fields coincide with material transport barriers. To calculate the FTLE fields, flow fields derived from the Regional Ocean Modeling System (ROMS) and wind fields were utilized. The combined effects of winds and currents in material transport in coastal and ocean environments were investigated. Comparison of LCSs derived by current only and current-wind combined flow showed that the results of current-wind combined flow cases match better the observation results from GOCI than those of current only cases. This implies that the distribution pattern of green algae patches would be controlled by the combined effect of the surface current and wind that was included LCS in terms of leeway effect.

ADDITIONAL INDEX WORDS: *Lagrangian particle tracking, Floating green algae detection, GOCI, Leeway effect.*

INTRODUCTION

Green algae blooms due to *Ulva prolifera* (previously known as *Enteromorpha prolifera*; Hayden *et al*., 2003) are commonly observed in Chinese coastal waters (Hu *et al*., 2010). During summer 2011, the image analysis of the world's first Geostationary Ocean Color Imager (GOCI) and various field observations showed the recurrent massive floating green algae bloomed in the Yellow Sea (YS) and East China Sea (ECS) (Son *et al*., 2012b, 2015, Figure 1). One of massive green algae blooms was detected at offshore area near Qingdao, China on 13 June 2011. After one month, they were suddenly appeared in the central part of the YS/ECS and even near the west coast of Korea. During *in situ* hydrographic cruises conducted in the early July 2011 in the YS and on the west coast of Korea, the presence of patches of the floating green algae was confirmed (Son *et al*., 2015).

This expansion of the floating green algae bloom to the west coast of Korea is a rather unusual event. To elucidate the pathway of the floating green algae patches and the governing factors, Son *et al*. (2015) conducted Lagrangian particle tracking modeling experiments. They demonstrated that in addition to the ocean current dominant southerly winds during June and July 2011 caused the green algae to detach from the coast and move to the east toward the west coast of Korea. The previous study was more about the overall movement of the patches over longer time scale (*i.e*., months). However, the structure of the dispersion pattern of bloom patches in shorter term (*i.e*., hours to days), the main theme of this study, was not investigated.

In this study we utilized the Lagrangian Coherent Structures (LCSs) analysis to unravel the effects of winds and currents on the dispersion of macroalgae bloom patches (or floated materials) in marine environments. Analysing LCSs such as stable and unstable manifolds is one emerging technologies for characterizing Lagrangian pathways and trajectories in aquatic environments (Beron-Vera *et al*., 2013; Griffa *et al*., 2013; Olascoaga and Haller, 2012; Peacock and Haller, 2013). LCS approach assumes that unstable manifolds such as ridges (*i.e*., high values) in the finite-time Lyapunov exponent (FTLE) fields coincide with material transport barriers.

By far, most of LCS studies have applied either surface flow fields or wind fields in geophysical applications. None of

DOI: 10.2112/SI75-248.1 received 15 October 2015 accepted in revision 15 January 2016
*Corresponding author: ypark@kiost.ac.kr.
©Coastal Education and Research Foundation, Inc. 2016

study analyzes combined effects of winds and currents in material transport in coastal and open ocean environments. In this study, the FTLE fields were computed from gridded trajectories using both flow fields estimated by current fields from the Regional Ocean Modeling System (ROMS) and wind fields from a regional atmospheric model (Park *et al.*, 2015) in the YS and ECS during summer 2011.

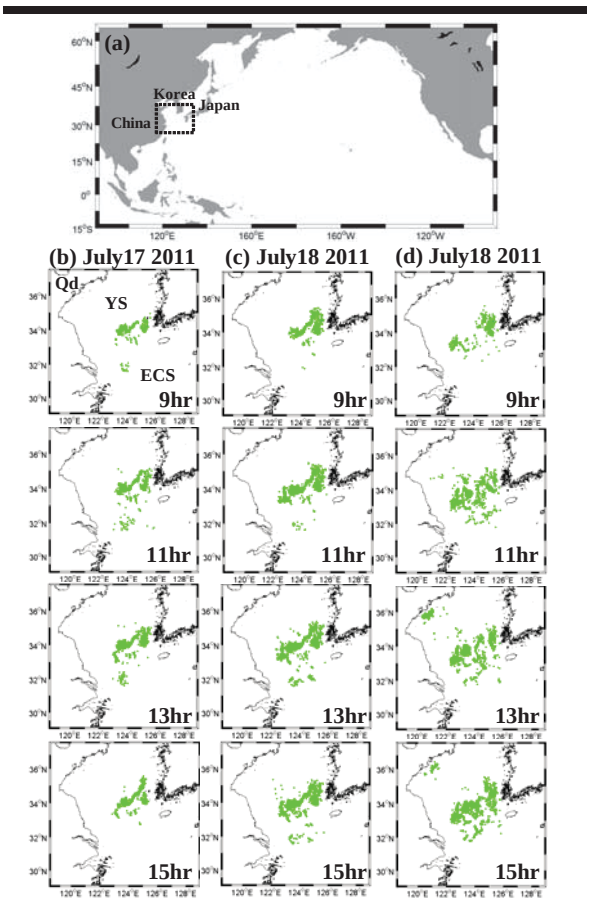

Figure 1. (a) The map of the North Pacific and its marginal seas. The retangle indicates our study area, a part of the Yellow Sea and East China Sea. The distribution of the floating green algae on (b) 18 July, (c) 19 July, and (d) 20 July 2011 from GOCI images (ECS : East China Sea, YS: Yellow Sea, Qd: Qingdao, China).

METHODS

Hourly GOCI data collected from Korea Ocean Satellite Center (KOSC) (http://kosc.kiost.ac.kr/) were used to detect massive floating green algae blooms in the YS and ECS. The Lagrangian coherent structure was then calculated using high resolution regional ocean model output and wind fields.

Satellite data processing

Son *et al.* (2012b) suggested that the spectral response of the green algae is a function of reflection at 555, 745, and 865 nm and absorption at 660 and 680 nm. An Index of floating Green Algae for GOCI (IGAG) based on multiple spectral band ratios was defined;

$$IGAG = \frac{R_{rc}(555) + R_{rc}(660)}{R_{rc}(745) - R_{rc}(660)} + \frac{R_{rc}(745)}{R_{rc}(660)} \quad (1)$$

Here R_{rc}, the Rayleigh reflectance, estimated with 6S R_{rc} (Vermote *et al.*, 1997).

$$R_{rc} = \frac{\pi \times L_t^*}{F_0 \times \cos\theta_0} - R_r \quad (2)$$

where L_t^* is the calibrated sensor radiance after adjustment for ozone and other gaseous absorption, F_0 is the extraterrestrial solar irradiance at data acquisition time, θ_0 is the solar zenith angle. The thresholds of the IGAG methods of > 0 (Son *et al.*, 2012b) indicated floating green algae in the oceanic environment as shown in Figure 1b-1e.

Lagrangian Coherent Structure

LCS enables to make predictions of pathways of tracers (Beron-Vera *et al.*, 2013; Olascoaga and Haller, 2012; Peacock and Haller, 2013). Out of numerous ways to measure stretching, the FTLE is selected in this study to show the flow geometry of general time-dependent systems. This approach is based on the assumption that unstable manifolds such as ridges (*i.e.*, high values) in the FTLE fields coincide with material transport barriers. One may consider a generic hyperbolic point and its associated stable and unstable manifolds. If we integrate two points that are initially on either side of a stable manifold forward in time, then these points will eventually diverge from each other. Likewise, if we started two points on either side of an unstable manifold, then these points would quickly diverge from each other if their trajectories are integrated backward in time. This is why these manifolds are often called separatices or repelling ridges: they separate trajectories. The FTLE, denoted by $\sigma_{t_0}^T(x)$, is a scalar value which characterizes the amount of stretching about the trajectory of point over the time interval [t, t+T], as:

$$\sigma_{t_0}^T(x) = \frac{1}{|T|} \cdot \ln\sqrt{\lambda_{\max}(\Delta)} \quad (3)$$

where $\Delta = \frac{d\phi_{t_0}^{t_0+T}(x)^*}{dx} \cdot \frac{d\phi_{t_0}^{t_0+T}(x)}{dx}$. When a particle at x, an arbitrary point at time t_0, is advected by the flow during time period T, it will be at $\sigma_{t_0}^{t_0+T}(x)$. The convention M* denotes the adjoint (transpose) of M, and $\lambda_{\max}(\Delta)$ denotes the maximum eigenvalue of Δ.

Our analysis of the pathways of green algae patches is based on surface velocity fields obtained from the ROMS, which is a three-dimensional, free-surface, hydrostatic, split-explicit, primitive equation, finite difference numerical model (Song and Haidvogel, 1994). ROMS has been widely used for the study of regional ocean circulation in the area of our interest (*e.g.*, Kim *et al.*, 2013; Lee *et al.*, 2011). The model domain (24~42.5°N, 113.9~133.5°E) includes the Bohai Sea, the Yellow Sea, the East China Sea, and the northwestern part of Pacific Ocean. Nominal horizontal grid spacing is about 8

km and 30 terrain-following levels are used in vertical direction. Bottom topography data were interpolated from 30-s gridded bathymetric data and ETOPO5 of National Geophysical Data Center.

The wind fields are derived from a regional atmospheric model operated by Korea Institute of Ocean Science and Technology (KIOST). Horizontal grid spacing of the regional atmospheric model is approximately 12 km, and there are 38 vertical layers. Wind output is stored every 3 hour and then interpolated into 1 hour interval to match with currents output time step when calculating LCS fields. In space, the wind data are also interpolated onto the ROMS grid.

To estimate leeway speed contributed by the surface wind, the drift rate is assumed as 3% of wind speed with the drift angle of zero (Youssef and Spaulding, 1993). Hourly output of currents were lineary superimposed with hourly-interpolated wind outputs for the entire domain. Figure 2 shows the difference of vectors between currents only and wind-current combined cases.

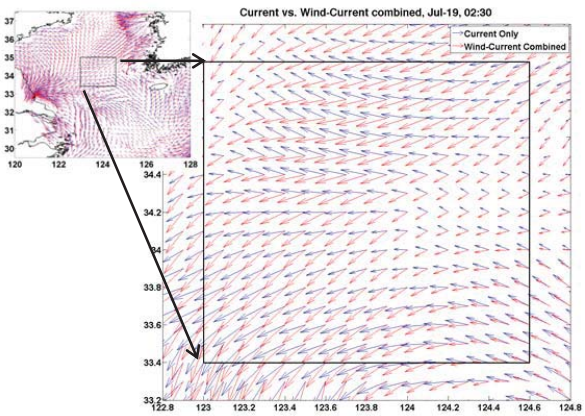

Figure 2. Surface currents from the ocean circulation model (blue arrows) and the combination of the surface currents and leeway effect (red arrows) on 19 July 2011.

RESULTS

This section describes the temporal variability and pathway of green algae based on the GOCI data. The distribution and pathway of the algae were then compared and analyzed using the FTLE fields

Distribution and pathway of floating green algae

Here we present the distribution pattern of the algae whose in depth description can be found in Son *et al*. (2015) for completeness. During the summer 2011, the floating green algae events recurred in this same area, as well as in offshore, clear waters of the YS and ECS, which was determined from satellite data and various field observations (Figure 1; Son *et al*., 2012b). Son *et al*. (2012b) showed that the massive floating green algae patches covering a large area offshore from Qingdao, China were detected on 13 June 2011. The temporal evolution pattern of observed massive patches around offshore Qingdao were similar to those during summer 2008 (*e.g*., Hu and He, 2008; Liu *et al*., 2009).

One month later, on 18-20 July 2011, the large amount of floating green algae were detected offshore in the YS and ECS (Figure 1b-1d). An interesting feature from the satellite data is that the patches of floating green algae extended across the middle of the YS and were linked from west to east direction, an apparent transoceanic transport of the massive floating algae. The floating green algae blooms were also found in the middle of the ECS and extended to near Jeju Island (Figure 1). On 20 July 2011, the patches of the floating green algae in GOCI image were found in two areas, offshore Qingdao and the southern part of YS (Figure 1d). Persistent patches of the floating green algae were shown near Qingdao, which lasted over one month period. By analyzing both satellite data and numerical particle trajectory simulation results, Son *et al*. (2015) showed that it might be linked to the migration of green algae patches originated from Jiangsu Province, China. They also noted that larger area of dense floating green algae were present near the west coast of Korea, whereas spatially coarse coverage of less-dense floating green algae occurred in the ECS.

LCSs and the dispersion processes

Figure 3 shows example cases of forward FTLE using only surface currents only versus combined flow fields with currents and wind on 19 July 2011. Ridges in forward FTLE (*i.e*., yellow and red colors) represent tearing apart and repelling materials (*e.g*., green algae patches) on either side of the ridge. Thus, the ridges can be regarded as maximum bounds of green algae patches transported. On the contrast, smaller values (blue color) in forward FTLE indicate attracting ridges, where green algae patches get aggregated. In the case of currents only, the repelling ridges were present in the direction parallel to east-west in the central part of YS (*e.g*., white box in Figure 3a), which implies that the green algae could be separated into north and south patches by those repelling bound. In the case of current and wind combined, on the other hand, the repelling ridges with large FTLE (red color) were located outside of that white box with NE-SW direction. Rather, small FTLE (blue color) dominates that central part of the box, indicating potential presence of green algae in that direction.

In addition to the forward LCS, we also calculated backward FTLE estimates for both cases of currents only and wind-current combined. Figure 4 shows the temporal variation of backward FTLE fields between 18 and 19 July. Small values (blue color) in backward FTLE indicate attracting ridges, where materials get aggregated. One may note that the location of blue ridge in the white box (124°N, 34.5°E) moved to the southwest from 18 July to 19 July.

DISCUSSION

Comparison between LCSs using current only vs. current-wind combined cases show that the results of current-wind case (*e.g*., Figure 3b) matches better the observation results from GOCI (*e.g*., Figure 1d in this paper and Figure 11 of Son *et al*. (2012b)) than those of current only cases. This implies that the transport of green algae patches would be controlled by the combined effect of surface current and wind leeway.

Thus, in order to predict the pathway and fate of green algae bloom, it is necessary to understand the pattern of both wind and current, that is consistent with the findings in the particle trajectory numerical simulation in Son *et al*. (2015).

In Figure 4, southwest movement of attracting ridges (*i.e*., blue color) during 18-19 July might indicate the aggregated materials (*e.g*., patches of green algae) can be moved toward southwest direction during that period. It is consistent with findings in Figure 11 of Son *et al*. (2012b) based on hourly satellite image analysis (Figure 1b-1d). ROMS outputs depict that the surface currents were directed to the west on 19 July (blue arrows in Figure 2), while wind-current combined vectors headed to the southwest (red arrows in Figure 2). This southwest movement of the repelling ridge in backward FTLE, and thus the movement of aggregation patches of green algae detected by satellite image analysis, was likely due to the combined effects of winds and currents. However, this trend was not observed in the LCS field with current only (not shown in the paper).

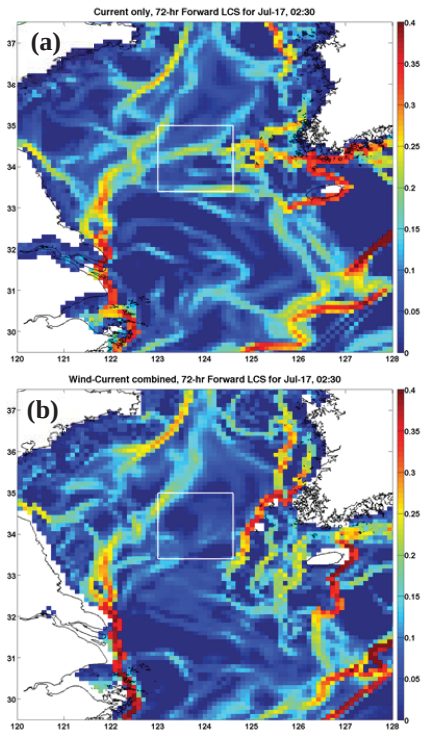

Figure 3. Forward LCS results with current only (a), and wind and current combined (b). Ridges in forward FTLE (red colors) represent tearing apart and repelling materials on either side of the ridge. So, these ridges can be regarded as maximum bounds of materials transported.

Green algae in the study area are known to be *Ulva prolifera* from previous studies (*e.g*., Hayden *et al*., 2003; Lee *et al*., 2011; Liu *et al*., 2009). The patches of such green algae are generally floating at the sea surface with increasing sub-surface stratification from the spring to the summer (Son *et al*., 2012a). Although some portions are submerged, the movement of these green algae patches would be subjective to the surface current as well as wind drift. In our experiments, we do not have enough field data to prove how much the wind drift influences the movement of green algae. Instead, we assumed that the wind drift of those floating patches can be similar to other floating materials like thin oil slick in oceanic environments, and thus we applied 3% of wind drift factor as suggested by Youseff and Spaulding (1993). As part of sensitivity test, we also applied the range of 2 or 4% of wind drift factor found in Yourseff and Spaulding's work, and calculated both forward and backward FTLE for 3 month of data sets. The results that match best with the satellite observation were cases with 3%. This sensitivity experiment results indicate this 3% factor would be a reasonable assumptions for the wind drift of the floating green algae patches.

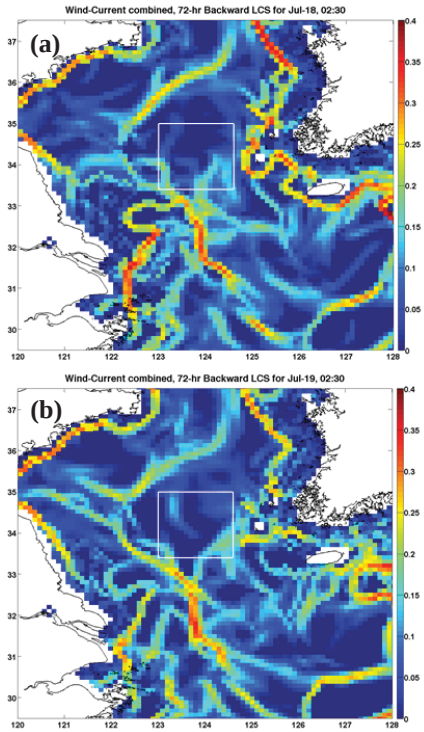

Figure 4. Backward LCS results with wind and current combined for (a) 18 July and (b) 19 July 2011. Small value (blue color) region in backward FTLE indicates attracting ridges, where materials get aggregated.

CONCLUSIONS

GOCI images were collected every hour during the day time, generating 8 images per day (Ryu and Ishizakak, 2012). This high temporal resolution of ocean color images provides a great potential for studying water quality and sediment

transport (*e.g.*, Kim *et al*., 2014; Son *et al*., 2014). Satellite iamges themselves sometime may not be enough in explainging the governing processes of environmental changes. If satellite data are combined with dynamic system analysis, dynamic features of materials (*e.g.*, pollutants or sediments transport pattern) could be unravel extensively, In this study we combined LCS technique with satellite data, to explain physical processes govening green algae bloom across the Yellow and East China Sea.

GOCI data shows the extension of green algae bloom patches and their evolution over time. Ridges in FTLE fields computed from (1) current-only and (2) combined wind-current cases represent tearing apart and repelling green algae patches. The results of current-wind cases match better the distribution of green algae patches observed from GOCI than those of current only cases because the current-wind cases include the wind effects in LCS by considering leeway effect. Wind may control not only long-term migrations but also short-term dispersion patterns.

ACKNOWLEDGMENTS

This research was supported by projects titled “Development of satellite based ocean carbon flux model for seas around Korea”, " Development of Korea Operational Oceanographic System (KOOS), Phase 2", “Environmental risk assessment of microplastics in the marine environment” funded by the Ministry of Oceans and Fisheries, Korea and performed as a collaborative research project of "Scientific big data, scientific data, big data platform, complex event processing, semantic technology" funded by the Korea Institute of Science and Technology and KIOST, and "Analysis and detailed report on Jeju marine environmental Satatus" funded by KIOST.

LITERATURE CITED

Beron-Vera, F.J.; Wang, Y.; Olascoaga, M.J.; Goni, G.J., and Haller, G., 2013. Objective detection of oceanic eddies and the Agulhas Leakage. *J. Phys. Oceanogr.*, 43, 1426-1438.

Griffa, A.; Haza, A.; Ozgokmen, T.M.; Molcard, A.; Taillandier, V.; Schroeder, K.; Chang, Y., and Poulain, P.-M., 2013. Investigating transport pathways in the ocean. *Deep-Sea Research II*, 85, 81-95.

Hayden, H.S.; Blomser, J.; Maggs, C.A.; Silva, P.C.; Stanhope, M.J., and Waaland, J.R., 2003. Linnaeus was right all along:Ulva and Enteromorpha are not distinct genera. *European Journal of Phycology*, 38, 227-294.

Hu, C.; Li, D.; Chen, C.; Ge, J.; Muller-Karger, F.E.; Liu, J.; Yu, F., and He, M.-X., 2010. On the recurrent *Ulva prolifera* blooms in the Yellow Sea and East China Sea. *Journal of Geophysical Research*, 115, C05017.

Hu, C. and He, M.-X., 2008. Origin and offshore extent of floating algae in Olympic sailing area. *EOS Trans AGU*, 89(33), 302-303.

Kim, C.-S.; Cho, Y.-K.; Choi, B.-J.; Jung, K.T., and You, S.H., 2013. Improving a prediction system for oil spills in the Yellow Sea: Effect of tides on subtidal flow. *Marine Pollution Bulletin*, 68(1-2):85-92.

Kim, Y.H.; Im, J.H.; Ha, H.K.; Choi, J.K., and Ha, S.H., 2014. Machine learning approaches to coatal water quality monitoring using GOCI satellite data, *GIScience and Remote Sensing*, 51, 158-174.

Lee, J.H.; Pang, I.C.; Moon, I.J., and Ryu, J.H., 2011. On physical factors that controlled the massive green tide occurrence along the southern coast of the Shandong Peninsula in 2008: A numerical study using a particle-tracking experiment. *Journal of Geophysical Research*, 116: C12036, doi:10.1.

Liu, D.; Keesing, J.K.; Xing, Q., and Shi, P., 2009. World’s largest macroalgal bloom caused by expansion of seaweed aquaculture in China. *Marine Pollution Bulletin*, 58, 888-895.

Olascoago, M. and Haller, G., 2012. Forecasting sudden changes in environmental pollution patterns. *Proceedings of National Academy of Science USA*,109, 4738.

Park, K.-S.; Heo, K.-Y.; Jun, K.; Kwon, J.-I.; Kim, J.; Choi, J.-Y.; Cho, K.-H.; Choi, B.-J.; Seo, S.-N.; Kim, Y.; Kim, S.-D.; Yang, C.-S.; Lee, J.-C.; Kim, S.-I.; Kim, S; Choi, J.-W., and Jeong, S.-H., 2015. Development of the Operational Oceanographic System of Korea. *Ocean Science Journal*, 50(2): 353-369.

Peacock, T. and Haller, G., 2013. Lagrangian coherent structures: the hidden skeleton of fluid flows. *Physics Today*, 66, 41.

Ryu, J.H. and Ishizaka, J., 2012. GOCI data processing and ocean applications. *Ocean Science Journal*, 47(3), 221.

Son, Y.B.; Gardner, W.D.; Richardson, M.J.; Ishizaka, J.; Ryu, J.H.; Kim, S.-H., and Lee, S.H., 2012a. Tracing offshore low-salinity plumes in the Northeastern Gulf of Mexico during the summer season by use of multispectral remote-senisng data. *Journal of Oceanography*. 68, 743-760.

Son, Y.B.; Min, J.E., and Ryu, J.H., 2012b. Detecting massive green algae (*Ulva prolifera*) blooms in the Yellow Sea and East China Sea using Geostationary Ocean Color Imager (GOCI). *Ocean Science Journal*, 47(3), 359-375.

Son, Y.B.; Choi, B.-J.; Kim, Y.H., and Park, Y.-G., 2015. Tracing floating green algae blooms in the Yellow Sea and the East China Sea using GOCI satellite data and Lagrangian transport simulations. *Remote Sensing of Environment*, 156, 21-33.

Son, S.H.; Kim, Y.H.; Kwon, J.I.; Kim, H.C., and Park, K.-S., 2014. Characterization of spatial temporal variation of suspended sediments in the Yellow and East China Seas using satellite ocean color data. *GIScience and Remote Sensing*, 51, 212-226.

Song, Y. and Haidvogel, D.B., 1994. A semi-implicit ocean circulation model using a generalized topography-following coordinate system. *Journal of Computational Physics*, 115(1), 228-244.

Vermote, E.F.; Tanre, D.; Deuze, J.L.; Herman, M., and Morcette, J.J., 1997. Second simulation of the satellite signal in the solar spectrum, 6S: An overview. *IEEE T. Geosci. Remote.*, 35, 675-686.

Youssef, M. and Spaulding, M., 1993. Drift, current under the action of wind and wave. in: *Proceedings of the Sixteenth Arctic and Marine Oil Spill Program Technical Seminar* (Calgary, AB, Canada), pp. 587–615.

Journal of Coastal Research	SI	75	1242 - 1246	Coconut Creek, Florida	2016

Quantitative Behaviour Characteristics Analysis of GPS Buoy in Rip Current Generation

Dongseob Song [†], Giyoung Kim [‡§*], and Junglyul Lee [††]

[†]Department of Earth and Environmental Enginnering
Kangwon National University
Samcheok, South Korea

[††]Department of Civil and Environmental Engineering,
Sungkyunkwan University,
Suwon, South Korea

[‡] Department of Environmental and Ocean Construction Enginnering
Kangwon National University
Samcheok, South Korea

[§]Dokdo Research Center
Korea Institute of Ocean Science and Technology
Wuljin, South Korea

www.cerf-jcr.org

www.JCRonline.org

ABSTRACT

Song, D.S; Kim, G.Y., and Lee, J.L., 2016. Quantitative behaviour characteristics analysis of GPS buoy in rip current generation. *In:* Vila-Concejo, A.; Bruce, E.; Kennedy, D.M., and McCarroll, R.J. (eds.), *Proceedings of the 14th International Coastal Symposium* (Sydney, Australia). *Journal of Coastal Research*, Special Issue, No. 75, pp. 1242 - 1246. Coconut Creek (Florida), ISSN 0749-0208.

GPS buoys have been used to acquire sea level change data, current measurements and other oceanic variables in sea for the purposes of vertical datum determination, tide correction, radar altimeter calibration, ocean environment and marine pollution monitoring. The occurrence of rip currents in the Haeundae beach, which is one of the most famous beaches in South Korea, has been threatening beach-goer security in summer season annually. Therefore, we adopted a GPS buoy system for an experiment which is to investigate rip current velocity; it is sporadic and may quickly upsurge within minutes due to larger arriving wave groups or nearshore flow uncertainties. In this study, for high accurate positioning of buoy equipment, a Satellite Based Argumentation System DGPS data logger was deployed to investigate within floating object, and it can be acquired three-dimensional coordinate or geodetic position of buoy with continuous NMEA-0183 protocol during 24 hours. The wave height and current profile measured by in-situ Acoustic Doppler Current Profilers in a cross-shore array were compared with the GPS-derived current velocity, it is being clearly increased before and after generation of rip current, and wave period also was lengthened when a rip current generated. The results presented in this study indicate that by using the GPS buoy system is a reasonable alternative for the measuring of rip current behaviour.

ADDITIONAL INDEX WORDS: *GPS buoy, Rip current, Haeundae beach.*

INTRODUCTION

Rip currents can be caused by longshore current interaction, including offshore flow through a rip channel in sandbars, natural variability of incident wave heights, and irregular wave caused by artificial structures. Rip currents are a menacing phenomenon to swimmers and influence beach erosion (COMET, 2012). It is widely known that the pattern of behaviour of a rip current strongly depends on subtle alongshore bathymetric variations, and it is difficult to predict when and where a rip current will be generated.

In Korea, one of the main coastal hazard concerns in summer are rip currents, which is a jet-like current of water that generally extend from near the shoreline. Dozens of people during three years (2007~2009) were caught in rip currents in Haeundae beach, which is the most famous beach for summer vacation, and the events received media attention (Song and Bae, 2011). Therefore the rip current in Haeundae beach has become the abiding interest of many ocean scientists and central and local government officers as shown Figure 1.

Figure 1. Study area and rip currents event in Haeundae beach in 2012.

DOI: 10.2112/SI75-249.1 received 15 October 2015 accepted in revision 15 January 2016
*Corresponding author: kkgin@kiost.ac.kr
©Coastal Education and Research Foundation, Inc. 2016

The first national investigation project for rip currents in Haeundae was established by the Korean Meteorological Administration (KMA). Observing rip currents was conducted in order to define their causes and mechanisms so their generation can be predicted (Song and Bae, 2011). The first numerical prediction model for nearshore rip currents using wave height, wave period, and incident wave angle was demonstrated (Lee *et al*., 2013). In order to understand beach erosion and rip current problem and obtain solutions for countermeasure at Haeundae beach, Kim *et al*. (2013) conducted historical investigations, field observations, laboratory experiments, and numerical simulations. Kim *et al*. (2013) developed a software package called the HAECUM (HAEundae CUrrent Model) to provide a user-friendly simulation tool as a rip forecasting system, and the automated HAECUM based on Matlab was updated to predict wave-induced currents for public safety (Lee *et al*., 2014). Also, the KMA operational forecasting system for rip current based on the HAECUM was introduced (Eom *et al*., 2014). The numerical studies of a rip current generation in Haeundae beach were condcuted in order to understand the mechanisms of rip generation (Ha *et al*., 2014; Lee *et al*., 2014; Shin *et al*., 2014). Additionally, rip current analysis methods using CCTV image were applied to measure rip current velocity (Hwang *et al*., 2014; Yoon *et al*., 2014). Lim *et al*. (2014) measured waves and currents in Haeundae beach using two AWAC (Acoustic Wave And Current). They suggested that relatively weak waves from the SSW and S directions were generated by southwesterly winds in spring and summer, whereas strong waves were predominant coming with directions of E and ESE controlled by northeasterly and northwesterly winds. Choi *et al*. (2014) described the result of a real-time rip current warning system. The system produced the warning index and the grade of danger of a rip current base don real-time observations.

In order to obtain the quantitative behaviour characteristics of rip current generation at Haeundae beach, various observation methods were undertaken. Among them, the GPS (Global Positioning System) buoys to acquire sea level change data, current measurements and other oceanic variables in sea, such as vertical datum, tide correction, radar altimeter calibration, ocean environment and marine pollution monitoring. GPS drifter designed to measure the surf zone circulation has been developed and field tested by Schmidt *et al*. (2003). Watson *et al*. (2008) presented results from a novel application of a GPS-equipped buoy to achieve an *in situ* calibration of the tide gauge, solving for scale, vertical offset, and sea state–dependent bias parameters. Figure 1 shows the various platform types of GPS buoy which were developed for oceanic research purposes. The objective of this study is to detect the rip current velocity in the using Lagrangian GPS buoy data. Recently, McCarroll *et al*. (2013) deployed participants with attached GPS to establish the escape strategy against rip current, and used the GPS drifters to obtain Lagrangian measurements of rip flow.

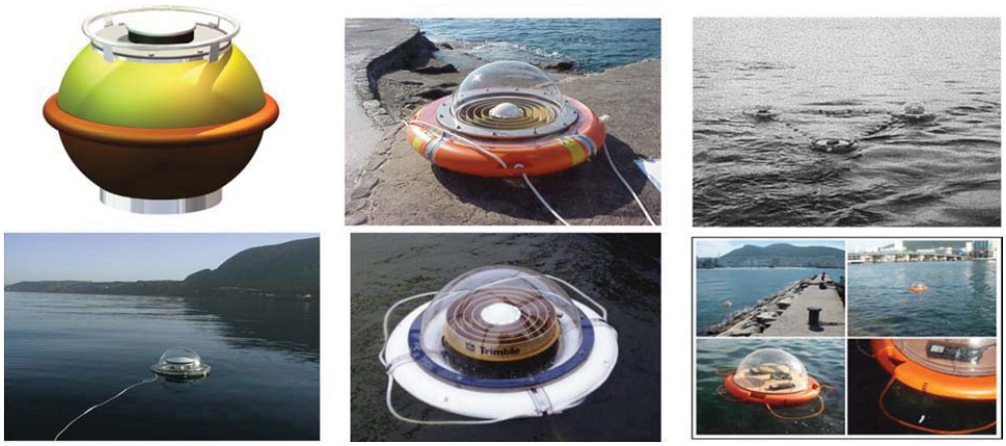

Figure 2. Various platform types of GPS buoy.

METHODS

Understanding current circulation in the near-shore region is a necessary component to protect natural hazard in the coastal zone. Current circulation patterns were obtained from tracking the movement of floating objects that included ships and drift buoys (Ohlmann *et al*., 2005). Many coastal scientists have been investigating rip currents by using field observations and measurements, laboratory measurements and wave tank experiments, and computer and numerical modeling. Rip current velocity is intermittent and may rapidly increase within minutes due to larger incoming wave groups or nearshore circulation instabilities. It is significant to consider that changes in rip current velocity occur in response to changes in incident wave height and period as well as variations in water level (COMET, 2012). Austin *et al*. (2010) demonstrated that the peak rip flow speed of 1.3 m/s, by using the 12 GPS-tracked Lagrangian surf zone drifter data, were recorded around low tide when the joint effects of dissipation and morphological constriction were maximized. Lagrangian techniques have been widely used in the study of oceans and large lakes, both for fundamental fluid dynamics and as for environmental problems. The data provided by current-following drifters or buoys are particularly valuable in observing the spatial structure of the flow field and providing

a different insight into the flow dynamics than that which can be obtained from Eulerian data (Austin *et al*., 2013). MacMahan *et al*. (2009) used two different low-cost, handheld GPS units and four different position-correcting configurations and they evaluated them to determine their practicality in measuring surf-zone currents.

Development of GPS buoy

On 2010, we developed our first GPS buoy system from research grant supported by the Korean Meteorological Administration (KMA) to detect velocities and directions of rip current based on the typical life ring platform type as shown in Figure 1. Figure 3(a) is a first GPS buoy system and photo of field experiment. However, they were useless in a surf zone due to the irregular wave force. We found out that GPS buoy must be including low-cost, simplicity, compact size, reusability, and great maneuverability in deployment, that were emphasized by Sabet *et al*. (2011) and Johnson *et al*. (2003). Therefore, we redesigned a new GPS drifter buoy system to more appropriate in the surface layer of the surf zone environment at Haeundae beach. Newly designed GPS buoy system can not only be easily affected by physical force below sea level in, but is also unaffected by breaking water, as shown in Figure 3(b).

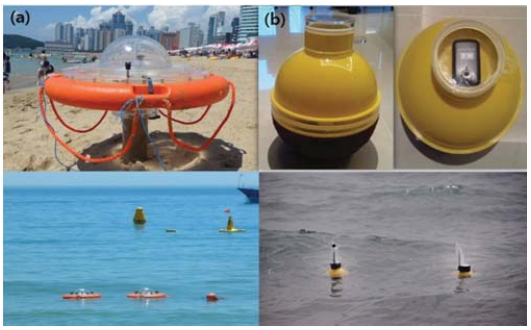

Figure 3. GPS buoy for detecting characteristics of rip current. (a) First development product on 2010. (b) Second buoy product on 2011.

The main platform is approximately globular compartment with middle diameter of 25 cm, length of 30 cm, and the head internal instrument frame, which can be mounted on the GPS receiver, can easily close and open rapidly with rotating cover. The GPS receiver is the Satellite Based Argumentation System (SBAS) DGPS data logger, and it is currently used to investigate with a floating platform. The DGPS data logger can be measured positioning data per 1 second with continuous NMEA-0183 protocol during 24 hours (Song and Bae, 2011). In order to prevent the loss of the buoy, the ring was added to tie a rope on the head side of platform.

Field experiment

Velocity is the rate of change of position and its determination requires measurements of distance and time component. GPS is accurate for the determination of velocity when moving at relatively constant speed. In order to investigate the cause of rip current generation in Haeundae beach, eight observation methods were deployed: Closed Circuit Television (CCTV), current and wave direction equipment, shoreline monitoring with GPS equipment, surf zone depth, tides, waves, Automated Weather System (AWS), as well as GPS buoys. The incident waves were measured by directional wave observation buoy which is located 1 km offshore. The Acoustic Doppler Current profilers (ADCP) and several current meters were installed to measure longshore current and rip current.

Bathymetry of the Haeundae beach was measured on 7 August and 12 November 2007, (Figure 4(a)). The presence of several oversized submerged rocks located a short distance from the beach lead to significant differences in the wave forcing and the uneven sea bed morphology. Figure 4(b) shows the trajectories of five new GPS buoys, and Lagrangian observations obtained using GPS buoys were presented within the surf zone large rotational circulation, as well as alongshore current patterns. The behaviour patterns of buoys appear to spread and dissipate outside the surf zone.

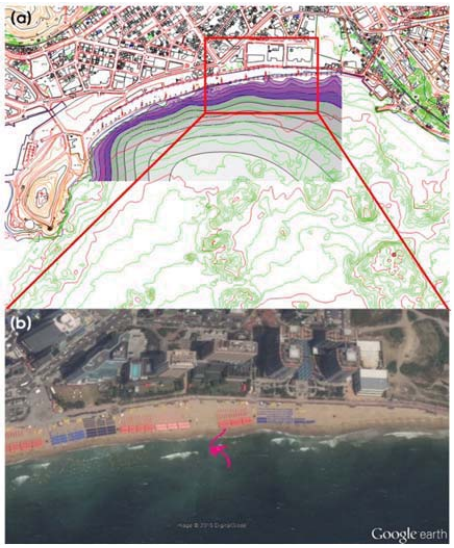

Figure 4. (a) Bathymertry plot and equal depth of water map in Haeundae beach. (b) Trajectories of GPS buoys.

RESULTS

To evaluate the performance of the new designed GPS buoys in a rip current, we deployed five GPS buoys in Haeunda beach. Due to many swimmers on the beach, we had difficulty in operating the GPS buoys in the surfzone. Nevertheless, the one of GPS drift buoys was successful to measure a rip current velocity on August 06, 2011. The left panel of Figure 5 shows the captured CCD images when the rip current occurred in the beach, and right panel is the rip current velocity which was detected by the GPS buoy during 7 minutes. The velocity, including positon and heading information was recorded every 5 minutes. As a result, it was found that the rip current was strongly generated to southward from the shore, as shown in Figure 5(a). The maximum

velocity of rip current is recorded at 14:00:30 on August 06, and it is about 1.37 m/s. The average of velocity is 0.44 m/s during 7minutes. The maximun velocity value is similar to the result of Yoon *et al*. (2014), that they suggested the 1.12 m/s calculated by video image analysis on August 10, 2012. Earlier studies have shown that the velocity of rip current ranges from 0.5 m/s to below 1.0 m/s, and the fastest velocity exceeds 2 m/s in the case of mega-rip on embayed beaches (MacMahan *et al*., 2006).

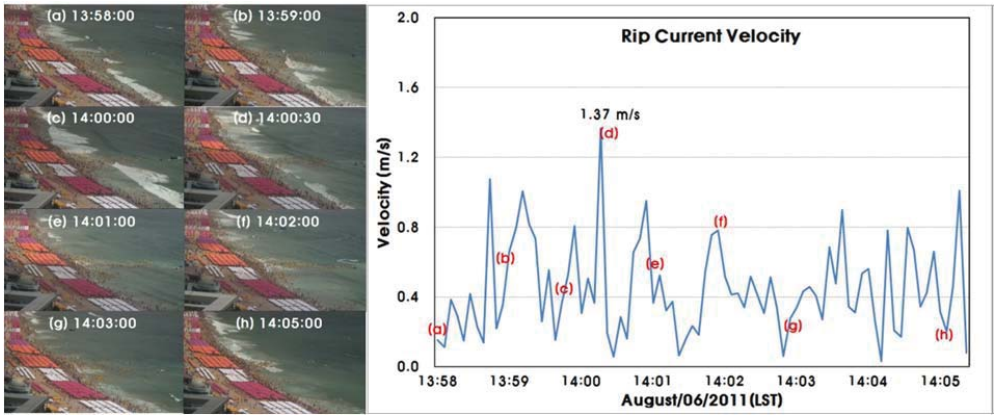

Figure 5. Rip current event in Haeundae beach. (a) CCD images captured during 7 minutes on August 6th, 2011. (b) Rip current velocity detected by GPS drift buoy during rip current generating.

Figure 6 present the timeseries of the hourly height and period in terms of significant wave and maximum wave during August 6, 2011. The height and period of significant wave is 0.93 m and the 5.4 second when the rip current generated.

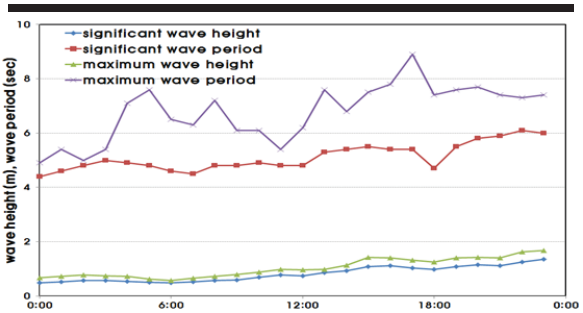

Figure 6. Timeseries of significant wave and maximum wave during August 6th, 2011.

DISCUSSION

In the past few years, rip currents at Haeundae beach have been intensively studied due drowning fatalities and subsequent media coverage. Since the last decade, there have been a substantial number of field studies and numerical analysis of rip current generation. Most studies of field observations on the subject of rip currents have been used to understand beach morphology. Measurements describing the forcing related to transient rip currents are desired in particular, since these motions may provide the initial perturbation for the generation of rip current.

CONCLUSIONS

The GPS system provides simultaneous information of location and time, in almost all weather conditions. Using these data, we can understand current pattern, speed and flow direction. In this sutdy, the GPS buoy system for measuring of rip current has been developed and tested. The results indicate that by using the GPS buoy system is a reasonable alternative for the measuring of rip current behaviour, as well as a lottoral current investigation for coastal erosion monitoring.

LITERATURE CITED

Austin, M.J.; Scott, T.M.; Brown, J.; Brown, J.; MacMahan, J.; Masselink, G., and Russell, P.E., 2010. Temporal observations of rip current circulation on a macro-tidal beach. *Continental Shelf Research*, 30(9), 1149-1165.

Austin, M.J.; Scott, T.M.; Russell, P.E., and Masselink, G., 2013. Rip current prediction: development, validation, and valuation of an operational tool. *Journal of Coastal Research*, 29(2), 283–300.

Choi, J.; Lim, C.H., and Yoon, S.B., 2014. A rip current warning system based on real-time observations for Haeundae Beach, Korea. *In:* Lee, J.L.; Leatherman, Stephen P., and Lee, J. (eds.), *Proceedings, 3rd International Rip Current Symposium (Busan, Republic of Korea). Journal of Coastal Research*, SI 72, 56-62.

COMET, 2012. *Rip Currents: Nearshore Fundamentals*. http://www.meted.ucar.edu/marine/ripcurrents/NSF/download.php.

Eom, H.; Yun, J.H.; Jeong, C.K.; Seo, J.W., and You, S.H., 2014. Introduction to KMA operational forecasting System for rip current. *In:* Lee, J.L.; Leatherman, Stephen P., and Lee, J. (eds.), *Proceedings, 3rd International Rip Current*

Symposium (Busan, Republic of Korea). Journal of Coastal Research, Special Issue, No. 72, pp. 63-68.

Ha, T.; Jun, K.; Yoo, J., and Park, K.S., 2014. Numerical study of rip current generation mechanism at Haeundae Beach, Korea. *In:* Lee, J.L.; Leatherman, Stephen P., and Lee, J. (eds.), *Proceedings, 3rd International Rip Current Symposium (Busan, Republic of Korea). Journal of Coastal Research*, Special Issue, No. 72, pp. 179-183.

Hwang, J.S.; Yun, H.S.; Suh, Y.C.; Lee, J., and Kang, S.C., 2014. Rip current research using a CCTV image analysis including swimmer detecting techniques at Haeundae Beach, Korea. *In:* Lee, J.L.; Leatherman, Stephen P., and Lee, J. (eds.), *Proceedings, 3rd International Rip Current Symposium (Busan, Republic of Korea). Journal of Coastal Research*, Special Issue, No. 72, pp. 33-38.

Johnson, D.; Stocker, R.; Head, R.; Imberger, J., and Pattiaratchi, C., 2003. A compact, low-cost GPS drifter for use in the oceanic nearshore zone, lakes, and estuaries. *Journal of Atmospheric and Oceanic Technology*, 20(12), 1880–1884.

Kim, H.; Jin, J.Y.; Jang, C.; Yoo, H.J., and Hwang, D.H., 2014. Simulation of seasonal bathymetric change at Haeundae Beach with two representative wave settings. *In:* Lee, J.L.; Leatherman, Stephen P., and Lee, J. (eds.), *Proceedings, 3rd International Rip Current Symposium (Busan, Republic of Korea). Journal of Coastal Research*, Special Issue, No. 72, pp. 173-178.

Kim, K.-H.; Shin, S. and Widayati, A.Y.W., 2013. Mitigation Measures for Beach Erosion and Rip Current. *In:* Conley, D.C., Masselink, G., Russell, P.E. and O'Hare, T.J. (eds.), *Proceedings 12th International Coastal Symposium (Plymouth, England). Journal of Coastal Research*, Special Issue No. 65, pp. 290-295.

Kim, I.C.; Lee, J.L., and Lee, J.Y., 2013. Verification of rip current simulation using a two-dimensional predictive model, HAECUM. *In:* Conley, D.C., Masselink, G., Russell, P.E. and O'Hare, T.J. (eds.), *Proceedings, 12th International Coastal Symposium. Journal of Coastal Research*, Special Issue No.65, pp. 726-730.

Lee, J.Y.; Jun, K.C.; Lee, S.C., and Lee, J.L., 2013. A study on a predictive index for danagerous rip current generation at Haeundae beach. *In:* Conley, D.C., Masselink, G., Russell, P.E. and O'Hare, T.J. (eds.), *Proceedings 12th International Coastal Symposium (Plymouth, England). Journal of Coastal Research*, Special Issue No. 65, pp. 754-759.

Lee, J.; Yoo, C., and Lee, J.L., 2014. Introduction to automated system in HAECUM (HAEundae Current Model. *In:* Lee, J.L.; Leatherman, Stephen P., and Lee, J. (eds.), *Proceedings, 3rd International Rip Current Symposium (Busan, Republic of Korea). Journal of Coastal Research*, Special Issue, No. 72, pp. 81-84.

Lee, W.D.; Shin, S.W.; Jeong, Y.M., and Hur, D.S., 2014. Numerical studies on rip current control using scenefriendly structures at Haeundae Beach, Korea. *In:* Lee, J.L.; Leatherman, Stephen P., and Lee, J. (eds.), *Proceedings, 3rd International Rip Current Symposium (Busan, Republic of Korea). Journal of Coastal Research*, Special Issue, No. 72, pp. 69-74.

Lim, H.S.; Kim, C.S.; Lee, H.J.; Shim, J.S.; Kim, S.J; Park, K.S., and Chun, I., 2014. Variability of residual currents and waves in Haeundae using long-term observed AWAC data. *In:* Lee, J.L.; Leatherman, Stephen P., and Lee, J. (eds.), *Proceedings, 3rd International Rip Current Symposium (Busan, Republic of Korea). Journal of Coastal Research*, Special Issue, No. 72, pp. 166-172.

MacMahan, J.; Brown, J., and Thornton, E., 2009. Low-cost handheld global positioning system for measuring surf-zone currents. *Journal of Coastal Research*, 25(3), 744–754.

MacMahan, J.H.; Thornton, E.B.; Stanton, T.P., and Reniers, A.J., 2005. RIPEX: Observations of a rip current system. *Marine Geology*, 218(1), 113-134.

McCarroll, R.J.; Brander, R.W.; MacMahan, J.H.; Turner, I.L.; Reniers, A.J.H.M.; Brown, J.A.; and Bradstreet, A., 2013. Assessing the effectiveness of rip current swimmer escape strategies, Shelly Beach, NSW, Australia . *In:* Conley, D.C., Masselink, G., Russell, P.E. and O'Hare, T.J. (eds.), *Proceedings 12th International Coastal Symposium (Plymouth, England), Journal of Coastal Research*, Special Issue No. 65, pp. 784-789.

Ohlmann, J.C.; White, P.F.; Sybrandy, A.L., and Niiler, P.P., 2005. GPS-cellular drifter technology for coastal ocean observing systems. *Journal of Atmospheric and Oceanic Technology*, 22(9), 1381-1388.

Sabet, B. S. and Barani, G.A., 2011. Design of small GPS drifters for current measurements in the coastal zone. *Ocean and Coastal Management*, 54(2), 158-163.

Schmidt, W.E.; Woodward, B.T.; Millikan, K.S.; Guza, R.T.; Raubenheimer, B., and Elgar, S., 2003. A GPS-tracked surf zone drifter. *Journal of Atmospheric and Oceanic Technology*, 20(7), 1069–1075.

Shin, C.H.; Noh, H.K.; Yoon, S.B., and Choi, J., 2014. Understanding of rip current generation mechanism at Haeundae Beach of Korea: Honeycomb waves. *In:* Lee, J.L.; Leatherman, Stephen P., and Lee, J. (eds.), *Proceedings, 3rd International Rip Current Symposium (Busan, Republic of Korea). Journal of Coastal Research*, Special Issue, No. 72, pp. 11-15.

Song, D.S. and Bae, H.K., 2011. Observation and forecasting of rip current generation in Haeundae beach, Korea plan and experiment. *Proceedings of the 11th International Coastal Symposium. Journal of Coastal Research*, Special Issue No. 64, 946 – 950.

Watson, C.; Coleman, R., and Handsworth, R., 2008. Coastal tide gauge calibration: a case study at Macquarie Island using GPS buoy techniques. *Journal of Coastal Research*, 24(4), 1071-1079.

Yoon, S.B.; Park, W.K., and Choi, J., 2014. Observation of rip current velocity at an accidental Event by using video imange Analysis. *In:* Lee, J.L.; Leatherman, Stephen P., and Lee, J. (eds.), *Proceedings, 3rd International Rip Current Symposium (Busan, Republic of Korea). Journal of Coastal Research*, Special Issue, No. 72, pp. 16-21.

Journal of Coastal Research	SI	75	1247 - 1251	Coconut Creek, Florida	2016

A New Computation Method of Bottom Shear Stress under Tsunami Waves

Hitoshi Tanaka[‡], Mohammad B. Adityawan[†*], Yuta Mitobe[‡], and Wahyu Widiyanto[‡]

[‡]Department of Civil Engineering, Tohoku University, Sendai, Japan

[†]Water Resources Engineering Research Group, Faculty of Civil and Environmental Engineering, Institut Teknologi Bandung, Bandung, Indonesia

www.cerf-jcr.org

www.JCRonline.org

ABSTRACT

Adityawan, M.B.; Tanaka, D., Mitobe, Y., and Widiyanto, W., 2016. A new computation method of bottom shear stress under tsunami waves, *In:* Vila-Concejo, A.; Bruce, E.; Kennedy, D.M., and McCarroll, R.J. (eds.), *Proceedings of the 14th International Coastal Symposium* (Sydney, Australia). *Journal of Coastal Research*, Special Issue, No. 75, pp. 1247 - 1251. Coconut Creek (Florida), ISSN 0749-0208.

The tsunami propagation in the river as well as sediment transport is highly affected by the bed stress beneath the wave. Unfortunately, most numerical models use an empirical method such as Manning's *n*, which was developed for steady flow. A new method in numerical modelling to assess bed stress and sediment transport induced by wave is developed based on the boundary layer approach. The boundary layer has a significant effect on the bed stress under unsteady flow. Bed stress under unsteady flow may exhibit phase shift and sign change to the free stream velocity. Recently, Simultaneous Coupling Method (SCM) was developed and verified by combining Shallow Water Equation (SWE) and k-ω model. The simplicity of SWE was maintained while k-ω model was used to assess the bed stress from the boundary layer. The velocity from SWE is assumed as the free stream velocity, which is used as the boundary condition for k-ω. The calculated bed stress from k-ω is used in SWE to obtain water depth and velocity. In this study, SCM is further developed by simulating a tsunami wave propagation around the Kitakami River mouth and verified using a laboratory experiment. The results show good comparison between the numerical and experimental.

ADDITIONAL INDEX WORDS: *Bed stress, boundary layer, numerical model, tsunamis.*

INTRODUCTION

The Great East Japan Tsunami of 2011 severely destroyed the affected coastal area. The tsunami caused significant changes to the morphology of coasts and estuaries. It was also found that the tsunami eroded sand spits at some river mouths and the wave itself propagated further upstream (Adityawan *et al*., 2012a, Adityawan *et al*., 2014, Tanaka *et al*., 2014a, Tanaka *et al*., 2014b). Therefore, it is important to understand the tsunami propagation into rivers and the tsunami-induced sediment transport. Numerical models as well as laboratory experiments are required to have a better understanding of the phenomenon.

The tsunami propagation in the river and the tsunami-induced sediment transport are highly affected by the bed stress beneath the wave. Unfortunately, most numerical models use an empirical method such as Manning's *n* to estimate the bed stress under a tsunami wave, which was usually developed for steady flow. Although they are capable of simulating the water level and velocity of a tsunami propagation with good accuracy, yet they are incapable of providing details on the bed stress. Therefore, a new method in the numerical modelling is needed to accurately assess this problem (Sugawara *et al.*, 2014).

The bed stress beneath an unsteady motion is highly influenced by the boundary layer beneath it. However, the commonly used empirical approach is usually derived from the vector relation of the bed stress to the free stream velocity and water depth. This relation fails to describe the bed stress behavior under an unsteady wave motion accurately, which exhibits a significant phase difference (Tanaka and Thu, 1994). The bed stress under an unsteady wave motion is influenced by both the velocity and acceleration related terms, and the phase lag (Kabiling and Sato, 1983, Nielsen, 2002). In addition, the bed stress under an unsteady wave motion changes its sign in the deceleration phase to the opposite direction of the free stream velocity (Liu *et al.*, 2007).

A 2D depth averaged equation such as Shallow Water Equation (SWE) is well known for its relatively good accuracy and its efficiency for simulating various cases of the tsunami wave propagation and run up. Most conventional SWE models still use the Manning approach to estimate the bed stress. Recently, Simultaneous Coupling Method (SCM) was developed to assess the bed stress beneath an unsteady wave motion (Adityawan and Tanaka, 2012b). It has also been used to simulate an experimental case of a dam break with good results (Adityawan and Tanaka, 2013). SCM couples SWE with the k-ω model. It simulates the water level and velocity based on SWE and estimates the bed stress from the boundary layer based on the k-ω model. Thus, SCM benefits from the simplicity of SWE while maintaining an accurate estimation of the bed stress from the boundary layer. This model is more efficient than those based on Reynolds-Averaged Navier-Stokes (RANS) equations. RANS based models are mainly used for special purposes. They may provide better results than depth-averaged model, but computation time is about one order of magnitude greater (Biscarini et al. 2010), and they are usually used only for special purposes. On the other hand, SCM has more flexibility in practical applications. In this study, SCM was used to assess the bed stress under an experimental case of a tsunami wave propagation around the Kitakami River, Japan. The experiment

DOI: 10.2112/SI75-250.1 received 15 October 2015 accepted in revision 15 January 2016
*Corresponding author: mbagus_st@yahoo.com
©Coastal Education and Research Foundation, Inc. 2016

was conducted at the Tsukuba Research Institute (Fukushima *et al*., 2013).

METHODS

SCM consists of two governing equations. SWE and the k-ω model. The 2D SWE equation consists of the mass and momentum conservations as shown below in Equations 1 and 2, consecutively.

$$\frac{\partial h}{\partial t}+\frac{\partial hU_i}{\partial x_i}=0 \quad (1)$$

$$\frac{\partial U_i}{\partial t}+U_i\frac{\partial U_j}{\partial x_i}+\frac{\partial(h+z_b)}{\partial x_i}+\frac{\tau_{iz}}{\rho h}=0 \quad (2)$$

where h is the water depth, U is the depth averaged velocity at x (i=1) and y (i=2), t is time, z_b is the bed elevation, g is gravity, ρ is the water density. τ is the bed stress. The governing equations above are solved using MacCormack predictor corrector scheme. The Manning equation is commonly used to estimate the bed stress. The Manning equation to calculate bed stress at x direction is given below.

$$\frac{\tau_{xz}}{\rho}=\frac{gn^2U\sqrt{U^2+V^2}}{R_h^{1/3}} \quad (3)$$

Here, n is the Manning roughness coefficient, and R_h is the hydraulic radius. SCM replaces Manning's n with the boundary layer approach.

The boundary layer approach provides a more accurate bed stress assessment under an unsteady wave motion as previously explained. SCM assessed the bed stress based on the Navier-Stokes equation in the stream wise component as follows:

$$\frac{\partial u_i}{\partial t}+u_j\frac{\partial u_i}{\partial x_j}=-\frac{1}{\rho}\frac{\partial P_i}{\partial x_i}+\frac{1}{\rho}\frac{\partial \tau_{ij}}{\partial z} \quad (4)$$

The equation above is simplified by assuming a 1D vertical flow distribution of the 2D horizontal velocity. The velocity component along z (i=3) is practically zero (w=0). The x and y distances are much larger than the z distances, and the fact that the boundary layer is very thin. Thus, the horizontal acceleration term in the above equation can be neglected too (Sana and Shuy, 2002, Suntoyo and Tanaka, 2009), which leads to the zero value of the second term in the left hand side of the equation.

$$\frac{\partial u_i}{\partial t}=-\frac{1}{\rho}\frac{\partial P_i}{\partial x_i}+\frac{1}{\rho}\frac{\partial \tau_{iz}}{\partial z} \quad (5)$$

with u is the velocity at location z in x and y direction from the bed. Outside the boundary layer, t = 0, and u =U, and therefore.

$$\frac{\partial u_i}{\partial t}=\frac{\partial U_i}{\partial t}+\frac{1}{\rho}\frac{\partial \tau_{iz}}{\partial z} \quad (6)$$

where bed stress is given as:

$$\frac{\tau_{iz}}{\rho}=(\nu+\nu_t)\frac{\partial u_i}{\partial z} \quad (7)$$

The turbulence closure model is based on the k-w model (Wilcox, 1998).

$$\frac{\partial k}{\partial t}=\tau_{iz}\frac{\partial u_j}{\partial z}-\beta^* k\omega+\frac{\partial}{\partial z}\left[\left(\nu+\sigma^*\nu_t\right)\frac{\partial k}{\partial z}\right] \quad (8)$$

$$\frac{\partial \omega}{\partial t}=\alpha\frac{\omega}{k}\tau_{iz}\frac{\partial u_j}{\partial z}-\beta\omega^2+\frac{\partial}{\partial z}\left[\left(\nu+\sigma\nu_t\right)\frac{\partial \omega}{\partial z}\right] \quad (9)$$

ω is the ratio of turbulence dissipation rate ε to the turbulent kinetic energy k, and may be regarded as a characteristic time scale of the turbulence. Eddy Viscosity is defined as the ratio of k and ω.

$$\nu_t=\frac{k}{\omega} \quad (10)$$

The values of the closure coefficients (Wilcox, 1988) are β= 3/40, β* = 0.09, α = 5/9, and σ = σ* = 0.5. Finite difference central scheme is applied to solve the governing equations in time and space. The boundary condition at the bottom is no slip boundary. At the free stream, it is assumed that the velocity gradient, turbulent kinetic energy gradient and the dissipation rate gradient are zero.

SCM calculates the water depth and free stream velocity from SWE. The calculated velocity is used to estimate the bed stress using the k-ω model. It should be noted here that SCM could only be used when the boundary layer thickness is less than half of the water depth. More details on the method can be found in the reference (Adityawan et al, 2012).

MODEL SETUP

An experimental study of the tsunami wave propagation on the Kitakami River was carried out (Fukushima *et al*., 2013). The sand spit around the river mouth of this river was severely eroded by the 2011 tsunami. It is important to assess the bed stress accurately in this area in relation to the induced sediment transport. Therefore, SCM is employed at the grids on the river mouth. The model domain is shown in Figure 1.

The model domain was divided by a 10x10 meter rectangular grid. This grid is used in the SWE model. The grid for the k-ω model starts at 0.01 m and increased exponentially by a factor of 1.01. Here, SCM is only used around the river mouth (Figure 1). The Manning roughness value for SWE is set at 0.025 while the *ks* value for SCM is set at its equivalent value of 46 mm. The wet dry boundary condition is given as a water depth threshold of 1cm. A water depth bellow this value is a dry grid with zero velocity.

The incoming wave profile was measured (Figure 2, point 01L. 010, and 01R) in the experiment and applied in the numerical model as the boundary condition on the right hand side of the model domain. The initial water level is set at -0.34 m as in the experiment. In the experiment, a weir was located in the river on the left hand side of the domain and therefore, the critical velocity above the weir is used as the left boundary condition in the river. The upper and lower domain use a closed boundary condition.

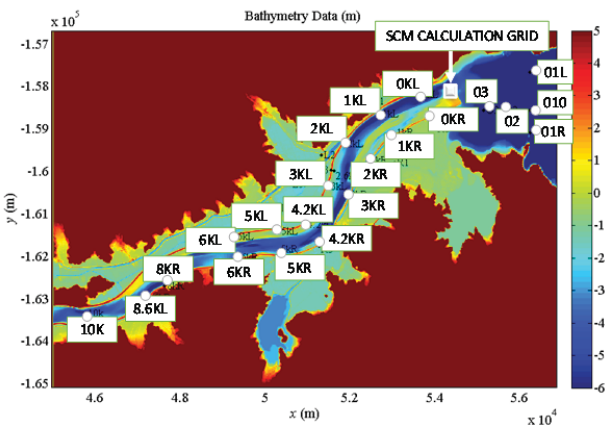

Figure 1. Model Domain

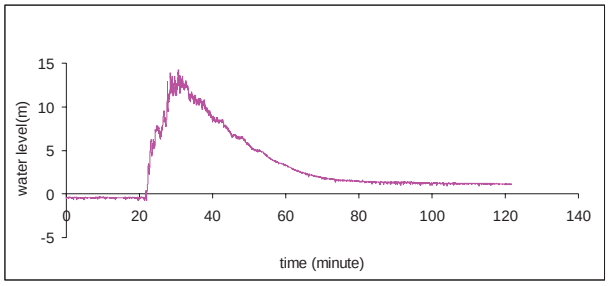

Figure 2. Incoming wave height.

The river and the shoreline in the experiment were protected by the embankment and thus, the tsunami wave propagates only in the river. There was no overland flow. The experiment measured the water level data at the left and right side of the river.

RESULTS

The simulation and experiment results are both shown using the same scale for comparison purposes and to have a better understanding of the wave propagation process as reported by Fukushima *et al*., 2013. The water level over time on the domain is shown in Figure 3. The model is clearly capable of reproducing the tsunami wave propagation at sea and its propagation in the river. It is also clearly shown that the incoming wave enters the river mouth and propagates upstream.

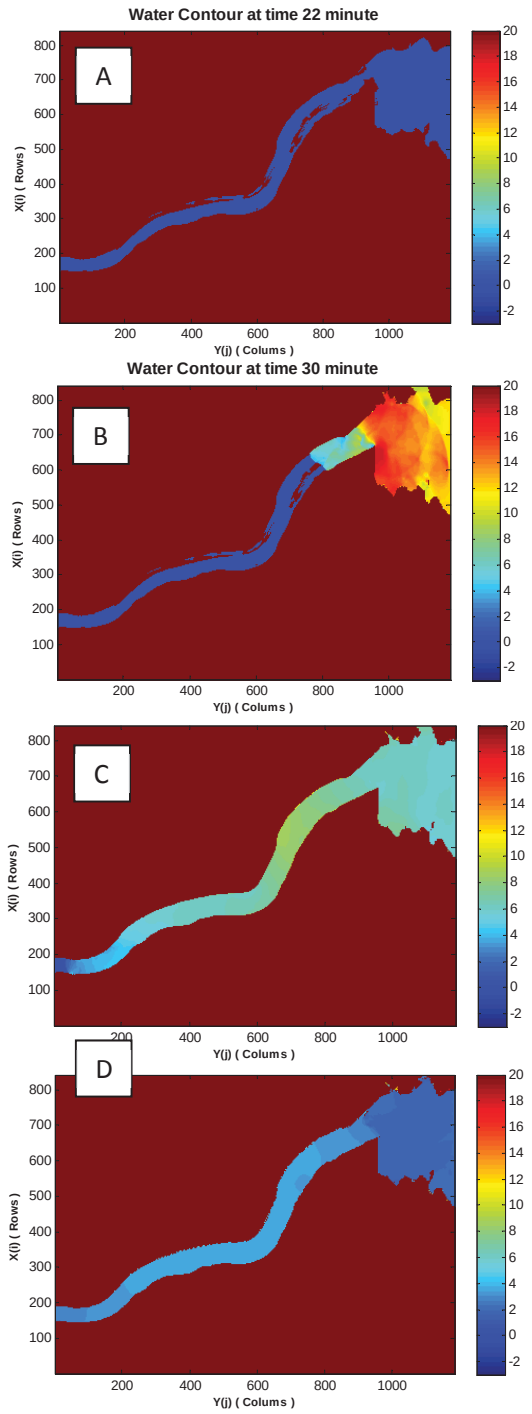

Figure 3. Water level at (A) 22 minutes (B) 30 minutes (C) 50 minutes (D) 80 minutes.

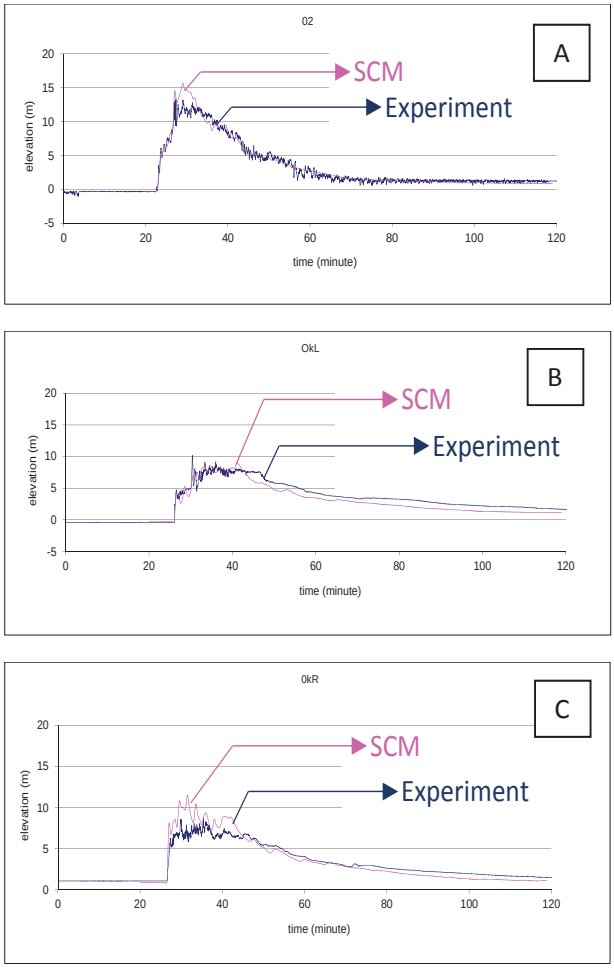

Figure 4. Simulated and measured water level in the experiment (A) Point 02 (B) Point 0kL (C) Point 0kR.

The incoming wave travels approximately 2 kilometers from the boundary to the shoreline and enters the river within approximately 4 minutes. The water level from the experiment and the numerical simulation at point 02 (sea), 0kL (left of the river mouth), and 0kR (right of the river mouth) are shown in Figure 4, A to C, respectively. The tsunami wave height before it enters the river mouth entrance may reach up to 15 meters (point 02). It was greatly reduced as it propagates in the river. Here the wave height is approximately 10 meters (points 1KL and 1KR). The tsunami wave continues to propagate to the upstream end of the domain, traveling for approximately 12 kilometers in the river as the wave height gradually decreases. Overall, the calculated water level from the numerical model shows good comparison to those measured from the experiment.

SCM calculates the area around the river mouth since this area was greatly affected by the tsunami-induced sediment transport as mentioned previously. The bed stress profiles were investigated further and compared to those obtained from Manning approach as shown in Figure 5. It should be noted here that SCM works at the early stage of the tsunami wave propagation. The boundary layer thickness grows fast and reaches the SCM limitation within approximately 1 minute.

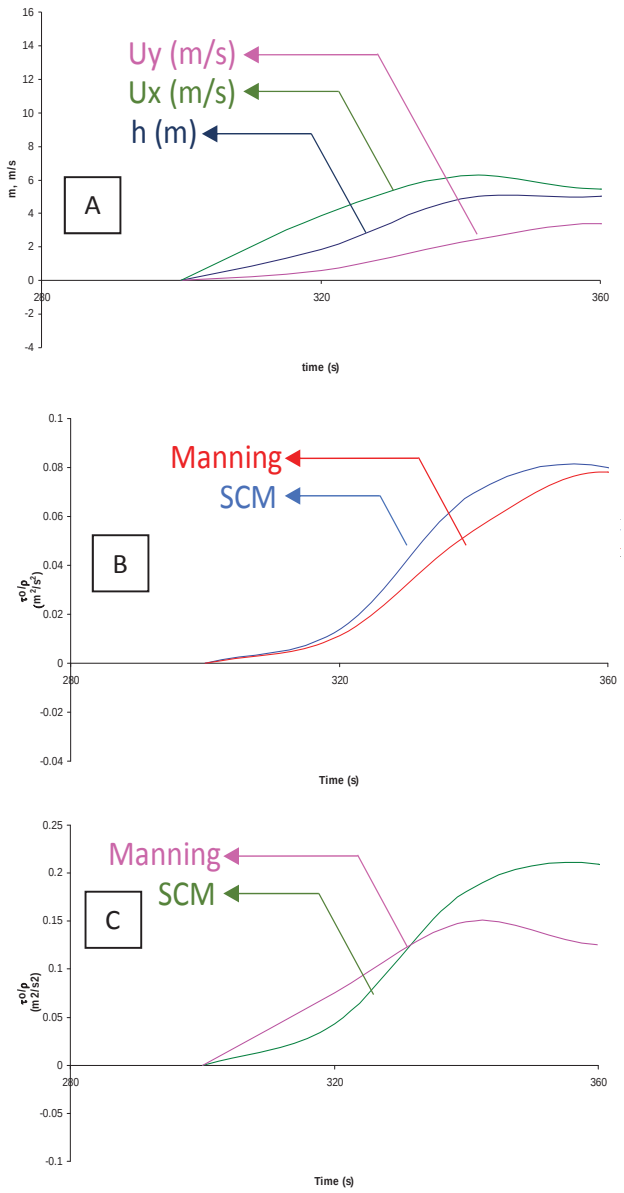

Figure 5. Bed stress comparison (A) water level and velocity (B) bed stress on x direction from SCM and Manning (C) Bed stress on y direction from SCM and Manning. **initial time level at 20 minutes*

It can be seen that the bed stress profile from a Manning approach is similar to the velocity profile. However, the early stage of the incoming tsunami wave is highly unsteady. Therefore, a more accurate bed stress assessment from the boundary layer is more suitable. Here, bed stress obtained from SCM shows the known effect of unsteadiness. The bed stress shows a significant phase lag to the velocity. In general, the maximum bed stress is higher in SCM, especially in the y direction, which is the dominant direction of the incoming tsunami wave.

CONCLUSIONS

Simultaneous Coupling Method (SCM) has been successfully applied to assess the tsunami-induced bed stress. SCM was used to simulate an experimental case of a tsunami in the Kikatami River, Japan. The river mouth was severely eroded by the 2011 tsunami and therefore this area requires a bed stress assessment from the boundary layer.

The model reproduced the wave propagation process from the sea boundary to the upstream end of the river. The incoming wave height was greatly reduced as it enters the river and propagates upstream. The calculated water level from the numerical simulation shows good comparison with the measured water level from the experiment.

SCM estimates the bed stress around the river mouth from the boundary layer. The boundary layer thickness grows fast beyond the SCM limitation. Thus, SCM can only use the boundary layer approach at the early stage of the wave, which is highly unsteady. The estimated bed stress shows a phase difference between the bed stress and the velocity, which is a known behavior of bed stress under an unsteady wave motion. The Manning approach cannot explain this behavior. In addition, the estimated bed stress magnitude is higher than that from the Manning approach.

An accurate bed stress assessment is useful in understanding the sediment transport process. Therefore, SCM is shown here as a valuable tool in assessing the sediment transport under an unsteady wave motion. It has been shown that SCM can be used for practical application in real case scenarios. SCM can be further developed to cover the boundary layer thickness up to the surface. Hence, it can cover the whole wave duration.

ACKNOWLEDGMENTS

The authors wish to express their gratitude to National Institute for Land and Infrastructure Management, Japan for providing us the valuable experimental data.

LITERATURE CITED

Adityawan M.B.; Roh, M.; Tanaka, H.; Mano, A., and Udo, K., 2012. Investigation of tsunami propagation characteristics in river and on land induced by The Great East Japan Earthquake 2011, *Journal of Earthquake and Tsunami*, 6, 1250033: 22 pages.

Adityawan, M.B. and Tanaka, H., 2012. Bed stress assessment under solitary wave runup, *Earth, Planet, Space Journal, Special Issue: Tsunami*, (64), 945–954.

Adityawan, M.B., and Tanaka, H., 2013. Dam break wave simulation using the simultaneous coupling method, *Proceedings of 35th IAHR Congress*, 9795-9802.

Adityawan, M.B.; Tanaka, H., and Lin, P., 2013. Boundary layer approach in the modeling of breaking solitary wave runup, *Coastal Engineering*, 73, 167–177.

Adityawan, M.B.; Dao, N.X., Tanaka, H.; Mano, A., and Udo, K., 2014, Morphological changes along the Ishinomaki Coast induced by the 2011 Great East Japan Tsunami and the relationship with coastal structures. *Coastal Engineering Journal*, 56(3), 1450016: 21 pages.

Biscarini, C.; Di Fransesco, S., and Manciola, P., 2010. CFD modeling approach for dam break flow studies, *Hydrol. Earth Syst. Sci.*, 14, 705-718.

Fukushima, M.; Matsuura, T., and Hattori, A., 2013. Experimental study on the characteristics of river tsunami, *Journal of JSCE B-2 (Coast. Eng.)*, 69(2), I_261-I_265. (*in Japanese*)

Kabiling, B. and Sato, S., 1993. Two-dimensional nonlinear dispersive wave-current model and three-dimensional beach deformation model, *Coastal Engineering in Japan*, 36, 195–212.

Liu, P.L.F.; Park, Y. S., and Cowen, E. A., 2007. Boundary layer flow and bed shear stress under a solitary wave, *Journal of Fluid Mechanics*, 135, 449–463.

Nielsen, P., 2002. Shear stress and sediment transport calculations for swash zone modeling, *Coastal Engineering*, 45, 53–60.

Sana, A., and Shuy, E. 2002. Two-Equation turbulence models for smooth oscillatory boundary layers, *Journal of Waterway, Port, Coastal, Ocean Eng.*, 38, 38-45.

Sugawara, D.; Goto, K., and Jaffeb, B.E., Numerical models of tsunami sediment transport — Current understanding and future directions, *Marine Geology*, 352, 295-320.

Suntoyo, and Tanaka, H., 2009. Effect of bed roughness on turbulent boundary layer and net sediment transport under asymmetric waves. *Coastal Engineering*, 56(9), 960-969.

Tanaka, H., and Thu, A., 1994. Full-range equation of friction coefficient and phase difference in a wave-current boundary layer, *Coastal Engineering*, 22, 237–254.

Tanaka, H.; Adityawan, M.B., and Mano, A., 2014a. Morphology change at the Nanakita River mouth after The Great East Japan Tsunami, *Coastal Engineering*, 86, 14–26.

Tanaka, H.; Kayane, K.; Adityawan, M.B.; Roh, M., and Farid, M., 2014b. Study on the relation of river morphology and tsunami propagation in rivers, *Ocean Dynamics*, 64(9), 1319-1332.

Wilcox, D.C., 1988. Reassessment of the scale determining equation for advanced turbulence models, *AIAA Journal*, 26(11), 1299–1310.

Journal of Coastal Research	SI	75	1252 - 1256	Coconut Creek, Florida	2016

Characteristics of Beach Erosion due to the 2011 Tohoku Earthquake and Tsunami and Its Recovery across the Entire Inundated Area

Kaoru Tojo † **and Keiko Udo**‡

†Department of Civil and Environmental Engineering, Tohoku University, Sendai 980-8579, Japan
kaoru1307@potential1.civil.tohoku.ac.jp

‡International Research Institute of Disaster Science, Tohoku University, Sendai 980-8579, Japan
udo@irides.tohoku.ac.jp

www.cerf-jcr.org

www.JCRonline.org

ABSTRACT

Kaoru, T. and Udo, K., 2016. Analysis of beach erosion because of the 2011 Tohoku earthquake and tsunami. *In:* Vila-Concejo, A.; Bruce, E.; Kennedy, D.M., and McCarroll, R.J. (eds.), *Proceedings of the 14th International Coastal Symposium* (Sydney, Australia). *Journal of Coastal Research*, Special Issue, No. 75, pp. 1252 - 1256. Coconut Creek (Florida), ISSN 0749-0208.

The 2011 Tohoku earthquake and tsunami caused the disappearance of beaches over a wide area because of inundation accompanying the land subsidence caused by the earthquake and because of tsunami erosion. This study aims to investigate the general characteristics of the 2011 earthquake and tsunami and identify the factors that caused beach damage. The study focuses on 74 beaches from Aomori Prefecture to Chiba Prefecture, including those where the damage was insignificant. Satellite and aerial image analyses demonstrated that the main factor in beach disappearance was not inundation following land subsidence caused by the earthquake but erosion because of sediment transport by the tsunami. There were many cases where a significant increase in the amount of beach retreat occurred when the tsunami overflowed a seawall, leading to the collapse of the seawall. It was also quantitatively confirmed that beach erosion could have been significantly reduced by the survival of the seawall. Three years after the 2011 tsunami and earthquake, the recovery rates differed between beaches on the Sanriku coast and those in other areas. The rate was ≤25% for many beaches on the Sanriku coast of the Rias terrain and ≥75% throughout the south of the Sendai plain.

ADDITIONAL INDEX WORDS: *Beach erosion, nationwide, overflow depth, tsunamis.*

INTRODUCTION

Large-scale beach damage has occurred in recent years, as exemplified by the 2004 Sumatra earthquake and tsunami and the 2011 Tohoku earthquake and tsunami. In the 2004 case, research has been conducted on beach erosion and its recovery process (*e.g.*, Liew *et al.*, 2010; Choowong *et al.*, 2009) and impact assessment of the coastal environment (Szczucinski *et al.*, 2006) on the Aceh coast of Sumatra, Indonesia, and near the Phang Nga province, Thailand. For Aceh, the erosion extended approximately 500 m inland and beaches were catastrophically destroyed by the tsunami, which is said to occur approximately every 500 years. In the 2011 case, research on beach erosion and its recovery process in the southern Sendai Bay coast (Udo *et al*., 2013; Takamura *et al*., 2014); the relationship between beach erosion and river mouth location and coastal structures (Tanaka *et al*., 2011); estuary sandbar outburst and its recovery (Hirao *et al*., 2012); and large-scale topography deformation and the associated factors causing structural damage (Nagasawa *et al*., 2012) has occurred. Beach damage occurred over a wide area from Iwate Prefecture to Fukushima Prefecture and the erosion reached up to several hundred meters inland in the areas with significant damage; natural recovery would be reportedly difficult for many of these beaches.

The mechanisms and recovery processes of large-scale erosion have been reported; however, most of these studies focus on areas with significant damage. There have been no studies quantitatively analyzing beach damage in areas where the damage was insignificant.

It is known that beach damage by an earthquake and tsunami is induced by inundation accompanying the land subsidence caused by the earthquake and erosion because of sediment transport by the tsunami. In this study, we focused on beach damage and examined its characteristics over a wide area from Aomori Prefecture to Chiba Prefecture. In order to investigate the factors that affect beach damage, we included beaches where the extent of damage was low.

METHODS

Study area

The coastal study area consists of 74 sites (Figure 1a), where the inundation height was measured and sandy beaches were confirmed. These were selected from a total of 396 sites with pebble beach, sandy beach, and muddy beach from Shiriyazaki, Aomori Prefecture to Kujukuri, and Chiba Prefecture, as described by the vegetation survey report of the second basic research on nature conservation, Ministry of Environment (1978). Shoreline extension at each site was about 0.1–10 km.

DOI: 10.2112/SI75-251.1 received 15 October 2015 accepted in revision 15 January 2016
*Corresponding author: kitsune_france126@icloud.com
©Coastal Education and Research Foundation, Inc. 2016

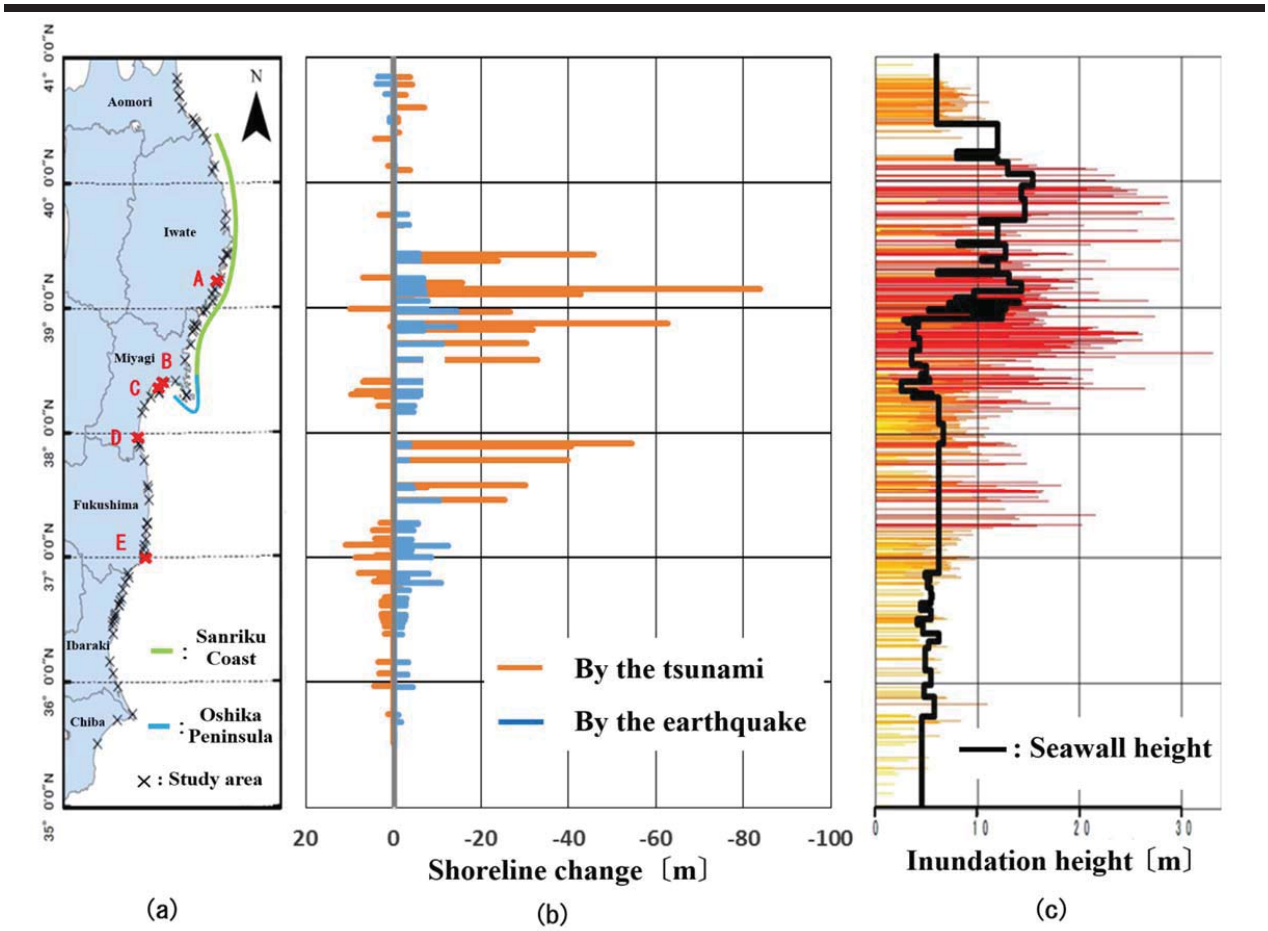

Figure 1. (a) Study area. (b) Spatial distribution of average shoreline change caused by the earthquake and tsunami, respectively. (c) Spatial distribution of inundation height and seawall height (distribution of seawall height is averaged throughout the coastal area even where a seawall was not installed).

For each site within the study area, we confirmed the status of beach erosion and other coastal features, such as seawall collapse, using satellite images and aerial photographs. Also, we used the shoreline change as a beach damage index and the overflow water depth determined from the inundation and seawall height as a tsunami force index. We then investigated the relationship between these variables to analyze the characteristics of beach damage.

Calculation of shoreline change

The shoreline change data used in this study were for every 50 m of shoreline extension, as obtained from the Biodiversity Center of Japan, Ministry of the Environment (2013). The shoreline status before the tsunami was determined visually from IKONOS satellite images photographed from November 4, 2000 to January 16, 2010. There is a possibility that shoreline change occurred during this period before the earthquake and tsunami; however, consideration of the long-term satellite images for several decades before the 2011 earthquake event (Udo *et al.*, in press) showed that such change was relatively small compared to the damage caused by the earthquake and tsunami. Data for the period after the 2011 tsunami were taken from aerial photos produced by the Geographical Survey Institute (GSI) from March to July 2011. The time difference of the extracted shoreline was four months, except for Chiba Prefecture (photographed in February 2012) and Fukushima Prefecture (photographed in April 2012). The shoreline change data included both shoreline changes caused by beach inundation following land subsidence because of the earthquake and those affected by sediment transport because of the tsunami. In order to separate these two impacts, we initially calculated the shoreline change caused by the earthquake by multiplying the beach slope and the vertical crustal deformation provided by GSI (2011, 2013). Next, we determined the shoreline change caused by the tsunami by deducting the shoreline change caused by the earthquake from the shoreline change data.

Estimation of overflow depth

Existing studies have reported that beach erosion is exacerbated at points where the seawall collapsed (*e.g.,* Udo *et al.*, 2015) and that seawall damage increases when the overflow water depth increases (Ministry of Land, Infrastructure, Transport and Tourism, 2011). Therefore, we made an analysis using overflow water depth as an indicator of tsunami force on a sandy beach. We estimated the overflow water depth of each coastal site by deducting the seawall height from the inundation height obtained by the 2011 Tohoku Earthquake Tsunami Joint Survey (TTJS) Group (2011) and the seawall height data of each regional coast from Aomori Prefecture to Chiba Prefecture (Aomori Prefectural Government, 2013; Iwate Prefectural Government, 2011; Miyagi Prefectural Government, 2012; Fukushima Prefectural Government, 2011; Ibaraki Prefectural Government, 2012; Chiba Prefectural Government, 2013).

Calculation of post-disaster recovery rate

We obtained the recovery rate by dividing the recovery area by the erosion area for the river mouth sandbar and the coastal site where significant erosion occurred. Using satellite images from Google Earth, we determined the eroded area immediately after the 2011 tsunami (March 14, 2011 to March 24, 2011) and before the tsunami (April 4, 2005 to March 21, 2010). We then determined land recovery area from the images immediately after the tsunami and after a further three years (March 24, 2014 to April 13, 2014). Artificially recovered area was excluded from the calculation.

RESULTS

Spatial distribution of the average shoreline change caused by the earthquake and tsunami

Figure 1b shows the spatial distribution of average shoreline change caused by the earthquake and tsunami at each site of the study area. The average shoreline change was obtained by dividing the sum of shoreline change every 50 m by the shoreline extension.

We found that beach damage from erosion caused by the tsunami was more significant than that from inundation caused by the earthquake. The level of subsidence was approximately 5 cm in Aomori Prefecture and 10 cm in Chiba Prefecture, and the level of subsidence was found to increase as it approached the epicenter, *e.g.*, 1 m or more of ground subsidence occurred in the Oshika Peninsula close to the epicenter. Shoreline change caused by the earthquake was approximately 5 m in Chiba Prefecture and 10 m in the Rias region. There was no relationship between the level of crustal movement and the shoreline change caused by the earthquake.

Relationship between the average overflow water depth and the tsunami-induced shoreline change

Figure 1c shows inundation height and average seawall height at each beach, with the differences corresponding to overflow water depth. Comparing Figure 1b and 1c, the amount of shoreline retreat was small in Aomori, Ibaraki, and Chiba prefectures, where the tsunami overflow water depth was relatively low. On the other hand, at many sites from Iwate Prefecture to Fukushima Prefecture where overflow water depth was relatively high, the amount of shoreline retreat was large. However, a clear relationship was not necessarily observed between the overflow water depth and the amount of shoreline retreat. From the analysis of satellite images, it was confirmed that localized erosion occurred in many places such as seawall breach points (Figure 2a and 2d) and river mouths (Figure 2c and 2e).

Figure 2. Examples of beach erosion from satellite images (locations of (a) to (e) correspond to A to E in Figure 1a). Red dash lines show the seawall locations; Blue arrows show the river mouth locations.

To identify the local characteristics of the erosion, we considered the seawall status at the rear of the beach as one of the following three cases: 1) where the seawall was collapsed or undeveloped, 2) where the seawall remained, and 3) where the seawall remained but the river mouth exists in the vicinity of the beach. Figure 3 shows the relationship between the overflow water depth and the shoreline change every 50 m at each coastal site. When the seawall remained, the amount of shoreline retreat was small even if the overflow water depth was large. The inundation height exceeded the seawall height

where the seawall was collapsed. The amount of retreat was greater at points where the seawall collapsed and in the vicinity of river mouths. The main causes of shoreline retreat were found to be local erosion because of seawall collapse and an increase in river mouth width.

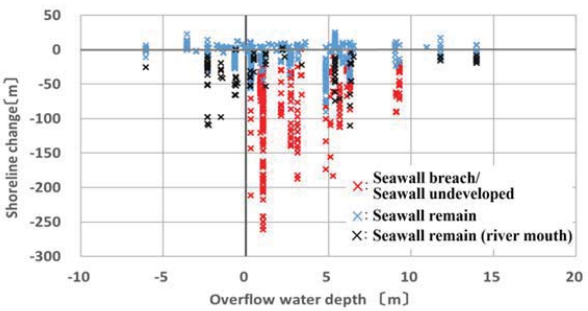

Figure 3. Relationship between the average overflow water depth (calculated by deducting seawall height from inundation height) and tsunami-induced shoreline change every 50 m.

Spatial distribution of the recovery rate

Figure 4 shows the spatial distribution of the recovery rate at each selected beach and sandbar. Three years from the 2011 tsunami and earthquake, the recovery rates differed between beaches on the Sanriku coast and in other areas. The rate was 25% or less for many beaches on the Sanriku coast of the Rias terrain and 75% or more throughout the south of the Sendai plain.

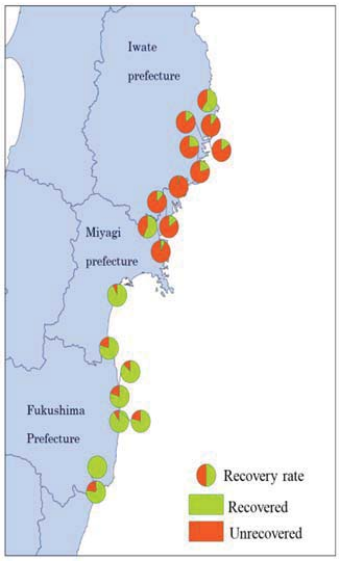

Figure 4. Spatial distribution of the recovery rate at each selected beach and sandbar.

DISCUSSION

Some shoreline changes caused by the tsunami were positive (advancing). These were caused by the error that occurred where an earthquake-induced shoreline change that was greater than the shoreline change data. We determined the shoreline change caused by the tsunami by deducting the earthquake-induced shoreline change from the shoreline change data. It is considered that such an error occurred because the shoreline change data included data relating to the recovery process up until the day of satellite image acquisition; this would have caused an underestimation of shoreline change. Another reason is that beach slope was defined as uniform at each site and a constant value was used.

There was no relationship recognized between the level of crustal movement and the shoreline change caused by the earthquake. This is because of the differences in slope between each site. The slope on the Sanriku coast of the Rias terrain is relatively steep, *i.e.*, 1/10, and that on the coasts of the plains is relatively gradual, *i.e.*, 1/30.

The main causes of shoreline retreat were local erosion because of the collapsed seawall and an increase in river mouth width. This is considered to occur because of local erosion induced by tsunami-return flows that were concentrated in areas of lower elevation (*e.g.*, Udo *et al.*, 2013; Nagasawa *et al.*, 2012). However, we occasionally found shoreline retreats of >50 m where the seawall remained. This was found in relatively low-elevation areas such as in rice fields deep behind a valley terrain of Rias; even if seawall collapse did not occur at this location, a collapse of the seawall was noted in surrounding areas (Figure 2b).

The recovery rates differed between the Sanriku coast and in other areas. As noted by Liu (2013), shortages in the supply of sediment from nearby rivers and shores must influence beach recovery.

CONCLUSIONS

In this study, we analyzed the characteristics of beach damage caused by the 2011 earthquake and tsunami across the entire inundated area, including beaches with an insignificant level of damage. The results of the analysis indicated that the major factor causing damage was not beach inundation because of subsidence caused by the earthquake but beach erosion because of sediment transport by the tsunami. Local erosion, such as the expansion of the river mouth and erosion at the seawall breach point, was the main cause of significant beach erosion by the tsunami and did not induce a uniform retreat of the shoreline. Where the tsunami overflowed and the seawall was collapsed, erosion tended to be significant. This suggests that if seawalls had not been broken, erosion could have been mitigated considerably. On the other hand, there was no clear relationship observed between the overflow water depth and beach erosion. Three years after the 2011 tsunami and earthquake, the recovery rates differed between the beaches on the Sanriku coast and those in other areas. The rate was 25% or less at many beaches on the Sanriku coast of the Rias terrain and 75% or more throughout the south of the Sendai plain.

ACKNOWLEDGMENTS

The authors would like to thank the Biodiversity Center of Japan for providing coastline change dataset. This research was supported by the Special Project Research of IRIDeS (International Research Institute of Disaster Science, Tohoku University).

LITERATURE CITED

Aomori Prefectural Government, 2013. http://www.pref.aomori.lg.jp/kotsu/build/tunami-kentokai.html.

Biodiversity Center of Japan, Nature Conservation Bureau, Ministry of the Environment, 1978. *Vegetation survey report of the second basic research of nature conservation.* http://www.biodic.go.jp/kiso/fnd_f.html.

Biodiversity Center of Japan, Nature Conservation Bureau, Ministry of the Environment, 2013. *2012 Survey of the Natural Environment in the Pacific coast of Tohoku district Summary.* http://www.shiokaze.biodic.go.jp/24sokuhou.html.

Chiba Prefectural Government, 2011. http://www.reconstruction.go.jp/topics/main-catl/sub-catl-3/20130801_chiba01asahi.pdf.

Choowong, M.; Phantuwongraj, S.; Charoentitirat, T.; Chutakositkanon, V.; Yumuang, S., and Charusiri, P., 2009. Beach recovery after 2004 Indian Ocean from Phang-nga, Thailand. *Geomorphology*, vol. 104, pp. 134–142.

Geospatial Information Authority of Japan, 2011. http://www.gsi.go.jp/chibankansi/chikakukansi40005.html.

Geospatial Information Authority of Japan, 2013. http://mekira.gsi.go.jp/JAPANESE/h23touhoku_2years.html.

Hirao, R.; Tanaka, H.; Adityawan, M, B.; Umeda, M.; Mano, A., and Udo, K., 2012. Breaching of Sandy Coast and Spit Due To The 2011 Tsunami and Their Recovery. *Journal of Japan Society of Civil Engineers*, Ser. B2, 68, pp. I_581–I_585.

Fukushima Prefectural Government, 2011. http://www.pref.fukushima.lg.jp/uploaded/attachment/10267.pdf.

Ibaraki Prefectural Government, 2011. http://www.pref.ibaraki.jp/bukyoku/doboku/01class/class06/kaigan/tsunamisinnsui/index.html.

Iwate Prefectural Government, 2011. http://www.pref.iwate.jp/kasensabou/kasen/fukkyuu/008326.htm.

Liew, S, C.; Gupta, A.; Wong, P, P., and Kwoh, L, K., 2010. Recovery from a large tsunami mapped over time: The Ache coast, Sumatra. *Geomorphology*, vol.114, pp. 520–529.

Liu, H., 2013. Dynamic changes of coastal morphology following the 2011 Tohoku Tsunami. *Proceedings of the 7th International Conference on Asian and Pacific Coasts* (Bali, Indonesia), pp. 594–601.

Ministry of Land, Infrastructure, Transport and Tourism, 2011. *The second Tsunami Protection committee in coast.* http://www.mlit.go.jp/river/shinngikai_blog/kaigantsunamitaisaku/dai02kai/.

Miyagi Prefectural Government, 2012. http://www.pref.miyagi.jp/uploaded/attachment/108393.pdf

Nagasawa, G. and Tanaka, H., 2012. Analysis of Structural Damages with massive Geomorphic Change due to Tsunami. *Journal of Japan Society of Civil Engineers*, Ser. B2, 68, pp. I_1361–I_1365.

Szczucinski, W.; Chaimanee, N.; Niedzielski, P.; Rachlewicz, G.; Saisuttichai, D.; Tepsuwan, T.; Lorenc, S., and Siepak, J., 2006. Environmental and Geological Impacts of the 26 December 2004 Tsunami in Coastal Zone of Thailand-Overview of Short and Long-Term Effects. *Polish J. Environ. Stud.*, 15(5), 793–810.

Takamura, M.; Udo, K., and Takeda, Y., 2014. Characteristics of beach morphology change and sediment budget in Yamamoto Beach, Miyagi Prefecture before and after the 2011 Tohoku Earthquake and Tsunami. *Proceedings of the 22th Global Environment Symposium* (Tokyo, Japan), pp. 31–35.

Tanaka, H.; Mano, A., and Udo, K., 2011. Beach Morphology Change Induced by The 2011 Great East Japan Earthquake Tsunami. *Journal of Japan Society of Civil Engineers*, Ser. B2, 67, pp. I_571–I_575.

The 2011 Tohoku Earthquake Tsunami Joint Survey (TTJS) Group, 2012. http://www.coastal.jp/ttjt/index.php.

Udo, K.; Takeda, Y.; Tanaka, H., and Mano, A., 2013. Beach Morphology Change of Southern Sendai Coast due to 2011 Tohoku Earthquake Tsunami. *Journal of Japan Society of Civil Engineers*, Ser. B2, 69, pp. I_1391–I_1395.

Udo, K.; Takeda, Y.; Tanaka, H., and Mano, A., 2015. Effect of Submarged Breakwaters on Coastal Morphology Change due to Tsunami. *Journal of Japan Society of Civil Engineers*, Ser. B3. (in press)

Udo, K.; Tojo, K.; Takeda, Y.; Tanaka, H., and Mano, A. Characteristics of Shoreline Retreat due to the 2011 Tohoku Earthquake and Tsunami and Its Recovery after Three Years. *Tsunami and Earthquakes in Coastal Systems, Advances in Natural and Technological Hazards Research.* (in press)

Journal of Coastal Research	SI	75	1257 - 1261	Coconut Creek, Florida	2016

Measurement and Model Simulations of Hydrodynamic Parameters, Observations of Coastal Changes and Experiments with Indicator Sediments to Analyse the Impact of Storm St. Jude in October, 2013

www.cerf-jcr.org

Hannes Tõnisson[†*], Ülo Suursaar[‡], Victor Alari[§†], Merle Muru[§], Reimo Rivis[†], Are Kont[†], and Marili Viitak[††]

[†]Institute of Ecology, Tallinn University
Tallinn, Estonia
[§†]Institute of Coastal Research, Helmholtz-Zentrum
Geesthacht, Geesthacht, Germany
[††]Marine Systems Institute, Tallinn University of
Technology, Tallinn, Estonia

[‡]Estonian Marine Institute, University of Tartu
Tallinn, Estonia
[§]Institute of Ecology and Earth Sciences
University of Tartu, Tartu, Estonia

www.JCRonline.org

ABSTRACT

Tõnisson, H.; Suursaar, Ü.; Alari, V.; Muru, M.; Rivis, R.; Kont, A.; and Viitak, M., 2016. Measurement and model simulations of hydrodynamic parameters, observations of coastal changes and experiments with indicator sediments to analyse the impact of storm St. Jude in October, 2013. *In:* Vila-Concejo, A.; Bruce, E.; Kennedy, D.M., and McCarroll, R.J. (eds.), *Proceedings of the 14th International Coastal Symposium* (Sydney, Australia). *Journal of Coastal Research*, Special Issue, No. 75, pp. 1257 - 1261. Coconut Creek (Florida), ISSN 0749-0208.

The aim of the study is to analyse the meteorological parameters, hydrodynamic conditions and coastal changes caused by a severe European storm referred to as St. Jude (Christian). It crossed the Baltic Sea on 27-29 October 2013. At Cape Kelba in the west Estonian archipelago, wave parameters were measured by RDCP and simulated by two wave models. Shoreline and topographic changes were recorded before and after the storm by RTK-GPS device. Simultaneous experiments with painted sediments were carried out to analyse sediment transport patterns and wave impact on the nearshore sea bed. It was the most significant storm in Estonia since 2007 with wind gusts up to 33 m/s and local storm surge height 1.5 m. The measured significant wave height reached 3.4 m at the 5.5 m deep point near the geomorphic study site. Modelling study indicated some wave-current-surge interaction effects. The distal section of the Kelba Spit elongated by about 12 m, but only minor changes were registered in the proximal part of the spit. The painted sediments placed on the sea bed at depths from 2-6 m were swept up to 20 m towards the shore.

ADDITIONAL INDEX WORDS: *Extra-tropical cyclones, wave modelling, sediment transport, Baltic Sea.*

INTRODUCTION

Anticipated sea level rise and increasing storminess caused by global climate warming calls for a better understanding of storm-related phenomena in the coastal zone. Although there is no consensus yet as to whether the frequency and intensity of storms has increased or will increase in the future (e.g. Feser *et al*., 2015), storm-related losses seem to be increasing worldwide (Emanuel, 2005). Also, the height of storm surges as well as extent of coastal destruction has increased in the eastern section of the semi-enclosed Baltic Sea (Hünicke *et al*., 2015).

The eastern coast of the Baltic Sea is exposed to the westerlies of moderate latitudes (55°-60° N) and to extratropical cyclones which occasionally pass from west to east (Suursaar *et al*., 2015). Owing to the variable wind fields of a travelling cyclone and the resulting difficulty in determining its track, storm-related impacts from a cyclone can be hard to predict (e.g. Tõnisson *et al*., 2008). And, notwithstanding advances in the modelling of marine hydrodynamic conditions, such modelling is mostly performed in grid-sizes of one or a few kilometers and using meshes which do not necessarily represent processes in the surf and the swash zone. Yet, it is the surf and the swash zone where waves dissipate or reflect their remaining energy after propagation from the open sea towards the coast (Brocchini and Baldock, 2008), and where their actual geomorphic outcome is formed. However, hydro- and morphodynamic processes appear in mixed scales there and are notoriously difficult to study. Although swash/surf zone hydrodynamics and sediment transport have been extensively studied over the past decades, a number of complex case studies and field experiments are still needed for a better description of the near-bed sediment dynamics.

Using *in situ* measurements of waves, repeated observations for coastal processes, and different types of wave- and hydrodynamic models, we attempt to analyse the coastal hydrodynamic and morphodynamic processes during a powerful windstorm designated to as "St. Jude" that significantly impacted the UK, Netherlands, Germany and Denmark. It was the first and the most influential cyclone of the 2013/14 storm season crossing the Baltic Sea on 27-29 October 2013.

Located in the eastern section of the Baltic Sea, the Cape Kelba study site on Harilaid Peninsula (Figure 1) is open to the

DOI: 10.2112/SI75-252.1 received 15 October 2015 accepted in revision 15 January 2016
*Corresponding author: Hannes.Tonisson@tlu.ee
©Coastal Education and Research Foundation, Inc. 2016

strongest winds (SW, W) and highest waves (Hünicke *et al*., 2015) of the region. The cape consists of a series of beach ridges forming an approximately 2 km long spit with a maximum crest height of 3.8 m above sea level (a.s.l) in its proximal part. The distal part consists of well-rounded crystalline gravel, pebble, cobble and boulders (Tõnisson *et al*., 2013). The accumulation of new beach ridges gradually elongates the spit while historical changes in shoreline position and contour reflect past changes in wind and wave climate (Suursaar *et al*., 2015). The 5 m isobath is about 150-200 m west from the shoreline and the 50 m isobath lies about 10-15 km away. The tides are negligible (less than 10 cm) in this region, and the major hydrodynamic agents acting on the seashores are waves and relatively infrequent storm surges.

The objectives of this study are: (1) to present a detailed meteorological and hydrodynamic analysis of the St. Jude storm; (2) to analyze wave-current interaction and wave transformation processes in the swash zone during the storm; and, (3) to analyze the relationships between coastal changes, meteorological parameters and hydrodynamic conditions during the storm.

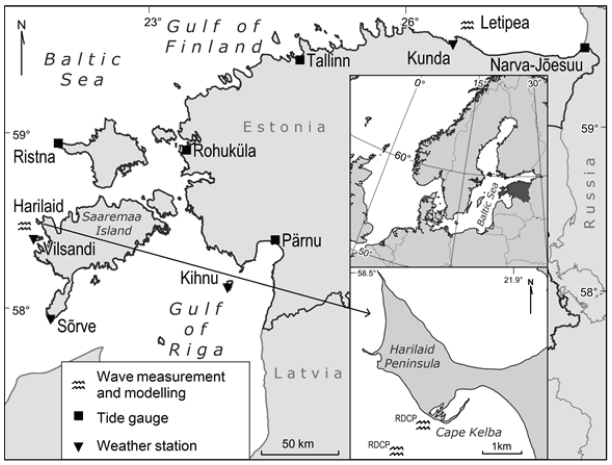

Figure 1. Study area.

METHODS

The wind data from nearby Vilsandi and Sõrve meteorological stations (located 7 and 60 km, respectively, south of Cape Kelba) were used to assess the meteorological conditions and to provide the forcing data for the hydrodynamic study (Figure 1). We used the data on 1-hour sustained wind speeds, wind gust speeds and mean wind directions. For sea level data, we used data from the Ristna tide gauge station, which is the closest (50 km north) to the study site, the Pärnu and Narva gauges being located farther along the Estonian coast. Both meteorological stations and the tide gauge station are operated by the Estonian Environment Agency (EEA).

Wave measurements were carried out at a depth of 5.5 m, 0.2 km off Cape Kelba (58°28′N, 21°49′E; Figure 1) from 29 July to 3 November 2013 using an oceanographic measuring complex RDCP-600. Prior to that, wave measurements were also carried out 1.5 km off Cape Kelba over the period from 20 December 2006 to 23 May 2007, which also included a notable storm. The latter measurements taken at a depth of 14 m gave hourly information on waves, currents and turbidity, and enabled us to calibrate and fine-tune a local point-model (LCPM; Suursaar, 2013) for wave hindcasts covering the period from 1966 to 2014 on hourly basis. To study the spatial patterns of wave fields around the Cape and to explain the shoreline changes, a spectral wave model SWAN (cycle III, version 40.91) was used. It is a third-generation wave model developed at the Delft University of Technology (Booij *et al*., 1999). The model was run in a non-stationary mode with a 15´ integration time step. The horizontal grid size was 1´ along latitudes and 2´ along longitudes, and the model domain covered the entire Baltic Sea. A nested grid with a resolution of 1 km was used to simulate waves in the Estonian coastal waters. The modelling period covered the St. Jude storm as well as the period one week prior to it. Physical processes, such as wave-wave interactions, whitecapping, wind input, bottom friction and depth-induced breaking were included; and, the linear growth term for wind growth was activated (Alari, 2013). The wave model was forced by the gridded High Resolution Limited Area Model – HIRLAM winds for the Baltic Sea with a horizontal resolution of 0.1 degrees.

In order to study the wave-current-surge interaction during the storm for the HIROMB-EST model (High Resolution Operational Model of the Baltic Sea; Lagemaa *et al*., 2011), sea-surface elevation and current data with 0.5 nm horizontal resolution were used.

The shoreline of Cape Kelba and beach profiles were measured during the routine annual survey on 30 July 2013. Shoreline measurements and precise leveling were carried out using an RTK-DGPS device with an accuracy of 1 cm in vertical and horizontal scales. The volume of disposed sediments in the active zone of each profile was calculated, with the active zone being defined as the zone from the mean shoreline to the highest elevation of the storm waves' impact (Tõnisson *et al*., 2013). The study site was revisited after the storm on 2 November 2013 and on 1 August 2014. Wave run-up and sea-levels were also recorded after the storm by reference to the location of physical manifestations of the storms' presence (e.g., ridges of debris).

In order to evaluate sediment dispersement, three sizes of sediment particles were collected from the local beach and painted with non-fluorescent asphalt paints (1-2.5 cm, yellow; 2.5-5 cm, red; 5-10 cm, blue). They were then stacked in piles, placed at depths of 1-10 m in one meter depth intervals. The piles were positioned with GPS and photographed. The sediment piles were then monitored on 1 August 2013, 2 November 2013 and 1 August 2014. Additional painted sediment tests were carried out in the swash zone on 31 July 2013 where the painted sediments were placed in a continuous line from -0.5 to +1.3 m. The material was monitored twice, the first time on the following day and the second time just after St Jude came through. The direction of sediment transport, maximum and average distances from the sources and the elevations of the painted sediment particles were analysed.

RESULTS AND DISCUSSION

The 2013-2014 storm season above north-western Europe began in October 2013 and lasted until the end of January 2014. Following the westerlies, a series of extra-tropical cyclones (including St.Jude, Hilde, Xaver, *etc.*) crossed the Baltic Sea.

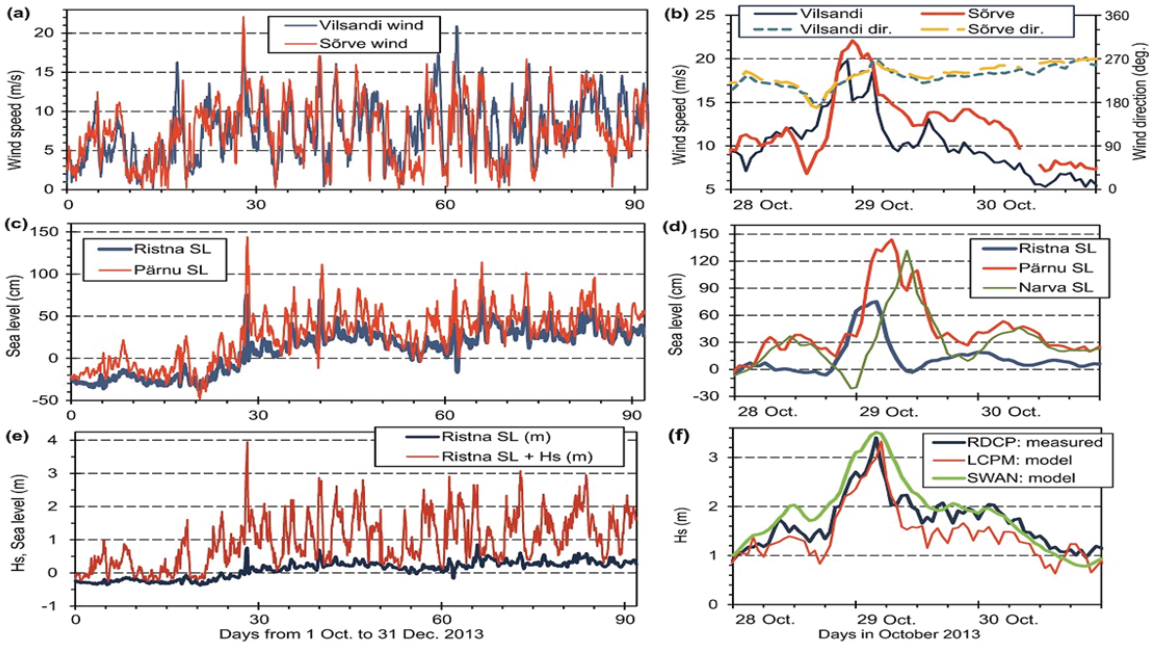

Figure 2. Measured wind conditions at Sõrve and Vilsandi over a longer period (a) and during the St.Jude (b); measured sea level heights (SL) at selected tide gauges (c, d); Hindcast Hs wave heights combined with the sea level height at nearby Ristna gauge (e), and comparison of measured wave heights at the 5.5 m deep location with the LCPM hindcast results for the 14 m deep location, as well as the SWAN results for the closest gridcell (f).

The storms were highly destructive over most of the northern Europe, but reached Estonia, in a somewhat dissipated state.

Meteorological and hydrological description of St. Jude

The first in this series of storms was St. Jude, known also as Cyclone Christian (in Germany), Carmen (in UK), or Allan (in Denmark). It formed in the northwest Atlantic on 26 October. The area of low pressure travelled eastward as a kind of explosive cyclone and made its landfall early on 28 October near the Isle of Wight, UK. The centre of the cyclone continued across the North Sea and over southern Finland with its most devastating winds on the right hand side of its track. Record-breaking wind gust speeds from it were recorded both in the Netherlands (up to 41 m/s) and in Denmark (up to 53 m/s).

In Estonia, the strongest winds (from SW-W) were recorded in western Saaremaa Island leaving northern Estonia relatively unharmed. The maximum 1h-sustained wind speeds were 19.8 m/s at Vilsandi, 22.1 m/s at Sõrve (Figure 2ab), and 23.2 m/s at nearby Roomassaare on 29 October (from 00:00 to 05:00 UTC at different stations). The wind gust speeds reached 30-32 m/s in those stations, all located 60 km or less to the south from the Cape Kelba study site. The cyclone also caused a storm surge in the eastern Baltic Sea. The tide gauge at Ristna, located the closest to Cape Kelba, showed a 80 cm high surge (Figure 2cd). Located in the nodal part of the elongated and essentially tideless Baltic Sea, the Ristna region is not surge-prone (Hünicke *et al*. 2015). The maximum sea level at the Pärnu gauge recorded a surge of 144 cm at 07:00 UTC. And, at Narva-Jõesuu, the sea level rose from the initial -21 cm to a high of 132 cm by 10:00 UTC, 11 hours after 7 UTC (Figure 2d). The storm surge heights remained relatively modest only because St.Jude was the first cyclone of the season and the mean (background) Baltic sea level was not yet elevated. If the initial sea level had been above 50 cm, which is frequently observed in late autumn (Suursaar *et al*., 2015), the storm surges both at Pärnu and Narva might have been well above the critical value of 150 cm.

The direct wave measurements taken at a depth of 5.5 m (relative to mean sea level state and about 200 m off Cape Kelba using RDCP yielded the highest Hs value of 3.4 m (Figure 2f) and the maximum waves reached 5.2 m at 04:00 UTC. Initially, the waves approached Cape Kelba from the southwest, but turned west during the peak of the storm. The peak wave period was 10 s and the energy wave period reached 6.9 s. Located along the same cross-shore transect but about 1 km seaward, the previously calibrated LCPM (Suursaar, 2013), being representative of the 14 m deep location, yielded the maximum Hs wave height at 3.33 m (Figure 2f). There was only a slight height difference as well as a one hour mismatch in peak timing between the estimates. The elevated values of the RDCP relative to LCPM suggest that this 5.5 m deep measurement site might have been in the shoaling/breaking zone for the 1.5-3 m high waves or some wave-surge interaction occurred (see the next chapter). Significant wave height simulated with the SWAN model (Figure 3a) reached 7 m in the Baltic Proper, and up to 4.5 m in the Gulfs of Riga and Finland. In terms of wave height only, St Jude was one of the most powerful autumn storms in half a century based on historical hindcasts (Alari, 2013).

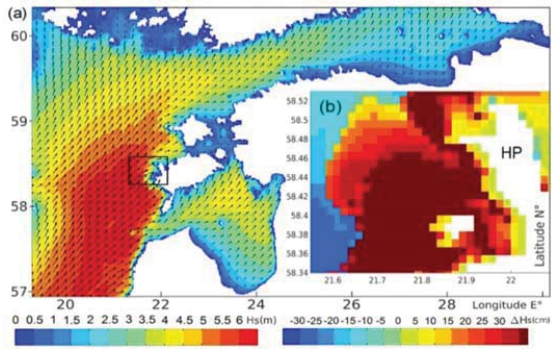

Figure 3. Simulated with the SWAN model, field of significant wave height on 29 October 2013 at 04:00 UTC (a). Wave height increment/decrement calculated as a difference between the simulation with currents+surge interaction and the control run for the Harilaid Peninsula (HP) region (b).

While a subsequent powerful storm referred to as Ivar (or, Seija) struck on 13 December bringing NW winds and raising the sea level at Narva Bay to 168 cm, its impact was felt mainly on North Estonia, and so ultimately was not as consequential as St. Jude which impacted more of Estonia overall. It was the most powerful storm in Estonia in some years, even slightly more powerful than the preceding notable storm Ulli on January 2012 (Tõnisson *et al*., 2013). Still, the meteorological and hydrodynamic manifestations of storms Hanno (on 14 January 2007) and Gudrun/Erwin (on 9 January 2005) remain the most significant for Estonia, with Gudrun being the most infamous (and least dissipated) of the Baltic Sea storms, characterized by a sea level measurement of 275 cm (starting from an already elevated Baltic Sea level for the season) and severe destruction along the Estonian coast (Tõnisson *et al*., 2008).

Wave-current-surge interaction

Various shallow sea effects, including wave-current-surge interaction, are rarely taken into account in coastal zone wave modelling (Alari, 2013). While the wave field evolution during the St.Jude storm (Figure 2f, 3a) was simulated using additional surface current velocity and surge height input, the wave height increments varied by up to 35 cm (Figure 3b). In relative terms this implies a change of up to 20% in the significant wave height. Most of the change (up to 30 cm) at the Cape Kelba study site was caused by elevated water level as the higher water level reduces the wave energy dissipation otherwise caused by bottom friction and wave breaking. Therefore, more wave energy propagates towards the coast. This effect was limited to about a 10-km wide zone, and it disappeared in sea areas that were more than about 30 m deep.

Coastal changes during the storm and in winter 2013/14

The distal part of Cape Kelba elongated by 12 m and shifted westward by 7 m as a result of sediment dispersal across the Cape. As the yearly elongation of the spit for the 12-month period ending in August 2014 was 60 m, the portion attributable to St. Jude contributed only about 20%. Some minor changes (less than 2 m) were registered in the proximal part of the Cape. Despite powerful waves, the relatively low sea-level hindered the storm's impact (Figure 4).

Analysis of the cross-shore profiles revealed that despite relatively low sea-level, the wave run-up reached 2.9 m a.s.l., which is very close to the maximum significant wave height measured 200 m from the shoreline. High waves removed up to a 0.6 m thick layer of gravel from the area between 1.2 m and 3.0 m a.s.l on the exposed western slope of the Cape, and deposited it on the lower slope in between the mean sea level and up to 1.2 m in elevation. The active sections of the shore profiles lost about 13% of their volume. The accumulation zone starts just after the area where the Cape curves to the northeast. There, freshly accumulated deposits provide up to 1/3 of the volume of the shore profiles' active sections. The profiles in the most distal section show some mixed signs: significant erosion on the seaward side and accumulation on the leeward side of the Cape. As the spit is about 1.5 m high in the distal part, the wave run-up could have reached over 1.5 m causing the sediments roll-over and shifting the whole Cape to the west by 5-7 m.

Revisiting the site at the beginning of November, we did not find any piles of painted sediments deeper than the beginning of the sandy bottom (7.5 m isobath), where the entire area was covered by a thick layer of freshly accumulated sand. We assume that the sand covered the sediment piles. The pile at 7 m depth was somewhat distorted and the pile at 6 m depth was dispersed over a 0.5 m wide and 8 m long shoreward directed band. No sediments were found at 5 m depth, but the sea bed showed signs of extensive erosion. There were several freshly formed holes and depressions around bigger boulders. The sediments placed at a depth of 4 and 3 m were dispersed along a 20 m long and 1 m wide shoreward directed band. We did not find any painted sediments at less than 2 m depth.

Some of the sediments that were placed as a continuous line from -0.5 m to 1.3 m during the field work between 31 July and 1 August 2013 and that moved alongshore at the rate of about 2.5 m/h in moderate wind (7 m/s) conditions during the summer were found after the storm. We found a few painted red particles 350 m towards the tip of the Cape from the initial position. The furthest yellow and blue particles were found 330 and 285 m, respectively, from their original location. The fact that we found some painted particles in such a mobile environment indicates a relatively thin mobile layer of sediments. All the painted particles were found at elevations between 0.95 and 1.18 m a.s.l. Waves near Cape Kelba typically break at 2-4 m depths, but this zone is capable of extending up to 5.5 m during strong storms. Gravel, pebble and cobble particles are first transported shorewards. Longshore sediment transport usually occurs in the swash zone (less than 2 m). According to Bagnold (1963), the wave-generated flow speed outside the breaking zone should be over 160 cm/s to move the particles with 1-10 cm diameter. The sediments reaching the foreshore are the most mobile.

While most of the paint wore off in three months, we could still identify yellow particles and particles with rough surfaces after that time. Burying under fresh deposits and physical wear were probably the main factors why we were not able to find painted particles on the surface of the distal part of the Cape a year later. However, the sediments placed in the sea were still clearly visible in August 2014, and no changes were identified compared to the situation immediately after St Jude.

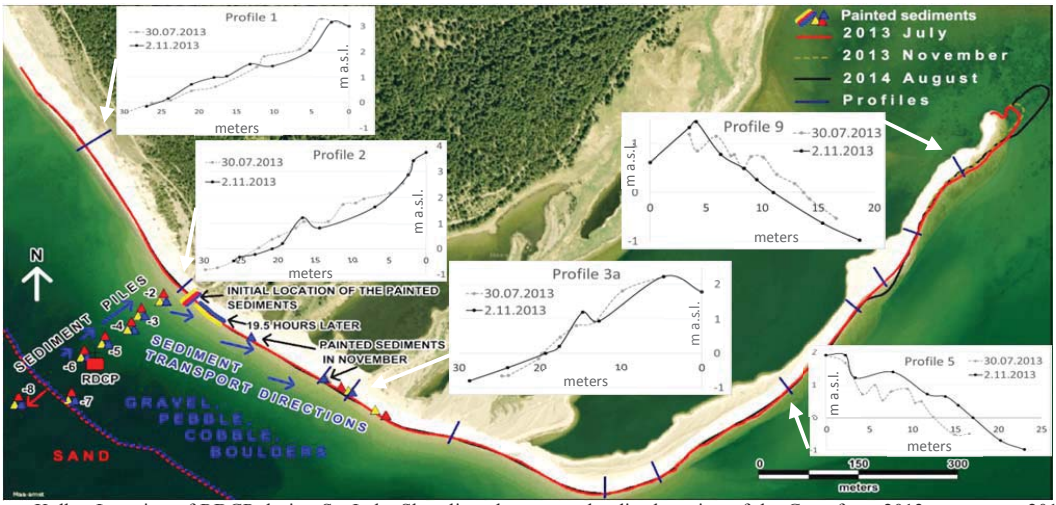

Figure 4. Cape Kelba. Location of RDCP during St. Jude. Shoreline changes at the distal section of the Cape from 2013 summer to 2014 summer. Profile changes during St. Jude. Painted sediment piles and main patterns in the movement of painted sediments.

CONCLUSIONS

The hydrodynamic study showed that wave action combined with the sea level height were the main hydrodynamic agents shaping the shores of Cape Kelba, while currents contributed to lateral drift of the material suspended by the waves. Despite the extreme meteorological parameters of the St Jude storm, its impact was modest even along the well-exposed shores of western Estonia mainly because of the low sea level. The breaking zone of storm waves at Cape Kelba may extend seaward during violent storm events with low sea level. In this active bottom erosion and sediment transport zone the particles with 1-10 cm diameter are usually transported shorewards.

Based on this case study, we can conclude that the combination of high waves and relatively low sea-level may cause significant erosion on up to 6 m deep sea bed while minimal changes are registered on the shore. Slight erosion occurs in higher parts of the shore and accumulation in the distal part of the Cape. Such storms with low sea level bring up additional material to the swash zone, possibly stabilizing the shore system and building small ridges that act as natural protection against subsequent storm impacts occurring at elevated sea-levels.

ACKNOWLEDGMENTS

This study was financially supported by the ESF Grant 9191, institutional research funding IUT18-9 of the Estonian Ministry of Education and Research and by the Estonian Research Council grant PUT595. Special thanks to D.A.Willis

LITERATURE CITED

Alari, V., 2013. Multi-Scale Wind Wave Modeling in the Baltic Sea. Tallinn: Tallinn University of Technology, PhD Thesis, 134 p.

Bagnold, R.A., 1963. Mechanics of marine sedimentation. *In:* M.N.Hill, ed., *The Sea*, Vol. 3. New York: Wiley and Sons, pp. 507-528.

Booij, N.; Ris, R.C., and Holthuijsen, L.H., 1999. A third-generation wave model for coastal regions 1. Model description and validation. *Journal of Geophysical Research C: Oceans*, 104 (C4), 7649-7666.

Brocchini, M. and Baldock, T.E., 2008. Recent advances in modelling swash zone dynamics: Influence of Surf–Swash interaction on nearshore hydrodynamics and morphodynamics. *Reviews of Geophysics,* 46, RG3003.

Emanuel, K., 2005. Increasing destructiveness of tropical cyclones over the past 30 years. *Nature* 436, 686-688.

Feser, F.; Barcikowska, M.; Krueger, O.; Schenk, F.; Weisse, R., and Xia, L., 2015. Storminess over the North Atlantic and northwestern Europe-A review. *Quarterly Journal of the Royal Meteorological Society*, 141(687), 350-382.

Hünicke, B.; Zorita, E.; Soomere, T.; Madsen, K.S.; Johansson, M., and Suursaar, Ü., 2015. Recent change - Sea level and wind waves. *In:* The BACC II Author Team (Ed.). *Second Assessment of Climate Change for the Baltic Sea Basin*, p.155-185. Springer.

Lagemaa, P.; Elken, J., and Kõuts, T., 2011. Operational sea level forecasting in Estonia. *Estonian Journal of Engineering*, 17(4), 301-331.

Suursaar, Ü., 2013. Locally calibrated wave hindcasts in the Estonian coastal sea in 1966–2011. *Estonian Journal of Earth Sciences*, 62, 42-56.

Suursaar, Ü.; Jaagus, J., and Tõnisson, H. 2015. How to quantify long-term changes in coastal sea storminess? *Estuarine Coastal and Shelf Science*, 156, 31-41.

Tõnisson, H.; Orviku, K.; Jaagus, J.; Suursaar, Ü.; Kont, A., and Rivis, R., 2008. Coastal Damages on Saaremaa Island, Estonia, Caused by the Extreme Storm and Flooding on January, 9 2005. *Journal of Coastal Research*, 24, 602-614.

Tõnisson, H.; Suursaar, Ü.; Rivis, R.; Kont, A., and Orviku, K., 2013. Observation and analysis of coastal changes in the West Estonian Archipelago caused by storm Ulli (Emil) in January 2012. *Journal of Coastal Research*, Special Issue No. 65, pp. 32-837.

Journal of Coastal Research	SI	75	1262 - 1266	Coconut Creek, Florida	2016

Tsunami Inundation Modelling in Estuaries: Sensitivity to Variation in Tide from an Emergency Management Perspective.

Olivia A. Wilson †, **Hannah E. Power**†

† School of Environmental and Life Sciences
Faculty of Science and IT
University of Newcastle
Sydney, Australia

www.cerf-jcr.org

www.JCRonline.org

ABSTRACT

Wilson, O.A and Power. H.E., 2016. Tsunami Inundation Modelling in Estuaries: Sensitivity to Variation in Tide from an Emergency Management Perspective., *Proceedings of the 14th International Coastal Symposium* (Sydney, Australia). *Journal of Coastal Research*, Special Issue, No. 75, pp. 1262 - 1266. Coconut Creek (Florida), ISSN 0749-0208.

Using tsunami modelling case studies in Port Jackson (Sydney Harbour), this paper assesses the sensitivity of tsunami modelling to variations in tidal data inputs. Four distinct model setups were all run twice with different tide data inputs. The tide inputs differed in the tidal stage with one input as a leading trough wave (a wave trough followed by a wave peak) and one input as a leading peak wave (a wave peak followed by a trough). One tidal wavelength coincides with the typical duration of a earthquake generated tsunami wave train, which is approximately 12 hours. The model results were assessed primarily for their differences from the perspective of emergency hazard management. It was found that maximum inundation area, maximum current speed and maximum wave height had negligible differences. Momentum results were consistent with the direction of tidal movement. It was concluded that for the outputs required by emergency management services, either a leading trough or leading peak tidal wave is suitable for tsunami modelling in estuaries.

ADDITIONAL INDEX WORDS: *Tsunamis, Tsunami Modelling, Tide Data, Sydney Harbour.*

INTRODUCTION

Earthquake generated tsunami events dominate the causes of tsunami worldwide (UNESCO, 2015) and such events can generate tsunami wave trains with a duration in excess of 12 hours (Burbidge *et al.*, 2008). The geomorphology of estuaries is known to affect tsunami propagation in several ways. During a tsunami event, estuaries can experience increased wave amplification (e.g. Cochard et al., 2008), very high current speeds (e.g. Beccari, 2009) as well as extreme inundation and runup (e.g. Tanaka et al., 2012, Tolkova, 2013). In New South Wales (NSW), Australia, estuaries have been identified by the NSW State Emergency Services (SES) as a key area of research for tsunami impact emergency planning (NSW SES, 2008).

Port Jackson is home to Sydney Harbour and NSW's largest population centre. The estuary is classified as a Drowned River Valley (DRV), Tide Dominated Estuary (TDE) under the Roy *et al.*, (2001) classification system and has complex geomorphology. There is both geological and historical evidence for tsunami affecting NSW (Dominey-Howes, 2007), and the SES has identified NSW as having a 'moderate' tsunami threat (NSW SES, 2008).

There are several programs available to accurately model potential tsunami. The open source software ANUGA is a widely used hydrodynamic model that has been validated for tsunami propagation and inundation (Hinwood & Mclean, 2012, Nielsen *et al.*, 2012). For tsunami propagation and transformation, ANUGA solves the non-linear shallow water equations, which have been shown to provide a good description of tsunami behaviour (Titov & Synolakis, 1988). The following inputs are required to run a tsunami model:

- elevation data
- tsunami wave data
- tidal data
- friction values

This paper focuses on the sensitivity of maximum inundation area, maximum current speeds and wave height to relative tide-tsunami phasing in the context of a Port Jackson tsunami modelling project. Port Jackson experiences semi-diurnal tides and should a tsunami event occur, it is likely that it will continue to have an impact over several stages of the tidal cycle.

The management of modelling resources during such a project is extremely important as it is computationally intensive and requires significant amounts of processing time. Therefore it is important to determine how different inputs are likely to affect outputs, so that optimum variables can be selected to get results with the broadest application.

METHODS

Tsunami modelling inputs were collated for ANUGA open source software. ANUGA uses these inputs to generate a triangular mesh detailing elevation, depth and friction data for

DOI: 10.2112/SI75-253.1 received 15 October 2015 accepted in revision 15 January 2016
*Corresponding author: olivia.wilson@newcastle.edu.au
©Coastal Education and Research Foundation, Inc. 2016

each cell and then calculates the propagation of the boundary wave condition across the mesh. Mesh cell resolution within Port Jackson was specified as less than 30m^2.

The tide data sensitivity was determined by analysing the results of several models in Port Jackson.

Port Jackson tsunami model inputs were determined as follows:

Elevation data of the highest quality and resolution (final grid was a minimum of 30m^2 grid resolution) available were obtained from several sources and, where necessary adjusted or reprojected into WGS 84 UTM 56S and the vertical datum Australian Height Datum (AHD)/Mean Sea Level (MSL). Tsunami wave input data was taken from Geoscience Australia's Probabilistic Tsunami Hazard Assessment (PTHA) of Australia. The PTHA tsunami are based on probabilistic source events and are modelled to the 100m depth contour surrounding Australia (Burbidge *et al.*, 2008). The tsunami wave forms are expressed as the wave amplitude and momentum through time for a given source zone and return period at defined hazard points along the 100m depth contour.

Predicted tide gauge data from the Middle Harbour tide gauge (33°49'31.56", 151°15'30.72") from January 2015 was used for this study. The tide data was shifted from the vertical datum 'Zero Fort Denison' to MSL, a difference of 0.925m. The spring tides with the greatest tidal range in this month were extracted for use with the model.

It should be noted that the leading peak and leading trough tidal signals are not exact mirror replicas but are extracted from actual tide data where the respective peaks and troughs occurred. Therefore the wave parameters differ slightly, which will be considered in the results. See Table 1 for details of tidal cycles used in model inputs:

Table 1*: Details of Tidal Cycles used in Model Inputs*.

Tidal Cycle	Maximum Amplitude (m)	Minimum Amplitude (m)	Tidal Range (m)
Peak Trough	0.97	-0.80	1.77
Trough Peak	1.02	-0.66	1.68

A generic friction value of Mannings "n=0.02," was applied to the entire model domain. This value is considered suitable for sand/gravel and has been validated in previous studies (Cardno, 2013). Table 2 details the tsunami models that were run.

TsuDAT waves and Tide Data were summed to provide the overall ANUGA boundary condition wave input as is shown in Figure 1. This assumes a liner interaction, which is a limitation to the study, given non-linear relationships have been observed (eg Kowalik & Proschutinsky, 2010).

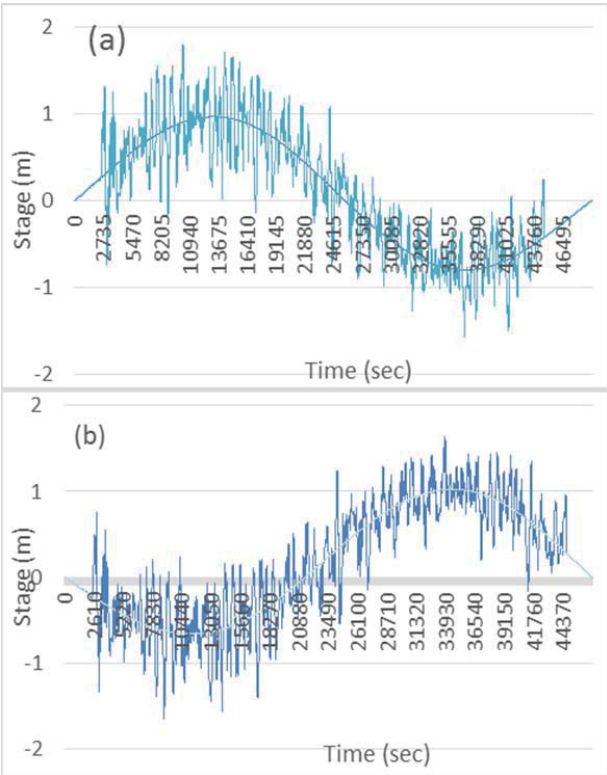

Figure 1. ANUGA Boundary Condition: TsuDAT wave and tide Data summed. Tide data is spring tides from January 2015. (a) TsuDAT wave 58173 from the Puysegur source zone with a 5000 year return interval and a leading peak tidal signal. (b) TsuDAT wave 58173 from the Puysegur source zone with a 5000 year return interval and a leading trough tidal cycle.

Table 2: *Tsunami Model Setup Details: TsuDAT wave and tidal data inputs.*

Model #	Source Zone Trench	Return Interval (years)	PTHA (TsuDAT) wave ref.	Tide
1	New Hebrides	1,000	50122	Leading Peak
2	New Hebrides	1,000	50122	Leading Trough
3	Puysegur	1,000	58244	Leading Peak
4	Puysegur	1,000	58244	Leading Trough
5	New Hebrides	5,000	50149	Leading Peak
6	New Hebrides	5,000	50149	Leading Trough
7	Puysegur	5,000	58173	Leading Peak
8	Puysegur	5,000	58173	Leading Trough
9	New Hebrides	10,000	50034	Leading Peak
10	New Hebrides	10,000	50034	Leading Trough

RESULTS

Results comparing models with leading trough and leading peak waves are given for several parameters including maximum inundation area, maximum current speeds for

specified locations, and maximum wave amplitude for specified locations.

Maximum inundation area is a useful comparison in terms of potential impact. It is defined as the total area that is inundated at any point during a modelled tsunami event. Maximum inundation areas for tidal inputs of both leading trough and leading peak are compared in Figure 2.

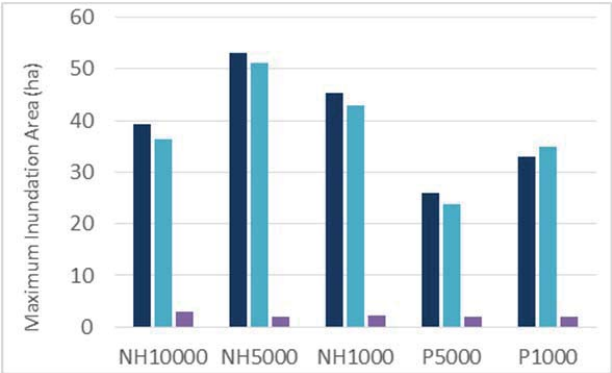

Figure 2. Inundation Area Comparison for the results of all models. NH represents New Hebrides source zone waves and P, Puysegur source zone waves. Numbers represent return interval in years.

There is not a significant difference between models run with a peak-trough tide when compared to models run with a trough-peak tide. Differences in inundation area did not exceed 8% of the mean maximum inundation area, where mean maximum inundation area was taken as the average of the both the leading peak wave model and the leading trough wave model. Four models had a greater area of inundation with a peak-trough tide input and one (P1000) had a greater area of inundation with a trough-peak input, although those difference were not large enough to be considered significant. Table 3 details the inundation areas illustrated in Figure 2.

Maximum speed rasters were also extracted from each model output. Five locations were selected to compare maximum speeds in each model. The test locations are provided in Figure 3.

No significant difference in maximum current speed was observed between models with peak-trough tidal cycles and models with trough-peak tidal cycles, see Figure 4.

Table 3: *Model Output Maximum Inundation Areas*.

Wave and TsuDAT reference number	Leading Peak Maximum Inundation Area (ha)	Leading Trough Maximum Inundation Area (ha)	Difference (m^2)	Difference as a % of the mean
NH10000 #50034	39.324	36.348	2.976	7.87
NH5000 #50149	53.202	51.138	2.064	3.96
NH1000 #50122	45.300	43.026	2.274	5.15
P5000 #58173	25.860	23.883	1.977	7.95
P1000 #58244	33.081	35.013	1.932	5.67

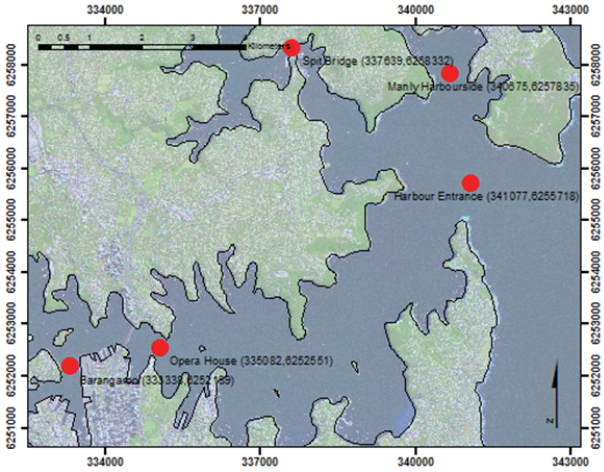

Figure 3: Port Jackson Test Locations. Positions given in WGS84 UTM56 coordinates.

However, given the different tidal stage, the current directions were opposite to each other. This pattern is the same as would be expected without a tsunami event. An example is provided for a 1000 year return interval wave from the Puysegur Trench source zone in Figure 5.

Maximum wave amplitude (defined in ANUGA as maximum stage; wave amplitude above MSL) occurred at high tide, so in this sense tidal stage had an effect on the timing of maximum wave height. The differences between maximum wave height for the models with a trough-peak tidal input and peak-trough tidal input were not significant. See Table 4 for detailed examples.

DISCUSSION

From the results presented in this paper there are negligible differences in tsunami model outputs between leading trough and leading peak tidal wave inputs. The results presented are consistent with the parameters used in emergency hazard management. Maximum inundation area, maximum current speed and maximum wave amplitude data are all useful to port and harbour authorities and emergency planners. Such macro analysis may account for the negligible differences, however when modelling for general emergency management, these are the ouputs that are used. When prioritising a spread of models for this purpose, these results should be considered and running several models with different tide inputs would not need to be a priority over other variables, such as a greater spread of tsunami wave inputs.

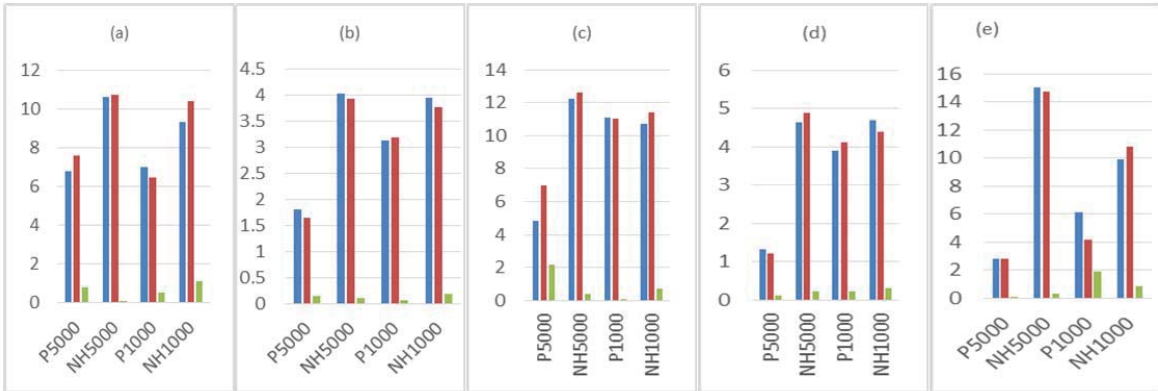

Figure 4: Maximum Speed Comparisons for Specified Locations, given in m/s. (a) Manly Harbourside (b).Opera House (c).Spit Bridge (d) Barangaroo (e) Harbour Mouth.

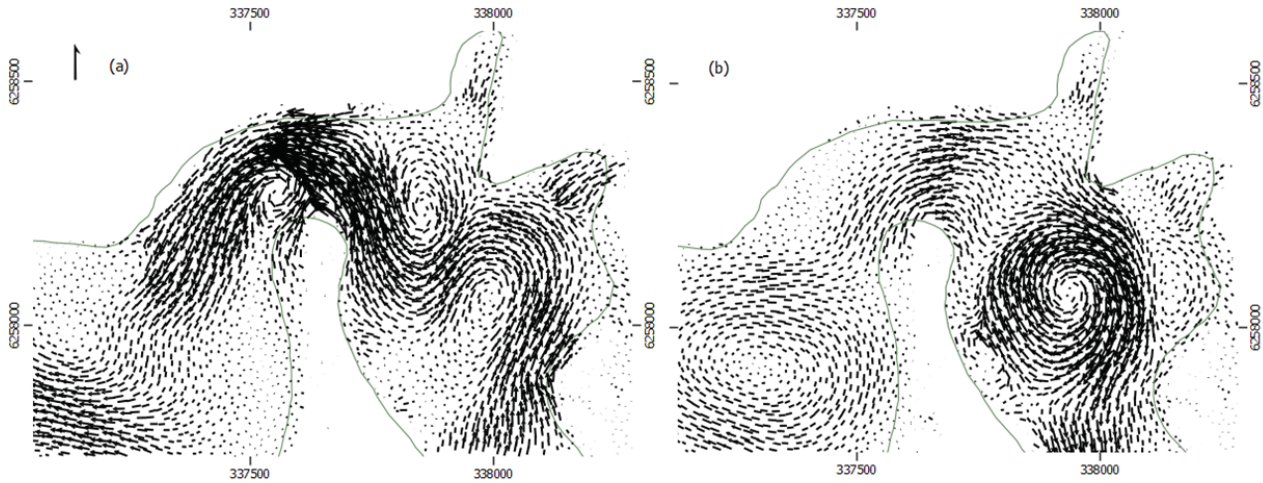

Figure 5. : Current Direction at the Spit Bridge location. (a) Puysegur source wave at a 1000 year return interval with a trough peak tide input. Taken from Timestep 131 (26,000 sec), where 'Timestep' is the step sequence number at the model duration time when the results are output.(b). Puysegur source wave at a 1000 year return interval with a peak trough tide input. Taken from Timestep 131 (26,000 sec).

Table 4: *Maximum wave height comparison for New Hebrides source waves of 1000 and 5000 return intervals at the Harbour Entrance and Spit Bridge locations.*

Location	Source Zone	Return Interval (years)	Leading Trough Max Wave Height (m)	Leading Peak Max Wave Height (m)	Difference (m)
Harbour Entrance	New Hebrides	1000	3.88	4.01	**0.13**
Harbour Entrance	New Hebrides	5000	5.25	5.35	**0.10**
Spit Bridge	New Hebrides	1000	2.60	2.59	**0.01**
Spit Bridge	New Hebrides	5000	2.58	3.10	**0.52**

Examination of results in greater detail would possibly elucidate other differences, such as water accumulation at different tidal stages or modulation of the tsunami wave by tide as detailed in the work of Tolkova, Tanaka *et al*., 2015.

There are limitations to this study, including the assumed linear effects between tide data and tsunami and the comparison of just leading peak and leading trough tidal inputs. Further tide

inputs such as one focussing on the peak and one on the trough could also show some differences.

CONCLUSIONS

For tsunami models with leading trough and leading peak tidal wave inputs, there is negligible difference in maximum inundation, maximum current speed and maximum wave amplitude. Maximum wave incident time however differs according to when high tide occurs and this should be taken into account when considering an emergency response.

When considering the choice of tidal input for tsunami modelling, tide should be considered in conjunction with maximum wave heights and where they occur along a tsunami wave train. For the most conservative outcome, maximum wave height should be modelled to coincide with high tide.

ACKNOWLEDGMENTS

Funding for this project was provided by NSW Police and Emergency Services with extensive support from NSW Office of Environment and Heritage and Geoscience Australia.

Specific thanks go to Robert Jacobs of the Manly Hydraulics Laboratory who was extremely helpful in providing tidal data, Edwina Foulsham and David Hanslow of the Office of Environment and Heritage for their ongoing support and data provision and NSW Roads and Maritime Services for data contributions.

LITERATURE CITED

Beccari, B. (2009). "Measurements and Impacts of the Chilean Tsunami of May 1960 in New South Wales, Australia." *Report by NSW SES*, State Headquarters.

Burbidge, D. et al. (2008). "A Probabilistic Tsunami Hazard Assessment for Australia." *Geoscience Australia*.

Cardno (2013). "NSW Tsunami Inundation Modelling and Risk Assessment*." NSW State Emergency Service and the Office of Environment and Heritage*.

Cochard, R., Ranamukhaarachchi, S. L., Shivakoti, G. P., Shipin, O. V., Edwards, P. J., Seeland, K. T. (2008). The 2004 tsunami in Aceh and Southern Thailand: A review on coastal ecosystems, wave hazards and vulnerability. *Perspectives in Plant Ecology, Evolution and Systematics*, 10(1), 3-40.

Dominey-Howes, D. (2007). "Geological and historical records of tsunami in Australia." Marine Geology 239(1-2): 99-123.

NSW *SES State Emergency Management Committee*, S. E. M. (2008). "New South Wales Tsunami Emergency SubPlan, A SubPlan of the New South Wales Disaster Plan (DISPLAN),."

Hinwood, J. B. and E. J. McLean. (2012). "Effects of the March 2011 Japanese Tsunami in Bays and Estuaries of SE Australia." *Pure and Applied Geophysics,* 170(6-8): 1207-1227.

Kowalik, Z and Proshutinsky, A. (2010). "Tsunami-tide interactions: A Cook Inlet case study." *Continental Shelf Research*. 30(6): 633-642.

Nielsen, O., Roberts, S., Gray, D., McPherson, A., and Hitchman, A. (2005). MODSIM 2005 International Congress on Modelling and Simulation. Modelling and Simulation Society of Australia and New Zealand, December 2005, pp. 518-523.

Roy, P. S., Williams, R. J., Jones, A. R., Yassini, I., Gibbs, P. J., Coates,B., West, R. J., Scanes, P. R., Hudson J. P. and Nichol. S. (2001). "Structure and Function of South-east Australian Estuaries." *Estuarine, Coastal and Shelf Science* 53, 351-384.

Tanaka, H., Tinh, N. X., Umeda, M., Hirao, R., Pradjoko, E., Mano, A., Udo, K. (2012). Coastal and estuarine morphology changes induced by the 2011 Great East Japan Earthquake Tsunami. *Coastal Engineering Journal,* 54(01), 1250010.

Titov, V.V., and Synolakis, C.E. (1988). Numerical modelling of tidal wave runup *Journal of Waterway, Port, Coastal, and Ocean Engineering* 124 (4), 157-171.

Tolkova, E. (2013). Tide−Tsunami Interaction in Columbia River, as Implied by Historical Data and Numerical Simulations. *Pure and Applied Geophysics*, 170(6-8), 1115-1126.

Tolkova, E., Tanaka, H. and Roh, M. (2015). "Tsunami Observations in Rivers from a Perspective of Tsunami Interaction with Tide and Riverine Flow." *Pure and Applied Geophysics*, 172(3-4): 953-968.

UNESCO (2015). "International Tsunami Information Centre." http://itic.ioc-unesco.org/index.php?option=com_content&view=category&layout=blog&id=1160&Itemid=1077&lang=en

Journal of Coastal Research	SI	75	1267 - 1271	Coconut Creek, Florida	2016

Probabilistic Tsunami Hazard Analysis — Application to Maanshan Nuclear Power Plant in Taiwan

En-Chi Wu[†], Wan-Hua Ma[†], Yen-Lung Chen[†], Han-Lun Wu[‡], Kai-Cheng Hu[‡], Shih-Chun Hsiao[†*], and Yuan-Chieh Wu[††]

[†] Department of Hydraulic and Ocean Engineering
National Cheng Kung University
Tainan, Taiwan

[‡] Assistant Research Fellow
Tainan Hydraulics Laboratory
National Cheng Kung University
Tainan, Taiwan

[††] Associate Research Fellow
Institute of Nuclear Energy Research
Atomic Energy Council
Taoyuan, Taiwan

www.cerf-jcr.org

www.JCRonline.org

ABSTRACT

Wu, E.C.; Ma, W.H., Chen, Y.L.; Wu, H.L.; Hu, K.C.; Hsiao, S.C. and Wu, Y.C., 2016. Probabilistic Tsunami Hazard Analysis — Application to Maanshan Nuclear Power Plant in Taiwan. *In:* Vila-Concejo, A.; Bruce, E.; Kennedy, D.M., and McCarroll, R.J. (eds.), *Proceedings of the 14th International Coastal Symposium* (Sydney, Australia). *Journal of Coastal Research*, Special Issue, No. 75, pp. 1267 – 1271. Coconut Creek (Florida), ISSN 0749-0208.

In the past twelve years, two earthquakes of magnitude 9.0 have occurred in the western Pacific. These earthquakes resulted in tsunamis, causing tremendous casualties, such as the nuclear disaster in Japan on March, 2011. Taiwan is an island located in the circum-Pacific belt, along which approximately 90% of the world's largest earthquakes take place. To prevent hazards, probabilistic tsunami hazard analysis (PTHA) is applied to nuclear power plants in the coastal regions of Taiwan. The approach developed here allows for the selection of reasonable tsunamis generated from distant earthquakes in the Manila Trench. Two types of uncertainty are considered: aleatory uncertainty and epistemic uncertainty. Concerning the aleatory uncertainty of modeling, a validation of prediction results is conducted against observed data. And a logic tree is introduced to help with epistemic uncertainty and set up different series of source parameters. In addition, a numerical model is used to simulate tsunami propagation and wave height. Under the assumptions of the logic tree and numerical modeling, the relationship between annual probability and maximum tsunami wave height can be obtained. Finally, tsunami hazard maps can be produced and the safety assessment of nuclear power plants can be carried out. The results provide useful information for engineering design and hazard prevention.

ADDITIONAL INDEX WORDS: *Probabilistic tsunami hazard analysis, Maanshan nuclear power plant.*

INTRODUCTION

The 2004 Indian Ocean and the 2011 Tohoku tsunami events devastated coastal areas. The Tohoku tsunami events resulted in the Fukushima Daiichi nuclear crisis. These hazards prompted experts and scholars to deliberate the possibility of a tsunami and nuclear disaster in Taiwan, which is a geologically active island. There are some tsunami records in Taiwanese historical documents. In consideration of nuclear crisis and other probable calamities caused by tsunamis, probabilistic tsunami hazard analysis (PTHA) provides a means of evaluating nuclear power plants in coastal regions.

PTHA has been developed for over 40 years. The method is derived from probabilistic seismic hazard analysis (PSHA), which is a methodology that quantifies the rate of exceeding ground-motion levels given all probable earthquakes. The numerical simulation of PSHA was first formalized by Cornell (1968). Lin and Tung (1982) modified PSHA and applied it to tsunami events, calculating the probability of exceedence of tsunami wave heights. Rikitake and Aida (1988) applied PTHA in Japan, but the aleatory variability of the tsunami wave height was not considered in their study. However, the Pacific Gas and Electric (PG&E) Company (2010) indicated that wave heights are significantly underestimated without considering aleatory variability. The issue of proper treatment of variability for tsunami wave heights is important and thus PG&E has made modifications to the approach used by Rikitake and Aida. In the present study, a methodology for conducting PTHA for the Maanshan Nuclear Power Plant in Taiwan is developed based on the investigation of PG&E.

Traditionally, numerical models have usually been applied to deterministic tsunami hazard analysis (DTHA). DTHA simulates a specific scenario, whereas PTHA considers all possible causes of a tsunami. The deterministic method is faster and easier to operate when used to determine the impact of historically large earthquakes. The probabilistic method uses geologists' opinions to obtain probable tsunami scenarios and

DOI: 10.2112/SI75-254.1 received 15 October 2015 accepted in revision 15 January 2016
*Corresponding author: schsiao@mail.ncku.edu.tw
©Coastal Education and Research Foundation, Inc. 2016

consider uncertainties. The probabilistic method produces hazard maps and hazard curves, which provide information about maximum tsunami wave heights in different return periods. PTHA produces more comprehensive results than those of DTHA and it can be utilized to estimate the probability of exceedance of sea level for engineering designs.

METHODS

PTHA combines the rate of earthquakes that generate tsunamis with the assumed distribution of tsunami wave heights. According to the report of PG&E (2010), the probabilistic tsunami hazard from earthquakes is given by:

$$\nu_{EQK}(W_{tsu} > z) = \sum_{i=1}^{N_{FLT}} N_i(M_{min}) \iint_{mLoc} f_{m_i}(M) f_{Loc_i}(Loc) P(W_{tsu} > z|M, Loc) dMdLoc \quad (1)$$

where $\nu_{EQK}(W_{tsu} > z)$ is the annual rate of tsunami wave heights exceeding z , W_{tsu} is the tsunami wave height, N_{FLT} is the number of faults, $N_i$is the i^{th}earthquake whose moment magnitude scale is over M_{min}, and f_{m_i} and f_{Loc} are probability density functions the of seismic scale and ruptured location, respectively. $P(W_{tsu} > z|M, Loc)$ is the conditional probability of exceeding wave height z. Assuming that the maximum tsunami wave heights have a log-normal distribution, the conditional probability is given by:

$$P(W_{tsu} > z|M, Loc) = 1 - \Phi\left(\frac{\ln z - \ln\left(\widehat{W}_{tsu}(M,Loc)\right)}{\sigma_{EQK}}\right) \quad (2)$$

where Φ is the cumulative normal distribution, $\widehat{W}_{tsu}$ is the median wave height, and σ_{EQK} is the standard deviation, which is also the aleatory variability of the tsunami wave height from earthquakes in natural log units.

In reality, only a limited number of representative scenarios can be considered. Therefore, the annual rate of exceeding wave height may be simplified to:

$$\nu_{EQK}(W_{tsu} > z) = \sum_{i=1}^{N_{FLT}} \sum_{j=1}^{NS_i} rate_{ij} P\left(W_{tsu} > z|M_{ij}, Loc_{ij}\right) \quad (3)$$

where $rate_{ij}$ is the rate of the i^{th}earthquake in the j^{th}scenario. To estimate the rate of tsunamigenic earthquakes in the Manila Trench, the empirical formulas given by Jing *et al*. (2013) are used:

$$\log_{10} N = 8.92 - 1.09M \quad (4)$$

$$rate_{ij} = \frac{1}{P_M} = \frac{N}{T} \quad (5)$$

where P_M is the return period, T is the time period of the seismic record, and N is the number of earthquakes with magnitudes greater than or equal to the given magnitude M.

Overall, we propose an approach similar to that proposed by PG&E (2010). Synthetic tsunami waveforms from numerical modeling and the rates of occurrence for tsunamigenic earthquakes are used to calculate the annual rate of exceeding wave height, which is representative of the probabilistic tsunami hazard.

Uncertainty Analysis

Generally, uncertainties exist in probability analysis. PTHA distinguishes two kinds of uncertainty, namely aleatory and epistemic (Senior Seismic Hazard Analysis Committee, SSHAC, 1997). Aleatory uncertainty is due to the random nature of earthquake occurrence, and epistemic uncertainty results from a lack of knowledge or data. These uncertainties are widely used in PSHA and PTHA. Thio (2010) considered the model to be the source of aleatory uncertainty and source parameters to be the source of epistemic uncertainty. This concept is applied in the present study.

The main source of aleatory uncertainty is modeling uncertainty. In order to verify the correctness of the model, we modeled historical tsunami events and compared the computed maximum wave heights with the observed data. Epistemic uncertainty can be expressed through the use of logic trees, which are normally adopted to set up different series of source parameters. The different scenarios are represented as branches of a logic tree. The weightings of the branches represent alternative hypotheses and interpretations. They are usually determined based on a questionnaire survey of tsunami and earthquake experts.

Numerical model

The numerical model plays a significant role in the accuracy of simulation results. The Cornell Multi-grid Coupled Tsunami (COMCOT) model developed at Cornell University is adopted in this study. COMCOT has been validated by many laboratory experiments and historical tsunami events, such as the 1992 Flores Islands tsunami (Liu *et al*., 1995), 2003 Algerian tsunami (Wang and Liu, 2005), and 2004 Indian Ocean tsunami (Wang and Liu, 2006). In COMCOT, the explicit staggered leap-frog finite difference method is applied to solve shallow water equations in both spherical and Cartesian coordinates. The moving boundary scheme decides the distribution of the shoreline. A nested grid configuration makes moving from global to local scales convenient. COMCOT is capable of simulating a tsunami life cycle, including tsunami generation, propagation, run-up, and inundation. A more detailed description can be found in the COMCOT user manual (Wang, 2009).

Logic Tree

A logic tree is necessary to consider epistemic uncertainty. The Institute of Nuclear Energy Research provides a logic tree with 72 possible scenarios. The logic tree consists of four branches (Figure 1), namely segmentation, which is the breaking up of 22 faults crossing the Manila Trench (Figure 2), the maximum seismic scale, rupture location, and focal depth. The complete logic tree and specification of fault parameters can be found in the thesis of Ma (2015).

Among these parameters of tsunamigenic earthquakes, dislocation of the fault plate and the maximum seismic scale are calculated from the empirical formulas proposed by Wells and Coppersmith (1994).

$$1.02 \times \log_{10} A = M_w - 3.98 \quad (6)$$

$$M_w = \frac{2}{3} \times (\log_{10} M_o - 9.1) \quad (7)$$

$$D = \frac{M_o}{\mu A} \quad (8)$$

$$\mu = 3 \times 10^{10} \ (N/m^2) \quad (9)$$

where A is the source area, M_w is the moment magnitude scale, M_o is the seismic moment, D is the dislocation of the fault plate, and μ is the modulus of rigidity. Without the weighting of the logic tree, we assume that the branches have equal weights.

PTHA is here applied to the Maanshan Nuclear Power Plant, which is located in southern Taiwan, near the Manila Trench. Therefore, this study simulates the distant tsunami sources along the Manila Trench as earthquake scenarios. The calculation process is shown in Figure 3.

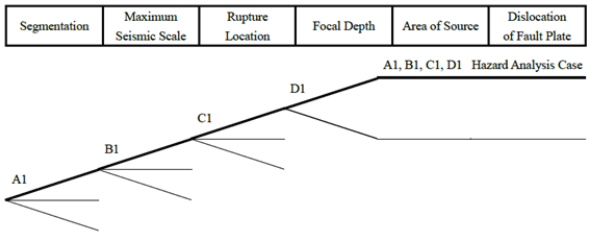

Figure 1. Outline of logic tree approach used in present research.

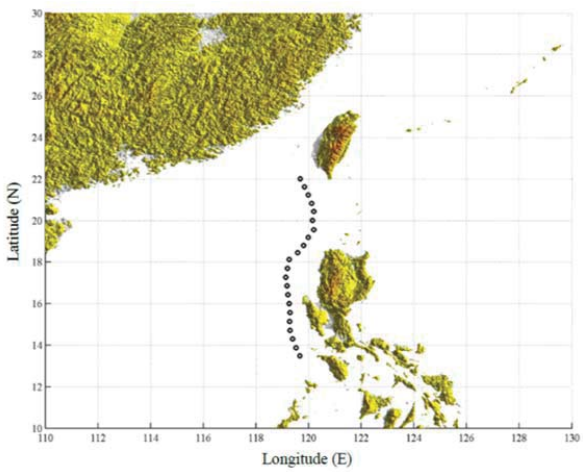

Figure 2. The Manila Trench consisting of 22 faults in the logic tree.

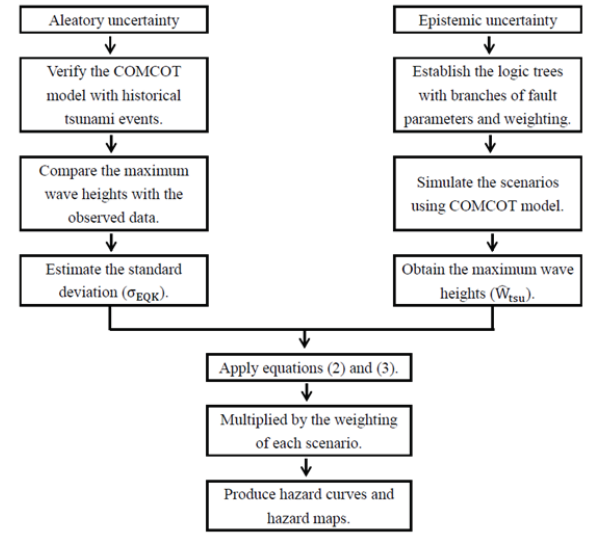

Figure 3. Calculation process of PTHA.

RESULTS

In order to determine aleatory variability, two historical tsunami events, the 2006 Pingtung earthquake and the 2011 Tohoku earthquake, were simulated using three layers of the nested grid configuration. The parameters for fault models in COMCOT are shown in Table 1. In addition, topographic data were obtained from the ETOPOT1 relief model of the National Oceanic and Atmospheric Administration and the Ocean Data Bank of the National Science Council. We collected the simulated maximum wave heights from various stations and compared them with the observed data, as shown in the Figure 4 and Figure 5. The other comparisons can be found in the thesis of Ma (2015). Assuming that the distribution is log-normal, the standard deviation, σ_{EQK}, was calculated as 0.57. (Thio, 2010).

$$\sigma_{EQK} = \sqrt{\frac{\sum_i^n (\ln x_i - \ln \bar{x})^2}{n-1}} \quad (10)$$

where x_i is the maximum wave height of observation divided by the simulation, $\bar{x}$ is the mean value, and n is the number of data.

Table 1. *Parameters of historical tsunami events (Harvard CMT; Wu et al., 2008)*

Historical Events	2006 Pingtung earthquake	2011 Tohoku earthquake
Epicenter Location	20.31° E, 21.36° N	143.05° E、37.52° N
Focal Depth	19600 (m)	20000 (m)
Length of Source Area	37400 (m)	450000 (m)
Width of Source Area	18700(m)	150000 (m)
Dislocation of Fault Plate	1.2 (m)	18 (m)
Strike Direction	165°	203°
Dip Angle	30°	10°
Slip Angle	-76°	88°

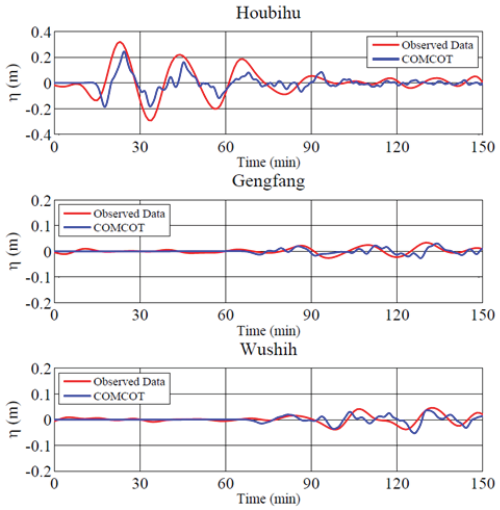

Figure 4. Time series of observed data and simulated data at Houbihu, Gengfang, and Wushih stations for 2006 Pingtung earthquake.

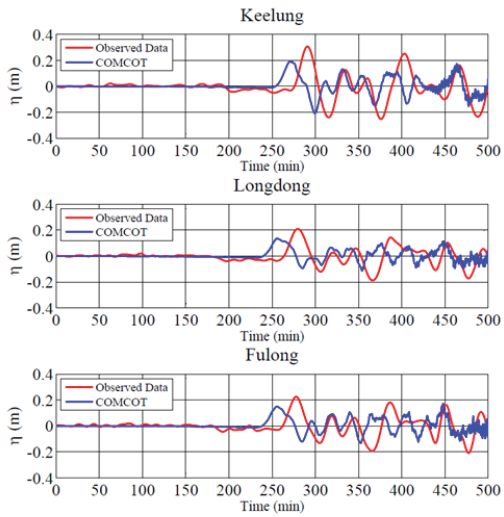

Figure 5. Time series of observed data and simulated data at Keelung, Longdong, and Fulong stations for 2011 Tohoku earthquake.

Hazard Curve

Each path of the logic tree generates a tsunami hazard curve. We simulated these scenarios using COMCOT with five layers of the nested grid configuration and determined the maximum wave heights in each location, which are considered to be the median value, $\widehat{W}_{tsu}$, of the log-normal distribution. After applying equation (2), we obtained the cumulative normal distribution and the annual rate of tsunami waves exceeding a specify height. The other scenarios were similarly used. The probabilities were multiplied by the weightings and the results were combined (Figure 7). However, the upper tail of the tsunami wave height distribution is not well constrained. Therefore, the log-normal distribution is truncated at three standard deviations, which is recommended by Thio (2010). Finally, by mapping the relationship between wave height and annual rate, the overall probabilistic tsunami hazard curve was obtained.

Take two gauges as an example. Gauge 1 is located in the ocean in southern Taiwan and gauge 2 is located near the shore of the Maanshan Nuclear Power Plant (Figure 6). As shown in Figure 7, at a given wave height, gauge 2 has a higher annual rate than that of gauge 1

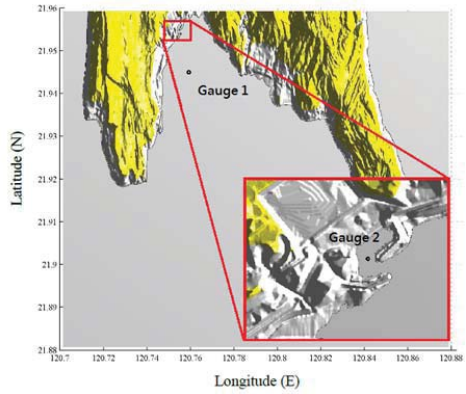

Figure 6. Locations of gauge 1 (120.759200°E, 21.945000°N) and gauge 2 (120.754372°E, 21.954929°N).

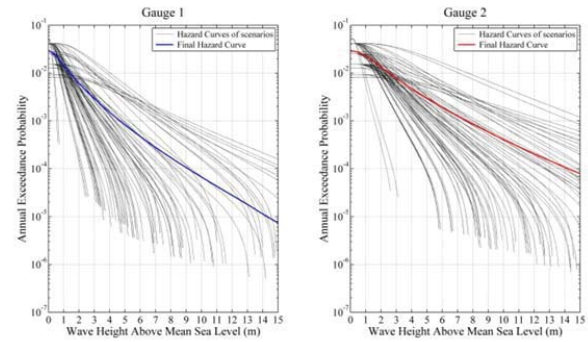

Figure 7. Hazard curves for gauge1 and gauge 2, which combine the probabilities of various scenarios.

Hazard Map

In addition to tsunami hazard curves, probabilistic tsunami hazard maps were also obtained, which show the maximum run-up and ebbing of tsunami waves under specific return periods.

The hazard maps in Figures 8 and 9 respectively display the distribution of maximum and minimum water levels around the Maanshan Nuclear Power Plant in annual exceedance probability of 1% and 0.2% respectively. Both the high and low water levels caused by tsunamis are harmful to the nuclear

power plant. It is reasonable to see a higher tsunami hazard in the longer return period.

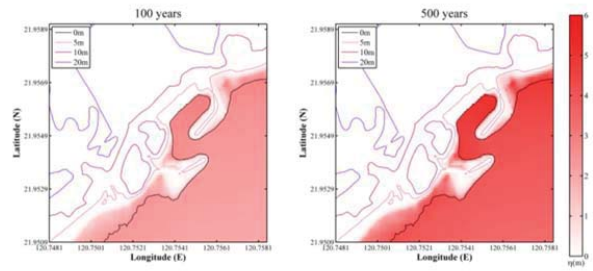

Figure 8. Hazard maps of maximum water level distribution for return periods of 100 and 500 years.

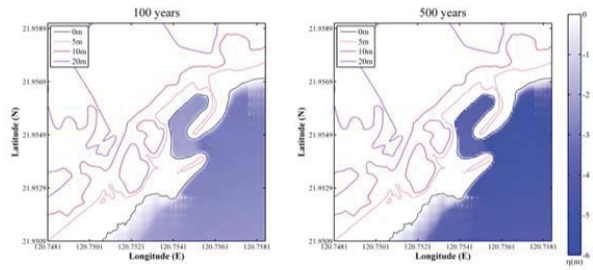

Figure 9. Hazard maps of minimum water level distribution for return periods of 100 and 500 years.

CONCLUSION

PTHA based on the theory of PG&E (2010) that considers the aleatory and epistemic uncertainties suggested by Thio (2010) was applied here. We obtained the aleatory uncertainty from model-data comparisons and epistemic uncertainty was considered by simulating every path of the logic tree provided by the Institute of Nuclear Energy Research, Taiwan. PTHA combines the probabilities of numerous probable scenarios and gives a more complete consideration than does DTHA for risk assessment.

Only the impact of distant earthquakes of the Manila Trench was considered in PTHA. For a more thorough study, more tsunami sources, such as landslide-induced tsunamis, should also be considered. Furthermore, the effects of tides and storms on sea level cannot be ignored. Although a comprehensive PTHA method takes more effort to conduct, the results could offer helpful information for engineering design and risk assessment.

ACKNOWLEDGMENTS

This research was supported by the Institute of Nuclear Energy Research, Taiwan, R.O.C., under grant 1042001INER034 and the Ministry of Science and Technology, Taiwan, R.O.C., under grant NSC 101-2628-E-006-015-MY3.

LITERATURE CITED

Cornell, C. Allin., 1968. Engineering seismic risk analysis. *Bulletin of the Seismological Society of America*, 58(5), 1583-1606.

Jing, H. H., Zhang, H., Yuen, D. A., & Shi, Y., 2013. A Revised Evaluation of Tsunami Hazards along the Chinese Coast in View of the Tohoku-Oki Earthquake. *Pure and Applied Geophysics*, 170(1-2), 129-138.

Lin, I. and C.C. Tung., 1982. A preliminary investigation of tsunami hazard. *Bulletin of the Seismological Society of America*, 72(6), 2323-2337.

Liu, P. L. F., Cho, Y. S., Yoon, S. B., & Seo, S. N., 1995. Numerical simulations of the 1960 Chilean tsunami propagation and inundation at Hilo, Hawaii. In: *Tsunami: Progress in prediction, disaster prevention and warning*. The Netherlands, Springer, pp. 99-115.

Ma, W. H., 2015. Methodology of Probabilistic Tsunami Hazard Analysis - Application to the Area of the Maanshan Nuclear Power Plant. Tainan, Taiwan: National Cheng Kung University, Master's thesis, 69p.

Pacific Gas and Electric Company., 2010. *Methodology for probabilistic tsunami hazard analysis: Trial application for the Diablo Canyon Power Plant site.* Presentation to the PEER Workshop on Tsunami Hazard Analyses for Engineering Design Parameters, Berkeley, CA.

Senior Seismic Hazard Analysis Committee, and Budnitz, R. J., 1997. *Recommendations for probabilistic seismic hazard analysis: guidance on uncertainty and use of experts* , Washington, DC: US Nuclear Regulatory Commission, Volume 1.

Thio, H.K., Somerville, P., Polet., 2010. *Probabilistic tsunami hazard in California. Pacific Earthquake Engineering Research Center*, PEER Report 2010/108 University of California Berkeley, 331p.

Wang, Xiaoming., 2009. *User manual for COMCOT version 1.7* , Cornel University, 65p.

Wang, X.M. and P.L.F. Liu, 2005. *Preliminary simulation of 1986 and 2002 Taiwan Hualien tsunami.* Cornell University, Ithaca.

Wang, X.M., and P.L.F. Liu, 2006. An analysis of 2004 Sumatra earthquake fault plane mechanisms and Indian Ocean tsunami. *Journal of Hydraulic Research*, 44(2), 147-154.

Wells, D. L., and Coppersmith, K. J., 1994. New empirical relationships among magnitude, rupture length, rupture width, rupture area, and surface displacement. Bulletin of the seismological Society of America, 84(4), 974-1002.

Wu, T. R., Chen P.F., W.T. Tsai, and G.Y. Chen, 2008. Numerical study tsunami excited by 2006 Pingtung earthquake doublet. *Terr. Atmos. Ocean. Sci*., 19(6), 705-71

Journal of Coastal Research	SI	75	1272 - 1276	Coconut Creek, Florida	2016

Erodibility assessment of Armour Blocks causing Damage to Breakwaters

Dong Hoon Yoo[†] and Hak Soo Lim[‡*]

[†]Department of Civil Engineering
Ajou University
Suwon 16499, Korea

[‡] Operational Oceanography Research Center
Korea Institute of Ocean Science and Technolgy
Ansan 15627, Korea

www.cerf-jcr.org

www.JCRonline.org

ABSTRACT

Yoo, D.H. and Lim, H.S., 2016. Erodibility assessement of Armour Blocks causing Damage to Breakwaters. *In:* Vila-Concejo, A.; Bruce, E.; Kennedy, D.M., and McCarroll, R.J. (eds.), *Proceedings of the 14th International Coastal Symposium* (Sydney, Australia). *Journal of Coastal Research*, Special Issue, No. 75, pp. 1272 - 1276. Coconut Creek (Florida), ISSN 0749-0208.

Empirical equations such as the Hudson, van der Meer-de Jong, and Yoo equations were compared for estimating the armour block weight of the breakwater by introducing an incremental factor based on the Hudson equation. The equation for deriving the critical wave height of erosion at the structure toe was developed for additional consideration of the armour-blocked breakwater stability. All empirical equations were reformed according to the Hudson equation, which has been widely employed in engineering design, and an incremental factor was added to each reformed empirical equation. This factor reflects the characteristics of each empirical equation. The equation in the present study incorporates wave including wave height at the local depth in the place of interest. The wave celerity was calculated using the modified solitary wave theory, which is valid for a wide range of applications. The equation for deriving the critical wave height of erosion was employed to test the sea bottom stability, and its inclusion improved the credibility by up to 87.7%. By employing the local value of wave celerity at the place of interest, the new Yoo-Lim equation was significantly improved over the previous estimation, as published by Yoo who introduced the wave action slope to define the local condition of wave motion.

ADDITIONAL INDEX WORDS: *Armour block weight, breakwater, sea bottom erosion, incremental factor, modified solitary wave theory.*

INTRODUCTION

In order to ensure the stability of a breakwater, the armour blocks should have sufficient weight so as to be locked tight and the structure toe should not be eroded by incoming waves. The Hudson equation (1959) has been widely employed as a traditional empirical equation to estimate the minimum weight of armour block. But the equation is known to have defects because it does not consider wave period and/or wave steepness. In recent years van der Meer (1987, 1999) introduced Iribarren number so as to include the effects of wave steepness in his empirical equation of armour block weight. He has developed the empirical equation of minimum weight of TTP armour block for surging waves, and de Jong (1996) for plunging waves, considering wave steepness which is the ratio of wave height to wave length. It is possible to adopt wave height at the place of interest, but the adaptation of wave length at the place of interest is not possible because the wave length varys rapidly from offshore to inshore, and the definition of wave length is not clear. In shoaling waters the offshore wave length may be far longer than the inshore wave length. The use of deep water wave length is unavoidable for the estimation of wave steepness even at the shoaling depth. It causes distorted wave steepness, and it might to be the drawback when the Iribarren number is used for the estimation of armour block weight.

DOI: 10.2112/SI75-255.1 received 15 October 2015 accepted in revision 15 January 2016
*Corresponding author: hslim@kiost.ac.kr
©Coastal Education and Research Foundation, Inc. 2016

Instead the wave action slope suggested by Yoo and Jung (2003) has a clear definition, which is the ratio of wave celerity. The local values of wave celerity at the place of interest can be clearly obtained even at shoaling waters, and an empirical equation of armour block weight has been developed using the wave action of slope. The wave celercity is evaluated by using the modified solitary wave theory. Incremental parameters are introduced to express various empirical equations clearly with the Hudson equation as the basis.

The sea bottom is highly erodible at the front face of breakwater by incoming and/or reflected waves. Wave period and the size of bottom materials have to be considered as well as wave height in order to describe the condition of erosion. The critical value of wave height for erosion is formulated with considering wave period and the size of bottom materials. The failure cases of eastern coast of the Korean Peninsula have been tested using various empirical equations and the equation of critical wave height for erosion.

METHODS

Various empirical equations have been reviewed and incremental factors had been suggested with the Hudson equation as the basis.

Hudson equation

Weight ratio and stability number are defined as follows:

$$\eta = \frac{W}{\rho_s g H^3} \quad (1)$$

$$\delta = \frac{H}{(s-1)\phi_n} \quad (2)$$

where η is the weight ratio, δ is the stability number, W is the weight of armour block, ρ_s is the density of armour block, g is the acceleration due to gravity, H is the wave height, ϕ_n is the norminal diameter of armour block defined by $W = \rho_s g \phi_n^3$, and we obtains the relation as follows: $(s-1)^3\eta = \delta^{-3}$.

Hudsion (1959) simplified the effects of breakwater slope, suggested the empirical equation as follows:

$$W = \frac{\rho_s g H^3}{K_D (s-1)^3 R} \tag{3}$$

where K_D is an empirical parameter depending on the type of armour block, s is the specific gravity, and R is the breakwater slope.

The Hudson equation (3) has been widely employed because of its simplicity, although it does not reflect sufficiently well the effects of wave condition. The Hudson equation is taken as the basis, and the incremental factor ξ is formulated as the weight ratio as follows:

$$W = \frac{\xi \rho_s g H^3}{K_D (s-1)^3 R} \tag{4}$$

The incremental factor ξ is computed by :

$$\xi = \eta K_D (s-1)^3 R = K_D R \delta^{-3} \tag{5}$$

van der Meer and de Jong Formula

Van der Meer (1999) conducted laboratory experiments of TTP armour block only for the case of $R = 1.5$ and for surging waves, and de Jong (1996) for plunging waves. Their equation is expressed as follows:

$$\delta = \begin{cases} (8.6E_N + 3.94)M_i^{+0.2} & (I_i < I_c) \\ (3.8E_N + 0.85)M_i^{-0.2} & (I_c < I_i) \end{cases} \tag{6}$$

where the wave steepness $M_i = H/L_o$, H is the wave height at the place of interest, L_o is the deep water wave length, $E_N = (E/\sqrt{N})^{0.5}$, N is the number of incident waves, E is the ratio of transformed distance of armour block to the length of armour block, $I_i$is the Iribarren number, I_c is the critical Iribarren number. For the case of TTP $E = 0.1$ is considered as the very dangerous status. Equation (6) can be used only for $R = 1.5$, but it can be transformed into a general form as follows. $M_i = I_i^{-2}R^{-2}$ as $I_i = M_i^{-0.5}R^{-1}$. $R = 1.5$ is introduced and a general form is deduced using the Iribarren number as follows:

$$M_i^{0.2} = I_i^{-0.4}(1.5)^{-0.4} = 0.85 I_i^{-0.4} \tag{7}$$

Therefore

$$\delta = (8.6E_N + 3.94)M_i^{0.2} = (7.3E_N + 3.4)I_i^{-0.4} \tag{8}$$

Furthemore for surging waves ($I_c < I_i$)

$$M_i^{-0.2} = I_i^{0.4}(1.5)^{0.4} = 1.18 I_i^{0.4} \tag{9}$$

Then

$$\delta = (3.8E_N + 0.85)M_i^{-0.2} = \frac{1.18}{\sqrt{1.5}}(3.8E_N + 0.85)\sqrt{R} I_i^{0.4}$$
$$= (3.6E_N + 0.8)I_i^{0.4}\sqrt{R} \tag{10}$$

Therefore

$$\delta = \begin{cases} (7.3E_N + 3.4)I_i^{-0.4} & (I_i < I_c) \\ (3.6E_N + 0.8)I_i^{0.4}\sqrt{R} & (I_c < I_i) \end{cases} \tag{11}$$

When $E = 0.1$, and $N = 3000$, $E_N = 0.043$, we have

$$\xi = \begin{cases} 0.14 M_i^{-0.6} S^{0.2} & (I_i < I_c) \\ 8.04 M_i^{+0.6} R^{0.7} & (I_c < I_i) \end{cases} \tag{12}$$

When $E = 0.1$, and $N = 1000$, $E_N = 0.056$, then we obtain

$$\xi = \begin{cases} 0.13 M_i^{-0.6} S^{0.2} & (I_i < I_c) \\ 6.97 M_i^{+0.6} R^{0.7} & (I_c < I_i) \end{cases} \tag{13}$$

where $S = R^{-1}$, $I_c = 4.5S^{0.63}$. The armour block weight is normally computed by using the equation for plunging waves, but in the case of a very mild slope it is calculated by using the equation for surging waves.

Yoo and Lim Formula

Yoo *et al*. (2010) considered that the wave particle velocity should represent the velocity acting on the breakwater. Drag force F_D is generally expressed by $F_D = \rho C_D V^2 A$ (ρ; water density, C_D; drag coefficient, V; particle velocity, A; projected area), and the Hudson equation assumes $V = \sqrt{gH}$. On the other hand Yoo *et al*. (2010) suggested to use the maximum wave particle velocity for the effective velocity and the maxium wave particle velocity is proposional to the wave celerity. They proposed a new non-dimensional number, 'wave action slope', and developed the empirical equation of armour block weight using the wave action slope as follows:

$$\eta = (s-1)^{-3} C_Y S_Y \tag{14}$$

where $S_Y = SF^2$, $S = R^{-1}$, $F = c/\sqrt{gh}$, c is the wave celerity, S_Y is the wave action slope, C_Y is the empirical parameter primarily depending on the type of armour block. Introducing equation (14) into equation (5) yields :

$$\xi = K_C S_Y R \tag{15}$$

where

$$K_C = K_D C_Y \tag{16}$$

Because $S_Y = SF^2$,

$$\xi = K_C F^2 \tag{17}$$

When water depth is very shallow, the modified solitary wave theory is more advantageous than the Stokes wave theories. Hedges and Kirgoez (1981) has modified the solitary wave theory so that it is valid in deep waters. Their theory is expressed by the modified dispersion relation:

$$\sigma^2 = gk\tanh k(h+H) \tag{18}$$

The modified dispersion relation is approximated as follows:

$$k(h+H) = \frac{\sqrt{Y_S}}{1-0.167Y_S} \tag{19}$$

where $Y_S = \frac{\sigma^2(h+H)}{g}$.

Then

$$c = \frac{\sigma(h+H)}{\sqrt{Y_S}}(1-0.167Y_S) \tag{20}$$

$$F^2 = \frac{c^2}{gH} = (1-0.167Y_S)^2 \frac{h+H}{H} \tag{21}$$

Therefore

$$\xi = K_C(1 - 0.167Y_S)^2 \frac{h+H}{H} \quad (22)$$

where K_C is given by equation (16).

Erosion of Structure Toe of Breakwater

Erosion of bottom materials occurs when the bottom shear stress exceeds a critical shear stress, i.e.

$$u_{*c} < u_* \quad (\tau_c < \tau) \quad (23)$$

where $u_* = \sqrt{\tau/\rho}$, τ is the sea bed shear stress, u_{*c} is the critical shear velocity which is primarily a function of bottom material diameter, and ρ is the water density. The shear velocity of wave motion is given by:

$$u_* = \sqrt{C}u_b \quad (24)$$

where C is the wave friction factor, and u_b is the maximum particle velocity at the sea bottom, given by:

$$u_b = \frac{\sigma a}{\sinh kh} \quad (25)$$

where $a = \frac{H}{2}$. The wave friction factor C is a function of roughness ratio ε ($=\frac{k_w}{A_b}$), k_w is the roughness height, and A_b ($= \frac{a}{\sinh kh}$) is the maximum excursion length of the sea bed. It is expressed by a power law as follows:

$$C = \zeta\varepsilon^\eta \quad \left(\varepsilon = \frac{k_w}{A_b}\right) \quad (26)$$

where $\zeta = 0.18$, $\eta = 0.7$ for $0.05 < \varepsilon < 0.5$, $\zeta = 0.23$, $\eta = 0$ for $0.5 < \varepsilon$, and $\zeta = 0.11$, $\eta = 0.5$ for $\varepsilon < 0.05$. The critical shear velocity u_{*c} is a function of bottom material diameter as follows:

$$u_{*c} = \gamma N_\phi^\delta \sqrt{(s-1)g\phi} \quad (27)$$

$$N_\phi = \frac{\phi\sqrt{(s-1)g\phi}}{\nu} \quad (28)$$

where ϕ is the diameter of bottom material, ν is the viscosity of water. The critical Froude number F_{*c} $(= u_*/\sqrt{(s-1)g\phi})$ is a function of diameter number N_ϕ $(= \phi\sqrt{(s-1)g\phi}/\nu)$. From Shields' laboratory experimental results several workers found optimum values of γ and δ as described by Yoo *et al*. (2000) and Yoo and Lim (2013). For the case of big size bed material, i.e., $2400 < N_\phi$, γ = 0.24 and δ = 0.

The hyperbolic sine function of equation (25) can be also expressed by a power law as follows:

$$\sinh kh = \alpha Y^\beta \quad (29)$$

where $Y = \sigma^2 h/g$, $\sigma = 2\pi/T$, T is the wave period and h is the water depth. As described by Yoo and Lim (2013), $\alpha = 1.08$, $\beta = 0.52$ for $Y < 0.16$, and $\alpha = 1.19$, $\beta = 0.57$ for $0.16 < Y < 0.4$.

The critical erosion condition is then represented as follows:

$$\gamma N_\phi^\delta \sqrt{(s-1)g\phi} < \frac{\sqrt{C}\sigma a}{\sinh kh} \quad (30)$$

$\delta = 0$ when the size of bed material is big enough ($2400 < N_\phi$), and introducing $C = \zeta\varepsilon^\eta$ and eq. (29) into eq. (30) yields:

$$\gamma\sqrt{(s-1)g\phi} < \frac{\sqrt{\zeta}\varepsilon^{\frac{\eta}{2}}\sigma a}{\alpha Y^\beta} \quad (31)$$

Assuming $k_w = 2\phi$ gives rise to:

$$B_Y \left(\frac{\phi}{H}\right)^{1-\eta} Y^{\beta(2-\eta)-1} h < H \quad (32)$$

where

$$B_Y = \gamma^2(s-1)2^{2(1-\eta)}\zeta^{-1}\alpha^{2-\eta} \quad (33)$$

Assuming $s = 2.6$, $\zeta = 0.18$, $\eta = 0.7$ valid for $0.05 < \varepsilon < 0.5$, and γ =0.24 and δ=0 valid for $2400 < N_\phi$, we obtain

$$C_Y h < H \quad (34)$$

where

$$C_Y = 0.86\left(\frac{\phi}{H}\right)^{0.3} Y^{-0.32} \quad (35)$$

Equation (35) is widely acceptable in a practical situation. If the water depth at the front of breakwater is shallower than 60% of the wave height, the value of C_Y is 1.6 ($= 0.6^{-1}$). Depending on the ratio of diameter to the wave height (ϕ/H) and the value of Y, C_Y may vary greater than 1.6 or less.

RESULTS

The status of 119 breakwaters at 12 harbour sites are analyzed in the eastern coast of the Korean Peninsula. 57 breakwaters of 119 TTP breakwaters were damaged, and the information of seriously damaged breakwaters are presented in Table 1.

Waves can break as any type between plunging and surging in a practical situation. Therefore bigger values of armour block weight when the formula of van der Meer and de Jong is employed. The modified solitary wave theory is considered to be more accurate than the Stokes 4th order theory in shallow waters, and thus the wave celerity is computed by using the modified solitary wave theory when applying Yoo and Lim's empirical equation to estimate the armour weight. To check the bottom erosion the diameter of bottom materials are assumed to be 0.3 m which is expected to be the maximum value.

Various empirical equations are applied to the damaged breakwaters, and the computational results are compared with the results of the Hudson equation. 30 sites among 57 damaged breakwaters are considered safe using the Hudson equation, 19 using the M-J (var der Meer and de Jong) equation, and 13 using the Y-L (Yoo and Lim, the present study) equation. It might be because the Hudson equation does not reflect the effects of wave steepness and wave period at all. Particularly when the water depth is deep (Nos. 3, 6, 7, 28, 29, 93, 94) the seven sites are evaluated to be instable when using the Y-L equation which implys the effect of wave celerity.

On the other hand 13 sites are considered safe (Decision: OK) using the Y-L equation. Among them the water depth are shallower than 5.6 m at 8 sites (Nos. 23, 24, 25, 26, 32, 65, 108, 119), the breakwater slopes are very mild at 2 sites (Nos. 32, 65). As presented in Table 1, most sites have high potential for erosion of bottom material when the diameters of bottom materials are assumed to be 0.3 m. It means that breakwaters can be in danger even when the armour blocks are heavy enough to withstand against the incoming waves with the armour block weight computed by using the advanced equations like the M-J equation or the Y-L equation. Considering the sites (Nos. 13, 16,

24, 32, 65, 108) of possible bed erosion as NG (no good), the total NG sites are evauated as 50 sites among 57 sites.

Among the OK (satisfactory) sites, the wave heights at several sites (Nos. 13, 16, 25, 26, 101, 106, 111, 119) suggested are considered too small so that the expected design wave heights are deduced from the armour block weights of the Hudson equation in Table 1. Applying the deduced wave heights, such OK sites are re-counted as NG sites using the M-J equation or the Y-L equation except No. 23. On the other hand the two sites of No. 32 and No. 65 are counted as NG when applying the M-J equation while counted as OK when applying the Y-L eqution. It is because of the very mild slope, where surging waves may occur due to the very mild slope. R=10 for the case of No. 32 and the required armour block weight is estimated 31.2 ton when using the M-J equation. It is, therefore, found that the extremely mild slope renders more dangerous situation to the breakwaters. The wave height of the incoming waves suggested 7.4 m at the water depth of 3.5 m, where wave breaking is expected to occur, and hence the real wave height is expected to be much smaller than 7.4 m. Due to the very small water depth the value of armour block weight estimated by using the Y-L equation is also very small in comparision with the applied weight. On the other hand the M-J equation estimates 31.2 ton because the incoming breaking waves are counted as surging. Such extremely mild slope incurs the surging-type wave breaking so that mild slope does not guarantee always the stability of breakwaters. 56 sites (except No. 23) among 57 sites are counted as NG, when using the present model to estimate the armour block weight with the deduced wave height and considering the bottom material erosion.

CONCLUSIONS

Various empirical equations for the estimation of armour block weight are expressed by introducing the incremental factor ξ on the basis of the Hudson equation so that the relative characteristics of each equation is clearly defined. Van der Meer (1987) described the behavious of armour block in relation with wave steepness, percolation, degree of damaged, etc., and Yoo *et al*. (2013) introduced the wave action slope to define the local condition of wave motion. When applying the M-J equation to the cases of damaged breakwaters, 66.7% (38/57) is counted as NG for the design. On the other hand when applying the present model (Y-L equation), 77.2% (44/57) as NG. If erosion test is made on the OK sites 6 sites are found erodible in the bottom materials. Therefore 87.7% (50/57) is counted as NG when applying the Y-L equation for the estimate of armour block weight and erosion condition of bottom materials.

In addition the wave heights of the incoming waves are considered too small at several sites so that the expected wave heights are deduced from the armour block weights of the Hudson equation. Applying the deduced wave heights to the M-J equation, 80.7% (46/57) is counted as NG. Furthermoure applying those to the Y-L equation, 91.2% (52/57) as NG. The rate of NG increases upto 98.2% (56/57) when considering the erosion condition applying the Y-L equation for the estimate of armour block weight with the corrected wave heights.

About half of the damaged breakwaters in the eastern coast of the Korean Peninsula are counted as safe when applying the Hudson equation for the estimate of armour block weight. When applying the M-J equation 11 more sites are counted as NG, and when applying the Y-L equation 18 more sites as NG. The original M-J equation has been suggested for R=1.5, but introducing the relation of the Iribarren number and wave steepness with the bed slope yields a general form of M-J equation applicable to any bed slope. The present model, Y-L equation, is considered most reliable for the eatimate of armour block weight, because it employs the local value of wave celerity at the place of interest.

ACKNOWLEDGMENTS

This research was supported by the project entitled “Development of Coastal Erosion Control Technology” and “Development of Safe Voyage Planning System for Vessels Operating in Northern Sea Route” funded by the Ministry of Oceans and Fisheries, Korea. This paper is the achievements of the dedication and passion of Dr. Yoo, Dong-Hoon who passed away March, 2015.

LITERATURE CITED

De Jong, R.J., 1996. Wave transmission at low-crested structures Stability of tetrapods at front, crest and rear of a low-crested breakwater. MSc thesis, Delft University of Technology.

Hedges, T.S. and Kirkgoz, M.S., 1981. An experimental of the transformation zone of plunging breakers. *Coastal Engineering*, 4, 319-333.

Hudson, R.V., 1959. Laboratory investigation of rubble-mound breakwaters. *J. Waterways and Harbors Division*, ASCE, 85(WW3), 93-121.

Shields, A., 1936. Anwendung der ahnlichkeits-mechanik und der turbulenz for schung auf die geshiebe bewegung. Mitt. der Preuss. Versuchanst. fur Wasserbau und Schiffbau, Heft 26, Berlin, Germany.

van der Meer, J.W., 1987. Stability of breakwater armor layers - design formulae. *Coastal Engineering*, 11, 219-239.

van der Meer, J.W., 1999. Design of concrete armor layers. *Proceedings of Coastal Structures'99 (Rotterdam, Netherland)*, 213-221.

Yoo, D.H. and Jung, P.K., 2003. Weight of breakwater armor unit, *Proceedings of Korean Society of Coastal and Ocean Engineers*, 290-293.

Yoo, D.H. and Lim H.S., 2013. Computation of armor block weight and erosion of damaged breakwater. *Journal of KOSHAM*, 13(4), 279-286.

Yoo, D.H.; Shin, S.H., and Lim, H.S., 2000. Computation of bed load transport in rivers, *Journal of Korea Water Resources*, 33(6), 711-723.

Yoo, D.H.; Yoon, J.J., and Jung, P.G., 2010. New improvement of breakwater armor weight estimation. *Proc. Int. Ass. Hydr. Res.*, 122-129.

Yoo, D.H.; Yoon, J.J.; Yoo, J.; Lim, H.S., and Choi, J.Y., 2013. Local parameter for armor weight estimation. *Journal of Coastal Research*, SI65, 422-427.

Table 1. *Assessment of Armour block weight of damaged breakwaters*

Port	No.	h (m) DL(-)	H_s(m) (deduced value)	T_p(s)	Applied weight		Hudson		van der Meer-de Jong (M-J)		Yoo-Lim (Y-L)		Bottom Erosion
					W(ton)	1:R	Required W(ton)	Decision	Required W(ton)	Decision	Required W(ton)	Decision	Decision (Hc-m)
Guryongpo	3	10.0	5.5	12	12.5	1:3.0	8.3	OK	15.5	NG	14.5	NG	NG (5.3)
	6	11.5	6.1	12	20.0	1:2.0	17.0	OK	25.5	NG	29.7	NG	NG (5.6)
	7	11.5	6.1	12	25.0	1:1.5	22.7	OK	27.7	NG	39.6	NG	NG (5.6)
Pohanggu	9	4.5	5.0	11	10.0	1:1.3	14.4	NG	15.7	NG	17.7	NG	NG (2.9)
	12	6.5	4.5	11	10.0	1:1.3	10.5	NG	10.8	NG	16.3	NG	NG (3.9)
	13	7.4	4.5(5.2)	11	12.5	1:2.0	6.8(10.5)	OK	9.5(15.9)	OK(NG)	11.3(16)	OK(NG)	NG (4.1)
	15	7.7	5.2	11	12.5	1:2.0	10.5	OK	15.9	NG	16.2	NG	NG (4.2)
	16	8.0	5.2(6.2)	11	20.0	1:2.0	10.5(18)	OK	15.9(30)	OK(NG)	16.5(25)	OK(NG)	NG (4.3)
	17	6.3	4.2	11	8.0	1:2.0	5.5	OK	7.4	OK	8.8	NG	NG (3.9)
Hupo	23	4.0	2.6(3.6)	12	5.0	1:3.0	0.9(2.3)	OK	1.4(3.4)	OK	1.5(3.3)	OK	OK (3.5)
	24	2.5	3.1	12	5.0	1:1.5	3.0	OK	5.0	NG	3.7	OK	NG (2.4)
	25	5.6	3.1(3.9)	12	5.0	1:2.3	2.0(4.4)	OK	3.6(6.2)	OK(NG)	4.1(7.1)	OK(NG)	OK (4.2)
	26	5.3	3.1(3.9)	12	5.0	1:2.3	2.0(4.4)	OK	3.6(6.2)	OK(NG)	4.0(6.9)	OK(NG)	OK (4.0)
	28	13.5	4.2	12	12.5	1:1.5	7.4	OK	10.4	OK	18.9	NG	OK (7.1)
	29	16.5	4.2	12	12.5	1:1.5	7.4	OK	10.4	OK	21.4	NG	OK (8.1)
Imwon	32	3.5	7.4	12	12.5	1:10.0	6.1	OK	31.2	NG	5.8	OK	NG (2.3)
	33	11.0	8.4	12	20.0	1:2.0	44.3	NG	38.8	NG	61.0	NG	NG (5.0)
Samcheok	39	7.0	7.4	12	12.5	1:2.0	30.3	NG	28.6	NG	36.9	NG	NG (3.8)
	40	7.0	7.4	12	12.5	1:2.0	30.3	NG	28.6	NG	36.9	NG	NG (3.8)
	44	10.0	7.4	12	12.5	1:2.0	30.3	NG	28.6	NG	43.3	NG	NG (4.8)
	45	9.0	7.4	12	12.5	1:2.0	30.3	NG	28.6	NG	41.2	NG	NG (4.5)
	46	9.0	7.5	12	20.0	1:2.0	31.5	NG	29.6	NG	42.6	NG	NG (4.5)
	47	9.0	7.4	12	20.0	1:2.0	30.3	NG	28.6	NG	41.2	NG	NG (4.5)
	48	9.8	7.5	12	20.0	1:2.0	31.5	NG	29.6	NG	44.3	NG	NG (4.7)
	51	4.0	4.0	12	3.0	1:2.0	4.8	NG	6.5	NG	6.4	NG	NG (3.1)
	52	7.0	4.0	12	3.0	1:2.0	4.8	NG	6.5	NG	8.5	NG	NG (4.5)
	53	8.0	4.5	12	5.0	1:2.0	6.8	NG	8.7	NG	12.1	NG	NG (4.8)
	54	7.0	4.9	12	12.5	1:1.5	11.7	OK	15.0	NG	18.3	NG	NG (4.3)
DongHae	56	8.0	7.4	12	40.0	1:1.5	40.4	NG	40.5	NG	52.2	NG	NG (4.1)
	57	9.0	7.4	12	40.0	1:1.5	40.4	NG	40.5	NG	55.0	NG	NG (4.3)
	61	6.0	8.0	12	20.0	1:1.3	58.9	NG	58.9	NG	64.8	NG	NG (3.3)
	62	9.0	6.6	12	12.5	1:2.0	21.5	NG	21.8	NG	31.5	NG	NG (4.6)
Mukho	65	3.0	4.5	12	5.0	1:4.0	3.4	OK	6.9	NG	3.8	OK	NG (2.4)
	66	3.0	4.5	12	5.0	1:1.3	10.5	NG	14.6	NG	11.7	NG	NG (2.4)
	67	4.0	5.8	12	5.0	1:1.5	19.5	NG	22.5	NG	21.6	NG	NG (2.7)
	68	4.0	5.7	12	20.0	1:1.5	18.5	OK	21.6	NG	20.6	NG	NG (2.7)
	74	8.0	7.8	12	20.0	1:2.0	35.5	NG	35.5	NG	44.4	NG	NG (4.1)
	75	11.0	7.5	12	20.0	1:2.0	31.6	NG	31.6	NG	46.8	NG	NG (5.1)
	76	11.6	7.5	12	20.0	1:2.0	31.6	NG	31.6	NG	48.0	NG	NG (5.3)
	81	8.0	4.5	12	5.0	1:3.0	4.5	OK	5.3	NG	8.1	NG	OK (4.8)
	82	5.0	4.5	12	8.0	1:1.5	9.1	NG	12.3	NG	12.6	NG	NG (3.4)
Okgye	93	15.5	6.1	12	32.0	1:1.3	26.1	OK	30.2	OK	53.8	NG	OK (6.9)
	94	13.5	6.1	12	32.0	1:1.3	26.1	OK	30.2	OK	49.9	NG	OK (6.3)
Jumunjin	101	8.0	3.6(4.6)	12	5.0	1:3.0	2.3(4.9)	OK	3.4(8.2)	OK(NG)	4.8(8.5)	OK(NG)	OK (4.8)
	102	9.0	5.1	12	5.0	1:2.0	9.9	NG	11.7	NG	17.2	NG	NG (5.0)
	103	13.0	7.4	12	12.5	1:2	30.3	NG	51.0	NG	49.2	NG	NG (5.8)
	104	8.5	5.4	12	12.5	1:1.3	18.1	NG	22.6	NG	29.4	NG	NG (4.7)
	105	8.5	4.7	12	12.5	1:2	7.8	OK	10.0	NG	13.8	NG	OK (4.9)
	106	9.0	4.7(6.3)	12	20.0	1:2	7.8(18.7)	OK	10.0(29)	OK(NG)	14.3(28)	OK(NG)	OK (5.1)
Sokcho	108	5.0	4.0	12	12.5	1:1.3	7.4	OK	11.0	OK	11.0	OK	NG (3.6)
	109	13.0	6.5	12	20.0	1:2	20.5	NG	32.0	NG	36.7	NG	NG (6.0)
	111	13.0	3.0(4.5)	12	12.5	1:1.3	3.1(10.5)	OK	5.5(19.8)	OK(NG)	10.2(25)	OK(NG)	OK (7.6)
Geojin	113	8.0	3.2	12	5.0	1:2	2.5	OK	3.8	OK	5.6	NG	OK (5.3)
	115	8.0	4.2	12	12.5	1:1.5	7.4	OK	10.4	OK	13.7	NG	OK (4.9)
	116	8.0	4.2	12	12.5	1:1.5	7.4	OK	10.4	OK	13.7	NG	OK (4.9)
	117	8.0	5.2	12	20.0	1:1.5	14.0	OK	17.3	OK	22.6	NG	NG (4.6)
	119	5.0	1.5(2.5)	12	3.0	1:1.5	0.34(2.9)	OK	0.9(3.4)	OK(NG)	1.0(5.2)	OK(NG)	OK (3.9)
NG / total							30/57		38(46)/57		44(52)/57		41/57
Reliability (%)							47.4		66.7(80.7)		77.2(91.2)		71.9

Journal of Coastal Research	SI	75	1277 - 1281	Coconut Creek, Florida	2016

Minimisation of the Uncertainty in Estimation of Extreme Coastal Wave Heights

Zai-Jin You[†*], Baoshu Yin[†], Zezhou Ji[‡], and Cong Hu[†*]

[†*] Centre for Ports and Coastal Disaster Prevention & Mitigation
School of Civil Engineering, Ludong University
Yantai 264025, China

[†] Chinese Academy of Sciences, Qingdao, China
[‡] CCC First Harbor Consultants Ltd, Tianjin, China
[†*]School of Civil Engineering, University of Queensland
St Lucia QLD 4072, Australia

www.cerf-jcr.org

www.JCRonline.org

ABSTRACT

You, Z.J., Yin, B.S., Ji, Z.Z., and Hu, C., 2016. Minimisation of Uncertainty in Estimation of Extreme Waves. *In:* Vila-Concejo, A.; Bruce, E.; Kennedy, D.M., and McCarroll, R.J. (eds.), *Proceedings of the 14th International Coastal Symposium* (Sydney, Australia). *Journal of Coastal Research*, Special Issue, No. 75, pp. 1277 - 1281. Coconut Creek (Florida), ISSN 0749-0208.

Accurate information on extreme wave conditions is often required for inshore and offshore structure designs, coastal inundation and erosion hazard studies, coastal construction planning, and coastal port operations. Estimates of extreme wave heights are commonly extrapolated from historical wave records based on extreme-value theory. Although a large number of studies have been undertaken to develop and improve methodologies in extreme wave analysis, there still exists much uncertainty in estimates of extreme waves. This study is to investigate main causes of this uncertainty based on historical wave buoy data collected off the NSW coast of Australia. It is found that the uncertainty is caused mainly by short wave record, missing storm wave data, different methods for generation of return wave height data, too low/high POT thresholds, subjective plotting positions, unsuitable distribution functions, different distribution parameter estimators, and ad-hoc criteria on selection of the best-fit function. The likelihood errors of the uncertainty are evaluated and the detail on how to minimise the uncertainty is also proposed.

ADDITIONAL INDEX WORDS: *Extreme Waves, Return Wave Height, Extreme-value Theory, POT, GEV, GPD*

INTRODUCTION

There are a large number of studies undertaken to develop and improve methodologies for extreme wave analysis (Goda, 1987, Kamphius, 2001; You, 2007). The commonly-adopted approach is to extrapolate historical wave record to return wave heights with different return periods based on extreme-value theory. The general calculation procedure is illustrated in Figure-1 of You (2007). Some of the main steps include extracting statistically independent extreme wave data; selecting suitable candidate distribution functions to fit to the extracted extreme wave data, determining the best-fit function, and extrapolating the best-fit function to extreme wave heights.

Two methods are often used to extract storm peak wave height data from historical wave record: the Peaks-Over-Threshold (POT) and the Annual *n*-Largest (ANL). The POT method picks up different numbers of storm peak wave heights per year but with the same threshold value, while the ANL method extracts the same number of storm peak wave heights per year but with different thresholds. The use of different threshold values is found to affect estimates of extreme wave heights (Sartini et al, 2015; Vanem, 2015). Similarly, the uncertainty in the ANL method is caused by the factor of the number of storm peak wave heights per year (2011).

Different plotting positions were suggested to estimate the empirical probability distribution of observed storm peak wave heights, which are often required to fit to or compare with calculated extreme wave heights. Many of the plotting positions were derived to give the unbiased median of ordered extreme values. Fig.II-8-5 of CEM (2002) lists five plotting position formulas for different distribution functions. However, You (2012) derived a unique plotting position based on the definition of return period, and the derived plotting position formula is independent of distribution functions.

Several distribution functions with long upper tail are often applied in extreme wave analysis. These functions may be classified into three groups: i) the Generalized Extreme-Value distribution GEV, ii) the Generalized Pareto Distribution GPD, and iii) the normal probability functions (e.g. Pearson-III, Weibull, Lognormal). Isaacson and MacKenzie (1981) stated that there might be no strong theoretical reasons for preferring one distribution function to another and the best-fit distribution might often be chosen from several distribution functions specially developed for extreme values. The first two groups of distribution functions generally require different methods to extract the data on extreme wave heights, i.e., GDP uses the POT, and GEV applies the ANL method, while the last group of distribution functions can use the data from both the POT and ANL methods.

There are three parameter estimators used to determine the distribution parameters, namely, the method of moments (MM), the maximum likelihood method (ML), and the least-squares method (LS). The MM is the most straightforward method, but only valid for candidate distribution functions whose statistical mean, standard deviation and skewness can be derived analytically. The LS method is applied for candidate distribution functions that can be transformed into linear equation. The ML is generally applied to nearly most distribution functions, but does have converging problems with some three-parameter functions such as GPD and Weibull. Carter and Challenor

DOI: 10.2112/SI75-256.1 received 15 October 2015 accepted in revision 15 January 2016
*Corresponding author: b.you@uq.edu.au
©Coastal Education and Research Foundation, Inc. 2016

(1983) assessed the three estimators and found that there was no one obviously better in estimating the FT-I two parameters. Mazas and Hamm (2011) preferred the ML to the LS and MM methods. You (2012) also discussed the applicability of the three parameter estimators.

This study is to investigate main causes of the uncertainty in extreme wave analysis and to propose methods on how to minimise this uncertainty.

STUDY DATA

Long-term wave buoy data, which were collected in the Tasman Sea off the NSW coast of Sydney, Australia since 1976 (see Figure-1), are used in this study to quantitatively investigate main causes of the uncertainty in extreme wave analysis. The time-series wave buoy data were recorded on paper chart for 10min every 6hr before 1976, and for 17min every 6hr after digital loggers were introduced in 1976, and for 34min every 1hr after fully programmable loggers were developed in mid 1984. Prior to the development of the fully programmable data loggers, a greater percentage of the wave data loss was due to wave buoy logger failure. Small coastal storms with their duration less than 6hr could not be fully recorded before 1984 due to the fact that the data sampling interval of 6hr was used. The NSW wave data quality collected after 1984 has been improved significantly.

Figure 1. Long-term wave buoy data collected at seven permanent wave stations along the NSW coast of Australia in the Tasman Sea.

UNCERTAINTY

Wave Record Length

The length of wave record may be one of the most dominant factors causing the uncertainty in extreme wave analysis. As a rule of thumb, for example, the ISO standard (ISO, 2005) recommends that the return period of extreme waves calculated be four times less than the length of wav record, but no theoretical reasoning was given. You and Lord (2008) studied the correlation of storm storm severity or power Ω with annual mean SOI index on the NSW coast. Figure-2 shows how storm wave heights measured off the coast of Sydney are affected by El Nino/La Nina Southern Oscillation (ENSO), a quasiperiodic climate pattern.

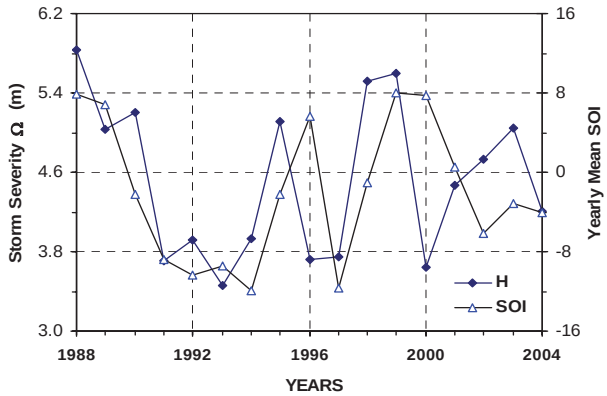

Figure 2. Annual variation of storm severity Ω or average storm wave heights measured off the coast of Sydney, Australia (You and Lord, 2008).

It can be seen from Figure 2 that the storm wave heights are generally smaller in El Nino years than those in La Nino years. This implies that extreme wave heights extrapolated from the wave data collected in El Nino years are expected to be smaller than those in La Nino years. This uncertainty can be minimised if the length of wave record is much longer than the period of ENSO. Addition to the ENSO effect, there are many other oceanographic and meteorological drivers causing long-term fluctuations of storm wave heights. Thus, a minimum length of wave record used in extreme wave analysis is required to be the multiple periods of the ENSO and other drivers.

Coastal Storm Types

Storm peak wave heights, which are extracted from individual storm events of time-series wave record, are shown to vary with different storm types. Figure 2 shows that the storm intensity Ω or storm power on the NSW coast varies with storm type, where Ω is defined by You and Lord (2008) as

$$\Omega=\left[\frac{1}{\lambda}\sum_{i=1}^{i=n}H_i^2\right]^{0.5}=\left(\frac{n}{\lambda}\right)^{0.5}\times\left(\frac{\sum H_i^2}{n}\right)^{0.5}=f\times H_{rms} \qquad (1)$$

where Ω is measured in meters, λ is the number of storms per year averaged over many years of the wave record, n is the number of storms in one year, H_i is a storm peak wave height, H_{rms} is the root-mean-square wave height and f may be called the relative frequency of occurrence of coastal storms.

The storm-by-storm method is applied to extract individual storm event from the seven NSW wave records. Each extracted storm event is then assigned to one of the eight synoptic storm types classified for the NSW coast (Shand et al., 2011). With this approach, the storm frequency and intensity for the eight classified storm types (TL, CL, TC, AI, ETL, ITL, STL, SSL) are shown in Figure 3. It can be seen that Ω varies with storm type. For a given location, however, Ω may be assumed to be stationary with time when the record length is sufficiently long.

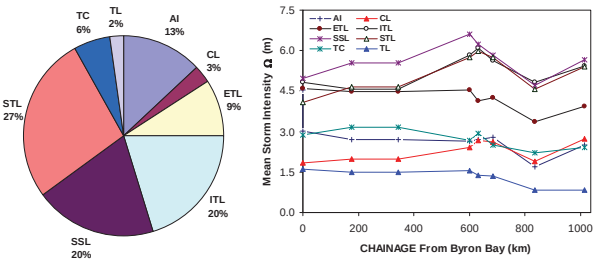

Figure 3. Coastal storm types analysed from long-term offshore wave data collected off the NSW coast of Byron Bay, Coffs Harbor, Crowdy Head, Sydney, Botany Bay, Port Kembla, Bateman Bay and Eden.

Missing Storm Data

Missing storm data in the wave record is another main cause of the uncertainty in extreme wave analysis. Figure 4 shows the comparison of return wave heights extrapolated from the wave data (1987-2009) of Sydney with those from the wave data (1977-2009) of Byron Bay (You, 2011). The return wave heights extrapolated from the wave record of Byron Bay are shown to be much smaller than those of Sydney. The difference between the 1-in-100 year return wave heights estimated from the two wave records is about 1.5m. This difference is found to be due to the fact the wave rider buoy of Byron Bay often failed to record wave data during large storm events. Therefore, whenever possible, hind-cast wave data should be used to fill storm wave data gaps before estimates of return wave heights can be calculated.

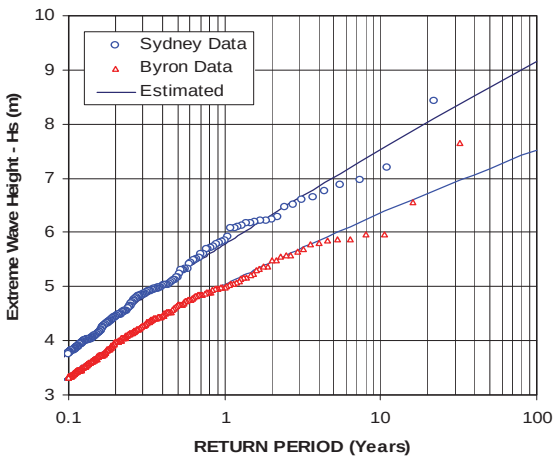

Figure 4. Estimates of return wave heights extrapolated from the wave record of Byron Bay with heavy losses of storm wave data are compared with those of Sydney (You, 2011).

Extraction of Extreme Wave Data

Three commonly-used methods are often used to generate extreme wave height data from time-series wave record, i.e. the storm-by-storm (SBS), peaks-over-threshold (POT) and annual *n*-largest (ANL) methods. The SBS method generates a set of storm peak wave height data by picking up storm peak wave heights of individual storm events identified from the time-series wave record. The POT method, which is similar to the SBS method, may be considered as a special case of the SBS method when its threshold is equal to the storm peak wave height of the smallest storm in the SBS method. The annual *n*-largest method (ANL) picks up *n* largest storm peak wave heights every year to generate a set of extreme wave height data. The annual maximum method (AM) is a special case of the ANL method when *n*=1.

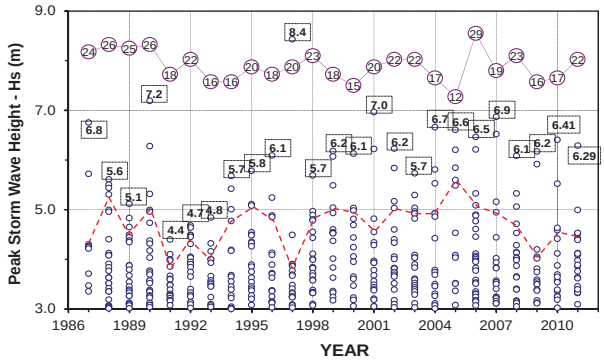

Figure 5. A set of storm peak wave height data extracted from the wave buoy data of Sydney with the POT and ANL methods.

As shown in Figure 5, in the POT method, the number of storm peak wave heights per year λ varies from year to year (the number in circle), but the same threshold of H_t=3m is used for all storm events, while in the ANL method, the number of peak storm wave heights per is kept as a constant (e.g. *n*=4), but different threshold values (the red dashed line) are used to obtain the annual *n* largest storm peak wave heights. The variable parameter λ of the POT will cause the uncertainty in estimating the total number of storm events over a return period T_r and also increase confidence intervals of return wave heights calculated. The uncertainty of the ANL method results from the use of the constant number of storm events every year by ignoring the fact that multiple storm events can fall in the same year and be much larger than those selected in many other years.

Generation of Return Wave Data

The data on return wave heights (T_r, H) can then be generated from the storm wave data in Figure 5. The return period T_r is defined as an average time interval between successive storm events of a given storm wave height being equalled or exceeded (CEM, 2002), from which T_r could be simply estimated as

$$T_r = \frac{T}{n}, \qquad (2)$$

where *T* is the length of wave record in years and *n* is the number of peak storm wave heights being equalled or exceeded.

Figure 6 shows the comparison of the return wave data (T_r, H) of the POT method with those of the ANL method (*n*=1, 2, 3, 5, 8 16). The return wave data analysed with the POT and ANL methods are shown to merge into one dataset when *n*>16 in Figure-6. In other words, if the return wave height data analysed with the POT and ANL methods are not the same, estimates of return wave heights calculated with GEV of the ANL method

are expected to be different from those with GDP of the POT method.

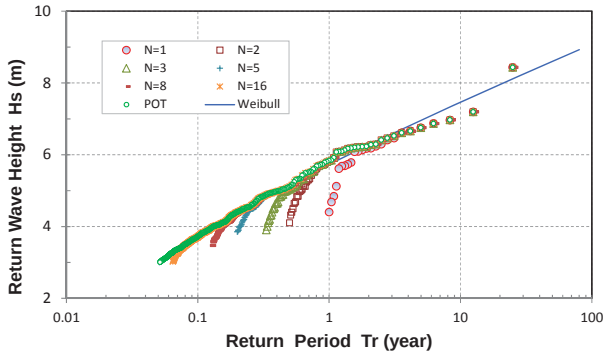

Figure 6. The data on return wave heights analysed with the POT method are compared with those with the ANL method (n=1, 2, 3, 5, 8, 16).

Estimation of POT Thresholds

The threshold H_T in the POT method determines the number of storm peak wave heights per year as shown in Figure 5. If H_T is set too low, a large number of unwanted small non-storm waves and possibly statistically dependent waves may be selected and subsequently affect accuracy of extreme wave heights estimated. On the other hand, if H_T is set too high, there are not enough data points to be generated from the wave record. As suggested by You (2012), the threshold H_T can be taken to be equal to the storm peak wave height of the smallest storm event identified locally. If available, air pressure data can be used to identify all storm events together with time-series wave data. It should be noted here that in Figure-6, different values of H_T will affect only the lower portion of return wave heights smaller than H_T, but not the upper portion of return wave heights larger than H_T.

Selection of Plotting Positions

The empirical distribution of storm peak wave heights is often estimated from this generalized plotting position formula

$$Q(\hat{H} \geq H) = \frac{j-a}{m+b}, \tag{3}$$

where j is the jth peak storm wave height ranked in descending order, m is the total number of storm events observed, and a and b are constants. The values of a and b are often chosen so that the median of the ordered extreme values is assigned a percentile rank of 50%. Many of the common plotting positions are members of a family b=1-2a.

In extreme wave analysis, however, a small probability Q of extreme waves with return period T_r is often estimated from the definition of return period as

$$Q = \frac{1}{T_r \lambda}, \tag{4}$$

from which and Eq.(2), a unique plotting position formula can be directly derived as

$$Q = \frac{1}{T_r \lambda} = \frac{n}{T} \times \frac{T}{m} = \frac{n}{m}, \tag{5}$$

where λ=m/T and T_r=T/n are applied. Thus, Eq.(5) is only the plotting position formula with n≤(m-1) to estimate the empirical distribution of observed storm peak wave heights.

Choice of Candidate Distribution Functions

In extreme wave analysis, a variety of probability distribution functions are often used for extrapolation of extreme wave heights. The commonly-used distribution functions may be classified into three groups: the Generalised Extreme Value distribution (GEV) of the ANL method, the Generalised Pareto distribution (GPD) of the POT method, and general probability distribution functions (pdfs) with long upper tail (e.g. Lognormal, Weibull, Pearson-III). When the POT and ANL methods generate the same set of return wave height data as shown in Figure 7, the classified three groups then reduce to one group only. Isaacson and MacKenzie (1981) stated that there might be no strong theoretical reasons for preferring one distribution function to another and the best-fit distribution might often be chosen from several distribution functions specially developed for extreme values. As suggested by You (2011), four distribution functions should be sufficient to be used in extreme wave analysis, namely, the FT-I, Weibull, GPD-II, Pearson-III as shown in Figure 7.

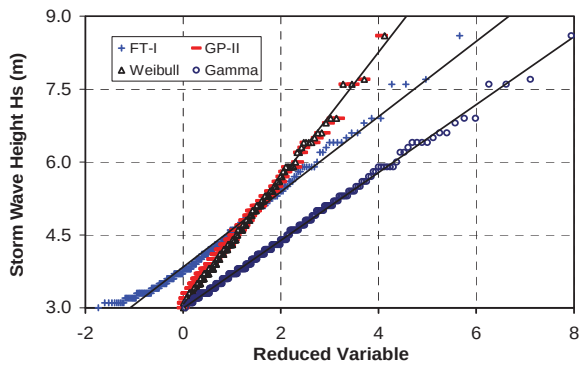

Figure 7. The FT-I, GP-II, Weibull and Gamma functions are fitted to the hindcast storm wave data of Mazas and Hamm (2011).

Selection of Parameter Estimators

Three distribution parameter estimators are commonly used to determine the parameters of candidate distribution functions: the method of moments (MM), the least-squares method (LS) and the maximum likelihood method (ML). The LS method may also be considered as a special case of the ML (You, 2012). The MM estimates the distribution parameters by equalling the moments of mean, variance and skewness calculated from the data to those derived from the distribution function. This method is applicable only to those functions, of which the first three moments can be derived analytically. The LS estimates the distribution parameters by transforming the distribution function into linear equation and then fitting the linear equation to the data (T_r, H) to obtain the distribution parameters. This method is only applicable to those functions that can be transformed into the linear equation. The ML method evaluates the distribution parameters by making it maximum the multiplication of the

probability density function for individual observations with respect to each distribution parameter. The ML is applicable to most distribution function, but becomes difficult in estimating three parameters of Weibull, GEV, GDP and Pearson-III (Mazas and Hamm, 2011).

Criteria on Goodness of Fit

The most commonly-used criterion on how to select the best-fit distribution function of candidate distribution functions is the sum of squares of the error (SSE)

$$SSE = \sum_{i=1}^{m} (H_i - H)^2 \qquad (6)$$

where H_i is the *i*th measured wave height and H is the estimated wave height. You (2011) extended the LS method to derive new criteria (W-1) and $|W\text{-}1|^{0.5}$ to select the best-fit distribution function, where |W-1|=0 gives the best fit to the return wave data. Four different criteria are compared in Figure 9, where the LS method is used to estimate the parameters of the GDP-II. The indicators SSE, R^2 and (W-1) are shown to insensitively vary with the shape parameter |α|, but $|W\text{-}1|^{0.5}$ is much more sensitive to the change of α than (W-1), SSE and R^2. The correlation coefficient R^2 of the regression line, which is also equivalent to *SSE*, has been commonly used as an indicator for the goodness of fit for the LS method. The value of R^2 is shown to converge slowly around the true value, but $|W\text{-}1|^{0.5}$ is shown to converge much faster than R^2 or SSE and *W*.

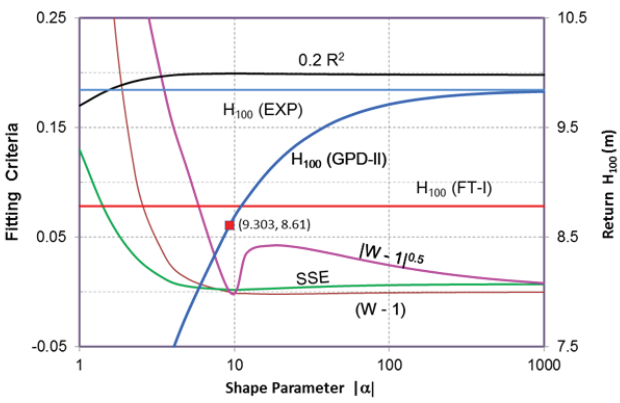

Figure 9. Four criteria are used to estimate the GDP-II parameters from the wave record of Sydney with the LS method.

CONCLUSIONS

The uncertainty in extrapolating one wave record to return wave heights has been investigated quantitatively based on the long-term wave records collected off the NSW coast of Australia in the Tasman Sea. Most of the uncertainty is found to be caused by short record length, missing storm wave data, too high/low POT thresholds, unsuitable candidate distribution functions, subjective plotting positions, improper distribution-parameter estimators, and ad-hoc criteria on the goodness of fit.

In order to minimise this uncertainty, 1) the return period T_r of extreme wave heights to be calculated is preferred to be four times less than the length of wave record to be extrapolated, 2) whenever possible, hind-cast wave data should always be used to fill storm wave data gaps in the wave record before estimates of extreme waves are calculated, 3) the storm-by-storm or POT method is preferred to generate storm wave data, 4) the POT threshold is taken as the peak storm wave height of the smallest storm event identified locally, 5) the data on return wave height and the empirical distribution are estimated uniquely as Q=n/m, 6) only four candidate distribution functions, the FT-I, Weibull, GDP-II and Pearson-III/Gamma, are required to fit to storm wave data and select the best-fit distribution of them, 7) the LS method is preferred to determine the distribution parameters, 8) The criterion |W-1| is used to assess the goodness of fit.

LITERATURE CITED

CEM, 2002. Chapter 8: Hydrodynamic analysis and design conditions. *U.S Army Corps of Engineers,* Coastal and Hydraulics Laboratory.

Carter, D.J.T and Challenor, P.G., 1983. Methods of fitting the Fisher-Tippett Type 1 extreme value distribution. *Ocean Engineering*, 10, 191-199.

Goda, Y., 1988. On the methodology of selecting design wave height. *The 21st Intl Conference on Coastal Engineering*, ASCE, 899-913.

ISO, 2005. Petroleum and natural gas industries specific requirements for offshore structures. Part-1 Metocean design & operating considerations. Intl. Standards Organization, Geneva.

Issacson, M.S and Mackenzie, N. G, 1981. Long-term distributions of ocean waves: A review: *J. Waterways, Port, Coastal & Ocean Eng*, 107, 93-109.

Kamphuis, J.W, 2000. Introduction to Coastal Engineering and Management. World Scientific, Singapore.

Mazas and Hamm, 2011. A multi-distribution approach to POT methods for determining extreme wave heights. *Coastal Engineering*, 58, 385-394.

Sartini, L, Mentaschi, L and Besio, G. 2015. Comparing different extreme wave analysis models for wave climate assessment along the Italian coast, Coastal Eng., 100, 37-47.

Shand, T.D, Carley, J.T, You, Z.J and Cox, R J. 2011. Long-term trends in NSW coastal wave climate and derivation of extreme design storms. *The 20th NSW Coastal Conference*.

You, Z.J. and Yin, B.S., 2006. Estimation of extreme coastal waves from time series of wave data. *China Ocean Eng.*, 20, 225-241.

You, Z.J., 2007. Extrapolation of extreme wave height with a proper probability distribution function. *Australasian Coasts and Ports Conference*, Melbourne.

You, Z. J. and Lord, D., 2008. Influence of the El Nino Southern Oscillation on the NSW coastal storm severity. *Journal of Coastal Research*, 24, 203-207.

You, Z. J., 2011. Extrapolation of historical coastal storm wave data with best-fit distribution function. *Australian Journal of Civil Engineering*, 9, 73-82.

You, Z. J., 2012. A multi-distribution approach to POT methods for determining extreme wave heights: Discussion. *Coastal Engineering*, 61, 49-52.

Vanem, E., 2015. Uncertainties in extreme value modelling of wave data in a climate change perspective. *J. Ocean Eng. Mar. Energy*. DOI 10.1007/s40722-015-0025-3.

Journal of Coastal Research	SI	75	1282 - 1286	Coconut Creek, Florida	2016

Restoration of the Chandeleur Barrier Arc, Louisiana

Duncan M. FitzGerald[†], Ioannis Georgiou[‡], and Mark Kulp[‡]

[†]Department of Earth and Environment
Boston University
Boston, MA, USA

[‡]Department of Earth and Environmental Sciences
University of New Orleans
New Orleans, LA, USA

www.cerf-jcr.org

www.JCRonline.org

ABSTRACT

FitzGerald, D.M., Georgiou, I., and Kulp, M., 2016. Restortation of the Chandeleur Barrier arc. Louisiana. *In:* Vila-Concejo, A.; Bruce, E.; Kennedy, D.M., and McCarroll, R.J. (eds.), *Proceedings of the 14th International Coastal Symposium* (Sydney, Australia). *Journal of Coastal Research*, Special Issue, No. 75, pp. 1282 - 1286. Coconut Creek (Florida), ISSN 0749-0208.

The north-south trending barrier arc of the Chandeleur Islands protects valuable wetlands and reduces hurricane impacts in southeastern Louisiana. Avulsion of the lower Mississippi River ~ 1500 ka led to reworking of the St. Bernard deltaic headland concentrating sand and producing the proto-Chandeleur Islands. During the same period, landward interior delta plain erosion and subsidence formed Chandeleur Sound. Since the 1980's, isolation from new sand sources, high rates of relative sea-level rise (5 mm/yr), and hurricane impacts have produced a low transgressive barrier, periodically breached by numerous hurricane passes. Much of the sand eroded during storms is transported laterally to the ends of the barrier arc and lost from the system. A sustainable restoration plan for the barrier chain involves massive sand nourishment (from Hewes Point and St Bernard shoals ~ 285 x 10^6 m^3) while accommodating its natural landward migration. Sand would be placed along existing barrier segments to build beaches and foredune ridges. Additional sand would widen and elevate recurved spits at hurricane passes. Sand would also be pumped behind the barriers to create a broad intertidal and subtidal sand sheet would provide a platform for barrier migration during transgression. Foredune ridges, recurved spits, and intertidal rear platforms would be vegetated to help stabilize these sand deposits and provide integrity. Finally, 15 large subtidal troughs would be excavated perpendicular and landward of the barrier arc, each filled with a 10^6 m^3 of sand. This plan emphasizes landward sand transport during storms and gradual reintroduction of sand during transgression.

ADDITIONAL INDEX WORDS: *Barrier island restoration, transgressive coast, sand nourishment*

INTRODUCTION

The Chandeleur Islands define a barrier arc extending 80-km along the eastern edge of southern Louisiana's coastal zone in the north-central Gulf of Mexico (Figures 1, 2). The barrier complex consists of small (< 2 km length) to longer (~10 km length) islands that historically have been divided into the northern islands (semi-continuous barrier arc), southern islands (Curlew, Grand Gosier, and Breton Islands) and western islands (North Harbor and Freemason Islands).

The Chandeleur Island chain was formed from the marine-reworking of the St. Bernard delta complex (Penland *et al.*, 1988), which was an active distributary of the Mississippi River between ~3,600 and ~1,500 yrs before present (Törnqvist *et al.*, 1996). After avulsion of the lower Mississippi River to the Lafourche delta complex, the St. Bernard deltaic headland was eroded and reworked concentrating sand that developed into the proto-Chandeleur Islands. At the same time, much of the interior St. Bernard delta plain subsided and was eroded to form what is now Chandeleur Sound. This process detached the Chandeleur Islands from its fluvial source thereby decreasing the sediment supply and ultimately forming a transgressive barrier arc. The island chain is particularly vital to Louisiana because it flanks the eastern side of the Mississippi River Delta Plain, thereby: 1) partially sheltering the Biloxi saltmarsh from fair-weather wave swell, 2) regulating estuarine salinity and circulation (Reyes *et al.*, 2005), 3) buffering New Orleans and its surrounding areas during the passage of tropical cyclones (Stone *et al.*, 2005), and collectively 4) providing a unique coastal habitat that comprises the Breton National Wildlife Refuge. Given the important mult-funtionality of the Chandeluer Islands and their present deteriorated condition, numerous restoration plans have periodically been suggested to rebuild the island chain (Lavoie *et al.*, 2009; Thomson *et al.*, 2010; FitzGerald *et al.*, 2015). This paper briefly discusses the erosional history and the dynamic nature of the Chandeleurs and then presents a plan to revitalize the northern barrier arc that accommodates storms and a transgression of the barrier system.

PHYSICAL SETTING

Significant wave heights in the northern portion of the barrier islands are 0.45 m (long-term hourly average for 25 years) with heights in excess of 1 m occurring approximately 4 percent of the year, while 2-m waves have return periods of less than 1 percent. Dominant winds are from the southeast to northwest reflecting the passage of frontal systems. These wave conditions produce a longshore sediment transport rate between 65,000 to 100,000 m^3/yr that is bidirectional due to the arcuate nature of the island trend (Georgiou and Schindler, 2009). During the longterm evolution of the island chain, northerly longshore sand transport along the northern portion of the chain has deposited a 150 x 10^6 m^3 of sand at Hewes Point (Figures 1, 2). This volume based on bathymetry between 1880 and 2006 (Miner *et al.*,

DOI: 10.2112/SI75-257.1 received 15 October 2015; accepted in revision 15 January 2016.
*Corresponding author: dunc@bu.edu
©Coastal Education and Research Foundation, Inc. 2016

2006) cannot be explained by the yearly wave regime, rather this massive accumulation of sand can only be reconciled by invoking much greater sand transports rates during major hurricane events (Georgiou and Schindler, 2009).

The islands have a mean tidal range of 0.4 m that increases to 0.5 m during spring tide conditions. The relative sea-level rise (RSLR) rate for the region (~0.5 cm/yr; Miner *et al*., 2007) is subsidence-driven, like most of the eastern coast of Louisiana, U.S.A. (Tornqvist *et al.*, 2008). The high RSLR coupled with the lack of new sand resouces and the large longshore loss of sand during strong wave energy events during hurricanes, averaging 5.77 x 10^6 m^3/year (Kulp *et al.* 2007; Miner *et al.* 2009) has severely starved the island chain of sediment.

PRESENT-DAY TRENDS

The islands are currently located on the middle to inner Louisiana continental shelf, and the northern islands are in *Transgressive Stage* of the Penland *et al.* (1988)'s barrier model. During the 1855-1989 period, the islands lost approximately 1000 hectares, which translates to nearly 475 m in average barrier width (McBride *et al.*, 1992). This erosion constitutes some of the highest barrier island losses in the country. Fearnley *et al.* (2009) noted that the islands have decreased noticeably in subaerial extent, but have not moved landward appreciably within historic times compared to some other Louisiana barrier island systems.

During an earlier evolutionary stage when the Chandeleur Islands contained more sand and had a more continuous and robust barrier footprint, and before the islands became segmented due to storm erosion and sand loss, a nodal point existed along the northern barrier arc that defined a divergence in longshore sediment transport directions. During this stage, sand moved northward accumulating at Hewes Point shoal (Figure 1) and was transported southward to nourish Curlew, Grand Gosier, and Breton Islands (Figure 2). As the sand reservoir at the nodal point and along the entire barrier system diminished, possibly due to fewer distributary sand-filled channels in the subsurface, sand transport to the south was greatly reduced and many of the southern islands periodically were converted to subtidal shoals.

Fearnley *et al.* (2009) asserted that major historical changes to the Chandeleur system are event driven and that the future long- term evolution and viability of the barrier chain will be controlled by the frequency and magnitude of tropical cyclones. Evidence of this trend is demonstrated by pre- and post-Katrina imagery (Sallenger *et al.*, 2009). In fact, between 2002 and 2008, the Chandeleurs were impacted by five major hurricanes and several other moderate tropical storms (Figure 3; Hu *et al.*, 2012). Collectively, these storms largely stripped the islands of sand with little recovery by 2007 (Kulp *et al.* 2007). Following Hurricanes Katrina and Rita, much of the Chandeleurs were characterized by marsh islands with broad washover fans and extensive flood-tidal deltas.

Projected future increases in the rate of relative sea-level-rise, hurricane frequency and hurricane intensity will further threaten the islands' ability to retain its sand resources and maintain its integrity. The combined alongshore losses of sand to Hewes Point, offshore losses during storms, and onshore sand transport filling an increasingly deeper backbarrier water column due to subsidence will ultimately deplete the Chandeleur Islands of its sand reservoirs.

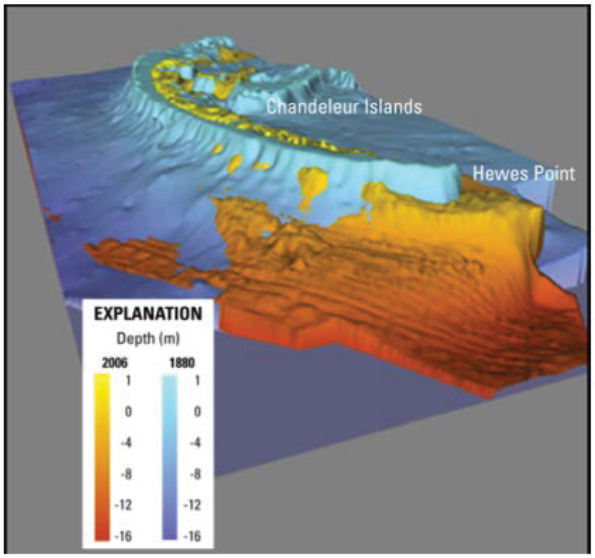

Figure 1. Digital elevation model of the Hewes Point shoal region and Chandeluer Islands looking south. Hewes Point contains 150 x 10^6 m^3 of sand (from Miner *et al.* 2007)

Fearnley *et al.* (2009) estimated that during the next 20 years the island system will be converted to an inner-shelf shoal (Stage 3 of the Louisiaan barrier model of Penland *et al*., 1988). This prediction is based on linear regressions of island areas coupled with projections of historical cyclone frequencies and analysis of high-resolution ortho-photos (Figure 4). The highly degraded nature of the island chain over the past 10 yrs is the impetus for this plan to restore the islands.

PROPOSED RESTORATION MODEL

Future restoration of the Chandeleur Island chain will require a substantial input of sediment and a sand input system that maximizes the longevity of the nourishment project by accommodating the major processes controlling sand dispersal vectors and providing a barrier architecture that encourages sand conservation. The major conditions that will impact barrier-wide restoration include:

1. Diverging longshore transport along southern barrier arc.
2. Overall landward barrier retreat.
3. Overwash at specific sites, ranging to barrier-wide overwash depending on storm intensity and relief of northern barriers.
4. High rate of sea level rise (5 mm/yr).
5. A deeply eroding shoreface (~ 8m).
6. Southern barrier arc of broad sand shoals with intermittent intertidal and supratidal shoals separated by tidal inlets.
7. Barriers anchored to marsh islands with eel grass beds in the north & small vestiges of marsh and mangrove to the south.
8. Many hurricane passes bordered by recurved spits and backed by intertidal to subtidal flood deltas (0.2 – 1.0 km).
9. Existence of subsurface distributaries that contribute sand to the retreating barrier system.

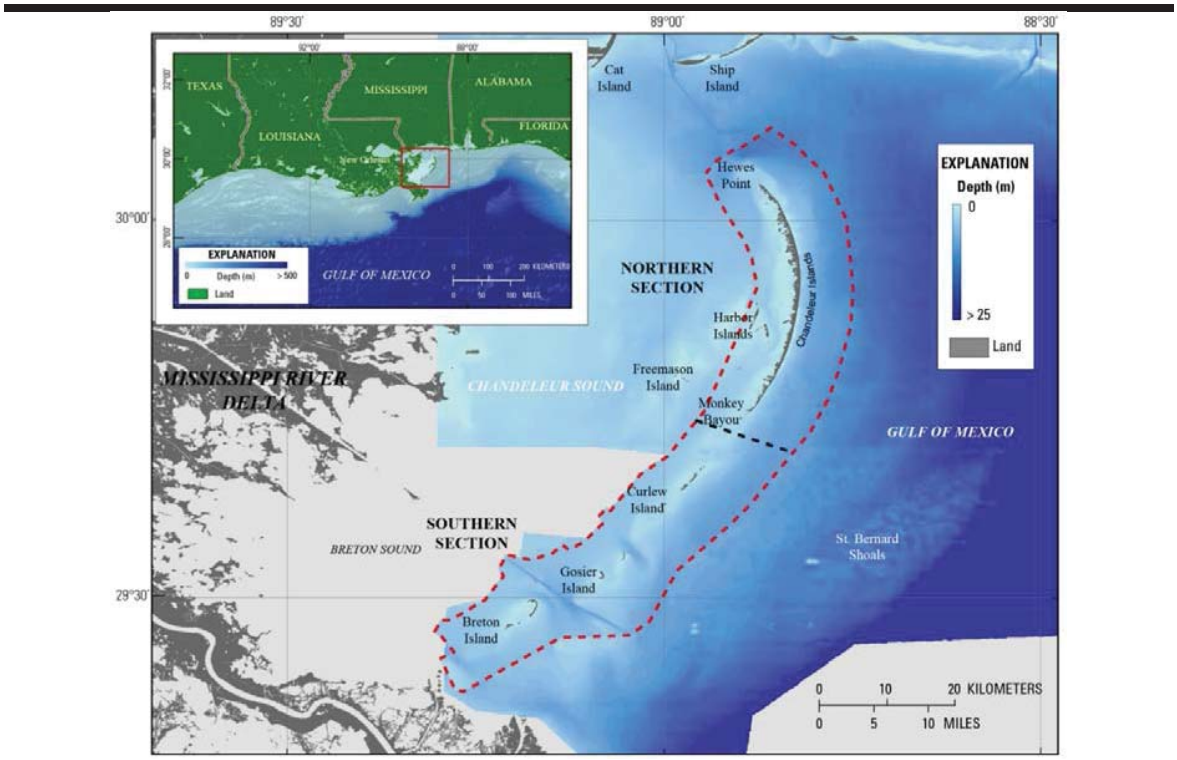

Figure 2. Location of Chandeleur Islands flanking the southeast coast of Louisiana (from Kindinger et al, 2013).

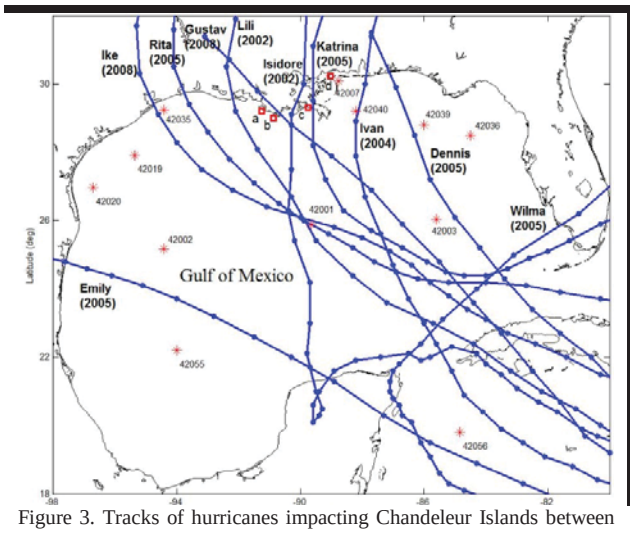

Figure 3. Tracks of hurricanes impacting Chandeleur Islands between 2002 and 2008 (from Hu *et al.*, 2012).

One of the beneficial aspects of restoring the Chandeleur Islands is that there are abundant nearby sediment resources including 150 x 10^6 m^3 of sand at Hewes Point (Miner *et al.*, 2007) and vast sand reservoirs contained in the Saint Bernard shoals (135 x 10^6 m^3; Rogers *et al.*, 2010). The importance of maintaining a healthy sandy barrier complex was recognized more than 20 years by Penland et al (1992) who provided a two dimensional view of various ways to rebuild the Chandeleur barriers.

However, this plan was intentionally piecemeal and site specific because in the early 1990's the barrier system was much more robust than it is today with extensive vegetated dunes, some ephemeral hurricane passes, and a vigorous rear barrier system of marsh and mangrove. The plan presented here is more aggressive due to the deteriorated nature of the barrier system; it draws on other ideas for revitalizing the island chain (Penland *et al.*, 1992; Lavoie *et al.*, 2009; Thomson *et al.*, 2010).

A measure of the magnitude of the restoration effort and the quantity of sand needed to restore the barrier complex is gaged by the almost complete dispersal of 3.7 million m^3 of sand that was placed in front and on top of the barrier during the summer and fall of 2010 as part of BP's response to keep the islands from being oiled (FitzGerald *et al.*, 2015). It is likely that most of the sand berm that was removed during Hurricane Isaac in late August of 2012 was transferred onshore and along shore.

Most importantly, a successful restoration plan must accommodate the strong longshore transport system and its divergent nodal point, as well as the susceptibility of the barrier system to hurricane overprinting. It is also important that a large enough quantity of sand be placed along the barrier to ensure that a single storm (erosional event) does not completely remove or redistribute this valuable sand resource.

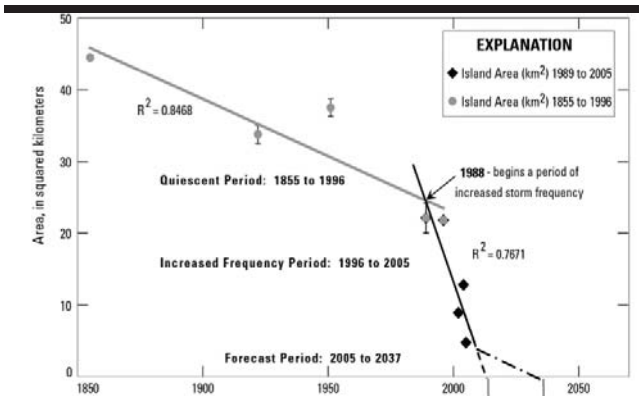

Figure 4. Projected conversion of islands to subtidal shoal based on linear regression analysis of decreasing island areas and increased storm frequency beginning in 1996. Future disappearance of the northern Chandeleur Islands assumes a storm frequency similar to 1989 to 2010, or the previous trend 1855 to 1996, and appended with 2008 and 2010 data. Lower dashed regression line represents predicted change according to the 1855-1996 period (from Fearnley *et al.*, 2009).

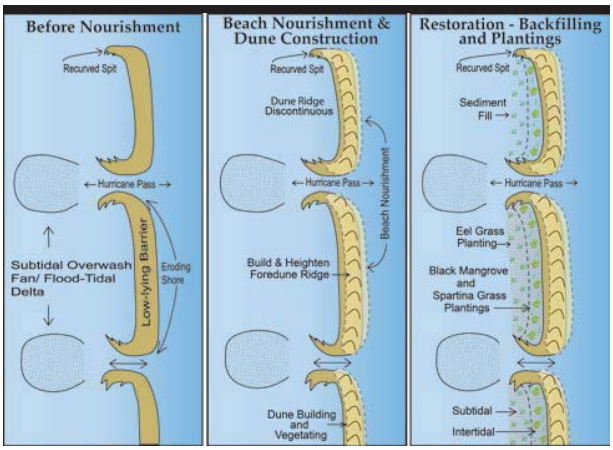

Figure 5. Generalized restoration plan for the segmented barriers along the northern Chandeleur Islands.

The restoration plan is conceptualized in Figure 5 and presented in detail in Figure 6. The plan depicts individual island segments, but is intended for the entire northern barrier arc. The volume of sand required for the individual components of barrier restoration are computed in Table 1. This plan takes advantage of the existing tidal passes that characterize the much of northern barrier system. Sand would be placed along the upper portion of the barrier building a moderately wide beach and dune system. The beach would be overfilled with sand to allow for some wave transfer of sand to nearshore during the construction of an equilibrium foreshore. Locally, tidal inlets and small breaches would produce natural breaks in nourishment area. Total width of renourished beach would be approximately 250 m with a thickness of approximately 1 m. Dune restoration would simultaneously be completed along barrier segments to create dunes 20-m wide at the base and 10-m wide at the top, with a height of 1.5 m (Figures. 5 and 6; Table 1). Dunes would be planted with appropriate vegetation to help capture the transport of aeolian sediment.

In some locations the foredune ridge should contain low areas that would permit overwashing during storms. In a regime of accelerating sea-level rise, it is beneficial to promote sand movement onshore during storms rather than solely offshore and alongshore where it may be lost from the barrier system. Tidal passes serve a similar function as the low areas in dune systems and provide large conduits through which sand can be transported landward, especially during storms where extensive flood-tidal delta shoals are formed. It is envisioned that waves will also transport sand along the sides of the inlets, building recurved spits. During the ongoing transgression it is expected that these deposits (washovers, flood-tidal deltas, recurved spits) will nourish the landward migrating barriers by sand being reintroduced into the littoral zone.

Immediately behind the barriers, the lagoon/bay waters should be filled with sand to an intertidal elevation with a width of approximately 100 m. This intertidal, backbarrier apron would be approximately 0.5-m thick and vegetated with Smooth Cordgrass and stands of Black Mangrove. These plants will trap suspended sediment and overwash sand while their roots and rhizomes will help to bind and stabilize the sediment. Seaward of the intertidal apron a subtidal apron of sediment 400-m wide and 0.5-m thick would be constructed and planted with beds of seagrass to stabilize the subtidal region. Not only will the seagrass beds add integrity to the backbarrier, but they will also provide an important habitat, food source, and feeding grounds for numerous faunal and infaunal species

Another strategy in our plan to restore the Chandeleur Islands, involves placing large sand reservoirs at numerous locations along the backside of the barrier arc as suggested by Lavoie *et al.* (2010). In this part of the plan, sand would be placed in troughs perpendicular to the shoreline trend. The troughs would be located in existing low areas such as inactive channels to decrease excavation costs. Trough dimensions would vary according to the characteristics of the site (bathymetry, existing vegetation, stratigraphy, proximity to tidal passes) but would have general dimension of: 2-3 m thick, 300 to 400-m wide, and 1-km long with dikes constructed along the sides of the deposit. The 3-m deep troughs would be excavated mostly below mean low water to prevent mobilization of the sand during a major hurricane (Category #3-5 hurricanes). The dikes would perform a similar function and would help stabilize the sand during minor storm events as well as large ones. We envision that approximately 15 reservoir sand troughs be constructed along the barrier arc having a total sand volume of about approximately 15 million m^3 (Table 1).

ACKNOWLEDGMENTS

This work was funded by Lake Pontchartrain Basin Foundation. We thank John Lopez and Mike Miner for constructive reviews.

Table 1. *Dimensions and Volumes Required for Restoration*

	Beach Restoration	Dune Restoration	Rear Barrier Sand Apron	Sand Trench Reservoiurs
Template Scale	5 segments 5.5 km long	5 segments 5.5 km long	5 segments 5.5 km long	15 segments 1 – 2 km apart
Fill dimensions	5.5 km long 250 m wide 1 m thick	5.5 km long 1.5 m high 10 m high top, 20 m base, Avg. Width = 15 m	100 m wide intertidal apron, 0.5 m thick, planted with *Spartina* 400 m wide subtidal platform, 0.5 m thick, planted with subquatic vegetation	Variable and 1000 m long, 400 m wide, 2 – 3 m thick
Vol.per segment (m^3)	1,375,0000	123,750	1,375,000	1,000,000
Total vol. for each phase (m^3)	6,875,000	618,750	6,8754,000	15,000,000

Total estimated for full implementation of sand nourishment program = ~ 30,000,000 m^3

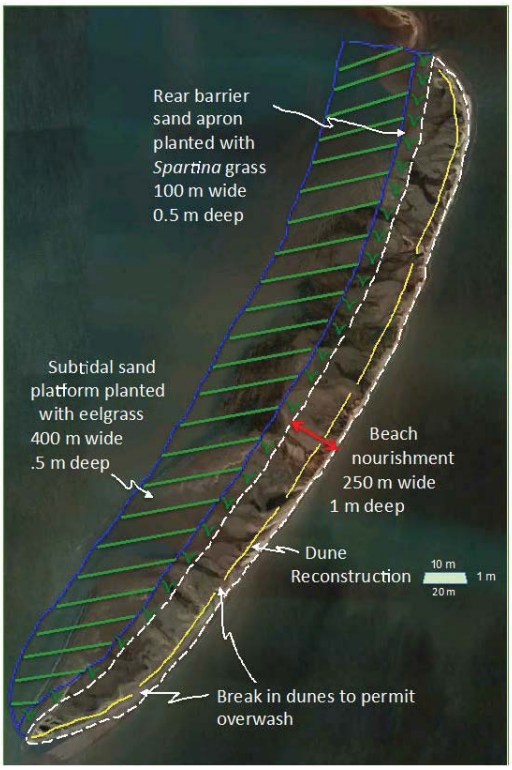

Figure 6. Conceptualized plan to restore island segments.

LITERATURE CITED

Fearnley, S. Miner, M. D., Kulp, M. A., Bohling, C, and Penland, S., 2009, Hurricane impact and recovery shoreline change analysis of the Chandeleur Islands, Louisiana, USA: 1855 to 2005, *GeoMarine Letters*, 29, 455-466.

FitzGerald, D., Georgiou, I., Kulp, M., and Miner, M., 2015, Chandeleur Islands: Post-berm Analysis and Island Renourishment Plan, *UNO*, Lake Pontchartrain Basin Foundation. 56 p.

Georgiou, I.Y., Schindler, J., 2009, Wave forecasting and longshore sediment transport gradients along a transgressive barrier island; Chandeleur Is., LA, *GeoMarine Letters*, 29, 467-476.

Hu, K., Chen, Q., and Fitzpatrick, P., 2012, Assessment of a Parametric Surface Wind Model for Tropical Cycles in the GoM, Advances in Hurricane Research - Modeling, Meteorology, Preparedness and Impacts, Dr. Kieran Hickey (Ed.), ISBN: 978-953-51-0867-2.

Kulp, M. FitzGerald, D. M., Miner, M., Georgiou, I., and Penland, S., 2007, The demise of the Chandeleur Islands in southeast Louisiana: Not Yet!, GSA Abs. with Prog, 39, 69.

Lavoie, D., Miner, M., Georgiou, I. Y., Fearnley, S., Sallenger, A. H., Williams, S. J., Twichell, D., Flocks, J., and Kulp, M., 2009, Sand resources, regional geology and coastal processes of the Chandeleur Islands coastal system-an evaluation of the Breton Nat. Wildlife Refuge: *U.S.G.S*. SI Report 2009-5252, 180 p.

Miner, M., Kulp, M., Rogers, B., 2007, Historical Shoreline and Bathymetric Changes of the Chandeleur Islands: Assessment of St. Bernard Shoals as Potential Sand Resource for Barrier Nourishment.

McBride, R. Penland, S., Hiland, M., Williams, S., Westphal, K. A., Jaffe, B. E., and Sallenger, A. H., Jr., 1992, Analysis of barrier shoreline change in Louisiana from 1853 to 1989, in: Williams,

S., Penland, S., and Sallenger, A., eds., *Louisiana barrier island erosion study-atlas of barrier island shoreline changes in LA* (1853 to 1989): USGS I-2150-A, p. 36-97.

Penland, S., Boyd, R. , and Suter, J. R., 1988, Transgressive depositional systems of the Mississippi Delta Plain; a model for barrier shoreline and shelf sand development, *Journal of Sedimentary Research*, 58, 932-949.

Penland, S. and others, 1992, Barrier island erosion and wetland loss in Louisiana, in Williams, S., Penland, S., and Sallenger, A. eds., Louisiana barrier island erosion study-atlas from 1853 to 1989: *U.S.G.S.* M.I.S. I-2150-A, p. 2-7.

Reyes, E., Geogiou, I., Reed, D., and McCorquodale, A., 2005, Using models to evaluate the effects of barrier islands on estuarine hydrodynamics and habitats: a numerical experiment, *Journal of Coastal Research*, SI 44, p. 176-185.

Rogers, B., Kulp, M.A., and Miner, M., 2009, Late Holocene chronology, origin and evolution of the St. Bernard Shoals, northern Gulf of Mexico, *GeoMarine Letters*, 29, 379-394.

Rosati, J., and Stone, G., 2007, Critical width of barrier islands and implication for engineering design. *Coastal Sediments*, 7, ASCE, 14 p.

Törnqvist, T. and others, 1996, A revised chronology for the Mississippi River Subdeltas, *Science*, 273, 1693-1696.

Thomson, G., Miner, M., Wycklendt, A., Rees, M. Swigler, D., 2010, MRGO Ecosystem Restoration Feasibility Study Chandeleur and Breton Islands. Boca Raton, Florida: *Coastal Planning & Engineering*, Inc. 96 p.

Journal of Coastal Research	SI	75	1287 - 1291	Coconut Creek, Florida	2016

Identification and Mapping of Marine Submerged Aquatic Vegetation in Shallow Coastal Waters with WorldView-2 Satellite Data

Tin Hoang[†‡*], Rodrigo Garcia[††§], Michael O'Leary[†], and Ravi Fotedar[†]

[†]Department of Environment and Agriculture, Faculty of Science and Engineering, Curtin University, Bentley, Perth, Western Australia 6102, Australia

[‡]Center for Coastal Management and Development Studies, Hue University of Sciences, Thua Thien Hue, 8454, Vietnam

[††]Remote Sensing and Satellite Research Group, Department of Physics and Astronomy, Curtin University, Bentley, Perth, Western Australia 6102, Australia

[§]School for the Environment, University of Massachusetts Boston, Boston, Massachusetts 02125, USA

www.cerf-jcr.org

www.JCRonline.org

ABSTRACT

Tin, H.; Garcia, R.; O'Leary, M., and Fotedar, R., 2016. Identification and Mapping of Marine Submerged Aquatic Vegetation in Shallow Coastal Waters with WorldView-2 Satellite Data. *In:* Vila-Concejo, A.; Bruce, E.; Kennedy, D.M., and McCarroll, R.J. (eds.), *Proceedings of the 14th International Coastal Symposium* (Sydney, Australia). *Journal of Coastal Research*, Special Issue, No. 75, pp. 1287 - 1291. Coconut Creek (Florida), ISSN 0749-0208.

Marine submerged aquatic vegetation (MSAV) naturally occurs on rubble and dead coral substrates in temperate and tropical coastal regions. During the growing season, MSAV develops to form dense canopy seaweed beds that play a vital role in coastal marine ecosystems and offer great potential to chemical, pharmaceutical, and bio-energy industries. At present, the total biomass and the distribution of the MSAV beds along the coast of Western Australia (WA) are not fully identified and quantified. Therefore, the application of satellite remote sensing data with high spatial resolution for examining the MSAV beds is required. The main objective of the present study was to assess and map the distribution of MSAV at two sites; Rottnest Island and Point Peron, Rockingham, WA, using WorldView-2 (WV2) satellite data. These study sites are important marine protected areas in WA waters with extraordinary documented biodiversity. By means of quantitative quadrat techniques, the MSAV canopy covers and fresh biomass data from the ground truth observations were assessed from September 2012 to December 2014. At Point Peron, the fresh biomass of *Sargassum* in the inter-tidal zone reached 5651.7±754.5, 5218.9±192.6, 1136.6±526.4, and 3472.2±434.2 g m^{-2} for spring, summer, fall, and winter, respectively. The overall accuracy of the minimum distance method was employed and yielded the highest accuracy rates of 90.93% (Kappa coefficient, $\kappa = 0.96$) and 97.13% ($\kappa = 0.96$) for Rottnest Island and Point Peron, respectively. The Mahalanobis classification with overall accuracy yielded 90.66% ($\kappa = 0.88$) and 94.16% ($\kappa = 0.85$) for Rottnest Island and Point Peron, respectively. The study results revealed that WV2 satellite data provided evidence of the high accuracy of MSAV classification.

ADDITIONAL INDEX WORDS: *clear shallow waters, marine habitat mapping, satellite remote sensing.*

INTRODUCTION

High spatial resolution satellite remote sensing is an effective tool for monitoring, evaluating and mapping biodiversity and natural resources in coastal areas (Green *et al.*, 1996; Gibbons *et al.*, 2006). There are numerous studies that have used high-resolution satellite images for identifying and mapping coastal habitats such as coral reefs (Benfield *et al.*, 2007), sea grass meadows (Guimarães *et al.*, 2011), mangroves (Heenkenda *et al.*, 2014; Ibrahim *et al.*, 2015), macroalgae (Garcia *et al.*, 2015; Tin, O'Leary, and Fotedar, 2015), and freshwater/ salt marsh (Carle, Wang, and Sasser, 2014). However, these studies mostly utilized sensors with fewer than four spectral bands in the visible domain, which limited the detailed classification of vegetation (Feilhauer *et al.*, 2013). To overcome the limitations, in October 2010, a WV2 satellite was successfully launched into orbit and began to acquire high spatial resolution images, 0.5-m for panchromatic and 2-m for multispectral images, and high spectral resolution (eight bands) including four additional spectral bands with additional near-infrared, coastal-blue, yellow, and red-edge bands (Updike and Comp, 2010).

Evaluation and validation of the feasibility of the new spectral bands of WV2 satellite data on identifying and mapping MSAV in coastal habitats are a necessity. This work not only contributes to scientific research but also provides useful information for managers, conservationists, and coastal planners, and is particularly relevant for marine conservation parks' authorities. The main objectives of the present study were: 1) validating the feasibility of the WV2 satellite data for identifying and mapping MSAV in coastal habitats; 2) evaluating three machine learning algorithms/classification methods, Mahalanobis distance (MDiP), supervised minimum distance (MiD), and spectral angle mapper (SAM), for mapping the diversity of MSAV.

DOI: 10.2112/SI75-258. 1 received 15 October 2015; accepted in revision 15 January 2016.
*Corresponding author: tin.hoangcong@postgrad.curtin.edu.au
©Coastal Education and Research Foundation, Inc. 2016

METHODS

In this section, we present a description of the study area, spectral reflectance measurements, WorldView-2 images acquired, processing methods, and the accuracy assessment used in this study.

Study area

Rottnest Island and Point Peron, Rockingham are recognized as biodiversity hotspots of the WA coast and have been selected as pilot study sites for the region. The tidal range of the WA coast is relatively low (± 1 m). Rottnest Island is located off the WA coast approximately 19 km from the port of Fremantle, while Point Peron is a large limestone region at Shoalwater Islands Marine Park on the Rockingham coast (Figure 1). The study sites are dominated by canopy forming macroalgae such as *Sargassum* sp., *Ecklonia* sp., sea grass (*Amphibolis* sp., *Posidonia* sp.), and other associated MSAV species such as *Ballia* sp., *Metagoniolithon* sp., *Asparogopsis* sp., *Gracilaria* sp., and *Ulva* sp.

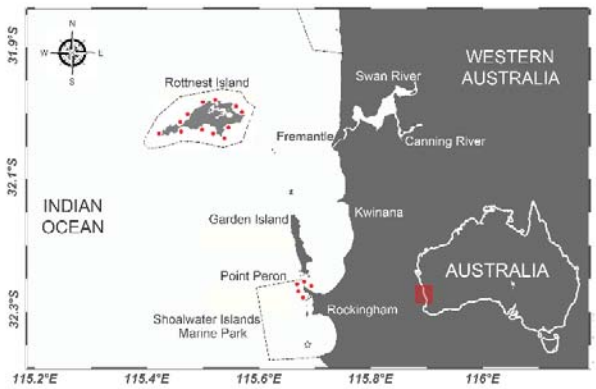

Figure 1. Map showing the selected study locations along the Western Australian coast, Australia. The dashed lines symbolize marine protected areas' boundaries.

Field surveys and vegetation classes

The purpose of mapping mainly focuses on the abundance of habitats. Consequently, broad-scale field surveys were conducted as much as possible. We used a combination of both scuba and free diving methods to collect ground truth data of the dominant habitat types. Ten and three survey transects were carried out at Rottnest Island and Point Peron, respectively (Figure 1). Along the transects, MSAV samples, in the depth range between 0.2 and 3.5 m, were collected and underwater photographs taken.

The classification of benthic habitats at the two study sites was based on a hierarchal classification scheme that included three levels and five classes (Figure 2). Classification at level 1 was based on the pixel reflectance value that best separated vegetated and non-vegetated benthos. The non-vegetated level 1 substrates were subdivided into sandy and limestone substrates by means of reflectance characteristics. Likewise the vegetated level 1 substrates were classed as either macroalgae and sea grass by means of spectral reflectance and the ground truthing from the field survey data. Level 3 classification, including five different habitat classes, largely depended on the characteristics of spectral reflectance to divide them into two groups of canopy algae and algae turf. The group of sea grass, sand, and limestone was also similar to level 2.

Spectral reflectance measurement and processing

Twenty-two MSAV samples that included macroalgae, sea grass, sand and limestone substrates were collected at Point Peron (32.2715 ºS, 115.6865 ºE), WA on August 22, 2014. The MSAV samples were preserved in cold containers and transported to the Curtin Aquatic Research Laboratory within four hours of collection. The samples were then identified to species level and their spectral reflectance was measured by an ASD Hi-Res FieldSpec® 4 portable spectroradiometer (1-nm resolution, 350−2500 nm coverage). All samples were placed on a non-reflective black tray and measured from nadir position (~10º). Thirty replicates were measured for each sample.

WorldView-2 image acquistion

Two WV2 scenes covering the Rottnest Island and Point Peron, Rockingham regions were acquired for study areas in WA coastal waters. The selected WV2 were captured on February 7 and October 28, 2013 for Point Peron, Rockingham and Rottnest Island, respectively. The captured time of the satellite corresponds to Australian mid-spring and late summer, coinciding with the most dominant MSAV habitat development, particularly the canopy macroalgae such as *Sargassum* and *Ecklonia* (Tin, O'Leary, and Fotedar, 2015; Kendrick and Walker, 1994).

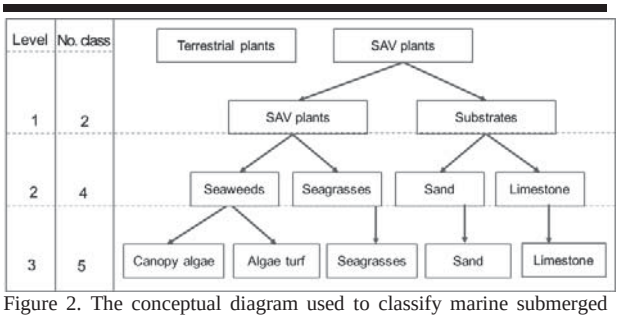

Figure 2. The conceptual diagram used to classify marine submerged aquatic vegetation habitats in clear shallow coastal waters.

Remote sensing image processing

The WV2 digital numbers were first converted to top of atmosphere surface reflectance values with the procedure given by Updike and Comp (2010). The FLAASH algorithm in ENVI 4.7 was then used for atmospheric correction. High-resolution panchromatic data (0.5-m) were fused with the lower resolution multispectral bands (2-m) to create a colorized high-resolution dataset.

Accuracy assessment

Overall classification accuracy was calculated by dividing the total number of calculated pixels by the total error pixel in the

classification process; overall classification accuracy was measured in units of percent. Index error (error matrices) was used to calculate the user's and producer's accuracy. In particular, the error matrix (user's accuracy) was used to determine the accuracy of the object's classification and Kappa coefficient index (κ) of n parameter estimation.

RESULTS

In this section, we describe the marine submerged aquatic vegetation types, spectral reflectance characteristics, mapping MSAV distribution, and results of accuracy assessment.

Marine submerged aquatic vegetation distribution substrates

According to field surveys, the distribution area of MSAV at selected sites in WA coast is mainly distributed on the limestone substrates within depths ranging from 0.2 to 3.5 m. The major subtrates are sandy and limestone rock.

Spectral reflectance characteristics

The results of the PCA analysis measuring the surface spectral reflectance of 19 MSAV groups and three substrate types showed that all MSAV groups in shallow coastal waters (<3 m) can be divided into four main groups: brown macroalgae, red macroalgae, green macroalgae, and benthic substrate groups. The sea grass group has two dominant species, *Posidonia* sp. and *Amphibolis* sp. The results from in-air spectral measurements showed that the sand and limestone substrates were completely different from the reflectance spectra of the other MSAV species (Fearns *et al*., 2011). The peak spectral reflectance values of brown macroalgae species were usually at 550 nm. Brown and red macroalgae usually have longer wavelengths and could have more than one maximum point (580 and 650 nm) (Figure 3). Regression between in situ and WV2 satellite-derived spectral reflectance, based on the classification results PCA and we found that all species of MSAV and substrates can be classified into/divided into four main groups. Therefore, in this present study, four major substrate habitats including sea grass, mixed MSAV, turf algae, canopy algae, and two main benthos substrate types including bare limestone and sand were selected for habitat mapping.

Mapping the distribution of MSAV

The results of the MDiP, MiD and SAM classification methods revealed that the distribution area differed with each method (Figures 4 and 5). The MDiP classifier showed that the mixed SAV was in deep waters. Sea grasses were identified as the dominant habitat and were usually distributed in the shallow waters where a sandy bottom is the most dominant. With the MiD classifier, sea grass was also identified as the highest distributed habitat that included the deep water areas. Canopy algae, algae turf, and sand were also interpreted similarly to the results of the MDiP method. Likewise, the SAM classifier expressed the sketchy interpretation results and unclear pattern of some sea grass, mixed SAV, and sand. Canopy algae and algae turf were not presented clearly either. At Point Peron, fresh biomass of *Sargassum* at the inter-tidal zone reached 5651.7±754.5, 5218.9±192.6, 1136.6±526.4, and 3472.2±434.2 gram per square meter (g m^{-2}) for spring, summer, fall, and winter, respectively.

Accuracy assessment

In Rottnest Island, the confusion matrix showed that the highest overall accuracy was achieved with the MiD classification method (90.93%), followed by the MDiP classification method (90.66%). The lowest overall accuracy was found in the SAM classification method with a value of 49.93%. In particular, the MiD classification methods had user's accuracy ranging from 86.9% for mixed MSAV to 100% for the bare limestone class. In the MiD classification methods, all identified classes had a user's accuracy greater than 70%.

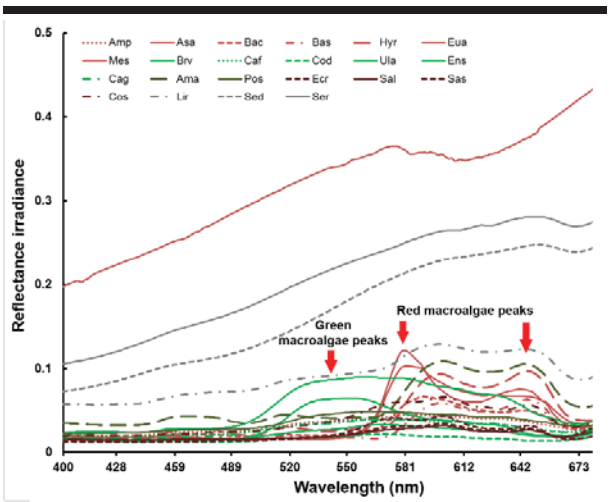

Figure 3. The in-air spectral signatures of the main inter-tidal submerged aquatic vegetation species and substrates in WA. Note: Sal = *Sargassum linearifolium*, Sas = *S. spinuligerum*, Ecr = *Ecklonia radiata*, Cos = *Colpomenia sinuosa*, Asa = *Asparagopsis armata*, *Hyr* = *Hypnea ramentacea*, Bas = *Ballia* sp., Amp = *Amphiroa anceps*, Eua = *Euptilota articulata*, Bac = *Ballia callitrichia*, Mes = *Metagoniolithon stelliferum*, *Ula* = *Ulva australis*, *Ens* = *Entermorpha* sp., Cod = *Codium duthieae*, Cag = *Caulerpa germinata*, Caf = *C. flexis*, Brv = *Bryopsis vestita*, Ama = *Amphibolis antartica*, Pos = *Posidonia* sp., Sed = Sediment, Ser = Sediment/Rubble, Lir = Limestone rocks with red coralline algae covering.

Producer's accuracy ranged from 43.8% for the canopy algae class and 100% for both sea grass and sand classes. Five out of six classes had a producer's accuracy greater than 70%, excluding the canopy algae class with 43.8%. User's accuracy of the MDiP classifier gave only the sea grass class less than 70% (66.6%), while the remaining classes were greater than 70%. Producer's accuracy of canopy algae was 45.7%, while the remaining classes had values greater than 70%. The user's accuracy of SAM had an accuracy value greater than 70%. Two out of the six classification classes had producer's accuracy of less than 70%, including canopy algae and sand.

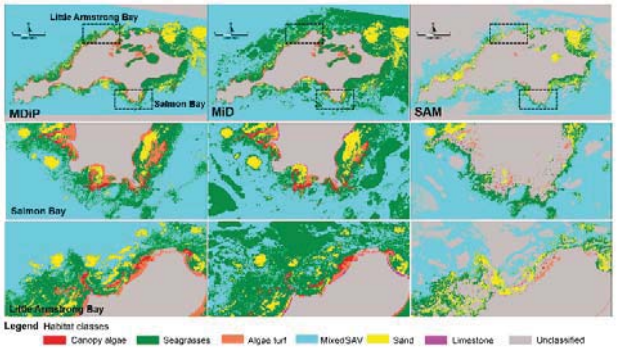

Figure 4. Comparison of classification results from three different classifier methods, MDiP, MiD, and SAM, at Rottnest Island study sites.

At Point Peron, the overall accuracy of the MiD classifier also reached the highest value of 97.13% (coefficient κ = 0.94). The MDiP classifier with general accuracy value reached 94.16% (κ = 0.88), and the lowest value SAM classifier a value of 88.43% (κ coefficient = 0.74). In the classification results of the MiD classifier, only the producer's accuracy of the bare limestone class was 68.58%' none of the classes had classification results less than 70% in terms of both user's and producer's accuracy. Similarly to the MDiP classifier, only the user's accuracy of the canopy algae class was valued at 66.7%; the remaining classes in terms of both user's and producer's accuracy were greater than 70%. The SAM classifier gave two out of six classes user's accuracy values lower than 70% including canopy algae and sand. The remaining results for both user's and producer's accuracy were above 70%.

DISCUSSION

Rehabilitation and development of MSAV habitats is currently one of the priority activities in ecosystem conservation, including freshwater ecosystems (Harwell and Havens, 2003; Herrera-Silveira and Morales-Ojeda, 2009; Yuan and Zhang, 2008). However, assessing the growth and mapping the current state of distribution of MSAV on a large scale is very time-consuming and labor-intensive not only because of geographical issues but also because of seasonal and weather variations (Yuan and Zhang, 2008). The results of this study can be compared with those of the recent studies that used high-resolution satellite imagery for mapping of shallow coastal vegetation. Fearns (2011) used HICO hyperspectral images in mapping marine vegetation that showed the optical model could classify 80% of the image pixels. Of those, approximately 50% of pixels were distinguished as sea grass and sand and 90% were classified as macroalgae (Fearns *et al.*, 2011). Regarding the optimum depth for classification satellite remote sensing imagery, this present study showed a similar trend to that of Reshitnyk and colleagues (2014) as results suggested that WV2 imagery can provide the finest interpretation of eelgrass, and brown and green macroalgae habitats at depths above <3.0 m.

The overall accuracy of the classification outcomes in the present study is higher than that of the study by Kumar and colleagues (2015) when using support vector machine (SVM), artificial neural network (ANN), and SAM classification methods for classifying crop and non-crop canopy in India. The highest overall accuracy found in SVM and ANN algorithms was 93.45% and 92.32%, respectively. Likewise, the SAM method has low accuracy among the classification methods (74.99%) (Kumar *et al.*, 2015). In this study, MDiP and MiD methods demonstrated potential for identifying and mapping MSAV with WV2 multispectral high-spatial resolution (MHSR) satellite imagery. This was validated by the highest overall accuracy (greater than 90%) for both study sites in WA. The MDiP method showed that mixed MSAV was in deep waters rather than shallow coastal waters.

This study supports the feasibility of previous studies suggesting that MHSR satellite data (*e.g.* QuickBird, WV2) would be suitable for mapping benthic macroalgae cover in regions of very high heterogeneity (Vahtmäe and Kutser, 2007). In addition, the MHSR imagery data combined with field surveys in coastal shallows are a perfect fit. However, hyperspectral airborne imagery (HAI) is an advantageous imagery source which have the abundantly information to assess coastal marine habitats due to its hyperspectral characteristic bands, regardless data acquire price. HAI is still very expensive compared with MHSR as it is collected by separate regions for each study purpose (Yuan and Zhang, 2008).

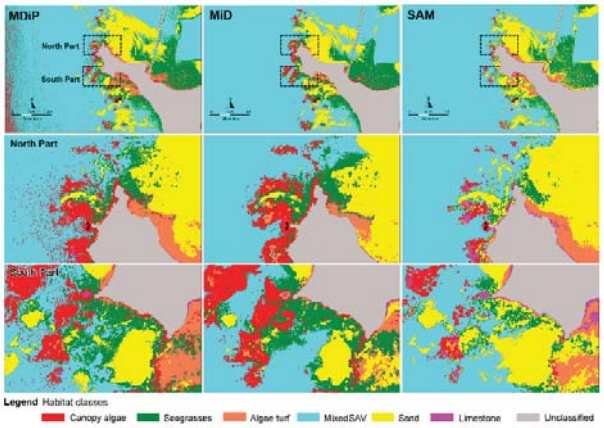

Figure 5. Comparison of classification results of three different classifier methods, MdiP, MiD, and SAM, at Point Peron study sites.

The similarity of reflectance spectra of sea grass species to those of other macroalgae groups is owed to their biological characteristics. A study of sea grass distribution by remote sensing in Bourgneuf Bay (France) for *Zostera marina* and *Z. noltii* species showed reflectance spectra distinct from micro and macroalgae, particularly in the wavelength used NIR band (Barillé *et al.*, 2010). Our results for in-air measurement and reflectance spectra of 22 MSAV species showed that two sea grass species, *Posidonia* sp. and *Amphibolis* sp., had reflectance spectra characterized by green and red macroalgae groups, respectively. As either they can have many different emphytes algae on the leaves' surface or they were on older stages in the life cycle when the leaves' pigments was changing. A similar

pattern was found by Yuan and Zhang (2008), who found that the spectral reflectance ratios of submerged aquatic species decreased with the aging MSAV species (Yuan and Zhang, 2008). This can be explained by the aging vegetation, decaying, and appearing of emphytes organisms on their leaves, branches, thallus' surface. Therefore, spectral reflectance not only reflects the host species but is also affected by many other fouling organisms.

CONCLUSIONS

This work demonstrates a case study using high spatial resolution satellite images in evaluating MSAV identification and distribution in shallow coastal waters. The major advantages of increasing the number of spectral bands and spatial resolution are better detection ability and MSAV distribution map with clear water column as WA coastal waters. The results revealed that both MDiP and MiD classification methods showed better evidence for the greater accuracy of MSAV classification results than the SAM classification method. Classification results also showed a full representation of the distribution of MSAV groups in shallow coastal areas.

ACKNOWLEDGMENTS

The authors would like to acknowledge the support of the Australian Award Scholarships, the Department of Environment and Agriculture, and the Department of Physics and Imagery, Curtin University.

LITERATURE CITED

Benfield, S.L.; Guzman, H.M.; Mair, J.M., and Young, J.A.T., 2007. Mapping the distribution of coral reefs and associated sublittoral habitats in Pacific Panama: a comparison of optical satellite sensors and classification methodologies. *International Journal of Remote Sensing*, 28(22), 5047–5070.

Carle, M.V.; Wang, L., and Sasser, C.E., 2014. Mapping freshwater marsh species distributions using WorldView-2 high-resolution multispectral satellite imagery. *International Journal of Remote Sensing*, 35(13), 4698–4716.

Fearns, P.R.C.; Klonowski, W.; Babcock, R.C.; England, P., and Phillips, J., 2011. Shallow water substrate mapping using hyperspectral remote sensing. *Continental Shelf Research*, 31(12), 1249–1259.

Feilhauer, H.; Thonfeld, F.; Faude, U.; He, K.S.; Rocchini, D., and Schmidtlein, S., 2013. Assessing floristic composition with multispectral sensors–A comparison based on monotemporal and multiseasonal field spectra. *International Journal of Applied Earth Observation and Geoinformation*, 21, 218–229.

Garcia, R.A.; Hedley, J.D.; Tin, H.C., and Fearns, P.R.C., 2015. A method to analyze the potential of optical remote sensing for benthic habitat mapping. *Remote Sensing*, 7(10), 13157–13189.

Gibbons, P.; Zerger, A.; Jones, S., and Ryan, P., 2006. Mapping vegetation condition in the context of biodiversity conservation. *Ecological Management & Restoration*, 7, S1–S2.

Green, E.P.; Mumby, P.J.; Edwards A.J., and Clark C.D. 1996. A review of remote sensing for the assessment of tropical coastal resources. *Coastal Management*, 21(1), 1–40.

Guimarães, M.H.M.E.; Cunha, A.H.; Nzinga, R.L., and Marques, J.F., 2011. The distribution of sea grass (*Zostera noltii*) in the Ria Formosa lagoon system and the implications of clam farming on its conservation. *Journal for Nature Conservation*, doi: 10.1016/j.jnc.2011.07.005.

Harwell, M.C., and Havens, K.E., 2003. Experimental studies on the recovery potential of submerged aquatic vegetation after flooding and desiccation in a large subtropical lake. *Aquatic Botany*, 77(2), 135–151.

Heenkenda, M.; Joyce, K.; Maier, S., and Bartolo, R., 2014. Mangrove species identification: comparing WorldView-2 with aerial photographs. *Remote Sensing*, 6(7), 6064–6088.

Herrera-Silveira, J.A., and Morales-Ojeda, S.M., 2009. Evaluation of the health status of a coastal ecosystem in southeast Mexico: Assessment of water quality, phytoplankton and submerged aquatic vegetation. *Marine Pollution Bulletin*, 59(1–3): 72-86.

Ibrahim, N.A.; Mustapha, M.A.; Lihan, T., and Mazlan, A.G., 2015. Mapping mangrove changes in the Matang mangrove forest using multi temporal satellite imageries. *Ocean & Coastal Management*, 114, 64–76.

Kendrick, G.A., and Walker, D.I., 1994. Role of recruitment in structuring beds of *Sargassum* spp. (Phaeophyta) at Rottnest Island, Western Australia. *Journal of Phycology*, 30(2), 200–208.

Kumar, P.; Gupta, D.K.; Mishra, V.N., and Prasad, R., 2015. Comparison of support vector machine, artificial neural network, and spectral angle mapper algorithms for crop classification using LISS IV data. *International Journal of Remote Sensing*, 36(6), 1604–1617.

Reshitnyk, L.; Costa, M.; Robinson, C.; and Dearden, P., 2014. Evaluation of WorldView-2 and acoustic remote sensing for mapping benthic habitats in temperate coastal Pacific waters. *Remote Sensing of Environment*, 153, 7–23.

Tin, H.C.; Michael, J.O., and Ravi, F., 2015. Remote-sensed mapping of *Sargassum* spp. distribution around Rottnest Island, Western Australia using high spatial resolution WorldView-2 satellite data. *Journal of Coastal Research*, doi:10.2112/jcoastres-d-15-00077.1.

Updike, T, and Comp, C., 2010. Radiometric use of WorldView-2 imagery. *In*: DigitalGlobe (ed.), Vol. 1.0, pp. 17. Longmont, USA: DigitalGlobe corporate.

Vahtmäe, E., and Kutser, T., 2007. Mapping bottom type and water depth in shallow coastal waters with satellite remote sensing. *Journal of Coastal Research*, SI 50 (Proceedings of the 9th International Coastal Symposium), 185–189. Gold Coast, Australia.

Yuan, L., and Zhang, L.-Q., 2008. Mapping large-scale distribution of submerged aquatic vegetation coverage using remote sensing. *Ecological Informatics*, 3(3), 245–251.

Journal of Coastal Research	SI	75	1292 - 1296	Coconut Creek, Florida	2016

Integrating Seafloor Habitat Mapping and Fish Assemblage Patterns Improves Spatial Management Planning in a Marine Park

Hamish A. Malcolm[1], Alan Jordan[2], Arthur L. Schultz[3], Stephen D.A. Smith[3], Tim Ingleton[4], Edwina Foulsham[4], Michelle Linklater[4], Peter Davies[4], Renata Ferrari[5], Nicole Hill[6], Vanessa Lucieer[6]

[1] Marine Ecosystems, NSW Department of Industry, 32 Marina Drive Coffs Harbour NSW 2450, Australia.
[2] Marine Ecosystems, NSW Department of Industry, Locked Bag 1, Nelson Bay, NSW 2315, Australia.
[3] Southern Cross University, National Marine Science Centre, Charlesworth Bay, Coffs Harbour, NSW 2450, Australia.
[4] NSW Office of Environment and Heritage, 59 Goulburn St, Sydney, NSW 2000, Australia.
[5] University of Sydney, Edgeworth David Bld., Science Road, NSW 2006, Australia.
[6] Institute for Marine and Antarctic Studies, University of Tasmania, Private Bag 129, Hobart, TAS 7001, Australia

www.cerf-jcr.org

www.JCRonline.org

ABSTRACT

Malcolm, H.A., Jordan, A., Schultz, A.L., Smith, S.D.A., Ingleton, T., Foulsham, E., Linklater, M., Davies, P., Ferrari, R., Hill, N., and Lucieer, V., 2016. Integrating seafloor habitat mapping and fish assemblage patterns improves spatial management planning in a marine park. *In:* Vila-Concejo, A.; Bruce, E.; Kennedy, D.M., and McCarroll, R.J. (eds.), *Proceedings of the 14th International Coastal Symposium* (Sydney, Australia). *Journal of Coastal Research*, Special Issue, No. 75, pp. 1292 - 1296. Coconut Creek (Florida), ISSN 0749-0208.

Marine Protected Areas (MPAs) are important spatial mechanisms for managing human activities, if effectively planned. The Solitary Islands Marine Park (SIMP), covering 720 km^2 of coastal waters in New South Wales, Australia, includes reef and unconsolidated habitats up to 17 km from shore and 75 m depth. When established in 1991, there was limited knowledge of biotic patterns, seafloor habitats and habitat-biotic relationships in the multiple-use SIMP, which constrained effective conservation planning. Subsequent mapping of sub-tidal habitats from aerial photography and single-beam acoustics improved habitat representation following rezoning in 2002 using Comprehensive, Adequate, Representative (CAR) principles and assisted site selection for diver surveys of fishes, a key surrogate taxon. In 2006, a swath acoustic mapping program commenced, which mapped ~35% of the MPA. This has produced high-resolution data on seafloor habitats, including depths >50 m. Bathymetry and backscatter layers have facilitated targeted deployment of Baited Remote Underwater Video (BRUV) to test hypotheses about associations between fishes and physical habitat characteristics. Strong and persistent patterns in fish assemblage composition in relation to particular habitat characteristics provided the basis for a Habitat Classification Scheme (HCS) to be refined with the following categories: substratum (consolidated, unconsolidated), cross-shelf position (inshore, mid, offshore) and depth (shallow, intermediate, deep). Further refinement of unconsolidated substratum into gravel and sand habitats, which were mapped using backscatter layers, improves this classification. The HCS, which integrates habitat and biotic patterns, greatly increases the potential for effective spatial management planning in the SIMP when used with spatial planning tools (e.g. Marxan).

ADDITIONAL INDEX WORDS: *MPA; Solitary Islands Marine Park; biodiversity; Marxan.*

INTRODUCTION

Marine Protected Areas (MPAs) are important spatial mechanisms for conservation and resource management providing they are effectively planned (Stewart *et al.* 2003). A key principle often underpinning spatial planning within an MPA is efficient representation of biodiversity within 'no take' sanctuaries (Friedlander *et al.* 2003; Stevens and Connolly 2005; Gladstone 2007). Planning that aspires to fulfil this principle requires spatial knowledge of biota, or suitable surrogates, at scales relevant to an MPA (Williams and Bax 2001).

In particular, fishes are an important biotic group in a marine park due to their ecological, social, and economic value (Gell and Roberts 2003; Shears and Babcock 2003). However, knowledge of their occurrence and abundance is often spatially constrained at the scale of a planning area (Curley *et al.* 2002; Gladstone 2007). A surrogacy approach can lessen spatial bias associated with this constraint (Ferrier 2002; Smith 2005).

Biotic patterns have been shown to relate to abiotic variables, such as seafloor complexity, at a range of scales (Curley *et al.* 2002; Gratwicke and Speight 2005; Moore *et al.* 2011). Where strong relationships occur, abiotic variables can be applied as surrogates for biodiversity, especially where biotic data is scarce (Ferrier 2002). Advances in acoustic technologies permit high resolution data to be acquired over broad areas of the seafloor more easily than biological data, including fishes (Rees *et al.* 2013). Integrating fish assemblage patterns and seafloor habitat mapping, as a biodiversity surrogate, can improve spatial management planning in a marine park for fishes (Williams and Bax 2001; Ferrier 2002) as well as fortuitously represent other groups with similar patterns (Bridge *et al*. 2015).

When established in 1991, there was limited knowledge of biotic patterns, seafloor habitats and habitat-biotic relationships in the Solitary Islands Marine Park (SIMP). This study is a synthesis of various fish and habitat studies undertaken within the SIMP since then. The objective of this study is to demonstrate how improved habitat mapping and knowledge of fish assemblage patterns, and their integration, has enhanced the capacity for effective spatial management planning in this MPA.

DOI: 10.2112/SI75-259. 1 received 15 October 2015; accepted in revision 15 January 2016.
*Corresponding author: hamish.malcolm@dpi.nsw.gov.au
©Coastal Education and Research Foundation, Inc. 2016

Background

The subtropical SIMP is located in a tropical-temperate transition in New South Wales (NSW) on the east coast of Australia and includes rocky reef and unconsolidated habitats extending up to 17 km from the mainland coast and to a maximum depth of 75 m. A prominent oceanographic feature in the SIMP is the East Australian Current (EAC), a western boundary current which predominantly jets through this region. The existing zoning plan for the SIMP (developed in 2002) based on Comprehensive, Adequate, Representative (CAR) principles, differs strongly from the initial plan developed in 1991 when the SIMP was established (Figure 1). During establishment, general naval bathymetric charts and sounding data were a proxy for habitat maps (e.g. Figure 2A) and biotic information and some of the human pressures driving establishment of this MPA were focused on shallow rocky reefs around islands of the Solitary Islands Group (Pollard 1981).

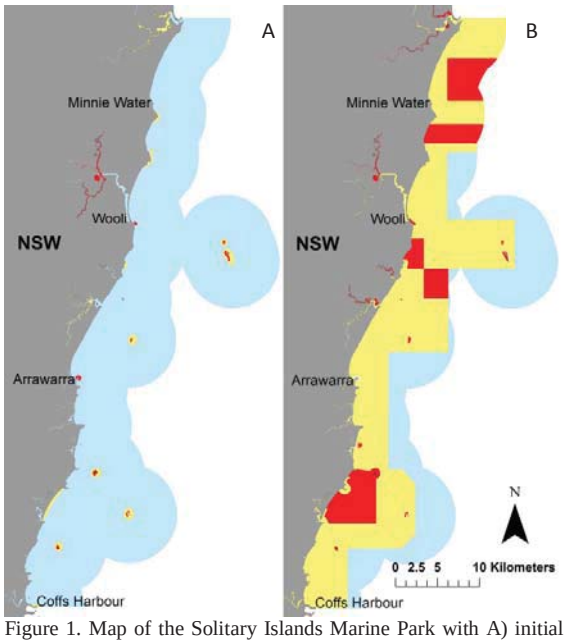

Figure 1. Map of the Solitary Islands Marine Park with A) initial 1991 zoning plan and B) 2002 zoning plan. Blue (mid shade) = General Use Zone where fishing can occur; Yellow (light shade) = Refuge Zone (in 1991). Yellow (light shade) = Habitat Protection Zone (in 2002) where trawling is prohibited; Red (dark shade) = Sanctuary Zone where 'no fishing' is permitted.

METHODS

To improve habitat mapping in the decade following establishment of the SIMP in 1991, a combination of aerial photography (near shore reef habitats to ~15 m depth) and single-beam each-sounder (cross-shelf transects) were used (Mau *et al.* 1998; NSWMPA 2000). This was combined with bathymetric chart data to interpret and map reef habitats in a Global Information System (GIS) using ArcMap software. The single-beam echo-sounder survey involved 22 cross-shelf transects running from shore to the seaward extent of the SIMP and spread-out along the length of the SIMP (approximately 80 km). The seafloor was categorised as reef or non-reef based on the strength of the sounder return signal and ground-truthing at selected sites was conducted using a downward facing camera (Mau *et al.* 1998). These maps, together with coarse bathymetry information and benthic biotic data, were used to develop a preliminary Habitat Classification System (HCS). The map of the preliminary HCS and the spatial area within habitat categories, informed the rezoning of the SIMP in 2002. After 2002, these maps (e.g. Figure 2B) were also used to facilitate site selection for broad-scale diver surveys of fishes, which are a key taxon for shallow (<25 m) reef communities.

To markedly improve mapping since 2005, high-resolution maps of seabed habitats in the SIMP have been generated with swath acoustic data (Figure 2C). These data (depth and sidescan backscatter data gridded at 2 to 5 m resolution) were collected with a GeoSwath interferometric sidescan sonar and details on acoustic parameters, data collection, and post-processing are reported in Jordan *et al.* (2010). This swath acoustic mapping covers ~35% of the SIMP at the time of this synthesis. Polygon shapefiles of reef were produced for all areas surveyed and compared and aligned to the previous habitat map for the SIMP. In areas of overlap, boundaries mapped from swath acoustic data were used preferentially. To facilitate systematic planning at the park-wide scale, a habitat layer covering the SIMP, was created using a combination of these data.

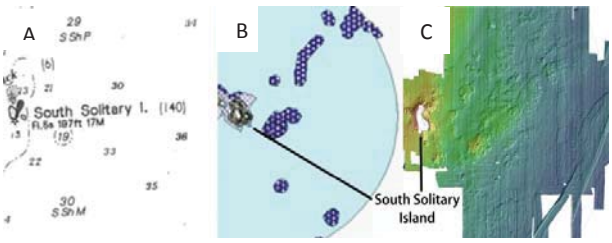

Figure 2. Evolution of available habitat maps from A) 1991, B) 2002 to C) 2011 showing the area around South Solitary Island as an example. A) numbers represent soundings (fathoms); B) dark areas represent reef; C) color ramp showing bathymetry overlaid on backscatter.

To examine potential cross-shelf fish assemblage patterns, 68 shallow reef sites (<25 m depth) were surveyed using a 30-minute roving diver count. These covered, as broadly as possible, the geographic range of shallow reefs in the SIMP, based on the preliminary HCS map. During counts, the relative abundance of every fish species observed was recorded using a $\log_5$ estimate (Malcolm *et al.* 2010a).

To examine potential fish assemblage patterns with depth, 56 reef sites (ranging from 15 to 75 m depth range) were also surveyed using Baited Remote Underwater Video (BRUV). These sites were pre-selected in GIS, using geoswath mapping layers, to cover a spatially-broad depth-range of reef in the SIMP (Malcolm *et al.* 2011). At each site, three replicate BRUVs were deployed in similar depths, at least 200 m apart for independence, for a period of 30 min (Harasti et al. 2015). A standard BRUV system was used as comprehensively described elsewhere (Cappo *et al.* 2004). From each deployment, the MaxN for each species was recorded (Malcolm *et al.* 2011).

MaxN is the maximum number of individuals of each species observed in a video frame at any one point of time during the 30-min sample.

To examine fish assemblage patterns on unconsolidated sediments, the most extensive seafloor habitat in the SIMP (~80%), a range of BRUV surveys were undertaken. These examined patterns in relation to distance from reef, broad depth categories, and 'type' of substrata based on back-scatter intensity (Schultz *et al.* 2012; Schultz *et al.* 2014; Schultz *et al.* 2015). Grab samples were used to ground-truth sediment type.

To integrate fish patterns and habitat data, combinations of multivariate statistical approaches in PRIMER were used (Clarke and Warwick 2001; Anderson *et al.* 2008). Visual patterns (Hierarchical Clustering, non-metric Multi-Dimensional Scaling (nMDS)), multivariate correlations (BIOENV, DistLM), and multivariate comparisons (PERMANOVA) were used to compare and test fish assemblage patterns with various predictor variables that could potentially influence those patterns (e.g. distance from shore, reef type, dominant benthos, latitude, depth range, depth, sediment type, etc.). Combinations of these analyses were used to determine which factors best explained biotic patterns from the different fish studies. These were then used to refine the HCS.

To systematically identify the most-suitable areas to represent HCS categories in sanctuary zone, the algorithm software Marxan was used (Ball and Possingham, 2000). The SIMP was subdivided into a grid of 3712 planning units, each 500 m x 500 m square. A range of planning scenarios were considered based on percentage of area in sanctuary (10%, 20%, 30%) and whether the existing (2002) zoning scheme was forcibly included or not in the Marxan solutions (Malcolm *et al.* 2012). The selection algorithm (simulated adaptive annealing with iterative improvement) used a set of 1000 runs (selections of sets of areas), each with 1,000,000 iterations. The selection frequency was the number of times (out of 1000) each planning unit was selected, with the higher the frequency the more irreplaceable that planning unit is in achieving a solution for that particular scenario.

RESULTS

A preliminary HCS was developed in 2000 (NSWMPA 2000) and used (non-systematically) to help develop a draft (2001) and a final zoning plan in 2002 (NSWMPA 2001, 2002). This preliminary HCS defined six habitats, consisting of unconsolidated substrata and five reef categories (inshore, mid-shelf shallow, mid-shelf deeper, offshore, submerged pinnacle) loosely based on depth and distance from mainland coast. Categories combined a maximum depth-range with a minimum depth to which those reefs rose. This made it impossible to separate categories and map them in the absence of accurate bathymetric information. Some areas of reef were therefore mapped as 'mixed' (NSWMPA 2000). In 2002, protected 'no take' sanctuary zone area increased from 0.02% to ~12%. While representation of sanctuary zones considerably increased for the mapped inshore and mid-shelf reef categories, no deep reefs (nor deeper unconsolidated habitats) were included.

Fish surveys since 2002 have found distinct spatial patterns in the SIMP. The fish assemblages found on reef and unconsolidated substrata strongly separate from each other.

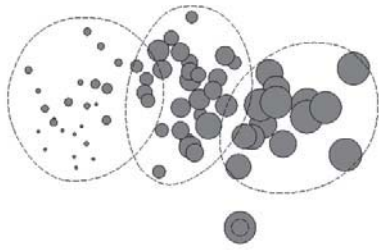

Figure 3. nMDS plot of fish assemblages. Example showing patterns cross-shelf – larger bubble = greater distance from mainland coast, n = 68 roving diver sites, stress = 0.15. Dashed lines = dissimilarity level (50%) which showed multivariate structure from SIMPROF analysis.

There are very strong cross-shelf (Figure 3) and depth patterns in reef fish assemblages. There are also depth and grain-size (gravel, sand) patterns in fishes of unconsolidated substrata.

These strong biotic patterns, in combination with knowledge of other biotic patterns in this region, have enabled a more clearly-defined HCS to be developed. This differs from the previous classification system by using a systematic hierarchical approach that integrates biotic pattern (Table 1).

Table 1. *Habitat Classification System Developed for the SIMP*

Substrata	Depth	Distance/Sed	% in sanctuary
Reef	Shallow	Inshore	13
		Mid	21
		Offshore	30
	Intermediate	Inshore	5
		Mid	28
		Offshore	1
	Deep	Offshore	0
Unconsolidated	Shallow	Sand/Gravel	19
	Intermediate	Sand/Gravel	11
	Deep	Sand/Gravel	0

Distance/Sed = distance from mainland coast or sediment grain-size (sand, gravel). Shallow < 25 m; Intermediate 25 - 50 m; Deep > 50 m; Inshore < 1.5 km from the mainland coast; Mid = 1.5 to 6 km from the mainland coast; Offshore > 6 km from the mainland coast. There is no deep habitat < 6 km from the coast. Mapping to differentiate sand and gravel habitats, based on backscatter layers is still required at the SIMP-wide scale.

Some categories lack representation in sanctuary zones in relation to the existing percentage overall (~12%) in the SIMP (Table 1). Marxan analyses of the HCS habitat categories (but without differentiation between gravel and sand habitats), systematically indicated where placement of sanctuaries would most-effectively achieve their representation. This included identification of the most irreplaceable areas (*i.e.* those areas selected most frequently in the set of 1000 runs). In particular, the two areas where the SIMP is widest cross-shelf were a focus in the selection frequency maps that Marxan analyses generated (Malcolm et al 2012).

DISCUSSION

Our understanding of the distribution of seabed habitats has improved substantially in the 25-year history of the Solitary

Islands Marine Park (SIMP) as a result of hydrographic mapping and complementary biotic surveys to determine patterns at the park-wide scale. This has enabled an evolving and improving integration of habitat and biotic patterns for use in spatial management planning. Sanctuaries in the initial zoning plan in 1991 were focused on island-associated shallow reef, and covered ~0.02% of the SIMP. The rezoning in 2002 incorporated 'biodiversity representation' as a planning principle (ANZECC TFMPA 1998) and this benefited from the improved resolution of maps and the development of a preliminary HCS. The preliminary HCS (developed 2000), with categories based on echosounder transects and drop camera surveys (Mau *et al.* 1998; NSWMPA 2000), represented the initial steps in integrating biotic pattern and habitat. However, it did not effectively represent biological patterns, at least not for reef fish, as it was strongly constrained by the spatial extent of biotic data and mapping available at that time.

Geoswath mapping since 2005 has provided significant, high-resolution broad-scale coverage (~35%) of the seafloor at the SIMP-wide scale. This has greatly improved the capacity for integrating biota and habitat by enabling both mapping of habitats and spatial analysis of various geomorphic metrics. This mapping has also facilitated the aquisition of biotic data from deeper reefs (Jordan *et al.* 2010).

There are very strong patterns in reef fish assemblages and biogeography in this region both cross-shelf and with depth (Malcolm *et al.* 2010b; Malcolm *et al.* 2011). Correspondingly, distance from the mainland coast and depth also influences the patterns of various invertebrate taxa and macro-algae in the SIMP (Harriott *et al.* 1994; Malcolm *et al.* 2010a; Harrison and Smith 2012). An important driver in these patterns is the tropical, southward-flowing East Australian Current (EAC), which has a stronger influence offshore (Malcolm *et al.* 2010c). The EAC delivers tropical larvae, drives cross-shelf and depth patterns in phytoplankton, and creates a cross-shelf sea-temperature differential (Armbrecht *et al.* 2015). The fish assemblages of unconsolidated substrata strongly separate from fish assemblages on reef, and show depth-related patterns (Schultz *et al.* 2014). They are also influenced by the type of sediment present (Schultz *et al.* 2015). It is possible that gravel provide a more consolidated and rugose seafloor compared to sands at the cm scale, and are thus more suitable substrata for the attachment of sessile benthos.

These strong patterns in fish assemblage composition in relation to particular habitat characteristics provided the basis for a refined HCS (Table 1). All the refined HCS reef categories have some unique biodiversity values in terms of representing assemblages of species, individual species, abundance of species, and biogeographic influences (Malcolm *et al.* 2010a; Malcolm *et al.* 2011; Schultz *et al.* 2014; Schultz *et al.* 2015).

Biodiversity conservation and maintenance of ecosystem services are major objectives for MPAs globally, with effective placement of 'no take' sanctuaries an important mechanism for helping to achieve these (Worm *et al.* 2006; Lester *et al.* 2009). Offshore reef categories are poorly represented in SIMP sanctuaries in regard to current global best practice within MPAs (Gaines *et al.* 2010). Marxan analyses have systematically demonstrated where improved spatial representation in these categories could best be achieved. Incorporating further mapping, predictive modelling, and the most recent HCS in Marxan analyses will continue to improve spatial management planning in this MPA.

CONCLUSIONS

The Habitat Classification System, by integrating habitat and biotic pattern, has increased the potential for effective spatial management planning in the SIMP, especially when used with systematic spatial planning tools such as Marxan. The integration of habitat and biotic pattern in multiple-use MPAs elsewhere can like-wise improve the capacity for effective spatial planning.

ACKNOWLEDGMENTS

Thanks everyone that has helped with surveys over the years.

LITERATURE CITED

Anderson, M., Gorley, R., and Clarke, K.,2008. Permanova+ for PRIMER: Guide to software and statistical techniques.

ANZECC TFMPA, 1998. Guidelines for Establishing the National Representative System of Marine Protected Areas. *Environment Australia*, Canberra.

Armbrecht, L. H., Schaeffer, A., Roughan, M., and Armand, L. K., 2015. Interactions between seasonality and oceanic forcing drive the phytoplankton variability in the tropical-temperate transition zone (~30°S) of Eastern Australia. *Journal of Marine Systems*, 144, 92-06.

Ball, I.R., Possingham, H.P., 2000. Marxan (V1.8.2): Marine reserve design using spatially explicit annealing, a manual. University of Queensland.

Bridge, T. C. L., Grech, A. M., and Pressey, R. L., 2015. Factors influencing incidental representation of previously unknown conservation features in marine protected areas. *Conservation Biology*, Early View Online, 00, 1-12.

Cappo, M., Speare, P., and De'ath, G., 2004. Comparison of baited remote underwater video stations (BRUVS) and prawn (shrimp) trawls for assessments of fish biodiversity in inter-reefal areas of the Great Barrier Reef Marine Park. *J. Exp. Mar. Biol. Ecol.*, 302, 123-152.

Clarke, K. R., and Warwick, R. M., 2001. Change in marine communities: an approach to statistical analysis and interpretation. PRIMER-E, Plymouth.

Curley, B. G., Kingsford, M. J., and Gillanders, B. M., 2002. Spatial and habitat-related patterns of temperate reef fish assemblages: implications for the design of Marine Protected Areas. *Mar.Freshwater Res.*, 53, 1197-1210.

Ferrier, S., 2002. Mapping spatial pattern in biodiversity for regional conservation planning: where to from here? *Systematic Biology*, 51, 331-363.

Friedlander, A., Sladek Nowlis, J., Sanchez, J. A., Appeldoorn, R., Usseglio, P., McCormick, C., Bejarano, S., and Mitchell-Chui, A., 2003. Designing effective marine protected areas in Seaflower Biosphere Reserve, Colombia, based on biological and sociological information. *Conservation Biology*, 17, 1769-1784.

Gaines, S.D., Lester, S.E., Grorud-Colvert, K., Costello, C., and Pollnac, R., 2010. Evolving science of marine reserves: new developments and emerging research frontiers. *Proceedings of the National Academy of Science*, 107, 18251–18255.

Gell, F. R., and Roberts, C. M., 2003. Benefits beyond boundaries: the fishery effects of marine reserves. *Trends in Ecology and Evolution*, 18, 448-455.

Gladstone, W., 2007. Requirements for marine protected areas to conserve the biodiversity of rocky reef fishes. *Aquatic Conservation: Marine and Freshwater Ecosystems*, 17, 71 - 87.

Gratwicke, B., and Speight, M. R., 2005. The relationship between fish species richness, abundance, and habitat complexity in a range of shallow tropical marine habitats. *Journal of Fish Biology*, 66, 650-667.

Harasti, D., Malcolm, H.A., Gallen, C., Coleman, M.A., Jordan, A., and Knott, N.A., 2015. Appropriate set times to represent patterns of rocky reef fishes using baited video *Journal of Experimental Marine Biology and Ecology* 463: 173-180

Harriott, V. J., Smith, S. D. A., and Harrison, P. L., 1994. Patterns of coral community structure of subtropical reefs in the Solitary Islands Marine Reserve, Eastern Australia. *Marine Ecology Progress Series*, 109, 67-76.

Harrison, M. A., and Smith, S. D. A., 2012. Cross-shelf variation in the structure of molluscan assemblages on shallow, rocky reefs, in subtropical eastern Australia. *Marine Biodiversity*, 42, 203-216.

Jordan, A., Davies, P., Ingleton, T., Mesley, E., Neilson, J., and Pritchard, T. R., 2010. Seabed habitat mapping of continental shelf waters of NSW. NSW Department of Environment Climate Change and Water Occasional Paper Series 209.

Lester, S. E., Halpern, B. S., Grorud-Colvert, K., Lubchenco, J., Ruttenberg, B. I., Gaines, S. D., Airamé, S., and Warner, R. R., 2009. Biological effects within no-take marine reserves:a global synthesis. *Marine Ecology Progress Series*, 384, 33-46.

Malcolm, H. A., Smith, S. D. A., and Jordan, A., 2010a. Using patterns of reef fish assemblages to refine a Habitat Classification System for marine parks in NSW, Australia. *Aquatic Conservation:Marine and Freshwater Ecosystems*, 20, 83-92.

Malcolm, H. A., Jordan, A., and Smith, S. D. A., 2010b. Biogeographical and cross-shelf patterns of reef fish assemblages in a transition zone. *Marine Biodiversity*, 40, 181-193.

Malcolm, H. A., Davies, P., Jordan, A., and Smith, S. D. A., 2010c. Variation in sea temperature and the East Australian Current in the Solitary Islands region between 2001 to 2008. *Deep Sea Research II: The East Australian Current - Its Eddies and Impacts*, 58, 616-627.

Malcolm, H. A., Jordan, A., and Smith, S. D. A., 2011. Testing a depth-based Habitat Classification System against the pattern of reef fish assemblages (15 - 75m) in a subtropical marine park. *Aquatic Conservation: Marine and Freshwater Ecosystems*, 21, 173-185.

Malcolm, H. A., Foulsham, E., Pressey, R. L., Jordan, A., Davies, P. L., Ingleton, T., Johnstone, N., Hessey, S., and Smith, S. D. A., 2012. Selecting zones in a marine park: Early systematic planning improves cost-efficiency; combining habitat and biotic data improves effectiveness. *Ocean and Coastal Management*, 59, 1-12.

Mau, R., Byrnes, T., Wilson, J., and Zann, L., 1998. The distribution of selected continental shelf habitats and biotic communities in the Solitary Islands Marine Park. Report to the NSW Marine Parks Authority.

Moore, C. H., Van Niel, K., and Harvey, E. S., 2011. The effect of landscape composition and configuration on the spatial distribution of temperate demersal fish. *Ecography*, 34, 425-435.

NSW MPA, 2000. *Solitary Islands Marine Park, Planning Issues and Option Paper*. NSW Marine Parks Authority Report.

NSW MPA, 2001. *Overview of the proposed changes to the Solitary Islands Marine Park*. NSW Marine Parks Authority Report.

NSW MPA, 2002. *Overview of the zoning plan: Solitary Islands Marine Park*. NSW Marine Parks Authority Report.

Pollard, D. A., 1981. *Solitary Islands Marine Reserve Proposal*. New South Wales Fisheries Proposal.

Rees, M. J., Jordan, A., Price, O. F., Coleman, M. A., and Davis, A. R., 2013. Abiotic surrogates for temperate rocky reef biodiversity: implications for marine protected areas. *Diversity and Distributions*, 20, 284-296.

Schultz, A. L., Malcolm, H. A., Bucher, D. J., and Smith, S. D. A., 2012. Effects of reef proximity on the structure of fish assemblages of unconsolidated substrata. *PLoS ONE*, 7(11), e49437. doi:10.1371/ journal.pone. 0049437.

Schultz, A. L., Malcolm, H. A., Bucher, D. J., Linklater, M., and Smith, S. D. A., 2014. Depth and medium-scale spatial processes influence fish assemblage structure of unconsolidated habitats in a subtropical marine park. *PLoS ONE*, 9(5): e96798. doi:10.1371/ journal.pone. 0096798.

Schultz, A. L., Malcolm, H. A., Linklater, M., Jordan, A. R., Ingleton, T., and Smith, S. D. A., 2015. Sediment variability affects fish community structure in unconsolidated habitats of a subtropical marine park. *Marine Ecology Progress Series*, 532, 213-226.

Shears, N. T., and Babcock, R. C., 2003. Continuing trophic cascade effects after 25 years of no-take protection. *Marine Ecology Progress Series*, 246, 1-16.

Smith, S. D. A., 2005. Rapid assessment of invertebrate biodiversity on rocky shores: where there's a whelk there's a way. *Biodiversity and Conservation*, 14, 3565-3576.

Stevens, T., and Connolly, R. M., 2005. Local-scale mapping of benthic habitats to assess representation in a marine protected area. *Marine and Freshwater Research*, 56, 111-123.

Stewart, R. R., Noyce, T., and Possingham, H. P., 2003. Opportunity cost of ad hoc marine reserve design decisions: an example from South Australia. *Marine Ecology Progress Series*, 253, 25-38.

Williams, A., and Bax, N. J., 2001. Delineating fish-habitat associations for spatially based management: an example from the south-eastern Australian continental shelf. *Marine and Freshwater Research*, 52, 513-536.

Worm, B., Barbier, E. B., Beaumont, N., Duffy, J. E., Folke, C., Halpern, B. S., Jackson, J. B. C., Lotze, H. K., Micheli, F., Palumbi, S. R., Sala, E., Selkoe, K. A., Stachowicz, J. J., and Watson, R., 2006. Impacts of biodiversity loss on ocean ecosystem services. *Science*, 314, 787-790.

Journal of Coastal Research	SI	75	1297 - 1301	Coconut Creek, Florida	2016

Spatial Variation in Carbon Storage: A Case Study for Currambene Creek, NSW, Australia

Christopher J. Owers[†*], Kerrylee Rogers[†], Debashish Mazumder[‡], and Colin D. Woodroffe[†]

[†]GeoQuEST research centre
School of Earth and Environmental Science
University of Wollongong
Wollongong, Australia

[‡]Australian Nuclear Science and
Technology Organisation (ANSTO)
Sydney, Australia

www.cerf-jcr.org

www.JCRonline.org

ABSTRACT

Owers, C.J.; Rogers, K.; Mazumder, D., and Woodroffe, C.D., 2016. Spatial Variation in Carbon Storage: A Case Study for Currambene Creek, NSW, Australia. *In:* Vila-Concejo, A.; Bruce, E.; Kennedy, D.M., and McCarroll, R.J. (eds.), *Proceedings of the 14th International Coastal Symposium* (Sydney, Australia). *Journal of Coastal Research*, Special Issue, No. 75, pp. 1297 - 1301. Coconut Creek (Florida), ISSN 0749-0208.

Quantifying carbon storage in coastal wetland environments is important for identifying areas of high carbon sequestration value that could be targeted for conservation. This study combines remote sensing and sediment analysis to identify spatial variation in soil carbon storage for Currambene Creek, New South Wales, Australia to establish whether vegetation structure influences soil carbon storage in the upper 30 cm. Wetland vegetation was delineated to capture structural complexity within vegetation communities using Light detection and ranging (Lidar) point cloud data and aerial imagery with an object-based image analysis approach. Sediment cores were collected and analysed for soil carbon content to quantify below-ground carbon storage across the site. The total soil carbon storage in the upper 30 cm for the wetland (59.6 ha) was estimated to be 3933 ± 444 Mg C. Tall mangrove were found to have the highest total carbon storage (1420 ± 198 Mg C), however are particularly sensitive to changes in sea-level as they are positioned lowest in the intertidal frame. Conservation efforts targeted at protecting areas of high carbon sequestration, such as the tall mangrove, will lead to a greater contribution to carbon mitigation efforts.

ADDITIONAL INDEX WORDS: *Coastal wetlands, mangrove, saltmarsh, object-based image analysis, loss on ignition, vegetation structure.*

INTRODUCTION

Saline coastal wetlands, particularly mangrove and saltmarsh, are globally recognised as valuable sinks of organic carbon (Barbier *et al*., 2011; Chmura *et al*., 2003). These environments are important for mitigating climate change by sequestering atmospheric carbon in plant biomass through photosynthesis. Organic material from biomass is subsequently sequestered within sediments for long periods until broken down by microbes (Duarte *et al*., 2005). Current knowledge of the spatial and temporal variation of carbon storage in these systems, both carbon storage in plant biomass and carbon storage in sediments, is limited (Gilman *et al*., 2008; Mcleod *et al*., 2011). Capturing spatial variation in carbon storage is important for evaluating carbon stocks within wetland ecosystems, and targeting areas for conservation and restoration that will more efficiently sequester carbon. This is particularly significant given projected changes in sea level, as the influence of sea-level rise on processes that drive carbon sequestration, such as sedimentation, soil biogeochemistry, and primary productivity, will vary spatially and temporally in wetlands (see review by Mcleod *et al*., 2011).

Current soil carbon estimates for wetlands largely focus on major vegetation communities, such as mangrove and saltmarsh (Chmura *et al*., 2003; Saintilan *et al*., 2013). Soil carbon storage may vary within these communities due to variation in structural forms of vegetation. These structural variations include species composition, height and density of vegetation. Established mangroves are often taller and have larger canopies than younger or stunted mangroves. This is likely to influence the depth of root zones, with taller mangroves having extensive and more developed roots than shorter, immature mangroves (Ong *et al*., 2004). Saltmarsh vegetation structure varies with species composition. *Juncus kraussii* and *Sporobolus virginicus* differ in height and density which is likely to influence plant biomass and soil carbon storage. Identifying variation in vegetation is useful for managing ecosystem services (Ewel *et al*., 1998). Capturing variation in vegetation structure may be important to improve estimates of soil carbon storage within a wetland.

This study aims to establish whether vegetation structure influences soil carbon storage in the upper 30 cm and whether this variation in vegetation is an important component when estimating total soil carbon storage within a wetland. This was achieved by combining remote sensing and carbon content analysis from sediment cores to provide an estimate of total below-ground soil carbon storage in the upper 30 cm of a wetland. Remote sensing was used to delineate wetland vegetation structure and capture vegetation complexity in greater detail than previous wetland vegetation mapping (Chafer, 1998; Oliver *et al*., 2012; Saintilan and Wilton, 2001). Sediment core extraction across the site in several vegetation forms will enable estimates of landscape scale carbon storage that are more accurate than approaches used previously (Howe *et al*., 2009; Rogers *et al*., 2013). In combination, this approach demonstrates the spatial variability of below-ground carbon storage. This is an important consideration when developing

DOI: 10.2112/SI75-260. 1 received 15 October 2015; accepted in revision 15 January 2016.
*Corresponding author: cjo766@uowmail.edu.au
©Coastal Education and Research Foundation. Inc. 2016

conservation and restoration priorities for coastal wetlands, particularly considering potential changes in vegetation composition due to sea-level rise.

Study area

Currambene Creek is a mature barrier estuary situated in Jervis Bay (35.0653ºS, 150.7347ºE) , New South Wales (Roy *et al*., 2001). The estuary supports temperate saline coastal wetlands comprising mangrove and saltmarsh. Mangroves are commonly positioned lower in the tidal frame than saltmarsh. Jervis Bay has a semi-diurnal tidal range of approximately 2 metres. Two species of mangrove are present in this region; predominantly *Avicennia marina* and also *Aegiceras corniculatum*. Commonly present saltmarsh species include *Sporobolus virginicus*, *Samolus repens*, *Juncus krausii* and *Sarcocornia quinqueflora* (Clarke, 1993).

METHODS

Wetland vegetation was delineated to structural forms using Lidar and aerial imagery coupled with an object-orientated image analysis (OBIA) approach (Owers *et al*., in review). These structural forms included: three classifications of mangroves based on height and diameter at breast height (DBH), tall mangrove (> 3 m height, > 15 cm DBH), shrub mangrove (1.3 – 3 m height, < 15 cm DBH), and dwarf mangrove (< 1.3 m height); saltmarsh species that were classified as rush (*Juncus krausii*), or herbs, grasses and sedges (*Sporobolus virginicus*, *Samolus repens*, *Sarcocornia quinqueflora*); mixed and sparse vegetation areas that comprised ecotone communities of mangrove and saltmarsh, where sparse vegetation had a sandy surface substrate; and *Casuarina glauca* woodlands that were positioned at higher elevations beyond tidal inundation. The OBIA methodology utilised the multiresolution segmentation algorithm to derive image objects from the remote sensing data that were then classified using the nearest neighbor algorithm. A hierarchical approach for segmentation and classification was used to delineate vegetation structural forms of mangrove and saltmarsh independently by initially delineating vegetation communities (see Owers *et al*., in review). The vegetation structural classification was validated using groundtruthed data. Spatial extents were extracted for each vegetation structure.

Sediment cores (twelve in total) were collected and analysed for soil carbon content and sediment characteristics. Core locations were selected to capture the spatial variability of vegetation structure, including position in the landscape and variation in environmental gradients such elevation and distance to shoreline (Figure 1c). Each core was analysed for soil carbon content and sediment characteristics to 30 cm depth and sub-sampled at depths of 0-2 cm, 2-4 cm, 5-6 cm, 10-15 cm, 15-16 cm, 20-21 cm, 25-26 cm, 30-31 cm. Particle size distributions were determined for all samples using a Malvern Mastersizer 2000. Wet samples were weighed and then dried at 60°C to a constant weight to estimate dry bulk density. Each sub-sample was then homogenised by grinding to a fine powder using a Retsch three-dimensional Vibrator Mill (Type-MM-2:Haan, Germany). Carbon content for all twelve cores was calculated using the Loss on Ignition (LOI) method in accordance with Ball (1964). Percent LOI was calculated to give an estimate of the percentage of organic matter present in the sample.

Commonly, percent organic matter is converted to percent carbon on the basis of relationships established for mangrove and saltmarsh elsewhere (Howard *et al*., 2014). These established relationships were assessed to determine if they were appropriate for use in this study. Of the twelve sediment cores, four (4) were selected to be analysed for percent carbon content using a dry combustion technique; more specifically using continuous flow isotope ratio mass spectrometer (CF-IRMS) at the Australian Nuclear Science and Technology Organisation (ANSTO) in accordance with Mazumder *et al*. (2010). These cores were selected to capture the dominant vegetation communities at Currambene Creek; mangrove (1 core), mixed ecotone (1 core), and saltmarsh (2 cores). The selected cores were 140 cm in length and analysed at 5 cm intervals. Established LOI to carbon conversion equations for mangrove (Kauffman and Donato, 2011) and saltmarsh (Craft *et al*., 1991) were compared against percent carbon in this study to assess their validity for use in this study. Analysis of variance (ANOVA) was used to establish whether carbon content estimated using these conversion equations differed from the quantitative assessments of carbon undertaken using dry combustion techniques. On the basis of this analysis (results presented later), the percent carbon results from the four sediment cores were used to develop unique LOI carbon conversion equations to reliably estimate carbon content using LOI at this study site. After testing for normal distribution, non-parametric generalised linear models were used to determine whether there were significant differences in the relationship between percent LOI and percent carbon for the different vegetation communities. On the basis of these results conversion equations were generated using linear regression analysis, with LOI as the fixed variable and carbon content as the dependent variable. Post hoc Tukeys HSD was performed to establish the appropriate equation to calculate carbon content for *Casuarina*.

After identifying the statistical distribution of our data, statistical analyses were also carried out to determine relationships between particle size, soil depth and carbon content, as well as vegetation structure and carbon content. Generalised linear models were selected for carbon bulk density as the distribution was log normal (log normal distribution, $p = 0.15$); ANOVA was used to establish relationships between carbon content as the data was found to be normally distributed ($p = 0.96$). All statistical tests completed in this study were carried out using a 0.05 level of significance.

Below-ground soil carbon content (C g cm^{-3}) was estimated by multiplying bulk density and percent carbon. Soil carbon content for each sediment core was estimated by fitting a linear model between each soil sub-sample and aggregating each centimetre interval. The area of each vegetation structure, delineated by remote sensing, was multiplied by the corresponding soil carbon content to determine the carbon storage of the system.

RESULTS

Vegetation was delineated to capture the structural morphology and complexity across Currambene Creek (Figure 1d). This map classification was validated to an accuracy of 95% (kappa coefficient of agreement = 0.932).

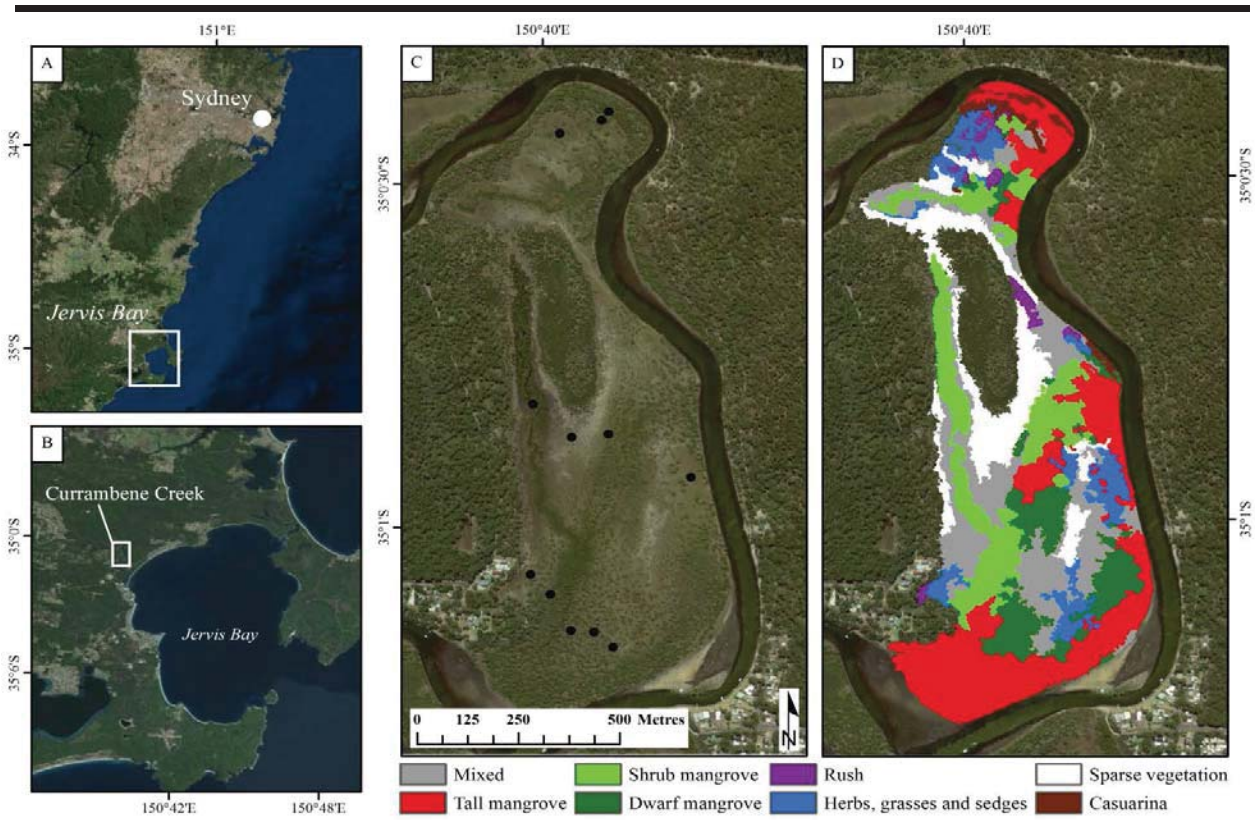

Figure 1. Location of (a) Jervis Bay and (b) Currambene Creek; (c) sediment core locations within the wetlands adjacent to Currambene Creek; and (d) vegetation structural classification. Data source: Imagery © ESRI Basemaps and Land and Property Information (LPI) NSW. Vegetation structural classification from Owers *et al*. (in review).

We found that carbon content estimated using established conversion equations was significantly different to quantitative estimates of carbon content for both mangrove ($p < 0.001$) and saltmarsh ($p < 0.001$). Furthermore, generalised linear models demonstrated that no significant relationship exists between percent carbon and vegetation community ($p = 0.44$), however the interaction between vegetation community and LOI was significant ($p = 0.0022$). Consequently, three separate equations for calculating carbon from LOI were generated for mangrove, saltmarsh and mixed vegetation communities (Figure 2). Post hoc Tukeys HSD indicated that *Casuarina* percent LOI was not significantly different to Tall mangrove ($p < 0.001$). Hence, the mangrove conversion equation was used to estimate carbon content for *Casuarina*.

Soil carbon content in the upper 30 cm varied on the basis of vegetation structure ($p = 0.0319$). Carbon storage was highest for *Casuarina* followed by tall mangrove > shrub mangrove > dwarf mangrove > rush saltmarsh > mixed > herbs, grasses and sedges > sparse vegetation (Table 1). However, total carbon storage within the wetland for each vegetation type was mediated by the spatial extent of each vegetation type; tall mangrove had the greatest area (16.1 ha) and constituted the largest carbon storage, while *Casuarina* had the second lowest storage, despite having the highest carbon content in the upper 30 cm. Similarly sparse vegetation had lower carbon content in the upper 30 cm than both saltmarsh forms; however the total carbon storage was similar to the combined carbon storage of all saltmarsh vegetation. Soil carbon increased with depth ($p < 0.001$) and was inversely related to mean particle size ($p < 0.001$). The total soil carbon storage in the upper 30 cm for the wetland was estimated to be 3933 ± 444 Mg C.

DISCUSSION

Variation in vegetation structure is an important component when estimating soil carbon storage within a wetland. In this study we found soil carbon content in tall mangrove to be higher than shrub mangrove, which is higher than dwarf mangrove (Table 1). This variation would not be captured if soil carbon estimates for mangrove were not delineated to capture structural variation. Similarly for saltmarsh and mixed vegetation, where variation exists between species composition and substrate, capturing wetland vegetation structure distinguishes vegetation complexity that was not demonstrated in previous research (Chafer, 1998; Oliver *et al*., 2012; Saintilan and Wilton 2001). Current estimates of below-ground carbon storage rarely

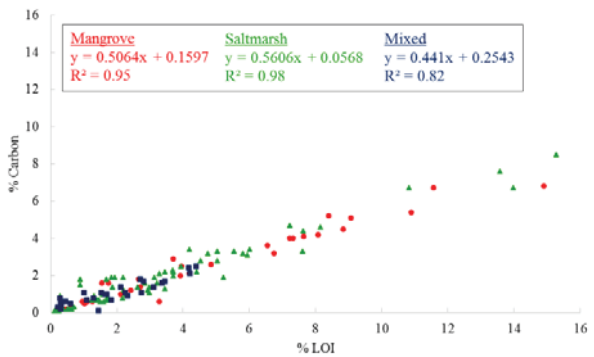

Figure 2. Relationship between percent carbon and percent LOI for mangrove (red, circle), saltmarsh (green, triangle) and mixed (blue, square) vegetation communities used to develop LOI conversion equations.

consider variation in structural forms of wetland vegetation. Sediment cores are often taken in vegetation communities; mangrove, saltmarsh, mixed, *Casuarina*, and results are extrapolated to estimate carbon storage at the landscape level using manually delineated vegetation areas from aerial photography (Howe *et al*., 2009; Rogers *et al*., 2013). Failing to capture variation in vegetation structure can result in erroneous estimates of carbon storage across the landscape. Aggregating the data presented in this study for vegetation communities yields a total soil carbon storage of 3845 ± 1114 Mg C in the upper 30 cm for Currambene Creek. When soil carbon content variation due to vegetation structure is captured, the total soil carbon storage in the upper 30 cm for Currambene Creek is 3933 ± 444 Mg C. For this study using vegetation communities to estimate total soil carbon storage in the upper 30 cm gives an underestimate with larger uncertainty. Further research is required to confirm if these differences may be even greater due to the limited depth of sediment core analysis presented in this study. A component of further research is to analyse sediment cores to 1.5 m depth, enabling a better estimate of total soil carbon storage in the system.

Services provided by coastal ecosystems are spatially and temporally variable (Barbier *et al*., 2011; Ewel *et al*., 1998). We found that carbon storage varies with vegetation structure within vegetation communities. Tall mangrove had the highest total carbon storage (1420 ± 198 Mg C) due to the combination of high soil carbon content and large spatial extent. *Casuarina* and rush saltmarsh where shown to be important carbon stores despite having the smallest spatial extents. Rush saltmarsh was shown to have the highest soil carbon content of the saltmarsh and mixed ecotone communities, however had the smallest total carbon storage in the upper 30 cm due to small spatial extent. Capturing variation in carbon storage services provided by these vegetation structures is an important tool for management as it highlights where different ecosystem services are concentrated. This is important for directing management towards improving specific services within an ecosystem, particularly efforts to improve climate change mitigation.

Exposure of ecosystem services to coastal processes is spatially complex. Capturing spatial variability in carbon storage services enables pressures of climate change to these services to be better distinguished. Sea-level rise, projected to increase between 0.18m and 0.59m by the end of this century (IPCC, 2013), poses significant concern for the vulnerability of current carbon storage and may limit future carbon sequestration. Tall mangrove are positioned lowest in the intertidal frame and are therefore particularly sensitive to erosion related to sea-level rise or other anthropogenic activities such as boating and wake-related erosion (Gilman *et al*., 2008; Mosisch and Arthington, 1998). Increased pressure to dredge the channel for navigation purposes may also have significant implications for the capacity of these systems to adapt. In contrast, wetland vegetation that occupies areas in the upper intertidal frame is sensitive to the effects of coastal squeeze; the inability of coastal vegetation to migrate landward with rising sea levels due to natural or artificial impediments (Doody, 2004). *Casuarina* and rush saltmarsh occupy areas in the upper intertidal frame, increasing their vulnerability to coastal squeeze and subsequent degradation. This has been observed at Currambene Creek as a considerable extent of rush saltmarsh has been degraded due to human interference.

Table 1. *Below-ground soil carbon content in the upper 30 cm for each vegetation structure.*

Vegetation structure	Soil carbon content (Mg C ha^{-1})	Area (ha)	Total soil carbon storage (Mg C)
Tall mangrove	88.5	16.1	1420 ± 198
Shrub mangrove	79.2	9.1	722 ± 153
Dwarf mangrove	74.5	6.7	498 ± 37
Mixed	50.7	12.4	628*
Sparse vegetation	31.3	8.1	255*
Herbs, grasses and sedges	41.7	4.8	200 ± 27
Rush	55.1	1.2	65*
Casuarina	118.3	1.2	145*
	Total	59.6	3933 ± 444

*standard deviation could not be calculated due to insufficient replicates

Identifying spatial variability in carbon storage services can aid targeted management for improving carbon sequestration potential and protecting current carbon stores from pressures of climate change. Mangrove and saltmarsh have some capacity to adapt to accelerated sea-level rise by accumulating sediment and adjusting their elevation in the soil profile relative to sea level (Rogers *et al*., 2013). This requires contributions from both autochthonous and allochthonous sources of sediment for vertical accretion (Saintilan *et al*., 2013). Activities in the catchment may reduce the availability of allochthonous material to aid elevation adjustment as the sea rises. Similar adaptive capacity has been demonstrated for landward migration of wetland vegetation (Rogers *et al*., 2013). Removing artificial impediments to facilitate landward migration may increase carbon sequestration potential by preventing further losses of vegetation and encouraging recolonisation.

CONCLUSIONS

Ecosystem services are not spatially homogenous throughout coastal wetlands, and we have demonstrated that carbon storage services varied on the basis of vegetation structure. Similarly, exposure to coastal processes is spatially complex, with lower intertidal areas being particularly sensitive to sea-level rise related erosion, and upper intertidal areas sensitive to the effects of coastal squeeze. Identifying spatial variability in carbon storage services can aid targeted management for improving carbon sequestration potential and protecting current carbon stores from pressures of climate change. In particular we found that tall mangrove fringing Currambene Creek exhibited the greatest carbon mitigation ecosystem services, yet was also particularly sensitive to coastal processes and management activies occurring within the catchment, including sea-level rise and dredging.

ACKNOWLEDGMENTS

This research was supported by a UOW postgraduate scholarship awarded to C. Owers. K. Rogers receives funding from the Australian Research Council (FT130100532). The authors would like to thank Daniel Owers, Kirti Lal, Tsun-You Pan and Catherine Bowie for fieldwork assistance as well as John Morrison (UOW), Barbora Gallagher (ANSTO) and Scott Allchin (ANSTO) for laboratory assistance.

LITERATURE CITED

Ball, D.F., 1964. Loss-on-ignition as an estimate of organic matter and organic carbon in non-calcareous soils. *Journal of Soil Science*, 15(1), 84-92.

Barbier, E.B.; Hacker, S.D.; Kennedy, C.; Koch, E.W.; Stier, A.C., and Silliman, B.R., 2011. The value of estuarine and coastal ecosystem services. *Ecological Monographs*, 81(2), 169-193.

Chafer, C.J., 1998. *A Spatio-temporal Analysis of Estuarine Vegetation Change in the Minnamurra River, 1938-1997*. Minnamurra Estuary Management Committee, 43p.

Chmura, G.L.; Anisfeld, S.C.; Cahoon, D.R., and Lynch, J.C., 2003. Global carbon sequestration in tidal, saline wetland soils. *Global Biogeochemical Cycles*, 17(4), 1–12.

Clarke, P., 1993. Mangrove, saltmarsh and peripheral vegetation of Jervis Bay. *Cunninghamia*, 3(1), 231 – 253.

Craft, C.B.; Seneca, E.D., and Broome, S.W., 1991. Loss on Ignition and Kjeldahl Digestion for Estimating Organic Carbon and Total Nitrogen in Estuarine Marsh Soils: Calibration with Dry Combustion. *Estuaries*, 14(2), 175-179.

Doody, J.P., 2004. "Coastal squeeze" – an historical perspective. *Journal of Coastal Conservation*, 10, 129-138.

Duarte, C.M.; Middelburg, J.J., and Caraco, N., 2005. Major role of marine vegetation on the oceanic carbon cycle. *Biosciences*, 2, 1-8.

Ewel, K.C.; Twilley, R.R., and Ong, J.E., 1998. Different kinds of mangrove forest provide different goods and services. *Global Ecology and Biogeography Letters*, 7, 83-94.

Gilman, E.L.; Ellison, J.; Duke, N.C., and Field, C., 2008. Threats to mangroves from climate change and adaptation options: A review. *Aquatic Botany*, 89, 237-250.

Howard, J.; Hoyt, S.; Isensee, K.; Telszewski, M. and Pidgeon, E. eds 2014. Coastal blue carbon: methods for assessing carbon stocks and emissions factors in mangroves, tidal saltmarshes, and seagrasses. UNESCO, International Union for Conservation of Nature, Arlington.

Howe, A.J.; Rodríguez, J.F., and Saco, P.M., 2009. Surface evolution and carbon sequestration in disturbed and undisturbed wetland soils of the Hunter estuary, southeast Australia. *Estuarine, Coastal and Shelf Science*, 84, 75-83.

IPCC, 2013. Climate Change 2013: The Physical Science Basis. Contribution of Working Group I to the Fifth Assessment Report of the Intergovernmental Panel on Climate Change. Cambridge University Press, Cambridge, United Kingdom and New York, NY, USA, 1535p.

Kauffman, J.B. and Donato, D.C., 2011. Protocols for the measurement, monitoring and reporting of structure, biomass and carbon stocks in mangrove forests. Bogor, Indonesia: Centre for International Forestry Research (CIFOR). 37p.

Mazumder, D.; Iles, J.; Kelleway, J.; Kobayashi, T.; Knowles, L.; Saintilan, N., and Hollins, S., 2010. Effect of acidification on elemental and isotopic compositions of sediment organic matter and macro-invertebrate muscle tissues in food web research. *Rapid Communications in Mass Spectrometry*, 24, 2938-2942.

Mcleod, E.; Chmura, G.L.; Bouillon, S.; Salm, R.; Björk, M.; Duarte, C.M.; Lovelock, C.E.; Schlesinger, W.H., and Silliman, B.R., 2011. A blueprint for blue carbon: toward an improved understanding of the role of vegetated coastal habitats in sequestering CO_2. *Frontiers in Ecology and the Environment*, 9(10), 552–560.

Mosisch, T.D. and Arthington, A.H., 1998. A review of literature examining the effects of water-based, powered recreational activities on lakes and rivers. *Lakes and Reservoirs: Research and Management*, 3, 1-17.

Oliver, T.S.N.; Rogers, K.; Chafer, C.J., and Woodroffe, C.D., 2012. Measuring, mapping and modelling: an integrated approach to the management of mangrove and saltmarsh in the Minnamurra River estuary, southeast Australia. *Wetlands Ecology and Management*, 20(4), 353–371.

Ong, J.E.; Gong, W.K. and Wong, C.H., 2004. Allometry and partitioning of the mangrove, *Rhizophora apiculate*. *Forest Ecology and Management*, 188, 395-408.

Owers, C.J.; Rogers, K, and Woodroffe, C.D., (in review). Identifying spatial variability and complexity in wetland vegetation using an object-based approach. *International Journal of Remote Sensing*.

Rogers, K.; Saintilan, N., and Copeland, C., 2013. Managed Retreat of Saline Coastal Wetlands: Challenges and Opportunities Identified from the Hunter River Estuary, Australia. *Estuaries and Coasts*, 37, 67-78.

Roy, P.S.; Williams, R.J.; Jones, A.R.; Yassini, I.; Gibbs, P.J.; Coats, B.; West, R.J.; Scanes, P.R.; Hudson, J.P., and Nichol, S., 2001. Structure and Function of South-east Australian Estuaries. *Estuarine, Coastal and Shelf Science*, 53, 351-384.

Saintilan, N.; Rogers, K.; Mazumder, D., and Woodroffe, C., 2013. Allochthonous and autochthonous contributions to carbon accumulation and carbon store in southeastern Australian coastal wetlands. *Estuarine, Coastal and Shelf Science*, 128, 84-92.

Saintilan, N. and Wilton, K., 2001. Changes in the distribution of mangroves and saltmarshes in Jervis Bay, Australia. *Wetlands Ecology and Management*, 9, 409-420.

Journal of Coastal Research	SI	75	1302 - 1306	Coconut Creek, Florida	2016

Beaches Morphological Variability Along a Complex Coastline (Sinis Peninsula, western Mediterranean Sea).

Simone Simeone†, Giovanni De Falco†, Giovanni Quattrocchi†, Luca Palombo θ, Andrea Cucco†

†† Istituto perl Ambiente Marino Costiero. IAMC – CNR. U. O. Oristano, loc Sa Mardini 09072 Torregrande, Oristano

θ Fondazione IMC ONLUS, loc Sa Mardini 09072, Torregrande, Oristano

www.cerf-jcr.org

www.JCRonline.org

ABSTRACT

Simeone, S., De Falco, G., Quattrocchi, G., Palombo, L., Cucco, A. 2016. Beaches morphological variability along a complex coastline (Sinis Peninsula, western Mediterranean Sea). In: Vila-Concejo, A.; Bruce, E.; Kennedy, D.M., and McCarroll, R.J. (eds.), Proceedings of the 14th International Coastal Symposium (Sydney, Australia). Journal of Coastal Research, Special Issue, No. 75, pp. 1302 - 1306. Coconut Creek (Florida), ISSN 0749-0208.

Wave climate, sediments, topographic features and tides influence the morphology and the short-term dynamics of beaches. The interactions between these different forcings affect the features of the beach system. In this work the morphological beach responses in relation to the most energetic period of the year were studied in a coastline with high geomorphological complexity. Three beaches, located along the Sinis Peninsula (western Mediterranean Sea, western Sardinia), were monitored for about 6 months. In order to estimate morphological changes, repetitive beach profiles were acquired by means of Differential Global Positioning System. Wave data were collected by an offshore wave buoy and the grainsize features of each beach was determined. A coupled 3D hydrodynamics–wave, finite element model was also applied in order to investigate the current dynamics and the wave propagation along the selected coastal area. During the monitoring period, the beaches experienced relevant changes when consecutive storms occurred. In sediment deprived embayed beaches, the presence of headlands interacting with waves, favored beach rotation and lead to a crenulate shape of the shoreline. In addition, on sediment abundant beach, cross-shore sediment transport and simultaneous shoreline retreats were observed during storms events. Finally, the effects on the wave heights and directions, due complex coastline features of the Sinis Peninsula, were discussed in relation to the morphodynamics response of each beach.

ADDITIONAL INDEX WORDS: *beach recovery, storms, numerical model, beach morphology*

INTRODUCTION

Wave climate, sediment grain size, topographic features and tides can profoundly influence the dynamics of beaches as well as their morphology (Short 1996). The interactions between these factors or alternatively a single factor can influence the characteristics of the beach system. In addition, geological inheritance and the presence of headlands can influence shoaling processes, beach shape and sediment transport in both the submerged and emerged beach (Simeone *et al.*, 2013). Beaches in the Mediterranean Sea experience drastic modifications in morphology and grainsize composition during intense storms and extreme meteorological and marine events, while the effects of tide result negligible (Basterretxea *et al.*, 2004). The geomorphical contexts of coastline can influences the beach response to storms and the presence of buried and emerged beachrock in the proximity of shoreline can affect beach morphodynamics (Vousdoukas *et al.*, 2007). The underlying geology set the limits of morphological evolution and the volume of accommodation space for sediments. Moreover an important factor influencing the beach response, that can be considered as a geological inheritance, is the nature and source of available sediments (Jackson *et al.*, 2005). Morphological changes on beaches are the results of the interplay between the wave forcing with the aforementioned geological controls factors. In fact the storm parameters such as wave height, peak period and wave direction drive the beach response (Loureiro *et al.*, 2014). Furthermore the pre storm morphology seems to be very important on the evolution of beach morphology (Vousdoukas *et al.*, 2012).

The aim of this study was to investigate the morphological beach response, during the most energetic period of the year in terms of storm occurrence. During the studied period, the effects of wave climate was monitored along a coastline characterized by a complex geomorphological setting.. An interdisciplinary approach, consisting on using both numerical and experimental methods was followed to investigate the morphological changes as well as the natural recovery of beaches during winter period.

In particular, the morphological variability of the beach profiles on the sub-aerial part was analyzed by using a Differential Global Positioning System. Wave data recorded by an off shore wave buoy located about 70km north of study area, were used to determine the wave climate. Finally, a high resolution coupled waves-currents numerical model was applied to reproduce the temporal and spatial variability of the main wave features along the whole investigated area during the main storms. The influence of both large and local scale forcings were simulated and the obtained data have been used to investigate the relationship between the morphological changes and the wind waves features in the study area.

STUDY AREA

DOI: 10.2112/SI75-261. 1 received 15 October 2015; accepted in revision 15 January 2016.

*Corresponding author: simone.simeone@cnr.it

©Coastal Education and Research Foundation, Inc. 2016

The The study area is located in the Sinis Peninsula, on the western coast of the island of Sardinia in the western Mediterranean (Figure 1). The geological setting of the Sinis peninsula includes a sequence of volcanic and sedimentary rocks (marls, sandstone and limestone) dating from the Neogene to the present (Marini and Murru, 1977) and several rocky outcrops and headlands characterize the coastline.

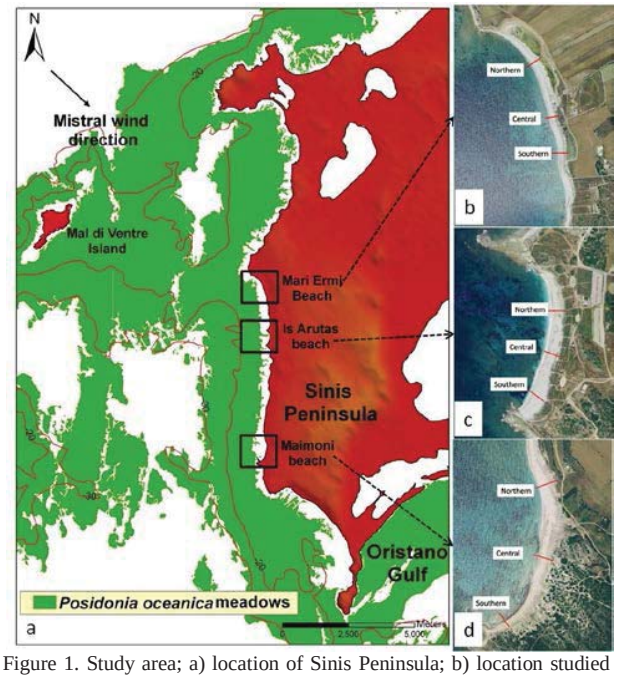

Figure 1. Study area; a) location of Sinis Peninsula; b) location studied beaches; c) position of beach profiles on each beach,

Studied beaches are located in the northern, central and southern sectors of the Sinis Peninsula (Figure 1a). The northern beach, named Mari Ermi (ME hereafter, see Figure 1b) is a beach ridge about 1 km in length, and about 60m wide. Beach sediment is mainly composed of coarse siliciclastic sand and gravel, with a carbonate content of about 20% (De Falco *et al.*, 2003). The orientation of the shoreline, is influenced by the presence of a rocky cape which encloses the beach to the north (Figure1b). The central beach, named Is Arutas (IA hereafter, see Figure 1c), is an embayed beach with a length of 500m, and about 60m of maximum cross shore beach width. The sediment is wholly siliciclastic and composed mainly of very coarse sand and granule (Simeone *et al.*, 2013). A rocky seafloor characterizes the whole submerged domain of the beach. Patchy Posidoniaoceanica meadows colonize the seafloor from a depth of about 5 - 10 m. The southern beach, named Maimoi (MA hereafter, see Figure 1d), is about 1 km in length and 60 m in cross shore beach width, from the toe of the dune up to the shoreline. Sediments of the emerged beach are composed a siliciclastic coarser fraction, mainly located on the foreshore and a finer biogenic carbonate fraction mainly in the backshore, in the dune field and in the submerged beach. The submerged sandy beach is characterized by fine sand (De Falco *et al.*, 2003), however in the central area limited shallow rocky outcrops occur. This beach can be considered as a sediment abundant beach, whereas ME and IA where the sediments are mainly relict, can be considered as sediment deprived beaches.

The prevailing winds are mainly from the north-west (Mystral), often in form of severe storms, especially during winter. In autumn and winter, southwestern winds (Libeccio) are also important (Corsini *et al.*, 2006). The tides are negligible with a maximum water displacement < 0.2 m (Cucco *et al.*, 2006).

METHODS

The morphological variability of beaches was investigated by the analyses of beach profiles variabilty. Wave data, recorded by an off shore wave buoy located about 70 km north of the study area, were used to determine the wave climate. Finally, a high-resolution hydrodynamic and waves numerical model was applied to reproduce the temporal and spatial variability of the main wave features along the Sins coast. The obtained data were used to investigate the relationship between the morphological changes and the wind waves features in the study area.

Table 1. *Summary of the features of studied beaches.*

	Mari Ermi			Is Arutas			Maimoi		
Beach Length (m)	ca 1200			ca 500			ca 1000		
Profile scaling (m)	450			150			300		
	Profile location			Profile location			Profile location		
	N	C	S	N	C	S	N	C	S
Repetition		7			6			7	
Profile length (m)	80	75	60	55	52	50	45	37	40
Min depth (m)		-1			-1			-1	
D50 (mm)	2.74	1.92	1.96	1.82	1.78	1.94	1.98	1.85	1.68
Ws (m/s)	0.33	0.25	0.26	0.24	0.23	0.25	0.26	0.24	0.23
Avg. Ws (m/s)		0.28			0.24			0.24	
Averaged (ξ_0)	1.03	0.94	0.94	1.00	0.97	0.88	0.96	0.92	0.78

N = north, C = centre, S = south

Beach Morphology and Sediments

In order to evaluate the beach morphology and the variability of the different areas of the sub-aerial beach, 3 profiles for each beach were realized (7 times for ME and MA and 6 times for IA) (Figure 1b-c-d, Table 1). Measured beach profiles started from the landward boundary of the beach, marked by the presence of vegetation or other features (man-made structures or physical limits), up to a depth of about 1meter below sea level. For each profile, a position point (X, Y, Z) was collected every 2.5m with the DGPS System. The variations of beach profile volumes (m^3 m^{-1}, corresponding to the section resulted from differences between two profiles consecutive in time, realized on same location: North, Central, South for each beach) were also calculated.

Wave Climate

The wave parameters, including the significant wave height Hs (m), the maximum wave height and the period T (s), were measured by an offshore buoy located in the northwest of Sardinia (Alghero buoy; ISPRA-R.O.N). These data were used

to define the wave climate on the western side of Sardinia. The averaged Iribarrean number (ξ_0) was calculated for each mean beach profile and obtained as the averaged value considering the whole surveyed period (Table 1). Furthermore the dimensionless fall velocity Ω (Dean, 1973) (mean values for the period between topographic surveys, as showed in Vousdoukas *et al.*, 2012) was calculated for each beach

$$\Omega = Hb/wsT \quad (1)$$

the breaking wave height Hb (m) used to compute Ω was derived from the Komar and Gaughan (1972) formula:

$$Hb = 0.39g^{0.2}(TH_0)^{0.4} \quad (2)$$

where g is the acceleration due to gravity, T the wave period (s) and H_0 (m) the significant deeper wave height and ws (m s^{-1}) the averaged settling velocity (Table 1). To define the strength of the storms occurred during the monitored period the 'storm power index', as defined in Karunarathna *et al.* (2014), was calculated:

$$Ps = Hs^2 maxD \quad (3)$$

Where Hs max (m) is the maximum significant storm wave height, D is the duration of the storms (hours), Ps is expressed in (m^2 h).

Numerical model

The SHYFEM3D-WWM is a coupled 3D hydrodynamic and wave model based on the finite element method (Umgiesser *et al.*, 2004, Cucco *et al.*, 2012). The wave module was adopted to reproduce the wind wave propagation in the study area, as directly influenced by the wind action, and the wave nonlinear interactions with the sea floor.

The wave module is a phase averaging numerical model, which solves the wave action equations (WAE) by means of the finite element integration method. WAE describe the net source terms defined by the energy input due to wind, the nonlinear interaction in deep and shallow water, the energy dissipation due to white capping and depth induced wave breaking and the energy dissipation due to bottom friction. A comprehensive description of the numeric is found in Roland *et al.* 2009.

The model integration domain includes the whole Western Mediterranean Sea, from the Gibraltar Strait to the western Sardinian. An unstructured mesh based on triangular elements were implemented covering the whole interested area with a spatial resolution varying between 10 km for the open ocean and 50m for the Western Sardinian shallow waters area. The model was already applied with success to simulate the wave propagation in the same area (Simeone *et al.*, 2014). In this study, ad hoc numerical simulations were carried out to reproduce the wave fields in the area as generated by typical storm events from North-West and from West (see Figure 2) that characterized the investigated period. Wind data from the high-resolution atmospheric model SKIRON, were used as model upper boundary conditions.

RESULTS

Figure 3a displays the significant wave heights and peak wave periods, recorded by the Alghero wave buoy during the surveyed period. Events with higher significant wave heights occurred from October 2010 to late January 2011 with peak periods up to 12 seconds. The highest wave height was recorded in November

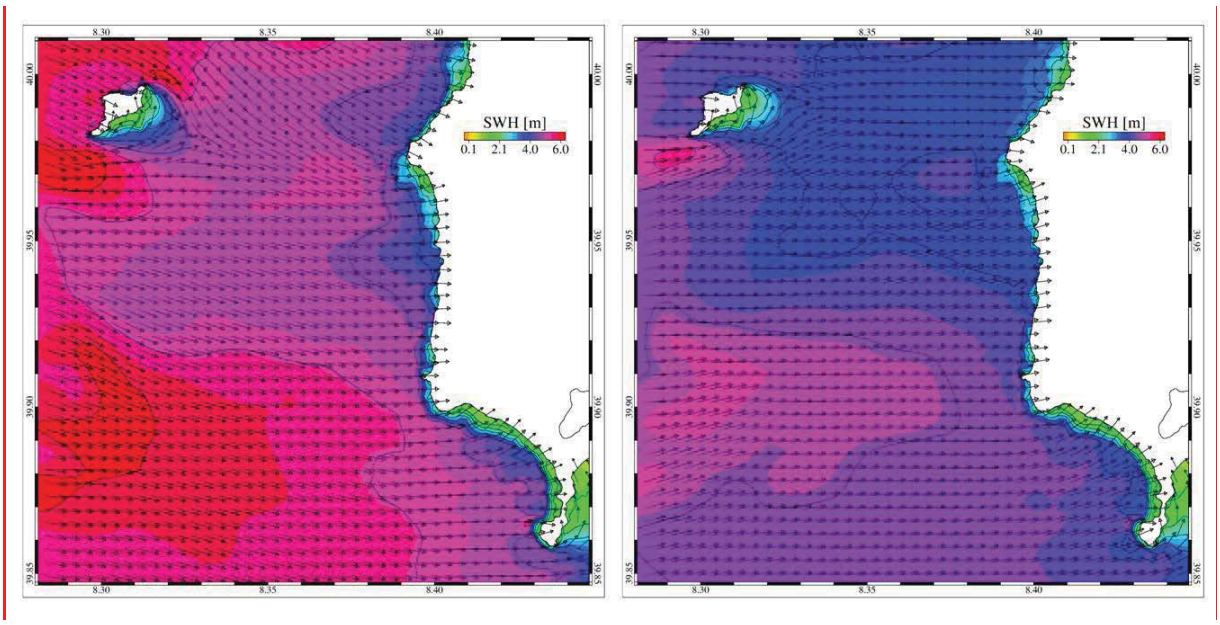

Figure2: Model results: wave height approaching the coastline of the Sinis Peninsula during typical intense storms. Left panels: Northwesterly storm. Right panel; Westerly storm.

16th 2010 (6.65m). During the entire survey period, the majority of the events resulted preferentially from NW direction (Mistral), however W events were also recorded.

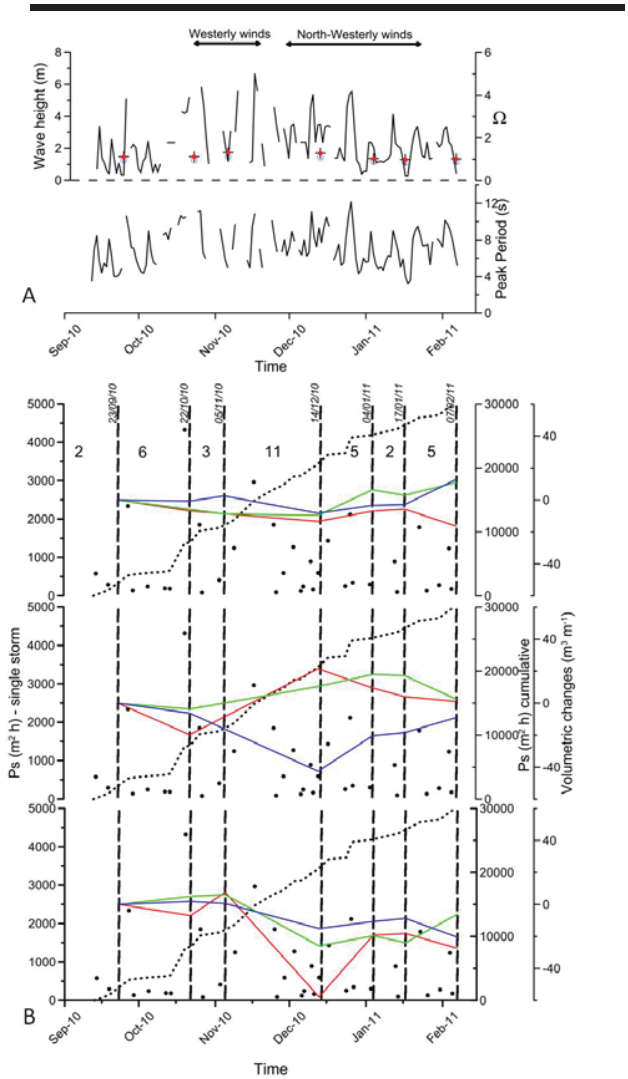

Figure 3. A: maximum measured offshore wave height and peak period. B: volumetric variation along the profiles of ME, IA and MA; lines: blue = south profiles; green = center profiles; red = north profiles. Dots represent the singles 'storm power index' (values in left y-axis); dotted lines represent the cumulative 'storm power index' (values in the right y-axis); dashed vertical lines represent the date of topographic survey.

Figure 3b reports the volumetric changes ($m^3\ m^{-1}$) along each profile, the Ps of the single storms, the cumulative value of the Ps and the number of storms occurred between each topographic survey.

The dimensionless fall velocity remained close to 1 (Reflective state) for each beach and for the whole surveyed period. The averaged Iribarrean number ($\xi 0$) calculated along each beach profile was about 1 and the breaking waves type considered as plunging type ($0.5 < \xi\ 0 < 3.3$). Major changes occurred on IA and MA beaches from November to January. On ME beach the cumulative volume changes resulted lower in comparison to the other two studied beaches. The cumulative Ps curve shows as the storms become strongest from late October up to late January. The beach profile changes did not exceed 25 m^3m^{-1} on ME beach, accounted for a maximum value of 41 m^3m^{-1} on IA beach and for about 60 m^3m^{-1} on MA. Main changes occurred from October to January along IA and MA and on late January on ME.

According to the displayed beach profiles it is possible to infer that the ME beach has minor variations.,The IA beach displays an accretion of the Northern profile and a contextual erosion of the Southern profile, related to a beach rotation process due to the wave provenance direction. Each surveyed profile along the MA beach shows an erosion between November and December 2010, that leads to a lowering of the beach level and a generalized shoreline retreat during.

The main storm events occurred during the study period were reproduced by the numerical model. In Figure 2 and 4 the distribution of the significant wave height (SWH hereafter) during typical intense storm from Northwest and West are reported for the whole area and for the northern and southern sector of the Sinis Peninsula where the 3 beaches are located.

Wave direction during NW storms approach the Sinis coast mainly from WNW bending to West approaching to the coastline (see Figure 2). The shallow water area between Sinis Peninsula and Mal di Ventre influences the wave energy distribution along the northern and southern coastal sectors, dumping the SWH to values lower than 6 m (see Figure 4 and Figure 5).Wave direction during W storm approach the Sinis coast mainly from West-Southwest with a westward bending of the wave ray approaching to the coast. Only the northern sector is partially sheltered by the shallow areas located in front of the Mal di Ventre Island.

DISCUSSION & CONCLUSION

Wave forcing can be considered as the main factor promoting changes on beach morphology and intense storms can cause severe erosion on beaches (Vousdoukas *et al.*, 2012). The beach responses to single or multiple storms and the consequent beach recovery depend on the beach features and should be considered as site specific (Karunarathna *et al.*, 2014). Our study highlighted that high variability, along three specific beaches of the Sinis peninsula, occurs when the frequency of intense storms increase (Ps values of storms increase from late October, see Figure 3). As depicted in Figure 4, no evidence of significant differences between the SWH approaching to coast, computed for the two storms events (NW and W) on the three sites, were found. In particular, on ME beach and MA beach the wave field near the coast is similar for both NW and W storm events with the same SWH and direction. Conversely, on the IA beach, even if the SWH is similar, the wave direction was different during the two events. A difference of about 20° was found between the wave ray main direction, computed during the NW and W storms. This reflects the morphological behavior of the IA beach, where a beach rotation was observed. During W storms the southern profile was eroded and simultaneously, an accretion

of the northern profile occurred. Opposite trend was found when NW storms were more frequent.

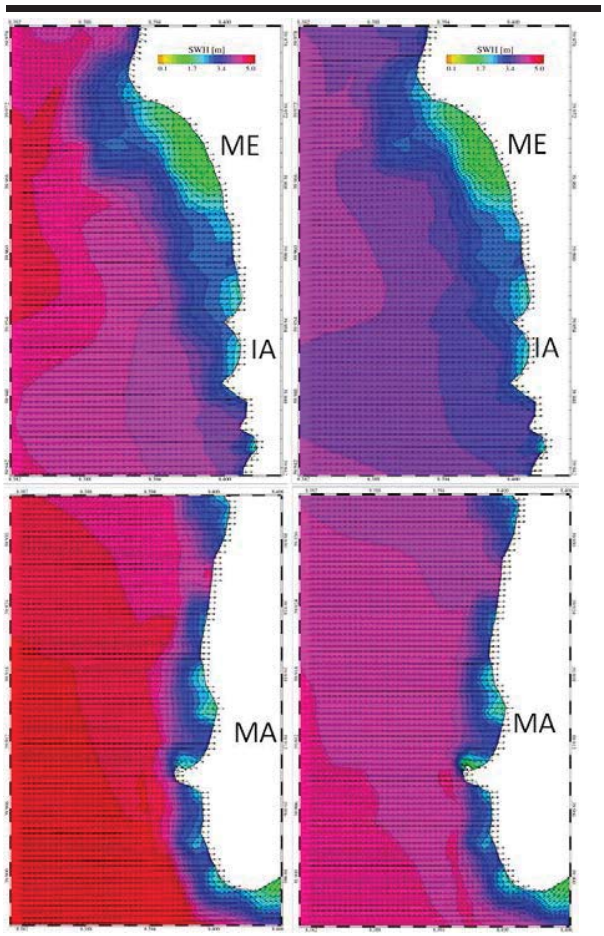

Figure 4. Models results: wave height approaching ME, IA and ME beach during intense storms. Left panels: North westerly storm. Right panel: Westerly storm.

On ME where the changes on beach profiles were less relevant, the wave height and directions were also subjected to the effect of the rocky shallow water, located in front and on the north side of the beach. Along the MA beach the approaching wave directions were influenced by the shallow submerged rocky outcrops in northern and southern area. During the most energetic storms on this beach, the waves eroded sediment from the sub aerial part that could have been deposed on the submerged domain promoting a cross-shore exchange between sub aerial and submerged beach.

Finally, this study highlights that the site-specific conditions of the beach are one of the main factors influencing the beach response to storms, in particular along coastlines with high geomorphological complexity, as in the Sinis Peninsula.

AKCNOWLEDGEMENTS

This work is founded by RITMARE project (founded by Italian Ministry of University and Scientific Research).

LITERATURED CITED

Basterretxea, G.; Orfica, A.; Jordi, A.; Casas, B.; Lynett, P.; Liu, P.L.F.; Duarte, C. M., and Tintoré, J., 2004. Seasonal Dynamics of a Microtidal Pocket Beach with Posidoniaoceanica Seabed (Mallorca, Spain).*Journal of Coastal Research*, 20 (4), 1155-1164.

Cucco, A., Sinerchia, M., Ribotti, A., Olita, A., Fazioli, L., Sorgente, B., Perilli, A., Borghini, M., Schroeder, K., Sorgente, R., 2012. A high resolution real time forecasting system for predicting the fate of oil-spills in the Strait of Bonifacio (western Mediterranean). *Marine Pollution Bulletin*, 64, 6, 1186–1200

Cucco A.; Perilli A.; De Falco G.; Ghezzo M., and Umgiesser, G., 2006. Water circulation and transport timescales in the Gulf of Oristano. *Chem. Ecol*., 22 (1), 307-331.

Corsini, S., Franco, L., Inghilesi, R., Piscopia, R., 2006. Atlante delle onde nei mari Italiani – Italian Waves Atlas. Roma, Italy: Agenzia per la Protezione dell'Ambiente e per i servizi Tecnici, 152 p.

Dean, R.G. 1973. Heuristic models of sand transport in the surf zone. Engineering dynamics in the surf zone. *Proc. firs Aust. Conf. CoastalEng. Inst. Eng., Australia*, 208-214.

De Falco, G., Molinaroli, E., Baroli, M., Bellacicco, S., 2003. Grain size and compositional trends of sediment from Posidoniaoceanica meadows to beach shore, Sardinia, Western Mediterranean. *Estuarine Coastal and Shelf Science*, 58, 299-309.

Jackson, D.W.T., Cooper, J.A.G., Del Rio, L. 2005. Geological control of beach morphodynamic state. *Mar. Geo.*, 216, 297-314.

Karunarathna H., Pender, D., Ranasinghe, R., short, A.D., Reeve, D. 2014.The effect of storm clustering on beach profile variabilty. *Mar. Geo*., 348, 103-112.

Komar, P.D., Gaughan, M.K. 1972. Airy wave theory and breaker wave prediction. proc. *13th Coast. eng. Conf. ASCE*, 405-418.

ISPRA- *Rete OndametricaNazionale*. URL: http://www.telemisura.it; accessed from September 12, 2010 to May 15, 2011.

Loureiro C., Ferreira, O., Cooper, J.A.G. 2014. Non-uniformity of storm impacts on three high energy embayed beaches. *J. Coastal. Res.*, S.I. 70, 326-331.

Marini, A. and Murru, M., 1977.Rilevamento geologico della penisola delSinis (Sardegna centro meridionale*). Rendiconti Seminario Facoltà di Scienze Università di Cagliari*, 24, 95-108.

Roland, A,.Cucco, A., Ferrarin, C., Hsu, TW, Liau, JM, Ou, SH.,Umgiesser, G., Zanke.U.,2009. On the development and verification of a 2-D coupled wave-current model on unstructured meshes. *Journal of Marine Systems* 78, S244-S254.

Short, A.D., 1996. The role of wave height, period, slope, tidal range and embaymentisation in beach classifications: a review. *RevistaChilena de Historia Natural*, 69, 589-604

Simeone, S., De Falco, G., Quattrocchi, G., Cucco., A. 2014 Morphological changes of a Mediterranean beach over oneyear (San Giovanni di Sinis, western Mediterranean) *Journal of Coastal Research*, 217-222

Simeone, S., Palombo, L., and De Falco, G., 2013. Morphodynamics of a Nontidal Embayed Beach: The Case Study of Is Arutas (Western Mediterranean*). Journal of Coastal Research.*, 29 (6a): 63-71.

Umgiesser, G., Canu, D.M., Cucco, A., Solidoro, C., 2004. A finite element model for the Venice lagoon: development, set up, calibration and validation. *Journal of Marine Systems.*, 51, 123–145

Vousdoukas, M.I. Almeida, L.P.M., Ferreira, O. 2012. Beach erosion and recovery during consecutive storms at steep sloping, meso tidal beach. *Earth Surface Processes and Landforms*, 37, 583-593.

Vousdoukas, M.I., Velegrakis, A.F., Plomaritis, T.A. 2007. Beachrock occurrence, characteristics, formation mechanism and impacts. *Earth Science Revues*, 85(1), 23 – 46,

Journal of Coastal Research	SI	75	1307 - 1311	Coconut Creek, Florida	2016

Textural facies and distribution of surface sediments and morphology on Korean tidal flats

YoungSook Baek[†*], SuHwan Lee[†], SangHoon Lee[†], Han-Joon Kim[†], Hyeong-Tae Jou[†], and SangOk Ryu[‡*]

[†]Korean Seas Geosystem Research Center, Korea Institute of Oceanscience and Technology, Ansan 426-744, Korea

[‡]Institute of Tidal Flat Research, Mokpo National University, 61 Dorim-ri, Muan-gun, Jeonnam, Korea.

www.cerf-jcr.org

www.JCRonline.org

ABSTRACT

Baek, Y.S.; Lee, S.H.; Lee, S.H.; Kim, H.-J.; Jou, H.-T., and Ryu, S.O., 2016. Textural facies and distribution of surface sediments and morphology on Korean tidal flats. *In:* Vila-Concejo, A.; Bruce, E.; Kennedy, D.M., and McCarroll, R.J. (eds.), *Proceedings of the 14th International Coastal Symposium* (Sydney, Australia). *Journal of Coastal Research*, Special Issue, No. 75, pp. 1307 - 1311. Coconut Creek (Florida), ISSN 0749-0208.

The aim of this study is to understand the regional distribution patterns of surface sediment together with morphology and to infer regional transport and sedimentation along the western and southwestern coast of Korea. Based on the analysis of 1027 surface sediment samples at 74 tidal flats and the morphologic profiles at 29 tidal flats obtained from estuarine, open coast, embayment, and islands along the western and southwestern coasts of Korea, tidal flats were divided spatially into four sectors; 1) Gyeonggi (GG), 2) Chungcheong (CH), and 3) Western Jeonnam (WJ) and 4) Southern Jeonnam (SJ). The tidal flats in the CH sector exhibit coarser (or more sandy) sediment facies and steeper slope gradient, probably resulting from more influence of waves on tidal-flat sedimentation caused by the geomorphic conditions of relatively straight coastline and non-barrier systems. The common occurrence of tidal channels on tidal flats in the WJ and SJ sectors could be ascribed to the fine-grained (or muddy) faceis and the gentle slope gradient. From GG (north) to SJ (south) sector along the coastline, the content (%) of fine-grained sediments increases. Fine-grained sediments supplied from the Han and Keum rivers in the western coast of Korea appear to have been transported to the south along the western and southwestern coast of Korea by Korea Coastal Currents (KCC). The fine-grained sediments settled on the tidal flats by the tidal currents and a residual coastal current.

ADDITIONAL INDEX WORDS: *tidal flat, surface sediments, morphology, Korea Coastal Currents, East Asian Winter Monsoon, Korea*

INTRODUCTION

Tidal flats along the western and southwestern coast of Korea extensively occur at various geomorphic settings of open coast, embayment and island margin with highly indented coastline and composed of diverse textural sediments. Types (or textures) of surface sediments, their distribution and morphology on tidal flats are generally influenced by various factors, such as sediment sources and physical oceanographic condition (tidal range, tide-/wind-driven currents, wave, climate, *etc.*) (Klein and Sanders, 1964; Golbuu *et al*., 2003). Regional pattern of surface-sediment characters on Korean tidal flats cannot be easily understood because of various specific conditions as follows. Korean tidal flats have been strongly influenced by strong winter storm waves with calm summer conditions caused by East Asian Winter Monsoon (Choi *et al*., 2004; Yang *et al*., 2005; Chang and Flemming, 2006; Baek and Chun, 2010; Choi *et al*., 2013; Baek *et al*., 2015). Morphologic characteristics, such as tidal channel systems, barrier-lagoon systems, salt marshes, and supratidal flats rarely occur at Korean tidal flats, compared to tidal flats in other nations (Frey *et al*., 1989; Alexander *et al*., 1991; Yang *et al*., 2005).

DOI: 10.2112/SI75-262.1 received 15 October, 2015; accepted in revision 15 January, 2015
*Corresponding author: duuri@kiostt.ac
©Coastal Education and Research Foundation, Inc. 2016

In this study, we analyze 1027 surface sediment samples at 74 tidal flats and topographic data at 29 tidal flats along the western and southwestern coast of Korea, and relation between spatial distribution of the sediments and morphology. Through these analyses, this study aims to understand the regional distribution patterns of surface sediment together with morphology and to infer general transport and sedimentation of fine-grained sediments along the western and southwestern coast of Korea.

Background

After the 1960s, about 1,428 km^2 of the tidal flats disappeared due to reclamation in the western and southern Korea. As a result of reclamation, coastlines become straightened and sediments supply from rivers is reduced. The western coast of Korea is characterized by many islets and irregular coastlines with large tidal ranges. Tidal range increases northward, generally over a 4 m in mean tidal range (KOHA, 2014). Tidal flats along the western coast of Korea have been classified as macro-tidal environments (Davis, 1964). Compared to the northern and southern parts of the western coast, the central (or middle) part is relatively straight (Figure 1). The southern coast of Korea is characterized by a highly curved coastline and numerous, small to large-sized islands (Figure 1). In the southern coast of Korea, tidal range decreases eastward, from 2–4 m in the western part (meso-tidal environment) to less than 2 m in the eastern part (micro-tidal environment) (KOHA, 2014).

Figure 1. Map showing the distribution of tidal flats along the western and southern coasts of Korea. The tidal flats are spatially divided into four sectors; 1) Gyeonggi (GG), 2) Chungcheong (CH) and 3) Western Jeonnam (WJ), 4) and Southern Jeonnam (SJ).

METHODS

Along the western and southwestern coast of Korea, we obtained 1027 surface sediment samples at 74 tidal flats and topographic data at 29 tidal flats in late summer (september) from 2009 to 2014. Standard sieving and pipetting methods were used for grain-size analyses, and the textural parameters were calculated by using the graphic method (Ingram, 1971). Textural classification of the surface sediments was performed by using Folk's diagrams (Folk, 1970). Tidal-flat morphological data were acquired using real-time kinematic (RTK) GPS, with a 10 mm for horizontal accuracy and 20 mm for vertical accuracy. In this study, tidal flats are geographically (or spatially) divided into four sectors; 1) Gyeonggi (GG), Chungcheong (CH), and Western Jeonnam (WJ) and 4) Southern Jeonnam (SJ).

RESULTS

Morphological characters

In the Gyeonggi (GG) sector, tidal flats wider than 3 km commonly occur (Figure 2A). Most tidal flats in the GG sector show the upward convex surface topography (Figure 2A). Sand dunes are generally present on the middle and lower parts of the tidal flats in the GG sector. Slope gradients in the GG sector are mostly less than 0.1 °. But tidal flats along islands have steeper slope gradient, over 0.2°. In the Chungcheong (CH) sector, most tidal flats exhibit convex-upward topography at the upper part and concave-upward one at the lower part (Figure 2B). Overall gradient of tidal-flat surface in the CH sector is steeper (over 0.1°) than that in the GG sector. Tidal channels in the GG and CH sectors are rarely present (Figure 2B). Tidal flats in the Western Jeonnam (WJ) sector show very gentle gradient, less than 0.1° (Figure 2C). Some tidal flats along the islands in the WJ sector, where are directly connected to Yellow Sea, show slope gradient of more than 0.1°. The WJ sector is characterized by common occurrence of tidal channels on tidal flats (Figure 2C).

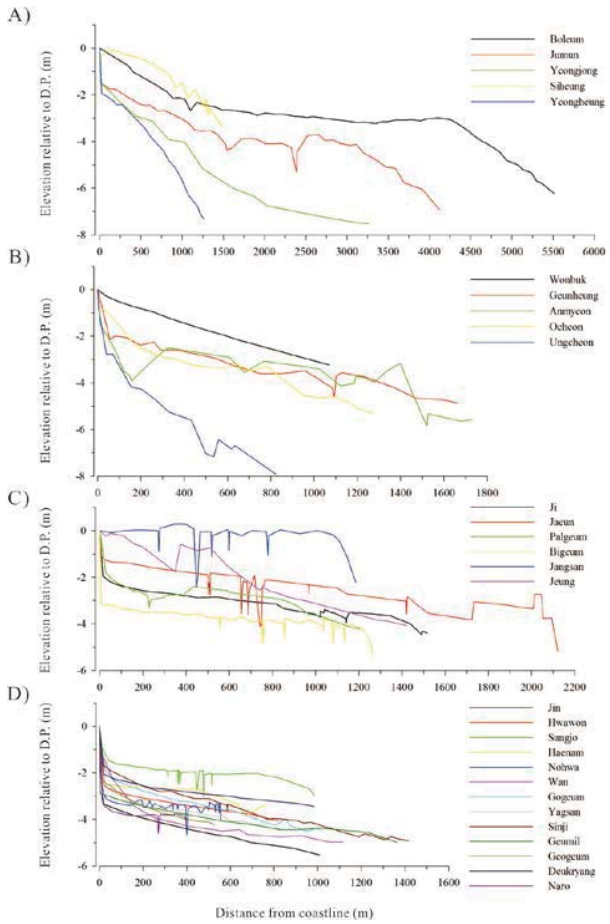

Figure 2. Morphologic profiles of (A) Gyeonggi, (B) Chung-cheong and (C) western Jeonnam, (D) southern Jeonnam and (E) Gyeongnam tidal flats in Korea.

The tidal flats in the Southern Jeonnam (SJ) sector have generally concave-upward morphology in the upper parts and convex-upward one in the lower parts, respectively. Most tidal flats in the SJ sector show a gentle slope gradient of 0.1–0.2° (Figure 2D). On the tidal flats in the SJ sector, tidal

channels are commonly developed on the middle flat (Figure 2D). Most of the tidal flats in the WJ and SJ sectors have steep slope gradient at the uppermost parts because of the reclamation dykes.

The WJ and SJ sectors are characterized by the common occurrence of tidal channels on the tidal flats (Figure 2). Most tidal channels in the WJ sector are more than about 10 m wide and ca. 1 m deep (Figure 3). In contrast, the tidal channels in the SJ sector have smaller dimension (<10 m wide, 1 m deep) than those in the WJ sector (Figure 3). The large-scale tidal channels in the WJ sector are generally connected to the subtidal zones that act as passages through which tides flow into the tidal flats.

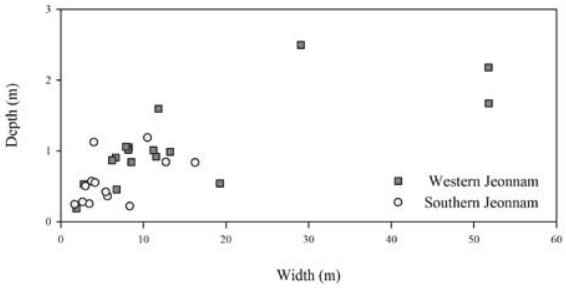

Figure 3. Plot of width and depth of tidal channels on tidal flats in the WJ (red dot) and SJ (blue dot) sectors.

Textural classification of surface sediments

In the GG sector, surface sediments are classified into the 5 sedimentary facies; S facies (24.3%), zS facies (27%), sZ facies (32.8%), Z facies (13.8%), and mS facies (2.1%). Although the most prevalent sedimentary facies is sZ, S and zS facies are dominant at 53.4% (Figure 4A).

Surface sediments in the CH sector are classified into three major sedimentary facies including S facies (30.9%), zS facies (28.9%), and sZ facies (28.4%) with four minor sedimentary facies consisting of mS facies (3.1%), sM facies (1.6%), Z facies (5.7%), and M facies (1.5%) (Figure 4B). Sandy facies (S, zS, and mS) are 62.9% in constituent percentage, and are more prevalent than those in the GG sector.

Surface sediments in the WJ sector are characterized by two major sedimentary facies; Z facies (51.3%) and M facies (16.4%). Minor sedimentary facies include S facies (6.3%), zS facies (5.9%), mS facies (4.2%), sZ facies (9.7%), sM facies (5%), sC facies (0.5%), and C facies (0.8%) (Figure 4C). In the tidal flats of the WJ sector, clayey facies (sC and C) are present, even though these facies are not observed in tidal flats of the GG and CH sectors.

Seven sedimentary facies on tidal flats in the SJ sector are classified; S facies (8.9%), zS facies (1.8%), mS facies (8.5%), sZ facies (12.5%), sM facies (9.4%), Z facies (17%), and M facies (42%) (Figure 4D). The mud faices (M) is mostly dominant in the SJ sector. Surface sediments in the SJ sector contain finer sediments (mud-sized) than those in the WJ sector.

DISCUSSION

Many tidal flats in the GG and WJ sectors have underwent a seasonal variation in sedimentation, deposition being dominated by mud in summer and sand in winter, because of monsoonal wind (Yang *et al*., 2005; Chang and Flemming, 2006; Baek and Chun, 2010). However, the seasonal variation in sedimentation is not obvious in the CH sector where sandy facies (S, zS and sZ) are present in all seasons (Yang *et al*., 2006; Fig 4). The CH sector is characterized by relatively straight (N–S-oriented) coastline without barrier systems at the seaward area (Figure 1). These geomorphic conditions could increase the effect of waves on tidal-flat sedimentation in the CH sector. In the other sectors (GG, WJ and SJ), the irregular coastline, embayment and many islands have acted as the barriers against the wave influence. The slope gradient of tidal flat can be affected by grain size (Smithson *et al*., 2002). The steeper slope gradient of the CH sector could be ascribed to coarser sediments than the other (GG and WJ) sectors.

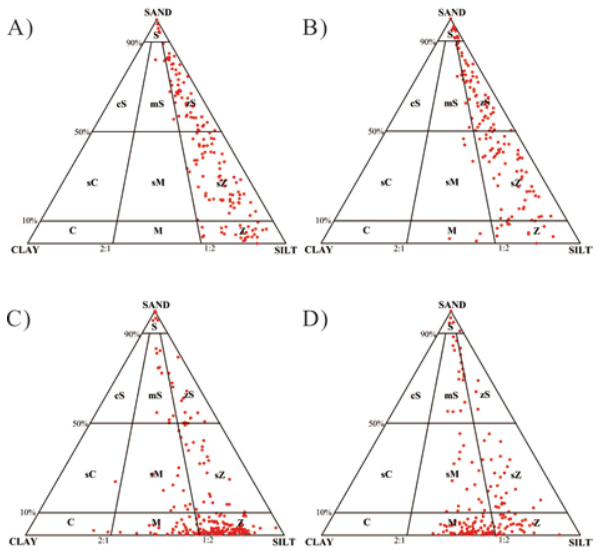

Figure 4. Ternary diagrams sand, silt, and clay contents (%) of tidal-flat surface sediments; (A) Gyeonggi (GG), (B) Chungcheong (CH), (C) Western Jeonnam (WJ) and (D) southern Jeonnam (SJ) sectors.

In the study area, tidal channels are mainly observed in the WJ and SJ sectors. These sectors are characterized by very irregular, rugged coastline with various scale of embayments and bays (Figure 1) and very gentle slope gradient (Figure 2). These geomorphic conditions protect the tidal flat against the wave influences. Therefore, tidal flats in the WJ and SJ sectors would be clamer and more stabl environments and include higher contents of clay sediments. These depositional conditons (muddy faceis and gentle slope gradient) could easily form tidal channels in the WJ and SJ sectors (Hughes, 2012). In the WJ sector, the tidal channels in the middle–lower flats are directly connected to the subtidal zone (Figure 3). Linkage of tidal

channels on tidal flats to the subtidal zone can be considered one of important factors for sediment distribution on tidal flats by acting passageway for sediments in-and-out on the tidal flat (Wells *et al*., 1990; Choi *et al*., 2013). The more occurrence of coarser sediments (sands and silts) in the WJ sector than SJ sector could be explained by the tidal channels on the flats connected to the subtidal zone.

As evident from Figs 4, the fine-grained sediments increased from GG to SJ sector (*i.e*., from north to south). The tidal flats in the WJ and SJ sectors consist mostly of fine-grained facies (M and Z). In contrast, the tidal flats in the GG and CH sectors consist mostly of sandy faceis (S and mS). Sediment distribution and transport on tidal flat can be affected by prevailing oceanic processes (waves, tides, and currents), sediment supply, and morphology (Flemming, 1981; Walsh and Nittrouer, 2009; Normandeau *et al*., 2013; Szczygielski *et al*., 2015). Most fine-grained sediments along the western coast of Korea have been generally supplied form Han and Keum rivers (Chough and Kim, 1981; Park and Khim, 1990). The fine-grained sediments supplied from these rivers have been re-suspended in the coastal areas by monsoonal wind during from late fall to early spring, and then transported southward along the coast by Korea Coastal Currents (KCC) (Wells *et al*., 1985; Lee and Chough, 1989). The southward transport of fine-grained sediments could be supported by V/Al ratio of fine-grained (>6 ϕ) sediments; the southward increase in V/Al ratio along the western coast of Korea (Cho *et al*., 1999). The fine-grained sediments transported by the Korea Coastal Currents (KCC) are deposited in sheltered tidal flat of bays and estuaries by the residual currents during calm summer weather (Cho and Kim, 1995; Kim and Bae, 2012). The overall southward transport of fine-grained sediments can explain the southward fining trend of surface sediments on tidal flats along the western coast of Korea.

CONCLUSIONS

The tidal flats along the western and southwestern coast of Korea are spatially separated into four sectors including Gyeonggi (GG), Chungcheong (GH), Western Jeonnam (WJ) and Southern Jeonnam (SJ). The tidal flats in the CH sector exhibit coarser (or more sandy) sediment facies and steeper slope gradient, probably resulting from more influence of waves caused by the geomorphic conditions of relatively straight coastline and non-barrier systems. The common occurrence of tidal channels on tidal flats in the WJ and SJ sectors could be ascribed to the fine-grained (or muddy) facies and the gentle slope gradient. Along the western coast of Korea, fine-grained sediments are mostly supplied from Han and Keum rivers. The Korea Coastal Current (KCC) with re-suspension of fine-grained sediments in the coastal areas by strong winter storm waves could generally transport the fine-grained sediments southward along the western and southwestern coast of Korea. These conditions probably cause the fining trends of tidal-flat sediments to the south (i.e., from the GG to WJ and SJ sectors).

ACKNOWLEDGMENTS

This work has been supported by Development of Technology for CO2 Offshore Geological Storage, funded by the Ministry of Oceans and Fisheries, Korea (PM58551), the the project funded by the Korea Meteorological Industry Promotion Agency, and the program of ‘Marine Geology and Geological Structure in the Korean Seas’ funded by Ministry of Oceans and Fisheries.. We appreciate the assistances provided by Jeon, C.G. and Ahn, S.H. (Korea Institute of Ocean Science & Technology) and Choi, S.R., and Park, J.H. and Lee, J.H. (Coastal manegements and Technology Institute) in the field and laboratory works.

LITERATURE CITED

Alexander, C.R.; Nittrouer, C.A.; CeMaster, D.J.; Park, Y.A., and Park, S.C., 1991. Macrotidal mudflats of the southwestern Korean coast: model for interpretation of intertidal deposits. *Journal of Sedimentary Petrology*, 61, 805-824.

Baek, Y.S. and Chun, S.S., 2010. The preliminary study about the formation of fluid mud layer during summer in the Duuri open coast tidal flat, southwestern coast of Korea. *Journal of the Geological Society of Korea*, 3, 291-303 (in Korean with English abstract).

Baek, Y.S.; Chun, S.S., and Kim, J.K., 2015. Spatio-temporal zonation by ichnocoenoses combined with sedimentary facies in the Yeochari tidal flat (Ganghwa Island), the Han River estuary of Korea. *Geoscience Journal*, 1-15.

Chang, T.S. and Flemming, B.W., 2006. Sedimnentation on a wave-dominated, open-coast tidal flat, southwestern Korea: Summer tidal flat-winter shoreface-discussion. *Sedimentology*, 53, 687-691.

Cho, Y.G.; Lee, C.B., and Choi, M.S., 1999. Geochemistry of surface sediments off the southern and western coasts of Korea. *Marine Geology*, 159, 111-129.

Cho, Y. K. and Kim, K., 1995, Characteristics and origin of the cold water in the South Sea of Korea in summer. *Journal of Oceanology of Society of Korea*, 19, 414-421 (in Korean with English abstract).

Choi, K.S. and Dalymple, R.W., 2004. Tecurring tide-dominated sedimentation in Kuonggi Bay (west coast of Korea): sililarity of tidal deposits in late Pleistocene and Holocene sequences. *Marine Geology*, 212, 81-96.

Choi, K.S.; Hong, C.M.; Oh, C.R., and Jung, J.H., 2013. Morphologic evolution of macrotidal estuarine channels in Gonso Bay, west coast of Korea: implications for the architectural development of inclined heterolithic stratification. *Marine Gology*, 346, 343-354.

Chough, S.K. and Kim, D.C., 1981. Dispersal of Fine-Grained Sediments in the Southeastern Yellow Sea: A Steady-State Model. Journal of Sedimentary Petrology, 51(3), 721-728.

Davies, J.L., 1964. A morphogenic approach to world shorelines. *Geomorphologie*, 8, 127-142.

Flemming, B.W., 1981. Factors controlling shelf sediment dispersal along the southeast African continental margin. *Marine Geology*, 42, 259–277.

Flemming, B.W., 2000. A revised textural classification of gravel-free muddy sediments on the basis of ternary diagrams. Continental Shelf Research, 20, 1125-1137.

Fley, R.W.; Howard, J.D.; Han, S.J., and Park, B.K., 1989. Sediments and sedimentary sequences on a modern macrotidal flat, Inchon, Korea. *Journal of Sedimentary Petrology*, 59, 28-44.

Folk, R.L.; Andrews, P.B., and Lewis, D.W., 1970. Detrital sedimentary rock classification and nomenclature for use in

New Zealand. *New Zealand Journal of Geology and Geophysics*, 13, 937-968.

Golbuu, Y.; Victor, S.; Wolanski, E., and Richmond, R.H., 2003. Trapping of fine sediment in a semi-enclosed bay, Palau, Micronesia. *Estuarine, Coastal and Shelf Science* 57, 1-9.

Hughes, Z.J., 2012. Tidal Channels on Tidal Flats and Marshes, Principles of Tidal Sedimentology. *In*; Davies, R.A. and Dalrymple, R.W.(eds), *Springer Science and Business Media*, pp. 269-300.

Ingram, R.L., 1971, Sieve analysis. *In*: Carver (eds.) *Procedures in Sedimentary Petrology*. Wiley, New York, pp. 49–67.

Kim, D.S. and Bae, S.W., 2012. Understanding the Flow Properties by a Numerical Modeling in the South Sea of Korea. *Journal of the Korean Society of Marine Environment and safety*, 18, 295-307.

Klein, G.deV. and Sanders, J.E., 1964. Comparison of sediments from Bay of Fundy and Dutch Wadden Sea tidal flats. *Journal of Sedimentary Petrology*, 34, 19-24.

Korea Office of Hydrographic Affairs (KOAH), 2014. Tide Tables. Seoul, Korea, Volume 1, 250 p.

Lee, H.J. and Chough, S.K., 1989. Sediment distribution, dispersal and budget in the Yellow sea. *Marine Gology*, 87, 195-205.

Normandeau, A.; Lajeunesse, P., and St-Onge, G., 2013. Shallow-water longshore drift-fed submarine fan deposition (Moisie River Delta, Eastern Canada). *Geo-Marine Letters*, 33, 391–403.

Park, Y.A. and Khim, B.K., 1990. Clay minerals of the recent fine-grained sediments on the Korean continental shelves. Continental Shelf Research, 10, 1179-1191.

Smithson, P.; Addison, K., and Atkinson, K., 2002. *Fundamentals of the physical Environment*. Third ed. Routledge, London, 627p.

Szczygielski, A.; Stattegger, K.; Schwarzer, K.; da Silva, AGA.; Vital, H., and Koenig, J., 2015. Evolution of the Parnaíba Delta (NE Brazil) during the late Holocene. *Geo-Marine Letters*, 35, 105–117.

Walsh, J.P. and Nittrouer, C.A., 2009. Understanding fine-grained river-sediment dispersal on continental margins. *Marine Geology*, 263, 34–45.

Wells, J. T.; Park, Y. A., and Choi, J. H., (1985). Storm-induced fine sediment transport, west coast of South Korea. *Geo-Marine Letters*, 4, 177-180.

Wells, J.T.; Adams, C.E.; Park, Y.A., and Frakenberh, E.W., 1990. Morphology, sedimentology and tidal channel processes on a high-tide-range mudflat, west coast of South Korea. *Marine Geology*, 95, 111–130.

Yang, B.C.; Dalymple, R.W., and Chun, S.S., 2005. Sedimentation on a wave-dominated, open-coast tidal flat, southwestern Korea: Summer tidal flat-winter shoreface-discussion. *Sedimentology*, 52, 235-252.

Yang, B.C.; Dalymple, R.W.; Chun, S.S., and Lee, H.J., 2006. Transgressive Sedimentation and stratigraphic evolution of a wave-dominated macrotidal coast, western Korea. *Marine Geology*, 235, 35-48.

Journal of Coastal Research	SI	75	1312 - 1316	Coconut Creek, Florida	2016

Mud Deposition on a Macrotidal Beach: Dasari Coastal Dune, West Coast of Korea

Tae Soo Chang[†*], Hun Jun Ha[†], and Seok Hwi Hong[†]

[†]Petroleum and Marine Research Division, Korea Institute of Geoscience and Mineral Resources
Daejeon, Republic of Korea

www.cerf-jcr.org

www.JCRonline.org

ABSTRACT

Chang, T.S., Ha, H.J., and Hong, S.H., 2016. Mud deposition on a macrotidal beach: Dasari coastal dune, West Coast of Korea. *In:* Vila-Concejo, A.; Bruce, E.; Kennedy, D.M., and McCarroll, R.J. (eds.), *Proceedings of the 14th International Coastal Symposium* (Sydney, Australia). *Journal of Coastal Research*, Special Issue, No. 75, pp. 1312 - 1316. Coconut Creek (Florida), ISSN 0749-0208.

Along the macrotidal west coast of Korea, numerous pocket-type or embayed sand beaches are exposed to wave energy and strong tidal processes. They are generally characterized by almost 1 km wide intertidal zones and relatively steep beach gradients. Among these, peculiar muddy beaches occur along the Dasari macrotidal shoreline, midwest coast of Korea. The Dasari beach is generally composed of three sectors; a currently eroding inland coastal dune, a steep and narrow sand beach, and a wide, gently seaward sloping intertidal flat. Unlike other sand beaches on tide-dominated coasts, sediments in the intertidal zone show an unexpected shoreward decrease in mean grain size, fine sands on the lower flat getting finer and finally becoming muddy on the upper flat at the transition between the beach and the intertidal flat. Topographic surveys reveal that the intertidal zone is located below mean sea level without the occurrence of any shore-parallel bars, these features being characteristic of wide low-tide terraces. In particular, the mud flats have a smooth morphology, probably leading to extensive wave energy dissipation. The sand on the narrow beach may be associated with erosion of foredunes during storms coinciding with high tide, rather than the influence of onshore transport across the mud flat. The source of both the fine-grained sediments of the mud flat and the sand of the beach is currently still unclear.

ADDITIONAL INDEX WORDS: *intertidal mud flat, high-tide sand beach, tide-dominated beach.*

INTRODUCTION

The west coast of Korea (*i.e.*, the eastern Yellow Sea) is dominated by a semidiurnal tidal regime with a spring tidal range exceeding 4 m along the entire shoreline. The extensive tidal flats lining the indented coast are world reknown (Chough *et al*., 2004). Large areas of these tidal flats have been reclaimed and diked over past centuries for industrial or agricultural purposes. In addition to the well-known tidal flats, numerous macrotidal beaches occur between larger estuaries and embayments. These beaches are mostly of the small embayed type, being bounded by rocky headlands on either side (Lee and Yoo, 2012; Lee, 2014).

Previous studies have shown that the macrotidal beaches along the west coast of Korea can be divided into two sectors, a narrow high-tide beach and a wide, relatively low-gradient intertidal flat (Lee and Yoo, 2012; Kim and Lee, 2013; Lee *et al*., 2013; Lee, 2014). The high-tide beaches have steep slope gradients ranging from 5 to 10 degrees, their widths generally not exceeding 100 m. The intertidal zones, by contrast, are characterized by very low gradients of under 1 degree. They commonly extend seaward up to 1 km and in many cases display small shore-parallel or slightly shore-oblique ridge-and-runnel sytems or intertidal sand bars, these being season-dependent. Due to the monsoonal climate, high waves associated with northwesterly winds during winter cause significant erosion and offshore sand transport (Lee and Yoo, 2012). The beaches are, however, regularly remolded by the strong tide, especially during summer. These contrasting energy situations along the west coast have been given considerable attention in the past (Yang *et al*., 2005).

The beach sands along the west coast have mean grain sizes that gradually fine seaward, as is commonly the case on other macrotidal beaches. Mean grain sizes generally range from 1.0 to 2.0 phi near the shore, and from 2.0 to 3.0 phi in the offshore.

Unlike the sandy character of other macrotidal beaches, the offshore sector of the Dasari beach, Seocheon County, midwest Korea (Figure 1), is distinctly muddy. On the other hand, and similar to other macrotidal beaches (*e.g.*, Anthony *et al*., 2002; Anthony and Dolique, 2004; Dolique and Anthony, 2005; Short and Woodroffe, 2009), the beach of the Dasari coast can be divided morphologically into two characteristic sectors, a narrow high-tide beach and a wide intertidal flat exposed at low tide. However, the Dasari beach differs distinctly from the other macrotidal beaches in that the intertidal flats consist of muddy sediment, with mean grain sizes increasing seaward. There are no intertidal bars, the intertidal zone being flat and featureless in morphology.

In this context, the Dasari beach was investigated with the aim to better understand the processes controlling the deposition of mud on the intertidal flat and sand on the beach. For the purpose of the study, five evenly spaced monitoring transects

DOI: 10.2112/SI75-263.1 received 15 October, 2015; accepted in revision 15 January, 2015
*Corresponding author: tschang@kigam.re.kr
©Coastal Education and Research Foundation, Inc. 2016

crossing the intertidal flat from the beach were repeatedly surveyed both topographically and sedimentologically.

Background

The Dasari beach is located in the southern part of the Biin Bay, Seocheon County, midwestern Korea, ca. 10 km north of the Geum river mouth (Figure 1). The beach is of the small embayed type, being about 1 km in length and bounded by rocky headlands both in the north and the south (Figure 2). The NNW-SSE alignment of this beach differs from that of other beaches along the west coast in that it does not directly face NW. At the northern end, a small stream channel exists, which becomes disconnected seaward during low tide. Freshwater input from the stream is very minimal. A small sandy spit extends towards the north, so that the stream channel is often closed. The low-lying bedrock basement, ca. 1 m high, is only exposed on the northern intertidal flat.

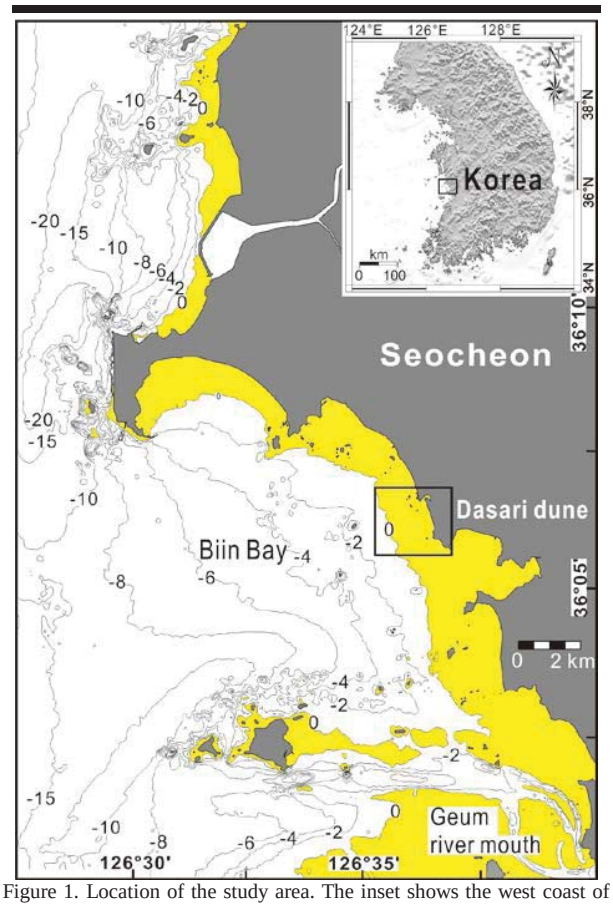

Figure 1. Location of the study area. The inset shows the west coast of the Korean Peninsula. The black box in the figure outlines the Dasari macrotidal coast. The color in yellow is the tidal flat zone.

The beach is generally composed of three geomorphological components, an inland eolian dune, a narrow sand beach and a wide intertidal flat (Figure 2). Foredunes are currently being actively eroded, resulting in about 2.8 m retreat per year (Choi *et al*., 2014). NW oriented parabolic dunes are well-developed, although the dunes are at present partly covered by pine trees. The narrow, steeply sloping high-tide sand beach is located topographically above mean sea level. The tidal flat, by contrast, is situated below mean sea level. It is very flat, almost 1 km wide and characterized by a lack of morphological features.

The tides in the region are semidiurnal with a mean spring tidal range of about 6 m, which places it into the upper macrotidal regime (Flemming, 2005; 2012). The maximum tidal amplitude reaches about 3.5 m at spring tide. Waves generally propagate from the SW. The significant wave height recorded at an offshore bouy is about 3.0-4.0 m under stormy conditions, while the peak period is 8-10 seconds. The largest and smallest waves occur in winter and summer, respectively. The main longshore transport is from south to north, as documented by the northward prograding sand spit.

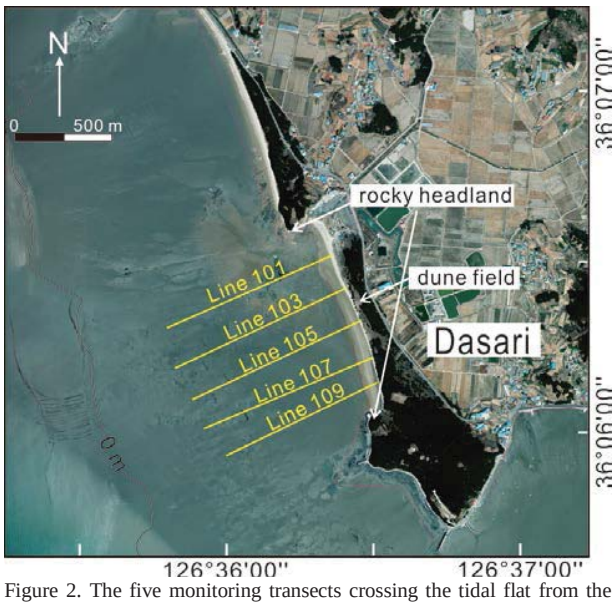

Figure 2. The five monitoring transects crossing the tidal flat from the Dasari coast. Note that the narrow beach (in white) grades into a wide intertidal flat (in greenish gray).

METHODS

The present study is largely based on observations and measurements along the five control transects crossing the intertidal flat and beach (Figure 2). Three times of beach profiling was performed along the transects in May, July-August and September-October in 2015. The morphology of the beach-tidal flat was surveyed with a virtual reference station global positioning system (VRS-GPS). At the same time, surface sediments of 62 samples were taken on the beach and the intertidal flat in May 2015.

Grain-size analyses of the sediments were carried out by the sieve and pipette methods for the sand and mud fractions, repectively. Sand fractions were sieved at 0.25 phi intervals to attain grain-size frequency distributions. The samples were processed according to standard laboratory procedures (Carver,

1971). All textural parameters presented in this study were calcualted following Folk and Ward (1957) and Folk (1966).

RESULTS

Beach-tidal flat morphology

As the Dasari tidal flat-beach is located topographically above the lowest low-water level, the entire area is exposed during low tide, while being completely submerged at high tide. The topographic surveys clearly reveal that the Dasari macrotidal beach can be divided into at least two distinct morphological sectors, a narrow high-tide beach and a wide low-tide intertidal flat (Figure 3).

The beach is typically located near the high tide level and hence above mean sea level. Its width varies between about 100 m in the norther part and almost 50 m at the southern end. The beach slope ranges from 2-5 degrees, being steeper in the south and more gentle in the north. The wider the beach, the gentler the gradient of the beach slope. Topographically, the southern part of the beach terminates slightly below mean sea level, whereas in the north it ends slightly above mean sea level.

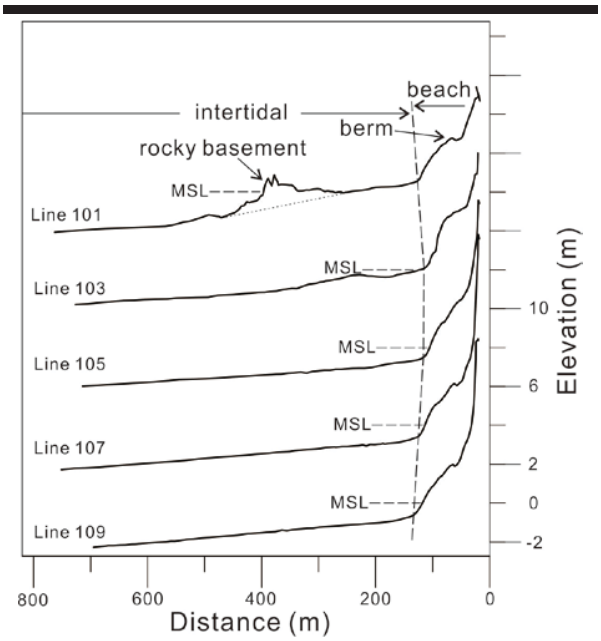

Figure 3. Topographic profiles of the Dasari tidal flat-beach transects surveyed by a VRS-GPS system. It is clearly evident that a pronounced morphological change occurs at mean sea level (MSL), which separates a narrow, steep-gradient beach from a very wide tidal flat.

The seaward intertidal flat has a rather flat and featureless topography (Figure 3). The intertidal zone as a whole extends up to 1.0-1.5 km seaward during spring tide, the muddy tidal flat sector being very much wider than the sandy beach. The slope gradient of the tidal flat is extremely low, amounting to less than 1 degree. As shown by the topographic profiles, the tidal flat is located entirely below mean sea level. Morphologically, the tidal flat is featureless, there being no topographic highs or lows, except for some outcrops of basement rock in the north. The southern part of the tidal flat is lower than the northern part. Under calm conditions, the tidal area is inundated from south to north.

Distribution patterns of surface sediments

The spatial distribution pattern of mean grain sizes of the surficial sediments is illustrated in Figure 4. The beach is composed of medium to fine sand with mean grain sizes of 2.0-3.0 phi, whereas the sediment of the intertidal flat mostly consists of very fine sand to muddy sand with mean grain sizes of 3.5-4.5 phi. The northern part of the tidal flat is dominated by medium sand with mean grain sizes ranging from 2.0 to 2.5 phi.

Spatially, mean grain sizes become coarser toward the beach and the northern tidal flats, whereas they generally become finer toward the transition zone between the tidal flat and the beach. The finest sediments actually occur in this transition zone.

The general mean grain size pattern shows that the Dasari beach can be divided into two distinct zones based on grain size (Figure 5), shoreward fining on the tidal flat and shoreward coarsening on the beach. The turning point in the grain size trend occurs at the transition from the tidal flat to the beach, the pattern thus coinciding with the morphological subdivision of the system. As clearly evident in Figure 5, mean grain sizes on the tidal flat get slightly finer toward the shore and eventually become muddy at the transition to the beach. Landward of the transition, the beach sediment abruptly gets coarser, consisting of medium sand with a mean grain size of 2.0 phi.

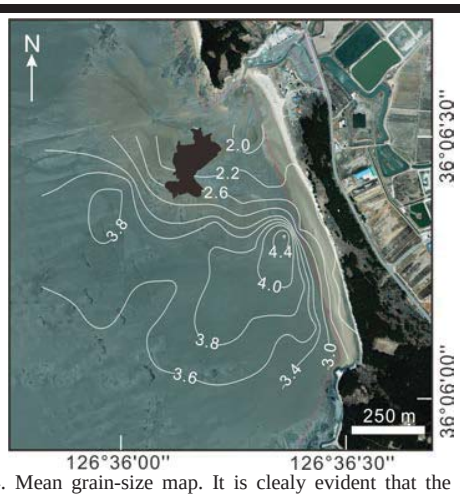

Figure 4. Mean grain-size map. It is clealy evident that the sediment becomes overall finer toward the shore on the tidal flat, but abruptly coarser on the beach.

DISCUSSION

As seen in Figure 3, the beach-tidal flat profiles reveal that the northern area is topographically higher than the southern area. The beach segment is also wider in the north. In the north the tidal flat-beach profiles are overall less concave than in the south, which are strongly concave. The morphological character of the

Dasari beach system suggests a sediment surplus in the northern area but a deficiency in the south (King, 1972; Masselink and Hughes, 2003; Chang and Flemming, 2006; Short and Woodroffe, 2009). Widening of the beach toward the north and the northward growth of the small sand spit support the notion of alongshore sand transport from the south. The transport pattern implies that the southern part of the beach experiences severe erosion, unless one would assume a sediment supply from offshore to onshore. However, a cross-shore transport is highly unlikely, as the sand would have to bypass the tidal mud flat. The tidal mud flat thus appears to represent an energy barrier that prevents cross-shore sand transport.

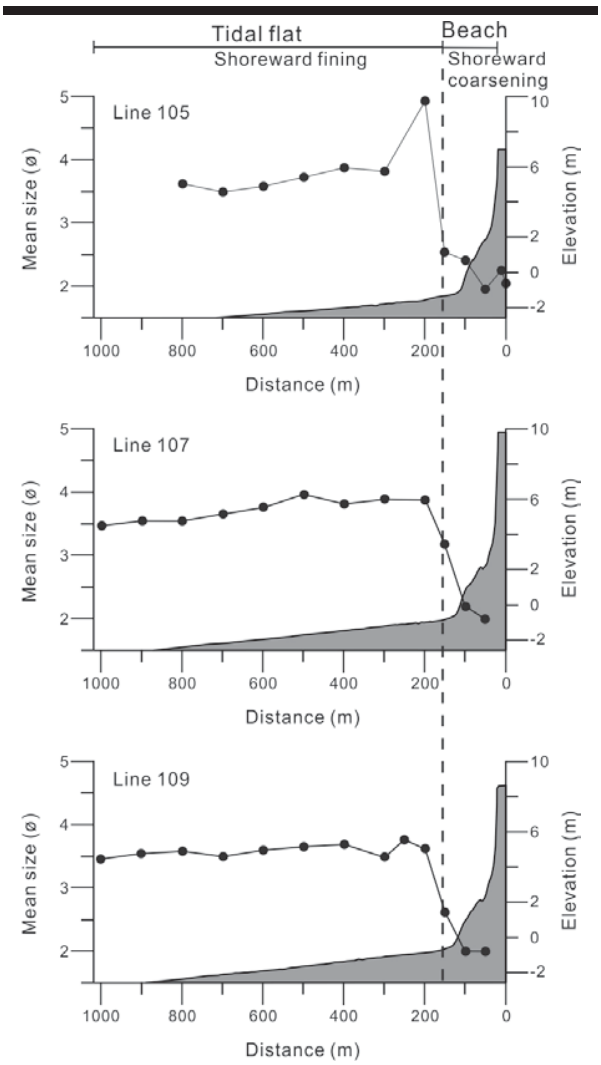

Figure 5. Cross-shore variation in mean grain size along the beach-tidal flat profiles. Mean grain sizes at first decrease and then increase shoreward, the turning point being coincident with the change in morphology.

The general distribution pattern of the sediment reveals a shoreward fining-to-coarsening trend from the seaward tidal flat to the beach, the turning point being located at the transition to the beach where an abrupt change in mean grain size occurs (Figure 5). Interestingly, the abrupt change in the grain-size trend coincides with the change in morphology. This suggests that the tidal flat is modulated by the tide, whereas the beach is controlled by wave action. The interplay between tidal and wave processes generates a narrow and steep gradient toward the high-tide sand beach and a wide and very low gradient across the low-tide mud flat on the seaward side (Short and Woodroffe, 2009).

The source of mud is problematical. The small stream at the northern end of the beach, which is currently gate-closed, does not supply enough mud to the shoreline to explain the extensive mud blanket on the tidal flat, as the discharge (*i.e*., drainage basin) of the stream is too small. On the other hand, the Geum river (see the location in Figure 1), located ca. 10 km south of the Dasari beach, delievers large quantities of fine-grained sediments to the coast and may thus be a potential source. However, previous studies have demonstrated that the sediments delivered by the Geum river are entirely confined to the estuary, being incapable of escaping to the sea (Kim *et al*., 2006). Furthermore, any mud that may escape from the estuary would be preferentially transported toward the south by the southward coastal current driven by the winter monsoon (Lee, 2014). Further studies are thus required to reveal the origin of the fine-grained sediments on the Dasari beach.

The source of the sand on the narrow beach is most probably located in the foredunes, which are being eroded by storms coinciding with high tide (Choi *et al*., 2014; Yi *et al*., 2015), rather than the offshore, from where it would have to bypass the tidal mud flat. In the long run, the Dasari beach may become sediment deficient, unless sand is supplied from other beaches located to the the north and south. In that case, the sand would have to bypass the headlands on both sides of the beach. As in the case of the mud source, this aspect also requires attention in the future.

CONCLUSIONS

The Dasari macrotidal beach, which is ca. 1.0 km in length and 1.5 km in width, is located along the tide-dominated coast of Seocheon County, midwest Korea. Topographic surveys reveal that the beach is composed of two morphologically distinct sectors, a narrow high-tide beach along the shore, and a wide and very low-gradient intertidal flat in the offshore. In contrast to other macrotidal beaches of the Korean west coast, the surficial sediments of the tidal flat are surpringly muddy, with mean grain sizes ranging from 3.5 to 4.5 phi. Grain-size analyses show that there are two contrasting grain size trends, a shoreward fining trend on the intertidal flat and a shoreward coarsening trend on the beach. The abrupt change in the mean grain size trend occurs at the transition from the tidal flat to the beach, being coincident with a pronounced change in morphology.

The peculiar high-tide sand beach fronted by a wide tidal mud flat is probably controlled by storm wave action coinciding with high tide. The wide low-tide mud flat, by contrast, seems to be predominantly modulated by the tide, particularly at times when

waves are small. The interplay between waves and tides imprints a shoreward fining-to-coarsening pattern in grain size, the former being associated with the featureless low-tide mud flat, the latter with the steep high-tide beach. Further studies are required to elucidate the source of not only the mud but also of the sand. In addition, the preservation potential of the mud on longer-term scale needs to be assessed.

ACKNOWLEDGMENTS

This study was supported by a research grant from the Korean Ministry of Oceans and Fisheries (PJT200538 and NP2014-003). The authors would like to thank Dr. Kwang Hee Choi (National Institute of Environmental Research) for introducing the unique mud flat fronting the Dasari sand beach to the authors.

LITERATURE CITED

Anthony, E.J. and Dolique, F., 2004. The influence of Amazon-derived mud banks on the morphology of sandy headland-bound beaches in Cayenne, French Guiana: a short- to long-term perspective. *Marine Geology*, 208: 249-264.

Anthony, E.J.; Gardel, A., Dolique, F., and Guiral D., 2002. Short-term changes in the plan shape of a sandy beach in response to sheltering by a nearshore mud bank, Cayenne, French Guiana. *Earth Surface Processes and Landforms*, 27, 857-866.

Carver, R.E., 1971. *Procedures in Sedimentary Petrology*. New York: Wiley-Interscience, 653p.

Chang, T.S. and Flemming, B.W., 2006. Sedimentation on a wave-dominated, open-coast tidal flat, south-western Korea: summer tidal flat-winter shoreface-discussion. *Sedimentology*, 53, 687-691.

Choi, K.H.; Chang, T.S., Choi, J.-H., Kim, Y., and Lee, S.Y., 2014. Burial storm deposits recorded at the coastal dunes, Dasari, Chungnam Province. *Journal of the Geological Society of Korea*, 50(4), 539-549. (in Korean)

Chough, S.K.; Lee, H.J., Chun, S.S., and Shinn, Y.J., 2004. Depositional processes of late Quaternary sediments in the Yellow Sea: a review. *Geosciences Journal*, 8(2), 211-264.

Dolique, F. and Anthony, E.J., 2005. Short-term profile changes of sandy pocket beaches affected by Amazon-derived mud, Cayenne, French Guiana. *Journal of Coastal Research*, 21(6), 1195-1202.

Flemming, B.W., 2005. Tidal environments. *In*: Schwartz, M. (ed). *Encyclopedia of Coastal Science*. Berlin: Springer, pp. 1180-1185.

Flemming, B.W., 2012. Siliciclastic back-barrier tidal flats. *In*: Davis Jr., R.A. and Dalrymple, R.W. (eds), *Principles of Tidal Sedimentology*. Dordrecht: Springer, pp. 231-267.

Folk, R.L. and Ward, W.C., 1957. Brazos River bar: a study in the significance of grain size parameters. *Journal of Sedimentary Petrology*, 27, 3-26.

Folk, R.L., 1966. A review of grain-size parameters. *Sedimentology*, 6, 73-93.

Kim, T.I.; Choi, B.H., and Lee, S.W., 2006. Hydrodynamics and sedimentation induced by large-scale coastal developments in the Keum River Estuary, Korea. *Estuarine, Coastal and Shelf Science*, 68, 515-528.

Kim, T.R. and Lee, J.H., 2013. The difference in wave environments between intertidal sand beaches and mud flats. *Journal of Coastal Research*, Special Issue, 65, 517-522.

King, C.A.M., 1972. *Beaches and Coasts*. London: Edward Arnold, 580p.

Lee, H.J. and Yoo, J., 2012. Macrotidal beach processes dominated by winter monsoon: Byunsan, west coast of Korea. *Journal of Coastal Research*, 28, 1177-1185.

Lee, H.J., 2014. A review of sediment dynamical processes in the west coast of Korea, eastern Yellow Sea. *Ocean Science Journal*, 49(2), 85-95.

Lee, J.-M.; Park, J-Y., and Choi, J-Y., 2013. Evaluation of sub-aerial topographic surveying techniques using total station and RTK-GPS for applications in macrotidal sand beach environment. *Journal of Coastal Research*, Special Issue, 65, 535-540.

Masselink, G. and Hughes, M.G., 2003. *Introduction to Coastal Processes and Geomorphology*. New York: Oxford University Press Inc., 354p.

Short, A.D. and Woodroffe, C.D., 2009. *The Coast of Australia*. Cambrige: Cambridge University Press, 288p.

Yang, B.C.; Dalrymple, R.W., and Chun, S.S., 2005. Sedimentation on a wave-dominated, open-coast tidal flat, southwestern Korea: summer tidal flat-winter shoreface. *Sedimentology*, 52, 235-252.

Yi, S.; Chang, T.S., Choi, J.-H., and Kim, J.C., 2015. Paleostorm deposits detection at the sand dune of west coast of South Korea based on palynomorphs. *Journal of the Geological Society of Korea*, 51(3), 327-332. (in Korean)

Journal of Coastal Research	SI	75	1137 - 1321	Coconut Creek, Florida	2016

The Economic Benefit of Coastal Erosion Control in Korea

Jeong-In Chang[†*] Sungsoon Yoon[†]

[†] Department of Marine Policy Research,
Korea Maritime Institute, Busan, South Korea

www.cerf-jcr.org

www.JCRonline.org

ABSTRACT

Chang, J.I. and Yoon, S., 2016. The Economic Benefit of Coastal Erosion Control in Korea. *In:* Vila-Concejo, A.; Bruce, E.; Kennedy, D.M., and McCarroll, R.J. (eds.), *Proceedings of the 14th International Coastal Symposium* (Sydney, Australia). *Journal of Coastal Research*, Special Issue, No. 75, pp. 1317 - 1321. Coconut Creek (Florida), ISSN 0749-0208.

The Korean coastal zone is regarded as a highly valuable environmental asset and provides important space for human life. Korean counties with a coastline have a deep interest in finding the most appropriate and sustainable management policy for their coastal resources and ecosystems. Korean coastal zone is now experiencing environmental pressure and is under threat from a diverse range of destructive forces. Thus, this study analyzes the economic benefits of Korea's coastal erosion control project (CECP). The main results of the study are as follows. (1) First, the study identifies the benefit factors of coastal erosion control, such as damage control services, recreational services, and other coastal ecosystem services. (2) Second, this study assesses the economic benefits of the CECP in Korea by applying choice experiment, a non-market valuation method. The annual benefit is estimated at 31,824 KRW (26.56 USD) per household, and the total annual economic benefit of the CECP is estimated at 587.7 billion KRW (490.8 million USD). The findings provide policymakers with a useful methodological framework and quantitative information for decision making on costal management policy.

ADDITIONAL INDEX WORDS: *beach erosion control, economic benefit, willingness to pay, choice experiment*

INTRODUCTION

The Korean coastal zone is now regarded as a highly valuable environmental asset that provides important space for human life. In Korea, 27.1% of the population lives in a coastal area, and 70% of industrial complexes are located there (Ministry of Oceans and Fisheries, 2015). The percentage of Korean tourists who visited coastal zone increased from 49.5% in 2000 to 69.1% in 2010 (Ministry of Land Transport and Maritime Affairs, 2011). However, the risk factors in coastal zone, such as rising sea level, natural disasters, and coastal erosion, have also increased. The damage resulting from issues such as abnormal waves, tsunamis, and super storms reached 431 billion KRW (384 million USD) between 2007 and 2012, representing 67.1% of the nation's total disaster damage.

Coastal erosion has increased due to coastal development and climate change. Coastal erosion issues accounted for 70% of the 580 coastal maintenance projects submitted in 2008. A series of 120 erosion monitoring tests found erosion in 44% of the tested areas in 2005 and 73% in 2012. Video monitoring of the subject areas shows that beach width has shrunk by 3.5%. The natural causes of erosion include waves, currents, and wind; artificial causes include the installation of coastal and river structures, the extraction of marine sand, and dredging.

The Korean government recently discovered that the main causes of erosion were the construction of coastal structures, the extraction of marine sand, and disruptions to currents (MOF, 2014). As demand for coastal use has increased despite the government's budgetary constraints, assessments for suitability or feasibility are required for the optimal use of coastal zone. The coastal erosion control project (CECP) is an infrastructure project that deals with issues, such as revetment, underwater revetment, and beach nourishment, that induce social benefits rather than private ones. Defining the total economic benefit of erosion control in a way that considers its environmental and non-market benefits requires an assessment process that takes economic benefits and project costs into account.

Therefore, this study attempts to measure the economic benefit of the CECP. To this end, the study employs the choice experiment (CE) approach, which offers a promising opportunity to explore the social benefits of the CECP by considering various related attributes. The study is expected to provide policymakers with quantitative information useful in cost–benefit analysis of the CECP. The remainder of this paper is organized as follows. The next section describes the main factors in the benefits and costs of the CECP and reviews several case studies. Then, the paper explains the valuation method and econometric models used to derive the respondents' willingness to pay. The final section discusses the results and provides a conclusion.

BACKGROUND

The first step in CECP assessment is defining the main benefit and cost factors. The benefit and cost of a public project are divided by the social and private factors (Table 1/Yoon and Chang, 2011). The private cost of a project comprises such costs as construction cost, operating cost, land acquisition cost, and

DOI: 10.2112/SI75-264.1 received 15 October, 2015; accepted in revision 15 January, 2015.
*Corresponding author: jeongin0906@gmail.com
©Coastal Education and Research Foundation, Inc. 2016

Table 1. Cost and Benefit Factors of CECP (Yoon and Chang, 2011)

Contents		Coastal improvement project	
		Coastal Erosion Control Project (protecting from erosion, flooding, *etc.*)	Waterfront park project
Cost	Private Cost	Construction cost, operating cost, land acquisition cost, reserve fund, *etc.*	Construction cost, operating cost, land acquisition cost, reserve fund, *etc.*
	Social Cost	Damaging coastal natural landscape with artificial structures	Environmental cost for excess use of waterfront park
Benefit	Private Benefit	-	-
	Social Benefit	- Disaster prevention (agricultural, industrial, residential damage mitigation in hinterland) - Coastal landscape improvement - Coastal environment improvement (water quality, ecological environment, natural restoration) - Public access improvement	- Coastal tourism and public access improvement - Coastal landscape improvement - Educational value - Coastal environment improvement (water quality, ecological environment, natural restoration) - Improvement of residential environment
Indirect Effect		Employment inducing effect, Regional economic effect, (produce inducing effect, value added inducing effect *etc.*)	

Table 2. *Literature review on assessing CECP (Chang and Yoon, 2014)*

Type of project	Researcher	Site	Benefit factors	Economic value [99% confidence interval]	Unit	Methods
Erosion mitigation on sandy beaches	MLTM (2009)	Busan Haundae	Recreation value	110,900	KRW/visit/person (2009)	Travel cost method
		Gangneung Gyungpodae	Recreation value	119,690		Travel cost method
		Busan Haundae	Damage cost for beach erosion width 10% decreasing width 30% decreasing	 - 32,493 - 64,986		Choice experiment
		Gangneung Gyungpodae	Damage cost for beach erosion width 10% decreasing width 30% decreasing	 - 35,069 - 70,138		Choice experiment
	MOMAF (2006)	Gangneung Gyungpodae	Recreational value	135,951 [124,119–154,160]	KRW/visit/person (2006)	Contingent valuation method
		Busan Haundae		137,565 [120,584–175,621]		
		Geoje Hakdong		96,329 [85,583–127,882]		
		Chungnam Daecheon		103,468 [94,445–115,251]		
		Jeonnam Yulpo		62,797 [54,187–79,044]		
		Incheon Youngjongdo		80,245 [71,894–92,051]		
		Ulwangli				
		Jeonbuk Buan Gyukpo		76,292 [67,458–110,378]		
Coastal forest	Chang and Yuk (2009)	Anmyeondo Kkotji beach	- Protecting from disaster (agricultural, residential damage mitigation in hinterland)	1,793.5 [1,487.5–2,203.1]	KRW/year/household (Seoul and Metropolitan Area household)	Contingent valuation method
			- Coastal landscape - Recreational value	1,541.5 [1,278.5–1,893.6]	KRW/year/household (Non Metropolitan area household)	

reserve fund. The private benefits of CECP are hard to quantify; most factors are driven by social dimensions such as disaster prevention (e.g., agricultural, industrial, residential damage mitigation in hinterland), coastal landscape improvement, coastal environment improvement (e.g., water quality, ecological environment, natural restoration), coastal tourism, and public access improvement. The regional and national economic effects of construction determined via inter-industry linkage analysis are classified as indirect effects during the construction period.

The economic assessment of coastal public projects has attracted much attention recently. However, empirical applications to coastal improvement appear to be scarce. Several examples are reviewed below (Table 2; Chang and Yoon, 2014).

(i) Cost of damage through beach erosion

A representative case study is a cost–benefit analysis of an erosion preventing project by the MLTM (2009). It measures the recreational benefits and damage costs of the erosion of a sandy beach based on visitor responses using a two-stage analysis (the travel cost method and conjoint analysis method).

(ii) Recreational value of beaches

The Ministry of Maritime Affairs and Fisheries (MOMAF) estimated the willingness to pay (WTP) for representative sandy beaches using the contingent valuation method (CVM) in 2006.

(iii) Coastal forest

Chang and Yuk (2009) estimated the economic value of the coastal forest at Anmyeondo Kkotji beach using the CVM. The coastal forest plays an important role in wind breaking and shifting sand prevention and as a place for relaxation and enjoying the landscape. The coastal forest project is an efficient measure for coastal improvement. The study estimated the total benefit of the coastal forest at 27,732 million KRW per year in 2009.

METHOD

What, then, is the total economic benefit of coastline protection? This study analyzes the economic benefit of the project using non-market valuation via the CE model, which has been widely used in the environmental field as a survey method to measure people's preferences. The CE allows respondents to systematically evaluate tradeoffs between multiple attributes using a random utility model, the multinomial logit (MNL) model, developed by McFadden (1973). This is useful because many policies are more concerned with changing the level of attributes of environmental goods rather than with losing or gaining an environmental goods as a whole (Hanley *et al.*, 1998). The CE allows respondents to systematically evaluate the trade-offs between multiple environmental attributes and/or between environmental and non-environmental attributes (Lee and Yoo, 2009). This tradeoff process may encourage respondents to introspect their responses; it also facilitates checking for consistency among response patterns, as the CE asks respondents the same questions several times in different questionnaires.

To identify the important attributes of the benefit of the CECP, we selected a set of four attributes, such as damage reduction, beach restoration, eco-waterfront space, and price drawing from the literature review. Each attribute (except price) has three levels. Table 3 presents these attributes and shows how each level was defined. Damage reduction attribute comprises level 1, damage reduction for the construction structure such as through revetment, and level 2, involving the hinterland. Beach restoration attribute refers to the extension of width and widening of recreation space on the beach. The eco-waterfront space attribute refers to the addition of eco-friendly facilities such as coastal trails and small eco-parks near the beach. The price attribute is defined as the additional annual income tax per household, which was likely to be familiar to the respondents. This price refers to the WTP of damage reduction and environmental improvement of the CECP. The lower bound is zero and the upper bound is 12,000 KRW. This is divided into five levels. We employed the orthogonal main effects design, which is effective in isolating the effects of individual attributes on choice. The ability to incorporate this orthogonality is an important advantage of the CE over revealed-preference random utility models, which attributes are often found to be highly correlated with one another (Hanley *et al.*, 1998). The orthogonal main effects design was implemented using the SPSS 12.0 package.

Table 4 shows an example of choice set. The CE's questions presented three alternatives, of which two represented a hypothetical environmental situation and the third represented a fixed alternative with "do nothing scenario". The survey was conducted during 1 August 2014. We conducted 670 person-to-person interviews in all parts of the country with heads of households or housewives between the age of 20 and 65, taking into account the characteristics of the households. Sampling and fieldwork were done by interview- experts from professional polling firms. To maximize the scope of the questions and answers, the interviews were carried out on randomly selected respondents at the respondents' residences.

Table 3. *Attributes and levels of the benefit of CECP*

Attributes	Levels	
Damage reduction (range)	Current level	Nothing
	Level 1	For coastal structure
	Level 2	For coastal structure + hinterland village and agricultural land
Beach restoration (width)	Current level	Nothing
	Level 1	1.5 times the width
	Level 2	2 times the width
Eco-waterfront space	Current level	Nothing
	Level 1	Coastal trails
	Level 2	Coastal trails + Eco- space
Price (WTP per household per year by Income Tax)	Current level	0
	Level 1	3,000 KRW (2.5 USD)
	Level 2	5,000 KRW (4.2 USD)
	Level 3	8,000 KRW (6.7 USD)
	Level 4	12,000 KRW (10.0 USD)

Table 4. *Example of choice set used for survey*

Q. Please, Choose most preferred alternative.

No : 1 (ID=31)	Alternative A	Alternative B	
Damage reduction	Coastal structure	Coastal structure + hinterland village and agricultural land	Do Nothing
Beach restoration	1.5 times the width	Nothing	
Eco-waterfront space	Nothing	Coastal trails	
Price	8,000 KRW	10,000 KRW	
	☐A	☐B	☐Neither

The random utility model is used to explain individual choices by specifying functions for the utility derived from the available alternatives (for details, see Lee and Yoo (2009)). The utility function for CECP can be expressed as a linear function of the attribute vector (X_1, X_2, X_3, X_4) = (Damage reduction, Beach restoration, Eco-waterfront space, Price). For each attribute, the marginal willingness to pay (MWTP) represents the marginal rate of the substitution between the price and that attribute.

RESULTS

The sample statistics of respondents are shown in Table 5. The average age of respondents was 45.78 and their monthly household incomes were 4.16 million KRW (3,479 USD). The estimation results of each coefficient of all the attributes in the utility function, shown in Table 6, are statistically significant at the 1% level. The sign of all coefficients are positive except price, indicating that as the level of attributes increases, the utility of household increases. The estimates of the household's MWTP are presented in Table 7. The average MWTP per household for reducing the erosion damage of level 1 is 5,708.6 KRW (4.77 USD). The respective *t*-values are 9.32, indicating that the hypothesis whereby MWTP is zero cannot be rejected at the 1% level. The MWTP for the beach restoration is estimated to be 5,514 KRW (4.60 USD) for a beach that is 1.5 times wider. The average WTP per household for CECP on level 2 for each alternative is 31,825 KRW (26.58 USD) per year.

Table 5. *Sample statistics of respondents*

Variables	Unit	Mean	Standard deviation
Age	Year	45.78	9.33
Household monthly income	10,000 KRW	416.6	275.86
Education level	Year	6	2.37
			13.96

Table 6. *Estimation results*

Variables	Estimates	*t*-statistics
β_{11} (Damage level 1)	0.434	7.086**
β_{12} (Damage level 2)	0.630	8.998**
β_2 (Beach restoration)	0.419	11.402**
β_{31} (Eco-waterfront space level 1)	0.628	10.009**
β_{32} (Eco-waterfront space level 2)	1.231	16.684**
β_4 (Price)	0.760E-04	8.445**
Number of observations [a]	2,680	
Log-likelihood	-2,693.143	
Wald statistics	461.61	
(p-value)[b]	(0.00)	

** indicates significance at the 1% level.

[a]*Each respondent was asked to answer for 4 choice sets*

[b]*The hypothesis is that all the parameters are jointly zero.*

Table 7. *Estimates of marginal willingness to pay*

(unit: KRW per household per year)

Attributes		MWTP (*t*-statics)	95% confidence interval [a]
Damage reduction	Coastal structure	5,708.6 (9.317**) 4.77 USD	4,358.1 – 7,379.2
	Hinterland village and agricultural land	2,579.8 (2.812**) 2.15 USD	1,039.0 - 4,125.9
Beach restoration	1.5 times the width	5,513.9 (10.543**) 4.60 USD	4,755.2 – 6,506.1
Eco-Waterfront space	Coastal trails	8,261.6 (7.338**) 6.90 USD	6,600.8 – 10,433.3
	Eco- space	7,922.7 (6.602**) 6.62 USD	7,318.2 – 8,918.9

** indicates significance at the 1% level

[a]*The 95% confidence intervals for the estimates of MWTP were computed by the use of the Monte Carlo simulation technique.*

Table 8. *Total economic benefit*

(unit: KRW per year)

Attributes	WTP	The number of households	Total economic benefit

Damage reduction	8,288.4		
Beach restoration	7,351.8		
Eco-Waterfront space	16,184.3		
Total	31,824.6	18,467,628	587.7 billion KRW 490.8 million USD

DISCUSSION

The estimation results show that the households' WTP of recreational attribute is higher than those of damage reduction or beach restoration. The higher WTP for the recreational attribute implies that they place more weight on the actual use value of the coastal zone. However, we found the respondents also evaluated their CECP option value highly. The aggregated WTP for damage reduction and beach restoration efforts was 15,639 KRW per year; these attributes are intimately related to the residents of the coastal zone.

The total annual economic benefit of the CECP is estimated at 587.7 billion KRW (490.8 million USD) by multiplying the households' annual WTP with the number of national households, 18,467,628 in 2014 (Table 8). When comparing it to the cumulative investment amount for the CECP of 818 billion KRW (54.5 billion KRW per year) from 2000 to 2014, the annual social benefit of the CECP is greater than the annual construction cost. Aside from the recreational attribute (Eco-waterfront space), the annual economic benefit of the two attributes was estimated at 288.8 billion KRW (241.2 million USD).

CONCLUSIONS

This study analyzes the economic benefit of the CECP, a coastal public project, using a non-market valuation method. The economic valuation results imply that Korea's coastal zone is a valuable national asset, as well as a place for recreational activities and residential areas. The results of the analysis can give decision makers quantitative information on social preferences for policy and its benefits. This study also introduces the categories and main factors of the economic benefits of the CECP in Korea. It offers profound insight into valuing the economic benefits of the CECP. More specific and accurate analyses could be carried out by developing economic cost-benefit analysis guide-lines for the CECP. This may provide a framework for preliminary and post-hoc feasibility assessments.

LITERATURE CITED

Chang J. I.; Lee J. S. and Shin C. O., 2011, Analyzing Consumer's Preference for the Potential Value of Coastal Wetland Ecotourism Using Contingent Choice Method, *Ocean and Polar Research*, 33(2), 149-157.

Chang, J. I. and Yuk G.H., 2009, Economic Value of Coastal Buffer Zone: The Coastal Forest, *Proceedings of Joint Conference of the Korean Society for Marine Environmental Engineering* (Changwon, Korea), 305p.

Chang, J. I. and Yoon S., 2014, The Economic Benefit of the Coastal Improvement Project in Korea, *Proceedings of OCEANS'14 MTS/IEEE Conference* (Taipei, Taiwan).

Hanley, N.; Wright, R.E., and Adamowicz, W., 1998. Using choice experiments to value the environment. *Environmental and Resource Economics* 11, 413–428.

Lee, J.S. and Yoo, S.H., 2009, Measuring the Environmental Cost of Tidal Power Plant Construction: A Choice Experiment Study, *Energy Policy*, 37, 5069-5074.

McFadden, D., 1973. *Conditional logit analysis of qualitative choice behavior*. *In*: Zarembka, P. (ed.), Frontiers in Econometrics. New York: Academic Press.

Ministry of Land, Transport and Maritime Affairs (MLTM), 2009, *The 4th Study on the Development of Technologies for Preventing Coastal Erosion: Economic Valuation and Validity Analysis*, Seoul, Korea: Ministry of Land, Transport and Maritime Affairs Publication.

Ministry of Maritime Affairs and Fisheries (MOMAF), 2006, *The Study on the Development of Management and Assessment Model by Beach Types*,108p.

Ministry of Oceans and Fisheries (MOF), 2015, *Coastal Basic Investigation*, Sejong, Korea: Ministry of Oceans and Fisheries Publication, 401p.

Ministry of Oceans and Fisheries, 2014, *The Second Adjusted General Plan for Coastal Improvement*, Sejong, Korea: Ministry of Oceans and Fisheries Publication, 52p.

Ministry of Land, Transport and Maritime Affairs, 2011, *The Research on the Establishment of Marine Tourism Statistics and development of Static Program*, pp. 128-129.

Yoon S. and Chang, J.I., 2011, *The Study on Coastal Improvement Project Effects and Benefit Enhancement Measures*, Seoul Korea: Korea Maritime Institute. pp. 51-52.

Yoo S. H. and Chang, J.I., 2013, The Economic value of Marine Ecosystem in Korea: A preliminary assessment, *Proceedings of the 1st International Workshop on Spatial Management Tools toward Creative and Viable Coastal Societies* (Seoul, Korea), pp. 84-96.

Journal of Coastal Research	SI	75	1322 - 1326	Coconut Creek, Florida	2016

Partitioning of Grain-size Component Populations in Bimodal Sediments

Tae-Jin Choi†, Jun-Yong Park‡*, and Jin-Yong Choi †

† Department of Oceanography,
Kunsan National University
Gunsan, South Korea

‡ Marine Environments & Conservation Research Division,
Korea Institute of Ocean Science and Technology (KIOST)
Ansan, South Korea

www.cerf-jcr.org

www.JCRonline.org

ABSTRACT

Choi, T.J.; Park, J.Y., and Choi, J.Y., 2016. Partitioning of Grain-size Component Populations in Bimodal Sediments, *Proceedings of the 14th International Coastal Symposium* (Sydney, Australia). *Journal of Coastal Research*, Special Issue, No. 75, pp. 1322 - 1326. Coconut Creek (Florida), ISSN 0749-0208.

Most continental shelf sediments show bi- and/or poly-modal patterns consisting of overlapping components in the grain-size distribution (GSD), which generally reflect various environmental conditions as well as multiple sources of sediment. Because the laser-diffraction method is accurate and requires only a few grams, it is useful for analyzing cores with complex sedimentary structures of alternating coarse and fine lamina. In this study mathematical method of the partitioning of component (PCP) is applied to high-resolution GSD analysis for a sediment core collected from the central Yellow Sea (14YS-PC-3, 261 cm). Coarser and finer components within the GSDs of the core sediments with a typical bi-modal pattern were separated by PCP method, and then the textural parameters of each component were recalculated. The upper part (0-75 cm) of the core consists of homogenous muddy sediments of about 8.31 Φ in mean grain size, while bi-modal muddy sands with 6-7 Φ in Mz are predominant at the lower part. Mz of the coarse components are about 4.13 Φ and remain constant throughout the core. The fine components are, however, in a range of 5.52 Φ to 8.71 Φ in Mz showing a typical fining-upward trend, and the amounts of fine component tend to increase upward. This result indicates that the fine component is a main factor determining Mz in the lower part (deeper than 75 cm). The trends of GSD by PCP might be related to the status of depositional energy level during the transgression stage of the Holocene period. Consequently, application of PCP to precise GSD data, together with the geochemical, palaeontological and age-dating data, can contribute to the better understanding of sediment sources and comprehensive paleo-environmental conditions.

ADDITIONAL INDEX WORDS: *PCP, Grain-size distribution, Curve-fitting, Laser-diffraction method.*

INTRODUCTION

The grain-size distribution (GSD) patterns and textural parameters of sediment samples have been generally used as environmental proxies to find out sediment sources, transportation and deposition processes, and sedimentary environments (Tanner, 1964; Middleton, 1976; Ashley, 1978; Bagnold and Barndorff-Nielsen, 1980). Generally most sediments on continental shelf show bi- and/or poly-modal distribution consisting of overlapping components in GSD (McCave and Syvitski, 1991). Considering that each component in multi-modal pattern reflects different depositional processes as well as multiple sources preserving information about depositional environment, it is necessary to separate out information of individual characteristic components from GSD of bulk samples.

Early study for partitioning of component populations (PCP) introduced by Visher (1969) was to separate subpopulations at breaks between fitted straight-line segments of cumulative probability plots on the assumption that all the subpopulations are truncated distributions (Sun, 2004). This graphical method was, however, nonobjective and imprecise to yield a particular sample (Middleton, 1976; Ashley, 1978). As a different approach, the quantitative method based on a cumulative distribution function was introduced, which was related with hydraulic sediments, but this approach was not diversely adopted (Kranck *et al*., 1966a, b; Passe, 1997).

Recently, mathematical methods have been developed using curve-fitting function that statistically finding out GSD of optimal component populations using a computer program. These curve-fitting methods have been applied to studies on reconstruction of paleo-oceanographic environments (Sun *et al*., 2002; Sun *et al*., 2004; Leys *et al*., 2005). Compared with the graphical methods, these mathematical methods, together with high-resolution grain size analysis technique using laser diffraction size analyzer (LDSA), generally show precise reconstructions of depositional environments. LDSA has been vigorously adapted in grain-size analysis for sediment cores with complex sedimentary structures of alternating coarse and fine lamina, because it requires only a few grams of the samples and analyze them within a very short time of several tens of seconds (Prins *et al*., 2002; Sun *et al*., 2004; Xiao *et al*.,2006; Nagashima *et al*., 2007).

In this study we examined the application of a mathematical approach for partitioning the grain-size components using the

DOI: 10.2112/SI75-265.1 received 15 October, 2015; accepted in revision 15 January, 2015
*Corresponding author: jypark@kiost.ac.kr
©Coastal Education and Research Foundation, Inc. 2016

GSD data measured by LDSA with sediment core samples collected from the central Yellow Sea continental shelf.

METHODS

Materials and grain-size analysis

Prior to the application, tests were made on piston cores collected from North Pacific deep sea (580 cm in total length) and from freshwater Daecheong Lake in Korea (67 cm in total length).

Four samples were selected from the two cores:

i) P-1 and P-2: subsamples on the North Pacific core at 11-cm and 250-cm depths; and

ii) L-1 and L-2: subsamples on Daecheong Lake core at 9-cm and 17-cm depths.

It is obvious that deep sea sediments consist mainly of abyssal clays of about few ㎛ in size and also coarser-grained biogenic materials. Their GSDs show typical bi-modal distribution, and therefore are the best samples to test the PCP procedure. Lacustrine samples are also considered to represent the different populations in GSD due to influences of the typical monsoonal climate of Korea.

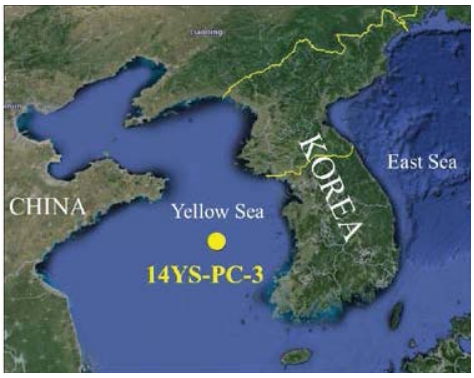

Figure 1. Core sampling site (14YS-PC-3, 83-m water depth) in the Yellow Sea of a typical epicontinental sea (Image source: GoogleEarth).

A piston core of 261-cm long was collected from central Yellow Sea of 83-m water depth (14-YS-PC-3) (Figure 1). After spliting the core in half, photographs and manual descriptions were made in detail. A series of subsamples were obtained from one-half of the core for water content, geochemical, mineralogical and paleontological analysis. For grain size analysis, about 3 gram of subsamples were collected at an interval of 1 cm. After oven-dried, pre-treatment procedures were made on the sediment samples following the standard method using distilled water and hydrogen peroxide to remove sea salts and organic matters. Hydrogen chloride was not treated in order to reserve carbonate materials of biogenic origin.

All the bulk samples were analyzed using the OASIS laser diffraction particle size analyzer with high degree of precision and accuracy (Choi *et al*., 2013; Choi, 2014) that has a working range from 0.1 to 8,750 ㎛ based on the Fraunhofer diffraction theory (Sympatec, Germany). Prior to the LDSA analysis, the samples were ultrasonically treated for a short time within 10 sec and were dispersed in a 2% Calgon solution during 24 hours. For the pretreated samples the LDSA analysis was conducted to obtain high-resolution grain-size distributions with a 0.1-Φ size resolution, followed by applying the mathematical PCP method to the resulted GSDs for separating grain-size components from them. Textural parameters of bulk samples and separated components were calculated by the method of moments.

Partitioning of the Grain-size Component Populations

PCP was processed using the curve-fitting functions of the MATLAB software to find the best curve-fit and separate major components from the grain-size distribution data of each bulk sample. Goodness of fit of the separated components was estimated by the fitting error (FE). It is basically assumed that the grain-size distributions of natural sediments follow the Gaussian function that has been used widely in sedimentology (Middleton, 1976; Ashley, 1978).

Procedures for PCP were performed as follows (Figure 2):

i) First curve fitting is conducted for a bulk sample, assuming that the bulk sample is unimodal with a single peak signal. If its result on FE is less than 5%, the bulk sample is determined to be unimodal. Otherwise, the sample is considered as bi- and/or poly-modal;

ii) In the case of FE > 5% from the first curve fitting, then second curve fitting is performed to find two peak-signals, assuming that the bulk sample is bimodal. If the FE of the second curve fitting is less than 5%, the bulk sample is determined to be bimodal, otherwise it is considered to be polymodal; and

iii) Until FE becomes less than 5%, additional curve fitting(s) is (are) performed for the polymodal sample.

Finally, the amount and grain-size distribution statistics of the individual components separated from the bulk samples are recalculated.

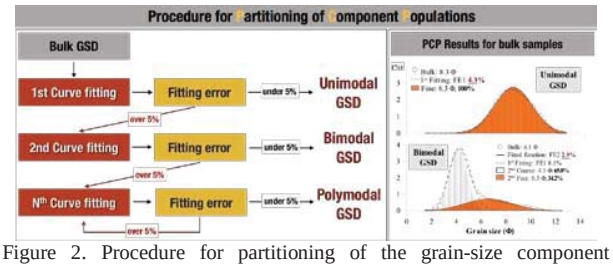

Figure 2. Procedure for partitioning of the grain-size component populations.

RESULTS

Test results of the PCP method with the deep-sea (P-1 and P-2) and lacustrine (L-1 and L-2) samples are summarized and illustrated in Table 1 and Figure 3, respectively. Results applied to the core sediment (14-YS-PC-3) are also illustrated in Figure 4. Final results yielded acceptable fitting functions within the given fitting error (FE) of less than 5%.

Deep-sea sediments

Bulk sediments of P-1 and P-2 have 8.1 Φ and 8.8 Φ in the mean size, respectively, but represent obvious bimodal GSD patterns. Results of PCP show two distinct components of the

coarse and fine fractions in the GSDs just as expected (Figure 3P-1 and P-2). The amounts of each component are noticeably different between the P-1 and P-2. Coarse-grain population of biogenic origin reaches 36% in P-1, but less than 10% in P-2. Decreasing amounts of the biogenic materials with depth are considered to represent the dissolution and fragmentation of biogenic materials, mostly foraminifera. Mean sizes of the coarse populations, therefore, decrease from 5.4 Φ in P-1 to 5.8 Φ in P-2. Although the amounts of the fine populations are different between the two samples, their mean grain sizes and modal grain sizes remain almost same at about 9.0 Φ, indicating the similar and continuous depositional conditions in abyssal environment for sediment P-1 and P-2.

Table 1. *Mean sizes of the bulk samples and the subpopulations separated by the PCP method.The P and L samples represent deep-sea and lacustrine sediments, respectively. FE represents the fitting error.*

Smples (core depth)	Bulk	1st curve fitting		2nd curve fitting				
				Coarse component		Fine component		
	Mz (Φ)	Mz (Φ)	FE1 (%)	Mz1 (Φ)	Content1 (%)	Mz2 (Φ)	Content2 (%)	FE2 (%)
P-1 (11 cm)	8.1	-	21.0	5.4	36.2	8.9	63.8	**3.4**
P-2 (250 cm)	8.8	-	6.0	5.8	9.1	9.0	90.9	**2.7**
L-1 (1 cm)	8.4	8.2	**4.7**	-	-	-	-	-
L-2 (17 cm)	7.1	-	8.9	6.0	48.9	8.1	51.1	**3.4**

Lacustrine sediments

L-1 and L-2 have about 8.4 Φ and 7.1 Φ in mean grain size, respectively and their GSD patterns look like they have uni-modal distributions. When applying PCP to L-1, it was, as expected, proved to be unimodal because the FE of the 1st curve fitting was 4.7%. The differences of textural parameters between the bulk sample and the curve-fitted component of L-1 are less than 0.2 Φ in mean size and peak mode (Figure 3L-1). Most of the errors occur in both the fine- and the coarse-tailed ranges because curve-fitting procedure enforces the symmetric distribution. On the other than, L-2 was identified as having a bimodal GSD pattern, although the GSD pattern of the bulk sample looked like a unimodal distribution (Figure 3L-2). FE is calculated 8.9% in 1st curve fitting but decreases less than 4 % in second fitting, suggesting that L-2 is composed of two overlapping components of a bi-modal distribution. Its coarse component has 6.0 Φ, 6.2 Φ and 48.9 % in mean size, mode and content, respectively, while its fine component has 8.1 Φ, 8.2 Φ and 51.1%, corresponding closely with those of L-1.

The lacustrine sediments are considered to represent the dynamic seasonal changes in depositional condition due to the typical monsoonal climate in Korea; rainy summer season of large sediment input and dry winter with no supply. The coarse population in L-2 is, therefore, interpreted as the materials supplied during the episodic events such as heavy rains in summer.

Application of PCP to the core sediments

Sediment core of Yellow Sea (Figure 1) is clearly separated into upper part of muddy sediment in dark olive gray (5Y 3/2) and lower part of sand and mud intercalated structures in dark grayish brown color (2.5Y 4/2). Mean sizes of its bulk samples show a wide range of variation of 4.1 to 8.6 Φ. Biogenic materials are scarce in the whole core, escept shell fragments at around 220 cm. Characteristically, the bulk sediments show noticeably different GSD patterns between upper and lower part (Figure 4a). The upper part (0-75 cm) of the core consists of homogenous muddy sediments having uni-modal GSD patterns and 8.3 Φ in mean size, whereas bimodal muddy sands with 4.1 to 7.6 Φ in mean are predominant at the lower part (Figure 4a and b).

When applying the PCP method to the bulk GSD results, coarse components have about 4.1 Φ in mean size consistently throughout the lower part but do not exist in the upper part (Figure 4a). Fine components of the lower part have a range of 5.5 to 8.0 Φ in mean size and show a typical fining-upward trend with content increase (Figure 4a). This trend corresponds closely to the mean-size trend of the bulk sediments, indicating that the fine component is a main factor determining textural charateristics in the whole core. Muddy sediments in the upper part are homogenous, and their mean sizes remain constant regardless of changes in depth. However, the detailed trend of mean grain-size variation exhibits a particular pattern; the fining-upward trend from 75 cm to 23 cm turns into coarsening-upward from 23 cm to the sruface, where mean grain sizes decrease from 8.4 Φ to 8.2 Φ (Figure 4a-1).

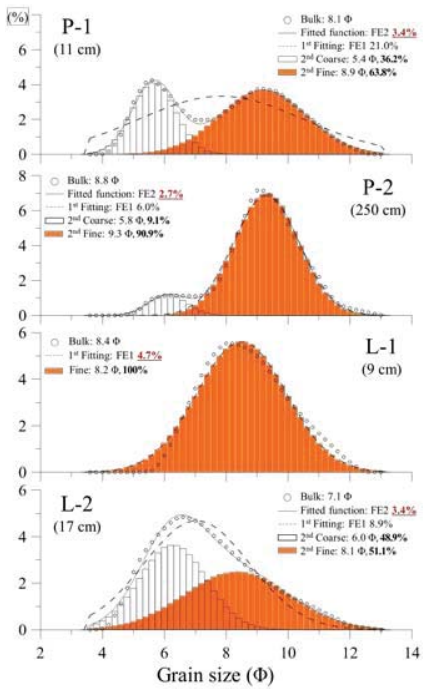

Figure 3. Curve-fitting tests of the GSD curves for deep-sea (P-1, P-2) and lacustrine (L-1, L-2) sediments by the PCP method.

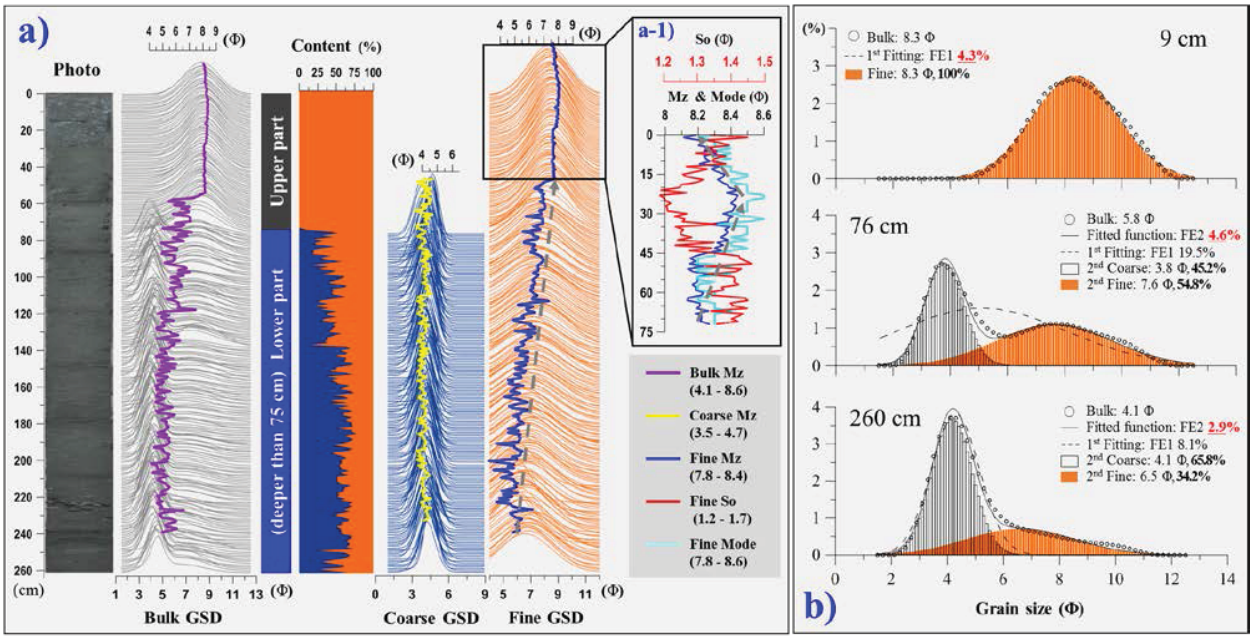

Figure 4. Results of the PCP analysis for the Yellow Sea 14YS-PC-3 core. a) Vertical profiles of textral parmeters of the bulk samples and the individual components separated by the PCP method. The upper and lower parts of the core show different trends in Mz based on 75 cm. The fine component is a main factor determining mean size and variation trend in the whole core. b) Detailed results of the PCP-analysis for the bulk samples at 9, 76 and 260 cm in core depth.

DISCUSSION

The main objective of this study is to present a mathematical approach to separate out the modal components from GSD of bulk sediments. This method is able to provide detailed information on sediment sources, depositional processes and the characteristics of sedimentary environments for each separated components.

Because deep-sea sediments consist mainly of abyssal clay of detrital origin and also the carbonate materials of biogenic origin, GSD of the pelagic deposits is generally bimodal. P-1 and P-2 from the deep-sea core show typical bimodal patterns in their GSD. It is appropriate to apply PCP to these samples since their FEs are lower than 3.0% after bi-modal separation. The difference in amount of each modal population between P-1 and P-2 is significant, especially in content of coarse component with 36.2% and 9.1%, respectively. The coarse components are considered to be foraminifera. Therefore, its decrease might result from is regarded as removal of carbonates by dissolution after burial. In conjunction with geochemical and age-dating data of a sediment core, PCP will be very useful for reconstructing paleoenvironmental events such as climate changes and glacial-interglacial events more precisely.

The lacustrine core sample of L-2 also show bi-modal patterns, although it looks like it has a unimodal distribution. Its result is interpreted as the mixture of two different depositional processes. Considering the monsoonal climate pattern in Korea, the coarser-grained component could be characterized by heavy-rain events in summer. The fine component, on the other hand, is considered to be the normal deposit during spring and fall of low precipitaion seasons. It is possible, therefore, to apply PCP to establishing seasonal depositional regimes, although these need to be investigated by further works.

When applying PCP to the continental shelf core, it clearly shows a reason that we should apply PCP to GSD. Especially, when sediment materials are the mixures of several population showing bi-modal distribution like the case of the lower part of the 14YS-PC-3 core, it is very hard or almost impossible to induce sedimentologic interpretations. Individual grain-size components should be separated out from the bulk samples for adequate interpretation. From the results of the PCP analysis for the Yellow Sea core, we found out several interesting results. First, the fine component is a main factor determining the mean grain-size variation trend in the whole core. Second, the coarse component at the lower part of the core shows consistant mean size and GSD pattern, which suggests that the coarse sediments were transported from the same origin. And finally, the fine component shows a typical upward-fining trend in the lower part, but alternating tendency in the upper part. The vertical GSD trends by PCP might be closely related to the status of depositional energy level during the transgression stage of the Holocene period. Although there still exist many intractable problems in explain the provenance and the depostional evolution in Yellow Sea due to its environemental complexity (Yang *et al.*, 2003), the high-resolution grain-size analysis technique using of PCP might be a valuable tool for better

understading of them in combination with geochemical, mineralogical and paleontological analysis data.

CONCLUSIONS

We apply PCP to high-resolution GSD analysis measured by LDSA for lacustrine, deep-sea and continental-shelf sediment cores. As summarized as follows:

i) The LDSA is a very useful method for analyzing sediment cores with complex sedimentary structures of alternating coarse and fine lamina.

ii) The PCP results indicate that the depositional processes of the lacustrine, deep-sea, and continental-shelf sediments might be related to the seasonal cycle of sedimentary processes, paleoclimate and sea-level changes, respectively.

In conclusion, application of the PCP method to high-resolution GSD can contribute to better understanding of sediment sources and comprehensive paleo-environmental conditions, in conjunction with the geochemical, palaeontological and, especially, age-dating data.

ACKNOWLEDGMENTS

This research was a part of the project titled “Integrated management of marine environment and ecosystems around Saemangeum” funded by the Ministry of Oceans and Fisheries, South Korea. The study has been partially funded by the PM58731 and PE99332 Research grant from the Korea Institute of Ocean Science and Technology (KIOST) and by 2014 and 2015 SMG Research supported by the Rural Research Institute (RRI) of the Korea Rural Community Corporation.

LITERATURE CITED

Ashley, G.M., 1978. Interpretation of polymodal sediments. *Journal of Geology*, 86, 411–421.

Bagnold, R.A. and Barndorff-Nielsen, O., 1980. The pattern of natural size distributions. *Sedimentology*, 27, 199–207.

Choi, T.J.; Park, J.Y.;Jeong, E.Y., and Choi, J.Y., 2013. Sand Grain-size Analysis Using a Laser Diffraction Analyzer. *Asia Oceania Geosciences Society*, 140p.

Choi, T.J., 2014. Sediments grain-size analysis using a laser-diffraction size analyser. Gunsan-si, Jeollabuk-do: Kunsan National University, Master’s thesis, 78p.

I. N. McCave and James P. M. Syvitski., 1991. Principles and methods of geological particle size analysis. In: James P. M. Syvitski (ed.) Principles, Methods and Application of Particle Size Analysis. Cambridge: Cambridge University Press. pp. 3-21.

Kranck, K.; Smith, P.C., and Milligan, T.G., 1996a. Grain-size characteristics of fine-grained unflocculated sediments: I. ‘One-round’ distributions. *Sedimentology*, 43, 589–596.

Kranck, K.; Smith, P.C., and Milligan, T.G., 1996b. Grain-size characteristics of fine-grained unflocculated sediments: II. ‘Multi-round’distributions. *Sedimentology*, 43, 597–606.

Leys, J.; McTainsh, G.; Koen, T.; Mooney, B., and Strong, C., 2005. Testing a statistical curve-fitting procedure for quantifying sediment populations within multi-modal particle-size distribution. *Earth Surface Processes and Landforms*, 30, 579-590.

Middleton, G.V., 1976. Hydraulic interpretation of sand size distributions. *Journal of Geology*, 84, 405–426.

Nagashima, K.; Tada, R.; Matsui, H.; Irino, T.; Tani, A., and Toyoda, S., 2007. Orbital- and millennial-scale variations in Asian dust transport path to the Japan Sea, *Palaeogeography, Palaeoclimatology, Palaeoecology*, 247, 144-161.

Passe, T., 1997. Grain size distribution expressed as tanh-functions. *Sedimentology*, 44, 1011–1014.

Sun, D.; Bloemendal, J.; Rea, D.K.; Vandenberghe, J.; Jiang, F.; An, Z., and Su, R., 2002. Grain-size distribution function of polymodal sediments in hydraulic and Aeolian environments, and numerical partitioning of the sedimentary components. *Sedimentary geology*, 152, 263-277.

Sun, D.; Bloemendal, J.; Rea, D.K.; An, Z.; Vandenberghe, J.; Jiang, F.; Lu, H.; Su, R., and Liu, T., 2004. Bimodal grain-size distribution of Chinese loess, and its palaeoclimatic implications. *CATENA*, 55, 325-340.

Tanner, W.F., 1964. Modification of sediment size distributions. *Journal of Sedimentary Petrology*, 34, 156–164.

Visher, G.S., 1969. Grain size distribution and depositional processes. *Journal of Sedimentary Petrology*, 39, 1074 – 1106.

Xiao, S.B.; Li, A.C.; Liu, J.P.; Chen, M.H.; Xie, Q.; Jiang, F.; Li, T.G.; Xiang, R., and Chen, Z., 2006. Coherence between solar activity and the East Asian winter monsoon variability in the past 8000 years from Yangtze River-derived mud in the East China Sea. *Palaeogeography, Palaeoclimatology, Palaeoecology*, 237, 293-304.

Yang, S.Y.; Jung, H.S.; Lim, D.I., and Li, C.X., 2003. A review on the provenance discrimination of sediments in the Yellow Sea. *Earth-Science Reviews*, 63(1-2), 93-120.

Journal of Coastal Research	SI	75	1327 - 1331	Coconut Creek, Florida	2016

A Laboratory Experiment on beach profile evolution induced by two wave conditions dominated in the Haeundae Coast of Korea

Junwoo Choi[†*], Min Roh[†], and Young Taek Kim[†]

[†] Coastal Research Lab., Korea Institute of Civil Engineering & Building Technology
Goyang, Korea

www.cerf-jcr.org

www.JCRonline.org

ABSTRACT

Choi, J.; Roh, M., and Kim, Y.T., 2016. A Laboratory Experiment on beach profile evolution induced by two wave conditions dominated in the Haeundae Coast of Korea. *In:* Vila-Concejo, A.; Bruce, E.; Kennedy, D.M., and McCarroll, R.J. (eds.), *Proceedings of the 14th International Coastal Symposium* (Sydney, Australia). *Journal of Coastal Research*, Special Issue, No. 75, pp. 1327 - 1331. Coconut Creek (Florida), ISSN 0749-0208.

A laboratory experiment was performed by using the scaled-down conditions (*i.e.*, 1/10) of the two dominant waves (i.e, a storm wave and a normal wave) obtained from the statistical analysis of wave data measured at the Haeundae coast during 3 years. The storm and normal waves did alternately evolve the beach profile from a constant slope and each of the wave conditions was maintained to reach its quasi-equilibrium state. The observation was conducted in the surf zone and the swash zone during the alternation of the 1-hr storm-erosion condition and the 2-hr normal-accretive condition. The storm-erosion condition generated the longshore bar-crest and trough and the steep berm, and the normal-accretion condition reduced the bar and trough. The subsequent quasi-equilibrium beach profile was reasonably agreed to the beach profile of the Haeundae beach.

ADDITIONAL INDEX WORDS: *Storm wave, normal wave, surfzone, morphological change.*

INTRODUCTION

The global warming has increased the sea levels and the extreme events of typhoons and storm surges. And they have accelerated the beach erosion. The dynamic change of the coastal morphology became one of the severe natural disasters. The coastal erosion of South Korea has been also recognized as in a dangerous situation, and many researchers are working on the beach erosion problems.

In the investigation of coastal morphology movable bed hydraulic experiments play an important role and has limitations caused by the scale effect. In order to overcome the scale effect, Kraus and Smith (1994) and Arcilla *et al.* (1994) had carried out the movable bed laboratory experiment on the level of real scale beach. In succession, the large-scale experiments have been performed by some limited researchers (Alsina *et al.*, 2012; Williams *et al.*, 2012; Yoon and Cox, 2010). The large-scale experiments were too restrictive to perform various experiment cases due to the incredible cost for their facilities. On the other hand, the various movable bed experiments in the laboratories, which are smaller than the real scale, have been achieved by some researchers (*e.g.*, Srisuwan *et al.*, 2015; Berni *et al.*, 2013). Baldock *et al.* (2011) also mentioned that the experiment results of the real scale and the laboratory scale agreed with each other, qualitatively.

For morphological changes in the cross-shore profile, Hoefel and Elgar (2003) suggested the mechanism of the sandbar offshore migration caused by the undertow due to wave breaking and of the sandbar onshore migration caused by the skewness of flow velocity and its acceleration toward the coast. The further researches (*e.g.*, Berni *et al.*, 2013; Fernandez-Mora *et al.*, 2015) confirmed the mechanism and provided the methods utilizing the mechanism for the numerical model development.

The erosion issue on the Haeundae coast (Yang *et al.*, 2010) has been debated and is an ongoing research topic among many Korean researchers. This study presents a laboratory experiment which observes the evolution of beach profile on the influence of a scaled-down wave sequence representing the wave condition dominated in the Haeundae coast of Korea. The observation was conducted in the surf zone and swash zone. The beach profile change and the wave height were observed during the experiments.

EXPERIMENTAL SETUP

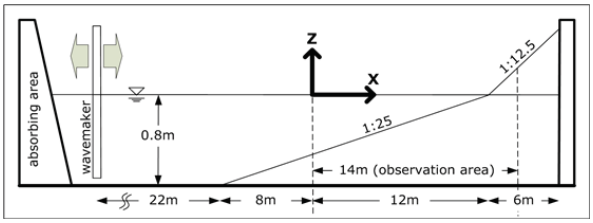

Figure 1. Sketch of experimental set-up and intial beach profile.

The present laboratory experiment was carried out on the two-dimensional wave flume with dimensions 48 m × 1 m × 2 m located in Korea Institute of Civil Engineering and Building Technology (KICT) as shown in Figure 1. The sand grains with D_{50}=0.18mm was chosen for the present experiment. Note that

DOI: 10.2112/SI75-266.1 received 15 October, 2015; accepted in revision 15 January, 2015
*Corresponding author: jwchoi@kict.re.kr
©Coastal Education and Research Foundation, Inc. 2016

one of the sand samples obtained from the Haeundae coast is approximately D_{50}=0.4mm. In addition, for the initial state of the laboratory experiment, the constant slope was set to be 0.04 in the surfzone and was set to be 0.08 in the swash zone which were chosen based on the slope of the Haeundae Coast. The incident wave condition was determined by the distribution based on the joint statistics of the significant wave height and period obtained from data measured for 3 years at the Haeundae coast. And the monochromatic wave conditions was used for the narrower surfzone and the less variation of the wave-breaking points than the random wave condition does.

The parameters of the incident wave conditions for the experiment and the corresponding values for the target area are summarized in Table 1. The fall velocity of the sand grain (D_{50}=0.18mm) was approximately 2cm/s suggested by Rouse (1937). In case that the scale of the laboratory experiment is assumed to be 1/10 of the target area, the fall velocity of the sand grain of the target area is 6.3(=$2\sqrt{10}$) cm/s. This value is close to the fall velocity of the sand grains with D_{50}=0.4mm which corresponds to a sample of the sand grains of the Haeundae coast. Thus, the present laboratory experiment satisfied the undistorted froude model of Kriebel *et al.* (1986). However, there might be the scale effects caused by the different scale ratios of boundary layers, sand ripples and so on, in the model experiment.

Table 1. *Wave parameter of experiment and target area.*

		Model	Prototype
Storm wave	wave height (H)	0.3 m	3 m
	wave period (T)	4 s	12.5 s
Normal wave	wave height (H)	0.1 m	1 m
	wave period (T)	2 s	6.3 s
Sediment (D_{50})		0.18 mm	0.4 mm
Sediment fall velocity (w_s)		2 cm/s	6.3 cm/s
Slope		0.04	0.04

Various beach profile parameters, which are used to classify an erosion condition and an accretion condition of the experiment beach profiles, are presented in Table 2. The beach profile parameters of the model and the target prototype were evaluated based on the initial profile slope and the incident wave condition. The surf similarity parameter is expressed as follows,

$$\xi = \tan\alpha / \sqrt{H/L_o} \quad (1)$$

where, tanα is the beach slope, and L_o is the deep-water wavelength (Battjes, 1974). The spilling breaker and the plunging breaker are usually classified by the surf similarity parameter of 0.5, and it has been said that the accretion conditions are dominant during the spilling breaker whereas the erosion conditions are dominant during the plunging breaker. However, Wright and Short(1984) suggested the modified surf parameter, for which the bottom slope at the wave breaking position is used in order to take into account the local effect. In addition, Yoon and Cox(2010) mentioned that the surf similarity parameter is not sufficient to determine the erosion state and accretion state of the morphological response. Based on the original surf similarity parameter, the storm wave case and the normal wave case in this experiment belong in the range of the spilling breaker representing the accretion conditions. The Dean number Ω_D(Dean, 1973) is presented as follows.

$$\Omega_D = H/Tw_s \quad (2)$$

According to the Dean number, the present two experiment cases are in a range of $1<\Omega_D<5$ that indicates the combinations of plunging breaker and spilling breaker (Wright and Short, 1984). For the Dean number, Hattori and Kawamata (1980) proposed the modified Dean number evaluated by including the local bottom slope and the wave height at the breaking location. In addition, Dalymple (1992) and Kraus and Mason (1993) proposed the profile parameter as follows,

$$P_s = gH^2/Tw_s^3 \quad (3)$$

where, g is the gravity acceleration. For the monochromatic waves, the erosion and accretion condition are categorized by 10,400 of the profile parameter of Eq. (3). In other words, the storm wave cases belong in the range of the erosion condition and the normal wave cases belong in the range of the accretion condition.

Table 2. *Parameters of beach profile according to wave condition.*

	Storm condition		Normal condition	
	Model	Prototype	Model	Prototype
Surf parameter	0.36	0.36	0.32	0.32
Dean number	3.75	4	2.5	2.65
Profile parameter	27,600	32,700	6,130	7,210

In order to measure the changes of beach profile and the surface motions, the experimental time with wave generation was determined based on the time-period in which the beach profile was stabilized under each of the wave conditions. The experimental time was set to 60 min for the storm wave case and 120 min for the normal wave cases. The total observation of the beach profile was carried out during 480min. In other words, the normal wave case was performed from the initial slope to 120min, and subsequently, the storm wave case was performed during 60 min. In succession, the experiment was performed during 120 min in the normal wave condition, during 60min in the storm wave condition, and during 120min in the normal wave condition. The observation area was set to be 14-m length area ranged from the coordinate orgin (*i.e.*, the 30m location from the wavemaker shown in Figure 1) to the swash zone. The beach profile changes were measured every 3 min for the rapid change on the storm wave condition and every 6 min for the gradual change on the normal wave condition. During the recess, in which the wave generation was stopped to measure the beach profile and restarted, the morphological changes were relatively small and assumed to be ignored.

EXPERIMENTAL RESULTS

Figure 2 presents the beach profile evolution due to the alternate repeat of the normal wave case and the storm wave case. Figure 2(a) shows the evolution of the beach profile in the storm wave condition during 120-180min and Figure 2(b) shows the evolution of the beach profile in the normal wave condition during 180-300min. For the storm wave case, the beach profile was rapidly changed for approximately 12min, which involves

the generation of the sand-bar crest and trough (x=5m and x=7m), and became relatively stable during the rest of 60min. The swash zone near the coastline (x=12m) became steeper gradually during 60min. Even outside of the surfzone, the erosion process appeared due to the undertow and nonlinear wave oscillatory flow. For the normal wave case, the crest and trough of the sand bar, which are formed due to the storm wave, were slowly decayed during 120 min, whereas the profile changes at the other locations are relatively small.

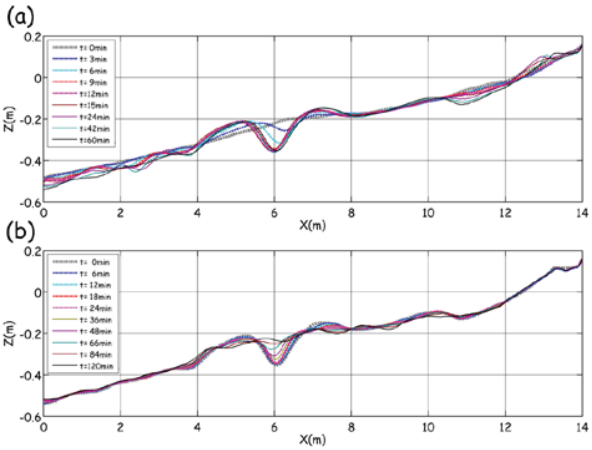

Figure 2. (a) Beach profile evolution stack, and beach profiles under (b) the storm wave condition (120-180min) and (c) normal wave condition (180-300min).

The formula of net sediment transport, Q (Baldock *et al.*, 2011) was used to evaluate the sediment transport due to the erosion and the accretion under the repeated storm wave and normal wave conditions.

$$Q(x_i) = Q(x_{i-1}) + \int_{x_{i-1}}^{x_i} M \frac{\Delta z_b}{\Delta t} dx \qquad (4)$$

where, $Q(x_i)$ is the net sediment transport rate, Δt is the measurement time interval of each condition, and Δz_b is the beach changes in the measurement time interval of each condition. As shown in Figure 3, the net sediment transport rate was calculated from the initial position, which was set to x=14 with no morphological change, to the direction of the wave generation.

From the net sediment transport rate of the storm wave conditions (t=180min and t=360min) shown in Figure 3, it was found that the erosion was processed by the sediment transfer from the observation region toward the deep water. The erosion rate in the first storm wave condition was larger than that in the second storm wave condition. The accretion process at the swash zone was occurred as well as the erosion rate was reduced in the second storm wave condition. The relatively small amount of erosion was processed from the initial constant slope profile under the first normal wave condition (t=120min). However, the accretion was processed by the deposition inside of the surfzone in the normal wave conditions (t=300min and t=480min) from the beach profile deformed by the storm wave. As a result, the erosion occurrence was processed in the storm wave condition, and the accretion occurrence was processed in the normal wave condition.

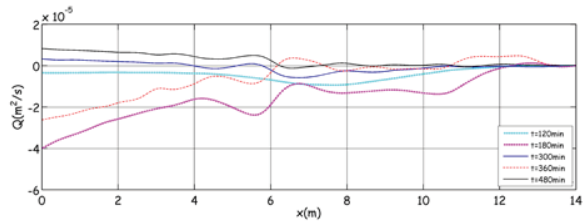

Figure 3. Net sediment transport rate along the distance under the storm wave case (t=180min, t=360min) and the normal wave case (t=120min, t=300min, t=480min).

From the analysis of the net sediment transport, it can be inferred that the overall equilibrium state of the beach profile was attained by the repeat conditions of the normal wave and the storm wave. The beach profile at the equilibrium state was obtained by the final normal wave case as shown in Figure 3. For the comparisons between the experimental result and the field observations, Figure 4 presents the down-scaled (*i.e.*, 1/10) beach profiles of the Haeundae coast and the Duck field experiment. The present experimental beach profile at the equilibrium state reasonably agreed with the down-scaled Haeundae beach profile. The development of terrace was successfully reproduced in the present experiment, and the slope of the swash zone reasonably agreed with the slope of the swash zone at the Haeundae coast rather than the milder slope of the Duck coast.

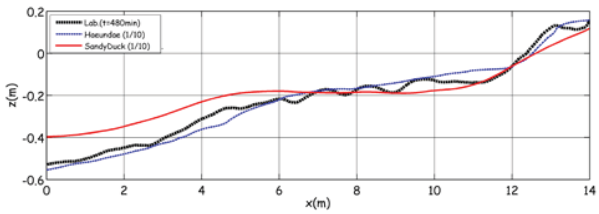

Figure 4. Beach profiles of the present result at the quasi-equilibrium state (black dotted line), the Haeundae coast (blue dotted line; 1/10 scale), and the SandyDuck experiment (red line; 1/10 scale).

Figure 5(a) presents the wave height distributions evaluated by using the water surface elevation data measured during 60 min (*i.e.*, 120-180min) in the storm wave condition, and the corresponding beach profiles. Note that the wave height was calculated by using the zero-up crossing method. The wave height distribution shows a rapid reduction from the start point (i.e., approximately x=4.5m) of the wave breaking which presented the feature of plunging breakers. The rapid reduction of wave height was kept up to approximately x=6m and the wave heights decreased gradually because of wave breaking due to the shallower water depth. From the distributions of wave heights and beach profiles, it can be inferred that the crest and trough of the sandbar at x=5~7m are caused by the first strong wave breaking. The three distributions of the wave height and

the beach profile in the figure were evaluated by using the first 6-min data, the last 6-min data, and the whole data of the 60 min-long measurements, respectively. From the distributions, it can be seen that the wave heights was varied according to the time variation of the beach profiles. As mentioned earlier, the beach profile evolution weakened after 12 min, and the trough of the sandbar was slightly moved back and forth. This was confirmed by the result that the wave heights evaluated by using the last 6-min data were relatively close to the wave height evaluated by using the whole data of the 60 min-long measurements. Because the observable changes were not significant in the beach profile and the wave height during the rest, it can be assumed that the experiment beach profile became the quasi-equilibrium state as being close to 60 min in the storm wave condition.

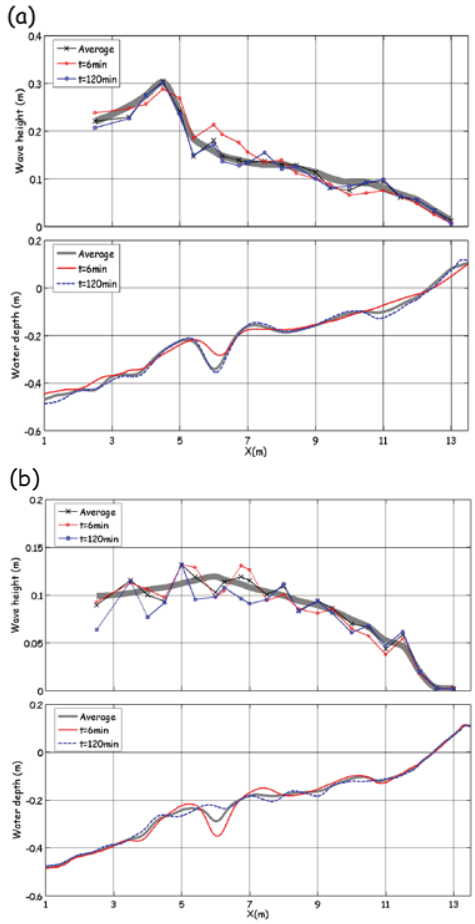

Figure 5. Distributions of wave height and beach profiles under (a) the first storm wave condition and (b) the second normal wave condition.

Since the monochromatic waves were chosen for the incident waves, the beach profile was evolved by the rapid wave breaking and the narrower surfzone. On the other hand, the effect of the partial standing wave was found in the observed wave height distribution (Wang and Kraus, 2005). Note that the spectral analysis (not presented in this paper) showed that the infragravity waves (Symonds *et al.*, 1982) were not revealed in the measurements. For random wave conditions, the effects might be hided by the phase interaction of random waves with spectral frequencies. The effects might cause the wave shape, and thus affect the skewness of the flow velocity and its acceleration(Liu and Tajima, 2014). Subsequently, the change of their skewness might affect the morphological change. Note that the wave height distribution presented as the gray line in Figure 5(a) indicates the sketch of the trend line excluding the phase interaction effect due to the reflective waves.

Figure 5(b) presents the wave height distributions evaluated by using the surface elevation data measured during 120 min (*i.e.*, *t*=180-300min) in the normal wave condition, and the corresponding beach profiles. The three distributions of the wave height and the beach profile in the figure were evaluated by using the first 6-min data, the last 6-min data, and the whole data of the 120min-long measurements, respectively. The wave height distribution shows a relatively gradual reduction from the start point (*i.e.*, approximately *x*=6-7m) of the wave breaking which presented the feature of spilling breakers. And the wave heights decreased gradually because of wave breaking according to the shallower water depth. As mentioned in the results of the storm wave case, the wave height distribution of the normal wave case also uncovers the effect of the wave reflection and the surfbeat. The effect of the phase interaction with the reflective waves in the normal wave case seems to be stronger than that in the storm wave case. This is because of the relatively clear wave phase, which is less dissipative during the wave breaking with the spilling breaker. During the process of sediment transport, the trough (*i.e.*, at *x*=6m) and crests of the sandbar were decayed by the onshore migration mechanism interacted with the offshore migration mechanism and the oscillatory flow effect (Hoefel and Elgar, 2003). As being close to *t*=300 min in the normal wave case, it was shown that the evolution of the beach profile gradually weakened and the experiment beach profile became the quasi-equilibrium state.

CONCLUSIONS

The movable bed laboratory experiment was carried out in a two-dimensional wave flume for qualitative understanding the mechanism of sediment transport on the cross-shore direction of the Haeundae beach. The storm and normal waves did alternately evolve the beach profile, and each of the wave conditions was maintained to reach its quasi-equilibrium states up to 120min under the normal wave condition and up to 60min under the storm wave condition. The trough and crests of the sandbar appeared in the storm wave case and the slope of the swash zone increases, whereas the sandbar was decayed in the normal wave case. From the analysis of the net sediment transport, it was confirmed that the erosion process of the sediment transport was dominant in the storm wave condition, whereas the accretion process of the sediment transport was dominant in the normal wave condition. Furthermore, the characteristics of the final equilibrium beach profile after the 480min-experiment was represented by the sandbar formation and the development of terrace in the surfzone, and the relatively steep slope of the swash zone. The characteristics

reasonably agreed with those of the beach profile of the Heaundae.

The results of the present experiment is not sufficient to discuss the erosion and the accretion problems of the Haeundae coast without the longshore transports. Nevertheless, it is expected that the present observation data are used to verify the algorithm of the cross-shore beach evolution in the numerical model for the simulation of the beach erosion and accretion..

ACKNOWLEDGMENTS

This study was performed by a project of ‘‘Development of coastal erosion control technology (No. 20130023)’’ sponsored by the Ministry of Oceans and Fisheries.

LITERATURE CITED

Alsina, J.M.; Cáceres, I.; Brocchini, M., and Baldock, T.E., 2012. An experimental study on sediment transport and bed evolution under different swash zone morphological conditions. *Coastal Engineering*, 68, 31-43.

Arcilla, A.S.; Roelvink, J.A.; O’Connor, B.A.; Reniers, A., and Jimeniz, J.A., 1994. The Delta flume ’93 experiment. *Proc. Coastal Dynamics ’94*, ASCE, 488-502.

Baldock, T.E.; Alsina, J.A, and Caceres, I., 2011. Large-scale experiments on beach profile evolution and surf swash zone sediment transport induced by long waves, wave groups and random waves, *Coastal Engineering*, 58, 214-227.

Battjes, J.A., 1974. Surf similarity, paper presented at *14th Int. Conf. on Coastal Eng., Coastal Eng. Res. Counc.*, Denmark.

Berni, C.; Barthélemy, E., and Michallet, H., 2013. Surf zone cross-shore boundary layer velocity asymmetry andskewness: an experimental study on a mobile bed. *Journal of Geophysical Research*, 118, 2188-2200.

Dalrymple, R.A., 1992. Prediction of storm/normal beach profiles. *Journal of Waterway, Port, Coast., Ocean Eng.*, 118:2(193), 193-200.

Dean, R.G., 1973. Heuristic models of sand transport in the surf zone, in Engineering Dynamics of the Coastal Zone: *First Australian Conference on Coastal Eng*., Sydney, pp.208-214.

Fernández-Mora, A.; Calvete, D.; Falqués, A., and de Swart, H.E., 2015. Onshore sandbar migration in the surf zone: new insights into the wave-induced sediment transport mechanisms. *Geophysical research letters*, 42(8), 2869-2877.

Hattori, M. and Kawamata, R., 1980. Onshore-offshore transport and beach profile change. *In Proceedings of the 17th Conf. on Coastal Eng*. ASCE, Sydney, Australia, pp.1175-1193.

Hoefel, F. and Elgar, S., 2003. Wave-induced sediment transport and sandbar migration. *Science*, 299, 1885-1887.

Kraus, N.C. and Smith, J.M., 1994. SUPERTANK Laboratory Data Collection Project, Tech. Report CERC-94-3, U.S. Army Engineer Waterways Experiment Station, MS, Vol 1-2.

Kraus, N.C. and Mason, J.M., 1993. Discussion of ‘Prediction of storm/normal beach profiles’ by Robert A. Dalrymple (March/April, 1992, Vol. 118, No. 2). *Journal of Waterway, Port, Coastal, Ocean Engineering*, 119:4(468), 468-470.

Kriebel, D.L; Dally, W.R., and Dean, R.G., 1986. Undistorted froude model for surf zone sediment transport. *Coastal Engineering*, 20, 1296-1310.

Liu, W. and Tajima, Y., 2014. Image-based study of breaking and broken wave characteristics in front of the seawall. *In Proceedings of the 34th Conf. on Coastal Eng.*, ASCE, Seoul.

Rouse, H., 1938. Nomogram for the settling velocity of spheres. National Research Council, Washington, DC. 57-64.

Srisuwan, C.; Work, P.; Karasu, S., and Özölçer, İ., 2015. Beach profile model with size-selective sediment transport. I: Laboratory experiment and sensitivity study. *Journal of Waterway, Port, Coastal, Ocean Engineering*, 141(2), 04014032.

Symonds, G.; Huntley, D.A. and Bowen, A.J., 1982. Two-dimensional surf beat: long wave generation by a time-varying breakpoint. *Journal of Geophysical Research*, 87, 492-498.

Wang, P. and Kraus, N.C., 2005. Beach profile equibrium and patterns of wave decay and energy dissipation across the surf zone elucidated in a large-scale laboratory experiment. *Journal of Coastal Research*, 21(3), 522-534.

Williams, J.J.; Buscombe, D.; Masselink, G.; Turner, I.L., and Swinkels, C., 2012. Barrier dynamics experiment (BARDEX): Aims, design and procedures. *Coastal Engineering*, 63, 3-12.

Wright, L.D. and Short, A.D., 1984. Morphodynamic variability of surf zones and beaches: A synthesis, *Marine Geology*, 56, 93-118.

Yoon, D.-D. and Cox, D.T., 2010. Large-scale laboratory observations of wave breaking turbulence over an evolving beach. *Journal of Geophysical Research*, 115, C10007.

Journal of Coastal Research	SI	75	1332 - 1336	Coconut Creek, Florida	2016

A Boussinesq Modeling of a Rip Current at the Daechon beach in Korea

Junwoo Choi [†*] **and Hyung Suk Kim**[‡]

[†] Coastal Research Lab., Korea Institute of Civil Engineering and Building Technology, Gyang, Republic of Korea

[‡] Hydro Science and Engineering Research Dept., Korea Institute of Civil Engineering and Building Technology, Gyang, Republic of Korea

www.cerf-jcr.org

www.JCRonline.org

ABSTRACT

Choi, J., and Kim, H. S., 2016. A Boussinesq modelling of a rip current at Daechon beach in Korea. *In:* Vila-Concejo, A.; Bruce, E.; Kennedy, D.M., and McCarroll, R.J. (eds.), *Proceedings of the 14th International Coastal Symposium* (Sydney, Australia). *Journal of Coastal Research*, Special Issue, No. 75, pp. 1332 - 1336. Coconut Creek (Florida), ISSN 0749-0208.

The rip current of the Daechon beach, characterized by dissipative beach profiles and macro tides, was investigated by numerical simulations of nearshore circulations. The numerical simulation was performed by the Boussinesq model, FUNWAVE. The simulation confirmed that the rip current was induced by alongshore non-uniformity of wave energy and involved the vortex mechanism at the ends of wave crest, especially in honeycomb wave pattern. The patterns of nearshore currents were varied according to various tide elevations, because of the change of water depth. The simulation also presented that a longshore current, developed due to the mega cusp beach of the Daechon coast, became a feed current of the rip current through the gap of ends of wave-crests. Even though the beach is the very dissipative beach as well as the macro tidal beach, the likelihood of dangerous rip current should be watched when the tidal condition in favour of developing rip current encounters the incident wave conditions sufficient to develop rip current.

ADDITIONAL INDEX WORDS: *Numerical simulation, dissipative beach, macro tides, FUNWAVE.*

INTRODUCTION

Accidental rip currents have become a social issue at the Haeundae beach in the Korean Peninsula in which dozens of swimmers rescued from rip currents have been reported every recent years (Choi *et al*., 2014; Yoon *et al*., 2014). In 2010 and 2012, rip current accidents with four casualties were reported at the Daechon beach, which is another popular beach located in the western sea of South Korea. Owing to weather change (or global warming), the Korean Peninsula is now becoming more subtropical in climate, and beach-goers are expected to increase more and more. Even researchers have a question whether rip currents can occur at beaches of the west coast of the Korean Peninsula, characterized by dissipative beach profiles with very gentle slope and macro tides. This study investigates the rip current at the Daechon beach, which is one of the typical beaches in the west coast of the Korean Peninsula, by using the numerical simulations.

It has been known that rip currents observed in the nearshore region are generated due to the longshore variations of wave energy which is caused by alongshore non-uniformities in the surfzone related to various reasons such as instability of mean motions and nonlinear interactions of waves influenced by topography (Darlymple, 1975, 1978; Tang and Dalrymple, 1989). In other words, when wave energy reduced partially in the longshore direction, the gradient of wave-induced excess momentum flux occurs, and then the strong jet-like flow, called rip current, evolves through the lower-energy zone (*i.e.*, rip channel) toward the open sea. The numerical simulation of rip current has been performed by either using a combination of wave model and current model using the radiation-stress concept (Haas *et al*., 2003; Yu and Slinn, 2003) or using the Boussinesq model including its approximated vorticity correction (Chen *et al*., 1999; Johnson and Pattiaratchi, 2006).

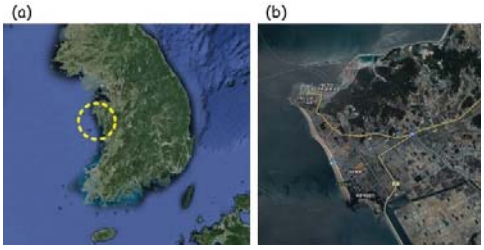

Figure 1. Location (a) and satellite image of Daechon beach in the Korea Peninsula.

In this study, the numerical simulation was performed by the Boussinesq model, FUNWAVE (Chen *et al*., 1999; Chen *et al*., 2003) which is one of the most advanced model for simulating rapid wave-induced current (*i.e.*, rip current), since it resolves wave-phase interactions and generating, evolving and dissipating vortex. The numerical simulations were performed

DOI: 10.2112/SI75-267.1 received 15 October, 2015; accepted in revision 15 January, 2015
*Corresponding author: jwchoi@kict.re.kr
©Coastal Education and Research Foundation, Inc. 2016

based on surveying data involving the topographical characteristics of the Daechon. In addition, we investigated rip-current occurrence varied according to various wave height, wave period, tidal levels, and spectral wave conditions dependent on directional and frequency spreading.

OBSERVATIONS

A CCTV camera, which was installed by Korea Hydrographic and Oceanographic Administration (KHOA), captured several rip current events for around 3 hours from 9:00 to 13:00 on the 13th of August, 2012. The CCTV image shown in Figure 2 presents the events of rip current occurred at the Daechon beach. In the figure, rip currents are seen by flowing swimmers with floating tubes toward the sea between the wave crest-lines with white turbulences caused by wave breaking. Even though the observed rip current event, which has very smaller scales than the rip current at the Haeundae beach (Yoon *et al*., 2014; Choi *et al*., 2014) in the south coast of the Korean Peninsula, the video image shows the possibility of rip current at the Daechon beach. It can be also expect that the larger incident waves can generate a larger rip current event. At the time of the rip current event, the observation presents 0.6m-significant wave height, 6s-significant wave period, and 5m-tidal elevation based on the datum level (*i.e.*, the approximated lowest low tide). Note that the range of the tidal elevation at the Daechon beach is about 12m.

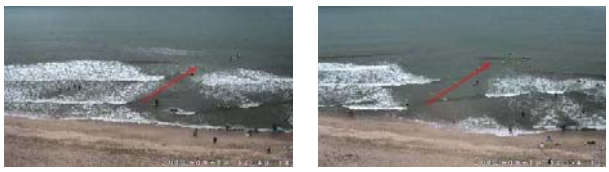

Figure 2. Snapshots of rip current observed at the Deachon beach at 12:46 (left) and 12:54 (right) on the 13th of August, 2012.

In general, rip currents occur at low tide better than at high tide, since the surfzone becomes relatively wide at low tide and thus alongshore non-uniformities inside the wider surfzone increase. Even though it can be difficult to generate rip current over the very shallow water depth near the lowest tidal elevation and the very steep slope neat the highest tidal elevation, the surfzone can be developed near the mean sea level with a mild beach slope to generate rip currents. This can be shown in the results in the next section. In addition, since the Daechon beach become a sand beach at the high tide as well as a mud beach at the low tide, beach-goers enjoy the beach in different ways at the high tide and the low tide.

NUMERICAL MODEL

To simulate wave-induced nearshore circulations in this study, FUNWAVE (Chen *et al*., 1999; Chen *et al*., 2003; Johnson and Pattiaratchi, 2006), a nonlinear Boussinesq model was employed since it has been used for investigation of rip current in many previous studies and is one of the most advanced model for simulating rip currents. This model is capable of simulating rapid rip currents under most sea environments influenced by random waves with wave-phase interactions. The present model was the version of Chen *et al*. (2003) in which the original governing equation for irrotational flow into the equation was modified to take into account rotational flow by inserting an approximated vorticity terms to its momentum equation. Also, random waves were generated by using internal wave-maker based on time series obtained from superposition of linear waves with random phase lags according to the target wave spectrum. The FUNWAVE model has been validated in many previous studies mentioned above, and thus the detailed description is referred to the previous studies.

MODEL SET-UP

The topography of the Daechon coast used in the numerical simulation is shown in Figure 3. Figure 3(a) shows the water depth at the medium tide, which is 5m-sea level above the datum level (i.e., the approximated lowest low tide level), and Figure 3(b) shows the water depth at the high tide, which is 10m-sea level above the datum level. As shown in Figure 3, there are some submerged shoals in the Daechon coast (*i.e.*, (X=710m, Y=2570m), (X=800m, Y=400m), (X=1500m, Y=2020m)) which become the reef over the surface at the lowest tide.

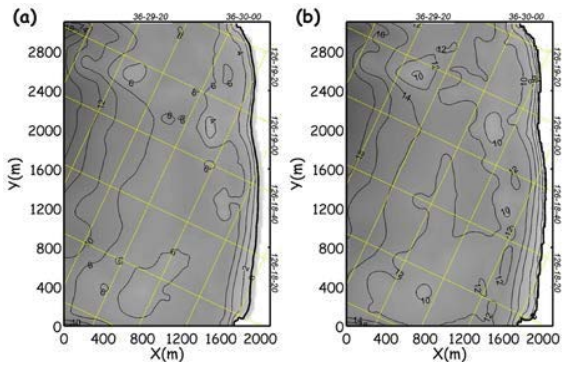

Figure 3. Topography of Daechon beach for numerical simulation near (a) the mean sea level (5m-tide elevation) and (b) the high tide (10m-tide elevation). The contour unit is m and the grid indicates the latitudinal and longitudinal lines.

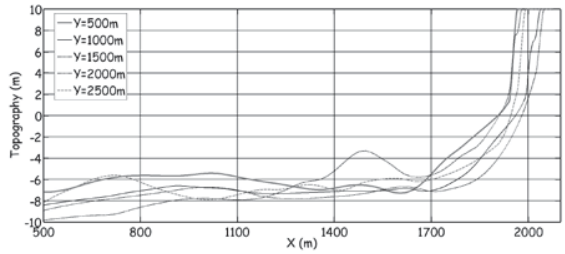

Figure 4. Beach profiles of the Daechon beach at several longshore locations at the low tide.

Due to the submerged shoals, the incident waves are transformed by refraction and the transformation induces the non-uniformities of wave energy in the longshore direction in the surfzone. It is difficult to say that the topography is not in

favor of generating rip currents, especially near the mean sea level. As shown in the figure, the *x-y* coordinates of the topography was transformed from the latitude-longitude coordinates and rotated around the point chosen to be an arbitrary origin. To utilize periodic boundary condition, the topography was rotated 25°in the counterclockwise direction and its lateral regions with around 200m-wide area were modified to be peripheral. This periodic lateral boundary condition was set to avoid the lateral boundary errors. The spatial grids Δx=1.3m and Δy =2.0m, and their total numbers are 1631 in the *x*-direction, and 1561 in the *y*-direction. The internal wave-maker was set at *x*=150m and 140m-wide sponge absorption boundaries were set behind the wave-generation line.

The cross-shore profiles of the topography shown in Figure 3(a) were shown in Figure 4 with presenting the water depth at the 5m-tidal elevation. As mentioned earlier, the low tide reveals so shallow water depth to dissipate waves far from the shoreline, and the high tide reveals so steep slope to break waves near the shoreline. However, the sufficient surfzone can be developed near the mean sea level (around –3m~+2m) with a mild beach slope to generate rip currents.

In order to perform numerical simulation of the rip current event at the Daechon coast, the random waves with 1.0m-significant wave height and 10s-peak wave period were chosen by using the bathymetry at the 5m over the datum level. And the peak wave direction was set to be the perpendicular to the coastline (S65W). The chosen wave conditions are arbitrary since there is no reliable measurement of the 13th of August, 2012, in which the rip current event (Figure 2) were recorded, except the tidal elevation. The arbitrary wave condition was chosen by performing various model tests to reproduce a rip current similar to that in the snapshot of Figure 2. Note that the comparison between the observation and the results may be discussed only in a qualitatively manner. The random wave spectra were constructed by using the JONSWAP frequency spectrum distribution and the wave directional spectrum distribution of power cosine function. The spreadings of wave spectra were controlled by using the peak enhancement parameter γ =9.0 and the circular root-mean-square spreading σ_θ =10° (Choi *et al.*, 2014). Note that the frequency spectrum becomes narrower as γ increases and the directional spectrum becomes narrower as σ_θ decreases. In addition, to analyze rip current likelihood according to various sea environments, we simulates nearshore circulations of the Daechon coast using the wave conditions with various wave heights, wave periods, tidal elevations, spreadings of the wave spectra. Note that the perpendicular direction to the coastline indicates S65W since the topography was rotated as mentioned earlier. For the random wave generation, each energy density spectrum is decomposed into 165 wave components and they are linearly superposed with random phase-lags. The computational time step is 0.05 sec. The friction factor was set to be 0.0015 and the other physical and empirical coefficients were set to be equal to the fault values in the model manual.

NUMERICAL SIMUATIONS

The numerical simulations of nearshore circulation including rip current are performed based on the topography (Figure 3a). The numerical results presenting the free surface elevation and the distribution of wave height are shown in Figure 5. The panel (a) of Figure 5 presents a snapshot of the free surface elevation at the time after 50-wave period from wave generation, and the bright light side indicates wave crest and the dark shade side indicates wave trough. The distribution of wave height in the panel (b) of Figure 5 was obtained by using 30-wave-period data of the free surface elevation after the 50-wave period, and it was evaluated by the definition of zeroth-moment wave height written as $H_s = 4\sqrt{\langle \eta^2 \rangle}$ where η indicates the computed free surface elevation, and $\langle (\ ) \rangle$ presents the 30-wave-period average.

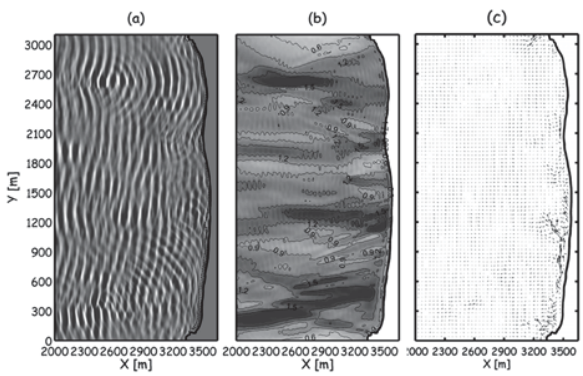

Figure 5. (a) Free surface displacement (shading) and (b) wave height (unit: m) resulted from t=60T after wave generation begins and (c) vector plots of wave-induced currents obtained at t=120T (incident wave condition: H_s=1.0m, T_p=10s, wave direction from S65W with γ=9.0, σ_θ=10°). The broken lines in panel (a) indicate the region where relatively intense wave-breaking occurs.

From the free surface elevation shown in Figure 5(a), it was found that the waves are significantly transformed by refraction due to the topographical characteristics of the Daechon coast such as the submerged shoals. Also, from the distribution of wave height shown in Figure 5(b), it was found that the alongshore variation of wave height is caused by focusing and defocusing of waves due to wave refraction over the topography. And the low wave-height areas of an alongshore-varied distribution can play a role in a rip channel without respect to a topographical rip channel. In addition, the broken line presented in Figure 5(a) indicates the wave-breaking region. The alongshore variation of the wave-breaking lines is also an implication for the alongshore non-uniformities which is a necessary condition for rip currents.

Figures 5(c) and 7 show the vector plots presenting the rip currents evolve and flow out through the relatively low wave-height region which is caused by directional wave group behavior due to wave refraction over the topographical characteristics of the coast. Based on the numerical simulation, the rip current at the Daechon beach can be characterized by that the rip current was developed by the feed current, which is a longshore current caused the mega-cusp pattern of the beach, and was travelled toward the sea through the relatively low wave energy area (*i.e.*, the gap of ends of wave-crests). Figure 6 shows

a magnification of Figure 5(a) and (b) presenting the distributions of free surface displacement and wave height and Figure 7 shows a magnification of Figure 6 presenting the vectors of wave-induced current. From the magnifications for focusing rip currents, it was found that the locations of rip current are almost fixed at the lower wave height area which is not related to a topographical rip channel. The non-topographical rip channel seems to be formed by nodal lines due to directional wave group behavior. The relatively low wave height distribution was also inferred from the wave-breaking region presented by the thick broken lines.

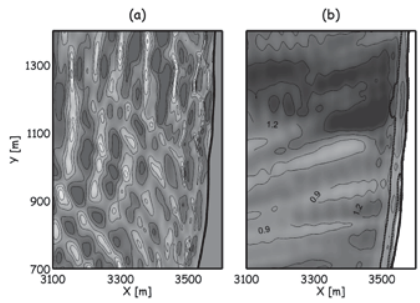

Figure 6. Zoomed figure of Figure 5. (a) free surface displacement (shading) and (b) wave height (unit: m) resulted from t=80T after wave generation begins (incident wave condition: H_s=1.0m, T_p=10s, wave direction from S65W with γ=9.0, σ_θ =10°). The broken lines in (b) indicate the region where relatively intense wave-breaking occurs.

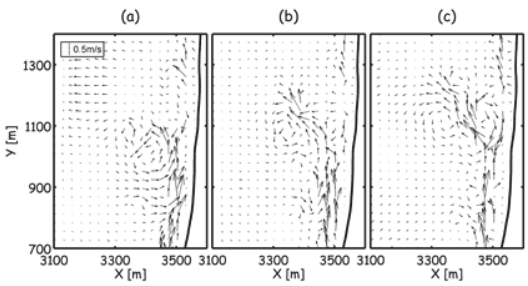

Figure 7. Zoomed figure of Figure 6. vector plots of wave-induced currents obtained at (a) t=40T, (b) t=80T, and (c) t=120T after wave generation begins (incident wave condition: H_s=0.8m, T_p=10s, wave direction from S65W with γ =9.0, σ_θ =10°)

As mentioned earlier, the rip current of the present simulation can be characterized as that a longshore current, developed due to the mega cusp beach, become a feed current of the rip current through the gap of ends of wave crests in the form of honeycomb-patterned waves. In a qualitative manner, the rip current event recorded at the 13th of August, 2012, shown in Figure 2 has the similar pattern of the result in the numerical simulation. Basically, the simulation confirmed that the rip current was induced by alongshore non-uniformity of wave energy and involved the vortex mechanism at the ends of wave crest. Note that in the directional random wave environments, the gaps of the wave-crests and the honey-comb-pattern waves are not as clear as those in the monochromatic wave environments. It can be worth to mention that the nearshore current including rip currents varied according to the tidal elevation which changes water depth of the topography. From the results, it can be inferred that rip current events can be seen at the Daechon beach when the sufficient large and long waves would propagate toward the beach at near the mean sea level which happens twice every day. Subsequently, the people, who enjoy the beach at the event, would be caught by the rip current.

DISCUSSION

This section describes the likelihoods of rip current at the Daechon coast based on the simulation results varied according to the sea condition scenarios. The numerical simulations were performed by using various boundary conditions according to the scenarios of sea conditions representing the observable quantities. Choi *et al*. (2013) describes the way how to evaluate the rip current likelihood from the simulation results as below: In a simulation case, the likelihood of rip current was defined by the rate of the time period, during which the rip current velocity is larger than the threshold velocity, over the total simulation time. For this, the rip current velocity was defined as the maximum seaward cross-shore current velocity in the computational domain, and the threshold velocity was defined as an arbitrary velocity regarded to overwhelm the resistance of swimmers.

The examples of the distribution of the rip current likelihood quantified according to the sea scenarios are shown in Figure 8. Figure 8(A) shows the distribution of rip current likelihood according to wave height and period at the 5m-tidal level without any variation of the other conditions. The figure presents that as the incident wave height and period increase, the rip current likelihood increases. This can be explained by that the stronger gradient of wave energy and flux, which is caused by the larger breaking waves with higher wave height and longer wave period, can induce the stronger rip currents. Figure 8(B) shows the likelihood distribution according to tidal elevations. The figure presents that the rip current likelihood become larger at the lower tide, which is generally accompanied by a wider surfzone with more non-uniform longshore variations. As mentioned earlier, the width of surfzone proportional to the slope of the Daechon beach is varied according to the tidal elevation. As shown in Figures 3 and 4, the slope of the beach become relatively gentle below the 6m-tidal level based on the datum level, thus, Figure 8(B) presents that the rip current likelihood is much higher below the 6m-tidal level than the others. Though the results are not presented in this study, as being the lower tide, the wave-induced currents are stronger and the more complicated near the reefs at the low tide and the submerged shores at the high tide. The distribution of rip current likelihood according to wave directions was shown in Figure 8(C). Note that the zero direction indicates S65W which presents the direction perpendicular to the shoreline. In general, the waves, which has the more perpendicular direction to the shoreline, induce more significant rip currents. The figure presents that the rip current likelihood increases as the wave direction become close to –20° which is almost the waves propagate from the west. The results might be induced by the mega-cusp beach pattern generating the feed current of rip

current. The distribution of rip current likelihood according to spreading of wave spectra shown in Figure 8(D). The swell waves with narrower spectra in the frequency and directional domain induce more significant rip currents. This is because the swell waves, which are refracted over a submerged shoal and are transformed into a few slightly different directional waves, tend to induce relatively strong longshore variations at the nearshore region with honeycomb crest-patterns. The distributions of rip current likelihood qualitatively agree with the general mechanism of rip current induced by the breaking waves and represent the local characteristics of rip current at the Daechon coast.

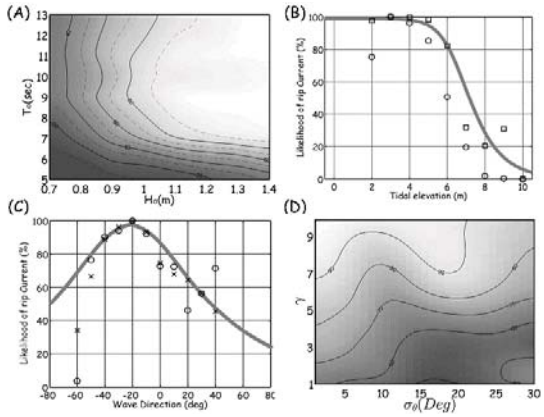

Figure 9. Distributions of rip current likelihood (%) varied according to (a) significant wave height and period of random incident; (b) tidal elevation; (c) peak wave direction; (d) spreading of frequency and directional spectrum with the incident wave condition H_s=1.0m and T_p=10s (γ=9.0 and σ_θ =10°) with wave direction S65W over DL+5m for the tidal elevation

CONCLUSIONS

A fully nonlinear Boussinesq model, FUNWAVE was utilized to perform the numerical simulation of rip current occurred at Daechon coast in South Korea. To compare the numerical result with the rip current event recorded in a video image at the beach in a qualitative manner, we presented a simulation in which the tidal elevation is near the mean sea elevation with a wide surf zone due to its gentle slope. The simulation presented that a longshore current, developed due to the mega cusp beach of the Daechon coast, became a feed current of the rip current through the gap of ends of wave-crests. The numerical results agreed with the rip current event qualitatively. The numerical results showed the honeycombed wave pattern, which produces alongshore non-uniformity of wave energy, and thus, it might generate the rip current in this site. It was confirmed that at lower tide the rip currents increase and strengthen and the rip circulations became complicated in the nearshore area. Even though the Daechon beach is the very dissipative beach as well as the macro tidal beach, the likelihood of dangerous rip current should be watched when the tidal condition in favour of developing rip current encounters the incident wave conditions sufficient to develop rip current.

ACKNOWLEDGMENTS

This study was performed by a project of ”Investigation of large swell waves and rip currents and development of the disaster response system (No. 20140057)” sponsored by the Ministry of Oceans and Fisheries.

LITERATURE CITED

Bae, J.S.; Yoon, S.B., and Choi, J., 2013. Boussinesq modelling of a rip current at Haeundae Beach in South Korea. *In:* Conley, D.C.; Masselink, G.; Russell, P.E., and O'Hare, T.J. (eds.), *Proceedings 12th International Coastal Symposium* (Plymouth, England), *Journal of Coastal Research*, Special Issue No. 65, pp. 654-659.

Chen, Q.; Dalrymple, R.; Kirby, J.; Kennedy, A., and Haller, M., 1999. Boussinesq modelling of a rip current system. *Journal of Geophysical Research*, 104, 20617-20637.

Chen, Q.; Kirby, J.T.; Dalrymple, R.A.; Shi, F., and Thornton, E.B., 2003. Boussinesq modeling of longshore current. *Journal of Geophysical Research*, 108(C11), 26-1-26-18.

Choi, J.; Lim, C.H., and Yoon, S.B., 2014. A rip current warning system based on real-time observations for Haeundae Beach, Korea. *In:* Lee, J.L.; Leatherman, Stephen P., and Lee, J. (eds.), *Proceedings, 3rd International Rip Current Symposium* (Busan, Republic of Korea), *Journal of Coastal Research*, Special Issue No. 72, pp. 56–62.

Dalrymple, R.A., 1975. A mechanism for rip current generation on an open coast. *Journal of Geophysical Research*, 80, 3485-3487.

Dalrymple, R.A., 1978. Rip currents and their causes. *16th international Conference of Coastal Engineering*, 1414-1427.

Haas, K.; Svendsen, I.; Haller, M., and Zhao, Q., 2003. Quasi-three-dimensional modeling of rip current systems. *Journal of Geophysical Research*, 108 (C7), 3217.

Johnson, D. and Pattiaratchi, C., 2006. Boussinesq modelling of transient rip currents. *Coastal Engineering*, 53, 419-439.

Tang, E.-S. and Dalrymple, R.A., 1989. Nearshore circulation: rip currents and wave groups. *Advances in Coastal and Ocean Engineering*. Plenum Press, New York, 205-230.

Yoon, S.B.; Park, W.K., and Choi, J., 2014. Observation of rip current velocity at an accidental event by using video image analysis. *In:* Lee, J.L.; Leatherman, Stephen P., and Lee, J. (eds.), *Proceedings, 3rd International Rip Current Symposium* (Busan, Republic of Korea), *Journal of Coastal Research*, Special Issue No. 72, pp. 16–21.

Yu, J. and Slinn, D., 2003. Effects of wave-current interaction on rip currents. *Journal of Geophysical Research*, 108 (C3), 3088.

Journal of Coastal Research	SI	75	1337 - 1341	Coconut Creek, Florida	2016

Analysis of Positioning Accuracy Using Multi Differential GNSS in Coast and Port Area of South Korea

Wonseok Jang[†*], Hansan Park[‡], Kiyeol Seo[†], Youngki Kim[†],

[†]Korea Research Institute of Ships & Ocean Engineering (KRISO), 32, Yuseong-daero Daejon 305-343, South Korea

[‡]Korea Institute of Ocean Science and Technology (KIOST), 787, Heanro, Ansan 426-744 South Korea

www.cerf-jcr.org

www.JCRonline.org

ABSTRACT

Jang, W.S., Park, H.S., Seo, K.Y., and Kim, Y.K., 2016. Analysis of positioning accuracy using differential GNSS in the coast and port area of South Korea. *In:* Vila-Concejo, A.; Bruce, E.; Kennedy, D.M., and McCarroll, R.J. (eds.), *Proceedings of the 14th International Coastal Symposium* (Sydney, Australia). *Journal of Coastal Research*, Special Issue, No. 75, pp. 1337 – 1341. Coconut Creek (Florida), ISSN 0749-0208.

Obtaining high-accuracy position information in coastal environments is very important. To obtain high-accuracy and high-precision positioning data at low cost, the use of a GPS augmentation system is an appropriate approach. Recently, in addition to GPS, the number of different types of satellite navigation systems is growing; such a system is called a GNSS (Global Navigation Satellite System). The positioning accuracy for every available GNSS is improved compared to the accuracy obtained using only GPS. However, to date, there are no RTCM standards for differential GNSS, except for DGPS. Because the RTCM DGNSS standard and DGNSS receiver did not exist until now, experiments related to GNSS positioning using DGNSS in coastal areas and ports have not been performed. Thus, the creation of GNSS (GPS, GLONASS, BeiDou) correction data is presented in this paper. Moreover, the positioning accuracy was measured using GNSS and its correction data. This experiment was performed for 5 ports in South Korea. The results indicate that the measured positioning accuracy using GNSS correction data should be considered applicable to both coastal and port environments..

ADDITIONAL INDEX WORDS: *positioning at port area, multi-DGNSS, combined GPS/GLONAS/BeiDou*

INTRODUCTION

Obtaining high-accuracy positioning is very important for the various forms of work conducted in coastal and port areas, such as surveying and analyzing coastal geomorphological changes, managing and controlling port facilities, and tracking container box locations. The most common of the many positioning methods uses a navigation satellite. Until recently, there was only one satellite navigation system, the Global Positioning System (GPS). However, currently, various navigation satellite systems, e.g., the United States' GPS, Russia's GLONASS, China's BeiDou, the EU's Galileo, and Japan's QZSS, are available. The GLONASS is currently in full operation. The Galileo system aims to be fully operational in 2020. These satellite navigation systems are called Global Navigation Satellite Systems (GNSSs). GPS standalone positioning, which is the conventional positioning method, has at most 4 meter (horizontal) and 10 meter (vertical) position errors. In many cases of GPS positioning in coastal and port environments, the number of available satellites is small because of shielding from structures and other facilities. If the number of available satellites is small, then the DOP value decreases and the position error exceeds 10 m (horizontal) and 20 m (vertical). This position accuracy is inappropriate because of the high position accuracy needed for coastal applications, such as coastal surveys and port facility management and control. Alternatively, if the positioning is conducted using the multi-GNSS, then the DOP improves. Because of the improved DOP value, positioning using combined GNSS can achieve consistently high position accuracy in confined environments.

There are various GNSS positioning methods that can be used for applications requiring high positioning accuracy. Among the GNSS positioning methods, real-time kinematic (RTK), network RTK and differential GPS (DGPS) are widely used as high-accuracy positioning methods (Grant *et al.*, 2003). If the RTK and network RTK methods are used, an extremely high accuracy positioning result (millimeter scale) can be achieved. This high accuracy is the primary advantage of the RTK and network RTK methods. However, the RTK method is cumbersome because it requires the installation of a RTK base station; the cost of the RTK equipment is high. The other method, i.e., network RTK, can solve the RTK's installation problem. The network RTK method does not require the installation of a RTK base station, so it has an operational advantage. However, the cost of the network RTK equipment is very high, similar to that of the RTK equipment. The network RTK method also suffers from the problem that it cannot be used outside of the network. Although the network RTK service of South Korea covers most inland area, the coverage is lacking in coastal and port areas. Most coastal and port areas in South Korea are located outside the network RTK's network coverage. Therefore, the network RTK method is difficult to use in the coastal areas of South Korea. For environmental and cost reasons, the differential GPS (DGPS) method is primarily used in the coastal and port areas. The South Korean government operates 17 DGPS reference stations, which cover all of South Korea. The DGPS method's positioning

DOI: 10.2112/SI75-268.1 received 15 October, 2015; accepted in revision 15 January, 2015
*Corresponding author: cws0714@kriso.re.kr
©Coastal Education and Research Foundation, Inc. 2016

accuracy is generally 0.5~1 m (static). That accuracy is lower than that of the RTK and network RTK methods; however, it can cover a very wide area, including the coastal and port areas, and the cost of the DGPS equipment is relatively low, making its functionality high in coastal areas. As stated above, the deployment of GNSS is gradually increasing; thus, the DGPS method can be applied to GNSS. For applying the DGPS method to GNSS, new RTCM standards are being enacted by the Radio Technical Commission for Maritime Services (RTCM), namely the Differential Navigation Systems Reference Stations and Integrity Monitors (DGNSS RSIM) version 1.3 and differential GNSS services version 2.4. After enacting the new DGNSS standards, they will be applied to all of the DGPS reference stations in South Korea. In addition, a DGPS reference station will be developed for the DGNSS reference station. The future DGNSS reference station in South Korea will provide the correction information for GPS, GLONASS, Galileo, QZSS and BeiDou. Currently, GPS, GLONASS and BeiDou can also be used in South Korea. Several studies have been performed to test the positioning accuracy of multi-GNSS for changing GNSS environments.

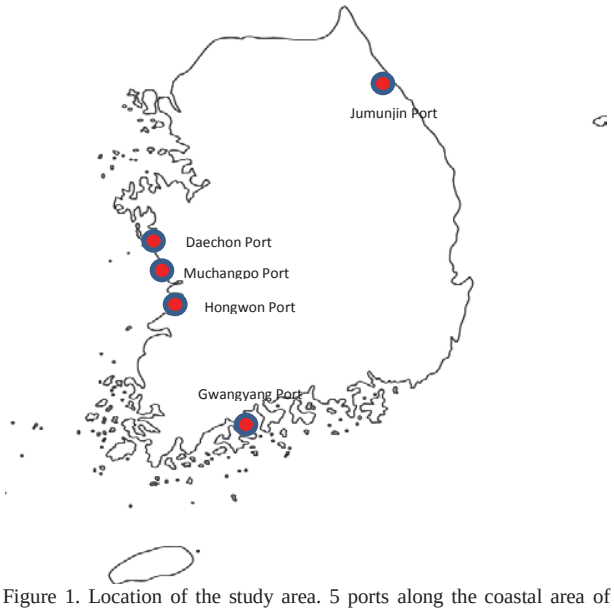

Figure 1. Location of the study area. 5 ports along the coastal area of South Korea were selected.

Yamada *et al.* (2008) developed experiments to test the positioning accuracy of kinematic surveying using GPS and combined GPS/GLONASS. According to the experiment results, the possible positioning time and positioning performance of combined GPS and GLONASS is higher than that of using only GPS . The experiment results of combined GPS/BeiDou were based on the studies of Choi, Cho, and Lee (2014). That experiment demonstrated that the positioning accuracy of the combined GPS/Beidou method is lower than that of using only GPS, but higher than that of using only BeiDou. These results show that the positioning accuracy using combined multi-GNSS is better that using only one GNSS. Although these studies include multi-GNSS for positioning, the positioning method did not use DGPS correction information, such as pseudorange correction (PRC) and range rate correction (RRC). Positioning in coastal and port environments requires high accuracy, although the non-differential GNSS positioning method cannot satisfy such requirements. In addition, the selected study area was inland; thus, the accuracy for coastal areas was not determined. Most coastal and port areas have a complex radio wave environment. Therefore, GNSS positioning experiments should be performed in coastal and port areas, not inland.

Therefore, this study used combined multi-differential GNSS (GPS, GLONASS, and BeiDou) for coastal and port areas in South Korea and evaluated the suitability of the combined multi-DGNSS's position accuracy for coastal and port requirements. For this experiment, 5 ports were selected in South Korea: 3 ports were located in the western coastal area, 1 port was located in the southern coastal area, and 1 port was in the eastern coastal area. The experiment was performed to verify whether the network RTK method is serviceable in the coastal area. The experiment generated each GNSS's pseudorange correction (PRC) information for differential GNSS positioning and determined the multi-differential GNSS positioning using raw measurements acquired from each study area and pseudorange corrections (PRCs). Furthermore, we also analyzed each study area's positioning accuracy using combined multi-DGNSS to determine its suitability in coastal and port areas.

METHODS

Verification of Network RTK's availability

Currently, a virtual reference station (VRS), which is one of the network RTK stations, is available in South Korea. To verify the network RTK availability (VRS), we installed a VRS receiver at the study locations and verified the ambiguity fixing. The test duration was three hours at each study location. Figure 2 shows the experiment equipment. We used the TOPCON VRS receiver to verify the network RTK availability and Trimble NetR9 to acquire each GNSS's raw measurements.

Figure 2. Experiement equipment. Trimble Zephyr GNSS antenna, Trimble NetR 9, Topcon VRS(GRS-1) and its antenna.

The verification results for the network RTK availability are shown in Table 1, showing that network RTK (VRS) availability was identified for the Daechon Port, but not at the other sites.

Table 1. *Network RTK availability at the study locations. Location coordinate system is ECEF (Earth-Centered Earth-Fixed).*

Name	Location coordinate (X,Y,Z)	*NetworkRTK*
Daechon	-3060878.457,4134932.933,3757550.145	O
Muchangpo	-3065888.498,4137648.178,3750518.292	X
Hongwon	-3066843.454,4144489.544,3742229.035	X
Gwangyang	-3214372.378,4140582.235,3621656.890	X
Jumunjin	-3160061.481,3925598.227,3896514.601	X

Combined positioning using GPS, GLONASS and BeiDou

GPS, GLONASS, and BeiDou use different coordinate systems. For the combined multi-DGNSS positioning, each of the GNSS's coordinate systems should be unified. For the unification of the coordinate systems, all of the GNSS's coordinate systems were transferred to the World Geodetic System 84 (WGS84). The GLONASS coordinate system is PZ-90. In the case of GLONASS, the formula proposed by Bazlov (1999) was used for the coordinate transformation (Lee *et al.*, 2012). To calculate GLONASS's satellite position, the fourth-order Runge-Kutta method proposed in the GLONASS Interface Control Document (Russian Institute of Space Device Engineering, 2008) was used. For the PZ90 system, the calculated GLONASS satellite position's coordinate, was converted to the WGS84 coordinate system using the following expression (Rossbach, Habrich, and Zarraoa, 1996):

$$\begin{bmatrix} x \\ y \\ z \end{bmatrix}_{WGS84} = (1 - 0.012 \cdot 10^{-6}) \begin{bmatrix} 1 & 0.82 \cdot 10^{-6} & 0 \\ 0.82 \cdot 10^{-6} & 1 & 0 \\ 0 & 0 & 1 \end{bmatrix} \begin{bmatrix} x \\ y \\ z \end{bmatrix}_{PZ90} - \begin{bmatrix} 1.1m \\ 0.3m \\ 0.9m \end{bmatrix} \quad (1)$$

The BeiDou's coordinate system is the Chinese Geodetic Coordinate System 2000 (CGCS 2000). According to the BeiDou Interface Control Document (China Satellite Navigation Office, 2013), CGCS 2000 and WGS84 are nearly the same. Therefore, we did not convert BeiDou's coordinate system. BeiDou consists of three satellite constellations, i.e., GEO, IGSO, and MEO. The ephemeris of IGSO and MEO are similar to GPS, whereas GEO is different. Thus, the IGSO and MEO positions (orbits) can be used to calculate the GPS orbit model. To calculate BeiDou GEO's satellite position, the following equations were used (China Satellite Navigation Office, 2013):

$$\Omega_k = \Omega_0 + \dot{\Omega} t_k - \dot{\Omega}_e t_{0e} \quad (2)$$

$$\begin{cases} X_{GK} = x_k \cos \Omega_k - y_k \cos i_k \sin \Omega_k \\ Y_{GK} = x_k \cos \Omega_k - y_k \cos i_k \sin \Omega_k \\ Z_{GK} = y_k \sin i_k \end{cases} \quad (3)$$

Where where Ω_k is the corrected longitude of the ascending node in the CGCS 2000 system, t_k is the computed time from the ephemeris reference time, t_0e is the ephemeris reference time, i_k is the corrected inclination, Ω ̇ is the rate of right ascension, and Ω ̇_e is the Earth rotation parameter of used in the CGC S2000 system, and x_k and y_k are the position coordinates of the satellite calculated on the orbital plane. Moreover, X_GK,Y_GK,and Z_GK are the satellite position coordinates in the inertial system. The satellite position in the CGCS 2000 coordinate system is finally then calculated using equation (4).using

$$\begin{Vmatrix} X_K \\ Y_K \\ Z_K \end{Vmatrix} = R_Z(\dot{\Omega}_e t_k) R_X(-5^o) \begin{vmatrix} X_{GK} \\ Y_{GK} \\ Z_{GK} \end{vmatrix} \quad (4)$$

where,

$$R_X(\psi) = \begin{bmatrix} 1 & 0 & 0 \\ 0 & +\cos\psi & +\sin\psi \\ 0 & -\sin\psi & +\cos\psi \end{bmatrix}, R_Z(\psi) = \begin{bmatrix} +\cos\psi & +\sin\psi & 0 \\ -\sin\psi & +\cos\psi & 0 \\ 0 & 0 & 1 \end{bmatrix}$$

Next, each GNSS's PRC can be calculated (Seo *et al.*, 2014). The equations of each GNSS's PRC is as follows:

$$\begin{aligned} \text{GPS PRC} &= -1 \times (\text{PR} - \text{TR} - \text{cSe} - \text{cRe} - \text{Tgd}) \\ \text{GLN PRC} &= -1 \times (\text{PR} - \text{TR} - \text{cSe} - \text{cRe} - \tau_{gps}) \\ \text{BDS PRC} &= -1 \times (\text{PR} - \text{TR} - \text{cSe} - \text{cRe} - \tau_{gps}) \end{aligned} \quad (5)$$

If we do not know each study location's position, we cannot calculate the true range. The known position was obtained from the National Geographic Information Institute's homepage or the integrated reference position's notice sign at the study site. The tTrue rRange (TR) is the actual distance between a satellite and a GNSS receiver. The pPseudorange (PR) is the pseudo-distance between a satellite and a GNSS receiver. Moreover, cSe is the sSatellite cClock eError, cRe is the rReceiver cClock Errorerror, Tgd is the L1-L2 gGroup dDelay, and τ_gps is the time difference between two GNSS systems. Finally, the least squares method is was used for localization using with the combined multi-DGNSS approach.

RESULTS

To obtain the position errors, combined multi-DGNSS positioning experiments using each of the calculated PRCs and the acquired GNSS raw measurement data were performed. The results are shown in Figure 3. Each line denotes the position error: the east error (blue), the north error (red), the up error (gray) and the horizontal position error (yellow). Each experiment was conducted for 6 hours.

The Daechon Port and Hongwon Port exhibited stable position errors. The variability in the position error for the Muchangpo Port and Gwangyang Port was high. Despite the high variation in the position errors, the root-mean-square values of the position errors at all of the study locations were at the centimeter level (less than 1 meter). This result is shown in Table 2.

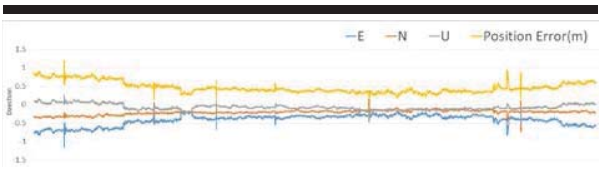

Daechon Port, measured on July 14, 2014

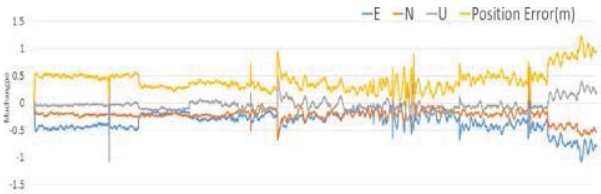

Muchangpo Port, measured on July 15, 2014

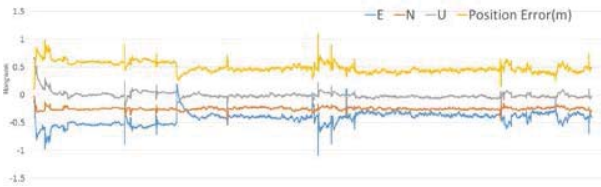

Hongwon Port, measured on July 16, 2014

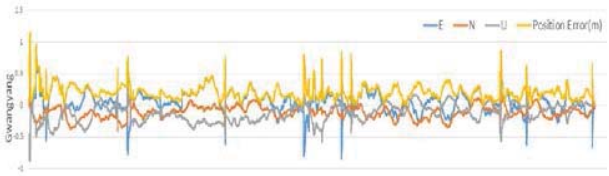

Gwangyang Port, measured on September 19, 2015

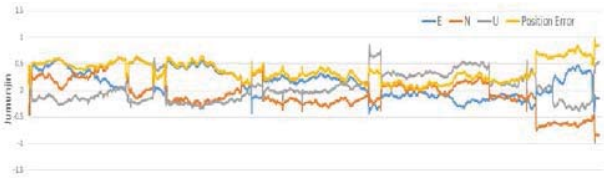

Jumunjin Port, measured on September 26, 2015

Figure 3. The combined-multi Differential GNSS's Position errors at each sutdy location.

Table 2. *The positioning result using combined multi-DGNSS at each site.*

Name	Position Errors(RMS)			
	East	North	Up	Horizontal Error
Daechon	0.44052	0.21672	0.09911	0.68371
Muchangpo	0.39095	0.24738	0.12075	0.64981
Hongwon	0.43592	0.25121	0.06702	0.70317
Gwangyang	0.19249	0.14301	0.18934	0.45696
Jumunjin	0.29316	0.29820	0.25743	0.61080

DISCUSSION

The network RTK method cannot be used at many coastal and port areas in South Korea because they are located outside of the coverage area of the VRS service. According to Table 1, only the Daechon Port can use the network RTK service. Combined multi-DGNSS positioning may be a viable alternative to the network RTK method. Numerous combined multi-DGNSS satellites are also advantageous. There are many facilities, containers, buildings, large ships and natural screening at coastal and port areas. These obstacles can shield radio waves. Therefore, GPS receivers cannot use all of the visible satellites in a complex area. In this environment, the combined multi-DGNSS positioning method, which uses many satellites, can achieve a higher positioning accuracy than using only one GNSS.

Figure 4 shows the variation in the GPS, GLONASS and BeiDou satellites counts at the Jumunjin Port on September 26, 2015. If using only GPS, then the number of available satellites was 6-8. However, in the case of combined multi-DGNSS, the number of available satellites increased to 16-22. The minimum number of GLONASS satellites was two due to shielding. When the number of GLONASS satellites was two, the number of available GPS satellites decreased. However, BeiDou's available satellite count remained unchanged. When shielding occurred, BeiDou was not influenced because it is located outside of the shield effect coverage area. Table 2 shows the positioning results for the combined multi-DGNSS method at each study site. The east, north and up (ENU) and horizontal position errors were all less than one meter (RMS, within 95% confidence level). In the case of the Gwangyang Port, the ENU error exhibited unstable errors, although its position errors (shown in Table 2) were small. The reason for this pattern is probably because of the carrier-to-noise Ratio (CNR). The Gwangyang Port has many facilities and large ships; thus, the satellite signal can be easily influenced by noise. More surveys are required in this area; thus, we will restudy the Gwangyang Port to understand this noise.

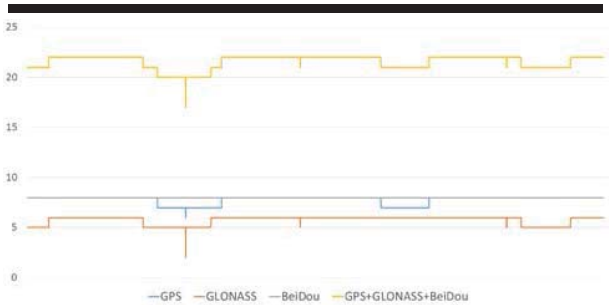

Figure 4. Number of GNSS satellites at Jumunjin Port, as measured on September 26, 2015

The International Maritime Organization (IMO) proposed the GNSS position accuracy in IMO Resolution A-915 for future maritime fields. According to A-915, the positioning accuracy limit in coastal and port areas is less than 10 meters and less

than 1 meter, respectively. Table 3 summarizes the IMO's positioning requirements. In this study, the experimental results for the combined multi-DGNSS positioning accuracy in the studied coastal and port areas met the IMO requirements. The maximum horizontal position accuracy was 0.68 meters at the Daechon Port.

Table 3. *The requirements of future marine positioning by IMO Resolution A915.*

Area	Horizontal(m)	Alert Limit
Ocean	10	25
Coastal	10	25
Port approach	10	25
Port	1	2.5
Inland waterway	10	25

However, the combined multi-DGNSS positioning accuracy did not appear to achieve the best results. That method can improve the GNSS's dilution of precision (DOP) because it uses many available GNSS satellites. However, the signal quality of GLONASS and Beidou is relatively low compared to that of GPS. Therefore, although combined multi-DGNSS positioning uses many GNSS satellites, its positioning accuracy is not the best (Song *et al.*, 2014). Moreover, the BeiDou system is a GNSS system that is still under development; thus, its quality of orbit error and satellite clock error are unstable (Wang *et al.*, 2015). The quality of the GLONASS system's satellite signal is also lower than that of GPS. Thus, the performance of combined multi-differential GNSS positioning is similar to DGPS. However, using only the DGPS positioning method cannot ensure the best performance in complex environments, such as port areas, which are conducive to many shielding effects. As a result, the DGPS method cannot use many satellites and achieve a stable DOP value. Therefore, although the signal quality is poor, combined multi-DGNSS positioning is a suitable method in coastal and port areas. Moreover, the signal quality of GLONASS and Beidou is rapidly improving; thus, the performance of combined multi-DGNSS positioning will continuously improve. In most of coastal and port areas, which require high positioning accuracy, the combined multi-DGNSS method will be very useful.

CONCLUSIONS

Because the availability of GNSS has increased, the combined multi-differential GNSS positioning method can be used. In South Korea, three GNSS systems are available. In this paper, we calculated the pseudorange correction (PRC) of the GPS, GLONASS and Beidou systems that are available in South Korea and performed combined multi-differential GNSS positioning based on GNSS code-pseudorange measurements and pseudorange correction information. To obtain the GNSS raw measurements at the studied coastal and port areas, we installed a GNSS receiver at 5 ports in South Korea and performed the positioning experiments. The positioning accuracy in the studied coastal and port areas was found to be less than 1 meter. The best accuracy was 0.45 meter. This accuracy will improve in the future; thus, the proposed combined multi-DGNSS method was found to be suitable for use at coastal and port areas.

ACKNOWLEDGMENTS

This research was conducted as part of the project titled 'Development of Multi-purpose Reference Station Technologies for Augmentation System [PMS3280]', funded by the Ministry of Oceans and Fisheries, Korea, and 'Development of Foundation Technologies of Multi-sources Integrated Navigation for Maritime Precise Tasks[PES1960]', funded by the Korean Research Institute of Ships & Ocean Engineering.

LITERATURE CITED

Choi, B.K., Cho, C.H., Lee, S.J., 2014. Combined GPS/BeiDou Positioning Performance in South Korea, *Journal of Positioning, Navigation, and Timing*, 3(4), 149-154

Grant, A., Last, D., and Kuncheva, L. 2003, Marine DGNSS Availability and Continuity, *Journal of Navigation*, 56, 353-369.

ICD-BeiDou, 2013. BeiDou Navigation Satellite System Sugnal In Space Interface Control Document version 2.0, China Satellite Navigation Office. pp 35-45.

ICD-GLONASS, 2008. GLONASS Interface Control Document version 5.1, Coordinational Scientific Information Center Russian Space Forces, Moscow. pp 30-44.

Lee, H.S., Park, K.D., Kim, D.S., Sohn,D.H., 2012. Analysis of integrated GPS and GLONASS double difference relative positioning accuracy in the simulation environment with lots of signal blockage, *Journal of Navigation and Port Research*, 36(6), 429-435

Roβbach, U., Habrich, H., Zarraoa N. 1996. Transformation parameter Between PZ90 and WGS84, Proceedings of the 9th International Technical Meeting of the Satellite Division of the Institute of Navigation, ION GPS-96, Kansas City, Missouri.

Seo, K.Y., Kim, Y.K., Jang, W.S., Park, S.H., 2014. Method of Differential Corrections Using GPS/Galileo Pseudorange Measurement for DGNSS RSIM, *Journal of Navigation and Port Research*, 38(4), 373-378

Song, W., Yi, W.,Lou, Y., Shi,C., Yao, Y.,Liu, Y., Mao, Y., Xiang Y., 2014. Impact of GLONASS pseudorange inter-channel biases on satellite clock corrections, *GPS Solutions*, 18(3), 323-333

Wang, G., Kees de Jong, Zhao, Q., Hu, Z., Guo, J., 2014. Multipath analysis of code measurements for BeiDou geostationary satellites, *GPS Solutions*, 19(1), 129-139

Yamada, H,. Takasu, T,. Kubo, N,. Yasuda,. 2008. Evaluation of Positioning Accuracy with Differential GPS/GLONASS, ION GNSS *Proceedings of the 21st Technical Meeting of the Satellite Division*, Savannah, GA. 16-19

Journal of Coastal Research	SI	75	1342 - 1346	Coconut Creek, Florida	2016

Coastal Water Quality Modeling in Tidal Lake: Revisited with Groundwater Intrusion

Chang S. Kim[†*], Jinah Kim[†], Haksoo Lim[†], Younghoon Jeong[‡], and Kwang Soon Park[†]

[†]Operational Oceanography Research Center,
Korea Institue of Ocean Science and Technology (KIOST)
Ansan, South Korea

[‡]Department of Ocean Science,
Kunsan National University
Kunsan, South Korea

www.cerf-jcr.org

www.JCRonline.org

ABSTRACT

Kim C.S.; Kim J.; Lim H.; Jeong Y. and Park K.S., 2016. Coastal water quality modelling in a tidal lake: Revisited with groundwater Intrusion. *In:* Vila-Concejo, A.; Bruce, E.; Kennedy, D.M., and McCarroll, R.J. (eds.), *Proceedings of the 14th International Coastal Symposium* (Sydney, Australia). *Journal of Coastal Research*, Special Issue, No. 75, pp. 1342 - 1346. Coconut Creek (Florida), ISSN 0749-0208.

A new method for predicting the temporal and spatial variation of water quality, with accounting for a groundwater effect, has been proposed and applied to a water body partially connected to macro-tidal coastal waters in Korea. The method consists of direct measurement of environmental parameters, and it indirectly incorporates a nutrients budget analysis to estimate the submarine groundwater fluxes. Three-dimensional numerical modeling of water quality has been used with the directly collected data and the indirectly estimated groundwater fluxes. The applied area is Saemangeum tidal lake that is enclosed by 33km-long sea dyke with tidal openings at two water gates. Many investigations of groundwater impact reveal that 10 ~ 50% of nutrient loading in coastal waters comes from submarine groundwater, particularly in the macro-tidal flat, as in the west coast of Korea. Long-term monitoring of coastal water quality signals the possibility of groundwater influence on salinity reversal and on the excess mass outbalancing the normal budget in Saemangeum tidal lake. In the present study, we analyze the observed data to examine the influence of submarine groundwater, and then a box model is demonstrated for quantifying the influx and efflux. A three-dimensional numerical model has been applied to reproduce the process of groundwater dispersal and its effect on the water quality of Saemangeum tidal lake. The results show that groundwater influx during the summer monsoon then contributes significantly, 20% more than during dry season, to water quality in the tidal lake.

ADDITIONAL INDEX WORDS: *Water quality, groundwater, Saemangeum tidal lake, numerical water quality model.*

INTRODUCTION

Fresh water in the land flows into the ocean through surface water or groundwater. The submarine groundwater can be either the direct intrusion of fresh water through soil or re-circulated seawater that has intruded through sediment pores. It has been reported that fresh water groundwater of takes approximately 6% of river runoff (Burnett *et al*., 2003) while the re-circulated seawater groundwater is approximately 48% of the discharge volume of river runoff (Zektzer *et al*., 1973). The groundwater impact on the tidal flats of the study area, Saemangeum (hereafter SMG) tidal lake, has been subject to uncertainty due to the moderately complex composition of of the sandy silt environment (Jeong *et al*., 2014). The coastal environmental setting and coastal hydraulic construction are well described in an earlier paper of Kim *et al*. (2011). The water quality in the tidal lake directly influences the seawater quality and consequently the coastal environment would be vulnerable to poor water quality in the lake. Determination of the pollutant and nutrient loading from the land requires a more or less quantitative understanding of the processes occurring in the tidal lake and the coastal system. In this study, we used field data observed during 2009 ~ 2010 in SMG tidal lake (Figure 1). The observed data for nutrients include the fluxes in the surface flow and submarine groundwater. The model input from the bottom layer to represent the groundwater influx was optimally distributed based on the estimated nutrient budget analysis using a one-dimensional box model.

To keep good water quality in tidal lake and adjacent coastal waters, a model system to predict the temporal and spatial variation of water conditions, including groundwater influence, is required.

METHODS

Field Data

The SMG tidal lake and coastal waters (Figure 1) show very unique and complex processes in water transport and biogeochemical changes due to the partly enclosed water body. The water quality in environments such as the SMG would be controlled by hydrodynamics, biogeochemical and benthic processes. The terrain loads of nutrients flow in the lake through rivers, precipitation, submarine groundwater and seawater exchange. The present study notably includes the submarine groundwater in the water body system, to quantify the water quality, investigate the material budget and to predict the future environmental condition. To fulfill all needeed procedures, the observation, budget study and numerical modeling of water quality are described below.

DOI: 10.2112/SI75-269.1 received 15 October, 2015; accepted in revision 15 January, 2015
*Corresponding author: surfkim@kiost.ac.kr
©Coastal Education and Research Foundation, Inc. 2016

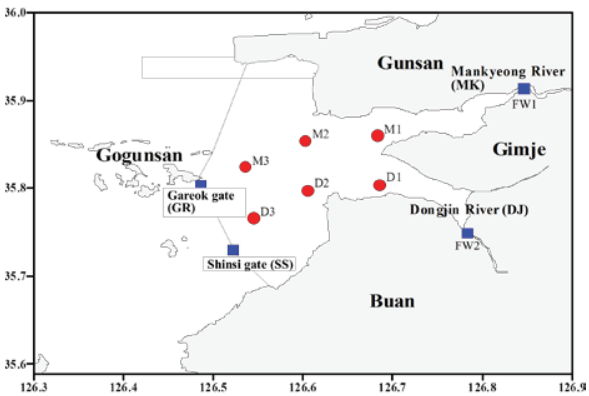

Figure 1. Sampling stations for the material budget study. MK and DJ denote the major rivers and GR and SS denote the water gates. The 6 major stations represent the perception area of submarine ground waters.

Field observations were conducted during March ~ October in 2009 and in 2010 in the SMG tidal lake. Samples were collected at the surface and bottom layers at 6 stations in the lake (Figure 1). Continuous monitoring has been also implemented at two sluice gates; Shinshi (SS) and Gareok (GR) gates as shown in Figure 1.

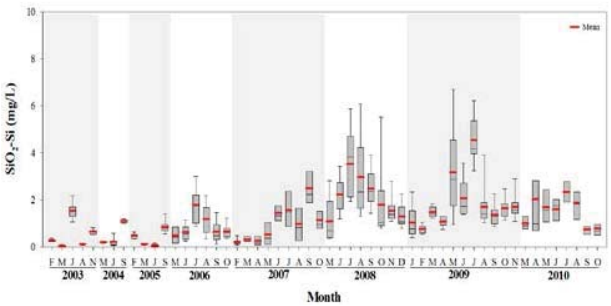

Figure 2. Annual variation of SiO_2-Si concentration in the surface water of SMG tidal lake. High concentration of SiO_2-Si occurs in the rainy season during June ~ August. Notably, a moderately high concentration shows in April 2010 due to an episodic stormy condition.

Figure 2 illustrates the annual variation of silicate concentration of surface water in the SMG tidal lake. Among many nutrient salts, the silicate has been observed as an index variable for excess-loading from submarine groundwater in the SMG coastal area in Korea (Lee *et al*., 2009). As shown in Figure 2, the silicate concentration dramatically increases after 2006. There was an engineering event in 2006 with full closure of the sea dyke that separates the coastal waters from the tidal lake. Particularly, increased precipitation was recorded during the summer monsoon season after 2006, which implies that the main transport carrier of the silicate would be the fresh water discharge from rivers and submarine groundwater in the rainy season. It is not surprising that the portion of fresh water volume in the tidal lake kept increasing after the year 2006 upon completion of the sea dyke. The closure of the sea dyke prohibits the fresh water from mixing with coastal waters.

It is more clearly shown that there is coherent relationship between the silicate concentration and fresh water discharge by examining the seasonal variation in Figure 2. Furthermore, it would be interesting to investigate the degree to which submarine groundwater contributed to the entire fresh water content of the tidal lake. This process is important for estimating the excess loading of nutrient salts added by groundwater to the tidal lake. To clarify the budget of nutrient salts in the lake, we have analyzed the material flux in the closed system of the tidal lake with field observed data (KIM *et al*., 2005; Lee *et al*., 2009).

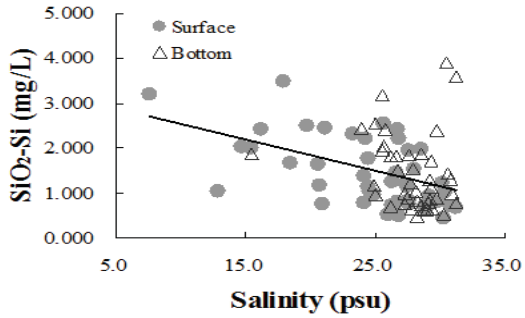

Figure 3. Relation between salinity and concentration of SiO_2–Si in the surface and bottom waters. It is noticeable that significantly high concentrations of silicate in the bottom layer are observed in highly stratified water. The line simply connects the cluseter of bottom water concentrations with typical concentrations of surfce waters.

In Figure 3, the maximum monthly mean concentration reaches approximately at 2,300 mg/L in surface layer in July, while the maximum monthly mean in the bottom layer shows approximately 2,400 mg/L in July. The silicate concentration at the seabed is somewhat higher than the surface water. The maximum occurring in July throughout the water column indicates the role of fresh water discharge during the rainy season. The horizontal distribution shows that higher concentrations occur near the river mouths while the bottom waters show higher silicate concentrations near the stations close to the GR water gate. Figure 3 illustrates the relationship between the salinity and the concentrations of SiO_2-Si in the surface and bottom waters. The silicate salts in the surface layer behave as an conservative process while the silicate at the bottom behaves as an additive material, indicating that the bottom concentrations arise from the presence of submarine groundwater.

Material Budget Study

To estimate the material budget in the tidal lake, we use the conceptual box model that enforces a balance between the influx and efflux crossing over the boundaries, including the sea surface and the sea bed.

It is assumed that the materials entered into the tidal lake undergo physical, chemical and biogeochemical processes but in

changed form are found in quantites that are accountable to the material budget. By analyzing the material budget study (Hong *et al*., 2000; Jeong *et al*., 2006), we investigate the importance of submarine groundwater for coastal water quality.

The fluxes of material that flow in and out of the control box are estimated by multiplying the flow rate by the concentration, and then the net fluxes are obtained using the following approaches.

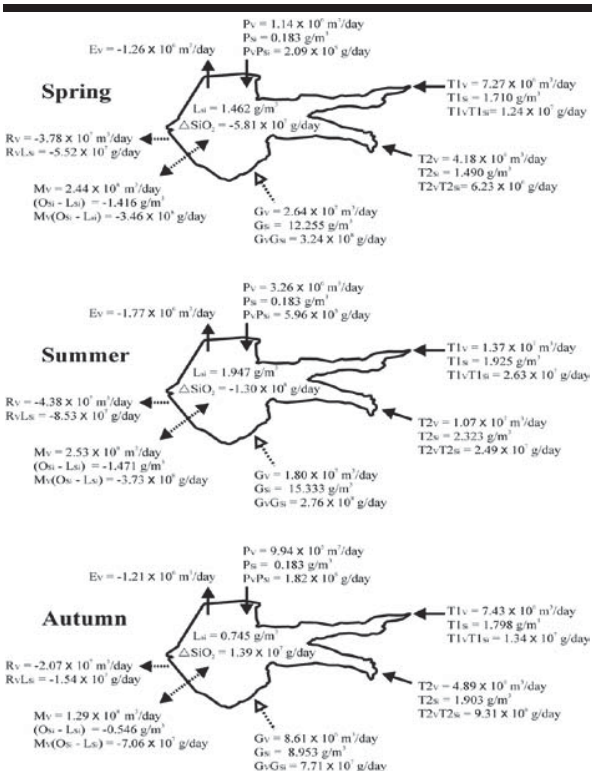

Figure 4. Seasonal change in influx and efflux of SiO_2-Si budget in the SMG tidal lake.

(1) The inflow volume of fresh water is provided daily by national flood control system run by Korea government agency. Annual fresh water discharge from the MK and DJ rivers is approximately 4,000 × 10^6 m^3/year.

(2) Seawater transport volume is estimated using the difference of seawater levels between the inner and outer sites. The flow rate is obtained by multiplying the water surface area by the difference in the surface water level. The observed difference in seawater levels are 0.61 m/day in spring, 0.63 m/day in summer and 0.32 m/day in autumn. Corresponding transport volumes of seawater are 2.44×10^8 m^3/day in spring, 2.53×10^8 m^3/day in summer and 1.29×10^8 m^3/day in autumn. Usually in spring the water level difference is relatively high due to the sudden spring breakout of stormy weather with heavy rains (Lie *et al*., 2008).

(3) Net seawater transport volume from the lake to the outer sea is estimated by dividing the salt flux (Mv·△Salinity) by the the average salinity of the inner lake.

(4) Water exchange at the water surface is the balance between the precipitation and evaporation. The meteorological data are obtained at adjacent meteorological stations.

(5) Salt transport is estimated by using the following equation with the assumption of the elements being conserved:

$$Mv(Os - Ls) + T1v \cdot T1s + T2v \cdot T2s + Pv \cdot Ps = Rv \cdot Ls + Ev \cdot Es.$$

Mv, is the seawater transport volumen; T1v the fresh water discharge from MK river: T2v the fresh water discharge from DJ river; Pv the precipitation volumen: Rv the residual transport volumen; Ev the evaporation volume. Os and Ls are the mean salinity of the outer sea and the mean salinity of the inner lake, respectively. T1s, T2s, Ps, and Es are respectively the salinities of the MK and DJ rivers and of precipitation and evaporation. However, the salinity of river waters, precipitation and evaporation are set to zero.

(6) The volume of submarine groundwater upwelled into the lake is estimated as the difference between the total inflow volume (rivers, precipitation and flood current through sluice gates) and outflow (evaporation and ebb current through sluice gates). The estimated volume of submarine groundwater is 16.0 m^3/m^2/year (Hwang *et al*., 2005). It is lower than the groundwater intrusion measured in Yeoja Bay Korea using a radioactive method, but higher than 7.0 m^3/m^2/year measured in Florida (Corbett et al., 1999) and 5.6 m^3/m^2/year in Point Judith.

(7) The water budget is calculated according to the following equation:

$$Rv + Ev = T1v + T2v + Pv + Gv$$

where Gv is the volume of submarine groundwater. The material budget is applied to estimate the budgets of total organic carbon (TOC), total nitrogen (TN), total phosphorus (TP), and SiO_2-Si. The material budget is obtained by multiplying the water flux and concentration of each variable. The total influx (Q_{influx}) and efflux(Q_{efflux}) are given as follows:

$$Q_{influx} = Mv \cdot (O_c - L_c) + T1v \cdot T1c + T2v \cdot T2c + Pv \cdot Pc + Gv \cdot Gc$$

$$Q_{efflux} = Rv \cdot L_C$$

where the subscript c stands for the concentration of the variable. We have used the observed field data for the nutrient variables. It is assumed that the characteristics of submarine groundwater are similar to that of pore water as suggested by Burnett *et al*. (2003).

Three-Dimensional Water Quality Modeling

The coastal water quality model, ROMS-ICM, has been fully described in the earlier work of Kim *et al.* (2011), hence we skip the details. To enhance the model predictability of the groundwater effect, model input from the benthic layer has been added In this study. In addition to the surface flow condition, we are ready to add the submarine groundwater condition with known flux budget that is obtained from the box model. As a simple prognostic asset test, the ground water flux at designated cells in the central basin have been supplied with 50% of riverine fluxes.

The loadings from surface flow and atmospheric deposition have been eliminated from consideration due to the insignificant effects during the land development.

RESULTS

Nutrient Budget Analysis

(1) Water Budget

The fresh water inflows to the tidal lake are 7.27×10^6 m^3/day (MK river) and 4.18×10^6 m^3/day (DJ river) in spring, 1.37×10^7 m^3/day (MK river) and 1.07×10^7 m^3/day (DJ river) in summer, and 7.43×10^6 m^3/day (MK river) and 4.89×10^6 m^3/day (DJ river) in autumn, showing a peak in summer due to the rainy monsoon.

The differences between precipitation and evaporation are -1.21×10^5 m^3/day (negative means more evaporation) in spring, 1.50×10^6 m3/day in summer and -2.17×10^5 m^3/day in autumn, showing a net loss of lake water through evaporation except during the summer.

The residual transport volumes are 3.78×10^7 m^3/day in spring, 4.38×10^7 m^3/day in summer and 2.07×10^7 m^3/day in autumn, showing peak transport of lake water to the sea in summer. The upwelling volumes of submarine groundwater are 2.64×10^7 m^3/day in spring, 1.80×10^7 m^3/day in summer and 8.61×10^6 m^3/day in autumn. The peak value in spring is believed due to the relatively big difference in water level and large amount of runoff in spring.

(2) Salt Budget

Assuming the salinity of river flow as 0 psu, the salt mass flowing into the tidal lake is estimated at 1.03×10^9 kg/day in spring. Based on salt balance between the inflow and outflow, the same amount of salt must be carried out to the sea by the ebb current. The net water transport flowing out through the sluice gates can be obtained by dividing the salt mass by the mean salinity of lake water. The process yields the net (residual) transport heading to the sea as -3.78×10^7 m3/day that is close to the estimate in the water budget study. The same approach yields the salt masses as 9×10^9 kg/day in summer and 5.47×10^8 kg/day in autumn.

In this paper, we illustrate the result of the material budget for SiO_2-Si among many other nutrient variables such as TOC, TP and TN through the MK and DJ rivers and according to the season in Table 1. The net transport of SiO_2-Si in spring and summer is toward the outer sea, while in autumn the transport is toward the tidal lake.

Table 1. *Flux-In (+) and Flux-Out (-) of SiO_2-Si in the tidal lake* (g/day).

	Spring	Summer	Autumn
SiO_2-Si Transport	1.87×10^7	5.11×10^7	2.27×10^7
Water exchange	-3.46×10^8	3.73×10^8	-7.06×10^7
Residual flow	-5.52×10^7	-8.53×10^7	-1.54×10^7
Precipitation	2.09×10^5	5.96×10^5	1.82×10^5
Groundwater	3.24×10^8	2.76×10^8	7.71×10^7
Net transport	-5.81×10^7	1.30×10^8	

Predictability of Water Quality

A calibration has been done to see whether the seasonal variation and episodic events (as shown in April 2010 in Figure 2) on the concentration of TN, TP and dissolved oxygen (DO).

Among the several stations of calibration points shown in Figure 1, station M3 is a representative place for the water quality in the tidal lake. The station M3 covers the area of very active mixing between the fresh water of river runoff and the seawater coming through the SS water gate at the dyke.

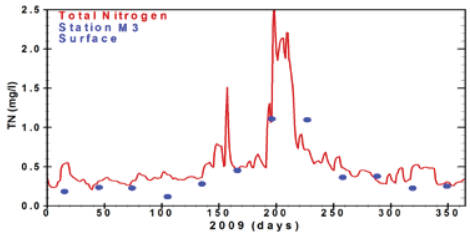

Figure 5. Comparison of observed and computed annual cycles of TN representing the water quality in SMG tidal lake in 2009.

Figure 5 shows the observed (dot) and computed (line) annual variation of total nitrogen. The annual mean of the TN observed in the entire tidal lake in 2009 is around 0.5 mg/l, ranging from 0.2 mg/l in a normal condition to 2.5 mg/l in stormy conditions in the summer monsoon or in an episodic event releasing abnormally high loading upstream (Lie *et al.*, 2008). The computed TN reproduces reasonably well the stormy conditions in summer and event-like release of high concentrations.

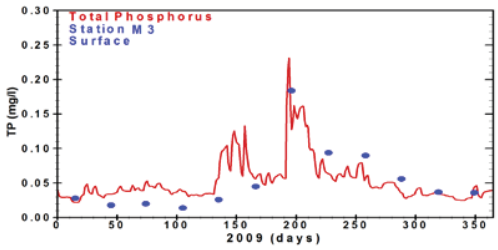

Figure 6. Comparison of observed and computed annual cycle of TP representing the water quality in SMG tidal lake in 2009.

Figure 6 illustrates the comparison of observed and computed TP. The computation of TP also is consistent with the observed values as the case of TN.

CONCLUSIONS

In this study, we have investigated the asset test on the predictability of submarine groundwater impact on coastal water quality in the SMG tidal lake and adjacent coastal waters. Monthly observed field data have been analyzed to quantify the contribution of submarine groundwater. Field data shows evidently significant additions to the total loading of nutrient salt in the tidal lake. Analysis of the material budget was conducted using a box model that attributes the excess loading of nutrient

salt to submarine groundwater intrusion. During the rainy season of spring and summer, the groundwater contributions are nearly the same order as the riverine fluxes. A three-dimensional water quality model (ROMS-ICM) that consists of a hydrodynamic model ROMS and eutrophication model CE-QUAL-ICM (Kim *et al*., 2011) was used for water quality modeling and prediction.

The model also has been calibrated to reproduce the annual cycle of major water state variables such as temperature, salinity, chlorophy-ll, chemical oxygen demand (COD), DO, TP, TN and etc. Major loadings of nutrients are from river flows and controlling points at seawater gates. The three-dimensional water quality model ROMS-ICM shows an excellent performance at predicting the annual cycle of nutrient fluxes in surface layer as well as in the bottom layer, indicating the importance of groundwater intrusion.

ACKNOWLEDGMENTS

This study was partly supported by the research project, “Development of Korea Operational Oceanographic System (KOOS PhaseII)” funded by Ministry of Ocean and Fisheries Korea.

LITERATURE CITED

Burnett, W. C.; Bokuniewicz, H.; Huettel, M.; Moore, W. S., and Taniguchi, M., 2003. Groundwater and pore water inputs to the coastal zone. *Biogeochemistry*, *66*(1-2), 3-33.

Corbett, D. R.; Chanton, J.; Burnett, W.; Dillon, K.; Rutkowski, C., and Fourqurean, J. W., 1999. Patterns of groundwater discharge into Florida Bay. *Limnology and Oceanography*, *44*(4), 1045-1055.

Hwang, D. W.; Kim, G.; Lee, Y. W., and Yang, H. S., 2005. Estimating submarine inputs of groundwater and nutrients to a coastal bay using radium isotopes. *Marine Chemistry*, *96*(1), 61-71.

Hong, S. J.; Lee, D. I.; Kim, D. M., and Park, C. K., 2000. Material budgets in the Nakdong River estuary with simple box model. *Journal of the Korean Society for Marine Environment & Energy*, *3*(3), 50-57.

Jeong, Y.H.; Kim, C.S. and Yang, J.S., 2014. Estimation of Addition and Removal Processes of Nutrients from Bottom Water in the Saemangeum Salt-Water Lake by Using Mixing Model. *Journal of the Korean Society for Marine Environment & Energy*, 17, 1-12.

Jeong, Y. H.; Kim, Y. T.; Kim, K. H.; Kim, S. Y.; Kim, B. H., and Yang, J. S., 2006. Mass Balance of Salts, DIP, DIN and DON in the Gomso Tidal Flat. *The Sea*, *11*(2), 68-81.

Kim, C. S.; Lim, H. S., and Cerco, C. F., 2011. Three-dimensional water quality modeling for tidal lake and coastal waters with ROMS-ICM. *Journal of Coastal Research, SI60, 10681072*.

KIM, G.; HWANG, D. W.; RYU, J. W., and LEE, Y. W., 2005. Environmental and ecological consequences of submarine groundwater discharge in the coastal areas of the Korea peninsula. *The Sea*, *10*(4), 204-212.

Kim, J. G.; Kim, D. M., and Yang, J. S., 2000. Estimation of material budget for Keum river estuary using a Box Model. *Journal of the Korean Society for Marine Environment & Energy*, *3*(4), 76-90.

Lee, K. S., and Jun, S. K., 2009. Material Budgets in the Youngsan River Estuary with Simple Box Model. *Journal of the Korean Society for Marine Environment & Energy*, *12*(4), 248-254.

Lie, H. J.; Cho, C. H.; Lee, S.; Kim, E. S.; Koo, B. J., and Noh, J. H., 2008. Changes in marine environment by a large coastal development of the Saemangeum reclamation project in Korea. *Ocean and Polar Research*, *30*(4), 475-484.

Zektzer, I. S.; Ivanov, V. A., and Meskheteli, A. V., 1973. The problem of direct groundwater discharge to the seas. *Journal of Hydrology*, *20*(1), 1-36.

Journal of Coastal Research	SI	75	1347 - 1351	Coconut Creek, Florida	2016

The Impacts of Debris Torrents in Caribbean Coast of Honduras, Central America

Sungduk Kim†, Hojin Lee†, and Kye-Won Jun††*

†The School of Civil Engineering,
Chungbuk National University,
Cheongju, South Korea

††Graduate School of Disaster prevention,
Kangwon National University,
Samcheok, South Korea

www.cerf-jcr.org

www.JCRonline.org

ABSTRACT

Kim, S.;Lee, H., and Jun, K.W., 2016. The impacts of debris torrents in Caribbean coast of Honduras, Central America. *In:* Vila-Concejo, A.; Bruce, E.; Kennedy, D.M., and McCarroll, R.J. (eds.), *Proceedings of the 14th International Coastal Symposium* (Sydney, Australia). *Journal of Coastal Research*, Special Issue, No. 75, pp. 1347 - 1351.Coconut Creek (Florida), ISSN 0749-0208.

One of the main contributing factors in creating debris torrents is heavy rainfall. Global climate changes have led to an increase in localized downpours, causing an increase in torrent occurrences as well. The purpose of this experiment is to utilize numerical simulation for the analysis of debris torrents in their behaviour and mechanism. The numerical simulation is comprised of equations calculating mass continuity and momentum in order to consider erosion, deposition, and the combination of them both. The Finite Difference Method is applied to analyze the debris torrents. The numerical model of present study was applied to four rivers in Omoa and Puerto Cortes, Honduras (Central America). Out of the four rivers, the Cuyamel River exhibited the greatest value of water discharge and water depth, and the Tulian River showed the biggest runoff real volume value for the debris torrents.It is deduced that high levels of sediment concentration affect the environment surrounding the ocean in areas consisting of both mountain areas and the ocean.

ADDITIONAL INDEX WORDS:*Debris torrents, climate change, sediment concentraion, Honduras.*

INTRODUCTION

In October of 1998, a Category 5 hurricane called Mitch struck Central America. Mitch is considered one of the most devastating hurricanes to strike the Western hemisphere within the past two centuries. Among the five countries within Central America, Honduras experienced the most impact from hurricane Mitch, and the Eastern Caribbean region of Honduras suffered the most damage. The storm caused as many as 11,000 casualties, left over 1.5 million homeless, which is 20% of the population, and wrecked over one third of the nation (Hellin and Haigh, 1999; Hellin *et al.*, 1999). In combination with the hurricane's heavy rainfalls, the fundamental cause behind the damage is due to the impacts of the saturated soil and the debris torrents of the bare hillsides. As a result, the residents of the hillside regions suffered the greatest damage.

Climate changes are observed to affect debris torrents. Globally, debris torrents are occurring at a higher rate, thus increasing the number of casualties and damaged territories on a larger scale. The damage is caused by the water supplied from the upstream region of the debris torrent flowing downstream with high mobility, mixing with fractured rocks and sediments caused by erosion and deposition. On a spatial-temporal scale, disasters caused by debris torrents are nonhomogeneous and occur irregularly, making it difficult to predict for. Therefore, it is important to combine forces and take preventive measures in understanding the mechanisms and characteristics of catastrophe.

DOI: 10.2112/SI75-270.1 received 15 October, 2015; accepted in revision 15 January, 2015
*Corresponding author: kwjun@kangwon.ac.kr
©Coastal Education and Research Foundation, Inc. 2016

In this study, the district of Honduras' Caribbean coast connected to Guatemala's earthquake zone and the four main rivers is chosen for further analysis of the attributes of debris torrents including their water discharge and water depth. The results of the study show that the districts of Omoa and Puerto Cortes of the Honduras Caribbean Coast exhibit a variety of inclined slopes that help provide useful information in predicting debris torrent occurrences and establishing preventive measures.

METHODS

The governing equations used to interpret the solid-liquefied mixture of the debris torrents are the continuity equation of water flow, which satisfies mass conservation, and the continuity equation of sediment particle, as shown in (1) and (2) respectively.

$$\frac{\partial A}{\partial t} + \frac{\partial Q}{\partial x} = \beta B \tag{1}$$

$$\frac{\partial (Ch)}{\partial t} + \frac{\partial (CM)}{\partial x} = C_* \beta \tag{2}$$

Where, A is area of flow section, Q is flow discharge, β is erosion velocity or deposition velocity, B is width of channel, C is sediment concentration in debris torrents, M is flow discharge per unit width, h is water depth, and C_* is maximum sediment concentration in the bed.

To calculate erosion or deposition velocity β the following equation is used (Takahashi *et al.*, 1992).

For deposition,

$$\beta = \alpha' \cdot \frac{C_\infty - C}{C_*} \cdot \frac{M}{d_m} \tag{3}$$

For the erosion,

$$\beta = \alpha \cdot \frac{C_{T\infty}}{C_* - C_{T\infty}} \cdot \frac{M}{d_m} \times \left\{ 1 - \frac{C}{C_\infty} \frac{\rho_m}{\rho} \frac{\tan\phi - (C_T / C_{T\infty})(C_\infty / C)\rho / \rho_m \tan\theta}{\tan\phi - \tan\theta} \right\} \tag{4}$$

where α is erosion coefficient, α=0.007, α' is deposition coefficient, α'=0.01, $C_\infty$is the equilibrium sediment concentration, C_T is the volume concentration of the total solid fraction, $C_{T\infty}$is the equilibrium of the total solids, $\rho_m$is the mixture density of water and sediment(ρ_m=(σ-ρ)C+ρ), σ is the density of sediment particle, θ is the angle formed by the bed slope and water surface elevation, ϕ is the internal friction angle of the sediment .

To understand the movability of the solid-liquefied mixture flow, the momentum equation is applied; (5) shows the momentum conservation equation of the solid-liquefied mixture flow.

$$\frac{\partial M}{\partial t} + \frac{\partial(\frac{Q^2}{AB} + gA\cos\theta)}{\partial x} = gh\sin\theta - \frac{\tau_b}{\rho_m} \tag{5}$$

Where, g is gravity acceleration and τ_b is the bottom shear stress. The changes in the thickness of soil strata due to erosion and deposition of the bed surface can be calculated with the following equation (6):

$$\beta = -\frac{\partial \xi}{\partial t} \tag{6}$$

Where, ξ is the deposition thickness of the bed measured from the original bed surface elevation.

The solid-liquefied mixture must satisfy the mass and the balance of the mass-momentum equation in order to observe the following equation (7) with (1), (2), and (5) in its conservative form (Chow, 1959).

$$\frac{\partial \mathbf{V}}{\partial t} + \frac{\partial \mathbf{\Omega}}{\partial x} = \mathbf{E} \tag{7}$$

Were, $\mathbf{V} = \begin{bmatrix} A \\ M \end{bmatrix}$, $\mathbf{\Omega} = \begin{bmatrix} Q \\ \frac{Q^2}{AB} + gA\cos\theta \end{bmatrix}$, $\mathbf{E} = \begin{bmatrix} \beta B \\ gh\sin\theta - \frac{\tau_b}{\rho_m} \end{bmatrix}$

The equilibrium sediment concentration based on the particles' movement of the debris flow can be observed with the following equation (8).

$$C_\infty = \frac{\rho_m \tan\theta}{(\sigma - \rho_m)(\tan\phi - \tan\theta)} \tag{8}$$

Equation (8) shows that depending on tanθ, the following information can be classified: stony debris torrents, immature debris torrents, and turbulent debris torrents (Takahash, 1997).

Debris torrents are greatly affected by heavy rainfalls and the rainfalls' intensity brought upon by climate changes. Therefore, knowledge of discharge of debris torrents between intervals of elapsed time is important in the prediction and thereby the prevention of the disaster.

Therefore, the numerical model used by Kim and Lee (2015) is implemented for this study and the Finite Difference Method (FDM) is applied to effectively analyse debris torrents of various elapsed time intervals.

Honduras widely covers the Central American isthmus, covering an area of about 112,000km^2. The climate of the Honduras Caribbean coast experiences seasonal easterly trade winds, causing the rainy season to last up to eight months each year.Annually, the annual rainfall exceeds 2000 mm and the average air temperatures range between 25°C and 29°C.In addition, this region in located within the hurricane belt and is connected to the earthquake zone of Guatemala (Bommer and Rodriguez, 2002).Therefore, such factors cause Honduras to always suffer from debris-torrents related disasters.

The following study analysed the characteristics and the discharge of debris torrents for four main rivers situated in two districts of the Honduras Caribbean coast, Puerto Cotes and Omoa. The four main rivers are the Tulian river,Masca river, Coto river, and the Cuyamel river.

Figure 1. Location of the selected study area at Caribbean coast in Honduras (Image source: Google map©).

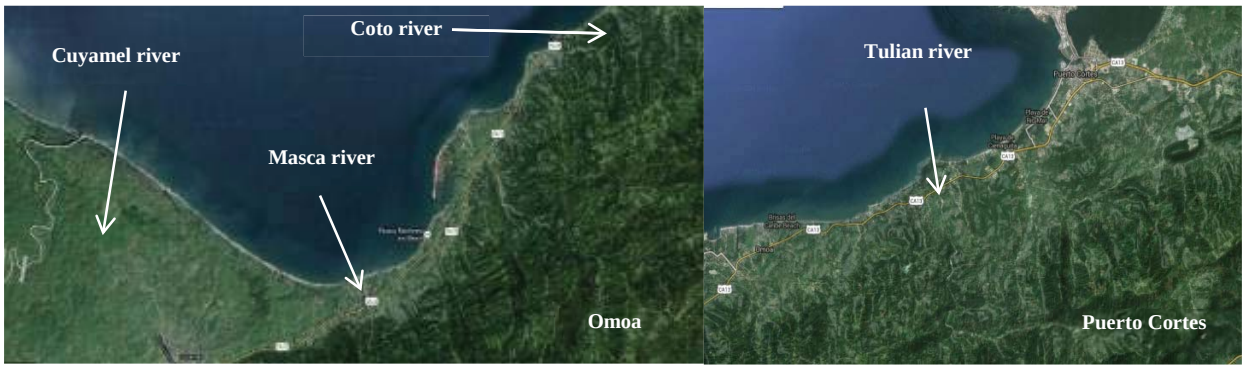

Figure 2. Topographic maps of four rivers at Caribbean coast in Honduras (Image source: Google map©).

The data of rainfall intensity from 1998 of Hurricane Mitch are used as input data for the experiment, where the maximum rainfall intensities ranged from 138mm/hr (2-minute period) to 58.4 mm/ hr (60-minute period).Figure 1 shows the target site of the experiment.

RESULTS

Figure 2 is the topographic map of three of Omoa's watershed areas and one of Puerto Corete's watershed areas.

The following information is the drainage area (in square kilometres) and the main channel length (in kilometres) of the four rivers listed respectively: Tulian river 7.8km^2 and 7.6 km, Coto river 6.2km^2 and 2.8 km, Masca river 5.2km^2 and 1.2 km, and Cuyamel river 10km^2 and 2.2 km.

The conditions for calculating the numeral simulation are given. The supply water discharge is calculated using the rational formula using the values of rainfall intensity and rainfall runoff. The predicted value of rainfall intensity for all the four rivers were uniformly set with the average maximum range of 98.2mm/hr given by Hurricane Mitch of 1998, and for each river the supply water discharge was set using the watershed area of the upper stream.

The supply water discharge values are 212.77m^3/sec for Tulian river, 169.12 m^3/sec for Coto river, 141.84 m^3/sec for Masca river, and 272.78 m^3/sec for Cuyamel river.

In the designated area, the depth of suspended sediments is set to Dp=10m for the stabilization of the saturated sediment layer.

The mean diameter of sediment is d_m=30cm, the volume concentration of sediment in the static bed is C_*=52%, the density of sand particle is σ=2.65g/cm^3, and the internal friction angle of a sand is $tan\ \phi$=0.7. The time lapse of the simulation was 360 seconds.

Figure 3 is a graph that exhibits the flow discharge and flow water depth of the designated watershed points at the Tulian river after the debris torrents reached the downstream over a 360 seconds time period. In Figure 3, the y-axis labels the flow discharge and the flow water depth, whereas the x-axis shows time elapses; from 288 meters to 2,448 meters are the points chosen from upstream towards downstream.Figure 3 shows that the peak flow discharge in the fastest time lapse occurred at the downstream 2,448 m point. On the other hand, the flow discharge line at the upstream 288 m point showed a more gradual slope.

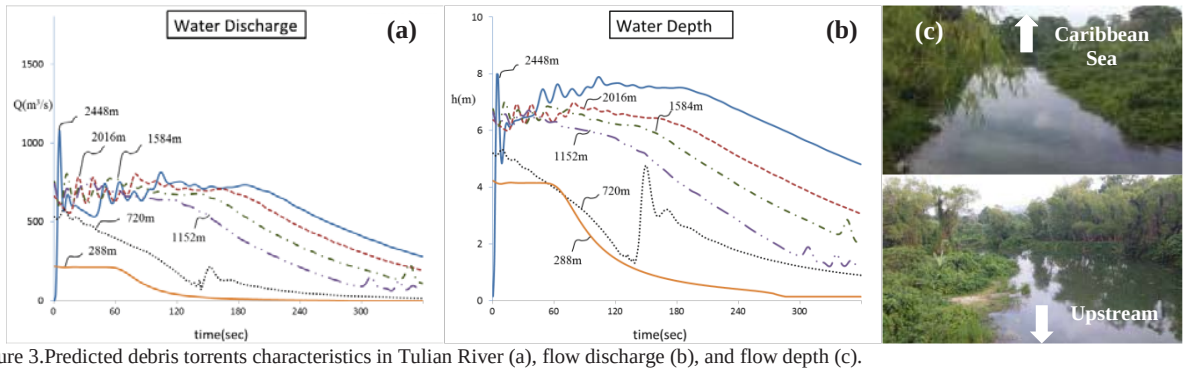

Figure 3.Predicted debris torrents characteristics in Tulian River (a), flow discharge (b), and flow depth (c).

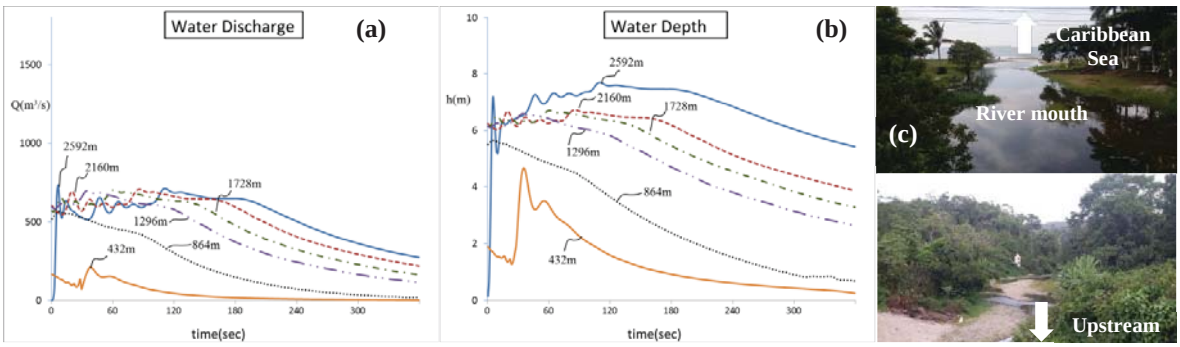

Figure 4. Predicted debris torrents characteristics in Coto River (a), flow discharge (b), and flow depth (c).

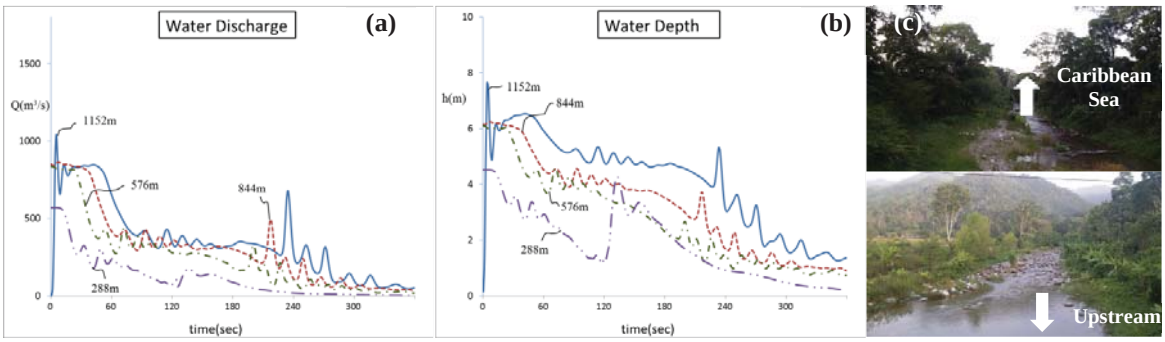

Figure 5. Predicted debris torrents characteristics in Masca River (a), flow discharge (b), and flow depth (c).

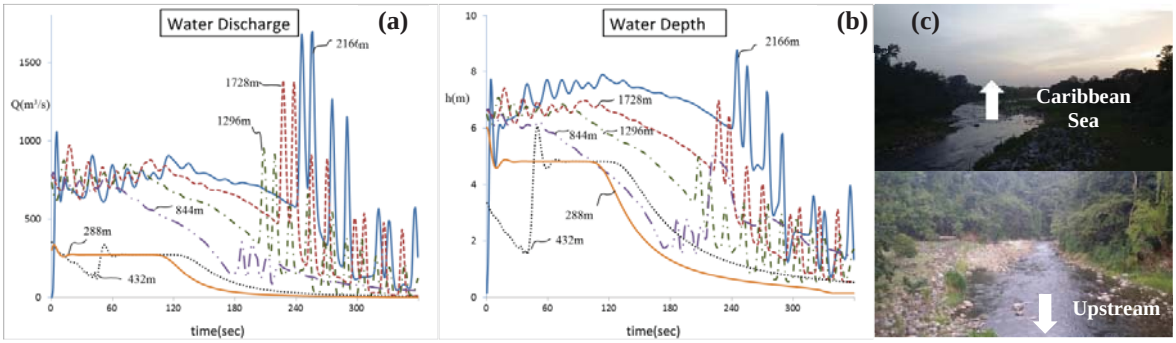

Figure 6. Predicted debris torrents characteristics in Cuyamel River (a), flow discharge (b), and flow depth (c).

The half point for all the main rivers showed fluctuation in the debris torrents, thus revealing distributions of high water discharge. As strong rainfall intensities develop from debris torrents of upstream mountainous areas, erosion and deposition repeatedly persist, thus causing much damage particularly around the mountainous area.

The depth of flow water shows similar conditions of water discharge. However, near the upstream 720 m point at around 150 seconds, a big height difference in water depth is observed. The simulation result states the real volume of runoff debris torrents is about 136,080 m^3.

In Figure 4, the peak water discharge value of the Coto river is small. The water depth value was high at the upstream 432 m point. In the case for Coto river, the flow rate exhibits an increase in water depth value from upstream continually towards downstream. The simulation result states the real volume of runoff debris torrents is about 120,962 m^3.

Figure 5 shows that compared to the previous two rivers, the water discharge values of Masca river continually increase up to

the 60 secs point, and the downstream 1,152 m and 844 m points exhibit fluctuations at the 240 secs point. Among the four main rivers, Masca river has the shortest length, which may explain why the debris torrents show a faster arrival at the designated end point. The simulation result states the real volume of runoff debris torrents is about 67,630 m^3.

Figure 6 shows that in the case of Cuyamel river, a high water discharge is seen spread along the downstream and then the water discharge fluctuates greatly between the 240 secs and the 300 secs time interval. It is deduced the high water discharge is due to the increase in supply water discharge caused by the wide watershed area and the long downstream length. The simulation result states the real volume of runoff debris torrents is about 124,417 m^3.

DISCUSSION

The erosion and deposition model established the numerical model where the governing equations consist of calculating for mass conservation and momentum conservation; the Finite Difference Method was applied and the results for each main river were inputted into a graph.

The supply water discharge values in four rivers are to be set up for simulating the program.

The flow discharge and flow water depth of the designated watershed points at the Tulian river after the debris flows reached the downstream over a 360 seconds time period in Figure 3. In Figure 3, the peak flow discharge in the fastest time lapse occurred at the downstream 2,448 m point. On the other hand, the flow discharge line at the upstream 288 m point showed a more gradual slope.

The peak water discharge value is small and the flow rate exhibits an increase in water depth value from upstream continually towards downstream in Figure 4. The water discharge values continually increase up to the 60 secs point and fluctuations at the 240 secs point in Figure 5. A high water discharge is seen spread along the downstream and then the water discharge fluctuates greatly between the 240 secs and the 300 secs time interval in Figure 6.

CONCLUSIONS

In 1998, Honduras suffered much destruction from Hurricane Mitch. The destruction was mainly caused by the debris torrents provoked by the heavy rainfalls on the mountainous sloped areas. This study analysed the water discharge and water depth of the debris torrents located in the four main rivers situated in the Honduras Caribbean coast.

As the supply water discharge increases, the peak flow discharges shows a steeper slope and after a certain time period passes, the high water discharge undergoes a fluctuation.

At the mountainous upstream locations, strong rainfall intensities provoke a repeated circle of erosion and deposition which results in debris torrents causing much damage along the mountainous terrains.

Out of the four main rivers, the greatest values for water discharge and water depth are seen in the Cuyamel river, whereas the greatest value for runoff debris torrents of 136,080m^3 is seen for the Tulian river.

The analysis of the various slopes within the districts of Omoa and Puerto Cortes of the Honduras Caribbean Coast help provide information to predict future debris torrent events and establish preventive precautions.

ACKNOWLEDGMENTS

This research was supported by Basic Science Research Program through the National Research Foundation of Korea(NRF) funded by the Ministry of Education (2013R1A1A4A01010397).

LITERATURE CITED

Chow, V.T., 1959. *Open channel hydraulics*. MacGraw-Hill Book Coorperation, 5p.

Hellin, J. and Haigh, M.J., 1999. Rainfall in Honduras during Hurricane Mitch. *Weather*, 54(1), 350-359.

Hellin, J.; Haigh, M.J., and Marks, F., 1999. Rainfall characteristicsof hurricane Mitch. *Nature*, 399, 316-317.

Bommer, J.J. and Rodrı´guez, C.E., 2002. Earthquakeinduced landslides in Central America. *Engineering Geology*, 63, 189-220.

Kim, S. and lee, H., 2015. A study of the debris flow activity on the one-steped channel slope. *Soil and Water Research*, 10(1), 32-39.

Map of Omoa and Puerto Cortes, Honduras, 2015. http://maps.google.com

Takahashi, T., 2007. Debris Flow: Mechanics, Prediction and Countermeasures. Tokyo: Taylor & Francis, 37-45.

Takahashi, T.; Nakagawa, H.; Harada, T. and Yamashiki, Y. 1992.Routing debris flows with particle segregation. *Journal of Hydraulic Engineering*, 118(11), 1490–1507.

Journal of Coastal Research	SI	75	1352 - 1356	Coconut Creek, Florida	2016

Study on Rip Current Generated by Submerged Breakwaters: Field Observation and Numerical Simulation

In Ho Kim [†], Woo Dong Lee[‡], Sungwon Shin[††], Jin Hoon Kim[†], Dong Soo Hur[‡*], and Won Chul Cho[∞]

[†] Kangwon National University, Dept. of Environmental and Ocean Construction Engineering, Samcheok, Rep. of Korea

[‡] Gyeongsang National University, Department of Ocean Civil Engineering, Tongyeong, Rep. of Korea

[††] Kangwon National University, Environmental Technology Research Institute, Samcheok, Rep. of Korea

[∞] Chung-Ang University , Department of Civil and Environmental Engineering, Seoul, Rep. of Korea

www.cerf-jcr.org

www.JCRonline.org

ABSTRACT

Kim, I.H.; Lee, W.D.; Shin, S.; Kim, J.H.; Hur, D.S., and Cho, W.C., 2016. The Study on Rip Current Generated by Submerged Breakwaters: Field Observation and Numerical Simulation. *In:* Vila-Concejo, A.; Bruce, E.; Kennedy, D.M., and McCarroll, R.J. (eds.), *Proceedings of the 14th International Coastal Symposium* (Sydney, Australia). *Journal of Coastal Research*, Special Issue, No. 75, pp. 1352 - 1356. Coconut Creek (Florida), ISSN 0749-0208.

Jetties and submerged breakwaters have been constructed at Gangmun beach, Korea, for the past several years in order to protect the beach and to secure the estuary channel. However, drowning accidents due to rip currents have often occurred in the gap between the jetty and the submerged breakwater. In this study, field observations and numerical simulations were performed to understand the mechanism of the rip current occurrences at Gangmun beach. The field investigation included the geomorphological change as well as the rip current occurrences. Three-dimensional numerical simulations were carried out to find out the occurrence mechanism of the rip currents and the countermeasure for the rip current reduction. The results showed that the mean water level difference between the gap and the area behind the submerged breakwater induced the rip currents. The numerical model results also showed that the drainage channel in the submerged breakwater can reduce the rip current magnitude.

ADDITIONAL INDEX WORDS: *Rip current, submerged breakwater, field observation, numerical modeling.*

INTRODUCTION

Rip currents are especially hazardous because it can be difficult to identify their occurrence and they are often encountered by people who have no experience with ocean waves or currents. Rip currents are jets of water issuing through the breaker line that carry sand off-shore. These currents can sometimes be observed occurring somewhat periodically down a long straight beach. They also occur under piers, alongside jetties and groins, in the center of embayments formed by headlands, and at breaks in sandbars and offshore breakwaters. The seaward velocities of rip currents can be more than 2m/s, and the rip currents contribute to the death toll at beaches by carrying unwary swimmers directly offshore into deep water.

Shepard (1936) firstly observed and studied the rip currents. Bowen (1969) and Sonu(1972) mentioned the role of a radiation stress and the bottom bathymetry in the longshore and rip current generations. They explained the mechanism of longshore currents generated by normally and obliquely incident waves based on the radiation stress introduced by Longguet-Higgins and Stewart (1962, 1964). Darlymple and Lozano (1978) suggested that the wave refraction due to the rip currents varies wave heights.

DOI: 10.2112/SI75-271.1 received 15 October, 2015; accepted in revision 15 January, 2015
*Corresponding author: dshur@gnu.ac.kr
©Coastal Education and Research Foundation, Inc. 2016

The site of the present study is Gangmun beach which is located at Gangneung city, Korea. Submerged breakwaters, jetties (training dikes) and a groin have been constructed to protect the eroding beach. On July 5th, 2014, four people drifted offshoreward due to the rip current, three of them were rescued, but one of them drowned in the area. In this study, we tried to figure out the relationship between the morphological change and the rip current occurrence through the field observation and numerical simulation before and after the construction. Moreover, this study suggests a countermeasure for the rip current reduction.

STUDY AREA

Gangmun beach is located at Gangneung city, Gangwon province and belongs to a littoral drift cell that extends from the Gangneung port (south) to the Sachun port (north). The shoreline is about 9.17 km long and includes several beaches including Gangmun beach as shown in Figure 1.

Training dike construction was started in 1996 and was completed in 2001 to secure the estuary channel from the Gyungpo lake at the northern part of Ganmun beach. After that, beach sands were rapidly disappeared and the city extended the training dike, but it could not prevent the pavement for parking area near the beach from collapsing. Even though the beach area was stabilized after a submerged breakwater and a groin (right-

Figure 1. Littoral drift cell of the study area (upper panel) and the Gangmun beach.

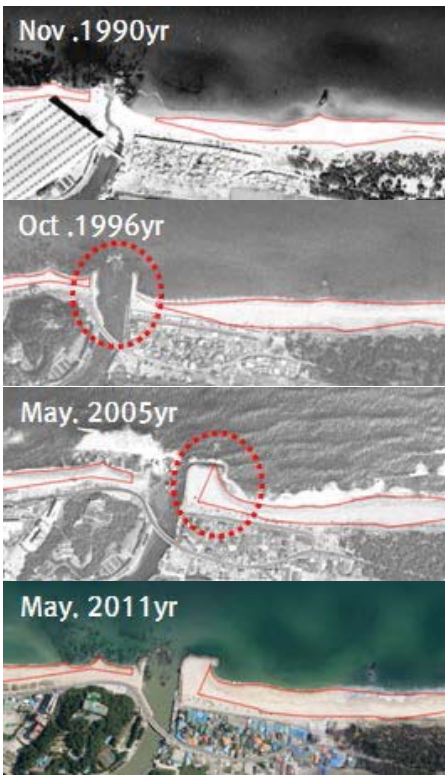

Figure 2. Historical aerial photographs of Gangmun beach

hand side of the submerged beakwater in the bottom panel of Figure 1) construction in 2013, the rip currents are still threatening swimmers. Figure 2 shows the historical aerial photographs of Gangmun beach from 1990 to 2013.

FIELD OBSERVATION

Bottom bathymetry near Gangmun beach was clearly changed in between pre-construction and post-construction of the submerged breakwater and groin as shown in Figure 3.

The bathymetry survey results showed that there were crescentic sandbars near the shoreline before the construction (Figure 3(a)). However, the survey result in June 2014, shows that the water depth in the seawater exchange channel (a gap between the training dike and the submerged breakwater) increased while the water depth behind the breakwater decreased as shown in Figure 3(b). In June 2015, the seawater exchange channel was deeper so that the rip channel was formed as shown in Figure 3(c).

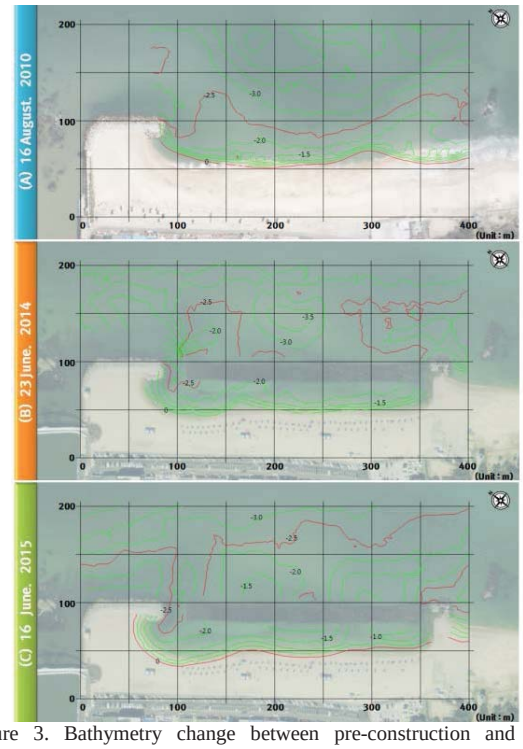

Figure 3. Bathymetry change between pre-construction and post-construction at Gangmun beach

Figure 4. Field observation for tracking the rip currents by using GPS buoys. "+" symbols represent the starting location of the buoys.

The rip current and wave observations were performed on July 19, 2014, September 30, 2015, and October 3, 2015 as shown in Figure 4. During the first observation, the incident wave came in SE direction (120 degrees) with the significant wave height of 0.2 m. The rip current was tracked by using the specially designed buoy for the rip current measurements. All the buoys near the seawater exchange channel drifted offshoreward as shown in Figure 4(a).

The rip current velocities were calculated by using GPS signals mounted on the buoy and ranged from 3.51 m/s to 6.36 m/s. Figure 4(b) shows the result during the second observation. The incident waves also came in SE direction (120 degrees) with the significant wave height of 1.2m. Five buoys were dropped in the area behind the submerged breakwater (cross symbols) and they were driven northward by the longshore current. A buoy dropped in the seawater exchange channel drifted offshoreward at the speed of 0.47 m/s.

On the contrary, rip currents did not occur when the incident wave came in NE or E direction during the third observation and the buoys slowly moved offshoreward over the submerged breakwater (Figure 4(c)).

NUMERICAL SIMULATIONS

A Three-dimensional numerical model based on the Large-Eddy Simulation (LES-WASS-3D, Lee and Hur, 2014) was employed to predict the rip currents under the measured bathymetry and wave conditions. The simulation results provided the wave height distribution, mean currents and the vertical profiles of horizontal wave velocities in Gangmun beach. The computational grid size in x,y, and z-directions were 4 m, 4 m, and 0.5 m respectively and the vertical grid size (z-direction) near the free surface elevation was set to 0.25 m to track the water surface elevation more precisely. After performing SWAN (Simulating WAves Nearshore) model simulation by using the offshore wave buoy, the wave height and period at the seaward boundary of LES-WASS-3D were set to 1.9 m and 11 seconds respectively.

Figure 5 shows the computational domain of LES-WASS-3D and the results include the wave height and mean current distributions. P1 and P2 in the top panel of Figure 5 are the points of interest for the mean current velocity profile. The middle panel of Figure 5 shows the wave height distribution normalized by the incident wave height. In this figure, the wave heights near the seawater exchange channel were larger than those near the submerged breakwater because the water depth near the channel was deeper. Mean current distribution was plotted in the bottom panel of Figure 5. The figure clearly shows the return flow through the channel.

Figure 6 shows the vertical profiles of the mean currents in P1 (onshore) and P2 (offshore). In this figure, the mean currents of the upper layer (above 0.5 m from the surface) are heading to the onshore direction and those of lower layer go to the offshore direction. The simulation results showed that the maximum and vertically averaged current velocities at P1 were 1.11 m/s, -0.68 m/s and those at P2 were 2.05 m/s, -0.86 m/s respectively. Therefore, the depth-averaged velocities are in the offshore direction.

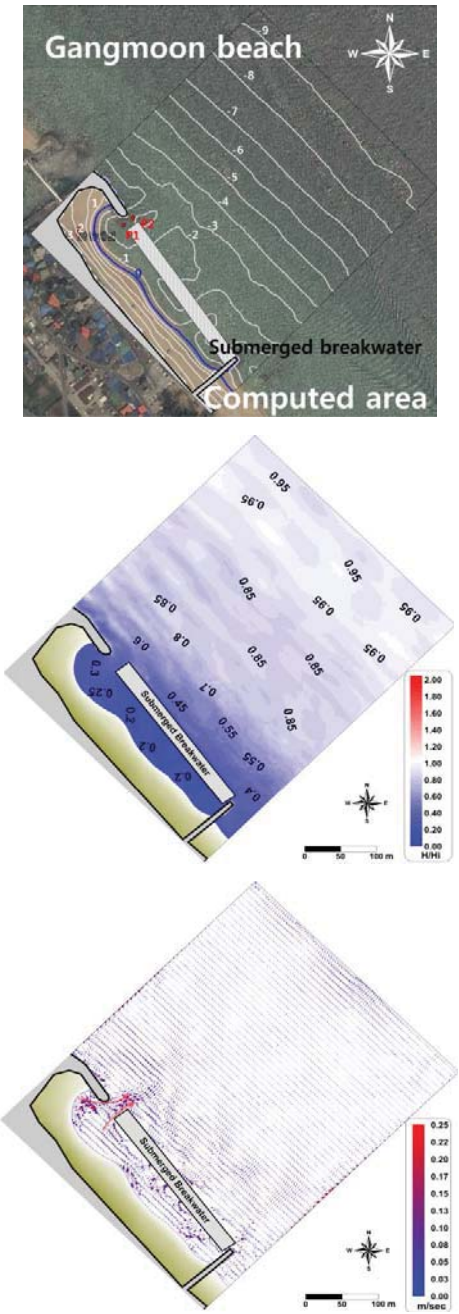

Figure 5. LEW-WASS-3D results: Computational domain (top) of the model; wave height (middle) and mean current (bottom) distributions.

Numerical simulations were also carried out to find the effective way to control the rip currents. Figure 7 shows the two different countermeasure scenarios to control rip currents. Method-1 separated the submerged breakwaters by the gap and method-2 installed drainage channels at the lower part of the submerged breakwater. Both of the methods were aimed to reduce the water surface increase behind the structures.

Figure 8 shows the vertical profiles of the calculated mean current velocities at P1 and P2 in Figure 4 (a) under the present setting (general shape), method-1, and method-2. The simulation results showed that method-1 reduced the rip current velocities by 18 % (maximum velocity) and 21 % (vertically averaged velocity) at P1, and by 18 % (maximum velocity) and 21 % (vertically averaged velocity) at P2 compared to those in the present setting. Similarly, method-2 also reduced the rip current velocities by 24 % (maximum velocity) and 25 % (vertically averaged velocity) at P1, and by 12 % (maximum velocity) and 15 % (vertically averaged velocity) at P2. Therefore, the proposed countermeasures for rip current control based on both two methods can reduce the rip current velocities by approximately 20 % compared to the present setting. However, even if both two methods showed similar performance near the seawater exchange channel, there could possibly be another rip channel near the gap between the submerged breakwaters in the case of method-1.

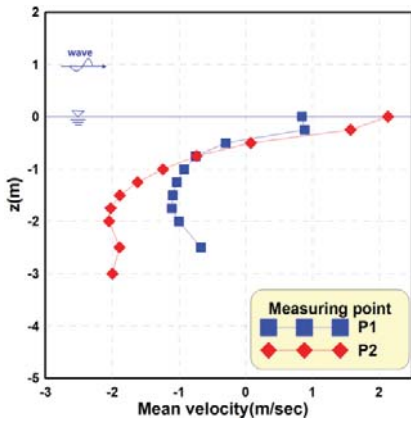

Figure 6. Numerical simulation results for mean current velocities. Positive values represent the onshore direction.

CONCLUSION

Field observations and numerical simulations were carried out to investigate the relationship between the rip current occurrence and the coastal structures for beach erosion control at Gangmun beach, Korea. The field observation results showed that the shoreline was stabilized after the construction of the submerged breakwater and groin even with the seasonal change. However, the bottom bathymetry has been changed and, especially, the area near the seawater exchange channel became deeper compared to the adjacent area. The rip currents were successfully tracked and measured through the seawater exchange channel.

The numerical model successfully predicted the rip currents near the channel. Therefore, this study shows that the submerged breakwater increases the mean water level behind the

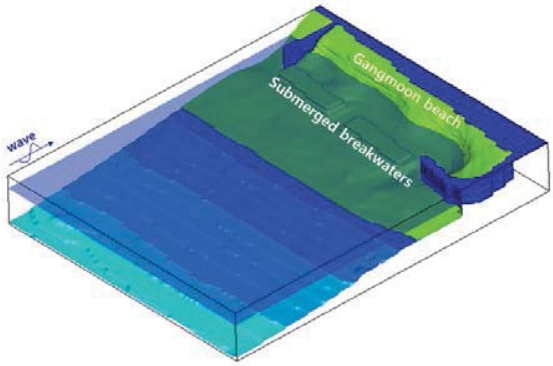

(a) Method -1: two separated submerged breakwaters by a gap

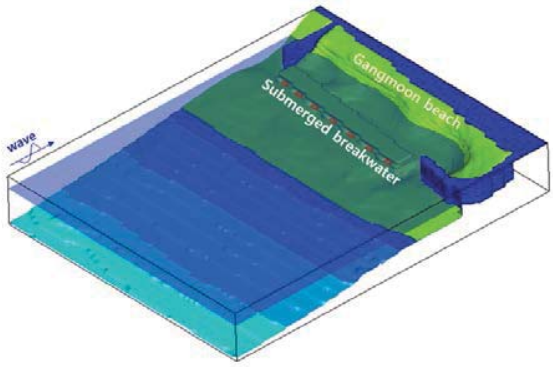

(b) Method -2: drainage channels at the lower part of the breakwater

Figure 7. Numerical model setup for the countermeasure to control rip currents.

submerged breakwater and induces the rip currents near the seawater exchange channel.

Numerical simulations were also carried out to investigate the countermeasures for the rip current control and the model results showed that installing either the gap between the submerged structures or the drainage channel at the lower part of the structures can reduce the rip current velocities by about 20 %.

ACKNOWLEDGMENTS

This paper is a part of the results of a Research Project titled "Development of Coastal Erosion Control Technology" funded by the Ministry of Oceans and Fisheries, Korea and a "Grant (12-RTIP-B01)" from Regional Technology Innovation Program by Ministry of Land, Infrastructure and Transport of Korean government, and this support was greatly appreciated.

LITERATURE CITED

Bowen, A. J. 1969. Rip currents: 1. Theoretical investigations, *Journal of Geophysical Research*, 74, 5467 – 5478.

Dalrymple, R. A. and Lozanno, C.J. 1978. Wave-current Interaction Models for Rip Currents. *Journal of Geophysical Research*, 83(C12), 6063-6071.

Lee, W.D. and Hur, D.S. 2014. Development of a 3-D Coupled Hydro-Morphodynamic Model between Numerical Wave Tank and Morphodynamic Model under Wave-Current Interaction. *Journal of the Korean Society of Civil Engineers*, 34(5), 1463-1476. (in Korean)

Stepard, F.P. 1936. Undertow Rip Tide or Rip Current, *Science*, 84, 181-182.

Longuet-Higgins, M. S. and Stewart, R. W. 1962. Radiation stress and mass transport in gravity waves, with application to 'surf beats'. *Journal of Fluid Mechanics*, 13(4), 481–504.

Longuet-Higgins, M. S. and Stewart, R. W. 1964. Radiation stresses in water waves; a physical discussion, with applications. *Deep Sea Research*, 11(4), 529–562.

Sonu, C. J. 1972. Field Observation on Nearshore Circulation and Meandering Currents, *Journal of Geophysical Research*, 77, 3232-3247.

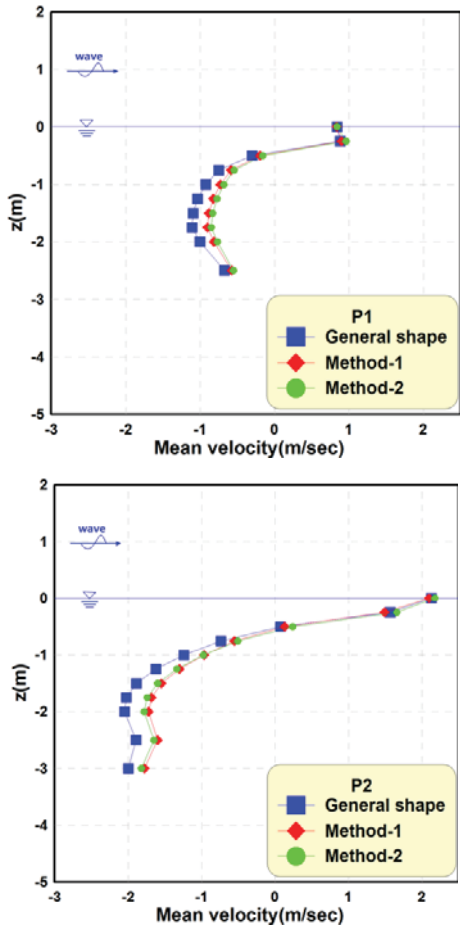

Figure 8. Numerical simulation results for mean current velocities. Positive values represent the onshore direction.

Journal of Coastal Research	SI	75	1357 - 1361	Coconut Creek, Florida	2016

Effects of Obliquely Incident Waves on Overtopping for Vertical Walls

Young-Taek Kim†, Sungwon Shin‡, Jun-Woo Choi †, and Jong-In Lee††*

†Hydro Science and Engineering Research Institute
Korea Institute of Civil Engineering and Building Technology
Goyang, Republic of Korea

‡Division of Climate Change and Interdisciplinay Research
Korea Envionment Institute
Sejong, Republic of Korea

††Department of Marine and Civil Engineering
Chonnam National University
Yeosu, Republic of Korea

www.cerf-jcr.org

www.JCRonline.org

ABSTRACT

Kim, Y.T.; Shin, S.W.; Choi, J.W., and Lee, J.I., 2016. Effects of oblique waves on overtopping for vertical walls. *In:* Vila-Concejo, A.; Bruce, E.; Kennedy, D.M., and McCarroll, R.J. (eds.), *Proceedings of the 14th International Coastal Symposium* (Sydney, Australia). *Journal of Coastal Research*, Special Issue, No. 75, pp. 1357 - 1361. Coconut Creek (Florida), ISSN 0749-0208.

In determination of the crest height of a vertical structure against attacking of obliquely incident waves, most of existing studies have suggested to use the overtopping reduction factor due to incident angles. However, they have not considered the amplification of wave heights and the spatial distribution of wave overtopping. In this study, a spatial distribution of wave overtopping along a vertical structure is experimentally investigated and also the wave overtopping reduction factors (γ) for incident wave angle is suggested. When the incident angle becomes larger, the wave overtopping reduction factor decreases almost linearly. EurOtop (2007) suggested the constant γ for β>45°, however the decreasing γ was calculated from this study.

ADDITIONAL INDEX WORDS: *Wave overtopping, vertical wall, wave overtopping reduction factor*

INTRODUCTION

When designing a port and harbor structures, the layout of outskirt structures such as main breakwaters is usually set by the primary wave directions, while the pier and other berth facilities at the inner harbor structures, which are shielded by the main breakwaters, are placed after accounting for several factors such as the operation of the harbor and geographical conditions.

In the process of designing the coastal structure, it is thought that the waves were propagating perpendicularly to the structures in general. A lot of researches on wave overtopping have been conducted using two-dimensional hydraulic and numerical tests since 1980s (Owen, 1980; Franco *et al*., 1994; van Gent *et al*., 2007; EurOtop, 2007; Goda, 2009; Victor and Troch, 2012; van der Meer and Bruce, 2014). And the other factors such as incident angle are concerned to reduce or increase the effects to the structures. It is known that the wave pressure and overtopping for obliquely incident waves are smaller than those for normally incident waves.

However, in actual sea areas, there is a very high possibility that oblique incident waves could propagate to the structures, except in particular situations. The port structures at the vicinity of entrance of port, which is covered by main breakwater, could be usually the faced to the obliquely incident waves. Figure 1 shows the example of them.

Most studies on wave overtopping have been based on the condition in which the incident waves are perpendicular to the structures. And the effects of incident angle on wave overtopping was concerned with the ratio of overtopping quantities of perpendicularly incident waves to the obliquely incident waves by using exponential function type overtopping formula (van der Meer and Janssen, 1995; Franco and Franco, 1999; EurOtop, 2007; Andersen and Burcharth, 2009). The wave overtopping reduction factor (γ_β) has been applied to the above studies.

Franco and Franco (1999) built a model of 11.7 m with two freeboards, and simultaneously measured the quantity of overtopping waves at each location, while Andersen and Burcharth (2009) measured the quantity at one location by

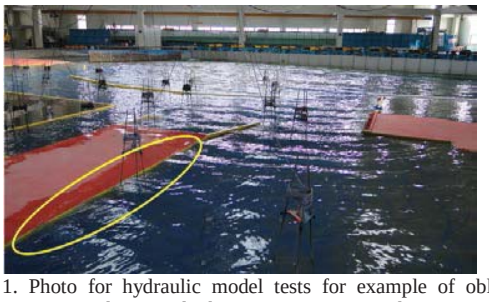

Figure 1. Photo for hydraulic model tests for example of obliquely incident wave into the inner harbor port structures at the vicinity of the entrance of harbor.

DOI: 10.2112/SI75-272.1 received 15 October, 2015; accepted in revision 15 January, 2015
*Corresponding author: jilee@chonnam.ac.kr
©Coastal Education and Research Foundation, Inc. 2016

installing a model with a length of 5 m in a tank of 18 m × 13 m. As seen in these examples, earlier studies involved measuring quantities of overtopping waves by using a short model in a relatively small tank, and were interested in the change of those quantities with respect to the angle of incidence itself, rather than with the interaction between the propagating waves along the structures and the structures.

EurOtop (2007) suggested the effect of oblique waves on wave overtopping as followings. For non-impulsive conditions, the following equation could be used.

$$\frac{q}{\sqrt{gH_{m0}^3}} = 0.04\exp\left(-\frac{2.6}{\gamma}\frac{R_c}{H_{m0}}\right) \qquad (1)$$

where γ is the wave overtopping reduction factor for incident angle and is given by

$$\begin{aligned} &\gamma = 1 - 0.0062\beta, \quad for \quad 0^0 < \beta < 45^0 \\ &\gamma = 0.72 \qquad\qquad for \quad \beta > 45^0 \end{aligned} \qquad (2)$$

and q is the wave overtopping volume per unit meter per second ($m^3/s/m$), g is the acceleration of gravity, H_{m0} and R_c are the significant wave height and the freeboard, respectively. β is the incident angle in degrees. When the incident wave angle (β) increased, the wave overtopping decreased. However, the angle is larger than 45 degrees, the effect of obliqueness is same. And also γ does not show the spatial distribution of wave overtopping along structures.

In this study, the wave overtopping for obliquely incident waves along the vertical walls was measured. The wave overtopping reduction factor for the condition that β is larger than 45° would be suggested. And the spatial distribution of wave overtopping would be investigated. The results would be compared with EurOtop (2007). EurOtop is the most recent wave overtopping calculation manual.

MODEL SETUP AND TEST CONDITION

The present model tests were performed in the shallow water basin at Korea Institute of Civil Engineering and Building Technology (KICT). The multidirectional wave generator was applied to the tests, which could create the regular wave, a single-and multi-directional irregular waves. Each wave-generation board connected to the driving part and has 0.5 m width and 1.1m height, which comprises of 50 driving parts and the total widths are 30 m. The generator is electric servo piston type. The size of wave basin is 42 m long, 36 m wide and 1.2 m deep. No active absorption on the wave paddles was used, however the passive absorption was applied. The crushed stone beaches were placed at the rear end and both side wall of the basin and behind the wave generator. The crushed stones were arranged at a slope of 1:10 and 1:3 on the opposite side of wave generator and side wall of water tank to minimize the reflective wave, respectively.

The test models were made of acrylic panel and length of each model is 1.2m. The length of vertical wall was total 6 m and the layout of model is shown in figure 2. Figure 3 is the sketch of vertical wall model. As shown in figure 3, the freeboard could be easily changed and the guide wall stands at an interval of 0.4 m. These guide walls had a role in gathering the overtopped waters into the overtopping box behind the vertical wall.

The test was conducted changing the freeboard height (R_c) of the vertical structure to analyze the overtopping characteristics of the vertical structure. The freeboard is R_c = 0.050, 0.075, 0.100, and 0.125 m. The water depth at toe of vertical wall is 0.5m. There is no slope at wave basin and the water depth is constant. Random waves were applied to the tests with Bretschneider- Mitsuyasu spectrum. The target wave height H_{s0}

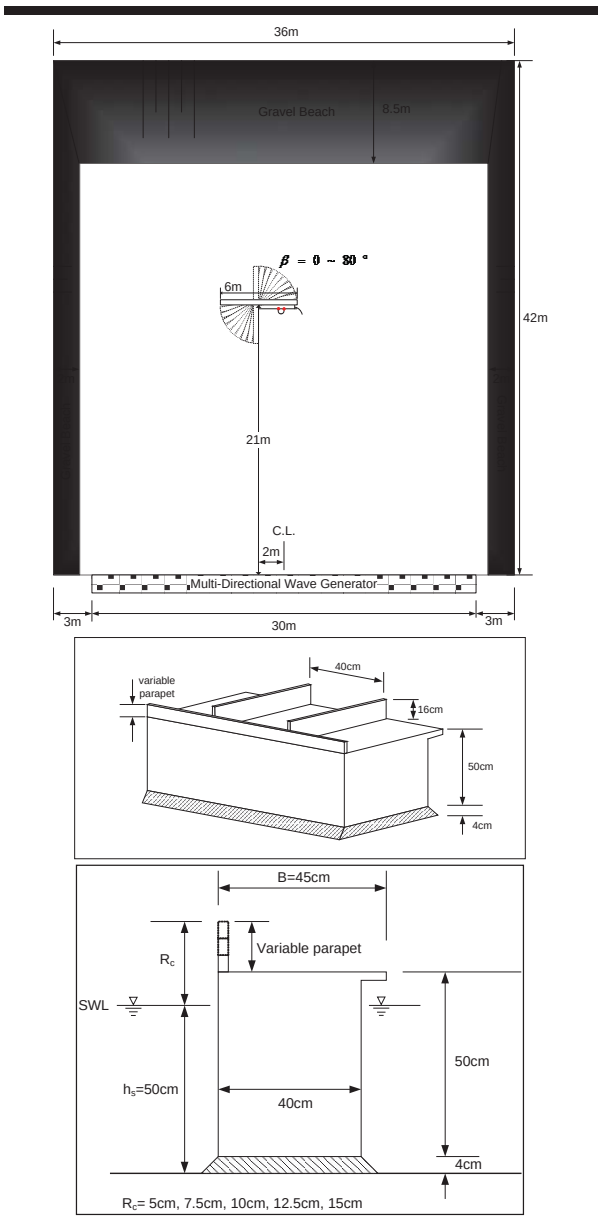

Figure 2. Schematic sketch of wave basin and test model

is 0.050, 0.075, and 0.100m. The significant wave period is T_{s0} = 1.19, 1.38, 1.57 and 1.98 s. The incident angle, that is, the angle between the wave direction and the vertical wall is β= 0°~80°. β is the incident angle between wave crest line and structure, that is, β=0° means the normally incident condition. Table 1 is the summary of test conditions.

Table 1. *Summary of test condition*

Properties	Values
Significant wave period (T_{s0})	1.19, 1.38, 1.57, 1.98 s
Target wave height (H_{s0})	0.050, 0.075, 0.100, 0.125 m
Freeboard (R_c)	0.050, 0.075, 0.100, 0.125, 0.150 m
Incident wave angle (β)	0~80 degree (step=10°)

Figure 3 shows the model setup for β = 50 degree and measuring gages. The capacity type wave gages and turbine type flow meters were used to measure the wave height and overtopping. 1,000 waves were generated to measure the wave overtopping quantity. The overtopping volume was calculated to the averaged values for time and width (q, $m^3/s/m$). The wave gages were located in front of the vertical wall and the distance between wave gage and vertical wall was 0.05 m. The capacity type wave gages and flow meter

Figure 3. Photo for model setup and snap shot of experiment for β=5°

TEST RESULTS

Wave heights and overtoppings along the vertical wall were measured for each test section. Wave overtoppings were analyzed with the method of earlier studies (van der Meer and Janssen, 1995; Franco and Franco, 1999; Andersen and Burcharth, 2009) The wave overtopping reduction factor (γ), which is explained in equation (1) and (2), was also applied to the analysis.

Although a lot of tests listed in Table 1 were conducted, the selected results would be shown in the followings. Figure 4 shows the results for wave height distribution along vertical wall for β = 50°, R_c = 0.05, 0.15 m and H_s = 5, 12.5cm. The measured wave heights (H_s) were normalized with target incident wave height (H_{s0}). It could be known that the wave heights were amplified along vertical wall and the normalized wave heights were almost constant at about 2.0. When comparing the results, the dimensionless wave heights for lower freeboard (upper figure) was smaller than those for higher freeboard (lower figure). This is thought that the wave height could not be amplified or reflected from vertical wall due to wave overtopping for lower freeboards. Also the dimensionless wave heights for smaller wave heights (solid label) is comparatively larger than those for higher wave height (empty label) due to the similar reasons, that is, the overtopping did not occur for relatively lower wave heights against higher freeboards.

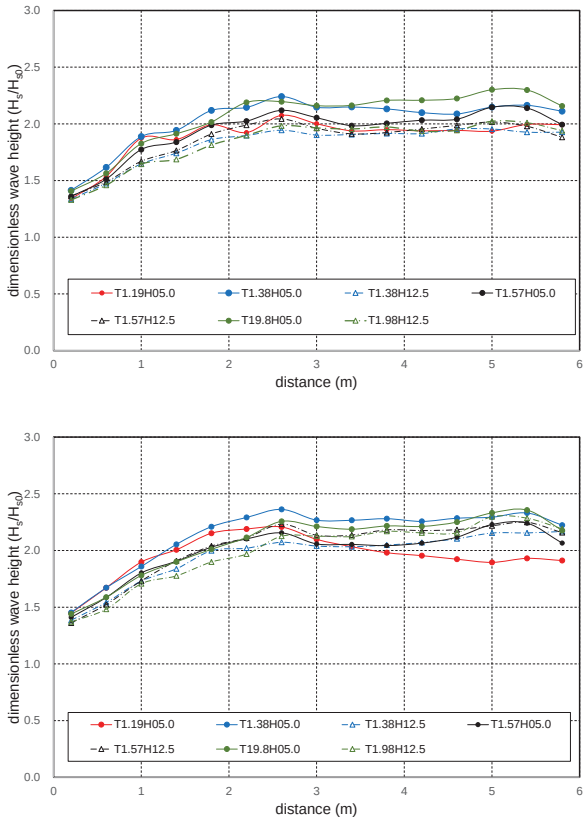

Figure 4. Wave height distribution along vertical wall for β=50°. The top figure shows the wave height distribution for R_c =0.05 m (up) and the bottom shows for R_c=0.15 m (down)

Figure 5 shows the distribution of dimensionless wave overtopping ($Q=q/\sqrt{gH^3}$) along vertical wall for the similar condition as Figure 4, β=50°, R_c= 0.05, 0.15 m and H_s = 5, 10, 12.5cm. The similar trends were observed between wave heights and wave overtopping. The wave overtopping rates were larger for relatively higher wave heights (triangle) against lower freeboards condition rather than lower wave heights (circle). The effects of wave periods were not clear, however, when the wave periods were longer, the wave overtopping increased. The wave overtopping rates were changing along vertical wall, however, the wave overtopping rate were increasing from x = 0 m and the almost similar for the range of 3~5 m.

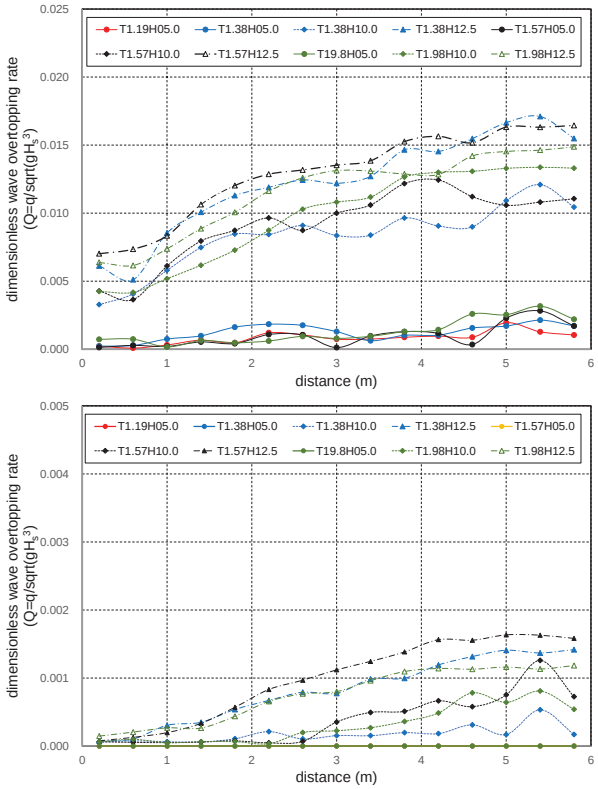

Figure 5. Distribution of dimensionless wave overtopping rate along vertical wall for β=50°. The top figure shows for R_c =0.05 m (up) and the bottom shows for R_c=0.15 m (down)

Figure 6 is the Q-R relationship at x=1 and 5m for β=50° from the starting point of vertical wall using equations (1). It could be seen that the slope of Q-R relationship for x = 1 m is relatively steeper rather than that for x = 5 m. This means that wave overtopping is larger at x = 5 m. From equation (1) and (2), when the waves were propagating normal to the structure (β=0°), the wave overtopping reduction factor is γ=1.0. When q, H_s, *and* R_c could be known and measured, the reduction factor (γ) could be calculated.

DISCUSSION

On the basis of the analysis of these experimental data, the wave overtopping reduction factors along vertical wall could be investigated. EurOtop (2007) suggested the effect of incident angle only. In this study the wave overtopping reduction factors were calculated for each location along the vertical wall and the distribution was investigated.

The distribution of wave overtopping using reduction factor (γ) is shown in Figure 7. When the incident wave angle becomes larger, the wave overtopping reduction factor decreases. This means that the oblique incidence brought about the reduction of wave overtopping. And the distribution of overtopping reduction factor was changing along the vertical wall. The wave overtopping reduction factor shows the similar trends with Mach stem waves at the range of β = 50~70°. The results for wave overtopping could be extended with Mach stem waves later.

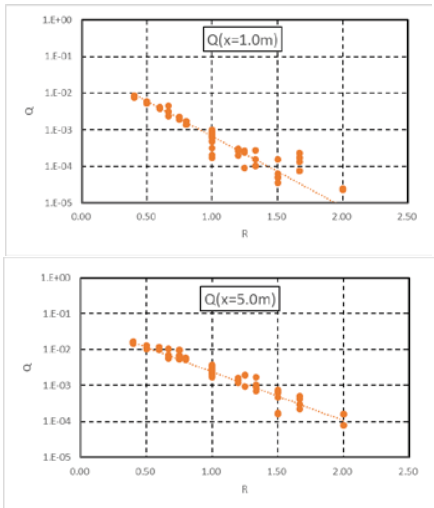

Figure 6. Wave overtopping at x=1.0 and 5.0m along vertical wall for β=50°.

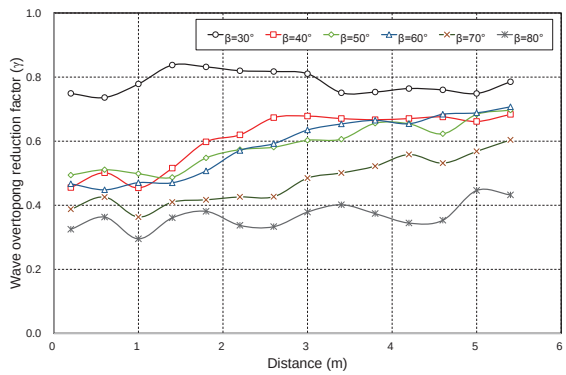

Figure 7. Wave overtopping along vertical wall with reduction factor (γ)

The comparison between EurOtop (2007) and this study is shown in Figure 8. Although the distribution of γ is changing along vertical wall, the almost constant values were shown between the range of 3~5 m. The averaged values were calculated from these range and the results could be plotted at figure 8. EurOtop(2007) suggested the constant γ for β>45°, however the decreasing γ was calculated from this study. When the incident wave angle is very oblique, the crest height of structure could be lower and the construction budget could be also down.

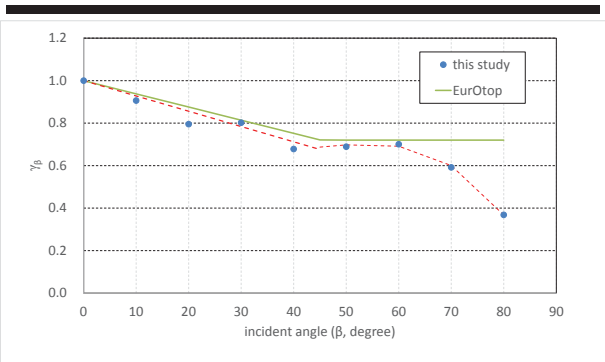

Figure 8. Comparison of reduction factor (γ) from this study with EurOtop.

CONCLUSIONS

In this study, hydraulic model test for measuring the wave height and overtopping along vertical walls were conducted.

Most of the wave propagation studies about obliquely incident waves to the vertical wall were non-wave overtopping conditions. The wave height distribution along vertical wall for overtopping and non-overtopping condition was measured. The wave heights were amplified along vertical wall and the normalized wave heights were almost constant at about 2.0. However, it could be known that the wave overtopping reduces the amplification of wave height along vertical wall. The dimensionless wave heights for lower freeboard was relatively smaller than those for higher freeboard. This is because that the wave height could not be amplified or reflected from vertical wall due to wave overtopping for lower freeboards.

EurOtop (2007) only suggested the reduction factor for each incident wave angle (β). In this study, the wave overtopping reduction factor were analyzed and the distribution of wave overtopping reduction factors along vertical walls were suggested.

The obliquely incident waves propagating along vertical wall generated the different wave overtopping for each location, that is, the wave overtopping rates are increasing from the start point of vertical wall and they were stabilized at the range of 3~5m. These distribution of overtopping reduction factor were suggested in this study. And by using the reduction factor for these range (3~5 m), the new wave overtopping reduction factors (γ) were suggested and compared for same condition. EurOtop (2007) suggested the constant γ for β>45°, however the decreasing γ was calculated from this study.

ACKNOWLEDGMENTS

This work was partially supported by the Korea Institute of Marine Science & Technology Promotion funded by Ministry of Oceans and Fisheries (No. 20110131) and the National Research Foundation of Korea(NRF) grant funded by the Korea government(MSIP) (No. 2011-0030040).

LITERATURE CITED

Anderson T.L. and Burcharth H.F., 2009. Three-dimensional investigation of wave overtopping on rubble mound structures, *Coastal Engineering*, 56, 180-189.

EurOtop, 2007. *European Overtopping Manual, Wave overtopping of sea defences and related structures: Assessment Manual*. Eds. Pullen, T., Allsop, N.W.H.,Bruce T, Kortenhaus A, Schüttrumpf H, Van der Meer J.W., www.overtopping-manual.com

Franco, L.; de Gerloni, M., and van der Meer, J., 1994. Wave overtopping on vertical and composite breakwaters. *Proceedings of 24th International Conference on Coastal Engineering*, ASCE, New York, 1030–1044.

Franco, C. and Franco, L., 1999. Overtopping Formula for Caisson Breakwaters with Nonbreaking 3D Waves. *Journal of Waterway, Port, Coastal, and Ocean Engineering*, 125(2), 98-108.

Goda, Y., 2009. Derivation of unified wave overtopping formulas for seawalls with smooth, impermeable surfaces based on selected CLASH data sets. *Coastal Engineering*, 56(4), 385–399.

Owen, M. W., 1980. *Design of sea walls allowing for wave overtopping*. Rep. EX 924, Hydraulics Research, Wallingford, U.K

van der Meer, and Janssen, J.P.F.M., 1995. Wave run-up and wave overtopping at dikes. ASCE. In: *Wave forces on inclined and vertical wall structures*, ed. N. Kobayashi and Z. Demirbilek, pp. 1-27.

van der Meer and Bruce, T., 2014. New physical insights and design formulae on wave overtopping at sloping and vertical structures. *Journal of Waterway, Port, Coastal, and Ocean Engineering*, DOI:10.1061/(ASCE)WW.1943-5460.0000221.

van Gent, M. R. A.; Van den Boogaard, H. F. P., Pozueta, B., and Medina,J. R., 2007. Neural network modelling of wave overtopping at coastal structures. *Coastal Engineering*, 54(8), 586–593.

Victor, L. and Troch, P., 2012. Wave overtopping at smooth impermeable steep slopes with low crest freeboards. *Journal of Waterway, Port, Coastal, and Ocean Engineering*, 135(5), 372-385.

Journal of Coastal Research	SI	75	1362 - 1366	Coconut Creek, Florida	2016

Morphodynamic behaviors of macrotidal ridge and runnel beaches during winter: The case of Baeksajang Beach, South Korea

Chan Woong Kim[†], Young Ho SHIN[‡], Keun Bae Yu[†], and Hosahng Rhew[††*]

[†] Department of Geography
Seoul National University
Seoul, Republic of Korea

[‡] BK21plus 4-Zero Land Space Creation Group
Seoul National University
Seoul, Republic of Korea

[††] Department of Geography Education
Chonbuk National University
Jeonju, Republic of Korea

www.cerf-jcr.org

www.JCRonline.org

ABSTRACT

Kim, C.W.; Shin, Y.H.; Yu, K.B., and Rhew, H., 2016. Morphodynamic behaviors of macrotidal ridge and runnel beaches during winter: The case of Baeksajang Beach, South Korea. *In:* Vila-Concejo, A.; Bruce, E.; Kennedy, D.M., and McCarroll, R.J. (eds.), *Proceedings of the 14th International Coastal Symposium* (Sydney, Australia). *Journal of Coastal Research*, Special Issue, No. 75, pp. 1362 - 1366. Coconut Creek (Florida), ISSN 0749-0208.

Macrotidal ridge and runnel beaches respond to external forces in a morphodynamic manner that involves morphological and sedimentological changes. In this study, we investigated morphodynamic responses of Baeksajang Beach, one of the macrotidal ridge and runnel beaches on the west coast of South Korea during the winter when high energetic conditions prevail. Landward migrations of intertidal ridges were predominant over the whole period, but bars on the upper and lower part of the beach profiles showed different behaviors. The position of mean sea level was associated with different upper and lower bar behaviors. The erosional and depositional phases alternated alongshore, implying net alongshore sediment transport. Textural characteristics responding to external forces were twofold: the occurrence of overall coarsening that correlated well with elevation, and the presumable generation of transport-origin grain size trends. Grain size trend analysis (GSTA) identified the overall transport patterns compatible with topographic changes, while cross-shore components were more represented than alongshore ones due to elevation-related coarsening effect. The apparent beach state is not well predicted by the morphodynamic indices even under high energy conditions like winter season, implying the delayed morphological adjustment. These suggest that local constraints such as sediment budget and geology might be no less critical than external energy conditions in macrotidal ridge and runnel beaches as observed in this study.

ADDITIONAL INDEX WORDS: *intertidal bar, onshore migration, dimensionless fall velocity, relative tide range*

INTRODUCTION

Macrotidal ridge and runnel beaches are interesting morphodynmic features that have long engaged many coastal geomorphologists (Anthony *et al.*, 2004; Levoy *et al.*, 2000). Macrotidal ridge and runnel beaches are characterized by semipermanent or permanent intertidal bars alternating with troughs, which have been considered as morphological responses to time-varying interactions between waves and tides (Anthony, 2009). The growth or destruction, configurations and migration patterns of intertidal bars in macrotidal ridge and runnel beaches are affected by external forces such as stormy waves combined with tidal modulations (Masselink *et al.*, 2007). At the same time, they also control the dissipation of external forces as boundary constraints (Aagaard *et al.*, 2006; Reichmüth and Anthony, 2007). Such morphodynamic interactions are one of the key processes in governing the marine energy dissipation and alongshore variations of wave impacts. Macrotidal ridge and runnel beaches are, in a sense, energy-dissipating systems via sediment transport related to morphological changes.

Dynamic behaviors of intertidal bars imply spatial and temporal variability in textural characteristics of surficial sediment. Surficial sediment usually becomes coarser in response to higher energy conditions, and better sorted under the operation of more preferential agents (Prothero and Schwab, 1996). Sediment transport is also considered to leave the observable grain size trends from which net transport patterns can be extracted (Gao and Collins, 1992; McLaren and Bowles, 1985; Pedreros *et al.*, 1996). However, textural behaviors of macrotidal ridge and runnel beaches have been investigated less than morphological behaviors, with some exceptions. For example, Levoy *et al.* (2000) mentioned that median grain size tended to be coarser towards a high tidal zone. Masselink *et al.* (2007) reported the lack of clear links between morphological and sedimentological changes during bar formation and migration. Textural responses in macrotidal ridge and runnel beaches need more investigations in terms of morphodynamic responses.

Macrotidal ridge and runnel beaches are well observed along the west coast of South Korea (hereafter, Korea) in open and embayed settings. Though the west coast of Korea is well known for high tidal ranges and vast stretches of tidal flat, wave actions

DOI: 10.2112/SI75-273.1 received 15 October, 2015; accepted in revision 15 January, 2015
*Corresponding author: serious53@jbnu.ac.kr
©Coastal Education and Research Foundation, Inc. 2016

cannot be neglected especially during the winter when the strong northwesterly winds blow due to the East Asian Winter Monsoon (Yang and Chun, 2001; Yang *et al.*, 2005).

The primary aim of this study is to describe the temporal and spatial behaviors of morphological and textural characteristics in the macrotidal ridge and runnel beach of Baeksajang Beach (BB) during the winter season. BB is located at the northwestern part of Anmyeon Island (Figure 1A). The northern part of BB is connected to the multiple spits, conspicuously extending northwest and having recursive distal features (Kim *et al*., 2015). The Baeksajang port for fishery holds the northern coast behind the spits, facing the Baeksa Channel between the island and mainland. The mean tidal range is 4.31m ranging from 2.65m (neap tides) and 5.98m (spring tides). Flood and ebb tides flow along the tidal channel in the north-south direction. The maximum flood and ebb current velocity both have similar values around 0.8m/s (Korea Hydrographic and Oceanographic Administration, 2011-12). During the winter to early spring, wave energy flux is much higher than during other seasons (Figure 1B). Therefore, morphodynamic responses of BB can be clearly identified during this season.

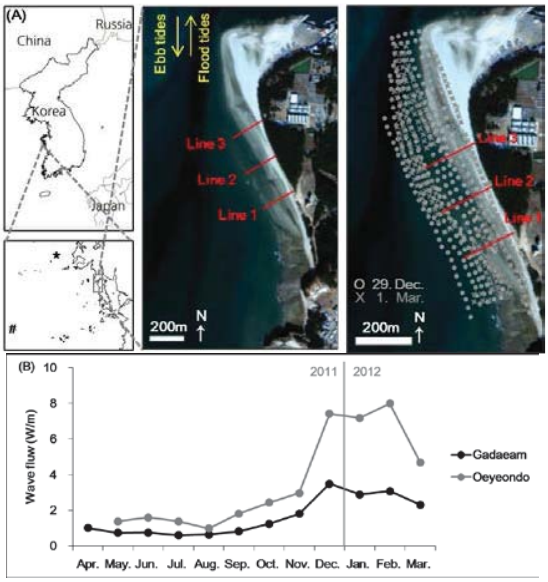

Figure 1. (A) Location of study area. Two symbols in left-low inset (* and #) indicate the location of Gadaeam light and Oeyeondo Buoy. (B) Monthly variation of wave energy flux near BB. The winter to early spring season (Dec. to Mar.) have the highest values, indicating the most energetic conditions near BB during this period.

METHODS

The morphological and sedimentological response patterns of BB were investigated by topographic surveys coupled with surficial sediment analysis. Topographic surveys were carried out along the three 200m long transects set up at the southern, central, and northern parts of BB using the total station (Figure 1A). For minimizing the variations related to the spring-neap cycle, surveys were conducted 2-3 days after the spring tides. Topographic surveys were conducted on a biweekly basis from early July 2011 to late March 2012. In this paper, four profile survey datasets measured on December 26, 2011, January 27, 2012, February 23, 2012, and March 24, 2012, were selected for analysis in order to compare morphological responses with textural patterns.

Sediment samples were collected twice on December 29, 2011 (n=301) and March 1, 2012 (n=252). The coordinates and elevation of sampling points were measured by the total station. For grain size trend analysis (GSTA), all samples were obtained from the upper 10cm of the bed during the low tide (Gao and Collins, 1992; Gao *et al.*, 1994). All samples were dry-sieved at half-Φ intervals in the range from -2 to 4Φ. The proportion of particles finer than 4Φ turned out to be negligible in all samples. Size parameters such as mean size, sorting, and skewness were calculated using GRADISTAT (Blott and Pye, 2001), following Folk and Ward (1957).

GSTA was applied to particle size data for estimating net sediment transport pathways at BB. Two spatial trends are considered to represent sediment pathways: finer, better sorted, more negatively skewed (F, B, -) and coarser, better sorted, more positively skewed (C, B, +) (Gao and Collins, 1992; McLaren and Bowles, 1985). In this research, GSTA, proposed by Gao and Collins (1992) and refined by Chang *et al.* (2001) was adopted to identify net sediment transport patterns at BB. The characteristic length is equal to 100m, which was obtained from variogram analysis for all size parameters. Instead of using raw data, interpolated data was utilized to minimize the undesirable influences such as boundary effects and incomplete spatial coverages (*e.g.*, Asselman, 1999; Gao *et al.*, 1994).

RESULTS

The main findings of this study can be divided into two sections: morphological responses and textural responses with net sediment transport pattern obtained by GSTA. The first section describes monthly changes of beach profiles.

Morphological responses

The overall pattern of morphological responses at BB shows two characteristics: the landward migrations of intertidal ridges and alongshore alternations between erosional and depositional phases. The former patterns were observed at all three transects. The ridges on the upper and lower part of the profiles both migrated toward the shores. The distinction between them was the degree of shape deformation. The ridges on the upper part of the profiles were mostly welded to the steep upper beach face, losing their undulated features into the flat surface. The counterparts on the lower part moved toward the shore, maintaining their overall shapes.

However, such migration patterns should not be directly interpreted as the sediment accumulation on the upper part of the profiles at BB. Temporal changes in sediment store along the three transects show more dynamic behaviors. Line 1, the southern transect, shows the erosional phase during Periods 1 and 2 (December 26-January 27; January 27-February 23), but the depositional phase during Period 3 (February 23-March 24). The erosional volume of Period 1 was almost ten times as much as that of Period 2. Afterwards, sand accumulation proceeded

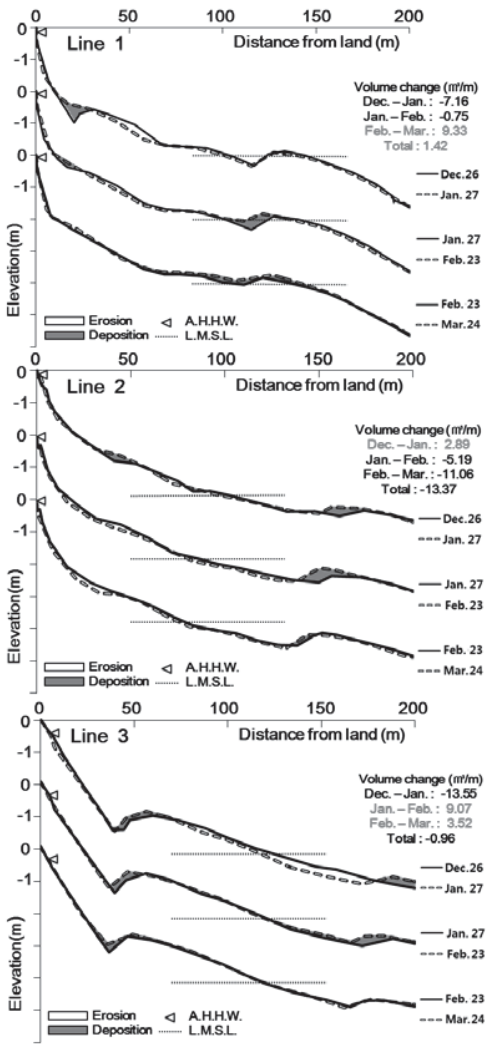

Figure 2. Responses of beach profiles. A.H.H.W. means approximately highest high water. L.M.S.L. means local mean sea level.

during Period 3 as much as the original sand store along Line 1 was excessively recovered.

The erosion occurred mostly on the seaside of the ridges, while deposition tended to concentrate in the troughs behind the ridges. On the contrary, Line 2, the central transect, reveals the continuously increasing sediment loss during the monitoring period except for Period 1. Regarding the upper part, a small ridge migrated onshore, almost welded into the steep beach face during Period 1. Afterwards, continuous erosion occurred over the whole upper beach. While the ridge on the lower part grew bigger, the significant sand supply must have originated from the upper part of the beach profiles. Line 3 shows another behavior. Overall, this profile shows the continuous recovery phase after the early severe loss of sediment. Through all periods, the ridge on the upper part grew and migrated onshore. The ridge on the lower part, which must have been formed by offshore sand transport in the erosional phase, also migrated toward the shore during the recovery phase. However, the final sediment store along the profile did not reach the original level. The alongshore alternations between erosional and depositional phases indicate a net alongshore sediment transport.

Textural responses and net sediment transport pattern

The comparison of two sediment datasets obtained at the early period and late period of monitoring reveals that beach surficial sediment became coarser (2.23 to 1.76Φ), more poorly sorted (0.58 to 0.62Φ), and less negatively skewed (-0.23 to -0.16). T-statistics indicates that mean size and skewness except sorting are significantly changed. The observed p-values are less than 1%, which means removal of fine sediment or transportation of coarse sediment caused by stronger wave conditions during winter (Hails, 1967).

Among the textural parameters, mean grain size correlates well with elevation (Figure 3). The coarser sediment has a tendency to be found on higher areas and such correlation pattern became more conspicuous after winter season. Therefore, the energetic conditions strengthen the coarsening trend from low to high areas. Such patterns represent a landward increase of surf and swash energy as the water depth becomes shallow near the shore (Niedoroda *et al.*, 1985). The other two parameters, sorting and skewness, show weak correlations with elevation, and did not change significantly during the winter.

GSTA shows different net sediment transport patterns for the two datasets (Figure 4). Each dataset represents the energetic conditions before December 29 and before March 1. While the net sediment transport pattern before December 29 is generally characterized by offshore transport, the longshore transport pattern is partly identified in a southerly direction along the lower intertidal bar between Line 1 and Line 2. The net sediment transport pattern identified from the dataset obtained on March 1 indicates convergence zones (Line 1, Line 3) alternating divergent zones (Line 2).

Such pattern seems to be compatible with the recovery phase along Line 1 and Line 3, and the erosional phase along Line 2. GSTA seems to capture cross shore signals rather than alongshore ones. The possible reason why alongshore signals were not enough effectively identified will be discussed in the next section.

DISCUSSION

Morphological behaviors of BB indicate that the MSL plays a key role in intertidal bar dynamics. Bars above MSL tend to become flat, welded to a steeper beach face, whereas those below MSL tend to grow, moving onshore. Erosion tends to be concentrated upon the area in between these bars. Such difference might be associated with dominance shift between swash and surf, and observed in similar sites (*e.g.*, Masselink *et al.*, 2007). Multiple bars also control the sediment transport behaviors in BB. Aagaard *et al.* (2006) attributed onshore migration of bars to their action as a filter that only passes the onshore mean and oscillatory components of sediment transport. Once the runnel has infilled, the offshore transport component becomes dominant. Such behaviors were clearly observed along.

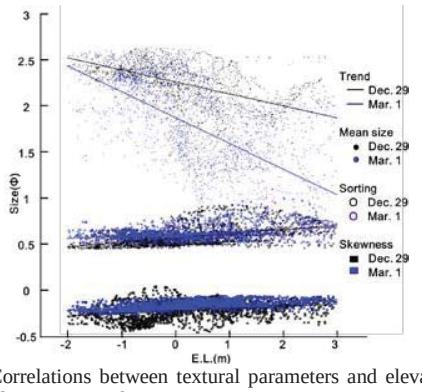

Figure 3. Correlations between textural parameters and elevation. E.L. means the elevation over the Korean Datum.

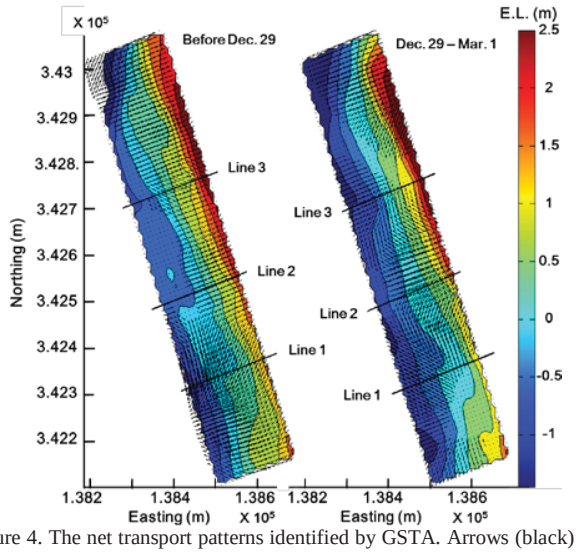

Figure 4. The net transport patterns identified by GSTA. Arrows (black) indicate the net transport patterns.

Line 2. Therefore, the intertidal bars might involve shifts between erosional phases and depositional phases at BB

GSTA-based net sediment transport pattern in BB seems biased upon cross-shore transport rather than longshore transport. This might be because of the elevation-related coarsening effect shown in Figure 3. This relationship implies (F, B, -) that trends exist toward the direction in which elevation decreases. The grain size trend (F, B, -) in a cross-shore direction might be winnowing-origin rather than transport-origin. Previous research reporting successful application of GSTA appear to be carried out at the areas with gentle slope or weak cross-shore gradient (*e.g.*, Gao *et al.*, 1994; Pedreros *et al.*, 1996). The removal of elevation-related coarsening signals from data might be needed for the effective use of GSTA in an environmental setting like BB.

Beach morphology is often regarded as a representation of morphodynamic beach state. Two morphodynamic indices, dimensionless fall velocity (Ω) and relative tidal range (RTR), are widely used to predict the beach state (Masselink and Short, 1993). These two indices, however, fail to predict the beach state of BB. Whereas BB should be the non-barred dissipate in terms of these indices (Table 1), beach profiles of BB are similar to the low tide bar and rip or barred dissipate. The shape of intertidal bars at BB is also similar to slip-face ridges that Wijnberg and Kroon (2002) refer to as the bar type developed under microtidal to mesotidal settings. In other words, the realized beach morphology of BB appears to be compatible with the beach state for reduced wave or tidal energy.

Although such discrepancy can simply be regarded as exceptional, it might also be attributed to the fact that energetic approaches often neglect local constraints such as geology and sediment budget, which are associated with the response time for morphological adjustment. Jackson *et al.* (2005) discussed this issue with cases around the north coast of Ireland. They indicated that inherited geological factors could be more important to beach morphology than contemporary dynamics. Ridge and runnel structures of BB might reflect geological constraint and sediment budget here as well as energetic conditions, which need more investigation.

Table 1. *State Parameters for beach classification (Masselink and Short, 1993). H_b is calculated using wave period (T, sec) and deepwater wave height (H_0, m) from Gadaeam and Oeyeondo (values in parentheses) buoy data managed by Korea Meteorological Administration, using the equation by Komar and Gaughan (1972); T = wave period(sec); RTR = relative tide range (MSR/H_b), MSR = mean spring tide range (m) of the study area; Ω = dimensionless fall velocity*

Month	H_b(m)	T(sec)	RTR	Ω
Dec.	1.01(1.37)	4.63(5.60)	5.90(4.36)	5.40(6.29)
Jan.	0.94(1.35)	4.50(5.24)	6.36 (4.42)	5.94(7.10)
Feb.	0.96(1.41)	4.80(5.45)	6.20 (4.23)	6.31(7.82)
Mar.	0.86(1.14)	4.70(4.98)	6.96 (5.24)	5.73(6.92)
Average	0.94(1.33)	4.66(5.28)	6.33 (4.50)	5.82(7.25)

CONCLUSIONS

In this research we investigated the morphological and sedimentological responses of macrotidal ridge and runnel beaches during the winter when high energy conditions prevail. The field measurement of beach profiles and textural characteristics show that the upper bars and lower bars behave in a different manner while landward migration is dominant at BB. The erosional or depositional phases alternate in a longshore direction, implying net alongshore sediment transport.

GSTA identifies the overall transport patterns compatible with topographic changes, while cross shore trends are much more represented rather than alongshore signals. Landward coarsening trend, which is often identified in a beach environment and is strengthened during the winter, might weaken the clarity of a transport-origin trend. The Removal of elevation-related signals might be required to apply GSTA to similar environmental settings.

The apparent beach state of BB is not predicted well by the morphodynamic indices of Ω and RTR. This might be due to other controls such as the geology or sediment budget rather than marine energy conditions, which need more investigation.

ACKNOWLEDGMENTS

We thank the '4-Zero Land Space Creation Group' at Seoul National University for supporting the research. The corresponding author also thank the financial support for writing from the project titled 'Development of integrated estuarine management system', funded by the Ministry of Oceans and Fisheries, Korea.

LITERATURE CITED

Aagaard, T.; Hughes, M.; Møller-Sørensen, R. and Andersen, S., 2006. Hydrodynamics and Sediment Fluxes across an Onshore Migrating Intertidal Bar. *Journal of Coastal Research*, 22(2), 247-259.

Anthony, E.J.; Levoy, F., and Monfort, O., 2004. Morphodynamics of intertidal bars on a megatidal beach, Merlimont, Northern France. *Marine geology*, 208(1), 73-100.

Anthony, E.J., 2009, *Shore Processes and Their Palaeoenvironmental Applications.* Amsterdam: Elsevier, 519p.

Asselman, N.E.W., 1999. Grain-size trends used to assess the effective discharge for floodplain sedimentation, River Waal, the Netherlands. *Journal of Sedimentary Research*, 69(1), 51-61.

Blott, S.J. and Pye, K., 2001. GRADISTAT: a grain size distribution and statistics package for the analysis of unconsolidated sediments. *Earth surface processes and Landforms*, 26(11), 1237-1248.

Chang, Y.H.; Scrimshaw, M.D., and Lester, J.N., 2001. A revised grain-size trend analysis program to define net sediment pathways. *Computers and Geosciences*, 27(1), 109-114.

Folk, R.L. and Ward, W.C., 1957. Brazos River bar: a study in the significance of grain size parameters. *Journal of Sedimentary Research*, 27(1), 3-26.

Gao, S. and Collins, M., 1992. Net sediment transport patterns inferred from grain size trends based upon definition of "transport vectors". *Sedimentary Geology*, 81(1), 47-60.

Gao, S.; Collins, M.B.; Lanckneus, J.; De Moor, G., and Van Lancker, V., 1994. Grain size trends associated with net sediment transport patterns: An example from the Belgian continental shelf. *Marine Geology*, 121(3), 171-185.

Hails, J.R., 1967. Significance of statistical parameters for distinguishing sedimentary environments in New South Wales, Australia. *Journal of Sedimentary Research*, 37(4), 1059-1069.

Jackson, D.W.T.; Cooper, J.A.G., and del Rio, L., 2005. Geological control of beach morphodynamic state. *Marine Geology*, 216(4), 297-314.

Kim, C.W.; Shin, Y.H., and Yu, K.B., 2015, Changes of beach profiles and sediment properties in Baeksajang sandspit beach, west coast of Korea, during winter season. *The Geographical Journal of Korea*, 49(1), 117-131. (in Korean)

Komar, P.D. and Gaughan, M.K., 1972. Airy wave theory and breaker height prediction. *Proceedings of the 13th Conference of Coastal Engineering* (Vancouver, Canada), pp. 405-418.

Korea Hydrographic and Oceanographic Administration. http://www.khoa.go.kr.

Korea Meteorological Administration. http://www.kma.go.kr.

Levoy, F.; Anthony, E.J.; Monfort, O., and Larsonneur, C., 2000. The morphodynamics of megatidal beaches in Normandy, France. *Marine Geology*, 171(1), 39-59.

Masselink, G. and Short, A.D., 1993. The effect of tide range on beach morphodynamics and morphology: a conceptual beach model. *Journal of Coastal Research*, 9(3), 785-800.

Masselink, G.; Auger, N.; Russell, P., and O'hare, T., 2007. Short-term morphological change and sediment dynamics in the intertidal zone of a macrotidal beach. *Sedimentology*, 54(1), 39-53.

McLaren, P. and Bowles, D., 1985. The effect of sediment transport on grain-size distributions. *Journal of Sedimentary Petrology*, 55(4), 457-470.

Niedoroda, A.W.; Swift, D.J.P., and Hokins, T.S., 1985. The shoreface, *In:* Davis, R.A. (ed.), *Coastal Sedimentary Environments*, 2nd ed. New York: Springer-Verlag, pp. 533-624.

Pedreros, R.; Howa, H.L., and Michel, D., 1996. Application of grain size trend analysis for the determination of sediment transport pathways in intertidal areas. *Marine Geology*, 135(1), 35-49.

Prothero, D.R. and Schwab, F., 1996. *Sedimentary Geology: An Introduction to Sedimentary Rocks and Stratigraphy,* New York: W.H. Freeman, 575p.

Reichmüth, B. and Anthony, E.J., 2007. Tidal influence on the intertidal bar morphology of two contrasting macrotidal beaches. *Geomorphology*, 90(1), 101-114.

Wijnberg, K.M. and Kroon, A., 2002. Barred Beaches. *Geomorphology*, 48(1), 103-120.

Yang, B.C. and Chun, S.S., 2001. A seasonal model of surface sedimentation on the Baeksu open-coast intertidal flat, southwestern coast of Korea. *Geosciences Journal*, 5(3), 251-262.

Yang, B.C.; Dalrymple, R.W., and Chun, S.S., 2005. Sedimentation on a wave-dominated, open-coast tidal flat, south-western Korea: summer tidal flat–winter shoreface. *Sedimentology*, 52(2), 235-252.

Journal of Coastal Research	SI	75	1367 - 1371	Coconut Creek, Florida	2016

Numerical Simulations of Flow Patterns and Possible Implications for Deposition around Circular Patches of Vegetation

Hyung Suk Kim [†*], Junwoo Choi[†], and Moonhyeong Park[†]

[†] Hydro Science and Engineering Research Institute
Korea Institute of Civil Engineering and Building Technology
Goyang, Republic of Korea

www.cerf-jcr.org

www.JCRonline.org

ABSTRACT

Kim, H. S.; Choi, J., and Park, M., 2016. Numerical simulations of flow patterns and possible implications for deposition around circular patches of vegetation. *In:* Vila-Concejo, A.; Bruce, E.; Kennedy, D.M., and McCarroll, R.J. (eds.), *Proceedings of the 14th International Coastal Symposium* (Sydney, Australia). *Journal of Coastal Research*, Special Issue, No. 75, pp. 1367 - 1371. Coconut Creek (Florida), ISSN 0749-0208.

This study presents flow patterns and possible deposition around circular patches of vegetation using a two-dimensional numerical model. Because flow can pass through the patch, the formation of the von-Karman vortex street is delayed and its position moves further downstream as solid volume fraction (SVF) increases. The vortex downstream of the patch is formed as SVF≥0.08. When the two patches are very close to each other, a single vortex street is formed. As the distance between two patches is large, the effect of the interaction is weak and the vortex is developed behind individual patches. The possible deposition region is associated with SVF and configuration of the patches and thus it can provide the process on bed morphodynamics with vegetation.

ADDITIONAL INDEX WORDS: *Deposition, Numerical model, Patch of vegetation, Vortex street*

INTRODUCTION

Flow through a porous obstruction is observed in rivers and coastal regions. Aquatic and terrestrial vegetation are representative porous obstructions. Vegetation reduces average velocity and decreases in the bed shear stress. Thus, vegetation can stabilize bed and change spatial distributions of erosion and deposition. Vegetation also acts as a protection for riverbanks and shorelines due to changes in turbulence structure and wave energy (Temmerman *et al*., 2007). In addition, vegetation improves water quality and provides a variety of ecosystem by trapping nutrients and heavy metals.

There are many researches on vegetation hydrodynamics to estimate bulk drag coefficient and to study diffusion within vegetation (Nepf, 1999; Tanino and Nepf, 2008). Most studies have been conducted in the flume that covers vegetation over the entire width. However, vegetation can be observed in patches with finite length and width which is more common in the fields. Recently, few studies have described finite patch of vegetation (Chen *et al*., 2012; Kim *et al*., 2015; Meire *et al*., 2014; Zong and Nepf, 2012). Zong and Nepf (2012) conducted laboratory experiments to investigate flow structures behind a circular patch of vegetation composed of a circular array of cylinders. Because flow passes through the patch, the steady region is formed directly downstream of the patch. This flow delays the onset of vortex development. Zong and Nepf (2012) described that the length of the onset of vortex was associated with solid volume fraction(SVF), $\phi = N(d/D)^2$, where N is the number of cylinders, d is the diameter of individual cylinders and D is the diameter of the patch. For 0.05≥SVF, no large-scale Karman vortex street is formed. When SVF is larger than 0.05, shear layers at both sides of the patch are developed downstream and a large-scale Karman vortex street is formed at some distance behind the patch. Chen *et al*. (2012) carried out the flume experiment on flow structure and deposition behind a circular patch of vegetation. There are two peaks of turbulence. The first peak is observed at the leading edge of the patch due to stem-scale turbulence generated by each stem. The second peak occurs downstream of the patch, resulting from patch-scale turbulence. This is produced by interaction between shear layers from the patch. The position of onset of a large-scale vortex shifts closer to the patch as SVF increases. In addition, the turbulence intensity increases with an increase in SVF. The spatial distribution of sediment is highly affected by flow structure behind the patch and high turbulence reduces deposition. Meire *et al*. (2014) investigated flow and deposition around an adjacent pair of patches of emergent vegetation, which was modeled by circular cylinders. The distance between patches is crucial factor to influence patterns of flow and deposition behind the patches.

In recent years, computer resources and techniques are developed and thus numerical simulations are efficient and economic tools to investigate flow structures around the patches. Several numerical studies on flow and turbulence structures behind a circular patch of vegetation have been conducted (Nicolle and Eames, 2011; Chang and Constantinescu, 2015; Lima *et al*., 2015). In most of the numerical simulations, vegetation elements are simplified as rigid circular cylinders and each element is treated by a high-resolution grid. Nicolle and Eames (2011) conducted numerical simulations using highly resolved two-dimensional direct numerical simulation (DNS) to study the vortex development behind a circular patch of

DOI: 10.2112/SI75-274.1 received 15 October, 2015; accepted in revision 15 January, 2015
*Corresponding author: hskim0824@kict.re.kr
©Coastal Education and Research Foundation, Inc. 2016

vegetation. The numerical simulation used a constant diameter of cylinders at a low Reynolds number (Re_D = 2100). Their results showed that for SVF≤0.05, shear layers formed at both sides of the patch are not interacted and the von Karman vortex is absent. On the other hand, the von Karman vortex street is formed downstream of the patch as 0.05<SVF<0.15, and the flow structure is similar to that of a solid cylinder of same diameter for SVF≥0.15.This is a same trend of Zong and Nepf's experiments. Chang and Constantinescu (2015) conducted fully three-dimensional large eddy simulation (LES) to study flow and turbulence structure through and around a circular patch. Detailed flow and turbulence structures within and behind the patch are captured, and the drag and lift forces on individual elements are evaluated. Lima *et al.* (2015) investigated flow patterns around two neighboring circular patches of vegetation using the computational fluid dynamic code FLUENT. Various configurations are examined with different intervals between two patches. The results showed that flow characteristics are affected by interaction between adjacent patches of vegetation and can propose feedbacks on evolution of vegetated landscapes.

The above numerical studies have used highly resolved numerical models and vegetation elements are resolved using fine meshes. This approach is able to reproduce a large-scale vortex and small-scale eddies generated by individual elements. However, this computation is still expensive and time consuming. If small-scale turbulence is modeled, the practical approach that vegetation is considered by adding source terms to the momentum and turbulence transport equations can be adopted (Choi and Kang, 2006; Kim, 2013). This approach does not demand high resolution grids, so that computation is efficient and adequate for engineering purposes.

The main objective of this paper is to investigate flow structure and possible deposition around a patch and two neighboring patches using a two-dimensional depth-averaged model. For isolated patch, numerical simulation is conducted with different SVF. For two neighboring patches, the patch distance is varied in the lateral direction. The flow structure and possible implications for deposition around and behind the patches are examined.

NUMERICAL MODEL

A depth-averaged, two-dimensional numerical model was employed to simulate the flow field with vegetation. The governing equations were based on continuity equation and momentum equations considered SVF by vegetation. The source terms for vegetation were added to momentum and turbulence transport equations. For more details, please refer to Kim (2013).

MODEL SET-UP

The numerical simulations are based on experiments of Zong and Nepf (2012). The experiment was conducted in a flume with 13 m long and 1.2 m wide (Figure 1a). The circular patch of vegetation composed of circular cylinders was located in the middle of channel. The diameter of circular cylinders, d, was 6 mm and the diameter of the circular patch was 0.22 m. The inflow velocity, u_0, was 0.098 m/s and water depth, h, was 0.133 m which corresponded to Re_D = 21,560 and Fr=0.09.

In numerical simulation, the uniform velocity is imposed at the inlet boundary and Neumann boundary condition is set at the downstream boundary. The no-slip boundary condition is used at both lateral sides. For isolated patch, several SVF is considered with ϕ=0.03, 0.05, 0.08, 0.09, 0.14, 0.36, 1.0. For two neighboring patches, the influence on distance between two patches, s, in the lateral direction is investigated and s/D=1.0, 1.18, 1.45, 2.0, 2.63 are considered with SVF=0.14. The number of meshes for the isolated patch is 50,000 and the fine meshes (Δ=0.01m) are placed around the patch. For two neighboring patches, the computational domain is double as shown in Figure 1b and the number of meshes is also twice in the lateral direction. The time-step size is 0.005 s which is satisfied in a courant number of less than 0.3 to ensure numerical stability.

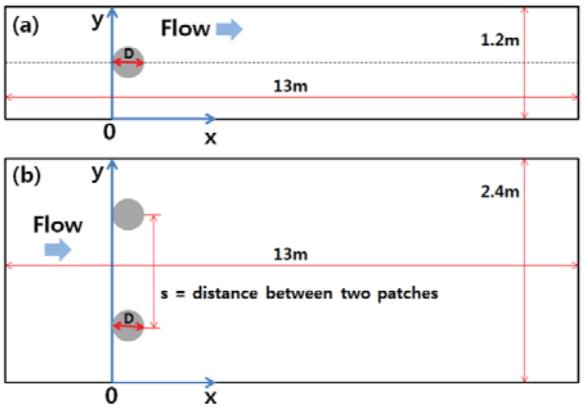

Figure 1. Computational doamin for (a) single patch and (b) two patches.

RESULTS

The numerical model is validated by comparing experimental data of a single patch with SVF=0.08. Figure 2 shows longitudinal profiles of streamwise and lateral velocities along a transect of the center of a patch and a transect of a lateral edge of the patch, respectively. The streamwise velocity begins to decrease from upstream of the patch and the velocity continues to decelerate after entering the patch. Downstream of the patch, the velocity is almost uniform until x/D=3.2. This region is called the steady wake region (Zong and Nepf, 2012). Beyond steady wake region, the velocity rapidly increases back to bulk velocity of upstream boundary but the velocity is slightly lower than the bulk velocity. As shown in Figure 2, the lateral velocity begins to increase from upstream of the patch with a distance of a patch diameter (D), which indicates that the diversion of flow occurs from upstream of the patch. The lateral velocity reaches a maximum value at $0<x<D$ which implies that the diversion of flow is strong around the leading edge of the patch. After the maximum value, the lateral velocity rapidly decreases until the end of the patch. Then, the velocity becomes constant but the negative velocity is observed at $3<x<10$ which means that the flow moves to the centerline of the patch. The velocity profiles of numerical simulation are in good agreement with experimental data. Notably, the diversion of flow and the

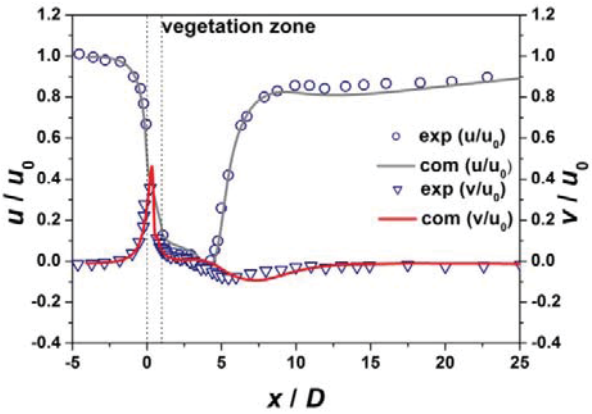

Figure 2. Comparison between measured and simulated velocities of longitudinal profiles. The streamwise velocity(u) is at the centerline of the patch and the lateral velocity(v) is at the lateral edge of the patch.

deceleration of the streamwise velocity are accurately reproduced.

Figure 3 presents instantaneous vorticity fields downstream of a solid body and a circular patch of vegetation. For SVF=1.0(solid body), flow around a solid body attaches to body surface and detaches from it. A von-Karman vortex street is formed behind a solid body. Vortices are observed and shed periodically downstream of a solid body. In contrast to the solid body, a circular patch is porous structure, meaning that flow can pass through the interior of the patch. Thus, as the flow encounters the patch, there is a flow through the patch and the other flow diverges from the patch. It can be seen in Figure 3b that the two shear layers are developed individually at the lateral edges of the patch. However, there is no interference between two shear layers, and thus the von-Karman vortex is not formed behind the patch. This is because the flow diverging from the patch is still small, so that high momentum interrupts the interaction between two shear layers. When SVF $\geq$ 0.08, the two shear layers merge at some distance and shear instability occurs. Then, the von-Karman vortex street is developed behind the patch. The initiation of the von-Karman vortex is observed at x/D=7.0, 4.6, 2.6, 1.5 for SVF=0.08, 0.09, 0.14, 0.36, respectively. As SVF decreases, the von-Karman vortex street originates further downstream. The steady wake region decreases with increasing SVF. Thus, an increase in the steady wake region results in delay of initiation of vortex development. The strength of the vortices in the street increases with an increase in SVF. The flow structure behind the patch for SVF=0.36 becomes similar to that of a solid body and the von-Karman vortex street is formed directly downstream of the patch. On the other hand, Zong and Nepf (2012) showed that the vortex development is initiated as SVF > 0.05. In the present simulation, the von-Karman vortex street is developed as SVF $\geq$ 0.08, which is larger than that of the experiment. This is due to fact that small-scale motion induced by individual elements in the patch is not resolved.

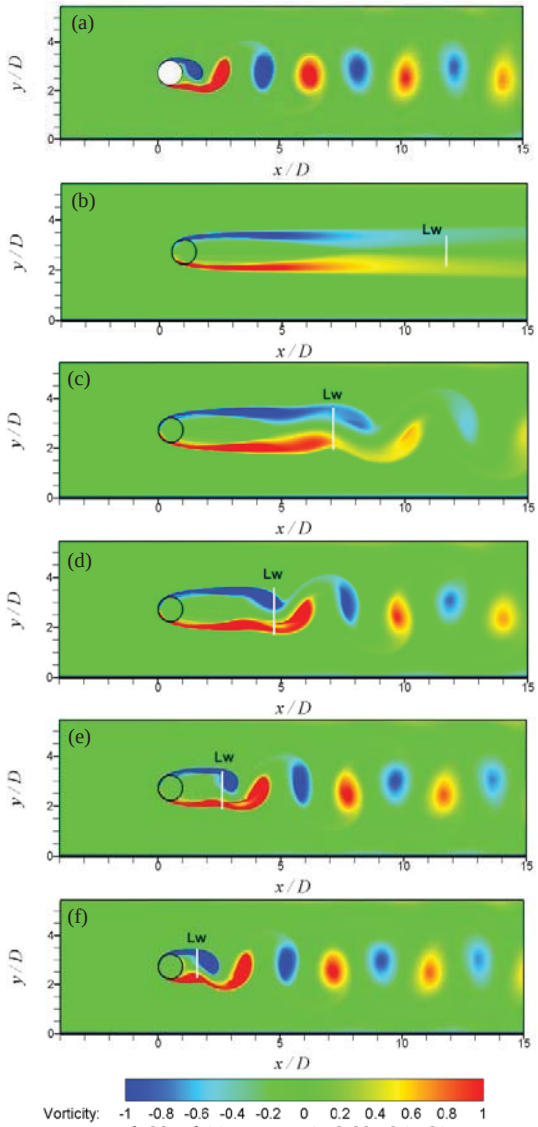

Figure 3. Vorticity fields of (a) SVF=1.0(Solid body), (b) SVF=0.05, (c) SVF=0.08, (d) SVF=0.09, (e) SVF=0.14, (f) SVF=0.36. L_w indicates the location of maximum turbulence kinetic energy.

Williamson (1996) presented that the location of the initiation of the von-Karman vortex street corresponds to that of maximum turbulence kinetic energy (TKE). In Figure 3, the location of maximum value is marked with white bars (L_W). When shear instability occurs downstream of the patch, the location of maximum TKE is consistent with that of the vortex initiation.For a single patch, the flow patterns are influenced by SVF whereas for aligned patches, the flow structure is strongly associated with interpatch distance. Figure 4 shows instantaneous vorticity fields for two neighboring patches in a side-by-side arrangement.

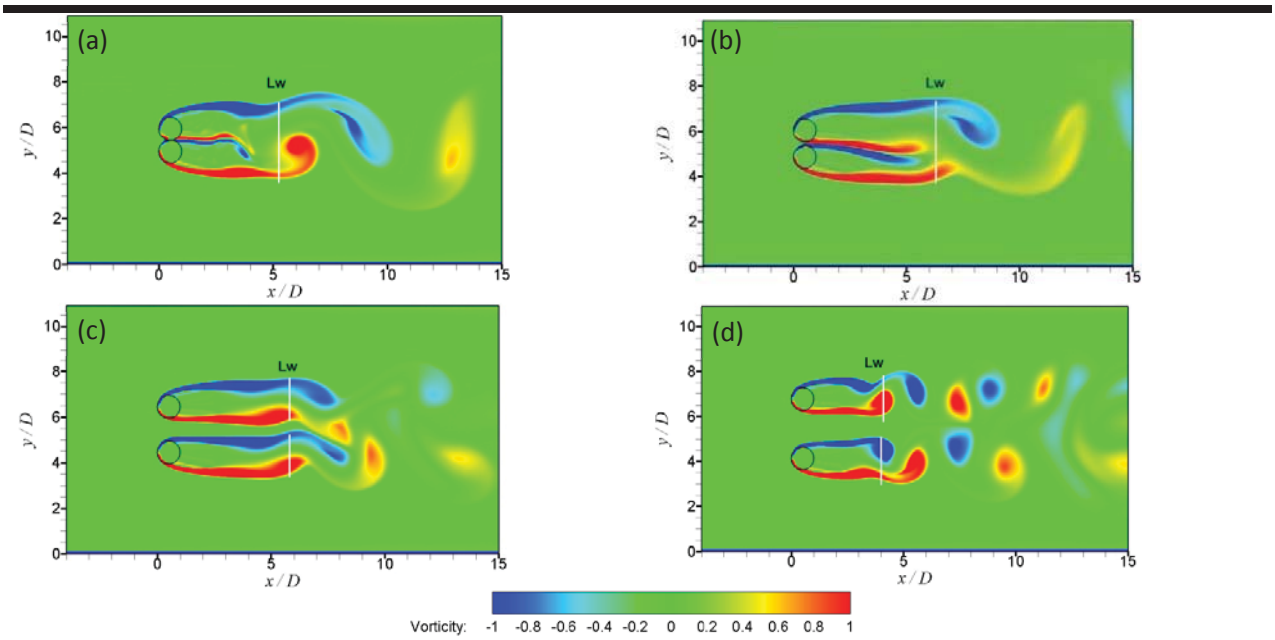

Figure 4. Vorticity fields of (a) s/D=1.0, (b) s/D=1.18, (c) s/D=2.0, (d) s/D=2.63. L_w denotes the location of maximum turbulence kinetic energy.

For s/D=1.0 and 1.18, a single Karman vortex street is formed downstream of two patches, which is similar behavior to that of the single patch. However, there is a jet-like flow between two patches, which increases in the streamwise extent of steady wake region. As the jet-like flow increases, the steady wake region increases. Thus, the formation of the von-Karman vortex is delayed. The shear instability only appears from the outside shear layers and shedding occurs downstream of two patches. For s/D=1.45, 2.0, 2.63, the von-Karman vortex is developed behind individual patches, which indicates that shear layers from each patch interact to form the von-Karman vortex. For s/D=2.0, shear layers from individual cylinders are interfered and the vortex is developed downstream of each patch. However, a single vortex street is produced in the combined wake of the patches. For s/D=2.63, the vortex street is observed behind the each patch which exhibits a symmetric flow pattern. This indicates that the effect of the jet-like flow is almost negligible.

The patch of vegetation is widely known for potential region of deposition. The deposition of sediment is related to decreased velocity region. The critical velocity of sediment is a function of the particle size. In order to examine enhanced deposition with the patches, we consider critical velocity, u/u_0<0.5, representing fine particles (Lima *et al*., 2015). Even though we don't consider specific particle sizes, the hypothesis can infer potential regions of enhanced deposition around and behind the patches.

Figure 5 presents the deposition region around and downstream of the patches. For SVF=0.05, deposition is only found downstream of the patch, which means that there is still high velocity within the patch. The deposition area (DA_1/D^2) is 7.84. For SVF=0.14, deposition is observed within and behind the patch, and the deposition area is 3.94. For a single patch, the deposition area decreases with an increase in SVF, which corresponds to diminishing steady wake region with SVF. As SVF is high, the negative feedback is provided because the potential of new growth decreases. For neighboring two patches, SVF is 0.14 and thus the result of a single patch with SVF=0.14 (Figure 5b) is used as the reference to investigate the impact of interaction between two patches. The deposition area for two neighboring patches (DA_2) is normalized by DA_1. For s/D=1.0, the deposition pattern resembles that of a single patch with two times the diameter of the patch. However, the deposition area ($DA_2/2DA_1$) is 2.22. For s/D=1.45, the deposition is observed behind each patch and a secondary deposition area appears, which is consistent with the experimental result of Meire *et al*. (2014). The deposition area is 3.42 which is much greater than that of s/D=1.0 due to the secondary deposition area. For s/D=2.63, the deposition area is totally separated, although the deposition area is 1.3, which is slightly greater than $DA_2/2DA_1$=1.0. The deposition area is the maximum when the secondary deposition is present. As the deposition area of two neighboring patches is separated, it decreases and is equal to $2DA_1$.

CONCLUSIONS

This study investigates flow fields and possible regions for deposition around and downstream of the patches using a two-dimensional numerical model. For a single patch, a von Karman vortex street is formed due to interaction between shear layers. As SVF≥0.08, the von Karman vortex street is formed downstream of the patch. However, When SVF<0.08, no vortex is developed downstream of the patch due to the high flow exiting the patch. The initiation position of the vortex street is delayed as SVF decreases. The maximum TKE appears behind the patch due to the patch-scale vortex, corresponding to the

formation of the von-Karman vortex street. For two neighboring patches, a single Karman vortex street is formed when the patches are very close. As the distance between two patches becomes larger, the vortex is formed downstream of individual patches.

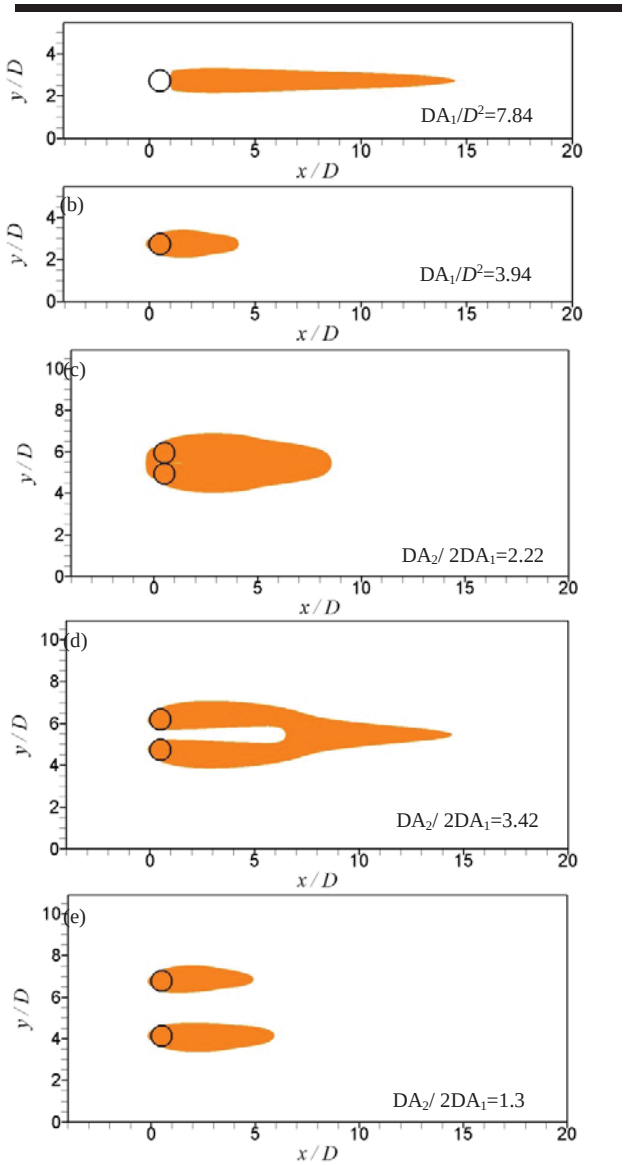

Figure 5. Deposition region identified by the color for $u/u_0 < 0.5$. (a) SVF=0.05 (single patch), (b) SVF=0.14 (single patch), (c) s/D=1.0 (SVF=0.14), (d) s/D=1.45 (SVF=0.14), (e) s/D=2.63 (SVF=0.14).

The possible deposition region is associated with SVF and configuration of the patches. The deposition area increases with diminishing SVF. When there is a small gap between two patches, the deposition area is enhanced. The deposition area is similar to that of a single patch as the gap becomes large. The results show that flow patterns and potential of deposition are influenced by SVF and patch configuration, which may impact the bed evolution with vegetation.

ACKNOWLEDGMENTS

This study was performed by a project of ”Investigation of large swell waves and rip currents and development of the disaster response system (No. 20140057)” sponsored by the Ministry of Oceans and Fisheries.

LITERATURE CITED

Chang, K. and Constantinescu, G., 2015. Numerical investigation of flow and turbulence structure through and around a circular array of rigid cylinders. *Journal of Fluid Mechanics*, 766, 161-199.

Chen, Z.; Ortiz, A., Zong, L., and Nepf, H., 2012. The wake structure behind a porous obstruction and its implications for deposition near a finite patch of emergent vegetation. *Water Resource Research*, 48, W09517.

Choi, S. and Kang, H., 2006. Numerical investigations of mean flow and turbulence structures of partly vegetated open-channel flows using the Reynolds stress model. *Journal of Hydraulic Research*, 44(2), 203-217.

Kim, H;. S., Kimura, I., and Shimizu, Y., 2015. Bed morphological changes around a finite patch of vegetation. *Earth Surface Processes and Landforms*, 40(3), 375-388.

Kim, H. S., 2013. Impact of finite vegetation patches on flow and bed morphology in open channels: Hokkaido University, Ph.D. dissertation.

Lima, P.; Janzen, J., and Nepf, H., 2015. Flow patterns around two neighboring patches of emergent vegetation and possible implications for deposition and vegetation growth. *Environmental Fluid Mechanics*, 15, 881-898.

Meire, D.; Kondziolka, J., and Nepf, H., 2014. Interaction between neighboring vegetation patches: Impact of flow and deposition. *Water Resource Research*, 50(5), 3809-3825.

Nepf, H., 1999. Drag, turbulence and diffusivity in flow through emergent vegetation. *Water Resource Research*, 35(2), 479-489.

Nicolle, A., and Eames, I., 2011. Numerical study of flow through and around a circular array of cylinders. *Journal of Fluid Mechanics*,679, 1-31.

Tanino, Y., and Nepf, H., 2008. Laboratory investigation of mean drag in a random array of rigid, emergent cylinders. *Journal of Hydraulic Engineering*, 134(1), 34-41.

Temmerman, S.; Bouma, T. J., and Van de Koppel, J., 2007. Vegetation causes channel erosion in a tidal landscape. *Geology*, 35(7), 631-634.

Williamson, C. H. K., 1996. Vortex dynamics in the cylinder wake, *Annual Review of Fluid Mechanics*, 28, 477-539.

Zong, L., and Nepf, H., 2012. Vortex development behind a finite porous obstruction in a channel. *Journal of Fluid Mechanics*. 691, 368-391.

Journal of Coastal Research	SI	75	1372 - 1376	Coconut Creek, Florida	2016

Analysis of Beach Deformation according to Nourishing Sand in Haeundae Beach, Korea

Woo Dong Lee[†], In Ho Kim[‡], Jong Sung Yoon[††], Won Chul Cho[∞] and Dong Soo Hur[†*]

[†] Gyeongsang National University, Department of Ocean Civil Engineering Tongyeong, Republic of Korea

[‡] Kangwon National University, Dept. of Environmental and Ocean Construction Engineering Samcheok, Republic of Korea

[††] Inje University, Department of Civil Engineering, Gimhae, Republic of Korea

[∞] Chung-Ang University , Department of Civil and Environmental Engineering, Seoul, Republic of Korea

www.cerf-jcr.org

www.JCRonline.org

ABSTRACT

Lee, W.D., Kim, I.H., Yoon, J.S., Cho, W.C. and Hur, D.S., 2016. Analysis of beach deformation according to nourishing sand in haeundae beach, Korea. *In:* Vila-Concejo, A.; Bruce, E.; Kennedy, D.M., and McCarroll, R.J. (eds.), *Proceedings of the 14th International Coastal Symposium* (Sydney, Australia). *Journal of Coastal Research*, Special Issue, No. 75, pp. 1372 - 1376. Coconut Creek (Florida), ISSN 0749-0208.

This study has analyzed the beach deformation characteristics of Haeundae Beach, which is one of the most representative beaches of S.Korea, after beach nourishment through monitoring and performing a numerical simulation. This study was able to analyze the beach deformation characteristics after beach nourishment in depth (e.g. variations in coastline, beach profile and the area and volume of beach, and beach stabilization process) in line with the results of marine geophysical survey (Do *et al.*, 2015). This study surveyed the marine morphological changes around Haeundae Beach caused by Typhoon Neoguri, but morphological changes did not show in the water level of over 3m. In addition, this study was not only able to identify the short-term advance and retreat of coastline in the beach profile due to Typhoon Neoguri, but also understand this phenomenon on the basis of the results of wave field analysis using Numerical Wave Tank (NWT). Furthermore, this study was able to find that NWT and the coupling calculation of Contour-line model simulated the changes of coastline due to Typhoon Neoguri almost similarly. NWT and the coupling calculation of Contour-line based on long-term monitoring are expected to greatly contribute to understanding the beach deformation characteristics due to beach nourishment in future.

ADDITIONAL INDEX WORDS: *Nourishing sand, Morphological change, Monitoring, NWT (Numerical wave tank), Contour-line model*

INTRODUCTION

Haeundae beach, which is one of the most representative beaches of S. Korea is located in a city (Figure 1). The average width and area were 58.6m and 88,658 $m^{2,}$ respectively, in 2007, but they were significantly reduced to 42.5m and 62,129 m^2 respectively in 2007. Thus the Ministry of Maritime Affairs and Fisheries of S. Korea promotes 5-year "Sandy Beach Restoration Project" from 2015. As a result of 2 times of beach nourishment, the average width and area were increased by more than 2 folds - 100m and 146,006 m^2 respectively. The primary beach nourishment was 407,000m^3 up until Feb. 28, 2014, and the secondary beach nourishment was 186,000m^3 up until Mar. 31, 2015.

Currently, the width and area have slightly been reduced since the completion of beach nourishment, which is a phenomenon indicating the stabilization of nourishing sand. Thus to discuss the stabilization of beach after beach nourishment, this study has been monitoring the beach, section, and sounding after the completion of beach nourishment. In addition, it analyzed the hydraulic characteristic in the vicinity of Haeundae Beach, using Numerical Wave Tank (NWT; Hur et al, 2012) and predicted the variations in coastline by applying the results of the analysis to contour-line model.

Haeundae is a symbolic beach of S.Korea, so many studies were carried out in the past. In particular, there are many studies conducted on the offshore current around Haeundae Beach since offshore current commonly takes place in the same area. For a representative example, Kim *et al.* (2013) and Lee *et al.* (2014) discussed the generation mechanism of offshore current using 2D prediction model and 3D predication model respectively; Yoon *et al.* (2014) investigated and analyzed the flow velocity of offshore current using a video analysis; and Choi *et al.* (2014) reviewed the establishment of offshore current alarm system through real-time observation. In addition, Do *et al.* (2015) conducted monitoring of waves and tidal current after the primary beach nourishment and reported the analysis results, and Lim *et al.* (2014) predicted wave induced current by combining a flow model (ROMS) and a wave model (SWAN). This study conducted monitoring and a numerical simulation for the morphological change for the purpose of analyzing the characteristics of beach deformation in Haeundae Beach after beach nourishment. This study ultimately aimed to investigate the beach stabilization process after beach nourishment by analyzing the results in a comprehensive manner.

DOI: 10.2112/SI75-275.1 received 15 October, 2015; accepted in revision 15 January, 2015.
*Corresponding author: dshur@gnu.ac.kr
©Coastal Education and Research Foundation, Inc. 2016

MONITORING SYSTEM

As shown in Table 1, beach nourishment for the area of 407,000m3 was carried out from Nov. 2013 till Feb. 2014, and monitoring has been carried out on a regular basis from Mar 8, 2014 until today. Until today, PS (Profile Survey), BS (Beach Survey), CS (Coastline Survey) and Sounding were performed 13 times, 15 times, 23 times, and 2 times, respectively. 53 sections were surveyed through PS and the beach areas surveyed through BS are shown in Figure 2.

During the monitoring period, 3 festivals took place (Table 1). During this period, artificial beach deformation occurred due to the mobilization of heavy equipment. The first festival took place from Jun. 5 to 9, 2014; the second festival, Busan Film Festival took place from Jun. 2 to 11, 2014; and the third festival, Sand Festival took place from May 29 till Jun. 1, 2015. 5 typhoons hit Haeundae Beach in 2014. The results of wave analysis performed by Do *et al.* (2015) are listed in Table 2. Thus this study reviewed the results of 10-month monitoring of the beach deformation from the primary beach nourishment until the commencement of the secondary beach nourishment, and at the same time, performed an in-depth analysis of the morphological change due to the 8th Typhoon Neoguri and Halong in 2014.

Figure 1. Beach targeted areas for monitoring (Haeundae beach, Busan, South Korea).

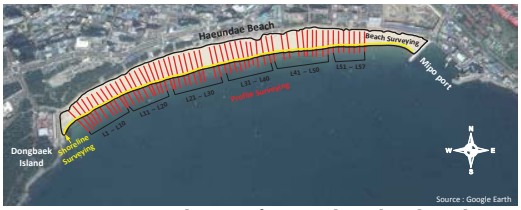

Figure 2. Survey area and range for coastline, beach and section of Haeundae Beach.

MONITORING RESULTS

The results of 17 coastline surveys, which were performed once every month since the primary beach nourishment, are expressed in Figure 3, where the solid lines in rainbow colors are No. 3 (Apr. 25), No. 5 (May 24), No. 7 (Jun. 27), No. 9 (Jul. 11), No. 11 (Aug. 28), No. 13 (Sept. 22), and No. 15 (Oct. 24); while the solid line is No. 17 (Nov. 21).

Figure 3 shows the advance/retreat of coastline due to artificial influence (e.g. festivals) as well as the influence of seasons and typhoon. The results of comprehensive analysis until the commencement of the secondary beach nourishment show the overall retreat of coastline.

Table 1. *The summary of monitoring in Haeundae beach, South Korea*

No	Date		Survey			Season	Event
			PS	CS	BS		
01		Mar. 28.	○				Nourishment (407000m^3)
02		Apr. 11.	○				
03		Apr. 25	○	○		Spring	
04		May 9	○	○			
05		May 23	○	○			Sand festival
06		Jun. 13	○	○			
07		Jun. 27	○	○			
08	2014	Jul. 8	○	○		Summer	Typhoon Neoguri
09		Jul. 11	○	○			
10		Aug. 1		○	○		Typhoon Nakri and Halong
11		Aug. 28		○	○		
12		Sept. 12		○	○		
13		Sept. 22		○	○		
14		Oct. 6		○		Fall	Sand festival Typhoon Phafone and Vongfong
15		Oct. 24		○	○		
16		Nov. 7		○	○		
17		Nov. 21	○	○	○		
18		Dec. 5		○	○		
19		Jan. 7		○	○		
20		Feb. 23		○		Winter	Nourishment (186000m^3)
21	2015	Mar. 12		○	○		
22		Mar. 21	○	○	○		
23		May 29		○	○		Sand festival
24		Jun. 25	○	○	○	Summer	
25		Sept. 4	○	○	○	Fall	
	Total		13	23	15		

Table 2. *The observed wave results during typhoons by Do et al.(2015)*

	Neoguri	Nakri	Halong	Phafone	Vongfong
H_s (m)	2.59	3.52	2.42	2.40	3.97
H_{max} (m)	3.78	5.32	3.66	3.56	5.77
T_p (sec)	11.78	7.46	9.00	9.41	10.46
T_s (sec)	10.63	7.80	8.74	8.95	9.61
D_p (deg)	180.8	155.3	113.2	109.3	117.4
SPR (deg)	18.67	26.54	26.55	28.71	21.74
Date (peak)	Jul. 9 22:00	Aug. 3 04:00	Aug. 10 05:00	Oct. 6 04:00	Oct. 13 14:00
Duration (H_s>1m)	26 Hr	71 Hr	72 Hr	71 Hr	115 Hr

To analyze the resultant variations in beach profile, the sections showing the most significant variations and the sections showing the least variations are expressed in Figure 4. In addition, the sections showing the most significant advance/retreat of coastline after Typhoon Neoguri, which caused the most significant variations since the primary beach nourishment, are expressed in Figure 5.

Figure 4 (a) shows L3 which is the section showing the most significant advance of coastline and the height of L25 showing the least retreat of coastline (see Figure 2). The omitted results

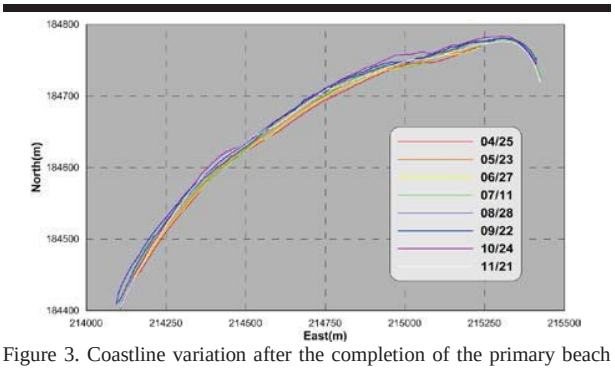

Figure 3. Coastline variation after the completion of the primary beach nourishment.

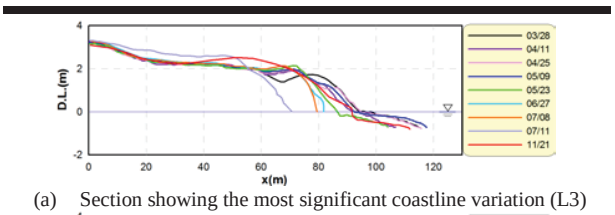

(a) Section showing the most significant coastline variation (L3)

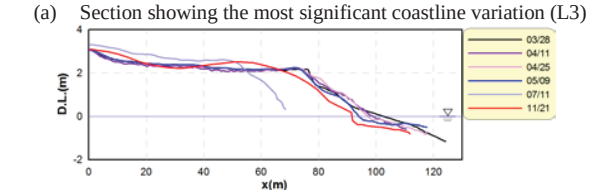

(b) Section showing the least coastline variation (L25)

Figure 4. Section variation of Haeundae after the completion of the first nourishment.

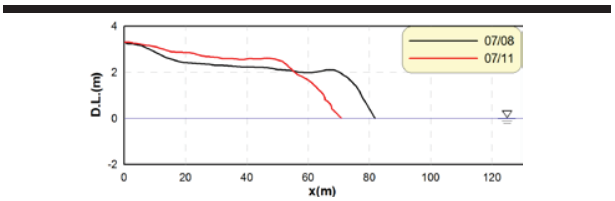

(a) Section showing the most significant retreat of coastline (L3)

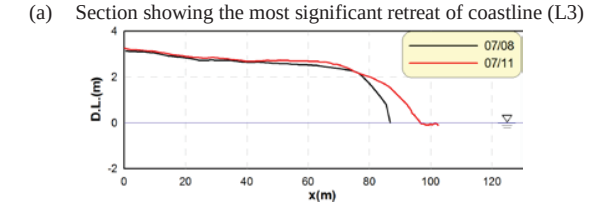

(b) Section showing the most significant advance of coastline (L19)

Figure 5. Comparison of section between before and after Typhoon Neoguri.

couldn't be measured because of festival. As aforementioned in Figure 4, the coastline repeats advancing and retreating, and then gradually recovers after the significant erosion due to Typhoon Neoguri. During this period, in L3 section and L25, coastline retreated 4.55m and 22.64m, respectively.Figure 5 (a) shows L3 section showing the most significant retreat of coastline due to Typhoon Neoguri and the height of L19 showing the most significant advance of coastline (see Figure 2).

Figure 5 indicates the most significant variations in beach profile due to the tsunami and wave accompanied by typhoon. In L3 showing the most significant retreat of coastline, the coastline retreated 10.30m and in L19 section it advanced 9.54m. This phenomenon is expected to significantly affect the area and volume of beach. This phenomenon will be addressed later.

In order to comprehensively analyze the characteristics of beach deformation, the area and volume of the areas for beach surveying in Figure 2 are expressed in Figure 6, where blue color indicates beach nourishment; red color indicates typhoon; lime green color indicates festival; circles (O) indicates the area of beach; and triangle (Δ) indicates land beach.

In Figure 6, the area of beach gradually decreases after the primary beach nourishment; rapidly increases due to sand festival (Jun. 05-09); and then repeats increasing and decreasing due to the variations in coastline. And then it rapidly decreases in a short period time after No. 15 (Oct. 24), which is identical to the results of the study conducted by Do *et al.* (2015). In other words, E-type wave direction showing significant appearance frequency of 78% significantly changes in Nov (i.e. S-type: 30.4%, SE-type: 22.4%, and E-type: 44.9%). In addition, the beach profile doesn't seem to be greatly influenced by Typhoon Neoguri. This is probably because that, as discussed earlier, the advance and retreat of coastline took place in a similar manner. Meanwhile, the volume of beach gradually decreases after the primary beach nourishment and sharply decreases due to Neoguri and then remains unchanged, implying that the nourishing sand reaches a plateau to some extent.

Figure 7 illustrates the morphology surveyed using sounding and beach survey from Aug 10-11, 2014 before and after Typhoon Halong, which affected Haeundae Beach. (a) is the morphology before the typhoons and (b) is the morphology after the typhoons. In Figure 7, there is no morphological change, especially in the water level of more than -3m. Given the significant wave height of 2.24m as shown in Table 2, it seems that sand moved significantly within foreshore area in which fluid activity is active.

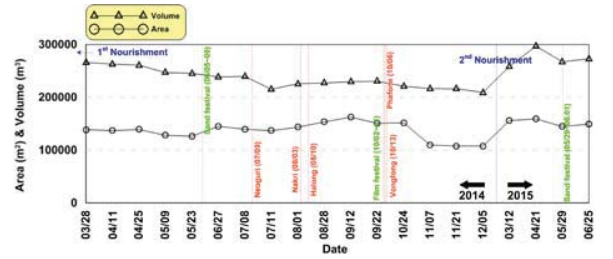

Figure 6. Variations in the area and volume of Haeundae Beach.

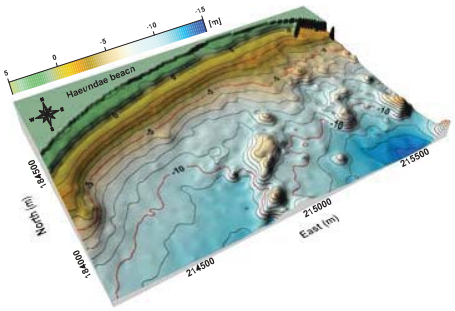

(a) Before the invasion of Typhoon (Jul. 17)

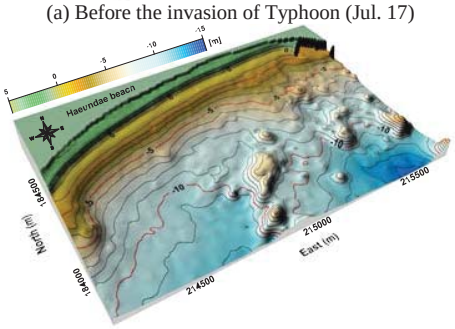

(b) After the invasion of Typhoon (Aug. 16)

Figure 7. Changes of water level and morphology of Haeundae after the invasion of Typhoon Neoguri.

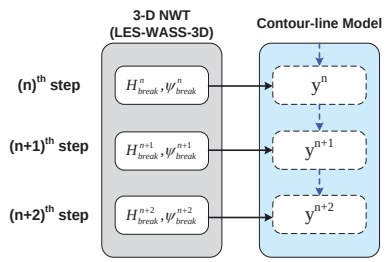

Figure 8. Coupling procedure between NWT and contour-line model.

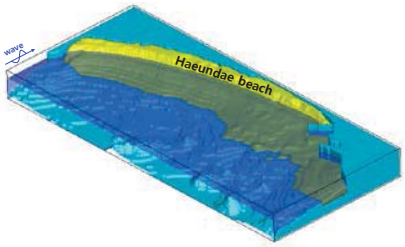

Figure 9. Definition sketch of 3-D numerical wave tank used for modeling of Haeundae beach.

Based on the above results of monitoring, this study analyzed variations in the area and volume of coastline and beach, and variations in beach profile due to the Typhoon Neoguri and variations in water level due to the Typhoon Halong. And then this study analyzed the characteristics of beach deformation through a numerical simulation based on the results of monitoring.

NUMERICAL ANALYSIS METHOD

A numerical analysis was conducted using Numerical Wave Tank (NWT; Hur et al, 2012) and counter-line model coupling calculation suggested by Uda and Kawan (1996).

Figure 8 is the conceptual diagram of the coupling analysis method of NWT and Counter-line model. The height of breaking wave and wave direction for respective morphologies were calculated using NWT and the results were used as the incidence conditions for counter-mile model. Where, H_{break} is the height of breaking wave and ψ_{break} is the wave direction at the time of wave breaking.

Non-reflected wave generation system which was applied to the numerical wave tank is shown in Figure 9.

The water level of over -5m in the numerical wave tank was processed as permeable beach and the rest areas were processed as impermeable beach, taking account of the beach sand with the porosity of 0.4 and average diameter of 0.05cm.

For the conditions of incident wave, the significant waves at the time of Typhoon Neoguri observed by Do *et al.* (2015) listed in Table 2 were used. For the conditions for NWT calculation, the horizontal grid size of 3.75-7.5m, the vertical grid size, and the calculation time interval of 1/50ses were applied.

ANALYSIS OF BEACH DEFORMATION

The wave height and average flow distribution calculated using NWT at the time of Typhoon Neoguri are expressed in Figure 10 and 11. Figure 10 indicates the spatial wave distribution calculated at the time of Typhoon Neoguri using NWT. Increased blue section indicates increased wave height.

Figure 10 indicates the significant differences in wave height reaching coastline due to morphological influence. In particular, relatively low wave height can be found in 4 places. This phenomenon is expected to cause the imbalance of littoral wave energy to develop wave-induced current.

Figure 11 indicates the significant development of offshore current in the areas showing low littoral wave height in the wave distribution as mentioned earlier. In addition, the littoral current develops towards the areas where offshore current occurs. The wave-induced current developed in this manner is expected to greatly affect beach deformation.

Figure 12 shows the results of a comparison of coastline deformation between before and after the Typhoon Neoguri. Dotted line indicates the coast line surveyed before the typhoon; blue solid line is the coastline surveyed after the typhoon; and red solid line is the coastline calculated by the coupling calculation using NWT and contour-line model. For the calculation time, this study considered 26-hour influence on Haeundae as shown in the study of Do *et al.* (2015) and conducted a simulation using x-direction calculation interval of 10m and the calculation time interval of 60sec.

As shown before in Figure 12, the coastline slightly advanced due to the sand from the both sides of the area where offshore current occurs due to meeting of two wave-induced currents. In addition, in the area where significant wave-induced current occurs from the west to the east, the overall sand moves, which

causes the coastline to have the tendency of retreating. Thus this study was able to analyze the characteristics of beach deformation due to Typhoon Neoguri on the basis of the results of wave calculation using NWT.

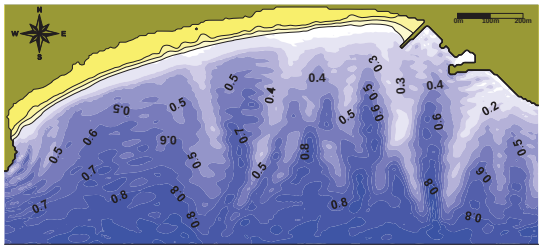

Figure 10. Spatial distribution of wave heights at the time of Typhoon Neoguri.

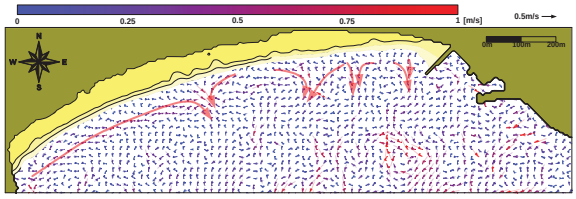

Figure 11. Spatial distribution of wave-induced currents at the time of Typhoon Neoguri.

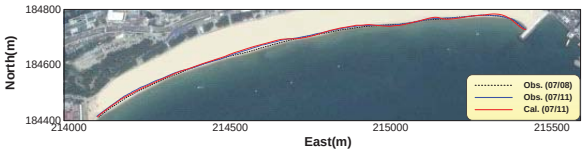

Figure 12. Comparison of coastline between before and after Typhoon Neoguri.

Meanwhile, the advance and retreat of the coastline surveyed using coupling calculation are greater than the results of survey No. 9 (Jul. 11), yet showing very similar tendency. This implies that the results are slightly exaggerated because this significant wave continued to work for 26 hours, though the significant wave observed at the time of Typhoon Neoguri did not continue to work. This studywas able to understand the beach deformation process due to the beach nourishment through site monitoring and coupling procedure. In addition, the coupling analysis suggested in this study is expected to help predict the beach deformation after the secondary beach nourishment.

CONCLUSIONS

This study monitored and calculated the coupling for the topographical change in order to analyze the deformation characteristics of beach after beach nourishment for the Haeundae Beach. Here are the analyis results.

1. Coastline measurement showed the change process (advance/retreat) after the beach nourishment.
2. It was able to compare and analyze the form of beach after the beach nourishment, and between before and after the invasion of Typhoon Neoguri from the measurement of cross section of beach.
3. Invation of Typhoon Halong changed little of submarine topography with 3m or more of water level.
4. By analyzing and combining the aforementioned results and oceanphysics study (Do *et al.*, 2015), it was able to understand the deformation characteristics of beach by the beach nourishment and invation of Typhoon Neoguri.
5. It was able to analyze the change characteristics of coastline due to the invation of Typhoon Neoguri by analyzing the wave and flow field using NWT.
6. The coastline calculated by coupling NWT and contour-line model showed very similary tendency with the coastline of No. 9 (Jul. 11).

It was able to understand the deformation process of beach by beach nourishment through the site monitoring and coupling calculation. The coupling analysis suggested in this study will help in predicting beach deformation after 2 times of beach nourishment.

ACKNOWLEDGMENTS

This research was a part of the project titled “development of coastal erosion control technology” funded by the Ministry of Oceans and Fisheries, Korea.

LITERATURE CITED

Choi, J.W., Lim, C.H. and Yoon, S.B., 2014. A rip current waring system based on real-time observations for Haeundae beach, Korea. *Proceeding of the 3rd International Rip Current Symposium* (Busan, South Korea). *Journal of Coastal Research*, Special Issue No. 72, 56-62.

Do, K.D., Yoo, J.S., Lee, H.J., Do, J.D. and Jin, J.Y., 2015. Field observations of spatial structure of hydrodynamics including waves and currents in the Haeundae coast. *Journal of Korean Society of Coastal and Ocean Engineers*, 27(4), 228-237 (in Korean).

Hur, D.S., Lee, W.D. and Cho, W.C., 2012. Three-dimensional flow characteristics around permeable submerged breakwaters with open inlet. *Ocean Engineering*, 44, 100-116.

Kim, I.C., Lee, J.L., and Lee, J.Y., 2013. Verification of rip current simulation using a two-dimensional predictive model, HAECUM. *Proceedings of the 12th International Coastal Symposium* (Plymouth, England). *Journal of Coastal Research*, Special Issue No. 65, 726-730.

Lee, W.D., Shin, S.W., Jeong, Y.M. and Hur, D.S., 2014. Numerical studies on rip current control using scenefriendly structures at Haeundae beach, Korea. *Proceeding of the 3rd International Rip Current Symposium* (Busan, South Korea). *Journal of Coastal Research*, Special Issue No. 72, 69-74.

Lim, H.S., Kim, C.S., Shim, J.S., Park, K.S., and Chun, I.S., 2014. Simulation of wave-induced current in Haeundae. *Korea Society of Civil Engineers, Civil Expo & Conf.*, 351-352 (in Korean).

Yoon, S.B., Park, W.K. and Choi, J.W., 2014. Observation of rip current velocity at an accidental event by using video image analysis. *Proceeding of the 3rd International Rip Current Symposium* (Busan, South Korea). *Journal of Coastal Research*, Special Issue No. 72, 16-21.

Uda, T. and Kawano, S., 1996. Development of a predictive model of contourline change due to waves. *Japan Society of Civil Engineers, JSCE*, 539(II-35), 121-139 (in Japanese).

Journal of Coastal Research	SI	75	1377 - 1381	Coconut Creek, Florida	2016

Application of EurOtop to Improve Simulations of Coastal Inundations due to Wave Overtopping

Hwa-Young Lee†, Seung-Won Suh‡*

†Disaster Information Research Division
National Disaster Management Institute
Ulsan, Republic of Korea

‡Department of Ocean Science and Engineering
Kunsan National University
Kunsan, Republic of Korea

www.cerf-jcr.org

www.JCRonline.org

ABSTRACT

Lee, H.Y. and Suh, S.W., 2016. Application of EurOtop to improve simulations of coastal inundations due to wave overtopping. *In:* Vila-Concejo, A.; Bruce, E.; Kennedy, D.M., and McCarroll, R.J. (eds.), *Proceedings of the 14th International Coastal Symposium* (Sydney, Australia). *Journal of Coastal Research*, Special Issue, No. 75, pp. 1377 – 1381. Coconut Creek (Florida), ISSN 0749-0208.

To simulate wave-induced overtopping on coastal dikes, a method has been proposed by incorporating the empirical formulas of EurOtop into the storm surge model ADCIRC+SWAN. This approach was found to be efficient and reasonably acceptable through the model validation and sensitivity tests performed on an idealized basin using a hypothetical storm onslaught even under the assumption of a gradually varied flow for a small value of overtopped volume. The hindcasting inundation simulation results on a real case at the Busan coast, Korea, during the typhoon Maemi in 2003 showed quite a similar pattern of inundation area compared with the watermark investigations. This approach could simulate overtopping and overland flow with only a 3% additional computation time of the storm surge model for small parallel clusters of 64 cores. Moreover, it can address various dike types, surface armoring conditions, and rapidly varying ambient wave characteristics of height, period, and incident angle with sea-level change. Thus, we can conclude that it can be applied in real-time forecasting even on artificial coasts to minimize coastal inundation hazards and vulnerability.

ADDITIONAL INDEX WORDS: *Storm surge, coastal hazard, ADCIRC+SWAN, artificial coast, typhoon.*

INTRODUCTION

Global warming and expected sea-level rise are now constantly occurring, and the associated extreme storm surges continuously threaten low-lying areas in the Korean coast. However, because of the recent national development in industries, some remarkable portions, *e.g.*, 54% of the entire coast, has been reinforced by humans. This artificial treatment along the coast can directly affect not only the coastal hydrodynamics but also be affected by external forces in case of storm occurrences. In particular, for water fronts, levees, and harbors with upright or similar coastal structures, coastal hazards caused by storm surge inundation occur differently in natural coastal areas.

During the period of a storm onslaught to artificial coasts, inundation caused by overtopping on dikes or coastal structures appears more disastrous than storm surge inundations because several meters of wave run-up height and overtopping precede the surge inundation due to the coupling effects of atmospheric depression, strong wind stress, and tidal nonlinear interactions with wave and geophysical characteristics. Moreover, although the overtopping rate is normally small compared with the surge inundation volume, it should be carefully and reasonably considered in coastal disaster prevention purposes by considering the inner flood runoff volume during storm periods. To estimate the overtopping volume, in-situ or hydraulic experiments (Owen, 1980; Aminti and Franco, 1988; Van der Meer and Jassen, 1995) have been widely applied. However, empirical equations are basically formulated based on limited experiments or in-situ observations, which are only applicable to restricted cases for structural design.

To minimize the uncertainty or limitations arising from the empirical formulas, especially owing to the development of numerical schemes and computer hardware, different and efficient overtopping research works have been conducted using the volume of fluid, Boussinesq simulation, and so on (Hu *et al.*, 2000; Lynett *et al.*, 2010). In addition to the numerical applications, more approaches using artificial neural network theory (Van Gent *et al.*, 2007) to minimize uncertainties that arise from the empirical formula, and hybrid computation of numerical schemes that consider wave run-up, overtopping interaction with tide (Chini and Stansby, 2014; Dugor *et al.*, 2014) have been conducted. Demirbilek *et al.* (2009) proposed the coupling of local phase-resolving one-dimensional Boussinesq approximation with the global two-dimensional wave–tide coupled model to enhance computational efficiency.

In the present study, we focus our efforts to efficiently incorporate the wave overtopping mechanism to improve the objective of coastal inundation simulation in case of storm surge attack on coastal structures. The overtopping volume over typical structure types can be easily computed from the EurOtop manual (Pullen *et al.*, 2007) using the time-varying force conditions, which are extracted from the ADCIRC (ADvanced CIRCulation model) + SWAN (Simulating Waves Nearshore) model (Dietrich *et al.*, 2011) that incorporates wave and tide

DOI: 10.2112/SI75-276.1 received 15 October, 2015; accepted in revision 15 January, 2015
*Corresponding author: suh@kunsan.ac.kr
©Coastal Education and Research Foundation, Inc. 2016

interactions. Hence, this approach could be applied by introducing the run-up and overtopping rates in not only the freeboard height cases, *i.e.*, before surge inundation, but also without the freeboard case according to the existing normal wet–dry or broad weir treatment on vertical structures (Luettich *et al.*, 1992; Dawson *et al.*, 2011).

METHODS

In the simulation of the wave overtopping rates during storm surge onslaught, we implement the EurOtop module into a well-designed circulation and wave model, namely, ADCIRC+SWAN. Here, a brief description of the coupling methods and conceptual approach of overland-inundated volume routing are introduced, together with the inevitable limitations and assumptions.

EurOtop module

EurOtop (Pullen *et al.*, 2007) can analyze and predict wave overtopping for flood defense against wave action. EurOtop can evaluate the overtopping volume for vertical and sloped sea dike coastal structures, embankments, and sea walls. It can account for three principal types of sea defense structures: sloping sea dikes and embankment seawalls; armored rubble slopes and mounds; and vertical, battered, or steep walls.

The schematic diagram in Figure 1 shows the coupling of a EurOtop overtopping module using the storm surge model ADCIRC+SWAN to predict coastal inundation, including wave run-up and overtopping, on coastal structures. Among several dike types, plain slope and vertical dikes are implemented in this study because a composite slope or a berm type of dike can be considered as a slope type when sufficiently resolved numerical grids are applied by introducing wet–dry treatment. Diverse incoming ambient wave and structural armoring conditions are incorporated. Overtopping calculations are performed when the freeboard, which is defined as the distance between the sea level and crest of the dike, is greater than or equal to zero. When the sea surface exceeds the crest level, storm surge modeling is done similar to that in natural coastal area without considering the wave overtopping.

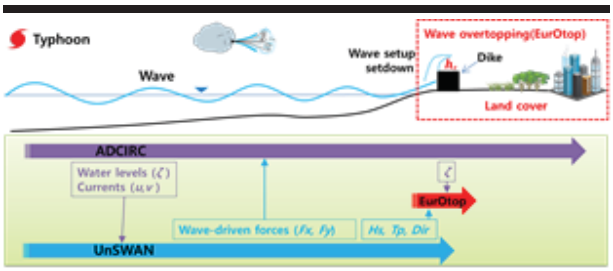

Figure 1. Schematic diagram of a wave overtopping module with a storm surge model.

The ambient sea level and incoming wave conditions are calculated and renewed in the ADCIRC+SWAN coupled storm surge model every 10 min. The information on water surface elevation (ζ), significant wave height (H_s), period (T_p), and directions (Dir) is input to the EurOtop module to calculate the run-up and overtopping. With this information, the newly proposed module continuously determines the proper structure type and overtopping equation to provide exact calculation of the time-varying wave overtopping rates for every 10 min.

Incorporating hydraulic gradient and step method

The background of coastal dikes or levees are usually paved or artificially treated. However, after the overtopping, the volume of sea water flows to the inner landward direction following hydraulic gradients. The overtopping volume is normally smaller than the surge-inundated volume. Thus, we assume that the volume of each wave attack can be summed to the next ambient wave condition, *i.e.*, the overland runoff induced by wave overtopping is computed once every 10 min of interaction interval of the wave run-up, overtopping, and surge model. Because, the volume is assumed small, we sum up the volume and the landward flow by considering friction loss due to bottom roughness in its hydraulic energy. Thus, assumption of gradually varied flow of the overtopped volume is introduced in computing the water surface to calculate the overland-inundation length and depth.

The computation procedure is composed of two parts. First, the overtopped rates considering frictional loss due to the width of the dikes is transferred landward. Then, the surface profiles that define the downstream depth are continuously computed through the standard step method. As described earlier, a gradually varied flow assumption is applied to minimize computational overburden in solving the fully non-linear shallow water flow. Thus, this spreads to the land direction, and to calculate the distance, the standard step calculation process, such as Equation (1), is applied (Chaudhry, 2007).

The computation details are described as follows: first, initial depth y_1 of the overtopped volume is calculated to meet the threshold value of 0.1 m as the assumed overland flow condition unless the volume is accumulated in the next step. In the computation, we assume 0.015 as the Manning's bottom friction coefficient when the surface is covered by concrete materials. The water surface profile and the corresponding depth are then calculated via iterative procedure such as the Newton or the trial-and-error methods until they satisfy an acceptable computational accuracy criterion of 0.001 m. After finalization, the overtopped volume is conveyed to the landward direction with frictional loss.

The energy balance equation can be represened in terms of the depths y_1 and y_2 at the points x_1 and x_2 of upstream and downstream, respectively.

$$F(y_2) = y_2 + \frac{\alpha_2 Q^2}{2gA_2^2} + \frac{1}{2}S_{f_2}(x_2 - x_1) + z_2 - z_1 - y_1 - \frac{\alpha_1 Q^2}{2gA_1^2} + \frac{1}{2}S_{f_1}(x_2 - x_1) = 0 \quad (1)$$

where S_f is the friction slope represented by $S_f = V^2 n^2 / R^{4/3}$, V is the traveling velocity, n is the friction coefficient, R is the hydraulic radius, A is the area of the channel assumed as rectangular type, α is the energy coefficient, Q is the overtopping rate, g is gravitational acceleration, and z is the bottom elevation at the corresponding location.

Storm surge model

Because of the complex geometry of the dikes, we need to represent the precise topography and bathymetry in the storm surge model. For this purpose, the ADCIRC model (Luettich *et al.*, 1992) is applied, which is considered as one of the widely used models in coastal and ocean simulation. Although it has great capability in surge inundation modeling, it still does not account for the wave run-up and overtopping on artificial coastal structures. Thus, we incorporate it as the base surge prediction model to provide precise time-varying deterministic wave overtopping inundations. In this study, the coupled ADCIRC+SWAN (Dietrich *et al.*, 2011) is applied.

The grid system used in actual application is named NWP-G116k_2014, which has 116,480 nodes and 204,926 elements with the shortest distance of 100 m near the west and south coasts of Korea. This system is based on the previous grid structure of the NWP-G116k by Suh *et al.* (2015). In the grid-construction process, we focus on retaining the nodal densities to resolve the shallow regions, especially below 10 m depth; thus, 53.9% of the total nodes are used to represent the shallow coastal areas. The bathymetry data are based on ETOPO1 (Amante and Eakins, 2009). Eight major tidal constituents (M_2, S_2, N_2, K_2, K_1, O_1, P_1, and Q_1) from FES2004 (Lyard *et al.*, 2006) are applied on the open boundary (Suh *et al.*, 2015).

RESULTS

To test the feasibility of the proposed overtopping coupling with storm surge modeling, a hypothetical case on an idealized basin is tested. The basin is composed of a semi-circle coastal area with a radius of 60 km and a land area of 10 km by 10 km, where an upright-type dike with a crest level of 4 m is set.

The bathymetry of the coastal area is set according to a linear slope with the deepest part of 25 and 5 m at the toe of the dike and the coastal line, respectively, as shown in Figure 2. As an open boundary condition for the tidal force, we set an M_2 amplitude of 2.9 m, which is a typical semi-diurnal amplitude at the Gyeonggi Bay on the west coast of Korea (Suh *et al.*, 2014). Thus, no inundation is expected because of the free elevation of at least 1 m. In this idealized basin, a hypothetical typhoon with central pressure intensity of 960 hPa with 40 $m^3 \cdot s^{-1}$ of maximum wind speed (similar to historical Typhoon Bolaven in 2012) approaches following the track from the southwest to the northeast direction and makes a landfall just north of the target land area, as shown in Figure 2.

The simulated results show that the maximum tidal elevation in front of the dike is 3.1 m, enforced by the open boundary condition of the M_2 tidal wave, *i.e.*, this event could not induce inundation. Moreover, another hypothetical typhoon approaches and passes the target area, where the significant wave height reaches 2.2 m; however, no storm surge inundation occurs. Nevertheless, even if the combined maximum surge height does not go over the crest of the dike, wave-induced overtopped volumes, computed using this newly proposed scheme, appear after 4.1 days after the simulations and display maximum value when the typhoon makes a landfall. This test case clearly shows that the performance of the wave overtopping coupling approach on upright dike condition is feasible in actual application. The maximum overtopped rates marked as 0.25 $m^3 \cdot s^{-1} \cdot m^{-1}$ and the time-varying volume are shown in Figure 2. In addition, to determine and acquire the sensitivities of the overtopping variations with respect to the structure types, model tests using different slopes (e.g., vertical, 1:1.5 and 1:2) and surface conditions armored by traditional tetrapod for a dike that provides a reduction factor of 0.38 are simulated.

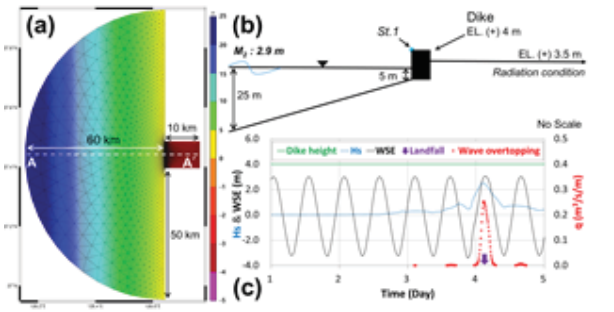

Figure 2. (a) Idealized basin with a hypothetical typhoon track. (b) Cross section (A–A′) indicating freeboard. (c) Resulting time series of the wave-induced overtopping at St. 1.

After confirming the feasibility and obtaining insight of the wave overtopping incorporated module through EurOtop into ADCIRC+SWAN on an idealized basin tests, we applied it to real inundation due to wave overtopping that occurred in a Korean coast. Using water-mark survey and historical records, we considered the water fronts in Busan area where paved roads adjacent to the coastal lines are parallel to the vertical type dikes with tetrapod armoring, and open harbor yards are well developed in the northern parts, as shown in B1, B2, and B3 in Figure 3. The detailed information on the dike structures for the A1 and A2 areas have a 1:2 slope with tetrapod, A3 is vertical, B1 and B3 have a slope of 1:1.25 and covered with tetrapod, and B2 is vertical.

These areas are exposed to open sea and were damaged by typhoon Maemi in 2003. The typhoon was recorded as one of the strongest typhoons with a super-storm intensity and is not expected to return for 100 years. It made a landfall on September 12, 2003, in the southern coast of Korea following the tracks shown in Figure 3(b). The maximum wind speed was 40 $m^3 \cdot s^{-1}$, and the central pressure of the typhoon was 950 hPa at landfall time. We used the best track data of Typhoon Maemi released by the Joint Typhoon Warning Center located in Hawaii. The wave overtopping simulation induced by storm waves were performed for 6.5 days from September 7, 2003 0000Z (UTC) to September 12, 2003 1200Z (UTC), covering the period of the typhoon onslaught in the Korean coast and land. During the Typhoon Maemi onslaught, 593,000 m^2 of coastal low-lying areas had been inundated due to wave overtopping. This information was based on the water mark and public testimony; thus, it suffers from limitation for quantitative comparison purposes. Although our simulated results showed that only 170,000 m^2 of areas were inundated, the trend of the overtopped area are coincided with the historical inundation area where comparable data are available, as shown in Figure 4. The numerical results showed that the maximum surge height due to

the typhoon was 1.5 m, and the wave-induced overtopping lasted for 5 h around typhoon landfall time.

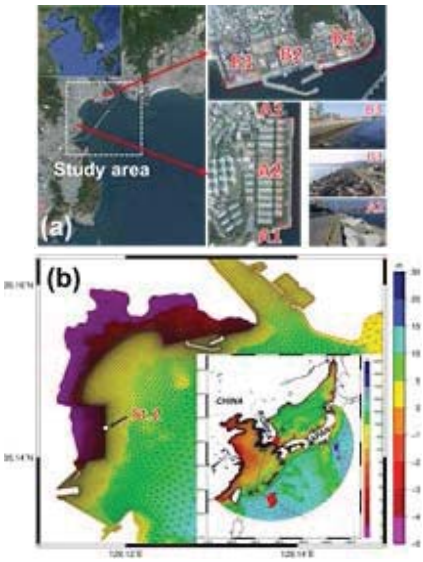

Figure 3. (a) Images of study area, Busan, Korea. (b) Grid structure with depth distribution.

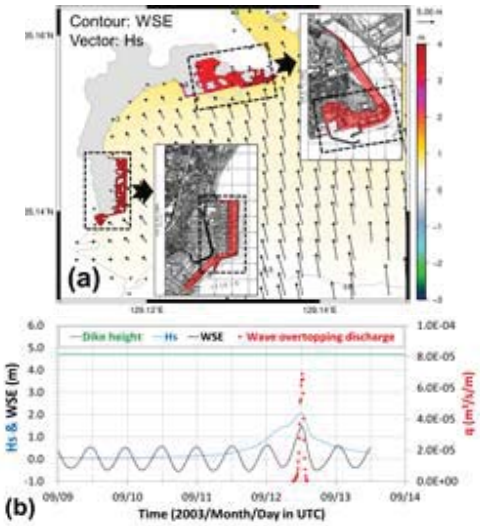

Figure 4. (a) Comparison of the simulated result with flooded water marks. (b) Resulting time series of the wave-induced overtopping at St.2 in Figure 3 (b).

Although the storm surge inundation was not seen because the crest of the dike height of 3.42–4.85 m was higher than the significant wave height of 2–3 m. This trend lasted until just after landfall time on September 12, 2003, 1200Z (UTC).

DISCUSSION

In this paper, we propose an advanced overtopping scheme by simplifying the dike type and incorporating ambient wave conditions to the EurOtop module compared with previous approaches (Chini and Stansby, 2014; Dugor *et al.*, 2014). Inundation simulations induced by wave overtopping have been studied by some researchers (Hu *et al.*, 2000; Lynett *et al.*, 2010 Van Gent *et al.*, 2007; Chini and Stansby, 2014; Dugor *et al.*, 2014) based on empirical or diverse numerical approaches. However, their results could not be directly applied in various types of dikes and in time-varying wave conditions.

Although EurOtop suffers from the limitation of validity in the parameter ranges used in their empirical curve fit (Lynett *et al.*, 2010), in the current study, we try to improve the efficiency in the numerical simulations. Moreover, we assume gradually varied flow of the overtopped volume flow for the artificially treated overland surface. As a result of incorporating the energy loss due to traveling distance, the peak flow rates could be reduced by at least 35% when the distance is longer than 10 m with respect to the minimum width of 1 m of the dike crest. However, this approach can be valid only in restricted cases of flat dike crest and the overtopped volume is not very large to solve a fully non-linear flood routing. Although some overestimation in the quantity could occur, this proposed scheme could provide reasonable and acceptable results. However, precise representation of the dike dimension and overland characteristics should be provided with a finely resolved unstructured grid to determine the realistic overtopping rates and associated inundation mechanism. In the implementation of the step method, an efficient iterative computation can minimize the computational time. At any rate, the overall computational burden only increases by 3% when 64 cores of parallel processors are used compared with that without incorporating the overtopping in the normal storm surge modeling using ADCIRC+SWAN.

One of the main difficulties in improving the performance of the proposed scheme is the lack of observation data on wave overtopping volume, inundation area, and height. Although we satisfactorily reproduced and suggested an efficient wave overtopping in the storm surge simulation, further study on incorporating diverse conditions might still be needed to calibrate, verify, and improve the applied parameters. However, under the some limitations of computing the empirical overtopping rates and assumption of overland hydraulics on the dike crest, this proposed storm surge inundation model that considers wave overtopping can be applied in coastal hazard-mitigation activities. In addition, because the extra numerical burden is within an acceptable threshold, this scheme could enhance the development of coastal disaster prevention plan and real-time forecasting of storm surge inundation even on artificially treated coast.

CONCLUSIONS

Numerical simulations of storm surge inundation have been mainly focused on the vulnerability of low-lying coastal area to define or determine the possible inundation area and depth. However, along artificially developed coastal areas, frequent inundation due to wave overtopping occurs even though the sea level does not meet the surge elevation. Such inundation is the result of wave overtopping induced by strong wave onslaught. In this paper, we have proposed an efficient modeling approach to

reproduce and simulate such wave-induced overtopping inundation before and/or during main storm surge by introducing empirical formulas of overtopping for various types of coastal dikes. For efficient coupling, we combined the EurOtop overtopping module with the coupled surge model. Not only the variety of coastal structure types, *i.e.*, vertical or slopped with or without armoring materials but also diverse time-varying ambient wave conditions of the wave height, period, and direction were considered. In addition to the overtopping volume estimation, we provided overland inundation simulation through a dike crest by introducing a gradually varied flow to maintain numerical efficiency under the assumption that the overtopped volume is not large to trace the inundated water surface.

Through numerical tests of a hypothetical case, we determined that this proposed method could efficiently and effectively reproduce wave overtopping with freeboard even if the sea level remains under the top crest level. Sensitivity tests on increased traveling distance of the overtopped volume to landward showed reasonable degradation of the energy slope of the water surface line, and hence, this scheme could provide acceptable inundation height and spreading information. The assumption of an overland gradually varied flow and the application of the standard step method should be profoundly investigated in a future research. At any rate, more intensive observation or hydraulic tests should be conducted to validate this approach because inundation induced by wave overtopping is not considered as important compared with the main storm surge inundation. However, the overburden of computation is only within 3% of the total computation using ADCIRC+SWAN. Thus, we suggest that incorporating the overtopping inundation to the storm surge model can be applied in real-time forecasting to estimate the coastal hazards on any artificial coasts by wave onslaught before or during storm passages.

ACKNOWLEDGMENTS

This research is a part of the projects entitled “A study on enhancement of element techniques in hazard information map for safe coastal activities” of the Honam Sea Grant program and “Countermeasure system against hazards of typhoons and tsunamis in harbor zones–Stage 2” funded by the Ministry of Oceans and Fisheries, Korea.

LITERATURE CITED

Amante, C. and Eakins, B.W., 2009. *ETOPO1 1 Arc-Minute Global Relief Model: Procedures, Data Sources and Analysis.* Boulder, Colorado: National Geophysical Data Center Marine Geology and Geophysics Division, *NOAA Technical Memorandum NESDIS NGDC-24*, 19p.

Aminti, P. and Franco, L., 1988. Wave overtopping on rubble mound breakwaters. *Proceedings of the 21th International Conference Coastal Engineering* (Malaga,), pp. 770-781.

Chaudhry, M.H., 2007. *Open-Channel Flow. 2nd Ed.*, New York; London: Springer, 523p.

Chini, N. and Stansby, P.K., 2014. Coupling TOMAWAC and EurOtop for uncertainty estimation on wave overtopping predictions. *Advances in Hydroinformatics*, Springer Hydrogeology, 117-127.

Dawson, C.; Kubatko E.J.; Westerink, J.J.; Trahan, C.; Mirabito, C.; Michoski, C., and Panda, N., 2011. Discontinuous Galerkin methods for modeling hurricane storm surge. *Advance in Water Resources*, 34, 1165-1176.

Demirbilek, Z.; Nwogu, O.G.; Ward, D.L., and Sanchez, A., 2009. *Wave Transformation Over Reefs: Evaluation of One-Dimensional Numerical Models*. Vicksburg, MS: U.S. Army Corps of Engineers, *Report ERDC/CHL TR-09-1*, 208p.

Dietrich, J.C.; Zijlema, M.; Westerink, J.J.; Holthuijsen, L.H.; Dawson, C.; Luettich Jr, R.A.; Jensen, R.E.; Smith, J.M.; Stelling, G.S., and Stone, G.W., 2011. Modeling hurricane waves and storm surge using integrally-coupled, scalable computations. *Coastal Engineering*, 58(1), 45-65.

Dugor, J.; Rihouey, D., and Lang, P., 2014. Flood modelling on Ile de Ré during Xynthia. *The 21st Telemac & Mascaret User Conference* (Grenoble, France), pp. 15-17.

Hu, K.; Mingham, C.G., and Causon, D.M., 2000. Numerical simulation of wave overtopping of coastal structures using the non-linear shallow water equations. *Coastal Engineering*, 41(2000), 433-465.

Luettich, R.A.; Westerink, J.J., and Scheffner, N.W., 1992. *ADCIRC: An Advanced Three-Dimensional Circulation Model for Shelves Coasts and Estuaries Report 1*, Vicksburg, MS: US Army Corps of Engineers Waterways Experiment Station, *Dredging Research Program Technical Report DRP-92-6*, 141p.

Lyard, F.; Lefevre, F.; Letellier, T., and Francis, O., 2006. Modelling the global ocean tides: Modern insights from FES2004. *Ocean Dynamics*, 56, 394-415.

Lynett, P.J.; Melby, J.A., and Kim, D.H., 2010. An application of Boussinesq modeling to hurricane wave overtopping and inundation. *Ocean Engineering*, 37(2010), 135-153.

Owen, M.W., 1980. *Design of Seawalls Allowing for Wave Overtopping*. Wallingford, UK: Hydraulics Research Station, *Report No. EX924*, 39p.

Pullen, T.; Allsop, N.W.H.; Bruce, T.; Kortenhaus, A.; Schüttrumpf, H., and Van der Meer, J.W., 2007. *EurOtop: Wave Overtopping of Sea Defences and Related Structures: Assessment Manual*. 178p.

Suh, S.W.; Lee, H.Y., and Kim, H.J., 2014. Spatio-temporal variability of tidal asymmetry due to multiple coastal constructions along the west coast of Korea. *Estuarine, Coastal and Shelf Science*, 151, 336-346.

Suh, S.W.; Lee, H.Y.; Kim, H.J., and Fleming, J.G., 2015. An efficient early warning system for typhoon storm surge based on time-varying advisories by coupled ADCIRC and SWAN. *Ocean Dynamics*, 65(5), 617-646.

Van der Meer, J.W. and Janssen, J.P.F.M., 1995. Wave run-up and wave overtopping at dikes. *In*: Kobayashi, N., and Demirbilek, Z. (eds.), *Wave Forces on Inclined and Vertical Wall Structures*. New York: ASCE, pp. 1-27.

Van Gent, M.R.A.; Van den Boogaarda, H.F.P.; Pozuetaa, B., and Medinab, J.R., 2007. Neural network modelling of wave overtopping at coastal structures. *Coastal Engineering*, 54, 586-593.

Journal of Coastal Research	SI	75	1382 - 1386	Coconut Creek, Florida	2016

The Scour Depth Prediction of the Submarine Pipeline Area on the Algorithm of the Radial Basis Function

Hojin Lee †, Sungduk Kim†*, and Kye-Won Jun††

†The School of Civil Engineering,
Chungbuk National University,
Cheongju, South Korea

††Graduate School of Disaster Prevention,
Kangwon National University,
Samcheok, South Korea

www.cerf-jcr.org

www.JCRonline.org

ABSTRACT

Lee, H.; Kim, S., and Jun, K.W., 2016. The scour depth of the submarine pipeline area on the algorithm of the Radial Basis Function. *In:* Vila-Concejo, A.; Bruce, E.; Kennedy, D.M., and McCarroll, R.J. (eds.), *Proceedings of the 14th International Coastal Symposium* (Sydney, Australia). *Journal of Coastal Research*, Special Issue, No. 75, pp. 1382-1386. Coconut Creek (Florida), ISSN 0749-0208.

The submarine pipeline is a facility that requires frequent usage for transporting substances like crude oil or gas. Failures in the submarine pipeline can cause marine pollution and the cost to restore the induced damage can be great. Therefore, it is important to consider several impact factors that can help secure the stability of the submarine pipeline during its installment. Scour is one of the factors that cause great damage to submarine pipelines. In this study, existing experimental data from previous experiments are analyzed in order to predict scour depth and deduce the main parameters affecting scour. The deduced parameters are used and analyzed by the Radial Basis Function Neural Network (RBFN) for the prediction of scour depth.

ADDITIONAL INDEX WORDS: *Submarine pipeline, marine pollution, scour, Radial Basis Function Neural Network (RBFN).*

INTRODUCTION

Submarine pipelines are frequently installed near the coastal regions for the convenient transport of crude oil and gas. For the convenience of import and export, the industrial parks located in the coastal regions are growing in scale, and as a result, the number of submarine pipeline installments is increasing as well. The submarine pipelines must be able to endure the conditions of the marine environments of installment in order for the functions to be easily conducted; thus details must be attentively considered during the installment process. Because the maintenance of the submarine pipeline is particularly difficult, the systematic review process is taken seriously during the pipeline's construction to prevent damage.

One of the main factors to consider within the design process during installment is scour. When scours localize beneath the submarine pipeline, a dynamic force is pressed onto the pipeline in the form of vibration or the pipeline undergoes self-burial as additional static and dynamic load occurs. As a result, marine pollution can occur due to pipeline failure and the cost to restore the damage would be high. In order to establish proper countermeasure steps against scour, an accurate and deeper analysis of scour is needed. There are various factors that affect scour.

In the past, the main method to predict for scour involved using the hydraulic experiment based on empirical formulas. With the development of technology, computers and numerical methods can now incorporate and run the numerical model, the statistical method, the artificial intelligence model, and the hydraulic model test altogether.

DOI: 10.2112/SI75-277.1 received 15 October, 2015; accepted in revision 15 January, 2015
*Corresponding author: soungdoug@hotmail.com
©Coastal Education and Research Foundation, Inc. 2016

In this study, an artificial neural network is applied to the methods used to predict the scour depth caused by waves within the submarine pipeline's vicinity. The results of the hydraulic model are set as input data: (D) for pipeline diameter, (T) for wave period, (H) for wave height, (d) for water depth, the Keulegan-Carpenter number, and the modified Ursell number. These values will be applied into the RBF Algorithm-based neural network model for scour depth prediction.

METHODS

In this paper, the data from Table 1 are used for the neural networks method along with the results obtained by the hydraulic model test (Oh *et al.*, 2002; Sümer and Fredsøe, 1990). The measurements of the two-dimensional wave generation tank are the following: 1 m in height, 0.8 m in width, and 25 m in length.

In Table 1, the following information are presented: D for pipe diameter, T for wave period, H for wave height, d for water depth, the Keulegan-Carpenter (KC) number, and the Modified Ursell number(U_{RF}).

The KC number and the Ursell number(U_{RF}) are defined with the following equations (1) and (2).

$$KC = \frac{U_m T}{D} \tag{1}$$

$$U_{RP} = \frac{U^3 T^2}{D^2 d^3} \tag{2}$$

In the equation listed above, U_m is the maximum water particle velocity on the bed in the absence of the pipe, and L represents wave length.

In the results of the previous hydraulic model test, the *KC* number and the Ursell number are proposed as main contributing factors to scour depth (Sümer and Fredsøe, 1990; Çevik and Yüksel, 1999).

Table 1. *Data used in Neural Network model*

no	*D(m)*	*T(m)*	*H(m)*	*d(m)*	*KC*	U_{RF}	*S/D*
1	0.09	1	0.048549	0.33	0.817392	0.775804	0.088889
2	0.08	1	0.08	0.48	0.861587	1.636296	0.092822
3	0.09	1.5	0.051977	0.33	1.889391	2.850241	0.111111
4	0.06	1	0.093535	0.33	2.362179	12.4827	0.116667
5	0.09	1	0.11071	0.33	1.863943	9.199387	0.122222
6	0.09	1	0.113556	0.33	1.911856	9.927201	0.122222
7	0.04	1	0.08	0.48	1.723174	6.545185	0.13127
8	0.06	1	0.079063	0.33	1.996701	7.538914	0.133333
9	0.06	1	0.111309	0.33	2.811048	21.03656	0.15
10	0.08	1.5	0.08	0.48	2.404883	5.618757	0.155077
11	0.09	2	0.047179	0.33	2.537269	4.162302	0.155556
12	0.09	3	0.05713	0.33	4.932188	17.73599	0.155556
13	0.09	2.5	0.034299	0.33	2.410797	2.606227	0.166667
14	0.06	1.5	0.100955	0.33	5.504588	46.98936	0.166667
15	0.04	1	0.091876	0.33	3.480411	26.61768	0.175
16	0.02	1	0.08	0.48	3.446349	26.18074	0.185643
17	0.09	2.5	0.092272	0.33	6.485514	50.74153	0.188889
18	0.09	3	0.080935	0.33	6.987349	50.42824	0.2
19	0.04	1	0.112927	0.33	4.277857	49.42623	0.2
20	0.08	1.5	0.16	0.48	4.809766	44.95005	0.219312
21	0.09	1.5	0.131352	0.33	4.77467	45.99878	0.222222
22	0.09	1.5	0.16604	0.33	6.035566	92.91166	0.222222
23	0.08	2	0.11	0.48	5.199565	29.89282	0.228026
24	0.09	2	0.143559	0.33	7.720575	117.2689	0.244444
25	0.06	1.5	0.127181	0.33	6.934557	93.94663	0.25
26	0.04	1.5	0.097293	0.33	7.957368	94.63289	0.25
27	0.09	3	0.105265	0.33	9.087794	110.9461	0.255556
28	0.02	1	0.16	0.48	6.892698	209.4459	0.262539
29	0.08	2	0.16	0.48	7.563004	91.99172	0.275009
30	0.09	2.5	0.111311	0.33	7.823707	89.07752	0.277778

The RBFN (Radial Basis Function Network) is applied in this paper to predict for scour depth. According to the studies

conducted by Broomhead and Lowe (1988), and Moody and Darken (1989), the Radial Basis Functional Network (RBFN) is a network based on the radial function making much progress within similar topics of study.

Multi-layer Perception (MLP) is a network with a high classification performance level; however, a couple of its

Table 1. *Continued*

no	*D(m)*	*T(m)*	*H(m)*	*d(m)*	*KC*	U_{RF}	*S/D*
31	0.08	3	0.11	0.48	8.182214	84.99641	0.286046
32	0.04	1	0.11143	0.33	4.221143	47.48635	0.3
33	0.06	2.5	0.06733	0.33	7.098625	44.35697	0.3
34	0.04	1.5	0.088804	0.33	7.263085	71.96099	0.3
35	0.06	3	0.061559	0.33	7.97179	49.92438	0.3
36	0.06	2	0.101033	0.33	8.150254	91.9721	0.3
37	0.04	3	0.094214	0.33	18.30082	402.6852	0.3
38	0.02	1.5	0.08	0.48	9.619532	89.9001	0.310154
39	0.08	2.5	0.16	0.48	10.12043	153.0102	0.318126
40	0.04	2.5	0.08	0.48	10.12043	76.5051	0.318126
41	0.09	2	0.106031	0.33	5.702325	47.24868	0.322222
42	0.04	2	0.11	0.48	10.39913	119.5713	0.322477
43	0.08	3	0.16	0.48	11.9014	261.5667	0.344984
44	0.04	3	0.08	0.48	11.9014	130.7834	0.344984
45	0.04	1.5	0.15588	0.33	12.74911	389.2006	0.35
46	0.06	2.5	0.163172	0.33	17.2033	631.3563	0.35
47	0.06	3	0.06502	0.33	8.420003	58.8277	0.366667
48	0.04	2.5	0.11	0.48	13.9156	198.8834	0.373036
49	0.06	1.5	0.123814	0.33	6.750985	86.6815	0.383333
50	0.06	2	0.089851	0.33	7.248242	64.69052	0.383333
51	0.02	2	0.08	0.48	15.12601	183.9834	0.388922
52	0.06	3	0.139949	0.33	18.12325	586.615	0.4
53	0.02	2	0.11	0.48	20.79826	478.2851	0.456051
54	0.04	2	0.191923	0.33	23.22352	1418.52	0.475
55	0.06	2.5	0.186227	0.33	19.63393	938.5573	0.483333
56	0.06	2	0.194256	0.33	15.67053	653.7233	0.5
57	0.04	2	0.146987	0.33	17.78608	637.2235	0.55
58	0.02	2	0.16	0.48	30.25202	1471.868	0.550018

drawbacks are found in its learning time and local minimum values. In contrast, the RBFN has a higher learning speed along with a simpler constitution. Its high level of classification performance also proves to be an excellent advantage. Similar to MLP, RBFN is constructed with an input layer, hidden layer, and an output layer; its basic structures are seen in figure 1.

The structure of this neural network is similar to prior neural networks while the internal functions are radically different. In the input of prior neural networks, only the vector's input pattern and the bias term were used. The RBFN incorporates not only these but its stochastic internal function provides the distribution, the average value, and the standard deviation of the given input. The RBFN consists of a number of algorithms and usually the algorithm is learned by two stages. In other words, algorithms are learned by the division of the hidden layer and the output layer (Hush and Horne, 1993). Figure 2 shows the study of RBFN. Table 2 shows the statistical indicators used in this paper.

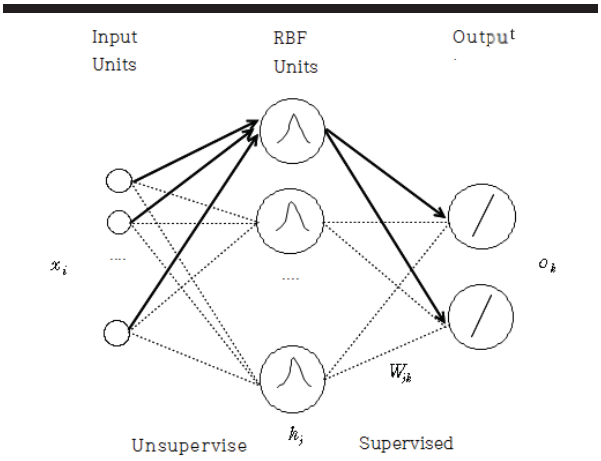

Figure 1. The traditional radial basis function network

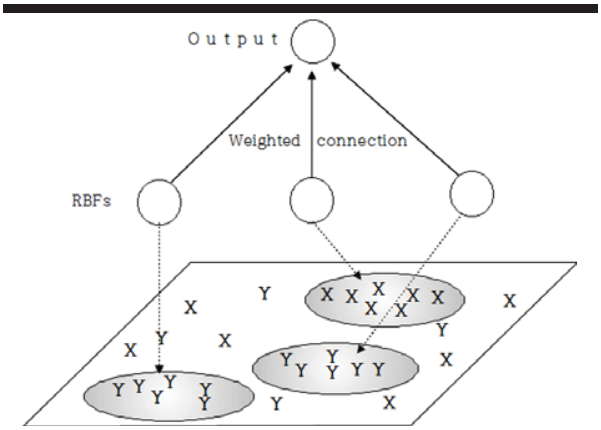

Figure 2. Leanring of the Radial Basis Functional Network (RBFN).

Table 2. *Indices for statistical test*

No	Index	Relation equation
1	CC	$\frac{1}{N}\sum_{i=1}^{N}\left(\frac{X_i - X_{in}}{\sigma_X}\right)\left(\frac{Y_i - Y_{in}}{\sigma_Y}\right)$
2	R^2	$1-\frac{\sum_{i=1}^{N}(X_i - Y_i)^2}{\sum_{i=1}^{N}(X_i - Y_{in})^2}$
3	RMSE	$\frac{1}{N}\sqrt{\sum_{i=1}^{N}(X_i - Y_i)^2}$
4	MAPE(%)	$\frac{1}{N}\sum_{i=1}^{N}\left(\frac{\lvert X_i - Y_i\rvert}{X_i}\right)$

Here, the measure value is X_i, the calculated value is Y_i, the average of the measured values is X_{in}, the average of the calculated values is Y_{in} , the standard deviation of the measured value is σ_X, the standard deviation of the calculated value is σ_Y, the number of data is N. Using the Radial Basis Function Network, the input data is constructed like the following for the calculation of the relative scour depth *S/D*.

Firstly, the foundational input values are set with the following independent factors: the pipe diameter (*D*), the wave period (*T*), the wave height (*H*), and the water depth (*d*); these values are combined to set the non-dimensional parameters for the *KC* number and the modified Ursell number, U_{RP}.

A correlation analysis was implemented on the relative scour depth based on the parameters of the input data; the high input data showed combined correlation. The parameters of the correlationships are shown in Table 3.

Table 3. *The correlation coefficient of between relative scour depth and parameter*

parameter	Correlation coefficient
D(m)	-0.48
T(m)	0.44
H(m)	0.55
d(m)	0.11
KC	0.88
U_{RP}	0.74

Table 4. *Construction of the Radial Basis Functional Network (RBFN)*

Model	Input	Spread Coefficient	Output
Case1	D, T, H, d, KC, U_{RF}		
Case2	D,T,H		
Case3	KC, U_{RF},H	2.0	S/D
Case4	KC, U_{RF}		
Case5	KC		
Case6	U_{RF}		

The KC, U_{RP}, and the H values that showed over 50% of correlation were focused to construct a combination of the input data. Table 4 shows the set and type of the input data used for RBFN application. The Matlab software was used to construct a model for RBFN learning and prediction.

RESULTS

Out of the 58 input data, 46 data have been chosen for training, whereas the remaining 12 were used for testing. Table 5 shows the results of the training and the prediction. The correlationship coefficient (CC) of RBFN's training results was over 0.9 for all the six model cases; the coefficient of determination (R2) was within the 0.81~0.94 range, the RMSE (Root Mean Square Error) was within 0.018~0.034, and the MAPE (Mean Absolute Percentage Error) turned out between 7.28~13.25%.

Analysis of the training result show that the Case 3 model constructed by the input data, KC, U_{RP}, H, exhibited the highest prediction. Based on even the existing results of the hydraulic model test, it can be inferred that the KC number and the U_{RP} number greatly impacts scour depth.

Table 5. *Predicted results of training*

Model	CC	R2	RMSE	MAPE(%)
Case1	0.94	0.89	0.02596	7.96
Case2	0.95	0.90	0.02517	8.47
Case3	0.97	0.94	0.01874	7.28
Case4	0.93	0.86	0.02939	9.32
Case5	0.92	0.85	0.03026	9.16
Case6	0.90	0.81	0.03421	13.25

Figure 3 and 4 show the training results for Case 1 and 3 respectively. Table 6 shows the application of the 12 data inputs that did not undergo training applied into the RBFN.

The results show that the CC for the Case 3 Model was is 0.94, the RMSE is 0.083, and MAPE is 8.37%, therefore showing an outstanding case of predictability. The accuracy of the prediction can be ranked by the following order, Case 3 > Case 4 > Case 6 > Case 5 > Case 2 > Case 1. Figure 5 shows the predicted results of relative scour depth when applied to RBFN.

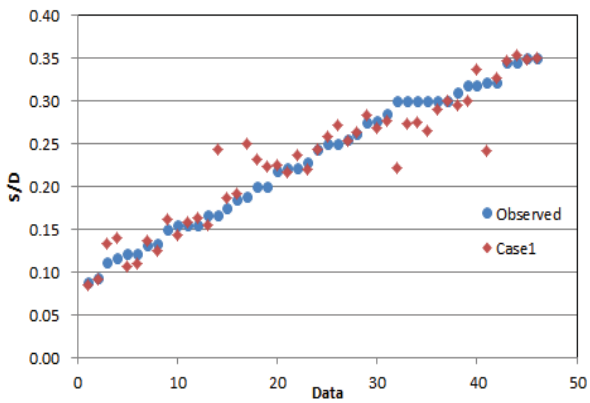

Figure 3. Training Results for Case 1 Model Using RBFN.

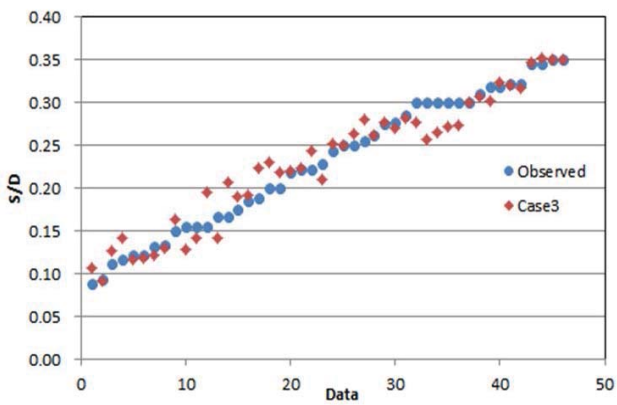

Figure 4. Training Results for Case 3 Model Using RBFN

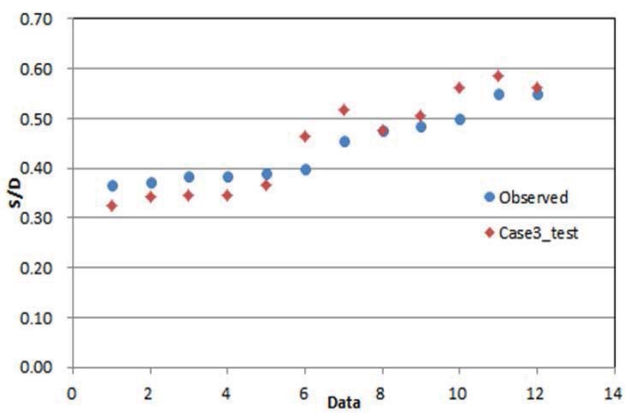

Figure 5. The predicted results of S/D

Table 6. *RBFN Testing*

Model	CC	R2	RMSE	MAPE(%)
Case1	0.72	0.51	0.09615	13.97
Case2	0.74	0.54	0.09904	14.07
Case3	0.94	0.91	0.06145	8.37
Case4	0.85	0.72	0.08640	11.34
Case5	0.78	0.61	0.08357	10.45
Case6	0.79	0.63	0.09230	10.69

DISCUSSION

The frequently used facility for transport of crude oil or gas is the submarine pipeline. The high convenience that comes with such utility has caused the numbers of installments to increase. Because the pipeline transports substances like crude oil, damages to the pipeline can lead to marine pollution. The cost to fixing the damage and restoring the pollution is high. With scour being one of the main factors that affect the submarine pipelines, it is necessary to correctly assess and predict for scour depth before installing the pipeline.

The correlationship coefficient was over 0.9 for all the six model cases and the Case 3 model constructed by the input data.

Based on even the existing results of the hydraulic model test, it can be inferred that the *KC* number and the U_{RP} number greatly impacts scour depth. The CC for the Case 3 showing an outstanding case of predictability. The accuracy of the prediction can be ranked by the following order, Case 3 > Case 4 > Case 6 > Case 5 > Case 2 > Case 1 (Figure 2 and 4).

CONCLUSIONS

In this paper, data from previous hydraulic model tests results are analyzed to deduce the parameters that affect scour formation. A correlation analysis is conducted between the deduced parameters and the relative scour depth; a set of parameters with high correlationships was constructed.

The results were inputted into the RBFN method to predict for the relative scour depth. The tendencies of the predicted results and the measured values were well simulated in the Case 3 model. In the future, it is regarded that data needs to be continuously collected for input use in order to improve the accuracy of the scour depth prediction model.

ACKNOWLEDGEMENTS

This research was supported by a grant(15RDRP-B066173-03) from Regional Development Research Program funded by Ministry of Land, Infrastructure and Transport of Korean government.

LITERATURE CITED

Broomhead, D.S. and Lowe, D., 1988. Multivariable functional interpolation and adaptive networks. *Complex Systems*, 2, 321-355.

Çevik, E. and Yüksel, Y., 1999. Scour under Submarine Pipelines in Waves in Shoaling Conditions. *Journal of Waterway, Port, Coastal, Ocean Engineering*, 125(1), 9–19.

Hush, D.R. and Horne, B.G., 1993. Progress in supervised neural networks. *IEEE Signal Processing Magazine*, 10(1), 8-39.

Moody, J. and Darken, C.J., 1989. Fast learning in networks of locally-tuned processing units. *Neural Computation*, 1(2), 291-294.

Oh, H.S.; Lee, H.J., and Kim, K.H., 2002. Local scour properties below submarine pipeline in waves. *Journal of the Korean Society of Civil Engineers*, 22(4-B), 539-549.

Sümer, B.M. and Fredsøe, J., 1990. Scour below pipelines in wave. *Journal of Waterway, Port, Coastal and Ocean Engineering*, 116(3), 308-323

.

Journal of Coastal Research	SI	75	1387 - 1391	Coconut Creek, Florida	2016

Second-mode semidiurnal internal tides on the continental slope of the southwestern East/Japan Sea

Hee-Yeol Lee[†], Jae-Hun Park[‡*], Chanhyung Jeon[‡], Seongbong Seo[†§], Dong Guk Kim[†], Young-Gyu Park[†§], Hong Sik Min[†], and Sug-Dae Kim[†]

[†]Ocean Circulation and Climate Research Center
Korea Institute of Ocean Science and Technology
Ansan, Korea

[‡]Department of Ocean Sciences
Inha University,
Incheon, Korea

[§]Department of Integrated Ocean Sciences
Korea University of Science and Technology
Daejeon, Korea

www.cerf-jcr.org

www.JCRonline.org

ABSTRACT

Lee, H.Y.; Park, J.H.; Jeon, C.; Seo, S.; Kim D.G.; Park, Y.G.; Min H.S., and Kim, S.D., 2016. Second-mode semidiurnal internal tides on the continental slope of the southwestern East/Japan Sea. *In:* Vila-Concejo, A.; Bruce, E.; Kennedy, D.M., and McCarroll, R.J. (eds.), *Proceedings of the 14th International Coastal Symposium* (Sydney, Australia). *Journal of Coastal Research*, Special Issue, No. 75, pp. 1387 - 1391. Coconut Creek (Florida), ISSN 0749-0208.

Energetic second-mode semidiurnal internal tides with a three-layer-like structure were observed from time series of 26-hour-long 2 hourly velocity profiles collected on the continental shelf-slope of the southwestern East/Japan Sea during a spring tidal period in early November 2013. Modal-fitted baroclinic semidiurnal signals using a least-squared method demonstrate that the kinetic energy of second-mode semidiurnal internal tides is comparable to the first-mode ones. In order to understand physical processes affecting the enhanced generation of the second-mode internal tides and their spatio-temporal variations, we utilize 30-month long numerical simulation outputs from a real-time ocean forecasting system of the East/Japan Sea. The model includes realistic oceanic circulation and stratification together with tides of 16 major components. The analysis results reveal that the most energetic second-mode semidiurnal internal tides generate during fall months when the main thermocline was located near the mid-depth (100–150 m) over the continental shelf-slope. It appears that the deepened mixed layer together with the enhanced mid-depth stratification induced by the increased flow through the western channel of the Korea Strait provide a second-mode favorable stratification condition near the internal tide generation region. This study has an implication that the seasonally-varying second-mode semidiurnal internal tides would have an impact on the tide-induced ocean mixing in the southwestern East/Japan Sea.

ADDITIONAL INDEX WORDS: *Second-mode semidiurnal internal tide, stratification, seasonal variation*

INTRODUCTION

The East/Japan Sea is a mid-latitude marginal sea connected to the North Pacific Ocean through the Korea, Tsugaru, and Soya Straits. The Korea Strait with a mean water depth of about 150 m is the widest among the three straits, and has an abruptly-changing topography in its northern part (Figure 1). It is divided into the western and eastern channels by the Tsushima Island. Tsushima Warm Current (TWC) through the western and eastern channels flows along the Korean and Japanese coast, respectively. Cold waters (1−3°C) beneath the TWC flow southward along the Korean coast and reach to the continental shelf-slope of the southwestern East/Japan Sea (Kim and Chung, 1984).

Internal tides are internal waves that are ubiquitous in the stratified seas and generate through the interaction between barotropic tides and bottom topography changes. Around northern part of the Korea Strait, the barotropic M_2 tidal currents are strong toward the direction across the continental shelf and slope, and hence energetic semi-diurnal internal tides generate there and propagate into the open basin (Jeon *et al*., 2014; Park and Watts, 2006).

Internal tides are classified by their vertical structures such as first-, second-, or higher-modes. For instance, second-mode internal tidal currents exhibit a three-layer-like vertical structure with an in-phase relationship between the upper and lower layers and an out-of-phase relationship between the upper and middle layers. Among the internal wave types, first-mode internal tides are extensively observed and investigated, while second- or higher-mode internal tides, which received less attention, have been documented by few observational studies (*e.g.*, Park *et al*., 2006; Yang *et al*., 2009).

Field experiments on the continental shelf and slope in the southwestern East/Japan Sea were designed to investigate semidiurnal internal tide generation once a year during 2012−2014. During a spring tidal period in early November 2013, 26-hour-long 2-hourly time series of velocity profiles, spanning from the surface to ~260 m about 10 m above the bottom, exhibited the semidiurnal variation with a typical feature of the second-mode semidiurnal internal tides. This is the

DOI: 10.2112/SI75-278.1 received 15 October, 2015; accepted in revision 15 January, 2015
*Corresponding author: jaehunpark@inha.ac.kr
©Coastal Education and Research Foundation, Inc. 2016

first observational evidence showing existence of energetic second-mode interal tides in this region. In this study, we examine what background conditions around the observation site can cause the energetic generation of second-mode semidiurnal internal tides. By analyzing data-assimilated numerical simulation outputs, we demonstrate that the seasonally-varying background stratification and the volume transport through the western channel of the Korea Strait play key roles in the seasonal modulation of second-mode semidiurnal internal tide generation around the study area.

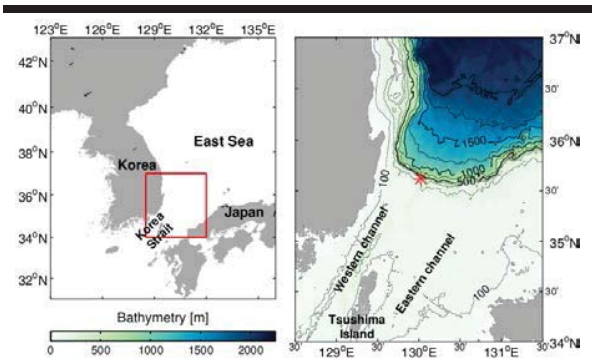

Figure 1. Observation site (red asterisk). Bottom topography from STRM30_plus (http://topex.ucsd.edu/WWW_html/srtm30_plus .html) is color contoured every 50 m with 100-m interval contours.

METHODS

Time-series of conductivity-temperature-depth (CTD) casts at 35° 37.21′N, 130° 01.41′E (water depth: ~260 m, red asterisk in Figure 1) were collected once a year from 2012 to 2014 using Sea-Bird 911 plus, 24-Hz sounder. This site is very close to the semidiurnal internal tide generation region in the southwestern East/Japan Sea (Jeon *et al*. 2014). Simultaneous measurements of horizontal current were conducted using a 300-kHz RDI Lowered ADCP (LADCP) attached to the CTD rosetted sampler. Three sets of CTD and LADCP casts were collected during two spring tidal periods, September 2012 and November 2013, and a neap tidal period, May 2014. Additionally, time series of shipboard ADCP (SADCP) were collected during the 2013 cruise (Table 1).

Table 1. *Observation periods, time intervals and conducted instruments.*

Observation periods and time interval	Instruments
`12. 09. 1-2. 04:00–05:00 / 1 hour	CTD, LADCP
`13. 11. 2-3. 02:30–04:30 / 2 hours	CTD, LADCP, SADCP
`14. 05. 9-10. 04:00–03:00 / 2 hours	CTD, LADCP

Since our intermittent observations are not enough to understand what can cause the energetic generation of second-mode semidiurnal internal tides, we utilize numerical simulation results from RIAMOM developed by the Research Institute for Applied Mechanics of Kyushu University, Japan (Jeon *et al*, 2014). RIAMOM was chosen because it includes realistic oceanic circulation and stratification together with tides of 16 major components. It was forced by hourly atmospheric forcing from the Japan Meteorogical Agency Meso-Scale model. Using the RIAMOM outputs, Jeon *et al*. (2014) demonstrate that seasonal variation of stratification can significantly modulate the generation and propagation of semidiurnal internal tides in the East/Japan Sea. In this study, we utilize hourly model outputs of a 30-month period from January 2012 to June 2014, which includes our three observation periods.

The observed time series of temperature profiles agree well with those from simulations during the three observation periods (Figure 2). Especially, RIAMOM realistically reproduces semidiurnal fluctuation of the thermocline caused by semidiurnal internal tides around the observation site. Time series of northward velocity profiles from simulations also agree well with those from observations during the two spring tidal periods (Figure 3), while they show somewhat different features from velocity observations during the neap tidal period. Nevertheless, overall performance of RIAMOM in reproducing the internal tides around the observation site is good enough to investigate their energy distribution changes in both spatial and temporal aspects.

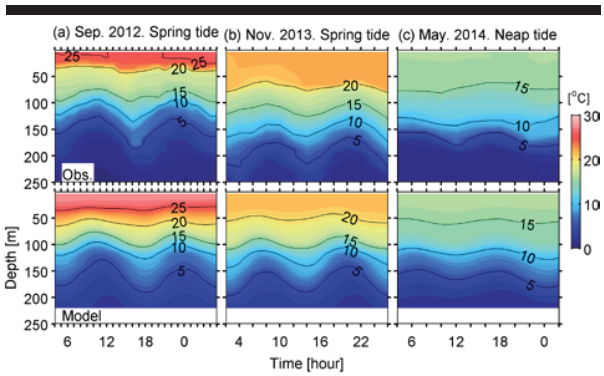

Figure 2. (Upper panels) Time series of temperature profiles (°C) from observations, and (Lower panels) simulations. Columns are for (a) 1–2 September 2012, (b) 2–3 November 2013, and (c) 9–10 May 2014.

Time series of temperature profiles obtained in early September 2012 and November 2013 show internal waves having an energetic semidiurnal periodicity in the thermocline (Figure 2). Temperature profiles observed in 2013 exhibit well-developed mixed layer of about 60 m, ticker than that observed in 2012. They show inapparent seasonal thermocline when compared with those in early September 2012. Time series of CTD-measured profiles obtain in May 2014 show that semidiurnal internal tides become significantly weak during the neap tidal period.

Time series of LADCP-measured velocity profiles in early September 2012 indicate the dominance of semidiurnal currents occurring in full depth (Figure 3). These results imply that the observation site is occupied by relatively strong barotropic tidal currents during this spring tidal periods. Time series of LADCP velocity profiles in May 2014 confirm the weakness of semidiurnal currents at the observation site. A complicated mixture of higher baroclinic modes and weak barotropic velocity are found during this neap tidal period.

Figure 4 shows time series of velocity profiles from LADCP and SADCP measurements in early November 2013. Overall they exhibit similar features with dominant semidiurnal fluctuations. Both velocity time series show alternating opposite currents occurring across the bottom of the mixed layer and the layer < 5°C (see Figure 2b). This three-layer-like velocity structure corresponds to the typical characteristics of second-mode internal tides.

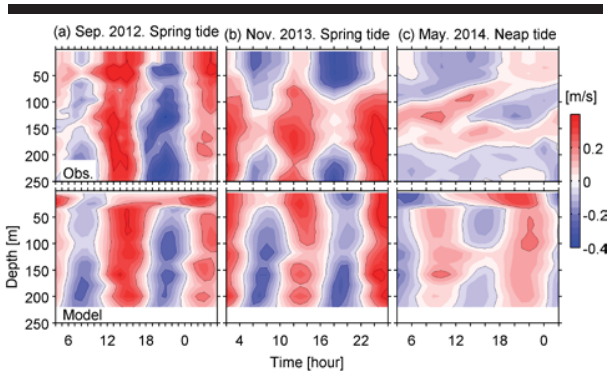

Figure 3. (Upper panels) Time series of northward velocity profiles from observations, and (Lower panels) simulations. Columns are for (a) 1–2 September 2012, (b) 2–3 November 2013, and (c) 9–10 May 2014.

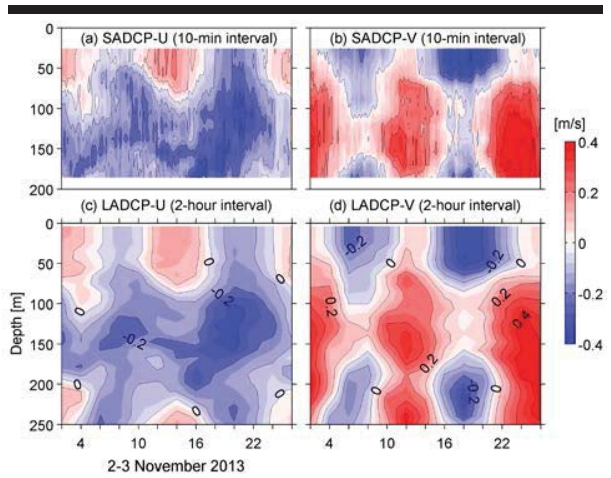

Figure 4. Time series of (a) eastward, and (b) northward velocity measured from SADCP in 10-min interval. The bottom two rows of panels show the 2-hourly time series of (c) eastward, and (d) northward velocity measured from LADCP.

We investigate the temporal changes of the first- and second-mode semidiurnal internal tide energies from the observations and RIAMOM outputs near the observation site. To estimate the potential energy of internal tides, temperature fluctuations are converted into vertical displacements (ζ). Barotropic currents are obtained by depth average of currents and baroclinic currents are the residuals from the estimated barotropic currents. Then, complex amplitude of the M_2 harmonics were estimated using harmonic analysis for ζ and baroclinic currents.

To calculate a modal decomposition of vertical modes, we first solve a linear internal wave propagation equation (Munk, 1997),

$$\frac{d^2\zeta}{dz^2} + \left(\frac{\omega}{C}\right)^2 \left[\frac{N^2(z)-\omega^2}{\omega^2-f^2}\right]\zeta = 0. \quad (1)$$

Here, C is the horizontal propagation phase speed of internal waves, ω is the wave frequency, N is the buoyancy frequency, and z is the vertical coordinate. Then, the calculated modal functions are least squares fitted to each M2 harmonics. Finally, these values are used to calculate the depth-integrated potential and kinetic energy by

$$Ep_n = \frac{1}{4}\int_{-H}^{0} \rho_0 (N^2|\zeta_n|^2)\, dz, \text{ and} \quad (2)$$

$$Ek_n = \frac{1}{4}\int_{-H}^{0} \rho_0 (|u_n|^2 + |v_n|^2)\, dz, \quad (3)$$

where H is the water depth, ρ_0 is the mean density, u and v are zonal and meridional components of velocity, and n is the mode number (Merrifield and Holloway, 2002). Here, we calculated the first 5 modal potential and kinetic energies from both observations and RIAMOM outputs.

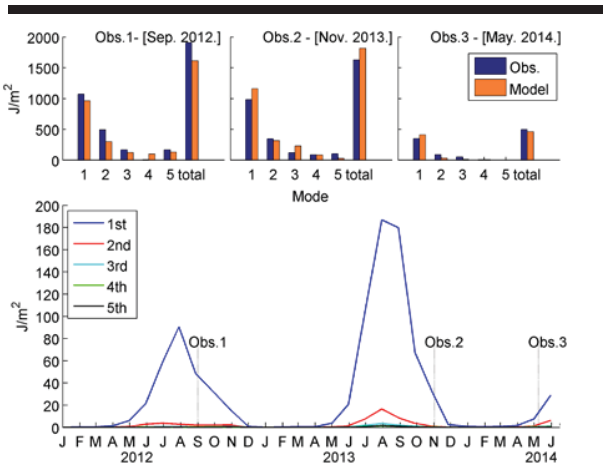

Figure 5. (Upper panels) The first 5 modal potential energies of semidiurnal internal tides calculated from observations (blue bars) and RIAMOM outputs (orange bars). (Lower panel) Time series of monthly-mean modal potential energy calculated from RIAMOM outputs during 30 months. Our observation times are indicated by vertical dotted lines.

RESULTS

The top three panels in Figure 5 show the first 5 modal potential energies during our observation periods. The blue and orange bars indicate potential energy of observation and model for each mode, respectively. The potential energy in measurements reveals dominant first-mode energy at all observation times. The potential energies from model outputs agree well with those from observations with dominant first-mode energy.

The bottom panel in Figure 5 shows time series of monthly-mean modal potential energy during the 30-month period of RIAMOM. The first-mode potential energy shows a significant seasonal variation with the highest values in summer and the lowest in winter, consistent with Jeon *et al*. (2014). Time series of second-mode potential energy also reveal seasonal variation, but relatively weaker than those of the first mode.

The kinetic energy of the first 5 modes calculated using model outputs during the three measurement periods agree well with those of observations (Figure 6). The first-mode energy is the largest in September 2012, while the second-mode energy is relatively stronger than other mode energies in November 2013 and May 2014.

The monthly-mean first-mode kinetic energy for the 30-month period reveals the seasonal variation with a peak in summer and a minimum in winter (blue line in Figure 6). The second-mode kinetic energy (red line) also shows a seasonally-varying feature with a gradual increase from March to November except in August 2013 and a rapid drop in early winter. In August 2013, due to the increase of cold water inflow near the bottom (not shown), the stratification is changed to reduce the second-mode energy. These results support that second-mode kinetic energy is relatively dominant during spring and fall months, which includes our second and third observation periods.

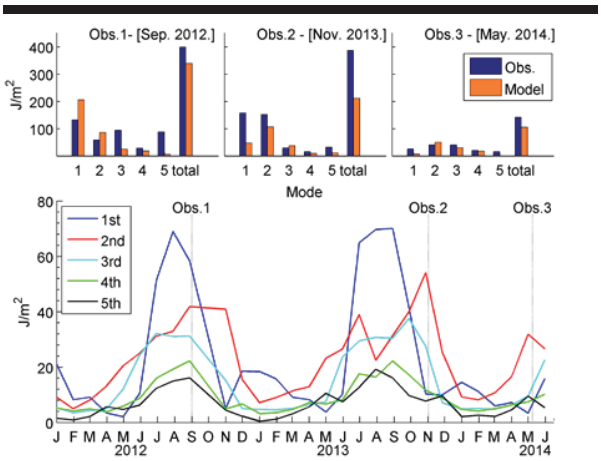

Figure 6. (Upper panels) Modal kinetic energy of semidiurnal internal tides calculated from observations (blue bars) and model outputs (orange bars). (Lower panel) Time series of monthly-mean modal kinetic energy calculated from model outputs during 30 months. Our observation times are indicated by vertical dotted lines.

DISCUSSION

Jeon *et al*. (2014) suggest that seasonal stratification exerts a dominant influence on the semidiurnal internal tides in the East/Japan Sea. Li and Farmer (2011) show that the background current can modulate the generation of internal tides in the South China Sea. For more insight into the pattern of second-mode kinetic energy, we investigate background conditions such as the seasonal stratification variation and the western channel of Korea Strait transport which may influence on the modal energy changes of semidiurnal internal tides in the southwestern East/Japan Sea.

The top panel in Figure 7 shows time series of monthly-mean density profiles near the observation site during the 30-month of RIAMOM run. Relatively light waters (σ_θ< 25 kg m^{-3}) appear in the upper layer from June to November. Outcrops of σ_θ = ~26 kg m^{-3} waters are formed in every February. The permanent pycnocline of σ_θ= 26−27 kg m^{-3} appears between 100 and 200 m.

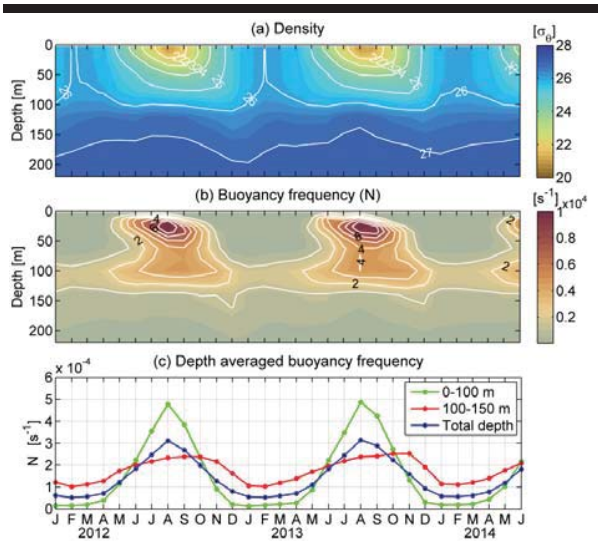

Figure 7. Time series of monthly-mean (a) density and (b) buoyancy frequency profiles, and (c) depth-averaged buoyancy frequency at 0−100 m (green), 100−150 m (red), and total depth (blue).

The monthly-mean buoyancy frequency profiles near the observation site clearly show the seasonal variation in the upper layer (Figure 7(b)). The buoyancy frequency of the middle layer (100−150 m) shows weaker seasonality than that of the upper layer. During winter, the buoyancy frequency of the middle layer becomes stronger than that of the upper layer.

The layer-averaged buoyancy frequencies of the middle layer (red line) exhibit changes correlated with the second-mode kinetic energy shown in the bottom panel of Figure 6: the magnitudes of buoyancy frequency of the middle layer gradually increase from spring to fall and have maximum values in fall. Correlation coefficient between second-mode energy and buoyancy frequency of the middle layer is 0.92. This result suggests that the enhanced second-mode kinetic energy around our observation site should be significantly affected by the seasonality of stratification there.

Yang *et al*. (2009) suggest that a density structure with a main pycnocline near the middle depth could be favorable for the development of second-mode internal tides. Figure 8 plots the buoyancy frequency profiles for odd months during 2012−2013. The middle layer with gradually-enhanced stratification (increased buoyancy frequency) from spring to fall in our observation site divides into two uniform density layers above and below the thermocline.

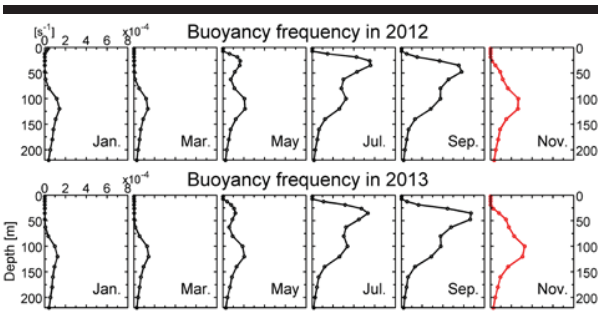

Figure 8. The buoyancy frequency profiles from RIAMOM outputs for odd months during 2012−2013.

Time series of the volume transport in the western channel of the Korea Strait (blue line) estimated from the RIAMOM reveal a seasonal variation correlated with those of the second-mode kinetic energy (red line) of the semidiurnal internal tides during the 30 months (Figure 9). Like the second-mode kinetic energy, the transport through the western channel increase from spring to fall and decreases in the winter months. Their similar trend results in a correlation coefficient of 0.90 between them. In fall, the volume transport through the western channel of the Korea Strait increases and the mixed layer deepens. These processes can produce the enhanced stratification structure in the middle layer (100−150 m) as shown in Figures 7 and 8, which provide the second-mode favorable three-layer-like stratification around the northern part of the Korea Strait.

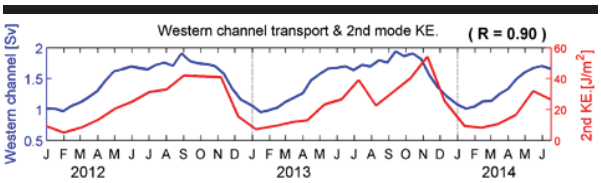

Figure 9. Time series of monthly-averaged volume transport of the TWC into the East/Japan Sea through the western channel of the Korea Strait (blue) and the second-mode kinetic energy of the semidiurnal internal tides (red, see Figure 6).

CONCLUSION

In this study, we reported an existence of energetic second-mode semidiurnal internal tides from observations on the continental slope of the southwestern East/Japan Sea in early November 2013. We used 30-month long data-assimilated model outputs to understand what can impact on the generation of this enhanced second-mode internal tide energy. Our analyses showed that the deepened mixed layer together with the enhanced mid-depth stratification related with the increased through flow in the western channel of the Korea Strait created a second-mode favorable three-layer-like vertical structure around the observation site during the fall months.

The dominant first-mode potential energies appear on both observations and simulations during our observation periods. Monthly-mean potential energies of the first mode calculated from model outputs are dominant during the summer months and weakest during winter months. Monthly-mean kinetic energies are complicated. The first-mode kinetic energy is similar to the first-mode potential energy pattern. The kinetic energy of the second-mode gradually increases from spring to fall and even has larger values than the first mode some times in spring and autumn. The second or higher-mode internal waves tend to dissipate their energy locally, which would be able to enhance the local ocean mixing (*e.g.*, Alford, 2003). Thus, this study has an implication that the seasonally-varying second-mode semidiurnal internal tides would have an impact on the tide-induced ocean mixing in the southwestern East/Japan Sea.

ACKNOWLEDGMENTS

This work was supported by a KIOST in-house grant (PE99293) and by projects titled “Development of satellite based ocean carbon flux model for seas around Korea” and “Development of Technology for CO2 Marine Geological Storage” funded by Ministry of Ocean and Fisheries, Republic of Korea. RIAMOM runs were supported by the Supercomputing of the Research institute for Applied Mechanics of Kyushu University. This work was supported by INHA UNIVERSITY Research Grant (INHA-52561).

LITERATURE CITED

Alford, M.H., 2003. Redistribution of energy available for ocean mixing by long-range propagation of internal waves. *Nature*, 423(6939), 159-162.

Jeon, C.; Park, J.H.; Varlamov, S.M.; Yoon, J.H.; Kim, Y.H.; Seo, S.; Park, Y.G.; Min, H.S.; Lee, J.H., and Kim, C.H., 2014. Seasonal variation of semidiurnal internal tides in the East/Japan Sea. *Journal of Geophysical Research: Oceans*, 119(5), 2843-2859.

Kim, K. and Chung, J.Y., 1984. One the salinity-minimum and dissolved oxygen maximum layer in the East Sea. *Elsevier oceanography series*, 39, 55-65.

Li, Q., and Farmer, D.M., 2011. The Generation and Evolution of Nonlinear Internal Waves in the Deep Basin of the South China Sea. *Journal of Physical Oceanography*, 41(7), 1345-1363.

Merrifield, M.A., and Holloway, P.E., 2002. Model estimates of M2 internal tide energetics at the Hawaiian Ridge. *Journal of Geophysical Research: Oceans*, 107(C8), 5-1-5-12.

Munk, W., 1997. Once again: once again-tidal friction. *Progress in Oceanography*, 40(1), 7-35.

Park, J.H.; Andres, M.; Martin, P.J.; Wimbush, M., and Watts, D.R., 2006. Second-mode internal tides in the East China Sea deduced from historical hydrocasts and a model. *Geophysical research letters*, 33(5), L05602.

Park, J.H. and Watts, D.R., 2006. Internal Tides in the Southwestern Japan/East Sea. *Journal of Physical Oceanography*, 36(1), 22-34.

Yang, Y.J.; Fang, Y.C.; Chang, M.H.; Ramp, S.R.; Kao, C.C., and Tang, T.Y., 2009. Observations of second baroclinic mode internal solitary waves on the continental slope of the northern South China Sea. *Journal of Geophysical Research: Oceans*, 114(C10), C10003.

Journal of Coastal Research	SI	75	1392 - 1396	Coconut Creek, Florida	2016

Wave-induced current simulated by wave–current coupled model in Haeundae

Hak Soo Lim[†*], Insik Chun[‡], Jae-Seol Shim[†], and Chang S. Kim[†]

[†]Operational Oceanography Research Center
Korea Institute of Ocean Science and Technology
Ansan 15627, Korea

[‡]Department of Civil Engineering
Kokuk University
Seoul 426-744, Korea

www.cerf-jcr.org

www.JCRonline.org

ABSTRACT

Lim, H.S.; Chun, I.; Shim, J.S., and Kim, C.S., 2016. Wave-induced current simulated by wave–current coupled model in Haeundae. *In:* Vila-Concejo, A.; Bruce, E.; Kennedy, D.M., and McCarroll, R.J. (eds.), *Proceedings of the 14th International Coastal Symposium* (Sydney, Australia). *Journal of Coastal Research*, Special Issue, No. 75, pp. 1392 - 1396. Coconut Creek (Florida), ISSN 0749-0208.

The wave-induced current in Haeundae, at the southeastern end of the Korean Peninsula, is one of the main causes of beach erosion. The Korean government recently initiated a beach restoration project for Haeundae beach to protect the famous beach against wave-induced currents generated by waves during summer and winter. To mitigate beach erosion, two submerged breakwaters and a sand nourishment program were initiated in 2013. With the support of the Korean government, we have also started an R&D project to develop coastal erosion control technology in order to understand the processes of beach erosion by measuring sediment transport and hydrodynamics in Haeundae coastal waters, including the development of a numerical simulation method. The aim of this study is to understand the main processes of wave-induced currents that cause erosion at Haeundae beach by considering wave and tide interactions, using a wave–current coupled model compared with long-term observed wave and current data. We found that the cross-shore current during summer is mainly caused by the eddies produced by wave-induced currents generated by strong high waves during a Typhoon approaching from the SSW and S directions. During other seasons, a longshore current is produced by swell waves coming from the E and ESE directions. In comparisons with the measured data, we also found that the wave-induced current is well simulated by a wave–tide coupled model in Haeundae with a coastal environment of wave and tide interaction.

ADDITIONAL INDEX WORDS: *Wave-induced current, wave-tide interaction, coastal processes, beach erosion.*

INTRODUCTION

Haeundae, located at the southeastern end of the Korean Peninsula, has a 1.6 km long coastline with a 60 m wide famous sand beach facing Tsushima Island and the Korea Strait. Haeundae has shallow water (<30 m), small tidal range (<1.2 m), and weak tidal currents (<1 m/s), waves (H_s < 4 m), and winds (<15 m/s) which vary seasonally. The end of the pocket-like beach is surrounded by Dongbaek Island at the western end of the coast, and Dalmaji hill, at the eastern end. The Chuncheon stream, once located in the middle of the beach, supplied fresh water and suspended sediment transport through the 1940s until it lost functionality due to coastal area development.

The beach is currently being eroded mainly by the recent ongoing coastal development, such as the construction of Mipo Port at the eastern end of the beach near Dalmaji hill, and revetments near the beach, as well as the disruption of river sediment inflow into the beach. Additionally, the beach has retreated due to high waves developed by nearby Typhoons during summer and fall, and the swell waves propagated by strong winds from the northwest and northeast during winter (Lim *et al.*, 2014). The Korean government recently started a restoration project in 2013 to mitigate beach erosion via a massive beach nourishment program and two submerged breakwaters at both ends of the beach to prevent offshore flow of sediment. To support the restoration project, in July 2013, we initiated a long-term observation and numerical simulation as part of the government R&D project to develop a coastal erosion control system.

The wave-induced current prediction software package HAECOM (Kim *et al.*, 2010) was developed recently with the goal of preventing people from being swept away by rip currents in Haeundae in the summer. The GUI-based forecasting system predicts rip currents generated by wave-induced currents simulated by one-way coupled hydrodynamic and wave models. To predict sediment transport in Haeundae coastal waters by high waves in summer and winter, the numerical simulation system CST3D (Kim *et al.*, 2013) was adopted to reproduce the bathymetric change during the period of beach erosion in 2007. The wave-induced current was simulated by the EFDC hydrodynamic one-way model, linked to the SWAN wave model for wave information, to calculate the radiation stress in the momentum equation of the flow model.

Recently, Lim *et al.* (2014) analyzed the variability of waves and currents in Haeundae using the long-term wave and current measurements observed by Acoustic Wave and Current meters (AWACs) near the beach, together with a wave–tide coupled nearshore current simulation using the ROMS-SWAN modeling system.

DOI: 10.2112/SI75-279.1 received 15 October, 2015; accepted in revision 15 January, 2015
*Corresponding author: hslim@kiost.ac.kr
©Coastal Education and Research Foundation, Inc. 2016

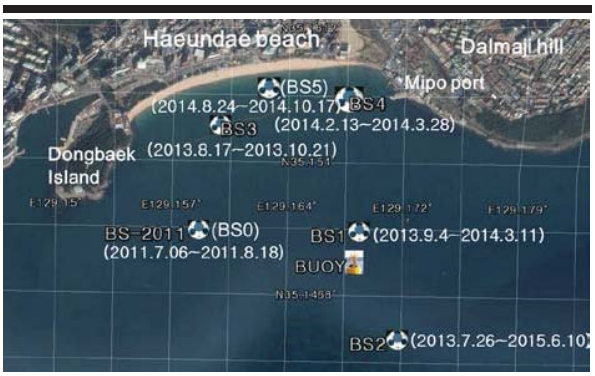

Figure 1. Location of study area. Observation stations and periods of AWAC wave and current measurements in Haeundae coastal waters at the southeastern end of the Korean Peninsula.

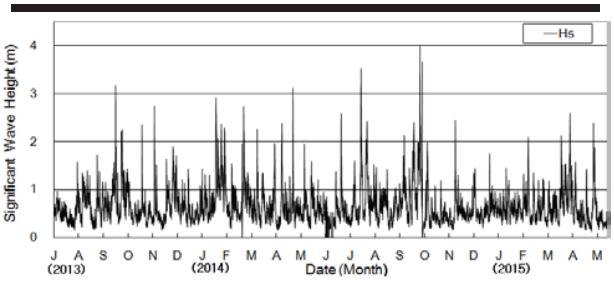

(a) Significant wave height (m) at BS2

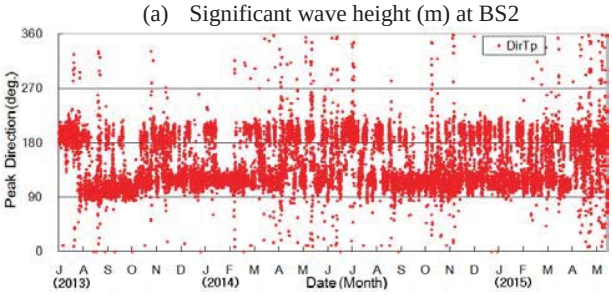

(b) Peak wave direction (°) at BS2

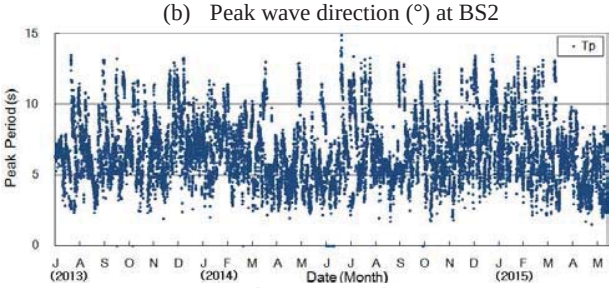

(c) Peak wave period (s) at BS2

Figure 2. Time series of (a) significant wave height, (b) peak wave direction, and (c) peak wave period at station BS2 from long-term observation by an AWAC from July 25, 2013 to June 10, 2015.

METHODS

In order to understand the coastal water processes, wave and current data were measured and analyzed to calibrate the wave and current coupled modeling system and validate the model results. Long-term field observations were designed and conducted in Haeundae coastal waters (Figure 1) as part of the measurements for the development of a coastal erosion control system. At station BS2, which was deployed at the mean water depth of 22 m, wave and currents have been observed by an AWAC since July 25, 2013. Figure 2 shows the significant wave height, peak wave direction, and peak wave period estimated from observed data from July 26, 2013 to June 10, 2014. At station BS3, which was deployed at the western part of Haeundae, with a mean water depth of 8 m, an AWAC measured the waves and currents from August 17 to October 21, 2013. At stations BS4 and BS5, with mean water depths of 6 m and 4 m, respectively, the waves and currents were also measured in winter and summer of 2014.

We estimated the residual currents from the current data observed nearshore of Haeundae beach for comparison with simulated wave-induced currents. The IOS Tidal Package, T_TIDE (Pawlowicz *et al.*, 2002) was used to estimate the residual current, eliminating the predicted tidal current from the observed raw current. Figure 3 shows the time series of the bottom residual current and regression curve for the residual current based on the bottom current measured at stations BS3, BS4, and BS5.

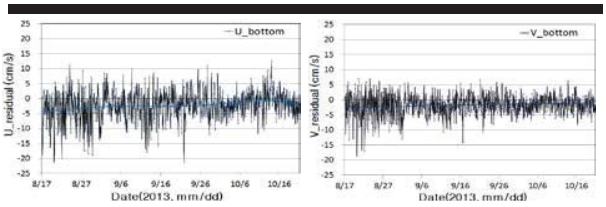

(a) U, V at BS3

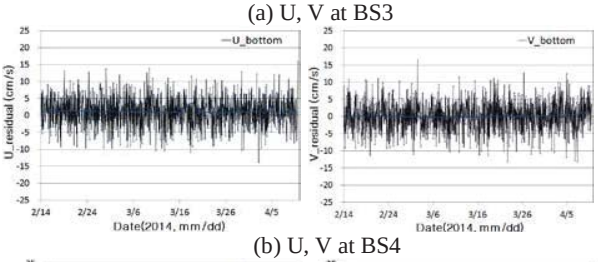

(b) U, V at BS4

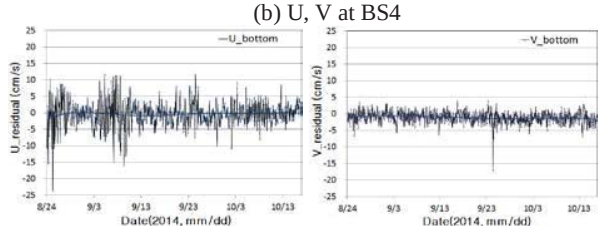

(c) U, V at BS5

Figure 3. Time series of bottom residual current at (a) BS3, (b) BS4, and (c) BS5 observed nearshore of the beach, derived from measured current data, eliminating predicted tidal current estimated by T_TIDE.

Wave and current coupled modeling

A numerical simulation using a wave and current coupled model, ROMS-SWAN (Warner *et al.*, 2008), was conducted to determine the wave-induced current in Haeundae with a typical condition of swell waves (H_s: 2.5 m, T_p: 12 s) coming from SSW in summer, and ESE in winter. The two-way coupled model has been used for a variety of applications in Korean coastal waters, especially by the Korea Operational Oceanographic System (KOOS) to provide predicted data on a 72-hour basis to the public for the prevention of coastal disasters and safe navigation in harbors and ports (Lim *et al.*, 2013a).

The down-scaled Haeundae hydrodynamic model ROMS (Haidvogel *et al.*, 2008; Lim *et al.*, 2013b) uses a high-resolution grid (288 × 144) with a cell size of 15 m horizontally and 5 layers vertically covering 129.15–129.19°E and 35.14–35.16°N. Figure 4 shows the computational model domain and bathymetry in Haeundae. In the middle of the Haeundae coastal waters near the beach, two parallel shoals are located orthogonally to the coastline. For the open tidal boundary, we used 10 major tidal constituents, including semi-diurnal tidal constituents (K_1, O_1, P_1, and Q_1) and diurnal tidal constituents (M_2, S_2, N_2, and K_2) derived from a global model of ocean tides, TPXO7 (Egbert *et al.*, 2002). The detailed model configuration was described by Lim *et al.* (2014). The phase-averaged spectral wave model SWAN (Booij *et al.*, 1999) two-way coupled with ROMS at the interval of 4 min also used the same model domain and bathymetry for the wave and current interaction. Figure 5 shows the simulated significant wave height and the direction of the swell waves coming from SSW in summer and ESE in winter estimated by long-term observed wave data at station BS2. Most of the waves coming from SSW reach the middle of Haeundae beach, especially behind the shoals, because of the wave breaking and shoaling effect. However, the waves coming from ESE are significantly decreased near the shallow waters because of wave breaking and refraction.

In this paper, we simulated a wave-induced current to investigate the coastal processes and beach erosion by swell waves. We compared the results of a wave and tide coupled simulation with the results of a wave only simulation to examine the effect of wave–current interaction, and validated the results using the estimated residual currents observed by AWACs.

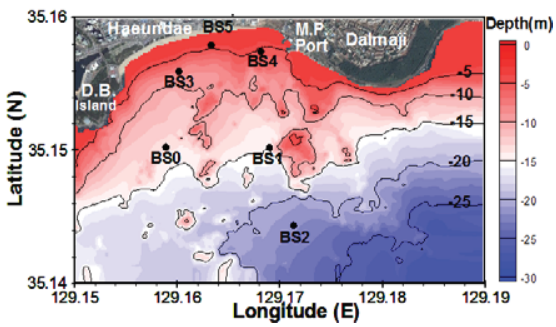

Figure 4. Computational domain and bathymetry of Haeundae coastal waters for the simulation of wave-induced current using ROMS-SWAN.

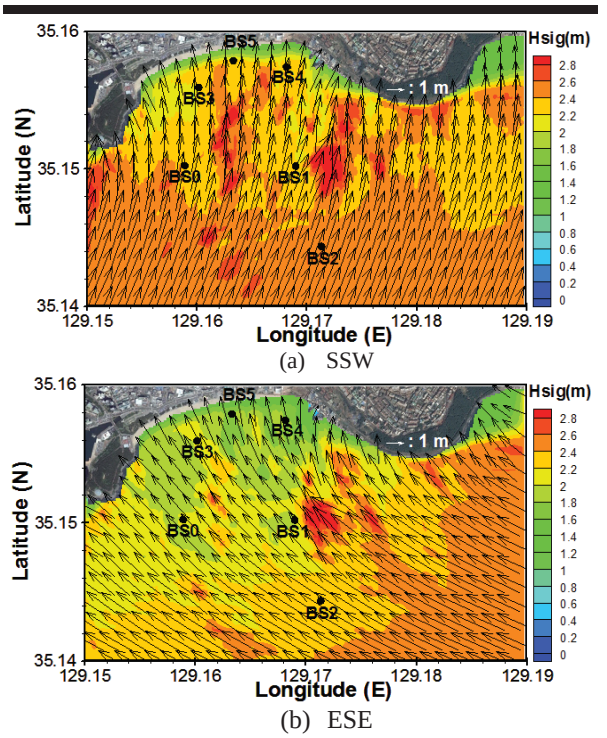

(a) SSW

(b) ESE

Figure 5. Significant wave height and direction simulated by SWAN model for swell waves (H_s: 2.5 m, T_p: 12 s) coming from (a) SSW in summer, and (b) ESE in winter.

RESULTS

We analyzed the seasonal variability of waves and currents using two-year long observations of waves and currents in Haeundae coastal waters. By statistical analysis, we found that swell waves (H_s: 2.5 m, T_p: 12 s) in the summer are propagated from SSW, generated in the South China Sea by typhoons passing nearby the Korean Peninsula. On the other hand, swell waves in fall and winter are propagated from ESE, generated in the East Sea by seasonal strong winds.

To estimate the average residual current from the observed current data, we applied a moving average method with a fortnightly data window, MSf (327.86 h) and two times MSf (Kim *et al.*, 2009; Lim *et al.*, 2014). Figure 6 shows the averaged bottom residual current, driven by a wave-induced current and eliminating the tidal current using a moving average method. The longshore currents measured in summer 2013 at station BS3, west of Haeundae beach, flows toward Dongbaek Island at a speed of 4–5 cm/s. The longshore current measured in summer 2014 at station BS5, in the middle of the beach, flows south at a speed of 2 cm/s. On the other hand, the longshore current measured in winter 2014 at station BS4, east of the beach near Mipo port, flows eastward at a speed of 3 cm/s. The offshore averaged residual current at stations BS1 and BS2

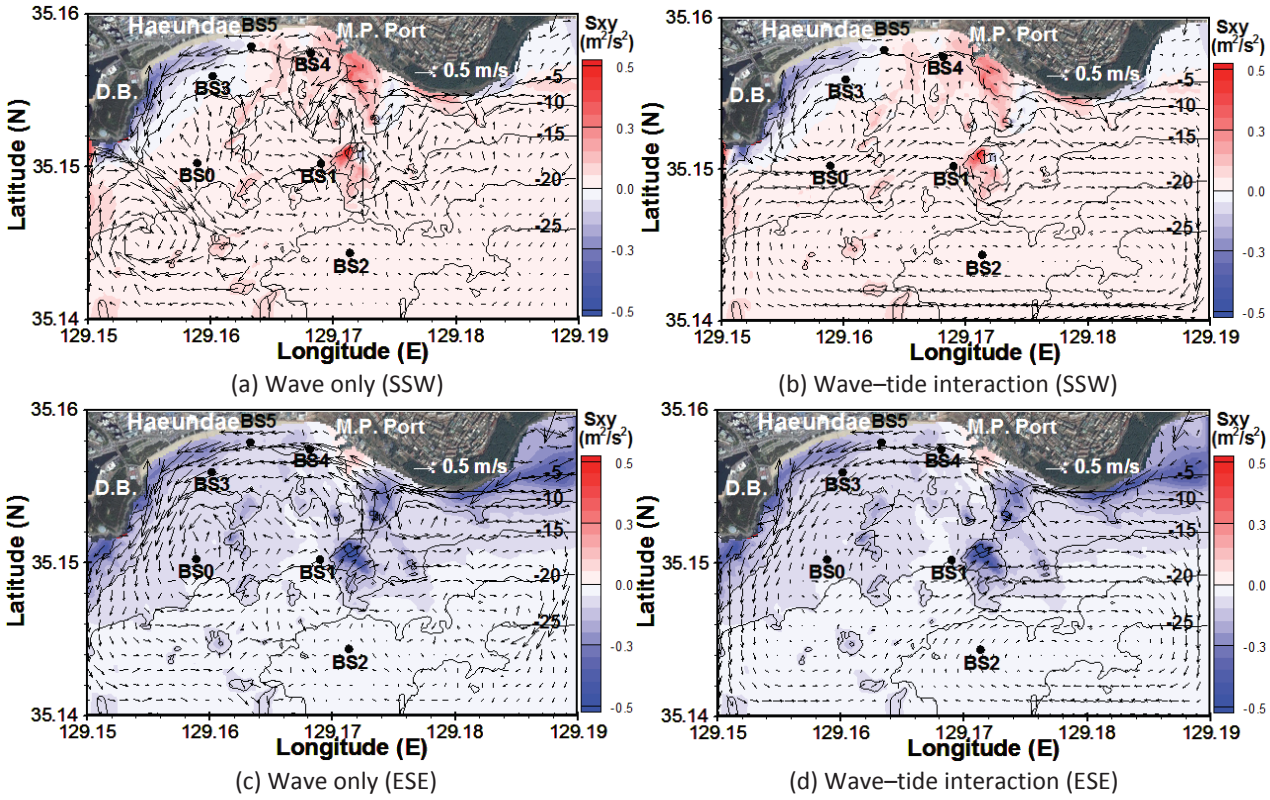

Figure 7. Bottom wave-induced current and horizontal radiation stress (S_{xy}) simulated by the ROMS-SWAN model under wave conditions of 2.5 m wave height and 12 s for different wave directions; (a, b) SSW and (c, d) ESE with/without wave–tide interaction.

flows northeast, similar to the ebb tide, at a speed of 9–10 cm/s. The flow direction at station BS0 during storms was opposite.

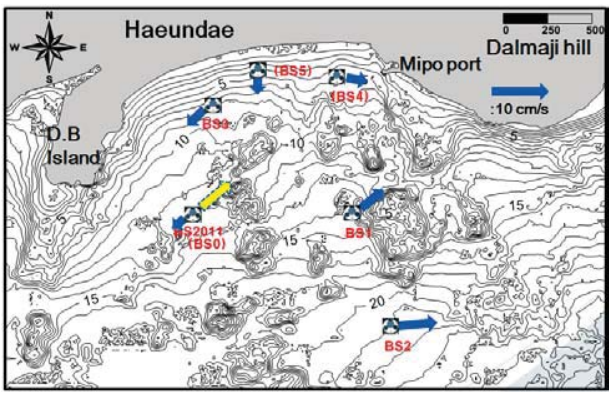

Figure 6. Averaged bottom residual currents in Haeundae coastal waters estimated by bottom-mounted AWAC flow data. Dotted arrow at the station BS0 means opposite residual current by storm waves in 2011.

Wave-induced current by wave–tide interaction

The wave-induced current was simulated separately using ROMS-SWAN, which is coupled through the Model Coupling Toolkit (MCT). SWAN provides the wave height, direction, and period to ROMS to calculate the radiation stresses, and ROMS also provides currents, surface elevation, and bathymetry to SWAN at certain intervals (Warner *et al.*, 2008). First, we simulated the wave-induced current without a tidal current boundary condition, calculating radiation stresses using the ROMS momentum equation using SWAN wave information every 4 min. Second, we simulated the wave-induced current using the ROMS model with a tidal current boundary condition, calculating the radiation stresses in ROMS using SWAN wave information. The ROMS-SWAN model exchange wave and flow information every 4 min for the wave–tide interaction.

Figure 7 shows the simulated bottom wave-induced current with swell waves coming from SSW and ESE, without and with wave–tide interaction. The simulated wave-induced current at station BS3 is well matched with the estimated averaged residual currents. Compared with the simulated results with swell waves coming from SSW in the summer, we found that the wave-induced current is separated at the station between BS5 and BS4, flowing westward and eastward. From the wave

and current coupled simulation, we also found that the speed of the longshore current along the coastline increased because of eddies generated by wave–tide interactions.

CONCLUSIONS

A numerical simulation using a wave and current coupled model (ROMS-SWAN) was conducted to determine the wave-induced current, which is one of the major causes of beach erosion in Haeundae during summer and winter. The wave-induced current simulated by seasonal swell waves (H_s: 2.5 m, T_p: 12 s) come from SSW in summer and ESE in winter. We compared the wave-induced current with averaged residual currents observed by a bottom-mounted AWAC nearshore of the beach. The speed and direction of residual currents were obtained using IOS T_TIDE and a moving average method with a fortnightly period (MSf).

By comparing the measured and simulated results, we found that the cross-shore current generated by swell waves in summer is mainly caused by the eddy which is separated in the middle of the beach by wave-induced currents generated by strong high waves coming from the SSW and S directions. In other seasons, a longshore current from swell waves is caused by the wave-induced current generated by strong swell waves coming from the ESE and E directions. This is consistent with surveyed beach erosion near the surf zone in summer and the observed sediment transport toward Dongbaek Island on the western end of Haeundae beach in winter (Kim *et al.*, 2012), respectively.

The wave-induced current simulated by the wave–current coupled model generates a strong longshore current along the coastline in winter and also generates counter-clockwise strong eddies near Dongbaek Island in summer, which are consistent with observed data. The simulated results show that the wave-induced current needs to be simulated by a wave–current coupled model that considers wave–tide interaction where tides exist in Haeundae coastal waters.

ACKNOWLEDGMENTS

This research was supported by the projects entitled “Development of Coastal Erosion Control Technology” and “Development of Safe Voyage Planning System for Vessels Operating in Northern Sea Route” funded by the Ministry of Oceans and Fisheries, Korea. The partial support by the project entitled “Development of Functional Technology for Coastal Erosion Control” funded by the Korea Institute of Ocean Science & Technology is also greatly appreciated.

LITERATURE CITED

Booij, N.; Ris, R.C., and Holthuijsen, L.J., 1999. A third-generation wave model for coastal regions, Part Ⅰ, Model description and validation. *Journal of Geophysical Research*, 104(C4), 7649-7666.

Egbert, G. D. and Erofeeva, S. Y., 2002. Efficient inverse modeling of barotropic ocean tides. *Journal of Atmospheric Oceanic Technology*, 19, 183-204.

Haidvogel, D.B.; Arango, H.; Budgell, W.P.; Cornuelle, B.D.; Curchitser, E.; Lorenzo, E.D.; Fennel, K.; Geyer, W.R.; Hermann, A.J.; Lanerolle, L.; Levin, J.; Mcwilliams, J.C.; Miller, A.J.; Moore, A.M.; Powell, T.M.; Shchepetikin, A.F.; Sherwood, C.R.; Signell, R.P.; Warner, J.C., and Wilkin, J., 2008. Ocean forecasting in terrain-following coordinates: formulation and skill assessment of the Regional Ocean Modeling System. *Journal of Computational Physics*, 227, 3595-3624.

Kim, C.S.; Lim, H.S.; Kim, J.A., and Kim, S.J., 2009. Residual flow and its implication to macro-tidal flats in Kyunggi Bay estuary of Korea. *Journal of Coastal Research*, SI56, 976-980.

Kim, H.; Ahn, J.; Jang, C.; Jin, J.Y., and Jung, B., 2013. Extention of piecewise exact solution method for two- and three- dimensional fluid flows. *Journal of Vibroengineering*, 15(3), 1243-1254.

Kim, I.C.; Lee, J.Y., and Lee, J.L., 2010. Generation mechanism and numerical simulation of rip current at Haeundae beach. *Journal of Korean Society of Coastal and Ocean Engineers*, 23(1), 70-78.

Kim, S.Y.; Jeong, J.B., and Lee, B.K., 2012. Seasonal variation of surface sediment distribution and transport pattern offshore Haeundae beach area. *Journal of the Korean Society of Oceanography*, 17(1), 16-24.

Lim, H.S.; Chun, I.S.; Kim, C.S.; Park, K.S.; Shim, J.S., and Yoon, J.J., 2013a. High-resolution operational coastal modeling system for the prediction of hydrodynamics in Korea using a wave-current coupled model. *Journal of Coastal Research*, SI65, 314-319.

Lim, H.S.; Kim, C.S.; Park, K.S.; Shim, J.S., and Chun, I.S., 2013b. Down-scaled regional ocean modeling system (ROMS) for high-resolution coastal hydrodynamics in Korea. *Acta Oceanologica Sinica*, 32(9), 50-61.

Lim, H.S.; Kim, C.S.; Lee, H.J.; Shim, J.S.; Kim, S.J.; Park, K.S., and Chun, I.S., 2014. Variability of residual currents and waves in Haeundae using long-term observed AWAC data. *Journal of Coastal Research*, SI72, 166-172.

Pawlowicz, R.; Beardsley, B., and Lentz, S., 2002. Classical tidal harmonic analysis including error estimates in MATLAB using T_TIDE, *Computers and Geosciences*, 28, 929-937.

Warner, J.C.; Sherwood, C.R.; Signell, R.P.; Harris, C.K., and Arango, H.G., 2008. Development of a three-dimensional, regional, coupled wave, current, and sediment-transport model. *Computers & Geosciences*, 34, 1284-1306.

Journal of Coastal Research	SI	75	1397 - 1401	Coconut Creek, Florida	2016

Recent record-breaking high ocean waves induced by typhoons in the seas adjacent to Korea

Il-Ju Moon[†], Minyeong Kim[†]∞, Minsu Joh[‡], Jooneun Ahn[‡], Jae-Seol Shim[§], and Jinyoung Jung[§]

[†]Typhoon Research Center, Jeju National University Jeju, South Korea

[‡]Supercomputing Center, National Institute of Supercomputing and Networking, Korea Institute of Science and Technology Information, Daejeon, Korea

[§]Operational Oceanography Research Center, Korea Institute of Ocean Science & Technology, Ansan, Korea

www.cerf-jcr.org

www.JCRonline.org

ABSTRACT

Moon, I.-J., Kim, M.; Joh, M., Ahn, J., Shim, J.-S., and Jung, J., 2016. Recent record-breaking high ocean waves induced by typhoons in the seas adjacent to Korea. *In:* Vila-Concejo, A.; Bruce, E.; Kennedy, D.M., and McCarroll, R.J. (eds.), *Proceedings of the 14th International Coastal Symposium* (Sydney, Australia). *Journal of Coastal Research*, Special Issue, No. 75, pp. 1397 - 1401. Coconut Creek (Florida), ISSN 0749-0208.

Estimation of extreme wave heights (EWHs) is the most important factor in the design of coastal structures such as breakwaters. In Korean coasts, the most EWHs occur during typhoon events. Recently, a number of ocean wave buoys have been deployed in the seas adjacent to Korea. This enables the measurement of record-breaking high waves during passages of recent strong Typhoons Kompasu (1007), Muifa (1109), Bolaven (1215), and Sanba (1216). This study investigates the characteristics of extreme waves during the passages of typhoons using buoy measurements and a numerical model. The wave simulations using WAVEWATCH III show that the model has the capability to reproduce the most EWHs during the four aforementioned typhoons with high accuracy, which guarantees an explanation of the mechanisms on the causes of such high wave generations over these regions. The analysis reveals that the occurrence of EWHs is influenced by not only storm intensity (i.e., maximum wind speed), but also the size, translation speed, and track of typhoons. Particularly, the record-breaking maximum wave height of 19.7 m observed during Typhoon Bolaven was the combined result of high winds, fast translation speed, big size, and straight track of Bolaven, which can maximize the increase of the dynamic fetch and duration.

ADDITIONAL INDEX WORDS: *Extreme high waves, typhoon, wave modeling.*

INTRODUCTION

The observation and estimation of extreme wave heights (EWHs) is important both scientifically, for the design of breakwaters, drilling platforms, and seabed mining facilities, as well as operationally, for the predictions of potentially hazardous conditions for ship navigation and coastal regions. In many cases, EWHs occur during tropical cyclone (TC, also called typhoon or hurricane) events with intense and fast-varying winds (Moon *et al*., 2003; Kim *et al*., 2014). The existence of gigantic maximum wave heights *(Hmax*) during hurricanes or typhoons has been reported from all over the world's oceans. Wang *et al*. (2005) reported a *Hmax* of 27.7 m derived from a deep-sea pressure gage in the northern Gulf of Mexico during the passage of hurricane Ivan in 2004. Holliday *et al*. (2006) discovered a recorded *Hmax* of 29.1 m from the Shipborne Wave Recorder onboard RRS Discovery in the northeast Atlantic Ocean. Most recently, Liu *et al*. (2008) measured a *Hmax* of 32.3 m from a discus buoy deployed near northeast Taiwan in the western Pacific, during the event of Typhoon Krosa on 6 October 2007, which could potentially be the largest *Hmax* ever recorded.

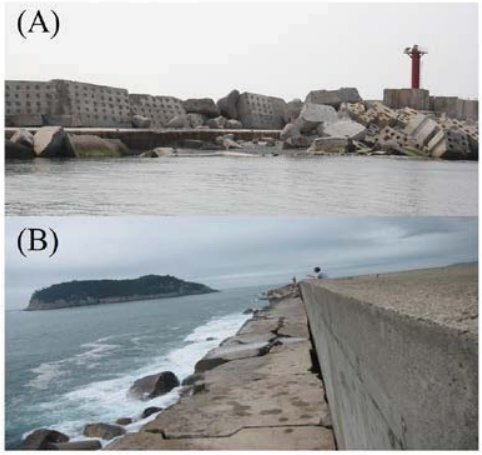

Figure 1. Pictures of breakwaters in (A) Gageodo and (B) Seogwipo, which were damaged by Typhoons Muifa (1109) and Bolaven (1215).

In the seas adjacent to the Korean peninsula (KP) including the Yellow Sea, the South Sea, and the East China Sea, such

DOI: 10.2112/SI75-280.1 received 15 October, 2015; accepted in revision 15 January 2016.

∞Corresponding author: nimbleyoung@hanmail.net

©Coastal Education and Research Foundation, Inc. 2016

extraordinarily huge waves have never been measured until now. This is most likely due to the relatively shallow water depths in these regions, the limited dynamic fetch for wave growth due to a bay-like shape surrounded by land, and the smaller intensity of storms compared to those in tropical regions. The lack of wave measurements in these areas also appears to contribute to the missing high wave observations.

Recently, a number of ocean wave buoys have been deployed in the seas adjacent to the KP. Fortunately some buoys that were located in the passage of recent strong Typhoons Kompasu (1007), Muifa (1109), Bolaven, (1215), and Sanba (1216), measured record-breaking high waves in these regions. This study investigates the characteristics of the observed extreme waves using an ocean wave model during the passages of the four typhoons that caused great damage to the coastal area (Figure 1), with a special focus on examining the occurrence mechanism of the extreme waves.

A brief outline of the dataset and wave model used in the present study is described in the next section. The third section describes the validations of simulated waves with observational data, and also explains the characteristics of extreme waves under typhoon forcing. The summary and conclusions are given in the last section.

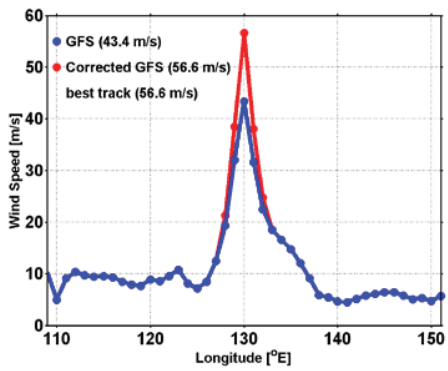

Figure 2. Comparisons of wind speed (cross section passing through the storm center at 20°N) between original GFS and corrected GFS for Typhoon Sanba at 06Z 14 September 2012. The numbers in the brackets are the maximum wind speeds at the section.

METHODS

Information on four typhoons was obtained from the best track archives of the Regional Specialized Meteorological Center (RSMC) in Tokyo. The data consist of the names of the TCs, their central positions (latitude and longitude), their minimum surface central pressures, and their maximum sustained wind speeds (MSWS: 10-min averaged maximum winds to the nearest 5 kts) measured every 6 hours.

The surface winds for typhoons, used as input data to the wave model, were obtained from the National Centers for Environmental Prediction's (NCEP) Global Forecast System (GFS). In this study, GFS winds near the storm core are modified using a weighted correction proportional to the distance (up to 223 km) from the position with the maximum difference in order to reduce the difference of the MSWS between GFS and best track (Figure 2). This modification allows us to resolve the problem of GFS winds, which usually underestimate the wind speed at a storm core due to its low spatial resolution (1 degree).

Wave data, *Hmax*, and significant wave height (*Hs*), are obtained from three separate sources: (1) three ocean buoys (Chilbaldo, Geojedo, Marado) from the Korean Meteorological Agency (KMA); (2) the Ieodo Ocean Research Station (IORS); and (3) five ocean buoys from the Korea Hydrographic and Oceanographic Administration (KHOA). Among them, KOGA-S01, IORS, and KOGA-S04 are open ocean sites, and KOGA-S01 is located in the southernmost point. Locations and pictures of the buoys and IORS are presented in Figure 3.

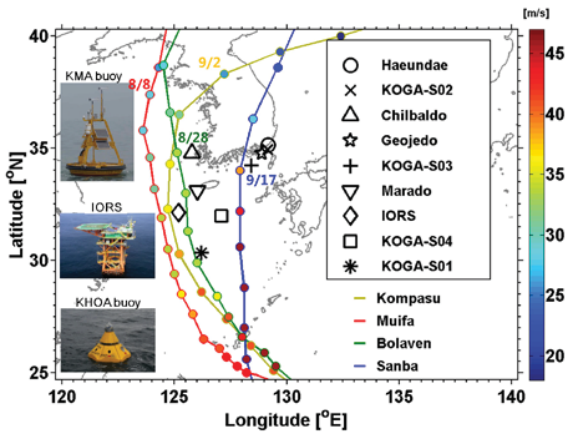

Figure 3. Tracks of Typhoons Kompasu (1007), Muifa (1109), Bolaven (1215), Sanba (1216), and locations of moored buoys and the ocean station. Colors of the filled-in circles represent the maximum wind speed of typhoon every 6 h. Date is indicated by [month/day].

The wave model used in the present study is WAVEWATCH III (WW3), which is developed at the National Oceanic and Atmospheric Administration (NOAA)/NCEP. The WW3 has been used in many research programs to study surface wave dynamics, and also as the operational wave model of NCEP for global and regional wave forecasts (Tolman 2002; Tolman *et al*. 2002). The WW3 explicitly accounts for wind input, wave–wave interaction, and dissipation due to whitecapping and wave–bottom interaction. It solves the spectral action density balance equation for directional wavenumber spectra. The source terms of the WW3 use wind–wave interaction according to Chalikov and Belevich (1993), as modified by Tolman and Chalikov (1996) and Tolman (1999), discrete interaction approximation (DIA) for nonlinear interactions (as in WAM), dissipation from Tolman and Chalikov (1996), and bottom friction as in the Joint North Sea Wave Project (JONSWAP, as in most WAM models). A detailed description of the model is given by Tolman (1999) and Moon *et al.* (2003).

The wave model used in this study is a two-way nest version of the WW3, in which the results calculated from higher-resolution nests are transferred to coarse domain. The model consists of three domains: the global domain (1º×1º spatial grid resolution extending from 75ºS to 75ºN and 180ºE to 180ºW), the northwestern (NWP) domain (1⁄12º×1⁄12º, extending from 17º to 50ºN and 115º to 155ºW), and the Korean peninsula (KP) domain (1⁄30º×1⁄30º, extending from 29º to 41ºN and 120º to 135ºW). This two-way interacting system with high-resolution nests is necessary to resolve the quickly varying wave fields associated with a typhoon.

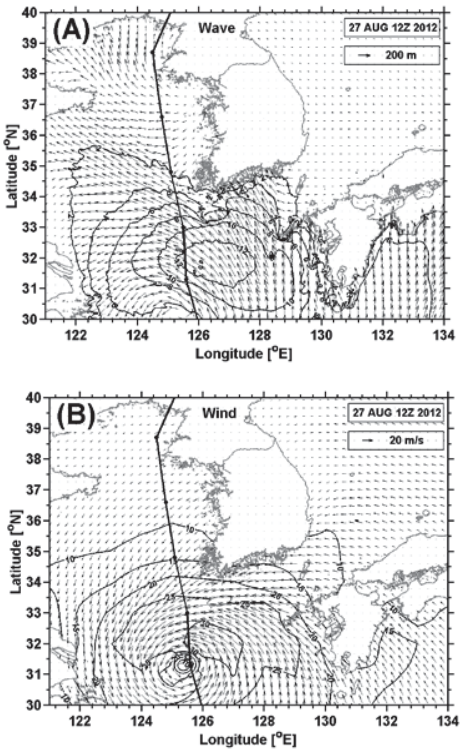

Figure 4. Distributions of (A) simulated *H*s and (B) wind speed for Typhoon Bolaven at 12Z 27 August 2012. In (A), contours and arrows represent *H*s and dominant wave direction/wavelength, respectively. The arrow length is proportional to the dominant wavelength. Solid line with dot is the track of Bolaven every 6 h.

RESULTS

Figure 4a shows distributions of *Hs* (contours), dominant wave directions (arrows), and dominant wavelengths (proportional to the arrow length) for Typhoon Bolaven at 12Z 27 August 2012, simulated by the present model. The *Hs* reached 14.4 m in the East China Sea, at which time the maximum wind speed was 33.4 m/s. The peak *Hs* and lengths are found in the right forward quadrant of a typhoon's center and propagate in the same direction as the typhoon. The asymmetric distributions are distinct in both fields of winds (Figure 4A) and waves, which appear to be due to the high storm translation speed (above 9 m/s). The high and long waves mostly propagated to the southern coasts of the KP and Jeju Island (Figure 4B).

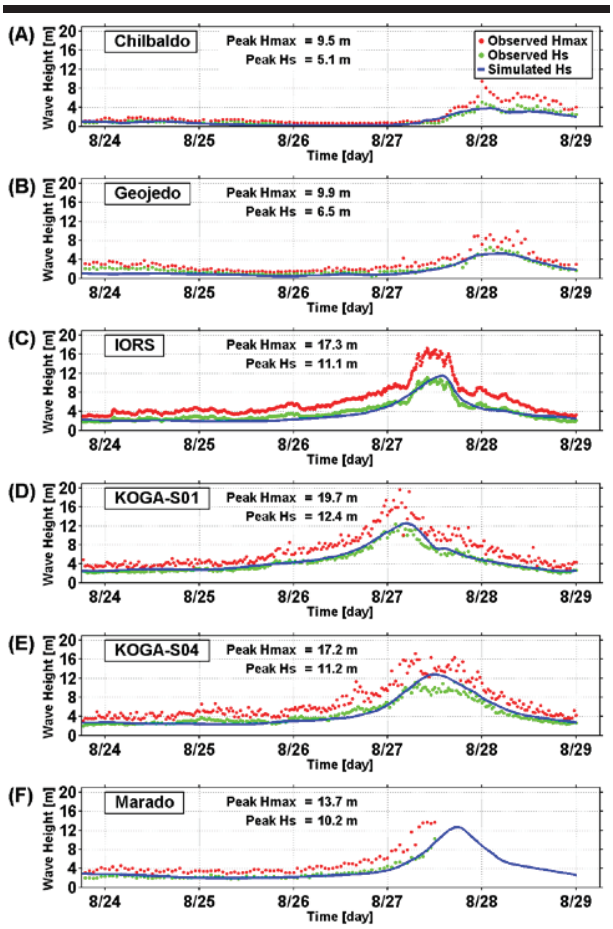

Figure 5. Comparisons of significant wave height (*H*s) between model (blue line) and observation (green dot) during the passage of typhoon Bolaven (1215) at (A) Chilbaldo, (B) Geojedo, (C) IORS, (D), KOGA-S01, (E) KOGA-S04, and (F) Marado. Red dots represent the observed maximum wave height.

Figure 5 shows a comparison of *Hs* between the model (blue line) and observations (green dot) for Typhoons Bolaven at Chilbaldo, Geojedo, IORS, KOGA-S01, KOGA-S04, and Marado. The peak *Hs* at these points reached 5.1, 6.5, 11.1, 12.4, 11.2, and 10.2 m, respectively. At that time, the *Hmax* (red dot) reached 9.5, 9.9, 17.3, 19.7, 17.2, and 13.7 m. The *Hmax* at all points except Geojedo were the largest ever recorded in the individual regions. The same comparisons were made for Typhoon Sanba at Chilbaldo, Geojedo, Haeundae, KOGA-S02, KOGA-S03, and Marado (Figure 6). The peak *Hs* at these points reached 4.8, 9.6, 5.4, 80, 10.8, and 6.2 m, respectively. At that

time the *Hmax* reached 6.1, 13.4, 6.9, 11.4, 15.5, and 10.3 m. The *Hmax* at Geojedo was the highest ever recorded in this region. The time series of *Hmax* and *Hs* for Typhoons Kompasu and Muifa also reveal that some values almost approached the highest records although they did not break the records set by Bolaven and Sanba (not shown).

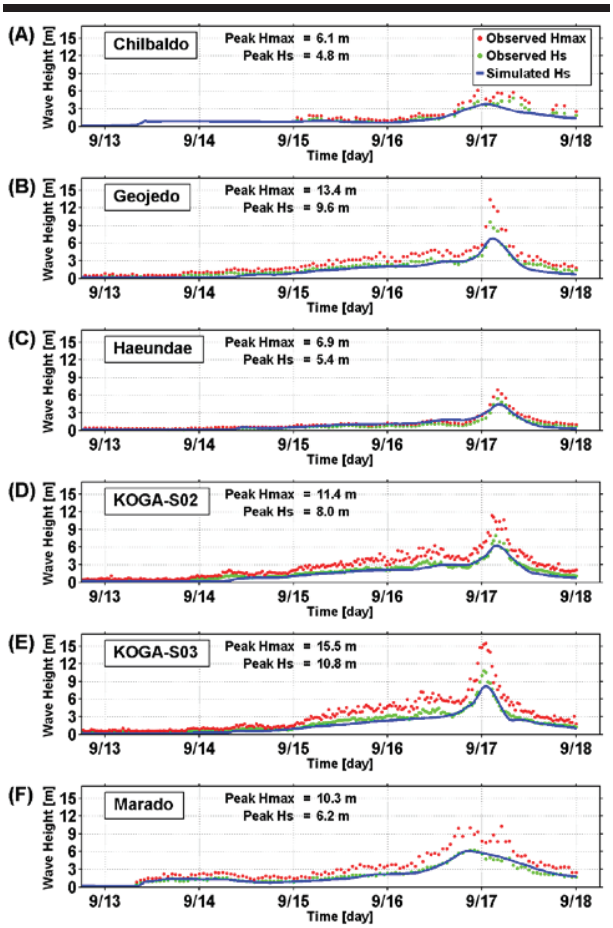

Figure 6. Same format as in Figure 5, but for typhoon Sanba (1216) at (A) Chilbaldo, (B) Geojedo, (C) Haeundae, (D), KOGA-S02, (E) KOGA-S03, and (F) Marado.

The simulated *Hs* are generally in good agreement with the observations throughout all typhoon passages (Table 1). The computed peak *Hs* are also well matched with their corresponding observations, although the model had a tendency to underestimate the peak values at some points. The estimated rms errors between simulated and observed *Hs* during the passage of Typhoons Kompasu, Muifa, Bolaven, and Sanba were 0.75 m, 0.58 m, 0.55 m, 0.44 m, respectively. This statistics suggest that the present model is capable of simulating *Hs* with high accuracy under typhoon forcing, which guarantees that the model results can be used in examining the causes of record-breaking extreme wave generations over these regions.

Table 1. *Bias and rms errors of significant wave height for Typhoons Kompasu, Muifa, Bolaven, and Sanba.*

Hs	Kompasu	Muifa	Bolaven	Sanba
Bias [m]	0.03	-0.35	-0.10	-0.22
Rmse [m]	0.75	0.58	0.55	0.44

It is important to investigate the spatial distribution of the severest wave conditions generated by typhoons from the perspective of structural engineers. Figure 7 compares the swath pictures of *Hs*, which show the maximum values at each grid point throughout the passages of each typhoon. For all typhoons, the higher waves appear to the right of the typhoon along their tracks. The areas with the higher waves extended to Jeju Island along the tracks. It is interesting that Jeju Island appears to play a role of breakwater that prevents high waves from propagating to the southern coasts of the KP.

The spatial patterns reveal that Bolaven produced the highest *Hs* for broad areas. Kompasu and Muifa showed also a similar spatial pattern to Bolaven in their tracks similarly passed through the left side of Jeju Island in a straight manner, but they were different in that their magnitudes of *Hs* were weaker than those of Bolaven. It should be noticed that the peak *Hs* of Kompasu is lower than that of Bolaven in the East China Sea, although the wind speed of Kompasu is much higher than that of Bolaven (Figure 8A & 8B; Figure 3).

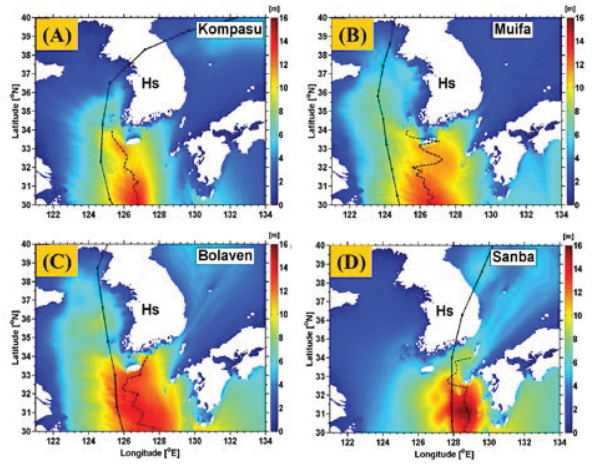

Figure 7. Swaths of *Hs* during the passage of Typhoons (A) Kompasu, (B) Muifa, (C) Bolaven, and (D) Sanba. Solid lines are the storm track. Dotted lines represent locations of the maximum *Hs* along the latitude of track.

In addition to wind speed, the dynamic fetch and duration are crucial factors that determine wave growth. It is known that as the storm translation speed (STS) becomes comparable to the

group speed of dominant waves, the waves to the right of the typhoon track are exposed to prolonged forcing from wind. These waves become “trapped” within the typhoon (resonance effect or dynamic fetch) and grow continuously (Moon *et al.*, 2003; Kim et al., 2014). In the case of Bolaven, size of the storm is the largest among 4 typhoons, the STS (8–10 m/s) was very similar to the group speed of dominant waves (Figure 8D), and the track was straight. These factors appear to maximize the increase of the dynamic fetch and duration for Bolaven, resulting in the production of the highest waves. This explains how Bolaven broke the observational high wave records in these regions although Bolaven was not the strongest typhoon based on the historical best-track archives of the RSMC.

Sanba has the strongest winds in the East China Sea (Figure 8b), but its track was different from the others (Figure 3), i.e., passing through the eastern side of Jeju Island close to Kyushu Island and finally making landfall over the southern coast of the KP. The peak *Hs* for Sanba is found near Kyushu Island reaching 16 m, which was the highest among the simulated *Hs* for 4 typhoons in the East China Sea. When Sanba made landfall, the extreme high waves (*Hs* = 13.4 m) were observed at Geojedo buoy, which was the highest ever recorded in this region.

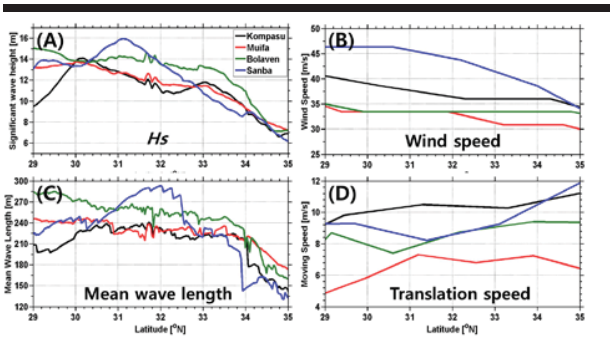

Figure 8. Variations of peak (A) *Hs*, (B) wind speed, (C) wavelength, and (D) storm translation speeds along the latitude of track (dotted lines in Figure 7) for Typhoons Kompasu, Muifa, Bolaven, and Sanba.

CONCLUSIONS

Recently record-breaking high ocean waves were measured from ocean buoys and research stations during the passage of Typhoons Kompasu (1007), Muifa (1109), Bolaven (1215), and Sanba (1216). This study simulated the extreme waves and investigated the mechanisms of high-wave generation by using a high-resolution wave model that allows a two-way interacting nest, as well as improving surface winds used for the input data of wave model. The comparisons of the model results with observations reveal that the present model was capable of simulating *Hs* with high accuracy under typhoon forcing. Spatial distributions of the maximum *Hs* for 4 typhoons show that Bolaven produced the highest *Hs* for broad areas, although the maximum wind speed of Bolaven was not the highest. In Bolaven’s case, we found that its large size, fast translation speed similar to the group speed of dominant waves, and its straight track maximized the increase of the dynamic fetch and duration, leading to the generation of high waves. The present measurements and modeling results for extreme waves induced by the four typhoons suggest that the update of design waves in these regions is required.

ACKNOWLEDGMENTS

This work has been performed as a subproject of KISTI's project *“Building Response System for National-Wide Issues Based on High-performance Supercomputer”* as well as a part of the project titled "*Construction of Ocean Research Stations and their Application Studies*" funded by the Ministry of Oceans and Fisheries, Korea.

LITERATURE CITED

Chalikov, D.V. and Belevich, M.Y., 1993. One-dimensional theory of the wave boundary layer. *Bound.-Layer Meteorology*, 63, 65–96.

Holliday, N.P.; Yelland, M.J.; Pascal, R.; Swail, V.R.; Taylor, P.K.; Griffiths, C.R., and Kent, E., 2006. Were extreme waves in the Rockall Trough the largest ever recorded?, *Geophysical Research Letters*, 33, L05613, doi:10.1029/2005GL025238.

Kim, C.S.; Lim, H.S.; Jeong, J.Y.; Shim, J.S.; Moon, I.-J.; Oh, Y.J., and You, H.K., 2014. Responses of coastal waters in the Yellow Sea to Typhoon Bolaven, *Journal of Coastal Research*, 70, 278–283.

Liu, P.C.; Chen, H.S.; Doong, D.-J.; Kao, C.C., and Hsu, Y.-J. G., 2008. Monstrous ocean waves during typhoon Krosa, *Annales of Geophysicae*, 26, 1327–1329.

Moon, I.-J.; Ginis, I.; Hara, T.; Tolman, H.; Wright, C.W., and Walsh, E.J., 2003. Numerical simulation of sea-surface directional wave spectra under hurricane wind forcing, *J. Phys. Oceanogr.*, 33, 1680–1706.

Tolman, H.L., 1999. User manual and system documentation of WAVEWATCH-III version 1.18. Tech. Note 166, Ocean Modeling Branch, NCEP, *National Weather Service, NOAA, U.S. Department of Commerce*, pp. 110.

Tolman, H.L., 2002. Validation of WAVEWATCH III version 1.15 for a global domain. *NOAA/NWS/NCEP/OMB Tech. Note 213, pp. 33.*

Tolman, H.L.; Balasubramaniyan, B.; Burroughs, L.D.; Chalikov, D.; Chao, Y.Y.; Chen, H.S., and Gerald, V.M., 2002. Development and implementation of wind-generated ocean surface wave models at NCEP. *Weather Forecasting*, 17, 311–333.

Tolman, H.L. and Chalikov, D., 1996. Source terms in a third-generation wind wave model. *Journal of Physical Oceanography*, 26, 2497–2518.

Wang, D.W.; Mitchell, D.A.; Teague, W.J.; Jarosz, E., and Hulbert, M.S., 2005. Extreme waves under Hurricane Ivan, *Science*, 309, 896, doi:10.1126/science.1112509.

Journal of Coastal Research	SI	75	1402 - 1406	Coconut Creek, Florida	2016

Vertical Structure of Rip-currents in the Nearshore Circulation

Sangyoung Son [†], Tae-Hwa Jung[‡*], and Fengyan Shi[††]

[†]School of Civil, Environmental, and Architectural Engineering
Korea University
Seoul, South Korea

[‡]Department of Civil and Environmental Engineering
Hanbat National University
Daejeon, South Korea

[††]Center for Applied Coastal Research
University of Delaware
Delaware, USA

www.cerf-jcr.org

www.JCRonline.org

ABSTRACT

Son, S.; Jung, T.H., and Shi, F., 2016. Vertical structure of rip-currents in the nearshore circulation. *In:* Vila-Concejo, A.; Bruce, E.; Kennedy, D.M., and McCarroll, R.J. (eds.), *Proceedings of the 14th International Coastal Symposium* (Sydney, Australia). *Journal of Coastal Research*, Special Issue, No. 75, pp. 1402 - 1406. Coconut Creek (Florida), ISSN 0749-0208.

A number of numerical models have been proposed over the past few decades to investigate rip currents in nearshore circulation zones. Rip currents are the offshore-directed flow generated mainly by wave breaking and momentum transfer over varying topography and they are important in relation to the management of coastal preservation, maintenance, and development. To date, a number of rip current studies have been conducted using depth-integrated two-dimensional (2D) or quasi-three-dimensional (3D) models based on wave-averaged formulations. However, compared with 3D hydrodynamic numerical models, these models are not capable of providing the accurate vertical profiles of current velocity. In this study, we examine the vertical variation of velocities induced by rip-currents using a phase-resolving, 3D Non-Hydrostatic WAVE model (NHWAVE) where an idealized rip channel is used to generate nearshore circulation. The vertical variation of velocities for several locations is investigated and compared with a depth-integrated numerical model for better understanding of depth-dependent hydrodynamics.

ADDITIONAL INDEX WORDS: *Non-hydrostatic model, rip-currents, nearshore circulation.*

INTRODUCTION

A rip current is an offshore-directed flow occuring in a nearshore circulation zone, and the phenomena was first described by Shepard *et al.*, (1941) through work conducted at the Scripps Institute of Oceanography. The generation mechanisms involoved in the creation of rip currents can be largely categorized as bathymetric variations and wave-wave interaction. Variations in bottom topography cause wave to break at different locations, thereby resulting in variation in alongshore shoreward mass transport (set-up); variations in the wave setup then induce a pressure gradient that drives offshore-directed flow. Dalrymple (1975) determined the mechanism of wave-wave interaction and showed that two obliquely incident waves with same periods, but different directions can induce a zero-amplitude line perpendicular to the coast, causing water particles to move along this line. In addition to these two mechanisms, alongshore currents and shear stability can give rise to rip currents (see Dalrymple *et al.*, 2011 for details).

Nearshore circulations have a great impact on sediment transport pattern and thus induce changes in coastline or beach morphology. The unexpected offshore-directed flow poses a considerable danger to swimmers. It was reported that more than one thousand people have been rescued by lifeguards on Korean beaches during the last decade.

Rip currents have been the subject of investigation for a number of decades. An initial theoretical approach was presented by Bowen (1969), wherein the nearshore circulation was explained using radiation stresses previously suggested by Longuet-Higgins and Steward (1964). Radiation stresses defined as the excess momentum flux from waves causes the longshore variation of wave field, and this variation generates offshore-directed flow known as rip-currents. In a follow-up study, Bowen and Inman (1969) conducted experimental studies and field observations and found that incident waves generate standing edge waves and the interaction between the incident and edge waves produce onshore flow, a longshore current in the surf zone and an offshore-directed flow. Noda (1974) attempted to determine theoretical approach to the generation mechanism of rip currents using the radiation stresses as a driving force and showed that wave interaction with bottom topography produces wave-induced nearshore circulation. A change in approach was then introduced by Le-Blond and Tang (1974), who considered that the rip current is caused by wave-current interaction and not wave-bottom interaction. Dalrymple and Lozano (1978) then extended the ideas presented in this study to describe a rip current cell. However, this study declared that the results of Le-Blond and Tang (1974) were invalid because of a mathematical error.

In addition to theoretical studies, laboratory experiments, and field observations, numerical studies have been conducted to investigate wave-induced currents. Noda (1974) derived a

DOI: 10.2112/SI75-281.1 received 15 October, 2015; accepted in revision 15 January, 2016
*Corresponding author: thjung@hanbat.ac.kr ©Coastal Education and Research Foundation, Inc. 2016

nearshore circulation equation using a two-dimensional (2D) shallow water equation and a stream function. He also calculated the wave height and propagation direction using geometric optics ray theory (Munk and Arthur, 1952). Kobayashi *et al.*, (1997) developed a time-dependent depth-averaged model to consider longshore currents in the surf zone. In addition, Damgaard *et al.*, (2002) used a 2D depth-averaged model to investigate the morphological evolution of a rip channel system. Furthermore, other researchers such as Ozkan-Haller and Li (2003), Kennedy and Kirby (2003), and Long and Ozkan-Haller (2005) investigated the nearshore circulation using depth-integrated shallow water equations. In addition to these shallow water equations, Boussinesq-type equations have been used to study nearshore circulation (Chen *et al.*, 1999; Johnson and Pattiaratchi, 2006). However, although depth-averaged numerical models deliver reasonable results for the generation of longshore or offshore direction flows, they do not provide the vertical distribution of velocity profiles. Therefore to consider the vertical variation of physical values, quasi three-dimensional (3D) or wave-averaged 3D model have been used for nearshore circulation (Haas *et al.*, 2003; Dronen and Deigaard, 2007; Haas and Warner, 2009; Chen *et al.*, 2014).

In this study, we examine vertical variations of velocities in rip currents using the 3D Non-Hydrostatic WAVE model (NHWAVE) developed by Ma *et al.*, (2012) that solves incompressible Navier-Stokes equations in the sigma coordinates. Rip currents are generated using a simple rip channel, and the vertical variation of mean velocities is calculated for several locations. To enable an in-depth understanding, the present results are compared with those of a depth-integrated Boussinesq model.

GOVERNING EQUATIONS

To simulate the 3D behavior of water particles, the incompressible Navier-Stokes equation in Cartesian coordinates is adopted as

$$\frac{\partial u_i}{\partial x_i^*} = 0 \tag{1}$$

$$\frac{\partial u_i}{\partial t^*} + u_j \frac{\partial u_i}{\partial x_j^*} = -\frac{1}{\rho}\frac{\partial p}{\partial x_i^*} + g_i + \frac{\partial \tau_{ij}}{\partial x_j^*} \tag{2}$$

where x_i^* are the Cartesian coordinates; (i, j)=1,2,3 is a tensor notation denoting the x^*, y^* and z^* directions, respectively; u_i is the velocity component corresponding to x^*; ρ is the water density; $g_i=-g\delta_{i3}$ is the gravitational acceleration. In addition, τ_{ij} is the turbulent stress defined as

$$\tau_{ij} = \nu_t \left(\frac{\partial u_i}{\partial x_j^*} + \frac{\partial u_j}{\partial x_i^*} \right) \tag{3}$$

where ν_t is the turbulent kinematic viscosity. The governing equation can be transformed as follows using the σ-coordinate

$$\frac{\partial D}{\partial t} + \frac{\partial Du}{\partial x} + \frac{\partial Dv}{\partial y} + \frac{\partial \omega}{\partial \sigma} = 0 \tag{4}$$

$$\frac{\partial \mathbf{U}}{\partial t} + \frac{\partial \mathbf{F}}{\partial x} + \frac{\partial \mathbf{G}}{\partial y} + \frac{\partial \mathbf{H}}{\partial \sigma} = \mathbf{S}_h + \mathbf{S}_p + \mathbf{S}_\tau \tag{5}$$

where $U=(Du,Dv, Dw)^T$. Fluxes and source terms are given by

$$\mathbf{F} = \begin{pmatrix} Duu + \frac{1}{2}gD^2 \\ Duv \\ Duw \end{pmatrix}, \mathbf{G} = \begin{pmatrix} Duv \\ Dvv + \frac{1}{2}gD^2 \\ Dvw \end{pmatrix}, \mathbf{H} = \begin{pmatrix} u\omega \\ v\omega \\ w\omega \end{pmatrix} \tag{6}$$

$$\mathbf{S}_h = \begin{pmatrix} gD\frac{\partial h}{\partial x} \\ gD\frac{\partial h}{\partial y} \\ 0 \end{pmatrix}, \mathbf{S}_p = \begin{pmatrix} -\frac{D}{\rho}\left(\frac{\partial p}{\partial x} + \frac{\partial p}{\partial \sigma}\frac{\partial \sigma}{\partial x^*}\right) \\ -\frac{D}{\rho}\left(\frac{\partial p}{\partial y} + \frac{\partial p}{\partial \sigma}\frac{\partial \sigma}{\partial y^*}\right) \\ -\frac{1}{\rho}\frac{\partial p}{\partial \sigma} \end{pmatrix}, \mathbf{S}_\tau = \begin{pmatrix} DS_{\tau_x} \\ DS_{\tau_y} \\ DS_{\tau_z} \end{pmatrix} \tag{7}$$

where p represents dynamic pressure.

To track the free surface elevation, Eq. (4) is integrated from 0 to 1 with bottom and free surface boundary conditions as

$$\frac{\partial D}{\partial t} + \frac{\partial}{\partial x}\left(D\int_0^1 u d\sigma\right) + \frac{\partial}{\partial y}\left(D\int_0^1 v d\sigma\right) = 0 \tag{8}$$

To solve Eqs. (4) and (5), combined finite-volume and finite-element schemes are used with a Godunov-type method. If the pressure is defined at the cell center, it is not easy to apply the pressure boundary condition at the free surface. Therefore, the pressure is defined at the vertically facing cell faces and the rest variables are defined at the cell center to solve the Riemann problem. In addition, the momentum equations are solved by a second-order Godunov-type finite volume method, and the HLL approximate Riemann solver (Harten *et al.*, 1983) is used to calculate fluxes at the cell faces (See Ma *et al.*, 2012 for details). The validation of the present model has been presented in previous papers and is therefore not addressed here (Ma *et al.*, 2012; Ma *et al.*, 2013; Ma *et al.*, 2014).

RESULTS

Rip currents were generated using an idealized rip-channel configured based on the typical rip-channel bathymetric feature in Duck, North Carolina (Yu and Slinn, 2003). A small modification was made to the bathymetry using only a center rip channel with a larger channel depth, compared with Yu and Slinn (2003), as shown in Figure 1. The bottom profile is given by

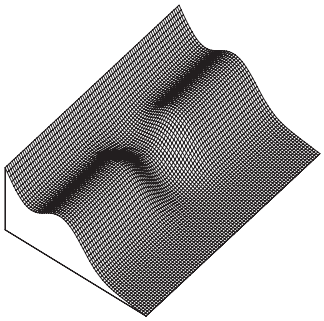

Figure 1. Idealized rip channel

$$h(x,y) = h_0(x) - h_0(x)\varepsilon \sin\left(\frac{2\pi y}{\lambda}\right)\exp\left[-5\left(\frac{x-x_c}{x_c}\right)^2\right] \qquad (9)$$

where

$$h_0(x) = \left(a_1 - \frac{a_1}{\gamma_1}\right)\tanh\left(\frac{b_1 x}{a_1}\right) + \frac{b_1 x}{\gamma_1} - a_2 \exp\left[-5\left(\frac{x-x_c}{x_c}\right)^2\right] \qquad (10)$$

with x_c=80, β_1=0.075, β_2=0.0064, a_1=2.97, a_2=1.5, ε=0.4, b_1=tan β_1, and γ_1= tan β_1/ tan β_2.

Waves were generated in the source region located at 440 m < x < 450 m, and 100 m of the sponge layer was placed at the right boundary of the computational domain to minimize re-entering waves from boundary wall as shown in Figure 2. The periodic boundary condition was imposed along the side wall. Grid sizes were 2.0 and 2.5 m in the x and y directions, respectively, and thus, the number of grids in the x and y directions became 280 and 256, respectively. The water column was divided into 20 layers in the vertical direction. A monochromatic wave with a height of 0.65 m $(H/h \approx 0.05)$, and a period of 10.0 s $(kh \approx 0.79)$ was used to generate the rip currents, where H is the incident wave height, h is the water depth in the source region, and k is the wavenumber corresponding to h.

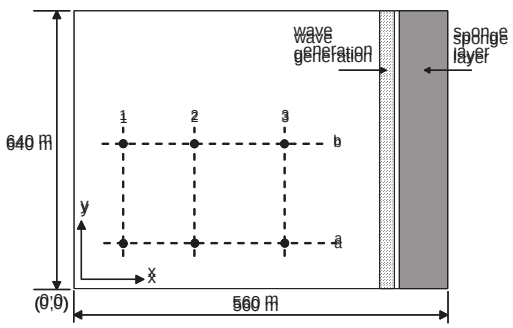

Figure 2. Schematic diagram of computational domain.

Figure 3 shows the wave height distribution averaged over 1,000 s < t < 2,000 s, where t is the time. It was observed that waves propagating over bar crest break earlier than those propagating along bar trough. As a result, increased wave setup by wave breaking drives nearshore circulation as shown in Figure 4. Because of the deeper channel depth used in the present study, less wave breaking is observed inside the rip channel compared with the cases of Yu and Slinn (2003). As a result, strong wave reflections from the beach cause standing wave patterns as indicated by the stems shown in Figure 3.

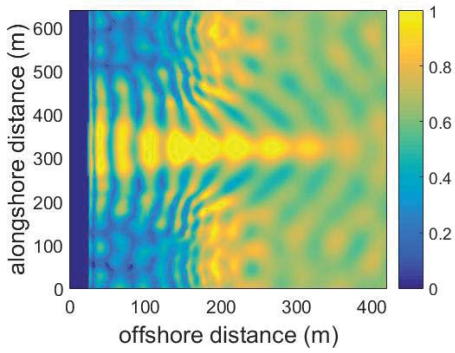

Figure 3. Wave height distribution averaged over 1,000< t <2,000 s.

Figure 4 shows the depth- and phase- averaged horizontal velocity vectors. Instantaneous velocities are averaged over 1,000 s < t < 2,000 s as done for the wave height calculation. It is clearly evident that the mean currents move toward the center of the bar channel near coastline and then return to the offshore region. Circulation cells can also be found outside the surfzone. The general circulation pattern is similar to the result of Yu and Slinn (2003), except that the present result shows a strong rip current jet towards outside of the surfzone. The more significant rip channel characteristics with a deeper channel make the circulation more bathymetrically controlled.

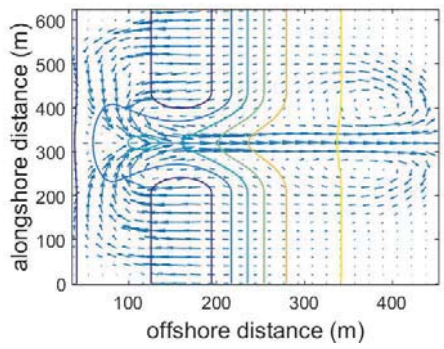

Figure 4. Depth and phase averaged horizontal velocity vector for the computational domain.

Figure 5 shows the vertical variation of horizontal velocities for different wave heights at several points at Transect a and Transect b, as denoted in Figure 2. Point a-2 is at the sandbar location and b-2 is around the rip channel location. The circles represent results from a Boussinesq model which will be discussed in the next section. Transect b is along the rip channel and measures the vertical profiles of rip current from the inside surfzone (b-1, b-2) to the outside surfzone (b-3). It can be observed that the seaward directed flow is strong at the center of the rip channel (b-2) and reduces the magnitude offshore (b-3). The current velocities in the alongshore direction, measured along this transect are very small. The vertical variations of the rip currents can be observed but not significant. In Transect a which is the transect crossing the sandbar, the landward directed currents can be predicted, particularily at the sandbar location (a-2). An alongshore directed flow can be found between the sandbar and the beach (a-1). Current velocities offshore are very small as shown at Point a-3. The vertical variation of the landward current is more significant at the sandbar location, compared with the rip current observed at the rip channel.

As expected, the strength of the nearshore circulation increases with an increase of incident wave height. However, the trends of vertical variation in current velocities are similar between the two cases with different incident wave heights.

DISCUSSION

The motivation of the study is to demonstrate 3D structure of a rip-current system predicted by a phase-resolving, 3D wave model. In order to get a typical rip current flow pattern, we configured a bathymetry and wave conditions where rip currents can be strongly controlled by a rip channel, versus the studies which were focused on instabilities caused by wave-current interaction. Our results show that the 3D structure of rip current can be observed but is not expectedly significant. However, the results still distinguish the results from a depth-integrated model below.

As mentioned in the introduction, rip currents can be modeled by a phase-resolving Boussinesq-type model sush as in Chen *et al.*, (1999). Here, we adopt FUNWAVE-TVD, a fully nonlinear Boussinesq model with a TVD solver (Shi *et al.*, 2012) to conduct the same case of H/h=0.5 as in the NHWAVE simulations.

To make comparisons between NHWAVE and FUNWAVE-TVD, the results from FUNWAVE-TVD are superimposed in Figure 5 as denoted by circles. The magnitude of the rip current predicted by FUNWAVE-TVD is generally same as the NHWAVE predictions, especially at the rip channel location (Figure 5, b-2). FUNWAVE-TVD predicts slightly smaller landward current at the sandbar location (a-2) comapred to NHWAVE. Most importantly, the vertical variations of current velocity predicted by FUNWAVE-TVD are less significant than NHWAVE predictions as observed in both seaward currents and landward currents.

It has been recognized, in theory, that the Boussinesq model can lead very poor predictions of wave-induced undertow. The vertical profiles of horizontal velocity from a Boussinesq model are always uniform below the wave trough, due to the Boussinesq long-wave theory and inviscid assumption even for breaking waves. Lynett (2006) proposed an ad-hoc method which uses the concept of roller and post-processes Boussinesq results. The roller effects are added locally on breakers in order to get better vertical profiles of wave-induced current velocity compared to the profiles directly from the Boussinesq model. However, it is questionable that the local roller effects could yield better predictions of the vertical profile in the rip current case because of the three-dimensionality. In particular, the depth-integrated model does not properly represent the mixing mechanisms which cause the vertical variation of the wave-induced circulations.

CONCLUSIONS

To consider vertical variation of horizontal velocity in the nearshore circulation, a 3D non-hydrostatic wave model was applied to rip-channel bathymetry. The results showed a generation of nearshore circulation and a decrease of horizontal velocity near the bottom. However, the depth-integrated model (FUNWAVE-TVD) did not show vertical variations of horizontal velocity, which is important in relation to the dispersive mixing. When the wave height was relatively large, a small circulation was observed in the off-shore region of rip-channel. However, the 3D structure of a rip-current system needs to be further investigated with a complete turbulence closure scheme and detailed analysis of mixing processes associated with wave breaking.

ACKNOWLEDGMENTS

This publication is supported by the Basic Research Program (NRF-2012R1A1A1011884) of the National Research Foundation of Korea, funded by the Ministry of Education, Science and Technology.

LITERATURE CITED

Bowen, A.J., 1969. Rip currents 1. Theoretical investigations. *Journal of Geophysical Research*, 74(23), 5467-5478.

Bowen, A.J. and Inman, D.L., 1969. Rip currents 2. Laboratory and field observations. *Journal of Geophysical Research*, 74(23), 5479-5490.

Chen, Q.; Dalrymple, R.A., and Kirby, J.T., 1999. Boussinesq modeling of a rip current system. *Journal of Geophysical Research*, 104(C9), 20,617-20,637.

Chen, J.-L.; Shi, F.; Hsu, T.-J., and Kirby, J.T., 2014. Nearcom-TVD – A quasi-3D nearshore circulation and sediment transport model, *Coastal Engineering*, 91, 200-212.

Dalrymple, R.A. and Lozano, C.J., 1978. Wave-current interaction models for rip currents. *Journal of Geophysical Research*, 83(C12), 6063-6071.

Dalrymple, R.A.; MacMahan, J.H.; Reniers, J.H.M., and Nelko, V., 2011. Rip currents. *Annual Review of Fluid Mechanics*, 43(1), 551-581.

Damgaard, J.; Dodd, N.; Hall, L., and Chesher, T., 2002. Morphodynamic modelling of rip channel growth, *Coastal Engineering*, 45(3-4), 199-221.

Dronen, N. and Deigaard, R., 2007. Quasi-three-dimensional modelling of the morphology of longshore bars, *Coastal Engineering*, 54, 197-215.

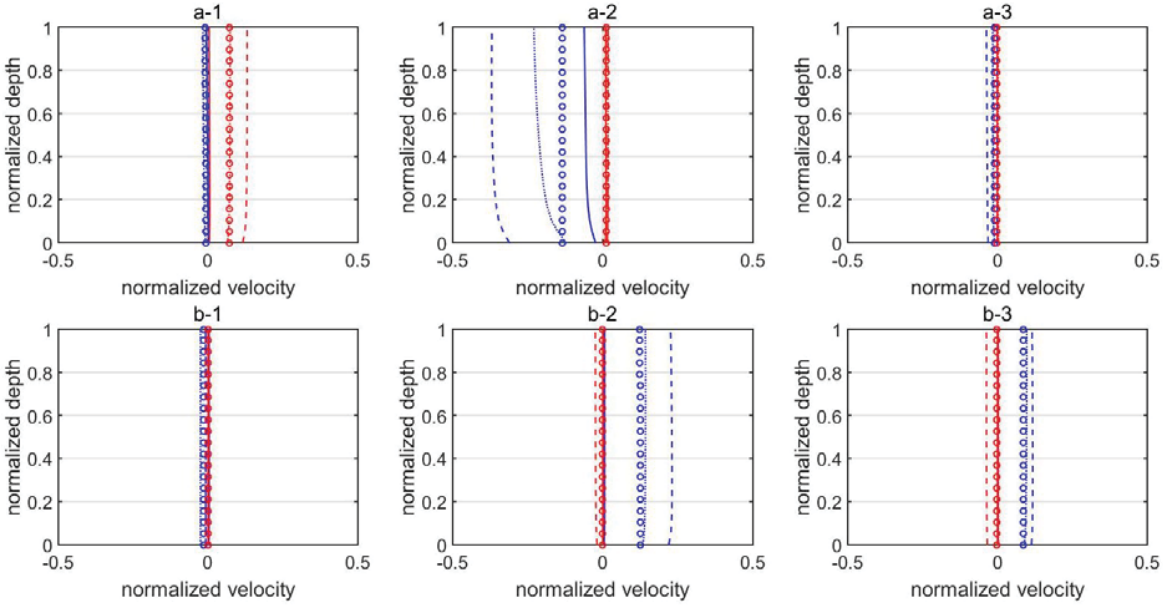

Figure 5. Vertical distribution of horizontal velocities for different wave heights at several points (blue: x-direction, red: y-direction, solid: *H/h*=0.01, dot: *H/h*=0.05, dash: *H/h*=0.1, circle: FUNWAVE-TVD (*H/h*=0.05)).

Haas, K.A. and Warner, J.C., 2009. Comparing a quasi-3D to a full 3D nearshore circulation model: Shorecirc and Roms, *Ocean Modelling*, 26, 91-103.

Haas, K.A.; Svendsen, I.A.; Haller, M.C., and Zhao, Q., 2003. Quasi-three-dimensional modeling of rip current systems. *Journal of Geophysical Research*, 108(C7), 1-21.

Harten, A.; Lax, P., and van Leer, B., 1983. On upstream differencing and Godunov-type schemes for hyperbolic conservation laws. *Society for Industrial and Applied Mathematics*, 25(1), 35-61.

Johnson, D. and Pattiaratchi, C., 2006. Boussinesq modelling of transient rip currents. *Coastal Engineering*, 53, 419-439.

Kennedy, A.B. and Kirby, J.T., 2003. An unsteady wave driver for narrow banded waves: modeling nearshore circulation driven by wave groups, *Coastal Engineering*, 48, 257-275.

Kobayashi, N.; Karjadi, E.A., and Johnson, B.D., 1997. Dispersion effects on longshore currents in surf zones, *Journal of Waterway, Port, Coastal, and Ocean Engineering*, 123(5), 240-248.

Long, J.W. and Ozkan-Haller, H.T., 2005. Offshore controls on nearshore rip currents, *Journal of Geophysical Research*, 110(C12007), 1-21.

Longuet-Higgins, M.S. and Steward, R.W., 1964. Radiation stresses in water waves; a physical discussion with applications. *Deep-Sea Research*, 11, 529-562.

Lynett, P., 2006. Wave breaking velocity effects in depth-integrated models. *Coastal Engineering*, 53, 325-333.

Ma, G.; Shi, F., and Kirby, J.T., 2012. Shock-capturing non-hydrostatic model for fully dispersive surface wave processes, *Ocean Modelling*, 43-44, 22-35.

Ma, G.; Kirby, J.T., and Shi, F., 2013. Numerical simulation of tsunami waves generated by deformable submarine landslides, *Ocean Modelling*, 69, 146-165.

Ma, G.; Chou, Y.-J., and Shi, F., 2014. A wave-resolving model for nearshore suspended sediment transport, *Ocean Modelling*, 77, 33-49.

Munk, W.H. and Arthur, R.S., 1952. *Gravity Waves*. 13. Wave intensity along a refracted ray. National Bureau of Standards Circular 521, Washington D.C., 95-108.

Noda, E.K., 1974. Wave-Induced Nearshore Circulation, *Journal of Geophysical Research*, 79(27), 4097-4106.

Ozkan-Haller, H.T. and Li, Y., 2003. Effects of wave-current interaction on shear instabilities of longshore currents. *Journal of Geophysical Research*, 108(C5), 1-19.

Shepard, F.P.; Emery, K.O., and La Fond, E.C., 1941. Rip currents: a process of geological importance. *Journal of Geology*, 49(4), 337-369.

Shi, F.; Kirby, J.T.; Harris, J.C.; Geiman, J.D. and Grilli, S.T., 2012. A high-order adaptive time-stepping TVD solver for Boussinesq modeling of breaking waves and coastal inundation, *Ocean Modelling*, 43-44, 36-51

Yu, J. and Slinn, D.N., 2003. Effects of wave-current interaction on rip currents. *Journal of Geophysical Research*, 108(C3), 1-19.

Journal of Coastal Research	SI	75	1407 - 1411	Coconut Creek, Florida	2016

Evaluating of Coastal Erosion Status from CEMP results in Eastern Coast, South Korea

Dongseob Song [†], Inho Kim[†*], Jaeseok Choi[‡], and Hyungseok Lee[††]

[†]Department of Earth and Environmental Enginnering
Kangwon National University
Samcheok, South Korea

[‡] Department of Environmental and Ocean Construction Enginnering
Kangwon National University
Samcheok, South Korea

[††]Department of Civil and Environmental Engineering
Hanzhong University
Donghae, South Korea

www.cerf-jcr.org

www.JCRonline.org

ABSTRACT

Song, D.S; Kim, I.H.; Choi, J.S., and Lee, H.S., 2016. Evaluating of Coastal Erosion Status from CEMP results in Eastern Coast, South Korea. *In:* Vila-Concejo, A.; Bruce, E.; Kennedy, D.M., and McCarroll, R.J. (eds.), *Proceedings of the 14th International Coastal Symposium* (Sydney, Australia). *Journal of Coastal Research*, Special Issue, No. 75, pp. 1407 - 1411. Coconut Creek (Florida), ISSN 0749-0208.

The Gangwon province, which is located in the mid-eastern part of the Korean Peninsula, started the Coastal Erosion Monitoring Program (CEMP) on 2006 and has been currently progressing. The CEMP in the eastern coast of Gangwon province is carried out in all the 41 littoral drift cells. In this study, we compared and evaluated a level of beach erosion based on the four years CEMP results. The indicators for coastal erosion evaluation in South Korea are consists of the beach width change (40 points), the beach area change (30 pts), the hinterland risk vulnerability (20 pts), the population (5 pts) and the nature conservation value (5 pts). The coastal erosion levels from the absolute evaluation point by the indicators were separated four phases through the A phase (stable, and well preserved beach with over 90 evaluation indicator points), the B phase (occurred an accretion or erosion, but relatively stable beach with 70~89 pts), the C phase (damage on beach or hinterland caused from erosion will be appeared, and with 50~69 pts), and the D phase (occurring heavy damage on beach or hinterland by continuous erosion with below 50 pts) on the 41 littoral drift sectors, which are including 79 beaches. The evaluation result shows that a serious erosion phenomenon in the eastern coast area of Korea has been increasing. Especially, the eroded beach sectors with the C and D phase were extremely increased in 2014 (A=0, B=18, C=47, D=14), compared with the monitoring result in 2010 (A=5, B=26, C=31, D=17).

ADDITIONAL INDEX WORDS: *Coastal erosion monitoring program,Gangwon province, coastal erosion level.*

INTRODUCTION

Coastal erosion is directly related to the loss of land and property in coastal areas and is thought to significantly increase the risk of flooding along hinterland areas. Therefore, beach erosion problem is a considerable hazard that the government can disregarded. Coastal erosion has become anomalous and widespread in the coastal zone of many East Asian countries, owing to multiple actions of various oceanicographic forces, industrialization and urbanization, population growth along a coast, within a river, a creek, and offshore.

Caia *et al*. (2009) reported a relationship between coastal erosion and sea level rise, storm waves and tides, and the influence of global climate changes on coastal erosion along the coastal zone of China. They emphasized three precautions to prevent aggravating coastal erosion as facing the impact of climate change. First, public awareness of coastal nature protection should be increased, and a new consciousness for disaster control planning needs to be popularized. Second, the health of the coastal environment and ecosystems needs to be maintained to guarantee the stability and security of the coast. In the future, based on countermeasure research and the integrated planning and supervision of sustainable coastal development, the government should draft an exploitation and utilization plan, make feasible policy for scientific management, and especially promote legislation to enhance coastal erosion control. Finally, strong administrative law for coastal protection should be established.

In Japan, beaches have been eroding since the 1970s as a result of the artificial structure construction. Approximately 3,000 fishing ports and 1,000 commercial ports have been constructed nationwide, as well as 2,532 large dams being built in the upstream areas of large rivers. Due to the man-made facility developments, a quite potamic sand supply has considerably decreased resulting in shoreline recession around the river mouths (Uda, 2010).

According to Isobe (1998), Japan is prone to seaborne natural disasters, including typhoon-induced flooding and high waves, and tsunamis or tidal waves. In addition, Japan's coastline is

DOI: 10.2112/SI75-282.1 received 15 October, 2015; accepted in revision 15 January 2016.
*Corresponding author: kimih@kangwon.ac.kr
©Coastal Education and Research Foundation, Inc. 2016

prone to erosion. Thus, prevention of disasters related to typhoons, tsunamis, and erosion is one important functional aspect of coastal zones that must take into account in any Integrated Coastal Zone Management (ICZM) schemes developed in Japan.

Since the establishment of the Kaohsiung Export Processing Zone in 1965, the first free trade zone in Asia, Taiwan established the various export processing zone, such as Taichung Export Processing Zone and the Nantze Export Processing Zone. In otherwise, the coastal areas in Taiwan are under heavy pressures of rapid development and incompatible uses (Chiau, 1998). On the basis of the result of the most recent survey in Taiwan, more than 80% of the island's sandy coasts have undergone erosion over the past 3 decades (Hsu *et al*., 2007). In response to the problems that have occurred in the coastal zone, Taiwan is actively undertaking several coastal zone management programs to balance and optimize environmental protection, public uses and socioeconomic development.

The erosion problems continue to be increased globally, and South Korea in East Asia is no exception. Kim and Lee (2011) reported that the coastal erosion in the eastern part of Gangwon Province has taken place more seriously along the 300km shoreline in Korea. They mentioned that the beaches in this area are heavily influenced by the presence of recent coastal defense projects that include groins, detached breakwaters and seawall.The ICZM Plan by the Ministry of Oceans and Fisheries (MOF) in South Korea, established in August 2000, the Coastal Erosion Monitoring Program (CEMP), which was supported by the Coastal Zone Management Act, has been implementing to evaluate the state and features of coastal erosion with quantitative field surveying data and numerical analyses (Song *et al*., 2013). The objective of Korean CEMP was the prevention of marine disasters, but it was not drafted from the viewpoint of integrated management of the coastal zone.

Coastal erosion can be defined as the recession of sand sediment from the coast by sea level fluctuating, wave and tidal current action, storms, coastal dynamics and/or the human activities, typically causing a landward retreat of the coastline. Beach erosion is mainly caused by the spatial imbalance in longshore sand transport. Accordingly, on a coast that has been formed under the premise that a large volume of sand was supplied from rivers or sea cliffs, beach is inevitable when sand supply is markedly reduced or longshore sand transport is blocked by breakwaters (Seino *et al*., 2015). The most common method for coast erosion status is the acquiring of beach profile (Shepard and Inman, 1950).

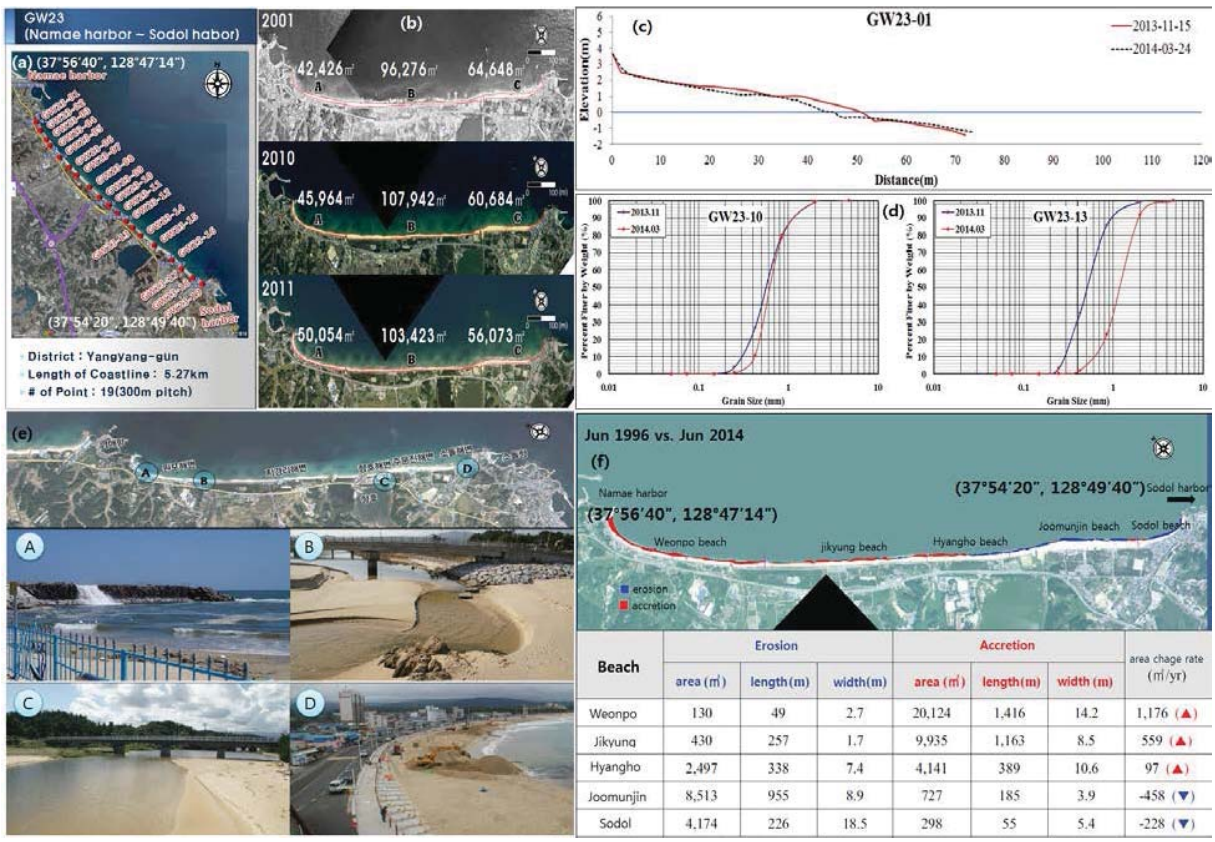

Beach	Erosion			Accretion			area chage rate (㎡/yr)
	area (㎡)	length(m)	width(m)	area (㎡)	length(m)	width (m)	
Weonpo	130	49	2.7	20,124	1,416	14.2	1,176 (▲)
Jikyung	430	257	1.7	9,935	1,163	8.5	559 (▲)
Hyangho	2,497	338	7.4	4,141	389	10.6	97 (▲)
Joomunjin	8,513	955	8.9	727	185	3.9	-458 (▼)
Sodol	4,174	226	18.5	298	55	5.4	-228 (▼)

Figure 1. Example of monitoring product by CEMP. (a) Information on littoral cell at the GW23, (b) Aerial photo analysis, (c) Beach cross-shore profile at GW23-1, (d) Median grain size, (e) Spot survey, (h) Monitoring overall results.

Therefore, the coastal monitoring approach in the Korea's CEMP has been focused on the change of beach width, beach profile, and grain size, producing beach face slope, erosion rate and scaling factor from the survey of the beach profile.

The Gangwon province, which is test area in this work and it is located in the mid-eastern part of the Korean Peninsula, started the CEMP on 2006 and has been currently progressing. The CEMP in the eastern coast of Gangwon province is carried out in all the 41 littoral drift cells (Song *et al*., 2013). Figure 1 is the example of monitoring proudcts from the CEMP result at the GW23 (GangWon23), which is one of the 41 littoral drift cells and it is located between the Namae harbor and the Sodol harbor in the Yangyang-gun district. Figure 1(a) represents the overall local situation, including the location of control points which are used for beach profile surveying, the length of coastline, and the administrative district information. Shown in Figure 1(b) are the analyzed results of coastline change from the aerial photos. Figure 1(c) is beach cross-shore profile, and the median grain size from a sieve analysis is shown in the diagram in Figure 1(d). Figure 1(e), (f), (g) is the timeseries of beach width, beach area, and median grain size during four years, respectively. Figure 1(h) depicts the comprehensive result of coastal erosion status.

Table 1. *Overall ndicators and points for evaluating of coastal erosion*

Indicator	Points	Evaluating criteria
Beach width	40	degrees of change in beach width
Beach area	30	degrees of change in beach area
Hinterland	20	degrees of risk vulnerability in hinterland
Population	5	population in hinterland
Conservation	5	nature conservation value

Table 2. *Erosion status from evaluation diagnosis of beach*

Level	Points	Erosion status of beach
A (stable)	over 90	well preserved beach
B (regular)	70~89	occurred an accretion or erosion, but relatively stable beach
C (concern)	50~69	damage on beach or hinterland caused from erosion will be appeared
D (serious)	below 50	occurring heavy damage on beach or hinterland by continuous erosion

METHODS

We conducted beach profiles, using the Global Navigation Satellite System (GNSS) surveying with the Virtual Reference System (VRS) which is known to overcome degradation of the location accuracy of a mobile station caused by the lack of spatial correlation of the errors as the length of the baseline increases, in the all of 41 littoral drift cells during four years. Based on beach erosion monitoring results, we evaluated a level of coastal erosion status at each beach after setting up of valuation items and standards, which were capable to estimate beach erosion and/or deposit condition. The indicators for evaluating coastal erosion in South Korea are consists of the beach width change (40 points), the beach area change (30 pts), the hinterland risk vulnerability (20 pts), the population (5 pts) and the nature conservation value (5 pts), as shown in Table 1.

The coastal erosion levels from the absolute evaluation points by the indicators were separated four phases through the A phase (stable, with over 90 points), the B phase (regular, with 71~89 pts), the C phase (with 50~70 pts), and the D phase (serious, below 50 pts) on the 41 littoral drift sectors, which are including 79 beaches (Table 2).

Evaluation methodology of beach width

In order to reflect both the short- and long-term change in the coastal erosion assessment, the beach width surveying result in 2014 year should be compared with the width value of the previous year (2013 year) and on the beginning year (2010 yearr). And then the comparison results are converted to the rate of change. The weighted values for each rate of change are the 0.7 when the quantitative beach width on 2014 year is compared with the observed values on 2010 year, and the 0.3, which is another weighted value, is applied in the comparison with the 2013 year. The detailed evaluation methodology is as follows.

$$\mathrm{X} = \left(\frac{width_{2014} - width_{2010}}{width_{2010}} \times 100\right) \times 0.7$$

$$\mathrm{Y} = \left(\frac{width_{2014} - width_{2013}}{width_{2013}} \times 100\right) \times 0.3 \qquad (1)$$

$$\mathrm{Z} = X + Y$$

$$\text{Beach width point} = 10 + (15 + Z)$$

where, the 15 in the formula of beach width point is a basic point in the Gangwon province.

If the Z is greater than or equal to 15%, then the beach width point is the 40 pts, and it is less than -20%, the 15 pts will be allotted.

Evaluation methodology of beach area

The calculating method of X and Y in Eq. (1) and the weighted values for the evaluating beach area is same as the case of evaluating beach width. However, the computing method of beach area point is different, as shown in Eq. (2).

$$\text{Beach area point} = 5 + ((20 + Z) \times 0.625) \qquad (2)$$

The 30 pts will be allotted when the Z is greater than or equal to 20%, and the 5 pts will be recorded when the Z is below -20%.

Evaluation methodology of hinterland risk vulnerability

The evaluation methodology of hinterland risk vulnerability suggested by the MOF is based on the presence of artificial facilities on the beach. If there is no erosion in the beach, the 20 points will be given. When there is artificial facilities, such as coastal road, public beach park, private house and etc., in the hinterland where the erosion is progressing, the evaluating point range is lower than in the case of no artificial facilities. The reason for this is to take into account the loss of lives and the damage of facilities caused by the beach erosion. The detailed description is shown in Table 3.

Evaluation methodology of population

The population evaluation is based on the result of taking a census of the population for the residents and visitors in the hinterland of pertinent beach. Especially, the range of hinterland for the census of the populuation is set up about 500m from the mean high water to the first road or property line as coastal landward boundaries which are defined by the National Coastal Zone Management Act of Korea (Figure 2). The formula of population evaluation follow as:

$$\text{Population point} = 6 - \log_{10} F \qquad (3)$$

where, $F = (\text{residents} \times 0.9) + (\text{visitors} \times 0.1)$

Even if the population point will be excess 5 pts or less than 1 pts in Eq. (3), the maximum is 5 pts and the minimum is 1 pt.

Table 3. *Evaluation methodology of hinterland risk vulnerability*

Points	Status	Method of point calculation		
20	no erosion area		-	
12 ~ 20	case of no artificial facilities in erosion area	Max. points under 20	Point formula 12+((20+E) ×0.467)	Min. points over 12
5 ~ 12	case of artificial facilities in erosion area	Max. points under 12	Point formula 12+((12+E) ×0.467)	Min. points over 5

where, E = erosion rate

Figure 2. Example of coastal landward boundaries in hinterland by National Coastal Zone Management Act.

Evaluation methodology of conservation value

The value of nature conservation would be evaluated with the fact of existence or nonexistence of man-made construction inside a shoreline. The evaluation target area is included that the designated area by the Marine Environment Management Act, the Wetlands Conservation Act, the Natural Parks Law, as well as the area where is not designated by the legal management. The each point about conservation value is listed in Table 4.

Table 4. *Evaluation methodology of nature conservation value*

Points	Evaluating method
5	In case of the existence of man-made construction in the coastal area where is not designated by legal management
3	In case of the nonexistence of man-made construction in the coastal area where is not designated by legal management
1	The coastal area where is designated by the laws

RESULTS

The administrative divisions which are adjacent to the ocean in the Gangwon province is divided into 4 cities (*si*) and 2 counties (*gun*). The names are Sokcho city, Gangneung city, Donghae city, Samcheok city, Goseong county, and Yangyang county (Figure 3).

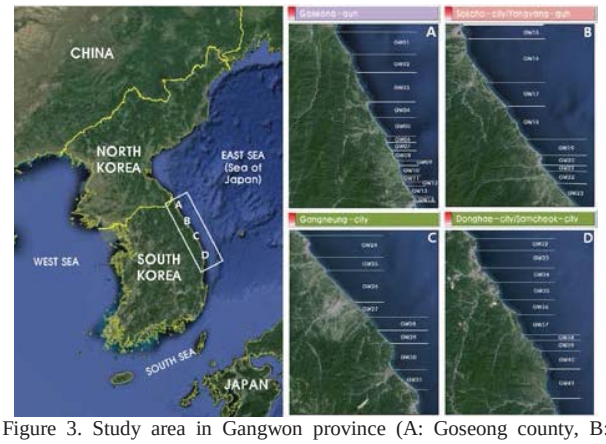

Figure 3. Study area in Gangwon province (A: Goseong county, B: Sokcho city and Yangyang county, C: Gangneung city, D: Donghae city and Samcheok city).

As referred to hereinbefore, we assessed the coastal erosion status about the 41 littoral drift, and compared the level of beach erosion based on the CEMP results during four years. Figure 4 represents the erosion evaluating results of 79 beaches. The evaluation result shows that a serious erosion phenomenon in the eastern coast area of Korea has been increasing. Especially, the eroded beach sectors with the C and D phase were extremely increased in 2014 (A=0, B=18, C=47, D=14), compared with the monitoring result in 2010 (A=5, B=26, C=31, D=17).

DISCUSSION

Above all, the thing to be emphasized is that the erosion state in the Goseong county is significantly processing. The stable and well preserved four beaches at 2010 year, such as Hwajinpo, Machajin, Sampo, and Jajakdo, were changed to the B and C phase status. It can be seen from Figure 4 that the situations of beaches in Yangyang county are also going to worse. Generally, the eroded beaches with the D phase on 2010 year were decreased than 2014 year, due to the coastal improved project, which were implemented by the MOF and some parts of the

local government. However, it seems that the risks and vulnerabilities associated with coastal hazards due to beach erosion problem extend along the coastline area of Gangwon province.

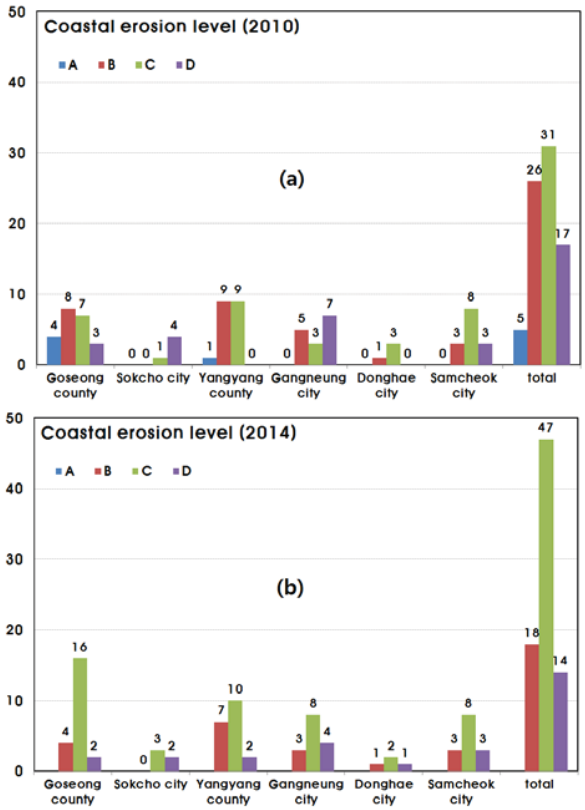

Figure 4. Costal erosion state in Gangwon province. (a) Evaluating result on 2010 year. (b) Evaluating result on 2014 year.

CONCLUSIONS

In this work, we present a case study of severe coastal erosion level from the beach erosion monitoring result under the action of CEMP in the Gangwon province. The quantitative assessment of coastal change in the study areas pointed out that much of populated beaches have fallen under vulnerable conditions due to chronic shoreline erosion. The long-term accumulated monitoring data with concern for beach erosion would be provided as fundamental reference data in maximizing the coast environmental enhancement. Consequently, quantitative criteria and assessment of erosion level of natural beach throughout the monitoring result would take an important role when a policy maker will decide to invest budget to local government.

LITERATURE CITED

Caia, F.; Sua, X.; Liub, J.; Lib, B., and Leia, G. 2009. Coastal erosion in China under the condition of global climate change and measures for its prevention. *Progress in Natural Science*, 19(4), 415-426.

Chiau, W.-Y., 1998. Coastal zone management in Taiwan: a review. Ocean and Coastal Management, 38(2), 119-132.

Hsu, T.-W.; Lin, T.-Y., and Tseng I.-F., 2007. Human Impact on Coastal Erosion in Taiwan. *Journal of Coastal Research*, 24(4) 961–973.

Isobe, M., 1998. Toward Integrated Coastal Zone Management in Japan, *ESENA Workship, Energy-Related Marine Issues in the Sea of Japan* (Tokyo, Japan), pp. 1-7.

Kim, I.H. and Lee. J.L, 2011. Beach Monitoring and Beach Management of Gangwon coast. In: Micallef, A. (ed.), *MCRR3-2010 Conference Proceedings, Journal of Coastal Research*, Special Issue No. 61, pp. 8-13.

Seinoa, S; Uda, T.; Ohtanib,Y., and Ohkib, Y. 2015. Essential Aspects of Beach Erosion - Lessons from Devastation of Ichinomiya Coast, Japan, *Procedia Engineering*, 116, 446-453.

Shepard, F.P. and Inman, D.L., 1950. Nearshore water circulation related to bottom topography and refraction. *Trans. Amer. Geophys. Union*, 31, 196– 212.

Song, D.S.; Kim, I.H., and Lee, H.S., 2013. Preliminary study of 3D Assessment of Coastal Erosion by Data Integration between Airborne LiDAR and DGPS Field Observations, *Proceedings 12th International Coastal Symposium (Plymouth, England), Journal of Coastal Research*, Special Issue No. 65, pp. 1445-1450.

Uda, T. 2010. Japan's Beach Erosion: Reality and Future Measures. *World Scientific*, 429p.

Journal of Coastal Research	SI	75	1412 - 1416	Coconut Creek, Florida	2016

Seasonal Changes in Sediment Characteristics on the Tidal Flat in Geunso Bay, West Coast of Korea

Han Jun Woo[†], Jeongwon Kang[†*], Jun-Ho Lee[†], and Seok Jang[‡]

[†]Korean Seas Geosystem Research Center, Korea Institute of Ocean Science & Technology, 787 Haeanro, Ansan, 15627, Korea

[‡]Maritime Security Research Center, Korea Institute of Ocean Science & Technology, 787 Haeanro, Ansan, 15627, Korea

www.cerf-jcr.org

www.JCRonline.org

ABSTRACT

Woo, H.J.; Kang, J.; Lee, J.-H., and Jang, S., 2016. Seasonal changes in sediment characteristics on the tidal flat in Geunso Bay, west coast of Korea. *In:* Vila-Concejo, A.; Bruce, E.; Kennedy, D.M., and McCarroll, R.J. (eds.), *Proceedings of the 14th International Coastal Symposium* (Sydney, Australia). *Journal of Coastal Research*, Special Issue, No. 75, pp. 1412 - 1416. Coconut Creek (Florida), ISSN 0749-0208.

Geunso Bay, located in Taean, western Korean Peninsula, is a semi-enclosed-type bay with a mean tidal range of about 6 m. Tidal flats are largely developed along the sides of the bay. A digital elevation model showed that 95% of the total area of the bay is tidal flat. Observations in both winter and summer of 2009 revealed that the surface sediments in the bay were mainly muddy sand, and the sediments were classified into five sedimentary facies: sandy silt, slightly gravelly sandy mud/sandy mud, slightly gravelly muddy sand/muddy sand, silty sand, and sand. In the eastern tidal flat, the annual sedimentation rate ranged from –71.3 to 12.4 mm/year, with a net erosion rate of –15.0 mm/year. Erosion was dominant on the tidal flat in the middle part of the bay, whereas deposition occurred in the western tidal flat in winter and spring, with a net deposition rate of 10.8 mm/year. Suspended sediments were supplied to the bay in relatively large amount in winter and spring and were transported in an anti-clockwise direction. Winter waves played a limited role in the seasonal variation in sedimentation due to the southwestward-opening bay mouth. It seems that the supply of suspended sediments and the circulation pattern of tidal currents are the most important factors for seasonal variations in sediments on the Geunso tidal flat.

ADDITIONAL INDEX WORDS: *Monsoon, Sedimentary cycle, Semi-enclosed tidal flat, Transport vector.*

INTRODUCTION

Tidal flats along the western coast of Korea have developed under mesotidal and macrotidal regimes (4 to 10 m) in a SW–NE direction as a result of Holocene transgression over the Yellow Sea basin (Lee *et al*., 2004; Ryu *et al*., 2004; Yang *et al*., 2006; Lee and Ryu, 2007). Because the western coast is mostly open to the Yellow Sea, the dispersal and transport of suspended sediments along the coast is associated with tidal flat sedimentation in coastal bays (Lee *et al*., 1999; Ryu, 2003). The Asian monsoon climate creates markedly contrasting summer and winter sedimentary processes between the tidal flats and the dispersal of nearshore suspended matter (see schematic diagram by Lee and Chu, 2001). In summer, river-derived fine sediments accumulate preferentially on the nearby tidal flats after summertime flooding events. During winter, high waves and wind-generated currents produce high hydrodynamic effects on the fine-grained sediments at the surface of the tidal flats on the open coast, generating a southward-directed nearshore suspended plume along the coast. Therefore, the muddy and coarse-grained sediments are actively winnowed and eroded by winter waves and currents and transported to the coastal area (Lee *et al*., 1999; Jo and Lee, 2008). In the summer mild season, tidal currents carry suspended sediments from the near-coast region to tidal flats in the bays (Lee, 2014).

There are four types of tidal flats on the western coast of Korea, depending on the geographic form of the coastline (Koh and Khim, 2014): (1) embayed (e.g., Hwangdo), (2) semi-enclosed (e.g., Garolim, Gomso, Hampyong, and Muan), (3) estuarine (Ganghwa), and (4) open-coast (Baeksu) types. Different sedimentary cycles exist between the open-coast and semi-enclosed bay types. Generally, seasonal variations in the textural characteristics and the accumulation of sediments on open-coast tidal flats are closely related to the seasonal sedimentary processes, namely deposition in summer and erosion in winter. However, on tidal flats of semi-enclosed bays, the controlling factors of the seasonal sedimentary characteristics vary depending on factors such as bay shape, hydrodynamic conditions, and artificial structures. For example, the major influences on seasonal variation in sedimentation are tidal currents in the Garolim (Lee and Jo, 2003), a combination of tidal currents, waves, and heavy rainfall in Gomso (Kang, *et al*., 2014), tidal currents, monsoon storms, and bay morphology in Hampyong (Ryu, 2003), and tidal currents and rainfall in Muan Bay (Ryu, *et al*., 2004).

DOI: 10.2112/SI75-283.1 received 15 October, 2015; accepted in revision 15 January 2016.
*Corresponding author: jwkhang7@kiost.ac.kr
©Coastal Education and Research Foundation, Inc. 2016

Geunso Bay, located in Taean in the western Korean Peninsula, is a semi-enclosed type of bay with no direct sediment input from on-land rivers (Figure 1). The mouth of the bay is narrow and open to the southwest to the Yellow Sea. The main tidal channel occurs along the eastern side of the bay. The tide is typically semidiurnal, with a mean tidal range of approximately 6 m. Tidal flats are largely developed all along both sides of the bay. A digital elevation model (DEM), which was generated using the waterline method based on remotely sensed data and water depth data of the subtidal zone measured by an echo-sounding survey, showed that the elevations of the tidal flat were about 200–300 cm (Eom *et al*., 2012). A hydro-hypsographic analysis (Oertel, 2001) based on DEM showed that the total area of the bay is about 31 km^2 and that tidal flats occupy 95% of the total area (Choi *et al*., 2011). The hydraulic turnover time (HTT) is 1.0 tidal cycle, indicating a well-flushed bay (Choi *et al*., 2011).

In this study, we attempted to understand sedimentation in the semi-enclosed tidal flat of Geunso Bay by monitoring the seasonal sediment characteristics and the sedimentation rates in the tidal flat.

METHODS

Surface sediments for sedimentological analysis were sampled at 45 stations in Geunso Bay in February 2009 (winter season) and August 2009 (summer season) (Figure 1). The sand and mud fractions were separated by wet sieving through a 63-micron stainless-steel sieve after removing organic matter and carbonates with 10% H_2O_2 and 0.1 N HCl, respectively. The grain-size distributions were determined by standard sieving (Folk, 1968) and a Sedigraph 5100 particle size analyzer at half-phi intervals. The inclusive graphic method was used to determine sediment type, mean size, sorting, skewness, and kurtosis (Folk and Ward, 1957).

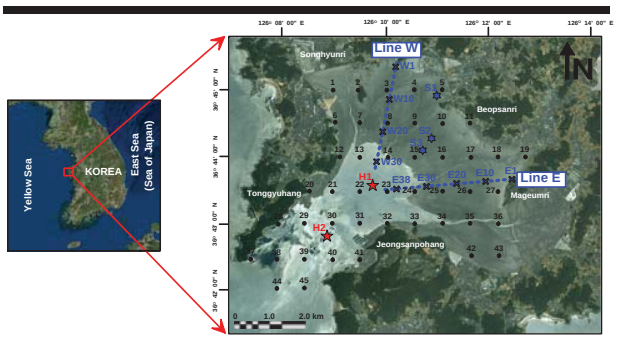

Figure 1. Location and Landsat ETM+ image of the tidal flat in Geunso Bay. The map of the study area (right) shows two transect lines and three stations (S1, S2, S3) for geomorphic measurements, 45 surface sediment sampling stations, and two stations (H1, H2) for hydrodynamic measurements.

Geomorphic changes caused by sediment deposition/erosion were checked for 1 year along two transects (E and W; east and west side of the tidal flat) and at three stations (S1 to S3) in the middle part of the tidal flat from February 2009 to February 2010 (Figure 1). The S1, S2, and S3 stations, located on the tidal flat at the middle of the bay near Beopsanri (Figure 1), were offset by about 500 m, 1,500 m, and 2,000 m toward the direction of the bay mouth, respectively. Elevation was measured using a leveling instrument (Pentax Pal 2S Level) and a differential global positioning system (DGPS). Sedimentation rates were determined by burying a plate at sub-bottom depth and periodically measuring the change in depth between the tidal flat surface and sedimentation plate. Surface sediments for examination of sedimentary processes were taken at stations of the two transect lines at 2-month intervals for 1 year.

Figure 2. Distribution of surface sediments in Geunso Bay in (A) winter and (B) summer.

RESULTS

The surface sediments in Geunso Bay were classified into five sedimentary facies: sandy silt, slightly gravelly sandy mud/sandy mud, slightly gravelly muddy sand/muddy sand, silty sand, and sand. In winter 2009 (Figure 2A), surface sediments on the tidal flat were composed mainly of poorly sorted muddy sand and silty sand. Sandy mud sediment was dominant on the upper tidal flat, and silty sand sediment was dominant on the subtidal flat. The percentages of sand content ranged from 14.8 to 98.7%, with increasing sand content from the shoreline to the subtidal area. In summer 2009 (Figure 2B), the surface sediments consisted mainly of muddy sand in the central and eastern parts of the tidal flat and sandy mud in the western part of the tidal flat. Sand sediments were distributed in the subtidal areas near Tonggyuhang and Jeongsanpohang The percentages of sand content ranged from 9.7 to 98.8%, with relatively low values in the central part of the tidal flat. Compared to the sedimentary facies in winter, muddy sand sediments on the tidal flat extended to the subtidal area and sandy mud sediments in the western part of the flat extended southward in summer. The silty sand sediments on the tidal flat in winter changed to muddy sand sediments in summer.

Two transect lines (Lines E and W) on the tidal flat were used to monitor changes in surface morphology, sediment characteristics, and sedimentation rates from February 2009 to February 2010. Line E on the tidal flat, located in the eastern part of the bay, had a gentle slope of 0.08° and extended 3,800 m toward the bay mouth (Figure 3A). The mean sea level on Line E was located at about 2,500 m from the shoreline. The sediment on the tidal flat along Line E was dominated by poorly sorted sandy mud from the shoreline to 1,600 m and by muddy sand between 1,800 m and 3,600 m. Sand content increased from the shoreline to the subtidal area. The area between 2,000 m and 3,800 m from the shoreline comprised clam farms. Line W, located at Songhyunri in the western part of the bay, had a gentle slope of 0.10° (Figure 3B). Its length to the bay mouth was 3,100 m, and it exhibited ripples, well-developed small tidal channels, tidal channels and creeks, and sand bars (see the photographs). The mean sea level was located about 900 m from the shoreline. Therefore, the area above mean sea level in the western part of the tidal flat was relatively smaller than that in the eastern part. The sediment of the tidal flat along Line W was dominantly poorly sorted sandy mud from the shoreline to 200 m and muddy sand between 200 m and 3,100 m. The sediment at station S1 consisted of slightly gravelly sandy mud, whereas the sediment at stations S2 and S3 was composed of poorly sorted sandy mud.

The seasonal variations in sedimentation rate during a year on the tidal flats of Geunso Bay are shown in Figure 4. Generally, the sediments on Line E showed mostly erosion in winter and spring and deposition in summer. In autumn, deposition and erosion occurred within 1,000 m and beyond 1,000 m from the shoreline, respectively (Figure 4A). During the year, on Line E, sediments were deposited within a distance of 800 m from the shoreline and were eroded in the interval from 800–1,800 m from the shoreline, with a net erosion rate of –15.0 mm/year. On Line W (Figure 4B), surface sediments were deposited in winter and spring and eroded from spring to summer. The annual sediment accumulation rate on Line W was as high as 51.7 mm/year, with a net deposition rate of 10.8 mm/year. The stations (S1, S2, and S3) on the tidal flat in the middle of the bay showed dominantly erosion of surface sediments during the year. The mean annual sedimentation rates at stations S1, S2, and S3 were –19.2, –27.9, and –35.1 mm/year, respectively (Figure 4C).

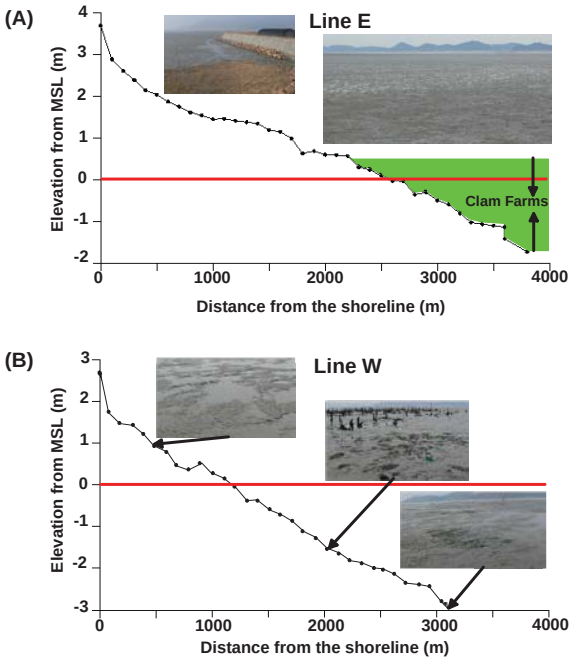

Figure 3. Elevation from MSL along (A) Line E and (B) Line W.

DISCUSSION

Previous studies using hydrodynamic measurements were carried out in the subtidal area during 2006 and 2007 using an acoustic Doppler current profiler (ADCP) and a YSI 6600 sonde (KORDI, 2007). The maximum velocities of tidal currents were about 80 cm/s during flood tide at a subtidal site (H1) and about 90 cm/s during ebb tide at the bay mouth (H2) (Figure 1). A numerical model of the residual tidal currents in the bay showed that residual currents with speeds <5 cm/s existed in two clockwise flows, one each in the eastern and western tidal flats. The direction of the tidal currents was flow to the northeast during flood tide and flow out to the southwest during ebb tide (KORDI, 2010). This seems to cause developments of the tidal flats along the sides of the bay.

However, the seasonal variations in sedimentation revealed reverse cycles of sedimentation on the eastern and western tidal flats of the bay. On Line W, accumulation was dominant during winter and spring, whereas on Line E, deposition occurred within 800 m from the shoreline in summer and autumn. The distributions of surface sediments in winter and summer 2009 showed that the area of muddy sand sediment on the tidal flat expanded in summer toward the Line E (Figure 2), indicating that fine-grained sediments were transported eastward in the bay

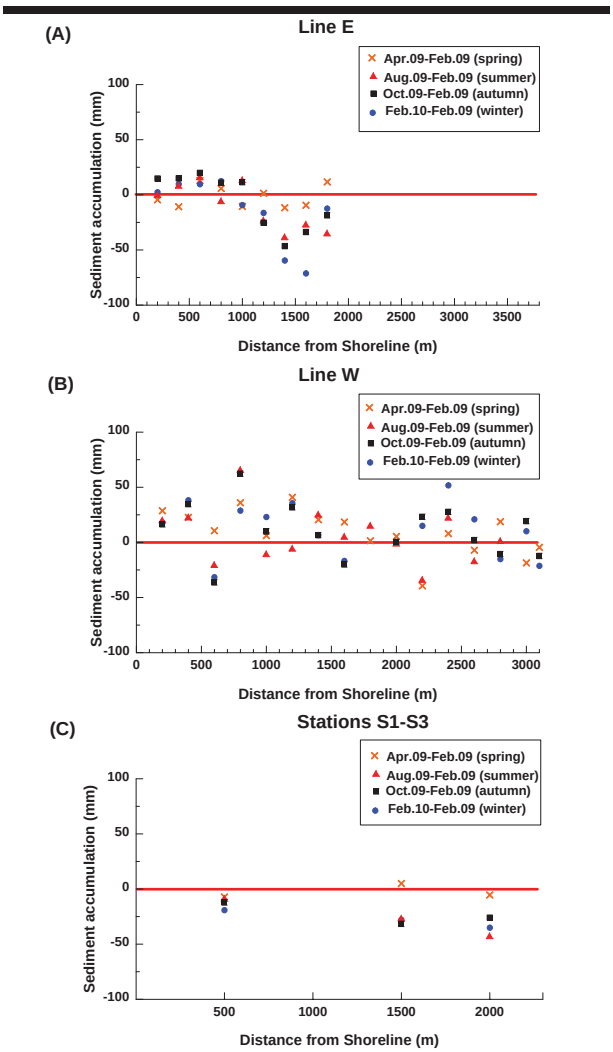

Figure 4. Seasonal changes of surface sediment accumulation rates along (A) Line E, (B) Line W, and (C) at stations S1, S2, and S3 in Geunso tidal flat from February 2009 to February 2010. The seasonal and net sedimentation rates were calculated by subtracting the initial value for February 2009.

in summer. The mean grain sizes of sediments on the tidal flat were relatively coarser in summer.

This sediment movement may be associated with the circulation of tidal currents as mentioned above. In addition, the suspended sediment concentrations at the bay mouth (H2) were relatively higher (10–40 mg/l) in winter and spring and were lower (about 10 mg/l) in summer. Therefore, the relatively high supply of suspended materials into the bay in winter resulted in the appearance of various sedimentary facies and accumulation of sediments on the tidal flat toward Line W (Figure 2A). During summer, under the small supply of suspended sediments, the tidal flat was eroded by tidal currents, but transport sediments toward Line E (Figure 2B).

CONCULSIONS

The geomorphic changes caused by sediment deposition/erosion for the year on Line E showed that deposition occurred in summer and from the shoreline to a distance of 800 m in autumn, whereas erosion was dominant in winter and spring and occurred beyond 1,000 m from the shoreline in autumn. On Line W, deposition occurred from winter to spring, and erosion was dominant in summer.

An examination of the patterns of sedimentation revealed that considerable sediment was supplied from the bay mouth to the western side of the tidal flat and deposited in winter and spring; winnowed and/or eroded fine-grained materials were then transported eastward in the bay in summer. It seems that the supply of suspended sediments and the circulation pattern of tidal currents are the most important factors for the seasonal variation in sediments on the tidal flat in Geunso Bay. The net sedimentation for the year showed that net deposition occurred in the western tidal flat and within 800 m from the shoreline in the eastern tidal flat, whereas net erosion occurred in the middle tidal flat and beyond 800 m from the shoreline in the eastern tidal flat of the bay (Figure 5).

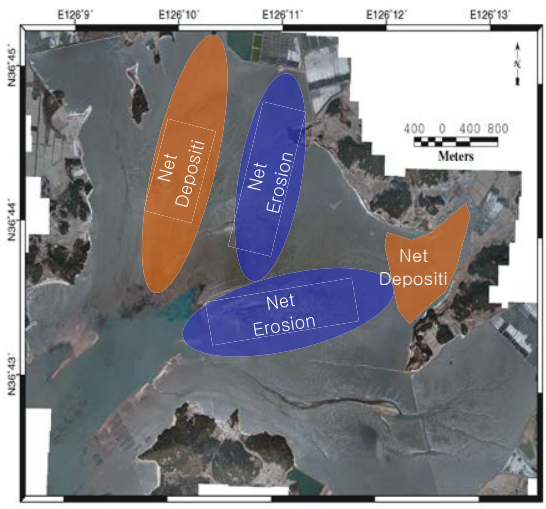

Figure 5. Schematic diagram of net sedimentation in Geunso tidal flat.

ACKNOWLEDGMENTS

This research was a part of the project titled “Studies on sediments, waters and biota to understand major environment factors in rehabilitation of degraded tidal flats” and “Study of Coastal Environment Change for Management of Nakdong Estuary” funded by the Korea Institute of Ocean Science and Technology (KIOST).

LITERATURE CITED

Choi, J.K.; Ryu, J.H.; Woo, H.J., and Eom, J., 2011. A study on the flushing characteristics in Geunso bay using hydro-

hypsographic analysis. *Journal of Korean Wetlands Society*, 13(1), 45-52.

Eom, J.; Choi, J.K.; Ryu, J.H.; Woo, H.J.; Won, J.S., and Jang, S., 2012. Tidal channel distribution in relation to surface sedimentary facies based on remotely sensed data. *Geosciences Journal*, 16(2), 127-137.

Folk, R.L. and Ward, W.C., 1957. Brazos river bar: a study in the significance of grain size parameters. *Journal of Sedimentary Petrology*, 27, 3-26.

Folk, R.L., 1968. Petrology of Sedimentary Rocks. Austin, Texas: Hemphill's, 170p.

Jo, H.R. and Lee, H.J., 2008. Sediment transport processes over a sand bank in macrotidal Garolim Bay, west coast of Korea. *Geosciences Journal*, 12(3), 243-253.

Kang, J.; Woo, H.J.; Lee, Y.-K., and Son, Y.B., 2014. Seasonal sedimentary processes of the macrotidal flat in Gomso Bay, Korea. In: Green, A.N. and Cooper, J.A.G. (eds.), *Proceedings 13th International Coastal Symposium . Journal of Coastal Research*, Special Issue No. 70, pp. 157-163.

Koh, C.H. and Khim, J.S., 2014. The Korean tidal flat of the Yellow Sea: physical setting, ecosystem and management. *Ocean and Coastal Management*, 102(B), 398-414.

KORDI, 2007. *Assessment on the flux at the sediment-water boundary and ecological role of intertidal flat*. Ansan, *BSPE 97703-1925-3*, 332p.

KORDI, 2010. *Studies on sediments, waters and biota to understand major environmental factors in rehabilitation of degraded tidal flats*. Ansan, *BSPE 98462-2253-5*, 583p.

Lee, H.J. and Chu, Y.S., 2001. Origin of inner-shelf mud deposit in the southeastern Yellow Sea: Huksan Mud Belt. *Journal of Sedimentary Research*, 71, 144-154.

Lee, H.J. and Jo, H.R., 2003. Sedimentological and hydrodynamical monitoring of modern sediments in Garolim Bay on the west coast of Korea. *In*: Chi, B.H. and Park, Y.A. (eds.), *Proceedings of Workshop on Sedimentation in the Yellow Sea* (Seoul, Korea), pp. 323-344.

Lee, H.J. and Ryu, S.O., 2007. Role of the giant Saemangeum dyke in sedimentation at the mouth of an estuarine complex. *Marine Geology*, 239, 173-188.

Lee, H.J., 2014. A review of sediment dynamical processes in the west coast of Korea, eastern Yellow Sea. *Ocean Science Journal*, 49(2), 85-95.

Lee, H.J.; Chu, Y.S., and Park, Y.A., 1999. Sedimentary processes of fine-grained material and the effect of seawall constructionin the Daeho macrotidal flat-nearshore area, northern west coast of Korea. *Marine Geology*, 157(3-4), 171-184.

Lee, H.J.; Jo, H.R.; Chu, Y.S., and Bahk, K.S., 2004. Sediment transport on macrotidal flats in Garolim Bay, west coast of Korea: significance of wind waves and asymmetry of tidal currents. *Contimental Shelf Research*, 24, 821-832.

Oertel, G.F., 2001. Hypsographic, hydro-hypsographic and hydrological analysis of coastal bay environments, Great Machipongo Bay, Virginia. *Journal of Coastal Research*, 17(4), 775-783.

Ryu, S.O., 2003. Seasonal variation of sedimentary processes in a semi-enclosed bay: Hampyong bay, Korea. Estuarine *Coastal and Shelf Science*, 56, 481-492.

Ryu, S.O.; Lee, H.J., and Chang, J.H., 2004. Seasonal cycle of sedimentary process on mesotidal flats in the semi-enclosed Muan Bay, southern west coast of Korea: culminating summertime erosion. *Continental Shelf Research*, 24, 137-147.

Yang, B.; Dalrymple, R.W.; Chun, S.S., and Lee, H.J., 2006. Transgressive sedimentation and stratigraphic evolution of a wave-dominated macrotidal coast, western Korea. *Marine Geology*, 235, 35-48.

Journal of Coastal Research	SI	75	1417 - 1421	Coconut Creek, Florida	2016

Rip Currents Generated by Distant Typhoons at Haeundae Beach of Korea: Forecast and Warning

Sung Bum Yoon[†], Ji Hoon Song[‡], Min Roh[§], and Junwoo Choi [§*]

[†]Dept. of Civil, Environmental and Plant Engineering, Hanyang University - ERICA Campus, Ansan, Republic of Korea

[‡]Dept. of Civil and Environmental Engineering, Hanyang University, Seoul, Republic of Korea

[§] Coastal Research Lab., Korea Institute of Civil Engineering and Building Technology, Gyang, Republic of Korea

www.cerf-jcr.org

www.JCRonline.org

ABSTRACT

Yoon, S.B.; Song, J.H.; Roh, M., and Choi, J., 2016. Rip Currents Generated by Distant Typhoon at Haeundae Beach of Korea: Forecast and Warning. *In:* Vila-Concejo, A.; Bruce, E.; Kennedy, D.M., and McCarroll, R.J. (eds.), *Proceedings of the 14th International Coastal Symposium* (Sydney, Australia). *Journal of Coastal Research*, Special Issue, No. 75, pp. 1417 - 1421. Coconut Creek (Florida), ISSN 0749-0208.

A rip current warning system, which estimates the rip current risk level based on the real-time incident wave conditions measured near the beach and the database pre-calculated using the Boussinesq wave model (Choi *et al.*, 2014), has been in operation at several beaches in South Korea. The warning system has been proved to be highly effective to reduce the rip current accidents in the beaches. However, it also suffers from the shortage of lead time of issuing the warning. In this study, the warning system was improved by forecasting the wave condition at the beach in advance with sufficiently long lead-time which was achieved by using the wave data of an ocean buoy deployed far from the beach towards the typhoon generating area. The empirical relation between the wave conditions at the two buoys was obtained to predict the wave condition at the Haeundae coast. The wave conditions predicted with 11-hour lead time agree reasonably well with those measured at the Haeundae coast.

ADDITIONAL INDEX WORDS: *Nearshore current, warning system, ocean buoy, Boussinesq wave model.*

INTRODUCTION

Haeundae is one of the most beautiful beaches in Korea, visited by millions of beach-goers every summer. However, Haeundae beach is also notorious for frequent and strong rip currents, where every recent year, hundreds of swimmers are reported as rescued. Studies by Bae *et al.*,(2013) and Yoon *et al.* (2014) have proposed the generation mechanisms of rip currents observed at Haeundae beach in a local viewpoint. For example, the alongshore non-uniform wave energy caused by the variations of incident waves and nearshore topography induces the rip currents. On the other hand, in a macro perspective, origins of the waves inducing the rip current events have not been studied.

At the Haeundae beach, dangerous rip currents occur mainly within the summer season, on sunny days with no local wind. Many people are caught by the rip current in the relatively calm sea and weather conditions. The incident waves generating rip currents are nearly monochromatic with the wave period of 7-13 seconds. These swell-like waves are supposed to be generated by distant typhoons as shown in Figure 1. From the characteristics of swells, it can be inferred that spectral wind waves might be generated by strong winds of a typhoon formed in Philippine Sea and some of them propagate with suffering in their dispersions and dissipations during the travel toward the south coast of the Korean Peninsula, especially to the Haeundae coast.

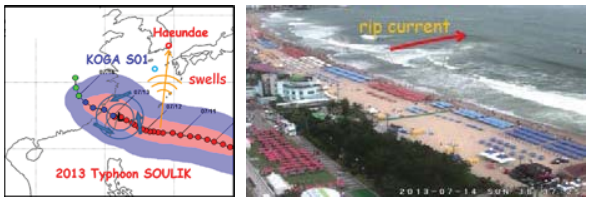

Figure 1. Swells and rip currents generated by Typhoon SOULIK in 2013 at the Haeundae beach.

In order to protect swimmers from rip current accidents, Choi *et al.* (2014) proposed a method for a rip current warning system, and Korea Hydrographic and Oceanographic Administration (KHOA) has established and operated the rip current warning system to several beaches including the Haeundae beach. The rip current warning system estimates the rip current risk level based on the real-time incident wave conditions measured near the beach and the database pre-calculated using the Boussinesq wave model, FUNWAVE (Chen *et al.*, 1999; Chen *et al.*, 2003; Johnson and Pattiaratchi, 2006; Choi *et al.*, 2015). However, the warning system is

DOI: 10.2112/SI75-284.1 received 15 October, 2015; accepted in revision 15 January 2016.
*Corresponding author: jwchoi@kict.re.kr
©Coastal Education and Research Foundation, Inc. 2016

suffering from the shortage of warning lead time since the observation of the warning system should be near the location of the seaward boundary of the numerical simulations.

This study investigates the swell waves inducing the rip currents at the Haeundae beach through analyzing the meteorological data (*i.e.*, typhoon tracking data) and the wave observations at a location 160km southward away from Jeju Island, Korea (*i.e.*, the ocean buoys of KHOA) and at near the Haeundae coast. To improve the rip current warning system with longer forecast lead-time, this study proposes the way to predict the wave condition at the Haeundae coast by using the relationship between the wave conditions at the two buoys. Section 2 describes the local mechanism to generate the dangerous rip current event at the Haeundae beach and the rip current warning system being in operation to the beach. Section 3 describes the way how to predict the wave condition of the Haeundae coast based on the ocean buoy observation far from the beach. Section 4 describes the prediction method that was applied to the algorithm of the rip current warning system.

BACKGROUND

Yoon *et al.* (2012) and Shin *et al.* (2014) described that the refraction of waves propagating over the central submerged shoal in the offshore can make the waves of honeycomb pattern at Haeundae beach as shown in the left panel of Figure 2. The waves of honeycomb pattern are generated by transformation when two wave trains propagate with slightly different directions (*i.e.*, interference pattern) in a shallow water. The nodal lines of the honeycomb pattern, which have the low wave-height areas of an alongshore-varying distribution, can play a role of a rip channel without respect to a topographical rip channel. The CCTV image shown in the right panel of Figure 2 presents the rip current generation process at the Haeundae beach. The honeycomb waves caused by the refraction of incident waves over the central shoal of the Haeundae coast break on the beach, thus generate rip currents along the nodal line of honeycomb waves.

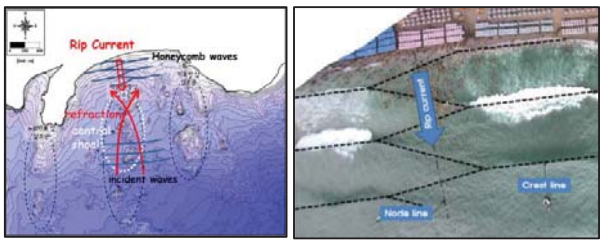

Figure 2. Schematic sketch of a rip current generated along the nodal line of honeycomb waves over topography (left) and video image (right) at the Haeundae beach on Aug. 10, 2012 (Yoon *et al.*, 2014).

A real-time rip current warning system was constructed to help mitigate against rip current accidents at Haeundae beach (Choi *et al.*, 2014). As shown in Figure 3, the system produces a real time sequence of index to quantify the risk and the likelihood of rip current based on the real time observations such as waves, currents, and tide. The index is estimated by using the rip current likelihoods derived from the results of various numerical simulations with various sea conditions using the Boussinesq wave model, the parameters of which correspond to the observation quantities. The rip current warning system takes into account the effects of wave height, wave period, wave direction, wave spectrum (*i.e.*, frequency-directional spreading), longshore currents, and tidal elevation on the rip current likelihood. The real-time observations, video image and the rip current warning index were provided to the coast guards at the beach by using the web-service (Figure 4) and the text service.

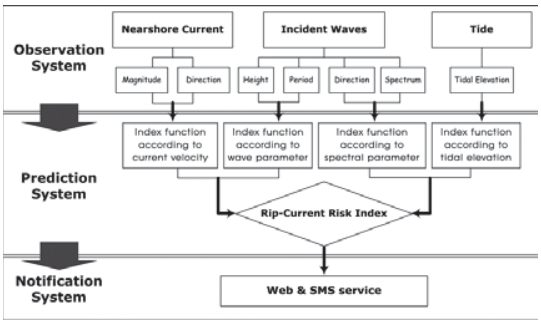

Figure 3. Conceptual flow chart of the real-time rip current warning system (Choi *et al.*, 2014).

The rip current warning system has been operated for three years since 2012 at the Haeundae beach, and its performance was proved to be successful. However, the system is suffering from the shortage of warning lead-time, since the observation of the warning system should be near the location of the seaward boundary of the numerical simulations.

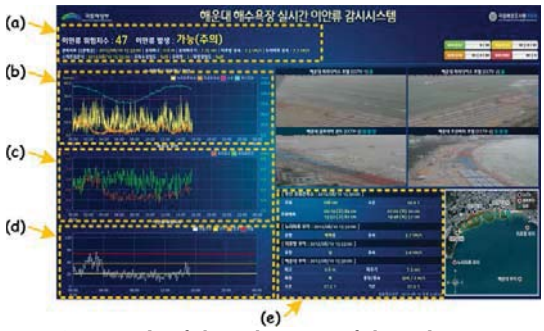

Figure 4. An example of the web-service of the real-time rip current warning system of KHOA including (a) the summary of observations and rip current index and level, (b) the observed tidal elevation and current velocities, (c) the wave height and period, (d) the rip current warning index, and (e) the other observations (Choi *et al.*, 2014).

METHODS

The warning system, which uses the real-time wave data measured at the buoy deployed at the Haeundae coast (*i.e.*, 1.5km from the coastline), is more accurate than other warning systems based on the forecasting wave conditions. However, the warning cannot be issued in advance. This section describes the way how to improve the rip current warning system by extending the lead-time of wave forecasting at the Haeundae coast. The modified warning system utilizes the wave data

measured at the KOGA-S01 buoy deployed far upwave towards the swell-generating open sea as shown in Figure 5.

The present technique estimates the wave information at the Haeundae coast with 11 hours of lead-time using the empirical correlation between the wave characteristics of wave heights, periods and directions measured at the KOGA-S01 buoy and the Haeundae buoy. Note that the observation buoy supports the significant wave height, the significant wave period, and the peak wave direction at every 30 min.

Figure 5. Location of KOGA-S01 buoy of KHOA.

In order to find the empirical correlation between the two measured wave data sets, the swell components were approximately extracted from the total measured waves, and the data sets of excess-swell-waves at the two locations were compared with each other. As using Eq. (1) and Eq. (2), the excess-swell-waves at each buoy are separated from the total measured waves by eliminating the antecedent-wind-waves, which can be assumed to be locally generated by winds, at each buoy.

$$H_{se} = \sqrt{{H_s}^2 - {H_{sb}}^2} \tag{1}$$

$$H_{he} = \sqrt{{H_h}^2 - {H_{hb}}^2} \tag{2}$$

where H_{se} indicates the excess-swell-wave height at the KOGA-S01 buoy, H_s denotes the total wave height measured at the KOGA-S01 buoy, H_{sb} represents the antecedent-wind-wave height at the KOGA-S01 buoy. H_{he} indicates the excess-swell-wave height at the Haeundae buoy, H_h indicates the total wave height at the Haeundae buoy, and H_{hb} indicates the antecedent-wind-wave height at the Haeundae buoy. The antecedent-wind-wave height was evaluated by using the average of 24 values (*i.e.*, equivalent to 12 hours) of the wave height paired with the wave period less than 6 s recorded at each present time. Note that the way how to divide the swell waves with the wind waves in the observations should be further studied for the future researches. From the comparison of the excess-swell-waves at the two locations for the several significant events (*e.g.*, as seen later in Figures 7 and 8), their cross-correlation suggests approximately 11 hr time-lag between them. Then, the correlation between the excess-wave height at the Haeundae buoy and the 11 hr lagged excess-wave height at the KOGA-S01 buoy was assumed to satisfy Eq. (3).

$$H_{he} = \alpha\, H_{se} \tag{3}$$

where α is the ratio between the excess-wave heights at the two locations, H_{he} and H_{se}, which can be obtained using Eq. (4) in terms of the wave direction θ measured at the KOGA-S01 buoy as shown in Figure 6.

$$\alpha = -0.0559\,\theta^2 + 0.5424\,\theta - 0.8351 \tag{4}$$

where θ indicates the 11-hr lagged wave direction (rad.) measured at the KOGA-S01 buoy. Subsequently, the wave height, H_h, and the wave period, T_h, at the Haeundae buoy can be predicted by using Eqs. (5) and (6), respectively.

$$H_h = \sqrt{{H_{he}}^2 + {H_{hb}}^2} \tag{5}$$

$$T_h = \frac{T_{hb}{H_{hb}}^2 + \beta T_s\, {H_{he}}^2}{{H_h}^2} \tag{6}$$

where T_h indicates the predicted wave period at the Haeundae coast, T_{sb} indicates the wave period of antecedent-wind-wave at the KOGA-S01 buoy, T_s indicates the wave period measured at the KOGA-S01 buoy, and β represents a tuning parameter (=1.15).

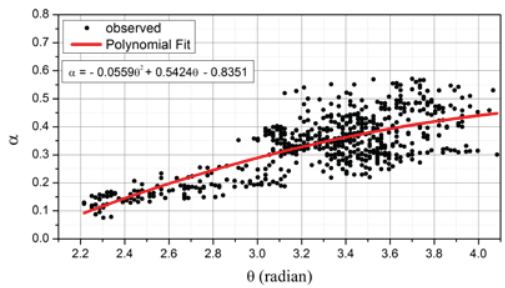

Figure 6. Ratio, α, between the excess-wave height measured at Haeundae beach, H_{he}, and the 11-hr lagged wave height measured at KOGA-S01, H_{se} ($\alpha = H_{he}/\,H_{se}$).

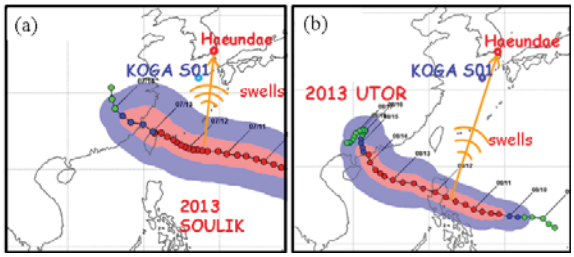

Figure 7. Paths of typhoons occurred in 2013, (a) Typhoon SOULIK, (b) Typhoon UTOR

RESULTS

Based on the empirical formula (1)-(6), the wave conditions at the Haeundae coast can be forecasted with 11 hr lead-time based on the real-time wave data measured at the KOGA-S01 buoy. In order to verify its applicability, the empirical formula were applied to the cases of swell events, which are generated by two typhoons, SOULIK and UTOR occurred in 2013 as shown in Figure 7.

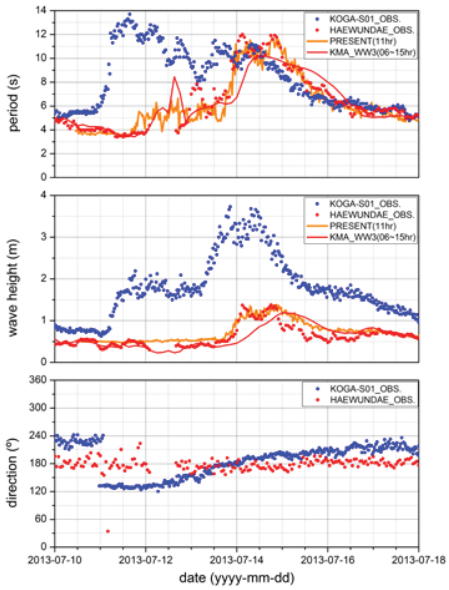

Figure 8. Comparison of time histories of wave information measured and forecasted at Haeundae beach for the case of swells generated by Typhoon SOULIK of 2013.

During the periods of the two typhoons, strong rip currents were reported at the Haeundae beach. The forecasted wave parameters were compared with the measured data observed at the Haeundae buoy. The results are shown in Figure 8 for the case of Typhoon SOULIK and in Figure 9 for the case of Typhoon UTOR. In addition, the present results are compared with the wave parameters predicted by Korea Meteorological Administration (KMA) which have 12 hr lead-time for the Haeundae coast. Note that the KMA data provides the 3 hr interval wave forecasts with 3 days lead-time for the near-field of Korean sea by running the WaveWatch3 global wave model based on predicted meteorological data. As a result, the forecasted wave data (*i.e.*, height and period) with 11 hr lead-time at the Haeundae beach agree reasonably well with the real-time measured data as shown in Figures 8 and 9. On the other hand, the wave data predicted by KMA for the 2013 Typhoon UTOR fail to give the swells at the Haeundae beach as shown in Figure 9. This might be because the performance of the wave forecast system managed by KMA is poor for the swells generated by distant typhoons. The swell induced by the 2013 Typhoon UTOR is captured by the KOGA-S01 buoy, and the present forecast method gives a satisfactory prediction at the Haeundae beach because the present technique uses directly the wave condition measured at the KOGA-S01 buoy.

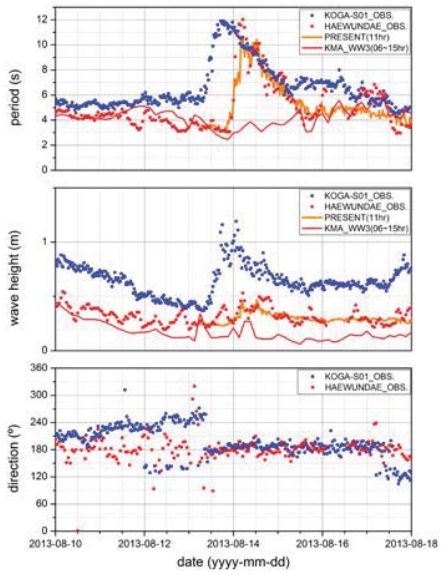

Figure 9. Comparison of time histories of wave information measured and forecasted at Haeundae beach for the case of swells generated by Typhoon UTOR of 2013.

Since the forecasted wave information is used as input wave data for the rip current warning system, the occurrence of rip current at the Haeundae beach can be forecasted 11 hours in advance. The present forecasting technique was applied to the rip current warning system for the cases of Typhoon SOULIK and Typhoon UTOR. The results as well as the time interval of rip current events at the Haeundae beach are shown in Figures 10 and 11. In the figures, the warning indices evaluated by using the measured data and the forecasted data at the Haeundae coast are compared with each other. The forecast warning index was evaluated by using the forecasted wave height and wave period. The waves are assumed to be from the south. On the other hand, the real-time warning index was evaluated by using the measured wave height, wave period, wave direction, spreading of wave spectrum, and tidal elevation. Note that for the forecast warning index, the spreading of wave spectrum was set to the values in most favor of generating rip currents.

Figure 10 shows the events in the 13th and 14th of July 2013 due to typhoon SOULIK, and Figure 11 shows the events in the 14th of August 2013 due to typhoon UTOR. It should be mentioned that even though the performance of the real-time warning system was proved to be successful, the system do not completely predict the actual time when rip currents occur. The forecast warning system involves the forecast wave data which are less accurate than the measurements at the Haeundae coast. Therefore, the forecast warning system is technically less accurate than the real-time warning system. Nevertheless, the forecast waning index can be produced in advance with 11 hr lead-time. On top of this, it agrees reasonably well with the real time warning index. Consequently, it can be said that the present

forecast rip current warning system is capable to be utilized for supplementing the real-time warning system.

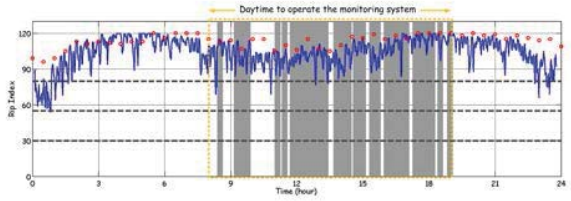

Figure 10. Comparison of time series of rip-current warning index in the 14th of July 2013 during the period of Typhoon SOULIK. The red circles indicate the forecasted warning index and the blue line indicates the real-time warning index. The gray broken lines of 30, 55 and 80 emphasize warning levels and the vertical wide gray bands indicate the rip current events.

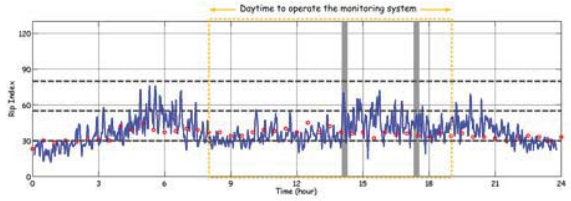

Figure 11. Comparison of time series of rip-current warning index in the 14th of August 2013 during the period of Typhoon UTOR. The legends are same as in Figure 10.

CONCLUSIONS

The rip current warning system, which estimates the rip current risk level based on the real-time measured near the beach and the data base pre-calculated using Boussinesq wave model, is in operation for the Haeundae beach. Even though the warning system has been effective to reduce the rip current accidents in the beach, it has the shortage of lead-time of issuing the warning. This study improved the rip current warning system through predicting the wave conditions at the beach in advance with sufficiently long lead-time by using the ocean buoy far from the beach. The prediction was achieved by the empirical relationship between the measurements at the two wave buoys. The predicted wave parameters with 11 hours lead-time agree reasonably well with those measured at the Haeundae coast. In addition, the present technique was applied to the rip current warning system for the cases of Typhoon SOULIK and Typhoon UTOR. The forecast warning index agreed with the real-time warning index as well as can be produced in advance with 11hr lead-time. Therefore, it can be expected that the present forecast rip current warning system is utilized for supplementing the rip current warning system.

ACKNOWLEDGEMENT

This study was performed by a project of “Investigation of large swell waves and rip currents and development of the disaster response system (No. 20140057)” sponsored by the Ministry of Oceans and Fisheries. We thank KHOA for making the extensive observations and the ongoing effort for data collection.

LITERATURE CITED

Bae, J.S.; Yoon, S.B., and Choi, J., 2013. Boussinesq modelling of a rip current at Haeundae Beach in South Korea. *In:* Conley, D.C.; Masselink, G.; Russell, P.E., and O’Hare, T.J. (eds.), *Proceedings 12th International Coastal Symposium* (Plymouth, England), *Journal of Coastal Research*, Special Issue No. 65, pp. 654-659.

Chen, Q.; Dalrymple, R.; Kirby, J.; Kennedy, A., and Haller, M., 1999. Boussinesq modelling of a rip current system. *J. of Geophys. Res.*, 104, 20617-20637.

Chen, Q.; Kirby, J.T.; Dalrymple, R.A.; Shi, F., and Thornton, E.B., 2003. Boussinesq modeling of longshore current. *J. of Geophys. Res.*, 108(C11), 26-1-26-18.

Choi, J.; Kirby, J.T., and Yoon, S. B., 2015. Boussinesq modeling of longshore currents in the Sandy Duck experiment under directional random wave conditions. *Coastal Engineering*, 101, 17-34.

Choi, J.; Lim, C.H., and Yoon, S.B., 2014. A rip current warning system based on real-time observations for Haeundae Beach, Korea. *In:* Lee, J.L.; Leatherman, Stephen P., and Lee, J. (eds.), *Proceedings, 3rd International Rip Current Symposium* (Busan, Republic of Korea), *Journal of Coastal Research*, Special Issue No. 72, pp. 56–62.

Johnson, D. and Pattiaratchi, C., 2006. Boussinesq modelling of transient rip currents. *Coastal Engineering*, 53, 419-439.

Shin, C.H.; Noh, H.K.; Yoon, S.B., and Choi, J., 2014. Understanding of rip current generation mechanism at Haeundae Beach of Korea: Honeycomb waves. *In:* Lee, J.L.; Leatherman, Stephen P., and Lee, J. (eds.), *Proceedings, 3rd International Rip Current Symposium* (Busan, Republic of Korea), *Journal of Coastal Research*, Special Issue No. 72, pp. 11–15.

Yoon, S.B.; Kwon, S.J.; Bae, J.S., and Choi, J., 2012. Investigation of characteristics of rip current at Haeundae Beach based on observation analysis and numerical experiments. *J. of the Korean Society of Civil Engineers*, 23(4B), 243-251. (in Korean)

Yoon, S.B.; Park, W.K., and Choi, J., 2014. Observation of rip current velocity at an accidental event by using video image analysis. *In:* Lee, J.L.; Leatherman, Stephen P., and Lee, J. (eds.), *Proceedings, 3rd International Rip Current Symposium* (Busan, Republic of Korea), *Journal of Coastal Research*, Special Issue No. 72, pp. 16–21.

Journal of Coastal Research	SI	75	1422 - 1426	Coconut Creek, Florida	2016

Study of the Residual Flow and Salinity during the Spring and Neap Tides at the Seokmo Channel, South Korea

Byung Il Yoon[†], Nakyong Choi[‡], Bon-Ho Gu[†], Jong Wook Kim[†], Jin Il Song[†], Chaewook Lim[†], Myung-Seok Kim[†], and Seung-Buhm Woo[†*]

[†]Department of Ocean Science
College of Natural Science, Inha Univesity
Incheon, South Korea

[‡]Pangyo R&D Center, Samsung Heavy Industries
Gyeonggi-do, South Korea

www.cerf-jcr.org

www.JCRonline.org

ABSTRACT

Yoon, B.I.; Choi, N.Y.; Gu, B.H.; Kim, J.W.; Song, J.I.; Lim, C.W.; Kim, M.S., and Woo, S.B., 2016. Study of the residual flow and salinity during the spring and neap tides at the Seokmo channels, South Korea. *In:* Vila-Concejo, A.; Bruce, E.; Kennedy, D.M., and McCarroll, R.J. (eds.), *Proceedings of the 14th International Coastal Symposium* (Sydney, Australia). *Journal of Coastal Research*, Special Issue, No. 75, pp. 1422 - 1426. Coconut Creek (Florida), ISSN 0749-0208.

The Seokmo (SM) channel of Gyeonggi Bay, located in the South Korea, exhibits unique and complex estuarine circulation characteristics. This study analyzed the salinity observations, and the cross-sectional variations in the residual current and strengths of stratification by tidal current, along two cross-channels transects, during the 13-hour periods of the spring and neap tides, respectively. The cross-sectional averaged residual velocity, at the northern entrance of the SM channel, showed a seaward directional flow of 0.05 m/s during the neap tide, and 0.21 m/s during spring tide. At the southern entrance, the residual current showed two-layer circulation with a landward flow in the bottom layer, and a seaward flow in the surface layer. The spatial characteristics of the landward residual current, at the southern entrance are different for the eastern and western sides of the channel, depending on the spring and neap tidal cycles. The variation in the location of the observed landward residual current, caused by the changes in spring and neap tidal cycles, and the correlation between this variation and the stratification, were analyzed using the Richardson number. At the northern and southern end of the SM channel, a landward residual current appeared in the location that Richardson number was large. These results suggested that the cross-sectional residual current pattern, at the SM channel, changes depending on freshwater and topographical influences, and is sensitive to tidal changes, such as changes in the spring and neap tidal cycles.

ADDITIONAL INDEX WORDS: *Residual current, stratification, Richardson number, Seokmo (SM) channel.*

INTRODUCTION

Gyeonggi Bay, which is located in the west coast of South Korea, is a semi-closed coastal region (Figure 1a). This estuary has a predominantly semidiurnal tide, with spring and neap tidal ranges of approximately 8.0 and 3.5 m, respectively and, due to large tidal range, the tidal flat has developed extensively. The estuarine circulation is both unique and complex, as it is connected to intricate coastlines and a high number of waterways (*e.g.*, Park *et al.*, 2002; Yoon and Woo, 2013). The seasonal variation of the freshwater discharge from the Han River has a significant effect on the estuarine circulation. The Seokmo (SM) channel, which is the key subject area of this study, has a width of 1.4 km and a length of 15.9 km, and it is located in the west of Ganghwado (Figure 1b).

The tidal residual currents in Gyeonggi Bay have been studied by Kim *et al*. (2009), Lee *et al.* (2012), and Yoon and Woo (2013). Previous studies of the SM channel have either analyzed the entire channel using a mooring point or have used numerical models, and, for this reason, it was not possible to carry out studies successfully on the overall current and salinity distribution of the channel. Therefore, the objective of our research was to understand the cross-sectional residual current characteristics, during the spring and neap tidal cycles.

METHODS

Observations of the SM channel were conducted at an interval of a 1-hour, for duration of 13 hours, over a period of 4 days, between August 24 and August 31, 2011. Regarding the observation equipment, a 600-kHz acoustic Doppler current profiler (ADCP) was used for Line 1, situated at the northern end of the SM channel (Figure 1c), and Line 2 situated at the southern end (Figure 1d). Additionally, the salinity was observed using Conductivity-Temperature-Depth (CTD) profiles at several observation stations in the SM Channel, as well as at same locations as the observation lines where the ADCP was used (Figure 1b).

The tidal ranges during the observation period, provided by the Korea Hydrographic and Oceanographic Administration, were 2.5 and 9.3 m for the neap and spring tides, respectively. Additionally, freshwater discharge data was collected in order to compare the change in magnitude of the tidal current because freshwater discharge has a significant influence on the tidal flow of the SM channel (Kim *et al.*, 2009).

DOI: 10.2112/SI75-285.1 received 15 October, 2015; accepted in revision 15 January 2016.
*Corresponding author: sbwoo@inha.ac.kr
©Coastal Education and Research Foundation, Inc. 2016

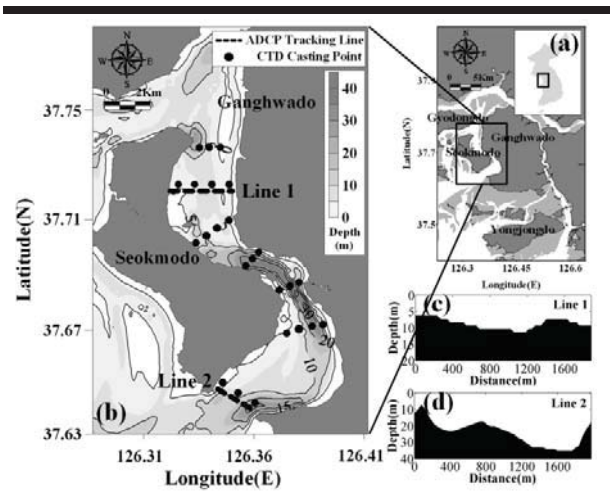

Figure 1. The study area (a) and field measurement locations of ADCP transects (b) for Lines 1 and 2. Mean depth at the north (c) and south (d) entrance of the Seokmo channel.

The ADCP raw data had a 4-stage conversion process. First, we used the method described previously by Valle-Levinson and Atkinson (1999), and obtained a single value for the averaged 10-sets of raw data. In the second stage, we removed the portion of the data which had a scale value (percent good) beam correlation of below 80% and velocity error greater than 10% of the averaged current value obtained from the averaged horizontal grid data. In the third stage, the angles were transformed. We transformed the velocities into a true north coordinate system (7-degree), and in order to correct for the vessel error, we applied the vessel speed calibration (Joyce correlation) method used by Joyce (1989). The principal component analysis is a method used to linearly transform the *u* (east-west direction) and *v* (south-north direction) components, extracted from the current data (ADCP), into a new coordinate system with longitudinal and transverse directions. This enables us to perform an analysis of the most dominant component (Preisendorfer and Mobley, 1988).

In the last stage of the data processing, we additionally transformed the data into vertical and horizontal Sigma coordinates. Due to ADCP cross-sectional observations were performed in this study area, it is difficult to construct the same grid for not only the changes in the vertical sea-level height (with respect to time, and to the spatial locations of the observations), but also for the horizontal coordinates correspond to the distance. To resolve this problem, this study included a transformation of the z-level velocities, which was verified by Lee *et al*. (2012), transforming them into a horizontal Sigma grid. Constructing a vertical and horizontal Sigma grid is useful because the entirety of the data, from all of the water layers, can be used in regions with large tides, such as the subject region of this study.

RESULTS

Figure 2 depicts the maximum flood and ebb currents during the spring and neap tides, for Lines 1 and 2. As the figure shows the cross-sections of the channel as viewed from the south, the

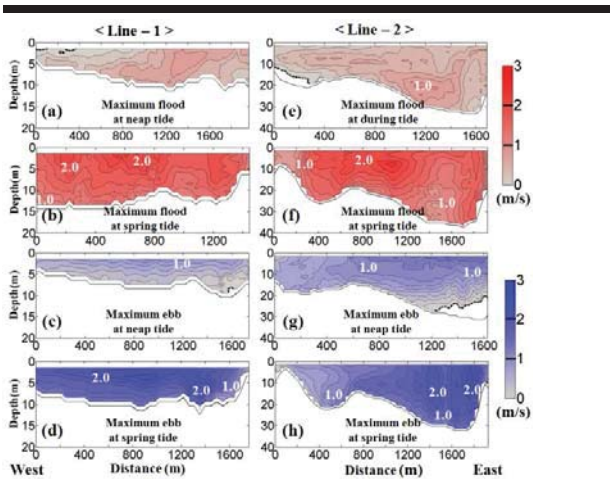

Figure 2. The along-channel current distribution at Lines 1 and 2 (towards the north). The figures on the left-hand side represent Line 1, and the figures on the right-hand side represent Line 2. The water depth (bathymetry) for (a)-(d) is difference because transects of Line 1 are difference according to spring and neap tide.

left and right sides of the figure represent the west and east directions, respectively.

For Line 1, during the neap tide, the ebb current appeared to be stronger than the flood current by more than 0.20 m/s. The maximum flood current was 0.89 m/s (Figure 2a) and maximum ebb current was 1.36 m/s (Figure 2c). Significantly higher currents were found during the spring tide, where a flood current of 1.84 m/s (Figure 2b) and an ebb current of 2.41 m/s (Figure 2d) were observed. For Line 2, a flood current of 0.98 m/s (Figure 2e) and an ebb current of 1.56 m/s (Figure 2g) were observed during neap tide, while a flood current of 2.39 m/s (Figure 2f) and an ebb current of 2.53 m/s (Figure 2h) were observed during spring tide. We found that the maximum current of Line 2 was greater than that of Line 1, but that the averaged cross-sectional current, during the spring tide, was greater for Line 1 than for Line 2.

The current at the surface layer appeared to be relatively high compared to that of the bottom layer. This was because of the bottom friction and freshwater discharge at Lines 1 and 2. In the case of Line 2, the current was relatively high on the east side compared to the west. In Line 2, the direction of the cross-section was from the south to the north, while the water flowed from the south-to-west to north-to-east directions, rather than the south-to-north direction, as was determined by the PCA analysis results (not shown).

Due to the aforementioned topographical reasons, the flow magnitude is greater than the eastern side. For the neap tide, the dotted line indicates the 0 (zero) line, classifying the region that flows in the opposite direction to the cross-sectional fluid flow. Therefore, we inferred that the flow caused by the strong

freshwater discharge is the reason why the current flows in the opposite direction, despite it being the maximum current. The SM channel is a region greatly affected by the freshwater discharge; therefore, there is a clear difference in the current distributions between the surface and bottom layers.

The M_2 and M_4 tidal components were removed from the value of each cell that was repeatedly observed, and the calculated value was defined as the residual current (Lwiza *et al*., 1991).

$$v_0 = v - \sum A_n \cos(\omega_n - \phi_n) \quad (1)$$

Here, v refers to the averaged 13-hour velocity in the axial direction (along-channel velocity), and v_0 refers to the residual velocity. A_n refers to the amplitude, ω_n refers to the angular velocity and ϕ_n refers to the phase angle. In the above equation, the v_0 value that remains after considering the phases of the M_2 and M_4 tidal components is defined as the residual current.

Figure 3 shows the cross-sectional and vertical residual current distributions at several stations located on the cross-section, during the neap and spring tides. The black dotted line in the residual current distribution plot represents the 0 m/s line, and the black dotted line in the average salinity distribution plot represents the 5 psu line. During the neap tide, at Line 1, the seaward residual current (maximum current: 0.34 m/s) was dominant through the entire surface layer due to the freshwater discharge. In the bottom layer, the landward residual current (maximum current: 0.13 m/s) was dominant.

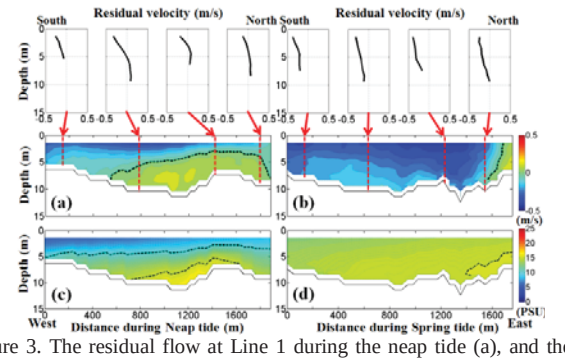

Figure 3. The residual flow at Line 1 during the neap tide (a), and the spring tide (b). The vertical profiles of the residual current at selected sites (red dotted line) in the transects are shown in the upper region of the figure. The bottom panel shows the tidally mean salinity during the observation period (c and d).

The landward residual current was found to be moving toward the east, which is on the right hand side of the channel cross-section (Figure 3a). Additionally, the averaged salinity was observed to be high in the east, which is the region where the landward residual current is illustrated (Figure 3c). The vertical structure of the residual current is different for the spring and neap tides. In the case of Line 1, during the neap tide, the ebb-directional residual current appeared in the surface layer, whereas the flood-directional residual current was strongest at the center of the cross-section.

During spring tide, the maximum landward residual current was 0.13 m/s in the bottom layer, where the averaged salinity was higher than that of the neap tide. The seaward residual current component, with a maximum velocity of 0.40 m/s, was found (Figure 3b). At this point, the landward directional residual current in the bottom layer was observed in a region further to the east, during the spring tide, than was observed during the neap tide. In contrast to the neap tide, the flood current during spring tide showed a similar distribution to that of the cross-section, whereas the ebb current was lower to the east of the channel. Therefore, the landward residual current for the spring tide was found to move more eastward than the neap tide. We hypothesized that this finding was due to the friction that resulted when the observation line at the east of the channel was not observed completely because of the tidal flat.

Similar to Line 1, the cross-sectional residual current and the averaged salinity distribution during the neap and spring tides, for Line 2, are illustrated in Figure 4. During the neap tide for Line 2, the seaward residual current of 0.54 m/s, and the landward residual current, with a maximum current of 0.43 m/s at the right hand side of the channel cross-section, are shown (Figure 4a). As in Line 1, the surface layer contained a dominantly seaward residual current, whereas a landward current, with a high salinity, was found throughout the eastern side of the channel. The residual current appeared in the eastern side of the channel, had a similar pattern of maximum current. During the spring tide, the ebb-directional residual current was observed at the eastern side of the channel, whereas a two-layer circulation pattern appeared at the western side.

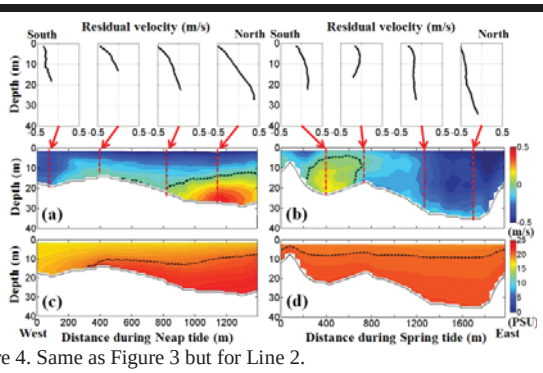

Figure 4. Same as Figure 3 but for Line 2.

During the spring tide, the landward residual current, with a maximum current of 0.22 m/s, and a seaward residual current component, with a value of 0.68 m/s, were observed (Figure 4b), and, due to mixing the salinity was evenly distributed (Figure 4d). The seaward residual current component was strongly apparent, and, unlike during the neap tide, the landward residual current component was found to be moving to the west, which is to the left hand side of the channel cross-section.

DISCUSSION

As shown from the observation results, the SM channel showed a significant difference in salinity between the northern and southern ends throughout the entire channel. In regions

similar to the SM channel, the difference in the density, due to the salinity variation, had a significant effect on the residual flow (*e.g.*, Geyer, 1987). Additionally, because the SM channel region is largely affected by freshwater discharge, when we examined the distribution of the average salinity, the two layer salinity structure was clearly apparent, as a result of the vertical salinity difference. Moreover, when we examined the distribution of the residual current, the distribution pattern of the cross-sectional residual current varied between the spring and neap tide, for Lines 1 and 2. In the case of Line 1, the landward residual current in the bottom layer, during the spring tide, appeared to occur closer to the eastern side, compared to during the neap tide, whereas, for Line 2, it appeared to occur closer to the western side during the spring tide, compared to during the neap tide. These variations suggest that the relationship between the spring and neap tides, during which the landward residual current appears, is different for Line 1 than for Line 2. In order to establish the relationship between the spring and neap tides, we analyzed the relationship between the degree of stability and the residual current during the observation period.

The stability within the cross-section of the channel can be expressed using the Richardson number (*Ri*), which is an index that represents the ratio of the buoyancy frequency (N^2) and to the stress of the vertical velocity (S^2)

$$Ri = -\frac{g}{\rho}\frac{\partial\rho/\partial z}{[(\partial U/\partial z)^2+(\partial V/\partial z)^2]} = \frac{N^2}{S^2} \quad (2)$$

Here, g refers to the gravity, ρ refers to the density, U refers to the across-channel velocity, V refers to the along-channel velocity and z refers to depth. Through experimentation and observation, a range of 0.25-0.33 was proposed as the limit of the shear instability of the *Ri* (Simpson and Briiter, 1979). If the *Ri* is less than this threshold, the shape of the stratification section appears linear, depending on the depth (Geyer, 1987). However, if the *Ri* is greater than this threshold, the direction of the velocity may appear to be different, or the difference in the velocity may be significant.

In order to compare the characteristics of the variation of the residual current in the SM Channel, the *Ri* was determined based on the observation results. Here, we applied the density value that was calculated using the salinity value that was observed from the CTD profiles. In addition, both the current and density are required to find the *Ri*, and the current value used here to find the *Ri* is the current that corresponds to the location of the CTD observation.

Figure 5 illustrates the *Ri*, in addition to the distribution of the residual current. When the *Ri* value is significantly changed, the direction of the current changes (Framinan *et al*., 2008). It was suggests that the change in the residual current has a significant influence on the change in stratification (Prandle, 1981). In regions where the flood-directional residual current appears in the bottom layer, we can see that the *Ri* becomes abnormally large. Similar results were found for both Line 1 and Line 2 during the neap tide as well as during the spring tide. Because this comparison is between the *Ri* for 1 hour and the residual current, we cannot use the threshold used in previous studies. However, this result still shows that the region in the bottom layer, where the landward residual current occurs is very unstable.

The *Ri* becomes larger when the landward residual current in the bottom layer is observed for all flood tides. However, low *Ri* values were observed at a point 1400 m from the western side of the channel during the ebb tide of the neap period and a point 1600 m from the western side of the channel during the ebb tide of the spring period even though a landward residual current occurred in the bottom layer. This phenomenon occurred because there was no stratification during the ebb tide; however, stratification did occur during the flood tide, causing the formation of a landward residual current in the bottom layer. Additionally, during the neap period, when we found that the *Ri* became significantly large at the center of channel during the flood tide, and that the *Ri* became significantly large in the eastern side of the channel during ebb tide, the unstable velocity pattern, during the flood and ebb tides, was found to have moved from the center to the eastern side of the channel. This result indicates that the levels of instability in the stratification and velocity were different for the flood and the ebb tides.

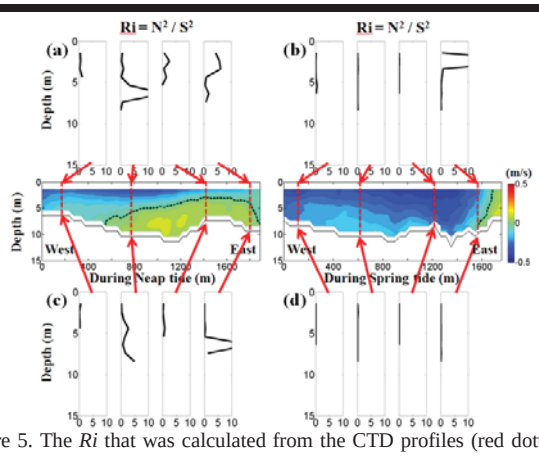

Figure 5. The *Ri* that was calculated from the CTD profiles (red dotted line) for Line 1. The results during neap and spring tides are shown in the left and right panel, respectively, during the flood tide: (a) and (b), and ebb tide: (c) and (d). For comparison, the residual velocity is shown in the center of the figure (flowing towards the north).

Figure 6 shows the *Ri* and residual currents for Line 2, in the same way as it was shown for Line 1. In the region where the landward residual current occurs in the bottom layer, with respect to the channel cross-section, the *Ri* is large and unstable. A large *Ri* was found in the region with a landward residual current in the bottom layer during the spring tide; however, during the neap tide, the *Ri* value was large in the western side, despite the fact that the landward residual current was not observed. The reason for this is that, for Line 2, the current appeared to be greater in the western side of the cross-section than in the eastern side; therefore, the *Ri* value was greater. This finding also demonstrated that the change in the vertical stability, in the transverse direction within the cross-section, was much greater during the neap tide than during the spring tide.

As shown in previous studies comparing the stability and the residual current, the comparison between the *Ri* and the residual current, in this study, demonstrated that in a region with a large *Ri*, the residual current for the channel cross-section presents different patterns in the surface layer than in the bottom layer.

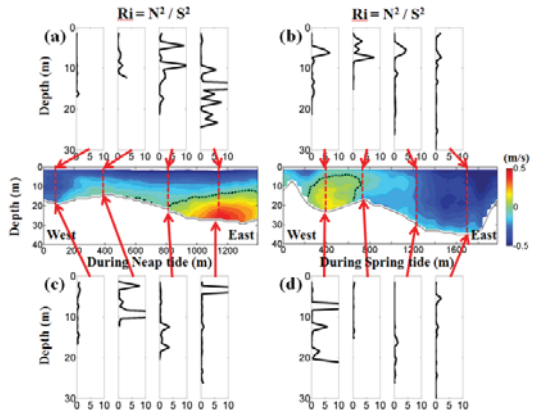

Figure 6. Same as Figure 5 but for Line 2.

Although the stability was not likely to be the reason for the occurrence of a landward residual current into the bottom layer as observed via a cross-sectional observation, one of the characteristics of the residual current that changes in the SM channel is exhibited through the stability.

CONCLUSIONS

In this study, the cross-sectional current and salinity distributions were observed during a continuous 13-hour period, at 2 different cross-sections which located at the northern and southern ends of the SM channel, South Korea. The residual current component, in the cross-section at the northern end of the SM channel, showed a seaward flow, whereas landward flows were found at the southern end. However, a landward residual current was observed in the bottom layer in every channel cross-section, thus clearly indicating a two-layer circulation structure.

As a result of analyzing the *Ri*, which is an index that represents the stability of the channel cross-section, we found that it increased in regions where the landward residual current appeared in the bottom layer during both the flood and ebb tides. These results indicated that in some regions of the cross-section, the stratification is stronger where vertical mixing does not actively occur. Thus, we cannot state that the stratification is the reason for the varying distribution patterns of the landward residual current in the bottom layer at the northern and southern ends of SM channel. However, using this analysis, we found that the landward residual current in the bottom layer occurred at a value which represents the stratification.

ACKNOWLEDGMENTS

This research was a part of the project titled ‘Development of integrated estuarine management system’, funded by the Ministry of Oceans and Fisheries, Korea. Additionally, this work was supported by INHA UNIVERSITY Research Grant.

LITERATURE CITED

Framinan, M.; Valle-Levinson, A., and Sepulveda, H. 2008. Tidal variations of flow convergence, shear, and stratification at the Rio de la Plata estuary turbidity front. *Journal of Geophysical Research*, 113(C8), 1-17.

Geyer, W.R. and Smith, J.D., 1987. Shear instability in a highly stratified estuary. *Journal of Physical Oceanography*, 17(10), 1668-1679.

Joyce, T.M., 1989. On in situ “calibration” of shipboard ADCPs. *Journal of Atmospheric and Oceanic Technology*, 6(1), 169-172.

Kim, C.S.; Lim, H.S.; Kim, J.A., and Kim, S.J., 2009. Residual flow and its implication to macro-tidal flats in Kyunggi Bay estuary of Korea. *Journal of Coastal Research*, Special Issue No. 56, 976-980.

Lee, D.H.; Yoon, B.I.; Kim, J.W.; Gu, B.H., and Woo, S.B., 2012. The cross-sectional mass flux observation at Yeomha channel, Gyeonggi Bay at spring tide during dry and flood season. *Jouranl of Korean Society of Coastal and Ocean Engineers*, 25(1), 16-25.

Lwiza, K.M.M.; Bowers, D.G., and Simpson, J.H., 1991. Residual and tidal flow at a tidal mixing front in the North Sea. *Continental Shelf Research*, 11(11), 1379-1395.

Park, K.; Oh, J.-H.; Kim, H.-S., and Im, H.-H., 2002. Case study: mass transport mechanism in Kyunggi Bay around Han River mouth, Korea. *Journal of Hydraulic Engineering*, 128(3), 257-267.

Prandle, D., 1981. Salinity intrusion in estuaries. *Journal of Physical Oceanography*, 11(10), 1311-1324.

Preisendorfer, R.W. and Mobley, C.D., 1988. Principal component analysis in meteorology and oceanography. *Developments in Atmospheric Science*. Amsterdam, 425p.

Simpson, J.H. and Britter, R., 1979. The dynamics of the head of a gravity current advancing over a horizontal surface. *Journal of Fluid Mechanics*. 94(3), 477-495.

Valle-Levinson, A. and Atkinson, L.P., 1999. Spatial gradients in the flow over an estuarine channel. *Estuaries*, 22(2), 179-193

Yoon, B.I. and Woo, S.B., 2013. Tidal asymmetry and flood/ebb dominance around the Yeomha channel in the Han River Estuary, South Korea. *Journal of Coastal Research*, Special Issue No. 65, 1242-1246.

Journal of Coastal Research	SI	75	1427 - 1431	Coconut Creek, Florida	2016

Development of a near real-time forecasting system for storm surge and coastal inundation

Jong-Joo Yoon †, Jae-Seol Shim ‡*

† ChungNam Institute, Chungcheongnam-do training road 73-26, Gongju, South Korea

‡ Korea Institute of Ocean Science & Technology(KIOST), 787 Haean-ro, Sangnok-gu, Ansan, South Korea

www.cerf-jcr.org

www.JCRonline.org

ABSTRACT

Yoon, J.J. and Shim, J.S., 2016. Development of a near real-time forecasting system for storm surge and coastal inundation. *In:* Vila-Concejo, A.; Bruce, E.; Kennedy, D.M., and McCarroll, R.J. (eds.), *Proceedings of the 14th International Coastal Symposium* (Sydney, Australia). *Journal of Coastal Research*, Special Issue, No. 75, pp. 1427 - 1431. Coconut Creek (Florida), ISSN 0749-0208.

Climate change is resulting in an increase in disastrous effects, such as sea level rise, intensity and frequency of storms, abnormal waves, and storm surges, in densely populated coastal areas. In particular, the coast of Korea was repeatedly damaged by storm surge and subsequent inundation caused by the approach of strong typhoons. Therefore, it is desirable to accurately forecast storm surge height and coastal inundation. In this study, a rapid, near real-time forecasting system was developed for addressing coastal inundation. A primary study of this system for operational forecasting using typhoon advisories was conducted and applied for the 2012 typhoon Sanba. To develop this forecasting system, a systematic investigation of storm surge impacts to the Korean coast was conducted using the unstructured grid model, FVCOM. This model was employed to simulate near-future storm surges and their corresponding inundation characteristics. Observed surges and inland inundation data were used to validate the model with satisfactory results. In this forecasting system, full automatic computations according to typhoon advisories were conducted for each typhoon invasion and uploaded to the disaster warning system. Less than one hour from starting the calculation, all pre- and post-processing was completed using parallel clusters. We also collected field measurements to compare with simulated inundation results for typhoon Sanba. The forecasting simulation results agreed with the observational data. The system developed in this study could be useful as a pre-warning system to prompt preparation of detailed evacuation plans that address storm surge inundation problems.

ADDITIONAL INDEX WORDS: *Storm surge, Operational prediction system, TC96, FVCOM, Numerical simulation.*

INTRODUCTION

As the intensity and frequency of typhoons increase because of climate change, risk of inundation damage caused by storm surge in major coastal cities is likely to grow. These coastal disasters have a tendency to take place on a large scale and are hard to predict. Korea has extended the range of use of coastal areas through reclamation projects. Consequently, coastal disaster damage could increase significantly in those areas. In order to establish a coastal management plan to minimize disaster damage, it is necessary to develop technology for responding to coastal inundation.

Typhoon Maemi, which struck South Korea in September 2003, destroyed about $4.2 billion worth of property and resulted in 131 human casualties. In November 2013, typhoon Haiyan hit the Philippines and left about 8000 people dead. Therefore, it is urgent that measures to protect property and lives against these coastal disasters be established. The sole use of structures such as shore protection and coastal dykes, however, cannot completely prevent damages due to storm surges and high waves. In addition to these structural measures, non-structural hazard mitigation measures such as forecasting systems are also important because they allow people to promptly prepare for disaster and mitigate the scale of damage.

To accurately predict the areas that storm surge might affect, fine-grid ocean numerical models that comprehensively consider oceanic conditions such as tide, surge, and waves should be established in conjunction with accurate fine-grid meteorological model. GIS Database, which identifies geographical features of coastal areas by systematically combining land elevation and water level data, should also be deployed. In this study, we accurately simulated the typhoon wind field to estimate the surge height and predict inundation area during a typhoon landing. We established the storm surge model using simulated meteorological results. Based on the storm surge model, we operated the coastal inundation forecasting system, targeting major low-lying coastal areas. The system was designed to generate near real-time forecasting data regarding inundation while a typhoon was landed.

The U.S. has experienced massive damages from hurricanes over time. For this reason, the SLOSH (Sea, Lake, and Overland Surges from Hurricanes) model is run by the National Hurricane Center (NHC) under the National Oceanographic and Atmospheric Administration (NOAA) to forecast maximum wave height and probabilistic wave height throughout the

DOI: 10.2112/SI75-286.1 received 15 October, 2015; accepted in revision 15 January 2016.
*Corresponding author: jsshim@kiost.ac
©Coastal Education and Research Foundation, Inc. 2016

country (Glahn *et al.*, 2009). Additionally, a storm surge forecasting system using the ADCIRC model is operated to predict storm surge in real-time as a storm approaches (Fleming *et al.*, 2008; Forbes *et al.*, 2010; Blanton *et al.*, 2012).

The research status in Korea, however, was not mature compared to these developed cases. As such, an accurate and immediate storm surge forecasting system coupled with the storm forecast issued by the Korea Meteorological Administration (KMA) has begun development. The storm surge forecasting system suggested in this study has been run and used to predict the occurrence of inundation since 2012. While typhoons rarely directly affected the Korean Peninsula from 2013 to 2015, four typhoons hit the peninsula in 2012. Typhoon Sanba hit the southern coast in September 2012 and was expected to cause significant damage because its intensity and tracking path were similar to typhoon Maemi, which caused record-breaking coastal damage. In fact, massive damages and losses occurred in several low-lying areas on the southern coast of Korea due to storm surge and high waves.

In this study, we evaluated the performance of the inundation prediction system that was used when typhoon Sanba struck South Korea in 2012. We also conducted an inundation trace investigation for the areas damaged by inundation after the typhoon passed so as to estimate the system's applicability.

ESTABLISHMENT OF OPERATING SYSTEM

Operating storm surge prediction system

The storm surge and coastal inundation forecasting system predicts real-time storm surge conditions. Once a typhoon forms, several agencies, such as the KMA, Japan Meteorological Agency (JMA), and Joint Typhoon Warning Centre (JTWC), issue a real-time advisory and typhoon information every six hours. The typhoon advisory includes forecast information about tracking path and typhoon intensity.

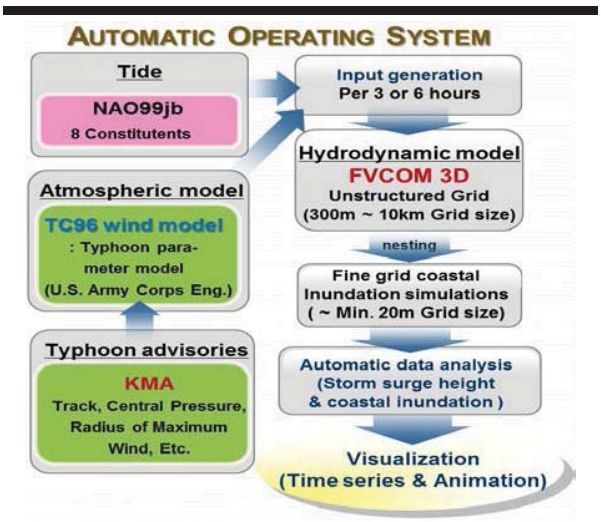

Figure 1. Flow chart of the near real-time storm surge inundation prediction system.

The storm surge forecasting system immediately executes a numerical ocean model, making use of the data in these typhoon advisories. The system generates 72-hour short-term prediction results in nearly real-time, including sea level with tides and surges, variation of currents, and areas likely to be inundated.

Figure 1 illustrates a flow chart of the near real-time storm surge inundation prediction system suggested by this study. During a typhoon, the meteorological data from a typhoon wind model (TC96) is used to estimate surge height. To simulate inundation caused by storm surge, an additional simulation is conducted for the nesting grid, extending computation coverage to low-lying coastal areas. A critical characteristic of this system is fast computing in response to typhoon warning updates. The system proposed in this study has relatively prompt forecasting capability; it can produce 72-hour prediction information within one hour of obtaining the typhoon data. The generated results are immediately sent to the local authority for coastal disaster prevention. The system continues to update the forecast results in accordance with typhoon advisory updates.

Typhoon wind model and storm surge model

To simulate the surge that occurs as a typhoon moves, accurate meteorological forecast data is essential. It is also important to choose a suitable sea-surface wind model to reproduce temporal and spatial variation of the typhoon wind field. Additionally, typhoon parameters necessary for calculating sea-surface wind need to be estimated accurately. For the ocean, there generally is not enough observation data readily available. Therefore, it is necessary to make use of satellite observation and numerical model analysis data in order to precisely analyze a typhoon. To estimate surge height, it is necessary to consider temporal and spatial data of sea-surface wind and atmospheric pressure field as external forces. In this study, TC96, which is a planetary boundary layer (PBL) model, was used to estimate wind and atmospheric pressure fields under typhoon conditions. Primary input parameters for TC96 comprised center position of typhoon, minimum center pressure, and radius of maximum wind. The TC96 wind model was introduced by Cardone *et al.* (1994) and Thompson and Cardone (1996), with support from the U.S. Army Corps of Engineers.

A 3-D finite-volume ocean model, FVCOM (Finite-Volume Coastal Ocean Model; Chen *et al.*, 2006) adopting a triangular grid was used to estimate storm surge. FVCOM employs the finite-volume method (FVM). FVCOM combines a numerical calculation flow of the finite-difference method (FDM) and a triangular unstructured grid system of the finite-element method (FEM). FVCOM balances the efficiency of discrete characteristics of FDM with the geometric flexibility of FEM. The wet/dry treatment method is also applied to simulate coastal inundation. Further model details are noted by Yoon and Shim (2013).

Mesh generation and boundary conditions

In the case of storm surge along Korea's southern coast, spatial variation tends to increase due to local geological influence. To better account for this spatial variation, fine-grid bathymetry data is required. To simulate storm surge height, it is particularly important to generate an exact water depth grid using bathymetry data.

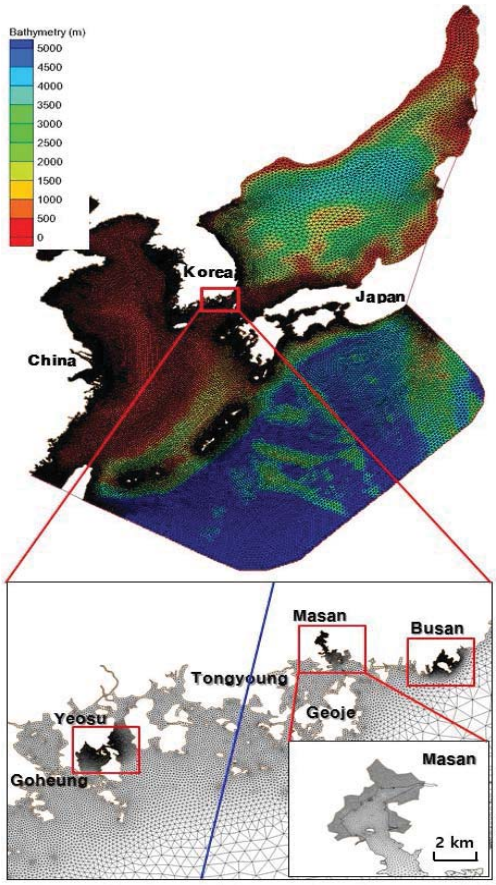

Figure 2. Overview of model domain, grid composition, and bathymetry distribution. Blue line represents moving track of typhoon Sanba.

Grid mesh used to simulate storm surge covered an extensive region including the Yellow, East (Japan), and East China Seas, as illustrated in Figure 2. The grid system was composed of unstructured triangular mesh in which the minimum grid size (close to the coastal area) was about 300–400 m. To simulate inundation in coastal land areas such as Yeosu, Masan, and Busan, the grid was extended to areas with elevations less than 10 m, and the minimum grid size was reduced to 20–30m. The total number of nodes was 136,570; the total number of elements was 258,482. Storm surge height was estimated in 3-D simulations. The vertical grid comprises eleven sigma layers. Water depth data were obtained from the digital nautical chart published by the Korea Hydrographic and Oceanographic Administration (KHOA); water depth data for areas outside the coastal area were obtained from ETOPO1 data (Amante and Eakins, 2008). Eight major tidal components of NAO99jb (Matsumoto *et al.*, 2000) were used as input to harmonic constants applied to open boundaries of the model.

OPERATION CASE OF STORM SURGE INUNDATION PREDICTION SYSTEM

Typhoon Sanba

Typhoon Sanba was the strongest typhoon that hit Korea in 2012. When it landed on the southern coast, it moved rapidly at speeds up to 43 km/hr. It had a maximum instantaneous wind speed over 40 m/s, barometric pressure of about 960 hpa, 60 mm/hr of heavy rain, and more than 1 m of maximum surge height during coastal landfall.

Figure 3. Cases of storm surge inundation damage in Masan by Typhoon Sanba, 2012.

During typhoon Sanba, the storm surge inundation prediction system was operated with every typhoon information update (KMA) at 3 hours intervals. Typhoon data that were released at 7 AM (LST) on September 17, 2012, the moment before typhoon landing, were applied to this study. Tracks of typhoon Sanba looked similar to that of Maemi in 2003. These typhoons maintained their circular shape until landfall on the coast.

When typhoon Maemi arrived, extreme storm surge and high tide were observed in some areas around Yeosu, Masan, and Tongyoung (Figure 2). Similar to typhoon Maemi, typhoon Sanba was expected to cause significant inundation damage to major coastal cities because it was anticipated to come during high tide. Fortunately, the worst inundation damage was avoided because maximum storm surge height occurred just after high tide. Inundation damage, however, could not be avoided in some coastal regions near Masan and Tongyoung (Figure 3).

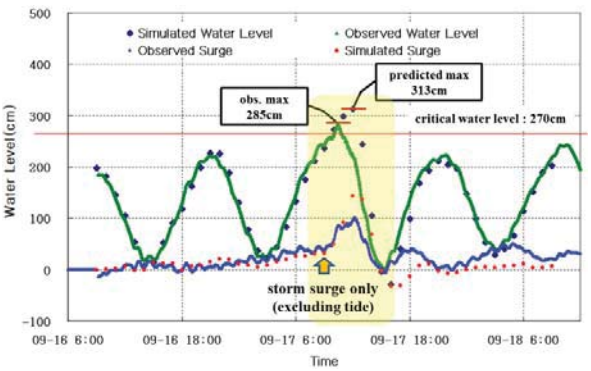

Figure 4. Comparisons of storm surge time variations at Masan tidal station during typhoon Sanba.

Results of storm surge inundation prediction

Figure 4 shows the predicted values of storm surge height for typhoon Sanba in Masan. This figure compares simulated results to observed data recorded by the tidal station. The estimated value of maximum water level including tide was about 313 cm at 12:00 PM (LST) on September 17, while the observed record was 285 cm at 10:30 AM on the same day. The prediction of maximum surge height excluding tide was simulated as 150 cm, while the observed record was 102 cm. Therefore, deviation of maximum surge height was about 48 cm.

The gap between observed and simulated results might be caused by several reasons. The first reason might be that recorded maximum surge height occurred one to two hours later than maximum tide level (during the ebb tide). Second, typhoon forecast data such as typhoon track and minimum central pressure (KMA), could contain errors. Third, primary external forces, such as wind and pressure field generated by the sea-surface wind model, might not exactly reproduce the meteorological field. Figure 5 compares the observed and simulated wind and air pressure time variations at Masan tidal station; wind speed was overestimated in comparison to the observed data.

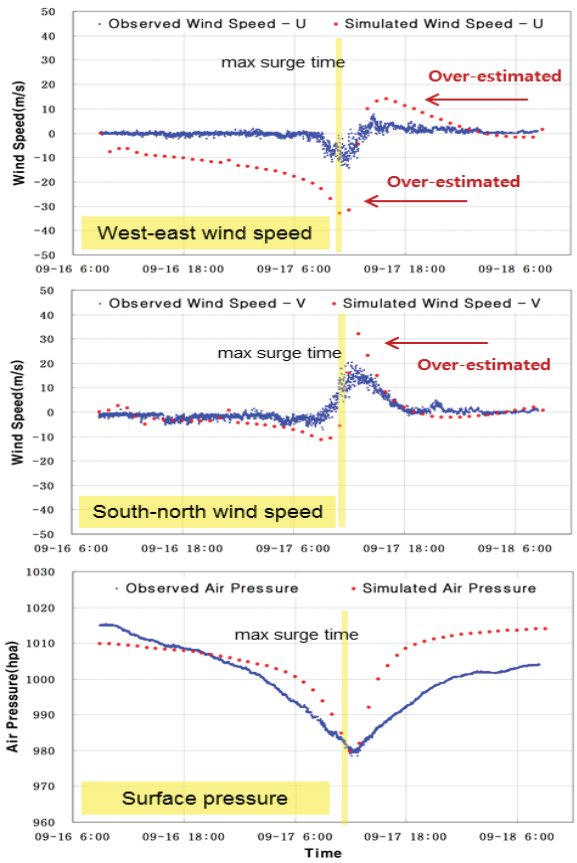

Figure 5. Comparisons between observed and simulated wind and air pressure time variations at Masan tidal station during Typhoon Sanba.

Maximum surge height simulated by the inundation prediction system was overestimated compared to the observed data; this was because simulated wind speed data was overestimated. To improve this wind simulation error, we refined the typhoon sea-surface wind model by noting that wind speed passing through the land surface could be mitigated by land surface friction (Yoon el al., 2014). This refinement improved the accuracy of the inundation prediction system.

Figure 6 shows the distribution of the maximum inundation area and height simulated by the inundation prediction system during typhoon Sanba. The simulation predicted that inundations up to 1 m would occur at Dong-Seodong, Jung-Angdong, Hae-Undong, and Bong-Amdong, which are located in low-lying coastal zones. Fortunately, the actual inundation was less than predicted since the strength of the typhoon was reduced upon landing. The data generated by this prediction system was immediately sent to the local authority so that it could be used to predict locations and times where damage might occur. The data was also used to issue warnings that allowed local residents to evacuate safely from the risky area.

Field Investigation of Damage by Surge Inundation (Masan)

Inundation caused by typhoon Sanba affected an extensive area along the southern coast of Korea, including Masan, Jinhae, Tongyoung, and Yeosu. The situation may have worsened in low-lying areas when seawater backflow occurred because sewage pipes, which are connected to the ocean, fully filled with seawater, especially at high tide. If heavy rainfall coincided with the typhoon, cities flooded severely even without storm surge inundation. Some coastal areas facing open sea without breakwater, like Yeosu, experienced significant damage by inundation due to wave overtopping. In this study, an inundation trace survey was conducted for Masan, Tongyoung, Jinhae, and Yeosu immediately after typhoon Sanba so that a wide variety of post-disaster data could be collected, including statements by eyewitnesses and photos taken when the region was inundated. This data could be useful for determining the accuracy of the inundation prediction model.

Figure 6 illustrates the distribution of inundated areas at Masan where the worst flooding damage happened. In this investigation, we explored the spatial distribution of major inundated areas and boundaries, however, we did not obtain precise inundation height due to lack of a digital altimeter. According to Figure 6, which compares observed and simulated inundation area, the simulation reproduced the inundation area well at industry complex zones like Bong-Amdong and residential and retail zones such as Dong-Seodong, Jung-Angdong, and Hae-Undong.

The primary characteristic of low-lying coastal zones is that rainfall easily causes flooding because sewage pipes connected to the sea fill with seawater at high tide and cannot release water. Inundation occurring under these circumstances is highly likely to lead to significant expansion of damages because there is no outlet for excess water. To overcome this problem, it will be necessary to apply the integrated numerical model including coastal inundation and urban flooding in the next step.

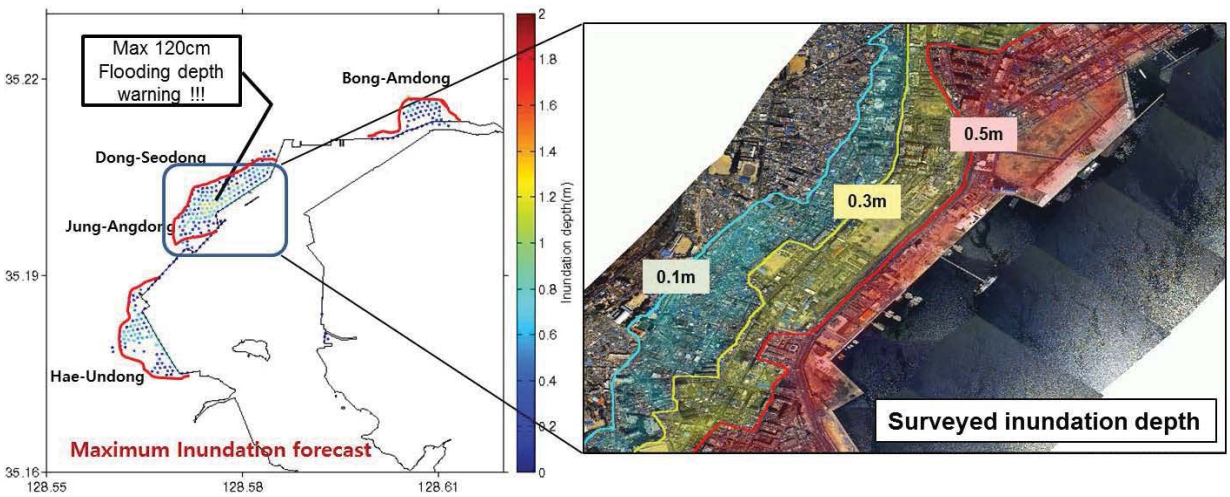

Figure 6. Simulated (dotted color) and observed (red line) inundation area at Masan during Typhoon Sanba.

CONCLUSION

In this study, we established a near real-time prediction system for estimating surge height and the storm surge inundation. The system is expected to forecast damages during typhoon landings on the Korean Peninsula. Applicability of this system was examined by comparing observed and simulated surge height for typhoon Sanba on September 17, 2012. The spatial distribution of inundated areas was relatively accurately simulated with respect to the observed data. It should be noted, however, that some errors occurred in the estimation of surge height. If we can improve the accuracy of sea-surface wind generation by investigating the cause of the error, the ability of this system to predict coastal disaster damages by simulating near future inundation will significantly increase.

ACKNOWLEDGEMENT

This research was supported by the basic research program of ChungNam Institute. This research was also a part of a project entitled “Construction of Ocean Research Station and their Application Studies” which were funded by the Ministry of Oceans and Fisheries, South Korea.

LITERATURE CITED

Amante, C., and Eakins, B.W., 2008. *Etopo1 1 arc-minute global relief model: procedures, data sources and analysis.* National Geophysical Data Center, Boulder, Colorado, NOAA Technical Memorandun NESDIS NGDC-24, 25 p.

Blanton, B.; McGee, J.; Fleming, J.; Kaiser, C.; Kaiser, H.; Lander, H. & Kolar, R., 2012. Urgent computing of storm surge for North Carolina's coast. *Procedia Computer Science*, 9, 1677-1686.

Cardone, V.J.; Cox, A.T.; Greenwood, J.A. and Thompson, E.F., 1994. Upgrade of tropical cyclone surface wind field model. US Army Corps of Engineers, *Waterways Experiment Station*, Miscellaneous paper CERC-94-14, 101 p.

Chen, C.; Beardsley, R.C. and Cowles, G., 2006. An unstructured grid, finite-volume coastal ocean model (FVCOM) system. *Oceanography- Washington Dc - Oceanography Society*, 19(1), 78-89.

Fleming, J.G.; Fulcher, C.; Luettich, R.A.; Estrade, B.D.; Allen, G.D. and Winer, H.S., 2008. A real time storm surge forecasting system using ADCIRC. *Estuarine and Coastal Modeling X*, 373-392.

Forbes, C.; Luettich Jr, R.A.; Mattocks, C.A. and Westerink, J.J., 2010. A retrospective evaluation of the storm surge produced by Hurricane Gustav (2008): Forecast and hindcast results. *Weather and Forecasting*, 25(6), 1577-1602.

Glahn, B.; Taylor, A.; Kurkowski, N. and Shaffer, W.A., 2009. The role of the SLOSH model in National Weather Service storm surge forecasting. *National Weather Digest*, 33(1), 3-14.

Matsumoto, K.; Takanezawa, T. and Ooe, M., 2000. Ocean tide models developed by assimilating TOPEX/POSEIDON altimeter data into hydrodynamical model: a global model and a regional model around Japan. *Journal of Oceanography*, 56(5), 567-581.

Thompson, E.F. and Cardone, V.J., 1996. Practical modeling of hurricane surface wind fields. *Journal of Waterway, Port, Coastal, and Ocean Engineering*, 122(4), 195-205.

Yoon, J.J. and Shim, J.S., 2013. Estimation of storm surge inundation and hazard mapping for the southern coast of Korea. *Journal of Coastal Research*, Special Issue No. 65, pp. 856-861.

Yoon, J.J.; Shim, J.S.; Park, K.S. and Lee, J.C., 2014. Numerical experiments of storm winds, surges, and waves on the southern coast of Korea during Typhoon Sanba: the role of revising wind force. *Natural Hazards and Earth System Science*, 14(12), 3279-3295.

Journal of Coastal Research	SI	75	1432 - 1436	Coconut Creek, Florida	2016

Analysis of long-period sea-level variation around the Korean Peninsula

Jong-Ju Yoon[†*]

[†]Seohaean Research Institute affiliated with ChungNam Institute,
Climate Change Response Research Center,
43-1 Shingyoung-ri Hongbuk-myon Hongseong, South Korea

www.cerf-jcr.org

www.JCRonline.org

ABSTRACT

Yoon, J.J., 2016. Analysis of long-period sea-level variation around the Korean Peninsula. *In:* Vila-Concejo, A.; Bruce, E.; Kennedy, D.M., and McCarroll, R.J. (eds.), *Proceedings of the 14th International Coastal Symposium* (Sydney, Australia). *Journal of Coastal Research*, Special Issue, No. 75, pp. 1432 - 1436. Coconut Creek (Florida), ISSN 0749-0208.

Regional long-term changes in sea level were investigated at 19 tidal stations located around the Korean Peninsula using more than 30 years of tide-gauge data. Regression analysis was applied to these data, and general trends of long-term change (1960–2014) in RSL (relative sea level) were estimated at each station. The results showed that the rates of RSL rise around Korea were higher than the global mean. Rates of RSL rise were relatively small along the western coast (average of 2.0 mm/yr.), large along the southern and eastern coasts (average of 2.8 and 3.6 mm/yr., respectively), and very large around Jeju Island (average of 3.8 mm/yr.). The rate of RSL rise near the coast of Jeju Island was about twice the world ocean mean. Interannual variations in sea-level rise around Korea showed regional differences. According to recently Fifth Assessment Report of IPCC, the rate of sea-level rise could accelerate throughout the 21st century. This should be considered when designing coastal structures in order to prevent coastal disasters.

ADDITIONAL INDEX WORDS: *Relative sea level, Sea-level rise, Interannual variation, Regression analysis.*

INTRODUCTION

Various problems may occur at sea and especially in coastal areas as a result of climate change. It is critical to develop countermeasures for coastal disasters that may result from rising sea level and increased intensity of typhoons. In particular, sea-level rise resulting from global warming may cause inundation of low-lying areas, coastal erosion, seawater influx into rivers and groundwater, rising river levels, variations of tidal levels, and waves intensity increment. It is to be expected that residential areas, ecosystems, water resources, transportation, tourism, and various industrial activities would be adversely affected. Sea-level rise directly affects the safety of various coastal facilities by changing design height estimation and indirectly affects these facilities via ocean waves or inundation.

Research by the IPCC (Intergovernmental Panel on Climate Change) has resulted in a wide range of forecast estimates of future sea-level rise. According to the Third Assessment Report of IPCC (2001), the global mean value of sea-level rise may have reached 1.8 mm/yr. by the end of the past century, and the forecasted mean value of sea-level rise, assuming that greenhouse gases continue to increase as they have been, was estimated to be 0.09–0.88 m by 2100. However, according to the Fourth Assessment Report (IPCC, 2007), the forecast range of sea-level rise was narrowed to approximately 0.18–0.59 m. The recently revised Fifth Assessment Report (IPCC, 2014) reported that sea-level rise reached 1.7 (1.5–1.9) mm/yr. in 1901–2010 and could be expected to increase up to 0.63 m by 2100. In previous studies, Flemming (1982) suggested a 0.2 mm/yr. average rate of sea-level rise for the past 2,000 years; and Warrick *et al*. (1996), Douglas (1997), and Church *et al*. (2001) estimated a 2.0 mm/yr. rate for the last century. Houghton *et al*. (1996) suggested that the pattern of rapid sea-level rise was a result of global warming.

For Korea, a 40-year (1961–2000) analysis based on TOPEX/Poseidon (T/P) satellite data reported rates of sea-level rise for the total area and the southern portion of the East (Japan) Sea to be 5.4 ± 0.3 and 6.6 ± 0.4 mm/yr., respectively (Kang *et al.*, 2004). In addition, Ha *et al.* (2006), using complex satellite data (1993–2005), reported annual rates of sea-level rise of 5.0, 3.6, and 3.7 mm/yr. for the East (Japan), South, and Yellow Seas, respectively; an average rate of 3.9 mm/yr. was reported for the whole region, which is 1.3 times the mean global rate.

However, the challenge of responding to changing predicted rates of sea-level rise when designing coastal structures expected to survive for a long period of time remains. In other words, the magnitude of rates of sea-level rise affect estimations of design sea level, and projected increases of local coastal wave action. Nevertheless, most experts agree that sea level is being elevated by increasing atmospheric and seawater temperatures caused by global warming. This sea-level rise is occurring gradually; as such, gradual adaptations are also required.

Sea-level variability varies regionally. Sea-level variation is determined mainly by atmospheric forcing and total ocean volume, temperature of the seawater column, and shape of the seafloor. Total seawater volume and seawater temperature vary

DOI: 10.2112/SI75-287.1 received 15 October, 2015; accepted in revision 15 January 2016.
*Corresponding author: yjj1230@naver.com
©Coastal Education and Research Foundation, Inc. 2016

with respect to climate change, but seafloor topography is generally neglected because the rate of change due to geological activity is small. When estimating sea level in a specific region, however, local land subsidence or uplift should be considered.

Most studies of sea-level variation around Korea have utilized data analysis of coastal tidal data. Recently, Jeon (2008) presented rates of relative sea-level (RSL) rise after analyzing long-term tide-gauge data from 21 tidal stations that had been accumulating data for more than 20 years. This study indicated that rates of RSL rise were 1.2, 3.4, and 1.4 mm/yr. for the eastern, southern, and western coasts, respectively.

In this study, the long-term variability of sea level was estimated by using linear regression to analyze data from tidal stations with the goal of providing useful information to estimate design sea level for design of coastal structures. In addition, regional and seasonal features of sea-level variation were analyzed and presented.

METHODS

Tidal stations of the KHOA (Korea Hydrographic and Oceanographic Administration) are a source of long-term, continuous data that can be used to analyze sea-level variation in Korea. In this study, hourly mean sea-level data from 19 tidal stations, at which the observation period was greater than 30 years, were used for analysis. The maximum time period of the observational data used was 1960–2014. The periods of data for each tidal station are listed in Table 1. The coastal area around Korea was divided into three sections: eastern, southern, and western coasts. The annual and seasonal mean rates of RSL rise that were obtained through linear regression for each tidal station are presented in Table 1.

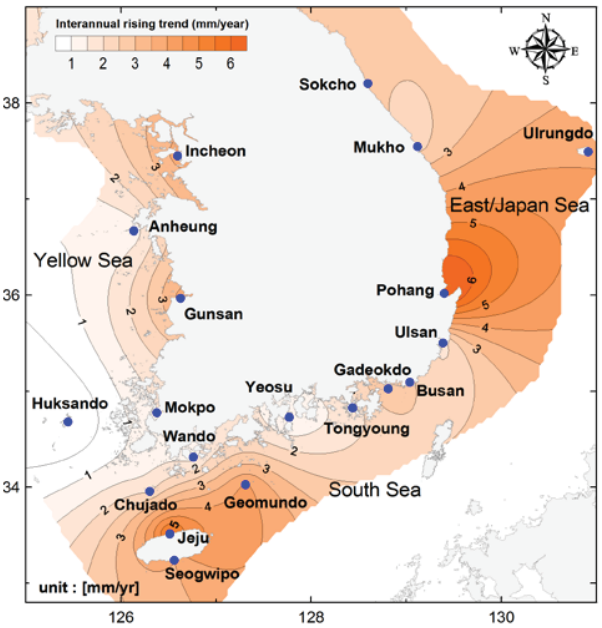

Figure 1. Annual rates of RSL rise around the Korean peninsula.

Table 1. *Information on tidal stations and linear trends (mm/yr.) of RSL rise.*

Area	Tidal Station		Interannual Trend (mm/yr.)		Seasonal Trend (mm/yr., 1985–2014)				
	Name	Total Period	Rising Rate 1	Unified Period	Rising Rate 2	Winter (Jan-Mar)	Spring (Apr-Jun)	Summer (Jul-Sep)	Fall (Oct-Dec)
East (Japan) Sea	Sokcho	1974-2014	2.4	1985-2014	2.6	3.0	3.1	1.6	2.7
	Mukho	1966-2014	1.2		2.3	2.9	2.6	0.9	2.8
	Ulrungdo	1979-2014	3.1		3.9	2.8	4.5	2.8	5.5
	Pohang	1972-2014	4.6		7.2	7.1	8.1	6.2	7.5
	Ulsan	1965-2014	1.0		1.8	1.6	2.3	1.0	2.2
	area mean		**2.5**		**3.6**	**3.5**	**4.1**	**2.5**	**4.1**
South Sea	Busan	1963-2014	2.5	1985-2014	2.6	2.6	2.8	1.9	3.0
	Gadeokdo	1977-2014	2.5		3.0	3.1	3.3	2.0	3.7
	Tongyoung	1977-2014	2.0		1.7	1.3	2.0	1.3	2.3
	Yeosu	1968-2014	1.5		0.9	2.3	1.2	-1.5	1.7
	Wando	1983-2014	1.4		1.3	2.1	1.4	-0.5	2.2
	Geomundo	1982-2014	4.3		4.1	5.0	4.4	2.2	4.6
	Chujado	1984-2004	2.0		1.9	3.8	2.1	-1.1	2.8
	Jeju	1965-2014	5.4		5.8	6.0	5.8	4.8	6.4
	Seogwipo	1985-2014	3.5		3.5	4.0	4.2	2.3	3.5
	area mean (Jeju Coast)		**3.8**		**3.8**	**4.7**	**4.1**	**2.1**	**4.3**
	area mean		**2.8**		**2.8**	**3.4**	**3.0**	**1.3**	**3.4**
Yellow Sea	Incheon	1960-2014	0.9	1985-2014	3.7	4.3	4.1	2.6	4.0
	Anheung	1987-2014*	1.2		1.2	2.0	1.5	-0.4	2.0
	Gunsan	1981-2014	3.4		3.7	4.8	3.6	1.9	4.3
	Mokpo	1960-2014	1.4		1.5	2.0	1.5	-0.2	2.8
	Huksando	1970-2014	0.5		-0.1	0.2	0.2	-1.4	0.2
	area mean		**1.5**		**2.0**	**2.7**	**2.2**	**0.5**	**2.7**
average of all areas			**2.4**		**2.8**	**3.2**	**3.1**	**1.4**	**3.4**

The locations of the tidal stations and estimated results for the spatial distribution of annual RSL rise rates are shown in Figure 1. The data for modified period were summarized over years (1985–2014) in this figure.

Previous studies of sea-level variation analysis include a variety of approaches: variation rate estimation for extreme high tides (Kang *et al.*, 2006), long-period component analysis of 18.6 years (Thompson, 1986), and analysis of the correlation between MSL (mean sea level) from satellite data and sea surface temperature (Ha *et al.*, 2006). In this study, the regional distribution of sea-level variation in the coastal area was estimated directly using long-term tide-level observation data covering the entire coast of Korea. Features of seasonal variation were also analyzed. The results of regression analysis may include variability related to the analysis period and length, and also may show differences depending on the filtering and error correction of the original data applied to the analysis. In this study, in order to enhance the reliability of the data, monthly MSL and RSL data were estimated by analyzing the hourly mean tidal gauge data of KHOA. In the case of an absence of monthly data due to a short-term period of missing measurements, the monthly mean value was estimated from the available data; when data was missing for more than 2 months, however, the entire year was excluded from the regression analysis. At the Incheon, Gunsan, and Mokpo sites in the Yellow Sea, artificial environmental changes occurred, such as extensive harbor work, construction of an estuary dam and tidal embankment, and the transfer of the tidal station installation (Kang *et al*., 2005). Transfers of major tidal stations were performed at the following sites: Incheon (1975, 1999), Wando (2005), Ulsan (2006), Gunsan (2007), and Huksando (2007). Also, the downward adjustment of the datum level for tidal observations at Mokpo (20.0 cm in 1982 and 3.3 cm in 2003) was considered in this analysis.

DISCUSSION AND RESULTS

The long-term variation of RSL observed at each tidal station on the eastern, western, and southern coasts of Korea is shown in Figure 2. These results represent relative distributions of the long-term sea-level variability observed at each tidal station. The distributions generally show a moderate rising trend, even though the magnitude differs by station. When implementing regression analysis by assuming that RSL variation is a linear function of time (years), the slope represents the rate of RSL rise; a similar rising trend is seen across all coasts (Table 1).

Figure 3 shows the linear trend at each station. The line connecting the dots in the figure represents the variation of annual RSL. Linear trends of the variation are shown in red for 1985–2014 and black for the total period at each station. The annual rates of RSL rise were determined to be 3.6, 2.8, and 2.0 mm/yr. on the eastern, southern, and western coasts of Korea, respectively, and approximately 2.8 mm/yr. overall. For the southern coast, considering only the sites at Geomundo, Chujado, Jeju, and Seogwipo near Jeju Island, the mean rate was the highest of all estimated rates at 3.8 mm/yr., which is about twice that of the world ocean (1.7 mm/yr.; IPCC AR5, 2014). Differences among regional rates of sea-level rise were significant, even along the same coast. For example, Pohang and Ulsan stations on the eastern coast showed significant deviations of 7.2 and 1.8 mm/yr., respectively. On the eastern coast, particularly low MSL values were represented in 1993, 1996, and 1997. In summer during these periods, low sea surface level was recorded not only in the Yamato basin but also by T/P satellite observations (Hirose and Ostrovskii, 2000). This trend is considerably affected by ocean currents. According to the results of Gordon and Giulivi (2004), the sea level of the Korea Straits and East (Japan) Sea is lower (higher) when the Kuroshio Current is strong (weak). Therefore, an analysis of long-term sea-level variation on the eastern and southern coasts of Korea should be conducted simultaneously with an analysis of long-term annual changes of the Kuroshio Current.

Our estimated rates of RSL rise were similar to those of Jeon (2008). When comparing with the results of this study, an overall increment of RSL rising rate was represented especially in the eastern coast. The rates of rise at Mukho, Pohang, and Ulsan showed a substantial increase from existing rates of 0.1, 2.0, and -0.3 mm/yr. to 2.3, 7.2, and 1.8 mm/yr., respectively. Furthermore, on the southern coast, a distribution similar to the existing rate of RSL rise was represented, but only the rate at Seogwipo (3.5 mm/yr.) was somewhat less than the existing rate of 7.3 mm/yr. On the western coast, the rate of RSL rise at Huksando, -0.1 mm/yr., was considerably less than the existing rate of 3.0 mm/yr. At Gunsan, the rate increased from an existing value of 1.0 to 3.7 mm/yr.

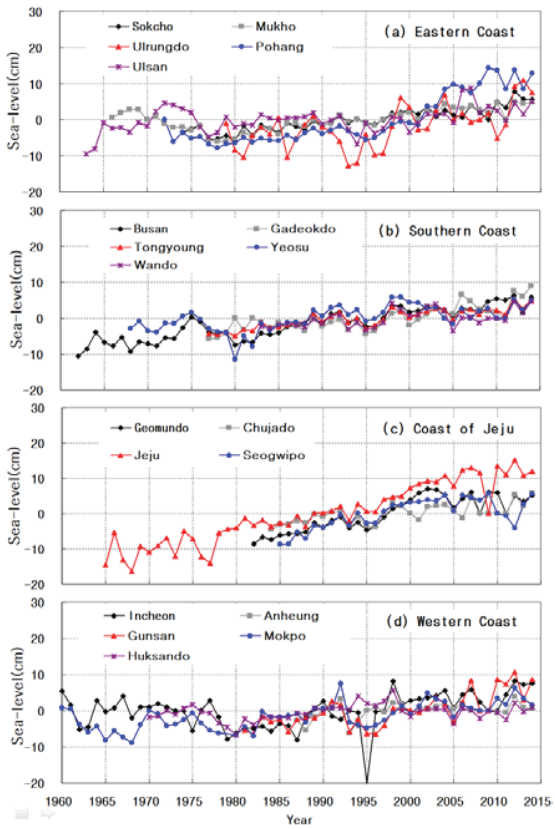

Figure 2. Interannual variation in RSL around the Korean Peninsula.

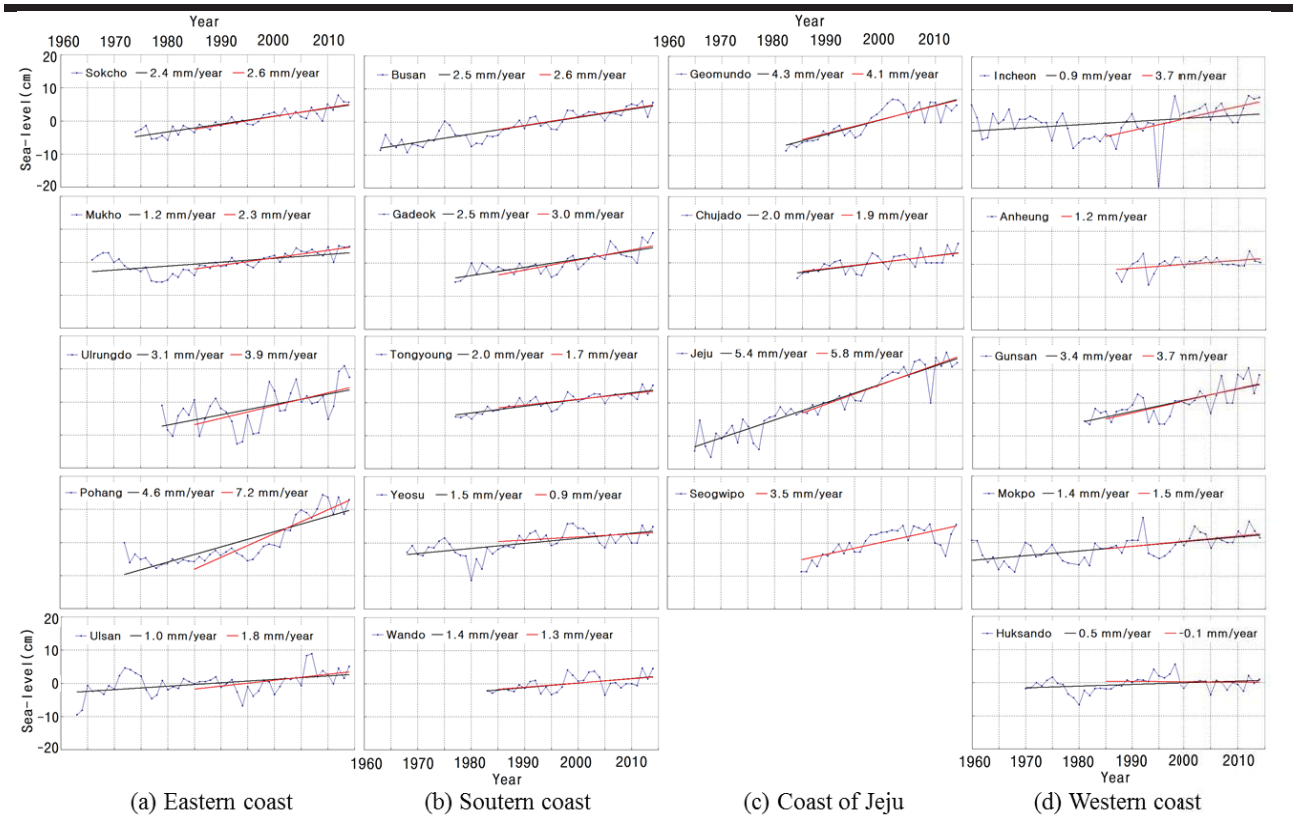

Figure 3. Linear trends (black line: whole period, red line: 1985–2014) and interannual variation in RSL (dotted blue line) at tide-gauge stations.

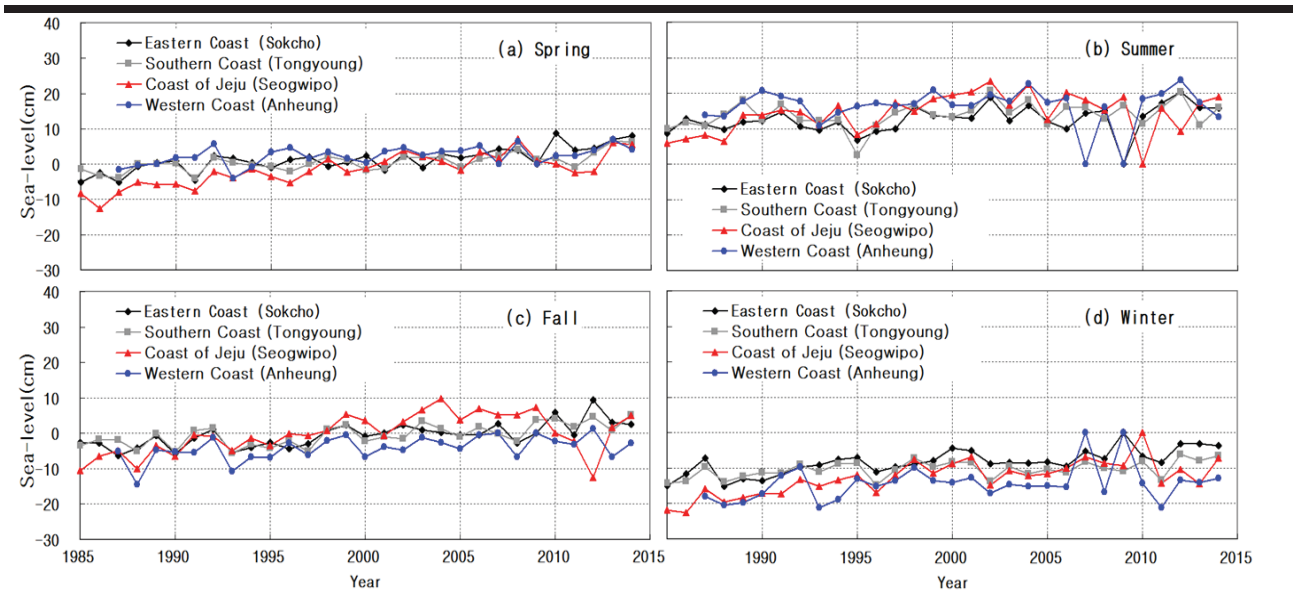

Figure 4. Seasonal variation of RSL for (a) spring, (b) summer, (c) fall, and (d) winter.

Figure 4 shows the seasonal change of RSL variation for each coast, and Table 1 lists the rate of RSL rise by season. These values were estimated by regression of three-month MSL values. RSL was highest in summer followed by spring, fall, and

winter. The seasonal rate of RSL rise was highest (3.4 mm/yr.) in the fall along the entire coast. However, this value decreased to 1.4 mm/yr. in summer. One reason that the RSL rise in summer was relatively low could be the combined effect of concentrated summer precipitation and seasonal variation of the Kuroshio Current.

CONCLUSION

Sea-level variation trends, including the influence of climate change, were investigated based on an analysis of long-period tidal observation data. Data from 19 tidal stations, for which the tidal observation record extended for more than 30 years, were used. Linear regression analysis was performed to assess long-term changes in annual MSL at each station.

Along the coast of Korea, RSL variation generally exhibited a clear rising trend. The rate of rise on the southern coast was particularly high. It may be possible to predict future sea-level variability by analyzing trends of RSL variation based on regional long-term observations. It was estimated that RSL increased by 3.6, 2.8, and 2.0 mm/yr. off the eastern, southern, and western coasts of Korea, respectively. The overall mean rate of rise was determined to be about 2.8 mm/yr. This value is much higher than the global mean, 1.7 mm/yr. (IPCC AR5, 2014). In addition, even within same coastal area, there was wide variation in regional RSL rising trends. The RSL rising rate around Jeju Island was about twice the global mean. The seasonal rate of RSL rise was relatively high in spring, fall, and winter and relatively low in summer.

Rising sea levels may cause coastal erosion, lowland inundation, and increased damage to coastal cities by flooding. Rising sea level must be considered for coastal disaster prevention when designing coastal structures. When applying these long-term variation factors to an actual construction plan, it would be desirable to estimate design sea level by summarizing research results for the northwestern Pacific area and the data from neighboring countries, including Japan and China, along with the results of this study.

ACKNOWLEDGEMENT

We would like to thank our editor and anonymous reviewers for their helpful and constructive comments. This research was supported by the basic research program of ChungNam Institute.

LITERATURE CITED

Church, J.A.; Gregory, J.M.; Huybrechts, P.; Kuhn, M.; Lambeck, K.; Nhuan, M.T.; Qin, D. and Woodworth, P. L., 2001. *Climate change 2001: the scientific basis: Contribution of Working Group 1 to the Third Assesment Report of the Intergovernmental Panel*, 639-694.

Douglas, B.C., 1997. Global Sea rise. A redetermination. *Surveys in Geophysics*, 18, 279-292.

Flemming, N.C., 1982. Multiple regression analysis of earth movements and eustatic sea-level change in the United Kingdom in the past 9000 years. *Proceedings of the Geologists' Association*, 93(1), 113-125.

Gordon, A.L. and Giulivi, C.F., 2004. Pacific decadal oscillation and sea level in the Japan/East Sea. *Deep-Sea Research I*, 51, 653-663.

Ha, K.J.; Jeong, K.Y.; Jang, S.R. and Kim, K.Y., 2006. Variation of the sea surface height around the Korean peninsula with the use of multi-satellite data (Topex/Poseidon, Jason-1, ERS, Envisat) and its association with sea surface temperature. *Korean Journal of Remote Sensing*, 22(6), 519-531. (in Korean)

Hirose, N. and Ostrovskii, A.G., 2000. Quasi-biennial variability in the Japan Sea. *Journal of Geophysical Research*, 105(C6), 14011-14027.

Houghton, J.T.; Meira Filho, L.G.; Callanger, B.A.; Harris, N.; Kattenberg, A. and Maskell, K., 1996. *Climate Change 1995*. Intergovernmental Panel on Climate Change, Cambridge University Press, Cambridge.

IPCC, 2001. *Climate Change : The scientific basis. Contribution of Working Group I to the Third Assessment Report of the Intergovernmental Panel on Climate Change*. Cambridge University Press, Cambridge.

IPCC, 2007. *Climate Change : The physical basis. Contribution of Working Group I to the Fourth Assessment Report of the Intergovernmental Panel on Climate Change*. Cambridge University Press, Cambridge.

IPCC, 2014. *Climate Change 2013: The physical science basis: Working group I contribution to the fifth assessment report of the Intergovernmental Panel on Climate Change*. Cambridge University Press, Cambridge.

Jeon, D.C., 2008. Relative sea-level change around the Korean peninsula. *Ocean and Polar Research*, 30(4), 373-378.

Kang, J.W.; Moon, S.R. and Oh, N.S., 2005. Sea level rise at the southwestern coast. *Journal of Korean Society of Civil Engineers*, 25, 151-157. (in Korean)

Kang, J.W.; Moon, S.R. and Park, S.J., 2006. Frequency Analysis of Extreme High Water Level Considering Tide/Surge Characteristic Changes. *Journal of Korean Society of Civil Engineers*, 26, 99-106. (in Korean)

Kang, S.K.; Cherniawsky, J.Y.; Foreman, M.G.G.; Min, H.S.; Kim, C.H. and Kang, H.W., 2004. Patterns of recent sea level rise in the East/Japan Sea from satellite altimetry and in situ data. *Journal of Geophysical Research*, 110, doi:10.1029/2004JC002565.

Thompson K.R., 1986. North Atlantic sea level and circulation. *Geophysical Journal of Royal Astronomical Society*, 87, 15-32.

Warrick, R.A.; Le Provost, C.; Meier, M.F.; Oerlemans, J. and Woodworth, P.L., 1996. *Changes in sea level Climate Change 1995 Intergovernmental Panel on Climate Change, Cambridge University Press, Cambridge*, 12, 20.

Journal of Coastal Research	SI	75	1437 - 1442	Coconut Creek, Florida	2016

Analyzing the relationship of meiobenthic community with geochemical factors in a coastal rocky shore of the East/Japan Sea, Korea

Ki Young Choi[†*], Won Gi Min[†], Young Il Kim[†], and Hyun Soo Rho[†]

[†] East Sea Research Institute
Korea Institute of Ocean Science & Technology
Uljin, Korea

www.cerf-jcr.org

www.JCRonline.org

ABSTRACT

Choi, K.Y., Mim, W.G., Kim, Y.I., and Rho, H.S., 2016. Analyzing the relationship of meiobenthic community with geochemical factors in a coastal rocky shore of the East/Japan Sea, Korea. *In:* Vila-Concejo, A.; Bruce, E.; Kennedy, D.M., and McCarroll, R.J. (eds.), *Proceedings of the 14th International Coastal Symposium (Sydney, Australia). Journal of Coastal Research*, Special Issue, No. 75, pp. 1437 - 1442. Coconut Creek (Florida), ISSN 0749-0208.

A study was performed to understand the geochemical factors that influence the spatial distribution of the meiobenthic community on the rocky shore of Hujeong, a typical eastern coast in Korea. Eleven sediment samples were collected from the study area; meiobenthos were separated from each other and analyzed for characteristics such as grain size, total organic carbon, and major and trace elements. A total of 9 meiobenthic animal groups were identified, and benthic harpacticoids were found to predominate in most samples with a mean meiofaunal density of 680 indiv 10 cm^{-2} and biomass of 294 µg 10 cm^{-2}. The principal component analysis (PCA), constructed considering both biotic and abiotic variables, accounted for 60.3% of the total variance. The PC 1 axis explained 46.5% of the total variance and was correlated with nematodes. The PC 2 axis explained 13.8% of the remaining variance and was correlated with polychaetes, ostracods, and halacaloideans. The score plot obtained from the PCA, helped identify three main groups in the benthic environment. Group-I is associated with the nearby beach stations that are affected by terrestrial inputs. Group-II is categorized as stations around sandy sediments and bed rocks, which are relatively stable areas. Group-III includes stations affected by external, offshore environmental factors.

ADDITIONAL INDEX WORDS: *Meiofauna, trace elements, sand and rocky shore, East/Japan Sea.*

INTRODUCTION

Subtidal rocky reefs provide habitats for diverse assemblages of marine organisms, and also influence the structure of the benthic faunal communities inhabiting the nearby soft-sediments (Davis *et al*., 1982; Ambrose and Anderson, 1990; Posey and Ambrose Jr., 1994; Barros, 2005). The fluctuations in these assemblages might be caused by the changes in the intensity of movement of water, direction of currents, rates of erosion or sedimentation, organic content of sediments, and in numbers or types of predators (Barros, 2005).

Benthic infauna are most frequent1y used to monitor the biological effects of environmental1 changes in the marine systems. In particular, meiofauna are a good indicator of the environmental conditions and changes in their density, diversity, structure and functioning may indicate alterations in the system (Schratzberger *et al*., 2000). Meiobenthic communities provide information of great interest because of their important role in the marine benthic food chains (Heip *et al*., 1985; Moens *et al*., 2005; Alves *et al*., 2013). In comparison to macrofauna, meiofauna exhibit smaller sizes, higher abundances, shorter response times, rapid turnover rates, and absence of a planktonic phase. As a result, meiofauna are more sensitive towards environmental factors and usually serve as monitoring organisms (Coull and Chandler, 1992; Schratzberger *et al*., 2000).

In order to understand how meiobenthic communities respond to the geochemical factors, 11 stations around Huam, a typical eastern coastal area in Korea, were sampled for meiofauna and a number of environmenta1 variables were measured. The main objectives in this study were: (1) to assess the spatial trends in meiofauna collected at inshore and offshore locations around Huam; (2) to analyze the relationship between the distribution patterns of observed meiofauna species and the geochemical properties of the sediments in order to understand the environmental variables that influence the spatial distribution of meiobenthic communities.

METHODS

Hujeong, a sandy and rocky beach, is mid-eastern coast of Korea and faces the East/Japan Sea (Figure 1). The tidal range for this area is 0.10 m – 0.30 m with depths of 1.5 to 6.5 m at low tide. A total of 11 upper-5-cm sediment samples were collected using a Van Veen grab in June 2014, and they were placed in LDPE bags and frozen immediately after sampling until environmental variables analysis.

DOI: 10.2112/SI75-288.1 received 15 October, 2015; accepted in revision 15 January 2016.
*Corresponding author: sberri@kiost.ac
©Coastal Education and Research Foundation, Inc. 2016

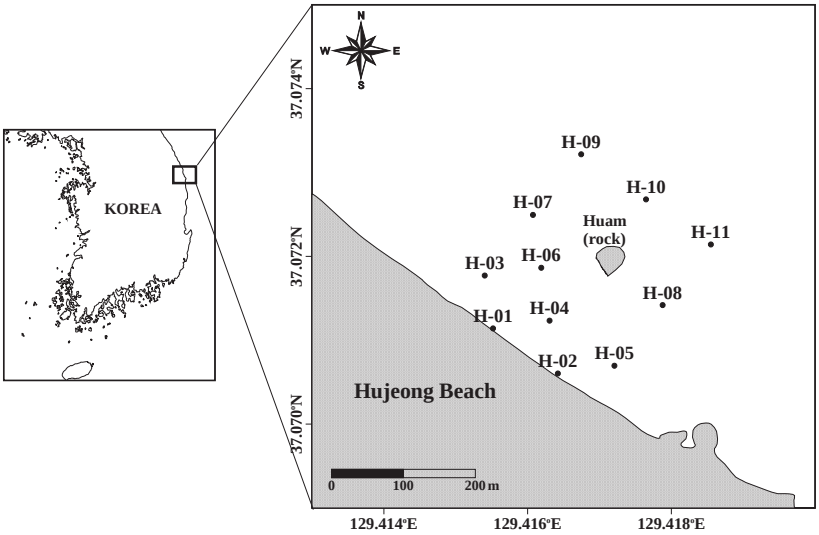

Figure 1. Location of sampling stations in the study area.

The sediment grain size was analyzed by wet sieving after pretreating the sediment samples with H_2O_2 and HCl to remove the organic matter and carbonate fractions. After sieving, weight percentages of below 4 Φ and over 4 Φ were obtained for the coarse sediments and fine-grained sediments, respectively, using an automatic particle size analyzer (Sedigraph 5100, Micromeritics). The mean grain size (Mz) and other particle size characteristics of the sediment samples were statistically treated and classified by the method of Folk (1954).

For measuring the total organic carbon, the freeze-dried samples were grinded uniformly and dried for 24 hours at 80 ℃ in a drying oven and carbonate was removed by adding 1 M HCl. After acid treatment, the total contents of organic carbon were measured using an elemental analyzer (EA 1112, Thermo). For the QA/QC analysis, the standard reference materials (SRM) MESS-3 and 1941b of Canada (NRC-CNRC) were analyzed using the same methods as for the sediment samples and the results for both the cases were compared.

For determining the total metal concentration, sediment samples were analyzed for total concentration of Al, Fe, Mn, Li, Cr, Co, Ni, Cu, Zn, As, Cd, and Pb. Approximately 20 mg of grounded and dried samples were digested using closed Teflon® vessels with the mixture acids of HNO_3, $HClO_4$, and HF (Merck, Suprapur®) on a hot plate at 180°C for 12 h. The completely dissolved samples were diluted in 1% HNO_3 for further analysis. Sample solutions and reagent blanks were analyzed using inductively coupled plasma mass spectrometry (ICP-MS, Thermo X series). The standard reference material of MESS-3 (National Research Council Canada) was analyzed simultaneously with the sample to identify the QA/QC values for this study, and the recoveries ranged from 93 to 110 % for the analyses.

Sediment samples for the analysis of meiofauna were collected using a Van Veen grab (0.025 m^2) from the study area. From the bulk sediment samples collected using the grab, subsamples were recovered using 3 acryl sub-corers (diameter 3.4 cm), by slicing the samples up to the depths of 5 cm from the surface, and then fixing them with 5 % neutralized formalin mixed with Rose Bengal. The samples were size fractioned using sieves with variable mesh apertures (1 mm, 500 μm, 250 μm, 125 μm, 63 μm, and 37 μm); subsequently, the animals were identified and counted under a stereo-microscope. The biomasses of meiofauna were calculated using the method of standard ash free dry weight per individual for four major meiobenthic animal groups by Shirayama (1983).

A Principal component analysis (PCA) of the environmental variables was performed to identify the distribution patterns of meiofauna depending on the geochemical factors in the study area. PCA is a data reduction procedure, the main goal of which is to provide an easy visualization of the relationships existing among the variables determined in large or complex data sets (Filgueiras *et al*., 2002; Passos *et al*., 2010). Prior to the calculation of the environmental parameter resemblance matrix based on Euclidean distance, the environmental variables (mean grain size, TOC, Al, Fe, Mn, Li, V, Cr, Co, Ni, Cu, Zn, As, Cd, Pb and meiofaunal abundance) were square-root transformed and normalized.

RESULTS

The mean grain size (Mz) of surface sediments in the study area was from slightly gravelly sand to sand, i.e., 0.51–2.14 Φ with an average of 1.20 ± 0.41 Φ. The smallest size particles were recorded at station H-09 located in the near offshore (Table 1). The concentrations of TOC in the study area ranged 0.026–0.066 % with an average of 0.039 ± 0.012 %. At stations near the shoreline (H-03, H-04, and H-05), TOC concentrations were relatively higher than at other stations.The concentrations of metals in surface sediments varied, with individual ranges recorded to be 2.45–7.03 % for Al, 0.29–2.00 % for Fe, 96–259 mg kg^{-1} for Mn, 10.9–28.4 mg kg^{-1} for Li, 6.8–34.1 mg kg^{-1} for V, 4.0–28.6 mg kg^{-1} for Cr, 1.5–4.1 mg kg^{-1} for Co, 2.0–11.1 mg kg^{-1} for Ni, 1.7–7.2 mg kg^{-1} for Cu, 8.3–47.7 mg kg^{-1} for Zn, 3.5–10.4 mg kg^{-1} for As, 0.021–0.051 mg kg^{-1}

Table 1. *Geochemical characteristics of sediments in the study area*

St.	Mz	TOC	Al	Fe	Mn	Li	V	Cr	Co	Ni	Cu	Zn	As	Cd	Pb
	Φ	%	%	%	mg kg^{-1}										
H-01	0.51	0.026	4.06	0.79	96	17.4	9.0	6.2	1.6	2.0	7.2	14.8	7.3	0.039	15.6
H-02	0.94	0.027	2.45	0.29	183	10.9	6.8	4.0	1.5	11.1	1.7	8.3	3.5	0.021	11.0
H-03	1.02	0.066	5.79	0.72	107	12.0	14.2	7.3	1.5	2.3	2.2	16.0	5.1	0.022	18.7
H-04	1.17	0.047	4.64	1.22	112	16.4	20.7	9.0	2.4	3.3	2.6	24.1	7.5	0.030	13.4
H-05	1.08	0.041	4.64	1.46	155	18.4	25.9	13.4	3.3	7.0	5.7	23.8	6.3	0.032	13.2
H-06	1.31	0.036	5.83	1.42	217	18.6	25.6	10.2	2.2	3.4	4.0	27.7	5.6	0.051	19.8
H-07	1.55	0.048	6.14	1.10	119	21.7	22.6	15.1	2.2	4.7	3.0	23.1	7.8	0.043	19.1
H-08	1.09	0.034	5.82	0.86	111	18.1	16.1	10.7	2.2	4.0	2.8	23.0	4.9	0.029	20.7
H-09	2.14	0.039	7.03	2.00	201	28.4	31.3	21.4	4.1	7.6	7.2	41.3	10.4	0.051	19.0
H-10	1.33	0.035	5.56	1.78	259	25.5	34.1	28.6	4.0	7.9	5.6	47.7	8.5	0.031	18.7
H-11	1.10	0.028	4.80	0.97	127	21.2	11.8	5.6	1.7	2.7	3.2	24.3	5.0	0.035	10.5

for Cd, and 10.5–20.7 mg kg^{-1} for Pb (Table 1). In samples from H-09 and H-10, the concentrations of Mn were higher than 200 mg kg^{-1}, and the concentrations of V, Cr, Co, Ni, Cu, Zn, and As were also much higher than those in the other samples. In samples from H-06, H-07, and H-09, the concentrations of Cd were higher than 0.04 mg kg^{-1} and those of Pb were higher than in the other samples.

Nine major taxa were identified from samples collected at the stations during the sampling period; harpacticoids was the most dominant taxon (57.5 %), followed by nauplius (19.9 %) and nematodes (17.4 %). All other taxa, including benthic foraminifera (2.7 %), ostracods (2.0%), polychaetes (0.4%), turbellarians (0.1%), halacaloideans (0.08 %), and bivalves (0.05%), accounted for less than 3% of the total.

Meiofaunal abundance ranged from 135 indiv 10 cm^{-2} at H-06 to 1458 indiv 10 cm^{-2} at H-11 (Table 2), and the number of taxa present varied from five (H-7 , H-08, H-09, and H-11) to eight (H-02 and H-05). Relatively higher densities (over 900 indiv 10 cm^{-2}) of meiofauna were recorded at the inner shore of the Huam (H-04 and H-05) and offshore stations (H-10 and H-11) than at other stations. Biomass of meiofauna ranged from 50.6 µg 10 cm^{-2} at H-06 to 652.0 µg 10 cm^{-2} at H-04 (Table 3). Relatively higher values of biomass were recorded at shoreline areas (H-01 and H-02) and the inner shore of the Huam (H-04) than at other stations.

Table 2. *Abundance of meiofauna in the study area (unit: indiv 10 cm^{-2})*

	H-01	H-02	H-03	H-04	H-05	H-06	H-07	H-08	H-09	H-10	H-11
Harpacticoids	273	161	421	804	484	45	307	177	109	577	947
Nauplius	106	107	21	453	354	13	2	41	6	88	300
Nematodes	8	78	112	39	73	71	93	93	331	258	143
Benthic foraminifera	15	21	5	10	21	2		52	8	13	54
Ostracods	45	41	5	10	26			3	3		15
Polychaetes	8	8		3	3	2	2			2	
Turbellarians		2			2					5	
Halacaloideans		2				2	2				
Bivalves			2		2						
Total	455	419	565	1319	965	135	404	365	458	942	1458

Table 3. *Biomass of meiofauna in the study area (unit: µg 10 cm^{-2})*

	H-01	H-02	H-03	H-04	H-05	H-06	H-07	H-08	H-09	H-10	H-11
Copepods	185.9	55.5	196.0	392.3	146.1	30.9	85.5	45.0	20.6	106.3	268.8
Nematodes	0.6	13.3	50.6	12.9	33.5	11.7	24.4	27.9	94.7	66.7	37.0
Benthic foraminifera	1.5	2.1	0.9	1.1	2.3	0.1	0.0	6.2	0.8	2.9	6.5
Others	357.1	344.6	14.3	245.8	99.0	7.9	72.1	11.3	24.4	89.4	27.8
Total	545.1	415.6	261.8	652.0	280.9	50.6	181.9	90.4	140.5	265.2	340.1

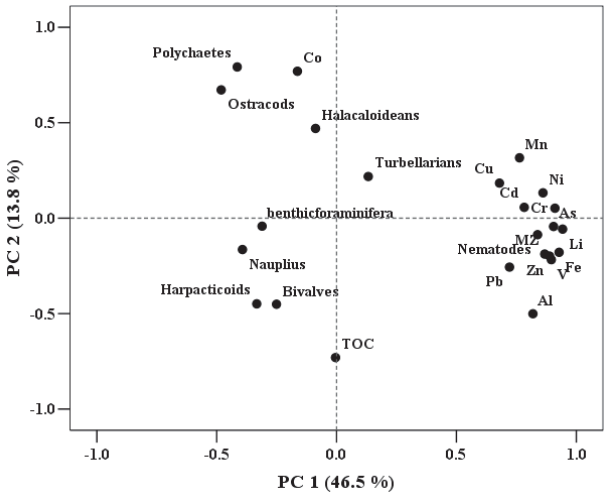

Figure 2. Plots of the principal component loads.

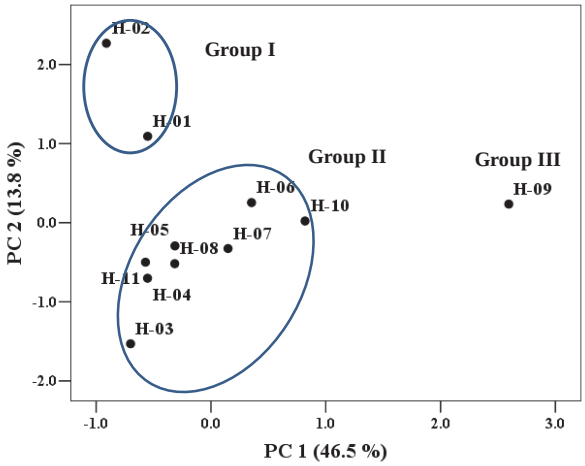

Figure 3. Scatter plot of the scores on the principal components.

Two principal components were extracted, and they explained approximately 60.3 % (PC 1: 46.5 %; PC 2: 13.8 %) of the information in the initial variables (Figure 2).

Factor 1 (PC 1) represented 46.5 % of the total variance and had strong positive loadings (> 0.7) on the concentrations of Al, Fe, Mn, V, Li, Cr, Ni, Cu, Zn, As, Cd, and Pb and Mz. PC1 was correlated with the abundance of nematodes, and it could be interpreted as an indicator of terrestrial origin. Most metals showed high positive loadings on Mz, Al, Fe, and Li, and these metals had a terrestrial origin.

Factor 2 (PC 2) accounted for 13.8 % of the total variance and was characterized by positive loading of Co, which was correlated with the abundance of polychaetes, ostracods, and halacaloideans. Another positive loading of TOC was correlated with the abundance of harpacticoids and bivalves and played an important role in determining the spatial distributions of these meiofauna.

A score plot from the PCA, showed three main groups in the benthic environment (Figure 3). Group-I was associated with nearby beach stations affected by terrestrial input. Group-II was categorized as stations around sandy sediments and bed rocks, which are relatively stable areas. Group-III was related with the stations affected by external offshore environmental factors

DISCUSSION

Results from this study indicate that differences in species composition of the meiobenthic communities between different locations provide sensitive environmental status. Meiofauna species distribution patterns were explained well by variables derived from concentrations of trace metals and TOC. The concentrations of correlated trace metals were relatively low at most stations and an unlikely cause of biological effects and might indicate input of terrestrial origin in the study area.

Concentration of TOC explained the abundance of Nauplius, Harpacticoids, and Bivalves at the inner shore of the Huam and relatively low concentrations of Cr, Co, Cu, and Pb in this area were correlated with high abundance of these meiofauna.

CONCLUSIONS

An investigation was carried out to understand the response of meiobenthic communities to geochemical factors in sediments. Samples were collected from the Huam, which is a typical eastern coastal area in Korea. Environmental variables such as Mz, TOC, Al, Fe, Mn, Li, V, Cr, Co, Ni, Cu, Zn, As, Cd, and Pb, and meiofaunal abundances were investigated in 11 surface sediment samples.

The meiofauna community mainly comprised individuals from nine taxonomic groups of which harpacticoids, nauplius, and nematodes were the three dominant groups accounting for 57.5 %, 19.9 %, and 17.4 % of the total individuals, respectively.

In the PCA, the two principal components accounted for 60.3 % of the total variance in the data set. The results suggest that the concentrations of V, Cr, Ni, Cu, Zn, As, Cd, and Pb are strongly correlated, and these elements may be derived from terrestrial sources, whereas Co, and TOC might have come from a different source. Further, the contributing sites responsible for the geochemical factors that are associated with distributions of meiofauna were identified through the PCA.

ACKNOWLEDGMENTS

This research was a part of the project titled "Deep-sea Environment & Ecosystem Project of East Sea with Advanced Scientific Technology (PE99399)" funded by Korea Institute of Ocean Science & Technology.

LITERATURE CITED

Alves, A.S.; Adão, H., Ferrero, T., Marques, J.C., and Patrício, J., 2013. Benthic meiofauna as indicator of ecological changes in estuarine ecosystems: The use of nematodes in

ecological quality assessment. *Ecological Indicators*, 24, 462-475.

Ambrose, R.F., and Anderson, T.W., 1990. Influence of an artificial reef on the surrounding infaunal community. *Marine Biology*, 107, 41–52.

Barros, F., 2005. Evaluating the importance of predation on subtidal benthic assemblages in sandy habitats around rocky reefs. *Acta Oecologica*, 27, 211–223

Coull, B.C., and Chandler, G.T., 1992. Pollution and meiofauna: field, laboratory, and mesocosm studies. *Oceanography and Marine Biology: An Annual Review*, 30, 191–271.

Davis, N.; VanBlaricom, G.R., and Dayton, P.K., 1982. Man-made structures on marine sediments: effects on adjacent benthic communities. *Marine Biology*, 70, 295–303.

Filgueiras, A.V.; Lavilla, I. and Bendicho, C., 2002. Chemical sequential extraction for metal partitioning in environmental solid samples. *Journal of Environmental Monitoring*, 4, 832–857.

Folk, R.L., 1954. The distinction between grain size and mineral composition in sedimentary-rock nomenclature. *Journal of Geology*, 62, 344-359.

Heip, C.H.; Vincx, M., and Vranken, G., 1985. The ecology of marine Nematoda. *Oceanography and Marine Biology: An Annual Review*, 23, 399–489.

Moens, T.; Bouillon, S., and Gallucci, F., 2005. Dual stable isotope abundances unraveltrophic position of estuarine nematodes. *Journal of the Marine Biological Association UK*, 85, 1401–1407.

Passos, E.A.; Alves, J.C., dos Santos, I.S., Alves, P.H., Garcia, C.A., and Costa, A.S., 2010. Assessment of trace metals contamination in estuarine sediments using a sequential extraction technique and principal component analysis. *Microchemical Journal*, 96, 50–57.

Posey, M.H. and Ambrose Jr., W.G., 1994. Effects of proximity to an offshore hard-bottom reef on infaunal abundances. *Marine Biology*, 118, 745–753.

Schratzberger, M.; Gee, J.M., Rees, H.L., Boyd, S.E., and Wall, C.M., 2000. The structure and taxonomic composition of sublittoral meiofauna assemblages as an indicator of the status of the marine environment. *Journal of the Marine Biological Association UK*, 80, 969–980.

Shirayama Y., 1983. Size structure of deep-sea meio- and macrobenthos in the western Pacific. *Internationale Revue der gesamten Hydrobiologie*, 68, 799-810.

Journal of Coastal Research	SI	75	1442 - 1446	Coconut Creek, Florida	2016

Influence of wave direction on uplift force of sloping high piled wharf

Chen Jia[†], Yan Yixin[†], Chen Guoping[†], and Tan Huiming[†, ‡*]

[†] College of harbor coastal and offshore engineering
Hohai University
Nanjing, China

[‡] State Key Laboratory of Hydrology-Water Resources
and Hydraulic Engineering, Hohai University
Nanjing, China

www.cerf-jcr.org

www.JCRonline.org

ABSTRACT

Chen, J.; Yan, Y.X.; Chen, G.P., and Tan, H.M., 2016. Influence of wave direction on uplift force of sloping high piled wharf. *In:* Vila-Concejo, A.; Bruce, E.; Kennedy, D.M., and McCarroll, R.J. (eds.), *Proceedings of the 14th International Coastal Symposium* (Sydney, Australia). *Journal of Coastal Research*, Special Issue, No. 75, pp. 1442 - 1446. Coconut Creek (Florida), ISSN 0749-0208.

Based on the experiment carried out in this study, the effect of incoming wave direction on uplift force acting upon high piled wharf deck has been analyzed. The main influencing factors have been taken into account, which include the wave incident angle, wave types, period, wave height, height of wharf deck.For the regular and irregular wave, the testing results showed that the oblique wave incoming angle was the main influencing factor on uplift force in both with and without current circumstances. The current direction has effect on the decreasing trend of total uplift force. Moreover, the simplified formula on uplift force under oblique wave without current was proposed. The comparison between the observed and calculated results illustrated that the accuracy of the proposed formula can mainly satisfy the requirements in practice.

ADDITIONAL INDEX WORDS: *oblique wave, wave uplift force, wave direction, lab test.*

INTRODUCTION

The ocean waves have great threats on the safety of the coastal structures, such as high piled wharf, artificial island, bay bridge, etc. The decks of coastal structures can be destroyed under the wave uplift force in some extreme situations. In order to decrease the wave uplift force acting on structure decks, the levels of decks for the offshore structures are usually designed above the mean sea level. However, for the onshore structures, such as high piled wharf and landing stage, the deck levels are often below the mean water level, so the influences of the wave uplift force cannot be ignored in the design of coastal structures. The main methods on wave forces acting on coastal structures are theoretical analysis, numerical modeling and laborotory experiments (Bozorgnia *et al*., 2013; Huang and Xiao, 2009; Kataoka *et al*., 2013; Wang *et al*., 2011). EI.Ghamry (1963) conducted the experiment of uplift force on offshore and onshore high piled wharf, the process of wave impact on structure has been analyzed, and the distribution of uplift force on horizontal plate followed the Rayleigh distribution. Sun *et al*. (2011) proposed a spectral analysis of wave uplift loads on a horizontal deck, and the wave uplift force spectrum on the underside of the deck is obtained. Kataoka *et al*. (2013) made analysis on the wave forces acting on the superstructures of two highway bridges affected by the 2011 Tohoku tsunami by combining 2-D FDM and a numerical wave flume.Chen *et al*. (2010) developed a laboratory setup to investigate irregular wave uplift loads on exposed high-pile jetties. The results showed that the pressure distribution length associated with the maximum uplift force was equivalent to the wave contact width, the statistical distribution of loads obeys the Weibull distribution. Kweon *et al*. (2011) conducted hydraulic model test to measure the wave pressure acting on a breakwater model, and the difference between the method proposed by Kweon *et al*., and the wave force measured at a different time without a phase difference has been discussed. A series of physical experiments on the wave uplift force have been conducted by Liu *et al*. (2010). Based on the results, two experiential formulas for calculating the maximum wave displacement around the pillars and the wave uplift force on superstructure of a pillar wharf were presented respectively. Due to the complexity of influencing factors on wave uplift forces, the uplift forces varied greatly with the changing of wave characteristics and deck arrangement. The calculating results by using different formulas usually cannot meet the agreement very well. Furthermore, the perpendicular wave uplift force on structure was taken into account for most researches and engineering specifications.The influences of wave direction and current were always considered for most coastal structures in reality, but the uplift force of oblique wave and the influences of current were not considered seriously.

In this study, the effects of incoming wave direction and wave-current interaction on uplift force acting upon high piled wharf deck has been analyzed based on laboratory experiment, and the main influencing factors have been taken into account, such as wave incident angle, wave types, period, wave height, height of wharf deck. According to the oberved data, the simplified formula on uplift force under oblique wave has been proposed. Results shown that the accuracy of calculating results sould satisfy the requirements in practice.

METHODS

DOI: 10.2112/SI75-299.1 received 15 October 2015; accepted in revision 15 January, 2015
*Corresponding author: thming@hhu.edu.cn
©Coastal Education and Research Foundation, Inc. 2016

The experiment was conducted in a wave tank(shown in Figure 1), which has a size of 50m (length) ×17.5 m (width) ×1.5 m (depth). On one side of the wave tank, the wave generator was set to generate both regular and irregular waves, and on the opposite side, a energy dissipation slope was installed. The water pump group has been adopted to generate steady flow with different magnitudes and directions.

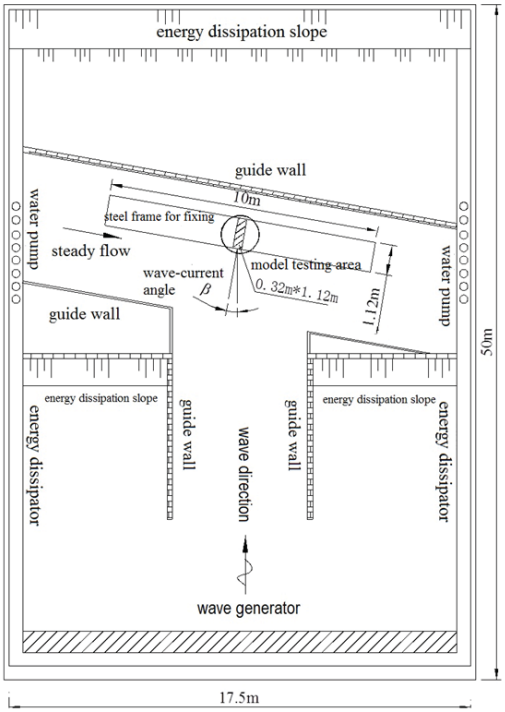

Figure 1.The wave tank arrangement.

The testing onshore sloping high piled wharf structure was shown in Figure 2. The laboratory model has been used based on the similarity law of Froude number, and the model scale was 1:50. The structure model was made of plexiglasswith a length of 10.0 m and width of 1.12 m. The testing area was set in the middle of the structure to reduce the boundary effect, which has a legth of 0.32 m. To avoid the displacement of the structure induced by waves during the experiment, the model decks were fixed by steel frame in wave tank, but the level and angle can be adjusted conveniently. The pressure transducer and total force transducer have been arranged on the decks and used to measure the wave uplift force. The instrument arrangement and model high piled wharf structure can be seen in Figure 3 and 4, respectively.

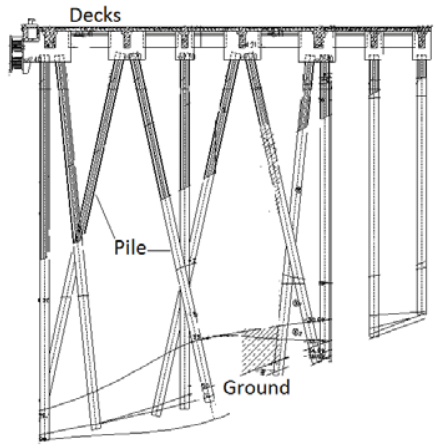

Figure 2. The sketch of the sloping high piled wharf.

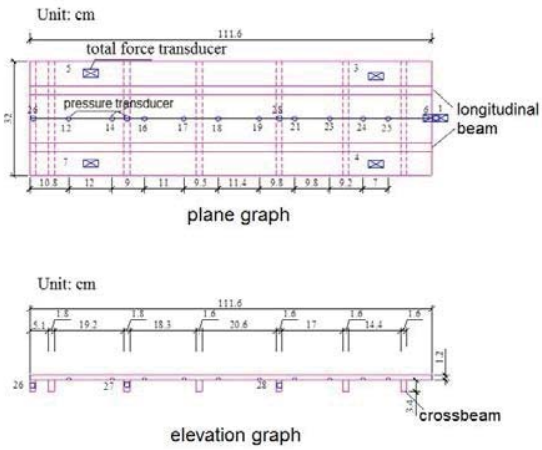

Figure 3. Instrument arrangement.

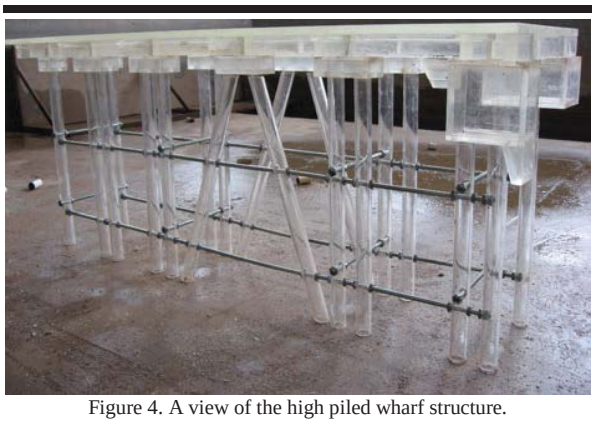

Figure 4. A view of the high piled wharf structure.

Both regular and irregular waves have been adopted in the model testing, and the JONSWAP spectrum was applied to produce irregular wave. The duration of generating regular wave was 50 s, that of irregular wave was 3-5 min, and the wave number was 120-150. The current velocity was controlled by the pump flow discharge. The wave incoming angle β (angle between wave direction and normal line of wharf structure) was adjusted by changing model structure position. The wave-current angle α was the angle between wave direction and flow direction (shown in Figure 5). The model testing sketch was illustrated in Figure 6. Considering the process of wave impact, the sampling interval was 1/125 s. The testing parameters have been listed in table 1.

Table 1. *Testing parameters of physical model*

Content	Parameters
water depth (d) /m	0.4
slope	1:2
regular wave height ($\overline{H}$) /cm	6.40, 9.23, 12.07
irregular wave height (Hs) /cm	4.5, 6.5, 8.5
wave period (T) /s	1.0, 1.38, 1.54
wave incoming angle (β) /°	-60, -45, -30, -15, 0, 15, 30, 45, 60
flow velocity (U) / m/s	0, 0.14, 0.21, 0.28, 0.35
freeboard height ($\triangle h$) /cm	2.5，5.5，7.5，11.5

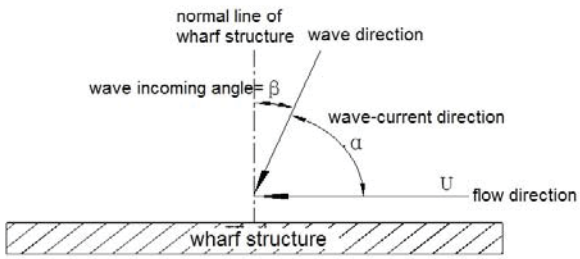

Figure 5. Sketch of wave incoming angle and wave-current direction.

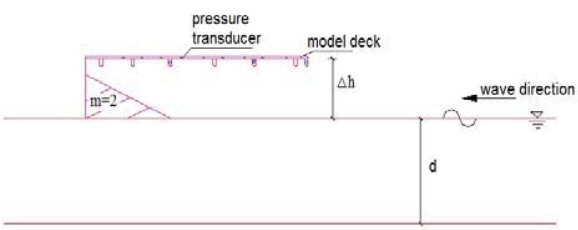

Figure 6. Model testing sketch.

RESULTS

The wave and current were the main controlling factors in the lab testing. The effects of incoming wave direction on uplift force have been analyzed under two circumstances seperatedly, with and without cuurent.

Effects of the incoming wave direction on total uplift force without current

As for the oblique wave, the incoming wave direction was the main influence factor on uplift force, and the incoming wave direction was measured with the wave incoming angle β in the test. In order to analyze the influence of wave direction on the total uplift force acting on structure without current, the total uplift force influencing factor has been introduced.

$$K_{\beta,0} = P_{\beta,0} / P_0 \qquad (1)$$

where the subscript variable β means wave incoming angle and the subscript label 0 means without current. $P_{\beta,0}$ is the total uplift force under the impact of oblique wave with different incoming angles; P_0 means the total uplift force under the impact of perpendicular wave without current.

The influences of wave incoming angle β on the total uplift force influencing factor $P_{\beta,0}$ under regular and irregular wave have been illustrated in Figure 7-8. The total uplift force influencing factor was always less than 1, and the total uplift forces of oblique wave were smaller than that of perpendicular wave for both regular and irregular waves. With the increase of wave incoming angle, the effective wave acting area decreased and the total uplift forces acting upon structure decreased obviously for both regular and irregular waves. Moreover, the wave reflection stacking has been weakened due to the reduction of acting surface area, and the interaction of oblique wave and slope bank led to the Mach reflection phenomenon. Due to Mach reflection, the wave incoming angle has effect on the wave reflection induced by slope, with the increase of wave incoming angle, the superimposed effect of incoming and reflecting waves weakened and the phase deviation intensified, so the total uplift force decreased rapidly.

Based on the testing results and analysis above, the total uplift force of oblique wave acting on sloping high piled wharf was affected by many factors, such as wave incoming angle, wave height, wave period, freeboard height, etc.However, the wave incoming angle β was the most important influencing factorbased on the non-linear fitting method and 90% guarantee rate.Therefore, the total uplift force influencing factor can be calculated by the following equation.

$$K_{\beta,0} = ((1+\cos^4(\frac{2\pi\beta}{360}))/2)^2 \qquad (2)$$

where, β is the wave incoming angle. The comparisons between the measured and calculated results can also be seen in Figure 7 - 8. The results showed that the accuracy of calculated results can satisfy the requirements in practice.

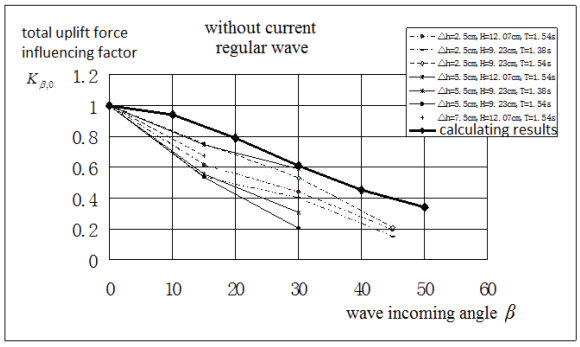

Figure 7. Comparisons of the measured total uplift force influencing factor in the cases with regular wave.

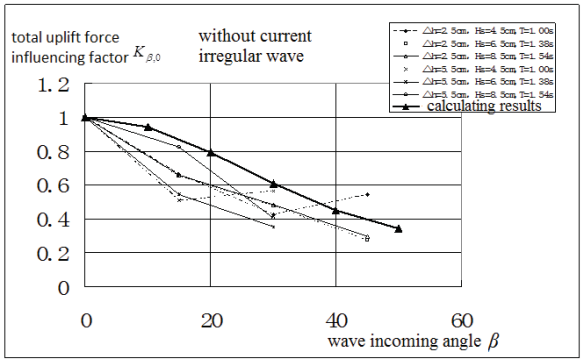

Figure 8. Influence of irregular wave incoming angle on total uplift force.

Effects of the incoming wave direction on total uplift force with current

The effects of wave direction on total uplift force with current have been shown in Figure 9 - 12. When the wave incoming angle β was larger than zero, the wave and current were in the same direction. The wave incoming angle smaller than zero meant the wave and current were in the opposite direction. Based on the measured data, when the incoming angle (β) increased from 0 to 30º, the total uplift force influencing factor decreased rapidly; when β >30º, the decreasing trend turned slower with the increase of wave incoming angle. When the wave and current were in the opposite direction, the changing trend of total uplift force influencing factor varied. When-15º<β<0, the total uplift force influencing factor increased with the increase of wave incoming angle, but the value of total uplift force influencing factor was always smaller than 1; when -30º <β<-15º, the total uplift force influencing factor decreased rapidly with the increase of wave incoming angle; when β <-30º, the decreasing trend of total uplift force influencing factor became shower with the increase of wave incoming angle.

According to theexperiment, the wave incoming angle has main influence on the total uplift force. When the wave incoming angle larger than 15º, the total uplift force was always smaller than that induced by perpendicular wave without current; when the wave incoming angle smaller than 15º and the wave and current were in the opposite direction, the total uplift force influencing factor was almost equal to 1; when the wave and current were in the same direction, the decreasing trend of total uplift force influencing factor was more rapid than that of wave and current in the opposite direction.

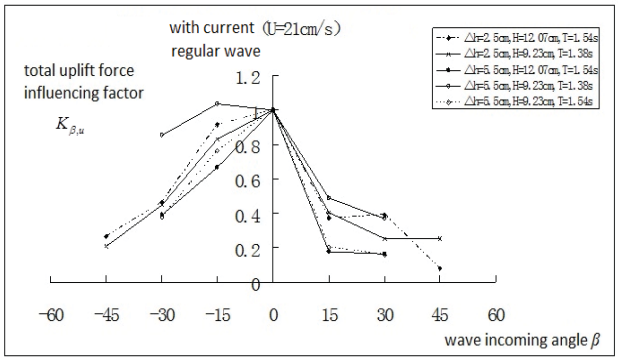

Figure 9. Influence of regular wave incoming direction on total uplift force with current (U = 21 cm/s).

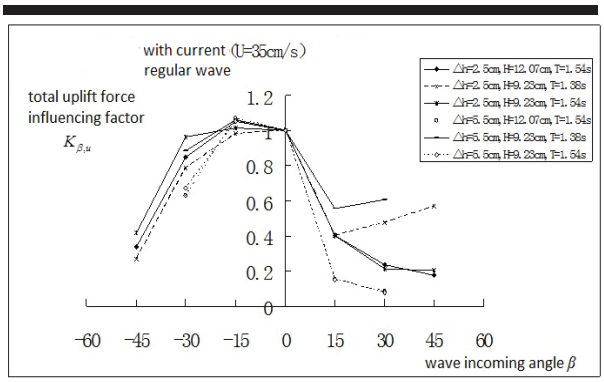

Figure 10. Influence of regular wave incoming direction on total uplift force with current (U = 35 cm/s).

CONCLUSIONS

The wave uplift force has great impact on the decks of coastal structures, which can lead to serious damage in some extreme circumstances. In order to analyze the influences of incoming wave direction on uplift force, a series of lab tests have been conducted in the wave tank, and the main influencing factors have been taken into account, which include the wave incident angle, wave types, period, wave height, height of wharf deck. Furthermore, the wave-current interaction has also been considered. According to the lab testing, the main results are as follows:

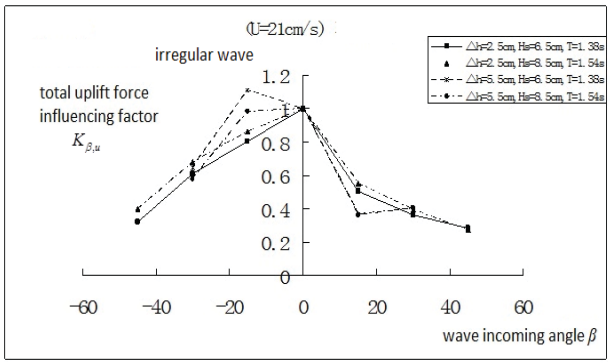

Figure 11. Influence of irregular wave incoming direction on total uplift force with current (U = 21 cm/s).

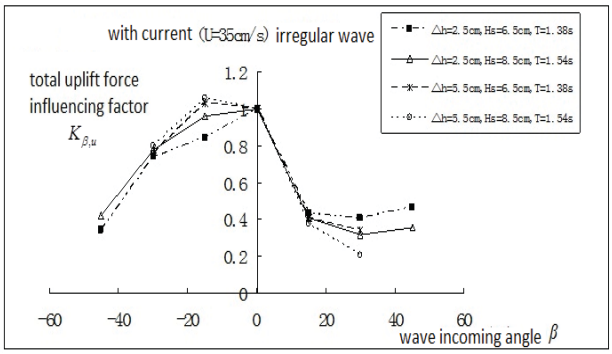

Figure 12. Influence of irregular wave incoming direction on total uplift force with current (U = 35 cm/s).

(1) With increased wave angle, the wave reflection stacking has weakened due to the reduction of acting surface area, and the interaction of oblique wave and slope bank led to the Mach reflection phenomenon.

(2) The total uplift forces of oblique wave were always smaller than that of perpendicular wave for both regular and irregular waves. With the increase of wave incoming angle, the total uplift forces acting upon the structure decreased obviously for both regular and irregular waves without current.

(3) The simplified formula on uplift force under oblique wave has been proposed, and the accuracy of calculated results can satisfy the requirements in practice.

(4) For the wave-current interaction situation, the wave incoming angle was still the primary influencing factor on uplift force. When the wave incoming angle was larger than 15°, the total uplift forces were smaller than those under perpendicular wave without current. When the wave incoming angle was smaller than 15°, the current direction has effect on the decreasing trend of total uplift force acting upon the structure.

ACKNOWLEDGMENTS

This research is supported by the Fundamental Research Funds for the Central Universities (2013B31414) and Specialized Research Fund for the Doctoral Program of Higher Education of China (20130094120019) The authors would also like to thank the reviewers for their valuable suggestions.

LITERATURE CITED

Bozorgnia, M.; Lee, Jiinjen and Raichlen, Frederic, 2011. Wave structure interaction: Role of entrapped air on wave impact and uplift forces. *Coastal Engineering Proceedings*, 1(32), 57.

Chen, Guoping; Meng, Yanqiu and Yan, Shichang, 2010. Experimental investigation of irregular wave uplift force on deck of exposed high-pile jetties. *China Ocean Engineering*, 24(1), 67-78.

El Ghamry, O. A., 1963. *Wave forces on a dock.* Technical Rep. No. HEL-9-1, Hydraulic Engineering Laboratory, Institute of Engineering Research, Univ. of California, Berkeley, Calif.

Huang, Wenrui and Xiao, Hong, 2009. Numerical modeling of dynamic wave force acting on Escambia bay bridge deck during Hurricane Ivan. *Journal of Waterway, Port, Coastal and Ocean Engineering*, 135(4), 164-175.

Kataoka, Shojiro; Kaneko, Masahiro, 2013. Estimation of wave force acting on bridge superstructures due to the 2011 Tohoku tsunami. *Journal of Disaster Research*, 8(4), 605-611.

Kweon, Hyuckmin; Oh, Sangho and Choi, Younghwan, 2013. Experimental study on the method of estimating the vertical design wave force acting on a submerged dual horizontal plate. *International Journal of Naval Architecture and Ocean Engineering*, 5(4), 569-579.

Liu, Haiyuan; Chen, Hanbao; Zheng, Baoyou and Gu, Hanbin, 2010. Experimental study on wave uplift force imposed on the superstructure of a pillar wharf. *Proceedings of the 5th International Conference on Asian and Pacific Coasts*, APAC 2009, v 4, 207-211.

Sun, Jiawen; Sun, Zhaochen; Liang, Shuxiu and Zheng, Kun, 2011. Spectral analysis of random wave uplift force on a horizontal deck. *Journal of Hydrodynamics*, 23(1), 81-88.

Wang, K-H.; Dai, Ziping and Lee, Hong Sik, 2011. Modeling Wave Run-up along a Sloping or a Moving Wall Boundary. *Journal of Coastal Research*, 27(6): 1159-1169.

Journal of Coastal Research	SI	75	1447 - 1451	Coconut Creek, Florida	2016

Land Subsidence Survey and Policy Development in Pantai Mutiara, Jakarta Bay, Indonesia

Hansan Park[†*], Suk-jae Kwon[‡], Safwan Hadi [††]

[†]Ocean Policy Institute
Korea Institute of Ocean Science and Technology
Ansan, Korea

[‡]Marine Biodiversity Institute of Korea
Seochun, Korea

[††]Center for Marine and Coastal Development
Institute of Technology Bandung
Bandung, Indonesia

www.cerf-jcr.org

www.JCRonline.org

ABSTRACT

Park, H.; Kwon, S.J., and Hadi, S., 2016. Land Subsidence Survey and Policy Development in Pantai Mutiara, Jakarta Bay, Indonesia. *In:* Vila-Concejo, A.; Bruce, E.; Kennedy, D.M., and McCarroll, R.J. (eds.), *Proceedings of the 14th International Coastal Symposium* (Sydney, Australia). *Journal of Coastal Research*, Special Issue, No. 75, pp. 1447 - 1451. Coconut Creek (Florida), ISSN 0749-0208.

The coastal flooding caused by land subsidence is one of major social problems in the coastal area of Jakarta bay, Indonesia. To develop a land subsidence response planning, 3D topographic survey is conducted by using the Terrestrial LIDAR and GPS in Pantai Mutiara. The Terrestrial LIDAR survey results show that the survey site has mean elevation of -0.31m with the highest elevation of 0.31m and lowest -0.99m. Considering that A.H.H.W. (Approximate Highest High Water) is 0.51m, many areas of the survey site are lying below the A.H.H.W. The subsidence happened from 1994 to 2012, subsided about 1.8m and the average rate of about 0.095m. The last stand which keeps the area from flooding and inundation is the dikes built around the area. Although the dikes are still functioning, the heights of the dikes are getting lower and uneven due to subsidence and partial reconstruction. We can conclude that flooding vulnerability of this area depends on the height of the dikes. In order to develop practical policies, we make the distribution maps, expected time of dike flooding, height and cost of dike heightening, through considering land subsidence rate, sea level rising rate, storm surge height and A.H.H.W.

ADDITIONAL INDEX WORDS: *land subsidence, terrestrial LIDAR, coastal policy.*

INTRODUCTION

Indonesia has a vast territorial lands stretching 5,100km East-West and 1,600km North-South with the second longest coastal lines in the world. It is an archipelago country having abundant biodiversity and rich in natural resources. The study site of this study (Figure 1), Jakarta, is one of rapidly developing capital cities in the world. The rate of development is considered problematic as it is located at a disaster prone coastal area. As the development precedes, the problems such as land subsidence, coastal flooding, garages, and water pollution have emerged.

Over the period of 1982–1997, subsidence ranging from 20 to 200 cm is evident in several places in Jakarta. In general the land subsidence exhibits spatial and temporal variations, with the rates of about 1 to 15 cm/year. A few locations can have the subsidence rates up to about 20-25 cm/year (Abidin *et al.*, 2009). It was found out that the spatial and temporal variations of land subsidence depend on the corresponding variations of groundwater extraction, coupled with the characteristics of sedimentary layers and building loads above it.

Land subsidence in Jakarta can be caused by four factors, namely: excessive groundwater extraction, load of buildings and constructions, natural consolidation of alluvium soil, and tectonic activities. Up to now, any information is not yet available about the contribution of each factor on the subsidence at each location and their spatial variation. In the case of Jakarta, tectonic activities seem to be the least dominant factor, while excessive groundwater extraction is considered to be one of the dominant factors. The first three factors will have a close relation with urban development activities in Jakarta and its surrounding areas (Abidin *et al.*, 2009).

The varied rates of subsidence increase the possibility of the collapse of dikes, sea walls and coastal structures. Therefore, it is important to identify the exact rate of subsidence at various locations in order to predict it's the impacts and to develop a response plan at a specific location. For this purpose, it is imperative to avail precise 3D data at various locations. However, currently available data is the 1:25,000 resolution map which was produced during the 1990s. The map is outdated and obsoletes for developing subsidence response.

The objective of this study is to develop a land subsidence response planning through conducting 3D topographic survey for land subsidence in vulnerable area, analyzing quantitatively the rate of the subsidence, and making a material for policy decision such as maps.

DOI: 10.2112/SI75-300.1 received 15 October, 2015 accepted in revision 15 January, 2015
*Corresponding author: hansanpark@kiost.ac.kr
©Coastal Education and Research Foundation, Inc. 2016

Figure 1. The satellite image of the study site (white box). (satellite image: maps.google.com)

METHODS

As one of the purposes of this study is to obtain the rate of subsidence, it is important to secure the absolute height of the site because the reference point installed on the ground also can be subsided. We used the absolute height obtained from GPS (Global Positioning System) ellipsoidal height and corrected to the MSL (Mean Sea Level) by bench mark data.

For the 3D topographical data, we used the Terrestrial LIDAR (LIght Detection And Ranging). LIDAR obtains more than several million to tens of million point data through scanning at once. Each point of scanned data has 3D coordination information (x, y, z). So we can quantitatively analyze for many purposes such as 3D topographical characteristics. In this study, we used the Optech (ILRIS 36D) and Leica (C-10) Terrestrial LIDAR which was operated on a tripod or roof of car.

The scanning of Terrestrial LIDAR was conducted at the rooftop of a 27-story condominium on Oct. 2011 and Feb. 2013. Based on the data obtained from pre-scan, possible scanning range and density of data were identified. Also to compensate the loss areas due to shades, more than 30 additional scanning points at the ground level were selected and scanned.

Terrestrial LIDAR data were processed as: 1) processing reference point, 2) alignment, 3) data verification, and 4) data modification. Reference points measured by GPS and total-station were built up as a network of points. Through the alignment process, all of terrestrial LiDAR data sets were positioned on the same coordinate system. After that, horizontality of the aligned data was adjusted using the reference points corrected to MSL. For verification of aligned data, 60 points in the Terrestrial LIDAR data were compared with the validation points measured by total-station. The root mean square error (RMSE) of deviations was 1.91 cm. To clean the LiDAR data, odd or out-of-the-place data (outliers) were removed from aligned data. Odd data includes dust in the atmosphere, and interference caused by sun light and insects. Land, roads, and buildings were extracted from LIDAR data by removing useless data such as cars, people, plants, and trees. The data were converted to the DEM (Digital Elevation Model) format which is useful for 3D topographic analysis or mapping.

RESULTS

The LIDAR data can be colored in accordance with their elevation (Figure 2). In this figure, blue color represents the areas below MSL and other colors represent above MSL.

Overall color of the survey area is in greenish color but most of the roads are in bluish color which means they are lower than MSL. West side roads are slightly higher than sea-level. Buildings and trees are expressed in yellowish and brownish colors and buildings are shown about 20m high.

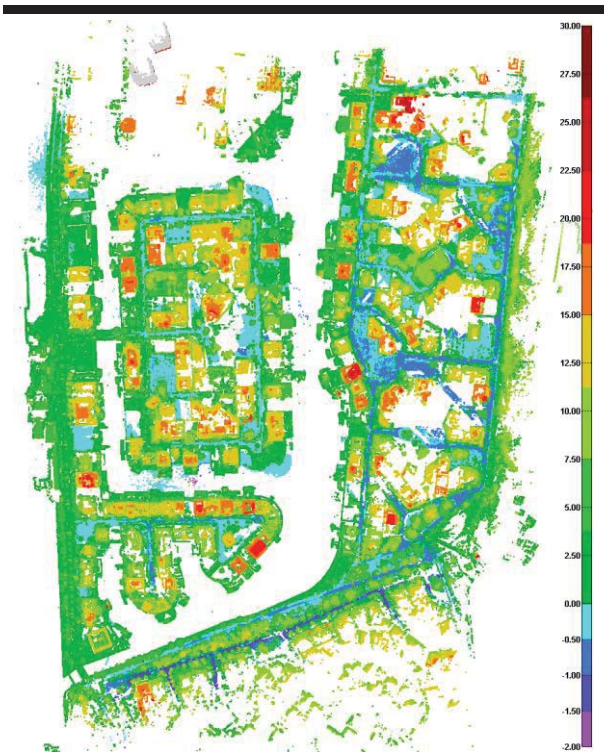

Figure 2. Points cloud in colored elevation of Pantai Mutiara.

Most of the real estates in Pantai Mutiara are owned by individuals. The owners can modify their lands including the bare ground. Therefore, we used public roads for analyzing topographic characteristics.

Figure 3 shows the satellite image of the site with roads in a color elevation format. Table 1 shows the mean elevation of the three sections of the survey area. The west section shows the highest mean elevation with 0.08m whereas the east section being the lowest with -0.62m and the middle section with -0.21m. The average elevation of roads is -0.31m having a lower value than MSL. All the roads are lower than the highest tidal height (0.51m). This means that dikes are preventing the inundation of sea water and vulnerable to inundation and flooding even if some parts of dikes are

damaged by natural disasters. Partially, land becomes lower toward the east section.

Figure 3. The height distribution of major roads in Pantai Mutiara.

Table 1. Elevation of roads in each section (unit: m)

Section	West	Middle	East	Overall
Mean Elevation	0.08	-0.21	-0.62	-0.31
Highest Elevation	0.31	0.17	0.15	0.31
Lowest Elevation	-0.12	-0.70	-0.99	-0.99
Standard Deviation	0.06	0.14	0.14	0.31

For calculating the land subsidence rate, we compare the data obtained from terrestrial LIDAR and GPS survey in 2011 and 2013. And 8 positions survey data at the time of the complete reclamation in 1994 were obtained from a construction company. Only one position was exactly coincided with the GPS survey positions of this study hence direct comparison was possible. Other 7 positions were compared with LIDAR data. Moreover, we gathered GPS data from previous research or survey. Table 2 shows the summary of land subsidence rate calculated from previous GPS survey and site survey. The total period was set from 1944 to 2012 because Feb. 2013 survey data could not represent all of 2013.

As shown in Table 2, the average rate of subsidence turned out to be -0.113m/yr. The subsidence rate was the highest during 2010–2011 and the lowest during 2010–2011 with -0.078m/yr. The Terrestrial LIDAR survey results confirm the continuing subsidence from 2011 to 2012 with 0.171m in Pantai Mutiara.

Table 2. Land subsidence rate for each time period in Pantai Mutiara

Period	Subsidence (m)	Subsidence rate (m/y)	Reference
1994 – 2012	-1.815	-0.095	site survey
2000 – 2010	-1.123	-0.112	previous GPS survey
2008 – 2009	-0.085	-0.085	previous GPS survey
2009 – 2010	-0.138	-0.138	previous GPS survey
2010 – 2011	-0.078	-0.078	previous GPS survey
2011 – 2012	-0.171	-0.171	site survey
	Average	-0.113	

Coastal flooding vulnerability should be considered with the level of possibility of flooding. In Pantai Mutiara, flooding will occur when the function of the dike have been lost by any reason include subsidence of dike or rising of seawater level. Moreover, as most of the Pantai Mutiara areas are already below MSL, flooding that happens in one region will affect the entire Pantai Mutiara area. Therefore, flooding vulnerability of this area is depending on possibility of overtopping at the dikes by seawater.

The factors affecting overtopping include land subsidence, sea-level rise, tidal height, and storm surge. The rate of sea-level rise is assumed to be 7mm/yr at all times (MoE, 2007). Tidal height used the highest tidal height. When the storm surge happens, sea-level rise due to tropical low pressure and wave height should be considered for total wave height. However, this study only can utilize existing data on sea-level under tropical low pressure and wave height. Tidal height during the tropical low pressure was selected as 30cm which was happened during tropical low pressure Hagibis (Ningsih *et al.*, 2011). Wave height was obtained as 20cm considering the actual data (MoE, 2007).

In sum, the following equation was derived for possible flooding height:

Possible flooding height = land subsidence
+ 7mm/yr (sea-level rise due to Climate change)
+ 0.51m (Jakarta highest tidal height)
+ 0.3m (tidal height during tropical low pressure)
+ 0.2m (highest wave height)

In above equation, all the factors are constants except for subsidence and sea-level rise. In order to assess land subsidence in the near future, quantitative analysis incorporating all the factors affecting the subsidence is necessary. However, as there is no information on geotechnical engineering survey and analysis of land subsidence. The land subsidence estimation is made through mathematical regression of existing data. Mathematical regression is a technique for obtaining assumed values of land subsidence. Thus, it should be note that the values of land subsidence may contain errors.

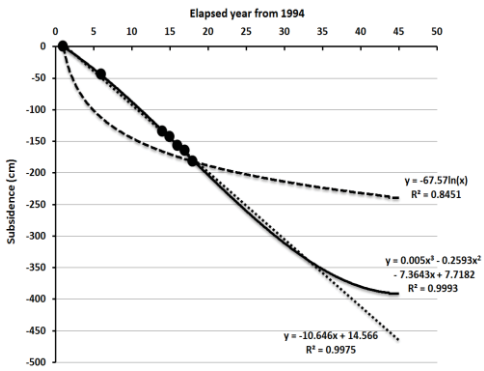

Figure 3. Mathematical regression results of subsidence in Pantai Mutiara.

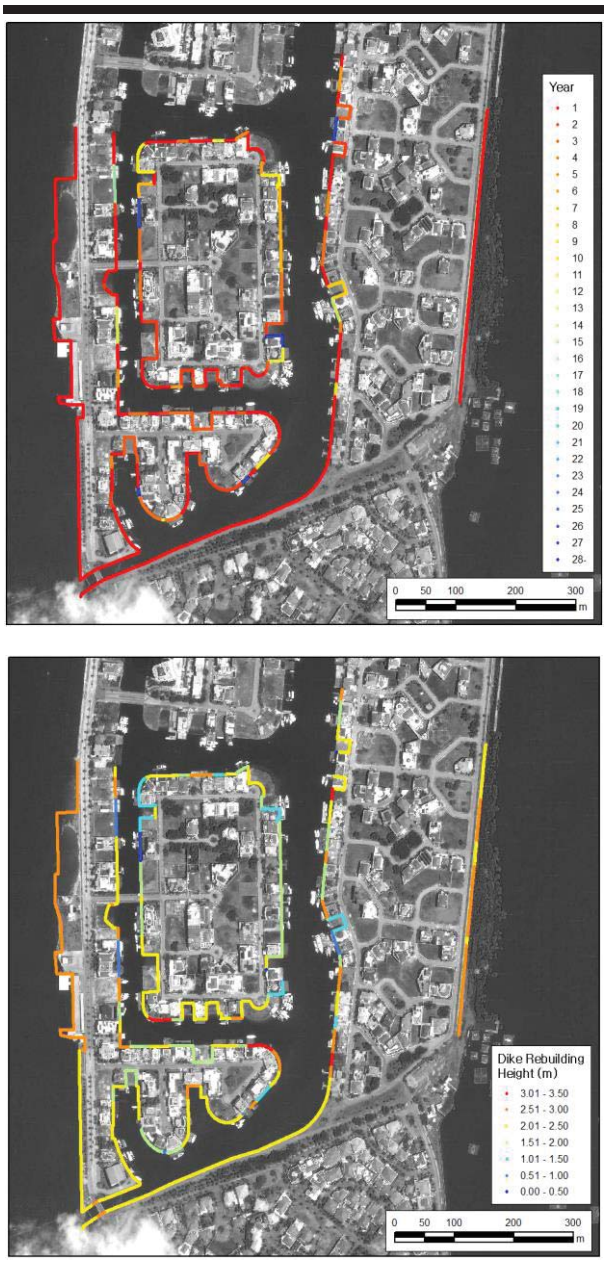

Figure 4. Prediction of timing of dike flooding (top), Height of dike heightening in Pantai Mutiara in 2039 (bottom).

The estimations were made by using a linear regression, a cubic equation regression and a log regression (Figure 3). The linear regression is congruous with R^2 value of 0.997. Linear regression can be applied under the assumption that subsidence is continuously happening. However, subsidence is gradually reduced when the time elapses. Thus, linear regression is considered not suitable. As for the log regression, it can better represent the subsidence trend as the first phase shows significant subsidence with less subsidence as time lapses. However, actual survey data do not agree well with the log regression result with low value of R^2 as 0.8451. Especially, regression result predicted -1.2m subsidence in 2000 but actual measured data was 0.5m which suggests significant deviation between two data. The cubic equation regression predicts low subsidence at initial stage with increasing subsidence with time lapse then stabilizing at final stage. This prediction method provided the highest value of R^2 and predicted that there will be no more subsidence after 45 years. Through this method, initial subsidence shows almost linear subsidence.

Among the three methods, it can be seen that the cubic equation regression is the optimum method for predicting the land subsidence in Pantai Mutiara which was adopted by this study. According to the cubic equation regression, about 10cm subsidence will be happening every year until the year 2022 and then subsidence will be reduced until the complete stop in the year 2039. Total subsidence is calculated as 2.11m and the possible flooding height is calculated to be 3.31m by sea-level rise, highest tidal height and storm surge wave.

Figure 4(top) shows that when the dike flood will occur according to the possible flooding height. The present dike heights were extracted from the terrestrial LIDAR data. In this map, the colored values denote the time (year) reaching the flooding height under the assumption that subsidence rate is the same for the entire area. This map provides important information on the timing of dike reconstruction and embankment.

As shown in this figure, the dikes in red color can be flooded within few years and the dikes in blue color can be flooded in 20 years. In this figure, the singular point is that many dikes colored in red. This implies that not only in the near future but even at present flooding can be happening under extreme weather events such as storm surges.

For making practical political measures, we made two more maps. One is the height of dike heightening distribution map when the subsidence will be stopped (Figure 4 bottom). Another is the cost of dike heightening cost map. These three maps can directly provide information about when, where, how high, and how much money to protect the area from coastal flooding.

DISCUSSION

In order to protect coastal flooding in Pantai Mutiara, a few countermeasure options can be considered such as dike heightening, pumping system expansion, ground embankment, and set back. The pumping system, however, is the facility to remove flood seawater, not the facility to prevent flooding. The options of ground embankment and set back are unrealistic since they may involve demolition of the existing buildings or abandonment of the area. Therefore, dike heightening can be the most appropriate, cost-effective solution for the given situation.

The Dike heightening of course cannot prevent fundamentally the problem of the land subsidence because this study shows that there seems to be no tendency of gradual decrease of land subsidence (Table 2, Figure 3). Therefore, a solution for the cause generating land subsidence is

mandatory and prohibition of groundwater extraction is widely known for the issue (Abidin *et al.*, 2009, 2011). In order to prohibit extracting groundwater, it is necessary to expand the waterworks system. However, we cannot wait until the waterworks system is sufficiently established because the recent rate of land subsidence is reaching to about 10 cm/yr. Furthermore, even if groundwater extraction becomes prohibited right away, the groundwater table has been already become low and the land subsidence may continue for a while. Therefore, dike extension can be the inevitable, urgent solution.

Besides, the study site is the area a company owns and develops. In terms of coastal management, the company, rather than the government, is responsible for ongoing inundation. Thus, this area could be an exceptional case which is not applicable to general coastal management policy for Jakarta Bay. Nevertheless, there has not been any specific, realistic research conducted in Jakarta Bay, which proposes solutions like this study. Local officials and policymakers were quite impressed by the results of this study. Local residents actually became aware of the results and requested the government and the company to heighten the dike. Consequently, the company heightened the dike for about 50 cm in 2014. Furthermore, through the results of this study local and central government realized again the severity of land subsidence and commenced to prepare solutions such as topographical survey on the whole coastal area in Jakarta Bay. Therefore, even though a research is carried out in a limited area during the short period, it can be considerably effective to develop coastal management policies that the research results draw attention of policy makers through presenting relative issues specifically and realistically.

CONCLUSIONS

In order to develop a land subsidence response planning, 3D topographic survey is conducted by using the Terrestrial LIDAR and GPS in Pantai Mutiara, in Jakarta Bay. We can identify that the survey site has mean elevation of -0.31m with the highest elevation of 0.31m and lowest -0.99m. Considering that the highest tidal height is 0.51m, many areas of the survey site are lying below the highest tidal height.

The last stand which keeps the area from flooding and inundation is the dikes built around the area. Although the dikes are still functioning, the heights of dikes are getting lower and uneven due to subsidence. We can conclude that flooding vulnerability of this area is depending on the height of dikes. In order to develop practical policies, we made the distribution maps of the expected time of dike flooding, the height of the dike heightening for preventing coastal flooding and the dike heightening cost through considering land subsidence rate, sea level rising rate, storm surge height and A.H.H.W.

Those results can be varied by the subsidence expectation because of insufficient geotechnical engineering research data. However, it was meaningful to create this material for policymakers to prevent imminent issues.

ACKNOWLEDGMENTS

This research was supported by the KIOST project "Study on Establishment of Integrated Coastal Management Program in Jakarta Bay Area, Indonesia III" (PG48810) funded by the Expo 2012 Yeosu Korea Foundation.

LITERATURE CITED

Abidin H.Z.; Andreas, H.; Gumilar, I.; Gamal, M.; Fukuda, Y., and Deguchi, T., 2009. Land Subsidence and Urban Development in Jakarta (Indonesia), *7th FIG Regional Conference Spatial Data Serving People: Land Governance and the Environment – Building the Capacity Hanoi, Vietnam*, pp. 19-22.

Abidin H.Z.; Andreas, H.; Gumilar, I.; Fukuda, Y.; Pohan, Y.E., and Deguchi, T., 2011. Land subsidence of Jakarta (Indonesia) and its relation with urban development, *Nat Hazards*, 59(3), 1753-1771

Beutler, G.; Bock, H.; Brockmann, E.; Dach, R.; Fridez, P.; Gurtner, W., and Weber, R., 2001. *Bernese GPS software version 4.2.* Astronomical Institute, University of Berne, 515.

MoE (Ministry of Environment), 2007. *Indonesia Country Report: Climate Variability and Climate Change, and their Implication*. Ministry of Environment, Republic of Indonesia, Jakarta.

Ningsih, N.S.; Suryo, W., and Anugrah, S.D., 2007. Study on Characteristics of Residual Water Level in Jakarta, Semarang, and Surabaya Waters–Indonesia and Its Relation to Storm Events in November 2007. *International Journal of Basic & Applied Sciences*, 11(5), 31-37

COASTAL EDUCATION AND RESEARCH FOUNDATION

5130 NW 54th Street
Coconut Creek, FL 33073, U.S.A.

Officers of the Foundation
Founded in 1983 by: Charles W. Finkl, Sr. (Deceased),
Charles W. Finkl, Jnr., Rhodes W. Fairbridge (Deceased),
and Maurice L. Schwartz (Deceased)

President & Executive Director:
Charles W. Finkl

Senior Vice President & Assistant Director:
Christopher Makowski

Secretary:
Heather M. Vollmer

Executive Assistant:
Barbara Russell

Regional Vice Presidents

North America
James R. Houston
Victor V. Klemas
Orrin H. Pilkey, Jr.

Western Europe
Carlos Pereira da Silva
Michael Phillips
Marcel J.F. Stive

South America
Omar Defeo

Eastern Europe
Kazimierz K. Furmanczyk

Southeast Asia
Nobuo Mimura

Oceania
Charles Lemckert
Vic Semeniuk
Andrew D. Short

Board of Directors (Trustees)

J. Andrew G. Cooper
Charles W. Finkl
Erlend J. Frederickson
Gary B. Griggs
James R. Houston
Robert Huff
Joseph T. Kelley
Victor V. Klemas
Charles Lemckert
Chris Makowski
Carlos Pereira da Silva
Michael Phillips
Orrin H. Pilkey, Jr.
Norbert P. Psuty
Elijah W. Ramsey, III
Vic Semeniuk
Andrew D. Short
Daniel J. Stanley
Marcel J.F. Stive
Allan Williams

Lifetime Members

Frédéric Bouchette
Yong-Sik Cho
Nicholas K. Coch
Hany Elwany
Björn Kjerfve
Charles Lemckert
Charles Thibault
Erik van Wellen
Ya Ping Wang
Wei Zhang

Patron Members

Luis Antonio Buenfil-Lopez
Georges Chapalain
Carl H. Hobbs, III
Timothy W. Kana
Norbert P. Psuty
Giovanni Randazzo
Robert S. Young

CERF Society Information

The Coastal Education and Research Foundation *[CERF]* is a nonprofit society dedicated to the advancement of the coastal sciences. The Foundation is devoted to the multi-disciplinary study of the complex problems of the coastal zone. The purpose of CERF is to help translate and interpret coastal issues for the public and to assist professional research and public information programs. The Foundation specifically supports and encourages field and laboratory studies on a local, national, and international basis. Through the medium of scientific publications, television, and radio CERF brings accurate information to the public and coastal specialists on all aspects of coastal issues in an effort to maintain or improve the quality of shoreline resources.

Because CERF is concerned with broad environmental issues, our efforts concentrate on significant problems such as maintenance of good quality (potable) water with adequate supply, and hazards associated with potential beach erosion, flooding, and susceptibility of developed shorelines to storm surge and wave attack. By focusing attention on these potential man-made and natural hazards, it is hoped that our research efforts will help others improve the quality of life in diverse coastal areas. CERF thus aims to stimulate awareness of coastal (marine and freshwater shorelines) land and water problems; initiate and foster research and innovation to promote long-term coastal productivity; establish an educational forum for the debate of contentious coastal issues; and develop new principles and approaches for enlightened coastal management, and encourage their adoption and use.

☐ CERF MEMBERSHIP ☐

Members are individuals that support the aims of the foundation through personal and group efforts or by donations. Memberships are available in different categories with privileges.

Subscription information is available online at www.cerf-jcr.org. Subscriptions office: Allen Press, Inc., P.O. Box 1897, Lawrence, KS 66044, U.S.A. CERF@allenpress.com

Editor-in-Chief

Charles W. Finkl Ph.D., CSci, CMarSci, FIMarEST, CPGS, CPSSc, PWS, M.ASCE

Dr. Charles W. Finkl is President and Executive Director of the Coastal Education and Research Foundation *[CERF]*, publisher of the JCR. Charlie, a founding editor of the *Journal of Coastal Research*, has served as Editor-in-Chief for the past 30 years. He is a Research Professor in the Department of Geosciences at Florida Atlantic University in Boca Raton, Florida. He received his Bachelor and Master of Science degrees from Oregon State University and the Ph.D. from the University of Western Australia. He is a member of more than 20 professional societies and has published more than 200 professional papers, books, and reports. He is a Chartered Marine Scientist (CMarSci) [Institute of Marine Engineering, Science and Technology], Certified Professional Geological Scientist (CPGS) [American Institute of Professional Geologists (AIPG)], Certified Professional Soil Scientist (CPSSc) [American Registry of Certified Professionals in Agronomy, Crops, and Soils], and a Professional Wetland Scientist (PWS) [Society of Wetland Scientists]. Charlie has field experience in parts of the USA, Caribbean area, Brazil, Honduras, Russia, South Africa, Western Europe, Australasia, and South Pacific islands. He is also the Series Editor of the Encyclopedia of Earth Sciences Series that is published by Springer (Germany). There are more than twenty-eight volumes in the Series and about twenty-five are available online. Charlie also serves on the Editorial Board of the *International Journal of Environmental Studies* (Routledge) and is an occasional peer reviewer for many other professional journals.

Charlie has interests and expertise in the general areas of surficial geology, coastal and marine geomorphology (including coastal classification), coastal/marine biophysical environments, exploration geochemistry, soils and weathering (regolith geology), coastal zone management and engineering applications or impacts on natural systems (including erosion control and shore protection), coastal hydrology including submarine freshwater and mineralized seeps, subaerial and marine structural geology, natural hazard mitigation in coastal zones, marine environments and coastal wetland protection and restoration, and remote sensing (*e.g.,* land cover classification in coastal wetlands, advection-diffusion turbidity plumes in coastal waters, delineation of bottom types and sand resources), effluent disposal and pollution of wetlands and estuaries, water resources mapping and conservation, time series studies of wetland hydroperiod and soil moisture.

Official Meeting of CERF
International Coastal Symposium (ICS)

The International Coastal Symposium (ICS) was originally set up by Per Bruun (deceased) and Charlie Finkl as the official meeting of the Coastal Education and Research Foundation (CERF), with one of the first meetings being held in Hilton Head, South Carolina, in 1993. After the repeated success of these meetings, CERF moved the ICS to the international scene holding these conferences in conjunction with local sponsors in Australia, Brazil, Iceland, New Zealand, Northern Ireland, Poland, and Portugal. The ICS brings together delegates from all over the world to collaborate and discuss the most current coastal research studies and projects. During the ICS 2014, which was held in Durban, South Africa, a grand celebration took place to mark the 30th Anniversary of CERF and the JCR. Our next ICS meeting is scheduled for March of 2016 in Sydney, New South Wales, Australia. For more information, please visit www.cerf-jcr.org.

One Tree Island Research Station
The University of Sydney

Geocoastal Research Group, School of Geosciences
The University of Sydney

www.grgusyd.org
www.geosci.usyd.edu.au